

# Proceedings of the Fifteenth Australasian Fluid Mechanics Conference

## Plenary papers

### The Batchelor lecture

**AFMC00184** Small-scale turbulence: how universal is it?

R. A. Antonia, P. Burattini

### Keynote lectures

**AFMC00038** Computing turbulent channels at experimental Reynolds numbers

J. Jimnez, J. C. del lamo

**AFMC00067** Gravity currents in nature and industry

H. E. Huppert

### Invited lectures

**AFMC00036** Spin-up flow of an incompressible fluid

J. S. Park, J. M. Hyun

**AFMC00065** The energetics of horizontal convection

R. W. Griffiths, G. O. Hughes

**AFMC00235** Very large-scale structures observed in DNS of turbulent channel flow with passive scalar transport

H. Kawamura, H. Abe, Y. Matsuo

**AFMC00255** Effects of subtle and dramatic changes to initial conditions on a jet's turbulent structure, mixing and combustion

G. J. Nathan, J. Mi, G. J. R. Newbold, D. S. Nobes, Z. T. Alwahabi

## Contributed papers

**AFMC00012** The cut-off frequency of constant temperature hot-wire systems in turbulent velocity measurements

J. D. Li

**AFMC00013** The effect of Coriolis force on Marangoni convection

I. Hashim, W. Sarma



- AFMC00014** Dam break wave propagation on abrupt drops: an experimental study  
H. Chanson
- AFMC00015** A new solution for ocean waves propagating over a sloping beach  
D.-S. Jeng, B. R. Seymour
- AFMC00016** Simultaneous field measurements of turbulence and water quality in a sub-tropical estuary in Australia  
H. Chanson, R. Brown, J. Ferris
- AFMC00017** 2D velocity-field analysis using triple decomposition of motion  
V. Kolar
- AFMC00019** Numerical simulation of drop formation in a T-shaped microchannel  
J. L. Liow
- AFMC00020** Flow of nonlinear viscoelastic fluid in concentric rotating cylinders with relative rotation  
M. Mirzazadeh, F. Rashidi, S. H. Hashemabadi
- AFMC00021** Behaviour of water droplets falling in oil under the influence of an electric field  
M. Chiesa, J. A. Melheim
- AFMC00022** Electrocoalescence modeling: an engineering approach  
M. Chiesa
- AFMC00023** Partially-reflecting characteristic-based boundary conditions  
R. Olsen, I. R. Gran
- AFMC00024** Feasibility study using computational fluid dynamics for the use of a turbine for extracting energy from the tide  
D. A. Egarr, T. O'Doherty, S. Morris, R. G. Ayre
- AFMC00025** A numerical study of the application of radial basis function and generalised smoothed particle hydrodynamics to CFD  
J. Ha
- AFMC00028** The effect of zero-mean suction on Görtler vortices: a receptivity approach  
J. P. Denier

- AFMC00029** The safe basin erosion of a ship in waves with single degree of freedom  
X. Wu, L. Tao, Y. Li
- AFMC00030** Exchange flow between continuously stratified reservoirs  
Andrew McC. Hogg, Peter D. Killworth
- AFMC00031** Simulation of the dam break problem and impact flows using a NavierStokes solver  
K. Abdolmaleki, K. P. Thiagarajan, M. T. Morris-Thomas
- AFMC00032** Numerical study of moist air flow through the Ludwig tube  
M. Tanaka, S. Matsuo, R. Nishizaki, H. D. Kim, T. Setoguchi
- AFMC00034** Measurement and modelling of controlled beach groundwater levels under wave action  
L. S. Ang, C. H.-Y. Sum, T. E. Baldock, L. Li, P. Nielsen
- AFMC00035** Drag reduction on bluff bodies using a rotating device  
S. E. Robson, N. A. Ahmed
- AFMC00039** Radial turbine with pitch-controlled guide vanes for wave energy conversion  
M. Takao, Y. Fujioka, H. Ito, T. Setoguchi
- AFMC00040** The zeroth law of turbulence in steady isotropic turbulence  
B. R. Pearson, T. A. Yousef, N. E. L. Haugen, A. Brandenburg, P.-. Krogstad
- AFMC00041** The stability of decaying pipe flow  
N. Jewell, J. P. Denier
- AFMC00042** Effect of delta wing's leading edge geometry to vortex breakdown  
Sutthiphong Srigrarom
- AFMC00043** Outflow from a plume impinging on a horizontal boundary  
N. B. Kaye, G. R. Hunt
- AFMC00044** On transient flow in a ventilated filling box  
G. R. Hunt, N. B. Kaye
- AFMC00045** A study of base drag optimization using mass bleed  
Y. K. Lee, H. D. Kim, S. Raghunathan

- AFMC00046** Modelling chemical reaction in a scalar mixing layer  
B. L. Sawford
- AFMC00047** Velocity measurement in turbulent boundary layer of drag-reducing surfactant solution  
M. Itoh, S. Tamano, K. Yokota, M. Ninagawa
- AFMC00049** Numerical investigation of unsteady flow and heat transfer in wavy channels  
Mohammad Zakir Hossain, A. K. M. Sadrul Islam
- AFMC00052** Surface-flow patterns in oscillating-triangular-jet nozzles  
S. K. Lee, P. V. Lanspeary, G. J. Nathan, R. M. Kelso
- AFMC00053** Influence of vegetation height and density on turbulent boundary layer  
P. Gualtieri, G. Pulci Doria, L. Taglialatela
- AFMC00054** The transport of sediment over a sloping breakwater  
A. J. Hogg, D. Pritchard
- AFMC00055** Preliminary identification of flow regimes in a mechanically oscillated planar jet  
M. Riese, G. J. Nathan, R. M. Kelso
- AFMC00056** Turbulent stress invariant analysis: clarification of existing terminology  
A. J. Simonsen, P.-. Krogstad
- AFMC00058** A physical model of the turbulent boundary layer consonant with the structure of the mean momentum balance  
J. Klewicki, P. McMurtry, P. Fife, T. Wei
- AFMC00059** Dynamics of a transient wave group breaking on a beach  
T. E. Baldock
- AFMC00060** Detonation modelling of corner-turning shocks in PBXN-111  
J. P. Lu, F. C. Christo, D. L. Kennedy
- AFMC00061** The external flow structure of a naturally precessing fluidic jet  
Chong Yau Wong, Richard M. Kelso, Graham J. Nathan
- AFMC00062** An investigation of the influence of nozzle aspect ratio on the velocity field of turbulent plane jet  
R. C. Deo, J. Mi, G. J. Nathan

- AFMC00063** The anomalous refraction of shock waves in gases  
L. F. Henderson, E. G. Puckett, P. Colella
- AFMC00064** Autocorrelation functions and the determination of integral length with reference to experimental and numerical data.  
P. L. O'Neill, D. Nicolaides, D. Honnery, J. Soria
- AFMC00066** Experimentalnumerical investigation of a bend diffuser-configuration  
A. J. Simonsen, P.-. Krogstad
- AFMC00068** Numerical studies on turbulent separated flows in high-velocity transient motors  
V. R. Sanal Kumar, H. D. Kim, B. N. Raghunandan, T. Setoguchi
- AFMC00069** The effect of turbulence on cloud droplet collision rates  
C. N. Franklin, P. A. Vaillancourt, M. K. Yau, P. Bartello
- AFMC00070** Low-Reynolds-number stirring in simple devices  
S. M. Cox
- AFMC00072** Bubble entrapment during water drop impacts  
D. E. Cole, J. L. Liow
- AFMC00073** Scaling analysis and direct simulation of unsteady natural convection cooling of fluid with  $Pr \ll 1$  in a vertical cylinder  
Wenxian Lin, S. W. Armfield
- AFMC00074** Effects of axial pulsing on unconfined vortex breakdown  
S. Khalil, K. Hourigan, M. C. Thompson
- AFMC00075** The aerodynamic forces on a series of tennis balls  
F. Alam, S. Watkins, A. Subic
- AFMC00076** Topographically trapped finite-amplitude kink solitons  
S. R. Clarke
- AFMC00077** Linear and nonlinear acoustic behaviour of outlet nozzles  
W. H. Moase, M. J. Brear, C. Manzie
- AFMC00078** Optimal nose shaping for delayed boundary-layer separation in laminar plane-symmetric and axisymmetric flow  
T. W. Mattner, E. O. Tuck, J. P. Denier

- AFMC00079** The unsteady near-wake of a simplified passenger car  
G. Vino, S. Watkins, P. Mousley, J. Watmuff, S. Prasad
- AFMC00080** Convective exchange between two connected chambers  
M. A. Coman, G. O. Hughes, R. C. Kerr
- AFMC00081** Lamb vector properties of swirling jets  
W. Kollmann, G. Umont
- AFMC00082** Measurements of temperature and water vapour concentration in a scramjet combustor  
A. D. Griffiths, A. F. P. Houwing
- AFMC00083** Preliminary examination of a round jet initial condition anomaly for the k- turbulence model  
E. J. Smith, J. Mi, G. J. Nathan, B. B. Dally
- AFMC00084** Modelling of transient behaviour in a Francis turbine power plant  
Tzuu Bin Ng, G. J. Walker, J. E. Sargison
- AFMC00085** Skin friction CFD calculation for complex flow: turbulent flow along an external corner  
K. A. M. Moinuddin, P. N. Joubert, M. S. Chong
- AFMC00086** Influence of free-stream turbulence on wakewake interaction in an axial compressor  
A. D. Henderson, G. J. Walker, J. D. Hughes
- AFMC00087** Experiments and modeling of impinging jets and premixed stagnation flames  
J. M. Bergthorson, D. G. Goodwin, P. E. Dimotakis
- AFMC00088** Effect of grid geometry on the scale-by-scale budget of decaying grid turbulence  
P. Lavoie, R. A. Antonia, L. Djenidi
- AFMC00089** Some hydrodynamic characteristics of an air-cushion supported concrete gravity structure  
B. Chenu, M. T. Morris-Thomas, K. P. Thiagarajan
- AFMC00090** Study of micro shock waves and cavitation generated by Ho:YAG laser beam for medical application  
S. H. R. Hosseini, K. Takayama

- AFMC00091** Experimental review of devices to artificially thicken wind tunnel boundary layers  
J. E. Sargison, G. J. Walker, V. Bond, G. Chevalier
- AFMC00093** The entrance length for fully developed turbulent channel flow  
K. Lien, J. P. Monty, M. S. Chong, A. Ooi
- AFMC00095** The development and use of dynamic pressure probes with extended cones of acceptance (ECA)  
Simon Watkins, Peter Mousley, Gioacchino Vio
- AFMC00096** The effect of particle concentration on the coefficient of drag of a spherical particle  
D. S. Dodds, J. Naser
- AFMC00097** Periodic forcing of baroclinic basin-scale waves in a rotating stratified basin  
G. W. Wake, J. Gula, G. N. Ivey
- AFMC00098** An internal solitary wave parameterization for hydrodynamic lake models  
L. Boegman, G. N. Ivey, J. Imberger
- AFMC00100** Differential diffusion: often a finite-mixing length effect  
Peter Nielsen, Ian A. L. Teakle
- AFMC00101** Shedding some light on  $\alpha$ -factors  
I. A. L. Teakle, P. Nielsen
- AFMC00102** Modelling gas-liquid bubbly flows  
G. H. Yeoh, J. Y. Tu
- AFMC00103** Numerically modelling blockage effects on the flow between flat plates  
M. D. Griffith, K. Hourigan, M. C. Thompson
- AFMC00104** Effects of turbulence manipulation in skimming flows: an experimental study  
C. A. Gonzalez, H. Chanson
- AFMC00105** Hydrodynamic performance of a surfboard fin  
P. A. Brandner, G. J. Walker

- AFMC00106** Effect of localised wall suction on the small-scale motion in a turbulent boundary layer  
O. Oyewola, L. Djenidi, P. Burattini, R. A. Antonia
- AFMC00107** Pressure measurements on an automobile side rear view mirror  
R. Jaitlee, F. Alam, S. Watkins
- AFMC00111** A numerical comparison of forced and free vibration of circular cylinders at low Reynolds number  
J. S. Leontini, M. C. Thompson, K. Hourigan
- AFMC00112** Vortex wake and energy transitions of an oscillating cylinder at low Reynolds number  
B. E. Stewart, J. S. Leontini, K. Hourigan, M. C. Thompson
- AFMC00113** Comparison of flow characteristics of 45 forward and 45 backward facing proximal anastomosis models: a particle image velocimetry study  
W. F. Ji, L. P. Chua, T. M. Zhou, S. C. M. Yu
- AFMC00117** Dynamic measurement of differential buffet pressure  
J. H. Watmuff, G. Vio, S. Watkins, B. Hill
- AFMC00118** Evidence of the -1-law in a high Reynolds number turbulent boundary layer  
T. B. Nickels, S. Hafez, I. Marusic, M. S. Chong
- AFMC00120** Characterising roof ventilators  
A. Revel, B. P. Huynh
- AFMC00121** Laminar-turbulent transition of a boundary layer by a single roughness element in an inlet region of a circular pipe  
M. Ichimiya
- AFMC00122** Model for anomalous scaling of turbulent structure functions  
T. S. Lundgren
- AFMC00123** Noise emission in large aspect ratio cavities  
G. Guj, R. Camussi, A. Di Marco, A. Ragni
- AFMC00124** Analysis of the propeller wake by pressure and velocity correlation  
M. Felli, F. Di Felice, G. Guj, R. Camussi

- AFMC00127** Dominant spanwise Fourier modes, and the existence of very large scale coherence in turbulent boundary layers  
N. Hutchins, B. Ganapathisubramani, I. Marusic
- AFMC00128** Dual-plane PIV investigation of structural features in a turbulent boundary layer  
I. Marusic, B. Ganapathisubramani, E. K. Longmire
- AFMC00129** Numerical study of flow and forced heat transfer of Robertson-Stiff fluid flowing axially through concentric annuli  
Aliakbar Heydari Gorji, Fariborz Rashidi
- AFMC00130** Numerical analysis of turbulent convective heat transfer processes in a square-sectioned U-bend duct  
Sassan Etemad, Bengt Sundn
- AFMC00131** The internal wave field generated by the body and wake of a horizontally moving sphere in a stratified fluid  
James W. Rottman, Dave Broutman, Geoff Spedding, Patrice Meunier
- AFMC00133** Direct injection of natural gas/liquid diesel fuel sprays  
T. R. White, B. E. Milton, M. Behnia
- AFMC00134** The turbulent wind environment of birds, insects and MAVs  
S. Watkins, G. Vino
- AFMC00135** Coherent structure dynamics in jets from irregular shaped nozzles  
J. Hart, J. Naser, P. Witt
- AFMC00137** CFD investigation of particle deposition around bends in a turbulent flow  
A. Hossain, J. Naser
- AFMC00138** A steady filling box solution with zero net buoyancy flux  
G. O. Hughes, R. W. Griffiths, J. C. Mullarney
- AFMC00140** Experimental investigation of a rectangular slot-burner in the presence of cross-flow for different jet velocity ratios  
S. Ahmed, J. Naser, J. Nikolov, C. Solnordal, W. Yang, J. Hart
- AFMC00141** Direct and large eddy simulation of a turbulent channel flow with roughness on one wall  
S. Leonardi, F. Tessicini, P. Orlandi, R. A. Antonia



- AFMC00143** Evolution of a turbulent wedge from a streamwise streak  
J. H. Watmuff
- AFMC00145** Response of ocean circulation to variable wind forcing  
A. E. Kiss, C. Mnesguen
- AFMC00146** A directional event detector for conditional laser imaging  
P. V. Lanspeary, S. K. Lee
- AFMC00148** Investigations on the closure of laminar separation bubbles  
R. L. Thomas, J. P. Gostelow
- AFMC00150** Flow measurements in microchannels using a MicroPIV system  
Wing T. Lai, Rajan K. Menon
- AFMC00151** Experimental investigation of impinging axisymmetric turbulent fountains  
Paul Cooper, Gary R. Hunt
- AFMC00154** Axisymmetric jet control using passive grids  
R. Lehman, S. Rajagopalan, P. Burattini, R. A. Antonia
- AFMC00155** Flows within a cylindrical cell culture bioreactor with a free-surface and a rotating base  
J. Dusting, J. Sheridan, K. Hourigan
- AFMC00156** Effect of initial conditions on the far field of a round Jet  
P. Burattini, R. A. Antonia, S. Rajagopalan
- AFMC00157** Numerical analysis of a hydrocyclone in a recirculating aquaculture system  
Eunpil Kim, Gul Chang, Jung In Yoon
- AFMC00158** Turbulence models and boundary conditions for bluff body flow  
M. E. Young, A. Ooi
- AFMC00159** Non-Newtonian flow behaviour in particulate suspensions under magnetic fields  
H. See
- AFMC00160** Modelling of solid wall boundaries in computational acoustics  
R. C. Z. Cohen, A. Ooi, R. Widjaja

- AFMC00161** Unsteady RANS simulation of high Reynolds number trailing edge flow  
D. Ang, L. Chen, J. Tu
- AFMC00162** Air entrainment by free falling streams of particles  
Zeqin Liu, Paul Cooper, Peter W. Wypych
- AFMC00163** Experimental investigation of flow-induced vibration in a parallel plate reactor fuel assembly  
Mark Ho, Guang Hong, A. N. F. Mack
- AFMC00164** Flow past a cylinder with free hemispherical ends: comments on grid independence and wake symmetry characteristics  
G. J. Sheard, Mark C. Thompson, K. Hourigan
- AFMC00166** Three-dimensional instabilities and transition in pulsatile stenotic flows  
H. M. Blackburn, S. J. Sherwin
- AFMC00167** Three-dimensional quasi-periodic instabilities of two-dimensional time-periodic flows  
H. M. Blackburn, J. M. Lopez, F. Marques
- AFMC00168** Fire behaviour studies of combustible wall linings applying Fire Dynamics Simulator  
A. Z. Moghaddam, K. Moinuddin, I. R. Thomas, I. D. Bennetts, M. Culton
- AFMC00170** Free surface monitoring using image processing  
P. D. M. Brady, M. Boutounet, S. Beecham
- AFMC00171** A numerical study of enhanced micro-channel cooling using a synthetic jet actuator  
V. Timchenko, J. Reizes, E. Leonardi
- AFMC00173** Identification of aerodynamic sound source in the wake of a rotating circular cylinder  
A. Iida, A. Mizuno, R. J. Brown
- AFMC00174** Dynamic analysis of airflow features in a 3D real-anatomical geometry of the human nasal cavity  
H. Tang, J. Y. Tu, H. F. Li, B. Au-Hijleh, C. C. Xue, C. G. Li
- AFMC00175** Nonlinear dynamics of thermoacoustic instability using a kinematic, premixed flame model  
N. Karimi, M. J. Brear, S. H. Jin

- AFMC00176** Mean flow characteristics of a micro-injector induced swirling jet  
I. K. Toh, P. O'Neill, D. Honnery, J. Soria
- AFMC00177** Simulation of vehicle A-pillar aerodynamics of various yaw angles  
N. M. Murad, J. Naser, F. Alam, S. Watkins
- AFMC00178** Active flow control over a NACA 0015 airfoil using a ZNMF jet  
A. Tuck, J. Soria
- AFMC00179** Velocity distribution in an asymmetric diffuser with perforated plates  
M. N. Noui-Mehidi, J. Wu, I. Sutalo
- AFMC00180** Gap effect on Taylor vortex size between rotating conical cylinders  
M. N. Noui-Mehidi, N. Ohmura, K. Kataoka
- AFMC00181** A blob insertion technique for the vortex blob method  
C. Macaskill
- AFMC00183** Design and calibration of a wind tunnel with a two-dimensional contraction  
J. E. Sargison, G. J. Walker, R. Rossi
- AFMC00186** Radiant heating of a bio-oil droplet: a quest for a suitable model and scaling of pre-explosion conditions  
J. Y. Hristov, V. Stamatov, D. R. Honnery, J. Soria
- AFMC00187** Thin-film flow in open helically-wound channels  
Y. M. Stokes, S. K. Wilson, B. R. Duffy
- AFMC00188** Effect of pulsation rate on spray-spreading rate in an isothermal environment  
L. Stamatova, D. Honnery, V. Stamatov, J. Ghajel, J. Soria
- AFMC00189** Flow structure around a finite-length square prism  
H. F. Wang, Y. Zhou, C. K. Chan, W. O. Wang, K. S. Lam
- AFMC00190** Active control of vortex-airfoil interactions  
M. M. Zhang, Y. Zhou, L. Cheng

- AFMC00191** A two-dimensional analysis of the effect of a rotating cylinder on an inverted aerofoil in ground effect  
S. Diasinos, T. J. Barber, E. Leonardi, S. D. Hall
- AFMC00192** PIV measurements in a square backward facing step  
M. Piirto, A. Karvinen, H. Ahlstedt, P. Saarenrinne, R. Karvinen
- AFMC00193** Stabilisation of a trapped vortex for enhancing aerodynamic flows  
A. Bouferrouk, S. I. Chernyshenko
- AFMC00195** Development of a fast response pressure probe for use in a cavitation tunnel  
P. A. Brandner, D. B. Clarke, G. J. Walker
- AFMC00196** Linear stability of natural convection on an evenly heated vertical wall  
G. D. McBain, S. W. Armfield
- AFMC00197** An investigation of flow over a two-dimensional spherical cavity  
C. C. Beves, T. J. Barber, E. Leonardi
- AFMC00198** Mixing characteristics of a notched-rectangular jet and a circular jet  
J. Mi, P. Kalt, G. J. Nathan
- AFMC00199** Preliminary investigations of vortex rings and jets in cross flow  
E. R. Hassan, R. M. Kelso, G. M. Schneider, T. C. W. Lau
- AFMC00200** Observations on high Reynolds number turbulent boundary layer measurements  
S. Hafez, M. S. Chong, I. Marusic, M. B. Jones
- AFMC00202** The effect of density ratio on the mean spread rate of a low pressure drop oscillating jet nozzle  
G. England, P. A. M. Kalt, G. J. Nathan, R. M. Kelso
- AFMC00203** Flow visualisation of a pitching and heaving hydrofoil  
Timothy C. W. Lau, Richard M. Kelso, Eyad R. Hassan
- AFMC00204** A numerical study of a circular cylinder in the wake of an airfoil  
C. Y. Zhou, C. W. Sun, Y. Zhou, L. Huang

- AFMC00205** The influence of mass loading on particle distribution in the near field of a co-annular jet  
C. H. Birzer, P. A. M. Kalt, G. J. Nathan, N. L. Smith
- AFMC00207** Flow visualisation of forced flow control over inclined airfoils  
K. L. Powell, K. Parker, J. Soria
- AFMC00208** On collective oscillations of bubble chains and arrays  
E. M. B. Payne, R. Manasseh, A. Ooi
- AFMC00209** Role of plant buildings in a power station acting as barrier to the wind affecting the natural draft cooling tower performance  
Ghulam Amur, Brian Milton, John Reizes, Jafar Madadnia, Simon Beecham, Peter Brady, Homa Koosha
- AFMC00210** Towards a universal criterion for predicting vortex breakdown in swirling jets  
A. J. Fitzgerald, K. Hourigan, M. C. Thompson
- AFMC00212** A numerical study of heat transfer from a cylinder in cross flow  
K. Szczepanik, A. Ooi, L. Aye, Gary Rosengarten
- AFMC00213** Impact of outlet boundary conditions on the flow properties within a cyclone  
St. Schmidt, H. M. Blackburn, M. Rudman
- AFMC00215** An experimental study of the jet of a boat propeller  
A. Loberto, R. J. Brown, M. K. Kwek, A. Iida, H. Chanson, S. Komori
- AFMC00216** Airflow distribution through the radiator of a typical Australian passenger car  
H. Jama, S. Watkins, C. Dixon, E. Ng
- AFMC00217** Spreading radius of fountains after impinging on a free surface  
C. J. Lemckert
- AFMC00218** Preliminary estimation methods for sizing detention basins in Queensland  
C. J. Scraggs, C. J. Lemckert
- AFMC00219** Design and experimental issues with heat exchangers for microfluidics  
G. Rosengarten, J. Cooper-White, Guy Metcalfe

- AFMC00221** Investigation of the mean flow pattern in zero-net-mass-flux elliptical-jets in cross-flow using planar-laser-induced fluorescence  
J. Arnaud, S. Tomar, J. Soria
- AFMC00222** Flow past an impulsively started oscillating elliptical cylinder  
T. L. Chng, T. T. Lim, J. Soria, K. B. Lua, K. S. Yeo
- AFMC00223** Wake structures of a heaving airfoil  
G. Y. Oo, K. B. Lua, K. S. Yeo, T. T. Lim
- AFMC00224** Structure of a zero-net-mass-flux round jet in crossflow  
S. Tomar, J. Arnaud, J. Soria
- AFMC00225** Dynamic testing of aircraft models in a water tunnel  
Lincoln P. Erm
- AFMC00226** Stereoscopic PIV measurements behind a 3D flapping foil producing thrust  
K. Parker, K. D. von Ellenrieder, J. Soria
- AFMC00227** Analysis of local flame propagation in gas explosions with multiple obstacles  
D. J. Park, A. R. Green, Y. C. Chen
- AFMC00228** Stereoscopic PIV measurements of the flow past a circular cylinder at Reynolds number 15000  
K. Parker, K. D. von Ellenrieder, J. Soria
- AFMC00230** Further study of spray combustion in a simple turbulent jet flow  
Yung-Cheng Chen, Sten H. Strner, Assaad R. Masri
- AFMC00231** Laminar flow in a periodic serpentine channel  
N. R. Rosaguti, D. F. Fletcher, B. S. Haynes
- AFMC00232** Simulating the deformation of Newtonian and non-Newtonian drops through a micro-fluidic contraction  
D. J. E. Harvie, M. R. Davidson, J. J. Cooper-White
- AFMC00233** DNS of turbulent heat transfer in a channel flow with a streamwisely varying thermal boundary condition  
Y. Seki, H. Kawamura

- AFMC00237** Numerical simulation of heat and mass transfer in a natural draft wet cooling tower  
N. Williamson, M. Behnia, S. Armfield
- AFMC00238** Three-dimensional transition in the buoyancy boundary layer on an evenly heated vertical wall  
S. W. Armfield, G. D. McBain
- AFMC00239** Transient behaviour of the fuel spray from an air-assisted, direct fuel injector  
S. H. Jin, M. J. Brear, G. Zakis, H. C. Watson, C. Xavier
- AFMC00240** How to describe turbulent energy distributions without the Fourier transform  
P. A. Davidson, B. R. Pearson, P. Staplehurst
- AFMC00243** Oscillations of the horizontal intrusion in a side-heated cavity  
F. Xu, J. C. Patterson, C. Lei
- AFMC00244** Numerical studies of contoured shock tube for murine powdered vaccine delivery system  
Y. Liu, N. K. Truong, M. A. F. Kendall
- AFMC00245** Application of transport PDF approach for modelling MILD combustion  
F. C. Christo, B. B. Dally
- AFMC00246** The transient behaviour of a differentially heated cavity with isoflux boundaries  
S. Jiracheewanun, S. W. Armfield, M. Behnia, G. D. McBain
- AFMC00247** Flow response to periodic heating and cooling in a reservoir  
Chengwang Lei, John C. Patterson, Yong Sha
- AFMC00248** Numerical method for the simulation of front evolving fibre suspension flow using level set method  
H.-S. Dou, N. Phan-Thien, B. C. Khoo, K. S. Yeo, R. Zheng
- AFMC00249** Instability of fluid material systems  
H.-S. Dou, N. Phan-Thien
- AFMC00251** Simulation of turbulence pressure fluctuations on cylinders in axial flow  
M. J. Woods, M. K. Bull

**AFMC00252** An experimental study of sudden release of bentonite suspensions down an inclined chute

H. Chanson, S. Jarny, L. Tocquer, P. Coussot

**AFMC00253** Comparing RANS models for flow and thermal analysis of pin fin heat sinks

B. Moshfegh, Robert Nyiredy

**AFMC00254** A study of the global differences between axisymmetric turbulent free jet flames from a smooth contraction and a pipe with well defined boundary conditions

A. S. Langman, G. J. Nathan, P. J. Ashman

**AFMC00256** Control of liquid sloshing in flexible containers: Part 1. Added mass

Birhan U. Gzel, Marija Gradinscak, S. Eren Semercigil, zden F. Turan

**AFMC00257** Control of liquid sloshing in flexible containers: Part 2. Top straps

Marija Gradinscak, Birhan U. Gzel, S. Eren Semercigil, zden F. Turan

**AFMC00258** Towards a valveless electro-rheological valve

Tam D. Truong, S. Eren Semercigil, zden F. Turan

**AFMC00259** Adverse pressure gradient turbulent boundary layer flows: Part 1: flow development

C. M. Anderson, . F. Turan, B. Brzek, L. Castillo

**AFMC00260** Adverse pressure gradient turbulent boundary layer flows: Part 2: scaling of Reynolds stress

B. Brzek, L. Castillo, C. M. Anderson, . F. Turan



## Small-Scale Turbulence: How Universal Is It?

R.A. Antonia and P. Burattini

Discipline of Mechanical Engineering  
University of Newcastle, NSW, 2308 AUSTRALIA

### Abstract

Kolmogorov's similarity hypotheses and his 4/5 law are valid at very large Reynolds numbers. For flows encountered in the laboratory, the effect of a finite Reynolds number and of the inhomogeneity associated with the large scales can affect the behaviour of inertial range scales significantly. This paper focuses on the source of inhomogeneity in two types of flows, those which are dominated mainly by a decay of energy in the streamwise direction and those which are forced, usually through a continuous injection of energy at large scales. Results based on a parameterization of the second-order velocity structure function indicate that the normalized third-order structure function approaches 4/5 more rapidly for forced than for decaying turbulence. These trends are supported by measurements and numerical data in these two flow types.

### Introduction

There is little doubt that the similarity hypotheses proposed by Kolmogorov [36] (or K41) and their subsequent revision ([38] or K62) have had a major impact on turbulence research (e.g., [11,13,26,47,49,50,58,61]). A fundamental element of these hypotheses is the assumption that the small scale motion, which includes the dissipative and inertial ranges, is isotropic. Also, K41 and K62 require that the Reynolds number is very large so that the small scale motion is independent of the invariably anisotropic large scale motion. The major outcome of the first similarity hypothesis is the prediction

$$\langle (\delta u^*)^n \rangle = f_{un}(r^*), \quad (1)$$

where the increment  $\delta u \equiv u(x+r) - u(x)$  ( $u$  is the velocity fluctuation along  $x$ ; the separation  $r$  is aligned with  $x$ , and the angular brackets denote averaging). For each value of  $n$ ,  $f_{un}$  is a universal function, in the sense that it is expected to depend only on  $r^* \equiv r/\eta$  ( $\eta \equiv (\nu^3/\langle \epsilon \rangle)^{1/4}$  is the Kolmogorov length scale,  $\nu$  is the kinematic viscosity and  $\langle \epsilon \rangle$  is the mean energy dissipation rate). The asterisk denotes normalization by the Kolmogorov velocity scale  $u_K \equiv (\nu \langle \epsilon \rangle)^{1/4}$  and/or  $\eta$ . The second similarity hypothesis yields the famous inertial range ( $\eta \ll r \ll L$ ;  $L$  is an integral length scale) result

$$\langle (\delta u^*)^n \rangle = C_{un} r^{*n/3}, \quad (2a)$$

when K41 is used ( $C_{un}$  is a universal constant). With K62,

$$\langle (\delta u^*)^n \rangle = C_{un}^{\dagger} r^{*\zeta_{un}}, \quad (2b)$$

where the exponents  $\zeta_{un}$  may depart from  $n/3$  due to the effect of intermittency in the dissipation rate ( $C_{un}^{\dagger}$  may differ slightly from  $C_{un}$ ).

An important "exact" relation between  $\langle (\delta u)^2 \rangle$  and  $\langle (\delta u)^3 \rangle$  was obtained by Kolmogorov [37], starting with the

Karman-Howarth [35] equation for homogeneous isotropic turbulence,

$$-\langle (\delta u)^3 \rangle = 4/5 \langle \epsilon \rangle r - 6\nu \frac{d}{dr} \langle (\delta u)^2 \rangle. \quad (3)$$

A detailed derivation of Eq.(3) was provided by Batchelor [11]. More recently, the assumptions underlying the Kolmogorov equation have been revised [26,41] and formalized more rigorously [32]. A matched asymptotic expansion approach has been used by Lundgren [44] to obtain the same result. In the inertial range, the viscous term can be neglected and (3) reduces to the 4/5 law, viz.

$$-\langle (\delta u)^3 \rangle = (4/5) \langle \epsilon \rangle r \quad \text{or} \quad -\langle (\delta u^*)^3 \rangle = (4/5) r^*. \quad (4)$$

It is important to underline that (3) and (4), as well as the hypotheses in K41 and K62, apply only at very large Reynolds numbers. It is not surprising, therefore, that for flows normally encountered in the laboratory, Eq.(1) appears to be satisfied only in the dissipative range (typically  $r^* \leq 10$ ) (see §7 of [19] and [53]); although the evidence is not altogether convincing especially when the isotropic form of  $\langle \epsilon \rangle$ , viz

$$\langle \epsilon \rangle_{\text{iso}} = 15\nu \langle (\partial u / \partial x)^2 \rangle \quad (5)$$

is used in forming  $\delta u^*$  and  $r^*$ . With a few exceptions, the laboratory data also indicate an asymptotic approach to Eq.(2a) (or Eq.(2b)) and Eq.(4) as the Reynolds number (usually represented by  $R_\lambda$  and defined by  $\langle u^2 \rangle^{1/2} \lambda / \nu$ , where  $\lambda$  is the

Taylor microscale  $\langle u^2 \rangle^{1/2} / \langle (\partial u / \partial x)^2 \rangle^{1/2}$ ) increases. When  $R_\lambda$  is finite, deviations from Eqs.(2), (4) and indeed (5) can be quite significant. When  $R_\lambda$  is fixed, the deviations may also depend on the nature of the flow, thus casting doubt on any claim of universality. For the same flow and  $R_\lambda$ , departures from Eqs.(2) and (5) can still depend on the initial conditions that are used. It seems reasonable to ascribe these deviations to a lack of homogeneity in laboratory flows, the source of inhomogeneity depending on a number of parameters, such as the Reynolds number, type of flow and initial conditions.

In deriving Eq.(3), Kolmogorov ignored the nonstationary or nonhomogeneous term (space or time derivative term, respectively). This term has since been considered by a number of authors (e.g., Danaila et al [21], Lindborg [41], Qian [54,55], Lundgren [43]) in the context of decaying homogeneous isotropic turbulence. There have also been attempts at identifying this nonstationarity in more complicated flows, e.g. the centreline region of a fully developed channel flow (Danaila et al. [22]), a homogeneous uniform shear flow (Casciola et al. [18], Danaila et al. [20], Qian [55,56]) and the region near the axis of a circular jet (Danaila et al. [24]). Forcing has been used in physical experiments (e.g., Moisy et al. [46]) to achieve stationarity. Stationary isotropic turbulence is often studied numerically by adding a forcing term to the Navier-Stokes equation (e.g., [26,30]).

It should also be recalled that, at the relatively large Reynolds numbers which occur in the atmospheric surface layer, the evidence in support of the “4/5” law is rather inconclusive. This is partly due to the uncertainty in estimating  $\langle \varepsilon \rangle$ . The data of Sreenivasan and Dhruva [60] for  $R_\lambda \approx 10^4$  indicated, however, that there is no discernible range over which  $d\langle(\delta u)^3\rangle/dr$  is constant over a convincing range. This raises some concern since the existence of the inertial range has been traditionally linked to the linear increase of  $\langle(\delta u)^3\rangle$  with  $r$ . These authors further noted that an inertial range could not be identified unambiguously from the local slopes of the even-order moments of  $\delta u$ . They also stressed the difficulty of discussing the scaling of  $\langle(\delta u)^n\rangle$  effectively without first understanding the effects of finite shear and finite  $R_\lambda$ . The previous observations can only fuel speculation about the meaningfulness of the scaling exponents that have been inferred from laboratory data and also the corresponding inferences regarding the departures of these exponents from the K41 predictions. For example, Lindborg [41] noted that “in order to test intermittency theories experimentally, it is necessary to recover Kolmogorov’s law with good accuracy in a sufficiently broad range of scales. Otherwise there is no reason to put faith in possible observed deviations from the K41 theory”.

In this paper, the focus is almost exclusively on the effect the inhomogeneity has on what is loosely referred to as the scaling range or restricted scaling range. We adopt the approach previously used by Danaila et al. [21–23], which consists in extending Eq.(3) to a statement which, in essence, expresses a scale-by-scale energy budget for a particular flow. Previously published data as well as new measurements for grid turbulence and along the axis of a circular jet are examined with the aim of quantifying possible differences in the inhomogeneity among various flows. Specifically, we distinguish between flows which are dominated by the decay of turbulent energy along the main flow direction—such as grid turbulence, jets and wakes—and flows which have been forced. In experiments, forcing can be achieved by stirring the flow with moving boundaries [46], introducing body forces or with zero-net mass-flow-rate jets [14,32]. In numerical simulations, it is usually achieved by continuously injecting energy at low wavenumbers [30]. We also examine how the asymptotic K41 result may be reached in these two flow categories.

### Inhomogeneity in Decaying and Forced Flows

In this section, we give examples of how the inhomogeneity can affect relation (3) in decaying flows. The modified form of this relation can be written as

$$-\langle(\delta u)^3\rangle = 4/5\langle\varepsilon\rangle r - 6\nu \frac{d}{dr}\langle(\delta u)^2\rangle + I_u \quad (6)$$

where  $I_u$  represents the inhomogeneity associated with the large scale motion. For decaying grid turbulence, [21]

$$I_u \equiv 3U/r^4 \int_0^r \omega^4 \frac{d}{dx}\langle(\delta u)^2\rangle d\omega \quad (7a)$$

where  $U$  is the mean velocity in the  $x$  direction and  $\omega$  a dummy integration variable. For forced turbulence, Moisy et al [46] obtained (using [51])

$$I_u \equiv -2/7\langle\varepsilon\rangle r^3/L_f, \quad (7b)$$

where  $L_f$  is an integral scale which characterises the forcing. A similar expression is given by Gotoh et al [30] and Fukayama et

al [26]. Since  $I_u$  is negative, its presence in Eq.(6) is to keep the magnitude of  $-\langle(\delta u)^3\rangle$  below its asymptotic value of  $4\langle\varepsilon\rangle/5$ .

As a consequence, measured values of  $-\langle(\delta u^*)^3\rangle$  cannot exceed  $4r^*/5$ , unless  $\langle\varepsilon\rangle$  is evaluated incorrectly. Note that Eq.(6) should provide a more reliable indirect means of estimating  $\langle\varepsilon\rangle$ .

A more general form of Eq.(6) is the corresponding transport equation for the energy structure function  $\langle(\delta q)^2\rangle \equiv \langle(\delta u)^2\rangle + \langle(\delta v)^2\rangle + \langle(\delta w)^2\rangle$  ( $v$  and  $w$  are velocity fluctuations in the  $y$  and  $z$  directions, respectively), e.g. [24],

$$-\langle\delta u(\delta q)^2\rangle = 4/3\langle\varepsilon\rangle r - 2\nu \frac{d}{dr}\langle(\delta q)^2\rangle + I_q \quad (8)$$

with

$$I_q \equiv (2U/r^2) \int_0^r \omega^2 \frac{d}{dx}\langle(\delta q)^2\rangle d\omega \quad (9)$$

for decaying homogeneous isotropic turbulence. Note that now 4/5 has been replaced by 4/3. One advantage of Eq.(8) over Eq.(6) is that it allows a more meaningful comparison with the transport equation for  $\langle(\delta\theta)^2\rangle$ , where  $\theta$  is the scalar fluctuation (e.g. [3]). Another advantage, [21], is that, for small  $r$ , it is consistent with a more general form of  $\langle\varepsilon\rangle$  than  $\langle\varepsilon\rangle_{\text{iso}}$ , i.e.

$$\langle\varepsilon\rangle_q = 3\nu \langle(\partial u/\partial x)^2 + (\partial v/\partial x)^2 + (\partial w/\partial x)^2\rangle \quad (10)$$

whereas, at sufficiently large  $r$ , it reproduces the turbulent energy budget, viz.

$$\langle\varepsilon\rangle = -\frac{U}{2} \frac{d\langle q^2\rangle}{dx} \quad (11)$$

(without the need to assume isotropy at large scales, i.e.  $\langle q^2\rangle = 3\langle u^2\rangle$ ; such an assumption is invalidated in most grid turbulence experiments because  $\langle u^2\rangle$  is typically larger than  $\langle v^2\rangle$  or  $\langle w^2\rangle$  by nearly 20%). As noted by Antonia et al [9], the presence of  $I_u$  in Eq.(6), or  $I_q$  in Eq.(8), allows compliance with two important classical results. The energy budget is retrieved at large  $r$ , whilst the decay of  $\langle\varepsilon\rangle$  or, equivalently, the enstrophy in homogeneous turbulence, is correctly reproduced in the limit of  $r \rightarrow 0$ .

For reasons mentioned above we have preferred to validate Eq.(8), instead of Eq.(6), using (new) measurements obtained in grid turbulence and along the axis of a circular jet. Both these flows offer advantages in the present context. In grid turbulence,  $\langle\varepsilon\rangle$  can be inferred reliably from Eq.(11); from an experimental viewpoint, this can be exploited usefully, e.g. for assessing any possible degradation to the high wavenumber part of the spectrum, e.g. [57]. Along the axis of a circular jet it can be shown that the structure functions should satisfy similarity, when normalized by the energy and Taylor microscale [16]. Because  $R_\lambda$  is constant along the axis, other combinations of normalising scales, such as  $(\eta, u_k^2)$  and  $(L, \langle q^2\rangle)$ , should also result in the collapse of the structure functions.

### Experimental Details

The grid turbulence tunnel has a working section of 350 mm  $\times$  350 mm and is 2.4 m long. A biplane square mesh

grid ( $M = 24.8$  mm with  $4.76$  mm square rods and a solidity of  $0.35$ ) is placed at the entrance section and measurements are made on the centreline at  $x = 52M$ , where the turbulence is approximately locally homogeneous and isotropic. The mean streamwise velocity is about  $6 \text{ ms}^{-1}$ .

The jet exits from a contraction (85:1 area ratio). The exit diameter,  $D$ , is  $55$  mm. Data are taken on the axis, at a distance of  $40D$  downstream of the exit, where the mean velocity in the streamwise direction is about  $4.5 \text{ ms}^{-1}$ .

The velocity was measured with in-house hot wires, operated with in-house constant temperature anemometer circuits. The hot wire (Pt-10% Rh) was etched to a diameter of  $d_w$  of  $2.5 \mu\text{m}$  and an active length  $l_w$  so that the ratio  $l_w/d_w$  was approximately 200. The CTA circuits were operated at an overheat ratio of 1.5, with a cut-off frequency set at approximately 15 kHz. The sampling frequency,  $f_s$ , was 8 kHz for the grid turbulence and 12.6 kHz for the jet measurements while the analog filters were set at  $f_s/2$ . The anemometer signals were digitized into a PC using a 16-bit AD board. The geometrical angle between the wires was nearly  $90^\circ$ . The calibration of the X-wire was performed using a look-up-table (LUT) method [15]. A comparison between LUT and the effective angle method showed that the former gives more reliable results when the velocity is below about  $6 \text{ ms}^{-1}$ . With LUT, the velocity and velocity derivative statistics, in both grid turbulence and the far field of the circular jet, were in closer (but far from perfect) agreement with isotropy than when the effective angle calibration was used. Corrections for the spatial attenuation of the hot-wires (using the method outlined in Zhu and Antonia [64]) and Taylor's hypothesis (following [34]) have been applied.

### Comparison of Experimental and Numerical Data with Eqs.(6) and (8)

All the measured terms in Eq.(8) are shown in Fig.1 (grid turbulence) and Fig.2 (jet axis). All terms have been normalized by dividing by  $\langle \epsilon \rangle r$ . The determination of  $\langle \epsilon \rangle$ , as given by Eq (10), has been used in each case. For grid turbulence,  $\langle \epsilon \rangle_q$  was within 5% of the value estimated from measurements of  $\langle q^2 \rangle$  via Eq (11). Use of  $\langle \epsilon \rangle_{\text{iso}}$  resulted in Eq (11) being satisfied within 10%. In the jet experiment,  $\langle \epsilon \rangle_q$  was in satisfactory (5%) agreement with the measured energy budget along the axis. This budget included turbulent advection and production via the normal stresses (the turbulent diffusion was found to be negligible) but ignored the pressure diffusion term; although justification for this latter assumption is lacking, the use of  $\langle \epsilon \rangle_{\text{iso}}$ , instead of  $\langle \epsilon \rangle_q$ , resulted in a 17% imbalance in the budget for  $\langle q^2 \rangle$ . In estimating  $I_q$  use was made of similarity [7], viz.

$$\langle \delta q^2 \rangle = \langle q^2 \rangle f(r/\lambda) \quad (12)$$

$$-\langle \delta u (\delta q)^2 \rangle = \langle q^2 \rangle^{\frac{3}{2}} g(r/\lambda) \quad (13)$$

For grid turbulence, where  $f$  and  $g$  determine the shape of the structure functions and are dependent only on  $r/\lambda$  (not on  $x$ ),

$$I_q \equiv \underbrace{(U/r^2) \langle q^2 \rangle \lambda^2 \frac{d\lambda}{dx} \int_0^{r/\lambda} (\omega/\lambda)^3 f' d(\omega/\lambda)}_{I_{q2}}$$

$$+ \underbrace{(U/r^2) \lambda^2 \frac{d\langle q^2 \rangle}{dx} \int_0^{r/\lambda} (\omega/\lambda) f d(\omega/\lambda)}_{I_{q1}} \quad (14)$$

On the jet axis,  $I_q$  is given by

$$I_q \equiv I_{q1} + I_{q2} + \underbrace{(2/r^2) \frac{dU}{dx} \langle q^2 \rangle \lambda^3 \int_0^{r/\lambda} (\omega/\lambda)^2 (e-h) d(\omega/\lambda)}_{I_{q3}} \quad (15)$$

where  $I_{q1}$  and  $I_{q2}$  are indicated in Eq (14). The prime denotes a derivative with respect to the similarity variable  $(\omega/\lambda)$ . The extra term  $(I_{q3})$  represents the contribution from the difference between the longitudinal and radial structure functions, viz.

$$\langle (\delta u)^2 \rangle = \langle q^2 \rangle e(r/\lambda) \quad (16)$$

$$\langle (\delta v)^2 \rangle = \langle q^2 \rangle h(r/\lambda) \quad (17)$$

In forming  $\langle (\delta q)^2 \rangle$ , we have assumed that  $\langle (\delta v)^2 \rangle = \langle (\delta w)^2 \rangle$  so that  $\langle (\delta q)^2 \rangle = \langle (\delta u)^2 \rangle + 2\langle (\delta v)^2 \rangle$  and consequently  $\langle v^2 \rangle = \langle w^2 \rangle$ , so that  $\langle q^2 \rangle = \langle u^2 \rangle + 2\langle v^2 \rangle$ . Justification for the similarity scales  $\langle q^2 \rangle$  and  $\langle \lambda \rangle$  was provided by George [29] who considered the spectral equations for decaying homogeneous isotropic turbulence and also Antonia et al. [7] and Danaila et al. [23] who considered the transport equation for  $\langle (\delta q)^2 \rangle$ .

In the jet, the first term of Eq.(14),  $I_{q1}$ , involving the decay of  $\langle q^2 \rangle$ , was estimated after applying a least squares fit to the axial profiles of  $\langle q^2 \rangle$  over the range  $38 \leq x/D \leq 42$ . The decay of the mean velocity was estimated in the same way, for the last term  $I_{q3}$ . Finally, a fit to the streamwise variation of  $\lambda$  was used to estimate  $I_{q2}$ . A more general definition of  $\lambda_q (= 5\nu \langle q^2 \rangle / \langle \epsilon \rangle_q)$ , and consequently  $R_\lambda = \langle q^2 \rangle^{1/2} \lambda_q / 3^{1/2} \nu$  [2]), which takes into account the three velocity components, has been used in analysing these data.

The linear vertical scale in Figs 1 and 2 provides a more severe test of how closely Eq.(8) is satisfied by the measurements than the logarithmic scale used in previous papers [9,51]. The imbalance, or difference between 4/3 and the remaining normalized terms in Eq.(8), is satisfactory, especially for Fig.1. The imbalance (dashed lines in Figs. 1 and 2) is larger for the jet than for grid turbulence. There may be several reasons for this. More assumptions were made [24] in the derivation of Eq.(15) than for Eq.(7a). The turbulence intensity in the jet is about 25%, much larger than that for grid turbulence (2.5%). This may introduce an additional uncertainty due to the use of Taylor's hypothesis (although modified, following [34]) and the neglect of the binormal component (the out-of-plane velocity component not resolved by the X-wire).

It is noteworthy, however, that at  $r \approx \lambda_q$  the balance is almost exact, implying that  $\langle \epsilon \rangle$  can be estimated from Eq.(8), once the second- and third-order structure functions are known. The major difference between Figs 1 and 2 reflects, to a large extent, the higher value of  $R_\lambda$  in the jet. Correspondingly, the maximum

value of  $-\langle \delta u (\delta q)^2 \rangle / \langle \varepsilon \rangle r$  is twice as large in Fig.2 than in Fig.1. Accordingly, the likelihood of a scaling range is bigger for Fig.2 than Fig.1. This range can be very roughly inferred from the intersections of the distribution corresponding to this term with those for the viscous term and for  $I_q$ . The locations of these crossings are denoted by  $r_l$  and  $r_h$  in the figures. The difference  $(r_h - r_l)$  is significant in Fig.2 but negligible in Fig.1, so that a scaling range would be most tenuous for Fig.1. The separate contributions to  $I_q$  are also included in Figs 1 and 2. The major contribution comes from  $I_{q1}$ , the term associated with the streamwise decay of  $\langle q^2 \rangle$ ; in this sense, the central region of the jet resembles grid turbulence for which this is the dominant term (see Eq.(8)). One may expect a similar behaviour to apply along the centreline of wakes, but not in a pipe or a channel, because of the streamwise inhomogeneity; here, the effect of turbulent diffusion along the wall-normal direction cannot be ignored. The contributions from  $I_{q2}$  are not negligible around  $r \approx \lambda_q$  (Fig.1) and  $r \approx 10\lambda_q$  (Fig.2).  $I_{q3}$  becomes largest at the largest  $r/\lambda_q$ .

The DNS data for box turbulence of Fukayama et al. [26] (replotted here on a linear scale) are shown in Fig.3. Results for both decaying and forced turbulence, obtained at the same  $R_\lambda (\approx 70)$ , are included. There is almost no difference between the viscous terms, reflecting the normalization by  $\eta$  (e.g., [2]). The maximum value of  $-\langle (\delta u)^3 \rangle / \langle \varepsilon \rangle r$  is larger for forced turbulence, reflecting the smaller value of  $I_u$  in this case. The difference between the forced and decaying values of  $I_u$  is only likely to increase, as  $R_\lambda$  is increased. Unfortunately, DNS data for decaying box turbulence at large  $R_\lambda$  are not yet available. That the influence of  $I_u$  (or  $I_q$ ) on scales corresponding to the peak in  $-\langle (\delta u)^3 \rangle / \langle \varepsilon \rangle r$  should diminish as  $R_\lambda$  increases can be readily inferred from available data in decaying grid turbulence. The data in [62] are reproduced in Fig. 4; although the  $R_\lambda$  range is limited, the trend is unmistakable. The magnitude of  $I_u$ , estimated here from the measured values of  $\langle (\delta u)^2 \rangle$  and  $\langle (\delta u)^3 \rangle$  and assuming the validity of Eq.(5), decreases with  $R_\lambda$  at least as rapidly as that of the viscous term.

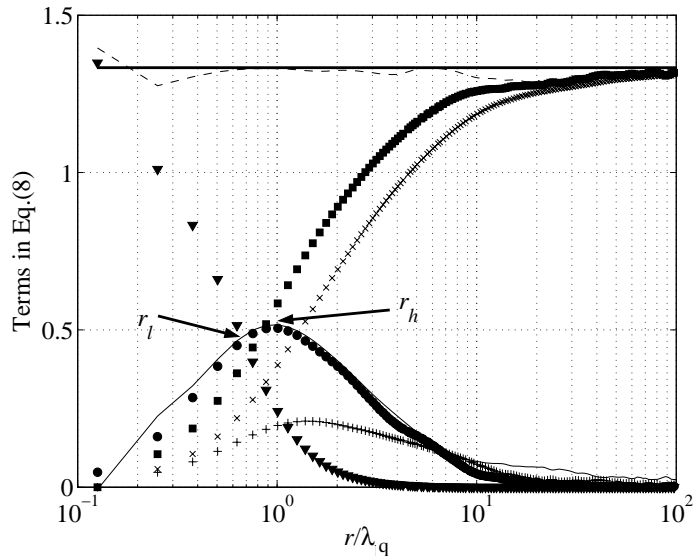


Figure 1: Terms in Eq.(8), divided by  $\langle \varepsilon \rangle r$ , for grid turbulence ( $R_\lambda \approx 50$ ).  $\nabla$ , viscous term;  $\bullet$ , third-order structure function;  $\blacksquare$ ,  $I_q$ ;  $\times$ ,  $I_{q1}$ ;  $+$ ,  $I_{q2}$ ;  $\cdots$ ,  $I_{q3}$ ; solid line: calculated third-order structure function using Eq.(8); solid thick line: 4/3; dashed line: sum of the viscous term, third-order structure function term and  $I_q$ .

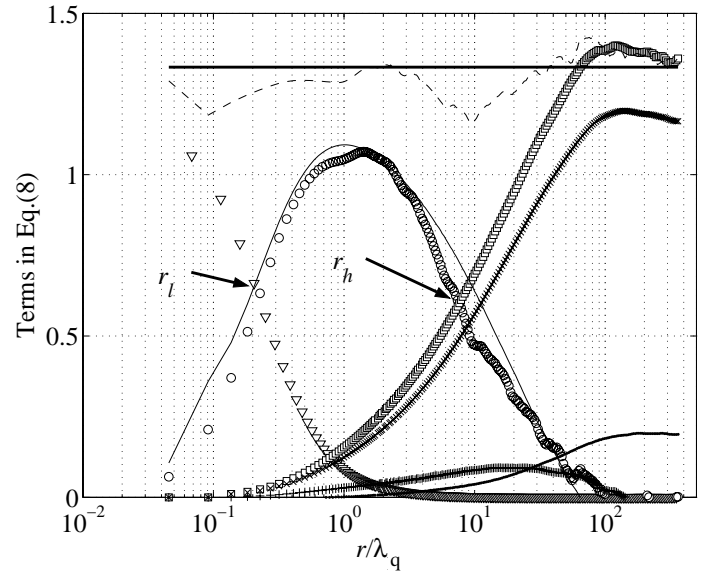


Figure 2: Terms in Eq.(8), divided by  $\langle \varepsilon \rangle r$ , for the jet ( $R_\lambda \approx 363$ ).  $\nabla$ , viscous term;  $\circ$ , third-order structure function;  $\square$ ,  $I_q$ ;  $\times$ ,  $I_{q1}$ ;  $+$ ,  $I_{q2}$ ;  $\cdots$ ,  $I_{q3}$ ; solid line: calculated third-order structure function using Eq.(8); solid thick line: 4/3 limit; dashed line: sum of the viscous term, third-order structure function term and  $I_q$ .

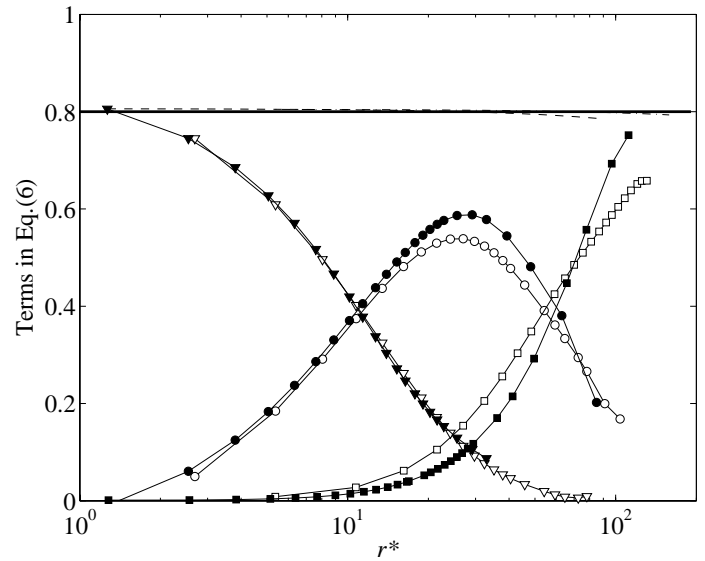


Figure 3: Terms in Eq.(6), divided by  $\langle \varepsilon \rangle r$ , using the DNS data of Fukayama et al [26] at roughly the same  $R_\lambda (\approx 70)$ . Filled-in symbols: forced turbulence; open symbols: decaying turbulence.  $\circ$ ,  $\bullet$ : third-order structure function;  $\blacksquare$ ,  $\square$ :  $I_q$ ;  $\blacktriangledown$ ,  $\triangledown$ : viscous term; dashed line: sum of the viscous term, third-order structure function term and  $I_q$ .

For a fixed  $R_\lambda$ ,  $I_u$  (or  $I_q$ ) may not be universal, even within the same flow type. For example, in the similarity region of decaying grid turbulence, the shape of the normalized form of  $I_q$  has been found to depend on the geometry of the grid [40]. A less sensitive dependence on the initial condition at the nozzle exit of a round jet has been reported in [17]. In this case the third-order structure functions, in the far field of the jet, remained unchanged under modified initial conditions. For the wake data of [10] (where 5 wake generators were used), Fig.5,  $I_u$  was inferred indirectly from measurements of  $\langle (\delta u)^2 \rangle$  and  $\langle (\delta u)^3 \rangle$  by assuming the validity of Eq.(6). Although  $R_\lambda$  is nominally constant in Fig.5, the peak of  $-\langle (\delta u)^3 \rangle / \langle \varepsilon \rangle r$  and the magnitude of  $I_u$  exhibit significant variations as the initial conditions are changed. It can be argued that different levels of large scale organisation in each flow can lead to differences in  $I_u$ , and they can produce differences in the departure from the 4/5 law. It is not difficult to

imagine that such departures can be reflected in differences in scaling exponents (e.g., [10]). The reasonable collapse of the viscous term in Fig.5 reflects mainly the constant value of  $R_\lambda$ ; an improved collapse at small  $r$  would be expected if  $r$  is normalized by  $\eta$  rather than  $\lambda$ . The lack of collapse of the third-order structure term in Fig.5 seems all the more significant given that, in each wake,  $R_\lambda$  is constant along  $x$ , so that a similarity based on  $\lambda$  seems appropriate.

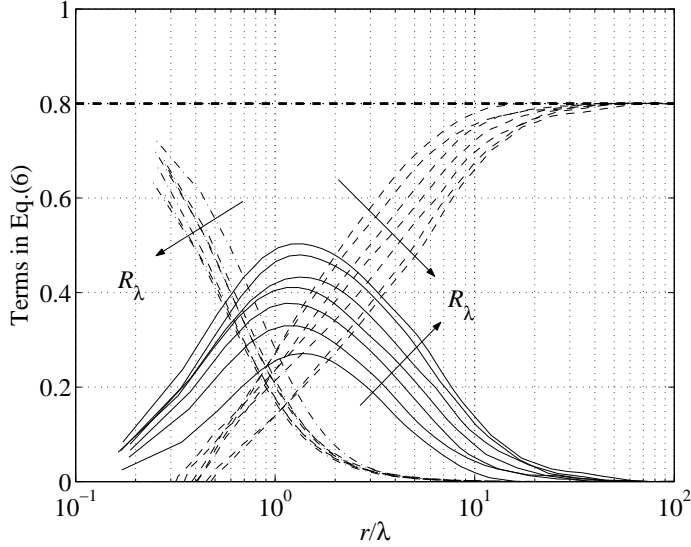


Figure 4: Variation with  $R_\lambda$  of the terms in Eq.(5), divided by  $\langle \epsilon \rangle r$ , for the grid turbulence data of [62] ( $R_\lambda$  increases between 27 and 100 in the direction of the arrows). Solid line:  $-\langle (\delta u^*)^3 \rangle r^{*-1}$ ; dashed line:  $I_u$  (calculated by difference from Eq.(6)); dash-dotted line: viscous term; dashed horizontal line: 4/5.

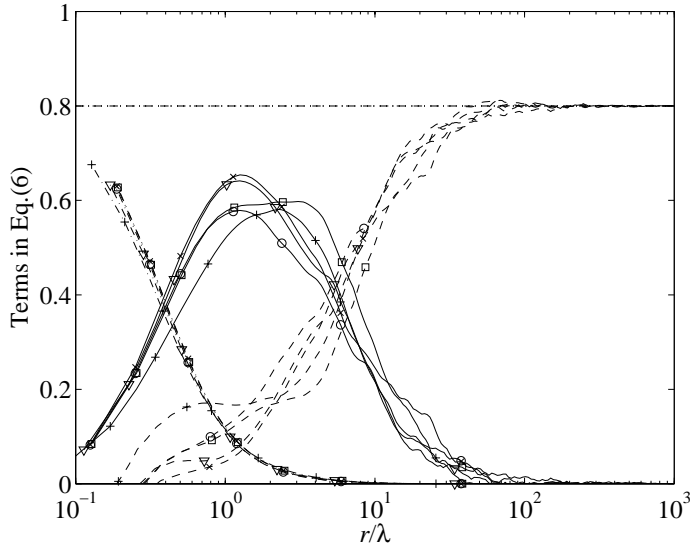


Figure 5: Terms in Eq.(6), divided by  $\langle \epsilon \rangle r$ , for the turbulent wake data of [10] at nominally the same  $R_\lambda$  ( $\approx 200$ ).  $\square$ : plate;  $\circ$ : circular cylinder;  $\nabla$ : square cylinder;  $\times$ : screen cylinder;  $+$ : screen strip; solid line: third-order structure function; dash-dotted line: viscous term; dashed line: inhomogeneous term, calculated by difference from Eq.(6); dash-dotted horizontal line: 4/5.

Distributions of  $-\langle \delta u (\delta q)^2 \rangle$  were calculated from Eq.(8) starting with the measured distributions of  $\langle (\delta q)^2 \rangle$  and assuming similarity based on  $\lambda$  and  $\langle q^2 \rangle$ . The agreement between these calculations (solid lines in Figs. 1 and 2) and the measurements is quite satisfactory, providing some indirect

support for the validity of Eq.(8) and the assumptions made in estimating its terms.

### Extrapolation to Large $R_\lambda$

Clearly, it is important to ascertain how quickly the maximum value of  $-\langle \delta u (\delta q)^2 \rangle$  divided by  $\langle \epsilon \rangle r$  or  $\langle (\delta u)^3 \rangle$  divided by  $\langle \epsilon \rangle r$  approaches its asymptotic value of 4/3 or 4/5. This has been the objective of many investigations. Our main interest here is to examine the  $R_\lambda$  dependence of this term in conjunction with that for the viscous and inhomogeneous terms in Eq.(8). To this end, we follow the approach by Antonia et al. [7] who used a description of  $\langle (\delta u^*)^2 \rangle$  [25,39] which extends from the smallest (Kolmogorov) scale to the integral scale  $L$ ,

$$\langle (\delta u^*)^2 \rangle = (r^{*-2}/15)(1 + \beta r^{*-2})^{2c-2} / (1 + (r^*/r_{cu}^*)^2)^c \quad (18)$$

where  $r_{cu}^*$  is identified with the crossover between the dissipative and inertial ranges,  $c \equiv (1 - \zeta_u/2)$  and  $\beta \equiv L^{*-1}$ . Eq.(18) is essentially a modification, for finite Reynolds numbers, of the model for  $\langle (\delta u^*)^2 \rangle$  first proposed by Batchelor [12] with  $\beta=0$ .

To obtain  $\langle (\delta q^*)^2 \rangle$ , use is made of the isotropic relation

$$\langle (\delta q^*)^2 \rangle = \left( 3 + r^* \frac{d}{dr^*} \right) \langle (\delta u^*)^2 \rangle. \quad (19)$$

For isotropic turbulence,  $\lambda^* = 15^{1/4} R_\lambda^{1/2}$ ,  $\langle q^{*2} \rangle = (3/15^{1/2}) R_\lambda$  and  $L^* \equiv 15^{-3/4} C_\epsilon R_\lambda^{3/2}$ , where  $L$  has been identified with  $C_\epsilon \langle q^2 \rangle^{3/2} / \langle \epsilon \rangle$ . The dimensionless energy dissipation rate parameter  $C_\epsilon$  is expected to become constant at sufficiently large  $R_\lambda$  but its magnitude should depend on the initial conditions. This is true in both experiments, e.g. [4], or simulations, e.g. [58] and references therein. In general, one expects the shape of  $\langle (\delta u^*)^2 \rangle$  (and  $\langle (\delta q^*)^2 \rangle$ ) to depend on the type and level of organisation in a particular flow (e.g. [40]), which may in any case reflect the influence of the initial conditions. Here, we have assumed a value of 1 for  $C_\epsilon$ , as in [7].

We have also assumed that  $r_{cu}^* \equiv (15C_{u2})^{3/4}$ , with a value of 2 for the Kolmogorov constant  $C_{u2}$ . The K41 value of 2/3 was assigned to  $\zeta_u$ , i.e. intermittency was ignored (calculations taking into account intermittency on  $\langle (\delta u^*)^2 \rangle$  did not show significant differences). Although  $C_{u2}$ ,  $\zeta_u$  and  $r_{cu}^*$  may vary slowly with  $R_\lambda$  (e.g. [5]) at small  $R_\lambda$  we believe that the present estimates of  $I_u$  (or  $I_q$ ) and  $-\langle (\delta u)^3 \rangle$  (or  $-\langle (\delta u)(\delta q)^2 \rangle$ ) should be sufficiently reliable to provide a first-order indication of how the Kolmogorov's asymptotic result may be approached.

Calculations of  $-\langle (\delta u)^3 \rangle / \langle \epsilon \rangle r$  are shown in Fig.6 together with those for the viscous term and  $I_u$  in Eq.(6). As  $R_\lambda$  increases, the latter two distributions shift to the left and right respectively, thus increasing the relevance of an inertial range. Nonetheless, the attainment of such a range requires values of  $R_\lambda$  well in excess of  $R_\lambda = 10^4$ . Even at  $R_\lambda = 10^6$ , it would appear that the extent of this range is limited; the difference between  $-\langle (\delta u)^3 \rangle / \langle \epsilon \rangle r$  and 4/5 is smaller than 1% over  $\approx 2.8$  decades in  $r/\lambda$  but the shape

of  $-\langle(\delta u)^3\rangle/\langle\epsilon\rangle r$  indicates that this quantity exhibits a maximum. Perhaps not surprisingly,  $\langle(\delta u^*)^2\rangle/r^{*2/3}$  appears to reach its assumed asymptotic value of 2 (the Kolmogorov constant) at  $R_\lambda \approx 10^4$  (Fig.7). The grid turbulence data ( $R_\lambda = 100$ ) of Zhou & Antonia [62] have been included to show that relation (18) approximates the measured data adequately.

The variation with  $R_\lambda$  of the calculated maximum value of  $-\langle(\delta u^*)^3\rangle r^{*-1}$  is shown in Fig.8. The calculation (solid line) is in good agreement with measurements obtained in grid turbulence and along the centreline of a circular jet (note that here the 4/3 value has been rescaled to 4/5 for our data). The plane jet data of Pearson and Antonia [53] lie below this line, partly because  $\langle\epsilon\rangle_{\text{iso}}$  has been used instead of  $\langle\epsilon\rangle_q$ . For the jet and grid turbulence data of [28],  $\langle\epsilon\rangle_{\text{iso}}$  was used. The large scatter associated with the active grid turbulence data of [48] may in part reflect the uncertainty in the estimation of  $\langle\epsilon\rangle$  in this experiment. The above comments suggest that, evidently, caution is required when interpreting the good agreement of most of the experimental decaying turbulence data with the model. The model is unlikely to take fully into account the differences in the initial conditions that have been found to exist between different experiments. The variation in the peak value of  $-\langle(\delta u^*)^3\rangle r^{*-1}$

for various wake data (fig.5), at nominally the same  $R_\lambda$ , supports the idea that a universal distribution is unlikely. This idea is consistent with the view (e.g., [30]) that simple shear flows do not reach universal asymptotic states. The results from the model are in close agreement with the prediction (dash-dotted line) of Lundgren [43] for  $R_\lambda \gtrsim 200$ . For lower values of  $R_\lambda$ , the model based on Eq.(18) is in satisfactory agreement with the grid turbulence data of [62] (the difference between  $\langle\epsilon\rangle_{\text{iso}}$  or  $\langle\epsilon\rangle_q$  and the value of  $\langle\epsilon\rangle$  estimated with Eq.(11) is quite small for these data). The measured and numerical data obtained in forced turbulence (denoted by filled-in symbols) seem to follow a separate distribution (it is unlikely that this distribution is unique in view of the documented effects of initial conditions for this type of turbulence); clearly the approach to 4/5 is much more rapid for these data and a value of  $10^3$  for  $R_\lambda$  may be sufficient for this type of turbulence to reach the Kolmogorov asymptote. This value is somewhat larger than the maximum value ( $\approx 460$ ) for DNS data of Gotoh et al. [31]; this may need to be kept in mind when assessing DNS data with forcing. For decaying turbulence, a value of  $R_\lambda$  in excess of  $10^5$  (perhaps even  $10^6$ ) may be needed before the K41 asymptotic state is reached. This estimate is somewhat higher than that given in [63] where the Batchelor parameterization was used for modelling  $\langle(\delta u^*)^2\rangle$ .

The difference between  $r_h$  and  $r_l$  is of interest when enquiring into the possible existence of a scaling range. Fig.9 indicates that  $\log(r_h/r_l)$  varies linearly with  $\log R_\lambda$ . For  $R_\lambda \geq 10^4$ , this range is equivalent to considering 50% of the maximum of  $-\langle(\delta u^*)^3\rangle r^{*-1}$ . Qian [54] adopted a slightly different criterion for identifying the extent of the inertial range, but obtained a similar linear dependence on  $R_\lambda$  (his figure 8). We recognize that there is inevitable arbitrariness in the definition of a scaling range; nonetheless, the dash-dotted line in Fig.9 indicates that  $R_\lambda$  should exceed  $3 \times 10^5$  to achieve a 2 decades plateau in  $-\langle(\delta u^*)^3\rangle r^{*-1}$ .

The inset in Fig.9 shows that the location of the maximum of  $-\langle(\delta u^*)^3\rangle r^{*-1}$  approaches a constant value for  $r \approx 1.1\lambda$ . This trend appears to have been established for decaying turbulence [28,43,62]. However, Lundgren [43] showed that, in the case of linearly forced turbulence, the maximum is at a higher value,  $r \approx 1.23\lambda$ , implying a different behaviour for forced turbulence.

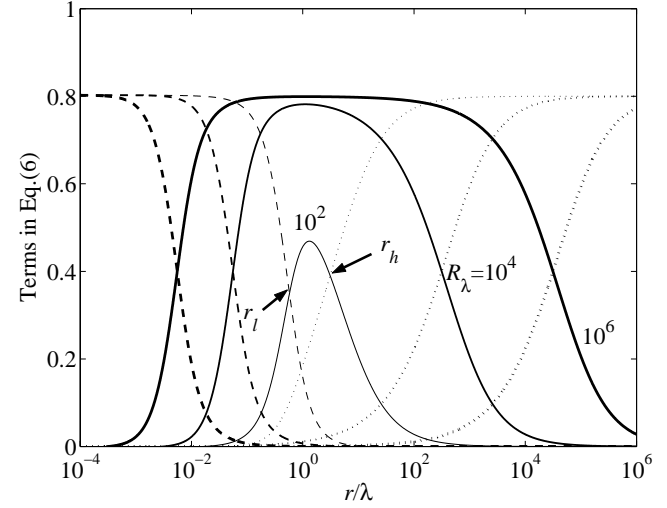


Figure 6: Variation with  $R_\lambda$  of the terms in Eq.(6), divided by  $\langle\epsilon\rangle r$ , derived from a model of decaying isotropic turbulence, Eq.(18). Solid line: third-order structure function; dotted line:  $I_u$ ; dashed line: viscous term.

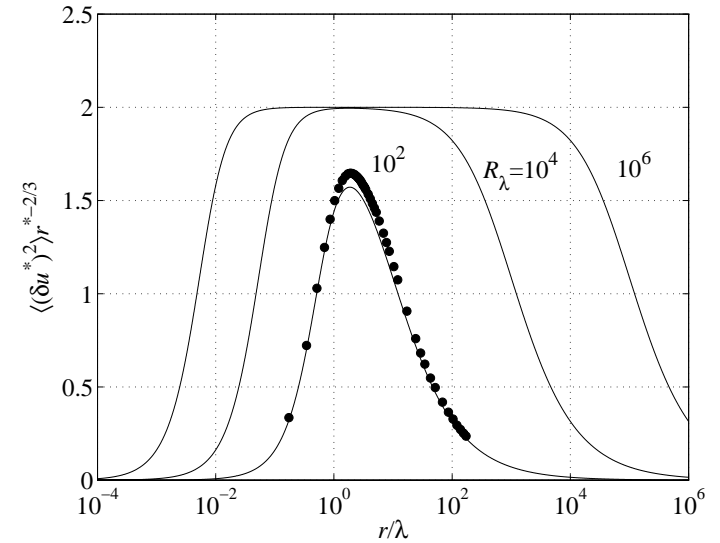


Figure 7: Kolmogorov-normalized second-order structure function of  $u$ , divided by  $r^{*2/3}$ . Solid lines: model Eq.(18);  $\bullet$ , measured grid turbulence data of [62] at  $R_\lambda = 100$ .

## Concluding Comments

The limiting values of 4/5 and 4/3, which appear in the stationary form of the transport equations for  $\langle(\delta u)^2\rangle$  and  $\langle(\delta q)^2\rangle$ , represent asymptotic states corresponding to large Reynolds numbers. For laboratory flows, deviations from these values can be significant; even in the atmospheric surface layer, the deviations may not be negligible. The inclusion of the non-stationarity or inhomogeneity (due mainly to the large scale motion) in the transport equation for  $\langle(\delta u)^2\rangle$  and  $\langle(\delta q)^2\rangle$  allows some assessment to be made on whether a scaling range, albeit of restricted extent, is possible. Experimental and numerical results obtained in a number of different flows indicate that the magnitude of the inhomogeneous term,  $I_u$  or  $I_q$ , can depend on various parameters, including initial conditions. In

particular, across the scaling range, the magnitude of  $I_u$  (or  $I_q$ ) is smaller for forced than decaying-type turbulence. Consistently, the maximum value of  $-\langle(\delta u^*)^3\rangle r^{*-1}$  approaches 4/5 more rapidly, as  $R_\lambda$  is increased, in forced than in decaying-type turbulence. This trend seems to be convincingly supported by both measured and numerical data. Antonia and Orlandi [1] noted that significant differences also existed for statistics of small-scale passive scalar ( $\theta$ ) fluctuations between forced and decaying homogeneous isotropic turbulence. One would expect that the  $R_\lambda$  variation of the maximum value of  $-\langle(\delta u^*)(\delta\theta^*)^2\rangle r^{*-1}$  will exhibit a similar behaviour, in terms of the difference between forced and decaying-type turbulence, to that in Fig. 8.

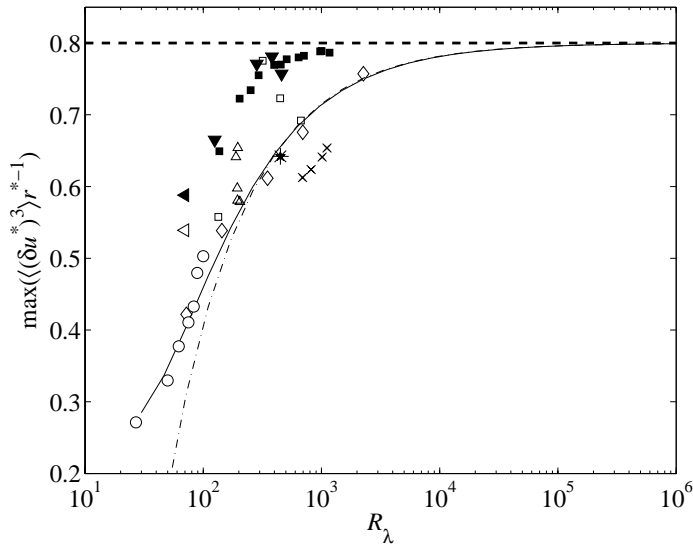


Figure 8: Variation with  $R_\lambda$  of the maximum of the normalized third-order structure function of  $u$ . Solid line: based on model Eq.(18);  $\blacktriangledown$ , DNS data for forced box turbulence [30];  $\blacktriangleleft$ , DNS data for forced box turbulence [26];  $\triangleleft$ , DNS data for decaying box turbulence [26];  $\blacksquare$ , measured forced turbulence data [46];  $\times$ , plane jet [53];  $\circ$ , grid turbulence [62];  $\diamond$ , values measured by [28];  $*$ , round jet (present data);  $\triangle$ , 2D wakes data [10]; dash-dotted line: model of [43];  $\square$ , grid turbulence [48]; dashed horizontal line: 4/5.

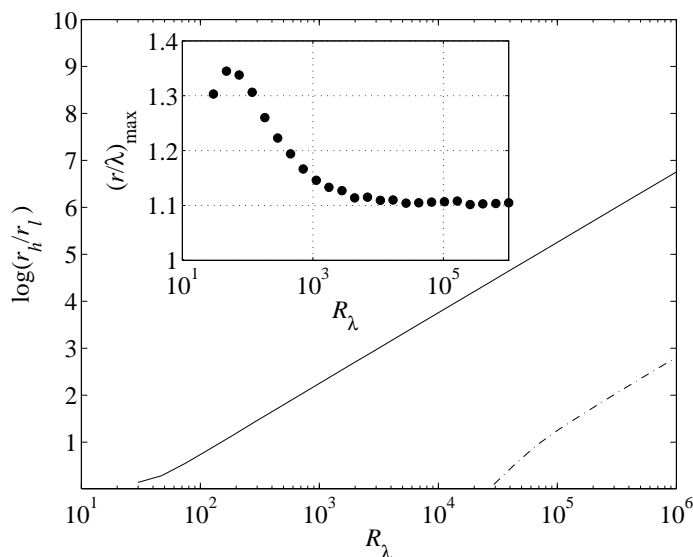


Figure 9: Dependence on  $R_\lambda$  of  $\log(r/r_l)$ , solid line. The dash-dotted line corresponds to a range where  $-\langle(\delta u^*)^3\rangle r^{*-1}$  is  $\geq 99\%$  of 4/5. Inset: location of the maximum value of the third-order structure function, divided by  $\langle\epsilon\rangle r$ , as a function of  $R_\lambda$ .

## Acknowledgements

The support of the Australian Research Council is acknowledged. We are especially grateful to L. Danaila for her major contributions to various aspects of this work, in particular the derivations of  $I_u$  in Eq.(7a) and  $I_q$  in Eq.(8).

## References

- [1] Antonia, R.A. and Orlandi, P., Effect of Schmidt Number on Small-Scale Passive Scalar Turbulence, *Appl. Mech Reviews*, **56**, 2003, 1-18.
- [2] Antonia, R.A. and Orlandi, P., Similarity of Decaying Isotropic Turbulence with a Passive Scalar, *J. Fluid Mech.*, **505**, 2004, 123-151.
- [3] Antonia, R.A., Ould-Rouis, M., Anselmet, F., Zhu, Y., Analogy between predictions of Kolmogorov and Yaglom. *J. Fluid Mech.*, **332**, 1997, 395-409.
- [4] Antonia, R.A. and Pearson, B.R., Effect of Initial Conditions on the Mean Energy Dissipation Rate and the Scaling Exponent. *Phys. Rev. E* **62**, 2000, 8086-8090.
- [5] Antonia, R.A., Pearson, B.R. and Zhou, T., Reynolds Number Dependence of Second-Order Velocity Structure Functions, *Phys. Fluids*, **12**, 2000, 3000-3006.
- [6] Antonia, R.A. and Smalley, R.J., Scaling Range Exponents from X-wire Measurements in the Atmospheric Surface Layer, *Boundary-Layer Meteorology*, **100**, 2001, 439-457.
- [7] Antonia, R.A., Smalley, R.J., Zhou, T., Anselmet, F., and Danaila, L., Similarity of energy structure functions in decaying homogeneous isotropic turbulence, *J. Fluid Mech.*, **487**, 2003, 245-269.
- [8] Antonia, R.A., Zhou, T., Danaila, L. and Anselmet, F., Scaling of the mean energy dissipation rate equation in grid turbulence, *J. of Turbulence*, **3**, 2002, 034.
- [9] Antonia, R.A., Zhou, T., Danaila, L. and Anselmet, F., Streamwise Inhomogeneity of Decaying Grid Turbulence, *Phys Fluids*, **12**, 2000, 3086-3089.
- [10] Antonia, R.A., Zhou, T. and Romano, G.P., Small-Scale Turbulence Characteristics of Two-Dimensional Bluff Body Wakes, *J. Fluid Mech.*, 2002, 67-92.
- [11] Batchelor, G.K., Kolmogoroff's Theory of Locally Isotropic Turbulence, *Proc. Camb. Phil. Soc.*, **43**, 1947, 533-559.
- [12] Batchelor, G.K., Pressure Fluctuations in Isotropic Turbulence, *Proc. Camb. Phil. Soc.*, **47**, 1951, 359-374.
- [13] Batchelor, G.K., *The Theory of Homogeneous Turbulence*, Cambridge University Press, Cambridge, Ma, 1953.
- [14] Birouk, M., Sarh, B. and Gokalp, I., An attempt to realize experimental isotropic turbulence at low Reynolds number, *Flow Turbul. Comb.*, **70**, 2003, 325-348.
- [15] Burattini, P. and Antonia, R.A., The Effect of Different X-wire Calibration Schemes on some Turbulence Statistics, Accepted for publication in *Expts. in Fluids*, 2005.
- [16] Burattini, P., Antonia, R.A. and Danaila, L., Similarity in the Far Field of a Turbulent Round Jet, Accepted for publication in *Phys. Fluids*, 2005.
- [17] Burattini, P., Antonia, R.A. and Rajagopalan, S., Effect of initial conditions on the far field of a round jet, To appear in proceedings of *15 AFMC*, 2004.
- [18] Casciola, C.M., Gualtieri, P., Benzi, R., Piva, R., Scale-by-scale budget and similarity laws for shear turbulence, *J. Fluid Mech.*, **476**, 2003, 105-114.
- [19] Chassaing, P., Antonia, R.A., Anselmet, F., Joly, L. and Sarkar, S., *Variable Density Fluid Turbulence*, Kluwer, 2002.
- [20] Danaila, L., Anselmet, F., Zhou, T., Turbulent Energy Scale-Budget Equations for nearly Homogeneous Sheared Turbulence, *Flow Turbul. Comb.*, **72**, 2004, 287-310.
- [21] Danaila, L., Anselmet, F., Zhou, T. and Antonia, R.A., A Generalization of Yaglom's Equation which accounts for the Large-scale Forcing in Heated Decaying Turbulence, *J. Fluid Mech.*, **391**, 1999, 359-372.

- [22] Danaïla, L., Anselmet, F., Zhou, T. and Antonia, R.A., Turbulent Energy Scale Budget Equations in a Fully Developed Channel Flow, *J. Fluid Mech.*, **430**, 2001, 87-109.
- [23] Danaïla L., Antonia, R.A. and Burattini, P., Progress in Studying Small Scale Turbulence using “exact” two-point equations. *New J. Phys.*, **6**, 2004, 128.
- [24] Danaïla, L., Burattini, P., Antonia, R.A., Large-scale effects in a self-preserving, axisymmetric turbulent jet, 2004, In preparation.
- [25] Dhruva, B., *An experimental study of high Reynolds number turbulence in the atmosphere*. PhD Thesis, 2000, Yale University.
- [26] Frisch, U., *Turbulence: the Legacy of A.N. Kolmogorov*, Cambridge University Press, Cambridge, Ma, 1995.
- [27] Fukayama, D., Oyamada, T., Nakano, T., Gotoh, T. and Yamamoto, K., Longitudinal structure functions in decaying and forced turbulence, *J. Phys. Soc. Jpn.*, **69**, 2000, 701-716.
- [28] Gagne, Y., Castaing, B., Baudet, C. and Malécot, Y., Reynolds Number Dependence of Third-order Velocity Structure Functions, *Phys. Fluids*, **16**, 2004, 482-485.
- [29] George, W.K., The decay of homogeneous isotropic turbulence. *Phys. Fluids A*, **4**, 1992, 1492-1509.
- [30] George, W.K. and Davidson L., Role of initial conditions in establishing asymptotic flow behavior, *AIAA J.*, **42**, 2004, 438-446.
- [31] Gotoh, T., Fukayama, D. and Nakano, T., Velocity field statistics in homogeneous steady turbulence obtained using a high-resolution direct numerical simulation, *Phys. Fluids*, **14**, 2002, 1065-1081.
- [32] Hill, R.J., Applicability of Kolmogorov’s and Monin’s equations of turbulence, *J. Fluid Mech.*, **353**, 1997, 67-81.
- [33] Hwang, W. and Eaton, J.K., Creating homogeneous and isotropic turbulence without a mean flow, *Expts. in Fluids*, **36**, 444-454, 2004.
- [34] Kahalerras, H., Malécot, Y., Gagne, Y. and Castaing, B., Intermittency and Reynolds number, *Phys. Fluids*, **10**, 1998, 910-921.
- [35] von Karman, T and Howarth, L., On the Statistical Theory of isotropic turbulence, *Proc. R. Soc. London A*, **164**, 1938, 192-215.
- [36] Kolmogorov, A.N., The Local Structure of Turbulence in Incompressible Viscous Fluid for very Large Reynolds Numbers, *Dokl. Akad. Nauk. SSSR* **30**, 1941, 299-303.
- [37] Kolmogorov, A.N., Dissipation of Energy in Locally Isotropic Turbulence, *Dokl. Akad. Nauk SSSR*, **32**, 1941b, 9-21.
- [38] Kolmogorov, A.N., A Refinement of Previous Hypotheses concerning the Local Structure of Turbulence in a Viscous Incompressible Fluid at High Reynolds Number, *J. Fluid Mech.*, **13**, 1962, 82-85.
- [39] Kurien, K.S. and Sreenivasan, K.R. Anisotropic Scaling Contributions to High-Order Structure Functions in High Reynolds Number Turbulence. *Phys. Rev. E*, **62**, 000, 2206-2212.
- [40] Lavoie, P., Antonia, R.A. and Djenidi, L., 2004. The Effect of Grid Geometry on the Scale-by-Scale Budget of Decaying Turbulence, To appear in proceedings of *15 AFMC*, 2004.
- [41] Lindborg, E., A note on Kolmogorov’s third-order structure function law, the local isotropy and the pressure-velocity correlation, *J. Fluid Mech.*, **326**, 1996, 343-356.
- [42] Lindborg, E., Correction to the Four-fifths Law due to Variations of the Dissipation, *Phys. Fluids*, **11**, 1999, 510-512.
- [43] Lundgren, T.S., Linearly Forced Turbulence, CTR Annual Research Briefs, 2003, 461-473.
- [44] Lundgren, T.S., Kolmogorov Turbulence by Matched Asymptotic Expansion, *Phys. Fluids*, **15**, 2003, 1074-1081.
- [45] Lundgren, T.S., Kolmogorov Two-thirds Law by Matched Asymptotic Expansion, *Phys. Fluids*, **14**, 2002, 638-642.
- [46] Moisy, F., Tabeling, P. and Willaime, H., Kolmogorov Equation in a Fully Developed Turbulence Experiment, *Phys. Rev. Lett.*, **82**, 1999, 3994-3997.
- [47] Monin, A.S., and Yaglom A.M., *Statistical Fluid Mechanics*, vol. 2, 1975, MIT press, Cambridge, MA.
- [48] Mydlarski, L., and Warhaft, Z., On the onset of high-Reynolds-number grid-generated wind tunnel turbulence, *J. Fluid Mech.*, **320**, 1996, 331-368.
- [49] Nelkin, M., Universality and Scaling in Fully Developed Turbulence, *Advances in Physics*, **43**, 1994, 143-181.
- [50] Nelkin, M., Turbulence in fluids, *Am. J. Phys.*, **68**, 2000, 310-318.
- [51] Novikov, E.A., Statistical balance of vorticity and a new scale for vortical structures in turbulence, *Phys. Rev. Lett.*, **71**, 1993, 2718-2720.
- [52] Orlandi, P. and Antonia, R.A., Dependence of the Non-stationary Form of Yaglom’s Equation on the Schmidt Number, *J. Fluid Mech.*, **451**, 2002, 99-108.
- [53] Pearson, B.R. and Antonia, R.A., Reynolds-number Dependence of Turbulent Velocity and Pressure Increments, *J. Fluid Mech.*, **444**, 2001, 343-382.
- [54] Qian, J., Inertial range and the finite Reynolds number effect of turbulence, *Phys. Rev. E.*, **55**, 1997, 337-342.
- [55] Qian, J., Slow Decay of the Finite Reynolds Number Effect of Turbulence, *Phys. Rev. E.*, **60**, 1999, 3409- 3412.
- [56] Qian, J., Scaling of structure functions in homogeneous shear-flow turbulence, *Phys. Rev. E*, **65**, 2002, 036301.
- [57] Schedvin, J.C., Stegen, G.R. and Gibson, C.H., Universal Similarity at High Grid Reynolds Numbers, *J. Fluid Mech.*, **65**, 1974, 561-579.
- [58] Sreenivasan, K., An update on the energy dissipation rate in isotropic turbulence, *Phys. Fluids*, **10**, 1998, 528-529.
- [59] Sreenivasan, K.R. and Antonia, R.A., The Phenomenology of Small-scale Turbulence, *Ann. Rev. Fluid. Mech.*, **29**, 1997, 435-472.
- [60] Sreenivasan, K.R. and Dhruva, B., Is there scaling in High-Reynolds-Number Turbulence, *Prog. Theor. Phys. Suppl.*, **130**, 1998, 103-120.
- [61] Sreenivasan, K.R., Dhruva, B. and Gil, I.S., The Effects of Large Scales on the Inertial Range in High-Reynolds-Number Turbulence, 1999, eprint arXiv:chao-dyn/9906041.
- [62] Zhou, T. and Antonia, R.A., Reynolds number dependence of the small-scale structure of grid turbulence, *J. Fluid Mech.*, **406**, 2000, 81-107.
- [63] Zhou, T., Antonia, R.A., Danaïla, L. and Anselmet, F., Approach to the Four-fifths ‘Law’ for Grid Turbulence, *J. of Turbulence*, **1**, 2000, 005.
- [64] Zhu, Y. and Antonia, R.A., Effect of Wire Separation on X-probe measurements in a Turbulent Flow, *J. Fluid Mech.*, **287**, 1995, 199-223.



## Computing Turbulent Channels at Experimental Reynolds Numbers

J. Jiménez<sup>1,2</sup> and J.C. del Álamo<sup>1</sup>

<sup>1</sup>School of Aeronautics, Universidad Politécnica  
28040 Madrid, SPAIN

<sup>2</sup>Centre Turbulence Research, Stanford University  
Stanford CA, 94305, USA

### Abstract

The availability of high-quality numerical simulations, with Reynolds numbers which are now in the range of  $Re_\tau = 2000$ , and which will probably be extended to  $Re_\tau \approx 4000$  in the near future, have revitalized the study of turbulence near walls in the last decade. Simulations can now be used to study the dynamics of the buffer and of the lower logarithmic layers in some detail, and some of the results obtained in that way are reviewed here. Particular attention is paid to the reasons for the failure of the scaling of the turbulence intensities with  $u_\tau$ , which are traced to different causes in the buffer layer and in the outer flow. While in the buffer layer the cause seems to be the growing scale disparity between the near-wall and outer-flow contributions, it is shown that in the outer flow some spectral ranges scale with the centreline velocity. The generation of the largest scales of the streamwise velocity component in the logarithmic layer is also studied, and shown to be consistent with the formation of large-scale passive wakes of smaller individual ejections. The latter are related to attached clusters of vortices extending from the buffer region into the logarithmic layer.

### Introduction

The study of turbulence near walls has experienced a renaissance in the last decade, largely because of the availability of high-quality numerical simulations. The numerical Reynolds numbers, now in the range of  $Re_\tau = 2000$ , allow for the first time the study in some detail of the dynamics of the buffer and of the lower logarithmic layers. The present and probable future status of direct simulations of turbulent channels, and some of the results obtained from them, are reviewed here.

Three issues are particularly addressed. Consider first the buffer and viscous layers. It has been known for some time that this part of the flow is relatively independent of the flow above it [17], and actually survives even when all the rotational fluctuations are artificially removed above  $y^+ \approx 60$ . This is in agreement with the fact that most of the mean velocity difference, of the turbulence production, and of the energy dissipation, reside in this region, which therefore sees the outer flow as a relatively weak perturbation of the local processes. These autonomous dynamics have been discussed elsewhere [9, 11, 15, 16], and will not be addressed here, but recent experimental results suggest that there are effects of the Reynolds number on the scaling of buffer-layer quantities [7]. They can only come from interactions with the outer flow, and they are also seen in simulations. We will review below some results obtained in the last few years, concerning their mechanism and their location in scale space.

The next question is the scaling of the structures both in the buffer and in the logarithmic layer. It follows from the study of the numerical energy spectra that the relation between the width and the length of the energy-containing structures is not straightforward, in the sense that both length scales are not proportional to each other, nor to the distance to the wall. Experi-

mental evidence for the latter lack of proportionality had already been found in [12, 19], but it has only been through numerical simulations that the former has been documented [2, 3, 14]. We will discuss below what the problem is, and what its solution appears to be.

Finally we address the question of the scaling of the velocity fluctuations in the logarithmic layer and in the outer layer. The classical view is that all the velocity fluctuations in wall flows should scale with the friction velocity  $u_\tau$  [30], but again the experimental evidence suggests otherwise [7], and it had already been noted in [31] that ‘inactive’ eddies, those not carrying Reynolds stresses, could scale in some other way. We will show that at least some eddies, those large enough to span the whole thickness of the flow, scale with the flow velocity at the centreline, and we will discuss the consequences that follow for the behaviour of the overall turbulence intensities at very high Reynolds numbers.

We use  $x$ ,  $y$  and  $z$  for the streamwise, wall-normal, and spanwise coordinates, and  $u$ ,  $v$  and  $w$  for the corresponding velocity components. The half-height of the channel, the pipe radius, and the boundary-layer thickness are denoted by  $h$ .

### Numerical simulations

There should be by now little doubt that careful numerical simulations of the Navier–Stokes equations are just different kinds of experiments, and that there is no reason to expect them to be less accurate than laboratory ones [23]. Some of their drawbacks, such as the artificial nature of some boundary conditions, are no worse than the artificial nature of the walls in wind tunnels and can, in both cases, be avoided by careful design. It is also not always clear that what we simulate is exactly the same thing that we would measure in the laboratory, but there is no reason why it should be. Simulations and experiments are equally valid idealizations against which to test theories and designs.

There is also no doubt that, once a flow has been successfully simulated, it can be observed more thoroughly than in a laboratory experiment. The cost of carrying out a large simulation is high, although not necessarily higher than that of building a large wind tunnel, but the instrumentation problems are simpler, and almost any observation that can be imagined can be made. While the results of laboratory experiments are often constrained by the instrumentation technology, those from numerical simulations are mainly limited by the ability of the researcher to ask the right questions.

Another advantage of simulations over laboratory experiments is the ease with which they can be adapted to perform ‘conceptual’ experiments, in which the equations of motion or the boundary conditions are changed to, in effect, ‘take the system apart’ [17]. This has always been a useful device in physics, and conceptual experiments have often been used to constrain physical theories by asking what would happen if a given ‘im-

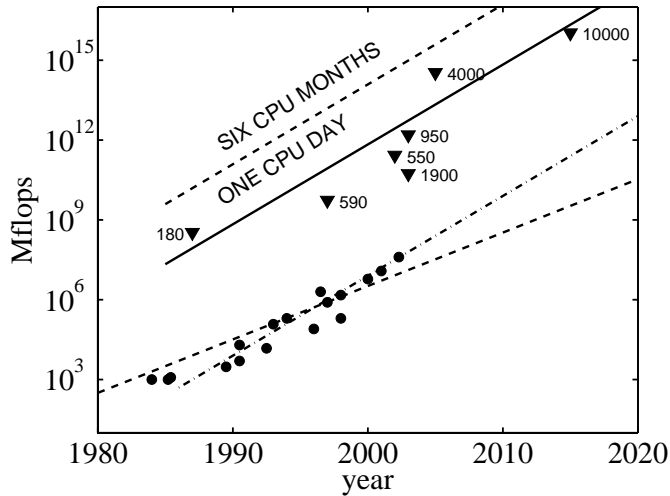


Figure 1: Evolution of direct channel simulations. ●, peak speeds of computers, in Mflops/s, as a function of the fabrication year. The two trend lines are for single- and multi-processor systems. The two upper lines are for total flops in one day and in six months of dedicated time at the computational speeds of the parallel trend line. ▼ are the estimated costs of the simulations in table 1.

$Re_\tau$	Box	Year	Points
180	$4\pi \times 4\pi/3$	1987 [21]	5 Mp
590	$2\pi \times \pi$	1996 [24]	40 Mp
550	$8\pi \times 4\pi$	2001 [2]	600 Mp
950	$8\pi \times 3\pi$	2003 [3]	4 Gp
1900	$\pi \times \pi/2$	2003 [3]	450 Mp
4,000	$8\pi \times 3\pi$	2005	130 Gp
10,000	$8\pi \times 3\pi$	2015	1.5 Tp

Table 1: Available and planned direct numerical simulations of turbulent channels. The box refers to the spatial periodicity of the spectral simulation contained in the table.

plausible’ modification were implemented. Think for example of the concept of potential inviscid flow. For such exercises to be useful, however, we should be able to answer the question that we have posed, and it is in that respect that many of the idealized systems of classical physics differ from complex ones, such as turbulence. While it might be possible with a pencil and paper, and with a lot of imagination, to decide what happens when two observers try to synchronize their clocks under certain conditions, the answer is often harder when trying to decide the outcome of a particular modification to a turbulent flow. Numerical simulations allow us to obtain answers to our conceptual experiments.

While those are clear advantages of simulations over laboratory experiments, the argument over their relative merits has often centred on the different question of which systems can be studied with each technique. It is often claimed that experiments can be run at higher Reynolds numbers than simulations. This question was reviewed in [13], where it was argued that the Reynolds number difference between laboratory and computation has been steadily eroding with the advances in computing technology, and that in many respects both are now comparable. This is particularly true when the magnitude of interest is something more complicated than the turbulence intensities, or even in some cases anything beyond the mean velocity profile.

In the particular case of turbulent channels, which will be the main subject of this paper, the friction Reynolds numbers of

the early simulations at  $Re_\tau = u_\tau h/\nu = 180$  [21] have now been multiplied by five [3]. A simulation at  $Re_\tau \approx 2000$  is also available, although the size of its computational box is too small to trust the results anywhere except very near the wall. The available simulations are summarized in table 1, and they overlap the experimental range. There are few well-documented laboratory channels at  $Re_\tau > 1000$ , and the main problem in validating the results of the simulations is now the lack of comparable experimental data.

The cost of these simulations is plotted in figure 1 against the historical and expected evolution of computer power. They cluster around one CPU-day of the fastest machine available at the time, showing that the barrier for larger simulations is more political than technological. None of the simulations in the figure were ran in the fastest available machine.

Two simulations still in the planning stage are included in table 1. The one at  $Re_\tau = 4000$  is at present in the advanced preparation phase, and will most probably be ready within the next two years. The simulation at  $Re_\tau = 10^4$  is a more distant prospect, but it holds a special place in the planing process. The two main ‘intrinsic’ open problems in wall-bounded turbulence are the interaction between the inner and the outer layers, and the dynamics of the logarithmic layer. Both require a sufficiently large Reynolds number.

The length of the dominant structures in the buffer layer is about 1000 wall units [14], while that of the global modes in the outer region is about five channel half-widths [2]. When  $Re_\tau = 10^4$ , the ratio between the two lengths is about 50, and probably large enough to be considered infinite from the point of view of their interaction. That Reynolds number also results in about a factor of ten between the upper and lower limits of the logarithmic layer [25]. Such a simulation can probably be considered as ‘asymptotically large’ from the point of view of clarifying the physics of wall-bounded flows at zero pressure gradient. It should be ready in about a decade.

It may be interesting at this point to discuss the question of the size of the computational box needed to simulate channels. We will see below that there are very long structures in turbulent wall-bounded flows, particularly for the streamwise velocity component, which contain a substantial fraction of the energy of the fluctuations. As long as the physics of those large scales, and of their interactions with other parts of the flow, is not completely understood, they have to be simulated to have any confidence in the results. As we will see below, this understanding has been achieved only in part, and many of the resulting scaling laws are still in doubt. Any new simulation at large Reynolds numbers, which is bound to be expensive and not easily repeated for some time, should use boxes large enough to include them.

With this in mind, there are still many things that can be learned from smaller boxes, in particular regarding the dynamics of the smaller scales in the absence of the larger ones [16, 17]. Something that usually does not work, however, is to use smaller computational boxes to save computer time. Consider for example the simulations in table 1. It is our experience that boxes in the order of  $L_x = 8\pi$  need to be run for about ten washouts ( $10L_x/U_c$ ) before the statistics of the larger scales are reasonably converged. Smaller boxes need to be run much longer, in part to accumulate enough statistics at the intermediate scales, and also because there is a tendency for the long Fourier modes in the centre of the channel to become ‘frozen’, producing spurious effects on the velocity fluctuation profiles which are not necessarily small. The problem is that short periodic boxes do not really lack long scales, but merely treat them as being in-

finitely long. The scales are in the simulation, but their dynamics are in general incorrect.

The box at  $Re_\tau = 1880$  in table 1, for example, had to be run for several hundred washouts before its statistics could be considered moderately converged. Even then the mean velocity profile cannot be trusted above the logarithmic layer. The same is true of the somewhat larger box at  $Re_\tau = 590$ , which also had to be run for hundreds of washouts before converging, and which even so retained a residual asymmetry in the velocity profile at the end of the simulation [24, private communication]. Our experience with intermediate boxes of size  $4\pi \times 2\pi$  is that they have to be run for about 80 – 100 washouts before the statistics converge in the outer region. These long integration times negate much of the gain in computer time which could be expected from using smaller boxes (although obviously not in memory usage), and they do so at the expense of decreasing the quality of the results. The consequence is that it usually pays to run the largest computational box compatible with the computer resources at hand, and that the main reason to use smaller boxes should be to simplify the physics, rather than to shorten the simulation time.

### The near-wall layer

It is well known [30] that wall-bounded turbulence over smooth walls can be described to a good approximation in terms of two sets of scaling parameters. Viscosity is important near the wall, and the length and velocity scales in that region are constructed with the kinematic viscosity  $\nu$  and with the friction velocity  $u_\tau$ . Everything in that region is expected to scale in wall units.

Far from the wall the velocity also scales with  $u_\tau$ , but the length scale is the flow thickness  $h$ . In the classical approximation the logarithmic region extends between the inner and the outer regions, because the only possible length scale is then  $y$  itself [30]. The velocity in the intermediate layer follows approximately

$$U^+ = \kappa^{-1} \log y^+ + A. \quad (1)$$

The viscous and buffer layers are extremely important for the flow as a whole. The ratio between the inner and outer length scales is the friction Reynolds number,  $Re_\tau$ , which ranges from 200 for barely turbulent flows to  $Re_\tau = 5 \times 10^5$  for large water pipes. The near-wall layer in the latter,  $y^+ \lesssim 150$ , is only about  $3 \times 10^{-4}$  times the pipe radius, but it follows from (1) that, even in that case, 40% of the velocity drop takes place below  $y^+ = 50$ . Turbulence is characterized by the expulsion towards the small scales of the energy dissipation, away from the large energy-containing eddies. In wall-bounded flows that separation occurs not only in scale space for the velocity fluctuations, but also in the mean velocity profile. The singularities are expelled both from the large scales, and from the centre of the flow towards the wall.

Because of this singular nature, the near-wall layer is not only important for the rest of the flow, but it is also essentially independent from it. That was for example shown by numerical experiments with ‘autonomous’ simulations [17] in which the outer flow was artificially removed above a certain wall distance  $\delta$ . The near-wall dynamics were unaffected as long as  $\delta^+ \gtrsim 60$ .

Understanding the structure of this part of the flow has practical implications. The velocity at the centreline,  $U_c^+ = (2/c_f)^{1/2}$ , determines the friction coefficient  $c_f$  when expressed in wall units, and we have seen that a large fraction of that velocity resides in the buffer layer. It is for this reason that the layer below  $y^+ \approx 100$  has been intensively studied. It is dominated by coherent streaks of the streamwise velocity and by quasi-streamwise vortices. The former are an irregular array of long

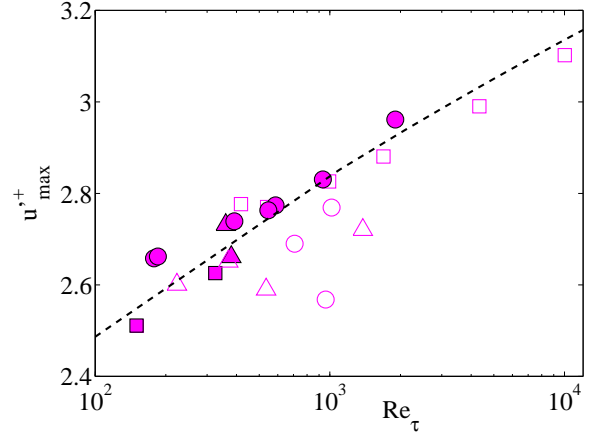


Figure 2: Maximum intensity of the streamwise velocity fluctuations as a function of the Reynolds number. In all cases the maximum is achieved near  $y^+ = 15$ .  $\square$ , boundary layers;  $\circ$ , channels;  $\triangle$ , pipes. Open symbols are laboratory experiments, and closed ones are computations. The dashed line is  $u'^{+2} \sim \log(20 Re_\tau)$ .

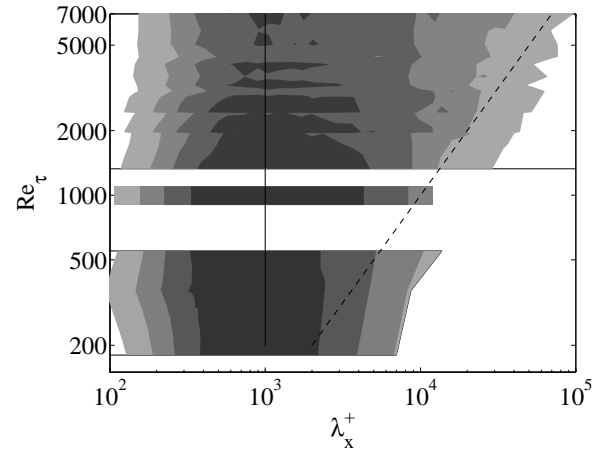


Figure 3: Longitudinal energy spectra  $k_x E_{uu} / u_\tau^2$  as a function of the wavelength  $\lambda_x = 2\pi/k_x$ , and of the Reynolds number, at  $y^+ = 20$ . Each horizontal line of the shaded area corresponds to a different Reynolds number. The upper block are laboratory boundary layers [10]. The lower one are numerical channels [2, 3]. The dashed line is  $\lambda_x = 10h$ , and the solid one is  $\lambda_x^+ = 1000$ . Adapted from [14].

( $x^+ \approx 1000$ ) sinuous alternating streamwise jets superimposed on the mean shear, with an average spanwise separation of the order of  $z^+ \approx 100$  [29]. The quasi-streamwise vortices are slightly tilted away from the wall [11], and stay in the near-wall region only for  $x^+ \approx 200$ . Several vortices are associated with each streak, with a longitudinal spacing of the order of  $x^+ \approx 400$ . The basic cell of wall-parallel dimensions  $400 \times 100$  wall units was also identified in [16] as the smallest dynamical periodic box able to self-sustain turbulence in the neighbourhood of the wall.

The intensity of the streamwise velocity fluctuations reaches a maximum around  $y^+ \approx 15$ , and classical theory implies that the maximum intensity should scale in wall units. It is clear from figure 2 that this is not true, and that the increasing trend is present both in the experimental and in the numerical results. This anomalous scaling is accompanied by other scaling failures in the buffer region. The most obvious is the form of the pre-multiplied energy spectrum, which was shown in [10] to contain two peaks, a short one at a streamwise wavelength  $\lambda_x^+ \approx 1000$ ,

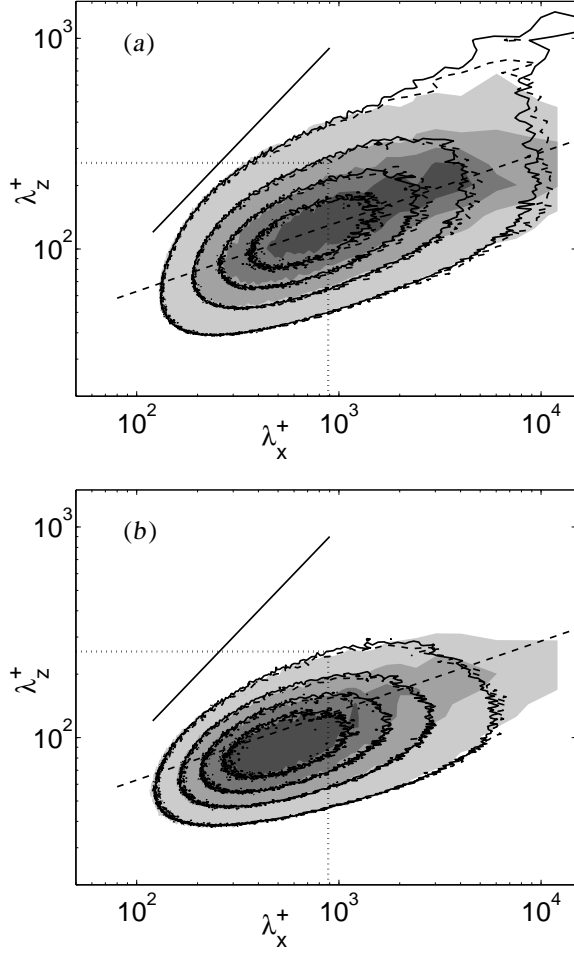


Figure 4: Two-dimensional spectral energy densities at  $y^+ = 16$ , in terms of the streamwise and spanwise wavelengths. Shaded contours are an autonomous flow [14] masked above  $y^+ = 60$ . Lines are full channels [3]. ----,  $Re_\tau = 550$ ; —,  $Re_\tau = 934$ . The solid diagonal line is horizontal isotropy,  $\lambda_x = \lambda_z$ , and the dashed one is  $\lambda_z \sim \lambda_x^{1/3}$ . The dotted rectangle is the approximate size of the minimal self-sustaining flow unit [16]. (a)  $k_x k_z E_{uu} / u_\tau^2$ . (b)  $-k_x k_z E_{uv} / u_\tau^2$ .

independent of  $Re_\tau$ , and a long one that scales in outer units as  $\lambda_x \approx 10h$ . A compilation of experimental and numerical spectra is found in figure 3. Since  $u^2$  is the integral of the energy spectrum, a nonclassical scaling of the latter almost automatically implies a similar nonclassical behaviour of the former.

The Reynolds-number dependence of the large scales can be also be seen in figure 4, which shows two-dimensional energy densities in the near-wall region. These spectra have at least three regions. On the lower left corner, at scales of the order of the minimum flow unit mentioned above, the two Reynolds numbers in the figure collapse well in wall units, and so does the autonomous flow that is also included. These are the structures involved in the nonlinear turbulence regeneration cycle, and they are present both in the spectrum of the energy and in that of the Reynolds stress. Both spectra continue towards longer wavelengths along a ridge with the anomalous power scaling  $\lambda_z \sim \lambda_x^{1/3}$ , which is present in the three flows. At the Reynolds numbers of the present simulations this spectral range also collapses in wall units, but the autonomous flow behaves differently, and it is not clear from the present data whether the ridge will become longer at higher Reynolds numbers, or whether the present data are already asymptotic. It was shown in [14] that the structures in this ridge are passive, in the sense that they are not involved in a two-way cycle. Their wall-normal velocity is

needed to create the streamwise-velocity structures, but not the other way around. It was also shown in [14] that the geometric relation between the smaller  $v$  structures in the minimal region and the longer  $u$ -structures along the ridge is consistent with the latter being wakes of the former. Their scaling is also consistent with this explanation. The similarity solution for wakes spreading in a simple shear under the action of a constant viscosity, both of which are good approximations near the wall, is

$$u \sim u(y/x^{1/3}, z/x^{1/3}). \quad (2)$$

Further support for the wake model will be provided in the next section.

The spectral region in which the three flows disagree most clearly is the upper right-hand corner, where the spectrum of the higher Reynolds number flow is longer and wider than that of the lower one. This component is completely absent in the autonomous flow, and is located around  $\lambda_x \times \lambda_z = 10h \times h$ . Its length thus agrees with the long-wavelength end of the spectra in figure 3. It is also the location of the ‘global’ modes identified in [2], which span the whole channel half-height and which will be the subject of a later section.

This strongly suggests that the growth of the intensity peak in figure 2 is due to large-scale outer flow structures. Note that, contrary to the other two spectral regions, this component is not present in the Reynolds-stress cospectrum, and is therefore ‘inactive’ in the sense of Townsend [31]. It has long been understood that, because the Reynolds stress defines  $u_\tau$ , the most likely reason for the failure of the wall scaling is the presence of inactive motions [31], and this is confirmed by the excellent collapse of the two full-channel cospectra in figure 4(b).

Note however that this correspondence is not automatic. The edge of the energy spectrum in figure 4(a) which is closest to the isotropic diagonal is missing in the cospectrum, but it scales very well in wall units.

### Wakes in the logarithmic region

As we move away from the wall, the form of the energy spectrum changes [2, 3]. Two spectra are shown in figure 5. The ridge of ‘wakes’ is also present in them, but it follows

$$\lambda_z \approx (y\lambda_x)^{1/2}, \quad (3)$$

rather than a cube-root law found in the viscous layer. This is also consistent with the model of a wake left by a compact structure, because in the logarithmic and outer layer the velocity is almost constant, and the diffusion of the wake is due to an eddy viscosity which, on dimensional grounds, is  $\nu_T \approx u_\tau y$ . The similarity solution is then [3]

$$u \sim u(y/x, z/(yx)^{1/2}). \quad (4)$$

For wavelengths shorter than  $\lambda_x \approx y$  the spectrum is bounded by (3) and by the line of horizontal isotropy,  $\lambda_z = \lambda_x$ , but longer structures are always anisotropic and follow the wake ridge. It was shown in [2, 3] that the structures of the wall-normal velocity  $v$  are effectively confined to the ‘isotropic’ region  $\lambda_x < y$ . Those eddies are detached from the wall, in the sense that the correlation of individual Fourier modes between the logarithmic and the buffer layer is very small. The height over which those correlations are large increases as the structures become longer. The eddies touch the wall when  $\lambda_x \approx y$ , and the attached eddies beyond that limit are the ones that cluster along the wake ridge.

The nature of the structures generating the wakes is discussed in [4], which studies the vorticity structures in the buffer and logarithmic layers. Vortices are defined as being formed by points in

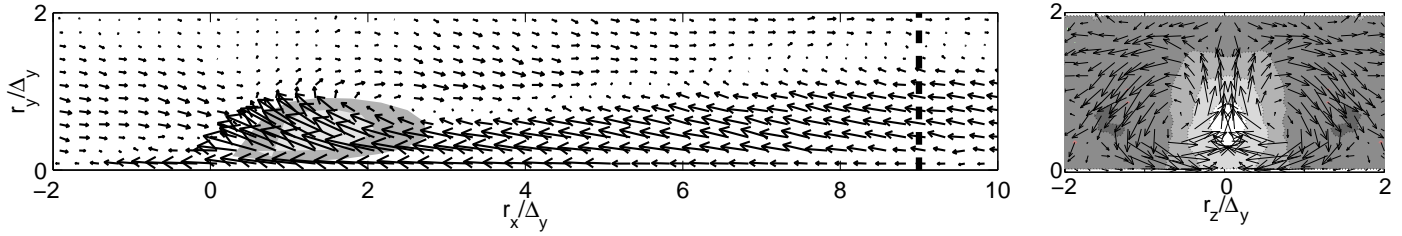


Figure 6: The left plot shows the perturbation velocity field,  $(u - U(y), v)$ , conditioned on the presence of a vortex cluster, on the  $x - y$  plane bisecting the bounding box of the cluster. The shaded area is the probability density function of finding a vortex. The right-hand plot is a section of the conditioned field in the cross plane marked in the left figure. The shaded contours are the perturbation streamwise velocity;  $u - U(y) = -0.3(0.1)0.1$ .  $Re_\tau = 550$ . Only clusters with  $y_{max}^+ > 100$  are included.

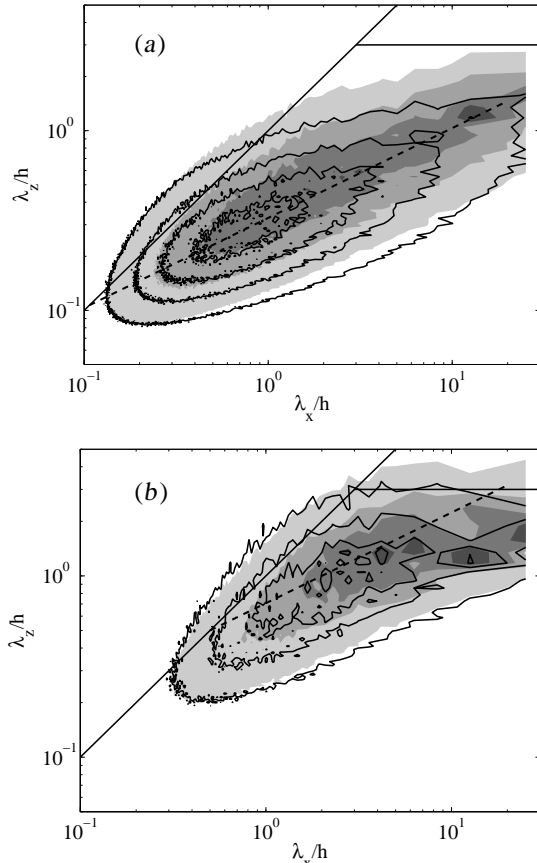


Figure 5: Two-dimensional spectral energy density  $k_x k_z E / u_\tau^2$ .  $Re_\tau = 934$ . The solid diagonal is  $\lambda_z = \lambda_x$ . The solid horizontal line is  $\lambda_z = 3h$ , and the dashed diagonal is  $\lambda_z = (y\lambda_x)^{1/2}$ . The shaded contours are the streamwise velocity; the lines are the Reynolds stress. (a)  $y/h = 0.1$ . (b)  $y/h = 0.5$ .

which the discriminant  $D$  of the velocity gradient tensor is larger than a properly-defined threshold [6]. Connected sets of such points are collected into individual vortex clusters, which break naturally into two distinct groups according to whether their lowest points are above or below a critical level around  $y^+ \approx 20$ . We will call the latter group attached and the former detached. The most interesting clusters are those attached to the wall and reaching into the logarithmic layer, above  $y^+ = 100$ . When each of them is inscribed into a parallelepipedal box aligned to the coordinate directions, the boxes are self-similar, with dimensions  $\Delta_z \approx 1.5\Delta_y$  and  $\Delta_x \approx 3\Delta_y$ . Note that for attached clusters it makes sense to associate  $\Delta_y$  with the height  $y$ , because  $y_{min}$  is small. When this is done, and when  $\Delta_x$  and  $\Delta_z$  are also equated to the streamwise and spanwise wavelengths, the dimensions of the bounding boxes roughly coincide with the location of the spectral peak for the wall-normal velocity  $v$ . The vortices them-

selves appear to be arranged as surfaces or shells within the boxes; while the volume of the bounding box increases as  $\Delta_y^3$ , the volume contained in points classified as vortices increases only as  $\Delta_y^2$ .

A conditionally-averaged flow field, based on the centres of the vortex boxes, and scaled with their vertical dimensions, shows a strong  $v$  ejection surrounded by two counterrotating vortices, as in a classical hairpin. The antisymmetry is only statistical and, as in the case of the buffer-layer vortices [28], there is little evidence for symmetry in individual vortex clusters.

When the conditionally-averaged flow field is extended down- and up-stream from the location of the vortex box, the result is that in figure 6. In the  $x - y$  streamwise plane bisecting the mean location of the box, the presence of a streamwise-velocity structure linked to the vortex cluster is clear. Its location with respect to the cluster is consistent with that of a wake. If we assume that the cluster is advected with the mean velocity at its centre of gravity, the flow closer to the wall is slower than the cluster, and the wake is *behind* the cluster. Above the centre of gravity, the mean flow is faster than the vortices, and the wake is *in front* of the cluster. The averaged vortical structure of the ramp in the transverse plane is shown in the right part of figure 6. It has two counterrotating vortices which are much larger than the size of the original vortex packet, and which are reminiscent of the downstream structure of the wake of a transverse jet in a boundary layer [8].

Similar ramp-vortex structures have been observed by previous investigators [1, 5], with geometric characteristics similar to those found here, but the present interpretation of their relation with the vortex packets is, to our knowledge, new. The results in [4] suggest that the shear layer which defines the top of the ramp is associated with detached vortex clusters, while the attached clusters are only found at the ramp origin. Note for example the absence of any coherent flow structure upstream of the vortex box in figure 6(a), except in the buffer layer. When the conditioned flow field is computed for the detached vortex clusters, the low-speed region extends symmetrically upstream and downstream of the box.

It is interesting to note that the above description is not restricted to ‘real’ vortices, but that it still holds when the flow is filtered to larger scales (up to  $200 \times 40 \times 100$  wall units in our experiments). Individual vortices are then smoothed, and what remains is only the integrated circulation over fairly large volumes. The velocity perturbations due to the ramps are of the order of  $u_\tau$ , and the total projected surface of the boxes bounding the wakes is enough to cover the whole wall with some overlap. The perturbation due to the wakes is therefore a substantial fraction of the total perturbation energy in the channel, as could be deduced from the spectra in figure 5.

Those spectra suggest that the wakes widen along the ridge (3) until  $\lambda_z \approx 2h$ . This effectively determines the longest wavelength in the spectrum, which is

$$\lambda_{x,max}/h \approx 4h/y. \quad (5)$$

This limit is longest at the bottom of the logarithmic layer, where  $y^+ \approx 100$  and  $\lambda_{x,max}/h \approx Re_\tau/20$ . These are very long structures that, even taking into account possible numerical factors, point to hundreds of boundary-layer thicknesses at high Reynolds numbers. Spectral peaks of the order of  $20h$  have been documented in experiments [12, 19], and they are probably limited by the length of the experimental records. The present simulations only reach to  $\lambda_x \approx 25h$  and, although longer to our knowledge than any other available simulation, they are not long enough to settle the matter. The one-dimensional streamwise premultiplied velocity spectra at the bottom of their logarithmic layers are still essentially flat at their longest wavelengths, as seen in figure 5(a). On the other hand, numerical experiments with shorter simulation boxes show very little difference in the part of the spectrum that is resolved by the simulations [3], suggesting that those very long structures are essentially passive and do not feed into the shorter ones. We have already noted that a short simulation box models long scales as being infinitely long, and the previous results suggest that, given enough time to randomize, structures longer than about  $5h$  behave as if they were dynamically infinite.

The shortening of the spectra above the lower logarithmic layer predicted by (5) had been previously noted experimentally, although without explanation [12, 19, 22].

An interesting question is whether the vortex clusters and the ramps discussed here are features of the whole logarithmic layer, or just of its lower edge. The probability density function  $p(\Delta_y)$  for the dimensions of the attached vortex clusters collapses well in wall units for different Reynolds numbers, with a maximum around  $\Delta_y^+ = 50$ . This suggests that the clusters are buffer-layer phenomena which should become negligible for most of the logarithmic layer when  $Re_\tau$  is large enough, but this is not necessarily so, and depends on the behaviour of  $p(\Delta_y)$ . The projected area of each vortex cluster on the plane of the wall is  $\Delta_x \Delta_z \approx 5\Delta_y^2$ , and for any p.d.f. decaying slower than  $\Delta_y^{-2}$  the largest clusters would be the ones covering most area. This would for example be the case for the distribution  $p(\Delta_y) \sim \Delta_y^{-1}$ , which was suggested in [27] on similarity grounds. In our simulations the decay of  $p(\Delta_y)$  depends on the threshold used to define the vortices, and there is little support for a self-similar distribution. But we are conscious of the limited extent of our logarithmic layers, and the matter remains under investigation.

### Global modes

The increase with the Reynolds number of the intensity of the streamwise velocity was justified above by noting that the pre-multiplied energy spectra are approximately flat in the long-wavelength regime, and that they become longer as  $Re_\tau$  increases. Since the total energy is the integral with respect to  $\log(\lambda_x)$  of the pre-multiplied spectrum, and since  $\lambda_x$  ranges between limits which scale respectively in wall and in outer units, it follows that  $u'^{+2}$  should increase as  $\log(h^+) = \log(Re_\tau)$ . This is the dashed line drawn in figure 2.

The same argument does not hold when comparing flows at a given value of  $y/h$ . The shorter end of the energy spectrum in the logarithmic and outer layers is the intersection of the wake line (3) with the isotropic locus  $\lambda_x = \lambda_z$ , which happens at  $\lambda_x \approx y$ . This is confirmed by the numerical spectra, as well as by the experimental limits of the classical  $k^{-1}$  spectrum [27]. The long-wavelength end is given by (5), and the range of the

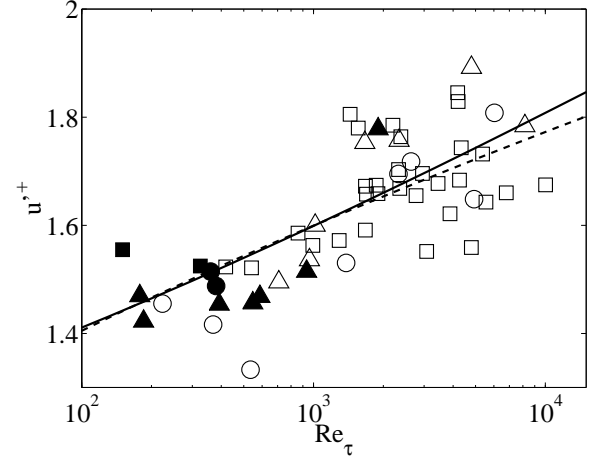


Figure 7: Scaling of the total energy of the streamwise fluctuations, as a function of the Reynolds number.  $y/h = 0.4$ .  $\square$ , boundary layers;  $\circ$ , channels;  $\triangle$ , pipes. Open symbols are laboratory experiments, and closed ones are computations. —,  $u'^{+2} \sim 1 + \alpha U_c^{+2}$ ; ----,  $u'^{+2} \sim \log Re_\tau$  [7].

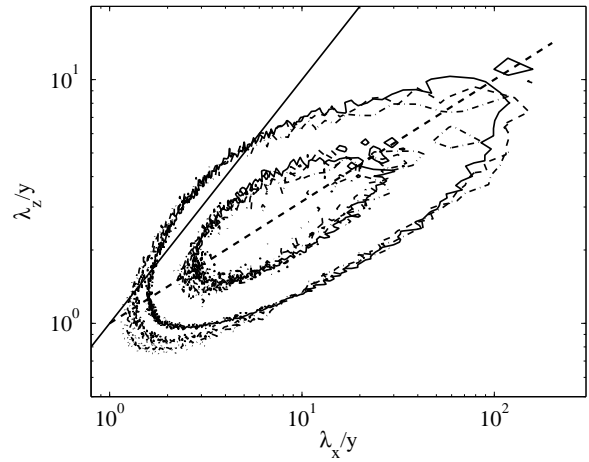


Figure 8: Premultiplied cospectra of the Reynolds stress in the logarithmic layer, as a function of  $\lambda_z/y$ . —,  $y/h = 0.1$ ; ----,  $y/h = 0.15$ ; -.-,  $y/h = 0.2$ .  $Re_\tau = 934$ .

spectral integral is therefore

$$\lambda_{x,max}/\lambda_{x,min} \approx 4h^2/y^2, \quad (6)$$

which is independent of  $Re_\tau$ . If the magnitude of the spectrum scales with  $u_\tau^2$ , arguments like this one allow us to estimate how  $u'^2$  depends on  $y/h$ , but they support the scaling of  $u'$  with  $u_\tau$ .

On the other hand, the experimental and numerical evidence compiled in figure 7 suggests that also in the outer layer the scaling of the fluctuations with  $u_\tau$  fails to apply [7].

The classical argument for the scaling of  $u'$  is that, since the total Reynolds stress is given by the momentum equation (in a channel) as  $u_\tau^2(1 - y/h)$ , and since the stress has to be carried by the product  $\langle u'v' \rangle$ , the easiest assumption is that both  $u'$  and  $v'$  scale with  $u_\tau$ . It was however noted by Townsend [31] that this argument does not apply to ‘inactive’ eddies which carry no Reynolds stresses. We already found such eddies in the upper edge of the buffer-layer spectra in figure 4, and it is clear from the observation of the higher contours of the energy spectra and of the Reynolds stress cospectra in figure 5, that the longest and widest eddies in the outer flow are also inactive.

There is a second argument that also supports the scaling  $u' \sim u_\tau$ . Assume an eddy of the self-similar family,  $y_{max} \sim y_{min} \sim y$ .



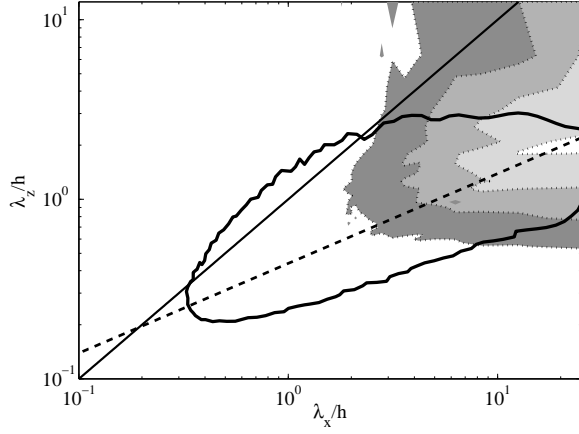


Figure 9: Correlation height for individual Fourier modes of the streamwise velocity. Contours are  $H_{uu}/h = 0.6(0.1)0.9$ . The  $k_x k_z E_{uu}$  spectrum at  $y = h/2$  is included for comparison.  $Re_\tau = 550$ .

If we think of the perturbation in  $u$  as coming from the mixing of the mean velocity profile, such as in the right-hand side of figure 6, we can estimate the perturbation generated by such an eddy as  $u' \approx U(y_{max}) - U(y_{min})$ , which in the logarithmic layer is approximately  $u_\tau \log(y_{max}/y_{min})$ . This also scales in wall units and, in conjunction with the argument in the previous paragraph, suggests that the Reynolds stress is carried in the logarithmic layer by self-similar eddies. This is supported by the cospectra in figure 8, which collapse well in terms of  $\lambda/y$  near their active peak, while the collapse deteriorates for the relatively-inactive shorter and longer wavelengths.

When the mixing argument is applied to attached modes, which are correlated from the wall to a given height  $y$ , it suggests that those modes should scale with  $U(y)$  instead of with  $u_\tau$ , especially if they are inactive. This argument would apply to all the wider modes in the logarithmic layer, but for most of them the experimental or numerical data is too scant to check the prediction.

There is however a set of modes in which the test can be carried, and for which there are results at high Reynolds numbers from laboratory experiments. Consider the correlation coefficient for a particular Fourier mode  $\hat{u}$  at two heights,

$$C_{uu}(k_x, k_z, y, y') = \frac{|\langle \hat{u}(k_x, k_z, y) \hat{u}^*(k_x, k_z, y') \rangle|}{(\langle |\hat{u}(k_x, k_z, y)|^2 \rangle \langle |\hat{u}(k_x, k_z, y')|^2 \rangle)^{1/2}}. \quad (7)$$

This is a real number between zero and one, which would be equal to unity for all  $y$  and  $y'$  if that particular mode were fully correlated across the full channel. We can define a ‘correlation height’,

$$H_{uu}^2(k_x, k_z) = \int_0^h \int_0^h C_{uu} dy dy', \quad (8)$$

which characterizes the depth over which the particular Fourier mode is correlated. In general  $H_{uu}$  increases as the wavelengths become longer and wider (see figure 9) and, for  $\lambda_x \gtrsim 6h$  all the modes are essentially correlated over the full half-channel. These global modes are particularly easy to analyse, because they do not interfere with any shallower structures at the same scales. A reference to figure 5 shows that they carry little Reynolds stress, and the previous argument suggests that they should scale with the centreline velocity  $U_c$ , instead of with  $u_\tau$ . Also, because the high correlation region in figure 9 spans most spanwise wavelengths, their intensity can be computed from laboratory spectra, which usually do not have spanwise information.

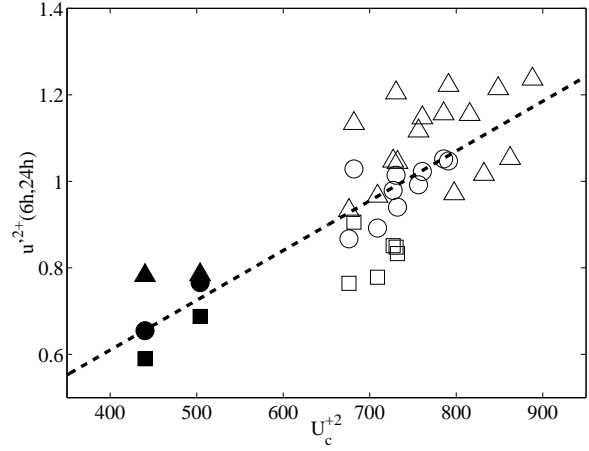


Figure 10: Scaling of the energy in the ‘global’ modes,  $6 < \lambda_x/h < 24$ , for numerical channels (solid symbols) and experimental boundary layers and pipes (open symbols).  $\Delta$ ,  $y/h = 0.1$ ;  $\circ$ ,  $y/h = 0.2$ ;  $\square$ ,  $y/h = 0.3$ . The dashed line goes through the origin.

This scaling is tested in figure 10, which plots the energy in the band  $6 < \lambda_x/h < 24$  as a function of the Reynolds number, and at three wall distances. Besides the numerical channels, the plot contains data from experimental boundary layers [10] and pipes [26]. The failure of the classical scaling is clear from the figure, and the proposed scaling with  $U_c^2$  works well.

We can now get back to the scaling failure of the total velocity fluctuations in figure 7. Since there is an active part of the spectrum which scales as  $u_\tau^2$ , and an inactive one which scales like  $U_c^2$ , we can expect that the total scales as  $u'^2 \sim 1 + \alpha U_c^2$ , which is the solid straight line in the figure. A different scaling  $u' \sim \log(Re_\tau)$  was proposed in [7] to fit the data, and it is also included in the figure. Even within the fairly wide range of Reynolds numbers compiled in figure 7, both scalings differ little, and it is unlikely that they will ever be distinguished through global measurements alone. They however predict different asymptotic behaviours at very large Reynolds numbers, and observations like the present one on the scaling of partial spectral ranges offer the best hope of deciding which argument is correct.

## Conclusions

We have briefly reviewed the present status of the understanding of the dynamics of turbulent flows near smooth walls, and given rational explanations for several of the scaling failures detected in experiments. This is a subject that, like most others in turbulence, is not completely closed, but which has evolved in the last two decades from empirical observations to relatively coherent theoretical models. It is also one of the first cases in turbulence, perhaps together with the structure of small-scale vorticity in isotropic turbulence, in which the key technique responsible for cracking the problem has been the numerical simulation of the flow.

The reason for the successes in the buffer layer is undoubtedly that the Reynolds numbers of the important structures are low, and therefore easily accessible to computation, while experiments are difficult.

The study of the logarithmic layer, on the other hand, requires massive computations at realistic Reynolds numbers, which only now are becoming available. It is in this area where the cost of computations and of laboratory experiments have to be weighted against their respective advantages. It is probably true

that both will forever be complementary. Note that we have used data from both sources whenever possible. But it is no longer true that Reynolds number alone is what separates ones from the others.

### Acknowledgements

The preparation of this paper was supported in part by the CICYT grant DPI2003-03434. The computer time needed for the  $Re_\tau = 550$  and 1880 simulations was made available by the CEPBA/IBM centre of the Universidad Polit cnica de Catalunya. We are most grateful to P. Zandonade and R.D. Moser for providing us with the raw data from the  $Re_\tau = 934$  simulation.

### References

- [1] Adrian, R.J., Meinhart, C.D. and Tomkins, C.D. Vortex organization in the outer region of the turbulent boundary layer, *J. Fluid Mech.* **422**, 1–54 (2000)
- [2] del  lamo, J.C. and Jim nez, J., Spectra of very large anisotropic scales in turbulent channels, *Phys. Fluids* **15** L41–L44 (2003)
- [3] del  lamo, J.C., Jim nez, J., Zandonade, P. and Moser, R.D., Scaling of the energy spectra of turbulent channels, *J. Fluid Mech.* **500**, 135–144 (2004)
- [4] del  lamo, J.C., Jim nez, J., Zandonade, P. and Moser, R.D., Self-similar vortex clusters in the attached logarithmic region, submitted *J. Fluid Mech.*
- [5] Christensen, K.T. and Adrian, R.J., Statistical evidence of hairpin vortex packets in wall turbulence, *J. Fluid Mech.* **431**, 433–443 (2001)
- [6] Chong, M.S., Perry, A.E. and Cantwell, B.J., A general classification of three-dimensional flow fields, *Phys. Fluids A* **2**, 765–777 (1990)
- [7] DeGraaf, D.B. and Eaton, J.K., Reynolds number scaling of the flat-plate turbulent boundary layer, *J. Fluid Mech.* **422**, 319–346. (2000)
- [8] Fric, T.F. and Roshko, A., Vortical structure in the wake of a transverse jet, *J. Fluid Mech.* **279**, 1–47 (1994)
- [9] Hamilton, J. M., Kim, J. and Waleffe, F., Regeneration mechanisms of near-wall turbulence structures. *J. Fluid Mech.* **287**, 317–348 (1995)
- [10] Hites, M.H., Scaling of high-Reynolds turbulent boundary layers in the national diagnostic facility. Ph.D. thesis, Illinois Institute of Technology (1977)
- [11] Jeong, J., Hussain, F., Schoppa, W. and Kim, J., Coherent structures near the wall in a turbulent channel flow. *J. Fluid Mech.* **332**, 185–214 (1997)
- [12] Jim nez, J., The largest structures in turbulent wall flows. In *CTR Annual Research Briefs*, 943–945. Stanford University (1998)
- [13] Jim nez, J., Computing high-Reynolds-number turbulence: will simulations ever replace experiments?, *J. of Turbulence* **22** (2003)
- [14] Jim nez, J., del  lamo, J.C. and Flores, O., The large-scale dynamics of near-wall turbulence, *J. Fluid Mech.* **505**, 179–199 (2004)
- [15] Jim nez, J., Kawahara, G., Simens, M.P., Nagata, M. and Shiba, M., Characterization of near-wall turbulence in terms of equilibrium and ‘bursting’ solutions, submitted to *Phys. Fluids*.
- [16] Jim nez, J. and Moin, P., The minimal flow unit in near wall turbulence. *J. Fluid Mech.* **225**, 221–240 (1991)
- [17] Jim nez, J. and Pinelli, A., The autonomous cycle of near wall turbulence, *J. Fluid Mech.* **389**, 335–359 (1999).
- [18] Jim nez, J. and Simens, M.P., Low-dimensional dynamics in a turbulent wall flow, *J. Fluid Mech.* **435**, 81–91 (2001).
- [19] Kim, K. C. and Adrian, R. J., Very large-scale motion in the outer layer. *Phys. Fluids A* **11**, 417–422 (1999)
- [20] Kim, J. and Hussain, F., Propagation velocity of perturbations in channel flow. *Phys. Fluids A* **5**, 695–706 (1993)
- [21] Kim, J., Moin, P. and Moser, R., Turbulence statistics in fully developed channel flow at low Reynolds number. *J. Fluid Mech.* **177**, 133–166 (1987)
- [22] Lawn, C.J., The determination of the rate of dissipation in turbulent pipe flow, *J. Fluid Mech* **48**, 477–505 (1971)
- [23] Moin, P. and Mahesh, K., Direct numerical simulation: A tool in turbulence research, *Ann. Rev. Fluid Mech.* **30** 539–578 (1998)
- [24] Moser, R.D., Kim, J. and Mansour, N.N., Direct numerical simulation of turbulent channel flow up to  $Re_\tau = 590$ , *Phys. Fluids* **11**, 943–945 (1999)
- [25]  sterlund, J.M., Johansson, A.V., Nagib, H.M. and Hites, A note on the overlap region in turbulent boundary layers, *Phys. Fluids* **12**, 1–4 (2000)
- [26] Perry, A.E. and Abell, C.J., Scaling laws for pipe-flow turbulence. *J. Fluid Mech.* **67**, 257–271 (1975)
- [27] Perry, A.E., Henbest, S. and Chong, M.S., A theoretical and experimental study of wall turbulence. *J. Fluid Mech* **165**, 163–199 (1986)
- [28] Robinson, S.K., Coherent motions in the turbulent boundary layer. *Ann. Rev. Fluid Mech.* **23**, 601–639 (1991)
- [29] Smith, C.R. and Metzler, S.P., The characteristics of low speed streaks in the near wall region of a turbulent boundary layer. *J. Fluid Mech.* **129**, 27–54 (1983)
- [30] Tennekes, H. and Lumley, J.L., *A first course in turbulence*, chapter 8. MIT Press (1972)
- [31] Townsend, A. A. *The structure of turbulent shear flows*, 2nd edn. Cambridge U. Press (1976)



## Gravity currents in nature and industry

H. E. Huppert

Institute of Theoretical Geophysics  
Department of Applied Mathematics & Theoretical Physics, University of Cambridge  
CMS, Wilberforce Road, Cambridge CB3 0WA UK

### Abstract

Gravity currents frequently occur in many natural and industrial situations. This article reviews the conceptual foundations used to understand and evaluate the evolution of gravity currents. Some of the latest results in specialised areas are highlighted. After an introduction, the paper ranges through the principal effects due to: low Reynolds number; compositional density differences; density differences due to dilute particulate matter; density differences due to concentrated particulate matter; and finally, the motion of a granular medium (with very little influence of the interstitial fluid). In addition, some effects due to permeable boundaries, rotation and propagation into an ambient which is either stratified or uniformly flowing will be considered.

### Introduction

Gravity currents occur whenever fluid of one density flows primarily horizontally into a fluid of different density. (Predominantly vertical motion is described more naturally as plumes and involves different concepts [1].) There are numerous natural and industrial occurrences of gravity current motions. These include: the spreading of honey on toast; the propagation of a relatively cold (and generally slightly wet) sea breeze, as happens so regularly on the East coast of Australia, across Canberra and at Perth (the Fremantle doctor); the outflow of the relatively warm and saline Mediterranean water through the Straits of Gibraltar into the Atlantic; the intrusion of giant umbrella clouds into the atmosphere following a volcanic eruption; and the flow of molten glass across a table to make sheet glass.

The first quantitative study of gravity currents was undertaken by von Kármán [2], who was asked by the American military to evaluate under what wind conditions poisonous gas released would propagate forward to envelop the enemy, rather than backwards to cause havoc to the troops who released the gas. Using Bernoulli's theorem, von Kármán showed that the velocity of the front,  $u$ , ahead of a layer of depth  $h$ , of relatively heavy fluid with density excess  $\Delta\rho$  over that of the atmosphere  $\rho_o$  was given by

$$u/(g'h)^{1/2} = Fr, \quad (1.1)$$

where the reduced gravity  $g' = \Delta\rho g/\rho_o$ ,  $g$  is the acceleration due to gravity and the Froude number,  $Fr$ , was evaluated by von Kármán to be  $\sqrt{2}$ . This is the condition to be applied at the nose of a current propagating at high Reynolds number  $Re = uh/\nu$ , where  $\nu$  is the kinematic viscosity.

Such was the reputation of von Kármán that (1.1) and the paper in which it appeared quickly became celebrated, even though von Kármán had not considered the effects of wind in the atmosphere or pointed out that in a particular situation (1.1) is but one equation for the two unknowns  $u$  and  $h$ . Benjamin [3] revisited the problem and argued that von Kármán had used Bernoulli's theorem incorrectly (by taking a contour through a turbulent region) and rederived (1.1) by the use of a momentum integral, or flow force as Benjamin called it. Benjamin expressed surprise that he obtained the same result as von Kármán, and was clearly

somewhat distressed by this. However, given that the starting point of both scientists was an (admittedly different) integral of the Euler equations, there was not any possibility that they could have arrived at a different result. In addition, since  $u$ ,  $g'$  and  $h$  are the only variables in the (time-independent) problem, the non-dimensional quantity  $u/(g'h)^{1/2}$  has to be a constant.

Expression of (1.1) has been used in (almost) all studies of gravity currents propagating at high Reynolds number as a form of conservation of momentum. Gravity currents propagating at low Reynolds number, behave quite differently, and, indeed, are not generally controlled at the front at all.

The next section briefly reviews the approach to studying low Reynolds number gravity currents, before continuing the above development for high Reynolds number currents, including the effects of particulate matter, permeable boundaries, rotation, intrusion into an ambient and, finally, the collapse of granular columns. The material is biased towards areas I have been involved with and know best. I hope this stance is understandable, though it means that a number of important contributions have not been mentioned.

### Viscous Gravity Currents

Viscous gravity currents propagate under a balance between viscous and buoyancy forces. In all problems so far solved the viscous fluid has been assumed to spread as a thin layer and the concept of lubrication theory has been appropriate. Thus the velocity profile is parabolic and conservation of mass leads to a governing partial nonlinear differential equation in space and time for the unknown free surface height  $h(\mathbf{x}, t)$  as depicted in figure 1. Thus, for example, for a current spreading along

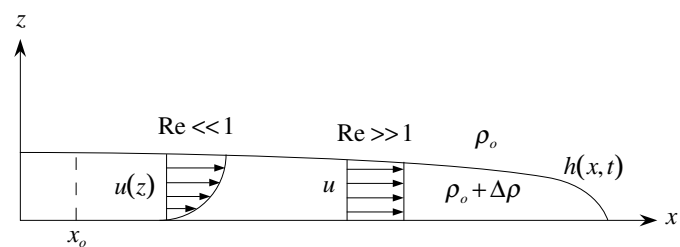


Figure 1: A sketch of a propagating gravity current showing the notation and parabolic velocity profile for  $Re \ll 1$  and the uniform velocity profile for  $Re \gg 1$ .

a horizontal base in either a wide channel or an axisymmetric situation, the governing equation is [4]

$$\frac{\partial h}{\partial t} - \frac{\beta}{x^n} \frac{\partial}{\partial x} \left( x^n h^3 \frac{\partial h}{\partial x} \right) = 0, \quad (2.1)$$

where  $\beta = \frac{1}{3}g/\nu$ ,  $n = 0$  in cartesian coordinates and  $n = 1$  in radial coordinates (where  $x$  is interpreted as the radius), under the assumption that the Bond number  $B = T/\rho l^2 \ll 1$ , where  $T$  is the surface tension and  $l$  some typical horizontal length, so

that surface tension effects along the interface and nose can be neglected. To the governing equation (2.1) must be added an overall volume conservation relationship of the form

$$\int_0^{x_N(t)} (2\pi x)^n h(x, t) dx = qt^\alpha, \quad (2.2)$$

where  $x_N(t)$  is the extent of the current and the volume is assumed to be  $qt^\alpha$ , where, for example,  $\alpha = 0$  represents a constant volume current and  $\alpha = 1$  a current fed at constant flux.

A similarity form of solution is easily obtained for (2.1) and (2.2) and is written as [4,5],

$$h(\mathbf{x}, t) = \zeta_N^{2/3} (q^{2-n}/\beta)^{1/(5-n)} t^{[(2-n)\alpha-1]/(5-n)} \Phi(\zeta/\zeta_N), \quad (2.3)$$

where the similarity variable

$$\zeta = (\beta q^3)^{-1/(5+3n)} x t^{-(3\alpha+1)/(5+3n)}, \quad (2.4)$$

$\zeta_N(\alpha, n)$  is determined by (2.2) and  $\Phi(w)$  satisfies the singular nonlinear differential equation

$$\begin{aligned} (w^n \Phi^3 \Phi')' + \frac{(3\alpha+1)}{(5+3n)} w^{1+n} \Phi' - \\ \frac{1}{(5-n)[(2-n)\alpha-1]} w^n \Phi = 0 \end{aligned} \quad (2.5)$$

$$\Phi(1) = 0. \quad (2.6)$$

The similarity variable (2.4) indicates immediately, with no further analysis, that the extent of the current is given by

$$x_N = \zeta_N (\beta q^3)^{1/(5+3n)} t^{(3\alpha+1)/(5+3n)}. \quad (2.7)$$

Experimental results for the rate of propagation of such viscous spreading are in excellent agreement with the theoretical determination [4-7]. The motivation for the original study was the availability of wonderful data on the spreading of the lava dome formed in the crater of the Soufrière of St Vincent in the West Indies after the eruption of 1979. The resultant lava dome slowly increased in volume, and spread horizontally for five months across the crater floor, by which time the pancake-shaped dome had a height of 130m, a mean diameter of 870m and a volume of  $5 \times 10^7 m^3$  [8]. Observations of the volume then indicated that  $\alpha = 0.66$ , which should lead to a radial time dependence, from (2.7), of  $(3\alpha+1)/8 = 0.37$ , in good agreement with the measured value of 0.39. In addition, (2.7) can then be inverted to determine the reasonable value for the kinematic viscosity of  $6 \times 10^7 m^2 s^{-1}$ . Considerable further work has been done to extend this initial model in order to be more realistic by including the effects of compressibility of the interstitial gas in the magma [9], and solidification of the thin upper carapace of the lava dome [10,11]. The theoretically determined shape, (2.3) has also been successfully used to describe the shape of the numerous lava domes recently observed on Venus [12].

The flow at low Reynolds number of a viscous fluid down a slope occurs in many different situations: the splattered wet mud down a car windscreen; liquid detergent on a slanted plate; and rainwater down the roof of a glass conservatory. A fundamental problem, which has acted as the foundation of further studies, is whether a broad band of viscous fluid, uniform in depth across the slope, can continue to flow in a fashion independent of the cross-slope coordinate. This situation was first

considered by Huppert [6] who showed, again under the assumption that  $B \ll 1$ , that there is a parabolic velocity profile and that the free surface  $h(x, t)$  is governed by

$$\frac{\partial h}{\partial t} + (g \sin \theta' / \nu) h^2 \frac{\partial h}{\partial x} = 0, \quad (2.8)$$

where  $x$  is the coordinate down the slope, which is inclined at angle  $\theta$  to the horizontal. By use of either the theory of characteristics or by similarity theory, Huppert showed that the appropriate theoretical solution of this two-dimensional flow was

$$h = (\nu / g \sin \theta)^{1/2} x^{1/2} t^{-1/2} \quad (2.9a)$$

for

$$0 \leq x < x_N = (9A^2 g \sin \theta / 4\nu)^{1/3} t^{1/3}, \quad (2.9b)$$

where  $A$  is the initial cross-sectional area of the current. The relationship (2.9a) indicates that at any time the free surface increases in thickness down the slope like the square root of the coordinate down the slope until the point  $x = x_N$  at which point the current ends (abruptly in this solution that neglects surface tension) and that at any point down the slope, once the current has passed overhead, its thickness decreases like the square root of time.

To test the validity of this theoretical prediction, Huppert conducted a series of experiments with different viscous fluids flowing down slopes of different angles to the horizontal. Initially the motion was virtually independent of the cross-slope coordinate and in good agreement with the predictions of (2.9). However, after some time the flow front spontaneously developed small amplitude waves of fairly constant wavelength across the slope. The amplitude of the waves increased in time as the maxima (point furthest down the slope) travelled faster than the minima. The wave length remained unaltered. For silicon oils the subsequent shape was a periodic, triangular front with tightly rounded maxima, connected by very straight portions at an angle to the slope, to extremely pointed minima. For glycerine, the shape was also periodic, though with much less tightly rounded maxima, again connected by extremely straight portions, almost directly down the slope, to very broad minima. To my knowledge no other shape has been seen for different fluids. The initial instability is due to the effects of surface tension, which were neglected in the two-dimensional analysis. Incorporating these effects at the tip, Huppert was able to show that the wavelength of the instability was well represented by

$$\lambda = (7.5A^{1/2} T / \rho g \sin \theta)^{1/3}, \quad (2.10)$$

independent of the co-efficient of viscosity, which only sets the timescale of the instability and its onset.

### Compositional Currents

In (almost) all situations, very soon after release, a current whose density difference is due to a dissolved component, such as salt, so that the density is conserved, propagates in such a way that its horizontal extent is very much larger than its vertical extent. Under the assumption that the Reynolds number is large, the balance is then between inertial and buoyancy forces and standard shallow water theory [13] can be applied. Alternatively, Huppert and Simpson [14] introduced the concept of a “box model”, which considers the simple model that results from assuming the current to evolve through a series of equal area rectangles, or equal volume cylinders, as appropriate, with no variations of any properties in the horizontal. (An integral justification of this approach is given in [15]). This approach leads immediately to the relationship

$$x_N = C(Fr)(g'A)^{(2-n)/6} t^{(4-n)/6}, \quad (3.1)$$

where  $C(\text{Fr})$  is dependent only on the Froude number and  $A$  is the cross-sectional area in two dimensions ( $n=0$ ) and the volume in three dimensions ( $n=1$ ) of the current. Even if mixing occurs the product  $g'A$  remains constant, and equal to the initial value.

The use of similarity theory [16-18] leads to a relationship which differs only in the premultiplicative constant in (3.1), and then only by a relatively small quantitative amount. (But that is the power of the correct dimensional constraints!)

Entrainment of ambient fluid into the flow has been investigated both theoretically and experimentally [19,20] by following the intrusion of an alkaline current into an acidic ambient. Entrainment takes place almost entirely at the head of the current owing to shear instabilities on the interface between the current and the ambient and by the over-riding of the (relatively less dense) ambient fluid as the head propagates over it. An entrainment or dilution ratio  $E$ , defined as the ratio of the volumes of ambient and original fluid in the head, which hence must be non-negative, can be shown by dimensional analysis, and was confirmed by experiment, to be independent of  $g'$ , and to be given in two dimensions by  $E = [1 - c_1 y_N / A_s^{1/2}]^{-c_2} - 1$ , where  $A_s$  is the cross-sectional area of fluid in the head at the end of the slumping phase (which occurs before the current has propagated about 10 lock lengths),  $y_N$  is the position of head beyond the slumping point [14], and  $c_1 \approx 0.05$  and  $c_2 \approx 1.5$  are empirical constants determined by the roughness of the floor.

### Particulate-laden Currents

When heavy (or possibly relatively less dense) particles drive the flow the major new addition to the advective effects is that the particles fall (or rise) out of the flow and the driving buoyancy continually decreases. Examples of this form of motion are the terrifying flows seen in lower Manhattan on September 11 and the awesome hot, ground-hugging pyroclastic flows which can be the life-threatening, destructive result of volcanic eruptions such as occurred recently at Pinatubo in Indonesia, Unzen in Japan and Montserrat in the Caribbean. After a sufficient number of particles have dropped to the ground, so that the bulk density of this hot flow is no longer greater than that of the surrounding atmosphere, the current can suddenly rise quite dramatically, taking much particulate matter high into the atmosphere.

The approach most frequently taken to analyse the sedimentation if the concentration is not too large is to assume that the (high Reynolds-number) flow is sufficiently turbulent to maintain a vertically uniform particle concentration in the main body of the current. However, at the base of the flow, where the fluid velocities diminish appreciably, the settling of particles occurs at the (low-Reynolds-number) Stokes velocity  $V_s$  in otherwise quiescent fluid. Quantitatively, this indicates that, neglecting particle *advection* for the moment and assuming that the particles are all of one size, if  $N_p$  (which is possibly a function of time and position) denotes the total number of particles per unit horizontal area in a layer of depth  $h$ , the change of  $N_p$  in time  $\delta t$ ,  $\delta N_p$ , due only to the sedimentation, is given by  $\delta N_p = -V_s C_0 \delta t$ , where  $C_0$  is the (number) concentration (per unit volume) just above the base of the flow. Vigorous turbulent mixing implies that  $C_0 = N_p / h$ , which (on taking the appropriate infinitesimal limits) indicates that  $dN_p / dt = -V_s N_p / h$ , a relationship which has been carefully verified by experiments [21]. Incorporation of advection of particles by the mean flow then results in

$$\frac{D}{Dt} \phi \equiv \frac{\partial \phi}{\partial t} + \mathbf{u} \cdot \nabla \phi = -V_s \phi / h, \quad (4.1)$$

where  $\phi$  is the volume concentration of particles.

Shallow water equations incorporating (4.1) are easily derived [17,18]. There are no similarity solutions and recourse, in general, has to made to numerical solution. There is very good agreement between the numerical solutions and experimental determinations carried out specially to test them.

Aside from numerical solutions, it is also possible to develop asymptotic, analytic solutions based on the smallness of  $\beta_S = V_s / (g'_0 h_0)^{1/2}$ , where  $g'_0$  is the *initial* reduced gravity of the system [15]. This is an example of the interesting problem which can be stated in general as the nonlinear partial differential equation

$$\mathcal{N}_1[\Phi(x, t)] = \epsilon \mathcal{N}_2[\Phi(x, t)], \quad (4.2)$$

where  $\mathcal{N}_1$  and  $\mathcal{N}_2$  are nonlinear operators in some spatial coordinate  $x$  and time  $t$ . For  $\epsilon \equiv 0$  there is a similarity solution to (4.2) and a special value of  $x, x_*$  say, such as that at the nose of the current, which increases continuously with time of the form  $x_* = f(t)$ . However, for  $\epsilon \neq 0$ , no matter how small, (4.2) does not have a similarity solution and eventually, for sufficiently large  $t, x_*$  attains a constant. Thus, in the style of singular perturbation problems, for sufficiently large  $t$  the solution for  $\epsilon = 0$  departs by as much as you like from solutions for  $\epsilon \ll 1$ . It must, on the other hand, be possible to obtain asymptotic solutions to (4.2) in a perturbative sense. Such a technique is constructed, in part, in [15].

When there is an external flow present, as originally put to von Kármán, the propagation of the current is significantly influenced, and in a different way if it is propagating with the ambient flow or against it. Hogg and Huppert [22,23] initiated an analysis and a series of laboratory experiments to investigate this case. They showed that in two dimensions the flow was dependent on the single non-dimensional parameter  $\Lambda = UA / (l_\infty^2 V_s)$ , where  $U$  is the effective mean external flow experienced by the current (shown in [22] to be 0.6 times the actual current),  $A$  is the cross-sectional area (or volume per unit width) of the fluid instantaneously released at the base of the flow, the reduced gravity of the particles of density  $\rho_p$  is given by  $g'_p = (\rho_p - \rho_a)g / \rho_a$ ,  $\rho_a$  is the density of the ambient and  $l_\infty = (g'_p \phi_0 A^3 / V_s^2)^{1/5}$ . The parameter  $\Lambda$  represents the ratio of the mean external velocity to the settling velocity of the particles. When  $\Lambda$  is small, (little effect of the flow in the ambient) the flow is roughly the same upstream or downstream. As  $\Lambda$  increases the effects of the flow in the ambient increase and the upstream flow is considerably restricted. However, even for large  $\Lambda$  there will still be some upstream propagation—much to the disbelief and then dismay of the government official who asked me to carry out this work in order to show that a new dredging technique which removed sand from the bottom of the harbour, by blowing high velocity water at it, would be totally removed by the outgoing tidal flow and not propagate at all upstream across the harbour and contaminate the highly valuable stocks of fish and oysters there! Figure 2 presents the theoretically determined maximum non-dimensional upstream distance of a particulate intrusion in a uniformly flowing ambient as a function of  $\Lambda$  and the laboratory experimental data obtained using various size particles. The agreement shown is excellent; and one of the best I have ever obtained in my career, and hence my pleasure with it.

Extensions of this idea to an axisymmetric (rather than line) source are summarised in [24,25] where the relevant parameters and shape of the current are carefully discussed. My clever graduate student, Anja Slim, [26] is also working in this area for her Ph.D. and has already developed a number of results with the final aim of understanding the details of how an initially vertically penetrating, particulate-rich, volcanic eruption column is

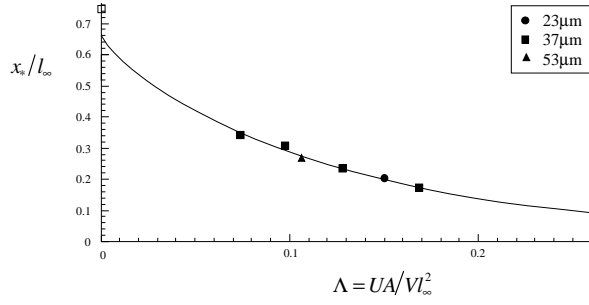


Figure 2: The theoretical prediction and experimental data of the maximum nondimensional upstream penetration of a particulate gravity current in a uniform flowing ambient,  $x_*/l_\infty$ , as a function of  $\Lambda = UA/(V_S l_\infty^2)$  for three different particle sizes.

influenced high in the atmosphere by the prevailing winds.

Further details of some of this work can be found in [27].

### Additional Effects

The preceding four sections have detailed some of the fundamental relationships for the propagation and evolution of a gravity current. Many other special effects are possible. We will describe some of these under the headings of: effects of a permeable boundary; intrusion below a stratified ambient; and effects of rotation.

### Permeable boundaries

There are many natural and industrial situations where a gravity current flows over a permeable boundary and seeps into it. Examples include protecting liquid-containing structures by surrounding them with a deep gravel bed, the seepage of tidal inflow up a beach and the everyday occurrence of honey seeping into toast. The most important new ingredient is that fluid from the current continuously seeps through the boundary, which reduces the volume of the current whose propagation must eventually cease.

The flow of the current at low Reynolds number was considered by Acton, Huppert and Worster [28]. The parabolic velocity profile in the current is augmented by a sink term in the local continuity equation which leads, in two dimensions, the only situation that has been investigated, to

$$\frac{\partial h}{\partial t} - \beta \frac{\partial}{\partial x} \left( h^3 \frac{\partial h}{\partial x} \right) = -(kg/v)(1 + h/l), \quad (5.1)$$

which takes the place of (2.1), where the term on the right hand side represents effects of the flow into the porous medium below, which is categorised by the intrinsic permeability of the medium  $k$  and  $l$  denotes the length of the current. In contrast to the situation for an impermeable boundary, (5.1) has a similarity solution only for the special case of  $\alpha = 3$ , for which the flux into the current at the origin just balances that out of the current through the permeable boundary. For other values of  $\alpha$  solutions of (5.1) must be obtained by numerical integration. This was done by Acton *et al.* [28], who also carried out special experiments to compare observational data on the length of the current as a function of time with their numerical solution. The result, as shown in figure 3, resulted in an extremely good comparison, with a final run-out length which scales with  $S_H = (A^2 k)^{1/3}$  for  $\alpha = 0$ . For  $\alpha < 3$  all currents eventually stop; for  $\alpha \geq 3$  all currents continue to propagate because the incoming flux overpowers the seepage. Note the similarity in concept between the slow loss of driving force due to seepage, considered here, and the loss of buoyancy due to slow particle fallout,

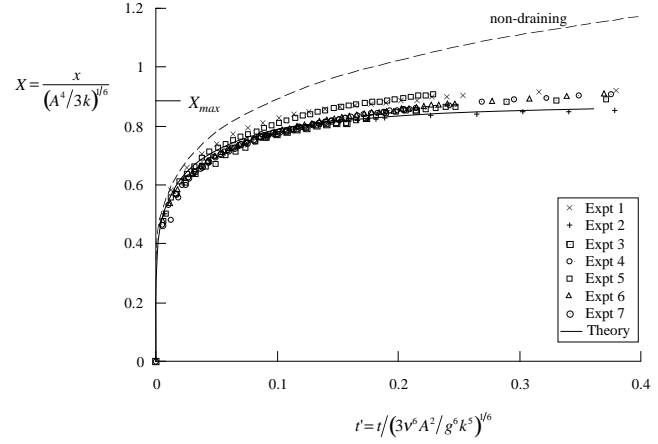


Figure 3: The nondimensional length of a low Reynolds number gravity current flowing over a permeable boundary as a function of the dimensionless time for seven different experiments. The solid curve is the theoretical prediction determined from numerical integration of (5.1) and the dashed line is the similarity solution for an impermeable boundary given by (2.7).

considered in Section 4. The general approach discussed there, as outlined in [15,29] has not been applied to this area, though it no doubt could be done so fruitfully.

When the current propagates at high Reynolds number the balance of forces are of course different, but the importance of seepage through the boundary is still paramount. This problem was initially considered by Thomas, Marino and Linden [30] and then extended by Ungarish and Huppert [31]. The latter solved numerically the shallow water equations governing mass and momentum for a two-dimensional geometry as well as obtaining analytical, box model solutions in both rectangular and axisymmetric geometries. This allowed closed form solutions for the extent of the current as a function of time and its final extent to be determined, which were in fair agreement with both the two-dimensional experiments carried out by Thomas *et al.* [30] and the numerical solutions.

### Propagation under the base of a stratified ambient

In all the foregoing discussion, it has been assumed that the ambient is homogeneous and not influenced in any way, in particular set into motion, by the intruding current. However, in both the atmosphere and in the oceans the ambient is stratified; and it immediately raises the question of why the solutions so far obtained are applicable in these more complicated, natural situations—or has something important been left out? What clearly has been left out of the homogeneous models is the possibility of exciting internal waves in the ambient by the propagation of the current. Viewed from another angle, the question that needs considering is what fraction of the potential energy stored in the original (unstable) buoyancy distribution is lost to the internal wave motion, in contrast to that which is put into the kinetic energy of motion and that which is dissipated. The first investigation of the influence of a stratified ambient was presented by Maxworthy *et al.* [32]. They investigated the propagation of a saline current below a linearly stratified saline ambient in a rectangular container. Their study was a combination of laboratory and numerical experiments. The numerical solutions, obtained from a full Boussinesq formulation, were in very good agreement with their measurements. They focused attention on the speed of propagation of the nose during the initial stage only, for which a good agreement between theory and numerical computation was obtained. Ungarish and Huppert [33] then extended this investigation by determining appropriate an-

alytical solutions. Using the methods of characteristics on the non-linear shallow water equations, which neglects the influence of waves in the ambient, they were able to obtain solutions for the front velocity as a function of the parameter  $S$ , defined as the ratio of the density difference between the fluid that makes up the bottom of the ambient and that at the top to the density difference between the fluid of the incoming current and that at the top. The results of their calculations, compared with the Maxworthy *et al.* experimental results, makes up figure 4.

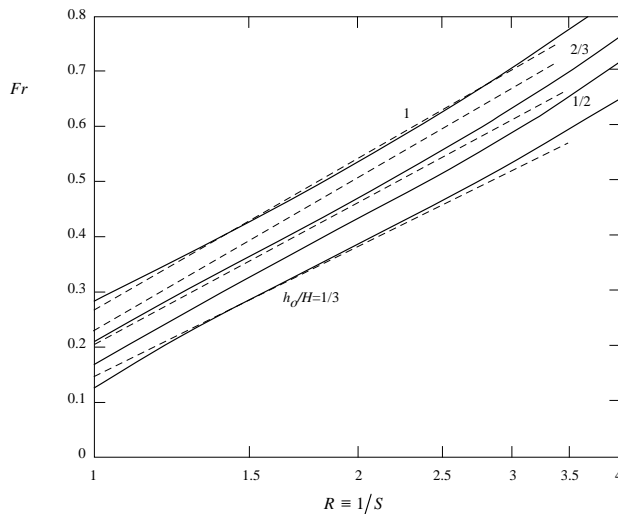


Figure 4: The Froude number, as a function of the logarithm of the inverse stratification parameter  $S$  for a high Reynolds number gravity current propagating beneath a stratified ambient for different initial depth ratios. The theoretical evaluation of Ungarish and Huppert [105], represented by the solid curves, are compared with the experimental results suggested by Maxworthy *et al* [32], represented by dashed curves

Ungarish and Huppert are currently considering how to incorporate the effects of stratified waves in the ambient. They intend first to solve a linear leewave model coupled to a deforming current and thereby evaluate the amount of energy that has gone into the waves. At the same time, they are carrying out laboratory experiments in which an array of conductivity probes will allow a direct sampling of the wave displacements in the ambient, from which, using sophisticated processes in signal analysis, the energy given up to the waves in the ambient will be determined as a function of  $S$  and the geometry of the container—a wave guide if  $l \gg H$ , the depth, and an effectively infinite medium into which the waves can radiate away if  $l \ll H$ .

#### Some effects of rotation

Rotational effects, which can be dominant, for example, in rapidly rotating systems in the laboratory, in industrial machines or due to the rotation of the Earth, brings in the initially counter-intuitive effect that fluid flows at right angles to the pressure gradient, in analogy with at least my experience of life, where you push in one direction and the result goes off in another—a concept which the naive, inexperienced young never understand! The effect of rotation on gravity currents can be particularly powerful in the presence of a boundary because a pressure gradient into the wall can easily be set up and drive a current which hugs the boundary [34]. These situations have been reviewed in detail by Griffiths [35].

An experimental investigation of axisymmetric gravity currents, where boundaries play no role, was carried out at the large rotating system housed in the Coriolis laboratory at the Laboratoire des Ecoulements Géophysiques et Industriels, Grenoble

by Hallworth, Huppert and Ungarish [36]. The major new feature of the results was the attainment of a maximum radius of propagation, attained in about one third of a period of revolution, in contrast to some theories which, totally unjustifiably, assume from the outset that the motion goes on for many rotation periods before anything interesting happens. The observed result had been predicted earlier by a theoretical investigation of the governing shallow water equations by Ungarish and Huppert [37], who evaluated that  $r_{max} \approx 1.6C^{1/2}$ , where  $C = \Omega_o/(h_o g')^{1/2}$ ,  $\Omega$  is the rotation rate of the instrument and the initial dense fluid, of reduced gravity  $g'$  was initially contained in the cylinder of radius  $r_o$  and height  $h_o$ . Thereafter the motion in the fluid consisted of a contraction/relaxation/propagation of the current with a regular series of outwardly propagating pulses. The frequency of these pulses was observed to be slightly higher than inertial, independent of  $h_o$  and  $g'$ , with an amplitude of the order of magnitude of half the maximum radius, as shown in figure 5.

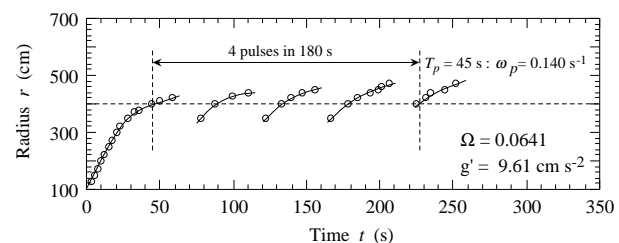


Figure 5: The radius of the leading edge of successive outward propagating fronts as a function of time for gravity currents intruding into a homogeneous, rotating ambient.

#### Concentrated Flows: Mud, Slurries and Landslides

As the concentration of particles increase, the statement of low concentration employed in driving (4.1) on the assumption that each particle sediments with its independent Stokes freefall speed  $V_s$  becomes less reliable. New effects must enter; and indeed, as the concentration becomes very high this situation relates more to mud flows than to the motion of suspended particles. Partly to investigate this problem, Hallworth and Huppert [38] carried out a systematic series of experiments on the instantaneous release of two-dimensional, heavy particle-driven gravity currents down a channel. Relatively low concentrations, with initial volume concentrations  $\phi_o$  in the range  $0 < \phi_o < 0.275$  were well described by the numerical solutions of (4.1) or the analytical box models associated with it, with the final runout length of the sedimented deposit increasing with  $\phi_o$ . Beyond this critical initial volume fraction of particles, the resulting dense current came to an abrupt halt at some point down the channel, depositing the bulk of its sediment load as a relatively thick layer of fairly constant thickness, characterised by a pronounced, steep snout. A very much thinner layer of sediment extended for some distance beyond the arrest point. This layer was deposited from the subsequent propagation of a slower moving, low concentration residual cloud and the final runout length of the sediment layer decreased with increasing  $\phi_o$ . This form of motion was observed for  $0.275 < \phi_o < 0.45$ , this upper limit being the approximate maximum for which Hallworth and Huppert were able to produce a fluid-like initial volume.

Over the last decade, for its obvious natural applications there has been considerable research to try to understand these high-concentration flows, exemplified by mud slides. Large mud flows can occur in mountainous regions after intense rains where they can move large boulders and even trees to cause enormous damage and loss of life and produce interesting al-

luvial fans. They also occur on submarine continental slopes, where they contribute to geomorphological evolution. There is hence considerable interest in both the geological and engineering community in such flows. Unfortunately, in contrast to all the work so far described in this article, for which it has been assumed that the constitutive relationship is Newtonian, it is quite definite that mud and the like are non-Newtonian. But how are they to be described? A plethora of rheological models have been proposed—power law, viscoplastic, Bingham plastic, Herschel–Bulkley, . . . Because of these different conceptual models, it is difficult to carry out systematic experiments which either test or verify any of these flows. Each person understandably views the possible contributions to the broad spectrum of science differently, but I find it unsatisfying working in areas where the fundamentals are on such shaky ground. Nevertheless, considerable activity has been shown in this area, which might be broadly and briefly summarised as follows.

The main new effect that enters is the possibility of a critical yield stress,  $\tau_o$ , below which there is no shear possible in the flow. (There are similarities here to some of the models for non-Newtonian lava flows, nicely reviewed in [39].) This leads to a variety of features which are unknown in Newtonian fluids, even in quite simple situations. For example, a uniform layer of fluid mud can remain stationary on an incline, if the depth of the mud or the slope of the incline is sufficiently small. When motion does occur it is generally investigated under two approximations: either the flow is so slow that inertia is neglected (the more usual case); or so fast that a boundary-layer approximation is appropriate. A variety of different initial set-ups have been solved for the motion of the mud and its final shape on a horizontal surface, down an inclined plane and over a gently sloped conical surface, representing a shallow basin or hill [40, 41]. Much further work in this area needs to be done before a good scientific understanding has been obtained and the results can be applied to the all-important area of hazard assessment, with the potential to save hundreds of thousands of lives and millions of wasted dollars.

### Granular flows

Partially motivated by recent interest in the flow of granular medium, my superb geological colleague, Steve Sparks, a student Gert Lube and I conducted a series of experiments in which various granular materials, initially contained in a vertical cylinder, were rapidly released onto a horizontal surface to spread out unhindered over it [42]. The materials were couscous, rice, dry sand, salt and sugar, all of which have different size and shape. The horizontal plane used was either wood, a smooth surface of baize lying on wood, a smooth transparent Plexiglas plane or a rough plane of sandpaper. The detailed spread of the granular material was independent of the explicit grains employed or the bounding surfaces. Eight different cylinders, in radius,  $r_i$ , from 1.7 to 9.7 cm, were used. Some experiments were recorded and later analysed on a digital high-speed video at 500 frames per second. After all motion had ceased, the profile of the resultant deposit was measured, to find the final runout radius,  $r_\infty$ , central cone height,  $h_\infty$ , and the steepest incline,  $\alpha$ , of the upper surface.

For all values of the initial aspect ratio  $a = h_i/r_i$ , where  $h_i$  is the initial height of the granular medium, there was a central undisturbed cone of material which did not partake in the motion, whose angle was close to  $60^\circ$ , corresponding to an aspect ratio of 1.7. This can be interpreted as an internal friction angle for the material. At the base, three different regions were captured by video during the collapse: a stationary circular region, of radius  $r_i$ ; a ring of previously deposited particles; and an outer ring of material which was still flowing. These last two regions

were divided by a moving interface that propagated outwards until the flow front came to rest.

Observations from the high-speed photography indicate that other aspects of the motion naturally divide themselves into three different regimes dependent on  $a$ . For initial aspect ratios  $a < 1.7$ , the upper surface of the released material was divided into an inner stationary circle (which remained at the initial height,  $h_i$ ) outside of which was flowing material. After the flow front had ceased propagating, a moving interface on the upper free surface appeared, which separated static from flowing particles and which propagated inward from the stationary front. For  $a < 1$  the final deposit consisted of an inner, undisturbed central region beyond which there was an axisymmetric, tapering frontal region with  $\alpha$  in the range of the angle of repose. For  $1 < a < 1.7$  the avalanching which occurred after the flow front had stopped moving removed the undisturbed central region.

For  $a > 1.7$  the entire upper surface flowed from the beginning of each experiment. Initially, the upper free surface remained undeformed and horizontal. After the column lost some height, deformation of the top occurred, to form a dome whose radius of curvature decreased with time. The final deposit had a steep central zone and an axisymmetric tapering frontal region with  $\alpha$  less than the angle of repose.

A transition in behaviour of collapse was evident from the video analyses to occur when  $a$  exceeds about ten. Immediately upon lifting the container the entire free surface began to flow. A flow front developed at the base of the column and propagated outwards while removing material from the centre. In contrast to lower initial aspect ratios, the upper surface of the column remained undeformed until its height sank to that of the neighbouring flat frontal region. Also, once the flow at the base had ceased, an interface between moving and stationary material appeared on the upper free surface but propagated outward from the centre to the flow front. The value of  $\alpha$  decreased monotonically with increasing  $a$ .

The quality of the observational data and the similarity of the results for the different materials suggest that, with the use of dimensional analysis, the data can be collapsed in a systematic way. The initial experimental set up is determined by  $r_i$ ,  $a$  and  $g$ , the acceleration due to gravity. Our ability to collapse all the data using only this input, and not any material properties, is a robust test for the assumption that no additional material property, such as the friction between individual grains, is needed to describe the motion.

The difference between the initial and final radius,  $\delta r = r_\infty - r_i$ , must be expressible as  $\delta r = r_i f(a)$ . A plot of  $\delta r/r_i$  makes up figure 6. For  $a < 1.7$ , because there is no motion of the inner region, the resultant expression must be independent of  $r_i$ , which requires that  $f(a) \propto a$ . From figure 6 we determine that the constant of proportionality which best fits the data is 1.3. For  $a > 1.7$  the best fit power law to the data for all grains is given by  $f(a) = 1.6a^{1/2}$ .

The final height at the centre is similarly expressible as  $h_\infty = r_i \eta(a)$ . Figure 6 also presents all the data for  $h_\infty/r_i$  as a function of  $a$ . For  $a < 1.7$ ,  $h_\infty = h_i$ , and so  $\eta(a) = a$ , as indicated by the data. For  $1.7 < a < c.10$  the best fit power law to the data is given by  $\eta(a) = 0.88a^{1/6}$ . For  $a > c.10$  there is a clear indication that  $h_\infty$  decreases with increasing  $a$ . This is in response to the wave that originates from the centre and removes material outwards. Unfortunately, the data are a little too scattered to be quantitatively analysed with confidence.

So far the parameter  $g$  has not entered our expressions because

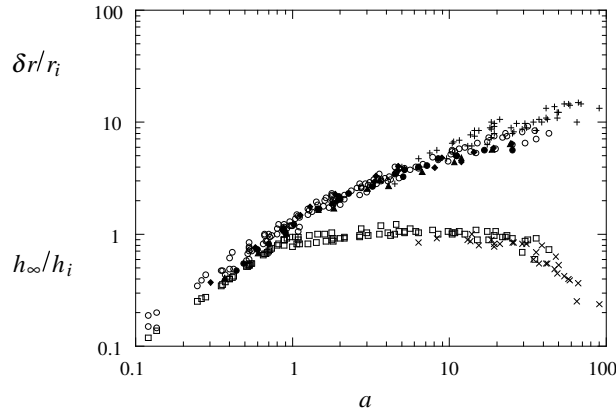


Figure 6: Nondimensional radial displacement and height at the centre of a pile of axisymmetric collapsing grains. Points marked with a cross are for experiments in which the cylinder was raised height  $H$  from the base before releasing the grains, and the aspect ratio is defined as  $(H + h_i)/r_i$ . This shows that in the final runout distance only maximum initial height is relevant (and initial radius).

it is the only input parameter for which time is involved in its dimensions, and  $\delta r, h_\infty/r_i$  are both independent of time. The value of  $g$  will affect the total time for collapse,  $t_\infty$ , which is defined as the time between the initiation of the experiment and that at which the flow front stops propagating. The high speed video allowed us to determine  $t_\infty$  reasonably accurately. By dimensions, it must be of the form  $t_\infty = (r_i/g)^{1/2}\psi(a)$ , for some function  $\psi(a)$ . A plot of  $t_\infty/(r_i/g)^{1/2}$  as a function of  $a$  is presented in figure 7. As before, for  $a < 1.7$ , an expression independent of

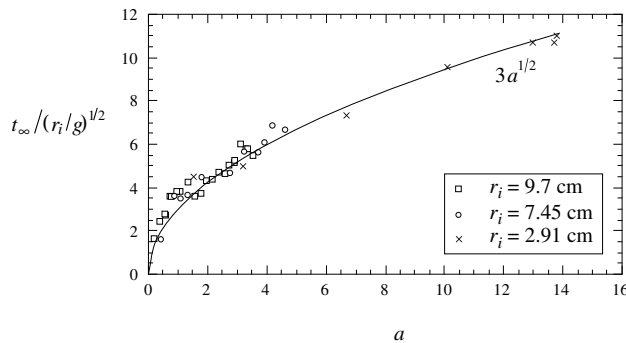


Figure 7: Nondimensional time until the grain front ceased motion as a function of  $a$ .

$r_i$  requires  $\psi(a) \propto a^{1/2}$ , which is consistent with the data for a constant of proportionality of 3.8. For  $a > 1.7$  the best fit power law through the data yields  $\psi(a) = 3a^{1/2}$ , which indicates that  $t_\infty = 3(h_i/g)^{1/2}$ . Note that the time taken for a particle to fall a height  $h_i$  under gravity is  $(2h_i/g)^{1/2}$ , which is just less than a half of  $t_\infty$ .

Further insight is obtained by an analysis of data on the radius of the flow front as a function of time,  $r(t)$ . For all flows there was a primary acceleration phase during which the acceleration was approximately constant between 0.25 g and 0.3 g. For  $a < 1.7$  this acceleration phase was followed by a phase of deceleration which came quite abruptly to a halt. For  $a > 1.7$  these two phases were separated by a phase of constant velocity of the flow front whose duration increased with increasing  $a$ . This phase of constant velocity has an analogue with the evolution of a fluid axisymmetric gravity current spreading at high Reynolds number, which also goes through a stage of constant velocity [14]. A fluid current then adjusts under a balance between buoy-

ancy and inertial forces, spreading like  $t^{1/2}$  [cf. (3.1)]—the same result as obtained for the granular collapse described here. This analogy, which uses quantitative relationships to describe the motion of the granular medium that are closely analogous to those used to describe the motion of density currents of Newtonian liquids, further strengthens our argument that intergranular frictional effects play a negligible role until the abrupt halt commences.

Obtaining the spreading relationships that our experiments have indicated remains a challenge for the future. A difficulty is that for at least half of the flow the concepts of shallow water theory, as applied by some to this problem, are false. In the meantime, a clue to understanding the emplacement we have observed may come from an interpretation of the final stages, when the spreading pile comes to a rapid halt. It has been suggested that granular materials can be considered in two states [43]: a static solid state, where intergranular forces at particle faces give the material strength; and a liquid state, exemplified by granular flows and fluidised beds, where the particles are in an agitated state and the system has negligible strength. The abrupt cessation of the motion of the granular flows that we observed can be likened to a phase change between two states [44]. In accord with the characterisation put forward in [45], the change of state can be envisaged as a kinetic process analogous to solidification of a true liquid. In the case of a granular medium, we suggest that as the flow decelerates, the granular temperature falls below a threshold value and frictional interactions between particles become dominant and the granular material converts to a static solid (or deposit).

## Conclusions

Since the propagation and evolution of gravity currents was first quantitatively analysed more than sixty years ago, a lot has been determined. The rates of propagation under many different situations have been evaluated, as described in the various sections of this article. The subject area has seen considerable active research over the last thirty years or so, primarily due to the influence of the giant names in the subject, including von Kármán [2], Benjamin [3] and Simpson [45]. Part of the drive for the research has come from the natural applications to flows in the oceans, atmosphere, on the Earth surface and also deep within the Earth along particular phase boundaries [5,46] as well as to many engineering and industrial problems.

## Acknowledgements

Many colleagues have helped me to understand the motion of gravity currents. I am grateful to each of them for their patience and wisdom.

## References

- [1] Turner, J.S. *Buoyancy effects in fluids*, Cambridge University Press 1979.
- [2] Von Kármán, T. The engineer grapples with nonlinear problems, *Bull. M. Math. Soc.* **46**, 1940, 615–683.
- [3] Benjamin, T.B. Gravity currents and related phenomena, *J. Fluid Mech.* **31**, 1968, 209–248.
- [4] Huppert, H.E. The propagation of two-dimensional and axisymmetric viscous gravity currents over a rigid horizontal surface, *J. Fluid Mech.* **121**, 1982, 43–58.
- [5] Huppert, H.E. The intrusion of fluid mechanics into geology, *J. Fluid Mech.* **173**, 1986, 557–594.
- [6] Huppert, H.E. The flow and instability of viscous gravity

currents down a slope, *Nature* **300**, 1982, 427–429.

[7] Huppert, H.E. Geological Fluid Mechanics. In: *Perspectives in Fluid Dynamics: A Collective Introduction to Current Research*, eds. G. K. Batchelor, H.K. Moffatt and M.G. Worster. Cambridge University Press, 2000, 447–506.

[8] Huppert, H.E., Shepherd, J.B., Sigurdsson, H. and Sparks, R.S.J. On lava dome growth, with applications to the 1979 lava extrusion of Soufriere, St. Vincent, *J. Volcanol. and Geotherm. Res.* **14**, 1982, 199–222.

[9] Jaupart, C. Effects on compressibility on the flow of lava, *Bull. Volc.* **54**, 1991, 1–9.

[10] Fink, J.H. and Griffiths, R.W. Radial spreading of viscous gravity currents in solidifying crust, *J. Fluid Mech.* **221**, 1990, 485–510.

[11] Fink, J.H. and Griffiths, R.W. Morphology, eruption rates, and rheology of lava domes; insights from laboratory models, *J. Geophys. Res.* **103**, 1998, 527–548.

[12] McKenzie D., Ford, P.G., Liu, F. and Pettengill, G.H. Pancake-like domes on Venus, *J. Geophys. Res.-Planet* **97(E10)**, 1992, 15967–15976.

[13] Whitham, G.B. *Linear and Nonlinear Waves*, Wylie, 1974.

[14] Huppert, H.E. and Simpson, J.E. The slumping of gravity currents, *J. Fluid Mech.* **99**, 1980, 785–799.

[15] Harris, T. C., Hogg, A. J. and Huppert, H.E. A mathematical framework for the analysis of particle-driven gravity currents, Appendix A, *Proc. Roy. Soc. A* **457**, 2001, 1241–1272.

[16] Chen, J.C. Studies on gravitational spreading currents, PhD thesis, California Institute of Technology, 1980.

[17] Bonnetaze, R.T., Huppert, H.E. and Lister, J.R. Particle-driven gravity currents, *J. Fluid Mech.* **250**, 1993, 339–369.

[18] Bonnetaze, R.T., Hallworth, M.A., Huppert, H.E. and Lister, J.R. Axisymmetric particle-driven gravity currents, *J. Fluid Mech.* **294**, 1995, 93–121.

[19] Hallworth, M.A., Phillips, J., Huppert, H.E. and Sparks, R.S.J. Entrainment in turbulent gravity currents, *Nature* **362**, 1993, 829–831.

[20] Hallworth, M.A., Huppert, H.E., Phillips, J. and Sparks, R.S.J. Entrainment into two-dimensional and axisymmetric turbulent gravity currents, *J. Fluid Mech.* **308**, 1996, 289–312.

[21] Martin, D. and Nokes, R. Crystal settling in a vigorously convecting magma chamber, *Nature*, **332**, 1988, 534–536.

[22] Hallworth, M.A., Hogg, A.J. and Huppert, H.E. Effects of external flow on compositional and particle gravity currents, *J. Fluid Mech.* **359**, 1998, 109–142.

[23] Hogg, A.J., Huppert, H.E. and Hallworth, M.A. Constant flux currents in external mean flows. *J. Fluid Mech.* (sub judice).

[24] Hogg, A.J. and Huppert, H.E. Two-dimensional and axisymmetric models for compositional and particle-driven gravity currents in uniform ambient flows. In: *Sediment Transport and Deposition by Particulate Gravity Currents. Spec. Publs. int. Ass. Sediment* **31**, 2001, 121–134.

[25] Hogg, A.J. and Huppert, H.E. Spreading and deposition of particulate matter in uniform fluids, *J. Hydraul. Res.* **39(5)**, 2001, 505–518.

[26] Slim, A.C. Ph.D. thesis, Cambridge University, 2005.

[27] Huppert, H.E. Quantitative modelling of granular suspension flows, *Phil. Trans. R. Soc.* **356**, 1998, 2471–2496.

[28] Acton, J.M., Huppert, H.E. and Worster, M.G. Two-dimensional viscous gravity currents flowing over a deep porous medium, *J. Fluid Mech.* **440**, 2001, 359–380.

[29] Harris, T.C., Hogg, A.J. and Huppert, H.E. Polydisperse particle-driven gravity currents, *J. Fluid Mech.* **472**, 2002, 333–372.

[30] Thomas, L.P., Marino, B.M. and Linden, P.F. Gravity currents over porous substrata, *J. Fluid Mech.* **366**, 1998, 239–258.

[31] Ungarish, M. and Huppert, H.E. High-Reynolds-number gravity currents over a porous boundary: shallow-water solutions and box model approximations. *J. Fluid Mech.* **418**, 2000, 1–23.

[32] Maxworthy, T., Lielich J., Simpson, J.E. and Meiburg, E.H. Propagation of a gravity current in a linearly stratified fluid, *J. Fluid Mech.* **453**, 2002, 371–394.

[33] Ungarish M. and Huppert H.E. On gravity currents propagating at the base of a stratified ambient, *J. Fluid Mech.* **458**, 2002, 283–301.

[34] Griffiths, R.W. and Hopfinger, E. Gravity currents moving along a lateral boundary in a rotating fluid, *J. Fluid Mech.* **134**, 1983, 357–399.

[35] Griffiths, R.W. Gravity currents in rotating systems. *Ann. Rev. Fluid Mech.* **18**, 1986, 59–89.

[36] Hallworth, M. A., Huppert H. E. and Ungarish, M. Axisymmetric gravity currents in a rotating system: experimental and numerical investigations, *J. Fluid Mech.* **447**, 2001, 1–29.

[37] Ungarish, M. and Huppert, H.E. The effects of rotation on axisymmetric, particle-driven gravity currents, *J. Fluid Mech.* **362**, 1998, 17–51.

[38] Hallworth, M.A. and Huppert, H.E. Abrupt transitions in high-concentration, particle-driven gravity currents, *Phys. Fluids* **10**, 1998, 1083–1087.

[39] Griffiths, R.W. The dynamics of lava flows, *Ann. Rev. Fluid Mech.* **32**, 2000, 477–518.

[40] Mei, C.C., Liu, K.-F. and Yuhi, M. Mud flows - slow and fast, *Geomorphological Fluid Mech.* (eds): Balmforth, N. and Provencale, A., Springer-Verlag 2001, 548–577.

[41] Yuhi, M. and Mei, C.C. Slow spreading of fluid-mud over a conical surface, *J. Fluid Mech.* (in press).

[42] Lube, G., Huppert, H.E., Sparks, R.S.J. and Hallworth, M.A. Axisymmetric collapses of granular columns, *J. Fluid Mech.* **508**, 2004, 175–199.

[43] Jaeger H.M., Nagel, S.R. and Behringer, R.P. Granular solids, liquids and gases, *Rev. Mod. Phys.* **68**, 1996, 1259–1273.

[44] Huppert, H.E. The fluid mechanics of solidification, *J. Fluid Mech.* **212**, 1990, 209–240.

[45] Simpson, J.E. *Gravity currents in the environment and the laboratory*, Cambridge University Press 1997.

[46] Kerr, R.S. and Lister, J.R. The spread of subducted lithospheric material along the mid-mantle boundary. *Earth Planet. Sci. Let.* **85**, 1987, 241–247.



## Spin-up flow of an Incompressible Fluid

J.S. Park<sup>1</sup> and J. M. Hyun<sup>2</sup>

<sup>1</sup>Department of Mechanical Engineering  
Halla University, Wonju, 220-712 KOREA

<sup>2</sup>Department of Mechanical Engineering  
KAIST, Taejeon, 305-702 KOREA

### Abstract

Spin-up flows of an incompressible homogeneous fluid have been reviewed. Characteristics of spin-up are followed by a summary of well-established previous papers along the orders : linear spin-up, weakly non-linear spin-up and non-linear spin-up. Discussions are given to open problems from previous analytic theories as comparing with full numerical solutions for Navier-Stokes equation.

### Introduction

Spin-up refers to the transient adjustment process of a confined fluid when the rotation rate of the container undergoes a change. Specifically, consider an incompressible viscous fluid which fills a closed circular cylindrical container [radius  $R$ , height  $H$ , aspect ratio  $H/R \sim O(1)$ ]. At the initial state, both the fluid and the cylinder are in rigid-body rotation about the longitudinal axis (z-axis) at rotation rate  $\Omega_i$ . At time  $t = 0$ , the rotation rate of the cylinder is increased abruptly to  $\Omega_f (\equiv \Omega_i + \Delta\Omega)$ . The transient motion of the fluid, in response to this abrupt alteration of the rotation rate of the container, constitutes the spin-up. For the majority of geophysical and technological applications, the flow is characterized by the smallness of the Ekman number  $E [\equiv \nu/\Omega_f H^2]$ , where  $\nu$  is the kinematic viscosity of fluid]. The condition  $E \ll 1$  leads to a boundary-layer-type global flow field, which consists of the inviscid interior, the Ekman and Stewartson boundary layers close to the solid walls of the container.

The pioneering treatise of Greenspan and Howard[11] considered the linear spin-up problem in which the Rossby number  $\varepsilon = \Delta\Omega/\Omega_f$  is small. By undertaking detailed theoretical analyses, it was shown that spin-up is substantially accomplished over the spin-up timescale  $E^{-1/2}\Omega_f^{-1}$ , which is an order-of-magnitude smaller than the diffusive timescale  $E^{-1}\Omega_f^{-1}$ .

The main ingredients of the adjustment process are the inviscid-boundary layer interactions, together with the angular momentum conservation in the inviscid interior. The essential flow character has since been verified by numerical simulations and laboratory experiments [see review articles by Benton & Clark [4], Duck & Foster [7]]. For definitiveness, the cylinder is oriented such that the central longitudinal axis is aligned in the vertical (z) axis, and the horizontal direction refers to the radial ( $r$ ) and azimuthal ( $\theta$ ) directions.

Efforts were made to extend the linear problem formulation of Greenspan and Howard [11] to nonlinear settings. For  $\varepsilon$  small, but finite, Greenspan and Weinbaum [12] carried out series expansions using  $\varepsilon$  to include higher-order terms, which rendered a weakly nonlinear theory. Wedemeyer [33], in a departure from the approach of Greenspan and Weinbaum [12], delineated the character of spin-up flow from the initiate state of

rest, i.e.,  $\Omega_i = 0$ ,  $\varepsilon = 1.0$ . When the container starts rotating from rest, Wedemeyer's solution demonstrated the existence of the radially-propagated velocity shear front. The interior inviscid fluid at smaller (larger) radii than the shear front moves toward (away from) the horizontal boundary layers. Venezian [28,29] generalized the analysis by Wedemeyer to the range  $0 \ll \varepsilon < 1.0$ . It is important to point out the difficulties associated with the above-stated flow models. The theory of Greenspan & Weinbaum [12] does not recover the nonlinear flow of Wedemeyer in the limit  $\varepsilon \rightarrow 1.0$ . Similarly, the solutions of Wedemeyer and Venezian do not reproduce completely the linear results of Greenspan & Howard as  $\varepsilon \rightarrow 0$ . These are indicative of the challenges ahead in unifying the linear and nonlinear solutions.

In 1970's and 1980's, numerical solutions to the full Navier-Stokes equations were obtained [16, 18, 32]. These endeavors verified the global flow field predicted by the previous theoretical studies. Further extensions were made by numerical simulations to explore spin-up with a free surface [5, 20, 21], turbulent flows[6], in a geostrophic flow [21], to name a few. In 1990's, different aspects of spin-up, somewhat modified from the classical models, were investigated. Examples include spin-up in a non-axisymmetric container [14, 26]. Also, spin-up flows were delineated when the shapes of the solid walls of the container were deformed. In summary, these are representative of the efforts to tackle more realistic situations.

In the present review, spin-up flows of an incompressible fluid will be dealt with. Spin-up of a stratified fluid and/or a compressible fluid is a separate topic, and a considerable body of research has been accumulated [2, 15, 17, 25, 30].

The longstanding problem areas in classical spin-up research may be summarized:

- (a) Nonlinear Ekman compatibility condition [19, 34],
- (b) Unifying the prediction of linear and nonlinear flow models [12, 28, 29],
- (c) On the viscous effects near the cylindrical sidewall [3, 19].

### General Problem Formulation

As stated previously, at the initial state, the rotation rate of the fluid and the cylindrical container is  $\Omega_i$ , and the rotation rate of the cylinder is increased instantaneously to  $\Omega_f$  [see figure 1]. The Rossby number,  $\varepsilon \equiv \Delta\Omega/\Omega_{ref}$ , where  $\Delta\Omega = \Omega_f - \Omega_i$ , is a measure of nonlinearity. Here, the reference rotation rate,  $\Omega_{ref}$ , is either  $\Omega_f$  or  $\Omega_i$ . For the nonlinear spin-up, it is convenient to set  $\Omega_{ref} = \Omega_f$ , and  $\Omega_i = (1 - \varepsilon)\Omega_f$ , as done in [28, 33]. In the case of a linear problem, it is customary to select  $\Omega_{ref} = \Omega_i$ ,  $\Omega_f = (1 + \varepsilon)\Omega_i$ , as in [11, 12]. In the present paper,  $\Omega_{ref} = \Omega_f$ , unless otherwise noted.

Nondimensionalization is made of the physical quantities of interest:

$$(r^*, z^*) = (r/H, z/H), \quad a^* = R/H, \quad t^* = t\Omega_{ref},$$

$$\vec{V}^* = \frac{\vec{V}}{\Omega_{ref}H}, \quad p^* = \frac{p}{\rho(\Omega_{ref}H)^2},$$

in which superscript  $*$  represents nondimensional quantities,  $t$  time,  $\vec{V}(\equiv(u, v, w))$  velocity vector in the (radial, azimuthal, axial) coordinate,  $\rho$  fluid density, and  $p$  pressure.

The governing time-dependent axisymmetric Navier-Stokes equations, in nondimensional form, are straightforward, after dropping  $*$ :

$$\frac{\partial u}{\partial t} + u \frac{\partial u}{\partial r} + w \frac{\partial u}{\partial z} - \frac{v^2}{r} = -\frac{\partial p}{\partial r} + E \left( \frac{\partial^2 u}{\partial r^2} + \frac{\partial}{\partial r} \left( \frac{u}{r} \right) + \frac{\partial^2 u}{\partial z^2} \right), \quad (1)$$

$$\frac{\partial v}{\partial t} + u \frac{\partial v}{\partial r} + w \frac{\partial v}{\partial z} + \frac{uv}{r} = E \left( \frac{\partial^2 v}{\partial r^2} + \frac{\partial}{\partial r} \left( \frac{v}{r} \right) + \frac{\partial^2 v}{\partial z^2} \right), \quad (2)$$

$$\frac{\partial w}{\partial t} + u \frac{\partial w}{\partial r} + w \frac{\partial w}{\partial z} = -\frac{\partial p}{\partial z} + E \left( \frac{\partial^2 w}{\partial r^2} + \frac{1}{r} \frac{\partial w}{\partial r} + \frac{\partial^2 w}{\partial z^2} \right). \quad (3)$$

In the above, the Ekman number  $E \equiv \nu / \Omega_{ref} H^2$ .

The associated initial and boundary conditions are stated:

$$u = v - (1 - \varepsilon)r = w = 0 \quad \text{at } t = 0; \quad (4a)$$

$$u = v - r = w = 0 \quad \text{at } z = \pm 1/2; \quad (4b)$$

$$u = v = \partial w / \partial r = 0 \quad \text{at } r = 0; \quad (4c)$$

$$u = v - a = w = 0 \quad \text{at } r = a. \quad (4d)$$

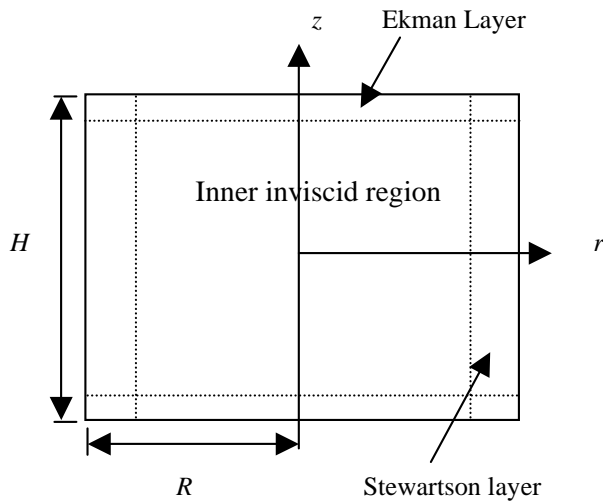


Figure 1. Coordinates and flow regime in the meridional plane

### Flow Regime

By inspecting the governing equations, the fact  $E \ll 1$  leads to the assertion that the overall flow field is of boundary-layer-type. It is advantageous to depict the character of the individual flow region [see figure 1].

### Horizontal Boundary Layers

The horizontal boundary layer, often termed the Ekman layer, forms near the (horizontal) endwall disks of the container. The fluid in this layer is propelled radially-outward due to the increased rotation rate ( $\Omega_i + \Delta\Omega$ ). This, in turn, causes suction in the axial direction of the inviscid interior fluid, which is known as the Ekman pumping. The crux of the argument is that, by way of the Ekman pumping, the rotating disk exerts control of the meridional (secondary) flow. The thickness of Ekman layer is scaled  $O(E^{1/2})$ , as can be inferred from the governing equations.

### Vertical Boundary Layer

The horizontal-propelled fluid flux in the Ekman layer, after reaching the vertical sidewall, is carried vertically along the cylindrical sidewall. Obviously, in order to meet the no-slip condition at the sidewall, a boundary layer is called for. This vertical boundary layer, which is termed the Stewartson layer, is to satisfy the no-slip condition for both the azimuthal and vertical directions. It has been established that the vertical layer consists of a double-layer structure, i.e.,  $O(E^{1/4})$ -layer for the azimuthal flow, and  $O(E^{1/3})$ -layer for the vertical flow. It should be mentioned that, in linear spin-up, the vertical boundary layer is less important in controlling the interior flow. However, in nonlinear spin-up, the influence of vertical layer is not insignificant in the determination of the interior fluid motion [1, 13].

### Inviscid Interior Region

For  $E \ll 1$ , the thicknesses of the above-stated boundary layers are thin and the bulk of the flow domain is essentially inviscid. In this region, the principal force balance is between the pressure gradient and Coriolis force. Also, the radial and azimuthal velocities are substantially uniform in the axial direction, i.e., the Taylor-Proudman column is maintained [8,9,10]. Thus, by treating the axial variations of flow properly, there is a possibility that the  $(r, z, t)$  dependent three-dimensional problem can be reformulated as a  $(r, t)$  dependent two-dimensional problem in the inviscid region.

### Linear Spin-up

Consideration is given to the transient flow when the rotation rate of the cylinder changes abruptly from  $\Omega_i$  to  $\Omega_f \equiv (1 + \varepsilon)\Omega_i$ . The problem is linearized under the assumption that the Rossby number  $\varepsilon \ll 1$ . In the original treatise of Greenspan and Howard [11], the governing equations were linearized under  $E \ll 1, \varepsilon \ll 1$ , and an analytical solution was secured by means of the Laplace transform. It should be pointed out that, in Greenspan & Howard [11], the reference rotation rate of the problem was chosen to be  $\Omega_i$ , not  $\Omega_f$ .

In a short duration  $t \sim O(\Omega_i^{-1})$  after the impulsive start-up of the cylinder, the Ekman boundary layer of thickness  $O(E^{1/2})$  is formed near the endwall disk of the cylinder. A complete mathematical solution is available for the linear Ekman layer, and the scales are  $u \sim O(\varepsilon), v \sim O(\varepsilon), w \sim O(\varepsilon E^{1/2})$ . Also, the axial variations of  $(u, v)$  are well-known spiral structure, as demonstrated in [10].

In the Ekman layer, the mass flux  $O(\varepsilon E^{1/2})$  of fluid is propelled radially outward, this sucks in the fluid in the inviscid interior. This creates an axial flow,  $w \sim O(\varepsilon E^{1/2})$ , which is termed the Ekman pumping, toward the disk. In the inviscid

interior, a concomitant radial flow,  $u \sim O(\varepsilon E^{1/2})$ , is induced. Therefore, in the inviscid interior, in order to satisfy angular momentum conservation, the angular velocity increases by way of vortex stretching, i.e., the spin-up process takes place. The bulk of interior fluid undergoes the spin-up process, and, therefore, the overall adjustment process is substantially accomplished over the spin-up timescale  $O(E^{-1/2})$ , not over the diffusion time scale  $O(E^{-1})$ .

The radial distance ( $d$ ) that a fluid parcel has travelled over the spin-up process is very small,  $O(\varepsilon)$ . This can be inferred from the fact that the distance is the product of the radial velocity scale  $u \sim O(\varepsilon E^{1/2})$  and the spin-up time scale  $O(E^{-1/2})$ .

The time-dependent velocity fields over the spin-up time scale (in the inertial frame) are described approximately [11]:

$$v = r + \varepsilon S(2t)r(1 - \exp(-E^{1/2}t)), \quad (5)$$

$$\Psi/\varepsilon = -rzE^{1/2}S(2t)\exp(-E^{1/2}t). \quad (6)$$

In which  $\Psi$  denotes the meridional stream function ( $u = \partial\Psi/\partial r, w = -\partial\Psi/\partial z$ ), and  $S(t)$  the Fresnel integral,

$$C(t) + iS(t) = \int_0^t (2\pi z)^{-1/2} \exp(iz) dz. \quad (7)$$

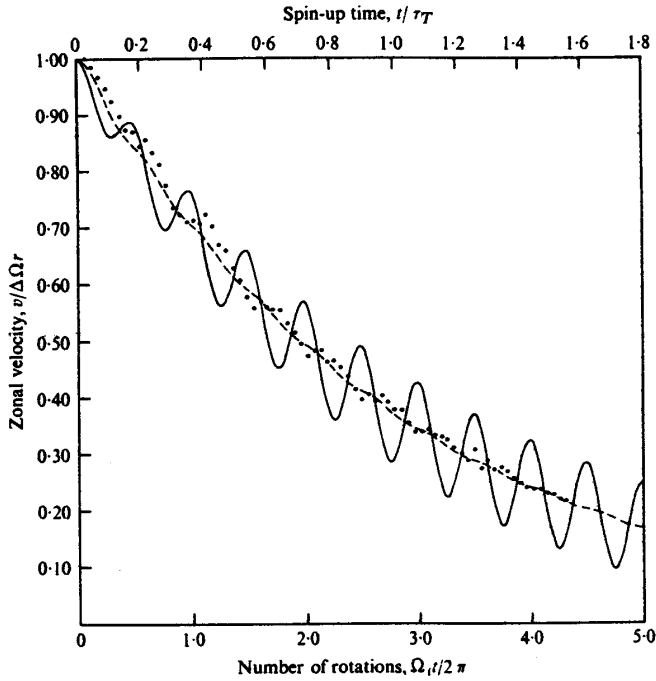


Figure 2. Comparison of the experiment results ( $E = 3.30 \times 10^{-3}, \varepsilon = 0.111$ ) with the analytical results of [11],  $\bullet \bullet \bullet$ , experimental data [31],  $-----$ , theory [eq.(3.18) of [11]],  $—————$ , approximate solution [eq.(5)], (printed from [31]).

The theoretical depiction of linear spin-up has since been validated by a multiple scaling analysis [28] as well as experiments [32] and numerical simulation [15] [see, see figure 2].

It is to be noted that the spin-up theory of Greenspan & Howard was developed under the assumption of two infinite disks. This also reinforces the observation that the role of the

cylindrical sidewall on the spin-up of interior fluid is insignificant. As remarked previously, the distance that a fluid parcel moves in the linear spin-up is  $d$ , which is much smaller than the thickness of vertical sidewall boundary layer  $O(E^{1/4})$ , i.e.,  $d \sim O(\varepsilon) \ll O(E^{1/4})$ . It implies that over the duration of spin-up, the fluid originating in the sidewall layer stays in this layer; the influence of the sidewall boundary layer is meager on the interior fluid. For the present closed container, however, the vertical boundary layer exists, and the structure of this layer has been a subject of another investigations [1, 14].

### Weakly Non-linear Spin-up

For  $\varepsilon$  small, but finite, Greenspan & Weinbaum [12] devised a nonlinear model from the afore-described linear model. They expressed the flow variable by series expansions of the Rossby number  $\varepsilon$ . In the course of analysis, due to the presence of the secular terms, the strained coordinate method by Poincare and Lighthill was introduced. Due to the complication in the analysis, expansions were obtained up to the second-order, i.e.,  $O(\varepsilon^2)$ . The result for the azimuthal velocity is shown :

$$v = r + \varepsilon(1 - \exp(-2\bar{t})) + O(\varepsilon^2), \quad (8)$$

$$\text{in which } E^{1/2}t = \bar{t} + \varepsilon\left(-\frac{1}{2}\bar{t} + \frac{2}{5}(1 - \exp(-2\bar{t}))\right). \quad (9)$$

This weakly nonlinear model of Greenspan & Weinbaum was shown to be consistent with the experiments in the range  $|\varepsilon| < 0.5$ .

Specifically, two issues are to be stressed:

- (1) Because of the nonlinear effect, in comparison to the linear theory, the time to reach the final state becomes shorter (longer) in spin-up (spin-down). Since the theory neglects the higher-order terms, it is not clear if the same conclusion is applicable when  $\varepsilon \sim O(1)$ . However, the later experiments and computations seem to be in support of the qualitative validity of the theory up to  $\varepsilon \sim O(1)$  [34]. It will be a challenge to supplement the theory to produce a more versatile analytical model [see figure 3].
- (2) As stated earlier, the theory of Greenspan and Weinbaum is for two infinite disks with no sidewall. Consequently, this theory is incapable of predicting the presence of the propagating velocity shear front which is a hallmark of nonlinear spin-up in a confined closed container. This is perhaps a more serious drawback of the theory [28, 29].

### Non-linear Spin-up

#### Wedemeyer Model ( $\varepsilon = 1.0$ )

An elegant theoretical model was put forth by Wedemeyer [33] about spin-up from rest ( $\varepsilon = 1.0$ ). In rapidly-rotating flow, the well-known axial uniformity of horizontal velocities in the inviscid interior (Taylor-Proudman column, i.e.,  $\partial u/\partial z = \partial v/\partial z = 0$ ) is exploited. A simplified equation for  $v$  is obtained:

$$\frac{\partial v}{\partial t} + u\left(\frac{\partial v}{\partial r} + \frac{v}{r}\right) = E\left(\frac{\partial^2 v}{\partial r^2} + \frac{\partial}{\partial r}\left(\frac{v}{r}\right)\right). \quad (10)$$

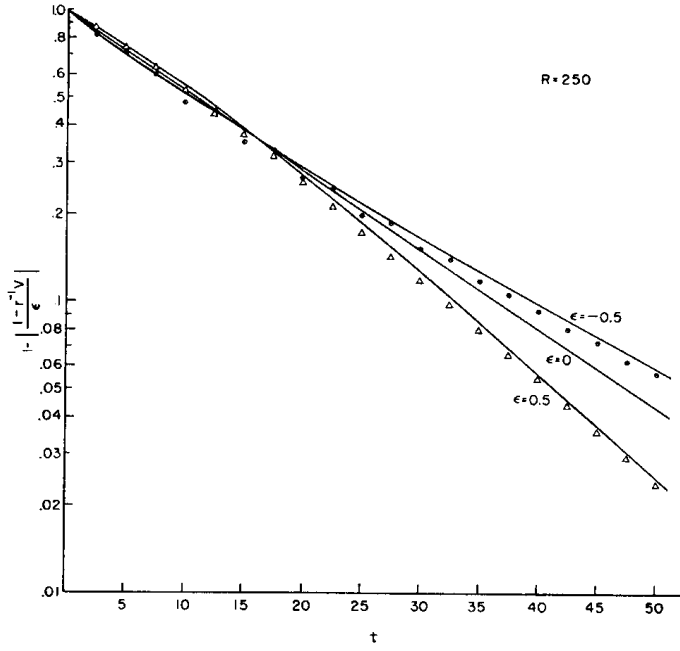


Figure 3. Comparisons between theory ( — ) of [11] and numerical data (  $\Delta$ ,  $\blacksquare$  ), ( printed from [12] ).

In order to solve the above equation, a relationship linking  $u$  and  $v$  is necessary. To this end, Wedemeyer made use of the numerical result of Rogers & Lance [23]. Furthermore, noting the inter-relations between the inviscid interior flow and the Ekman layer flow, Wedemeyer made the following assumptions:

- (a) the boundary layer flow is quasi-steady;
- (b) the finite geometry of the cylinder does not effect the boundary layer flux;
- (c) the interior fluid is in rigid-body rotation.

Combining the above assumption and the local similarity assumption based on the Rogers & Lance data, Wedemeyer arrived at an approximate relationship linking  $u$  and  $v$  :

$$u = E^{1/2}(v - r). \quad (11)$$

Substituting eq.(11) into eq.(10) yields

$$\frac{\partial v}{\partial \tau} + (v - r) \left( \frac{\partial v}{\partial r} + \frac{v}{r} \right) = E^{1/2} \left( \frac{\partial^2 v}{\partial r^2} + \frac{\partial}{\partial r} \left( \frac{v}{r} \right) \right). \quad (12)$$

Under  $E \ll 1$ , dropping the viscous terms in eq.(12) leads to

$$(i) \quad v = 0, w = 2E^{1/2}z, \quad (13a)$$

for the region ahead of the shear front, i.e.,  $r \leq ae^{-\tau}$

$$(ii) \quad v = \frac{1}{1 - \exp(-2\tau)} \left( r - \frac{a^2}{r} \exp(-2\tau) \right), \quad w = -\frac{2E^{1/2}z}{\exp(2\tau) - 1}, \quad (13b)$$

for the region behind the shear front, i.e.,  $r \geq ae^{-\tau}$ , where  $\tau = E^{1/2}t$ .

The Wedemeyer solution, Eq. (13a-b), successfully depicts much of the prominent flow characteristics. The existence of the propagating shear front and the global flow field and other nonlinear behavior are captured well in this model. However,

inconsistencies are discernible as well. For instance, the behavior of the Ekman pumping velocity  $w$  in both sides of the front is at variance with assumption (i). Also, the adoption of the numerical data of Rogers & Lance poses serious difficulty. According to the data of Rogers and Lance, the Ekman pumping takes place from the region of small angular velocity to that of large angular velocity. However, the Wedemeyer solution shows that, in the inviscid region behind the front ( $r \geq ae^{-\tau}$ ), the Ekman pumping is directed from the disk-region with a higher rotation rate to the inviscid-region with a lower rotation rate. These, and others, illustrate conflicting assumptions and solutions. Despite these shortcomings, the Wedemeyer solution provides overall flow pictures which are shown to be generally compatible with the numerical solutions [16, 18, 32]. The inconsistencies of Wedemeyer model have been pointed out [3, 16], but little serious efforts have been made to improve the fundamental foundation of the model.

#### Extension of the Wedemeyer Model ( $0 < \varepsilon \leq 1.0$ )

Expanding upon the approaches of Wedemeyer, Venezian [28-29] produced an analytical solution for the spin-up from a finite rotation rate ( $\Omega_i \neq 0$ ) to another finite rotation rate ( $\Omega_f \neq 0$ ) for  $0 < \varepsilon \leq 1.0$  :

$$v = \frac{r}{1 + \frac{\varepsilon}{1 - \varepsilon} \exp(-2\tau)} \quad (14a)$$

$$\text{at } r \leq a(1 - \varepsilon + \varepsilon \exp(-2\tau))^{1/2},$$

$$v = \frac{1}{1 - \exp(-2\tau)} \left( r - \frac{a^2}{r} \exp(-2\tau) \right) \quad (14b)$$

$$\text{at } r \geq a(1 - \varepsilon + \varepsilon \exp(-2\tau))^{1/2}.$$

The theoretical solution of Venezian demonstrates the salient nonlinear features for  $\varepsilon \sim O(1)$ , which include the spin-up from rest. However, difficulties are encountered as this solution attempts to recover the linear spin-up by letting  $\varepsilon \ll 1$ . In addition, it is unclear to come up with a physically convincing explanation about Wedemeyer's assertion that the propagating shear front represents the propagating of characteristic line.

One contribution of Venezian's model lies in the improved treatment of viscous terms in the vicinity of the front. Venezian, by a careful analysis of the thin viscous layer in the neighborhood of the shear front, gave a description of flow surrounding this front:

$$v = 4E^{1/4}(2\pi\eta)^{-1/2}(a\exp(\beta^2)\text{erfc}(\beta))^{-1}, \quad (15)$$

in which

$$\eta = \exp(2E^{1/2}t) - 1, \quad \beta^2 = a^2(r^2 \exp(2E^{1/2}t) - 1)^2 / 8E^{1/2}\eta, \text{ and } a \text{ being nondimensional radius of the container.}$$

The analytical solution of Venezian was shown to be generally compatible with the full Navier-Stokes numerical solutions, as displayed in figure 4. Clearly, the viscous solution of Venezian, in comparison to the Wedemeyer inviscid solution, is in better agreement with the numerical results. However, the discrepancies near the shear front are not in substantial.

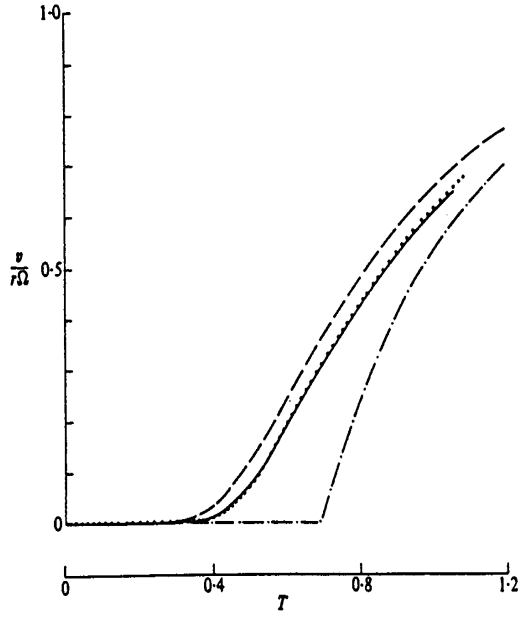


Figure 4. Time histories of azimuthal velocity ( $E = 9.18 \times 10^{-5}$ ). The vertical location is at mid-depth. The radial location is 0.5.  
 - - - - - , Wedemeyer's inviscid solution;  
 ———— , numerical results [16];  
 ..... , LDV measurements;  
 - . - . - , Venezian's profile [eq.(15)],  
 (printed from [16]).

### The Weidman Model

Weidman [34] noted that the linear Ekman pumping condition was the source of inconsistencies. From that standpoint, Weidman attempted to use a 7<sup>th</sup>-degree polynomial curve fitting to the numerical data of Rogers & Lance [23] [see figure 5].

$$\frac{\partial v}{\partial \tau} + F(v) \frac{\partial(rv)}{\partial r} = 0, \quad (16)$$

in which

$$F(s) = 4.8867s^7 - 21.06589s^6 + 38.23662s^5 - 38.45380s^4 \\ + 23.88193s^3 - 9.44264s^2 + 1.07258s + 0.88446.$$

Weidman [34] proceeded to make numerical integration and the results contained physically unrealistic flow descriptions near the shear front. In this connection, Benton [3] ascertained an inherent difficulty with the local similarity assumption in utilizing the data of Rogers & Lance [23]. The current trend is to find supplementary ideas to improve or refine the basic model of Wedemeyer. The recent endeavors by Konijnenberg & Heijst [19] also ascertained the need to modify the modeling of Ekman pumping.

### Concluding Remarks

The backbone of the modern study of spin-up is the Greenspan & Howard model of linear spin-up ( $\varepsilon \ll 1, E \ll 1$ ). The role of Ekman layer pumping, together with the meridional circulation, is clearly captured in the model. The overall transient process is accomplished over the spin-up time scale  $O(E^{-1/2}\Omega_f^{-1})$ .

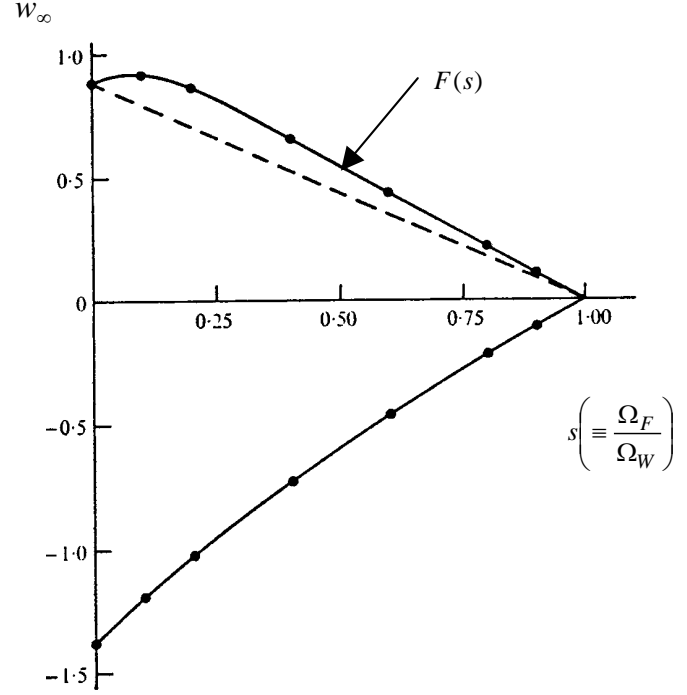


Figure 5. Nonlinear Ekman pumping velocity.  $w_\infty$  is Ekman pumping velocity at the boundary layer edge,  $\Omega_F$  angular velocity of the far-field fluid and  $\Omega_W$  angular velocity of the disk wall, (printed from [34]).

The expansion of the model to nonlinear ranges is a challenging issue. The limitation of the weakly nonlinear model is pointed out. The success and shortcomings of the Wedemeyer model ( $\varepsilon = 1.0$ ) are re-visited. The attempts to expand upon or improve this model are discussed.

The classical topic of spin-up is still alive, and some of the future directions are listed.

### References

- [1] Barcilon, V., Stewartson Layers in transient rotating fluid flows, *J. Fluid Mech.*, **33**, 1968, 815-825.
- [2] Bark, F.H., Meijer, P.S. & Cohen, H.I., Spin-up of a rapidly rotating gas, *Phys. Fluids*, **21**(4), 1978, 531-539.
- [3] Benton, E.R., Vorticity dynamics in spin-up from rest, *Phys. Fluids*, **22**, 1979, 1250-1251.
- [4] Benton, E.R. & Clark, J., Spin-up, *Ann. Rev. Fluid Mech.*, **6**, 1974, 257-280.
- [5] Cederlof, U., Free-surface effects on spin-up, *J. Fluid Mech.*, **187**, 1988, 395-407.
- [6] Cui, A. & Street, R.L., Large-eddy simulation of turbulence rotating convective flow development, *J. Fluid Mech.*, **447**, 2001, 53-84.
- [7] Duck, P.W. & Foster, M.R., Spin-up of homogeneous and stratified fluids, *Ann. Rev. Fluid Mech.*, **33**, 2001, 231-263.
- [8] Greenspan, H.P., On the transient motion of a contained rotating fluid, *J. Fluid Mech.*, **20**, 1964, 673-696.
- [9] Greenspan, H.P., On the general theory of contained rotating fluid motions, *J. Fluid Mech.*, **22**, 1965, 449-462.
- [10] Greenspan, H.P., *The theory of rotating fluids*, Cambridge Univ. Press, 1968.
- [11] Greenspan, H.P. & Howard, L.N., On a time dependent motion of a rotating fluid, *J. Fluid Mech.*, **17**, 1963, 385-404.
- [12] Greenspan, H.P. & Weinbaum, S., On nonlinear spin-up of a rotating fluid, *J. Math. & Phys.*, **44**, 1965, 66-85.

- [13] Heijst, G.J.F. van, The shear layer structure in a rotating fluid near a differentially rotating sidewall, *J. Fluid Mech.*, **130**, 1983, 1-12.
- [14] Heijst, G.J.F. van, Spin-up phenomena in non-axisymmetric container, *J. Fluid Mech.*, **206**, 1989, 171-191.
- [15] Hyun, J.M., Fowlis, W.W. & Warn-Varnas, A., Numerical solutions for spin-up of a stratified fluid, *J. Fluid Mech.*, **117**, 1982, 71-90.
- [16] Hyun, J.M., Leslie, F., Fowlis, W.M. & Warn-Varnas, A., Numerical solutions for spin-up from rest in a cylinder, *J. Fluid Mech.*, **127**, 1983, 263-281.
- [17] Hyun, J.M. & Park, J.S., Spin-up from rest of a compressible fluid in a rapidly rotating cylinder, *J. Fluid Mech.*, **237**, 1992, 413-434.
- [18] Kitchen, C.W.J., Navier-Stokes for spin-up in a filled cylinder, *AIAA J.*, **18**(8), 1980, 929-934.
- [19] Konijnenberg, J.A. van de & Heijst, G.J.F. van, Nonlinear spin-up in a circular cylinder, *Phys. Fluids*, **7**(12), 1995, 2989-2999.
- [20] Maars, L.R., Nonlinear and free-surface effects on the spin-down of barotropic axisymmetric vortices, *J. Fluid Mech.*, **246**, 1993, 117-141.
- [21] O'Donnell, J. & Linden, P.F., Free-surface effects on the spin-up of fluid in a rotating cylinder, *J. Fluid Mech.*, **232**, 1991, 439-453.
- [22] Reznik, G.M. & Grimshaw, R., Nonlinear geostrophic adjustment in the presence of a boundary, *J. Fluid Mech.*, **472**, 2002, 257-283.
- [23] Rogers, M.H. & Lance, G.N., The rotationally symmetric flow of a viscous fluid on the presence of an infinite rotating disk, *J. Fluid Mech.*, **7**, 1960, 617-631.
- [24] Saffman, P.G. & Baker, G.R., Vortex interactions, *Ann. Rev. Fluid Mech.*, **11**, 1979, 95-122.
- [25] Sakurai, T. Spin-down problem of rotating stratified fluid in thermally insulated circular cylinders, *J. Fluid Mech.*, **37**, 1969, 689-699.
- [26] Suh, Y.K. & Choi, Y.H., Study on the spin-up of fluid in a rectangular container using Ekman pumping models, *J. Fluid Mech.*, **458**, 2002, 103-132.
- [27] St-Maurice, J.P. & Veronis, G., A multiple-scaling analysis of the spin-up problem, *J. Fluid Mech.*, **68**, 1975, 417-445.
- [28] Venezian, G., Spin-up of a contained fluid, in *Topics in ocean engineering* editors C.I. Bretschneider, Gulf Publishing Co., 1969, 212-223.
- [29] Venezian, G., Nonlinear spin-up, in *Topics in ocean engineering* editors C.I. Bretschneider, Gulf Publishing Co., 1970, 87-96.
- [30] Walin, G. Some aspects of time-dependent motion of a stratified rotating fluid, *J. Fluid Mech.*, **36**, 1969, 289-307.
- [31] Warn-Varnas, A., Fowlis, W., Piaci S. & Lee, S.M., Numerical solutions and laser-Doppler measurements, *J. Fluid Mech.*, **85**, 1978, 609-639.
- [32] Watkins, W.B. & Hussey, R.G., Spin-up from rest: limitations of the Wedemeyer model, *Phys. Fluids*, **16**(9), 1973, 1530-1531.
- [33] Wedemeyer, E.H., The unsteady flow within a spinning cylinder, *J. Fluid Mech.*, **20**, 1964, 383-399.
- [34] Weidman, P.D., On the spin-up and spin-down of a rotating fluid. Part 1. & 2., *J. Fluid Mech.*, **77**, 1976, 685-735.

## The Energetics of Horizontal Convection

R. W. Griffiths and G. O. Hughes

Research School of Earth Sciences  
The Australian National University, Canberra ACT 0200, AUSTRALIA

### Abstract

Convection driven by a gradient of temperature or heat flux along one horizontal boundary produces a localized turbulent plume and an otherwise stably stratified circulation. Informed by laboratory observations of the steady-state convection, we examine the rate of production of available potential energy, rate of viscous dissipation and rate of conversion of turbulent kinetic energy to potential energy by vertical mixing. Given the heat flux through the flow, the requirement of a steady state in the interior determines the vertical turbulent diffusivity in the interior, and an expression is also found for the boundary layer thickness. Applied to the zonally-averaged meridional overturning of the oceans, where we allow for a turbulent transport coefficient at the sea surface, the energy arguments lead to a thermocline depth of 300 – 530m. For the estimated meridional heat flux of  $2 \times 10^{15}$  W, we predict an average diffusivity of  $\bar{\kappa}^* = O(10^{-5})$  m<sup>2</sup>/s, in agreement with measurements of vertical mixing. Also in agreement with previous estimates and ocean observations is the predicted rate of production of available potential energy ( $0.5 \times 10^{12}$  W), of which  $0.8 - 1.5 \times 10^{11}$  W is used to maintain the density structure.

### Introduction

Horizontal convection driven by a horizontal gradient of temperature or heat flux along the top or bottom boundary of a volume of fluid is remarkably different from the (more extensively studied) convection forced by a temperature difference applied between either two vertical boundaries or the bottom and top boundaries. In horizontal convection, the heat flux enters a horizontal boundary layer and is extracted at the same boundary, with little heat passing through the bulk of the interior of the volume. The heat flux is, however, achieved through a horizontal flow in the boundary layer. There must be a return flow, and in experiments using a monotonic temperature gradient along the base or surface of a rectangular box, this is observed to occur as a vertical buoyant plume at one end of the box, nearest the destabilizing heat flux [21, 22, 13]. The plume extends through the full depth of the box (although this aspect is sensitive to non-steady boundary conditions and side wall heat loss [13]). More gentle vertical flow, perhaps distributed through the volume, returns the fluid to the boundary layer in the region of stabilizing heat flux. The boundary layer dynamics have been described by Rossby [21]. However, it is not clear how the boundary fluxes drive a deep vigorous overturning, and how the interior maintains a steady state given an interior density stratification (or a buoyancy flux in the plume through all levels, as is required for the plume to penetrate through the depth). The global thermohaline circulation (or meridional overturning circulation) of the oceans is one possible, and particularly important, example of horizontal convection. Surface waters of the oceans are subject to net heating at equatorial latitudes (between approximately 20°S and 23°N based on a global annualized average) and to net cooling polewards of these latitudes [4]. The circulation of surface waters carries a net poleward transport of heat to maintain the balance, and highly localized downwelling at polar latitudes carries surface waters to abyssal depths [24, 21, 14, 19].

Much of the heat transport is a consequence of wind-driven surface flows. However, it is not clear whether the heat transport is passive [15, 5, 27, 28], or whether instead the thermal buoyancy flux associated with the meridional heat flux is a significant contribution to the driving forces in the momentum budget for the mean overturning flow. A separate question is whether the internal vertical mixing (which maintains the density structure of the oceans in the presence of the vertical components of the circulation) is substantially sustained by energy input from buoyancy-driven flow (hence by the heat flux) or whether the mixing is dominated by energy from tides and winds [14, 15, 5, 27, 28].

In current diffusive theories of the meridional overturning circulation the density structure throughout much of the ocean is maintained by a balance between slow upwelling of cold water and downward turbulent mixing of heat, for which the required vertical diffusivity (at least at depths between 1000m and 3000m) is of  $O(10^{-4})$  m<sup>2</sup>/s [14, 15]. The enormous amounts of mechanical energy (of order  $2 \times 10^{12}$  W) required to maintain such a large rate of vertical mixing are available only from the tides and the surface winds [15]. Consequently, it has been argued [5, 27, 28] that the thermal buoyancy cannot be the dominant driving force for the overturning circulation and that heat stored in the relatively warm equatorial surface waters must be carried passively towards high latitudes by the circulation. However, the argument appears to confuse the forces providing momentum to the mean overturning flow with sources of energy for the vertical mixing.

Dissipation and tracer measurements in the ocean interior [3, 9, 7, 12] on the other hand support a much smaller vertical diffusivity (of order  $10^{-5}$  m<sup>2</sup>/s) than that required by existing models. Recent data [23] also suggest that the basin-averaged diffusivity is less than a factor of three above that in the interior, despite the discovery of regions of very intense turbulence associated with topography [20, 10, 8]. Here we show that, given the estimated meridional heat flux in the oceans, a simple and self-consistent energy argument predicts both a mechanical energy flux in agreement with general circulation models and inferences from data, and a vertical diffusivity in agreement with measurements in the ocean interior. We conclude that the observed circulation can be driven by buoyancy fluxes at the surface and need not be reliant on energy input to mixing from winds and tides. A dynamical model and solution for the circulation is also required to demonstrate that a flow satisfying the energy requirements is possible and consistent with observations, and this will be presented elsewhere.

### Available Potential Energy Fluxes due to Surface Heating

In order to discuss the mechanical energy supplied to a box of fluid by differential heating along the surface (figure 1) we divide the flow driven into two regions – the surface boundary layer and the interior. Water in a portion of the surface boundary layer of depth  $h$  is supplied with heat at a rate  $q_h$  while heat is removed from the remainder of the surface waters at a rate  $q_c$  ( $= -q_h$ ). While we choose to describe the circulation in terms of the heat flux carried, this does not imply any particular boundary condition on heat flux or temperature. The hor-

horizontal variation of heat flux gives rise to a horizontal density gradient and flow (at a velocity  $u$ ) within the surface layer. The consequent horizontal mass flux in the boundary layer must be ejected into the interior for heat throughput to be maintained in the flow. Mass is returned to the surface boundary layer by a broad upwelling from the interior, as shown in figure 1. The boundary layer thickness  $h$ , which characterizes both the velocity and thermal structure, is therefore set by a balance between downward diffusion of heat from the surface and upward advection. Thus, conservation of heat in the boundary layer requires that

$$q_h = -q_c \sim \rho_r c_p \kappa_b A_h \frac{\delta T}{h} \sim \rho_r c_p \frac{A}{L} \delta T u h, \quad (1)$$

where  $\delta T$  characterizes both the vertical and horizontal temperature variation in the surface boundary layer,  $A$  and  $L$  are the cross-sectional area and length of the box, respectively,  $A_h$  is the cross-sectional area over which heating is applied,  $\kappa_b$  is the thermal diffusivity in the boundary layer,  $c_p$  is the specific heat, and  $\rho_r$  is a reference density. If the vertical velocity is zero at the surface ( $z = 0$ ) and  $h \ll L$  (an assumption that will be justified in the next section), the equations of continuity and heat transport require that

$$\frac{u}{L} \sim \frac{w}{h} \sim \frac{\kappa_b}{h^2}. \quad (2)$$

Observations from laboratory experiments and numerical solutions for horizontal convection show that the ejection of mass flux from the surface boundary layer occurs in a localized plume [21, 22, 18, 13], the dynamics of which we will examine below. For the moment it is necessary only to realise that water in the plume must be negatively buoyant to be ejected into the interior. Diffusion in the interior, together with zero flux conditions on the sidewalls and lower boundary, ensures that the flow is in a steady state only if the plume penetrates to the bottom [13]. The temperature variation in the plume required to drive this flow is denoted as  $\delta T'$ , which must also characterize the temperature variation in the interior. As water in the plume is relatively dense, the box has an amount of *available potential energy* (APE) equal to the potential energy that would be released by letting the fluid adjust adiabatically to static equilibrium. If  $\alpha$  is the coefficient of thermal expansion and  $g$  the gravitational acceleration, the buoyancy flux in the plume is  $F' = \rho_r g \alpha \delta T' u h A / L$  and represents the rate at which excess weight appears in the plume at the base of the boundary layer. As the plume falls through a depth  $H - h$  in reaching its level of neutral buoyancy, by equation (1) APE is generated at a rate

$$\dot{P}' \sim (H - h) F' = \frac{\alpha g (H - h) q_c}{c_p} \frac{\delta T'}{\delta T}, \quad (3)$$

where we have assumed the space occupied by the plume to be much less than the total volume of the box.

### Turbulent Mixing Energized by Convection

We now consider the dissipation of energy, which for a steady state exactly balances the supply of mechanical energy (equation 3). It has been shown [18, equation 3.4] that in a box of Boussinesq fluid forced only by a temperature difference (or heat flux) imposed along its top boundary, the volume-averaged rate of viscous dissipation of energy per unit mass,  $\bar{\epsilon}$ , is given by

$$\bar{\epsilon} = \kappa_b g \alpha \Delta \bar{T} / H, \quad (4)$$

where the uptake of heat at the boundary is characterized by the diffusivity  $\kappa_b$ , (which was assumed to be the molecular diffusivity), and  $\Delta \bar{T}$  is the temperature difference between horizontal averages at the top and bottom of the box. This result (equation 4) implies that the flow cannot be turbulent in the limit of

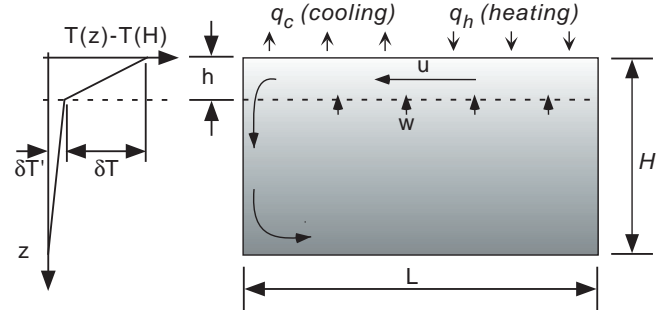


Figure 1: Schematic diagram of the convective flow driven in a box by differential heating along a horizontal boundary. Surface heat fluxes  $q_c$  and  $q_h (= -q_c)$  transfer heat to/from the boundary layer adjacent to the surface, maintaining a horizontal density gradient and a flow directed from the heated region to the cooled region. For sufficiently large heat fluxes most of the temperature variation occurs across the surface boundary layer, which occupies a small fraction of the total depth.

vanishing diffusivity or infinite fluid depth [18]. For density-stratified flow the vigour of turbulence can be measured by the parameter  $\epsilon / \nu N^2$ , where  $\epsilon$  is the local rate of viscous dissipation per unit mass,  $N = [-g\alpha(dT/dz)]^{1/2}$  is the local buoyancy frequency characterizing the density stratification and  $z$  is the depth [1]. Hence from equation (4), for general values of the diffusivity, horizontal convection in water must have a volume averaged  $\bar{\epsilon} / \nu N^2 \approx \kappa_b / \nu$ , which  $\sim 0.1$  if  $\kappa_b$  is set equal to the molecular diffusivity  $\kappa$ , no matter what the depth or heat flux. This value implies very weak or no turbulence [1].

On the other hand, equation (3) shows that for an imposed heat flux the total dissipation in the box (which must be equal to the mechanical energy input) increases in proportion to the heat flux  $q_c$  and depth  $H$ , and is independent of the viscosity and molecular diffusivity. The average dissipation per unit mass is therefore independent of  $H$  and inversely proportional to the area  $A$ . There is an apparent inconsistency with the results from equation (4). However, the value of  $\bar{\epsilon} / \nu N^2$  obtained above from equation (4) is based on the overall depth-averaged buoyancy frequency. Hence, the constraints imposed by equations (3) and (4) may both be satisfied if for a given fluid (water) we propose that below the surface layer ( $z > h$ ) the density gradient becomes small and the flow becomes turbulent when  $h \ll H$  (whereas for very large horizontal area, the temperature difference and dissipation rate vanish). Our later scaling analysis will indicate when this a priori assumption is invalid. We again characterize turbulent mixing in the density-stratified interior by a vertical diffusivity  $\kappa^*$  and use the usual relationship [17, 3, 7]

$$\kappa^* = \eta \left( \frac{\epsilon}{N^2} \right), \quad (5)$$

where  $\eta$  can be interpreted as the ratio of the turbulent energy used for vertical mixing to the energy dissipated by viscosity. The ratio  $\eta$  is commonly taken to be 0.2 [17], but an alternative formulation for weak turbulence [1] gives  $\eta = 0.47$  based on the molecular properties of seawater. The volume-averaged rate of viscous dissipation per unit mass will be given by

$$\bar{\epsilon} \approx \bar{\epsilon}' = \frac{1}{V'} \int_{V'} \epsilon dV' = \frac{\kappa_i^* g \alpha \delta T'}{\eta (H - h)}, \quad (6)$$



where  $V'$  is the volume of the interior (excluding the surface layer) and  $\bar{\epsilon}'$  is the volume-averaged rate of viscous dissipation per unit mass in the interior. We have assumed the cross-sectional area  $A$  to be independent of depth and defined an averaged interior diffusivity  $\kappa_i^*$  (which applies below the boundary layer). Setting equations (4) and (6) to be equal gives

$$\kappa_i^* = \kappa_b \eta \left( \frac{\overline{\Delta T}}{\delta T'} \right) \left( \frac{H-h}{H} \right). \quad (7)$$

The total rates  $\dot{W}'_{pe}$  and  $\dot{W}'_{ke}$  at which work is done by turbulence in the interior against gravity and against viscosity, respectively, can be summed to give the total rate of working

$$\begin{aligned} \dot{W}' &= \dot{W}'_{ke} + \dot{W}'_{pe} \\ &= \rho_r \int_{V'} \epsilon dV' + g \int_{V'} \kappa_i^* \frac{d\rho}{dz} dV' \\ &= g A \kappa_i^* \frac{1+\eta}{\eta} [\bar{\rho}(H) - \bar{\rho}(h)], \end{aligned} \quad (8)$$

where  $\rho$  is the density in the interior and the overbar denotes a horizontal average. Setting  $\dot{W}'$  in equation (8) equal to  $\dot{P}'$  in equation (3), along with  $\rho = \rho_0 [1 - \alpha(T - T_0)]$ , and then using equation (1) gives

$$\begin{aligned} \kappa_i^* &\sim \left( \frac{\eta}{1+\eta} \right) \left( \frac{(H-h)q_c}{\rho_r c_p A \delta T} \right) \\ &= \kappa_b \left( \frac{\eta}{1+\eta} \right) \left( \frac{H-h}{h} \right) \frac{A_h}{A}, \end{aligned} \quad (9)$$

where  $\delta T = \bar{T}(0) - \bar{T}(h) = \overline{\Delta T} - \delta T'$ . Combining equations (7) and (9) gives the temperature variation in the interior

$$\frac{\delta T'}{\overline{\Delta T}} \sim \frac{h}{H} (1+\eta) \frac{A}{A_h}. \quad (10)$$

By equations (7), (9) and (10), the assumption of a turbulent interior (where  $\kappa_i^* > \kappa$ ,  $\kappa_b \geq \kappa$ ) is seen to be valid when the surface boundary layer depth is much smaller than the basin depth, i.e.  $h/H \ll 1$ . The temperature drop  $\delta T$  across the surface boundary layer is then almost the same as the top-to-bottom temperature difference  $\overline{\Delta T}$ , where  $\delta T$  and  $h$  satisfy equation (1). As  $H/L < 1$  for the small aspect ratio basin geometry assumed here, the earlier assumption  $h/L \ll 1$  will be automatically satisfied. The interior flow will become non-turbulent at sufficiently small heat fluxes, as given by equation (1) when the surface boundary layer occupies the full depth. The molecular viscous stresses dissipate energy per unit mass at a rate given by equation (4), which in the non-turbulent flow is also equal to the rate of energy input required to maintain the density field by molecular diffusion.

Applying the results to the experiments of Mullarney *et al.* [13], where the boundary layer at the forcing boundary was laminar, we consider the case  $q_c = 140\text{W}$ , in which  $\delta T \sim \overline{\Delta T} \approx 17^\circ\text{C}$ . Here equations (1), (9) and (10) predict  $h \sim 0.007\text{m}$ ,  $\kappa_i^* \sim 0.4 - 0.7 \times 10^{-6} \text{ m}^2/\text{s}$  and  $\delta T' \sim 1.4 - 1.7^\circ\text{C}$  (for  $\eta = 0.2 - 0.47$ ). From equations (4) and (7),  $\bar{\epsilon}/vN_i^2 = \kappa_i^*/v\eta \sim \text{O}(3)$ , which indicates very weak turbulence in the interior and a diffusivity 3 to 5 times the molecular value for heat ( $A = 2A_h = 0.1875 \text{ m}^2$ ,  $L = 1.25 \text{ m}$ ,  $H = 0.2 \text{ m}$ ,  $\kappa = 1.47 \times 10^{-7} \text{ m}^2/\text{s}$ ,  $\rho_r = 1000 \text{ kg/m}^3$ ,  $c_p = 4184 \text{ J/kg/K}$ ,  $v = 7.6 \times 10^{-7} \text{ m}^2/\text{s}$ ). These predictions compare reasonably well with measurements:  $h = \text{O}(0.01) \text{ m}$  and  $\delta T'$  in the range  $0.34 - 3.5^\circ\text{C}$ , noting that the actual edge of the boundary layer is not well-defined and that the temperature profiles were not taken in the plume itself.

In applying the results to the oceans, we first note that equation (1) would predict the surface boundary layer (i.e. thermocline) thickness to be only a few metres based on a molecular thermal diffusivity. Instead, we expect a turbulent thermocline whose properties are determined primarily by wind-driven processes. Thus if the effective diffusivity in the thermocline is  $\kappa_b (\gg \kappa)$ , the volume-averaged viscous dissipation per unit mass  $\bar{\epsilon}_o$  throughout the oceans is then a factor of  $1/\eta$  larger than when the buoyancy uptake at the surface is by molecular diffusion (equation 4 with  $\kappa_b = \kappa$ ),

$$\bar{\epsilon}_o = \frac{\kappa_b g \alpha \overline{\Delta T}}{\eta H}. \quad (11)$$

Viscous dissipation by turbulence in the thermocline must also be allowed for in the energy budget. Equating the total viscous dissipation rate to the sum of the viscous dissipation rates in the interior and thermocline,

$$\int_V \bar{\epsilon}_o dV = \int_{V'} \epsilon dV' + \int_{V_b} \epsilon dV_b, \quad (12)$$

and substituting equation (5) gives

$$\kappa_b \overline{\Delta T} = \kappa_i^* \delta T' + \kappa_b \delta T, \quad (13)$$

where  $V_b$  is the volume incorporating the thermocline. Noting that  $\overline{\Delta T} = \delta T + \delta T'$ , equation (13) requires that the diffusivity is uniform throughout the flow, i.e.  $\kappa_b = \kappa_i^*$ . Physically this is because the diffusivity in the boundary layer is set by the external energy supplied (mainly from wind-driven turbulence). The total rate of working in the interior is still given by equation (8), but replacing  $\kappa$  with  $\kappa_b$  in equation (9) leads to the surprising conclusion that the thermocline thickness in this convection model is set by geometrical considerations alone, i.e.

$$\frac{h}{H} = \frac{A_h/A}{A_h/A + (1+\eta)/\eta}. \quad (14)$$

If heating is applied over one half of the surface area, as is approximately the case for the oceans ( $A_h/A = 0.5$ ), equation (14) predicts  $h/H \sim 0.08 - 0.14$  for  $\eta = 0.2 - 0.47$ . Substituting equation (14) into equation (1) and taking  $\alpha \delta T \approx \delta \rho / \rho_r$  gives

$$\kappa_i^* \delta \rho = \frac{\alpha q_c H}{c_p A [A_h/A + (1+\eta)/\eta]}, \quad (15)$$

where  $\delta \rho = \bar{\rho}(h) - \bar{\rho}(0)$ . It can also be shown using equation (5) that the density ratio

$$\frac{\delta \rho'}{\delta \rho} = \frac{\bar{\epsilon}'(H-h)}{\bar{\epsilon}_b h}, \quad (16)$$

where  $\delta \rho' = \bar{\rho}(h) - \bar{\rho}(H)$  and  $\bar{\epsilon}'$  and  $\bar{\epsilon}_b$  are the volume-averaged rates of dissipation per unit mass in the interior (equation 4) and the thermocline, respectively.

As  $\delta \rho' + \delta \rho = \bar{\rho}(0) - \bar{\rho}(H)$ , equation (16) would now close the problem if we knew the rate at which external energy was supplied to turbulence in the thermocline. However, without an estimate of this external input, we can only show that this scaling is consistent with measurements from the oceans. Taking  $H = 3780 \text{ m}$ , the average depth of the oceans [2], equation (14) predicts  $h$  to be  $300 - 530 \text{ m}$ . Using the globally averaged potential density profile from the Levitus 1994 dataset to estimate  $\delta \rho'$  and  $\delta \rho$  for the predicted thermocline depth (<http://iridl.ldeo.columbia.edu/SOURCES/LEVITUS94/>), we find  $\delta \rho' \sim 1.1 - 0.7 \text{ kg/m}^3$ ,  $\delta \rho \sim 2.0 - 2.4 \text{ kg/m}^3$  (for  $\eta = 0.2 - 0.47$ ). By equation (15), we then predict the diffusivity

$\kappa_i^* = \kappa_b = 2 - 3.2 \times 10^{-5} \text{ m}^2/\text{s}$ . This agrees nicely with available measurements of vertical mixing [23]. We have taken the total heat loss  $q_c$  from the oceans to be approximately  $4 \times 10^{15} \text{ W}$  ([4, p. 212], and inferred from hydrographic data, [11]), the surface area of the oceans  $A = 3.6 \times 10^{14} \text{ m}^2$  [2],  $\rho_r \sim 1025 \text{ kg/m}^3$ ,  $c_p \approx 3990 \text{ J/kg/K}$  for seawater at  $20^\circ\text{C}$  and atmospheric pressure [2] and  $\alpha = 2.54 \times 10^{-5} \text{ K}^{-1}$  for seawater at  $-2^\circ\text{C}$  [2], a temperature representative of the Weddell Sea outflow source water. Furthermore we predict that turbulence in the oceans has an intensity  $\bar{\epsilon}'/vN_i^2 = \bar{\epsilon}/vN^2 = \kappa_i^*/v\eta = \mathcal{O}(80)$ . However, we have not yet considered the sinking regions, where there will be a larger-than-average dissipation rate.

### Energy Fluxes in a Simple Circulation Model and Application to the Oceans

The above arguments are now applied to the ocean overturning by adopting an analytically more convenient model for the near-surface flow, a simple assumption about the interior flow, and recognising the deep sinking leg as a turbulent plume. Although the plume of interest in the oceans will be a slope current supplied by overflow from a sill, we discuss the simpler case of a vertical three-dimensional plume as shown in figure 2, where the plume originates at the surface. We first demonstrate that the energetics governing this situation are the same as those discussed for the more complex flow in figure 1. The structure of the surface layers in the oceans is more complicated than that sketched in figure 1. Heat transfer across the air-sea interface is not simply by molecular conduction, but also involves a combination of radiative and evaporative transfer, wave action and turbulence. We have demonstrated that the heat transfer in the water column is strongly influenced by external energy input (most probably through wind-driven turbulence). However, as we will show, forcing of the abyssal circulation is a result of the surface buoyancy flux.

We assume that the thermal forcing is constant on the overturning timescale. The rate of heat loss at the surface  $q_c$  produces a total buoyancy flux

$$F_T = \frac{\alpha g q_c}{c_p} \quad (17)$$

that is the sum of buoyancy fluxes over all regions of deep downwelling, which we assume to be plumes (we later assume that these are turbulent, but this restriction is not required at this stage). The rate of generation of APE at any level is equal to the local buoyancy flux multiplied by the distance the plume still has to fall. Thus, for the plume in figure 2 that falls through a depth  $D$ ,

$$\dot{P} = DF = \frac{\alpha g D q_c}{c_p}. \quad (18)$$

If this plume falls to the bottom,  $D = H$ . The flux of APE reduces rapidly through the surface layers to be equal to equation (3) at a depth  $z = h$ . Thus it is apparent that very little residual APE is required to drive the abyssal circulation. We proceed by applying the results for the abyssal circulation in figure 1 to the flow in figure 2 and we justify below why this approximation is valid.

Deep convection occurs in both the northern and southern hemispheres, but surface waters sink to the greatest depth at sites around the Antarctic to form Antarctic Bottom Water (AABW). Surface waters that sink in the north Atlantic are found in the abyssal ocean at levels above the AABW. This is consistent with the prediction, for turbulent plumes, that the plume with the greatest buoyancy flux reaches the bottom and dominates the density structure [6, 26]. From equation (18), this plume will also make the dominant contribution to the total  $\dot{P}$ . Therefore, we consider the flow due to a single southern hemisphere

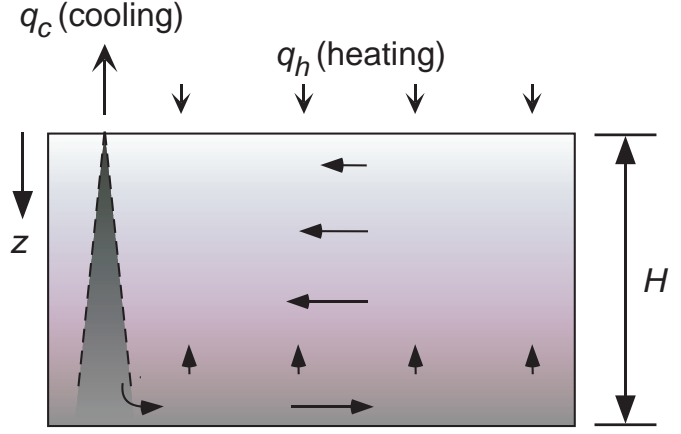


Figure 2: Schematic diagram of a model for horizontal convection (and the meridional overturning circulation of the oceans). Surface cooling at a rate  $q_c$  leads to a small region of downwelling (represented as a vertical plume) from the surface to the bottom in an idealized basin of depth  $H$  and cross-sectional area  $A$ . Heating at a rate  $q_h = -q_c$  is distributed over the surface allowing the flow to reach a steady state. Only one downwelling (that with greatest buoyancy flux in the oceans) is shown. If the sinking is turbulent, entrainment drives recirculation at depth.

plume as a first approximation to the global ocean (figure 2). Equations (17) and (18) predict that the southern hemisphere heat loss  $q_c$  of approximately  $2 \times 10^{15} \text{ W}$  [4, 11], leads to a buoyancy flux of  $F_T \approx 1.2 \times 10^8 \text{ N/s}$  (or equivalently, after dividing by the density,  $1.2 \times 10^5 \text{ m}^4/\text{s}^3$ ), and APE generation at a rate of  $\dot{P} \approx 0.47 \times 10^{12} \text{ W}$ . We have taken  $D = H = 3780 \text{ m}$ ,  $g = 9.81 \text{ m/s}^2$  and properties for seawater as given earlier. The coefficient of expansion is strongly temperature dependent, but we have used that for seawater at  $-2^\circ\text{C}$  ( $\alpha = 2.54 \times 10^{-5} \text{ K}^{-1}$  [2]) because the generation of available potential energy that may drive turbulence in the interior will be determined primarily by the density difference in the interior.

This predicted rate of APE generation compares with values calculated for the global ocean from an ocean general circulation model ( $0.3 \times 10^{12} \text{ W}$  [25]) and from observations of the density distribution and fluxes of heat and water at the surface ( $1.4 \pm 0.8 \times 10^{12} \text{ W}$  [16]). The latter value is based on small density gradients in the surface mixed layer and is likely to be an over-estimate [25]. The definition of the rate of generation (or flux) of potential energy (equation 18) avoids any estimates of the actual APE in the flow, and therefore does not require discussion of a reference energy state. Note, by equation (18), that the potential energy flux through the system is several thousand times smaller than the heat energy flux from which it arises, but that only the potential energy flux is of dynamical significance in the energy budget of the overturning circulation. In order to calculate the overturning circulation that could be supported by the input of available potential energy calculated above, let us assume that all of  $\dot{P}$  is converted to kinetic energy and that turbulent mixing in the density-stratified ocean is characterized by a vertical diffusivity  $\kappa^*$  that is the same at any point for heat, salt and, with a linear equation of state, also density [15]. For the situation in figure 2, the total rate of working by turbulence against gravity and against viscosity evaluates to

$$\dot{W} = \rho_r \int_V \epsilon dV + g \int_V \kappa^* \frac{d\rho}{dz} dV \quad (19)$$

$$= g A \kappa^* \frac{1 + \eta}{\eta} [\bar{\rho}(H) - \bar{\rho}(0)], \quad (20)$$

where  $V$  is the full volume (cf. equation 8). For a simple first

approximation to the oceans, we have again assumed the cross-sectional area  $A$  to be independent of depth and defined an average diffusivity  $\bar{\kappa}^*$  over the whole volume. Horizontal transports in the oceans are typically large enough to achieve horizontal density differences over most of the basin that are much smaller than the vertical difference [15], and we have implicitly assumed this to be the case. Recalling that  $\overline{\Delta T} = \delta T + \delta T'$ , equations (3), (8), (18) and (19) give

$$\frac{\dot{P}'}{\dot{P}} = \frac{(H-h)}{H} \frac{\overline{\Delta T}}{\delta T} \frac{\bar{\kappa}^*}{\kappa_i^*} \frac{\dot{W}'}{\dot{W}} \approx c \frac{\dot{W}'}{\dot{W}}. \quad (21)$$

For a laminar surface boundary layer with  $h \ll H$ ,  $\bar{\kappa}^*$  can be estimated by a volume average over the interior and boundary layer (i.e.  $H\bar{\kappa}^* = h\kappa_b + (H-h)\kappa_i^*$ ) and equations (7), (9) and (10) give  $c \approx 1$  in equation (21). For the turbulent surface boundary layer in the oceans,  $c \approx 1.1$  ( $\eta = 0.47$ ) –  $1.4$  ( $\eta = 0.2$ ), using our earlier scaling results and  $\bar{\kappa}^* = \kappa_i^*$ . Thus equation (21) shows that although the rate of energy generation  $\dot{P}$  in figure 2 is greater than the rate  $\dot{P}'$  for figure 1, the rate of dissipation  $\dot{W}$  in figure 2 is correspondingly greater than  $\dot{W}'$  for figure 1. Therefore,  $\dot{P} - \dot{P}' \approx \dot{W} - \dot{W}'$ , implying that the additional energy generated in the surface layer in figure 2 is also dissipated locally in the surface layer. Thus we expect the abyssal flows in figures 1 and 2 to be governed by equivalent energetics, and to not depend strongly on the detailed structure of the surface layers.

Equating  $\dot{W}$  in equation (19) to  $\dot{P}$  in equation (18) gives

$$\bar{\kappa}^* = \left( \frac{\eta}{1+\eta} \right) \left( \frac{\alpha q_c H}{Ac_p \Delta \bar{\rho}} \right) \quad (22)$$

where  $\Delta \bar{\rho} = \bar{\rho}(H) - \bar{\rho}(0)$ . Using the above values for the southern hemisphere heat flux, the surface area and average depth of the oceans, the molecular properties of seawater, and the bottom-to-surface density difference from the globally averaged potential density ( $\sigma_\theta$ ) profile obtained from the Levitus 1994 dataset ( $\bar{\rho}(H) - \bar{\rho}(0) = 3.1 \text{ kg/m}^3$ ), we again predict that turbulence could be supported in the ocean interior with an average diffusivity of  $\bar{\kappa}^* = 0.7 \times 10^{-5} \text{ m}^2/\text{s}$  ( $\eta = 0.2$ ) or  $1.4 \times 10^{-5} \text{ m}^2/\text{s}$  ( $\eta = 0.47$ ). Although buoyancy is not expected to be the only energy source, these predictions are remarkably consistent with measurements of  $\bar{\kappa}^* = O(10^{-5}) \text{ m}^2/\text{s}$  in the ocean interior [3, 9, 7, 12] and with the recent estimates of basin average diffusivities [23]. Of the available potential energy generated,  $0.8 - 1.5 \times 10^{11} \text{ W}$  is used to maintain the density structure.

## Conclusions

Our theoretical analysis of the energetics of horizontal convection is consistent with our recent laboratory experiments [13], and is also consistent with the dissipation theorem of Paparella & Young [18] in the case of a laminar surface boundary layer. The energy budget for the flow, along with a common-place relationship between turbulent mixing and viscous dissipation rates, leads to a prediction of the average interior mixing rate that is consistent with the measured ocean value. In this model, turbulent mixing in the interior is sustained as a consequence of the requirement that the upward diffusive buoyancy flux match the downward buoyancy flux in the sinking region. Thus the abyssal density gradient adjusts to allow sufficient vertical mixing. Among the factors that have not been taken into account is the seasonal salinity excess beneath sea ice, which will add to the buoyancy forcing at periods of maximum buoyancy flux. The tides and surface winds also will augment the buoyancy-driven circulation calculated here by supplying energy to interior turbulence (at a rate that is poorly known), which increases

the buoyancy uptake in the upper ocean. The spatial distribution of mixing from all three energy sources remains an open question.

## References

- [1] Barry, M. E., Ivey, G. N., Winters, K. B. and Imberger, J., Measurements of diapycnal diffusivities in stratified fluids, *J. Fluid Mech.*, **442**, 2001, 267–291.
- [2] Gill, A. E., *Atmosphere-Ocean Dynamics*, Academic Press, London, England, 1982.
- [3] Gregg, M. C., Scaling turbulent dissipation in the thermocline, *J. Geophys. Res.*, **94**, 1989, 9686–9698.
- [4] Houghton, J. T., Meira Filho, L. G., Callander, B. A., Harris, N., Kattenberg, A. and Maskell, K., *Climate change 1995: The science of climate change*, Cambridge University Press, Cambridge, England, 1996.
- [5] Huang, R. X., Mixing and energetics of the oceanic thermohaline circulation, *J. Phys. Oceanogr.*, **29**, 1999, 727–746.
- [6] Killworth, P. D. and Turner, J. S., Plumes with time-varying buoyancy in a confined region, *Geophys. Astrophys. Fluid Dyn.*, **20**, 1982, 265–291.
- [7] Kunze, E. and Sanford, T. B., Abyssal mixing: where is it not?, *J. Phys. Oceanogr.*, **26**, 1996, 2286–2296.
- [8] Ledwell, J. R., Montgomery, E. T., Polzin, K. L., Laurent, L. C. S., Schmitt, R. W. and Toole, J. M., Evidence for enhanced mixing over rough topography in the abyssal ocean, *Nature*, **403**, 2000, 179–182.
- [9] Ledwell, J. R., Watson, A. J. and Law, C. S., Evidence for slow mixing across the pycnocline from an open-ocean tracer release experiment, *Nature*, **364**, 1993, 701–703.
- [10] Lueck, R. G. and Mudge, T. D., Topographically induced mixing around a shallow seamount, *Science*, **276**, 1997, 1831–1833.
- [11] Macdonald, A. M., The global ocean circulation: a hydrographic estimate and regional analysis, *Prog. Oceanogr.*, **41**, 1998, 281–382.
- [12] Matear, R. J. and Wong, C. S., Estimation of vertical mixing in the upper ocean at Station P from chlorofluorocarbons, *J. Mar. Res.*, **55**, 1997, 507–521.
- [13] Mullarney, J. C., Griffiths, R. W. and Hughes, G. O., Convection driven by differential heating at a horizontal boundary, *J. Fluid Mech.*, in press.
- [14] Munk, W. H., Abyssal recipes, *Deep-Sea Res.*, **13**, 1966, 707–730.
- [15] Munk, W. H. and Wunsch, C., Abyssal recipes II: energetics of tidal and wind mixing, *Deep-Sea Res. I*, **45**, 1998, 1977–2010.
- [16] Oort, A. H., Anderson, L. A. and Peixoto, J. P., Estimates of the energy cycle of the oceans, *J. Geophys. Res.*, **99**, 1994, 7665–7688.
- [17] Osborn, T. R., Estimates of the local rate of vertical diffusion from dissipation measurements, *J. Phys. Oceanogr.*, **10**, 1980, 83–89.

- [18] Paparella, F. and Young, W. R., Horizontal convection is non-turbulent, *J. Fluid Mech.*, **466**, 2002, 205–214.
- [19] Pierce, D. W. and Rhines, P. B., Convective building of a pycnocline: laboratory experiments, *J. Phys. Oceanogr.*, **26**, 1996, 176–190.
- [20] Polzin, K. L., Toole, J. M., Ledwell, J. R. and Schmitt, R. W., Spatial variability of turbulent mixing in the abyssal ocean, *Science*, **276**, 1997, 93–96.
- [21] Rossby, H. T., On thermal convection driven by non-uniform heating from below: an experimental study, *Deep-Sea Res.*, **12**, 1965, 9–16.
- [22] Rossby, H. T., Numerical experiments with a fluid non-uniformly heated from below, *Tellus*, **50**, 1998, 242–257.
- [23] Rudnick, D. L., Boyd, T. J., Brainard, R. E., Carter, G. S., Egbert, G. D., Gregg, M. C., Holloway, P. E., Klymak, J. M., Kunze, E., Lee, C. M., Levine, M. D., Luther, D. S., Martin, J. P., Merrifield, M. A., Moum, J. N., Nash, J. D., Pinkel, R., Rainville, L. and Sanford, T. B., From tides to mixing along the Hawaiian ridge, *Science*, **301**, 2003, 355–357.
- [24] Stommel, H., On the smallness of sinking regions in the ocean, *Proc. Nat. Acad. Sci., Washington*, **48**, 1962, 766–772.
- [25] Toggweiler, J. R. and Samuels, B., On the ocean’s large-scale circulation near the limit of no vertical mixing, *J. Phys. Oceanogr.*, **28**, 1998, 1832–1852.
- [26] Wong, A. B. D. and Griffiths, R. W., Stratification and convection produced by multiple plumes, *Dyn. Atmos. Oceans*, **30**, 2001, 101–123.
- [27] Wunsch, C., Moon, tides & climate, *Nature*, **405**, 2000, 743–744.
- [28] Wunsch, C. and Ferrari, R., Vertical mixing, energy, and the general circulation of the oceans, *Ann. Rev. Fluid Mech.*, **36**, 2004, 281–314.

## Very large-scale structures observed in DNS of turbulent channel flow with passive scalar transport

H. Kawamura<sup>1</sup>, H. Abe<sup>2</sup> and Y. Matsuo<sup>2</sup>

<sup>1</sup>Department of Mechanical Engineering  
Tokyo University of Science, Noda-shi, Chiba, 278-8510 JAPAN

<sup>2</sup>Information Technology Center  
Japan Aerospace Exploration Agency, Jindaiji-higashi, Chofu, Tokyo 182-8522 JAPAN

### Abstract

Direct numerical simulation of a fully developed turbulent channel flow with passive scalar transport has been carried out at four Reynolds numbers, 180, 395, 640 and 1020, based on the friction velocity and the channel half width. The molecular Prandtl numbers are 0.025 and 0.71 where the working fluids are assumed to be mercury and air, respectively. It is shown that for both Prandtl numbers, very large-scale structures of the temperature fluctuations certainly exist in the outer layer at the given Reynolds numbers. Also, it is shown that at high Reynolds number, the very large-scale structures appear hierarchically in the outer layer for the two Prandtl numbers.

### Introduction

The understanding of heat and mass, i.e. scalar, transport mechanism in wall turbulence is of great importance in both the scientific and the engineering viewpoints.

Experimental studies on turbulent heat transfer in wall-bounded flows have been performed over past several decades, and important aspects on the scalar transport mechanism have been reported in the literature. For example, Bremhorst and Bullock[1] measured cross-spectra of turbulent heat and momentum transfer in a turbulent pipe flow, and suggested an almost perfect correlation between the streamwise velocity and the temperature fluctuations at low wavenumbers. Fulachier and Dumas[2] conducted an experiment in a turbulent boundary layer. They showed that except in the buffer region the temperature spectrum differs strongly from the streamwise velocity spectrum, and the spectrum of three velocity components is similar to that of the temperature fluctuation. Perry and Hoffmann[3] made a measurement in a slightly heated boundary layer, and examined the scaling law on the mean and fluctuating temperature for the velocity and thermal fields. Subramanian and Antonia[4] conducted an experiment in a slightly heated boundary layer at  $Re_\tau = u_\tau \delta / \nu = 371 \sim 2273$ , where  $u_\tau$  is the friction velocity,  $\delta$  the channel half width or boundary layer thickness and  $\nu$  the kinematic viscosity. They examined the Reynolds-number effect on mean temperature, temperature fluctuation, turbulent heat fluxes and turbulent Prandtl number. Antonia, Krishnamoorthy and Fulachier[5] investigated the correlation between the streamwise velocity and temperature fluctuations in the near-wall region. They indicated that the correlation coefficient of the streamwise turbulent heat-flux is large throughout the near-wall region, and its magnitude approaches unity at the wall.

On the other hand, owing to an evolution of numerical simulation technique, direct numerical simulation (DNS) has become an inevitable tool to examine turbulence phenomena. In wall turbulence, DNS of scalar transport has been first performed by Kim and Moin[6] in a turbulent channel flow at  $Re_\tau = 180$  with  $Pr = 0.2, 0.71$  and  $2.0$  using the uniform volumetric heating condition. Later, a lot of DNS studies on scalar transport have been performed in a turbulent channel flow at  $Re_\tau = 150 \sim 180$  with

a wider range of Prandtl numbers,  $Pr = 0.025 \sim 10.0$  [7-11], using various thermal boundary conditions, because the turbulent channel is simple in its geometry, and contains fundamental nature of wall turbulence. In these studies, the effects of the Prandtl number and of the thermal boundary conditions were fairly well examined. However, since these DNS studies were conducted at very low Reynolds numbers, the results obtained from DNS were not compared directly with the existing experimental results. Hence, there still remain several inconclusive issues such as Reynolds number dependence on turbulence statistics. Notably, the Reynolds-number effect on the peak values of the temperature variance and the turbulent heat-fluxes, and the behaviours of the turbulent Prandtl number and the time scale ratio have not reach a consensus because of the lack of sufficient information in the measurements.

Recently, with an aid of the development of computer power, DNS of a turbulent channel flow has been performed at relatively high Reynolds numbers. For the velocity field, the Reynolds-number effect on the root-mean-square velocity and vorticity fluctuations, and the scaling law of the energy spectra was carefully examined up to  $Re_\tau = 1900$  (see, for example, Moser, Kim and Mansour[12], Abe, Kawamura and Matsuo[13], del Álamo, Jiménez, Zandonade and Moser[14]). Also, considering the experimental evidence that an importance of the outer-layer effect, i.e. large-scale structures, increases with increasing Reynolds number, the behaviour of large-scale structures was investigated by several researchers (see, for example, del Álamo and Jiménez[15], Abe, Kawamura and Choi[16]).

For the scalar field, on the other hand, DNS studies of Reynolds- and Prandtl-number effects on turbulence statistics were limited to  $Re_\tau = 395$  (see, for example, Wikström and Johansson[17], Kawamura et al.[18, 19]), where firm conclusion on the Reynolds-number effect can hardly be drawn because the simulation at  $Re_\tau = 180$  includes the low Reynolds-number effect (see, for example, Moser et al.[12]). Recently, the present author's group has established DNS database up to  $Re_\tau = 1020$  with  $Pr = 0.025$  and  $0.71$  using a constant heat-flux boundary condition, where the Reynolds number of  $Re_\tau = 1020$  was chosen to be compared with the experimental results of Wei and Willmarth[20]. Using our DNS database, two DNS studies of turbulent heat transfer in a channel flow have been performed at  $Re_\tau \geq 395$ . Abe and Kawamura[21] reported turbulence thermal structures at  $Re_\tau = 180 \sim 640$  with  $Pr = 0.025$  and  $0.71$ . They showed that very large-scale structures of the temperature fluctuations appear clearly in the outer layer for  $Re_\tau = 640$  at each Prandtl number. Abe, Kawamura and Matsuo[22] examined the Reynolds- and Prandtl-number effects on wall variables such as surface heat-flux fluctuations at  $Re_\tau = 180 \sim 1020$  with  $Pr = 0.025$  and  $0.71$ . They showed that the effect of large scales increases with increasing Reynolds number even in the wall variables. However, except these studies, the Reynolds- and Prandtl-number effects on turbulence statistics and turbulence structures for the scalar field have not been reported for  $Re_\tau \geq 395$ .

Re <sub>τ</sub>	180	395	640	1020
Pr	0.025, 0.71	0.025, 0.71	0.025, 0.71	0.025, 0.71
L <sub>x</sub> × L <sub>y</sub> × L <sub>z</sub>	12.88 × 28 × 6.48	12.88 × 28 × 6.48	12.88 × 28 × 6.48	12.88 × 28 × 6.48
L <sub>x</sub> <sup>+</sup> × L <sub>y</sub> <sup>+</sup> × L <sub>z</sub> <sup>+</sup>	2304 × 360 × 1152	5056 × 790 × 2528	8192 × 1280 × 4096	13056 × 2040 × 6528
N <sub>x</sub> × N <sub>y</sub> × N <sub>z</sub>	256 × 128 × 256	512 × 192 × 512	1024 × 256 × 1024	2048 × 448 × 1536
Δx <sup>+</sup> × Δy <sup>+</sup> × Δz <sup>+</sup>	9.00, 0.20~5.90, 4.50	9.88, 0.15~6.52, 4.94	8.00, 0.15~8.02, 4.00	6.38, 0.15~7.32, 4.25
tu <sub>m</sub> /L <sub>x</sub>	49	50	14	10

Table 1. Computational box size, grid points, spatial resolution and sampling time period.

Therefore, in the present study, we use our DNS database of a fully developed turbulent channel flow with passive scalar transport up to Re<sub>τ</sub>=1020 at Pr=0.025 and 0.71. The wide range of Reynolds numbers and two quite different Prandtl numbers allow us to evaluate the Reynolds- and Prandtl-number dependence adequately. The main objectives of the present study are to report the Reynolds- and Prandtl-number effects on very large-scale structures of the temperature fluctuations in the outer layer, which will appear clearly at high Reynolds number.

In this paper, numerical methodology is described in the following section. In the section of results and discussion, the first part is focused on the Reynolds- and Prandtl-number effects on the turbulence statistics, which exhibits fundamental statistical nature of wall turbulence at relatively high Reynolds numbers. On the other hand, the second part is on those of the very large-scale structures in the outer layer.

### Numerical methodology

The governing equations for the velocity and scalar fields consist of the incompressible three-dimensional continuity, Navier-Stokes and energy equations. The flow is assumed to be a fully developed turbulent channel flow with a passive temperature field. It is driven by the streamwise mean pressure gradient. The temperature field is imposed through uniform heating on both walls, where the averaged heat flux is constant but the instantaneous one is time dependent.

The continuity and Navier-Stokes equations, respectively, are expressed as:

$$\frac{\partial u_i^+}{\partial x_i^*} = 0, \quad (1)$$

$$\frac{\partial u_i^+}{\partial t^*} + u_j^+ \frac{\partial u_i^+}{\partial x_j^*} = -\frac{\partial p^+}{\partial x_i^*} + \frac{1}{\text{Re}_\tau} \frac{\partial^2 u_i^+}{\partial x_j^{*2}} + \frac{\partial \bar{p}^+}{\partial x_i^*} \delta_{il}, \quad (2)$$

which are non-dimensionalized by the friction velocity  $u_\tau$ , the density  $\rho$  and the channel half width  $\delta$ . Here, the variables  $u$ ,  $p$ ,  $t$  and  $x$  are the velocity, pressure, time and location, and the subscript  $i=1, 2$  and  $3$  indicates the streamwise, wall-normal and spanwise directions, respectively. Note that the streamwise, wall-normal and spanwise velocities,  $u$ ,  $v$ , and  $w$ , and the streamwise, wall-normal and spanwise locations,  $x$ ,  $y$ , and  $z$ , are used interchangeably throughout this paper. The superscripts  $+$  and  $*$  indicate that the variables are normalized by wall units and the channel half width, respectively. The third term for right-hand side of Eq. (2) is the streamwise mean pressure gradient.

For the energy equation, the temperature difference  $\theta$  is introduced to be satisfied with the constant heat-flux boundary condition. Since the statistically averaged temperature increases linearly in the streamwise direction, the instantaneous temperature  $T^+(x^*, y^*, z^*)$  can be divided into the mean and fluctuating parts:

$$T(x^*, y^*, z^*) = \frac{d \langle \bar{T}_m^+ \rangle}{dx^*} x^* - \theta^+(x^*, y^*, z^*) \quad (3)$$

where  $\langle \bar{T}_m^+ \rangle$  is the mixed mean temperature. Considering the present configuration, the first term for the right-hand side of Eq. (3) can be obtained as  $d \langle \bar{T}_m^+ \rangle / dx^* = 2 / \langle \bar{u}_1^+ \rangle$ , where  $\langle \bar{u}_1^+ \rangle$  is the

bulk mean velocity. Hence, using the above transformation, the energy equation is expressed as

$$\frac{\partial \theta^+}{\partial t^*} + u_j^+ \frac{\partial \theta^+}{\partial x_j^*} = \frac{1}{\text{Re}_\tau \cdot \text{Pr}} \frac{\partial^2 \theta^+}{\partial x_j^{*2}} + \frac{2u_1^+}{\langle \bar{u}_1^+ \rangle}. \quad (4)$$

Note that the temperature is normalized by the friction temperature  $T_\tau (= Q_w / \rho c_p u_\tau)$ , where  $Q_w$  and  $c_p$  denote the averaged surface heat-flux and the specific heat at constant pressure, respectively. In the  $x$  and  $z$  directions, the periodic boundary condition is employed. In the  $y$  direction, the non-slip and no temperature fluctuations conditions are used for the velocity and thermal fields, respectively, which are expressed as

$$u_i^+ = \theta^+ = 0 \quad (y = 0 \text{ and } 2\delta). \quad (5)$$

For the time integration, a fractional step method proposed by Dukowicz and Dvinsky[23] is adopted, and a semi-implicit time advancement is used. For the viscous terms with wall-normal derivatives, the Crank-Nicolson method is used. For the other terms, the second-order Adams-Bashforth method is applied for Re<sub>τ</sub>=180, 395 and 640, and the low storage third-order Runge-Kutta method (Spalart et al.[24]) for Re<sub>τ</sub>=1020.

For the spatial discretization, the finite difference method is used. The numerical scheme proposed by Morinishi et al.[25] with the fourth-order accuracy is adopted in the streamwise and spanwise directions, whereas the second-order one is applied in the wall-normal direction. The computational box size ( $L_x$ ,  $L_y$ ,  $L_z$ ), number of grid points ( $N_x$ ,  $N_y$ ,  $N_z$ ), spatial resolution ( $\Delta x$ ,  $\Delta y$ ,  $\Delta z$ ) and sampling time period ( $tu_m/L_x$ ) are given in Table 1, where  $u_m$  denotes the bulk mean velocity. Detailed numerical methodology can be found in Kawamura et al.[18,19] and Abe et al.[13].

### Results and discussion

#### Turbulence statistics

In the classical theory, the mean temperature  $\bar{\theta}$  is expressed as

$$\frac{\bar{\theta}}{T_\tau} = f(y^+), \quad (6)$$

$$\frac{\bar{\theta}_c - \bar{\theta}}{T_\tau} = f\left(\frac{y}{\delta}\right), \quad (7)$$

where  $f$  and  $g$  represent the universal functions and the subscript  $c$  denotes the centreline value. The former and the latter are referred to as the law of the wall for the mean temperature and the temperature defect law, respectively. In our former work[22], we showed that the conductive sublayer follows the relation of Eq. (6), i.e.  $\bar{\theta}^+ = \text{Pr} y^+$ , for Re<sub>τ</sub>=180~1020 at Pr=0.025 and 0.71. On the other hand, Hoffmann and Perry[26] suggested from their measurements that the temperature defect law, i.e. Eq. (7), is valid in the outer layer. Figure 1 shows the temperature defect law for the Reynolds and Prandtl numbers investigated. In Fig. 1, the temperature defect profile for Pr=0.71 indeed shows a good collapse in the outer layer, whereas that for Pr=0.025 shows a noticeable increase in the whole region with increasing Re<sub>τ</sub>. The incomplete scaling for Pr=0.025 is due to the enhanced convective effect with increasing Reynolds number under the strong thermal conductive condition.

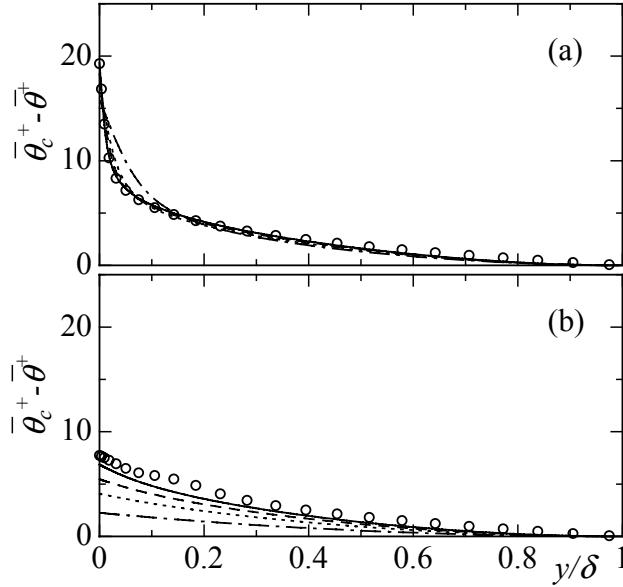


Figure 1. Temperature defect profile: (a)  $Pr=0.71$ ; (b)  $Pr=0.025$ .  
—,  $Re_\tau=1020$ ; ---,  $Re_\tau=640$ ; ..... ,  $Re_\tau=395$ ;  
- · - · - ,  $Re_\tau=180$ ; ○ , Kader[27] for  $Re_\tau=1020$ .

By integrating the area under the curve of the temperature defect profile, the Clauser thickness of the thermal boundary layer can be obtained as

$$\Delta_t = \int_0^1 \frac{\bar{\theta}_c^+ - \bar{\theta}^+}{T_\tau} dy^* \quad (8)$$

The obtained  $\Delta_t$  are summarized in Table 2, where the momentum Clauser thickness  $\Delta$  is also included for comparison. It is shown in Table 2 that  $\Delta_t$  for  $Pr=0.71$  does not vary noticeably for the given Reynolds numbers, whereas that for  $Pr=0.025$  increases appreciably with increasing Reynolds number. Also, it turns out from Table 2 that  $\Delta_t$  for  $Pr=0.71$  shows almost the same trend as  $\Delta$ , indicating a high similarity between the velocity and thermal fields for each Reynolds number. On the other hand,  $\Delta_t$  for  $Pr=0.025$  differs noticeably from  $\Delta$  independently of  $Re_\tau$ , suggesting the breakdown of the similarity between the velocity and scalar fields, i.e. the Reynolds analogy.

The behaviour of the temperature fluctuations  $\theta'$  is investigated using the probability density functions (PDFs). Figure 2 shows the PDFs of  $\theta'$  for the Reynolds and Prandtl numbers examined at several wall-normal locations compared with those of the streamwise velocity fluctuations  $u'$ . In the case of  $Pr=0.71$ , near the wall, the peak position of the PDF deviates to the negative value, and the tail extends to the large magnitude of the positive value, indicating that the sweep occurs less frequently but it contributes more significantly to the heat transport. Moving away from the wall, the peak position of the PDF shifts gradually to the positive value, and the negative tail becomes more prominent with increasing  $y^+$ . The Reynolds-number effect is noticeable in the positive and negative tails. As for the similarity between  $u'$  and  $\theta'$ , the high similarity is observed near the wall, whereas the similarity decreases gradually moving away from the wall.

In the case of  $Pr=0.025$ , the PDFs below  $y^+ \approx 10$  show almost the same behaviour independently of  $y^+$  for each  $Re_\tau$  due to the

$Re_\tau$	$\Delta$	$\Delta_\theta$	
		$Pr=0.71$	$Pr=0.025$
180	2.72	2.45	0.74
180[6]	2.7	2.4	-
395	2.69	2.34	1.27
640	2.72	2.43	1.64
1020	2.77	2.43	1.98

Table 2. Clauser thickness for the velocity and scalar fields.

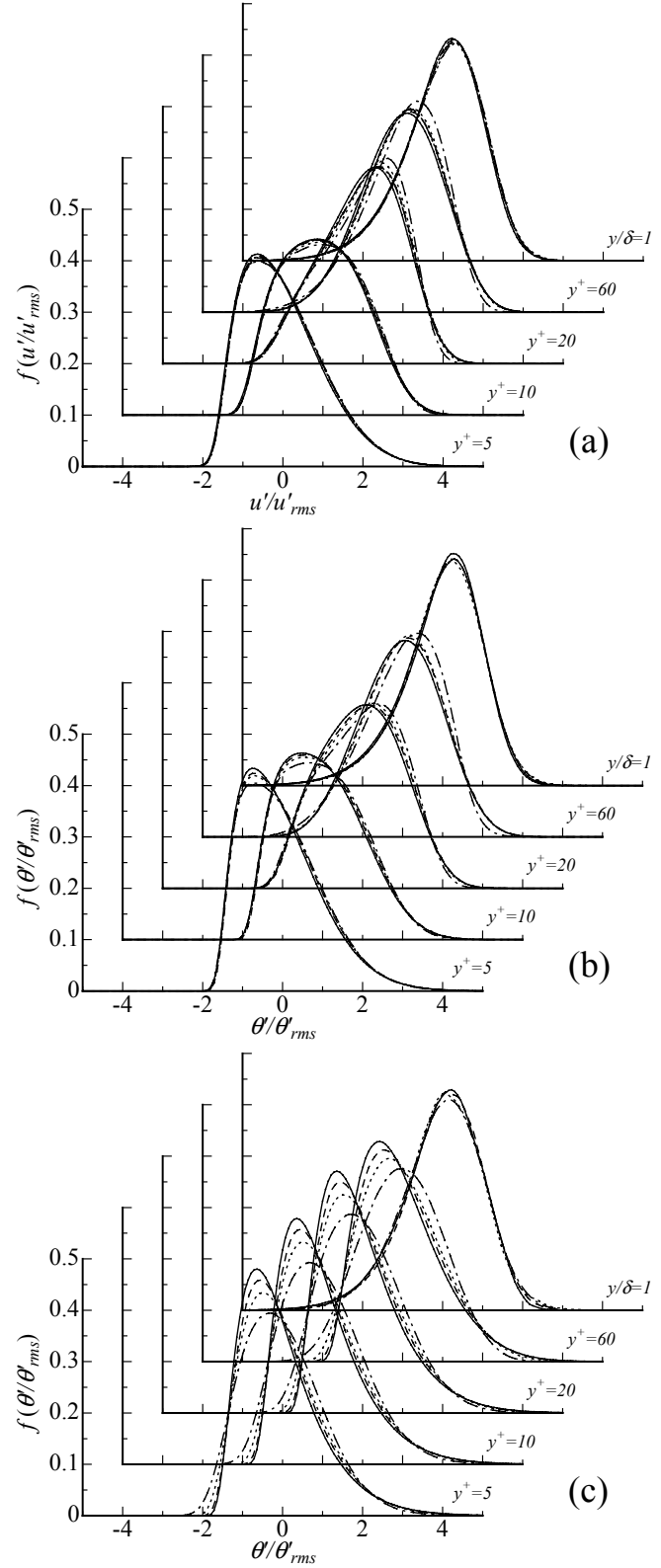


Figure 2. Probability density functions of  $u'$  and  $\theta'$ :  
—,  $Re_\tau=1020$ ; ---,  $Re_\tau=640$ ; ..... ,  $Re_\tau=395$ ;  
- · - · - ,  $Re_\tau=180$ . (a)  $u'$ ; — · — · — , Moser et al.[12] for  $Re_\tau=590$ ;  
(b)  $\theta'$  for  $Pr=0.71$ ; (c)  $\theta'$  for  $Pr=0.025$ .

strong conductive effect. Also, near the wall, the significant Reynolds-number effect appears. That is, the PDF is more positively skewed with increasing  $Re_\tau$  due to the enhanced convective effect. In the central region, on the other hand, the PDF is negatively skewed, and the Reynolds-number dependence is rather small.

The streamwise turbulent heat flux  $\overline{u'^+ \theta'^+}$  and its cross-correlation coefficient  $R_{u\theta} (= \overline{u' \theta'} / u'_{rms} \theta'_{rms})$  are given in Figs. 3 and 4, respectively, where the subscript  $rms$  denotes the root-mean-square value. It is shown in Fig. 3 that the peak value of  $u'^+ \theta'^+$  increases with increasing Reynolds number for each  $Pr$ .

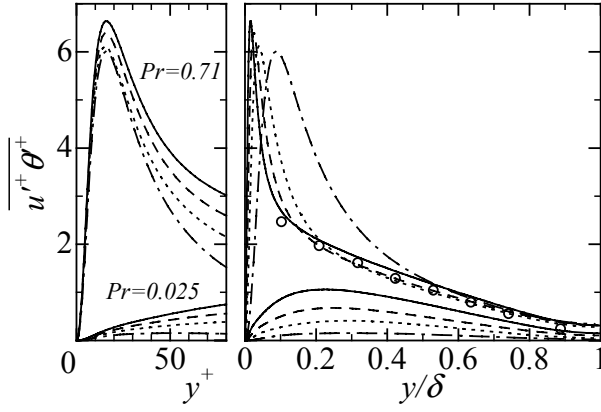


Figure 3. Streamwise turbulent heat flux: —,  $Re_\tau=1020$ ; ---,  $Re_\tau=640$ ; ..... ,  $Re_\tau=395$ ; - · - · ,  $Re_\tau=180$ ; ○ , Subramanian and Antonia[4] for  $Re_\tau \approx 1055$ .

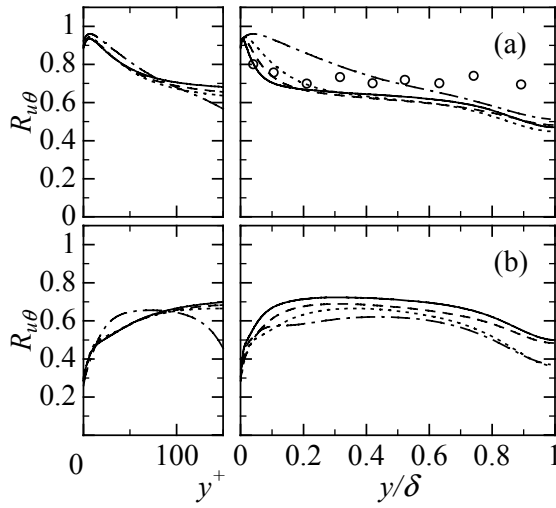


Figure 4. Correlation coefficient of the streamwise turbulent heat flux: (a)  $Pr=0.71$ ; (b)  $Pr=0.025$ . —,  $Re_\tau=1020$ ; ---,  $Re_\tau=640$ ; ..... ,  $Re_\tau=395$ ; - · - · ,  $Re_\tau=180$ ; ○ , Subramanian and Antonia[4] for  $Re_\tau \approx 1055$ .

The increasing rate for  $Pr=0.025$  from  $Re_\tau=180$  to 1020 is larger than that for  $Pr=0.71$ , indicating that the enhancement of the convective effect due to the increase in  $Re_\tau$  is more significant in the low  $Pr$  fluid than in the medium to high  $Pr$  one. Also, considering no constrained condition in the streamwise direction, the peak value of  $u'^+\theta'^+$  may continue to increase with increasing Reynolds number for both  $Pr$  cases.

In Fig. 4, the cross-correlation coefficient  $R_{u\theta}$  exhibits a quite different behaviour in the near wall region for each  $Pr$ . That is,  $R_{u\theta}$  for  $Pr=0.71$  shows a clear peak near the wall and decreases gradually toward the outer layer, whereas that for  $Pr=0.025$  shows no clear peak near the wall and increases gradually toward the outer layer. This difference must be attributed to the fact that  $\theta'$  for  $Pr=0.71$  is a near-wall marker, whereas that for  $Pr=0.025$  marks in a wider range of the flow region. However, in spite of these different characteristics of  $\theta'$ ,  $R_{u\theta}$  is scaled well with the inner variables at  $y^+ \leq 50$  for each  $Pr$  over  $Re_\tau=395$ . Also, we see that for  $Pr=0.71$ , the clear peak appears at  $y^+ \approx 7$  regardless of  $Re_\tau$ , and its peak value remains unchanged as 0.94 over  $Re_\tau=395$ , suggesting that near the wall, the high similarity between  $u'$  and  $\theta'$  at  $Pr=0.71$  does not change substantially over  $Re_\tau=395$ .

The wall-normal turbulent heat flux  $-v'^+\theta'^+$  and its cross-correlation coefficient  $-R_{v\theta} (= -\overline{v'\theta'}/v'_{rms}\theta'_{rms})$  are shown in Figs. 5 and 6, respectively. In Fig. 5, the total heat flux  $Q_{total}$  and the temperature gradient, i.e. molecular heat flux,  $(1/Pr)(d\bar{\theta}^+/dy^+)$ , are also included. It can be confirmed in Fig. 5 that for all the cases investigated, the total heat-flux reaches the

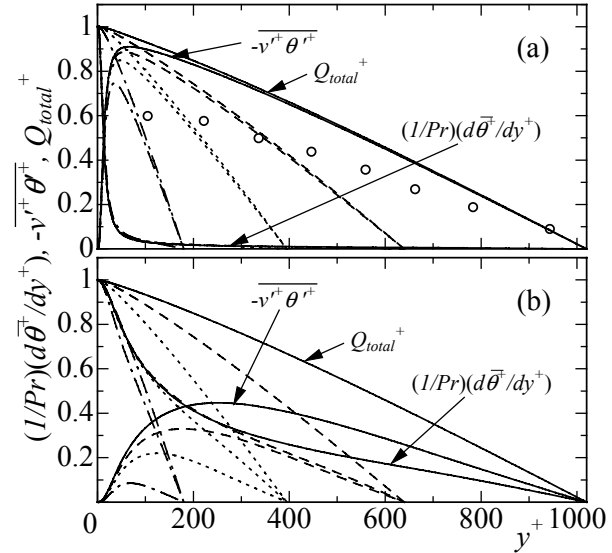


Figure 5. Wall-normal turbulent heat flux: —,  $Re_\tau=1020$ ; ---,  $Re_\tau=640$ ; ..... ,  $Re_\tau=395$ ; - · - · ,  $Re_\tau=180$ ; ○ , Subramanian and Antonia[4] for  $Re_\tau \approx 1055$ .

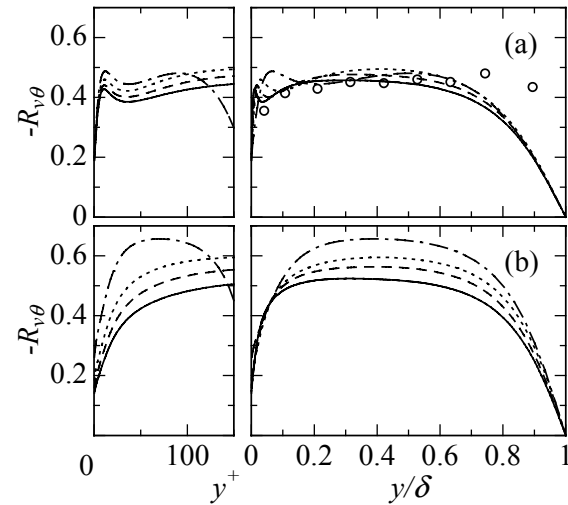


Figure 6. Correlation coefficient of the wall-normal turbulent heat flux: (a)  $Pr=0.71$ ; (b)  $Pr=0.025$ . —,  $Re_\tau=1020$ ; ---,  $Re_\tau=640$ ; ..... ,  $Re_\tau=395$ ; - · - · ,  $Re_\tau=180$ ; ○ , Subramanian and Antonia[4] for  $Re_\tau \approx 1055$ .

statistically steady state, indicating that the sampling average time is quite sufficient to discuss the Reynolds- and Prandtl-number effects on the turbulence statistics.

In Fig. 5, with increasing  $Re_\tau$ , the peak value of  $-v'^+\theta'^+$  increases and its peak position moves toward a larger  $y^+$  for each Prandtl number. In the case of  $Re_\tau=1020$ , the peak value of  $-v'^+\theta'^+$  is 0.90 ( $y^+ = 67$ ) and 0.45 ( $y^+ = 254$ ) for  $Pr = 0.71$  and 0.025, respectively. Interestingly, for  $Pr=0.025$ , the turbulent heat flux exceeds the molecular heat flux at  $y^+ > 200$  when  $Re_\tau$  reaches 1020, although the molecular contribution is still large throughout the channel at the given Reynolds numbers.

As for the cross-correlation coefficient  $-R_{v\theta}$ , a large difference between  $Pr=0.025$  and 0.71 exist in the near-wall region as seen in the behaviour of  $R_{u\theta}$ . For  $Pr=0.71$ , a close similarity between  $-R_{v\theta}$  and  $-R_{uv}$  (not shown here) is found near the wall independently of  $Re_\tau$ , suggesting that  $-v'^+\theta'^+$  and  $-u'^+v'^+$  are generated by approximately the same turbulence transport mechanism there. Also, the agreement between the present result and that of Subramanian and Antonia[4] is good except for the centre of the channel where flow characteristics between the channel and boundary layers are quite different. For  $Pr=0.025$ , on the other hand,  $-R_{v\theta}$  shows a lower value than that for  $Pr=0.71$



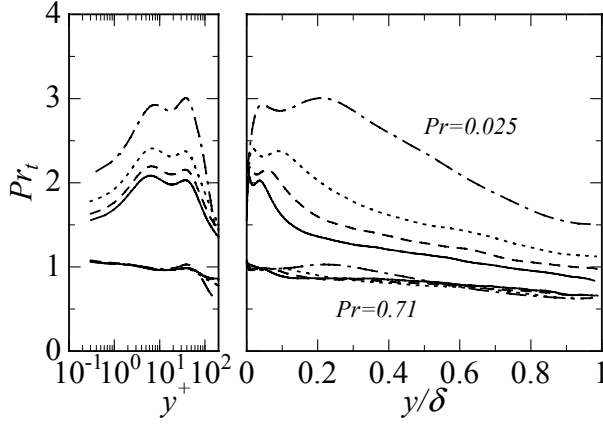


Figure 7. Turbulent Prandtl number; —,  $Re_\tau=1020$ ; ---,  $Re_\tau=640$ ; ..... ,  $Re_\tau=395$ ; -.-.-,  $Re_\tau=180$ .

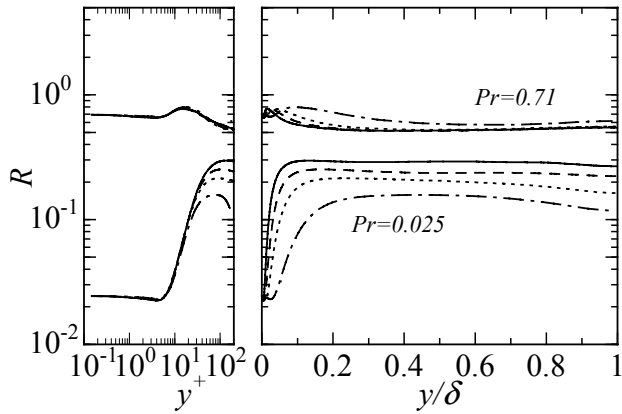


Figure 8. Time scale ratio; —,  $Re_\tau=1020$ ; ---,  $Re_\tau=640$ ; ..... ,  $Re_\tau=395$ ; -.-.-,  $Re_\tau=180$ .

near the wall and increases gradually toward the outer layer. Interestingly, in the outer layer,  $-R_{v\theta}$  decreases gradually with increasing  $Re_\tau$  due to the enhanced convective effect, which is in contrast to the behaviour of  $R_{u\theta}$  (see Figs. 4(b) and 6(b)).

Turbulent Prandtl number is defined as

$$Pr_t = \frac{\nu_t}{a_t} = \frac{\overline{u'^+ v'^+}}{\overline{v'^+ \theta'^+}} \cdot \frac{(d\overline{\theta'^+}/dy^+)}{(d\overline{u'^+}/dy^+)}, \quad (9)$$

which corresponds to the ratio of turbulent eddy viscosity  $\nu_t$  to thermal eddy diffusivity  $a_t$ . Figure 7 shows the turbulent Prandtl number for the Reynolds and Prandtl numbers calculated. For  $Pr = 0.71$ , as the wall is approached,  $Pr_t$  tends to be a constant value of 1.1 independently of  $Re_\tau$ . This coincides well with the low  $Re$  DNS results of Kim and Moin[6] and Antonia and Kim[28] in the channel flow with the uniform volumetric heating and that of Kong, Choi, and Lee[29] in the thermal boundary layer. In the centre of the channel,  $Pr_t$  decreases down to 0.65 independently of Reynolds number. Interestingly, in the case of  $Re_\tau=1020$ ,  $Pr_t$  stays at a roughly constant value of 0.86 at  $0.1 < y/\delta < 0.4$ . This is very close to the value of 0.9 which was often used in the calculation of turbulent heat transfer using turbulence modelling.

For  $Pr = 0.025$ , on the other hand,  $Pr_t$  shows a larger value than that of  $Pr = 0.71$  for all the Reynolds numbers. Nevertheless, with increasing  $Re_\tau$ ,  $Pr_t$  decreases appreciably and tends to approach unity. One may wonder if the near-wall limiting value of  $Pr_t$  for  $Pr=0.025$  also asymptotes to unity for extremely high  $Re$ . Considering the quite different behaviour of  $-R_{v\theta}$  between  $Pr=0.025$  and  $0.71$  in the near-wall region (see Fig. 6), it may be concluded that the near-wall value of  $Pr_t$  for  $Pr=0.025$  does not asymptote to unity for high Reynolds number.

With respect to the scaling law for  $Pr_t$  in the case of  $Pr=0.71$ , the inner scaling is valid up to  $y^+=100$ , while the outer one is in

the range,  $0.2 < y/\delta < 1$ , except for  $Re_\tau=180$ . On the other hand, in the case of  $Pr=0.025$ , no collapse is observed for the Reynolds number range investigated.

The time scale ratio is a quantity often used to estimate the dissipation rate of the temperature variance. It is defined as

$$R = \frac{\tau_\theta}{\tau_u} = \frac{\overline{\theta'^+{}^2} \varepsilon}{2k\varepsilon_\theta}. \quad (10)$$

Its wall asymptotic value is analytically equal to the molecular Prandtl number. Figure 8 shows the distribution of the time scale ratio for the given Reynolds and Prandtl numbers. Near-the wall, the limiting value of  $R$  becomes indeed  $Pr$  irrespective of Reynolds number. In the outer layer, the time scale ratio for  $Pr=0.71$  shows a good collapse with the outer scaling in the range,  $0.2 < y/\delta < 1$ , where  $R$  stays  $0.5 \sim 0.6$  and shows an almost plateau. This value is very close to that of  $0.5$ , which was often used in earlier turbulence modelling to obtain the dissipation rate of the temperature variance[30]. On the other hand, time scale ratio for  $Pr=0.025$  does not collapse for the given Reynolds numbers. Nevertheless, it is interesting to note that  $R$  tends to approach  $0.5$  with increasing Reynolds number even at  $Pr=0.025$ .

### Very large-scale structures

The large-scale structures are often referred to as the large-scale motions existing in the outer layer of the flow, and many experimental studies on the large-scale motions have been conducted for turbulent pipe, boundary layer and channel flows (see, for example, Kim and Adrian[31]; Adrian et al.[32]; Liu et al.[33]). Furthermore, Kim and Adrian[31] found that very large-scale motions which are much longer than the large-scale motions exist in the outer layer in a turbulent pipe flow.

Recently, DNS of turbulent channel flow at relatively high Reynolds numbers showed convincing evidence on very large-scale structures in the outer layer. For the velocity field, del Álamo and Jiménez[15] found that very large-scale structures of  $u'$  appear at  $y/\delta=0.5$  for  $Re_\tau=180$  and  $550$ , where the streamwise and spanwise size is about  $5\delta$  and  $2\delta$ , respectively. Abe, Kawamura and Choi[16] obtained the most energetic spanwise scale as  $1.3 \sim 1.6\delta$  for  $Re_\tau=180 \sim 640$ . For the thermal field, Abe and Kawamura[21] reported from their DNS results that there exist very large-scale structures of  $\theta'$  in the outer layer for  $Re_\tau=640$  with  $Pr=0.025$  and  $0.71$ . However, the spanwise organization of the very large-scale structures of  $\theta'$  has not been examined in detail. Therefore, we investigate here the behaviour of the very large-scale structures in the spanwise direction.

One-dimensional spanwise wavenumber energy spectra of the temperature fluctuations  $\theta'$  are defined as

$$\int_0^\infty \phi(k_z) dk_z = \theta'^2_{rms}, \quad (11)$$

where  $k_z$  is the spanwise wavenumber and  $\lambda_z$  the corresponding wavelength. The spanwise pre-multiplied energy spectra of the temperature fluctuations for  $Re_\tau=180, 395, 640$  and  $1020$  at  $Pr=0.025$  and  $0.71$  are given in Figs. 9 and 10, where spectral peaks at long wavelengths appear more clearly for high Reynolds number. Note that the wavelength where the pre-multiplied energy spectrum shows a maximum indicates the most energetic scale. In the case of  $Pr=0.71$ , with increasing  $Re_\tau$ , spanwise length scales are separated clearly, and small and large scales are scaled with the inner and outer variables, respectively. Near the wall, a clear peak appears at  $\lambda_z^+ \approx 100$  for each Reynolds number. Away from the wall, the peak moves to longer wavelengths. At  $y/\delta=0.5$ , a large peak appears at  $\lambda_z/\delta=1.3 \sim 1.6$  for all the  $Re_\tau$ , suggesting an existence of very large-scale structures of  $\theta'$  in the outer layer. This trend is also observed in the spanwise spectra of  $u'$  (not shown here). However, comparison of the spectra between  $u'$  and  $\theta'$  shows that the peak value of  $\theta'$  is much

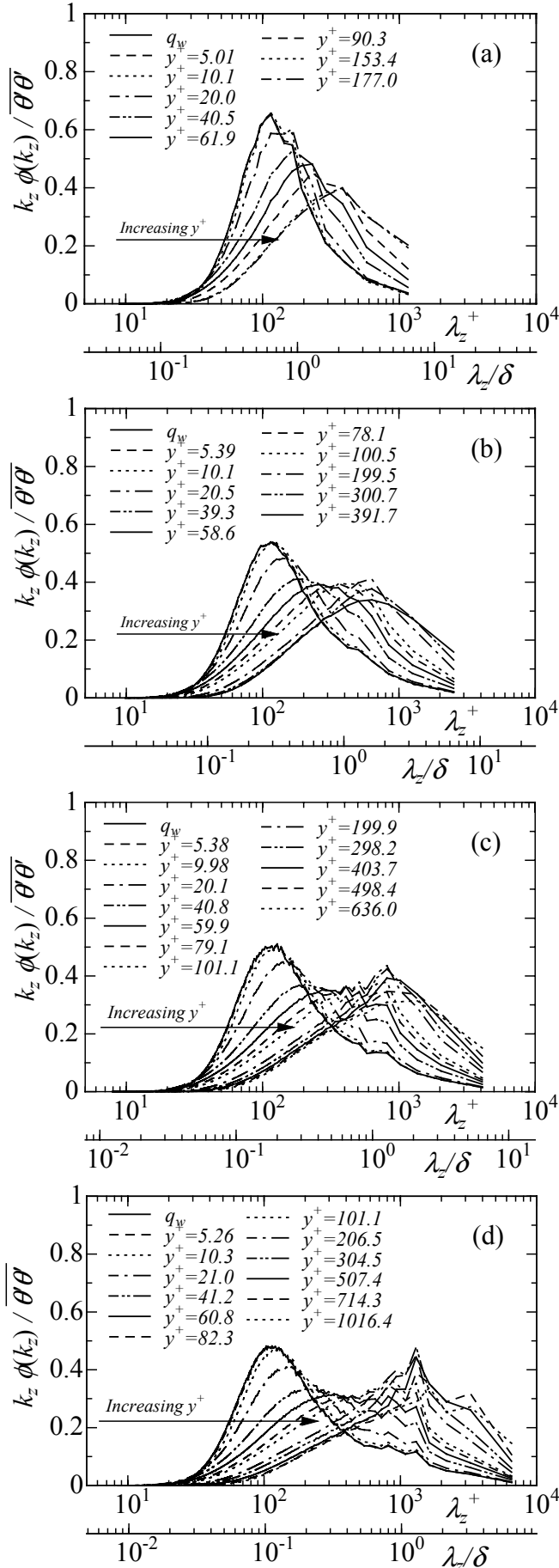


Figure 9. Spanwise pre-multiplied energy spectra of  $\theta'$  at  $Pr=0.71$ :  
(a)  $Re_\tau=180$ ; (b)  $Re_\tau=395$ ; (c)  $Re_\tau=640$ ;  $Re_\tau=1020$ .

smaller than that of  $u'$  in the outer layer, indicating a dissimilarity in the very large-scale structures between  $u'$  and  $\theta'$ . In the case of  $Pr=0.025$ , on the other hand, all the spectral peaks appear at long wavelengths regardless of  $y^+$  for all the Reynolds numbers. This may be yielded by the strong conductive effect throughout the channel. Interestingly, in the case of  $Re_\tau=1020$ , another large

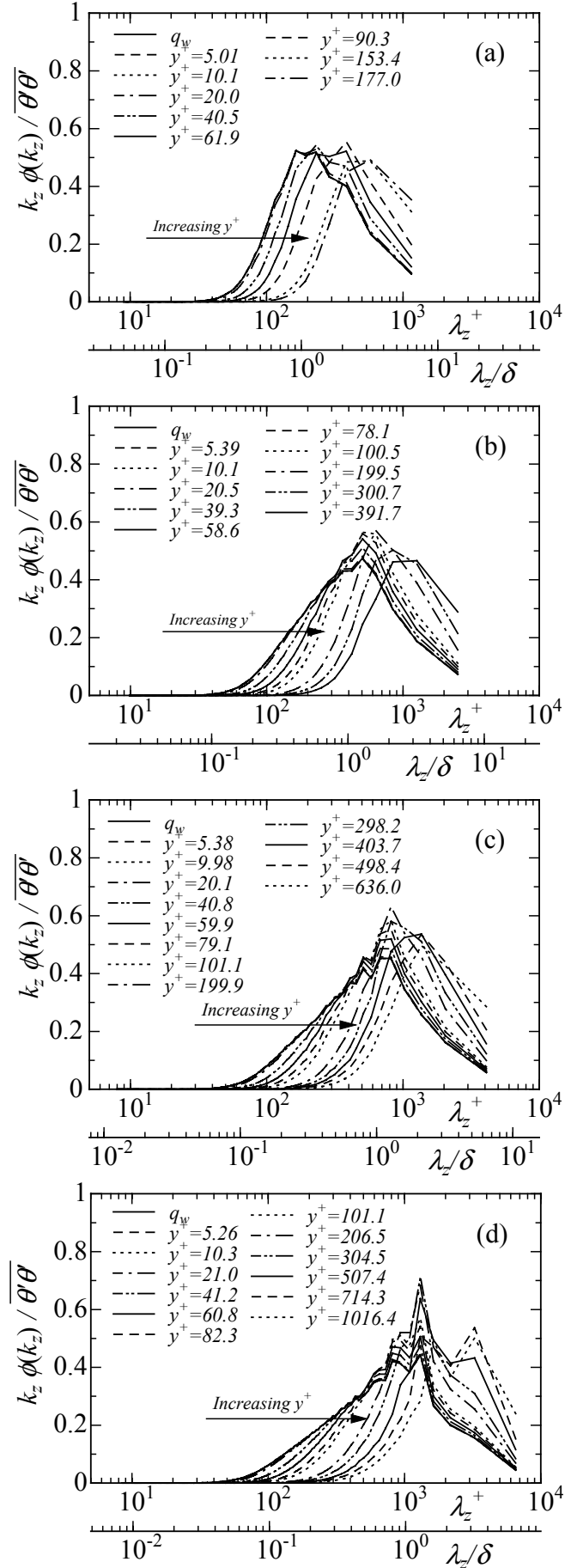


Figure 10. Spanwise pre-multiplied energy spectra of  $\theta'$  at  $Pr=0.025$ :  
(a)  $Re_\tau=180$ ; (b)  $Re_\tau=395$ ; (c)  $Re_\tau=640$ ;  $Re_\tau=1020$ .

peak appears at a long wavelength,  $\lambda_z/\delta \approx 0.9$ , at  $y/\delta \approx 0.2$  for the both  $Pr$  cases. Since this peak does not appear clearly at  $Re_\tau \leq 640$ , it may be closely associated with the enhanced nonlinear effect with increasing  $Re_\tau$ , indicating that there exist hierarchical very large-scale structures of  $\theta'$  in the outer layer at high Reynolds number for the two  $Pr$  fluids.

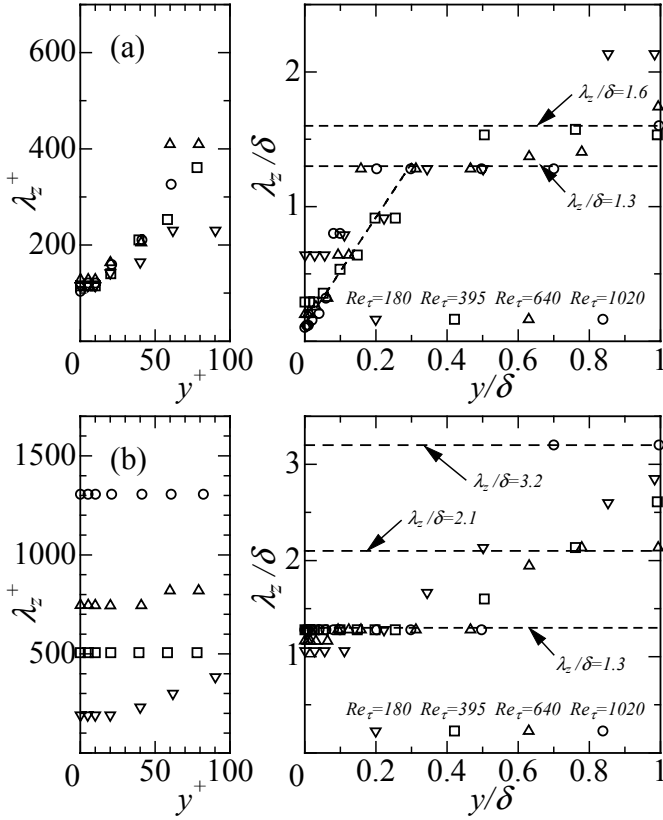


Figure 11. The most energetic spanwise wavelengths obtained from the pre-multiplied energy spectra of  $\theta'$  for  $Re_\tau=180, 395, 640$  and  $1020$ : (a)  $Pr=0.71$ ; (b)  $Pr=0.025$ .

The most energetic wavelengths (MEWs, hereafter) of  $\theta'$  are obtained from Figs. 9 and 10, and are presented in Fig. 11. Note that when the pre-multiplied spanwise spectrum shows a clear peak we have taken the most energetic wavelength, while when the spectrum shows a broad peak we have computed a least-square interpolating polynomial in the region where the spectrum shows the most energetic power. In Fig. 11, there appears a significant  $Pr$  dependence independently of Reynolds number. For  $Pr=0.71$ , the MEWs can be divided into three regions. Near the wall ( $y^+ < 10$ ), we see the MEWs at  $\lambda_z^+ \approx 100$ . Away from the wall ( $y^+ > 10$ ,  $y/\delta < 0.3$ ), the MEWs increase linearly with distance from the wall. In the outer layer ( $0.3 < y/\delta < 1$ ), the MEWs stay  $1.3 \sim 1.6\delta$  and show an almost plateau. On the other hand, for  $Pr=0.025$ , the MEWs can be categorized into two regions. Below  $y/\delta=0.5$ , the MEWs are obtained as  $1.3 \sim 2.1\delta$ , while those are  $2.1 \sim 3.2\delta$ , indicating that in the very low  $Pr$  fluid, only large-scale structures exist even in the near-wall region independently of  $Re_\tau$ .

We will show the variation of the very large-scale structures of  $\theta'$  as a function of the Reynolds number. The instantaneous temperature fluctuations for  $Re_\tau=180$  and  $1020$  at  $Pr=0.71$  are normalized by their own rms values at each  $y^+$ , and are shown in Fig. 12. This normalization allows us to evaluate the outer-layer structures adequately [16, 22]. Note that for Fig. 12(c), only the data in the range,  $y/\delta=0 \sim 0.2$ , are visualized in order to show instantaneous evidence of hierarchical very large-scale structures in the outer layer at high Reynolds number. It is obvious from Figs. 12(a) and (b) that for each  $Re_\tau$ , large-scale positive and negative temperature fluctuations appear alternatively in the spanwise direction. The spanwise spacing of the negative  $\theta'$  is about  $1.3 \sim 1.6\delta$  at  $y/\delta \approx 0.5$ , which agrees well with the wavelengths at which the spanwise pre-multiplied spectra show maxima in the outer layer. With increasing  $Re_\tau$ , very large-scale structures with wider scales appear in the outer layer, as expected. For  $Re_\tau=1020$ , another large-scale structures with a spanwise spacing,  $0.8 \sim 1.0\delta$  appear at  $y/\delta \approx 0.2$  (see Fig. 12(c)), suggesting the existence of the hierarchical very large-scale structures. Furthermore, the very large-scale structures of  $\theta'$  show much

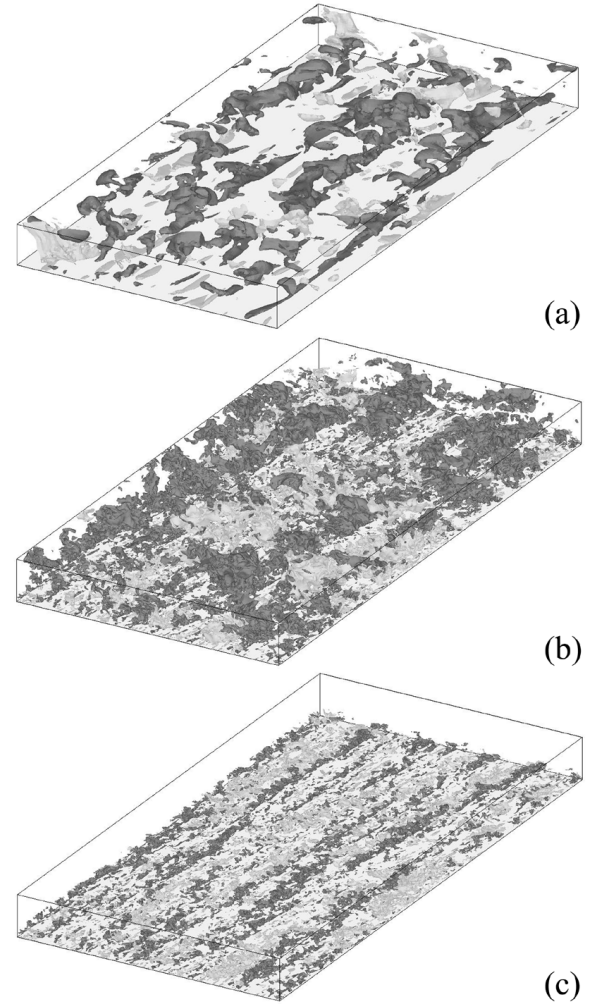


Figure 12. Iso-surfaces of the instantaneous temperature fluctuations normalized by their own rms value at each  $y^+$  for  $Re_\tau=180$  and  $1020$  at  $Pr=0.71$ : (a)  $Re_\tau=180$ ; (b)  $Re_\tau=1020$ ; (c)  $Re_\tau=1020$  (plotted in the range,  $y/\delta=0 \sim 0.2$ ). Light-gray,  $\theta'/\theta'_{rms} > 1.75$ ; dark-gray,  $\theta'/\theta'_{rms} < -1.75$ . The boxes visualized here are  $12.8\delta \times \delta \times 6.4\delta$  in  $x$ ,  $y$  and  $z$  directions. The direction of the flow is from bottom-left to top-right.

sharper gradient to the wall as compared with those of  $u'$  (not shown here). This temperature structure may be closely related to the temperature front reported by Chen and Blackwelder [34].

Similarly, the instantaneous temperature fluctuations for  $Re_\tau=180$  and  $1020$  at  $Pr=0.025$  are normalized by their own rms values at each  $y^+$ , and are shown in Fig. 13. Indeed, very large-scale structures with a spanwise spacing,  $1.3 \sim 1.6\delta$ , exist in the outer layer for each  $Re_\tau$ . Interestingly, the shapes of the structures do not change noticeably with increasing  $Re_\tau$ . Also, in the case of  $Re_\tau=1020$ , hierarchical very large-scale structures appear in the outer layer, as was shown at  $Pr=0.71$ .

## Conclusions

In the present study, we performed DNS of turbulent channel flow with passive scalar transport at  $Re_\tau=180, 395, 640$  and  $1020$  with  $Pr=0.025$  and  $0.71$ , and investigated the Reynolds- and Prandtl-number effects on the turbulence statistics and the very large-scale structures existing in the outer layer of the flow.

An investigation of the turbulence statistics showed that near the wall, the turbulent Prandtl number for  $Pr=0.71$  becomes  $1.1$  independently of  $Re_\tau$ , whereas that for  $Pr=0.025$  does not asymptote to unity even for  $Re_\tau=1020$ . Also, the near-wall limiting value of the time scale ratio becomes indeed  $Pr$  irrespective of Reynolds number. In the outer layer,  $Pr_t$  and  $R$  for  $Pr=0.71$  scale with the outer variable in the range,  $0.2 < y/\delta < 1$ .

An inspection of the very large-scale structures of  $\theta'$  in the outer layer revealed that for all the Reynolds numbers, there certainly exist very large-scale structures with a spanwise spacing,

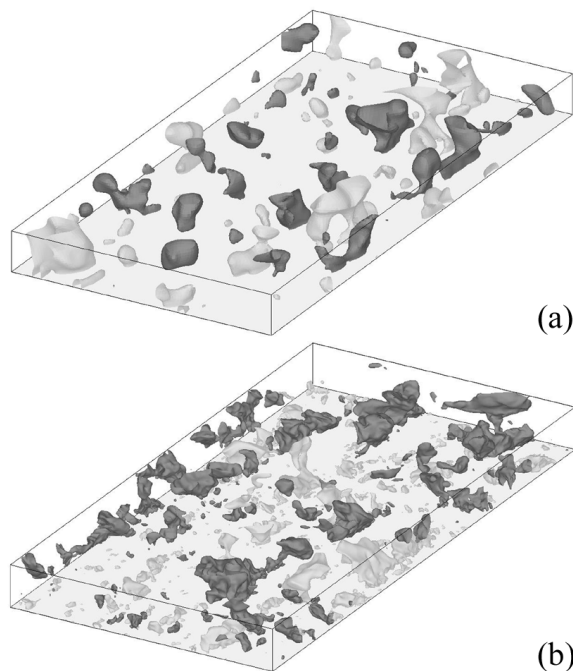


Figure 13. Iso-surfaces of the instantaneous temperature fluctuations normalized by their own rms value at each  $y^+$  for  $Re_\tau = 180$  and  $1020$  at  $Pr = 0.025$ : (a)  $Re_\tau = 180$ ; (b)  $Re_\tau = 1020$ . Light-gray,  $\theta'/\theta'_{rms} > 1.75$ ; dark-gray,  $\theta'/\theta'_{rms} < -1.75$ . The boxes visualized here are  $12.88 \times 6.48 \times 6.48$  in  $x$ ,  $y$  and  $z$  directions. The direction of the flow is from bottom-left to top-right.

$1.3 \sim 1.6\delta$  at  $y/\delta \approx 0.5$  at the two  $Pr$  cases. Also, in the case of  $Re_\tau = 1020$ , another large-scale structures with a spanwise spacing,  $0.8 \sim 1.0\delta$ , appear at  $y/\delta \approx 0.2$ . This indicates that hierarchical very large-scale structures exist in the outer layer, which may be closely associated with the enhanced nonlinear effect with increasing Reynolds number.

Ensemble averaged statistics are/will be presented at <http://murasun.me.noda.tus.ac.jp>.

## Acknowledgments

Computations were made with Numerical Simulator III at Computer Center of Japan Aerospace Exploration Agency, and also VPP5000 at Tokyo University of Science and Computer Center of Kyushu University.

## References

- [1] Bremhorst, K. and Bullock, K., Spectral measurements of turbulent heat and momentum transfer in fully developed pipe flow, *Int. J. Heat Mass Transfer*, **16**, 1973, 2141-2154.
- [2] Fulachier, L. and Dumas, R., Spectral analogy between temperature and velocity fluctuations in a turbulent boundary layer, *J. Fluid Mech.*, **77**, 1976, 257-277.
- [3] Perry, A. E. and Hoffmann, P. H., An experimental study of turbulent convective heat transfer from a flat plate, *J. Fluid Mech.*, **77**, 1976, 355-368.
- [4] Subramanian, C. S. and Antonia, R. A., Effect of Reynolds number on a slightly heated turbulent boundary layer, *Int. J. Heat Mass Transfer*, **24**, 1981, 1833-1846.
- [5] Antonia, R. A., Krishnamoorthy, L. V. and Fulachier, L., Correlation between the longitudinal velocity fluctuation and temperature fluctuation in the near-wall region of a turbulent boundary layer, *Int. J. Heat Mass Transfer*, **31**, 1988, 723-730.
- [6] Kim, J. and Moin, P., Transport of passive scalars in a turbulent channel flow, in *Turbulent shear flows 6*, editors J.-C. André et al., Springer-Verlag, Berlin, 1989, 85-96.
- [7] Lyons, S. L., Hanratty, T. J., and McLaughlin, J. B., Direct numerical simulation of passive heat transfer in a turbulent channel flow, *Int. J. Heat Mass Transfer*, **34**, 1991, 1149-1161.
- [8] Kasagi, N., Tomita, Y., and Kuroda, A., Direct numerical simulation of passive scalar field in a turbulent channel flow, *ASME J. Heat Transfer*, **114**, 1992, 598-606.
- [9] Kasagi, N. and Ohtsubo, Y., Direct numerical simulation of low Prandtl number thermal field in a turbulent channel flow, in *Turbulent shear flows 8*, editors F. Durst et al., Springer-Verlag, Berlin, 1993, 97-119.
- [10] Kawamura, H., Ohsaka, K., Abe, H., and Yamamoto, K., DNS of turbulent heat transfer in channel flow with low to medium-high Prandtl number fluid, *Int. J. Heat and Fluid Flow*, **19**, 1998, 482-491.
- [11] Na, Y. and Hanratty, T. J., Limiting behavior of turbulent scalar transport close to a wall, *Int. J. Heat Mass Transfer*, **43**, 2000, 1749-1758.
- [12] Moser, R. D., Kim, J., and Mansour, N. N., Direct numerical simulation of turbulent channel flow up to  $Re_\tau = 590$ , *Phys. Fluids*, **11**, 1999, 943-945.
- [13] Abe, H., Kawamura, H., and Matsuo, Y., Direct numerical simulation of a fully developed turbulent channel flow with respect to the Reynolds number dependence, *ASME J. Fluids Eng.*, **123**, 2001, 382-393.
- [14] del Álamo, J. C. and Jiménez, J., Spectra of the very large anisotropic scales in turbulent channels, *Phys. Fluids*, **15**, 2003, L41-L44.
- [15] del Álamo, J. C., Jiménez, J., Zandonade, P., and Moser, R. D., Scaling of the energy spectra of turbulent channels, *J. Fluid Mech.*, **500**, 2004, 135-144.
- [16] Abe, H., Kawamura, H., and Choi, H., Very large-scale structures and their effects on the wall shear-stress fluctuations in a turbulent channel flow up to  $Re_\tau = 640$ , *ASME J. Fluids Eng.*, 2004, to appear.
- [17] Wikström, P. M. and Johansson, A. V., DNS and scalar-flux transport modeling in a turbulent channel flow, in *Proc. of 2nd EF Conference in Turbulent Heat Transfer*, vol. 1, Manchester, UK, 1998, 6.46-6.51.
- [18] Kawamura, H., Abe, H. and Matsuo, Y., DNS of turbulent heat transfer in channel flow with respect to Reynolds and Prandtl number effects, *Int. J. Heat and Fluid Flow*, **20**, 1999, 196-207.
- [19] Kawamura, H., Abe, H., and Shingai, K., DNS of turbulence and heat transport in a channel flow with different Reynolds and Prandtl numbers and boundary conditions, in *Proc. of 3rd Int. Symp. Turbulence, Heat and Mass Transfer*, editors Y. Nagano et al., 2000, 15-32.
- [20] Wei, T. and Willmarth, W. W., Reynolds-number effects on the structures of a turbulent channel flow, *J. Fluid Mech.*, **204**, 1989, 57-95.
- [21] Abe, H. and Kawamura, H., A study of turbulence thermal structure in a channel flow through DNS up to  $Re_\tau = 640$  with  $Pr = 0.025$  and  $0.71$ , in *Proc. of 9th European Turbulence Conference*, 2002, 399-402.
- [22] Abe, H., Kawamura, H., and Matsuo, Y., Surface heat-flux fluctuations in a turbulent channel flow up to  $Re_\tau = 1020$  with  $Pr = 0.025$  and  $0.71$ , *Int. J. Heat and Fluid Flow*, **25**, 2004, 404-419.
- [23] Dukowicz, J. K. and Dvinsky, A. S., Approximate factorization as a high order splitting for the implicit incompressible flow equations, *J. Comp. Phys.*, **102**, 1992, 336-347.
- [24] Spalart, P. R., Moser, R. D., and Rogers, M. M., Spectral methods for the Navier-Stokes equations with one infinite and two periodic directions, *J. Comp. Phys.*, **96**, 1991, 297-324.
- [25] Morinishi, Y., Lund, T. S., Vasilyev, O. V., and Moin, P., Fully conservative higher order finite difference schemes for incompressible flow, *J. Comp. Phys.*, **143**, 1998, 90-124.
- [26] Hoffmann, P. H. and Perry, A. E., The development of thermal boundary layers on flat plates, *Int. J. Heat Mass Transfer*, **22**, 1979, 39-46.
- [27] Kader, B. A., Temperature and concentration profiles in fully turbulent boundary layers, *Int. J. Heat Mass Transfer*, **24**, 1981, 1541-1544.
- [28] Antonia, R. A. and Kim, J., Turbulent Prandtl number in the near-wall region of a turbulent channel flow, *Int. J. Heat Mass Transfer*, **34**, 1991, 1905-1908.
- [29] Kong, H., Choi, H., and Lee, J. S., Direct numerical simulation of turbulent thermal boundary layers, *Phys. Fluids*, **12**, 2000, 2555-2568.
- [30] Béguyer, C., Dekeyser, I., and Launder, B. E., Ratio of scalar and velocity dissipation time scales in shear flow turbulence, *Phys. Fluids*, **21**, 1978, 307-310.
- [31] Kim, K. C. and Adrian, R. J., Very large-scale motion in the outer layer, *Phys. Fluids*, **11**, 1999, 417-422.
- [32] Adrian, R. J., Meinhardt, C. D. and Tomkins, C. D., Vortex organization in the outer layer region of the turbulent boundary layer, *J. Fluid Mech.*, **422**, 2000, 1-54.
- [33] Liu, Z., Adrian, R. J. and Hanratty, T. J., Large-scale modes of turbulent channel flow: transport and structure, *J. Fluid Mech.*, **448**, 2001, 53-80.
- [34] Chen, C.-H.P. and Blackwelder, R. F., Large-scale motion in a turbulent boundary layer: a study using temperature contamination, *J. Fluid Mech.*, **89**, 1978, 1-31.

## Effects of subtle and dramatic changes to initial conditions on a jet's turbulent structure, mixing and combustion

G. J. Nathan<sup>1</sup>, J. Mi<sup>1</sup>, G. J. R. Newbold<sup>1</sup>, D. S. Nobes<sup>1</sup> and Z.T. Alwahabi<sup>2</sup>

Schools of Mechanical<sup>1</sup> and Chemical<sup>2</sup> Engineering, The University of Adelaide, South Australia 5005, Australia

### Abstract

Turbulent jet diffusion flames have been widely studied and have also found wide application in industrial burners. However, subtle or dramatic differences often exist between the configurations investigated by different research groups, and also between those investigated in laboratories and those used in industrial burner designs. Although the importance of initial conditions is well established as a general principal, many details of these influences are still only emerging. The present paper reviews previous work, and presents new results, of the effect of such differences on the non-reacting scalar field and on flames. Subtle differences are those arising from a round pipe, a smoothly contracting nozzle and sharp-edged orifice plate. Dramatic differences are generated by large-scale, unsteady precession of the emerging jet. The differences are related to the underlying large-scale organised motions. In a flame, these differences influence the global strain rate, and so the heat losses due to flame radiation and thermal NO<sub>x</sub> emissions. It is also shown that increased rates of mixing are not necessarily beneficial for a flame.

### Introduction

George [1] deduced analytically that turbulent free shear flows such as jets and wakes can converge asymptotically to a variety of different self-preserving states, depending on their individual initial conditions. It has since become recognized that all turbulent flows are sensitive to the inlet and boundary conditions, even in the far field. For this reason the mixing characteristics of turbulent jets from different devices are anticipated to be individually distinctive and the greatest of care is required to reproduce two experiments, or to allow viable comparisons between experiments and models. However the extent to which given changes may influence the flow or a flame is still relatively poorly documented or understood.

In turbulent combustion, mixing is often the rate-limiting step. Knowledge of this has stimulated the development of a wide range of practical mixing devices, first with a view to increasing flame stability and combustion intensity e.g. swirl and bluff bodies, and later to reduce NO<sub>x</sub> emissions, e.g. staged combustion. The rate-limiting importance of mixing is also the basis of physical modelling [52] and the first step in developing reliable mathematical and computational models. However, the interactions between turbulent mixing processes and combustion/chemical reactions are extremely complex. A wide range of chemical time-scales exist, from many gas-phase reactions that are typically faster than the mixing rates, to reactions such as those for soot formation, growth and oxidation, whose time-scale is typically longer than that of mixing. Hence the extent to which changes in initial conditions of a jet influence a flame is even more complex than on the flow alone.

Furthermore, accurate measurements, already difficult enough in cold-flow [53] are even much more difficult in flames. Consequently, many developments of turbulent combustion systems have to make use of both reacting and non-reacting investigations. This is particularly true in the systems that involve

highly unsteady flows, where the instantaneous flow differs dramatically from the mean flow, such as the precessing vortex core in swirling flows, e.g., [2].

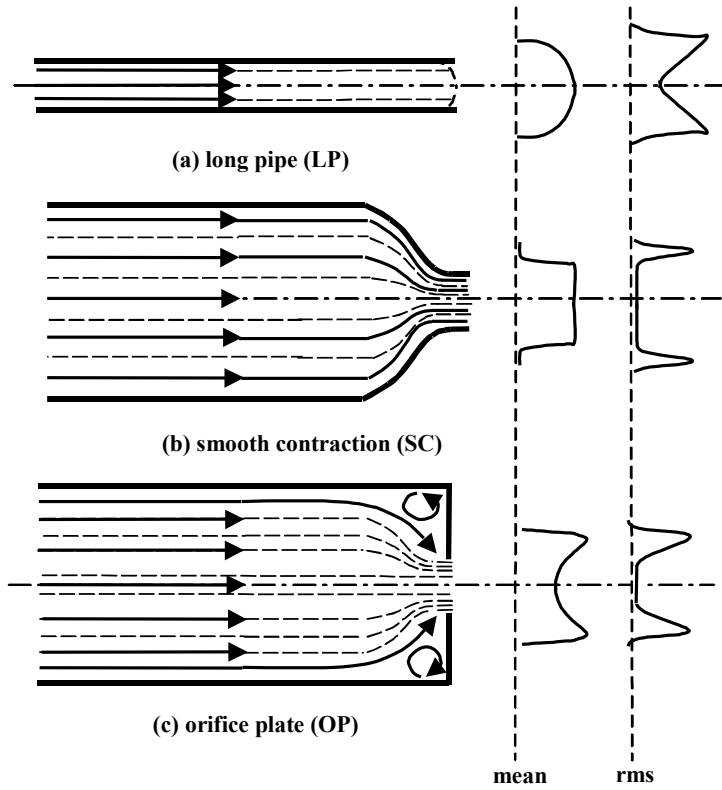
A common target of most of the developments of “enhanced mixing” combustion devices has been to increase the rate of entrainment of surrounding air as indicated, for example, by spreading rate of these jets. This appears to be based on the widely held assumption that increased mean mixing rates are necessarily desirable, although this has not been adequately assessed. One such approach has been to stimulate, or excite, the large-scale, coherent motions in the emerging jet, based on the knowledge that such motions play a dominant role in the gross transport processes in jets and jet flames. Perhaps the best-known approach is the use of acoustic excitation, either in jets [3], jet flames [4] or in pulsed combustion systems [5]. Another approach is the use of mechanically oscillating devices, e.g. [6-7], and fluidically excited devices [8]. Yet, another class of mixing device is the fluidic devices that produce a jet of large-scale precession [9] or flapping [10].

Despite the large number of investigations of jet mixing devices, several important aspects remain poorly understood. Of these, the present paper seeks to address the following issues:

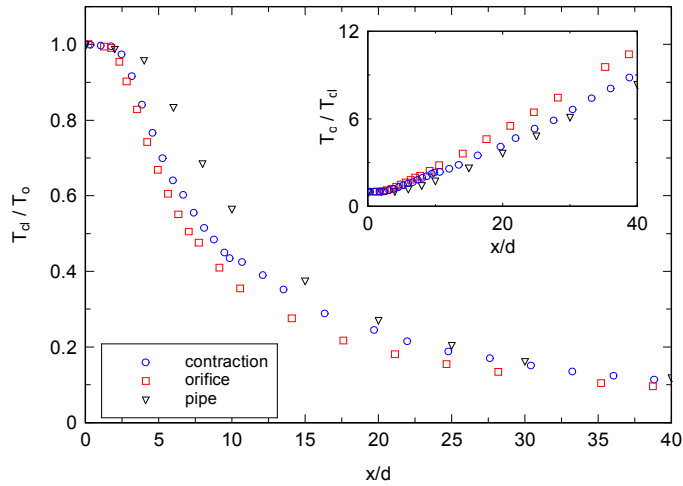
- The effect of initial conditions on jet's underlying turbulent structure and mixing behaviour,
- The near and far field flow and mixing behaviour in “excited” jets with highly unsteady initial flows,
- The implications of these differences in mixing on combustion performance.

### Effects of subtle differences in initial conditions

Turbulent jets from round nozzles have been extensively studied for many decades. The three most common classes of round nozzle are a smoothly contracting nozzle, a sharp-edged orifice plate and a long pipe. Where the length of a supply pipe is sufficient, typically at least 70 diameters, the flow within it is fully developed. A jet with a fully-developed-pipe initial flow has a mean velocity profile that closely approximates the well-known 1/7 power law and an “M” shaped rms profile (Fig. 1a). Such jets are moderately common in burners because of their simplicity and ease of manufacture. In contrast, jets issuing from an aerodynamically well-designed smoothly contracting nozzle have an initial mean velocity profile of that is approximately uniform or of a “top-hat” shape (Fig. 1b). They also have a low and uniform rms, except at the very edge of the jet where the shear is high. Jets from these nozzles are widely studied because the uniform initial velocity profile is well suited to analytical (and some numerical) investigations. They also have a lower pressure drop than a long pipe because the supply pipe is of larger diameter. Sharp edged orifice plates are also simple to manufacture and are therefore widely used. The sudden contraction on the upstream side of the plate results in the well-known “vena contracta”, where flow streamlines initially converge towards the jet axis. Their mean velocity is “saddle-backed” and the initial rms profile somewhere between those of the other two nozzles mentioned (Fig. 1c).



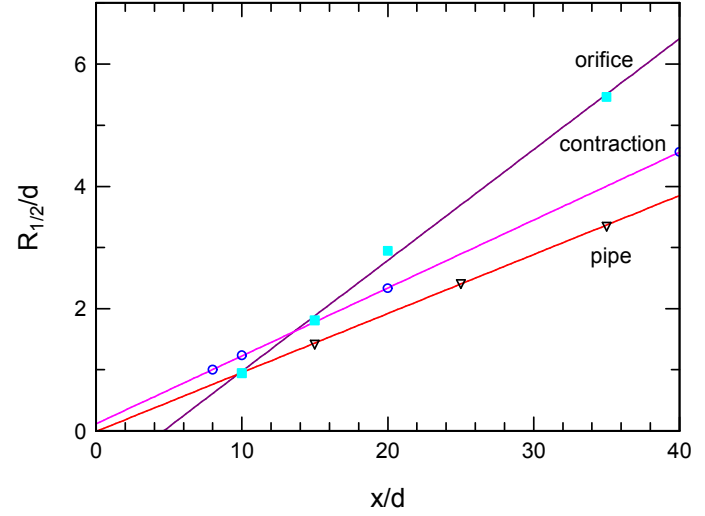
**Fig. 1.** Simplified representation of the initial velocity profiles of jets emerging from a long pipe, a smooth contraction and a sharp-edged orifice plate.



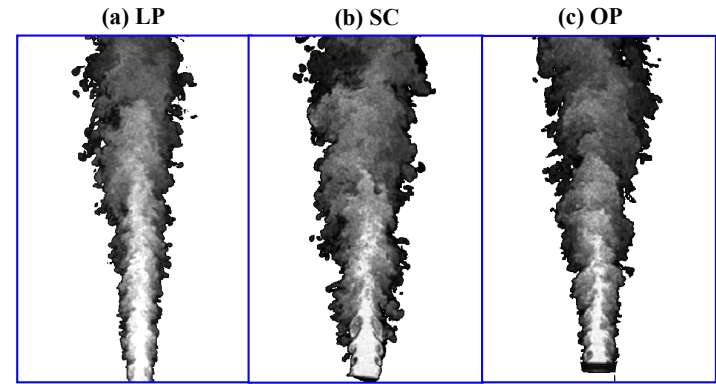
**Fig. 2.** Centreline variations of the mean scalar of the three jets [21].

The significance of initial conditions on the development of an axisymmetric jet-mixing layer near the nozzle exit has been well documented (e.g. [11-16]). However, until recently, they supported the classical belief that the influence of initial conditions of a flow decays rapidly with downstream distance to converge to a universal far-field flow with a fixed rate of spread and decay [17]. The classical view is that the differences in initial conditions result only in a shift in the location of the virtual origin of the jet (e.g. [18]), i.e. the “point” source in space from which the far-field mean flow emanates [19]. While this classical hypothesis was questioned analytically, e.g. by George [1], it has only recently been confirmed by experiments. Mi *et al.* [20-22] and Xu and Antonia [23] have shown that differences in initial conditions, as indicated by the exit velocity profiles, propagate throughout the entire field, affecting even the far-field spread rate, decay rate, and almost all turbulence statistics. The mean decay rate of the scalar fields of three jets of equal Reynolds number,  $Re$ , and diameter, but from different types of nozzles, is shown in Figure 2. It is clear that the decay rate for the orifice plate is the highest, followed by that from the smooth contraction

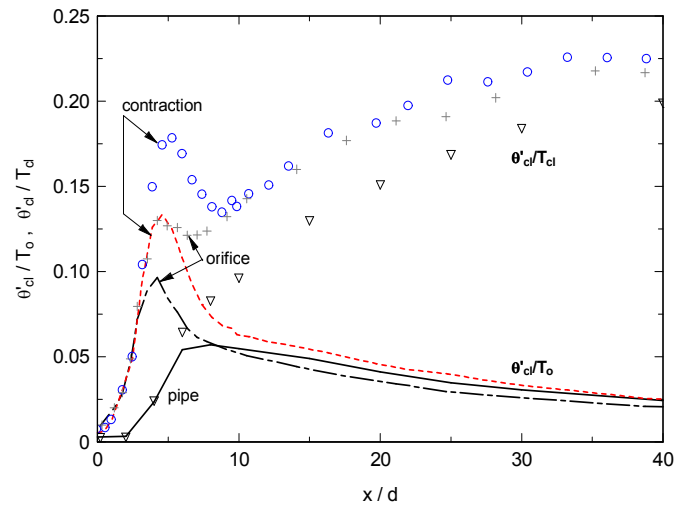
and then by that from the long pipe. Consistently, the rates of spread and decay of scalar advection are greatest in the orifice jet and lowest in the pipe jet (Fig. 3). The measurements also show that even the concept of a “virtual origin” of a classical jet is only an idealisation that is fundamentally flawed, since the virtual origin of the mean spreading rate is always different from that of the mean centre-line decay rate [20]. These values also depend upon the jet source conditions.



**Fig. 3.** Axial variations of the scalar half-radius of the three jets [21].



**Fig. 4.** Instantaneous planar Mie-scattering images of the scalar fields in (a) a LP jet, (b) a SC jet and (c) an OP jet [21].



**Fig. 5.** The normalised centreline scalar RMS of jets from an orifice plate, a smooth contraction nozzle and a long pipe [21]. Here  $\theta'$  is the rms of the fluctuations of the passive temperature marker,  $T_0$  is the initial temperature difference between the jet and ambient fluid, and  $T_{cl}$  is the local mean temperature difference on the jet centre-line.

Mi *et al.* [21] further showed, using Mie scattering images of the concentration that, as might be expected, the differences in the scalar flow are associated with differences in the underlying flow



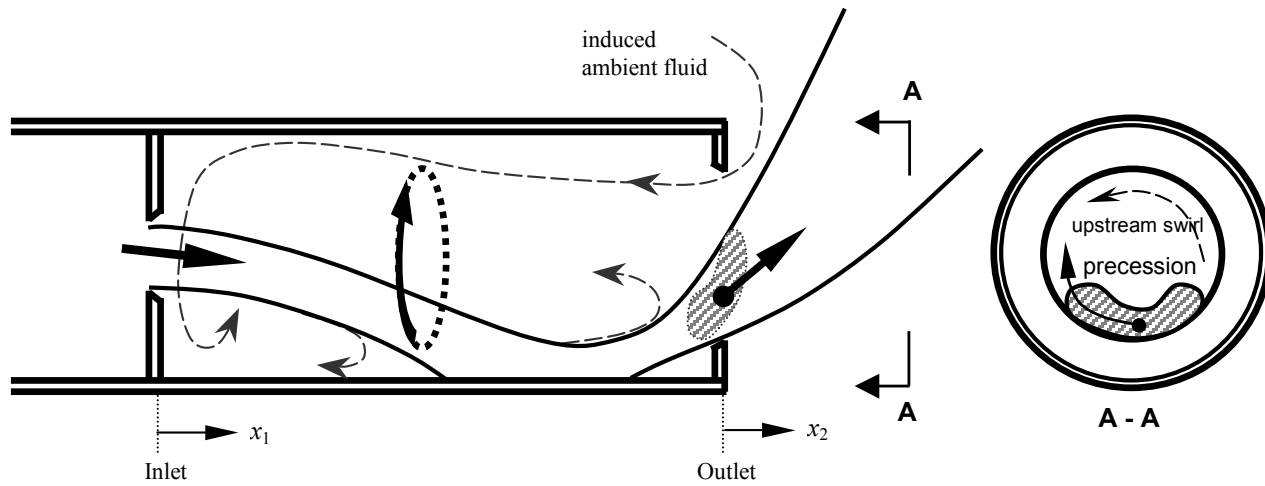


Fig. 6. A simplified schematic representation of the fluidic nozzle and the precessing jet flow [9].

structure (Fig. 4). This dependence is also reflected in the centreline variation of the scalar RMS (Fig. 5).

It should be noted that in these measurements the mixing of jet and ambient fluids was performed by slightly heating the jet relative to the ambient fluid, so providing a marker for the scalar. Here  $\theta'$  is the rms of the fluctuations of the passive temperature marker,  $T_0$  is the initial temperature difference between the jet and ambient fluid, and  $T_{cl}$  is the local mean temperature difference on the jet centre-line. In the near field, the locally normalised rms of fluctuations ( $\langle \theta'^2 \rangle^{1/2} / \langle T \rangle_{cl}$ ) exhibits a local maximum slightly downstream from the potential core for the SC and OP jets, but not for the pipe jet. The presence of the maximum is associated with the convergence of the primary coherent vortex rings generated by rolling up the thin initial shear layer (see Fig. 4). The absence of the maximum for the pipe jet is attributed to the much weaker coherence in the underlying flow structures associated with initially the fully-developed pipe flow [20]. The second important difference is that the far-field, asymptotic values of the two jet flows are also different, with that from the pipe being lower. Based on previous studies, Mi et al. [20] hypothesised that the differences in the underlying coherent structures also exist in the far field. Taken together, these results demonstrate that the far field of a jet does not forget its origin entirely. Given these differences in both the mean flow everywhere and especially in the initial flow where a lifted flame is stabilised, differences in a flame might also be expected, as discussed below.

#### Effects of highly unsteady initial flow on jet mixing

Precessing jets (PJ) are a class of highly unsteady flows which are of both scientific interest and practical significance because of the benefits found when used as industrial burners. Precession is the term used to describe the azimuthal oscillation of a flow about an axis. Examples in fluid mechanics include the precessing vortex core found in swirling flows [2] and precessing jet flows [9]. The former precession in swirl burners can have significance in the well-known combustion driven oscillations in gas turbine combustors.

Precessing jet flows have found application in rotary kilns where high radiant heat and low  $\text{NO}_x$  emissions are sought [24-25]. Direct comparison of the flames from a PJ nozzle and an optimized high momentum jet burner in a pilot-scale cement kiln simulator demonstrated a net increase in heat transfer of 4% and reduction in  $\text{NO}_x$  emissions by 30% [26]. These precessing flows can be generated naturally in an axisymmetric fluidic device [9,27] or by mechanical rotation of a nozzle device [28-29]. The registered trade name for the burners that utilise the fluidic PJ nozzle [30] is Gyro-Therm®.

The unsteady flow within and emerging from the fluidic PJ nozzle is illustrated schematically in Fig. 6. The dimensions of the chamber are such that the instantaneous jet reattaches asymmetrically within it and emerges from the chamber outlet at about  $45^\circ$  to the nozzle axis. The asymmetry is accompanied by a rotating pressure field so that the entire flow-field, including the emerging jet, precesses [9]. The flow within the chamber is complex, containing a large-scale reverse flow zone and a region of high swirl at the upstream end of the chamber. The frequency of the precession is two orders of magnitude lower than that of formation of the primary vortices in the SC free jet mentioned above (see Fig. 4b).

However, of particular interest to the present discussion, the precession of the emerging asymmetric jet causes a large increase in the initial spreading rate of the time-averaged jet relative to a “steady” jet, as clearly demonstrated by the concentration half-width contours of the FPJ flows in Fig. 7. An increase in initial spreading rate is not unique to the PJ nozzle. Alternative devices which have also achieved increased spreading include a fluidic device [8], mechanical devices [6] and acoustic devices [3, 31]. The increased initial spread led those authors to refer to their respective devices as “enhanced mixing” nozzles, under the assumption that increased spreading implies increased entrainment, and that increased entrainment implies enhanced mixing. However, while the arguments sound plausible, they may not necessarily be correct, at least for highly unsteady jets.

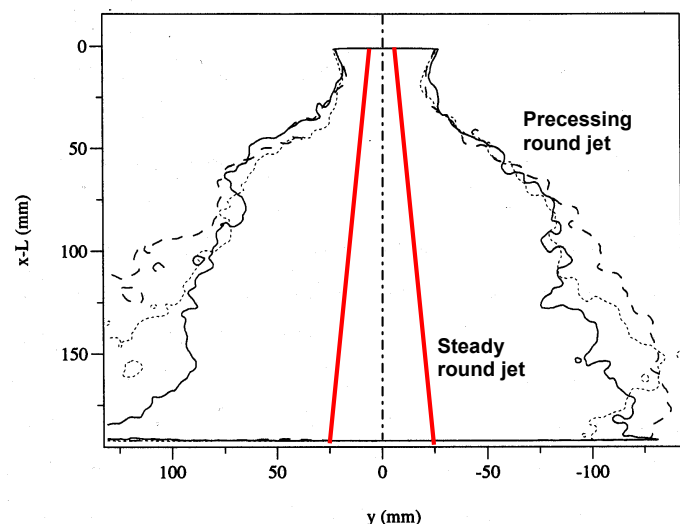


Fig. 7. Concentration half-width contours of the FPJ flows. The jet initial diameter is 7.3 mm [33]. —, Re = 37,000; ----, Re = 49,200; ····, Re = 61,500.

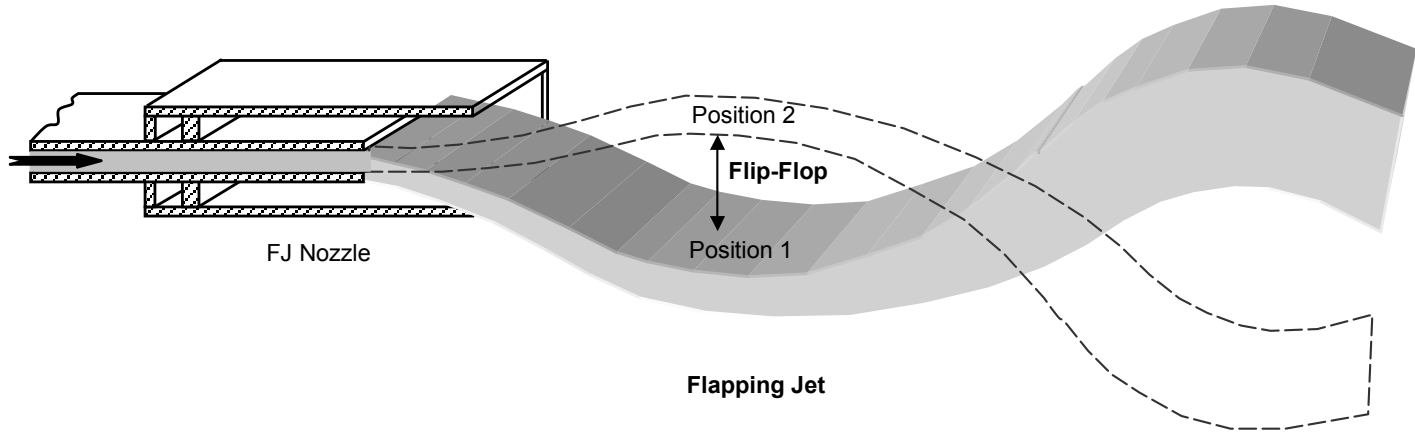


Fig. 8. A simplified schematic representation of the fluidic nozzle producing a pseudo two-dimensional flapping motion.

Mi and Nathan [10] used the fluidic device shown in Fig. 8 to generate a two-dimensional flapping jet that is broadly analogous to the azimuthal precessing motion. The chamber of this device is rectangular in cross-section, and the inlet nozzle is of smaller span than the chamber to provide a feed-back path and allow the pressure fields on either side of the jet to communicate. Their flow visualization and velocity measurements showed that this jet also produces a significant increase in the initial spreading rate of the jet [10]. The *initial rate* of entrainment outside the chamber is also higher, as shown by the volume flux measurements through various downstream cross-sections (Fig. 9). However, the *total* amount of ambient fluid entrained by the flapping jet was found to be less than that by the non-flapping counterpart (Fig. 9).

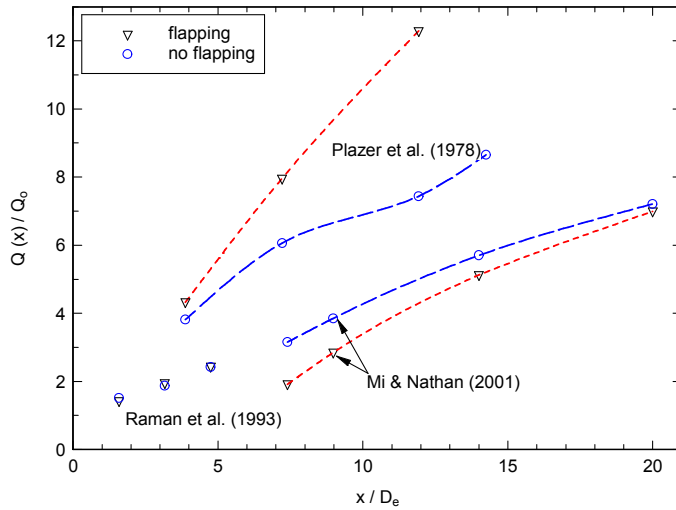


Fig. 9. Entrainment of the flapping jet relative to that of a steady jet [10].

Figure 9 presents a three-dimensional integral of the axial velocity flux through different transverse planes obtained in [10]. It is important to note that the axial coordinate is measured from the inlet plane of the nozzle chamber. This provides a direct comparison of the volume flux of fluid for the cases with the nozzle chamber present and removed. The volume flux is also normalized relative to the flow introduced through the nozzle. It shows that the initial *rate* of entrainment downstream from the chamber exit is greater for the flapping jet than the steady jet, consistent with the increased rate of spread resulting from the flapping motion. Nevertheless, the total volume flux for the flapping jet never actually reaches that of the steady jet counterpart. This is because the presence of the chamber walls inhibits the jet entrainment of ambient fluid from outside the chamber. That the presence of the nozzle chamber creates a net loss of entrainment is perhaps not unexpected given the fact that the chamber creates a pressure loss and the second law of thermodynamics. The mechanical flapping nozzle (no chamber) of Plazer et al. [7] was measured to produce a jet with significantly more ambient fluid entrained (Fig. 9). However this

measurement was only performed along one axis, so the finding relies on the assumption of two-dimensionality which is not necessarily correct.

We have also conducted scalar measurements for unsteady oscillating jets. Newbold [33] measured the concentration field of an unconfined precessing jet from the fluidic nozzle (FPJ). Parham [34] studied the effect of a co-flow and confinement on the same flow, while Nobes [35] measured the concentration field of a precessing jet from a mechanically rotating nozzle. The mechanical nozzle, shown in Fig. 10 and described in detail elsewhere [36], can provide well-defined and controllable initial conditions for the mechanical precessing jet (MPJ). One important finding of the work on the MPJ flow is the importance of the dimensionless frequency of precession, the precession Strouhal number,  $St_p = f_p d / u_e$ . Here  $f_p$  is the frequency of precession,  $d$  the nozzle exit diameter and  $u_e$  the bulk-mean exit velocity. As  $St_p$  approaches zero, the precession has negligible influence on the flow, and its trajectory remains at the exit angle. However, above a critical Strouhal number,  $St_c$ , precession causes the jet to “spiral” into a helix [28,29]. For  $St_p > 0.01$ , the helix converges upon itself within about 5 nozzle diameters from the exit plane [29]. This is associated with a low-pressure core associated with the asymmetric entrainment [36].

Figure 13 compares the average scalar mixing field of a non-

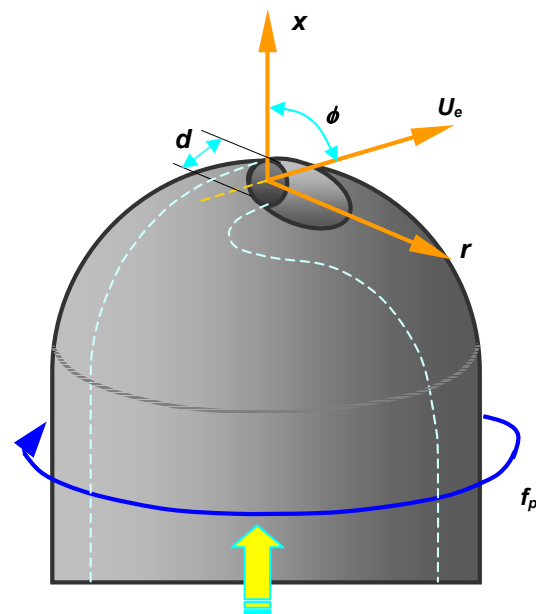


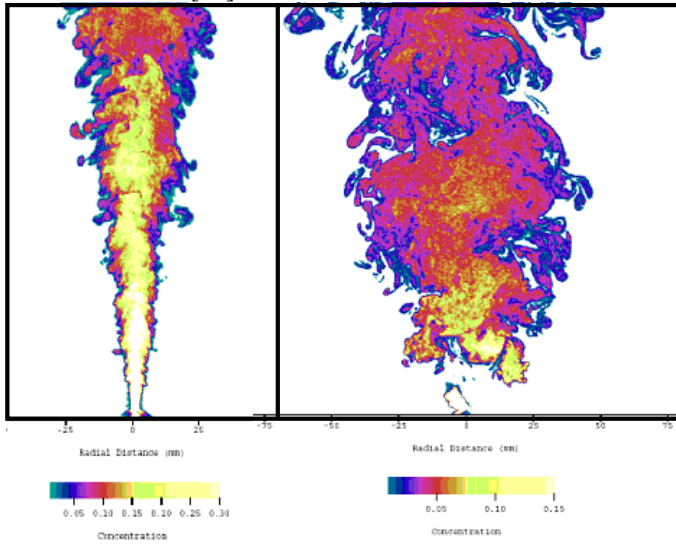
Fig. 10. Schematic representation of the MPJ nozzle that produces a PJ with well-defined and controllable initial conditions [27].

precessing round jet and the phase-averaged scalar field of the MPJ above  $St_c$ . The laser sheet cuts through the helix, which is evident for approximately one full turn. Downstream from the helix, the global jet undergoes a transition to a spreading rate

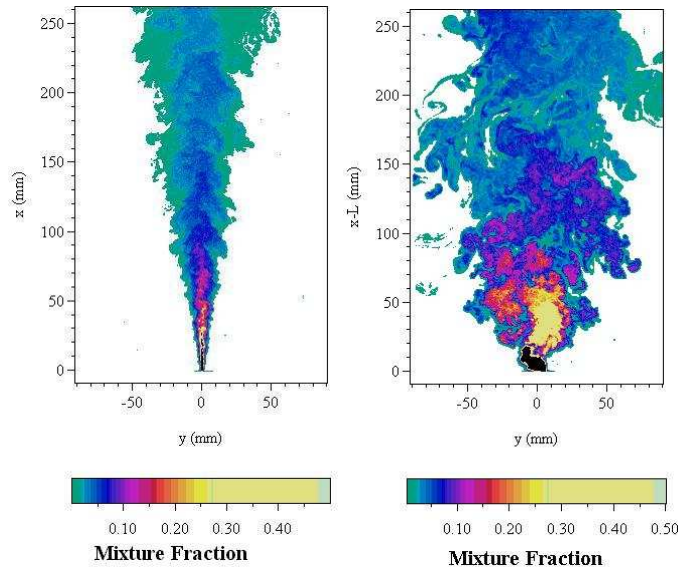


broadly comparable with that of a simple jet. Hence the rapid initial spreading rate does not extend into the far field (Fig. 13). The precessing motion also decays through the transition region, so that the phase-averaged scalar field is axi-symmetric for  $x/d > 15$  (Fig 13). In addition, frequency spectra reveal that neither the precession, nor any sub-harmonic, is evident beyond a downstream distance of about 12-15 nozzle diameters [29]. The near-field flow from the FPJ nozzle does differ from that of the MPJ in that it does not transcribe a clear helical trajectory. The initial structure is also highly non-uniform and more complex [32]. However a similar decay in precession is supported by the instantaneous images, which do not reveal any correlation between far-field structure and the position of the emerging jet.

Comparison of the instantaneous concentration measurements of the MPJ (Fig. 11) and FPJ (Fig. 12) suggests that, while there are significant differences in the details of the flow, especially in the near field, many of the gross features are similar. Importantly, both jets exhibit a rapid initial spreading followed by the convergence to a far-field flow. Likewise, broad features of their flames are similar [41].



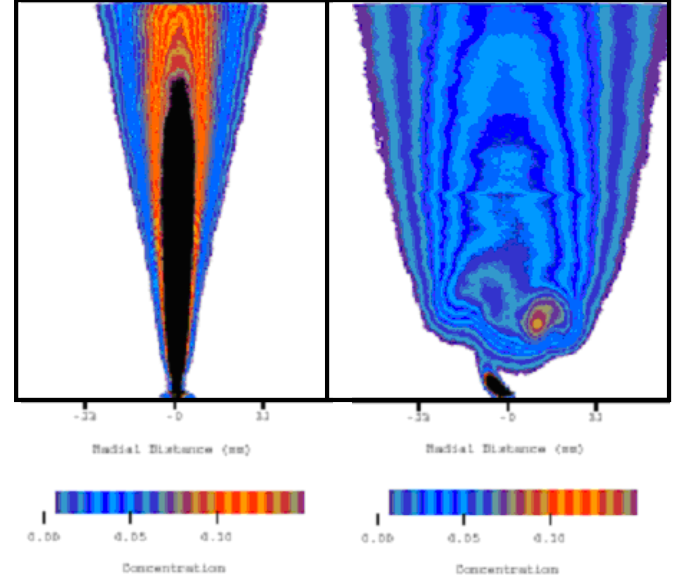
**Fig. 11.** The instantaneous non-reacting mixture fraction in a simple jet (left) and a mechanically precessing jet with  $St = 0.0126$  (right). The jet initial diameter is 3 mm and  $Re = 3,800$  [35].



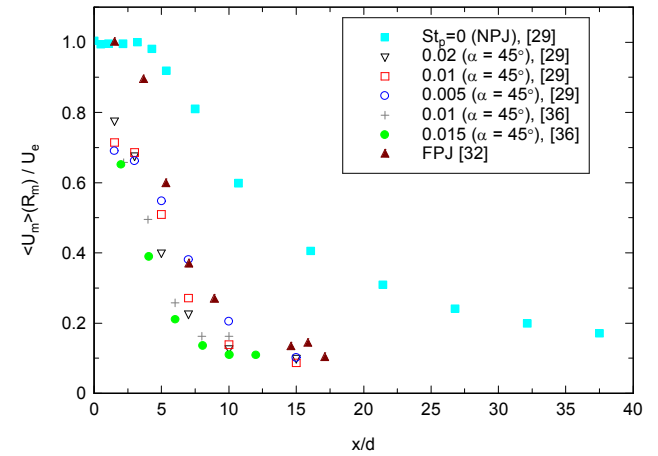
**Fig. 12.** Instantaneous non-reacting mixture fraction of the emerging simple jet (left) and a fluidic precessing jet (bottom). The jet initial diameter is 3 mm and  $Re = 20,000$  [33].

Figure 14 shows that the local phase-averaged maximum velocity,  $\langle U_m \rangle$ , of the “instantaneous” precessing jet flow in the near field ( $x/d < 15$ ), exhibits a substantially stronger decay than the equivalent,  $\langle U_c \rangle$ , of the non-precessing jet. This is consistent with the precession causing an increase in the strain on the jet.

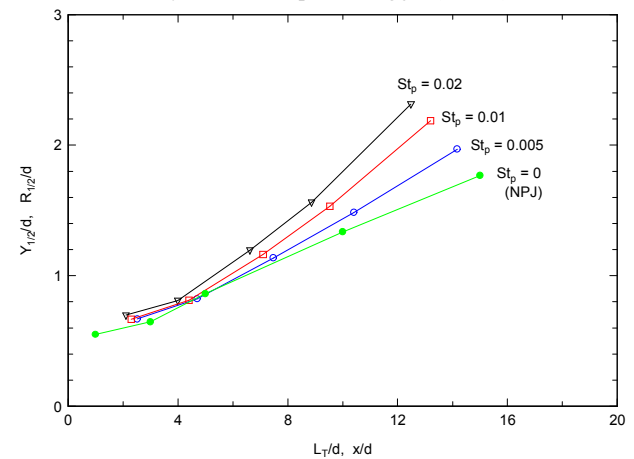
Consistently, the conditionally averaged half-width,  $Y_{1/2}$ , of the local precessing jet flows spreads more rapidly than does that of the half radius,  $R_{1/2}$ , of the non-precessing round jet (Fig. 15). Taken together, this implies that the precession of the entire jet promotes the *initial* entrainment of ambient fluid, consistent with the flapping jet discussed above. Figs. 14 and 15 also suggest that the initial velocity decay and spread rates of the precessing jet increase as the Strouhal number  $St_p$  increases. However, in the far field, the strain rates in the flows for  $St > St_c$  are reduced, as determined by two point spatial correlation contours of the scalar field for both the MPJ [35] and FPJ [33] flows.



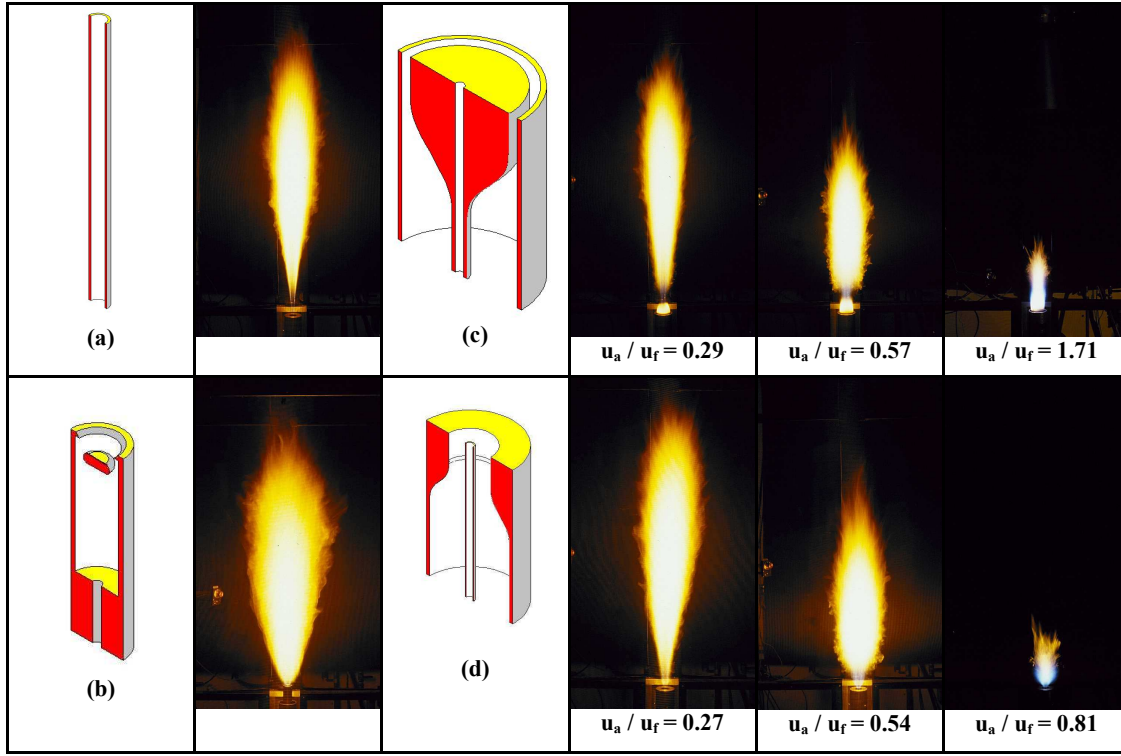
**Fig. 13.** Mean non-reacting mixture fractions of a non-precessing jet (left) and a MPJ with  $St = 0.0096$  (right). The jet initial diameter is 3 mm and  $Re = 3,800$  [34].



**Fig. 14.** Axial variations of local maxima of the conditionally averaged (“instantaneous”) precessing jet,  $\langle U_m \rangle(R_m)$  from the MPJ nozzle and the centreline  $\langle U_c \rangle$  decay for the non-precessing jet ( $\alpha = 0^\circ$ ) [29].



**Fig. 15.** Axial variations of the averaged half-width  $Y_{1/2}$  for the MPJ and the non-precessing jet ( $\alpha = 0^\circ$ ) [29].



**Fig. 16.** Time-averaged flames from (a) an axial jet nozzle, (b) a precessing jet nozzle, (c) a bluff-body nozzle, and (d) a swirling jet nozzle. All nozzles have the same central fuel pipe, are fired with propane and have identical fuel velocity,  $u_f$ , equating to  $Re_f = 20,000$  and are presented to scale [40].

### Effects of initial conditions on flames

The non-linear nature of flames means that they can be highly sensitive to initial conditions. For example, Dahm and Dibble [59] have shown both experimentally and theoretically that a co-flow velocity of the order of only 1% of the jet velocity leads to a reduction of the order of 50% in the blow out velocity compared with stagnant air. Likewise, a slight co-flow of the order of 2% has a dramatic effect on the length of pulsed flames [60]. However other aspects of initial and boundary conditions, such as the effect of initial velocity profile, have not been considered previously. Even the measurements of basic properties such as lift-off height and blow-off velocity as reported in text books [e.g. 54] do not raise the issue. Data is only presented for a single nozzle type (a long pipe), based on the pioneering measurements of Kalghatgi [55], and the lack of reference to possible effects of initial conditions evokes the tacit assumption that performance is independent of the nozzle type. However, our recent measurements [56] have shown that lift-off and blow-off velocities are 40% and 17% higher, respectively, for a smooth contraction than a long pipe, the asymptotic flame length of the smooth contraction is 13% greater and the radiant energy from the smooth contraction nozzle is lower.

A broader study of the effect of more significant changes to mixing on global flame performance was performed by Newbold *et al.* [40]. They compared the flames from four nozzles with dramatically different mixing conditions: a simple jet issuing from a long pipe, a PJ nozzle, a swirl jet and a bluff body jet. The flames were unconfined to avoid the influences of confinement, which can also be significant, and examined in with identical facilities to avoid subtle differences in conditions. The four burners were carefully designed to utilise the identical source conditions, including fuel nozzle geometry, (for the PJ nozzle this corresponds to the inlet to the nozzle chamber) and the same fuel flow rate. Each of these flames, as shown in Fig. 16, are dramatically different. However, before returning to a detailed

comparison of each, we will first discuss the key features of precessing jet flames, which are least well known.

When firing gas in the range  $St > St_c$ , the PJ flame is typically stabilised several nozzle diameters downstream from the burner. However the flame length is several hundred times the nozzle diameter. Hence nearly all of the combustion occurs *downstream* from the near-field region where precession is evident. Various investigations have confirmed that precession is also not evident for  $St > St_c$ , which is also the range in which the fluidic PJ nozzle operates [27]. Newbold *et al.* [37] identified and analysed the large-scale structures that propagate through the flame using the “volume rendering” technique of Mungal *et al.* [38]. This is constructed from a time-series of images of the edge of the flame, as determined from the visible light naturally emitted by it. They showed that the frequency of these large-scale motions is more than an order of magnitude lower than the precession frequency. Instead, in an open-flame environment, these large-scale motions are driven by buoyancy, while in a kiln they are driven by the confined, co-flowing environment. The independence from the precession frequency of the large-scale motions within the PJ flame is further supported by phase-averaged images of the OH radical excited by laser-induced fluorescence [39].

Although there seems to be no direct correlation between a PJ flame itself and the precession, the effect of precession within the upstream flow produces a dramatic influence on the flame. The rapid initial spreading produces a flame that is typically three times wider than the equivalent non-precessing axial jet flame with the same fuel and flow rate, although the length of the flame is only slightly shorter [40]. This results in a net increase in volume. Note again that the global characteristics of the flames from the MPJ and FPJ nozzles are similar, provided that the Strouhal number of precession is comparable [41].

The global mixing residence time of the fuel gases within a flame,  $\tau_G$ , can be defined as the flame volume divided by the volume flow-rate of fuel [42]. On this basis, Newbold *et al.* [40] compared the global mixing rate the four burner types shown in Fig. 16. Both the swirling and bluff body flows act to increase global mixing rates and flame strain relative to a simple jet, as evidenced by a reduced flame volume relative to the simple jet. In contrast, the PJ flame acts to decrease the global mixing rate and flame strain, which is related to the global strain rate defined by Rokke (1992 & 1994), as evidenced by an increased flame volume. Using an independent measurement of flame strain, also based on the volume rendering technique, Newbold *et al.* [43] found that PJ flames have a global flame strain that is an order of magnitude lower than that of a simple jet flame. This is consistent with the reduced far-field strain found in non-reacting measurements described above.

Flame strain rate has a dramatic effect on soot formation and flame radiation. This is because, unlike the primary reactions in a flame, the time-scales for the processes of soot formation, growth and oxidation are of the same order as the time-scales of mixing. The pioneering study by Kent and Bastin [44] shows that the soot volume fraction in a turbulent diffusion flame increases with decreased global strain, defined as  $u/d$  at the source. The same trend is also found by numerous fundamental studies of local flame strain in laminar flames. At strain rates below the soot-limiting critical strain rate, soot concentration decreases with increasing strain rate [45]. Decroix and Roberts [46] also found that the width of the soot field in a laminar counter-flow diffusion flame decreases linearly with the square root of the local strain rate. Our measurements have confirmed the trend in turbulent flames. The reduced strain in the far-field of PJ flames results in increased local soot volume fraction within the reaction zones and in three to six times more soot within comparable regions of the simple jet (SJ) flame [47]. The soot volume fractions within the bluff body (BB) flame are slightly lower, while the total soot within it is more than an order of magnitude lower [47]. It is important to make a distinction between the desirable presence of soot within a flame and the undesirable presence of soot emitted from a flame. Since the soot is consumed within the PJ flame envelope, its presence constitutes neither a loss of combustion efficiency nor an environmental threat.

The presence of soot within a flame acts to increase the flame emissivity. As solid particles, soot radiates incandescently over a wide range of wavelengths (i.e. broad-band), so radiating more effectively the narrow-band radiation from molecular processes. For this reason, lowering flame strain acts to promote flame radiation, both by increasing flame volume and by increasing the amount of soot within the flame [47], as described above. The effect of changing flame volume on flame radiation is shown in Fig. 17, where the radiant fraction,  $\chi_r$ , is defined as the percentage of the total energy of the flame that is released by radiation [40]. Perhaps surprisingly, the relationship is approximately linear across this wide range of flames spanning four different types of burners. Since the heat losses from a flame are typically dominated by radiation, this implies that the mean flame volume has a controlling influence on temperature for these flames. Flame radiation controls thermal NO<sub>x</sub> emissions from simple jet turbulent diffusion flames through its effect on flame temperature [42]. Newbold *et al.* [40] therefore concluded that the global flame strain, through its effect on radiation, has a controlling influence on thermal NO<sub>x</sub> emissions. The significance of this finding, in the context of modelling, is that the accurate prediction of mean flame volume and strain is of first order importance in predicting flame temperature, and hence, thermal NO<sub>x</sub> emissions, again highlighting the importance of mixing.

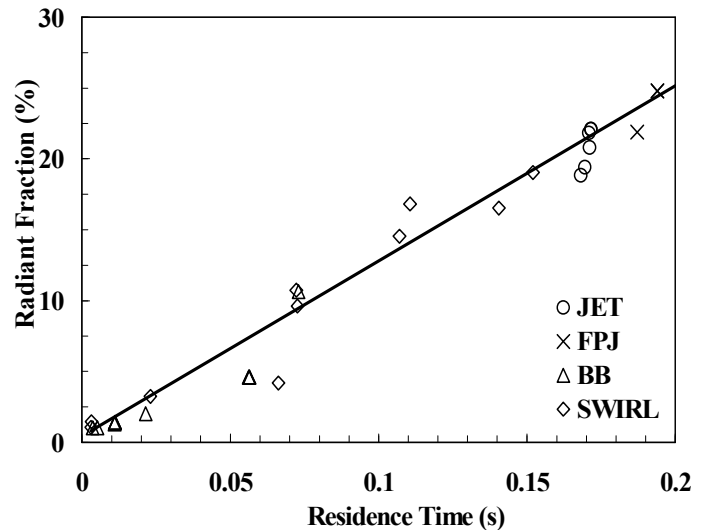


Fig. 17. The relationship between radiant fraction and global residence time for all of the flames in Fig. 16 [40].

In gaseous jet flames, the precessing flows with  $St > St_p$  result in lower global strain, and so, increased radiant heat transfer and lower thermal NO<sub>x</sub> emissions than simple jet, swirling jet and bluff-body jet flames [40]. This is further demonstrated by Pilot scale measurements in a cement kiln simulator which demonstrated that, relative to an optimised high momentum burner, the fluidic PJ flow provides about 4% increase in radiant heat-transfer and a shift in the profile toward the burner. Those measurements also revealed an equivalent reduction in NO<sub>x</sub> emissions, when corrected for differences in heat transfer, of about 30% [26]. These measurements are consistent with full-scale plant data. In natural-gas-fired cement [47] and lime [48] kilns, the precessing jet nozzle is found to typically provide a reduction in specific fuel consumption and/or increase in output by 5 to 10% and a reduction in NO<sub>x</sub> emissions by 30-50%. This reduction is significantly higher than the 5-10% difference at ambient conditions because the 800-1100°C air temperature in a rotary kiln means that NO<sub>x</sub> production is dominated by the thermal route, while prompt NO<sub>x</sub> is also significant at ambient temperature. The high temperatures in a kiln also increase the burn-out of any residual soot.

Similar trends are found to apply with the combustion of pulverised coal in cement kilns [49]. However, the combustion of solid fuels is more complex than that of gas. Unsteady effects are also significant, with precession enhancing the non-uniform distribution of particles, termed “clustering” [50].

## Conclusions

That differences in the initial flow from a jet, due to nozzle profile or co-flow for example, influence the downstream flow and flame is well established. However, the detailed nature, extent and underlying causes of these influences are still an area of active investigation. The issues which the present review has addressed are as follows. Firstly, it is clear that even subtle differences in the initial flow of a non-reacting flow do propagate into the far field, so that a jet never entirely forgets its origin. It is also evident that these differences relate to differences in the underlying flow structure, although the details of this remain to be resolved. This finding contradicts the classical belief that initial conditions influence only the near field and can be accounted for by a shift in the virtual origin. On the other hand, even with the introduction of dramatic differences to the initial flow, such as by precession of the entire jet at sufficiently high Strouhal numbers, the far-field flow may still converge to a flow which is broadly comparable with that of a simple jet. Hence, the classical belief appears to be true to the first order. At present

there is insufficient information to put bounds on the maximum and minimum rates of spread, decay and normalised fluctuations that can result from differences in initial conditions.

Secondly, the relationship between initial spreading rates and overall mixing is more complex than is often assumed. Those nozzles which produce a naturally occurring large-scale oscillation, either two-dimensional flapping or precession, do produce a large increase in the mean initial spreading and, with this, an increase in the initial rate of entrainment and scalar mixing. However, because of the energy losses within the nozzle itself, these devices may decrease the total entrainment or mixing relative to a simple jet. Also the far-field rates can be quite different from the near-field. Thus the total entrainment of a flapping jet from a fluidic device is less than that for the steady jet when the length of the nozzle chamber is accounted for [10]. Similarly the flame volume of both the fluidic [40] and mechanical [41] precessing jet nozzles are significantly larger than that of the steady jet counterpart with identical nozzle diameter, fuel and flow rate. Since the flame volume is a direct measure of the volume required to mix the fuel to the stoichiometric contour, the total mixing rate of the precessing flow is reduced. Hence the reduced overall mixing rate of the flame is broadly consistent with cold-flow measurements.

However, the finding which is arguably least well recognised is that there is no direct correlation between increased mean mixing rates and the “desirability” of flame performance. Despite the fact that precessing jet nozzles reduce the net mixing rate of a jet and jet flame, they can nevertheless provide significant benefits for those applications where high radiation is desirable. This is because radiation from gas flames is dominated by the contribution of soot, where it is present, since soot produces broadband, incandescent radiation while non-sooting flames only produce narrow-band radiation. The production of soot, in turn, is favoured by reduced strain rates. Hence low strain flames can be desirable, so long as the soot is burned out within the flame envelope. It should also be noted that, while in principle it is possible to produce low-strain rate flames by other means (e.g. by increasing the diameter of a nozzle), this is difficult to achieve in practice without increasing the flame length, which usually a constraining parameter in design.

For these reasons researchers in fluid-mechanics and combustion should take the greatest of care to ensure that initial and boundary conditions are well defined and fully specified. Care should also be exercised in use of the terms “enhanced mixing” or “better mixing”. They should not be as a synonym for increased mixing rates or without specifying how they are better, since some aspects of combustion benefit from reduced mixing rates.

## Acknowledgments

The present paper summarises research which has been undertaken over many years, predominantly with support of the Australian Research Council and FCT-Combustion Pty Ltd. The work has been undertaken collaboratively and the authors also wish to acknowledge that many colleagues, whose work is referenced, have contributed to the development of the ideas expressed here.

## References

- [1] George, W.K., *Recent Advances in Turbulence* (eds. Arndt, R.E.A. & George, W.K.), Hemisphere, New York, 1989, pp.39-73.
- [2] Syred, N., and Beer, J.M., Combustion in Swirling Flow: A Review, *Combust. & Flame*, **23**, 1974, 143-201.
- [3] Hill, W.G. Jr. and Greene, P.R., Increased Turbulent Jet Mixing Rates Obtained by Self Excited Acoustic Oscillations, *J. Fluids Engineering*, **99**, 1977, 520-525.

- [4] Gutmark, E., Parr, T.P., Hanson-Parr, D.M. and Schadow, K.C., On the role of large and small-scale structures in combustion control, *Combust. Sci. & Tech.*, **66**, 1989, 107-126.
- [5] Candel, S.M. (1992), “Combustion Instabilities Coupled by Pressure Waves and Their Active Control”, *Proc. Combustion Institute*, **24**, 1277-1296.
- [6] Simmons, J.M., Lai, J.C.S. and Platzter, M.F., Jet Excitation by an Oscillating Vane, *AIAA J.*, **19**, 1981, 673-676.
- [7] Platzter, M. F., Simmons, J. M. and Bremhorst, K., Entrainment characteristics of unsteady subsonic jets, *AIAA J.*, **16**, 1978, 282-284.
- [8] Viets, H., Flip-flop jet nozzle, *AIAA J.*, **13**, 1975, 1375-1379.
- [9] Nathan, G.J., Hill, S.J. and Luxton, R.E., An axisymmetric fluidic nozzle to generate jet precession, *J. Fluid Mech.*, **370**, 1998, 347-380.
- [10] Mi, J., and Nathan, G.J., Mixing characteristics of a flapping jet from a self-exciting nozzle, *Flow, Turb. & Combust.*, **67**, 2001, 1-23.
- [11] Bradshaw, P., The effect of initial conditions on the development of a free shear layer, *J. Fluid Mech.*, **26**, 1966, 225-236.
- [12] Flora, J.J. and Goldschmidt, V.M. *AIAA J.*, **7**, 1969, 2344-2346.
- [13] Hussain, F. & Clark, A.R. On the coherent structure of the axisymmetric mixing layer: a flow-visualization study, *J. Fluid Mech.*, **104**, 1981, 263-294.
- [14] Husain, D.Z. & Hussain, F., Axisymmetric mixing layer: influence of the initial and boundary conditions, *AIAA J.*, **17**, 1979, 48.
- [15] Yule, A.J. Large-scale structure in the mixing layer of a round jet, *J. Fluid Mech.*, **89**, 1978, 412-432.
- [16] Zaman, K. B. M. Q. & HUSSAIN, A. K. M. F., Natural large-scale structures in the axisymmetric mixing layer, *J. Fluid Mech.*, **138**, 1984, 325-351.
- [17] Richards, C.D. & Pitts, W.M., Global density effects on the self-preservation behaviour of turbulent free jets, *J. Fluid Mech.*, **245**, 1993, 417-435.
- [18] Townsend, A.A., *The Structure of Turbulent Shear Flow*. 2<sup>nd</sup> edition, 1976, Cambridge University Press.
- [19] Chen, C.J. & Rodi, W. *Vertical Turbulent Buoyant Jets – A Review of Experimental Data*. 1980, Pergamon.
- [20] Mi, J., Nobes, D.S. and Nathan, G.J., Influence of jet exit conditions on the passive scalar field of an axisymmetric free jet, *J. Fluid Mech.*, **432**, 2001, 91-125.
- [21] Mi, J., Nathan, G.J. and Nobes, D.S., Mixing characteristics of axisymmetric free jets from a contoured nozzle, an orifice plate and a pipe, *J. Fluid Eng., Trans ASME*, **123**, 2001, 878-883.
- [22] Mi, J. and Nathan, G.J., Momentum mixing characteristics of turbulent axisymmetric jets with different initial velocity profiles, to be submitted for *J. Fluid Mech.*
- [23] Xu, G. and Antonia, R. A., Effect of different initial conditions on a turbulent round free jet, *Expts. Fluids*, **33**, 2002, 677-683.
- [24] Manias, C.G. and Nathan, G.J., The Precessing Jet Gas Burner - A Low NO<sub>x</sub> Burner Providing Process Efficiency and Product Quality Improvements, *World Cement*, March, 1993, 4 -11.
- [25] Manias, C.G. and Nathan, G.J., Low NO<sub>x</sub> clinker production, *World Cement*, May, 1994, 21-26.
- [26] Parham, J.J., Nathan, G.J., Smart, J.P., Hill, S.J. and Jenkins, B.G., The relationship between heat flux and NO<sub>x</sub> emissions in gas fired rotary kilns, *J. Inst. Energy*, **73**, 2000, 25-34.
- [27] Mi, J. and Nathan, G.J. Self-excited Jet precession Strouhal Number and its influence on turbulent mixing characteristics, *J. Fluids & Structures*, **19**, 2004, 851-862.
- [28] Schneider, G.M., Froud, D., Syred, N., Nathan, G.J. and Luxton, R.E., Velocity Measurements in a Precessing Jet Flow using a Three Dimensional LDA System, *Expts. Fluids*, **23**, 1997, 89-98.
- [29] Mi, J., and Nathan, G.J. Statistical analysis of the velocity field in a mechanical precessing jet flow, *Phys. Fluids*, **17**(1), 2005, in press.
- [30] Luxton, R. E. and Nathan G. J., Mixing using a fluid jet, *Patent Application No PI4068/87*, Australian Patent Office, 1987.
- [31] Abell, C.J., Acoustic coupling in a turbulent flow, *Proc. 6<sup>th</sup> Australasian Hydr. & Fluid Mech. Conf.* (Adelaide), 1977, pp41-45.
- [32] Wong C.Y. Lanspeary P.V. Nathan G.J., Kelso, R.M. & O'Doherty, T., Phase-averaged velocity in a fluidic precessing jet nozzle and in its near external field, *Exp. Therm. Fluid Sci.*, **27**, 2003, 515.
- [33] Newbold, G.J.R., *PhD Thesis*, 1997, Department of Mechanical Engineering, The University of Adelaide.
- [34] Parham, J.J., *PhD Thesis*, 2000, Department of Mechanical Engineering, The University of Adelaide.
- [35] Nobes, D.S., *PhD Thesis*, 1998, Department of Mechanical Engineering, The University of Adelaide.

- [36] Schneider, G.M., *PhD Thesis*, 1996, Department of Mechanical Engineering, The University of Adelaide.
- [37] Newbold, G.J.R., Nathan, G.J., and Luxton, R.E., The Large Scale Dynamic Behaviour of an Unconfined Precessing Jet Flame, *Combust. Sci. and Technol.*, **126**, 1997, 71-95.
- [38] Mungal, M.G., Karasso, P.S. and Lozano, A., The visible structure of turbulent jet diffusion: Large-scale organisation and flame tip oscillation, *Comb. Sci. Tech.* **76**, 1991, 165-185.
- [39] Reppel, J., *PhD Thesis*, 2003, Department of Chemical Engineering, The University of Adelaide.
- [40] Newbold, G.J.R., Nathan, G.J., Nobes, D.S. and Turns, S.R., Measurement and prediction of NO<sub>x</sub> emissions from unconfined propane flames from turbulent-jet, bluff-body, swirl and precessing jet burners, *Proc. Combust. Inst.* **28**, 2000, 481-487.
- [41] Nathan, G.J., Turns, S.R. and Bandaru, R.V., The influence of jet precession on NO<sub>x</sub> emissions and radiation from turbulent flames, *Comb. Sci. Tech.*, **112**, 1996, 211-230.
- [42] Turns, S.R., and Myhr, F.H., *Combust. Flame* **87**, 1991, 319-335.
- [43] Newbold, G.J.R. and Nathan, G.J., The influence of changes to mixing on the sooting and NO<sub>x</sub> emission characteristics of unconfined turbulent jet diffusion flames, *Develop. Chem. Eng. & Min. Proc.* **7**, 1999, 361 – 374.
- [44] Kent, J. H. & Bastin, S. J., Parametric effect on sooting in turbulent acetylene diffusion flames, *Comb. & Flame* **56**, 1984, 29-42.
- [45] Vandsburger, I. M., Kennedy, I. M. and Glassman, I., Sooting counter-flow diffusion flames with varying velocity gradients” *Proc. Combust. Inst.* **20**, 1984, 1105-1112.
- [46] Decroix, M. E. & Roberts, W. L., Transient flow field effects on soot volume fraction in diffusion flames, *Comb. Sci. & Tech.* **160**, 2000, 165-189.
- [47] Qamar N.H., Nathan, G.J., Alwahabi, Z.T., and King, K.D., The effect of global mixing on soot volume fraction: Measurements in simple Jet, precessing jet and bluff body flames, *Proc. Combust. Inst.* **30**, 2004, to appear.
- [48] Videgar, R., Gyro-therm technology solves burner problems, *World Cement*, November, 1997.
- [49] Manias, C.G. Balendra, A.S. and Retallack, D.J., New combustion technology for lime production, *World Cement*, December, 1996.
- [50] Nathan, G.J. and Hill, S.J., Full scale assessment of the influence of a precessing jet of air on the Performance of pulverised coal flame in a cement kiln, *Proc. 6<sup>th</sup> Euro. Conf. Ind. Furn. & Boilers* (Eds: Reis, Ward & Leuckel), v. **1**, 2002, pp 155-168.
- [51] Smith, N.L., Nathan, G.J., Zhang, D.-K. and Nobes, D.S., The Significance of Particle Clusters in Pulverised Coal Flames, *Proc. Combust. Inst.* **29**, 2002, 797-804.
- [52] Rhine, J.M. and Tucker, R.J., *Modelling of Gas-Fired Furnaces and Boilers*, 1991, McGraw Hill.
- [53] Mi J. and Nathan G.J., The influence of probe resolution on the measurement of a passive scalar and its derivatives, *Expts. Fluids*, **34**, 2003, 687-696.
- [54] Turns, S. R., *An Introduction to Combustion; Concepts and Applications*, 2<sup>nd</sup> Ed., 2000, McGraw-Hill.
- [55] Kalghatgi G.T., Blow-out stability of gaseous jet diffusion flames. Part I: In Still Air, *Combust. Sci. & Technol.*, **26**, 1981, 233-239.
- [56] Langman, A.S., Nathan, G.J. and Ashman, P.J., A study of the global differences between axisymmetric turbulent free jet flames from a smooth contraction and a pipe with well defined boundary conditions, *15<sup>th</sup> Australasian Fluid Mechanics Conference*, 13-17 Dec, 2004, *The University of Sydney*.
- [57] Røkke, N.A., Hustad, J.E., Sønju, O.K., and Williams, F.A., *Proc. Combustion Institute*, **24**, 1992, 385-393.
- [58] Røkke, N.A., Hustad, J.E., and Sønju, O.K., *Combust. Flame* **97**, 1994, 88-106.
- [59] Dahm, W.J.A. and Dibble, R.W. Coflowing turbulent jet diffusion flame blowout, *Proc. Combust. Inst.*, **22**, 1988, 801-808.
- [60] Hermanson, J.C., Usowicz, J.E. and Johari, H., An Experimental Study of Isolated Turbulent Flame Puffs with a Co-Flow, *AIAA Paper* 2000-0813, 1-11.



# The Cut-Off Frequency of Constant Temperature Hot-Wire Systems in Turbulent Velocity Measurements

J. D. Li

School of Architectural, Civil and Mechanical Engineering  
Victoria University of Technology,  
PO BOX 14428, MCMC, Melbourne, 8001, AUSTRALIA

## Abstract

The analytical solution for the frequency response of a constant temperature hot-wire system at given turbulent velocity fluctuations are used to investigate the effects on the cut-off frequency of the hot-wire system under different operating conditions. It is found that the optimal frequency response of the hot wire system determined by the traditional square wave test cannot guarantee the stability of the hot wire system under velocity perturbations. It is also found that the cut-off frequency depends not only on the hot-wire length to diameter ratio, the mean velocity, the hot-wire materials, and the overheat ratio as previously found, but also on the physical wire length, the resistances used in the Wheatstone bridge, and the gain of the amplifier in the feedback loop. Hot-wire systems with preferred operating conditions are recommended.

## Introduction

Hot wires have been used for measuring velocities of turbulent gas flows for many years. Recently, Li [1] has for the first time derived an analytical solution for temperature fluctuations along a single hot wire when it is exposed to turbulent velocity fluctuations of different frequencies and wave numbers. The solutions show that attenuation to the velocity fluctuations exists at high frequencies and depends on the relative end-conduction heat loss from the hot wire to its supports. This result is consistent with the results obtained by Freymuth [2] based on intuitive argument and the numerical results of Morris and Foss [3] for a specific hot wire.

Li [1] used a simplified circuit for a hot-wire anemometer to analyse the frequency response of the combined hot wire and its anemometer with specific electronic components. The frequency response was investigated for given velocity fluctuations rather than introducing voltage perturbations as that normally performed during experiments through a square wave test. As Khoo et al. [4] pointed out, from a user's point of view, the cut-off frequency determined from the velocity fluctuation serves as a more accurate indicator of the overall frequency response of the hot-wire system. Li [1] found that even though the frequency response of the anemometer (as that determined from a square/sine wave test) can be very high, the cut-off frequency of the combined hot wire and its anemometer (it is called the hot-wire system here) can be low, and depends on the hot-wire length to diameter ratio, Reynolds numbers, overheat ratio, and the hot-wire material used. The analytical solutions were compared with the experimental results of Khoo et al. [4], who measured the frequency response of a hot-wire system by introducing velocity fluctuations to a marginally elevated and flush-mounted 5  $\mu\text{m}$  tungsten wire of 1.2 mm long. Li [1] found that the theoretical results agree remarkably well with the experimental results of Khoo et al. [4] at the similar operating conditions.

In turbulence measurements using hot wires, the wire length is in general kept at  $2l/d > 200$  following the recommendation of Champagne et al. [5]. Here  $2l$  is the length of the hot wire and  $d$  is the diameter of the hot wire. On the other hand, it has also been common experience that hot wires in general cannot resolve all the turbulence length scales when the Reynolds number is high. The reason for this is that, at high Reynolds numbers, the hot wire used is longer than the small length scales of the turbulence, and it can only measure an averaged turbulent velocity along the wire. In the past, it has always been assumed that the spatial resolution problem of the hot wire depends only on the length of the wire because of the falsely high cut-off frequency determined from the square wave test. In light of the results of Khoo et al. [4] and Li [1], this may not be the case.

In this paper, we will investigate the effects from using different electronic components in the hot-wire anemometer and hot-wire diameters on the cut-off frequency of the hot-wire system. For a given hot wire in a specific flow field, it will be shown that the electronic components used in the Wheatstone bridge and the feedback circuit in the anemometer can all affect the cut-off frequency of the hot-wire system, even though their effect on the cut-off frequency of the anemometer itself is normally small. It is also found that not only the cut-off frequency of the hot-wire system is in general much lower than that determined from the square wave test but also an optimally tuned frequency response using square wave test cannot always guarantee the stability of the system when performing measurements. Recommendations will be made on the operating conditions of the hot wire with anemometer using preferred electronic components.

## The hot-wire system and the theoretical solutions

In Li [1], the hot wire was assumed to be in cylindrical shape and is operated with an overheat ratio  $a$ , the ends of the hot wire are connected to the prongs (no stubs), and the hot wire is operated at constant temperature mode with the ambient temperature kept constant.

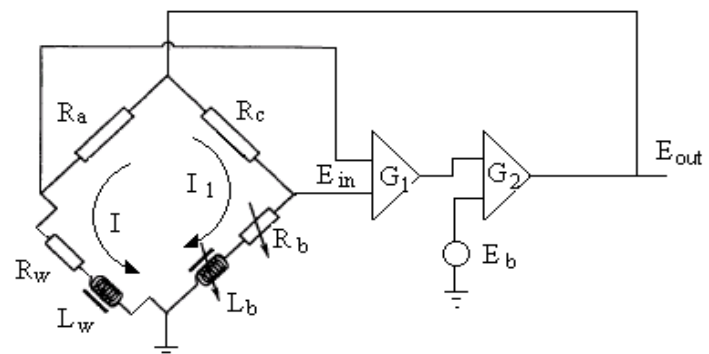


Figure 1. Schematic diagram of a constant temperature hot wire anemometer (CTHWA)

Figure 1 shows a schematic diagram of a Constant Temperature Hot-Wire Anemometer (CTHWA). In the figure,  $R_a$  and  $R_c$  are the two resistors in the upper arms of the Wheatstone bridge,  $R_w$  the hot wire resistance at the operating temperature,  $L_w$  the inductance from the hot wire cable,  $R_b$  and  $L_b$  the adjustable resistor and inductor for bridge balance,  $I$  and  $I_l$  the electrical currents in the Wheatstone bridge,  $G_1$  and  $G_2$  the gains of the two stage amplifiers,  $E_{in}$  and  $E_{out}$  the instantaneous voltages at the input and output of the amplifiers, and  $E_b$  is a mean voltage for offset.

The solution for the frequency response of the hot wire system including the hot wire and its anemometer, as according to Li [1], is

$$\frac{\tilde{e}_{out}'}{\tilde{u}_1'} = \frac{A}{B - CP} \quad (1)$$

where

$$\tilde{e}_{out}' = \frac{\tilde{e}_{out}}{E_{out}}, \quad \tilde{u}_1' = \frac{\tilde{u}_1}{U}$$

$$A = \frac{\chi \bar{Q}}{Y_s^2 Y^2} \frac{\sin(\beta)}{\beta} [1 - f(Y) - f(Y_s) + g(Y) + g(-Y)]$$

$$f(x) = \frac{\beta}{x^2 + \beta^2} \left( \frac{x \tanh(x)}{\tan(\beta)} + \beta \right)$$

$$g(x) = \frac{\beta}{2[(Y_s + x)^2 + \beta^2]} \left[ \frac{(Y_s + x)(\tanh(Y_s) + \tanh(x))}{\tan(\beta)} + \beta(1 + \tanh(Y_s) \tanh(x)) \right]$$

$$P = \frac{2\bar{Q}}{Y_s^2} \left[ \frac{\tanh(Y_s)}{Y_s} - 1 \right] +$$

$$\frac{2\bar{Q}^2}{\tau s} \left[ \frac{\tanh(Y_s)}{Y_s^3} - \frac{\tanh(Y)}{Y^3} + \frac{\tau s}{Y_s^2 Y^2} \right]$$

$$B = \frac{[(M''s^2 + M's + 1)\Sigma Z - KZ_0](R_a + R_w)}{KR_a R_0 (R_c + Z_b)}$$

$$C = \frac{R_a + R_w}{R_a + Z_w} \left[ 1 + \frac{(M''s^2 + M's + 1)\Sigma Z - KZ_0}{KR_a (R_c + Z_b)} \right]$$

$$Q = \frac{4I^2 R_{0x} \alpha}{\pi k_w} \left( \frac{l}{d} \right)^2, \quad \xi = 4Nu \frac{k_f}{k_w} \left( \frac{l}{d} \right)^2$$

$$Y = \sqrt{\xi - \bar{Q}}, \quad Y_s = \sqrt{\xi - \bar{Q} + \tau s}$$

$$\tau = \rho_w C_w \frac{l^2}{k_w}, \quad K = G_1 G_2, \quad \chi = -\frac{U}{Nu} \frac{dNu}{dU} \xi$$

$$\Sigma Z = (R_a + Z_w)(R_c + Z_b), \quad Z_0 = R_a Z_b - R_c Z_w$$

$$Z_w = R_w + L_w s, \quad Z_b = R_b + L_b s$$

Here  $s$  is the Laplace variable,  $\sim$  means the Laplace transform,  $M''$  and  $M'$  are the time constants of the feedback circuit as given by Freymuth [6] and they are connected to the Gain Bandwidth Product (GBP) of the amplifiers,  $u_1$  the time variation of the velocity fluctuation,  $U$  the mean velocity,  $Nu$  the Nusselt number,

$Re_w$  the Reynolds number based on the hot-wire diameter,  $k_w$  and  $k_f$  the thermal conductivities of the hot wire and the fluid respectively,  $R_0$  and  $R_{0x}$  the electrical resistance of the hot wire and that of per unit length at ambient temperature respectively,  $\alpha$  the thermal coefficient of electrical resistivity of the hot wire,  $\beta = kl$  the non-dimensional wave number of the velocity fluctuations along the hot wire, and over-bar means steady condition. For detailed derivation of these relationships, please refer [1].

Using equation (1), Li [1] shows that the cut-off frequency  $f_c$  of the hot-wire system with  $\beta = 0$  increases with increasing  $2l/d$ ,  $U$ , and  $a$ , and with decreasing  $k_w$ . Here frequency response is defined as the ratio between the square of the voltage fluctuations at the anemometer to the square of the velocity fluctuations at the hot wire at each frequency, and  $f_c$  is defined as the frequency where the frequency response has dropped by 3dB. It was found that this cut-off frequency is related to the relative heat loss from the end conduction.

### The cut-off frequency $f_c$ of the hot-wire system

Figure 2 shows the frequency response of the hot wire system of three wires in decibels:  $5\mu m$  tungsten wire,  $2.5\mu m$  tungsten wire and  $2.5\mu m$  Pt/Ir (90/10) wire all at  $2l/d = 200$ ,  $a = 0.5$ , and  $U = 10$  m/s. In calculating the results,  $R_a = 100 \Omega$ ,  $R_c = 1000 \Omega$ ,  $K = 1000$ ,  $L_w = 15\mu H$ ,  $GBP = 5 \times 10^7$ , the bridge was tuned with  $R_b = 9.98R_w$ ,  $L_b = \lambda L_w R_b / R_w$ , and  $\lambda = 1.00285-1.0026$  to achieve an optimal frequency for the CTHWA with an approximate 14.6% overshoot as that specified by Brunn [7]. The slight off balance of the Wheatstone bridge with  $R_b = 9.98R_w$  is consistent with the recommendation of Perry [8] and in practice this is achieved by adjusting the offset voltage  $E_b$ .

Figure 2 also shows the frequency response of the CTHWA and the attenuation of the hot wire to the velocity fluctuations for the  $5\mu m$  tungsten wire. The overshoot of the CTHWA can be clearly seen and the attenuation of the hot wire to the velocity fluctuation approaches a lower plateau at high frequency as that found in [1-3]. The cut-off frequencies of the CTHWA for the  $2.5\mu m$  wires are slightly higher than that given in the figure and are not shown for clarity. The cut-off frequency of the CTHWA determined from figure 2 is  $900kHz$ . This is also the cut-off frequency as determined from the impulse response using MATLAB, and that would be determined from the square wave test in practice. This high cut-off frequency for the CTHWA is because of the high GBP values used for the amplifiers and the circuit in figure 1 is an idealization of the actual hot-wire anemometer.

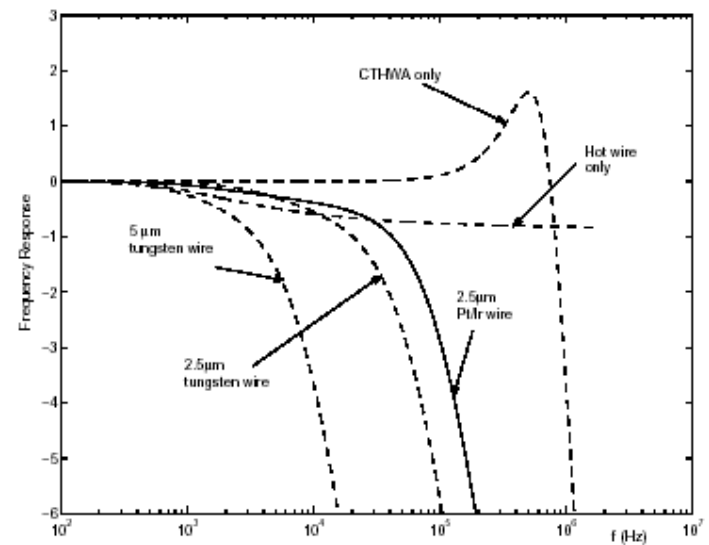


Figure 2 Frequency responses of hot wire and its anemometer

Figure 2 shows that the cut-off frequencies of the hot wire system are  $8.2\text{kHz}$  for the  $5\mu\text{m}$  tungsten wire,  $52\text{kHz}$  for the  $2.5\mu\text{m}$  tungsten wire and  $100\text{kHz}$  for the  $2.5\mu\text{m}$  Pt/Ir wire. These frequencies are much lower than that from the CTHWA alone, and depend strongly on the physical wire length and the wire materials. The time constants of the three wires are  $\tau = 3.8\text{ms}$  for the  $5\mu\text{m}$  tungsten wire,  $0.96\text{ms}$  for the  $2.5\mu\text{m}$  tungsten wire and  $5.6\text{ms}$  for the  $2.5\mu\text{m}$  Pt/Ir wire, respectively. The reason that the cut-off frequency of the  $2.5\mu\text{m}$  Pt/Ir wire is higher than that of the tungsten wire at the same diameter is because the thermal conductivity of the Pt/Ir wire is  $31\text{ W/mK}$  while that of the tungsten is  $174\text{ W/mK}$  even though the time constant of the former is much larger than the later.

Figure 2 shows that the cut-off frequency of the  $2.5\mu\text{m}$  wires are much higher than that of the  $5\mu\text{m}$  wire, and that of the  $2.5\mu\text{m}$  Pt/Ir wire is higher than that of the  $2.5\mu\text{m}$  tungsten wire. Thus it can be concluded that  $2.5\mu\text{m}$  Pt/Ir wire should be the preferred wire to use in turbulent measurements.

Figure 3 shows the effect of the amplifier GBP on the cut-off frequencies of the CTHWA and the hot-wire system for a  $2.5\mu\text{m}$  Pt/Ir wire. In figure 3,  $GBP = 10^6$ ,  $10^7$  and  $5 \times 10^7$  are used with  $\lambda = 1.042$ ,  $1.0049$  and  $1.0026$ , respectively, for optimal frequency response of the CTHWA. The other parameters are the same as those used in figure 2. It can be seen from figure 3 that the cut-off frequencies of the CTHWA are  $43\text{ kHz}$ ,  $380\text{ kHz}$  and  $1.1\text{ MHz}$ , while those of the hot-wire system are  $60\text{kHz}$ ,  $240\text{kHz}$  and  $100\text{kHz}$ , respectively, with  $GBP = 10^6$ ,  $10^7$  and  $5 \times 10^7$ . However, it can be seen from figure 3 that the frequency response of the hot-wire system is unstable at  $GBP = 10^6$  and thus should not be used even though the cut-off frequency of the hot-wire system is higher than that of the CTHWA. This also shows that the hot-wire anemometers tuned for optimal frequency response using the square wave test may not guarantee the stability of the hot-wire system. At  $GBP = 10^7$ , the cut-off frequency of the how-wire system is close to that of the CTHWA and higher than that at  $GBP = 5 \times 10^7$ . However, a close look at the results show that the frequency response of the hot-wire system with  $GBP = 10^7$  is close to loss its stability. With imperfections in the electronic components and at higher mean velocities, it is expected that the hot-wire system will loss its stability for a  $2.5\mu\text{m}$  Pt/Ir wire with  $GBP = 10^7$ . Because of this, it is recommended that  $GBP > 10^7$  should be used. However, hot-wire anemometers with  $GBP = 10^7$  may be used for  $5\mu\text{m}$  tungsten wires since the cut-off frequency for this wire is well below the cut-off frequency of the CTHWA at such GBP.

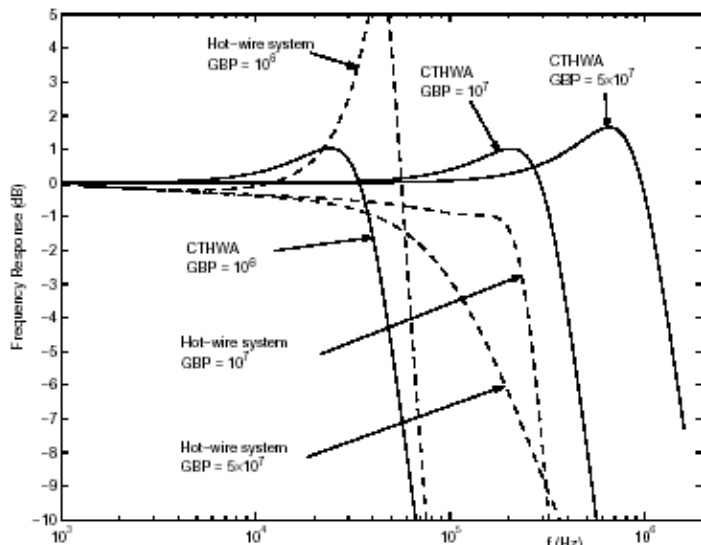


Figure 3 Effect of amplifier GBP on the cut off frequency

Figure 4 shows the effect of the feedback gain  $K$  on the cut-off frequency of the hot wire system. In the present analysis and that of [1], the two-stage amplifiers have been assumed to have the same gain, ie.  $G_1 = G_2$ . The hot wire used is a  $5\mu\text{m}$  tungsten wire. Again,  $L_b$  has been adjusted to have the optimal frequency response for the CTHWA. The other parameters used are the same as those in figure 2. The effect of  $K$  on the cut-off frequency of the CTHWA is small and only that at  $G = 1000$  is shown in figure 2. Of course, changing  $K$  will not affect the hot-wire attenuation. Figure 4 shows that the cut-off frequency of the hot-wire system increases from  $f_c = 8.2\text{kHz}$  at  $K = 1000$  to  $17\text{ kHz}$  at  $K = 2000$ . This shows that in case  $5\mu\text{m}$  tungsten wire has to be used for turbulence measurements, using high  $K$  values can increase the cut-off frequency of the hot-wire system. However, increasing  $K$  will also increase the amplification to the noise within the system such as the electronic noise, and this will in general reduce the signal to noise ratio of the system.

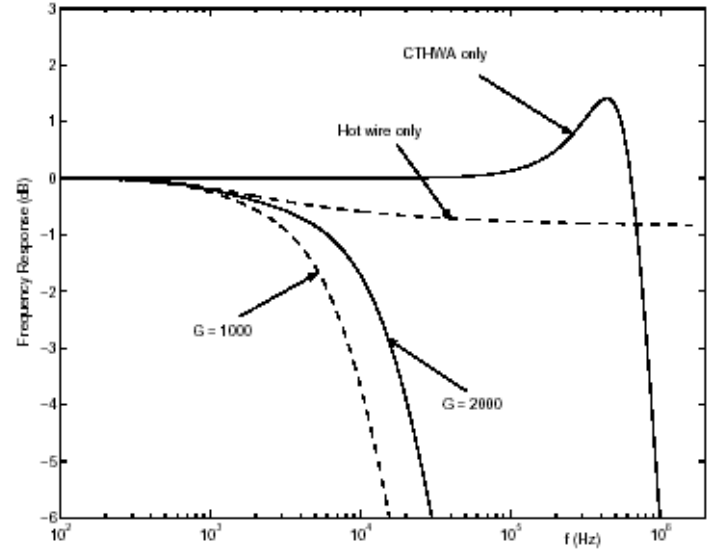


Figure 4 The effect of feedback gain on the cut-off frequency

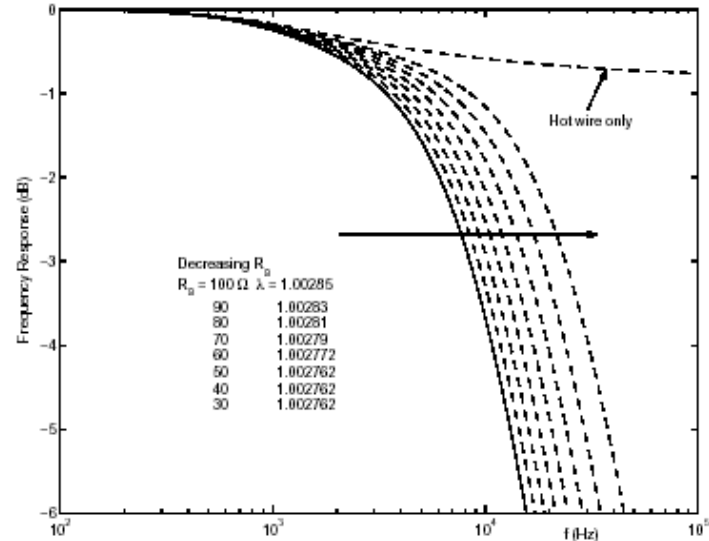


Figure 5 The effect of  $R_a$  on the cut-off frequency of the hot-wire system

Figure 5 shows another way to increase the cut-off frequency of the hot-wire system by reducing the resistance  $R_a$ . In the figure,  $5\mu\text{m}$  tungsten wire has been used and the ratio  $R_c/R_a = 10$  has been kept to have the bridge close to balance. In order to achieve the optimal frequency response for the CTHWA,  $\lambda$  has also been adjusted and the value is also given in figure 5 for each  $R_a$ . Figure 5 shows that the hot-wire system has a cut-off frequency  $f_c = 8.2\text{ kHz}$  with  $R_a = 100\ \Omega$  and this increases to  $f_c = 21\text{ kHz}$  at  $R_a = 30\ \Omega$ .



Figure 6 shows the effect of  $L_w$  on the cut-off frequency of the CTHWA and that of the hot-wire system for a  $5\mu\text{m}$  tungsten wire. Except the  $L_w$  and the  $\lambda$  values, other parameters are the same as those in figure 2. In practice,  $L_w$  is determined by the cable length of the hot-wire probe. Perry [8] suggested that for each meter of hot-wire cable there would be an effective  $5\mu\text{H}$  inductance. In the results presented so far,  $L_w = 15\mu\text{H}$  has been used, which corresponds to a  $3\text{m}$  long hot-wire cable. Figure 6 shows that changing  $L_w$  from  $5\mu\text{H}$  to  $30\mu\text{H}$  will reduce the cut-off frequency of the CTHWA from  $1.5\text{ MHz}$  to  $610\text{ kHz}$  while there is no appreciable change in the cut-off frequency of the hot-wire system. One interesting point can be noticed from figure 6 is that the overshoot peaks increase as  $L_w$  increase even though the overshoot determined from the zero and pole diagram using MATLAB has always been kept at around 14.7%. This is because the 14.7% overshoot determined from the zero and pole plot is based on the overshoot at the pole positions and the results shown in figure 6 include the effects from the zeros as well. Nevertheless, it will not affect the conclusions here.

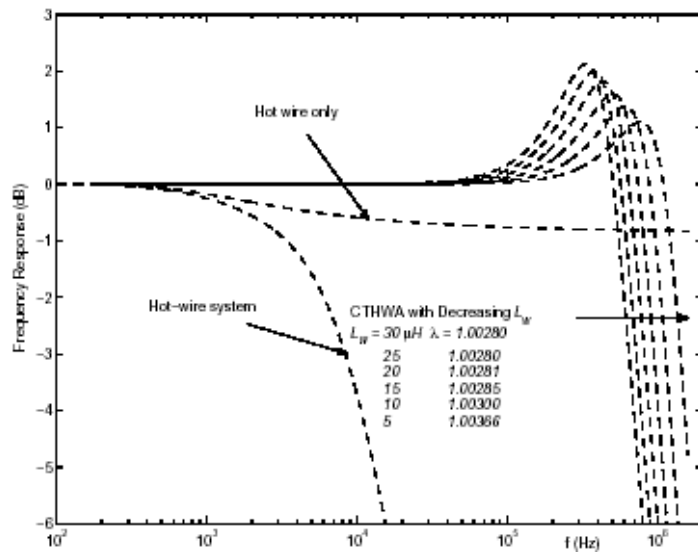


Figure 6 The effect of  $L_w$  on the cut-off frequency

The effect of  $R_b$  on the cut-off frequency of the hot-wire system has also been investigated. It is found that the cut-off frequency  $f_c$  of the CTHWA and the hot-wire system is not affected at all when  $R_b$  is changed from  $R_b = 9.98 R_w$  to  $R_b = .998 R_w$  ( $R_c$  is changed from  $1000\Omega$  to  $100\Omega$  to have the Wheatstone bridge being close to balance, and the overheat ratio has been kept the same).

### Conclusions and discussion

The cut-off frequency of the hot-wire system has been investigated by using the theoretical solution of Li [1]. It is found that the hot-wire diameter and the thermal conductivity of the hot-wire material have large effects on the cut-off frequency. The results show that  $2.5\text{mm}$  Pt/Ir wire would have a cut-off frequency in the order of  $100\text{ kHz}$  with a  $GBP > 10^7$ . This is probably sufficient for most of today's turbulence measurements.

The effect of the  $GBP$  of the amplifiers used in the feedback circuit is investigated and it is found that the square wave test for optimal frequency response may not guarantee the stability of the hot-wire system. In order to have a stable frequency response for the hot-wire system,  $GBP$  should be larger than  $10^7$  for  $2.5\mu\text{m}$  Pt/Ir wire.

In case  $5\mu\text{m}$  tungsten wires need to be used for turbulence measurements, it is found that increasing the overall gain  $K$  in the feedback circuit and using smaller resistance  $R_a$  in the Wheatstone bridge can both increase the cut-off frequency of the hot-wire system. However, hot-wire operator should keep in mind that using higher  $K$  may reduce the signal to noise ratio of the system. It is also found that reducing the resistance  $R_b$  or using shorter hot-wire cable (which results in smaller  $L_w$  value) will not increase the cut-off frequency of the hot-wire system, although the later can increase the cut-off frequency of the CTHWA.

One point that needs to be mentioned is the attenuation of the hot wire to the velocity fluctuation at high frequencies. The current investigation on the cut-off frequency of the hot-wire system assumes that the frequency response of the system approaches the attenuation curve from below as  $f_c$  is increased. Because of this, the measured velocity is that of being attenuated at high frequency. So far, there is no correction method available to take this attenuation effect into account. A calibration method similar to that of [4] is needed to calibrate the hot wire and check its frequency response in free stream flow.

### References

- [1] Li, J.D. Dynamic Response of Constant Temperature Hot-Wire System in Turbulent Velocity Measurements, *Meas. Sci. Technol.*, **15**, 2004, 1835-1847.
- [2] Freymuth, P. Engineering Estimation of Heat Conduction Loss in Constant Temperature Thermal Sensor, *TSI Quarterly*, **3**, 1979, issue 3.
- [3] Morris, S.C. and Foss, J.F., Transit Thermal Response of a Hot-Wire Anemometer, *Meas. Sci. Technol.*, **14**, 2003, 251-259.
- [4] Khoo, B.C., Cjew, Y.T., Teo, C.J. and Lim, C.P. Dynamic Response of Hot-Wire anemometer, Part III: Voltage-Perturbation versus Velocity Testing for near Wall Hot-Wire/Film probes, *Meas. Sci. Technol.*, **19**, 1999, 152-169.
- [5] Champagne, F.H., Sleicher, C.A. and Wehrmann, O.H. Turbulence Measurements with Inclined Hot Wires, Part 1: Heat Transfer Experiments with Inclined Hot Wires, *J. Fluid Mech.*, **28**, 1967, 153-175.
- [6] Freymuth, P. Frequency Response and Electronic Testing for Constant-Temperature Anemometers, *J. Phys. E: Sci Instrum.*, **10**, 1977, 705-710.
- [7] Brunn, H.H. *Hot-Wire Anemometry: Principals and Signal Analysis* Oxford University Press, Oxford, 1995.
- [8] Perry, A.E. *Hot-Wire Anemometry* Oxford University Press, 1982.

## The Effect of Coriolis Force on Marangoni Convection

I. Hashim and W. Sarma

School of Mathematical Sciences, Faculty of Science and Technology,  
Universiti Kebangsaan Malaysia, 43600 UKM Bangi, Selangor, Malaysia

### Abstract

The effect of uniform rotation on the onset of steady and oscillatory surface-tension-driven (Marangoni) convection in a horizontal fluid layer heated from below is considered theoretically. The theoretical analysis follows the usual small-disturbance approach of perturbation theory and leads, at the marginal state, to a functional relation between the Marangoni and Taylor numbers which is then computed numerically. We present numerically a necessary and sufficient condition for oscillatory Marangoni convection to occur in a rotating fluid layer with a deformable free upper surface.

### Introduction

The onset of surface-tension-gradients-driven (Marangoni) convection in a layer of fluid which is heated (or cooled) from below is a fundamental model problem for several material processing technologies, such as semiconductor crystal growth from melt, in the microgravity environment of space. As Schwabe [8] describes, typically in microgravity surface tension rather than buoyancy forces are the dominant mechanism driving the flow. In general, convection appears when a certain dimensionless parameter exceeds a critical value. This parameter is a Rayleigh number when the convection is induced by buoyancy effects due to variations in density and is a Marangoni number when surface-tension variations induce the convection.

In his pioneering work Pearson [6] showed that variation of surface tension with temperature will drive steady Marangoni convection in a fluid layer provided that the non-dimensional Marangoni number,  $M$ , (defined in the next Section) is sufficiently large and positive. Since for most fluids surface tension decreases with increasing temperature, this means that steady convection only occurs when the layer is heated sufficiently strongly from below. The most significant limitation of Pearson's [6] work was that it considered only the case of a non-deformable free surface, corresponding to the limit of strong surface tension. Scriven and Sterling [9], Smith [10] and Takashima [11] extended Pearson's [6] analysis by considering the effect of free surface deformation on the onset of steady convection and found that it dramatically destabilises the long wavelength modes. Vidal and Acrivos [14] and Takashima [12] showed numerically that oscillatory Marangoni convection is impossible when the free surface is non-deformable.

All of the work mentioned above excluded the effect of rotation of the fluid layer. The effect of rotation on Benard convection was first studied by Chandrasekhar [1]. Vidal and Acrivos [13] analysed the effect of rotation on Marangoni convection. McConaghy and Finlayson [4] re-examined Vidal and Acrivos' [13] conclusion on the possibility of oscillatory convection. Namikawa *et al.* [5] studied the case when both buoyancy and surface tension forces act together to cause the instability. Kaddame and Lebon [2, 3] investigated the onset of steady and oscillatory Benard-Marangoni convection with rotation.

In this work we use the classical linear stability theory to study the effect of rotation on the marginal curves for the onset of steady and oscillatory Marangoni convection. In particular, we

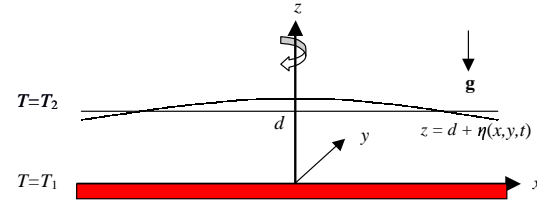


Figure 1: Sketch of the one-layer model.

show how the  $P_r$ - $T_a$  (where the Prandtl number  $P_r$  and the Taylor number  $T_a$  are defined in the next Section) parameter space is divided into domains in which steady or oscillatory convection is preferred, and in so doing we extend the work of Kaddame and Lebon [3].

### Mathematical Formulation

We wish to examine the stability of a horizontal layer of quiescent fluid of thickness  $d$  which is unbounded in the horizontal  $x$ - and  $y$ -directions. The layer is kept rotating uniformly around a vertical axis with a constant angular velocity  $\Omega$ . The layer is bounded below by a thermally conducting planar boundary and above by a free surface, subject to a uniform vertical temperature gradient (see figure 1).

The fluid is Boussinesquian with a mass density  $\rho$  assumed to vary linearly on the temperature

$$\rho = \rho_0[1 - \alpha_1(T - T_0)], \quad (\alpha_1 > 0), \quad (1)$$

where  $\alpha_1$  is the volume expansion coefficient and  $T_0$  a reference arbitrary temperature. The variations of surface tension  $\gamma$  with the temperature  $T$  is assumed in the form

$$\gamma = \gamma_0 - \tau(T - T_0), \quad (2)$$

where  $\gamma_0$  is a reference value of surface tension and  $\tau$  is the rate of change of surface tension with the temperature. The deformation of the interface is represented by the relation

$$z = d + \eta(x, y, t), \quad (3)$$

wherein  $\eta(x, y, t)$  is an *a-priori* unknown deformation with respect to the mean thickness  $d$ . In the reference state, the fluid is at rest with respect to the rotating axes and heat propagates only by conduction. When motion sets in, the velocity  $\mathbf{v} = (u, v, w)$ , pressure  $p$  and temperature  $T$  fields obey the usual balance equations of mass, momentum and energy (cf. Chandrasekhar [1]),

$$\nabla \cdot \mathbf{v} = 0, \quad (4)$$

$$\rho_0 \left[ \frac{\partial \mathbf{v}}{\partial t} + (\mathbf{v} \cdot \nabla) \mathbf{v} + 2\Omega \times \mathbf{v} \right] = -\nabla p + \mu \nabla^2 \mathbf{v} - \rho \mathbf{g} \mathbf{e}_z, \quad (5)$$

$$\frac{\partial T}{\partial t} + (\mathbf{v} \cdot \nabla) T = \kappa \nabla^2 T, \quad (6)$$

where  $\mathbf{g} = (0, 0, -g)$  is the gravitational field,  $\mathbf{e}_z = (0, 0, 1)$  is a unit vector in the  $z$ -direction,  $\mu$  is the viscosity,  $\kappa$  is the thermal

diffusivity and  $\nabla^2 = \partial^2/\partial x^2 + \partial^2/\partial y^2 + \partial^2/\partial z^2$  is the Laplacian operator.

At the deformable free surface,  $z = d + \eta(x, y, t)$ , the boundary conditions comprise of the kinematic, the heat flux, the two shear stress and the normal stress conditions which are given by, respectively,

$$\frac{\partial \eta}{\partial t} + u \frac{\partial \eta}{\partial x} + v \frac{\partial \eta}{\partial y} = w, \quad (7)$$

$$k \nabla T \cdot \mathbf{n} + hT = 0, \quad (8)$$

$$2\mu D_{nt} = \frac{\partial \gamma}{\partial T} \nabla T \cdot \mathbf{t}, \quad (9)$$

$$(p_a - p) + 2\mu D_{nn} = \gamma \nabla \cdot \mathbf{n}, \quad (10)$$

where  $h$  is the heat transfer coefficient,  $k$  is the thermal conductivity of the fluid,  $p_a$  is the pressure of the atmosphere,  $D_{ij}$  is the rate of strain tensor,  $\mathbf{t}$  and  $\mathbf{n}$  denote tangential and normal unit vectors, respectively. At the isothermal lower, rigid and plane, boundary we have the no-slip condition.

We introduce infinitesimal disturbances to the governing equations and boundary conditions by setting

$$(u, v, w, p, T) = (0, 0, 0, \bar{p}, \bar{T}) + (u', v', w', p', T'), \quad (11)$$

where the barred quantities are the basic state solutions and primed quantities represent the perturbed variables. A set of scales  $d$ ,  $d^2/\kappa$ ,  $\Delta T$  is chosen for distance, time and temperature, respectively. The perturbed quantities in normal mode forms are

$$\begin{bmatrix} w' \\ \theta' \\ \zeta' \\ \eta \end{bmatrix} = \begin{bmatrix} W(z) \\ \Theta(z) \\ K(z) \\ E \end{bmatrix} e^{i(a_x x + a_y y) + \sigma t}, \quad (12)$$

where  $a_x$  and  $a_y$  are wavenumbers of disturbances in the  $x$  and  $y$  directions, respectively.  $W$ ,  $\Theta$ ,  $K$  and  $E$  are amplitudes of vertical velocity, temperature, vertical vorticity and deflection of the free upper surface, respectively. The growth parameter  $\sigma$  is in general a complex variable denoted by  $\sigma = \sigma_r + i\sigma_i$ , where  $\sigma_r$  is the growth rate of the instability and  $\sigma_i$  is the frequency. If  $\sigma_r > 0$ , the disturbances grow and the system becomes unstable. If  $\sigma_r < 0$ , the disturbances decay and the system becomes stable. When  $\sigma_r = 0$ , the instability of the system, at the marginal state, sets in stationarily, provided ( $\sigma_i = 0$ ), or oscillatorily, provided ( $\sigma_i \neq 0$ ).

The governing equations of the perturbed state in dimensionless forms, assuming the Boussinesq approximation, are

$$(D^2 - a^2)(D^2 - a^2 - \sigma P_r^{-1})W - T_a^* DK = a^2 R^* \Theta, \quad (13)$$

$$(D^2 - a^2 - \sigma P_r^{-1})K = -DW, \quad (14)$$

$$(D^2 - a^2 - \sigma) \Theta = -W, \quad (15)$$

subject to

$$W - \sigma E = 0, \quad (16)$$

$$C_r^* [(D^2 - 3a^2 - \sigma P_r^{-1})DW - T_a^* K] - a^2(a^2 + B_o^*)E = 0, \quad (17)$$

$$(D^2 + a^2)W + a^2 M^* (\Theta - E) = 0, \quad (18)$$

$$D\Theta + B_i^* (\Theta - E) = 0, \quad (19)$$

$$DK = 0, \quad (20)$$

evaluated on the undisturbed position of the upper free surface  $z = \pi$ , and

$$W = \Theta = K = DW = 0, \quad (21)$$

evaluated on the lower rigid boundary  $z = 0$ , where the operator  $D = d/dz$  denotes differentiation with respect to the vertical coordinate  $z$  and  $a = (a_x^2 + a_y^2)^{1/2}$  is the horizontal wave number of the disturbance. The starred dimensionless numbers are defined by  $R^* = R/\pi^4$ ,  $M^* = M/\pi^2$ ,  $T_a^* = T_a/\pi^4$ ,  $C_r^* = \pi C_r$ ,  $B_i^* = B_i/\pi$ ,  $B_o^* = B_o/\pi^2$ , where the Rayleigh number,  $R = \alpha g \Delta T d^3 / \nu \kappa$ , where  $\nu$  is the kinematic viscosity, the Marangoni number,  $M = \gamma \Delta T d / \rho_0 \nu \kappa$ , the Taylor number,  $T_a = 4\Omega^2 d^4 / \nu^2$ , the capillary number,  $C_r = \rho_0 \nu \kappa / \gamma_0 d$ , the Biot number,  $B_i = h d / k$ , the Bond number,  $B_o = \rho g d^2 / \gamma$ , and the Prandtl number,  $P_r = \nu / \kappa$ . The Rayleigh number  $R$  accounts for buoyancy destabilising effect. The number  $M$  accounts for surface tension destabilising effect. The Taylor number  $T_a$  represents the square of the ratio between Coriolis and frictional forces. The capillary number  $C_r$  shows an idea of the rigidity of the upper free surface of the fluid layer. The Biot number  $B_i$  represents the heat flux flow through the interface, and the physical parameter Bond number  $B_o$  is the ratio between gravity effect in keeping the surface flat and the effect of surface tension in making a meniscus. The Prandtl number,  $P_r$ , stands for the ratio between thermal and heat diffusivities.

### Solution of the Linearised Problem

Combining equations (13)–(15) then gives a single linear eighth-order ordinary differential equation for  $\Theta$ ,

$$(D^2 - a^2 - \sigma) \left[ (D^2 - a^2)(D^2 - a^2 - \sigma P_r^{-1})^2 + T_a^* D^2 \right] \Theta + a^2 R^* (D^2 - a^2 - \sigma P_r^{-1}) \Theta = 0. \quad (22)$$

Equation (22) together with the boundary conditions (16)–(21) constitute a linear eigenvalue problem for the unknown temporal exponent  $\sigma$ . Relation (17) gives the expression for the surface deflection  $E$  in terms of the other quantities. In the general case  $\sigma \neq 0$  we seek solutions in the forms

$$W(z) = A C e^{\xi z}, \quad K(z) = B C e^{\xi z}, \quad \Theta(z) = C e^{\xi z}, \quad (23)$$

where the complex quantities  $A$ ,  $B$  and  $C$  and the exponent  $\xi$  are to be determined. Substituting these forms into the equations (13)–(15) and eliminating  $A$ ,  $B$  and  $C$  we obtain an eighth-order algebraic equation for  $\xi$ , namely

$$(\xi^2 - a^2 - \sigma) \left[ (\xi^2 - a^2)(\xi^2 - a^2 - \sigma P_r^{-1})^2 + T_a^* \xi^2 \right] + a^2 R^* (\xi^2 - a^2 - \sigma P_r^{-1}) = 0, \quad (24)$$

with eight distinct roots  $\xi_1, \dots, \xi_8$ . Denoting the values of  $A$ ,  $B$  and  $C$  corresponding to  $\xi_i$  for  $j = 1, \dots, 8$  by  $A_j$ ,  $B_j$  and  $C_j$  we can use equations (14) and (15) to determine  $A_j$  and  $B_j$  to be

$$A_j = -(\xi_j^2 - a^2 - \sigma), \quad B_j = -\frac{\xi_j A_j}{\xi_j^2 - a^2 - \sigma P_r^{-1}}, \quad (25)$$

for  $j = 1, \dots, 8$ . The boundary conditions (16)–(21) can be used to determine the eight unknowns  $C_1, \dots, C_8$  (up to an arbitrary multiplier), and the general solution to the stability problem is therefore

$$W(z) = \sum_{j=1}^8 A_j C_j e^{\xi_j z}, \quad K(z) = \sum_{j=1}^8 B_j C_j e^{\xi_j z}, \quad \Theta(z) = \sum_{j=1}^8 C_j e^{\xi_j z}. \quad (26)$$

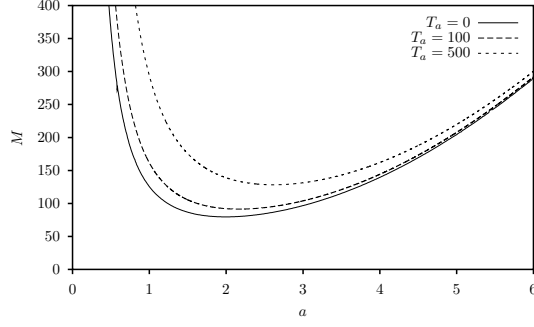


Figure 2: Numerically-calculated marginal curves for the onset of steady Marangoni convection plotted as functions of  $a$  in the case  $C_r = 0$  and  $B_i = 0$  for several values of  $T_a$ .

Imposing boundary conditions (16)–(21) yields a linear system  $\mathbf{PA} = \mathbf{0}$ , where  $\mathbf{A} = [A_1, \dots, A_8]^T$ . In general, the  $8 \times 8$  coefficient matrix  $\mathbf{P}$  (whose entries depend on  $a, M, R, \sigma, C_r, T_a, P_r, B_o$  and  $B_i$ ) is complex and may be rather complicated, and so, in general, it has to be calculated either numerically or symbolically using a symbolic algebra package. In this work we use both approaches. We use a FORTRAN 77 program employing the Numerical Algorithms Group (NAG) routine F03ADF to evaluate the determinant of  $\mathbf{P}$  using LU factorisation with partial pivoting. A modification of Powell's [7] hybrid algorithm, which is a combination of Newton's method and the method of steepest descent, implemented using NAG routine C05NBF is then used to find the eigenvalues of  $\mathbf{P}$  by solving the two non-linear equations obtained from the real and imaginary parts of the determinant of  $\mathbf{P}$ .

### Marginal Stability Curves

In this work we shall concentrate on the problem of the onset of steady and oscillatory Marangoni convection, i.e. we set  $R = 0$ . The marginal stability curves in the  $(a, M)$  plane on which  $\sigma_r = 0$  separate regions of unstable modes with  $\sigma_r > 0$  from those of stable modes with  $\sigma_r < 0$ . The critical Marangoni number for the onset of convection is the global minimum of  $M$  over  $a \geq 0$ .

For steady convection ( $\sigma = 0$ ), the dispersion relation  $F(a, M, C_r, T_a, B_o, B_i) = 0$  takes the linear form  $D_1 + MD_2 = 0$ , where  $D_1$  and  $D_2$  are two  $6 \times 6$  determinants which depend on the whole set of parameters of the problem except  $M$ . Given any set of values for  $R, T_a, C_r, B_i, B_o$ , we can determine the Marangoni number as a function of the wave number  $a$ .

Figure 2 shows typical marginal stability curves for the onset of steady Marangoni convection for various values of the Taylor number  $T_a$  in the case when the free surface is undeformable,  $C_r = 0$ , and insulating,  $B_i = 0$ . In this case the problem is independent of  $B_o$ . As a validation of our algorithm we found that as  $T_a \rightarrow 0$  the marginal curves tend to that obtained by Pearson [6] for the pure Marangoni problem without rotation,  $T_a = 0$ . Figure 2 clearly shows that in the cases investigated the effect of rotation is to stabilise the layer. Rotation introduces vorticity into the fluid which then causes the fluid to move in the horizontal planes with higher velocity. The velocity of the fluid perpendicular to the planes reduces, thus the onset of convection is inhibited (Chandrasekhar [1]).

While in practice the value of  $C_r$  may be very small (for a 1 cm layer of water open to air at  $20^\circ \text{C}$  we have  $C_r \sim 10^{-7}$ ) it will inevitably be non-zero. Figure 3 shows typical marginal stability curves for the onset of steady Marangoni convection for a range of values of  $T_a$  for  $C_r = 0.001$ ,  $B_o = 0.1$  and  $B_i = 0$ . As shown in figure 3 the marginal curves can have a local minimum value at  $a = 0$ . There exists a critical Taylor number, say  $T_{ac}$  be-

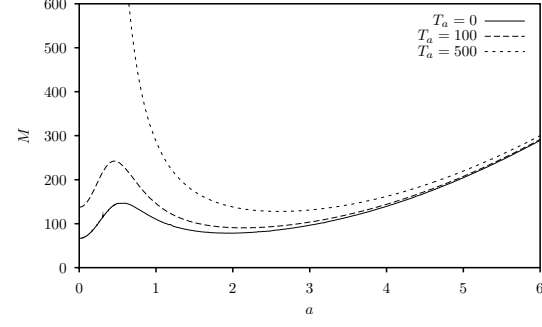


Figure 3: Numerically-calculated steady marginal curves for the onset of Marangoni convection plotted as functions of  $a$  in the case  $C_r = 0.001$ ,  $B_o = 0.1$  and  $B_i = 0$  for several values of  $T_a$ .

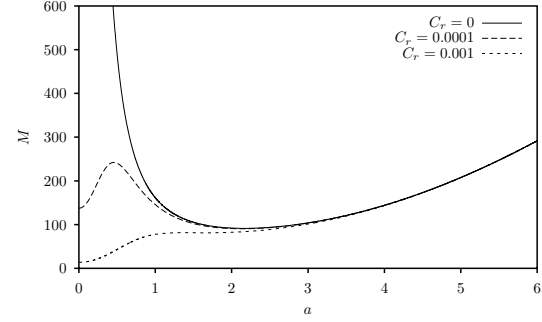


Figure 4: Numerically-calculated steady marginal curves for the onset of Marangoni convection plotted as functions of  $a$  in the case  $T_a = 100$ ,  $B_o = 0.1$  and  $B_i = 0$  for several values of  $C_r$ .

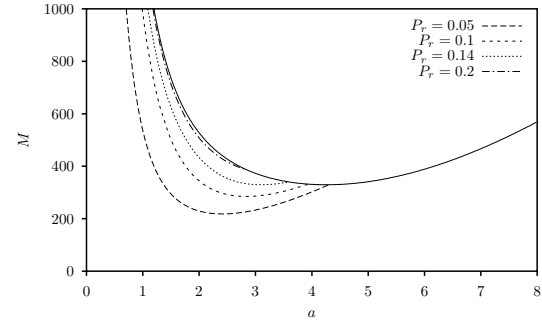


Figure 5: Numerically-calculated steady marginal curves for the onset of steady (solid) and oscillatory (dashed) Marangoni convection plotted as functions of  $a$  in the case  $C_r = 0$ ,  $T_a = 5000$ ,  $B_o = 0.1$  and  $B_i = 0$  for several values of  $P_r$ .

low which the onset of convection is at  $a = 0$  and above which the onset of convection is at  $a = O(1)$ . More interesting is the case when  $T_a = T_{ac}$  in which a competition between two different modes is possible. If the free surface is allowed to deform ( $C_r \neq 0$ ) then the marginal stability curves differ fundamentally from those in the case  $C_r = 0$  in the region  $a \ll 1$  and depend critically on  $T_a$  as depicted in figure 4. In the cases investigated in figure 4 variations in  $C_r$  has a minute effect on the marginal curves as  $a$  gets bigger.

Kaddame and Lebon [3] showed that convection can set in as oscillatory ( $\sigma \neq 0$ ) motions for the case when the free surface is flat, but no complete marginal curves were given. In figure 5 we plot both steady and oscillatory marginal curves in the case  $T_a = 5000$ ,  $C_r = 0$ ,  $B_o = 0.1$  and  $B_i = 0$  for several values of  $P_r$ . There exists a certain critical value of  $P_r = P_{rc}$  (depending on the other problem parameters) below which the onset of convection is oscillatory. In figure 6 we plot  $P_{rc}$  as a function of  $T_a$  in the case  $B_o = 0.1$  and  $B_i = 0$  for several values of  $C_r$ . Each curve in figure 6 defines the boundary between the steady and oscillatory domains. Points below each curve in figure 6 rep-

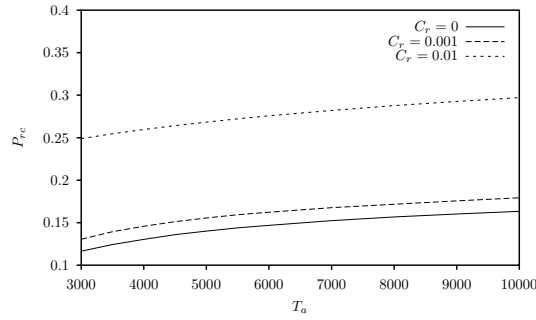


Figure 6: Numerically-calculated critical values of  $P_r$  below which oscillatory convection is preferred plotted as functions of  $T_a$  in the case  $B_o = 0.1$  and  $B_i = 0$  for several values of  $C_r$ .

resent parameter combinations  $(T_a, P_{rc})$  for which convection sets in as oscillatory motions, while points above each curve are those for which oscillatory convection is preferred. In the cases investigated, for a fixed value of  $T_a$ , increasing  $C_r$  has the effect of increasing  $P_{rc}$ .

### Conclusions

In this work we used classical linear stability theory to investigate the effect of rotation on the onset of steady and oscillatory Marangoni convection in a horizontal planar layer of fluid heated from below. The results showed the stabilising effect of the rotation and the possibility of the co-existence of two different modes at the onset of convection. In particular, we showed how the  $P_r$ - $T_a$  parameter space is divided into domains in which steady or oscillatory convection is preferred.

### Acknowledgments

The authors acknowledge the financial support from Malaysian Ministry of Science, Technology and Environment through IRPA grant no. 09-02-02-0078-EA206.

### References

- [1] Chandrasekhar, S., *Hydrodynamic and Hydromagnetic Stability*, Oxford University Press, Oxford, UK, 1961.
- [2] Kaddame, A. and Lebon, G., Bénard-Marangoni convection in a rotating fluid with and without surface deformation, *Appl. Sci. Res.*, **52**, 1994, 295–308.
- [3] Kaddame, A. and Lebon, G., Overstability in rotating Bénard-Marangoni cells, *Microgravity Quart.*, **4**, 1994, 69–74.
- [4] McConaghy, G. A. and Finlayson, B. A., Surface tension driven oscillatory instability in a rotating fluid layer, *J. Fluid Mech.*, **39**, 1969, 49–55.
- [5] Namikawa, T., Takashima, M. and Matsushita, S., The effect of rotation on convective instability induced by surface tension and buoyancy, *J. Phys. Soc. Japan*, **28**, 1970, 1340–1349.
- [6] Pearson, J. R. A., On convection cells induced by surface tension, *J. Fluid Mech.*, **4**, 1958, 489–500.
- [7] Powell, M. J. D., A hybrid method for nonlinear equations, in *Numerical Methods for Nonlinear Algebraic Equations*, editor P. Rabinowitz, Gordon and Breach, London, 1970, 87–114.
- [8] Schwabe, D., Surface-tension-driven flow in crystal growth melts, *Crystals*, **11**, 1988, 75–112.
- [9] Scriven, L. E. and Sternling, C. V., On cellular convection driven by surface-tension gradients: Effects of mean surface tension and surface viscosity, *J. Fluid Mech.*, **19**, 1964, 321–340.
- [10] Smith, K. A., On convective instability induced by surface-tension gradients, *J. Fluid Mech.*, **24**, 1966, 401–414.
- [11] Takashima, M., Surface tension driven instability in a horizontal liquid layer with a deformable free surface. I. Stationary convection, *J. Phys. Soc. Japan*, **50**, 1981, 2745–2750.
- [12] Takashima, M., Surface tension driven instability in a horizontal liquid layer with a deformable free surface. II. Overstability, *J. Phys. Soc. Japan*, **50**, 1981, 2751–2756.
- [13] Vidal, A. and Acrivos, A., The influence of Coriolis force on surface-tension-driven convection, *J. Fluid Mech.*, **26**, 1966, 807–818.
- [14] Vidal, A. and Acrivos, A., Nature of the neutral state in surface-tension driven convection, *Phys. Fluids*, **9**, 1966, 615–616.



## Dam Break Wave Propagation on Abrupt Drops: an Experimental Study

H. Chanson<sup>1</sup>

<sup>1</sup>Dept of Civil Engineering, The University of Queensland,  
Brisbane QLD 4072, AUSTRALIA

### Abstract

Flood waves resulting from dam breaks and flash floods have been responsible for numerous losses. In the present study, sudden flood releases were investigated down a large waterway with a succession of abrupt drops. A new experimental technique was developed to obtain instantaneous void fractions, bubble count rates and velocities using arrays of conductivity probes. The surging waters propagated as a succession of free-jets and horizontal runoff flow motion downstream of each abrupt drop. A strong aeration of the surge front was observed for all flow conditions. In the runoff region, instantaneous velocity measurements indicated a turbulent boundary layer region.

### Introduction

Surge waves resulting from dam breaks have been responsible for numerous losses of life (Fig. 1A). Related situations include flash floods, debris flow surges, surging waves in the swash zone, rising tides in dry estuaries and tsunami runup on dry land. In all cases, the surge front is a shock characterised by a sudden discontinuity and extremely rapid variations of flow depth and velocity. Despite a few early studies [1,2], current knowledge of dam break wave surging down rough surfaces is rudimentary and the aerated nature of the surging waters remains un-quantified, although clearly evidenced by photographs, movies and witness reports.

Hydraulic researchers have studied surging flows in laboratory facilities, but the findings have been sometimes contradictory. Some researchers highlighted a boundary layer region in the surging wave leading edge, including Mano [3] who studied unsteady wave runup using bubble tracer and high speed video, and Fujima and Shuto [4] who performed steady LDA (1 component) measurements on a conveyor belt. But Wang [5], based upon video observations, recorded a quasi-linear velocity profile at the head of two-phase debris flow, while Jensen et al. [6] using a PIV technique observed a quasi-uniform velocity profile in wave runup on a steep beach.

Research into highly-unsteady gas-liquid flow situations has been very limited, with a few exceptions. These include studies of cavitating flows [7] and void fraction measurements in breaking waves [8]. Nearly all works were performed in periodic flows enabling repeated measurements.

During the present study, surging waters were investigated in a large-size channel with a rough invert consisting of a succession of abrupt drops. The results provide new information on the wave front propagation, while unsteady two-phase flow measurements were conducted to gain new insights into the air-water flow characteristics and momentum exchanges.

### Experimental Setup

New experiments were performed in the 24 m long 0.5 m wide flume with a slope  $S_0 \sim 0.065$  ( $\theta = 3.4^\circ$ ) previously used by Chanson [9]. A precise flow rate was delivered by a pump controlled with an adjustable frequency AC motor drive Taian T-Verter K1/N1 (Pulse Width Modulated design), enabling an accurate discharge adjustment in a closed-circuit system. The flow was fed through a smooth convergent nozzle (1.7 m long), and the nozzle exit was 30 mm high and 0.5 m wide. The chute

consisted of a 2.4 m long horizontal section, immediately downstream of the nozzle, followed by 18 identical abrupt drops ( $h = 0.0715$  m), each followed by a 1.2 m long horizontal step.



(A) Lake Ha!Ha! Canada, July 1996 - Looking upstream at the breached dam (Courtesy of Natural Resources Canada)



(B) Present study:  $Q(t=0+) = 0.065 \text{ m}^3/\text{s}$ , step 16, looking at advancing surge (Courtesy of C.G. SIM and C.C. TAN)  
Fig. 1 - Photographs of dam break and resulting surging wave.

### Instrumentation

The flow rates in steady flow conditions were measured with a Dall tube flowmeter, calibrated on site with a sharp-crested weir, with an accuracy of about 2%. The surging flow was studied with high-shutter speed digital still- and video-cameras.

Air-water flow properties were measured with two systems. Air concentrations and bubble count rates were recorded with an

array of single-tip conductivity probes (needle probe design). Each probe consisted of a sharpened rod ( $\varnothing = 0.35$  mm) which was insulated except for its tip and set into a metal supporting tube acting as the second electrode. The second apparatus was a double-tip conductivity probe. The inner electrode was a Platinum wire ( $\varnothing = 0.15$  mm) and the outer electrode was a stainless steel surgical needle ( $\varnothing = 0.5$  mm). Each tip was identical and the distance between sensors was  $\Delta x_{tip} = 8.9$  mm. With both probe systems, the sensors were aligned along the flow direction and excited by an air bubble detector developed at the University of Queensland (UQ82.518) with a response time of less than  $10 \mu s$  and calibrated with a square wave generator. The probe output signals were scanned at 10 kHz per channel.

Data acquisition was triggered manually immediately prior to the flow arrival to have a minimum of 5 seconds of record. Visual observations showed that the wave front was roughly two-dimensional, and measurements were conducted on the centreline at several distances  $x$  from the step vertical face. At most locations, a single-tip conductivity probe (i.e. reference probe) was set on the invert, acting as a time reference, while the other probes were set at different elevations. In the free-jet region, the reference probe was set at the brink height (i.e.  $y = h$ ) to investigate the jet flow. Each experiment was repeated until sufficient data were obtained for each vertical profile.

The displacement of the probes in the vertical direction was controlled by a fine adjustment travelling mechanism with an error of less than 0.2 mm.

### Data Processing

Video-taped movies were analysed frame-by-frame. The error on the time was less than  $1/250$  s and the error on the longitudinal position of the wave front was  $\pm 1$  cm.

The conductivity probe signal outputs were processed using a single threshold technique. The threshold was set at 50% of air-water range. Unsteady void fractions  $C$  and bubble count rates  $F$  were calculated during a short time interval  $\tau$  such as  $\tau = \Delta X/V_s$  where  $V_s$  is the surge front celerity measured with the video-cameras and  $\Delta X$  is the control volume streamwise length. Preliminary tests indicated that the control volume length had to satisfy  $\Delta X \geq 70$  mm to contain a minimum of 5 to 20 bubbles [9]. The bubble count rate was calculated as:  $F = N_{ab}/\tau$  where  $N_{ab}$  is the number of bubbles detected during the time interval  $\tau$ .

Velocity data were calculated from individual droplet/bubbles events impacting successively the two probe sensors. The velocity was deduced from the time lag  $\delta t$  for air-to-water interface detections by both leading and trailing tips respectively. For each meaningful event, the interfacial velocity was calculated as:  $V = \Delta x_{tip}/\delta t$  where  $\Delta x_{tip}$  is the distance between probe sensor. The processing technique was compared successfully with video-observations of the shock front celerity and with the speed of ejected droplets.

### Boundary conditions

Before each run, the recirculation pipe system and convergent intake were emptied, while the channel was dry. The pump was rapidly started and reached nominal discharge  $Q(t=0+)$  in 5 sec.: that is, at least 10 sec. prior to the waters entering the channel. The discharge  $Q(t=0+)$  was maintained constant until the experiment end. Experiments were conducted for  $Q(t=0+) = 0.050, 0.060, 0.065$  and  $0.070$  m<sup>3</sup>/s.

For completeness, preliminary tests were conducted with the channel initially dry and wet. Visual observations demonstrated a major change in wave front shape in the presence of an initial film of water. Indeed, in presence of an initial water skin, the wave front was led by a positive surge that is completely different from surging waters on a dry bed [10,11].

### Basic Observations

For all flow conditions, visual observations and void fraction data demonstrated that the surging waters propagated as a succession of free-falling nappe, nappe impact and horizontal runoff (Fig. 2). At each step brink, the advancing surge took off as a free-jet, before impacting onto the downstream step around  $x = 0.2$  to  $0.3$  m. Nappe impact was associated with very significant spray and splashing, with water droplets reaching heights in excess of 0.5 m. Further, waters started to fill the cavity beneath the nappe, and the cavity became drowned after sometimes. The cavity filling process was however relatively slow compared to the surge propagation on each step. Downstream of nappe impact, the advancing waters ran off the step as a surge wave on dry bed.

The wave leading edge was highly aerated, in particular for the larger flow rates (Fig. 1B). Figure 1B emphasises the chaotic nature of wave front, with strong spray, splashing and wavelets. Water packets were commonly projected to heights greater than 3 to 5 step heights, while some droplets reached heights of more than 10 step heights. Visually laboratory experiments in the large-size flume had a similar appearance to prototype surging flows observed on Brushes Clough dam spillway and in Glashütte township.

The propagation of the wave front was recorded for a range of unsteady flow conditions. Wave front celerity data showed some flow acceleration in the first 4 to 6 steps. Further downstream, a gradual decay in celerity  $V_s$  was observed. The data were compared successfully with Hunt's [12] theory for dam break wave down sloping chutes. A fair agreement was achieved assuming an equivalent Darcy-Weisbach friction factor  $f = 0.05$ , irrespective of flow rate and chute configuration [4, Present study]. This flow resistance value is close to air-water flow measurement results in steady flow conditions yielding  $f \sim 0.047$  [13].

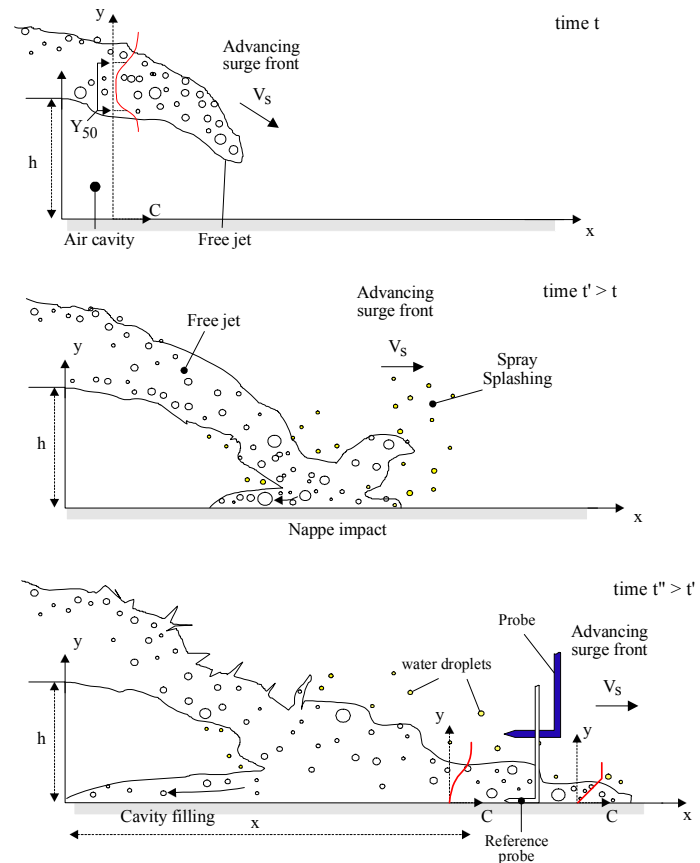


Fig. 2 - Definition sketch of advancing surging downstream of an drop.

### Void Fractions and Bubble Count Rate Distributions

Quasi-instantaneous measurements of void fractions in the free-

jet and in the horizontal runoff are presented in Figures 3 and 4 respectively. In each figure, instantaneous distributions for different times  $t$  are shown at a given location  $x$ , where  $t$  is the time from the first water detection by the reference probe. In Figures 3 and 4, the vertical axis is  $y/d_o$  where  $y$  is the vertical coordinate and  $d_o$  is a measure of the initial flow rate  $Q(t=0+)$ :

$$d_o = \frac{9}{4} \sqrt[3]{\frac{Q(t=0+)^2}{g W^2}} \quad (1)$$

$g$  is the gravity acceleration and  $W$  is the chute width.

In the free-jet region (i.e.  $x < 0.2$  to  $0.3$  m), interfacial aeration occurred at both upper and lower nappes. Instantaneous distributions of void fraction followed closely analytical solutions of the air bubble diffusion equation for upper and lower nappes:

$$C = \frac{1}{2} \left( \operatorname{erf} \left( \frac{y - Y_{50}}{2 \sqrt{\frac{D_t}{V_s} x}} \right) - 1 \right) \quad (2A)$$

$$C = \frac{1}{2} \left( 1 - \operatorname{erf} \left( \frac{y - Y_{50}}{2 \sqrt{\frac{D_t}{V_s} x}} \right) \right) \quad (2B)$$

where  $C$  is the void fraction,  $Y_{50}$  are the characteristic locations where  $C = 0.50$  in the nappe,  $D_t$  is an air bubble diffusivity,  $V_s$  is the surge front celerity, and the function  $\operatorname{erf}$  is the Gaussian error function:

$$\operatorname{erf}(u) = \frac{2}{\sqrt{\pi}} * \int_0^u \exp(-v^2) dv \quad (3)$$

Equations (2A) and (2B) were developed respectively for the upper and lower nappes of steady water jets, assuming constant bubble diffusivity [14,15]. They are compared with experimental data in Figure 3. The results show an increase in nappe thickness with increasing time at a given location. Note the start of cavity filling in Figure 3B.

In the nappe impact region and in the horizontal runoff, the void fraction distributions at the leading edge of the surging waters had a quasi-linear shape:

$$C = 0.9 \frac{y}{Y_{90}} \quad t \sqrt{g/d_o} < 1.0 \quad (4)$$

where  $Y_{90}$  is the height where  $C = 0.90$ . For larger times (i.e.  $t \sqrt{g/d_o} > 1.5$ ), the distributions of air concentration exhibited an inverted S-shape that was best described by the diffusion model:

$$C = 1 - \tanh^2 \left( K' - \frac{y}{2 D_o} + \frac{\left( \frac{y}{Y_{90}} - \frac{1}{3} \right)^3}{3 D_o} \right) \quad (5)$$

where  $K'$  and  $D_o$  are functions of the depth-averaged void fraction  $C_{\text{mean}}$  only [16].

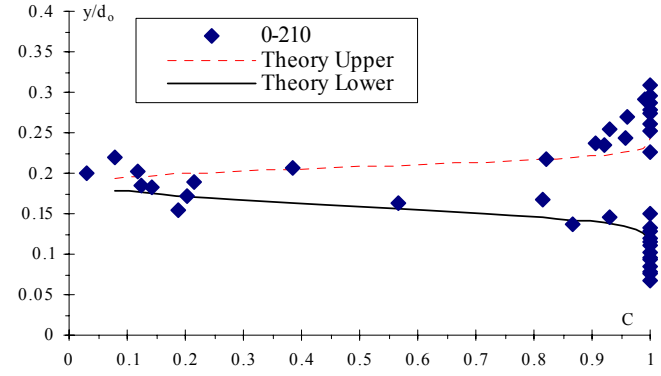
Typical instantaneous void fraction data are presented in Figure 4, in which they are compared with Equations (4) and (5). These are analytical solutions of the advective diffusion of air bubbles assuming respectively the following distributions of dimensionless turbulent diffusivity of air bubbles:

$$D' = \frac{C \sqrt{1-C}}{0.9} \quad t \sqrt{g/d_o} < 1.0 \quad (6)$$

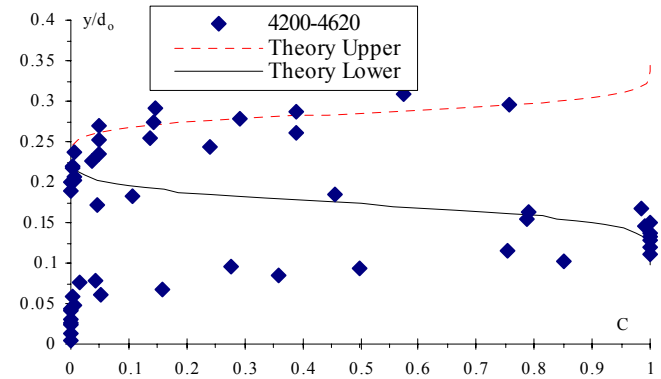
$$D' = D_o \left( 1 - 2 \left( \frac{y}{Y_{90}} - \frac{1}{3} \right)^2 \right)^{-1} \quad t \sqrt{g/d_o} > 1.5 \quad (7)$$

where  $D' = D_t / ((u_r)_{\text{Hyd}} \cos \theta Y_{90})$ ,  $(u_r)_{\text{Hyd}}$  is the bubble rise velocity in hydrostatic pressure gradient. Note that the shape of Equation (7) is similar to the sediment diffusivity distribution which yields to the Rouse distribution of suspended matter.

Bubble count rate data showed systematically large bubble count rates, hence large interfacial areas, at the surge leading edge, while the maximum bubble count rates tended to decrease with increasing time  $t$  towards steady flow values.



(A)  $t = 0.044$  s,  $\Delta X = 0.21$  m



(B)  $t = 1.87$  s,  $\Delta X = 0.42$  m - Note the start of cavity filling  
Fig. 3 - Dimensionless distributions of instantaneous void fractions in the free-jet flow region ( $Q(t=0+) = 0.070$  m<sup>3</sup>/s,  $d_o = 0.283$  m, step 16,  $x = 0.1$  m,  $V_s = 2.36$  m/s) - Comparison with Equations (2A) and (2B)

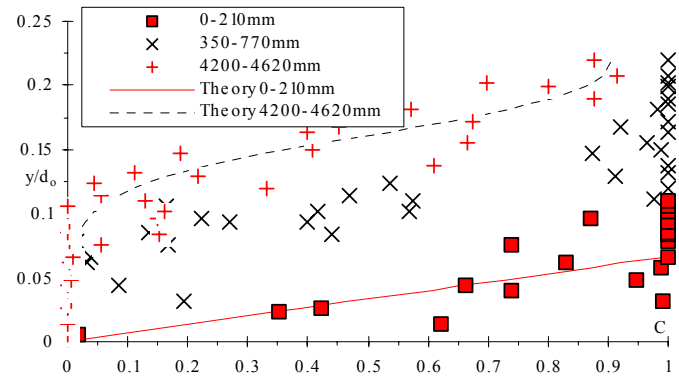


Fig. 4 - Dimensionless distributions of instantaneous void fractions in the horizontal runoff region ( $Q(t=0+) = 0.070$  m<sup>3</sup>/s,  $d_o = 0.283$  m,  $V_o = 0.48$  m/s, step 16,  $x = 0.8$  m,  $V_s = 2.57$  m/s) -  $t = 0.040$  [0-210], 0.210 [350-770], 1.66 s [4200-4620].

### Velocity Distributions

In the free-jet region ( $x < 0.3$  m), velocity distributions showed a quasi-uniform profile. Despite some scatter, the data suggested a reasonably uniform velocity distribution, although some high-speed water projections were observed in the initial instants.

Figure 5 presents typical instantaneous velocity data in the horizontal runoff region. Each data point represents the velocity of the first air-to-water interface at each position  $y$ . At the surge leading edge, the instantaneous velocity data compared reasonably well with an analytical solution of the Navier-Stokes equations (first Stokes problem) for startup flow (Fig. 5):



$$\frac{V}{U} = \operatorname{erf}\left(\frac{y}{2\sqrt{v_T t}}\right) \quad (8)$$

where  $U$  is a free-stream velocity,  $t$  is the time, and  $v_T$  is the momentum exchange coefficient. Dimensionless distributions of time-average velocity (over about 5 sec.) were typically quasi-uniform suggesting a potential flow region above the shear zone. The magnitude of time-average velocities was consistently smaller than the velocity of the first interface, possibly because of water projections ahead of the surging waters. The data further highlighted high levels of turbulence in the surging flow, with turbulence levels ranging from 20 to 100% with mean values of about 50%. These were consistent with observed turbulence levels in steady stepped chute flows [16,17].

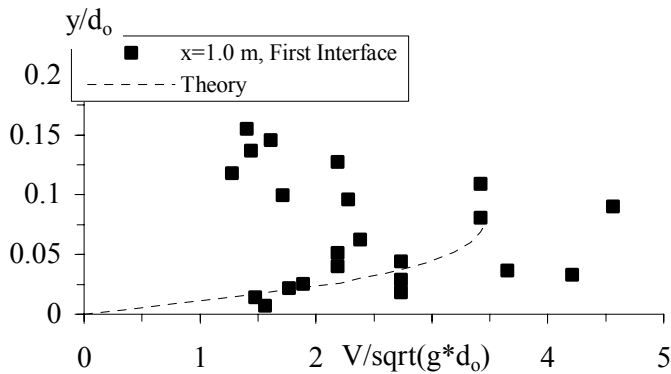


Fig. 5 - Instantaneous velocity distributions at surge leading edge in horizontal runoff ( $Q(t=0+) = 0.065 \text{ m}^3/\text{s}$ ,  $d_o = 0.27 \text{ m}$ , step 16,  $x = 1.0 \text{ m}$ ) - Interfacial velocity of first air-to-water interface ( $t < 0.12 \text{ s}$ ) - Comparison with Equation (8).

### Discussion

In the horizontal runoff flow, the data highlighted a boundary layer region next to the invert in the shock front (Fig. 5). The finding is consistent with earlier laboratory experiments [3,4]. The values of  $U$  and  $v_T$  (Eq. (8)) were determined from best data fit. Despite some scatter and crude approximations leading to Equation (8), the results implied a turbulent boundary layer. Based upon present void fraction and velocity measurements in horizontal runoff flow, the air bubble diffusivity  $D_t$  and eddy viscosity  $v_T$  which satisfy Equations (4) and (8) respectively yielded a ratio  $D_t/v_T$  of about unity in the surge front. The ratio  $D_t/v_T$  compares the effects of the difference in diffusion of a discrete bubble particle and small coherent fluid structure, as well as the effect of entrained air on the turbulence field. The result  $D_t/v_T \sim 1$  seems to suggest strong interactions between air bubble diffusion and momentum exchange processes.

### Conclusion

New experiments were conducted systematically in surging waters down a 24 m long chute with a succession of abrupt drops. Unsteady air-water flow measurements were performed in the surging waters using an array of conductivity probes. Visual observations showed that the surges propagated at a succession of free jets immediately downstream of each abrupt drop, nappe impact and horizontal runoff flow. The results showed quantitatively a strong aeration of surge leading edge. The void fraction distributions followed reasonably well analytical solutions of air bubble diffusion equation developed for steady flow conditions. In the horizontal runoff, velocity data showed the presence of an unsteady turbulent boundary layer next to the invert. Overall the results emphasised the complicated nature of the surging flow and its front.

It must be emphasised that present results were focused on a flat chute ( $3.4^\circ$ ) in which the horizontal runoff was a dominant flow

motion. On steeper slopes, preliminary observations suggested significantly more complicated processes.

### Acknowledgments

The writer thanks his students Chye-guan SIM, and Chee-chong TAN for their help and assistance.

### References

- [1] Dressler, R., Comparison of Theories and Experiments for the Hydraulic Dam-Break Wave, *Proc. Intl Assoc. of Scientific Hydrology Assemblée Générale*, Rome, Italy, 1954, **3** (38), pp. 319-328.
- [2] Escande, L., Nougare, J., Castex, L., and Barthet, H., Influence de Quelques Paramètres sur une Onde de Crue Subite à l'Aval d'un Barrage." *Jl La Houille Blanche*, 1961, (5) pp. 565-575.
- [3] Mano, A., Boundary Layer Developed near Surging Front." *Coastal Engineering in Japan*, 1994, **37** (1) pp. 23-39.
- [4] Fujima, K., and Shuto, N., Formulation of Frictions Laws for Long Waves on a Smooth Dry Bed, *Coastal Engineering in Japan*, 1990, **33** (1) pp. 25-47.
- [5] Wang, Z.Y., Initiation and Mechanism of Two Phase Debris Flow." *Proc. Conf. on Flood Defence'2002*, Ed. Wu et al., Science Press, New York, 2002, pp. 1637-1648.
- [6] Jensen, A., Pedersen, G.K., and Wood, D.J., An Experimental Study of Wave Run-up on a Steep Beach, *Jl of Fluid Mech.*, 2003, **486** pp. 166-188.
- [7] Stutz, B., and Reboud, J.L., Measurements within Unsteady Cavitation." *Experiments in Fluids*, 2000, **29** pp. 545-552.
- [8] Hwang, H.H., Chyan, J.M., and Chung, Y.C., Energy Dissipation and Air Bubbles Mixing inside Surf Zone." *Proc. 23rd Intl Conf. on Coastal Eng.*, ASCE, Venice, Italy, 1992, **1** (22) pp. 308-321.
- [9] Chanson, H., Sudden Flood Release down a Stepped Cascade. Unsteady Air-Water Flow Measurements. Applications to Wave Run-up, Flash Flood and Dam Break Wave, *Report CH51/03*, Dept of Civil Eng., Univ. of Queensland, Brisbane, Australia, 142 pages, 2003.
- [10] Henderson, F.M., *Open Channel Flow*, MacMillan Company, New York, USA, 1966.
- [11] Montes, J.S., *Hydraulics of Open Channel Flow*, ASCE Press, New-York, USA, 697 pages, 1998.
- [12] Hunt, B., Asymptotic Solution for Dam-Break Problems, *Jl of Hyd. Div.*, Proceedings, ASCE, 1982, **108** (HY1) pp. 115-126.
- [13] Chanson, H., and Toombes, L., Energy Dissipation and Air Entrainment in a Stepped Storm Waterway: an Experimental Study, *Jl of Irrigation and Drainage Engrg.*, ASCE, 2002, **128** (5) pp. 305-315.
- [14] Chanson, H., Study of Air Entrainment and Aeration Devices, *Jl of Hyd. Res.*, IAHR, 1989, **27** (3) pp. 301-319.
- [15] Brattberg, T., Chanson, H., and Toombes, L., Experimental Investigations of Free-Surface Aeration in the Developing Flow of Two-Dimensional Water Jets, *Jl of Fluids Eng.*, Trans. ASME, 1998, **120** (4) pp. 738-744.
- [16] Chanson, H., and Toombes, L., Strong Interactions between Free-Surface Aeration and Turbulence down a Staircase Channel, *Proc. 14th Australasian Fluid Mech. Conf.*, Adelaide, Australia, 2001, pp. 841-844.
- [17] Ohtsu, I., and Yasuda, Y., Characteristics of Flow Conditions on Stepped Channels, *Proc. 27th IAHR Biennial Congress*, San Francisco, USA, 1997, Theme D, pp. 583-588.

## A new solution for ocean waves propagating over a sloping beach

D.-S. Jeng<sup>1</sup> and B. R. Seymour<sup>2</sup>

<sup>1</sup>Department of Civil Engineering  
The University of Sydney, New South Wales 2006 AUSTRALIA

<sup>2</sup>Department of Mathematics, The University of British Columbia  
Vancouver V6T 1Z2 Canada

### Abstract

In this paper, the phenomenon of ocean waves propagating over a sloping beach is re-examined. Unlike previous analytical approximations, we propose an exact solution for a general case with arbitrary beach shape. Two different beach shapes are used as numerical examples. Numerical results demonstrate the significant influence of beach shapes on the water surface elevation and velocity.

### Introduction

The phenomenon of ocean waves transformation from offshore (deep water) to nearshore (shallow water) is particularly important for the design and protection of the coastline. This includes the topics of wave breaking, the stability of the coastline, and beach nourishment. Also, the transformation of wave energy in the nearshore region is a dominant factor in the design of coastal structures.

Since the perturbation technique was first applied to the development of ocean waves [12], the symmetric ocean waves in a uniform water depth has been widely studied since the 1980s. With the development of computational technique, the wave phenomenon in a uniform depth is no longer a mystery. However, in realistic environments, the seabed bottom is varied, the variation of the seabed bottom will affect the free surface fluctuation from deep to shallow water.

Numerous investigations for the ocean waves propagating over a sloping seabed have been carried out. Carrier and his co-author [1, 2] developed a series of analytical solutions for gravity waves propagating on water of variable depth. Their solutions have been limited to a beach with constant slope, although the solution for a beach with arbitrary bottom was suggested.

To date, the commonly used model for waves propagating over a sloping seabed is based on the wave model of a uniform depth, and then apply the conservation of energy flux to solve the wave fluctuation with varying depth step by step [3, 8]. This type of approaches cannot represent the effects of seabed bottom slope in the solution. A few researchers have attempted to directly take into account of slope in the whole problem [7]. However, their approaches only limited to the cases with a small slope and a small relative water depth. Recently, with advance of numerical schemes, the wave propagating over a sloping seabed even to wave breaking state can be solved numerically. For example, the parabolic wave model proposed by Li [9] has been widely used and extended to various situations [4, 10, 13]

Besides analytical approximations, significant advances have been made in developing mathematical models to describe fully non-linear and weakly dispersive waves propagating over an impermeable bottom [5, 6, 11]. Based on the inviscid fluid assumption, these models reduce the three-dimensional Euler equations to a set of two-dimensional governing equations. These equations are usually expressed in terms of the free sur-

face displacements and representative horizontal velocity components, which are either evaluated at a certain elevation, or depth averaged.

In this study, a new analytical solution is developed for the phenomenon of ocean wave propagating over a sloping beach. Unlike previous analytical approximations, we consider the beach with an arbitrary shape, rather than linear beach. Two types of beach shapes are used as examples, and their effects on the water surface elevation will be investigated.

### Theoretical Formulations

#### Boundary Value Problem

In this study, we consider the the ocean gravity waves propagating over a sloping beach, as depicted in figure 1. In the figure,  $h_a$  is the reference water depth far from the beach,  $h(x, t)$  is the water surface elevation, which is defined by

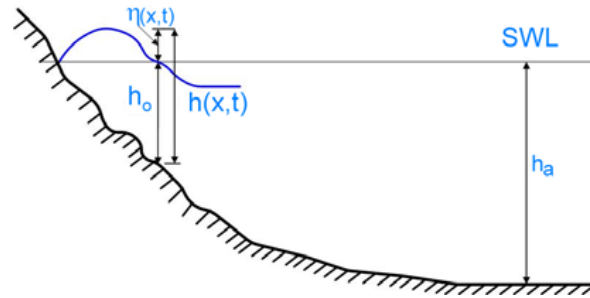


Figure 1: Geometry of the general propagation problem.

$$h(x, t) = h_o(x) + \eta(x, t), \quad (1)$$

where  $\eta(x, t)$  represents the fluctuation of water wave, and  $h_o(x)$  is the water depth at the location  $(x)$ .

Based on shallow water theory [1], the governing equations for the ocean waves propagating over an incompressible and inviscid fluid can be expressed in Eulerian system as

$$\frac{\partial u}{\partial t} + u \frac{\partial u}{\partial x} + g \frac{\partial \eta}{\partial x} = 0, \quad (2a)$$

$$\frac{\partial h}{\partial t} + \frac{\partial (uh)}{\partial x} = 0, \quad (2b)$$

where  $u$  is the velocity in the horizontal direction,  $t$  is the time,  $g$  is the gravitational acceleration, and the subscripts "x" and "t" denote the partial differentiation respective to  $x$  and  $t$ , respectively.

Now, we consider the problem in a Lagrangian system, and choose  $h_a$  as the reference height, the relationship between two co-ordinates is

$$\frac{\partial x}{\partial X} = \frac{h_a}{h(x,t)} = \frac{h_a}{h_o(x) + \eta(x,t)}. \quad (3)$$

To simplify the problem, we linearise (3) as,

$$\frac{\partial x}{\partial X} = \frac{h_a}{h(x,t)} \approx \frac{h_a}{h_o(x)}. \quad (4)$$

Then, the linearised governing equations in a Lagrangian system can be expressed as

$$\frac{\partial u}{\partial t} + g \frac{h_o}{h_a} \frac{\partial \eta}{\partial X} = 0, \quad (5a)$$

$$\frac{\partial \eta}{\partial t} + \frac{h_o^2}{h_a} \frac{\partial u}{\partial X} = 0. \quad (5b)$$

To simplify the mathematical expressions, we non-dimensionalise the whole problem with the following variables,

$$(X^*, \eta^*, h) = \frac{(X, \eta, h)}{h_a}, \quad t^* = \frac{t}{(h_a/\sqrt{gh_a})}, \quad (6)$$

where the superscript "\*" denote the non-dimensional parameters. To avoid the complicated mathematical expressions, the "\*" will be ignored, and all physical variables are non-dimensional parameters in the following section, unless specified.

Introducing (6) into (5a) and (5b), the governing equations can be re-written as

$$\frac{\partial u}{\partial t} + h_o \frac{\partial \eta}{\partial X} = 0 \quad (7a)$$

$$\frac{\partial \eta}{\partial t} + h_o^2 \frac{\partial u}{\partial X} = 0 \quad (7b)$$

### Analytical Solution

In this paper, we attempt to solve the above governing equations (7a) and (7b) analytically. Herein, we define a new variable,

$$\frac{dR}{dX} = \frac{1}{h_o^{3/2}} \quad (8)$$

which leads to

$$\frac{\partial u}{\partial t} + \frac{1}{\sqrt{h_o}} \frac{\partial \eta}{\partial R} \quad (9a)$$

$$\frac{\partial \eta}{\partial t} + \sqrt{h_o} \frac{\partial u}{\partial R} = 0 \quad (9b)$$

$$\frac{\partial^2 \eta}{\partial t^2} - \sqrt{h_o} \frac{\partial}{\partial R} \left( \frac{1}{\sqrt{h_o}} \frac{\partial \eta}{\partial R} \right) = 0 \quad (9c)$$

Let  $C(\epsilon) = \sqrt{h_o(X)}$ , we have

$$\frac{\partial^2 \eta}{\partial t^2} - C(R) \frac{\partial}{\partial R} \left( \frac{1}{C(R)} \frac{\partial \eta}{\partial R} \right) = 0 \quad (10a)$$

$$\frac{\partial^2 u}{\partial t^2} - \frac{1}{C(R)} \frac{\partial}{\partial R} \left( C(R) \frac{\partial u}{\partial R} \right) = 0 \quad (10b)$$

in which

$$R = \int_0^X \frac{ds}{C^3(s)} \quad \text{and} \quad X = \int_0^R C^3(s) ds \quad (11)$$

Note that (10a) contains the *beach shape function*,  $C(R) = \sqrt{h_o(X)}$ , which describes the variation in the beach profile with depth. In general, it is difficult to obtain analytical solutions for equations of the form (10a), However, an exact solution is possible using the approach of Varley and Seymour [14].

The general solution for (10a) can be expressed as

$$\eta = \sum_{n=0}^N f_n(R) \frac{\partial^{N-n} F}{\partial R^{N-n}} \quad (12a)$$

$$u = \sum_{n=0}^N e_n(R) \frac{\partial^{N-n} E}{\partial R^{N-n}} \quad (12b)$$

where  $f_o = 1/e_o = \sqrt{C(R)} = h_o^{1/4}(X)$ , and  $E$  and  $F$  satisfy

$$\frac{\partial E}{\partial t} + \frac{\partial F}{\partial R} = 0 \quad \text{and} \quad \frac{\partial F}{\partial t} + \frac{\partial E}{\partial R} = 0 \quad (13)$$

The function  $E$  and  $F$  can be expressed as

$$E = A(t+R) + B(t-R) \quad (14a)$$

$$F = -A(t+R) + B(t-R) \quad (14b)$$

where  $A(t+R)$  is given as the incident wave components, and  $B(t-R)$  is an unknown function, which needs to be determined later.

To find  $B$ , the following boundary conditions are required:

$$\eta \rightarrow 0 \quad \text{as} \quad C(R) \rightarrow 0 \quad (15a)$$

$$u \quad \text{bounded} \quad \text{as} \quad C(R) \rightarrow 0 \quad (15b)$$

Using  $N = 1$  as the first approximation, we have

$$\eta = \sqrt{C(R)} \frac{\partial F}{\partial R} + \ell_1 F \quad (16a)$$

$$u = \frac{1}{\sqrt{C(R)}} \frac{\partial E}{\partial R} + k_1 E \quad (16b)$$

With the boundary conditions, we have  $A(t) = B(t)$ , which gives us

$$E = A(t+R) + A(t-R) \quad (17a)$$

$$F = -A(t+R) + A(t-R) \quad (17b)$$

If we consider the incident wave  $A(x,t)$  as

$$A(x,t) = A_0 \cos\left(\frac{2\pi}{L}(x-ct)\right) = A_0 \cos\left(\frac{2\pi h_a}{L}(X^* - t^*)\right) \quad (18)$$

where  $L$  is the wavelength of incident wave in deep water,  $A_0$  is the amplitude of waves.

### Numerical Examples

In this paper, two types of beach profiles are used:

$$\text{case I: } h_o(R) = [0.5 \tanh(0.1R)]^4 \quad (19a)$$

$$\text{case II: } h_o(R) = R^4 \quad (19b)$$

Two different beach shapes are plotted in figure 2. As shown in the figure, Case I represents a case with gentle slope, which is a function of  $\tanh$ , while Case II represents a case of rapidly slope, which is a function of  $R(x)^4$ . In this study, we use  $h_a=0.05L$  as the reference water depth, because we are only concern with the case of shallow water. In the following discussion, the non-dimensional variables will be represented with "\*" superscripts.

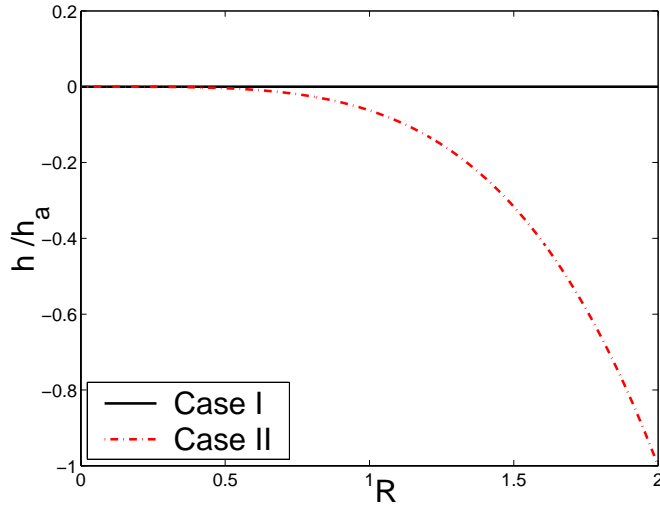


Figure 2: Two types of beach profiles.

With the beach profile shown in figure 2, the water surface elevations ( $\eta/h_a$ ) with different beach profile are illustrated in figure 3(a). As shown in the figure, functions of beach profiles significantly affect the water surface elevation ( $\eta$ ). The distribution of velocity versus horizontal distance ( $x/h_a$ ) is illustrated in figure 3(b). Again, significant influence of beach profile is found.

it is noted that the amplitude of the water surface elevation ( $|\eta|$ ) slowly increases as horizontal distance ( $x$ ) increases. It is because the present solution is only valid for the shallow water, i.e.,  $h_a/L < 0.05$ , which is based on the assumption of shallow water expansion. For the cases with intermediate water and deep water, the conventional Stokes wave theory should be used.

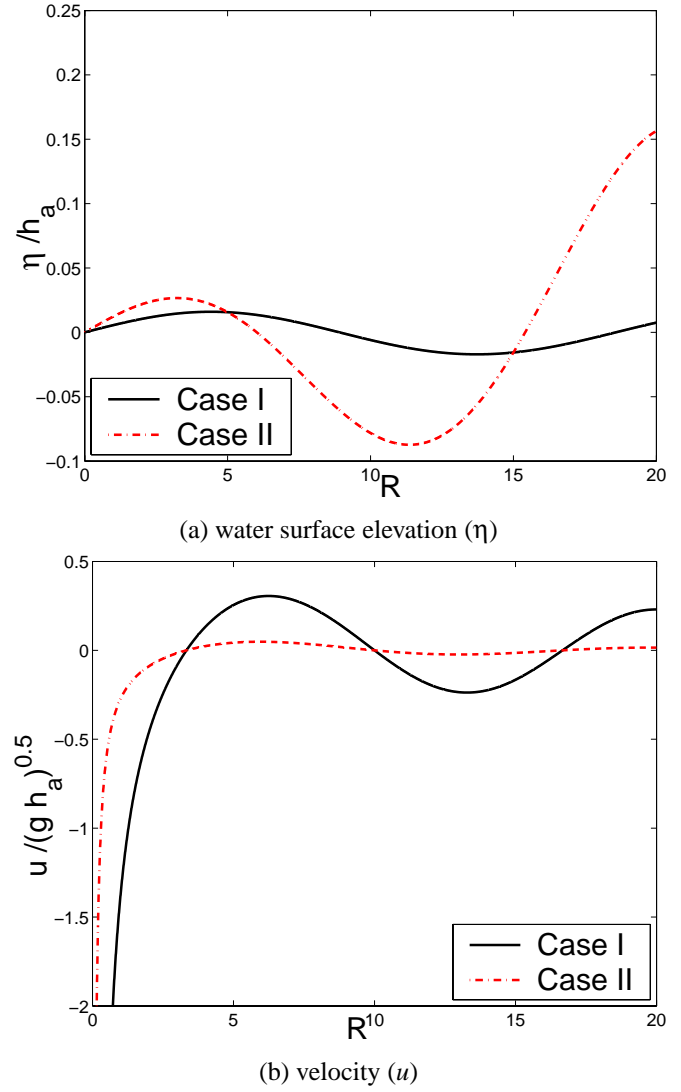


Figure 3: Comparison of (a) water surface elevation and (b) velocity with different beach profiles. ( $T=0.5$ )

### Conclusions

In this paper, an exact solution for ocean wave propagating over a sloping beach is derived. In the new analytical solution, an arbitrary beach shape is considered, which has been assumed to be a linear function in the past. Two different beach profiles are used as numerical examples. Numerical results demonstrate the significant effects of beach profile on the water surface elevation and velocity profiles.

### Acknowledgements

The authors are grateful for the support from Australian Research Council Discovery Grant #DP0450906 (2004-2007).

### References

- [1] Carrier, G.F. and Greenspan, H.P., Water waves of finite amplitude on a sloping beach, *J. Fluid Mech.*, **4**, 1958, 97-109.
- [2] Carrier, G.F., Gravity waves on water of variable depth, *J. Fluid Mech.*, **24**, 1966, 641-659.
- [3] Chen, Y.Y. and Hwung, H.H., Water waves propagating on beaches of arbitrary slope. *Proceeding of the 18th International Conference on Coastal Engineering, ASCE*, 1982, 811-822.

- [4] Ehrenmark, U.T. and Williams, P.S., Wave parameter tuning for the application of the mild-slope equation on steep beaches and in shallow water. *Coastal Engineering*, **42**, 2001, 17-34.
- [5] Gobbi and Kirby, J., Wave evolution over submerged sills: tests of a higher-order Boussinesq model, *Coastal Engineering*, **37**, 1999, 57-96.
- [6] Hsu, T.W. and Wen, C.C., A parabolic equation extended to account for rapidly varying topography. *Ocean Engineering*, **28**, 2001, 1479-1498.
- [7] Keller, J.B., Surface waves on water of non-uniform depth. *J. Fluid Mech.*, **4**, 1958, 607-614.
- [8] Le Mehaute, H. and Web, L., Periodic gravity wave over a gentle slope at a third-order of approximation. *Proceeding of the 9th International Conference on Coastal Engineering*, ASCE, 1964, 23-40.
- [9] Li, B., An evolution equation for water waves. *Coastal Engineering*, **23**, 1994, 227-242.
- [10] Li, B., Parabolic model for water waves. *Journal of Waterway, Port, Coastal and Ocean Engineering*, ASCE, **123**(4), 1997, 192-199.
- [11] Liu, P.L.F., Model equations for wave propagation from deep to shallow water, *Advances in Coastal and Ocean Engineering*, **1**, 1994, 125-158.
- [12] Stoke, G.G., On the theory of oscillatory waves. *Mathematical and Physical Papers*, Cambridge University Press, **1**, 1847, 314-326.
- [13] Suh, K.D., Lee, C. and Part, W.S., Time-dependent equations for wave propagation on rapidly varying topography. *Coastal Engineering*, **32**, 1997, 91-117.
- [14] Varley, E. and Seymour, B.R., A method for obtaining exact solutions to partial differential equations with variable coefficients. *Studies in Applied Mathematics*, **78**, 1988, 183-225.



## Simultaneous Field Measurements of Turbulence and Water Quality in a Sub-Tropical Estuary in Australia

H. Chanson<sup>1</sup>, R. Brown<sup>2</sup>, and J. Ferris<sup>3</sup>

<sup>1</sup>Dept of Civil Engineering, The University of Queensland, Brisbane QLD 4072, AUSTRALIA

<sup>2</sup>School of Mechanical, Manufacturing and Medical Engineering, Q.U.T., Brisbane QLD 4000, AUSTRALIA

<sup>3</sup>Water Quality Monitoring Group, E.P.A., Indooroopilly QLD 4068, AUSTRALIA

### Abstract

In natural systems, mixing is driven by turbulence, but current knowledge is very limited in estuarine zones. A series of detailed field studies was conducted in a small subtropical creek in eastern Australia. Hydrodynamic and physio-chemical parameters were measured simultaneously at high frequency to assess the complexity of the estuary and the interactions between turbulence and environment. The results provide an original data set to complement long-term monitoring. Unlike many such field observations, velocity and physio-chemistry (scalars) were measured herein with sufficient spatial and temporal resolutions to determine quantities of interest in the study of turbulence. In particular the results yielded contrasted outcomes, and the finding impacts on the selection of "key water quality indicators".

### Introduction

Mixing and dispersion of matter in estuaries is of considerable importance. Applications include sediment transport, smothering of seagrass and coral, release of wastewater into ecosystems including from treated sewage effluent, and storm-water runoff during flood events. Current knowledge is limited : e.g., the vertical mixing coefficient is often approximated by the depth-averaged momentum exchange coefficient, while transverse mixing and dispersion coefficients are assumed constant over relatively long distances. Both sets of assumptions are untrue. Predictions of contaminant dispersion in estuaries must be therefore based upon empirical mixing coefficients that are highly sensitive upon the natural system and must be measured in-situ. Experimental findings are accurate only "within a factor of 10" at best and they can rarely be applied to another system [1,2,3]. Although mixing is driven by turbulence, the interactions between hydrodynamics, physio-chemistry and ecology are rarely considered together. There has been very little research done on turbulent mixing and dispersion in complete estuarine systems, in particular in subtropical zones. One reason is the complex behaviour of an estuary.

A series of field studies were conducted in the estuarine zone of Eprapah Creek (Australia) in 2003. The purpose of field works was to assess the complexity of a small estuarine system, and the interactions between hydrodynamics and water quality. The results provide a new understanding of basic mixing process in sub-tropical estuaries, while the experience highlights important issues and practical considerations.

### Field site

Eprapah Creek (Long. 153.30°, Lat. -27.567°) is a sub-tropical stream located in the Redlands shire close to Brisbane city. Average hydrological conditions are listed in Table 1 for a 50-year period. Eprapah Creek flows directly to the Moreton Bay at Victoria Point (Fig. 1). It is basically 13.6 km long with about 3.8 km of estuarine zone. In the latter, the water depth is typically about 1 to 2 m mid-stream, the width is about 20-30 m and the tides are semi-diurnal with a range of about 1.5 m. The catchment (~ 39 km<sup>2</sup> area) is mostly urban in the lower reaches and semi rural/rural residential in the upper reaches. The estuary includes

two conservation areas hosting endangered species (e.g. koalas, swamp wallabies, sea eagles), some marinas and boat yards, and a sewage plant impacting heavily on the natural system.

Although water quality and ecology have been closely monitored at Eprapah Creek (Victoria Point QLD) for more than 30 years, the creek was heavily polluted in 1998 by illegal discharges of TBT and chemical residues. The catchment has been adversely affected by industrial poultry farms, land clearance and semi-urban development. Recent works included the constructions of new shopping centres and residential lots.

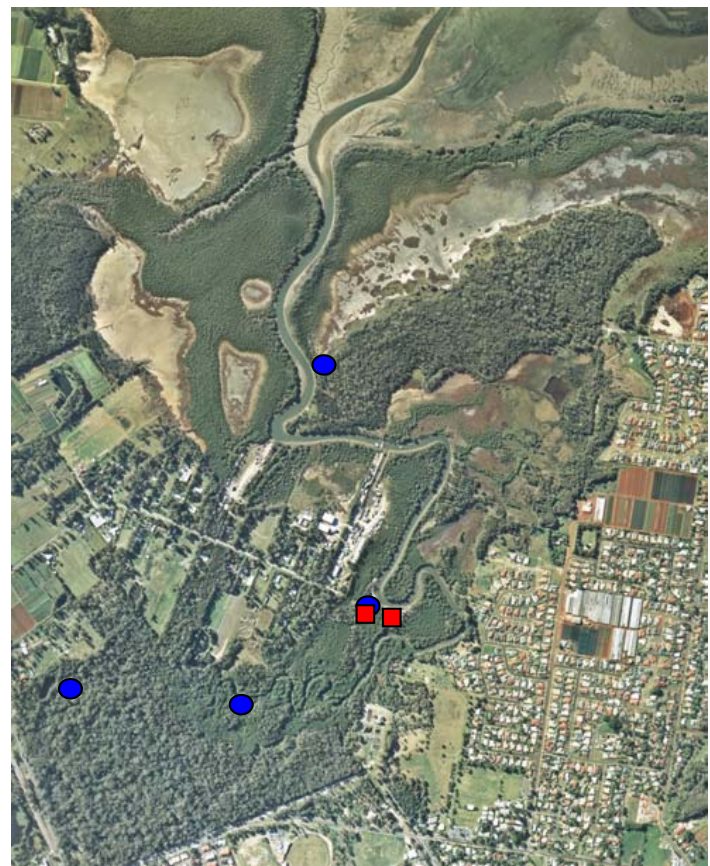


Fig. 1 - Aerial photograph of Eprapah Creek estuary (Courtesy of Queensland Department of Natural Resources and Mines, 2001)

Blue circle: water quality sampling station - Red square: instantaneous velocity and physio-chemical measurement sites.

### Experimental Methods

Field works took place on three different days (Table 2). They involved more than 80 people, including researchers, students, professionals and local community groups for a single-day each time. Tidal and weather conditions are summarised in Table 2. Several sites were simultaneously monitored at locations AMTD 0.6, 2, 2.1, 3.1, 3.4 and 3.8 km for Sites 1, 2, 2B, 3, 3B and 4 respectively, where AMTD is the upstream distance from river mouth. (Sites 1, 2, 3 and 4 are marked with a blue circle on Figure 1.) At each site, a series of hydraulic and water quality data were recorded from the bank: e.g., water elevations, surface

velocity, air and water temperatures, conductivity, pH, dissolved oxygen, turbidity. Most readings were taken every 15 to 30 minutes. Vertical profiles of physio-chemical parameters were conducted in the middle of the creek at several sites. They were performed at high tide and during ebb flow using a water quality probe YSI™6920 lowered from a boat drifting with the flow. Measurements included water temperature, conductivity pH, conductivity, dissolved oxygen content and turbidity taken every 20 to 50 cm.

Parameters	Value	Units
Air temperature at 09:00 :	20.5	°C
Average humidity at 09:00 :	67	%
Average wind speed at 09:00:	8.6	km/h
Average yearly rainfall :	1284.3	mm
Maximum monthly rainfall :	909.7	mm
Maximum daily rainfall :	241.0	mm
Average number of rainy days :	116	days/year
Average sunny days :	81	days/year
Average number of overcast days :	60	days/year

Table 1 - Average hydrological conditions in Eprapah Creek catchment for the period 1953-2003 (Ref.: Bureau of Met.)

	4 Apr. 2003	17 July 2003	24 Nov. 2003
Tides (Brisbane bar):	04:58 (0.53 m) 10:49 (2.02 m) 17:06 (0.43 m) 23:17 (2.20 m)	23:42 (2.41 m) 06:30 (0.46 m) 12:01 (1.73 m) 17:47 (0.45 m)	03:09 (0.09 m) 09:36 (2.52 m) 16:11 (0.34 m) 21:39 (1.91 m)
Study period:	06:00-18:00	06:00-14:05	07:00-16:00
ADV/YSI6600 record period:	10:10-14:05	06:10-14:05	09:18-15:55
Weather :	Sunny	Overcast	Overcast with few showers
Water temp. (°C) :	23.7 [20.4-28.4]	16.7 [15.5-18.5]	25.5 [22.7-28.0]
Air temp. (°C):	22.2 [15.5-29]	17.2 [10.5-21.5]	-- [19-29]
Conductivity (mS/cm):	34.5 [23.9-48.3]	37.2 [29.8-48.4]	50.0 [42.7-55.1]
D.O. (% sat):	0.85 [0.62-1.0]	0.82 (*) [0.66-1.06]	0.81 [0.76-0.85]
pH	6.8 [6.4-7]	7.4 [6.6-7.8]	7.8 (*) [7.4-8.0]
Turbidity (m Secchi)	0.68 [0.53-1.0]	0.84 [0.5-1.2]	--
Turbidity (NTU)	9.4 [5.8-13.9]	11.0 [7.2-24.6]	19.9 [7.1-43]

Table 2 - Summary of experimental flow conditions and measurements at Site 2 (AMTD 2 km) - Averages and extremes in brackets

At one site, a Sontek™ ADV velocimeter and a physio-chemical probe YSI™6600 were deployed and data-logged continuously at respectively 25 Hz and 0.2 Hz (or 0.5 Hz). The probes were located at Site 2B on 4 April and 24 Nov. 2003, and at Site 2 on 17 July 2003. They were installed about the middle of the channel in a moderate bend to the right when looking downstream (Fig. 2). The probes were located 14.2 m, 8.0 m and 10.8 m from the left bank on 4 April, 17 July and 24 Nov. 2003 respectively. The sensors were positioned 300 mm apart horizontally and held by a metallic frame sliding on two poles (Fig. 2A). All sensors were located 0.50 m beneath the free-surface and maintained at a constant depth below the free-surface for all studies. The probes were installed outside of the support system to limit the support wake effects. Further details on the experimental procedures are available in Chanson et al. [4].

### Data accuracy

For measurements from the bank, the data accuracy was about 1 cm for water level elevation, 0.2 to 0.5 °C for water temperature, 1 to 2% for conductivity, 0.2 to 0.5 for pH measurement with pH paper, 5 cm on turbidity Secchi disk length, 10% on the surface velocity and 5 to 10% on the dissolved oxygen concentration. With the water quality probes YSI6920 and YSI6600, the data accuracy was :  $\pm 2\%$  of saturation concentration for D.O.,  $\pm 0.5\%$  for conductivity,  $\pm 0.15^\circ\text{C}$  for temperature,  $\pm 0.2$  unit for pH,  $\pm 0.02$  m for depth,  $\pm 1\%$  of reading for salinity, and  $\pm 5\%$  for turbidity. No information was available on the data accuracy on chlorophyll levels.

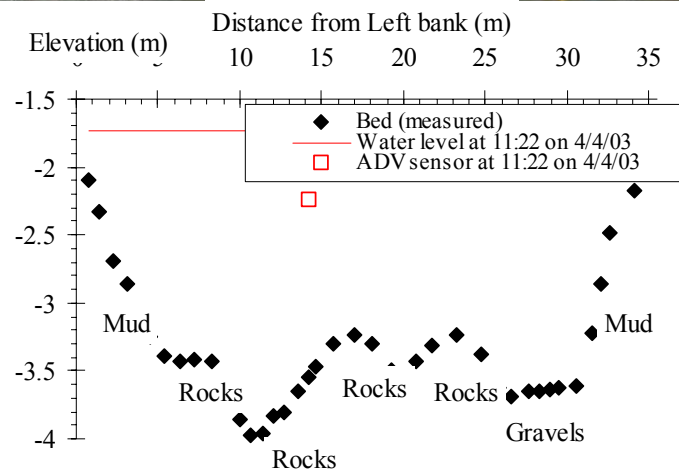


Fig. 2 - Simultaneous measurements of physio-chemistry and turbulence. (A) Probes in position, looking upstream. (B) River cross-section at Site 2B looking downstream.

### General Observations

For all studies, the tidal influence was felt up to Site 3B (AMTD 3.5 km) but not at Site 4. The latter site was basically a freshwater system each time. For the greatest tidal range (24 Nov. 2003), a very-shallow water zone was seen at low tide between Site 2B (AMTD 2.1 km) and the sewage plant (AMTD ~ 2.6 km) : i.e., depths less than 0.3 to 0.5 m. For such very low tides, the "bar" acted as a weir. It reduced drastically mass exchanges between upper and lower estuarine zones at low tides. Physio-chemical observations were conducted systematically from the bank and from a boat mid-stream at several longitudinal locations. Water temperature data were affected predominantly by the natural heating of the Sun, and by the flood tide bringing temperate waters from the Moreton Bay. Dissolved oxygen (DO) measurements showed more oxygenated downstream waters and



maxima around high tide. Basically dissolved-oxygen saturated waters were brought in by the flood tide. Turbidity data indicated consistently a greater water clarity at high tide and at beginning of ebb flow, while the observations were about constant along the creek. Water conductivity data followed the tidal cycle with an influx of saltwater during the flood flow and a reflux during the ebb in the intertidal zone, with an overall decrease in time-average conductivity with increasing distance from the mouth. A decrease in pH with increasing distance from the river mouth was consistently observed, suggesting slightly acidic waters in the upstream reach. Vertical profiles of water quality parameters showed that the distributions of water temperature, dissolved oxygen content, turbidity and pH were reasonably uniform for all studies. Conductivity data showed however some stratification with a fresh water lens above a saltwater wedge. The stratification was possibly the strongest on 4 April 2003 because of freshwater runoff.

### Short-Term Fluctuations

Short-term fluctuations in velocity and physio-chemical parameters were systematically investigated mid-estuary (AMTD 2 km). Turbulent velocity records, measured with the ADV, suggested distinct periods : i.e., a slack time around high and low tides, and some strong flushing during the flood tide (17/07/03) and ebb tides (4/04/03 & 24/11/03). Around high and low tides, the velocity magnitudes were small (i.e. less than 10 cm/s), and the velocity direction was highly fluctuating. The velocity magnitude increased with time after slack, and the strongest currents were observed during mid-ebb tides (4/04/03 & 24/11/03) with instantaneous velocities of about 0.2 to 0.35 m/s. Detailed records showed consistently significant time fluctuations of both velocity magnitude and direction, with fluctuations in instantaneous velocity directions of typically 20 to 30°. Instantaneous water quality results showed relatively small fluctuations of water quality parameters with time. These fluctuations were at least one order of magnitude smaller than observed turbulent velocity fluctuations. The findings might suggest that the estuary was reasonably well-mixed in terms of temperature, pH, DO and turbidity, although the turbulence was not homogeneous in the waterway.

Figures 3 and 4 present instantaneous velocity and physio-chemical data recorded on 4 April 2003. (For these data, the surveyed cross-section of the estuary is shown in Figure 2B.) Figure 3 presents instantaneous velocity magnitude  $|V|$  and direction  $\theta$ , with  $\theta = 0$  in the downstream direction and  $\theta > 0$  towards the left bank. In Figure 4, the right vertical axis corresponds to temperature and pH data, while the left vertical axis scales the dissolved oxygen content (DO) and salinity (ppt). In natural systems, the flow motion is characterised by unpredictable behaviour, strong mixing properties and broad spectrum of length scales [5]. There is however some coherence caused by bursting phenomena and large-scale vortical motion. The present data set highlighted large fluctuations of instantaneous velocity direction which is characteristic of the passage of coherent vortical structures (Fig. 3). The probability distribution functions of  $\theta$  were approximately Gaussian that is consistent with random turbulent processes.

In meandering channels, Blanckaert and Graf [6] highlighted the existence of a small outer bank recirculation cell. Such recirculation zones were systematically observed at Site 2 (AMTD 2 km). Toad fish, a relatively slow fish specie, were seen utilising these outer bend zones for feeding. Visual observations and toad fish behaviour indicated spatial and temporal variations of these recirculation regions. Their occurrence is important since outer bend cells contribute to a reduction in bend scouring. Their existence confirms that the turbulence was not homogeneous across the river.

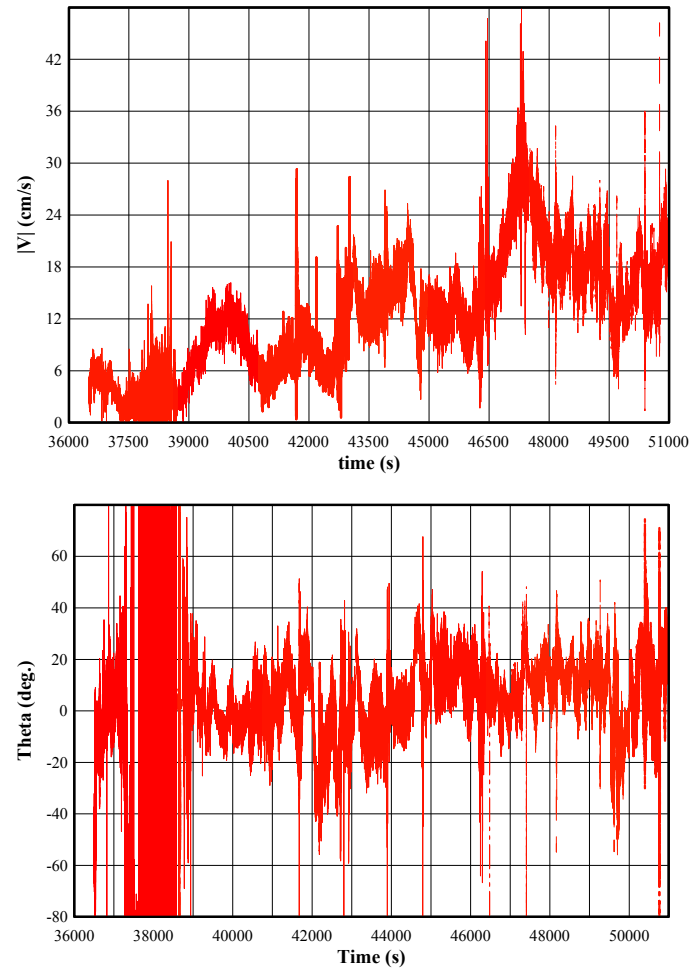


Fig. 3 - Instantaneous velocity measurements on 4 April 2003 during high tide slack and early ebb tide. The horizontal axis is the clock time in seconds with  $t = 0$  at 0:00. (A) Velocity amplitude  $|V|$ . (B) Velocity direction  $\theta$ .

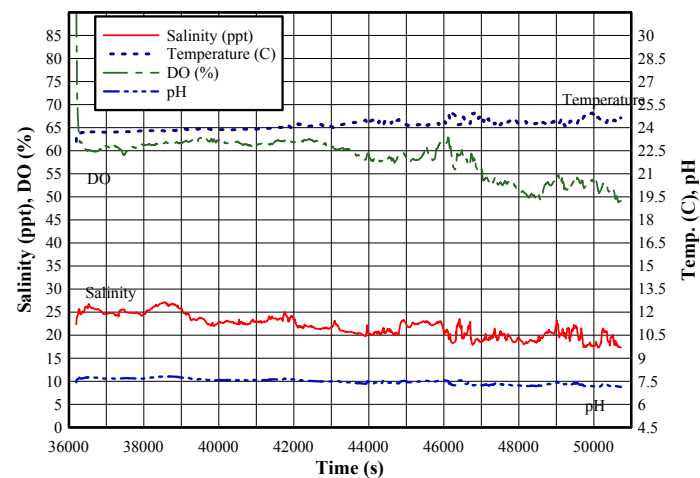


Fig. 4 - Instantaneous physio-chemical parameters on 4 April 2003 during high tide slack and early ebb tide.

### Discussion

Continuous measurements showed important fluctuations in instantaneous velocity and physio-chemical parameters caused by navigation (e.g. Fig. 2A). Boat passages were typically associated with large fluctuations in velocity for a few seconds, followed by a longer period, lasting for several minutes, of fluctuations in both velocity and physio-chemical parameters. While the data implied some mixing induced by wake waves and propeller motion, there were longer-lasting interactions between boat-induced turbulence and secondary circulation in the river. These might explain observations of significant fluctuations in turbidity, conductivity and temperature following boat passage.



A statistical analysis of instantaneous physio-chemical records was performed. The relevant time scales  $T_{0.5}$  were typically about 1 to 4 minutes for all parameters and flow periods, where  $T_{0.5}$  is the time delay for which the auto-correlation coefficient was 0.5.  $T_{0.5}$  must be a significant time scale for river mixing processes. The results showed further strong correlations between pH and conductivity that is consistent with both variables being related to ion concentration in water. pH data lagged typically by about 5-10 sec. behind conductivity data. Possible explanations might include mixing processes or difference in sensor response time.

## Experiences and Outcomes

### Practical Considerations

Careful preparation of field works is crucial. In particular, all the instrumentation must be thoroughly calibrated and tested beforehand. Present experience demonstrated recurrent problems with the ADV velocimeter evidenced by high levels of noise and spikes in the 3 velocity components. In the stream, the velocity fluctuations characterise the combined effects of the Doppler noise, velocity fluctuations and installation vibrations. Lemmin and Lhermitte [7] and Chanson et al. [8] discussed the inherent noise of an ADV system. Further spikes may be caused by aliasing of the Doppler signal. Goring and Nikora [9] discussed techniques to eliminate these. Some problem was also experienced with the vertical velocity component. Calibration tests in laboratory failed, possibly because of the effects of the wake of the stem. Since the probe was mounted vertically downlooking, vertical velocity data were discarded. Herein the ADV velocity data were cleaned by removing communication errors, low signal-to-noise ratio data ( $< 5\text{dB}$ ) and low correlation samples ( $< 70\%$ ), and they were "despiked" using an acceleration thresholding method. Yet, during periods of low velocity, the ADV Doppler noise and spikes predominated causing large fluctuations in velocity around zero. This can be observed in Fig 3B in the range 37,500-38,500 s. When the direction ( $\theta$ ) is calculated, this fluctuation is greatly increased because there is no predominant flow direction as shown during the corresponding time in Fig 3B. The writers' experience at Eprapah Creek suggests that most classical "despiking" techniques are unsuitable to estuarine data, and data errors may still exist in the present data sets.

### Personal experiences

Field works provided unique personal experiences to all people involved, and facilitated interactions between groups with different background and interests. Key interactions involved university researchers and students, local community, and government institutions. Field works contributed to the students' personal development and complemented traditional lectures, as strongly supported by anonymous student feedback [10]. Student comments emphasised their enhanced motivation. Group work contributed to new friendships and openings: e.g., between civil and environmental students, between students, academics and professionals involved in the studies. These personal experiences are at least as important as the academic and scientific experience, although this aspect is poorly understood from university hierarchy, administration clerks, managers and politicians.

### Definition of key water quality indicators

Overall this series of field measurements provided consistently contrasted outcomes in terms of natural system health. Fish sampling and bird observations suggested a dynamic eco-system [4]. Velocity measurements indicated high turbulence levels and a strong flushing process in the estuary. But other results highlighted poor physio-chemical parameters in the upstream

sections of the estuary. Serious concerns included low dissolved oxygen and pH levels (Sites 3 and 4), surface slicks (Sites 2 and 3), large numbers of exotic fish (e.g. Sites 3 and 4) competing with native fish species, and surface runoff (e.g. construction sites, shopping centres). All these results demonstrated on-going pollution in the estuary. Clearly a major issue is the definition of a limited number of "key indicators", which could describe the complexity of sub-tropical estuaries.

## Summary and Conclusion

Detailed investigations in a small subtropical estuary provided a broad range of simultaneous data encompassing hydrodynamics and physio-chemistry. The measurements yielded contrasted outcomes. While some results were positive, others demonstrated on-going pollution. Field works provided further unique personal experiences to all individuals involved.

The field results obtained at Eprapah Creek bring new lights into the complexity of the estuarine system, but also thought-provoking outcomes. It is clear that basic mixing processes are driven by turbulence. However its impact on a natural system cannot be comprehended without simultaneous measurements of hydrodynamic, physio-chemical and ecological parameters, implying substantial instrumentation, human resources and broad-based expertise. Genuine inter-disciplinary research is essential and it can offer new approaches: e.g., using fish activities to characterise recirculation zones in shallow waters.

## Acknowledgments

The writers thank Dr K. Warburton (UQ) and Dr I. Ramsay (Qld EPA) for their advice. They acknowledge the assistance of all participants, in particular the ECCLA group. H.C. and R.B. thank their students for their field work contributions.

## References

- [1] Ippen, A.T., *Estuary and Coastal Hydrodynamics*, McGraw-Hill, New York, USA, 1966.
- [2] Fischer, H.B., List, E.J., Koh, R.C.Y., Imberger, J., and Brooks, N.H., *Mixing in Inland and Coastal Waters*, Academic Press, New York, USA, 1979.
- [3] Chanson, H., *Environmental Hydraulics of Open Channel Flows*, Elsevier Science, Oxford, UK, 2004.
- [4] Chanson, H., Brown, R., Ferris, J., and Warburton, K., A Hydraulic, Environmental and Ecological Assessment of a Sub-tropical Stream in Eastern Australia: Eprapah Creek, Victoria Point QLD on 4 April 2003, *Report No. CH52/03*, Dept. of Civil Eng., Univ. of Queensland, Australia, 2003.
- [5] Nezu, I., and Nakagawa, H., *Turbulence in Open-Channel Flows*, IAHR Monograph, Balkema, The Netherlands, 1993.
- [6] Blankaert, K., and Graf, W.H., Mean flow and turbulence in open-channel bend, *Jl of Hyd. Engrg.*, ASCE, 2002, **127** (10) pp. 835-847.
- [7] Lemmin, U., and Lhermitte, R., ADV Measurements of Turbulence: can we Improve their Interpretation ? *Jl of Hyd. Engrg.*, ASCE, 1999, **125** (6) pp. 987-988.
- [8] Chanson, H., Aoki, S., and Maruyama, M., Unsteady Two-Dimensional Orifice Flow: a Large-Size Experimental Investigation, *Jl of Hyd. Res.*, IAHR, 2002, **40** (1) pp. 63-71.
- [9] Goring, D.G., and Nikora, V.I., Despiking Acoustic Doppler Velocimeter Data, *Jl of Hyd. Engrg.*, ASCE, 2002, **128** (1) pp. 117-126.
- [10] Chanson, H., Enhancing Students' Motivation in the Undergraduate Teaching of Hydraulic Engineering: the Role of Field Works, *Jl of Prof. Issues in Eng Educ. and Practice*, ASCE, 2004, **130** (4) pp. 259-268.

## 2D Velocity-Field Analysis Using Triple Decomposition of Motion

V. Kolář

Institute of Hydrodynamics, Academy of Sciences  
166 12 Prague 6, CZECH REPUBLIC

### Abstract

A straightforward application of the new triple decomposition of the local relative motion near a point to 2D velocity fields is presented. Unlike the Cauchy-Stokes double decomposition of motion into a pure straining motion and a rigid-body rotation the triple decomposition of motion aims, moreover, at the extraction of an *effective* pure shearing motion. It results in a more detailed flow description as the third term is responsible for a specific portion of vorticity labelled "*shear vorticity*" and for a specific portion of strain rate labelled "*shear strain rate*".

### Introduction

The concept of the triple decomposition of motion has been motivated by a longstanding problem of a vortex and vorticity expressed by the fact that "*solely vorticity cannot distinguish between swirling motions and shearing motions*", Kida and Miura [1] (this fact is emphasized also by Jeong and Hussain [2] and Cucitore, Quadrio and Baron [3]). Let us add an analogous statement for strain rate: "*solely strain rate cannot distinguish between straining motions and shearing motions*". Vorticity and strain rate reflect the conventional Cauchy-Stokes decomposition of the local relative motion near a point into two elementary homogeneous motions: a pure irrotational straining motion along principal axes of the rate of strain tensor (generally including a uniform dilatation) and a rigid-body rotation. In Kolář [4] an arbitrary instantaneous state of the local relative motion near a point is decomposed into three elementary motions—each described by an additive part of  $\nabla \mathbf{u}$  with a distinct tensor character—explicitly including an *effective* pure shearing motion. The first two elementary parts of the proposed triple decomposition remind, at least in tensor character, the two elementary parts of the conventional double decomposition,  $\nabla \mathbf{u} = \mathbf{S} + \mathbf{\Omega}$ , and represent their *residual* portions after extracting an *effective* pure shearing motion.

### Triple Decomposition of Motion

The algorithm of the triple decomposition of motion is briefly summarized below. For details, justification and discussion see Kolář [4] where three elementary motions are introduced in terms of a *virtually structured continuum*. The triple decomposition of the local relative motion near a point aims, basically, at the extraction of an *effective* pure shearing motion. It reads

$$\nabla \mathbf{u} = (\nabla \mathbf{u})_{\text{EL}} + (\nabla \mathbf{u})_{\text{RR}} + (\nabla \mathbf{u})_{\text{SH}} \quad (1)$$

where the three elementary homogeneous motions are described by additive parts of  $\nabla \mathbf{u}$ : a pure irrotational straining motion given by symmetric tensor  $(\nabla \mathbf{u})_{\text{EL}}$  (subscript "EL" reminds the term "elongation"), a rigid-body rotation given by antisymmetric tensor  $(\nabla \mathbf{u})_{\text{RR}}$ , and an *effective* pure shearing motion  $(\nabla \mathbf{u})_{\text{SH}}$  described below.

A general pure shearing motion (that is, at this stage, without specification of the term "*effective*") is defined by a "purely asymmetric tensor form" of  $\nabla \mathbf{u}$  fulfilling in a *suitable reference frame* (null tensors are excluded, the subscript  $/j$  denotes differentiation)

$$u_{i/j} = 0 \quad \text{OR} \quad u_{j/i} = 0 \quad (\text{for all } i, j). \quad (2)$$

The desired reference frame, showing an *effective* pure shearing motion "in a clearly visible manner" described by the form (2), is called a *basic reference frame* (BRF). In this frame, the local relative motion is decomposed in terms of additive parts of  $\nabla \mathbf{u}$  at a given point. In any other frames rotated with respect to the *basic reference frame* under an orthogonal transformation  $\mathbf{Q}$ , an arbitrary elementary part of  $\nabla \mathbf{u}$ , say  $\mathbf{A}_i$ , is described simply by  $\mathbf{Q}\mathbf{A}_i\mathbf{Q}^T$ . Note that the sum of additive parts  $\sum_i \mathbf{A}_i$  transforms as

$$\mathbf{Q} \left( \sum_i \mathbf{A}_i \right) \mathbf{Q}^T = \sum_i \mathbf{Q}\mathbf{A}_i\mathbf{Q}^T. \quad (3)$$

The triple decomposition then reads in the BRF (specified afterwards)

$$\begin{aligned} \nabla \mathbf{u} &\equiv \begin{pmatrix} u_x & u_y & u_z \\ v_x & v_y & v_z \\ w_x & w_y & w_z \end{pmatrix}^{\text{BRF}} \\ &= \begin{pmatrix} u_x & (\text{sgn } u_y) \text{MIN}(|u_y|, |v_x|) & \bullet \\ (\text{sgn } v_x) \text{MIN}(|u_y|, |v_x|) & v_y & \bullet \\ \bullet & \bullet & w_z \end{pmatrix}^{\text{BRF}} \\ &\quad + \begin{pmatrix} \text{purely} \\ \text{asymmetric} \\ \text{matrix} \end{pmatrix}^{\text{BRF}} \\ &= [\text{tensor core of } (\nabla \mathbf{u})]^{\text{BRF}} + [\text{tensor overhang of } (\nabla \mathbf{u})]^{\text{BRF}} \\ &= [(\nabla \mathbf{u})_{\text{EL}} + (\nabla \mathbf{u})_{\text{RR}}] + (\nabla \mathbf{u})_{\text{SH}} \end{aligned} \quad (4)$$

where (using simplified notation) subscripts  $x, y, z$  stand for spatial partial derivatives, and the remaining two non-specified pairs of off-diagonal terms in the first matrix of the decomposition are constructed strictly analogously as the specified one. The introduced frame-dependent *tensor-core matrix* is characterized by the symmetry in absolute values of components. This matrix determined above in the BRF is further decomposed into two parts as it represents a sum  $[(\nabla \mathbf{u})_{\text{EL}} + (\nabla \mathbf{u})_{\text{RR}}]$ . Note that each pair of off-diagonal terms of the *tensor-core matrix* is either symmetric or antisymmetric. The introduced frame-dependent *tensor-overhang matrix* has a purely asymmetric tensor form defined by (2) and represents in the BRF an *effective* pure shearing motion.

The BRF is determined from the condition

$$\| [\text{tensor core of } (\nabla \mathbf{u})]^{\text{BRF}} \| = \text{MIN over all frames} \quad (5)$$

where the symbol  $\| \dots \|$  denotes a standard tensor norm (frame-independent absolute tensor value). Alternatively, in terms of the Cauchy-Stokes double decomposition of  $\nabla \mathbf{u}$  (e.g. Truesdell and Toupin [5], Batchelor [6])

$$\nabla \mathbf{u} = \frac{1}{2} (\nabla \mathbf{u} + (\nabla \mathbf{u})^T) + \frac{1}{2} (\nabla \mathbf{u} - (\nabla \mathbf{u})^T) \equiv \mathbf{S} + \mathbf{\Omega}, \quad (6)$$

the BRF is determined from the condition

$$\left[ |S_{12}\Omega_{12}| + |S_{23}\Omega_{23}| + |S_{31}\Omega_{31}| \right]^{\text{BRF}} = \text{MAX over all frames} . (7)$$

It is clearly seen from (7) that the BRF, unlike the system of principal axes of  $\mathbf{S}$ , is determined *simultaneously* on the basis of a non-zero  $\mathbf{S}$  and a non-zero  $\mathbf{\Omega}$ .

Further, from the viewpoint of the double decomposition the *effective* pure shearing motion  $(\nabla \mathbf{u})_{\text{SH}}$  itself (i.e. separately) represents a certain coupling of a pure irrotational straining motion with a rigid-body rotation. Consequently, the *triple* decomposition of  $\nabla \mathbf{u}$  may be substituted by the *quadruple* decomposition of  $\nabla \mathbf{u}$  with two different (symmetric) strain-rate terms and two different (antisymmetric) vorticity terms

$$\begin{aligned} \nabla \mathbf{u} &= (\nabla \mathbf{u})_{\text{EL}} + (\nabla \mathbf{u})_{\text{RR}} + (\nabla \mathbf{u})_{\text{SH}} \\ &= (\nabla \mathbf{u})_{\text{EL}} + (\nabla \mathbf{u})_{\text{RR}} \\ &\quad + \frac{1}{2} [(\nabla \mathbf{u})_{\text{SH}} + ((\nabla \mathbf{u})_{\text{SH}})^T] + \frac{1}{2} [(\nabla \mathbf{u})_{\text{SH}} - ((\nabla \mathbf{u})_{\text{SH}})^T] \\ &= \mathbf{S}_{\text{RES}} + \mathbf{\Omega}_{\text{RES}} + \mathbf{S}_{\text{SH}} + \mathbf{\Omega}_{\text{SH}} \\ &= [\mathbf{S}_{\text{RES}} + \mathbf{S}_{\text{SH}}] + [\mathbf{\Omega}_{\text{RES}} + \mathbf{\Omega}_{\text{SH}}] = \mathbf{S} + \mathbf{\Omega} . \end{aligned} \quad (8)$$

These four terms (in the last two square brackets) are labelled "residual strain rate" and "shear strain rate", "residual vorticity" and "shear vorticity". Note that in the triple decomposition,  $\mathbf{S}$  and  $\mathbf{\Omega}$  are cut down in magnitudes to "share" their portions through the third term  $(\nabla \mathbf{u})_{\text{SH}}$  associated with a pure shearing motion as

$$\nabla \mathbf{u} = \mathbf{S}_{\text{RES}} + \mathbf{\Omega}_{\text{RES}} + (\nabla \mathbf{u})_{\text{SH}} . \quad (9)$$

### Triple Decomposition of Motion in 2D Fluid Flow

The nature of the proposed triple decomposition (and its physical justification) is straightforward in 2D fluid motion. To make the decomposition of motion clearly visible, the conventional double decomposition frequently uses as a reference frame the *shear-free frame* of principal axes of the strain-rate tensor. A uniform dilatation can be removed prior to further analysis of  $\nabla \mathbf{u}$  without loss of generality and an arbitrary 2D flow can be described (using simplified notation) in the system of principal axes by the form

$$\nabla \mathbf{u} = \begin{pmatrix} s & -\omega & 0 \\ \omega & -s & 0 \\ 0 & 0 & 0 \end{pmatrix}^{\text{PRINCIPAL AXES}} . \quad (10)$$

By a suitable rotation of coordinate axes we approach the desired BRF. For 2D rotational motion, the BRF corresponds to the *shear frame* in which the deviatoric strain-rate tensor has zeros on the leading diagonal and  $\nabla \mathbf{u}$  is given by

$$\nabla \mathbf{u} = \begin{pmatrix} 0 & s - \omega & 0 \\ s + \omega & 0 & 0 \\ 0 & 0 & 0 \end{pmatrix}^{\text{BRF}} . \quad (11)$$

In this frame, in the plane of 2D motion, there are only two characteristic "shearing interactions" of  $u_y dy$  with  $v_x dx$ , namely with the same or opposite rotational orientations, see Fig. 1. For both orientations, the magnitude of the resulting "superimposed" pure shearing motion is given simply by the difference of absolute values of  $u_y$  and  $v_x$ .

The present new approach is easy to demonstrate *geometrically* in 2D fluid motion in terms of the decomposition of vorticity  $\omega$  and strain rate  $s$ , see (10), (11), as shown in Fig. 1. In this figure the vorticity and strain-rate components are proportional to the infinitesimal changes of related characteristic angles during the infinitesimal change of time. In Fig. 1(a) the characteristic angles correspond to the *residual* vorticity  $\omega_{\text{RES}}$  (associated with the rigid-body rotation) and *shear* vorticity  $\omega_{\text{SH}}$  (associated with the

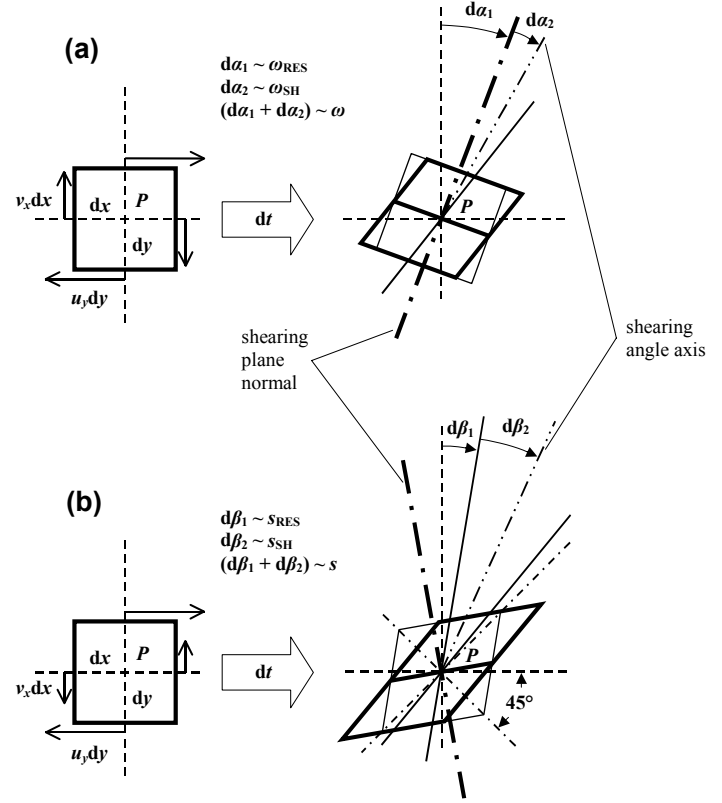


Figure 1 Geometrical interpretation of the triple decomposition in 2D fluid motion: (a) vorticity components, (b) strain-rate components.

pure shearing motion) while their sum is proportional to the *total* vorticity  $\omega$ . In Fig. 1(b) the characteristic angles correspond to the *residual* strain rate  $s_{\text{RES}}$  and *shear* strain rate  $s_{\text{SH}}$  while their sum is proportional to the *total* strain rate  $s$ . This "superimposing" geometrical construction is of virtual nature and applicable to infinitesimal motional changes only. However, it provides a clear qualitative insight and interpretation of the vorticity and strain-rate components.

Fig. 1 indicates two significant inherent features of the proposed decomposition. Firstly, the concept of the triple decomposition as defined by (4) implies (generally in 3D) that the corresponding components of the *residual* vorticity and *shear* vorticity have the *same signs in the BRF*. The same holds for the *residual* strain rate and *shear* strain rate. Secondly, Fig. 1 indicates a certain "principle of exclusivity" which is valid in 2D. The principle of exclusivity may be expressed for arbitrary 2D velocity fields representing an isochoric part of motion as

$$(\nabla \mathbf{u})_{\text{EL}}^{\text{2D}} = 0 \quad \text{OR} \quad (\nabla \mathbf{u})_{\text{RR}}^{\text{2D}} = 0 \quad (12a)$$

or, alternatively, in terms of  $\omega$  and  $s$  as

$$s_{\text{RES}} = 0 \quad \text{OR} \quad \omega_{\text{RES}} = 0 . \quad (12b)$$

The expressions (12a, b) say that a non-zero *residual* vorticity apparently existing only for the same rotational orientations of  $u_y dy$  and  $v_x dx$ , see Fig. 1, excludes the existence of a non-zero *residual* strain rate existing only for the opposite rotational orientations of  $u_y dy$  and  $v_x dx$ . Consequently, Fig. 1(a) represents an inevitable reduction of the three distinct terms of the triple decomposition to the form  $(\nabla \mathbf{u})_{\text{RR}} + (\nabla \mathbf{u})_{\text{SH}}$  while Fig. 1(b) represents the reduction to  $(\nabla \mathbf{u})_{\text{EL}} + (\nabla \mathbf{u})_{\text{SH}}$ .

Components of the triple decomposition of the local relative motion near a point and corresponding flow patterns for various flow situations in 2D isochoric fluid motion are shown in Fig. 2. All possible flow configurations near a point for fixed  $u_y$  and variable  $v_x$  are depicted in the corresponding BRFs. The points

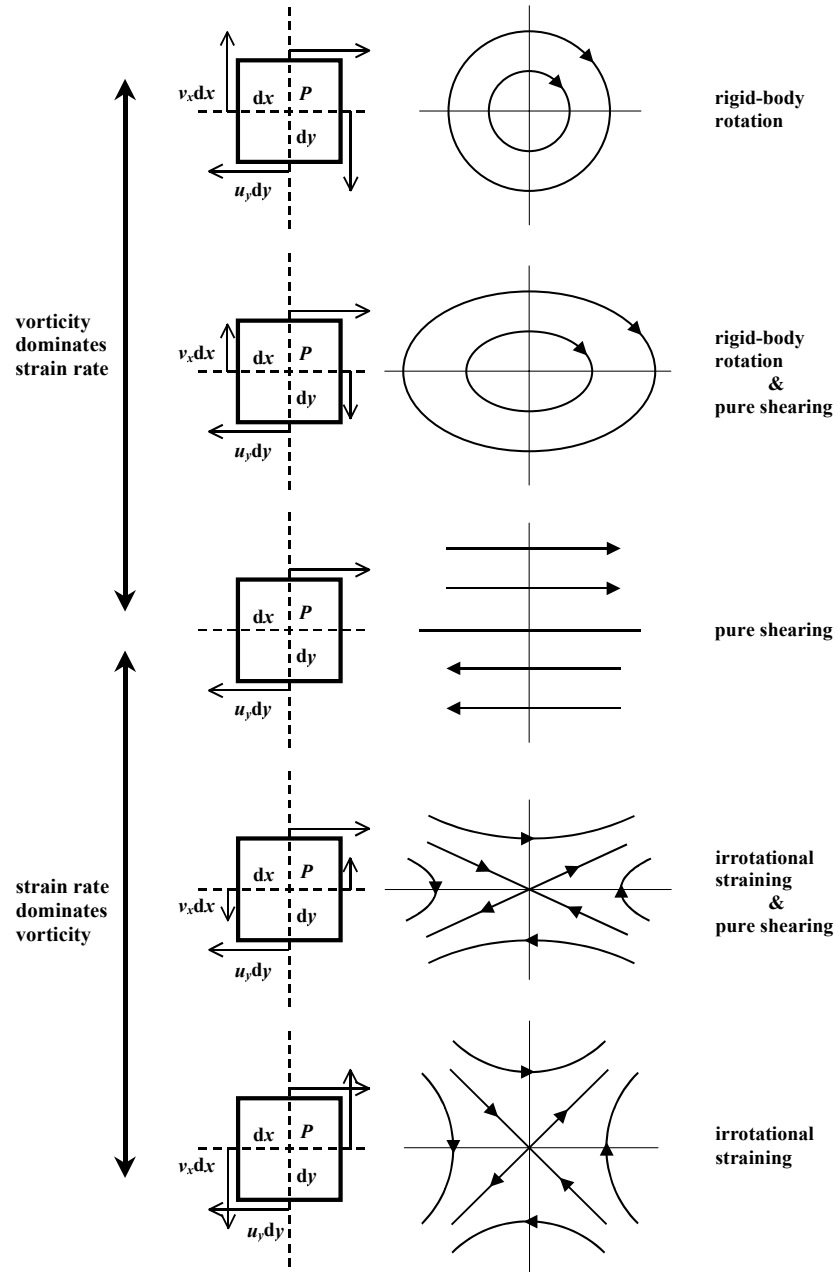


Figure 2 Components of the triple decomposition of motion and flow patterns for various flow situations in 2D fluid motion.

itself can be described as critical points and the local flow patterns correspond to the leading terms of a Taylor series expansion for the velocity field in terms of space coordinates (Perry and Chong [7], Chong, Perry and Cantwell [8]).

### Application of the Triple Decomposition of Motion to 2D Velocity-Field Analysis

Let us remind that a uniform dilatation can be removed prior to further analysis of  $\nabla \mathbf{u}$  without loss of generality and applicability to compressible flows. In terms of  $s$  and  $\omega$  introduced in (10) and (11) by a suitable rotation of coordinate axes

$$\begin{pmatrix} u_x & u_y & 0 \\ v_x & -u_x & 0 \\ 0 & 0 & 0 \end{pmatrix} \rightarrow \begin{pmatrix} s & -\omega & 0 \\ \omega & -s & 0 \\ 0 & 0 & 0 \end{pmatrix}^{\text{PR. AXES}} \rightarrow \begin{pmatrix} 0 & s-\omega & 0 \\ s+\omega & 0 & 0 \\ 0 & 0 & 0 \end{pmatrix}^{\text{BRF}}$$

where

$$|s| = \left( \sqrt{4u_x^2 + (u_y + v_x)^2} \right) / 2, \quad (13)$$

$$\omega = (v_x - u_y) / 2, \quad (14)$$

and their *residual* and *shear* components (note that these are of the *same signs in the BRF*) we can draw from (4) and (8) the following set of relations

$$s = s_{\text{RES}} + s_{\text{SH}}, \quad (15)$$

$$|s| = |s_{\text{RES}}| + |s_{\text{SH}}|, \quad (16)$$

$$s_{\text{SH}} = (\text{sgn } s)|\omega| \quad \text{for } |s| > |\omega|, \quad (17)$$

$$s_{\text{SH}} = s \quad \text{for } |s| < |\omega|, \quad (18)$$

$$s_{\text{RES}} = s - s_{\text{SH}} \quad \text{for } |s| > |\omega|, \quad (19)$$

$$s_{\text{RES}} = s - s_{\text{SH}} = 0 \quad \text{for } |s| < |\omega|, \quad (20)$$

$$\omega = \omega_{\text{RES}} + \omega_{\text{SH}}, \quad (21)$$

$$|\omega| = |\omega_{\text{RES}}| + |\omega_{\text{SH}}|, \quad (22)$$

$$\omega_{\text{SH}} = \omega \quad \text{for } |s| > |\omega|, \quad (23)$$

$$\omega_{\text{SH}} = (\text{sgn } \omega)|s| \quad \text{for } |s| < |\omega|, \quad (24)$$

$$\omega_{\text{RES}} = \omega - \omega_{\text{SH}} = 0 \quad \text{for } |s| > |\omega|, \quad (25)$$

$$\omega_{\text{RES}} = \omega - \omega_{\text{SH}} \quad \text{for } |s| < |\omega|. \quad (26)$$

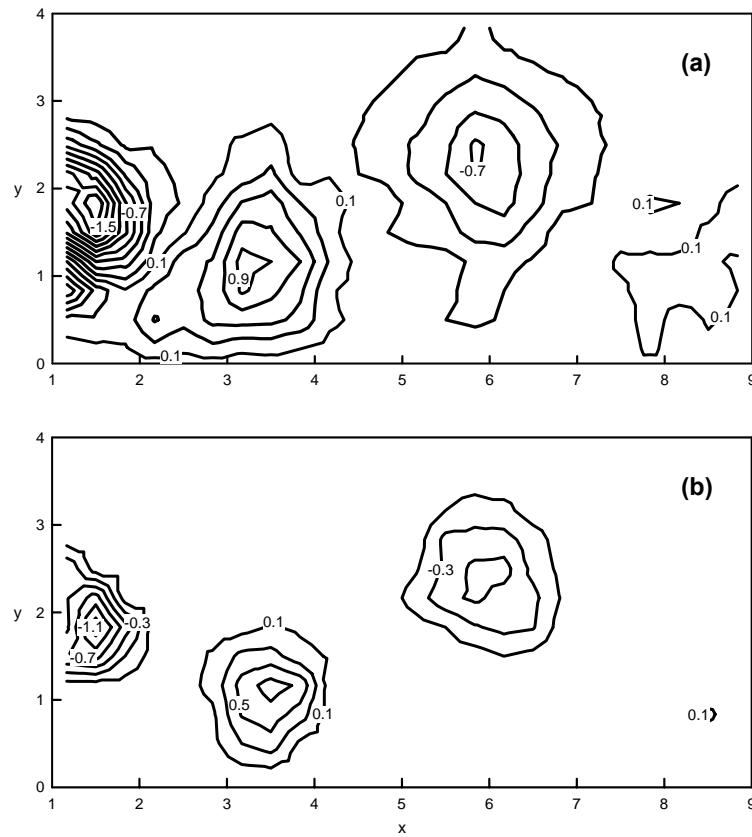


Figure 3 Comparison of (a) total vorticity and (b) *residual* vorticity for plane turbulent wake (velocity data taken from [9], phase 3, contour int. 0.2).

The case  $|s| = |\omega|$  represents a simple shear, hence an *effective* pure shearing motion is the only non-zero component of the triple decomposition of motion in this case.

A practical application of the present approach to the velocity data of the *nominally* plane turbulent wake of two side-by-side square cylinders by Kolář, Lyn and Rodi [9] is shown in Fig. 3.

It is clearly seen from Fig. 3 that by removing the shearing component of motion, that is after the extraction of an *effective* pure shearing motion by means of the triple decomposition of motion, we reach a more adequate picture of vortical structures. These structures are characterized exclusively by swirling motion in terms of the *residual* vorticity which is non-zero for  $|s| < |\omega|$  and determined from (24) and (26) using (13) and (14). The *residual* vorticity appears as the proper kinematic quantity to identify true vortex cores determining both their boundary and inner structure.

Similarly we can distinguish the *residual* strain rate from the total strain rate, for example, while describing the process of turbulence production in the saddle regions of the primary large-scale vortical structures in turbulent wakes.

## Conclusions

2D flow fields have been described in terms of the new triple decomposition of the local relative motion near a point. The triple decomposition of motion aims at the extraction of an *effective* pure shearing motion which is responsible for a specific portion of vorticity labelled "*shear* vorticity" and for a specific portion of strain rate labelled "*shear* strain rate". The triple decomposition of motion is closely associated with the so-called *basic reference frame* (BRF) where it is performed. Some fundamental issues have been pointed out: (i) *principle of exclusivity* holds between 2D *residual* vorticity and 2D *residual* strain rate for an isochoric part of motion, (ii) *residual* and *shear* components of both vorticity and strain rate have the *same signs* in the BRF. Considering arbitrary 2D velocity fields, simple relations have been derived for vorticity and strain-rate components.

The kinematic structure inferred from the triple decomposition of motion should help in the description and analysis of a wide variety of fluid-dynamical processes and fluid-flow phenomena. It may prove its usefulness for flow classification schemes as well as for complex rheological problems.

## Acknowledgments

This work was financially supported by the Grant Agency of the Academy of Sciences of the Czech Rep. through grant IAA2060302, and by the Academy of Sciences of the Czech Rep. through Inst. Res. Plan AV0Z2060917 and Prog. Basic Res. KSK2076106.

## References

- [1] Kida, S. & Miura, H., Identification and analysis of vortical structures, *Eur. J. Mech. B/Fluids*, **17**, 1998, 471-488.
- [2] Jeong, J. & Hussain, F., On the identification of a vortex, *J. Fluid Mech.*, **285**, 1995, 69-94.
- [3] Cucitore, R., Quadrio, M. & Baron, A., On the effectiveness and limitations of local criteria for the identification of a vortex, *Eur. J. Mech. B/Fluids*, **18**, 1999, 261-282.
- [4] Kolář, V., Triple decomposition of the local relative motion near a point, submitted to *J. Fluid Mech.*
- [5] Truesdell, C. & Toupin, R.A., The Classical Field Theories, in *Encyclopedia of Physics, Vol. III/1, Principles of Classical Mechanics and Field Theory*, Flügge, S. (editor), Springer-Verlag, 1960.
- [6] Batchelor, G.K., *An Introduction to Fluid Dynamics*. Cambridge University Press, 1967.
- [7] Perry A.E. & Chong M.S., A description of eddying motions and flow patterns using critical-point concepts, *Annu. Rev. Fluid Mech.*, **19**, 1987, 125-155.
- [8] Chong, M.S., Perry, A.E. & Cantwell, B.J., A general classification of three-dimensional flow fields, *Phys. Fluids A* **2**, 1990, 765-777.
- [9] Kolář, V., Lyn, D.A. & Rodi, W., Ensemble-averaged measurements in the turbulent near wake of two side-by-side square cylinders, *J. Fluid Mech.* **346**, 1997, 201-237.

## Numerical simulation of drop formation in a T-shaped microchannel

J.L. Liow<sup>1</sup>

<sup>1</sup>Mechanical Engineering Discipline, School of Engineering  
James Cook University, Qld, 4811 AUSTRALIA

### Abstract

The formation of water drops of specific size when sheared by a tetradecane stream at a T-junction in a microchannel was investigated numerically. The numerical results showed that the water drop sizes decreased with increasing tetradecane flow rate and decreasing interfacial tension. This is in agreement with published experimental results. During the formation of the water drops, two recirculating zones are formed in the water stream, a large one occupying most of the water drop, and a smaller one near the downstream corner of the T-junction. The smaller recirculating zone results in a high pressure spot.

### Introduction

In the last two decades, the emphasis on fluid flow in MEMS devices has been focused on the study of single fluid flows, involving only a gas or a liquid [4]. In contrast, the dispersion of the droplets of one fluid in a second immiscible fluid has received less attention. Nevertheless, there is a wide range of applications for multiphase flows in microchannels and such flows are found in naturally occurring systems. The ability to control and manipulate the drop size and frequency enables the drop formation process to be tailored. This is of immense importance as it allows the outcomes of the applications to be very specific. In recent years, the use of microchannels for the formation of drops of uniform and specific sizes has been shown experimentally to be feasible. However, there is a wide range of microchannel configurations that have been published and the drop formation processes are quite different for different configurations. The simplest configuration is the T-junction where one liquid shears a second liquid that flows in the perpendicular arm.

Early work by Thorsen *et al.* [13] showed that aliphatic straight chained hydrocarbons (HC) with 2% SPAN 80 were able to shear a normal flow of water to form a variety of drop shapes. The drop shapes were strongly dependent on the sharpness of the edges of the T-junction. Further work by Tabeling *et al.* [12] suggests that such drops can only be formed when the surface tension of the HC is significantly lowered by SPAN 80 used as the surfactant. The roughness of the channel surface also plays a critical role in the drop formation process. In contrast, Nisisako *et al.* [7] managed to form droplets without the use of surfactants albeit the channels they used were 100 – 500  $\mu\text{m}$  in width and 100  $\mu\text{m}$  in depth compared to 35  $\mu\text{m}$  in width for the work of Thorsen *et al.* [13] and Tabeling *et al.* [12]. Apart from channel size, there were a few significant differences between Thorsen *et al.* [13] and Nisisako *et al.* [7]. First, Nisisako *et al.* [7] used a sunflower oil where the fluid properties were not measured but sunflower oil does have a much higher kinematic viscosity than straight chained HC. Second, Nisisako *et al.* [7] produced their microchannels with a micromilling technique resulting in extremely sharp corners. Thorsen *et al.* [13] produced their microchannels from moulding with an acrylated urethane where the corners are much smoother.

Other more complex configurations include the use of multiple slits to focus the flow and produce drops that are much

smaller than the slit width [1], or the use of fine pores and stepped structures to try and produce reproducible drop sizes [11]. More complex network of T-junctions have been shown to enable drop size distributions to be controlled (Link *et al.* as referenced in [10]). The control of drop breakup is influenced significantly by the interfacial tension between the two fluids and Dreyfus *et al.* [3] have found that without the presence of Span80, drops do not form in microchannels of 20  $\mu\text{m}$  by 200  $\mu\text{m}$  cross section.

In this study, a T-junction microchannel is numerically simulated using a volume of fluid (VOF) code in 2D to determine the breakup of water drops entering into a flow of tetradecane. This is compared to the experimental result of Cole [2]. Although the depth of the channel may affect the drop formation, much information can be obtained of the behaviour of the drop break up characteristics in 2D prior to a full simulation in 3D.

### Mathematical formulation

Detailed description of the multifluid VOF (MFVOF) code has been published elsewhere [5] and only a brief description will be included here.

The distribution of the fluid species is tracked as a “colour”  $C$  where in the continuous limit within a computational domain represented by a 2D axisymmetric mesh,  $C(r, z)$  is the Heaviside function

$$C = \begin{cases} 1, & \text{if point } (r, z) \text{ is occupied by } C \text{ fluid;} \\ 0, & \text{otherwise.} \end{cases} \quad (1)$$

All interfaces throughout the computational domain are deduced from the spatial locations of the discontinuities in the distribution of  $C$ . The equations solved are:

*Equation of continuity*

$$\nabla \cdot \mathbf{U} = 0. \quad (2)$$

*Fluid species transport equation*

$$\frac{\partial C}{\partial t} + \nabla \cdot (\mathbf{U}C) = 0. \quad (3)$$

*Momentum equation*

$$\frac{\partial \mathbf{U}}{\partial t} + \nabla \cdot (\mathbf{U}\mathbf{U}) = -\frac{1}{\rho} \nabla P + \frac{1}{\rho} \nabla \cdot \boldsymbol{\tau} + \mathbf{g} + \frac{\mathbf{S}}{\rho}, \quad (4)$$

where  $\tau_{ij} = 2\mu S_{ij}$  and the rate of strain tensor,  $S_{ij} = (\partial u_i / \partial x_j + \partial u_j / \partial x_i) / 2$ . The effects of surface tension are incorporated in the surface force vector

$$\mathbf{S} = S_r \hat{i} + S_t \hat{j} = \sigma \kappa \hat{n}, \quad (5)$$

which is applied only at interfaces. The interfacial curvature  $\kappa$  and interfacial normal  $\hat{n}$  are functions of  $C$ . The density and viscosity distributions are dependent on the distribution of fluid throughout the flow domain, and are computed from  $C$  of the

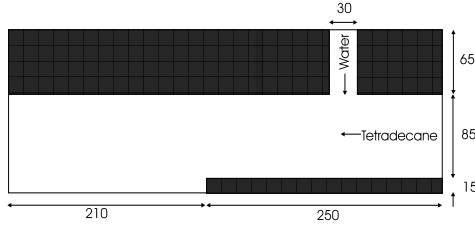


Figure 1: The simulation region. Dimensions are given in  $\mu\text{m}$ .

number of fluid species ( $nsp$ ) using weighted averages of the form

$$\rho = \sum_{l=1}^{nsp-1} C_l \rho_l + \left(1 - \sum_{l=1}^{nsp-1} C_l\right) \rho_{nsp}. \quad (6)$$

### Discretisation and Solution Algorithm

The equations are discretised on a uniform MAC mesh using second-order accurate conservative finite differencing schemes. The time advance of the solution from timestep  $n$  to  $n+1$  is achieved using a two-step projection method, which decomposes the algorithm for the flow solver into three core steps:

- estimate the solution at the next timestep by including all numerical schemes for modelling all physics in the problem,
- solve a Poisson equation, for which the source term is the divergence from a solenoidal velocity field,
- correct the momentum update velocity estimate, to update the velocity field to timestep  $n+1$ .

An explicit scheme is used in the MFVOF solution algorithm for the time advance. Second-order temporal accuracy is achieved using Euler time-stepping, which involves performing the two-step projection twice. The color function in the discretised problem is only an approximation of the Heaviside function, and on the mesh is interpreted as a fractional volume function. The value of  $C$  in interface cells is simply taken as the volume fraction of the mesh cell volume occupied by  $C$ -fluid.

### Layout of the microchannel

The T-junction microchannel simulated is shown in Figure 1. Water flows downwards in the vertical channel of  $30 \mu\text{m}$  and tetradecane flows in the horizontal channel of  $85 \mu\text{m}$  from right to left. Away from the T-junction, the horizontal channel widens to  $100 \mu\text{m}$  to allow the drops to disengage. The mesh used was a 64 and 192 cells in the vertical and horizontal directions respectively. The physical properties of the fluids are given in Table 1. No-slip boundary conditions were used and a flat inlet velocity profile was used for both liquids streams.

### Results

Simulations were carried out for varying tetradecane velocities for two different water inlet velocities with no surfactant added. The water droplets formed were uniform in size and shown in Figure 2. It was found that a straight line relationship could be obtained for water drops less than  $100 \mu\text{m}$  as a function of the tetradecane velocity. There was no difference in the diameter of the water drops for water flow velocities of 0.01 and 0.05 m/s. The relationship fitted is

$$d = -15.9 \ln V + 36.77, \quad (7)$$

Water	
Density	$998.2 \text{ kg/m}^3$
Viscosity	$1.0 \times 10^{-3} \text{ kg/(m}\cdot\text{s)}$
Tetradecane	
Density	$773.0 \text{ kg/m}^3$
Viscosity	$3.19 \times 10^{-3} \text{ kg/(m}\cdot\text{s)}$
Interfacial tension	$0.0442 \text{ N/m}$
Temperature	$20^\circ\text{C}$

Table 1: Properties of the fluids used in the simulation.

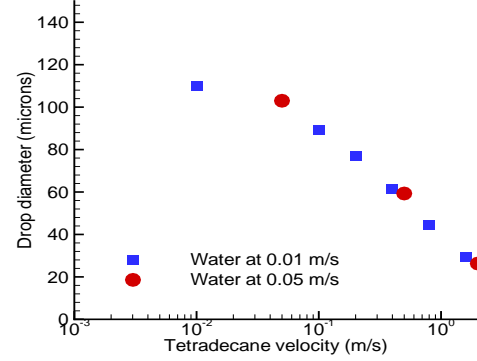


Figure 2: Water drop size as a function of tetradecane flow velocity.

where  $d$  is the water drop diameter in microns and  $V$  is the tetradecane velocity in m/s. A previous numerical simulation of a similar T-junction by Reedman [8] for a T-junction where both channels were  $30 \mu\text{m}$  in size is shown in Figure 3. It can be seen that a linear relationship exists for water drops formed that are smaller than  $50 \mu$  in diameter. However, as the water flow velocity is increased, the water drops formed increase in size for the same tetradecane flow rate so that there is a different linear relationship for each water flow velocity. The main difference between the current results and [8] is that in Reedman's results, the water drops formed are all larger than the channel width, while in the current work most of the drop sizes are smaller than the channel width. The experimental results of Nisisako *et al.* [7] and that of Liow and Cole [6] are shown in Figure 4. For water drops that are smaller or close to the oil/HC channel width, there is a straight line relationship. In Nisisako's case, the oil inlet channel is  $500 \mu\text{m}$ , and the water drops formed are all smaller than the oil channel and do not give rise to slug flow. For Liow and Cole, the lower tetradecane flow rates re-

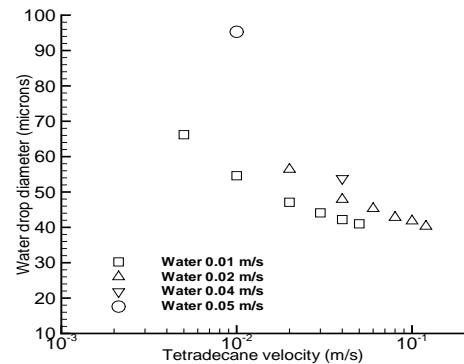


Figure 3: Results of Reedman [8] for water drop size as a function of tetradecane flow velocity for a  $30 \mu\text{m}$  width channel.

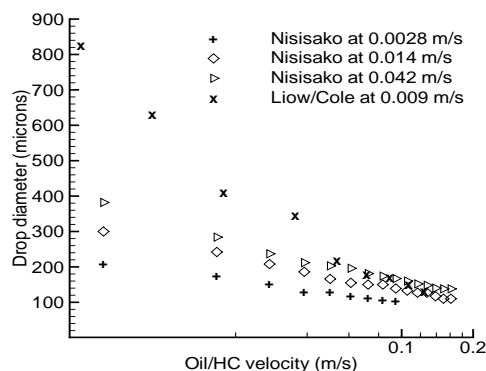


Figure 4: The experimental results of Nisisako [7] and Liow and Cole [6]. For Nisisako, the channel widths are 100  $\mu\text{m}$  for the water and 500  $\mu\text{m}$  for the oil. For Liow and Cole, the channel widths are both 250  $\mu\text{m}$ .

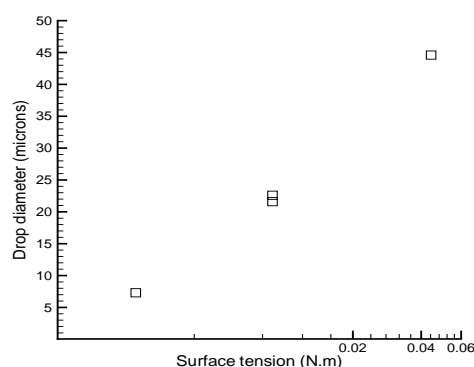


Figure 5: Effect of interfacial tension on the water drop size formed. The two data points for a interfacial tension of 0.0089 N/m were carried out at mesh resolution of  $64 \times 192$  and  $128 \times 384$ .

sult in large drops that slugs down the channel. Consequently, drops larger than 250  $\mu\text{m}$  do not follow the straight line fit for the smaller drops.

#### Effect of reducing interfacial tension

Experimentally [6, 10, 13] it has been shown that when surfactants are not used for the formation of water drops in small channels, the water and oil/HC streams form separate parallel flow channels. The reduction in interfacial tension was simulated for a case where the water and tetradecane flow velocities were 0.01 and 0.8 m/s respectively. Figure 5 shows the dramatic effect the drop size decreasing with a reduction in the interfacial tension. As the interfacial tension is reduced to 0.0089 N/m, satellite drops are formed. A high order resolution of the mesh used ( $128 \times 1024$ ) to check the results showed that satellite drops were not a result of the lower mesh resolution. Moreover, the large water drops formed differed only by 4% in diameter ( $1\mu\text{m}$ ) between the two mesh resolutions, which was of the order of 1 mesh size. This effect was not seen experimentally by [6] but the water/tetradecane flow ratios in the simulation are much higher. However, satellite drops have been found in the flow focussing experiments of Anna *et al.* [1]. For the control of drop sizes, the presence of the satellite drops as the interfacial tension is reduced means that smaller drops are always present. The presence of the satellite drops are not desired if the aim is to produce a fixed particle size. Figure 6 shows the drop formed for the three different surface tension cases. As the interfacial

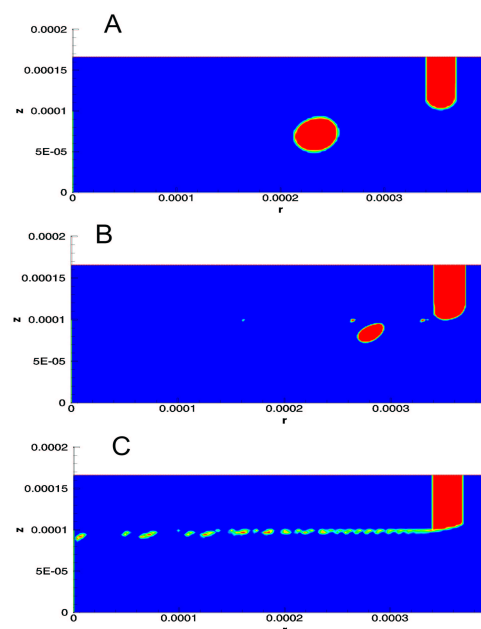


Figure 6: Drop formation for varying surface tension A: 0.0442 B: 0.0089 C: 0.0022 N/m. Water 0.01 m/s, Tetradecane 0.8 m/s.

tension is reduced, the drop is stretched much more in the flow. Interestingly, the satellite drops that are formed remain close to the channel boundary and hence move with a much lower velocity. This may provide a means of separating the larger and smaller drops if satellite drop formation is unavoidable.

#### Drop generation

Figure 7 shows the velocity vectors and associated pressure contours at the T-junction for the first four milliseconds from the numerical simulation. The drop detaches just after 4 ms. The velocity profile of the tetradecane stream is parabolic, the profile being established within a few  $\mu\text{m}$  from the inlet. The pressure gradient along the tetradecane channel decreases linearly with distance. In the first ms, the pressure in the water stream initially increases throughout the channel to overcome the interfacial forces to form a hemispherical cap. The velocity of the tetradecane stream creates a velocity gradient in the hemispherical cap resulting in a localised recirculating flow. The tetradecane stream also distorts the interface slightly resulting in an asymmetric pressure distribution around the hemispherical cap.

At 2 ms, the drop has protruded far enough that the tetradecane stream shears it in the downstream direction. The recirculating flow in the water section has grown in magnitude and is concentrated in the section that protrudes into the tetradecane section. The tetradecane approaching the water protrusion is forced to accelerate as the cross sectional area for flow is reduced. Far downstream, the tetradecane flow regains its parabolic flow profile. The velocity vectors show a smaller co-rotating recirculating flow at the downstream corner of the T-junction. The centres of the two recirculating zones show up in the pressure contours as a high pressure spot, with the smaller co-rotating recirculating zone having a higher peak pressure. The presence of the two recirculating zones that are in the same direction suggests that the flow set up by the tetradecane splits into two stream, the larger one moving into the drop that is being formed, while the smaller one moves towards the downstream corner.

At 3 ms and 4 ms, the smaller co-rotating recirculating zone continues to grow in size while the larger co-rotating zone moves out further into with the water drop. The pressure in the larger co-rotating zone smears out to a more uniform value,



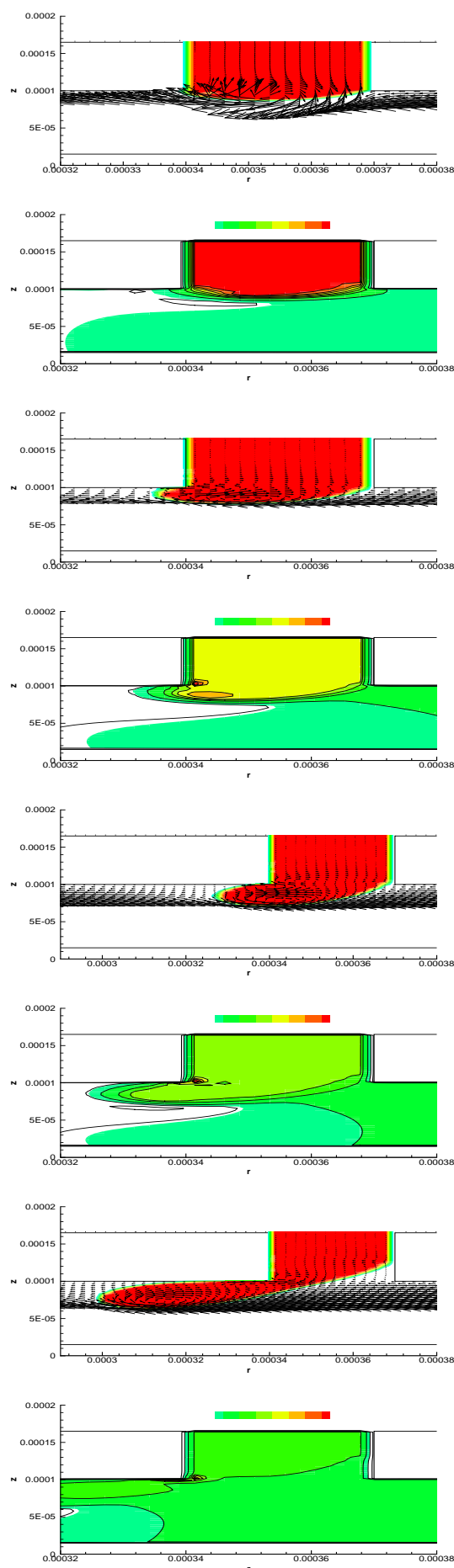


Figure 7: Velocity vectors and corresponding pressure contours at the T-junction for successive time intervals of 1, 2, 3 and 4 ms respectively from top to bottom. Water 0.01 m/s, Tetradecane 1.6 m/s.

as the drop grows rapidly since the interfacial forces holding the larger drop shape decreases when the drop is past a hemispherical shape. Throughout the growth of the water drop, the pressure at the downstream corner is still the highest. This has implications for drop formation in that the sharp corner significantly affects the pressure and flow characteristics in the formation of the water drop. The use of a rounded corner would be expected to reduce the pressure buildup there.

## Conclusions

This study of water drops forming into a stream of tetradecane at a microchanneled T-junction has shown that the water drop size decreases with increasing tetradecane velocity and decreasing interfacial tension. The numerical results are in line with published experimental results. It was found that a high pressure recirculating zone builds up at the downstream corner of the T-junction and the use of a rounded corner for controlling the drop formation process should be investigated in the future.

## References

- [1] Anna S. L., Bontoux N., and Stone H. A., Formation of dispersions using “flow focusing” in microchannels. *Applied Physics Letters*, **82**(2), 2003, 364–366.
- [2] Cole D. *Microdevice Construction and Application for Multiphase Microflows*. Final year thesis, James Cook University. 2003.
- [3] Dreyfus R., Tabeling P., and Willaime H., Ordered and disordered patterns in two-phase flows in microchannels. *Phys. Rev. Lett.*, **90**, 2003, 144505.
- [4] Gad-el-Hak M., The fluid mechanics of microdevices. The Freeman Scholar lecture. *J. Fluids Engng.*, **121**, 1999, 5–33.
- [5] Liovic P., Rudman M. and Liow J. L. Numerical modelling of free surface flows in metallurgical vessels. *Appl. Maths. Modelling*, **26**, 2002, 113–140.
- [6] Liow J. L., and Cole D. Drop formation in T-junction microchannels. in *Chemeca conference 2004*, Sydney, Australia, 2004, 6pp.
- [7] Nisisako T., Torii T. and Higuchi T., Droplet formation in a microchannel network. *Lab on a Chip*, **2**, 2002, 24–26.
- [8] Reedman, M. *Numerical simulation of microflows*. Final year thesis, James Cook University. 2002.
- [9] Stone, H. A. and Kim, S., Microfluidics: Basic issues, applications, and challenges. *AIChE Journal*, **47**(6), 2001, 1250–1255.
- [10] Stone H. A., Stroock A. D. and Ajdari A., Engineering flows in small devices: Microfluidics toward a lab-on-a-chip. *Annu. Rev. Fluid Mech.*, **36**, 2004, 381–411.
- [11] Sugiura S., Nakajima M., and Seki M., Interfacial tension driven monodispersed droplet formation from microfabricated channel array. *Langmuir*, **17**, 2001, 5562–5566.
- [12] Tabeling M., Some basic problems of microfluidics in *14th Australasian Fluid Mechanics Conference*, Adelaide University, Adelaide, Australia, 2001, 57–62.
- [13] Thorsen T., Roberts R. W., Arnold F. H. and Quake S. R., Dynamic pattern formation in a vesicle-generating microfluidic device. *Phys. Rev. Letters*, **86**, 2001, 4163–4166.

## Flow of a Nonlinear Viscoelastic Fluid in Concentric Rotating Cylinders with relative rotation

M. Mirzazadeh<sup>1</sup> and F.Rashidi<sup>1\*</sup> and S.H.Hashemabadi<sup>2</sup>

<sup>1</sup>Department of Chemical Engineering,  
Amir kabir University of Technology, 424 Hafez Ave, Tehran, IRAN

<sup>2</sup>Department of Chemical Engineering,  
Iran University of Science and Technology, 16844 Narmak, Tehran, IRAN

### Abstract

An analytical solution is presented for the steady and purely tangential flow of a viscoelastic fluid obeying the simplified form of Phan-Thien-Tanner (PTT) constitutive equation in a concentric annulus with relative cylinder rotation. The effect of fluid elasticity and aspect ratio on the velocity profile and fRe are investigated for two combinations of inner and outer cylinder rotation. The results show that the differences between the radial location of the minimum velocity and of the critical angular velocity compared with their Newtonian counterparts increase when the fluid elasticity increases. The results also show that fRe decreases with increasing fluid elasticity and radius ratio in the case of inner cylinder rotation.

### Introduction

An extensive bibliography of work on the flow of non-Newtonian liquids through annular channels is given in the recent paper by Escudier et al [1]. The flow of non-Newtonian fluids was studied in several works [2-6]. Cruz and Pinho [7] derived an analytical solution for helical flow within a concentric annulus of a fluid obeying the simplified form of the Phan-Thien-Tanner (SPTT) constitutive equation.

The PTT model is a non-linear viscoelastic constitutive equation derived using network theory by Phan-Thien and Tanner [8]. A distinctive advantage of the PTT model over most of the other similar constitutive equations is the inclusion of an elongational parameter  $\mathcal{E}$ . The flow of PTT viscoelastic fluids has been considered in several works by Oliveira and Pinho [9], Alves et al [10] and Hashemabadi et al [11].

The objective of the present investigation is to obtain velocity profiles as well as the coefficient of friction using an analytical method to solve the simplified form of PTT model in purely tangential flow between concentric rotating cylinders where the inner and outer cylinders are rotating with different angular velocities, for a wide range of fluid elasticity and radius ratios.

### Mathematical Formulation

We assume steady-state, laminar, purely tangential flow and neglect body forces in the momentum equation. We then have:

$$V_\theta = V_\theta(r) \quad , \quad V_r = V_z = 0 \quad (1)$$

Where  $V_r$ ,  $V_\theta$  and  $V_z$  are the radial, tangential and axial components of velocity profile, respectively.

The dimensionless form of the momentum equation for the  $\theta$  - direction is:

$$\frac{1}{r^{*2}} \frac{d}{dr^*} (\dot{\tau}^{*2} \tau_{r\theta}^*) = 0 \quad (2)$$

The simplified form of the PTT constitutive equation is as follows:

$$Z(tr\tau)\tau + \lambda \tau_{(1)} = \eta \dot{\gamma} \quad (3)$$

Where  $\eta$  is the viscosity coefficient of the model,  $\lambda$  is the

relaxation time,  $tr\tau$  is the trace of stress tensor and  $\tau_{(1)}$  is the convected time derivative of stress tensor:

$$\tau_{(1)} = \frac{D\tau}{Dt} - \{(\nabla V)^T \cdot \tau + \tau \cdot (\nabla V)\} \quad (4)$$

The stress coefficient,  $Z$ , has an exponential form:

$$Z(tr\tau) = \exp\left(\frac{\mathcal{E}\lambda}{\eta} tr\tau\right) \quad (5)$$

Where  $\mathcal{E}$  is the elongational parameter of the model. Eq. (5) may be linearized when the deformation rate of a fluid element is small which corresponds to the behaviour of weak flow according to Tanner's classification [12]:

$$Z(tr\tau) = 1 + \frac{\mathcal{E}\lambda}{\eta} tr\tau \quad (6)$$

### Exact solution for the simplified PTT model (SPTT)

For steady tangential annular flow Eq. (3) reduces to:

$$Z(tr\tau)\tau_{\theta\theta} = 2\lambda\dot{\gamma}\tau_{r\theta} \quad (7)$$

$$Z(tr\tau)\tau_{rr} = 0 \quad (8)$$

$$Z(tr\tau)\tau_{r\theta} = \eta\dot{\gamma} + \lambda\dot{\gamma}\tau_{rr} \quad (9)$$

Eq. (8) indicates  $\tau_{rr} = 0$ , hence the trace of the stress tensor will be equal to  $\tau_{\theta\theta}$ . Using Eq. (6) for the stress coefficient yields:

$$Z = 1 + \frac{\mathcal{E}\lambda}{\eta} \tau_{\theta\theta} \quad (10)$$

By dividing Eq. (9) by Eq. (7) the following for  $\tau_{\theta\theta}$  is obtained:

$$\tau_{\theta\theta} = \frac{2\lambda}{\eta} \tau_{r\theta}^2 \quad (11)$$

The shear rate  $\dot{\gamma}$  is obtained by substituting  $\tau_{\theta\theta}$  from Eq. (11) into Eq. (7) and using Eq. (10) for the stress coefficient:

$$\eta\dot{\gamma} = \tau_{r\theta} \left[ 1 + \frac{2\mathcal{E}\lambda^2}{\eta^2} \tau_{r\theta}^2 \right] \quad (12)$$

where the shear rate  $\dot{\gamma}$  is defined by:

$$\dot{\gamma} = r \frac{d}{dr} \left( \frac{V_\theta}{r} \right) \quad (13)$$

The dimensionless shear stress is obtained by integrating Eq. (2):

$$\frac{\tau_{r\theta}^*}{\tau_{wi}^*} = \frac{\kappa^2}{r^{*2}} \quad (14)$$

Where  $\tau_{wi}^*$  is the dimensionless wall shear stress on the inner cylinder and  $\kappa$  is inner to outer radius ratio ( $R_i / R_o$ ).

Combination of Eqs. (12) and (13) leads to:

$$(1-\kappa)^* r \frac{d}{dr} \left( \frac{V_\theta^*}{r} \right) = \left( 1 + 2\varepsilon We^2 \tau_{r\theta}^* \right) \tau_{r\theta}^* \quad (15)$$

The following normalizations have been used in Eq. (15):

$$r^* = \frac{r}{R_o}, \quad V_\theta^* = \frac{V_\theta}{V_c}, \quad \tau_{r\theta}^* = \frac{\tau_{r\theta}}{\eta V_c / \delta}, \quad We = \lambda \frac{V_c}{\delta} \quad (16)$$

Where  $We$  is the Weissenberg number,  $\delta$  is the annular gap ( $\delta = R_o - R_i$ ) and  $V_c$  is a characteristic velocity which is defined as follows:

$$V_c = \begin{cases} R_i \Omega_i & \Omega_o = 0 \\ R_o \Omega_o & \Omega_i = 0 \\ \bar{R} |\Omega_o - \Omega_i| & \Omega_i \neq \Omega_o \neq 0 \end{cases} \quad (17)$$

Where  $\bar{R}$  is the average radius ( $(R_o + R_i) / 2$ ). By substitution of  $\tau_{r\theta}^*$  from Eq. (14) into Eq. (15) and then integration of this equation, the dimensionless velocity profile is obtained, as follows:

$$\frac{V_\theta^*}{r^*} = - \frac{\kappa^2 \tau_{wi}^*}{(1-\kappa)^* r^{*2}} \left[ \frac{1}{2} + \frac{\varepsilon We^2 \kappa^4 \tau_{wi}^{*2}}{3 r^{*4}} \right] + C_2 \quad (18)$$

The boundary conditions are as follows:

$$\begin{array}{ccc} \text{Both} & \text{Inner} & \text{Outer} \\ r = R_i & V_\theta = R_i \Omega_i & R_i \Omega_i & 0 \end{array} \quad (19)$$

$$\begin{array}{ccc} r = R_o & V_\theta = R_o \Omega_o & R_o \Omega_o & 0 \end{array} \quad (20)$$

and in dimensionless form:

$$\begin{array}{ccc} r^* = \kappa & V_\theta^* = \frac{2\kappa}{(1+\kappa)|\beta-1|} & 1 & 0 \end{array} \quad (21)$$

$$\begin{array}{ccc} r^* = 1 & V_\theta^* = \frac{2\beta}{(1+\kappa)|\beta-1|} & 0 & 1 \end{array} \quad (22)$$

Where  $\beta$  is the outer to inner angular velocity ratio ( $\Omega_o / \Omega_i$ ). By introducing boundary conditions from Eqs. (21) and (22) into Eq. (18), and after mathematical simplification, the following cubic equation is obtained:

$$\tau_{wi}^{*3} + p \tau_{wi}^* + q = 0 \quad (23)$$

Where the constants  $p$  and  $q$  in Eq. (23) for the cases of both cylinder rotation, inner cylinder rotation and outer cylinder rotation are, respectively:

$$p = \frac{3(1-\kappa^2)}{2\varepsilon We^2 (1-\kappa^6)}, \quad q = \frac{-6(1-\kappa)(\beta-1)}{\varepsilon We^2 (1-\kappa^6) (1+\kappa)|\beta-1|} \quad (24)$$

$$p = \frac{3(1-\kappa^2)}{2\varepsilon We^2 (1-\kappa^6)}, \quad q = \frac{3(1-\kappa)}{\varepsilon We^2 (1-\kappa^6) \kappa} \quad (25)$$

$$p = \frac{3(1-\kappa^2)}{2\varepsilon We^2 (1-\kappa^6)}, \quad q = \frac{-3(1-\kappa)}{\varepsilon We^2 (1-\kappa^6)} \quad (26)$$

The real solution of Eq. (23) can be expressed as:

$$\tau_{wi}^* = \frac{1}{6} \sqrt[3]{-108q + 12\sqrt{12p^3 + 81q^2}} - 2p \sqrt[3]{-108q + 12\sqrt{12p^3 + 81q^2}} \quad (27)$$

By introducing boundary conditions from Eq. (21) or (22) into Eq. (18) and using  $\tau_{wi}^*$  from Eq. (27), the second constant  $C_2$  can be easily obtained.

For the limiting case of a Newtonian fluid ( $\varepsilon We^2 \rightarrow 0$ ), Eq. (18) reduces to:

$$\frac{V_\theta^*}{r^*} = - \frac{\kappa^2 \tau_{wi}^*}{2(1-\kappa)} \frac{1}{r^{*2}} + C_2 \quad (28)$$

By introducing boundary conditions from Eqs. (21) and (22) into Eq. (28), the following relations can be written to obtain  $\tau_{wi}^*$  and  $C_2$  for the cases of both, inner and outer cylinder rotation, respectively :

$$\tau_{wi}^* = \frac{4(\beta-1)}{(1+\kappa)^2 |\beta-1|} \quad C_2 = \frac{2(\beta-\kappa^2)}{(1+\kappa)(1-\kappa^2) |\beta-1|} \quad (29)$$

$$\tau_{wi}^* = - \frac{2}{\kappa(1+\kappa)} \quad C_2 = - \frac{\kappa}{(1-\kappa^2)} \quad (30)$$

$$\tau_{wi}^* = \frac{2}{(1+\kappa)} \quad C_2 = \frac{1}{1-\kappa^2} \quad (31)$$

These results are in full agreement with previous work such as that of Mahmud and Fraser [13].

An important parameter in engineering calculations is the product of the friction factor and the Reynolds number. In the present situation, the torque friction factor,  $f$ , can be defined as follows [14]:

$$f = \frac{\tau_w}{\rho V_c^2 / 2} \quad (32)$$

and the rotational Reynolds number as [6,14]:

$$Re = \rho V_c \delta / \eta \quad (33)$$

Using these definitions we can derive the following equations for the two special cases of inner and outer cylinder rotation ( $fRe_i$

and  $fRe_o$ ):

$$fRe_i = -2 \tau_{wi}^* \quad (34)$$

$$fRe_o = 2 \kappa^2 \tau_{wi}^* \quad (35)$$

## Results and Discussion

Velocity profiles are presented in figure 1, for different values of the angular velocity ratio ( $\beta$ ). As represented in this figure, the velocity profile shows a minimum value within the annular gap for  $\beta > \beta_c$ . The radial location of the minimum velocity can be determined from the following equation:

$$r_{\min}^* = \frac{\sqrt{6d(d^2 + 4a^2 - 2ad)}}{6d} \quad (36)$$

where

$$d = \sqrt[3]{(-108b - 8a^3 + 12\sqrt{(81b^2 + 12ba^3)})} \quad (37)$$

$$a = \frac{\kappa^2 \tau_{wi}^*}{2(1-\kappa)C_2} \quad (38)$$

$$b = \frac{5\varepsilon We^2 \kappa^6 \tau_{wi}^*}{3C_2} \quad (39)$$

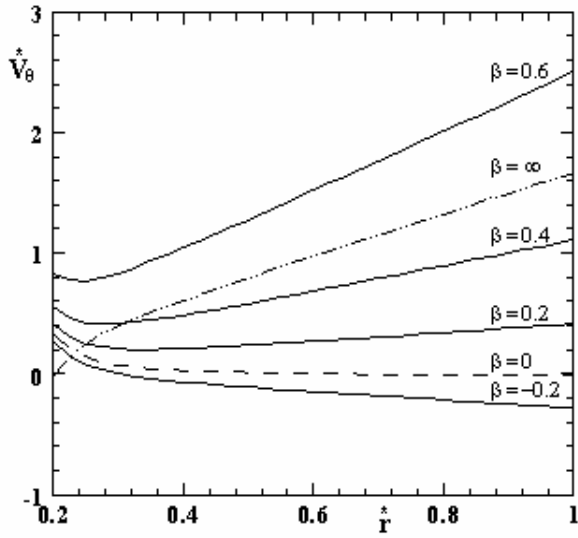


Figure 1. Effect of angular velocity ratio on velocity profile for  $\kappa = 0.2$  and  $\varepsilon We^2 = 10$ .

For the limiting case of a Newtonian fluid (i.e.  $\varepsilon We^2 \rightarrow 0$ ), we arrive at the well-known (see e.g. [13]) result:

$$r_{\min}^* = \kappa \sqrt{(1 - \beta) / (\beta - \kappa^2)} \quad (40)$$

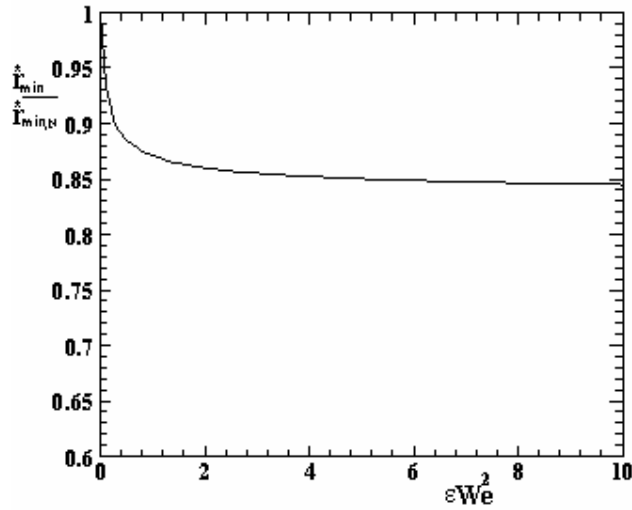


Figure 2. Effect of fluid elasticity,  $\varepsilon We^2$ , on the radial location of minimum velocity for  $\kappa = 0.5$ .

Figure 2, shows the location of minimum velocity ( $r_{\min}^*$ ), normalized with the corresponding Newtonian values (according to Eq. (40)) as a function of the non-dimensional viscoelastic group ( $\varepsilon We^2$ ). As can be seen, the departure from the Newtonian value increases with increasing fluid elasticity.

As can be seen from figure 1, the velocity profile exhibits a minimum when  $\beta$  is greater than a critical value ( $\beta_c$ ) which satisfies the following inequality:

$$\kappa < r_{\min}^* < 1 \quad (41)$$

Figure 3, shows the critical value of the angular velocity ratio,  $\beta_c$ , normalized with the corresponding Newtonian value ( $\beta_{c,N} = 2\kappa^2 / (1 + \kappa^2)$ ) as a function of the elasticity parameter ( $\varepsilon We^2$ ), for the various values of the radius ratio  $\kappa$ .

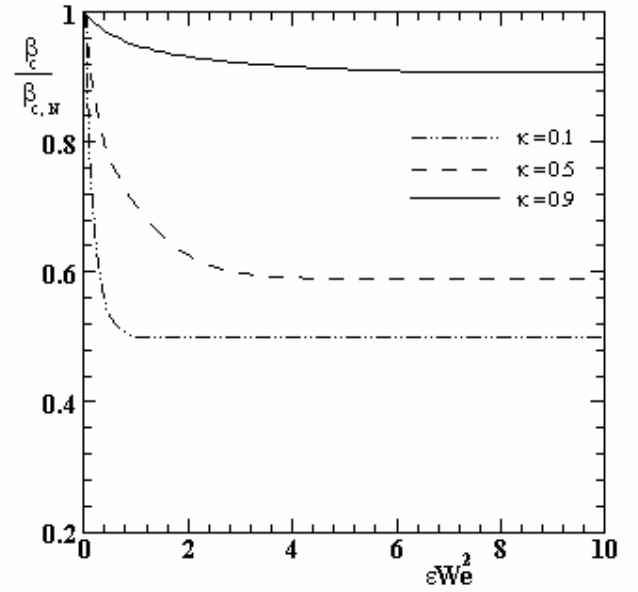


Figure 3. Effect of fluid elasticity,  $\varepsilon We^2$ , and radius ratio ( $\kappa$ ) on critical angular velocity.

For high values of  $\kappa$ , i.e. for a narrow annulus,  $\beta_c$  is only marginally different from the Newtonian value and is independent of elasticity for large value of  $\varepsilon We^2$ . For smaller radius ratios, for example  $\kappa = 0.1$ , the differences are about 50% at high Weissenberg number.

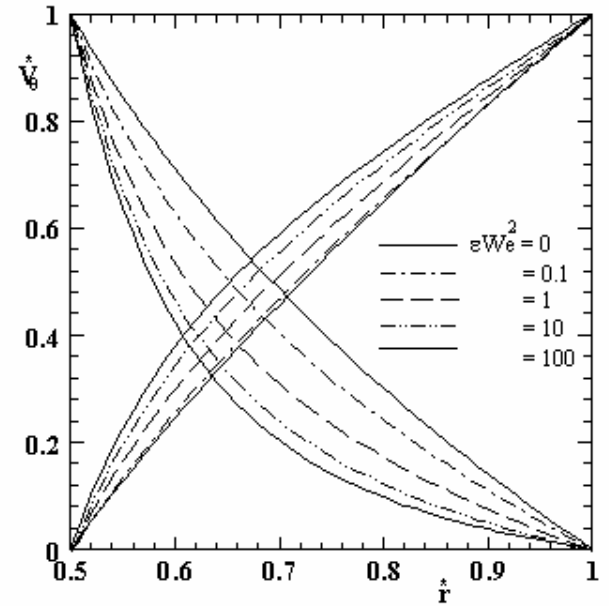


Figure 4. Effect of fluid elasticity,  $\varepsilon We^2$ , on the velocity profile in the both cases of inner and outer cylinder rotation for  $\kappa = 0.5$ .

Figure 4, shows the effect of fluid elasticity on the velocity profile for the two special cases of inner and outer cylinders rotation. As can be seen, by increasing fluid elasticity  $\varepsilon We^2$  the velocity profile differs from the Newtonian case, i.e. as the shear-thinning behaviour of the fluid increases. The viscosity function and shear-thinning behaviour of a PTT fluid is discussed in detail by Pinho and Oliveria [15] and Alvez, et al [10].

The influence of the radius ratio on the velocity profile for the two special cases of inner cylinder rotation and outer cylinder

rotation are shown in Figure 5. The results show that the profiles tend to take linear form with increasing  $\kappa$ .

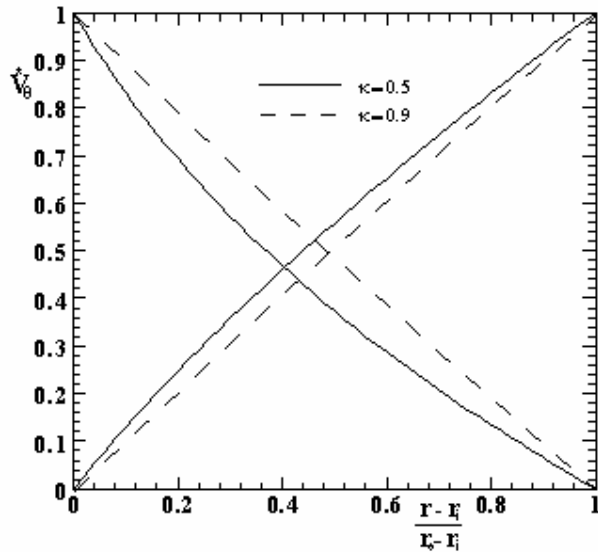


Figure 5 Effect of radius ratio on velocity profile in the both cases of inner and outer cylinder rotation for,  $\varepsilon We^2 = 0.01$ .

Figure 6, shows the effect of fluid elasticity on  $fRe$  which is normalized with the corresponding Newtonian value ( $fRe_{i,N} = 4 / \kappa(1 + \kappa)$ ) for the various radius ratios for the case of inner cylinder rotation

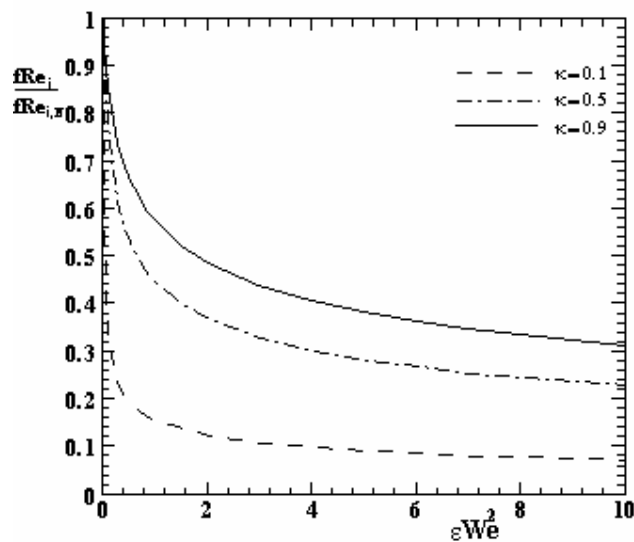


Figure 6. Effect of fluid elasticity,  $\varepsilon We^2$ , and radius ratio ( $\kappa$ ) on the ratio of viscoelastic to Newtonian friction factor ( $fRe_i / fRe_{i,N}$ ).

The decrease in  $fRe$  with increasing elasticity is again attributable to the shear-thinning behaviour of the PTT fluid. As can be seen from this figure, as  $\varepsilon We^2$  approaches zero the  $fRe$  values are in agreement with those for a Newtonian fluid [6 and 14]. These features of polymeric fluid have been investigated experimentally by Escudier et al. [16]. Their results showed that increasing fluid elasticity decreases friction factor. The same conclusion will be achieved if we plot  $fRe_o$  against  $\varepsilon We^2$ .

## Conclusion

An analytical solution has been derived for the steady-state, purely tangential flow in a concentric annulus with relative

rotation of the two cylinders of a viscoelastic fluid obeying the simplified form of the Phan-Thien-Tanner (PTT) constitutive equation. The results show that the difference between the radial location of minimum velocity and its corresponding Newtonian value increases when the fluid elasticity increases and that the same is true for the critical angular velocity. The results show that increasing the fluid elasticity increases the velocity gradient near the inner cylinder and so decreases the viscometric viscosity of the fluid (i.e. the fluid behaviour is increasingly shear-thinning) and in consequence  $fRe$ . The results also indicate that increasing the radius ratio decreases  $fRe$  in the case of inner cylinder rotation. With increasing radius ratio the velocity profile tends to take a linear form.

## References

- [1] Escudier, M.P. and Oliveira, P.J. and Pinho, F.T., Fully developed laminar flow of purely viscous non-Newtonian liquids through annuli including the effects of eccentricity and inner cylinder rotation, *Int. J. Heat Fluid Flow*, **23**, 2002, 52-73.
- [2] Batra, R.L. and Das, B., Flow of Casson fluid between two rotating cylinder, *Fluid Dyn. Res.*, **9**, 1992, 133-141.
- [3] Batra, R.L. and Eissa, M., Helical Flow of a Sutterby model Fluid, *Polym. - Plast. Technol. Eng.*, **33**, 1994, 489-501.
- [4] Eissa, M. and Ahmad, S., Forced convection Heat transfer of Robertson- Stiff fluid between two coaxial rotating cylinders, *Int. comm. Heat Mass Transfer*, **26**, 1999, 695-704.
- [5] Rao, I.J., Flow of a Johnson-Segalman fluid between rotating co-axial cylinders with and without suction, *Int. J. Non-Linear Mech.*, **34**, 1999, 63-70.
- [6] Khellaf, K. and Lauriat, G., Numerical study of heat transfer in a non-Newtonian Carreau- fluid between rotating concentric vertical cylinders, *J. Non- Newtonian Fluid Mech.*, **89**, 2000, 45-61.
- [7] Cruz, D.O.A. and Pinho, F.T., Skewed Poiseuille-Couette flow of SPTT fluids in concentric annuli and channels, *J. Non-Newtonian Fluid Mech*, 2004, Article in press.
- [8] Phan- Thien, N. and Tanner, R.T., A new constitutive equation derived from network theory, *J. Non- Newtonian Fluid Mech.*, **2**, 1977, 353-365.
- [9] Oliveira, P.J. and Pinho, F.T., Analytical solution for fully developed channel and pipe flow of Phan- Thien- Tanner fluids, *J. Fluid Mech.*, **387**, 1999, 271-280.
- [10] Alves, M.A. and Pinho, F.T. and Oliveira, P.J., Study of steady pipe and channel flows of single- mode Phan- Thien- Tanner fluid, *J. Non- Newtonian Fluid Mech.*, **101**, 2001, 55-76.
- [11] Hashomabadi, S.H. and Etemad, S.Gh. and Thibault, J. and Golkar Naranj, M.R., Analytical solution for dynamic pressurization of viscoelastic fluids, *Int. J. of Heat Fluid Flow*, **24**, 2003, 137-144.
- [12] Tanner, R.I., *Engineering Rheology*, Clarendon Press, oxford, 2000.
- [13] Mahmud, S. and Fraser, R.A., Analysis of entropy generation inside cylindrical annuli with relative rotation, *Int. J. Thermal Sci.*, **42**, 2003, 513-521.
- [14] Gazley, Jr.C. and Monica, C.S., Heat transfer characteristics of the rotational and axial flow between concentric cylinders, in *Trans. of the ASME., paper number 56-A-128*, Nov.25, 1956, 79-90.
- [15] Pinho, F.T. and Oliveira, P.J., Axial annular flow of non-linear viscoelastic fluid-an analytical solution, *J. Non- Newtonian Fluid Mech.*, **93**, 2000, 325-337.
- [16] Escudier, M.P and Presti, F. Smith, S., Drag reduction in turbulent pipe flow of polymers, *J. Non-Newtonian. Fluid Mech.*, **81**, 1999, 197-213.

## Behaviour of water droplets falling in oil under the influence of an electric field.

M. Chiesa<sup>1</sup>, J. A Melheim<sup>2</sup>

<sup>1</sup>Dept. of Energy Processes, SINTEF Energy Research, Norway, matteo.chiesa@sintef.no

<sup>2</sup>Dept. of Energy and Process Engineering, NTNU, Norway, jensm@pvv.ntnu.no

### Abstract

The use of electric field is a promising technique for separating stabile water-oil emulsions. Charges induced on the water droplets will cause adjacent droplets to align with the field and attract each other. The present work outlines the efforts to model the forces that influence the kinematics of droplets exposed to electric field when falling in oil. Mathematical models for these forces are briefly presented with respect to the implementation in a multi-droplet Lagrangian framework. The droplet motion is mainly due to buoyancy, drag, film-drainage, and dipole-dipole forces. Attention is paid to internal circulations, non-ideal dipoles, and the effects of surface tension gradients. Experiments are performed to observe the behavior of two falling water droplets exposed to an electric field perpendicular to the direction of their motion up to the droplets coalescence. The droplet motion is recorded with a high-speed CMOS camera. The optical observations are compared with the results from numerical simulations where the governing equations for the droplet motion are solved by the RK45 Fehlberg method with step-size control and low tolerances. Results, using different models, are compared and discussed in details. Observation concerning the contribution of the different forces acting on the water droplets kinematics is presented.

### Introduction

The oil extracted from offshore reservoirs will normally contain a large and, during the reservoir lifetime, increasing percentage of water in the oil. When the water-oil mixture is passed through the pressure relief valve an emulsion with a high percentage of small water drops is formed. Before the oil is pumped on-shore or into tankers, it is desirable to extract the water from this emulsion. Today the separation tanks are mainly built or operated as gravity separators with low flow rates and long residence times; lasting from minutes to tens of minutes. The residence time mainly depends on the sedimentation velocity of the smallest drops (e.g.  $d < 100 \mu\text{m}$ ). Electrostatic fields are to some extent used to help smaller drops to coalesce in to larger drops that sediment quicker as presented by Eow et al. [1]. The combination of an electric field and a moderate turbulent flow is a promising and compact technique for separating stabile water-oil emulsions, see Atten [2]. Charges induced on the water droplets will cause adjacent droplets to align with the field, attract each other and eventually coalesce. The sedimentation velocity increases proportionally to the square of the diameter, and therefore one wishes to get the smallest water droplets to coalesce into larger droplets. The present work outlines the forces that influence the kinematics of falling spherical droplets exposed to an electric field. Mathematical models for these forces are presented and discussed with respect to the implementation in a multi-droplet Lagrangian framework. The spherical droplet motion is mainly due to buoyancy, drag, film-drainage, and dipole-dipole forces. General and physically meaningful models for these forces are needed in order to establish simulation models for the behavior of water-oil emulsion.

In the present work, models for the forces that are believed to dictate the motion of droplets falling in oil under the influence

of an electric field are reviewed and discussed in details. A modeling framework that properly account for the effect of the different forces on the droplet motion is used as suggested by Chiesa et al. [3]. Experiments are performed to observe the behavior of two falling droplets released simultaneously into oil. The electrical field applied perpendicularly to the direction of the motion induces charges on the water droplets. This causes adjacent droplets to align with the field and attract each other. A comparison between observations and predictions is presented in order to assess the performance of the modeling framework used in this work.

### Theoretical background

The trajectory of a spherical droplet  $i$  is calculated by integrating Newton's second law. The law equates the droplet inertia with the forces acting on it, and reads:

$$\frac{dx_i}{dt} = v_i \quad (1)$$

$$m_i \frac{dv_i}{dt} = F_{\text{fluid}} + F_{\text{ext}} + F_{\text{d-d}}, \quad (2)$$

where  $m_i$ ,  $x_i$ , and  $v_i$  are the mass, position, and velocity of the droplet.  $F_{\text{fluid}}$  represents the vector of forces acting from the fluid on the droplet,  $F_{\text{ext}}$  is the external force vector, and  $F_{\text{d-d}}$  represents the inter-droplet force vector. Droplet tracking with droplet-droplet interaction has a high computational cost. It is therefore important to keep the computational work necessary to calculate the particle forces as low as possible since the forces have to be calculated for each particle. Finally models should be easily implementable in a numerical code.

In the following sessions, models for the forces that are believed to dictate the motion of droplets falling in oil under the influence of an electric field are reviewed and discussed in details. The modeling framework proposed by Chiesa et al. [3] is used in the present work. The electric force between the particle and the droplet is modeled with either the analytical expression obtained by Davis [4], the DID model by Siu et al. [5] or the point dipole model by Klingenberg et al. [6]. When describing the motion of a falling water droplet the effect of internal circulation induced in the droplet has to be taken into account. Internal circulation reduces the viscous part of the drag force and therefore the drag coefficient needs to be corrected in order to account for this reduction as outlined by Happel and Brenner [7]. Furthermore, the surface tension varies over the droplet surface by the effect of surfactant on the interface and by elongation of the droplet, caused by the electric field. This leads to interfacial stresses that inhibit the creation of internal circulation. LeVan [8] suggests how to take into account the effect of surface tension gradient in our numerical framework. The model proposed by Vinogradova [9] takes into account the slip between the liquid film and the approaching spheres.

### Modeling the fluid-droplet and body forces

Fluid droplet forces are transferred from the fluid to the droplets through friction and pressure difference. These forces are ex-

pressed exactly by the following surface integral:

$$\frac{1}{V_d} F_{\text{fluid}} = \frac{1}{V_d} \int_{\mathcal{A}_d} (-p_s n_d + \tau_d \cdot n_d) dA \quad (3)$$

where  $V_d$  is the volume of the droplet.  $p_s$  is the pressure at the droplet surface,  $n_d$  represents the unit outward normal vector and  $\tau_d$  is the shear stress tensor at the droplet surface. The pressure and the friction on the interface are unknown and Eq. (3) has to be modeled. In the Lagrangian framework, the models for the surface integral attempt to provide particular physical meanings.

The ‘*steady-state*’ **drag force** acts on a droplet in a uniform pressure field when there is no acceleration of the relative velocity between the droplet and the conveying fluid. The force reads:

$$F_d = \frac{1}{2} \rho_c C_d A |u - v| (u - v), \quad (4)$$

Surfactants on the interface and elongation of the droplet, caused by the electric field, give a variation in the surface tension. The surface tension gradient leads to interfacial stresses that inhibit the creation of internal circulation. The surface tension gradient is included in the formula by LeVan [8] for the drag coefficient:

$$C_d = \frac{24}{Re_d} \frac{3\lambda + 2 + 2\kappa(\mu_c r_d)^{-1} + 2/3\gamma_1(\mu_c |u - v|)^{-1}}{3\lambda + 3 + 2\kappa(\mu_c r_d)^{-1}}, \quad (5)$$

where also the surface dilational viscosity  $\kappa$  is taken into account. However, in the present work surface dilational viscosity is neglected,  $\kappa = 0$ . In Eq. (5) it is assumed that the interfacial tension varies as follows  $\gamma = \gamma_0 + \gamma_1 \cos \psi$  where  $\psi$  is measured from the front stagnation point.

The **virtual mass force**  $F_{vm}$  is an unsteady force that describes the acceleration of fluid when a particle and the fluid have a relative acceleration. It reads:

$$F_{vm} = \frac{\rho_c V_d}{2} \left( \frac{Du}{Dt} - \frac{dv}{dt} \right) \quad (6)$$

We assume that the droplets have no net charge, hence the electric field as a far field force can be neglected. On the other hand, the electric field gives rise to dipole-dipole interactions between the droplets, which are modeled as inter-droplet forces. Then the gravity is the only **external force** and the buoyancy force is given by:

$$F_b = (\rho_d - \rho_c) g V_d e_g \quad (7)$$

where  $g$  and  $e_g$  are the modulus and the direction of the gravity.

In the present work, the effects of the pressure gradient, the Basset history force and the lift forces have been neglected. The pressure difference over a small droplet is negligible due to the size of the droplets. The contribution from the gravity is handled separately. Lift forces are due to droplet rotation and shear forces, and can therefore be neglected when a rigid sphere or droplet is falling in a stagnant fluid. Due to the small size of the spheres and the high viscosity of the oil, the particle time scale is very small. Thereby follows that the Stokes number is small and the Basset history force can therefore be neglected [10].

### Modeling droplet-droplet forces

The inter-droplet forces are the film thinning forces, due to the drainage of the fluid between the droplets, and the electric forces due to polarization of the conductive water droplets.

The **film-thinning force** is caused by drainage of the liquid film between two approaching droplets. The derivation of the formulas usually requires that the gap between the particles is small  $h \ll a$  and that the flow is within Stokes regime  $Re_d h \ll a$ .  $a = (r_1 r_2)/(r_1 + r_2)$  is the reduced radius. When the particles are very close, a slip will occur and avoid a zero impact velocity. The formula of Vinogradova [9] for the film-thinning force includes a slip distance  $b$  and reads:

$$F_f = - \frac{6\pi\mu_c a^2 (v_r \cdot e_r)}{h} \left\{ \frac{2h}{6b} \left[ \left( 1 + \frac{h}{6b} \right) \ln \left( 1 + \frac{6b}{h} \right) - 1 \right] \right\} e_r. \quad (8)$$

The **electric forces** are due to polarization of the conductive water droplets. Consider an uncharged spherical droplet placed in an insulating medium. The droplet is furthermore subjected to an electric field  $E_0$ . The field outside a dielectric sphere of permittivity  $\epsilon_d$  corresponds exactly to the electric field of a dipole located at the sphere centre. The value of this dipole moment  $p$  depends on the sphere size, permittivity and the strength of the electric field. Due to the polarization of the droplet, the poles will have charges of same magnitude but opposite polarity, preserving zero net charge. In a homogeneous field, the net force on the droplet is zero. Subjected to an inhomogeneous field the droplet will experience a stronger field at one pole than at the other, resulting in a net force acting on the droplet in the direction of the field gradient, a phenomenon called dielectrophoresis. The resulting force is given by  $F = (p \cdot \nabla) E$ . If the permittivity of the drop  $\epsilon_d$  is higher than the permittivity of the surrounding medium  $\epsilon_{oil}$ , the drop will move towards the high field region. An inhomogeneous electric field may for instance be set up by nearby point charge or another dielectric droplet. In the latter case the electrostatic force attracts the two droplets, given that  $\epsilon_d > \epsilon_{oil}$ .

#### Point dipole model

For large droplet distances  $|d|/r_d \gg 1$  we can approximate the electrostatic interaction between two droplets as the force between two dipoles located at the sphere centres. This is frequently referred to as the *point-dipole* approximation. The forces in radial direction  $F_r$  and tangential direction  $F_t$  read [6]:

$$F_r = \frac{12\pi\beta^2\epsilon_{oil}|E_0|^2 r_2^3 r_1^3}{|d|^4} (3k_1 \cos^2 \theta - 1) \quad (9)$$

$$F_t = - \frac{12\pi\beta^2\epsilon_{oil}|E_0|^2 r_2^3 r_1^3}{|d|^4} k_2 \sin(2\theta), \quad (10)$$

where  $\theta$  is the angle between the direction of the electrical field  $E_0$  and the relative droplet position vector  $d$ .  $\beta$  is defined as:  $\beta = \frac{\epsilon_d - \epsilon_{oil}}{\epsilon_d + 2\epsilon_{oil}}$ .  $k_1 = 1$  and  $k_2 = 1$  in the point dipole approximation. The point-dipole model is not valid when the droplets are approaching each other. In the literature there are different approaches to find the dipole-dipole forces beyond the point dipole approximation for multiple particles of arbitrary size and position.

#### The multiple image method

A promising method, the *multiple image method*, was presented by Yu et al. [11]. The two first terms in the multiple image method gives the dipole induced dipole model (DID) [5], which is simple and numerical efficient. Siu et al. [5] show that the DID model is in good agreement with experimental values for  $|d|/r_1 > 0.1$  for equally sized conductive particles. The DID model reads as Eq. (9) and (10), where the coefficients  $K_1 \neq 1$  and  $K_2 \neq 1$ , see Siu et al. [5] for further details. In the limit  $|d| \rightarrow \infty$  the coefficients  $K_1$  and  $K_2$  approach unity and we recover the point dipole model given by Eq. (9) and (10).

### The analytical solution

Davis [4] found an analytical solution to Laplace's equation for two conducting spheres of arbitrary size, displacement and net charge, using bi-spherical coordinates. The exact solution for uncharged spheres is given by:

$$F_r = 4\pi\epsilon_{oil}|E_0|^2 r_2^2 \left( F_1 \cos^2 \theta + F_2 \sin^2 \theta \right) \quad (11)$$

$$F_t = 4\pi\epsilon_{oil}|E_0|^2 r_2^2 F_3 \sin(2\theta), \quad (12)$$

where the parameters  $F_1$ ,  $F_2$ , and  $F_3$  are complicated series depending on the ratios  $|d|/r_2$  and  $r_1/r_2$ . Unfortunately, the computational cost required for calculating  $F_1 - F_3$  is high in a multi-droplet situation. However, the exact solution is excellent for benchmarking other models in cases with two particles/droplets. For large drop separations  $|d|/r_1 \gg 1$  the force components  $F_1 - F_3$  approach the values of the point-dipole Eq. (9) and (10). For small separations  $|d|/r_1 < 1$ ,  $F_2$  and  $F_3$  takes constant values while  $F_1$  diverges, see Atten [2].

### Results and Discussions

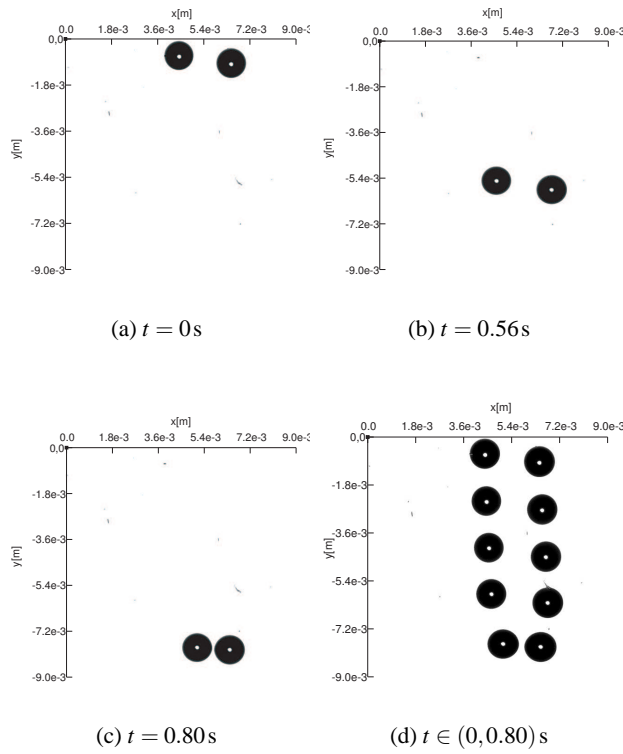


Figure 1: Experimental observation of the kinematic of two water droplets falling in a stagnant oil under the influence of an electric field.

Experiments are designed for visual observation of water droplets in oil under the influence of electric field stress, see [3]. Two sub-millimeters sized water droplets are released within an upper ground electrode from a glass capillary coated with gold to avoid static charge transfer from glass to the particle. The two water droplets fall freely in Nytro 10X oil and after  $t = 0.56$ s an electric 50Hz field of magnitude 280 V/mm is applied. The electric field is horizontally applied thus perpendicular to the direction of the droplets motion. A sinusoidal voltage with frequency 50Hz is used. Droplet interactions and coalescence are recorded with the Phantom V4 high speed CMOS camera.

Numerically, the governing equations (1) and (2) are solved with a Runge-Kutta Fehlberg 4-5 solver with step-size control.

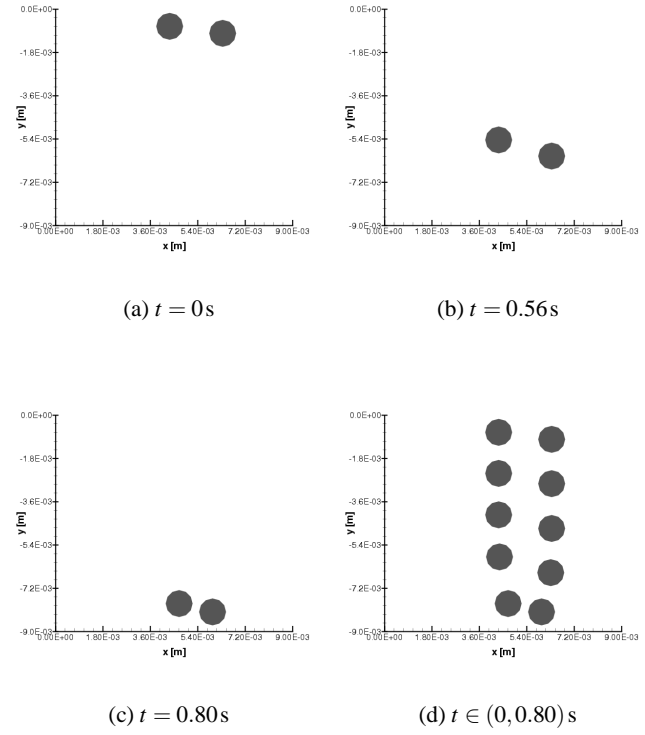


Figure 2: Visual prediction of the kinematic of two water droplets falling in a stagnant oil under the influence of an electric field. The models of Davis, LeVan, Vinogradova are employed.

Accurate simulations are ensured by using a relative tolerance of  $10^{-5}$  and an absolute tolerance of  $10^{-25}$ . The modeling framework outlined in [3] is used in the present work to predict the kinematics of two water droplets simultaneously released in oil. The radius of the smallest droplet placed on the left in the experiments is  $r_1 = 533\mu\text{m}$  and the radius of the biggest one is  $r_2 = 553\mu\text{m}$ . Uncertainty in measured droplet diameter is less than  $10\mu\text{m}$ . The position of the droplets is recorded with a high speed CMOS camera and it is digitally extracted from the sequential frames [3]. Fig. 1 shows a series of frames at different times. At time  $t = 0.0$ s, see Fig. 1 a) the droplets are released in the oil. The droplets fall down because of gravity and at time  $t = 0.56$ s an electric field perpendicular to the direction of the droplets motion is applied. Fig. 1 b) shows the droplets position at the instant when the field is applied. Fig. 1 c) shows the droplets position at time  $t = 0.80$ s, when the droplets are just about to coalesce. The electrical field induces charges on the water droplets and this causes adjacent droplets to align with the field and attract each other. Fig. 1 d) shows a sequence of frames taken at a time interval  $\Delta t = 0.20$ s where the effect of the electric field on the droplet kinematics is observable. The biggest droplet is observed to fall at a higher speed than the smallest one and therefore the angle between the center of the droplets and the normal to the droplets motion increases. This trend is reversed when a field normal to the droplet motion is applied and the droplets tend to align with the field. Fig. 2 shows a visual prediction of the kinematics of the two falling droplets when the Davis model is employed together with the models of LeVan, and Vinogradova as previously explained. The observed y-coordinates of the two droplets are here compared to the predictions obtained when using different models for the electric forces. Fig. 3 shows a comparison between the predicted and observed y-coordinate of the two droplets as a function of time. The Davis, the DID and the point dipole models are used to-



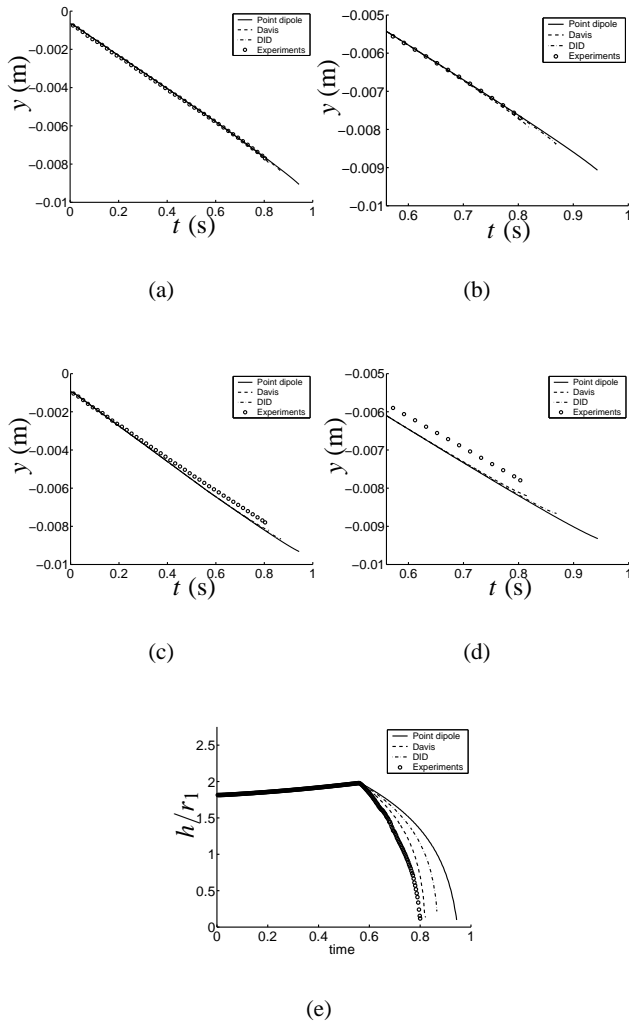


Figure 3: Observed and predicted vertical coordinate versus time of droplet 1 a), b) and of droplet 2 c), d). Different models for the electrical forces are adopted together with the models of LeVan, and Vinogradova.

gether with the models of LeVan, and Vinogradova to predict the time of coalescence and droplets kinematic of the droplets. The results obtained by the Davis model predict well the time of coalescence and the overall kinematic of the two droplets. The simulation obtained by the other two models overestimated the collision time. This result is coherent to the results presented by Chiesa et al. [3]. The point dipole model underestimates the effect of the electric forces on the kinematic of the droplets. In the numerical prediction, the biggest droplet is falling at a higher speed than the smallest one as observed in the experiment. The predicted fall of the smallest droplet up to time  $t = 0.56$  s agrees well with the experimental observations see Fig. 3a) and b). On the other hand the predicted fall of the biggest droplet is slightly overestimated, see Fig. 3c) and d). This is most probably due to the uncertainty related to the measured droplets size. There is not any reason to believe that the drag model needs to be reviewed in order to account for the vicinity of the other droplet. The drag force acting on the droplets is effected by the present of a second droplet in its vicinity when the droplets lye in the boundary layer of the neighboring one. In the present case, the boundary layer is very small due to the high viscosity of the oil in which the droplets are moving. The predicted and observed normalized distance  $h/r_1$  between the droplets centers as a function of time is plotted in Fig. 3e). The time to collision

predicted by means of the Davis equations well agrees with the coalescence time observed in the experiments.

## Observations

The motion of two fluid droplets simultaneously released in oil is predicted by means of the modeling framework proposed by Chiesa et al. [3]. The effect of internal circulation induced in the droplets is taken into account together with the variation of the surface tension of the droplets due to the electric field. The electric field is applied normally to the motion of the droplets after 0.56 s of free fall. The droplets tend to align with the field before they eventually coalesce with each other. This behavior is well predicted by the model proposed by LeVan Eq. (5) for the drag force, by Vinogradova Eq. (8) for the film-thinning force and the Davis' analytical expression. The use of different models to take into account the effect of electrical fields is also assessed. The 'time of coalescence' predicted by means of the Davis equations well agrees with the collision time observed in the experiments.

## References

- [1] J. S. Eow, M. Ghadiri, A. O. Sharif, and T. J. Williams. Electrostatic enhancement of coalescence of water droplets in oil: a review of current understanding. *Chem. Eng. J.*, 84:173–192, 2001.
- [2] P. Atten. Electrocoalescence of water droplets in an insulating liquid. *J. Electrostatics*, 30:259–270, 1993.
- [3] M. Chiesa, J. A. Melheim, A. Pedersen, S. Ingebrigtsen, and G. Berg. Forces acting on water droplets falling in oil under the influence of an electric field: numerical prediction versus experimental observations. *Submitted to European Journal of Mechanics*, 2004.
- [4] M. H. Davis. Two charged spherical conductors in a uniform electric field: forces and field strength. Rand. Corp. Memorandum RM-3860-PR, January 1964.
- [5] Y. L. Siu, T. K. Wan Jones, and K. W. Yu. Interparticle force in polydisperse electrorheological fluid: Beyond the dipole approximation. *Comput. Phys. Commun.*, 142:446–452, 2001.
- [6] D. J. Klingenberg, F. van Swol, and C. F. Zukoski. The small shear rate response of electrorheological suspensions. II. extensions betond the point-dipole limit. *J. Chem. Phys.*, 94(9):6170–6178, 1991.
- [7] J. Happel and H. Brenner. *Low Reynolds number hydrodynamics*. Martinus Nijhoff Publishers, The Hague, The Netherlands, 1983.
- [8] D. M. LeVan. Motion of droples with a Newtonian interface. *J. Colloid Interface Sci.*, 83(1):11–17, 1981.
- [9] O. I. Vinogradova. Drainage of a thin liquid film confined between hydrophobic surfaces. *Langmuir*, 11:2213–2220, 1995.
- [10] E. E. Michaelides. Hydrodynamic force and heat/mass transfer from particles, bubbles, and drops - the Freeman scholar lecture. *J. Fluids Eng. - Trans. ASME*, 125:209–238, March 2003.
- [11] K. W. Yu and T. K. Wan Jones. Interparticle forces in polydisperse electrorheological fluids. *Comput. Phys. Commun.*, 129:177–184, 2000.

## Electrocoalescence modeling: an engineering approach.

M. Chiesa<sup>1</sup>

<sup>1</sup>Dept. of Energy Processes, SINTEF Energy Research, Norway, matteo.chiesa@sintef.no

### Abstract

In a stagnant water-in-oil emulsion subjected to an external AC electrical field, charges induced on the water drops will cause adjacent drops to attract each other. Simulations and experimental observations are here compared. A discrete particle model of the emulsion is implemented and used to calculate the two-dimensional motion of the individual, spherical water drops directly from the forces acting on them. The hydrodynamic interaction between the drops and the interstitial oil phase is taken into account, together with the effect of the electrical field. In our model, coalescence is assumed to occur when two drops collide. Experiments have been performed to observe the behavior of water drops in oil exposed to a homogeneous electrical field. The optical observations are compared to the results obtained from the discrete particle model. Good agreement between the predicted and measured volumetric drop distribution is found for low water volume fractions.

### Introduction

The oil extracted from offshore reservoirs will normally contain a large and, during the reservoir lifetime, increasing percentage of water in the oil. When the water-oil mixture is passed through the pressure relief valve, an emulsion with a high percentage of small water drops is formed. Before the oil is pumped on-shore or into tankers, it is desirable to extract the water from this emulsion. Today the separation tanks are mainly built or operated as gravity separators with low flow rates and long residence times, lasting from minutes to tens of minutes. The residence time mainly depends on the sedimentation velocity of the smallest drops (e.g.,  $d < 100 \mu\text{m}$ ). Electrostatic fields are to some extent used to help smaller drops to coalesce into larger drops that sediment quicker. The sedimentation velocity increases proportionally to the square of the diameter of the drops. Frequently, investigations on electro-coalescence are done on emulsions focusing on bulk behavior. The understanding of the electrostatic mechanisms active in the electro-coalescence process is often quite superficial. Traditionally, electro-coalescers have utilized DC or pulsed DC fields and laminar liquid flow. However, recently, [1] showed that by applying a combined AC field and turbulence on the emulsion the coalescence rate is increased and the sedimentation time is significantly reduced. This effect on the coalescence is believed to be caused by the electric field around and between the drops. Polarization of the water drops is induced by the external electric field. The electrostatically induced field and forces increase when polarized water drops approach each other. Additionally, velocity fluctuations associated with the turbulent flow cause a high impact rate between drops.

One may model the electro-coalescence process by separating the coalescence efficiency that can be achieved when two drops come close to each other, and the collision rate between drops. One then needs to know how the magnitude, frequency and distribution of the electric field influence the coalescence efficiency and how turbulence and electric field forces influence the impact rate between drops. A numerical tool for the simulation of the electro-coalescence phenomena is implemented in the present work. The numerical simulator works as a design tool which gives research scientists and engineers the possibil-

ity of gaining an idea of the complex physics involved in the electro-coalescers.

The two-dimensional motion of each spherical drop can be directly calculated from the forces acting on it. The interaction between the drops and the interstitial oil phase as proposed by Michaelides [8], together with the effect of the electrical field on the kinematics of the drops as outlined by Davis [3], is taken into account. Our collision model is based on conservation laws for linear and angular momentum, and coalescence is assumed to occur when two drops collide. In the present paper, the numerical simulation tool is briefly presented and the validity of the model implemented for the calculation of electrical forces between drops is assessed. Numerical simulations of the electro-coalescence phenomena in a stagnant emulsion are performed and compared to experimental observations. Good agreement is observed between the predicted and measured volumetric drop distribution for water-in-oil emulsions with a water volume fraction below 2%.

### An analytical model for the electrical forces acting on the drops

When two water drops get close, the fields around the drops will mutually influence each other. Adding more drops will enhance this problem. Considering the difficulties due to these mutual influences one realizes that this approach is not feasible. A simplified model to calculate the electrical forces acting between the water drops is necessary to keep the problem easier to handle numerically. Lundgaard et al. [7] reviews a simplified analytical model for the electric force between two uncharged metallic spheres. The Laplace equation  $\nabla^2 \Phi = 0$  is solved in order to determine the resulting electric potential  $\Phi$  with which the field  $E$  is calculated from  $E = -\nabla \Phi$ . Davis [3] calculates the maximum electrical field on the sphere with radius  $r_2$  as:

$$E_{r_2}^{Max} = E_0 \cos \theta \cdot E_3 \quad (1)$$

where  $E_3$  is a function of the distance between the spheres normalized with the radius of the sphere itself.  $E_3(s/r_2)$  has a high value for small values of  $s/r_2$  see [3]. This means that the field of a drop with radius  $r_2$  is highly influenced by the presence of another drop in its vicinity. On the other hand, the electrical field is almost undisturbed by the presence of the drops when  $s/r_2 > 1$ . Let  $d$  be the distance between the drop centers:  $d = r_2 + r_1 + s$ . The components of the electrical force on the drop  $r_2$  see Davis [3], read:

$$F_r = 4\pi\epsilon_{oil}r_2^2E_0^2(f_1 \cos^2 \theta + f_2 \sin^2 \theta) \quad (2)$$

$$F_\theta = 4\pi\epsilon_{oil}r_2^2E_0^2f_3 \sin 2\theta \quad (3)$$

where  $f_{k=1,2,3}$  are expressed by a complicated series depending on the ratio  $s/r_2 \leq 1$ , see Lundgaard et al. [7]. One quickly realizes that even if the background field is low, the field and forces between adjacent drops from the induced polarization may become large. The electrical force becomes repulsive when the angle  $\theta \geq 54.7^\circ$ . Eq. (2)-(3) have a validity limited to a two-drop system, but in the present work they are used to calculate the electrical forces in a multi-drop system such as a water-in-oil emulsion with a low water content. This is considered to be

a satisfactory approximation as long as the water volume fraction in the emulsion is below 5%, ( $[H_2O] < 0.05$ ), see [2]. When going from a two drop model case to a multi drop case, one must be aware that the presence of the water drops in the emulsion between the electrodes will result in an increased stress in the oil. Generally, if one puts two dielectrics having different permittivities in series between two plane electrodes, the field in the higher permittivity dielectric will be reduced. The field in the lower permittivity dielectric will be enhanced compared to an average field magnitude  $|E| = V/d$  where  $V$  is the voltage and  $d$  the distance between the electrodes.

### The Discrete Element Method (DEM)

Consider  $n$  spherical drops that follow a trajectory given by:

$$m_i \frac{dv_i}{dt} = F_{i,flow} + F_{i,external} + F_{i,collisions} \quad (4)$$

$$\frac{dx_i}{dt} = v_i, \quad (5)$$

where  $i = 1, \dots, n$  and  $v_i$  are the velocities of the  $i$ th drop and where mass transfer has been neglected. Forces from the flow are drag forces, virtual mass forces etc, see for instance Michaelides [8]. Gravity is the typical external force. In the present study the dielectrophoretic forces between the drops due to an average electric field are also present, and have to be taken into account to describe the kinematics of the system of drops in a realistic way. Inter-drop and wall-drop forces are caused by collisions. The hard sphere model approach is used in the present work and a simplified version of the drop-wall collision model is used see [2]. A sequence of binary collisions needs to be handled, since collisions are assumed to happen instantaneously. The drop-drop collisions are considered in the present work to be ideally plastic, since coalescence is assumed to occur whenever two drops collide. The model used in the present work does not describe the complex physics of the coalescence phenomenon, however it is considered to be a satisfactory approximation for the present study. The velocity of the drop immediately after the collision is computed algebraically from the velocities of the drops immediately before the collision. Conservation of mass and momentum is fulfilled. A technique for sequencing multiple collisions within one basic time step is pointed out by Hoomans et al. [5] and is used in the present work. When the spherical drop moves in straight trajectories, the time until a collision between drop  $i$  and  $j$  occurs, is given by:

$$t_{ij} = \frac{-r_{ij} \cdot v_{ij} - \sqrt{(r_{ij} \cdot v_{ij})^2 - |v_{ij}|^2 (|r_{ij}|^2 - (r_i + r_j)^2)}}{|v_{ij}|^2}, \quad (6)$$

where  $r$  is the drop radius and

$$r_{ij} = x_i - x_j, \quad (7)$$

$$v_{ij} = v_i - v_j, \quad (8)$$

where  $x_i$  and  $v_j$  are the positions and velocities of the drops.

### Numerical solution procedure

The numerical solution follows the lines of Kuipers et al. [4]. The solution of the Navier-Stokes equations, require specification of the porosity  $\alpha$  and the drop  $x$ - and  $y$ - velocity components ( $v_x$  and  $v_y$ ) at the appropriate grid nodes. These values are obtained from the discrete particle model. For each particle, the indices  $i$  and  $j$  of the cell where its center of mass can be found, are stored. From this information  $\alpha(i, j)$  can be calculated based

on the area occupied by the particle cell  $i, j$ . Since the porosity is an important parameter which considerably influences the oil-phase motion, a detailed check for overlap is carried out in which multiple cell overlap is taken into account, see Hooman et al. [5]. In a computational cell, the porosity is defined as the ratio between the volume of the particles contained in the cell and the entire volume of the cell:

$$\alpha_g = 1 - \frac{2}{3} \frac{\sum A_p}{A_{cell}} \quad (9)$$

where  $A_p$  and  $A_{cell}$  are the drop volume and the cell volume respectively see Hooman et al. [5].

Firstly, the forces on the particles are recalculated, based on a recently updated velocity field. Events in this context are contact between two drops and contact between drop and wall. Based on the positions and velocities at the end of the previous time step, a new event queue is built. The events are handled, new events are detected, and the cell-particle list and the event queue are updated. The loop runs until no more events will happen during the actual time step.

The system of Eq. (4) is solved by a first order explicit Runge-Kutta (forward Euler) time discretization which reads:

$$y_{n+1} = y_n + dt y'_n, \quad y_0 = y(t_0), \quad (10)$$

where  $dt$  is the time step length and  $y$  is a general vector with the initial conditions  $y(t_0)$ . We desire to use a solver with better accuracy and stability properties than the forward Euler's method. The key point is the consistency between the calculations of the point of time a collision occurs and the movement of the particles. Therefore, the numerical scheme has to predict the positions linearly in  $dt$ , see Lubachevsky [6] and Sigurgeirsson [9]. During the time-step, only particles that are involved in a collision or a wall collision are moved. At the end of the time step, every particle is moved. Finally the volume fraction of particles is calculated.

### Experimental results

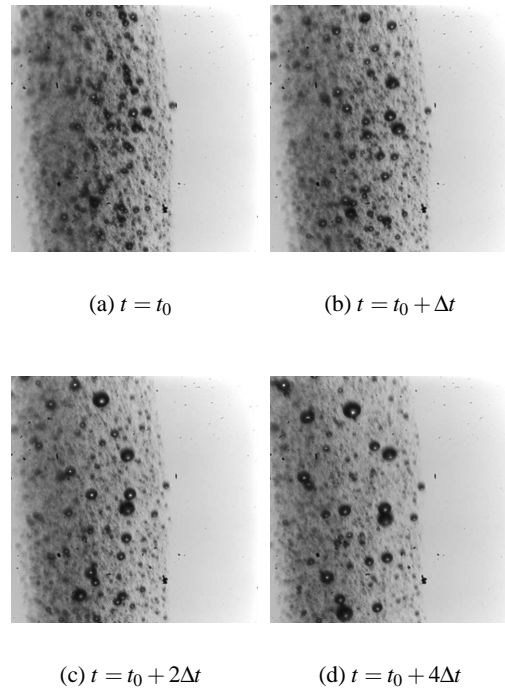


Figure 1: Water drop growth due to electro-coalescence.  $t = \sum_i (t_0 + i\Delta t)$  s with  $i = 0, 1, 2, 4$ .

Experiments are designed for visual observation of drops or water-in-oil emulsion exposed to electrical field, [7]. The electrode arrangement is placed inside a small test cell  $15 \times 15 \times 15 \text{ cm}^3$ . The test cell is mounted in a shadow-graphic setup using an optical bench. A water-in-oil emulsion where coalescence is achieved whenever the water drops collide is used in this experiment. The main goal with this experiment is to assess the effect of the electrical field on coalescence and in general on the kinematics of the water-in-oil emulsion. The emulsion is injected in a naphthenic oil under the effect of an electrical field  $E_0 \approx \pm 1.2 \times 10^5 \text{ V/m}$ . The density difference between the emulsion and the oil phase is small, and therefore the emulsion translates downwards slowly. This allows us to keep the camera focused at the same position during the whole experiment. A high-speed camera with a maximum frame rate

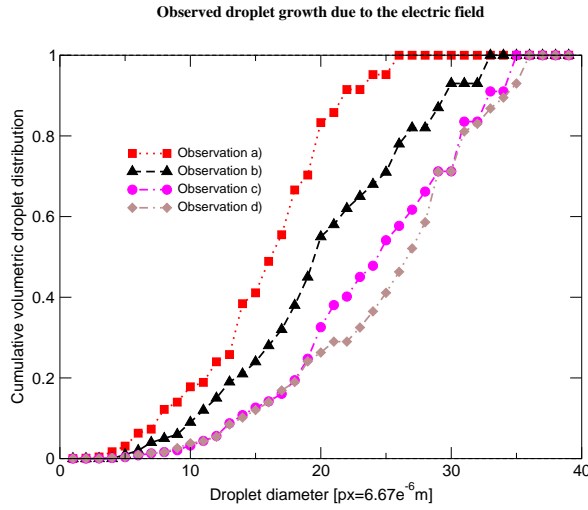


Figure 2: Cumulative volumetric drop distribution obtained from the photographs of Fig. 1

of 32000frames/sec is used to record the trajectory of the moving drops. The voltage source is a HV-amplifier (High Voltage) ( $\pm 20 \times 10^3 \text{ V}$ ,  $0 - 20 \times 10^3 \text{ Hz}$ ). A 50Hz sinusoidal voltage is used in these experiments. Fig. 1 shows four photographs of the emulsion taken at different times:  $t = \sum_i (t_0 + i\Delta t)s$  with  $i = 0, 1, 2, 4$ . The light grey zone in Fig. 1 represents the pure oil phase while the dark one is the emulsion injected in the pure oil phase. The black circles are the water drops. The size of the photographs is  $512 \times 512$  pixels. At the beginning, the water drops' average size is approximately  $20 \mu\text{m}$  while at time  $t = t_0 + 4\Delta t$  it has increased about 30%. The average drop size increases due to the effect of the electrical field acting on the emulsion.

Fig. 2 shows the cumulative volumetric drop distribution obtained from the photographs of Fig. 1. It is once again possible to observe how the water drops average size increases during the experiment.

### Numerical results

A numerical simulation of the water-in-oil emulsion is performed. First of all, a mesh independency study of the result is undertaken and a time step of  $10^{-6} \text{ s}$  is chosen. The experimental drop size distribution at time  $t = t_0$  is used at the beginning of the numerical simulation. A simplified model where the electrostatic, drag, Magnus, and gravitational forces are employed, is used in the present work.

Fig. 3 shows the numerical prediction of the water drop growth due to the effect of the electrical field acting on the emulsion. Fig. 3 resembles qualitatively what is observed in Fig. 1: the average drop size increases about 30%. The electro-coalescence phenomenon seems properly described by the simplified model

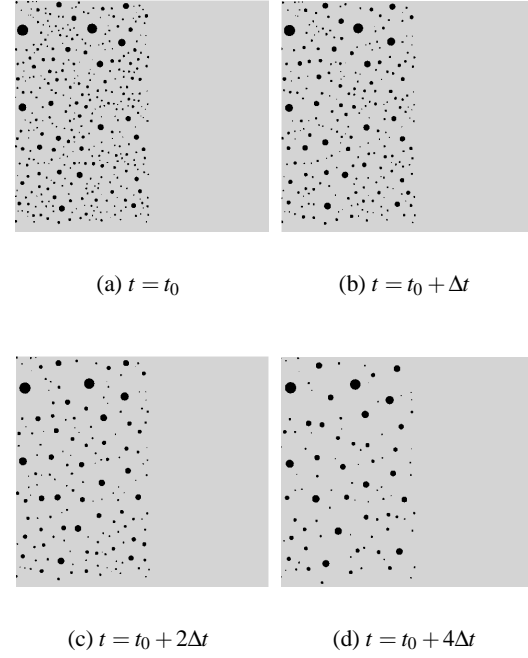


Figure 3: DEM prediction of the water drop growth due to electro-coalescence.

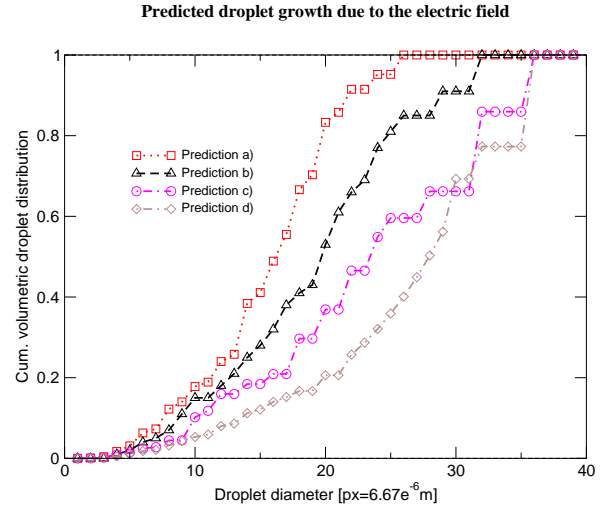
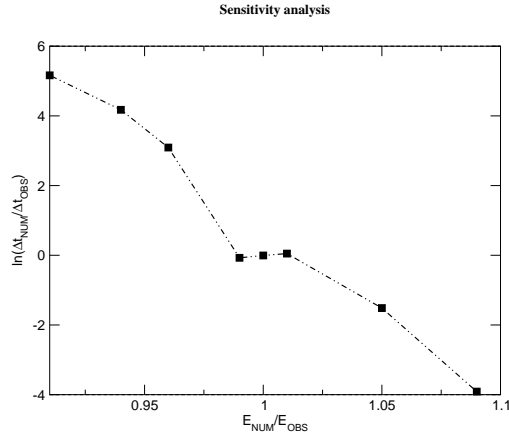


Figure 4: Cumulative volumetric drop distribution obtained from the numerical prediction of Fig. 3

used in the present work to quantify the magnitude of the electrical forces acting on the drops.

### Discussion

The numerical predictions obtained in the present work are strongly dependent on the magnitude of the electric field used in the calculation. Let  $\Delta t_{OBS}$  be the time interval between the observations (a) and (b) in Fig. 1 and  $\Delta t_{NUM}$  the time interval between the numerical predictions (a) and (b) in Fig. 3. Fig. 5 shows the dependency of the time interval ratio  $\Delta t_{NUM}/\Delta t_{OBS}$  on the magnitude of the electric field used in the numerical prediction. Let  $E_{OBS}$  be the measured electric field between the electrodes.  $E_{NUM}$  is the electric field used in the numerical calculation. The ratio  $E_{NUM}/E_{OBS}$  is varied between the interval  $[0.92 \ 1.08]$ . The electric forces due to the induced charges on the surface of the droplets play an important role on the behavior of the emulsion. A variation of the field magnitude of  $\pm 1\%$  does not affect significantly the time interval necessary



(a)

Figure 5: Dependency of the numerical predictions on the electric field magnitude used in the calculation.

to predict a droplet distribution similar to the one observed in the experiment. An overestimation of the electric field of 5% accelerate strongly the coalescence process and the time interval necessary to predict a droplet distribution similar to the one observed in the experiment is strongly reduced. An underestimation of the electric field has the opposite effect and the time interval necessary to experience a droplet distribution similar to the one observed in the experiment is strongly increased.

In Fig. 6, the cumulative volumetric drop distribution obtained from the experimental observation and from the numerical analysis are compared. Good agreement is observed. The electric field used in the numerical prediction is  $E_{NUM} = E_{OBS}$  and  $\Delta t_{NUM} \approx \Delta t_{OBS}$ .

The way the electrical forces acting on the drops are calculated in the present work has a limited validity. The good agreement observed indicates that the analytical model for the calculation of the electrical forces gives satisfactory results in the special case of stagnant emulsion considered in the present study. This agreement can be explained by the fact that the water volume fraction in the considered emulsion is below 2% and therefore the probability of finding more than one drop within twice the radius of the smallest drops is relatively low. In the present work, the initial fluid field is at rest. The movement of the drops due to the electrical forces acting on them is given by the drag and the gravitational force. The fluid starts moving because of the drop movement due to the interface momentum transfer term. The magnitude of the velocity field always remains insignificant and the flow regime is laminar.

## References

- [1] Atten, J. Electrocoalescence of water drops in an insulating liquid. *Journal of Electrostatics*, **30** pp. 258-370, 1993
- [2] Chiesa, M., Norheim, S., Pedersen, A and Lundgaard, L. Predicted and measured drop coalescence in an electrostatic field: an engineering approach Submitted to *International Journal of Engineering science*.
- [3] Davis, M. H. Two Charged Spherical Conductors in a Uniform Electric Field: Forces and Field Strength. *RM-3860-PR*, Rand Corporation, 1964

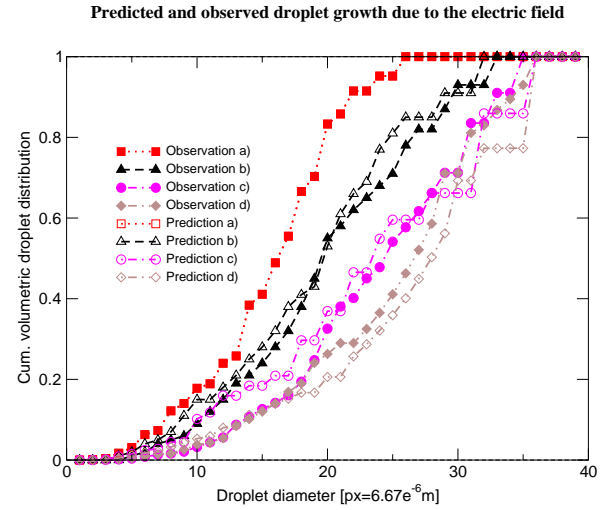


Figure 6: Comparison of the cumulative volumetric drop distribution obtained from the experimental observation and from the numerical analysis.

- [4] Kuipers, J. A. M., van Duin, K. J., van Beckum, F. P. H. and Van Swaaij, W. P. M. A numerical model of gas-fluidized beds. *Chemical Engineering Science*, **47**, 1913
- [5] Hoomans, B. P. B., Kuipers, J. A. M., Briels, W. J. and van Swaaij, W. P. M. Discrete particle simulation of bubble and slug formation in a two-dimensional gas-fluidised bed: A hard-sphere approach. *Chemical Engineering Science*, **51**(1):99–118, 1996.
- [6] Lubachevsky, B. D. How to Simulate Billiards and Similar Systems. *J. Comput. Physics*, **94** pp. 255, 1991
- [7] Lundgaard, L., Berg, G., Pedersen, A. and Nilsen, P. J. Electrocoalescence of water drop pairs in oil. *Proc. IEEE 14th International Conference on Dielectric Liquids* Graz, Austria, 2002
- [8] Michaelides, E. E. Hydrodynamic Force and Heat/Mass Transfer From Particles, Bubbles, and Drops - The Freeman Scholar Lecture *J. Fluids Eng. - Trans. ASME*, **125** pp.209-238, 2003
- [9] Sigurgeirson, H., Stuart, A. C. and Wan, W. L. Collision Detection for Particles in a Flow. *J Comput. Physics*, **172** pp. 766-807, 2001

## Partially-reflecting characteristic-based boundary conditions

R. Olsen<sup>1</sup>, I. R. Gran<sup>2</sup>

<sup>1</sup>Dept. of Energy and Process Engineering, NTNU, Norway, Robert.Olsen@sintef.no

<sup>2</sup>Dept. of Energy Processes, SINTEF Energy Research, Norway, Inge.R.Gran@sintef.no

### Abstract

In characteristic-based boundary formulations, reflecting boundary conditions are used where non-reflecting boundary conditions are not applicable. Physical boundary conditions are set through the incoming wave amplitudes. This work propose to estimate the incoming wave amplitudes with control functions. The method which previous works have used, is identified as P-controllers. This study examines P- and PI-controllers for Poiseuille flow. A new test, which assesses the quality of the boundary conditions, is used to evaluate the boundary conditions. Results are found to improve significantly when a numerical filter is applied.

### Introduction

Thompson [1, 2] presents a characteristic based way of developing boundary conditions for the Euler equations. This method is straightforward to implement, and to extend to other types of flow. Poinot and Lele [3] have developed this method further for direct numerical simulations of compressible flow, and Baum *et al.* [4] extend this to reactive multicomponent flow. Okong'o and Bellan [5] extend the method to real gas mixtures.

The key idea for characteristic-based boundary conditions (CBC) is to identify outgoing and incoming waves and then set the correct boundary conditions in terms of them. To ensure well posed and well behaved solutions, waves emerging from the computational domain must be calculated from the domain and not be specified. The CBC method is only strictly valid for hyperbolic systems, like the Euler equations. However, [3] use results from well-posedness analyses, extend CBC to the Navier-Stokes equations, and hence call it NSCBC (Navier-Stokes Characteristic Boundary Conditions). Characteristic-based boundary conditions have evolved to become an attractive way of solving the boundary problem, and have been used in a number of studies today.

### Characteristic-based boundary conditions

A general system in three dimensions is treated as locally one-dimensional, where the normal direction to the boundary is denoted by  $x_1$ . Terms from the other directions are passive in the analysis, meaning that the main effects of the flow are along the normal direction. To perform the analysis we need the primitive form of the equation system:

$$\frac{\partial U}{\partial t} + A \frac{\partial U}{\partial x_1} + C = 0. \quad (1)$$

Assume that  $A$  is diagonalizable, then a diagonal matrix,  $\Lambda$ , with the eigenvalues  $\lambda_i$  of  $A$  along the diagonal, can be obtained by the similarity transformation,

$$S^{-1}AS = \Lambda, \quad (2)$$

where  $\Lambda_{ij} = 0$  for  $i \neq j$  and  $\Lambda_{ij} = \lambda_i$  for  $i = j$ . The columns of the matrix  $S$  are the right eigenvectors,  $r_j$ , and the rows of the inverse matrix,  $S^{-1}$ , are the left eigenvectors,  $l_i^T$  of  $A$ . Multiply

Eq. (1) with  $S^{-1}$ ,

$$S^{-1} \frac{\partial U}{\partial t} + S^{-1}A \frac{\partial U}{\partial x_1} + S^{-1}C = 0, \quad (3)$$

and define  $\mathcal{L}$  as,

$$\mathcal{L} \equiv \Lambda S^{-1} \frac{\partial U}{\partial x_1} \equiv S^{-1}A \frac{\partial U}{\partial x_1}, \quad (4)$$

This gives the primitive form of the *Time-dependent boundary conditions*:

$$\frac{\partial U}{\partial t} + S\mathcal{L} + C = 0. \quad (5)$$

If the system was linearly hyperbolic with  $C = 0$  and  $A$  independent of  $U$ , then the change of variables to  $W = S^{-1}U$ , would give a set of wave equations,

$$\frac{\partial w_i}{\partial t} + \lambda_i \frac{\partial w_i}{\partial x} = 0, \quad (6)$$

with characteristic velocities  $\lambda_i$ . When  $\lambda_i > 0$ , the waves will propagate in the positive  $x$ -direction. It is then obvious that  $w_i$  cannot be specified at the right boundary, and that  $w_i$  must be specified at the left boundary. For a quasi-linear system like the Euler equations, it is not so simple anymore. However, it turns out that  $\lambda_i$  is the velocity and  $\mathcal{L}_i$  is the amplitude of the different waves and  $\mathcal{L}_i$  is the proper variable to specify at the boundary [1]. For outgoing<sup>a</sup> waves the  $\mathcal{L}_i$  are calculated from its definition, Eq. (4). Therefore write the outgoing  $\mathcal{L}_i$  as  $\mathcal{L}_i^+$  and incoming as  $\mathcal{L}_i^-$ . The eigenvector matrix  $S$  is also split into  $S^+$  and  $S^-$ , where  $S^+$  contains eigenvectors with positive eigenvalues. Eq. (5) now reads:

$$\frac{\partial U}{\partial t} + S^+ \mathcal{L}^+ + S^- \mathcal{L}^- + C = 0. \quad (7)$$

Since  $\mathcal{L}^-$  represents incoming waves, this is the only variable left to link the surroundings with the domain. Hence, all boundary conditions must be set through  $\mathcal{L}^-$ . The task is then to find equations for the unknown  $\mathcal{L}^-$  which represents different boundary conditions.

### Typical boundary conditions for the generalised system

If the time-derivative of a given quantity, like for instance the velocity, is to be specified, an equation for  $\mathcal{L}_i^-$  may be found from Eq. (7),

$$S_i^- \mathcal{L}^- = - \left( \frac{\partial U_i}{\partial t} + S_i^+ \mathcal{L}^+ + C_i \right). \quad (8)$$

For a wall at rest the proper boundary condition would be to set the velocity equal to zero at the wall and find the  $\mathcal{L}_i^-$  which gives  $\partial u / \partial t = 0$ . Non-reflecting boundary conditions may be achieved by setting the amplitude of the incoming wave to zero, i.e.  $\mathcal{L}_i^- = 0$ . This may, however, in some cases lead to drifting

<sup>a</sup>outgoing means that  $\lambda_i > 0$  at  $x = x_{\max}$  and  $\lambda_i < 0$  at  $x = x_{\min}$ .

values of the variable at the boundary and hence in the whole field. A way to overcome drifting values is to specify  $\partial U_i/\partial t$  using a PID controller (three-mode controller):

$$S_i^- \mathcal{L}^- = (S_i^- \mathcal{L}^-)^\circ + \frac{K_P}{T} \Delta U_i + \frac{K_I}{T^2} \int_0^t \Delta U_i d\tau + K_D \frac{\partial U_i}{\partial t}, \quad (9)$$

where  $\Delta U_i = (U_i - U_i^\infty)$ ,  $T$  is the integral time,  $K_P$  is the proportional gain,  $K_I$  is the integral gain,  $K_D$  is the derivative gain and a start term for the controller  $(S_i^- \mathcal{L}^-)^\circ$ . The start term can be based on an analytical solution, a previous simulation or simply set to zero. Inserting  $\partial U_i/\partial t$  from Eq. (7) gives:

$$S_i^- \mathcal{L}^- = \text{PID}(U_i) \equiv \frac{1}{(1 + K_D)} \cdot \left( (S_i^- \mathcal{L}^-)^\circ + \frac{K_P}{T} \Delta U_i + \frac{K_I}{T^2} \int_0^t \Delta U_i d\tau - K_D (S_i^+ \mathcal{L}^+ + C_i) \right). \quad (10)$$

The reasoning behind this method is presented in [6]. Now, the discussion continues with the Euler and the Navier-Stokes equations.

### Single-phase Euler equations

The Euler equations in one-dimension reads:

$$\frac{\partial}{\partial t}(\rho) + \frac{\partial}{\partial x}(\rho u) = 0, \quad (11)$$

$$\frac{\partial}{\partial t}(\rho u) + \frac{\partial}{\partial x}(\rho u^2 + p) = 0, \quad (12)$$

and the equation of state

$$p = \rho c^2, \quad (13)$$

where  $c$  is the speed of sound.

### Boundary matrices for the Euler equations

In this section, the boundary matrices for the Euler equations in one dimension, also referred to as the LODI (locally one-dimensional inviscid) relations are presented. The system vector, matrix and the eigenvalue matrix are

$$U = \begin{bmatrix} p \\ u \end{bmatrix}, \quad A = \begin{bmatrix} u & \rho c^2 \\ 1/\rho & u \end{bmatrix}, \quad \Lambda = \begin{bmatrix} u - c & 0 \\ 0 & u + c \end{bmatrix}. \quad (14)$$

The eigenvector matrix and the inverse

$$S = 1/2 \begin{bmatrix} 1 & 1 \\ -1/(\rho c) & 1/(\rho c) \end{bmatrix}, \quad S^{-1} = \begin{bmatrix} 1 & -\rho c \\ 1 & \rho c \end{bmatrix}. \quad (15)$$

When subsonic flow ( $|u| < c$ ) is assumed, the eigenvector matrix at the upper boundary, ( $x = x_{\max}$ ), is split into:

$$S^+ = 1/2 \begin{bmatrix} 1 \\ 1/(\rho c) \end{bmatrix}, \quad \text{and} \quad S^- = 1/2 \begin{bmatrix} 1 \\ -1/(\rho c) \end{bmatrix}. \quad (16)$$

We can also find  $\mathcal{L}^+$ ,

$$\mathcal{L}^+ = \mathcal{L}_2 = (u + c) \left( \frac{\partial p}{\partial x} + \rho c \frac{\partial u}{\partial x} \right). \quad (17)$$

### Non-reflecting boundary conditions

Eq. (5) now becomes:

$$\frac{\partial p}{\partial t} + \frac{1}{2}(\mathcal{L}_2 + \mathcal{L}_1) = 0, \quad (18)$$

and

$$\frac{\partial u}{\partial t} + \frac{1}{2\rho c}(\mathcal{L}_2 - \mathcal{L}_1) = 0. \quad (19)$$

$\mathcal{L}_2$  may be eliminated from the equations if we rewrite Eq. (19)

$$\mathcal{L}_2 = \mathcal{L}_1 - 2\rho c \frac{\partial u}{\partial t}, \quad (20)$$

and insert this in the pressure Eq. (18),

$$\frac{\partial p}{\partial t} - \rho c \frac{\partial u}{\partial t} + \mathcal{L}_1 = 0. \quad (21)$$

By setting  $\mathcal{L}_1 = 0$ , the non-reflecting boundary condition used by Rudy and Strikwerda [7] is found, see also the footnote on page 111 of Poinso and Lele [3].

It is known that specifying  $\mathcal{L}_1 = 0$  may lead to a drifting pressure, and by studying Eq. (18) and Eq. (19) it is easy to realize why it happens. First note that a steady solution is only possible when  $\mathcal{L}_2 = 0$ , or  $\partial p/\partial x = -\rho c \partial u/\partial x$ . When using the Euler equations in 1D it is often the case that  $\partial p/\partial x = \partial u/\partial x = 0$  in the steady solution and hence no drifting pressure will occur. A way to represent 2D viscous effects in a 1D-simulation is to use friction factors. By adding a wall friction term  $f|u|u$  to Eq. (19), Eq. (21) now becomes:

$$\frac{\partial p}{\partial t} - \rho c \frac{\partial u}{\partial t} + \mathcal{L}_1 = \rho c f|u|u. \quad (22)$$

When  $\mathcal{L}_1 = 0$  and  $\partial u/\partial t = 0$  is specified at the other boundary,  $\partial u/\partial t \rightarrow 0$  at this boundary as well. Eq. (22) is reduced to:

$$\frac{\partial p}{\partial t} = \rho c f|u|u. \quad (23)$$

It is now clear that the pressure will drift unless the velocity equals zero.

### Partially reflecting boundary conditions

A way to overcome the problem of drifting pressure was proposed by [7]:

$$\frac{\partial p}{\partial t} - \rho c \frac{\partial u}{\partial t} + k(p - p_\infty) = 0, \quad (24)$$

where  $p_\infty$  is the pressure at some reference state located at infinity. [8] studied the behaviour of a linearised Navier-Stokes system and claimed that the coefficient  $k$  should be of the form  $k = \sigma(1 - \mathcal{M}^2)c/L$ .  $\mathcal{M}$  is the maximum Mach number in the flow,  $L$  is a characteristic size of the domain, and  $\sigma$  is a constant. They derived an optimal value for  $\sigma$  around 0.27, but their tests showed that a value of 0.58 provides better results. [3] compared Eq. (24) and several other methods, they arrived at setting  $\mathcal{L}_1 = k(p - p_\infty)$  with  $\sigma=0.25$  and using this in all equations at the boundary. They also suggested that the method might perform better if an analytical expression for  $\mathcal{L}_1$  were available, then the expression for  $\mathcal{L}_1$  becomes:

$$\mathcal{L}_1 = \mathcal{L}_1^{\text{exact}} + k(p - p_\infty). \quad (25)$$

If we consider the procedure of modifying Eq. (24) in terms of control engineering, the methods of the previous section are recognised as controllers. Specifically, the methods used by [7] and [3] are recognised as P-controllers for  $\partial p/\partial t$ .

It is known from control engineering that a PID-controller performs better than a P-controller. With  $\Delta p = (p - p_\infty)$ , a PID-controller for  $\partial p/\partial t$  may be written as:

$$\mathcal{L}_1 = \frac{1}{1 + K_D} \left( \mathcal{L}_1^\circ + \frac{K_P}{T} \Delta p + \frac{K_I}{T^2} \int_0^t \Delta p d\tau - \frac{K_D}{2} \mathcal{L}_2 \right). \quad (26)$$



The P-controller of [3], Eq. (25), is found if we set  $\mathcal{L}_1^\circ = \mathcal{L}_1^{\text{exact}}$ ,  $K_P = kT$  and  $K_I = K_D = 0$ . [9] used the same approach as [3], at the inlet in addition to the outlet, i.e. by specifying  $\mathcal{L}_i^-$  on the form,

$$\mathcal{L}_i^- = K_{\text{in}}(u - u^\infty) + K_{\text{in}}(v - v^\infty). \quad (27)$$

Thus it makes sense to use a PID-controller at the inlet as well.

### Numerical methods

For the time integration, the five-stage, fourth order, explicit Runge-Kutta scheme of [10] is chosen, mainly because it is nearly as effective as the standard RK-schemes while only needing two storage registers for each equation.

### Finite differences (RKFD)

Eq. (1) is discretised in all points by replacing  $\partial/\partial x$  by finite difference operators. After each time step, the solution vector  $U$  is filtered by a filter function,

$$\tilde{U} = (1 + \zeta_D D_f)U, \quad (28)$$

where the filter coefficient  $\zeta_D$  is given by  $(-1)^{n+1}2^{-2n}$  for a  $(2n)$ th-order filter, and  $D_f$  is the dissipation matrix. Special care must be taken when  $\partial U_i/\partial t$  is given on the boundary or estimated by a P-controller. The easiest solution is to not filter the boundary point for  $U_i$ . When a PID-controller is used at the boundary, there is no need for special care since the controller makes sure that the solution slowly converges to the specified value.

A more thorough discussion of explicit filters and high-order finite difference operators can be found in Kennedy and Carpenter [11].

### Single-phase poiseuille flow

In order to check the implementation and to compare the different controlling methods, the plane channel of [3] is chosen.

### Problem description

A viscous fluid, with kinematic viscosity  $\nu = 2\text{ m}^2/\text{s}$  and speed of sound  $c = 300\text{ m/s}$ , flowing in a 2D plane channel, with length  $L = 10\text{ m}$  and half-height  $h = 1\text{ m}$ , is studied here.

The inflow conditions are:

$$u(0, y, t) = u_0 \left[ \cos\left(\frac{\pi y}{2h}\right) \right]^2, \quad (29)$$

$$v(0, y, t) = 0, \quad (30)$$

where  $u_0 = 30\text{ m/s}$  is the maximum inlet velocity. The Reynolds number is  $Re = u_0 h / \nu = 15$  and the Mach number is  $\mathcal{M} = u_0 / c = 0.1$ . An analytical solution may be found if this case is considered to be incompressible. A criterion for this is:

$$\frac{L}{h} \frac{\mathcal{M}^2}{Re} \ll 1. \quad (31)$$

For this computation,  $L/h Re^{-1} \mathcal{M}^2 = 0.007$  and the incompressible solution may be considered to be close to the exact one. The exact solution is:

$$\frac{\partial p^e}{\partial x} = -\frac{3}{2} Re^{-1} \rho u_0^2, \quad (32)$$

where

$$u(x, y, t) = u_m (1 - (y/h)^2), \quad (33)$$

and  $u_m$  is the maximum velocity:  $u_m = -\frac{1}{2\mu} \frac{\partial p^e}{\partial x} h^2$ . Initial values for the calculations are:

$$\begin{aligned} u(x, y, 0) &= u_0 \left[ \cos\left(\frac{\pi y}{2h}\right) \right]^2, \\ v(x, y, 0) &= 0, \\ \rho(x, y, 0) &= \rho_{\text{in}} = 1\text{ kg/m}^3. \end{aligned} \quad (34)$$

At the inlet, the velocity is specified and the unknown  $\mathcal{L}_i$  are found from the LODI relations, (Sec. ). At the outlet, the pressure is specified with a controller for  $\partial p/\partial t$ . For simplicity, the discussion is restricted to P- ( $K_I = K_D = 0$ ) and PI-controllers ( $K_D = 0$  in Eq. (26)):

$$\mathcal{L}_1 = \mathcal{L}_1^\circ + K_P \Delta p + \frac{K_I}{T} \int_0^t \Delta p d\tau, \quad (35)$$

$$\mathcal{L}_1^\circ = (u - c) \left( \frac{\partial p^e}{\partial x} - \rho c \frac{\partial u^e}{\partial x} \right), \quad (36)$$

where  $\partial u/\partial x^e$  is found from continuity of the exact solution. For the proportional term we take  $K_P = \sigma(1 - \mathcal{M}^2)c/L$  and the integral term is  $K_I = K_P$ .

### About the computations

The Navier-Stokes equations were discretised in the same manner at the boundary as in the inner domain. The domain was discretised with an equidistant  $21 \times 21$  grid and the spatial discretisations were obtained with an eight-order first-derivative operator. For the viscous terms, the first-derivative operator was applied twice. The solution was filtered after each time step with an eight-order explicit filter. The steady-solution found agrees with [3].

### Evaluation of the boundary conditions

In order to find out how good the boundary conditions are, they should be tested where something can be stated about their performance. Therefore a new test for the boundary conditions is presented.

In Fig. 1 three Channels A, B and C are shown, for clarity the figure is not drawn dimensionally correct. The length of Channel C in Fig. 1 is twice that of Channel A and Channel B. With this configuration, the obtained solution in Channel A can be compared with the solution in the first part of Channel C, and logically the solution obtained in Channel B can be compared with the solution in the second part of Channel C.

This test can be done since the PI-controllers have the ability to specify the pressure to any degree of accuracy. Note that to perform this test with a P-controller would be cumbersome, since it would require an iteration procedure to specify the pressure to a high degree of accuracy.

This approach will give an idea of the performance of the boundary conditions, furthermore it is even possible to extract approximate values of  $\mathcal{L}_i$  at  $x = L$  from Channel C and compare them with the values for Channel A and B. Here, however, the discussion is restricted to comparing the converged solution for the three cases.

**Boundary conditions for Channel C:** The same channel as earlier in this section is calculated, but now with length  $2L$ . The boundary conditions are the same as before, specifying the outlet pressure  $p_\infty$  with a PI-controller and setting the inlet velocity.

**Boundary conditions for Channel A:** To compute the first part of the channel, the same boundary conditions as for Channel C



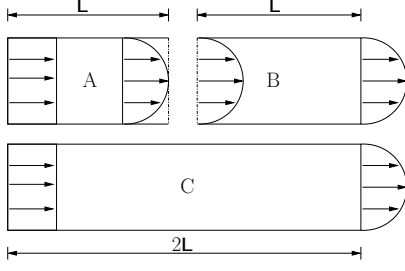


Figure 1: Test case for evaluating the boundary conditions.

were used, except that the pressure  $p_L = p_{x=L}$  obtained at  $x = L$  from Channel C was specified instead of  $p_\infty$ .

**Boundary conditions for Channel B:** A natural choice would be to specify boundary conditions for Channel B as for Channel A and Channel C. That is by reading the velocity profile at  $x = L$  in Channel C, and specify this at the inlet. However, this way of specifying boundary conditions is already tested for Channel A. Since the flow in Channel B is fully developed, boundary conditions for fully developed flow can be tested instead.

For the second part of the channel, a PI-controller was applied for the pressure at both the inlet and outlet, i.e. specifying  $p_L$  at the inlet and  $p_\infty$  at the outlet. According to theory, one more boundary condition must be specified at the inlet, so a P-controller for the  $v$ -velocity was used.

This problem was computed with the RKFD approach and gave excellent results. In order to compare and quantify the error, the relative difference between the simulations has been calculated. The relative error is defined by:

$$e(f) = \left| \frac{f_{2L} - f_L}{f_{2L}} \right|, \quad (37)$$

where  $f_{2L}$  is evaluated in Channel C.  $f_L$  is evaluated in Channel A when  $0 \leq x \leq L$  and in Channel B when  $L \leq x \leq 2L$ . The error is computed in all points, except where  $f_{2L}$  is zero. To simplify the comparisons, it makes sense to use the maximum of  $e(f)$  as a measure of performance.

In Tab. 1, Channel A and C are compared for three computations. The first column tells which variable is compared, and the second column at which point the comparison is done. For instance (mx,2) is at the maximum in  $x$ -direction and point 2 in the  $y$ -direction. In the next column, the label 2x-8f means that the spatial derivative operator is second-order, and the filter is eight-order.

The first to be read from the table is that the error goes significantly down when filtering is applied, and slightly down when the order of the spatial operator is increased. Second, when the error in the  $u$ -velocity is as low as  $1 \cdot 10^{-5}$  it is for most practical purposes zero. It is then reasonable to conclude that a filter should be applied when available. This is confirmed when the grid resolution is increased, since then the computations were unstable when filtering was not applied.

When comparing Channel B and C, similar results as when comparing Channel A and C are obtained.

### Concluding remarks

Characteristic based boundary conditions have been reviewed for single-phase flow. The method of avoiding a drifting pressure has been analysed, and this method turns out to be the implementation of a control function for estimating the incoming wave amplitude.

Table 1: Comparison of Channel A and C for the RKFD computations

$e(f)$	$(i, j)$	2x-NO	2x-8f	8x-8f
$u$	(mx,2)	0.0031	$9.6 \cdot 10^{-5}$	$6.45 \cdot 10^{-5}$
$u$	(2,2)	0.0013	$1.8 \cdot 10^{-5}$	$1 \cdot 10^{-5}$
$p$	any	$12 \cdot 10^{-7}$	$4.3 \cdot 10^{-7}$	$9 \cdot 10^{-8}$

The hypothesis of the use of control functions has been tested for single-phase, and been verified.

Particularly P- and PI-controllers have been tested with different arrangements. When the start term for the controller was zero, the P-controller gave the best convergence. However, it was not able to specify the imposed value. The PI-controller made it possible to specify a given value. Based on this the PI-controller was preferred. The case when the PI-controller have been used to set the inlet as well as the outlet had better performance in the tests, except on convergence. The case where the inlet values are set directly had almost as good results as the others. Therefore, setting the inlet values directly may in some cases be the best choice.

This work has been sponsored by the Research Council of Norway. \*

### References

- [1] Thompson K.W. Time-dependent boundary conditions for hyperbolic systems. *Journal of Computational Physics* 68 (1) (1987) 1–24.
- [2] Thompson K.W. Time-dependent boundary conditions for hyperbolic systems. II. *Journal of Computational Physics* 89 (2) (1990) 439–461.
- [3] Poinso T.J., Lele S.K. Boundary conditions for direct simulations of compressible viscous flows. *Journal of Computational Physics* 101 (1992) 104–129.
- [4] Baum M., Poinso T., Thévenin D. Accurate boundary conditions for multicomponent reactive flows. *Journal of Computational Physics* 116 (1994) 247–261.
- [5] Okong'o N., Bellan J. Consistent boundary conditions for multicomponent real gas mixtures based on characteristic waves. *Journal of Computational Physics* 176 (2002) 330–344.
- [6] Olsen R., Gran I.R. Estimation of incoming wave amplitudes for characteristic-based boundary conditions. Submitted to *Journal of Computational Physics*.
- [7] Rudy D.H., Strikwerda J.C. A nonreflecting outflow boundary condition for subsonic Navier-Stokes calculations. *Journal of Computational Physics* 36 (1980) 55–70.
- [8] Rudy D.H., Strikwerda J.C. Boundary conditions for subsonic compressible Navier-Stokes calculations. *Computers & Fluids* 9 (1981) 327–338.
- [9] Kim J.W., Lee D.J. Generalized characteristic boundary conditions for computational aeroacoustics. *AIAA Journal* 38 (11) (2000) 2040–2049.
- [10] Carpenter M., Kennedy C. Fourth-order 2n-storage runge-kutta schemes. Tech. Rep. NASA TM-109112, Langley Research Center, Hampton, VA, 1994.
- [11] Kennedy C.A., Carpenter M.H. Several new numerical methods for compressible shear-layer simulations. *Applied Numerical Mathematics* 14 (1994) 397–433.

## Feasibility Study Using Computational Fluid Dynamics for the Use of a Turbine for Extracting Energy from the Tide

D.A. Egarr<sup>1</sup>, T. O'Doherty<sup>1</sup>, S. Morris<sup>1</sup> and R.G. Ayre<sup>2</sup>

<sup>1</sup>Cardiff University, Queen's Buildings, The Parade,  
PO Box 925, Cardiff, CF24 0YF, Wales, UK

<sup>2</sup>Tidal Hydraulic Generators Ltd, 7 Dolan Court, Broad Haven,  
Haverford West, Pembrokeshire, SA62 3JN, Wales, UK

### Abstract

A 4 blade tidal turbine has been modelled using computational fluid dynamics and validated against experimental data prior to modelling a 3 blade turbine. This is the first stage in the process of optimising a turbine to extract energy from the tide. The 3 blade turbine has been modelled in a number of tidal flows between 0.51 and 3.09m/s (1 and 6 knots) and the power predictions studied as well as the magnitude of the force on the turbine. The redevelopment of the flow downstream from the turbine has also been studied.

### Introduction

The Kyoto agreement of 1997 was that each country that acceded the agreement will reduce or limit its greenhouse gas emissions by an amount agreed, such that the overall emissions of such gases is reduced by at least 5% compared to 1990 levels in the commitment period 2008 to 2012 [6]. It should be noted that the protocol acknowledges developing countries and in some cases, allows particular countries, such as Australia and Iceland to increase their emissions. For those that have to reduce emissions, alternative sources to fossil fuels are required for producing electricity. The British government currently has no plans for development of further nuclear power plants [4]. This leaves renewable sources of energy as a viable option to reduce greenhouse gases. The British government has 'confirmed a timetable up to 2015 when 15.4% of electricity generated in the UK is from renewable sources' [5]. One of the most popular renewable sources is wind energy, whereby a single turbine with 66m diameter rotor blades is capable of producing 1.5MW.

Another source of renewable energy is that harnessed from the sea. Recently, interest has focussed on capturing the energy in the tides. The gravitational force of attraction of the moon and sun on the earth and the rotation of the earth results in a rhythmic rise and fall of ocean levels relative to the coastline [1]. Thus, unlike wind and solar energy, tidal currents are predictable. In addition to this advantage the available power flux from the tide is around 500W/m<sup>2</sup> compared to 40W/m<sup>2</sup> for air. This is based on the density of water being some 815 times that of air and the tidal velocity of the order of 25% that of air. There is a large quantity of literature on the methods that can be utilised for extracting energy from the tides but the use of turbines in tidal streams, due to the advances in technology, is only now becoming reality with the world's first full scale offshore tidal turbine being constructed in 2003 [2].

This paper looks to assess the feasibility of energy generation from the tide, using the Computational Fluid Dynamic (CFD) package FLUENT. Initial models are validated against full scale experimental trials of a 4 blade turbine. Modelling of a 3 blade turbine has also been undertaken.

### Experimental trials

Tidal Hydraulic Generators Ltd. (THGL) undertook the experimental trials in 2002 on the Cleddau River near Milford

Haven in Pembrokeshire, UK, using a four blade, 5.5m diameter turbine. These trials were reported to be the first large scale tests to be undertaken on a river in the UK. The blades were constructed from Glass Reinforced Plastic (GRP) and held on a welded steel tube assembly. The turbine was mounted on a swivel system so that it could be easily lowered from the back of a barge during slack tide, shown in figure 1. When lowered, the turbine was held 3.35m, to the hub centre, below the surface. An RPM sensor disc measured the angular velocity of the turbine through a drive system. A load was applied, via a lever arm, to the drive shaft and thus the power extracted by the turbine could be determined using equation (4). Table 1 contains data measured in an average tidal flow of 0.9m/s (1.75 knots). Hence, with applied load, geometry and gear rates known the power generated was determined using equation (4).



Figure 1 (Provided by THGL © 2002). The 4 blade, 5.5m turbine on the Cleddau River during experimental trials.

The tidal flow varies due to the tide change, hence a constant tidal flow is therefore difficult to capture at which a set of data can be taken.

Series A		Series B	
Turbine angular velocity, / rad/s	Power, / W	Turbine angular velocity, / rad/s	Power, / W
1.49	1677	1.48	0
1.21	2724	1.26	1650
0.79	2820	1.05	1965
0.66	2464	0.87	2456
		0.64	2161

Table 1. Experimental data, measured in a 0.9m/s (1.75 knot) tidal flow (Data provided by THGL Ltd.)

The blade used in the experimental trials was surveyed to produce a set of vertex data. The vertices were connected to form a blade comprising of over 900 faces. Further 3D CAD

manipulation resulted in the blade comprising of 6 faces. This was used in the CFD modelling.

## Computational Fluid Dynamics

Computational Fluid Dynamics is a tool used in a variety of engineering fields, such as automotive, process and micro-processor. The CFD software solves the 'Reynolds Averaged Navier-Stokes' (RANS) equations and, depending on the viscous model chosen, relates the Reynolds stresses to the mean velocity gradients, or closes the RANS equation by solving transport equations for the Reynolds Stresses [3]. This yields a flow field for which quantities such as fluid velocity, pressure and turbulence can be obtained. The advantage of CFD is that it is relatively inexpensive compared to experimental trials; providing a validation is made between CFD and experimental data. This validation and further modelling of a 3 blade turbine is presented. This is the first stage of the optimisation of a turbine for extracting energy from the tide.

## Turbine Power

The maximum theoretical efficiency of a frictionless turbine, found to be 59.3%, was derived by A. Betz in 1920. The derivation of which is documented in many fluid mechanics texts such as White [7]. A real turbine is not frictionless, as is assumed by the derivation of the Betz limit, thus the force acting on the turbine is made up of the shear force on the turbine blades and the force due to the static pressure, hence

$$F = F_S + F_P \quad (1)$$

Where:  $F$  = Total force, N       $F_S$  = Shear force, N  
 $F_P$  = Static pressure force, N

To calculate the force on a turbine blade that has been divided into finite faces, the forces in the  $x$ ,  $y$  and  $z$  components must be considered. The force due to the static pressure is given by the product of the static pressure and the area vector of the face, hence, in the  $x$ -component

$$F_{Px} = p \cdot A_x \quad (2)$$

Where:  $F_{Px}$  = Force due to static pressure in  $x$ -component, N  
 $p$  = Static pressure acting on the element, N/m<sup>2</sup>  
 $A_x$  = Area vector of the face in  $x$ -component, m<sup>2</sup>

Similar expressions apply for the  $y$  and  $z$  component.

The torque is required only for the components of the forces in which the plane of the turbine lies. Hence, if the turbine axis is in the  $z$ -component, then only the forces in the  $x$  and  $y$  components are required and for simplicity, consider the case for the origin of the axis of rotation of the turbine at (0,0,0). Then the total torque acting on the turbine is the summation of the torque acting on each face. The torque on each face is given by the cross-product of the distance and force vectors, hence:

$$T = \sum_{n=1}^{n=N} [r_x F_y - r_y F_x] \quad (3)$$

Where:  $T$  = Torque, Nm  
 $r_x$  = Distance in  $x$ -component, m  
 $r_y$  = Distance in  $y$ -component, m  
 $F_x$  = Force vector in  $x$ -component (sum of shear force and static pressure force), N

$F_y$  = Force vector in  $y$ -component (sum of shear force and static pressure force), N

The power being extracted by the turbine is then given by:

$$P = T\omega \quad (4)$$

Where:  $\omega$  = Angular velocity of turbine, rad/s  
 $P$  = Extracted power, / W

The maximum power available to a turbine is the kinetic energy of the fluid in a stream tube whose diameter is equal to the diameter of the turbine. Thus:

$$P_{\max} = \frac{1}{2} \rho A v^3 \quad (5)$$

Where:  $P_{\max}$  = Power available, W  
 $\rho$  = Density of fluid, kg/m<sup>3</sup>  
 $A$  = Cross-sectional area of stream tube, m<sup>2</sup>  
 $v$  = Free stream velocity of fluid, m/s

This allows the efficiency of the turbine,  $\eta$ , to be defined as

$$\eta = 100 \cdot \frac{P}{P_{\max}} \quad (6)$$

## Meshing and grid dependency

A check for grid dependency was made by comparing two meshes created from tetrahedral elements; one comprising of 300 000 cells and two cell zones, with a non-conformal interface and the other 800 000 cells and one cell zone. The significance of a grid with two cell zones, with a non-conformal interface, is that averaging errors occur across the interface. This is an inherent problem when modelling rotational and/or translational parts. The difference in power prediction between the two grids was 0.32%, hence a grid of 300 000 cells was considered grid independent. The actual grid used comprised of 500 000 cells, shown in figure 2, to achieve a slightly higher resolution grid downstream of the turbine for studying the flow field. Custom sizing functions were used to attain a slightly higher quality grid in parts of the model.

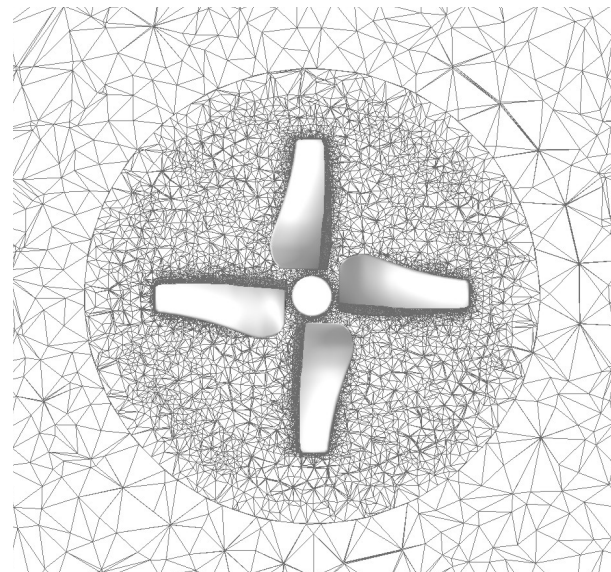


Figure 2. The 4 blade turbine and grid comprising 500 000 cells.

The topology of the region in which a tidal turbine can be located varies from site to site. It was felt that for assessing the power of the turbine and studying the flow field downstream from the turbine a domain the shape of a rectangular channel with a flat

bed would be sufficient and a free surface represented by a frictionless wall. A frictionless wall was chosen over the use of the 'Volume of Fluid' (VOF) multiphase model, because it was felt the extra computation time in using the VOF model was not justified, as the flow field around the free surface was not of interest. Initially, models were created with different widths, to choose a width of channel that minimised boundary effects, but which was sufficiently small to keep the grid size as low as possible.

The width of the channel chosen was approximately 6 times the turbine's diameter and the sides of the channel were specified as frictionless walls, to reduce boundary layer effects. In all the models, the turbine axis of rotation was parallel to the flow and a steady state solution was attained. This was justified by the fact that the turbine arrangement would allow the 'head' to swivel on a stanchion to face the tidal flow at all times. The inlet to the channel was specified as a velocity inlet, where a constant velocity was specified across the entire surface of the inlet. This ensured that the free stream velocity of the fluid approaching the turbine was that specified at the inlet. The velocity profile due to boundary layer effects adjacent to the bed of the model therefore developed within the model. In this region the grid was fairly coarse and had negligible, if any effect on the flow around the turbine. A range of turbulence intensities at the inlet were investigated and it was found that for the domain in which the turbine was being modelled, a turbulence intensity of 2% was appropriate.

### Validation

The CFD model of the 4 blade, 5.5m diameter turbine was simulated in a 0.9m/s (1.75 knot) tidal flow. The experimental data sets are small, since their collection was difficult and expensive. Hence, the experimental data in table 1 was averaged; a polynomial was fit to each set and at a number of angular velocities, the power for each polynomial calculated, for which an average was taken. Figure 3 shows good agreement between the CFD and an average of the experimental data. There is a 4% difference in peak power and approximately 15% difference in the angular velocity at which the peak power occurs.

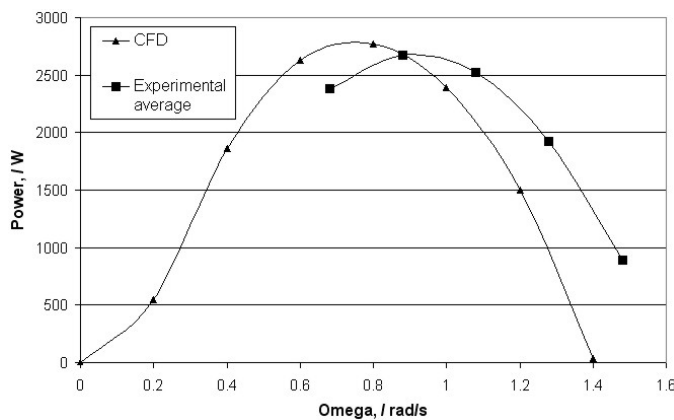


Figure 3. Comparison of CFD and experimental power for a 5.5m diameter turbine in a 0.9m/s (1.75 knot) tidal flow.

### 3 Blade Turbine

In order to reduce the cost of manufacture, a 3 blade turbine was preferable and to match the power of a 4 blade 5.5m diameter turbine, the diameter of the 3 blade turbine was increased to six metres. Thus, having acquired good agreement between CFD and experimental data, modelling of a 3 blade, 6m diameter turbine was undertaken, shown in figure 4, using a scaled version of the blade used for the four blade turbine.

To ensure that the optimum power from the 3 blade turbine was achieved, the blade pitch was investigated, to ensure that the blade setting was appropriate for the new geometry. Having established the maximum efficiency of the turbine at a minimum of 3 blade pitches, the optimum blade pitch was identified by

plotting efficiency vs. blade pitch and fitting a third order polynomial to the data. The pitch at which the turning point of the polynomial occurred was determined by means of differentiation of the polynomial. The turbine was then re-modelled at the estimated optimum blade pitch and the procedure repeated until the optimum blade pitch of 2.6° was attained. As this was the method utilised, the blade pitches for which efficiency data have been acquired are not evenly distributed in figure 5.

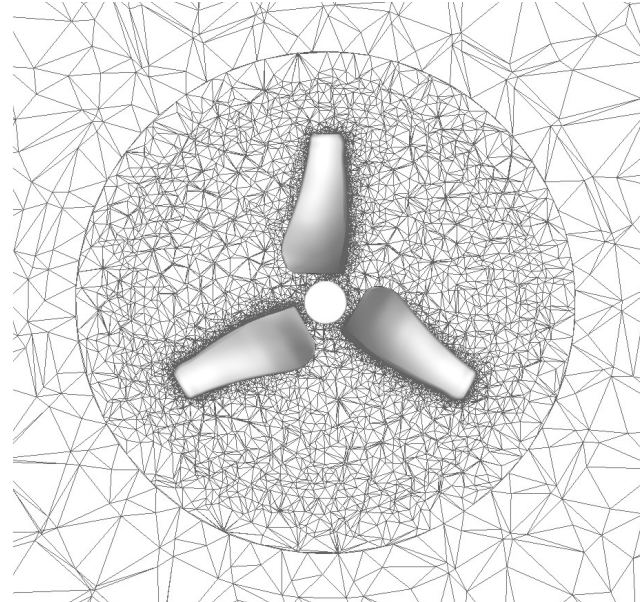


Figure 4. The 3 blade turbine and grid comprising 500 000 cells.

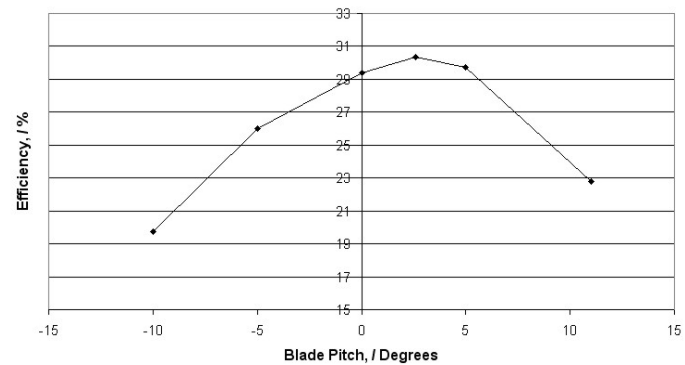


Figure 5. Variation in efficiency with blade pitch of a 3 blade, 6m diameter turbine in a 3.09m/s (6 knot) flow.

With the optimum blade pitch established, the turbine was modelled in a range of tidal flowrates. Figure 6 shows how the power varies with tidal flow.

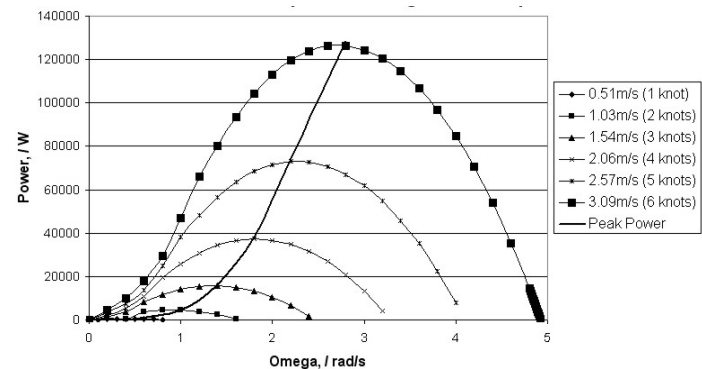


Figure 6. Three blade turbine power predictions for a range of current velocities (Blade pitch of 2.6 degrees at the tip).

From figure 6 it can be seen that there is a clear function between the maximum power attainable for the given turbine and the tidal flow, given by:

$$P = 4289v^3 = 5755\omega^3 \quad (7)$$



Where:  $v$  = Free stream velocity of fluid, m/s  
 $\omega$  = Angular velocity of turbine, rad/s

However, when considering the optimal power extraction by the turbine, the increasing force that is exerted on the turbine via the blades must be considered as the turbine would have to be supported by a structure anchored to or piled into the sea bed. The magnitude of the force on the turbine has therefore been considered at each tidal flow and angular velocity at which a data point is presented in figure 7.

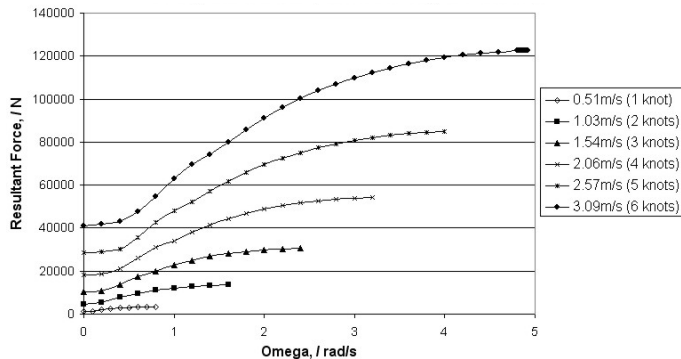


Figure 7. Force magnitude on the 3 blade turbine for a range of current velocities (Blade pitch of 2.6 degrees at the tip).

From figure 7, as the turbine approaches the free wheeling speed, the force on the turbine starts to plateau. This was investigated in more detail (indicated by the greater number of points in figures 6 and 7) as the turbine in a 3.09m/s (6 knot) tidal flow approaches the free wheeling velocity. The conclusion is that the peak force on the turbine appears to occur when the turbine is free wheeling.

As with wind turbines potential sites will exist where tidal turbine farms would be desirable. Hence where turbines could be in line with each other, then the development of the flow downstream from a turbine is of interest. This information will then aid the optimum positioning of additional turbines. Figure 8 shows the velocity magnitude of the fluid along the turbine axis at peak power extraction in a 3.09m/s (6 knot) tidal flow. The turbine is positioned at 0m. It can be seen that as the fluid approaches the turbine, the fluid in effect 'sees' the turbine and the velocity drops. The fluid velocity must clearly drop to zero as the axis passes through the turbine hub. Immediately behind the hub of the turbine there is a recirculation zone, which forces the velocity magnitude to peak and then drop. Once past this the fluid gradually recovers and reaches 90% of the free stream at approximately 70m downstream of the turbine i.e. approximately 12 turbine diameters. An 80% recovery is achieved however in the first 40m i.e. approximately 7 turbine diameters. This indicating that the closest position for a downstream turbine based on the velocity magnitude would be approximately 7 turbine diameters. Vortex shedding has also been examined and was found to decay considerably faster than the distance required for redevelopment of the flow.

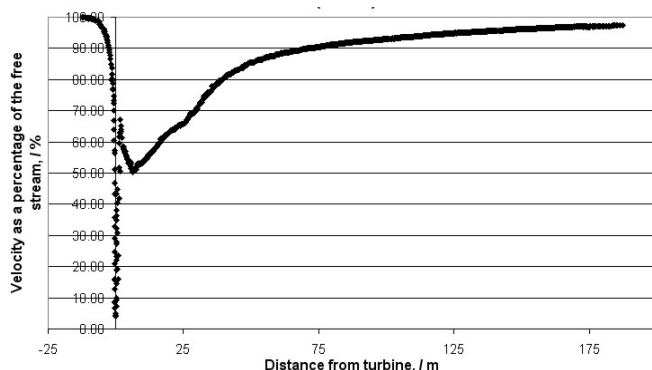
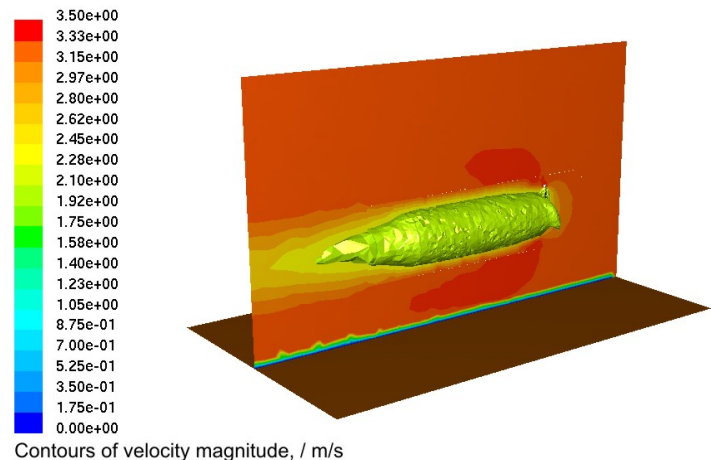


Figure 8. Development of the flow downstream from the turbine at peak power extraction in a 3.09m/s (6 knot) tidal flow.

This recovery in the downstream velocity is best illustrated in figure 9, which shows an iso-surface of velocity magnitude of

2.27m/s (74% of the free stream velocity) around the turbine, with all contours coloured by velocity magnitude. Here the flow is passing from right to left, with the turbine situated at the extreme right of the iso-surface. As the flow develops downstream, the envelope effectively collapses in on itself as the free stream velocity recovers.



Contours of velocity magnitude, / m/s

Figure 9. Contours of velocity magnitude in a 3.09m/s (6 knot) tidal flow.

## Conclusion

It has been found that in using CFD, a good prediction of power extraction by a turbine can be made. Work has concentrated on a 3 blade turbine, for which power predictions have been made at a number of flowrates. The force on the turbine has been investigated and found to peak at the free wheeling velocity. The redevelopment of the flow along the turbine axis has been investigated, as well as the velocity field around the turbine. Although the efficiency of this particular blade is 31%, the work presented here is the first stage in the process of detailed modelling of tidal turbines. More recent work has found that a tidal turbine can be designed to have an efficiency of 40 to 45%. The results presented here will differ slightly for an optimised turbine blade, but it is expected that the trend of the data will remain the same.

This work clearly indicates the feasibility for well designed tidal turbines, positioned in suitable tidal streams, to extract energy from the tide. Further work is to be undertaken to model an improved blade and other parameters such as scaling and improved boundary conditions.

## Acknowledgements

The authors wish to acknowledge THGL for the experimental data and for allowing publication.

## References

- [1] Baird, S., Tidal Energy, [www.iclei.org/EFACTS/TIDAL.html](http://www.iclei.org/EFACTS/TIDAL.html), 1993, [March 2004]
- [2] BBC News, Tidal energy turbine launches, 16/06/03, <http://news.bbc.co.uk/go/pr/fr/-/1/hi/england/devon/2992996.stm>, [March 2004]
- [3] Fluent Inc., Fluent Documentation, 2003
- [4] Grant, C., Government gets tough on green power, Feb. 2003, <http://thescotsman.scotsman.com/uk.cfm?id=230462003>, [October 2004]
- [5] Institution of Mechanical Engineering, UK, Professional Engineering, 10/12/03, Vol. 16, Number 21
- [6] Kyoto Protocol To the United Nations Framework Convention on Climate Change, <http://unfccc.int/resource/docs/convkp/kpeng.pdf>, [October 2004]
- [7] White, F.M., Fluid mechanics, Third Edition, 1979, McGraw Hill

## A Numerical Study of the Application of Radial Basis Function and Generalised Smoothed Particle Hydrodynamics to CFD

J. Ha

CSIRO Mathematical & Information Sciences  
Clayton, VIC, 3168, AUSTRALIA

### Abstract

Mesh free methods can be grouped into two approaches. One is based on field approximations such as moving least square approximations and radial basis functions (RBF) and the other is based on kernel approximations such as smoothed particle hydrodynamics (SPH). This paper presents a unified approach to implement the RBF and SPH methods for solving partial differential equations in general and for solving problems in computational fluid dynamics in particular.

There are many forms of RBF and SPH. This paper restricts attention to multiquadric and compactly supported RBFs and a particular SPH that satisfies certain completeness and reproducing conditions. Completeness and reproducing conditions enables SPH to incorporate boundary conditions in similar fashions to mesh based methods such as finite element. A number of numerical examples are presented to demonstrate the effectiveness of the two mesh free methods. Some remarks with respect to their computational efficiencies and implementation are also discussed.

### Introduction

Mesh free methods have attracted much attention recently. Two distinct directions are followed by these methods. One is based on field approximations such as radial basis functions (RBF), element free Galerkin and moving least square approximations. The other is based on kernel approximations such as smoothed particle hydrodynamics.

The kernel approximations used in the original SPH proposed by Lucy [15] and Gingold and Monaghan [7] fail to reproduce linear functions. Various approaches to remedy these inaccuracies have been reported in the literature. It has been shown that the kernel approximations can be corrected so that they reproduce linear functions exactly (see, for example, Belytschko et al. [1]. Other workers, such as Johnson and Beissel [9], Randles and Libersky [19], and Krongauz and Belytschko [11], developed corrected derivative methods. Essentially, these methods replace the standard SPH interpolant with more sophisticated interpolant that was constructed by imposing the consistency conditions. Liu et al. [13] showed that the reproducing kernel provides boundary correction as well as removing the tensile instability. Chen and Beraun [3], on the other hand, developed a generalised SPH method (GSPH) by applying the kernel estimate into the Taylor series expansion. Their formulation extends not only the ability of standard SPH to model partial differential equations with higher order derivatives but to enforce boundary conditions directly as well.

In the last decade or so, another group of mesh free methods that is based on the function approximation by RBFs either globally or compactly supported was developed to solve partial differential equations (see, for example, Kansa [10]). RBF interpolation is required to be exact at the nodes, so one drawback of these methods is the need to solve the full coefficient matrix arising from the function approximation. A common approach to im-

prove computational efficiency is to ensure sparsity, either by using functions of compact support, or by using domain decomposition (see, for example, Dubal [5]). In this paper, we applied the approach of SPH to RBF in using the nearest neighbours of a particle for estimating its derivatives. Thus, computer programs implementing the SPH and RBF methods can share the same structure. They differ only in their different estimates of the derivatives. The aim of this paper is to present the results of such implementation of RBF, and to compare them to GSPH. Most applications of standard SPH are to simulate compressible fluids. The second aim is to study the application of GSPH to two benchmark incompressible fluid problems for testing CFD codes. Also unlike standard SPH discretisation, all the numerical examples are obtained from substituting each term of the governing equations by their corresponding RBF or GSPH derivative approximations directly.

### Generalised SPH

Applying the kernel approximation to the Taylor series expansion for  $f(x)$  in the neighbourhood of  $x$ , Chen and Beraun [3] derived results that improve the approximation accuracy of SPH. In 1D, the GSPH approximation of a function  $f(x)$  and its first two derivatives are given in Equations (1)-(3). Higher derivatives can easily be derived.

$$f(x) = \frac{\int f(x')W(x-x',h)dx'}{\int W(x-x',h)dx'} \quad (1)$$

$$\frac{df(x)}{dx} = \frac{\int (f(x) - f(x')) \frac{dW}{dx} dx'}{\int (x-x') \frac{dW}{dx} dx'} \quad (2)$$

$$\frac{d^2f(x)}{dx^2} = \frac{\int (f(x) - f(x')) \frac{d^2W}{dx^2} dx' - \frac{df}{dx} \int (x-x') \frac{d^2W}{dx^2} dx'}{0.5 \int (x-x')^2 \frac{d^2W}{dx^2} dx'} \quad (3)$$

The same procedure can be followed to derive approximations for functions in higher dimensions. However, the derivative estimates for higher dimensions involve matrix inversion. It is clear that GSPH is computationally more expensive to use than conventional SPH. The extra terms in the above approximations can be interpreted as corrections to the boundary deficiency in the conventional SPH. The results are equivalent to some of the results of Liu et al. [13] and Krongauz and Belytschko [11] obtained from imposing certain completeness and consistency conditions. The above approximations are algebraically correct for a function if it is constant, for its first derivative if it is constant or linear, and for its second derivative if it is constant, linear or quadratic.

It is well appreciated that SPH is closely related to the finite element method. The main difference between the two methods is that the SPH kernel approximation of a function does not satisfy the Kronecker delta property. It is thus not possible to impose essential boundary conditions in conventional SPH. The inclusion of  $f(x)$  and  $df/dx$  in the above first and second derivative estimates enable the direct insertion of Dirichlet and Neumann boundary conditions, if they exist, in the GSPH method.

## Radial Basis Functions

The development of RBFs into a mesh free method for solving partial differential equations arises from the recognition that a radial basis function interpolant can be smooth and accurate on any set of nodes in any dimension. The starting point is that the approximation of a function  $f(\mathbf{x})$  for a set of distinct points  $\mathbf{x}_i, i = 1, \dots, N$  can be written as a linear combination of  $N$  RBFs.

$$f(\mathbf{x}) = \sum_{i=1}^N \alpha_i \phi(\|\mathbf{x} - \mathbf{x}_i\|) \quad (4)$$

where  $\phi(\|\mathbf{x} - \mathbf{x}_i\|)$  denotes a positive definite RBF. The unknown coefficients  $\alpha_i$  are to be determined from the system of equations formed by  $f(\mathbf{x}_j), j = 1, \dots, N$ . Once they are determined, the  $m$ -th spatial derivatives of  $f(\mathbf{x})$  are approximated by taking the  $m$ -th spatial derivatives of the RBFs.

$$\frac{\partial^m f}{\partial x^m} = \sum_{i=1}^N \alpha_i \frac{\partial^m \phi}{\partial x^m} \quad (5)$$

The application of Equations (4) and (5) provides the framework for the numerical solution of partial differential equations and their boundary conditions.

There are many RBFs either globally or compactly supported. An example of a globally supported RBF that is used extensively is multiquadric (MQ):  $\phi(r) = (r^2 + c^2)^{1/2}$ , where  $r = \|\mathbf{x} - \mathbf{x}_i\|$  and  $c > 0$ . It is well known that the shape parameter  $c$  strongly influences the accuracy of MQ approximation. An important unsolved problem is to find a method to determine the optimal value of  $c^2$ . To improve boundary treatment, methods using MQ usually have a polynomial of zero degree added to the right hand side of Equation 4.

The compactly supported RBFs are generally expressed in the form  $\phi(r) = (1 - r)_+^n p(r)$  (Wu [21] and Wendland [20]), and

$$(1 - r)_+^n = \begin{cases} (1 - r)^n & 0 \leq r < 1, \\ 0 & r \geq 1 \end{cases} \quad (6)$$

where  $p(r)$  is a prescribed polynomial. By replacing  $r$  with  $r/\delta$  for  $\delta > 0$ , the basis function has support on  $[0, \delta]$ . It is clear that the value  $\delta$  defines the band width of the coefficient matrix. In general, the smaller the value of  $\delta$ , the greater is the number of zero entries in the coefficient matrix resulting in lower accuracy. In the numerical results for compactly supported RBF, the Wendland function used is  $\phi(r) = (1 - r)^4(4r + 1)$ .

In this paper, we applied the approach of SPH to RBF in that only neighbouring particles within a given radial distance from the particle of interest are used in estimating the particle's derivatives. This has the advantage of avoiding the inversion of large coefficient matrix making problems requiring large number of nodes more amenable to numerical solution. In general, the larger the supporting region the higher is the accuracy of the approximation. The need to invert coefficient matrix makes the method more expensive than the generalised SPH.

## Numerical Examples

First, the GSPH and RBF approximations of  $\partial u / \partial x$  of the function  $u(x, y) = \sin(\pi r) + \cos(2\pi r)$  are studied, where  $r = \sqrt{x^2 + y^2} + 0.1$ . The L1-norms of error for a range of particle size and width of the supporting region are first computed to determine the optimal values of  $c^2$  and  $\delta$  to use for MQs RBF (MQRBF) and compactly supported RBF (CSRBF) respectively. Figure 1 compares the errors of GSPH with those

of CSRBF and MQRBF using the optimal values of  $c^2$  and  $\delta$  obtained but different supporting regions ranging from  $2h - 5h$ , where  $h$  denotes the smoothing length. It shows that the RBF methods give better accuracy than the generalised SPH at the expense of more computational effort.

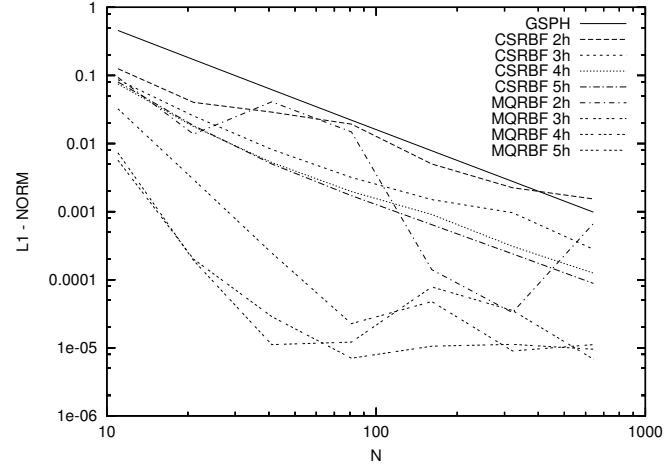


Figure 1: L1-norm errors for estimating  $\partial u / \partial x$ .

To demonstrate that the GSPH method can impose boundary conditions directly, the following heat conduction problem is solved in the domain  $0 \leq x \leq 1, 0 \leq y \leq 1$ , initial condition  $T(x, y, 0) = -1$ , Neumann boundary condition  $\partial T(x, 1, t) / \partial y = 0$  at  $y = 1$  and Dirichlet condition at the other boundaries  $T(0, y, t) = T(1, y, t) = T(x, 0, t) = 1$ .

$$\frac{\partial T}{\partial t} = \frac{\partial^2 T}{\partial x^2} + \frac{\partial^2 T}{\partial y^2} \quad (7)$$

where  $T$  denotes temperature and  $t$  time. Both RBF and GSPH give the result shown in Figure 2 and appear identical to the result obtained by Jeong et al. [8] who implement the boundary conditions to the conventional SPH in a different way.

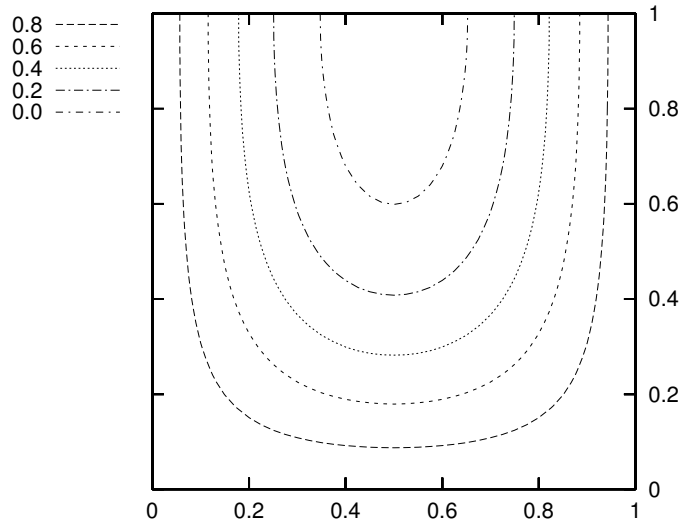


Figure 2: Temperature profiles at  $t = 0.08$ .

Next, the 3D Burger's equation is solved using GSPH and MQRBF and the numerical results are compared with the analytical solution.

$$\frac{\partial \mathbf{v}}{\partial t} + \mathbf{v} \cdot \nabla \mathbf{v} - \nu \nabla^2 \mathbf{v} = 0 \quad (8)$$



where  $\mathbf{v}$  and  $\nu$  denote velocity and viscosity respectively. The solution becomes more shock-like as the viscosity parameter decreases. Figure 3 compares L1-norm errors for GSPH and MQRBF for  $\nu = 0.05$ . The number of particles used is  $41 \times 41$ . In general, MQRBF gives a slightly more accurate result than GSPH.

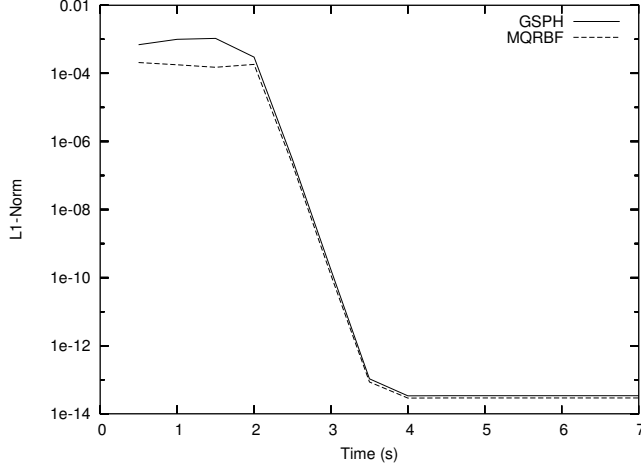


Figure 3: L1-norm errors for solving 3D Burger's equation.

To conclude this section, the GSPH method is applied to two standard CFD test problems - 2D lid-driven flow and natural convection in a square cavity. For the lid-driven cavity problem, the following Navier Stokes equation in 2D is solved

$$\frac{\partial \mathbf{v}}{\partial t} + \mathbf{v} \cdot \nabla \mathbf{v} + \frac{1}{\rho} \nabla p - \nu \nabla^2 \mathbf{v} = 0 \quad (9)$$

where  $p$  denotes pressure. The boundary conditions are  $\mathbf{v} = (1, 0)$  on  $y = 1$  and  $\mathbf{v} = (0, 0)$  on the other three sides of the unit square. For an incompressible fluid, the Navier Stokes equation is complemented by the incompressibility constraint,  $\nabla \cdot \mathbf{v} = 0$ .

In general, velocity  $\mathbf{v}^{n+1}$  at time  $t^{n+1}$  obtained by solving Equation (9) does not satisfy the incompressibility constraint. This constraint on velocity must be satisfied at all times. In this paper, the following steps are iterated until  $\nabla \cdot \mathbf{v} \approx 0$  is reached.

1.  $\Delta p_k^n = -\gamma \nabla \cdot \mathbf{v}_k^{n+1}$
2.  $\Delta \mathbf{v}_k^{n+1} = \Delta t \nabla (\Delta p_k^n)$

Here,  $k$  is the iteration counter and  $\Delta f_k = f_{k+1} - f_k$ . Upon convergence, the above procedure gives the new pressure  $p^{n+1}$  and divergent free velocity  $\mathbf{v}^{n+1}$  for time  $t^{n+1}$ . The parameter  $\gamma$  controls the rate of convergence and must satisfy the stability requirements  $0 \leq \gamma \leq (\Delta x)^2 / 4\Delta t$ . The iteration is equivalent to solving a Poisson equation for the pressure.

Figure 4 shows that the GSPH solutions for Reynolds number 1000 on a  $129 \times 129$  grid using 3 different kernels compare well with the benchmark solutions 1 and 2 of Ghia et al. [6] and Botella and Peyret [2] respectively. In the figure, W3 denotes the cubic spline kernel of Monaghan [17], W4 the quartic spline kernel of Liu et al [14] and W5 the quintic spline kernel of Morris et al. [18]. For this problem, W4 gives the best result and W5 the worst result.

For incompressible fluid flow in a differentially heated square cavity of side  $L$ , the following equations are solved

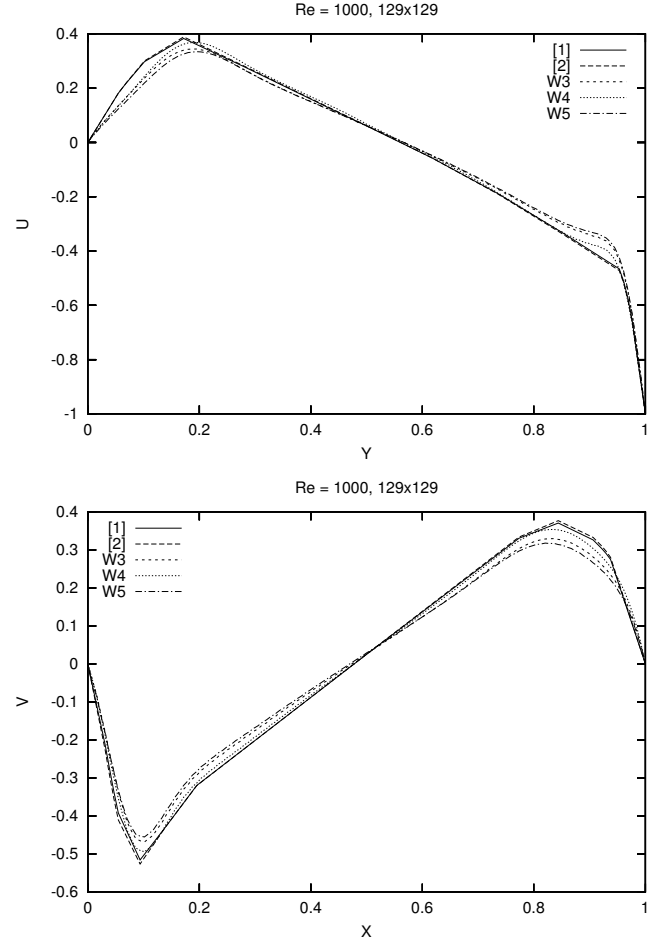


Figure 4: Comparison of lid-driven cavity results.

$$\frac{\partial \mathbf{v}}{\partial t} + \mathbf{v} \cdot \nabla \mathbf{v} + \frac{1}{\rho} \nabla p - \nu \nabla^2 \mathbf{v} = \beta(T - T_r)\mathbf{g} \quad (10)$$

$$\frac{\partial T}{\partial t} + \mathbf{v} \cdot \nabla T = \alpha \nabla^2 T \quad (11)$$

where  $\alpha$  denotes thermal diffusivity,  $\beta$  the coefficient of thermal expansion and  $\mathbf{g}$  the gravity. The initial conditions are  $\mathbf{v}(x, y, 0) = (0, 0)$  and  $T(x, y, 0) = T_r$ . The boundary conditions are  $\mathbf{v} = (0, 0)$  on cavity boundary,  $T(0, y, t) = T_h$ ,  $T(L, y, t) = T_c$ ,  $\partial T(x, 0, t) / \partial y = \partial T(x, L, t) / \partial y = 0$ . Here,  $T_r$ ,  $T_h$  and  $T_c$  denote the reference, hot and cold wall temperatures respectively. Table 1 shows that the GSPH results compares well with the benchmark solutions for Prandtl number 0.71 and Rayleigh numbers  $10^4 - 10^6$ . In the table, the numbers enclosed by [] and () are the results of Leal et al. [12] and de Vahl Davis [4] respectively.

	$\bar{u}_{\max}$	$\bar{y}$	$\bar{v}_{\max}$	$\bar{x}$
$Ra = 10^4$	[16.18]	[0.823]	[19.63]	[0.119]
	16.18	0.822	19.63	0.119
	(16.178)	(0.823)	(19.617)	(0.119)
$Ra = 10^5$	[34.74]	[0.855]	[68.62]	[0.066]
	34.76	0.853	68.64	0.0656
	(34.73)	(0.855)	(68.59)	(0.066)
$Ra = 10^6$	[64.83]	[0.850]	[220.6]	[0.0379]
	64.91	0.847	220.72	0.0375
	(64.63)	(0.850)	(219.36)	(0.0379)

Table 1: Comparison of natural convection results.

Even for unsteady problems, the pseudo-compressibility formulation may also be used above to enforce the incompressibility condition provided that some relations between the relevant parameters hold (Mendez and Velazquez [16]). In this method, the pseudo-compressibility equation  $\partial p / \partial \tau = -c \nabla \cdot \mathbf{v}$  is solved together with equation (9) or equations (10) and (11), where  $c$  is the pseudo-compressibility coefficient. For Reynolds numbers in the range of 100-1000,  $c$  values of 100 give accurate solutions. When steady solutions are sought,  $c$  values of 5-10 can be used. The pseudo-compressibility method gives almost identical results to the above two test problems and is computationally less expensive than solving the Poisson equation for pressure.

## Conclusions

This paper presents an unified approach to implement the RBF and SPH methods for numerical computations. The approach of SPH in using the nearest neighbours within the supporting region of a particle to estimate its derivatives of a function is applied to RBF. The size of supporting region depends on the smoothing kernel used in the case of SPH but is a parameter in the case of RBF. In the numerical examples considered in this paper, a supporting region of width  $3h$  for RBF gives accurate results provided that optimal values for the parameters  $c^2$  and  $\delta$  are used. There are attempts reported in the literature but it is still an important unsolved problem of how to determine the optimal value for these parameters.

The numerical examples presented in the last section demonstrated that GSPH and RBF give accurate results to the problems considered. Unlike conventional SPH, they have the advantage of being able to impose boundary conditions directly. Also, they are just as easy to implement as the conventional SPH. There is no dimensional difference between 1D, 2D and 3D as far as computer coding for their implementation is concerned. Apart from correcting the boundary deficiency problem, GSPH is less affected by particle disorder than conventional SPH because of the normalisation term in the denominator (refer to Equations 1-3).

## Acknowledgements

The author thanks Dr N. Stokes of CSIRO Mathematical and Information Sciences for valuable discussions.

## References

- [1] Belytschko, T., Krongauz, Y., Organ, D., Fleming, M. and Krysl, P., Meshless methods: An overview and recent developments, *Comput. Meth. Appl. Mech. Engng.*, **139**, 1996, 3-47.
- [2] Botella, O. and Peyret, R., 1998. Benchmark spectral results on the lid-driven cavity flow, *Computers & Fluids*, **27**, 421-433.
- [3] Chen, J.K. and Beraun, J.E., A generalized smoothed particle hydrodynamics method for nonlinear dynamic problems, *Comput. Methods Appl. Mech. Engrg.*, **190**, 2000, 225-239.
- [4] de Vahl Davis, G., Natural convection of air in a square cavity: a benchmark numerical solution, *Int. J. Numer. Methods Fluids*, **3**, 1983, 243-264.
- [5] Dubal, M.R., Domain decomposition and local refinement for multiquadric approximations. I: Second-order equations in one-dimension, *Int. J. Appl. Sci. Comput.*, **1**, 1994, 146-171.
- [6] Ghia, U., Ghia, K.N. and Shin, C.T., High-Re solutions of incompressible flow using the Navier-Stokes equations and a multigrid method, *Journal of Computational Physics*, **48**, 1982, 387-411.
- [7] Gingold, R. and Monaghan, J., Smoothed particle hydrodynamics: theory and application to non-spherical stars, *Mon. Not. Roy. Astron. Soc.*, **181**, 1977, 375-389.
- [8] Jeong, J.H., Jhon, M.S., Hallow, J.S. and van Osdol, J., Smoothed particle hydrodynamics: Applications to heat conduction, *Computer Physics Communications*, **153**, 2003, 71-84.
- [9] Johnson, G.R. and Beissel, S.R., Normalized smoothing functions for SPH impact calculations, *Int. J. Numer. Meth. Engng.*, **39**, 1996, 2725-2741.
- [10] Kansa, E.J., Multiquadrics - A scattered data approximation scheme with applications to computational dynamics - I. Surface approximations and partial derivative estimates, *Comput. Math. Appl.*, **19**, 1990, 127-145.
- [11] Krongauz, Y. and Belytschko, T., Consistent pseudo-derivatives in meshless methods, *Comput. Meth. Appl. Mech. Engng.*, **146**, 1998, 371-386.
- [12] Leal, M.A., Perez-Guerrero, J.S. and Cotta, R.M., Natural convection inside two-dimensional cavities: the integral transform method, *Communications in Numerical Methods in Engineering*, **15**, 1999, 113-125.
- [13] Liu, W.K., Jun, S., Adee, J. and Belytschko, T., Reproducing kernel particle methods for structural dynamics, *Int. J. Numer. Meth. Engng.*, **38**, 1995, 1655-1679.
- [14] Liu, M.B., Liu, G.R. and Lam, K.Y., Constructing smoothing functions in smoothed particle hydrodynamics with applications, *Journal of Computational and Applied Mathematics*, **155**, 2003, 263-284.
- [15] Lucy, L.B., A numerical approach to the testing of the fission hypothesis, *J. Astron.*, **82**, 1977, 1013-1024.
- [16] Mendez, B. and Velazquez, A., Finite point solver for the simulation of 2-D laminar incompressible unsteady flows, *Computer Methods in Applied Mechanics and Engineering*, **193**, 2004, 825-848.
- [17] Monaghan, J.J., Smoothed particle hydrodynamics, *Ann. Rev. Astron. Astrophys.*, **30**, 1992, 543-574.
- [18] Morris, J.P., Fox, P.J. and Zhu, Y., 1997. Modeling low Reynolds number incompressible flows using SPH, *J. Comput. Phys.*, **136**, 214-226.
- [19] Randles, P.W. and Libersky, L.D., Smoothed particle hydrodynamics: some recent improvement and applications, *Comput. Methods Appl. Mech. Eng.*, **139**, 1996, 375-408.
- [20] Wendland, H., Piecewise polynomial, positive definite and compactly supported radial functions of minimal degree, *Adv. Comput. Math.*, **4**, 1995, 389-396.
- [21] Wu, Z., Compactly supported positive definite radial functions, *Adv. Comput. Math.*, **4**, 1995, 283-292.

## The effect of zero-mean suction on Görtler vortices: a receptivity approach

J. P. Denier

School of Mathematical Sciences  
The University of Adelaide, South Australia 5005 AUSTRALIA

### Abstract

We consider the effect of zero-mean suction on the development of Görtler vortices in the boundary layer flow over a concavely curved surface. The zero-mean suction is assumed not to affect the basic boundary-layer flow and so can be modelling by modifying the impermeability condition at the surface to read  $v = \delta \cos \omega t$  where  $0 < \delta \ll 1$ . The problem is posed in terms of vortex receptivity and we demonstrate that small amplitude zero-mean suction with a frequency  $\omega$  satisfying  $\omega > 2.254G^{2/5}$  (where  $G$  is the Görtler number) serves to fully stabilise the most unstable Görtler vortex.

### Introduction

The use of boundary layer suction to control the process of transition to turbulence is one which has a long history in the scientific literature; this is reviewed in Schlichting [14]. Although the majority of earlier work on suction control has focused upon flat-plate boundary layers, and consequently on controlling the growth of Tollmien-Schlichting waves, there have been a number of studies on the effect of suction on centrifugal instabilities (that is, Görtler vortices). Görtler vortices arise in the boundary-layer flow over a concavely curved surface and are particularly relevant in the design of laminar flow aerofoils. For example, the laminar flow wing considered by Mangalam *et al.* [11] had appreciable regions of concave curvature on the underside of the airfoil. The introduction of concave curvature then presented the potential problem of an earlier transition to turbulence due to the development of a secondary instability on the streamwise aligned counter-rotating Görtler vortices.

The majority of theoretical work on the effect of suction on Görtler vortices has focused upon the asymptotic suction profile

$$\bar{u} = 1 - e^{-v_s y}, \quad \bar{v} = -v_s. \quad (1)$$

Kobayashi [9] and Floryan & Saric [7] showed that suction serves to stabilise Görtler vortices; the latter work demonstrating that a larger level of suction is required to stabilise Görtler vortices than is required to stabilise Tollmien-Schlichting waves. A similar result was reported by Lin & Hwang [10] in their computational study Görtler vortices on a heated concave surface. Myose & Blackwelder [12] undertook a series of experiments using isolated suction holes (placed in the low-speed region between the counter-rotating Görtler vortices) and were able to demonstrate that this method required two orders of magnitude less suction to control the breakdown of Görtler vortices, over a comparable area, when compared to an asymptotic suction profile approach. However, this study was concerned with controlling the secondary instability that occurs in Görtler vortex flows through the modification of the low-speed flow region and so did not suppress the development of the Görtler vortices themselves but controlled the onset of secondary instability.

Park & Huerre [13] also employed an asymptotic suction profile (given by (1) with  $v_s = 0.5$ ) in their study of the nonlinear development and subsequent secondary instability of Görtler vortices. Their work was not concerned with suction control but

was aimed at exploiting the fact that with a base flow given by (1) all issues regarding non-parallelism in the development of Görtler vortices could be side-stepped. It was the early work of Hall [8] that was the first to emphasise the fact that the Görtler vortex instability is crucially linked to the non-parallel evolution of the boundary-layer flow. Further recent work on suction control of Görtler vortices can be found in Balakumar & Hall [3].

Recently Denier [4] has reconsidered the stability of the asymptotic suction profile (1) in order to determine the level of suction required to fully stabilise the flow to Görtler vortices. By focusing on the most unstable Görtler vortex mode (whose structure is described in [6], [15]) it can be shown that suction will fully stabilise the flow when the level of suction, measured by  $v_s$  in (1), satisfies  $v_s > 0.3581G^{1/3}$ . Here  $G$  is the Görtler number, defined in (3).

In the past few years there has been considerable attention given to the problem of unsteady suction at the leading edge of an aerofoil. Here we consider the effect of an unsteady suction (that is, alternating suction and blowing) on the stability of Görtler vortices. We will assume that the suction profile has a **zero-mean** state; in other words we will assume that the suction velocity is prescribed at the surface and is proportional to  $\cos \omega t$ .

### Formulation

The equations governing the *linear* evolution of span-wise periodic disturbances to a boundary layer flowing over a curved surface are

$$\tilde{U}_x + \tilde{V}_y + ik\tilde{W} = 0, \quad (2a)$$

$$\tilde{U}_{yy} - k^2\tilde{U} = \bar{u}\tilde{U}_x + \tilde{U}\bar{u}_x + \bar{v}\tilde{U}_y + \tilde{V}\bar{u}_y, \quad (2b)$$

$$\tilde{V}_{yy} - k^2\tilde{V} = \bar{P}_y + G\chi\tilde{U}\bar{u} + \bar{u}\tilde{V}_x + \tilde{U}\bar{v}_x + \bar{v}\tilde{V}_y + \tilde{V}\bar{v}_y, \quad (2c)$$

$$\tilde{W}_{yy} - k^2\tilde{W} = ik\bar{P} + \bar{u}\tilde{W}_x + \bar{v}\tilde{W}_y, \quad (2d)$$

where  $2\pi/k$  is the spanwise-wavelength of the disturbance, an over-bar denotes a basic boundary-layer variable, a tilde denotes a disturbance quantity,  $x$  is the streamwise coordinate and  $y$  the usual boundary-layer variable. The precise form for the basic boundary-layer is relatively unimportant in what follows. We will simply assume that the boundary layer remains attached - Görtler vortices in separated flows were described by Denier & Bassom [5]. In what follows we take  $(\bar{u}, \bar{v})$  to be the streamwise and vertical velocity components within an attached boundary layer and so governed by Prandtl's boundary-layer equations

$$\begin{aligned} \frac{\partial \bar{u}}{\partial x} + \frac{\partial \bar{v}}{\partial y} &= 0, \\ \bar{u} \frac{\partial \bar{u}}{\partial x} + \bar{v} \frac{\partial \bar{u}}{\partial x} &= -\frac{\partial \bar{p}}{\partial x} + \frac{\partial^2 \bar{u}}{\partial y^2}, \end{aligned}$$

where  $\bar{p}_x = u_e(x)u_{ex}(x)$  denotes the streamwise pressure gradient. These must be solved subject to no-slip boundary conditions  $\bar{u} = \bar{v} = 0$  on  $y = 0$  and  $\bar{u} \rightarrow u_e$  as  $y \rightarrow \infty$ .

The important parameter appearing in (2) is the Görtler number  $G$  which is traditionally defined according to

$$G\chi = Re^{1/2}g_{xx} \quad (3)$$

where  $y = g(x)$  denotes the position of the wall and thus  $g_{xx}$  is the wall curvature, which is positive if the surface is concavely curved, and  $Re$  is the Reynolds number. For boundary-layer flows over a surface with even a moderate level of curvature the Görtler number is typically large due to the presence of the Reynolds number factor appearing in (3). Thus most boundary-layer applications involving Görtler vortices can typically be described as large Görtler number flows. This fact allows some considerable simplification of the fully parabolic system of equations (2) as has been described by Hall [8]. More importantly, it is the large Görtler number limit the most unstable vortex mode occurs (see Denier *et al.* [6] and Timoshin [15] for details). The wavelength of this mode scales as  $O(G^{-1/5})$  and it is confined to within a viscous layer of thickness  $O(G^{-1/5})$  situated at the wall. Furthermore the streamwise growth rate has magnitude  $O(G^{3/5})$  and in this regime the maximum growth rate of all vortex-like perturbations occurs.

Turning to the question of the physical boundary conditions appropriate to the flow we focus our attention on the problem of zero-mean suction (alternatively blowing) at the surface. By zero-mean we take to mean blowing whose time averaged behaviour shows no mean component and is therefore assumed to have no effect upon the mean-boundary layer flow. We will model this by prescribing the wall-normal perturbation velocity to be given by

$$\tilde{V} = \begin{cases} 0 & \text{if } x < \bar{x} \\ \delta F(J(x - \bar{x})) \exp(ikz + i\omega t) & \text{if } x \geq \bar{x} \end{cases} \quad (4)$$

where  $J$  is a constant that determines the streamwise extent of the active region of suction/blowing,  $2\pi/\omega$  is the suction frequency and  $0 < \delta \ll 1$  is a small parameter which sets the strength of the suction. We are therefore focusing on small amplitude perturbations to the basic boundary-layer flow induced by small amplitude blowing/suction. We have also assumed that the region of active blowing is spanwise periodic<sup>1</sup>; this is equivalent to assuming that there is a periodic array of finite suction slots located at  $x = \bar{x}$ .

In addition to this condition on  $\tilde{V}$  we must also impose the usual no-slip boundary conditions on the streamwise and spanwise velocity perturbations

$$\tilde{U} = \tilde{W} = 0 \quad \text{on } y = 0,$$

and the condition that the perturbation is confined to within the boundary layer

$$(\tilde{U}, \tilde{V}, \tilde{W}) \rightarrow 0 \quad \text{as } y \rightarrow \infty.$$

### Vortex receptivity

We focus our attention on the receptivity of the most unstable Görtler vortex to zero-mean suction. As noted earlier the most unstable Görtler vortex has a streamwise growth rate of  $O(G^{3/5})$  and is confined to an  $O(G^{-1/5})$  thick layer located at

<sup>1</sup>This assumption is not necessary. Indeed, a suction slot with a finite extent in *both* the streamwise and spanwise direction can be dealt with by simply taking the Fourier transform in  $z$ . This however unduly complicates the subsequent analysis and so we choose not to consider this problem here.

the wall. We therefore introduce a new stretched wall coordinate  $\phi = G^{1/5}y$  (where  $y$  is the usual boundary-layer coordinate). Led by the results of Denier *et al.* [6] and Timoshin [15] we consider perturbations to the basic flow in the form

$$(u, v, w, p) = (\bar{u}, Re^{-1/2}\bar{v}, 0, \bar{p}) + \delta(G^{-2/5}u_1, v_1, w_1, G^{1/5}p_1) \times \exp\left(ikz + G^{3/5} \int \beta(x)dx + i\omega t\right),$$

where  $\delta$  is the (infinitesimally) small perturbation amplitude of the zero-mean suction/blowing. In these expansions we have anticipated that the disturbance to the basic flow is of the same order of magnitude as the zero-mean suction/blowing velocity and so is of size  $O(\delta)$ . This fixes the amplitude of the vertical velocity perturbation term; the relative magnitude of the other terms is then a simple consequence of balancing terms in the continuity and momentum equations.

In order to determine the frequency at which the suction/blowing first affects the stability of the flow we must necessarily balance

$$\frac{\partial u}{\partial t} \sim \bar{u} \frac{\partial u}{\partial x}. \quad (5)$$

Within the viscous sub-layer the mean streamwise velocity expands as

$$\bar{u} = \mu y + \dots = \mu G^{-1/5} \phi + \dots,$$

where  $\mu = \bar{u}'(x, 0)$  is the wall shear; given our previous comments on the boundary layer remaining attached,  $\mu$  is taken to be positive. Taken with the fact that the streamwise growth rate of the most unstable Görtler vortex is  $O(G^{3/5})$  the balance expressed by (5) implies that  $\omega = O(G^{2/5})$  (or equivalently the frequency of the blowing/suction must be  $O(G^{-2/5})$ ). Thus it will be the, relatively, low frequency suction (through the periodic pumping) that will affect the stability of the flow.

In order to pose this problem in the form of a flow *receptivity* problem we suppose that the suction velocity is given by

$$v = \begin{cases} 0 & \text{if } x < \bar{x} \\ F(\tilde{J}G^{3/5}(x - \bar{x})) \exp(i\lambda G^{1/5}z + i\omega t) & \text{if } x \geq \bar{x} \end{cases} \quad (6)$$

where we have set the vortex wavenumber  $k = \lambda G^{1/5}$  thus allowing us to focus upon the wavenumber regime containing the most unstable Görtler vortex. To simplify matters let us define  $\tilde{x} = \tilde{J}G^{3/5}(x - \bar{x})$  and write

$$\begin{aligned} u &= u_0(\tilde{x}, \phi) + G^{-1/5}u_1(\tilde{x}, \phi) + \dots, \\ (\chi\mu^2G)^{-3/5}v &= v_0(\tilde{x}, \phi) + G^{-1/5}v_1(\tilde{x}, \phi) + \dots, \end{aligned}$$

Setting  $\omega = G^{2/5}\omega_0$  and substituting our expansions into the governing equation yields, to  $O(\delta)$ , the system of equations (in canonical form)

$$\left(\frac{\partial^2}{\partial \phi^2} - \frac{\phi}{\tilde{\lambda}^3} \frac{\partial}{\partial \tilde{x}} - 1 - \frac{i\tilde{\omega}}{\tilde{\lambda}^2}\right) \left(\frac{\partial^2}{\partial \phi^2} - 1\right) \tilde{v}_0 = -\frac{\phi \tilde{U}_0}{\tilde{\lambda}^2}, \quad (7a)$$

$$\left(\frac{\partial^2}{\partial \phi^2} - \frac{\phi}{\tilde{\lambda}^3} \frac{\partial}{\partial \tilde{x}} - 1 - \frac{i\tilde{\omega}}{\tilde{\lambda}^2}\right) \tilde{U}_0 = \frac{\tilde{V}_0}{\tilde{\lambda}^2}, \quad (7b)$$

which must be solved subject to the boundary conditions

$$\begin{aligned} \tilde{U}_0 = \tilde{V}_0' &= 0, \quad \tilde{V}_0 = F(\tilde{x}) \quad \text{on} \quad \phi = 0, \\ \tilde{U}_0, \tilde{V}_0, \tilde{V}_0' &\rightarrow 0 \quad \text{as} \quad \phi \rightarrow \infty. \end{aligned}$$

Here  $\tilde{\lambda}$  and  $\tilde{\omega}$  are the scaled wavenumber and frequency, respectively.

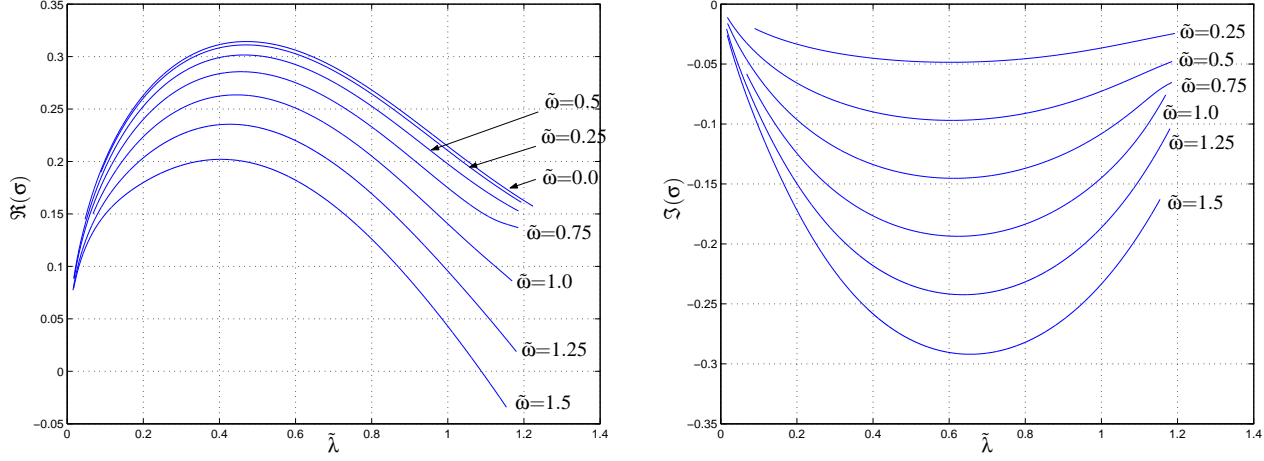


Figure 1: Plot of the first eigenvalue of system (8) for a variety of values of  $\tilde{\omega}$ . Shown is the (a) real part and (b) imaginary part of  $\sigma$  versus  $\tilde{\lambda}$ .

System (7) is most readily solved by taking the Laplace transform with respect to  $x$ . To this end we define

$$\hat{U}_0 = \int_0^\infty e^{-\sigma \tilde{x}} \tilde{U}_0(\varphi, \tilde{x}) d\tilde{x}, \quad \hat{V}_0 = \int_0^\infty e^{-\sigma \tilde{x}} \tilde{V}_0(\varphi, \tilde{x}) d\tilde{x}.$$

and upon taking the Laplace transform of system (7) we obtain

$$\left( \frac{\partial^2}{\partial \varphi^2} - \frac{\sigma \varphi}{\tilde{\lambda}^3} - 1 - \frac{i\tilde{\omega}}{\tilde{\lambda}^2} \right) \hat{U}_0 = \frac{\hat{V}_0}{\tilde{\lambda}^2}, \quad (8a)$$

$$\left( \frac{\partial^2}{\partial \varphi^2} - \frac{\sigma \varphi}{\tilde{\lambda}^3} - 1 - \frac{i\tilde{\omega}}{\tilde{\lambda}^2} \right) \left( \frac{\partial^2}{\partial \varphi^2} - 1 \right) \hat{V}_0 = -\frac{\varphi \hat{U}_0}{\tilde{\lambda}^3}, \quad (8b)$$

which must be solved subject to the boundary conditions

$$\hat{U}_0 = \hat{V}_0 = 0, \quad \hat{V}_0 = \hat{F}(\sigma) \quad \text{on} \quad \varphi = 0, \quad (8c)$$

$$\hat{U}_0, \hat{V}_0, \hat{V}_0' \rightarrow 0 \quad \text{as} \quad \varphi \rightarrow \infty, \quad (8d)$$

where  $\hat{F}(\sigma)$  is the transform of the function  $F(\tilde{x})$ . As noted by Denier *et al.* [6] this system has solutions which possess simple poles at  $\sigma = \sigma_j$  where  $\sigma_j$  is the  $j$ th eigenvalue of the homogeneous system (8),  $j = 1, 2, \dots$ . We therefore seek a solution to (8) in the form

$$(\hat{U}_0, \hat{V}_0) = \frac{\Delta_j (U_{0j}(\sigma_j, \varphi), V_{0j}(\sigma_j, \varphi))}{(\sigma - \sigma_j)} + (U_{1j}(\sigma_j, \varphi), V_{1j}(\sigma_j, \varphi)) + \dots \quad (9)$$

Substitution into (8) shows that  $U_{0j}, V_{0j}$  are the eigenfunctions of (8) corresponding to eigenvalue  $\sigma = \sigma_j$ . We will normalise these functions so that  $U_{0j}$  has a maximum value of unity. At next order we find that the functions  $U_{1j}, V_{1j}$  satisfy an inhomogeneous form of (8). Such an inhomogeneous equation only has a solution provided a solvability condition on the inhomogeneous terms is satisfied. In our case this solvability condition serves to determine the *receptivity coefficient*  $\Delta_j$  as

$$\Delta_j = \frac{\tilde{\lambda}^3 Q_2'''(0)}{\int_0^\infty \varphi \left[ Q_1 U_{0j} + Q_2 (V_{0j}' - V_{0j}) \right] d\varphi} \quad (10)$$

where  $Q_1$  and  $Q_2$  are the adjoint eigenfunctions satisfying the system

$$\left( \frac{\partial^2}{\partial \varphi^2} - \frac{\sigma \varphi}{\tilde{\lambda}^3} - 1 - \frac{i\omega}{\tilde{\lambda}^2} \right) Q_1 + \frac{\varphi}{\tilde{\lambda}^3} Q_2 = 0, \quad (11a)$$

$$\left( \frac{\partial^2}{\partial \varphi^2} - 1 \right) \left( \frac{\partial^2}{\partial \varphi^2} - \frac{\sigma \varphi}{\tilde{\lambda}^3} - 1 - \frac{i\omega}{\tilde{\lambda}^2} \right) Q_2 - \frac{1}{\tilde{\lambda}^2} Q_1 = 0, \quad (11b)$$

subject to the boundary conditions

$$Q_1 = Q_2 = Q_2' = 0 \quad \text{on} \quad \varphi = 0, \quad (11c)$$

$$Q_1, Q_2, Q_2' \rightarrow 0 \quad \text{as} \quad \varphi \rightarrow \infty. \quad (11d)$$

In order to complete the problem we must invert the transformed velocity field; to do this we must be more precise about the form of the function  $F$  appearing in (6). If we are interested in the effect of an isolated suction slot we can take  $F$  to be a function of compact support in which case  $F$  will not have any singularities in  $\sigma_r \geq 0$ . Then, as discussed above, the only singularities of (8) in  $\sigma_r \geq 0$  correspond to the simple poles discussed above the contour of integration for the inverse transform can be chosen parallel to the imaginary axis to the right of  $\sigma = \Re(\sigma_1)$ . The contour is then closed in the left-hand half plane  $\Re(\sigma) < \Re(\sigma_1)$  and the only contribution to the inverse Laplace transform then comes from the simple poles at  $\sigma = \sigma_j$ . Thus we obtain

$$(u_0, v_0) = \sum_{j=1}^{\infty} (U_{0j}, V_{0j}) \Delta_j \hat{F}(\sigma_j) e^{\sigma_j x} \quad (12)$$

so that for a given value of  $\tilde{\lambda}$  the effective coupling coefficient between the isolated (in  $x$ ) unsteady suction and the vortex field is  $\Delta_j \hat{F}(\sigma_j)$ .

## Results

The eigenvalue problem posed by (8) was solved by first discretising the system using second order accurate centred differences in  $\varphi$ . The homogeneous boundary condition  $\hat{U}_0$  on  $\varphi = 0$  was replaced with the normalisation condition  $\hat{U}_0' = 1$  on  $\varphi = 0$ . When these boundary conditions are implemented in the discretised version of (8) an inhomogeneous matrix equation is obtained which can readily be solved. Newton iteration is then performed on the eigenvalue  $\omega$  until the final boundary condition  $\hat{U}_0 = 0$  on  $\varphi = 0$  is satisfied, to within some pre-defined tolerance. An identical technique is used to solve the adjoint system (11); by noting that the adjoint system has the same eigenvalues as system (8) we have a useful check on the accuracy of our results.

The eigenvalues of system (8) are presented in figure 1 for a variety of values of the forcing frequency  $\tilde{\omega}$ . These show similar trends to those discussed in Bassom & Hall's [1] work on the effect of crossflow on Görtler vortices. In particular we note that for increasing frequency the vortices become stabilised at some finite value of the scaled wavenumber  $\tilde{\lambda}$ . Additionally

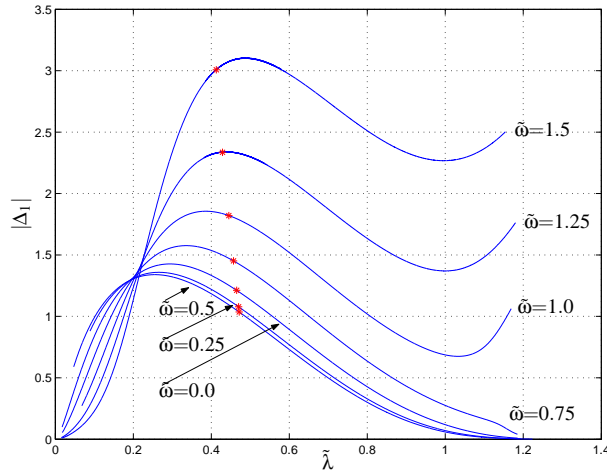


Figure 2: Plot of the magnitude of the receptivity coefficient  $|\Delta_1|$  for the first eigenvalue of system (8) versus wavenumber  $\tilde{\lambda}$ . The asterisk indicates the wavenumber location of the maximum growth rate (see Fig. 1a).

the magnitude of the largest growth rate  $\Re(\sigma)$  decreases with increasing frequency  $\tilde{\omega}$ .

The receptivity coefficient for the leading order eigenmode,  $|\Delta_1|$ , is given in figure 2. In order to interpret these results the values of the receptivity coefficient must be considered in the context of the streamwise response of the vortex disturbance which is given by (12). Thus the streamwise growth of the vortex is determined by the real part of  $\sigma$ . As figure 1 demonstrates increasing the frequency serves to reduce the growth rate. For sufficiently high frequencies the flow is completely stabilised, as is demonstrated by the *neutral curve* presented in figure 3. To the left of this curve the flow is unstable (over a finite band of vortex wavenumbers). The turning point in this curve is highlighted and occurs at  $\tilde{\omega} \approx 2.2542$ . Remembering that our analysis has focused upon the most unstable Görtler vortex we can then conclude that zero-mean suction of a frequency greater than  $2.2542G^{2/5}$  will stabilise the flow to Görtler vortices (or more precisely, promote spanwise periodic disturbances which decay downstream).

## Conclusions

We have shown that zero-mean suction can promote growing Görtler vortices in the boundary-layer flow over a concavely curved surface. If the frequency of the zero-mean suction is suitably high the vortices will decay immediately downstream of the source of the suction. Thus zero-mean suction provides a potential mechanism for the suppression of Görtler vortices.

## Acknowledgements

Thanks to S.R. Otto (R&A Rules Limited) and J.A.K. Stott (Bradford College) for some useful discussions on this problem. This work was funded by the Australian Research Council through Discovery Grant DP0210877.

## References

- [1] Bassom, A.P. and Hall, P., Vortex instabilities in three-dimensional boundary-layers – the relationship between Görtler and cross-flow vortices, *J. Fluid Mech.* **232**, (1991), 647.
- [2] Bassom, A.P. and Otto, S.R., Weakly nonlinear stability

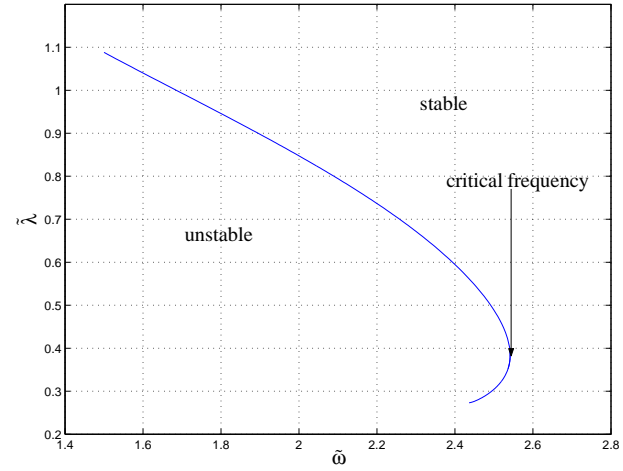


Figure 3: Plot of neutral wavenumber  $\tilde{\lambda}$  (at which  $\Re(\sigma) = 0$ ) as a function of the imposed frequency  $\tilde{\omega}$ .

of viscous vortices in three-dimensional boundary layers, *J. Fluid Mech.* **249**, (1993), 597.

- [3] Balakumar, P. and Hall, P., On the control of the fastest growing Görtler vortex, *Theor. Comp. Fluid Dyn.* **13**, (1999), 21.
- [4] Denier, J.P., The effect of suction on Görtler vortices, (in preparation).
- [5] Denier, J.P. and Bassom, A.P. On the existence of Görtler vortices in separated boundary layers. *Studies in Applied Mathematics* **96**, (1996) 247–271.
- [6] Denier, J.P., Hall, P. and Seddougui, S.O., On the receptivity problem for Görtler vortices: vortex motions induced by wall roughness, *Phil. Trans. R. Soc. Lond. A* **335**, (1991), 51–85.
- [7] Floryan, J.M. Saric, W.S., Effects of suction on the Görtler instability of boundary- layers, *AIAA J.* **21**, (1983), 1635.
- [8] Hall, P. The linear development of Görtler vortices in growing boundary layers. *J. Fluid Mech.* **126**, (1983), 357,
- [9] Kobayashi, R., Note on the stability of a boundary layer flow on a concave wall with suction, *J. Fluid Mech.* **52**, (1972) 269.
- [10] Lin, M.H. and Hwang, G.J., Numerical prediction of the formation of Görtler vortices on a concave surface with suction and blowing, *Int. J. Num. Meth. Fluids* **31**, (1999), 1281.
- [11] Mangalam, S.M., Dagenhart, J.R., Hepner, T.E., & Meyers, J.F., The Görtler instability on an airfoil, *AIAA Paper* (1985), **85-0491**
- [12] Myose, R.Y. and Blackwelder, R.F., Control of streamwise vortices using selective suction, *AIAA J.* **33**, (1995), 1076.
- [13] Park, D.S. and Huerre, P., Primary and secondary instabilities of the asymptotic suction boundary-layer on a curved plate, *J. Fluid Mech.* **283**, (1995), 249.
- [14] Schlichting, H., *Boundary-Layer Theory*, McGraw-Hill, Inc. (1979).
- [15] Timoshin, S., Asymptotic analysis of a spatially periodic unstable Görtler spectrum, *Fluid Dyn.* **25**, (1990), 25.

# The Safe Basin Erosion of a Ship in Waves with Single Degree of Freedom

X. Wu<sup>1</sup>, L. Tao<sup>1</sup> and Y. Li<sup>2</sup>

<sup>1</sup>School of Engineering, Griffith University, PMB50 GCMC, QLD9726 AUSTRALIA

<sup>2</sup>Department of Naval Architecture & Marine Engineering, South China University of Technology, CHINA

## Abstract

The safety of a ship is studied using the theory of "safe basin" in this paper. The safe basins of the single degree of freedom (rolling) in waves and winds are investigated. The influences of a static heel angle, waves and winds to the safe basin erosion are examined. It is found that the shape of the safe basin is changed when a static bias angle takes place, and the area of the safe basin decreases while the static heel angle increases, but the safe basin will begin to erode in waves or winds.

## Introduction

Current practice in the stability design of ships is based on the righting lever in still water (the GZ curve). Such an approach considers a ship in calm water, and imposes certain restrictions on the characteristics of the GZ curve. As a measure of the safety of a ship, the GZ curve gives a good description of the stability of a ship in still water, such as the initial metacentric distance (GM); the largest steady heeling force that the vessel can withstand without capsizing (maximum GZ); range of stability; and angle of deck edge immersion. However, large-amplitude ship motions are essentially transient due to the sudden appearance of waves and a gust of wind. Further, the ship capsizing, resulting from these nonlinear motions, is a dynamic process, the transient condition is therefore a much more useful measure of capsizing.

[13-15] first introduced the concept of "safe basin" to the study of the nonlinear ship rolling motion and capsizing. For a ship in still water experiencing a single-degree-of-freedom (1-DOF) roll motion due to initial disturbance, plotting the evolving solution of the 1-DOF dynamic system as a trajectory in phase space (with normalised roll angle and roll angular velocity as  $x$  and  $y$  axes respectively) rather than as a time history, [14,15] obtained a trajectory spiral into the origin as the ship comes to rest. Stationary steady solutions are represented in phase space by points, while periodic solutions appear as closed curves, such as the case of a ship in waves. Those stable solutions are called attractors, while the unstable solutions are called repellers. The combination of the domains of all attractors is termed the safe basin [9].

Marshfield [5] demonstrated the nonlinear character of the frequency response curve and the existence of bi-stability within a certain range around resonance through "Admiralty model tests". By applying the nonlinear dynamic system theory on the ship-capsizing problem, [9] and [16] considered the capsizing process as dynamically equivalent to the escape of a ball rolling in a potential well, i.e. a transient phenomenon. The significance of the new method of quantifying stability of a ship in waves is that the use of the transient capsizing diagram to assess the ship hull's capsizability, and the demonstration of considerable impact of bias on the maximum wave slope at which capsizing is still resisted. [3] extended the nonlinear dynamic system theory to the study of 1-DOF nonlinear rolling motion and capsizing of biased ships in random beam seas. Compared to the inertia effects and hydrostatic righting moments, the relatively small damping and wave excitation moments were treated as perturbations. Assuming an unperturbed system model, safe and unsafe areas were defined in the phase plane to distinguish the qualitatively different ship motions of capsizing and non-capsizing. Capsizing events were represented by solutions passing out of the safe region.

Finally, they presented the quantitative description of the influence of bias on the probability of capsizing in random beam seas, and concluded that the widening of the dangerous significant frequency range when bias is presented.

In this paper, a current-in-use cargo ship is used for the study of safe basin erosion. The nonlinear damping, which is very important to ship roll motion in waves, is obtained by an experiment of the ship model rolling in waves in a wave tank. Other coefficients in the roll motion equation of the ship in waves are obtained through theoretical methods. The safe basins with and without heel angle are discussed, and the safe basin erosions caused by the exciting wave spectrum and the pulse wind spectrum are investigated by using a quantitative method.

## Theoretical Formulation

A typical roll motion with single degree of freedom can be described as

$$(I + \Delta I(\omega))\ddot{\theta} + B(\omega)\dot{\theta} + C\theta = F_{wave}(t) + F_{wind}(t), \quad (1)$$

where  $\theta$  is the roll angle,  $\dot{\theta}$  and  $\ddot{\theta}$  are the first and second derivatives with respect to time,  $I$  is the total moment of inertia in roll,  $\Delta I(\omega)$  is the roll added mass coefficient,  $B(\omega)\dot{\theta}$  is the nonlinear damping moment,  $C\theta$  is the nonlinear restoring moment,  $F_{wave}(t)$  is the wave exciting moment, and  $F_{wind}(t)$  is the wind exciting moment. Various expressions of damping and restoring terms were used to simulate the nonlinear characteristics of roll motion. The commonly used representations are:

$$B(\omega)\dot{\theta} = B_L(\omega)\dot{\theta} + B_N(\omega)\dot{\theta}|\dot{\theta}|, \quad (2)$$

$$C\theta = C_0 + C_1\theta + C_3\theta^3, \quad (3)$$

where  $B_L$  and  $B_N$  are the linear and nonlinear damping coefficients respectively,  $C_1$  and  $C_3$  are the linear and third-order restoring force coefficients, and  $C_0$  is the bias moment which can arise due to wind, cargo, ship damage or the pull of a fishing net.

Eq. 1 is a frequency domain description since  $\Delta I(\omega)$  and  $B(\omega)$  are frequency-dependent due to the presence of the free surface. Following [7], the time-domain ship rolling motion equation can be written as:

$$(I + \Delta I(\infty))\ddot{\theta} + \int_0^\infty K(t - \tau)\dot{\theta}(\tau)d\tau + B_N\dot{\theta}|\dot{\theta}| + C_0 + C_1\theta + C_3\theta^3 = F_{wave}(t) + F_{wind}(t) \quad (4)$$

where  $\Delta I(\infty)$  is the hydrodynamic added mass coefficient evaluated at the infinite frequency limit;  $K(t)$  is the hydrodynamic rolling moment due to impulse roll velocity expressed as Eq. 5; and its integral is usually called the memory function, as it represents how roll-radiation moments depend on the history of rolling velocity.

$$K(t) = \frac{2}{\pi} \int_0^\infty (B_L(\omega) - B(\infty)) \cos(\omega t) d\omega. \quad (5)$$

Following [17], the wave exciting moment  $F_{wave}(t)$  can be expressed by

$$F_{wave}(t) = \int_0^\infty \frac{F_{wave}(\omega)}{\zeta_0} \cos(\omega t + \varepsilon(\omega)) \sqrt{2S_\zeta(\omega)} d\omega, \quad (6)$$



where  $F_{wave}(\omega)/\zeta_0$  is the response function of wave exciting moment in frequency domain;  $\varepsilon(\omega)$  is the response function of the phase difference in frequency domain represented by a random value between 0 and  $2\pi$ ; and  $S_\varepsilon(\omega)$  is the wave elevation spectrum represented by ITTC two-parameter formula:

$$S_\varepsilon(\omega) = \frac{A}{\omega^5} \exp[-B/\omega^4], \quad (7)$$

where  $A = 173H_{1/3}^2/T_z^4$ ,  $B = 691/T_z^4$ ,  $H_{1/3}$  is the significant wave height and  $T_z$  is the zero up-crossing wave period.

Following [1], the wind exciting moment  $F_{wind}(t)$  can be expressed as:

$$F_{wind}(t) = \frac{1}{2} C_m \rho_a A_w z_a u^2(t), \quad (10)$$

where  $C_m$  is the wind moment coefficient;  $\rho_a$  is the density of air;  $A_w$  is the wind area;  $z_a$  is the height of the wind area centre; and  $u(t)$  is the velocity of wind. In order to determine the safe basin erosion caused by the wind, the pulse wind spectrum different to that of [1] is adopted, and can be described by a Fourier series:

$$u(t) = u_0 + \sum_{i=1}^{\infty} u_i \cos(\omega_i t + \varepsilon_i), \quad (11)$$

where  $u_0$  is the average velocity of wind;  $\omega_i$  is the pulse frequency of wind velocity;  $\varepsilon_i$  is the phase difference of wind velocity; and  $u_i$  is the turbulent velocity of wind expressed as:

$$u_i = \sqrt{2S_u(\omega)d\omega}, \quad (12)$$

where the wind velocity spectrum can be represented by Von Karman spectrum [11],

$$S_u(\omega) = \frac{4\bar{u}^2 L_x^u}{\bar{U} [1 + (2c\omega(L_x^u/\bar{U}))^2]^{5/6}}, \quad (13)$$

where  $\bar{U}$  is the longitudinal mean wind speed;  $\omega$  is the frequency of pulse wind;  $L_x^u$  is the longitudinal turbulence integral length scale of longitudinal turbulence;  $\bar{u}^2$  is the variance of longitudinal turbulent velocity; and  $c$  is a constant that is the function of height of observation site and its surrounding terrain.

Since the general solution for nonlinear ordinary differential equation with 1-DOF describing roll motion of a ship in waves is unknown, the solution of Eq. 4 will be obtained by numerical simulation. The phase space consists of roll angle  $\theta$  (-1.5~1.5) and roll velocity  $\dot{\theta}$  (-0.31~0.31), and is divided into  $600 \times 620$  small areas. Eq. 4 with initial condition including the values of each small area is solved by using the Adams fourth-order trial and error method. If the solution can be obtained, the small area is called the domain of safe abstract marked black. The safe basin is obtained by the combination of the domains of all the safe attractors.

### Parameters and coefficients of the ship

The data of a current-in-use cargo ship introduced in our study are given in Table 1. The GZ curve of the ship is shown in Fig. 1. The linear and third-order restoring moment coefficients are obtained by the fitting of the GZ curve,  $C_1^* = 0.56725$  and  $C_3^* = -0.47992605$ .

Then the linear and third-order restoring force coefficients are:

$$C_1 = \Delta g C_1^*, \text{ and } C_3 = \Delta g C_3^*.$$

The linear damping is obtained by numerical computation using 3D Source Distribution Method, while nonlinear damping is

obtained by an experiment of the model ship rolling in irregular waves. The value of nonlinear damping  $B_N$  ( $= 2.502 \times 10^6 \text{ kg} \cdot \text{m}^2$ ), is finally obtained from roll time record in irregular waves using Random Decrement Technique. For details of the obtaining of nonlinear damping in an experiment, readers can refer to [4].

Length overall	105.9 m	L <sub>p</sub>	99 m	Displacement	6.2 x 10 <sup>6</sup> kg
Mean Draft	5.55 m	Inertial Radius of Roll	0.35 m	Centre of Gravity above Baseline	6.715 m
Breadth	16.0 m	Depth	9 m	Natural Period of Roll	23.55 s

Table 1. Principle dimensions of the cargo ship.

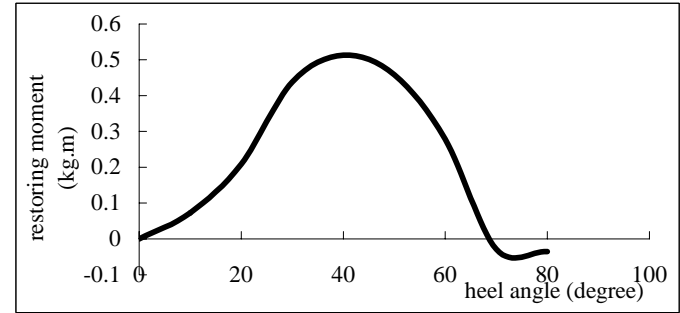


Fig. 1 GZ curve of the ship.

## Results and discussion

### Effects of heel angle

The safe basins with different heel angles without wind and waves are shown in Fig 2- Fig. 4. The intersection of the top line and bottom line is called a saddle, which is the position where the safe basin begins to disappear. The values of saddles with different initial heel angle  $\delta$  are shown in Table 2. Several significant differences between safe basins with or without heel angle can be observed from the figures: 1) The safe basin without heel angle, which is symmetric to x-axis and y-axis, is composed of a top and bottom curve, while the safe basin which is asymmetric to y-axis is closed by a curve when the heel angle appears; 2) The value of the left saddle is different from the value of the right saddle when the heel angle appears; 3) The area of safe basin decreases as the heel angle increases; 4) no safe basin erosion occurs if wind and waves are not considered.

Heel angle (rad.)	Values of left saddle (rad.)	Values of right saddle (rad.)
0	-1.0871	1.0871
0.01	-1.06756	0.9336
0.08	-1.03998	0.60985

Table 2 Values of saddle with different hell angles.

### Effects of waves

Fig. 5 and Fig. 6 are the safe basins in [10] and the present study respectively, using wave slope spectrum for the excitation parameters  $a/\omega_0^2 = 0.03$ ,  $\omega_N/\omega_0 = 0.9$  (equal to excitation parameters  $H_{1/3} = 6 \text{ m}$ ,  $\bar{T} = 10 \text{ s}$ ). However, the response function of the exciting moment in [10] is a sinusoidal response function, while the response function in the present study is a response curve obtained from theoretical calculation. As can be seen from the figures, excellent agreement is obtained, indicating the feasibility of present method. The safe basin using the ITTC spectrum with the same excitation parameter  $H_{1/3} = 6 \text{ m}$ ,  $\bar{T} = 10 \text{ s}$  is shown in Fig. 7. The quantitative results are obtained by an introduction of safe basin ratio  $A_s$ , a value of computational area divided by the safe basin area. The values of  $A_s$  in Fig. 6 and Fig. 7 are 0.548 and 0.352 respectively,

demonstrating the significant impact of the selection of wave spectrum on safe basin erosion. The adoption of the wave slope spectrum results in the evaluation of a larger safe basin area.

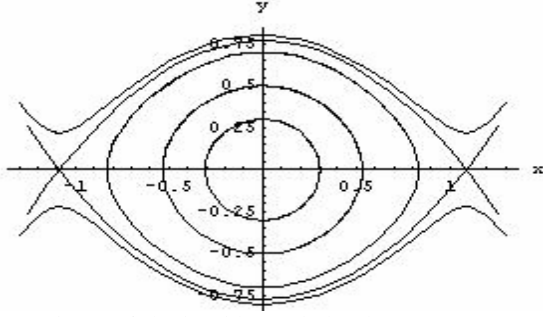


Fig. 2 Safe basin without wind and waves ( $\delta = 0$ )

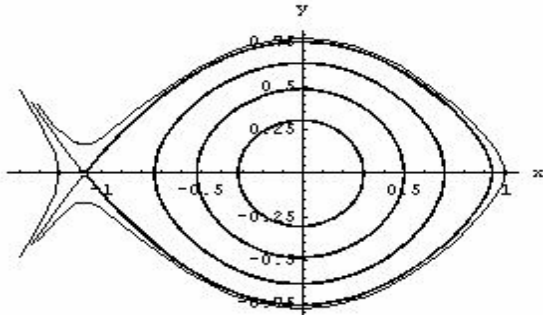


Fig. 3 Safe basin without wind and waves ( $\delta = 0.01$ )

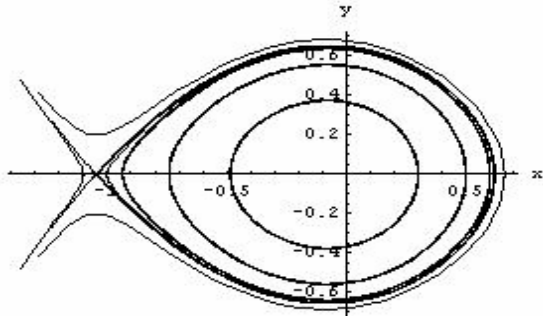


Fig. 4 Safe basin without wind and waves ( $\delta = 0.08$ )

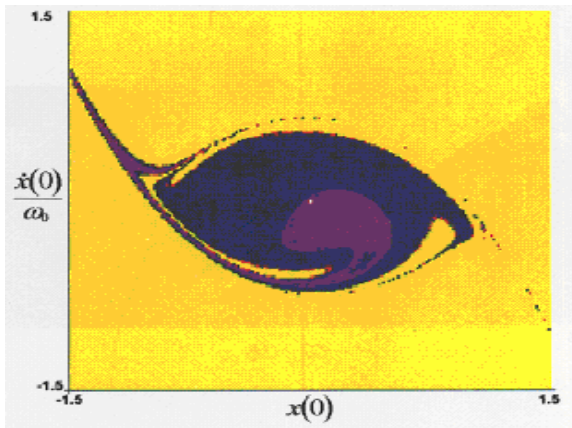


Fig. 5 Safe basin in waves using wave slope spectrum,  
 $a / \omega_0^2 = 0.03, \omega_N / \omega_0 = 0.9$ .

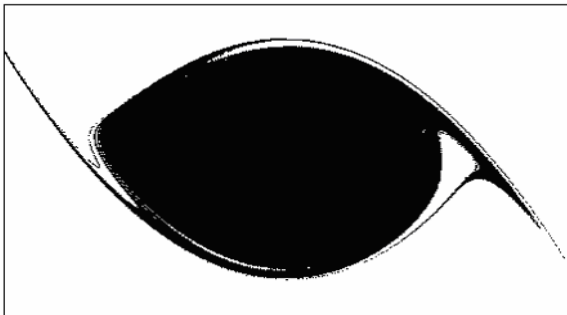


Fig. 6 Safe basin in waves using wave slope spectrum,  $H_{1/3} = 6\text{m}$ ,  
 $\bar{T} = 10\text{ s}$ .

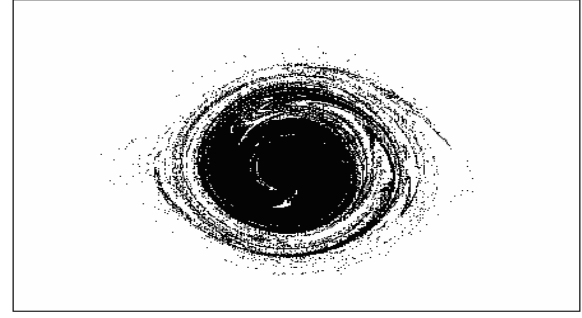


Fig. 7 Safe basin in waves using ITTC spectrum ( $H_{1/3} = 6\text{m}$ ,  $\bar{T} = 10\text{ s}$ ).

Fig. 8 and Fig. 9 show safe basins obtained using ITTC spectrum with different  $H_{1/3}$  and same  $\bar{T}$ . Fig. 10 is a safe basin obtained using ITTC spectrum with excitation parameters  $H_{1/3} = 6\text{ m}$ ,  $\bar{T} = 6\text{ s}$  (the same  $H_{1/3}$  as in Fig. 7). As can be seen, the higher the wave height  $H_{1/3}$ , the smaller the safe basin area. However, it appears that the effect of a wave period on the safe basin area is small. This is because the much longer natural roll period of the ship compared to the wave periods.

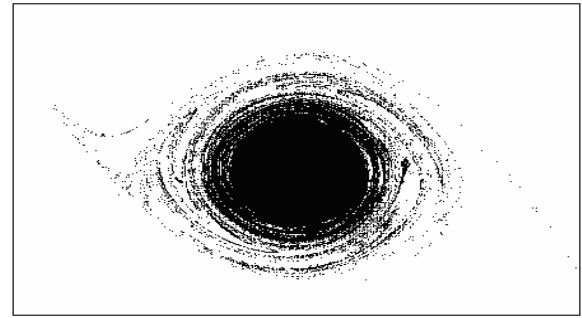


Fig. 8 Safe basin in waves using ITTC spectrum ( $H_{1/3} = 5\text{m}$ ,  $\bar{T} = 8\text{ s}$ ).

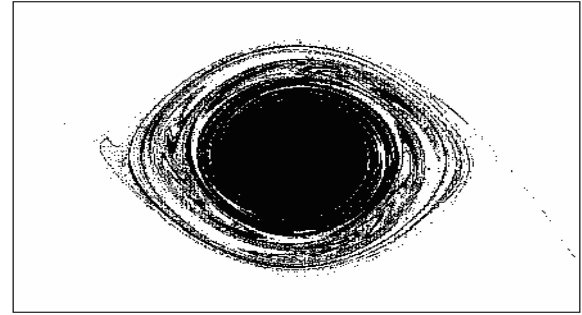


Fig. 9 Safe basin in waves using ITTC spectrum ( $H_{1/3} = 3\text{m}$ ,  $\bar{T} = 8\text{ s}$ ).

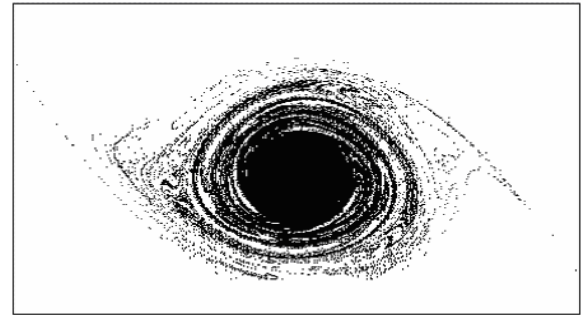


Fig. 10 Safe basin in waves using ITTC spectrum ( $H_{1/3} = 6\text{m}$ ,  $\bar{T} = 6\text{ s}$ ).

There is a significant difference in the shape of safe basin in waves in comparison with the safe basin in calm water without wind. The two sides of the boundary have extended outside, and even the unsafe attractors appear inside the safe basin, i.e. the safe basin erosion occurs. As can be seen, the ship is more dangerous under the higher wave height  $H_{1/3}$ , as the safe basin erosion area is larger.

### Effects of wind and waves

The velocity and turbulence statistics at the north-eastern coast of Taiwan under high-wind condition by [11], is selected as the environmental condition for the present study. The different wind parameters, also used by [2], are shown in Table 3.

When wind is considered, safe basin erosion occurs (see Fig. 11 for  $\bar{U} = 18.78$  m/s). Fig. 12 is the safe basin obtained using ITTC spectrum with wave excitation parameter  $H_{1/3} = 5$  m,  $\bar{T} = 8$  s and wind parameter  $\bar{U} = 15.58$  m/s. Compared to the safe basin in Fig. 8, it can be seen that their shapes are almost identical. However, the different safe basin ratios  $A_s$  (0.1410 in Fig. 8 and 0.1381 in Fig. 12) indicate that the effect of wind on the safe basin is not negligible.

### Conclusions

Ship capsizing has been studied using safe basin theory. The effects of initial heel angle, waves and winds on safe basin erosion have been discussed. The following conclusions can be drawn from the present study:

- The area of the safe basin is dependent on the heel angle. The larger the heel angle, the smaller the area of the safe basin. However, no safe basin erosion occurs if the ship is in calm water without wind.
- The wave exciting spectrum is found to have a significant effect on the safe basin erosion. The safe basin area is unreasonably large if the ideal wave spectrum is used.
- The wave height has a greater impact on safe basin erosion than the wave period. The pulse wind is also found to cause safe basin erosion. The random properties of wind and waves should be considered in the investigation of safe basin erosion.

### Acknowledgments

This research project was sponsored by the National Natural Science Foundation of China, Grant No.10072021.

### References

- [1] Belenky, V.L., Degtyarev, A.B. & Boukhanovsky, A.V., Probabilistic qualities of nonlinear stochastic rolling, *Ocean Engineering*, **25**(1), 1998, 1-25.
- [2] Bhattacharyya, R., *Dynamics of marine vehicles*, New York, Wiley & Sons Inc., 1978.
- [3] Jiang, B.Y.C., Troesch, A.W. and Shaw, S.W., Highly nonlinear rolling motion of biased ships in random beam sea, *J. of Ship Res.*, **40**(2), 1996, 125-135.
- [4] Li, Y.L. and Wu, X.R., Experimental Determination of Nonlinear roll Damping: a Technique for Data Processing (In Chinese), *J. of South China University of Tech.*, **30**(2), 2002, 79-82.
- [5] Marshfield, W.B., AMTE-NMI capsizing experiments, *Admiralty Research Establishment*, Haslar Gosport Hants, Report TM78011, 1978.
- [6] Odabashi, A.Y., Methods of analysing nonlinear ship oscillations and stability, Department of Shipbuilding and Naval Architecture, University of Strathclyde, Report No 08/73, 1973.
- [7] Ogilvie, T.F., Recent progress toward the understanding and prediction of ship motions, *Proc. 5th Symp. on Naval Hydrodynamics*, 1964, 3-80.
- [8] Oh, I., Nayfeh, A.H. and Mook, D., Theoretical and experimental study of the nonlinearly coupled heave, pitch and roll motions of a ship in longitudinal waves, *Proc. 19th Symp. on Naval Hydrodynamics*, **2**, 1992, 71-89.
- [9] Rainey, R.C.T. and Thompson, J.M.T., The Transient Capsizing Diagram - A New Method of Quantifying Stability in Waves, *J. of Ship Res.*, **35**(1), 1991, 58-62.

$H_{1/3}$ (m)	$\bar{T}$ (s)	$\bar{U}$ (m/s)	$L_x^u$	$\overline{u^2}$	$C$
3.0	6.0	12.35	-	-	4.023
5.0	8.0	15.58	40.8	9.516	4.023

Table 3 Wind conditions.

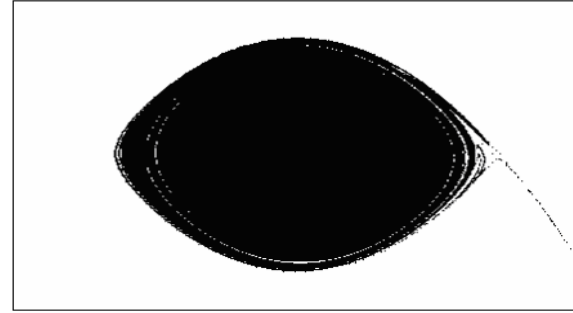


Fig. 11 Safe basin in wind ( $\bar{U} = 18.78$  m/s).

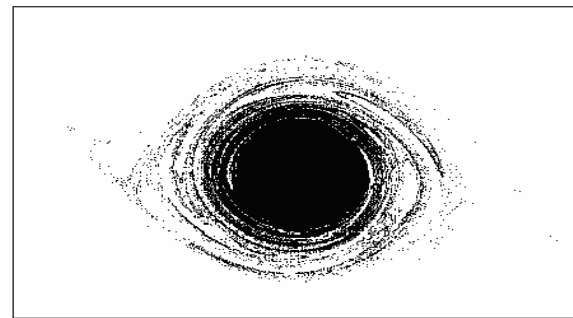


Fig. 12 Safe basin in wind and waves using ITTC spectrum ( $H_{1/3} = 5$  m,  $\bar{T} = 8$  s,  $\bar{U} = 15.58$  m/s).

- [10] Senjanvic, I. and Fan, Y., Numerical simulation of a ship capsizing in irregular waves, *Chaos, Solitons & Fractals*, **5**(5), 1995, 727-737.
- [11] Shiau, B.S., Velocity spectra and turbulence statistics at the northeastern coast of Taiwan under high-wind conditions, *J. of Wind Engineering and Industrial Aerodynamics*, **88**, 2000, 139-151.
- [12] Spyrou, K.J. and Thompson, J.M.T., The nonlinear dynamics of ship motions: a field overview and some recent developments, *Phil. Trans. Roy. Soc. Lond. A* **358**, 2000, 1735-1760.
- [13] Thompson, J.M.T. and Stewart, H.B., *Nonlinear dynamics and chaos*, New York, John Wiley & Sons Inc., 1987.
- [14] Thompson, J.M.T., Loss of engineering integrity due to the erosion of absolute and transient basin boundaries, *Proc. of IUTAM Symp. On the Nonlinear Dynamics in Engineering Systems*, 1989, 313-320.
- [15] Thompson, J.M.T., Transient basins: a new tool for designing ships against capsizing, *Proc. of IUTAM Symp. on the Dynamics of Marine Vehicles & Structures in Waves*, 1990, 325-331.
- [16] Thompson, J.M.T. and Soliman, M.S., Fractal control boundaries of driven oscillators and their relevance to safe engineering design, *Proc. of The Royal Society, London*, **A 428**, 1990, 1-13.
- [17] Van Oortmerssen, G., *The motions of a moored ship in waves*, Thesis, MARIN Publications No. 510, 1976.
- [18] Wellicome, J.F., An analytical study of the mechanism of capsizing, *Proc. 1st International Conf. on Stability of Ships and Ocean Vehicles*, University of Strathclyde, 1975.
- [19] Wright, J.H.G. and Marshfield, W.B., Ship roll response and capsizing behaviour in beam seas, *Transactions RINA*, **122**, 1980, 129-148.

## Exchange flow between continuously stratified reservoirs

Andrew McC. Hogg<sup>1</sup> and Peter D. Killworth<sup>2</sup>

<sup>1</sup>Research School of Earth Sciences  
The Australian National University, Acton, ACT, 0200, AUSTRALIA

<sup>2</sup>Southampton Oceanography Centre  
European Way, Southampton SO14 3ZH, UK

### Abstract

We provide a solution to inviscid steady exchange flow between continuously stratified reservoirs, where it is assumed that the flow in each direction is independently self-similar. The solution requires knowledge only of the two reservoir stratifications and an imposed net barotropic through flow, and includes regions of stagnant fluid which separate two counter-flowing, stably stratified layers. It is argued that these stagnant, or inactive layers, may play a role in oceanic and geophysical flows, but are inherently difficult to observe in field measurements.

### Introduction

Density driven exchange flow through a channel connecting two reservoirs occurs in many geophysical systems, in particular between ocean basins, between semi-enclosed seas and the open ocean, and at the mouth of estuaries. To first order, a solution for bi-directional exchange can be obtained by assuming a two-layer structure in the flow [1, 2, 7]. The two-layer hydraulic solution can be used to give a first order prediction of flow through a channel, assuming that the end reservoirs are homogeneous and that the fluid is inviscid, hydrostatic, non-rotating and incompressible. However geophysical flows are invariably more complicated than the two-layer theory. Here we present the results of a study into the influence of stable stratification in the reservoirs upon exchange flows.

Continuously stratified internal hydraulics was investigated by Killworth [5] for the case of uni-directional flow. In appendix A of that paper it was demonstrated that if inviscid bi-directional exchange between stratified reservoirs were to occur, then the vertical position of the streamline dividing the two counter-flowing regions can only occupy one position in the vertical: it must be flat everywhere. This result breaks down in two cases; first, when the density coordinates are discontinuous (that is, when the vertical gradient in density is zero) and second, when there is a discontinuity in density at the dividing streamline.

Engqvist [3] used a multi-layer formulation to include stratification into bi-directional exchange flows through a contracting channel. The multiple layers are divided into left- and right-flowing groups and if these two groups of active layers are separated by a central layer which has zero velocity, then the problem can be solved. The central stagnant layer has the effect of decoupling the two groups of layers so that control conditions for each group of layers independently satisfies Wood's [6] criteria for control of the selective withdrawal problem.

Motivated by the result of Killworth [5] we have investigated the problem of flow through a flat-bottomed contracting channel using analytical techniques and a two-dimensional numerical model. We extend Engqvist's [3] layered solution to continuously stratified flow. In addition we show a solution where the two active layers are allowed to make contact at one point. We proceed test this theory against the numerical model.

### Analytical model

#### The selective withdrawal problem

The derivation of selective withdrawal of an inviscid fluid from a stratified reservoir was originally due to Wood [6]. One assumes a single layer flow in which the reservoir density profiles and channel shape is known. The linear Bernoulli function for a Boussinesq fluid is written

$$B(x, z) = \frac{p + \rho g z}{\rho_0}, \quad (1)$$

where  $x$  is the horizontal coordinate,  $z$  denotes height,  $g$  acceleration due to gravity,  $\rho$  density,  $\rho_0$  the reference density and  $p$  pressure. Define  $\eta$ , the upstream height coordinate which follows streamlines (so that in the reservoir  $z = \eta$ ), and note that density conservation implies that  $\rho = \rho(\eta)$  only. Conservation of energy along a streamline is then simply

$$\frac{1}{2}u^2 + B = B_\infty, \quad (2)$$

where  $u$  is horizontal velocity and  $B_\infty(\eta)$  is the Bernoulli function in the upstream reservoir (where  $u = 0$ ).

Conservation of volume along a streamline can be written

$$ubz_\eta = Q(\eta), \quad (3)$$

where  $b(x)$  is the channel width and  $Q$  is the flux along the streamline. Equations (2) and (3) then allow solution of the selective withdrawal problem.

These equations are now applied to the withdrawal of a stably stratified fluid (with total upstream depth  $h$ ) through a contracting channel. The boundary conditions on the flowing layer include a solid surface on the lower boundary where  $z = 0$ , and a free upper surface with a density jump  $\delta\rho$ . We assume that flow within the layer is self-similar [6], or in other words the height and energy of a streamline can be separated into  $x$ - and  $\eta$ -dependent parts:

$$z(x, \eta) = \alpha(x)\eta, \quad (4)$$

$$B(x, \eta) = \alpha(x)B_\infty(\eta). \quad (5)$$

The factor  $\alpha(x)$  describes the reduction in height of a streamline from the upstream reservoir conditions.

The assumption of self-similarity allow us to write down a solution to this problem. The horizontal velocity  $u$  can be deduced from (2), and substituted into (3) to obtain

$$b(x)\alpha(x)(1 - \alpha(x))^{1/2} = \frac{Q(\eta)}{(2B_\infty(\eta))^{1/2}}. \quad (6)$$

The left hand side of (6) depends only upon  $x$ , while the right hand side is a function of  $\eta$ , implying that both sides are constant. The  $x$ -derivative of (6) gives

$$\frac{1}{b} \frac{db}{dx} = \frac{1}{\alpha} \frac{d\alpha}{dx} \left( \frac{3\alpha - 2}{2(1 - \alpha)} \right). \quad (7)$$



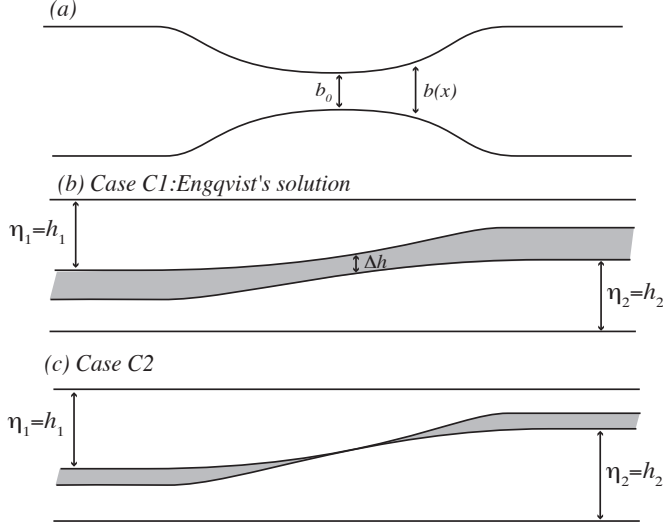


Figure 1: Schematic of stratified exchange flow. (a) Contracting channel in plan view; (b) case C1; Engqvist's solution for two decoupled layers separated by a minimum distance of  $\Delta h$ ; (c) case C2; solution where flowing layers touch at one (and only one) point. In both cases upstream stratification for each layer, and upstream height coordinate are known.

When there is a minimum in  $b(x)$ , then either  $d\alpha/dx = 0$  or  $\alpha = 2/3$ . The latter case was defined by Wood [6] as a point of hydraulic control, which enables us to find velocity and density everywhere provided that the withdrawal height  $h$  is known.

#### Application of self-similar flow to bi-directional exchange

We now apply Wood's self-similar solution to exchange flows, where we have two stably stratified reservoirs at either end of a channel which has a simple minimum in width. Two cases are considered, as depicted in figure 1. In both examples we allow for two active layers flowing in opposite directions, and use two upstream vertical coordinates ( $\eta_1$  for the upper layer, and  $\eta_2$  for the lower layer). The first scenario (case C1, figure 1(b)) is simply the continuous extension of the layered solution proposed by Engqvist [3], and we therefore refer to it as Engqvist's solution. In this solution there are two active layers which are divided by a stagnant, or inactive region in which we assume that vertical gradients of both velocity and density are zero. At some point in the channel the stagnant region has a minimum thickness which we call  $\Delta h$ . For this case we expect the density jump which bounds the flowing layers,  $\delta\rho$ , to be zero.

In the second case (C2, figure 1(c)), the two flowing layers touch at a single point. This is analogous to Engqvist's solution with  $\Delta h = 0$ , and  $\delta\rho$  finite. The inactive region still exists in this solution, and is of finite thickness throughout the length of the channel except for the point where the layers touch.

The solution of these equations requires knowledge of the upstream withdrawal height  $h_i$  for each layer. We have several restrictions which allow us to calculate these heights, namely that the two layers are closest at some point  $x_0$

$$\alpha_1(x_0)h_1 + \alpha_2(x_0)h_2 = 1 - \Delta h, \quad (8)$$

(where all heights have been nondimensionalised by the total height  $H$  of the channel). In addition there are conditions on the density of the streamlines bounding the active layers, namely

$$(C1): \quad \rho_1(h_1) = \rho_2(h_2) \quad \delta\rho = 0, \quad (9a)$$

$$(C2): \quad \Delta h = 0 \quad \delta\rho = \frac{\rho_2(h_2) - \rho_1(h_1)}{2}, \quad (9b)$$

where we have assumed that stagnant fluid has density which is the half-way between the densities on the streamline bounding either active layer.

One more condition on layer heights is required to close this problem. This condition is a specified barotropic flux  $q_0$  through the channel. For the cases shown here, we retain symmetry, so that  $q_0 = 0$ , and reservoir stratifications are linear and symmetric (although more general solutions are possible via iterative methods [4]). Because of this symmetry, the point  $x_0$  is found at the centre of the channel,  $\alpha_i(x_0) = \frac{2}{3}$ ,  $h_1 = h_2$  and (8) becomes

$$\Delta h = 1 - \frac{4}{3}h_i. \quad (10)$$

This is sufficient to close the problem.

#### Comparisons

We now test the theory (and, by implication, the self-similar assumption) by simulating stratified exchange flows with a hydrostatic 2-dimensional numerical model (see [4] for details). We compare the numerical and analytical solutions, to determine whether the assumption of self-similarity and the derived solution provide a suitable description of stratified exchange flows. In comparing the two solutions, we are primarily interested in whether the self-similar solution is selected by the numerical simulation, but note that we expect to see some differences due to the role of diffusion and viscosity in the simulations. Thus we anticipate that the numerical solution will be more diffuse, particularly close to the edge of the active layers, where discontinuities in velocity and density gradients are present in the analytical model.

In the two cases presented, both reservoirs are linearly stratified with the same density gradient (described by the top to bottom density difference  $\delta_v$ ), but the mean density of each reservoir is offset by a small amount (the horizontal density difference being  $\delta_H$ ). The ratio of vertical to horizontal density differences  $r_p = \frac{\delta_v}{\delta_H}$  governs whether solution C1 or C2 will be selected. For large values of  $r_p$  the stratification in the reservoirs is strong and solution C1 is expected. For small  $r_p$  solution C2 is possible.

#### Case C1

The analytical flow field is shown in figure 2(a) for the case  $r_p = 4$ . The numerical simulation, shown in panel (b), appears to be qualitatively similar; both solutions show anti-symmetric layers which accelerate through the contraction. A region of zero (or small) velocities divides the two flowing layers. The two lower panels in this diagram show the differences between the numerical and analytical solutions for the density (c) and velocity (d) fields as a percentage of the range in density and velocity respectively. These diagrams show that, to first order, the assumption of self-similarity applies in the numerical solution. Within the active layers the differences between the two solutions are generally very small ( $< 3\%$ ). Self-similarity deteriorates with distance along the channel, which is expected from the impact of diffusion and viscosity in the numerical solution.

The largest differences between the numerical and analytical solutions (10–15%) can be seen at the edge of the flowing layers, and within the inactive regions. The analytical solution predicts a discontinuity in the velocity gradient at the edge of the flowing layers, so that the diffusive flux in the numerical solution is expected to be large. Viscosity thus acts to thin the stagnant region in the centre of the channel (near  $x/L = 0$ ) so that it might appear from the numerical solution that the stagnant region does not extend to the centre of the channel. The velocit-

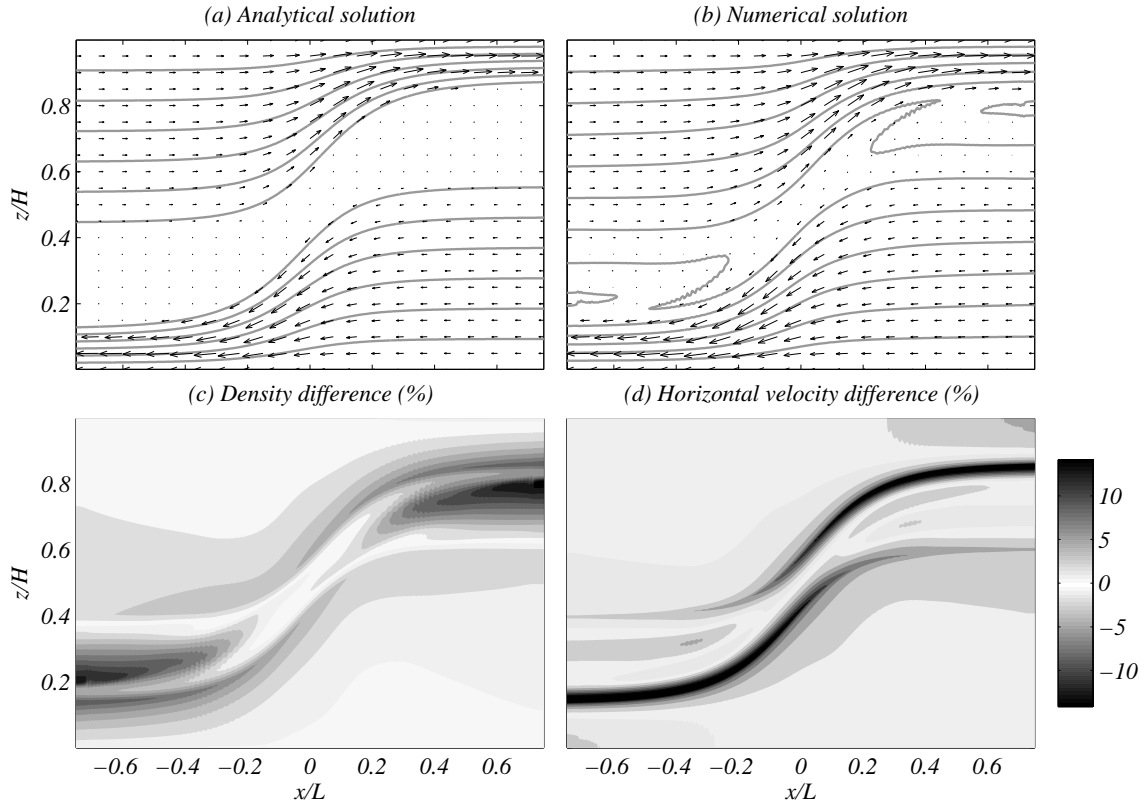


Figure 2: Engqvist's solution (case C1) with  $r_p = 4$  and  $q_0 = 0$ . Isopycnals (contours) and velocity (vectors) for (a) the self-similar analytical solution; (b) numerical simulations. (c) Difference in density and (d) difference in horizontal velocity.

ies in this region are small compared to velocities in the active layers, but the effects of recirculation can be seen in the density field. In fact, the largest errors in the density field are due to these recirculations, which produce a statically unstable density profile in the inactive parts of the flow. These unstable regions are allowed to develop, as the numerical convection routine is turned off. It is shown in Hogg and Killworth [4] that the addition of convection removes the unstable density fields without altering flow in the active layers.

### Case C2

A more stringent test of the self-similarity assumption is the case where stratification is further weakened, as shown in figure 3 so that the analytical solution requires that the layers meet at a point and the density jump,  $\delta\rho$  is finite. The implication of this solution is that some fluid from (say) reservoir 2 is dense enough that it might be exchanged, but that the requirement for self-similar flow, in combination with the existence of flow in layer 1, acts to block the passage of this dense fluid. The data shown in figure 3 supports the hypothesis that self-similar flow occurs in this case. This can be seen by the small differences ( $< 5\%$ ) within the two flowing layers. In this case there are discontinuities in both density and velocity at the edges of the flowing layers in the analytical solution. The result is that diffusion is large in the numerical solution so that differences between numerical and analytical predictions are as great as 20% at the edges of the layers, and also acts to reduce the total transport of each layer.

The analytical solution in figure 3 includes a finite width stagnant region everywhere except at  $x = 0$ . However the numerical solution (figure 3(b)) shows that the stagnant region is only observable there towards either end of the channel. This highlights the role of viscosity in thinning the stagnant region. One can infer from these simulations, which use the minimum vis-

cosity necessary for stability, that stagnant layers are unlikely to be observed in geophysical flows with reasonable values of viscosity. Nonetheless, the importance of self-similarity in the simulated flow indicates the relevance of the solution presented here as an estimate of exchange flux.

### Discussion

We have presented a method of calculating flow between stratified reservoirs assuming that flow within each of two active layers is self-similar. The simplification yielded by the assumption of self-similarity allows us to solve analytically for flow in both layers, producing a solution which predicts that parts of the fluid column are inactive. It is these inactive or stagnant regions which allow us to overcome the paradox raised by Killworth [5]. In that paper it was shown that if bi-directional stratified exchange flow were to occur, then the zero-velocity streamline can only occupy one vertical position. The self-similar solutions bypass this condition because the zero streamline(s) occur in regions of the flow where there is no vertical gradient in density.

We have proposed two self-similar cases which are solutions for stratified bi-directional flow through a flat-bottomed contracting channel. Confirmation of the solutions are difficult. The theory described here is inviscid by necessity, and yet we are using it as a theoretical model to describe flows which will always feel the effect of viscosity. This is true for observed geophysical flows, laboratory models and numerical simulations. Numerical simulation allows the greatest scope for comparison, since we can run the model such that viscosity and diffusion are minimised. These comparisons show the first order effect that viscosity and diffusion have upon the flow, and that the major elements of the theoretical solution can be identified in the simulated flows.

In the examples shown, the inactive regions are thinned by

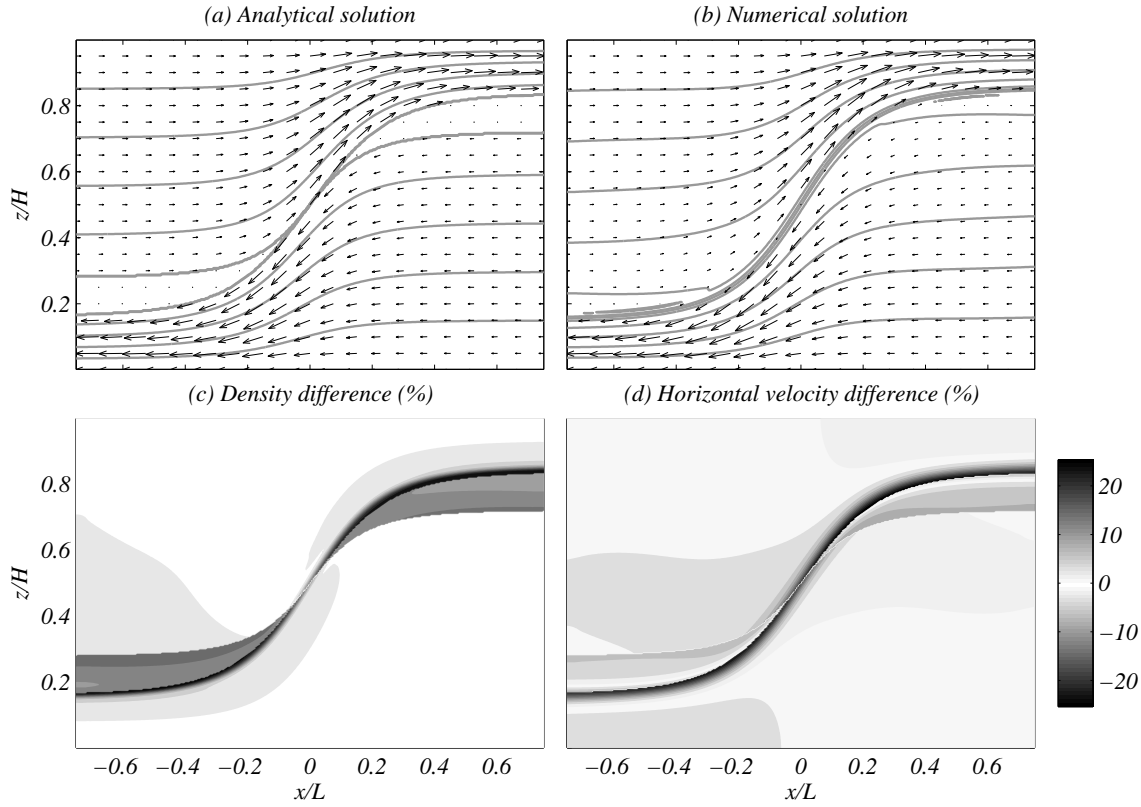


Figure 3: Case C2 using  $r_p = 1$  and  $q_0 = 0$ . Panels as for figure 2.

the transfer of momentum from the neighbouring active layers. This acts to mask the existence of the stagnant regions in the viscous case, and provides an explanation as to why the self-similar solution to stratified exchange flows has not been considered before as a general solution to this problem. There is unlikely to be any observational evidence indicating that a stagnant region plays a role in dynamic flows.

The stagnant layers which are specified in these analytical solutions present two difficulties. Firstly there is the question of how they form, and secondly how they connect to reservoir conditions. The former question presents little difficulty for case C1, where the stagnant layer is constrained in density by the fact that the bounding densities of the two active layers are equal. However, for case C2 we have (somewhat arbitrarily) chosen the stagnant layers to have density which is intermediate between the two bounding densities. It is important to stress that this density cannot be achieved by mixing in our inviscid solution. We have chosen this density as a suitable boundary condition on the active layers which allow computation of the solution.

Similarly, it is not possible for the homogeneous stagnant layers to connect smoothly to reservoir densities in a time dependent flow for either cases C1 or C2. A possible scenario is that convection (which is not included in these simulations) is important. One might expect this to alter the solution to some extent, however in hydraulically controlled flows such as these the solution is controlled at the throat of the contraction; so that the most relevant quantity is the density which acts as a boundary condition on the active layers there. For this reason the assumed homogeneous stagnant layers produce a solution which closely approximates the time dependent cases.

It may also be noted that the fast flowing layers do not match reservoir conditions. In realistic flows it would be expected that a transition to subcritical flow (probably via an internal hydraulic jump) would occur. We have omitted this possibil-

ity by ignoring hydraulic jumps in the analytical solution, and by setting the boundary conditions at the open boundaries of the numerical solution to allow supercritical flow to pass out of the model domain. Internal hydraulic jumps may well occur in more realistic flows, however the presence of stagnant layers means that the jump is insulated from the neighbouring active layer.

Despite these unresolved issues, the solutions presented here provide a simple resolution to a problem which has been assumed in the past to be too complicated to address. The solutions give useful and simple estimates for flux through a contraction in a channel between stratified reservoirs, and the problem can be solved analytically.

## References

- [1] Armi, L., The hydraulics of two flowing layers with different densities, *J. Fluid Mech.*, **163**, 1986, 27–58.
- [2] Dalziel, S. B., Two layer hydraulics: a functional approach, *J. Fluid Mech.*, **223**, 1991, 135–163.
- [3] Engqvist, A., Self-similar multi-layer exchange flow through a contraction, *J. Fluid Mech.*, **328**, 1996, 49–66.
- [4] Hogg, A. M. and Killworth, P. D., Continuously stratified exchange flow through a contraction in a channel, *J. Fluid Mech.*, **499**, 2004, 257–276.
- [5] Killworth, P. D., On hydraulic control in a stratified fluid, *J. Fluid Mech.*, **237**, 1992, 605–626.
- [6] Wood, I. R., Selective withdrawal from a stably stratified fluid, *J. Fluid Mech.*, **32**, 1968, 209–223.
- [7] Wood, I. R., A lock exchange flow, *J. Fluid Mech.*, **42**, 1970, 671–687.



## Simulation of The Dam Break Problem and Impact Flows Using a Navier-Stokes Solver

K. Abdolmaleki, K. P. Thiagarajan and M. T. Morris-Thomas

School of Oil and Gas Engineering  
The University of Western Australia, Crawley, WA, 6009 AUSTRALIA

### Abstract

The impact flow on a vertical wall resulting from a dam break problem is simulated using a Navier-Stokes (NS) solver. The NS solver uses an Eulerian finite volume method (FVM) along with a volume of fluid (VOF) scheme for phase interface capturing. The purpose of this study is to assess the accuracy of the solver for problems in the category of wave impacts. Previous experiments and other numerical solution techniques are compared with the solver's results. Different aspects of the flow such as free-surface elevation before and after the initial impact have been studied in depth. The pressure peak due to water impact on the vertical wall has also been analyzed. Water viscosity and air compressibility effects have been assessed. The significance of the time step and grid resolution are also discussed. Results show favorable agreement with experiments before water impact on the wall. However, both impact pressure and free-surface elevations after the impact depart from the experiments significantly. Hence the code is assessed to be good only for qualitative studies.

### Introduction

Hydrodynamics of free-surface flows that cause impact loads on the maritime structures, has not been fully understood. The impact loads are important in designing offshore and coastal structures. Typical problems such as green water loads on ships, wave run-up on offshore structures, slam loads and sloshing loads in tanks are important in the area of naval hydrodynamics. Available theories such as potential theory, which is commonly solved by a boundary element method (BEM), cannot be successfully applied to such problems. This is because, in addition to the free-surface geometrical complexities, discontinuities in the flow and air entrainment effects in these problems cannot be treated satisfactorily by the said theories [3].

New trends are towards direct numerical solutions of NS equations. It then becomes necessary to find a proper numerical method that best serves the above mentioned complexities. In fact, the need for a computational fluid dynamics (CFD) package for naval hydrodynamics problems is highly increasing. Different numerical techniques and packages are under investigation to explore a robust methodology to numerically simulate complex free-surface and impact problems. Among the large volume of literature written on this subject, [9] provides a good review and highlights the problems associated with numerical techniques.

The dam break problem was approached mathematically by Stoker [11]. For studying green water loads on ships, this problem was investigated experimentally by Zhou et al. [13]. The dam break flow with the consequent wall impact is widely used to benchmark various numerical techniques that tend to simulate interfacial flows and impact problems (see e.g. [1, 2, 4, 5, 8, 10]). This is due to the fact that this problem includes several features of existing problems in the area of marine hydrodynamics and coastal engineering. For example, in a *shipping of water* event, the problem includes: wave run-up on the ship bow; formation of a water height above the deck (dam

formation); high velocity shallow water flow (dam break); and impact of the flow on deck mounted structures (impact to the vertical wall) [2]. Therefore, the impact flow on a wall resulting from a dam break problem has scientific and practical importance.

This work uses FLUENT, a state of the art CFD package, which is widely used in both industry and academia. However, to the authors' knowledge, the software's strengths have not yet been proven in solving interfacial flow problems existing within the naval hydrodynamics framework. Therefore, the motivation of this work was to assess the software benchmark for this category of problems. The package uses a finite volume method to solve the NS equations and has several features for multi-phase flows. Among these, the VOF method is considered suitable for free-surface problems. We examine various grid sizes, time steps, air compressibility, water viscosity and turbulence effects to obtain the most realistic results from the solver. The problem dimensions are taken from [13] for comparative purposes.

### The Problem Setup

A schematic of the dam break model is presented in figure 1. In this model, the tank size is  $L = 3.22$  m and  $H = 2.0$  m and a column of water ( $L = 1.2$  m and  $H = 0.6$  m) is located in the left side of the tank. For impact pressure measurements on the downstream wall, similar to the experiments in [13], a point  $P(3.22$  m,  $0.16$  m) is defined on the wall. Free-surface elevations are recorded at stations  $h_1$  and  $h_2$  at distances  $x_1 = 2.725$  m and  $x_2 = 2.228$  m from the origin (left side wall) respectively. Notations  $h_1, h_2, x_1, x_2$  are selected to be consistent with [4, 13].

Water is considered viscous with a constant density of  $\rho_w = 998.2$  kg/m<sup>3</sup>. The density of air is also considered constant ( $\rho_a = 1.225$  kg/m<sup>3</sup>). The flow is modeled as both laminar and turbulent, however, the plotted results are from laminar model. As shown in figure 1, the boundary conditions are all set as *wall* conditions except for the tank top, which is set as *pressure outlet*. The pressure outlet boundary condition maintains a zero gauge pressure at the defined boundary, which is desired for the tank top.

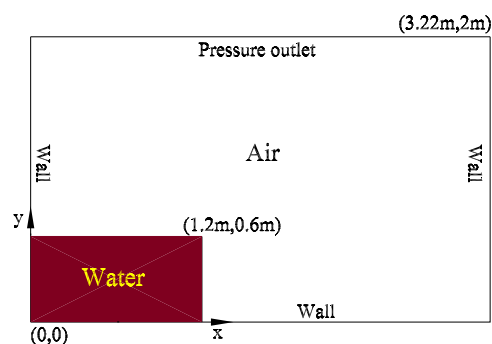


Figure 1: General layout of the dam break problem and boundary conditions.

## The Numerical Setup

With the VOF method, the software allows the use of the *seg-regated* solver only. This solver considers the integral form of the momentum and continuity equations, which are solved sequentially. Since these equations are naturally coupled, several iterations over the solution cycle must take place to provide convergence at each time step. During the iteration process, the Poisson equation, derived from the continuity and the linearized momentum equations, is used for pressure and velocity field corrections. The convergence criterion for the continuity equation and the velocity components was selected as 0.001. For further details on the solver refer to [6].

## Grid Size

The simple problem geometry allows for efficient discretisation of the domain using plane quadrilateral cells. Different grid sizes were examined to investigate the sensitivity and the accuracy of the results. The following grids were used; A1: 10mm×10mm, A2: 30mm×30mm, A3: 50mm×50mm, A4: 100mm×100mm and A5: mixture of 30mm×30mm and 15mm×15mm.

Uniform grid refining was observed to increase the computational burden as well as degrade the results. For example, for the case A1, the computation time increased dramatically and solutions did not converge at the initial water impact stage, even for  $\Delta t = 10^{-9}$  s. The accuracy of both the impact pressure and the free-surface elevations depended on the grid sizes. It was also found that the results were much more sensitive to the mesh size rather than the time step. The results for fluid pressure at point *P* approached an upper extreme for refined grid sizes. For example, A4 under-predicts the pressure peak at *P* whereas A1 gives a very steep and high pressure peak at *P*. For local averaging of the pressure, various approximation schemes such as *Facet Average Total Pressure* were used. All the used schemes' definitions are available at [6].

## Time Step

A proper time step, which provides converged results, is a function of grid size applied to the problem. For the case A5, considering  $\Delta t = 0.004$  and  $v_{fluid} = \sqrt{2gH} = 3.431$  m/s, the maximum value of the Courant number over the domain becomes  $C = v_{fluid}\Delta t/\Delta x = 0.91$ . This time step was observed to be too conservative since  $\Delta t = 0.01$  s was also applied and the solutions were similar and converged. For the cases A2, A3 and A4,  $\Delta t = 0.01$  s was sufficiently small to provide convergence during the entire simulation time. For the case A1, a time step of  $\Delta t = 10^{-9}$  s did not provide convergence at every time step - even with 80 iterations per time step.

In the plotted results, A5 was used for spacial discretisation with a time step of  $\Delta t = 0.004$  s. In A5 the grids were reduced to 15mm×15mm in the locations where the free-surface was expected. When an unsteady VOF calculation is performed in FLUENT, a time step different to the one used for the rest of the transport equations is defined for the volume fraction calculation. The time step is refined based on the input for the maximum Courant number allowed near the free-surface [6]. The Courant number for this purpose was 0.25. For the selected time steps, the solutions were all converged with the required number of iterations between 10 and 20.

## Description of The Flow

Figure 2 presents some snapshots of the flow at different times. A non-dimensionalised time,  $\tau = t(g/H)^{1/2}$ , where  $H$  is the initial water height, is used for explaining different stages of

the problem. At time  $\tau = 0$  (not shown in the figure) the water column is allowed to flow. A relatively high velocity and shallow water depth flow in the  $x$ -direction quickly forms (e.g.  $\tau = 2.02$ ). As time progresses, the flow impacts on the vertical wall at the opposite side of the tank. An upward water jet is suddenly formed that rises until gravity overcomes the upward momentum (around  $\tau = 4.04$ ). At this moment, the jet becomes thicker and the flow starts to reverse. Due to the oncoming flow, an adverse momentum gradient is created that results in an overturning wave (around  $\tau = 5.46$ ). This wave formation continues until the wave tip reconnects with the incident shallow water flow that now has less forward momentum. (before  $\tau = 6.06$ ). A sudden rise in pressure occurs at the reconnection point that is of the same order of magnitude as the pressure in wall impact. This is due to the existence of high relative momentum between fluid at the wave tip and the free-surface just before the attachment. A secondary but smaller overturning wave is created due to this impact and breaks in the same manner as the first wave (around  $\tau = 7.08$  and  $\tau = 8.69$ ). At this stage, the flow has become complicated as several big and small pockets of entrained air have been created due to the first and the subsequent impacts on the free-surface. For  $\tau > 8.69$ , the overall momentum of the flow has reduced considerably, therefore, analysis of the flow beyond this point is of no practical significance.

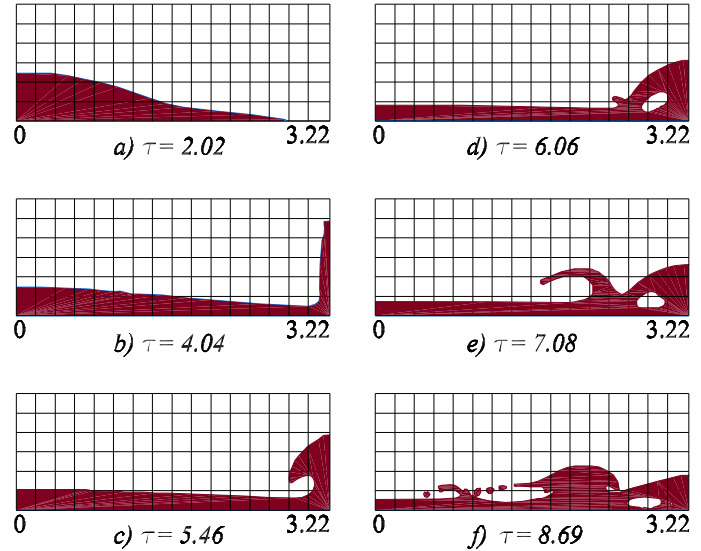


Figure 2: Dam break flow and impact against the tank wall.  $\tau = t(g/H)^{1/2}$ . Grids are based on case A5. The illustrated grid is of 20cm × 20cm in size and is a guide only.

## Free-surface Reconstruction

In wave-structure interaction problems, free-surface location relative to an immersed body is an indicator of the impact's extent on the body. For example, in green water incidents, the key feature of the problem is to find out the initial water surface elevation just before the flow starts to run over the deck [2]. The studied problem here includes the free-surface from the smoothest geometry at the early stages of the dam break, to the most violent geometry after the water impacts on the wall.

The VOF places the free-surface where the cells are partially filled with water. Therefore, refining the mesh should provide more accurate results. During simulations, it was observed that finer grids enabled smaller entrained air pockets created in the water to be captured more effectively. However, there were two problems with mesh refinement. Firstly, it had a negative impact on the convergence of solutions and secondly, as was reported in [12], no matter how fine the mesh was defined, there was an

artificially high velocity given to the air in the vicinity of the free-surface. Moreover, finer grids beyond a certain level, i.e. A5, did not improve the free-surface resolution significantly.

In a qualitative comparison, the breaking wave created after the initial impact was similar to other numerical works presented in [4, 8]. Figure 3 compares the total free-surface elevation with experimental records at stations  $h_1$  and  $h_2$ . Results closely agree until  $\tau \approx 6.5$  for both  $h_1$  and  $h_2$ . Beyond this point, the wave travelling opposite to the main flow, reenters the free-surface and creates inaccuracies in both the experimental and the numerical results. The same scale of disagreement can be seen in the results of other numerical methods [4, 8].

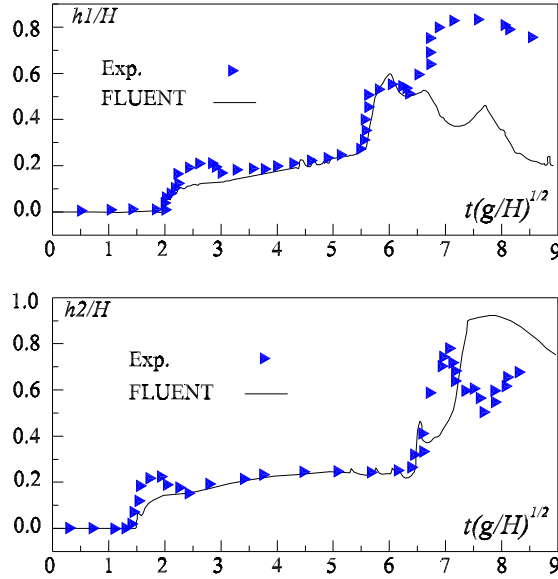


Figure 3: Total height  $h$  of the water at  $x_1 = 2.725$  m (top) and  $x_2 = 2.228$  m (down) from the origin. Experiment results are from [13].

A separate simulation was undertaken for studying initial stages of the dam break by tracing the water front location without existence of the downstream wall. The water column size was  $L = H = 5.7$  cm. The same study was undertaken in [4] to reproduce experiments documented in [7] by different numerical techniques. These numerical techniques are the BEM, Level set and smoothed particle hydrodynamics (SPH) methods. We have added our results in figure 4 for the purpose of comparison. The figure illustrates that all of the numerical methods agree reasonably well. Also as discussed in [4], the numerical results asymptotically approach the shallow water solution as time increases. However, deviation from the experiments shows a lower progressive velocity available in the experiments. This may be due to the imperfect initial conditions in the experiments and the physical effects not considered in the numerical model. At the earliest stages of the flow i.e.  $\tau < 1$ , the deviation is perhaps caused by the non-uniform breaking of the diaphragm in the experiments. For  $\tau > 1$ , the friction on the bottom becomes an important factor in creating turbulence and delaying the progress of the water front [4].

### Impact Pressure

The impact pressure at the point  $P$  can be averaged over time or location. Alternatively, it can be directly calculated (numerically only) at the point. In impact problems, as the spatial and temporal pressure gradients are high, any of the said approaches provide significantly different results. In fact, both time and local averaging underestimate the peak pressure because the peak value lasts less than  $t = 0.01$  s and the surrounding points do not

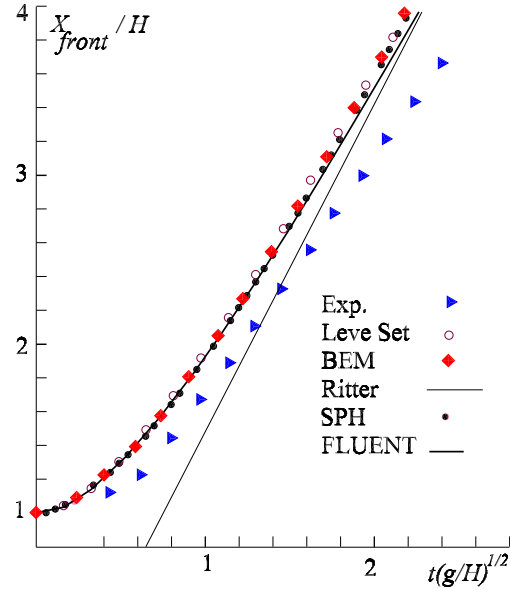


Figure 4: Time history of the water front toe evolution.  $t = 0$  is the start of the flow and  $X_{front}$  is the position of the water front [4].

reach their peak value at the same time as the central point. An exact pressure measurement at  $P$  cannot be determined experimentally as pressure sensors need an area to sense the impact pressure (in [13] this area is a circle with diameter of 90 mm). However, this value can be calculated numerically. Although in this case the pressure value for a mathematical point is averaged over the neighboring nodes, improvements can be achieved by grid refinement.

In this study, the local averaging and the value of the pressure at the point  $P$  are compared. Figure 5 shows the time history of the pressure at point  $P$ . Three sets of graphs are seen in the figure. These sets are; experimental results, numerical results measured at point  $P$  and numerical results averaged over an area corresponding to the pressure sensor diameter in experiments. Different approximation schemes are used for area averaging. All results predict the two pressure peaks at about the same time instant. However, the peak magnitudes are largely different over the different schemes. At the first peak, the closest results to the experiments are the *Facet Average Total Pressure* and *Vertex Average Total Pressure* schemes whereas the other three schemes (i.e. *Facet Maximum Total Pressure*, *Mass-Weighted Ave. Total Pressure* and *Vertex Maximum Total Pressure*) provide results close to the pressure measured at point  $P$  (vertex average). The second peak is under predicted by both *Facet Average Total Pressure* and *Vertex Average Total Pressure* schemes. That is perhaps because of entrained air effects, which are not well predicted by the code. Finally, the pressure at the mathematical point  $P$ , that could be calculated numerically, was found to be much higher than the pressures measured experimentally. The existence of such a high pressure peak could not be validated by comparison with experiments.

### Viscosity, Air Compressibility and Turbulence Effects

The viscosity of the water was found to be unimportant for this problem as the simulation results for viscous and inviscid options were similar. This is evidenced by [4], where although the inviscid model was chosen, the numerical results compare favorably with those shown in figure 4.

Air compressibility effects were checked by assuming air as an ideal gas and assuming an adiabatic process for air compres-



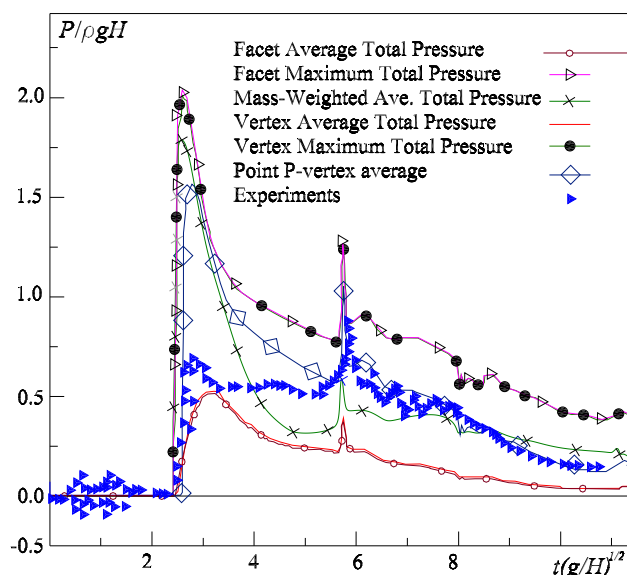


Figure 5: Impact pressures against downstream wall at point  $P(3.22m, 0.16m)$ . Plots are Experiment results [13], impact pressures measured at a mathematical point and averaged over an area corresponding to the pressure gauge. Different approximation schemes are plotted for area averaged case only.

sion. The software failed to simulate the whole process and unrealistic pressures appeared at the time instant of air cavity formation. This resulted in software interruption. Further studies are required to investigate the correct implementation of air compressibility as a user defined function. Finally, as was performed in [12],  $K - \epsilon$  theory was adopted to account for turbulence effects but the results were unsatisfactory and an artificial viscosity made the flow unrealistic.

## Conclusion

The state of the art CFD package, FLUENT, has been employed to assess its applicability in simulating free-surface problems. In particular, we have examined the classical dam break problem and subsequent water impact on a plane vertical wall. The FLUENT results for the initial stages of the problem closely agreed with other numerical techniques and experimental results. However, there was some disagreement in water tip location between numerical results and experiments. This is perhaps due to the imperfect initial conditions and some physical effects not numerically modeled. The numerical results for the total free-surface elevation at two stations,  $h_1$  and  $h_2$ , were in agreement while  $\tau < 6.5$ . The results disagree after the overturning wave reentered the free-surface i.e.  $\tau > 6.5$ .

The water impact pressure was numerically measured and compared with experiments. The impact pressure at point  $P$  on the wall, was measured by two methods using different averaging schemes. The averaged pressure over an area corresponding to the pressure gauge was more in line with the experimental results than the pressure measured at a mathematical point placed at the centre of the pressure gauge. Although the first peak agrees with the experimental measurements of [13], the second peak was largely underestimated. This suggests that FLUENT is acceptable for qualitative studies only.

In general, the problem after the initial impact could not be modeled with the desired accuracy. Further research is needed to strengthen the features of the software which are not suited for these types of applications. Free-surface reconstruction (complex geometry) including fluid discontinuity and the treat-

ment of entrained air are some of the areas that require further investigations.

## Acknowledgements

The first author gratefully acknowledges the funding support of the Ministry of Science, Research and Technology (MSRT) of Iran. The support of the Australian Research Council is also acknowledged.

## References

- [1] Brufau, P. and Garcia-Navarro, P., Two-dimensional dam break flow simulation, *Intl. J. Num. Meth. Fluids*, **33**, 2000, 35–57.
- [2] Buchner, B., *Green water on ship-type offshore structures*, Ph.D. thesis, Delft University Of Technology, The Netherlands, 2002.
- [3] Bulgarelli, U. P., Lugni, C. and Landrini, M., Numerical modelling of free-surface flows in ship hydrodynamics, *Intl. J. Num. Meth. Fluids*, **43**, 2003, 465–481.
- [4] Colagrossi, A. and Landrini, M., Numerical simulation of interfacial flows by smoothed particle hydrodynamics, *J. Comp. Phys.*, **191**, 2003, 448–475.
- [5] Greco, M., Faltinsen, O. M. and Landrini, M., Basic studies of water on deck, in *23rd Symp. on Naval Hydrodynamics*, Val de Reuil, France, 2000.
- [6] Inc., F., *FLUENT 6.1 User Guide*, Fluent Inc., Centerra Resource Park 10 Cavendish Court Lebanon, NH 03766, 2003.
- [7] Martin, J. C. and Moyce, W. J., An experimental study of the collapse of liquid columns on a rigid horizontal plane, *Philos. Trans. Roy. Soc. London, Ser. A*, **244**, 1952, 312–324.
- [8] Nielsen, K. B., *Numerical prediction of green water loads on ships*, Ph.D. thesis, Technical University Of Denmark, Lyngby, Denmark, 2003.
- [9] Scardovelli, R. and Zaleski, S., Direct numerical simulation of free-surface and interfacial flow, *Annu. Rev. Fluid Mech.*, **31**, 1999, 567–603.
- [10] Shin, S. and Lee, W. I., Finite element analysis of incompressible viscous flow with moving free surface by selective volume of fluid method, *Intl. J. Num. Meth. Fluids*, **21**, 2000, 197–206.
- [11] Stoker, J. J., *Water Waves: The Mathematical Theory with Applications*, Pure and Applied Mathematics, Interscience publishers, Inc., New York, 1957.
- [12] Wood, D. J., Pedersen, G. K. and Jensen, A., Modelling of run-up of steep non-breaking waves, *Ocean Eng.*, **30**, 2003, 625–644.
- [13] Zhou, Z. Q., Kat, J. O. D. and Buchner, B., A nonlinear 3-D approach to simulate green water dynamics on deck, Nantes, 1999, *7th Intl. Conf. Num. Ship Hydrodynamics*.

## Numerical Study of Moist Air Flow through the Ludwieg Tube

M. Tanaka<sup>1</sup>, S. Matsuo<sup>1</sup>, R. Nishizaki<sup>1</sup>, H.D. Kim<sup>2</sup> and T. Setoguchi<sup>1</sup>

<sup>1</sup>Department of Mechanical Engineering  
Saga University, 1 Honjo-machi, Saga, 840-8502 JAPAN

<sup>2</sup>School of Mechanical Engineering, Department of Mechanical Engineering  
Andong National University, Songchun-dong, Andong, 760-749 Korea.

### Abstract

A rapid expansion of moist air or steam in a supersonic nozzle gives rise to non-equilibrium condensation. If the latent heat released by condensation exceeds a certain quantity, the flow becomes unstable and a periodic flow oscillation occurs. In the present study, a numerical simulation of moist air flows in a supersonic nozzle was carried out using a special short duration supersonic wind tunnel, called a Ludwieg tube. In cases of nozzles with large throat height, the effects of initial relative humidity of the moist air on the flow field have been shown numerically. As a result, it was found that the characteristics of flow with occurrence of condensation were grouped into three types.

### Introduction

A short duration supersonic wind tunnel, called a Ludwieg tube (or a Tube wind tunnel) [1,2], is recently receiving a renewed interest in simulating a space transportation system [3,4], because it is easy to achieve high Mach number and Reynolds numbers with relatively low turbulence, compared with the conventional supersonic and hypersonic wind tunnels. However the short duration of steady flow makes the flow measurements in the Ludwieg tube extremely difficult.

Typical example of a supersonic flow with heat addition is often found in Laval nozzle with a non-equilibrium condensation of moist air or steam, which is rapidly expanded through the nozzle (homogeneous nucleation) [5,6,7]. According to some previous works, the non-equilibrium condensation of moist air results in considerable total pressure losses [8]. In general, the process of heat addition almost always leads to unsteady wave motions even in a supersonic flow field [9,10,11].

In heterogeneous condensation [12], the condensation of the vapor takes place on foreign nuclei; smoke and vapor from fires and various industries, dust from land surfaces, salt from oceans and particulate products from chemical reaction. Their presence in sufficient numbers leads to condensation near equilibrium at degree of supersaturation only slightly larger than unity.

Ludwieg tube has long been used to investigate the process of heat addition due to the condensation in the nozzle, since it provides well controlled flow conditions that permit operation with increased initial relative humidity and pressures [9,10]. From some previous researches, it was observed that the non-equilibrium condensation of moist air in a nozzle could lead to total pressure losses and flow instabilities as well [13]. However, detailed flow information with regard to time-dependent condensation in case of occurrence of condensation upstream of nozzle is not yet well known, since it is hard to reveal through experiments.

In the present study, a computational fluid dynamics work is applied to predict the condensation phenomena in the Ludwieg tube. The Ludwieg tube with a diaphragm downstream is simulated using the two-dimensional Navier-Stokes equations. In cases of

nozzles with large throat height (case with occurrence of condensation upstream of nozzle), the effects of initial relative humidity of the moist air on the flow field have been shown numerically.

### Computational analysis Governing Equations

For simplicity of the present computational analysis, several assumptions are made; there is no velocity slip and no temperature difference between condensate particles and medium gas flows, and thus the energy relaxation processes between two phases are not considered in the present analysis. Due to very small condensate particles, the effect of the particles on pressure field of flow can be neglected.

The governing equations are unsteady, two - dimensional, compressible, Navier-Stokes equations and a droplet growth equation [14]. The equations described for compressible viscous flow were discretized by the finite difference method. Third-order TVD finite difference scheme [15] with MUSCL approach was used for spatial derivative terms and second-order central difference scheme in discretizing viscous terms. The spatially discretized equations are integrated in time by means of a time splitting method that has the second order accuracy.

Baldwin-Lomax turbulence model is employed to close the governing equations [16]. The governing equations are mapped from the physical plane into a computational plane of a general transform and non-dimensionalized using the reference values at the initial conditions upstream of the nozzle.

### Initial and Boundary Conditions

Computational grids of the Ludwieg tube flow field for the present computational analysis is schematically shown in figure 1, which was also used for the previous experimental work by Matsuo et al. [17]. The number of grids is  $300 \times 60$ . The Ludwieg tube consists of the upstream high-pressure tube, the convergent-divergent nozzle, and the downstream low-pressure tube. The Ludwieg tube has a length of 1000 mm. A diaphragm is located at the origin ( $x = 0$ ) downstream of the nozzle throat, and separates the high and low-pressure tubes. The high and low-pressure tubes have the same height of  $H=38$  mm. The convergent-divergent nozzle with a throat height of  $h^*$  ( $= 24$  mm,  $27$  mm,  $30$  mm) is located at  $x = 302.5$  mm upstream of the diaphragm and is in the shape of circular arcs with the same curvature radius of  $R^*=155$  mm.

The pressures in the high and low-pressure tubes are defined as  $p_4$  and  $p_1$ , respectively. In the present study,  $p_4$  is kept constant at 101.3 kPa and the ratio of  $p_4 / p_1 (= p_{41})$  is 5.0. The initial flow conditions in the high-pressure tube are given by pressure  $p_4$ , relative humidity  $\phi_4$  and temperature  $T_4$ . In the present computations,  $T_4 (=T_1)$  is kept constant at 302 K. The initial relative humidity  $\phi_4$  is set at 0 %, 20 %, 40 %, 60 % and 80 %.

Moist air is used as the working gas and assumed to be thermally

and calorically perfect. Inlet and outlet boundaries are constrained to the free boundary conditions. No velocity slip wall is assumed on adiabatic wall condition. Furthermore, condensate mass fraction  $g = 0$  is given at the solid walls.

## Results and Discussions

Figures 2, 3 and 4 show the time-dependent characteristics of static pressure  $p$  on the centre line of the Ludwig tube in cases of  $\varphi_4 = 20\%$ ,  $40\%$  and  $80\%$ , respectively. The height of the nozzle throat in each figure is  $27\text{ mm}$ . The abscissa is the distance  $x$  measured from the diaphragm divided by the tube height  $H$ .  $t$  in figures 2(a), 3(a) and 4(a) is the elapsed time after the rupture of diaphragm. Broken lines in figures 2(b), 3(b) and 4(b) denote the distribution of the static pressure for  $\varphi_4 = 0\%$ .

As seen from figure 2, variations of the static pressure  $p$  are found in the region close to the nozzle throat and at slightly upstream part of nozzle. In this case, a condensation shock wave builds up periodically in the divergent nozzle section and it moves upstream through the throat [18]. This corresponds to the case of Type A in Table 1 as described later. The pressure variation is due to the

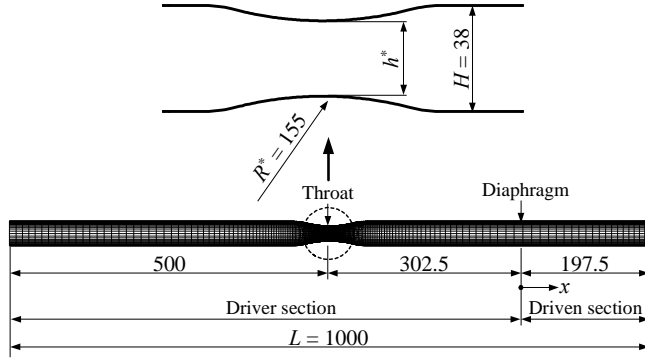
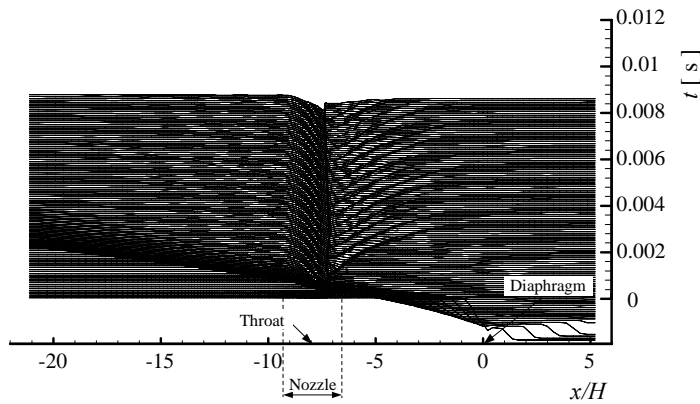
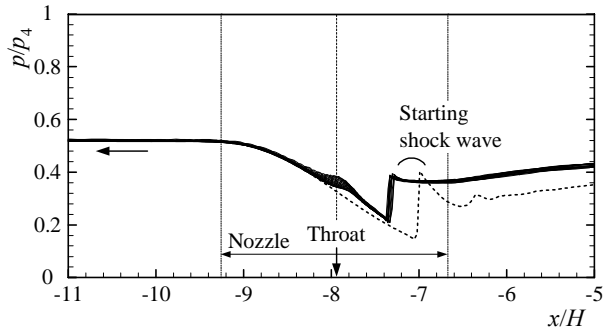


Figure 1. Computational grids ( Unit : mm ).



( a ) Wave diagram.

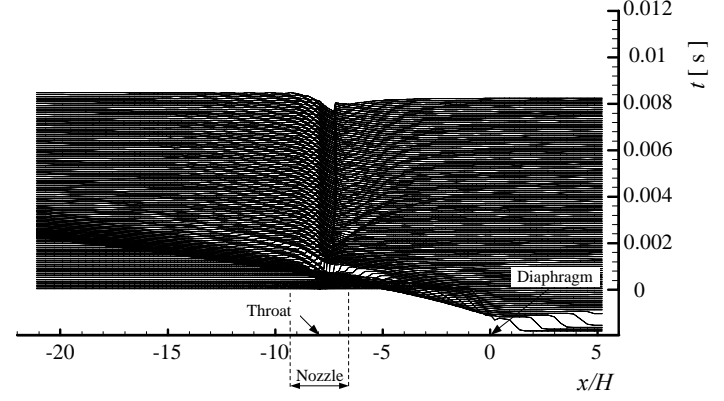


( b ) Distributions of static pressure (  $t = 7.86 \sim 9.45 \mu\text{s}$  ).

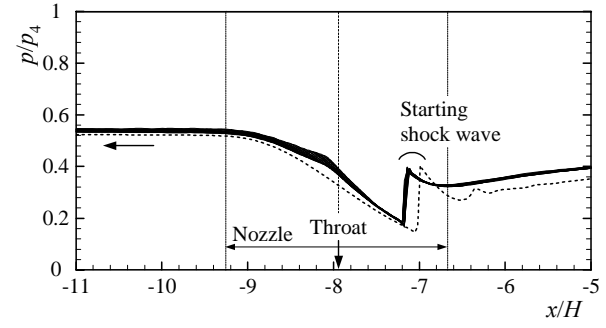
Figure 2. Time dependent distributions of static pressure (  $h^* = 27\text{ mm}$ ,  $\varphi_4 = 20\%$  ).

periodic excursions of the condensation shock wave. The variation of  $p$  for  $\varphi_4 = 40\%$  (figure 3) is similar to that for  $\varphi_4 = 20\%$  (figure 2).

In figure 4 (  $\varphi_4 = 80\%$  ), variations of the static pressure are not found in the region upstream of the nozzle throat. Furthermore, in

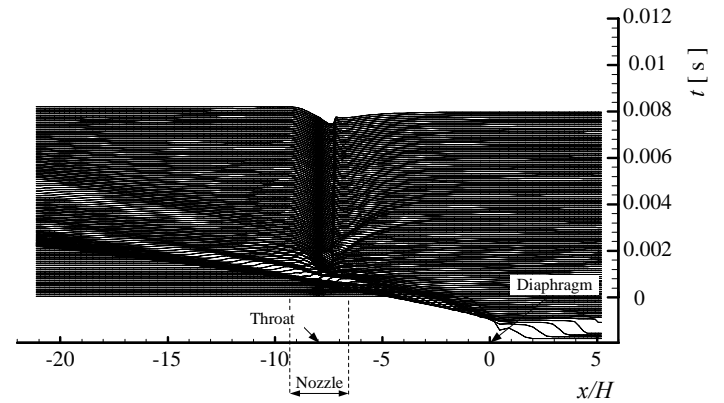


( a ) Wave diagram.

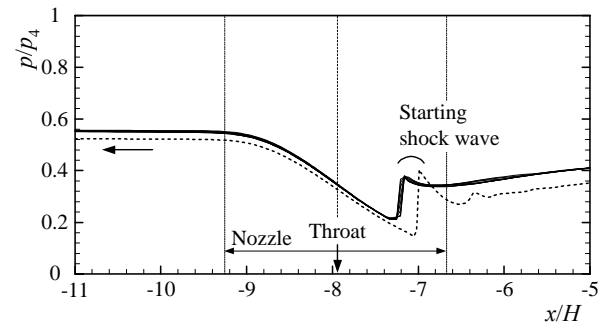


( b ) Distributions of static pressure (  $t = 7.87 \sim 9.43 \mu\text{s}$  ).

Figure 3. Time dependent distributions of static pressure (  $h^* = 27\text{ mm}$ ,  $\varphi_4 = 40\%$  ).



( a ) Wave diagram.



( b ) Distributions of static pressure (  $t = 7.84 \sim 9.42 \mu\text{s}$  ).

Figure 4. Time dependent distributions of static pressure (  $h^* = 27\text{ mm}$ ,  $\varphi_4 = 80\%$  ).

this region it is found that the static pressure value (solid lines in figures 3 and 4) is larger than that (broken lines) for  $\varphi_4 = 0 \%$ . This is due to the latent heat released by the non-equilibrium condensation. The variation of  $p$  for  $\varphi_4 = 60 \%$  was similar to that for  $\varphi_4 = 80 \%$  (figure 4).

Figures 5, 6 and 7 show the time-dependent characteristics ( $x - t$  diagram) of nucleation rate  $I$  (number of condensate nuclei per unit time and unit volume) and  $g$  (ratio of the condensate mass fraction to total mass flow through the Ludwig tube) on the centre line for  $\varphi_4 = 20 \%$ ,  $40 \%$  and  $\varphi_4 = 80 \%$ , respectively ( $h^* = 27 \text{ mm}$ ). Each line in these figures indicates the time increment of about  $0.08 \mu\text{s}$ . As seen from figure 5(a) ( $\varphi_4 = 20 \%$ ), the nucleation rate and condensate mass fraction start to increase rapidly at the position close to the nozzle throat. Furthermore, the condensate nuclei (nucleation rate) are not found in the region upstream of the nozzle.

In figure 6 ( $\varphi_4 = 40 \%$ ), the condensate nuclei seem to generate mainly in the region close to the nozzle throat and it is found even upstream of the nozzle periodically. The variation of  $g$  in the region close to the nozzle throat is larger than that in figure 5(b) and a larger amount of droplets are generated in that region. But it was not seen upstream of the nozzle.

In figure 7(a), the spatial distribution of the condensate nuclei seems to be of a narrow zone with a sharp peak and a large number of the condensate nuclei is generated even upstream of the nozzle as the time proceeds. The condensate mass fraction is seen in the whole region in contrast to the case of that in figures 5 and 6 (figure 7(b)). Furthermore, occurrence of the condensate mass fraction in the region upstream of the nozzle in figure 7(b) is due to that of the condensate nuclei in this region. The change of  $I$  and  $g$  for  $\varphi_4 = 60 \%$  was similar to that for  $\varphi_4 = 80 \%$ .

Table 1 shows the classification of the flow field with non-equilibrium condensation obtained by the present simulations.

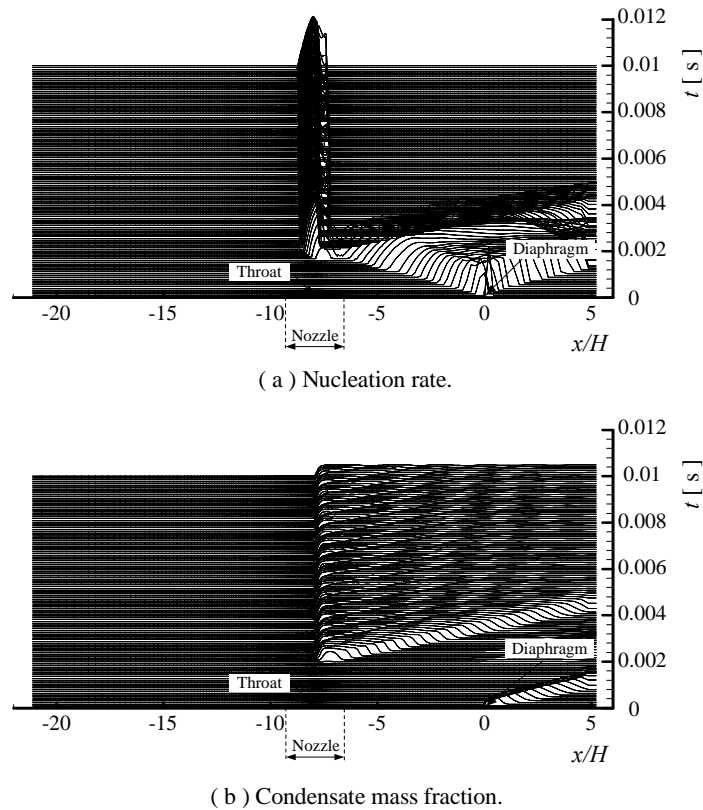


Figure 5. Time dependent distributions of condensate mass fraction and nucleation rate ( $h^* = 27 \text{ mm}$ ,  $\varphi_4 = 20 \%$ ).

From the point of view of occurrence of condensate nuclei and condensate mass fraction, and variation of the static pressure, there are three kinds of flow field with non-equilibrium condensation as follows :

A : At the upstream part of the nozzle, variations of the static pressure are slightly found. But occurrence of the condensate mass fraction and nucleus are not recognized. In the region of the nozzle throat, occurrence of the condensate mass fraction

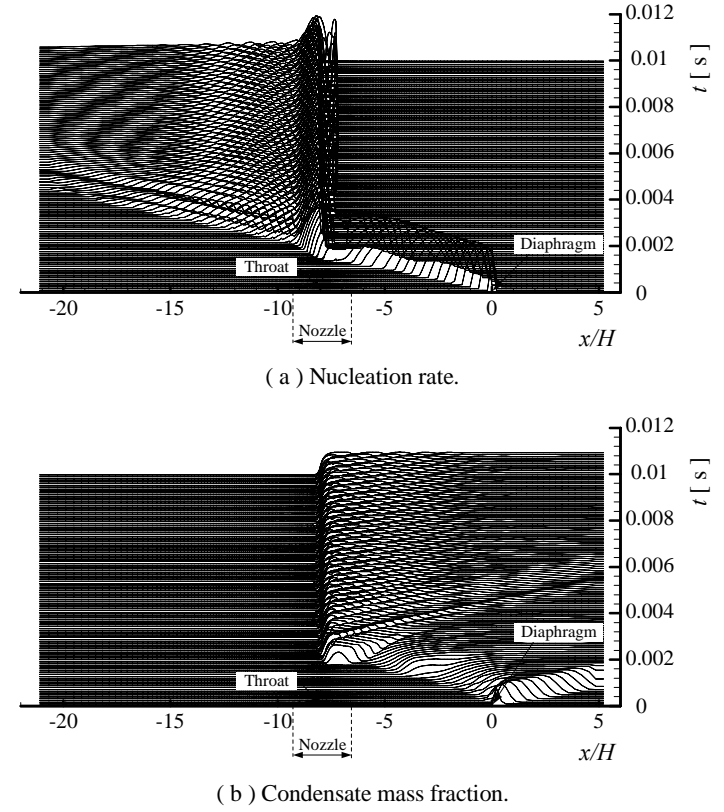


Figure 6. Time dependent distributions of condensate mass fraction and nucleation rate ( $h^* = 27 \text{ mm}$ ,  $\varphi_4 = 40 \%$ ).

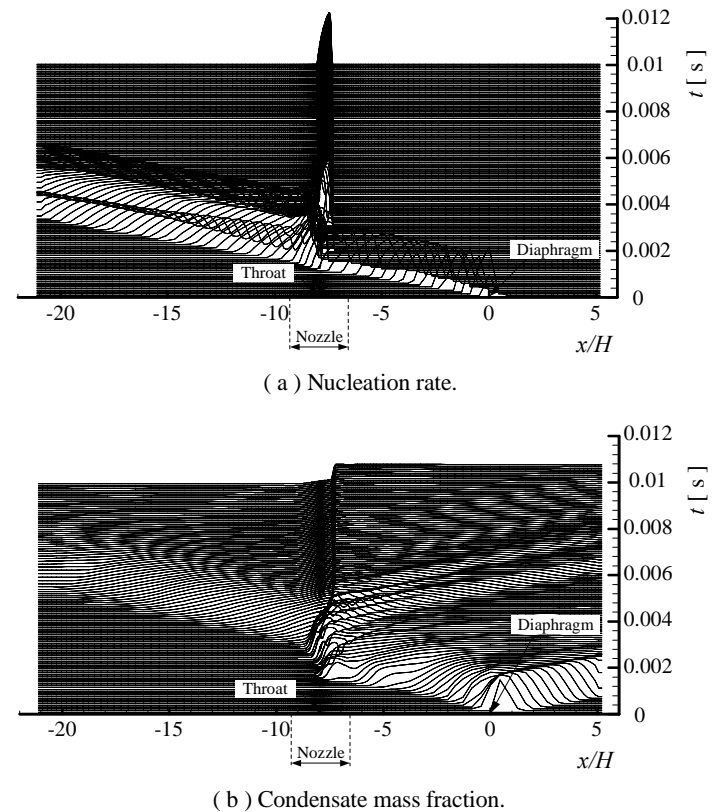


Figure 7. Time dependent distributions of condensate mass fraction and nucleation rate ( $h^* = 27 \text{ mm}$ ,  $\varphi_4 = 80 \%$ ).



and the nucleus, and variation of the static pressure are recognized.

B : At the upstream part of the nozzle, variations of the static pressure and occurrence of the nucleus are found. But occurrence of the condensate mass fraction are not found. In the region close to the nozzle throat, occurrence of the condensate mass fraction and the nucleus, and variation of the static pressure are recognized.

C : At the upstream part of the nozzle, variations of the static pressure are not found. Occurrence of the nucleus and the condensate mass fraction are found in this region.

As seen from Table 1, the flow field for case with large nozzle height is different from that (Type A) obtained from the previous researches [13].

Figure 8 shows a time dependent characteristics of  $p$ - $T$  diagram for  $\phi_4 = 20\%$ ,  $40\%$ ,  $60\%$  and  $80\%$  ( $h^* = 27$  mm). Solid line in this figure is a liquid-vapour saturation line. Each line denotes the variation of pressure and temperature of vapour at the position close to the maximum degree of supersaturation. As seen from this figure, the variation of vapour pressure and temperature becomes very complicated as time proceeds and the line for  $\phi_4 = 80\%$  approaches the saturation line as time proceeds in contrast to the cases of  $\phi_4 = 40\%$  and  $60\%$ . This means that the condensation proceeds heterogeneously and the relative position between a liquid – vapour saturation line and the position after time proceed does not depend on the value of initial relative humidity in driver section. The time-dependent variations of the line for Type C in Table 1 showed almost as the same tendency as that in figure 8.

## Conclusions

In order to investigate the time-dependent behavior of

		$\phi$ (%)			
		20	40	60	80
$h^*$ (mm)	24	A	A	B	C
	27	A	B	C	C
	30	B	C	C	C

Table 1. Classification of flow with condensation.

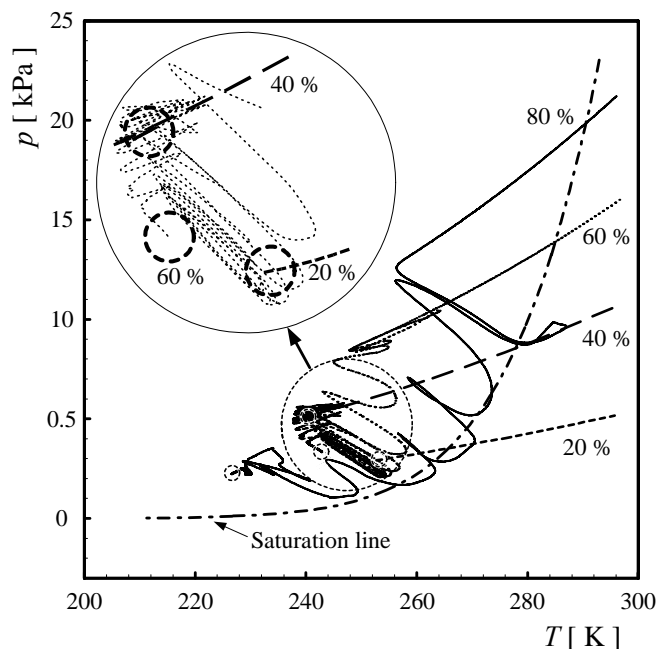


Figure 8.  $p$ - $T$  diagram ( $h^* = 27$  mm).

condensation of moist air through the Ludwig tube, a computational fluid dynamics work was applied to the two - dimensional, compressible, Navier - Stokes equations, fully coupled with the droplet growth equations. As a result, it was found that the height of the nozzle throat strongly effected the occurrence of condensation in the Ludwig tube and from the point of view of occurrence of nuclei and condensate mass fraction, and variation of the static pressure, three kinds of flow field with non-equilibrium condensation were obtained by the present simulations.

## References

- [1] Ludwig, H., Der Rohrwindkanal, *Zeitschrift für Flugwissenschaften*, **3**(7), 1955, 206-216.
- [2] Cable, A. J. & Cox, R. N., The Ludwig pressure tube supersonic wind tunnel, *The Aeronautical Quarterly*, **14**(2), 1963, 143-157.
- [3] Friehmelt, H., Koppenwaller, G. & Müller-Eigner, R., Calibration and first results of a redesigned Ludwig expansion tube, *AIAA/DGLR Fifth International Aerospace Planes and Hypersonics Technologies Conference*, AIAA-**93**(5001), 1993.
- [4] Schneider, S. P. & Haven, C. E., Quiet-Flow Ludwig Tube for High-Speed Transition Research, *AIAA J.*, **33**(4), 1995, 688-693.
- [5] Wegener, P. P. & Mack, L.M., Condensation in supersonic hypersonic wind tunnels, *Adv. In Appl. Mech.*, **5**, Academic Press, 1958.
- [6] Matsuo, K., Kawagoe, S., Sonoda, K. & Sakao, K., Studies of Condensation Shock Waves (part 1, Mechanism of their Formation), *Bulletin of JSME*, **28**, 1985, 2577-2582.
- [7] Schnerr, G. H., Homogene Kondensation in Sationären Transsonischen Strömungen durch Lavaldüsen und um Profile, Habilitationsschrift, Universität Karlsruhe (TH), Germany, 1986.
- [8] Kwon, S. B., Matsuo, K., Kawagoe, S. & Matsuo, S., Total Pressure Loss in Supersonic Nozzle Flows with Condensation, *JSME Int. J.*, **31**(1), 1988, 16-21.
- [9] Wegener, P. P. & Cagliostro, D. J., Periodic nozzle flow with heat addition, *Combustion Sci. and Tech.*, **6**, 1973, 269-277.
- [10] Matsuo K, Kawagoe S, Sonoda K and Setoguchi T. Oscillations of Laval nozzle flow with condensation (part 1), *Bulletin of JSME*, **28**(241), 1985, 1416-1422.
- [11] Adam, S. & Schnerr, G. H., Instabilities and bifurcation of non-equilibrium two-phase flows, *J. Fluid Mech.*, **348**, 1997, 1-28.
- [12] Wegener, P. P., *Nonequilibrium Flow*, Part 1, Marcel Dekker, 1969.
- [13] Matsuo, S., Tanaka, M., Setoguchi, T. & Kim, H. D., Numerical Visualization of Moist Air Flow through the Ludwig Tube, *Proc. of the 13<sup>th</sup> Int. Symposium on Transport Phenomena*, 2002, 151-156.
- [14] Sislian, J. P., Condensation of water vapour with or without a carrier gas in a shock tube, *UTLAS Report* **201**, 1975.
- [15] Yee, H. C., A class of high-resolution explicit and implicit shock-capturing methods, *NASA TM-89464*, 1989.
- [16] Baldwin, B.S. & Lomax, H., Thin layer approximation and algebraic model for separated turbulent flows, *AIAA Paper. No.78-257*, 1978.
- [17] Matsuo, K., Kawagoe, S., Sonoda, K. & Setoguchi, T., Oscillations of Laval nozzle flow with condensation (part 1, on the range of oscillations and their frequencies), *Bulletin of JSME*, **26**(219), 1983, 1556-1562.
- [18] Setoguchi, T., Matsuo, S., Shimamoto, K., Yasugi, S. & Yu, S., Passive control of unsteady condensation shock wave, *J. of Thermal Science*, **9**(4), 2000, 299-304.

## Measurement and Modelling of Controlled Beach Groundwater Levels Under Wave Action

L.S. Ang, C.H-Y. Sum, T.E. Baldock, L. Li, and P. Nielsen,  
Division of Civil Engineering, University of Queensland,  
St Lucia, Qld 4072, Australia

### Abstract

New laboratory scale experimental data are presented on the forcing of beach groundwater levels by wave run-up. The experimental setup simulates a coastal barrier dividing the ocean from a relatively constant back beach water level, conditions approximating a closed off lagoon system or beach aquifer. The data are critically compared to an advanced numerical model for simulating wave and beach groundwater interaction in the coastal zone, and provide the first experimental verification of such a model. Overall model-data comparisons are good, but some systematic discrepancies are apparent, and reasons for these are discussed.

### Introduction

Groundwater levels in beaches and across coastal barriers and atolls play an important role in the mixing of fresh and saline water and the overall flux of nutrients and pollutants across the land-ocean boundary. Depending on the gradient of the water table, water, nutrients or pollutants may flow landward [7] or seaward [4]. The watertable slope is dependent on boundary conditions on the beach face and the landward water table level (see figure 1). The latter may be fresh water from rainfall on to the barrier, or from a creek or estuarine system behind the coastal barrier. The beach face boundary condition is controlled by tidal oscillations and wave induced setup and run-up on the beach face.

The beach groundwater level also controls the degree of infiltration or exfiltration into the beach, which in turn may influence sediment mobility on the beach face and overall beach morphology (e.g. [3,10]). However, attempts to modify beach morphology by controlling groundwater levels or through beach drainage have had mixed success (e.g. [8]). In part this may be due to the complex interaction between wave run-up and groundwater and uncertainties over the influence of infiltration/exfiltration on sediment transport. While analytical and numerical models for beach groundwater have been verified against data at tidal frequencies [6,1], no verification has been carried out for forcing at wave frequencies.

This paper considers this issue and presents new experimental laboratory data which are critically compared to results from a recent numerical model [5]. The results suggest that the model provides a good overall description of the data, particularly for raised groundwater levels. However, the model tends to under estimate the groundwater levels for longer period waves, while overestimating them for shorter period waves. Possible reasons for this are discussed with regard to the inner surf zone and swash zone hydrodynamics.

### Background

Figure 1 shows a definition sketch of the coastal zone, where the backshore region consists of a coastal sand barrier/dune system dividing a creek, lagoon or estuary from the ocean. The water level in the creek, lagoon or estuary may oscillate at tidal

frequencies if the system is open to the ocean, or be relatively constant if closed, changing only with rainfall or input from the catchment. In that instance, the backshore water level is fixed at some elevation that may be higher, lower or similar to the mean ocean level, which will vary according to tidal stage. Thus at high tide the groundwater level at the beach boundary may be raised above that inland, whereas at low tide it may be lower. Wave run-up subsequently further influences the groundwater levels in the beach.

The present paper simulates this scenario in carefully controlled laboratory experiments and provides measurements of the piezometric head levels in the beach. These are compared to predictions from the BeachWin model of Li et al. [5]. The model couples the non-linear shallow water wave equations with the Laplace equation for saturated flow in the beach, including capillary effects. Previous applications of the model show realistic simulations of the groundwater response to waves, but it has yet to be tested against experimental data. Such testing is reported below.

### Experimental Setup

The experiments were carried out in a section of the Coastal Wave Basin at the University of Queensland. This section is approximately 30m long by 1.4m wide and was used with a working water depth of 0.5m. A model scale mobile sediment beach ( $d_{50}=0.84\text{mm}$ ) was setup in the basin (figure 2), behind which the water table was controlled by means of an overflow system. The water level in the basin was kept constant using a small inflow near the wavemaker and a weir. A set of 20 damped manometer tappings on the bed of the flume provided time-averaged mean piezometric head levels from offshore of the breakpoint to the back of the beach.

For each run the initial beach shape was plane (gradient 1:7.6) with the beach was regraded between runs. Prior to running waves, the watertable behind the beach was set at a chosen level (nominally 0 to  $\pm 0.075\text{m}$ ) relative to the offshore level and the piezometric head levels recorded. A series of regular waves were then generated by the wavemaker, with the beach profile and piezometric head levels recorded at intervals of 10-20 minutes for a one hour period. Wave periods ranged from 1-2.5s, with wave heights between 0.05m and 0.15m. A total of 10 different wave conditions were run, each with at least 3 different back beach controlled water levels. The relative back beach water levels and wave heights were set so as to simulate the typical tidal range and wave heights on a micro-meso tidal beach. Further details may be found in Sum [9].

### Modelling

The BeachWin model was setup identically to the experimental arrangement and using the measured hydraulic conductivity of the beach sediment (0.001m/s). The model was run in fixed beach mode, i.e. without profile evolution over time, to avoid errors in the sediment transport predictions feeding through into predicted piezometric head levels.

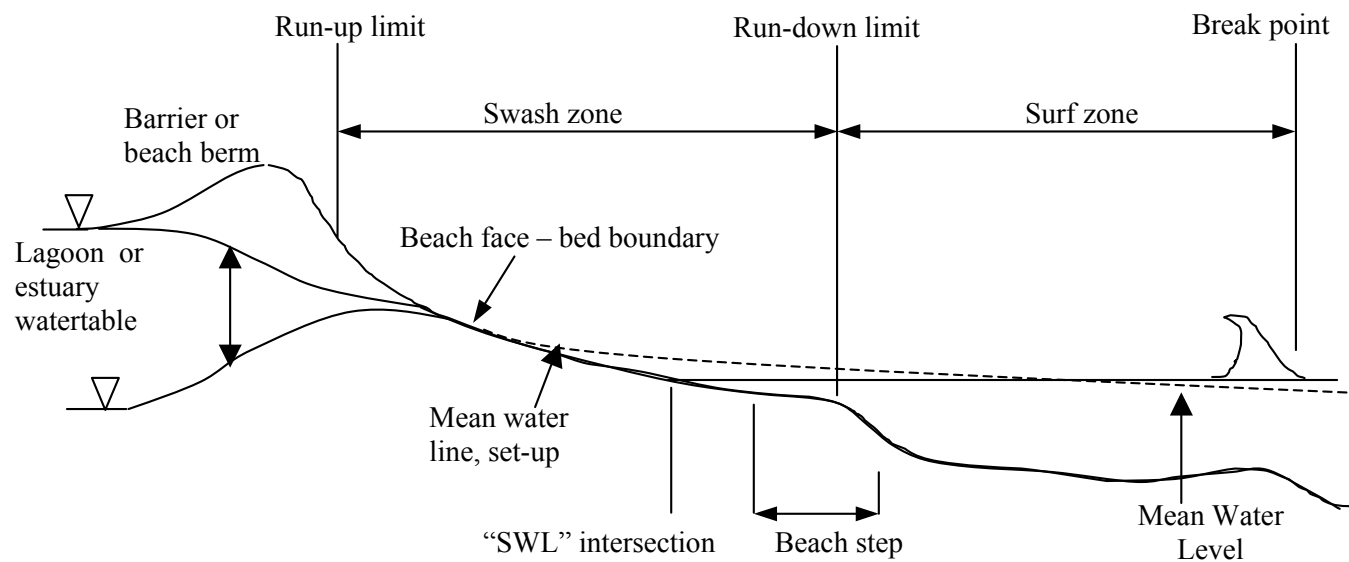


Figure 1. Definition sketch of nearshore zone, coastal barrier and beach groundwater levels.

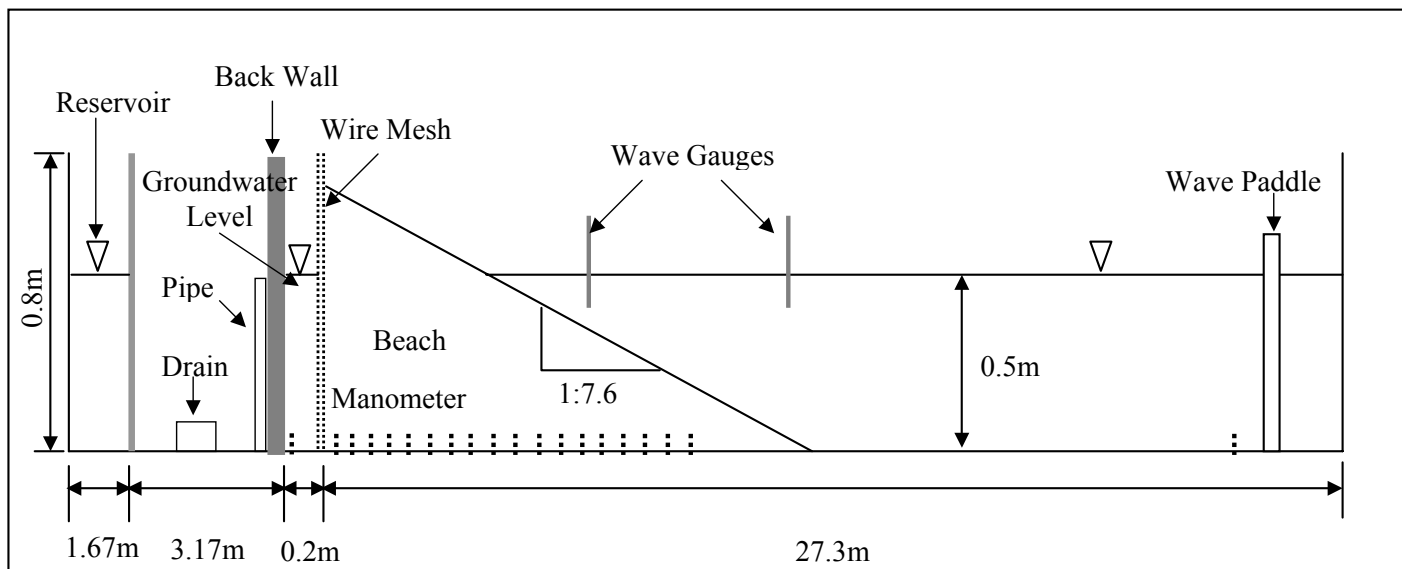


Figure 2. Wave flume, beach layout and instrumentation.

Model-data comparisons were therefore carried out only for measurements made at the first 10min sampling interval. At this time the groundwater level had reached equilibrium with the waves and beach morphology, but the changes in morphology from the initial plane state were small. Subsequent tests suggested that later changes in morphology lead to only minor changes in overall piezometric head levels. Differences between model predictions for small changes in morphology are also minor. Hence, taking the beach boundary as the initial plane state has a very minor effect on the model predictions and model-data comparisons.

## Results

Figure 3a shows an example of the initial beach profile, the beach profile after 10min, together with the still water line (SWL) and the measured and modelled piezometric heads (denoted BW). The wave conditions and back beach head level are indicated in the caption. While significant profile evolution occurs, this has little effect on the measured or modelled head levels, which are primarily governed by the back beach head level and the wave run-up limit [7]. In this instance the back beach head level was

controlled to be similar to the offshore water level, simulating a mid-tide condition, micro-tidal beach or spit between the arm of an estuary and the ocean.

Figure 3b shows the measured and modelled piezometric heads for the same wave conditions but with the back beach water level held lower than the offshore water level, simulating high tide conditions. Figure 3c shows similar data, but simulating low tide conditions (offshore water level below the back beach level). In both instances the model appears to overestimate the head levels in the surf zone ( $x=1.5\text{m}$  corresponds to the intersection of the initial beach profile and the SWL), but underestimates them in the swash zone and within the beach, particularly for the high tide scenario.

With a shorter wave period ( $f=0.6\text{Hz}$ ) but the same wave height ( $H=0.15\text{m}$ ), the model-data comparisons are good for the mid-tide and high tide conditions (figures 4a and 4b), but the model shows a systematic over-estimation of the head levels for the low tide case (figure 4c). The reason for this appears to be a significant overestimation of the wave setup in the inner surf zone and this may be related to the energy dissipation routine within the model.

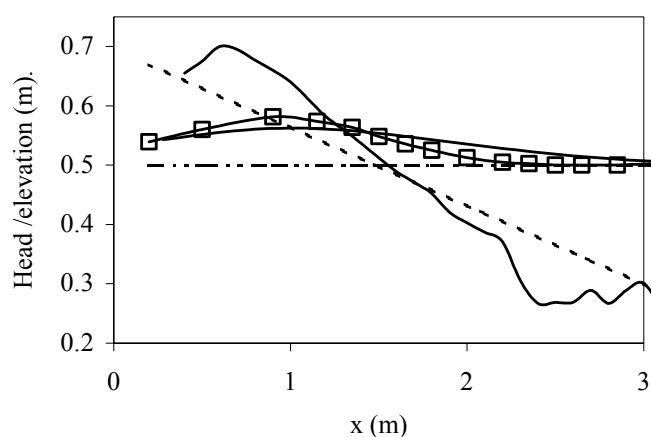


Figure 3a. Beach profile evolution and piezometric head.  
 $f=0.4\text{Hz}$ ,  $H=0.15\text{m}$ ,  $\text{TWL}=0.54\text{m}$ .  
 — BW; —□— measured; — · — SWL  
 --- profile,  $t=0$ ; — profile,  $t=10\text{mins}$ .

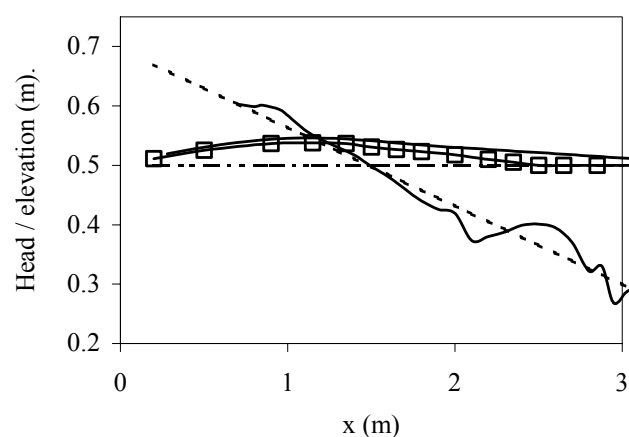


Figure 4a. Beach profile evolution and piezometric head.  
 $f=0.6\text{Hz}$ ,  $H=0.15\text{m}$ ,  $\text{TWL}=0.511\text{m}$ .  
 — BW; —□— measured; — · — SWL  
 --- profile,  $t=0$ ; — profile,  $t=10\text{mins}$ .

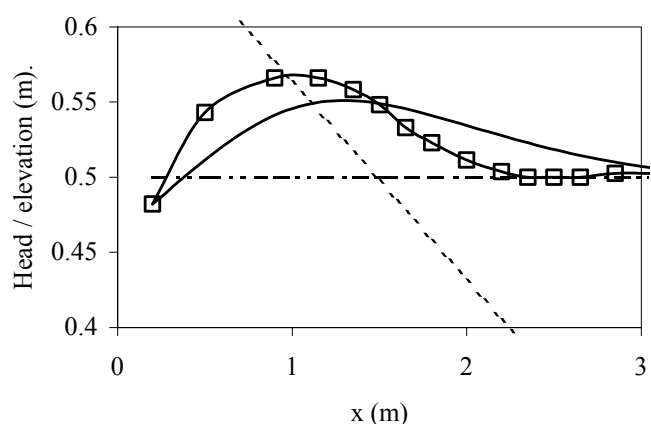


Figure 3b. Modelled and measured piezometric head,  
 $f=0.4\text{Hz}$ ,  $H=0.15\text{m}$ ,  $\text{TWL}=0.48\text{m}$ .  
 — BW; —□— measured; — · — SWL; --- profile,  $t=0$

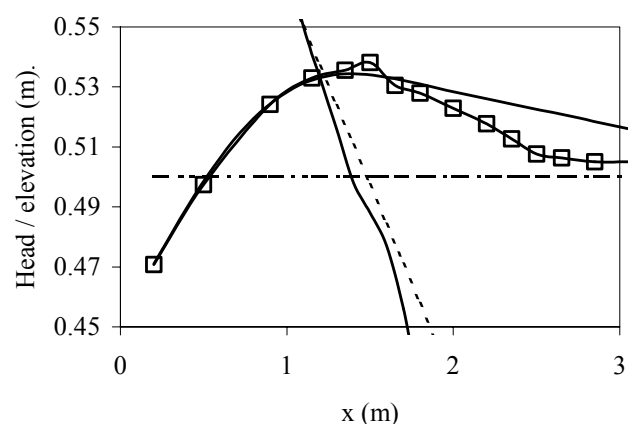


Figure 4b. Modelled and measured piezometric head,  
 $f=0.6\text{Hz}$ ,  $H=0.15\text{m}$ ,  $\text{TWL}=0.471\text{m}$ .  
 — BW; —□— measured; — · — SWL; --- profile,  $t=0$

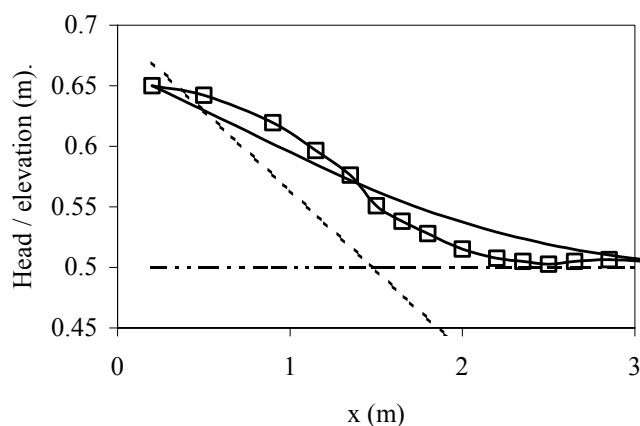


Figure 3c. Modelled and measured piezometric head,  
 $f=0.4\text{Hz}$ ,  $H=0.15\text{m}$ ,  $\text{TWL}=0.65\text{m}$ .  
 — BW; —□— measured; — · — SWL; --- profile,  $t=0$

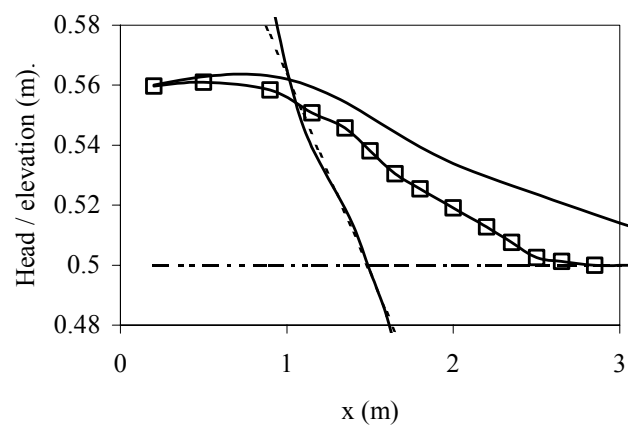


Figure 4c. Modelled and measured piezometric head,  
 $f=0.6\text{Hz}$ ,  $H=0.15\text{m}$ ,  $\text{TWL}=0.56\text{m}$ .  
 — BW; —□— measured; — · — SWL; --- profile,  $t=0$

The two main boundary conditions influencing the beach groundwater head levels are the back beach water level and the surf zone setup due to waves. These interact through the flow within the beach and model-data comparisons of this are illustrated in figure 5. For longer wave periods the back beach water level appears to have little effect on the head offshore of the initial shoreline (figure 5a and 5b), indicated by near constant

setup in the surf zone, irrespective of the back beach water level. The model results are in good agreement with the data in this respect. However, for the low-tide condition, the influence of the back beach water level is not so well predicted, as demonstrated by the different shape of the modelled and measured head profile (see also figure 3c).

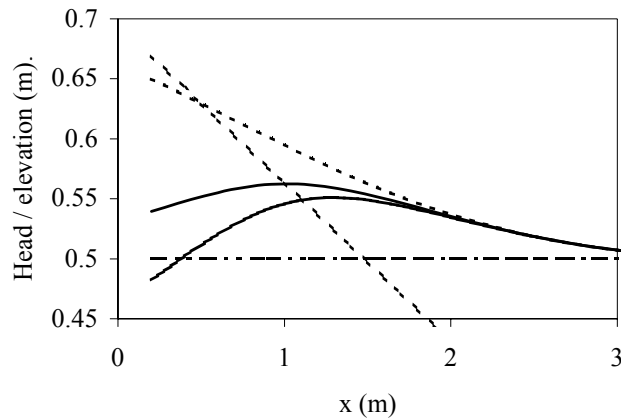


Figure 5a. Modelled piezometric head,  $f=0.4\text{Hz}$ ,  $H=0.15\text{m}$ , varying TWL, as figure 3 above.  
— · — SWL; — — — profile,  $t=0$

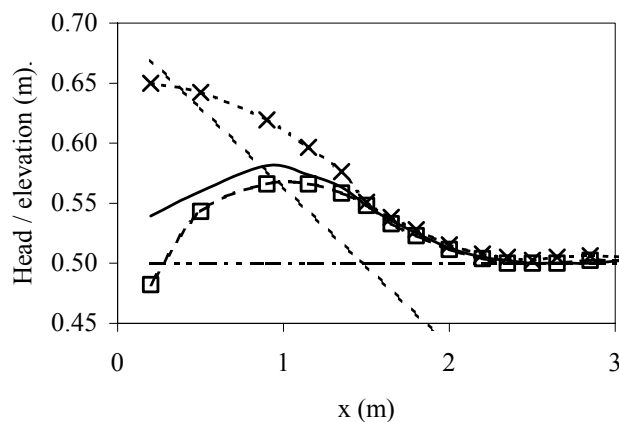


Figure 5b. Measured piezometric head,  $f=0.4\text{Hz}$ ,  $H=0.15\text{m}$ , varying TWL.  
— · — SWL; — — — profile,  $t=0$

For a shorter wave period and smaller wave height ( $f=1\text{Hz}$ ,  $H=0.1\text{m}$ ) the measured data show that the back beach ground water level can influence the setup in the inner surf and swash zones, with smaller setup observed for a lower overall beach groundwater (figure 6b). However, the model does not predict this, and indeed shows an opposite trend which does not seem entirely realistic. The observations are consistent with the influence of swash-swash interactions on nearshore setup, which becomes proportionally larger for shorter period waves [2]. While this interaction process can be simulated by the model, it is clear that some discrepancies remain.

### Conclusions

Numerical model results have been compared to new experimental laboratory data on beach groundwater levels forced by wave-runup. Overall model results are encouraging and suggest the model may be a useful tool to study wave-induced beach groundwater interactions. Model-data discrepancies appear to be a result of inaccurate prediction of the nearshore hydrodynamics, as opposed to poor representation of the internal flow in the beach.

### Acknowledgements

The authors gratefully acknowledge support and funding from the Australian Research Council, the CRC for Sustainable Tourism and the University of Queensland.

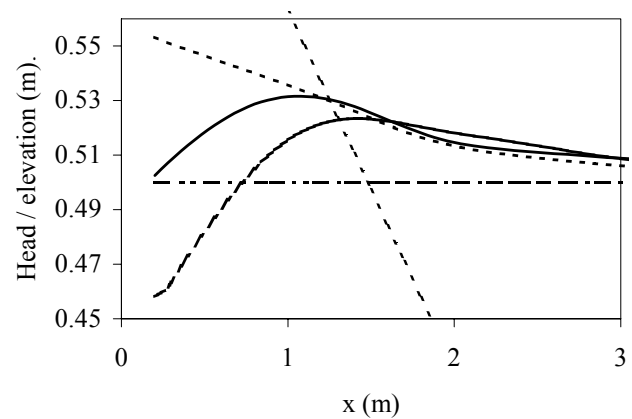


Figure 6a. Modelled piezometric head,  $f=1\text{Hz}$ ,  $H=0.1\text{m}$ , varying TWL.  
— · — SWL; — — — profile,  $t=0$

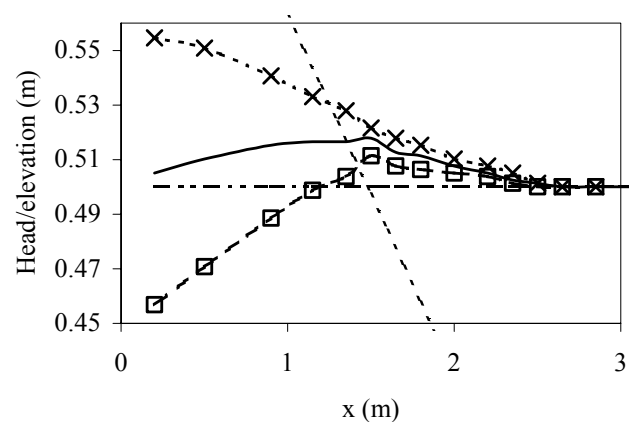


Figure 6b. Measured piezometric head,  $f=1\text{Hz}$ ,  $H=0.1\text{m}$ , varying TWL. — · — SWL; — — — profile,  $t=0$

### References

- [1] Baird, A.J., Horn, D.P. and Mason, T.E. Validation of a Boussinesq model of beach ground water behaviour. *Marine Geology*, 148, 1998, 55-69.
- [2] Baldock, T. E. and Holmes, P., Simulation and prediction of swash oscillations on a steep beach. *Coastal Engineering*, 36, 1999, 219-242.
- [3] Grant, U.S. Influence of the water table on beach aggradation and degradation. *J. Mar Res.*, 7, 1948, 655-660.
- [4] Li, L., Barry, D. A., Stagnitti, F. and Parlange, J.-Y. (1999): Submarine groundwater discharge and associated chemical input to a coastal sea, *Water Res. Research*, 35, 3253-3259.
- [5] Li, L., Barry, D. A., Pattiaratchi, C.B., and Masselink, G., BeachWin: modelling groundwater effects on swash sediment transport and beach profile changes. *Environmental Modelling & Software*, 17, 2002, 313-320.
- [6] Nielsen, P., Tidal dynamics of the watertable in beaches. *Water Resources Research*, 26, 9, 1990, 2127-2135.
- [7] Nielsen, P., Groundwater dynamics and salinity in Coastal Barriers, *J. Coastal Res.*, 15 (3), 1999, 732-740.
- [8] Oh, T.M. and Dean, R.G. Effects of controlled water table on beach profile dynamics. *Proc. Int. Conf. Coastal Engineering*, 3, 1994, 2449-2460.
- [9] Sum, CH-Y., Influence of beach groundwater levels on beach morphology. University of Queensland, 2004. 92pp.
- [10] Turner, I.L. and Masselink, G., Swash infiltration-exfiltration and sediment transport, *J. Geophys. Res.*, 103, 1998, 30813-30824.

## Drag Reduction on Bluff Bodies using a Rotating Device

S.E. Robson and N.A. Ahmed

School of Mechanical & Manufacturing Engineering  
The University of New South Wales, Sydney, NSW, 2052 AUSTRALIA

### Abstract

Drag plays a significant role in the overall force on aerodynamic bodies. In this paper a drag reducer in the form of a rotating ventilator is proposed for bluff bodies. The qualitative and quantitative investigations were conducted on the effects of this device mounted on the front end of a rectangular bluff body. Results indicate that the device decreases drag on the body significantly by approximately 50% at Reynolds numbers of  $3.5 \times 10^5$  and  $6.5 \times 10^5$ . The incorporation of this device also makes the drag of the body less Reynolds number dependant. Consequently the proposed configuration is more efficient at higher speed in comparison to the conventional configuration which did not have the device attached to it.

### Nomenclature

$C_D$  drag coefficient,  $\frac{D}{\frac{1}{2}\rho V^2 S}$

$D$  drag force

$L$  characteristic length

Re Reynolds number,  $\frac{\rho V L}{\mu}$

$S$  reference area, defined as frontal area

$V$  free stream velocity

$\mu$  free stream viscosity

$\rho$  free stream density

### Introduction

Bluff bodies are used in a wide variety of applications such as bridges, buildings and other infrastructure and transport vehicles. The forces and characteristics of the flow around these objects can be significant for example vortex shedding and galloping may cause structural vibration problems while excessive wind loads may cause static structural problems and/or excessive energy consumption. Extensive studies have been conducted into how to reduce wind loads and vibration loads on bluff bodies. Boundary layer control devices and streamlining of the body are the two major methods of reducing loading, 80% of which may be attributed to pressure drag.

Although a variety of techniques are currently used to reduce drag and consequently fuel consumption or required structural strength many have a limited range of application. The most popular forms of aerodynamic improvements for bluff bodies use passive flow control techniques that effectively streamline the shape such as steps [8], flow deflectors [15], fences [8], [12], rounded edges [5], [8] and [15], nose cones [15] and wake ventilation [6]. However, these devices have a limited operating envelope.

Boundary layer control using rotating control cylinders, on the other hand, has shown greater promise on various shaped bodies [1][7],[9]-[11], [13]. However, the requirement of large control power input and other associated costs have not made the techniques commercially viable at present [7], [13]. The ideal solution to the problem of drag reduction should be competitive on cost and applicable in a large range of realistic flow situations.

If the main functional purpose of the bluff body, which may be to hold a certain capacity [buildings and other infrastructure] or allow the conveyance of goods [transport vehicles] or passage of people and vehicles [bridges], is not to be compromised, the current rectangular shape of these bodies appears to be appropriate. The drag characteristics of a rectangular box exhibit a direct relationship with the sharpness of the corner. Most of the drag is produced by losses induced at the corner. The more rounded the corner the lower the losses and the drag. However, most transport vehicles and infrastructure require the useable storage or road space to be maximised and tend to have sharp corners and edges. Active methods of drag reduction such as control cylinders must have a minimum energy input.

In this paper, the use of a generic rotating ventilator as a form of low energy drag reducer is proposed for use on bluff bodies such as transport vehicles. An experimental investigation of a rectangular bluff body was conducted to demonstrate the viability of this novel concept. The ventilator is expected to produce an effect on the flow characteristics similar to a rotating cylinder but with the added advantage that it can be operated using natural wind without the need for any power input by the engine or any auxiliary unit. Another advantage of this configuration is that storage capacity is unaffected as it is mounted externally.

### Experimental Set Up

The bluff body was modelled as a rectangular box with dimensions of 0.3x0.3x0.5m. The ventilator was mounted on the front of the model with the axis of rotation parallel to the front surface and the bottom edge as depicted in Figure 1. A commercial wind driven ventilator, Edmonds model number GP130, was used in all experiments. A full description of the ventilator can be found in Rashid and Ahmed [14].

The 30" Open Circuit Open Jet Wind Tunnel in the Aerodynamics Laboratory at the University of New South Wales [2] was used to conduct the experiments. The test Reynolds numbers were selected to lie between  $3.5 - 6.5 \times 10^5$  with the major study at an Re of  $5.4 \times 10^5$  where the characteristic length is defined as the length of the bluff body. The model was mounted in the tunnel with provision for the angle of yaw to be adjusted. Measurements were taken at yaw angles of 0, 5, 10 and 15 degrees. The Reynolds number dependence of the zero angle case was examined at Re of  $3.6 \times 10^5$ ,  $4.5 \times 10^5$ ,  $5.4 \times 10^5$  and  $6.3 \times 10^5$ .

Tufts of synthetic woven thread were used for flow visualisation. A six axis Industrial Automation ATI DAQ F/T Gamma Load Cell was used to measure forces on the model. The load cell was

connected to a PCI-6034E National Instruments Data Acquisition Card. The data acquisition program provided by the manufacturer was used to convert the raw voltages into force output that was displayed on the monitor. The test section arrangement is shown in Figure 2.

Three configurations were tested. Configuration 1 was a plain box, Configuration 2 had the ventilator mounted on the box but rotation was prevented and Configuration 3 was the box with the ventilator free to rotate.

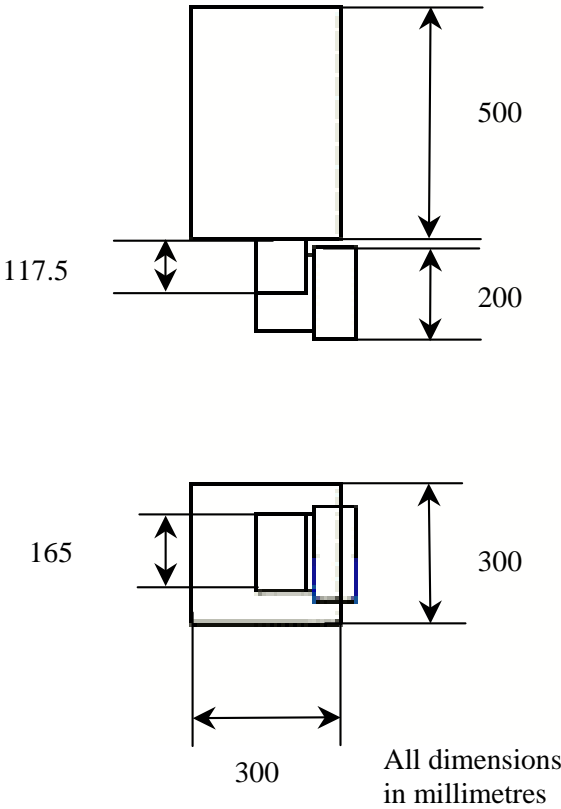


Figure 1. Bluff Body and Ventilator Model.

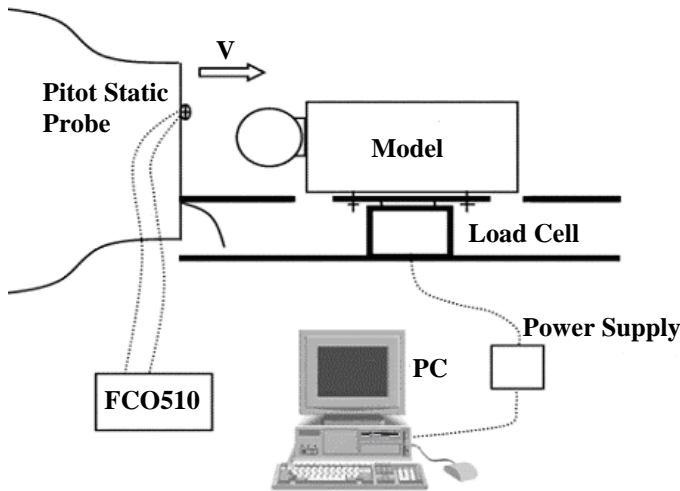


Figure 2. Test Section and Equipment Arrangement.

**Results and Discussion**  
**Qualitative Results**

Results of the flow visualisation are shown in Figure 3. There is an obvious improvement in flow attachment of Configuration 2 over Configuration 1. The improvement in Configuration 3 over Configuration 2 is however, less pronounced. There is further improvement in Configuration 3 where in row five, seven straight

tufts can be seen in this configuration as opposed to four straight tufts in Configuration 2. The increased straightening of the tufts is visible on most of the top surface and some of the side surface indicating improved streamlining and hence reduced drag of the body.

The flow visualisation indicates results similar to those found for rotating control cylinders on bluff bodies, which draw the flow back down onto the body, reducing separation [1], [7], [10][11] [13].

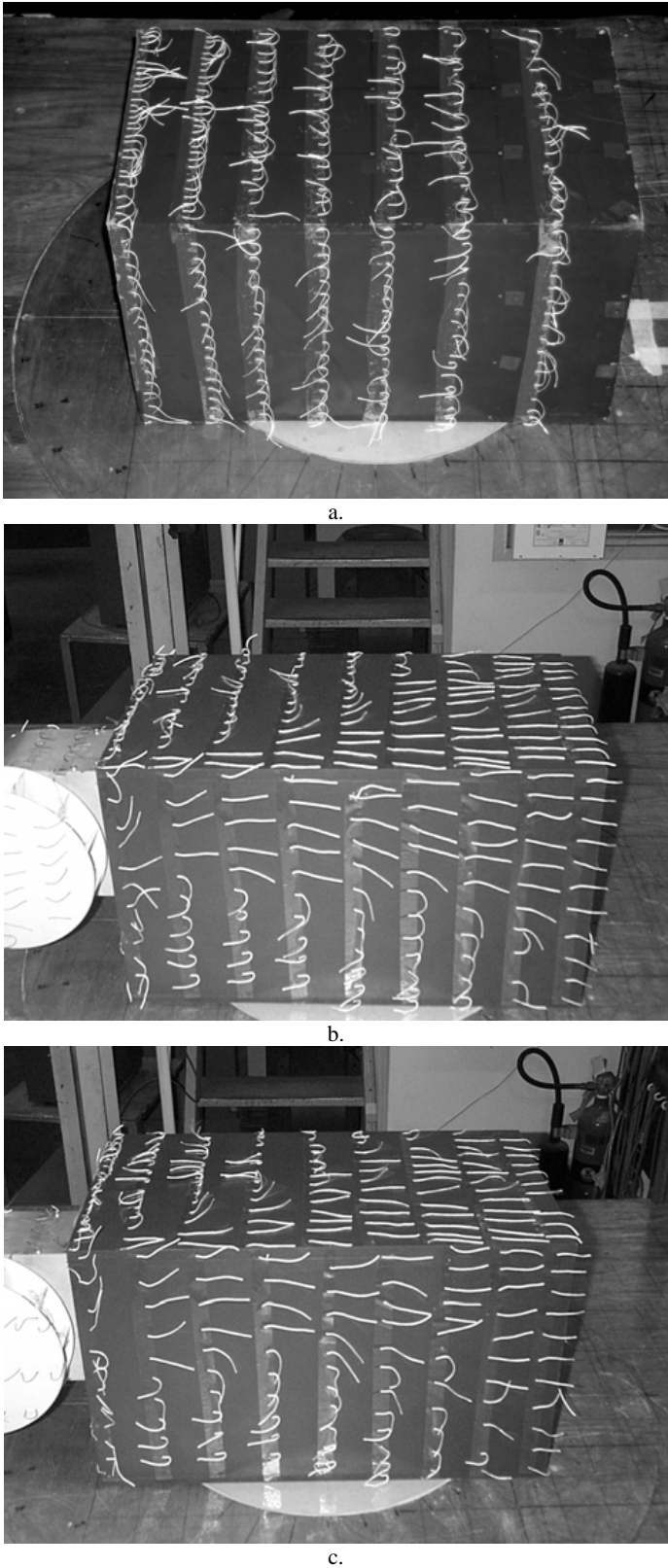


Figure 3. Flow Visualisation for  $Re = 5.4 \times 10^5$ .  
a. Configuration 1, b. Configuration 2, c. Configuration 3.



## Quantitative Results

Results of the quantitative investigation are presented in terms of drag force coefficients. The drag coefficient results shown in Figures 4 and 5 indicate a significant improvement due to the ventilators rotation. Data for Configuration 1 suggests the drag coefficient results were between 0.92 and 0.8 at yaw angles of 0 to 15 degrees. To obtain confidence in the data obtained, a check was made on the value of the drag coefficient for Configuration 1 using ESDU data sheet 71016 [4]. The data sheet gives a value of one for a surface mounted block which is close to the value obtained in this experiment for this configuration and corresponds within the bounds of the published uncertainty.

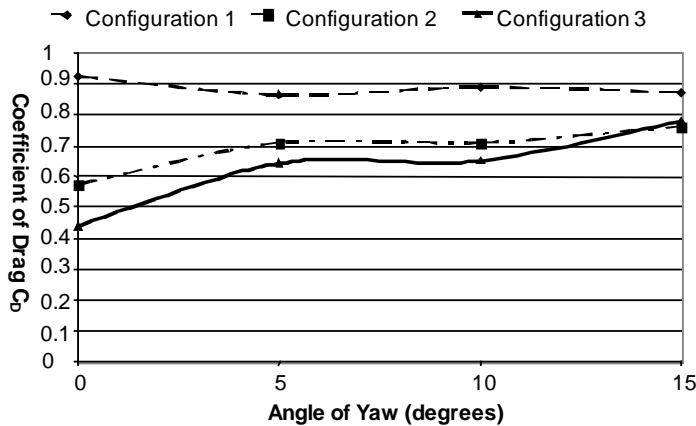


Figure 4. Variation of  $C_D$  at different angles of yaw for  $Re = 5.4 \times 10^5$ .

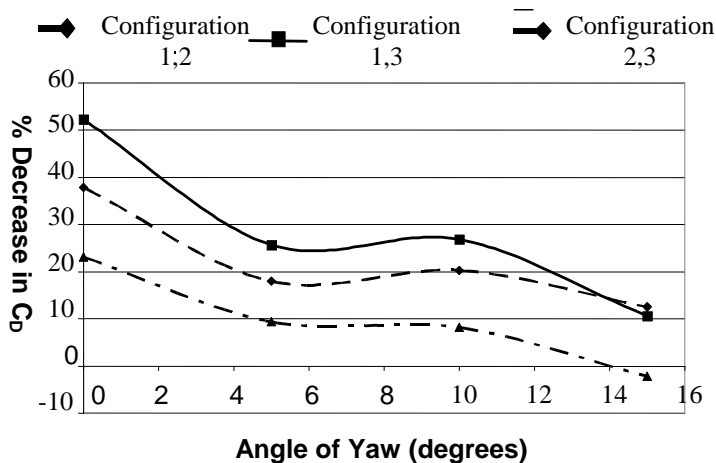


Figure 5. Percentage Decrease in Drag Coefficient for  $Re = 5.4 \times 10^5$ .

The effect of the ventilator is found to be most significant at 0 degrees angle of yaw with a decrease in drag coefficient of over 50%. At higher angles of yaw the improvement in drag coefficient is lower but is still significant. In the experiments the lowest recorded result was at 15 degrees angle of yaw where the result was still greater than 10 %.

Figure 6 indicates the Reynolds number dependence of the drag coefficient for Configuration 1 at zero angle of yaw; the dependence of Configurations 2 and 3 is much less significant. The drag reduction increases with Reynolds number from nearly 48% for a  $Re$  of  $3.64 \times 10^5$  to approximately 57% for a  $Re$  of  $6.4 \times 10^5$ .

The uncertainty of  $C_D$  was calculated to be  $\pm 1\%$  based on the values obtained for the base configuration (Configuration 1) at zero angle of yaw.

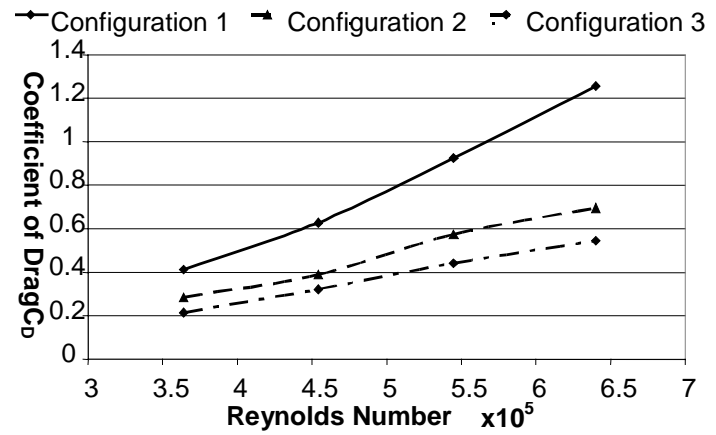


Figure 6. Reynolds Number Dependence of Drag Coefficient.

## Conclusions

The present study has demonstrated the viability of using a rotating ventilator as a form of drag reducer for bluff bodies. As far as the authors are aware this is a novel application of the device which has only been used in natural ventilation.

The experimental results presented in this paper indicate a clear improvement in the drag coefficient at all angles of yaw due to the rotating ventilator. A significant reduction in drag of over 50% at zero degrees angle of yaw was achieved. This is a very encouraging finding since the relative angle of yaw of the free stream is generally small and close to zero for most transport applications however other devices may need to be attached for flows dominated by high angles. Another useful finding is that the incorporation of the rotating ventilator makes the drag of the vehicle less Reynolds number dependent. This suggests that the positive attributes of this device are applicable over the whole range of the flow speeds and thus in the case of transport vehicles will be more economic for long-haul transportation on the open road.

It should be pointed out that only one ventilator was used in this study to demonstrate the concept. However, in normal operation it is envisaged that a series of ventilators would be attached to the body. Further work is progressing.

Finally, the drag reducer considered in this study has considerable operational and economic advantages. The price of the ventilator used is quite low, approximately US\$35 retail per unit, which is a very small percentage of the total vehicle cost. The device is easy to implement and costs nothing to operate. The method proposed here, therefore offers a cost effective, practical solution to a common problem of bluff body flows such as truck operation. The improved fuel efficiency resulting from the use of this concept will have significant positive impact on the bottom-line operating cost of these vehicles and also benefit the environment from reduced fuel emissions. In the case of other bluff bodies the reduced loading will result in reduced structural demands.

## Acknowledgments

The authors would like to thank Edmonds Products Pty Ltd and in particular Mr Allan Ramsay and Mr Derek Nunn for their enthusiastic support in the conduct of this experiment.

## References

- [1] Abu-Hijeh, B.A.K., Modifying a Reattaching Shear layer using a Rotating Cylinder, *Comp. and Fluids*, **29**, 2000, 261-273.

- [2] Ahmed, N. A. & Archer, R. D., Testing of a Highly Loaded Horizontal Axis Wind Turbines Designed for Optimum Performance, *Int. J. of Renewable Energy*, **25**, 2002, 613-618.
- [3] Editor, Active Flow Control-Bright Prospects and Basic Challenges, *J. of Aircraft*, **38**, 2001, 401.
- [4] ESDU, Fluid Forces, Pressures and Moments on Rectangular Blocks, *ESDU Data Sheet 71016*, 01 Nov 1978.
- [5] Gotz, H., Bus Design Features and Their Aerodynamic Effects, *Int. J. of Vehicle Design*, Technological Advances in Vehicle Design Series, SP3, Impact of Aerodynamics on Vehicle Design, 1983, 229 – 255.
- [6] Grosche, F.-R. & Meier, G.E.A., Research at DLR Göttingen on Bluff Body Aerodynamics, Drag Reduction by Wake Ventilation and Active Flow Control, *J. of Wind Eng. and Ind. Aerodyn.*, **89**, 2001, 1201-1218.
- [7] Kubo, Y., et al, Control of Flow Separation from Leading Edge of a Shallow Rectangular Cylinder through Momentum Injection, *J. of Wind Eng. and Ind. Aerodyn.*, **83**, 1999, 503-514.
- [8] Lajos, T., Drag Reduction by the production of a Separation Bubble on the Front of a Bluff Body, *J. of Wind Eng. and Ind. Aerodyn.*, **22**, 1986, 331-338.
- [9] Mittal, S., Control of Flow Past Bluff Bodies using Rotating Control Cylinders, *J. of Fluid. Struct.*, **15**, 2001, 291-326.
- [10] Modi, V.J., Moving Surface Boundary Layer Control: A Review, *J. of Fluid. Struct.*, **11**, 1997, 627-637.
- [11] Modi, V.J. & Deshpande, V.S., Fluid Dynamics of a Cubic Structure as Affected by Momentum Injection and Height, *J. of Wind Eng. and Ind. Aerodyn.*, **89**, 2001, 445-470.
- [12] Modi, V.J., St. Hill, S. & Yokomizo, T., Drag Reduction of Trucks through Boundary Layer Control, *J. of Wind Eng. and Ind. Aerodyn.*, **54/55**, 1995, 583-594.
- [13] Munshi, S.R., Modi, V.J. & Yokomizo, T., Fluid Dynamics of Flat Plates and Rectangular Prisms in the Presence of Moving Surface boundary Layer Control, *J. of Wind Eng. and Ind. Aerodyn.*, **79**, 1999, 37-60.
- [14] Rashid, D. H. & Ahmed, N. A., Study Of Aerodynamic Forces on a Rotating Wind Driven Ventilator. *Int. J. of Wind Eng.*, **27**, 2003, 63-72.
- [15] Stollery, J. & Garry, K. P., Techniques for Reducing Commercial Vehicle Aerodynamic Drag., *Int. J. of Vehicle Design*, Technological Advances in Vehicle Design Series, SP3, Impact of Aerodynamics on Vehicle Design, 1983, 210 – 228.



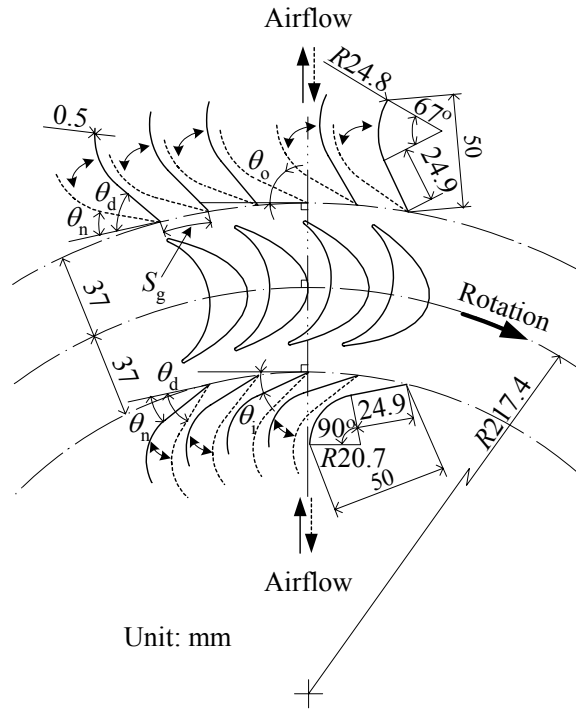


Figure 3. Configuration of turbine

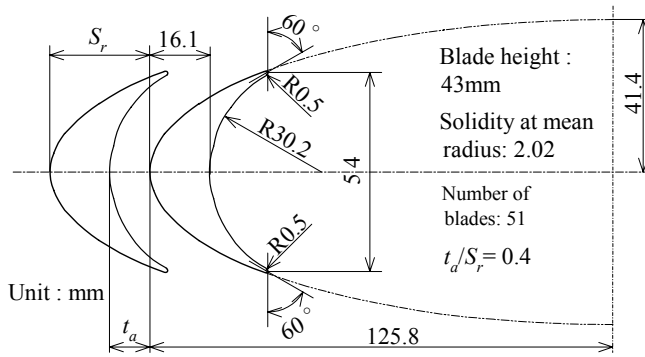


Figure 4. Rotor blade

equation (4) are obtained. Data for a range of flow coefficients are collected by varying flow rate or turbine angular velocity. Tests were performed with turbine shaft angular velocities  $\omega$  up to 68.1 rad/s and flow rates  $Q$  up to 0.275 m<sup>3</sup>/s. The Reynolds number based on the blade chord was approximately  $3 \times 10^4$  at conditions corresponding to the peak efficiency of the turbine. The measurement uncertainty in efficiency is about  $\pm 1\%$ .

The radial turbine shown in figure 2 was tested at a constant rotational speed under steady flow. The sign and magnitude of the torque of the motor-generator is servo controlled so as to hold the turbine speed constant even if the flow velocity is varying with time. The part of shroud casing and the part of disk covering the inner guide vane to the exit are flat and parallel to each other. The height of flow path of the turbine  $h$  (gap between the shroud casing and the disk) is 44 mm. The flow passage from inlet to inner guide vane entry has been shaped such that the flow area is constant along this passage. The turbine system has guide vanes before and behind the rotor so as to operate efficiently in a reciprocating airflow. They are set by pivots on the shroud casing wall as shown in figure 2. The pivots are located at the end of the guide vane chord close to the rotor. The guide vanes are controlled by the stepping motors, timing pulleys and timing belts. Each cascade of outer and inner guide vane changes the pitch angle simultaneously when the airflow direction changes. These guide vanes rotate between two angles, i.e., nozzle setting angle  $\theta_n$  (upstream side of

the rotor) and diffuser setting angle  $\theta_d$  (downstream one) as shown in figure 3. However, the pitch angle is set at a particular value because tests are performed under steady flow conditions in the study.

The guide vane geometries are shown in figure 3. The guide vane consists of a straight line and circular arc. Details of the guide vanes are given by chord length of 50mm; solidity of inner guide vane at  $r_R$  of 1.15; solidity of outer guide vane of 1.16. The nozzle setting angle  $\theta_n$  is only 15° for both the airflow direction. In order to clarify the effect of the diffuser setting angle  $\theta_d$  on the turbine characteristics  $\theta_d$  is 20° to 60° for the inner guide vane in the case of inhalation, and 30° to 90° for the outer guide vane in the case of exhalation. Rotor blade geometry is shown in figure 4 and is the same as what was used in previous studies [5, 6]. The blade profile consists of a circular arc and on the pressure side and part of an ellipse on the suction side. The ellipse has semi-major axis of 125.8mm and semi-minor axis of 41.4mm. Detailed information about the blade profile is as follows: chord length of 54mm; tip clearance of 1 mm; mean radius of  $r_R = 217.4$ mm; blade inlet (or outlet) angle of 60°; thickness ratio of 0.3. The blade is oriented such that the blade profile is tangent to a radial line at the maximum thickness point on the suction side which can be seen clearly for the second blade from the left in figure 3.

## Results and Discussion

Experimental results on the running characteristics of the turbine are expressed in terms of the torque coefficient  $C_T$ , input coefficient  $C_A$  and efficiency  $\eta$ , which are all plotted against the flow coefficient  $\phi$ . The various definitions are

$$C_T = T_o / \{ \rho (v_t^2 + U_R^2) A_R r_R / 2 \} \quad (1)$$

$$C_A = \Delta p Q / \{ \rho (v_t^2 + U_R^2) A_R v_R / 2 \} = \Delta p / \{ \rho (v_t^2 + U_R^2) / 2 \} \quad (2)$$

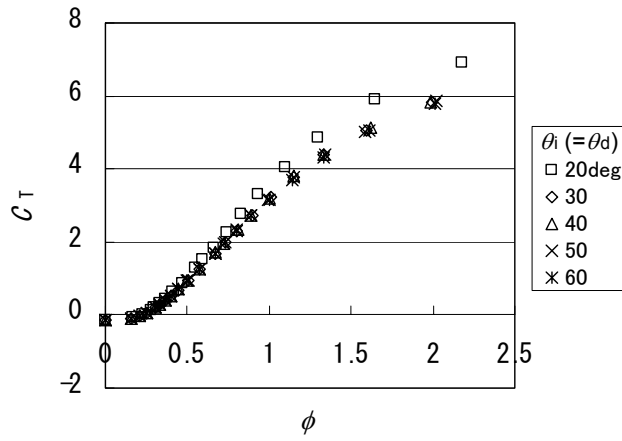
where  $\rho$  and  $U_R$  are density of air, rotational speed at  $r_R$ , respectively. Efficiency, which is the ratio of shaft power output to pneumatic power input, can be expressed in terms of the coefficients mentioned above:

$$\eta = T_o \omega / (\Delta p Q) = C_T / (C_A \phi). \quad (3)$$

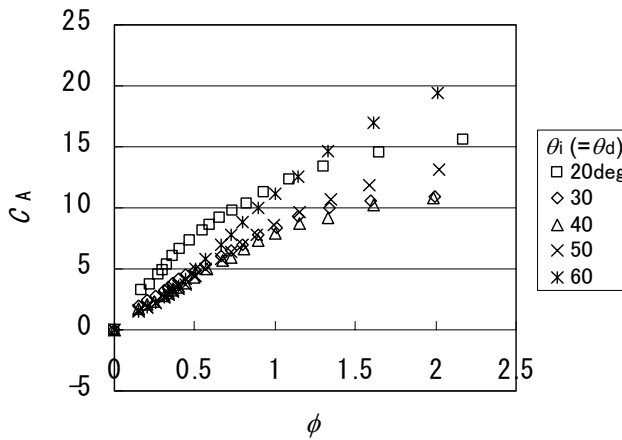
The flow coefficient is defined as

$$\phi = v_R / U_R. \quad (4)$$

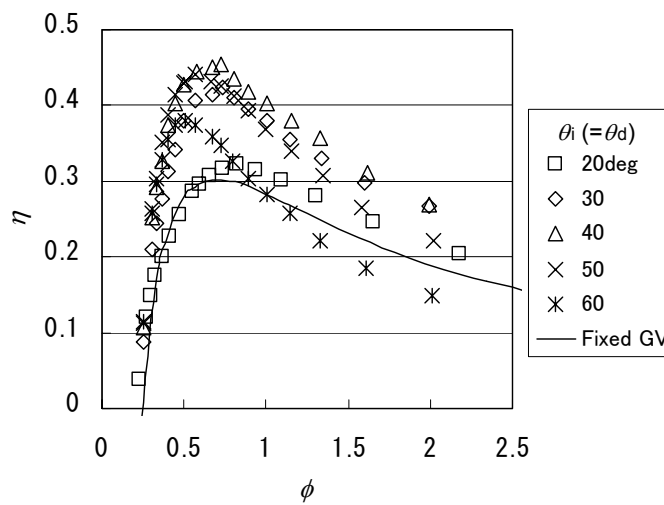
Figures 5 and 6 show the effect of setting angle of the inner guide vane on the turbine characteristics under steady flow conditions. In figure 5c the solid line represents the efficiency of the radial turbine with fixed guide vanes which has the optimum setting angle ( $\theta_i = \theta_o = 25^\circ$ ) [7]. When the flow direction is from atmosphere to settling chamber (i.e. inhalation) the inner guide vane is downstream of the rotor and it works as a diffuser. Consequently, the torque coefficient  $C_T$  is independent of  $\theta_i$  (figure 5a), whereas the input coefficient  $C_A$  decreases with increasing  $\theta_i$  for  $\theta_i \leq 40^\circ$  (figure 5b). Then,  $C_A$  increases with  $\theta_i$  for  $\theta_i \geq 40^\circ$ . Combining the above results and equation (3), it is evident that the highest efficiency occurs for the highest value of  $\theta_i = 40^\circ$  and its value is approximately 0.45 when the flow is 'from atmosphere' (figures 5c and 6). Moreover, it can be observed from figure 5c that the efficiency of the presented radial turbine is higher than that of the conventional radial turbine (i.e. the radial turbine with fixed guide vanes) by 0.15. Conversely, when the flow direction is from chamber to atmosphere (i.e. exhalation), the outer guide vane is downstream of the rotor and it works as a diffuser. Hence, the torque coefficient  $C_T$  is independent of  $\theta_o$  (figure 7a). Regarding  $C_A$ - $\phi$  characteristics,  $C_A$  decreases slightly with increasing  $\theta_o$  for  $\theta_o \leq 60^\circ$  and  $C_A$ - $\phi$  characteristics in the case of  $\theta_o \geq 60^\circ$  are almost the same (figure 7b). As a result,  $\eta$  increases with  $\theta_o \leq 60^\circ$  and remains



(a) Torque coefficient



(b) Input coefficient



(c) Efficiency

Figure 5. Effect of setting angle of inner guide vane on turbine characteristics (inhalation,  $\theta_o = \theta_n = 15^\circ$ )

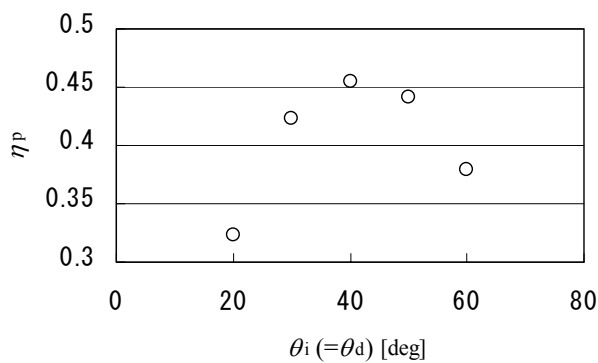
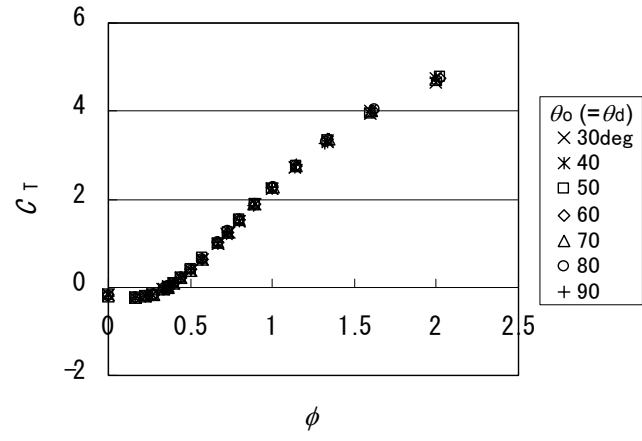
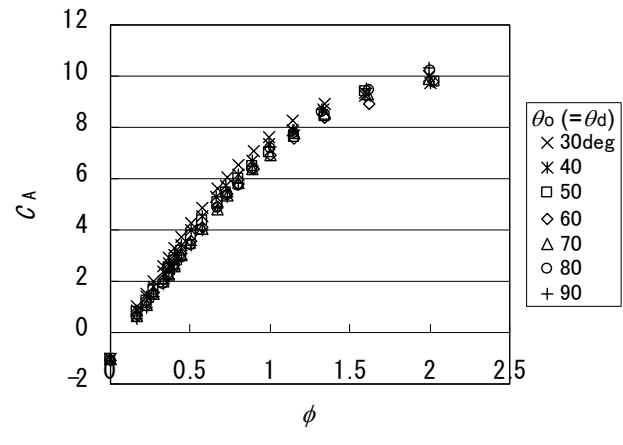


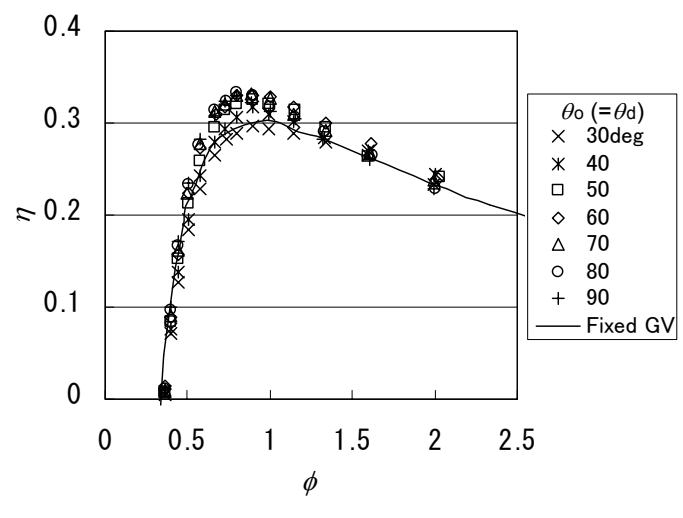
Figure 6. Effect of setting angle of inner guide vane on peak efficiency (inhalation,  $\theta_o = \theta_n = 15^\circ$ )



(a) Torque coefficient



(b) Input coefficient



(c) Efficiency

Figure 7. Effect of setting angle of outer guide vane on turbine characteristics (exhalation,  $\theta_i = \theta_n = 15^\circ$ )

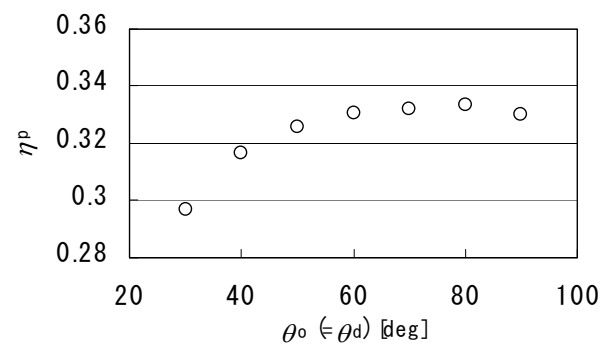


Figure 8. Effect of setting angle of outer guide vane on peak efficiency (exhalation,  $\theta_i = \theta_n = 15^\circ$ )

a stable situation at round 0.33 (figures 7c and 8). Its efficiency is higher than that of the conventional radial turbine by 0.03. Looking at the efficiency curves in figures 5c and 7c, it is seen that higher efficiencies are obtained when the flow is from atmosphere. Therefore, it has been concluded from the above results that the performance of the radial turbine can be improved by using pitch-controlled guide vanes.

### Conclusions

In order to develop a high performance radial turbine for wave energy conversion, a radial turbine with pitch-controlled guide vanes has been proposed and investigated experimentally by model testing. As the first step to an analysis the presented turbine, the experiment has been carried out under steady flow conditions in the study. Then, the results have been compared with those of a radial turbine with fixed guide vanes by previous studies. As a result, the performances of the presented radial turbine under steady flow conditions have been clarified. Furthermore, it seems that the presented radial turbine is superior to the conventional radial turbine, i.e., the radial turbine with fixed guide vanes.

### References

- [1] Kaneko, K., Setoguchi, T. & Raghunathan, S., Self-rectifying Turbine for Wave Energy Conversion, in *1st International Offshore Polar Engineering Conference*, **1**, 1991, 385-392.
- [2] Kaneko, K., Setoguchi, T. & Raghunathan, S., Self-rectifying Turbines for Wave Energy Conversion, *Int. J. Offshore Polar Engng.*, **2**(3), 1992, 238-240.
- [3] McCormick, M. E., Rehak, J. G. & Williams, B. D., An Experimental Study of a Bi-directional Radial Turbine for Pneumatic Energy Conversion, in. *Mastering Ocean through Technology*, **2**, 1992, 866-870.
- [4] McCormick, M. E. & Cochran, B., A Performance Study of a Radial Turbine, in *1st European Wave Energy Conference*, 1993, 443-448.
- [5] Setoguchi, T., Takao, M., Kinoue, Y., Kaneko, K., Santhakumar, S. & Inoue, M., Study on an Impulse Turbine for Wave Energy Conversion, *Int. J. Offshore Polar Engng.*, **10**(2), 2000, 145-152.
- [6] Setoguchi, T., Kaneko, K., Taniyama, H., Maeda, H. & Inoue, M., Impulse Turbine with Self-pitch-controlled Guide Vanes for Wave Power Conversion, *Int. J. Offshore Polar Engng.*, **6**(1), 1996, 76-80.
- [7] Setoguchi, T., Santhakumar, S., Takao, M., Kim, T.H. & Kaneko, K., A Performance Study of a Radial Turbine for Wave Energy Conversion, *J. Power and Energy*, **216**(A1), 2002, 15-22.
- [8] Veziroglu, T. N. (editor), *Alternative Energy Sources VI*, Vol. 3, Wind/Ocean/Nuclear/Hydrogen, Hemisphere Publishing Corporation, 1985, 169-181.

## The “zeroth law” of turbulence in steady isotropic turbulence

B. R. Pearson<sup>1</sup>, T. A. Yousef<sup>2</sup>, N. E. L. Haugen<sup>3</sup>, A. Brandenburg<sup>4</sup> & P. -Å. Krogstad<sup>2</sup>

<sup>1</sup>School of Mechanical, Materials, Manufacturing Engineering & Management.  
University of Nottingham, Nottingham NG7 2RD, UNITED KINGDOM.

<sup>2</sup>Dept. of Energy and Process Engineering, The Norwegian University of Science and Technology,  
Kolbjørn Hejes vei 2B, N-7491 Trondheim, NORWAY

<sup>3</sup>Department of Physics, The Norwegian University of Science and Technology,  
Høy skoleringen 5, N-7034 Trondheim, NORWAY

<sup>4</sup>NORDITA, Blegdamsvej 17, DK-2100 Copenhagen Ø, DENMARK

### Abstract

The dimensionless kinetic energy dissipation rate  $C_\epsilon$  is estimated from numerical simulations of statistically stationary isotropic box turbulence that is slightly compressible. The Taylor microscale Reynolds number ( $Re_\lambda$ ) range is  $20 \lesssim Re_\lambda \lesssim 300$  and the statistical stationarity is achieved with a random phase forcing method. The strong  $Re_\lambda$  dependence of  $C_\epsilon$  abates when  $Re_\lambda \approx 100$  after which  $C_\epsilon$  slowly approaches  $\approx 0.5$ , a value slightly different to previously reported simulations but in good agreement with experimental results. If  $C_\epsilon$  is estimated at a specific time step from the time series of the quantities involved it is necessary to account for the time lag between energy injection and energy dissipation. Also, the resulting value can differ from the ensemble averaged value by up to  $\pm 30\%$ . This may explain the spread in results from previously published estimates of  $C_\epsilon$ .

### Introduction

The notion that the mean turbulent kinetic energy dissipation rate  $\epsilon$  is finite and independent of viscosity  $\nu$  was originally proposed by G. I. Taylor[1]. Its importance is so recognized now that it is sometimes referred to as the “zeroth law” of turbulence. Its existence was assumed by von Kármán and Howarth, Loitsianskii and also, significantly, Kolmogorov[2] in establishing his celebrated similarity hypotheses for the structure of the inertial range of turbulence. Kolmogorov assumed the small scale structure of turbulence to be locally isotropic in space and locally stationary in time - which implies the equality of turbulent kinetic energy injection at the large scales with the rate of turbulent kinetic energy dissipation at the small scales. Although this view should be strictly applied only to steady turbulence, the mechanism of the dissipation of turbulent kinetic energy can be considered the most fundamental aspect of turbulence not only from a theoretical viewpoint but also from a turbulence modeling viewpoint. Indeed, the mechanism that sets the level of turbulent dissipation in flows that are unsteady is a difficult, if not intractable, aspect of turbulence modeling.

The rate of turbulent kinetic energy dissipation is determined by the rate of energy passed from the large-scale eddies to the next smaller scale eddies via a forward cascade until the energy is eventually dissipated by viscosity. Thus,  $C_\epsilon$  defined as,

$$C_\epsilon = \epsilon L / u'^3, \quad (1)$$

(here,  $L$  and  $u'$  are characteristic large length and velocity scales respectively) should be independent of the Reynolds number and of order unity. An increase in Reynolds number should only result in an increase in the typical wave number where dissipation takes place. In the past few years there have been a number of numerical (see Ref. [3] and references therein) and

experimental (see Refs. [4, 5] for recent results) efforts to determine the value of  $C_\epsilon$  and its dependence on the Reynolds number. Perhaps the most convincing of these are the numerical attempts since there is no re-course to one-dimensional surrogacy as there is for experiments. Notwithstanding this fact, there is good agreement, both numerically and experimentally, with the long held view that  $C_\epsilon$  is  $\sim O(1)$  when the Reynolds number is sufficiently high. The collection of isotropic simulation results for  $C_\epsilon$  shown in Ref. [3] indicates that “high enough” Reynolds number “appears” to be  $Re_\lambda \sim O(100)$ . Here,  $Re_\lambda (= u'^2 [15/\nu\epsilon]^{1/2})$  is the Taylor microscale Reynolds number. At higher  $Re_\lambda$  e.g.  $Re_\lambda \gtrsim 300$ , small  $Re_\lambda$  dependencies for  $C_\epsilon$ , such as that proposed by Lohse[6] cannot be ruled out. Measuring such  $Re_\lambda$  dependencies, either numerically or experimentally, will be close to impossible.

One unresolved issue is that raised by Sreenivasan[7]. After assembling all the then known experimental decaying grid turbulence data[8] and numerical data for both decaying and stationary isotropic turbulence he concludes that “the asymptotic value (of  $C_\epsilon$ ) might depend on the nature of large-scale forcing, or, perhaps, on the structure of the large scale.” He also demonstrates[9] in homogeneously sheared flows that the large structure does influence  $C_\epsilon$ . However, it might be argued that these results were obtained at low Reynolds numbers and the issue of a universal asymptotic value for  $C_\epsilon$  could still be considered open. Alternatively it could be argued that homogeneous shear flows and the like are strictly unsteady turbulent flows and the zeroth law, in its simplest guise, should not be expected to apply to such flows e.g. see Ref. [10]. The possibility of some characteristics of large-scale turbulence being universal should not be ruled out. The recent observation that input power fluctuations, when properly re-scaled, appear universal[11] may be construed to suggest the possibility of universality for  $C_\epsilon$ . The aim of the present work is to estimate  $C_\epsilon$  from direct numerical simulations (DNS) of statistically stationary isotropic turbulence and compare with previously reported DNS results (summarized in Fig. 3 of Ref. [3]) and experiments carried out in regions of low ( $dU/dy \approx dU/dy|_{\max}/2$ ) or zero mean shear. The present DNS scheme differs from methods already reported in that a high-order finite difference method is used. To our knowledge, these are the first finite difference results for  $C_\epsilon$ . Hence, it is worthwhile to test if different numerics and forcing at the large scales result in vastly different values for  $C_\epsilon$  to those already reported.

### Numerical Methods

The data used for estimating  $C_\epsilon$  are obtained by solving the Navier Stokes equations for an isothermal fluid with a constant kinematic viscosity  $\nu$  and a constant sound speed  $c_s$ . In



Run	$N$	$Re_\lambda$	$T_{tot}/T$	$\nu (\times 10^4)$	$\varepsilon (\times 10^5)$	$\Delta t/t_\kappa$	$L$	$\lambda$	$u'$	$\tau_{max}/T$	$C_\varepsilon$	$\eta$	$k_{max}\eta$
A	32	20	31	40	24	0.0190	1.9	1.2	0.071	0.15	1.2	0.128	2.1
B	64	42	30	15	22	0.0150	1.6	0.81	0.078	0.37	0.75	0.063	2.0
C	128	90	11	4.0	24	0.0150	1.3	0.43	0.084	0.62	0.54	0.023	1.5
D	256	92	19	4.0	21	0.0071	1.4	0.45	0.081	0.69	0.53	0.024	3.0
E	256	152	20	1.6	21	0.0110	1.4	0.29	0.084	0.74	0.49	0.012	1.5
F	512	219	7	0.80	25	0.0086	1.3	0.20	0.089	0.67	0.47	0.007	1.7

Table 1: Examples of DNS parameters and average turbulence characteristics.  $N$  is the number of grid points in each of the Cartesian directions,  $Re_\lambda$  is the Taylor microscale Reynolds number  $\equiv u'\lambda/\nu$ ,  $T_{tot}$  is the total run time after the run became statistically stationary,  $T$  is the eddy turnover time  $\equiv L/u'$ ,  $\Delta t$  is the run time increment,  $t_\kappa$  is the Kolmogorov time scale  $\equiv \nu^{1/2}\varepsilon^{-1/2}$ ,  $\lambda$  is the Taylor microscale  $\equiv u'\sqrt{15\nu/\varepsilon}$ ,  $\tau_{max}$  is the average time for the energy cascade from large to small scales, and  $\eta$  is the Kolmogorov length scale  $\equiv \nu^{3/4}\varepsilon^{-1/4}$ .

the numerical simulations the system is forced (stirred) using random transversal waves. The forcing amplitude is chosen such that the root mean square Mach number for all runs is between 0.13 and 0.15 which is not too dissimilar to that found in the wind-tunnel experiments to be discussed in the next section. For these weakly compressible simulations, the energies of solenoidal and potential components of the flow have a ratio  $E_{pot}/E_{sol} \approx 10^{-4}-10^{-2}$  for most scales; only towards the Nyquist frequency (henceforth  $k_{max}$ ) does the ratio increase to about 0.1. It is thus reasonable to assume that compressibility is irrelevant for the results presented here whilst at the same time the present results can be considered more comparable and relevant to experimental wind tunnel flows than the perfectly incompressible simulations published so far. The code has been validated in previous turbulence studies[12, 13] and the reader is especially referred to Ref.[14] for more information. The simulations are carried out in periodic boxes with resolutions in the range of  $32^3 - 512^3$  grid points. The box size is  $L_x = L_y = L_z = 2\pi$ , which discretizes the wave numbers in units of 1. The viscosity  $\nu$  is chosen such that the maximum resolved wave number  $k_{max}$  is always greater than  $1.5/\eta$ , where  $\eta = (\nu^3/\varepsilon)^{1/4}$  is the Kolmogorov length scale. To be consistent with previously published DNS studies, the total kinetic energy  $E$  is defined as,

$$E_{tot} = \frac{1}{2} \langle \mathbf{u}^2 \rangle = \frac{3}{2} u'^2 = \int_0^{k_{max}} E(k) dk, \quad (2)$$

the integral length scale  $L$  is defined,

$$L = \frac{\pi}{2u'^2} \int_0^{k_{max}} k^{-1} E(k) dk, \quad (3)$$

and the average turbulent energy dissipation rate is defined as

$$\varepsilon = 2\nu \int_0^{k_{max}} k^2 E(k) dk. \quad (4)$$

Angular brackets denote averaging over the box volume. After each run has become statistically stationary (typically 1-2 eddy turnovers  $T \equiv L/u'$ ) the average statistics are estimated for the remaining total run time. Table 1 summarizes the average statistics for each run. Comparing Runs C and D in Table 1 indicates that there is little difference in the average  $C_\varepsilon$  for simulations resolved up to  $\eta k_{max} = 1.5$  from  $\eta k_{max} = 3$ .

## Results

### Numerical results

In this section results for the higher order finite difference numerical simulations are presented. The simulations began with  $N = 32^3$  and each subsequent larger box size began with a velocity field interpolated from the previous box size. Figures

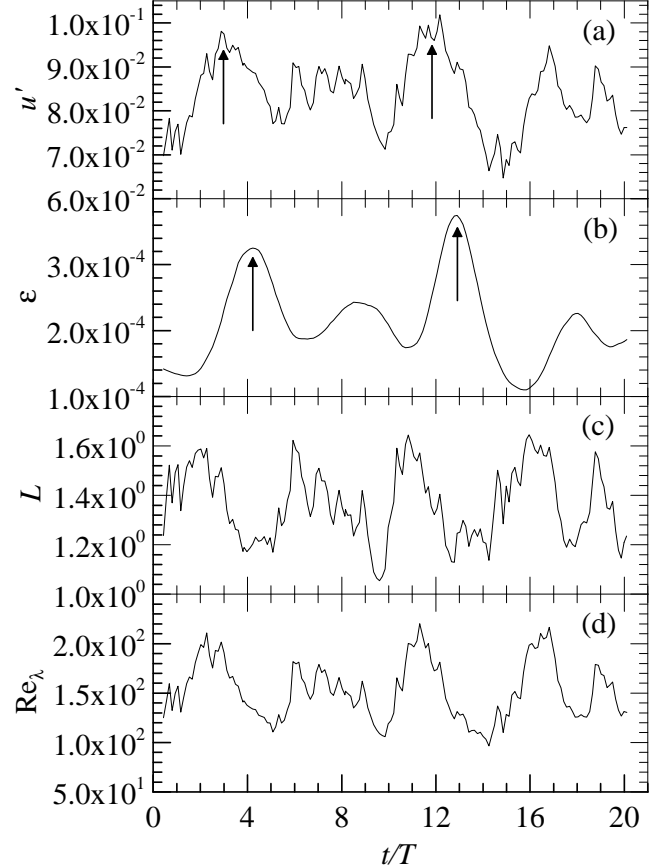


Figure 1: Example time series from Run E,  $N = 256^3$ , average  $Re_\lambda \approx 152$ . (a),  $u'$ ; (b),  $\varepsilon$ ; (c),  $L$ ; (d),  $Re_\lambda$ . Here, the eddy turnover time  $T = L/u'$ . The up arrows  $\uparrow$  indicate correlated bursts of  $u'$  and  $\varepsilon$ .

1(a)-(d) show example time series from Run E ( $N = 256^3$ ) for the fluctuating velocity  $u$ , the fluctuating integral length scale  $L$ , the fluctuating kinetic energy dissipation rate  $\varepsilon$  and the fluctuating Reynolds number  $Re_\lambda$  respectively. Initially, the turbulence takes a short amount of time to reach a statistically stationary state - a consequence of stabilizing the new run from the previously converged run. The fluctuating quantities shown in Figures 1(a)-(d) are not unlike those encountered in a wind tunnel. Indeed, Fig. 1(a) could easily be mistaken for a hot-wire trace of a turbulent flow. This is in stark contrast to some pseudo-spectral methods that use negative viscosity to maintain a constant energy level e.g. Ref. [3].

Given that the statistics are fluctuating, although they are statistically stationary, it is tempting to plot the instantaneous  $C_\varepsilon$  as a function of  $Re_\lambda$ . Figure 2 shows  $C_\varepsilon$  calculated in such a way. The  $Re_\lambda$  dependent trends are obviously not as expected. How-

ever, it is worth noting the apparent range for  $C_\varepsilon$  when  $Re_\lambda \gtrsim 50$  is  $\approx 0.3 - 0.7$  which is the range of previously published DNS results. This may explain the scatter in previously published DNS results if  $C_\varepsilon$  is calculated from a subjective choice of  $\varepsilon$ ,  $L$  and  $u'$  at a single time step e.g. as in Ref. [3]. The reason for the incorrect  $Re_\lambda$  dependence for  $C_\varepsilon$  can be gleaned from Figs. 1(a) and (b). Figure 1(a) shows that an intense burst in turbulent kinetic energy  $u^2$  (an example is noted by the arrow) can be observed some maximum time lag  $\tau_{\max}$  later in the turbulent kinetic energy dissipation rate [Figure 1(b), again noted by an arrow]. By noting that there is a strong correlation between intense events of  $u^2$  and  $L$  on the one hand and  $\varepsilon$  on the other hand it is possible to estimate  $\tau_{\max}$  from the maximum in the correlation between  $u'^3/L$  and  $\varepsilon$  by

$$\rho_{u'^3/L, \varepsilon}(\tau) = \frac{\overline{[u'^3(t)/L(t)] [\varepsilon(t+\tau)]}}{\overline{u'^3(t)/L(t)} \overline{\varepsilon(t+\tau)}}. \quad (5)$$

With this done for all runs it is possible to shift the time series of  $\varepsilon(t)$  for each run by its respective  $\tau_{\max}$  and correctly calculate the instantaneous magnitude of  $C_\varepsilon$  e.g. Fig. 3. Figure 4 shows the newly calculated  $Re_\lambda$  dependence of  $C_\varepsilon$  using the correct time lag  $\tau_{\max}$  for each of the runs. A number of comments can be made. Firstly, the dimensionless dissipation rate  $C_\varepsilon$  appears to asymptote when  $Re_\lambda \gtrsim 100$ . The asymptotic magnitude  $C_\varepsilon \approx 0.5$  is in good agreement with the consensus DNS results published so far i.e.  $C_\varepsilon \approx 0.4$  to  $0.5$  (see Ref. [3] and references therein). Having said this and given the present demonstration that it is incorrect to estimate  $C_\varepsilon$  from a single time snap shot it would be interesting to recalculate previously published results based on subjective choices of the quantities involved for estimating  $C_\varepsilon$  by using the entire time series. Lastly, the present results verify the use of a high-order finite difference scheme and also prove that the zeroth law applies to slightly compressible turbulence.

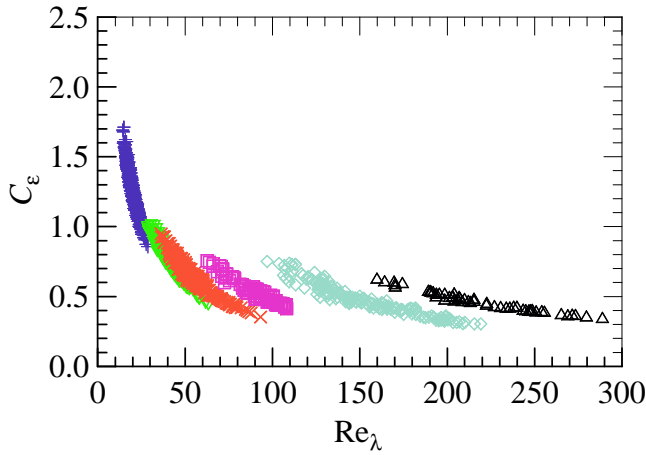


Figure 2: Incorrectly estimated  $C_\varepsilon$  as a function of  $Re_\lambda$ . +, Run A;  $\nabla$ , Run B;  $\times$ , Run C;  $\square$ , Run D;  $\diamond$ , Run E;  $\triangle$ , Run F. Ensemble averages can be found in (Table 1).

### Experimental results revisited

Results from experiments originally published in Refs. [4, 5], are updated here with more data within the range  $170 \lesssim Re_\lambda \lesssim 1210$ . Detailed experimental conditions can be found in Refs. [4, 5] and need not be repeated here. The main group of measurements are from a geometry called a NORMAN grid which generates a decaying wake flow. The geometry is composed of a perforated plate superimposed over a bi-plane grid of

square rods. The flow cannot be classed as freely decaying as the extent of the wind tunnel cross section ( $1.8 \times 2.7 \text{ m}^2$ ) is approximately  $7 \times 11 L^2$ . For all the flows presented in Ref. [4], signals of the fluctuating longitudinal velocity  $u$  are acquired, for the most part, on the mean shear profile centerline. For the NORMAN grid, some data is also obtained slightly off the center-line at a transverse distance of one mesh height where  $dU/dy \approx dU/dy|_{\max}/2$ .

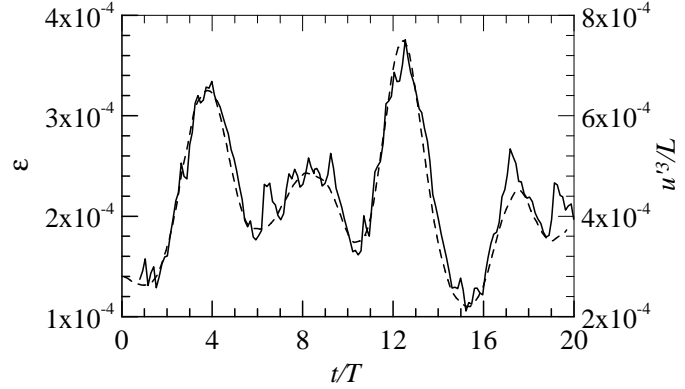


Figure 3: Example of the offset time series for Run E ( $\tau_{\max}^+ \approx 0.74$ ),  $N = 256^3$ , average  $Re_\lambda \approx 150$ . Note that the peak events are now well correlated. —,  $u'^3/L(t/T)$ ; - - -,  $\varepsilon([t - \tau_{\max}]/T)$ .

All data are acquired using the constant temperature anemometry (CTA) hot-wire technique with a single-wire probe made of  $1.27 \mu\text{m}$  diameter Wollaston (Pt-10% Rh) wire. Time lags  $\tau$  and frequencies  $f$  are converted to streamwise distance ( $\equiv \tau U$ ) and one-dimensional longitudinal wave number  $k_1$  ( $\equiv 2\pi f/U$ ) respectively using Taylor's hypothesis. The mean dissipation rate  $\varepsilon$  is estimated assuming isotropy of the velocity derivatives i.e.  $\varepsilon \equiv \varepsilon_{\text{iso}} = 15\nu \langle (\partial u / \partial x)^2 \rangle$ . We estimate  $\langle (\partial u / \partial x)^2 \rangle$  from the average value of  $E_{1D}(k_1)$  [the 1-dimensional energy spectrum of  $u$  such that  $u^2 = \int_0^\infty E_{1D}(k_1) dk_1$ ] and from finite differences  $\langle (\partial u / \partial x)^2 \rangle = \langle (u_{i+1} - u_i)^2 / (U f_s)^2 \rangle$ . For most of the data, the worst wire resolution is  $\approx 2\eta$  where  $\eta$  is the dissipative length scale  $\equiv \nu^{3/4} \varepsilon_{\text{iso}}^{-1/4}$ . The characteristic length-scale of the large-scale motions  $L$  is  $L_p$  and is estimated from the wave number  $k_{1,p}$  at which a peak in the compensated spectrum  $k_1 E_{1D}(k_1)$  occurs i.e.  $L_p = 1/k_{1,p}$ .

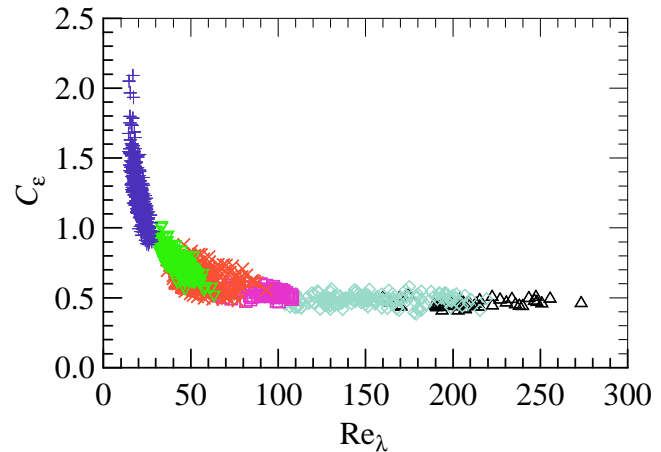


Figure 4: Correctly estimated  $C_\varepsilon$  as a function of  $Re_\lambda$ . +, Run A;  $\nabla$ , Run B;  $\times$ , Run C;  $\square$ , Run D;  $\diamond$ , Run E;  $\triangle$ , Run F. Ensemble averages can be found in (Table 1).

Figure 5 shows  $C_\varepsilon$  for the present data. For all of the data, a value of  $C_\varepsilon \approx 0.5$  appears to be the average value. Figure 5 confirms that  $C_\varepsilon$ , albeit a one-dimensional surrogate, measured in a number of different flows is independent of  $Re_\lambda$ . It could be argued that the rate of approach to an asymptotic value depends on the flow e.g. proximity to initial and boundary conditions. The asymptotic value  $C_\varepsilon \approx 0.5$  is in excellent agreement with the present DNS results. These experimental results are encouraging considering that wind-tunnel turbulence is always relatively young compared to DNS turbulence, e.g. the NORMAN grid turbulence has only of the order of 6 eddy turnover times in development by the time it reaches the measurement station.

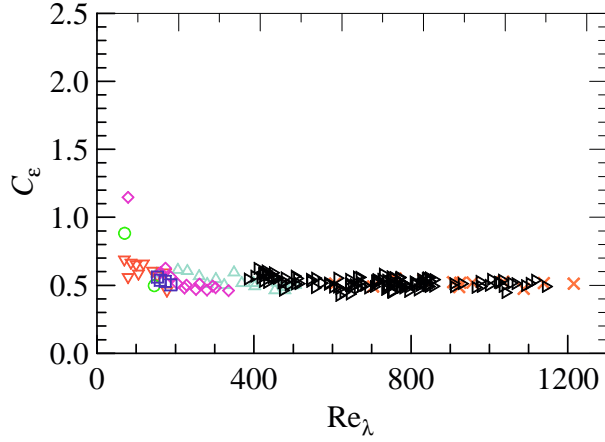


Figure 5: Normalized dissipation rate  $C_\varepsilon$  for different experimental flows.  $\square$ , circular disk,  $154 \lesssim Re_\lambda \lesssim 188$ ;  $\circ$ , golf ball,  $70 \lesssim Re_\lambda \lesssim 146$ ;  $\nabla$ , pipe,  $70 \lesssim Re_\lambda \lesssim 178$ ;  $\diamond$ , normal plate,  $79 \lesssim Re_\lambda \lesssim 335$ ;  $\triangle$ , NORMAN grid N1,  $152 \lesssim Re_\lambda \lesssim 506$ ;  $\times$ , NORMAN grid N2 (slight mean shear,  $dU/dy \approx dU/dy|_{max}/2$ ),  $607 \lesssim Re_\lambda \lesssim 1215$ ;  $\blacktriangleright$ , NORMAN grid N2 (zero mean shear),  $388 \lesssim Re_\lambda \lesssim 1120$ .

### Final remarks and conclusions

The present work has revisited the zeroth law of turbulence for both numerical simulations of statistically stationary isotropic turbulence and experiments. The numerical simulations are slightly compressible isotropic turbulence and the statistical stationarity is achieved with a random phase forcing applied at low wave numbers. The main result of the numerical simulations is the demonstration that  $C_\varepsilon$  should only be estimated with ensemble averaged quantities from the entire time series for which the statistics are stationary. If  $C_\varepsilon$  is to be estimated at each time snap shot it is necessary to correctly account for the time lag that occurs from the large scale energy injection to the fine scale energy dissipation. Even after correctly correlating the energy injection with the energy dissipation, the instantaneous value of  $C_\varepsilon$  can vary quite considerably (e.g.  $\pm 30\%$ ) over the extent of the simulation. Such a variation may account for the scatter in magnitude of  $C_\varepsilon$  in previously published results. Both the present numerical and experimental results suggest that the asymptotic value for  $C_\varepsilon$  is  $\approx 0.5$ . In light of this, the previously held view that the asymptotic value of  $C_\varepsilon$  may be dependent on the large scale energy injection could be suspect.

### Acknowledgments

We gratefully acknowledge the Norwegian Research Council for granting time on the parallel computer in Trondheim (Gridur/Embla) and the NTNU technical staff for assistance with the experiments.

### References

- [1] Taylor, G. I., The statistical theory of turbulence: Parts I-IV, *Proc. Roy. Soc. London* **A151**, 1935, 421-435.
- [2] Kolmogorov, A. N., The local structure of turbulence in an incompressible fluid for very large Reynolds numbers, *Dokl. Akad. Nauk. SSSR* **30**, 1941, 299-303.
- [3] Kaneda, K., Ishihara, T., Yokokawa, M., Itakura, K. and Uno, A., Energy dissipation rate and energy spectrum in high resolution direct numerical simulations of turbulence in a periodic box, *Phys. Fluids*, **15**, 2003, L21-L24.
- [4] Pearson, B. R., Krogstad, P. -Å. and van de Water, W., Measurements of the turbulent energy dissipation rate, *Phys. Fluids*, **14**, 2002, 1288-1290.
- [5] Pearson, B. R., Krogstad, P. -Å. and Johnson, G. R., Re dependence of the Kolmogorov constant and scaling, in *Reynolds Number Scaling in Turbulent Flow* (Ed. A. J. Smits) Kluwer Academic Publishers, 2003, 229-336.
- [6] Lohse, D., Crossover from high to low Reynolds number turbulence, *Phys. Rev. Lett.* **73**, 1994, 3223-3226.
- [7] Sreenivasan, K. R. An update on the energy dissipation rate in isotropic turbulence, *Phys. Fluids* **10**, 1998, 528-529.
- [8] Sreenivasan, K. R. On the scaling of the energy dissipation rate, *Phys. Fluids* **27**, 1984, 1048-1051.
- [9] Sreenivasan, K. R. The energy dissipation rate in turbulent shear flows, in *Developments in Fluid Dynamics and Aerospace Engineering*, (Eds. S. M. Deshpande, A. Prabhu, K. R. Sreenivasan, & P. R. Viswanath) Interline, Bangalore, India, 1995, p159.
- [10] Schumacher, J. Relation between shear parameter and Reynolds number in statistically stationary turbulent shear flows, *Phys. Fluids* **16**, 2004, 3094-3102.
- [11] Bramwell, S. T. Holdsworth, P. C. W. and Pinton, J.-F., Universality of rare fluctuations in turbulence and critical phenomena, *Nature* **396**, 1998, 552-553.
- [12] Dobler, W., Haugen, N. E. L., T. A. Yousef and Brandenburg, A., Bottleneck effect in three-dimensional turbulence simulations, *Phys. Rev. E*, **68**, 2003, 026304-1.
- [13] Yousef, T. A. Haugen N. E. L. & Brandenburg, A. Self-similar scaling in decaying numerical turbulence, *Phys. Rev. E*, **69**, 2004, 056303-1.
- [14] The PENCIL CODE is a cache-efficient high-order finite-difference code (sixth order in space and third order in time) for solving the compressible hydrodynamic and hydromagnetic equations. The code can be obtained from <http://www.nordita.dk/data/brandenb/pencil-code>.

## The stability of decaying pipe flow

N. Jewell and J. P. Denier

School of Mathematical Sciences  
The University of Adelaide, South Australia 5005 AUSTRALIA

### Abstract

We consider the decay and subsequent instability of the fully developed flow within a pipe of circular cross section when the pipe is suddenly closed.

### Introduction

The behaviour of the flow within a suddenly blocked pipe has important applications across a wide range of disciplines. Two such examples are the so called water-hammer effect which occurs when a valve is suddenly closed in a pipe and the rhythmic opening and closure of the *aortic valve* and the *pulmonic valve* in the heart during ventricular ejection. In both applications an unsteady flow develops which typically exhibits a transient turbulent state (see, for example, Refs. [3] and [13]).

It was the physiological applications that led Wienbaum & Parker [16] to first consider the problem of the decay of the flow in a suddenly blocked channel or pipe. They gave the problem its correct mathematical formulation and employed an approximate technique based upon the Pohlhausen method to describe the flow. This work allowed them to demonstrate that the decaying channel flow develops points of inflection thus suggesting that the flow would be susceptible to wave-like instabilities. The stability of the flow was subsequently considered by Hall & Parker [7] who employed a WKBJ style approximation, based upon the assumption of large flow Reynolds number, to derive a quasi-steady Orr-Sommerfeld equation describing the flow stability.

The theoretical result that the decelerating flow in a suddenly blocked pipe is unstable to wave-like disturbances is in qualitative agreement with *in vivo* measurements of turbulence levels in the ascending aorta (for example Ref. [13]). Hall & Parker [7] demonstrated that the decaying flow within a suddenly blocked channel is unstable, due to the inflectional nature of the stream-wise velocity profiles, for Reynolds numbers as low as  $O(10^2)$ . Some care must be taken in interpreting these results, since the quasi-steady approximation they employed requires the flow Reynolds number to be simultaneously large (for the asymptotic approximation to be valid) and finite (to justify retaining viscous terms in the resulting Orr-Sommerfeld equation).

One of the drivers of the renewed interest in the behaviour of the flow in a suddenly blocked pipe occurs in the water industry where considerable attention has been given to the problem of detecting leaks in pipeline systems using inverse transient techniques, see Ref. [10]. For this technique to be fully implemented it is necessary to be able to differentiate between damping due to leaks and damping due to unsteady friction resulting from the (possibly) turbulent flow within the pipeline. Current models for the unsteady friction within pipes, such as that of Vardy & Brown [15], are largely empirical and typically underpredict the amplitude and the phase of the pressure response within the pipeline. Recent work by Lambert *et al.* [9] suggests that this lack of agreement between theory and experiment may be largely due to the empirical nature of the friction models used. Their results highlight the need for an improved under-

standing of the flow within the unsteady boundary layer, both laminar and turbulent.

It is the aim of this paper to quantify the stability properties of the decaying flow in a suddenly blocked pipe.

### Formulation

Consider the pressure driven flow within a cylindrical pipe of non-dimensional radius  $r = 1$  which is suddenly blocked at  $x = 0$  at time  $t = 0$ , where  $(r, \theta, x)$  are the usual cylindrical polar coordinates and  $(v, w, u)$  is the corresponding velocity field. Prior to blockage the flow is assumed to be fully developed, laminar, Poiseuille flow with axial velocity given by  $u(r, x) = 1 - r^2$ .

As noted by Wienbaum & Parker [16], the pressure wave which results from the sudden valve closure acts to freeze the vorticity within the flow in the state which existed prior to the closure. Thus, provided the Mach number of the flow is small (which it invariably is for most pipeline applications), immediately after the passage of the pressure wave the vorticity distribution within the flow is the same as it was before the closure. Solving the vorticity equation demonstrates that immediately after the blockage, roughly two pipe radii downstream of the blockage, the flow is uni-directional and given by

$$u_0(r, x) = \frac{1}{2} - r^2 \quad (t = 0). \quad (1)$$

Following the blockage, the flow develops on the viscous diffusion time-scale  $\tau = Re^{-1}t = O(1)$ , where  $Re$  is the flow Reynolds number.

Assuming then that the flow within the blocked pipe is now uni-directional, we write  $(v, w, u) = (0, 0, U_0(r, \tau))$ . Substitution of this expression into the full Navier-Stokes equations yields

$$\frac{\partial U_0}{\partial \tau} = \frac{\partial^2 U_0}{\partial r^2} + \frac{1}{r} \frac{\partial U_0}{\partial r} + \phi'(\tau), \quad (2a)$$

which must be solved subject to

$$U_0(r, 0) = \frac{1}{2} - r^2, \quad 0 < r < 1, \quad (2b)$$

$$U_0(1, \tau) = 0 \quad \tau > 0. \quad (2c)$$

In (2a) the term  $\phi'(\tau)$  denotes the unsteady axial pressure gradient; this must be determined as part of the solution process. In order to do this we impose the condition that the integrated volume flux across any cross-section must vanish. Thus

$$\int_0^1 r U_0(r, \tau) dr = 0. \quad (2d)$$

The system (2) can be solved by two ways. The first involves taking the Laplace transform in  $\tau$ , solving the resulting ordinary differential equation and then taking the inverse Laplace transform to obtain the velocity field  $U_0(r, \tau)$ . Due

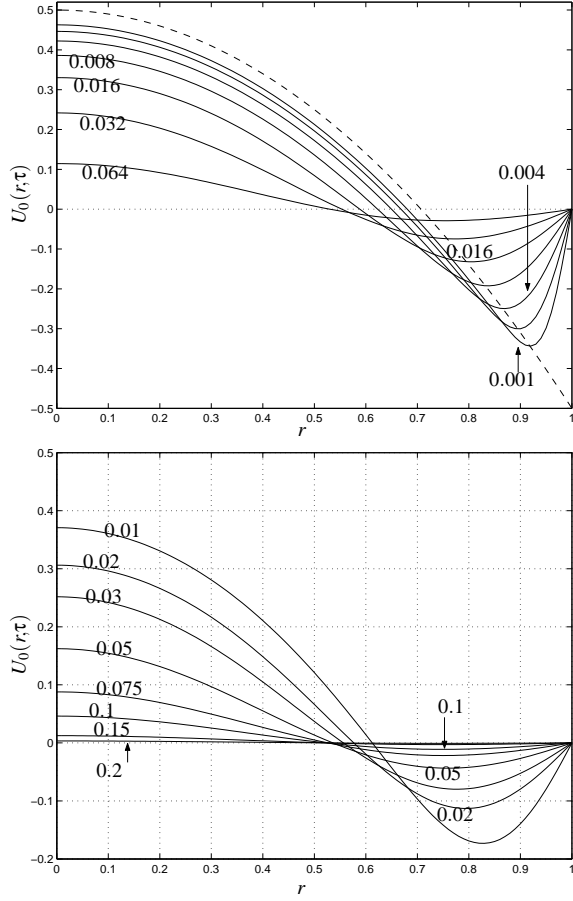


Figure 1: Plot of streamwise velocity  $U_0(r, \tau)$  versus  $r$  for times  $\tau$  as labelled.

to its complexity the inverse Laplace transform must be calculated numerically. The second approach involves discretizing the equation (2a), in both space and time, and solving the discretized system numerically. It is readily shown (see Refs. [8], [16]) that the streamwise pressure gradient term has a singularity at time  $t = 0$  in the form  $\phi'(\tau) = O(\tau^{-1/2})$  as  $\tau \rightarrow 0$  (this is a simple consequence of the impulsive nature of the blockage). For this reason a simple marching-in-time scheme, with initial conditions imposed at  $\tau = 0$ , is not suitable for solving (2). To use such a scheme an accurate small-time solution must be developed. Details of this can be found in Jewell & Denier [8]. For our purposes it is sufficient to note that, for small  $\tau$ , we can write

$$\phi(\tau) = -\frac{2}{\sqrt{\pi}}\tau^{1/2} + \frac{5}{2}\tau + O(\tau^{3/2});$$

the velocity field  $U_0(r, \tau)$  ( $0 < \tau \ll 1$ ) can be written in the form of an infinite power series in powers of  $\tau^{1/2}$  (details can be found in Ref. [8]).

This small  $\tau$  solution was taken as the starting-point for a Crank-Nicolson finite-difference marching scheme as follows. Given  $U_0(r, \tau)$  and  $\phi'(\tau)$  at time  $\tau_0$  we use the value of  $\phi'(\tau_0)$  as a guess for the value of  $\phi'(\tau_1)$  (where  $\tau_1 = \tau_0 + \Delta\tau$ ). The inhomogeneous discretized equations are then solved, subject to the boundary condition (2b) to give  $\tilde{U}_0(r, \tau_1)$ ; this will be the “correct” value if and only if the flux condition (2d) is satisfied. In general this will not be the case thus allowing us to set-up an iteration scheme, based upon the flux condition, which can be used to update  $\phi'(\tau_1)$ . We chose to employ Newton iteration for this task.

The results of our calculations are presented in figure 1 which show the decay of the streamwise velocity. For small times  $\tau$  we

observe the rapid change as the flow adjusts from the inviscid slip condition to the no-slip boundary condition on  $r = 1$ .

### Linear stability of the flow

To consider the stability of the flow we proceed in two ways. Firstly we undertake a classical linear stability analysis which invokes the *quasi-steady approximation* that the basic flow does not vary significantly over the  $O(t)$  time scale characteristic of Orr-Sommerfeld modes. We then relax the quasi-steady assumption thus taking into account the  $O(\tau)$  evolution of the basic flow and focus our attention on *transient pseudomodes*, that is, flow perturbations which are capable of significant transient growth.

### Normal mode analysis

Here we look for flow perturbations in the form

$$\begin{aligned} (\mathbf{u}, p) &= (0, 0, U_0(r, \tau), p) \\ &+ \varepsilon(U_r(r), U_\theta(r), U_x(r), P(r)) e^{i[\alpha(x - ct) + k\theta]}, \end{aligned} \quad (3)$$

where  $U_x, U_r$  and  $U_\theta$  are the axial, radial and circumferential velocity components respectively, and  $c$  denotes a complex-valued wave-speed. The diffusion time scale  $\tau$  is treated as a parameter (the quasi-steady approximation), along with the Reynolds number  $Re$ , the axial wavenumber  $\alpha$  and the azimuthal wavenumber  $k$  ( $k = 0, 1, 2, \dots$ ). The case  $k = 0$  corresponds to two-dimensional perturbations, that is  $U_\theta = 0$ . The governing equations for  $(\mathbf{U}(r), P(r))$  are

$$i\alpha(U_0 - c)U_x = -i\alpha P - U_0'U_r + Re^{-1}\mathcal{L}U_x, \quad (4a)$$

$$i\alpha(U_0 - c)U_r = -P' + Re^{-1}[\mathcal{L}U_r - r^{-2}U_r - 2ikr^{-2}U_\theta], \quad (4b)$$

$$i\alpha(U_0 - c)U_\theta = -ikr^{-1}P + Re^{-1}[\mathcal{L}U_\theta - r^{-2}U_\theta + 2ikr^{-2}U_r], \quad (4c)$$

$$0 = i\alpha U_x + \left(\frac{\partial U_r}{\partial r} + r^{-1}U_r\right) + ikr^{-1}U_\theta. \quad (4d)$$

where the operator  $\mathcal{L}$  is given by

$$\mathcal{L} = \frac{\partial^2}{\partial r^2} + \frac{1}{r} \frac{\partial}{\partial r} - (\alpha^2 + k^2 r^{-2}).$$

The full system (4a)–(4d) is to be solved subject to the no-slip condition  $\mathbf{U}(1) = \mathbf{0}$ . Boundary conditions at  $r = 0$  (adapted from [6]) are

$$k = 0: \quad U_r = 0, \quad U_x' = 0, \quad P' = 0. \quad (4e)$$

$$k = 1: \quad U_x = 0, \quad P = 0, \quad U_r' = 0, \quad U_c = i\alpha U_r. \quad (4f)$$

$$k > 1: \quad \mathbf{U} = \mathbf{0}, \quad P = 0. \quad (4g)$$

When discretized, system (4) reduces to a generalized eigenvalue problem for the complex wavespeed

$$\mathbf{A}(\mathbf{U}, \mathbf{P})^T = c\mathbf{B}(\mathbf{U}, \mathbf{P})^T. \quad (5)$$

Discretization was performed using an order- $N$  Chebyshev pseudospectral scheme, yielding an eigenvalue problem of approximate size  $3N$  or  $4N$ . The order  $N_{\min}$  required to resolve the first eigenvalue to five decimal places was found to range from fifteen to twenty five, depending on choice of parameters (provided that  $\tau \gtrsim 0.001$ ). Furthermore, resolution of the ten leading eigenvalues was generally possible at  $N = N_{\min} + 10$ .

The results from our calculations are given in figure 2. We note that the flow is unconditionally stable to axisymmetric modes

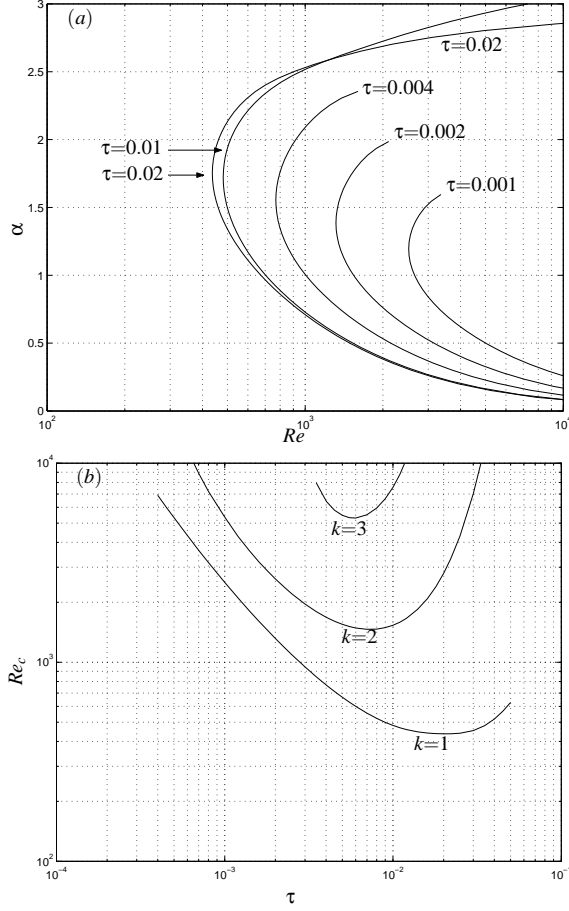


Figure 2: Plots of (a) Neutral-stability curves for blocked-pipe flow and (b) the corresponding critical Reynolds number for azimuthal wavenumbers  $k = 1, 2, 3$ . The solid line corresponds to the neutral-stability curves.

( $k = 0$ ). Neutral curves, for  $k = 1$ , are presented in figure 2a. From this figure we clearly observe the variation of the critical Reynolds number with time  $\tau$ . In figure 2b we plot the critical Reynolds number versus  $\tau$  for  $k = 1, 2, 3$ . The most unstable mode corresponds to  $k = 1$  and has a minimum critical Reynolds number of  $Re_c \approx 440$  which occurs at a time  $\tau = 0.02$ . These results are in qualitative agreement with those of Ref. [5].

It has long been known that eigenmodes predict long-term rather than short-term behaviour. Whether this is a reliable guide to short-term behaviour depends on whether the eigenmodes are orthogonal and non-degenerate: where this is not the case, transient growth may be possible even if all individual eigenmodes decay and we now turn our attention to this problem.

### Transient growth analysis

It is only in recent years that it has been recognised that the eigenmodes of some flows are not orthogonal. This is indeed the case for Couette and plane-Poiseuille flows. For these flows it is possible to describe a linear combination of eigenmodes which interfere destructively in the early stages, before separating out to produce significant transient growth in the intermediate stage (see Refs. [2], [12] and [14]). Eventually, in a purely linear model, this linear combination decays exponentially in accordance with classical predictions. This leads to the conjecture that in practice the transient may attain a critical amplitude beyond which non-linear effects destabilize the flow. This is supported by the numerical results presented in Refs. [1], [4] and [14].

There are two basic numerical techniques of linear transient analysis which are presented Refs. [2], [12] and [14]. We focus our attention on determining the *explicit transient pseudo-modes*. As in classical stability analysis, the pseudomode is considered to be a flow perturbation arising instantaneously at some time  $t = 0$ . Typically, it attains some amplification factor  $g = O(Re)$ , that is  $g_{\max} \approx (Re/Re_0)$  where  $Re_0 \ll Re_c$ , before decaying exponentially as  $t \rightarrow \infty$ .

The present problem differs in one important respect from Couette and Poiseuille flows: the basic flow for a blocked pipe is unsteady. To the extent that the quasi-steady assumption is valid, the explicit-transient technique is directly applicable. To this end, we denote the transient response by

$$\tilde{\mathbf{u}}(t) \equiv \tilde{\mathbf{u}}(t, r, x, \theta; \tau_0, Re, \alpha), \quad (6)$$

where  $t = 0$  and  $\tau = \tau_0$  denote the time of commencement. Let this transient be approximated by the  $J$  leading eigenmodes of the basic flow at time  $\tau_0$ :

$$\tilde{\mathbf{u}}(t) = \sum_{j=1}^J \gamma_j \tilde{\mathbf{u}}_j(t; \tau_0, Re, \alpha). \quad (7)$$

Following Trefethen *et al.* [14] we define the transient-growth factor via its energy norm over space as

$$g(t) = \frac{\|\tilde{\mathbf{u}}(t)\|}{\|\tilde{\mathbf{u}}_0\|} = \left( \frac{\gamma^* \mathbf{R}(t) \gamma}{\gamma^* \mathbf{R}_0 \gamma} \right)^{\frac{1}{2}} \quad (8)$$

where  $R_{jk}(t) = \langle \tilde{\mathbf{u}}_j(t), \tilde{\mathbf{u}}_k(t) \rangle$ . In order to relax the quasi-steady assumption we must track the temporal and spatial evolution of each of the original eigenmodes:

$$\tilde{\mathbf{u}}_j(t) = \exp \left[ -\int_0^t \tilde{\mathbf{A}}(\tau_0 + Re^{-1}t') dt' \right] \tilde{\mathbf{u}}_j(0) \quad (9)$$

where  $\tilde{\mathbf{A}}$  is the matrix evolution operator defined in Jewell & Denier [8]. The matrix-exponential was evaluated using the Matlab function `expm`, together with the formula

$$\tilde{\mathbf{u}}_j(t) = \exp \left[ -t \tilde{\mathbf{A}}(\bar{\tau}) \right] \tilde{\mathbf{u}}_j(0), \quad (10)$$

where  $\tilde{\mathbf{A}}(\bar{\tau})$  is understood to mean  $\tilde{\mathbf{A}}$  is evaluated using the mean basic flow for  $\tau_0 < \tau < (\tau_0 + Re^{-1}t)$ .

We calculate the maximum possible growth  $g^*(t)$  at some time  $t = t_1$ , obtaining what Trefethen *et al.* [14] have termed the Butler-Farrell optimum transient at  $t = t_1$ . Obtained by setting  $\partial g / \partial \gamma = \mathbf{0}$  at  $t = t_1$ , the Butler-Farrell transient corresponds to the dominant eigenmode of the generalized eigenvalue problem

$$\mathbf{R}(t_1) \gamma = \lambda \mathbf{R}_0 \gamma, \quad \text{with} \quad g^*(t_1) = \sqrt{\lambda_1(t_1)}. \quad (11)$$

Results are shown in Figures 3 and 4. Figure 3 shows the function  $g^*(t)$  for a variety of parameter values ( $Re, \tau_0$ ) and figure 4 shows  $g_{\max} \equiv \max \{g^*(t)\}$  as a function of Reynolds number. It is found that

$$g_{\max} \approx (Re/Re_0) \quad \text{where} \quad Re_0 \approx 120 \quad (Re < 1000). \quad (12)$$

The quasi-steady estimate  $g_{\max}(Re, \tau_0)$  proves to be reasonably accurate (provided that  $Re < Re_c(\tau_0)$ , where  $Re_c(\tau_0)$  is the classical critical value). This is due to the weak dependence of  $g_{\max}(Re, \tau_0)$  on  $\tau_0$ ; it does not demonstrate that the quasi-steady approximation is intrinsically valid. On the contrary, figure 3c shows that a given transient persists almost as long as the basic flow itself, continuing to grow until  $\tau \approx 0.05$ ; at this time the

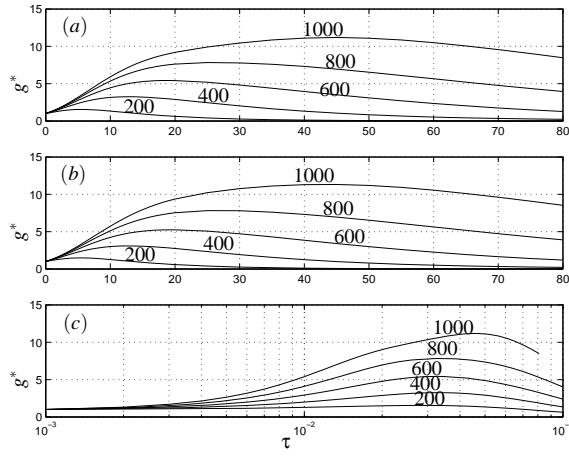


Figure 3: Butler-Farrell transient-growth profile  $g^*(t_1)$  for  $\alpha = 1.5$ . The transient commences at (a)  $\tau_0 = 0.001$  and (b)  $\tau_0 = 0.004$  and (c) as for (a) but plotted against  $\tau_1 = \tau_0 + Re^{-1}t_1$

viscous boundary-layer, which has grown from the pipe-wall almost fills the whole pipe (see Jewell & Denier [8] for details).

These results suggest that the precise classical value  $Re_c(\tau)$  is of limited physical significance. Below this limit, transient growth may be possible. Above it, transition to turbulence may not be realized – the basic flow may decay too soon to permit much growth of the dominant eigenmode.

To explore this idea further, we compare our results with those of Trefethen *et al.* [14] for Couette and plane-Poiseuille flows (Figure 4). Couette flow (for which  $Re_0 \approx 29$ ) is known to transition to turbulence in the range  $350 < Re < 3500$ ; Poiseuille flow ( $Re_0 \approx 71$ ) becomes turbulent for  $10^3 < Re < 10^4$ . On this basis we conjecture that transition-to-turbulence is usually associated with transient growth factors in the range 15 to 50. For the case of a blocked pipe, this corresponds to  $1100 \lesssim Re \lesssim 1800$ .

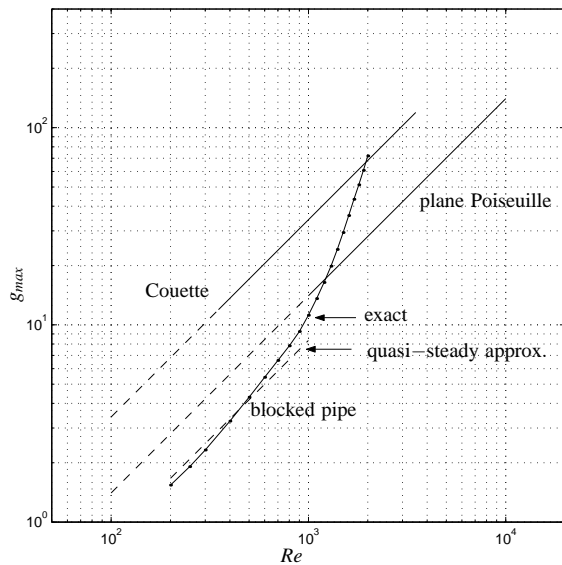


Figure 4: Maximum transient growth  $g_{\max} \equiv \max\{g^*\}$ . Corresponding results from Couette and plane-Poiseuille flows are provided for comparison (solid and dashed sections correspond to transitional and unstable flow, respectively).

## Conclusions

We have demonstrated that the flow within a suddenly blocked pipe is unstable to non-axisymmetric disturbances. The flow also supports modes which undergo transient growth. Comparison with Couette and plane Poiseuille flow suggests that these transients may play an important role in the transition process.

## Acknowledgements

NJ kindly acknowledges the support of an Australian Postgraduate Research Award.

## References

- [1] Baggett, J.S., Driscoll, T.A. and Trefethen, L.N. 1995 A mostly linear model of transition to turbulence. *Phys. Fluids* **7** (4), 833–8.
- [2] Butler, K.M. and Farrell, B.F. 1992 Three-dimensional optimal perturbations in viscous shear flow. *Phys. Fluids* **4** (8), 1637–1650.
- [3] Das, D and Arakeri, J.H. 1998 Transition of unsteady velocity profiles with reverse flow. *J. Fluid Mech.* **374**, 251–283.
- [4] Gebhart, T. and Grossman, S. 1994 Chaos transition despite linear stability. *Phys. Rev. E*, **5**, 3705–3712.
- [5] Ghidaoui, M.S. and Kolyshkin, A.A. 2002 A quasi-steady approach to the instability of time-dependent flows in pipes. *J. Fluid Mech.* **465**, 301–330.
- [6] Khorrami, M.R., Malik, M.R. and Ash, R.L. 1989 Application of spectral collocation techniques to the stability of swirling flows. *J. Comp. Phys.* **81**, 206–229.
- [7] Hall, P. and Parker, K.H. 1976 The stability of the decaying flow in a suddenly blocked channel. *J. Fluid Mech.* **75**, 305–314.
- [8] Jewell, N. and Denier, J.P. The instability of the flow in a suddenly blocked pipe. (in preparation).
- [9] Lambert, M.F., Vitkosky, J.P., Simpson, A.R. and Bergant, A. 2001 A boundary-layer growth model for one-dimensional turbulent unsteady pipe friction, in *Proc. Austral. Fluid Mech. Conf.* (ed. B. Dally), Adelaide, pp. 929–932.
- [10] Liggett, J.A. and Chen, L.-C. 1994 Inverse transient analysis in pipe networks. *J. Hydraul. Engin.* **120**, 934–955.
- [11] Parker, S.C. and Balachandar, S. 1999 Viscous and inviscid instabilities of flow along a streamwise corner. *J. Theor. Comp. Fluid Dyn.* **13**, 231–270.
- [12] Reddy, S.C. and Henningson, D.S. 1993 Energy growth in viscous channel flows. *J. Fluid Mech.* **252**, 209–238.
- [13] Sugawara, M. 1987 Blood flow in the heart and large vessels. *Med. Prog. Tech.* **12**, 65–76.
- [14] Trefethen, L.N., Trefethen, A.E., Reddy, S.C. and Driscoll, T.A. 1993 Hydrodynamic stability without eigenvalues. *Science* **261**, 578–584.
- [15] Vardy, A.E. and Brown, J. 1995 Transient, turbulent, smooth pipe friction. *J. Hydraul. Res.* **33**, 435–456.
- [16] Weinbaum, S. and Parker, K.H. (1975) The laminar decay of suddenly blocked channel and pipe flows. *J. Fluid Mech.* **69**, 729–752.



## Effect of delta wing's leading edge geometry to vortex breakdown

Sutthiphong Srigrarom

Division of Thermal and Fluid Engineering, School of Mechanical and Production Engineering,  
Nanyang Technological University, 639798, SINGAPORE

### Abstract

This paper studies the effect of delta wing's leading edge geometry (sharpness and bevel angle) to the vortex breakdown. At the apex, the flow separates and forms apex vortices, which may breakdown if the wing is at high angle of attack. Preliminary studies reveal that the initial circulation and/or swirl of the apex vortices are mostly created at the wing's apex vicinity. This initial circulation is the control parameter of vortex breakdown, and it is changed significantly by the wing's leading edge geometry. Here we study the leading edge sharpness and the bevel angle effects by means of flow visualization. For curvature effect, we compare two delta wings with sharp and rounded leading edges. The delta wing with sharp leading edge results in stronger apex vortices' initial circulation, and that the consequent vortex breakdown happens earlier than the rounded one. For bevel angle effect, we flip the delta wing with sharp leading edge vertically. When the delta wing is flipped, the apex vortices bifurcate into smaller vortices. We label these vortices as: primary, secondary and tertiary vortices. These vortices are convected downstream without breaking down.

### Introduction

The vortex breakdown is an abrupt enlargement of a vortex, where the axial filament emanating from the apex of a delta wing suddenly takes a spiral form. At times, a bubble form of the breakdown is also observed. Encapsulated within the spiral or bubble is a limited region of flow reversal near the vortex centerline, which is followed by highly turbulent flow.

Although there have been many theories of vortex breakdown, they mostly ignore the spiral form of the breakdown on the delta wing, which is more common, and instead focus on axisymmetric bubble breakdown in the pipe with swirling flow, because the latter is mathematically tractable. A recent comment (ref. 1) stating that "a comprehensive theory of vortex breakdown still does not exist" echoes similar comments made in 1977: "the embarrassing number of different theoretical notions has not, it must be admitted, led to satisfactory understanding of the flows observed." (ref. 2)

Recently, we proposed what we call a self-induction mechanism for the formation of vortex breakdown. Details of the mechanism can be found in Kurosaka (1998) (ref. 3), Srigrarom & Kurosaka (2000a, 2000b) (ref. 4 and 5). According to the theory, it is the initial circulation and/or swirl that causes the negative axial vorticity gradient within the apex vortices itself. Then, by its own self-induction, the apex vortices can pile-up and breakdown.

The apex vortices (and hence, their initial circulation) are created by the flow separation on the wing from the pressure side to the suction side of the delta wing. Consider figures 1 and 2, which show the computed viscous flow around the delta wing (from VSAERO® CFD code). For the delta wing positioned at high angle of attack ( $\alpha = 25^\circ$ ), the incoming flow streamlines at the apex will hit the wing, separate and form the apex vortices (figures 3 and 4). It is the leading edge that controls the vortices' turning radii, and that, their initial swirl. Therefore, we focus our attention to the sharpness and the curvature of the wing. We also consider the effect of the bevel angle by flipping the wing vertically to create different flow pattern. The investigation was done primarily by means of food coloring dye and Laser Induced Fluorescence (LIF) flow visualization in the water tunnel.

### Effect of leading edge shape

According to the self-induction mechanism theory, it is the initial vorticity gradient that leads to the chain of events leading to the formation of vortex breakdown. Suppose that we could reduce the initial vorticity gradient, then, theoretically, the vortex breakdown can be delayed or weakened. For the case of the delta wing with a sharp apex, the initial vorticity gradient is associated with the flow separated from the sharp corner at the apex of the wing. Therefore, to reduce the initial vorticity gradient, we could attempt to prevent flow separation by rounding the wing's apex.

To investigate the above concept, we have done pilot experiments by installing a curved wood attached to the apex of the delta wing, and tested at various usual vortex breakdown conditions in the water tunnel. The plexiglass delta wing 12 inches chord length and 1 inch thick (i.e. thickness to chord ratio,  $t/c = 1/12$ ) with 60-degree swept angle was used. This relatively thick delta wing was used, because we could observe the edge effect more visibly. The wing was set at angle of attack of 20 and 25 degrees, under incoming freestream flow of 5 cm/s, corresponding to Reynolds number of  $\sim 15000$  based on chord length ( $Re \equiv U_\infty c / \nu \sim 15000$ ). Red food-coloring dye was used for flow visualization. The wing was tested with and without the curved wood attachment for direct visual side-by-side comparison. We compare the results by examining the local flow at the apex, and the location of the vortex breakdown.

Let us consider the flow around the rounded leading edge of the curved wood attachment shown in figure 3, which was taken from side view. The wing was set at angle of attack of 25 degree. The flow remains mostly attached at the apex, with a mild separation. Therefore, the apex vortices would have reduced initial swirl, hence lesser axial vorticity gradient, compared to the one with the sharp leading edge case.

Figure 4 shows side-by-side comparison for the case of the wing at  $20^\circ$  angle of attack. Although, there is still vortex breakdown on the one with the curved wood attachment, the vortex breakdown is weaker, as noticeable by the gradual fading of the dye color. The location of the vortex breakdown is also delayed downstream, as observed by comparing  $L_1 > L_2$  in figure 4 (both  $L_1$  and  $L_2$  are measured from the delta wing's trailing edge). This means that smoothening the delta wing's apex to reduce the separation helps to lessen the initial vorticity gradient and weaken and delay the vortex breakdown, as expected. We also obtained the same results for the case of the wing at  $25^\circ$  angle of attack (figure 5)

### Effect of bevel angle

In the previous section, we discussed the effect of modifying the delta wing's apex shape, by which we could delay the vortex breakdown. The modification was done by rounding the sharp apex to a smooth curved one. Here we look into the effect of the bevel angle. We may change the delta wing apex and/or the leading edge, such that the incoming flow needs not to turn around the acute angle (see figure 6), which has smaller turning radius, and that, creates the apex vortices with causes strong initial swirl (circulation). Instead, the flow bends around the obtuse angle (milder turn), corresponding to larger turning radius, and that, creates the apex vortices causes weaker initial swirl

(circulation). We achieve this change by flipping it vertically flipped, as shown schematically, in figure 6.

Here we used the same delta wing with 12 inches chord length and 1 inch thick (i.e. thickness to chord ratio,  $t/c = 1/12$ ), and 60 degree swept angle ( $\phi = 60^\circ$ ) in the water tunnel. The incoming flow speed was 5 cm/s. The delta wing was at 25 degree angle of attack ( $\alpha = 25^\circ$ ). We first present the baseline result corresponding to its normal position as figure 7, which corresponds to strong swirl in apex vortex (on each side of the wing), and that where the usual vortex breakdown is observed.

For the delta wing at vertically flipped position as shown in figure 8, in comparison to the normal position wing as shown in figure 7, the flow at the apex turns at lesser angle, having larger turning radius, and that, apex vortex (on each side) has lesser initial swirl. Therefore, vortex breakdown is suppressed, as predicted by this changing the bevel angle manner.

Furthermore, for the case of vertically flipped wing, the apex vortices stay close to the wing and bifurcate into to multiple vortices, as shown in figures 9 and 10. We identify the multiple vortices as the primary, secondary and tertiary apex vortices, as shown schematically in figure 11.

Figures 12-15 taken by dye and figures 16-17 by LIF shows the eruption of the fluid near the wall. In general, it is well known that when a vortex is located in the vicinity of a solid surface, the boundary layer over the surface is drawn towards the vortex in an eruptive manner and forms a secondary vortex, which, for exactly the same reason, induces the tertiary vortex in turn. It is in this context that we interpret these figures. It should also be noted that, for all primary, secondary, and tertiary vortices, they are just convected downstream without breaking down.

## Conclusions

From the flow visualization results, we have studied the effect of leading edge's sharpness and bevel angle to the apex vortex. For

curvature effect, we compare two delta wings with sharp and rounded leading edges. The delta wing with sharp leading edge results in stronger apex vortices' initial circulation, and that the consequent vortex breakdown happens earlier than the rounded one. For bevel angle effect, we flip the delta wing with sharp leading edge vertically flipped. When the delta wing is flipped, the apex vortices bifurcate into smaller vortices, labelled as: primary, secondary and tertiary vortices. These vortices are convected downstream without breaking down.

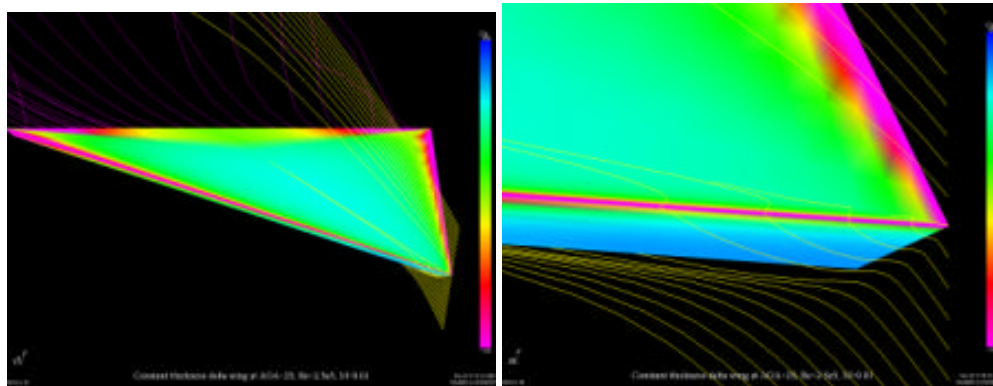
## Acknowledgments

In preparation of this paper, the author wishes to express his appreciative thanks to his research assistant –Mr. Nuttawut Lewpiriyawong, for providing suggestive comment and proofreading the manuscript.

## References

1. Spall, R.E., "Transition from Spiral- to Bubble-Type Vortex Breakdown", *Physics of Fluids*, Vol. 8, No.5, 1995, pp. 1330-1332.
2. Faler, J.H., and Leibovich, S., "Disrupted States of Vortex Flow and Vortex Breakdown", *Physics of Fluids*, Vol. 20, No.9, 1977, pp. 1385-1400.
3. Kurosaka, M., "Spiralling Shear Layers as a Cause of Vortex Breakdown", *Proceedings of the 8<sup>th</sup> International Symposium on Flow Visualization* [CD-ROM], National Library of Scotland, 1998.
4. Srigarom, S., and Kurosaka, M., "Shaping of Delta-Wing Planform to Suppress Vortex Breakdown", *AIAA Journal*, Vol. 38, No.1, 2000, pp.183-185.
5. Srigarom, S., and Kurosaka, M., "Surface Shaping to Suppress Vortex Breakdown on Delta Wings", *AIAA Journal*, Vol. 38, No.1, 2000, pp. 185-187.
6. Srigarom, S., "On the Formation of Vortex Breakdown over Delta Wings", *Ph.D. Dissertation*, University of Washington, 2001

## Figures



Figures 1 (left) and 2 (right): CFD results (VSAERO® CFD code) of flow around delta wing (left) and at the wing's apex (right).

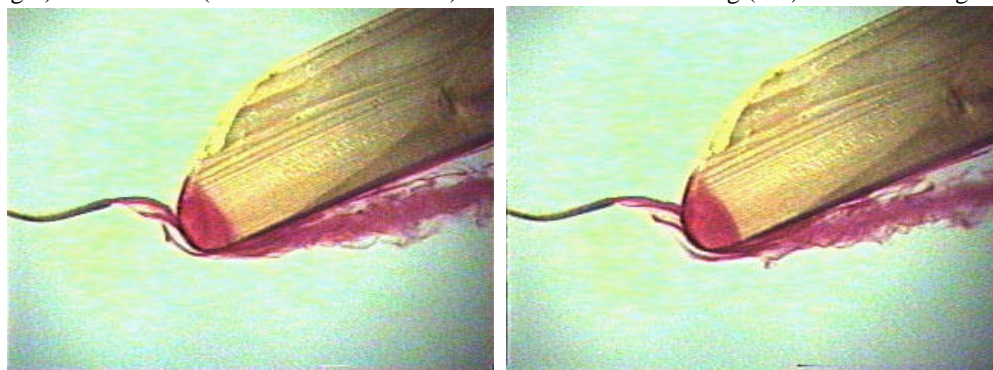


Figure 3: The flow around the curved wood attachment (= rounded leading edge).

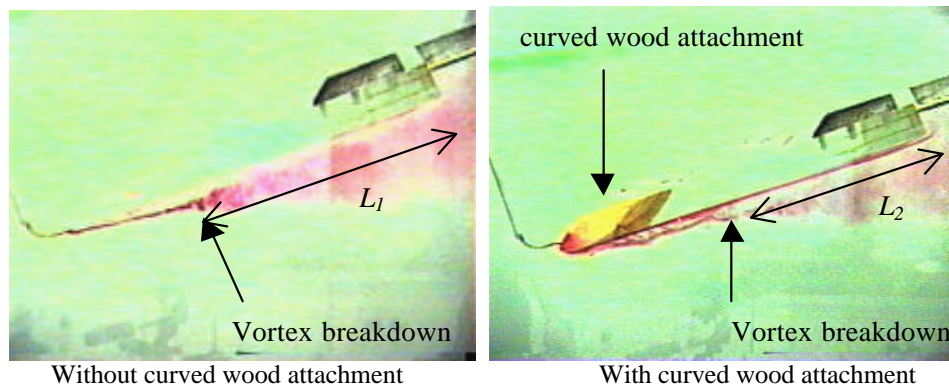


Figure 4: Vortex breakdowns on the wing, at  $\alpha = 20^\circ$  with curved wood attachment = rounded L.E. (right) and without = sharp L.E. (left).

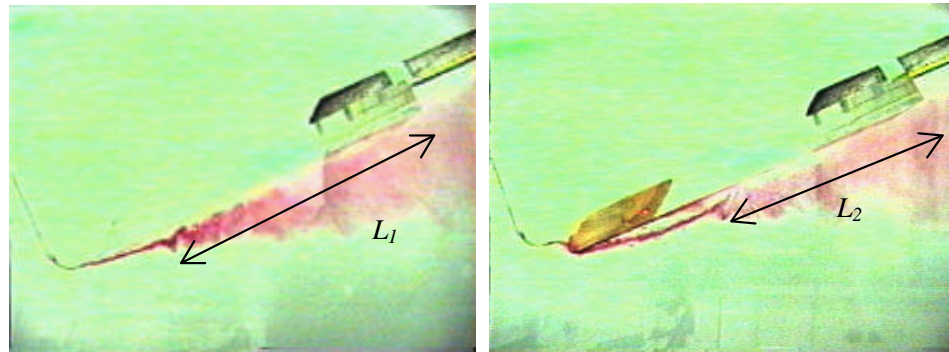


Figure 5: Vortex breakdowns on the wing, at  $\alpha = 25^\circ$  with curved wood attachment = rounded L.E. (right) and without = sharp L.E. (left).

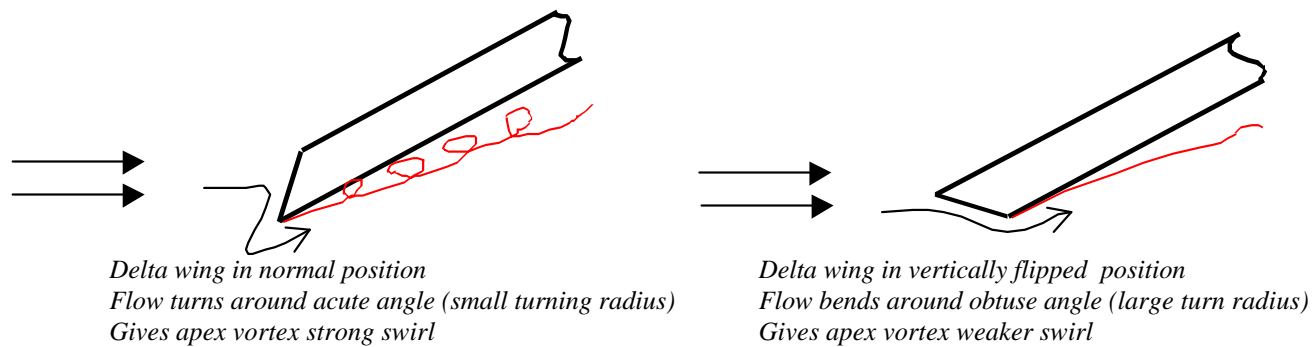


Figure 6: Schematic diagram: Flipping the delta wing vertically flipped results in changing initial circulation/swirl in apex vortex.

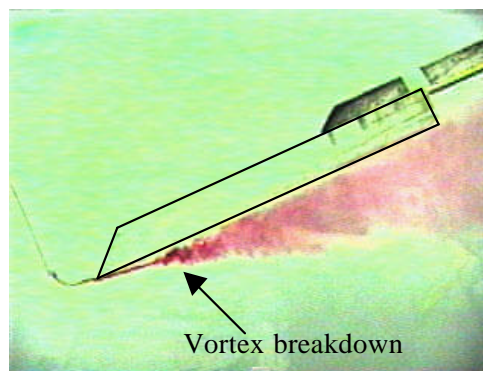


Figure 7: The  $\delta = 60^\circ$  delta wing with  $t/c = 1/12$ , mounted at normal position, at  $\alpha = 25^\circ$ . The line is drawn to indicate wing for clarity. The dye probe is visible at the left of the wing. The apex vortex has strong swirl and breaks down immediately.

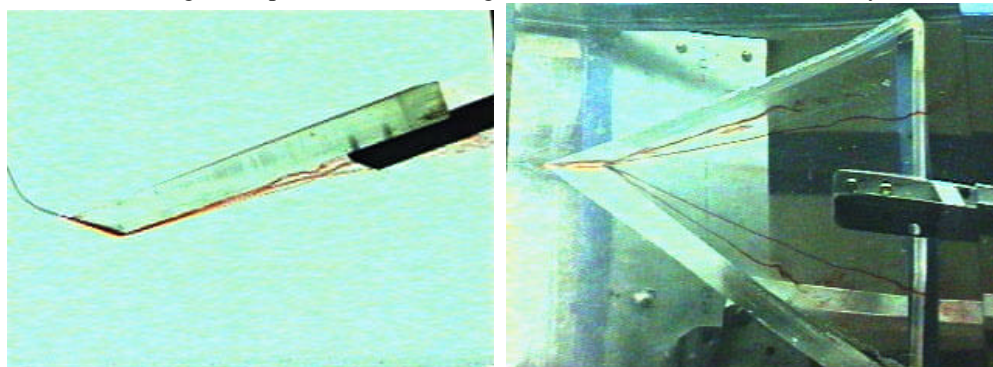


Figure 8: The  $\delta = 60^\circ$  delta wing with  $t/c = 1/12$ , mounted vertically flipped, at  $\alpha = 25^\circ$ . The apex vortex has weaker swirl, and that, no vortex breakdown exists. (Left: side view, Right: bottom view of the left figure).



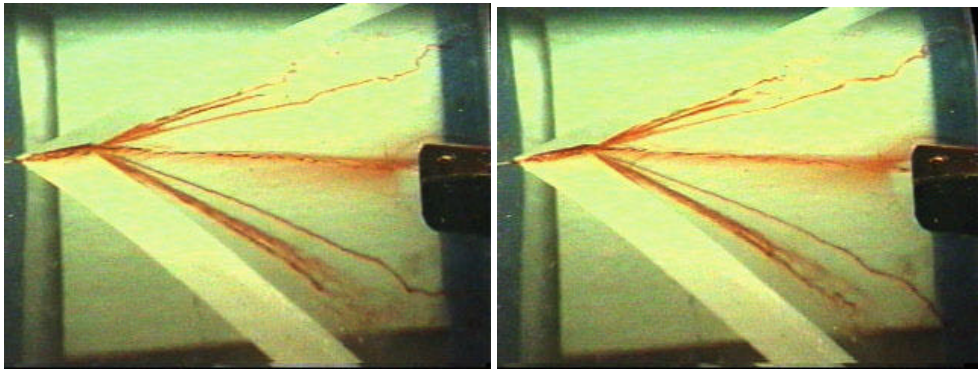


Figure 9: The vertically flipped  $\delta = 60^\circ$  delta wing with  $t/c = 1/12$  at  $\alpha = 25^\circ$ , entire view.

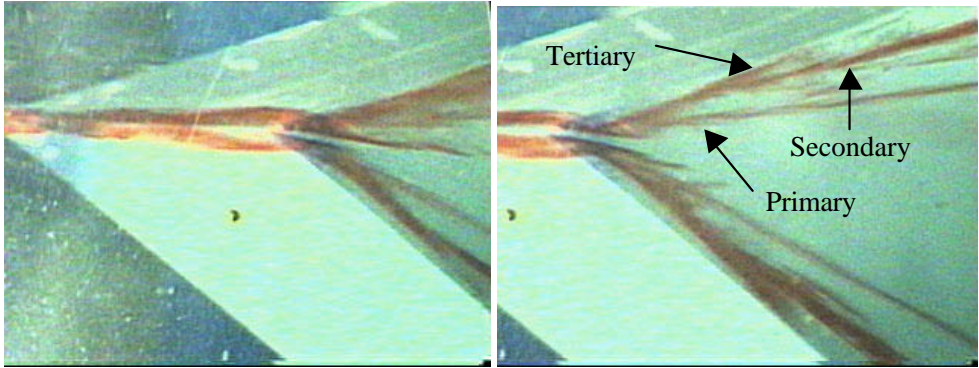


Figure 10: Close-up look of figure 9 at the apex.

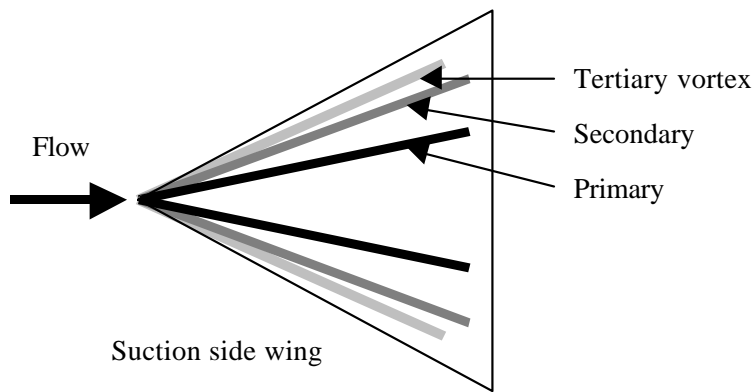
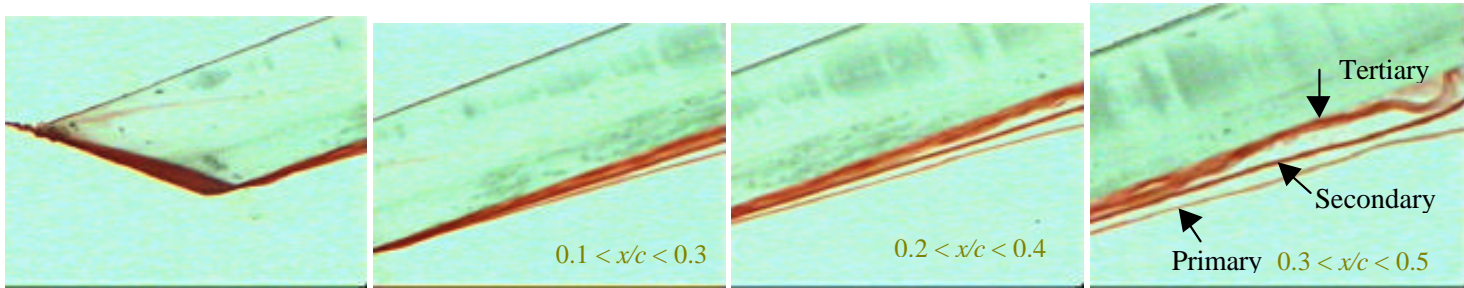
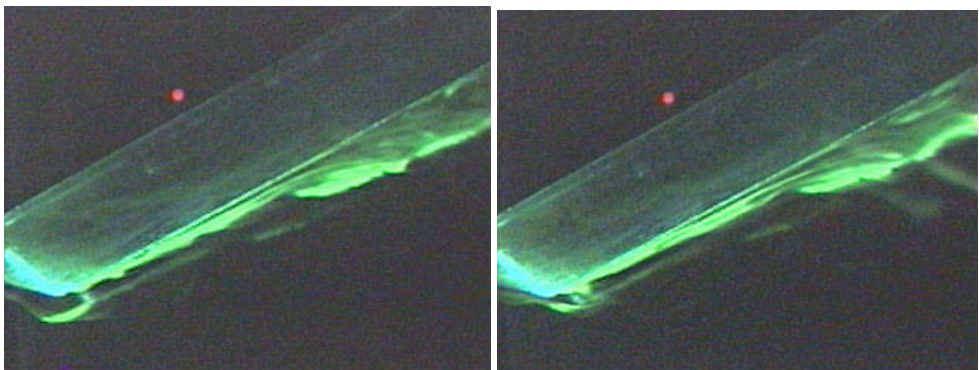


Figure 11: The diagram showing the primary, secondary and tertiary apex vortices.



Figures 12,13,14 and 15: The same wing as in figs. 9 and 10, close-up 1,2, 3 and 4 consecutively.



Figures 16 (left) and 17 (right): LIF of the secondary vortex's core plane 1 and 2.

## Outflow from a Plume Impinging on a Horizontal Boundary

N. B. Kaye and G. R. Hunt

Department of Civil and Environmental Engineering  
Imperial College London, London SW7 2AZ United Kingdom.

### Abstract

The radial outflow from a Boussinesq turbulent plume impinging on a horizontal boundary is examined both theoretically and experimentally. We gain insight into the transition from the vertical plume flow to the horizontal gravity current flow by drawing an analogy between classifying a constant buoyancy flux radial gravity current in terms of its source conditions and forced, pure and lazy plumes. Using dimensional arguments and existing experimental results for pure gravity currents and plumes, we demonstrate that the outflow will be initially jet like, before adjusting into a gravity current. This finding is supported by the results of our experiments.

### Introduction

We consider the collision of an axisymmetric turbulent plume flow with steady source conditions and a horizontal boundary in a quiescent environment. In practice these flows are relatively common, for example, a fire plume or thermal plume from a heat source in a room impinging on a ceiling (in this case a solid boundary), or a buoyant waste water plume reaching the surface of a sea into which it is pumped. In this work we restrict our attention to situations where the density difference between the plume and the surroundings is small compared with the density of the surroundings.

On impinging with the boundary the flow from the plume will spread horizontally outwards and in the far field develop into a constant flux radial gravity current. Near the point of impact, however, there is an adjustment region over which the flow develops into a pure gravity current - here we use 'pure' to refer to a current with a constant Froude number.

The details of this adjustment process and the radial extent over which this adjustment occurs are not well understood and form the motivation for the present study. Knowledge of the process of transition from vertical plume flow to horizontal gravity current flow is key to understanding a number of flows of practical interest. For example, when a thermal plume impinges on a ceiling in a confined room it spreads out and hits the side walls. In order to understand how far down the wall the heat or smoke will then initially descend requires an understanding of the dynamics of the initial outflow. Though not covered here, this problem is currently under investigation by the authors.

A schematic of the flow considered herein and the nomenclature adopted is given in figure 1. We denote the plume buoyancy flux by  $F$ , the vertical distance from the plume to the boundary by  $H$ , the radial coordinate by  $r$  and the thickness of the gravity current by  $\Delta(r)$ . We begin by stating a key result relating to the spread of constant flux radial gravity currents before considering the initial adjustment region. We then present a mathematical model for the bulk properties of the flow and compare our predictions to experimental measurements of the movement of the gravity current front.

In [3] a balance between the buoyancy force ( $\rho g' \Delta^2$ ) and inertial force ( $\rho r^2 \Delta / t^2$ ) was used to establish a relationship for the position of the front of the gravity current with time for

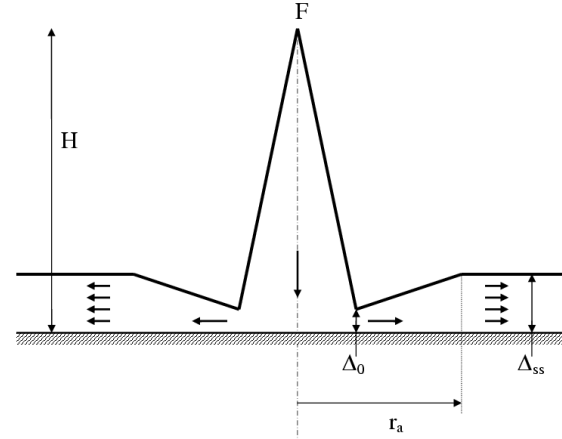


Figure 1: Schematic of the outflow from a plume impinging on a horizontal boundary showing the nomenclature adopted.

the inertial regime:

$$r = c_i F^{1/4} t^{3/4}. \quad (1)$$

Following on from this work [2] solve the governing equations and obtain the same time scalings as [3]. Experimental results suggest  $c_i = 0.84$ , hence

$$r = 0.84 F^{1/4} t^{3/4}. \quad (2)$$

This equation for the front movement implies a constant Froude number for the gravity current. If the 'source' conditions which characterise the supply of material to the current do not result in an identical Froude number, as will in general be the case, then there will be an adjustment region (in the near field) before the flow becomes a pure constant buoyancy flux radial gravity current (in the far field).

In this paper we draw an analogy between classifying radial gravity currents and classifying plumes in terms of their respective source conditions. We demonstrate that the adjustment region for the radial flow may be regarded as similar to either forced plumes [8] or lazy plumes [5] which themselves adjust to a pure plume in the far field. We also show that for a plume impinging on a horizontal boundary, the flow in the adjustment region is that of a forced radial gravity current regardless of the distance between source and boundary.

### Source Conditions and Length Scales

For a constant buoyancy flux radial gravity current the main parameters are the thickness ( $[\Delta] = L$ ), radial distance ( $[r] = L$ ), and buoyancy flux ( $[F] = L^4 T^{-3}$ ). The other parameters of note are the volume flux ( $[Q] = L^3 T^{-1}$ ) and momentum flux ( $[M] = L^4 T^{-2}$ ). Assuming that for the fully-developed flow the current has a constant thickness and velocity ( $v$ ) we can use dimensional analysis to develop scalings for the volume flux ( $2\pi r \Delta v$ ) and momentum flux ( $2\pi r \Delta v^2$ ) in terms of the thickness, radius and buoyancy flux:

$$Q \sim \Delta F^{1/3} r^{2/3} \quad \text{and} \quad M \sim \Delta F^{2/3} r^{1/3}. \quad (3)$$

The velocity of the current

$$v = \frac{dr}{dt} \sim F^{1/3} r^{-1/3}. \quad (4)$$

It is possible to derive the latter result by differentiating (2):

$$v = \frac{dr}{dt} = \frac{3 \times 0.84 F^{1/4}}{4t^{-1/4}} = 0.59 F^{1/3} r^{-1/3} \quad (5)$$

which can now be used to estimate the values of the constants in (3):

$$Q \approx 3.7 \Delta F^{1/3} r^{2/3} \quad \text{and} \quad M \approx 2.2 \Delta F^{2/3} r^{1/3}. \quad (6)$$

These equations give straightforward estimates of the volume and momentum flux at any given radial distance, but for chosen values of the fluxes  $Q$  and  $M$  they can also be inverted to provide an estimate of the radial distance a gravity current of buoyancy flux  $F$  would need to travel in order to obtain those flux values. It is in this sense that we define two radial length scales, the volume flux length scale ( $r_Q$ ) and the momentum length scale ( $r_M$ ):

$$r_Q = 3.7^{-3/2} \Delta_0^{-3/2} Q_0^{3/2} F^{-1/2} \quad (7)$$

$$r_M = 2.2^{-3} \Delta_0^{-3} M_0^3 F^{-2} \quad (8)$$

where the subscript 0 indicates the initial value. Note that the plume and current source buoyancy fluxes are identical as the environment is unstratified, thus  $F = F_0 = \text{constant}$ . Drawing an analogy with plume theory (see [5]) the gravity current can be regarded as ‘forced’ if  $r_M > r_Q$ , ‘lazy’ if  $r_M < r_Q$  and ‘pure’ if  $r_M = r_Q$ . We can also define a ratio of these length scales analogous to that for plumes:

$$\Gamma = \frac{r_Q}{r_M} = 1.5 \frac{Q_0^{3/2} \Delta_0^{3/2} F^{3/2}}{M_0^3}. \quad (9)$$

Again the flow in the adjustment region will be ‘forced’ for  $\Gamma < 1$ , ‘pure’ for  $\Gamma = 1$  and ‘lazy’ for  $\Gamma > 1$ .

For the case of a highly ‘forced’ gravity current one would expect a development region that behaved like a radial jet. For a smooth boundary this is a constant momentum flux flow with a linear growth in current thickness with radius. This linear radial growth is observed in the work of [7] and [6]. It is therefore a reasonable approximation that the transition region is ‘forced’ and will behave as a radial jet with a linear growth in thickness with radius and constant momentum flux (see, for example, [1]).

The ‘source’ conditions for the radial flow are those supplied by the pure plume of buoyancy flux ( $F$ ). Assuming top-hat profiles in the plume, the radius ( $b$ ) and volume flux ( $Q_p$ ) and momentum flux ( $M_p$ ) at the boundary can be expressed as:

$$b = \frac{6\alpha_t H}{5} = 0.15H \quad (10)$$

$$Q_p = \pi \left( \frac{5F}{8\pi\alpha_t} \right)^{1/3} \left( \frac{6\alpha_t H}{5} \right)^{5/3} = 0.16 F^{1/3} H^{5/3} \quad (11)$$

$$M_p = \pi \left( \frac{5F}{8\pi\alpha_t} \right)^{2/3} \left( \frac{6\alpha_t H}{5} \right)^{4/3} = 0.35 F^{2/3} H^{4/3} \quad (12)$$

where  $\alpha_t \approx 0.09\sqrt{2}$  (see [5]) is the plume entrainment coefficient appropriate for top-hat profiles. We now use (10) as the initial gravity current radius and using continuity we take (11) as the initial volume flux. However, it is likely that there will be

losses as the plume impinges on the solid boundary. We therefore assume that the initial gravity current momentum flux is given by  $\gamma M_p$ , for some constant  $\gamma$ . We can now establish the boundary conditions on the radial outflow, namely,

$$r_0 = 0.15H, \quad Q_0 = 0.16 F^{1/3} H^{5/3} \quad (13)$$

and

$$M_0 = \gamma M_p = 0.35 \gamma F^{2/3} H^{4/3}. \quad (14)$$

Therefore, for the initial outflow thickness we get

$$\Delta_0 = \frac{Q_0^2}{2\pi r_0 M_0} = \frac{0.068}{\gamma} H. \quad (15)$$

This implies that the initial outflow thickness increases as the energy loss (due to the change in flow direction) increases.

The next step is to evaluate the length scales defined in (7) and (8) using (15). This leads to

$$r_Q = 0.41 \gamma^{3/2} H \quad \text{and} \quad r_M = 7.1 \gamma^6 H, \quad (16)$$

or

$$\Gamma = 0.58 \gamma^{-9/2}. \quad (17)$$

We note the particularly sensitive dependence of  $r_M$  and  $\Gamma$  on  $\gamma$  and that (17) indicates that the flow is forced near the point of impingement provided  $\gamma > 0.53$ . It is expected that the losses will not be this significant and, therefore, we choose to model the transitional flow as a forced radial jet.

We will assume that the flow behaves as a turbulent radial momentum jet near the point of impingement with no loss in momentum flux as the flow spreads across the boundary. It is therefore expected to entrain ambient fluid and increase linearly in depth with radius [1]. This will increase the local value of  $\Gamma$  until it reaches the pure gravity current balance of  $\Gamma = 1$ . The flow will then behave as a radial gravity current as given by (2). For a momentum jet we know that:

$$\Delta = \frac{d\Delta}{dr} (r - r_0) + \Delta_0 \quad \text{and} \quad M = M_0 = \gamma 0.35 F^{2/3} H^{4/3} \quad (18)$$

where  $d\Delta/dr$  and  $\gamma$  are our unknown constants, and  $r_0$  and  $\Delta_0$  are given by (13) and (15), respectively. Carrying these unknowns through we can write expressions for the velocity  $v$  and volume flux  $Q$ :

$$v = \frac{\gamma^{1/2} \sqrt{0.33} F^{1/3} H^{2/3}}{\sqrt{2\pi r \Delta}} \quad \text{and} \quad Q = \sqrt{2\pi r \Delta} \gamma^{1/2} \sqrt{0.33} F^{1/3} H^{2/3}. \quad (19)$$

To leading order in  $r$  the outflow thickness is given by  $\Delta \approx \frac{d\Delta}{dr} r$ , hence, using (19) we estimate the movement of the front with time in the adjustment region as

$$\frac{dr}{dt} \approx \sqrt{\frac{0.35}{2\pi}} \sqrt{\frac{\gamma}{\frac{d\Delta}{dr}}} \frac{F^{1/3} H^{2/3}}{r}. \quad (20)$$

This leads to

$$r \approx 0.69 \left( \frac{\gamma}{\frac{d\Delta}{dr}} \right)^{1/4} F^{1/6} H^{1/3} t^{1/2} \quad (21)$$

to leading order in  $r$ .

We now introduce length and time scales based on the vertical separation  $H$  and the plume buoyancy flux  $F$ . Dimensionless time and radial distance, respectively, are given by

$$\tau = \frac{t}{H^{4/3} F^{-1/3}} \quad \text{and} \quad \phi = \frac{r}{H}. \quad (22)$$

This allows us to write expressions for the front movement with time in non-dimensional terms. In the initial forced adjustment region we get from (21):

$$\phi = 0.69 \left( \frac{\gamma}{\frac{d\Delta}{dr}} \right)^{1/4} \tau^{1/2} \quad (23)$$

and for the pure gravity current flow described by [2] we get

$$\phi = 0.84\tau^{3/4}. \quad (24)$$

In order to establish the value of the constant in (23) and the radial extent of the forced region we now turn to laboratory experiments.

### Experiments

A series of laboratory experiments were performed to examine the plume outflow. A negatively buoyant turbulent plume was created by injecting a salt solution (NaCl) at constant volume flow rate into a large visualisation tank filled with fresh water. The plume descended and impinged on a horizontal false bottom in the tank. As the radial flow from the plume spread out it was filmed using a CCD digital camera and the captured images processed using the software DigiFlow [4]. A schematic of the experimental setup is shown in figure 2.

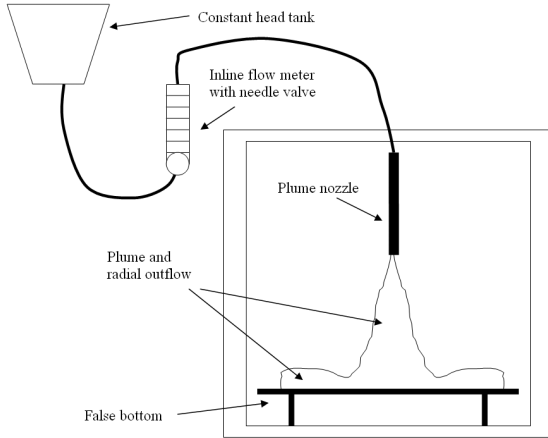


Figure 2: Schematic of experimental setup for tracking the front movement and thickness of the plume outflow.

### Jet region

The first set of measurements reported is the dependence of the adjustment radius ( $r_a$ ), see figure 1, on the separation distance ( $H$ ) for fixed plume source conditions. For these experiments the plume was dyed with Sodium Fluorescein and a thin vertical light sheet was projected up from below the tank. Once the outflow was fully established a time-averaged image (see figure 3 for a typical image) of the flow was taken and the radial distance ( $r_a$ ) at which the outflow was thickest measured. The separation  $H$  was varied from 5.5cm to 18.2cm. A plot of  $r_a$  against  $H$  is shown in figure 4. The line plotted is based on a best fit of the data forced through the origin and is given by

$$r_a = 0.66H. \quad (25)$$

### Front movement

Using the same experimental setup a series of experiments was run to measure the front position of the outflow as a function of time. In these experiments the apparatus was back lit and the



Figure 3: Time-averaged image of the outflow showing the radial growth in thickness near the source and adjustment to a constant thickness gravity current. The right-hand boundary of the image is the plume centreline. The outflow is the horizontal dark grey region.

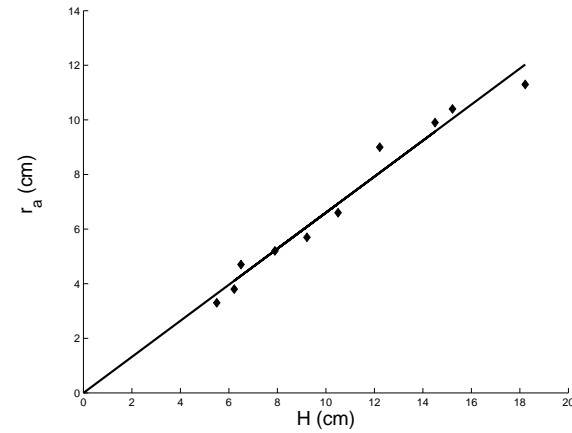


Figure 4: Plot of the radius  $r_a$  at which the outflow has maximum thickness as a function of the plume-boundary separation  $H$ . The line is given by  $r_a = 0.66H$ .

plume was dyed using a blue food colouring. A series of typical photos from these experiments is shown in figure 5.

A series of 5 experiments was performed, the plume-boundary separation and buoyancy flux are given in table 1. The plume was activated and the front movement was filmed. After each experiment was completed the film was reviewed and measurements of the front position against time were recorded. The time origin was taken as the moment the plume came into contact with the horizontal boundary. Measurements of front movement against time are plotted in figure 6.

Using the scalings given in (22) we can collapse all the data from figure 6 onto a single line. This scaled front movement is shown in figure 7. Based on our analysis we expect that for small  $\phi$  there would be a jet-like region where the front move-

Experiment	$H(\text{cm})$	$F(\text{cm}^4\text{s}^{-3})$	Symbol
A	47.5	255	+
B	50.5	255	×
C	21.5	255	*
D	32.3	182	★
E	7.1	122	○

Table 1: Experiment parameters for the five profiles presented in figures 6 and 7.



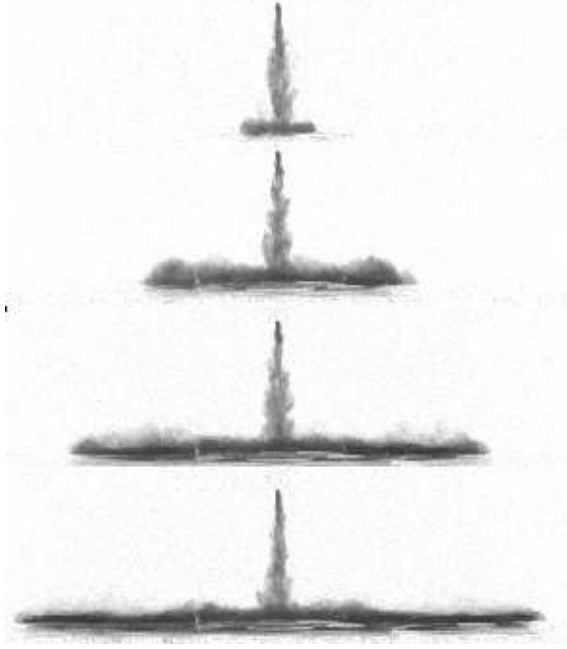


Figure 5: Series of digital images showing the descending plume and the horizontal outflow at various times during an experiment.

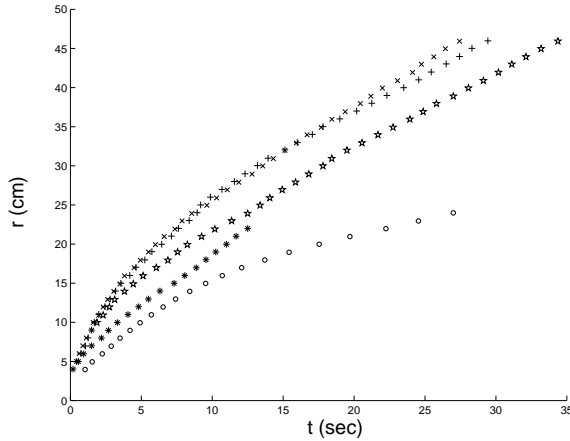


Figure 6: Plot of the front position  $r$  (cm) against time  $t$  (sec) for five experiments. + experiment A,  $\times$  experiment B, \* experiment C,  $\star$  experiment D and  $\circ$  experiment E.

ment scaled on  $\tau^{1/2}$  followed by a pure gravity current region where  $\phi \sim \tau^{3/4}$ . This behaviour is clearly seen in figure 7

### Conclusions

We have demonstrated that the outflow from a turbulent plume that impinges on a horizontal boundary behaves as a radial forced jet near the point of impingement. Downstream of this initially forced region the flow behaves as a constant buoyancy flux radial gravity current. Results of our experiments demonstrate that the adjustment region scales linearly on the vertical distance of the plume source from the horizontal boundary (see figure 4). We have also demonstrated that the dimensionless front position  $\phi = r/H$  can be described in terms of the non-dimensional time  $\tau = t/(H^{4/3}F^{-1/3})$  by (23) and (24). Experimental results have shown that the full description of the front movement with time is given by:

$$\phi = \begin{cases} 0.85\tau^{1/2} & \phi < 0.66 \\ 0.84\tau^{3/4} & \phi \geq 0.66. \end{cases} \quad (26)$$

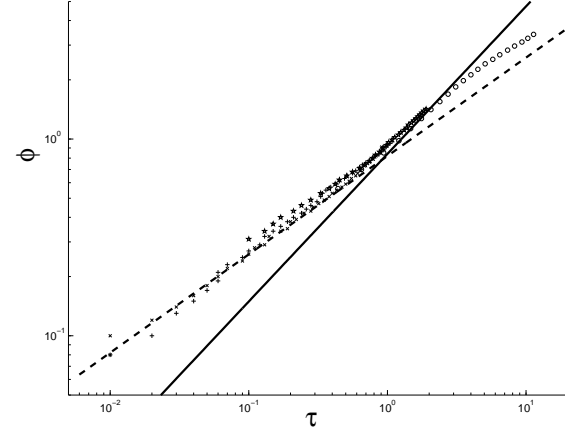


Figure 7: Non-dimensional front position  $\phi$  against time  $\tau$  showing the collapse of the experimental data and the ‘forced’ jet-like region near the point of impingement. The dashed line is given by  $\phi = 0.85\tau^{1/2}$ , cf. (23). The solid line is given by  $\phi = 0.84\tau^{3/4}$ . The discrepancy between the data and theory for large  $\phi$  is due to the increasing influence of viscous forces.

### Acknowledgements

NBK and GRH gratefully acknowledge the financial support of the EPSRC and BP through the BP Advanced Energy Programme in Buildings at Imperial College London, UK.

### References

- [1] Bakke, P., An experimental investigation of a wall jet., *J. Fluid Mech.*, **2**, 1957, 467–472.
- [2] Britter, R. E., The spread of a negatively buoyant plume in a calm environment., *Atmospheric Environment*, **13**, 1979, 1241–1247.
- [3] Chen, J. C. and List, E. J., Spreading of buoyant discharges., *Proc. 1976 ICHMT seminar on turbulent buoyant convection*, 171–182.
- [4] Dalziel, S. B., Rayleigh-taylor instability: experiments with image analysis., *Dyn. Atmos. Oceans*, **20**, 1993, 127–153.
- [5] Hunt, G. R. and Kaye, N. G., Virtual origin correction for lazy turbulent plumes., *J. Fluid Mech.*, **435**, 2001, 377–396.
- [6] Lawrence, G. A. and Maclatchy, M. R., Radially spreading buoyant flows., *J. Hydraulic Res.*, **39**, 2001, 583–590.
- [7] Lee, J. H. W. and Jirka, G. H., Vertical round buoyant jet in shallow water., *J. Hydraulics Div. Proc. ASCE*, **107**, 1981, 1651–1975.
- [8] Morton, B. R., Forced plumes., *J. Fluid Mech.*, **5**, 1959, 151–163.

## On Transient Flow in a Ventilated Filling Box

G. R. Hunt and N. B. Kaye

Department of Civil and Environmental Engineering  
Imperial College London, London, SW7 2AZ United Kingdom.

### Abstract

The transient flow driven by turbulent buoyant plumes rising from the floor of a ventilated filling box is examined. A rectangular box is considered and openings in the base and top of the box link the interior environment to a quiescent exterior environment of constant and uniform density. A theoretical model is developed for predicting the density stratification and the volume flow rate through the openings that lead to the known steady state. Predictions are compared with the results of small-scale analogue laboratory experiments in which saline solutions are used to create density differences in water tanks. The timescale for the flow to approach steady state depends on the relative magnitudes of two timescales; ( $t_f$ ) proportional to the time taken for fluid from the plume(s) to fill a closed box and ( $t_d$ ) the time taken to drain buoyant fluid from the ventilated box. Previous work has shown that the steady state is characterised by the dimensionless vent area  $A^*/H^2$  and we re-interpret this quantity as the ratio of the timescales ( $\mu = t_d/t_f$ ). For  $\mu > \mu_c$  the depth of the buoyant upper layer is shown to exceed, or 'overshoot', the steady layer depth during the initial transient. Applications include the natural ventilation of buildings and some implications of our results to building ventilation are discussed.

### Introduction

We consider the time-dependent stratification and flow induced by turbulent plumes in a ventilated box. Turbulent plumes in a sealed enclosure were examined by [1] in their 'filling box' paper. In a filling box, the plume rises to the top of the box and spreads laterally outwards to form a density interface between the plume outflow and the ambient fluid. This interface descends towards the plume source as ambient fluid is entrained into the plume and passes into the buoyant upper layer. [1] showed that the box fills with buoyant fluid on a timescale which depends on the floor area ( $S$ ) and height ( $H$ ) of the box, and the buoyancy flux ( $B$ ) of the plume. This resulted in the 'filling time',  $t_f$ , of

$$t_f \propto \frac{S}{B^{1/3} H^{-2/3}}. \quad (1)$$

[8] investigated ventilated boxes, including the draining of buoyant fluid from a box via openings in the top (of area  $a_t$ ) and base (of area  $a_b$ ) connecting to a quiescent external ambient. In the absence of mixing the time taken to flush the box, the 'draining time',  $t_d$ , is given by

$$t_d \propto \frac{S}{A^*} \left( \frac{H}{g'} \right)^{1/2} \quad (2)$$

where  $g' = g\Delta\rho/\rho$  is the reduced gravity of the buoyant layer,  $\Delta\rho$  the density contrast between the layers,  $\rho$  the density of the external ambient and  $A^*$  the 'effective' area of upper and lower openings such that  $a_b^* = 2^{1/2} c_b a_b$ ,  $a_t^* = 2^{1/2} c_t a_t$  and

$$\frac{1}{A^{*2}} = \frac{1}{a_b^{*2}} + \frac{1}{a_t^{*2}} \quad (3)$$

where  $c_b$  and  $c_t$  denote the loss coefficients associated with flow through the respective openings. This draining time is valid for uni-directional flow through the openings which usually requires that  $a_b$  is greater than or roughly equal to  $a_t$ , see [4]. For high Reynolds number flows  $c_b$  and  $c_t$  are normally assumed constant ( $\approx 0.6$ ).

[8] then consider a single continuous point source input of buoyancy at floor level and balance the draining flow rate with the supply flow rate from the plume and, thereby, examine 'emptying filling boxes', focussing on the steady states. A steady-state two-layer stratification is reached in which the upper buoyant layer drives a draining flow through the vents which is balanced by the filling flow from the plume. The steady upper layer depth ( $H - h$ ) depends only on the vent area, the box height and the plume entrainment coefficient ( $\alpha$ ):

$$\frac{A^*}{H^2 C^{3/2}} = \frac{\zeta_{ss}^{5/2}}{\sqrt{1 - \zeta_{ss}}} \quad (4)$$

where the subscript  $ss$  denotes 'steady state',  $C = \pi(5/2\pi\alpha)^{1/3} (6\alpha/5)^{5/3}$  and  $\zeta = h/H$ . Herein we use  $\alpha = 0.09$  which results in a value of  $C = 0.16$ . The steady interface height  $\zeta_{ss}$  is thus a function of the box geometry only and the entire problem may be regarded as geometric.

In this paper we re-interpret the parameter  $A^*/H^2 C^{3/2}$  in (4), previously regarded as a dimensionless opening area, as the ratio of the two competing timescales  $t_d$  and  $t_f$ , and examine the influence of these two times on the transient development of the flow. We begin by developing a theoretical model of the transients and then compare this with the results of analogue laboratory experiments. We discuss these results in the context of ventilation of a lecture theatre. Conclusions are then drawn.

### Mathematical model for the transient flow

Buoyancy is input from  $n$  equal non-interacting, localised point sources of buoyancy flux  $B$  at floor level ( $z = 0$ ) in a rectangular box of height  $H$  and cross-sectional area  $S$  (independent of height). Openings, of area  $a_b$  and  $a_t$ , in the base and top of the box, respectively, connect the interior environment to a quiescent exterior environment of constant density  $\rho$ . Buoyancy transfers between the boundaries of the box and the fluid in the interior are assumed negligibly small.

The turbulent plumes rising from the sources entrain ambient fluid and on reaching the top of the box spread radially outwards. Following [1] the details of the outward motion are ignored and an infinitesimally thin buoyant layer forms at time  $t = 0$  with an interface separating the layers. Over time the interface descends and increasingly buoyant fluid is fed into the layer. A pressure difference between the interior and exterior environments is thereby established which drives buoyant fluid out through the upper openings and draws in an equal volume of ambient fluid through the lower openings. Mixing between the inflowing fluid and the buoyant layer is assumed negligible and the flow through each opening is assumed to be unidirectional. As the layer deepens and increases in buoyancy, the volume flux

out of the box increases and begins to balance the volume flux fed into the buoyant layer by the plumes. After a finite time, a steady-state flow is approached in which the volume fluxes balance, the level of the interface is constant and the stratification consists of two homogeneous layers as confirmed in the experiments of [8]. Although one might expect a transient density profile similar to that of a filling box, for the purposes of modelling the movement of the interface we assume that the buoyant layer is well mixed throughout the transients.

The time rate of change of the buoyant layer thickness ( $H - h$ ) is governed by the difference between the volume flux of buoyant fluid supplied ( $nQ_p$ ) via the  $n$  buoyant plumes, and the volume flux out through the upper openings ( $Q_{out}$ ). Conservation of volume and buoyancy yield

$$\frac{dV}{dt} = nQ_p - Q_{out} \quad \text{and} \quad \frac{dVg'}{dt} = nB - B_{out} \quad (5)$$

respectively, where  $g'$  and  $V = S(H - h)$  are the average buoyancy and volume of the buoyant layer.  $B_{out} = g'Q_{out}$  is the flux of buoyancy out through the top openings. Introducing the non-dimensional interface height  $\zeta$  and reduced gravity  $\delta$ :

$$h = \zeta H \quad \text{and} \quad g' = \delta C^{-1} B^{\frac{2}{3}} H^{-\frac{5}{3}} \quad (6)$$

and using the plume flow rate scalings and the draining theory outlined by [8], the time rate of change of the buoyant layer depth and of the average layer buoyancy can be expressed as

$$\frac{d\zeta}{d\tau} = \frac{1}{\sqrt{\mu}} \sqrt{\delta(1 - \zeta)} - \sqrt{\mu} \zeta^{\frac{5}{3}} \quad (7)$$

$$\frac{d\delta}{d\tau} = \sqrt{\mu} \frac{1 - \zeta^{\frac{5}{3}} \delta}{1 - \zeta} \quad (8)$$

where the non-dimensional timescale  $\tau$  and parameter  $\mu$  are

$$t = \tau \sqrt{t_d t_f} = \tau \left( \frac{S^2}{nC^{\frac{1}{2}} A^* B^{\frac{2}{3}} H^{-\frac{2}{3}}} \right)^{\frac{1}{2}} \quad (9)$$

$$\mu = \frac{t_d}{t_f} = \frac{nC^{\frac{3}{2}} H^2}{A^*} \quad (10)$$

and the timescales  $t_d$  and  $t_f$  are defined as

$$t_d = \frac{C^{\frac{1}{2}} S H^{\frac{4}{3}}}{A^* B^{\frac{1}{3}}} \equiv \frac{S}{A^*} \left( \frac{H}{g'_p|_{z=H}} \right)^{\frac{1}{2}} \quad (11)$$

$$t_f = \frac{S}{nC B^{\frac{1}{3}} H^{\frac{2}{3}}} \quad (12)$$

$g'_p$  denotes the reduced gravity of the plume. Further details of the model and generalisation to both point and line source plumes are given in [7]. The initial conditions considered are those of an initially empty box:

$$\delta = 1, \quad \zeta = 1 \quad \text{at} \quad \tau = 0. \quad (13)$$

The timescale  $t_d$  is the ‘draining box’ time and is proportional to the time taken for a buoyant layer of depth  $H$  and of buoyancy equal to that in the plumes at height  $H$  to drain completely through openings of effective area  $A^*$ .  $t_f$  is the ‘filling box’ timescale for  $n$  non-interacting plumes each of buoyancy flux  $B$  (see [1]). In other words,  $t_d$  relates to the draining of a ventilated box in the absence of a supply of buoyancy and  $t_f$  relates to the filling of an unventilated box supplied with a constant buoyancy flux from sources at floor level.

## Theoretical Predictions

Solution of the governing equations (7) and (8) subject to (13) was achieved using a finite-differencing scheme. The key parameters examined are: the interface heights at maximum overshoot ( $\zeta_{over}$ ) and at steady state ( $\zeta_{ss}$ ), and the time taken to reach the maximum overshoot ( $\tau_{over}$ ) and the steady state ( $\tau_{ss}$ ). The time taken to reach the steady state is defined as the time taken for the ambient layer to reach 99% of its steady-state depth ( $|\zeta - \zeta_{ss}| < 0.01$ ). When the interface overshoots the steady state,  $\tau_{ss}$  is the time taken to overshoot and then settle back to 99% of the steady-state interface height. Numerical solutions for  $10^{-3} < \mu < 10^5$  from  $\tau = 0$  to  $\tau = 50$  were evaluated; the finishing time chosen allowed the interface height to reach steady state for the full range of  $\mu$  considered. The steady state is expected to be approached but never reached, however, given the (large) finish time of  $\tau = 50$  the flow approached close enough to the steady state of (4) to be graphically indistinguishable.

## Progress to steady state

The variation of the dimensionless volume flow rates, as supplied to ( $\sqrt{\mu} \zeta^{\frac{5}{3}}$ ) and draining out of ( $\sqrt{\delta(1 - \zeta)}/\sqrt{\mu}$ ) the buoyant layer, leading to the steady state is shown in figure 1 for  $\mu = 10$ . A rapid decrease in the volume flux supplied to the layer by the plume is predicted as the layer descends towards the plume source. The volume flux draining out increases more gradually. The lines shown intersect at the point of maximum overshoot (see figure 2), after which the volume flux out exceeds the volume flux supplied to the layer and the layer thins as it approaches the steady state.

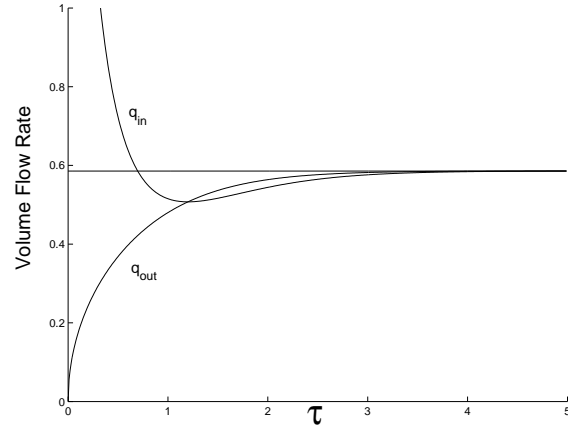


Figure 1:  $q_{in} = \sqrt{\mu} \zeta^{\frac{5}{3}}$  and  $q_{out} = \sqrt{\delta(1 - \zeta)}/\sqrt{\mu}$  against  $\tau$  for a point source plume and  $\mu = 10$ . The horizontal line represents the value of the volume fluxes at the predicted steady state (4).

Figure 2 shows profiles of  $\zeta$  as a function of  $\tau$ . An initial rapid deepening of the buoyant layer is predicted. For sufficiently large  $\mu$  the buoyant layer depth exceeds (or overshoots) the steady value and then thins as it approaches steady state. The initial rate of change of the buoyant layer depth increases with increasing  $\mu$ . The initial increase in layer depth results in the layer being supplied with increasingly buoyant fluid from the plumes, and thus a corresponding increase in the average buoyancy of the layer. The time taken to reach maximum overshoot can be seen to decrease as  $\mu$  increases.

## Amplitude of overshoot

For small values of  $\mu$  no overshoot is predicted (see figure 2) but for larger values of  $\mu$  the overshoot can be as high as 3.7% of  $H$  (this occurs at  $\mu \approx 41.4$ ). Although the overshoot typically is only a small fraction of the box height, it can be a significant

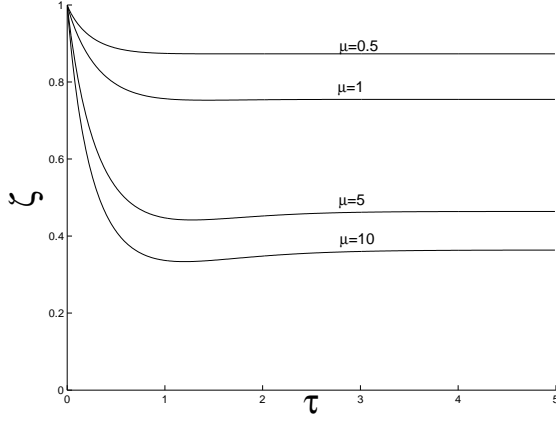


Figure 2:  $\zeta$  vs.  $\tau$  for point sources with  $\mu = \{0.5, 1, 5, 10\}$ .

fraction of the ambient lower layer depth when the lower layer is thin (i.e. for large  $\mu$ ).

#### Time taken to reach steady state

Figure 3 shows the time taken  $\tau_{ss}$  to reach the steady-state layer depth. The dashed line is the time to reach  $\zeta_{ss}$  the first time, i.e. as the interface descends. The solid line is the time taken to return to  $\zeta_{ss}$  after overshooting, i.e. as the interface ascends. For  $\mu < \mu_c$  there is no overshoot, and the layer merely increases to the steady layer depth. [7] predict that  $\mu_c = 0.27$  and provide an explanation for the ‘bulge’ in the plot.

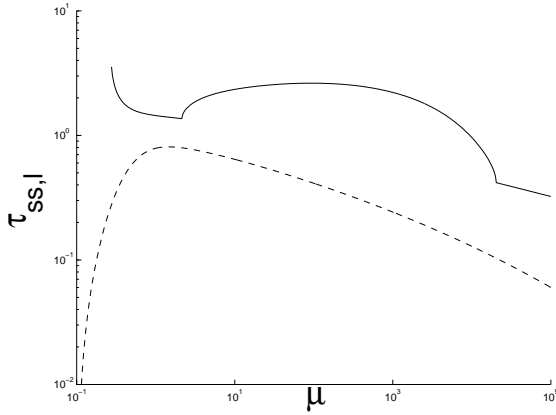


Figure 3: Time taken ( $\tau_{ss}$ ) to reach the steady layer depth during both the initial increase in layer depth (dashed line) and subsequent decay in layer depth towards the steady state (solid line).

#### Experiments

To test the validity of the modelling assumptions a series of small-scale laboratory experiments were performed in a large, clear-sided visualisation tank filled with fresh water. A clear Perspex box (cross section 0.5m×0.5m, height 0.2m) was immersed in the tank. Circular holes, of 3cm and 5cm diameter, in the top and bottom of the box (including a 1cm and a 0.5cm diameter hole in the bottom) could be opened or closed by removing or adding plugs. The range of  $\mu$  possible was  $0.1 < \mu < 35$ , however, for  $\mu > 10$  we were unable to reach the final steady state owing to the tank stratifying as saline solution flowed out of the box. Saline solution was supplied via constant head apparatus to a nozzle located in the centre of the box’s top face. The (constant) volume flow rate of supply was finely controlled with a needle valve and measured using an in-line flowmeter. Dye added to the supply aided visualisation and the apparatus

was diffusively back lit. The density of the ambient and supply was measured using an Anton Paar DMA 35N density meter (accuracy  $5 \times 10^{-4} \text{gcm}^{-3}$ ). The virtual origin of the plume source was located following [6]. An experiment was started by opening a tap supplying salt solution to the nozzle; the needle valve was pre-set so that the desired flow rate was achieved immediately. The upper opening area was typically a factor of two greater than the lower opening area in order to maintain a low inlet velocity. This low inlet velocity prevents the inflowing jets of fluid from disturbing the interface, and enabled a sharp interface to be maintained. However, due to the geometry of the box, for smaller values of  $\mu$  (larger vent areas) we were unable to maintain this ratio resulting in disturbances on the interface. The digital image analysis system DigiFlow [5] was used to track the interface. A horizontal average of each time frame was taken (excluding the plume region), and the point of highest vertical gradient in the intensity (buoyancy) profile was taken as the interface height.

#### Results

A descending turbulent plume developed below the nozzle and after impinging with the base of the box spread radially outwards as a saline gravity current. This outflow is considered in an accompanying paper by the authors at the 15th AFMC. On reaching the box walls a well-defined saline layer, with depth approximately equal to the width of the plume at the base of the box, was clearly visible. The current sloshed up the side walls of the box before slumping back downward. This produced wave-like disturbances which propagated along the interface between the layers before dissipating over time. The initial slumping also produced mixing between the layers, however, at later times the only fluid crossing the density step was that entrained into the plume. Saline drained out through the base openings and was replaced by fluid of ambient density which flowed in through the top openings. For most  $\mu$  the interfacial disturbances due to the flow through the openings were minimal and were wave-like with no mixing across the interface and, therefore, had no effect on the interface position. For small  $\mu$ , however, the disturbances were more significant.

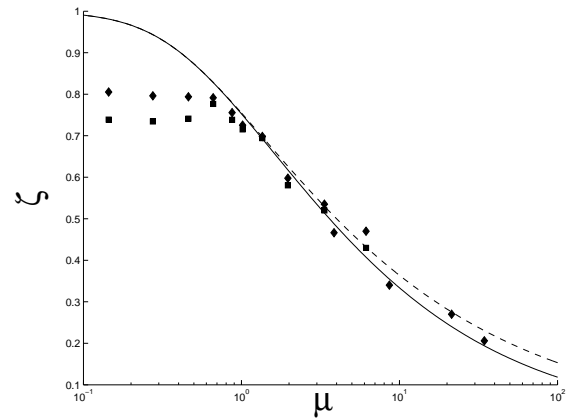


Figure 4: Predicted and measured values for  $\zeta_{over}$  (diamonds and dashed line) and  $\zeta_{ss}$  (squares and solid line).

During the initial transients the saline layer rapidly increased in depth (*cf.* figure 2) indicating that the draining rate was small compared with the supply rate to the layer from the plume. The subsequent development of the stratification within the box was observed to be dependent on the opening area:

(i) For relatively small openings ( $\mu > 1$ ) the buoyant layer initially deepened and the interface became horizontal and sharper as the initial slumping phase decayed away and the mixed fluid

at the interface was entrained into the plume. The layer depth increased to a maximum and then decreased to the steady-state depth. Other than the finite thickness of the initial outflow layer this is qualitatively in keeping with our model. Measurements of interface height show generally good agreement with theory for this range of  $\mu$  (see figure 4). There is also good agreement between our theoretical predictions of  $\tau_{over}$  and  $\tau_{ss}$  for  $\mu > 1$  (see figure 5) and our experiments.

(ii) For sufficiently large opening areas ( $\mu < 1$ ) a different flow regime was observed. Instead of the hydrostatic two-layer stratification modelled, the interface in the region below the open vents was broken up and mixed by the inflowing jets of ambient fluid. Away from the openings the interface was also unstable with waves persisting. A significant initial overshoot of the interface height was also observed due to these disturbances. The final average interface height was not observed to vary with  $\mu$  and was of the order of the plume width at  $z = H$ . Therefore, for  $\mu < 1$ , the experimental measurements of  $\zeta$  and  $\tau$  show poor agreement with our theoretical predictions.

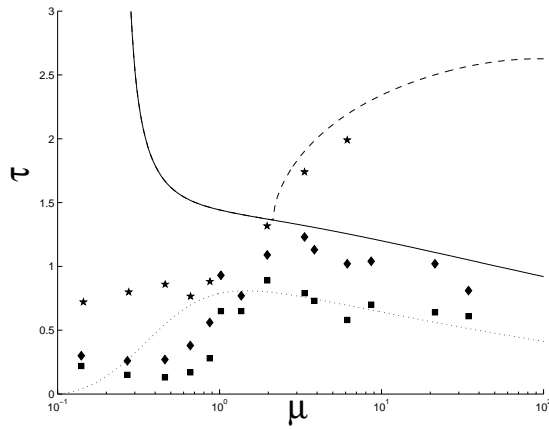


Figure 5: Predicted and measured values of  $\tau_{ss}$  and  $\tau_{over}$ . Squares and dotted line indicate the time taken to reach the steady-state height. Diamonds and solid line indicate the time taken to reach maximum overshoot  $\tau_{over}$ . Stars and dashed line indicate the time taken to settle back to the steady state.

## Discussion

Our model and experiments have shown that transient buoyancy-driven flow in a ventilated enclosure yields a reduced volume flow rate through the enclosure compared to the steady-state value and an overshoot of the buoyant upper layer for sufficiently large  $\mu$ . We now briefly discuss the implications of these transient phenomena in the context of a lecture room.

We consider a lecture theatre with floor area 300m<sup>2</sup>, height 6m and with 256 occupants. We assume that each occupant can be represented by a plume with a power output of 100W. We also assume an opening area of 1.5% of the floor area giving  $A^* = 2.9\text{m}^2$ . We model the heat input in two ways. Firstly as 256 individual plumes (one from each occupant) and secondly as a single plume (assuming they all merge near their source). The parameters used and resulting timescales are summarised in table 1. These values are representative of those used in ventilation models of actual buildings (see [9] & [3]).

The first point to note is the significant variation in  $\mu$  depending on how the heat is input. Also the time taken in both cases to reach steady state is of order a quarter of an hour. This means that for the first quarter of a one hour lecture the ventilation rates will be less than designed for using a steady-state model.

	256 plumes	single plume
# Plumes	256	1
$t_d$	54	8.5
$t_f$	0.25	11
$\sqrt{t_d t_f}$	3.8	10
$\mu$	201	0.8
$\tau_{over}$	0.8	1.5
$\tau_{ss}$	2.6	1.5
$t_{over}(\text{mins})$	3	14
$t_{ss}(\text{mins})$	10	14
Air changes/hr	6.6	3.9

Table 1: Typical lecture room parameter values and timescales for a floor area 300m<sup>2</sup>. Times are given in minutes. Buoyancy flux has been calculated using  $B = \frac{gP}{\rho T C_p}$  where  $P$  and  $T$  are the source power output (W) and temperature  $^{\circ}\text{K}$  [2], respectively.

## Conclusions

Transient flow in ventilated boxes driven by a sudden increase in buoyancy flux has been investigated. The transients are governed by the relative magnitudes of the draining ( $t_d$ ) and filling ( $t_f$ ) timescales as characterised by the parameter  $\mu = t_d/t_f$ . The layer depth may overshoot the steady-state depth for  $\mu > \mu_c$ . Results of laboratory experiments show good agreement with our predictions for  $\mu > 1$ . However, below this value, a constant thickness layer was measured and found to be independent of  $\mu$ .

## Acknowledgements

The authors gratefully acknowledge the financial support of BP through the BP Advanced Energy Programme in Buildings at Imperial College London, UK, and the EPSRC.

## References

- [1] Baines, W. D. and Turner, J. S., Turbulent buoyant convection from a source in a confined region., *J. Fluid Mech.*, **37**, 1969, 51–80.
- [2] Batchelor, G. K., Heat convection and buoyancy effects in fluids., *Quart. J. Roy. Met. Soc.*, **80**, 1954, 339–358.
- [3] Clancy, E. M., Derivation of simple ventilation and thermal models for a naturally ventilated auditorium with high internal heat gains., *Proc. 21st Int. AIVC Conf.*, 1–12.
- [4] Coffey, C. J. and Hunt, G. R., On the night purging of naturally ventilated enclosures - the effect of the relative area of openings., in *ROOMVENT 2004, 9th Intl. Conf. on Air Dist. in Rooms*, editor M. C. G. D. Silva, 2004.
- [5] Dalziel, S. B., Rayleigh-taylor instability: experiments with image analysis., *Dyn. Atmos. Oceans*, **20**, 1993, 127–153.
- [6] Hunt, G. R. and Kaye, N. G., Virtual origin correction for lazy turbulent plumes., *J. Fluid Mech.*, **435**, 2001, 377–396.
- [7] Kaye, N. B. and Hunt, G. R., Time-dependent flows in an emptying filling box., *J. Fluid Mech.*, **520**, 2004, 135–156.
- [8] Linden, P. F., Lane-Serff, G. F. and Smeed, D. A., Emptying filling boxes, the fluid mechanics of natural ventilation., *J. Fluid Mech.*, **212**, 1990, 309–335.
- [9] Quincy, R., Knowles, N. and Thomas, R., The design of assisted naturally ventilated theatres., *Proc. CIBSE National Conf.*, **1**, 1997, 83–90.

## A Study of Base Drag Optimization Using Mass Bleed

Y.K. Lee<sup>1</sup>, H.D. Kim<sup>1</sup> and S. Raghunathan<sup>2</sup>

<sup>1</sup>School of Mechanical Engineering  
Andong National University, Andong, 760-749, KOREA

<sup>2</sup>School of Aeronautical Engineering  
The Queen's University of Belfast, Belfast, NI, BT9 5AG, UK

### Abstract

Compressible base flows with mass bleed in a Mach 2.47 freestream have been numerically investigated to find a way to effectively control the base flow for base drag reduction. Axisymmetric, compressible, mass-averaged Navier-Stokes equations are solved using the standard  $k-\omega$  turbulence model, a fully implicit finite volume scheme and a multi-stage Runge-Kutta scheme. Various base flow characteristics are obtained by the change in the injection parameter, which is defined by the mass flow rate of the bleed jet non-dimensionalized by the product of the base area and freestream mass flux. The results obtained through the present study show that there is an optimum bleed condition that base pressure reaches a maximum value for all afterbody configurations tested, consequently leading to a minimum base drag, when the injection parameter changes.

### Introduction

Aerodynamic bodies such as missiles, projectiles, and rockets, generally, undergo significant deterioration of flight performance by drag. For these kinds of flight bodies, especially, the drag in the base region has the most significant contribution to total drag. At transonic speeds, for example, base drag constitutes a major portion up to 50 % of the total drag for typical projectiles at Mach 0.9 [1]. Base drag should, therefore, be considered separately from other pressure drag components. For this reason, the minimization of base drag has been an important issue to date, and considerable effort has been made to find suitable techniques for obtaining low base-drag shell design.

Base drag reduction can be achieved by afterbody boattailing [2], base bleed or base burning [3,4], some vortex suppression devices [5] and their combinations [6]. Such active or passive flow control techniques, basically, manipulate or alter the near-wake flowfield for an increase in base pressure and consequently reduce base drag. These drag control techniques have been applied in somewhat empirical manners to date due to a lack of understanding of viscous-inviscid flow interactions between a near-wake flow and a freestream.

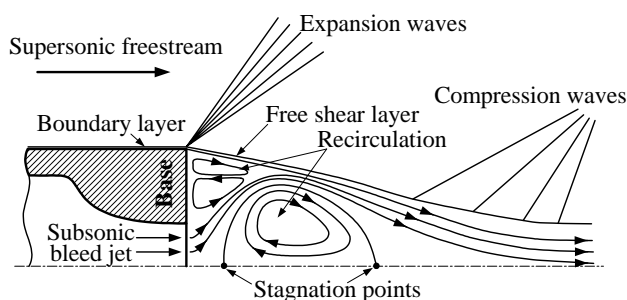


Figure 1. Supersonic base flow with mass bleed.

Figure 1 shows the schematic diagram of the supersonic base flow and afterbody model under consideration in the present computations. The supersonic freestream expands through a

Prandtl-Meyer expansion fan generated at the base corner, and the wall boundary layer developing along the body is separated at the corner and recompressed by compression waves at a certain downstream region. The interaction between two distinct flows inside and outside the separation leads to a free shear layer along the boundary of the flows and recirculating flows inside the separation. In the presence of low mass bleed into the separated region, such flow features can be significantly changed depending on the bleed mass flow rate for a given freestream Mach number and afterbody geometry [7].

According to a computational work conducted by Sahu et al. [1] using thin-layer Navier-Stokes equations, at transonic speeds of Mach 0.9 to 1.2, the use of mass bleed can reduce base drag by 40-80 %. However, the drag does not continuously decrease with increased mass bleed. An experimental study performed by Bourdon and Dutton [8] reported that an optimum condition giving the maximum base pressure was observed at a certain bleed mass flow rate for the given freestream Mach number of about 2.5. This important feature must be replicated with computational results, in order to be considered in aerodynamic design with reliability.

In the present study, a compressible base flow in a supersonic freestream at Mach 2.47 was numerically investigated. Computations have been conducted using axisymmetric mass-averaged Navier-Stokes equations with the standard  $k-\omega$  turbulence model [9]. The results are validated with experimental data [10] and also supported by detailed flow visualization to provide a better understanding of the physics of base flows controlled by a bleed jet.

### Numerical Simulations

#### Afterbody Model

Figure 2 shows the afterbody model used in the present CFD (computational fluid dynamics) analysis, taken from [10] for validation. In the figure,  $M$ ,  $p$ ,  $T$  are Mach number, pressure and temperature, and subscripts 0,  $j$  and  $\infty$  represent a total state, bleed jet and freestream, respectively. The bleed mass flow rate and the Mach number at the orifice exit  $M_e$  are calculated by isentropic relations, corresponding to the mass bleed under consideration. Regarding the model dimensions, the diameters of the model and orifice exit are given as  $R_b$  and  $R_e$ , respectively. The afterbody is taken for computations only up to a length of  $3R_b$  from the origin, which lies at the center of the orifice exit.

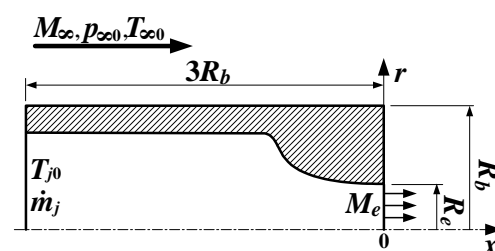


Figure 2. Afterbody model.

$M_\infty$	2.47	$T_{j0}$	293 K
$p_{\infty 0}$	470 kPa	$R_b$	25.40 mm
$p_\infty$	28.8 kPa		31.75 mm
$T_{\infty 0}$	300 K		38.15 mm
$Re_{unit}$	$46 \times 10^6 m^{-1}$	$R_e$	12.70 mm

Table 1. Details of CFD model and flow properties.

The details of model geometry and properties given to specify flow conditions are shown in Table 1, where  $Re_{unit}$  is the unit Reynolds number of the freestream.

### Numerical Methods

The present CFD study adopted a commercial computational code, FLUENT 6, in order to analyze complex flow interactions between a supersonic base flow and a subsonic bleed jet. Axisymmetric compressible mass-averaged Navier-Stokes equations governing the flowfield around an afterbody with mass bleed at the base were solved. The governing equations are discretized spatially and temporally using a fully implicit finite volume scheme and a multi-stage Runge-Kutta scheme [11], respectively in the code. To obtain accurate solutions for the base flow including separation regions, wakes, strong free shear layers and wave systems, suitable turbulence modeling is indispensable. Therefore, preliminary computations were carried out for several turbulence models and wall functions.

### Computational Domain and Analysis

Figure 3 shows the grid layout near the afterbody model and brief information of the computational domain used in the current CFD analysis with boundary conditions applied. It has been found that about 50,000 nodes are required to get grid-independent solutions with the computational domain used. Grids were clustered in the regions with large gradient near model surfaces and downstream of the base where the separation of a turbulent boundary layer and wave systems are expected to exist.

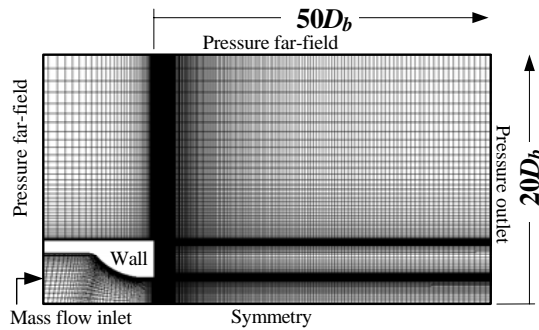


Figure 3. Computational grids.

The computational domain were set up with dimensions of  $50D_b$ , where  $D_b$  is the model diameter, downwards from the base and  $20D_b$  upwards from the model axis to ensure freestream conditions and thus to obtain better convergence. Freestream boundaries are identified with a combination of the pressure far-field and pressure outlet conditions as shown in the figure. Preliminary tests showed better convergence could be achieved using the combination rather than the use of the pressure far-field condition at all outer boundaries. To specify the freestream condition, the Mach number and static properties were applied to the boundaries.

Bleed air is injected through an orifice into the near wake region behind the model base. For obtaining various characteristics of mass bleed, the bleed mass flow rate  $\dot{m}_j$  applied to the mass flow inlet boundary is changed corresponding to the injection parameter  $I$  given as follows.

$$I = \frac{\dot{m}_j}{A_b \rho_\infty U_\infty} \quad (1)$$

where  $A_b$  is the base area, and  $\rho_\infty$  and  $U_\infty$  are the density and velocity of the freestream. With  $\dot{m}_j$ , total temperature and static pressure are given at the inlet boundary. Adiabatic and no-slip conditions are applied to the wall boundaries, and a symmetry boundary condition is applied to the domain axis. The properties used for the boundary conditions mentioned are given in Table 1.

Regarding testing conditions,  $I$  was changed from 0.004 to 0.032 for three base areas tested as the geometry of the orifice and freestream conditions are fixed. The area ratios ( $A_b/A_e$ ) calculated from  $R_b$  values given in Table 1 are 4.00, 6.25 and 9.00, respectively. With a proper grid size and computational domain obtained through preliminary tests, basically, solutions were considered converged when the residuals of mass and momentum equations dropped to  $1.0 \times 10^{-4}$ . The mass imbalance was also checked for flow inlet and outlet boundaries and it is less than  $\pm 0.1\%$  for converged solutions.

### Results and Discussion

For  $I = 0.0038$  and  $A_b/A_e = 6.25$ , Figure 4 shows grid dependency on the solution given here as axial velocity profiles at  $x/R_b = 1.0$  for several grid sizes. The velocity profiles presented have been computed using the standard  $k-w$  turbulence model. The radial distance  $r$  and the axial velocity  $U_x$  are normalized by  $R_b$  and  $U_\infty$ , respectively. The grid size has been tested in a range of about 20,000 to 63,500 nodes. In the figure, the profile inside the back flow region near the axis ( $r/R_b = 0.0$ ) has a relatively significant change for the grid sizes tested. Because grid sizes with more than 45,202 nodes give no more change in the profile, it is considered that 45,202 nodes are enough to have grid independent solutions for the given value of  $I$ . For larger  $I$  values, in this approach, it has been found that about 50,000 nodes can be used to simulate the flowfields under consideration.

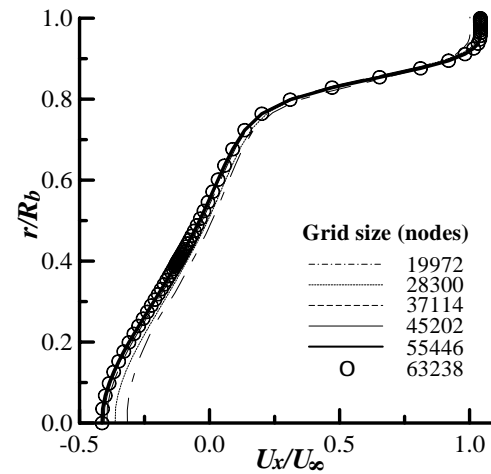


Figure 4. Velocity profiles at  $x/R_b = 1.0$  with a change in grid size ( $I = 0.0038$  and  $A_b/A_e = 6.25$ ).

With a proper grid size obtained through the approach mentioned above, several turbulence models and wall functions have been tested at  $I = 0.0038$  and  $A_b/A_e = 6.25$ , and base pressure values  $p_b$  normalized by  $p_\infty$  are given in Table 2. In computations, the grid system was set up to correctly calculate the near-wall flow by checking  $y^+$ , which was 50 to 200 for the turbulence models with wall functions and less than 1 for the  $k-w$  turbulence model. In comparison of computed values and a measured value taken from [10], the standard  $k-w$  turbulence model resulted in the closest



prediction of base pressure. The results also indicate that the effect of wall functions on base pressure predictions is insignificant for the geometry and testing conditions used in the present computations.

Turbulence Model		$p_b/p_\infty$
Standard $k-\omega$		0.602
RNG $k-\varepsilon$	SWF	0.569
	NWF	0.572
RSM	SWF	0.571
	NWF	0.580
Experimental, [10]		0.592

Table 2. Base pressure ( $I = 0.0038$  and  $A_b/A_e = 6.25$ ).

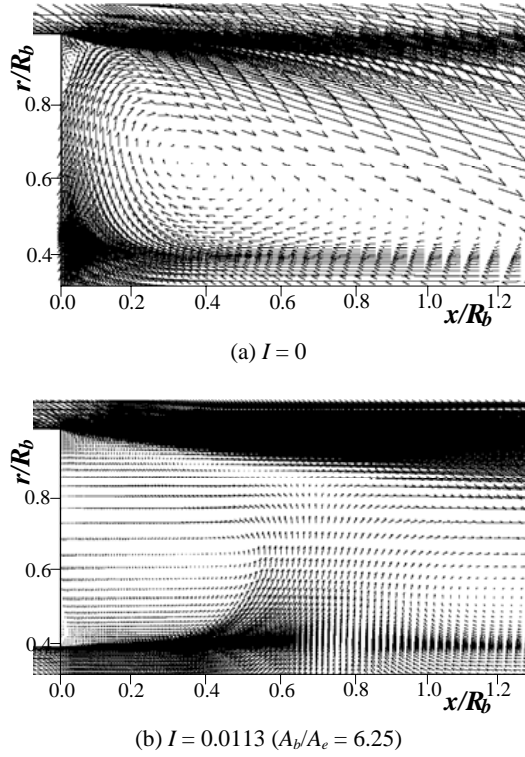


Figure 5. Velocity vectors near the base.

Figure 5 presents mean velocity vectors near the base with and without base bleed. In the figures, axial and normal distances are normalized by  $R_b$ . Without base bleed (The whole base region was treated as a wall.), a large and strong recirculating flow is observed. In general, for aerodynamic bodies, base drag rises due to a decrease in base pressure depending on such separation. As mass is injected into the separated region ( $I = 0.0113$ ), the recirculation near the model base becomes significantly weakened.

Base flows visualized computationally at  $A_b/A_e = 6.25$  are given in Figure 6 to help an understanding of the detailed flow structures. The computed images (upper half) have been developed by density gradients and these are given with corresponding axial velocity contours valued by  $U_x/U_\infty$  (lower half). Inside the separated region, two major recirculation areas are observed near the base and axis. With increased mass bleed, the  $x$ -directional directivity of the bleed jet increases, and then the upper recirculation (near the base) becomes stronger and the lower recirculation (near the axis) becomes weaker. These flow characteristics can be apparently shown though axial velocity contours. The lower recirculation moves downstream as  $I$  increases. At  $I = 0.0226$ , the lower separation is almost negligible. Therefore, it is expected that a further increase in  $I$  completely moves away the separation from the axis.

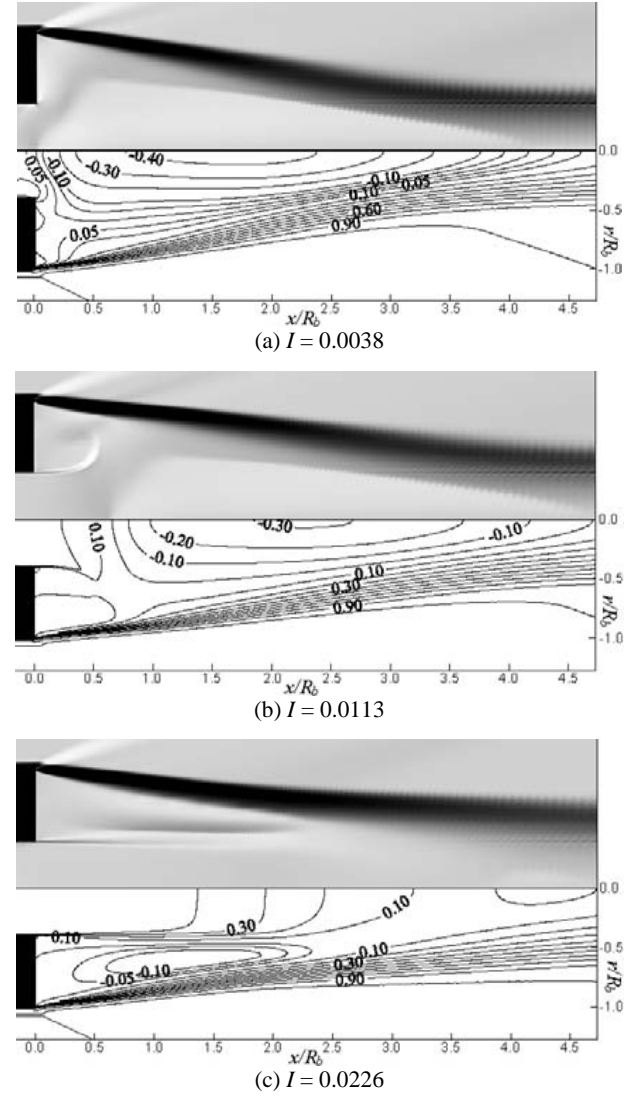


Figure 6. Computed images based on density gradients and  $U_x/U_\infty$  contours ( $A_b/A_e = 6.25$ ).

With a change in the injection parameter  $I$ , Figure 7 shows base pressure distributions for each base configuration tested. The pressure values estimated along the base are non-dimensionalized by the freestream pressure  $p_\infty$ . Without base bleed, in general, a large pressure gradient is existent and a very low-pressure region is formed around  $r/R_b = 0.65$  due to a strong recirculating flow along the base as observed in Figure 5(a). As  $I$  increases, however, such a gradient becomes smaller with an increased pressure level. When  $I$  increases over a certain value, consequently, the base pressure level decreases because the recirculation behind the base becomes strong again as shown in Figure 6(c). With an increased area ratio, this behaviour is found at relatively lower  $I$ . It can be also found that the base pressure level is higher at a smaller area ratio for given  $I$ .

In Figure 8, base pressure obtained through the present CFD method and an experiment [10] are presented with  $I$ . The base pressure values shown in the figure are obtained by the production of the area of the base wall and the pressure force acting on the wall. For all base configurations considered, as  $I$  increases, base pressure increases up to a maximum value and then decreases. The present computations predict the experimental result properly that the maximum base pressure, leading to minimum base drag, is obtained at  $I = 0.0148$  for  $A_b/A_e = 6.25$ . For a larger area ratio, this optimum condition occurs at relatively lower  $I$  and the maximum base pressure which can be achieved by use of mass bleed is lower. From the results discussed in this paper, it is considered that an increase and a

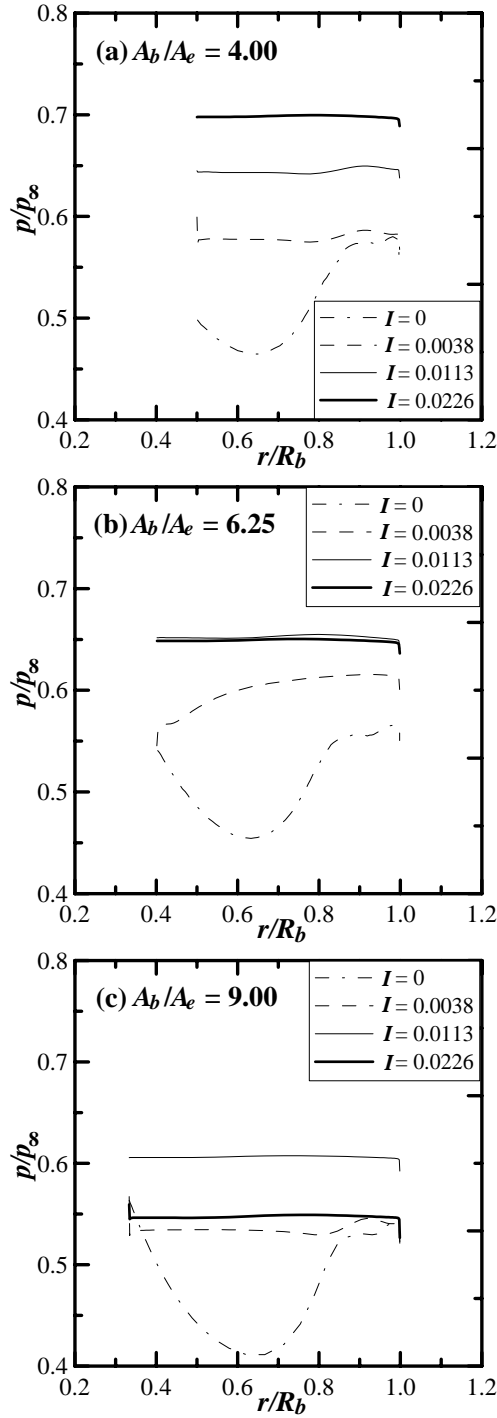


Figure 7. Base pressure distributions with a change in  $I$ .

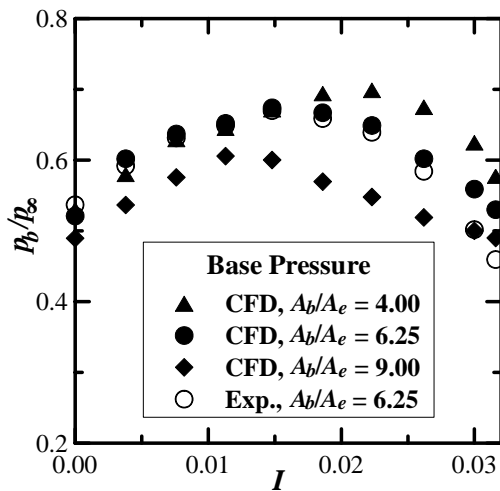


Figure 8. Area-averaged base pressure.

the flow structure characterized by the recirculation regions deformed depending on  $I$ , and the base drag control using mass bleed is more effective for smaller  $A_b/A_e$ .

## Conclusions

For a supersonic freestream of Mach 2.47, the base flow with and without mass bleed generated by an orifice was investigated by CFD as a tool. Axisymmetric, compressible, mass-averaged Navier-Stokes equations were computed using a two-equation turbulence model, standard  $k-\omega$ , a fully implicit finite volume scheme, and a multi-stage Runge-kutta scheme. The injection parameter and the ratio of base and orifice exit areas were changed to provide various characteristics of subsonic bleed jet flows injected into the severely separated region downstream of the afterbody base.

The results obtained through the present study show that the strong recirculating flows formed near the base and model axis were considerably weakened by use of mass bleed. A change in the mass flow rate of bleed jet led to a significant variation of the flow structure in the separation region behind the base. As the injection parameter increases over a certain value, base pressure distributions became almost uniform. For all afterbody configurations tested, during the mass bleed increase, the average base pressure reached a maximum value. This important feature as shown in a past experimental study could be validated successfully with the present numerical analysis. For a smaller base area, the optimum bleed condition, leading to minimum base drag, occurred at relatively larger mass bleed with better drag control performance.

## References

- [1] Sahu, J. & Nietubicz, C.J., Navier-Stokes Computations of Projectile Base Flow with and without Mass Injection, *AIAA Journal*, **23**(9), 1985, 1348-1355.
- [2] Viswanath, P.R. & Patil, S.R., Effectiveness of Passive Devices for Axisymmetric Base Drag Reduction at Mach 2, *Journal of Spacecraft and Rockets*, **27**(3), 1990, 234-237.
- [3] Wood, C.J., Visualisation of an Incompressible Wake with Base Bleed, *Journal of Fluid Mechanics*, **29**(2), 1967, 259-272.
- [4] Murthy, S.N.B. & Osborn, J.R., Base Combustion Effects on Base Pressure, Aerodynamics of Base Combustion, *Progress in Astronautics and Aeronautics*, AIAA, **40**, 1976, 307-338.
- [5] Nash, J.F., Quincey, V.G. & Callinan, J., Experiments on Two-Dimensional Base Flow at Subsonic and Transonic Speeds, *ARC R&M* 3427, 1966.
- [6] Addy, A.L., Thrust-Minus-Drag Optimization by Base Bleed and /or Boattailing, *Journal of Spacecraft and Rockets*, **7**(11), 1360-1362.
- [7] Bowman, J.E. & Clayden, W.A., Cylindrical Afterbodies in Supersonic Flow with Gas Ejection, *AIAA Journal*, **5**(8), 1967, 1524-1525.
- [8] Bourdon, C.J. & Dutton, J.C., Visualization of a Central Bleed Jet in an Axisymmetric, Compressible Base Flow, *Physics of Fluids*, **15**(2), 2003, 499-510.
- [9] Wilcox, D.C., *Turbulence Modeling for CFD*, DCW Industries, Inc., La Canada, California, 1998.
- [10] Mathur, T. & Dutton, J.C., Velocity and Turbulence Measurements in a Supersonic Base Flow with Mass Bleed, *AIAA Journal*, **34**(6), 1996, 1153-1159.
- [11] Jameson, A., Schmidt, W. & Turkel, E., Numerical Solution of the Euler Equations by Finite Volume Methods Using Runge-Kutta Time-Stepping Schemes, *AIAA paper*, AIAA 81-1259, 1981.

decrease in base pressure as changing mass bleed are decided by

## Modelling Chemical Reaction in a Scalar Mixing Layer

B.L. Sawford

Department of Mechanical Engineering  
Monash University, Clayton, VIC, 3800 AUSTRALIA

### Abstract

Statistics of passive and reactive scalar concentration in a scalar mixing layer are modelled using a Lagrangian particle model coupled to a micro-mixing model and using conserved scalar theory for the chemistry. Good agreement is obtained with laboratory experiments for passive scalar statistics. Reasonable agreement is obtained with laboratory data for reactive scalars on the edges of the mixing layer, but both the mean and variance are over-estimated in the middle of the layer. It is suggested that this discrepancy may be due to a flow instability in the experiments.

### Introduction

Modelling chemical reactions in turbulence is well-established in chemical engineering flows such as flames and other combustion devices, but is less advanced in environmental flows. The critical aspect of the problem is that the mean rate of reaction depends on the mean of the product of the instantaneous concentrations of the reactants, not on the product of the mean concentrations. Since both turbulent mixing and chemical reaction can affect this mean product, it is important to include both of these processes, and their interaction, in the model.

When a step change in temperature in a direction transverse to the flow is acted upon by turbulence, the interface between hot and cold fluid, which thickens with distance downstream, is known as a thermal mixing layer. More generally, when the transported scalar quantity is the concentration of some contaminant species, the interface is known as a scalar mixing layer. If the temperature difference is small, or the species dilute, the scalar material has no effect on the flow and the interface is known as a passive scalar mixing layer.

The scalar mixing layer has been studied experimentally in grid turbulence using both temperature [1] (and references therein) and chemical species [2]. Bilger et al. [2] also studied the reaction of two species introduced as separated streams upstream of the grid (see their figure 1 for a schematic of the configuration). Recently de Bruyn Kops et al. [3] studied reacting scalar mixing layers using direct numerical simulation.

The reacting scalar mixing layer is an important prototype for more complex and realistic configurations. On one hand, its simplicity and symmetry make it relatively easy to study. On the other hand it increases in scale with distance from the source, and is similar in this respect to plumes from localised sources which figure so prominently in atmospheric and other environmental applications. In this paper we use a Lagrangian model for the motion of fluid particles coupled to a simple micro-mixing model to represent the turbulent transport and mixing of a passive conserved scalar in a scalar mixing layer. We then use conserved scalar theory [2] in various limits to model the statistics of chemically reactive species.

### Transport and Mixing of a Conserved Scalar

In common with most theoretical approaches, for convenience we represent both the scalar mixing layer and the grid turbulence as non-stationary, spatially homogeneous analogues of the experimental systems which are stationary and inhomogeneous in

the stream-wise direction. This is achieved through the Taylor transformation  $x - x_0 = x' = Ut$  and requires that the stream-wise velocity fluctuations be small compared with the mean velocity  $U$ . For generality we allow the origin of the mixing layer  $x_0 = Ut_0$  to be non-zero. We thus represent the source of the conserved scalar as an instantaneous function of the cross-stream position  $z$

$$S(z, t) = c_0(1 - H(z))\delta(t) \quad (1)$$

where  $H(z)$  is the Heaviside function and we have taken the source concentration in the lower stream to be  $c_0$ . The scalar concentration statistics are thus functions of  $z$ ,  $t$  and the travel time from the grid to the source,  $t_0$ . Note that the time origin is the source release time.

Lagrangian theory relates the 1-point displacement statistics for independent marked fluid particles to the mean concentration of the scalar field [4]. Marked particles conserve the concentration assigned to them at the labeling time, which is usually associated with the source. Much success in modelling the mean concentration under a wide range of turbulence and scalar source conditions has been obtained using stochastic models in which the velocity  $\mathbf{u}$  and position  $\mathbf{x}$  along the trajectory of a marked fluid particle are treated as a joint continuous Markov process. For decaying grid turbulence we have

$$dw = -\frac{C_0 \varepsilon}{2\sigma_w^2} w dt + \frac{w}{2\sigma_w^2} \frac{\partial \sigma_w^2}{\partial t} + \sqrt{C_0 \varepsilon} d\xi \quad (2)$$

$$dz = w dt$$

where the deterministic terms ensure that the probability density function (pdf) for the Eulerian velocity component  $w$  is Gaussian with variance  $\sigma_w^2(t)$ ,  $C_0$  is the Lagrangian velocity structure function inertial sub-range constant [5],  $\varepsilon(t)$  is the rate of dissipation of turbulence kinetic energy and  $\xi$  is the Wiener process [6]. We represent  $\sigma_w^2$  and  $\varepsilon$  as power-law functions of travel time from the grid and take  $C_0 = 3$  [7].

Marked particle statistics generated using Eq. (2) produce concentration fluctuations because particles arriving at the receptor point in different realizations can have different concentrations according to their location with respect to the source at the labeling time. In order to account for the dissipation of scalar variance, we add to (2) an equation describing the evolution of the scalar concentration  $c$  along a trajectory. This is known as a micro-mixing model, and here we use the interaction by exchange with the conditional mean (IECM) model [8] for which

$$dc/dt = -(c - \langle c | w \rangle)/t_m \quad (3)$$

where  $\langle c | w \rangle$  is the conditional mean concentration given the velocity and  $t_m$  is the mixing time scale. This is perhaps the simplest mixing model to satisfy the ideal properties set down by Pope [9]. In particular it ensures that the mean concentration, and other 1-point statistics such as the flux and the conditional mean concentration, are unaffected by mixing and so can be calculated from marked particle statistics. Then, we have [10]

$$\bar{c}(z, t) = \frac{1}{2} c_0 \left[ 1 - \operatorname{erf} \left( z / \sqrt{2} \sigma_z \right) \right] \quad (4)$$

and

$$\langle c | w \rangle = \frac{1}{2} c_0 \left[ 1 - \operatorname{erf} \left( \frac{z - \rho_{wz} w \sigma_z / \sigma_w}{\sqrt{2} \sigma_z (1 - \rho_{wz}^2)^{1/2}} \right) \right] \quad (5)$$

where  $\sigma_z(t)$  is the dispersion of marked particles and the correlation between the velocity and position along a trajectory is  $\rho_{wz} = (\partial \sigma_w^2 / \partial t) / (2 \sigma_w \sigma_z)$ . For decaying grid turbulence Anand and Pope [11] give an analytical result for  $\sigma_z(t)$ . Although we do not show it explicitly, all these quantities also depend on the source time  $t_0$ .

The mixing model (3) implies a closure for the mean scalar dissipation conditional on the scalar concentration [10]

$$\langle \varepsilon_c | c \rangle = \kappa \langle \partial^2 c / \partial x_i^2 | c \rangle = -(c - \tilde{c}) / t_m \quad (6)$$

where  $\tilde{c}(c) = \int \langle c | w \rangle P(w | c) dw$ . Note that for simplicity we use the same notation for the physical variables  $c$  and  $w$  and their corresponding sample space variables.

Various researchers have recently shown that for developing scalar fields such as plumes from small sources, the mixing time scale grows linearly with time [7, 10]. We expect the scalar mixing layer to behave similarly since its thickness grows at the same rate as a line plume. Thus we take  $t_m = bt$  and determine the value of the constant  $b$  by fitting appropriate experimental data. For this purpose we use the most completely documented set of experimental results, those of Ma and Warhaft [1].

Thus we have finally a closed set of equations which can be solved for the velocity, position and concentration along a fluid trajectory. We used  $5 \times 10^5$  trajectories with initial positions (at  $t = 0$ ) distributed uniformly across the domain, initial velocities drawn from a Gaussian distribution with variance  $\sigma_w^2(0)$  and initial concentrations given by the source function (1). The computational domain spanned the region  $|z| \leq 0.2$  m, the width of the wind tunnel of Ma and Warhaft [1], with perfect reflection at the boundaries. Because the integration was stopped well before the width of the mixing layer (i.e.  $\sigma_z$ ) reached the width of the domain, the results are insensitive to the boundary conditions. At specified sampling times, the cross-stream position  $z$ , the concentration  $c$  and the velocity  $w$  were sorted jointly into bins of width  $0.2\sigma_z$ ,  $0.0125c_0$  and  $0.2\sigma_w$  respectively, so that joint statistics of velocity and concentration could readily be calculated as functions of cross-stream location and travel time. The mean wind speed and the turbulence decay power laws were taken from Table I of Ma and Warhaft [1].

Ma and Warhaft [1] introduced the initial step profile into the turbulence at the grid using an upstream “toaster” and at a range of distances down stream from the grid using a “mandoline”. When scaled by the width of the mixing layer all their data for the mean concentration profile collapse onto the error function profile (4). Figure 1 shows that the evolution of the root-mean-square (rms) concentration fluctuations  $\sigma_c$  on the centreline can be represented well if we choose a value  $b = 0.5$  for the constant of proportionality in the mixing time scale. This is lower than the value of 1.2 used by Sawford [7] to fit wind tunnel data for a line plume. The model with  $b = 0.5$  also represents very well profiles for the rms concentration (figure 2) and, although we do not show results here, for the skewness and kurtosis of concentration fluctuations across the mixing layer.

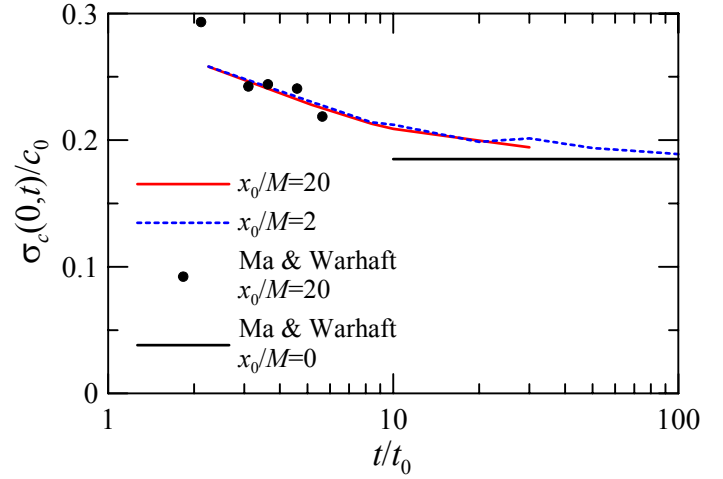


Figure 1. Comparison of model prediction for the centreline standard deviation of concentration fluctuations with the results of Ma and Warhaft [1] using a mixing time scale  $t_m = 0.5t$ .

The model results in figure 1 show that scaling in terms of  $t_0$  collapses results for different source locations, and that for large values of  $t/t_0$  the centreline rms is constant, as is also observed in the data. Thus, although we cannot explicitly model the case where the source is at the grid because the power-law representations of the turbulence diverge at the grid, we can approximate it by choosing  $x_0$  suitably small, so that at the distance of interest  $(x - x_0)/x_0$  is larger than about 50. This limit is of interest for the chemically reacting case, because  $x_0 = 0$  for the experimental results of Bilger et al. [2].

We calculated the pdf for the scalar concentration  $P(c)$  and the conditional scalar dissipation at a range of values of  $t/t_0$ . Details are given in Sawford [10]. For  $t/t_0$  greater than about two the results are well-fitted by the simple forms

$$\langle \varepsilon_c | c \rangle t_m / c_0^2 = A c^2 (1 - c)^2 \quad (7)$$

and

$$P(c) = B(\gamma) c^\gamma (1 - c)^\gamma \quad (8)$$

In the limit  $t/t_0 \rightarrow \infty$ , we found  $A = 0.4$ ,  $\gamma = 2$  and  $B(2) = 30$ . Integrating (7) over the pdf (8), substituting these limiting values and using the fitted time scale constant  $b = 0.5$ , we obtain the unconditional scalar dissipation

$$\langle \varepsilon_c \rangle / c_0^2 = 0.038 t^{-1} \quad (9)$$

The coefficient 0.038 may be compared with the value of 0.06 inferred by Bilger [12] from the data of Ma and Warhaft [1].

### Conserved Scalar Theory for Chemistry

Consider the second-order reaction



Then the chemical source terms for species  $A$ ,  $B$  and  $P$  are

$$w_A = w_B = -w_P = -k c_A c_B \quad (11)$$

where  $k$  is the reaction rate constant. Thus the quantity  $c_A - c_B$  is unaffected by reaction and is known as a conserved scalar, and its statistics are identical with those already discussed. Other conserved scalars can be defined for the system (10), but they are all essentially equivalent.

Now if species  $A$  is introduced in the upper stream (stream 1) with concentration  $c_{A,1}$  and species  $B$  is introduced in the lower stream with concentration  $c_{B,2}$  (as in [2]), then we can define the mixture fraction  $F$  for the conserved scalar by

$$F = (c_A - c_B + c_{B,2}) / (c_{A,1} + c_{B,2}) \quad (12)$$

with the boundary conditions  $F = 0$  in the lower stream and  $F = 1$  in the upper stream. Thus,  $1-F$  is equivalent to the normalised scalar concentration  $c/c_0$  in the Ma and Warhaft experiments [1].

We see from figure 2 that the conserved scalar results for the rms fluctuations are significantly lower than the model predictions and the thermal mixing layer results of Ma and Warhaft [1]. Li et al. [13] noted that this is at least partly due to an instability in the flow and by removing the instability they obtained improved agreement. Nevertheless, the reactive scalar results of Bilger et al. [2] have been affected by what is effectively excess mixing in the middle of the mixing layer.

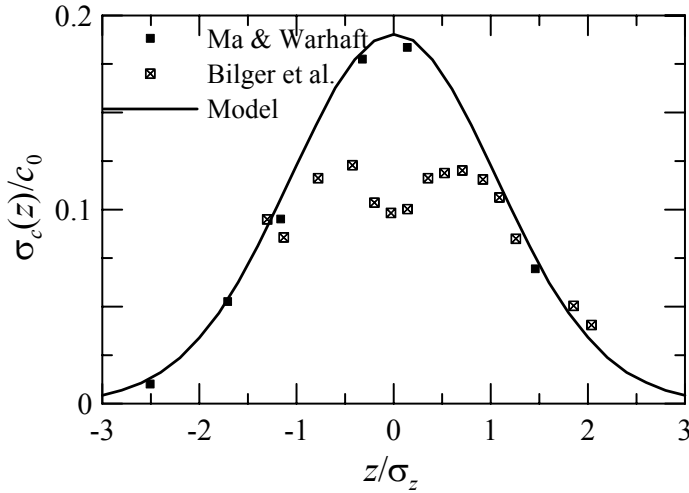


Figure 2. Comparison of model predictions for the cross-wind profile of rms concentration fluctuations with the conserved scalar results of Bilger et al. [2] at  $x'/M = 21$  and the passive scalar results of Ma & Warhaft [1] for  $x_0 = 0$ .

The conserved scalar concept is useful because in various limits and approximations the reactant concentrations  $c_A$  and  $c_B$ , and the product concentration  $c_P$ , can be written as functions of the mixture fraction. Thus in the limit of very slow reactions, the so-called frozen limit, the reactants are unaffected by chemistry, so we have

$$c_A^f = F c_{A,1}; \quad c_B^f = (1-F) c_{B,2}; \quad c_P^f = 0 \quad (13)$$

At the other extreme of very fast chemistry, reaction is so fast that species  $A$  and  $B$  cannot coexist, so from (12)

$$c_A^e = c_{A,1} (F - F_s) H(F - F_s) / (1 - F_s) \\ c_B^e = c_{B,2} (F_s - F) H(F_s - F) / F_s \quad (14)$$

where the stoichiometric mixture fraction  $F_s = c_{B,2} / (c_{A,1} + c_{B,2})$  is obtained by setting  $c_A = c_B$  in (12).

Another useful approximation is the so-called reaction-dominated limit, which assumes instantaneous mixing at the source followed by reaction for the travel time  $t$  from the source [2]. For  $F \neq F_s$

$$\frac{c_A^{rd}}{c_{A,1}} = \frac{F(F_s - F)}{F_s(1-F) \exp\{(F_s - F)N_D x'/M\} - F(1-F_s)} \\ \frac{c_B^{rd}}{c_{B,2}} = \frac{(F_s - F)}{F_s} + \frac{(1-F_s)c_A^{rd}}{F_s c_{A,1}} \quad (15)$$

and for  $F = F_s$

$$\frac{c_A^{rd}}{c_{A,1}} = \frac{F_s}{1 + F_s(1-F_s)N_D x'/M} \\ \frac{c_B^{rd}}{c_{B,2}} = \frac{(1-F_s)}{1 + F_s(1-F_s)N_D x'/M} \quad (16)$$

where the Damkohler number  $N_D = k(c_{A,1} + c_{B,2})M/U$  and  $M$  is the grid mesh length.

Finally, Klimenko [14] and independently Bilger [12] have developed the conditional moment closure (CMC) theory for the mean concentration of the reactive species conditional on the conserved scalar mixture fraction,  $\hat{Q}(F) = \langle c_A | F \rangle$  for example.

Bilger [12] shows that for the reacting mixing layer the CMC equation can be approximated by

$$\frac{\partial Q}{\partial \zeta} = -Q(Q - F + F_s) + \langle \varepsilon_F | F \rangle \frac{\partial^2 Q}{\partial F^2} \quad (17)$$

where  $Q = \hat{Q}/(c_{A,1} + c_{B,2})$  and  $\zeta = N_D x'/M$ . Bilger [12] modelled the conditional dissipation in (17) as  $\langle \varepsilon_F | F \rangle = \langle \varepsilon_F \rangle = 0.03t^{-1}$ , which is close to (9). We solved for  $Q$  as a function of  $\zeta$  and  $F$  using the conditional scalar dissipation (7) and also, for comparison, its unconditional approximation (9). We represented the numerical results for  $Q$  analytically by fitting to them the RDL formulae (16) and (17) with a retarded reaction progress variable  $\zeta(\zeta)$ . For  $\langle \varepsilon_F | F \rangle = 0$ , the CMC approximation reduces to the reaction-dominated limit.

Now using (13) - (17) we are able to calculate the reactant concentrations (or in the case of CMC, the conditional mean concentration) along a trajectory from the conserved scalar concentration, and can then calculate statistics of these reactant concentrations as a function of cross-stream location and travel time simply by averaging over trajectories.

### Results for reactive scalar statistics

In figure 3 we compare model predictions for the mean reactant concentration with the results of Bilger et al. [2] for  $F_s = 0.5$ ,  $N_D = 0.42$  (corrected by a factor of  $\sqrt{2}$  after Li et al. [13]) and  $Ut/M = 21$ . Note that reaction depletes the mean concentration more strongly in the low-concentration side of the mixing layer; i.e. in the lower layer for species  $A$  and the upper layer for  $B$ , so the profiles as a whole are shifted towards the high concentration side. There is also a greater differentiation between the different limits and models on the low-concentration side. As noted by Bilger et al. [2], the mean concentration tends to be closer to the equilibrium limit than the frozen limit. We see that on the edges of the mixing layer the CMC calculation is in excellent agreement with the experimental results, but in the middle of the layer the experimental results lie close to the equilibrium limit.

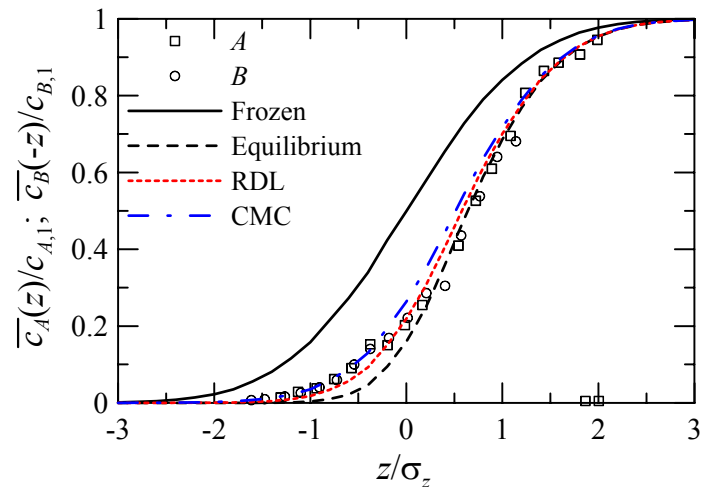


Figure 3. Comparison of model mean reactant concentrations as a function of position across the plume with experimental results [2] for  $F_s = 0.5$ ,  $N_D = 0.42$  and  $Ut/M = 21$ . Note that the plot for species  $B$  has been inverted in space.



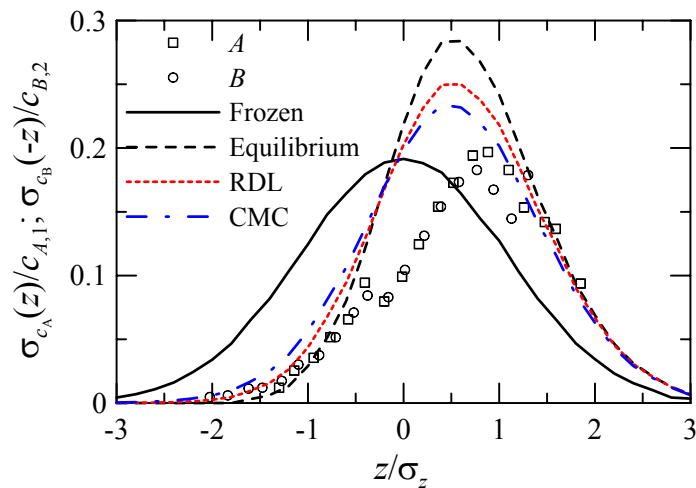


Figure 4. Comparison of model rms reactant concentrations as a function of position across the plume with experimental results [2] for  $F_s = 0.5$ ,  $N_D = 0.42$  and  $Ut/M = 21$ . Note that the plot for species  $B$  has been inverted in space.

The asymmetry about the centreline due to chemical reaction is even more obvious for rms fluctuations in reactant concentration as shown in figure 4, where the peak is clearly shifted towards the high-concentration side. Notice also that reaction reduces the fluctuations on the low-concentration side and increases them on the high-concentration side, as reflected by the trend from the frozen to the equilibrium results. Again the CMC model is in reasonable agreement at the edges of the mixing layer, but the experimental values are clearly lower than any of the theoretical estimates in the middle of the layer.

The discrepancy between the experimental results and the model predictions may be due to the effects of the flow instability reported by Li et al. [13]. The increased mixing due to this instability would tend to reduce the mean reactant concentration because the reactants are brought into closer contact. It would also have a direct effect in reducing fluctuations in the reactant concentrations.

For the case studied here, the CMC results using (7) and (9) are virtually indistinguishable and have not been plotted separately. This is not surprising because the unconditional value is within 30% of the conditional value for  $0.25 < F < 0.75$ , and values of the mixture fraction outside this range are rare, as shown by the pdf (8).

## Conclusions

We have used a Lagrangian stochastic trajectory model coupled with the IECM mixing model to calculate concentration statistics in a scalar mixing layer in decaying grid turbulence. We obtained good agreement with the results of Ma and Warhaft using a

mixing time scale  $t_m = 0.5t$ . We also used conserved scalar theory in various limits and approximations to calculate reactive scalar statistics, and compared our predictions with the results of Bilger et al. [2]. As has been previously documented [13], a flow instability in these experiments caused enhanced mixing in the middle of the mixing layer (compared with the thermal mixing layer). It seems likely that this enhanced mixing causes a significant reduction in both the mean and rms reactant concentrations in the middle of the mixing layer. Under the conditions studied here ( $F_s = 0.5$  and  $N_D = 0.42$ ) the modelling results show that replacing the conditional scalar dissipation by the unconditional dissipation in the CMC theory is an excellent approximation.

## References

- [1] Ma, B-K & Warhaft, Z., Some aspects of the thermal mixing layer in grid turbulence, *Phys. Fluids*, **29**, 1986, 3114-3120.
- [2] Bilger, R.W., Saetran, L.R. & Krishnamoorthy, L.V., Reaction in a scalar mixing layer, *J. Fluid Mech.*, **233**, 1991, 211-242.
- [3] de Bruyn Kops, S., Riley, J.J. & Kosály, G., Direct numerical simulation of reacting scalar mixing layers, *Phys. Fluids*, **13**, 2001, 1450-1465.
- [4] Sawford, B.L., Turbulent relative dispersion, *Annu. Rev. Fluid Mech.*, **33**, 2001, 289-317.
- [5] Monin, A.S. & Yaglom, A.M. *Statistical Fluid Mechanics*, Vol. 2., MIT Press, 1975.
- [6] Gardiner, C.W., *Handbook of Stochastic Methods for Physics Chemistry and the Natural Sciences*, Springer, 1983.
- [7] Sawford, B.L., Micro-mixing models of scalar fluctuations for plumes in homogeneous turbulence, *Flow Turb. Combust.*, **72**, 2004, 133-160.
- [8] Pope, S.B., The vanishing effect of molecular diffusivity on turbulent dispersion: Implications for turbulent mixing and the scalar flux, *J. Fluid Mech.*, **359**, 1998, 299-312.
- [9] Pope, S.B., *Turbulent Flows*, CUP, 2000.
- [10] Sawford, B.L., Conditional scalar mixing statistics in homogeneous isotropic turbulence, *New J. Phys.*, **6**, 2004, 55.
- [11] Anand, M.S. & Pope, S.B., Diffusion behind a line source in grid turbulence, in *Turbulent Shear Flows 4*, editors L.J.S. Bradbury, F. Durst, B.E. Launder, F.W. Schmidt and J.H. Whitelaw, Springer-Verlag, 1985, 46-52.
- [12] Bilger, R.W., Conditional moment closure for turbulent reacting flow, *Phys. Fluids*, **5**, 1993, 436-444.
- [13] Li, J.D., Brown, R.J. & Bilger, R.W., Experimental study of a scalar mixing layer using passive and reactive scalars, *Proc. 11<sup>th</sup> Australasian Fluid Mechanics Conf.*, University of Tasmania, 1992, 159-162.
- [14] Klimenko, A.Y., Multicomponent diffusion of various admixtures in turbulent flow, *Fluid Dyn.*, **25**, 1990, 327-334.

## Velocity Measurement in Turbulent Boundary Layer of Drag-Reducing Surfactant Solution

M. Itoh<sup>1</sup>, S. Tamano<sup>1</sup>, K. Yokota<sup>1</sup> and M. Ninagawa<sup>2</sup>

<sup>1</sup>Graduate School of Engineering, Nagoya Institute of Technology, Gokiso-cho, Showa-ku, Nagoya, 466-8555 JAPAN

<sup>2</sup>TOYOTA Motor Corporation, 1 Toyota-cho, Toyota, Aichi 471-8571 JAPAN

### Abstract

The influence of a drag-reducing surfactant on a zero pressure gradient turbulent boundary layer was investigated using a two-component laser-Doppler velocimetry (LDV) system. It was found that the streamwise turbulence intensity has an additional maximum near the center of the boundary layer, in addition to the near-wall maximum which appears in the canonical wall-bounded turbulent flow. At the location of the additional maximum, the skewness factor of streamwise turbulent fluctuation is zero.

### Introduction

Experimental studies on turbulent channel flow [1, 2, 3] and pipe flow [4, 5, 6] of a drag-reducing surfactant solution have yielded valuable knowledge, such as the stress defect and modification of turbulence structures. On the other hand, there have been no studies on the turbulent boundary layer, which is a typical external flow, of a drag-reducing surfactant solution, while the turbulent boundary layer of a polymer solution was recently investigated [7]. One rheological property of surfactant solutions is that the viscoelastic effect appears only when the shear rate becomes larger than a certain critical value [8]. Therefore, a study of the turbulent boundary layer mixing of the turbulent and potential flows in the surfactant solution will be helpful for understanding the mechanism of drag-reduction, which cannot be obtained by study of the internal flow or the polymer solution.

In the present study, the mean velocity and turbulence statistics were measured using a two-component LDV system in a zero pressure gradient turbulent boundary layer of a drag-reducing surfactant solution. The obtained results were compared with the matching statistics of water.

### Experimental Apparatus and Procedure

The experiments were conducted in a closed-loop water tunnel with a cross section of  $300 \times 300$  mm and a length of 1500 mm in which a test plate of  $20 \times 295 \times 1700$  mm was installed (see figure 1). A 2-mm diameter trip wire was fixed 100 mm downstream from the leading edge. The difference in free-stream velocities between the location of the leading edge of the test plate and the location 1000 mm downstream was less than 1%. We also confirmed that the freestream turbulence intensity was less than 2%.

The surfactant solution ( $C_{16}$ TASal) used here was a mixture of cetyltrimethyl ammonium chloride with sodium salicylate as counterion, which was dissolved in deionized water. The concentration was 75 ppm by weight. The shear viscosity  $\eta$  of the surfactant solution was measured at temperature  $T = 20.0 \pm 0.2^\circ\text{C}$  using a homemade

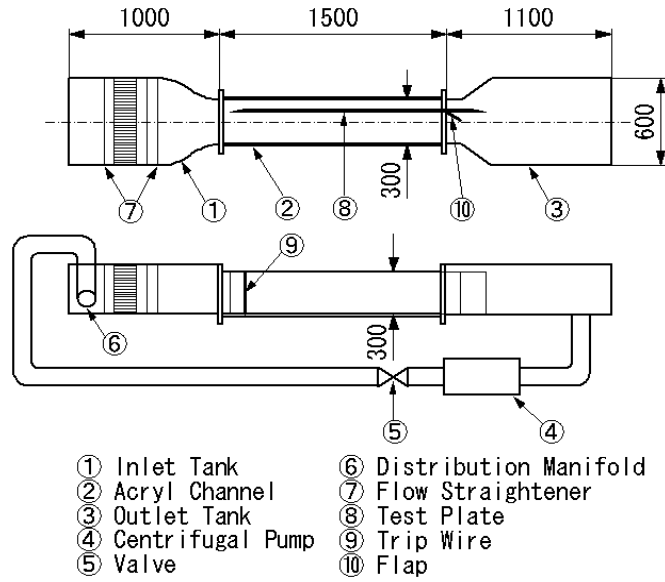


Figure 1: Experimental apparatus

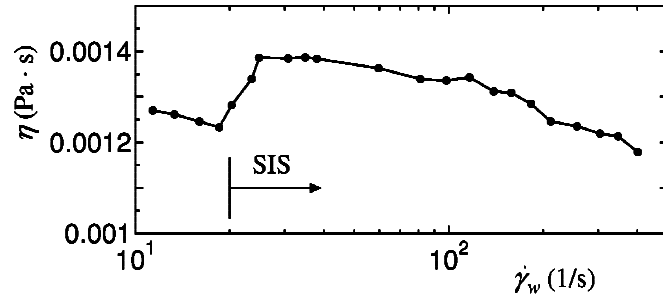


Figure 2: Shear viscosity as a function of the shear rate:  $C_{16}$ TASal, 75 ppm,  $T=20.0^\circ\text{C}$ .

capillary viscometer. Figure 2 shows that the shear viscosity increases suddenly at the shear rate  $\dot{\gamma}_w \simeq 20$  1/s by a factor of about 1.4 compared with that of water, this phenomena is called shear induced state (SIS) [8]. It has been suggested that SIS is strongly related to drag reduction, since in SIS the rod-like micelles form large structures that can directly affect turbulence structures.

The two-component LDV system (300 mW argon-ion laser) was used in back scatter mode. The LDV measurements under the free-stream velocity  $U_e \simeq 300$  mm/s and the fluid temperature  $T = 20.0 \pm 0.1^\circ\text{C}$  were made at the locations downstream from the leading edge  $x = 300, 500, 800$  and  $1000$  mm. The probe was tilted  $5^\circ$  with respect to the test plate surface. The flow was seeded with the nylon powder particles (the mean diameter is  $4.1 \mu\text{m}$  and the specific gravity is 1.02). Typical data rates in the location away from the wall were about 300 Hz, falling off to about 20 Hz very close to the wall. Data samples in the locations away from and near the wall were about 25000 and 5000, respectively.



Table 1: Boundary layer parameters and friction velocity

	C <sub>16</sub> TASal (75 ppm)				Water			
$x$ (mm)	$\delta$ (mm)	$\delta^*$ (mm)	$\theta$ (mm)	$u_\tau$ (mm/s)	$\delta$ (mm)	$\delta^*$ (mm)	$\theta$ (mm)	$u_\tau$ (mm/s)
300	12.7	2.91	1.63	13.2	14.8	3.15	2.14	15.3
500	16.8	3.71	2.04	10.6	22.7	3.94	2.72	15.0
800	20.5	4.50	2.47	9.5	29.1	4.82	3.36	14.3
1000	23.0	4.87	2.65	8.5	33.0	5.38	3.78	13.9

Table 2: Non-dimensional parameters of boundary layer

	C <sub>16</sub> TASal (75 ppm)				Water				
$x$ (mm)	$C_f$	$H$	$Re_\theta$	$Re_x$	$C_f$	$H$	$Re_\theta$	$Re_x$	%DR
300	$4.0 \times 10^{-3}$	1.788	357	$6.58 \times 10^4$	$5.2 \times 10^{-3}$	1.472	641	$8.99 \times 10^4$	25.6
500	$2.5 \times 10^{-3}$	1.817	444	$1.09 \times 10^5$	$5.1 \times 10^{-3}$	1.451	808	$1.49 \times 10^5$	50.1
800	$2.0 \times 10^{-3}$	1.821	535	$1.77 \times 10^5$	$4.6 \times 10^{-3}$	1.438	1002	$2.38 \times 10^5$	55.8
1000	$1.6 \times 10^{-3}$	1.833	601	$2.25 \times 10^5$	$4.3 \times 10^{-3}$	1.425	1136	$3.01 \times 10^5$	62.6

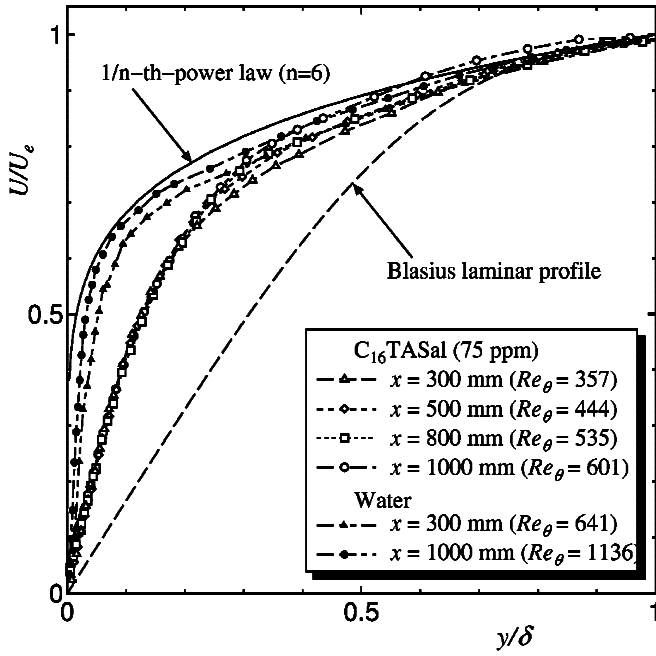


Figure 3: Mean velocity distribution

## Results

### Boundary Layer Parameters

The typical boundary layer parameters such as boundary layer thickness  $\delta$ , displacement thickness  $\delta^*$  and momentum thickness  $\theta$ , and the friction velocity  $u_\tau$  at  $x = 300, 500, 800$  and  $1000$  mm are shown in table 1 for the surfactant solution and water. The friction velocity  $u_\tau$  was obtained by estimating the wall shear stress from the mean velocity gradient at the wall for the surfactant solution and by the Clauser method for the water, respectively.

As the non-dimensional parameters of the boundary layer, the friction coefficient  $C_f = 2(u_\tau/U_e)^2$ , shape factor  $H = \delta^*/\theta$ , momentum-thickness Reynolds number  $Re_\theta = U_e\theta/\nu$ , where  $\nu$  is the kinematic viscosity, surface-length Reynolds number  $Re_x = U_ex/\nu$ , and drag reduction ratio %DR compared with those of water flow at the same positions and free-stream velocity are shown in table 2. It is found that the shape factor  $H$  increases with increasing drag reduction.

### Mean Velocity

The distribution of mean velocity scaled by the free-stream velocity is shown in figure 3. The solid and dashed

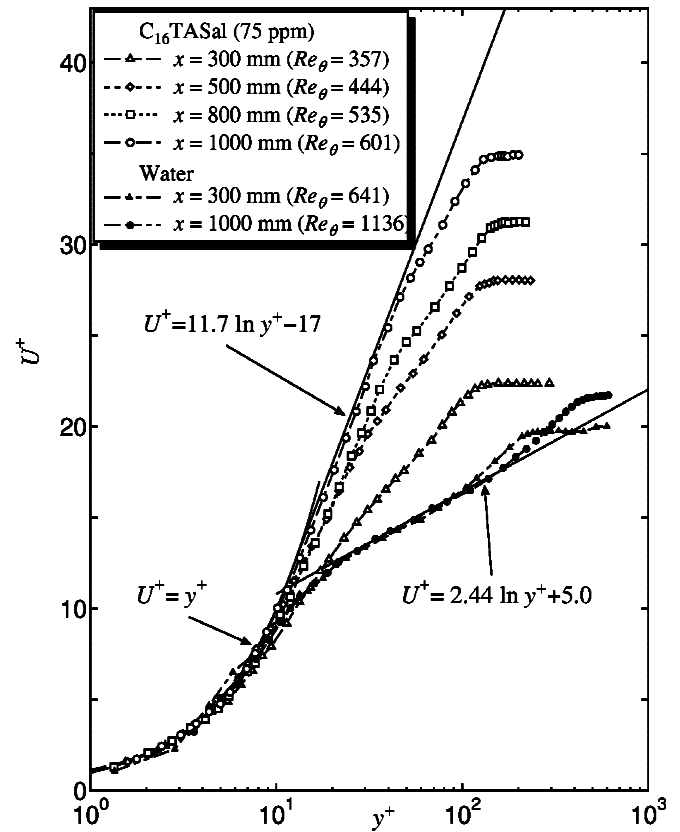


Figure 4: Mean velocity distribution.

lines in the figure represent 1/n-th-power law ( $n=6$ ) and the Blasius laminar profile, respectively. The mean velocities  $U/U_e$  near the wall ( $y/\delta \leq 0.2$ ) for the surfactant solution, whose profiles are collapsed for the different Reynolds numbers  $Re_\theta$ , are in about the middle between the mean velocity profile of the water and the Blasius laminar profile.

Figure 4 shows the profiles of mean velocity  $U^+ = U/u_\tau$  in the wall-coordinate  $y^+ = u_\tau y/\nu$ . We confirmed that the measurements for the water agreed well with the corresponding experimental and numerical data [9, 10]. The values of  $U^+$  for the surfactant solution increase with increasing  $Re_\theta$ , namely increasing the amount of drag reduction. For the surfactant solution at  $Re_\theta = 601$ , the elastic layer in which the velocity agrees with the Virk's ultimate profile ( $U^+ = 11.7 \ln y^+ - 17$ ) [11] exists for  $20 < y^+ < 30$ , in addition to the standard logarithmic region ( $60 < y^+ < 90$ ). The shear rates  $\dot{\gamma}_w$  were about

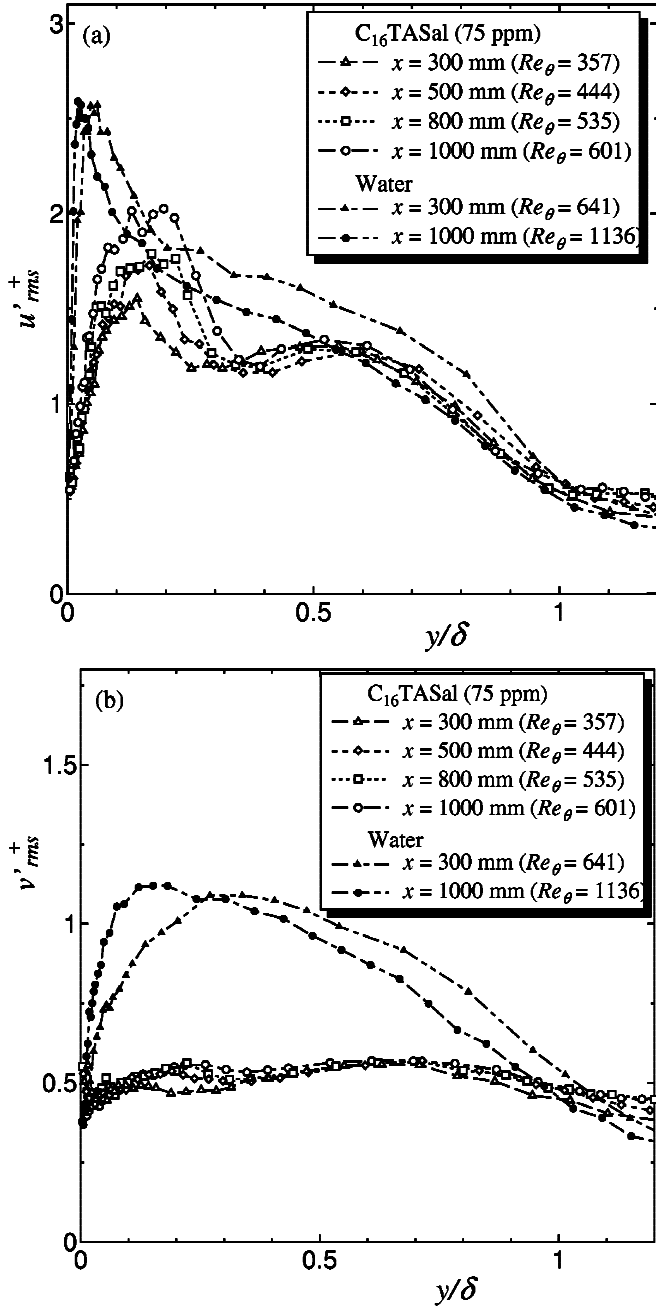


Figure 5: Distribution of turbulence intensity: (a) streamwise, (b) wall-normal

25 and 10 1/s at  $y^+ = 30$  and 60, respectively, indicating that the surfactant solutions were in SIS and not in SIS at  $y^+ < 30$  and  $y^+ > 60$ , respectively (see figure 2).

### Turbulence Statistics

The distributions of the streamwise and wall-normal turbulence intensities scaled by the friction velocity  $u'_{rms}^+$  and  $v'_{rms}^+$  are shown in figures 5(a) and 5(b), respectively. The streamwise turbulence intensity  $u'_{rms}^+$  of C<sub>16</sub>TASal increases downstream and is smaller than that of water because of the low-Reynolds number effect, as was also reported in a study on channel flow [1]. It was found that the streamwise turbulence intensity distribution has an additional maximum near the center of the boundary layer, where the solution is not locally in SIS due to the effect of mixing of the potential and turbulent flows, in addition to the standard maximum near the wall. This additional maximum has not been previously observed in the turbulent channel flow [1]. This may be because the large structures of micelles that form near the wall do not disappear suddenly at the center of the channel even

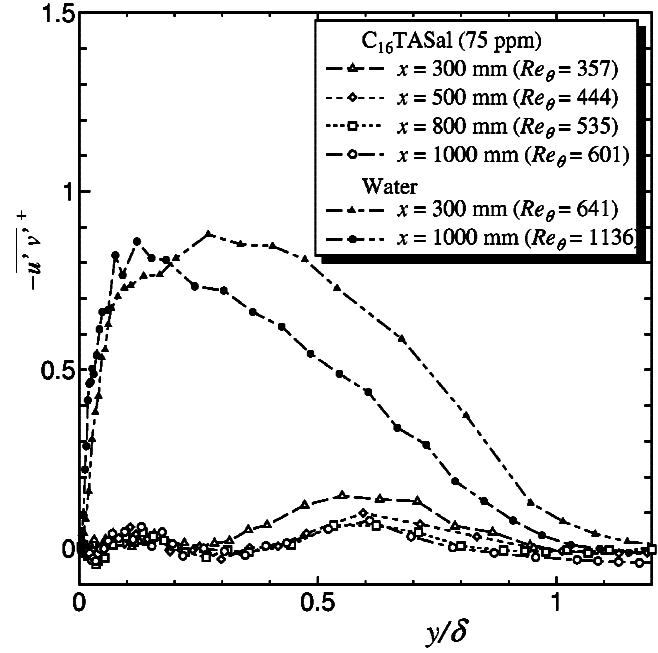


Figure 6: Distribution of Reynolds shear stress

if the shear rate is small there.

The wall-normal turbulence intensity  $v'_{rms}^+$  of the surfactant solution is much smaller than that of water and is almost constant across the boundary layer. In addition, the peak of  $v'_{rms}^+$  seen in the canonical wall turbulence does not appear.

Figure 6 shows the distributions of the Reynolds shear stress scaled by the friction velocity  $-u'v'^+$ . The Reynolds shear stress of C<sub>16</sub>TASal, which is much smaller than that of water, has a slight maximum near the center of the boundary layer.

The skewness factors of the streamwise and wall-normal turbulent fluctuations  $S_{u'}$  and  $S_{v'}$  are shown in figure 7 (a) and figure 7 (b), respectively. The maximum of  $S_{u'}$  appears at  $y/\delta \simeq 0.5$  for the surfactant solution, as not seen for the water. It is also found that the skewness factor  $S_{v'}$  are almost constant ( $S_{v'} \simeq 0$ ) near the outer edge of turbulent boundary layer in the surfactant solution.

Figure 8 shows the distributions of streamwise turbulence intensity  $u'_{rms}^+$ , Reynolds shear stress  $-u'v'^+$ , skewness and flatness factors of streamwise velocity fluctuation  $S_{u'}$  and  $F_{u'}$  for both C<sub>16</sub>TASal ( $Re_\theta = 601$ ) and water ( $Re_\theta = 641$ ), where dashed lines (a) to (d) represent the locations of  $S_{u'} = 0$ . For C<sub>16</sub>TASal,  $u'_{rms}^+$  and  $F_{u'}$  have the maximum and minimum, respectively, at the location of dashed line (b). This relationship for C<sub>16</sub>TASal observed at location (b) is qualitatively equal to that of water at location (a). Here the value of  $y/\delta$  at location (b) is larger than that of location (a), which indicates that the scale of the quasi-streamwise vortex for C<sub>16</sub>TASal is larger than that for water, as seen in the turbulent channel flow [3]. Note that the relationship between  $u'_{rms}^+$  and  $F_{u'}$  for C<sub>16</sub>TASal observed at location (d) is also equal to that of water at location (a).

### Conclusions

The influence of a drag-reducing surfactant on a zero pressure gradient turbulent boundary layer was investigated using a two-component LDV system. LDV measurements were made for four different momentum thick-

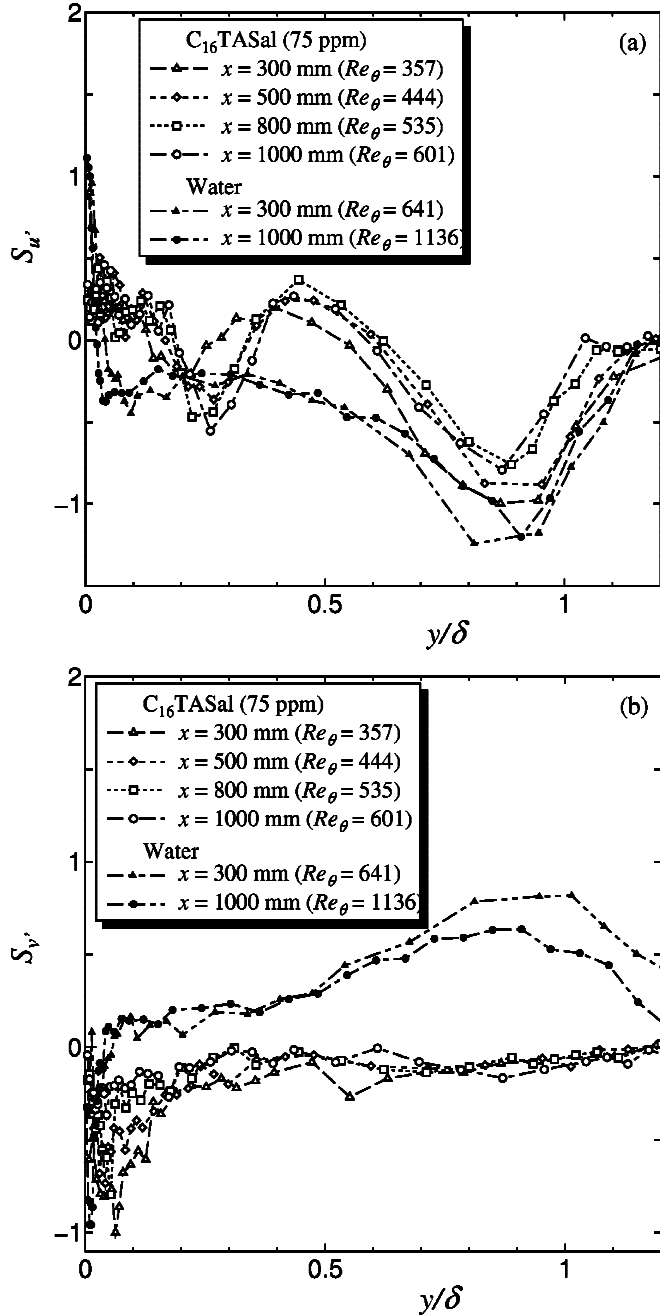


Figure 7: Skewness factor of turbulent fluctuation: (a) streamwise, (b) wall-normal

ness Reynolds numbers,  $Re_\theta = 357, 444, 535$  and  $601$ . The amount of drag reduction is from 25.6 to 62.6% when compared to a water flow at the same position and free-stream velocity. The mean velocity distribution in wall-coordinates indicates the existence of the elastic layer in addition to the standard logarithmic region. It is found that the streamwise turbulence intensity distribution has the additional maximum near the center of the boundary layer, where the solution is not locally in SIS due to the effect of mixing of the potential and turbulent flows. The location of additional maximum of streamwise turbulence intensity is corresponding to the location at which the skewness factor of streamwise turbulent fluctuation is zero.

## References

- [1] Warholic, M.D., Schmidt, G.M. and Hanratty, T.J., The Influence of a Drag-Reducing Surfactant on a Turbulent Velocity Field, *J. Fluid Mech.*, **388**, 1999, 1–20.

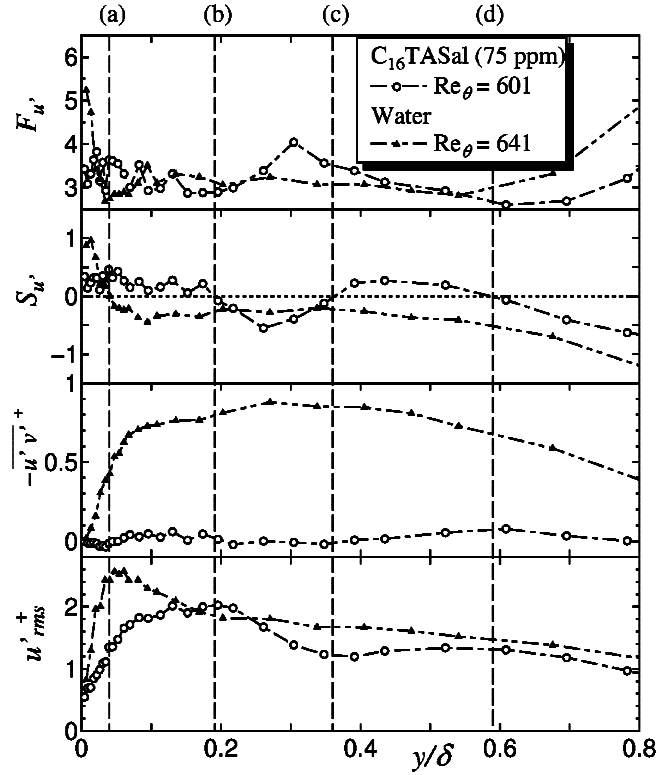


Figure 8: Streamwise turbulence intensity, Reynolds shear stress, skewness and flatness factors of streamwise turbulent fluctuation.

- [2] Kawaguchi, Y., Segawa, T., Feng, Z. and Li, P., Experimental Study on Drag-Reducing Channel Flow with Surfactant Additives-Spatial Structure of Turbulence Investigated by PIV System, *Int. J. Heat Mass Transfer*, **23**, 2002, 700–709.
- [3] Itoh, M. and Kurokawa, Y., Visualization of Turbulent Structure in the Drag-Reducing Flow of Aqueous Surfactant Solution, *Proc. 14<sup>th</sup> Australasian Fluid Mechanics Conference*, 2001, 877–880.
- [4] Chara, Z., Zakin, J.L., Severa, M. and Myska, J., Turbulence Measurements of Drag Reducing Surfactant Systems, *Exp. Fluids*, **16**, 1993, 36–41.
- [5] Hetsroni, G., Zakin, J.L. and Mosyak, A., Low-Speed Streak in Drag-Reduced Turbulent Flow, *Phys. Fluids*, **9** (8), 1997, 2397–2404.
- [6] Nowak, M., Time-Dependent Drag Reduction and Ageing in Aqueous Solutions of a Cationic Surfactant, *Exp. Fluids*, **34**, 2003, 397–402.
- [7] White, C.M., Somandepalli, V.S.R. and Mungal, M.G., The Turbulence Structure of Drag-Reduced Boundary Layer Flow, *Exp. Fluids*, **36**, 2004, 62–69.
- [8] Gyr, A. and Bewersdorff, H.-W., *Drag Reduction of Turbulent Flows by Additives*, Kluwer, 1995.
- [9] Ching, C.Y., Djenidi, L. and Antonia, A., Low-Reynolds-Number Effects in a Turbulent Boundary Layer, *Exp. Fluids*, **19**, 1995, 61–68.
- [10] Spalart, P.R., Direct Simulation of a Turbulent Boundary Layer up to  $Re_\theta = 1410$ , *J. Fluid Mech.*, **187**, 1988, 61–98.
- [11] Virk, P.S., Drag Reduction Fundamentals, *AIChE J.*, **21** (4), 1975, 625–656.

## Numerical Investigation of Unsteady Flow and Heat Transfer in Wavy Channels

Mohammad Zakir Hossain and A.K. M. Sadrul Islam

Department of Mechanical Engineering  
Bangladesh University of Engineering & Technology  
Dhaka 1000, Bangladesh

### Abstract

Two-dimensional Navier-Stokes and energy equations have been solved numerically for unsteady laminar flow in periodic wavy (sinusoidal and triangular) channels. The flow in the channels has been observed to be steady up to a critical Reynolds number. Beyond the critical Reynolds number the flow becomes self-sustained quasiperiodic oscillatory. This transition of flow occurs at lower Reynolds number for triangular channel relative to sinusoidal channel. The frequencies of oscillations, the friction factors and Nusselt numbers are reported.

### Introduction

A simple geometry of the flow passage that is relatively easy to fabricate and may be used to enhance the heat transfer rate is wavy, periodic channel. Wavy channel can provide significant heat transfer augmentation if operated in an appropriate (transitional) Reynolds number (Re) range. Therefore, wavy passages have been considered in several earlier studies as a means to enhance heat / mass transfer in compact exchange devices. Both corrugated and converging-diverging cross sections have been studied experimentally and numerically. An important observation made is that wavy passages do not provide any significant heat transfer enhancement when the flow is steady. However, if the flow is made unsteady (either through external forcing or through natural transitioning to an unsteady state) significant increases in heat exchange are observed. This is a result of complex interactions between the core fluid and boundary layer fluid through shear layer destabilization and self-sustained oscillations. It is in this regime that such passages can be very effective and our objective, therefore, has been to quantify such gains as well as penalties (increased pressure drop) through accurate and well resolved numerical computations of the unsteady flow and heat exchange processes.

Several literatures are available on steady state solutions of wavy channels [8,11,7,9,5,6]. Saidi et al. [8] studied laminar flow past a sinusoidal cavity. They presented how increase of flow velocity gave birth vortex inside a cavity and affected the hydrodynamic and the thermal performance. Wang and Vanka [11] reported higher values of friction factor for wavy channel compared to the parallel plate channel of same inter-wall spacing. Nishimura et al. [7] investigated flow characteristics such as flow pattern, pressure drop and wall shear stress in a channel with symmetric sinusoidal wavy wall. This study reported that at Reynolds number greater than 700, turbulent flow occurred owing to the onset of unsteady vortex motion. Sparrow et al. [9] presented the effect of inlet condition, inter wall spacing and protruding edge on fluid flow and heat transfer.

Studies on fully developed flow in periodic converging-diverging passages with uniform in-flow report a Hopf bifurcation at Re=130, followed by a series of bifurcations leading to chaos [2].

The flow was observed to be quasi-periodic with up to three fundamental frequencies and multiple sub- and super-harmonics in the Reynolds number range of 130-800. At 850, the flow became aperiodic with broad band frequency spectra of the velocity signals. Stone and Vanka [10] have presented numerical results on developing flow and heat transfer characteristics in a furrowed wavy channel. They found that at low Reynolds numbers, the flow in the wavy passage is steady, characterized by steady separation bubbles in the troughs of the waves. However, as the Reynolds number is increased beyond a modest value, the flow becomes unsteady, with the rolling up of the shear layers on the channel walls. When the flow becomes unsteady, there is increased mixing between the core and near-wall fluids, resulting in enhanced heat transfer rates and pressure drops.

The present paper deals with the flow structure and heat transfer of wavy channels at unsteady state with periodic boundary conditions. Two different types of surface waviness one sinusoidal channel and another triangular channel have been considered for the present investigation. For both of the geometry, individual minimum height has been varied to understand the flow and heat transfer behavior properly.

### Conservation Equations

In the present study, the flow is considered to be two-dimensional with no variation in the span wise direction. The governing equations for flow and energy transport can be written as:

$$\nabla \cdot \mathbf{u} = 0 \quad (1)$$

$$\frac{\partial \mathbf{u}}{\partial t} + \nabla \cdot (\mathbf{u}\mathbf{u}) = -\frac{1}{\rho} \nabla p + \nu \nabla^2 \mathbf{u} \quad (2)$$

$$\frac{\partial \mathbf{q}}{\partial t} + \nabla \cdot (\mathbf{u}\mathbf{q}) = \frac{1}{a} \nabla^2 \mathbf{q} \quad (3)$$

where  $\mathbf{u}$  is the velocity vector,  $\theta = (T - T_w)/(T_{b,in} - T_w)$ , and  $T_{b,in}$  is the bulk mean temperature of the flowing fluid at inlet,  $\nu$  and  $\alpha$  are kinematic viscosity and thermal diffusivity respectively.

### Computational Details

The base geometry (minimum height,  $H_{min} = 6\text{mm}$ , maximum height,  $H_{max} = 20\text{mm}$ , amplitude,  $a = 3.5\text{mm}$ , and wavelength,  $\lambda = 28\text{mm}$ ) considered in the present investigation are shown in figure 1. These geometrical configurations conform to the channel studied experimentally by Nishimura et al. [7] and numerically by Wang and Vanka [11]. Here minimum heights are varied keeping the others constant. As boundary conditions, no-slip conditions with a constant wall temperature are prescribed along the wall. Thus

$$u_w = 0, v_w = 0, \text{ and } \theta_w = 1.$$

A uniform velocity is prescribed at the inlet. At the stream wise direction, the following periodic boundary conditions (equation 4) are used to attain fully-developed flow.

$$u(0,y)=u(\lambda,y), v(0,y)=v(\lambda,y), \theta(0,y) = \theta(\lambda,y) \quad (4)$$

In this study, the integral forms of governing equations are discretized using control volume based Finite Volume method with collocated arrangement. The final discretized form of governing equations are solved iteratively using TDMA solver. Time integration is done using three time level method [1]. All the calculations are performed using  $64 \times 64$  grid size with a time step of 0.001sec. A systematic grid refinement test has been done using  $32 \times 32$ ,  $48 \times 48$  and  $64 \times 64$  grid sizes [3].

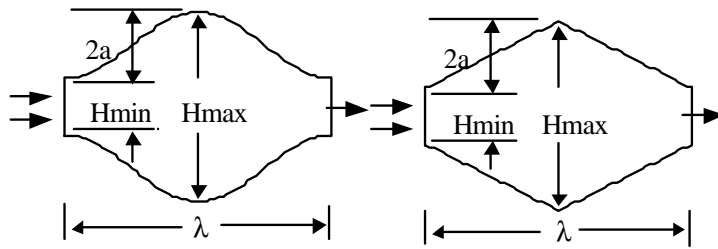


Figure 1. Detail geometry configurations of sinusoidal (left) and triangular (right) channels.

## Results and Discussion

Calculations were performed for several Reynolds numbers ( $Re = u_{avg,in} H_{min}/\nu$ ) from a low value to 500. It has been observed that at low Reynolds numbers, the flow in the wavy passages (both sinusoidal and triangular) is steady, characterized by steady separation bubbles in the troughs of the waves. With the increase of Reynolds number beyond a certain critical value the flow becomes unstable and bifurcates, with the rolling up of shear layers on the channel walls. The critical Reynolds numbers for both geometry are reported in table 1. It has been observed that the value of critical Reynolds number increased with the increase of  $H_{min}$  for sinusoidal channel, but it decreased in case of triangular channel. The transition to unsteady flow for triangular channel occurs at a lower Reynolds number than for the sinusoidal channel. This is the consequences of the fact that the edges of the triangular channel are relatively sharper than the edges of the sinusoidal channel, and thus contribute to the formation, at lower Reynolds number, of an unstable jet-pattern, which easily becomes unsteady.

$H_{min}$ (mm)	Critical Reynolds Numbers		Frequency (Hz)	
	Sinusoidal channel	Triangular channel	Sinusoidal channel	Triangular channel
	Stone & Vanka [10]	Present Prediction		
3	130	150	31	25
6	190	205	20	60
9	240	240	27	27

Table 1. Critical Reynolds number and Frequency of oscillation

Instantaneous streamline plot at  $Re = 300$  for both the channels are shown in figure 2. It has been shown [4] that steady flow yields recirculating vortices in each of the cavities, accompanied by straight cross flow. A single trapped vortex fills each of the cavities. But here at unsteady state separation vortices are formed in the wavy cavity at an earlier instant that is slowly engulf by the

shear layer. This interaction of the core fluid with the fluid in the cavities replenishes the thermal boundary layer and results in enhanced heat transfer. Corresponding temperature field at this Reynolds number is shown in figure 3.

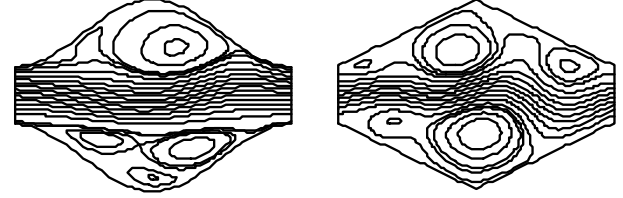


Figure 2. Instantaneous streamline plot for sinusoidal (left) and triangular (right) channel at  $Re = 300$ .

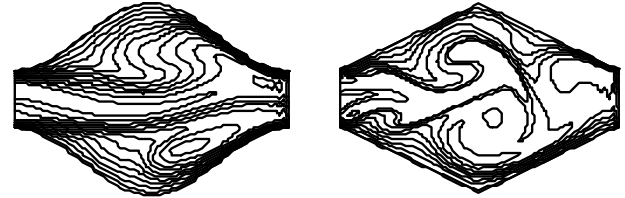


Figure 3. Temperature field for sinusoidal (left) and triangular (right) channel at  $Re = 300$ .

A velocity probe was arbitrarily placed at height of  $0.75H_{max}$  in the tallest part of the each of the channel. The time signal of the u-velocity at Reynolds number 300 at the probe height for sinusoidal and triangular channels and the corresponding FFT analyses are shown in figure 4 and 5 respectively. At this Reynolds number, self-sustained quasiperiodic oscillatory flow was observed. For sinusoidal channel the fundamental frequency was 20 with some of its harmonics as it is shown by the FFT analysis of the u-velocity. In the case of triangular channel, the fundamental frequency of oscillation was 60 and the FFT analysis is chaotic and shows multiple secondary harmonics. To find out cause for the higher value of the frequency of oscillation, the frequencies for the  $H_{min}$  of the closer values have been

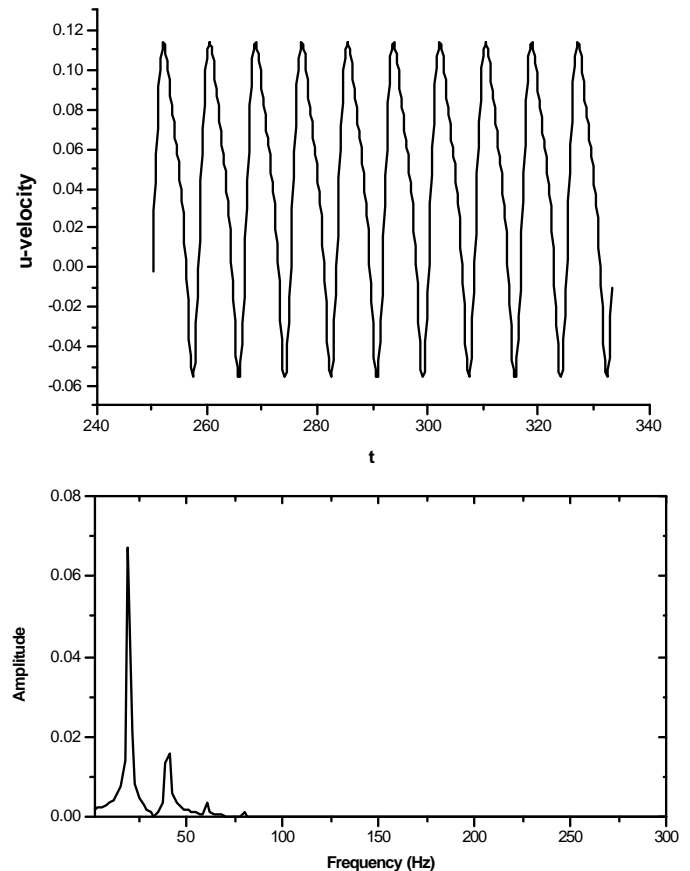


Figure 4. Time signal of u-velocity at  $Re = 300$  for sinusoidal wavy channel (top) and corresponding FFT (bottom) :  $H_{min} = 6mm$ .

obtained and frequencies for  $H_{\min}=4, 5, 7$  and  $8\text{mm}$  are found to be 40, 45, 24 and 26 respectively. Here, we got the frequencies of the flow disturbances are to be independent of  $Re$ , but function of the geometry, which is shown in table 1.

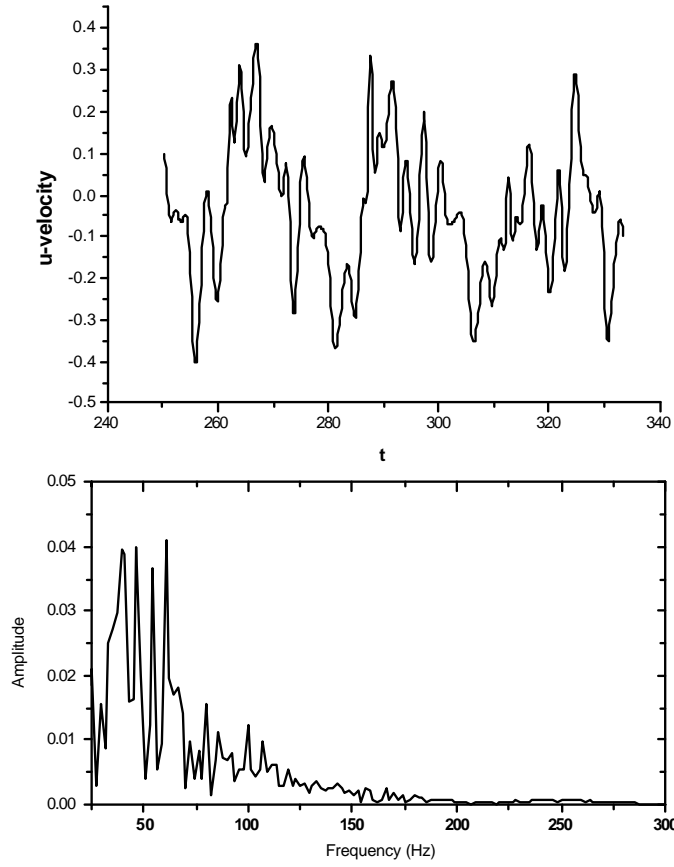


Figure 5. Time signal of u-velocity at  $Re = 300$  for triangular wavy channel (top) and corresponding FFT (bottom) :  $H_{\min} = 6\text{mm}$ .

A comparison of the time mean friction factor averaged over the wave length is shown in figure 6 for sinusoidal wavy channel of  $H_{\min} = 6\text{ mm}$ . The present prediction slightly under predicts the experimental data of Nishimura et al.[7] but shows a good agreement with the predicted values of Wang & Vanka [11]. In the steady regime the friction factor is approximately twice that of the planer channel. In the unsteady regime the friction factor is even more.

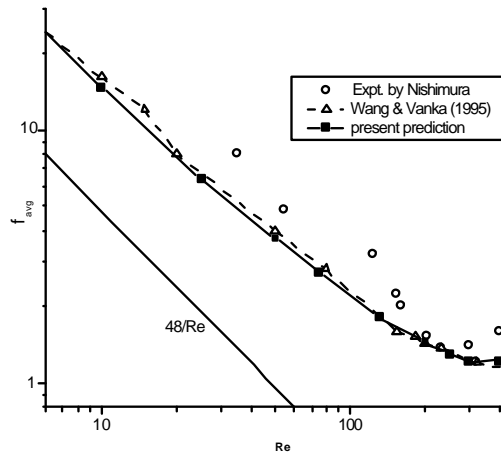


Figure 6. Comparison of present predicted average friction factor with Nishimura et. al. [7] and Wang & Vanka[11] for  $H_{\min} = 6\text{ mm}$  of sinusoidal wavy channel.

The effect of the aspect ratio (by changing the minimum height) on average friction factor(  $f_{avg} = 2\Delta p.D_h/\rho\lambda u_{avg,in}^2$  ) is shown in figure 7 for both the channels. Friction factor is higher in all

cases than the straight channel ( $48/Re$ ) for all Reynolds number, and with the decrease of  $H_{\min}$  friction factor increases. For the same  $H_{\min}$ , friction factor of triangular channel is lower than the sine-shaped (wavy) channel, this is because of less effective area of the triangular channel.

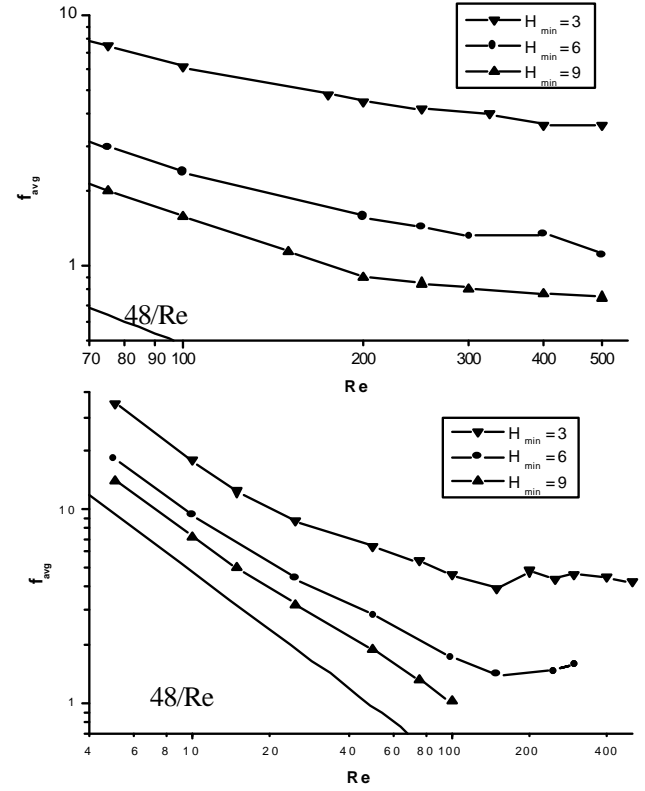


Figure 7. Effect of the minimum height on time averaged friction factor for sinusoidal channel (top) and triangular channel (bottom).

Figure 8 shows the time averaged friction factor and Nusselt number ( $Nu = hD_h/k$ ,  $D_h = H_{\min} + H_{\max}$ ) at various  $Re$  for both steady and unsteady flow in the sinusoidal channel. After slight increase in friction factor when the flow first becomes unsteady,

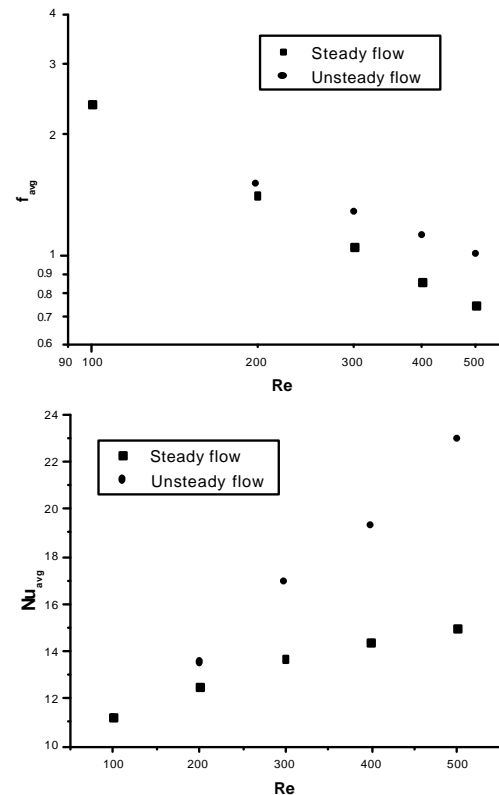


Figure 8. Time averaged friction factor (top) and Nusselt number (bottom) for the sinusoidal channel (base case).

time averaged friction factor continues to decrease with  $Re$ . However, the rate of this decrease slows down as  $Re$  is increased. On the other hand, Nusselt number increases with increase in  $Re$ . Steady flow gives modest increase in Nusselt number but unsteady flow gives rapid increase due to better mixing of core and near wall fluids, but this rate of increase again slows down as  $Re$  is increased more. Hence, there comes a point where the increasing  $Re$  renders diminishing benefits in heat transfer performance. The optimal value of  $Re$  depends on the specific criteria for evaluating performance, and on the dimensions of the passage. But it is known that wavy passages generally offer the best enhancement in the transitional regime.

Time mean Nusselt number averaged over the wave length for the sinusoidal and triangular channels of  $H_{min} = 6\text{mm}$  are shown in figure 9. The Nusselt number for both the cases is higher than that for a straight channel and increases with Reynolds number. The rate of increase of Nusselt number for triangular channel is higher than that of sinusoidal channel. At low Reynolds number (less than  $Re=275$ ) sinusoidal channel has higher heat transfer capability than a triangular channel but above  $Re=275$  the triangular channel gives more heat transfer.

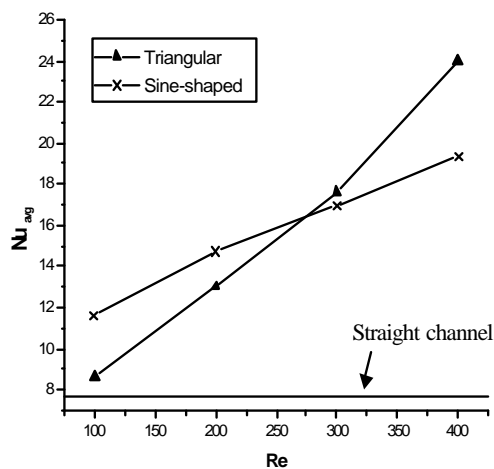


Figure 9. Average Nusselt number at different Reynolds number for  $H_{min} = 6\text{mm}$ .

## Conclusion

Fluid flow and heat transfer in periodic, corrugated channels have been numerically investigated at unsteady flow conditions using finite volume method for a fluid with Prandtl number 0.7, representative value for air. Periodic boundary conditions are used to attain the fully developed flow condition. Two different types of wavy geometry, sinusoidal and triangular, are considered. Effect of aspect ratio has been studied by changing

the  $H_{min}$  only. It has been observed that the flow becomes unstable with a self-sustained oscillation beyond a certain critical Reynolds number and thereby increase heat transfer rate. For sinusoidal channel the critical Reynolds number increases with the increase of  $H_{min}$ , but decreases in case of triangular channel. FFT analysis of the u-velocities shows that one fundamental frequency of oscillation prevails at all the Reynolds number for a particular geometry. The transition of flow occurs earlier, at lower Reynolds number, for triangular channel relative to sinusoidal channel.

## References

- [1] Ferziger, J and Peric, M: *Computational Methods for Fluid Dynamics*. Springer Verlag, Berlin Hedelberg, 1996.
- [2] Guzman, AM and Amon, CH: Transition to Chaos in Converging-Diverging Channel Flows: Ruelle-Takens-Newhouse Scenario, *Phys. Fluid*, **6**(6), 1994, 1994-2002.
- [3] Hossain, M Zakir: Numerical Investigation of Unsteady Flow and Heat Transfer in Wavy Channels. M.Sc. Engg. thesis, Dept. of Mech. Engg., Bangladesh University of Engineering and Technology (BUET), Dhaka, 2003.
- [4] Hossain, M. Z. and Islam, A.K.M.S., Fully Developed Flow Structures and Heat Transfer in Sine-Shaped Wavy Channels, *Int. Com. Heat Mass Transfer*, **31**(6), 2004, 887-896.
- [5] Mahmud, S; Islam, AKM Sadrul and Mamun, MAH: Separation Characteristics of Fluid Flow Inside Two Parallel Plates with Wavy Surface, *Int. J. Engng Sci.*, **40**, 2002, 1495-1509.
- [6] Mahmud, Shohel: *Numerical Investigation of Fluid Flow and Heat Transfer in Corrugated Channels*. M.Sc. Engg. thesis, Dept. of Mech. Engg., Bangladesh University of Engineering and Technology (BUET), Dhaka, 1999.
- [7] Nishimura, T, Ohori, Y and Kawamura, Y: Flow Characteristics In A Channel With Symmetric Wavy Wall For Steady Flow, *J. Chem. Engng Jap.*, **17**, 2002, 466-471.
- [8] Saidi, C, Legay, F and Fotch, BP: Laminar Flow Past a Sinusoidal Cavity, *Int. J. Heat Mass Transfer*, **30**(4), 1987, 649-660.
- [9] Sparrow, EM and Hossfeld, LM: Effect of Protruding Edges on Heat Transfer and Pressure Drop in Duct, *Int. J. Heat Mass Transfer*, **27**(10), 1987, 1715-1722.
- [10] Stone, K and Vanka, SP: Numerical Study of Developing Flow and Heat Transfer in a Wavy Passage, *ASME J. Fluid Engng.*, **121**, 1999, 713-719.
- [11] Wang, G and Vanka, SP: Convective Heat Transfer in Periodic Wavy Passages", *Int. J. Heat Mass Transfer*. **38**(17), 1995, 3219-3230.



## Surface-Flow Patterns in Oscillating-Triangular-Jet Nozzles

S. K. Lee, P. V. Lanspeary, G. J. Nathan and R. M. Kelso

School of Mechanical Engineering  
The University of Adelaide, Adelaide, South Australia, 5005 AUSTRALIA

### Abstract

A triangular-jet nozzle which usually produces an oscillating-jet flow can, for a narrow range of geometric parameters, produce a stationary deflected jet which reattaches to the internal surface of the nozzle. Surface-flow-visualisation images and surface-pressure maps from the stationary deflected jet contain a wealth of detail not available from similar experiments with the oscillating-jet flow. In the topological model constructed from this data, the most significant feature is a strong sink focus. The model suggests that most of the reverse flow through exit plane of the nozzle is attracted towards this sink focus before it is entrained by the jet flow and ejected from the nozzle.

### Introduction

Nathan et al. [5] have shown that a nozzle consisting of a circular inlet orifice and a chamber with an exit lip can produce a naturally oscillating jet flow. This device is known as the “fluidic-precessing-jet” (FPJ) nozzle because flow from the inlet orifice reattaches asymmetrically to the wall of the chamber. In the absence of a preferred azimuthal orientation, the reattaching flow “precesses” around the wall (Figure 1).

At an early stage, the FPJ nozzle was developed as an industrial natural-gas burner because the flame is shorter, more luminous and more resistant to “blow-off” than equivalent simple-turbulent-jet or “axial-jet” nozzles [6]. The higher luminosity can lead to a decrease of up to about 40% in nitrogen-oxide ( $\text{NO}_x$ ) emissions [7].

Nathan et al. [5] have also shown that, for reliable oscillation of the jet flow, the expansion ratio of the inlet-orifice diameter ( $D/d_1$ ) must be larger than 5.0, and length-to-diameter ratio of the chamber ( $L/D$ ) must be in the range  $2.60 < L/D < 2.80$ . Of these geometric criteria, the requirement for a small inlet orifice ( $D/d_1 \geq 5.0$ ) makes the fuel supply pressure much higher than for an axial-jet burner of the same outer diameter and (heat) capacity. This can be a costly problem if the supply pressure is inadequate; either the pressure must be increased or the burner must be larger.

Mi et al. [4] found that, if the inlet-orifice shape is changed from circular to triangular, jet oscillation occurs at orifice area expansion ratios as low as 4.0. For a fixed burner capacity, this allows

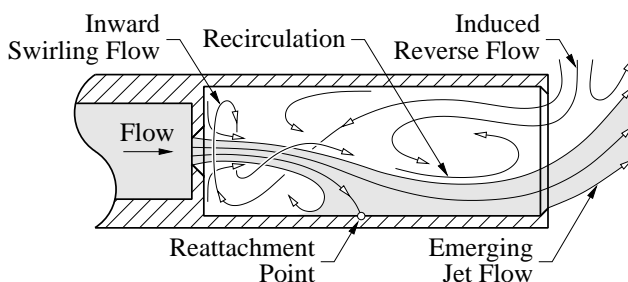


Figure 1: Schematic flow-field pattern for the “fluidic-precessing-jet” (FPJ) nozzle inferred from visualisation [5].

either a reduction in supply pressure by an order of magnitude or a reduction of the nozzle diameter by a factor of about two.

Lee et al. [3] have performed a parametric study of the “oscillating-triangular-jet” (OTJ) nozzle. Their results verify that oscillations occur at much smaller expansion ratios than in the FPJ and that, unlike an FPJ, oscillation is continuous rather than intermittent. In comparison with the FPJ, the jet spreading angle is smaller and varies more gradually over a wide range of  $L/D$  ratios and inlet-expansion ratios. This provides a capacity, by selecting appropriate  $L/D$  and inlet-expansion ratio, to design a nozzle with not only a much lower supply pressure than the FPJ nozzle, but also with a selectable jet spreading angle.

This paper reports the results of surface-flow-visualisation experiments. These are the first investigations of large-scale flow structure inside the OTJ nozzles.

### Experimental Technique

Figure 2 shows the oscillating-jet nozzle used for this investigation. Flow enters the nozzle chamber, which has an internal diameter  $D$ , through an equilateral triangular inlet-orifice plate and it leaves the chamber through an exit lip of diameter  $d_2 = 0.9D$ . There are four available inlet orifices with area expansion ratios of  $(D/d_{e1})^2 = 2.1^2, 2.5^2, 3.0^2$  and  $3.5^2$ , where  $d_{e1}$  is the “equivalent diameter” of the triangular orifice. The length of the chamber can be adjusted to any value within the range  $0.00 \leq L/D \leq 3.00$ . To permit visualisation of the internal flow, the chamber is made of Perspex tube.

The nozzle is connected to a compressed-air supply through a straight tube of diameter  $D_0 = 0.763D$  and length  $50D_0$ . At the upstream end of the tube is a flow conditioner consisting of a

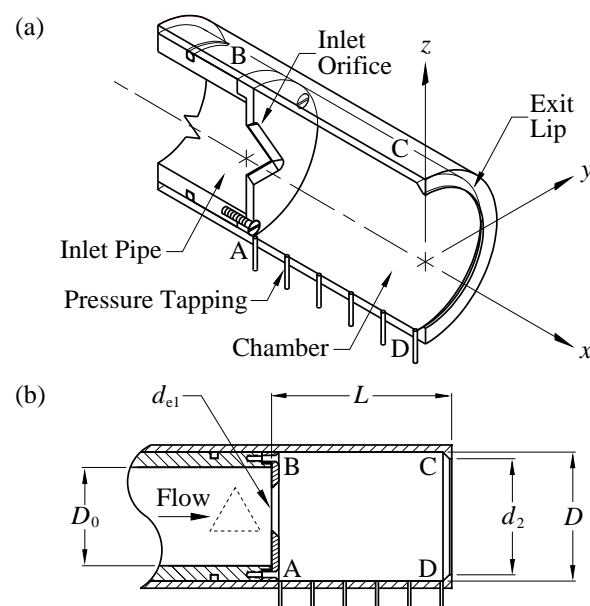


Figure 2: The “oscillating-triangular-jet” (OTJ) nozzle (a) components and (b) geometric parameters.

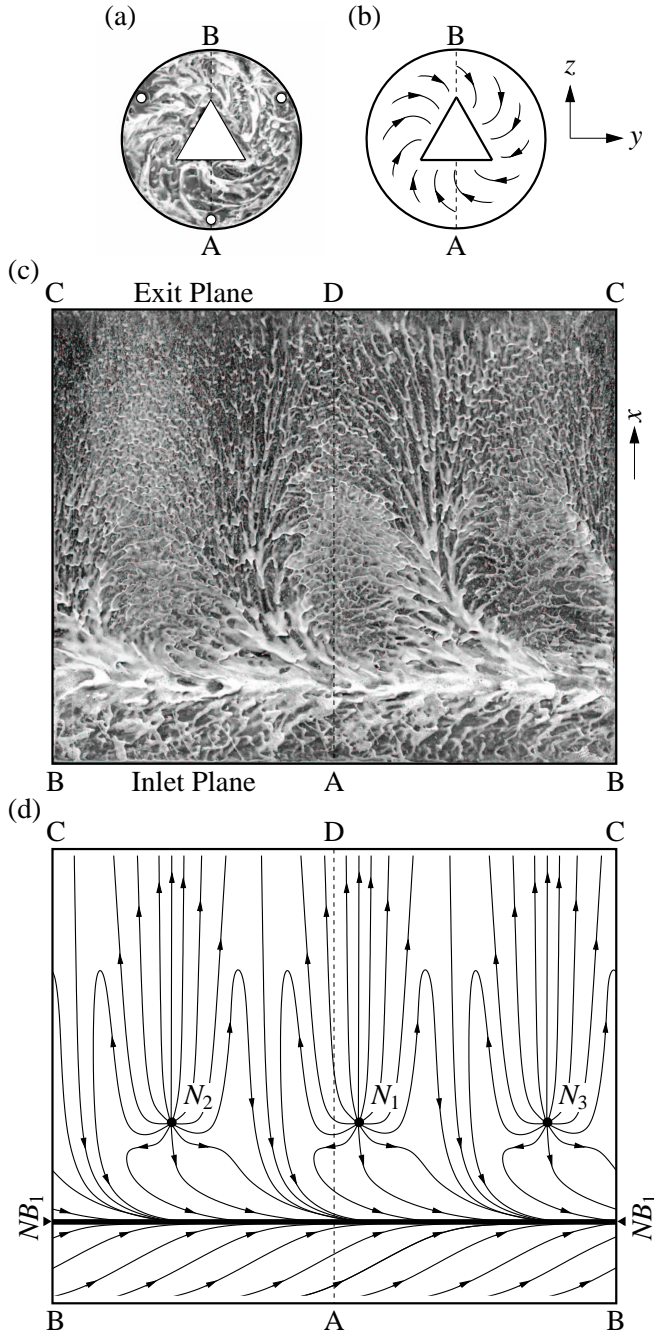


Figure 3: Oscillating triangular jet surface-flow visualisation pattern and streakline interpretation; (a, b) inlet plane, (c, d) cylindrical surface.  $D/d_{e1} = 3.5$  and  $L/D = 2.50$  at  $Re_1 = 70,000$ .

“honeycomb” (of plastic drinking straws) followed by a wire-mesh screen. Further details of the flow conditioning and of the ancillary equipment are provided by Lee et al. [3].

The method of flow visualisation is similar to the “china-clay” technique described by Bradshaw [1] and adopted by Nathan et al. [5] for investigating the surface-flow patterns in the FPJ nozzle. A transparent A4-size plastic sheet, 0.1 mm thick, is cut to the internal length and circumference of the nozzle chamber, and is then inserted so that it forms a new inner surface of the chamber. A viscous mixture of white toothpaste, corn-flour and water is painted uniformly onto the plastic sheet and is immediately exposed to the flow until the water evaporates (which takes about 12 minutes). To record the “streakline” pattern produced by the flow, the plastic sheet is removed from the nozzle and unrolled. Four “streakline” images were obtained for each flow condition. While the flow is producing a pattern on the plastic sheet, it also spreads paste over the back face of

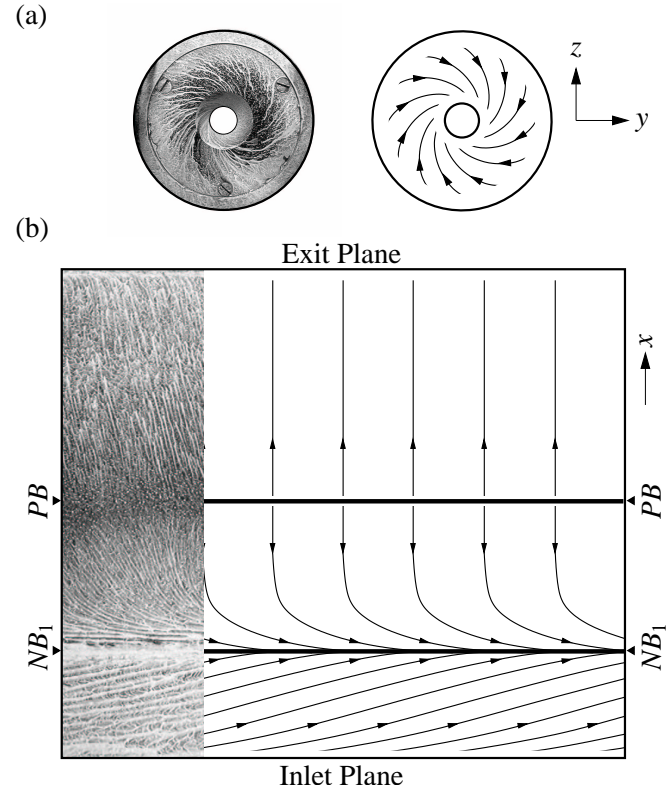


Figure 4: Fluidic precessing jet surface-flow visualisation pattern and streakline interpretation; (a) inlet plane, (b) cylindrical surface [5].  $D/d_{e1} = 6.4$  and  $L/D = 2.70$  at  $Re_1 = 280,000$ .

the chamber. The pattern thus formed on the inlet-orifice plate is also recorded as an image.

The flow visualisation is supplemented by measurements of static pressure from a row of six pressure tappings through the wall of the chamber (Figure 2). The distance between tappings is  $D/4$ . An azimuthal increment of  $30^\circ$  is obtained by rotating the chamber about its axis. For each measurement the signal from the pressure transducer was time averaged for 100 seconds on a digital oscilloscope.

#### Oscillating-Jet Flows

The flow-visualisation patterns and corresponding surface-streakline interpretations for the OTJ nozzle are shown in Figure 3. The expansion ratio is  $D/d_{e1} = 3.5$  and the chamber length is  $L = 2.50D$ . The other expansion ratios (2.1, 2.5 and 3.0) produce similar flow patterns.

The spiral pattern in Figure 3(a), which indicates a radially inward swirling flow at the inlet plane, is similar to that observed by Nathan et al. [5] in the FPJ nozzle (Figure 4(a)). In the interpretation of the flow field, this swirling flow (Figure 3(b)) is entrained into the flow from the inlet orifice.

In the OTJ nozzle, flow from the inlet orifice is deflected asymmetrically and reattaches to the cylindrical surface of the chamber. Azimuthal (or tangential) motion of the reattachment point appears as oscillation of the jet. Lee et al. [3] have shown that the preferred locations for the reattachment point are aligned azimuthally at midway between corners of the orifice. In Figures 3(c) and 3(d), these preferred locations are shown as nodes  $N_1$ ,  $N_2$  and  $N_3$ . In surface-flow visualisation of the FPJ nozzle [5], the moving reattachment point has no preferred direction and appears as a positive bifurcation, line  $PB$  in Figure 4(b).

The strongest feature in the OTJ flow-visualisation pattern (Figure 3(c)) is a circumferential “ring” ( $NB_1$ ) where converging

flow has caused a build-up or thickening of the paste. Nathan et al. [5] interpreted a similar feature in flow-visualisation patterns (Figure 4(b)) from the FPJ nozzle as a negative-bifurcation line. Surface-flow streaklines consistent with the flow-visualisation pattern of Figure 3(c) are drawn in Figure 3(d). These streaklines may approximate a time-average of flow in the OTJ nozzle but, like Figure 4(b), they do not provide much insight into the mechanism of the flow.

### Stationary-Deflected-Jet Flow

The behaviour of the flow in the OTJ nozzle and the behaviour of the jet emerging from the exit plane depend on expansion ratio ( $D/d_{e1}$ ), length ( $L/D$ ), and Reynolds number ( $Re_1$ ). In their parametric study, Lee et al. [3] found that, with  $L/D \leq 1$ , the flow from the inlet orifice remains axisymmetric, and there is no large-scale oscillation. For  $L/D$  between 1.25 and 3.00, the jet oscillates in a manner which produces the flow-visualisation pattern of Figure 3(c).

However, these are not the only flow regimes of the OTJ. For a very narrow range of “critical” values near  $L/D = 1.25$ , Lee et al. [3] observed that the jet from the “ $D/d_{e1} = 3.5$ ” orifice is deflected towards the wall, but does not oscillate. Increasing chamber length beyond this narrow but critical  $L/D$  range causes the deflected jet to oscillate. We would therefore expect a flow pattern produced by the stationary (or non-oscillating) jet to be related to the phase-averaged flow of an oscillating jet. Figure 5 shows that the surface-flow visualisation pattern for the stationary deflected jet is significantly different from the visualisation pattern for the oscillating jet. The most striking difference between Figure 5(c) and Figure 3(c) is that the built-up line of paste representing the negative-bifurcation line  $NB_1$  is no longer straight.

To assist with the interpretation of the flow-visualisation pattern we have measured the distribution of time-averaged static pressure on the internal cylindrical surface of the nozzle. This is presented in Figure 5(d) as contours of static-pressure coefficient,  $C_p = p_s/q_1$ , where  $p_s$  is the wall static pressure and  $q_1$  is the mean dynamic pressure of flow through the inlet orifice. The location of maximum pressure, shown as the  $C_p = 0.00$  contour, is the reattachment “point” of the deflected jet. In Figure 5(e), this is the “source” node  $N_1$ . Closer to the inlet plane and to each side of the pressure maximum, there is a region of minimum pressure ( $C_p = -0.13$ ). These coincide with large accumulations (or “blobs”) of paste in the flow-visualisation image (Figure 5(c)). Clearly observed rotation of the larger “blob” implies there is a “sink” focus at the corresponding pressure minimum. This is shown as  $F_1$  in Figure 5(e). The smaller “blob” is represented by focus  $F_2$ . The existence of saddles  $S_1$  and  $S_2$  is deduced from the rules of topology.

In the experiment (Figure 5(c)), paste spreads to the left and to the right of the reattachment node,  $N_1$ . Flow spreading to the left of  $N_1$  is drawn into focus  $F_1$  and flow spreading to the right is drawn into the negative-bifurcation line  $NB_1$ . Features  $F_1$  and  $NB_1$  are strong sinks where flow separates from the surface and they also induce a reversed flow through the exit plane (Figure 5(e)). Since the surface is cylindrical, and is continuous along the left and right edges of the diagram, flow which spreads circumferentially away from  $N_1$  must also converge towards a negative bifurcation which extends from the exit plane and into focus  $F_1$ . This negative bifurcation is shown in Figure 5(e) as the line  $NB_2$ . The complementary positive-bifurcation line  $PB_1$  extends from node  $N_1$  to the exit plane.

The strongly swirling surface flow between the inlet plane and  $NB_1$  (Figure 5(e)) is directed away from the edge  $BAB$ . The inward-spiral flow-visualisation pattern in Figure 5(b) also in-

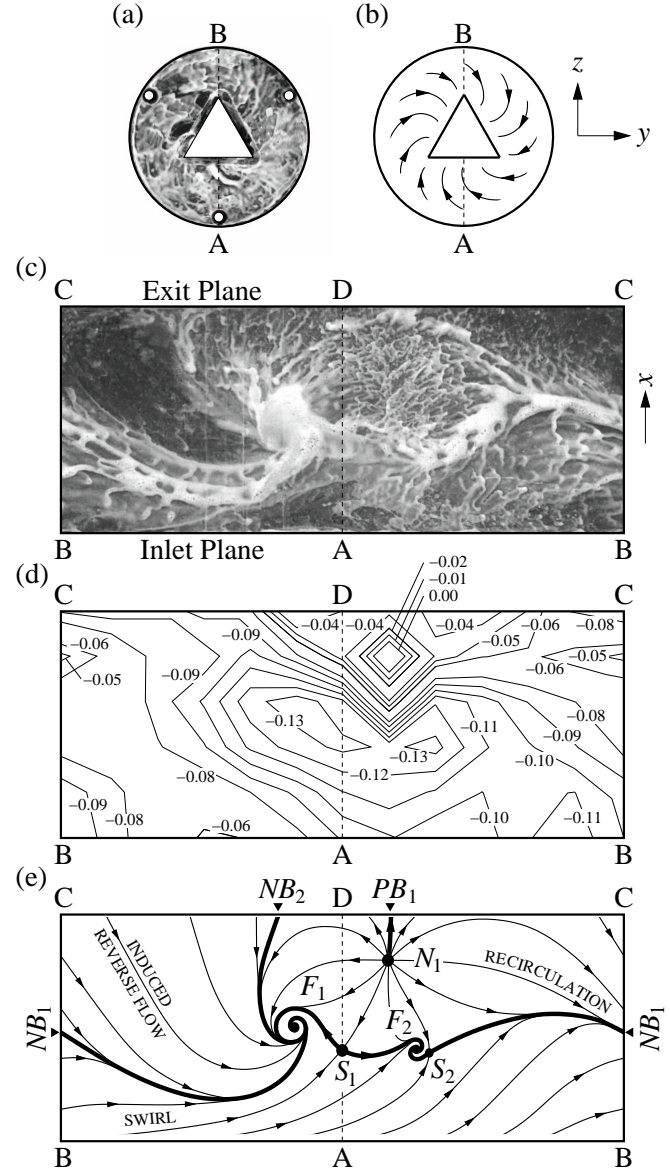


Figure 5: Surface-flow visualisation of the stationary deflected jet; (a, b) inlet plane, (c) cylindrical surface, (d) distribution of static-pressure coefficient,  $C_p$ , (e) streakline interpretation.  $D/d_{e1} = 3.5$  and  $L/D = 1.25$  at  $Re_1 = 70,000$ .

icates flow directed away from the perimeter  $BAB$ , and so continuity requires a positive-bifurcation line between the inward-spiral flow and the flow on the cylindrical surface. The positive bifurcation is shown in Figure 6(a) as the closed loop  $PB_2$ . In the side view, Figure 6(b), the positive bifurcation ( $PB_2$ ) is visible as saddles  $S_3$  and  $S_4$ . A topologically consistent side-view flow pattern (Figure 6(b)) is obtained by placing foci  $F_3$  and  $F_4$  in the swirling near-surface flow, and  $F_5$  in the recirculation region between the reattachment point  $S_7$  and the inlet plane [8].

### Flow at the Exit Plane

There are two regions of flow at the exit plane, the emerging-jet-flow region, and the induced-reverse-flow region. The contour plots in Figure 7 are of the time-averaged signal from a total-pressure tube (i.e. Pitot probe) placed sequentially at each of 241 points distributed over the exit plane of the nozzle. The results are plotted as a pressure coefficient based on  $q_1$ , the dynamic pressure at the inlet orifice. The Pitot probe is aligned parallel to the axis so that, when placed in the emerging jet flow, it provides an approximate measurement of jet-flow speed. When the probe is placed in the induced-reverse-flow region, the recorded pressure is *negative*.



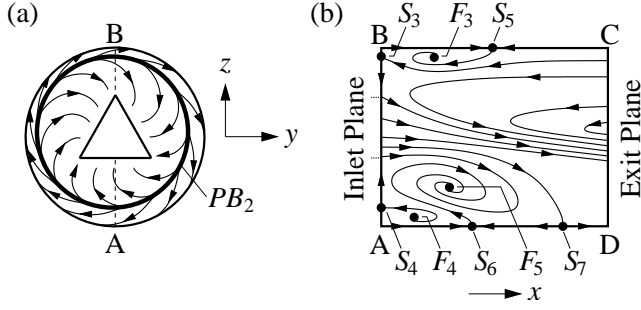


Figure 6: Flow topology of the stationary deflected jet in the oscillating-triangular-jet nozzle; (a) inlet plane, (b) azimuthal plane  $\overline{ABCD}$ .

Figure 7 shows that only an outer part of the jet shear layer reattaches to the side wall of the nozzle. The higher velocity part of the emerging jet ( $0.20 \leq C_p \leq 0.80$ ) is deflected by only a small amount ( $\approx D/9$ ) and discharges from the exit plane without interacting directly with the wall of the nozzle.

We propose the following model for flow near the reattachment node  $N_1$ . Focus  $F_1$  (Figure 5(e)) is the end of a line vortex which extends away from the internal surface of the OTJ nozzle. The vortex beginning at  $F_1$  is a feature of the turbulent shear layer of the deflected-jet flow and, as indicated by  $\overline{F_1 F_6}$  in Figure 8(a), it is drawn out of the OTJ chamber as a longitudinal vortex aligned with the axis of the nozzle. The weaker vortex beginning at  $F_2$  is also entrained and drawn out of the chamber on the other “side” of the deflected jet. As suggested by the Kelso model of the FPJ [2], the vortex  $F_5$  (Figure 6(b)) would be entrained by the jet flow so that it is stretched into the form of a horseshoe vortex. In Figure 8(b), the stretched legs of the horseshoe vortex are combined with the “legs” of the  $\overline{F_1 F_6}$  and  $\overline{F_2 F_7}$  vortices. This leads to a sketch of the non-axial components of the flow at the exit plane (Figure 8(b)). Saddle  $S_8$  corresponds to the positive bifurcation  $PB_1$  of Figure 5(e), and saddle  $S_9$  corresponds to the negative bifurcation  $NB_2$ .

### Conclusions

From flow visualisation and static-pressure measurements at the internal surface of the OTJ nozzle, the authors have identified a number of bifurcation lines and critical points in the stationary-deflected-jet flow observed by Lee et al. [3]. These are shown in Figures 5(e), 6 and 8(b). Although deflection of the jet centreline is only about  $D/9$ , there is a clearly observed reattachment node downstream of the inlet plane (or backward-facing step). Closer to the inlet plane and to each side of the reattachment node, flow separates from the surface at a strong sink focus,  $F_1$ , and a much weaker focus  $F_2$ . The surface-flow pattern indicates that much, and perhaps most of the reverse flow through the exit plane of the nozzle is attracted towards  $F_1$ . A rather dis-

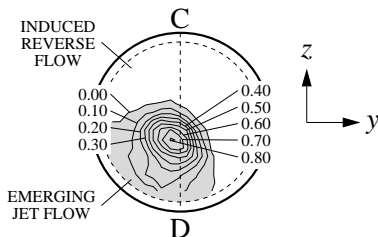


Figure 7: Stationary deflected jet at the nozzle exit plane; distribution of Pitot-pressure coefficient,  $C_p$ .  $D/d_{e1} = 3.5$  and  $L/D = 1.25$  at  $Re_1 = 70,000$ .

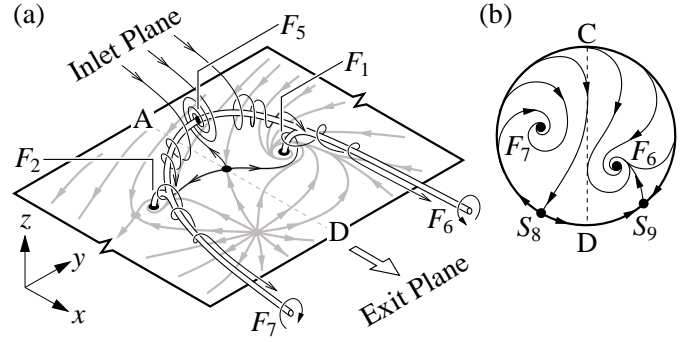


Figure 8: Stationary deflected jet; (a) “vortex skeleton” compatible with the foci in Figures 5 and 6, (b) schematic streamline pattern of in-plane velocity components at the nozzle exit plane.

torted circumferential negative bifurcation  $NB_1$  also flows into  $F_1$ . The vortices which terminate at  $F_1$  and  $F_2$  are features of the shear layer in the reattached flow, and so they are drawn through the exit plane as longitudinal counter-rotating vortex “legs”.

A topologically consistent model of flow between  $NB_1$  and the inlet plane is obtained by placing a positive-bifurcation loop on the back face of the nozzle.

### References

- [1] Bradshaw, P., *Experimental fluid mechanics*, Pergamon Press Ltd., Oxford, 1970.
- [2] Kelso, R. M., A mechanism for jet precession in axisymmetric sudden expansions, in *Proceedings of the Fourteenth Australasian Fluid Mechanics Conference*, The University of Adelaide, Adelaide, Australia, 2001, 829–832.
- [3] Lee, S. K., Lanspeary, P. V., Nathan, G. J., Kelso, R. M. and Mi, J., Low kinetic-energy loss oscillating-triangular-jet nozzles, *Experimental Thermal and Fluid Science*, **27**, 2003, 553–561.
- [4] Mi, J., Nathan, G. J., Luxton, R. E. and Luminis Pty. Ltd., *Naturally Oscillating Jet Devices*, Australian Patent Office, Application No.: PP0421/97, 1998.
- [5] Nathan, G. J., Hill, S. J. and Luxton, R. E., An axisymmetric ‘fluidic’ nozzle to generate jet precession, *Journal of Fluid Mechanics*, **370**, 1998, 347–380.
- [6] Newbold, G. J. R., Nathan, G. J., Nobes, D. S. and Turns, S. R., Measurement and prediction of  $\text{NO}_x$  emissions from unconfined propane flames from turbulent-jet, bluff-body, swirl, and precessing jet burners, in *Proceedings of the Combustion Institute*, Volume 28, 2000, 481–487.
- [7] Rapson, D., Stokes, B. and Hill, S. J., Kiln flame shape optimisation using a Gyro-Therm gas burner, *World Cement*, **26**(7), 1995, 2–5.
- [8] Schram, C., Rambaud, P. and Riethmuller, M. L., Wavelet based eddy structure eduction from a backward facing step flow investigated using particle image velocimetry, *Experiments in Fluids*, **36**, 2004, 233–245.

## **Influence of Vegetation Height and Density on a Turbulent Boundary Layer**

**P. Gualtieri, G. Pulci Doria and L. Tagliatela**

Department of Hydraulic and Environmental of Hydraulic Engineering Girolamo Ippolito  
University of Napoli Federico II  
Via Claudio 21 - 80125 Napoli - ITALY  
voice 0039-081-7683460 fax 0039-081-5938936 e-mail [paola.gualtieri@unina.it](mailto:paola.gualtieri@unina.it)

### **Abstract**

In last years vegetated surfaces problems are becoming more and more important in hydraulic research, whereas boundary layer problems are always a very important topic of fluid mechanics. In this paper the influence of submerged rigid vegetation on the development of a water equilibrium boundary layer in a rectangular channel is experimentally investigated. Vegetation is modelled through vertical cylinders inserted in the channel bottom: two different cylinders heights and two different cylinders densities have been considered, so that four different vegetation conditions have been investigated and always compared with the same boundary layer without vegetation. Local mean velocity distributions in four subsequent test sections have been measured through an LDA system. The main results obtained are the following ones: 1) vegetation presence increases boundary layer thickness; 2) with the investigated cylinders heights and densities the boundary layer behaves yet as an equilibrium one; 3) the equilibrium characteristics depend on either cylinders height or cylinders density; 4) it is possible to define an index which summarizes the aforementioned equilibrium characteristics.

### **Introduction**

#### **Vegetated surfaces problems**

It is generally agreed that vegetation increases flow resistance, changes backwater profiles and modifies sediment transport and deposition. In the past vegetation along rivers and on floodplains was traditionally regarded a nuisance and for this reason it has been usually eliminated. At the present in river restoration and environmental engineering natural river characteristics are sought after, implying that the physical habitat and flow conditions should be as close as possible to a pristine reach.

Much of the earlier work on the hydraulic properties of riverine vegetation was conducted by agricultural engineers who concentrated on determining roughness coefficients or developing design methods, rather than on obtaining a better understanding of the physical processes. Conventional approaches typically use reference publications for selecting a roughness coefficient, which groups all sources of flow resistance, including vegetation, into Manning's  $n$ . Significant advances have been made to gain a better understanding of flow phenomena in floodplain and wetland flows. A considerable amount of research has been carried out in developing resistance laws for channels with rigid vegetation, flexible vegetation, and various combinations.

Recently, several studies have focused on velocity profiles and turbulent characteristics of vegetated channels. Overall, an abundance of studies, however, is based on laboratory experiments with simple artificial roughness, whereas in fact natural vegetation exhibits a wide variety of forms and flexibility. In hydraulic analysis, non-submerged and submerged conditions are typically distinguished, and, in addition, two types of vegetation are usually defined: rigid (woody or arborescent plants) and flexible (herbaceous plants) [11, 12, 13, 15, 16].

#### **Boundary layer problems**

On the other side, the hydrodynamic behaviour of a boundary layer is one of the most important topics of fluid mechanics. The hydrodynamic laws which describe boundary layer behaviour are now reasonably well known. In particular, with regard to an air boundary layer, the non dimensional value of the pressure gradient along the flat plate is the most important parameter which controls the local mean velocity distributions along the direction orthogonal to the plate. In fact, if this parameter is kept constant along the plate, the boundary layer is called an "equilibrium boundary layer" and the non dimensional velocity distributions, represented as a velocity defect law, does not vary along the plate.

A more sophisticated type of boundary layer flow, much investigated in international literature [1, 8, 9, 10, 14], is the turbulent boundary layer under free stream turbulence.

Two of the authors worked in previous years on this research field [2, 3, 4, 5, 6], performing their experimental tests in a water channel. The investigated boundary layers were always equilibrium ones with zero-piezometric head gradient (condition that for water is equivalent to the zero- pressure gradient in air).

#### **Aim of the paper**

Authors are not acquainted of any presence, in the however growing scientific literature on vegetated streams, of the problem of vegetation effects on boundary layers.

In a recent paper [7] authors began to study how bottom vegetation can affect the development of a water boundary layer. In particular submerged rigid vegetation placed on the bottom of the channel was considered, and was modelled through groups of vertical cylinders, 4 mm diameter, placed in rectangular meshes  $5.0 \times 2.5 \text{ cm}^2$ ; each cylinder was 5 mm high in a first experimental condition and 10 mm high in a second experimental condition. A third experimental condition, without cylinders at all, was also obviously considered for comparison.

This paper is an advance of [7]. In particular either the investigated boundary layer flow or the heights of the cylinders modelling vegetation are the same ones as in [7], but the cylinders density has been increased: in fact they are placed in square meshes  $2.5 \times 2.5 \text{ cm}^2$ .

The main purpose of this paper is to deepen, employing also the results of [7], the mixed influence on boundary layer development of cylinders heights and densities.

### Experimental plant

The experimental plant represented in figure 1, carefully described in [7], has been used.

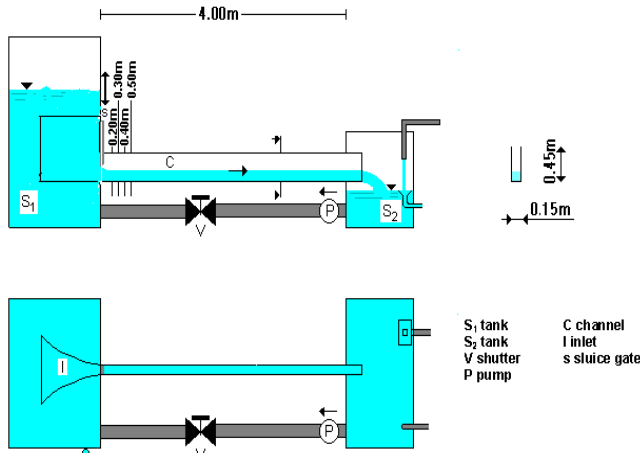


Figure 1. Experimental plant.

Its main device is a variable slope channel 4 m long and 15 cm wide, with plexiglas walls and bottom, coming out from a feeding tank supplied by a circulation pump. This tank feeds the channel through an adjustable rectangular sluice gate. The inlet towards the sluice gate is modelled through a suitable plexiglas device.

In the channel, until a distance of some decimetres from the sluice gate, a boundary layer flow is generated on the bottom. Moreover, due to feeding tank characteristics, this current showed, in every flow condition, a not at all negligible free stream turbulence.

The instantaneous velocity measurements and the local mean velocity values have been carried out through an LDA technique.

### Vegetation modelling

As already said, vegetation was modelled through groups of vertical cylinders placed in square meshes  $2.5 \times 2.5 \text{ cm}^2$ . In particular, they have been arranged in the following way. The longitudinal rows of cylinders were 2.5 cm far each another and 1.25 cm far from the lateral walls. The first cylinder of each row was placed 1.25 cm from the channel inlet (sluice gate section).

In this way, the whole arrangement was symmetric, the centreline of the channel bottom was free from cylinders and it was possible to carry out velocity distributions measurements on it. In particular the four test sections that have been chosen, likewise in [7], are at 20 cm, 30 cm, 40 cm, 50 cm respectively far from the channel inlet. These test sections were all placed exactly between two following rows, so that the measurement verticals lied exactly in the centre of each square mesh.

### Experimental surveys carried out and relative results

In order to compare all experimental conditions some fundamental hydraulic parameters have been kept constant and equal to the corresponding ones in [7].

The height of the sluice gate was always of 7.49 cm, and the height of the vena contracta was of 4.61 cm.

The head of the tank above the vena contracta was always of 10.34 cm and the velocity in the vena contracta was of 1.424 m/s. The flow-rate was of 9.85 l/s.

As in [7], in each condition, in order to have always an equilibrium boundary layer with zero-piezometric head gradient in the flow direction, the free surface was kept horizontal.

Therefore it has been necessary to change the slope of the channel in each experimental condition, because of the different bottom friction head losses without cylinders, with 5 mm and 10 mm cylinders heights. In particular in the two conditions 1.15% and 2.05% slopes were established, which can be compared to the 0.25% characteristic of smooth bottom condition. In such a manner, the hydraulic head was kept constant and equal to 10.34 cm also along the whole current in each flow condition; and the velocity in the external layer was 1.424 m/s everywhere.

In each experimental condition, local mean velocity distributions have been measured in the four aforementioned test sections. Such experimental velocity distributions, together with the smooth bottom velocity distribution, have been represented in figures 2, 3, 4, 5.

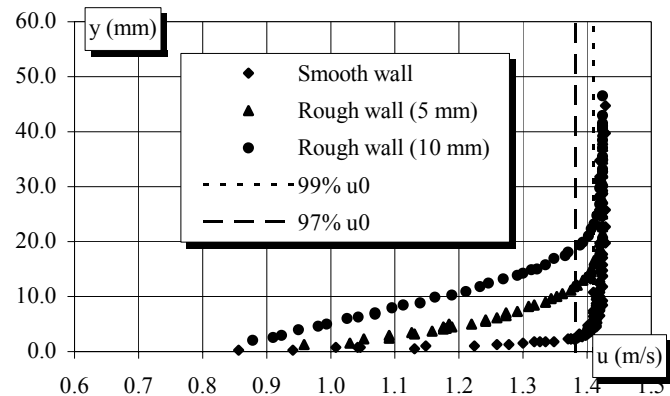


Figure 2. Velocity distributions in section 1 (20 cm from the inlet).

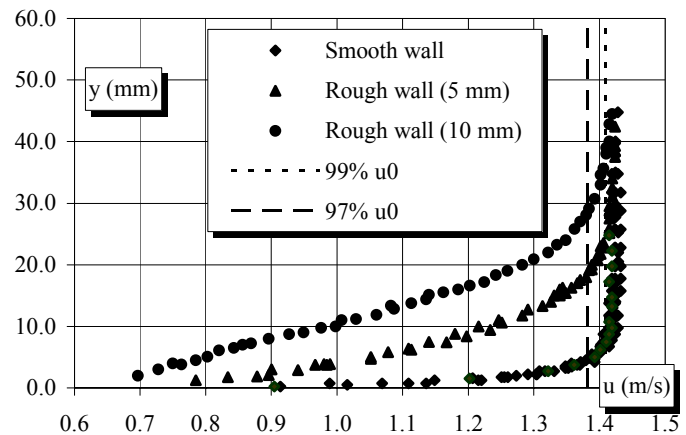


Figure 3. Velocity distributions in section 2 (30 cm from the inlet).

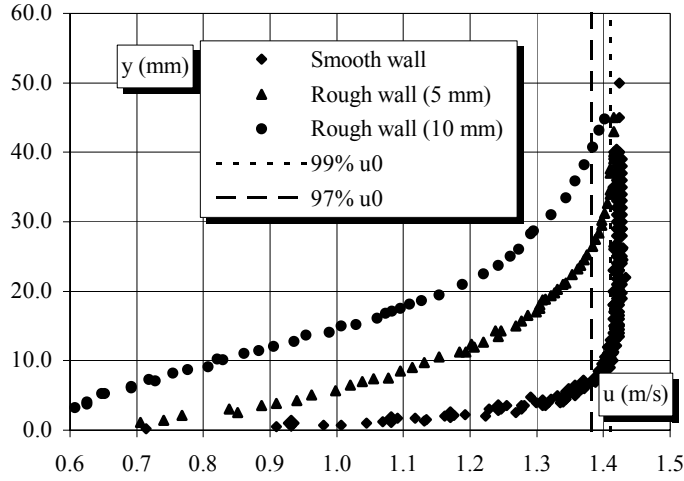


Figure 4. Velocity distributions in section 3 (40 cm from the inlet).

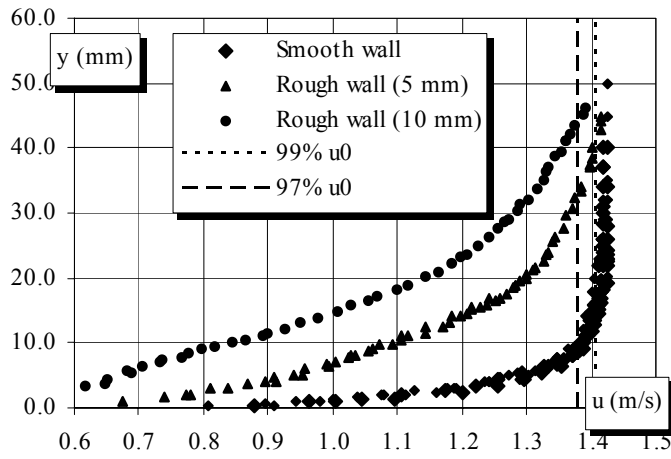


Figure 5. Velocity distributions in section 4 (50 cm from the inlet).

Some first qualitative results are immediately evident. First of all, the vegetation presence affects widely velocity distributions in boundary layers. In particular, because of the presence of vegetation, the boundary layer thickness grows and the velocity inside the boundary layer decreases. In particular, the values of the 99% boundary layer thickness ( $\delta_{99}$ ) in the four test sections (20 cm, 30 cm, 40 cm, 50 cm) are the following ones:

Smooth bottom: mm 3.8, 7.1, 10.9, 13.5.  
 5 mm cylinders height: mm 16.0, 26.3, 35.1, 44.0.  
 10 mm cylinders height: mm 22.0, 33.9, 47.7, 52.4.

These values have been evaluated through a special procedure fully described in [7], because it is difficult to read directly on the diagrams the  $\delta_{99}$ .

A further qualitative result is that it is possible to notice that no evidence appears, at first sight, of possible irregularities of the velocity distributions at the cylinders height.

At a deeper insight, it would be possible to observe, in the section 20 cm far from the sluice gate, a little irregularity (an elbow) in velocity distributions. This phenomenon is clearly caused by the greater resistance met by the current in its lower part where the cylinders are present, and it is related in literature about uniform or steady vegetated currents [17]. Either in [7] or in this paper it is not very evident because of the fairly low adopted cylinders densities.

In any case the conditions that produce the irregularity in the case of boundary layer must be deepened through further

experiments, which will be carried out in a next paper.

### Non dimensional velocity distributions and equilibrium characteristics

All the twelve velocity distributions reported in figures 2, 3, 4, 5 can be transformed in non dimensional ones through the  $u_0$  velocity in the external layer and the already obtained  $\delta_{99}$  values. In figure 6 non dimensional velocity distributions in three experimental condition (smooth bottom, 5 mm and 10 mm cylinders height) are reported.

A simple look to the figure shows clearly that the distributions relative to the same experimental condition but to different test sections overlap one another (with the almost invisible exception of the irregular points of the 20 cm test section) so that only three different diagrams appear, every one relative to a different vegetation condition (smooth bottom, 5 mm and 10 mm cylinders height).

In figure 7, in order to have a fruitful comparison, the correspondent diagram that had been presented in [7] is represented. It refers always to smooth bottom, 5 mm cylinders and 10 mm cylinders height, but to a lower vegetation density value (rectangular meshes  $5.0 \times 2.5 \text{ cm}^2$  instead of square meshes  $2.5 \times 2.5 \text{ cm}^2$ ). Also in this diagram the distributions relative to the same experimental condition but to different test sections overlap one another.

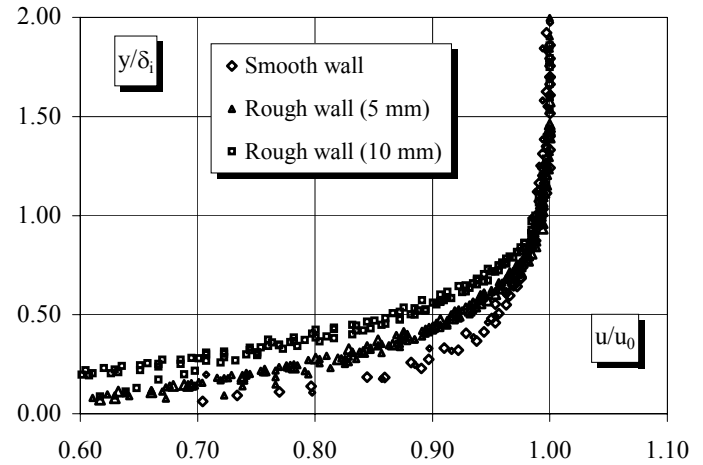


Figure 6. Non dimensional velocity distributions (square meshes).

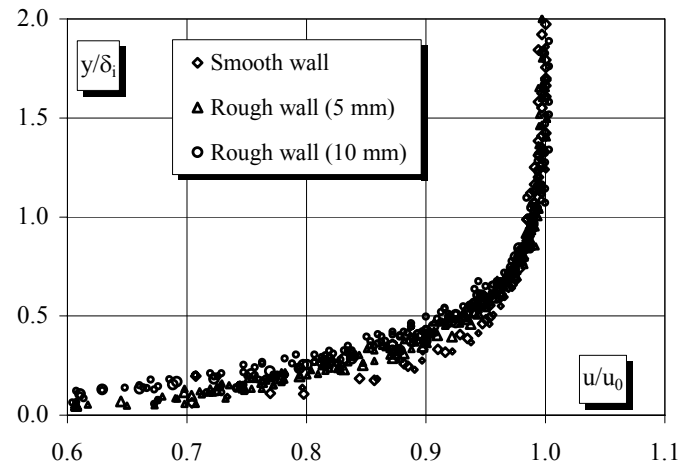


Figure 7. Non dimensional velocity distributions (rectangular meshes).

This behaviour represents the clear mark of the equilibrium state of the boundary layers in each experimental condition, not only in the case of smooth bottom, as it was obvious, but also in the cases of vegetated surfaces. This conclusion, as it



has been verified in [7], can be drawn also if the distributions are not represented in the theoretically requested shape of velocity defect laws. The circumstance that the boundary layers over vegetated surfaces appear to be equilibrium ones, at least in the considered conditions, is an intriguing result. In conclusion, therefore, except the few considered exceptions which regard only the inner part of the boundary layer and only the first test section, the considered boundary layers appear to be equilibrium ones: namely in each experimental condition their velocity distributions in different test sections superimpose one another.

### Difference of equilibrium conditions in different hydrodynamic current conditions

As already stressed, in both figures 6 and 7 it is clear that the three velocity distributions do not overlap. A direct comparison between the two figures shows that also distributions relative to the same cylinders height but different cylinders density do not overlap.

Therefore, in the considered experimental conditions, our pattern of vegetation does not produce the well known elbow in the velocity distributions, but, in any case, it influences the overall trend of the distributions themselves. This influence depends on cylinders either height or density.

It is even possible to define a simple shape index of the distributions, defined as the ratio  $\delta_{99}/\delta_{97}$  (with an obvious meaning of the symbols). This index is not based on displacement thickness and momentum thickness, as more typical in boundary layer literature, but has the advantage to be more immediately intelligible and measurable. The values of this shape index in the different experimental conditions are given in following table:

	0 mm	5 mm	10 mm
Zero density	1.65	1.65	1.65
Rect. mesh	1.65	1.50	1.40
Square mesh	1.65	1.38	1.25

Table 1. Table of the shape index

From this table, it is clear that this index varies with height and density of the cylinders: in particular it regularly decreases with cylinders either height or density.

### Conclusions

In recent years much attention has been paid to the problem of the behaviour of free stream currents with vegetated surfaces in relation to atmospheric or river flow problems. The study of the influence of vegetated bottom on the growth of turbulent boundary layer can let us deepen some further currents behaviour characteristics.

From the point of view of basic fluid mechanics, the most important conclusion coming from the analysis of the experimental results is that, in case of regular submerged rigid cylinders-shaped vegetation, the boundary layer flow, if the free surface is kept constant and excluding some minor exceptions, behaves as an equilibrium boundary layer.

Moreover the equilibrium conditions are different in the boundary layer without cylinders, or with cylinders of different heights or densities. These different equilibrium conditions can be summarized by a very simple shape index which depends on vegetation characteristics.

### Acknowledgements

The authors acknowledge very much the laboratory technician Franco Caiazzo, whose infinite patience was the fundamental tool in order to manufacture vegetation.

### References

- [1] Bandypadhyay, P.R. Reynolds Number Dependence of the Freestream Turbulence Effects on Turbulent Boundary the Layers *AIAA J.* **30(7)**, 1992, 1910-1912.
- [2] Gualtieri, P. & Pulci Doria, G. Non dimensional distribution of longitudinal integral length scales in a turbulent boundary layer *FLUCOME '97 Congress* Hayama, Japan, 1997, 161-166.
- [3] Gualtieri, P. & Pulci Doria, G. A proposal of a physically based thickness definition and of a new mean velocities distribution law in a turbulent boundary-layer on the ground of LDA measurements *13<sup>th</sup> Australasian Fluid Mechanics Conference*, Melbourne, Australia, 1998, 845-848.
- [4] Gualtieri, P. & Pulci Doria, G. 1999 Boundary Layer Intermittency Model *IUTAM Symposium on Geometry and Statistics of Turbulence*, Hayama, Japan, 1999, 379-384.
- [5] Gualtieri, P. & Pulci Doria, G. 2001 A Correct Model of Variance, Skewness, Kurtosis in Boundary Layer with Turbulent External Layer *14<sup>th</sup> Australasian Fluid Mechanics Conference*, Melbourne, Australia, 2001, 259-262.
- [6] Gualtieri, P. & Pulci Doria, G. 2003 A correct model of longitudinal integral length scales in boundary layer with turbulent external layer *2<sup>nd</sup> Int. Conf. on Heat Transfer, Fluid Mechanics, and Thermodynamics H.E.F.A.T.*, Victoria Falls, Zambia, 2003.
- [7] Gualtieri P., Pulci Doria G. & Tagliatela L. Effect of vegetation on boundary layer with turbulent free stream layer *2<sup>nd</sup> Int. Conf. on Fluvial Hydraulics RiverFlow 2004*, Napoli, Italy, 2004, 381-388.
- [8] Hancock, P.E. & Bradshaw, P. Influence of Free-Stream Turbulence on Turbulent Boundary Layers *J. Fluids Eng.* **105**, 1983, 284-289.
- [9] Hancock, P.E. & Bradshaw, P. Turbulent structure of a boundary layer beneath a turbulent free stream *J. Fluid Mech.* **205**, 1989, 45-76.
- [10] Hoffmann, J.A. & Mohammady, K. Velocity Profiles for Turbulent Boundary Layers Under Freestream Turbulence *J. Fluids Eng.* **113**, 1991, 399-404.
- [11] Kouwen, N. & Unny, T.E. Flexible roughness in open channels *J. Hydraulic Eng.* **99(5)**, 1973, 684-698.
- [12] Kouwen, N. & Unny, T.E. Flow resistance in vegetated waterways *Trans. ASCE* **24(3)**, 1981, 684-698.
- [13] Kouwen, N., Unny, T.E. & Hill, H.M. Flow retardance in vegetated channels *J. Hydraulic Eng.* **95(2)**, 1969, 329-342.
- [14] Meier, H.U. & Krepli, H.P. Influence of Freestream Turbulence on Boundary-Layer Development *AIAA J.* **18**, 1980, 11-15.
- [15] Nezu I. & Onitsuka Kouki Turbulent structures in partly vegetated open channels flows with LDA and PIV measurements *J. Hydraulic Research* **39(6)**, 2001, 629-642.
- [16] Stone, B. M. & Shen, H. T. Hydraulic Resistance of Flow in Channels with Cylindrical Roughness *J. Hydraulic Eng.* **128(5)**, 2002, 500-506.
- [17] Tsujimoto, T., Shimuzu Y. & Okada T. Turbulent open-channel flow over bed covered by rigid vegetation *J. Hydropscience and Hydraulic Eng.* **10 (2)**, 1992, 13-25.

## The transport of sediment over a sloping breakwater

A.J. Hogg<sup>1</sup> and D. Pritchard<sup>2</sup>

<sup>1</sup>Centre for Environmental & Geophysical Flows, School of Mathematics, University of Bristol, Bristol BS8 1TW, UK

<sup>2</sup>BP Institute for Multiphase Flow, University of Cambridge, Madingley Road, Cambridge CB3 0EZ, UK

### Abstract

We analyse the transport of suspended sediment by a single swash event on a sloping breakwater and investigate the effects of overtopping on the motion and the redistribution of particles. By deploying a Lagrangian frame of reference, we calculate the net transport by these flows and demonstrate that overtopping promotes the landwards transport of sediment, primarily because the backwash of the swash is significantly weakened. Furthermore we quantify the flux of sediment that is transported over the crest to be deposited behind the breakwater.

### Introduction

Wave breaking and collapse on a sloping beach or breakwater drives a rapid shallow flow under which the shoreline moves back and forwards across the ‘swash zone’. Such events may transport significant volumes of sediment by their erosive action or by the advection and deposition of pre-mobilised particulate. They therefore play a significant role in determining the morphology of a beach or a soft breakwater and in the accumulation of sediment in the region the behind the breakwater. Studies of sediment movement by these intense, transient events are in their infancy. Programmes of field measurements face significant challenges in determining the properties of these shallow flows, while mathematical models are limited due to incomplete understanding of the physical mechanisms that control the flows and of the subtle, yet highly nonlinear interactions that occur between the fluid and sediment phases.

The mechanics of the swash zone are determined by a number of physical processes including unsteady, gravitational-driven fluid motion, the development of turbulent structures within advancing flow and the percolation of the flow into the unsaturated, porous substrate (see the reviews of Butt & Russell[1] and Elfrink & Baldock[2]). It is generally thought, however, that the motion is primarily driven by the upslope, gravitational collapse of water to form a relatively shallow, transient flow (figure 1). Thus a leading-order description of the hydrodynamics may be based upon the use of shallow water equations in which hydraulic resistance is neglected. Shen & Meyer[8] derived a solution to these equations to model the flow up a planar beach following the collapse of a bore in which they showed that the shoreline undergoes a ballistic motion with a constant downslope acceleration due to gravity. This approach was recently extended by Peregrine & Williams[3] to model the flow that overtops a sloping breakwater on the assumption that at the crest of the breakwater the Froude number of the flow is equal to, or exceeds, unity.

In this paper we study theoretically the ability of these flows to transport sedimentary particles both as bed- and suspended load and we examine the net transport that occurs over a swash event. Throughout this paper we draw the distinction between ‘total load’ models of sediment transport in which the instantaneous flux of particles adjusts immediately to the local conditions and suspended load models for which advection by the suspending fluid is of considerable importance, so that there is a lag between changes in the hydrodynamics and the sediment

transport. Naturally for steady flows, these two approaches are identical. Our analysis couples sediment transport to the hydraulic model of Peregrine & Williams[3] and by treating the equations of motion in a Lagrangian frame of reference, we are able to make considerable analytical progress that obviates the need for lengthy numerical calculations and the associated difficulties of tracking the motion of the shoreline. Furthermore this analytical technique permits the robustness of our results to be examined by investigating the changes in the patterns of transport for particles with different physical properties, or by varying the empirical relationship between the flux of suspended particles and the flow speed. This Lagrangian technique has been recently applied to reveal the role of ‘settling lag’ for sediment transport by tidal currents and infra-gravity waves over inter-tidal regions [4],[5].

The paper is structured as follows. First, we formulate the hydraulic model, identify the relevant dimensionless parameters and review the overtopping solution of Peregrine & Williams[3]. We then calculate the associated patterns of sediment transport predicted by total load models and by the suspended load. Finally we summarise our results and draw some brief conclusions from this study.

### Shallow water model

We assume that the swash-flow is sufficiently shallow so that vertical fluid accelerations are negligible and the pressure adopts a hydrostatic distribution. Thence we employ the shallow water equations to model the conservation of fluid mass and momentum and the transport of suspended sediment, which is assumed to be sufficiently dilute so that it does not significantly supplement the density of the suspending fluid. Denoting the depth of the fluid by  $h$ , the depth-averaged velocity and mass concentration by  $u$  and  $c$ , respectively, and aligning the  $x$ -axis to be parallel to the planar surface of the breakwater which is inclined at an angle  $\theta$  to the horizontal (see figure 1), the governing equations are given by

$$\frac{\partial h}{\partial t} + \frac{\partial}{\partial x}(uh) = 0, \quad (1)$$

$$\frac{\partial u}{\partial t} + u \frac{\partial u}{\partial x} + g \cos \theta \frac{\partial h}{\partial x} = -g \sin \theta, \quad (2)$$

$$\frac{\partial c}{\partial t} + u \frac{\partial c}{\partial x} = \frac{m_e q_e - w_s c}{h}, \quad (3)$$

where  $g$  denotes gravitational acceleration,  $w_s$  is the settling velocity of the particles and  $m_e q_e$  is the rate of erosion from the bed per unit area. In this expression of the erosive flux,  $m_e$  is a dimensional constant and  $q_e$  is an empirically-determined function of the flow. (Pritchard & Hogg[6] provide a more complete derivation of these equations and discuss the approximations that underlie them). In this model we have neglected the feedback between the sediment movement and the fluid motion because morphological changes occur on a much slower timescale than the swash events[7].

Sediment is not eroded until the shear stress exceeds a threshold value and then the erosive flux is often modelled as a function of

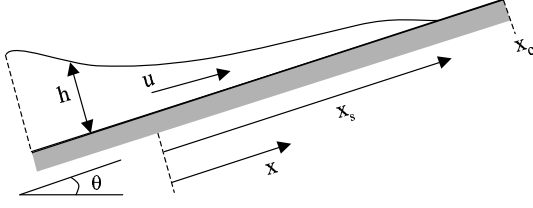


Figure 1: The flow configuration.

the excess shear stress. Although within the framework developed below, we could study any dependence of  $q_e$  upon the velocity and height of the flow, here, for brevity, we assume that  $q_e$  is proportional to  $u^2$  for the suspended load and we neglect the existence of a threshold for erosion. This follows Pritchard & Hogg[7], who demonstrated that the general patterns of erosion are robust to a wide range of parameterisations of the erosive flux. Furthermore these swash flows are relatively intense with peak velocities of approximately  $2 \text{ ms}^{-1}$ , whereas the threshold velocity for the erosion of fine sand is approximately  $0.25 \text{ ms}^{-1}$ . Thus apart from regions close to flow reversal, the neglect of the threshold for erosion does not appreciably affect the pattern of net sediment transport. However we stress that the calculations below could have included an erosion threshold, but this does not introduce any significant qualitative differences to the results. In the discussion that follows we define the instantaneous and net sediment fluxes by

$$q(x, t) = uhc \quad \text{and} \quad Q(x) = \int_{t_{in}(x)}^{t_{de}(x)} q \, dt, \quad (4)$$

where  $t_{in}(x)$  and  $t_{de}(x)$  are the times at which location  $x$  is inundated and denuded, respectively.

Following [3] we non-dimensionalise this system of equations using the lengthscale  $A/\sin\theta$  and the velocity scale  $(gA)^{1/2}$ , where  $2A$  is the vertical excursion of the swash event. Furthermore we nondimensionalise the height of the flowing layer by  $A/\cos\theta$  and the concentration field by  $m_e/w_s$ . Replacing the variables by their dimensionless counterparts, we find that the governing equations are given by

$$\frac{\partial h}{\partial t} + \frac{\partial}{\partial x}(uh) = 0, \quad (5)$$

$$\frac{\partial u}{\partial t} + u \frac{\partial u}{\partial x} + \frac{\partial h}{\partial x} = -1, \quad (6)$$

$$\frac{\partial c}{\partial t} + u \frac{\partial c}{\partial x} = E \frac{q_e(u) - c}{h}. \quad (7)$$

The residual dimensionless parameter in (5)-(7),  $E = w_s \cot\theta (gA)^{-1/2}$ , measures the rate at which the sediment concentration responds to the hydraulic conditions and will henceforth be termed the exchange rate. If  $E \gg 1$  then the concentration rapidly adjusts to the local conditions and  $c = q_e(u)$  to leading order. This regime corresponds to ‘total load’ models of sediment transport. Conversely if  $E \ll 1$  then the concentration field lags the local conditions and the sediment is mainly advected by the flow with little exchange with the bed. Typical values of  $E$  may be estimated as follows: for a steep breakwater,  $\tan\theta = 0.1$ , maximum velocities of a swash event may range from  $0.5$  to  $4 \text{ ms}^{-1}$ . Thus, as we show below, the velocity scale  $(gA)^{1/2}$  ranges from  $0.25$  to  $2 \text{ ms}^{-1}$ . If the surface of

the breakwater is composed of sand particles then the typical settling velocity is approximately  $10^{-2} \text{ ms}^{-1}$ . Combining these dimensional parameters, we find that the exchange rate parameter  $E$  is  $0.05 - 0.4$ .

A final important parameter is the dimensionless extent of the breakwater,  $x_c$ . This is the distance up the slope from where the bore is initiated to the crest of the breakwater. In terms of these dimensionless units, the flow overtops the breakwater if  $0 \leq x_c < 2$ .

We rewrite (7) in a Lagrangian frame of reference. Thus following fluid elements with position  $x_L(t; \xi)$ , where  $\xi$  labels the initial position, we find that

$$\frac{dc_L}{dt} = E \frac{q_e(u_L) - c_L}{h_L}, \quad \text{with} \quad \frac{dx_L}{dt} = u_L. \quad (8)$$

In this expression  $u_L = u(x_L, t)$  and  $h_L = h(x_L, t)$ . This may be integrated to give

$$c_L = c_0 \exp\left(-\int_0^t \frac{E}{h_L} dt'\right) + \int_0^t \frac{E q_e}{h_L} \exp\left(\int_{t'}^t \frac{E}{h_L} dt''\right) dt', \quad (9)$$

where  $c_0$  is the initial concentration. Thus in a Lagrangian frame of reference the concentration field may be represented as  $c_L \equiv c^{pr} + c^{en}$ , where  $c^{pr}$  equals the first term of the right-hand-side of (9) and denotes the concentration that is initially suspended within the collapsing bore and subsequently redistributed over the breakwater; and  $c^{en}$  corresponds to the second term of the right-hand-side of (9) and denotes the contribution from material eroded from the bed. In what follows we describe the evolution of  $c^{pr}$  and  $c^{en}$  separately.

### Overtopping flow

An overtopping solution to the shallow water equations was derived by Peregrine & Williams[3]. It models the advance of the shoreline up the breakwater, overtopping with Froude number of unity, or higher, at the crest of the breakwater and subsequent shoreline retreat. It is given by

$$u(x, t) = \begin{cases} -t & x < -t - \frac{1}{2}t^2 \\ \frac{2(t - t^2 + x)}{3t} & -t - \frac{1}{2}t^2 \leq x < x_{ch}(t) \\ \frac{2 - t - 2\sqrt{2(x_c - x)}}{3} & x_{ch}(t) \leq x \end{cases}, \quad (10)$$

$$\text{where} \quad x_{ch}(t) = \begin{cases} x_c & t < \sqrt{2x_c} \\ \sqrt{2x_c}t - \frac{1}{2}t^2 & t > \sqrt{2x_c} \end{cases}. \quad (11)$$

The height field is given by  $h = (2 - t - u)^2/4$  and the position of the shoreline,  $x_{sh}(t)$ , which is determined by  $h(x_{sh}, t) = 0$ , may be evaluated

$$x_{sh}(t) = \begin{cases} 2t - \frac{1}{2}t^2 & 0 \leq t < 2 - \sqrt{4 - 2x_c} \\ x_c & 2 - \sqrt{4 - 2x_c} \geq t < 2 \\ x_c - \frac{1}{2}(t - 2)^2 & 2 \geq t \end{cases}. \quad (12)$$

In figure 2 we plot Lagrangian trajectories (particle paths) under this flow, noting that the curve  $x = x_{ch}(t)$  corresponds to a contour of constant height, namely  $h = \frac{1}{9}(2 - \sqrt{2x_c})^2$ .

### Sediment transport: total load

We first consider sediment transport under a total load model. Figure 3 shows the net flux  $Q(x)$  across the truncated swash zone for various values of  $x_c$  and two total load models: equilibrium suspended sediment transport with  $q_e = u^2$  and the Bailard model in which total load is independent of depth ( $q = |u|^3 u$ ).

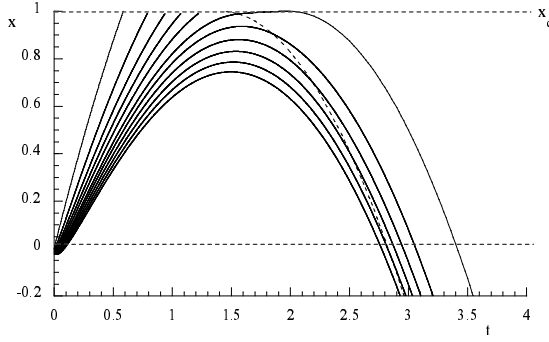


Figure 2: Selected Lagrangian trajectories,  $x_L(t)$ , under the overtopping flow (solid lines) when  $x_c = 1.0$ . Also plotted is the curve  $x = x_{ch}(t)$  across which the acceleration is discontinuous (dashed line).

Although the magnitudes of the net sediment fluxes are different, largely as a result of the choice of dimensionless variables, the patterns of transport are broadly similar.

First note that when there is no overtopping ( $x_c \geq 2$ ), then  $Q(x)$  increases monotonically to zero at  $x = 2$ . This implies that the flux is always offshore and that the breakwater/beach will be eroded all along its surface since  $dQ/dx > 0$ . The origin of this offshore transport is the asymmetry in the underlying hydrodynamics. Although the ballistic speed of the shoreline varies identically during the on- and off-shore phases of the motion, this is not the case behind the shoreline, where the backwash is prolonged. Thus this leads to greater sediment movement on the backwash and net offshore transport. It can be readily shown that this result is robust provided that the erosive flux is a monotonic function of the velocity [7].

When there is overtopping the net pattern of the sediment transport is somewhat different and there is now the possibility of on-shore transport because the backwash is diminished (see figure 3). When the swash zone is severely truncated, the effect of the backwash on total load is negligible, and most of the sediment movement is landward, with some deposition towards the crest of the breakwater. As the degree of truncation is reduced, the effect of the backwash reasserts itself, and net seaward transport is restored.

#### Sediment transport: suspended load

We now consider suspended sediment transport: figure 4 shows the net fluxes for the representative case  $q_e = u^2$  and  $E = 0.1$ , for four values of the cut-off point  $x_c$ .

Several points are evident in these figures. First note that  $Q^{en} > 0$  for locations close to the crest of the breakwater ( $|x_c - x| \ll 1$ ). In contrast to the total load models above, this landwards flux occurs even for a flow without overtopping ( $x_c = 2$ ). The mechanism for this landwards flux on the upper part of the breakwater is settling lag [4]: sedimentary material is eroded during the initial part of the swash event and deposited progressively as the flow reverses. On the backwash the flow also erodes material; however the concentration of suspended sediment does not adjust immediately to the local velocity and so even though the backwash lasts longer than the uprush, the landwards flux exceeds the seawards flux on the upper part of the breakwater. Pritchard & Hogg[7] show that the existence of a zone within which there is landwards transport remains robust to variations in the empirical erosion function ( $q_e$ ).

It is also noteworthy that the presence of the cut-off makes barely any difference to the landwards transport of internally

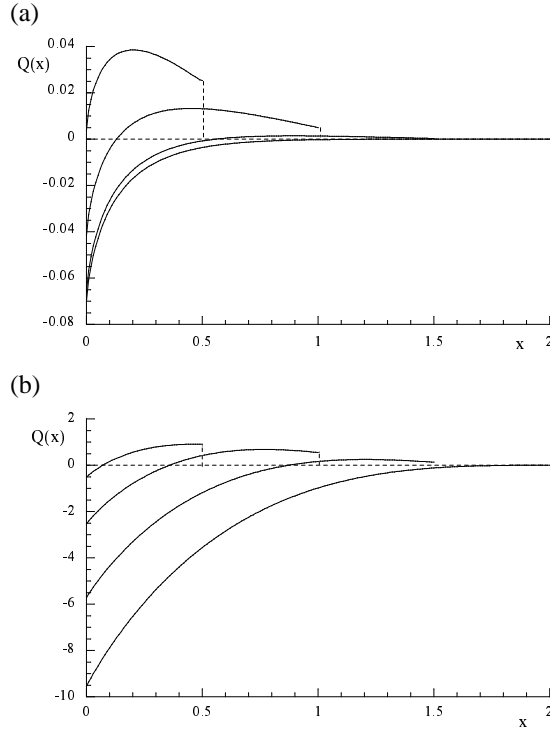


Figure 3: The net flux,  $Q(x)$ , across a breakwater with crest at  $x_c = 0.5, 1.0, 1.5$  and  $2.0$  for (a)  $q = u^3 h$ ; and (b)  $q = |u^3| u$  (Bailard model).

mobilised sediment (figure 4 a) or externally supplied sediment (figure 4 b), because unless  $x_c$  is very close to the origin of the swash event, most of the flow has reversed before it is affected by the overtopping. The difference which the overtopping does make is to the flow and sediment transport on the backwash, both of which are substantially reduced (although the spatial pattern is very similar to that under swash on an untruncated beach: compare the results for  $x_c = 0.5, 1.0$  and  $1.5$  with  $x_c = 2.0$ ).

As a result, there are substantial net fluxes in the landwards direction (figures 4 a and b). Some material passes over the top of the breakwater and is lost; for values of  $x_c$  around 1, however, a substantial quantity is deposited just seaward of  $x_c$  and then not re-entrained on the weak backwash; these intermediate values of  $x_c$  may cause a significant quantity of sediment to be deposited just below the crest of the breakwater, although the net effect is still generally erosional. The effect of truncation on the fate of externally supplied sediment (figure 4 b) is fairly insignificant, since most of this material has settled out before the backwash in any case.

The fluxes of sediment over the crest of the breakwater for the entrained material,  $Q^{en}(x_c)$ , and the pre-mobilised material,  $Q^{pr}(x_c)$ , exhibit rather different behaviours as  $E$  is varied. The material in suspension when the swash is initiated gradually settles out along the breakwater. As  $E$  increases, the rate of deposition also increases and so fewer particles remain in suspension at the crest of the breakwater. Thus as shown in figure 5, the flux of sediment lost over the breakwater diminishes monotonically with  $E$ . However, the amount of material mobilised within the swash zone which can be carried over the breakwater,  $Q^{en}(x_c)$ , shows a more complicated variation, because there are two competing effects. When the exchange rate parameter is sufficiently small, there is little erosion during the swash event ( $Q^{en} = O(E)$ ). Thus  $Q^{en}(x_c)$  increases with  $E$  for  $E \ll 1$ . Conversely when  $E$  is sufficiently large then the concentration of suspended sediment is in equilibrium with the local flow con-

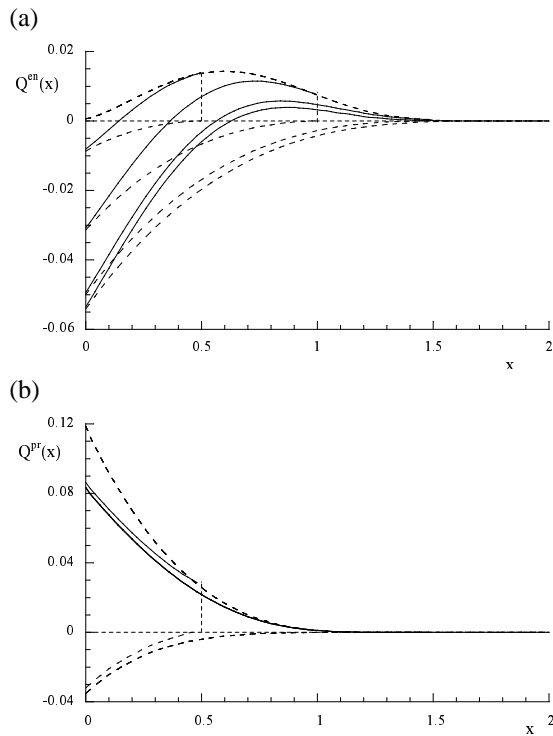


Figure 4: The net flux,  $Q(x)$ , across a breakwater with crest at  $x_c = 0.5, 1.0, 1.5$  and  $2.0$  for  $q_e = u^2$  and  $E = 0.1$  as a function of position: (a) Internally mobilised sediment,  $Q^{en}$ ; and (b) Pre-suspended sediment,  $Q^{pr}$ . The solid lines represent the net fluxes over the overtopping event; the dashed lines represent the contributions from the uprush and backwash components. (Note that in (b) the curves for  $x_c = 1.0, 1.5$  and  $2.0$  are indistinguishable.)

ditions and attains a constant value determined solely by the velocity and height at the crest ( $Q^{en} = O(1)$ , when  $E \gg 1$ ). Decreasing the exchange rate parameter in this regime increases the flux of sediment because material is advected over the crest that was mobilised lower down the breakwater where the velocity and rate of erosion are higher. These observations imply that there is a value of  $E$  for which  $Q^{en}(x_c)$  is maximised (figure 5). We note that such a maximum may act as a mechanism for segregating by size of the sediment that is carried over the breakwater, because transport is maximised for a particular value of  $E$  (and thus of  $w_s$ ).

The sediment flux at the crest also exhibits a complicated behaviour with the length of the breakwater ( $x_c$ ): longer breakwaters provide a longer-lived uprush and thus more time to entrain sediment, but they also reduce the velocity of the flow at the time when it reaches the crest. Overall, the latter effect dominates, and there is quite a strong decrease in fluxes at the crest as  $x_c$  increases. Increasing the length of the breakwater,  $x_c$ , also decreases the value of the exchange parameter,  $E$  at which the sediment flux is maximised.

## Conclusions

We have developed an analytical description of the transport of suspended sediment by a single swash event following the collapse and overtopping of a bore onto a sloping breakwater. Our analysis couples the hydrodynamic model of overtopping flow of Peregrine & Williams[3] to a sediment transport model and treats the equations in a Lagrangian frame of reference to determine the concentration of suspended sediment within the entire flow. It was particularly insightful to separate the transported sediment into contributions entrained during the swash event

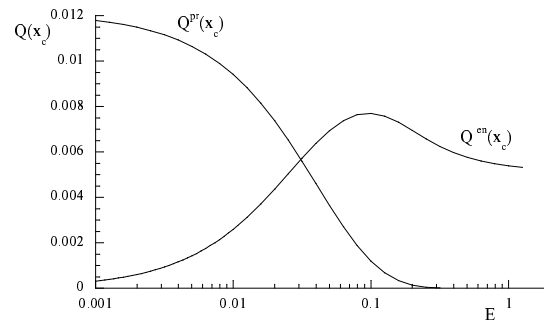


Figure 5: The net flux of sediment at the crest of the breakwater,  $Q(x_c)$ , as a function of  $E$  for  $q_e = u^2$  and  $x_c = 1.0$ . The internally mobilised,  $Q^{en}(x_c)$  and the presuspended components,  $Q^{pr}(x_c)$  are plotted separately.

and pre-suspended within the collapsing bore and to analyse their evolutions separately. We demonstrated that the effects of overtopping were to increase significantly the landwards transport of suspended sediment. This occurs because sediment is carried over the crest of the breakwater and because the backwash is weakened and becomes unable to mobilise sediment. Thus overtopping is likely to erode the face of the breakwater towards the seawards end of the swash zone, but there may be appreciable deposition close to the crest. Since the long-term effect of this erosion and deposition is to steepen the breakwater and make it less effective at dissipating wave energy, paradoxically the landwards movement of sediment may ultimately contribute to the degradation of the defence structure.

## Acknowledgements

AJH and DP acknowledge financial support from EPSRC (UK). DP also acknowledges funding from NERC (UK), award NE/B50188X/1.

## References

- [1] Butt, T. and Russell, P., Hydrodynamics and cross-shore sediment transport in the swash-zone of natural beaches: a review, *J. Coastal Res.*, **16**, 2000, 255–268.
- [2] Elfrink, B. and Baldock, T., Hydrodynamics and sediment transport in the swash zone: a review and perspectives, *Coastal Engineering*, **45**, 2002, 149–167.
- [3] Peregrine, D. H. and Williams, S. M., Swash overtopping a truncated plane beach, *J. Fluid Mech.*, **440**, 2001, 391–399.
- [4] Pritchard, D. and Hogg, A. J., Cross-shore sediment transport and the equilibrium morphology of mudflats under tidal currents, *J. Geophys. Res.*, **108**, 3313: doi:10.1029/2002JC001570.
- [5] Pritchard, D. and Hogg, A. J., On fine sediment transport by long waves in the swash zone of a plane beach, *J. Fluid Mech.*, **493**, 2003, 255–275.
- [6] Pritchard, D. and Hogg, A. J., Suspended sediment transport under seiches in circular and elliptical basins, *Coastal Engineering*, **49**, 2003, 43–70.
- [7] Pritchard, D. and Hogg, A. J., On the transport of suspended sediment by a swash event on a plane beach, *Coastal Engineering*, In press.
- [8] Shen, M. C. and Meyer, R. E., Climb of a bore on a beach. Part 3. Run-up, *J. Fluid Mech.*, **16**, 1963, 113–125.

## Preliminary Identification of Flow Regimes in a Mechanically Oscillated Planar Jet

M. Riese, G.J. Nathan, R.M. Kelso

School of Mechanical Engineering  
The University of Adelaide, SA 5005, AUSTRALIA

### Abstract

A plate with a large aspect ratio nozzle was mechanically oscillated in a near sinusoidal fashion with three ratios of oscillation stroke to nozzle diameter, namely 10, 5 and 2.5. A set of 210 different flow conditions was investigated in the laminar Reynolds number regime and visualized utilizing both the hydrogen bubble and dye trace technique. Three flow regimes were identified with the transition between them being dependent on a Strouhal number based on oscillation stroke, which is equivalent to a relative velocity ratio of the plate to the jet,  $|V|/U$ . The first regime identified occurs in the highest velocity ratio region and has been termed the Wall Vortex regime. Here a vortex detaches from the jet at the end of each stroke and stays attached to the plate. A second flow regime, termed the Mushroom Vortex regime exists at lower velocity ratios. Here a counter-rotating vortex pair forms within the jet at the end of each stroke. The third regime is called the Weaving Jet regime. Here the jet is ejected approximately normal to the plate but exhibits large-scale oscillations further downstream. All regimes were recorded and half sequences are presented here.

### Introduction

Jets find common usage in chemical and combustion processes, for example, and have therefore been widely studied. The orderly structures and flow instabilities within them have received special attention because they dominate the rate of spread and decay, etc. However, most research on the subject has been undertaken on round jets. Throughout the past decades it has been shown that it is possible to excite jets by acoustical [2], fluidic [10] and mechanical means [8]. Of these, the fluidic excitation has the greatest potential for application in harsh industrial environments, typically of furnaces and kilns, although each may have its niche. Significantly, relatively little effort has been spent on the investigation of stimulated planar jets and likewise, relatively few practicable applications have been conceived. One such device, which uses fluidic excitation is the planar flip-flop nozzle of Mi *et al.* [7]. This has been shown to yield significantly higher initial entrainment of the ambient fluid and initial spreading as well as an increase in large-scale mixing. While fluidically excited nozzles such as this are mechanically robust and can be employed in high temperature processes, they are not well suited to rigorous investigations at fundamental level. For example the oscillation frequency depends directly on the jet velocity and geometry, so preventing the possibility of their individual variation. In addition, the velocity profiles at the nozzle exit are neither uniform nor well defined, even if the inlet flow is.

In contrast, mechanically oscillated planar jets can be well defined and have been investigated since the 1970s. Simmons *et al.* [9] and Collins *et al.* [1] developed an apparatus consisting of a plenum chamber with a smooth contracting nozzle (length to height ratio, i.e. nozzle aspect ratio of 60) and a large oscillating vane positioned in the potential core.

This imposed an angular oscillation on the jet, resulting in higher initial jet spread and bulk fluid entrainment. Although the apparatus allowed for independent variation of the oscillation frequency and jet velocity, an angular velocity was introduced by the flapping of the vane increasing the complexity of the investigation. To reduce this complexity, a modified apparatus was employed by Galea [3] and Galea & Simmons [4]. Here one

of the nozzle plates was oscillated instead of a flapping vane, so modulating the nozzle width. Again an increase in jet spreading angle and bulk fluid entrainment was shown. The stroke of oscillation to nozzle diameter ratio was chosen to be  $\leq 0.1$ . These investigations as well as all other currently known investigations were undertaken at a  $St \sim 0.3$  trying to achieve the maximum amplification as described by [2].

To the authors' current knowledge, no investigations have been performed on a large aspect ratio oscillating nozzle with a stroke to nozzle diameter ratio greater than unity. To address this issue the present study performs a flow visualization study using a mechanical device to identify the flow regimes for a much wider range of oscillations than has been previously assessed.

### Experimental Set-up

Experiments were conducted in a water tunnel facility using dye traces or a hydrogen bubble wire as flow visualisation techniques. The oscillating plate (figure 1) consists of a sliding plate with a smooth radially contracting nozzle of aspect ratio,  $w/h = 16.5$ . It is driven by a crank-conrod mechanism with a near sinusoidal motion that provides a maximum motion deviation from pure simple harmonic motion (SHM) of 10%. The stroke length ( $S$ ) to nozzle height ( $h$ ) ratios ( $R$ ) investigated were 10, 5 and 2.5. By using the nozzle height to calculate the Reynolds number, the flows investigated were in the range  $Re = 253 - 1831$ . The frequencies of oscillation ranged from 0.25 Hz - 1.25 Hz. The flow visualization experiments were recorded with a 0.47-mega-pixel digital video camera resolving a pixel size of  $0.7\text{mm} \times 0.7\text{mm}$  in the case of the hydrogen bubble wire set-up and phase locked still images using a 6-mega-pixel digital SLR camera with a 50 mm standard lens resolving a pixel size of  $0.28\text{mm} \times 0.28\text{mm}$ . A set of 210 experimental conditions was investigated for different combinations of oscillation frequency, stroke to diameter ratios and  $Re$  using the hydrogen bubble wire method (Table 1). All recorded cases were examined to identify characteristic flow features. A limited set of conditions was repeated using dye visualization to confirm observations made in the preliminary experiments and to provide higher quality images.

Dye flow visualization experiments used a rake of small probes positioned stationary upstream from the oscillating plate along the vertical nozzle centreline to achieve evenly distributed dye flow through the nozzle. For both, the hydrogen bubble wire and dye, no buoyancy effect of the marker particles were noted. The oscillation of the plate translates the source of the jet with a perpendicular velocity, in a manner that closely approximates SHM and hence can be calculated as

$$V_i = \frac{S}{2} \times (2 \times \pi \times f) \times \cos(t \times 2 \times \pi \times f) \quad (1)$$

where

- $V_i$  = Instantaneous plate velocity ( $\text{m.s}^{-1}$ );
- $S$  = Oscillation stroke (m);
- $f$  = Oscillation frequency (Hz);
- $t$  = Time (s);

whereby the oscillation stroke is equal to twice the amplitude. Although  $V_i$  varies with time, for the purpose of a comparative study it is possible to characterize it based on the maximum value,  $|V|$ , at the centreline position, eliminating the cosine term from (1).



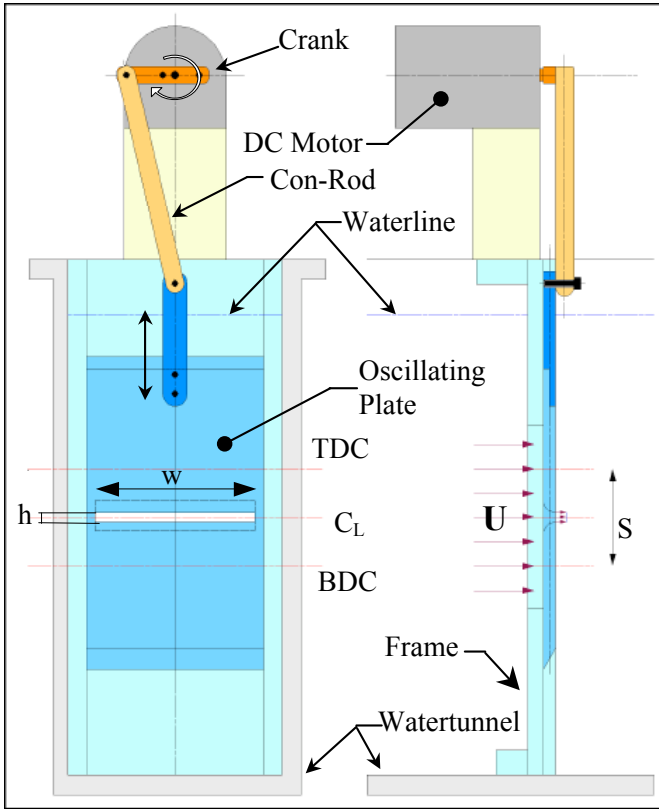


Figure 1. Mechanically Oscillating Planar Jet mechanism.  $S$  = oscillation stroke;  $C_L$  = oscillation centreline; TDC = top dead centre; BDC = bottom dead centre;  $h$  = nozzle width;  $w$  = nozzle length;  $U$  = jet mean velocity.

Variable	Unit	Values
Oscillation Frequency (f)	Hz	0.25 – 1.25 (Increments of 0.25 Hz)
Stroke/ Diameter Ratio (R)		10, 5, 2.5
Reynolds Number ( $Re_h$ )		253 – 1831 (Increments of 126)

Table 1. Investigation grid for hydrogen bubble wire flow visualisation experiments.

### Flow Regimes

From recorded footage one of three dominant flow regimes was found to exist in all of the amplitude-nozzle ratios investigated. These regimes have been termed, as follows

- the Wall Vortex regime
- the Mushroom Vortex regime
- the Weaving Jet regime

The ratio of the characteristic  $|V|/U$ , is equivalent to a Strouhal number based on the oscillation amplitude. As shown

$$St_S = \frac{|V|}{U} = \frac{S \times f}{U} \quad (2)$$

appears to be one of the most important scaling parameters. The characteristic features and conditions under which they occur, are assessed in turn.

### Wall Vortex Regime

A time sequence spanning a half-cycle of oscillation in the wall vortex regime is shown in figure 6. Note that the images of the flow have been rotated by  $90^\circ$  (to appear vertical) to assist in formatting the images in the available space. During the phase in the cycle, when the nozzle passes the oscillation centre line and the nozzle starts to decelerate, a small vortex forms behind the nozzle jet. When the nozzle reaches TDC or BDC, the vortex separates from the jet and remains approximately stationary at the point of detachment. TDC and BDC are the phase in the oscillation (approximately SHM), where the maximum deceleration followed by the maximum acceleration occurs. The vortex dissipates during the subsequent cycle and cannot be identified visually as a coherent feature by the phase in the

oscillation cycle when the nozzle reaches the opposite turning point. During the phase where the vortex can be identified as a coherent feature by visual inspection, it seems to grow steadily by entraining ambient fluid throughout the phase the vortex appears to be attached to the plate surface. Shortly before transition into the next regime a small counter- rotating vortex appears between the main vortex and the plate (figure 2), which is then “squashed” by the larger vortex. The Wall Vortex regime is situated in the highest range of  $|V|/U$  of the currently investigated cases.

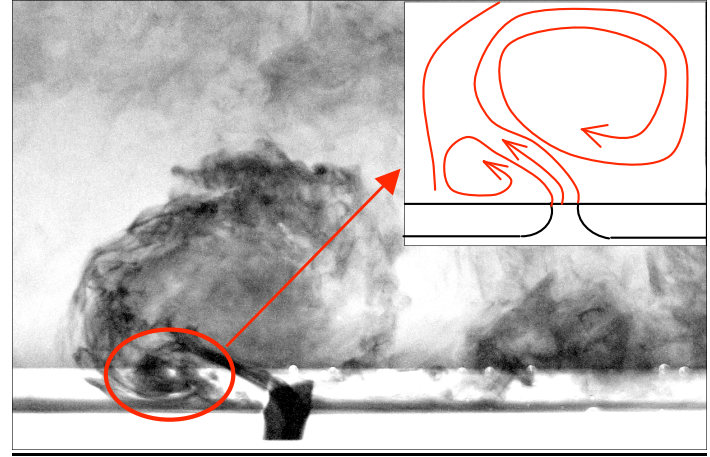


Figure 2. Wall vortex regime shortly before detachment of vortex structure and transition to the mushroom regime.

### Mushroom Vortex Regime

The mushroom vortex regime exists at a  $|V|/U$  range below the range of the wall vortex regime for each  $R$ . In this regime the jet momentum high enough to prevent the vortex formed at TDC and BDC from being attached to the oscillating plate and to form a counter- rotating vortex pair (figure 7). The motion of the plate causes the apparent angle between the jet and the plate to be large. However it should be noted that velocity measurements are required to obtain actual trajectories. The mushroom shape of the formed vortices bear some resemblance with vortex rings formed described by such likes as [5] (figure 3).

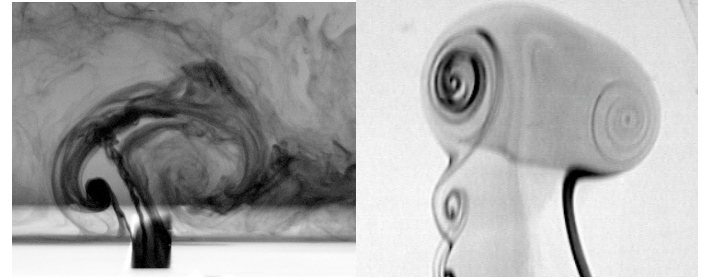


Figure 3. Mushroom vortex from mechanically oscillated planar jet (left) and vortex rings from jet as described by [5] (right) (Photo: E. Hassan [6]).



Figure 4. Jet in the weaving jet regime with inclusion of the flow field further downstream. Initially nearly straight jet shows high degree of oscillation in the far field.



### Weaving Jet Regime

The weaving jet regime occurs at a  $|V|/U$  range below the mushroom vortex range (figure 8). This regime is related to the mushroom vortex regime and in addition to the jet being more perpendicular to the oscillating plate during its initial ejection phases, the main difference is that no visible counter-rotating vortex pairs exist here. The initial near field of the jet is visually very similar to a steady flow jet, with two important differences. Firstly, the shear layer vortices are strongly magnified compared to a steady jet and secondly, they are larger on the trailing edge of the oscillating jet. Inspections of the flow field downstream from the initially straight jet (figure 4) shows that it subsequently develops a large-scale oscillation.

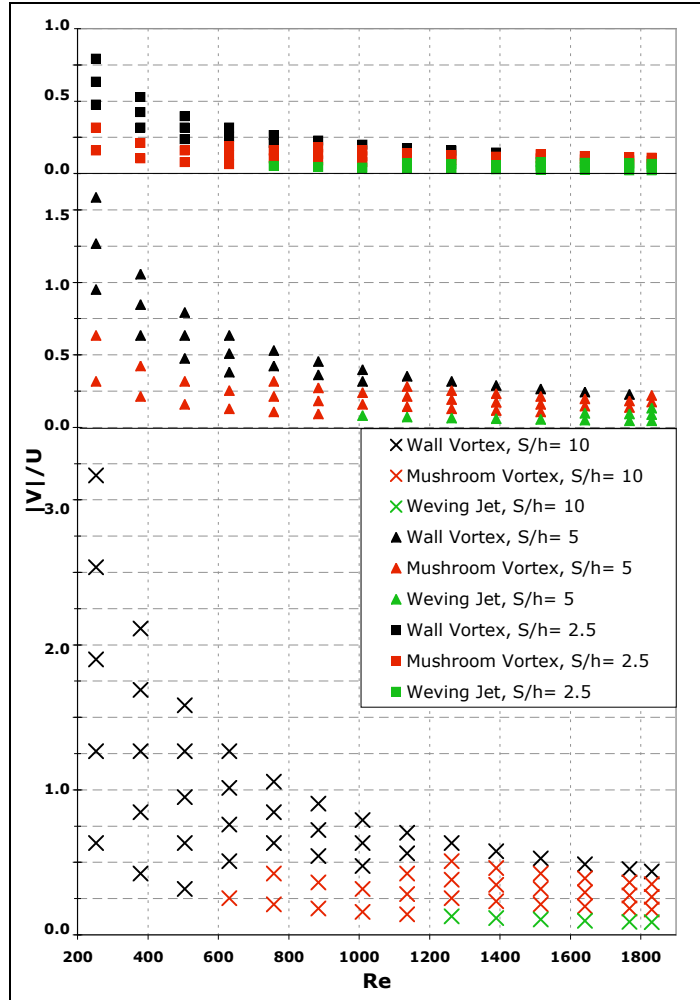


Figure 5. Flow regimes as identified for different  $S/h$ .

### Regime Boundaries

A systematic study was performed to identify which regime occurs in each of a wide combination of  $Re$ ,  $R$  and  $|V|/U$ . These were all performed with a fixed nozzle, so that varying the stroke causes a variation in  $R$ . The technique chosen for this investigation was the hydrogen bubble. The results can be seen in figure 5.

It can be seen that as expected the flow regimes follow the same sequence from Wall Vortex over Mushroom Vortex to Weaving Jet for all  $R$ . For each value of  $R$  regime boundaries seem to approach a constant value with increasing  $Re$  as the influence of viscous forces is reducing and it is expected that this trend continues in the transition and turbulent regime. However it can also be seen that for constant  $Re$  the regime boundaries are changing at different values of  $|V|/U$  for different  $R$ .

As all tests were carried out over a grid of discrete  $|V|/U$  values, which were determined prior to any knowledge of the flow to be encountered and solely governed by the achievable values, entrenched in the mechanical properties of the experimental apparatus are hence making it impossible to exactly determine the regime boundaries from the existing data.

As the three regimes do not suddenly change from one into the other, but rather gradually approach a different regime under varying flow conditions and hence the determination of the mode in each case was somewhat subjective. At the current moment it is unclear if any further flow regimes exist and what their characteristics are.

### Conclusions

From flow visualization of the transverse oscillation of the source of a planar jet, three flow regimes were identified and characterized. These flow regimes have not been documented previously and exhibits considerable differences to the flows observed by related investigations [3, 4, 9]. It should be noted that the present investigations were undertaken with a relatively small nozzle aspect ratio with a facility that was only able to produce flows in the laminar  $Re$  regime. Further investigations are planned with a new facility that provides better-controlled initial conditions, such as minimizing three-dimensional end-effects from the nozzle, and is also capable of operating within the turbulent  $Re$  regime. This work will redefine the regime boundaries and provide further detailed of each the flow regimes identified.

### Acknowledgments

The authors would like to acknowledge the ongoing support of the Australian Research Council and FCT International.

### References

- [1] Collins, D J, Platzer, M F, Lai, J C S & Simmons, J M, Experimental Investigations of Oscillating Subsonic Jets, *Conference Proceedings of Numerical and Physical Aspects of Aerodynamic Flows*, 1982, pp 575 – 587.
- [2] Crow, S C & Champagne F H, Orderly Structures in Jet Turbulence, *Journal of Fluid Mechanics*, No 3, Vol 48, Aug 1971, pp 547 – 591.
- [3] Galea, S C, *Excitation of a Plane Turbulent Jet by Nozzle Area Variation*, Master Thesis, University of Queensland, Australia, May 1983.
- [4] Galea, S C & Simmons, J M, Excitation of a Plane Jet by Periodic Perturbation of the Nozzle Area, *Eighth Australasian Fluid Mechanics Conference*, 1983, 13C.5 - 13C.8.
- [5] Gharib, M, Rambod, E & Shariff, K, *A universal time scale for vortex ring formation*, *Journal of Fluid Mechanics*, Vol 350, Apr. 1998, pp 121 –140.
- [6] Hassan, E & Riese, M, Personal unpublished communication, July 2004.
- [7] Mi, J, Nathan, G J, & Luxton, R E, Dynamic Oscillation of a Quasi-Planar Jet, *12th Australasian Fluid Mechanics Conference*, 1995, pp 119 – 122.
- [8] Schneider, G M, *Structures and turbulence characteristics in a precessing jet flow*, PhD Thesis, University of Adelaide, Australia, 1996.
- [9] Simmons, J M, Lai, J C S & Platzer, M F, Jet Excitation by an Oscillating Vane, *AIAA Journal*, No 6, Vol 19, June 1981, pp 673 – 676.
- [10] Viets, H, Flip-Flop Jet Nozzle, *AIAA Journal*, No 10, Vol 13, Oct 1975, pp 1375-1379.

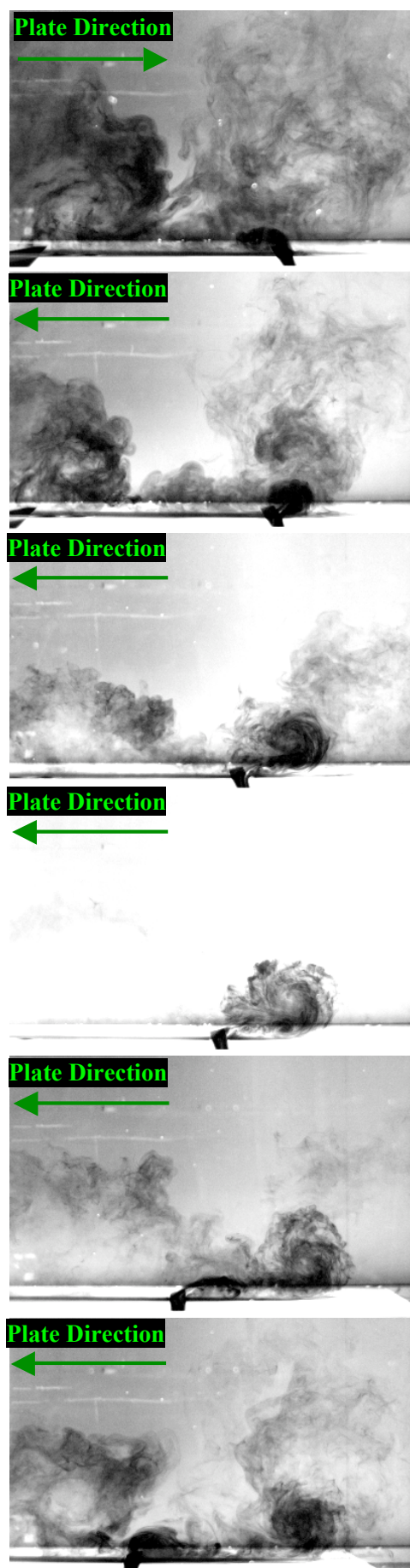


Figure 6. Pseudo sequence of a jet in the wall vortex flow regime (top to bottom). Vortex forms at TDC and BDC and stays attached to plate. Flow symmetrical across oscillation centreline.

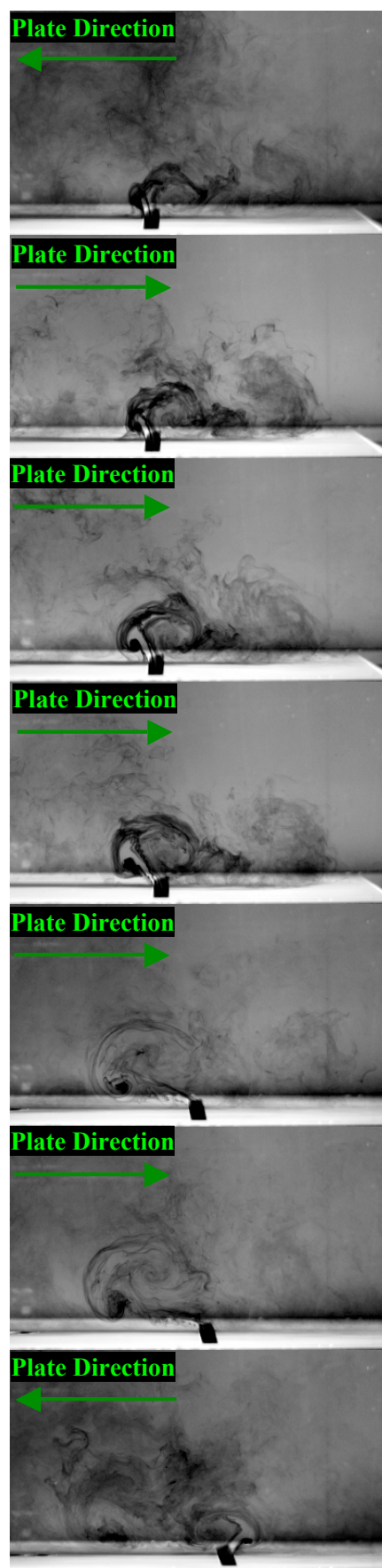


Figure 7. Pseudo sequence of a jet during the mushroom vortex flow regime (top to bottom). Jet forms counter-rotating vortex pair at TDC and BDC, which is detached from the oscillating plate. Flow symmetrical across oscillation centreline.

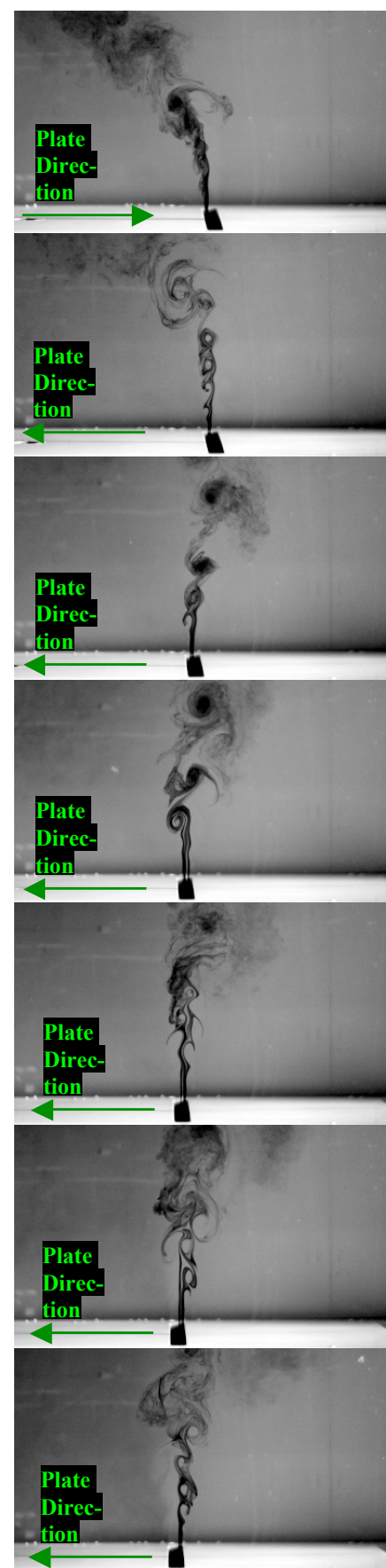


Figure 8. Pseudo sequence of a jet during the weaving jet flow regime (top to bottom). Jet does not form visible counter-rotating vortex pairs at TDC and BDC, shear layer vortex structures appear magnified on trailing edge of jet compared to steady jet flow. Flow symmetrical across oscillation centreline.

## Turbulent Stress Invariant Analysis: Clarification of Existing Terminology

A.J. Simonsen<sup>1</sup> and P.-Å. Krogstad<sup>2</sup>

<sup>1</sup>Present address: SINTEF Energy Research, Energy Processes. Kolbjørn Hejes v. 1b, N-7065 Trondheim, Norway

<sup>2</sup>Department of Energy and Process Engineering, The Norwegian University of Science and Technology, N-7491 Trondheim, Norway

### Abstract

As a means of studying the structure of the turbulence, the time mean invariants, defined according to the theory of Lumley [3] has proven to be a useful and popular tool. According to the theory there is a domain, known as the Lumley triangle, within which all realizable Reynolds's stress invariants must lie. The borders of this domain describes different states of the turbulent stress tensor. It has been found that there is some confusion in the terminology used when describing these states. The confusion is related to whether the notation is used to describe the shape of the stress tensor or the eddies of the turbulence. Choi and Lumley [1] noted the same controversy in terminology, but since the confusion is still found to exist the current work describes the fundamental relationships which exist between the shape of the stress tensor and it's invariants. Also an analysis is given to clarify the existing terminology.

### Introduction

Any symmetric tensor, like the stress tensor  $\tau_{ij}$ , may be divided into a traceless deviator,  $\tau'_{ij}$  and an isotropic part,  $\tau^\circ_{ij}$

$$\tau_{ij} = \tau^\circ_{ij} + \tau'_{ij} \quad (1)$$

where

$$\tau^\circ = \frac{1}{3} \tau_{kk} \delta_{ij} \quad (2)$$

and

$$\tau'_{ij} = \tau_{ij} - \frac{1}{3} \tau_{kk} \delta_{ij} \quad (3)$$

In the case of true isotropy all the elements in  $\tau'_{ij}$  would become zero. The non-dimensional form of the anisotropy tensor is given by

$$b_{ij} = \frac{\tau'_{ij}}{\tau_{kk}} = \frac{\tau_{ij}}{\tau_{kk}} - \frac{1}{3} \delta_{ij} \quad (4)$$

By using the Cayley-Hamilton theorem, the characteristic equation for any second order symmetric tensor may be written as

$$\sigma^3 - I_1 \sigma^2 + I_2 \sigma - I_3 = 0 \quad (5)$$

where the  $I$ 's are the first, second, and third invariants of the tensor and  $\sigma$  is the principal stress. The invariants are related to the tensor terms according to the relations

$$I_1 = b_{kk} \quad (6)$$

$$I_2 = -\frac{1}{2} b_{ij} b_{ji} \quad (7)$$

$$I_3 = \det(b_{ij})$$

where the flow has been assumed to be incompressible.

Assuming incompressible axisymmetric turbulence with  $y$  as the symmetry axis, and using cylindrical coordinates, the invariants may be expressed as

$$I_1 = 0 \quad (8)$$

$$I_2 = -\frac{1}{2} [b_{rr}^2 + b_{yy}^2 + b_{\theta\theta}^2 + 2b_{ry}^2]$$

$$I_3 = [b_{rr}b_{yy} - b_{ry}^2]b_{\theta\theta}$$

In solving the characteristic equation, equation (5), for a given set of invariants the eigenvalues and the related eigenvectors of the tensor are revealed. This gives the main stress directions of the stress tensor and their magnitude. Several solutions are possible depending on the stress field, but there are also definitive bounds with respect to the realizability of the flow which have led to the anisotropy invariant map (initially proposed by Lumley [3]) and therefore often referred to as the Lumley triangle) given in figure 1.

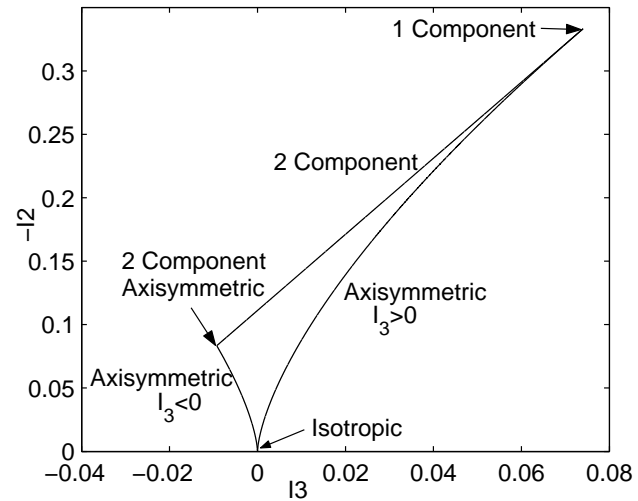


Figure 1: The anisotropy invariant map, AIM.

At the origin ( $I_2 = I_3$ ) the isotropic state is found. From this point two limiting lines are found where the flow is assumed to be axisymmetric (i.e.  $b_{ry} = 0$  and two of the diagonal elements are equal e.g.  $b_{rr} = b_{\theta\theta}$ ). This leads to the relation  $I_3 = \pm 2(-I_2/3)^{3/2}$ . Each of these lines have a limiting value. In the first case the two identical diagonal terms are smaller than the third element and tend to zero. This leads to a 1 component state of turbulence (1C in figure 1). The other possibility is that the two identical elements dominate so that the third component is ignorable. This leads to the two component axisymmetric state indicated in figure 1. The line joining 1- and 2-component axisymmetric turbulence represents the all other possible states where only two diagonal components exist.

As a tool in describing the state of the turbulence Lee and



Reynolds[2] designated different shapes of the stress field to the value of the invariants in equation (5) such as rod and disk like turbulence. However, in their description Lee and Reynolds were focusing on the turbulent eddies rather than the stress field itself. This has over the years lead to a confusion when describing the stress field since the characteristic shapes related to the stresses and the eddies are not generally the same. If not aware of this the axisymmetric limits of the Lumley triangle will be described by shapes that do not relate to the stress tensor the invariants represent.

In the following the relations between the stress field and the invariants are shown and then related to the shape of the stress tensor. This will be compared to the shape of the turbulent eddies for the same type of turbulence. It must be emphasized that this analysis does not have an influence on turbulence modelling, but have implications in understanding and visualization of the stress field. It must also be noted that the aim of the current paper is to clarify the terminology used.

### The characteristic shape related to the stress tensor

In terms of the stress tensor the visualization of the stress field is determined by the relative sizes of the three main stresses and the designations of the axisymmetric limits are based upon the following analysis. The Reynolds stress tensor,  $\tau_{ij}$ , is a second order symmetric tensor. As stated by the spectral theorem *every real symmetric matrix can be diagonalized by an orthonormal matrix*. In other words the Reynolds stress matrix,

$$\mathbf{T} = \tau_{ij} = \begin{pmatrix} \tau_{11} & \tau_{12} & \tau_{13} \\ \tau_{21} & \tau_{22} & \tau_{23} \\ \tau_{31} & \tau_{32} & \tau_{33} \end{pmatrix}$$

may be written as

$$\mathbf{T} = \mathbf{Q}\mathbf{\Sigma}\mathbf{Q}^{-1} \quad (9)$$

where

$$\mathbf{\Sigma} = \begin{pmatrix} \sigma_1 & 0 & 0 \\ 0 & \sigma_2 & 0 \\ 0 & 0 & \sigma_3 \end{pmatrix}$$

is the eigenvalue matrix of  $\mathbf{T}$  and  $\sigma_i$  are the eigenvalues.  $\mathbf{Q}$  is an orthonormal matrix with the properties

$$\mathbf{Q}\mathbf{Q}^{-1} = \mathbf{Q}\mathbf{Q}^T = \mathbf{I}. \quad (10)$$

Now, recalling that the stress,  $\mathbf{f}_\tau$ , in the direction of a vector  $\mathbf{n}$  is represented by the linear operator  $\mathbf{T}$  on  $\mathbf{R}^3$  ( $\mathbf{T}: \mathbf{R}^3 \rightarrow \mathbf{R}^3$  where both  $\mathbf{n}, \mathbf{f}_\tau \in \mathbf{R}^3$ ):

$$\mathbf{f}_\tau = \mathbf{T} \cdot \mathbf{n} \quad (11)$$

By the use of relation 9 and left-multiplying with  $\mathbf{Q}^{-1}$  this may be rewritten as

$$\mathbf{y} = \mathbf{Q}^{-1}\mathbf{f}_\tau = \mathbf{\Sigma}\mathbf{Q}^{-1}\mathbf{n} = \mathbf{\Sigma}\mathbf{x}, \quad (12)$$

which means that by changing the old coordinate system into a new coordinate system, coinciding with the principal axis of the stress tensor,  $\mathbf{T}$  becomes a diagonal matrix  $\mathbf{\Sigma}$  with the principal stresses of  $\mathbf{T}$  on its diagonal.

If  $\mathbf{x}$  is considered as the normalized stress vector of an isotropic field describing the unit sphere we have

$$\begin{aligned} \mathbf{x} &= \langle x_1, x_2, x_3 \rangle \\ \mathbf{x}^T \mathbf{x} = 1 &\Leftrightarrow x_1^2 + x_2^2 + x_3^2 = 1. \end{aligned} \quad (13)$$

Equation (12) is now representing a distortion of this stress vector due to the mapping  $\mathbf{T}$ . Left-multiplying equation (12) with  $\mathbf{\Sigma}^{-1}$  gives

$$\mathbf{x} = \mathbf{\Sigma}^{-1}\mathbf{y} \quad (14)$$

By using the equation (10) and the matrix relation

$$(\mathbf{A}\mathbf{B})^T = \mathbf{B}^T \mathbf{A}^T \quad (15)$$

the following is obtained

$$\mathbf{x}^T \mathbf{x} = \mathbf{y}^T \mathbf{\Sigma}^{-2} \mathbf{y} = 1 \quad (16)$$

or

$$\left(\frac{y_1}{\sigma_1}\right)^2 + \left(\frac{y_2}{\sigma_2}\right)^2 + \left(\frac{y_3}{\sigma_3}\right)^2 = 1 \quad (17)$$

where relation 13 is used. This describes the shape of a spheroid in the coordinate system  $(y_1, y_2, y_3)$ .

In order to establish a relationship between the shape of the stress tensor and the invariants of the anisotropy tensor we need to relate the eigenvalues of  $\mathbf{b} = (\frac{\mathbf{T}}{T_{kk}} - \frac{1}{3}\mathbf{I})$  and  $\mathbf{T}$ . From matrix theory we know that if for two matrices  $\mathbf{A}$  and  $\mathbf{B}$

$$\mathbf{A}\mathbf{B} = \mathbf{B}\mathbf{A} \quad (18)$$

then the matrices  $\mathbf{A}$  and  $\mathbf{B}$  share the same eigenvectors. Since the tensor  $1/3\delta_{ij}$  is equal to the identity matrix  $\mathbf{I}/3$ , relation 18 always holds between the matrices  $\mathbf{T}$  and  $\mathbf{I}$ . They therefore share the same eigenvector  $\mathbf{n}$  and the following relationship will hold.

$$\mathbf{b}\mathbf{n} = \left(\frac{\mathbf{T}}{T_{kk}} - \frac{1}{3}\mathbf{I}\right)\mathbf{n} \quad (19)$$

The relationship between the eigenvalues of  $\mathbf{b}$  and  $\mathbf{T}$  then becomes

$$\lambda_i = \frac{\sigma_i}{T_{kk}} - \frac{1}{3}. \quad (20)$$

For the non-dimensional anisotropy tensor,  $\mathbf{b}$ , related shapes of the ellipsoid formed by the Reynolds stresses are illustrated in figure 2 and characteristics of the flow are given in table 1.

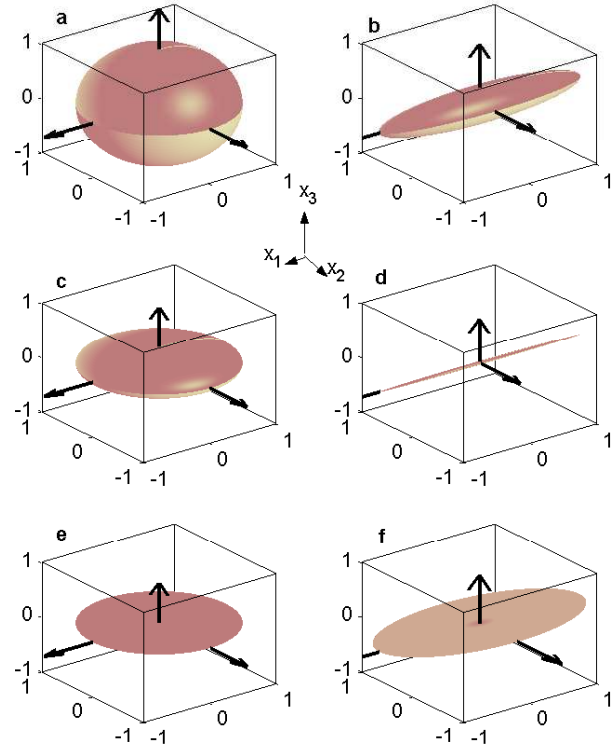


Figure 2: Illustration of the ellipsoid shapes formed by the Reynolds stress tensor in different regions of the flow.

State of turbulence	Invariants	Eigenvalues of $b_{ij}$	Shape of stress tensor (see eq. 17)	Symbol in figures 1 and 2
Isotropic	$I_2 = I_3 = 0$	$\lambda_i = 0$	Sphere	a, isotropic
Axi.sym. (One large $\lambda$ )	$-\frac{I_2}{3} = (\frac{I_3}{2})^{2/3}$	$0 < \lambda_1 < \frac{1}{3}, -\frac{1}{6} < \lambda_2 = \lambda_3 < 0$	Prolate spheroid	b, axisymmetric ( $I_3 > 0$ )
Axi.sym. (One small $\lambda$ )	$-\frac{I_2}{3} = (-\frac{I_3}{2})^{2/3}$	$-\frac{1}{3} < \lambda_2 < 0, 0 < \lambda_1 = \lambda_3 < \frac{1}{6}$	Oblate spheroid	c, axisymmetric ( $I_3 < 0$ )
One-comp.	$I_3 = \frac{2}{27}, I_2 = -\frac{1}{3}$	$\lambda_1 = \frac{2}{3}, \lambda_2 = \lambda_3 = -\frac{1}{3}$	Line	d, 1 Component
Two comp., axisym.	$I_3 = -\frac{1}{108}, I_2 = -\frac{1}{12}$	$\lambda_1 = \lambda_3 = \frac{1}{6}, \lambda_2 = -\frac{1}{3}$	Disk	e, 2 Component, (axisymmetric)
Two component	$-I_2 = 3(\frac{1}{27} + I_3)$	$\lambda_1 + \lambda_3 = \frac{1}{3}, \lambda_2 = -\frac{1}{3}$	Ellipsoid	f, 2 Component

Table 1: Characteristics of the turbulence stress tensor and anisotropic tensor.

### Clarification of Terminology

Now it is time to address the misconception encountered in the designation of the limits of Lumley's invariant map. Axisymmetric turbulence means that two of the principal stresses  $\sigma_i$ , or  $\lambda_i$ , are equal. Writing  $\mathbf{b}$  in terms of the principal direction we have

$$\mathbf{b} = \begin{pmatrix} \lambda_1 & 0 & 0 \\ 0 & \lambda_2 & 0 \\ 0 & 0 & \lambda_3 \end{pmatrix} \quad (21)$$

and for axisymmetric turbulence we have e.g.  $\lambda_2 = \lambda_3$ . Together with relationship 8,  $\lambda_1 + \lambda_2 + \lambda_3 = 0$ , this gives for the invariants  $I_2$  and  $I_3$

$$I_2 = -\frac{3}{4}\lambda_1^2, \quad I_3 = \frac{1}{4}\lambda_1^3 \quad (22)$$

From the previous analysis it is clear that if we have one large principal value  $\sigma_1$  and two equal but smaller principal values  $\sigma_2 = \sigma_3$ , the turbulence field will be stretched in the  $\mathbf{n}_{\sigma_1}$ -direction creating the prolate spheroid of figure 2 b). On the other hand, if  $\sigma_1$  is smaller than the other two, the shape of the stress tensor would be the oblate spheroid of figure 2 c). This gives the following relationship between the principal values, invariants, and shape.

$$\lambda_1 > 0 \Rightarrow I_3 > 0 \Rightarrow \text{Rod-like turbulence} \quad (23)$$

$$\lambda_1 < 0 \Rightarrow I_3 < 0 \Rightarrow \text{Disk-like turbulence} \quad (24)$$

Eliminating  $\lambda_1$  from the relations in 22 we get

$$I_3 = A \left[ 2 \left( -\frac{I_2}{3} \right)^{3/2} \right] \quad (25)$$

The term in the parenthesis will always be greater than zero since  $I_2 \leq 0$  (see equation (7)), so the sign of  $I_3$  will be determined by  $A$ . Comparing this with the statements 23 and 24,  $A$  will have the following values

$$A = \begin{cases} 1 & , \text{ Rod-like turbulence} \\ -1 & , \text{ Disk-like turbulence} \end{cases}$$

With respect to the invariant map of Lumley and in terms of the shape of the stress tensor this gives the designation of axes shown in figure 3.

The error in the designation encountered in articles and text-books is that the two axisymmetric limits with rod like and disk like turbulence are switched because some researchers talk about the shapes of the turbulent eddies rather than those of the stress tensor. In terms of vorticity the visualization of the turbulence would be opposite to that of the stresses. This may be exemplified by the flow through an axisymmetric contraction as shown in figure 4. Figure 4A) illustrates a streamwise vortex tube before and after a contraction. For an incompressible fluid the transport equation for vorticity is given by the Helmholtz equation

$$\frac{D\boldsymbol{\omega}}{Dt} = (\boldsymbol{\omega} \cdot \nabla) \mathbf{U} + \nu \nabla^2 \boldsymbol{\omega}, \quad (26)$$

where  $\mathbf{U}$  is the fluid velocity and the vorticity  $\boldsymbol{\omega}$  is defined by the curl of the velocity

$$\boldsymbol{\omega} = \nabla \times \mathbf{U}. \quad (27)$$

The first term on the right of (26) is called the vortex stretching term whereas the second term is a viscous diffusion term. Through the contraction the streamwise component of the vorticity  $\omega_1$  is increased by vortex stretching term since it includes the term  $\omega_1 \partial U_1 / \partial x_1$ .  $\partial U_1 / \partial x_1$  is positive due to the decrease in flow area and therefore a streamwise vortex tube is stretched and obtains a rod-like shape after the contraction. At the same time, due to the continuity requirement  $\nabla \cdot \mathbf{U} = 0$ , the vorticity in the directions normal to the streamwise direction,  $\omega_2$  and  $\omega_3$ , are attenuated.

For the turbulent stress tensor, on the other hand, the production of the streamwise turbulence component is suppressed by the secondary production term  $-\tau_{11} \partial U_1 / \partial x_1$  (see [4]).  $\tau_{11}$  is always positive and since the streamwise gradient is positive the production term will become negative. The result is that the stress ellipsoid, according to the analysis in the previous section, becomes flattened in the streamwise direction and obtains a disk-like shape as illustrated in figure 4B).

### Summary

The aim of the current paper is to clarify the terminology used when the axisymmetric limits of the Lumley triangle are related

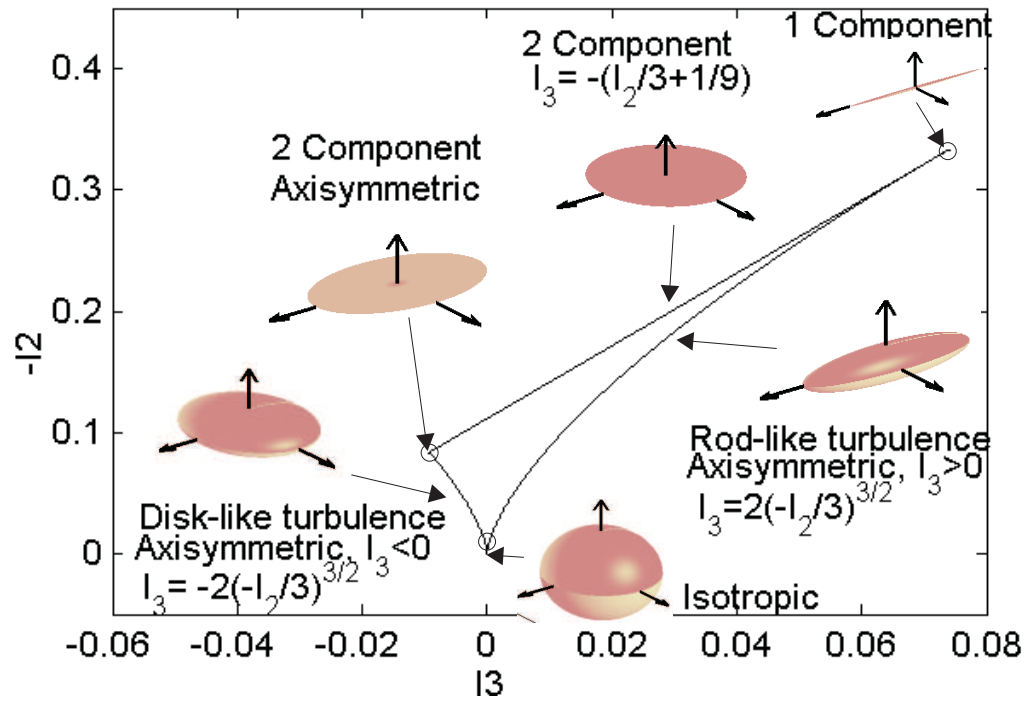


Figure 3: Anisotropy invariant map with correct designation of the axisymmetric states.

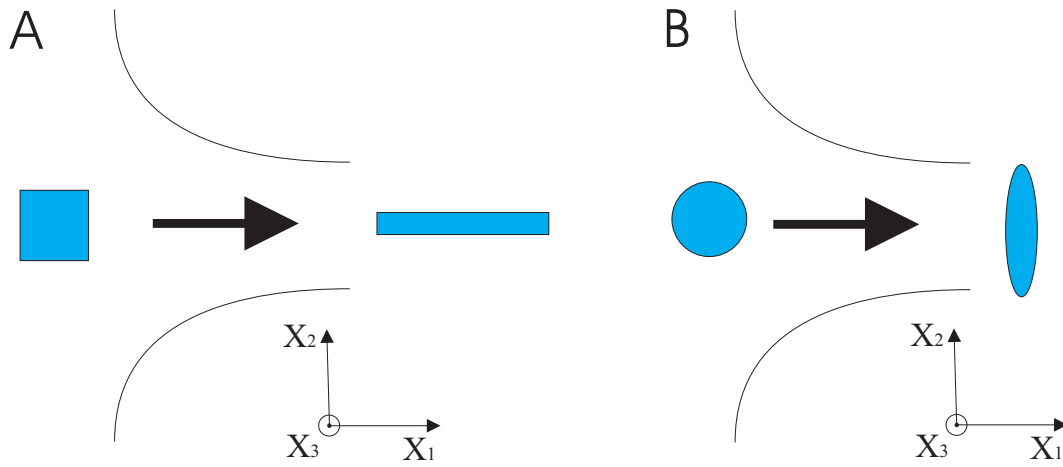


Figure 4: Illustration of streamwise vortex tube stretching(A) and stress ellipsoid deformation(B).

to shapes of the turbulence. As demonstrated by the above discussion the shape designated to the axisymmetric limits in the invariant map may be interpreted in two ways. Although this has no effect on turbulence modelling it does lead to some confusion when visualizing the turbulence. Since the invariant map itself is based on the turbulent stress tensor, it would be preferable that the designation of its axis is related to this quantity only.

## References

- [1] Choi, K. and Lumley, J., The return to isotropy of homogeneous turbulence, *J. Fluid Mech.*, **436**, 2001, 59–84.
- [2] Lee, M. and Reynolds, W., Numerical experiments on the structure of homogeneous turbulence, Technical Report Rep. TF-24, Thermoscience Division, Stanford University, 1985.
- [3] Lumley, J., Computational modelling of turbulent flows, *Adv.Appl.Mech.*, **18**, 1978, 123–176.
- [4] Torbergsen, L., *Experiments in turbulent pipe flow*, Ph.D. thesis, Norwegian University of Science and Technology, 1998.

## A Physical Model of the Turbulent Boundary Layer Consonant with the Structure of the Mean Momentum Balance

J. Klewicki,<sup>1</sup> P. McMurtry,<sup>1</sup> P. Fife<sup>2</sup> and T. Wei<sup>1</sup>

<sup>1</sup>Department of Mechanical Engineering, <sup>2</sup>Department of Mathematics  
University of Utah, Salt Lake City, Utah 84112 USA

### Abstract

Recent studies by the present authors have explored, both empirically and analytically, the nature by which the terms in the mean momentum equation, as applied to canonical turbulent wall flows, sum to zero as a function of distance from the wall. To establish a context for the present work, the previously unrecognized structural and Reynolds number scaling properties revealed in these previous studies are succinctly reviewed. These characteristics are then used as the basis for composing a physical model for the turbulent boundary layer. The model is constructed such that it appropriately embraces the dynamical structure of the mean flow, while remaining consistent with independent empirical observations. Implications of the proposed model relative to the well-established view of boundary layer structure are briefly discussed.

### Introduction

An established tack for describing turbulent wall flow structure begins with an examination of the distribution of the mean axial velocity as a function of distance from the wall,  $U^+(y^+)$ , in concert with an examination of the mean viscous stress profile,  $\partial U^+/\partial y^+(y^+)$ , relative to the magnitude of the Reynolds shear stress profile,  $T^+(y^+) = -\overline{uv}^+(y^+)$ . (In these expressions the superscript + denotes normalization by the kinematic viscosity,  $\nu$ , and the friction velocity,  $u_\tau = \sqrt{\tau_{wall}/\rho}$ , with  $\tau_{wall}$  and  $\rho$  being the mean wall shear stress and mass density respectively.) Such an analysis naturally leads to the well-accepted interpretations regarding the average dynamical characteristics of the constituent layers nearly universally employed to describe to boundary layer structure, e.g., [1]. Empirical data directly relevant to the mean momentum balance, however, reveal a layer structure that differs considerably from the sub, buffer, logarithmic and wake layers ascribed to the mean velocity profile [2]. Given this, the objectives of the present effort are to: *i*) outline the origin and basic features of this newly revealed dynamical layer structure, *ii*) propose a consistent physical model, and *iii*) briefly discuss the implications of this model relative to the more traditional view of boundary layer structure.

### Review of Momentum Balance Properties

An important premise underlying the layer structure to be described, and, in turn, the proposed model, is that the Reynolds Averaged Navier-Stokes (RANS) equation in its unintegrated form (and in this case as applied to boundary layer flow over a planar surface located at  $y = 0$ ),

$$U^+ \frac{\partial U^+}{\partial x^+} + V^+ \frac{\partial U^+}{\partial y^+} = \frac{\partial^2 U^+}{\partial y^{+2}} + \frac{\partial T^+}{\partial y^+}, \quad (1)$$

provides the primary description of mean flow dynamics. (Herein,  $x$  is the axial coordinate,  $y$  is the wall normal coordinate,  $U$  and  $V$  are the velocity components in the  $x$  and  $y$  directions respectively, upper case letters represent mean quantities, lower case letters denote fluctuating quantities, tilde denotes instantaneous quantities (i.e.,

$\tilde{u} = U + u$ ), an overbar denotes time averaging, and vorticity components are identified by their subscript.) The left side of Eq. 1 represents mean flow advection, while the right side terms represent the viscous and Reynolds stress gradients respectively. Since, for the flat plate flow, there are only these three distinct dynamical effects, the ratio of any two determine the nature by which the equation is balanced.

### Layer Structure

Wei et al. [2] explored the structure of boundary layer, pipe and channel flows by examining the ratio of the last two terms in Eq. 1. Interpretation of this ratio is as follows:

1. If  $|\frac{\partial^2 U^+}{\partial y^{+2}} / \frac{\partial T^+}{\partial y^+}| \gg 1$  then the Reynolds stress gradient term is negligible and Eq. 1 sums to zero essentially through a balance of the mean advection and viscous stress gradient terms.
2. If  $|\frac{\partial^2 U^+}{\partial y^{+2}} / \frac{\partial T^+}{\partial y^+}| \ll 1$  then the mean viscous stress gradient term is negligible and Eq. 1 sums to zero essentially through a balance of the mean advection and Reynolds stress gradient terms.
3. If  $|\frac{\partial^2 U^+}{\partial y^{+2}} / \frac{\partial T^+}{\partial y^+}| \simeq 1$  then the Reynolds stress and viscous stress gradients balance and are either greater or of the same order of magnitude as the mean advection term.

Relevant premier quality experimental and DNS data [3, 4, 5] were differentiated and the indicated ratio was examined as a function of distance from the wall,  $y^+ = yu_\tau/\nu$ , for differing Reynolds numbers,  $\delta^+$ , where  $\delta$  is the boundary layer thickness.

The sketch of Figure 1 depicts the behavior of the stress gradient ratio at any fixed  $\delta^+$ . As indicated, there exists a four layer structure. Layer I retains the character of the viscous sublayer, and in the boundary layer is a region where the viscous stress gradient nominally balances mean advection. In layer II the magnitude of the ratio is very close to unity, and thus is called the stress gradient balance layer. Across the mesolayer (layer III), the Reynolds stress gradient changes sign and the terms in Eq. 1 undergo a process of balance breaking and exchange [2, 6]. The net result of this process is that from the outer edge of layer III to  $y = \delta$  (i.e., layer IV) Eq. 1 is characterized by a balance between mean advection and turbulent transport via the Reynolds stress gradient.

### Reynolds Number Scaling Behaviors

The qualitative features of Fig. 1, depicted for a fixed Reynolds number, persist for the Reynolds number range currently accessible to inquiry. Quantitatively, however, this layer structure has been shown [2] to exhibit distinct Reynolds number dependencies relating to both the wall-normal extent of the layers and the velocity increment across each of the layers. Table 1 presents these scaling behaviors as normalized by inner variables. As is evident, layers I



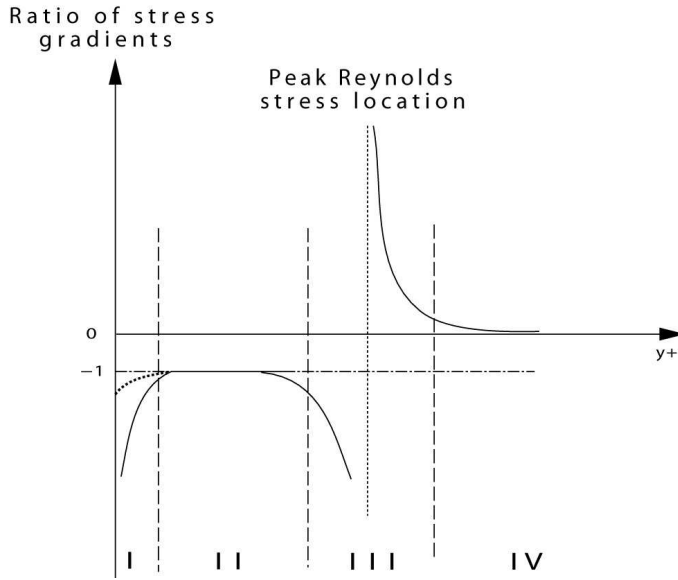


Figure 1: Sketch of the ratio of the viscous stress gradient to the Reynolds stress gradient (terms on the right side of Eq. 1) in a turbulent boundary layer at any given Reynolds number. Layer I is characterized by a balance between mean advection and the viscous stress gradient; dashed line. (Note that in a pipe this balance is between the mean pressure gradient and the viscous stress gradient.) In layer II the balance is between the viscous and Reynolds stress gradients. Layer III is a mesolayer in which all three terms in Eq. 1 are of the same order of magnitude, except that in a part of it, the Reynolds stress gradient is negligible. Layer IV is defined by a balance between mean advection and turbulent inertia.

and IV adhere (at least asymptotically) to the traditional inner and outer scalings respectively. On the other hand, layers II and III exhibit mixed scaling properties. The inner normalized thickness of layer II grows like the geometric mean of the Reynolds number defined as the ratio of outer to inner length scales (i.e.,  $\sim \sqrt{\delta^+}$ ), while its velocity increment remains a fixed fraction of  $U_\infty$ , independent of Reynolds number. Similarly,  $\Delta_{III}y^+ \sim \sqrt{\delta^+}$ , while its velocity increment is only about  $1.0u_\tau$ , independent of  $\delta^+$ . As discussed in detail by Wei et al. [2], these scaling behaviors differ considerably from the classical view of boundary layer structure, and are associated with the existence of a third fundamental length scale,  $\sqrt{\nu\delta/u_\tau}$ , that is intermediate to  $\nu/u_\tau$  and  $\delta$ .

layer	$\Delta y^+$ increment	$\Delta U^+$ increment
I	$O(1) \ (\simeq 3)$	$O(1) \ (\simeq 3)$
II	$O(\sqrt{\delta^+}) \ (\simeq 1.6\sqrt{\delta^+})$	$O(U_\infty^+) \ (\simeq U_\infty^+/2)$
III	$O(\sqrt{\delta^+}) \ (\simeq 1.0\sqrt{\delta^+})$	$O(1) \ (\simeq 1)$
IV	$O(\delta^+) \ (\rightarrow \delta^+)$	$O(U_\infty^+) \ (\rightarrow U_\infty^+/2)$

Table 1: Inner-normalized scaling behaviors of the layer thicknesses and velocity increments. Note that the layer IV properties are asymptotically attained as  $\delta^+ \rightarrow \infty$ .

The mean dynamics and scaling behaviors associated with layers II and III are central and apparently unique to the model proposed below, and thus are worthy of further discussion. Layer II is called the stress gradient balance layer since the dominant dynamical mechanisms are the viscous and Reynolds stress gradient terms on the right of Eq. 1; underlying their ratio being  $-1$  in Fig. 1. Contrary to the prevalent notion that boundary layer dynamics are inertially dominated outside the buffer layer (independent of  $\delta^+$ ), momentum balance data incontrovertibly reveal that an equal competition between viscous and inertial effects persists to a wall-normal distance near the peak in the Reynolds stress,  $T_{max}$ . Consistent with

the mathematical hierarchical structure revealed by Fife et al. [6], in the model posed below this competition is associated (in a time mean sense) with the vortical motions forming and evolving from the near-wall vorticity field. It is significant to note, however, that the balance in layer II comes about via two nearly equal but opposite decreasing functions that lose their dominance over mean advection as layer II transitions into layer III.

The scalings of Table 1 reveal that the layer II and III thicknesses are coupled such that their velocity increments adhere to outer and inner scaling respectively. These properties underlie new interpretations relating to, for example, the nature of the inner/outer interaction in boundary layers. In this regard it is relevant to note that major portions of layers II and IV and all of layer III reside within the bounds of the region of the mean profile that exhibits a logarithmic-like variation with  $y^+$ . The lower edge of layer II is fixed near the edge of the viscous sublayer (independent of  $\delta^+$ ), while the position of its outer edge extends to increasing  $y^+$  values like  $\sqrt{\delta^+}$  such that  $\Delta_{II}U = U_\infty/2$ . (Note that relative to outer scaling the position of the outer edge of layer II moves “inward” like  $1/\sqrt{\delta^+}$ .) Because of this positioning behavior for layer II, both end points of layer III vary with  $\delta^+$ . Thus, while the layer III thickness exhibits the same Reynolds number scaling behavior as layer II, its velocity increment is only  $\simeq 1u_\tau$  owing to the fact that with increasing  $\delta^+$  its position is located at increasing  $y^+$  locations in a region where  $U^+ \simeq \log(y^+)$ .

### Physical Model

Elements of a new physical model for the boundary layer are presented in the schematic of Figure 2. In contrast to the physical picture promoted by the traditional (sub, buffer, log and wake layer) view, this model is consistent with the properties of the mean momentum balance reviewed above. Associated with this are requisite nontrivial reinterpretations and modified insights relating to the description of flow physics. Conversely, it is recognized that any defensible model should also embrace the numerous independent empirical observations relating to, for example, boundary layer coherent motions. As evidenced below, the model presented in Figure 2 attempts to simultaneously satisfy these constraints.

A particularly prevalent and growing body of research supports the hypothesis that hairpin-like vortices constitute a basic building block of wall turbulence, e.g., [7, 8, 9, 10, 11, 12]. Broadly speaking, near-wall hairpin vortices are seen to form via redistribution of the intense sublayer vorticity field (mainly composed of  $\tilde{\omega}_z$ ), and during their development extend outward. While earlier flow visualization-based evidence indicated that these motions might extend from the sublayer to the edge of the boundary layer [9], an increasing and predominantly more recent body of results indicates that at some distance from the wall the boundary layer vortical motions lose connection with their sublayer/near-wall origin.

This “attached” – “detached” eddy decomposition of the vorticity field finds support from visual studies [13, 14, 15, 16], two-point vorticity correlations [14, 17, 18] and DNS and PIV studies [19, 12, 20]. Furthermore, the inclusion of detached eddies has been found to improve coherent motion-based model performance [21]. As depicted in Fig. 2, attached eddies are viewed as predominantly populating layer II, and to a decreasing degree with increasing  $y^+$  across layer III and into layer IV. Though a specific geometric form for the detached eddies is not completely established, direct measurements of near-wall  $\tilde{\omega}_z$  structure, the increasingly three-dimensional nature of the vorticity field with increasing distance from the surface, and data considerations relative to  $\vec{\nabla} \cdot \vec{\omega} = 0$  [22, 23, 16] support the expectation that at some distance from wall the characteristic coherent vortical motions become spatially localized and topologically form closed loops. Detached ed-

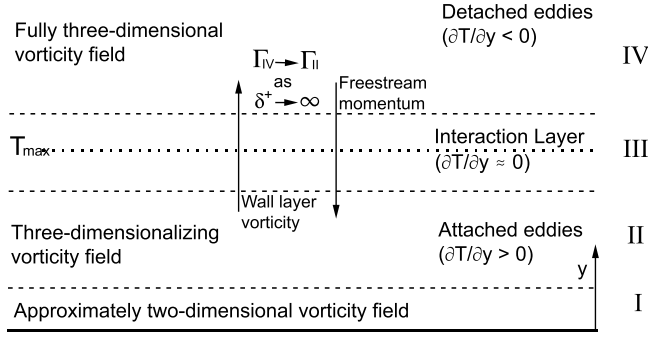


Figure 2: Schematic representation of some of the dynamical attributes of the proposed model for the turbulent boundary layer. Layer numbers are the same as those identified in Fig. 1.

dies are hypothesized to predominantly populate layer IV, and to a decreasing degree with decreasing  $y^+$  across layer III and into layer II. Of course, the simplest form of such an eddy is a vortex ring-like motion. Falco's earlier "typical eddy" observations [13, 15] support the existence of intermediate scale ring-like eddies in both the inner and outer regions. More recently, direct numerical simulations by Bake et al. [24] provide compelling evidence for the formation of vortex rings from the pinch-off of the legs of hairpin vortices during the latest stages of transition. Such a process was previously proposed by Falco as a mechanism for ring-like motion formation, and was explored numerically by Moin et al. [25]. Regardless of the exact geometric form of the detached eddies, however, an important characteristic feature is hypothesized to be that they contain positive  $\tilde{\omega}_z$ , i.e., having sign opposite  $\Omega_z$  [14, 22, 26, 17, 18].

The new insights derived from the properties of the mean momentum balance [2, 6] allow specific attributes to be associated with the attached/detached eddy structure proposed. For example, under the proposed model attached eddies form and evolve across layer II, and thus their dynamical signature is that they produce instantaneous contributions to positive  $-\partial\overline{uv}/\partial y$ . Similarly, the characteristic eddies of layer IV are detached. Therefore their dynamical signature is that they produce negative  $-\partial\overline{uv}/\partial y$ .

In the context of these dynamical signatures it is useful to examine the equation, e.g., [27, 28],

$$-\frac{\partial\overline{uv}}{\partial y} = \overline{v\omega_z} - \overline{w\omega_y} + \frac{\partial}{\partial x}(\overline{v^2} + \overline{w^2} - \overline{u^2}). \quad (2)$$

For turbulent channel flow the last term is identically zero, while for boundary layers this term is small, especially as  $\delta^+$  becomes large [28]. Thus, to a very good approximation, the gradient of the Reynolds stress is established by the difference of the indicated velocity vorticity correlations. Given this, the interpretation is that in layer II the attached eddies interact with the velocity field to generate a net positive sum, and in layer IV the detached eddies generate a net negative sum. The dominant terms in Eq. 1 indicate that the dynamics underlying the evolution of attached eddies are characterized by a competition between viscous shear forces and turbulent advection. Similarly, detached eddy dynamics in layer IV are characterized by a competition between mean flow and turbulent advection. The flow field interactions underlying Eq. 2 in either layer II or layer IV have recently been shown to be intermediate in scale [29]. Physically, the reason for this is attributable the fact that as  $\delta^+ \rightarrow \infty$  velocity spectra peak at decreasingly low wavenumber, while vorticity spectra peak at increasingly high wavenumber. According to Eq. 2, however, the velocity and vorticity fields must interact (i.e., correlate) over some wavenumber range in order for there to be a

net momentum transport via turbulent inertia.

## Discussion

The proposed model creates a new context for describing boundary layer processes. In this regard, three important issues are now briefly discussed. These concern *i*) inner/outer interactions, *ii*) coherent motion dynamics, and *iii*) scaling turbulence statistics. A more comprehensive discussion these issues in the context of the proposed model is forth-coming [30].

Given the proposed physical model, a central element of the inner/outer interaction would seem to have association with how the attached and detached eddies interact, and, in particular, how these interactions simultaneously accomplish a net outward transport of vorticity (associated with boundary layer growth) and a net inward transport of momentum (associated with the surface drag). The proposed model provides a rather clearly defined framework for identifying where in the layer the inner/outer interaction occurs (as a function of Reynolds number) and the competing mean dynamical effects at play. Overall, the velocity increment scalings suggest that as  $\delta^+ \rightarrow \infty$  a net outcome of the interaction is that the circulation (per unit length) associated with the outward transport of vorticity from layer II is asymptotically balanced by the net inward transport of momentum from layer IV.

Relevant to coherent motion dynamics, important questions would appear to relate to how the instantaneous dynamics of attached eddies produce the statistical features of layer II, and similarly how detached eddies produce the negative Reynolds stress gradient of layer IV. The respective physical interpretations (in the context of Eq. 2) are that *i*) the vortical motions in the region inside of  $T_{max}$  interact with the velocity field to act as a source term in Eq. 1, and *ii*) the vortical motions for  $y^+$  values greater than the position of  $T_{max}$  interact with the velocity field to act as a sink term.

Connected to the above *instantaneous-to-mean* perspectives is the somewhat converse issue of scaling turbulence quantities using the properties of the mean flow. That is, given the Reynolds number dependencies of the mean momentum field described above, such connections would permit the prediction of turbulence properties at arbitrary  $\delta^+$ . Relative to this, it is worth noting that the scaling hierarchy revealed by the analysis of Fife et al. [6] provides new insights. Furthermore, the layer scaling behaviors reflected in Table 1 constitute a broader set of velocity and length scale combinations than contained in the traditionally employed theory based on the assumption of a region of inner and outer overlap.

## Conclusions

A new framework for interpreting boundary layer dynamics is described herein. Notable features of this model include and incorporate the following.

- The  $y^+$  extent of the dynamical interaction characterized by a balance between viscous/inertial effects (Layer II) is both Reynolds number dependent and, in general, much larger than previously recognized in the traditional layer structure ascribed to boundary layers.
- Both the  $y^+$  position and extent of the region over which the inner/outer interaction occurs is Reynolds number dependent. The inner/outer interaction primarily occurs over a region in which the terms in the mean momentum equation undergo the balance breaking and exchange as described by Fife et al. [6].
- The Reynolds stress gradient has opposite dynamical contributions to the mean momentum equation for  $y^+$  positions on

the inside and outside of  $T_{max}$  respectively.

- To be fully understood, the dynamical layer structure of the mean momentum balance requires an extended/revised set of length and velocity information. These provide a broader context for scaling turbulence quantities.

## Acknowledgements

This work was supported by the National Science Foundation under grant CTS-0120061 (grant monitor, M. Plesniak), the Office of Naval Research under grant N00014-00-1-0753 (grant monitor, R. Joslin), and the Department of Energy under grant W-7405-ENG-48.

## References

- [1] Pope, S.B., *Turbulent Flow*, Cambridge University Press, 2000.
- [2] Wei, T., Fife, P., Klewicki, J. and McMurtry, P., Properties of the mean momentum balance in turbulent boundary layer, pipe and channel flows, *J. Fluid Mech.*, to appear, 2004.
- [3] Moser, R.D., Kim, J. and Mansour, N.N., Direct numerical simulation of turbulent channel flow up to  $Re_\tau = 590$ , *Phys. Fluids*, **11**, 1999, 943.
- [4] Zagarola, M.V. and Smits, A.J., Scaling of the mean velocity profile for turbulent pipe flow, *Phys. Rev. Lett.*, **78**, 1997, 239.
- [5] DeGraaff, D.B. and Eaton, J.K., Reynolds number scaling of the flat plate turbulent boundary layer, *J. Fluid Mech.*, **422**, 2000, 319.
- [6] Fife, P., Wei, T., Klewicki, J. and McMurtry, P., Stress gradient balance layers and scale hierarchies in wall bounded turbulent flows, *J. Fluid Mech.*, submitted, 2004.
- [7] Theodorsen, T., Mechanism of turbulence, in *2nd Midwestern Conference on Fluid Mechanics*, The Ohio State University, Columbus, OH, 1952, 1.
- [8] Wallace, J.M., On the structure of turbulent shear flow. A personal view, in *Developments in Theoretical and Applied Mechanics*, editors Chung, T.J. and Karr, G., University of Alabama, Department of Mechanical Engineering, Huntsville, Alabama, 1982, 1.
- [9] Head, M.R. and Bandyopadhyay, P., New aspects of turbulent boundary layer structure, *J. Fluid Mech.*, **107**, 1981, 297.
- [10] Perry, A.E., Henbest, S. and Chong, M.S., A theoretical and experimental study of wall turbulence, *J. Fluid Mech.*, **165**, 1986, 163.
- [11] Smith, C.R., Walker, J.D.A., Haidari, A.H. and Sobrun, U., On the dynamics of near-wall turbulence, *Phil. Trans. R. Soc. Lond. A*, **336**, 1991, 131.
- [12] Adrian, R.J., Meinhardt, C.D. and Tomkins, C.D., Vortex organization in the outer region of the turbulent boundary layer, *J. Fluid Mech.*, **422**, 2000, 1.
- [13] Falco, R.E., New results, a review and synthesis of the mechanism of turbulence production in boundary layers and its modification, *AIAA paper no. 83-0377*, 1983.
- [14] Klewicki, J.C., *On the Interactions Between the Inner and Outer Region Motions in Turbulent Boundary Layers*, Ph.D. Dissertation, Michigan State University, 1989.
- [15] Falco, R.E., A coherent structure model of the turbulent boundary layer and its ability to predict Reynolds number dependence, *Phil. Trans. R. Soc. Lond. A*, **336**, 1991, 103.
- [16] Klewicki, J.C., Self-sustaining traits of near-wall motions underlying boundary layer stress transport, in *Self-sustaining mechanisms of wall turbulence*, editor Panton, R.L., Computational Mechanics Publications, Southampton, UK, 1997, 135.
- [17] Klewicki, J.C. and Falco, R.E., Spanwise vorticity structure in turbulent boundary layers, *Int. J. Heat and Fluid Flow*, **17**, 1996, 363.
- [18] Metzger, M.M. and Klewicki, J.C., A comparative study of wall region structure in high and low Reynolds number turbulent boundary layers, *Phys. Fluids*, **13**, 2001, 692.
- [19] Robinson, S.K., Coherent motions in the turbulent boundary layer, *Ann. Rev. Fluid Mech.*, **23**, 1990, 601.
- [20] Ganapathisubramani, B., Longmire, E.K. and Marusic, I., Characteristics of vortex packets in turbulent boundary layers, *J. Fluid Mech.*, **478**, 2003, 35.
- [21] Perry, A.E. and Marusic, I., A wall-wake model for the turbulence structure of boundary layers. Part 1. Extension of the attached eddy hypothesis, *J. Fluid Mech.*, **298**, 1995, 361.
- [22] Klewicki, J.C., Gendrich, C.P., Foss, J.F. and Falco, R.E., On the sign of the instantaneous spanwise vorticity component in the near-wall region of turbulent boundary layers, *Phys. Fluids A*, **2**, 1990, 1497.
- [23] Rajagopalan S. and Antonia, R.A., Structure of the velocity field associated with the spanwise vorticity in the wall region of a turbulent boundary layer, *Phys. Fluids A*, **5**, 1993, 2502.
- [24] Bake, S., Meyer, D.G.W. and Rist, U., Turbulence mechanism in Klebanoff transition: a quantitative comparison of experiment and direct numerical simulation, *J. Fluid Mech.*, **459**, 2002, 217.
- [25] Moin, P., Leonard, A. and Kim, J., Evolution of a curved vortex filament into a vortex ring, *Phys. Fluids*, **29**, 1986, 955.
- [26] Klewicki, J.C., Murray, J.M. and Falco, R.E., Vortical motion contributions to stress transport in turbulent boundary layers, *Phys. Fluids*, **6**, 1994, 277.
- [27] Hinze, J.O., *Turbulence*, McGraw-Hill, 1975.
- [28] Klewicki, J.C., Velocity-vorticity correlations related to the gradients of the Reynolds stress in parallel turbulent wall flows, *Phys. Fluids A*, **1**, 1989, 1285.
- [29] Priyadarshana, P. and Klewicki, J.C., Reynolds number scaling of wall layer velocity-vorticity products, in *Reynolds Number Scaling in Turbulent Flow*, editor Smits, A.J., Kluwer Academic Publishers, 2003, 117.
- [30] Klewicki, J., McMurtry, P., Fife, P. and Wei, T., Physical models of wall turbulence consonant with the dynamical structure of the mean flow, *J. Fluid Mech.*, in preparation.

## Dynamics of a Transient Wave Group Breaking on a Beach

T.E. Baldock

Division of Civil Engineering, University of Queensland,  
St Lucia, Qld 4072, Australia

### Abstract

New experimental data are presented on the dynamics of a transient wave group breaking on a beach. The transient group is tracked during shoaling and wave breaking, together with the long waves forced during those processes. High spatial sampling enables novel resolution of the evolution of the wave envelope during breaking and the correlation between the envelope and the long waves. The data show a strong dynamic long wave setup in front of the group in shallow water. The amplitude of the dynamic setup is likely to be a function of beach slope, and larger on steeper beaches.

### Introduction

Wind and swell gravity water waves propagate towards the coastline in groups of high and low waves which shoal in shallowing water and eventually break on beaches. As a result of the dispersive nature of gravity waves, the groups are transient and evolve in space and time, with wave focusing potentially leading to the formation of extreme waves [1]. In addition to the formation of extreme waves, the focusing of wave energy and the wave height variation within the group forces low frequency long waves that propagate with the wave group [9]. In sufficiently shallow water the short waves within the group break at different depths, leading to further free long wave generation [12,4]. In both cases the shoreward propagating long waves may reflect at the shoreline and subsequently propagate offshore, which is how they were first identified by Munk [10] and Tucker [13].

The present paper considers this issue and presents a detailed analysis of the wave breaking process and the long waves forced by a large transient wave at the breakpoint. Carefully controlled laboratory experiments allow the direct identification of the incident and radiated long waves and this avoids difficulties associated with the analysis of non-linear shoaling waves and breaking waves. High data resolution enables direct identification of the relationship between the spatial variation of the short wave envelope and the long wave surface slopes, and this is consistent with radiation stress theory [9]. Cross-correlations between the long wave motion at different cross-shore locations suggest that the radiated long wave is generated in the surf and swash zones. A brief review of previous work follows, with the experimental setup and analysis techniques summarised in Section 3. Section 4 presents and discusses the experimental data, followed by final conclusions in section 5.

### Background

Long waves in the coastal zone are frequently termed surf beat as a result of their correlation with the breaking process [10,13], and are significant since they can modify the incident wave field and strongly influence sediment transport patterns. Much recent research has considered long wave forcing by regular wave groups and random waves on sloping beaches and clarified the forcing mechanisms [5,2,4]. Similarly, recent work has presented detailed analyses of the non-linear mechanics of transient wave groups in uniform depth [1,8] and such waves may now form the basis for design conditions for offshore structures.

However, studies on the propagation of transient wave groups over a sloping bed are much more limited, particularly during shoaling and wave breaking. Watson et al. [14] presented some results from numerical studies and limited comparisons with experimental data. Hunt [6] investigated the propagation of focused wave groups over a sloping bed and identified long wave generation in the surf and swash zones, but did not consider the long wave generation process in detail. Unfortunately, limitations on the wave generation technique also made it difficult to examine critically the long wave behaviour.

The identification of the details of wave breaking and long wave forcing for a particular set of experimental wave conditions is not trivial and complicated by a number of factors. These include the correct generation of non-linear waves and the absorption of radiated waves at the wavemaker in laboratory experiments (see section 3). Further, the analysis usually requires separation of the incident and reflected wave trains, for which no rigorous method exists for non-linear waves on a sloping bed.

In the present paper, we take advantage of the transient nature of the wave group and long wave to overcome these difficulties. The incident and radiated long waves are well separated in time, except very close to the shore, and can be identified directly in the time domain. In addition, high spatial sampling enables resolution of the instantaneous cross-shore structure of the short wave envelope and the long wave at sequential time intervals. This allows us to track the short wave breaking and the resulting long wave in space and time, which could only otherwise be achieved with an exact time-domain numerical model for shoaling and breaking transient waves.

### Experimental Setup

The experiments were carried out in a wave flume 18m long, 0.9m wide, with a working water depth,  $h$ , of 0.8m (Figure 1). A plane beach (gradient  $\beta=0.1$ ) starts 5.65m from the wave paddle. The origin of the horizontal co-ordinate,  $x$ , is taken as the intersection of the still water line with the beach face, positive onshore. Waves were generated by a hydraulically driven wedge type wave paddle using second order generation for long waves [3] and a digital feedback system that absorbs up to 60% (in amplitude terms) of waves radiated from the far end of the flume for frequencies at 0.1Hz, rising to over 90% above 0.4Hz.

Data were collected simultaneously from an array of five surface piercing resistance type wave gauges, mounted on a carriage above the flume, and a run-up wire within the swash zone. The absolute accuracy of these wave gauges is of order  $\pm 1$ mm, with a relative accuracy better than  $\pm 0.2$ mm. Further details of the wave flume, wave generation system and the instrumentation may be found in Baldock and Huntley [2]. Time-series data were collected from a total of 38 cross-shore locations, with the spatial separation between measurement positions varying between 0.2-0.6m offshore of the outermost breakpoint, reducing to 0.1-0.2m in the surf zone.

## Wave Flume

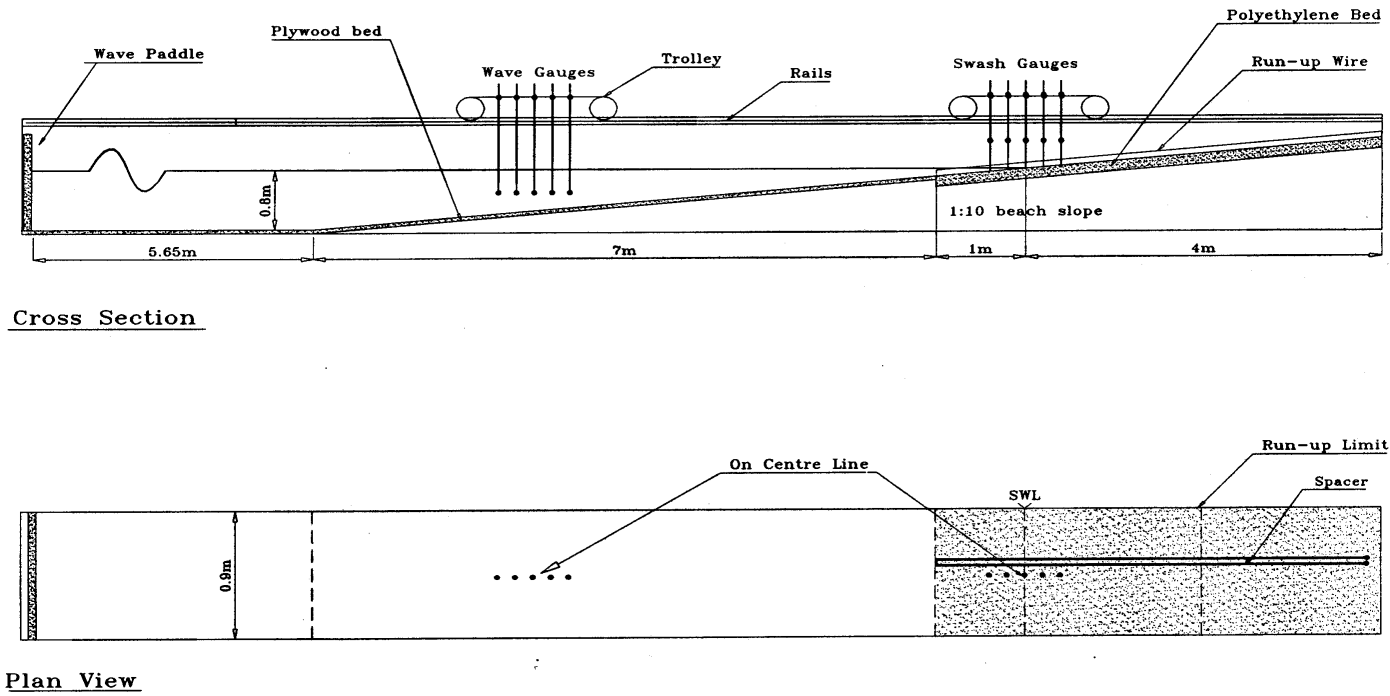


Figure 1. Wave flume and instrumentation.

The present paper examines data from a single transient focused wave group generated from a “top-hat” frequency spectrum. The central, upper and lower frequency limits for the 30 primary (linear) wave components of the spectrum were 1Hz, 1.2Hz and 0.8Hz, respectively, with a total group amplitude,  $A$ , defined by the linear sum of the amplitudes of the primary wave components and equal to 50mm. Long wave frequencies are defined as  $f < 0.4\text{Hz}$ , with the long wave components obtained by Fourier filtering the measured surface elevation data. Linear wave theory was used to focus the wave energy to generate a group dominated by a single large transient wave, so that a well developed large plunging breaker occurred 1.5-2m from the still water shoreline. At this location, the crest-trough height measured in the time domain just prior to breaking was 125mm. The smoothed short wave envelope was calculated from a Hilbert transform of low pass filtered ( $f < 1.5\text{Hz}$ ) surface elevation data [11].

### Results

Figure 2 shows the evolution of the focused wave group over the sloping bathymetry, together with the expected propagation path of the group centre, based on the linear group velocity. During propagation the energy is focused within a smaller region of space and time in comparison to the initial energy density at  $x = -11\text{m}$ ,  $t = 25\text{s}$ . In shallow water ( $x > -3\text{m}$ ) the group travels faster than expected from linear theory, a result of the highly non-linear waves generated during focusing and shoaling. This is illustrated further on figure 3, which shows the surface elevation of the wave envelope (a measure of the local energy density). Prior to wave breaking at  $x \approx -2.2\text{m}$ , the transient group is fairly symmetric about the main crest, both in the time domain and in space. After breaking, the majority of the short wave energy is dissipated or transferred to other frequencies within a distance of approximately 1m, or about 1 wavelength of the short waves.

During propagation of the wave group, energy is transferred to lower frequency bound long waves through radiation stress forcing [9]. These travel with the group, shoaling in shallow

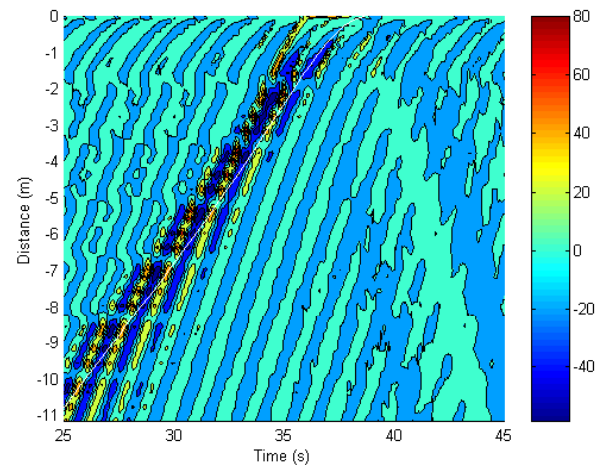


Figure 2. Space-time evolution of a focusing transient wave group. Colour bar on right indicates water surface elevation in mm. White line indicates expected propagation path based on group velocity.

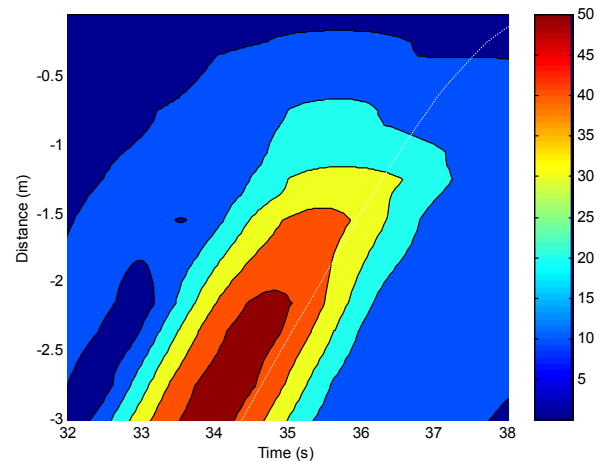


Figure 3. Space-time evolution of short wave envelope. Colour bar on right indicates elevation in mm. White line indicates expected propagation path based on group velocity.



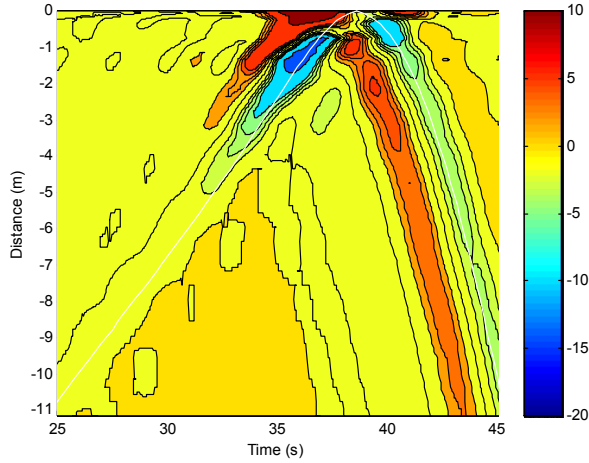


Figure 4. Space-time evolution of the low frequency ( $f < 0.4\text{Hz}$ ) surface elevation. Solid white lines indicate the expected shoreward and seaward propagation paths determined from the group velocity and the wave celerity, respectively.

water, and are frequently reflected from the shore as free waves after short wave breaking [4]. This is illustrated on figure 4, which shows the space-time evolution of the low frequency ( $f < 0.4\text{Hz}$ ) component of the surface elevation. A long wave trough propagates with the group as expected, and appears to reflect from the beach at  $t \approx 38\text{s}$  and propagate offshore at the free wave celerity. However, the notable feature in figure 4 is the dynamic setup or long wave preceding the group. Initially, this becomes significant in amplitude outside the breakpoint, at  $x \approx -3\text{m}$ , and subsequently grows very rapidly just before and after short wave breaking. This growth is consistent with high radiation stress gradients due to the wave height variation across the group. Further time-varying radiation stress gradients are induced by breaking [12]. This wave reflects from the beach at  $t \approx 36\text{s}$ , again propagating offshore with the celerity of a free wave. Of particular interest is that the bound long wave (trough) decreases significantly in amplitude during the reflection and radiation process, while the dynamic setup (crest) is largely unchanged in amplitude. This is considered further below. The radiated long waves propagate offshore, where they can be recorded without interference from the short wave group at a later time (figure 5). Note that on this figure the long waves are plotted on the right hand scale.

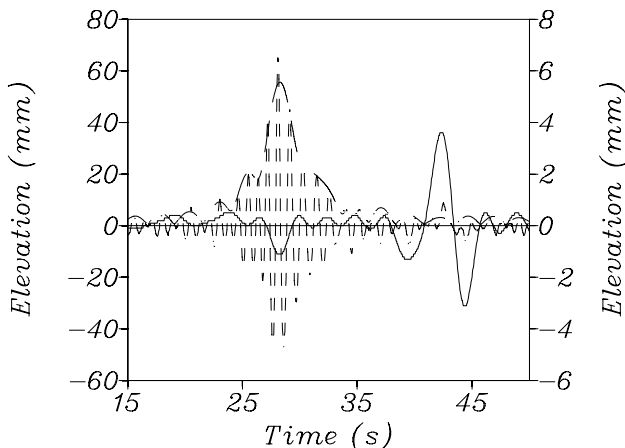


Figure 5. Wave group surface elevation and radiated long wave at  $x = -7.95\text{m}$ . ---, surface elevation; —, envelope; —, long wave (rhs).

Cross-correlations between the low frequency motion offshore ( $x = -11.15\text{m}$ ) and that further shoreward are shown on figure 6. In this instance the long wave signal in the nearshore leads that further offshore, whereas Janssen et al. [7] observed the opposite

on a much more mildly sloping beach under random wave conditions. The difference is that Janssen et al. [7] observed a reflected bound long wave that originally propagated from offshore to onshore, and then back. In contrast, these data show a new long wave generated through the shoaling and breaking process, reflected from the beach and then propagating offshore. Furthermore, the original incident bound long wave trough visible in figure 4 shows little correlation with the long waves observed further shoreward or at lags greater than zero. This implies that the original bound long wave is only a weak component of the overall radiated long wave. This analysis is complicated by the rundown that follows the large uprush at  $t \approx 36\text{s}$  (figure 4), which may well generate an offshore propagating long wave which is dominated by a wave trough [14]. It is therefore not possible to exactly determine if the radiated wave trough visible for  $t > 40\text{s}$  on figure 4 is a reflection of the incident bound wave present at  $x \approx -3\text{m}$ ,  $t \approx 34\text{s}$ . Indeed, weak autocorrelation at positive lags in the measured signal at  $x = -3\text{m}$  suggests that the radiated trough is strongly modified by the rundown.

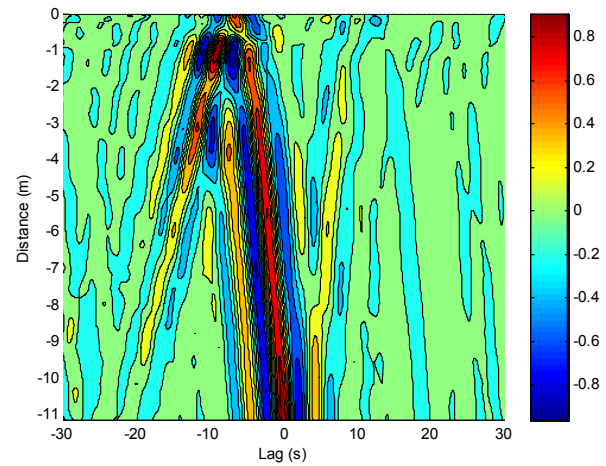


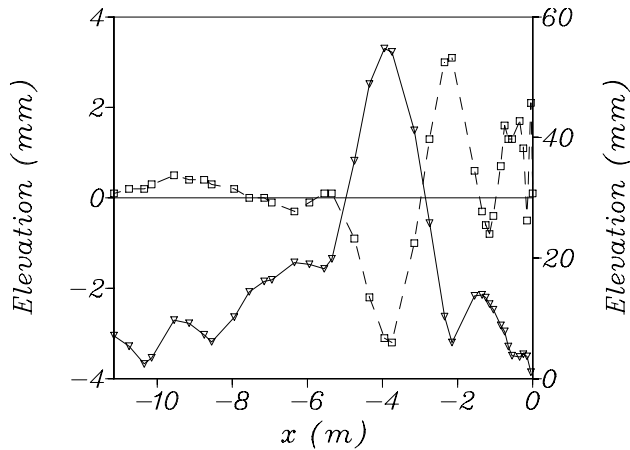
Figure 6. Cross-correlation between the low frequency motion at  $x = -11.15\text{m}$  and that further shoreward.

The high spatial sampling allows resolution of the instantaneous cross-shore structure of the short wave envelope and long wave. This novel experimental data is illustrated on figures 7a-c at three different times during the propagation of the wave group across the beach. Figure 7a&b show the group and long wave structure in the lead up to short wave breaking, while figure 7c shows the structure after breaking. In each case, the short wave envelope is plotted on the right hand scale. Prior to breaking, the gradients in short wave height lead to spatial variations in radiation stress which force the bound long wave (visible at  $x = -4\text{m}$ ) as well as some dynamic setup in front of the group ( $x = -2\text{m}$ ). Note that the changes in surface slope of the long wave exactly correspond with changes in gradient of the short wave envelope and hence radiation stress, in agreement with radiation stress theory.

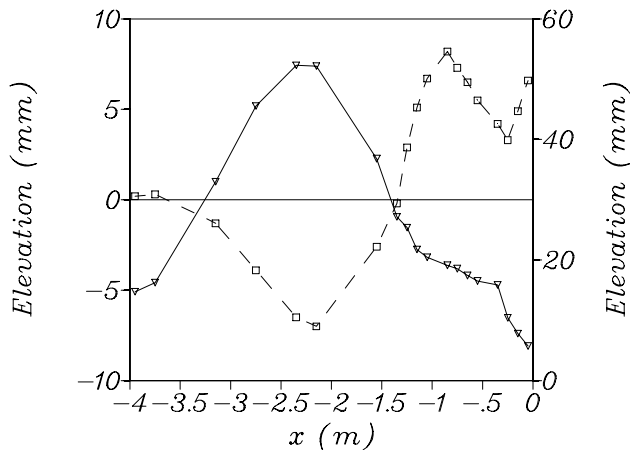
In shallower water, after breaking, a similar correlation is evident between the short wave envelope and long wave slope until the long waves reflect at the shoreline and the incident waves can no longer be identified easily. However, these data show the dynamic setup in front of the group is similar in amplitude to the incident bound long wave, which has not been observed on mildly sloping beaches, but is consistent with long wave forcing by random waves on the same beach [2].

This appears to be a combination of two factors. Firstly, on mildly sloping beaches wave breaking is more gradual, with breaking spread over a broader surf zone, and this leads to smaller radiation stress gradients overall. Secondly, to generate the large dynamic setup requires large radiation stress gradients

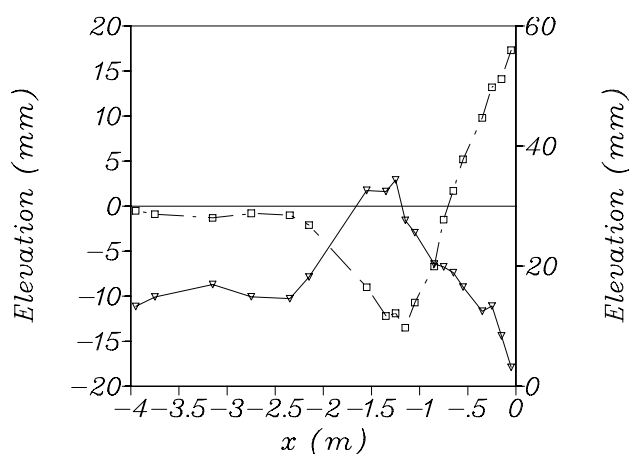
in very shallow water. This is possible on a steep beach, where wave breaking occurs closer to the shoreline and where the gradients in both wave height and water depth are large. Large dynamic setup is therefore likely on steep beaches, resulting in very different long wave generation from that on mildly sloping beaches. This is consistent with the previous work of Baldock and Huntley [2] and Battjes et al. [4].



a)  $t=32.88s$



b)  $t=34.76s$



c)  $t=36.24s$

Figure 7. Spatial variation of surface elevation envelope and low frequency surface elevation at the times indicated.

—□—, low frequency wave; —▽—, envelope (rhs).

## Conclusions

New experimental data have been presented on the dynamics of a transient wave group during shoaling and breaking. The transient wave group propagates faster than predicted by linear theory, a result of non-linear effects in shallow water. During wave breaking a dominant plunging breaker dissipates the short wave

energy over a narrow surf zone, leading to large radiation stress gradients. These lead to a large dynamic setup in front of the group in addition to the commonly observed setdown beneath the group. The dynamic setup forces free long waves which radiate offshore. The data show that the radiated wave is generated in the final stages of shoaling and in the surf zone, as opposed to being a reflection of the incident bound wave originating further offshore. Novel data show the spatial structure of the short wave envelope and long wave, and these are consistent with radiation stress theory and explain the observed dynamic setup. The magnitude of the dynamic setup and associated radiated long wave is expected to be a function of beach slope, and greater on steeper beaches.

## Acknowledgements

The authors gratefully acknowledge support and funding from the Australian Research Council, the CRC for Sustainable Tourism and the University of Queensland.

## References

- [1] Baldock, T. E., Swan, C. and Taylor, P. H. A laboratory study of non-linear surface waves on water. *Philos. Trans. R. Soc. Lond. A*, **354**, 1996, 649-676.
- [2] Baldock, T.E and Huntley, D.A.. Long wave forcing by the breaking of random gravity waves on a beach. *Proc. R. Soc. Lond. A*, **458**, 2002, 2177-2201.
- [3] Barthel, V., Mansard, E. P. D., Sand, S. E. and Vis, F. C. Group-bounded long waves in physical models. *Ocean Engineering*, **10**, 1983, 261-294.
- [4] Battjes, J. A., Bakkenes, H. J., Janssen, T.T., and van Dongeren, A. R., Shoaling of subharmonic gravity waves. *J. Geophys. Res.*, **109**, 2004, doi:10.1029/2003JC001863.
- [5] Guza, R. T. and Thornton, E. B.. Observations of surf beat. *J. Geophys. Res.*, **90**, 1985, 3162-3172.
- [6] Hunt, A., Extreme waves, overtopping and flooding at sea defences. DPhil thesis, University of Oxford, 2003, 255pp.
- [7] Janssen, T. T., Battjes, J. A. and Van Dongeren, A. R. Observations of long waves induced by short wave groups. *J. Geophys. Res.*, **108**, 2003, 3252-3264.
- [8] Johannessen, T.B and Swan, C., On the non-linear dynamics of wave groups produced by the focusing of surface water waves. *Proc. R. Soc. Lond. A*, **459**, 2003, 1021-1052.
- [9] Longuet-Higgins, M. S. and Stewart, R. W. Radiation stress and mass transport in gravity waves, with application to "surf beats". *J. Fluid Mech.*, **13**, 1962, 481-504.
- [10] Munk, W. H. Surf beats. *Trans. Am. Geophys. Union*, **30**, 1949, 849-854.
- [11] Sobey, R. J. and Liang, H-B. Complex envelope identification of wave groups. *Proc. 20th Int. Conf. Coastal Engng.*, 1986, 752-766, ASCE, New York.
- [12] Symonds, G., Huntley, D. A., and Bowen, A. J. Two-dimensional surf beat: long wave generation by a time-varying breakpoint. *J. Geophys. Res.*, **87**, 1982, 492-498.
- [13] Tucker, M. J. Surf beats: sea waves of 1 to 5 min. period. *Proc. R. Soc. London Ser. A*, **202**, 1950, 565-573.
- [14] Watson, G., Barnes, T. C. D. and Peregrine, D. H. The generation of low frequency waves by a single wave group incident on a beach. *Proc. 24th Int. Conf. Coastal Eng.*, ASCE, 1994, 776-790.



## DETONATION MODELLING OF CORNER-TURNING SHOCKS IN PBXN-111

J.P. Lu<sup>1</sup>, F.C. Christo<sup>1</sup> and D.L. Kennedy<sup>2</sup>

<sup>1</sup>Weapons Systems Division  
Defence Science and Technology Organisation  
P O Box 1500, Edinburgh, SA 5111 AUSTRALIA

<sup>2</sup>Orica Explosives, George Booth Drive  
PO Box 196, Kurri Kurri, NSW

### Abstract

An explicit finite element hydrocode, LS-DYNA, was used to model corner-turning shocks of a highly non-ideal PBXW-115 explosive. Unlike our previous work where the CPeX combustion model was used, this study has focused on the Ignition and Growth Reactive Model, which has been calibrated against experimental results. It was found that the Ignition and Growth Reactive Model performs as well as the CPeX model in predicting shock evolution around corners, yet both models were unable to accurately model the configuration of the brass confined explosive booster.

### Introduction

PBXW-115 explosive has been tailored and fully qualified as an underwater explosive. Known also as PBXN-111 in the US, and PBXW-115(Aust), it is composed of 43% ammonium perchlorate (AP), 25% aluminium (Al), 20% RDX and 12% HTPB binder. Modelling this highly non-ideal explosive is a challenging task. Non-ideal explosives refer to explosives that have a C-J (detonation) pressure, velocity, or expansion isentropically significantly different from those expected from equilibrium, steady-state calculations. To this end, calculations of an axisymmetric geometry were performed using an explicit finite element hydrocode, LS-DYNA.

Earlier studies of PBXW-115 performance [6-9], have used the CPeX (Commercial Performance of explosives) reaction model to characterise this explosive in a cylindrical geometries. Kennedy and Jones [4] have also used the CPeX to model corner turning shocks to predict the breakout times through the curved surfaces of bowl-shaped acceptor charges. In this paper the capability of the Ignition and Growth Reactive Model (IGRM) to calculate corner turning shocks, is evaluated against the CPeX model and experimental data.

### Model Description

The modelled geometry shown in Fig. 1, is based on the experiment of Forbes et al. [1,2]. The acceptor charges are spherically bowl-shaped PBXN-111 explosive. The curved surface of each bowl had a radius of curvature of 50.8 mm. The bowls were initiated through their flat rear surfaces by cylindrical boosters 50.8mm in diameter and 152mm in length. Two different booster configurations were modelled here. The first was bare Comp-B (RDX/TNT explosive) booster and the second was PBXN-111 booster confined in a brass tube of 16.9mm wall thickness. In both cases the boosters were initiated by Pentolite charges.

Due to geometrical symmetry an axisymmetric computational model was constructed. The boosters were modelled with the programmed burn model and JWL equation of state. The acceptors were modelled with the Ignition and Growth Reactive Model, and the brass tube was modelled with the plastic-kinematic material model.

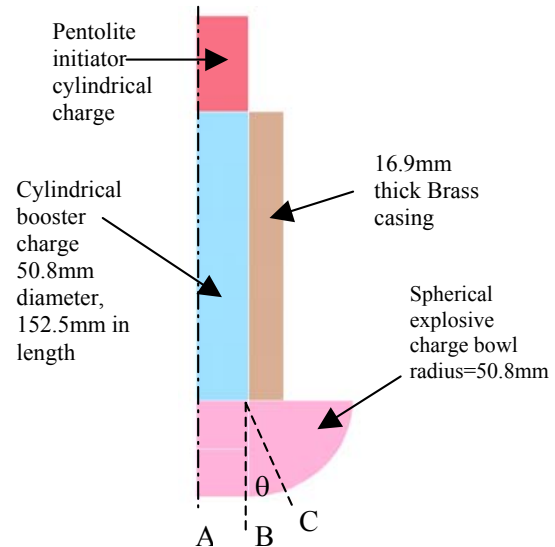


Figure 1. Schematic description of model geometry.

Both unreacted and combustion product equations of state are of Jones-Wilkins-Lee (JWL) form

$$P_{eos} = Ae^{-R_1 V} + Be^{-R_2 V} + \frac{\omega C_v T}{V} \quad (1)$$

where  $P_{eos}$  is pressure,  $V$  is relative volume,  $T$  is temperature, and  $A$ ,  $B$ ,  $R_1$ ,  $R_2$ ,  $\omega$  (the Gruneisen coefficient) and  $C_v$  (the average heat capacity) are constants.

For the programmed burn model used for the boosters, the effect of combustion on the pressure in the high explosive regions is computed using

$$P = P_{eos} \max(F_1, F_2) \quad (2)$$

The burn mass fractions ( $F_1$  and  $F_2$ ) that control the release of chemical energy are computed by

$$F_1 = \begin{cases} \frac{2(t - t_1) DA_{e, \max}}{3v_e} & \text{if } t > t_1 \\ 0 & \text{if } t \leq t_1 \end{cases} \quad (3)$$

$$F_2 = \frac{1 - V}{1 - V_{CJ}} \quad (4)$$

where  $t_I$  is an ignition time that is computed for each computational element by dividing the distance from the detonation point to the centre of the element by the detonation velocity  $D$ .  $A_{e,max}$ , and  $v_e$  are, respectively the maximum surface area and the volume of an element.

The JWL parameters and properties for Pentolite [10] that are used in the calculations are given in Table 1. Here  $\rho_0$ , and  $E_0$  are the material density and initial internal energy, respectively.

Parameter	Pentolite
$\rho_0$ (g/cm <sup>3</sup> )	1.65
$A$ (GPa)	531.77
$B$ (GPa)	8.933
$R_1$	4.6
$R_2$	1.05
$\omega$	0.33
$E_0$ (kJ/cm <sup>3</sup> )	8.0
$D$ (mm/ $\mu$ s)	7.36

Table 1: Material and JWL parameters for Pentolite explosives.

### Ignition and Growth Reactive Model

The Ignition and Growth Reactive Model is based on Tarver *et al.* [12] hypothesis that shock initiation of heterogeneous solid explosives should be modelled as at least a three-step process. The first step is the formation of hot spots created by various mechanisms (void closure, viscous heating, shear banding, etc.) during shock compression and the subsequent ignition (or failure to ignite due to heat conduction losses) of these heated regions. The second step in the process is assumed to be a relatively slow growth of reaction in inward and/or outward “burning” of the isolated hot spots. The third step in the shock initiation process is a rapid completion of the reaction as the reacting hot spots begin to coalesce. This model requires [11]:

- An unreacted explosive equation of state;
- A reaction product equation of state;
- A reaction rate law that governs the chemical conversion of explosive molecules to reaction product molecules; and
- A set of mixture equations to describe the states attained as the reactions proceed.

The chemical reaction rate equation in the three-term ignition and growth model is of the form [13]:

$$\frac{\partial F}{\partial t} = I(1-F)^b \left( \frac{\rho}{\rho_0} - 1 - a \right)^x + G_1(1-F)^c F^d P^y + G_2(1-F)^e F^f P^z \quad (5)$$

where  $F$  is the mass fraction of explosive ( $F=0$  implies no reaction,  $F=1$  implies complete reaction),  $t$  is time,  $\rho_0$  is initial density,  $\rho$  is current density,  $P$  is pressure, and  $I$ ,  $G_1$ ,  $G_2$ ,  $b$ ,  $x$ ,  $a$ ,  $b$ ,  $c$ ,  $d$ ,  $y$ ,  $e$ ,  $f$ , and  $z$  are constants. Upper threshold limits  $F_{mixg}$ ,  $F_{mxGr}$  and  $F_{mnGr}$  are set to limit the contributions of the three terms to respectively; a maximum reacted fraction  $F_{mixg}$  for the first term, a maximum fraction  $F_{mxGr}$  for the second term and a minimum fraction  $F_{mnGr}$  for the last term. Accordingly, the ignition rate is set equal to zero when  $F \geq F_{mixg}$ , the growth rate is set to zero when  $F \geq F_{mxGr}$ , and the completion rate is set to zero when  $F \leq F_{mnGr}$ . These limits are material dependant.

Table 2 lists the calibrated parameters in the Ignition and Growth Reactive Model for unconfined PBXN-111 [8,9].

Unreacted Equation of State and Constitutive Values			
$\rho_0$ (g/cm <sup>3</sup> )	1.792	$R_2$	3.6
$A$ (GPa)	4.06x10 <sup>3</sup>	$R_3 = \omega^* C_v$ (GPa/K)	2.09x10 <sup>-3</sup>
$B$ (GPa)	-133.9	Yield Strength (GPa)	0.2
$R_1$	7.2	Shear Modulus (GPa)	4.54
Reacted Product Equation of State and CJ Values			
$A$ (GPa)	372.9	$R_4 = \omega^* C_v$ (GPa/K)	4.884x10 <sup>-4</sup>
$B$ (GPa)	5.412	$E_0$ (KJ/cc)	12.95
$R_1$	4.453	$D_{cj}$ (mm/ $\mu$ s)	6.476
$R_2$	1.102	$P_{cj}$ (GPa)	20.84
Reaction Rate Parameters for 3 Term Model			
$I$ ( $\mu$ sec <sup>-1</sup> )	30	$G_2$ (GPa <sup>-z</sup> $\mu$ sec <sup>-1</sup> )	1.805x10 <sup>-03</sup>
$b$	0.6667	$e$	1.0
$a$	0	$f$	0.1111
$x$	4.0	$z$	2.0
$G_1$ (GPa <sup>-y</sup> $\mu$ sec <sup>-1</sup> )	0.045	$F_{mixg}$	0.015
$c$	0.6667	$F_{mxGr}$	0.25
$d$	0.1111	$F_{mnGr}$	0
$y$	1.0		

Table 2. Parameters for the Ignition and Growth of Reaction Model [8,9]  
Note:  $E_0$  is the internal energy.

These parameters are based on the assumption of the initial ignition and consumption of the RDX, the intermediate decomposition of the AP plus HTPB binder, and the later reaction of the aluminium.

For completeness of the presentation a brief description is also given on the CPeX model. Similar to the Ignition and Growth Reactive Model, the CPeX model represents the heat release rate as a three-term function in the form [4]

$$\frac{\partial F}{\partial t} = (1-F) \left( \frac{p_x a_h}{\tau_h} + \frac{p a_i}{\tau_i} + \frac{p a_f}{\tau_f} \right) \quad (6)$$

where  $F$  is the mass fraction of explosive,  $P$  is the pressure as computed from the JWL equation of state (Eq. 1). The three characteristics reaction times  $\tau_h$ ,  $\tau_i$ , and  $\tau_f$  are time constants of the hotspot, intermediate and final stages of the reaction, respectively. The  $a$  factors in Eq. 6, describe the assumed geometry of the burn front, controlling the switching on and off the hotspot, intermediate and final reaction rate terms. The detailed functional description of these factors, the function  $P_x$  and their calibrated values, are given in Ref.[4] and will not be repeated here.

### Results

Time-dependant calculations were performed over a total time of 45  $\mu$ sec. The time-step, which is adjusted automatically during the iterations, is selected to roughly correspond to the transient time of an acoustic wave through an element using the shortest characteristics distance in the computational domain. For numerical stability reasons, the size of time-step is scaled by a factor smaller than unity (0.9-0.67).

To compare the model with the experimental data [1,2], breakout time and pressure values are extracted from the model. Peak pressures at the outer surface of the bowl were presented as a function of a polar angle,  $\theta$  (see Fig.1). The breakout time is defined as the time of arrival of a detonation wave at a given location on the outer surface of the bowl, relative to the time of arrival of the first detonation wave at the flat bottom of the bowl at location (A) in Fig. 1.

Figure 2 shows pressure contours of the detonation wave (for the PBXW/Brass booster) in the bowl approximately 31 $\mu$ s, 33 $\mu$ s, 36 $\mu$ s and 39 $\mu$ s after initiating the Pentolite charge.

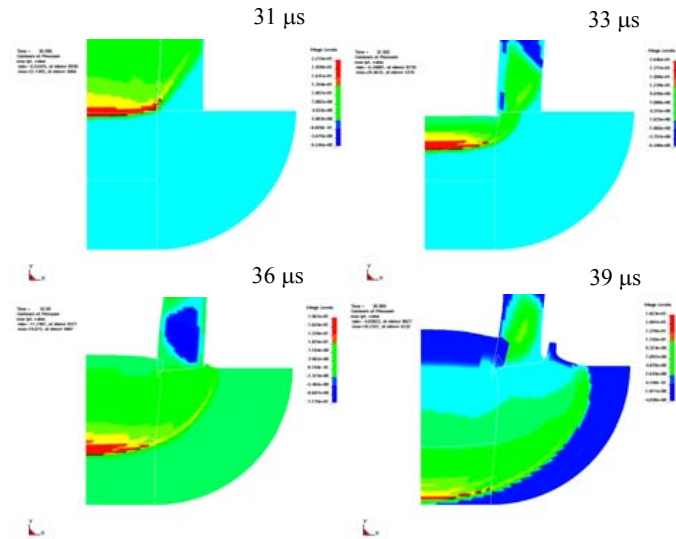


Figure 2: pressure (GPa) contours inside the bowl (for a PBXW/Brass booster configuration) 31 $\mu$ s, 33 $\mu$ s, 36 $\mu$ s and 39 $\mu$ s post initiation (note: pressure scales differ in each plot).

The figure shows the detonation front maintains almost a flat profile up to a 5 $\mu$ s after it enters the bowl, then it bends and begins to take the shape of the bowl. The model shows a slight increase in the peak shock pressure in the booster approximately 1 $\mu$ s after the shock entered the bowl, from ~21.5GPa to ~22.15GPa. The peak pressure then drops to 20.5GPa, 19.7GPa, and 18.2 GPa, respectively 2 $\mu$ s, 4 $\mu$ s, and 9 $\mu$ s after the shock enters the bowl.

It is interesting to note in Fig. 2, the time delay in the dynamic response of the brass tube. Tube deformation becomes obvious only a few microseconds after the detonation wave have entered the bowl. This is clearly illustrated in Fig. 2 at 31 $\mu$ s, which shows a flat detonation front entering the bowl at the explosive rear surface, while the oblique shock in the brass tube lags behind it. It is worth indicating the highly deformed computational elements of the brass tube were removed during iterations to reduce the possibility of numerical instability.

Burn mass fraction contours (F) for the PBXW/Brass booster configuration, inside the bowl are shown in Fig. 3. The figure shows a maximum of 62% and 65% mass burn fractions at 36 $\mu$ s and 39 $\mu$ s, respectively after the Pentolite initiation. This incomplete burnout of the explosives is consistent with typical burnout percentages of non-ideal explosives. Comparing the pressure (Fig. 2) and mass burn fraction (Fig. 3) contours, show a spatial lag of the reaction zone behind the detonation front.

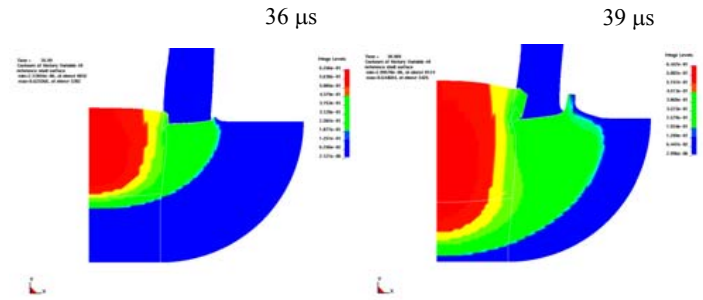


Fig. 3: Contours of mass burn fraction inside the bowl for a PBXW/Brass booster 36 $\mu$ s (left) and 39 $\mu$ s (right) post the Pentolite initiation.

Breakout times against angle ( $\theta$ ) are plotted in Fig. 4 for the COMP-B bowl charge and in Fig. 5 for the PBXW/Brass bowl charge. Results from the CPeX model [4] are also presented on the graphs.

For the COMP-B booster configuration, the results in Fig. 5 show that the Ignition and Growth Reactive Model predicts the breakout times reasonably accurate both in term of pressure magnitude and profile shape, consistent with the experiment. Both the IGRM and the CPeX models have comparable accuracy that is within the bounds of the experimental error, as shown in Fig.4.

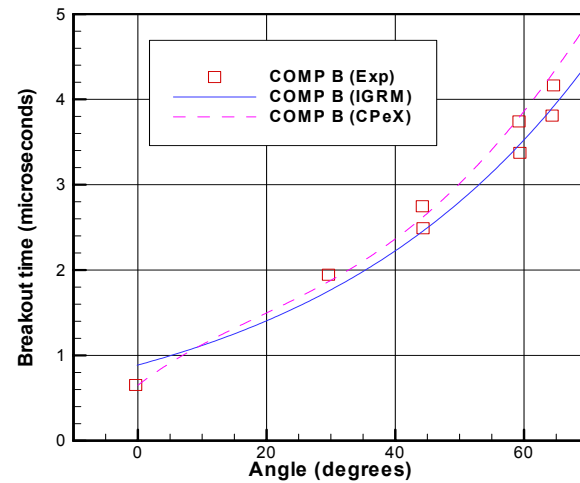


Fig. 4: A comparison between measured and calculated breakout times at various angular locations for a COMP-B booster, using the CPeX [4] and ignition and growth reactive model (IGRM).

However, for the PBXW/Brass booster configuration (Fig. 5), the IGRM performance is unexpectedly poor. The deviation of the calculated breakout times from the measured values increases with the angle, reaching a relative error of ~40% at an angle of 60 degrees. It is well known that having a brass casing (especially as thick as that used in this configuration) should increase the peak value and duration of the pressure delivered by the booster to the bowl charge, hence the breakout time through the outer edges of the bowl should be shortened. This was not the case here and no physical explanation can be found. Similar observations were made by Kennedy and Jones [4], who also could not find a physical explanation for this discrepancy.

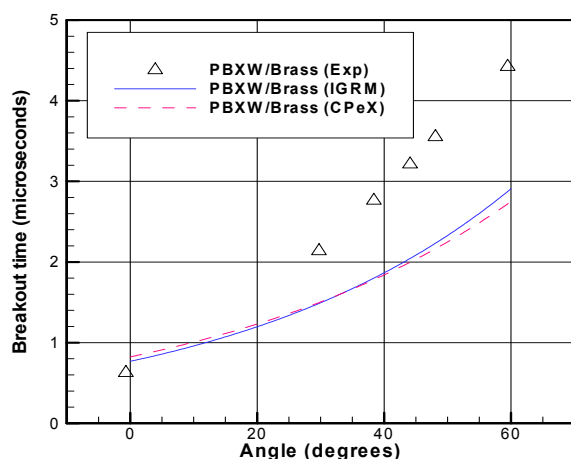


Fig. 5: A comparison between measured and calculated breakout times at various polar locations for PBXW/Brass booster, using the CPeX [4] and ignition and growth reactive model (IGRM).

It is worth mentioning that calculations were also performed using the IGRM (instead of the programme burn model) for the PBXN-111 booster, but did not yield any improvement in accuracy.

Considering the excellent agreement of the COMP-B booster configuration, the consistency and similarity of the results obtained by the IGRM and the CPeX models [4] for the PBXW/Brass booster configuration, implies that the current model parameters warrant further analyses for non-ideal explosives used in the complex geometries.

## Conclusions

The modelling results using the Ignition and Growth Reactive Model for the COMP-B booster configuration are within the bounds of experimental error. However for the PBXW/Brass booster configuration the IGRM results were poor in comparison to the experiment. Similar conclusions were also obtained using the CPeX model. Considering that the IGRM parameters were calibrated using unconfined charges as it is the case in the bowl charges of this study and the good agreement for the COMP-B booster configuration, the only plausible explanation for the discrepancies point out to the suitability of otherwise of the programmed burn model, which was used for the boosters. This would be the subject of our next investigation.

## References

- [1] Forbes, J.W., Lemar, E.R. and Baker R.N. (1989) *Detonation Wave Propagation in PBXW-115*, Proceedings of the 9<sup>th</sup> International Detonation Symposium, Office of the Chief of Naval Research, OCNR 113291-1, pp.806-815.
- [2] Forbes, J.W., Lemar, E.R., Sutherland G.T. and Baker R.N. (1992) *Detonation Wave Curvature, Corner Turning and Unreacted Hugoniot of PBXN-111*, NSWCCD/TR-92/164.
- [3] Jones, D.A., Kemister, G. and Borg, R.A.J. (1998) "Numerical simulation of detonation in condensed phase explosives", DSTO-TR-0705.
- [4] Kennedy, D.L. and Jones, D.A. (1993) *Modelling Shock Initiation and Detonation in the Non Ideal Explosive PBXW-115*, Proceedings of the 10<sup>th</sup> International Detonation Symposium, Boston, Mass., USA, 12-16 July, Office of Naval Research ONR 33395-12, pp. 665-674.
- [5] Lee, E.L. and Tarver C. M. (1980) *Phenomenological model of shock initiation in heterogeneous explosives*, Phys. Fluids, Vol. 23, pp.2362.
- [6] Lu, J.P. (2001) *Evaluation of the Thermochemical Code – CHEETAH 2.0 for Modelling Explosives Performance*, DSTO-TR-1199, AR-011-997, DSTO Technical Report, Melbourne, August.
- [7] Lu, J.P. and Kennedy, D.L. (2001) *Modelling of non-ideal explosive PBXW-115*, In PARARI 2001, Proceedings of 5<sup>th</sup> Australian Explosive Ordnance Symposium, 31 Oct. – 2 Nov., Canberra, Australia.
- [8] Lu, J.P., Dorsett, H. and Kennedy, D.L. (2002) *Simulation of Aquarium Tests for PBXW-115(Aust)*, Proceedings of the 12<sup>th</sup> International Detonation Symposium, San Diego, California, USA, 11-16 August.
- [9] Lu, J.P. and Kennedy, D.L. (2003) *Modelling of PBXW-115 Using Kinetic CHEETAH and the DYNA Codes*, DSTO-TR-1496, AR-012-899, DSTO Technical Report, Melbourne, September.
- [10] Lu, J.P., Anderson, J.G. and Christo, F.C. (2004) *Detonation Modelling of High Explosive Cylinders*, Proceedings of the 24<sup>th</sup> International Symposium of Shock Waves, 11-16 July, Beijing, China.
- [11] Murphy, M.J., Lee E.L., Weston, A.M. and Williams, A.E.(1993) *Modeling Shock Initiation in Composition B*, Proceedings of the 10<sup>th</sup> International Detonation Symposium, Boston, Mass., USA, 12-16 July, Office of Naval Research ONR 33395-12, pp.963-970.
- [12] Tarver, C.M., Hallquist, J.O. and Erickson, L.M. (1985) *Modeling Short Pulse Duration Shock Initiation of Solid Explosives*, Proceedings of the 8<sup>th</sup> International Detonation Symposium, Naval Surface Weapons Center, Albuquerque, NSWC MP 86-194, pp.951-961.
- [13] Tarver C.M. and Green L.G. (1989) *Using Small Scale Tests to Estimate the Failure Diameter of a Propellant*, Proceedings of the 9<sup>th</sup> International Detonation Symposium, Office of the Chief of Naval Research, OCNR 113291-1, pp.701-710.

## The External Flow Structure of a Naturally Precessing Fluidic Jet

Chong Y. Wong<sup>1</sup>, Richard M. Kelso<sup>1</sup> and Graham J. Nathan<sup>1</sup>

<sup>1</sup>School of Mechanical Engineering  
The University of Adelaide, Adelaide, SA, 5005 AUSTRALIA

### Abstract

A novel direction and phase-triggered Particle Image Velocimetry experiment has been applied to the near external field of a fluidic precessing jet nozzle. The results reveal significantly more detail of the flow structure than has been known previously. In particular three main vortex pairs which may contribute to the unsteady and mixing characteristics of the external fluid have been identified for the first time.

### Introduction

Unsteady precessing flow instabilities can occur within an axisymmetric nozzle of appropriate geometrical dimensions. They are of interest fundamentally because the mechanisms which generate them are still poorly understood. In practice, their occurrence can either be undesirable, as in milk driers [1] or desirable when applied to the combustion of gaseous and particulate fuels in a precessing jet burner [2]. The main advantage of the precessing jet burner lies in its mechanical simplicity, increased flame radiation and its low-NO<sub>x</sub> capabilities. Although this type of burner has been used since the early 1990s, the details of the underlying mechanism and structure of the external flow have yet to be identified.

Measurements of the external flow structure from fluidic precessing jet nozzles are limited. Nathan, Hill & Luxton [3] provided information on both the internal and external flow structure of a simple nozzle configuration (Figure 1) that produces a precessing jet. They deduced key features of the flow based on information from various flow visualisation techniques, such as China-clay surface flow visualisation, coloured dye visualisation, bubble visualisation and smoke visualisation. However, no quantitative information of the instantaneous flow structure could be obtained from their techniques.

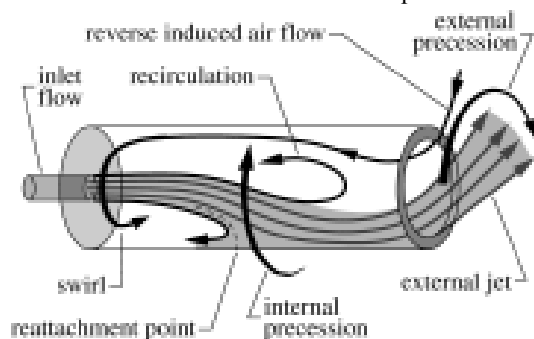


Figure 1. Flow-field of a fluidic precessing jet (Wong *et al.* [4]).

From the flow visualisation results of Nathan *et al.* [3], Kelso [5] analytically proposed that the internal jet precession is sustained by a “driving vortex” just downstream of a sudden expansion with a diameter expansion ratio of  $D/d=5$ . Computational fluid dynamic simulation by Guo *et al.* [1] for the same expansion ratio in a long downstream pipe at  $Re_d=10^5$  also revealed the motion of an internal precessing jet that generates similar surface flow patterns observed in a shorter downstream chamber used by Nathan *et al.* [3].

Newbold *et al.* [6] employed cross-correlation digital Particle Image Velocimetry (PIV) with a continuous Argon-ion laser beam modulated with an acousto-optic modulator on a fluidic precessing jet (FPJ) nozzle with a lip-and-centrebody arrangement. Due to the constraints of their optical arrangement their data suffered from severe out-of-plane particle movement. Hence, no details of the velocity near to the nozzle exit could be obtained from that investigation. However, an instantaneous image pair in the far-field appears to indicate some regions of flow reversals on the nozzle centreline, consistent with jet precession.

Nobes *et al.* [7] improved on the spatial resolution of the PIV arrangement and details of the flow near to the exit of the PJ could be quantified and studied. However, since their experiments were not phase-averaged, little can be said about the structure of the external jet.

Wong *et al.* [8] visually sorted their free-running PIV data into either a left-sided, or right-sided emerging precessing jet. They reported that the spatially-averaged emerging precessing jet has a centreline decay that is more rapid than a free turbulent jet with a uniform initial velocity distribution. However, their results suffered from directional ambiguity of the emerging jet.

The present paper describes an experimental technique which allows the emerging precessing jet to be directionally resolved and phase-averaged. Phase averaging the emerging jet reveals finer aspects of the ‘instantaneous’ precessing flow than has been previously studied.

### Experimental Details

Details of the FPJ nozzle and the phase-triggered PIV system are shown in Figure 2. The flow at the inlet plane is seeded with 1 $\mu$ m olive oil droplets and has a flat velocity distribution [4,8] with an inlet velocity  $u_i=55.0$  m/s giving a Reynolds number of  $Re_d=59,000$ . At this velocity, the precession frequency,  $f_p$ , is approximately 6Hz, giving a Strouhal number,  $St_d=0.0017$  based on  $u_i$  and  $d$ .

A pair of hot-wire (HW) anemometer probes (each being 1mm long Wollaston wire of 5mm nominal diameter) are positioned just downstream of the exit lip. The centre of the lag HW was located at  $x'/D_2=0.15$  ( $D_2=64$ mm and refers to the exit lip diameter) and  $r/D_2=0.58$  and was azimuthally offset from the lead HW by 24°. Both wires were previously adjusted to respond equally to the same flow before the offset was applied.

The signals from each HW are low-passed filtered at a cut-off frequency of 30Hz and passed into respective Schmitt Triggers (STs). These triggers output a high signal (+5V) each time the filtered signals exceed an arbitrary upper trigger voltage level (2/3 of +5V) and they output a low signal only if the input signal falls below a pre-determined lower trigger level. Fluctuating signals between these two ranges are ignored by the trigger.



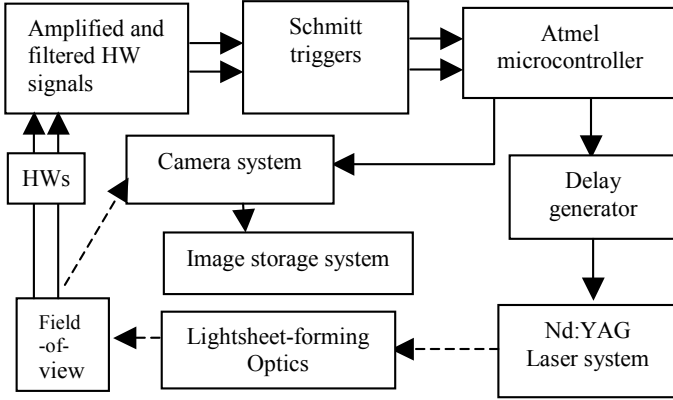
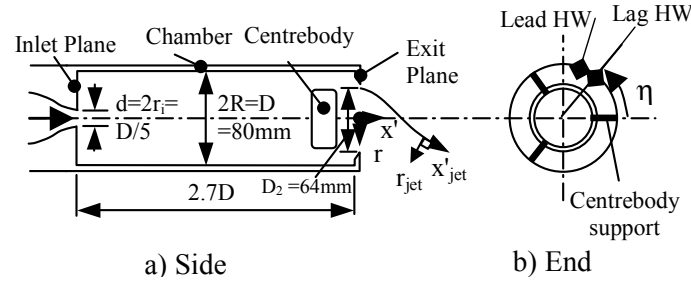


Figure 2. Details of the FPJ nozzle and the PIV system (solid and dashed arrows refer to electrical and light signals respectively).

The outputs from the Schmitt triggers are fed into the interrupt inputs of an 8-bit Atmel AT90S2313-10PC programmable microcontroller. This controller is responsible for generating a constant train of 10Hz pulses to a Stanford Research Systems pulse delay generator (DG-535) which regulates the flashlamp and Q-switch timing of a Quantel Brilliant Twins Nd:YAG laser operating at a wavelength of 532nm with a power of 180mJ per oscillator output. The output laser beam passes through a series of optical lenses to produce a lightsheet that is approximately 2 mm thick in the region of interest.

When the microcontroller determines that the lag ST is triggered after the lead ST and this event occurs within 2.5ms of the next laser clock pulse, the microcontroller activates the camera to record a pair of PIV images. In this way, only one precession direction is selected. A Kodak Megaplex ES1.0 camera which has an array of 1018 by 1008 pixels is used with an AF Zoom-Nikkor 70-300mm f/4-5.6D ED lens at an  $f\#$  of 5.6.

A total of 11 transverse planes ( $x'/D_2=0.11, 0.19, 0.27, 0.34, 0.42, 0.50, 0.58, 0.74, 0.89, 1.05$  and  $1.20$ ) were measured. The time interval between each laser pulse varies with distance downstream from the exit lip. It was  $15\mu s$  for  $0 < x'/D_2 < 0.58$ ,  $30\mu s$  for  $0.58 \leq x'/D_2 \leq 0.89$  and  $20\mu s$  for  $x'/D_2 > 0.89$ . An interrogation window size of 32 by 32 pixels with a 50% overlap was used (measurement volume is  $6.3\text{mm} \times 6.3\text{mm} \times 2\text{mm}$ ). A total of 12 planes ( $\eta = 0^\circ, 15^\circ, 30^\circ, 45^\circ, 60^\circ, 75^\circ, 90^\circ, 105^\circ, 120^\circ, 135^\circ, 150^\circ, 160^\circ$ ) were also interrogated in the longitudinal section, this time using an interrogation window size of 16 by 16 pixels (measurement volume is  $1.51\text{mm} \times 1.51\text{mm} \times 2\text{mm}$ ) and zero overlap. The time interval used here was  $15\mu s$ . Velocities from all the image pairs were calculated using PIVview 1.7's cross-correlation algorithm.

## Results

Nominally 50 instantaneous image pairs were averaged in each experimental plane. Axial vorticity results from each transverse section and tangential vorticity results from each longitudinal section are presented in Figures 3 and 4 respectively. The jet in

Figure 3 is precessing in a clockwise fashion, while the jet to the right of  $r/D_2=0$  in Figure 4 is moving out of the page.

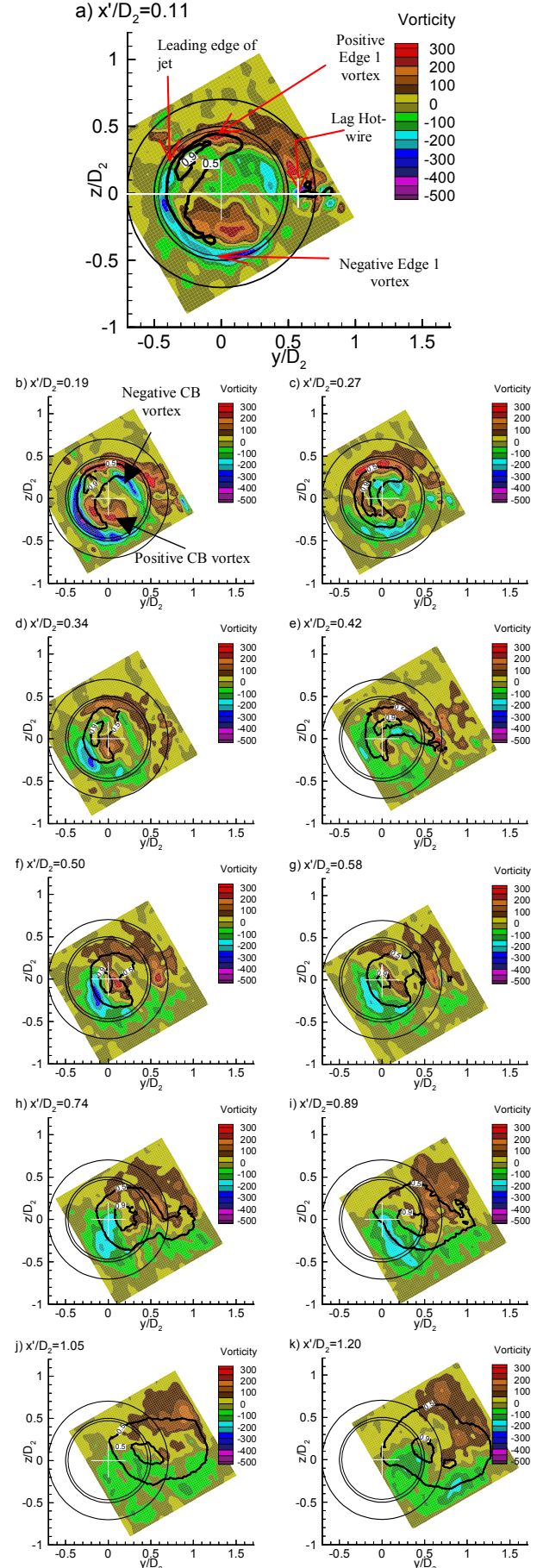


Figure 3. Axial vorticity results in the  $y$ - $z$  (transverse) section. Contours representing  $0.5$  and  $0.9 (v^2 + w^2)^{1/2}_{max}$  are overlaid on the coloured vorticity contours.

In Figure 3(a), a pair of vortices can be observed near to the central axis of the nozzle. Results from surface flow visualisation (Figure 5) of a non-precessing deflected jet using the same nozzle confirms that these central vortices (CB vortex pair) originate from a pair of foci on the downstream face of the centrebody. The CB vortices move closer to each other with downstream distance and finally annihilate each other by  $x'/D_2 \sim 0.5$  (Figure 6), or possibly reconnect to form a closed loop.

Another pair of vortices surrounding the CB vortices is also apparent. The ‘legs’ of this vortex form a pair of longitudinal vortices downstream from the centrebody. These appear as negative and positive vorticity regions as seen by a downstream observer. These vortices which depart the centrebody at an inclined angle (‘Edge 1’ vortex pairs) are thought to originate from the outer edges of the centrebody. Thus, this vortex pair appears as two kidney-shaped patterns near to the exit plane. The negative edge of this vortex initially follows the trajectory of the main jet fairly closely, but at  $x'/D_2 = 0.58$ , it departs, with increasing radius from the nozzle axis, in a direction opposite to the jet precession.

A third vortex pair is also found to sit slightly above the surface of the exit lip. It then lifts away from the lip at the rear side of the exiting jet at the position of the lag-hot-wire probe in figure 3a, approximately  $130^\circ$  to  $150^\circ$  from the centre of the emerging jet. This range of angles is similar to the separation angles of the surface flows in jets in cross flows [9]. The vorticity associated with this vortex pair (‘Edge 2 Vortex’) is labelled (Fig. 4a) and is most clearly seen in all of Figure 4. The trajectories of the two ‘legs’ of this vortex pair follow the same trend as the ‘Edge 1’ vortex pair (in terms of the y-z trajectory with downstream distance) albeit with a slight delay in phase. The presence of this vortex pair below the core of the jet was also detected in earlier phase-averaged LDA studies [4].

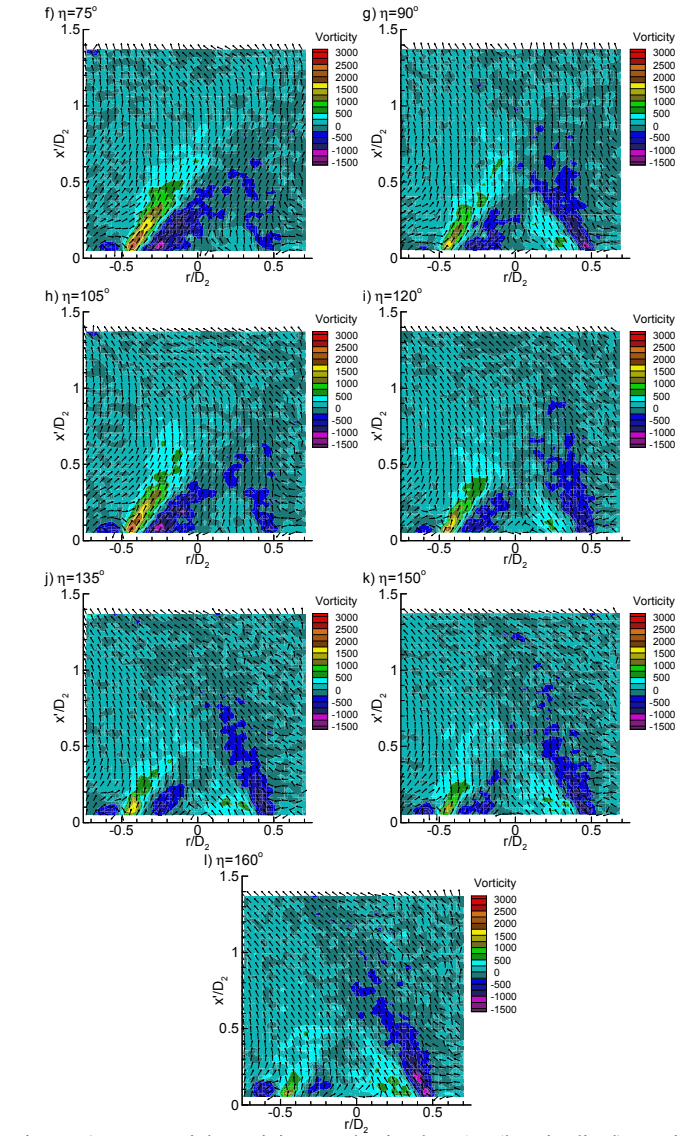
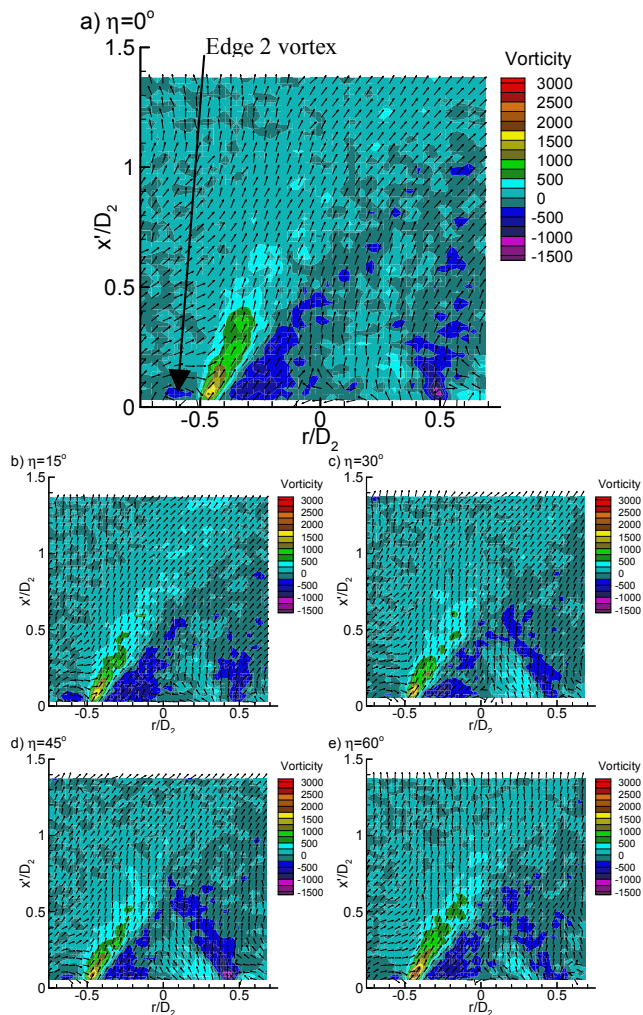


Figure 4. Tangential vorticity results in the  $x'$ - $r$  (longitudinal) section. Velocity vectors indicate direction only.

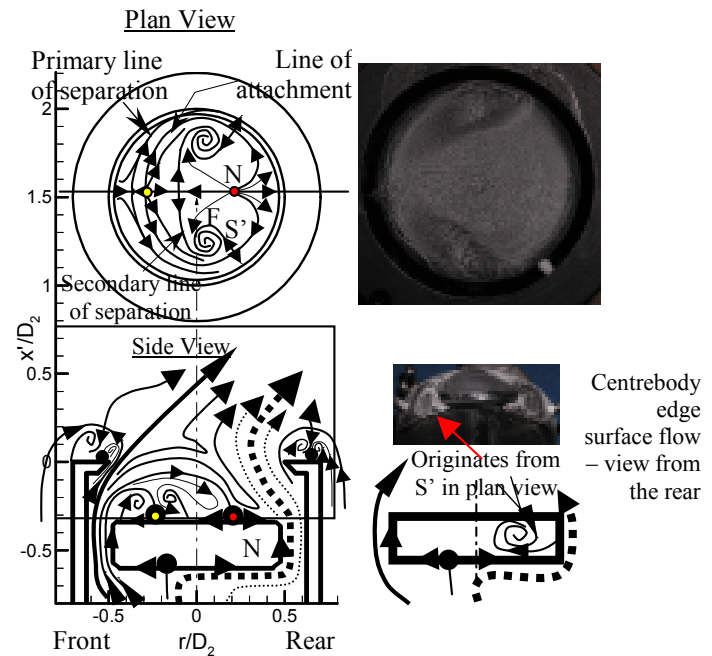


Figure 5. Pre-exit lip flow topology interpreted from PIV and surface flow visualisation experiments (top-right). Not to scale.



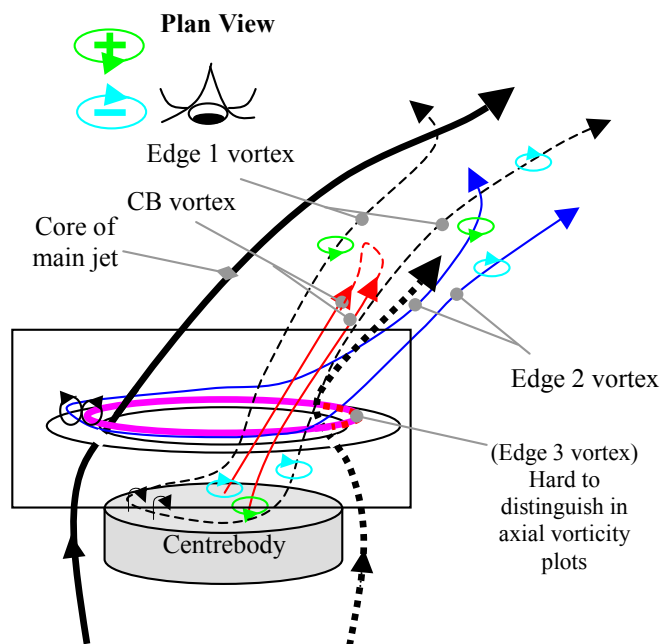


Figure 6. Overall flow topology interpreted from PIV and surface flow visualisation experiments.

Adjacent to the 'Edge 2 Vortex' is an 'Edge 3 Vortex' with a different sign of vorticity (at approximately  $r/D_2=0.5$  in Figure 4). This vortex is relatively small just off the edge of the field of view and Figure 6 illustrates the qualitative location of this small feature. Due to its small size, it is not further discussed here.

### Interpretation of results

By combining the PIV and surface flow visualisation results, the external structure of the precessing jet is qualitatively constructed as shown in Figures 5 and 6.

### Conclusions

The phase-averaged structure of an external precessing jet is revealed, for the first time, by means of a novel PIV experimental technique which resolves the phase and direction of the naturally precessing jet. The study found that at least three large-scale fluid vortex pairs exist in this flow:

- a 'Centrebody' vortex pair that originates from the foci on the downstream face of the centrebody;
- an 'Edge 1' vortex pair surrounding the inner 'CB vortex pair' and likely to originate from the edge of the centrebody, and
- an 'Edge 2' vortex pair that originates from the top surface of the exit lip.

A fourth vortex pair adjacent to the top surface of the exit lip is also deduced to be present, however, due to its small size, it is not examined further.

### Acknowledgments

CYW is thankful for the International Post-graduate Research Scholarship and the Adelaide University Scholarship. The help from Mr. Owen Lucas, who assisted in writing the code for the microcontroller, is also acknowledged. The facilities from the Turbulence, Energy and Combustion Group (The University of Adelaide) have been developed with support from the Australian Research Council, The University of Adelaide and FCT-combustion through the LIEF, LARGE and SPIRT grant schemes.

### References

- [1] Guo, B.Y., Langrish, T.A.G., Fletcher, D.F., Numerical simulation of unsteady flow in axisymmetric sudden expansions, *Trans. ASME: J. Fluids Eng.*, **123**, 2001, 574-587.
- [2] Manias, C.G., Nathan, G.J., Low  $\text{NO}_x$  clinker production, *World Cement*, **25**(5), 1994, 54-56.
- [3] Nathan, G.J., Hill, S.J. & Luxton, R.E., An axisymmetric 'fluidic' nozzle to generate jet precession, *J. Fluid Mech.*, **370**, 1998, 347-380.
- [4] Wong, C.Y., Lanspeary, P.V., Nathan, G.J., Kelso, R.M. & O'Doherty, T., Phase averaged velocity in a fluidic precessing jet nozzle and in its near external field, *J. Experimental Thermal and Fluid Science*, **27**, 2003, 515-524.
- [5] Kelso, R.M., A Mechanism for jet precession in axisymmetric sudden expansions, in *Proc. 14<sup>th</sup> Australasian Fluid Mechanics Conference*, editor B.B Dally, Adelaide, Australia, **2**, 2001, 829-832, 10-14 Dec.
- [6] Newbold, G.J.R., Nobes, D.S., Alwahabi, Z.A., Nathan, G.J. & Luxton, R.E., The application of PIV to the precessing jet nozzle, in *Proc. 12<sup>th</sup> Australasian Fluid Mechanics Conference*, editor R.W. Bilger, Sydney, Australia, **1**, 1995, 395-398, Dec.
- [7] Nobes, D.N., Newbold, G.J.R., Hasselbrink, E.F., Su, L., Mungal, M.G. & Nathan, G.J., *PIV and PLIF measurements in precessing and round jets*, Internal Report, Dept. Mech. Engng., University of Adelaide, Australia, 2002.
- [8] Wong, C.Y., Nathan, G.J. & Kelso, R.M., Velocity measurements in the near-field of a fluidic precessing jet flow using PIV and LDA, in *Proc. 3<sup>rd</sup> Australian Conference on Laser Diagnostics in Fluid Mechanics and Combustion*, Uni. of Queensland, Brisbane, Australia, Paper 4, 2002, 48-55, 2-3 Dec.
- [9] Fric, T.F., Roshko, A., Vortical structure in the wake of a transverse jet, *J. Fluid Mech.*, **279**, 1994, 1-47.

## An Investigation of the Influence of Nozzle Aspect Ratio on the Velocity Field of Turbulent Plane Jet

R. C. Deo, J. Mi and G. J. Nathan

Turbulence, Energy and Combustion [TEC] Group, School of Mechanical Engineering, Adelaide University, South Australia

### Abstract

The effect of nozzle aspect ratio ( $w/H$ ) (major axis to minor axis ratio) on the velocity field of a turbulent plane jet is investigated using a hot-wire anemometer. The aspect ratios investigated were in the range  $10 \leq w/H \leq 60$ . The initial turbulence intensity profiles exhibit a lower intensity at higher aspect ratios although this is probably caused by the nozzle whose profiles change with aspect ratio. The length of the potential core and the normalized mean and rms velocities are all found to be a function of  $w/H$ , in both the near and far field. Lower aspect ratio leads to faster decay of the mean velocity. Most investigations on aspect ratio effects have been on rectangular jets, hence this work is unique in its own right. Overall, the dependence of the current plane jet on aspect ratio is quite significant.

### Introduction

Plane jets are a class of fundamental turbulent shear flow that have been a subject of research interest mainly due to their relative simplicity. An ideal plane jet is a statistically two-dimensional flow, with a dominant mean flow in the axial ( $x$ ) direction, jet spread along the lateral ( $y$ ) direction and zero entrainment in the transverse ( $z$ ) direction. Side walls, placed in the  $x$ - $y$  plane are necessary to achieve this. Plane jets have received much attention, both experimental and modelling investigations.

Plane jets can exhaust from rectangular nozzles, either into the ambience or into a controlled co-flow. While many studies have indicated the importance of initial conditions (jet exit Reynolds number, nozzle aspect ratio, exit velocity profiles, nozzle geometry, presence or absence of co-flow and presence or absence of side walls), very few of these initial conditions have been systematically assessed. Previous work has tested to some degree, the effect of nozzle geometry [1], effect of nozzle exit turbulence on jet spreading [2], effect of presence/absence of sidewalls [3] and effect of jet exit Reynolds number [4, 5, 6]. However, the influence of nozzle aspect ratio for a plane jet has yet to be studied systematically.

Nozzle aspect ratio,  $w/H$ , is defined from the exit dimensions of the rectangular nozzle, where  $w$  and  $H$  are the dimensions of the short and long sides of the nozzle respectively. [7] assessed the influence of slot aspect ratio over the limited range,  $3.4 \leq w/H \leq 12$ . They used total head tubes and hot-wire anemometry, and suggested that their smallest aspect ratio jet exhibits quite different behavior to the larger aspect ratios. Later, [8] studied the aspect ratio dependence of unconfined rectangular jets between  $2 \leq w/H \leq 20$  using hot-wire anemometry. He found that the rate of near field mixing increases with increased three-dimensionality and hence with increasing aspect ratio up to  $w/H = 20$ . Their work also suggested that the shortest potential core, highest shear layer turbulent kinetic energy, highest Reynolds shear stresses and largest turbulent transport of Reynolds stresses, were found with the largest aspect ratio.

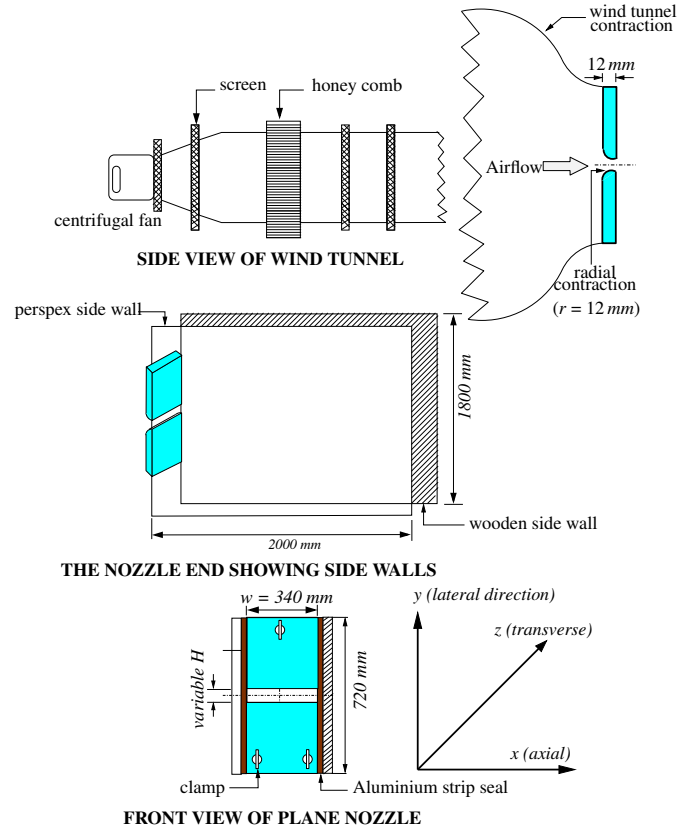


Figure 1: Schematic of the plane jet facility.

Given the distinctions in the velocity field of rectangular jets with different aspect ratios [8, 7], the velocity field of a plane jet may also depend on the aspect ratio. To verify our postulate, a preliminary investigation has been carried out using hot wire anemometry. We have used four aspect ratios for the investigation, which are  $w/H = 10, 20, 30$  and  $60$ . It has been also proposed that the nozzle aspect ratio has to be large - typically 50 to achieve a flow that is statistically 2-dimensional and free from end effects as stated in [9]. However, this hypothesis has not been tested experimentally. For these reasons, the current nozzle was designed to provide higher nozzle aspect ratios than previously studied (i.e.  $> 20$ ) and also higher than that proposed in [9] (i.e.  $> 50$ ).

Length $w$ (mm)	340	340	340	340
Width $H$ (mm)	34	17	11.33	5.6
Aspect Ratio $w/H$	10	20	30	60
$r/H$	0.353	0.706	1.059	2.143
Range of $x/H$	30	100	100	160

Table 1: Nozzle geometric parameters.

### Experimental Details

The plane jet facility, illustrated in Figure 1, is described in

detail elsewhere ([4]). Briefly, the nozzle has a  $90^\circ$  radial contraction machined into two plates of 12 mm thickness ( $r=12$  mm), separated by gap width,  $H$ , which is adjusted to allow the variation of the nozzle aspect ratio. Table 1 lists the nozzle geometric parameters and the nozzle aspect ratios selected. The nozzle aspect ratios were selected by studying previous measurements of rectangular jets by [7, 8] who showed that their three-dimensional flows are still show significant differences, even at their highest aspect ratios (i.e.  $w/H = 20$ ).

The plane jet, emerges from the radial contraction shown in Figure 1, into ambient air. Hot-wire anemometry was used to measure the axial ( $x$ ) centerline and lateral ( $y$ ) instantaneous velocities. Data were sampled at 18.4 kHz and 400,000 samples, were collected at every axial location. A three-dimensional traversing system, controlled via a tri-axial driven control switch, was mounted below the plane nozzle to enable measurements along all the 3-axes to an accuracy of  $\pm 0.5$  mm in all three directions. The extent of measurements along the axial direction are shown in Table 1 for each aspect ratio. The Reynolds number  $Re = U_{co}H/\nu$ , where  $H$  is the nozzle slot opening,  $U_{co}$  the jet exit velocity on the centerline and  $\nu$  the kinematic viscosity of air, was about  $1.65 \times 10^4$ .

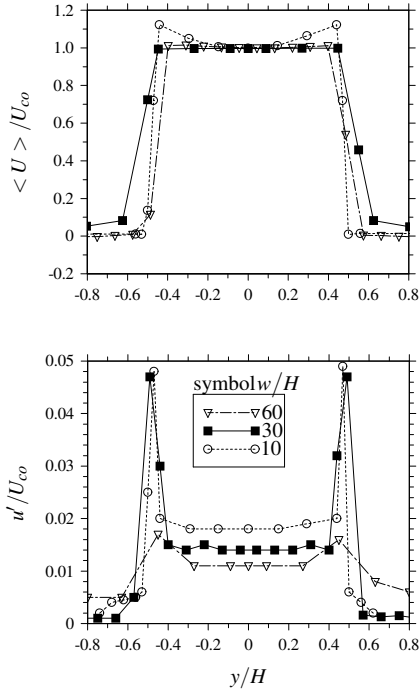


Figure 2: The normalized mean velocity profiles (top) and turbulence intensity fields (bottom), at different nozzle aspect ratios, at the nozzle exit plane.

## Results

Figure 2(top) presents the normalized initial velocity and turbulence intensity profiles, measured at  $x/H \approx 0.5$ , for the nozzle aspect ratios,  $w/H = 10, 30$  and  $60$ . Here,  $\langle U \rangle$  is the mean velocity and  $u'$  is the rms velocity. The mean profiles are *top-hat* for  $w/H = 30$  and  $60$ , and *saddle-backed* for  $w/H = 10$ . The top-hat profiles are typical of that from a smooth-contraction nozzle (e.g. [5], [1]) while the saddle-backed profile is a characteristic of a sharp-edged orifice type nozzle (e.g. [8]). The mean profile is uniform ( $\langle U \rangle / U_o \approx 1$ ) over the range  $-0.46 \leq y/H \leq 0.46$  for  $w/H = 30$  and over the range  $-0.4 \leq y/H \leq 0.4$  for  $w/H = 60$ . The figure shows that the initial velocity profiles also change with aspect ratio because  $r/H$  changes with  $w/H$ . The saddle-backed profiles for  $w/H$

$= 10$  are caused by the relatively small radius of the exit plates i.e.  $r/H = 0.353$ , because in this case, the nozzle tends to be of an orifice type.

The normalized initial turbulence intensity profiles (Figure 2 (bottom)) also show a significant variation on nozzle aspect ratio and  $r/H$ . Again, the central region has a nearly uniform turbulence intensity, ranging from 1 % to 1.8 %. It is evident that the initial turbulence intensity is lower ( $\approx 1$  %) for  $w/H = 60$  and higher ( $\approx 1.8$  %) for  $w/H = 10$ . The shear layers show peak turbulence intensities, which is the largest for  $w/H = 10$  and smallest for  $w/H = 60$ . Reduced central region and shear layer intensities are lower at higher aspect ratios, possibly due to reduced near field mixing (as shown later) for these case. Less interactive activity of the jet keeps the turbulence levels low. The dependence of the initial turbulence intensity on the nozzle aspect ratio suggests that this parameter is likely to influence both the near and far field characteristics of the plane jet flow. Hence the present assessment of the effect of aspect ratio is somewhat complicated by a secondary influence of the effect of different initial conditions.

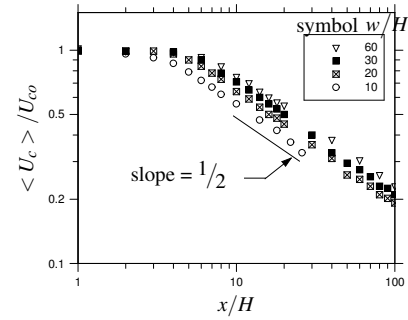


Figure 3: Evolution of the normalized mean streamwise velocity decay on the jet centerline, measured at different nozzle aspect ratios.

Figure 3 shows the normalized centerline velocity decay at various aspect ratios. (Note that  $\langle U_c \rangle$  is the mean velocity on the jet centerline). The plot reveals some interesting features. A strong dependence of the velocity decay on aspect ratio is evident. The length of potential core increases with the aspect ratio, even at  $w/H$  as high as 60. An opposite dependence was noted by [8] and [7] for their three-dimensional rectangular jet. The discrepancy is most likely to be an effect of nozzle type, rectangular for theirs versus planar for ours. However, their dependence suggests that current variations are not solely due to the different  $r/H$ , since this parameter was constant in their experiments. Potential core lengths have also been assessed for plane jets, but only at relatively low Reynolds numbers and for single aspect ratios. [10] studied plane jet at  $Re = 4200$ ,  $w/H = 5.8$ , [1] at  $Re = 32,550, 61,400$  and  $w/H = 44$  and [5] at  $1,000 \leq Re \leq 7,000$ ,  $w/H = 44$ . These investigators presented near field data of centerline velocity decay which shows the length of the potential core. Table 2 compares the potential core lengths obtained in past and present measurements. Overall, the measurements in the literature compare well with current findings, although there are some interesting differences, especially between those of rectangular jet investigations and plane jets. The trends of the unconfined rectangular jets in [8] are opposite to those for the present plane jet, with him measuring a decrease in potential core length with increasing aspect ratio.

The far field centerline velocity decay exhibits the usual

inverse-square relationship for a plane jet

$$\left[ \frac{U_{co}}{\langle U_c \rangle} \right]^2 = K_u \left[ \frac{x}{H} \right] + \frac{x_o}{H} \quad (1)$$

where  $K_u$  and  $x_o$  are constants determined by experiments. The values of the  $K_u$  are used to compare the effect of aspect ratio on the far field flow (Table 2). It is evident that the decay rate varies significantly with the nozzle aspect ratio. The highest decay is found for  $w/H = 10$  (with largest value of  $K_u$ ) and the lowest for  $w/H = 60$  (with smallest  $K_u$ ). The general trends of the centerline decay are presented in Figure 4.

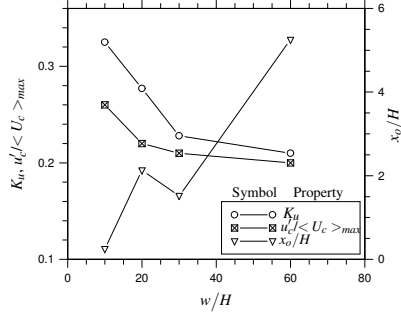


Figure 4: The dependence of some flow parameters on nozzle aspect ratio.

It is evident that the dependence of  $K_u$  on aspect ratio seems to be asymptotic as expected, with the difference at  $w/H = 30$  and  $w/H = 60$  being small. However, the present results are different to the measurements of [8], who did not use side walls. For example  $K_u = 0.277$  at  $w/H = 20$  for the present jet at while for his results  $K_u = 0.240$  at  $w/H = 20$ . Similarly,  $K_u = 0.325$  at  $w/H = 10$  for plane jet at while for his results  $K_u = 0.220$  at  $w/H = 10$ . This is probably attributable to the difference between rectangular and plane jets although a difference in Reynolds number may also play a small role. The results of [11] for  $w/H = 20$  and  $Re = 7,700$  for their smooth contraction plane nozzle show a lower decay rate at the same aspect ratio. This difference is probably due to the combined effect of lower Reynolds number and a different shaped radial contraction nozzle as stipulated in [4]. A similar explanation can be offered for the discrepancy in  $K_u$  for [5] and [1]. The results of [12] are consistently higher than those of current measurements for their plane jet at  $w/H = 120$  and  $Re = 34,000$ . This is consistent with a sharp-edged orifice, having a higher rate of decay than a smooth contraction. Overall, the constant,  $K_u$  in the measured range of  $w/H$  compares better with [8] and [12] for their orifice type nozzles rather than the smooth contraction nozzles of [5], [11] or [1]. This implies that our initial conditions are similar to that of a orifice type nozzle rather than a smooth contraction, even though the current nozzle is radially contoured. The dependence of the virtual origin  $x_o/H$  is clearly demonstrated in Figure 4. The figure also shows that  $x_o/H$  is not asymptotic even at  $w/H = 60$ , suggesting aspect ratio effect still dominates even at aspect ratio as high as 60. The dependence of centerline velocity decay rate  $K_u$  on the exit turbulence intensities cannot be conclusively evaluated from the current data, due to the combined influence of both  $r/H$  and  $w/H$ . However, the currently observed higher turbulence intensities correlate well with the corresponding higher decay rates, at smaller aspect ratios and vice versa for higher aspect ratios. This agrees totally with [2], who also observed faster decay and spreading rates when exit intensities were larger.

INVESTIGATION			PROPERTIES		
author(s)	$Re_H$ $\times 10^3$	$w/H$	$x_p$ $\times H$	$K_u$	$u'_c / \langle U_c \rangle_{max}$
current	16.5	10	2.0	0.33	0.26
	16.5	20	3.0	0.28	0.22
	16.5	30	4.0	0.23	0.21
	16.5	60	5.0	0.20	0.20

[8]	36.7	5	4.0	0.20	0.15
[8]	36.7	10	3.1	0.22	0.17
[8]	36.7	20	2.6	0.24	0.20
[11]	7.70	20	3.0	0.14	0.23
[5]	7.00	44	2.0	0.18	0.22
[1]	32.5	44	4.0	0.11	0.17
[12]	34.0	132	N/M	0.27	N/M

Table 2: Summary of current and literature work.<sup>1</sup>

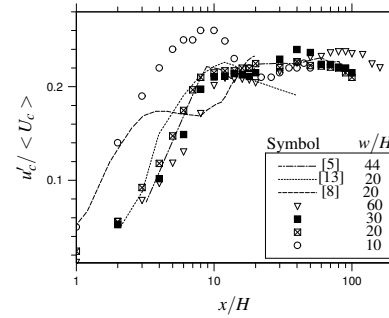


Figure 5: The axial centerline normalized rms at different nozzle aspect ratios.

Figure 5 shows the axial centerline normalized rms velocity. Clear trends are evident - the lowest aspect ratio jet ( $w/H = 10$ ) shows a dramatic transition in the rms in the immediate near field when compared with the higher aspect ratios. This is quite unexpected because the effect of nozzle aspect ratio is thought to be small in the near field and only to be significant in the transition and far fields. It is not possible to isolate the effects of initial conditions (Figure 2) and aspect ratio from the present data alone, and more data is required to determine whether this is a genuine effect of the aspect ratio. It is possible that both are contributing to the near field effect. The value of  $r/H$  (stated in Table 1) are quite small and this suggests that the flow emerging from the smallest aspect ratio nozzle is more like an orifice type plane nozzle rather than a smooth contraction nozzle. This makes the lowest aspect ratio jet quite different in the initial field, hence the rms are different in the near field. At  $x/H = 10$ , there are distinct peaks in the rms for all aspect ratios, with the highest aspect ratio having the smallest peak value. For verification, the peak values in rms at  $x/H = 10$  are listed Table 2 and also plotted in Figure 4. It is observable that the peak values in rms also seem to approach an asymptotic value at higher aspect ratios. It means that the rms is approaching its self-similar state faster when nozzle aspect ratio are larger, which is quite expected. The occurrence of a bigger peak for  $w/H = 10$  shows that the large-scale vortices are more coherent and organized than for  $w/H = 60$  for which

<sup>1</sup>Jet types - [8] rectangular jet sharp-edged orifice exit, [11] plane jet smooth contraction exit, [5] rectangular jet smooth contraction exit, [1] rectangular jet smooth contraction exit and [12] plane jet sharp-edged orifice exit

the near field peak is reduced.

Initial conditions are not expected to have a significant influence on the far field values of normalized rms. However, according to Figure 5, differences seem to persist even at  $x/H > 10$ . This means that the nozzle aspect ratio effect is maintained, even in the far field.

## Conclusions

A preliminary study has been carried out, to assess the effect of aspect ratio on a plane jet. The variation of  $w/H$  was achieved by varying the gap between two radially curved plates, which also cause a change in  $r/H$ , hence some changes in the initial conditions. At this point, it is not possible to separate the two influences, but the effects are significant enough to provide indicative trends of the effect of aspect ratio. Key results are:

1. It has been found that the normalized initial velocity profiles and turbulence intensity profiles are different when varying  $w/H$ . This, however, could be a direct effect of varying  $r/H$  for the nozzles rather than an influence of the aspect ratio. The normalized turbulence intensities in the central region (i.e.  $|y/H| \approx 0.5$ ) are 1 % for  $w/H = 60$  and increased up to 1.8 % when  $w/H = 10$ .
2. The length of the jet potential core is smaller at lower nozzle aspect ratio. This suggests that the rate at which ambient fluid is drawn into the jet (i.e. the mixing rate) in the near field, is greater when the nozzle has a smaller aspect ratio.
3. The rate of centerline velocity decay decreases with increasing aspect ratio. For example, for  $w/H = 10$ ,  $K_u = 0.325$  but for  $w/H = 60$ ,  $K_u$  decreases to 0.2. An aspect ratio dependence of the jet virtual origin,  $x_o/H$  has also been noted.
4. The centerline normalized rms are also sensitive to aspect ratio. In the near field, peak rms is found at  $x/H = 10$ , indicating a maximum deviation of the instantaneous centerline velocity from the mean. This means higher instabilities are likely to be caused by smaller nozzle aspect ratio in the near field. This is consistent with the above finding that rapid mixing in the near field occurs for lowest aspect ratio jet, hence faster engulfment of the ambient fluid into the jet causes biggest fluctuations of the instantaneous signal from its mean. It is also possible that a faster acceleration of large-scale coherent vortices occur at this location. In the far field, the normalized rms have not become asymptotic at the current range of measurements, although they approach it. The absolute magnitude also different.

The present findings are not conclusive because of the combined influences at different initial conditions ( $r/H$ ) and aspect ratio ( $w/H$ ). Nevertheless, the influences are of sufficient magnitude to warrant a more complete investigation where aspect ratio is varied for fixed initial conditions. Both, independent investigations on,  $r/H$  and  $w/H$  are now complete and the preliminary assessment of results suggest that the influence of  $r/H$  is even greater than  $w/H$ . Full documentation of the independent investigation on aspect ratio dependence, will be presented in near future.

## Acknowledgements

This research is a major focus of the main author's Ph.D, accomplished through the support of ARC and IPRS. Hence we wish to acknowledge ARC Discovery Grant and the IPRS funding. Special thanks for George Osborne (for hot-wire design/build up), Derek Franklin (for traverse setups and overall technical support) and Bill Finch for nozzle design support. \*

## References

- [1] Hussain A K M F and Clark A R . Upstream influence on the near field of a planar turbulent jet. *Phys. Fluids*, **20** (9):1100-1112, 1977.
- [2] Goldschmidt V W and Bradshaw P . Effect of nozzle exit turbulence on the spreading (or widening) rate of plane free jets. In *Proc. Joint Eng., Fluid Eng. and Appl. Mech. Conference*, ASME, 1-7, Boulder, Colorado, June 22-24 1981.
- [3] Hitchman G J , Strong A B , Slawson P R , and Ray G . Turbulent planar jet with and without confining walls. *AIAA J.*, **28**(10):1699-1700, 1990.
- [4] Deo R C , Mi J , and Nathan G J . An investigation of the effects of reynolds number on a turbulent plane jet. *J. Turbulence*, Under Review, 2004.
- [5] Namar I and Ötügen M V . Velocity measurements in a planar turbulent air jet at moderate reynolds numbers. *Exp. Fluids*, **6**:387-399, 1988.
- [6] Löfdahl L , H Abrahamsson , B Johansson , and T Hadzianagnostakis . On the reynolds number dependence of a plane two-dimensional wall-jet. *Doktorsavhandlingar vid Chalmers Tekniska Högskola*, **1292**:8pp, 1997.
- [7] Marsters G F and Fotheringham J . The influence of aspect ratio on incompressible turbulent flows from rectangular slots. *Aeronaut. Quart.*, **XXXI**, **4**:285-305, 1980.
- [8] Quinn W R . Turbulent free jet flows issuing from sharp-edged rectangular slots: The influence of slot aspect ratio. *Exp. Thermal. Fluid Sc.*, **5**:203-215, 1992.
- [9] Pope S B . *Turbulent Flows*. Cambridge University Press, UK, 2002.
- [10] Lemieux G P and Oosthuizen P H . Experimental study of behaviour of planar turbulent jets at low reynolds numbers. *AIAA J.*, **23**(12):1845-1846, 1985.
- [11] Brown L W B , Antonia R A , and Chambers A J . The interaction region of a turbulent planar jet. *J. Fluid Mech.*, **149**:355-373, 1984.
- [12] Heskestad G . Hot-wire measurements in a plane turbulent jet. *Trans. ASME, J. Appl. Mech.*, **32**:721-734, 1965.
- [13] Brown L W B , Antonia R A , Rajagopalan S , and Chambers A J . Structure of complex turbulent shear flows. In *Proc. IUTAM Symposium*, 411-419, Marcseille, 1982.

## The Anomalous Refraction of Shock Waves in Gases

L.F. Henderson<sup>1</sup> E.G. Puckett<sup>2</sup> and P. Colella<sup>3</sup>

<sup>1</sup>8 Damour Avenue, East Lindfield, N.S.W. 2070 Australia,

<sup>2</sup>Department of Mathematics and Institute of Theoretical Dynamics, University of California, Davis Ca 95616 USA,

<sup>3</sup>Center for Computational Science and Engineering, Lawrence Berkeley National Laboratory, Berkeley, California Ca 94720.

### Abstract

Anomalous refraction comprises at least five refracting shock systems. All need sonic or subsonic flow downstream for their existence, which is induced by overtaking downstream disturbances, thus the limiting sonic condition determines their onset. The wave impedances are also an important factor for their existence. The theory predicts a new system (ARe) that has not yet been observed. Numerical results for all these refractions and related systems are presented and some comparison is made with experiment.

### Introduction

Consider two gases, differing in composition and, or in state and meeting at a plane interface. A plane (i-) shock in the *incident* gas propagates parallel to, and towards (angle of incidence  $\alpha_i = 0^\circ$ ) the interface. The speed of sound in the gas is  $\alpha_{0i}$ . The i-shock crosses the interface and enters the *receiving* gas (with speed-of-sound  $\alpha_{0t}$ ) where it becomes the *transmitted* (t-) shock. In general a reflected wave which may be a shock (r-) or an expansion (e-) is sent back into the i-gas. By symmetry all the waves in the system are parallel to the interface. This phenomenon is *normal* (1-D) shock refraction.

There is (2-D) *oblique* shock refraction when  $\alpha_i > 0^\circ$  with respect to the upstream interface. If  $\alpha_i$  is sufficiently small the refraction is *regular* i.e. the gas between any two adjacent waves has a uniform state ( $v, s$ ) and speed ( $u$ ), figure 1(a). Here  $v$  is specific volume and  $s$ , is entropy. If ( $v, s, u$ ) are non-uniform between any wave pair, the refraction is *irregular*, figure 1(c). A regular (i, t, e) wave system (RRE) can be transformed into an irregular *anomalous refraction* (ARE) via a transitional system figure 1(b) by sufficiently increasing  $\alpha_i > \alpha_i^*$ . At  $\alpha_i = \alpha_i^*$  the *flow* Mach number is sonic at the foot of the i-shock,  $M_{i1} = 1$ . For  $\alpha_i > \alpha_i^*$ , the shock and the e-waves are steeper and the e-waves partly overrun the shock causing attenuation of part (i') of it, causing it to curve backwards. There is a sonic surface on the rear of i' and a distributed band of supersonic expansions emanating downstream from it. The refraction law [3] relates the angles  $\alpha_i$ ,  $\alpha_t$  at the interface,

$$U_i / \sin \alpha_i = U_t / \sin \alpha_t, \quad (1)$$

where  $U$  is shock speed. These angles determine the direction of flow of information. If for regular refraction  $0 < \alpha_i < 90^\circ$ , and  $\alpha_i > 90^\circ$  the i-shock *arrives* at the interface and the t-shock *leaves* it [4].

If  $\alpha_{0i} > \alpha_{0t}$  the refraction is *fast-slow* and vice-versa for *slow-fast*. ARE has appeared in experiments with the fast-slow combinations air / CO<sub>2</sub> and air / SF<sub>6</sub> [1] [2], figure 1(b). The results

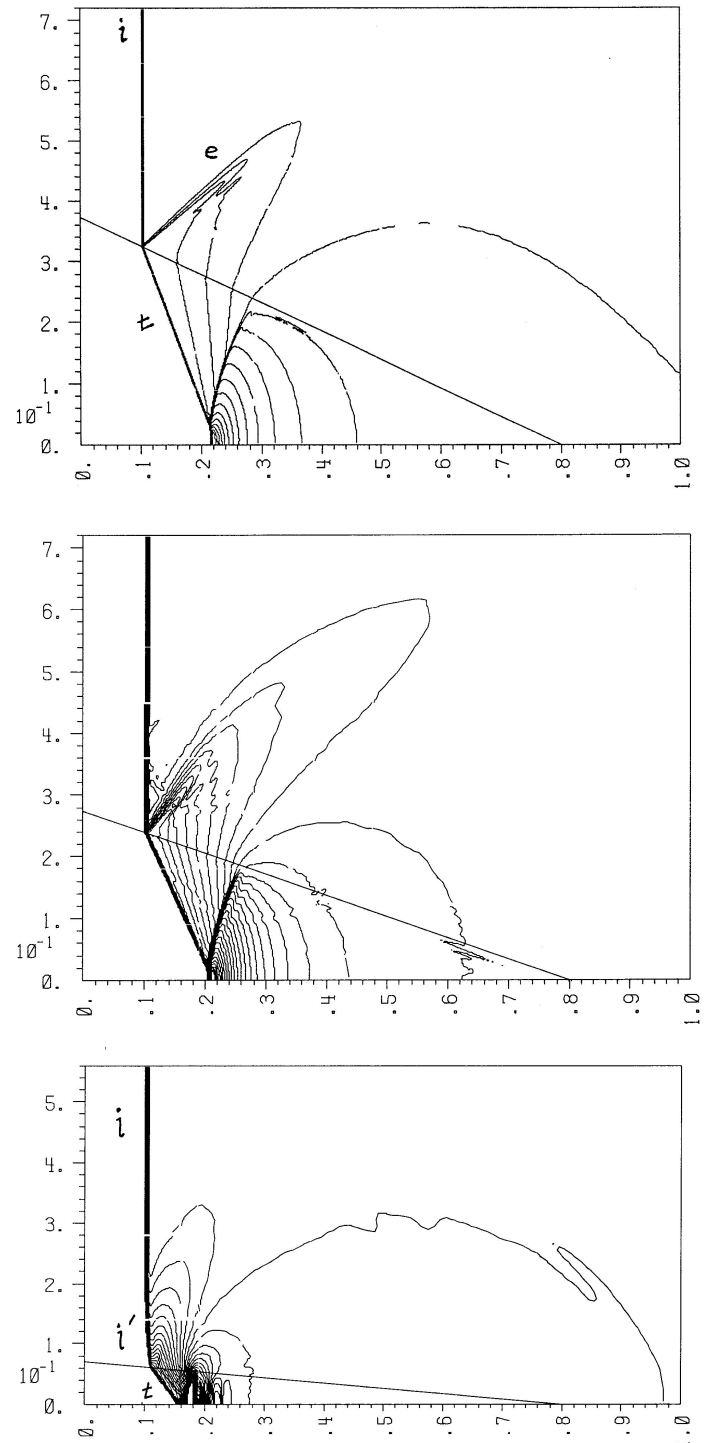


Figure 1. Computed Refracting Shock Systems in the Air-CO<sub>2</sub> Combination  $\xi_i = 0.85$ . a) Regular refraction with reflected expansion RRE; b) Transitional; c) Anomalous refraction ARE.



of a numerical study of ARE and related refractions are reported here and in forthcoming papers [5], [6]. A second order Godonov code was used to integrate the equations of motion that included the Euler equations. Some of the ARE experiments in [1], [2], were simulated numerically.

## Theory

In our earlier papers we defined the relative refractive index ( $\eta$ ) and the incident shock impedance ( $Z_i$ ) for *normal* shock refraction [3], [4],

$$\eta \equiv \frac{U_i}{U_t} \quad (2)$$

$$Z_i \equiv \pm(P_i - P_o)/U_{pi} \quad (3)$$

Where  $U_{pi} = u_i - u_o$  is the shock piston speed in rest frame coordinates,  $P$  is pressure,  $u$  is particle speed, and the subscripts 0,1 refer to conditions upstream and downstream of the incident i-shock. It follows from the shock momentum equation that the impedance is also the mass flux  $Z_i = \rho_0 u_0$  ( $\rho$  is density) through the shock [3]. The reflection and transmission coefficients are,

$$R \equiv \frac{(P_2 - P_1)}{(P_1 - P_2)} \equiv \frac{Z_r(Z_i - Z_t)}{Z_i(Z_r - Z_t)}, \quad (4)$$

$$T \equiv \frac{(P_t - P_o)}{(P_1 - P_o)} \equiv \frac{Z_t(Z_i - Z_r)}{Z_i(Z_t - Z_r)} \quad (5)$$

The  $R$ ,  $T$ , expressions are also valid for oblique shock refraction provided that the impedance is defined as,

$$Z_i \equiv \pm(P_i - P_o)/U_{pi} \cos \beta_i, \quad (6)$$

where  $\beta_i$  is the angle between the i-shock and the *deflected* gas interface. With similar definitions for the other shocks; an e-wave requires the denominator of (6) to be replaced by an integral [3]. Regular refraction solutions can be found from the algebraic Rankine-Hugoniot equations and the equations of states (EOS's) for the gases. Solutions for irregular refractions require numerical integration of the conservation equations. For ARE the i-shock Mach number  $M_i$  is typically small  $M_i \leq 1.7$  so it is sufficient to use the perfect gas EOS for each gas. In the important special case when the i- and t-shocks have equal impedances  $Z_i = Z_t$ , corresponding to  $\alpha_i = \alpha_p$ , and  $R = 0$ ,  $T = 1$ , there is no reflected wave and this condition is called *total transmission*. The system is reduced to a regular shock pair refraction (RSP) and both i- and t-shocks are plane. A more detailed study [6] shows that a convenient parameter space for refraction in any particular gas combination is  $(\xi_i, \alpha_i)$  where  $\xi_i \equiv P_o/P_i$  is the inverse shock strength. Each system has a unique parameter space in this plane. The domain boundaries are defined by the curves for  $\alpha_i = \alpha_p$ , and  $\alpha_i = \alpha_i^*$ ; for a perfect gas the latter curve can be found as the closed form expression,

$$\sin^2 \alpha_i^* = \frac{[(\gamma+1) + (\gamma-1)\xi_i]^2}{2\gamma[(\gamma+1) + (\gamma+1)\xi_i - 2\xi_i^2]} \quad (7)$$

A map of every refraction domain for Air/CO<sub>2</sub> is shown in figure 2. The ARE, ARe, ARc, are anomalous refractions, the upper case E signifies supersonic/sonic flow downstream of the reflected wave, the lower case e, and c, signifies subsonic expansion and compression respectively. RRR, RRE, refer to regular refraction with either a reflected shock or expansion, while MRR is an irregular Mach reflection refraction [4]. The ARE, ARe, and RRE, systems occur only for  $\alpha_i > \alpha_p$ , or  $Z_i > Z_t$  the ARc, RRR, and MRR, only for  $\alpha_i < \alpha_p$ , or  $Z_i < Z_t$ . It is shown elsewhere [6] that the AR boundary (7) may be used with some modification to predict the ARc  $\Leftrightarrow$  RRR transition.

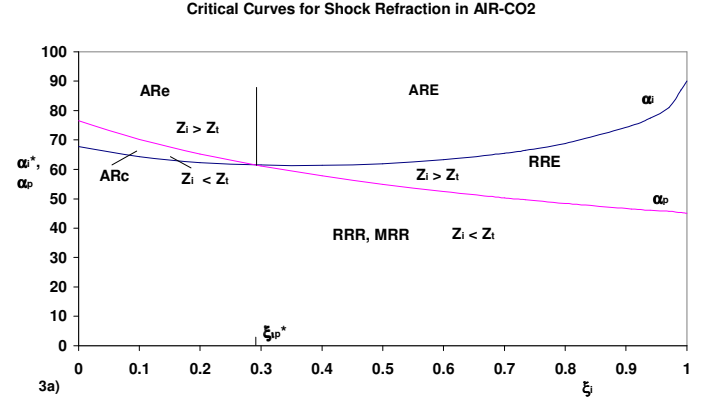


Figure 2. Critical Curves for Air-CO<sub>2</sub> for Anomalous Refraction and Equality of Impedance.

## Numerical Results

Returning to figure 1 it shows a transition sequence

RRE  $\Leftrightarrow$  ARE all for  $\xi_i = 0.85$  and  $\alpha_i > \alpha_p$ . The RRE where  $\alpha_p < 69^\circ < \alpha_i^*$  has a reflected Prandtl-Meyer expansion. The transitional system at  $\alpha_i^* = 71.116^\circ$  has sonic flow at the foot of the i-shock, followed by the P-M expansion. For ARE where  $\alpha_i = 85^\circ > \alpha_i^*$  some of the P-M waves overrun the i-shock producing the attenuated and curved i'-shock. But a remnant of the P-M wave still exists, which is contrary to the Jahn model. This remnant has been detected in experiment [2]. The ARE  $\Leftrightarrow$  ARE transition occurs when the remnant vanishes, so (7) applies at the foot of the i-shock. Figure 3 shows an ARc, an RSP, and an ARE all with  $\xi_i = 0.1$ . The disturbed part of the i-shock in the ARc leans slightly forward near the interface as it is overtaken by subsonic compressions;  $Z_i > Z_t$ ,  $\alpha_i^* < 67.24^\circ < \alpha_i$ . The RSP where  $\alpha_i = \alpha_p = 70.2^\circ$ , and  $Z_i = Z_t$ , is the transition system ARc  $\Leftrightarrow$  ARe. The disturbed part of the i-shock in the ARe, where  $\alpha_i = 85^\circ$ ,  $Z_i > Z_t$ , leans backwards as it is overtaken by subsonic expansions. The flow is subsonic downstream of an ARe, and sonic / supersonic for an ARE. The transition ARE  $\Leftrightarrow$  ARE is at the sonic condition  $\xi_i^*$  figure 2.

## Anomalous Refraction at a Slow-Fast Interface

In this case a regular refraction may disintegrate during transition to an irregular system. Specifically the t-shock moves ahead of the refraction point (node) and becomes a free precursor shock. These refractions have been observed by experiment for the Air/CH<sub>4</sub>, and CO<sub>2</sub>/He interfaces [1], [7]. The refraction law (1) is violated, along the interface,

$$U_t / \sin \alpha_t > U_i / \sin \alpha_i \quad (8)$$

In node fixed coordinates there is a streamline that coincides with the interface, and at this point it is deflected through an angle that exceeds an angle analogous to the detachment angle for the t-shock. This implies that a necessary condition for the onset of a t-precursor is that the flow downstream of it is either subsonic or at *most sonic* [6], which once more allows the application of the AR equation (7). Experiment show that for such a wave  $\alpha_t > 90^\circ$  so the t-wave now *arrives* at the interface and it transmits a side (s-) shock back into the initial gas which interacts with the i-shock. Numerical results agree with experiment [4]. But this means that the t-shock is undergoing *fast-slow* refraction; the t-s shock pair may be either a regular (RSP) or an irregular pair (ISP) refraction [5]. The latter paper has a detailed comparison of numerical results with experiments for the CO<sub>2</sub>/CH<sub>4</sub> combination. There are no disturbances ahead of the t-s pair so they can only be generated by the downstream shattering of the shock tube diaphragm. Thus a necessary condition for the existence of a t-precursor is for its downstream flow to be subsonic or at most sonic. At the sonic limit the AR condition (7) can again be applied.

### Evanescent Precursor Waves

The  $\alpha_i$  data from experiment shows that it is possible for a precursor t-shock to change into a distributed (evanescent) band of compressions. This also forces the s-wave to be also evanescent. It is assumed that every wavelet moves at the local speed of sound. Then for the leading wavelet  $U_i = a_{0i}$  and  $\alpha_i = v_i$ , where  $v_i$  is the Mach angle, and so by (8),

$$a_i / \sin v_i \geq U_i / \sin \alpha_i \Rightarrow a_i \geq U_i \sin v_i / \sin \alpha_i. \quad (9)$$

Thus an acoustic wave in the receiving gas travels at an equal or greater speed along the interface than the i-shock does in the incident gas. The equality defines the boundary between a shock and an evanescent wave,

$$\sin \alpha_{sc}^* \equiv U_i \sin v_i / a_i. \quad (10)$$

This relation is more general than others given in literature [6]. The refraction law and the equality of impedance condition for the leading t-s pair gives respectively,  $a_i / \sin v_i = a_i / \sin v_i$  and  $\rho_i a_i / \cos v_i = \rho_i a_i / \cos v_s$ .

They are valid for any wavelet pair in the t-s band. Figure 4 shows a computed evanescent precursor t-s wave system in a  $\text{CO}_2\text{-CH}_4$  gas combination with  $\alpha_i = 60^\circ$ ,  $\xi_i = 0.78$ .

### Conclusions

Anomalous refraction occurs for both the slow-fast and fast-slow gas combinations. It is necessary for AR that  $\alpha_i > \alpha_i^*$ . There are three AR systems for the fast-slow combination, ARE, ARc, ARE. The parameter spaces for their existence are shown in figure 2 for Air/ $\text{CO}_2$ . ARE and ARc and they have been observed in the cited experiments, but ARE is a new system predicted by the theory that has not yet been observed. Numerical evidence for all three systems in the corresponding parameter spaces of figure 2 are presented in figures 1, 3. The model proposed by Jahn becomes correct by the addition of a centered reflected expansion wave. There are two AR systems for the slow-fast combination, one with a precursor t-shock and the other where the precursor t-wave is evanescent.

The onset of all five AR systems is caused by disturbances arising downstream and overrunning a pre-existing system. The AR criterion (7) corresponds to sonic flow downstream, but if the flow becomes subsonic then a pre-existing system can be overrun.

The numerical data supports the theory and we found no counter examples to the theory either in the numerical or experimental results.

### References

- [1] Jahn, R. G., The Refraction of Shock Waves at a Gaseous Interface, *J. Fluid Mech.*, **1**, 1956, 457-489.
- [2] Abd-El-Fattah, A. M., & Henderson, L. F., Shock Waves at a Fast-Slow Gas Interface, *J. Fluid Mech.*, **86** 1978, 15-32.
- [3] Henderson, L. F., On the Refraction of Shock Waves, *J. Fluid Mech.*, **1989**, 365-386.
- [4] Henderson, L. F., Colella, P., Puckett, E. G., On the Refraction of Shock Waves at a Slow-Fast Gas Interface, *J. Fluid Mech.* **224** 1991, 1-27.
- [5] Puckett, E. G., Henderson, L. F., & Colella, P., The Anomalous Refraction of Shock Waves in Materials with General Equations of State, Part 1. The Shock Pair System *Proc. Roy. Soc. London*, In the press, accepted July 2004.
- [6] Puckett, E. G., Henderson, L. F., & Colella, P., The Anomalous Refraction of Shock Waves in Materials with General Equations of State, Part 2. Anomalous Wave Systems *Proc. Roy. Soc. London*, In the press, accepted July 2004.
- [7] Abd-El-Fattah, A.M., Henderson, L.F. & Lozzi, A. Precursor Shock Waves at a Slow-Fast Gas Interface *J. Fluid Mech.* **76** 1976, 157-176.

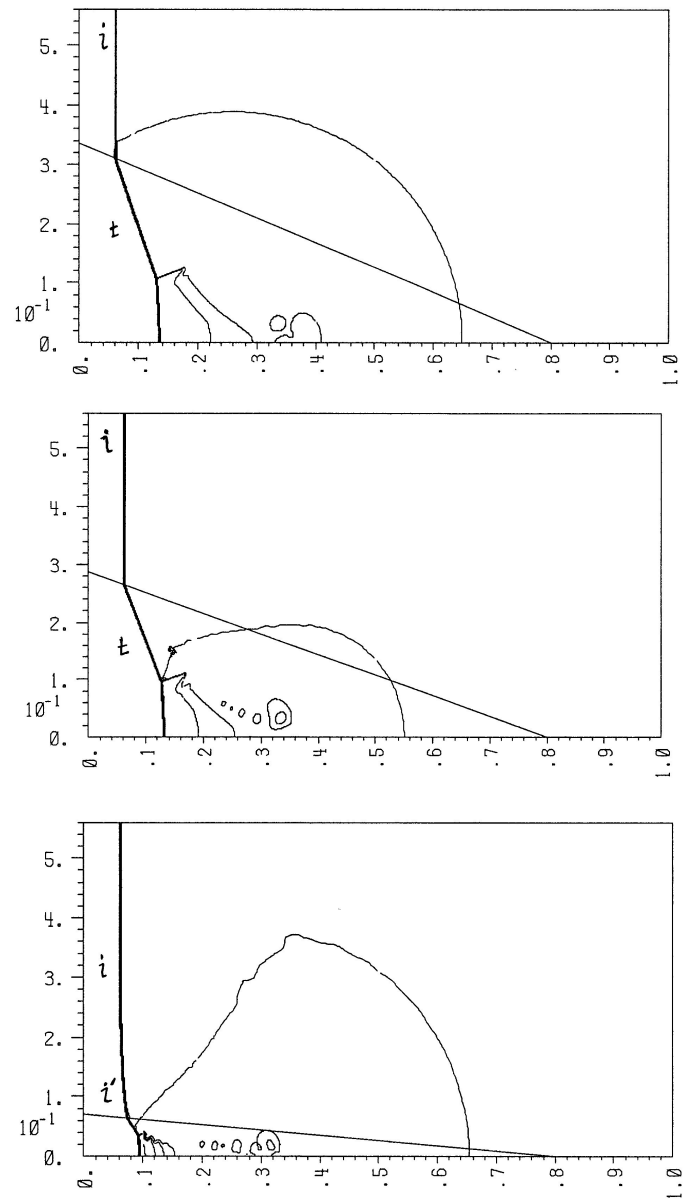


Figure 3. Computed Refracting Shock Systems in the Air- $\text{CO}_2$  Combination  $\xi_i = 0.1$ . a) ARc; b) RSP ; c) ARE

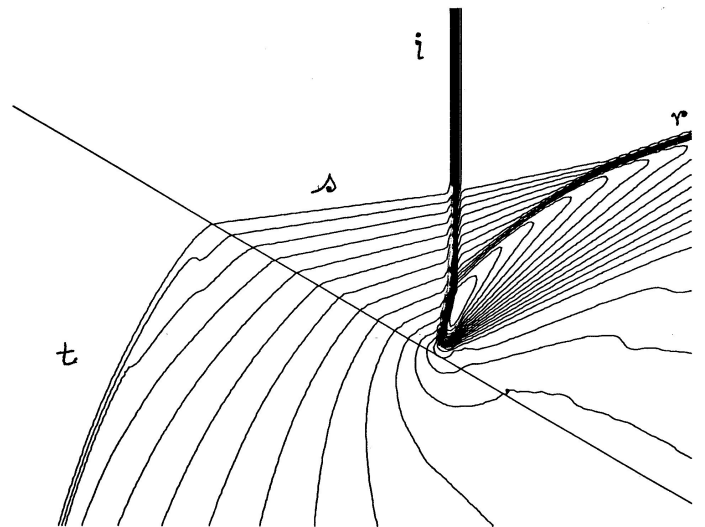


Figure 4. Free Precursor Irregular Refraction in the  $\text{CO}_2\text{-CH}_4$  Combination  $\xi_i = 0.78$ . a) Regular refraction with reflected expansion RRE; b) Transitional; c) Anomalous refraction ARE.

## Autocorrelation Functions and the Determination of Integral Length with Reference to Experimental and Numerical Data

P. L. O'Neill, D. Nicolaides, D. Honnery and J. Soria

Laboratory for Turbulence Research in Aerospace and Combustion, Department of Mechanical Engineering, Monash University, Victoria 3800, AUSTRALIA

### Abstract

Results from a particle image velocimetry (PIV) investigation of grid turbulence were recently compared with results from a direct numerical simulation (DNS) of homogeneous isotropic turbulence [5]. The comparison highlighted the difficulty of specifying an adequate spatial domain for numerical and experimental studies so that an accurate determination of integral length is obtained. Integral length is determined from the autocorrelation function, but the autocorrelation function is incorrect if the spatial domain is not sufficiently large. In general, the spatial domain in an experimental or numerical investigation is limited by restrictions on the experimental equipment or computational resources. Using the available spatial domain, an autocorrelation function is obtained from which the integral length is determined. The accuracy of the integral length is usually evaluated by comparing it to the spatial domain. If the spatial domain is sufficiently larger than the integral length, the integral length is judged to be accurate. However, how many times larger than the integral length does the spatial domain need to be?

### Introduction

Defining a length or time period that is characteristic of the largest scales in a turbulent flow is of importance both in defining a suitable area or volume for experimental and numerical investigations, and also to understanding the process of energy production and dissipation in the flow. In some cases a suitable scale can be defined by the physical constraints of the flow domain. For example, in pipe flow the diameter of the pipe is of the order of the largest eddies in the flow, and the ratio of the pipe diameter to mean velocity along the pipe is a good estimate of the time period required to describe the flow. In other cases where the largest scale is not obvious from the flow geometry, an integral scale can be defined that is a measure of the longest connection or correlation distance between two points in the flow that are separated either by distance or time [3]. In this paper, we determine the integral length scale of the velocity defined by:

$$\Lambda = \int_0^\infty R_{ii}(r, t) dr \quad (1)$$

where the double- $i$  subscript in  $R_{ii}(r, t)$  indicates the autocorrelation function (i.e. correlation of a velocity component with itself) defined by:

$$R_{ii}(r) = \frac{\langle u_i(x_i, t) u_i(x_i + r, t) \rangle}{\langle u_i^2 \rangle} \quad (2)$$

and  $r$  is the distance between two points in the flow. The autocorrelation function is longitudinal if  $r$  is parallel to  $u_i$ , and transverse if  $r$  is perpendicular to  $u_i$ , where  $u_i$  is the root-mean-square velocity in the  $i$ -direction.

### Results

#### Comparison of Experimental and Numerical Data

The experimental data cited in this paper is from a PIV investigation of grid turbulence. Details of the experiment can be

found in [5]. The experimental results are compared to numerical results from DNS of homogeneous isotropic turbulence. Details of the DNS can be found in [6].

In the case of the PIV data, the size of the spatial domain depended on the image acquisition equipment that was available. There was a balance between obtaining a sufficiently large experimental domain and accurately resolving the particles in the acquired images. The spatial domain was of size  $3\lambda$  where  $\lambda$  is the Taylor microscale determined from:

$$\lambda^2 = \frac{u_1^2}{\langle (\frac{du_1}{dx_1})^2 \rangle} \quad (3)$$

where  $u_1$  is the root-mean-square of the stream-wise component of velocity, and  $\frac{du_1}{dx_1}$  indicates the streamwise gradient of the streamwise velocity. For the DNS data the Taylor microscale is calculated from:

$$\lambda = \sqrt{\frac{15\nu u^2}{\epsilon}} \quad (4)$$

The kinetic energy dissipation ( $\epsilon$ ) is determined spectrally and  $\nu$  is the kinematic viscosity. The side-length of the three-dimensional simulation volume was greater than  $7\lambda$ , although the velocity field could be restricted to any spatial domain, including  $3\lambda$ .

Figure 1 compares the autocorrelation function obtained from the PIV data to that obtained from the DNS data using the entire available domain, and also restricting the domain to different values, including  $3\lambda$ . Both the longitudinal and transverse autocorrelation functions are shown. For the DNS data it would be expected that, once the spatial domain is large enough, there would be little change in the autocorrelation function when the spatial domain is increased. In the longitudinal case there is a significant difference between the autocorrelation function for a spatial domain of  $4.5\lambda$  and that for  $8\lambda$ , so it appears that a spatial domain of  $4.5\lambda$  is not sufficient to accurately determine the longitudinal integral length in this case. In the transverse case the autocorrelation functions found for a spatial domain of  $4.5\lambda$  and  $8\lambda$  are quite similar, but that for  $3\lambda$  is significantly different, so a spatial domain of  $3\lambda$  appears to be insufficient for an accurate determination of transverse integral length in this case.

It was noted in [5] that the autocorrelation functions obtained from the PIV data were different from previous experimental and numerical results. It appears from Figure 1 that the limited spatial domain of the PIV investigation may account for much of the deviation from past results. Also shown in 1 is the theoretical autocorrelation functions obtained by Townsend [8] for isotropic turbulence with uniform size structures and turbulence with a wide range of structure sizes.

#### Velocity Integral Length

The determination of the integral scale from equation (1) is not straight-forward [1]. The form of the autocorrelation function is such that it generally decreases rapidly to its first zero crossing, after which it may become negative and proceed to oscillate

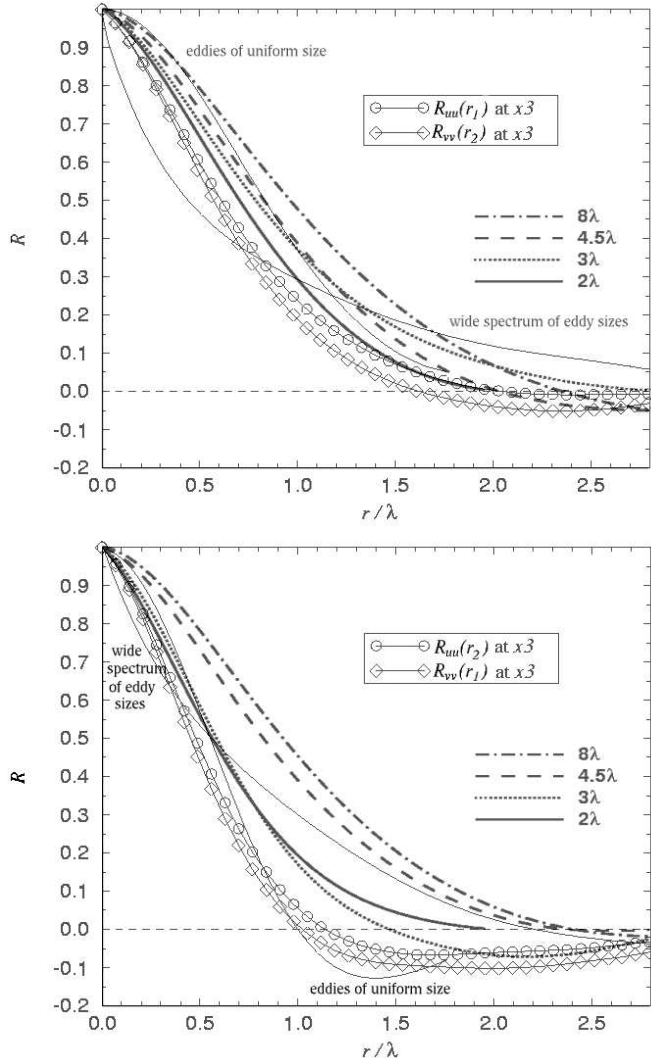


Figure 1: Longitudinal and transverse velocity autocorrelation functions obtained from DNS data by progressively restricting the spatial domain ( $Re_\lambda = 26$ ) compared to experimental data obtained using a spatial domain of  $3\lambda$  ( $Re_\lambda = 23$ ). Top: longitudinal autocorrelation; bottom: transverse autocorrelation.

about zero. While equation (1) involves the determination of the integral over an infinite domain, the domain of the autocorrelation function from experimental or numerical data is finite, and there is some uncertainty on how best to define the integration domain. For example, Tritton [9] described how, in the case of transverse autocorrelations, one might observe negative correlations, and further that the shape of the autocorrelation function following the first zero crossing may contain information about the structure of the turbulence. On the other hand, Yaglom [10] found that while the oscillations in the autocorrelation function may reflect the turbulence structure, they can also be described as “spurious” if a small number of data points are used to determine the autocorrelation function, and the error exceeds the quantity being estimated.

The integration domain for the determination of the integral length as a representative length scale of the turbulence can be specified in a number of ways. In this study we investigate the following four methods:

1. integrate over the entire available domain;
2. if the autocorrelation function has a negative region, integrate only up to the value where the autocorrelation function is a minimum [9];

3. integrate only up to the first zero-crossing [4]; or
4. integrate only up to the value where the autocorrelation function falls to  $1/e$  [9].

To investigate the effect of the spatial domain on the integral length determination, each of the four integration domains listed were used to determine the integral length from the longitudinal autocorrelation function of velocity. The spatial domain of the velocity field was progressively restricted. The results are shown in Figure 2. Note that measurements are with respect to a DNS grid size of  $2\pi$ , chosen so that wavenumbers are integer values.

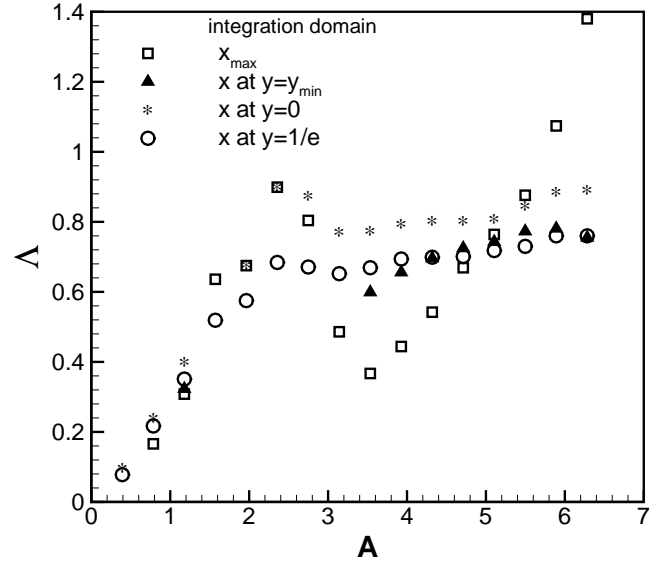


Figure 2: Integral length ( $\Lambda$ ) determined from DNS data ( $Re_\lambda = 26$ ) using four different integration domains and progressively restricting the spatial domain ( $A$ ).

It is expected that the effect on integral length of increasing the spatial domain would be to increase integral length up to a limit where further increasing the spatial domain has little or no effect, at which point the integral length is judged to be accurate. From Figure 2 this appears to be what happens for three of the four integration domains, but not for the case where the integration domain includes all the available data (i.e. integrating from  $x = 0$  to  $x = x_{max}$ ). The reason for this can be seen by considering Figure 3 which shows the autocorrelation function obtained for the entire available spatial domain. The boundary conditions for the DNS are periodic, and the effect of this can be seen in the form of the autocorrelation function, with very high values (close to 1) being obtained when the distance between correlated points is close to the side length of the grid. While this is a true representation of the autocorrelation function from the DNS data, it is not a fair representation for homogeneous isotropic turbulence, where the autocorrelation function would be expected to decay to zero within a sufficiently large spatial domain. It also leads to an erroneous measure of integral length if all the data is used in the evaluation, and that error can be seen in the continued increase in the integral length observed using this integration domain in Figure 2. The effect of the periodic boundary condition can also be seen in the fact that the integral length does not follow a gently increasing trend as the spatial domain is increased up to approximately 3, but increases significantly then reduces. For these reasons this integration domain is not used in the determination of integral length in the remainder of this study.

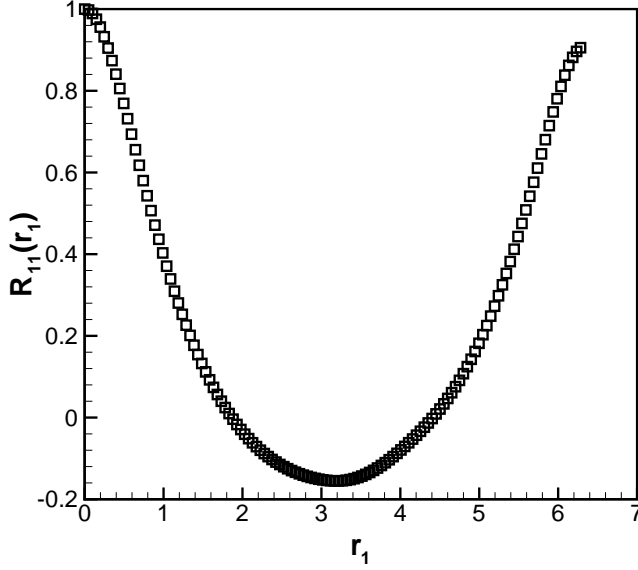


Figure 3: Longitudinal autocorrelation function obtained using the entire spatial domain available ( $Re_\lambda = 26$ ).

Of the three remaining integration domains, two of the methods give similar results (integration from zero to  $x$  at  $y = y_{min}$  and from zero to  $x$  at  $y = 1/e$ ). The first of these methods (zero to  $x$  at  $y = y_{min}$ ) has a disadvantage in that it often cannot be evaluated. If the autocorrelation function does not become negative and does not have a minimum value, the integration domain cannot be specified. The second of these two methods (from zero to  $x$  at  $y = 1/e$ ) discounts a large portion of the autocorrelation function and is expected to underestimate the integral length. For the remainder of the results presented in this study, the integration domain used in the evaluation of integral length is from  $x = 0$  to the first zero crossing of the autocorrelation function.

Having selected an integration domain, the question is: what is the minimum spatial domain that will ensure an accurate determination of integral length? In order to help answer this question, Figure 4 compares the integral length determined from the longitudinal autocorrelation function found for a range of  $Re_\lambda$  using a range of spatial domains. For all the  $Re_\lambda$  shown in Figure 4 it appears that increasing the spatial domain  $A$  above  $\sim 3.2$  only has a small effect on the evaluation of  $\Lambda$ . However, the number of integral lengths in the spatial domain for this determination is different for each of the four Reynolds numbers, the spatial domain being between  $\sim 4$  and  $\sim 5.5$  times greater than the integral length ( $\Lambda$ ). It is also noted that in one case an underestimate of integral length appears to be obtained, even though the spatial domain is approximately six times greater than the integral length. It appears from these results that the number of integral lengths required in the spatial domain in order to obtain the correct integral length may depend on the Reynolds number of the flow under investigation. A spatial domain greater than six times the integral length appears to be just sufficient for the worst case represented in Figure 4.

### Vorticity Integral Length

The results in the previous section indicate that a spatial domain equivalent to at least six integral lengths is required for determination of an accurate integral length from the longitudinal velocity autocorrelation function for the DNS results shown. Further investigations were undertaken to determine what spatial domain is required when determining the integral length scale for the vorticity.

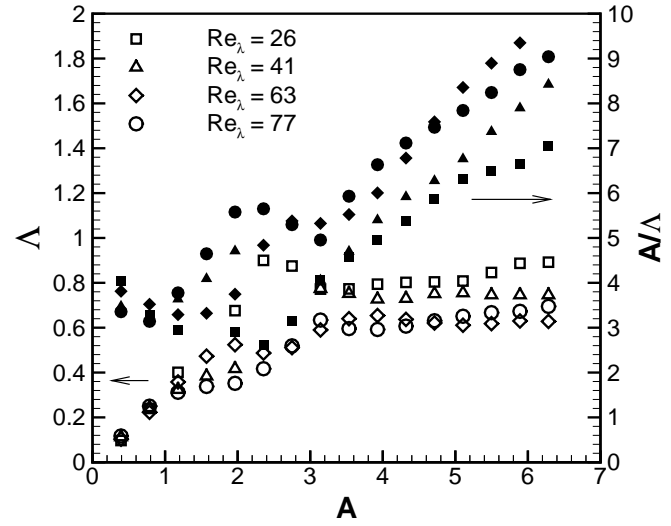


Figure 4: Integral length calculated from the longitudinal autocorrelation function over a range of spatial domains ( $A$ ). Also shown is the ratio of the spatial domain to integral length ( $A/\Lambda$ ). Results are shown for a range of  $Re_\lambda$ . Hollow symbols indicate  $\Lambda$ , filled symbols indicate  $A/\Lambda$ .

Using the same method for obtaining integral length, that is integrating up to the  $x$ -position of the first zero-crossing of the autocorrelation function, results are obtained for integral length of the vorticity from the transverse autocorrelation function. The results are presented in Figure 5. It appears that the spatial domain required for an accurate determination of vorticity integral length is smaller than needed for velocity integral length, being approximately 1.5 compared to 3.2. However, for all the  $Re_\lambda$  the number of multiples of vorticity integral length required in the spatial domain is larger, being between 4.5 and 7 times larger than the integral length compared to between 4 and 5.5 times larger for the velocity integral length. It is likely, however, that a spatial domain chosen to accurately resolve velocity integral length will also accurately resolve vorticity integral length.

### Conclusions

Integral length is important in characterising the structure of turbulence. It is a measure of the longest correlation distance between the flow velocity (or vorticity, etc) at two points in the flow field [3]. It is possible to extract an integral length from a numerical or experimental investigation of turbulence, it is however not possible to determine if the integral length so obtained is accurate.

In some of the archival literature a domain equivalent to at least two to three times the measured integral length is recommended for the accurate determination of integral length (eg. [2]). However a more recent citation states that a reasonable lower limit on the domain is eight integral length scales [7]. This recommendation is consistent with the results shown here, where it is found that, in the worst case, the spatial domain must be at least six times larger than the integral length. In the same reference [7] it states that the effect of limiting the spatial domain has not been studied systematically. In this paper a systematic approach to determining the effect of limiting the spatial domain is presented. The results have suggested that a spatial domain at least six times larger than the integral length is required for the two Reynolds numbers presented, however the results indicate that there may be a Reynolds number effect that should be considered. Further investigations may show that specifying a

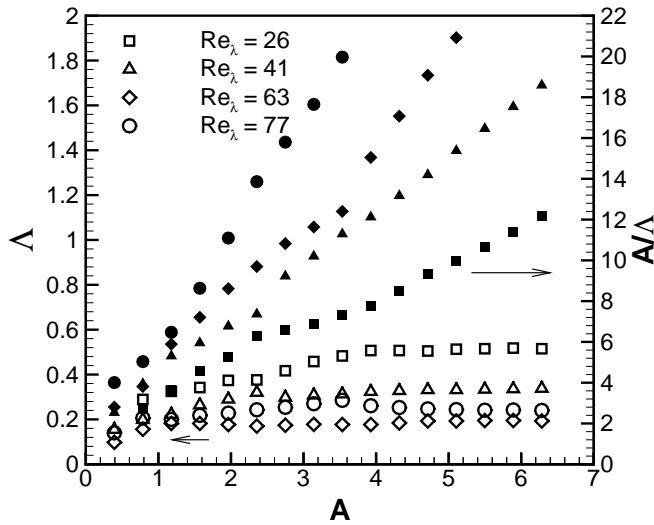


Figure 5: Integral length calculated from the autocorrelation function of vorticity over a range of spatial domains ( $A$ ). Also shown is the ratio of the spatial domain to integral length ( $L/\Lambda$ ). Results are shown for a range of  $Re_\lambda$ . Hollow symbols indicate  $\Lambda$ , filled symbols indicate  $A/\Lambda$ .

simple relationship between integral length and spatial domain is inappropriate.

In the case of the integral length of the vorticity it appears that the spatial domain required for determination of an accurate integral length for velocity will also be sufficient for determination of an accurate integral length for vorticity.

#### Acknowledgements

Use of the VPAC computing facilities is gratefully acknowledged.

#### References

- [1] Dias, N.L., Chamecki, M., Kan, A. and Okawa, C.M.P., A Study of Spectra, Structure and Correlation Functions and their Implications for the Stationarity of Surface-Layer Turbulence, *Boundary-Layer Meteorology*, **110**, 2004, 165–189.
- [2] Eswaran, V. and Pope, S.B., Direct Numerical Simulations of the Turbulent Mixing of a Passive Scalar, *Physics of Fluids*, **31**(3), 1988, 506–520.
- [3] Hinze, J.O., *Turbulence*, McGraw-Hill, 1975
- [4] Katul, G.G. and Parlange, M.B., Analysis of Land Surface Heat Fluxes using the Orthonormal Wavelet Approach, *Water Resource Research*, **31**, 1995, 2743–2749.
- [5] O'Neill, P.L., Nicolaides, D., Honnery, D. and Soria, J., Velocity, Velocity Gradient and Vorticity Statistics of Grid Turbulence Obtained using Digital Cross-Correlation PIV, submitted to *Experiments in Fluids*, 2004.
- [6] O'Neill, P.L. and Soria, J., The Relationship Between the Topological Structures in Turbulent Flow and the Distribution of a Passive Scalar with an Imposed Mean Gradient, submitted to *Fluid Dynamics Research*, 2004.
- [7] Pope, S.B., *Turbulent Flows*, Cambridge University Press, 2000.

[8] Townsend, A.A., *The structure of turbulent shear flow*, Cambridge University Press, 1976.

[9] Tritton, D.J., *Physical Fluid Dynamics*, Second Edition, Oxford University Press, 1988.

[10] Yaglom, A.M., *Correlation Theory of Stationary and Related Random Functions*, Volume 1: Basic Results, Springer Verlag, 1987.



## Experimental-Numerical investigation of a bend diffuser-configuration

A.J. Simonsen<sup>1</sup> and P.-Å. Krogstad<sup>2</sup>

<sup>1</sup>Present address: SINTEF Energy Research, Energy Processes. Kolbjørn Hejes v. 1b, N-7065 Trondheim, Norway

<sup>2</sup>Department of Energy and Process Engineering, The Norwegian University of Science and Technology, N-7491 Trondheim, Norway

### Abstract

The current work presents an experimental-numerical investigation of the flow in a special bend-diffuser configuration. Measured data of static pressure, time-mean velocity, and estimates of the skin friction are compared with the results from a numerical model. The main objective of the comparison was to obtain information on how well the numerical simulations using standard turbulence models, were able to reproduce the experimental data. Although the geometry is simple the combination of flow curvature and adverse pressure gradient generates complex flow physics.

### Introduction

Intercooling between different compressor stages are commonly used to reduce compressor work and thereby increase the total efficiency of gas turbine cycles. Effective intercooling is partly achieved by reducing the fluid velocity after compressors using diffusers. Since flow in diffusers are subjected to an adverse pressure gradient there is a potential danger for flow separation to occur which could lead to loss in performance as well as damage of downstream equipment. The aim of design is to keep the adverse pressure gradient as high as possible, but below a critical limit, by controlling the length versus outlet/inlet area-ratio of the diffuser. The configuration described in the current paper is tailored for applications where axial compressors are used and allowable axial length is limited. The new configuration turns the axial flow outwards radially through a axial-to-radial bend. After the bend a small stabilizing section with constant flow area follows before the diffusion process starts. Radial diffusers are not uncommon, but their main application is after a centrifugal compressor which, considering the importance of inlet boundary conditions on diffuser performance, is a completely different flow configuration.

### Experimental setup

Figure 1 shows a schematic view of the test rig. A centrifugal fan was used for air supply. The channels and settling chamber were made of galvanised plates while the models were made out of transparent plexiglass. Static pressure was measured with a linear response pressure transducer. The uncertainty of the static pressure measurements are within one percent. For the velocity measurements a  $2.5\mu\text{m}$  Platinum-rhodium(90/10%) single hot-wire wire was used. The hot-wire was calibrated in a separate unit and moved to the test rig without disconnecting the cable. It was carefully put into the probe-holder and inclined with the horizontal direction using a level tool. Measurement accuracy for mean velocity, taking into account high turbulence intensity, probe misalignment and calibration errors, is estimated to be within 6%. The distance from the wall to the first measurement point was measured with a telescope mounted on a micrometer. The channel wall was polished and gave a reflected image of the probe giving an accuracy roughly estimated to be of order  $0.1\text{mm}$ . Later, the wall position was op-

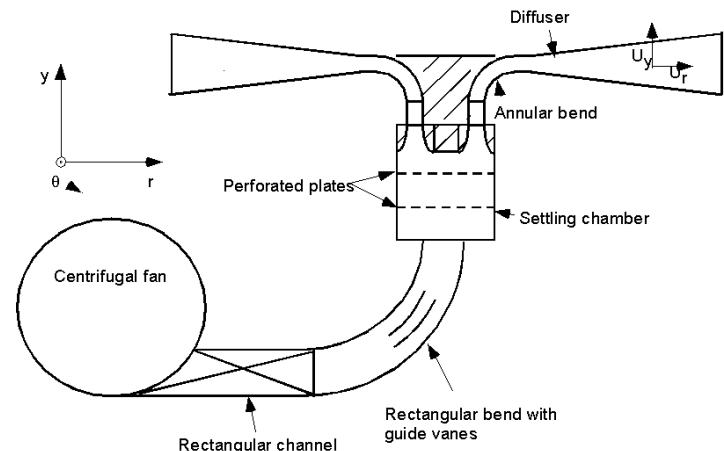


Figure 1: The figure shows the cross section when slicing the rig along the y axis.

timized with a wall function fit leading to a correction of the original value usually less than  $0.1\text{mm}$ . Figure 2 shows the different sections where velocity was measured and table 1 gives an overview of geometrical and flow related data.

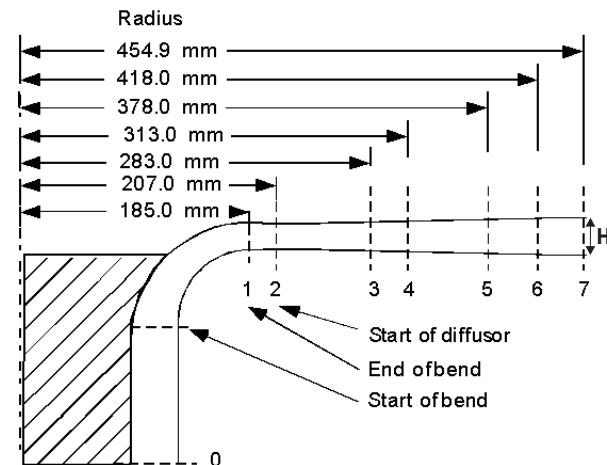


Figure 2: The figure shows an axisymmetric cross section of the model. The radial cross sections where the velocity was measured and skin-friction were measured and calculated are represented by the dashed lines (Number 1- 7).

### Numerical model

The numerical calculations were performed with the FLUENT code version 6.0 [2]. The code has several turbulence models incorporated and is easy to use. The numerical domain was identical to the geometry shown in Figure 2, and was modeled as being axisymmetric. Uniform mean velocity was set at section

Sec.	$y_c$	$r_c$	H	$ \bar{U} $	$Re_{Dh}$
#	[mm]	[mm]	[mm]	[m/s]	-
0	0	108.7	38.0	27.0	$8.0 \times 10^4$
1	284.0	184.8	22.3	27.0	$8.0 \times 10^4$
2	284.0	207.1	20.0	26.9	$7.2 \times 10^4$
3	284.0	283.0	23.3	16.9	$5.2 \times 10^4$
4	284.0	313.0	24.6	14.5	$4.7 \times 10^4$
5	284.0	378.0	27.5	10.7	$3.9 \times 10^4$
6	284.0	418.0	29.3	9.1	$3.5 \times 10^4$
7	284.0	454.9	31.0	7.9	$3.3 \times 10^4$

Table 1: Details of the geometry.  $y_c$  and  $r_c$  denote the position of the geometrical centerline at each of the dashed lines shown in figure 2.  $D_h = 2H$  is the hydraulic diameter and  $Re_{Dh}$  is the bulk flow Reynolds number.

0. This is close to the experimental conditions since a strong contraction upstream of section 0 in the experiment produced a nearly uniform velocity profile with very thin boundary layers. In agreement with observations from the experiment, the static pressure at the outlet was set to be uniform. At the walls the no slip condition was imposed. The grid was made up of  $80 \times 660$  quadrilateral cells in the wall normal and streamwise direction respectively, and grid independence was checked with two additional grids of  $70 \times 472$  and  $50 \times 660$  resolution. No major discrepancy was found in velocity and skinfriction between these three grids[7]. Towards the wall both the equilibrium and non-equilibrium law of the wall approach was found inadequate [7]. The first grid point was therefore placed well within the viscous sublayer ( $y^+ < 5$ ) and a two layer model was chosen. In the viscosity affected region,  $Re_y = \rho y \sqrt{k}/\mu < 200$ , the one equation model of Wolfstein [10] was used. In the fully turbulent region several turbulence models with a varying degree of complexity were employed ranging from the one-equation model of Spalart-Allmaras[8] to the Reynolds stress model given by Launder [4]. In the mid range complexity the two equation  $k - \epsilon$ -models of Launder and Sharma [5], often referred to as the standard  $k - \epsilon$  model (std), the "renormalization group" (RNG) [1], and the realizable  $k - \epsilon$  (Realz) model by Shih et al. [6] were used. In the buffer layer the turbulent viscosity was estimated with a blending function between the values calculated in the inner and outer regions [3]. Further details concerning the numerical code and turbulence models may be found in reference [2].

### Static Pressure

Static pressure was measured along radially directed planes, at the hub and boss surfaces (Figure 3). The static pressure recovery coefficient  $C_p(s) = (P(s) - P_{in})/\bar{q}_{in}$  quantify how much of the kinetic energy is recovered as static pressure energy,  $P$ , downstream the channel.  $s$  is the streamwise length measured from the first static pressure hole which was located 100mm downstream of section 0 in figure 2.  $\bar{q}_{in} = 1/2\rho|\bar{U}|^2$  is the kinetic energy of the mean flow, with velocity  $\bar{U}$  and density  $\rho$ , at  $s = 0$ . Figures 4 and 5 show comparisons between the measured, and calculated pressure recovery coefficient. The dotted vertical lines are the borders between the different zones of the configuration. 1) Inlet annular pipe, 2) Axial-Radial bend, 3) Stabilizer, and 4) Diffuser. As can be seen from the figure there is a reasonable degree of collapse between the computed, and the measured pressure distribution. Following the hub side surface the agreement is considered very good. There is a small deviation at the lower peak of  $C_p$  in the bend of about 5%. Along the boss side the agreement is also good although the relative deviation in the bend is considerably larger. With respect to the

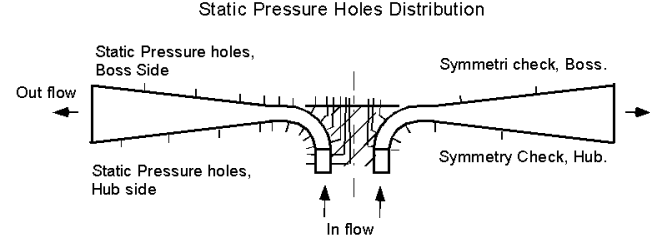


Figure 3: Distribution of static pressure holes (ry-plane of diffuser). The holes denoted as "Symmetric check" were only used in documenting the axisymmetry of the static pressure distribution.

form of the curves the agreement is good along both walls. Local peaks and abrupt changes in gradients coincide well with respect to the flow distance  $s$ . It is also to be noted that a small difference between the geometry used in the CFD, and the real geometry could result in discrepancies, especially in the narrowest regions of the flow. Table 2 gives a comparison of  $C_p$  at the diffuser outlet. As seen from the table all methods are within 5% of the experimentally obtained value with the RSM model being the closest.

Method	$C_p$	$(C_{p,cf} - C_{p,exp})/C_{p,exp}$ in %
Exp.	0.678	0
SA	0.6566	-3.2
$k - \epsilon_{std}$	0.7082	4.4
$k - \epsilon_{RNG}$	0.6986	3.0
$k - \epsilon_{realz}$	0.7054	4.0
RSM	0.6754	-0.4

Table 2: Comparisons of calculated and experimentally obtained pressure recovery at the diffuser outlet.

### Mean velocity

Figures 6 and 7 shows a comparison of calculated versus measured data of the normalized radial mean velocity component at the outlet of the bend (r185), and close to the outlet of the diffuser (r455). We clearly see that the choice of turbulence model results in largely deviating profiles. At r185 the  $k - \epsilon_{std}$  results in completely erroneous profiles indicating the peak of the velocity profile to be at the opposite side of the channel compared to the experimental results. The SA,  $k - \epsilon_{RNG}$  and  $k - \epsilon_{realz}$  represent the velocity profiles well while the RSM model performs less well. At the hub side we clearly see a large difference between the gradient of the RSM model and the experimental results. The RSM model also has some abnormal behavior at  $y/H \approx 0.7$  where it takes a distinct dip when approaching the wall. At r455 the SA model wrongly indicate a separation zone at the outlet and generally compare poorly with the measured profile. Among the two equation models we clearly see that the  $k - \epsilon_{RNG}$  and the  $k - \epsilon_{realz}$  models are in better agreement with the experimental data than the other models. Both these models estimate the velocity peak with reasonable accuracy and also the velocity descent from the peak towards the wall. The  $k - \epsilon_{realz}$  model clearly match the data best as seen when approaching the walls (especially at the hub side). Somewhat surprisingly the RSM model does not represent the current flow very well. It is more in error with respect to the experimental data than the  $k - \epsilon_{RNG}$  and the  $k - \epsilon_{realz}$  models. This is seen especially at the hub side wall where it overestimates the velocity largely and completely misses on the velocity gradient in the vicinity of the wall. The explanation for the rather poor behavior of the RSM model is for the time being not clear.

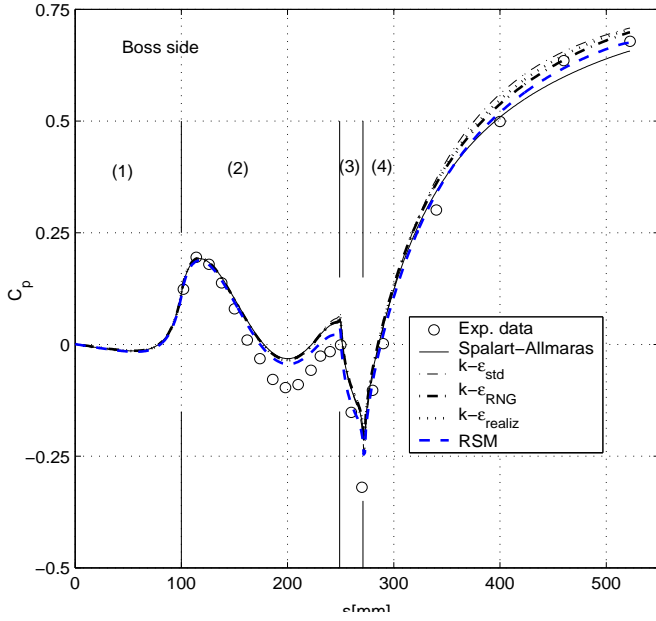


Figure 4: Comparison of experimental, and computed  $C_p$  values along the boss surface.

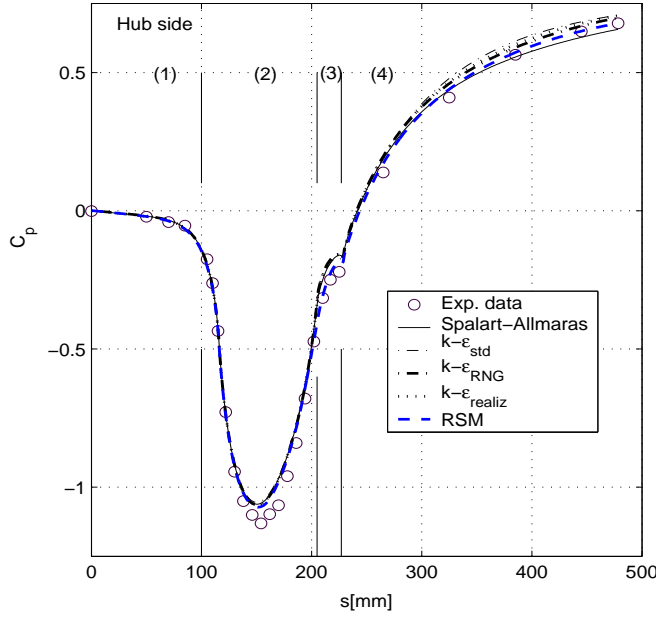


Figure 5: Comparison of experimental, and computed  $C_p$  values along the hub surface.

### Skin-friction

Due to the difficulty in accurately estimating the experimental skin-friction for the current flow three different methods were employed. The methods used were velocity fitting using the Musker-Granville function, dynamic head pressure measurements using a  $0.9\text{mm}$  diameter Preston tube, and the Von-Kármán momentum equation based correlation of White[9]. Figure 8 and Figure 9 show the comparison of the globally normalized skin-friction coefficient,  $C_f = 2\tau_w/\rho U_{r,in}^2$ , at the hub and boss sides respectively. At the hub side, in the diffuser, the three experimental based methods agree very well in the outer part, but are more scattered in the inner part of the diffuser. The simulation results however are scattered throughout most of the domain. The RSM model indicates a significantly higher  $C_f$  than the other models while the SA model is the lowest and pre-

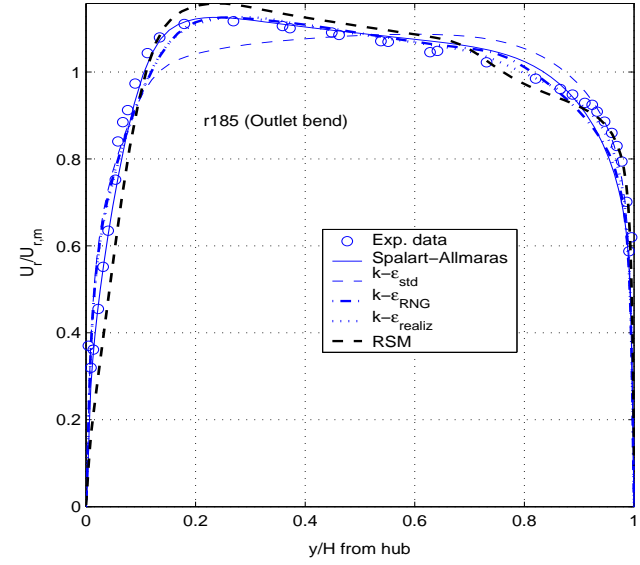


Figure 6: Calculated and measured  $U_r$  mean velocity at r185.

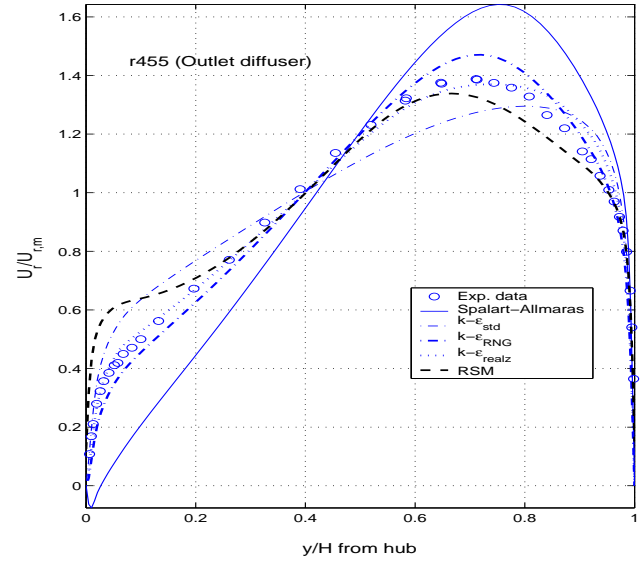


Figure 7: Calculated and measured  $U_r$  mean velocity at r455.

dicts separation at  $r \approx 275\text{mm}$ . The  $k-\epsilon_{RNG}$  and the  $k-\epsilon_{realiz}$  models agree well with each other but underpredict the experimental  $C_f$  towards the outlet. The  $k-\epsilon_{RNG}$  simulation is very close to separation at the hub side as we see from the included subfigure in Figure 8. The  $k-\epsilon_{std}$ , fits the experimental data best through the diffuser. At the boss side the experimentally based methods are less scattered and the agreement between simulations and the experiment is considerably better. At this side both the  $k-\epsilon_{std}$  and RSM model overpredicts the skin-friction slightly. The SA model underpredicts the  $C_f$  in the beginning of the diffuser but decays less rapidly compared to the other models and ends up overpredicting the  $C_f$  at the outlet. The  $k-\epsilon_{RNG}$  and the  $k-\epsilon_{realiz}$  models agree very well with the experiments.

The two first measurements in the figures are in the vicinity of the borders between the bend-stabilizer and stabilizer-diffuser respectively. At these positions  $C_f$  exhibits a discontinuous be-

havior due to the discontinuity in the gradient of the width with respect to the streamwise distance. In this region a small positioning error in the streamwise direction leads to large errors in  $C_f$ . Hence it is difficult to compare the experimental and computed distributions here. However, it appears that the experimental values lie within the ranges of the CFD values.

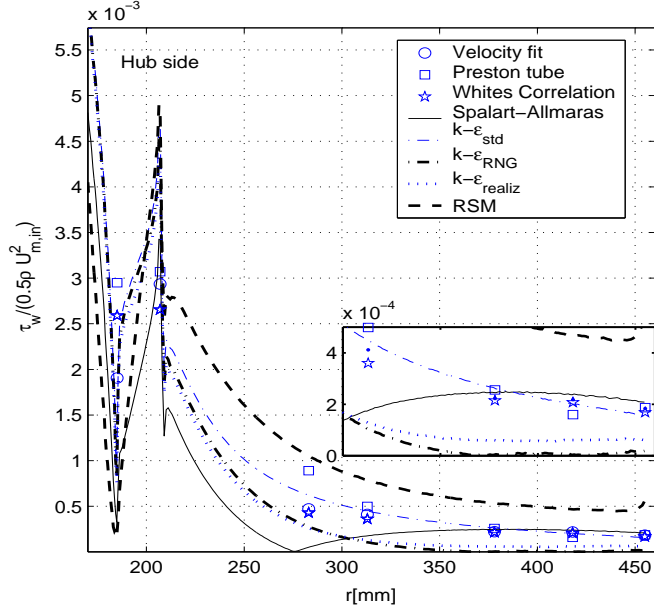


Figure 8: Comparison between calculated and experimentally obtained estimates of the skin-friction coefficient at the hub side of the channel.

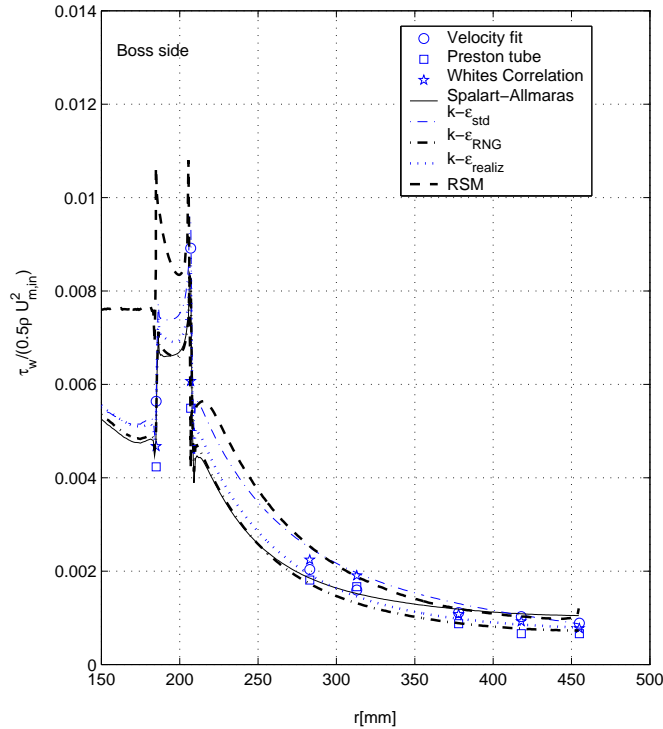


Figure 9: Comparison between calculated and experimentally obtained estimates of the skin-friction coefficient at the boss side of the channel.

## Summary

The current work describes the flow in an axial to radial bend-diffuser configuration. This configuration is used as a pressure recovery device behind axial compressors when axial space is limited. No prior reports on this particular flow configuration has been found. Radial diffusers are not uncommon, but normally there is a centrifugal compressor upstream of the diffuser. Mean velocity and static pressure has been measured and based on these data the skin-friction,  $C_f$ , has been calculated. The experimental data have been compared with numerical simulations using the Fluent software package. The comparisons show that with respect to the pressure recovery,  $C_p$ , the differences between the measured and calculated data are within 5%. The one equation turbulence model underestimates while the two equation models overestimate the measured value. The Reynolds stress model (RSM) agrees with the measurements to within 1%. The realizable  $k - \epsilon$  model, closely followed by the renormalized group model (RNG), clearly predicted the mean velocity best while the other models did not compare very well. Skin friction was predicted fairly well along the boss side surface while being less accurate along the hub surface. The one equation model incorrectly predicts a small separation zone along the hub side surface. A detailed investigation of the different turbulence models clarifying what causes the large differences in especially  $C_f$  and  $U_r$  has not been carried out yet.

## References

- [1] Choudhury, D., Introduction to the renormalization group method and turbulence modeling, Technical Report TM-107, Fluent Inc. Technical Memorandum, 1993.
- [2] Fluent Incorporated, Holmworth House, Corthworth Road, Sheffield, S11 9LP, UK, *Fluent 6.1 Users Guide*, 2003.
- [3] Jongen, T., *Simulation and Modeling of Turbulent Incompressible Flows*, Ph.D. thesis, EPF Lausanne, Switzerland, 1992.
- [4] Launder, B., Reece, G. and Rodi, W., Progress in the development of a reynolds-stress turbulence closure., *J. Fluid Mech*, **68**, 1975, 537–566.
- [5] Launder, B. and Sharma, D., *Lectures in Mathematical Models of Turbulence*, Academic Press, London, England, 1972.
- [6] Shih, T., Liou, W., Shabbir, A. and Zhu, J., A new k- eddy-viscosity model for high reynolds number turbulent flows - model development and validation., *Computers Fluids*, **24**, 1995, 227–238.
- [7] Simonsen, A., *Experimental and numerical investigation of a bend diffuser configuration*, Ph.D. thesis, Department of Energy and Process Engineering, The Norwegian University of Science and Technology, Trondheim, Norway, 2003.
- [8] Spalart, P. and Allmaras, S., A one-equation turbulence model for aerodynamic flows., *AIAA*, **0439**.
- [9] White, F., *Viscous fluid flow*, McGraw-Hill, 1991, second edition.
- [10] Wolfstein, M., The velocity and temperature distribution of one-dimensional flow with turbulence augmentation and pressure gradient, *Int. J. Heat Mass Transfer*, **12**, 1969, 301–318.



## Numerical Studies on Turbulent Separated Flows in High-Velocity Transient Motors

V.R. Sanal Kumar,<sup>1</sup> H.D. Kim,<sup>2</sup> B.N. Raghunandan,<sup>3</sup> and T. Setoguchi<sup>4</sup>

<sup>1,2</sup>School of Mechanical Engineering, Andong National University  
Andong, Kyeongbuk 760-749, KOREA

<sup>3</sup>Department of Aerospace Engineering, Indian Institute of Science  
Bangalore-12, Karnataka, INDIA

<sup>4</sup>School of Mechanical Engineering, Saga University  
Honjo-machi, Saga 840-8502, JAPAN

### Abstract

Numerical studies have been carried out to examine the starting transient flow features in high-performance solid rocket motors with non-uniform port geometry with the aid of a standard k- $\omega$  turbulence model. The parametric studies have been carried out to examine the geometry-dependent driving forces, which control the transient flow features of solid rockets with non-uniform ports. We concluded that the narrow port and long flow development ahead of the steep divergence are shown to favor flow separation, which might lead to high peak pressure, pressure-rise rate and thrust oscillations during the starting transient period of operation of high-velocity transient motors with divergent ports.

**Introduction** many modern high-performance solid rockets have grains with sudden expansion/divergence of port combined with high volumetric loading density, high throat to port area ratio ( $A_t/A_p > 0.56$ ) and large length-to-diameter ratio ( $L/D \geq 10$ ). Qualitatively these motors are referred as high-velocity transient (HVT) motors. Flow separation and recirculation caused by sudden changes in port geometry plays an important role in the design of these motors. The basic idea behind a solid rocket motor (SRM) is simple but its design is a complex technological problem requiring expertise in diverse sub disciplines to address all of the physics involved. The design optimization of high-performance rockets is more complex when the mission demands dual thrust. Dual-thrust motors with single chamber necessarily have non-uniform port geometry. Although, a great deal of research has been done in the area of solid rockets for more than six decades, the accurate prediction of the starting transient/ignition transient of high-performance solid rockets with non-uniform ports has remained an intangible problem [1-3]. The starting transient is usually defined as the time interval between the application of the ignition signal and the instant at which the rocket motor attains its equilibrium or the designed operating conditions. The two primary concerns during the starting transient are the overall time of the transient and the extent of the peak pressure. The overall time, that is, the delay in the development of full thrust must be kept within some limit and must be reproducible. This research topic, although interesting in its own right, has been motivated by several practical problems.

The motivation for the present study emanates from the desire to explain the phenomena or mechanism(s) responsible for the high pressure, pressure-rise rate, instabilities and pressure oscillations

often observed during the static tests and the actual flights of certain class of SRMs with non-uniform ports [3-6]. In this study attention is focused on idealized grain geometry with divergent port; deduced from the US Space shuttle's redesigned SRM, Ariane 5 SRM and Dual-thrust motor configurations. For technological reasons, large solid propellant boosters, such as US Space Shuttle and Titan SRMs or European Ariane 5 P230 are made from segmented propellant grains from three to seven segments with non-uniform ports according to the motor versions. Earlier works at the USA show that such grain segmentation conducted to low amplitude, but sustained pressure and thrust oscillations, on the first longitudinal acoustic mode frequencies [7-9]. Although such oscillations do not jeopardize the mission, they induce some penalties to the overall performance. Detailed studies on instabilities and pressure oscillations in solid rocket motors have been carried out by Yves Fabignon et al [7] at ONERA (2003). But none of these studies able to explain the cause(s) of the unexpected pressure peak, pressure-rise rate and thrust oscillations often observed in certain class of dual-thrust motors (DTMs) during the starting transient period of operation. Figure 1 shows a typical DTM configuration with narrow cylindrical port at the head-end followed by divergence region and star port at the nozzle-end. In such configurations, it is very likely that the flow separation would take place at transition locations.

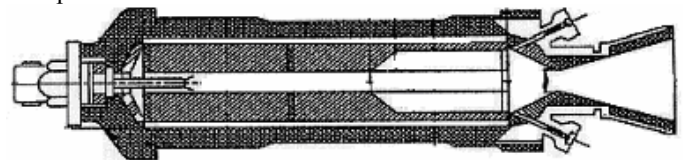


Figure 1. Typical dual-thrust motor.

In all the previous studies the features of turbulent separated flows are not examined in any motor with dual-thrust configuration [10]. With the advent of computational fluid dynamics (CFD) and available computer power, several numerical studies have been reported on the overall starting transient of SRMs in the recent past. Even though these studies have been helpful in interpreting many fundamental processes on starting transient, the understanding of pressure peak and pressure oscillations often observed in HVT motors has been elusive. In an attempt to resolve some of these problems and in the light of new findings [10, 11], a substantial revision of the existing idea is required. One such problem of urgency is to examine the starting transient flow features, without invoking the mass addition and combustion, of high-performance solid rockets with non-uniform ports. In this paper, using a two dimensional turbulence model, a diagnostic investigation is carried out to examine the geometry-dependent driving forces on the starting transient flow features of dummy (unignited) SRMs with dual thrust configuration. Note that it is often the practice in ignition studies to use dummy grains to obtain the physical insight into the starting transient flow features of SRMs *a priori*.

<sup>1</sup>Scientist/Engineer, Propulsion Group, Vikram Sarabhai Space Centre, India, Email: [rsanal@hotmail.com](mailto:rsanal@hotmail.com) (Currently at the Andong National University).

<sup>2</sup>Professor and Head

<sup>3</sup>Professor and Chairman

<sup>4</sup>Professor

### Numerical Method of Solution

The numerical simulations have been carried out with the help of a standard k- $\omega$  model. This turbulence model is an empirical model based on model transport equations for the turbulence kinetic energy ( $k$ ) and the specific dissipation rate ( $\omega$ ). This code solves standard k- $\omega$  turbulence equations with shear flow corrections using the coupled second order implicit unsteady formulation. The turbulence kinetic energy,  $k$ , and the specific dissipation rate,  $\omega$ , are obtained from the following two transport equations:

$$\frac{\partial}{\partial t}(\rho k) + \frac{\partial}{\partial x_i}(\rho k u_i) = \frac{\partial}{\partial x_j} \left( \Gamma_k \frac{\partial k}{\partial x_j} \right) + G_k - Y_k + S_k \quad (1)$$

$$\frac{\partial}{\partial t}(\rho \omega) + \frac{\partial}{\partial x_i}(\rho \omega u_i) = \frac{\partial}{\partial x_j} \left( \Gamma_\omega \frac{\partial \omega}{\partial x_j} \right) + G_\omega - Y_\omega + S_\omega \quad (2)$$

In the equations,  $G_k$  represents the generation of turbulent kinetic energy due to mean velocity gradient.  $G_\omega$  represents the generation of  $\omega$ .  $\Gamma_k$  and  $\Gamma_\omega$  represent the effective diffusivity of  $k$  and  $\omega$ , respectively.  $Y_k$  and  $Y_\omega$  represent the dissipation of  $k$  and  $\omega$  due to turbulence.  $S_k$  and  $S_\omega$  are user-defined source terms.

This model uses a control-volume based technique to convert the governing equations to algebraic equations, which can be solved numerically. The viscosity is determined from the Sutherland formula. An algebraic grid-generation technique is employed to discretize the computational domain. The present code has been validated and selected for capturing the fine flow features often observed in SRMs with non-uniform port. A typical grid system in the computational region is selected after the detailed grid refinement exercises. The grids are clustered near the solid walls using suitable stretching functions. In all the cases length of the first grid from the solid surfaces is taken as 0.1 mm. The motors geometric variables and material properties are known *a priori*. Initial wall temperature, inlet total pressure and temperature are specified. At the solid walls no-slip boundary condition is imposed. At the nozzle exit a pressure profile is imposed. The Courant-Friedrichs-Lewy number is initially chosen as 3.0 in all of the computations. Ideal gas is selected as the working fluid. The transient mass additions due to propellant burning are deliberately ignored in this model to examine the turbulent separated flow features discretely in solid rockets with non-uniform ports.

The numerical results corresponding to the experimental configuration and propellant properties reproduce many qualitative features such as secondary ignition and backward flame spread. These results are succinctly reported in the previous connected papers [12-16]. In this study consideration is given to examine the geometrical influence on turbulent separated flows in SRMs without any mass addition. Results of interests such as reattachment length, size of the recirculation bubble and the axial velocity variations are reported to illustrate the influence of transition region on the flow characteristics of turbulent mixed convection downstream of a solid rocket motor with divergent port. Such detailed results are needed for an integrated design and optimization of the high-performance solid rockets port geometry and its allied igniters with confidence.

### Results and Discussion

In the present numerical simulation two different physical models with different port geometries are examined. In the first phase low-velocity transient (LVT) motors ( $A_t/A_p \leq 0.56$ ,  $L/D \leq 10$ ) and in the second phase HVT motors are considered. The grid system (baseline case) in the computational region for LVT motor is shown in figure 2. Baseline values are selected based on the geometric configuration of a typical LVT motor ( $L/D = 4$ ,

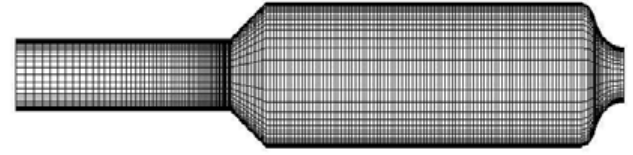


Figure 2. Grid system (180 x 30) in the computational region.

$X_s/d = 3$ ,  $d_t/D = 0.375$ ). Initial total pressure and temperature are given as the input to the code and a pressure profile is imposed at the exit. Except the geometric variable all other parameters are kept constant in the parametric studies.

Figure 3 shows the comparison of the axial velocity variation at a particular time interval for five different test cases. In the first three cases divergent location ( $X_s$ ) is varied, in the fourth case inlet diameter is increased by 50% and in the fifth case divergence angle,  $\alpha$  is increased from  $45^\circ$  to  $64^\circ$ . All the results reported are anticipated and giving corroborative evidences of the previous experimental and theoretical findings [10-16].

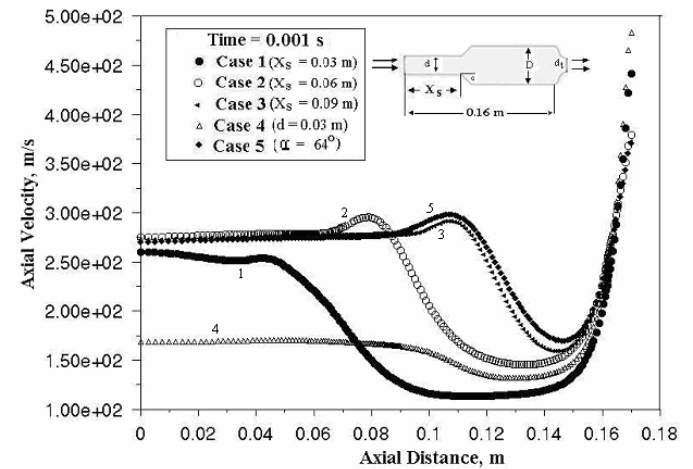


Figure 3. Demonstrating the influence of port geometry on the velocity variation along the axis (configuration is shown in inset).

It can be seen from figure 3 that, in three different cases (Case 2, 3 & 5), the axial velocity is relatively high at the divergence location. This can be explained with the help of boundary layer theory. Note that owing to the viscous friction, boundary layer will be formed on the walls (before the transition region) and their thickness will increase in the down stream direction to the divergence location. Since the volume of flow must be the same for every section, the decrease in rate of flow near the walls which is due to friction must be compensated by a corresponding increase near the axis. Thus the boundary layer growth occurs under the influence of an accelerated external flow. As a result, at larger distances from the inlet section velocity will be relatively high at the divergence location. This will cause flow separation far downstream of the divergence region. In the fourth case reported herein shown relatively low velocity at the axis due to high port area compared to the other four cases reported. Traditionally many solid rocket motor designers occasionally increases the port area of a solid rocket motor for reducing the unexpected pressures peak observed during the starting transient period. Note that such an increase in port area will negate the high performance nature of the rocket motor. Figure 4 depicts the velocity vectors at two different time intervals showing the formation of recirculation bubble and flow reattachment for a typical case. This figure gives a clear description about the flow development pattern at the expansion region during the starting transient period of operation of a typical solid rocket motor with divergent port. The recirculation bubble and the reattachment point are visible at the divergent region at time,  $t=0.006s$ . When time advances this region gradually expands and shifts towards the downstream and finally vanishes. Reverse flow can be



recognized up to  $t = 0.001$  s. This phenomenon is not observed in the forth case due to high inlet port area and low axial velocity.

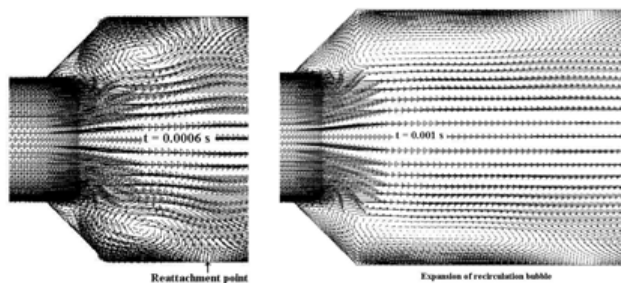


Figure 4. Sequence of pictures showing the formation of recirculation bubble and its expansion at two different intervals of time in an SRM with divergent port (Enlarged view).

In the first case flow recirculation tendency, leading for reattachment and secondary ignition, was found very less because location of the transition region was near to the head-end at the cost of the propellant loading density. When the transition location was fixed at far downstream of the SRM, the tendency of flow separation was found very high. This will lead to the formation of recirculation bubble and flow reattachment. Note that the flow reattachment will favour secondary ignition and that will cause the flow unsteadiness leading for an unacceptable high-pressure rise rate during the starting transient period of operation of solid rockets. Hence the prudent selection of the transition location within the given envelop, without diluting the high-performance nature of solid rocket motor, is critical for a designer. This task will be more complex in the case of HVT motor, which is discussed in the subsequent session.

In the second phase attention is focused on HVT motors with sudden enlargement of port, as has been observed in the case of Space Shuttle's Redesigned SRM. In the parametric study three different transition locations ( $X_s$ ) are considered. Figure 5 shows the grid system in the computational region of the baseline case.



Figure 5. Grid system in the computational region of an HVT motor.

An algebraic grid-generation technique is employed to discretize the computational domain. The total element in each case is fixed as 1328. The grids are clustered using suitable stretching functions for capturing the fine flow features during the transient period. Note that the inappropriate stretching of grids will lead to the inaccurate prediction of the reattachment point. An error in pinpointing the reattachment point will lead to the significant errors in the actual prediction of the location of secondary ignition, which will warrant the inaccurate performance prediction of HVT motors. The geometrical parameters are selected based on typical HVT motors. In all the cases, considered in this study, the length-to-diameter ratio and the throat-to-port area ratio are retained as constant values similar to a conventional HVT motor. The igniter jet flow and the material properties are retained as constant for examining the influence of location of the transition region on identical conditions. The ignition is not invoked in this analysis. At the solid walls no-slip boundary condition is imposed. Initial total pressure and temperature are prescribed at the inlet and a pressure profile is imposed at the nozzle exit. In the first numerical drill, for all the cases, the initial igniter total pressure is taken as  $2.25 \text{ kgf/cm}^2$ , and temperature as  $700 \text{ K}$ . The turbulent intensity is assumed as 10% at the inlet and the exit. At the given inlet hydraulic diameter, using the standard  $k-\omega$  model, the initial inlet turbulent kinetic energy is evaluated as  $306.93 \text{ m}^2/\text{s}^2$  and the corresponding specific dissipation rate is obtained as  $62569.78 \text{ s}^{-1}$ . The initial Courant-Friedrichs-Lewy number is chosen as 5 in all the cases.

Figure 6 is demonstrating the difference in velocity magnitude along the axis of an HVT motor with three different divergent locations at two different time intervals but with same initial and boundary conditions. In all the cases the velocity magnitude is found maximum at the transition location.

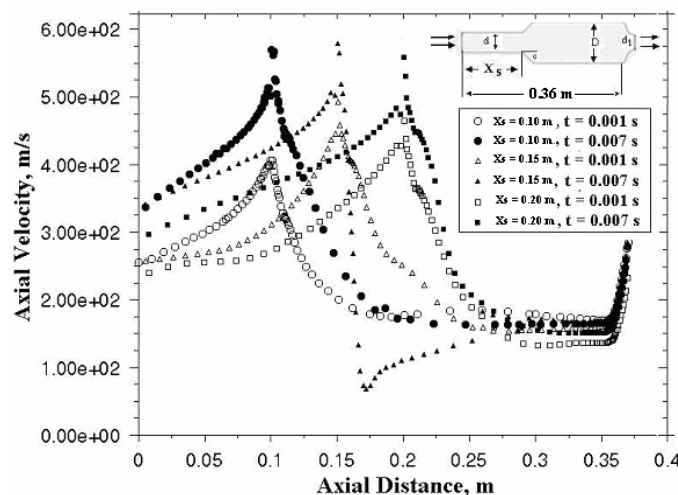


Figure 6. Demonstrating the difference in velocity magnitude along the axis of an HVT motor with three different divergent locations at two different time intervals but with same initial and boundary conditions.

As explained in the previous cases, in general, at larger distances from the inlet section ( $X_s$ ) velocity will be high at the step location due to the boundary layer effect. But figure 6 shows that the peak value of the axial velocity is relatively lower in the Case 3 ( $X_s = 0.20 \text{ m}$ ) than the Case 2 ( $X_s = 0.15 \text{ m}$ ). This will not contradict the argument reported earlier based on boundary layer effect because this difference is due to the altered variation of the entire flow field due to the nozzle end effect coupled with the geometry dependent driving forces and the corresponding compressibility effect. Through these diagnostic investigations, we observed that there is a limiting case of the location for transition for developing maximum axial velocity in any HVT motor due to its port geometry. In all the HVT motor cases, as anticipated, at the upstream the flow acceleration is found very high compared to the LVT motor cases reported earlier.

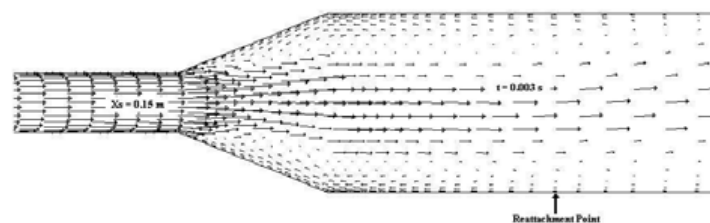


Figure 7. Velocity distribution showing the formation of the recirculation bubble and the reattachment point at the divergent region of the HVT motor of Case 2 ( $X_s = 0.15 \text{ s}$ ) at time,  $t = 0.003 \text{ s}$  (Enlarged view).

The separated flow characteristics such as size of the separation bubble, flow redevelopment and heat transfer in the recirculation region are known to depend on Reynolds number upstream of the divergent region and its height. In the HVT motor cases considered here the reattachment point is found to lie around 1.5 - 3 times of the divergent height, as estimated, which is relatively higher than the LVT cases considered in this study. Figure 7 depicts the velocity vectors at time,  $t = 0.003 \text{ s}$  showing the formation of recirculation bubble and flow reattachment for the case  $X_s = 0.15 \text{ m}$ . Reverse flow can also be recognized in this figure. We can easily infer from this figure that the implication of the secondary ignition will be more severe in the case of HVT motors because the location of the secondary ignition will be closer to the reattachment point, which is observed far downstream than LVT motor cases. From these results one can assert that the flow instability, pressure-rise rate and the ignition pressure peak will be more prominent in HVT motors than LVT

motors. We also observed that in all the cases, due to the flow instability, the near wall temperature was found non-uniform along the curved surface and as a result the heat flux values will be discontinuous. This will warrant the discontinuous ignition leading for multiple flame fronts in HVT motors with divergent port. The velocity, density and temperature fluctuations are not independent, being related, also through pressure fluctuations, by the mass balance equation, the energy balance equation, and the constitutive equation of the fluid. So suppression and control of one parameter will be a meaningful objective for rocket motor design optimization. We also discerned that under certain conditions, the flow gets accelerated to a higher Mach number ( $M > 1$ ) near the transition region of an HVT motor with divergent port but without any geometrical-throat! A shock wave cannot exist unless the Mach number is supersonic; therefore the flow must have accelerated through a throat which is sonic. As argued above, owing to the viscous friction, boundary layer will be formed on the walls (before the transition region) and their thickness will increase in the down stream direction to the divergent location leading to the formation of a momentarily *fluid-throat* at the transition location. This might lead to the formation of shock waves in certain class of HVT motors with divergent port. Note that the downstream of the shock the flow has an adverse pressure gradient, usually leading to wall boundary-layer separation and reattachment.

From these studies one can deduce that the thrust/pressure oscillations, pressure-rise rate and unexpected peak pressure often observed in solid rockets with non-uniform ports are presumably contributed due the joint effects of the geometry dependent driving forces and the chamber gas dynamic forces. The present study is expected to aid the designer for conceiving the physical insight into problems associated with the prediction and the reduction of the peak pressure, the pressurization rate and thrust oscillations during the starting transient period of operation of solid rockets with non-uniform ports.

### Concluding Remarks

It is indeed accepted that no single turbulence model is universally accepted as being superior for all class of problems. However, the experience gained through our studies prompted to choose k- $\omega$  model for the diagnostic investigation of the oscillatory behavior of thrust transient of solid rockets with non-uniform ports. Through these diagnostic investigations, we observed that there is a limiting case for transition location for forming peak velocity in any HVT motor due to the nozzle end effect coupled with the port geometry and the chamber gas dynamics effects. The shock waves, the boundary layer thickness and the turbulence are rather familiar notion: yet it is not easy to define in such a way as to cover the detailed flow characteristics comprehended in HVT motors. The shock waves in HVT motor will alter the turbulence level and this new turbulence level will alter the location of reattachment and secondary ignition. The shock wave formed presumably due to the *fluid-throat* effect is an area that needs to be contemplated in detail. We concluded that the narrow port and long flow development ahead of the steep divergence are shown to favour flow separation, which might lead to high pressure-rise rate and ignition over pressure during the starting transient of SRMs with non-uniform ports. The zone of the secondary ignition for many laboratory tests and the location of the reattachment point for SRMs with divergent port in the present numerical studies are found around 0.8-3.0 times of the step height. Therefore, one can conclude that the secondary ignition occurs inside the initial recirculation bubble. The preheating of the propellant in this zone before the arrival of the flame at the transition region therefore appears important, which however not invoked in this analysis. The present study leads to say that a prudent selection of the port geometry is one of

the challenging tasks for any HVT motor designer for getting reliability, repeatability and payload capability of any launch vehicle with credence.

### Acknowledgment

The KOSEF under the overseas research program for promoting cooperation in the field of science and technology between India and South Korea has supported this work and acknowledged the same by the first author.

### References

- [1] Peretz, A., Kuo, K.K., Caveny, L.H., & Summerfield, M., Starting transient of solid propellant rocket motors with high internal gas velocities, *AIAA Journal*, Vol. 11, No. 12, 1973, 1719-1729.
- [2] Kumar, M. and Kuo, K. K., 1983, Flame spreading and overall ignition transient, *Prog. Astronaut. & Aeronaut.*, 90, 1983, 305-60.
- [3] Salita, M., Modern ignition transient modelling (Part 1): Introduction and Physical Models, *AIAA Paper*, No. AIAA 2001-3443.
- [4] Raghunandan, B.N., *Diagnostic investigation of ignition problems in high-performance rocket motors*, Final Technical Report, AE Department, IISc, Bangalore, India, Report No. ISTC/AE/BNR/043, 1995.
- [5] Sanal Kumar, V. R., and Raghunandan, B. N., A ballistic explanation of ignition peak of low velocity transient motors, *Proceedings of the 2nd IHEM Conference and Exhibit*, IIT Chennai, India, 8-10 Dec., 1998, 371-375.
- [6] Luke, G. D., Eager, M. A., and Dwyer, H. A., Ignition transient model for large aspect ratio solid rocket motors, *AIAA paper*, No. AIAA 96-3273.
- [7] Fabignon, Y., Dupays, J., Avalon, G., Vuillot, F., Lupoglazoff, N., Casalis, G and Prevost, M, Instabilities and pressure oscillations in solid rocket motors, *Aerospace Science and Technology*, 7, 2003, 191-200.
- [8] Brown, R.S., Dunlap, R., Young, S.W., and Waugh, R.C., Vortex shedding as a source of acoustic energy in segmented solid rockets, *Journal of Spacecraft and Rockets* 18(4), 1981, 312-319.
- [9] Manson, D.R., Folkman, S.K., Behring, M.A, Thrust oscillations of the space shuttle solid rocket booster motor during static tests, *AIAA paper* . No. AIAA 79-1138.
- [10] Raghunandan, B. N., Sanal Kumar, V. R., Unnikrishnan, C and Sanjeev, C., 2001, Flame spread with sudden expansions of ports of solid propellant rockets, *Journal of Propulsion and Power*, Vol. 17, No. 1, 2001, 73-78.
- [11] Sanal Kumar, V.R., Thermoviscoelastic characterization of a composite solid propellant using tubular test, *Journal of Propulsion and Power*, Vol.19, No.3, 2003, 397-404.
- [12] Raghunandan, B.N., Madhavan, N.S., Sanjeev, C and Sanal Kumar, V. R., Studies on flame spread with sudden expansions of ports under elevated pressure, *Defence Science Journal*, 46 (5), 1996, 417-423.
- [13] Sanal Kumar, V. R., and Unnikrishnan, C., Raghunandan, B.N., 2000, Studies on ignition transients of solid rocket motors with non-uniform ports, *AIAA Paper*, No.2000-3701.
- [14] Unnikrishnan, C., Sanal Kumar, V. R., and Raghunandan, B.N., Internal flow simulation of solid rockets using an unsteady Navier Stokes solver, *AIAA Paper*, No.2001-3450.
- [15] Sanal Kumar, V. R., and Unnikrishnan, C., Raghunandan, B.N., Effect of flame spread mechanism on starting transients of solid rocket motors, *AIAA Paper*, No. 2001-3854.
- [16] Sanal Kumar, V. R., Unnikrishnan, C., Kim, H.D., Raghunandan, B. N., and Setoguchi, T., 2004, Simulation of flame spread and turbulent separated flows in solid rockets, *AIAA paper*, AIAA 2004-3375.

## The Effect of Turbulence on Cloud Droplet Collision Rates

C.N. Franklin<sup>1</sup>, P.A. Vaillancourt<sup>2</sup>, M.K. Yau<sup>1</sup> and P. Bartello<sup>1,3</sup>

<sup>1</sup>Department of Atmospheric and Oceanic Sciences  
McGill University, Montreal, Quebec, H3A 2K6 CANADA

<sup>2</sup>Recherche en Prévision Numérique  
Meteorological Service of Canada, Dorval, Quebec, H9P 1J3 CANADA

<sup>3</sup>Department of Mathematics and Statistics  
McGill University, Montreal, Quebec, H3A 2K6 CANADA

### Abstract

Direct numerical simulations of an evolving flow field have been performed to explore how turbulence affects the motion and the collisions of cloud droplets. Large numbers of droplets are tracked through the flow field and their positions, velocities and collision rates have been found to depend on the eddy dissipation rate of turbulent kinetic energy. The radial distribution function, which is a measure of the preferential concentration of droplets, increases with eddy dissipation rate. The clustering is most pronounced for 15 and 20  $\mu\text{m}$  droplets, which is the largest radius ratio considered, increasing to more than twice the value for a homogeneous Poisson distribution. This increase from the value for sedimenting droplets in a quiescent flow, together with an increase in the mean radial relative velocity of colliding droplets, leads to increases in the geometric collision kernel of up to almost 4 times the corresponding gravitational kernel. The greatest increase in the collision efficiency is observed for the smallest radius ratio. Interacting 5+20  $\mu\text{m}$  droplets collide almost 3 times more frequently when turbulent accelerations are included in their equation of motion as compared to the purely gravitational case. The lowest dissipation rates had the greatest effect on the collision kernel that includes the hydrodynamic forcing between interacting droplets for the smallest radius ratio considered. The most energetic flow field produced the largest increase in this kernel for the droplets of 15 and 20  $\mu\text{m}$  in radius and this was the most significant increase observed of more than 9 times the gravitational kernel. These increases are expected to play an important role in the broadening of the drop size distribution and the initiation of rain.

### Introduction

The time of transition from cloud droplet growth by condensation to that of effective collision and coalescence is an outstanding issue in cloud physics. Turbulence has long been postulated to reduce the time it takes to produce rain drops by accelerating the growth of droplets in the size range of 5 to 30  $\mu\text{m}$  in radius. Due to the complexity of the problem, previous studies of turbulence-droplet interactions made use of statistical techniques and numerous assumptions about the flow field and the motion of the droplets and hence there is a lot of discrepancy between the results. With the increase in computational power we are now in a position to be able to use direct numerical simulations (DNS) of the flow field to investigate the effect of turbulence on the collisions of droplets. DNS have the advantage of explicitly resolving the dissipation range dynamics, which has been shown to have the most influence on the local particle accumulation and settling rate of small particles whose diameter is less than that of the small eddies of the flow [9].

As demonstrated by Sundaram and Collins [6] the collision kernel can be expressed by two statistical quantities of the particle phase; the radial distribution function  $g(R)$  and the

particles' relative velocity  $|w|$ . When an inertial particle interacts with a turbulent structure, because of centrifugal forces the particles will tend to cluster or become preferentially concentrated in regions of the fluid with low vorticity and increased pressure in the boundaries between eddies. Since an increased local particle density means that there is an increased probability of finding two droplets closely separated in the flow, consequently there is an increase in the collision rate or kernel. Wang *et al.* [10] extended this work and demonstrated that the spherical geometry is the correct form to use in the problem of collision in a turbulent flow field and thus the collision kernel,  $\Gamma$ , for droplets of radius  $r_1$  and  $r_2$  is given by

$$\Gamma = 2\pi R^2 \langle |w_r| \rangle g(R) \quad (1)$$

where  $R$  is the sum of the droplet radii and the radial relative velocity  $w_r$  is defined as  $w \cdot \mathbf{R}/|\mathbf{R}|$ , where  $\mathbf{R}$  is the separation vector for the droplets' positions. For droplets falling only under the force of gravity, the collision kernel is expressed by (1) with  $g(R)$  equal to 1 and  $\langle |w_r| \rangle$  equal to half of the difference in the terminal velocities of the droplets. The collision kernel can also be defined in terms of the direct counting of collisions as

$$\Gamma = n_c \Omega / dt N_1 N_2 \quad (2)$$

where  $n_c$  is the average number of collisions per time step,  $\Omega$  is the volume,  $dt$  is the time step and  $N$  is the number of droplets from the respective size group.

### Numerical Methods

The turbulent flow field is generated by solving the Navier-Stokes equations using a pseudo-spectral model. For a detailed description of the model see Vaillancourt *et al.* [8]. The initial kinetic energy is specified and throughout the simulation energy is forced into the large scales of the flow to produce a statistically stationary field. Four numerical simulations are performed with the number of grid points  $N^3$  equal to  $80^3$ ,  $120^3$ ,  $180^3$  and  $240^3$ . The computational domain is fixed for all experiments at  $10 \times 10 \times 10 \text{ cm}^3$ , thus we increase in spatial resolution from a grid length of 0.125 cm to 0.04166 cm. Periodic boundary conditions are imposed in all three directions. The flow field that is generated by the model is homogeneous and isotropic and this structure is expected to be representative of the small-scale flow of adiabatic cloud cores. It is this region of the cloud where one would expect to find the large droplets needed to initiate effective collision-coalescence growth, as the main body of the cloud typically has lower water contents. The average eddy dissipation rates,  $\epsilon$ , for the simulations are 95, 280, 656 and  $1535 \text{ cm}^2 \text{ s}^{-3}$ , which span the range of observed values in cumulus clouds. Even though the Reynolds numbers of the flows ( $R_\lambda$  increases from 33 to 55) are much smaller than those of atmospheric turbulence, the Kolmogorov scales are close to atmospheric values and it is these scales that have the most influence on droplet motion.

25 000 droplets of each of the two sizes being considered are tracked in the simulations. Due to the small volume fraction occupied by droplets we neglect any modification that the droplets may have on the turbulence and only consider binary collisions. The equation of motion for the droplets is

$$\frac{d\mathbf{V}(t)}{dt} = \frac{1}{\tau_p} (\mathbf{U}[\mathbf{X}(t), t] - \mathbf{V}(t)) + \mathbf{g} \quad (3)$$

where  $\mathbf{V}(t)$  is the droplet velocity at time  $t$ ,  $\mathbf{U}$  is the flow field,  $\mathbf{X}$  is the droplet position,  $\mathbf{g}$  is gravity and  $\tau_p$  is the droplet inertial response time based on the Stokes drag force, which is a function of the droplet mass, size and the dynamic viscosity of air. The droplets are randomly distributed in the domain once the turbulent flow field has reached a statistically stationary state. To ensure there is no influence of the initial conditions on the results, the droplet positions and velocities are allowed to evolve in time before the calculation of the collision statistics begins. For a description of the collision detection scheme see Franklin *et al.* [2].

### Geometric Collision Kernels

The collision statistics have been calculated for collisions between a collector droplet of 20  $\mu\text{m}$  in radius and droplets of sizes 5, 10 and 15  $\mu\text{m}$ . These sizes have been chosen as it is collisions between droplets in the range of 5 to 30  $\mu\text{m}$  that are needed to allow some large droplets to grow to a size that will initiate effective coalescence. If turbulence is to significantly reduce the time it takes to produce rain drops, the collision kernel for small droplets must increase from the gravitational collision kernel. Figure 1 shows the sensitivity of the collision kernels to the turbulent forcing. The turbulent kernels calculated from (2) for the 3 droplet size combinations all show a fairly linear response to increasing dissipation rates. For the lowest dissipation rate the turbulent kernels are only marginally larger than the corresponding gravitational kernel. However, as the dissipation rate increases the turbulent kernels increase, with the largest radius ratio (15+20  $\mu\text{m}$ ) giving the greatest increase of almost 4 times the gravitational case. These increases are significant and are expected to influence the evolution of the drop size distribution. The physical mechanisms responsible for these increases are discussed in the following section.

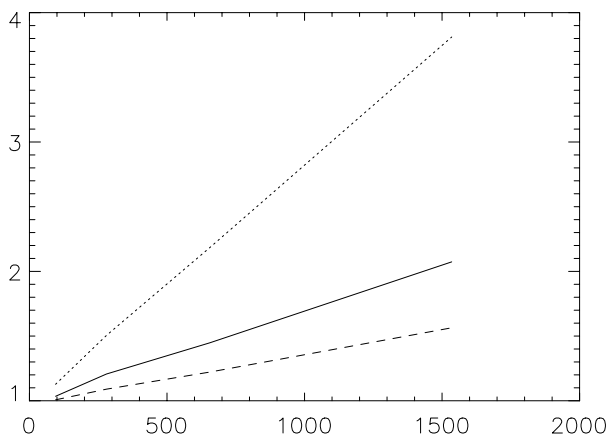


Figure 1. The turbulent collision kernel normalised by the corresponding gravitational kernel as a function of average eddy dissipation rate ( $\text{cm}^2 \text{s}^{-3}$ ). The dotted line is the normalised collision kernel for the 15 and 20  $\mu\text{m}$  droplets, the solid line is for the 10 and 20  $\mu\text{m}$  droplets and the dashed line is for the 5 and 20  $\mu\text{m}$  droplets.

### Radial Relative Velocity and Preferential Concentration

As shown in (1) the collision kernel is partly a function of the relative velocity between droplets. Just as the differential inertia effect due to gravitational acceleration defines the relative velocity in a quiescent flow, this effect also contributes to the relative velocities amongst droplets in a turbulent flow. The

turbulent flow field can change the droplets' velocities by two physical processes. The first is the inertial bias which causes droplets to accumulate in the peripheries of local vortical structures. The second process is caused by the droplets tending to move on the downflow sides of these vortices due to particle inertia, the local velocity field and the way the droplets generally approach these structures from above [9]. The quantity that is input into the collision kernel calculation is the mean radial relative velocity of the droplet pairs that are separated by a slightly larger distance than that required for a collision. The reason being that the non-uniform flow field results in a local non-uniform relative velocity distribution [11]. The other kinematic quantity that can change the collision kernel is the preferential concentration of the droplets. In a bidisperse system the clustering is determined by the correlation between particle concentrations of the two size groups. Zhou *et al.* [12] demonstrated that particles of different sizes will tend to cluster in different regions of the flow field due to the different inertial responses to the flow accelerations.

Table 1 and figure 2 show that for small radius ratios, that is the 5+20  $\mu\text{m}$  case, the increase in the turbulent collision kernel that is illustrated in figure 1 results mostly from increases in the radial relative velocities between droplets. The spatial distribution of these droplets in the two lowest dissipation rate flows show no spatial correlations, as  $g(R)$  is close to 1 which is the value for a homogeneous Poisson distribution. For the two highest dissipation rates, the droplets become preferentially concentrated with a maximum value of  $g(R)=1.1296$ , which demonstrates that in this case the chances of seeing two droplets, one from each size category, closely separated in the flow is approximately 13% greater than the purely gravitational case.

	$\epsilon$	95	280	656	1535
5+20	$\langle  w_r  \rangle_n$	1.0120	1.0684	1.1624	1.3500
	$g(R)$	0.9905	1.0023	1.0517	1.1296
10+20	$\langle  w_r  \rangle_n$	1.0119	1.0630	1.2214	1.5099
	$g(R)$	1.0274	1.1949	1.2311	1.3672
15+20	$\langle  w_r  \rangle_n$	1.0181	1.1169	1.3283	1.7801
	$g(R)$	1.1158	1.3966	1.6912	2.1679

Table 1. Preferential concentration  $g(R)$  and the normalised mean radial relative velocity  $\langle |w_r| \rangle_n$  between droplets that are closely separated in the domain, for the three size combinations of droplets in the four different flow fields with increasing dissipation rates  $\epsilon$  ( $\text{cm}^2 \text{s}^{-3}$ ). The velocities have been normalised by the corresponding gravitational values.

For collisions between the droplets of 10 and 20  $\mu\text{m}$  in radius, the increase in the collision kernel is comparable between the two kinematic quantities across the four simulations. For the largest radius ratio, the 15 and 20  $\mu\text{m}$  case, the large increases shown in figure 1 can be attributed to increases predominately in the clustering of the droplets. However,  $w_r$  also shows the largest increase from the corresponding gravitational value for this size combination of droplets. The reason why turbulence has the greatest impact for this case is primarily because of the droplet Stokes number. The Stokes number is the ratio of the particle inertial response time  $\tau_p$  to the Kolmogorov time scale of the flow. The effect of turbulence has been demonstrated to have the most effect on  $g(R)$  for both non-sedimenting and sedimenting monodisperse droplets when this number is of order 1 [6,9]. The Stokes numbers of cloud droplets are small [7] and the largest Stokes number in our simulations is 0.48, which is the value for the 20  $\mu\text{m}$  droplet in the most energetic flow. The trend for the effect of turbulence on the droplet clustering to increase with increasing Stokes number is demonstrated by the results in table 1 and shows support for the hypothesis of Kolmogorov scaling for the radial distribution function. It is important to note however, that the Stokes number does not take into consideration

the effect of the terminal velocity of the droplets. The gravitational forcing means that the time of interaction between an eddy and a particle will be reduced and thus the Stokes number does not describe all aspects of the interaction between droplets and the turbulent flow field. This is clear from the lack of Stokes number scaling for the normalised radial relative velocities. Results for other size combinations of droplets are necessary before an appropriate nondimensional parameter to describe the interaction can be determined.

### Collision Efficiencies

When two droplets approach one another, the fluid they push aside as they move through a medium interacts with the other droplet and tends to prevent the droplets from colliding. As the Reynolds numbers of the droplets in this study are quite small, with the largest value being 0.1, we can use the Stokes flow as a good approximation to represent the hydrodynamic flow field and as a consequence neglect any wake effects. To determine the relative motion between two interacting droplets we use the superposition method whereby the flow field of one drop is superimposed onto the flow field of the other drop. In this method each droplet is assumed to be influenced by the fluid motion around the other droplet in isolation. Details on the implementation of the Stokes disturbance flow solution to a three-dimensional framework are given in Franklin *et al.* [2].

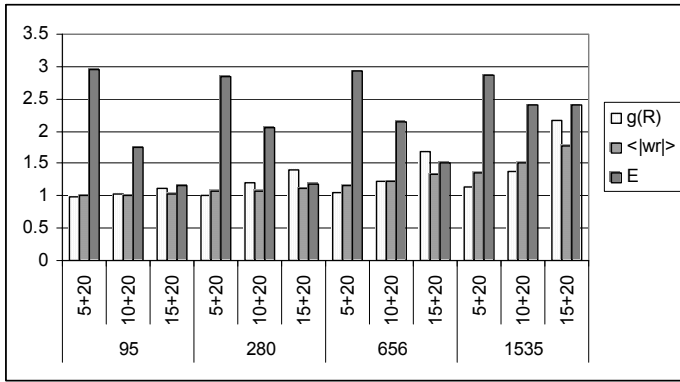


Figure 2. The contribution of the three effects (the radial distribution function  $g(R)$ , the radial relative velocity  $\langle |w_r| \rangle$  and the collision efficiency  $E$ ), to the increase in the turbulent collision kernel. The quantities have been normalised by the corresponding gravitational values. The results are presented as a function of average eddy dissipation rate ( $\text{cm}^2 \text{s}^{-3}$ ) for the three size combinations.

To test the algorithm developed to calculate the hydrodynamic forces between interacting droplets, we first applied it to the case of droplets only falling under the force of gravity. The collision efficiency is defined to be

$$E = \frac{\text{no. of collisions with hydrodynamics}}{\text{no. of collisions with no hydrodynamics}} \quad (4)$$

The turbulent collision efficiencies have been calculated by taking the background flow field to be fixed over the time of interaction. This methodology was adopted by Pinsky *et al.* [4], who showed that the turbulent flow evolves over much longer time and length scales compared to those of the hydrodynamic interaction. The initial separation distance is prescribed to be 20 times the radius of the largest droplet, 0.04 cm, as this is the typical value used in previous theoretical studies. The results were calculated by taking the positions and velocities of all of the collision pairs in the previous geometric collision kernel experiments with no hydrodynamic forces. The colliding droplets were interpolated backwards in time until the drops were separated by the prescribed distance and then the drops were allowed to move towards one another with their velocities being modified by the forces of gravity, the constant background velocity of the turbulent flow field and the hydrodynamic effect from the flow field around the interacting droplet. The values of

$E$  obtained for the gravitational cases are 0.09 for the 15+20  $\mu\text{m}$  droplets, 0.08 for the droplets of 10+20  $\mu\text{m}$  and 0.05 for the 5+20  $\mu\text{m}$  droplets. These values are well within the fairly broad range of other theoretical studies. Such a large range exists due to the necessary use of approximations and the lack of definitive experimental work for comparison.

Figure 2 shows how the collision efficiencies change with respect to the dissipation rates of the four numerical simulations. The efficiencies have been normalised by the corresponding gravitational values and all results show that the inclusion of turbulent accelerations in droplet motion acts to increase the efficiencies for all sizes and all flows considered. The largest increase in  $E$  is for collisions between the droplets of radius 5 and 20  $\mu\text{m}$ . For this size combination the turbulent collision efficiency is almost three times the gravitational value. For the 10+20  $\mu\text{m}$  case the collision efficiency increases from 1.7 times the gravitational case at the dissipation rate of about  $100 \text{ cm}^2 \text{s}^{-3}$  to 2.4 times greater for the most energetic flow field. The turbulent collision efficiency has the least change from the gravitational efficiency for the largest radius ratio, increasing from 1.15 to 2.4 times for the 15+20  $\mu\text{m}$  droplets. Figure 1 shows that turbulence has the greatest effect on the geometric collision kernel for this size combination, however for the collision efficiency, figure 2 shows that turbulence has the least effect on these sizes. The reason for this is the small gravitational collision efficiency for the 5+20  $\mu\text{m}$  droplets.  $E$  is determined by the relative velocities between interacting droplets and as table 1 shows  $\langle |w_r| \rangle_n$  for the 5+20 and the 15+20  $\mu\text{m}$  cases are comparable. The difference in the gravitational collision efficiencies for these radius ratios is much larger. Therefore when one compares the increase in the collision efficiency when the effects of turbulence are included, the small radius ratio has a greater sensitivity.

### Turbulent Collision Kernels with Hydrodynamic Forces

Turbulent coalescence is governed by three processes: collision due to particle-turbulence interactions; collision efficiency due to particle-particle hydrodynamic interactions, and; coalescence efficiency as determined by surface sticking characteristics. Laboratory studies of colliding cloud droplets have shown that the coalescence efficiency is near unity [1]. Since detailed observations of the coalescence efficiency for small size droplets is inherently difficult to obtain in real clouds, previous theoretical studies have assumed that the collection efficiency is equal to the collision efficiency. Thus the problem of droplet growth through collection in a turbulent flow reduces to determining the collision rates that include hydrodynamic forcing.

Figure 3 shows the turbulent collision kernels that include the hydrodynamic forcing normalised by the corresponding gravitational kernel, that is

$$(E \times \Gamma)_{\text{turb}} / (E \times \Gamma)_{\text{grav}} \quad (5)$$

In this figure each of the three normalised contributions in figure 2 have been multiplied together to give the total effect of the turbulence. For low dissipation rates turbulence has the most impact on the small radius ratios. For the 5+20  $\mu\text{m}$  droplets at the dissipation rate of about  $100 \text{ cm}^2 \text{s}^{-3}$ , the increase in  $E \times \Gamma$  is substantial at 3 times the gravitational value. This increases with increasing eddy dissipation rate to a value of more than 4 times the corresponding gravitational value. For the intermediate droplet pair of 10+20  $\mu\text{m}$ , the increases range from almost 2 to 5 times the gravitational case across the four flow fields. The increase for the 15+20  $\mu\text{m}$  droplets is quite modest for the least energetic flow, however it is for this droplet pair that we see the greatest effect of turbulence. The increase is greater than 9 times



the gravitational case for the largest radius ratio in the most energetic flow.

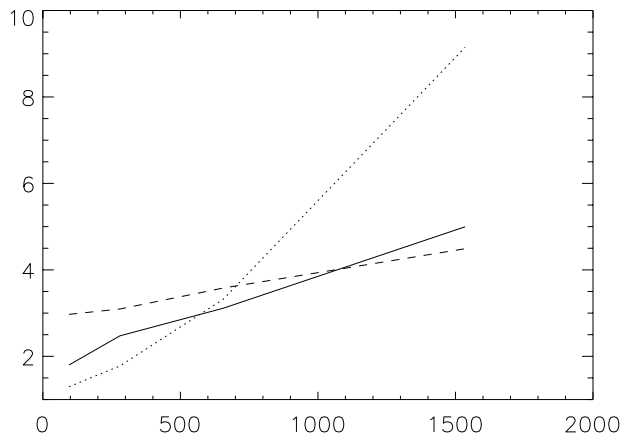


Figure 3. The turbulent collision kernel that includes the hydrodynamic forcing normalised by the corresponding gravitational kernel as a function of average eddy dissipation rate ( $\text{cm}^2 \text{s}^{-3}$ ). The dotted line is the normalised collision kernel for the 15 and 20  $\mu\text{m}$  droplets, the solid line is for the 10 and 20  $\mu\text{m}$  droplets and the dashed line is for the 5 and 20  $\mu\text{m}$  droplets.

### Conclusions

The effect of turbulence on the collision rates of small cloud droplets has been explored by the use of a direct numerical simulation of the flow field. By implementing an efficient scheme to detect collisions, large numbers of droplets have been explicitly tracked as they move throughout the turbulent flow. The collision rates and characteristics of the droplets at the time of collision have been investigated. Four numerical simulations with increasing rates of eddy dissipation have been performed. As the intensity of the turbulence increases the deviation from gravitational statistics becomes greater. The turbulent geometric collision kernel that does not include the hydrodynamic forces between interacting droplets is greater than the corresponding gravitational kernel for each of the droplet size combinations considered. The turbulent collision kernel increases fairly linearly with increasing dissipation rate for each of the three size combinations. Turbulence has the most effect on the largest radius ratio, the 15+20  $\mu\text{m}$  droplets. In this case the turbulent kernel is greater than the gravitational one by 1.1 times for the least energetic flow and 3.8 times for the most energetic flow. Analysis of the two kinematic quantities responsible for changes in the kernel shows that the increases in the geometric collision kernel for the small radius ratio droplets were predominately caused by increases in the relative radial velocities. For the 10+20  $\mu\text{m}$  droplets, the increases in the kernel were caused by both increases in the relative radial velocities and the clustering of the droplets. The large increase for the 15+20  $\mu\text{m}$  droplets was mostly due to the preferential concentration of the droplets, however, this size combination also had the largest increase in the relative radial velocities. This is because these droplets have the largest Stokes numbers and it has been shown that for the radial distribution function, the interaction between particles and turbulence is maximised when the Stokes number is of order 1.

The collision efficiency results presented are for the simplified problem of two interacting droplets, whereby the flow field is stationary over the time of interaction. Another assumption in the calculation of the collision efficiencies is that only those droplets that collide geometrically can collide when the hydrodynamic interactions are accounted for. For an initial separation distance of 0.04 cm, the collision efficiencies increased the least for the 15+20  $\mu\text{m}$  droplets. For this case the collision efficiency increase ranged from 1.2 to 2.4 times the gravitational value across the four dissipation rates. The 10+20  $\mu\text{m}$  case showed similar increases of 1.7 to 2.4 times the gravitational value and the collision efficiencies for the 5+20  $\mu\text{m}$  droplets had the greatest increase of almost 3 times.

The overall turbulent coagulation process is governed by the product of the geometric collision kernel and the collision and coalescence efficiencies. Taking the coalescence efficiency to be 1, the increases that we have seen in both the geometric collision kernel and the collision efficiency translate into significant increases in the product of these two quantities. The lowest dissipation rates explored in this study have the greatest effect on the small radius ratio of more than 3 times the corresponding gravitational value. This is an encouraging result as it is at the beginning of the cloud lifetime when the dissipation rates are modest that collisions between small droplets will have the most effect on expediting the production of rain drops. The collision kernels that include the hydrodynamic forcing for the 5+20 and the 10+20  $\mu\text{m}$  droplets increase linearly with dissipation rate from 3.0 and 1.8 times the gravitational values up to 4.5 and 5.0 times respectively. Low energy turbulence has the smallest influence on the collision kernel with hydrodynamic forces for the largest radius ratio. For this case the 15+20  $\mu\text{m}$  droplets show increases of 1.3 and 1.8 times the gravitational case for the two lowest dissipation rates. However, the effect of turbulence is the most dramatic for this size combination, which for the most energetic flow has an increase of more than 9 times the gravitational value. These increases are significant and are expected to influence the evolution of the drop size distribution and accelerate the growth of rain drops.

### Acknowledgments

This work was supported by the Canadian Foundation for Climate and Atmospheric Sciences.

### References

- [1] Beard, K.V., Durkee, R.I. & Ochs III, H.T., Coalescence Efficiency Measurements for Minimally Charged Cloud Drops, *J. Atmos. Sci.*, **59**, 2002, 233-243.
- [2] Franklin, C.N., Vaillancourt, P.A., Yau, M.K. & Bartello, P., Collision Rates of Cloud Droplets in Turbulent Flow, submitted to *J. Atmos. Sci.*, 2004.
- [3] Klett, J.D. & Davis, M.H., Theoretical Collision Efficiencies of Cloud Droplets at Small Reynolds Numbers, *J. Atmos. Sci.*, **30**, 1973, 107-117.
- [4] Pinsky, M., Khain, A. & Shapiro, M., Collisions of Small Drops in a Turbulent Flow. Part I: Collision Efficiency. Problem Formulation and Preliminary Results, *J. Atmos. Sci.*, **56**, 1999, 2585-2600.
- [5] Saffman, P.G. & Turner, J.S., On the Collision of Drops in Turbulent Clouds, *J. Fluid Mech.*, **1**, 1956, 16-30.
- [6] Sundaram, S. & Collins, L.R., Collision Statistics in an Isotropic Particle-laden Suspension. Part I: Direct Numerical Simulations, *J. Fluid Mech.*, **335**, 1997, 75-109.
- [7] Vaillancourt, P.A. & Yau, M.K., Review of Particle-Turbulence Interactions and Consequences for Cloud Physics, *Bull. Amer. Meteor. Soc.*, **81**, 2000, 285-298.
- [8] Vaillancourt, P.A., Yau, M.K. & Grabowski, W.W., Microscopic Approach to Cloud Droplet Growth by Condensation. Part I: Model Description and Results without Turbulence, *J. Atmos. Sci.*, **58**, 2001, 1945-1964.
- [9] Wang, L.-P., & Maxey, M.R., Settling Velocity and Concentration Distribution of Heavy Particles in Homogeneous Isotropic Turbulence, *J. Fluid Mech.*, **256**, 1993, 27-68.
- [10] Wang, L.-P., Wexler, A.S. & Zhou, Y., On the Collision Rate of Small Particles in Isotropic Turbulence. Part I: Zero-inertia Case, *Phys. Fluids*, **10**, 1998, 266-276.
- [11] Wang, L.-P., Wexler, A.S. & Zhou, Y., Statistical Mechanical Description and Modelling of Turbulent Inertial Particles, *J. Fluid Mech.*, **415**, 2000, 117-153.
- [12] Zhou, Y., Wexler, A.S. & Wang, L.-P., Modelling Turbulent Collision of Bidisperse Inertial Particles, *J. Fluid Mech.*, **433**, 2001, 77-104.



## Low-Reynolds-number stirring in simple devices

S. M. Cox<sup>1</sup>

<sup>1</sup>School of Mathematical Sciences, University of Adelaide, Adelaide, SA 5005 AUSTRALIA

### Abstract

We examine two models for stirring devices that operate at low Reynolds number. In each, elliptical paddles are used to stir a vat of fluid. In the first model, a single paddle stirs an infinite expanse of inviscid fluid; in the second, three paddles stir a highly viscous fluid. Such models are clearly a caricature of any real mixing device, but they do allow accurate simulation in a genuinely time-dependent geometry, appropriate for impeller-driven mixers. The first model is simple enough to yield an exact expression for the velocity field and so allow numerical particle tracking to be carried out to high precision. The choice of a suitable mode of operation of the device is essentially a matter of optimising the system parameters. In our second model, we show how, by the use of more than one stirring element, a high quality of stirring can be *built in*, giving a design that performs well, regardless of the exact system parameters, such as paddle design or fluid rheology.

### Introduction

Many modern applications of fluid mixing pose a particular challenge because the associated flows are laminar, with low Reynolds number. (The Reynolds number  $Re = UL/\nu$ , where  $U$ ,  $L$  and  $\nu$  are, respectively, a typical velocity scale, a typical length scale and the kinematic viscosity of the fluid.) An example is the mixing in microfluidic devices such as used in the biotechnology industry. Fortunately for such applications, it is now well established [2] that good mixing can be achieved in slow laminar flows, provided that fluid particles undergo *chaotic* motions. The challenge is thus to design devices and corresponding modes of operation that achieve this end, of the *chaotic advection* of fluid particles [1].

The stirring effectiveness of chaotic advection was first shown in rather artificial ‘devices’ [1, 2], chosen because an exact mathematical expression is available for the velocity field, and hence numerical simulation of extreme accuracy is possible; these simple models were entirely adequate for the pedagogical purpose at hand. Over the past twenty years or so, a wide variety of increasingly sophisticated mathematical models have been developed for simple mixing devices [2]. Most rely on a tuning of the system parameters to optimise the mixing quality that is achieved.

A recent significant theoretical advance in the design of laminar mixers is the work of Boyland, Aref and Stremler [3], which concerns stirring achieved by topologically nontrivial motions of three or more stirring elements (e.g., rods used to stir a fluid in a vat). Given only the topology of the motions of the stirring elements, it is possible to compute a rate of stretch of material lines. The fluid rheology, e.g., whether Newtonian or otherwise, is unimportant. Of course, given such moderate input information, the theory does not specify the size of the chaotic region generated by the boundary motions, nor does it specify exactly which material lines enjoy (at least) the predicted rate of stretch. However, in both experiments [3] and numerical simulations [6] the associated designs seem to work remarkably well.

This paper begins by introducing a model for a simple stirring ‘device’, comprising a single elliptical paddle in an infinite vat

of fluid. This model is clearly unrealistic in assuming an infinite expanse of fluid, but it possesses an important feature of all batch mixers, that the geometry of the device changes with time as the stirring element sweeps through the fluid. By contrast, many of the first experimental and numerical studies of chaotic advection were carried out in the *eccentric annular mixer* (see [2] for an account of the history), whose geometry is fixed. As with all other simple models, the elliptic paddle requires careful tuning of its mode of operation to stir the fluid effectively.

We then discuss how this design can be made somewhat more realistic, by adopting a finite geometry and employing more than one stirring element (and a viscous fluid model). In this second model, while different degrees of effectiveness are still possible by varying the system parameters, we shall see that a certain quality of mixing is built in once a topologically non-trivial motion of the stirring elements is specified.

### Stirring with a single paddle

One of the simplest stirring devices is a paddle. Consider the flow in two dimensions generated by the motion of an elliptical paddle. For simplicity, we take the fluid to be inviscid, and occupying the entire infinite region exterior to the paddle. This is clearly not intended as a practical model for reality, but it has enough complication to generate chaotic advection yet enough simplicity to permit an exact (classical) mathematical solution for the velocity field.

We consider irrotational flow, in which case the streamfunction  $\psi(x, y, t)$  satisfies Laplace’s equation

$$\nabla^2 \psi = 0.$$

In order to stir the fluid, the paddle must execute some motion: the ‘stirring protocol’. It is necessary to select an appropriate protocol that stirs the fluid effectively. Our goal will be to generate a significant region in which fluid particles undergo chaotic motion, characterised by exponential-in-time separation of neighbouring particles. By contrast, stirring is less effective in regular regions, with algebraic-in-time separation of fluid particles. In two dimensions, time dependence of the streamfunction is necessary for chaos. Some immediate candidates for stirring protocols are readily seen to generate exclusively regular particle motions, since they correspond to steady streamlines in an appropriate frame of reference. Examples are: (i) a paddle whose axis is fixed, and which rotates about this axis (i.e., an ‘impeller’), because the streamfunction is steady in a frame co-rotating with the paddle; and (ii) a paddle that sweeps around in a large circle, one ‘nose’ always pointing towards the centre of the circle, for a similar reason.

The streamfunction  $\psi$  is most readily constructed in elliptical coordinates  $(\xi, \eta)$ , given by

$$x = c \cosh \xi \cos \eta, \quad y = c \sinh \xi \sin \eta,$$

for an ellipse centred at the origin, with major axis of length  $2a$  along the  $x$ -axis, and minor axis of length  $2b$  along the  $y$ -axis. The constant  $c = \sqrt{a^2 + b^2}$ . If the ellipse is translating

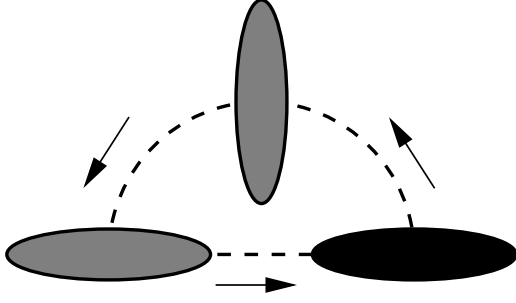


Figure 1: A semi-circular stirring protocol for an elliptical paddle. The ellipse starts at right, moves counterclockwise around the semicircular path, then straight along the  $x$ -axis. One loop around the circuit defines a single period of the stirring protocol.

with velocity  $(U, V)$  and is rotating about its axis with angular velocity  $\omega$ , then the appropriate solution to Laplace's equation that satisfies the no-penetration condition on the perimeter of the ellipse is [7, 9]

$$\psi = Ae^{-\xi}(Ub\sin\eta - Vacos\eta) + \frac{1}{4}\omega(a+b)^2e^{-2\xi}\cos 2\eta,$$

where  $A = [(a+b)/(a-b)]^{1/2}$ . Corresponding formulae hold for an ellipse centred elsewhere or in a different orientation, but they are easily obtained by appropriate rotation or translation of the axes, and are not given here.

Given the streamfunction, we track fluid particles by solving for each particle the Lagrangian equations of motion, i.e., the coupled ODEs

$$\dot{x} = u(x, y, t), \quad \dot{y} = v(x, y, t), \quad (1)$$

where  $u = \psi_y$  and  $v = -\psi_x$ , subject to an appropriate initial condition for each particle.

A simple stirring protocol that cannot essentially be reduced to steady flow through a change of frame of reference is illustrated in Figure 1. Here the ellipse moves along a semicircular path. On the curved part of the path, the ellipse rotates about its axis so as to point one nose towards the centre of the arc; on the straight part of the path, the ellipse does not rotate about its axis ( $\omega = 0$ ). In this example, the circle has diameter 3, while  $a = 2$  and  $b = 1$ . This is clearly only one possible stirring protocol; its key feature from the point of view of successfully generating chaotic fluid particle trajectories is that the paddle cannot be brought to rest by moving to a new frame of reference, unless the change of frame is itself time dependent.

One simple, mostly qualitative, diagnostic of the stirring quality is the Poincaré map. Here the positions of a few fluid particles are followed by integrating (1) in time. The positions of the particles are then plotted stroboscopically, after  $1, 2, \dots$  periods of the stirring protocol: where the eye sees closed curves in the Poincaré map, there is *regular* motion of fluid particles; where the eye sees a random collection of dots, there is *chaotic* motion.

Figure 2 shows the Poincaré map associated with the protocol in Figure 1. There are two large regular regions visible, and a significant *chaotic sea*; indeed the bulk of the fluid, sufficiently far from the ellipse, undergoes regular particle motion. One may attempt to devise a better stirring protocol, in the sense of one that increases the size of the chaotic region, or one that increases the stretch rate experienced by fluid elements (this latter, *quantitative* diagnostic of the stirring clearly requires a more sophisticated measure than the 'by-eye' examination of the Poincaré map). One might choose a less symmetrical path for the paddle, or a different paddle aspect ratio; one might adopt a more

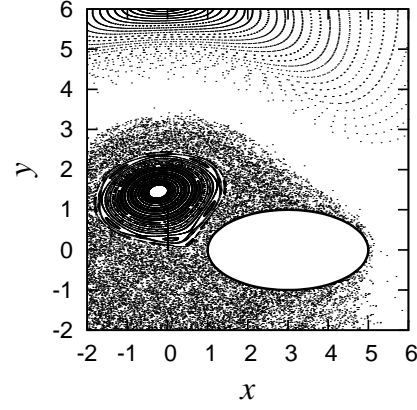


Figure 2: Poincaré map for the stirring protocol in Figure 1, with parameter values as indicated in the text.

sophisticated model for the fluid than the simple inviscid, irrotational one used here; one might confine the fluid in a finite vat. But with a single paddle, the only option is to tune the stirring protocol and the other parameters of the system to obtain the desired end of improved stirring performance. It is in the nature of chaotic flows that the resulting, tuned stirring protocol has an unfortunate susceptibility to further parametric perturbations; this is an undesirable feature of any real mixer, since one would like the design to be largely insensitive to the precise details of the underlying design.

The next section indicates how this parametric fussiness can be avoided, and high quality stirring can be 'built in' by the simple device of using multiple stirring elements.

### Stirring with a multiple paddles

There does not appear to be a simple analytical expression available for the flow driven by  $n$  elliptical paddles, when  $n > 1$ . In computing such a flow, we must therefore resort to a numerical evaluation of the velocity field. Since numerical errors grow geometrically in the simulation of chaotic particle motions, it is highly desirable to have a means of computing the velocity field with a truncation error smaller than that introduced by the time integration routine for the fluid particles. Such a method has been described elsewhere [6, 10] when the stirring elements have circular cross-section; the method allows simulation in finite or infinite domains, and of either inviscid, irrotational flow or highly viscous (Stokes) flow. The method uses a complex-variable formulation of the problem: the complex potential  $w(z, z^*, t)$  is subject to either Laplace's equation

$$\frac{\partial^2 w}{\partial z \partial z^*} = 0 \quad (2)$$

or the biharmonic equation

$$\frac{\partial^4 w}{\partial^2 z \partial^2 z^*} = 0 \quad (3)$$

in a time-dependent multiply connected geometry (here  $z^*$  is the complex conjugate of  $z$ ).

The corresponding streamfunction takes the form

$$\psi = f(z) + f^*(z^*)$$

or

$$\psi = z^* f(z) + z f^*(z^*) + g(z) + g^*(z^*),$$

respectively, in the models (2) or (3), for some analytic functions  $f$  and  $g$ . The solution for  $f$  (or for  $f$  and  $g$ , as appropriate)

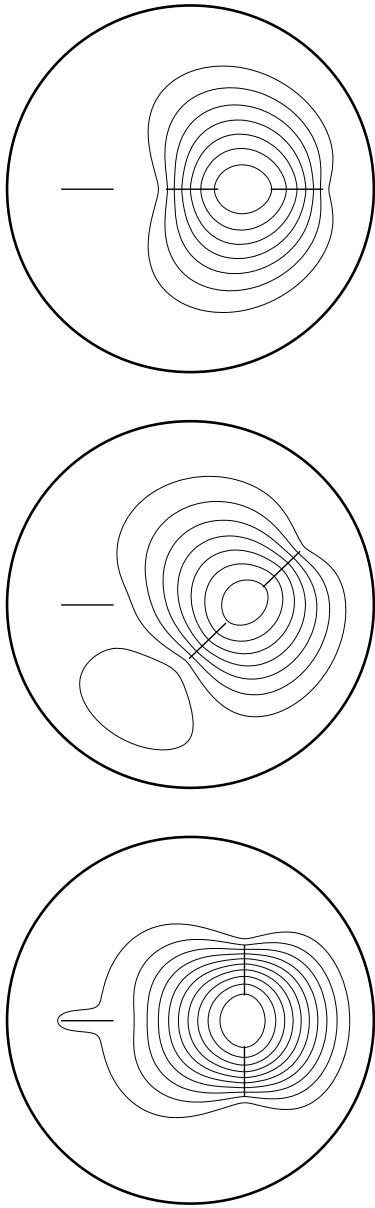


Figure 3: Instantaneous streamlines at three instants during an exchange of the rightmost pair of stirring elements.

is sought in the form of a finite system of singularities (located inside the stirring elements, and hence not in the physical fluid domain) together with Laurent series centred in each stirring element. The coefficients of the singularities and the terms in the Laurent series are determined numerically by minimising the squared error in the boundary conditions; the series coefficients decay geometrically and so only a few terms (around 10 to 20) need be kept in order to generate a highly accurate velocity field.

If the same expansions are used for elliptical paddles, they do not converge so rapidly and they struggle to provide an acceptable level of accuracy when the paddles depart from circular symmetry. However, if the component of the solution associated with each paddle is modified, by making a suitable conformal mapping of the ellipse, parametrised by  $z = z(\theta)$ , say, to a circle, parametrised by  $Z = \exp i\theta$ , say, and the complex potential is written in terms of  $Z$  rather than  $z$ , then the series become spectrally convergent once more, and the velocity field can readily be computed, almost down to machine precision. The extraordinary accuracy is maintained even down to ellip-

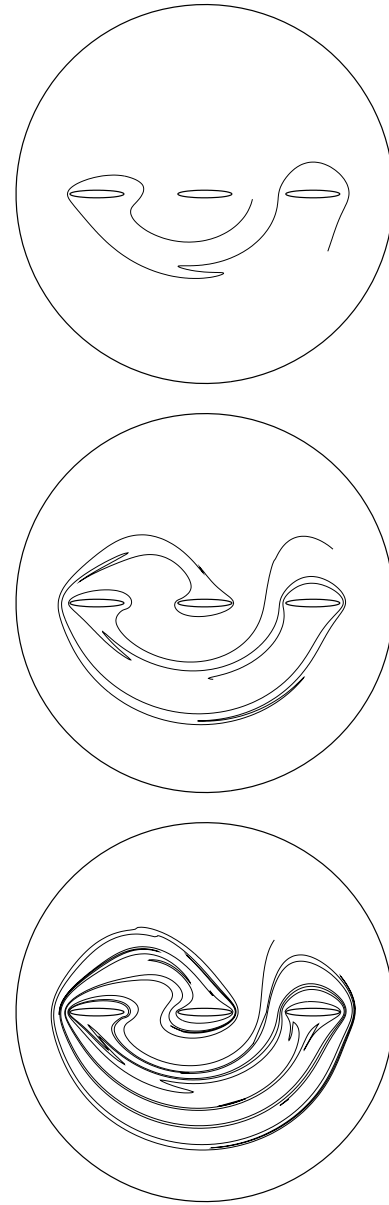


Figure 4: The stretching of a line element, initially of unit length and located between the points  $(2/7, \pm 1/2)$  under the stirring protocol described in the text. The vat is a unit circle, centred at the origin.

tical paddles of extreme aspect ratio (we have computed flows down to  $b/a = O(10^{-7})$ ). In fact, by an appropriate conformal mapping, exactly flat paddles, of zero mathematical width, can be simulated by this method, with no numerical difficulties.

The numerical method allows an arbitrary number of stirring elements, of different sizes and aspect ratios, translating and rotating in arbitrary fashion. We illustrate in Figure 3 Stokes flow with  $n = 3$  stirring rods, in a circular vat. Each elliptical paddle has aspect ratio  $b/a = 10^{-3}$  and length  $2a = 2/7$ ; the radius of the vat is scaled to unity. The three paddles initially lie equispaced along the real (horizontal) axis. The figure illustrates the instantaneous flow pattern as the positions of the rightmost pair are exchanged; the exchange is accomplished by rotating the centres  $c_1$  and  $c_2$  of the two paddles about the point  $c_3$  mid-way between  $c_1$  and  $c_2$ . As the paddles are moved, they are rotated about their axes so as always to ‘point towards’  $c_3$ . Note that the flow at any instant is smooth and laminar.

Topologically nontrivial motions involving three stirring ele-

ments are readily constructed by considering motions that correspond to nontrivial *plaiting* or *braiding* motions [3]. One such motion is achieved by moving the stirring rods according to the following protocol: first the right-hand pair are interchanged, in a counterclockwise motion, then the new left-hand pair are interchanged, but clockwise. This pair of interchanges constitutes a single period of operation of the device (i.e., one application of the stirring protocol); it is akin to the natural plaiting of three strands of hair.

The batch stirring device described above, with multiple stirring elements, serves as a simplified model for commercial planetary mixers. Although it now becoming apparent that topologically nontrivial motions such as described above build in a high mixing quality, standard batch mixers do not at present employ any such stirring protocol (but see [8]). It might superficially appear that a complicated system of gearing is necessary to generate the motions described in the previous paragraph, and that this might be the reason for the commercial vacuum; however, with some ingenuity, topologically equivalent motions are readily accomplished with only simple gearing, such as already used on commercial devices, together with fixed baffles [6].

The evolution of a line element of unit initial length is shown in Figure 4, after one, two and three applications of the stirring protocol. (In this case we have increased the aspect ratio of the paddles so that  $a = 1/7$  and  $b = 1/50$ , so the finite thickness of the paddles can be seen.) The number of points in the line has been dynamically increased where necessary to maintain adequate resolution. The requirement of good resolution effectively constrains accurate calculations of the length of the line element to two or three further periods of the stirring protocol beyond those illustrated in Figure 4. We find that the length of the line after one, two and three periods of the protocol is, respectively, 4.3, 14 and 42. The dramatic rate of line stretch is relatively insensitive to the exact motions of the stirring elements or their exact dimensions. This is the hallmark of a topologically chaotic mixer design.

## Conclusions

We have illustrated in this paper a simple model for a stirring ‘device’ that uses a single elliptical paddle in an infinite expanse of inviscid fluid undergoing irrotational motion. While this is not intended as a true model for any realistic device, it is a good pedagogical tool for illustrating the concept of chaotic advection, using no more than a basic undergraduate knowledge of classical hydrodynamics and the numerical solution of ordinary differential equations. In this respect, it is in the same spirit as Aref’s ‘blinking vortex flow’ [1], although (marginally) more realistic, in possessing no flow singularities (these play havoc with numerical computations of the evolution of material lines). The model allows one to experiment (numerically) to find good stirring protocols by varying the system parameters, including the path taken by the stirring element and its shape and size.

Better than this parametric optimisation is to use topological ideas to build in some degree of mixing quality [3, 6, 8]. Then the stirring device that is so designed operates ‘robustly’ in the sense that it remains insensitive to the nature of the fluid being mixed and to its exact specifications, provided the topology of the motion of the stirring elements is unaltered.

So far we have, as illustrated here, simulated flows in the two mathematically ‘easy’ limits (for a Newtonian fluid at zero and infinite Reynolds numbers) and it would be highly desirable to investigate the effectiveness of the topologically designed stirring devices for a Newtonian fluid at finite Reynolds number [5], or for other fluids. Results from the two cases already studied [6] show a promising indication of the robustness of the

topological designs, but clearly further research is warranted.

Finally, we note that one important question that needs to be considered with any mathematical model is its degree of applicability. To address this question in the present context, we have performed laboratory experiments on a batch mixer with a single stirring element (of circular cross-section) [4]. Our results indicate that the two-dimensional Stokes flow approximation performs well for genuinely small Reynolds numbers (e.g.,  $Re = O(10^{-3})$ ). However, when the Reynolds number is merely moderate ( $Re = O(1)$ ), there are significant changes to the streamlines of the flow. Furthermore, the flow is no longer quasi-steady (i.e., it depends on more than just the *instantaneous* motions of the boundaries). However, for *topologically chaotic* flows generated using three or more stirring elements, we expect a much greater degree of robustness of the results to changes in the Reynolds number. Of course, the requisite experiments to demonstrate this have not yet been performed (but see [3]); we hope in the future to carry out such experiments, which may provide strong validation of the topologically chaotic theory.

## Acknowledgements

I am grateful to Matthew Finn, whose Matlab routines formed the basis of the FORTRAN77 code used to generate the numerics in Figures 3 and 4.

## References

- [1] Aref, H., Stirring by chaotic advection, *J. Fluid Mech.*, **143**, 1984, 1–21.
- [2] Aref, H., The development of chaotic advection, *Phys Fluids*, **14**, 2002, 1315–1325.
- [3] Boyland, P.L., Aref, H. and Stremmer, M.A., Topological fluid mechanics of stirring, *J. Fluid Mech.*, **403**, 2000, 277–304.
- [4] Clifford, M.J., Cox, S.M. and Finn, M.D., Reynolds number effects in a laminar chaotic mixer with changing geometry, *Chem. Eng. Sci.*, **59**, 2004, 3371–3379.
- [5] Dennis, S.C.R. and Young, P.J.S., Steady flow past an elliptic cylinder inclined to the stream, *J. Eng. Math.*, **47**, 2003, 101–120.
- [6] Finn, M.D., Cox, S.M. and Byrne, H.M., Topological chaos in inviscid and viscous mixers, *J. Fluid Mech.*, **493**, 2003, 345–361.
- [7] Lamb, H. *Hydrodynamics*, 6th ed., Cambridge University Press, 1932.
- [8] MacKay, R.S., Complicated dynamics from simple topological hypotheses, *Phil. Trans. R. Soc. Lond. A*, **359**, 2001, 1479–1496.
- [9] Morton, W.B., On the displacements of the particles and their paths in some cases of two-dimensional motion of a frictionless liquid, *Proc. R. Soc. Lond. Ser. A*, **89**, 1914, 106–124.
- [10] Price, T.J., Mullin, T. and Kobine, J.J., Numerical and experimental characterization of a family of two-roll-mill flows, *Proc. R. Soc. Lond. Ser. A*, **459**, 2003, 117–135.

## Bubble Entrapment During Water Drop Impacts

D.E. Cole<sup>1</sup> and J.L. Liow<sup>1</sup>

<sup>1</sup>Mechanical Engineering Discipline, School of Engineering  
James Cook University, Qld, 4811 AUSTRALIA

### Abstract

In the splash of a liquid drop on a deep pool of water, bubble entrapment occurs over a limited range of Froude number. Using high speed video photography at framing rates between 10000-100000 fps, the bubble entrapment regime was studied for water drops impacting on a deep pool of water. It is known that a high speed jet accompanies the entrapment of a bubble. In this study it was found that preceding the appearance of the high speed jet, a series of high speed droplets, having diameters up to a magnitude smaller than droplet previously observed, appears. The speed of these droplets were 50% higher than those formed from the high speed jets. We believe that these smaller high speed droplets were the result of a focusing of the ejecta sheet into a thin high speed jet. This thin high speed jet breaks up rapidly on formation and cannot be observed above the bath free surface. In conjunction with the upward high speed jet, an entrapped bubble was found to be expelled downwards from the cavity with a high speed downward jet of liquid penetrating into the bubble. If the high speed downward jet penetrated far enough into the bubble, such that its length exceeded Rayleighs wavelength for instability, it broke up to form a single drop within the bubble. The entrapped drop would then bounce around inside the bubble before the drop coalesced with the bulk liquid through a coalescence cascade with a geometric similarity given by  $We = 8$ .

### Introduction

The impact of a water drop on a deep pool of water has been studied for almost a hundred years, beginning with the spark photography of Worthington [13]. Applications of liquid-liquid impacts include gas injection metallurgy, fire suppression systems [5] and behaviour of the worlds oceans. When the water drop impacts, a range of phenomena subsequent to the impact have been observed. The occurrence of these phenomena have been detailed by Rein [9] and Liow [2], and shown to be primarily dependent on the Froude number (defined as  $Fr = u^2/(gd)$ ) and to a lesser extent, the Weber number (defined as  $We = \rho u^2 d / \sigma$ ). At low Froude numbers, the water drop coalesces with the pool and forms a vortex ring that is propagated into the pool water. At higher Froude numbers, a cavity is formed after impact. With still increasing Froude numbers, the cavity formed collapses to entrap an air bubble with the formation of a high speed water jet; this connection was first observed by Rein [9]. Subsequently, based on physical arguments, Oguz and Prosperetti [7] derived scalings for the lower and upper limits for the occurrence of the high speed jet based on as  $We \approx Fr^{1/5}$  and  $We \approx Fr^{1/4}$  respectively. Fitting to experimental measurements [7], the lower and upper limits are  $We = 41.3Fr^{0.179}$  and  $We = 40Fr^{0.247}$ . Liow [2] results suggest that the range for the formation of a high speed jet is larger than the range for the bubble entrapment, more so for the lower limit. For Froude numbers larger than those in the region where the high speed jet is found, the cavity does not entrap a bubble and a thick slow jet is formed after the cavity collapses.

The formation of the entrapped bubble occurs very rapidly, in the order of less than 1 millisecond. High speed cinematic re-

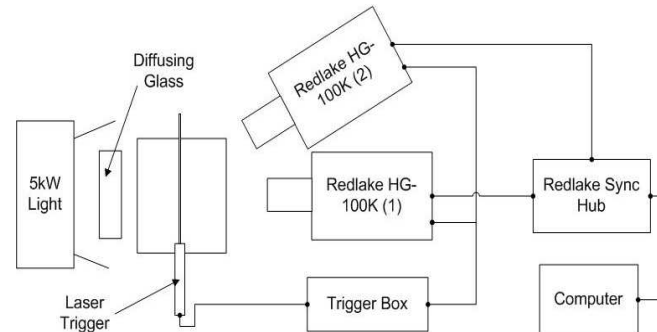


Figure 1: Schematic of the experimental apparatus.

sults at 5000 fps for two specific cases [1] show that the bubble entrapment process is not fully captured at those speeds. Their results show that the cavity base stagnates prior to bubble entrapment.

Although the events leading up to bubble entrapment is well known and published, the process of bubble entrapment is still not fully understood as the duration is extremely short. Moreover, the process of the formation of the high speed jet and the subsequent motion of the entrapped bubble has not been studied in any detail. In this paper, a high speed video study of the bubble entrapment process was conducted to capture events that have a lifetime of less than 1 ms.

### Experimental

The experimental setup is shown schematically in Figure 1. Apart from the high speed video and lighting, the experimental setup uses the same equipment as that of Liow [2] where water drops of approximately 2 mm diameters are formed at regular intervals. A pair of high speed video cameras, Redlake HG-100K, are used here, to provide synchronised details above and below the water bath. The resolution of the high speed video is dependent on the framing rate,  $1504 \times 1128$  pixels at 1000 fps,  $512 \times 512$  at 5000 fps and  $352 \times 352$  at 10000 fps with a minimum exposure of  $5 \mu s$ . A Nikon Micro 105 mm lens on f11 was used and positioned so that each pixel in the image represented a  $12 \mu m$  square. The drops were released from different heights to vary the impact velocity. The diameter of the drop was used as the characteristic length scale and the ratio of the drop diameter to impact velocity provided the characteristic time scale. A 5kW Arri fresnel lamp was used to provide the back illumination.

### Results and Discussion

The results presented here deals with specific phenomena that have not been reported or have been reported with insufficient details in the published literature.

#### Thin High Speed Jet

The high speed jet phenomena has generated considerable interest since Rein [9] linked the high speed jet to bubble entrapment. Zeff *et al.* [14] suggested that the high speed jet resulted

from a singularity. An early explanation by Oğuz and Prosperetti [7] suggested that this was due to the cavity base having a high momentum and was still travelling downwards while the cavity sides collapsed inwards. Liow [2] showed experimentally that the cavity base motion stagnates prior to bubble entrapment and suggested that a nonlinear capillary wave travelling down the cavity wall balances the upward momentum of the cavity base enabling the cavity sides to close in, trapping the bubble. This experimental observation was confirmed by Elmore *et al.* [1].

Figure 2 shows a sequence of drops generated from the impact of a water drop ( $Fr = 110$ ,  $We = 100$ ) in the region of thin high speed jet formation. On close observation, it was found that prior to the emergence of the high speed jet, a series of even smaller droplets was found to be ejected at high velocities. The small droplets did not necessarily follow the same upward trajectory as the high speed jet suggesting the presence of an initial thin high speed jet preceding the high speed jet. This thin high speed jet would be fairly short in length prior to breakup. The smallest droplets observed from this thin high speed jet occupied 1 to 2 pixels corresponding to  $18 \mu\text{m}$  in diameter. The previous smallest drops resulting from the high speed jet were in the order of  $70 \mu\text{m}$  [2]. The size of droplets from the thin high speed jet is below the resolution of [2] and [9] and the current measurements suggest that it could be up to an order of magnitude smaller in size. The highest speed of a thin high speed jet droplet was calculated at over 15 m/s. In comparison, previous measurement of the speed of the high speed jet have been less than 10 m/s. The thin high speed jet disappears from view within 2 ms. Morton *et al.* [6] numerical simulations of the high speed jet does not show the presence of the thin high speed jet and this could be due to the grid resolution  $\approx 25 \mu\text{m}$ . Although a low pressure region was identified at the cavity base where positive vorticity was generated, Morton *et al.* did not provide a pressure map for the time when the cavity wall met to entrap the bubble. The presence of high speed jets suggest that a high pressure region must form at the impact site of the walls.

Figure 2 shows that the thin high speed droplet sizes that emerge into view are not necessarily a succession of the smallest to the largest. Droplets 1 and 4 are the smallest but droplet 4 has a slower velocity than droplets 2 and 3 that preceded it. The drops move at different speeds and coalescence can take place. The drop pair 9-10 coalesces to form drop A (Figure 2:v-vi) and 12-13 coalesces to form drop C (Figure 2:ix-x). Drop pair A-11 further coalesce to form B (Figure 2:viii-ix). Thirteen individual drops were identified prior to the appearance of the larger drop (labelled 14) in the high speed jet.

The exact mechanism that gives rise to this thin high speed jet is not known as attempts to video into the cavity was not successful as there was insufficient lighting. A probable mechanism of this thin high speed jet is the formation of a thin ejecta spray [12]. Weiss and Yarin[12] showed that during the first millisecond of contact between the drop and the impact surface, a thin axisymmetric ejecta sheet arises travelling horizontally to the impact surface and subsequently evolving into a range of shapes [11]. Thoroddsen has shown experimentally that such an ejecta sheet can have an initial speed more than 10 times the drop impact velocity. During the contact of the cavity walls to form the entrapped bubble, the impact is similar to that of a drop impact on a surface where the ejecta sheet is formed. In this case, the collapsing cavity is focussing towards a central point and the ejecta sheet formed reduces to an axisymmetric jet. This is observed as the thin high speed jet and precedes the high speed jet, which is formed by the large bulk of the fluid behind the impact point being re-directed up and downwards after impact.

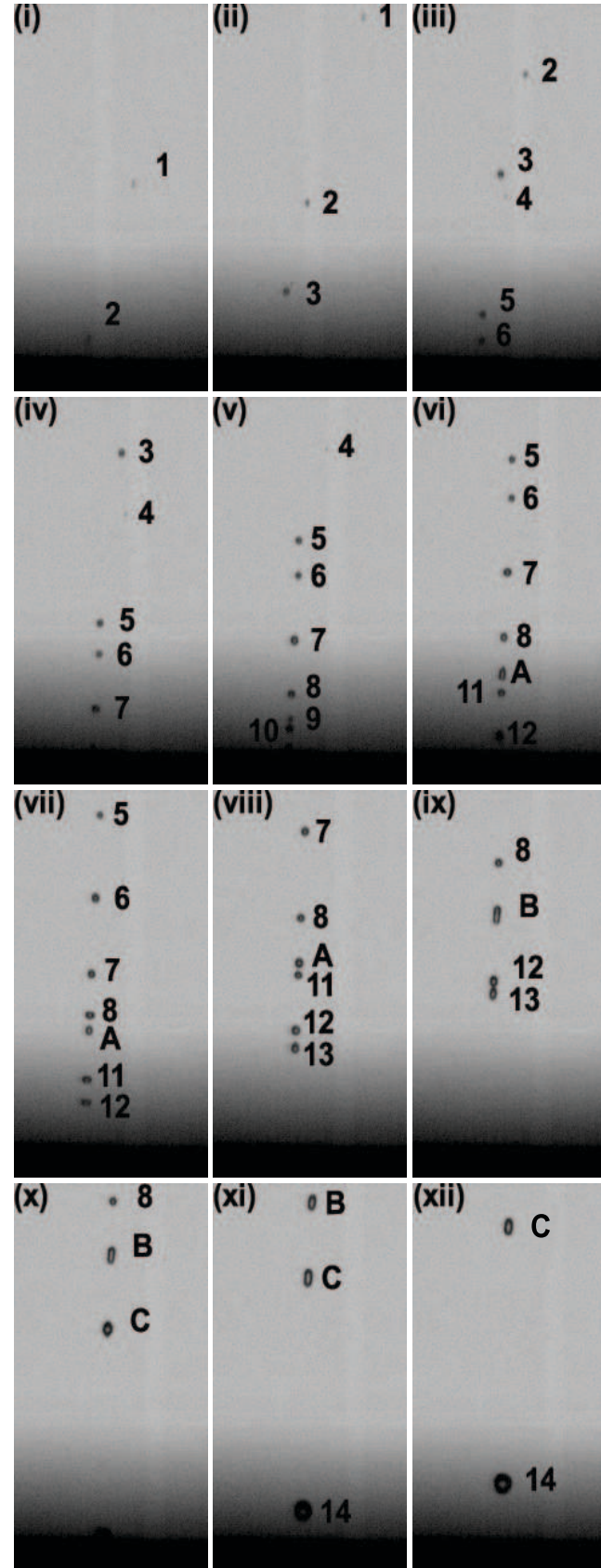


Figure 2: A sequence of twelve images of the thin high speed jet at  $100\mu\text{s}$  interval (10000 fps). Weber =100, Froude = 110. The individual drops are given numeric identities, while the coalesced drops are given alphanumerical identities. The first frame start at 13.7 ms after drop impact.



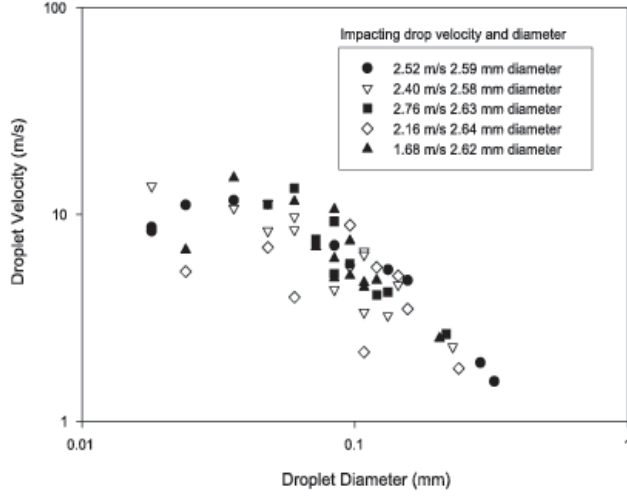


Figure 3: Droplet speed versus diameter from five different drop impacts. Each drop impact gives rise to 10-15 droplets.

Figure 3 shows a plot of the droplet diameter versus speed obtained from a number of observations. The speed was taken between the earliest two frames that the droplet was seen to emerge above the free surface, *i.e.* prior to coalescing if the droplets coalesced. The speed decreases logarithmically with the droplet diameter for droplet diameters larger than  $100\ \mu\text{m}$ . For smaller droplet diameters, there is a large spread in the speeds measured and the results suggest that the droplet speed is independent of the droplet diameter. There is a gap between the  $150$  and  $200\ \mu\text{m}$  where no droplets having those diameters were found. A larger drop impact sample would be required to ascertain if this anomaly actually exists or just due to the small sample size. In the analysis of the droplet diameters and speed, it was found that the small fast moving droplets tend to be clustered together at the beginning and are skewed in shape while in flight. Moreover, the string of droplets does not rise vertically from the cavity, but rather the first few droplets are ejected at an angle from the axis of symmetry. After a short time,  $\approx 600\ \mu\text{s}$ , the following droplets start to rise vertically from the cavity. This was found in all the experimental videos obtained so far.

### Bubble Entrapment

The impact of the walls to entrap a bubble results in a high speed jet. It is expected that an equal but opposite jet should result, travelling downwards with the entrapped bubble. Although [1] alluded to the presence of a downward jet, they provided no evidence of it. Figure 4 shows the presence of the downward jet. The downward jet reaches the opposite surface of the entrapped bubble but does not penetrate it. The tip of the downward jet detaches to form a water droplet within the bubble. The downward jet does not always follow a vertical downward path and can be angled up to  $45^\circ$  in any direction from the vertical. Previous observations of this phenomena has only been observed using glycerol mixtures to slow down the bubble collapse phase (Lohse [3]) suggesting that the time scale for the process is strongly viscosity dependent. This phenomena has a number of similarities with the detachment of an air bubble formed at an orifice. Under certain conditions, a water jet penetrates into the bubble that is detached from a nozzle [4]. The acoustic signal emanated from the entrapped bubble has been used by Pumphrey and Elmore [8] to locate the region where bubble entrapment occurs, and [4] has used the detaching bubble acoustic to determine the size of the bubble formed from nozzles in industrial processes. However, for the bubble detaching from a nozzle, there has not been any reports of whether a

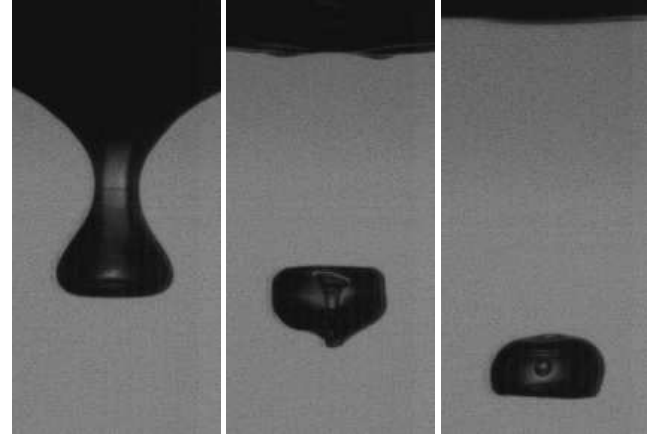


Figure 4: Three frames from a sequence showing the detachment of the entrapped bubble captured at 10000 fps. (Left) Cavity shape prior to snap off. (Middle) A jet penetrates the entrapped bubble  $500\ \mu\text{s}$  after snap off. (Right) Jet breaks up with a drop (diameter of  $140\ \mu\text{m}$ ) detached from the tip,  $600\ \mu\text{s}$  after snap off.

high speed jet is formed that travels back into the nozzle.

In some cases where the jet did not extend to the lower extremity of the air bubble, the jet would rapidly retract without leaving any fluid entrapped in the bubble. When the jet did break up in the entrapped drop, the length of the jet exceeded Rayleigh's wavelength of instability,  $\lambda = 4.508D$ , where  $D$  is the diameter of the downward jet. From the middle image in Figure 4 the diameter of the jet was estimated to be  $108\ \mu\text{m}$  resulting in  $\lambda = 487\ \mu\text{m}$ . The length of the jet in this case is  $528\ \mu\text{m}$  thereby satisfying the conditions for instability and resulting in the jet breaking up. The size of the entrapped droplet that detached from the downward jet is shown in the right image in Figure 4 and is approximately  $144\ \mu\text{m}$  in diameter.

Figure 5 shows the subsequent motion of the drop within the entrapped bubble. The drop bounces inside the bubble before coalescing with the bulk fluid. The coalescing gives rise to a capillary wave that propagates over the bubble surface as well as a smaller secondary drop. The formation of progressively smaller drops during the coalescence process has been documented by Thoroddsen [10] for a drop on a flat liquid surface. The disturbance is quickly damped out and the air bubble returns to its spherical shape. The secondary drop remains visible for a moment before coalescing with the bulk fluid. This coalescing process again propagates a capillary wave over the bubble surface but of reduced amplitude and without any further drop formation. Elmore *et al.* [1], using dyed impacting drops, claimed that the downward jet consisted of the impacting fluid. This would suggest that the drop formed within the bubble consists of the impacting drop fluid. In the current experiments, some of the impacting drops were dyed but the backlighting used did not allow a conclusive determination of the source of the fluid of the drop formed in the bubble.

Thoroddsen [10] suggested that the process of one droplet coalescing and spawning a secondary drop is controlled by a dimensional similarity given by a constant  $We = d^3/L^3$ , where  $d$  is the diameter of the first drop formed and  $L$  is the diameter of the second drop formed. In this study, for every case where the secondary drop was produced and could be measured, the secondary drop was always found to be close to half the diameter of the first drop giving a constant  $We = 8$ .

The bubble entrapment process is extremely rapid. The camera was set to 30000 fps ( $128 \times 136$  pixels) in an attempt to capture

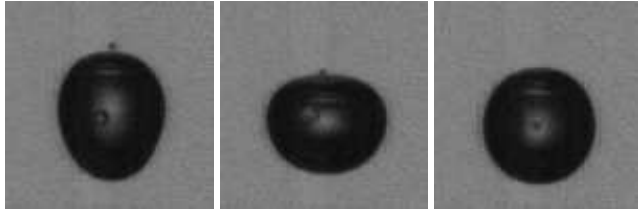


Figure 5: (Left) Formation of a liquid drop within the gas bubble. Entrapped drop  $\approx 96 \mu\text{m}$  (Middle) Exact moment of coalescence 3.9 ms after the first appearance of the primary entrapped drop (Right) Secondary entrapped drop dia.  $48 \mu\text{m}$ . Bubble size is  $\approx 660 \mu\text{m}$

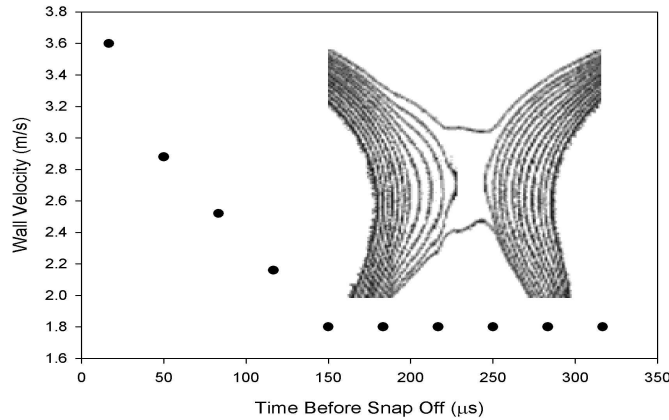


Figure 6: Cavity wall velocity versus time taken at 30000 fps tracking the velocity of the walls prior to bubble entrapment. Pixel outline of cavity walls prior to snap off shown in inset.

the evolution of the cavity walls prior to bubble entrapment. Figure 6 shows the velocity of the collapsing cavity walls moments before bubble entrapment. Approximately  $150 \mu\text{s}$  before bubble break off, the left side of the cavity rapidly increases in velocity while the right side retains at a constant velocity. These actions result in an asymmetric acceleration of the cavity walls prior to bubble entrapment. To examine in more detail how the bubble snap off, the camera was set to 100000 fps ( $32 \times 24$  pixels). However, using such a low resolution meant that the evolution of the cavity profile in the moments before snap off could not be tracked. The smallest wall to wall distance prior to bubble entrapment captured was  $72 \mu\text{m}$ . This is almost half the distance of  $156 \mu\text{m}$  from the 30000 fps sequence. The snap off of the bubble occurs in less than  $10 \mu\text{s}$ , in agreement with the fact the timescale for the snap off process is of the order of 0.2 ns. However, the local asymmetry of the cavity is a departure from most events involving liquid drop breakup problems. For example the break up of a liquid jet or snap off of a drop are axisymmetric. This implies that the cavity undergoes significantly more deformation before snap off than is described in the 30000 fps sequence. Therefore, to further understand how bubble entrapment actually occurs framing rates in excess of 100000 fps with greatly improved resolution would be required.

## Conclusions

This study has sought to gain a deeper understanding of the fluid mechanics occurring during bubble entrapment using high-speed video photography with framing rates of 10000-100000 fps. Analysis of the high speed jet showed that a string of smaller high speed droplets preceded the high speed jet with speeds 50% greater than those for the high speed jet breakup. These droplets were an order of magnitude smaller than what had been observed before. It was concluded that these smaller

high speed droplets were the result of a focussing of the ejecta sheet into a thin high speed jet. This thin high speed jet then broke up rapidly on formation and cannot be observed above the bath free surface.

During the entrapment of the air bubble, the cavity walls were found to accelerate inwards in an asymmetric fashion where the left wall accelerated faster, relative to the centre line, than the right wall in the last  $150 \mu\text{s}$  before bubble snap off. A high speed downward jet was observed in many cases of the entrapped bubble. If the high speed downward jet travelled far enough into the bubble, it broke up to form a single drop within the bubble. The bubble then bounced around the bubble until it coalesced with the bulk liquid through a coalescence cascade with a geometric similarity given by  $We = 8$ .

## Acknowledgements

The equipment for this study was funded through an ARC LIEF grant.

## References

- [1] Elmore, P. A., Chahine, G. L. and Oğuz, H. N., Cavity and flow measurements of reproducible bubble entrapment following drop impacts. *Exp. Fluids*, **31**, 2001, 664–673.
- [2] Liow, J.L., Splash Formation by spherical drops, *J. Fluid Mech.*, **427**, 2001, 73–105.
- [3] Lohse, D. Bubble puzzles. *Physics Today*. **56(2)**, 2003, 36–41.
- [4] Manasseh R., Yoshida, S. and Rudman, M., Bubble formation processes and bubble acoustic signals. *Third International Conference on Multiphase flow*, 1998, Lyon, France, June 8-12.
- [5] Manzello, S.L, Yang, J.C. and Cleary, T.G. On the Interaction of a Liquid Droplet with a Pool of Hot Cooking Oil, *Fire Safety Journal*, **38(7)**, 2003, 651–659.
- [6] Morton, D. E., Rudman, M. J. and Liow, J. L., An investigation of the flow regimes resulting from splashing drops. *Phys. Fluids*, **12**, 2000, 747–763.
- [7] Oğuz H. N. and Prosperetti, A., Bubble entrapment by the impact of drops on liquid surfaces. *J. Fluid Mech.*, **219**, 1990, 143–179.
- [8] Pumphrey, H. C. and Elmore, P. A., The entrainment of bubbles by drop impacts. *J. Fluid Mech.*, **220**, 1990, 145–165.
- [9] Rein, M., The transitional regime between coalescing and splashing drops, *J. Fluid Mech.*, **306**, 1996, 145–165.
- [10] Thoroddsen, S. T., and Takehara, K., The coalescence cascade of a drop. *Phys Fluids*, **12(6)**, 2000, 1265–1267.
- [11] Thoroddsen, S. T., The ejecta sheet generated by the impact of a drop. *J. Fluid Mech.*, **451**, 2002, 373–381.
- [12] Weiss, D. A. and Yarin, A. L., Single drop impact onto liquid film: neck distortion, jetting, tiny bubble entrapment, and crown formation. *J. Fluid Mech.*, **385**, 1999, 229–254.
- [13] Worthington, A.M., On impact with a liquid surface. *Proc. Roy. Soc.*, **34**, 1882, 217–230.
- [14] Zeff, B.W., Kleber, B., Fineberg, J. and Lathrop, D.P., Singularity dynamics in curvature collapse and jet eruption on a fluid surface, *Nature*, **403**, 2000, 401–404.

## Scaling analysis and direct simulation of unsteady natural convection cooling of fluid with $Pr < 1$ in a vertical cylinder

Wenxian Lin<sup>1,2</sup> and S. W. Armfield<sup>1</sup>

<sup>1</sup>School of Aerospace, Mechanical & Mechatronics Engineering,  
The University of Sydney, NSW 2006, AUSTRALIA

<sup>2</sup>Solar Energy Research Institute, Yunnan Normal University,  
Kunming, Yunnan 650092, P. R. China

### Abstract

The unsteady natural convection cooling of fluid with  $Pr < 1$  in a vertical cylinder with an imposed lower temperature on vertical sidewalls is dominated by three distinct stages of development, *i.e.* the boundary-layer development stage adjacent to the sidewall, the stratification stage, and the cooling-down stage, respectively. Various scaling laws to describe the unsteady flow behavior at these respective stages are developed with scaling analysis and are verified and quantified by direct numerical simulation with selected values of the aspect ratio of the cylinder  $A$ , the Rayleigh number  $Ra$ , and the Prandtl number  $Pr$  in the ranges of  $1/3 \leq A \leq 3$ ,  $10^6 \leq Ra \leq 10^{10}$ , and  $0.01 \leq Pr \leq 0.5$ .

### Introduction

Cooling/heating a body of fluid in an enclosure via natural convection with an imposed temperature difference or heat flux on the enclosure boundary is widely encountered in nature and in engineering settings, and the understanding of its transient flow behavior is of fundamental interest and practical importance. In the past decades, extensive experimental, numerical, and analytical studies have been conducted on this issue, although mainly on the more specific case of a rectangular cavity with differentially heated sidewalls (see, *e.g.* [1, 2]).

Patterson and Imberger [3] used a scaling analysis in their pioneering investigation of the transient behavior that occurs when the opposing two vertical sidewalls of a two-dimensional rectangular cavity are impulsively heated and cooled by an equal amount. They devised a classification of the flow development through several transient flow regimes to one of three steady-state types of flow based on the relative values of  $Ra$ ,  $Pr$ , and  $A$ . This Patterson-Imberger flow model has since occupied the center stage of research into understanding natural convection flow in cavities, and numerous investigations subsequently focused on diverse aspects of the model (see, *e.g.* [4, 5, 6, 7]).

The majority of the past studies have focused on fluids with  $Pr \geq 1$  owing to their relevance in theoretical and practical applications. Natural convection flows with  $Pr < 1$  are very important as well, in such applications as the Earth's liquid core convection, crystal growth in semiconductors, melting processes, etc., not to mention those using air and other gases as the working medium. However, studies on unsteady natural convection flows of fluids with  $Pr \ll 1$  resulting from heating/cooling vertical boundaries, together with studies on the effect of  $Pr$  variation, are scarce. This scarcity, together with the apparently incomplete understanding of  $Pr \leq 1$  flows, motivates the current study.

### Scaling Analysis

Under consideration is the flow behavior of cooling a quiescent isothermal Newtonian fluid with  $Pr < 1$  in a vertical cylinder by unsteady natural convection due to an imposed fixed lower

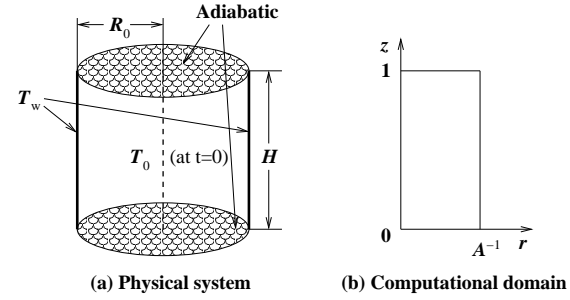


Figure 1: A sketch of the physical system considered and the computational domain used for numerical simulations.

temperature on the vertical sidewalls. The cylinder has a height of  $H$  and a radius of  $R_0$ , as sketched in Fig. 1. It is assumed that the fluid cooling is the result of the imposed fixed temperature  $T_w$  on the vertical sidewalls while all the remaining boundaries are adiabatic and all boundaries are non-slip, and the fluid in the cylinder is initially at rest and at a uniform temperature  $T_0$  ( $T_0 > T_w$ ). It is also assumed that the flows are laminar.

The governing equations of motion are the Navier-Stokes equations with the Boussinesq approximation for buoyancy, which together with the temperature transport equation can be written in the following two-dimensional form,

$$\frac{1}{R} \frac{\partial(RU)}{\partial R} + \frac{\partial V}{\partial Z} = 0, \quad (1)$$

$$\begin{aligned} \frac{\partial U}{\partial t} + \frac{1}{R} \frac{\partial(RUU)}{\partial R} + \frac{\partial(VU)}{\partial Z} = -\frac{1}{\rho} \frac{\partial P}{\partial R} \\ + \nu \left\{ \frac{\partial}{\partial R} \left[ \frac{1}{R} \frac{\partial(RU)}{\partial R} \right] + \frac{\partial^2 U}{\partial Z^2} \right\}, \end{aligned} \quad (2)$$

$$\begin{aligned} \frac{\partial V}{\partial t} + \frac{1}{R} \frac{\partial(RUV)}{\partial R} + \frac{\partial(VV)}{\partial Z} = -\frac{1}{\rho} \frac{\partial P}{\partial Z} \\ + \nu \left[ \frac{1}{R} \frac{\partial}{\partial R} \left( R \frac{\partial V}{\partial R} \right) + \frac{\partial^2 V}{\partial Z^2} \right] + g\beta(T - T_0), \end{aligned} \quad (3)$$

$$\frac{\partial T}{\partial t} + \frac{1}{R} \frac{\partial(RUT)}{\partial R} + \frac{\partial(VT)}{\partial Z} = \kappa \left[ \frac{1}{R} \frac{\partial}{\partial R} \left( R \frac{\partial T}{\partial R} \right) + \frac{\partial^2 T}{\partial Z^2} \right], \quad (4)$$

where  $U$  and  $V$  are the radial ( $R$ -direction) and vertical ( $Z$ -direction) velocity components,  $t$  is the time,  $P$  is the pressure,  $T$  is the temperature,  $g$  is the acceleration due to gravity,  $\beta$ ,  $\nu$  and  $\kappa$  are the thermal expansion coefficient, kinematic viscosity and thermal diffusivity of the fluid, respectively. The gravity acts in the negative  $Z$ -direction.

The flow considered here is dominated by three distinct stages of development, *i.e.* the boundary-layer development stage, the

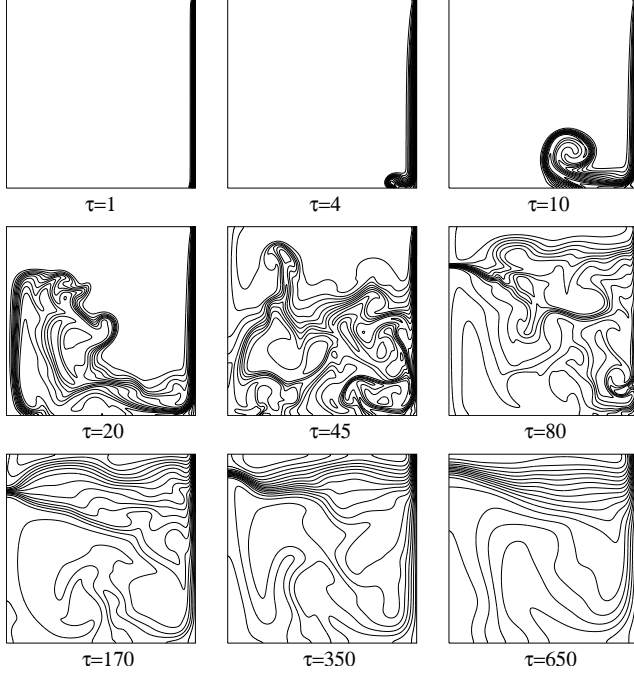


Figure 2: Numerically simulated temperature contours at the stages of the boundary-layer development (top row), the stratification (middle row), and the cooling-down (bottom row), respectively, for  $Ra = 10^8$ ,  $A = 1$ , and  $Pr = 0.1$ .

stratification stage, and the cooling-down stage, respectively, as illustrated in Fig. 2, where numerically simulated temperature contours are shown for the three stages for the specific case of  $Ra = 10^8$ ,  $Pr = 0.1$  and  $A = 1$ , where  $Ra$ ,  $Pr$  and  $A$  are defined as

$$Ra = \frac{g\beta(T_0 - T_w)H^3}{\nu\kappa}, \quad Pr = \frac{\nu}{\kappa}, \quad A = \frac{H}{R_0}.$$

In this case the boundary-layer development is seen in the temperature contours adjacent to the righthand, cooled, wall, with the boundary-layer development completed by around  $\tau = 10$ , where  $\tau$  is the dimensionless time, made dimensionless by  $H^2/(\kappa Ra^{1/2})$ . The cooled fluid ejected by the boundary layer acts to fill and stratify the domain, seen in the stratification stage, from  $\tau = 20$  to  $80$ . Finally the stratification is gradually reduced in the cooling-down stage of the flow, for  $\tau > 170$ . In this section, scaling relations will be developed for the relevant parameters characterizing the flow behavior at these respective stages of flow development.

The vertical boundary layer adjacent to the cooled sidewall experiences a start-up stage, followed by a short transitional stage before reaching a steady-state stage. The parameters characterizing the flow behavior at this development stage are the thermal boundary-layer thickness  $\Delta_T$ , the maximum vertical velocity  $V_m$ , the time  $t_b$  for the boundary-layer development to reach the steady state, and the Nusselt number  $Nu$  across the sidewall.

Heat is initially transferred out through the vertical wall from the fluid by conduction after the initiation of the flow, resulting in a vertical thermal boundary layer of thickness  $O(\Delta_T)$  adjacent to the wall, where at height  $Z$ , from Eq. (4), the balance between the inertial term  $O([T_0 - T_w]/t)$  and the conductive term  $O(\kappa[T_0 - T_w]/\Delta_T^2)$  dominates the flow, which gives,

$$\Delta_T \sim \kappa^{1/2} t^{1/2}, \quad (5)$$

or, in dimensionless form,

$$\delta_T = \frac{\Delta_T}{H} \sim Ra^{-1/4} \tau^{1/2}, \quad (6)$$

in which “ $\sim$ ” means “scales with” and  $\tau = t/(H/V_0)$  is the dimensionless time, where  $V_0 = \kappa Ra^{1/2}/H$  is the characteristic velocity scale. During this start-up stage, the dominant balance in Eq. (3) for  $Pr < 1$  is that between the inertia force  $O(V_m/t)$  and the buoyant force  $O(g\beta[T_0 - T_w])$ , which gives

$$V_m \sim g\beta(T_0 - T_w)t \sim \frac{Ra\nu\kappa}{H^3}t, \quad (7)$$

or, in dimensionless form,

$$v_m = \frac{V_m}{V_0} \sim Pr\tau, \quad (8)$$

After the start-up stage, the dominant balance at height  $Z$  in Eq. (4) gradually shifts from that between the inertial term  $O([T_0 - T_w]/t)$  and the conductive term  $O(\kappa[T_0 - T_w]/\Delta_T^2)$  to that between the inertial term and the convective term  $O(V_m[T_0 - T_w]/[H - Z])$ , until the latter balance becomes fully dominant and the thermal boundary-layer development then reaches its steady-state stage. The inertia-convective balance in Eq. (4) gives

$$\frac{T_0 - T_w}{t} \sim \frac{V_m[T_0 - T_w]}{H - Z}. \quad (9)$$

Using Eqs. (5) and (7), this leads to

$$t_b \sim \left[ \frac{H - Z}{g\beta(T_0 - T_w)} \right]^{1/2} \sim \frac{H^2}{\kappa Ra^{1/2} Pr^{1/2}} \left( 1 - \frac{Z}{H} \right)^{1/2}, \quad (10)$$

or, in dimensionless form,

$$\tau_b = \frac{t_b}{(H/V_0)} \sim \left( \frac{1 - z}{Pr} \right)^{1/2}, \quad (11)$$

which represents the local time scale for the thermal boundary layer at height  $Z$  to reach the steady state, where  $z = Z/H$  is the dimensionless vertical coordinate.

At time  $t_b$ , the thermal boundary layer at height  $Z$  reaches its steady-state thickness scale  $\Delta_{T,b}$ , which, from Eq. (5), is as follows,

$$\Delta_{T,b} \sim \kappa^{1/2} \left[ \frac{H - Z}{g\beta(T_0 - T_w)} \right]^{1/4} \sim \frac{H^{3/4} (H - Z)^{1/4}}{Ra^{1/4} Pr^{1/4}}, \quad (12)$$

or, in dimensionless form,

$$\delta_{T,b} = \frac{\Delta_{T,b}}{H} \sim \left( \frac{1 - z}{Pr Ra} \right)^{1/4}, \quad (13)$$

and the steady-state vertical velocity scale  $V_{m,b}$  at height  $Z$  within this thermal boundary layer is, from Eq. (7), as follows,

$$V_{m,b} \sim \frac{\kappa Ra^{1/2} Pr^{1/2}}{H} \left( 1 - \frac{Z}{H} \right)^{1/2}, \quad (14)$$

or, in dimensionless form,

$$v_{m,b} = \frac{V_{m,b}}{V_0} \sim [(1 - z)Pr]^{1/2}. \quad (15)$$

The heat transfer across the vertical sidewall is represented by the following local Nusselt number  $Nu$  at height  $Z$ ,

$$Nu \sim \left[ \frac{R_0}{(T_0 - T_w)} \frac{\partial T}{\partial R} \right]_{R=R_0}. \quad (16)$$

Therefore, during the start-up stage,

$$Nu \sim \frac{R_0}{\Delta_T} \sim \frac{R_0}{\kappa^{1/2} t^{1/2}} \sim \frac{1}{A} Ra^{1/4} \tau^{-1/2}, \quad (17)$$

and at the steady-state stage,

$$Nu_b \sim \frac{R_0}{\Delta_{T,b}} \sim \frac{(PrRa)^{1/4}}{A(1-Z/H)^{1/4}} \sim \frac{1}{A} \left( \frac{PrRa}{1-z} \right)^{1/4}, \quad (18)$$

Equations (6), (8), and (17) clearly show that during the start-up stage, the boundary-layer development on the vertical sidewalls is independent of  $z$ , however, as shown by (13), (15), and (18), the boundary-layer development and the heat transfer across the vertical sidewall become  $z$  dependent at the steady-state stage of the boundary-layer development.

Once the boundary layer is fully developed, the fluid in the cylinder is gradually stratified by the cooled fluid ejected from the boundary layer, starting from the bottom of the cylinder. The time  $t_s$  for the full stratification of the whole fluid in the cylinder will be at the moment when the volume of the cooled fluid ejected from the boundary layer is equal to the volume of the cylinder. The rate of flow of fluid through the boundary layer is characterized by  $\Delta_{T,b} V_{m,b}$ , and therefore the time to full stratification is characterized by

$$t_s \sim \frac{HR_0}{\kappa Ra^{1/2}} \left( \frac{Ra}{Pr} \right)^{1/4}, \quad (19)$$

which is in dimensionless form as follows,

$$\tau_s = \frac{t_s}{(H/V_0)} \sim \frac{1}{A} \left( \frac{Ra}{Pr} \right)^{1/4}. \quad (20)$$

After the full stratification, the fluid in the cylinder is continually cooled down until the whole body of fluid has the same temperature as that imposed on the sidewalls. The appropriate parameters to characterize this cooling-down process are the time  $t_f$  for the fluid to be fully cooled down, the average fluid temperature  $T_a(t)$  over the whole volume of the cylinder at time  $t$ , and the average Nusselt number on the cooling wall.

As the fluid cooling-down is achieved by maintaining a fixed temperature  $T_w$  on the vertical sidewalls while keeping the top and bottom boundaries adiabatic, all the heat used to fully cool down the fluid in the cylinder must pass through the sidewalls, and then energy conservation in the cylinder requires that,

$$\rho c_p V_c (T_0 - T_w) \sim t_f A_s k \frac{(T_0 - T_w)}{\Delta_{T,b}}, \quad (21)$$

where  $V_c = \pi R_0^2 H$  is the volume of the fluid in the cylinder,  $A_s = 2\pi R_0 H$  is the surface area of the sidewall,  $k$  is the thermal conductivity of fluid, and  $\Delta_{T,b}$  is the average thermal boundary-layer thickness which is calculated as follows,

$$\Delta_{T,b} = \frac{1}{H} \int_0^H \Delta_{T,b} dZ. \quad (22)$$

Therefore,  $t_f$  has the following scaling relation,

$$t_f \sim \frac{R_0 \Delta_{T,b}}{\kappa} \sim \frac{R_0 H}{\kappa (PrRa)^{1/4}}, \quad (23)$$

where  $\kappa = k/(\rho c_p)$ , which is in dimensionless form as follows,

$$\tau_f = \frac{t_f}{(H/V_0)} \sim \frac{1}{A} \left( \frac{Ra}{Pr} \right)^{1/4}. \quad (24)$$

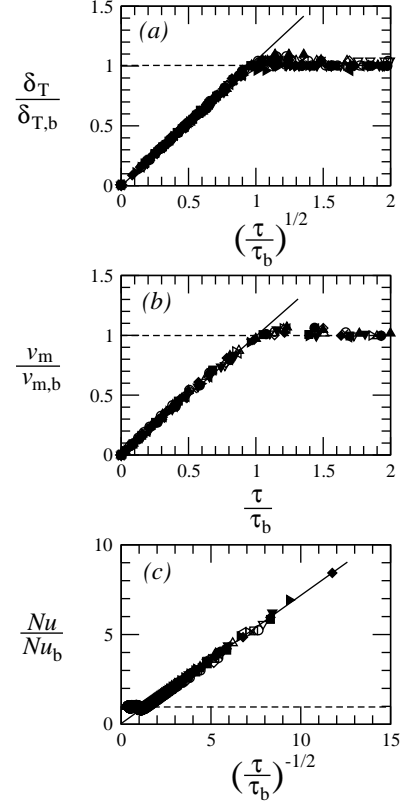


Figure 3: Numerical results for (a)  $\delta_T / \delta_{T,b}$  plotted against  $(\tau / \tau_b)^{1/2}$ ; (b)  $v_m / v_{m,b}$  plotted against  $\tau / \tau_b$ ; and (c)  $Nu / Nu_b$  plotted against  $(\tau / \tau_b)^{-1/2}$ . solid line, linear fit for the start-up stage; dashed line, linear fit for the steady-state stage.

The decay of the average fluid temperature  $T_a(t)$  is expected to obey an exponential relation[8], that is,

$$\frac{T_a(t) - T_0}{T_0 - T_w} = e^{-f(Ra, Pr, A)t} - 1, \quad (25)$$

where  $f(Ra, Pr, A)$  is some function of  $Ra$ ,  $Pr$ , and  $A$ , which is in dimensionless form as follows

$$\theta_a(\tau) = e^{-C_f A \left( \frac{Pr}{Ra} \right)^{1/4} \tau} - 1, \quad (26)$$

where  $C_f$  is a constant of proportionality which will be determined below by numerical results.

### Numerical results

In this section, the scaling relations obtained above will be validated and quantified by a series of direct numerical simulations with selected values of  $A$ ,  $Ra$ , and  $Pr$  in the ranges of  $1/3 \leq A \leq 3$ ,  $10^6 \leq Ra \leq 10^{10}$ , and  $0.01 \leq Pr \leq 0.5$ . A total of 12 simulation runs have been carried out for this purpose. Specifically, results have been obtained with  $Ra = 10^6$ ,  $10^7$ ,  $10^8$ ,  $10^9$ , and  $10^{10}$ , while keeping  $A = 1$  and  $Pr = 0.1$  unchanged, to show the dependence of the scaling relations on  $Ra$  (Runs 1-5); the runs with  $A = 1/3$ ,  $1/2$ ,  $1$ ,  $2$ , and  $3$ , while keeping  $Ra = 10^8$  and  $Pr = 0.1$  unchanged, have been carried out to show the dependence on  $A$  (Runs 6-7, 3, and 8-9); and the runs with  $Pr = 0.01$ ,  $0.05$ ,  $0.1$ , and  $0.5$ , while keeping  $Ra = 10^8$  and  $A = 1$  unchanged, have been carried out to show the dependence on  $Pr$  (Runs 10-11, 3, and 12), respectively.

Detailed information about the numerical algorithm, mesh construction, initial and boundary conditions, and numerical accuracy tests can be found in [5, 6].

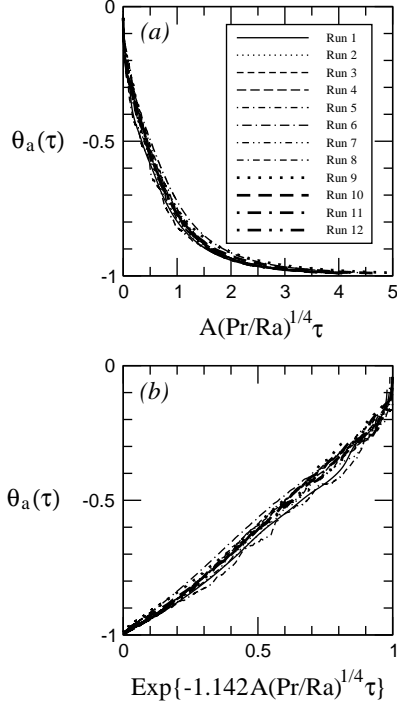


Figure 4: Numerical results for  $\theta_a(\tau)$  plotted against (a)  $A(Pr/Ra)^{1/4}\tau$  and (b)  $e^{-1.142A(Pr/Ra)^{1/4}\tau}$  for all simulation runs.

The numerical results for  $\delta_T$ ,  $v_m$ , and  $Nu$  at the boundary-layer development stage are plotted as a ratio with respect to their steady-state values against the scaled times  $\tau/\tau_b$  in Fig. 3. The results for  $\tau/\tau_b < 1$  fall onto a straight line, confirming the scaling laws at the start-up stage, while the results for  $\tau/\tau_b \geq 1$  fall onto a horizontal line, confirming the scaling laws at the steady-state stage. The numerically quantified scaling laws are therefore as follows,

$$\tau_b = 2.395 \left( \frac{1-z}{Pr} \right)^{1/2}, \quad (27)$$

$$\delta_{T,b} = 4.845 \left( \frac{1-z}{PrRa} \right)^{1/4}, \quad (28)$$

$$v_{m,b} = 0.872[(1-z)Pr]^{1/2}, \quad (29)$$

$$Nu_b = \frac{0.519}{A} \left( \frac{PrRa}{1-z} \right)^{1/4}, \quad (30)$$

$$\overline{Nu}_b = \frac{0.658}{A} (PrRa)^{1/4}. \quad (31)$$

$$\delta_T = 3.131Ra^{-1/4}\tau^{1/2}, \quad (32)$$

$$v_m = 0.364Pr\tau, \quad (33)$$

$$Nu = \frac{0.803}{A} Ra^{1/4}\tau^{-1/2}, \quad (34)$$

$$\overline{Nu} = \frac{1.018}{A} Ra^{1/4}\tau^{-1/2}. \quad (35)$$

The numerical results show that  $\tau_s$  can be well approximated by the following expression

$$\tau_s = \frac{0.313}{A} \left( \frac{Ra}{Pr} \right)^{1/4}. \quad (36)$$

which clearly demonstrate that the scaling law (20) is correct for the stratification stage.

The numerical results also show that  $\tau_f$  can be well approxi-

mated by the following expression

$$\tau_f = \frac{4.031}{A} \left( \frac{Ra}{Pr} \right)^{1/4}, \quad (37)$$

where  $\tau_f$  was determined as the time at which  $\theta_a(\tau_f) = -0.99$ , which clearly demonstrate that the scaling law (24) is correct for the cooling-down stage. Therefore, the full expression for the time decay of  $\theta_a$ , Eq. (26), is obtained as

$$\theta_a(\tau) = e^{-1.142A\left(\frac{Pr}{Ra}\right)^{1/4}\tau} - 1. \quad (38)$$

The numerical results presented in Fig. 4 show that all sets of data fall onto a single curve, indicating that the scaling relation (26) is correct.

## Conclusions

The cooling down behavior of a fluid contained in a vertical cylinder subjected to isothermal boundary condition on the vertical walls is examined via scaling analysis and direct numerical simulation. Scaling laws have been obtained for the development time and properties of the initial vertical thermal boundary layer, of the stratification time and of the full cooling down time. The scalings have been obtained for  $Pr < 1$ , yielding different relations from those obtained for  $Pr > 1$ . For instance the scaling relations for the time development of the boundary layer, stratification and full cooling down stages are  $\tau_b \sim (1-z)^{1/2}Pr^{-1/2}$ ,  $\tau_s \sim Ra^{1/4}Pr^{-1/4}/A$ ,  $\tau_f \sim Ra^{1/4}Pr^{-1/4}/A$  respectively for  $Pr < 1$ , and  $\tau_b \sim (1-z)^{1/2}$ ,  $\tau_s \sim Ra^{1/4}/A$ ,  $\tau_f \sim Ra^{1/4}/A$  respectively for  $Pr > 1$  [6]. It is seen that for  $Pr > 1$  the scaled quantities are independent of  $Pr$ , while for  $Pr < 1$  they show a  $Pr$  dependency.

## Acknowledgements

The financial support of the Australian Research Council, via an Australian Postdoctoral Fellowship (Grant No. DP0449876), the National Natural Science Foundation of China (Grant No. 10262003), and the Natural Science Foundation of Yunnan Province of China (Key Project, Grant No. 2003E0004Z) are gratefully acknowledged.

## References

- [1] Gebhart, B., Jaluria, Y., Mahajan, R.L. and Sammakia, B., *Buoyancy-Induced Flows and Transport*, Hemisphere, 1988.
- [2] Hyun, J.M., Unsteady bouyant convection in an enclosure, *Adv. Heat Transfer*, **24**, 1994, 277–320.
- [3] Patterson, J.C. and Imberger, J., Unsteady natural convection in a rectangular cavity, *J. Fluid Mech.*, **100**, 1980, 65–86.
- [4] Bejan, A., *Convection Heat Transfer* (2nd Edn.), John Wiley & Sons, 1995.
- [5] Lin, W. and Armfield, S.W., Direct simulation of natural convection cooling in a vertical circular cylinder, *Int. J. Heat Mass Transfer*, 1999, **42**, 4117–4130.
- [6] Lin, W. and Armfield, S.W., Natural convection cooling of rectangular and cylindrical containers, *Int. J. Heat Fluid Flow*, **22**, 2001, 72–81.
- [7] Lin, W. and Armfield, S.W., Long-term behavior of cooling fluid in a rectangular container, *Phys. Rev. E*, **69**, 2004, 056315.
- [8] Mills, A.F., *Heat Transfer* (2nd Edn.), Prentice Hall, 1999.



## Effects of Axial Pulsing on Unconfined Vortex Breakdown

S. Khalil, K. Hourigan and M.C. Thompson

Fluid Laboratory for Aeronautical and Industrial Research (FLAIR)

Department of Mechanical Engineering PO BOX 31

Monash University, Clayton, Victoria 3800, AUSTRALIA

### Abstract

The experimental investigation undertaken explores the response of low Reynolds number ( $300 < Re < 1000$ ) unconfined swirling jets undergoing vortex breakdown to axial pulsing. In particular particle visualisation in conjunction with 2-D PIV has allowed a detailed examination of the effect of axial pulsing on shear-layer flow structures and vortex breakdown, as the pulsing frequency and amplitude is varied. A range of Reynolds numbers and swirl numbers is considered. Extremely promising results have been obtained revealing that pulsing at the natural shedding frequency results in substantial downstream shift of the mean breakdown position. Furthermore, application of low-level forcing at the natural frequency intensifies the shear-layer vortices considerably.

### Introduction

Experimental research into vortex breakdown and vortex breakdown control techniques has been undertaken for the past 50 and 40 years respectively [2,8]. The importance of understanding this phenomenon, and how to control it, is of immense importance for applications such as heat exchangers and combustion control, but none more pronounced than in the aeronautical industry.

Studies have shown that the swirl number, defined as the ratio of azimuthal to axial velocity, is a useful parameter to determine whether vortex breakdown will occur [1]. Either slowing the azimuthal velocity or increasing the axial velocity can lower the swirl number. This can have a stabilizing effect by delaying vortex breakdown, or even lead to the recreation of the vortical core after breakdown has occurred [8]. Vortex breakdown can therefore be considered as a reversible phenomenon with respect to its ability to pass between the pre-breakdown and post-breakdown states. However, it should be kept in mind that the transition to the breakdown state is hysteretic and to re-establish the pre-breakdown state may require the swirl number to drop well below the critical value for the onset of breakdown.

Controlling this phenomenon by introducing well-defined perturbations into the flow field by implementing unsteady blowing techniques has been conducted previously on delta wings with great success. As pointed out in a review paper by [9], Werle (1954) was the first investigator to implement blowing as a means of controlling breakdown. Werle found that blowing downstream along the core delayed or eliminated breakdown, while blowing upstream caused breakdown to spontaneously occur or to move further upstream. Further studies of vortex breakdown control techniques applied to the flow over delta wings by [3,11,13] have revealed the most effective positions to implement control mechanisms are those close to the point of vortex conception and downstream of breakdown. The unsteady nature of breakdown, especially at higher Reynolds number, introduces difficulties in positioning a downstream control device; hence, in practice, the optimum control location is

upstream of breakdown or at the point of conception of the vortex core.

Although both continuous and pulsed blowing or suction cause a delay in the formation of the breakdown structure, there are certain advantages displayed by the pulsed approach. [10] concluded from their investigation of continuous blowing along the core that the downside of that technique is the large amount of energy required for its effective implementation. [12,13] experimented with both steady and pulsed trailing-edge blowing and found that intermittent blowing during the upward pitching of a delta wing was the most effective means of shifting the vortex breakdown location downstream. [4] conducted several experimental investigations into control methods including tangential suction and blowing, steady suction, and alternate tangential suction and blowing, all applied along the leading edge. Although all the above-mentioned control techniques delayed breakdown, the most effective was found to be alternating blowing and suction. [5] studied the effects of oscillatory jets exiting through spanwise slots along a NACA 0015 airfoil. Their results demonstrated "*the effectiveness of pulsed blowing as a tool to increase lift and reduce drag* (by enhancing the wake profile), *especially when compared to the relative ineffectiveness of steady blowing under similar conditions.*" [6] showed that pulsed blowing parallel to the leading edge was almost twice as effective in delaying vortex breakdown as continuous blowing, with the best results achieved at the natural shedding frequency of the shear layer. Further advantages of unsteady pulsing or blowing lies in the reduced energy use and the ability to maintain an unchanged mean jet momentum or mass flow as required/desired.

In this study employing unsteady pulsing to control breakdown of an effectively unconfined vortex core, an initial study of the shear layer and corresponding shedding frequency was undertaken. Subsequently, an examination of the resulting breakdown structure and its movement, both locally and globally, was carried out. The primary aim of this investigation was to uncover which frequencies and amplitudes of pulsing create the greatest movement of the vortex-breakdown (upstream) stagnation point.

### Experimental Setup

The swirling flows generated in this experiment were created by a similar method to that of [1,15], and consisted of a pressure-driven swirling water jet which discharges into a large tank. The swirl is imparted by means of an electric servomotor, which rotates a honeycomb within a settling chamber. A schematic of the apparatus is shown in Figure 1.

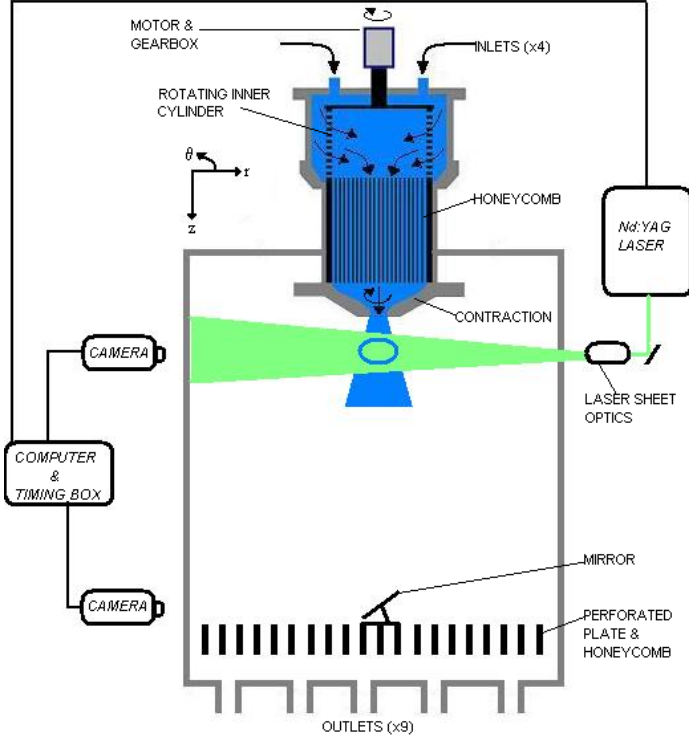


Figure 1: Experimental setup. Note: Laser sheet is rotated for both horizontal and vertical plane cross-sections.

A smooth axial velocity is generated by a laminar pulse-less disc pump, creating a closed circuit with accurate control of axial flow rates. It also enables a more realistic simulation of a pulsing mechanism, which could be used in combustion chambers or in flight. Pulsing is achieved via an inline computer-controlled proportional-lift solenoid valve. Previous studies (see [9]) have examined steady and unsteady suction and blowing of separate flows, which join the vortical structure somewhere along its path to control vortex breakdown. This experiment is novel in that it pulses the actual vortical structure in the axial direction at the point of generation. The flow rate, which in turn determines the axial Reynolds number, is controlled to within  $\pm 1\%$  by a frequency inverter connected to the disc pump and an electronic flow meter.

The azimuthal velocity component is imparted to the flow via the vortex generator. The vortex generator consists of a motor and two concentric cylinders, similar to that used by [1]. The underlying principle is to set the axially flowing fluid into a solid body rotation before passing through a contraction. The fluid in the outer cylinder passes through the upper part of inner cylinder through an arrangement of holes. In order to set the flow into laminar solid-body rotation, (i.e. a Rankine vortex), the flow is then passed through a honeycomb located in the lower part of the rotating inner cylinder. The swirling jet then passes through a smooth converging nozzle, which is attached to the outer cylinder and is fixed, i.e. non-rotating. In order to avoid flow separation, the contraction zone is designed according to Mikhail (1979)'s optimum contraction design method. The exit diameter of the contraction zone is  $D = 2R = 39.5\text{mm}$ . A frequency inverter and servomotor control the frequency of rotation to within  $\pm 0.5\%$ .

The vortex generator is partly submerged in a square cross-section ( $650\text{mm} \times 650\text{mm} \times 1500\text{mm}$ ) transparent Perspex tank into which the swirling jet is discharged. Such a configuration allows the simulation of an almost unconfined vortex due to the large ratio of tank to jet area ( $\sim 345$ ). Recirculation currents were found to be almost non-existent in all cases.

An intercooler setup was also incorporated to ensure minimal temperature gradients within the tank to avoid thermal convection currents. The intercooler involved passing the cooler outflow over the warmer inflow via an intercooler core. In order to ensure slow-moving outlet flow, and to minimise pressure gradients caused by the outlet pipes, a perforated plate, acting as a honeycomb, is placed at the bottom of the test tank. This also had the advantage of retarding any whirlpool effect from occurring. Water consistency and temperature uniformity was vigilantly monitored with highly sensitive thermometers at specified locations around the whole circuit. The maximum temperature difference between the swirling jet and fluid within the test tank was found to be  $0.5^\circ\text{C}$ .

In order to characterise this experiment the following non-dimensional variables were used based on a cylindrical  $(r, \theta, z)$  coordinate system. The swirl number  $S$  provides a measure for the ratio of azimuthal velocity  $U_\theta$  and axial velocity  $U_z$ .

$$S = \frac{2U_{\theta\max}}{U_{z\max}} = \frac{2U_\theta(r=R/2)}{U_z(r=0)}. \quad (1)$$

At the critical swirl number,  $S_c \sim 1.3$ , vortex breakdown is found to occur independent of the Reynolds number and nozzle diameter [1]. The Reynolds number characterises the axial flow component, and is based on the jet diameter  $D = 2R$  and average axial velocity  $\bar{U}_z$  which is extracted from the mean mass flow rate  $\bar{m}$ .

$$Re = \frac{2\bar{U}_z R}{\nu}. \quad (2)$$

Furthermore, the Strouhal number non-dimensionalises the frequency of pulsing,  $f$ ,

$$St = \frac{2fR}{\bar{U}_z}. \quad (3)$$

The sinusoidal variation in mass flow during pulsing is characterised by the *Peak Mass Flow Variation* (PMFV).

$$m_v = \frac{\bar{m} - m_{\min}}{\bar{m}} = \frac{m_{\max} - \bar{m}}{\bar{m}}. \quad (4)$$

Here,  $m_{\min}$  and  $m_{\max}$  are the minimum and maximum mass flow rates, respectively.

### Data Acquisition

For both visualisation and PIV measurements, the water was seeded with spherical polyethylene ( $25\mu\text{m}$ ) particles with an SG of 0.9. In order to create minimal disturbance to the flow the particles were continuously feed into the flow as far upstream as possible. The injection rate was controlled via a piston-controlled injection chamber and a gravity-feed device. Particles were illuminated via a combination of stage lights and lasers. For PIV, the particles were illuminated using a laser sheet generated by a frequency doubled Nd:YAG laser at  $532\text{nm}$  and  $400\text{mJ}$  in  $5\text{ns}$  bursts.

Flow visualisations were conducted using a 5 mega-pixel Minolta digital camera and a Kodak ES4 CCD 4 mega-pixel camera, which was also used to acquire the raw PIV images. The ES4 CCD camera was used at both  $30\text{hz}$  ( $1024 \times 1024$  pixels) and

double shutter mode at 5ms and an 8Hz sequence between image pairs. PIV was used for quantitative measurements of axial and swirl profiles in order to obtain the swirl number.

PIV was performed using a cross-correlation type analysis, with the dynamic range enhanced using an iterative approach to select the Sample Window Size (SWS) by starting at 128 x 128 to a final window size of 16 x 16 with a an overlap of 50%. By performing the analysis in this fashion the largest displacement vectors are determined by using a large SWS. The accuracy and spatial resolution is increased by then reducing the SWS and offsetting successive pairs of sample windows by the displacement calculated from the previous iteration. Erroneous vectors are rejected by comparing them to a local fit of the data (in an absolute sense) and any vector which deviates from that fit (by more then 2 pixels in this case) are rejected and replaced by the local fit. Vorticity is calculated using a second-order least-squares fit in X and Y (6 terms) and then analytically differentiating this equation to obtain the derivatives i.e. the vorticity.

## Results & Discussion

An examination of the (helical) vortex structures forming at the edge of the unforced swirling jet was conducted by using long exposure (0.5sec) images spanning a period of 120 seconds. A sample frame is shown in Figure 2.

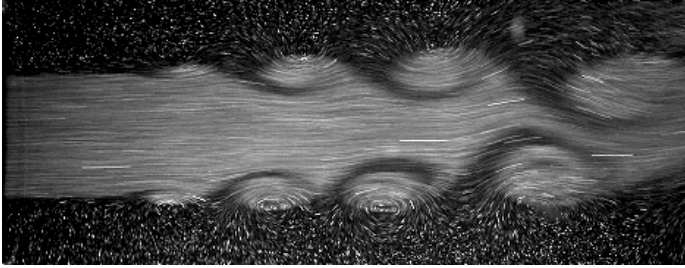


Figure 2: Shear layer shedding of a swirling Jet at  $Re=900$ ,  $S=0.3$ .

A spectral analysis of the data revealed that the shear-layer Strouhal number is independent of the swirl number, in agreement with [7]. Furthermore, over the Reynolds number range tested, the Strouhal number is independent of Reynolds number to within two standard deviations of the mean and is fixed at  $St = St_n = 0.78 \pm 0.01$ , as shown in Figure 3. The shear layer first sheds at approximately one to two nozzle diameter downstream in all cases and appeared to periodically shed in small bursts with durations and delays of the same order as the natural shedding frequency of the structure.

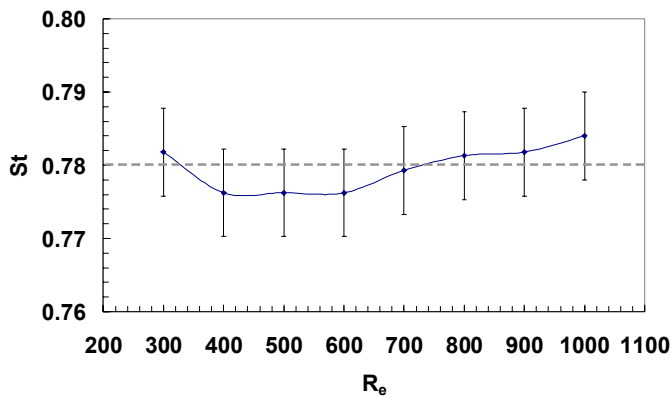


Figure 3: Shear-layer Strouhal number as a function of Reynolds number.  $S_m$  is shown by a dashed line.

By sinusoidally pulsing the swirling jet mass flow rate  $m$ , in the form  $m = \bar{m} + (m_{\max} - \bar{m}) \sin(2\pi f t)$ , it is possible to alter the vorticity within the shear layer (see Figure 4), hence altering the vortex-shedding frequency at the point of its conception.

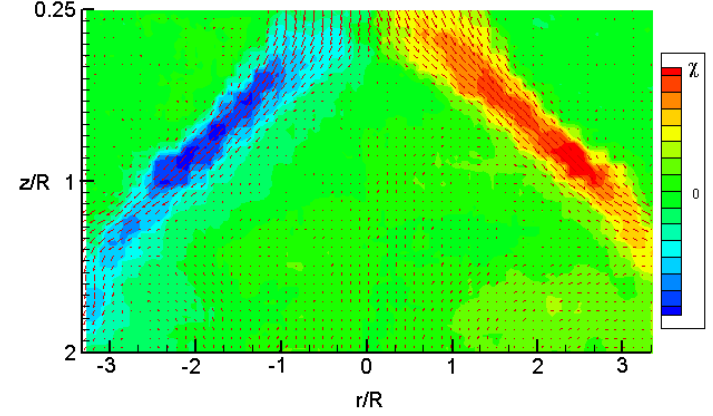


Figure 4: Vorticity  $\chi$  plot of a swirling jet undergoing breakdown with no pulsing ( $m_0=0$ ) at  $Re=600$   $S=1.36$ .

The vortex shedding frequency was easily controlled when pulsing was conducted at  $S_t < 2S_m$ . The shedding frequency of the swirling jet was found to lock onto low frequencies up to approximately twice the un-pulsed or natural frequency of shedding. Above this critical value, the flow below the stagnation point where the shedding becomes apparent is unresponsive to the imposed perturbation and the jet sheds at its natural frequency independent of the amplitude of the perturbation. As is the case with most stability problems, the shear layer is unreceptive when pulsing is conducted far from that of the natural frequency.

The effect of pulsing at various Strouhal numbers on breakdown was determined by flow visualisation. The breakdown stagnation point  $Z_b$  was found to move further downstream as the pulsing Strouhal number approached the natural Strouhal shedding frequency (see Figure 5) in agreement with the experiments conducted by [6] using delta wings. To obtain significant downstream movement of the breakdown position, pulsing must be conducted at  $St = St_n \pm 10\%$ .

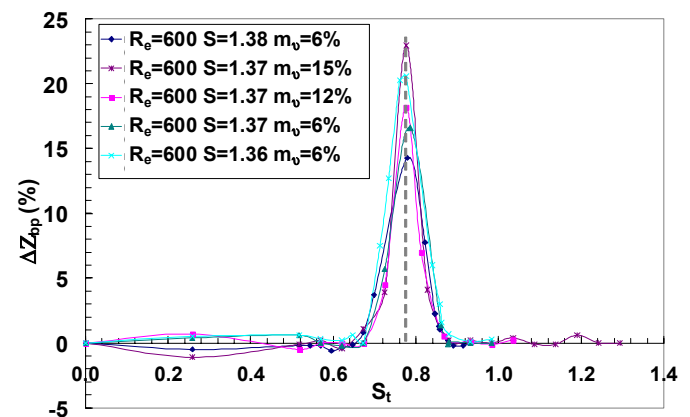


Figure 5: Pulsed breakdown position  $Z_{bp}$  as a percentage of the un-pulsed breakdown position  $Z_b$  (where:  $\Delta Z_{bp} = (Z_{bp} - Z_b)/Z_b$ ) for various Swirl and PMFV values at  $Re=600$ . Similar results occur for the other Reynolds numbers tested.

Some key findings are that axial pulsing within the hysteretic range at which breakdown exists has the ability to revert the core to the non-breakdown state, with PMFV values as low as  $m_0=6-12\%$ . An established breakdown moves downstream as PMFV values increase, however, the shift begins to plateau at  $m_0>30-40\%$ . For higher amplitudes, large fluctuations in the stagnation



point position are observed. It is not uncommon to experience relative shifts of up to  $\Delta Z_{bp} = 50\%$  at  $S = S_c$  and  $St = 0.78$ , with higher swirl stabilizing the structure, in agreement with [7], and lowering  $\Delta Z_{bp}$ . Flow visualisations at  $St = 0.78$  (Figure 6) shows that axially pulsing the breakdown at this frequency increases the concentrations of vorticity within the shear layer and excites the shear-layer resonance.

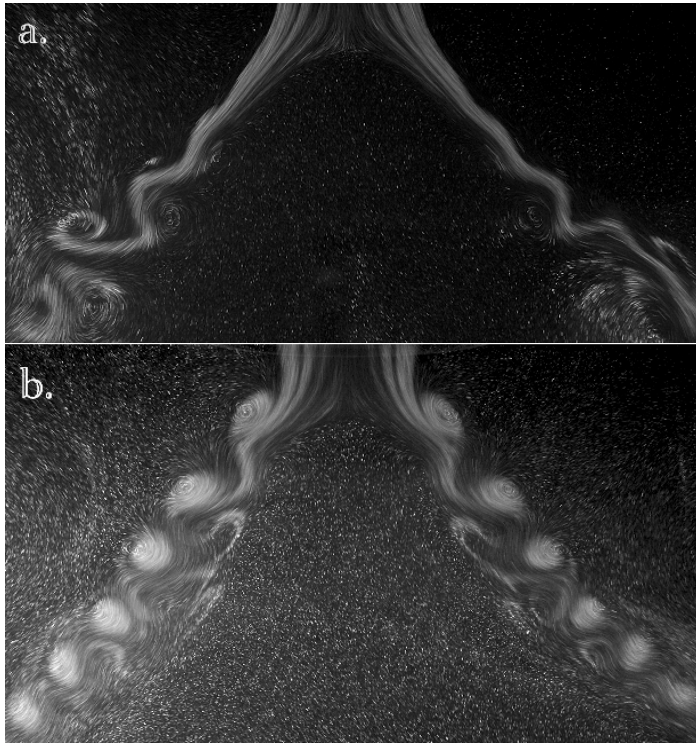


Figure 6: (a) Unpulsed breakdown  $m_0=0$  at  $Re=600$ ,  $S=1.41$ ; (b) pulsed breakdown  $m_0=6\%$ ,  $St=0.78$  at  $Re=600$ ,  $S=1.41$  clearly showing increased vorticity concentrations in the shear layer resulting in increased  $\Delta Z_{bp}$ .

The modifications to the shear layer structure and the highly periodic shedding at  $St = 0.78 \pm 10\%$  has the effect of forcing the stagnation point further downstream. From observations it was also interesting to see that the stagnation point without pulsing was consistently further upstream than the axial position at which the shear layer begins to shed. Whereas when axial pulsing was applied at  $St = 0.78 \pm 10\%$ , the axial location at which shedding begins moved further upstream closer to the jet outlet consistently higher than the stagnation point which moved downstream. The reason for the stagnation point movement downstream could be that the shear layer vorticity concentrations effectively modify the mean axial and azimuthal velocity profiles so that breakdown is delayed. This hypothesis is still under investigation.

## Conclusions

The application of axially pulsing to swirling jets undergoing vortex breakdown can have some profound effects on the resulting structure. The following can be concluded from this preliminary experimental investigation:

1. For an unforced swirling jet, the Strouhal number of shedding is independent of Reynolds number and swirl number, and is fixed at  $St = St_n (= 0.78)$ .
2. For the forced case, the shedding frequency of the swirling jet was found to lock onto low frequencies up to approximately  $2St_n$ . Above this critical value, the flow below the stagnation point is not receptive to the higher frequency pulsing and the jet sheds at its natural frequency, independent of the amplitude of the forcing.

3. To obtain significant downstream movement of the breakdown position, pulsing must be conducted close to the natural frequency, i.e., at  $St = St_n \pm 10\%$ .

4. Axial pulsing within the hysteretic range over which breakdown exists has the ability to destroy the breakdown structure all together with PMFV values as low as  $m_0=6-12\%$ . It is possible to shift the breakdown structure by up to 50% at  $S = S_c$  and  $St = 0.78$ .

5. The increased vorticity concentrations within the shear layer and the highly periodic shedding at  $St=0.78 \pm 10\%$  has the effect of forcing the stagnation point further downstream, delaying breakdown as shedding now occurs closer to the nozzle exit.

## References

- [1] Billant, P., J.-M. Chomaz, et al. (1998). *Experimental study of vortex breakdown in swirling jets*. Journal of Fluid Mechanics **376**(Dec 10): 183-219.
- [2] Delery, J. M. (1994). *Aspects of vortex breakdown*. Prog. Aerospace Sci. **30**: 1-59.
- [3] Er-El, J. and A. Seginer (1986). *Effects of spanwise blowing on pressure distribution and leading-edge vortex stability*. 15th Congress of the International Council of the Aeronautical Sciences, London, ICAS-86-2.5.1, September 1986.
- [4] Gu, W., O. Robinson, et al. (1993). *Control of vortices on a delta wing by leading-edge injection*. AIAA J **31**(7): 1177-1186.
- [5] Hites, M., H. Nagib, et al. (2002). *Lift enhancement using pulsed blowing at compressible flow conditions*. Israel (TAU), 306, Moscone Center.
- [6] Johari, H. and J. Moreira (1996). *Delta wing vortex manipulation using pulsed and steady blowing during ramp-pitching*. J Aircraft **33**(2): 452-453.
- [7] Loiseleux, T., J. M. Chomaz, et al. (1998). *Effect of swirl on jets and wakes: Linear instability of the Rankine vortex with axial flow*. Physics of Fluids **10**(5): 1120-1134.
- [8] Lucca-Negro, O. and T. O'Doherty (2001). *Vortex breakdown: A review*. Progress in Energy and Combustion Science **27**(4): 431-481.
- [9] Mitchell, A. M. and J. Delery (2001). *Research into vortex breakdown control*. Progress in Aerospace Sciences **37**(4 May): 385-418.
- [10] Mitchell, A. M., P. Molton, et al. (2000). *Control of vortex breakdown by along-the-core blowing*. AIAA Fluids 2000.
- [11] Owens, D. B. and J. Perkins (1995). *Vortex suppression on highly-swept wings by suction boundary-layer control*. 33rd AIAA Aerospace Sciences Meeting and Exhibit, Reno, NV.
- [12] Vorobieff, P. V. and D. O. Rockwell (1996). *Multiple-actuator control of vortex breakdown on a pitching delta wing*. AIAA J **34**(10): 2184-2186.
- [13] Vorobieff, P. V. and D. O. Rockwell (1998). *Vortex breakdown on pitching delta wing: control by intermittent trailing-edge blowing*. AIAA J **36**(4): 585-589.
- [14] White, F. M. (1999). *Fluid Mechanics*. Boston, U.S.A., McGraw-Hill.
- [15] Wu, M. M., A. Garcia, et al. (1992). *Instabilities in a swirling jet*. Bull. Am. Phys. Soc. **37**(8): 1789-1790.

## The Aerodynamic Forces on a Series of Tennis Balls

F. Alam, S. Watkins and A. Subic

School of Aerospace, Mechanical & Manufacturing Engineering  
 RMIT University, Melbourne, VIC 3083, AUSTRALIA

### Abstract

The aerodynamic properties of typical tennis balls as a function of Reynolds numbers have been reported in the open literature. However, the results are somewhat different as each study indicated differences in drag coefficients. The primary objective of this paper is to study the aerodynamic drag of tennis balls used in major tournaments around the world. Results presented in this paper are at steady conditions (no spin involved).

### Introduction

Tennis is one of the most popular games in the world. The International Tennis Federation (ITF) is actively considering how to slow down the speed of tennis balls in order to make the game more attractive to spectators by increasing the diameter of the ball or some other way. The aerodynamic properties of a tennis ball will play a vital role in this process. However, not many studies have been conducted on aerodynamics of tennis balls. Several studies on the aerodynamic drag and lift of a typical tennis ball as a function of Reynolds numbers have been reported in the open literature (Mehta and Pallis [1], Chadwick and Haake [2], Cooke [3], Stepanek [4]). There is a significant variation of aerodynamic drag coefficients and it is not clear if this variation is due to experimental techniques or to other effects such as the relative position of the seam. It is well known that aerodynamic properties are significantly affected by the spin of a ball thus the motion and flight path of the ball. Although several studies on aerodynamic drag, lift and surface (fuzz) effects have been conducted there are still gaps in understanding. Therefore, a project is being undertaken in the School of Aerospace, Mechanical and Manufacturing Engineering of RMIT University to study the effects of spin on aerodynamic properties of a series of tennis balls. As a part of this large project, a separate study on steady state (without spin) aerodynamic forces and moments has been conducted on a series of new tennis balls used in the Australian Open Tennis Championship. The aerodynamic drag coefficients are compared with the published work in order to understand the variation.

### Experimental Procedure and Equipment

The aerodynamic forces and their moments were measured for a range of Reynolds numbers based on ball diameters and tunnel air speeds (40 km/h to 140 km/h with an increment of 20 km/h air speeds) as a function of seam orientation. Six tennis balls have been selected for this work as they are officially used in the Australian Open Championship. These balls are: Dunlop 3 Ti, Dunlop 2 Grand Prix, Kennex Pro, Tretorn Micro X, Tretorn Plus and Penn Tennis Master Series. Their average diameters are: 65.5 mm, 65.5 mm, 64.0 mm, 65.0 mm, 64.5 mm and 63.5 mm respectively. The diameter of the ball was determined using an electronic calliper. The width was adjusted so that the ball can slide through the opening with minimum effort. Diameters were measured across several axes and averaged. All balls were brand new. Fuzz structures of these balls are slightly different from each other. A special mounting support device was designed to hold each ball and spin up to 3500 rotations per minute (RPM),

see Figures 2 and 3. The motorised device was mounted on a 6 component force balance (type JR-3).

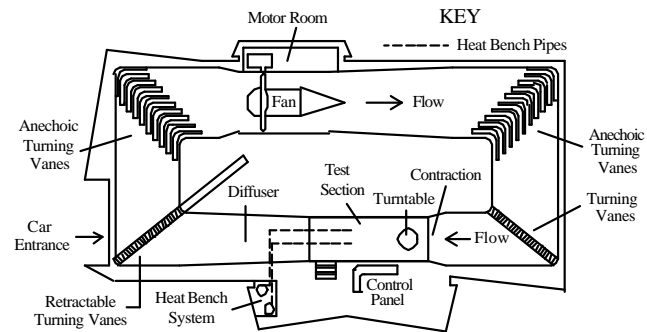


Figure 1: A Plan View of RMIT Industrial Wind Tunnel



Figure 2: Experimental Set Up in Tunnel's Test Section



Figure 3: Motorised Ball Supporting Device mounted on a 6-Component Force Balance

Figure 2 shows the experimental set up in the wind tunnel test section. The distance between the bottom edge of the ball and the tunnel floor was 350 mm, which is well above the tunnel's boundary layer and considered to be out of ground effect. Each ball was tested at 4 seam positions (at 0, 90, 180 and 270 degrees). The seam positions for all 6 balls are shown in Figures



4 to 9. Experiments were performed in RMIT University Industrial Wind Tunnel. A plan view of RMIT Industrial Wind Tunnel is shown in Figure 1. This is a closed test section, closed return circuit wind-tunnel with a maximum speed of 145 km/h. The rectangular test section dimension is 3 m (wide) x 2 m (high) x 9 m (long) with a turntable to yaw suitably sized objects. The tunnel was calibrated before conducting the experiments and tunnel air speeds were measured via a modified NPL (National Physical Laboratory) ellipsoidal head Pitot-static tube (located at the entry of the test section) connected to a MKS Baratron Pressure sensor. Purpose made computer software was used to compute all 6 forces and moments (drag, lift, roll, yaw moment, pitch moment and roll moment) and their non-dimensional coefficients. Since the blockage ratio was extremely low no corrections were made.

## Results and Discussion

In order to obtain aerodynamic forces and moment for each ball, the motorised supporting device was tested first and then subtracted from the forces and moments of ball and support assembly. The forces and moments were converted to non-dimensional parameters such as drag, lift and side forces coefficients and their respective moment coefficients. Only drag coefficients are presented in this work and they are plotted against the speeds. Figures 10 to 13 show the drag coefficient variation with velocities for seam position 1, seam position 2, seam position 3 and seam position 4 for all 6 balls.

The Tretorn Plus ball had the highest average drag coefficient and Dunlop 3 Ti and Penn Master Series had the lowest average drag coefficient at all Reynolds numbers tested (see Figures 5 and 6). All balls have relatively high drag coefficients at 40 km/h. However, Tretorn Micro X had the lowest drag at 40 km/h for seam position 2. At higher speeds, the fuzz becomes more streamlined and reduces the turbulent boundary layer and local flow separation. Drag coefficients reduce with an increase of Reynolds numbers and remain almost constant at higher Reynolds numbers. It is well known that flow separation that exists at lower Reynolds numbers will reduce at higher Reynolds numbers. Seam orientation had no significant effect on drag coefficients at high Reynolds numbers as expected. However, seam orientation has noticeable effects on drag coefficients at lower Reynolds numbers for all balls. The highest effects on drag coefficients by seam orientation have been noted for the Tretorn Plus (seam position 1). The averaged drag coefficients for all four seam positions and Reynolds numbers are shown in Figure 14 and Table 1. Overall drag coefficients (averaged) for all Reynolds numbers and seam positions for Tretorn Plus, Tretorn Micro X, Kennex Pro, Dunlop 2 Grand Prix, Dunlop 3 Ti and Penn Master Series 0.69, 0.62, 0.62, 0.61, 0.59 and 0.59 respectively. However, the averaged drag coefficients for all seam positions and Reynolds numbers (except 40 km/h) are lower and they are: 0.64 (Tretorn Plus), 0.62 (Tretorn Micro X), 0.60 (Kennex Pro), 0.59 (Dunlop 2 Grand Prix), 0.57 (Dunlop 3 Ti) and 0.58 (Penn Master Series).

It may be noted that a separate study conducted by Alam et al. [3, 4] showed the overall drag coefficients for some other balls such as Bartlett, Wilson DC 2, Wilson US Open 3, Wilson Rally 2, Slazenger 1 and Slazenger 4 are 0.71, 0.68, 0.66, 0.60, 0.60 and 0.57 respectively under the same test conditions used in this work (eg., 40 to 140 km/h with an increment of 20 km/h).

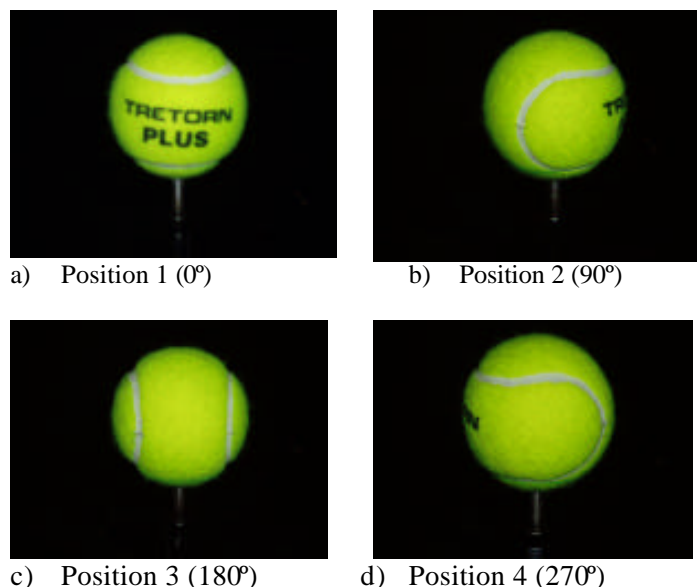


Figure 4: Orientation of Seam Towards Wind Direction (Tretorn Plus)

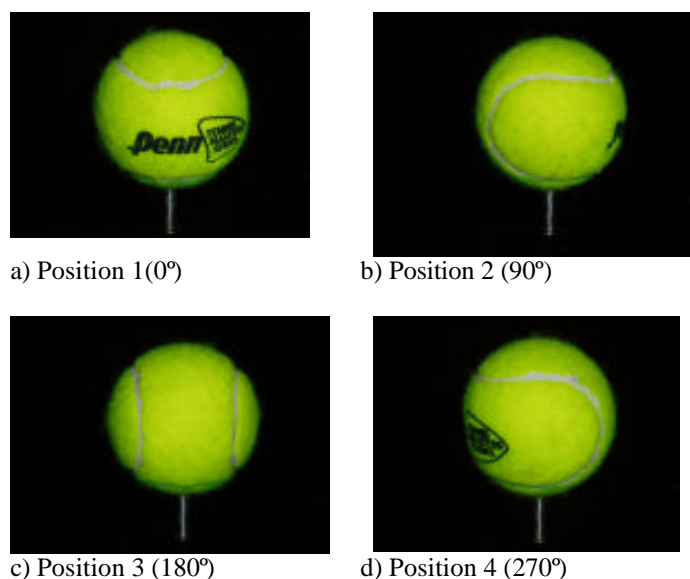


Figure 5: Orientation of Seam Towards Wind Direction (Penn Master Series)

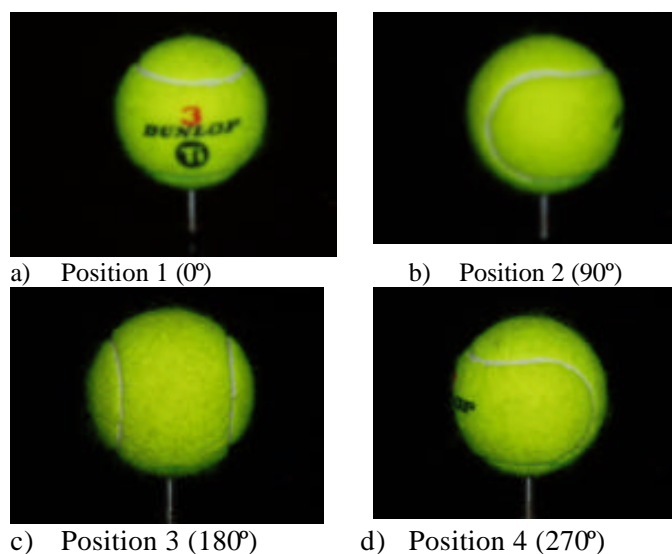


Figure 6: Orientation of Seam Towards Wind Direction (Dunlop 3 Ti)



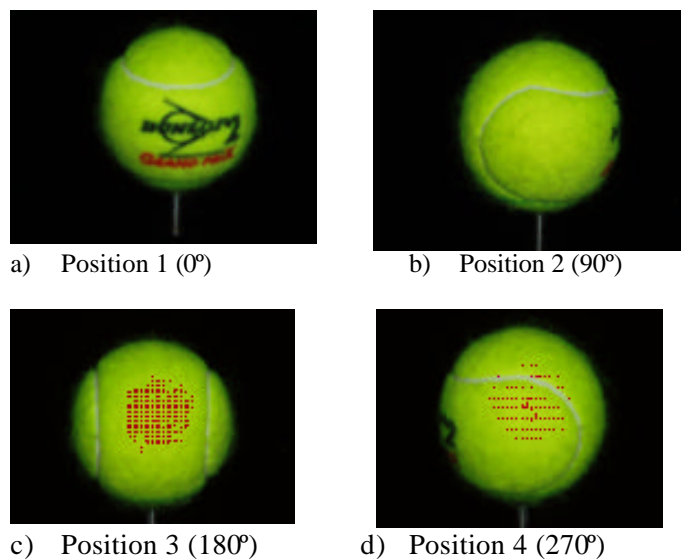


Figure 7: Orientation of Seam Towards Wind Direction (Dunlop 2 Grand Prix)

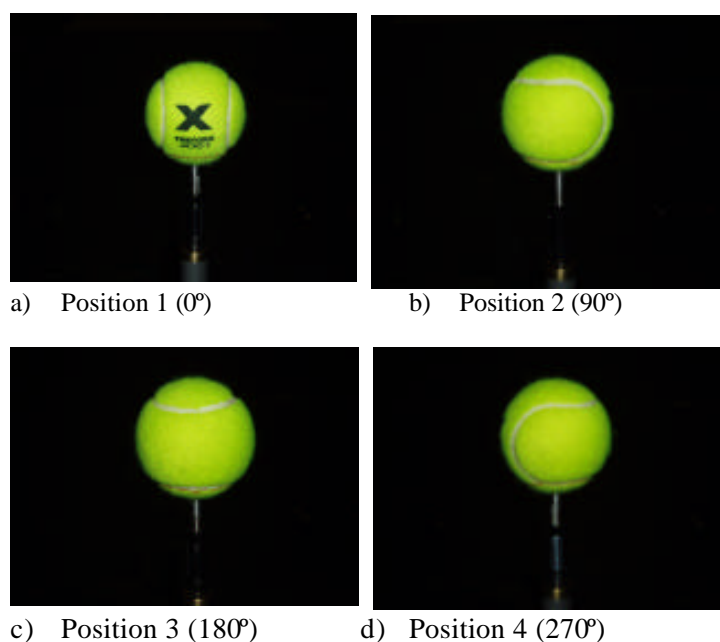


Figure 8: Orientation of Seam Towards Wind Direction (Tretorn Micro X)

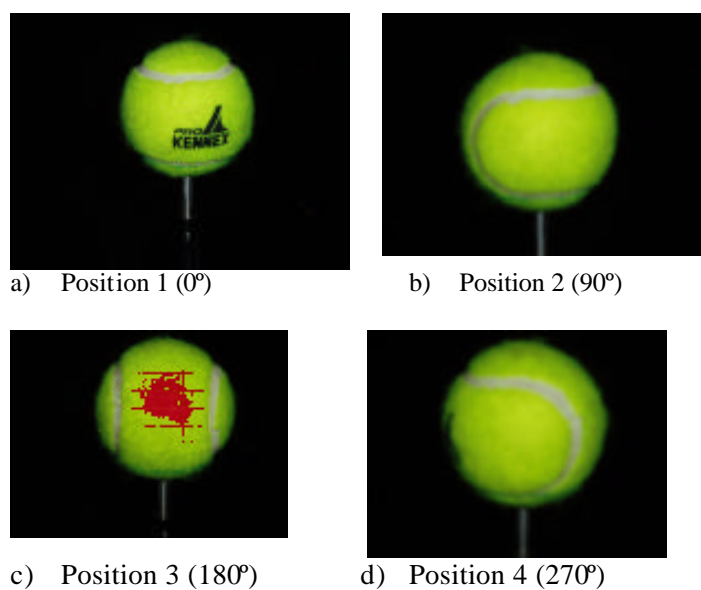


Figure 9: Orientation of Seam towards Wind Direction (Kennex Pro)

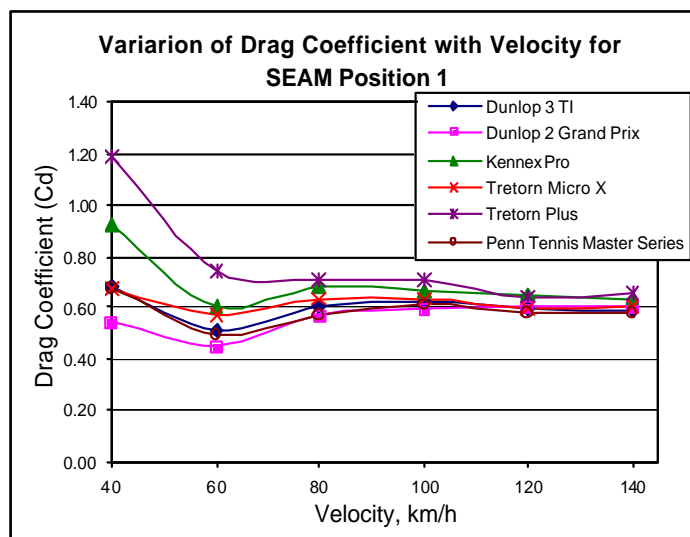


Figure 10: Drag Coefficient Variation with Velocity, SEAM Position 1

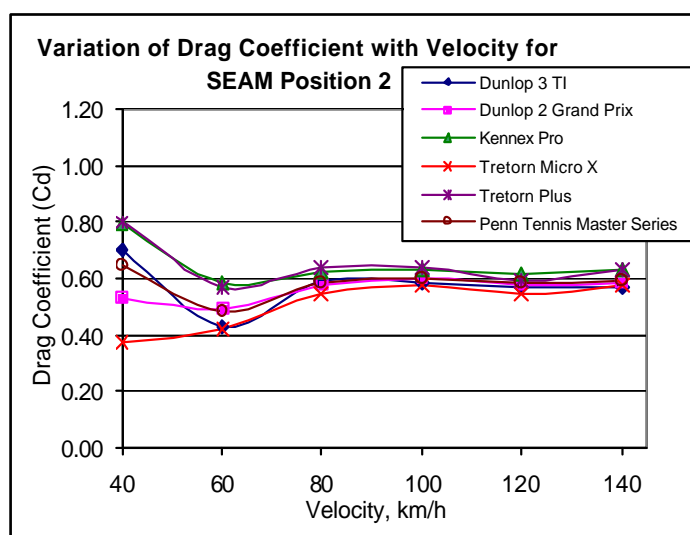


Figure 11: Drag Coefficient Variation with Velocity, SEAM Position 2

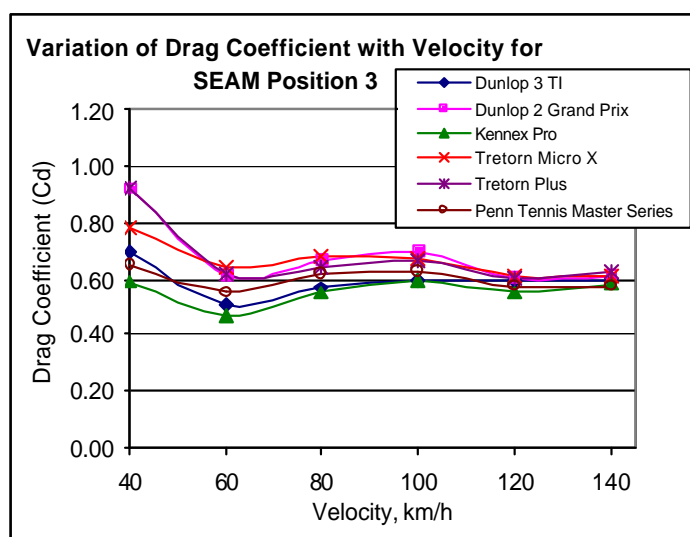


Figure 12: Drag Coefficient Variation with Velocity, SEAM Position 3

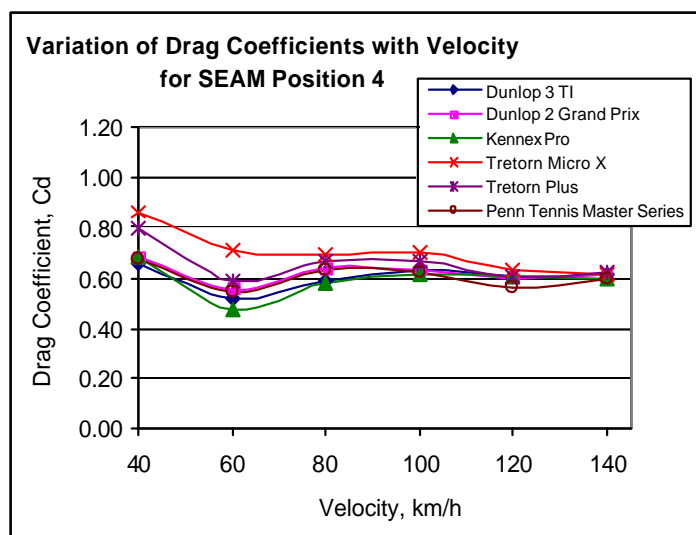


Figure 13: Drag Coefficient Variation with Velocity, SEAM Position 4

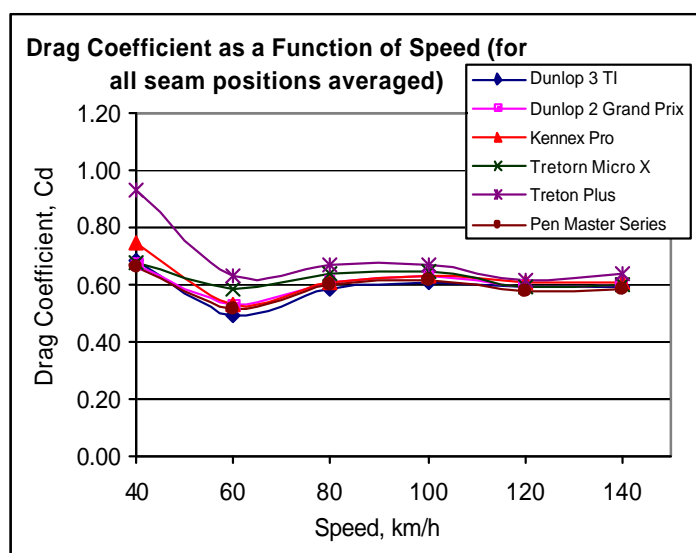


Figure 14: Averaged Drag Coefficient Variation with Velocity (for all 4 SEAM Positions)

Table 1: Averaged Drag Coefficients for all 6 Balls

Dunlop 3 Ti			Dunlop 2 Grand Prix		
Speed	Averaged Cd	Averaged Cd	Averaged Cd	Averaged Cd	
km/h	All seam pos.	All seam pos. & speeds	All seam pos.	All seam pos. & speeds	
40	0.69	0.59	0.67	0.61	
60	0.49		0.53		
80	0.58		0.61		
100	0.61		0.63		
120	0.59		0.59		
140	0.59		0.60		

Kennex Pro			Penn Master Series		
Speed	Averaged Cd	Averaged Cd	Averaged Cd	Averaged Cd	
km/h	All seam pos.	All seam pos. & speeds	All seam pos.	All seam pos. & speeds	
40	0.75	0.62	0.66	0.59	
60	0.53		0.52		
80	0.61		0.60		
100	0.63		0.61		
120	0.61		0.57		
140	0.61		0.58		

Tretorn Micro X			Tretorn Plus		
Speed	Averaged Cd	Averaged Cd	Averaged Cd	Averaged Cd	
km/h	All seam pos.	All seam pos. & speeds	All seam pos.	All seam pos. & speeds	
40	0.68	0.62	0.93	0.69	
60	0.59		0.63		
80	0.64		0.67		
100	0.65		0.67		
120	0.60		0.61		
140	0.60		0.64		

## Conclusions

The following conclusions have been made from the work presented here:

- Seam orientation has effects on drag coefficients at a very low Reynolds numbers. The magnitude of drag coefficient variations largely depends on seam and fuzz geometry.
- The "Tretorn Plus" possesses the highest drag coefficient and the "Dunlop 3 Ti and Penn Master Series" has the lowest aerodynamic drag coefficient.
- The averaged drag coefficients of all six new tennis balls (studied in this work) are between 0.59 to 0.69.

## Acknowledgments

The authors would like to express their sincere thanks to Mr Ian Overend, Mr Jeremy Luci and Mr Gilbert Atkins, School of Aerospace, Mechanical and Manufacturing Engineering, RMIT University for providing technical assistance.

## References

- Alam, F., Watkins, S. and Subic, A., "Effects of Spin on Aerodynamic Properties of Tennis Balls", Accepted for *The 5<sup>th</sup> International Conference on Sports Engineering*, 13-16 September, University of California, Davis, USA, 2004.
- Alam, F., Watkins, S. and Subic, A., "The Aerodynamic Drag of a Rugby Ball and Australian Rules Foot Ball", *Proceedings of the 5<sup>th</sup> Bluff Body Aerodynamics and Applications (BBAA V)*, 11-15 July, pp 211-214, Ottawa, Canada, 2004.
- Alam F., Watkins S. and Subic A., "The Effects of Surface Structures on Aerodynamic Properties of Tennis Balls", *Proceedings of the 2<sup>nd</sup> BSME-ASME International Conference on Thermal Engineering*, Vol. 1, pp 357-362, ISBN: 984-32-1003-4, 2-4 January, Dhaka, Bangladesh, 2004.
- Alam F., Subic A. and Watkins S., "An Experimental Study on the Aerodynamic Drag of a Series of Tennis Balls", *Sports Dynamics: Discovery and Application (edited by Subic A., Trivailo P. and Aam F.)*, pp 295-300, ISBN 0864592728, RMIT University, Melbourne, Australia, 2003.
- Chadwick, S. G. and Haake, S. J., "The drag coefficient of tennis balls", *The Engineering of Sport: Research, Development and Innovation*, pp 169-176, Balckwell Science, 2000.
- Cooke, A. J., "An overview of tennis ball aerodynamics", *Sports Engineering*, 3 (2), pp 123-129, 2000.
- Mehta, R. D. and J. M. Pallis, "The aerodynamics of a tennis ball", *Journal of Sports Engineering*, No 4, Vol 4, 2001.
- Mehta, R. D., "Aerodynamics of Sports Balls", *Annual Review of Fluid Mechanics*, 17, pp 151-189, 1985.

## Topographically trapped finite-amplitude kink solitons

S.R. Clarke

School of Mathematical Sciences,  
Monash University, Vic. 3800, AUSTRALIA

### Abstract

The evolution of internal wave fronts in an approximately linearly stratified fluid is considered where the fluid is contained in a channel with localized variations in width. It is assumed that there is an oncoming flow such that the long-wave speed of an internal wave mode is near zero. A variable coefficient finite-amplitude equation is presented which governs the wave evolution for uniform flows and rectangular channels, and it is shown that in these circumstances forced waves can be neglected. The interaction of kink soliton solutions of this finite-amplitude equation are considered.

### Introduction

In [2] the dynamics of weakly nonlinear internal wave fronts, or columnar disturbances, contained in a rectangular channel of variable width were considered in the transcritical limit (i.e. long-wave speed approximately zero), with uniform oncoming flow and weak contractions. There it was shown that the evolution was governed by a variable coefficient Korteweg–de Vries (KdV) equation, as the effective velocity experienced by the fronts accelerates within the contraction. The solutions of this equation for a step initial condition were considered in detail. For negative steps or rarefaction fronts it was demonstrated that steady solutions could evolve in the vicinity of the contraction which exhibited two types of hydraulic control: normal controls where the long-wave speed was zero at the maximum topographic perturbation and virtual controls where the long-wave speed was zero away from this point. For positive steps or compression fronts the interaction with the contraction was shown to be intrinsically unsteady, with solitary waves being generated on the downstream side of the contraction and propagating upstream.

The weakly nonlinear KdV model breaks down for two important circumstances; nearly linearly stratified fluids and two-layer fluids where the layer depth is approximately half the total depth. In the former case finite-amplitude effects must be included ([3]), and in the latter cubic nonlinearity resulting in an extended Korteweg–de Vries (eKdV) equation ([4]).

As solutions of the constant coefficient KdV equation with step initial conditions are unsteady, the interaction of fronts with a contraction in the weakly nonlinear KdV model must be unsteady and is dependent to some degree on the time that the front has evolved over before it reaches the contraction. To obtain steadily propagating front solutions in the long-wave limit requires at a minimum cubic nonlinearity, as opposed to the quadratic nonlinearity in the KdV equation. The eKdV equation has such steadily propagating step solutions, known as kinks or kink solitons or topological solitons. These kink solitons are also valid solutions for an approximately linearly stratified fluid. The investigation of kink solitons interacting with contractions is thus of significance for three reasons. Firstly, unlike finite-amplitude undular bores or rarefactions, the interaction of kink solitons has no weakly nonlinear analogue. Second, observations suggest that kink solitons, like non-topological solitons, appear to be robust nonlinear structures, and so their interac-

tion with topography is of physical importance, especially in exchange type flows. Finally, kink solitons are steadily propagating structures and consequently their interaction can be considered independent of their starting position relative to the contraction.

In the next section the equations which govern the near-critical propagation of waves in a contraction are discussed. Forced waves are also generated for approximately linear stratification; it is shown that for rectangular channels and uniform oncoming flows these waves are of smaller amplitude and evolve on a longer timescale and hence can be ignored. In the final section solutions for kink solitons interacting with contractions are presented.

### Near-critical waves in a contraction

Consider the inviscid, nondiffusive flow of a stratified fluid in a channel. A Cartesian coordinate system  $h(x, y, z)$  is introduced, where  $h$  is the undisturbed height of the free-surface above the origin,  $x$  is the horizontal coordinate along the channel,  $y$  is the transverse coordinate and  $z$  is the vertical coordinate, being positive upwards. The density is  $\rho_0\rho(z - \zeta)$  where  $\zeta$  is the non-dimensional vertical particle displacement. The Boussinesq parameter, which characterizes the strength of the density perturbation, is then defined as  $\beta = \rho(0) - \rho(1)$ . The reduced gravity is then  $g' = \beta g$ , where  $g$  is the acceleration due to gravity, and the normalized buoyancy frequency  $N(z)$  is

$$N^2 = -\frac{\rho'}{\beta\rho} (= M). \quad (1)$$

The time is  $(h/g')^{\frac{1}{2}}t$ , while the fluid velocities are  $(g'h)^{\frac{1}{2}}N_0h(u, v, w)$ , the free surface displacement is  $eh\eta$ , where the binary parameter  $e$  is 0 for a rigid lid boundary condition and 1 for a free surface condition, and finally the pressure is  $\rho_0gh(P(z) + \beta p)$ , where  $P' = -\rho$ .

The waves in the channel are assumed to have amplitude  $O(\alpha)$  and wavelength  $O(\mu^{-1})$ . It is assumed that this is also the lengthscale of the perturbation of the contraction, which has amplitude  $O(\varepsilon)$ . For both  $\mu$  and  $\varepsilon$  it is assumed  $\varepsilon, \mu \ll 1$ . Therefore, introduce

$$(x, y, t) = \mu^{-1}(x', y', t'), \quad (2)$$

and define the side boundaries

$$b'_{\pm} = \pm b'_0(1 + \varepsilon f_{\pm}). \quad (3)$$

The mean perturbation is

$$f = \frac{1}{2}(f_+ + f_-). \quad (4)$$

A mean flow  $\bar{u}$  exists in the channel, which can be assumed to be independent of  $x$  and  $y$ . At this point no other restrictions are placed on  $f_{\pm}$  and  $\bar{u}$ . Hence,

$$(u, v, w) = (\bar{u} + \alpha u', \varepsilon v', \mu \alpha w'), \quad p = \alpha p', \quad \zeta = \alpha \zeta', \quad \eta = \alpha \beta \eta', \quad (5)$$

and primes are ignored hereafter.

### Forced waves

As shown in [1] near criticality four cases of forced evolution equations apply in these circumstances:

- (F1) If  $\bar{u}$  and  $f$  vary with height the appropriate choice for  $\alpha$  and  $\mu$  is

$$\alpha = \mu^2 = \varepsilon^{\frac{1}{2}}, \quad (6)$$

and no restriction is placed on  $\beta$ . The flow is assumed to be close to criticality, hence  $\bar{u}$  can be written as

$$\bar{u} = U(z) - c + \varepsilon^{\frac{1}{2}} \Delta + O(\varepsilon), \quad (7)$$

where  $c$  is the long-wave speed of the resonant mode and  $\Delta$  is a detuning constant. A long timescale is introduced:

$$\tau = \varepsilon^{\frac{1}{2}} t, \quad (8)$$

and a perturbation solution for  $\zeta$  is sought in  $\varepsilon^{1/2}$  of the form

$$\zeta = A(x, \tau) \phi(z) + \varepsilon^{\frac{1}{2}} \zeta^{(1)} + O(\varepsilon), \quad (9)$$

where  $\phi$  is the long-wave mode with speed  $c$  for the shear  $U(z)$ . Then it can be shown that  $A$  satisfies

$$A_\tau + \Delta A_x + r A A_x + s A_{xxx} = -F_x, \quad (10)$$

where the forcing function  $F$  is proportional to an integral of  $f$  over the height of the fluid and  $r$  and  $s$  are constants. The Boussinesq limit corresponds here to  $\beta \rightarrow 0$ . In general, this will only marginally affect the coefficients of (10). In this case, in terms of the original variables, the characteristic amplitude and timescale for the forced waves is  $O(\varepsilon^{\frac{1}{2}})$  and  $O(\varepsilon^{-\frac{3}{4}})$  respectively.

- (F2) When  $\bar{u}$  is constant with height and the stratification is uniform, i.e.

$$M = 1 + O(\beta), \quad (11)$$

the nonlinear term in (10) is  $O(\beta)$ , where typically  $\beta \ll 1$ , and the derivation of (F1) does not apply in this limit. This was alluded to in [1]; the appropriate choice of parameters in this case is

$$\alpha = 1, \quad \mu^2 = \varepsilon, \quad \beta = \sigma \varepsilon. \quad (12)$$

The expressions (7), (8) and (9) are again used with  $\varepsilon^{1/2}$  replaced everywhere by  $\varepsilon$  and the simplification that  $U_z \equiv 0$ . Then a similar evolution equation for  $A$  to that derived by [3] will result. The nonlinear term in this case is  $O(\sigma)$ , therefore in the Boussinesq limit  $\sigma \rightarrow 0$ , with all else unchanged, it would be expected that any forced wave will grow without being limited by nonlinear effects until it overturns. In this case, in terms of the original variables, the characteristic amplitude and timescale for the forced waves is  $O(1)$  and  $O(\varepsilon^{-\frac{3}{2}})$  respectively.

- (F3) In the joint limit when  $\beta \rightarrow 0$  and  $\bar{u}$  and  $f$  are independent of height the forcing term in (10) disappears. However, it was demonstrated in [1] that resonance will still occur due to Boussinesq effects. Here

$$\alpha = \mu^2 = \varepsilon, \quad \beta = \sigma \varepsilon, \quad (13)$$

and the same expressions for  $\bar{u}$ ,  $\tau$  and  $\zeta$  are introduced as for (F2). Subsequently it can be shown that  $A$  satisfies

$$A_\tau + (\Delta A)_x + r A A_x + s A_{xxx} = \gamma \Delta_x. \quad (14)$$

The coefficient of the forcing term,  $\gamma$ , is  $O(\sigma)$ , clearly in the Boussinesq limit the forced wave vanishes. In this case, in terms of the original variables, the characteristic amplitude and timescale for the forced waves is  $O((\beta \varepsilon)^{\frac{1}{2}})$  and  $O(\beta^{-1} \varepsilon^{-\frac{1}{2}})$  respectively.

- (F4) Finally, for uniform stratification the nonlinear term in (14) vanishes. To derive a forced nonlinear evolution equation the appropriate choice of parameters is now

$$\alpha = \mu^2 = \varepsilon^{\frac{1}{2}}, \quad \beta = \sigma \varepsilon^{\frac{1}{2}}. \quad (15)$$

The same expressions for  $\bar{u}$  and  $\tau$  are introduced as in (F3), however as the expansion for  $\zeta$  occurs in powers of  $\varepsilon^{1/2}$  (9) is introduced. The perturbation expansion must be taken to second order to demonstrate that  $A$  again satisfies a version of (14). For this equation the coefficient of both the nonlinear term,  $r$ , and the forcing,  $\gamma$  are  $O(\sigma)$ . In this case, in terms of the original variables, the characteristic amplitude and timescale for the forced waves is  $O(\varepsilon^{\frac{1}{2}})$  and  $O(\beta^{-1} \varepsilon^{-\frac{3}{4}})$  respectively. In the limit  $\sigma \ll 1$  forced waves will still be generated, however they take an infinitely long time to form.

Other types of resonance can occur in a contraction apart from the generation of forced waves. For example shear fronts propagating towards a contraction can become trapped and resonate. The analysis of (14) in the limit  $\gamma \rightarrow 0$  in [2] clearly demonstrates this. For each of the above circumstances we can therefore consider the amplitude of the quasi-steady solution which form in a contraction due to this interaction and the timescale for its formation. In (F1) and (F2) the amplitudes and timescales are identical to the forced waves, therefore the only effect of a shear front will be to perturb one quasi-steady solution of (10) to another quasi-steady solution. However, for (F3) the amplitude and timescales are respectively  $O(\varepsilon)$  and  $O(\varepsilon^{-\frac{3}{2}})$ , while for (F4) they are  $O(\beta^{-1} \varepsilon)$  and  $O(\varepsilon^{-\frac{5}{4}})$ . In these latter two cases, since typically  $\varepsilon \gg \beta$  the amplitudes for these unforced waves are larger than the corresponding forced waves, while the timescales the unforced waves form over are smaller than those for the forced waves. This suggests that the forced waves studied in the cases (F3) and (F4) are only relevant if there are no unforced waves in the vicinity of the contraction, in particular, when these unforced waves are shear fronts. In conclusion, if there are shear fronts in the vicinity of the contraction, for (F1) and (F2) these can be ignored, while for (F3) and (F4) the forced waves can be ignored. Thus we are led to consider the appropriate evolution equations for unforced waves.

### Unforced waves

Two equations describe the general evolution of unforced waves in these circumstances. The appropriate equation is dependent on the stratification:

- (U1) In the limit  $\sigma \rightarrow 0$  of (F3), which corresponds to making the Boussinesq approximation, the forcing disappears and the amplitude satisfies the variable coefficient KdV equation

$$A_\tau + (\Delta A)_x + r A A_x + s A_{xxx} = 0. \quad (16)$$

This equation was studied in detail in [2]. In particular it was shown that in the limit  $r \rightarrow 0$  and for long contractions the amplitude could grow without bounds if the sign of the  $\Delta$  changed within the contraction. This leads us to consider the appropriate evolution equation for uniform stratification, for which  $r = 0$  in the Boussinesq limit.

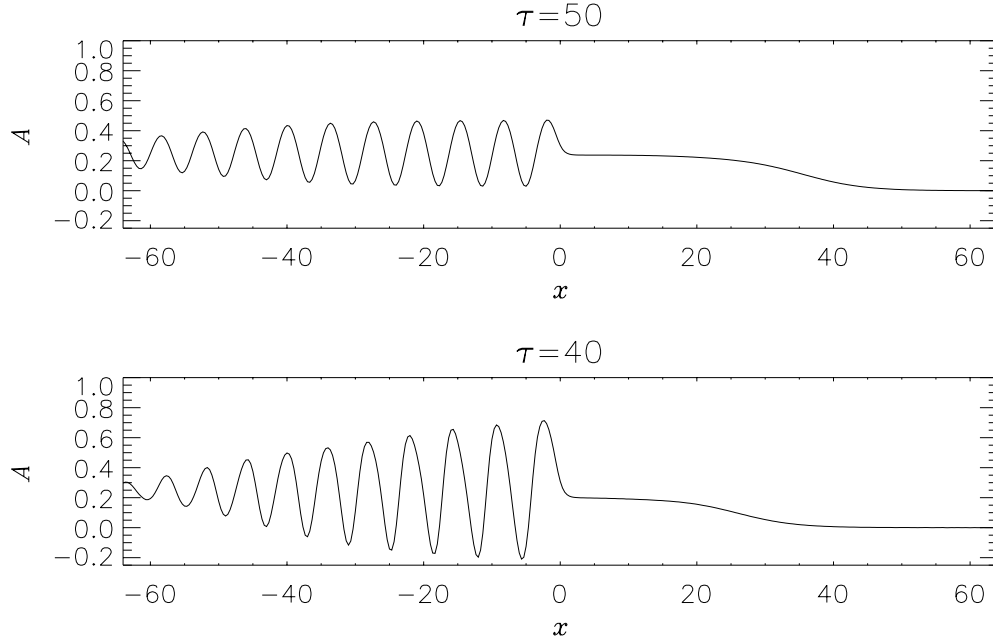


Figure 1: Interaction of a finite-amplitude kink soliton in a contraction demonstrating the effect of changing the width of the contraction. In both panels  $q = -2$ ,  $r = \frac{3}{4}$  and  $\Delta_0 = 1$ . For the upper panel  $\Delta_1 = \frac{1}{2}$  and for the lower panel  $\Delta_1 = 1$ .

(U2) Case (F4) suggests that resonant shear fronts will attain an asymptotic amplitude  $O(\beta^{-1}\epsilon)$ . Therefore, since typically  $\beta \ll \epsilon$  finite-amplitude effects must be considered. The derivation of the appropriate equation is summarized here. Introducing the same scalings as in (F2), a perturbation solution for  $\zeta$  is sought of the form

$$\zeta = cA(x, \tau)\phi + \epsilon\zeta^{(1)} + O(\epsilon^2), \quad (17a)$$

where

$$\phi = \sin n\pi z, \quad c = \frac{1}{n\pi}, \quad (17b)$$

and  $n$  is a positive, nonzero integer. Define  $z(\xi, A)$  to be the solution of

$$\xi = z - \frac{A}{\pi} \sin n\pi z, \quad (18)$$

which has a unique solution if  $|A| < 1$ . If this condition is violated then the wave has overturned, however providing it is satisfied then the amplitude satisfies the integro-differential equation

$$\int_{-\infty}^{\infty} K(A, A') A'_{\tau} dx' + \Delta A + \frac{c^3}{2} (\sigma m(A) + A_{xx}) = 0, \quad (19a)$$

where

$$\Delta = \hat{\Delta} + cf, \quad (19b)$$

$$K(A, A') = \pi^2 \int_0^1 \frac{\partial z}{\partial A} \left[ \frac{\partial z'}{\partial A'} \left( 1 + \frac{\partial z'}{\partial \xi} \right) - (z - z') \frac{\partial}{\partial \xi} \left( \frac{\partial z'}{\partial A'} \right) \right] d\xi, \quad (19c)$$

$$m(A) = 2\pi^4 \int_0^1 (z - \xi) X_{eff}(\xi) z_A d\xi + \frac{A^2}{3} (1 - (-1)^n) - e(2A - (-1)^n 3A^2 + A^3), \quad (19d)$$

and for  $n > 1$   $X_{eff}$  is a smoothed version of the buoyancy frequency perturbation:

$$X_{eff}(\xi) = \sum_{k=0}^{n-1} X \left( \frac{1}{n} \left( k + \frac{1}{2} (1 - (-1)^k) + (-1)^k \xi \right) \right). \quad (20)$$

#### Finite-amplitude waves.

We now consider finite-amplitude solutions for kink solitons in a contraction; however before proceeding a few comments can be made concerning (19). Equation (19) can be normalized by introducing

$$\tau^* = \alpha^{-\frac{3}{2}} \frac{c^3 \tau}{2}, \quad \Delta^* = \frac{2\alpha\Delta}{c^3}, \quad \sigma^* = \alpha\sigma, \quad x^* = \alpha^{-\frac{1}{2}} x, \quad (21)$$

where  $\alpha$  is some positive, arbitrary constant. Then, dropping the asterisks, the amplitude satisfies

$$\int_{-\infty}^{\infty} K(A, A') A'_{\tau} dx' + \Delta A + \sigma m(A) + A_{xx} = 0. \quad (22)$$

Consider the term  $\sigma m(A)$  of (22). Let

$$X(z) = az - b. \quad (23)$$

Thus

$$m(A) = \frac{A}{c^2} \left( \frac{a}{2} - b \right) + \frac{A^2}{3} (1 - 4a) (1 - (-1)^n) - e(2A - (-1)^n 3A^2 + A^3), \quad (24)$$

which, as noted in [3], contains no terms of order greater than cubic. The linear terms of  $\sigma m(A)$  can be incorporated in the velocity, hence  $\sigma m(A)$  can in general be written as

$$\sigma m(A) = \frac{1}{2} r A^2 + \frac{1}{3} q A^3, \quad (25)$$

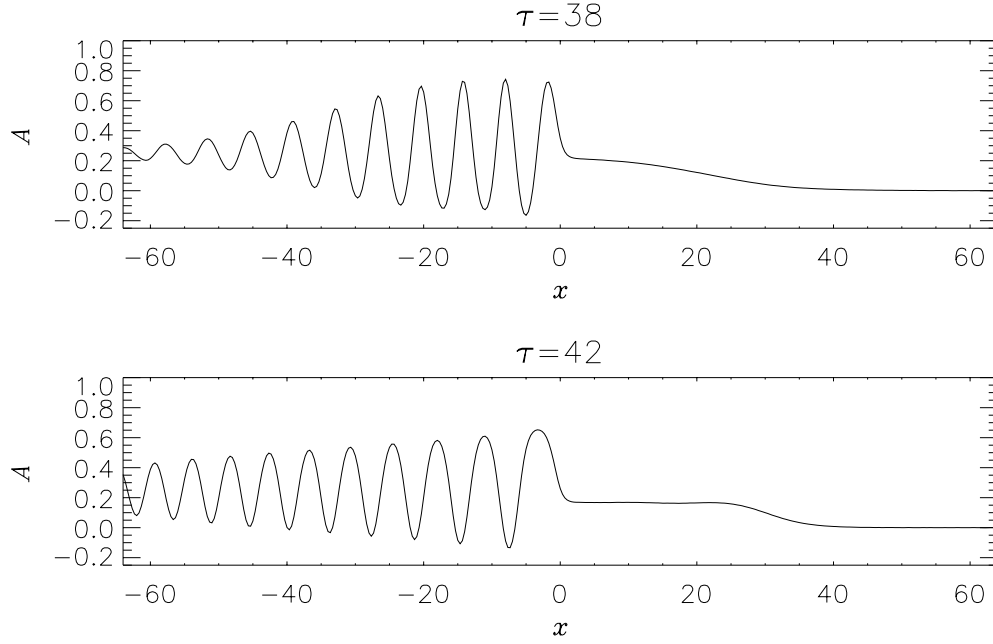


Figure 2: Interaction of a finite-amplitude kink soliton in a contraction demonstrating the effect of changing the strength of the stratification. In both panels  $\Delta_0 = 1$  and  $\Delta = \frac{1}{2}$ . For the upper panel  $q = -1$  and  $r = \frac{3}{8}$ , while in the lower panel  $q = -4$  and  $r = \frac{3}{2}$ . The upper panel of figure 1 is intermediate between these two figures.

where, the only limitation at this point is that  $q = -3e\sigma \leq 0$ . For  $\Delta \equiv 0$ , (22) has kink soliton solutions (see [5]):

$$A = \frac{\Lambda}{2}(1 - \tanh \kappa(x - V\tau)), \quad (26a)$$

where

$$\Lambda = -\frac{2r}{3q}, \quad \kappa = \left(-\frac{q\Lambda^2}{8}\right)^{\frac{1}{2}}, \quad V = \frac{r\Lambda}{3}. \quad (26b)$$

Thus we assume an initial condition

$$A = \frac{\Lambda}{2}(1 - \tanh \kappa(x - x_0)), \quad (27)$$

where  $x_0 < 0$  and  $\Lambda$  and  $\kappa$  are as specified by (26). The velocity perturbation is assumed to be here of the form:

$$\Delta(x) = \Delta_0 - \Delta_1 \operatorname{sech}^2(x/x_a), \quad (28)$$

and by an appropriate definition of  $\alpha$  in (21) we can assume  $x_a = 1$ . The results presented here are largely independent of the exact form of the topography, provided it is smoothly varying with a single extrema and characteristic lengthscale.

Figures 1 and 2 show some selected solutions which demonstrate significant effects of the interaction of kink solitons with a contraction. The system which is solved is (19) with (25), (28) and (27). The numerical simulations use a synthesis of the methods used by [3] and [2]. This involves differentiating (19), resulting in a Volterra integral equation of the second type for  $A_\tau$  at each time step. Spatial derivatives are evaluated by removing the step in  $A$  and using pseudospectral methods for the residual function.

In figure 1 the effect of changing the width of the contraction is shown. For narrow contractions, as typified by the upper panel, the kink soliton is able to pass through the contraction with an insignificant reduction in the amplitude. After the generation

of transient waves a steady, constant amplitude lee wave then forms downstream of the contraction. For larger contractions the transmitted front is reduced correspondingly. Further simulations suggest that for the parameters of figure 1 there is no transmitted wave for  $\Delta_1 \geq 3$ . Downstream of the contraction it appears that no steady lee wave train has formed, even though the upstream behaviour is no longer transient. Shortly after the time shown the simulation was halted due to overturning.

The effect of changing the stratification strength is shown in figure 2. As with figure 1 the transmitted front decreases as this effect strengthens. Secondly, increasing nonlinearity dampens the growth of the downstream lee wave. For weak stratification a constant amplitude lee wave starts to evolve just prior to the simulation being halted, while for the stronger stratification it appears that a downstream plateau starts to evolve which at large times would result in a steady hydraulically controlled solution in the vicinity of the contraction.

\*

## References

- [1] S.R. Clarke and R.H.J. Grimshaw. Resonantly generated internal waves in a contraction. *J. Fluid Mech.*, 274:139–161, 1994.
- [2] S.R. Clarke and R.H.J. Grimshaw. Weakly nonlinear internal wave fronts trapped in contractions. *J. Fluid Mech.*, 415:323–345, 2000.
- [3] R. Grimshaw and Z. Yi. Resonant generation of finite-amplitude waves by the flow of a uniformly stratified fluid over topography. *J. Fluid Mech.*, 229:603–628, 1991.
- [4] T.R. Marchant and N.F. Smyth. The extended Korteweg-de Vries equation and the resonant flow of a fluid over topography. *J. Fluid Mech.*, 221:263–288, 1990.
- [5] J.W. Miles. On internal solitary waves. *Tellus*, 31:456–462, 1979.



## Linear and Nonlinear Acoustic Behaviour of Outlet Nozzles

W. H. Moase, M. J. Brear and C. Manzie

Department of Mechanical & Manufacturing Engineering  
The University of Melbourne, VIC, 3010 AUSTRALIA

### Abstract

The response of outlet nozzles to upstream flow perturbations of varying magnitudes is investigated by numerically solving the quasi-one-dimensional Euler equations. Results are compared to the analytic linear solutions of Marble & Candel for compact and finite length choked nozzles, and those of Rienstra for open nozzles. It is demonstrated that the nonlinear response of the choked exit nozzle is very close to the linear analytic response at forcing amplitudes that are representative of those observed in combustors experiencing limit cycle, thermoacoustic instability. Although jet formation at an open end cannot be represented by quasi-one-dimensional flow, the numerical simulations suggest that the behaviour is slightly more nonlinear than for a choked outlet at the same forcing magnitudes, but still closely in agreement with the analytic linear solutions.

### Introduction

Whenever combustion occurs in a duct, coupling between the flame and the duct acoustics can result in unstable behaviour often referred to as ‘thermoacoustic’ instability. Under many circumstances, the amplitude of the limit cycles can be large enough to cause flame blowout, structural damage, or unacceptable noise. The feedback process between the acoustic disturbances produced by the flame and the acoustic excitation of the flame involves the reflection of disturbances off the outlet of the combustor, which is typically a choked nozzle. In the case of experimental test rigs, it is not always possible for the outlet of the combustor to be choked and instead it is common to have an open outlet exhausting into a large plenum.

Marble & Candel [5] determined the linear response of both compact and finite length choked nozzles. Stow et al. [7] developed theory and performed numerical simulations of the linearised Euler equations for an annular duct, showing that, even in the three-dimensional case, Marble & Candel’s analysis for compact nozzles still holds. In their analysis of finite length choked nozzles, Marble & Candel assumed the stream-wise velocity profile of the steady part of the flow throughout the nozzle is linearly distributed. Stow et al. offered an alternative low-frequency asymptotic analysis for finite length nozzles which allows for an arbitrary stream-wise steady velocity profile and also for the difference between finite length and compact nozzle responses to be approximated as an end-correction. Rienstra [6] performed an extensive low Strouhal number asymptotic analysis for the linear acoustic behaviour of an open outlet.

In a typical thermoacoustic limit cycle, the amplitude of the pressure perturbations can be 10% of the mean pressure [3]. Under such conditions it is useful to know whether the assumptions of linearity made by Marble & Candel [5], Stow et al [7] and Rienstra [6] are still valid. The purpose of this paper is therefore to investigate the response of an outlet nozzle to varying amplitude disturbances in order to determine the validity of a linear analysis under conditions when, for example, a combustor is in a limit cycle. The response of the outlet nozzle to upstream flow perturbations is determined by numerically solving the nonlinear quasi-one-dimensional Euler equations. As

this paper is primarily concerned with the effect of a small disturbance assumption, comparison is only made with Marble & Candel’s and Rienstra’s analyses for choked and open outlets respectively. It is demonstrated that, even for relatively large amplitude disturbances, the response can be accurately represented by these linear boundary conditions.

### Theory

Neglecting diffusive and viscous effects, the system is governed by the continuity, Euler (momentum) and energy equations. In this paper, a quasi-one-dimensional form is used

$$\frac{\partial \rho}{\partial t} = -\frac{\partial u \rho}{\partial x} - \rho u \left( \frac{1}{A} \frac{dA}{dx} \right), \quad (1)$$

$$\frac{\partial u}{\partial t} = -u \frac{\partial u}{\partial x} - \frac{1}{\rho} \frac{\partial p}{\partial x}, \quad (2)$$

$$\frac{\partial p}{\partial t} = -u \frac{\partial p}{\partial x} - \gamma p \frac{\partial u}{\partial x} - \gamma p u \left( \frac{1}{A} \frac{dA}{dx} \right), \quad (3)$$

where  $p$  is the pressure,  $u$  the velocity,  $\rho$  the density, and  $A$  the cross-sectional area.

### Linearisation of the Equations of Motion

A given flow property  $G(x, t)$ , may be split into its steady-flow value  $\bar{G}(x)$  and a perturbation  $G'(x, t)$ . The Euler equations can then be linearised to first-order in the perturbation quantities. In a region of spatially uniform steady flow, assuming disturbances with time dependence  $\exp(i\omega t)$  this gives

$$\frac{p'}{\gamma \bar{p}} = \left[ P^+ e^{-i\omega x/(\bar{u} + \bar{c})} + P^- e^{-i\omega x/(\bar{u} - \bar{c})} \right] e^{i\omega t}, \quad (4)$$

$$\frac{u'}{\bar{c}} = \left[ P^+ e^{-i\omega x/(\bar{u} + \bar{c})} - P^- e^{-i\omega x/(\bar{u} - \bar{c})} \right] e^{i\omega t}, \quad (5)$$

$$\frac{s'}{c_p} = \frac{p'}{\gamma \bar{p}} - \frac{\rho'}{\bar{\rho}} = \left[ \sigma e^{-i\omega x/\bar{u}} \right] e^{i\omega t}, \quad (6)$$

where  $c$  is the speed of sound and  $s$  is the entropy. So to first-order the unsteady field is composed of three characteristics: a pressure wave  $P^-$  traveling upstream at the speed of sound relative to the steady flow; a pressure wave  $P^+$  traveling downstream at the speed of sound relative to the steady flow; and an entropy disturbance  $\sigma$  convecting with the steady flow. In fact, even in spatially non-uniform flow, it can be shown that the entropy disturbances convect at the *local* flow velocity without change. In other words  $s'/c_p$  is purely a function of  $t - \int dx/\bar{u}$ .

### Compact Choked Nozzle

A nozzle can be considered compact if it has no storage capacity. Taking the nozzle entrance to be the origin of the system, this means that at  $x = 0$ ,  $M' = 0$  if the nozzle is choked at the throat. The Mach number perturbation can be expressed in terms of the pressure, velocity and density fluctuations to give

$$\frac{p'}{\bar{p}} = 2 \frac{u'}{\bar{u}} + \frac{\rho'}{\bar{\rho}}. \quad (7)$$

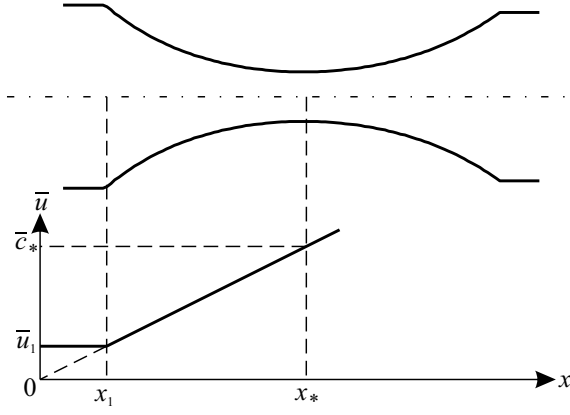


Figure 1: Relationship between choked nozzle geometry and steady velocity distribution.

This is Marble & Candel's [5] well known boundary condition for a compact choked nozzle. Substitution of equations (4)–(6) into (7) yields expressions for the reflection coefficients  $R_s$  and  $R_p$ , the amplitude of the reflected upstream traveling pressure wave due to incoming entropy and pressure disturbances respectively

$$\frac{P^-}{\sigma} = R_s = \frac{\bar{M}}{2 + (\gamma - 1)\bar{M}}, \quad (8)$$

$$\frac{P^-}{P^+} = R_p = \frac{2 - (\gamma - 1)\bar{M}}{2 + (\gamma - 1)\bar{M}}. \quad (9)$$

### Choked Nozzle of Finite Length

In a finite length nozzle, it is not correct to assume that there is zero storage capacity and that the steady flow field is uniform. The analysis must start back at the linearised Euler equations. To ease the algebraic burden of solving the linearised Euler equations, Marble & Candel [5] assume that the steady part of the velocity profile throughout the nozzle increases linearly with position. Furthermore, the origin of the co-ordinate system will no longer be considered the start of the nozzle. Instead,  $x = 0$  is the location where the extrapolated nozzle steady velocity profile reaches zero. Subscript 1 designates quantities at the nozzle entrance, and subscript \* designates quantities at the nozzle throat. Thus the nozzle length is  $x_* - x_1$ . The relationship between the nozzle geometry and steady velocity is illustrated in figure 1. For convenience, Marble & Candel also introduce the non-dimensional time  $\tau = \bar{c}_* t / x_*$ , non-dimensional position  $\xi = (x/x_*)^2$  and reduced frequency  $\Omega = x_* \omega / \bar{c}_*$  where the excitation frequency is  $\omega$ . For periodic disturbances,

$$\frac{p'}{\gamma \bar{p}} = P(\xi) \exp(i\Omega \tau), \quad (10)$$

$$\frac{u'}{\bar{u}} = U(\xi) \exp(i\Omega \tau), \quad (11)$$

$$\frac{s'}{c_p} = \sigma \exp\left(i\Omega \left[\tau - \ln \sqrt{\xi/\xi_1}\right]\right). \quad (12)$$

Substituting equations (10)–(12) into the linearised Euler equations gives

$$\xi(1 - \xi) \frac{d^2 P}{d\xi^2} - \left[2 + \frac{2i\Omega}{\gamma + 1}\right] \xi \frac{dP}{d\xi} - \frac{i\Omega(2 + i\Omega)}{2(\gamma + 1)} P = -\frac{i\sigma\Omega}{2(\gamma + 1)} \left(\frac{\xi}{\xi_1}\right)^{-i\Omega/2}, \quad (13)$$

$$(2 + i\Omega)U = -(\gamma + 1)(1 - \xi) \frac{dP}{d\xi} + \sigma \left(\frac{\xi}{\xi_1}\right)^{-i\Omega/2}. \quad (14)$$

Equation (14) can give  $U(\xi)$  if  $P(\xi)$  is known.  $P$  can be found by solution of equation (13) which is of the hypergeometric form — a unique solution can only exist if more information is known about the problem. The pressure disturbance is regular at the nozzle throat, but the location  $\xi = 0$  occurs before the nozzle inlet and is out of the domain of interest for this problem. Thus it doesn't matter if a singularity in the solution occurs at  $\xi = 0$ . Using this information, it is possible to find both a particular  $P_p(\xi)$  and homogeneous  $P_h(\xi)$  solution to equation (13) such that  $P = P_p + kP_h$ , where  $k$  is a constant, and each solution has the form

$$\sum_{n=0}^{\infty} a_n (1 - \xi)^{n+m}. \quad (15)$$

In order to find  $k$  it is necessary to couple the solution to the wave system of the approaching flow. As the flow approaching the nozzle is spatially uniform, equations (4)–(6) hold, giving

$$U(\xi_1) = (2P_1^+ - P(\xi_1)) / \bar{M}_1, \quad (16)$$

so given the magnitudes of the incoming pressure wave  $P_1^+$  and the entropy disturbance  $\sigma$ , equation (16) can be substituted into (14) to close the solution for  $P(\xi)$ .

### Open Outlet

In practice, the exhaust from an open outlet forms a jet. The acoustic interaction with the shear layer of the jet separating from the outlet cannot be modelled with a quasi-one-dimensional analysis. Rienstra [6] provides an extensive low Strouhal number asymptotic analysis of the flow and, in comparison with experiments, concludes that the employment of a Kutta condition at the trailing edge of the pipe outlet is essential in accurately determining the acoustics both within and outside the duct. For zero Strouhal number flow, Rienstra's analysis gives a pressure reflection coefficient of  $-1$ , accurate to first-order in the flow perturbations. In the absence of a Kutta condition, to first-order, Rienstra gives the same pressure reflection coefficient as that given by a simple application of the one-dimensional mass, momentum and energy conservation laws:

$$R_p = -(1 + \bar{M}) / (1 - \bar{M}). \quad (17)$$

Comparison of this reflection coefficient with numerical simulations of the nonlinear quasi-one-dimensional Euler equations may shed some light on the nonlinear effect of high amplitude disturbances on an open outlet when the Kutta condition is employed.

### Numerical Solver

The quasi-one-dimensional Euler equations were solved using fourth-order Runge–Kutta time-stepping and a fourth-order Padé spatial finite differencing scheme. These schemes have very small inherent dissipation and give a highly accurate representation of wave propagation [4]. System excitation was caused by sinusoidally varying the relevant outgoing characteristic at the inflow boundary. The system inflow boundary was placed very close to the nozzle entrance so that the nonlinear propagation of the excitation characteristic from inflow boundary to nozzle entrance was negligible. Simulations were run for sufficiently long periods of time to ensure that transients were not present in the final results.

A common source of error in numerical acoustics is the artificial reflection of disturbances from the system boundaries. In the absence of spurious disturbances, boundary conditions that

are nonreflecting in the linear characteristics are given by Giles [2]. As spurious waves can travel at speeds that are significantly different to those of physical waves, a scheme as basic as Giles' can cause reflection of spurious waves. For this reason, discretely nonreflecting boundary conditions were employed as given by Colonius [1]. The chosen scheme was third-order accurate about the Nyquist frequency (spurious) and fourth-order accurate about the steady state (physical) for incoming waves, and fifth-order accurate about the Nyquist frequency for outgoing waves. The chosen boundary conditions resulted in very small reflection of all spurious and physical waves present in typical simulations.

The numerical scheme was validated by solving a number of model problems including the linear propagation of small magnitude waves, and nonlinear wave steepening in large pressure wave propagation. These simulations conformed well with theoretical predictions. The close agreement between the results given by the numerical solver for small amplitude disturbances and the linear analytic solutions presented in this paper is in itself a convincing validation. Initial tests were performed using a number of grid densities and boundary locations. The results were independent of boundary location and converged with increasing grid density. For typical simulations, it was necessary to use around 1000 data points to gain a well resolved solution.

## Discussion

Measurement of the linear characteristics in a nonlinear system can be achieved by re-casting equations (4)–(6) in terms of the characteristics to give the following definitions

$$p^+(x, t) = \frac{1}{2} \left( \frac{p'}{\gamma \bar{p}} + \frac{u'}{\bar{c}} \right), \quad (18)$$

$$p^-(x, t) = \frac{1}{2} \left( \frac{p'}{\gamma \bar{p}} - \frac{u'}{\bar{c}} \right), \quad (19)$$

$$\frac{s'}{c_p}(x, t) = \frac{p'}{\gamma \bar{p}} - \frac{\rho'}{\bar{\rho}}. \quad (20)$$

As already mentioned, the excitation characteristic is sinusoidal in time. In a linear system, that would mean that the pressure wave reflected from the nozzle is also sinusoidal. However, the temporal nature of the reflected pressure wave may be different for a nonlinear system. A question then arises as how to measure its magnitude. At the nozzle inlet, it is easy to take a full steady state period of the reflected pressure wave  $p_{ss}^-(t)$ , and its Fourier transform  $\mathcal{F}$ . The magnitude of the response can be considered the Fourier component occurring at the excitation frequency,  $\mathcal{F}_\omega$ . The nonlinearity is indicated by the difference between the output and its mode occurring at the excitation frequency. In a normalised form, this can be expressed as

$$\kappa = \frac{||\mathcal{F}_\omega| \cos(2\pi\omega t + \arg(\mathcal{F}_\omega)) - p_{ss}^-(t)||_2}{||p_{ss}^-(t)||_2}, \quad (21)$$

where  $||\cdot||_2$  denotes the  $\ell^2$ -norm. When  $\kappa = 0$ , the output signal is sinusoidal at the input frequency which infers a linear response. When  $\kappa = 1$ , all of the output occurs at frequencies other than the input frequency, suggesting the output is not at all linearly related to the input.

Simulations were performed in order to measure the reflection coefficients  $R_p$  and  $R_s$  for a 'compact' choked nozzle over a range of Mach numbers. In order to ensure compactness, a value of  $\Omega = 0.01$  was used. The results of these simulations are shown in figure 2. Even when the excitation characteristics are as large as 0.1, the numerically determined reflection coefficients are very close to the first-order approximation of Marble & Candel [5]. This was a surprising result and of practical

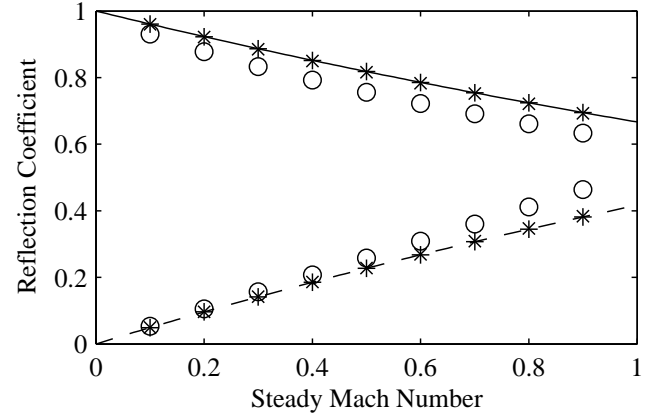


Figure 2: Steady Mach number dependence of the reflection coefficient of a choked exit nozzle with  $\Omega = 0.01$ . Marble and Candel's compact result for  $|R_p|$  in solid line and  $|R_s|$  in dashed line. Simulations for:  $\sigma, P^+ = 0.5$  ( $\circ$ );  $\sigma, P^+ = 0.1$  ( $\times$ ); and  $\sigma, P^+ = 0.001$  ( $+$ ).

interest since the pressure perturbations during thermoacoustic limit cycles can be 10% of the steady state pressure. For excitation characteristics of 0.5, a significant deviation from the linear approximation is evident, although perturbations of this magnitude are unlikely to occur in thermoacoustic limit cycles.

Further simulations were performed to measure the effect of finite nozzle length on  $R_s$  for a choked exit with a steady approach Mach number of 0.61 (the same Mach number as that studied by Marble & Candel [5]). Care was taken to ensure that the geometry enforced a linear steady velocity profile along the nozzle. Figure 3 shows a Bode plot of the entropy reflection coefficient for a finite length nozzle. It is clearly observed that the effect of finite nozzle length is to filter out the reflection of high frequency oscillations. This indicates that in the stability analysis of many real systems with a choked outlet nozzle, only the low frequency modes of vibration are of interest. Again the agreement between Marble & Candel's first-order approximation and the numerical results is surprising, even for  $\sigma = 0.1$ . Shown below the Bode plot is the nonlinearity measure  $\kappa$ . Although the higher amplitude excitation still gives a similar reflection coefficient to the linear model, some small nonlinearity is detected in the waveform of the response. Figure 4 gives an example of the degree of nonlinearity observed by comparing  $p^-(t)$  at the nozzle entrance to its component at the excitation frequency with  $\kappa = 0.05$ . Note that the time-averaged value of the nonlinear perturbation is non-zero.

Numerical simulations were also performed for the quasi-one-dimensional flow through an open outlet. The open geometry was represented by a smooth fractional area change of 100 occurring over a length of 0.005 of the incoming wavelength. This ensured that the outlet was both compact and emptying into an approximately infinite plenum. As discussed earlier in this paper, such a flow is not physical due to separation of the flow from the outlet, and formation of a jet. Nonetheless, figure 5 compares the linear analytic expression to those found numerically. The agreement between the numerical simulations and the analytical results for  $R_p$  is good, although the open outlet is slightly more nonlinear than the choked outlet.

## Conclusions

The Euler equations have been solved numerically for the case of quasi-one-dimensional flow through outlet nozzles. The reflection coefficients have been found for open, compact choked and finite length choked nozzles. For perturbation amplitudes

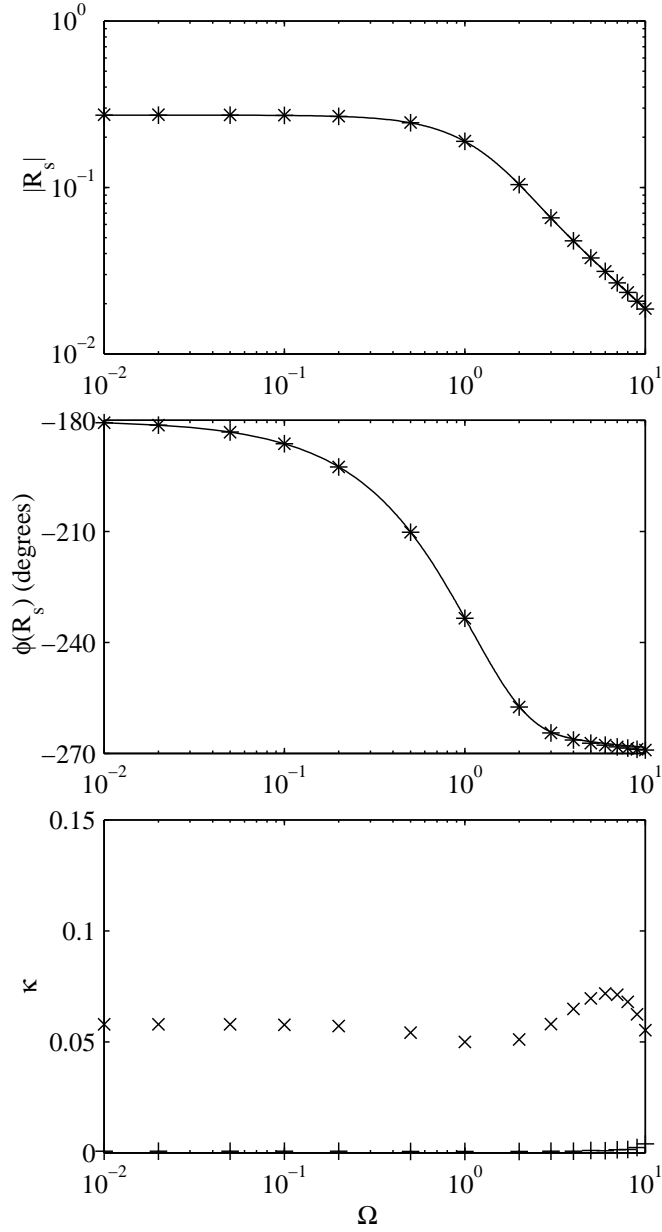


Figure 3: Reduced frequency dependence of entropy reflection coefficient of a choked nozzle with  $\bar{M} = 0.61$ . Solid line: Marble and Candel's finite length result. Simulations for:  $\sigma = 0.1$  ( $\times$ ); and  $\sigma = 0.001$  (+).

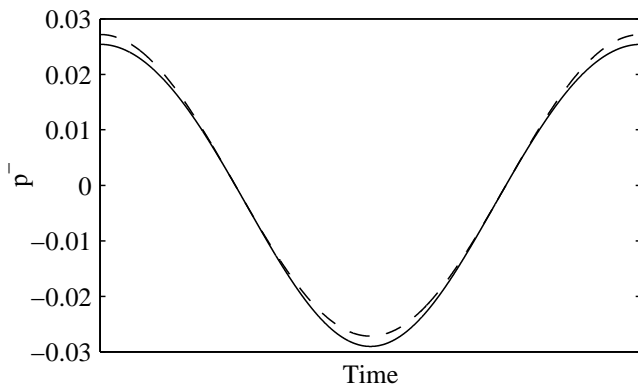


Figure 4: Reflected pressure wave from a choked exit nozzle as a function of time. Actual waveform shown in solid line, and its Fourier component at the excitation frequency shown in dashed line.  $\bar{M} = 0.61$ ,  $\Omega = 0.1$  &  $\sigma = 0.1$ .

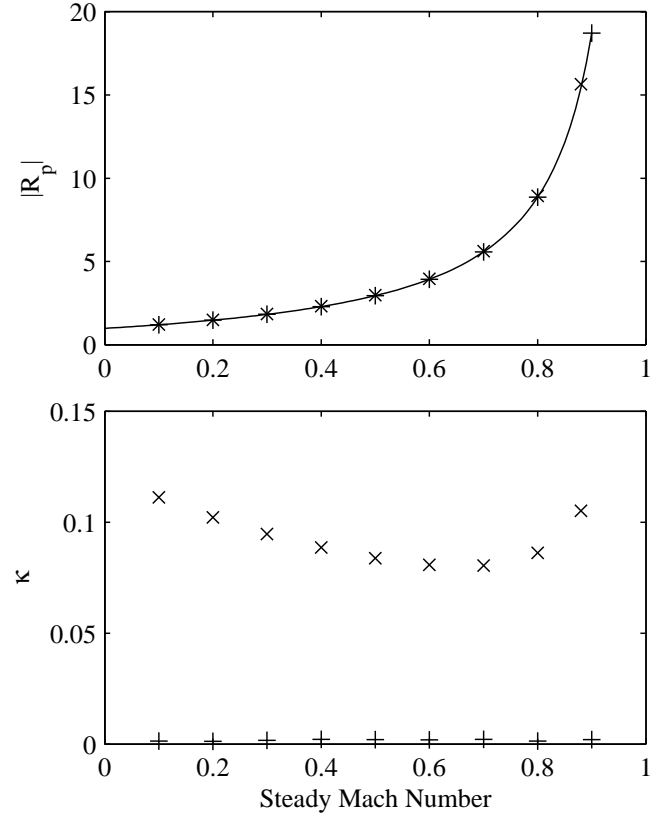


Figure 5: Dependence of reflection coefficient on steady Mach number. Analytical linear result in solid line. Simulations for:  $P^- = 0.001$  (+); and  $P^- = 0.1$  ( $\times$ ).

as big as 10% of their corresponding steady flow quantities, a small non-linearity is observed, but the reflection coefficients are very closely represented by linear approximations. This suggests that in the analysis of typical thermoacoustic limit cycles, the outlet will be close to linear and the boundary conditions of Marble & Candel as well as Rienstra are applicable.

## References

- [1] Colonius, T., Numerically Nonreflecting Boundary and Interface Conditions for Compressible Flow and Aeroacoustic Computations, *AIAA Journal*, **35**, 1997, 1126–1133.
- [2] Giles, M.B., Nonreflecting Boundary Conditions for Euler Equation Calculations, *AIAA Journal*, **28**, 1990, 2050–2058.
- [3] Langhorne, P.J., Reheat Buzz: an Acoustically Coupled Combustion Instability. Part I: Experiment, *J. Fluid Mech.*, **193**, 1988, 417–443.
- [4] Lele, S.K., Compact Finite Difference Schemes with Spectral-Like Resolution, *J. Comput. Phys.*, **103**, 1992, 16–42.
- [5] Marble, F.E. and Candel, S.M., Acoustic Disturbance from Gas Non-Uniformities Convected Through a Nozzle, *J. Sound Vib.*, **55**, 1977, 225–243.
- [6] Rienstra, S.W., A Small Strouhal Number Analysis for Acoustic Wave-Jet Flow-Pipe Interaction, *J. Sound Vib.*, **86**, 1983, 539–556.
- [7] Stow, S.R., Dowling, A.P. and Hynes, T.P., Reflection of Circumferential Modes in a Choked Nozzle, *J. Fluid Mech.*, **467**, 2002, 215–239.

where  $\mathbf{X}(s_i) = (X_i, Y_i)$  is the  $i$ -th node. The point (ring) source locations are given by  $\hat{X}_i = X_i - \gamma \Delta s n_x(s_i)$  and  $\hat{Y}_i =$

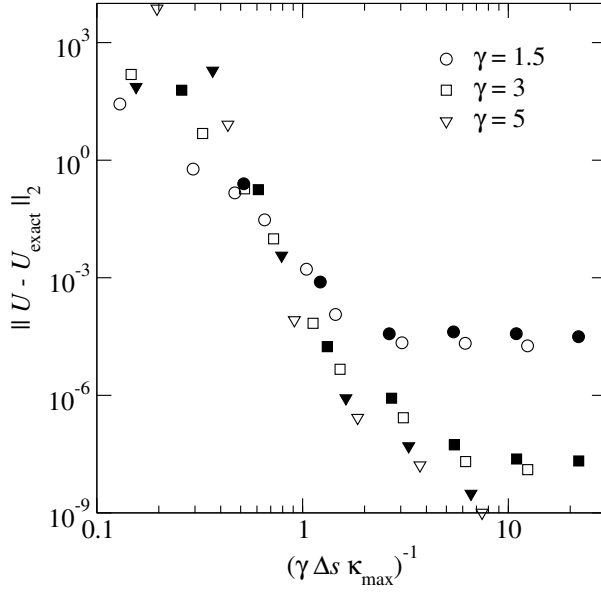


Figure 2: Surface velocity error for spheroids of aspect ratio 4 (open symbols) and 2 (closed symbols).

$\max[0, Y_j - \gamma \Delta s n_y(s_j)]$ , where  $\Delta s$  is the local node spacing and  $\gamma$  is a parameter measuring the source's distance inside the boundary relative to  $\Delta s$ .

Figure 2 shows the surface velocity error for prolate spheroids of aspect ratio 2 and 4. The optimal value of  $\gamma$  depends on both the grid spacing,  $\Delta s$ , and the maximum curvature,  $\kappa_{\max}$ . When  $\gamma \Delta s \kappa_{\max} \lesssim 1$ , that is, when the radius of curvature is similar in magnitude to the offset distance of the ring sources, the error is large, independent of  $\gamma$ . For prolate spheroids and ellipses, the maximum curvature occurs at the nose and, in this implementation, some of the point or ring sources are forced onto the plane or axis of symmetry. More generally, it is reasonable to expect that the point/ring source techniques will experience difficulty whenever the radius of curvature becomes small in comparison to the offset distance of the sources.

### Boundary-layer flow

Using the Görtler and (in the case of axisymmetric flow) Mangler transformations, the boundary-layer equations [5] reduce to

$$f_{\eta\eta\eta} + f f_{\eta\eta} + \beta(\xi)(1 - f_{\eta}^2) = 2\xi(f_{\eta}f_{\xi\eta} - f_{\xi}f_{\eta\eta}) \quad (10)$$

where

$$\eta = \frac{U(s)}{v\sqrt{2\xi}}n, \quad \psi(s, n) = v\sqrt{2\xi}f(\xi, \eta), \quad (11)$$

$(s, n)$  are coordinates parallel and normal to the surface, respectively,  $\psi(s, n)$  is the streamfunction,  $U(s)$  is the local surface velocity obtained from the potential solution,  $v$  is the kinematic viscosity, and subscripts on  $f$  denote differentiation. For plane-symmetric flows,

$$\xi = \frac{1}{v} \int_0^s U(s) ds \quad \text{and} \quad \beta(\xi) = 2v \frac{U'(s)}{U^2(s)} \xi. \quad (12)$$

For axisymmetric flows, the Mangler transformation is also applied, giving

$$\xi = \frac{1}{v} \int_0^s U(s) Y^2(s) ds \quad \text{and} \quad \beta(\xi) = 2v \frac{U'(s) Y^2(s)}{U^2(s)} \xi. \quad (13)$$

Equation (10) is subject to the boundary conditions

$$f(0) = 0, \quad f_{\eta}(0) = 0, \quad \text{and} \quad f_{\eta}(\infty) = 1, \quad (14)$$

	Plane-symmetric		Axisymmetric	
	$\eta - f(\eta)$	$f_{\eta\eta}(0)$	$\eta - f(\eta)$	$f_{\eta\eta}(0)$
Box method	0.6480	1.2328	0.8046	0.9278
Schlichting [5]	0.6480	1.2326	0.8047	0.9277

Table 1: Boundary-layer solver validation for self-similar stagnation point flow. Note that  $\eta - f(\eta)$  should be evaluated in the limit  $\eta \rightarrow \infty$ , but is here evaluated at  $\eta = 5$ .

and solved using the Keller Box method [5]. Second-order accurate finite difference and interpolation schemes are used to discretize (10) and a Newton method is used to solve the resulting nonlinear difference equations at each streamwise station. Adaptive Romberg integration is used to evaluate the integrals in (12) and (13). Second order finite differences are used to evaluate  $U'(s) = dU/ds$ . The far-field boundary condition is applied at  $\eta = 5$ . Consideration of plane-symmetric and axisymmetric stagnation point flow yields  $\beta(0) = 1$  and  $\beta(0) = 1/2$ , respectively.

Table 1 compares published results for self-similar stagnation point flow with those calculated using the Box Scheme solver with 100 nodes. This is not a complete check of the solver because the right-hand-side of (10) vanishes for self-similar boundary-layer flows. For plane-symmetric flow past a circular cylinder, the combined potential and boundary-layer solvers predict a separation angle of  $104.3^\circ$ , compared with a published value  $104.5^\circ$  [5]. For axisymmetric flow past a sphere, the combined potential and boundary-layer solvers predict a separation angle of  $104.6^\circ$ , compared with published values in the range  $103.6\text{--}109.6^\circ$  [6]. These values are obtained using 100 nodes in both the circumferential and wall-normal directions and first-order interpolation between circumferential grid points.

### Optimization

A discrete optimization problem is obtained by defining a discrete design or control vector,  $\mathbf{x}$ , whose components determine the forebody node positions according to

$$\mathbf{X}(s_i) = x_i \mathbf{n}_0(s_i) + \mathbf{X}_0(s_i), \quad i = 1, \dots, M, \quad (15)$$

where  $x_i$  is the  $i$ -th component of  $\mathbf{x}$ ,  $\mathbf{n}_0$  and  $\mathbf{X}_0$  are the normal and position vectors of a reference (initial) geometry, and  $M$  is the number of nodes on the forebody. Note that the objective function is still linear with respect to  $\mathbf{x}$ . The discrete constraints are

$$g_i(\mathbf{x}) = -\tau(s_i) \leq 0 \quad (16)$$

$$g_{i+M}(\mathbf{x}) = -X_s(s_i) \leq 0 \quad (17)$$

where  $i = 1, \dots, M$ . Although there are  $2M$  constraints, only a maximum of  $M$  can be active.

Using the boundary-layer solver described above, it is not possible to continue solutions downstream of the separation point due to the presence of the Goldstein singularity. It is therefore necessary to use an optimization algorithm that generates shape iterates that are always feasible, that is, unseparated. We use the Feasible Direction Interior Point (FDIP) method [2, 3]. With the above definitions, application of the algorithm to the present problem is straightforward.

The FDIP method is a gradient-based algorithm. For our problem, the objective function is linear, so analytical computation of  $\nabla f(\mathbf{x})$  is trivial. Finite differences are used to compute  $\nabla g_i(\mathbf{x})$ . Although expensive, this is satisfactory for sufficiently small problems, such as those presented in this paper. The Lagrangian Hessian is set to the identity matrix, resulting in a first-order method. A smoothing operator is applied to updates to help preserve shape regularity [4].



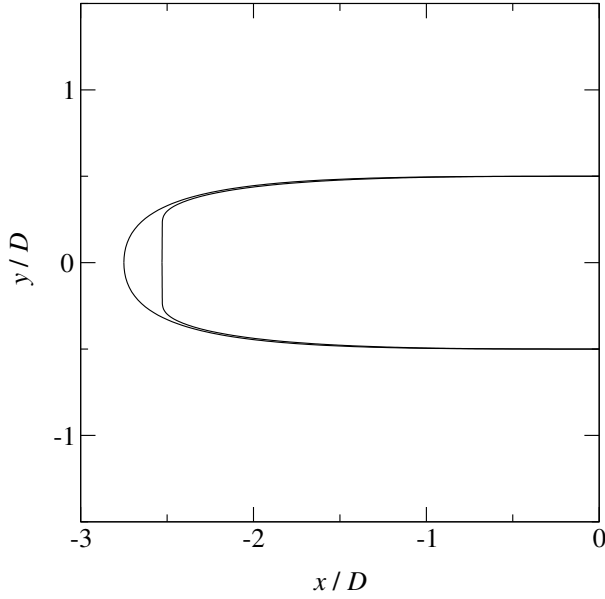


Figure 3: Initial and optimized forebody after 30 iterations for plane-symmetric flow.

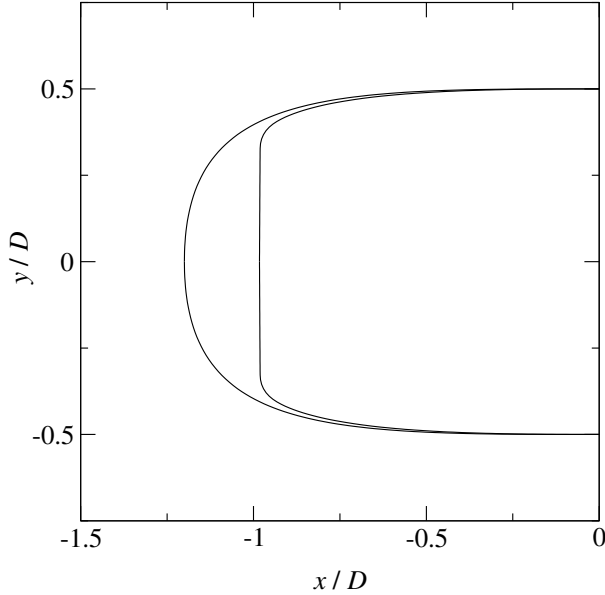


Figure 4: Initial and optimized forebody after 30 iterations for axisymmetric flow.

## Results

Figures 3 and 4 show the initial and optimized shapes for plane-symmetric and axisymmetric flow, respectively. In each case, the initial forebody geometry is specified as the lowest order Chebyshev polynomials that satisfy  $Y(0) = 0$ ,  $Y(s_0) = D/2$ ,  $Y_s(s_0) = 0$ ,  $Y_{ss}(s_0) = 0$  and  $X(0) = -L_{\text{init}}$ ,  $X_s(0) = 0$ , and  $X(s_0) = 0$ .  $L_{\text{init}}$  is chosen sufficiently large to obtain a feasible initial geometry. The results are obtained with  $\gamma = 3$ ,  $N = 800$ ,  $M = 240$ ,  $L_A/D = 8.56$  for the plane-symmetric case and  $\gamma = 3$ ,  $N = 400$ ,  $M = 100$ , and  $L_A/D = 3.38$  for the axisymmetric case. Calculations are terminated when progress stalls, or when the curvature and shear stress profiles develop significant grid-scale oscillations. These features are rejected because they are not retained upon grid refinement.

Figures 5 and 6 show the pressure coefficient,

$$c_p \equiv \frac{p - p_\infty}{\frac{1}{2} \rho U_\infty^2} = 1 - \left( \frac{U}{U_\infty} \right)^2, \quad (18)$$

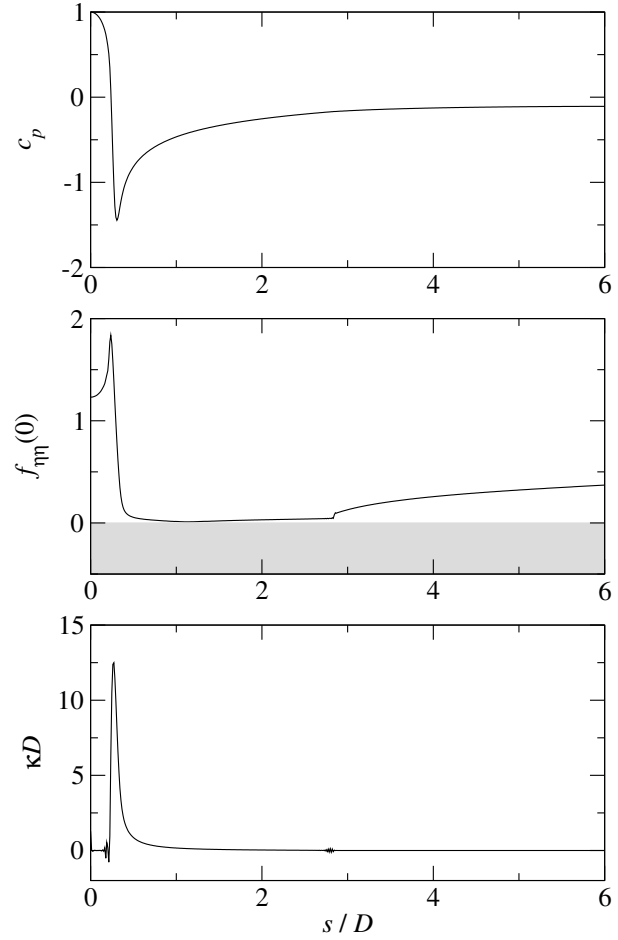


Figure 5: Pressure coefficient, shear stress, and curvature after 30 iterations in the plane-symmetric case. The junction is located at  $s_0/D = 2.84$ . The shaded area indicates separated (infeasible) solutions.

$f_{\eta\eta}$  evaluated at the wall ( $\eta = 0$ ), and the curvature for the plane-symmetric and axisymmetric case, respectively. Note that at any streamwise station,  $f_{\eta\eta}(0)$  is proportional to the wall shear stress,  $\tau$ , and is a convenient nondimensional substitute. The maximum curvature, maximum shear stress, and minimum pressure coefficient are clearly correlated. The optimization algorithm drives the geometry towards an almost discontinuous curvature variation. This causes curvature overshoots, as the splines struggle to resolve such features. The optimal geometry consists of an essentially flat-plate stagnation-point flow with a favourable pressure gradient up to the point of maximum curvature. Between this point and the junction with the aftbody, an approximately zero shear-stress surface is obtained.

The effect of aftbody length,  $L_A$ , is shown in Figure 7. Upstream influence can only enter through the pressure coefficient. The plane-symmetric case is more sensitive to aftbody length than the axisymmetric case and there appears to be some residual effect at  $L_A/D = 5.39$ .

## Discussion

The limitations of the flow solvers used in this paper are widely understood. Potential flow and first-order boundary-layer theory provide an accurate prediction when the Reynolds number is large and large-scale separation and transition do not occur. As the flow in the vicinity of the forebody is attached by design and separation occurs far downstream, we expect the present approximations to be qualitatively meaningful. Higher order effects, such as boundary-layer displacement effects, are ignored, as are the effects of instability and transition to turbulence that

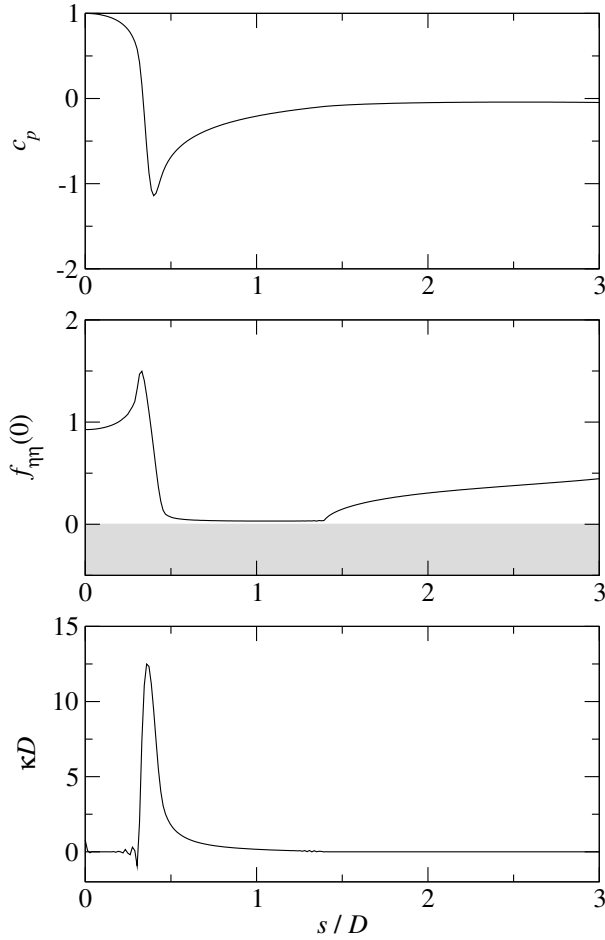


Figure 6: Pressure coefficient, shear stress, and curvature after 30 iterations in the axisymmetric case. The junction is located at  $s_0/D = 1.39$ . The shaded area indicates separated (infeasible) solutions.

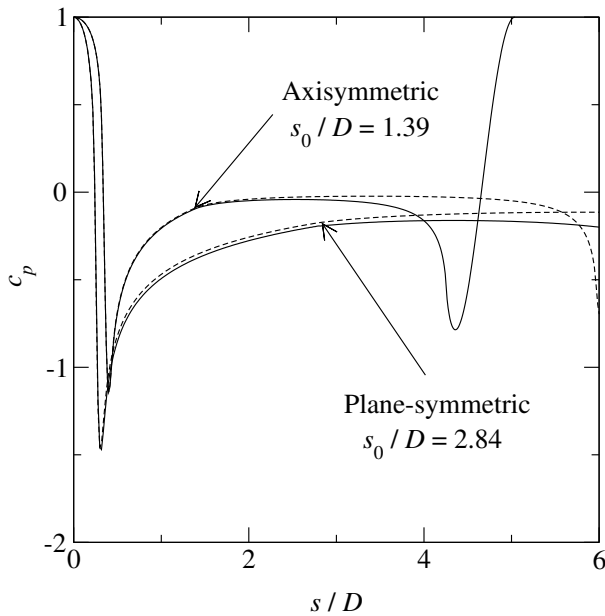


Figure 7: Effect of aftbody length on pressure coefficient profiles for plane-symmetric (solid line,  $L_A/D = 5.39$ ; dashed line  $L_A/D = 8.56$ ) and axisymmetric (solid line,  $L_A/D = 3.38$ ; dashed line  $L_A/D = 5.09$ ) cases.

will occur at sufficiently large Reynolds number. The zero shear stress surface is rather sensitive to perturbations in the geometry, suggesting that displacement effects may be important in a physical flow. The adverse pressure gradient associated with the zero shear stress surface implies the existence of an inflection point in the boundary-layer velocity profiles, hence the boundary layer will be particularly susceptible to instability. It is likely the forebody geometry will need to be modified to take these effects into account. This is the subject of future work.

Another important factor in the physical flow is sensitivity to angle of incidence. The optimized forebody geometries exhibit rather sharp corners. We expect that such features would promote separation in the presence of small angles of incidence. This is also the subject of future work.

The optimizing algorithm can find solutions of the discrete problem with lower values of the objective function than the examples shown here. Approaching these solutions, the shapes tend to lose regularity, with large oscillations in the curvature causing similar oscillations in the streamwise shear stress profiles. As mentioned above, such solutions are rejected, but a rational criterion for doing this has not been developed. As a result, it is not possible to be certain how well-converged the solutions are.

## Conclusions

Classic flow solvers are combined with the FDIP optimization algorithm to obtain minimum-length forebody geometries free from separation. The optimal geometry consists of an essentially flat plate normal to the flow, connected to the aftbody by a smooth surface with almost zero shear stress. For the plane-symmetric case, the minimum forebody aspect-ratio was approximately 2.5, compared with approximately 1.0 for the axisymmetric case.

## Acknowledgements

This project is supported by Australian Research Council Discovery Project DP0211479.

## References

- [1] Cao, Y., Schultz, W. W. & Beck, R. F., Three-dimensional desingularized boundary integral methods for potential problems, *Int. J. Numer. Meth. Fl.*, **12**, 1991, 785–803.
- [2] Herskovits, J. & Santos, G., On the computer implementation of feasible direction interior point algorithms for nonlinear optimization, *Struct. Optimization*, **14**, 1997, 165–172.
- [3] Herskovits, J., Feasible direction interior-point technique for nonlinear optimization, *J. Optimiz. Theory App.*, **99**, 1998, 121–146.
- [4] Mohammadi, B. & Pironneau, O., *Applied Shape Optimization for Fluids*, Oxford University Press, Oxford, 2001.
- [5] Schlichting, H. & Gersten, K., *Boundary Layer Theory*, Springer-Verlag, Berlin, 2000.
- [6] White, F. M., *Viscous Fluid Flow*, McGraw-Hill, New York, 1974.

## The Unsteady Near-Wake of a Simplified Passenger Car

G. Vino<sup>1</sup>, S. Watkins<sup>1</sup>, P. Mousley<sup>2</sup>, J. Watmuff<sup>1</sup> and S. Prasad<sup>1</sup>

<sup>1</sup> School of Aerospace, Mechanical and Manufacturing Engineering  
RMIT, Melbourne, Australia

<sup>2</sup>Turbulent Flow Instrumentation Pty Ltd, Tallangatta, Australia

### Abstract

The time-averaged and time-dependant nature of the wake of a simplified passenger vehicle (Ahmed model) has been investigated experimentally. Time-averaged results of the far-wake showed good agreement to previously published work, although the near-wake structure was found to be somewhat different, complementing findings made through flow visualisation. Time-dependant analysis revealed that the shedding behind the model is analogous to vortex shedding behind simple bluff bodies, with most of the fluctuations confined to the axial and vertical directions. In addition, the shedding characteristics on the slant showed very similar behaviour to the vertical base, indicating strong turbulent mixing between the two regions, emphasizing time-averaged findings and complementing the proposed flow topology.

### Introduction

There exists a large database of information directed towards understanding flow structures in the wake of simplified passenger vehicle geometries. Until recently, the bulk of literature has only been successful in elucidating regions in the wake where the flow direction is dominantly in the streamwise sense. In addition, much of this work has been limited to time-averaged behaviour, due to the complexity associated with time-varying flows that exhibit significant flow angles, and sometime complete reversals.

The purpose of this research is to further the understanding of flow in the near-wake of a well-known simplified passenger vehicle geometry.

The use of simplified forms of passenger vehicles has proven extremely useful in terms of understanding the fundamental flow characteristics associated with more complex passenger cars [5]. Although many types of simplified passenger vehicle geometries have been investigated, one of the most popular has been the Ahmed model, after [1]. From flow visualisation and time-averaged measurements, the hypothesised flow patterns of Ahmed et al are summarized in Figure 1. It is important to note that some of the time-averaged results presented indicate that certain complex flow regions (i.e. large flow angles including reversals) were not successfully captured during sampling, although this was not discussed in detail.

The size and strength of the C-pillar vortices were found to be very dependant on the base slant angle. As the base slant angle reached 30 degrees from the horizontal, the separated bubble on the slanted edge grows in size forming a dominant low-pressure horseshoe vortex on the backlight. This low-pressure region then draws in and strengthens the C-pillar vortices. Overall, the base pressure is significantly reduced, resulting in a significant rise in drag. Beyond a slant angle of 30 degrees, the separated flow is no longer able to reattach down the slanted edge, thus reducing the strength of the C-pillar vortices. Hence, at slant angles above 30 degrees the flow pattern is accompanied by a significant rise in base pressure and therefore reduction in drag. The "critical" 30-degree high-drag backlight configuration was used in this investigation.

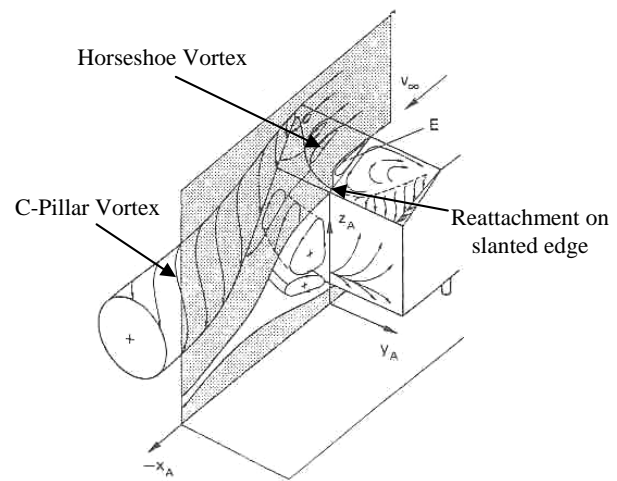


Figure 1. Proposed high-drag vortex system for the Ahmed model geometry [1].

This paper will further elucidate the complex behaviour in this near-wake region through a detailed experimental investigation into the time averaged and unsteady flow characteristics.

### Experimental Arrangement

A 1/4 scale Ahmed model geometry was used in this investigation, with the rear slant angle held constant at 30 degrees. All tests in this investigation were conducted in the RMIT Industrial Wind Tunnel. The wind tunnel is a closed-jet and fixed-ground type, and is able to generate flow speeds of up to 43 m/s, with a longitudinal turbulence intensity of 1.5%. The wind-tunnel blockage ratio was equal to 1.9%, based on maximum projected frontal area of the Ahmed model, which was deemed suitable in that relevant flow structures would not be significantly affected by the presence of the wind tunnel walls. No corrections were made for blockage.

Time-averaged and time-varying surface pressure measurements were measured with a Dynamic Pressure Measurement System (DPMS), supplied by Turbulent Flow Instrumentation Pty Ltd. Tests were conducted at a range of speeds between 20 and 35 m/s. Silicon tubes of 0.8 mm diameter were inserted at each surface pressure tap and connected to the DPMS. As described in [5] and [2], the oscillatory pressures through these tubes undergo an amplitude variation and phase lag that is frequency dependant. Therefore, the pressure signals measured by the transducers were linearised to correct for the amplitude and phase distortion. The correction technique used is based on a Fourier transform technique (see [3]) and consists of obtaining the Fourier transform of the measured signal at the transducer, dividing this by a tubing transfer function (that relates the dynamic pressure at the transducer to that at the point of measurement), and transforming the result back to the time domain via an Inverse Fourier transform.

In order to obtain a more complete representation of the flow field, off-body flow measurements were taken at three downstream transverse planes in the wake of the model. Single

point flow measurements were conducted at a wind tunnel speed of 35 m/s using a 13-hole, high frequency response pressure probe. This pressure probe, known as the ECA (Extended Cone of Acceptance) Probe, was also supplied by Turbulent Flow Instrumentation. It is of the multi-hole type and has a flow acceptance cone of about  $\pm 135^\circ$ , resolving all three components of velocity and local static pressure up to frequencies of about 1 KHz. For more information on the design, validity, steady state and dynamic calibration of the probe, refer to [12].

## Results

### Time-Averaged Results

Figure 2 shows the off-body flow patterns at the rear of the model through smoke injection. In the top figure the smoke was injected at the end of the roof centerline, while the smoke patterns shown in lower figure originated at the top of the C-pillar as shown. The wake pattern shows excellent agreement with [10], in that the flow over the backlight shows a large separation bubble over the entire centerline, consequently aiding the generation of a strong trailing vortex from the C-pillar, which is very well defined. It is important to note however that unlike the proposed flow pattern of [1], the flow along the centreline does not fully reattach before leaving the base, but forms part of the wake behind.

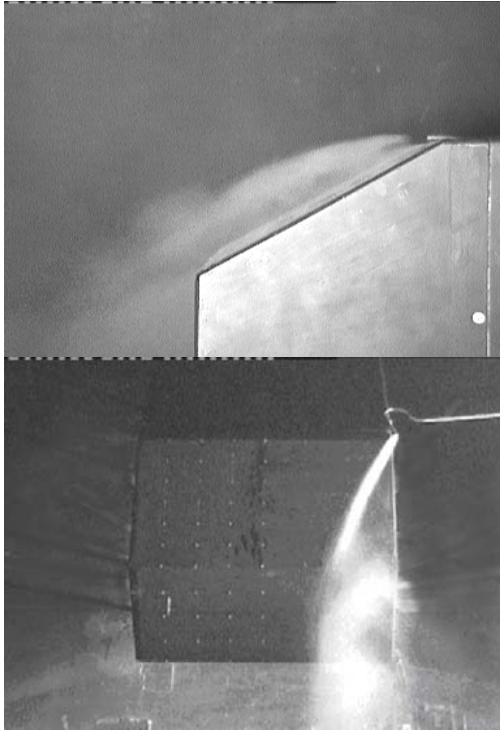


Figure 2. Off-body smoke flow patterns at rear end of the model.

Figure 3 shows the corresponding surface skin friction patterns on the backlight and vertical base. It is evident that the flow from the roof separates at the top of the backlight, which is consistent with smoke flow patterns. Just inboard of the C-pillars, there exists a separation line extending through the entire length of the backlight. This line makes an angle of approximately 7 degrees relative to the C-pillar, comparing well to results obtained by [10] and [1]. It has been widely accepted that this separation line is a result of the C-pillar vortex separating as it spirals along the backlight.

Further inboard there is a large separated region that extends to the base of the backlight. Many authors have also revealed the existence of this large separated region, which is bordered by the trailing vortex impingement lines. These impingement lines also agree with smoke patterns shown in Figure 2. Within this region exist significant levels of reverse flow making a radiating pattern originating from main stable foci located just below the top

corners of the backlight. The presence of these foci corresponds to the work of [11]. In addition, unlike [1] whereby this reverse flow region was fully enclosed and assumed an arch shaped horseshoe vortex (see Figure 1), this region takes on a 'D - like' shape, with a central tail at its base. This central tail, which is relatively thin, does not show any sign of reattachment but instead exhibits flow reversals right up until the rear of the model. A similar shaped detached flow region was also found by [10]. Thus, it is envisaged that the separated flow over the slant reattaches along the vortex impingement lines, but not in the small region between.



Figure 3. Rear end surface skin friction patterns.

On the vertical base, there exists a well-defined line that makes the shape of an arch. The patterns suggest that the flow originates at the periphery of this arch and radiates towards the top and sides of the base. Within the arch, patterns made during model preparation (i.e. applying surface oil solution) are significant, indicating low levels of energy within this region. This suggests that the flow just off the surface of the vertical base is characterised by a dominant arch-shaped recirculation bubble. It is envisaged that a counter-rotating vortex is created below, which is fed below by the flow coming from the underbody and above by this large arch vortex, although this is not discernable from Figure 3.

Figure 4 shows the mean velocity vectors measured with the ECA probe along the plane of symmetry and Figure 5 shows the corresponding calculated streamline pattern. Thus far, this complex near-wake flow region has proven difficult to capture due to the limitations associated with hot-wire and pressure probes measuring flow reversals, however, flow structures within this region were successfully captured with the 13-hole probe.

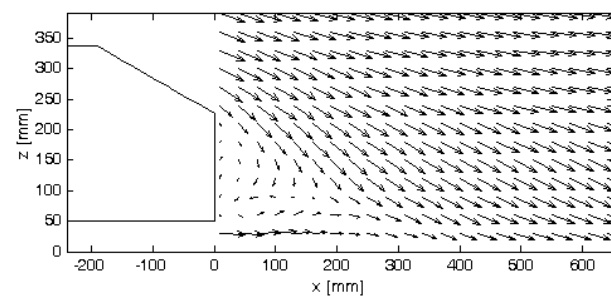


Figure 4. Velocity vectors measured along the symmetry plane in wake of model.

Through the use of PIV, [7] were also able to capture flows in the near-wake, although the data published and conclusions drawn were somewhat limited to far-wake characteristics.

Immediately behind the vertical base, a well-defined separation at the top and bottom of the vertical base is apparent, enclosing a clear recirculatory flow region. Two recirculatory bubbles are observed, one above the other, and in opposing directions. The higher bubble covers the upper region of the

vertical base, while the lower bubble, which rotates in the opposite direction, does not appear to interact with the surface. This finding agrees with skin friction patterns of Figure 3, which indicated that a single recirculation bubble interacted with the vertical rear surface.

Towards the upper portion of the separated region it is clear that the circulation zone is drawing fluid from the separated flow above the slanted edge. Thus, the flow over the slanted edge, at least along the centreline, does not reattach on the slant before separating at the base, which emphasises flow patterns in Figure 3. This is in contrast to the flow topology of Ahmed et al [1], which suggests that flow above the central region of the slant is characterised by a large separation bubble that reattaches before separating again at the base. Thus, the closed horseshoe vortex proposed by Ahmed et al is in fact partially open, and mixes with the upper recirculation bubble on the vertical base. As a result, the flow leaving the top of the model assumes much larger angles to the slant.

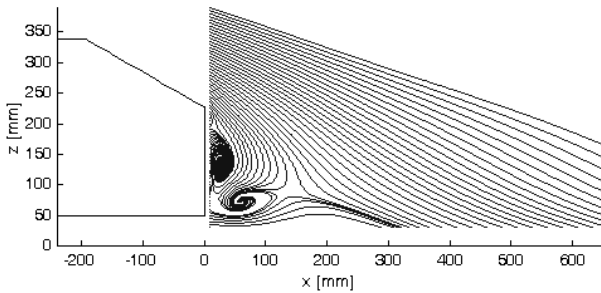


Figure 5. Streamlines along the symmetry plane in wake of model.

This finding also agrees with the work of [11], which shows that the horseshoe vortex on the slant was not closed but mixed with the flow in the wake. It is important to note that the model used by [11] had a slant angle of just 25 degrees, which would only act to promote reattachment. Thus, this new proposed flow topology is not limited to slant angles very close to and above the critical geometry (i.e. 30 degrees rear slant angle).

## Unsteady Results

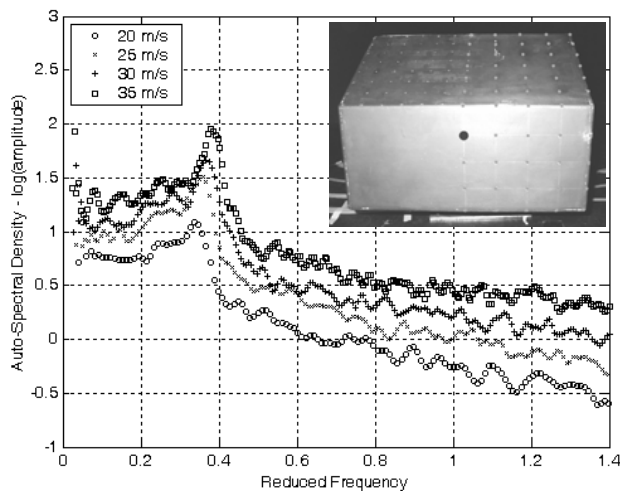


Figure 6. Auto-spectral Density function of a selected surface pressure tap on the rear of the model.

Although only shown here for a single location (see Figure 6), spectral analysis of time-signals of various surface pressure taps on the rear slant and vertical base revealed a single dominant shedding frequency of 40 Hz at the highest test Reynolds number, which corresponds to a Strouhal number 0.39 (based on the square root of model frontal area). Some sensitivity of the Strouhal number was also observed within the Reynolds number range tested. Readings from pressure taps on both the vertical

base and slanted edge indicate high energies are also associated with the shedding.

Figure 7 shows the correlation between time signals of surface pressure taps at the top and bottom of the vertical base, corresponding to the two-recirculatory bubbles, one above the other, shown in Figure 1 and Figure 5. Firstly, we see that the phase estimate near the non-dimensional shedding frequency of 0.39 suggests that the shedding is 180 degrees out of phase, implying alternate shedding. Thus, the recirculatory bubbles located behind the vertical base (see Figure 5) are analogous to the well-known von Karman vortex shedding behind bluff bodies, particularly square cylinders, shedding alternately at a Strouhal number of about 0.39. For the test speed range used here, Reynolds numbers (based on square root of frontal area) were between  $5.5 \times 10^5 < Re < 7.7 \times 10^5$ .

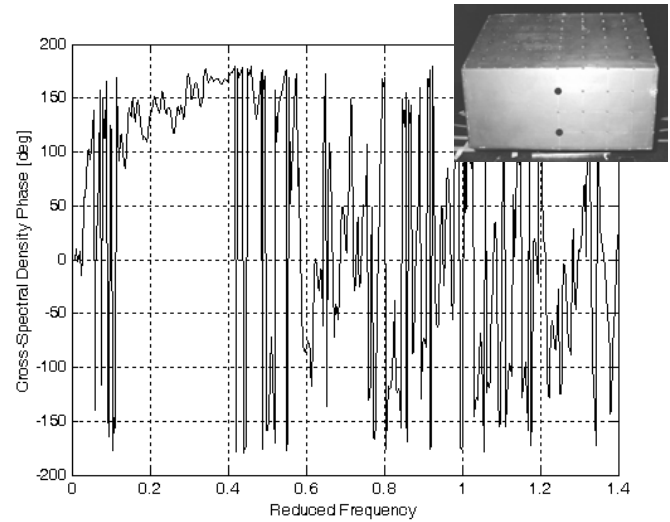


Figure 7. Cross-spectral Phase estimate between selected surface pressure taps on the vertical base.

It is known that at such high Reynolds numbers, circular cylinders exhibit significant losses in periodic flow (see [8]) due to the boundary layer undergoing transition to turbulence, creating a smaller wake, and accompanied by diminishing shedding characteristics. However, square cylinders tend to exhibit well-defined shedding behaviour up to Reynolds numbers well beyond those investigated here due to the separation locations being fixed irrespective of Reynolds number, which result in well-defined separated shear layers at opposite sides of the wake.

Time-averaged results suggest that the flow over the slant mixes with the upper recirculation bubble behind the vertical base. Figure 8 shows the correlation of shedding characteristics between pressure taps on the slant and upper region of the vertical base. At a reduced frequency of 0.39, the two regions correlate close to 0 degrees, suggesting that they are in phase. Thus, the fluctuations on the slanted edge shed simultaneously with the upper separation bubble on the vertical base. This result emphasizes that the detached flow region on the slant and recirculation bubble on the vertical base are in fact a single large separated flow region.



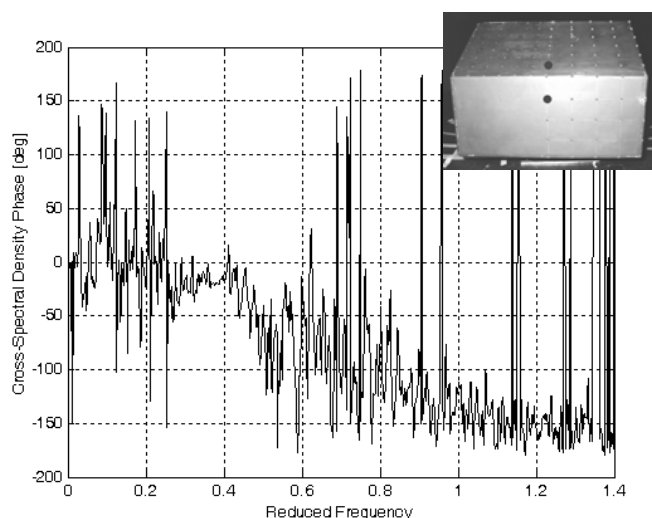


Figure 8. Cross-spectral Phase estimate between surface pressure taps on the slant and vertical base.

### Proposed Flow Topology

Figure 9 highlights the important time-averaged flow features found from this investigation, with surface patterns drawn as limiting streamlines (i.e. lines of surface shear stress) on the right hand side of the model, and off-body flows on the left.

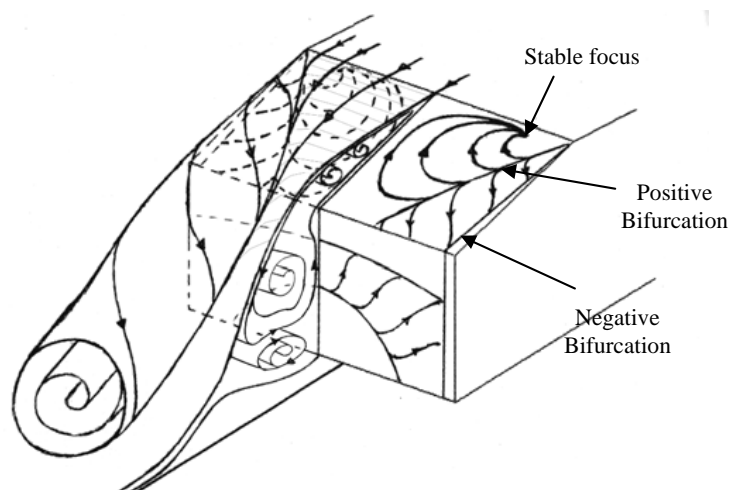


Figure 9. Proposed topological flow structure of the Ahmed model with critical geometry.

Clearly, the impingement of the trailing vortex along the C-pillar is shown. This impingement can be considered as a classic example of a positive bifurcation in terms of the 'critical point theory' described in [7] and [3]. Here, a streamline from the oncoming streamsurface (i.e. the trailing vortex surface) bifurcates into two at the line. On one side of this positive bifurcation, the flow tends toward a stable focus in a spiralling path, as it interacts with the flow reversals inside the detached flow region on the slant. On the other side, the path taken by the vortex as it interacts with the surface is shown. Note that the vortex separates at approximately 7 degrees to the C-pillar. Although not found in results of this study, possibly due to limited resolution of flow maps, [10] showed that a smaller, counter rotating, vortex existed above the small region between the line and C-pillar. As such, this 7-degree separation line can be viewed as a negative bifurcation, in which two streamlines appear to combine into one.

On the vertical base, the limiting streamlines indicate the path of the upper separation bubble, which causes significant levels of upwash on the surface. Note the horseshoe shape made by the bubble as it extends to the sides of the model. No

hypothesis is made for the regions above and below this bubble since results failed to reveal any definite path.

Off the body, the combination of the detached flow over the backlight and recirculation bubble on the vertical base is shown. It is important to note that although the detached flow region on the slanted edge only fails to reattach in the small region between the trailing vortices, it does reattach along the positive bifurcation lines. Also, it was found that this region was highly unsteady, so the time-averaged flow topology should only serve as an approximate representation. Finally, the dominant trailing vortex generated at the C-pillar is also shown, with its path illustrating that the vortex core tends to move downward as it flows downstream.

### Concluding Remarks

The complex nature of the near- and far-wake of the Ahmed model geometry has been investigated. Surface friction patterns and time-averaged results revealed that the separated flow region over the slanted edge does not fully reattach further down the slant, but instead mixes with the large separated region behind the vertical base. The two regions consequently exhibit similar time-dependant behaviour.

Spectral characteristics of surface pressure signals also revealed that the recirculation bubbles found behind the vertical base could be seen as analogous to longitudinal vortices in a von Karman vortex street.

### References

- [1] Ahmed, S.R., Ramm, G. & Faltin, G., Some Salient Features of the Time-Averaged Ground Vehicle Wake, *Society of Automotive Engineers*, 1984, 840300.
- [2] Bergh, H. & Tidjeman, H., Theoretical and Experimental Results for the Dynamic Response of Pressure Measuring Systems, *National Aero And Aeronautical Research Institute*, 1965, NLR-TR F.238.
- [3] Hooper, J. D. and Musgrove, A. R., Reynolds stress, mean velocity, and dynamic static pressure measurement by a four-hole pressure probe, *Journal of Experimental Thermal and Fluid Science*, **15**, 1997, 375-383.
- [4] Hornung, H. & Perry, A. E., Some Aspects of Three-Dimensional Separation, Part 1: Streamsurface Bifurcations, *Z. Flugwiss. Weltraumforsch* **8**, 1984, 77-87.
- [5] Iberall, A. S., Attenuation of Oscillatory Pressures in Instrument Lines, U.S. *Department Of Commerce, National Bureau Of Standards* **45**, 1950, RP2115.
- [6] Le Good, G. & Garry, K. P., On The Use of Reference Models in Automotive Aerodynamics, *Society of Automotive Engineers*, 2004, 04B-25.
- [7] Lienhart, H. & Becker, S., Flow and Turbulence Structure in the Wake of a Simplified Car Model, *Society of Automotive Engineers*, 2003, 2003-01-0656.
- [8] Perry, A. E. & Chong, M. S., A Description of Eddying Motions and Flow Patterns Using Critical-Point Concepts, *Annual Rev. Fluid Mechanics* **19**, 1987, 125-155.
- [9] Roshko, A., Perspectives on Bluff Body Aerodynamics, *Journal Of Wing Engineering And Industrial Aerodynamics* **49**, 1993, 79-100.
- [10] Sims-Williams, D.B., Self-Excited Aerodynamic Unsteadiness Associated with Passenger Cars, PhD Thesis, University Of Durham.
- [11] Spohn, A. & Gillieron, P. 2002 Flow Separations Generated by a Simplified Geometry of an Automotive Vehicle, *IUTAM Symp*. 2001.
- [12] Vio, G. & Watkins, S. 2004 A Thirteen-Hole Probe for Measurements in Bluff Body Wakes, *Fifth International Colloquium on Bluff Body Aerodynamics and Applications*, Canada, 2004.



## Convective Exchange between two Connected Chambers

M. A. Coman, G. O. Hughes and R. C. Kerr

Research School of Earth Sciences  
The Australian National University, Canberra ACT 0200, AUSTRALIA

### Abstract

High Rayleigh number convection is studied experimentally in a differentially heated cavity that consists of two connected chambers. We investigate how the circulation, the temperature field and the transport of heat and mass depend on the height of the barrier separating the chambers. We find that the temperature fields in the chambers are very different and that a complex flow structure evolves to accommodate the heat and mass transports. Surprisingly, both of these transports are found to have little dependence on the barrier height, and only begin to decrease rapidly when the barrier height becomes very large.

### Introduction

Convection in a two-dimensional differentially heated cavity has been extensively studied, motivated by a wide range of engineering applications [1, 2, 3, 4, 7]. At high Rayleigh numbers, a strong boundary layer circulation (figure 1) accommodates most of the mass and heat fluxes: a buoyant plume rises up the heated endwall, flows along the top of the cavity, falls down the cooled endwall as a dense plume, and then returns along the bottom of the cavity [2, 3, 4]. Fluid in the cavity interior or 'core' is nearly stagnant and has a temperature field that varies linearly with depth and is independent of longitudinal position [1, 7].

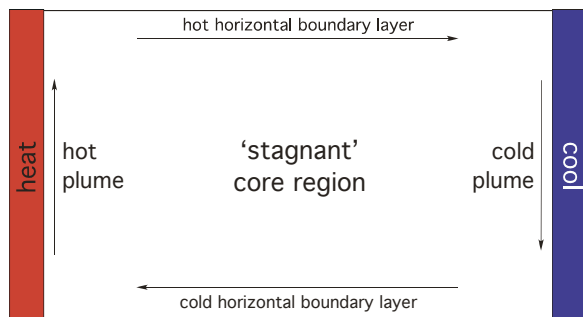


Figure 1: Schematic of the boundary layer circulation in a differentially heated cavity at high Rayleigh number (no barrier).

In many geophysical, environmental and industrial situations convective circulation is strongly influenced by complex bottom topographies or building geometries [5, 6, 8]. As a step towards understanding these more complex flows, we have placed a barrier in the cavity interior that blocks the boundary layer circulation and changes the flow significantly. In this paper we describe how the flow changes as a function of barrier height and present measurements of the modified heat and mass transports in the cavity.

### Experimental Apparatus & Methods

The experimental set-up is illustrated in figure 2. The experiments were carried out in a tank of length  $L = 302$  mm, height  $H = 196$  mm and width  $W = 150$  mm. The base, lid and side-walls were made of Perspex, with heat exchangers as endwalls. Each heat exchanger was kept at a constant temperature by recirculating water from a temperature-controlled bath. The tem-

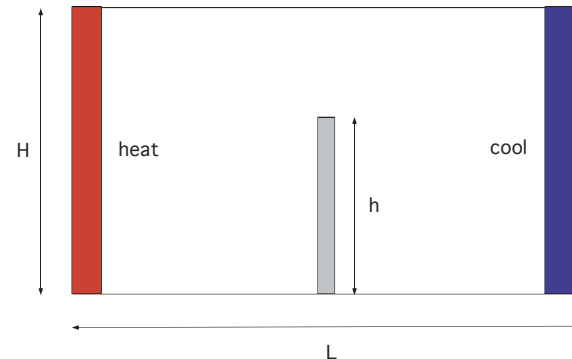


Figure 2: Experimental configuration (elevation view).

perature in the heat exchangers was monitored using embedded thermistors. Water was used as the working fluid in the tank. Four holes along the length of the tank in the centre of the lid accommodated flow visualisation and temperature measurements. This ensured all visualisation and measurements were subject to minimal influence from the sidewalls. Barriers of the same width as the tank and of height  $h = 36$  mm, 56 mm, 76 mm, 96 mm, 116 mm, 136 mm, 156 mm and 176 mm, were inserted half way along the tank at the bottom so as to create two connected chambers of equal size. The barriers were made of 20 mm thick Styrofoam with rubber sealing on the three sides touching the tank to ensure minimal conductive heat transfer and no water leakage between chambers. Heat loss from the tank was minimised by double glazed Perspex sidewalls. In addition, the tank was insulated on all sides with Styrofoam. The insulation on the two sidewalls was removed only when photos and temperature profiles were being collected. The heat loss from the tank was found to be minimal, about 1% of the total convective heat flux in the no barrier case.

In each experiment the tank was carefully filled using de-aired water to reduce the amount of bubbles present. Two free standing thermistors were placed in the interior of the tank, one in the middle of each chamber. Temperatures were logged on a PC and when the readings from all the thermistors were constant (after typically 15 hours), the system was considered to have reached thermal equilibrium.

Once at equilibrium, temperature profiles through the two chambers and through the depth above the barrier were measured. Potassium permanganate crystals and food dye were introduced into the flow through the holes in the tank lid. A slide projector was placed a few metres behind the tank illuminating a sheet of tracing paper attached to the back of the tank. The tracing paper acted as a light diffusing screen, against which the dye could be easily seen. A Nikon D100 digital camera was used to take photos during the experiments. Horizontal velocity measurements were made in the centre of the tank, above the barrier, in order to determine the mass and heat fluxes in the flow. Approximately vertical dyelines were generated by dropping potassium permanganate crystals through the flow. Pho-

tographs were taken at intervals between two and sixty seconds, and the velocities calculated (with an accuracy of  $\pm 5\%$ ) using the horizontal displacement in dye line positions from one photo to the next.

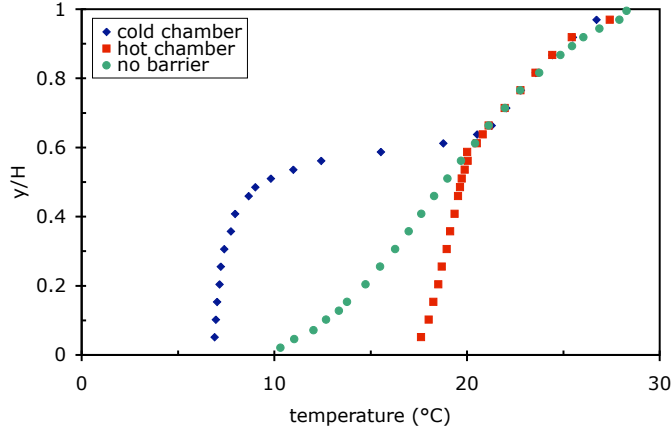


Figure 3: Steady-state temperature profiles through the two chambers for  $A_B = 0.59$ . The steady-state temperature profile at the centre of the tank for the flow with no barrier is also shown.

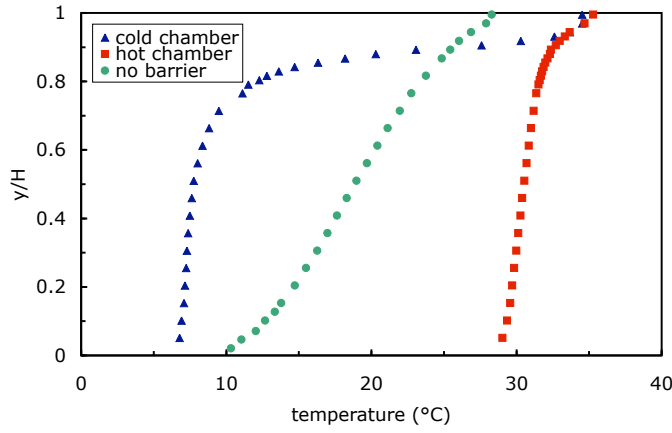


Figure 4: Steady-state temperature profiles through the two chambers for  $A_B = 0.90$ . The steady-state temperature profile at the centre of the tank for the flow with no barrier is also shown.

In this flow there are four important parameters: the Rayleigh number

$$Ra = \frac{\alpha g \Delta T H^3}{\nu \kappa} = 5 \times 10^9, \quad (1)$$

the Prandtl number

$$Pr = \frac{\nu}{\kappa} = 7, \quad (2)$$

the aspect ratio

$$A = \frac{H}{L} = 0.65, \quad (3)$$

and the barrier aspect ratio

$$A_B = \frac{h}{H}, \quad (4)$$

where  $g$  is the gravitational acceleration,  $\alpha$  is the expansion coefficient,  $\Delta T$  is the applied temperature difference between the two endwalls,  $\nu$  is the kinematic viscosity and  $\kappa$  is the thermal diffusivity.

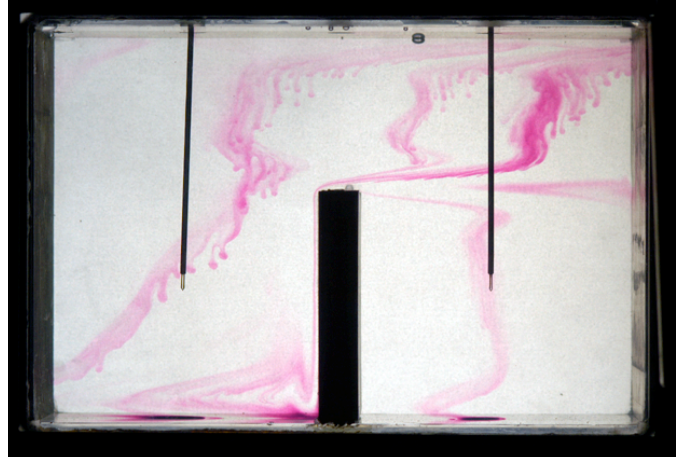


Figure 5: Visualisation of the flow for  $A_B = 0.59$ . Initially vertical dye streaks were generated by dropping potassium permanganate crystals at three positions: the centre of the tank and aligned horizontally with the thermistors (visible in the centre of each chamber).

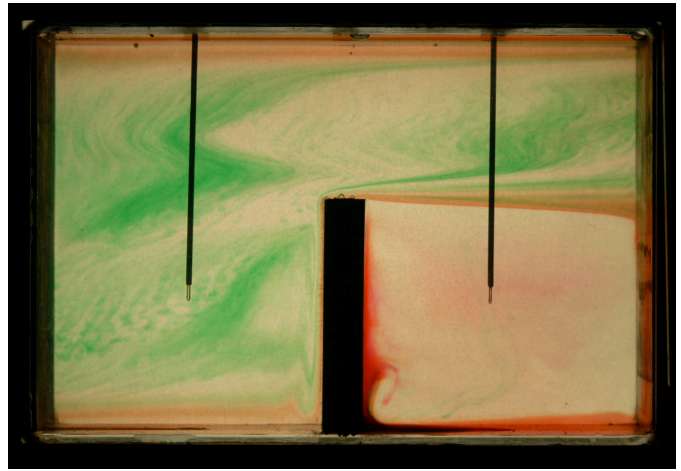


Figure 6: Visualisation of the flow for  $A_B = 0.59$ . Red dye was introduced into the boundary layer at the bottom of each chamber and at a later time green dye was added to the interior of the tank.

In this paper only  $A_B$  is varied, by changing the barrier height  $h$ . The other parameters are fixed as we are using the same tank, keeping water as the working fluid, and using an applied temperature difference  $\Delta T = 45^\circ\text{C}$  (the heated endwall had a temperature  $T_{hot} = 50^\circ\text{C}$  and the cooled endwall had a temperature  $T_{cold} = 5^\circ\text{C}$ ).

### Qualitative Observations

When a barrier is inserted into the cavity, fluid in the cold horizontal boundary layer in figure 1 is prevented from flowing all the way to the hot plume. Instead the outflow from the cold plume pools and slowly fills the right chamber in figure 2. Eventually, the coldest water totally fills this chamber to the height of the barrier, creating a ‘cold chamber’ whose final steady-state temperature profile contrasts dramatically with the temperature profile in the adjacent ‘hot chamber’ (see figures 3 and 4). The presence of a barrier has a significant effect on the temperature profile at the uppermost levels in the tank only when the gap above the barrier is small (compare figures 3 and 4).

Figures 5 and 6 show visualisations of the steady state circulation for  $A_B = 0.59$ . The hot plume (not visible) rises up the heated endwall and detains to form the hot horizontal boundary layer. The cold plume forms at the top of the cooled endwall and flows down the plate, but splits into two at around the height of the barrier. The coldest fluid from the inner part of the plume (against the endwall) continues to flow downwards, but the fluid in the outer part of the plume is not cold enough to penetrate into the cold chamber: it instead detains and flows horizontally towards the barrier. Along the way, the intruding flow is combined with upwelling fluid from the cold chamber to produce a strongly stratified overflow at the barrier (see figure 8). This flow then plunges over the side of the barrier forming a fast downflowing plume. In a manner very similar to a plume entering a stratified environment, the momentum of the downflowing fluid causes it to overshoot and then oscillate about its level of neutral buoyancy in the heated chamber (figures 5 and 6). As the overflow is strongly stratified, only the very coldest fluid immediately adjacent to the barrier is observed to reach the tank bottom, while the remainder enters the interior of the heated chamber at a range of different levels (figures 5 and 6). This fluid is then gradually drawn towards the lower part of the heated endwall, where it is entrained into the hot plume.

In the cold chamber, the flow is primarily driven by the cold sidewall plume, which produces a slow upwelling return flow (figure 6). The cold chamber is also weakly stirred by a small amount of heat transfer through the barrier (less than 3% of the total amount).

### Quantitative Results

The exchange flow above the barrier was found to be strongly dependent on the barrier height (see figure 7). In the no barrier case (figure 7 a), we observed strong boundary layer flows at the top and bottom, with a weak uniform shear in the interior (cf. figure 1). With the addition of a small barrier (figure 7 b), the top half of the flow is similar to the no barrier case (figure 7 a), but the bottom half is significantly different: the return flow occurs in a thinner layer with a much faster velocity. This barrier overflow also generates horizontal shear layers in the overlying fluid (cf. [9]), which are identified by a local maximum or minimum in the velocity profile. As  $h$  is increased, the region of uniform shear in the interior steadily decreases until it disappears at  $A_B = 0.59$  (figure 7 c). When  $h$  is increased further, the number of shear layers decreases from six (for  $A_B = 0.59$ ) to four (for  $A_B = 0.69$ , see figure 7 d), and then to a simple bi-directional exchange flow for the highest barrier (figure 7 e), where a layer of warm water flowing towards the cooled endwall overlies a cooler layer overflowing the barrier.

In figure 8, the temperature profile above the barrier is shown for a number of different barrier heights. As the barrier height is increased, two main effects are observed. First, the temperature gradient in the barrier overflow systematically increases. Second, the temperature profiles are shifted to warmer temperatures. However, the temperature gradient above the barrier appears to be unchanged (cf. figures 3 and 4).

From integration of the velocity profiles in figure 7, we determined the volume flow per unit width from the hot chamber to the cold chamber, as a function of the barrier height (figure 9). The volume flow was expected to decrease steadily with increasing barrier height. However, for modest barrier heights, no such decrease was observed (and there is a suggestion of a maximum in flow rate at around  $A_B \sim 0.4$ ). A substantial decrease in volume flow was only apparent when the barrier height became very large ( $A_B > 0.8$ ), which satisfies the constraint that the volume flow must go to zero as  $h \rightarrow H$  (and the gap closes).

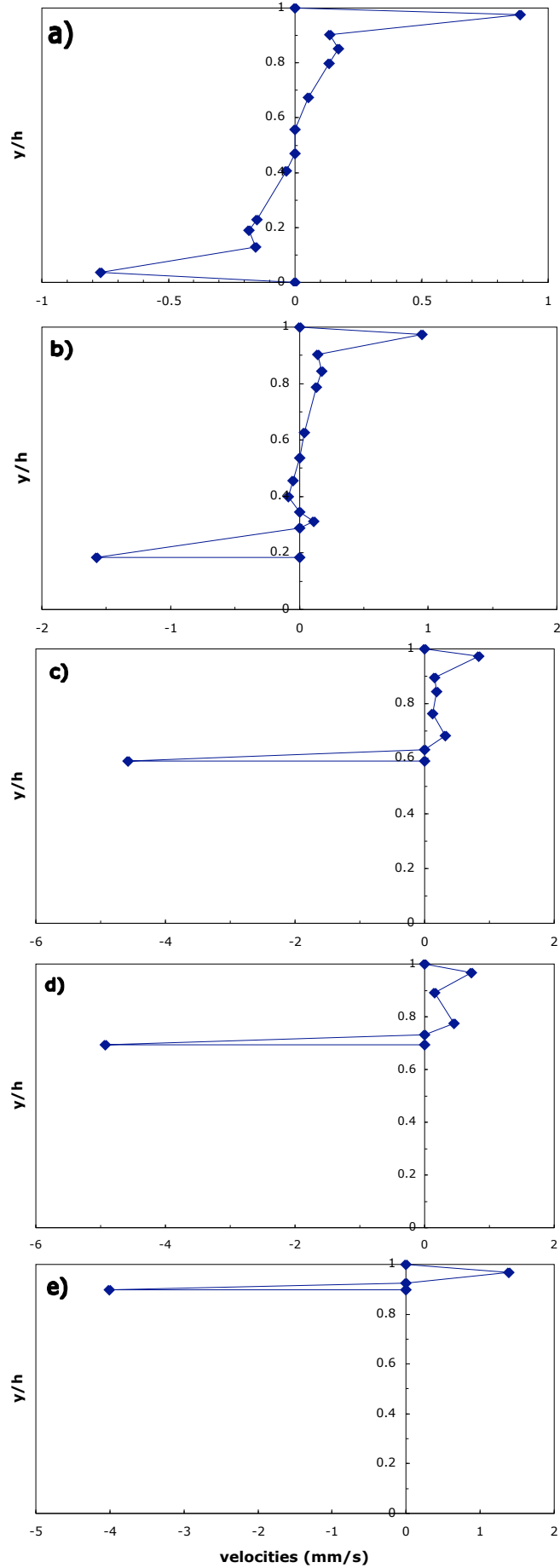


Figure 7: Velocity profiles above the barrier for a)  $A_B = 0$ , b)  $A_B = 0.18$ , c)  $A_B = 0.59$ , d)  $A_B = 0.69$ , e)  $A_B = 0.90$ . The points on the plots in (c) – (e) correspond to heights at which the velocity was either zero or a local maximum/minimum. Note that the horizontal scale differs for each plot.

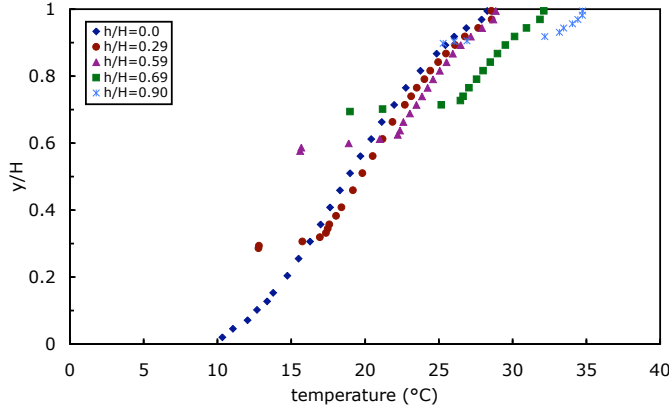


Figure 8: Temperature profiles above the barrier for  $A_B = 0, 0.29, 0.59, 0.69, 0.90$ .

From the measured velocity and temperature profiles, we determined the heat transport per unit width  $q$  across the barrier

$$q = \rho c_p \int_h^H u T dy, \quad (5)$$

where  $\rho$  is the density,  $y$  is the vertical coordinate and  $c_p$  is the specific heat of water at constant temperature. The Nusselt number is then given by

$$Nu = \frac{q}{k \Delta T} \quad (6)$$

where  $k$  is the thermal conductivity of water. The measured Nusselt numbers are plotted in figure 10 as a function of barrier height. We had anticipated that the heat transport would steadily decrease with increasing barrier height. However, no decrease was observed for modest barrier heights, and a rapid decrease in heat transport was found when  $A_B > 0.8$  (satisfying the constraint that the heat transport must go to zero as  $h \rightarrow H$ ).

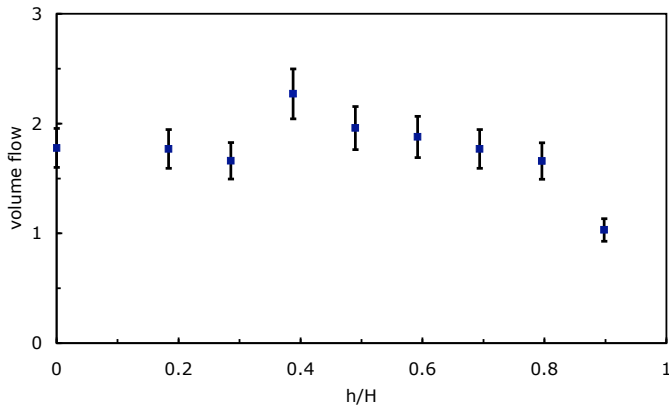


Figure 9: Volume flow per unit width (in  $10^{-5} \text{ m}^2/\text{s}$ ) exchanged through the gap above the barrier as a function of  $A_B$ .

## Conclusions

We have studied the convective flow in two connected chambers by placing a partial-height barrier into a cavity with differentially heated endwalls. The introduction of the barrier severely disrupts the transport of heat and mass in the boundary layers and plumes adjacent to the cavity walls. Temperature profiles in the cavity are dramatically modified, with the formation of a very cold chamber and a moderately warmer chamber. An unexpected flow structure arises to accommodate the exchange

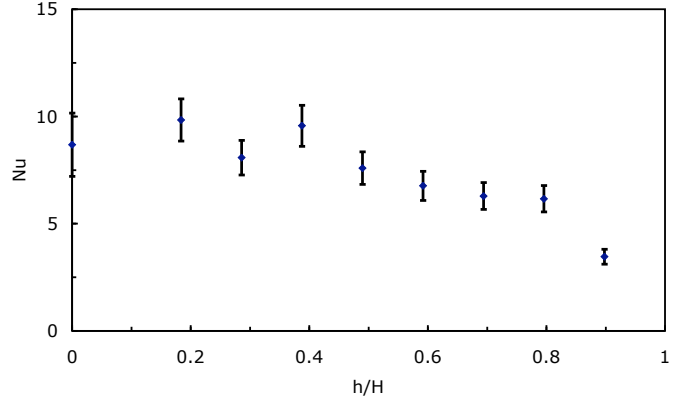


Figure 10: Measured Nusselt number as a function of  $A_B$ .

of fluid between the chambers. Contrary to intuition the heat and mass transport is little changed by the presence of a moderate barrier, and only begin to decrease rapidly when the barrier height becomes very large (when  $A_B > 0.8$ ). The complex dynamics responsible for this behaviour are currently being studied.

## Acknowledgements

Technical assistance from Tony Beasley and Brad Ferguson is gratefully acknowledged. We also thank Ross Griffiths for help throughout this project.

## References

- [1] Bejan, A., Al-Homoud, A. A. and Imberger, J., Experimental study of high-Rayleigh number convection in a horizontal cavity with different end temperatures, *J. Fluid Mech.*, **109**, 1981, 283-299.
- [2] Bejan, A. and Tien, C. L., Laminar Natural Convection Heat Transfer in a Horizontal Cavity with Different End Temperatures, *J. Heat Transfer*, **100**, 1978, 641-647.
- [3] Cormack, D.E., Leal, L. G and Seinfeld J. H., Natural convection in a shallow cavity with differentially heated end walls. Part 2, *J. Fluid Mech.*, **65**, 1974, 229-246.
- [4] Imberger, J., Natural convection in a shallow cavity with differentially heated end walls. Part 3, *J. Fluid Mech.*, **65**, 1974, 247-260.
- [5] Linden, P. F., The fluid mechanics of natural ventilation, *Annu. Rev. Fluid Mech.*, **31**, 1999, 201-238.
- [6] Lin, Y. J. P. and Linden, P. F., Buoyancy-driven ventilation between two chambers, *J. Fluid Mech.*, **463**, 2002, 293-312.
- [7] Simpkins, P. G. and Chen, K. S., Convection in horizontal cavities, *J. Fluid Mech.*, **166**, 1986, 21-39.
- [8] Wong, A. B. D. and Griffiths, R. W., Two-basin filling boxes, *J. Geophys Res.*, **106**, 2001, 26929-26941.
- [9] Wong, A. B. D., Griffiths, R. W. and Hughes, G. O., Shear layers driven by turbulent plumes, *J. Fluid Mech.*, **434**, 2001, 209-241.

# Lamb vector properties of swirling jets

W. Kollmann<sup>1,2</sup> and G. Umont<sup>2</sup>

<sup>1</sup>MAME Dept, University of Melbourne, Vic.3010, Australia

<sup>2</sup>MAE Dept, University of California Davis, CA 95616, USA

## Abstract

Swirling jets show at Reynolds numbers in the transitional and low turbulence regime several competing flow forms due to shear and centrifugal instabilities. The swirling flow in jets at swirl numbers high enough to generate breakdown bubbles is simulated numerically using an accurate Navier-Stokes solver in cylindrical coordinates. The vector lines for vorticity and the Lamb vector are computed and analyzed in detail. The main result is that the set of critical points of the Lamb vector field contains stable and unstable manifolds characterizing high shear regions.

## Introduction

The interpretation of flow fields can be guided by vector lines associated with vector properties of the flow. It is well known that streamlines, pathlines and streaklines generated by the velocity field give a unique picture of a steady flow, but differ significantly for unsteady flows as simple examples show (Hama, [1]). Turbulent flows are always unsteady and it is important to study vector lines generated by a variety of vector fields to gain an understanding of the kinematics and the dynamics of the flow. Velocity, vorticity and Lamb vector fields in axisymmetric, swirling jets are considered for this purpose with the emphasis on the Lamb vector. The Lamb vector is the cross product of vorticity and velocity and is, therefore, an indicator of regions of a flow field where vorticity is nonzero. It shares with velocity and vorticity critical points, but possesses additional critical points where the flow is locally Beltrami, i.e. a pure corkscrew motion.

Swirling jets show at Reynolds numbers in the transitional and low turbulence regime several competing flow forms due to shear and centrifugal instabilities ([3], [5], [4]). The swirling flow in jets at supercritical swirl numbers generating breakdown bubbles is simulated numerically using a hybrid spectral - finite difference method for the solution of the Navier-Stokes solver in cylindrical coordinates. The vector lines for vorticity and the Lamb vector are generated for this flow and analyzed in detail.

## Numerical Method

The hybrid spectral finite-difference method developed in [6] is applied to solve the Navier-Stokes equations in cylindrical coordinates. The details including the verification of its accuracy and convergence properties are presented in [6] and [7]. The method takes advantage of the fact that smooth functions are periodic with respect to azimuthal variable and the discrete Fourier transform [8] is applicable, which is for axisymmetric flows reduced to a single mode. The axial and radial directions are discretized using finite difference methods with formal accuracy at inner points up to 8<sup>th</sup> order. The time integrator is an explicit 4<sup>th</sup>-order state space Runge-Kutta method that requires minimal storage (see [6]). The Poisson/Helmholtz equations for streamfunction and pressure modes (see for [6] details) are solved using LU-decomposition (LINPACK, see Dongarra et al.[9]) combined with deferred corrections for bandwidth reduction.

## Evolution of vector lines

The vector lines associated with vorticity and the Lamb vector are used as indicators for the variation of the swirling jet flow with time and the change of boundary conditions. The properties of the Lamb vector are discussed first.

## Properties of the Lamb vector

The Lamb vector is defined as the cross product of velocity and vorticity

$$\mathbf{L} \equiv \mathbf{v} \times \nabla \times \mathbf{v} \quad (1)$$

It has interesting properties that can be exploited for the analysis of recirculation zones. The notion of the critical structure of the Lamb vector field is helpful for this analysis. It is defined as the set of points where  $\mathbf{L} = 0$  and all stable and unstable manifolds intersected with the hull of the support of the vorticity field. The Lamb vector is trivially zero in irrotational zones, hence these regions are excluded. It will be shown that the critical structure of the Lamb vector field is particularly well suited for the detection of shear layers.

It is easy to show that the momentum balance for incompressible fluids can be rearranged in terms of vorticity. It emerges in the Lamb-Gromeka form as (the volume force is assumed to have a potential  $\Phi$ )

$$\frac{\partial v_\alpha}{\partial t} - L_\alpha = -\frac{\partial}{\partial x_\alpha} \left( \frac{1}{2} v_\beta v_\beta + \frac{p}{\rho} + \Phi \right) - \frac{1}{Re} \varepsilon_{\alpha\beta\gamma} \frac{\partial \omega_\gamma}{\partial x_\beta} \quad (2)$$

This form of the momentum balance shows that viscosity has no influence on momentum transport if vorticity is zero, the viscous term is the curl of vorticity which is called flexion vector (Truesdell [2]). The left side of (2) is not acceleration since the gradient part of the convective acceleration is combined with the pressure and the potential of the volume force. If vorticity is zero, it follows from the Stokes theorem that velocity has also a potential and (2) leads to a Bernoulli theorem [2].

The Lamb-Gromeka form of momentum balance (2) contains the Lamb vector (1) representing the rotational part of the convective acceleration in the sense that the curl of the convective acceleration is equal to the curl of the Lamb vector. The Lamb vector furnishes a geometric interpretation of the case of steady inviscid flow with nonzero vorticity. The momentum balance (2) emerges then in the form

$$\nabla H = \mathbf{L} \quad (3)$$

where  $H$  denotes the Bernoulli head

$$H = \frac{1}{2} v_\beta v_\beta + \frac{p}{\rho} + \Phi \quad (4)$$

Equation (3) can be interpreted as follows: The gradient of  $H$  is in the direction normal to the surface formed by streamlines and vortex lines. This surface has the Lamb vector as normal vector and is called Lamb surface. It follows that the gradient has only one nonzero component normal to the Lamb surface



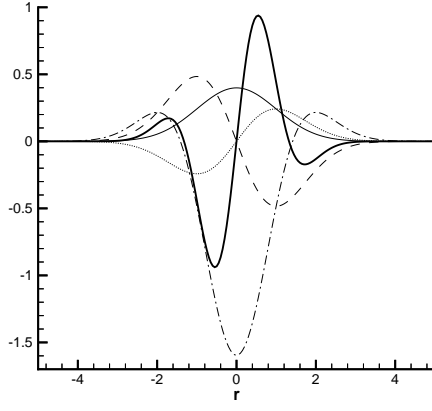


Figure 1: Velocity ( $v_\theta$  dashed line,  $v_z$  thin full line), vorticity ( $\Omega_\theta$  dotted line,  $\Omega_z$  dot-dashed line) and the Lamb vector component  $L_r$  (thick full line) for the swirling column example ( $\sigma_\theta = \sigma_z = 1$ ,  $S = 2$ ).

and we obtain the result that  $H = \text{constant}$  on the Lamb surface. This relation is satisfied for steady inviscid vortical flows and the Bernoulli head  $H$  depends in general on the particular Lamb surface chosen.

Further properties of the Lamb vector follow from the properties of velocity and vorticity. Elementary vector identities show that the Lamb vector can be represented by

$$L_\alpha = \frac{\partial}{\partial x_\alpha} \left( \frac{1}{2} v_\beta v_\beta \right) - v_\beta \frac{\partial v_\alpha}{\partial x_\beta} \quad (5)$$

This form can be seen as the difference between the gradient of the kinetic energy and the convective acceleration. The divergence of the Lamb vector is nonzero even for incompressible flows, given by

$$\frac{\partial L_\alpha}{\partial x_\alpha} = \omega_\alpha \omega_\alpha - \frac{\partial v_\alpha}{\partial x_\beta} \frac{\partial v_\alpha}{\partial x_\beta} + \frac{\partial^2}{\partial x_\alpha \partial x_\alpha} \left( \frac{1}{2} v_\beta v_\beta \right) \quad (6)$$

The example of linear Couette flow  $v_1 = Ax_2$ ,  $v_2 = v_3 = 0$  generates the divergence  $\nabla \cdot \mathbf{L} = A^2$ , where the Lamb vector is oriented in the positive  $x_2$  direction  $L_\alpha = \delta_{\alpha,2} A^2 x_2$ . The Lamb vector field can be interpreted as the flow (regarding the Lamb vector as velocity) generated by a uniform distribution of sources with strength  $A^2$ . This vector field has the  $x_1$ -axis as unstable manifold.

The evolution of the Lamb vector is for incompressible Newtonian fluids governed by the pde

$$\frac{D\mathbf{L}}{Dt} = -\frac{1}{\rho} \boldsymbol{\omega} \times \nabla p + \mathbf{v} \times (\boldsymbol{\omega} \cdot \mathbf{s}) + \frac{1}{Re} \nabla^2 \mathbf{L} \quad (7)$$

(where  $\mathbf{s} = \frac{1}{2}(\nabla \mathbf{v} + \nabla \mathbf{v}^T)$  denotes the rate of strain) which follows at once from mass and momentum balances. The Lamb vector is created or destroyed by two distinct processes. The first source term is the cross product of vorticity and the pressure gradient. It is zero if these two vectors are aligned and it is always present in plane flows. The second source is analogous to the vortex stretching term in the vorticity equation. It is easy to show that it is zero for plane flows and that it produces exponential growth in three-dimensional flows if the Lamb vector is aligned with the eigenvector of the rate of strain tensor associated with the middle (positive) eigenvalue. The critical structure of the Lamb vector field is a point set containing the

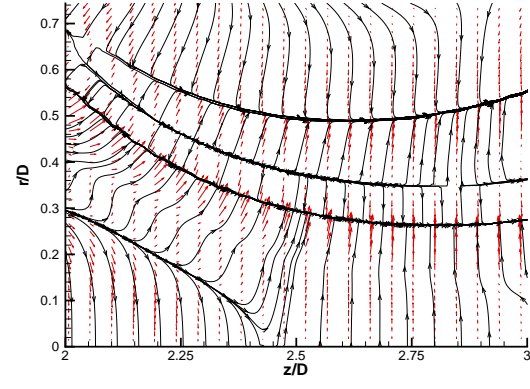


Figure 2: Detail of the Lamb vector lines at  $t = 154.8$  for  $Re = 2000$  and swirl number  $S = 1.40$ . The Lamb vector field is shown as red arrows

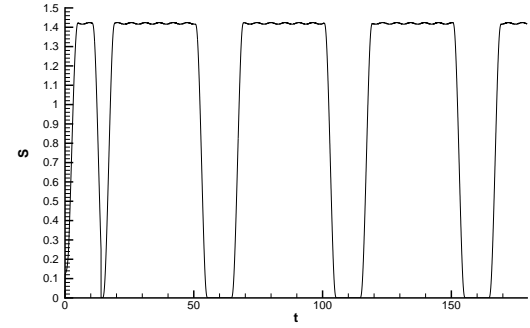


Figure 3: Swirl number as function of time for  $Re = 2000$  and swirl number  $S = 1.4$ .

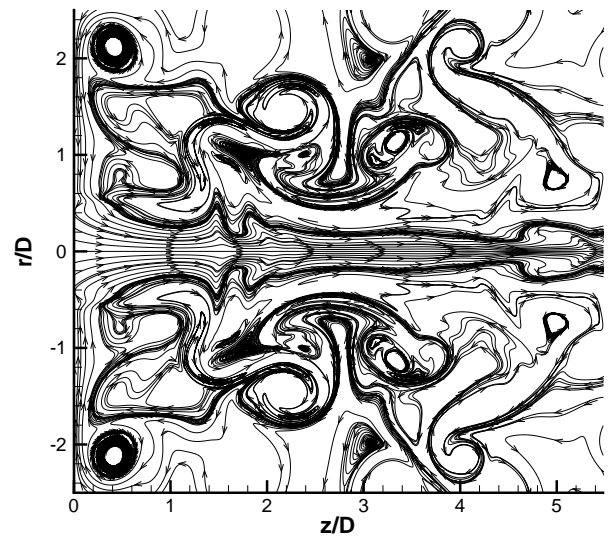


Figure 4: Vorticity lines at  $t = 154.8$  for  $Re = 2000$  and swirl number  $S = 1.40$ .



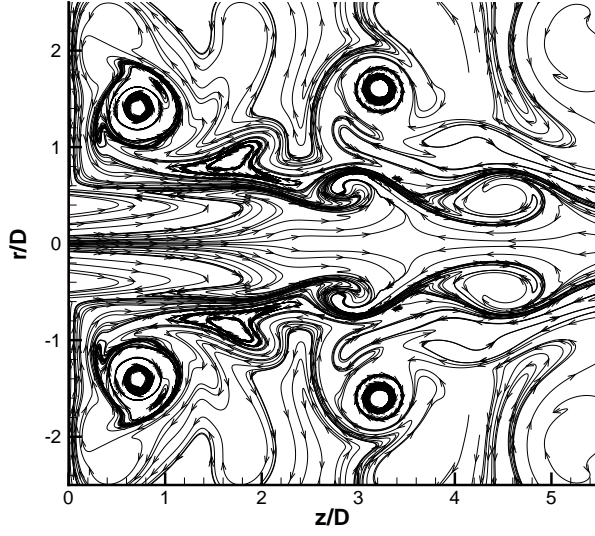


Figure 5: Vorticity lines at  $t = 167$  for  $Re = 2000$  and swirl number  $S = 1.4$ .

critical point sets for velocity and vorticity as the definition (1) shows. In addition to the critical points for velocity and vorticity, Beltrami points, where velocity and vorticity are aligned, appear in the critical set of the Lamb vector.

#### Example for Lamb vector lines

The properties of the Lamb vector lines can be illustrated in an example. A swirling column of fluid is considered with velocity given in cylindrical coordinates by

$$v_r = 0, \quad v_\theta(r) = -\frac{rS}{\sigma_\theta^3 \sqrt{2\pi}} \exp\left(-\frac{r^2}{2\sigma_\theta^2}\right),$$

$$v_z(r) = \frac{1}{\sigma_z \sqrt{2\pi}} \exp\left(-\frac{r^2}{2\sigma_z^2}\right)$$

The vorticity components follow from their definitions at once

$$\Omega_r = 0, \quad \Omega_\theta(r) = \frac{r}{\sigma_z^3 \sqrt{2\pi}} \exp\left(-\frac{r^2}{2\sigma_z^2}\right),$$

$$\Omega_z(r) = -\frac{S}{\sigma_\theta^3 \sqrt{2\pi}} \left(2 - \frac{r^2}{\sigma_\theta^2}\right) \exp\left(-\frac{r^2}{2\sigma_\theta^2}\right)$$

The Lamb vector for this parallel flow has only one nonzero component

$$L_r = \frac{S^2}{\sigma_\theta^6 \sqrt{2\pi}} r \left(2 - \frac{r^2}{\sigma_\theta^2}\right) \exp\left(-\frac{r^2}{\sigma_\theta^2}\right) - \frac{r}{\sigma_z^4 \sqrt{2\pi}} \exp\left(-\frac{r^2}{\sigma_z^2}\right)$$

This implies that the radial locations where  $L_r = 0$  (see the thick line in fig.1, which has apparently three roots) are in fact stagnation lines in the  $r - z$  plane for the Lamb vector. In particular, the symmetry axis for axi-symmetric flows is in general stagnation line for the Lamb vector. The example indicates that two critical structures appear in a rotating fluid column: The center being an unstable manifold (line source) surrounded by a stable manifold (cylindrical surface). This is the situation that is emerging in the simulation of the swirling jet as shown in fig.6, 7 and in greater detail in fig.2. The details in the latter figure show the presence of several stable and unstable manifolds with the Lamb vectors as red arrows. The axis  $r = 0$  changes from stable (sink) to unstable (source) with increasing  $z/D$ .

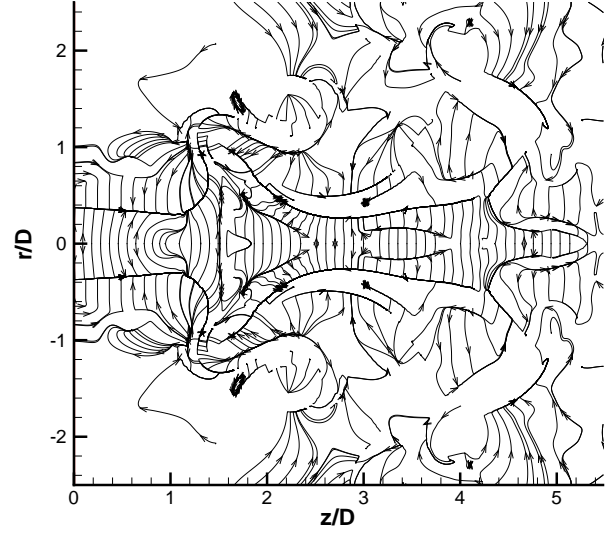


Figure 6: Lamb vector lines at  $t = 154.8$  for  $Re = 2000$  and swirl number  $S = 1.4$ .

The Lamb vector lines away from the critical structure can be explained for regions where Bernoulli holds. Consider a streamline where the Bernoulli head  $H$  is constant, then is the Lamb vector parallel to the gradient of the Bernoulli head according to (3), hence orthogonal to the streamline. This is evident in fig.6, fig. 7 and fig.2.

#### Results for axi-symmetric flows

The simulation of axi-symmetric swirling jets were done for the Reynolds number  $Re$  defined by

$$Re \equiv \frac{v_z(0, z_0)D}{\nu} \quad (8)$$

the present results are for  $Re = 2000$ , and the swirl number  $S$  defined by Billant et al. [5] as

$$S \equiv \frac{2v_\theta(R/2, z_0)}{v_z(0, z_0)} \quad (9)$$

where  $z_0 = 0.4D$  ( $D$  is the nozzle diameter), in the range  $S = 1.0 - 1.45$ , the present value is  $S = 1.4$ . The resolution was set to  $121 \times 251$  gridpoints in radial and axial direction for the fourth order discretization of the non-convective spatial derivatives and the fifth order upwind-biased scheme for the convective terms. The entrance boundary conditions are a smooth top-hat profile for the axial velocity and a smooth profile for the azimuthal velocity with the maximum at  $r/D = 0.25$ . The entrance conditions were varied in time in cyclical fashion to follow the creation and destruction of the recirculation zones. The wind-down and wind-up phases of the entrance conditions are controlled with a  $C^\infty$ -function (partition of unity) interpolating smoothly between the maximal and minimal values. The variation of the swirl with time at the entrance boundary is given in fig.3. Four wind-down and wind-up cycles are computed and the results are presented in terms of vector lines for vorticity and the Lamb vector.

#### Vector line results

The entrance boundary conditions for the azimuthal and the axial velocity are varied in time in a cyclical pattern to generate identical conditions with respect to the boundary conditions shifted by a finite time interval. The variation of the resulting swirl number (9) with time is given in fig.3. The third

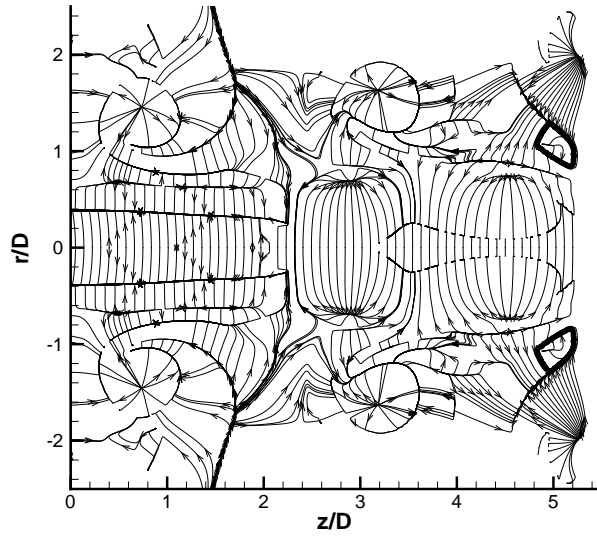


Figure 7: Lamb vector lines at  $t = 167$  for  $Re = 2000$  and swirl number  $S = 1.4$ .

and fourth cycle of wind-down and wind-up in the time intervals  $[100, 120]$  and  $[150, 170]$  are suitable for the structural investigation as the flow is sufficiently developed. The states at  $t = 154.8$  and  $t = 167$  are selected in the winding-down and winding-up phases of the fourth cycle, the two times correspond approximately to the same value of the Swirl number  $S = 0.7$ . The corresponding vector line pictures for the associated wind-down and wind-up states are presented in fig.4, fig. 6 at  $t = 154.8$  (Vorticity lines) and fig.5, fig.7 at  $t = 167$  (Lamb vector lines). The vortex lines in fig.4 and fig.5 in the subdomain  $\mathcal{D}_1 \equiv [4, 5.2] \times [0, 1]$  show different connectedness, hence are topologically different in the two corresponding states.

The Lamb vector lines in fig.6 and fig.7 are in parts of the flow domain, where Bernoulli holds, orthogonal to the streamlines and possess critical points and stable and unstable manifolds where it does not hold. The manifolds are dominant and their number changes between the corresponding states of the flow. In particular, the subdomain  $\mathcal{D}_1$  contains at  $t = 154.8$  stable and unstable manifolds, which form a source point at the wind-up phase at  $t = 167$ . The core region in  $0 \leq z \leq 2$  and  $0 \leq r \leq 0.5$  at  $t = 167$  forms a swirling column of fluid as presented in the example above.

## Conclusions

The simulation of axi-symmetric swirling flows in jets at super-critical Swirl numbers shows that repeated self-similar variation of the entrance boundary conditions does not produce topologically equivalent flow states as measured by the vector lines of vorticity and the Lamb vector. The comparison of corresponding states in the down and upwinding phases produce critical structures which are topologically different. The Lamb vector lines possess stable and unstable manifolds indicating regions of high shear in addition to isolated critical points.

## References

- [1] Hama, F. (1962), "Streaklines in a perturbed shear flow", *Physics of Fluids* **5**, 644-650
- [2] Truesdell, C.A. (1954), "The kinematics of vorticity", Indiana University Press, Bloomington, Indiana.

- [3] Leibovich, S. (1978), "The structure of vortex breakdown", *Annual Rev. Fluid Mech.* **10**, 221-246
- [4] Shtern, V. and Hussain, F. (1998), "Instabilities of conical flows causing steady bifurcations", *JFM* **366**, 33-85
- [5] P. Billant, J. Chomaz and P. Huerre (1999), "Experimental study of vortex breakdown in swirling jets", *J. Fluid Mech.* **376**: 183-219.
- [6] W. Kollmann and J.Y. Roy (2000), "Hybrid Navier-Stokes solver in cylindrical coordinates I: Method", *Computational Fluid Dynamics Journal* **9**, 1-16.
- [7] W. Kollmann and J.Y. Roy (2000), "Hybrid Navier-Stokes solver in cylindrical coordinates II: Validation", *Computational Fluid Dynamics Journal* **9**, 17-22.
- [8] Canuto, C., Hussaini, M.Y. and Zang, T.A. (1988), "Spectral Methods in Fluid Dynamics", Springer-Verlag, Berlin.
- [9] J.J. Dongarra and C.B. Moler and J.R. Bunch and G.W. Stewart (1979), "LINPACK user's guide", SIAM Philadelphia

## Measurements of Temperature and Water Vapour Concentration in a Scramjet Combustor

A. D. Griffiths<sup>1</sup> and A. F. P. Houwing<sup>1</sup>

<sup>1</sup>Department of Physics, The Faculties  
The Australian National University, ACT, 0200 AUSTRALIA

### Abstract

Two-line, time-multiplexed diode laser absorption spectroscopy is applied to a scramjet combustor to measure water vapour concentration and temperature at sampling rates of up to 20kHz. The measurement is made in the supersonic, expanding exhaust region of the combustor and is shown to be repeatable and able to resolve differences between different operating conditions.

### Introduction

For many years, hypersonic airbreathing propulsion has been promoted as an economical alternative to rocket propulsion for payload deployment into low earth orbit [3]. This has motivated many fundamental studies of scramjet flows (e.g. [6]), a significant number of which were undertaken in a free-piston shock tunnel [10]. Some of this earlier work used schlieren, luminosity or fluorescence imaging or floor or sidewall pressure measurements. The aim of the current work is to use a diode laser absorption technique (tunable diode laser absorption spectroscopy, or TDLAS) to measure temperature and water vapour density within a hydrogen-fueled scramjet. In so doing, we intend to make a unique contribution to fundamental scramjet research, demonstrating for the first time the viability of a diode laser absorption system for supersonic combustion measurements in a pulsed facility. In addition, we expect to provide data suitable for comparison with theoretical results produced by computational fluid dynamical (CFD) simulation of the flow within the scramjet.

### Theoretical background

The application of absorption spectroscopy, using diode lasers, for thermometry and species measurement has been well established previously for environmental measurements, combustion studies and gasdynamic measurements [1]. The theory that underpins the technique is also well established (e.g. [1]) so only a brief outline of the theory is presented here.

As a monochromatic beam from a diode laser passes through an absorbing medium, the transmitted intensity of the beam,  $I$ , is related to the initial intensity,  $I_0$ , by the Beer–Lambert relation

$$I = I_0 \exp(-k_v l) \quad (1)$$

where  $k_v$  is the frequency-dependant absorption coefficient and  $l$  is the path length travelled by the beam. The product  $k_v l = \log(I_0/I)$  is termed the spectral absorbance.

If an absorption line, of species  $i$  in some gas mixture, is sufficiently isolated from other spectral features then  $k_v$  is a function of the strength,  $S(T)$ , and shape,  $g(v)$  where  $\int g(v) dv = 1$ , of the absorption line and the number density,  $N_i$ , of the molecular species. This relation is given by

$$k_v = S(T) g(v) N_i \quad (2)$$

so that  $k_v$ , as well as depending on frequency, depends on the temperature,  $T$ . For the case of multiple overlapping spectral lines,  $k_v$  is treated as a sum over the individual spectral lines.

If  $S(T)$  is known, then equation (2) can be used to find  $N_i$  by integrating absorbance over frequency. This requires knowledge of the temperature, which can be found by probing a second absorption line.

Thermometry relies on the dependence of line strength on temperature [8],

$$S(T) = S(T_0) \frac{Q(T_0) \exp(-c_2 E''/T)}{Q(T) \exp(-c_2 E''/T_0)} \times \frac{[1 - \exp(-c_2 v_0/T)]}{[1 - \exp(-c_2 v_0/T_0)]} \quad (3)$$

where the line strength measured at a reference temperature,  $S(T_0)$  is scaled to an arbitrary temperature  $T$ . This scaling function depends on the lower-state energy of the transition,  $E''$ , the frequency of the transition,  $v_0$ , and the total internal partition sum of the molecule,  $Q$ , which can be computed using the method of Fischer *et al.* [2]. Also appearing in the expression is the second radiation constant,  $c_2 = hc/k$  where  $h$  is Planck's constant,  $c$  is the speed of light and  $k$  is Boltzmann's constant.

From equation (3) we see that if we choose two spectral lines of different  $E''$  and similar  $v_0$  then the ratio

$$R(T) = \frac{S_1(T)}{S_2(T)} = \frac{S_1(T_0)}{S_2(T_0)} \exp \left[ -c_2 (E''_1 - E''_2) \left( \frac{1}{T} - \frac{1}{T_0} \right) \right] \quad (4)$$

is a function only of  $T$ . Therefore, if an experimental system is arranged in such a way so as to measure the integrated spectral absorption of two spectral lines with different lower-state energies then both temperature and species concentration can be deduced. Furthermore, the sensitivity of the thermometry can be tuned to a particular temperature range by choosing spectral lines with appropriate  $E''$ .

### Experimental Configuration

The experimental system that was built for this purpose is shown in figure 1. Two diode lasers (Laser Components SPECILAS DFB diodes operating near 1390nm) produced the probe beam for the system. These diodes exhibit narrow line width and no mode hops were observed in the tuning range. The laser frequency was tunable across around  $10 \text{ cm}^{-1}$  by controlling the temperature and injection current of the laser. Temperature control was used to tune the lasers into the region of a target absorption line and then current modulation was used to scan the two lasers alternately across approximately  $0.5 \text{ cm}^{-1}$ . Current modulation allowed for a repetition rate of up to 20kHz, but meant that the laser power varied by a factor of two over a scan. Modulation was applied to the external modulation input of the diode laser controllers (ILX LDC 3700B).

The first laser was tuned to a water vapour absorption line at  $7181.15570 \text{ cm}^{-1}$  while the second laser was tuned to a line at  $7179.7519 \text{ cm}^{-1}$ . The second line is around 70 times weaker than the first at room temperature with this ratio dropping as temperature increases. The strength of the line near  $7181 \text{ cm}^{-1}$  at room temperature necessitated flushing of the exposed beam

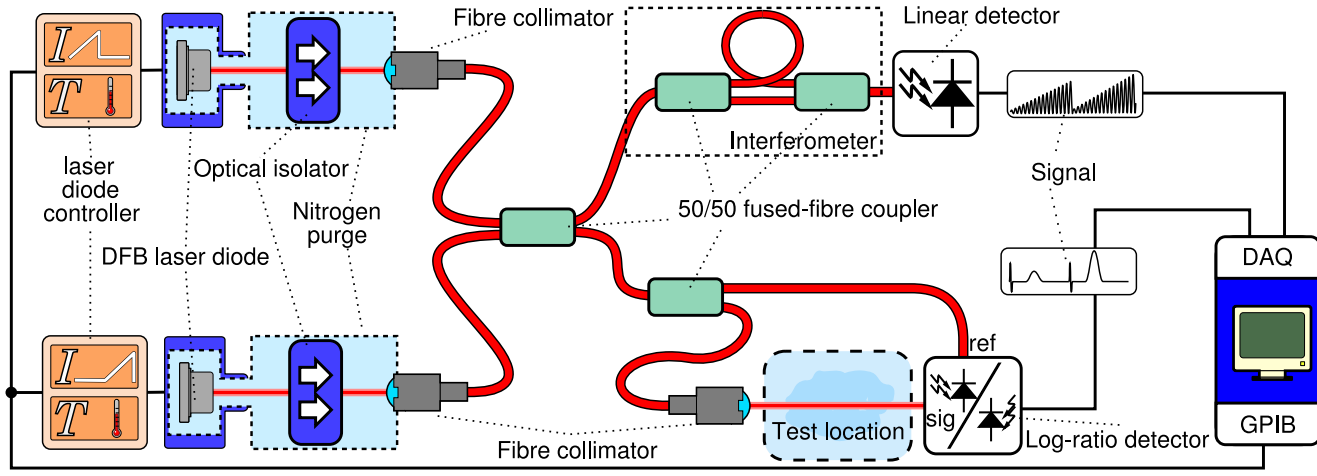


Figure 1: Experimental layout.

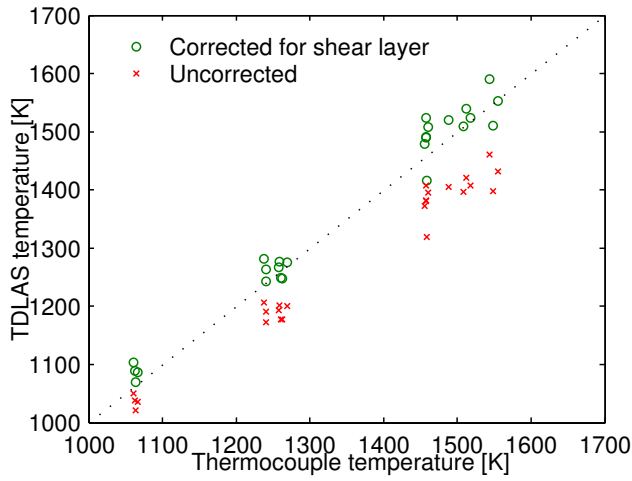


Figure 2: Temperature in a flame measured with a thermocouple compared with TDLAS. Systematic deviations are visible if a homogeneous beam path is assumed but temperature agrees well if the line-of-sight profile is specified.

path with a purge gas (nitrogen). This purge region was not very large since the beam was coupled into fibre-optics after leaving the laser housing and passing through an optical isolator.

The fibre-optic network then delivered the beam to the measurement location—the scramjet combustor or, during calibration, a flat flame burner—and to a fibre-optic interferometer which measured the relative frequency of the laser as it was scanned across the absorption line.

The remaining component of the laser light was split again with half going to the reference channel of a log-ratio detector and half passing through the test area to the signal channel of the detector. This detector [4] has been used previously for diode laser absorption spectroscopy [1] because of its ability to suppress the modulation of laser power due to injection current modulation, among other useful features. It produces a voltage

$$V = -G \log(I_{\text{ref}}/I_{\text{sig}} - 1), \quad (5)$$

where  $G$  is the gain of the detector and  $I_{\text{ref}}$  and  $I_{\text{sig}}$  are the reference and signal photocurrents respectively, which is readily converted to absorbance. The detector exhibits the best bandwidth and noise characteristics when the output voltage is adjusted to be around 0V, which is achieved when  $I_{\text{ref}} \approx 2I_{\text{sig}}$ .

After losses through the fibre optic network,  $I_{\text{sig}} \approx 100 \mu\text{W}$  near the centre of a scan.

The output of the balanced detector and the interferometer were digitised with a PC based data acquisition board (National Instruments PCI-6110E) at 5 MS/s then processed to obtain the spectral absorbance,  $k_{\nu}l$ , as a function of frequency. Spectral lines were then fit to this data, using the Voigt line shape for  $g(\nu)$  in equation (2), thereby obtaining  $R$ .

This process was complicated by the appearance of an additional spectral line at high temperature. This line was not predicted by the HITRAN database and overlapped the line near  $7181 \text{ cm}^{-1}$ . To compensate for this, a two-line fit was used for the  $7181 \text{ cm}^{-1}$  region with the value of  $S_{7181}$  taken from the strength fitted to the original, target line.

Before deployment to the tunnel, the system was tested in a premixed burner [7] and where temperature was measured with an S-type thermocouple. The thermocouple temperature was corrected for radiation losses, a correction of up to 30 K. Best results were obtained by using reference strengths,  $S(T_0)$ , measured by Toth [11] and then using parameters in the 2000 edition of the HITRAN database [9] to scale the strengths with temperature. The TDLAS temperature also required a correction since the beam passed through the cooler shear layer of the flame. This was applied by measuring the flame temperature profile with a thermocouple traverse, assuming that the shape of this distribution was constant and modelling the water vapour concentration based on the temperature distribution.

When this correction was applied, the comparison between thermocouple and TDLAS temperature was good, as shown in figure 2. While the assumption of homogeneous properties along the beam path results in a systematic offset that increases with temperature, the systematic error is below 1% when the above-mentioned correction was applied.

Following determination of the temperature, equation (3) can be used to find the strength of either of the two absorption lines and equation (1) applied to find the water vapour concentration. If temperature is determined in this way, either of the two absorption lines can be used to produce the same numerical result.

## Scramjet measurements

### Flow facility and scramjet model

Measurements using diode laser absorption spectroscopy were carried out in a model scramjet in the T3 shock tunnel at the



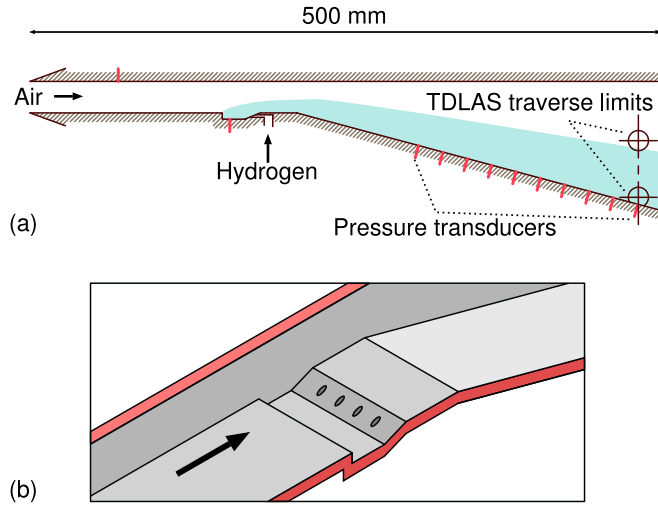


Figure 3: The scramjet model used in these experiments. Part (a) shows the duct cross section, including a sketch of water vapour distribution. The cavity geometry, with injector ports, is shown in (b).

Australian National University. This facility [5, 10] can produce flow conditions to simulate hypersonic flight, but the test duration, at around 3 ms, is short. Apart from modifications to the downstream geometry—a diverging duct instead of a straight duct—and addition of TDLAS equipment, this work used the same scramjet model and flow conditions as Neely *et al.* [5]. This model was developed for combustor studies and, therefore, does not include an intake. As a result, the tunnel was configured to produce the conditions, shown in table 1, that would be present after the intake of a hypersonic vehicle in flight.

Temperature	$1160 \pm 50 \text{ K}$
Pressure	$80 \pm 6 \text{ kPa}$
Velocity	$2790 \pm 30 \text{ ms}^{-1}$
Density	$0.23 \pm 0.01 \text{ kgm}^{-3}$
Mach number	$4.16 \pm 0.09$

Table 1: Conditions at the combustor intake at 1.5 ms. These are nominally the same as ref [5] and representative of a vehicle flying at around Mach 10.

After leaving the contoured nozzle of T3, the main flow entered the scramjet combustor, shown in figure 3. It first traveled down a rectangular duct of height 25 mm and width 52 mm until reaching a cavity in the floor of the duct. The cavity was designed to produce a recirculation zone for flame-holding, and hydrogen was injected into the cavity from four injector ports in the sloping rear face. Temperatures in this part of the duct were high enough for self-ignition of the fuel–air mixture, initiating water vapour production. The rate of hydrogen injection was set by the desired fuel–oxygen equivalence ratio [5]. For this work two fuel-lean equivalence ratios were used, ‘high’ with  $\phi = 0.47 \pm 0.01$  at 1.5 ms and ‘low’ with  $\phi = 0.153 \pm 0.005$  at 1.5 ms where uncertainties represent the standard deviation of the shot-to-shot scatter.

Aft of the cavity, the flow was expanded by a  $15^\circ$  ramp in the floor of the duct. This reduced the temperature of the flow to within the range where the lines chosen for this work are effective for thermometry and reduced the pressure, increasing the peak absorption.

The laser beam for TDLAS was aligned horizontally across the scramjet duct perpendicular to the flow in this region of lower temperature. The beam could be traversed vertically across the duct covering the region where cross-flow variation in water vapour was expected—from 5.6 mm above the duct floor to 50.6 mm above the duct floor, thus accessing half of the duct’s vertical extent. The beam centre was 482 mm downstream of the scramjet inlet.

The duct was instrumented with piezoelectric PCB pressure transducers along its centreline. Pressure readings showed evidence of the presence of supersonic combustion for both equivalence ratios.

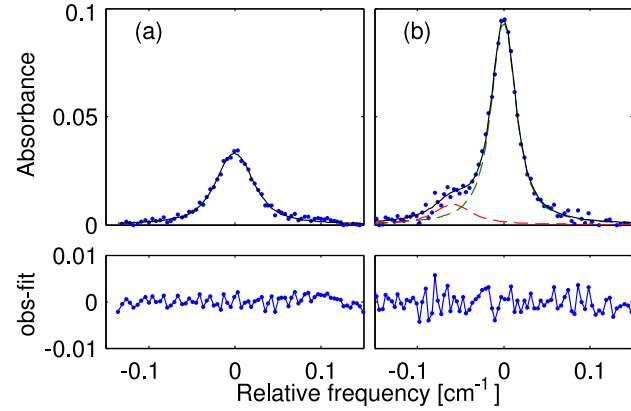


Figure 4: Single-sweep absorption data, and fits, from a high  $\phi$  run showing (a) the line near  $7179.7 \text{ cm}^{-1}$  and (b) the two lines near  $7181 \text{ cm}^{-1}$  with the components shown as dashed lines.

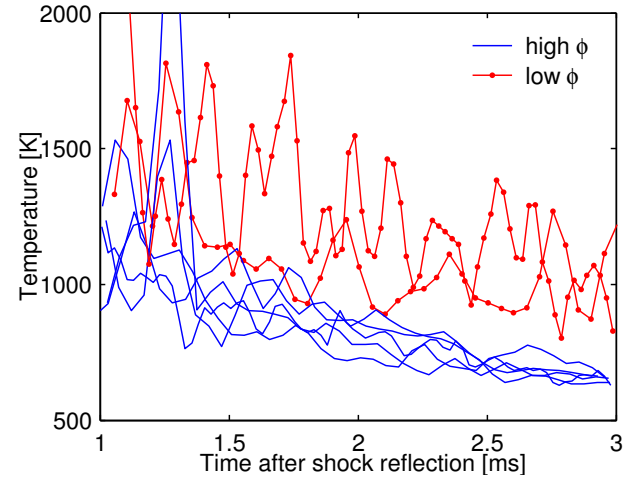


Figure 5: Temperature measured at 10.6 mm from duct floor for two different equivalence ratios.

### TDLAS results

In order to test the viability of TDLAS as a diagnostic in the combustor, repeated measurements were carried out at 10.6 mm from the bottom of the duct and 482 mm from the inlet. This location was chosen after a preliminary survey of the traverse showed the presence of water vapour at a suitable temperature for thermometry.

The absorption signal measured at this location showed adequate signal-to-noise ratio and Voigt profiles showed good fits to the data. A single Voigt profile was used for the line near  $7179.8 \text{ cm}^{-1}$ , shown in figure 4 (a), while two Voigt profiles

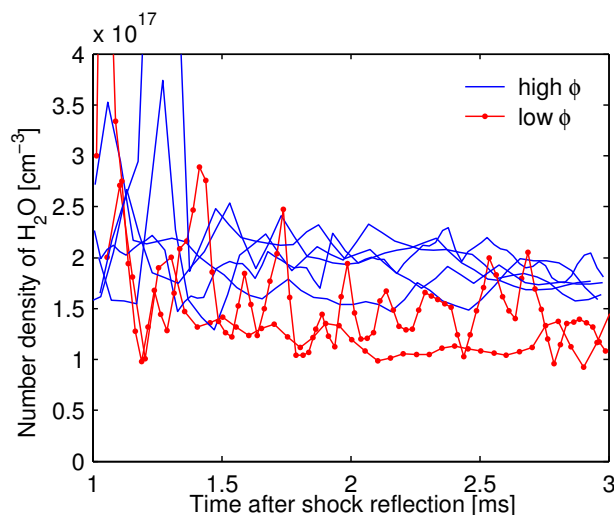


Figure 6: Water vapour number density derived from the same data set as figure 5.

were used in order to distinguish the two lines near  $7181\text{ cm}^{-1}$ , as shown in figure 4 (b), with the stronger of these two lines being the targeted transition. The absorption lines shown are for single laser scans, since the short test time of the facility precludes averaging multiple scans, taken during a high equivalence ratio run. Similar quality of fit can be seen in runs where the equivalence ratio was low.

Processing absorption signals from multiple runs of the tunnel results in the temperature and water vapour number density as shown in figures 5 and 6 respectively. Temperature and number density histories from seven tunnel runs are plotted together with five examples of the low equivalence ratio case and two of the larger one. Most of these were acquired at 10kHz, however two were acquired at 20kHz and show equally successful operation at the higher sampling rate.

Considering the results at 2ms after shock reflection, we observe a greater concentration of water vapour when equivalence ratio is higher, as expected. The temperature variation with equivalence ratio, however, runs contrary to expectation. Furthermore, the temperature result is highly repeatable with a clear distinction between the two cases.

Within each tunnel run there is also a clear trend. The time from 1 – 3ms is within the nominal test time for these tunnel operating conditions, however no steady state is apparent in the temperature results. On the contrary, a downwards trend is apparent for both equivalence ratio cases, although a plateau may be hidden by the large variability in the measurements.

## Discussion

The result here that is the most difficult to explain is the increase in temperature following a decrease in equivalence ratio. Furthermore, if we temporarily accept this relationship to hold, an explanation for the decrease in temperature over the facility test time is apparent. Over this time, while the hydrogen mass flux remains approximately constant, the air mass flux steadily decreases resulting in an increase in the equivalence ratio over the test time and, in agreement with our initial observation, a decrease in temperature.

A key to understanding why this is the case may lie in the fact that TDLAS is sensitive only at a point; possibly the hot region of the flow is moved up the duct when equivalence ratio is increased. Furthermore, if there is significant non-uniformity over

the beam path, the inferred temperature is not simply an average over the beam path due to the nonlinear relationship between temperature and line strengths. Rather, it can be weighted towards cold regions of the flow where the  $7181\text{ cm}^{-1}$  line is particularly strong. This effect was seen to be important in flame-based calibration, and may be more pronounced in the combustor.

More work is needed in order to understand this, and CFD work is planned in the near future. Direct comparison of these results with those obtained with CFD is also expected to be instructive.

## Conclusions

While interpretation remains difficult, the feasibility of using diode laser absorption spectroscopy for scramjet measurements in a pulsed facility has been established. The sampling rate achieved was high enough to indicate trends over the test time of the facility and the results were clearly different when the fuel–air equivalence ratio was varied. Planned CFD calculations should provide a better understanding of the physical processes occurring in the scramjet combustor.

## References

- [1] Allen, M. G., Diode laser absorption sensors for gas dynamic and combustion flows, *Meas. Sci. Technol.*, **9**, 1998, 545–562.
- [2] Fischer, J. et al., Total internal partition sums for molecular species in the 2000 edition of the HITRAN database, *J. Quant. Spectrosc. Ra.*, **82**, 2003, 401–412.
- [3] Heiser, W. H. and Pratt, D. T., *Hypersonic Airbreathing Propulsion*, AIAA, 1994.
- [4] Hobbs, P. C. D., Ultrasensitive laser measurements without tears, *Appl. Optics*, **38**, 1997, 903–920.
- [5] Neely, A. et al., Hydrocarbon and hydrogen-fuelled scramjet cavity flameholder performance at high flight Mach numbers, in *12th AIAA International Space Planes and Hypersonic Systems and Technologies Conference*, 2003, AIAA 2003-6989.
- [6] O’Byrne, S., Doolan, M. and Houwing, A. F. P., Analysis of thermal choking processes in a model scramjet engine, *J. Propul. Power*, **16**, 2000, 808–814.
- [7] Prucker, S., Meier, W. and Stricker, W., A flat flame burner as calibration source for combustion research: Temperatures and species concentrations of premixed  $\text{H}_2/\text{air}$  flames, *Rev. Sci. Instrum.*, **65**, 1994, 2908–2911.
- [8] Rothman, L. S. et al., The Hitran molecular spectroscopic database and Hawks (Hitran Atmospheric Workstation) 1996 edition, *J. Quant. Spectrosc. Ra.*, **60**, 1998, 665–710.
- [9] Rothman, L. S. et al., The HITRAN molecular spectroscopic database: edition of 2000 including updates through 2001, *J. Quant. Spectrosc. Ra.*, **82**, 2003, 5–44.
- [10] Stalker, R. J., Development of a hypervelocity wind tunnel, *Aeronaut. J.*, **76**, 1972, 374–384.
- [11] Toth, R. A., Extensive measurements of  $\text{H}_2^{16}\text{O}$  line frequencies and strengths: 5750 to  $7965\text{ cm}^{-1}$ , *Appl. Optics*, **33**, 1994, 4851–4863.



## Preliminary Examination of a "Round Jet Initial Condition Anomaly" for the k- $\epsilon$ Turbulence Model

E.J. Smith, J. Mi, G.J. Nathan and B.B. Dally

School of Mechanical Engineering  
The University of Adelaide, SA, 5005 AUSTRALIA

### Abstract

The current numerical study assesses the capability of the k- $\epsilon$  (epsilon) model to predict downstream trends of round jets with varying initial conditions. The numerical model was compared with experimental data for three jets issuing from a smooth contraction, a sharp-edged orifice and a long pipe respectively. The results show that, while the initial conditions are similar, the downstream trends predicted from the model are opposite to those obtained from experiments. This is deduced to follow from the fact that two-equation models do not account for the effect of large-scale coherent structures, and thus provides further evidence that the turbulence "constants" are not universal.

### Introduction

Townsend [16] argued that turbulent flows should achieve true self-similarity when they become asymptotically independent of initial conditions. This has led to the "argument" that 'turbulence forgets its origins'. However, analytical results of George [3] dispelled this by showing that the entire flow is influenced by the initial conditions, resulting in a variety of initial-condition-dependent self-similar states in the far field.

This analytical work has been supported by experiments [8-10, 17]. Mi et al. [8, 9] compared downstream scaling mixing characteristics for round jets issuing from a smooth contraction (SC) nozzle, a sharp edged orifice plate (OP) and a long pipe (LP). Xu and Antonia [17] compared effects of downstream velocity decay between round jets issuing from a LP and SC nozzle. These investigators concluded that differences seen in the downstream decay are directly related to the underlying turbulence structure of the jet in the near field or the jet exit conditions. Those initial conditions known to affect downstream characteristics include Reynolds number and initial turbulence, as characterised by the nozzle exit radial profiles of mean velocity and turbulence intensity.

The above experimental studies [8-10, 17] showed that the flow emerging from the OP exhibited the highest decay rate and the widest spreading angle, followed by the smooth contraction nozzle and then the LP. This same trend in spread and decay rates for round jet flows was also found numerically for a SC and OP by Boersma et al. [1] using DNS (direct numerical simulation). However no direct comparison of these flows appears to have been performed before using Reynolds Averaged Navier-Stokes (RANS) models. The present paper seeks to perform such an investigation using the k- $\epsilon$  model.

### Different Round Nozzle Flows

The exit profiles for the three round jets are distinctly different. The radial velocity profile ( $\langle U \rangle(r)$ ) for the SC nozzle is approximately uniform (i.e. "top hat") while the LP is initially fully developed, and so is well described by the one-seventh-power law. The radial velocity profile for the OP is quite different again, being "saddle backed" with the highest velocity at the edge of the jet. The initial turbulence intensity ( $\langle U' \rangle(r)/U_c$ ) from each nozzle is also different. For the SC nozzle the mean

turbulence intensity is low (about 0.5%) except at the edges ( $r < 0.45d$ ) where it increases to ~8%. In contrast, the relative turbulence intensity for the LP is generally much higher throughout the exit plane. It typically varies between 3% to 9.5% [9]. The OP is roughly between these extremes. Variations in jet exit conditions are shown schematically in figure 1.

The flows upstream from the three nozzle exit planes are also quite different. For the SC it undergoes a large radial contraction, but with no separation, while the sudden contraction of the OP produces an upstream separation so that the initial flow has a slight radial inflow at the edge and the well-known "vena contracta". For the LP, the upstream flow is axial in the mean, although the turbulence is high.

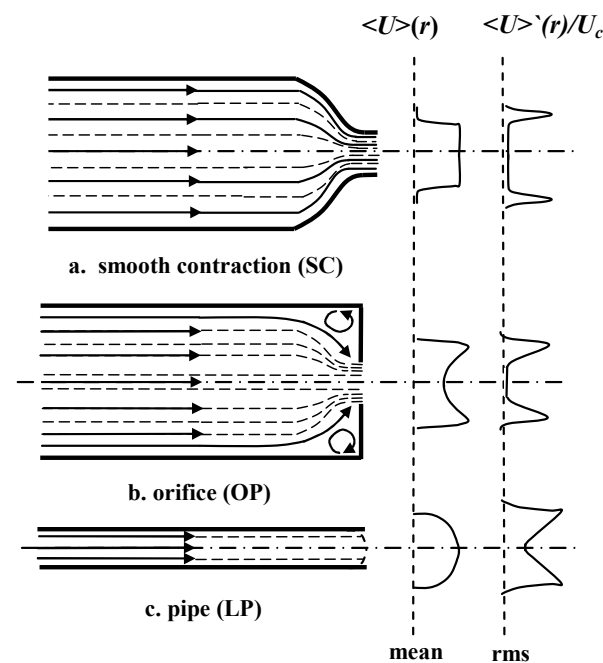


Figure 1. Schematic diagram showing flow upstream and downstream from (a) smooth contraction, (b) orifice plate, and (c) long pipe.

### k- $\epsilon$ Turbulence Model

Today, even with the successful development of DNS and LES (large eddy simulation) for turbulent flows, the most popular models for round jet flows and industrial modelling are the two-equation Reynolds Averaged Navier Stokes (RANS) models. Of these, the k- $\epsilon$  two-equation model accounts for 95% or more of the industrial use at present [4]. This form of model is easy to solve, converges relatively quickly, is numerically robust and stable, is able to solve large domains and high Reynolds numbers and requires minimal computational expense, which is important for industrial models.

All two-equation models are based on the Boussinesq approximation, Eq. (1), and the turbulent kinetic energy equation, Eq. (2). The Boussinesq approximation is used to approximate the Reynolds stress tensors introduced by the Reynolds averaging

of the conservation equations (where isotropic turbulence is assumed). The turbulent kinetic energy equation describes the physical processes of the turbulence throughout the flow.

The second equation of the k- $\epsilon$  model, the specific dissipation rate equation, Eq. (3), contains the dissipation rate,  $\epsilon$ , which describes the rate of energy transfer from the large energy containing scales, characterised by integral scales, to the smaller dissipating scales, characterised by the Kolmogorov scales. Turbulent flows contain a spectrum of length scales, the intensity and distribution of which, depends upon the initial and boundary conditions. Predicting the role of each length scale is very computationally expensive and is avoided by these two equation models.

$$\tau_{ij} = 2\nu_T S_{ij} - \frac{2}{3}k\delta_{ij} \quad (1)$$

$$\frac{\partial k}{\partial t} + U_j \frac{\partial k}{\partial x_j} = \tau_{ij} \frac{\partial U_i}{\partial x_j} - \varepsilon - D + \frac{\partial}{\partial x_j} \left[ \left( \nu + \frac{\nu_T}{\sigma_k} \right) \frac{\partial k}{\partial x_j} \right] \quad (2)$$

$$\frac{\partial \varepsilon}{\partial t} + U_j \frac{\partial \varepsilon}{\partial x_j} = C_{\varepsilon 1} \frac{\varepsilon}{k} \tau_{ij} \frac{\partial U_i}{\partial x_j} - C_{\varepsilon 2} f_2 \frac{\varepsilon}{k} + \frac{\partial}{\partial x_j} \left[ \left( \nu + \frac{\nu_T}{\sigma_\varepsilon} \right) \frac{\partial k}{\partial x_j} \right] + E \quad (3)$$

The closure coefficients and auxiliary relations for the standard k- $\epsilon$  model are defined by Launder et al. [5], where the empirical turbulence constants within the dissipation rate term are defined as  $C_{\epsilon 1}=1.44$  and  $C_{\epsilon 2}=1.92$ . However,  $C_{\epsilon 1}$  and  $C_{\epsilon 2}$  are non-universal and need to be adjusted for different classes of flow. This is consistent with turbulence being non-universal and dependent on initial boundary conditions [4].

The standard  $k-\epsilon$  model with the standard constants predicts the velocity field of a two-dimensional plane jet quite accurately, but results in large errors for axisymmetric round jets. Although the standard  $k-\epsilon$  model matches the spreading rate of the round jet more accurately than other two equation models it still overestimates it by 40% [14]. This "round-jet plane-jet anomaly" results from the numerous simplifying assumptions in all RANS models, and is further evidence of the non-universality of turbulence. It is also this work which prompted the title of the present investigation.

To tailor the k- $\epsilon$  model for solving round jet flows the turbulence constants  $C_{\epsilon 1}$  and  $C_{\epsilon 2}$  can be modified. Modifications to the turbulence constants have been suggested by McGuirk and Rodi [7], Morse [11], Launder et al. [5], and Pope [14]. All modifications involve the turbulence constants becoming functions of the velocity decay rate and jet width. For self-similar round jets it was found that modifications made by Morse [11], and Pope [14] lead to  $C_{\epsilon 1}$  having a fixed value of 1.6.

To examine the impact of the modifications to the accuracy of the k- $\epsilon$  model when used for round jets, Dally et al. [2] compared the use of the Morse [11] and Pope [14] modifications with the standard k- $\epsilon$  constants ( $C_{\epsilon 1}=1.44$  and  $C_{\epsilon 2}=1.92$ ) and a fixed value for  $C_{\epsilon 1}=1.6$  with  $C_{\epsilon 2}=1.92$ . It was found that the modifications by Morse and Pope did improve the accuracy of the k- $\epsilon$  model when compared to the standard k- $\epsilon$  constants. However the fixed value of  $C_{\epsilon 1}=1.6$  with  $C_{\epsilon 2}=1.92$  matched the experimental results the closest. The k- $\epsilon$  model with  $C_{\epsilon 1}=1.6$  with  $C_{\epsilon 2}=1.92$  is referred to as the ‘modified’ k- $\epsilon$  model for improved prediction of round jet flows.

The modified k- $\epsilon$  model is expected to provide a similar relationship between decay and spreading rates as found in the experimental measurements discussed previously. However, it is unknown whether the modified k- $\epsilon$  model is suitable for all round jet flows, or if further model modification is required to predict each of the round jet nozzles.

## Numerical Method and Code Validation

The numerical investigation was performed in a low velocity co-flow, with  $U_a/U_{co}=0.05$ , rather than in ambient air, to provide as definitive boundary conditions as possible. This co-flow satisfies the velocity criterion of Maczynski [6] and Nickels and Perry [12] in which the effect of a slight co-flow on the jet mixing is deemed to be negligible. As such, it allows the calculations to be compared with the relevant experiments, since all direct comparisons of the different initial conditions were performed with no co-flow.

The Reynolds number at the jet exit for all three nozzle types was  $Re = 28,200$ . To allow scalar (mixture fraction) data to be extracted (the results of which will be presented in future publications), the numerical model used Hexane (with modified density and molecular weight to match water) within the jet stream. Water was used as the working fluid within the control volume and also as the fluid in the co-flow. This allows direct comparison with experimental data obtained in our laboratory [13]. From the point of view of the calculation it makes no difference if the working fluid is water or air, so long as the Reynolds number is matched.

For the LP case, the computational domain extends 20 diameters upstream from the jet exit to ensure fully developed pipe flow, and a developed co-flow. For the SC and OP cases, the initial jet flow is specified directly at the jet exit but the co-flow boundary is not changed. The computational domain extends 105 diameters downstream from the jet exit, to ensure capture of data in the self-similar region, and 37 diameters in the radial direction to ensure that wall effects are negligible. A schematic diagram of the computational domain is shown in figure 2. Grid cells were placed closer together near to the jet walls and further apart with increasing distance from the jet exit. Grid independence is ensured for the geometry. The commercially available CFD program CFX 4.4dp is used for all calculations. CFX uses a finite volume formulation over a structured mesh.

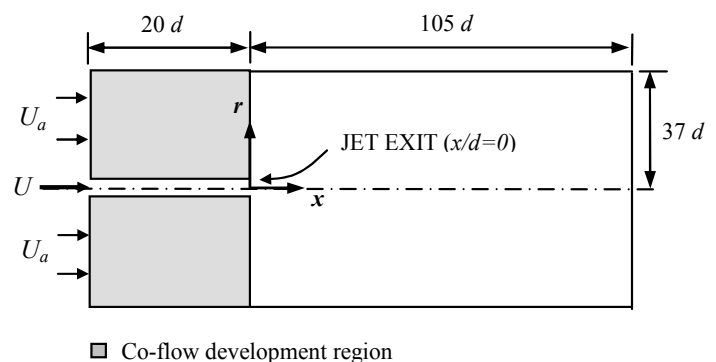


Figure 2. Schematic diagram of the computational domain.

A steady state k- $\epsilon$  model is applied with 2-D axisymmetric assumption; the k- $\epsilon$  model is modified for improved prediction of round jet flows by using the constants  $C_{\epsilon 1} = 1.6$  and  $C_{\epsilon 2} = 1.92$  recommended by Dally et al. [2]. Convergence was considered to be complete when the ratio of mass residuals to mass entering the jet was less than  $1 \times 10^{-6}$ .

The flow is assumed to be non-reacting, steady state and incompressible. A "Mixed is Burnt" subroutine is used to extract the passive scalar data, mean and RMS mixture fraction. Temperature is under-relaxed to prevent heat release and remains constant at 293K.

To obtain a fully developed pipe flow at the jet exit (shown in figure 2) the flow is initiated 20 diameters upstream from the jet exit. The resulting profiles for jet exit velocity and turbulence intensity are shown in figure 3. To check the modelling technique, comparison was made between numerical and measured LP data [13], and overall the numerical method predicted the LP flow as measured by Parham [13] reasonably well (Refer to Smith et al. [15]). Hence the assumptions for grid resolution, initial and boundary conditions associated with the LP are considered sufficient. The modelling technique can therefore, confidently be applied for prediction of the flows emerging the OP and SC nozzles.

For prediction of the downstream flow emerging the OP and SC nozzles the boundary condition at the jet exit is modified. The appropriate mean velocity and turbulence intensity profile for each jet is specified directly as the boundary condition at the jet exit (figure 2). Other boundary conditions remain unchanged and are the same as those applied to the LP. This approach also ensures that the co-flow around the nozzle is the same for all jets, since it does not introduce differences in the external shape of the supply pipe. Thus, allowing reasonable comparison with experimental data obtained in ambient air where there is no external boundary layer.

## Results and Discussion

Velocity and turbulence intensity profiles obtained from the numerical model at  $x/d=0.5$  are shown in figure 3 and correspond closely to those found experimentally by Mi et al. [9]. Hence the initial conditions for the three nozzles are well represented by the numerical model.

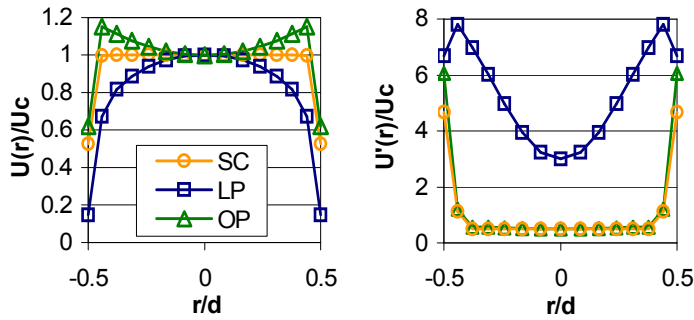
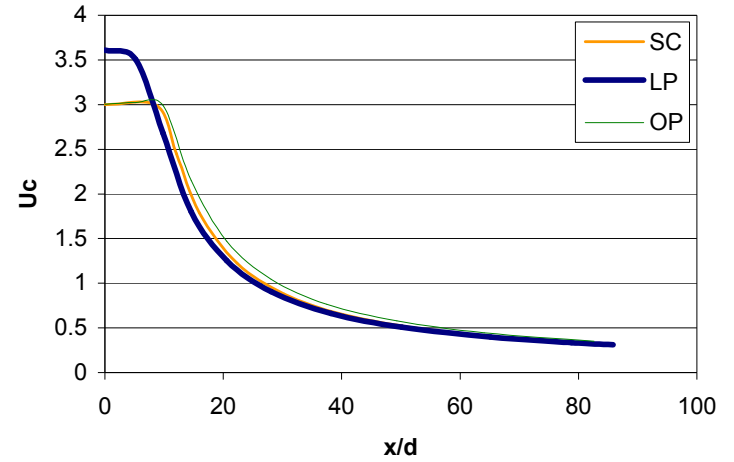


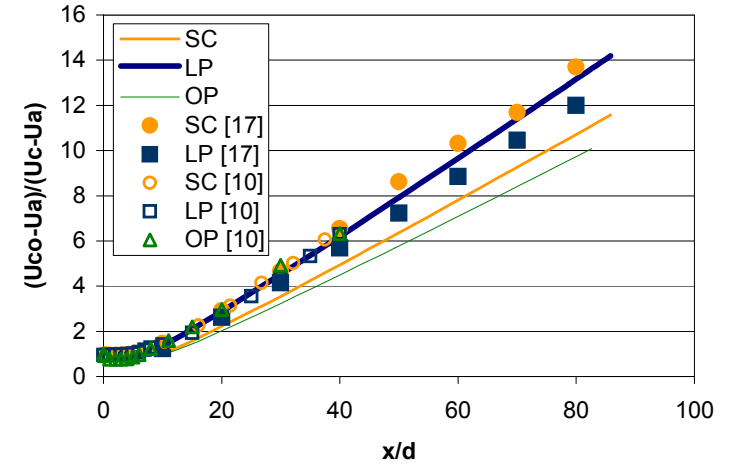
Figure 3. Radial profiles of velocity ( $U$ ) and rms ( $u'$ ) values obtained at  $x/d=0.05$  for jets issuing from the smooth contraction (SC), orifice (OP) and pipe jet nozzles (LP), (a)  $U(r)/U_c$ ; (b)  $u'(r)/U_c$ .

A comparison of the downstream velocity decay rates for the three round jet nozzles is shown in figure 4. It is shown in figure 4(a) that the centre-line velocity of the LP begins to decay immediately from the nozzle exit, i.e. it has no "potential core", unlike that from the other two nozzles. This trend agrees with experiments [10]. However the potential core of the SC and OP ends at  $x/d \approx 10$  so that their length is about twice as long as the measured value. Another difference is that the OP has the shortest measured potential core, over which its centreline velocity is not uniform [10, 17]. In the present case of modelling, the centreline velocity of the LP has the greatest rate of decay and the OP the lowest, as is seen more clearly in the inverse decay rate (Figure 4b). This trend is opposite to that found in the experimental [10] and DNS [1] studies.

The decay and spreading rates obtained from the current numerical study are compared with the experimental results of Mi and Nathan [10] and Xu and Antonia [17] (figures 4b and 5). The decay rates obtained from the  $k-\epsilon$  model, for the round jet flows, are within the expected range as that found experimentally, confirming the reliability of the calculations. However the relationship in decay rates between the three nozzles is opposite to the expected results, as can be seen in figures 4b and 5.



a. Centreline decay



b. Normalised centreline decay

Figure 4. Axial decay of velocity for jets issuing from the smooth contraction (SC), orifice (OP) and long pipe (LP).

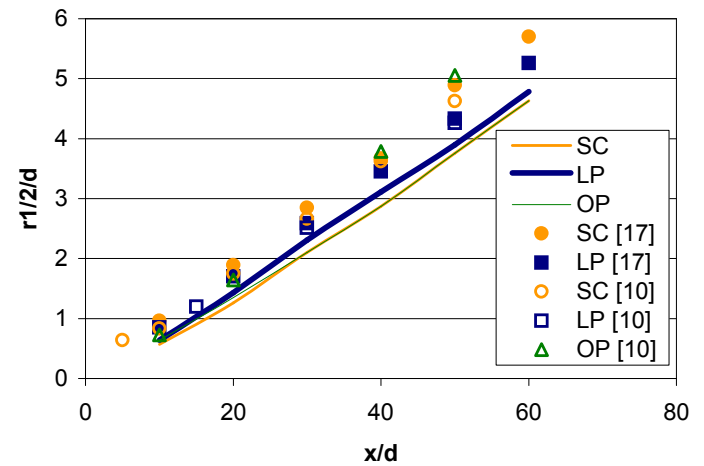


Figure 5. Comparison between experimental and numerical data for downstream radial half width decay for jets issuing from the smooth contraction (SC), orifice (OP) and long pipe (LP).

These results indicate that the k-ε model does not reproduce the measured trends of the effect of initial conditions on mean jet behaviour. In seeking to find an explanation for this, it is first noted that the calculated trend in spreading rate matches the trend in the total amount of initial turbulence intensity. That is, the LP has the highest initial turbulence intensity and is also predicted to have the highest rate of spread and decay, while the SC has the lowest of each. The inverse relationship between mean and fluctuating velocity in the k-ε model is found in the turbulent kinetic energy equation, Eq. (4). When the turbulence intensity ( $I$ ) is high, the initial turbulent kinetic energy ( $k$ ) is also high, thus creating higher initial decay rates.

$$I = \frac{\sqrt{\frac{2}{3}k}}{U} \quad (4)$$

It is further noted that RANS models do not model turbulence structure, but seek to account for differences in turbulence by appropriate selection of the turbulence constants. Although the SC has low initial turbulence, it produces highly coherent large-scale structures, while a LP produces a much lower level of coherence due to its higher overall initial turbulence, and the structure of the OP is different again [9, 17]. These differences are clearly not accounted for in the k-ε model. The non-universality of turbulence in the three jets therefore suggests that it is inappropriate to use a single set of turbulence "constants" for all initial conditions for a round jet, but rather that they should be calibrated for each of the three initial flows.

## Conclusion

Previous work [17, 10] has shown that the mean velocity decays most rapidly for the orifice jet and slowest for the pipe jet. This has been supported by direct numerical simulation (DNS) [1]. However when applying the k-ε model to calculate round jets, it is the long pipe that is found to decay most rapidly.

The failure of the model to reproduce the measured trends under different initial conditions is linked to the differences in underlying structure which are not accounted for in the model. It further suggests that, while initial differences in underlying flow structures are inevitably reflected in differences in initial velocity profiles, the information contained in the initial mean and RMS axial-velocity profiles is insufficient to allow the adequate reproduction of the flow.

## Acknowledgements

The authors wish to thank the Australian Research Council (ARC), the Sugar Research Industry (SRI) and Fuel and Combustion Technology (FCT) for their support of this work.

## References

- [1] Boersma B.J., Brethouwer G., Nieuwstadt, F.T.M., A numerical Investigation on the Effect of the Inflow Conditions on the Self Similar Region of a Round Jet, *Phys Fluids*, **10**, 1998, 899-909.
- [2] Dally, B.B., Fletcher, D.F. and Masri, A.R., Flow and Mixing Fields of Turbulent Bluff-Body Jets and Flames, *Combust. Theory Modelling*, **2**, 1998, 193-219.
- [3] George, W.K., The Self-Preservation of Turbulent Flows and Its Relation to Initial Conditions and Coherent Structures, *Recent Advances in Turbulence*, Ed. Arndt, R.E.A. and George, W.K., 1989.
- [4] George, W.K., Wang, H., Wollblad, C. and Johansson, T.G., Homogeneous Turbulence and its Relation to Realizable Flows, *14<sup>th</sup> AFMC*, Adelaide, Australia, 2001, 41-48.
- [5] Launder, B.E., Morse, A.P., Rodi, W., and Spalding, D.B., The Prediction of Free Shear Flows – A comparison of Six Turbulence Models, *NASA SP-311*, 1972.
- [6] Maczynski, J.F.J., A round jet in an ambient co-axial stream, *J. Fluid Mech.*, **13**, 1962, 597-608.
- [7] McGuirk, J.J. and Rodi, W., The Calculation of Three-Dimensional Turbulent Free Jets, *1<sup>st</sup> Symp. On Turbulent Shear flows*, editors F. Durst, B.E. Launder, F.W. Schmidt and J.H. Whitelaw, 1979, 71-83.
- [8] Mi, J., Nobes, D.S. and Nathan, G.J., Influence of jet exit conditions on the Passive Scalar Field of an Axisymmetric Free Jet, *J. Fluid Mech.*, **432**, 2001, 91-125.
- [9] Mi, J., Nathan, G.J. and Nobes D.S., Mixing Characteristics of Axisymmetric Free Jets From a Contoured Nozzle, an Orifice Plate and a Pipe, *J. Fluids Eng.*, **123**, 2001, 878-883.
- [10] Mi, J. and Nathan, G.J., Momentum Mixing Characteristics of Turbulent Axisymmetric Jets with Different Initial Velocity Profiles, to be submitted for, *J. Fluid Mech.*, 2004.
- [11] Morse, A.P., Axisymmetric Turbulent Shear Flows with and without Swirl, *Ph.D. Thesis*, London University, 1977.
- [12] Nickels, T.B. and Perry, A.E., An experimental and theoretical study of the turbulent co-flowing jet, *J. Fluid Mech.*, **309**, 1996, 157-182.
- [13] Parham, J.J., Control and Optimisation of Mixing and Combustion from a Precessing Jet Nozzle, *Ph.D. Thesis*, The University of Adelaide, Australia, 2000.
- [14] Pope, S.B., An Explanation of the Round Jet/Plane Jet Anomaly, *AIAA Journal* **16**, 3, 1978.
- [15] Smith, E.J., Nathan, G.J. and Dally, B.B., Assessment of the Robustness of the k-ε Model to Variations in Turbulence Constants for Simulation of Increased Jet Spreading, *EMAC 2003 Proceedings*, editors R.L. May and W.F. Blyth, 2003.
- [16] Townsend, A.A., The Structure of Turbulent Shear Flow, 2<sup>nd</sup> Edition, Cambridge University Press, 1996.
- [17] Xu, G. and Antonia, R.A., The Effect of Different Initial Conditions on a Turbulent Round Jet, *Experiments in Fluids*, **33**, 2002, 677-683.

## Nomenclature

$C_{\epsilon 1}$	Dissipation rate equation production constant
$C_{\epsilon 2}$	Dissipation rate equation dissipation constant
$d$	Pipe exit diameter
$D$	$D = 2\mu \left( \frac{\partial k^{\frac{1}{2}}}{\partial x_i} \right)^2$
$E$	$E = 2\mu \nu_T \left( \frac{\partial^2 U}{\partial x_i \partial x_i} \right)^2$
$I$	Turbulence intensity ( $u'/u_{avg}$ )
$k$	Kinetic energy of turbulent fluctuation per unit mass
$r$	Radial distance
$Re$	Reynolds number
$r$	Radial distance
$r_{1/2}$	Half width, value of radius at which axial velocity is half centreline value
$U$	Axial component of velocity
$U_a$	Co-flow velocity
$U_c$	Centreline velocity
$U_{co}$	Jet exit centreline velocity
$S_{ij}$	Mean strain rate tensor, $S_{ij} = \frac{1}{2} \left( \frac{\partial U_i}{\partial x_j} + \frac{\partial U_j}{\partial x_i} \right)$
$x$	Axial distance
$\delta_{ij}$	Kronecker delta
$\epsilon$	Dissipation per unit mass
$\mu$	Dynamic molecular viscosity
$\nu$	Kinematic molecular viscosity
$\nu_T$	Kinematic eddy viscosity
$\sigma_k$	Turbulent Prandtl number for kinetic energy (k-ε)
$\sigma_\epsilon$	Turbulent Prandtl number for dissipation rate (k-ε)
$\tau_{ij}$	Specific Reynolds stress tensor ( $-\overline{u'_i u'_j}$ )

## Modelling of Transient Behaviour in a Francis Turbine Power Plant

Tzuu Bin Ng, G.J. Walker and J.E. Sargison

School of Engineering  
The University of Tasmania, Hobart, TAS, 7001 AUSTRALIA

### Abstract

This paper presents a nonlinear mathematical model of the Francis turbine for a single-machine hydroelectric power plant. Several model refinements have been proposed to improve the capability of the existing industry models to simulate the transient operations of the power station. The new model is evaluated by full-scale field tests involving both steady and transient operations. Significant improvement in accuracy is demonstrated. However, there remain some frequency-dependent discrepancies for short penstock installation that appear to be associated with unsteady flow within the turbine.

### Introduction

The increasing interconnection of individual power systems into major grids has imposed more stringent quality assurance requirements on the modelling of power plants. Power systems are nowadays operated closer to capacity limits than in the past. Hence, a review of the commonly used models for the hydraulic systems in the hydroelectric power plant is warranted to accurately identify and minimise transient stability problems. This is particularly relevant for islanding, load rejection and black start after power system restoration cases where large changes in the power output or system frequency are expected.

The commercial PSS/E package [5], which is commonly used to simulate the behaviour of the hydroelectric power plant, involves both hydraulic and electrical system components. It uses a conventional turbine model developed by authors from the Institute of Electrical & Electronics Engineers (IEEE) [10]. The current study is specifically concerned with the hydraulic modelling aspects of the Francis type reaction turbine incorporated in the PSS/E package. The IEEE model is improved to incorporate a nonlinear model, which is used to examine the transient phenomena associated with changing turbine load to meet fluctuating system demand.

The present paper will focus on the operation of a simple power plant with a single Francis turbine and a short penstock. This eliminates the need to consider travelling pressure wave phenomena in a long waterway conduit and the problem of more complex governor and hydraulic interactions that frequently occur in multiple-machine stations. Significant elements of the hydraulic model developed here are:

1. nonlinear modelling of Francis turbine characteristics;
2. allowance for water column inertia and unsteady flow effects in the turbine and draft tube;
3. nonlinear Guide Vane (GV) function for Inlet Guide Vane (IGV) operation;
4. correct allowance for effects of changing turbine speed and supply head.

Prediction of the original and improved IEEE models using Matlab Simulink software will be compared with the results of

full-scale field tests on the Mackintosh power station conducted by Hydro Tasmania. Details of the Mackintosh power station are illustrated in Figure 1. The plant has a short penstock, unrestricted reservoir and tailrace, and no surge chamber. The turbine flow or power output is controlled by hydraulically operated guide vanes.

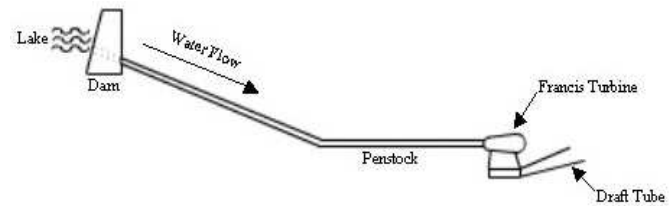


Figure 1: Scheme of the Mackintosh hydro power plant.

### Description of the Power Plant Model

#### Conventional IEEE Model

The linearized equations originally designed for implementation on analogue computers are still widely used in the power industry. They are suitable only for investigation of small power system perturbations or for first swing stability studies. Nonlinear simulations have been increasingly utilized from the early 1990s [1,2,10] with the availability of greater computing power and the demands of more complex power system distribution grids. Although a nonlinear IEEE model [10] as shown in Figure 2 has been introduced in the time domain simulations, it has oversimplified some important features of the hydraulic system.

For a short-penstock, single-machine station where travelling pressure wave (water hammer) effects are relatively insignificant, the inelastic water column theory using the linear momentum equation for incompressible flow is usually applied in the waterway conduit:

$$\bar{Q} = \frac{1}{T_w} \int (\bar{H}_o - \bar{H} - \bar{H}_f) dt \quad (1)$$

where  $\bar{Q}$  = per-unit turbine flow

$\bar{H}_o$  = per-unit static head between reservoir and tailrace

$\bar{H}$  = per-unit static head at the turbine admission

$\bar{H}_f$  = per-unit conduit head losses

$T_w$  = water time constant =  $\sum Q_{rated} L_i / g A_i h_{rated}$

$L_i$  = length of the conduit section  $i$

$A_i$  = area of the conduit section  $i$

$g$  = gravitational acceleration

$Q_{rated}$  = rated flow rate

$h_{rated}$  = rated head

The conduit head losses in equation (1) were usually ignored in the IEEE model for simplicity [10]. These losses could easily amount to around 5% of the total available head at rated flow and are not always a constant even for a simple hydro plant such as Mackintosh. Hence, the inclusion of the conduit losses is considered desirable [9].

No provision is made in the inelastic model to account for unsteady flow effects in the turbine and draft tube caused by changing GV position. Although these effects may be insignificant for a station with a relatively long penstock, they will be more important for station like Mackintosh where the water column inertia is small.

In this generic model, the Francis turbine is depicted as an orifice with constant discharge coefficient for a particular guide vane setting [6,9]. The flow rate through the turbine is modelled by a simple orifice flow relation:

$$\bar{Q} = \bar{G} \sqrt{\bar{H}} \quad (2)$$

The guide vane (GV) function  $\bar{G}$  in the existing model [10] is assumed to vary linearly with the guide vane opening only. In reality, the slope of this function will vary with flow coefficient and Reynolds number over the full range of turbine operations [4] and it should properly be modelled as a nonlinear function. A similar approach is implemented in the 1994 model of De Jaeger et al. [1].

The turbine power output for the IEEE model is evaluated from:

$$\bar{P}_m = A_t \bar{H} (\bar{Q} - \bar{Q}_{nl}) - D \bar{G} (\bar{N} - \bar{N}_{rated}) \quad (3)$$

=  $f(C_Q)$  where  $\bar{P}_m$  = per-unit turbine power output  
 $A_t$  = turbine gain factor  
 $\bar{Q}_{nl}$  = per-unit no-load flow  
 $D$  = speed-damping factor  
 $\bar{N}$  = per-unit turbine rotational speed  
 $\bar{N}_{rated}$  = per-unit rated turbine rotational speed

The no-load flow  $\bar{Q}_{nl}$  is used to correct for the bearing friction and the windage losses in both turbine and generator [2]. The turbine gain factor  $A_t$  allows for other internal flow losses. However, the resulting linearized model is not very accurate [9]. The damping factor  $D$  in the IEEE model is introduced to allow for efficiency changes resulting from varied operating conditions; a constant value of  $D=0.5$  has been used for Francis turbine modelling [10].

### Problems with Existing IEEE Model

The current IEEE model does not use dimensionless turbine characteristics. Equation (3) is inappropriate and could lead to significant error when the change in turbine operating conditions is large. In particular, the speed-damping factor  $D$  used in the model is unrealistic for the Francis turbine operation. The power (and the efficiency) change with speed may be positive or negative depending on the GV position, and their rates of change also vary with GV position [4].

Damping effects due to head changes are also neglected in the existing model. In fact, changing the turbine net head ( $H$ ) will also change the flow rate of the machine ( $Q$ ). At a constant turbine speed ( $N$ ), this also changes the flow coefficient  $C_Q \propto Q/N$  and moves to a different turbine operating point and efficiency. The magnitude is similar to the speed damping effect and must be taken into account in the simulation [4].

Hence, dimensionless turbine performance curves should be employed to correctly represent the hydraulic turbine operation. Figure 3 shows a typical efficiency curve for the Francis turbine. For incompressible flow, the turbine operation is accurately described by the dimensionless relation:

$$C_H = f(C_Q, Re) \quad (4)$$

where  $C_Q$  = flow coefficient =  $Q / Nd^3$   
 $C_H$  = head coefficient =  $gH / N^2 d^2$   
 $Re$  = Reynolds number =  $4Q / \pi v d$   
 $d$  = characteristic turbine diameter  
 $v$  = dynamic viscosity of water

Changes with  $Re$  are relatively slow and for small variations in  $Re$  the turbine performance can be approximated by:

$$(5)$$

The net turbine head may vary due to transients or changes in the supply head. Similar operating conditions ( $C_Q$ ,  $C_H$  constant) with varying speed require that  $H \propto N^2$ ,  $Q \propto N$  and therefore  $Q \propto H^{0.5}$ , as assumed in equation (2). This is incorrect for a power plant that has been governed to maintain a constant runner speed in order to keep the AC frequency constant within the grid, in which case  $C_Q$  must vary with  $H$  for GV fixed.

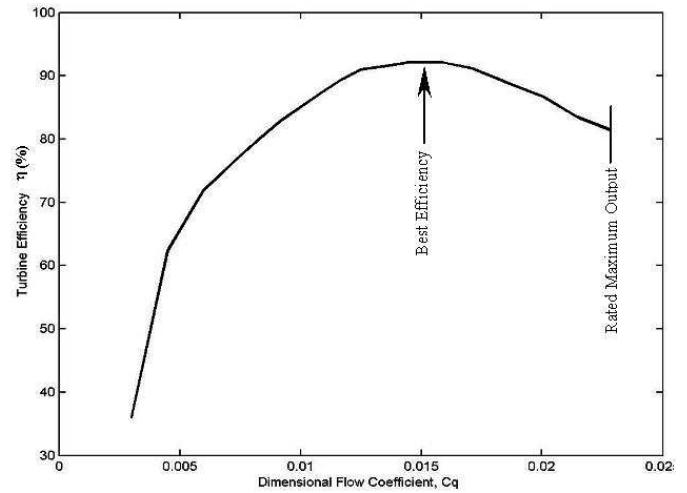


Figure 3: Typical efficiency curve ( $\eta \sim C_Q$ ) for Francis Turbine.

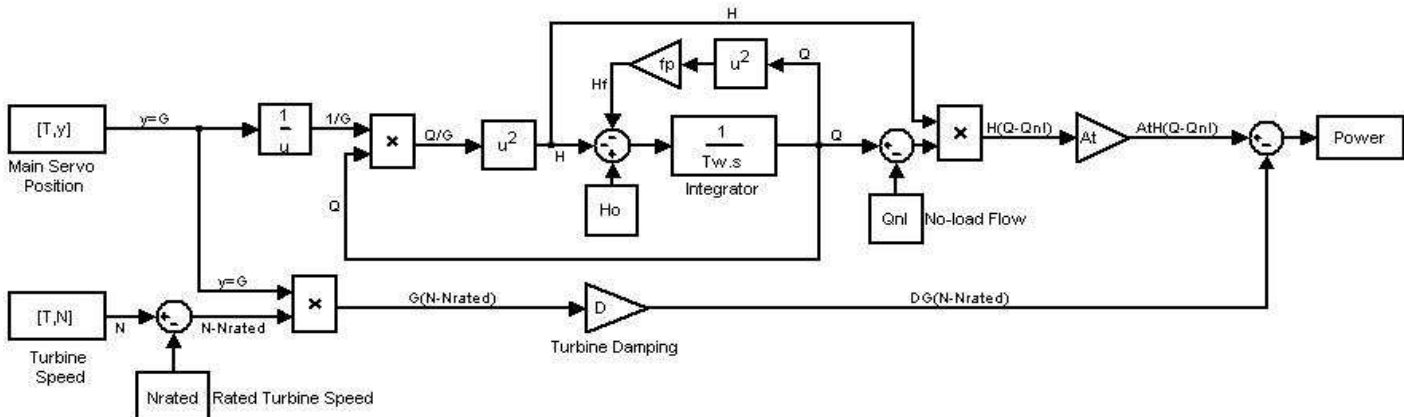


Figure 2: Block diagram for 1992 nonlinear IEEE turbine model [10].



### New Features of the Proposed Model

The earlier IEEE model illustrated in Figure 3, with its simplified turbine and guide vane characteristics, could not adequately represent all the transient behaviour observed in the field tests. Such simplifications are no longer necessary with modern computing power. Thus, additional nonlinear features have been adopted here to improve accuracy of the turbine model.

1. A lookup table is included in the model to implement a nonlinear GV function. The table combines two nonlinear relationships: the GV angle varies nonlinearly with the main servo movement; and the GV function varies nonlinearly with the GV movement. A quadratic term is introduced to provide a simple non-linear relation between flow and gate opening. This term can be tuned to match the observed steady state power output.
2. A lookup table for the efficiency vs. flow coefficient is used to replace the turbine gain and damping factor. This procedure incorporates damping effects due to both speed and head changes as well as the losses in the turbine. The lookup table is constructed using a combination of data from full-scale steady-state tests, simulations and model test results. No further correction for variation from rated head is required with this arrangement [4].
3. A first order filter block (gate time delay) can be included to model the unsteady effects associated with gate movement. It has not been used in the present work, but will be implemented later when adequate data becomes available from computational studies, field tests or laboratory model tests.

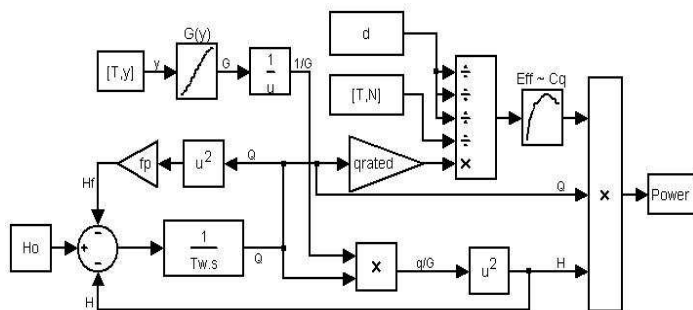


Figure 4: Block diagram for new proposed turbine & waterway model.

## Field Test Procedure

A test program was developed in cooperation with Hydro Tasmania to evaluate the improved turbine and waterway model for the single-machine Mackintosh power station. The tests consisted of frequency deviation tests, Nyquist tests and the steady-state measurements [7]. The power output, main servo position, generator frequency (or turbine speed), and the static pressure at turbine admission were recorded during the tests [8].

The frequency deviation and Nyquist tests give a quantitative measure of the plant behaviour if the generator is supplying an isolated load [7]. A large injected signal to the governor is applied in the frequency deviation test to cause a large step change in the guide vane position. A smaller oscillatory signal is injected in the Nyquist test to move the guide vane sinusoidally about a given average position. This is repeated at various frequencies. Steady-state measurements were carried out to obtain the turbine characteristics with respect to the change in guide vane position [8]. The test results are used in combination with the model test data to determine the characteristic curves of the Francis turbine. Due to the influence of the remainder of the power system, it was not possible to vary the machine speed

during field tests. Testing these aspects would require laboratory model tests or a full-scale machine isolated from the grid.

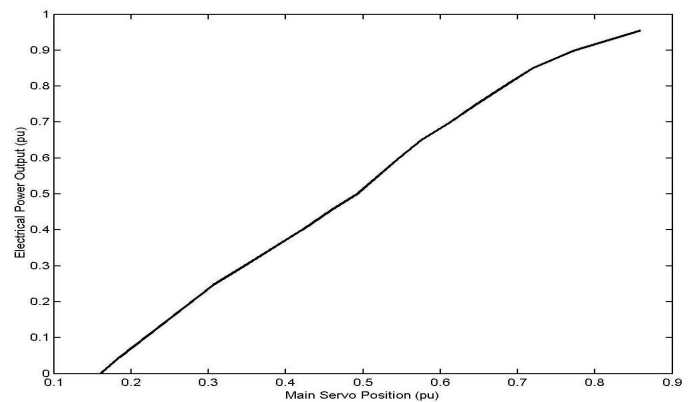


Figure 5: Steady state test measurement for Mackintosh power station.

## Modelling and Simulation

A Matlab/Simulink program was used for testing of the new turbine model. The Simulink code can readily be translated into the Fortran-based PSS/E package used for predicting overall power system response to disturbances. Hydraulic parameters for the original and improved turbine models are listed in Table 1.

Description of the Model Parameter	Value
Rated flow rate, $Q_{\text{rated}}$ ( $\text{m}^3 \text{s}^{-1}$ )	149.7
Rated power output, $P_{\text{rated}}$ (MW)	79.9
Rated speed, $N_{\text{rated}}$ (rpm)	166.7
Rated head, $h_{\text{rated}}$ (m)	61
Water time constant, $T_w$ (s)	3.16
Conduit head loss coefficient, $f_p$	0.0004
Damping factor, $D$	0.50
Turbine Gain, $A_t$	1.48
No-load Unit flow, $Q_{nl}$	0.16

Table 1: Hydraulic parameters for the original and improved turbine models of the Mackintosh power station.

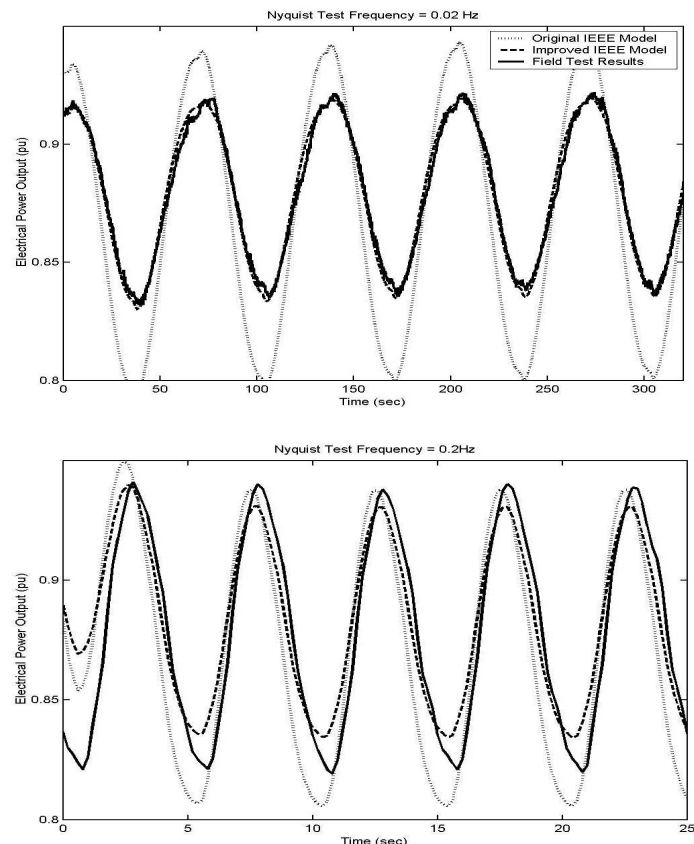


Figure 6: Simulated and measured responses of the Mackintosh power station. Nyquist tests are performed at test frequencies of 0.02 Hz (low speed) and 0.2 Hz (high speed) respectively. Available static head is 61m.

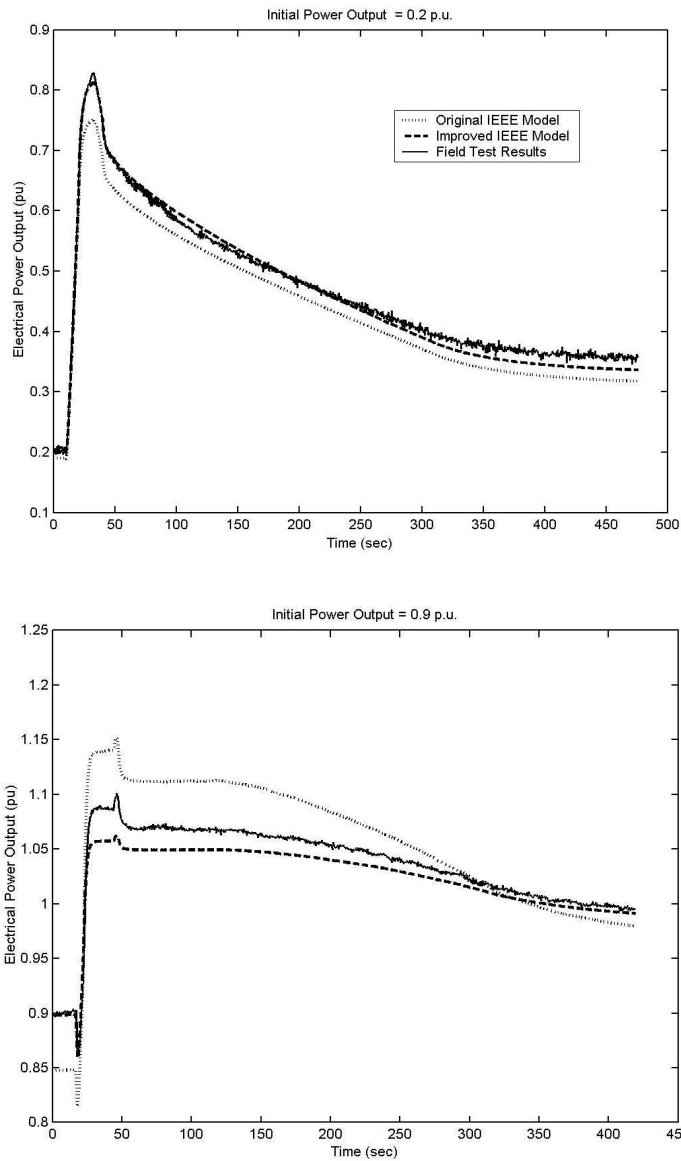


Figure 7: Simulated and measured responses of the Mackintosh power station following a step change in the load. The tests are conducted at low and high initial power outputs respectively. Available static head is 65m.

As shown in Figures 6 and 7, the new model has better simulated the magnitude of power fluctuations when the plant is subjected to a frequency disturbance. The improvements are more obvious when the turbine is operating at high load and the guide vane is moving at a faster rate. However, the new model still shows a retraceable phase lag between the measured and the simulated power outputs, which increases in magnitude with guide vane oscillation frequency.

The well-tested electro-mechanical model for the governor operation is unlikely to have been a significant cause of error. The remaining discrepancies are most likely due to unsteady flow effects in the Francis turbine. In general, the flow pattern in the Francis turbine does not change instantaneously with the gate movement and thus a time lag in flow establishment through the runner and draft tube may occur. The lag may change as the operating condition of the machine changes [4].

This unsteady effect, however, should not be such a significant problem for power stations with relatively long waterway conduits and high water inertia [4]. The inertia effect of the water column in such cases is expected to dominate any unsteady flow effects of the Francis turbine operation. Hence, unsteady flow studies should be focused on the stations with relatively short penstocks. This is the subject of the ongoing research.

## Conclusions

An improved nonlinear turbine and waterway model suitable for Francis turbine operation has been proposed. Comparisons between simulation and full-scale test results have demonstrated significant improvements in accuracy. However, there remain some frequency-dependent discrepancies for short penstock installation that appear to be associated with unsteady flow within the turbine.

## Acknowledgments

The authors thank Hydro Tasmania and University of Tasmania for the funding of this research project and facilitations of field tests. The authors also gratefully acknowledge the contributions of K. Caney, P. Rayner, P. Vaughan, and M. Wallis of Hydro Tasmania for their contribution to this project.

## References

- [1] De Jaeger, E., Janssens, N., Malfliet, B., & Van De Meulebrooke, F., Hydro Turbine Model for System Dynamic Studies, *IEEE Trans. Power Sys.*, **9**, 1994, 1709–1715.
- [2] Hannet, L.N., & Fardanesh, B., Field test to validate hydro turbine-governor model structure and parameters, *IEEE Trans. Power Sys.*, **9**, 1994, 1744–1751.
- [3] IEEE Task Force on Overall Plant Response, Dynamic models for steam and hydro turbines in power system studies, *IEEE Trans. Power Apparatus and Sys.*, **92**, 1973, 1904–1915.
- [4] Ng, T.B., Walker, G.J., & Sargison, J.E., Turbine and Waterway modelling: Investigation and Development of Improved Models Stage II report, School of Engineering, University of Tasmania, Tech. Rep. 19/03. 2003.
- [5] Power Technologies Inc., PSS/E the proven integrated program for power flow, short circuit and dynamic simulation. [www.pti-us.com](http://www.pti-us.com), 27 July 2004.
- [6] Ramos, H. & Almeida, A.B., Dynamic orifice model on water hammer analysis of high or medium heads of small hydropower schemes, *J. Hydraul. Res.*, **39**, 2001.
- [7] Rayner, P. & Ho, S., Devils Gate Power Station – Dynamic Modelling and Tasmanian Electricity Code Compliance Assessment, Hydro Electric Corp., Tasmania, Australia. Tech. Rep. GEN-112475-Report-1, 2003.
- [8] Rayner, P. & Rai, P., Machine Test Guidelines (Rev. 2), Hydro Electric Corp., Tasmania, Australia. Tech. Rep. GEN-0201-TR-0002. 1999.
- [9] Walker, G.J. & Sargison, J.E., Turbine and Waterway Modelling: Investigation and Development of Improved Models Stage I Report, School of Engineering, University of Tasmania, Tech. Rep. 19/02. 2002.
- [10] Working Group on Prime Mover and Energy Supply Models for System Dynamic Performance Studies, Hydraulic Turbine and Turbine Control Models for System Dynamic Performance Studies, *IEEE Trans. Power Sys.*, **7**, 1992, 167–179.

## Skin Friction CFD Calculation for Complex Flow: Turbulent Flow along an External Corner

K. A. M. Moinuddin<sup>1</sup> P. N. Joubert<sup>2</sup> and M. S. Chong<sup>2</sup>

<sup>1</sup> Centre for Environmental Safety and Risk Engineering  
Victoria University of Technology, PO Box 14428, Melbourne City MC, VIC-8001 AUSTRALIA

<sup>2</sup>Department of Mechanical and Manufacturing Engineering  
The University of Melbourne, VIC-3010 AUSTRALIA

### Abstract

RSM (Reynolds Stress Model) simulations of turbulent flow on a streamwise external corner were carried out using the CFD code FLUENT to obtain skin friction. Both wall function and near-wall treatment approaches were used. Experimental data from an earlier experimental study [J. Fluid Mech. 511 (2004) 1], measured at the streamwise station  $x = 0.54$  m was used as the inlet condition for the numerical simulation. The objective of the numerical investigation is to determine the accuracy of RSM prediction of skin friction coefficients ( $C_f$ ) for a complex three-dimensional flow. Calculated values were compared with the experimental data and only wall function model data is found to be in reasonable agreement.

### Introduction

Commercial CFD softwares are widely used to calculate various forms of drag in number of engineering applications. Most of these applications are complex in nature. Since experimental investigation of complex flow, such as turbulent flow along an external corner has been conducted [1, 2], it is worthwhile to find whether CFD calculations can replicate the measured skin friction data.

In the earlier studies of [1, 2] the details of turbulent boundary layer development over a 6 m long external corner were investigated using hot-wire anemometry in a large closed circuit wind tunnel. Mean streamwise velocities were also measured using a Pitot-static tube. The first measurement point of the mean velocity profile was taken as Preston tube measurement of  $C_f$ . This quantity was also calculated using a Clauser chart. Details are presented in [1].

For this numerical simulation a commercial Computational Fluid Dynamics (CFD) software, FLUENT 6.0, was used adopting a Reynolds Stress Model (RSM). For the details of the numerical scheme, grid configuration and boundary conditions, refer to [3]. A brief description with emphasis to grid configuration is presented in the next section. In FLUENT calculation, wall can be treated with three different approaches: (a) near-wall model (based on [4, 5]), (b) standard wall function model [6] and (c) non-equilibrium wall function model [7]. The current study utilizes all three models.

### Numerical technique

Incompressible turbulent flow along streamwise corners was considered. The geometry and co-ordinate systems are displayed in figure 1(a). Two different sets of grids (one consisting of 588,000 and the other of 507,000 hexahedral elements) were generated. The first set was created for the near-wall RSM model, where the grids are clustered closely to the wall to ensure that the first computational node is at  $y^+ < 5$  (for the current study  $y^+ \approx 1$ ) as per FLUENT guidelines (assuming that the  $u^+ = y^+$  relationship exists in that region). In addition, a very

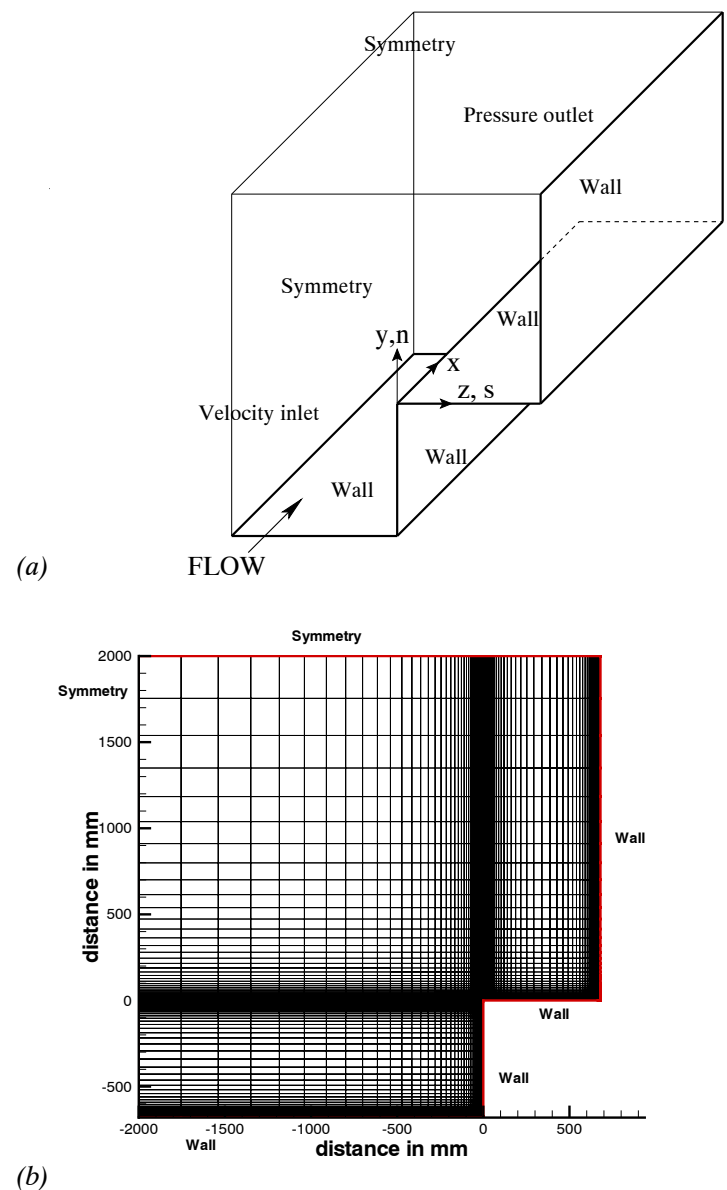


Figure 1: (a) Flow configuration of streamwise corner for numerical simulation (not to scale). (b) Mesh distribution on the cross section of the flow domain. Figures are presented looking upstream.

fine grid was generated near the streamwise corners to capture the correct secondary flow structures.

Traditionally, in most of the commercially available CFD codes, including FLUENT, the preferred mode of simulation is the wall function approach. For this approach, FLUENT suggests that the first computational grid should be set at  $30 < y^+ < 60$  (assuming that log-law exists in that region). This necessitates the need for the second set of grids with the first computational

node at  $y^+ \approx 30$ . The same guideline applies for both standard and non-equilibrium wall functions.

Experimental data measured at the streamwise station at 0.54 m was used as the inlet condition for the numerical simulation. Off-the-wall boundary conditions are normally used for both near-wall and standard wall function approaches in FLUENT. In the wall function approach (both standard and non-equilibrium), the viscosity-affected region is not resolved. Instead, semi-empirical formulae known as “wall functions” are used to bridge the viscosity-affected region between the wall and the fully turbulent region. To compute the values of the mean velocity components, Reynolds stresses and dissipation rate ( $\epsilon$ ) at the first node off-the-wall separate wall functions are used. In the near-wall model the viscosity-affected region is usually resolved all the way to the wall. However, similar to the standard wall functions, enhanced wall functions are used to compute the quantities at the first grid off-the-wall for the FLUENT near-wall model. This is a deviation from the original Launder and Shima model [8], where flow to be calculated all the way down to the wall, setting zero values of all the velocity and Reynolds stress components. These boundary conditions have been discussed elaborately in [3]. The convergence of the calculation is determined by monitoring the residual versus iteration curves. The simulations are conducted until these curves are flattened.

## Results

In figure 2(a), the spanwise  $C_f$  profiles, at  $x=4.565$ m, from all three runs (simulations) are plotted. In addition, near-wall method data from [3] is shown, in which  $y^+ \approx 3$ . All profiles have similar trends, except very close to the corner. Unexpectedly, near-wall method values are much higher than the wall function method values. The FLUENT near-wall model calculates wall shear stress based on the assumption that the law  $u^+ = y^+$  exists in the viscous sublayer. Therefore, despite calculating approximately correct values of the mean velocity, a very minor inaccuracy may result in an erroneous local skin friction coefficient ( $C_f$ ). Although emphasis is given on the importance of setting  $y^+ \approx 1$  in [5], a simulation with  $y^+ < 5$  does not provide much variation.

In figure 2(b) all the current numerical profiles, as well as profile from [9], are normalised by  $C_{f2D}$ , the  $C_f$  value in the 2-D region. A length scale  $s_{2D}$  is also used, which represents spanwise distance from the corner where the nominal 2-D region approximately starts. For the [9] profile  $s_{2D}$  is the distance between the corner and the wall bisector. The profiles are found to have excellent similarity, except very close to the corner. Besides differences in flow geometry, the study of [9] adopted a coarse grid for the external corner. All these may have contributed to the larger difference close to the corner.

The  $C_f$  is usually measured in mild 3-D flows using a Preston tube. The experimental data of [1] (obtained using a Preston tube) is compared with both wall function model data in figure 3. Overall a very good agreement is observed. However, data from the near-wall model is not plotted in this figure. Correlating figure 2(a), it is clear that the near-wall model grossly overpredicts  $C_f$  values all along the model.

Unlike the experimental finding, at  $x=1.07$  m multiple peaks are not found in the numerical profiles and the values of the peaks (close the corner) are smaller compared to the experimental data. Overall the non-equilibrium model better predicts the data at this station compared to standard wall function model.

In figure 4, the comparison of both wall function model data with the experimental data (obtained using a Clauser chart) is

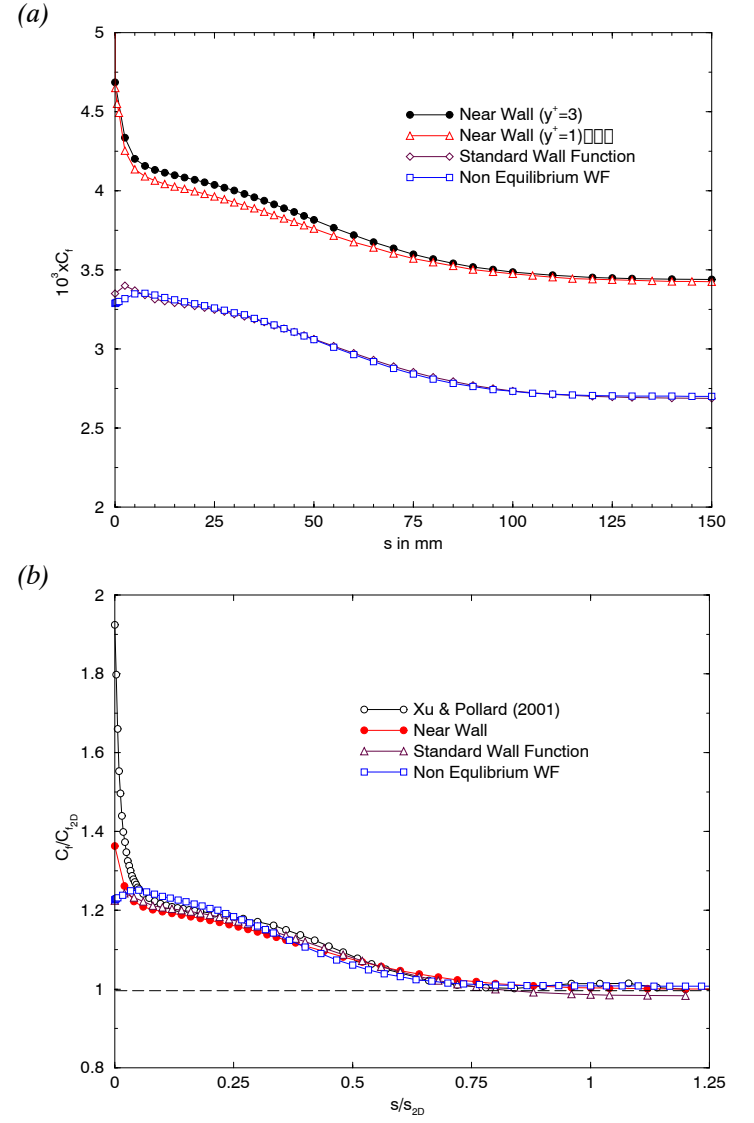


Figure 2: (a) Comparison between absolute spanwise  $C_f$  profiles from all current numerical simulations. (b) Comparison of normalised spanwise  $C_f$  profiles from current numerical simulations and [9].  $s_{2D}$  represents spanwise distance from the corner where the nominal 2-D region approximately starts.

presented for five streamwise stations. The numerical data is found to be significantly lower compared to the experimental data derived from a Clauser chart. This difference is larger at the upstream stations (i.e.  $x=1.07$  m and 2.17 m) compared to the downstream stations. However, at  $x=1.07$  m prediction by non equilibrium model is comparatively better. The difference between the wall function data and the Clauser chart data is the same order of magnitude as the difference between the Clauser chart data and the Preston tube data, which is given in the fourth column of table 1.

2-D values for $C_f$ distribution			
Station (in mm)	Clauser Chart	Preston tube	Diff.
$x, s=1070, 40$	$3.637 \times 10^{-3}$	$3.315 \times 10^{-3}$	9.71
$x, s=2170, 100$	$3.087 \times 10^{-3}$	$2.869 \times 10^{-3}$	7.07
$x, s=3385, 100$	$2.941 \times 10^{-3}$	$2.765 \times 10^{-3}$	6.70
$x, s=4565, 100$	$2.880 \times 10^{-3}$	$2.735 \times 10^{-3}$	5.30
$x, s=5010, 100$	$2.878 \times 10^{-3}$	$2.731 \times 10^{-3}$	5.38

Table 1:  $C_f$  values in the nominal 2-D region at various streamwise station. distribution. The fourth column shows the difference between two methods as a percentage.

Although in the experimental study, the shape of the spanwise  $C_f$  profile are different at early and downstream streamwise

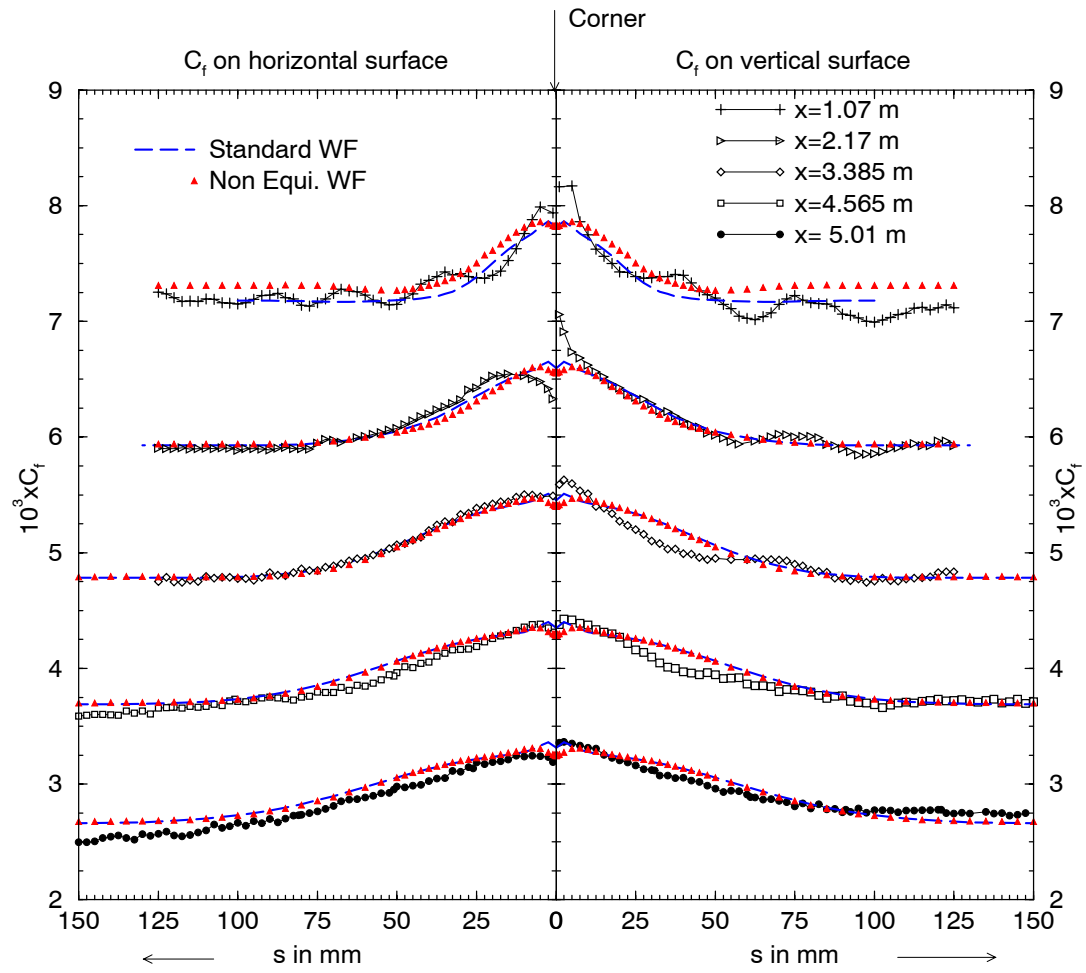


Figure 3: Comparison of spanwise  $C_f$  profiles from both wall function model simulations with that from the experimental data (based on Preston tube). Profiles for each streamwise station are shifted 1 unit upwards from the downstream one except at  $x=5.01$ m.

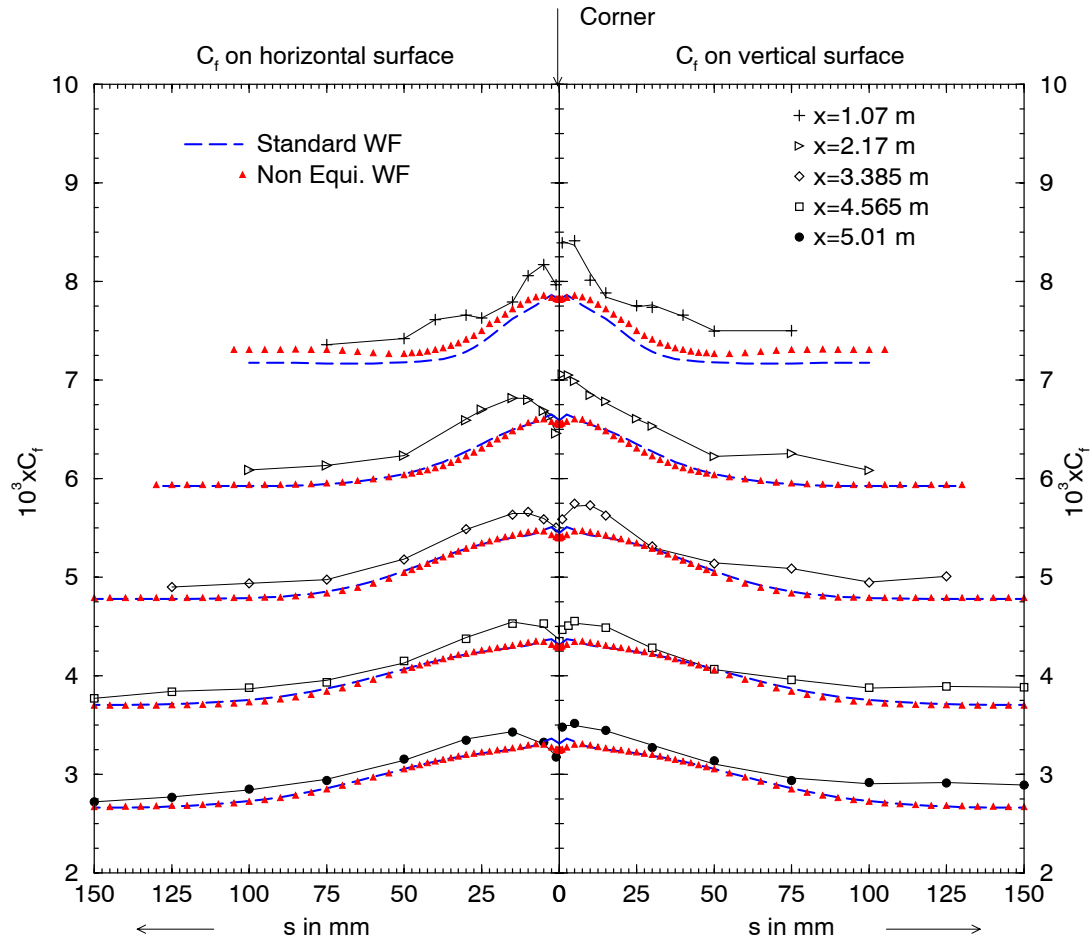


Figure 4: Comparison of spanwise  $C_f$  profiles from both wall function model simulations with that of experimental data (derived from a Clauser chart). Profiles for each streamwise station are shifted 1 unit upwards from downstream one except at  $x=5.01$ m.

stations (presented in [1]), these profiles are found to have a similar shape all along the model in the numerical study. It is observed that similar to the experimental findings, in the numerical studies with wall function model, the maximum value of  $C_f$  occur away from the streamwise corner. As one moves away from the location of the maximum, the  $C_f$  decays exponentially towards the two-dimensional region. The location of the maximum  $C_f$  from the standard wall function model data is found to be closer to the corner ( $s \approx 2.5$  mm) compared to that from the experimental findings ( $s < 5$  mm at early station and  $s < 10$  mm downstream). However these locations from the non-equilibrium model are found to be similar to that from the experimental study.

## Conclusions

Numerical simulation based on an RSM model is performed for the flow along an external corner. The current study shows that in an ideal situation the boundary layer develops symmetrically about the external corner bisector and therefore, the  $C_f$  distribution is symmetrical too. The  $C_f$  distribution from the wall function model simulation is found to be in reasonable agreement with the experimental work. However, the near-wall model simulation grossly overpredicts the  $C_f$  values. This problem has been traced back by [3] to the fact that a serious error is involved with the wall boundary conditions (enhanced wall functions) for Reynolds stresses. Therefore, it is suggested that for the near-wall model, instead of using off-the-wall boundary conditions, flow to be calculated all the way down to the wall setting zero values of all the velocity and Reynolds stress components (as done in [8]).

## Acknowledgements

The authors gratefully acknowledge the assistance of Dr. A. Ooi for his valuable advice during this study.

## References

- [1] Moinuddin, K. A. M., Joubert, P. N., Chong, M. S. and Hafez, S. Experimental investigation of turbulent boundary layer developing along a streamwise external corner (Chine), *Exp. Thermal and Fluid Science*, **27**(5), 2003, 599–609.
- [2] Moinuddin, K. A. M., Joubert, P. N. and Chong, M. S. Experimental investigation of turbulence-driven secondary motion on a streamwise external corner. *J. Fluid Mech.*, **511**, 2004, 1–23.
- [3] Moinuddin, K. A. M., Joubert, P. N., A. Ooi and Chong, M. S. RSM Simulation of turbulence-driven secondary motion over a streamwise external corner: Comparison with experimental result *Trans. ASME I, J. Fluid Eng.* (under review).
- [4] Chen, H. C. and Patel, V. C. Near-wall turbulence models for complex flows including separation. *AIAA Journal* **26**(6), 1988, 641–648.
- [5] Malan, P. and Kim, S.-E. A unified wall treatment for turbulent flows-Part 1: Hydrodynamics. *Fluent Internal Publication* January, 2000 (unpublished).
- [6] Launder, B. E. and Spalding, D. B. The numerical computation of turbulent flows. *Comput. Methods Appl. Mech. Eng.* **3**, 1974, 269–289.
- [7] Kim, S.-E. and Choudhury, D. A near wall treatment using wall functions sensitized to pressure gradient. In *ASME FED Vol. 217, Separated and Complex Flows*. ASME, 1995.
- [8] Launder, B. E. and Shima, N. Second-moment closure for the near-wall sublayer: Development and application. *AIAA Journal* **27**(10), 1989, 1319–1325.
- [9] Xu, H. and Pollard, A. Large eddy simulation of turbulent flow in a square annular duct. *Phys. Fluids*, **13**, 2001, 3321–3337.



## Influence of Free-Stream Turbulence on Wake-Wake Interaction in an Axial Compressor

A. D. Henderson<sup>1</sup>, G. J. Walker<sup>1</sup> and J. D. Hughes<sup>2</sup>

<sup>1</sup>School of Engineering, University of Tasmania  
Hobart, Tasmania 7001, AUSTRALIA

<sup>2</sup>Rolls-Royce plc, Derby DE248BJ, UK

### Abstract

A turbulence generating grid has been used to increase the level of free-stream turbulence inside a 1.5 stage axial compressor to values typical of an embedded stage in a multi-stage machine. Hot-wire measurements taken in the rotor-stator axial gap have been ensemble-averaged to determine periodic fluctuations in turbulence level and velocity. These results are compared to measurements made at low turbulence levels without the turbulence grid. Increasing levels of free-stream turbulence are shown to reduce the magnitude of periodic disturbances produced by viscous interaction between the inlet guide vane (IGV) and rotor blade wakes.

### Introduction

Unsteady flow in aeroengines is well known to influence many aspects of performance. Despite this, unsteady effects are not generally considered in current design methods due to the high level of complexity involved. There is now a large research effort to improve understanding of unsteady flow phenomena. One common source of unsteadiness in multi-stage compressors is the periodic disturbance produced by the viscous wakes of upstream blade rows. The relative flow past a blade leaves a wake region that is characterised by high levels of turbulence and lower relative velocity. These wakes are convected downstream to the next blade row, where they are chopped into segments as they pass through the blade passages. The velocity variation across the passages due to the circulation around the blades causes a rotation of the wake segments, as earlier described by Smith [6]. These segments leave the passages and then interact with the wakes shed from the blade row causing their dispersion. A typical wake dispersion pattern is shown in figure 1.

Low speed single-stage research compressors are commonly used for making detailed studies of many flow phenomena. The flow conditions are generally different from multi-stage industrial turbomachinery which operate at higher levels of turbulence due to the mixing of wakes over a large number of blade rows. Industrial machines also operate at high speeds with significant compressibility effects, a difficult environment for taking measurements. Experience has shown that many types of flow phenomena remain the same in nature in both types of machine. Consequently, low speed single stage compressors remain a widely used research tool.

Earlier studies of wake-wake interaction in the low speed research compressor at the University of Tasmania were conducted by Lockhart and Walker [3], who took hot-wire anemometer measurements of the flow in the rotor-stator axial gap. They observed that the rotor wake decay varied with circumferential position and proposed this was due to an interaction with wakes from the IGV blade row. They presented a model for the wake dispersion process similar to that shown in figure 1.

Some years later, Walker et al. [8] and Walker et al. [9] took more detailed hot-wire measurements in the rotor-stator axial gap using high speed data acquisition. The measurements were processed to calculate ensemble-averaged velocity and turbulence level. The results showed an accumulation of rotor-wake fluid on the suction side of the IGV wakes due to a restriction of the rotor wake relative flow by viscous interactions with the adjacent IGV wake segments. Results taken for different load cases showed that the rotor wake segments were turned by a larger amount as the level of loading was increased. Similar processes occur in axial turbines but the higher blade loadings produce a much larger distortion of wakes from upstream rows.

Recently Chow et al. [1] used particle image velocimetry (PIV) to study the wake-wake interaction in a 2-stage axial turbomachine. They observed regions where rotor wake fluid was collected into turbulent hot spots. They also observed a significant distortion or kinking of the rotor wakes. These observations indicate a greater amount of wake-wake interaction than has been found in the other research described here. This could be explained by their different turbomachine geometry.

The objective of the current research is to study how the wake-wake interaction process is influenced by increased levels of free-stream turbulence, such as those found in multi-stage turbomachinery.

### Experimental Details

#### Research Compressor

Air enters the compressor radially through a cylindrical inlet 2.13m in diameter and 0.61m wide. The flow passes through a 6.25:1 contraction, where it turned 90° to the axial direction. The compressor has three blade rows: inlet guide vanes (IGV), rotor, and stator as shown in figure 1. The stationary blade rows both have 38 blades and the rotor has 37 blades, giving space/chord ratios of 0.99 and 1.02 respectively. The blade profiles were based on a British C4 section with a constant chord length of 76.2mm and an aspect ratio of 3.0. The blade profiles were stacked about a radial axis to achieve free-vortex flow and 50% reaction at mid-blade height at design flow conditions. The test section annulus is constant in area with hub and casing diameters of 0.69m and 1.14m respectively. The flow passes through an annular diffuser before discharging through a cylindrical throttle at exit. The throttle can be automatically adjusted to achieve the desired compressor load. The rotor is directly coupled to a 30kW DC motor via a long shaft. The speed is controlled by an analogue feedback loop with a computer controlled reference voltage. The speed control for a fixed set point was within  $\pm 0.1\text{RPM}$ .

Instruments are inserted into the test section through an axial slot in the casing wall. A probe traversing rig on the outside allows accurate positioning in axial and radial directions.

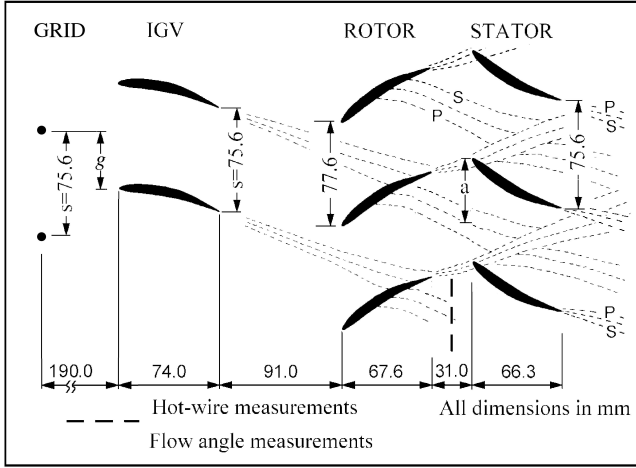


Figure 1: Cross section of the research compressor showing the mid-passage blade row configuration and a typical instantaneous wake-dispersion pattern: S = suction side P = pressure side.

The IGV and stator blade rows are held in movable rings which allow circumferential traversing over 2 blade pitches via stepper drives. This enables the stationary blade rows to be aligned circumferentially relative to each other and the fixed turbulence grid as indicated by the variables (a) and (g) shown in figure 1.

The background turbulence level of the research compressor was raised using a turbulence generating grid similar to that of Place et al. [4], who mainly focused on measuring machine performance and turbulence characteristics. The design goal was 4% turbulence intensity at entry to the stator row, which is typical of multi-stage machine operation. This was achieved by installing a turbulence grid at the start of the test section as shown in figure 1. The grid consisted of 38 radial rods of 7.94mm diameter, each spanning between rings fixed to the hub and casing. A constraint was placed on the maximum pressure loss so that the full range of test load cases could be reached. The number of rods was made equal to the number of blades in the stationary rows so that every blade in a stationary row would experience the same disturbance field. The selection of rod diameter and the grid position was primarily based on the data given in Roach [5], assuming isotropic decay of turbulence in a zero pressure gradient over an estimated mean flow path length between the turbulence grid and stator row.

### Measurement Techniques

The compressor was operated at a constant blade Reynolds number ( $Re = U_{mb}c/\nu = 120000$ ) based on mid-blade rotor speed ( $U_{mb}$ ) and blade chord ( $c$ ). Compressor load was controlled by setting the flow coefficient ( $\phi = u_{ref}/U_{mb}$ ), where the reference flow speed ( $u_{ref}$ ) was measured by a pitot-static tube located upstream of the test section. Ring tapings on the intake contraction were calibrated prior to installation of the turbulence grid to measure the compressor flow coefficient. The flow coefficient was set to a medium load condition ( $\phi = 0.675$ ) during the beginning of each test and was not adjusted during testing.

The hot-wire measurements were made using a single wire Dantec 55P05 probe with sensor aligned in the radial direction. The probe support was rigidly fixed between two stator blades

with the wire position in the centre of the rotor-stator gap at mid-blade height. A circumferential traverse was completed by moving the stator row and probe over one whole blade pitch keeping the IGV row fixed. The hot-wire probe was operated with a TSI IFA100 constant temperature anemometer. The frequency response of the system was estimated using a square wave test to be greater than 70kHz. The anemometer voltage was offset, amplified and low pass filtered at 20kHz before data acquisition at 50kHz. The offset and gain settings were optimised to maximise the signal range for input to the data acquisition card. Data were recorded on a Pentium II computer with an United Electronic Industries WIN30DS card. The sampling process was triggered once per revolution by a pulse from an encoder attached to the rotor shaft. Measurements were taken at 32 circumferential steps across a blade passage. In each position 512 data traces were recorded, each containing 1024 samples. This corresponds to approximately 6 wake passing periods.

The probe was calibrated using an in-situ method developed by Solomon [7]. In this method a local velocity coefficient  $U/U_{mb}$  was measured with a pre-calibrated three hole probe over a range of rotor speeds. A direct calibration was made by replacing the three hole probe with the hot-wire probe and repeating the process. Solomon [7] also investigated calibrating the probe in a different wind tunnel and then re-assembling it in the compressor for measurement. However this was found to introduce large errors caused by changes in lead contact resistances. The in-situ method eliminated this requirement and was found to be fast and repeatable.

### Data Analysis

The hot-wire traces were processed using the ensemble averaging technique detailed in Evans [2]. Walker et al. [8] and Walker et al. [9] later adapted and refined this method in their research. A brief summary of their method follows.

Instantaneous velocity is commonly expressed in terms of a time mean  $\bar{u}$  and associated fluctuating component  $u'$ . The flow under examination has strong periodic events and can also be defined in terms of an ensemble-averaged velocity  $\langle u \rangle$  and fluctuating component  $u''$ . This may be expressed as

$$u = \bar{u} + u' = \langle u \rangle + u'' \quad (1)$$

The ensemble-averaged velocity field observed by a stationary probe downstream of the rotor is circumferentially periodic with a wavelength equal to the IGV pitch. It retains this periodicity through the stator due to the equal numbers of IGV and stator blades. It may be calculated by phase lock averaging a sufficiently large number of records  $N$  for each time instant  $t_i$ . This is expressed by

$$\langle u \rangle(t_i) = \frac{1}{N} \sum_{k=1}^N \{u(t_i)\}_k \quad (2)$$

The periodic unsteadiness is evaluated over an integral number of blade-passing periods and non-dimensionalised by the local free-stream velocity  $U$ . This is expressed by

$$\tilde{T}u = (\langle u \rangle - \bar{u})_{rms}/U \quad (3)$$

The true random unsteadiness is given by

$$Tu = u''_{rms}/U \quad (4)$$

The total turbulence level or overall unsteadiness is given by

$$Tu_D = u'_{rms}/U \quad (5)$$

Assuming the periodic and random turbulence levels are statistically independent they may be related by

$$Tu_D^2 = \tilde{T}u^2 + Tu^2 \quad (6)$$

## Results and Discussion

Figure 2 shows processed results of the hot-wire measurements in the rotor-stator gap for the test cases with and without the turbulence grid. The shaded contour plots show ensemble-averaged velocity  $\langle u \rangle$ , non-dimensionalised by pitchwise averaged time mean velocity  $\bar{u}_s$ . The line contours show ensemble-averaged disturbance level  $\langle Tu \rangle$  in 1% intervals. The vertical axis (w/s) is circumferential position (w) divided by the rotor blade pitch (s). Time is shown on the horizontal axis, non-dimensionalised by the rotor passing period. This convention shows the earliest measurements on the right ( $t^* = 0$ ). The results have been replotted over a second passage by assuming the flow is periodic in the pitchwise direction. The plot represents the instantaneous view of the unsteady flow field on a cylindrical surface at mid-span radius, which would result from the flow convecting unaltered from the measuring station with zero whirl.

The rotor wakes are clearly defined by bands of high turbulence level running diagonally across the plots. These are diagonal due to the changing probe position relative to the fixed rotor position where triggering starts. The IGV wakes are shown by the horizontal segments with slightly higher than average turbulence level in the passage. This contrasts with the dispersion pattern shown in figure 1 because the whirl component of velocity has not been included. The IGV wakes are hardly visible in the high turbulence case, indicating that the elevated free-stream turbulence has accelerated their mixing out.

The contours of ensemble-averaged velocity provide further detail of the wake-wake interaction processes. The rotor wakes are clearly identified by bands of low level velocity which correspond well with the bands of high turbulence. The IGV segments have lower velocity than the mean velocity in the passage. These zones also correlate well with the contours of turbulence. At the intersection of wake streets, the lower energy fluid of the rotor wake accumulates near the suction surface side of the IGV wake. This leads to circumferential variations in the rotor wake thickness and local regions of high turbulence and lower velocity. The test case with the turbulence grid shows significantly reduced interaction. The rotor wakes fluctuate little in thickness and turbulence intensity. The flow in the passage is also much more uniform than in the case without the grid. This suggests that the higher level of free-stream turbulence has mixed out the IGV wakes. A reduction in periodic flow field at entry to the rotor may also alter the wake shedding process and contribute to a more uniform rotor wake. In particular, there should be smaller fluctuations in rotor blade trailing edge boundary layer thickness due to reduced unsteadiness in the transition process on the blade surface.

The line graphs on the left hand side of figure 2 show time mean values of turbulence level and velocity against circumferential position. Apparent turbulence level  $Tu_D$  is shown with the periodic component  $\tilde{T}u$  and random component  $Tu$ . In both cases, the random component is greater in the IGV wake. The case with higher turbulence shows only a very slight increase at the

location of the IGV wake. Significant periodicity occurs at the position where the low energy rotor wake fluid has collected. This also corresponds to a minimum of time mean velocity. The periodic unsteadiness peaks are essentially absent with the turbulence grid installed.

The turbulence intensity between blade wakes was only slightly lower than the design value of 4%. The small deviation from design was most likely due to the neglected effects of changing stream velocity.

## Conclusions

A study of increasing inlet turbulence level in a 1.5 stage axial compressor has shown a strong influence on wake-wake interactions. Hot-wire measurements taken in the rotor stator gap were used to calculate ensemble-averaged velocity and turbulence. At low levels of inlet turbulence the results showed strong periodic fluctuations in rotor wake thickness and ensemble-averaged velocity. At high levels of inlet turbulence the periodic fluctuations were significantly reduced. This indicates that viscous interaction processes will be much smaller in magnitude for embedded blade rows in a multi-stage axial turbomachine.

## Acknowledgments

The financial support of Rolls-Royce plc is gratefully acknowledged.

## References

- [1] Chow, Y., Uzol, O. and Katz, J., Flow non-uniformities and turbulent "hot spots" due to wake-blade and wake-wake interactions in a multistage turbomachine, *ASME Journal of Turbomachinery*, **124**, 2002, 553–563.
- [2] Evans, R. L., Turbulence and unsteadiness measurements downstream of a moving blade row, *ASME Journal of Engineering for Power*, **122**, 1975, 131–139.
- [3] Lockhart, R. C. and Walker, G. J., The influence of viscous interactions on the flow downstream of an axial compressor stage, in *Proceedings of the 2nd International Symposium on Air Breathing Engines*, Sheffield, UK, 1974.
- [4] Place, J. M. M., Howard, M. A. and Cumpsty, N. A., Simulating the multistage environment for single-stage compressor experiments, *ASME Journal of Turbomachinery*, **118**, 1996, 706–716.
- [5] Roach, P. E., The generation of nearly isotropic turbulence by means of grids, *International Journal of Heat and Fluid Flow*, **8**, 1987, 82–92.
- [6] Smith, L. H., Wake dispersion in turbomachines, *ASME Journal of Basic Engineering*, **88**, 1966, 688–690.
- [7] Solomon, W. J., *Unsteady Boundary Layer Transition on Axial Compressor Blades*, Ph.D. thesis, University of Tasmania, 1996.
- [8] Walker, G. J., Hughes, J. D., Köhler, I. and Solomon, W. J., The influence of wake-wake interactions on loss fluctuations of a downstream axial compressor blade row, *ASME Journal of Turbomachinery*, **120**, 1998, 695–704.
- [9] Walker, G. J., Hughes, J. D. and Solomon, W. J., Periodic transition on an axial compressor stator - Incidence and clocking effects. Part I - Experimental data, *ASME Journal of Turbomachinery*, **121**, 1999, 398–407.

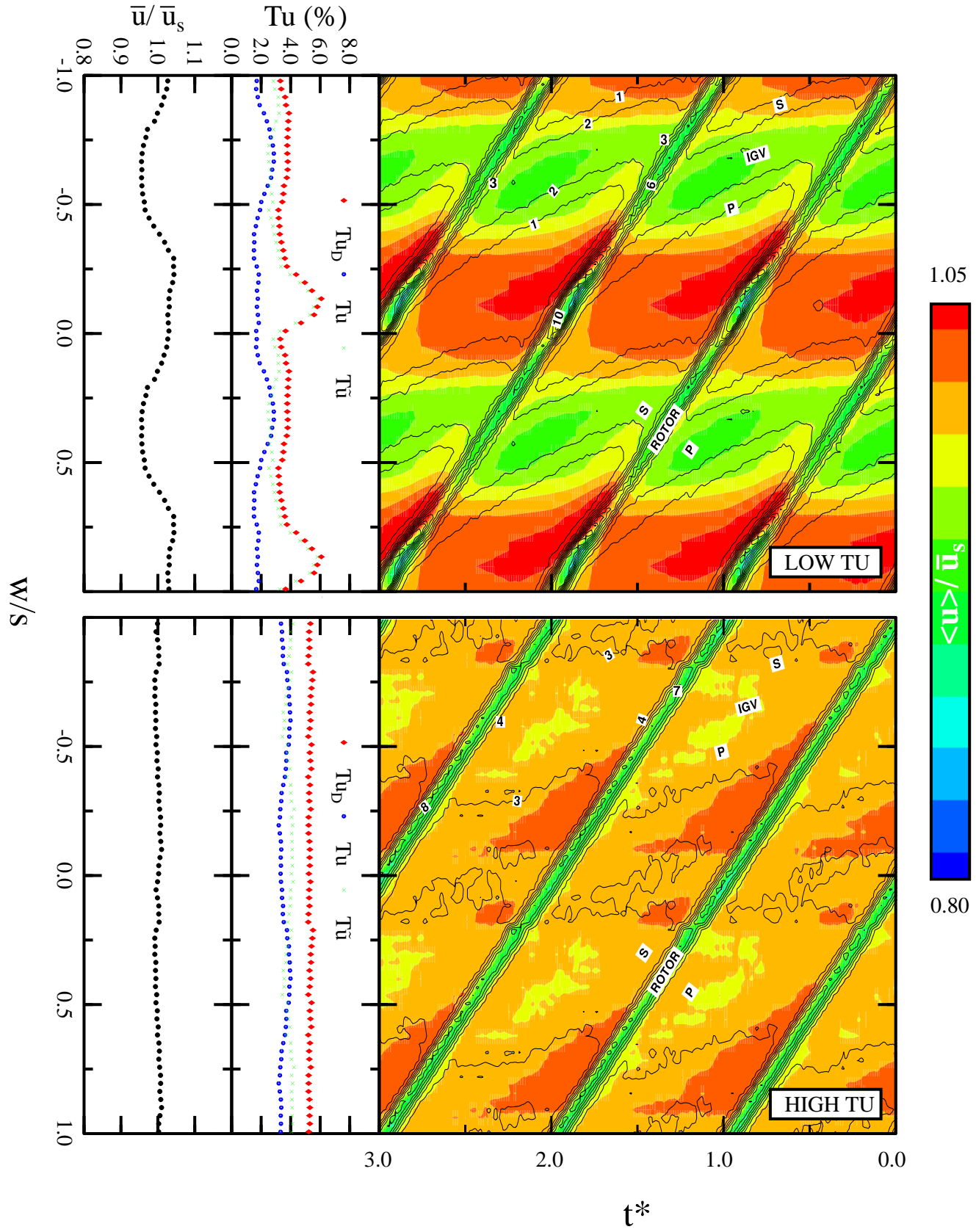


Figure 2: Variation of ensemble-averaged velocity with turbulence level for low (top) and high (bottom) levels of free-stream turbulence. Hot-wire measurements taken in the rotor-stator passage at with a flow coefficient  $\phi = 0.675$  and blade Reynolds number  $Re = 120000$ . Shaded contours show ensemble-averaged velocity  $\langle u \rangle / \langle u_s \rangle$ . Line contours show ensemble-averaged turbulence level  $\langle tu \rangle$  in 1% intervals.

## Experiments and Modeling of Impinging Jets and Premixed Stagnation Flames

J. M. Bergthorson<sup>1</sup>, D. G. Goodwin<sup>2</sup>, and P. E. Dimotakis<sup>1</sup>

<sup>1</sup>Graduate Aeronautical Laboratories  
California Institute of Technology, Pasadena, CA, 91125, USA

<sup>2</sup>Department of Mechanical Engineering  
California Institute of Technology, Pasadena, CA, 91125, USA

### Abstract

Non-reacting impinging laminar jets and premixed methane-air flames are studied experimentally and numerically. Axial velocity measurements are performed using Particle Streak Velocimetry (PSV). The nozzle pressure drop is measured concurrently to determine the Bernoulli velocity. For cold impinging jets, scaling by the Bernoulli velocity collapses the centerline axial velocity profiles onto a single curve that is independent of the nozzle-plate separation distance. Cold-flow velocity profiles can be modeled using an error function with a single, Reynolds number dependent, parameter. Velocity data for cold impinging jets and premixed methane-air flames are compared to one-dimensional simulations with multi-component transport and full chemistry (GRI-Mech 3.0). Near-stoichiometric flames are studied as a function of the nozzle-stagnation plate separation distance. At constant Bernoulli velocity, flame profiles also collapse independently of separation distance. The results indicate that the one-dimensional streamfunction model can accurately capture both non-reacting and reacting stagnation flow if appropriate boundary conditions are specified.

### Introduction

Premixed laminar flames offer a useful environment for validating chemical-kinetic mechanisms of hydrocarbon fuels. Studies that can be referenced to chemical kinetics over a variety of conditions (*e.g.*, equivalence ratio, ambient pressure, strain-rate field) are desirable. The approach here relies on detailed measurements of strained flames in a jet-wall stagnation flow. This geometry has boundary conditions that can be accurately specified, facilitating simulation and comparisons with experiment.

Velocity data for impinging jets in the nozzle-plate separation distance  $L$  to nozzle-diameter  $d$  ratio range of  $0.5 \leq L/d \leq 1.5$  are not widely available. In addition, although stagnation flows have been employed in a large number of laminar flame studies, direct comparisons between flame measurements and simulations are sparse. When comparisons have been made, inlet velocity boundary conditions are treated as free parameters to align measured and simulated profiles (*e.g.*, [5]). This work targets the hydrodynamics of impinging jets and the effects of chemical reaction and the resulting heat release on this flow.

Velocity profiles are measured using Particle Streak Velocimetry (PSV) [1]. Concurrent measurements of the nozzle pressure drop are used to define the Bernoulli velocity  $U_B$ . Impinging jets are studied as a function of  $L$  at imposed strain rates (Reynolds numbers) of interest in laminar flame studies. Near-stoichiometric premixed methane-air flames are studied at constant  $U_B$ , as a function of  $L$ . One-dimensional (1D) simulations of cold and reacting stagnation flows are performed using *Cantera* to assess the streamfunction model employed [1, 2]. This work is part of an ongoing investigation into the performance of flow, transport and chemistry models for premixed hydrocarbon flames.

### Experiments

A room-temperature, atmospheric-pressure jet is generated from a contoured nozzle with an exit diameter of  $d = 10$  mm that impinges on a constant-temperature (water-cooled) copper stagnation plate. Three K-type thermocouples are embedded on the centerline, spaced vertically between the stagnation and cooled surface, to allow monitoring of wall temperature and temperature gradients. Fuel and air mass flow rates are set using sonic metering valves and monitored concurrently (Omega FMA868-V-Methane and FMA872-V-Air, calibrated using a Bios DryCal ML-500). Estimated uncertainty in the mass-flow measurement of the air and fuel streams is 0.5%, resulting in an uncertainty of 0.7% in the equivalence ratio  $\Phi$ .

The pressure difference between the jet plenum interior and a point just outside the jet-core flow region is measured with a 1 torr full-scale differential-pressure transducer (BOC Edwards W57401100 and W57011419). The Bernoulli velocity,

$$U_B = \sqrt{\frac{2\Delta p}{\rho[1 - (d/d_p)^4]}}, \quad (1)$$

is then calculated, where  $\Delta p$  is the nozzle static pressure drop,  $\rho$  the fluid density,  $d$  the nozzle exit diameter, and  $d_p$  the plenum (inner) diameter. Pressure, mass-flow, and temperature data are acquired simultaneously with digital-image acquisition, allowing accurate specification of simulation boundary conditions.

### Particle Streak Velocimetry (PSV)

Flow velocities along the jet centerline are measured using Particle Streak Velocimetry (PSV) [1]. The implemented PSV methodology yields low-fractional-error axial-velocity data, while requiring a low particle-seed density. Low particle loading reduces flame disturbances. A single PSV image can capture the entire velocity field, making it ideal for short-run-time experiments. A sample PSV image for impinging-jet flow is shown in figure 1. The measurements rely on micron-sized alumina particles and ceramic microspheres.

A Coherent I-90 Ar<sup>+</sup> laser, operated at 2 – 3 W, provides the PSV illumination source. Two cylindrical lenses generate a thin laser sheet ( $\approx 200 \mu\text{m}$ ) in the field of view. An Oriel (Model 75155) chopper with a 50% duty-cycle wheel modulates the laser beam. The chopper wheel is placed at a laser-beam waist to minimize on-off/off-on transition times. Chopping frequencies are in the range,  $1 \text{ kHz} \leq \nu_c \leq 2 \text{ kHz}$ , with  $\nu_c$  optimized depending on flow velocity. PSV image data are recorded at 4 fps using the in-house-developed “Cassini” CCD [1]. Magnification ratios are close to 1:1 using a Nikon 105 mm,  $f/2.8$  macro lens (with a 514.5 nm bandpass filter).

Local velocities,  $u(x)$ , are estimated from streak pairs as,  $u(x) \cong \Delta X(x)/\Delta t$ , yielding  $u_I = L_I/\tau_c$  and  $u_{II} = L_{II}/\tau_c$ , where  $\tau_c = 1/\nu_c$  (chopping period) and  $L_I = x_{2s} - x_{1s}$  and  $L_{II} = x_{2e} - x_{1e}$  are the distances from the start/end of one streak to the start/end of

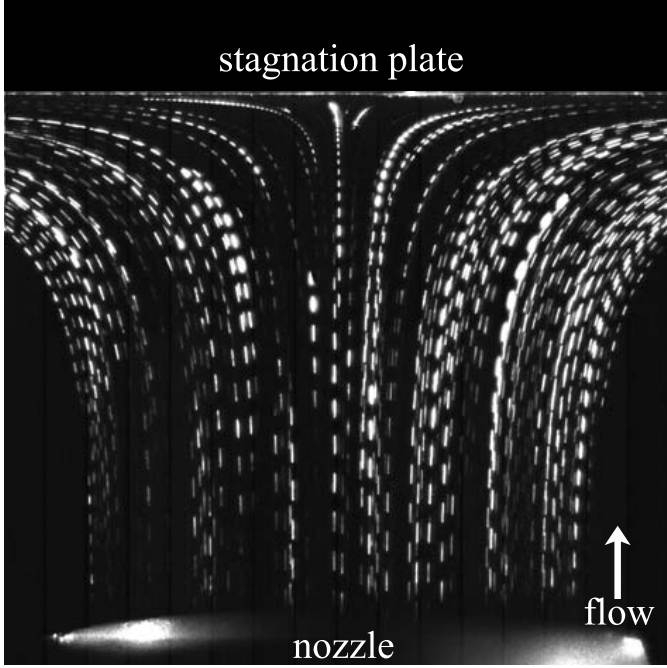


Figure 1: PSV in impinging-jet flow ( $L/d = 1.0$ ).

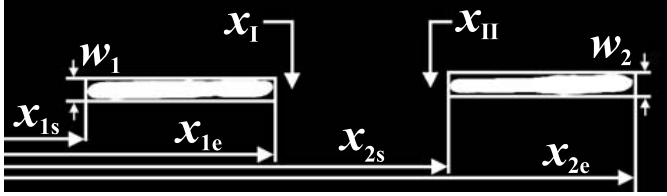


Figure 2: PSV measurement technique.

the next, respectively. The velocity estimate  $u_I$  is located at  $x_I = (x_{1s} + x_{2s})/2 + (w_1 + w_2)/4$ , where  $x_{is}$  is the spatial location of the start of the  $i^{\text{th}}$  streak and  $w_i$  is the width of the  $i^{\text{th}}$  streak. Similarly,  $u_{II}$  is located at  $x_{II} = (x_{1e} + x_{2e})/2 - (w_1 + w_2)/4$ , where  $x_{ie}$  is the location of the end of the  $i^{\text{th}}$  streak (cf. figure 2). Using the same intensity threshold on a streak pair removes systematic errors in applying the Lagrangian time interval  $\tau_c$  to the spatial extent of each streak. The PSV analysis technique yields an rms error of  $\approx 0.01 U_B$ . See [1] for additional details on PSV.

### Simulations

Axisymmetric stagnation flow and premixed flame simulations are performed using the *Cantera* reacting-flow software package [1, 2]. The 1D model for stagnation flows relies on a stream-function  $\psi(x, r) = r^2 U(x)$ , with  $U(x) = \rho u/2$ , where  $u$  is the axial velocity. The momentum equation then becomes,

$$2U \frac{d}{dx} \left( \frac{1}{\rho} \frac{dU}{dx} \right) - \frac{1}{\rho} \left( \frac{dU}{dx} \right)^2 - \frac{d}{dx} \left[ \mu \frac{d}{dx} \left( \frac{1}{\rho} \frac{dU}{dx} \right) \right] = \Lambda. \quad (2)$$

In this formulation,  $\Lambda \equiv (1/r) dp/dr$  and must be a constant. Treating  $\Lambda$  as unspecified, four boundary conditions are imposed on this third-order ordinary differential equation at  $x = 0$  and  $x = \ell$ , with  $0 < \ell \leq L$  a suitably chosen interior point, e.g.,  $U(0) = 0$ ,  $U'(0) = 0$ ,  $U(\ell) = \rho_0 u_\ell/2$ ,  $U'(\ell) = \rho_0 u'_\ell/2$ , where  $\rho_0$  is the density of the (cold) gas mixture, and  $u_\ell$  and  $u'_\ell$  are the velocity and velocity gradient at  $x = \ell$ . Energy and species equations are also solved with specification of inlet composition, inlet temperature, and stagnation-wall temperature boundary-conditions. The simulations use a multi-component transport model and the GRI-Mech 3.0 kinetics mechanism. A (multi-component) no-flux boundary condition for species is assumed at the wall.

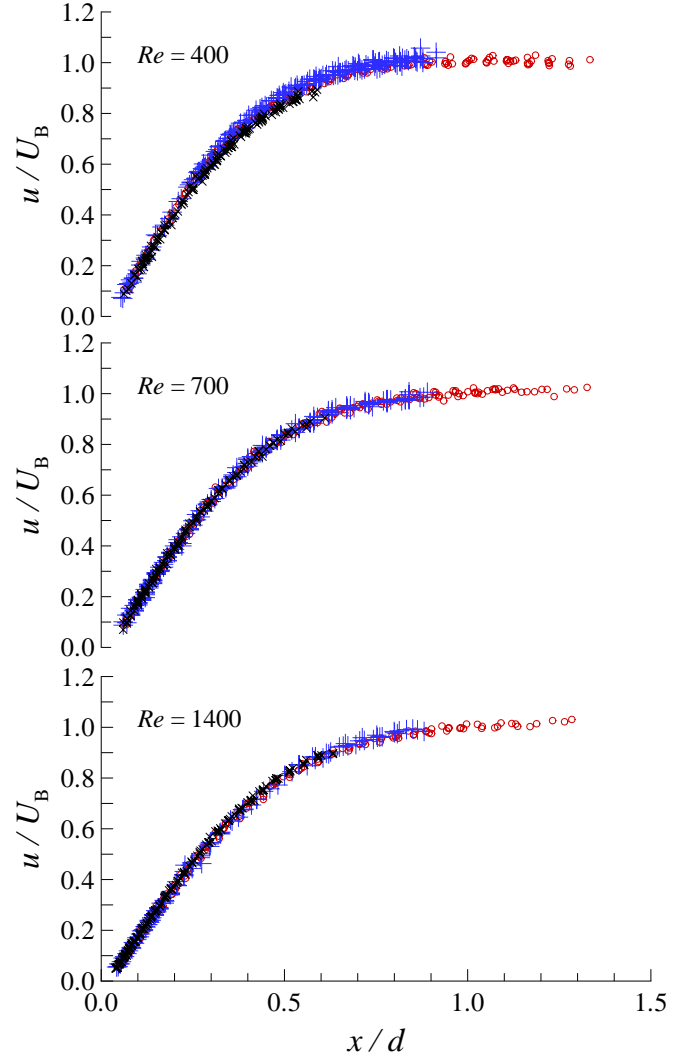


Figure 3: Comparison of velocity (scaled by  $U_B$ ) versus axial distance from plate (scaled by  $d$ ) at three nominal Reynolds numbers and  $L/d = 1.4$  ( $\circ$ ),  $1.0$  ( $+$ ), and  $0.7$  ( $\times$ ).

### Results

Cold impinging-jet velocity data are reported at three nominal Reynolds numbers,  $Re \equiv \rho d U_B / \mu \cong 400, 700$ , and  $1400$ , and three nozzle-to-stagnation plate separation distance to nozzle-diameter ratios,  $L/d \cong 0.7, 1.0$ , and  $1.4$ . Figure 3 compares measured axial velocities, scaled by the Bernoulli velocity, for three  $L/d$  ratios at three Reynolds numbers. The velocity profiles collapse on a single curve, independent of  $L/d$ , if axial velocities are scaled by  $U_B$ . An axial velocity deficit at the jet-exit develops as the separation distance is decreased due to the influence of the stagnation point on the nozzle flow [6]. Notably, the velocity and its gradient adjust to maintain self-similarity, with the Bernoulli velocity scaling the flow.

In their study of cold turbulent jets, Kostiuk *et al.* [4] showed that opposed-jet or impinging-jet velocity data are well characterized by an error function. Their error function contained three adjustable parameters: the velocity at infinity  $U_\infty$ , a strain-rate parameter  $\alpha$ , and a wall-offset length  $\delta/d$ ,

$$u(x)/U_\infty = \text{erf}[\alpha(x/d - \delta/d)]. \quad (3)$$

Figure 3 indicates that an error function also characterizes laminar impinging-jet flow. The experimental data in figure 3 suggest that the appropriate velocity scale for laminar impinging jets is the Bernoulli velocity, i.e.,  $U_\infty = U_B$ . From one-dimensional viscous stagnation-flow theory [7], the scaled-



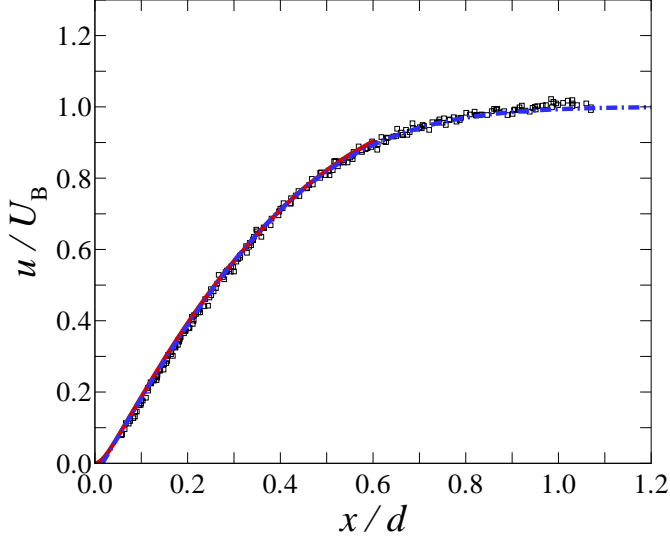


Figure 4: Cold-flow velocity profile corresponding to a  $\Phi = 0.9$  methane-air flame ( $Re = 1100, L/d = 1.2$ ). ( $\square$ ) exp. data, (solid red line) 1D simulation, (dot-dash blue line) error function.

$Re$	$\alpha$	$\delta/d$	$\epsilon_{rms}/U_B$
400	2.21	0.027	0.017
700	2.00	0.020	0.010
1400	1.88	0.015	0.011

Table 1: Error-function fit parameters and resulting error  $\epsilon_{rms}$ .

offset length  $\delta/d$ , which is proportional to the wall-boundary-layer thickness, can be related to the strain-rate parameter  $\alpha$ , such that,  $\delta/d(Re, \alpha) = 0.7575 \sqrt{1/(Re\alpha)}$ . Thus, the only free parameter in this error-function is the Reynolds-number dependent strain-rate parameter  $\alpha = \alpha(Re)$ . The axial velocity field for an axisymmetric impinging laminar jet is then fully specified by the Bernoulli velocity  $U_B$ , since the Reynolds number, in turn, derives from it. The error function was fit to each experimental profile by adjusting  $\alpha$  to minimize the root-mean-squared (rms) error  $\epsilon_{rms}$ . For each  $Re$ , the strain-rate parameter  $\alpha$  was averaged over the range  $0.7 \leq L/d \leq 1.4$ . This single  $\alpha(Re)$  dependence was subsequently used in all error-function fits to determine the resulting rms error  $\epsilon_{rms}$ . The fit parameters and  $\epsilon_{rms}$  are shown in table 1.

Cold and reacting stagnation flows are studied for a near-stoichiometric,  $\Phi = 0.9$ , methane-air ( $CH_4$ -air) flame to determine the effect of heat release on the fluid mechanics and the ability of the one-dimensional simulations to capture the flow. The nozzle-stagnation plate separation distance  $L$  is varied at constant  $\Phi$  to study the hydrodynamics at constant chemistry. Figure 4 shows the measured velocity data for a cold-flow at  $Re \cong 1100$  and  $L/d = 1.2$ . Velocities are scaled by  $U_B$  and axial-distances by  $d$ . The error-function profile with  $\alpha = 1.95$ , interpolated for  $Re = 1100$ , is included and accurately models the flow. Exploiting the inviscid, constant-density solution to equation (2), which is a parabola, a quadratic is fit to the velocity profile in the range  $0 \leq x/d \leq 0.8$ . The values  $u_\ell$  and  $u'_\ell$  are calculated from the fit at  $x = \ell$ , with  $U(\ell) = \rho_0 u_\ell/2$  and  $U'(\ell) = \rho_0 u'_\ell/2$  then specifying the boundary conditions. In this work,  $\ell/d$  is fixed at 0.6. As can be seen, the one-dimensional model accurately captures the flowfield if velocity boundary conditions are specified in this manner.

Figure 5 shows velocity profiles for a  $\Phi = 0.9$  methane-air flame at  $L/d = 1.2$  and  $Re \cong 1100$ . The cold-flow (error-function) profile is also included for comparison. Simulation boundary

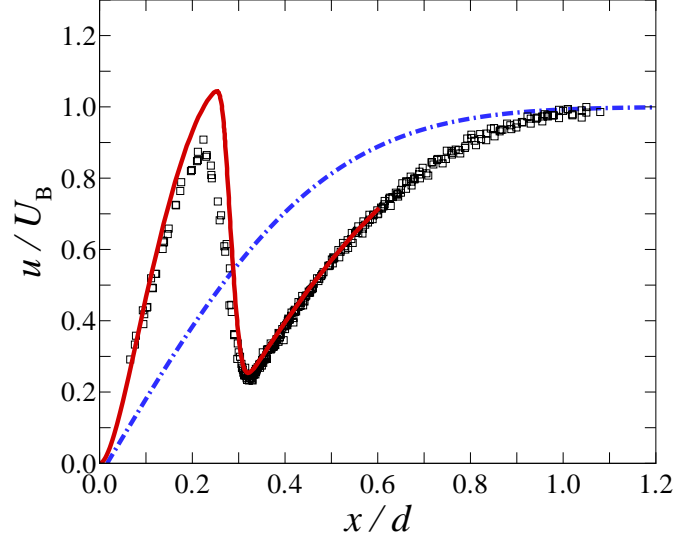


Figure 5:  $CH_4$ -air flame profiles ( $\Phi = 0.9, L/d = 1.2$ ). ( $\square$ ) exp., (solid red line) 1D sim., (dot-dash blue line) error-function.

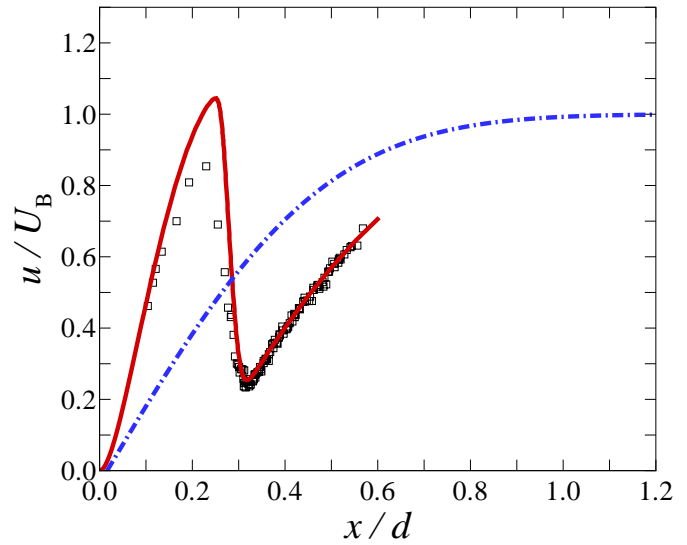


Figure 6:  $CH_4$ -air flame profiles ( $\Phi = 0.9, L/d = 0.6$ ). Legend as in figure 5.

conditions are specified from a fit to the cold-flow portion of the profile ( $0.35 < x/d < 0.80$ ) to determine  $u_\ell$  and  $u'_\ell$ . The simulated velocity profile is in good agreement with experiment, but predicts a higher post-flame velocity than measured. The PSV chopping frequency was optimized for the cold upstream region and not for this high-velocity, high-curvature region of the flow. While accounting for this brings experiment and simulation closer, it does not account for the difference. The flame produces a virtual stagnation point that alters the flowfield, although the strain rate,  $\sigma = du/dx$ , upstream of the flame is very close to that of the cold flow. Figure 6 depicts measured and simulated velocity profiles for a  $\Phi = 0.9$  methane-air flame at  $L/d = 0.6$  and  $Re \cong 1100$ . Again, good agreement is seen except for an overprediction of post-flame velocities. A nozzle-exit-velocity deficit is evident compared to the cold flow.

A comparison of experimental velocity profiles at variable  $L/d$  and constant  $U_B$  is given in figure 7. The velocity profiles collapse on a single curve, independent of  $L/d$ , if the Bernoulli velocity is held constant. As all datasets were recorded for essentially the same flame, the agreement between experiment and simulation for  $L/d = 0.8$  and  $1.0$  is consistent with that

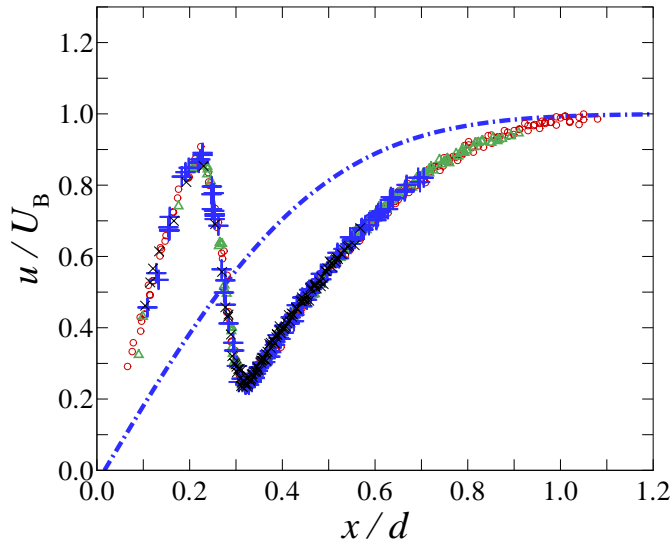


Figure 7: CH<sub>4</sub>-air flame profiles ( $\Phi = 0.9$ ) at:  $L/d = 1.2$  ( $\circ$ ),  $L/d = 1.0$  ( $\triangle$ ),  $L/d = 0.8$  ( $+$ ), and  $L/d = 0.6$  ( $\times$ ). Cold-flow error function is also included (dot-dash blue line).

seen in figures 5 and 6. The imposed strain rate  $\sigma$  can be defined as the maximum slope of the velocity profile upstream of the flame. The strain rate for the flames presented in figure 7 is  $\sigma \cong 360\text{s}^{-1}$ . This is very close to the maximum strain rate for the cold-flow profile of  $\sigma \cong 365\text{s}^{-1}$  (cf. figure 4). This flame is not close to extinction conditions, as verified experimentally and predicted numerically. The “global strain rate” has been defined as the nozzle-exit velocity divided by the nozzle-stagnation point separation distance (e.g., [8]). For the flames studied here the global strain rate varies from  $140\text{s}^{-1}$  at  $L/d = 1.2$  to  $190\text{s}^{-1}$  at  $L/d = 0.6$ . This indicates that the global strain rate, based on the centerline nozzle-exit velocity, does not provide a good surrogate for the strain rate imposed on the flame. However, Kobayashi and Kitano [3] found a good correlation between the global strain rate based on the mean nozzle-exit velocity and the velocity gradient upstream of the flame. This may be due to their different definition of global strain rate. Figure 8 plots the product of the simulated velocity and density profiles, scaled by the cold-flow density  $\rho_0$  and  $U_B$ . The profile of  $\rho u$  is composed of two stagnation flows with different gradients in the cold and hot regions of the flow.

## Conclusions

Velocity profiles are measured, using PSV, in impinging jets and methane-air stagnation flames. For impinging jets, velocity profiles are found to collapse when scaled by the Bernoulli velocity. These profiles are well characterized by an error-function model in terms of a single, Reynolds number dependent, parameter. One-dimensional simulations can accurately capture the flow if the boundary conditions are correctly specified. Near-stoichiometric flames are studied as a function of the nozzle-stagnation plate separation distance. The flames are simulated using a one-dimensional model with multi-component transport and full chemistry (GRI-Mech 3.0). Good agreement is found between experiment and simulation. Flame velocity profiles collapse to a single curve at a fixed Bernoulli velocity, independent of the separation distance. The strain rate in the reacting flow is very close to that of the corresponding impinging jet. The results indicate that the global strain rate, based on the centerline nozzle-exit velocity, is not a good surrogate for the applied strain to the flame as it is dependent on the separation distance, while the maximum velocity gradient upstream of the flame is not. The profile of the product of the density and veloc-

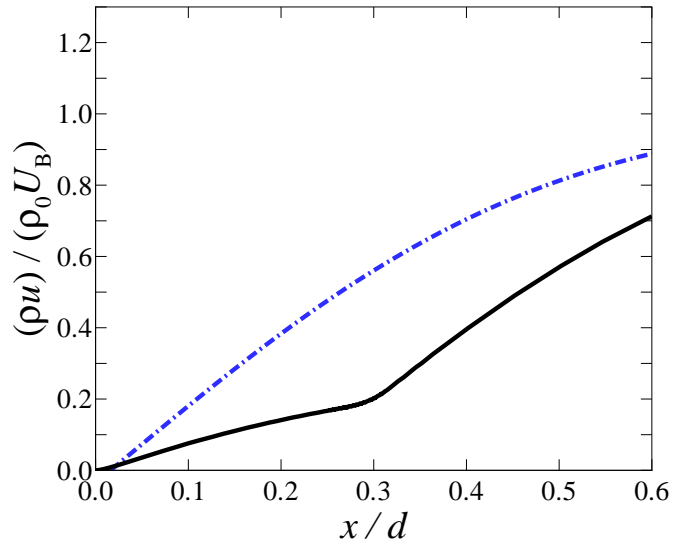


Figure 8: Simulated CH<sub>4</sub>-air flame profile of  $\rho u$  at  $\Phi = 0.9$  (solid black line). Cold-flow error function (dot-dash blue line).

ity indicates that the reacting flow is characterized by two stagnation flows with different gradients. Ongoing research targets the effect of the imposed strain rate on premixed hydrocarbon flames and the performance of transport and chemistry models.

## Acknowledgements

We would like to acknowledge discussions with T. W. Mattner and K. Sone, as well as contributions by D. Lang to digital imaging, and G. Katzenstein to mechanical design. The work was funded by AFOSR Grant F49620-01-1-0006, whose support is gratefully acknowledged.

## References

- [1] Berghthorson, J. M., Goodwin, D. G. and Dimotakis, P. E., Particle streak velocimetry and CH laser-induced fluorescence diagnostics in strained, premixed, methane-air flames, *Proc. Combust. Inst.*, **30**, (in press).
- [2] Goodwin, D. G., An open-source, extensible software suite for CVD process simulation, in *Proc. of CVD XVI and EuroCVD Fourteen*, Electrochem. Soc., 2003, 155–162.
- [3] Kobayashi, H. and Kitano, M., Effects of equivalence ratio on the extinction stretch rate of cylindrical premixed flames, *Combust. Sci. Technol.*, **89**, 1993, 253–263.
- [4] Kostiuk, L. W., Bray, K. N. C. and Cheng, R. K., Experimental study of premixed turbulent combustion in opposed streams: Part I - non-reacting flow field, *Combust. Flame*, **92**, 1993, 377–395.
- [5] Law, C. K., Sung, C. J., Yu, G. and Axelbaum, R. L., On the structural sensitivity of purely strained planar premixed flames to strain rate variations, *Combust. Flame*, **98**, 1994, 139–154.
- [6] Rolon, J. C., Veynante, D., Martin, J. P. and Durst, F., Counter jet stagnation flows, *Exp. Fluids*, **11**, 1991, 313–324.
- [7] Schlichting, H., *Boundary layer theory*, McGraw-Hill Book Company, Inc., New York, 1960, 81–83.
- [8] Zhang, H. and Egolfopoulos, F. N., Extinction of near-limit premixed flames in microgravity, *Proc. Combust. Inst.*, **28**, 2000, 1875–1882.

## Effect of Grid Geometry on the Scale-by-scale Budget of Decaying Grid Turbulence

P. Lavoie, R. A. Antonia and L. Djenidi

Discipline of Mechanical Engineering  
University of Newcastle, Callaghan, NSW, 2308 AUSTRALIA

### Abstract

The approximately homogeneous, isotropic turbulence (HIT) produced by three grids with different geometries was measured over the range  $30 \leq x/M \leq 80$ . The scale-by-scale budget of decaying grid turbulence obtained from the transport equation for  $\langle (\delta q)^2 \rangle$  is used to study the effect of grid geometry in an attempt to quantify the influence of initial conditions of the turbulence decay. Although  $R_\lambda$  is too small for a scaling range to exist, the initial conditions show negligible effect on scales smaller than  $\lambda$ . The solidity of the grid influences only the very large scales. The shape of the grid elements can significantly affect the overall shape of the inhomogeneous term in the transport equation for  $\langle (\delta q)^2 \rangle$ .

### Introduction

Theoretical studies of decaying homogeneous, isotropic turbulence (HIT) have classically eliminated initial conditions from the problem with the assumption of infinite Reynolds number and invoking Kolmogorov's theory [12], although early presentations of the theory included a discussion of their possible effect on the decay [5]. Initial condition effects remained absent from HIT theory, which is the basis of most modern turbulence models, despite experimental and, more recently, DNS results that supported the importance of initial conditions via the unexplained wide scatter in  $m$ , the decay exponent [8, 10, 16].

Theoretical work by George [9], herein referred to as G92, argues for the importance of initial conditions and derives a self-similar theory for HIT that includes the effect of initial conditions and applies at finite Reynolds number. Although the derivation of the theory is strictly correct and some of its parts are supported by experimental and numerical data [2, 3, 17], certain aspects of the theory are argued to have no physical basis [9, 15]. G92 expects that the decay exponent will change with initial conditions. However, the analysis of Speziale and Bernard [15], referred herein as SB, predicts a universal decay that is reached asymptotically with time. Their analysis shows that the scatter in previously reported  $m$  could be due to some experimental data having been sampled in the transition zone prior to the universal decay state.

Alternatively, Mohamed and LaRue [13] suggested the scatter could be due to inconsistencies in the way different authors fitted the power-law to their respective measurements. These authors then proposed a procedure to estimate the parameters of the power-law, which they argued to be consistent and rigorous. When this was applied to their and other previously published data, they found a reduction in the scatter that pointed to a weak or non-existent dependence on initial conditions. However, the decay exponent thus obtained,  $m = -1.3$ , is significantly different from the value  $-1$  predicted by classical theories [5, 10].

As highlighted by this discussion of references [9, 13, 15], there remains much confusion and controversy regarding the actual cause of the scatter reported for  $m$ . Furthermore, George *et al.* [10] and Mohamed and LaRue [13] showed that the esti-

mation of  $m$  includes sizable uncertainties, which suggests that this variable may not be sensitive enough to show the effects of initial conditions on decaying HIT clearly. The difficulty with the study of initial conditions is that neither the initial conditions themselves nor their effects are easily quantifiable. This is particularly true in experimental work where the initial energy distribution over the turbulent scales can hardly be controlled or measured. This also makes comparisons between experimental and numerical results very difficult. It is the purpose of this paper to show that the scale-by-scale budget of the turbulence generated by three grids of different geometry can be used to quantify in a non-ambiguous manner the effect that initial conditions have on the approximately homogeneous, isotropic turbulence generated by these grids.

### Background

Grid turbulence provides a good approximation of decaying HIT and offers a direct measure of the mean dissipation rate from the turbulence kinetic energy decay, viz.

$$\langle \epsilon \rangle_d = -\frac{U}{2} \frac{d \langle q^2 \rangle}{dx}. \quad (1)$$

Danaila *et al.* [7] revisited the classical Kolmogorov “four-fifths law” [11] which relates the second- and third-order structure functions, viz.

$$-\langle (\delta u)^3 \rangle + 6\nu \frac{d}{dr} \langle (\delta u)^2 \rangle = \frac{4}{5} \langle \epsilon \rangle r, \quad (2)$$

where  $\delta u \equiv u(x+r) - u(x)$  is the difference in streamwise velocity fluctuations between two points separated by a distance  $r$  along the streamwise directions,  $\langle \epsilon \rangle$  is the mean kinetic energy dissipation rate and  $\langle \rangle$  denote an ensemble average. It is well known that equation (2) is only balanced for very small separations, typically of the order of a few Kolmogorov lengths,  $\eta \equiv \nu^{3/4} \langle \epsilon \rangle^{-1/4}$ , for the small and intermediate Reynolds numbers obtained in most experiments. In an attempt to study the effect of large-scale inhomogeneities on the small scales of turbulence, Danaila *et al.* [7] obtained a transport equation for  $\langle (\delta q)^2 \rangle$  from the Navier-Stokes equation for decaying grid turbulence, viz.

$$-\langle (\delta u) (\delta q)^2 \rangle + 2\nu \frac{d}{dr} \langle (\delta q)^2 \rangle - \frac{U}{r^2} \int_0^r s^2 \frac{\partial}{\partial x} \langle (\delta q)^2 \rangle ds = \frac{4}{3} \langle \epsilon \rangle r, \quad (3)$$

where  $\langle (\delta q)^2 \rangle \equiv \langle (\delta u)^2 \rangle + \langle (\delta v)^2 \rangle + \langle (\delta w)^2 \rangle$  and  $s$  is a dummy variable. Equation (3) is an extension of equation (2) with the addition of an inhomogeneity term. Also, the former takes into account the three velocity components, instead of only  $u$  in equation (2). It is important to note here that the inhomogeneous term in equation (3) is a consequence of the streamwise decay of the turbulence and that, for box turbulence

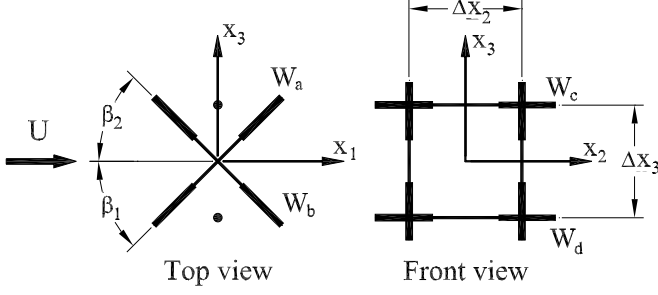


Figure 1: One-component vorticity probe.  $\Delta y \simeq 1.0$  mm,  $\Delta z \simeq 1.3$  mm,  $\beta_1 \simeq \beta_2 \simeq 45^\circ$ . All wires have a diameter of  $2.5 \mu\text{m}$  and were etched from Wollaston (Pt-10% Rh) material to a length of approximately 0.5 mm.

where there is no mean flow, it would take the form of a time-wise decay [14]. An important feature of equation (3) is that it can be used as a scale-by-scale budget of the turbulence [1, 6].

Following G92, Antonia *et al.* [3] derived the conditions for which equation 3 satisfied similarity. Their analysis yielded the following self-similar forms for the second- and third-order structure functions,

$$\langle (\delta q)^2 \rangle = \langle q^2 \rangle f\left(\frac{r}{\lambda}\right) \quad (4)$$

and

$$-\langle (\delta u)(\delta q)^2 \rangle = \left[ \frac{\langle q^2 \rangle^{3/2}}{3^{1/2} R_\lambda} \right] g\left(\frac{r}{\lambda}\right), \quad (5)$$

respectively, where  $\lambda$  is the Taylor microscale, defined here as

$$\lambda^2 = 5\nu \frac{\langle q^2 \rangle}{\langle \epsilon \rangle_d}, \quad (6)$$

and  $R_\lambda$  is taken as

$$R_\lambda = \frac{\langle q^2 \rangle^{1/2} \lambda}{3^{1/2} \nu}. \quad (7)$$

Under these conditions,  $f$  and  $g$  are independent of  $x$  and the turbulence decays following a power-law of the form

$$\langle q^2 \rangle = a \left( \frac{x}{M} - \frac{x_o}{M} \right)^m, \quad (8)$$

where  $x_o/M$  is the virtual origin,  $m$  is the power-law exponent and  $a$  is a constant of proportionality. Detailed derivation and discussion of this theory can be found in [3].

When equations (1), (4), (5) and (8) were applied to equation (3), Antonia *et al.* [3] obtained a self-similar form for the scale-by-scale budget, viz.

$$g + 2f' - \left[ \frac{5\Gamma_1}{m} \left( \frac{r}{\lambda} \right)^{-2} - 10\Gamma_2 \left( \frac{r}{\lambda} \right)^{-2} \right] = \frac{20}{3} \left( \frac{r}{\lambda} \right), \quad (9)$$

where  $\Gamma_1$  and  $\Gamma_2$  are given by

$$\Gamma_1 \equiv \int_0^{r/\lambda} \left( \frac{s}{\lambda} \right)^3 f' d\left( \frac{s}{\lambda} \right) \quad (10)$$

$$\Gamma_2 \equiv \int_0^{r/\lambda} \left( \frac{s}{\lambda} \right)^2 f d\left( \frac{s}{\lambda} \right). \quad (11)$$

Equation (9) can be written symbolically as  $A + B + [\text{INH}] = C$ , where INH represents the total streamwise inhomogeneous term.

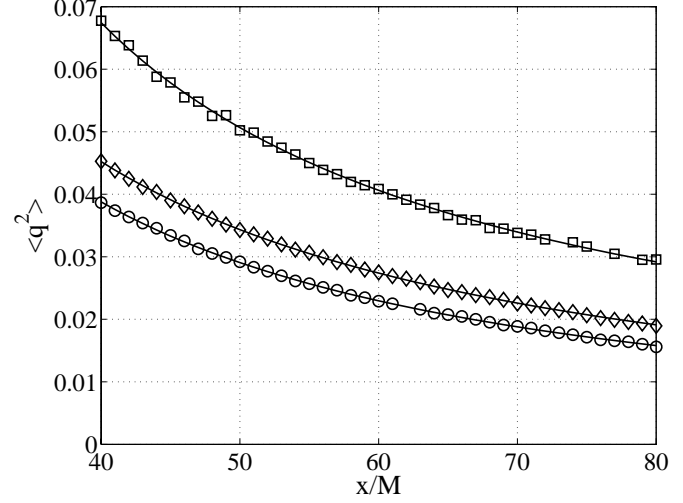


Figure 2: Streamwise variation of  $\langle q^2 \rangle$  behind the three grids (Sq35,  $\square$ ; Rd35,  $\circ$ ; Rd44,  $\diamond$ ) compared to the fitted power-laws (fitting parameters summarized in table 1).

### Experimental Details

The measurements presented here were made with a one-component vorticity probe, which consists of parallel wires and a X-wire. Figure 1 gives a schematic of the probe with typical dimensions. A vorticity probe was used to obtain more complete measurements of the turbulence behind the grids. Vorticity results are however not presented here. The wires were operated with in-house constant-temperature circuits at an overheat ratio of 0.5. The signals were then amplified and low-pass filtered at a cut-off frequency of  $f_c$ , which varied depending on the grid and  $x/M$ .  $f_c$  was selected to correspond to the onset of electronic noise and was of the order of  $f_k \equiv U/2\pi\eta$ , the Kolmogorov frequency. The signals were sampled at a frequency  $f_s \geq 2f_c$  and digitized with a 16 bit A/D converter for a duration of 60 to 300 seconds.

Three biplane grids were used, all with the same mesh size  $M = 24.76$  mm. The geometry of the grids was varied by changing the shape of the bars cross-section and the solidity of the grid. The first grid, Sq35, was made with square bars and solidity  $\sigma \equiv d/M(2 - d/M) = 0.35$ . The other two grids, Rd35 and Rd44, were both manufactured with round rods but with  $\sigma = 0.35$  and  $\sigma = 0.44$ , respectively. The grids were placed downstream of the contraction (area ratio of 9:1) of an open-circuit wind tunnel. The length of the working section was 2.4 m and its cross-sectional area at the contraction was 350 mm  $\times$  350 mm (the floor of the tunnel was slightly inclined to provide zero pressure gradient). The probe was traversed along the centerline of the working section. Measurements were made between  $x/M = 30$  and  $x/M = 80$  in steps of one mesh length with a mean velocity  $U = 6.4$  m/s ( $R_M = UM/\nu \approx 10,400$ ) for all three grids. The mean turbulent statistics obtained with the vorticity probe were corrected for spatial resolution following the method described in Zhu and Antonia [18]. The flow was assumed to be axisymmetric so that  $v$  and  $w$  statistics are taken to be equal. The measurements of  $w$  and  $uw$  correlations were taken from the X-wire, while the average of the two single wires was used for  $u$ .

### Results

The decay exponent for each grid was obtained here by fitting equation (8) in the range  $40 \leq x/M \leq 80$  with the MatLab routine NLINFIT. Initial estimates for  $a$  and  $m$  were obtained by assuming  $x_o/M = 0$  and applying a linear regression to  $\log(\langle q^2 \rangle)$

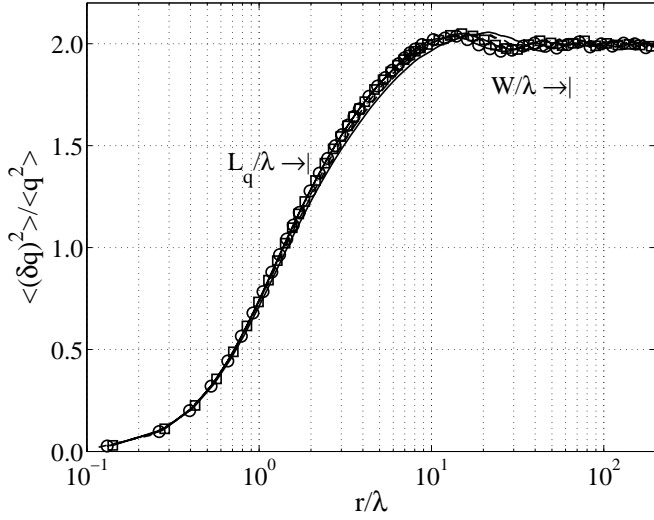


Figure 3: Second-order turbulent energy structure function for *Rd44*.  $x/M = 30$ , —;  $x/M = 40$ , - - -;  $x/M = 50$ , - · - ·;  $x/M = 60$ , · · · · ·;  $x/M = 70$ , □-□-□-;  $x/M = 80$ , ○-○-○-.

Grid	$m$	$\frac{x_o}{M}$	$\frac{\langle u^2 \rangle}{\langle w^2 \rangle}$	$R_\lambda$	$\lambda$ mm	$L_q$ mm	$\eta$ mm
<i>Sq35</i>	-1.13	3	1.48	41.1	5.36	13.7	0.42
<i>Rd35</i>	-1.31	0	1.40	30.0	5.23	10.2	0.48
<i>Rd44</i>	-1.28	0	1.39	33.4	5.32	10.8	0.47

Table 1: Decay law parameters and other basic turbulence characteristics obtained at  $x/M = 60$  for the three grids.

vs.  $\log(x/M)$ . The power-laws obtained are compared graphically in figure 2 to the measured  $\langle q^2 \rangle$ . Figure 3 presents  $\langle (\delta q)^2 \rangle$  normalized according to G92 for *Rd44* and shows that similarity is only reached approximately for  $x/M \geq 40$ . The plots for *Sq35* and *Rd35* lead to the same conclusions and are not shown here. The three criteria suggested by Mohamed and LaRue [13] were met before  $x/M = 40$ ; namely  $S_u = \langle u^3 \rangle / \langle u^2 \rangle^{3/2}$  was zero,  $S_{\partial u / \partial x} = \langle (\partial u / \partial x)^3 \rangle / \langle (\partial u / \partial x)^2 \rangle^{3/2}$  was constant and  $\langle \epsilon \rangle_{iso} \equiv 15\nu \langle (\partial u / \partial x)^2 \rangle$  was equal to  $\langle \epsilon \rangle_d$  within 10%. Note here that the results of the scale-by-scale budgets presented are insensitive to errors in  $m$  and therefore the method of determining  $m$  used was deemed sufficient for the purposes of this paper.

We shall concentrate our analysis to the measurements obtained at  $x/M = 60$  since the results do not change significantly with location for  $40 \leq x/M \leq 80$ , due to the quasi-self-similar turbulence decay. The location  $x/M = 60$  presents a good compromise between probe resolution, which improves with increasing  $x/M$ , the degradation of the signal-to-noise ratio with  $x/M$  and increasing confinement of the turbulence due to the finite width of the tunnel. A few basic quantities measured at this location are summarized in table 1. Note that the integral length scale  $L_q$  is defined here as

$$L_q = \frac{1}{\langle q^2 \rangle} \int_0^{r_o} B_{q,q}(r) dr, \quad (12)$$

where  $B_{q,q}$  is calculated here as

$$B_{q,q} = \langle q(x)q(x+r) \rangle = \langle u(x)u(x+r) \rangle + 2\langle w(x)w(x+r) \rangle \quad (13)$$

and  $r_o$  is the first zero crossing of  $B_{q,q}$ .

Figure 4 compares the function  $f(r/\lambda)$  measured behind each grid at  $x/M = 60$ . The ratio  $W/\lambda$ , where  $W$  is the width of

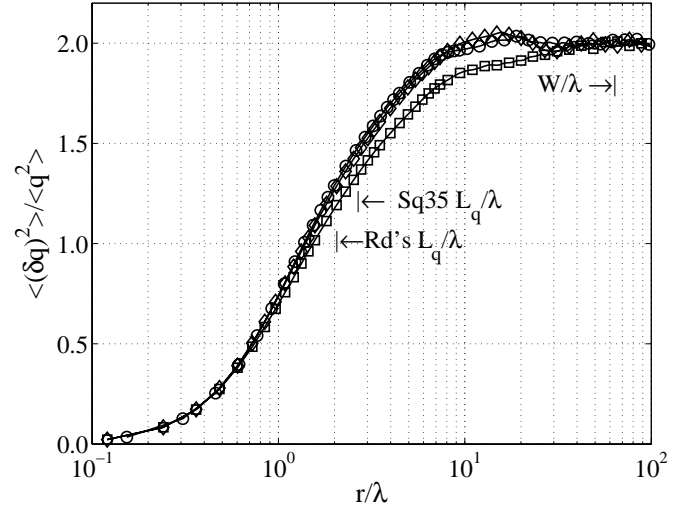


Figure 4: Second-order turbulent energy structure function measured at  $x/M = 60$  behind three grid geometries: *Sq35*, □; *Rd35*, ○; *Rd44*, ◇. Indicated are the ratios  $W/\lambda$ , which is approximately equal for the three grids at  $x/M = 60$ , and  $L_q/\lambda$ , which is roughly equal for *Rd35* and *Rd44*.

the tunnel, is included to provide an indication of the values of  $r/\lambda$  that may be affected by the size of the tunnel. For  $r/\lambda < 1$ , the normalized structure functions are nearly equal for the three grids. In the range  $1 \leq r/\lambda \leq 7$ , the difference between *Rd35* and *Rd44* is within 1.4%, which is the estimated statistical uncertainty, while *Sq35* shows a clear departure from the two round-rod grids by  $r/\lambda = 1$ . Figure 4 establishes that  $f(r/\lambda)$  for *Sq35* approaches the asymptotic value of 2 monotonically from below. This is contrasted to *Rd35* and *Rd44* for which  $f(r/\lambda)$  overshoots the asymptote before it settles to 2 as  $r/\lambda \rightarrow \infty$ . This overshoot for the round-rod grids suggests that the large turbulent scales behind these two grids are more periodic in nature than those for *Sq35*. The stronger overshoot and oscillations at large separations outside the measurement scatter for *Rd44* imply that the periodic structures of *Rd44* are stronger than for *Rd35*.

The scale-by-scale budgets compensated with  $(r/\lambda)$  for the three grids are compared in figure 5. As shown, the left-side of equation (9) equals  $20/3$  to  $\pm 10\%$  at all separations. In the range  $r/\lambda < 1$ , the balance is very sensitive to inaccuracies in the estimate of  $\lambda$ , while at larger separations, the main uncertainty comes from the statistical convergence of  $g(r/\lambda)$ . For the current experiments there is no separation between the scales responsible for the dissipation of turbulence and the scales affected by INH, which is not surprising given the low  $R_\lambda$ . It is also clear that INH does not differ significantly for the three grids up to about  $r/\lambda = 1$ . While the inhomogeneous term for *Sq35* deviates from that of the two round-rod grids for  $r/\lambda \geq 1$ , there is little difference between *Rd35* and *Rd44* until  $r/\lambda > 8$ . These observations indicate that the three grid geometries studied here have little effect on the turbulent scales ranging from  $\eta$  to  $\lambda$ . However, the shape of the bar cross-section show an influence on scales as small as  $\lambda$ . The solidity of the round-rod grids appears to impact only on scales much larger than  $L_q$ .

### Concluding Comments

The effect of grid geometry was studied using the turbulent energy structure function and the related scale-by-scale budget. The small Reynolds numbers of the current experiment prohibited the formation of a proper separation between the scales responsible for the turbulence dissipation and those affected by the inhomogeneity of the flow. Despite the low  $R_\lambda$ , the three

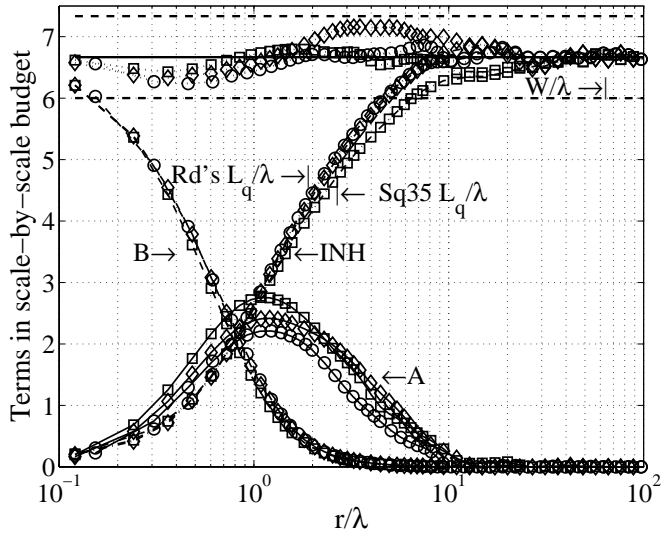


Figure 5: Comparison between the energy budget behind the three grids (*Sq35*,  $\square$ ; *Rd35*,  $\circ$ ; *Rd44*,  $\diamond$ ) at  $x/M = 60$ .  $A(r/\lambda)^{-1}$ , —;  $B(r/\lambda)^{-1}$ , ---;  $INH(r/\lambda)^{-1}$ , - · -;  $(A+B+INH)(r/\lambda)^{-1}$ , ······. The thick horizontal line is at  $20/3$  and the horizontal dotted lines represent  $\pm 10\%$ . Also indicated for reference are the ratios  $W/\lambda$  and  $L_q/\lambda$ .

different grid geometries studied here had little effect on scales ranging between  $\eta$  and  $\lambda$ . Overall, the shape of the bars exhibited a stronger influence on the energy containing scales than the grid solidity. This latter parameter was only important for  $r/\lambda \geq 8$  and mainly affected the periodicity of large organized structures. The questions of how the grid geometry produces different turbulent states and how these affect important parameters, such as the power-law energy decay exponent, remain however undetermined.

A detailed study of the turbulence from very close to the grid up to the quasi-self-similar region is required to answer the first of these questions. The complexity of the flow field and reduced scales of the turbulence near the grid make hot-wire measurements more difficult and uncertain. Other methods of flow measurements, such as PIV [4], can however be employed to corroborate and complement hot-wire data.

A more detailed understanding of the effect of grid geometry on approximately homogeneous, isotropic turbulence is the subject of continued work. The scale-by-scale budget for grid turbulence, which was shown to capture quantitatively the effect the grid-geometry in this paper, should prove to be an invaluable tool in the study of decaying HIT.

#### Acknowledgements

The authors would like to acknowledge the support of the Australian Research Council and the Australian Government.

#### References

- [1] Antonia, R. A. and Burattini, P., Small scale turbulence: how universal is it?, in *15th Australasian Fluid Mechanics Conference*, University of Sydney, 2004.
- [2] Antonia, R. A. and Orlandi, P., Similarity of decaying isotropic turbulence with a passive scalar, *J. Fluid Mech.*, **505**, 2004, 123–151.
- [3] Antonia, R. A., Smalley, R. J., Zhou, T., Anselmet, F. and Danaila, L., Similarity of energy structure functions in de-

caying homogeneous isotropic turbulence, *J. Fluid Mech.*, **487**, 2003, 245–269.

- [4] Avallone, G., De Gregorio, F. and Romano, G. P., PIV measurements in grid turbulence, in *5th International Symposium on Particle Image Velocimetry*, Busan, Korea, September 22–24, 2003.
- [5] Batchelor, G. K., *The Theory of Homogeneous Turbulence*, Cambridge University Press, 1953.
- [6] Burattini, P., Antonia, R. A. and Rajagopalan, S., Effect of initial conditions on the far field of a round jet, in *15th Australasian Fluid Mechanics Conference*, University of Sydney, 2004.
- [7] Danaila, L., Anselmet, F. and Antonia, R. A., An overview of the effect of large-scale inhomogeneities on small-scale turbulence, *Phys. Fluids*, **14**, 2002, 2475–2484.
- [8] Gad-el-Hak, M. and Corrsin, S., Measurements of the nearly isotropic turbulence behind a uniform jet grid, *J. Fluid Mech.*, **62**, 1974, 115–143.
- [9] George, W. K., The decay of homogeneous isotropic turbulence, *Phys. Fluids*, **4**, 1992, 1492–1509.
- [10] George, W. K., Wang, H., Wollbald, C. and Johansson, T. G., Homogeneous turbulence and its relation to realizable flows, in *14th Australasian Fluid Mechanics Conference*, Adelaide University, 2001, 41–48, 41–48.
- [11] Kolmogorov, A., Dissipation of energy in locally isotropic turbulence, *C. R. Acad. Sci. U.R.S.S.*, **32**, 1941, 16–18.
- [12] Kolmogorov, A., The local structure of turbulence in incompressible viscous fluid for very large Reynolds number, *C. R. Acad. Sci. U.R.S.S.*, **30**, 1941, 301–305.
- [13] Mohamed, M. S. and LaRue, J. C., The decay power law in grid-generated turbulence, *J. Fluid Mech.*, **219**, 1990, 195–214.
- [14] Pope, S. B., *Turbulent Flows*, Cambridge University Press, 2000.
- [15] Speziale, C. G. and Bernard, P. S., The energy decay in self-preserving isotropic turbulence revisited, *J. Fluid Mech.*, **241**, 1992, 645–667.
- [16] Uberoi, M. S. and Wallis, S., Effect of grid geometry on turbulence decay, *Phys. Fluids*, **10**, 1967, 1216–1224.
- [17] Wang, H. and George, W. K., The integral scale in homogeneous isotropic turbulence, *J. Fluid Mech.*, **459**, 2002, 429–443.
- [18] Zhu, Y. and Antonia, R. A., The spatial resolution of hot-wire arrays for the measurement of small-scale turbulence, *Meas. Sci. Tech.*, **7**, 1996, 1349–1359.



## Some hydrodynamic characteristics of an air-cushion supported concrete gravity structure

B. Chenu, M. T. Morris-Thomas and K. P. Thiagarajan

School of Oil and Gas Engineering  
The University of Western Australia, Crawley, WA, 6009 AUSTRALIA

### Abstract

The tow out of a concrete gravity structure (CGS) through shallow water is assisted by employing an air-cushion for draft reduction purposes. This requires an understanding of the effect of the air-cushion on the stability and dynamics of the CGS. In this present work, experiments were performed on 1:100 scale models of typical concrete gravity substructure configurations at the University of Western Australia. Three models of dimensions 0.5m length x 0.5m width x 0.1m draft were considered. The experimental campaign focused on determining the effect of the air-cushion on the metacentric height and, coupled with the water depth, on the added mass and natural frequency in heave and pitch of each model. The experimental results illustrate that the air cushion reduces the stability of the vessel and influences both the natural frequency and added mass in heave and pitch. Compartmentalising the air-cushion and varying the water depth affects the hydrodynamic characteristics of the floating structure.

### Introduction

The use of air-cushions to support floating bodies is well known. These bodies range from high speed surface effect ships to very large floating structures such as the mobile offshore base (MOB) used in military logistic applications. A floating body, supported by an air-cushion, comprises rigid - or flexible for surface effect ships - vertical side walls that penetrate below the main structure and exterior free-surface thus trapping a column of air. These vertical side walls must penetrate the free-surface to a sufficient depth to maintain an excess air pressure in the interior chamber. For surface effect ships, the air cushion typically supports 80% of the structures weight with the remainder supported by buoyancy. This weight balance is described by

$$M = \rho \left( V_0 + \frac{p_0}{\rho g} A_i \right), \quad (1)$$

where  $M$  is the structure mass,  $\rho$  is the density of water,  $V_0$  is the displaced volume,  $A_i$  is the air-cushion surface area, and  $p_0$  is the excess air pressure contained within the cushion. The excess pressure contained within the air-cushion determines the static water plug height  $h_w$  - measured from the keel to the interior free-surface - through the hydrostatic relation  $p_0 = \rho g(T - h_w)$  where  $T$  is the draft (see Figure 1).

The tow out of a concrete gravity structure (CGS) through shallow water is another application of an air-cushion support. In this context, the primary use of the air-cushion is to elevate the structure to avoid seabed contact during tow out operations. However, a consequence of this approach is a reduced hydrodynamic stability due to a destabilising moment produced by the depressed interior free-surface. Moreover, the reduced stiffness in angular motions can shift the natural frequency into the frequency space of significant wave energy. This is particularly important when the CGS is towed through shallow channels open to long period swells.

Early work on the use of air-cushion support for floating structures predominately concentrates on surface effect ships with

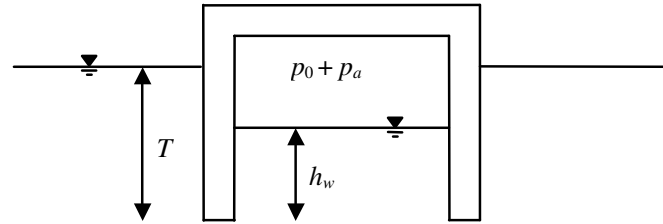


Figure 1: Schematic of an air-cushion supported floating body.

and without forward speed (see Kaplan et al. [3], and for a good literature review, Graham and Sullivan [1]). An examination of the added mass of a surface effect ship was considered by Kim and Tsakonas [4] where the authors describe the entrained air as a pulsating pressure distribution on the free-surface. In 2-dimensions, this approach was considered by Malenica and Zalar [6] to study the heave added mass and radiation damping of an air-cushion supported floating body with rigid side walls. Using a boundary integral equation method Guret and Hermans [2] extended the work of Malenica and Zalar to investigate transfer functions for the heave and the interior vertical free-surface displacement of an air-cushion supported body in regular waves. A 3-dimensional approach is given by Lee and Newman [5] and Pinkster [7] using the boundary integral equation method. The work of Pinkster [7] is particularly notable as the author considered an air-cushion structure with various compartmental configurations. It is thought that compartmentalising the air-cushion reduces its effect on the hydrodynamic stability of the body. An air-cushion supported floating body has been studied experimentally in regular waves by both Thiagarajan et al. [11], and Pinkster and associates [8, 9]. The studies performed by [10] demonstrate that an air-cushion supported box exhibits a higher pitch response when compared to a closed bottom box model of similar geometry.

In this present work we experimentally study the effect of water plug height and compartmentalisation of an air-cushion on the metacentric height, heave and pitch natural frequency and added mass of an air-cushion supported box model. Moreover, we also consider the influence of water depth on the heave and pitch natural frequency added mass values.

### Experimental Campaign

Experiments were conducted in a circular tank of height 1m and diameter 1.65m. During testing, the models were positioned in the centre of the tank using a rigidly mounted linear voltage displacement transducer (LVDT). Three models were used in the experimental campaign: a simple closed bottom box configuration with no air-cushion; a one compartment air-cushion supported open bottom box model (see Figure 2, denoted 1-C); and a nine compartment air-cushion supported open bottom model (see Figure 3, denoted 9-C). For each model, the water plane area measured 0.5m x 0.5m and the draft was held constant at 10cm. For the two air-cushion supported structures, the height of the air-cushion was varied such that the water plug height consisted of the following values  $h_w=3\text{cm}$ , 4cm, 5cm and 6cm. These heights were controlled by adjusting valves located on



Figure 2: The one compartment air-cushion box model, 1-C.



Figure 3: The nine compartment air-cushion box model, 9-C.

the deck of the cushion models (see Figures 2 and 3). Moreover, through these valves, the pressure inside the air-cushion was monitored using pressure transducers. The main particulars of each model, including the vertical centre of gravity  $z_G$  relative to the quiescent free-surface position and the pitch radius of gyration  $r_{22}$ , are given in Table 1.

The metacentric height, denoted  $\overline{GM}$ , of each model and water plug configuration was determined using a standard inclining experiment whereby a known ballast mass was displaced along the model's centreline. The inclination was recorded using a tilt sensor and the metacentric height determined by the following relation:

$$\overline{GM} = md / \tan \vartheta, \quad (2)$$

where  $m$  is a known mass,  $d$  is the known mass displacement from its initial position and  $\vartheta$  is the inclination induced by the mass displacement. The maximum induced inclination for all tests was  $\vartheta = \pm 5$ -degrees.

The natural frequency of each model in heave and pitch was determined by free oscillation experiment. Whereby, in the mode of interest, the model was given a small initial displacement or rotation and allowed to return to its initial position. Initial displacements of 2.5cm and 5-degrees were used in heave and pitch respectively. Vertical displacements were recorded by an LVDT and pitch rotations by a tilt sensor. The displacement time traces were digitised at 30Hz and logged by a personal computer for data analysis. In addition to the natural frequencies in heave and pitch, the added mass and damping of each model at the natural frequency was determined. Only the added mass values are presented here. The water plug height was varied to investigate its influence on the added mass and natural frequency of the 1-C and 9-C models. It was found that the recorded air pressure (cf. Table 1) inside the chamber follows (1) to within 5% error.

The natural frequencies in heave and pitch are given by the following expressions:

$$\omega_{0,3} = \sqrt{\frac{k_{33}}{M + \mu_{33}}}, \quad \omega_{0,5} = \sqrt{\frac{Mg\overline{GM}}{Mr_{22}^2 + \mu_{55}}}, \quad (3)$$

where  $k_{33}$  denotes the the heave restoring stiffness and  $\mu_{33}$  and  $\mu_{55}$  are the added mass values in heave and pitch respectively. The heave restoring stiffness includes both hydrostatic and acoustic - arising from the compressibility of the air-cushion - contributions. The stiffness of each model in heave was experimentally determined and found to be  $k_{33} = 2.43\text{kN/m}$ ,  $2.18\text{kN/m}$  and  $3.07\text{kN/m}$  for the closed bottom box, 1-C and 9-C models respectively. The closed bottom stiffness is very close to the theoretical value of  $\rho g A_0 = 2.45\text{kN/m}$ . The natural frequency added mass values were determined from (3).

## Result and Discussion

The experimental results are now discussed with particular regard to: the influence of the water plug height and air-cushion compartmentalisation on the metacentric height; and the influence of the water plug height, air-cushion compartmentalisation and water depth on the natural frequency of oscillation and added mass in heave and pitch. The water plug height and water depth are normalised by the draft  $T$ . To incorporate the effect of the air-cushion (1), the added mass values are normalised according to  $\mu_{33}^* = \mu_{33}/M$  and  $\mu_{55}^* = \mu_{55}/Mr_{22}^2$  for heave and pitch respectively.

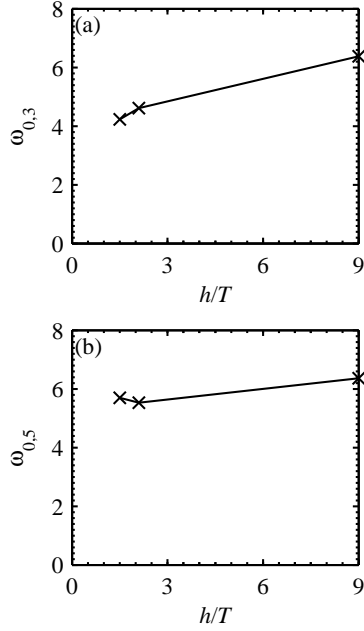
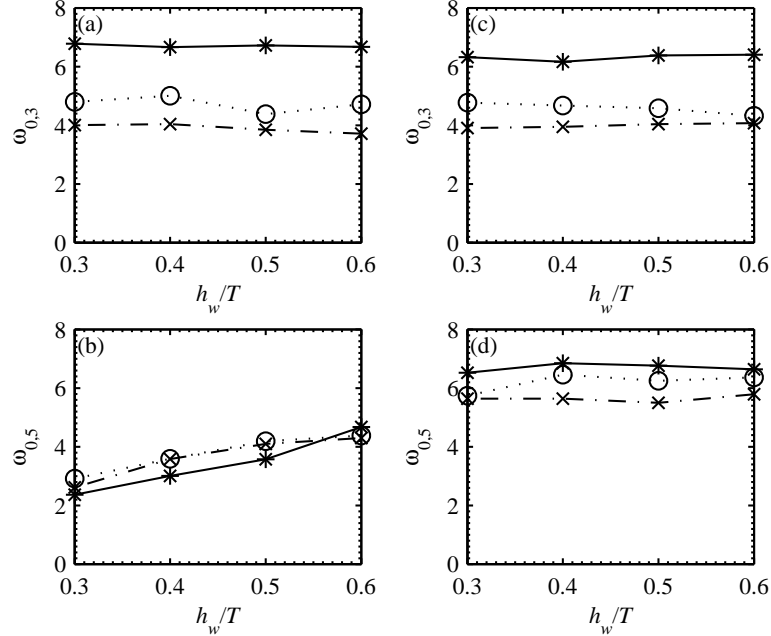
### Metacentric Height

For each model configuration, the inclining experiment results are provided in Table 1 for the  $\overline{GM}$  and hydrostatic restoring coefficient  $Mg\overline{GM}$ . It is immediately evident that the addition of a single compartment air-cushion reduces the  $\overline{GM}$  and thus destabilises the model. Compartmentalising the cushion, as in the 9-C model, reduces the destabilising effect of the air-cushion. However, we note that we cannot directly compare the  $\overline{GM}$  values of the two cushion models and the box model due to the large difference in their body masses. This was unavoidable since we required the under water geometry of the models to be similar for added mass and natural frequency comparisons. To circumvent this, the hydrostatic restoring coefficients  $Mg\overline{GM}$  provides insight. Subsequently, we notice that  $Mg\overline{GM}$  is of the same order of magnitude for both the box and 9-C models. Furthermore, in general the restoring moment is larger for the 9-C model than that of the box. This could be caused by each individual compartment behaving as it were in heave when the structure is tilted, thus providing an additional restoring moment. However, it is thought that if one were to construct a nine compartment and box model of equal mass, then one would expect the  $\overline{GM}$  of the box model to be a little larger than the nine compartment model. In contrast, the similar masses of the single and nine compartment cushion models allows direct comparison of the  $\overline{GM}$  values.

The water plug height demonstrates a positive effect on the metacentric height of the cushion models. For instance, increasing  $h_w$  by a factor of 2 approximately doubles the  $\overline{GM}$  of the cushion models. This is physically caused by a reduced destabilising couple acting on the side walls for increasing  $h_w$  due to the reduced air pressure inside the air-cushion. It should be pointed out that the standard free-surface correction formula for internal fluid tanks (see Pinski and Meevers Scholte [9] for instance) for the  $\overline{GM}$  does not take such effects into account and cannot be used for air-cushion supported structures.

Table 1: The characteristic of each model and water plug configuration.

Model	$h_w$ (cm)	Mass (kg)	$r_{22}$	$V_0$ (m <sup>3</sup> )	$z_G$	$p_0$ (kPa)	$\overline{GM}$ (m)	$Mg\overline{GM}$ (Nm)
Box	-	24.25	0.152	0.0250	-0.010	0	0.172	40.8
1-C	3	16.38	0.142	0.0062	0.014	0.526	0.013	2.06
	4	14.48	0.152	0.0062	0.011	0.456	0.036	5.10
	5	13.78	0.150	0.0062	0.007	0.342	0.045	6.06
	6	11.98	0.160	0.0062	0.011	0.251	0.063	7.42
9-C	3	16.94	0.144	0.0066	0.006	0.477	0.241	40.0
	4	14.99	0.152	0.0066	0.002	0.446	0.305	44.9
	5	13.29	0.157	0.0066	-0.005	0.354	0.373	48.6
	6	11.44	0.170	0.0066	-0.009	0.264	0.466	52.3


 Figure 4: The natural frequency  $\omega_0$  of the closed bottom box model in heave (a) and pitch (b) versus the normalised water depth  $h/T$ .

 Figure 5: The natural frequency in heave and pitch of the 1-C and 9-C models versus the normalised water plug height  $h_w/T$ : (a), 1-C heave; (b), 1-C pitch; (c), 9-C heave; (d), 9-C pitch. Three water depth conditions are considered:  $h/T = 1.5$ , ( $-\cdot-\cdot-\cdot-\cdot-$ );  $h/T = 2.1$ , ( $\cdots\circ\cdots$ ); and deep water, ( $-\ast-$ ).

### Free Oscillation

Measured results, from the free oscillation experiments, of the heave and pitch natural frequencies are illustrated in Figure 4 for the closed bottom box model and Figure 5 for the two air-cushion models. Three normalised water depths are considered whereby  $h/T = 1.5, 2.1$  and  $9$ . For  $h/T > 9$ , we assume that the seabed does not affect the surrounding fluid pressures induced by the free oscillation of the body. Consequently,  $h/T = 9$  is considered a deep water condition.

The experimental results in heave demonstrate that  $\omega_{0,3}$  is susceptible to the water depth parameter  $h/T$  and reasonably insensitive to the water plug height parameter  $h_w/T$  (cf. Figures 5a and 5c). For instance, in deep water both the 1-C and 9-C cushion models exhibit a heave natural frequency of  $\omega_{0,3} \approx 6.3$  rad/s across the range of  $h_w/T$  values examined. Furthermore, the fact that  $\omega_{0,3}$  is similar for both the 1-C and 9-C models suggests that compartmentalisation has little influence on  $\omega_{0,3}$ . The experimental values of  $\omega_{0,3}$  versus  $h/T$  demonstrates that  $\omega_{0,3}$  is remarkably similar for each model regardless of air-cushion configuration.

For the 1-C model in pitch, whilst the water depth does not appear to significantly influence  $\omega_{0,5}$ ,  $h_w/T$  appears to be a far more important parameter. For instance, Figure 5b shows that  $\omega_{0,5}$  linearly increases by approximately 2 rad/s between  $h_w/T = 0.3$  and  $0.6$ . Presumably, this is caused by an increased  $\overline{GM}$  for increasing  $h_w/T$  (cf. Table 1). In contrast, the 9-C

model behaves in a similar fashion to the heave results whereby  $\omega_{0,5}$  is relatively insensitive to  $h_w/T$ . This suggests that compartmentalising the air-cushion reduces the effect of  $h_w$  on  $\omega_{0,5}$ . Moreover, compartmentalising the air-cushion almost trebles the magnitude of  $\omega_{0,5}$  for small  $h_w/T$ . This significant change in  $\omega_{0,5}$  would undoubtedly be an important air-cushion design consideration.

Measured results of the natural frequency added mass in heave and pitch for each model configuration are illustrated in Figures 6 and 7. Apart from  $\mu_{55}^*$  for the 1-C model, the measured results indicate that both  $\mu_{33}^*$  and  $\mu_{55}^*$  consistently increases as  $h/T$  decreases. This is due to an increased surrounding fluid pressure when the model oscillates in the vicinity of the seabed - this is generally true regardless of body geometry (see Yeung [12]). For the 1-C model, it is interesting to note that  $\mu_{55}^*$  exhibits very small and slightly negative  $\mu_{55}^*$  for small  $h_w/T$  (cf. Figure 7b). Furthermore, the measured results suggest that the natural frequency pitch added mass, for the 1-C model, is relatively insensitive to water depth. At present, this result cannot be explained and is under continued investigation.

The experimental results show that the water plug height exhibits a significant influence on both the heave and pitch added mass. For the nine-compartment model in particular,  $\mu_{55}^*$  increases from 2.6 at  $h_w/T = 0.3$  up to 3.7 at  $h_w/T = 0.6$  for  $h/T = 1.5$  (see Figure 7d). Furthermore, compartmentalising the air-cushion significantly increases the magnitude of  $\mu_{55}^*$  (cf.

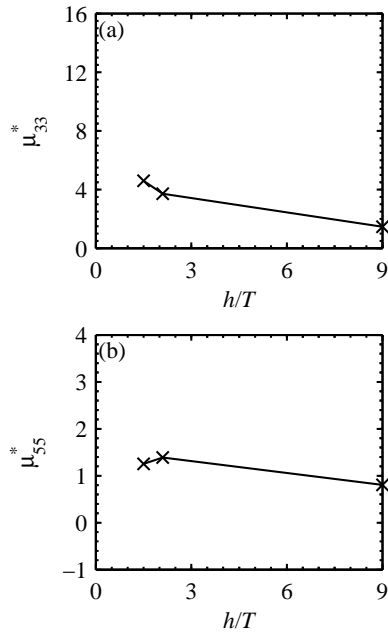


Figure 6: The normalised added mass of the closed bottom box model versus the normalised water depth  $h/T$ : (a), heave  $\mu_{33}^*$ ; and (b), pitch  $\mu_{55}^*$

Figures 7b and 7d). It is reasonable to expect that this increase in  $\mu_{55}^*$ , through compartmentalising the air-cushion, would offer important pitch motion reduction consequences.

## Conclusions

The present work has experimentally examined the metacentric height, natural frequencies, and added mass of a closed bottom box model and two cushion models in heave and pitch. The two cushion models differ by the cushion compartmentalisation into one single compartment and one nine-compartment model. The results demonstrate that the inclusion of an air-cushion reduces the metacentric height. However, this can be circumvented by compartmentalising the air-cushion. Increasing the water plug height has a positive effect on the metacentric height. We find that the cushion compartmentalisation is mostly important to the pitch natural frequency and both heave and pitch added mass values. Generally, the water plug height was found to be an important parameter for both the heave and pitch natural frequency added mass. However, for the natural frequency in pitch, the water plug height seems only to influence the 1-compartment cushion model. The measured results indicate that the water depth influences the heave natural frequency and both heave and pitch added mass regardless of air cushion configuration.

## Acknowledgements

The experiments were conducted as part of a research project supported by Minerals and Energy Research Institute of Western Australia (MERIWA), with financial support of Woodside Energy, Concrete Offshore Structures Industry Subgroup, and Ove Arup and Partners.

## References

- [1] Graham, T. A. and Sullivan, P. A., Pitch heave dynamics of a segmented skirt air cushion, *J. Ship Res.*, **46**, 2002, 121-137.
- [2] Guret, R. and Hermans, A. J., An air cushion under a floating offshore structure, *Proc. 16th Intl. Workshop on Water Waves and Floating Bodies*, Hiroshima, Japan, 2001, 1-4.

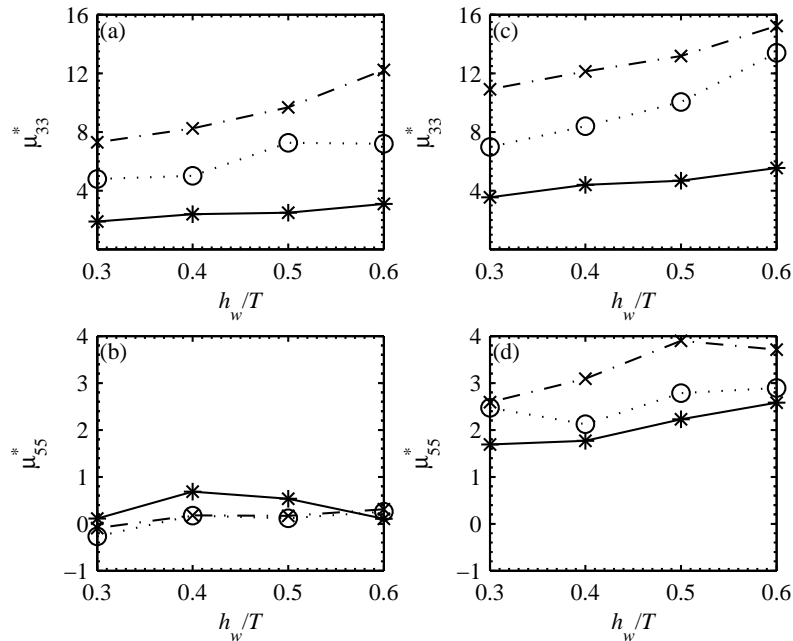


Figure 7: The added mass in heave and pitch of the 1-C and 9-C models versus the normalised water plug height  $h_w/T$ : (a), 1-C heave; (b), 1-C pitch; (c), 9-C heave; (d), 9-C pitch. Three water depth conditions are considered:  $h/T = 1.5$ , ( $-\cdot-\cdot-\cdot-$ );  $h/T = 2.1$ , ( $\cdots\circ\cdots$ ); and deep water, ( $-\ast-$ ).

- [3] Kaplan, P., Schneider, J. and Goodman, T. R., Motions of air cushion vehicles (ACV) in waves, in *Intl. Symp. on the Dynamics of Marine Vehicles and Structures in Waves*, editors R. Bishop and W. Price, 1975, 227-234.
- [4] Kim, C. H. and Tsakonas, S., An analysis of the heave added mass and damping of a surface-effect ship, *J. Ship Res.*, **25**, 1981, 44-61.
- [5] Lee, C. H. and Newman, J. N., Wave effects on very large floating structures with air cushions, *Marine Structures*, **13**, 2000, 315-330.
- [6] Malenica, Š. and Zalar, M., An alternative method for linear hydrodynamics of air cushion supported floating bodies, in *Proc. 15th Intl. Workshop on Water Waves and Floating Bodies*, Caesarea, Israel, 2000, 1-4.
- [7] Pinkster, J. A., The effect of air cushions under floating offshore structures, *Proc. BOSS'97*, 1997, 1-17.
- [8] Pinkster, J. A. and Fauzi, A., The effect of air cushions under floating offshore structures, in *Proc. 2nd Intl. Conf. Hydroelasticity in Marine Technology*, Fukuoka, Japan, 1998, 497-509.
- [9] Pinkster, J. A. and Meevers Scholte, E. J. A., Behaviour of a large air-supported MOB at sea, *Marine Structures*, **14**, 2001, 163-179.
- [10] Thiagarajan, K., Morris-Thomas, M. T. and Spargo, A., Heave and pitch response of an offshore platform with air cushion support in shallow water, in *Proc. 23rd Intl. Conf. Offshore Mech. and Arctic Eng.*, Vancouver, Canada, 2004, paper 51469.
- [11] Thiagarajan, K. P., Sow, H. E., Ronalds, B. F. and Hill, A. B., Vertical motions of a concrete gravity structure supported by air cushions in shallow water, in *Proc. Offshore Mech. and Arctic Eng.*, New Orleans, USA, 2000, paper 4191.
- [12] Yeung, R. W., Added mass and damping of a vertical cylinder in finite-depth waters, *Appl. Ocean Res.*, **3**, 1981, 119-133.

## Study of Micro Shock Waves and Cavitation Generated by Ho:YAG Laser Beam for Medical Application

S. H. R. Hosseini and K. Takayama

Nanomedicine Division, Tohoku University Biomedical Engineering Research Organization (TUBERO),  
Tohoku University, Sendai 980-8577, Japan

### Abstract

For medical application of underwater shock waves as a less-invasive approach, a reliable micro shock wave source is required. The present paper reports progress in production of underwater micro shock waves by direct irradiation of laser beam through an optical fiber. Energy source was a Q-switched Ho:YAG laser with 91 mJ/Pulse energy measured at the end of a 0.60 mm diameter glass optical fiber. The generation and propagation of underwater shock waves from the optical fiber were quantitatively visualized by double exposure holographic interferometry. Sequential flow visualizations revealed that plasma generated by the laser beam, drove spherical shock waves in water. Heat induced flow in front of the fiber vanished after 100 ms. Peak overpressures were measured at various stand-off distances by needle hydrophones. Effects of the optical fiber end configuration on the shock waves strength were clarified. The weak shock waves produced by this method have potential to be applied for precise medical procedures such as revascularization in neurosurgery.

### Introduction

For applying shock waves to sensitive and precise medical procedures like revascularization therapies and neurosurgery, generation of underwater micro shock waves plays an important role. Such delicate applications make limits on usage of conventional underwater shock wave sources like shock wave reflection and focusing over half-ellipsoidal cavity so-called Extracorporeal Shock Waves ESW [2], micro explosives [4], or electric sparks [1]. In the present study a Q-switched Holmium: Yttrium Aluminum Garnet (Ho:YAG) laser and a 0.60 mm glass optical fiber are used. Advantages of this method over previous shock wave sources are two order of magnitude reductions in focusing area if compared with ESW and elimination of product gases of micro explosives.

From another point of view, Ho:YAG laser has been intensively used in medical therapies [3, 5, and 8]. However, mechanism of its effectiveness has not yet been well clarified.

Nakahara and Nagayama [6] studied underwater shock waves emanated from roughened end surface of an optical fiber by pulse laser input using shadowgraph technique. Their qualitative study limited to visualization of shock waves at its early stage. Shaw et al. [9] and Tong et al. [11] showed production of cavitation bubble after laser beam focusing in water. Schiffrers et al. [7] by using high speed Schlieren photography studied the collapse of a laser-generated cavity near a rigid boundary. In their experimental study they focused Nd:YAG laser beam by focusing lenses.

The present research aims to clarify quantitatively: (i) process of the shock wave generation by direct laser beam irradiation through the optical fiber, (ii) effects of the fiber end configuration on the shock wave strength, (iii) growth and behaviour of the generated cavitation bubble, and (iv) structure of heat induced flow in front of the fiber.

### Materials and Methods

Energy source was a Q-switched Ho:YAG laser (Nippon Infrared Industries Co., Ltd.) with  $90 \pm 10\%$  mJ/Pulse energy measured at the end of a 0.60 mm diameter glass optical fiber, pulse duration of 200 ns, and wavelength of 2.1  $\mu\text{m}$ . The laser beam was transmitted through the optical fiber.

Double exposure holographic interferometry was used for quantitative flow visualization [10]. Figure 1 shows a schematic diagram of the optical set-up. The optical arrangement consists of two paraboloidal schlieren mirrors (P.M.) of 200 mm dia. and 1,000 mm in focal length. A beam splitter transmitted 60% of source light intensity to an object beam and 40 % to a reference beam. Mirrors (M) were used to make the light path lengths of object beam and reference beam identical with each other. Light source was holographic double pulse ruby laser (Apollo Laser Inc. 22HD, 25 ns pulse duration, 1J per pulse). Visualization laser light of object beam was diverged with a lens (L), collimated with the 200 mm dia. paraboloidal mirror, and illuminated the test section. As seen in Fig. 1, the image of phenomenon in the test section was focused with a focusing lens and was collected on the holographic film placed on a film holder. This method is called image holography so that the result is identical with Mach Zehnder interferometry. Reference and object beams were then superimposed on a holographic film. The films were 100 mm x 125 mm AGFA GEVAERT 10E75 sheet films. Double exposure holographic interferometry was used. The first laser exposure was carried out before triggering of the Ho:YAG laser and the second exposure was synchronized with the propagation of the shock wave at the test section with a proper delay time.

The constructed holograms were later reconstructed by illuminating them with an Argon-Ion laser beam (514.5 nm wave length and 1 watt). The reconstructing laser beam was adjusted by diverging and converging lenses as shown in figure 2. Neo Pan SS 100 mm x 125 mm sheet films were used to record

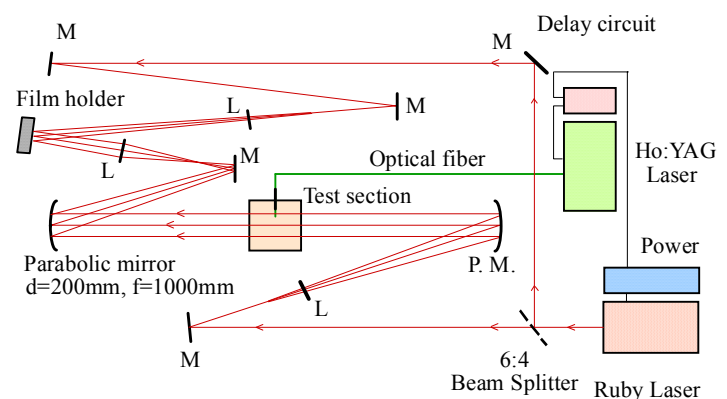


Figure 1. A schematic diagram of holographic interferometric optical arrangement.



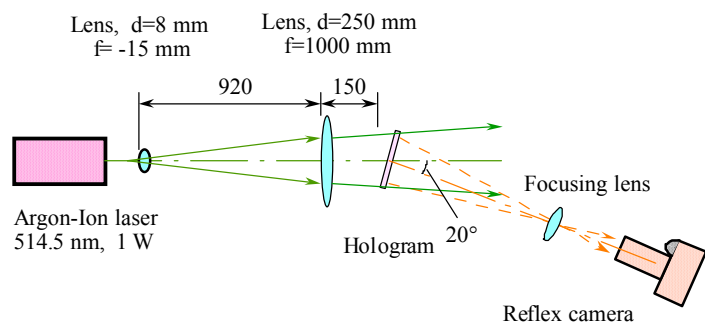


Figure 2. A schematic diagram of optical setup for reconstruction of holograms.

reconstructed images.

Figure 3 shows a schematic of the experimental set up for pressure measurement. A stainless steel container equipped with observation windows was used. The optical fiber and pressure transducers were exactly aligned in lateral, horizontal, and vertical directions. PVDF needle hydrophones with 0.5 mm sensitive dia. and 50 ns rise time (Imotec Messtechnik, Germany) were used for pressure measurements.

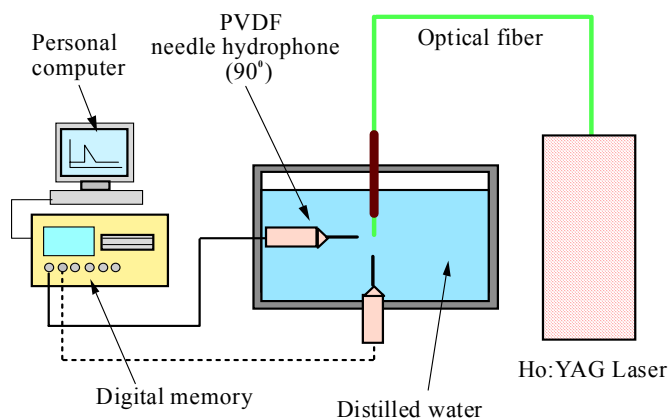
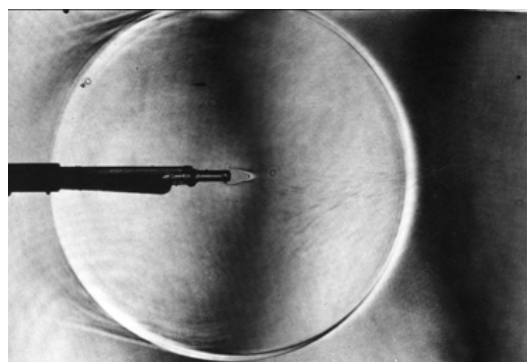
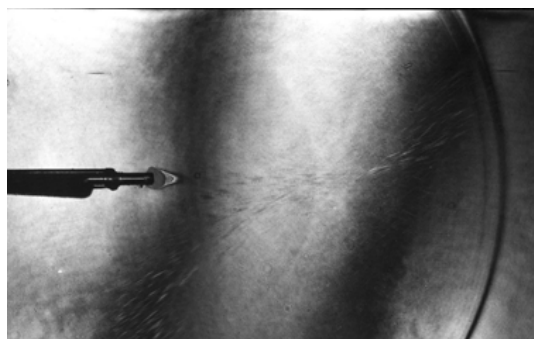


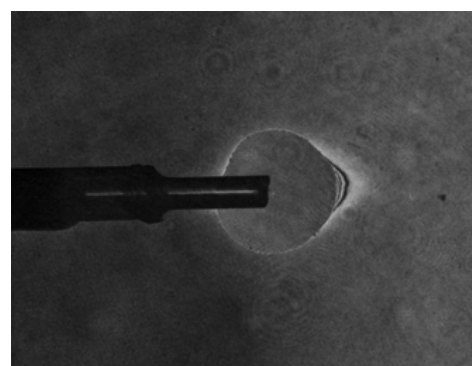
Figure 3. Experimental set up for pressure measurement.



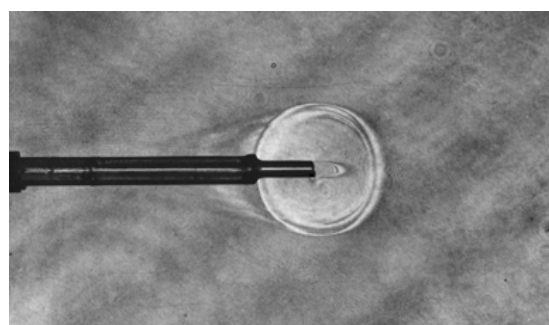
(c) 6.5  $\mu$ s



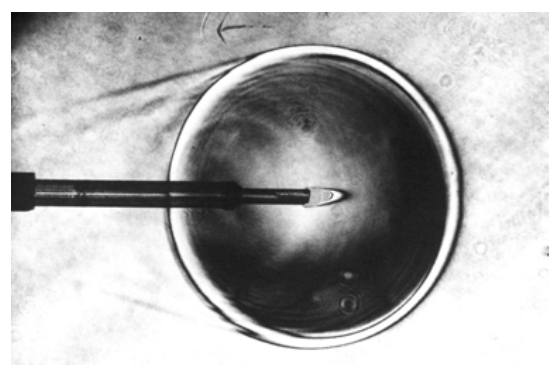
(d) 12.5  $\mu$ s



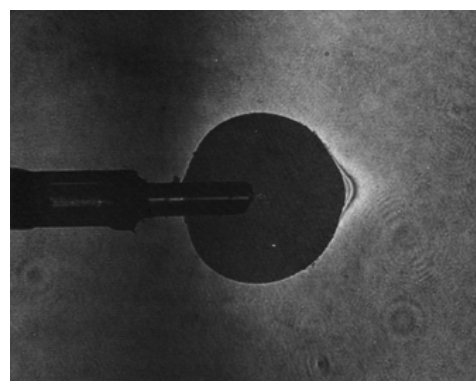
(e) 100  $\mu$ s



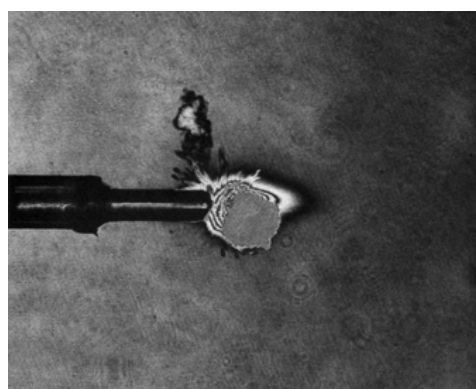
(a) 1.7  $\mu$ s



(b) 4  $\mu$ s

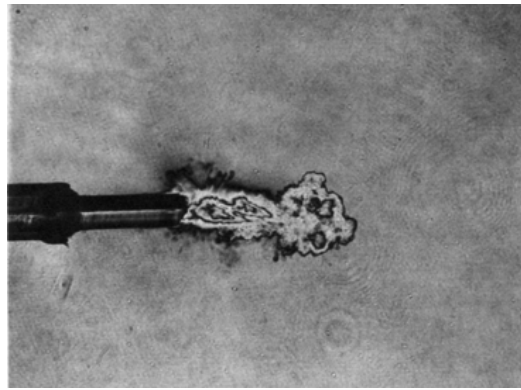


(f) 200  $\mu$ s

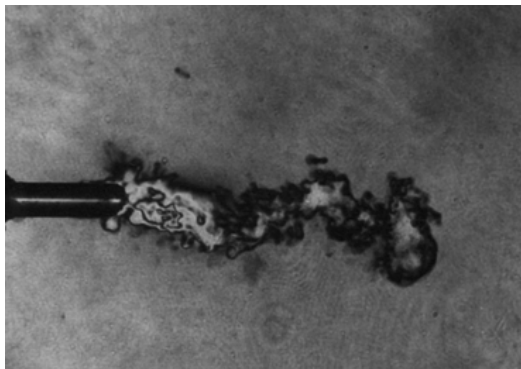


(g) 300  $\mu$ s

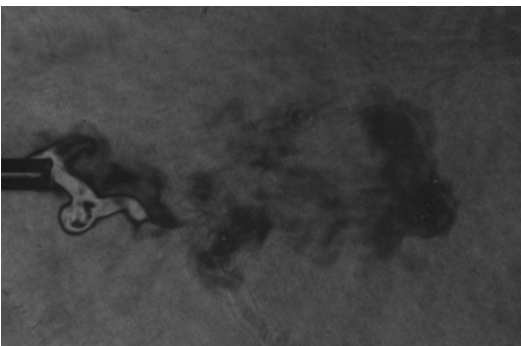




(h) 700  $\mu$ s



(i) 2 ms



(j) 10 ms

Figure 4. Sequential infinite fringe holograms of the underwater shock waves and the vapor cavities produced by Ho:YAG laser beam irradiation from roughened end 0.60 mm glass optical fiber.

## Results and discussion

### Flow visualization

Figure 4 shows sequential infinite fringe interferograms of generation and propagation of the underwater shock waves from roughened end of the optical fiber. Figure 4a, 1.7  $\mu$ s after shock wave production, shows a 2.55 mm radius spherical shock wave in water. The shock wave generation associated with the laser breakdown in the water. The laser interaction produced micro plasma in the water and heated the liquid in front of the fiber. The plasma drove spherical shock wave in water. This process followed by formation of a high temperature vapor cavity. Wave propagation through the optical fiber produced a conical precursor wave which is clearly observable in figure 4a. Figures 4b, c, and d show the sequence of the spherical shock wave propagation at 4, 6.5, and 12.5  $\mu$ s, respectively. In front of the optical fiber in figure 4b at 4  $\mu$ s the vapor bubble of about 0.41 mm dia. is observed and fringes next to it indicate the high temperature of that zone. In figures 4b-d first shock wave followed by another shock with about 0.6 mm radial distance and shock front had a fold shape. This process might be related to Ho:YGA laser irradiation from the optical fiber. A random or rough end surface of the fiber can produce diffuse transmission

of the laser beam and separate focal areas with different energies. This made a delay for distinct plasma generations and shock waves. Figures 3e-f, at 100 and 200  $\mu$ s, show cavitation bubble of 1.15 and 1.6 mm radius, respectively. The high temperature in front of the fiber resulted in higher growth of the vapor cavity in that direction. Figure 4g, at 300  $\mu$ s, shows the cavitation bubble after its first collapse. By that moment secondary cavity is produced which is observable in front of the fiber in figure 4g. By elapse of time heat dissipation in front of the fiber can be seen in figures 4h-j.

### Pressure measurement

Pressure histories at various stand-off distances  $R$  were measured. In order to determine the strength of the laser generated and cavitation induced shock waves, different kind of surface finished optical fibers were examined. Results are shown in figure 5. By increasing the roughness of the optical fibers end, stronger shock waves were produced. Figure 6 shows enlarged views of the fiber ends referring to figure 5. As can be seen by making the fiber end sharper, higher overpressures were obtained. Figure 7 shows pressure histories for a hyperboloidal end optical fiber at  $R=4.0$  mm. At 280  $\mu$ s collapse of the cavitation bubble produced a secondary strong pressure pulse. Figure 8 shows a hologram of underwater shock wave for hyperboloidal end optical fiber. An integrated single shock wave in figure 8 refers to effective laser focusing in front of the hyperboloidal fiber, so that production of higher strength shock wave became possible. Variation of laser generated cavitation pressure pulses with stand-off distances in front of the fiber ( $0^\circ$ ) and perpendicular to the fiber ( $90^\circ$ ) is shown in figure 9. Good agreement between two measurements with  $0^\circ$  and  $90^\circ$  angles is obtained. Spherical shock waves became more uniform by propagation as can be seen in figure 9.

### Conclusions

The obtained results are summarized as follows:

- 1) A Q-switched Ho:YAG laser and an optical fiber were used for production of underwater spherical micro shock waves.
- 2) Using double exposure holographic interferometric quantitative flow visualization generation process and propagation of shock waves were observed. Behaviour of the induced cavitation bubbles was clarified.
- 3) Effects of the optical fiber end configuration on the shock waves strength were studied.
- 4) The weak shock waves produced by this method have potential to be applied for precise medical procedures such as revascularization in neurosurgery.

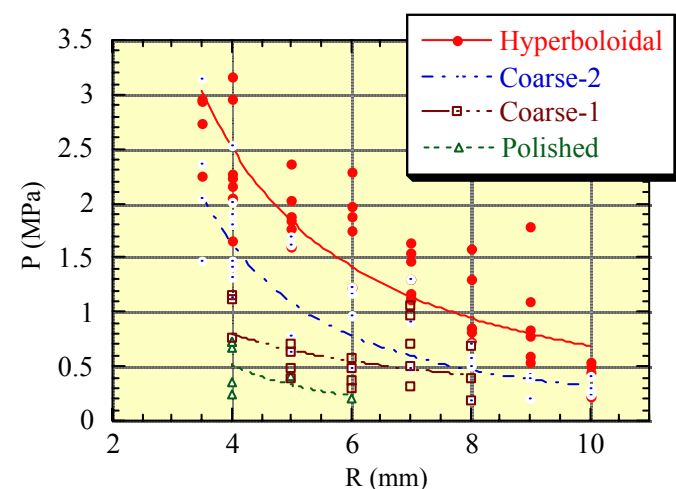


Figure 5. Effects of the optical fiber end configuration on peak overpressure.

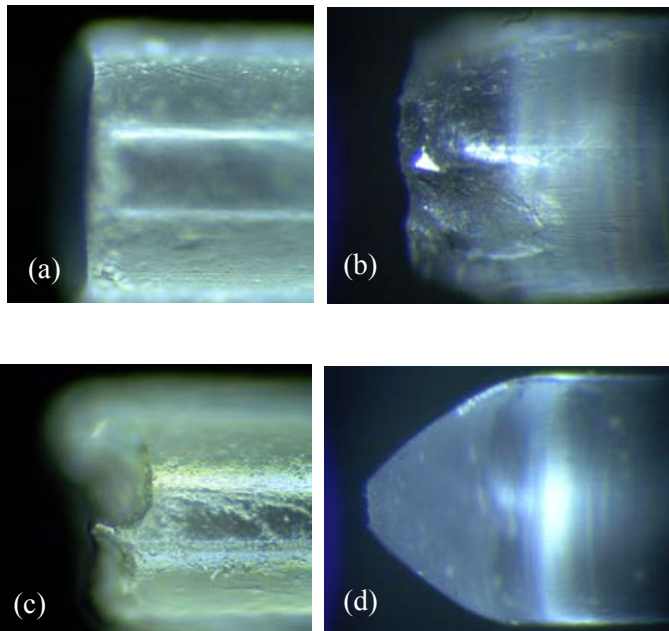


Figure 6. Photographs of the optical fibers referring to figure 5: (a) Polished, (b) Coarse-1, (c) Coarse-2, (d) hyperboloidal.

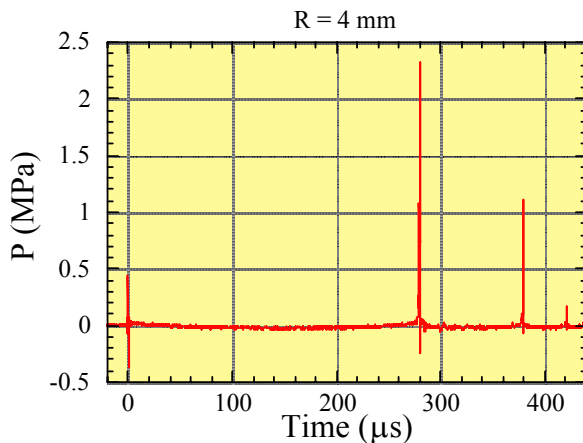


Figure 7. Pressure histories measured in water at R=4.0 mm from the hyperboloidal end optical fiber.

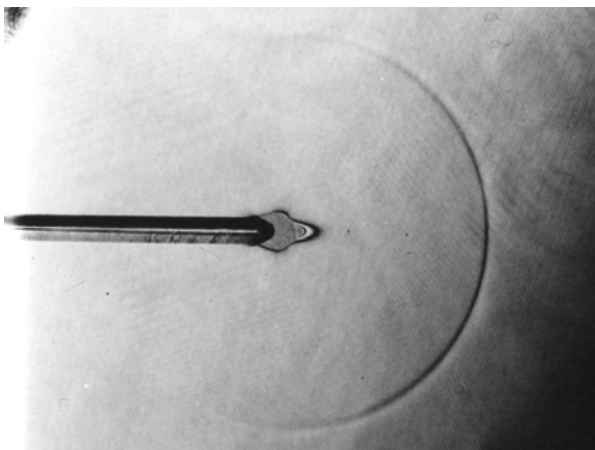


Figure 8. Infinite fringe hologram of the underwater shock wave produced 3.2  $\mu$ s after Ho:YAG laser beam irradiation from hyperboloidal end optical fiber.

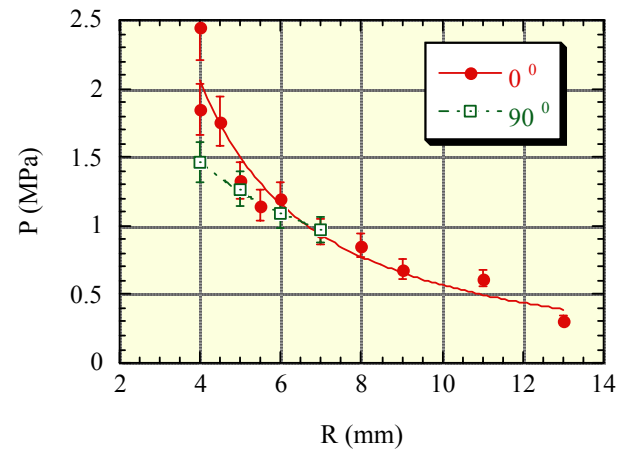


Figure 9. Variation of peak overpressure of the laser induced underwater shock waves with stand-off distance from the optical fiber of figure 4.

## References

- [1] Fernstroem, I. & Johansson B., Percutaneous pyelolithotomy. A new extraction technique, *Scan. J. Urol. Nephrol.* **10**, 1976, 257-259.
- [2] Heustler, E., Destruction of kidney stones by means of auto focused guided shock-waves, 2nd European Congress Ultrasonic and Medicine, 1975.
- [3] Johnson, D.E., Cromeens, D.M., Price, R.E., Transurethral incision of the prostate using the Holmium:YAG laser, *Laser in Surg. and Medicine* **12**, 1992, 364-369.
- [4] Kodama, T., Takayama, K., Nagayasu, N., Uenohara, H., Yoshida, M., A basic study of shock wave revascularization therapy for cerebral embolism, *Neurosonology* **10**, 1997, 79-83.
- [5] Koslin, M.G. & Martin, J.C., The use of the Holmium laser for temporomandibular joint arthroscopic surgery, *J. Oral. Maxillofacial Surg.* **51**, 1993, 122-123.
- [6] Nakahara, M. & Nagayama, K., Water shock wave emanated from roughened end surface of an optical fiber by pulse laser input, *J. Material Proc. Tech.* **85**, 1999, 30-33.
- [7] Schiffers, W.P., Shaw, S.J., Emmony, D.C., Acoustical and optical tracking of the collapse of a laser-generated cavitation bubble near a solid boundary, *Ultrasonics* **36**, 1998, 559-563.
- [8] Shapshay, S.M., Rebeiz, E.E., Bohigian, K., Hybels, R.L., Artez, H.T., Pankratov, M.M., Holmium: Yttrium Aluminum Garnet laser-assisted endoscopic sinus surgery: Laboratory experience, *Laryngoscope* **101**, 1991, 142-149.
- [9] Shaw, S.J., Jin, Y.H., Schiffers, W.P., Emmony, D.C., The interaction of a single laser-generated cavity in water with a solid surface. *J. Acoust. Soc. Am.* **99** (5), 1996, 2811-2824.
- [10] Takayama, K., Application of holographic interferometry to shock wave research, *Proc SPIE* **398**, 1983, 174-181.
- [11] Tong, R.P., Schiffers, W.P., Shaw, S.J., Blake, J.R., Emmony, D.C., The role of splashing in the collapse of a laser-generated cavity near a rigid boundary, *J. Fluid Mech.* **380**, 1999, 339-361.

# Experimental review of devices to artificially thicken wind tunnel boundary layers

J.E. Sargison<sup>1</sup>, G.J. Walker<sup>1</sup>, V. Bond<sup>2</sup>, G. Chevalier<sup>2</sup>

<sup>1</sup>School of Engineering

University of Tasmania, Private Bag 65, Hobart, Tasmania, 7001, AUSTRALIA

<sup>2</sup>Ecole Polytechnique de l'Universite de Nantes, FRANCE

## Abstract

Three devices that artificially increase the thickness of the boundary layer in a wind tunnel working section have been tested. These included a serrated fence to disturb the flow, and the use of various secondary jet arrays injected into the boundary layer through the bounding surface. Momentum and turbulence profiles in the boundary layer downstream from the thickening devices were measured. The greatest boundary layer thickness was achieved using an array of varying diameter crossflow jets with the jet diameter reducing with distance downstream. However, the fence thickener and a plate with varying jets increasing in diameter downstream produce a boundary layer with momentum and turbulence profiles more typical of a natural equilibrium boundary layer.

## Introduction

Aeronautical wind tunnels are generally designed to minimise the thickness of the boundary layer on the wall in the working section, in order to maximise flow uniformity. However, there are occasions when such wind tunnels are used for non-aeronautical research and a thicker boundary layer is required in order to simulate the physical phenomenon being modelled. A typical application of the present work is to model the boundary layer at the stern of a high-speed catamaran vessel for studies of the flow in flush type waterjet propulsion intakes [1]. Other applications include modelling the atmospheric boundary layer for studies of wind turbine performance.

Atmospheric scale boundary layer simulations in wind engineering use isolated spires of height equal to the thickened boundary layer thickness to introduce the momentum deficit [6]. However this technique may introduce undesirable spanwise variations in the flow. A previous study of techniques to artificially thicken the boundary layer [2] demonstrated the usefulness of arrays of crossflow jets and boundary layer fences. That work has been expanded to include a different, larger boundary layer fence geometry, and the use of an array of varying diameter jets with the large jets downstream. In addition the development of the thickened boundary layer has been studied in more detail by measuring the turbulence and momentum profiles at four planes downstream from the thickener location.

## Nomenclature

$B$  Constant  
 $H$  Shape factor =  $\delta^*/\theta$   
 $K$  Constant  
 $Q$  Total flow rate (m<sup>3</sup>/s)  
 $Re_\delta$  Reynolds number =  $\rho u \delta / \nu$   
 $U$  Mainstream velocity (m/s)  
 $c_f$  skin friction coefficient  
 $q$  Flow rate per metre width (m<sup>3</sup>/s/m)  
 $u$  Velocity (m/s)  
 $u^+ = u/u^*$

$u^*$  Shear velocity =  $(\tau_w / \rho)^{1/2}$

$y^+ = y u^* / \nu$

$y$  Distance from wall (mm)

$\delta^*$  Boundary layer displacement thickness

$\delta$  Total boundary layer thickness based on 99% velocity

$\theta$  Boundary layer momentum thickness

$\nu$  Kinematic viscosity (m<sup>2</sup>/s)

$\rho$  Density (kg/m<sup>3</sup>)

$\tau_w$  Wall shear stress

## Experimental Technique

### Boundary layer thickening devices

The devices used to disturb the boundary layer are shown in Figures 1-3. The devices were installed immediately upstream of the wind tunnel working section, in a location where the natural boundary layer was fully turbulent with a total boundary layer thickness of 16.7mm,  $Re_\theta = 1510$ . The natural boundary layer thickness at the midplane of the wind tunnel working section was 22.4 mm,  $Re_\theta = 5160$ .

The fence thickener was inserted into the wind tunnel with the triangular 'spikes' angled at 40° to the wind tunnel wall and their tips pointing downstream. The spikes were at a pitch of 20 mm and 20 mm high in the plane of the spike. The regular and varying hole thickeners were connected to an intake pipe with bell mouth nozzle to measure the flow rate of air ingested into the working section. The plates were located in the sidewall of the wind tunnel, with the downstream edge of the plate 100mm upstream from the start of the wind tunnel working section. The regular hole plate had a hole diameter of 2.3 mm at a pitch of 6.3 mm. The varying hole plate had hole diameters 10, 7.5, 5.5, 4, 3, 2, 1.5 mm (Table 1). The standard installation of the varying holes plate was to have the largest diameter holes upstream. This plate was also tested in a reversed configuration, with the largest holes downstream.



Figure 1a. Fence thickener.

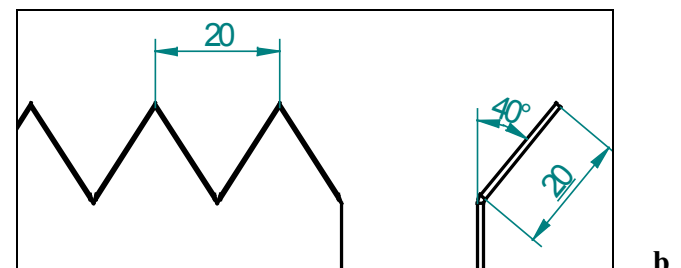


Figure 1b: Fence 'spike' geometry (dimensions in mm).



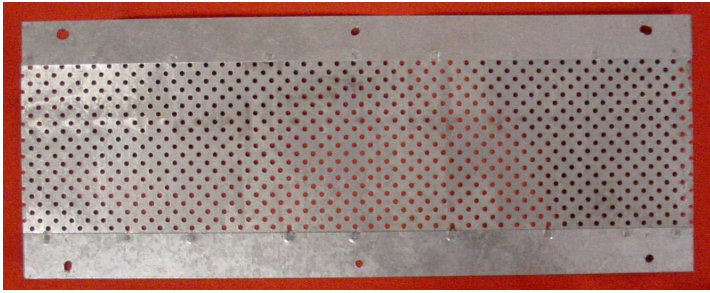


Figure 2. Regular hole thickener.

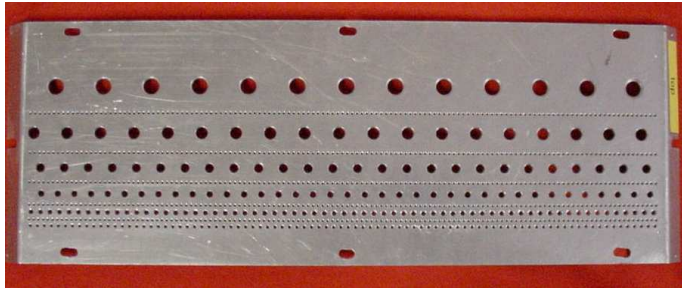


Figure 3. Varying hole thickener.

Hole dia (mm)	Total no. holes	No. Rows	Dist from leading edge (mm)	Lateral pitch (mm)
1.5	660	5	22.8, 43.3, 57.8, 68.0, 75.8	3.0
2.0	88	1	78.8	4.5
3.0	66	1	72.0	7.6
4.0	37	1	62.8	10.6
5.5	26	1	51.0	15.2
7.5	18	1	34.0	21.2
10.0	13	1	7.5	30.3

Table 1: Hole distribution for varying hole thickener (Fig 3.).

### Experimental configuration

The closed circuit wind tunnel in the Aerodynamics Laboratory at the University of Tasmania was used for the present work. This wind tunnel has a 615mm square working section with corner fillets and length 1.2m. It is preceded by a 9:1 area ratio contraction of similar cross-section.

The boundary layer thickening plates were located upstream of the working section in as shown in the schematic in Figure 4. The wind tunnel was operated at nominally 23 m/s. The plates could be easily interchanged, and the air intake system removed when the fence thickener was used.

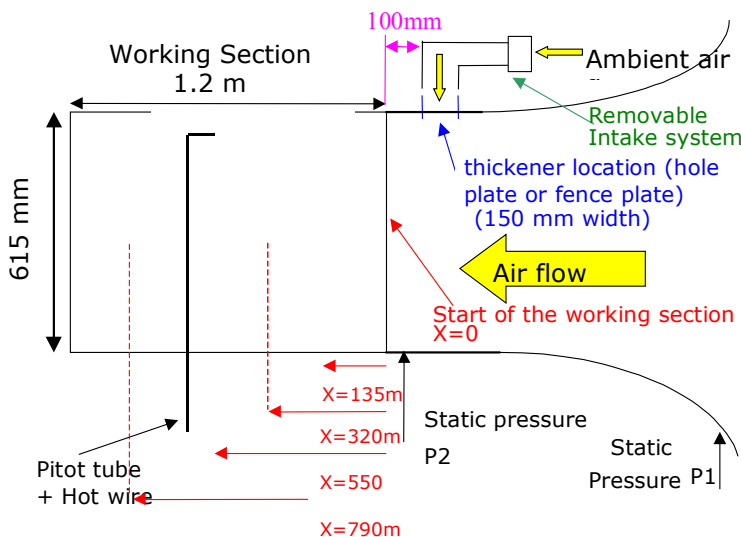


Figure 4. Wind tunnel configuration (not to scale).

The flow rate of ingested air was controlled by the pressure difference between ambient pressure and the lower static pressure

in the wind tunnel at the thickener location. The measured flow rates for the three different intake configurations are outlined in Table 2. The flow rates were nominally constant between hole configurations, at the maximum level possible with the pressure difference available. The influence of flow rate on boundary layer thickness will be the subject of future research.

	$Q(\text{m}^3/\text{s})$	$q(\text{m}^3/\text{s}/\text{m})$
Varying holes	0.0401	0.100
Regular holes	0.0420	0.104
Varying holes reversed	0.0408	0.101

Table 2. Secondary flow rate through hole thickeners.

A boundary layer traverse at the thickener location demonstrated that the undisturbed boundary layer was fully turbulent at the thickener location with a displacement thickness,  $\delta^* = 1.03 \text{ mm}$  and boundary layer thickness Reynolds number,  $Re_\theta = 1510$ . The boundary layer was traversed with a 1.26mm diameter pitot tube and hot wire probes at distances 135, 320, 550 and 790 mm downstream from the start of the working section to study the development of the natural and perturbed boundary layers. The DISA 55M Constant Temperature Anemometer was used with a single axis hot wire probe (Dantec 55P11), with sensor normal to the mean flow.

## Results

### Boundary layer parameters

The boundary layer parameters for the natural boundary layer (no thickening) and the thickened boundary layers formed using the four thickening devices summarised in Table 3 demonstrate that all of the devices achieved some level of boundary layer thickening.

$x$	$\delta^* (\text{mm})$	$\theta (\text{mm})$	H	$Re_\theta$	$c_f$
<b>Natural</b>					
135 mm	1.545	1.244	1.242	2900	0.00347
320 mm	2.067	1.630	1.268	3800	0.00326
550 mm	2.834	2.215	1.279	5160	0.00306
790 mm	3.848	3.033	1.269	7070	0.00292
<b>Fence</b>					
135 mm	4.891	3.698	1.323	8620	0.00266
320 mm	6.032	4.725	1.277	11010	0.00285
550 mm	6.391	5.124	1.247	11940	0.00292
790 mm	6.944	5.560	1.249	12960	0.00279
<b>Varying holes</b>					
135 mm	6.400	4.044	1.583	9420	0.00181
320 mm	6.419	4.554	1.410	10610	0.00230
550 mm	6.751	5.074	1.331	11820	0.00256
790 mm	7.172	5.525	1.298	12870	0.00260
<b>Regular holes</b>					
135 mm	5.430	3.719	1.460	8670	0.00213
320 mm	5.948	4.430	1.343	10320	0.00260
550 mm	6.793	5.308	1.280	12370	0.00285
790 mm	6.760	5.383	1.256	12540	0.00279
<b>Varying holes reverse</b>					
135 mm	5.511	4.040	1.364	9410	0.00254
320 mm	5.712	4.418	1.293	10290	0.00279
550 mm	6.178	4.900	1.261	11420	0.00285
790 mm	6.518	5.216	1.250	12150	0.00277

Table 3. Measured boundary layer parameters .

## Momentum profiles

The velocity profiles at the end of the working section downstream of the boundary layer thickening devices are shown in Figure 5. At this location, the boundary layers are fully developed and there is little difference in the momentum thickness produced. The momentum deficit produced by the varying holes device is concentrated near the wall. The fence is more effective in producing a momentum deficit in the outer region of the boundary layer. The profiles downstream of the regular hole plate and the reversed varying hole plate are similar.

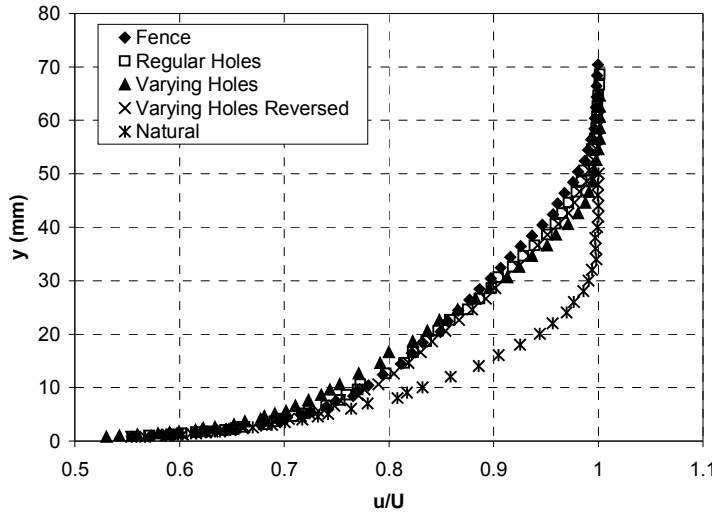


Figure 5. Velocity profiles for established boundary layers (790 mm).

The quality of the thickened boundary layer velocity distribution is determined by comparing with the standard law of the wall following Coles [4] with  $K=0.393$  and  $B=5.56$ . The wall shear stress,  $\tau_w$ , was measured using a 1.26mm diameter Preston tube (extending only into the transition region between the viscous sub-layer and fully turbulent log layer) with the calibration data provided by Patel [3]. An adjacent wall tapping provided the static pressure for the Preston tube measurement.

Hence the wall shear velocity,  $u^*=(\tau_w/\rho)^{1/2}$ , was determined and the velocity profiles could be compared using the inner-law variables:

$$u^+ = \frac{\ln y^+}{K} + B \quad \text{where } u^+ = \frac{u}{u^*} \text{ and } y^+ = \frac{yu^*}{\nu} \quad (1)$$

The thickened boundary layers all show a greater region of wall similarity (Figure 6) than the natural boundary layer, as might be expected from the higher Reynolds number for these cases. A small undershoot of the law of the wall is noticeable in the outer part of the wall layer for all the thickening devices. The wake region is very similar for the fence, regular holes and varying holes (reversed) devices. The varying holes thickener produced a significantly higher wake component with an associated increase in shape factor  $H$ .

Development of the momentum thickness and shape factor with distance downstream of the thickening devices is shown in Figures 7 and 8. The increase in momentum thickness is comparable for all the devices tested, but the variation with streamwise distance is less regular for the fence and varying holes devices.

The development of the boundary layer momentum thickness along the wind tunnel working section (Figure 7) highlights the dramatic increase in  $\theta$  that can be achieved using these techniques. The increase in  $\theta$  with downstream location for the regular holes does not appear to be monotonic, indicating that this technique may not be suitable for use with models requiring some development of the boundary layer.

The fence and the varying holes (reversed) show the most rapid return to an equilibrium condition, as demonstrated by the shape factor variation with streamwise distance (Figure 8). The boundary layer created by the varying holes plate demonstrated the largest disturbance of shape factor, which was not fully at equilibrium even at the downstream measurement location. The superior performance of the fence and varying holes reversed devices is clearly due to the fact that their initial perturbations from equilibrium are smaller in magnitude. The different performance of the injection devices, particularly the varying holes in normal and reversed configurations demonstrates that hole configuration is important in controlling the boundary layer.

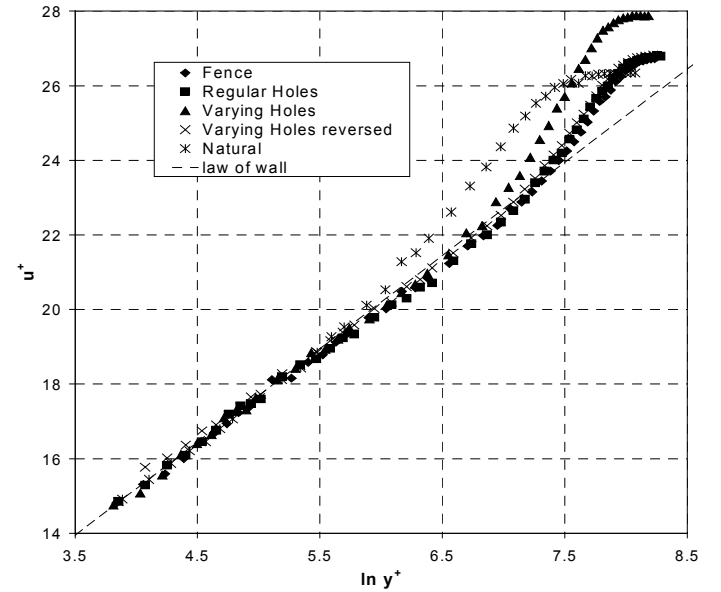


Figure 6. Velocity profiles compared with law of the wall (790 mm).

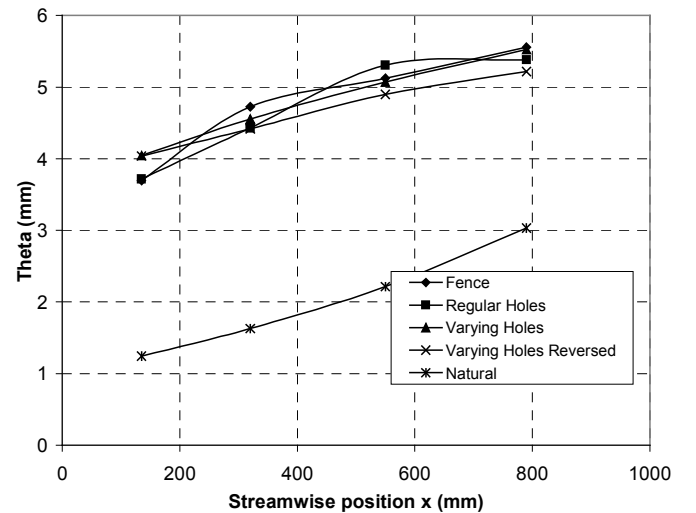


Figure 7. Development of boundary layer momentum thickness.

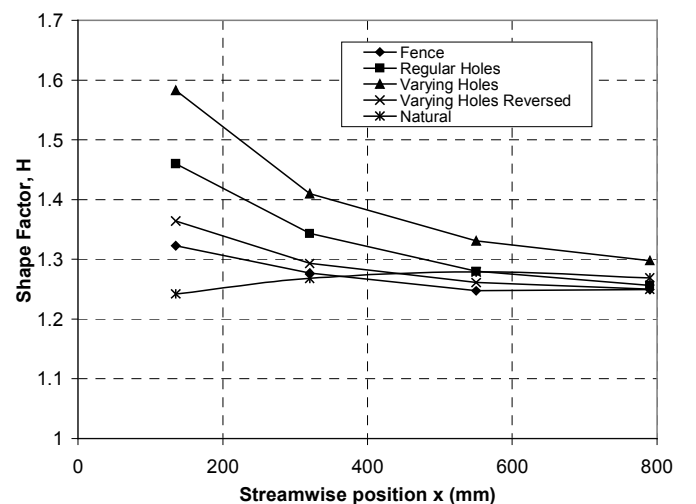


Figure 8. Development of boundary layer shape factor.

## Turbulence Profiles

Figure 9 compares the turbulence profiles at  $x = 550$  mm for the natural boundary layer and various thickening devices. The turbulence levels in the natural boundary layer slightly exceed those reported by Klebanoff [5] in the wall region. Wall vibration may have been a factor in this apparent increase.

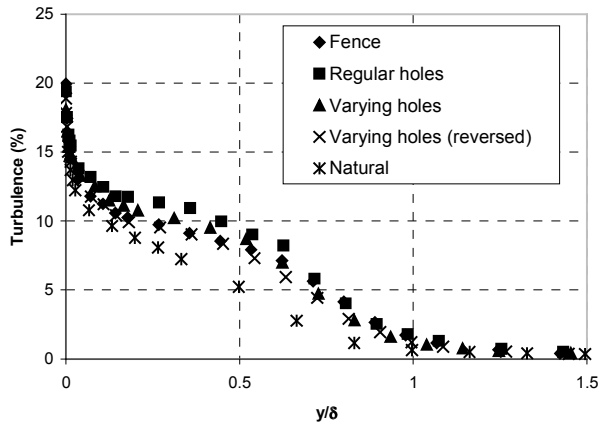


Figure 9. Comparison of turbulence profiles at  $x=550$  mm for natural boundary layer and various thickening devices.

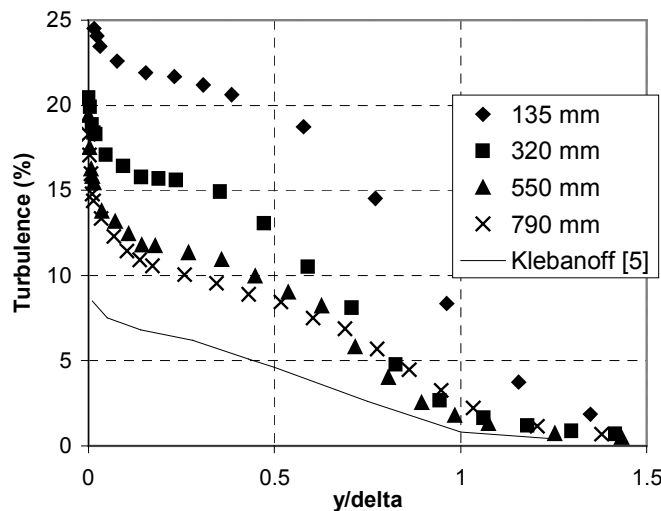


Figure 10. Turbulence profile for regular hole device boundary layers (Largest increase in b.l. turbulence).

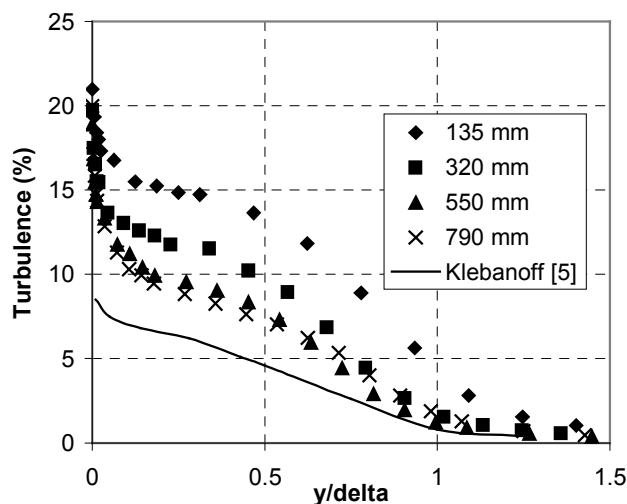


Figure 11: Turbulence profile for varying hole (reversed) device boundary layers (Smallest increase in b.l. turbulence).

All of the thickening methods produce an elevation of turbulence level over the natural boundary layer values for  $0.2 < y/\delta < 0.7$ . This increase in turbulence may be associated with the

streamwise vortex structure introduced to create the mixing required to produce the desired momentum profile.

Figures 10-11 show the streamwise development of boundary layer turbulence profiles for the regular holes and the varying holes (reversed) devices, which respectively produced the greatest and least turbulence elevation of all the thickening devices. The turbulence profiles have essentially stabilised by  $x = 550$  mm, about  $10\delta$  (thickened) downstream of the device.

## Conclusions

The present work has demonstrated that the boundary layer can be artificially thickened by naturally aspirating jets, or by a boundary layer fence. The momentum profiles have demonstrated that up to a trebling of the momentum and displacement thickness of the natural boundary layer can be achieved.

The passive serrated fence and active injection type devices were all found capable of producing comparable degrees of boundary layer thickening. The regular holes and varying holes device were less satisfactory in that they produced higher levels of turbulence and a slower return to equilibrium with distance downstream. The performance of the fence and varying holes (reversed) devices were closely comparable. These are capable of establishing a reasonably developed momentum boundary layer a distance of  $10\delta$  (thickened) downstream of the device. A trebling of the natural boundary layer thickness was achieved. All of the thickening devices produced significantly elevated turbulence levels in the central region of the boundary layer, which may be associated with the streamwise vortex structure introduced to achieve the required mixing.

The measured velocity and turbulence profiles in the artificially thickened boundary layers indicate that the preferred thickening devices are the fence and the array of jets with the largest jets downstream. This choice is based on obtaining a realistic velocity profile, compared with the law of the wall, and retaining a turbulence profile most similar to the natural boundary layer.

## References

- [1] Roberts, J.L., The influence of hull boundary layers on waterjet intake performance, PhD thesis, University of Tasmania, 1998.
- [2] Roberts, J.L. and Walker, G.J., Artificial thickening of wind tunnel boundary layers via an array of cross-flow jets, *Experimental Thermal and Fluid Science*, **27**, 2003, 583-588.
- [3] Patel, V.C., Calibration of the Preston tube and limitations on its use in pressure gradients, *Journal of Fluid Mechanics*, **23**, 1965, 185-208.
- [4] Schlichting, H., 1979, "Boundary-Layer Theory", Seventh Edition, McGraw-Hill Book Company, New York.
- [5] Klebanoff, P.S., Characteristics of turbulence in a boundary layer with zero pressure gradient, NACA Rep. No. 1247, 1955.
- [6] Standen, N.M., A spire array for generating thick turbulent shear layers for natural wind simulation in wind tunnels, LTR-LA-94, National Aeronautical Establishment, NRC Canada, May 1972.



## The Entrance Length for Fully Developed Turbulent Channel Flow

K. Lien, J. P. Monty, M. S. Chong and A. Ooi

Department of Mechanical Engineering  
The University of Melbourne, Parkville, 3010 AUSTRALIA

### Abstract

An experimental investigation into the entrance length for fully developed turbulent flow in a smooth channel was undertaken. The Reynolds number based on channel height were approximately  $40 \times 10^3$ ,  $105 \times 10^3$ , and  $185 \times 10^3$ . Mean velocity profiles were taken with a Pitot-static tube between distances of 70 and 205 heights from the inlet. A vertical shift—the direct result of a change in skin friction—is found to be the most salient indication of under-development in the velocity profile. It is suggested that commonly used criteria for fully developed flow may be inadequate to detect these first instances of under-development.

### Nomenclature

$a$	channel half-height
$A$	universal constant
$C_f$	skin friction coefficient
$d_p$	Pitot-tube diameter
$h$	channel height (internal)
$K_\tau$	Karman number: $K_\tau = U_\tau h/\nu$
$p$	static pressure
$Re$	Reynolds number: $Re = \bar{U}h/\nu$
$U$	local mean streamwise velocity
$\bar{U}$	mean/bulk streamwise velocity
$U^+$	non-dimensional $U$ : $U^+ = U/U_\tau$
$U_{CL}$	centreline velocity
$U_{max}$	maximum streamwise velocity
$U_\tau$	friction velocity: $U_\tau = \sqrt{\tau_w/\rho}$
$x$	distance in streamwise direction from channel inlet
$y$	distance normal to the channel wall; wall distance
$y^+$	non-dimensional wall distance: $y^+ = yU_\tau/\nu$
$\delta$	boundary layer thickness
$\eta$	non-dimensional wall distance: $\eta = y/a'$
$\kappa$	universal Karman constant
$\nu$	kinematic viscosity
$\rho$	air density
$\tau_w$	wall shear stress: $\tau_w = \frac{1}{2}\rho\bar{U}^2C_f$

### Introduction

Duct flow is commonly encountered in engineering. The precise nature of the evolution of turbulent flow through a duct, however, requires further investigation despite over a century of research. Any further understanding of the theoretical mechanisms that underlie such a phenomenon must necessarily rely on observation. But, for observation to be accurate, experiment must be exact.

The most basic requirements for a rigorous study of fully developed two-dimensional channel flow is clearly a knowledge of the channel dimensions necessary for its establishment. The minimum aspect ratio of 7:1 postulated by Dean [3] has provided experimentalists with a reliable standard for the achievement of nominally two-dimensional flow. By contrast, there is a distinct scarcity of thorough investigations on the minimum entrance length for fully developed flow—probably due to the many challenges such a study encounters. Efforts to compile in-

formation from existing literature have revealed data that is scattered and unreliable. Present-day experimentalists are still without a definitive guide to the necessary length for an intended experimental facility.

One such effort to compile channel flow data was made by Dean [3], who noted that references to the entrance length were generally vague, if not entirely omitted—which is surely symptomatic of the inadequacy of the current state of knowledge. The lengths (from inlet to measuring station) that he did find ranged widely from 23 to 300 heights. Notable among Dean's sources is the seminal work of Laufer on turbulent channel flow, which was performed at a length of some 55 heights. His later work on turbulent pipe flow [4] claimed full flow development at 30 diameters based on “the measured mean velocity distribution” (p.421). Similarly, in his paper on turbulent pipe flow, Nikuradse [7] concluded from a comparison of mean velocity profiles at successive streamwise lengths that the flow was fully developed by 40 diameters.

No absolute minimum length has been established, but the lengths of Laufer and Nikuradse were substantially exceeded by a large number of those surveyed by Dean. Furthermore, none of the more recent investigations that have employed more stringent criteria have been found to claim entrance lengths much lower than 100, casting doubts on the state of the flow in these classical works. Patel [8], for example, in a dedicated study of entrance length, found a minimum length of 100 pipe diameters for sufficiently high Reynolds numbers. Zanon, Durst, and Nagib [10] claim a sufficient channel length at 115 heights based on the oft-cited work of Comte-Bellot. Zagarola [9] applied numerous checks to find a pipe entrance length of 160 diameters was adequate for all but the lowest Reynolds number.

This investigation aims to help fill what appears to be a critical gap in the current knowledge of turbulent duct flow.

### The Test Facility and Experimental Equipment

The channel flow facility (shown in Figure 1) is situated in the Walter Bassett Laboratory at the University of Melbourne. With a width of 1170 mm and a height of 100 mm giving an aspect ratio of 11.7:1, the existence of a region of nominally two-dimensional flow in the channel is ensured. Spanwise measurements of mean flow quantities in the channel by Monty, Jones and Chong [6] have since confirmed this. Furthermore, at 22.5 m (or 225 $h$ ), the length of the channel working section was considered to be ample for the attainment of fully developed flow.

The air flow is driven by a centrifugal fan capable of volume flow rates of up to 3.51 m<sup>3</sup>/s. A diffuser and a settling chamber, which house a honeycomb screen and a series of 12 fine-mesh screens, serve to straighten the incoming air and minimise turbulence at the channel entrance. The two-dimensional, 9:1 area ratio contraction—achieved by splicing together a cubic and quadratic curve—is designed to avoid flow separation and deliver uniform flow to the channel inlet (at  $x/h = 0$ ). The effectiveness of the facility to this point in producing the desired uniform flow was verified by mean velocity profiles at a number

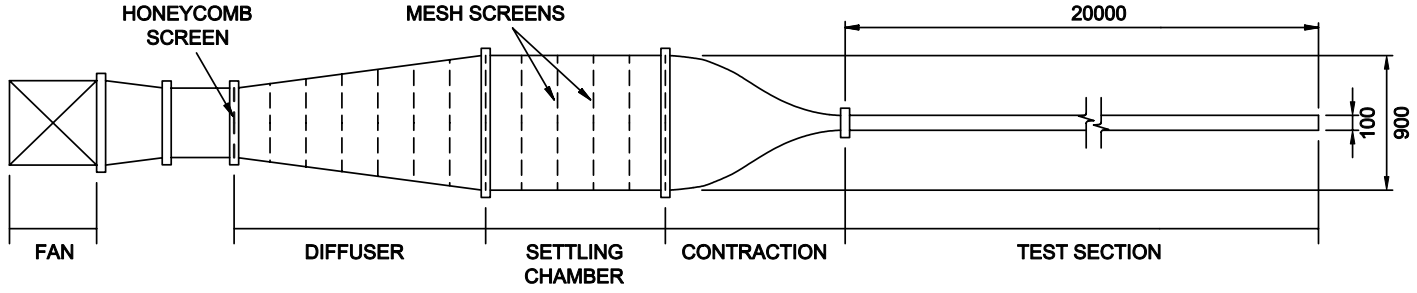


Figure 1: The channel flow facility (side view).

of spanwise locations. At the inlet the entire perimeter is lined with a 100-mm wide strip of 80-grit sand paper to promote immediate transition to turbulence, thereby shortening the length required for the flow to reach a fully developed state.

The channel itself is constructed from  $1220 \times 2440 \times 18$  mm Medium Density Fibreboard (MDF) that has been repeatedly varnished and sanded and, finally, waxed on one side to achieve the required finish for a smooth wall investigation. The floor boards are supported against deflection under load by three 6-mm thick extruded aluminium alloy C-section joists. Two 3-mm thick aluminium alloy C-section beams were bolted between the channel floor and ceiling boards to serve as the channel side walls. Wooden stiffeners glued onto the upper side of the channel at regular intervals constrain any deflection of the channel ceiling to within 0.5%.

Six measuring stations were successively installed along the centreline of the completed channel at a streamwise distances of  $x/h = 205, 176, 148, 128, 94$ , and  $70$ . Four stainless steel pressure taps were inserted into the upper surface of the channel along the centreline at intervals of approximately  $25h$ , starting at  $x/h = 120$ . The finished taps were inspected for burrs and other defects, and were tested against a removable static pressure probe before use.

All mean velocity measurements for this investigation have thus far been performed using a stainless steel Pitot-static tube with an outer diameter of 1 mm. The Pitot-static tube was connected to a MKS Baratron pressure transducer. The output from the transducer was sampled by a computer equipped with a 16-bit Microstar 4000a Data Acquisition Processor (DAP) board.

## Experimental Procedure and Data Analysis Methods

### Measurements

Mean velocity profiles were taken at each of the six stations for Reynolds numbers of approximately  $40 \times 10^3$ ,  $105 \times 10^3$ , and  $185 \times 10^3$ . Air temperature and pressure were measured before and after the collection of each mean velocity data set. Their respective values were adjusted when necessary. The fully developed streamwise pressure drop,  $dp/dx$ , was obtained by applying a linear curve fit to readings from the four wall-mounted pressure taps. Scatter within 1% was considered acceptable. This was also done before and after each data set.

### Wall Distance

The initial wall distance was found by first traversing the Pitot tube down until it pressed against the channel wall. It was then traversed back upwards an incremental distance of 0.05 mm, where a reading was taken and compared to the previous reading. This process was repeated until a noticeable difference between two consecutive readings was seen. This reading was then taken to correspond to a wall distance of  $y = 0.05$  mm.

This method relies on the specification of a rather arbitrary threshold value and was not found to be reliably precise (with an error of  $\pm 0.05$  mm). The effect of this inaccuracy in the measurement of the wall distance, however, diminishes with each successive  $y$  value, such that the impact of the error on the velocity profile away from the wall is marginal.

### Mean Flow Parameters and Non-dimensional Quantities

The local mean velocities are calculated from the Pitot-static tube data, and the MacMillan correction for shear ( $\Delta y = 0.15d_p$ ) [5] is applied to the wall distances. The bulk velocity,  $\bar{U}$ , is then evaluated from a numerical integration of the velocity profile, which thereby enables the computation of the Reynolds number,  $Re$ , based on channel height. The wall shear stress,  $\tau_w$ , is calculated for *fully developed*, two-dimensional channel flow from a momentum balance equation:

$$\tau_w = -\frac{h}{2} \left[ \frac{dp}{dx} \right], \quad (1)$$

which has been validated by Monty *et al.* for this channel in [6]. From this, values for the friction velocity,  $U_\tau$ , and the Karman number,  $K_\tau$ , for fully developed flow are obtained.

Now, velocity defect for internal flow is conventionally given by  $(U_{CL} - U)/U_\tau$ , where  $U_{CL}$  for fully developed channel flow would correspond to a wall distance equal to largest length scale,  $a = h/2$ , and be equivalent to  $U_{max}$ . The case of developing channel flow, however, is essentially a study of boundary-layer flow: the channel centreline is no longer necessarily an axis of symmetry, and the equivalence of  $U_{CL}$  to  $U_{max}$  is no longer guaranteed. As consistency demands that the velocity defect vanishes at  $\eta = 1$ ,  $U_{max}$  is chosen as a more appropriate and general reference velocity, and  $\eta$  is accordingly redefined:  $\eta = y/\delta$ , where  $y = \delta$  when  $U = U_{max}$  such that  $\delta$  is comparable to the local mean thickness of the developing boundary layer.

### Local Wall Shear Stress: The Clauser-Plot Method

The wall shear stress for the *developing* flow is determined by the Clauser-plot method [2], which is based on the assumption of the existence of a universal logarithmic region for constant pressure turbulent boundary layer flow. Here, the section of the velocity profile described by the Prandtl's law of the wall (the inner flow region) overlaps that described by von Karman's velocity-defect law (the outer flow, or core, region). This overlap region can be represented in terms of inner-scaled and outer-scaled variables, respectively, by

$$U^+ = \frac{1}{\kappa} \ln y^+ + A \quad (2)$$

and

$$\frac{U_{max} - U}{U_\tau} = -\frac{1}{\kappa} \ln \eta + B, \quad (3)$$

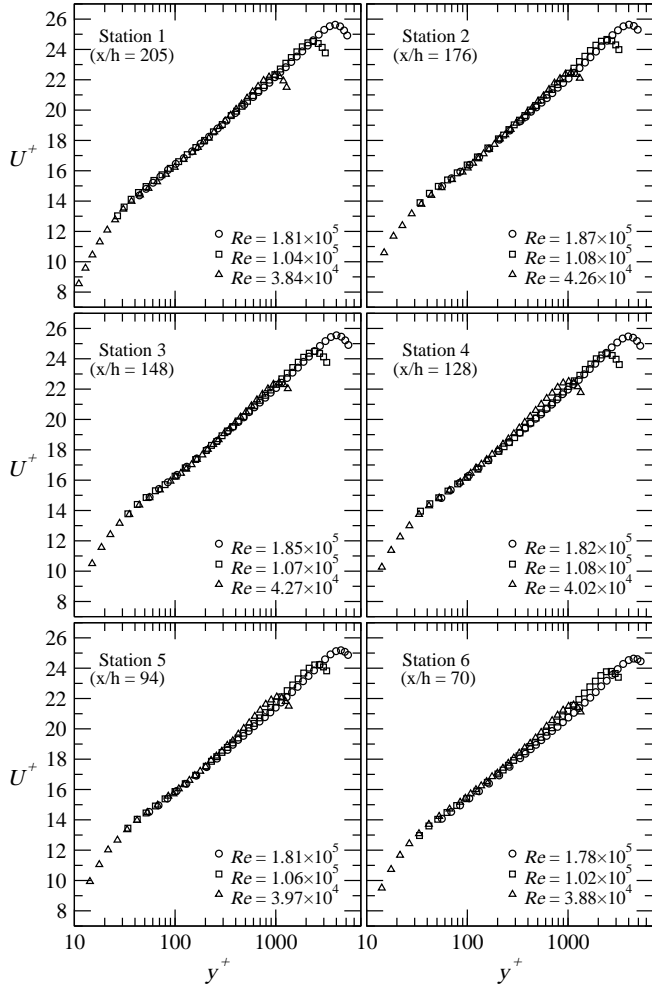


Figure 2: Mean velocity profiles, where  $y^+$  and  $U^+$  are scaled with the fully developed  $U_\tau$ . Profiles are shown for  $Re \approx 40 \times 10^3$ ,  $105 \times 10^3$ , and  $185 \times 10^3$ , at each of the six stations.

where  $A$  and  $\kappa$  are universal constants, and  $B$  is dependent on large-scale flow geometry. The Clauser values of  $U_\tau$  were used as an alternative scaling for the mean velocity data, some of which will be presented in the following section.

## Results and Discussion

Figure 2 shows the mean velocity profiles for the three Reynolds numbers from each of the six stations. This data is found to be consistent with previous unpublished results in this facility by Monty (Monty, J.P., 2004, pers. comm.). The inner flow variables  $y^+$  and  $U^+$  in this figure remain scaled with  $U_\tau$  found by Eq. (1). Because it is unlikely that the flow is fully developed at the more upstream stations, this scaling means that the collapse of all of the inner flow data is not ensured. Nevertheless, these plots show that the data is in good agreement with the general form of the inner-scaled logarithmic law; the existence of the universal overlap region is well supported. That inner flow similarity is still apparent for data from any single given station suggests that dependence of entrance length on Reynolds number is weak.

Also notable in Figure 2 is a small, but discernible increase in the size of the wake as the inlet is approached—particularly at the lowest Reynolds number. What is perhaps not clear, however, is the vertical shift of the profiles that results from the use of the fully developed value of  $U_\tau$ . The subplots in Figure 3 show the superposition of velocity profiles from all stations for the respective values of  $Re \approx 40 \times 10^3$  and  $185 \times 10^3$ . The use of appropriate velocity scales would see all the data collapse

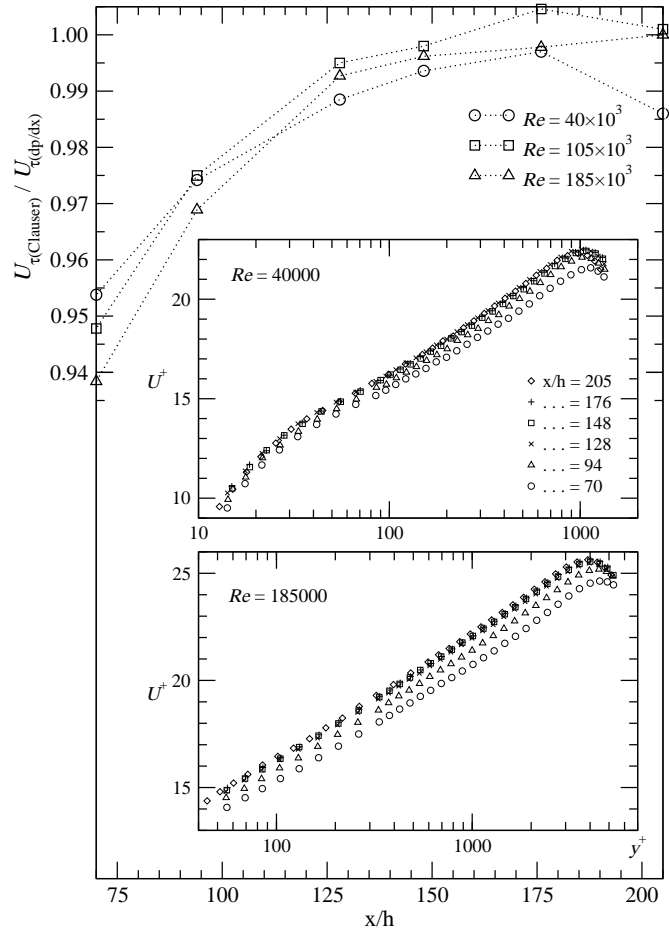


Figure 3: Ratio of  $U_\tau$  for developing flow to that of the fully developed flow, for  $Re \approx 40 \times 10^3$ ,  $105 \times 10^3$ , and  $185 \times 10^3$ . Inset plots show the mean velocity profiles, where  $y^+$  and  $U^+$  are scaled with the fully developed  $U_\tau$ . Profiles are shown for  $Re \approx 40 \times 10^3$  (top) and  $185 \times 10^3$  (bottom) at all six stations.

onto a single profile. Instead, only the profiles from stations downstream of a distance just short of  $x/h \approx 128$  (i.e., stations 1 to 4) appear to do so. Profiles taken below this channel length are increasingly shifted downwards as the inlet is approached.

It should be remarked that this is a surprising finding as it was expected that, as the inlet was approached, under-development would first be evidenced in a change in the structure of the wake. As such, the first instance of vertical shift prompted a systematic inspection of the equipment and repeated measurements in search of a source of error. Subsequent measurements have firmly established an undeniable pattern that is certainly not a product of error. It is thus suggested that the inappropriateness of the velocity scale implied by the vertical shift in the profiles is indicative of the changing wall shear stress in the entrance region of the channel. The actual values of the friction velocity that enable the collapse of the profiles (found via the Clauser-plot method, taking  $\kappa = 0.395$  and  $A = 4.65$  from the aggregated station 1 data) were plotted as a ratio to the fully developed friction velocity in Figure 3. This ratio is proportional to the observed vertical shift.

Though the scale on this plot is greatly magnified, a slight, but definite increasing trend in the shear stress is evident as the flow moves along the channel towards full development. It is encouraging that the trend seen here towards the end of the entrance region would seem to be in accord with that observed by Byrne, Hatton, and Marriott [1]. Their measurements, spanning from channel inlet to some 36 heights for Reynolds numbers ranging from 100,600 to 221,000, suggest an initial decrease in shear

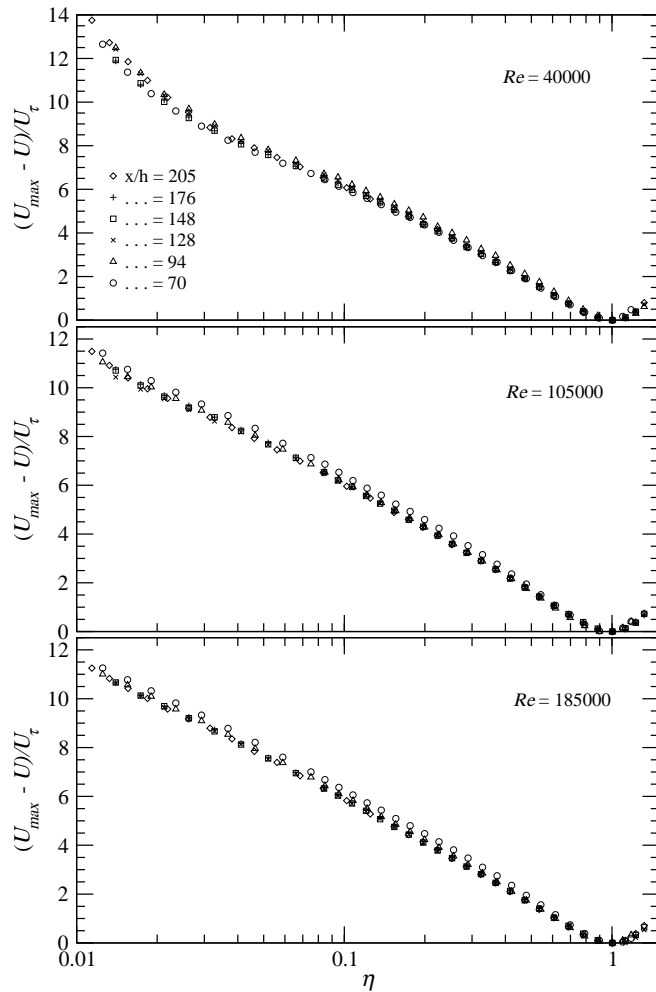


Figure 4: Velocity-defect profiles, where  $\eta$  and  $U_{\text{def}}$  are scaled with local  $U_\tau$  obtained by the Clauser-plot method. Profiles are shown for  $Re \approx 40 \times 10^3$  (top),  $105 \times 10^3$  (middle), and  $185 \times 10^3$  (bottom) at all stations.

stress within the first 20 heights, wherein the fully developed value is overshoot, before a final increase to the constant value. Significantly, no clear dependence of shear stress development on Reynolds number is observed from the data in Figure 3.

Upon closer inspection of Figure 3, it may appear that constancy of the shear stress is not convincingly achieved. Consider, however, that experimental error in the calculated value of  $U_\tau$  from Eq. (1) is of the order of  $\pm 0.5\%$ . In addition, the error associated with the use of the Clauser chart may be greater, especially at the lowest Reynolds number (as can be seen from the plot) where as few as three points may occur in the logarithmic region. Hence, while it is certain that the shear stress, and therefore the flow, is still developing up to  $x/h \approx 130$ , nothing conclusive can be inferred from this plot beyond that length.

The under-development of the flow at stations 5 and 6 suggested by the above inner-scaled profiles is substantiated in Figure 4. Their properly scaled velocity-defect profiles—at least those of the two higher Reynolds numbers—are found to increasingly diverge from those of the other stations away from  $\eta = 1$ , which is particularly reflective of the larger wakes seen earlier. (It has yet to be determined whether the failure of the station 6 data at  $Re \approx 40 \times 10^3$  to follow this trend is a genuine phenomenon, or simply a matter of experimental error; though the latter is suspected.)

## Conclusions and Further Research

This preliminary study shows that under-development in rela-

tion to the velocity profile is first manifested as a vertical shift, which is likely to be indicative of a change in the skin friction. Tests for fully developed flow that seek changes in the wake structure of the velocity profile may not detect the earliest instances of under-development. Moreover, testing for fully developed flow commonly involves two measurements over a distance that is substantially shorter than that separating the measuring stations used in this investigation. It was seen that even at these intervals observable changes in the mean velocity profiles are slight; shorter intervals may therefore not be adequate to resolve the vertical shift seen here with any certainty.

It is estimated from the present data that a minimum length of  $130h$  is required for flow to become sensibly constant with streamwise direction, although a more conservative entrance length of  $150h$  could be recommended.

Mean velocity profiles alone, however, would not constitute a thorough study of the development of turbulent channel flow. Measurements of turbulence quantities by hot-wire anemometry are underway.

## Acknowledgments

Thanks to the Defence Science and Technology Organisation for supplying additional funding for this research project.

## References

- [1] Byrne, J., Hatton, A. and Marriott, P., Turbulent flow and heat transfer in the entrance region of a parallel wall passage, in *Proc. Instn Mech. Engrs* 1969–70, 1971, volume 184, 697–712, 697–712.
- [2] Clauser, F., Turbulent boundary layers in adverse pressure gradients, *J. Aero. Sci.*, **21**, 1954, 91–108.
- [3] Dean, R., Reynolds number dependence of skin friction and other bulk flow variables in two-dimensional rectangular duct flow, *J. Fluids Engng*, **100**, 1978, 215–223.
- [4] Laufer, J., The structure of turbulence in fully developed pipe flow, NACA Report 1174, 1952.
- [5] MacMillan, F., Experiments on pitot tubes in shear flow, Report R & M 3028, Aero. Res. Council., 1956.
- [6] Monty, J., Jones, M. and Chong, M., On the wall shear stress in fully developed turbulent channel flow, in *Proc. Tenth Asian Congress of Fluid Mechanics*, Peradeniya, Sri Lanka, 2004.
- [7] Nikuradse, J., Gesetzmäßigkeiten der turbulenten strömung in glatten rohren, *Forschung auf dem Gebiet des Ingenieurwesens*, **3**, 1932, 1–36, (Translated in NASA TT F-10, 359, 1966.).
- [8] Patel, R., A note on fully developed turbulent flow down a circular pipe, *Aeronaut. J.*, **78**, 1974, 93–97.
- [9] Zagarola, M., *Mean-flow scaling of turbulent pipe flow*, Ph.D. thesis, Princeton University, 1996.
- [10] Zanon, E.-S., Durst, F. and Nagib, H., Evaluating the law of the wall in two-dimensional fully developed turbulent channel flows, *Phys. Fluids*, **15**, 2003, 3079–3089.

## The Development and Use of Dynamic Pressure Probes With Extended Cones of Acceptance (ECA)

Simon Watkins<sup>1</sup> Peter Mousley<sup>2</sup> and Gioacchino Vano<sup>1</sup>

<sup>1</sup>School of Aerospace, Mechanical & Manufacturing Engineering  
RMIT University, AUSTRALIA

<sup>2</sup>Turbulent Flow, Tallangata, AUSTRALIA

### Abstract

The development and use of multi-hole pressure probes for measurements in time-varying flows is outlined. An FFT-based dynamic calibration technique is used that permits enhanced dynamic response from relatively robust probes. To enable high turbulence flows to be measured, including flow reversals, a probe with an extended cone of acceptance is described including validation in a variety of turbulent and smooth flows. The pressure-based probes can be used for a range of measurements that would normally be outside the scope of HWA, LDA and PIV. Some applications are described.

### Introduction and Aims

Measurement of turbulence in “real-world” industrial flows with instruments that are primarily designed for laboratory applications is problematic. Such flows are frequently complex and may have temperature variations and/or particulate loads and can include measurements from moving vehicles (cars, trains, planes, etc). Currently the three main techniques used; hot-wire anemometry (HWA), laser-Doppler anemometry (LDA) and particle image velocimetry (PIV) have limitations in timely documentation of industrial flows. Drawbacks are often cost, complexity of hardware and software, the requirement of seeding (for optical methods if particulate levels are low) and the inability to cope with significant levels of vibration due to the optics needing careful alignment.

The method detailed in this work is pressure-based, where the differences between pressures sensed on the different faces of a probe are related to the velocity vector and static pressure. This technique is not new; multi-hole pressure probes have been used for measuring the time-averaged flow velocity (including the pitch and yaw angles of the flow relative to the probe) for several decades and the interested reader is referred to Schulze et al. [14] and Ower and Pankhurst [13] for details. However in recent years the method has been extended to permit relatively rapid time-varying measurements to be made, via the use of dynamic calibrations coupled with fast Fourier transform (FFT) techniques. The first step is to convert the pressure signal measured by each transducer to the frequency domain using a FFT. This provides a frequency spectrum of the pressure signal. The second step is to divide the frequency spectrum by the complex transfer function, also known as the frequency response function, of the pressure tubing. The transfer function may be determined either numerically or experimentally. The final step is to transform the linearised frequency spectra back to the time domain, using an inverse FFT, to produce undistorted pressure signals as seen by the Probe head. These undistorted pressure time-records are used to determine the time-varying velocity vector and static pressure estimates from the calibration surfaces.

Robust systems now exist that can accurately capture fluctuating flows up to 2000Hz with angular variations of pitch and yaw fluctuation of up to 90 degrees. Typically such probes have four or five faceted faces with a centrally disposed pressure tap (which when aligned into the flow corresponds to the total pressure). Recently this “zone of acceptance” has been extended

to encompass much higher fluctuating flow angles via the use of an increased number of faces. The aim of this paper is to give an overview of the techniques and to also give examples of validation and use of such systems.

### Overview of Technique

The pressure registered by a square headed tube with the open end facing an oncoming fluid stream has a response to angle of inclination to the flow (i.e. the yaw or pitch angle) that is closely sinusoidal. This response is exploited in multi-hole probes by having a system of several parallel tubes in close proximity with each offering a different orientation to the flow. Historically these were constructed by soldering or brazing four or five tubes together (along their length) and turning the end of the tube “stack”. This provided a chamfered end at, usually, 45 degrees, resulting in each tube presenting a face that was inclined at 45 degrees to the flow when the axis of the tube system was parallel to the mean flow axis. Thus yawing and pitching of either the tube system or the flow gives pressure differentials across pairs of tubes that can be related to the magnitude of velocity and the angles between the probe axis and the flow. Calibration is effected by putting the instrument in known flows and changing the speed and inclination of the probe to the flow. Recent manifestations of the system include probe heads that are machined from solid such as the probe shown in Figure 1.

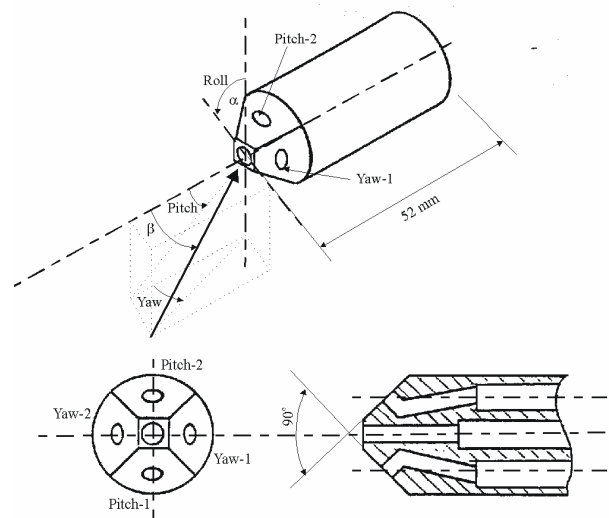


Figure 1: The Head of a Typical Five Hole Pressure Probe, from [1].

Such multi-hole probes usually have five pressure taps as shown, although to obtain flow magnitude, direction (yaw and pitch angles up to 45 degrees) and static pressure only four independent pressure taps are needed. Five holes are sometimes used for ease of manufacture although sometimes it is required to obtain flow angles in excess of 45 degrees and/or enhanced accuracy through redundancy. For these reasons several researchers have used probes with many pressure ports, see for example Cogotti [4] who used a 14 hole probe to provide time-

averaged surveys of the wakes of several car geometries. However this probe was relatively large (28 mm x 6 mm).

The response time of the system is the combined response time of the flow stabilization time around the head, the tubing system and the pressure transducers (including their effective internal volumes). This has meant that until fairly recently the use of pressure probes has generally been limited to time-averaged quantities. These have included total and static pressures, velocity, vorticity and other derived quantities such as “micro drag” maps, eg see Cogotti [5].

### Improvement of Frequency Response

In order to extend the use of such probes into measuring time-dependent quantities, the response time can be reduced by physical design. This requires a minimization of tubing lengths and volumes (including the “filling in” of excess volume in the pressure transducer) or using MEMS technology to mount the responding diaphragm on the probe surface. However a drawback of the latter method is that the probe loses some robustness. Alternatively, knowledge of the dynamic response of the head/tube/transducer system can be used to reconstruct the original time series resulting in a robust probe that has a good dynamic response. The first analytical models and dynamic calibration appears to be the work of Berg and Tijdeman [2] with other relevant work including that of Irwin et al. [9] and Lewis and Holmes [10].

The advent of the PC and routines to rapidly permit FFTs and inverse FFTs of large numbers of data points, now means a reconstruction of the original “undistorted” time data can be achieved in a timely manner. Thus the frequency response of a relatively robust yet inherently slow instrument can now be optimized such that it can replace some of the more conventional, yet less robust, instrumentation.

### Improving the Angular Response

Four or five hole probes accept flow angles of up to about  $\pm 45$  degrees. One such manifestation is the High-Frequency Cobra Probe. With reference to Figure 2, the principle of operation is to relate the pressure field detected by four pressure tap locations on the faceted head to the magnitude of the instantaneous local velocity vector, the flow yaw and pitch angles and the instantaneous static pressure.

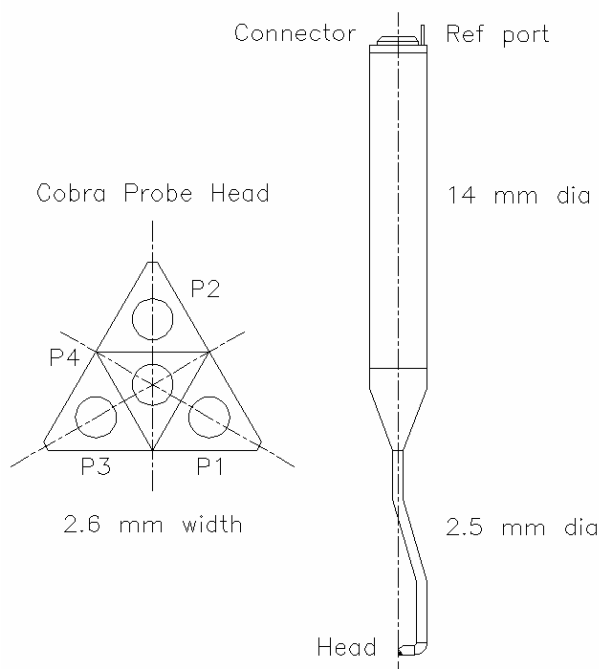


Figure 2: The High-Frequency Cobra Probe.

Pressure signals measured by the transducers in the Probe body are linearised to correct for amplitude and phase distortions that are inherent in the system, using a dynamic calibration procedure as previously described. The four pressure values are then converted to non-dimensional ratios. These are used as the independent variables that are related to the four dependent variables of total pressure, dynamic pressure, yaw angle and pitch angle through pre-calculated calibration surfaces. Thus there are three stages in the calibration process; static calibration of the four pressure transducers by applying steady pressures; generation of calibration surfaces from yawing and pitching the probe in known flow and; dynamic calibration via the application of known fluctuating pressures measured via a reference dynamic transducer.

The calibration surface lookup is performed for all samples (usually 5000 samples per second) to produce time varying values of velocity, pitch and yaw angles and static pressure. Mean and time dependent data can then be displayed and saved to disk, as can other data such as turbulence intensity, Reynolds stresses etc.

To enable large flow angles to be accepted the number of faces has to be increased. Very large flow angles are encountered in flow close to the back of bluff bodies or (under very light wind conditions) atmospheric turbulence and recently a 13-hole probe offering an extended cone of acceptance has been developed, see Figure 3. The probe head is manufactured from a 6mm cube and fitted to a stem of 4 mm diameter.

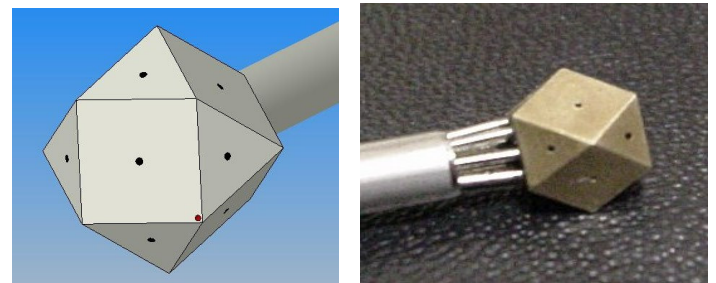


Figure 3: Thirteen Hole ECA Probe.

### Validation of the ECA Probe

Measurements have been made in flows of low and high turbulence and swirling flows. Results were compared with similar measurements from the Cobra Probe - which has been the subject of extensive prior validation. This prior work includes comparison of turbulence quantities with known instrumentation such as HWA. Hooper and Musgrove [7, 8] compare measurements of mean velocity and Reynolds stresses in pipe flow and found very good agreement except relatively close to the wall where wall proximity affects measurements. Further details of validation can be found in Chen et al. [3].

Data from both the ECA and Cobra Probes in low turbulence flow included comparative measurements of turbulence intensities – see Figure 4 - where both probes measured turbulence intensities that were very close to the freestream intensity of 1.7% (measured with HWA). Other tests included rolling the probe axially through a wide range of angles and comparing the resolved axial velocity under several speeds – good agreement was found and details can be found in Vano and Watkins [15].

Grid-generated turbulence of 32% (at 20 grid spacings downstream) was also used to compare the integral length scales calculated via the autocorrelation method - see Figure 5. The corresponding scales from the ECA and Cobra Probes were 117 and 123 mms. In smooth flow, spectra revealed there was no obvious vortex shedding from the probe. NB vortex shedding from the head might be expected at a Strouhal number of 0.15 to 0.2 using Strouhal numbers for spheres in the relevant Reynolds number range.



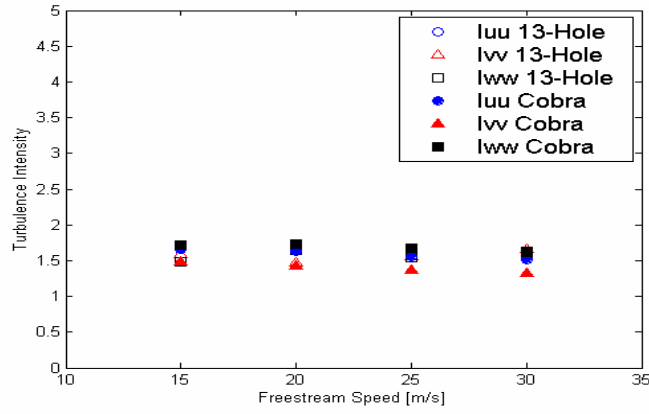


Figure 4: Measured Intensities in 1.7% Intensity Flow.

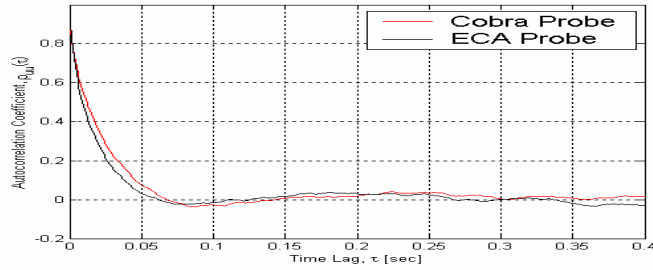


Figure 5: Autocorrelation Functions ECA vs Cobra.

Time histories of angle fluctuations demonstrate that instruments with 45 acceptance angles can miss significant proportions of turbulent fluctuations for high turbulence levels. Figures 6 and 7 show data 20 characteristic lengths downstream of a grid. Note that data that do not fall within the calibration zone are flagged by software and not plotted. 90% of data fall on the calibration surfaces of the Cobra Probe compared to 98% for the ECA Probe (zones of acceptance are 45 and 135 degrees respectively). When Probes were moved to 10 grid spacings downstream the figures are 64% and 95%. A PDF plot of the flow angle from the ECA Probe illustrates why, see Figure 8.

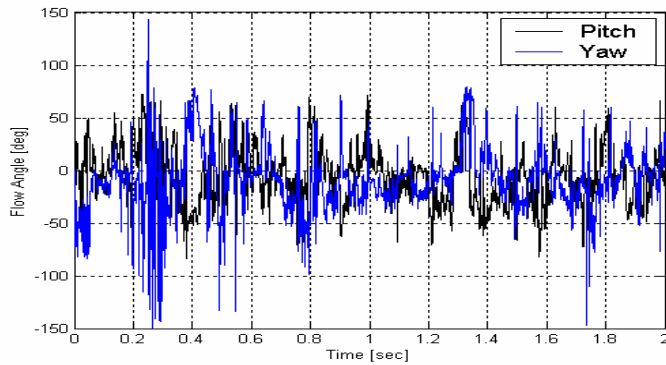


Figure 6: Flow Angles at 20 Grid Spacings – ECA.

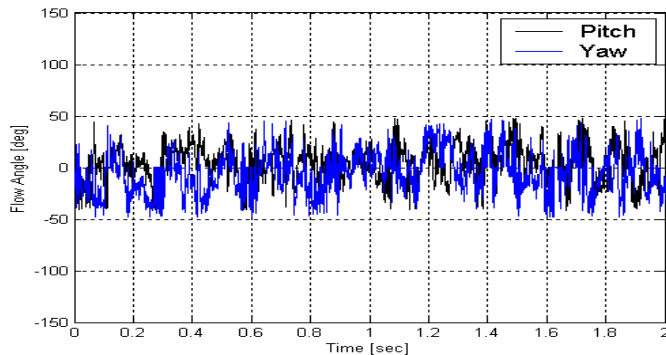


Figure 7: Flow Angles at 20 Grid Spacings – Cobra.

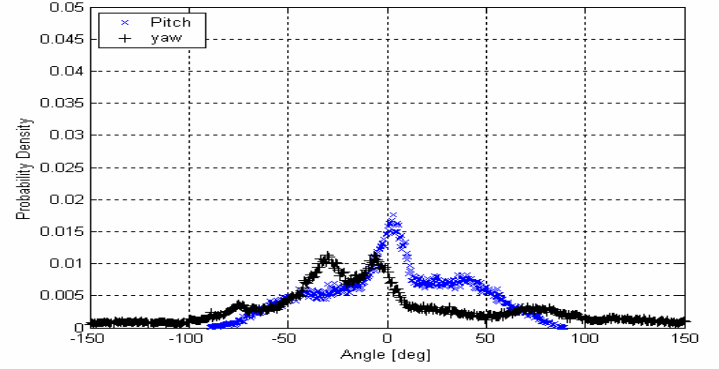


Figure 8: PDF of Angles at 10 grid Spacing – ECA.

### Examples of Use

The robustness of the pressure-based systems has enabled new measurements to be made including roadside measurements of the turbulence in the wake of commercial vehicles, Mousley and Watkins [11]. They used a bank of 3 Cobra probes fixed to the ground in order to document the flow field for spray suppression studies.

In order to better understand the on-road environment for more realistic CFD and EFD simulations, systems have been fitted to moving vehicles to measure turbulence quantities as perceived from the moving vehicle. This is useful in understanding the “real” turbulent environment as opposed to the relatively smooth conditions that exist in vehicle wind tunnels or the boundary conditions in most CFD simulations. This has also enabled understanding of the link between the transient in-cabin noise and the external velocity fluctuations, see Watkins et al. [16]. Examples of a bank of four Cobra probes used to further understanding of the flow environment of birds and micro air vehicles traversing atmospheric winds is given in Watkins and Melbourne [17].

Recent work has included mapping the flow through car radiator cores and measuring the flow field around ventilated disc brake rotors whilst rotating with a smaller version of the Cobra probe (head width of 1.6 mm). This has enabled surveys of relatively small jets and wakes such as exiting flows from heat exchangers Ng et al. [12].

### Concluding Remarks and Future Possibilities

A considerable advantage of the pressure-based method is that the probes are robust and the only periodic calibration required is a static calibration of the pressure transducers. However despite a very large angle of acceptance care still needs to be taken in choosing a suitable flow/probe alignment angle and until a 360 degree system is developed this will remain the case.

It is interesting to note that Hooper and Musgrove [8] claim that such systems can measure moments between the fluctuating pressure and velocity which are not possible with other systems, leading to new insights into turbulence modelling for CFD codes.

One of the original uses of the probes were to measure strongly swirling flow in industrial cyclones (for details see Hooper and Watkins, [6]). A planned extension of this work is to attempt measurements in flows with low loads of fine particulates.

## Acknowledgement

The fine machining of Bernard Smith is much appreciated. Examples of use have been supplied by the postgraduates of the Vehicle Aerodynamics Group at RMIT and the financial support of the ARC is also acknowledged.

## References

- [1] Anon <http://www-g.eng.cam.ac.uk/whittle/current-research/hph/pressure-probes/pressure-probes.html>
- [2] Berg H. and Tijdeman H., "Theoretical and Experimental Results for the Dynamic Response of Pressure Measuring Systems", National Aerospace Laboratories (Netherlands) Rep. NLR-TR F238, 1965.
- [3] Chen, J., Fletcher, D.F., Haynes, B.S. and Hooper, J.D. Validation Of The Cobra Probe Using Turbulence Measurements In Fully Developed Pipe Flow. Proc. 13th Australasian Fluid Mech. Conf., Melbourne, 1998.
- [4] Cogotti A, "Flow-Field Surveys Behind Three Squareback Models Using a New Fourteen Hole Probe", SAE Paper 870243, SAE International Congress and Exposition, Detroit, Michigan, February 1987.
- [5] Cogotti A, "Prospects for Aerodynamic Research in the Pininfarina Wind Tunnel", FISITA paper 905149, XXIII FISITA Congress, Turino, May 1990.
- [6] Hooper, J. and Watkins S., "Mean Velocity, Reynolds Stress and Static Pressure Measurements in an Air Cyclone", in proceedings of the 14th Australasian Fluid Mechanics Conference, Adelaide University, 9-14 December, 2001.
- [7] Hooper, J.D. and Musgrove, A.R. "Pressure Probe Measurements of Reynolds Stresses and Static Pressure Fluctuations in Developed Pipe Flow", Proc. 12th Australasian Fluid Mechanics Conference, Sydney, Australia, 1995.
- [8] Hooper, J.D. and Musgrove, A.R. "Reynolds stress, mean velocity and dynamic static pressure measurement by a four hole pressure probe." Experimental Thermal and Fluid Science Vol. 15 Pt 3, (1997)
- [9] Irwin H. Cooper K. R. and Girard R., "Correction of Distortion Effects Caused by Tubing Systems in Measurement of Fluctuating Pressures", Journal of Industrial Aerodynamics, 5, pp 93-107, 1979
- [10] Lewis R. E., and Holmes J. "A Dynamic Calibration Rig For Pressure Tubing and Transducers", 1st Workshop on Industrial Aerodynamics", July 3-5 1984, CSIRO Highett, Australia.
- [11] Mousley P.D, Watkins S, "A Method of Flow Measurement About Full-Scale and Model-Scale Vehicles", in Society of Automotive Engineering (USA) Transactions – Journal of Passenger Cars, 2000, SAE 2000-01-087, also in SP 1524, ISBN 0-7680-0574-4.
- [12] Ng E., Watkins S., Johnson P. J. and Mole L., "Use of a Pressure-Based Technique for Evaluating the Aerodynamics of Vehicle Cooling Systems", in Vehicle Aerodynamics Studies", ISBN 0-7680-0935-9, pp 71-86, 2002
- [13] Ower E. and Pankhurst R. C., "The Measurement of Airflow", Pergamon Press, UK, 1977, ISBN 0-08-021282.
- [14] Schulze M., Ashby G. C. and Erwin J. R., "Several Combination Probes for Surveying Static and Total Pressure and Flow Direction", N.A.C.A. TN-2830.
- [15] Vino G. and Watkins S., "A Thirteen Hole Probe for Measurements in Bluff Body Wakes", 5th Int. Coll. on Bluff Body Aerodynamics and Applications, July 11-15 NRC, Canada, 2004.
- [16] Watkins S, Riegel M and Wiedemann J., "The Effect of Turbulence on Wind Noise", invited paper, 4th Int. Stuttgart Symposium, FKFS/Stuttgart University, 20-22nd February 2001 in Automotive and Engine Technology, Expert-Verlag, ISBN 3-8169-1981-2.
- [17] Watkins S. and Melbourne W. H., "Atmospheric Turbulence and Micro Air Vehicles", 18th Bristol International Conference on Unmanned Air Vehicle Systems, Bristol University, UK, March 31 - April 2, 2003.

## The Effect of Particle Concentration on the Coefficient of Drag of a Spherical Particle.

D.S.Dodds<sup>1,2</sup> and J.Naser<sup>1,2</sup>

<sup>1</sup>CRC for Clean Power from Lignite  
Mulgrave, Vic, 3170 AUSTRALIA

<sup>2</sup>School of Engineering and Science  
Swinburne University of Technology, Vic, 3122 AUSTRALIA

### Abstract

In the simulation of dilute gas-solid flows such as those seen in many industrial applications, the Lagrangian Particle Tracking method is used to track packets of individual particles through a converged fluid field. In the tracking of these particles, the most dominant forces acting upon the particles are those of gravity and drag. In order to accurately predict particle motion, the determination of the aforementioned forces becomes of the upmost importance, and hence an improved drag force formula was developed to incorporate the effects of particle concentration. This study examines the individual effects of particles located both perpendicular and parallel to the flow direction, as well as the effect of a particle entrain within an infinite matrix of evenly distributed particles. Results show that neighbouring particles perpendicular to the flow (Model II) have an effect of increasing the drag force at close separation distances, but this becomes negligible between 5-10 particle diameters depending on particle Reynolds number ( $Re_p$ ). When entrained in an infinite line of particles co-aligned with the flow (Model I), the drag force is remarkably reduce at close separation distances and increases as the distance increases. The results of the infinite matrix of particles (Model III) show that, although not apparent in the individual model, the effect of side particles is experienced many particle diameters downstream.

### Introduction

CFD (Computational Fluid Dynamics) is utilised to model many industrial flows for a number reasons ranging from the design stage to monitoring flows where experimental measurements are unavailable. One such area is the distribution piping on a coal-fired burner as used by the coal industry in the generation of electricity. These flows consist of a carrier fluid, transporting particles from the mill to the burner outlet. Due to the low mass loadings (10%) of coal, the use Lagrangian Particle Tracking is the most appropriate, where the air flow field is solved using the full Navier-Stokes equations, and then packets of particles are individually tracked through the fluid according to Newton's 2<sup>nd</sup> law of motion. The motion of a particle is governed by the following equation:

$$m_p \frac{du_p}{dt} = \sum F \quad (1)$$

where the forces affecting the particle include the drag force and gravity force, and to a lesser extent, the added mass and Basset forces. For small particles such as those used in coal industry ( $d < 100 \mu m$ ), the drag and gravity forces become the most dominant and as such the determination of these forces is of the upmost importance in the accurate prediction of the particle phase motion.

The drag force of a spherical particle is calculated using the following theoretical formula:

$$F_D = \frac{1}{2} C_D \rho A V_{rel}^2 \quad (2)$$

where  $C_D$  is the coefficient of drag,  $A_p$  is the frontal projected area and  $V_{rel}$  is the relative velocity between the particle and the carrier fluid. The most common approach to determine the drag force on a particle is using the standard drag coefficient curve, which is based on experimental studies of a sphere in unbounded fluid flow. The most commonly accepted approximation of this curve is given by the following equation:

$$C_D = \frac{24}{Re} (1 + 0.15 Re^{0.687}) \quad Re < 1000 \quad (3)$$

As it can be seen, the above equation is solely a function of the local particle Reynolds number, and as such, discounts other effects that may affect the drag on a particle. In a situation whereby particles are relatively spread out, this assumption can be correctly employed to accurately predict particle motion, but in many industrial flows, it is impossible to assume that the distribution will be such that particles will not interact and in turn will affect each others motion. Kuan [2] found that reducing the drag coefficient to 65% of the standard  $C_D$ , predicted particle velocities better matched those of the validating experimental results of a vertical gas-particle flow. These results are based on a mass loading of 0.3, which corresponds to an average particle concentration, or particle volume fraction, of  $1.5 \times 10^{-4}$ . Although this is considered to be dilute flow, the interactions between particles cannot be ignored, which has been common practice in the past due to computer limitations and a lack of understanding of the interaction phenomenon.

A number of researchers have tried to measure the influence on the drag force of a particle in the presence of other particles [1, 3-6]. Liang [1] experimentally measured the forces in a number of particle orientations. The main findings of this research show that the drag force experienced by a particle is significantly affected by surrounding particles, more so when the particle are co-aligned. The work of Liang [1] looked at three particles co-aligned and at separation distances up to 7 particle diameters, which corresponds to a particle volume fraction of approximately  $10^{-3}$ .

It is necessary to assume that for a given particle concentration, that the particles are evenly distributed throughout the cell. Using this assumption it is possible to relate volume fraction to a uniform separation distance using the follow relation:

$$c = \frac{\pi d^3}{6L^3} \quad \text{or} \quad \frac{L}{d} = \sqrt[3]{\frac{\pi}{6c}} \quad \text{or} \quad \frac{X+d}{d} = \sqrt[3]{\frac{\pi}{6c}} \quad (4)$$

where  $c$  is the volume fraction,  $L$  is the distance between particle centres,  $X$  is the distance between particle surfaces and  $d$  is the particle diameter (See figure 1).

In order to extend this work to investigate the effects at lower concentration values,  $10^{-4}$ , which is common in many dilute phase industrial flows, a full CFD study of this work was undertaken. To gain confidence in the ability of the software to predict the trends outside of the experimental work, validation of Liang's work [1] will also be presented. The extension will include the individual effects of particle aligned both perpendicular and parallel to the flow direction, and also the final set of results will pertain to an infinite matrix of particles.

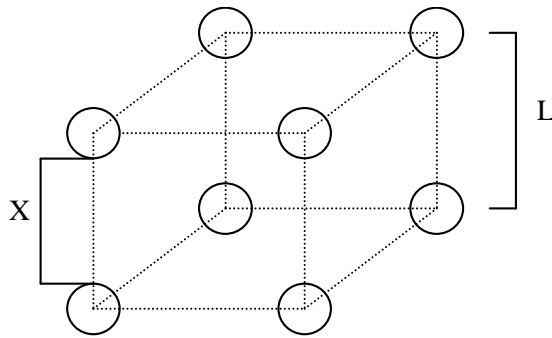


Figure 1 Particle Arrangement assuming even distribution.

### Governing Equations

As the range of Reynolds numbers of the simulated flows in this study are well within the bounds for laminar flow, the continuity and momentum equations take the forms:

$$\nabla \cdot \mathbf{U} = 0 \quad (5)$$

$$\nabla \cdot (\rho \mathbf{U} \mathbf{U}) = -\nabla p + \mu \nabla^2 \mathbf{U} \quad (6)$$

where  $\mathbf{U}$  is the velocity vector and  $p$  is the pressure. Boundary conditions will be discussed within the different models.

### Results and Discussion

#### Model Validation

In order to extend the work experimental work of Liang [1], it was necessary to simulate the published experimental results to give confidence that CFX 5.6 could accurately predict the flows and forces. The set-up consisted of three co-aligned particles of 1.58cm diameter inside a plexi-glass circular pipe of 15.24 cm diameter.

To accurately replicate the experimental conditions, a fully developed laminar pipe flow condition is used at the inlet boundary:

$$u = u_0 \left( 1 - \frac{r^2}{R^2} \right) \quad (7)$$

where  $u_0$  is the flow velocity at the centre of the pipe. No slip wall boundary conditions were applied to the particle surface and the pipe walls.

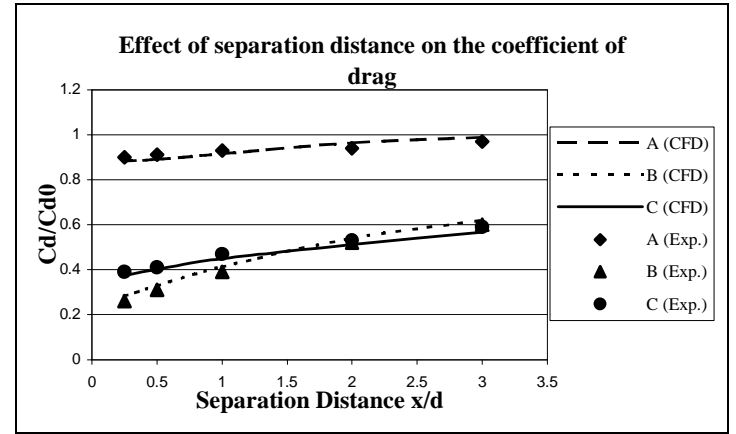


Figure 2 Validation of Liang's Experimental work at  $Re=54$

The fluid used in both the experiments and simulation was a glycerin/water solution approximately 82% glycerin with a density of  $1206 \text{ kg/m}^3$  and a viscosity of  $0.057$ . For consistency to same fluid was used for all models in this paper.

Figure 2 shows the comparison between the experimental work of Liang [1] and the CFD results where A, B and C refer to the leading, middle and trailing particles respectively. It can be seen that the present simulation quite accurately replicates the experimental results even picking up the region at a separation distance of approximately 1.5 where the middle starts to experience more drag than the trailing particle.

#### Model I.

This model contains an infinite number of particles co-aligned with the flow direction. A single particle was simulated using wall boundaries, with free slip boundary conditions, at a distance of 20 particle diameters to ensure negligible effects on the flow results. A periodic boundary condition was utilized in the stream wise direction and a body force is applied to the fluid to ensure that the momentum was conserved throughout the simulation. The fluid field was initialized with a  $u$  velocity as no inlet boundary conditions were specified. To ensure the simulation predictions were correct, this method was used to calculate the force on a isolated particle by conducting simulations with a separation distance of 60 and 80 particle diameters and compared the simulated forces with the theoretical forces using the standard approximating formula for  $C_D$ . The error difference between the CFD results and the theoretical values were within 3%, and given the fact that the formula for  $C_D$  is only an approximation it would be virtually impossible to expect any greater accuracy.

The results from this model (See Figure 3) show that at smaller separation distances, the  $C_D/C_{D0}$  ratio becomes much smaller than unity, due manly to the fact that the fluid does not have time to return to its previously uniform state before it encounters the next particle. As the Reynolds number increases this difference becomes greater. Figure 3 shows that even up to a separation distance of 20 particle diameters, the limit of this study, that there is still a noticeable effect especially at higher Reynolds numbers.

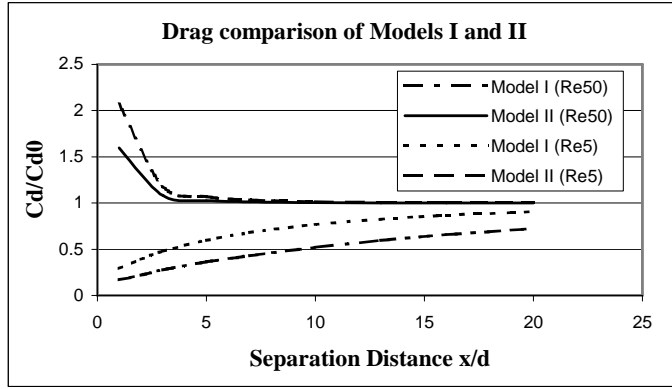


Figure 3 Comparison of Drag Coefficients for Models I and II

### Model II.

Model II consists of a single line of infinite particle along perpendicular to the flow direction. This model has been simulated using symmetry boundaries on the four walls running parallel to the flow. Although grid independency was completed for all models, Model II required a geometry independence test also. A number of different stream wise length models were tested to ensure that the drag force results were unaffected. It was found that as long as the stream wise length is at least twice as long as the separation distance, the results were unaffected. As in the stream wise direction, only a single particle was being simulated, the standard inlet and outlet boundary conditions were utilised. A uniform velocity profile was applied to the inlet boundary and a pressure boundary to the outlet. The results show that at small separation distances (See Figure 3) the drag experienced by the particle is drastically increased due to the squeezing effect of the flow as the flow area is reduced around the particle. As the coefficient of drag is highly affected by Reynolds number, it is worth noting that a lower Reynolds numbers the squeezing effect more pronounced. Depending on Re number, the effects of side neighbouring particles becomes negligible at a separation distance between 5-10 particle diameters.

### Model III.

Model III consists of a combination of Models I and II representing an infinite matrix of particles. Figure 4 shows that the effect of neighbouring particle perpendicular to flow cause a dramatic rise in the experienced drag force due to the squeezing of the flow between the particles as mentioned in Model II.

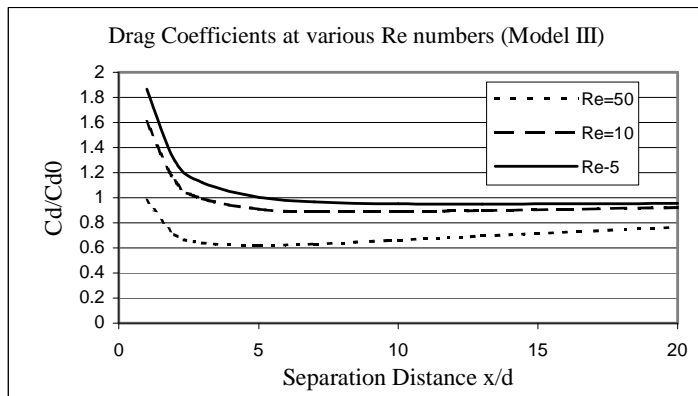


Figure 4 Drag Coefficients for Model III at Various Reynolds numbers.

Also beyond a separation distance of 5 particle diameters the  $C_D/C_{D0}$  ratio slowly approaches unity. This is due to influence of results witnessed in Model I, although it must be pointed out that the  $C_D/C_{D0}$  ratios are higher than those seen in Model I. This

difference has been highlighted in figure 5. In figure 5 the influence of Model II can be seen to be negligible but there is significance difference between Models I and III. This difference means that although not noticeable in Model II, the effects of neighbouring perpendicular particles do indeed effect the flow structure further downstream than first thought.

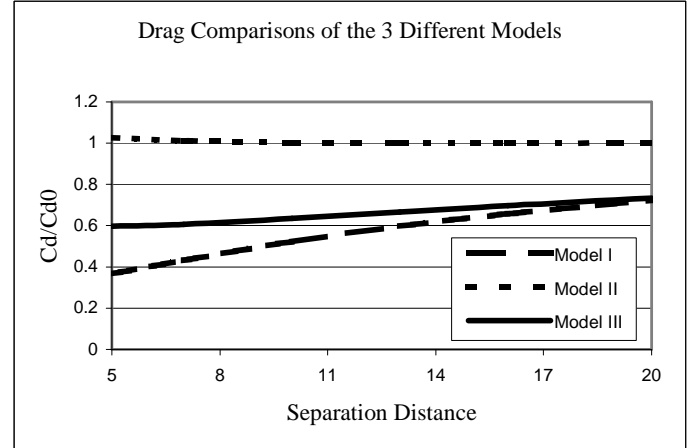


Figure 5 Comparison of the drag coefficient of the 3 models at Re=50

Figure 6 shows the normalised velocity contours of comparative simulations of Models I and III (Re = 20 and separation distance = 16d). The contours of model III carry over the squeezing effect so noticeable in the results of Model II, with the individual contours being smaller in both horizontal and vertical directions. These smaller contours mean that the average velocity in the vicinity of the particle is higher and as such we see higher drag forces experienced than those seen in Model I.

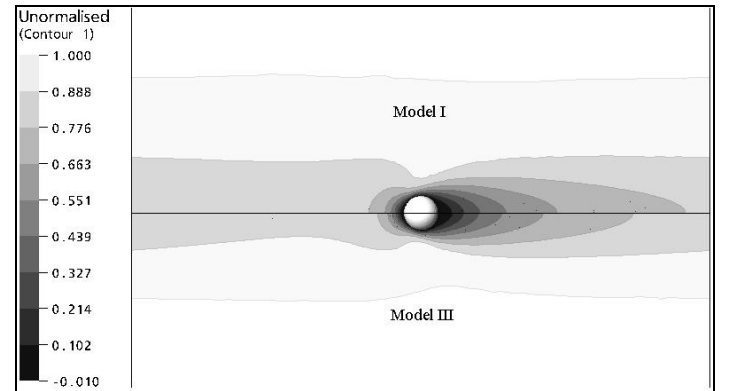


Figure 6 The Velocities at Re=20 for Models I and III

### Curve Fitting

To development of a new approximation for  $C_D$  that is a function of Reynolds number and particle volume fraction, a Least Squares Curve Fitting program was used. The generic form of the equation was chosen as:

$$C_D = \frac{24}{Re} \left( 1 + 0.15 Re^{0.687} + a \left[ \text{Log} \left( \sqrt[3]{\frac{\pi}{6C}} \right) \right]^b + c [\text{Log}(Re)]^d \right) \quad (8)$$

where C is the particle volume fraction, Re is the local particle Reynolds number and a, b, c and d are unknown constants. Solving for these unknowns, the equation that best fits the data was found to be:

$$C_D = \frac{24}{Re} \left( 1 + 0.15 Re^{0.687} + 0.000353 \left[ \log \left( \sqrt[3]{\frac{\pi}{6C}} \right) \right]^{15.93} - 0.16 [\log(Re)]^{3.62} \right) \quad (9)$$

The above is valid for re numbers ranging from 1 to 50 and particle volume fractions ranging from 0.00005 to 0.01. It is appropriate to specify these limits on the volume fraction because at higher volume fractions, the Lagrangian particle tracking is less accurate due to the lack of particle-particle interactions, which become the dominant factor in particle motion.

### Conclusion

A validating study of Liang's experimental work was conducted to test the ability of CFX 5.6 to predict flow patterns and drag forces on three co-aligned particles at several separation distances and Reynolds numbers. The study showed that the software was able to quite accurately predict the drag forces and even picked up the region highlighted in the experimental work where the middle particle began to experience more drag than the trailing particle. This validation gave confidence to extend the work to larger separation distances corresponding to lower particle volume fraction so as to develop a new coefficient of drag approximation to include the effects of volume fraction as well as Reynolds number. Three model configurations were studied to examine the individual effects of particle arrangement on the experienced drag of a particle. Model I consisted of an infinite number a co-aligned stream wise particles and results showed that a significant reduction in drag force was experienced by the particle, compared to that of an isolated particle, especially at small separation distances and higher Reynolds numbers. Model II consist of an infinite line of particles perpendicular to the flow direction. At very close separation distances, the experienced drag force increased due to increase in velocity as the flow is forced between the neighbouring particles. Beyond a separation distance of 5-7 particle diameters, the effects become negligible on the measured particle. But to the contrary when the two models were combined, forming Model III, an infinite matrix of particles, the effects of the side particles seem to have an effect on particles downstream up to 20 particles diameters

downstream. Comparing Models I and III a distinguishable difference is noticed in reduction of the drag force seen in Model I. A new approximation for the coefficient of drag for use with dilute flows has been developed according to the data of this study.

### Acknowledgements

The author gratefully acknowledges the financial and other support received for this research from the Cooperative Research Centre (CRC) for Clean Power from Lignite, which is established and supported under the Australian Government's Cooperative Research Centres program.

Also the author would to acknowledge the financial support of the Australian Postgraduate Award (APA) through Swinburne University of Technology.

### References

- [1] Liang, S-C., Hong, T. and Fan, L-S. Effects of Particle Arrangements on the Drag Force of a Particle in the Intermediate Flow Regime. *Int. J. Multiphase Flow*, **22**, 1996, 285-306.
- [2] Kuan, B. and Schwarz, P. Numerical prediction of particulate flows with dilute suspension in a vertical upflow circular duct: A parametric study. DMR-1930, CSIRO-Minerals, Clayton, Australia, 2002.
- [3] Lee, K. C. Aerodynamic interaction between two spheres at Reynolds numbers around  $10^4$ . *Aeronaut. Q.* **30**, 1979, 371-385.
- [4] Tsuji, Y., Morikawa, Y. & Fujiwara, Y. Pipe flow with solid particles fixed in space. *Int. J. Multiphase Flow*, **11**, 1985, 177-188.
- [5] Tsuji, Y., Morikawa, Y. & Terashima, K. Fluid-dynamic interaction between two spheres. *Int. J. Multiphase Flow*, **8**, 1982, 71-82.
- [6] Zhu, C., Liang, S.-C. & Fan, L.-S. Particle wake effects on the drag force of an interactive particle. *Int. J. Multiphase Flow*, **20**, 1994, 117-129.



## Periodic Forcing of Baroclinic Basin-Scale Waves in a Rotating Stratified Basin

G. W. Wake<sup>1</sup>, J. Gula<sup>2</sup> and G. N. Ivey<sup>1</sup>

<sup>1</sup>Centre for Water Research, Faculty of Engineering, Computing and Mathematics  
The University of Western Australia, WA, 6907 AUSTRALIA

<sup>2</sup>Ecole Normale Supérieure de Cachan  
61 Avenue du Président Wilson, Cachan, 94235 FRANCE

### Abstract

A laboratory study is used to investigate the baroclinic basin-scale response to an imposed external periodic forcing. It is shown that near-resonant periodic forcing results in the generation of Kelvin and Poincaré modes of the basin which satisfy the initial condition as well as a forced response. Forcing at the resonant frequency results in the amplification of the Kelvin mode as well as higher harmonics of the forcing frequency, thus providing a mechanism by which energy may be transferred directly from a periodic basin-scale external forcing to higher frequency internal waves. Despite the resonant amplification of the Kelvin wave, there is little suggestion of nonlinear steepening of the basin-scale wavefront and the transfer of energy to higher frequency waves previously noted in the non-rotating analogue of the experimental study considered here.

### Introduction

The hydrodynamics of small to medium stratified water bodies unaffected by rotation has been studied extensively (for a detailed review see [9]). Recent work has noted that a single basin-scale external forcing event (due to the wind) excites a baroclinic basin-scale wave response which exhibits nonlinear steepening of the wavefront resulting in the transfer of up to 20% of input energy to shorter wavelength waves after some time [8, 5]. These shorter wavelength waves may then propagate to the lake boundary where they break, resulting in enhanced vertical transport of pollutants in this region [13, 4]. The temporal evolution and, hence, the energy pathways of these basin-scale waves was found to be dependent on the amplitude of the initial forcing and the ambient stratification [8].

In large stratified lakes, the hydrodynamics are influenced by the Earth's rotation, so that the progressive baroclinic response to a single basin-scale external forcing event consists of basin-scale Kelvin and Poincaré waves which propagate in a cyclonic or anticyclonic fashion around the lake boundary [7, 1]. A recent laboratory study [14] demonstrated that in a circular domain, the temporal evolution of the Kelvin and Poincaré waves excited by a single forcing event was essentially linear with frictional effects at the boundaries steadily dissipating wave energy. The authors concluded that rotation acts, via Ekman dynamics, to damp the wave motion before one can observe significant nonlinear behaviour associated with the basin-scale wave.

Field observations in large stratified water bodies subject to periodic forcing by the wind have noted amplification of the gravest natural mode of the basin (a Kelvin wave in most instances), when the forcing events occur at approximately the resonant frequency [2, 11]. Resonant forcing of the wave response may result in a sufficient increase in amplitude that nonlinear wave behaviour (e.g., steepening of the wavefront, wave/wave interactions) may be observed which, in turn, would modify the energy pathways for the basin-scale waves and may provide an explanation for the high frequency waves observed in large stratified lakes [12, 4].

The objective of this paper is to use a laboratory experiment to determine the influence of periodic forcing on the energy pathways of baroclinic basin-scale waves in rotating stratified basins.

### Laboratory Facility

The experiments were conducted in a 95 cm diameter cylindrical perspex tank of depth 50 cm filled with a two-layer density stratified fluid. The tank was mounted on a rotating turntable that revolved counterclockwise at a constant rate  $\Omega = f/2$  (figure 1). In a typical experiment, the tank was filled with fresh water to the desired upper layer depth and allowed to spin up into solid body rotation. A saline solution was then carefully introduced beneath the lighter, fresher water until the desired lower layer depth was achieved. A semi-cylindrical perspex insert (closed at the bottom), attached via a pulley system to a small DC motor mounted on the rotating turntable frame, was initially positioned at the free surface over one half of the circular domain.

A basin-scale external forcing was modelled by oscillating the insert, using an eccentric crank and arm attached to the DC motor, so that over one forcing period the free surface over half of the tank was depressed 1.5 cm before being restored to its initial position. The observed response to such a forcing was predominantly baroclinic in nature. Periodic forcing was obtained by repeatedly driving the insert at a constant frequency of oscillation  $\sigma$ . The interface displacement created by forcing the free surface was sampled at 5 Hz at three positions by ultrasonic internal wave gauges [10] that were positioned along a radial transect perpendicular to the insert (figure 1).

The radius of the semi-cylindrical forcing mechanism was equal to the radius  $R_0$  of the cylindrical tank, as shown in figure 1. The baroclinic Rossby radius of deformation is given by  $R = c_0/f$  where  $c_0 = (g'H_2/(H_1 + H_2))^{1/2}$  is the baroclinic phase speed and  $g' = g(\rho_2 - \rho_1)/\rho_2$ , where  $g$  is acceleration due to gravity and  $\rho_2$  and  $\rho_1$  is the density of the upper ( $H_1$ ) and lower ( $H_2$ ) layer depths respectively, thus defining the Burger number  $S = R/R_0$ , that provides a measure of the relative importance of stratification versus rotation [1]. The inertial frequency  $f$  and the baroclinic phase speed  $c_0$  where varied so that  $S$  varied between 0.5 and 0.25. The total fluid depth was 20 cm while the ratio of the layer depths  $H_1/H_2 = 1$ . All densities were measured with a digital densimeter.

### Timescales

The experimental configuration presented in figure 1 suggests three timescales that may be important in determining the baroclinic basin-scale wave response to periodic forcing.

The time taken for rotation to influence the hydrodynamics is

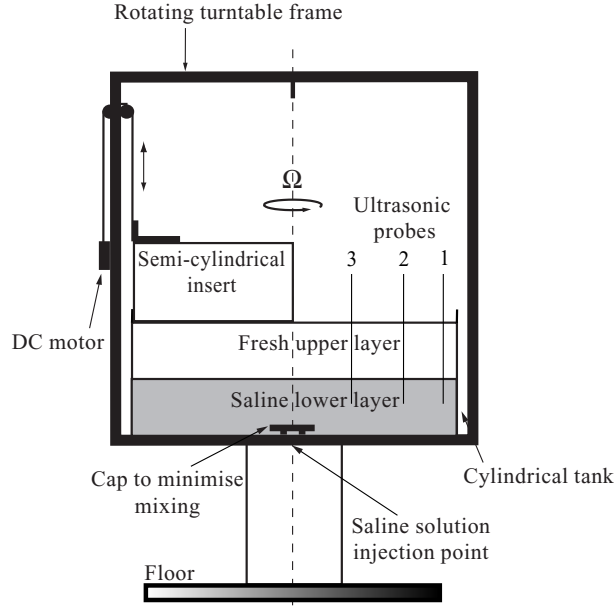


Figure 1: The experimental facility. The three ultrasonic wave gauges were positioned 3 cm, 13 cm, and 38 cm from the tank sidewall.

given by the inertial period

$$T_I = \frac{2\pi}{f}. \quad (1)$$

The closed nature of the circular basin introduces a second timescale

$$T_N = \frac{2\pi}{\omega}, \quad (2)$$

where  $\omega$  is the frequency of the gravest natural mode of the basin (a Kelvin wave for the range of  $S$  considered here). This timescale characterizes the time taken for the Kelvin wave to propagate around the basin.

The periodic nature of the forcing introduces a third timescale

$$T_F = \frac{2\pi}{\sigma}, \quad (3)$$

where  $\sigma$  is the frequency of the forcing.

## Results

### Single Forcing Event

Consider first the baroclinic response following a single oscillation of the forcing mechanism (step forcing). Interface displacement and time series measured by the radial array of ultrasonic wave gauges are presented in figure 2 (a) for  $S = 0.5$ . The transient response to the forcing event is similar to the laboratory experiments of [14], consisting of multiple frequencies which decay in time with no wave motion evident after  $30 T_I$ . Comparison of time series between positions 1 and 3 clearly shows that the interface displacement amplitude decays offshore. Power spectra of the interface displacement time series in figure 2 (a) is shown in figure 2 (b). Two waves of significance can be identified for this run: a sub-inertial (Kelvin) and a super-inertial (Poincaré) wave with non-dimensional frequencies ( $\omega/f$ ) of 0.55 and 1.51 respectively.

The frequencies of the natural modes for a circular basin containing a two-layer stratification can be predicted using the

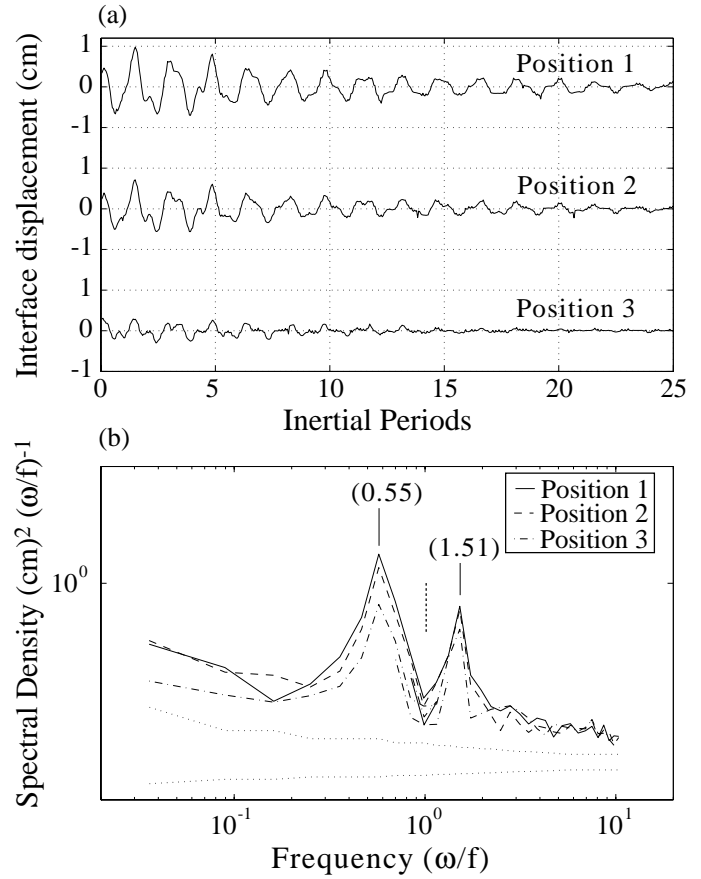


Figure 2: (a) Time series of the interface displacement for  $S = 0.5$  following a step forcing. (b) Power spectra of the interface displacements shown in (a). The wave frequency  $\omega$  is scaled by  $f$  with the dashed vertical line identifying the inertial frequency  $f$ . Spectra have been smoothed in the frequency domain to improve confidence, with the 95% confidence level is given as the difference between the two dotted lines at a prescribed frequency [3].

dispersion relations derived by [7]. For  $S = 0.5$ , the gravest mode of the basin is an azimuthal mode one, radial mode one Kelvin wave predicted to have a non-dimensional frequency of 0.65 while the azimuthal mode one, radial mode one Poincaré wave has a non-dimensional frequency of 1.51. The good agreement between observed and predicted frequencies suggests (see also [14]) that such a frequency comparison can be used to identify the structure of the basin-scale modes observed following a single forcing event

### Periodic Forcing

The baroclinic response subject to continuous forcing is illustrated in figure 3. Comparing the response to a step forcing presented in panel (a) with that observed for periodic forcing shown in panel (b) it is clear that there is an amplification of the interface displacement with the wave period being determined by the forcing period  $T_F$ . Once the forcing has ceased, however, the wave period is determined by the period of gravest (Kelvin) mode of the basin  $T_N$  and the rate of internal wave decay is comparable to what is observed following a single forcing event. Moreover, the baroclinic response appears to behave in an analogous fashion to a damped mass-spring system. In particular, when the forcing period  $T_F$  is similar to the period of gravest (Kelvin) mode of the basin  $T_N$ , there is evidence of wave beating during continuous forcing (see figure 3 (b)). When the

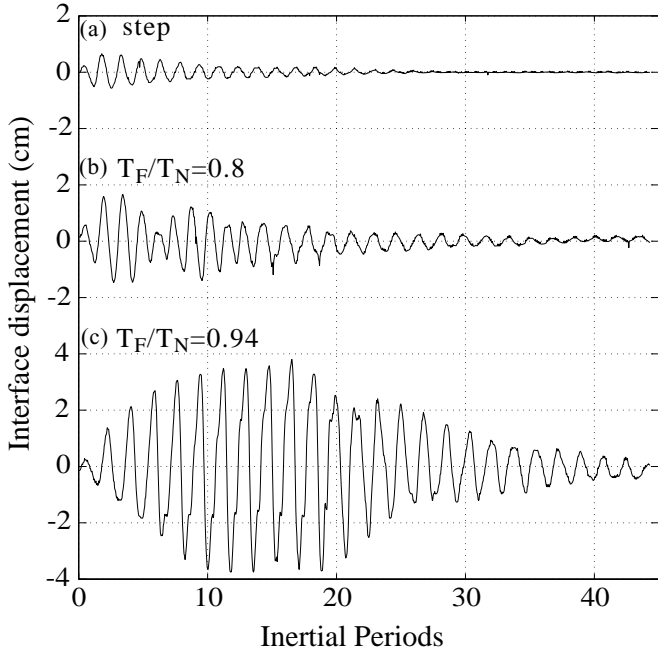


Figure 3: Time series of interface displacement recorded at position 1 for  $S = 0.5$  subject to (a) a step forcing (b) 10 forcing events with  $T_F/T_N = 0.8$  (c) 10 forcing events with  $T_F/T_N = 0.94$ .

non-dimensional forcing period  $T_F/T_N \approx 1$ , resonant forcing is observed, with a noticeable amplification of the interface displacement which reaches a steady state after approximately 5 forcing events and is sustained for the duration of the periodic forcing event (see figure 3 (c)).

Figure 4 demonstrates the amplification of the interface displacement as  $T_F/T_N \rightarrow 1$ . Note that maximum amplification is achieved when the dimensionless forcing period is slightly less than 1 ( $T_F/T_N = 0.94$ ), due to the influence of frictional effects, which is consistent with analytically derived results for the classical damped mass-spring system forced at resonance [6]. As noted earlier, frictional dissipation by complicated Ekman dynamics plays an important role in determining the hydrodynamics in the current experimental configuration [14].

Now consider the power spectra of interface displacement time

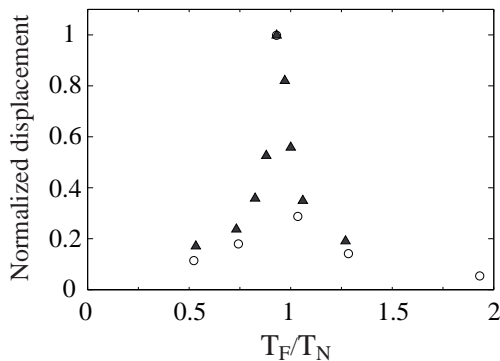


Figure 4: Normalized interface displacement recorded at position 1 as a function of the dimensionless forcing period  $T_F/T_N$  for  $S = 0.5$  (filled triangles) and  $S = 0.25$  (circles). Steady state interface displacements were measured after 20 forcing events and are normalized by the interface displacement at resonance  $T_F/T_N = 0.94$ .

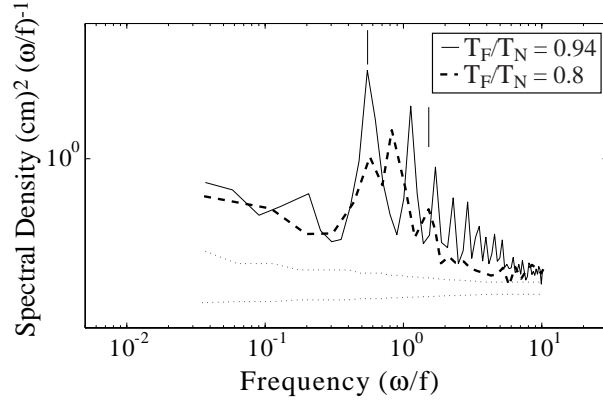


Figure 5: Power spectra of the interface displacement recorded at position 1 for  $S = 0.5$  subject to 20 forcing events with  $T_F/T_N = 0.8$  and  $T_F/T_N = 0.94$ . The solid vertical lines indicate the frequency of the natural modes of the basin (see figure 2 (b)) which satisfy the imposed initial condition. Spectra were smoothed in a similar manner to figure 2

series following near-resonant ( $T_F/T_N = 0.8$ ) and resonant ( $T_F/T_N = 0.94$ ) periodic forcings presented in figure 5. As noted earlier in figure 2, two modes of the basin are observed following a step forcing: a Kelvin and Poincaré wave. When  $T_F/T_N = 0.8$ , these natural modes of the basin are observed but there is also a third peak which dominates the power spectra corresponding to the forcing frequency at  $\omega/f = 0.7$ .

When forcing at the resonant frequency, the dominant spectral peak is now associated with the Kelvin wave (the frequency of which now coincides with the forcing frequency) but at least 4 other spectral peaks can be clearly identified with non-dimensional frequencies of 1.1, 1.66, 2.24, and 2.80, respectively. The non-dimensional forcing frequency is 0.55 (the Kelvin wave frequency), suggesting that the higher frequency waves are harmonics of the resonant forcing frequency.

The interface displacement time series observed when forcing at the resonant frequency can be bandpass filtered to isolate the contribution of the Kelvin wave and the higher frequency harmonics. The filtered signals for the Kelvin wave and the first harmonic of the forcing frequency are presented in figure 6. It is evident that forcing at the resonant frequency not only results in amplification of the gravest mode of the basin but also essentially simultaneously the first harmonic until a steady state interface displacement is achieved which is then sustained until the periodic forcing ceases.

Nonlinear steepening of the basin-scale wavefront and the subsequent transfer of energy to higher frequency waves after some time, previously noted in non-rotating stratified basins, does not readily explain these observations due to the fact that energy resides in the higher frequency waves almost immediately after initiation of the resonant forcing (see figure 6 (b)). Instead, the results presented here suggest that energy may be transferred directly from the basin-scale external forcing to higher frequency internal waves which are harmonics of the resonant forcing frequency.

## Conclusions

We have investigated the baroclinic basin-scale wave response to periodic forcing in a rotating stratified basin. It was demonstrated that the response was analogous to a damped string-mass system with continuous forcing at near-resonant forcing resulting in the generation of Kelvin and Poincaré modes of the basin

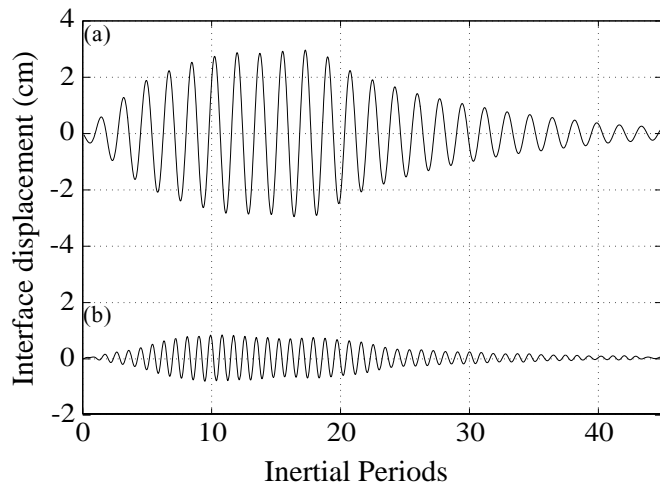


Figure 6: Bandpass filtered time series of interface displacement recorded at position 1 for  $S = 0.5$  subject to 10 forcing events with  $T_F/T_N = 0.94$  for (a) the Kelvin wave, (b) first harmonic of the forcing frequency.

which satisfy the initial condition as well as a forced response. Forcing at the resonant frequency resulted in the amplification of the Kelvin mode as well as higher harmonics of the forcing frequency thus providing a mechanism by which energy may be transferred directly from a periodic basin-scale external forcing to higher frequency internal waves. The exact nature of this transfer mechanism remains to be determined and will be the focus of subsequent studies. Despite the resonant amplification of the Kelvin wave, there was little suggestion that this mechanism was associated with nonlinear steepening of the basin-scale wavefront and the transfer of energy to higher frequency waves.

#### Acknowledgements

This research was funded by the Australian Research Council and the Centre for Sustainable Mining Lakes and forms Centre for Water Research reference ED1867.1 GW.

#### References

- [1] Antenucci, J. P. and Imberger, J., Energetics of long internal gravity waves in large lakes, *Limnol. Oceanogr.*, **46**, 2001, 1760–1773.
- [2] Antenucci, J. P. and Imberger, J., The seasonal evolution of wind/internal wave resonance in Lake Kinneret, *Limnol. Oceanogr.*, **48**, 2003, 2055–2061.
- [3] Bendat, J. S. and Piersol, A. G., *Random Data: Analysis and Measurement Procedures*, Wiley, New York, 2000, third edition.
- [4] Boegman, L., Imberger, J., Ivey, G. N. and Antenucci, J. P., High-frequency waves in large stratified lakes, *Limnol. Oceanogr.*, **48**, 2003, 895–919.
- [5] Boegman, L., Ivey, G. N. and Imberger, J., The energetics of large-scale internal wave degeneration in lakes, *J. Fluid Mech.*, submitted for review.
- [6] Boyce, W. E. and DiPrima, R. C., *Elementary differential equations and boundary value problems*, Wiley, New York, 1992, fifth edition.
- [7] Csanady, G. T., Large-scale motion in the Great Lakes, *J. Geophys. Res.*, **72**, 1967, 4151–4162.
- [8] Horn, D. A., Imberger, J. and Ivey, G. N., The degeneration of large-scale interfacial gravity waves in lakes, *J. Fluid Mech.*, **434**, 2001, 181–207.
- [9] Imberger, J., 'Flux paths in a stratified lake - a review' in *Physical Processes in Lakes and Oceans*, AGU Press, 1998.
- [10] Michallet, H. and Barthélemy, E., Ultrasonic probes and data processing to study interfacial solitary waves, *Experiments in Fluids*, **22**, 1997, 380–386.
- [11] Rueda, F. J., Schladow, S. G. and Ó. Pálmarsson, S., Basin-scale wave dynamics during a winter cooling period in a large lake, *J. Geophys. Res.*, **108**, 2003, art. no. 3097.
- [12] Saggio, A. and Imberger, J., Internal wave weather in a stratified lake, *Limnol. Oceanogr.*, **43**, 1998, 1780–1795.
- [13] Thorpe, S. A., Turbulence and mixing in a Scottish loch, *Phil. Trans. P. Soc. Lond. A*, **286**, 1977, 125–181.
- [14] Wake, G. W., Ivey, G. N. and Imberger, J., The temporal evolution of baroclinic basin-scale waves in a rotating circular basin., *J. Fluid Mech.*, in Press.

## An Internal Solitary Wave Parameterization for Hydrodynamic Lake Models

L. Boegman, G. N. Ivey and J. Imberger

Centre for Water Research, The University of Western Australia, WA, 6009 AUSTRALIA

### Abstract

A laboratory based closure scheme is presented to parameterize the evolution and subsequent degeneration of high-frequency internal waves in geophysical numerical models. These waves are typically not resolved by discretized governing equations. Our results are suitable for inclusion into field-scale hydrodynamic and water-quality models applied to lakes or reservoirs. In such systems the high-frequency waves result from the non-hydrostatic degeneration of the wind forced basin-scale internal seiche and are believed to sustain a quasi-steady flux of 20% of the introduced wind energy to the benthic boundary layer.

### Introduction

Reservoirs are constructed to impound water for later release, hydroelectric power generation and flood control. Reservoirs and natural lakes are often subject to water-quality problems, for example those situated in agricultural regions may suffer nutrient loads via runoff that are in excess of the assimilative capacity of the waterbody. A primary tool for diagnosing poor water-quality and formulating remediation strategies is the coupled hydrodynamic and water-quality model [4]. The predictive capability of such models is limited by the ability of the hydrodynamic scheme to simulate the temperature, salinity and physical transport processes affecting the biogeochemical cycle. In turn, practical field-scale hydrodynamic models (e.g. CE-QUAL-W2, DYRESM, ELCOM and POM) are hindered by their inability to resolve small-scale dynamics. Fortunately, the fundamental energy flux from the surface wind field to the basin-scale internal wave field may be adequately simulated [7]. However, modelling the down-scale degeneration of the basin-scale motions into high-frequency internal waves has not been addressed and remains a challenge to all modellers [6]. This degeneration process is not described by the governing hydrostatic equations [8] and the high-frequency waves typically have wavelengths of order 100 m [1], much smaller than the feasible grid spacing of field-scale hydrodynamic models [6].

The down-scale energy flux has significant implications for hydrodynamic modelling. Laboratory experiments suggest that in most lakes the basin-scale internal waves will degenerate into progressive solitary waves through nonlinear steepening [9]. During this process, up to 20% of the available potential energy (APE) input by the wind may be found in the solitary wave field [2]. As the high-frequency internal waves shoal upon sloping topography, up to 80% of the incident wave energy may be lost to dissipation and mixing [3] with between 5% and 25% [11] of the incident energy (1% to 5% of the APE) being converted through diapycnal mixing to an irreversible increase in the potential energy of the water column. The localized nature of these mixing events in space and time may strongly influence biogeochemistry within the littoral zone [10].

The aim of this paper is to parameterize the unresolved internal wave dynamics in terms of parameters that are easily computed from the resolved flow (e.g. wind speed and direction, boundary slope, quiescent stratification, etc.). This parameterization must accomplish the following.

- Quantify the energy transfer to progressive high-frequency internal waves.
- Determine the traveltime until the high-frequency internal waves shoal upon sloping topography.
- Quantify the energy loss from the incident high-frequency wave packet and the fraction of energy being converted through diapycnal mixing to an irreversible increase in the potential energy of the water column (mixing efficiency).
- Determine the position upon the slope where the waves break.

To do so we use results from the laboratory experiments by [11], [9], [2] and [3].

### The Internal Solitary Wave Parameterization

During the summer months a stratified lake will typically possess a layered structure consisting of an epilimnion, metalimnion and hypolimnion. If the vertical density gradient is abrupt through the metalimnion, the lake may be approximated as a simple two-layer system [9] of depth  $h_1$  and density  $\rho_1$  over depth  $h_2$  and density  $\rho_2$ , where  $H = h_1 + h_2$  is the total depth and  $L$  denotes the basin length. Internal waves may be initiated within a stratified lake by an external disturbance such as a surface wind stress  $\tau$ . This stress advects surface water toward the lee-shore, thus displacing the internal layer interface through a maximum excursion  $\eta_o$  as measured at the ends of the basin. The excursion is dependent upon the strength and duration of the wind event. A steady state tilt of the interface is achieved when a steady wind blows for at least one quarter of the fundamental seiche period (defined below) [13] and  $\eta_o$  may be calculated from the integral of the shear velocity  $u_* = \sqrt{\tau/\rho_o}$  as

$$\eta_o \approx \frac{Lu_*^2}{g'h_1}, \quad (1)$$

where  $\rho_o$  is a reference density and  $g' = g(\rho_2 - \rho_1)/\rho_2$  is the reduced gravity at the interface [12]. To first order, the APE introduced by the tilted interface is given as [2]

$$\text{APE} = \frac{16gL(\rho_2 - \rho_1)\eta_o^2}{\pi^4}. \quad (2)$$

Upon termination of the wind stress, the period of the fundamental basin-scale internal standing wave (or seiche) for the two-layer system is

$$T_i = \frac{2L}{c_o}, \quad (3)$$

where  $c_o = \sqrt{(g'h_1h_2)/(h_1 + h_2)}$  is the linear long-wave speed.

Moderate forcing ( $0.3 < \eta_o/h_1 < 1.0$ ) results in the development of a nonlinear surge and dispersive solitary wave packet (figure 1) [14, 9, 2]. The temporal development of the nonlinear

surge may be quantified by the nonlinearity parameter defined in [2] as

$$I = \frac{\alpha \eta_o}{c_o}, \quad (4)$$

where the nonlinear coefficient  $\alpha = \frac{3}{2}c_o(h_1 - h_2)/(h_1 h_2)$ . If the interface is at mid-depth,  $\alpha$  vanishes, steepening can not occur and there is no production of solitary waves. As the progressive nonlinear surge steepens, its length scale decreases until non-hydrostatic effects become significant and the wave is subject to dispersion. This occurs as  $t \rightarrow T_s$ , leading to the steepening timescale [9]

$$T_s = \frac{L}{\alpha \eta_o}. \quad (5)$$

Steepening is eventually balanced by dispersion and the surge degenerates into a high-frequency internal solitary wave packet. The horizontal length scale  $\lambda$  of a particular wave is [5]

$$\lambda^2 = \frac{12\beta}{a\alpha}, \quad (6)$$

where the dispersive coefficient  $\beta = \frac{1}{6}c_o h_1 h_2$ . Note the inverse relationship between the wavelength  $\lambda$  and amplitude  $a$  for the nonlinear waves and that  $a \sim \eta_o$  [8].

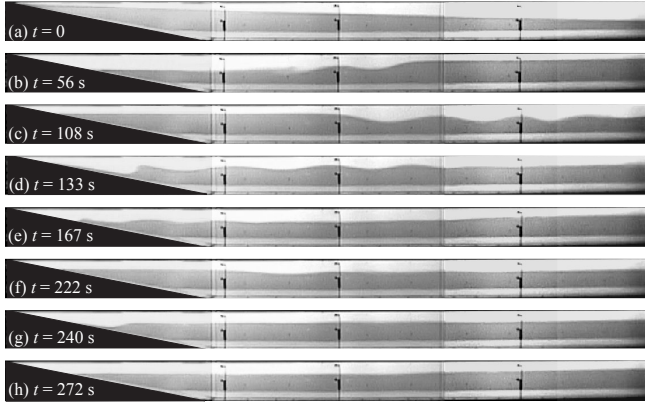


Figure 1: Video frames showing the wave field evolving from the initial condition of upwelling at the slope in (a). The surge and internal solitary wave packet are propagating to the right in (b), (c) and (f) and to the left in (d), (e) and (g). Wave breaking is shown to occur upon the slope. For this experiment  $h_1/H = 0.29$  and  $\eta_o/h_1 = 0.90$ . The apparent dye-free layer near the tank bottom is a spurious artifact of light reflection. Reproduced from [3].

#### Temporal energy transfer to high-frequency waves

From the laboratory experiments, we have quantified the temporal evolution of the energy in the high-frequency internal solitary waves. This was accomplished by integrating the square of the interfacial displacement associated with the passage of each wave. Interfacial displacement timeseries were recorded using ultrasonic wavegauges as depicted in figure 1. In figure 2a this energy is shown as contours normalized by the APE, where the vertical axis ( $\alpha \eta_o/c_o$ ) indicates the relative magnitudes of the linear and nonlinear components of the internal wave field [3] and the horizontal axis ( $T_i$ ) reveals how the system evolves in time.

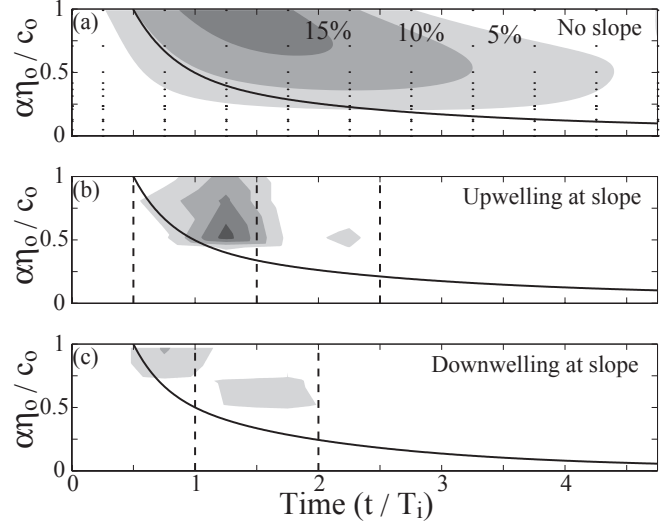


Figure 2: Evolution of the internal wave energy  $E_{ISW}/\text{APE}$ : (a) Normalized energy for the case of no slope. Contours are least-squares fit to the data points (indicated by  $\cdot$ ) as described in the text. Normalized energy for the initial conditions of (b) upwelling and (c) downwelling along a 0.145 slope. In all panels the contours are presented as a percentage of the APE introduced at  $t = 0$  with a contour interval of 5%. The ratio  $T_s/T_i$  for a particular  $\alpha \eta_o/c_o$  is indicated by  $—$ . The times at which the solitary wave packet shoals upon the sloping beach are denoted with  $- -$ . Reproduced from [3].

For systems where  $\alpha \eta_o/c_o \rightarrow 1$ , the energy in the solitary waves  $E_{ISW}$  is shown to increase to as much as 20% of the APE. For the experiments shown in this figure, the end walls of the domain were vertical, thus favouring wave reflection over breaking and the energy in the solitary wave packet was ultimately lost to viscosity on timescales of order  $3T_i$  to  $5T_i$ . The contours in figure 2a are calculated from the data points through fitting a third-order two-dimensional polynomial to the data in a least-squares sense with a RMS error of 3% of the APE. The equation for the polynomial is

$$\begin{aligned} \frac{E_{ISW}}{\text{APE}} = & 0.0169I^2T_i^3 - 0.0346I^2T_i^2 - 0.1693IT_i^2 \\ & - 0.2624I^2T_i + 0.1714I^2 + 0.0081IT_i^3 \\ & + 0.6896IT_i - 0.2301I - 0.0021T_i^3 \\ & + 0.0259T_i^2 - 0.0821T_i + 0.0292. \end{aligned} \quad (7)$$

#### Traveltime of the Progressive Internal Waves

The solitary wave packet evolves from the large-scale flow at  $t \approx T_s$  (figure 2a and [9]). This packet will first encounter sloping topography after traveltimes of  $T_s/T_i = 0.5, 1.5, 2.5$ , etc. and  $T_s/T_i = 1, 2, 3$ , etc. for the initial conditions of upwelling (figure 2b) and downwelling (figure 2c) along the slope, respectively [3]. Clearly, significant energy is lost from the high-frequency internal wave field due to wave breaking at the boundary. The actual time at which a particular solitary wave packet shoals, may be computed as the travletime appropriate to the forcing direction (upwelling or downwelling along the slope) subsequent to  $t = T_s$ .

#### Mixing and Dissipation Due to Wave Breaking

The ratio of the beach slope  $S$  to the wave slope ( $a/\lambda$ ) is commonly used to classify breaking surface waves. This ratio may



be expressed as the off-shore form of the Iribarren number  $\xi$ ,

$$\xi = \frac{S}{(a/\lambda)^{1/2}}. \quad (8)$$

The Iribarren number has also been shown to be appropriate for internal waves, describing the energy loss along the slope, the mixing efficiency and the breaker type [3]. However, the difficulty in measuring the unresolved parameters  $\lambda$  and  $a$  necessitates recasting  $\xi$  in terms of the resolved flow variables. To do so a knowledge of the internal wave profile is required.

In figure 3, published observations (as described in [2]) suggest that when the inverse Wedderburn number, which is given for our two-layer system as

$$W^{-1} = \frac{\eta_o}{h_1} \sim \frac{a}{h_1}, \quad (9)$$

is greater than 0.4 the internal solitary waves will have a  $\text{sech}^2$  profile and  $a/\lambda \sim \alpha\eta_o/c_o$  [2], hence (8) becomes

$$\xi_{\text{sech}} = \frac{S}{(\alpha\eta_o/c_o)^{1/2}}. \quad (10)$$

Conversely for  $W^{-1} < 0.4$ , the progressive internal waves will have a sinusoidal profile,  $a/\lambda \sim f\eta_o/c_o$  and (8) becomes

$$\xi_{\text{sin}} = \frac{S}{(f\eta_o/c_o)^{1/2}}. \quad (11)$$

From figure 3 we take the wave frequency  $f \sim 10^{-4}$  Hz.

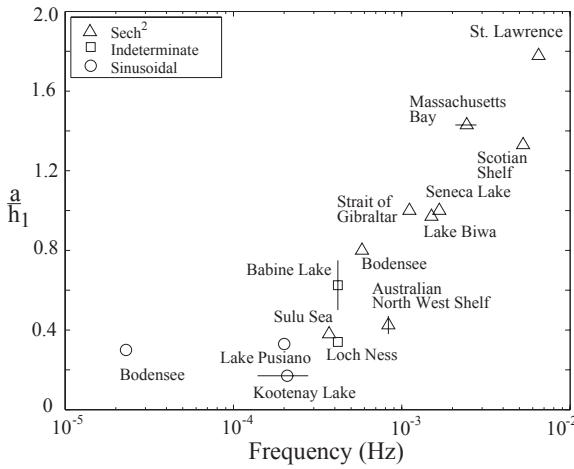


Figure 3: Observations of progressive internal waves as reported in [3]. A relationship between the wave nonlinearity ( $a/h_1 \sim \eta_o/h_1$ ), profile (see legend) and frequency ( $f$ ) is shown. Reproduced from [3].

The high-frequency internal solitary wave packets have been observed to break upon encountering sloping topography (figure 1). In figure 4, the reflection coefficient  $R = E_r/E_i$  (where  $E_r$  and  $E_i$  are the energy in the reflected and incident wave packets, respectively) and mixing efficiency are expressed as functions of  $\xi$  for individual breaking events (data from [11] and

[3]). For small  $\xi$ , the wave slope is steep relative to  $S$ , spilling breakers are observed,  $R \rightarrow 0$ , viscosity dominates and mixing efficiencies are small. Conversely, for waves with very large  $\xi$ ,  $R \rightarrow 1$ , buoyancy dominates and the collapsing breakers again induce minimal mixing. Intermediate to these extremes inertia dominates and plunging breakers develop with gravitational instabilities that drive mixing efficiencies peaking near 25%. As the incident waves contain as much as 25% of the APE, it implies that 6% of the APE may be converted by diapycnal mixing to an irreversible increase in potential energy in the near boundary regions.

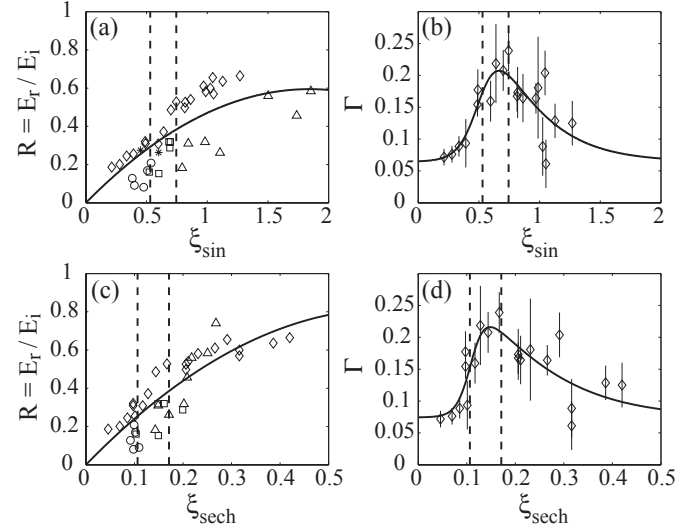


Figure 4: Reflection coefficient ( $R$ ), mixing efficiency ( $\Gamma$ ) and breaker type classified according to the various forms of the Iribarren number: (a) breaker type and  $R$  versus  $\xi_{\text{sin}}$ , (b) breaker type and  $\Gamma$  versus  $\xi_{\text{sin}}$ , (c) breaker type and  $R$  versus  $\xi_{\text{sech}}$  and (d) breaker type and  $\Gamma$  versus  $\xi_{\text{sech}}$ . The — lines demarcate the breaker classifications and are inferred in panels b and d from panels a and c, respectively. The lines of best fit are described in the text and the symbols are: ( $\circ$ ) spilling breakers, ( $\Delta$ ) collapsing breakers, ( $\square$ ) plunging breakers, ( $\diamond$ ) from [11] and ( $*$ ) Lake Pusiano. Reproduced from [3].

Using the least-squares regressions presented in figure 4, both  $R$  and  $\Gamma$  may easily be evaluated for a particular  $\xi$ . The regressions are

$$R(\xi) = a_1 \xi^2 + a_2 \xi \quad (12)$$

and

$$\Gamma(\xi) = b_1 + b_2 \left( \frac{1}{1 + \exp \left[ \frac{-(\xi - b_3 + b_4/2)}{b_5} \right]} \right) \times \left( 1 - \frac{1}{1 + \exp \left[ \frac{-(\xi - b_3 - b_4/2)}{b_6} \right]} \right). \quad (13)$$

In figure 4a and 4b ( $W^{-1} < 0.4$  and  $\xi \equiv \xi_{\text{sin}}$ ),  $a = [-0.1751 \ 0.6454]$  and  $b = [0.0646 \ 0.4863 \ 0.4913 \ -0.0747 \ 0.0820 \ 0.3385]$ . In figure 4c and 4d ( $W^{-1} > 0.4$  and  $\xi \equiv \xi_{\text{sech}}$ ),  $a = [-2.0852 \ 2.6105]$  and  $b = [0.0744 \ 0.3967 \ 0.1019 \ -0.0186 \ 0.0147 \ 0.1198]$ . Note that the standard error associated with (12) is approximately  $\pm 0.1$ .

### Breaker Position

As a wave travels along the slope it steepens,  $a$  increases and the streamlines approach vertical. During steepening, the maximum horizontal fluid velocity in the direction of wave propagation will increase more rapidly than the wave velocity and a limiting amplitude may be achieved where the velocities in the wave crest become equal to the phase velocity. This limit is defined as the *breaking limit* and the location on the slope where this limit is observed is the *breaking point*. In [3] the breaking limit is shown to occur along the slope where  $a \sim h_1$  (figure 5). Assuming the wave-slope interaction is sufficiently rapid that mixing and reflection do not occur prior to wave breaking, the breaking limit may be found for an initial wave characterized by the off-shore parameters  $a$  and  $\lambda$  (ie.  $a\lambda = \text{constant}$  [3]). Progressing incrementally along the slope in  $x$  according to  $h'_2 = H - h_1 - (H/L_s)x$ , where  $L_s$  is the slope length and the  $'$  denotes a quantity that is variable in  $x$ , we discretely evaluate  $c'_o$ ,  $\alpha'$  and  $\beta'$  with  $h_1 = \text{constant}$ . Substitution into (6) gives

$$\lambda' = \frac{12\beta'}{\alpha'a\lambda} \quad (14)$$

which may be rearranged as

$$a' = \frac{12\beta'}{\alpha'\lambda^2}. \quad (15)$$

Note the transformation of the wavelength-amplitude dependence in (6) to a wavelength-initial condition dependence in (14). Assuming the off-shore wave characteristics may be approximated as  $a \sim \eta_o$  and  $\lambda \sim c_o/(10^{-4}\text{Hz})$  for  $W^{-1} < 0.4$  or  $\lambda \sim \sqrt{12\beta/\eta_o\alpha}$  for  $W^{-1} > 0.4$ , equations (14) and (15) may be used to determine the location  $x$  along the slope where the breaking limit  $a' \sim h_1$  occurs.

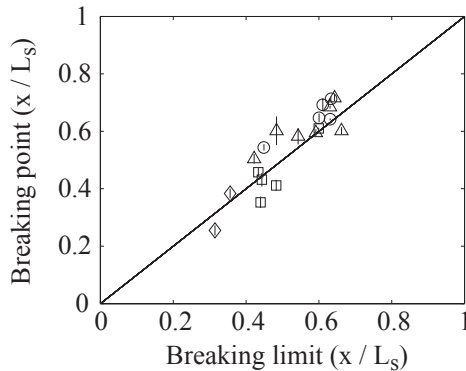


Figure 5: Theoretical breaking limit versus measured breaking point. The breaking limit is determined as the position on the slope where  $a' \sim h_1$  from (14) and (15). The symbols are as follows: ( $\circ$ ) spilling breakers, ( $\Delta$ ) collapsing breakers, ( $\square$ ) plunging breakers, ( $\diamond$ ) shoaling undular jump. Error bars denote uncertainty in determining the breaking point due to parallax (shows maximum and minimum position). Reproduced from [3].

### Conclusions

We have presented a parameterization for the inclusion of high-frequency internal waves into hydrodynamic lake models. This scheme accounts for the generation, propagation and breaking of the waves at the lake boundary. The parameterization is in

terms of the resolved time averaged quantities  $h_1$ ,  $h_2$ ,  $\rho_1$ ,  $\rho_2$ , the longitudinal wind direction (ie. upwelling or downwelling along the slope), the integral of  $\tau$  over  $t > T_i/4$  and the basin morphology  $L$  and  $S$ .

### Acknowledgements

We thank David Horn and Hervé Michallet for the raw data used to generate figure 2a and figure 4b and d, respectively. This research has been funded by the Australian Research Council. This paper forms CWR reference ED-1867-LB.

### References

- [1] Boegman, L., Imberger, J., Ivey, G. N. and Antenucci, J. P., High-frequency internal waves in large stratified lakes, *Limnol. Oceanogr.*, **48**, 2003, 895–919.
- [2] Boegman, L., Ivey, G. N. and Imberger, J., The energetics of large-scale internal wave degeneration in lakes, *J. Fluid Mech.*, (Accepted).
- [3] Boegman, L., Ivey, G. N. and Imberger, J., Experiments on shoaling internal waves in closed basins, *Limnol. Oceanogr.*, (Accepted).
- [4] Chapra, S. C., *Surface water-quality modeling*, McGraw-Hill, 1997.
- [5] Djordjevic, V. D. and Redekopp, L. G., The fission and disintegration of internal solitary waves moving over two-dimensional topography, *J. Phys. Oceanogr.*, **8**, 1978, 1016–1024.
- [6] Hodges, B. R., Imberger, J., Laval, B. and Appt, J., Modeling the hydrodynamics of stratified lakes, in proceedings *Hydroinformatics Conference*, Iowa Institute of Hydraulic Research, 2000.
- [7] Hodges, B. R., Imberger, J., Saggio, A. and Winters, K., Modeling basin-scale internal waves in a stratified lake, *Limnol. Oceanogr.*, **45**, 2000, 1603–1620.
- [8] Horn, D. A., Imberger, J. and Ivey, G. N., Internal solitary waves in lakes - a closure problem for hydrostatic models, in proceedings *11th Aha Huliko Hawaiian winter workshop - Internal gravity waves II*, University of Hawaii, 1999.
- [9] Horn, D. A., Imberger, J. and Ivey, G. N., The degeneration of large-scale interfacial gravity waves in lakes, *J. Fluid Mech.*, **434**, 2001, 181–207.
- [10] MacIntyre, S., Flynn, K. M., Jellison, R. and Romero, J. R., Boundary mixing and nutrient fluxes in Mono Lake, California, *Limnol. Oceanogr.*, **4**, 1999, 512–529.
- [11] Michallet, H. and Ivey, G. N., Experiments on mixing due to internal solitary waves breaking on uniform slopes, *J. Geophys. Res.*, **104**, 1999, 13467–13477.
- [12] Monismith, S. G., Wind-forced motions in stratified lakes and their effect on mixed layer shear, *Limnol. Oceanogr.*, **30**, 1985, 771–783.
- [13] Spigel, R. H. and Imberger, J., The classification of mixed-layer dynamics in lakes of small to medium size, *J. Phys. Oceanogr.*, **10**, 1980, 1104–1121.
- [14] Thorpe, S. A., Asymmetry of the internal seiche in Loch Ness, *Nature*, **231**, 1971, 306–308.

## Differential Diffusion: Often a Finite-Mixing Length Effect

Peter Nielsen & Ian A L Teakle

Department of Civil Engineering, The University of Queensland  
Brisbane, AUSTRALIA 4072, i.teakle@uq.edu.au

### Abstract

Many instances of differential diffusion, i.e., different species having different turbulent diffusion coefficients in the same flow, can be explained as a finite mixing length effect. That is, in a simple mixing length scenario, the turbulent diffusion coefficient has the form  $K = w_m l_m \left[ 1 + O\left(\frac{l_m}{L_c}\right)^2 \right]$  where,  $w_m$  is the mixing

velocity,  $l_m$  the mixing length and  $L_c$  the overall distribution scale for a particular species. The first term represents the familiar gradient diffusion while the second term becomes important when  $l_m/L_c$  is finite. This second term shows that different species will have different diffusion coefficients if they have different overall distribution scales. Such different  $L_c$ s may come about due to different boundary conditions and different intrinsic properties (molecular diffusivity, settling velocity etc) for different species. For momentum transfer in turbulent oscillatory boundary layers the second term is imaginary and explains observed phase leads of shear stresses ahead of velocity gradients.

### Introduction

Understanding and modelling natural and industrial processes requires in very many cases understanding of turbulent mixing. The present paper addresses an aspect of turbulent mixing, which is still not well understood namely, differential diffusion. The term differential diffusion refers to the observation of different turbulent diffusion coefficients  $K$  defined by

$$K = - \frac{\text{turbulent mixing flux density}}{\text{concentration gradient}} \quad (1)$$

for different species in a given flow.

In physical oceanography, the species in focus are usually, momentum, heat and salt, and differential diffusion of these has been argued by Gargett [4] to be an important player in many oceanographical processes. Laboratory experiments, e.g., Turner [13], Nagata & Komori [9] and Jackson & Rehmann [7] have shown differential diffusion of heat and salt. Turner [13] and Jackson & Rehmann [7] found  $K_{\text{heat}} > K_{\text{salt}}$ , and this has been rationalized, by Turner [13] and others, as being due to heat having a greater molecular diffusivity than salt. However, Nagata & Komori [9] found the opposite, i.e.  $K_{\text{heat}} < K_{\text{salt}}$ , in experiments which had a different geometry. Hence, differential diffusion cannot be totally due to differences in molecular diffusivity.

The idea that species with greater molecular diffusivity should diffuse more rapidly in turbulence has also been applied to various species in flame combustion by Kronenburg & Bilger [8]. Chanson ([1], [2]) has reported data, which show differential diffusion of momentum and bubbles in supercritical free surface flows. Differential diffusion of momentum and different sediment sizes has been documented for steady flows by Coleman [3] and Graf & Cellino [5] and for oscillatory flows by Nielsen [10] p 220.

Nielsen & Teakle [11] reconsidered the simple mixing length scenario of Figure 1, where parcels with vertical spacing  $l_m$ , the mixing length, are swapping positions traveling with vertical speed  $w_m$ , the mixing velocity.

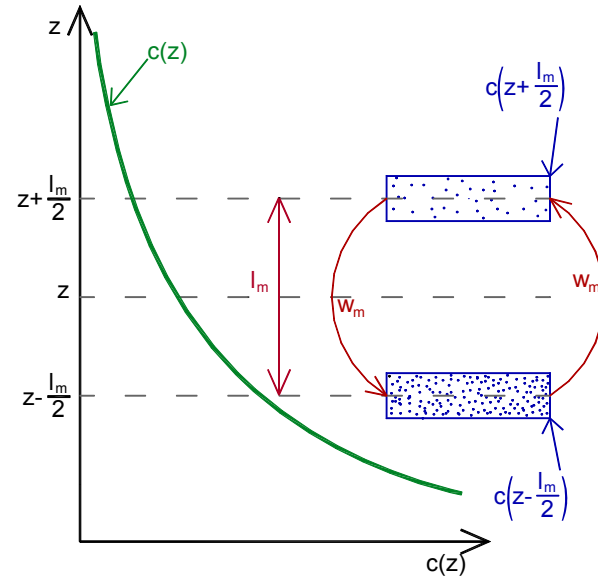


Figure 1: A simple mixing length scenario involving a single mixing length  $l_m$  and corresponding mixing velocity  $w_m$ .

The resulting flux density is then

$$\begin{aligned} q_m &= w_m \left[ c\left(z - \frac{l_m}{2}\right) - c\left(z + \frac{l_m}{2}\right) \right] \\ &= -w_m l_m \frac{dc}{dz} \left[ 1 + O\left(\frac{l_m}{L_c}\right)^2 \right] \end{aligned} \quad (2)$$

which, by the definition (1), gives the diffusion coefficient

$$K = w_m l_m \left[ 1 + O\left(\frac{l_m}{L_c}\right)^2 \right] \text{ of which the second term offers an}$$

explanation for differential diffusion as a finite mixing length effect. Examples are given below.

### Steady Sediment Suspensions

Consider sediment particles with a range of settling velocities  $w_s$  suspended in the same turbulent flow, and adopting velocity fluctuations with the same statistics as those of the fluid. The turbulent swapping process in Figure 1 then creates an upward flux density given by (2), which in a steady situation is balanced by the settling flux  $-w_s c(z)$  i.e.,

$$w_m \left[ c\left(z - \frac{l_m}{2}\right) - c\left(z + \frac{l_m}{2}\right) \right] - w_s c(z) = 0 \quad (3)$$

In general ( $w_m$ ,  $l_m$ ) may be functions of  $z$ . However, the essence of differential diffusion as a finite mixing length effect is captured by

the simple case of homogeneous turbulence, i.e., constant ( $w_m$ ,  $l_m$ ). In this case Equation (3) has solutions of the form

$$c(z) = C_o e^{-z/L_s} \quad (4)$$

with

$$L_s = \frac{l_m}{2 \sinh^{-1}(\frac{w_s}{2w_m})} \quad (5)$$

$$= \frac{l_m w_m}{w_s} \left[ 1 + \frac{1}{24} \left( \frac{w_s}{w_m} \right)^2 + \dots \right]$$

The corresponding diffusion coefficient is given by

$$K_s = \frac{q_m}{-\frac{dc}{dz}} = \frac{w_m [c(z - \frac{l_m}{2}) - c(z + \frac{l_m}{2})]}{-\frac{dc}{dz}} \quad (6)$$

$$= w_m l_m \left[ 1 + \frac{1}{24} \left( \frac{w_s}{w_m} \right)^2 + \dots \right]$$

This result quantifies differential diffusion for different sand sizes in homogeneous turbulence. It is however also in general qualitative agreement with data from river flows, where the turbulence is not homogeneous, see e.g., Coleman [3], Graf & Cellino [5]. Indeed, van Rijn [14] suggested the empirical correction factor

$$\beta = \frac{K_s}{v_t} = 1 + 2 \left( \frac{w_s}{u_*} \right)^2 \quad (7)$$

for dealing with the observed differential diffusion of momentum (with diffusion coefficient  $v_t$ ) and different sand fractions in natural rivers. Van Rijn's formula is seen to have the same dependence upon  $w_s/w_m \sim w_s/u_*$  as the finite mixing length result (6).

We acknowledge that the example, which leads to (6), does not deal with all details, i.e., in a natural scenario, particles with different settling velocities, and hence different response times  $w_s/g$ , do not get identical turbulent velocity statistics ( $\sim$  same  $w_m$ ). However, this is usually totally overshadowed by the finite-mixing-length-effect. That is, the two act in opposite directions, but all the experimental data show  $K_s$  to be an increasing function of  $w_s$  as predicted by the finite-mixing-length model.

### The importance of boundary conditions

The above example, of sediment particles with different  $w_s$  but statistically identical velocity fluctuations in homogeneous turbulence, can also be used to illustrate the importance of boundary conditions for the occurrence of differential diffusion. Consider point injections of such sediments into an infinite, homogeneous turbulence field, Figure 2. Each sediment type will then form a cloud, which sinks at an average rate of  $w_s$ . At the same time, each cloud grows in accordance with the theory of Taylor [12], i.e., the vertical extent  $\sigma_z$  of each cloud grows in accordance with

$$\sigma_z(t) = \sqrt{2 w'^2 \int_0^t \int_0^\theta \rho_{ww}(\tau) d\tau d\theta} \quad (8)$$

where  $\rho_{ww}$  is the autocorrelation function for  $w(t)$ . This standard deviation, or cloud size, is independent of  $w_s$  under the assumption of identical fluctuation statistics. There is thus no differential diffusion in Taylor's infinite, unsteady scenario. Differential diffusion only occurs when a boundary condition, e.g.,  $c(0,t) \equiv C_o$ , as in the example above, is enforced.

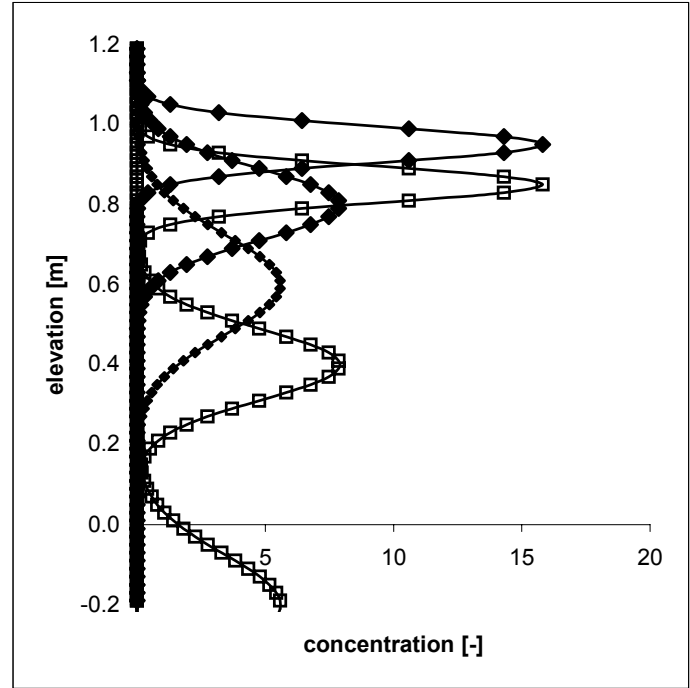


Figure 2: Successive concentration profiles  $c(z,t)$ , after 5, 10 and 20 seconds of particles with  $w_s=1\text{cm/s}$  ( $\blacklozenge$ ), and  $3\text{cm/s}$  ( $\square$ ) respectively settling with statistically identical velocity fluctuations after being released as point injections at  $z=1\text{m}$  at  $t=0$ . At any time the concentration profiles have the same shape, irrespective of  $w_s$ .

### Finite Mixing Length Effects on Eddy Viscosities

Steady current profiles, e.g., the log-profile can be understood in terms of a mixing length model where only the first term (the gradient term) of (2) is retained. That is however not possible for oscillatory turbulent flows. The most obvious feature of oscillatory turbulent boundary layers, which requires finite mixing length terms, is the observed phase lead of local shear stresses ahead of the local velocity gradients, cf Figure 3.

In a formalism with real-valued eddy viscosities, shear stresses  $\tau(z,t)$  being out of phase with the local velocity gradients  $\partial u / \partial z$

leads, through the usual definition,  $v_t = \frac{\tau / \rho}{\partial u / \partial z}$  to wildly

variable  $[-\infty; \infty]$  eddy viscosities. Alternatively one can (for the simple harmonic case) use constant, but complex-valued eddy viscosities with argument equal to the phase lead of  $\tau(z,t)$  relative to  $\partial u / \partial z$ . The complex-valued eddy viscosities are however just nominal and rather ad hoc tools. In the following, we make the case that the phase lead of  $\tau(z,t)$  relative to  $\partial u / \partial z$  is in fact a finite-mixing length effect. In this case the finite mixing length term in (2) is imaginary corresponding to the observed phase shift between  $\tau(z,t)$  relative to  $\partial u / \partial z$ .

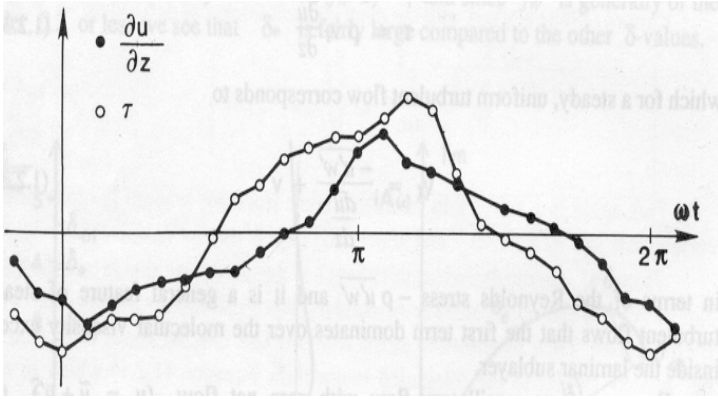


Figure 3: Velocity gradient and shear stress in a turbulent oscillatory boundary layer. The stress leads the velocity gradient. Measurements by Jonsson & Carlsen [6].

To show this we first note that, in the simple mixing length scenario in Figure 1 the upward flux of  $x$ -momentum ( $= -\tau$ ) is

$$-\tau = w_m \left[ \rho u(z + \frac{l_m}{2}) - \rho u(z - \frac{l_m}{2}) \right] \quad (9)$$

The velocity in a simple harmonic oscillatory boundary layer flow is often expressed in terms of the free stream velocity  $u_\infty(t)$  and the complex velocity defect function  $D(z)$  defined by

$$u(z, t) = A \omega e^{i\omega t} [1 - D(z)] = u_\infty(t) [1 - D(z)] \quad (10)$$

in terms of which the shear stress is

$$\frac{\tau(z, t)}{\rho} = \frac{\partial}{\partial t} \int_z^\infty [u_\infty(t) - u(z', t)] dz' = i \omega \int_z^\infty D(z') dz' \quad (11)$$

In combination with (9) this leads to the finite mixing length momentum equation

$$\frac{d}{dz} \left\{ w_m \left[ D(z + \frac{l_m}{2}) - D(z - \frac{l_m}{2}) \right] \right\} = i \omega D(z) \quad (12)$$

This equation must, with the relevant expressions for  $l_m(z)$  and  $w_m(z)$  be solved with the boundary conditions  $D(0) = 1$  and  $D(\infty) = 0$ . By letting  $l_m$  tend to zero, one sees that Equation (12) is the finite-mixing-length equivalent to the laminar

$$v \frac{d^2 D}{dz^2} = i \omega D \quad (13)$$

which, with the above mentioned boundary conditions has the solution

$$D = e^{-\sqrt{\frac{i\omega}{v}} z} \quad (14)$$

To see the essence of the finite mixing length effect on the momentum flux (9) and hence on  $v_t$  it suffices to consider the simplest scenario: homogeneous turbulence with constant  $(l_m, w_m)$ . In this case, the momentum equation (12) has an analogous solution to the " $l_m \rightarrow 0$  solution" (14).

Inserting a solution of this form, i.e.,  $D = e^{\alpha z}$ , into (12) leads to the following expression for  $\alpha$

$$\alpha = -\sqrt{\frac{i\omega}{w_m l_m}} \left( 1 - \frac{1}{48} \frac{i\omega l_m}{w_m} - \dots \right) \quad (15)$$

This expression for the exponent shows by comparison with the laminar solution (14) that the eddy viscosity is given by

$$v_t = w_m l_m \left( 1 + \frac{1}{24} i \frac{l_m}{w_m / \omega} + \dots \right) \quad (16)$$

where the second, imaginary term shows that the phase lead of  $\tau$  ahead of  $\partial u / \partial z$  develops as  $l_m$  becomes large compared with the vertical scale  $L_\omega = w_m / \omega \sim u_* / \omega$  defined by the mixing (friction) velocity and the wave frequency. For very slow oscillations the second term vanishes and the classical von Karman-Prandtl mixing length theory suffices.

### Differential Diffusion at an Interface

Consider mixing at an interface as in Figure 4. The density variation may be due to temperature, salinity or suspended sediment. Horizontal fluid momentum may vary in a similar fashion at the interface.

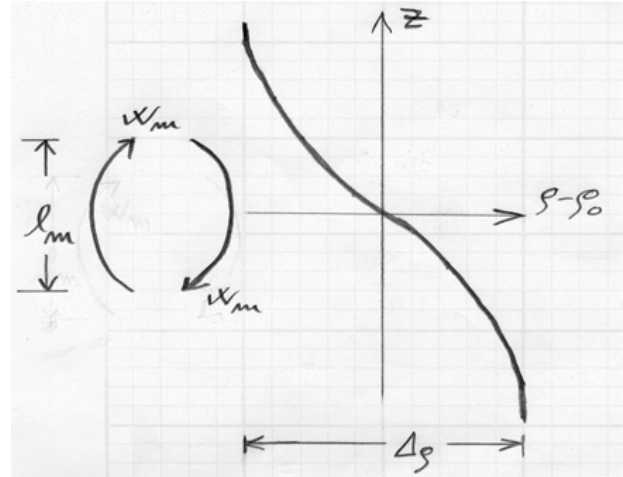


Figure 4: Assumed density distribution at an interface where turbulent mixing can be described by Equation (2) in terms of a single mixing length  $l_m$  and a single mixing velocity  $w_m$ .

Consider density as an example and, for simplicity, assume that the density profile is given by

$$\rho(z) = \rho_0 - \frac{\Delta \rho}{2} \tanh\left(\frac{z}{L}\right) \quad (17)$$

In this situation the mixing flux corresponding to the mixing length  $l_m$  and the mixing velocity  $w_m$  is

$$\begin{aligned} q_m &= w_m \left[ \rho(z - \frac{l_m}{2}) - \rho(z + \frac{l_m}{2}) \right] \\ &= -w_m l_m \frac{d\rho}{dz} \left[ 1 - \frac{1}{12} \left( \frac{l_m}{L} \right)^2 [1 - 3 \tanh^2(\frac{z}{L})] \right] \end{aligned} \quad (18)$$

which for  $z \ll L$  is simplified to

$$q_m \approx -w_m l_m \frac{d\rho}{dz} \left[ 1 - \frac{1}{12} \left( \frac{l_m}{L} \right)^2 \right] \quad (19)$$

The second term, the finite mixing length term, thus indicates greater diffusion coefficients for species with greater  $L$ . Equation (19) could thus explain the observed differential diffusion of salt and temperature with  $K_s < K_t$  if the mixing length  $l_m$  is a finite fraction of the distribution scales and if the scale for the temperature  $L_t$  is greater than that of salt,  $L_s$ . In this case a positive feed back loop exists: Greater  $L \Rightarrow$  greater  $K \Rightarrow$  greater  $L \dots$

Jackson & Rehmann [7] found that the differentiation disappears when the mixing gets very vigorous. That could also be explained by (19). That is, if the mixing is enhanced essentially by increasing  $w_m$  while  $l_m$  is more or less fixed. Both of  $L_t$  and  $L_s$  will then increase compared with  $l_m$  and the second term in the bracket (the finite mixing length effect) becomes insignificant.

## Conclusions

In classical mixing length models, including those of Prandtl and von Karman, only the first term, the gradient term, is maintained in the Taylor expansion of the turbulent mixing flux:

$$\begin{aligned} q_m &= w_m \left[ c \left( z - \frac{l_m}{2} \right) - c \left( z + \frac{l_m}{2} \right) \right] \\ &= -w_m l_m \frac{dc}{dz} \left[ 1 + O \left( \frac{l_m}{L_c} \right)^2 \right] \end{aligned} \quad (2)$$

This leads to  $K=w_m l_m$  for all species in a given flow. In other words, differential diffusion is not anticipated by these models, at least not for species with the same  $w_m$ ,  $l_m$ . On the other hand, differential diffusion is quite commonly observed even for species between which no significant differences in  $w_m$ ,  $l_m$  are expected.

We have shown that keeping just one more term yields explanations for a number of conundrums related to turbulent mixing. That is, the second term in the mixing flux, which becomes important when  $l_m/L_c$  is finite, can explain that different sediment sizes suspended in the same flow display  $K$ -values which increase with increasing settling velocity.

For the mixing of momentum, salt and heat at an interface, Equation (2) also holds a possible explanation for differential diffusion. That is, if one species, for some reason, has a greater  $L$ , the finite mixing length terms will make it diffuse faster and thus provide a positive feedback loop for this difference.

While the classical theory of Taylor [12] does include finite mixing length effects in a Lagrangian sense, these are not expressed in terms of differential diffusion until steady boundary conditions are enforced.

For the transfer of momentum in turbulent oscillatory boundary layers the finite mixing length term is imaginary and explains observed phase leads of shear stresses ahead of velocity gradients.

## References

- [1] Chanson, H., Air Bubble Diffusion in Supercritical Open Channel Flow, *Proc 12th Australasian Fluid Mech Conf*, Sydney, Australia, R W Bilger Ed, **2**, 1995, 707-710.
- [2] Chanson, H., *Air Bubble Entrainment in Free-Surface Turbulent Shear Flows*, Acad Press, London, UK, 1997.
- [3] Coleman, N., Flume studies of the sediment transfer coefficient, *Water Resources Res*, **6(3)**, 1970, 801-809.
- [4] Gargett, A E., Differential diffusion: an oceano-graphical primer, *Progress in Oceanography*, Pergamon, **56**, 2003, 559-570.
- [5] Graf, W H & M Cellino, Suspension flows in open channels; experimental study, *J Hydr Res*, **40(4)**, 2002, 435-447.
- [6] Jonsson, I G & N A Carlsen, Experimental and theoretical investigations in an oscillatory turbulent boundary layer, *J Hydraulic Res*, **14**, 1976, 45-60.
- [7] Jackson, R P & C R Rehmann, Laboratory measurements of differential diffusion in a diffusively stable turbulent flow, *J Phys Oceanogr*, **33**, 2003, 1592-1603.

- [8] Kronenburg, A & R W Bilger, Modelling of differential diffusion effects in non-premixed non-reacting turbulent flow, *Physics of Fluids*, **9(5)**, 1997, 1435-1447.
- [9] Nagata, K & S Komori, The difference in turbulent diffusion between active and passive scalars in stable thermal stratification, *J Fluid Mech*, **430**, 2001, 361-380.
- [10] Nielsen, P., *Coastal bottom boundary layers and sediment transport*, World Scientific, Singapore, 1992.
- [11] Nielsen, P & I A L Teakle (2004): A finite mixing length theory for the turbulent diffusion of momentum and suspended sediment, *Physics of Fluids*, **16(7)**, 2004.
- [12] Taylor, G.I., Diffusion by continuous movements, *Proc London Mathematical Society*, **20**, 1921, 196-212.
- [13] Turner, J., The influence of molecular diffusivity on turbulent entrainment across a density interface, *J Fluid Mech*, **33**, 1968, 639-656.
- [14] Van Rijn, L.C., Sediment Transport, Part II: Suspended Load transport, *J Hydr Eng*, ASCE, **110(11)**, 1984, 1613-1641.



## Shedding Some Light on $\beta$ -factors

I.A.L. Teakle<sup>1</sup> and P. Nielsen<sup>1</sup>

<sup>1</sup>Division of Civil Engineering  
The University of Queensland, QLD, 4076 AUSTRALIA

### Abstract

The use of a Fickian (infinitesimal-mixing-length) framework for the case of turbulent mixing can necessitate the use of ad hoc modifications (e.g.  $\beta$ -factors) in order to reconcile experimental data with theoretical expectations. This is because in many cases turbulent mixing occurs on scales which cannot be considered infinitesimal. In response to this problem a Finite-Mixing-Length (FML) model for turbulent mixing was derived by Nielsen and Teakle [10]. This paper considers the application of this model to the scenario of suspended sediment in steady, uniform channel flows. It is shown that, unlike the Fickian framework, the FML model is capable of explaining why  $\beta$ -factors are required to be an increasing function of  $w_s/u_*$ . The FML model does not on its own explain observations of  $\beta < 1$ , seen in some flat-bed experiments. However, some potential reasons for  $\beta < 1$  are considered.

### Introduction

Fickian (gradient) diffusion is the usual theoretical framework applied to modelling the turbulent suspension of sediment. However, measurements of actual suspended sediment profiles in the laboratory and in the field demonstrate that pure gradient diffusion models are not capable of satisfactorily performing this task. In particular, a strong dependence of the observed Fickian sediment diffusivity,  $\varepsilon_{Fick}$ , on sediment settling velocity,  $w_s$ , has been clearly established by experiments covering a large range of flow situations from laboratory channels, to rivers and even to wave flumes and coastal locations involving oscillatory flows. This positive dependence, ( $\uparrow \varepsilon_{Fick}$  for  $\uparrow w_s$ ) implies that the larger, more inert particles are mixed more efficiently by the turbulence than their less heavy counterparts. Coleman [3] obtained an experimental dataset that clearly demonstrated this phenomena, see figure 1. This seemingly strange nature of apparent Fickian sediment diffusivities has typically necessitated the application of ad hoc modifications ( $\beta$ -factors) to this parameter for modelling purposes.

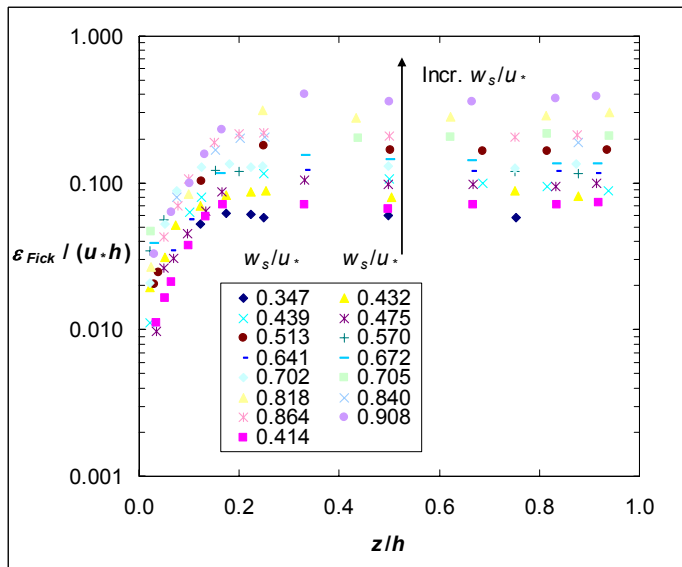


Figure 1. Coleman's [3] dataset clearly showing  $\uparrow \varepsilon_{Fick}$  for  $\uparrow w_s$ .

$\beta$  is defined as the ratio of the apparent Fickian diffusivity of sediment and of momentum (the eddy-viscosity,  $\nu_t$ ),  $\beta = \varepsilon_{Fick} / \nu_t$ . This parameter describes the relative turbulent mixing efficiency of momentum compared with sediment in the same flow.  $\beta$ -factors greater than and less than 1 have been observed in turbulent channel and river flows. However, a universally observed feature is the strong dependence in a given series of experiment of  $\beta$  on the ratio,  $w_s/u_*$ .

Nielsen [9] explains that the observed behaviour is due to the importance of large-scale convective transport mechanisms in turbulent mixing. However, the assumption implicit in the derivation of the gradient diffusion framework is that mixing occurs on purely infinitesimal scales. Nielsen and Teakle [10] derived a new Finite-Mixing-Length (FML) framework for turbulent diffusion which is capable of explaining the observed trend of increasing  $\varepsilon_{Fick}$  with increasing  $w_s/u_*$ . However, some other features of the data such as  $\beta < 1$  for flat-bed laboratory experiments could not be reconciled with the FML model alone. In order to investigate possible improvements to the model, some of the dynamic interactions that may occur between sediment and fluid are also qualitatively considered.

### Finite-Mixing-Length Model

Nielsen & Teakle [10] consider in detail the derivation of the FML theory and its application to a number of simple situations. The following section will provide a brief summary of this work. Turbulent mixing is capable of generating a net vertical flux of suspended sediment which can be quantified in terms of the simplified scenario involving the swapping of fluid parcels (including suspended sediment) shown in figure 2.

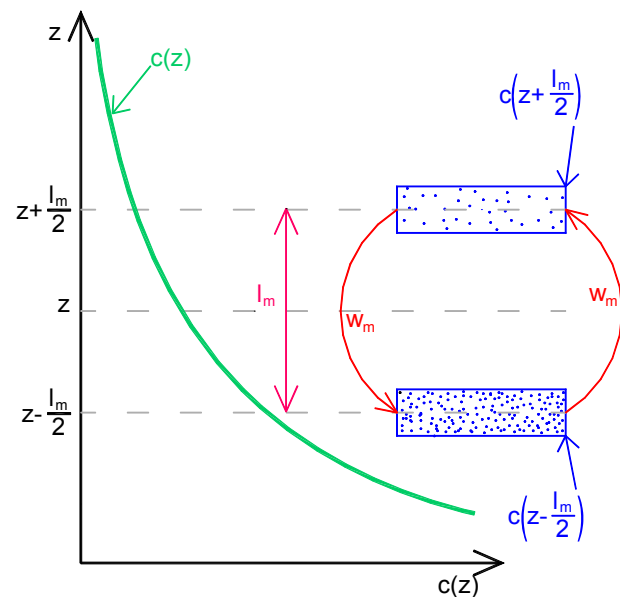


Figure 2. The upward sediment flux due to turbulent mixing can be understood in terms of swapping fluid-sediment-mix parcels over a vertical distance  $l_m$ .

The resulting sediment flux density is,

$$q_m = w_m \left[ c(z - l_m/2) - c(z + l_m/2) \right] \quad (1)$$

and by Taylor expansion of  $c(z \pm l_m/2)$ ,

$$q_m = -w_m l_m \frac{\partial c}{\partial z} \left[ \sum_{n=1}^{\infty} \left\{ \frac{l_m^{(2n-2)}}{(2n-1)! 2^{(2n-2)}} \frac{\partial^{(2n-1)} c}{\partial z^{(2n-1)}} \right\} \right] \quad (2)$$

$$= -w_m l_m \frac{\partial c}{\partial z} \left[ 1 + \frac{l_m^2}{24} \frac{\partial^3 c}{\partial z^3} + \dots \right]$$

The term in front of the brackets is the familiar gradient diffusion flux. The higher order terms disappear for the case of infinitesimal mixing length,  $l_m \rightarrow 0$ , demonstrating that Fickian diffusion is only a particular limit of the more general turbulent mixing scenario. It is the effect of the higher-order terms for cases of finite  $l_m$  which can account for much of the previously irreconcilable behaviour of suspended sediment profiles in turbulent flows.

### Apparent Fickian Diffusivities

The sediment continuity equation for a 1D vertical, steady scenario can be written,

$$q_m - w_s c(z) = 0 \quad (3)$$

If the gradient diffusion framework is adopted, the mixing flux is simply assumed to be,

$$q_m = -\varepsilon_{Fick} \frac{\partial c}{\partial z} \quad (4)$$

Using Eqs. (2), (3) and (4) it can be seen that, according to the FML framework, the apparent Fickian diffusivity is,

$$\varepsilon_{Fick} = -\frac{w_s c(z)}{\frac{\partial c}{\partial z}} = w_m l_m \left[ 1 + \frac{l_m^2}{24} \frac{\partial^3 c}{\partial z^3} + \dots \right] \quad (5)$$

Therefore,  $\varepsilon_{Fick}$ , is not purely a function of the turbulence parameters  $w_m$  and  $l_m$ , it is also dependent on the higher order terms in Eq. (5). The nature of these higher order terms can be more clearly seen by considering an exponential concentration distribution,

$$c(z) = c(z_0) e^{-\frac{(z-z_0)}{L_c}} \quad (6)$$

Substituting this into Eq. (2) gives for the mixing flux,

$$q_m = -w_m l_m \frac{\partial c}{\partial z} \left[ 2 \frac{L_c}{l_m} \sinh \left( \frac{l_m}{2L_c} \right) \right] \quad (7)$$

$$= -w_m l_m \frac{\partial c}{\partial z} \left[ 1 + \frac{1}{24} \left( \frac{l_m}{L_c} \right)^2 + \dots \right]$$

From Eq. (7) it can be seen that the higher order terms are zero and the turbulent mixing process is correspondingly Fickian only for the limit of  $l_m/L_c \rightarrow 0$ , i.e. when the turbulent mixing length is small compared with the distribution length-scale  $L_c$ . Coarser particles (larger  $w_0$ ) are seen to have larger  $\varepsilon_{Fick}$  than fine particles due to the fact that they have a relatively smaller  $L_c$  (and hence larger higher order terms according to Eq. (7)) in a given turbulent mixing regime.

### FML Concentration Distributions

For a couple of simple turbulent mixing scenarios the FML model predicts concentration distributions that are analogous to the corresponding Fickian distributions:

#### Homogeneous Turbulence; constant $w_m$ and $l_m$

In this case the concentration profile derived from the pure gradient diffusion theory (combining Eqs. (3) and (4)) gives an exponential distribution, Eq. (6), where the distribution length-scale is given by,

$$L_c = \frac{l_m w_m}{w_s} \quad (8)$$

The FML framework (combining Eqs. (1) and (3)) gives an analogous solution to (6), however in this case the distribution length-scale is,

$$L_c = \frac{l_m}{2 \sinh^{-1} \left( \frac{w_0}{2w_m} \right)} \quad (9)$$

$$= \frac{l_m w_m}{w_s} \left( 1 + \frac{1}{24} \left( \frac{w_0}{w_m} \right)^2 - \dots \right)$$

Figure 3 illustrates this relationship and demonstrates that the Fickian approximation is exact for  $w_m/w_s \rightarrow 0$ , while it underestimates  $L_c$  for finite  $w_s/w_m$ . Interestingly, van Rijn's [12] empirical  $\beta$ -factor formula shows a similar dependence on  $w_s/u_*$  to Eq. (9),

$$\beta = 1 + 2 \left( \frac{w_s}{u_*} \right)^2 \quad (10)$$

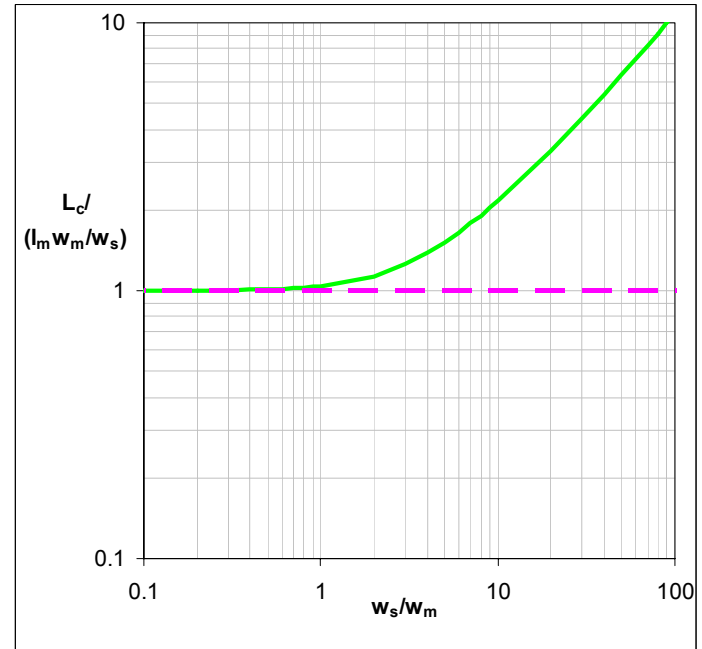


Figure 3. Solid line showing finite-mixing-length model exponential lengthscale,  $L_c$ , for homogeneous turbulence compared with the corresponding Fickian prediction (dotted line).

#### Constant Stress Layer; linear $l_m(z)$ and constant $w_m$

This turbulence distribution is usually assumed to apply to the “constant-stress-layer” in wall-bounded shear flows, e.g. Pope [11]. In particular Nielsen and Teakle [10] made the general assumption that,

$$l_m(z) = \lambda z, \text{ and} \quad (11)$$

$$w_m = \gamma u_* \quad (12)$$

where,  $u_* \equiv \sqrt{\tau_0/\rho}$  is the bed, friction-velocity. This is similar to Prandtl's mixing-length hypothesis except that Prandtl made the further assumptions that  $\gamma = 1$ ,  $\lambda = \kappa$ , and that the mixing process was Fickian in nature.

Nielsen and Teakle [10] sought a unified and consistent turbulent mixing model for both momentum and sediment for the constant stress layer. Firstly, considering the FML model (figure 2) applied to momentum transfer with mixing parameters given by Eqs. (11) and (12), they got,

$$-\rho u_*^2 = \gamma u_* \left[ \rho u \left( z - \frac{\lambda}{2} z \right) - \rho u \left( z + \frac{\lambda}{2} z \right) \right] \quad (13)$$

This equation is found to satisfy the usual logarithmic velocity profile,

$$u(z) = \frac{u_*}{\kappa} \ln \left( \frac{z}{z_0} \right) \quad (14)$$

when  $\lambda$  and  $\gamma$  satisfy,

$$\gamma \ln \left( \frac{1 + \lambda/2}{1 - \lambda/2} \right) = \kappa \quad (15)$$

This equation approaches the Fickian limit  $\lambda \gamma \rightarrow \kappa$  as  $\lambda \rightarrow 0$ . Physically  $\lambda = 2$  is the upper limit in the mixing scenario of figure 2.

The sediment distribution obtained using the Fickian approximation is a power-function in the case of a constant-stress-layer,

$$c(z) = c(z_0) \left( \frac{z}{z_0} \right)^{-\frac{w_s}{\lambda \gamma u_*}} \quad (16)$$

The FML model also yields a power-function for the sediment distribution,

$$c(z) = c(z_0) \left( \frac{z}{z_0} \right)^p \quad (17)$$

where  $p$  satisfies,

$$\left( 1 - \frac{\lambda}{2} \right)^p - \left( 1 + \frac{\lambda}{2} \right)^p = \frac{w_s}{\gamma u_*} \quad (18)$$

The FML model approaches the Fickian distribution,  $p = -w_s/(\lambda \gamma u_*)$ , when  $w_s/u_* \rightarrow 0$ . As  $\lambda \rightarrow 0$  the homogeneous FML solution (figure 3) is approached. The strength of the FML mixing enhancement is determined by the magnitude of the mixing length gradient,  $\lambda$ . This raises the issue of how the model parameters  $\lambda$  and  $\gamma$  should be chosen. In the Fickian mixing scenario  $w_m$  and  $l_m$  only ever appear in combination, i.e.  $w_m l_m$ , therefore in the Fickian model it does not matter how these terms proportionately contribute to the mixing. However, in the FML model (Eq. (5)) the relative size of the mixing length is seen to determine the strength of the FML effects. Therefore, in this case the model parameters will be chosen to best match the available constant-stress-layer data.

### Comparison With Experimental Data

The most convenient way to compare the model with experimental data makes use of the  $\beta$ -factor,

$$\beta = \frac{\mathcal{E}_{Fick}}{v_t} = \frac{-w_s c(z)}{\frac{\partial c}{\partial z}} \bigg/ \frac{\tau}{\rho \frac{\partial u}{\partial z}} \quad (19)$$

For the constant-stress-layer case (log-function velocity and power-function sediment distribution) this gives,

$$\beta = -\frac{1}{\kappa p} \frac{w_s}{u_*} \quad (20)$$

The comparison of the FML model with data is shown in figure 4, for three different choices of  $\lambda$ . The data points were obtained by only considering the constant-stress-layer portion ( $z/h < 0.5$ ) of the concentration profiles from channel and river flow experiments. In order to maintain a consistent approach between datasets, some of which did not include detailed velocity measurements, it was assumed that  $\kappa$  (in effect the velocity gradient) maintained its clear-water value of 0.4 in all cases, even though this was demonstrated not to necessarily be the case where velocity measurements were available.  $\beta$  is seen to be an increasing function of  $w_s/u_*$  in good qualitative agreement with the data. The choice of larger values of  $\lambda$  produces a stronger

increase with  $w_s/u_*$ . The slope of the data suggests that  $\lambda = 1.9$  best describes the increase of  $\beta$  with  $w_s/u_*$ . This has an interesting physical interpretation when it is considered that as  $\lambda \rightarrow 2$  the mixing scenario shown in figure 2 corresponds to mixing between an upper parcel and a lower parcel that always originates from the vicinity of the bed.

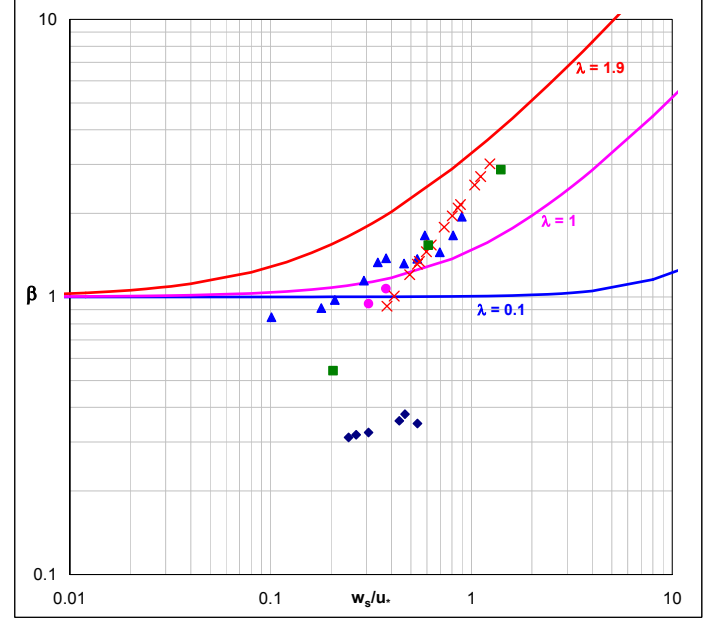


Figure 4 Lines showing theoretical  $\beta$ -values for the constant stress layer model. Experimental  $\beta$ -values from the constant stress layer of channel flows;  $\diamond$  Graf & Cellino (no bedforms) [6],  $\bullet$  Graf & Cellino (bedforms) [2],  $\blacktriangle$  Anderson (Enoree River) [1],  $\times$  Coleman [3],  $\square$  Coleman [4].

While the FML model predicts increasing  $\beta$  with increasing  $w_s/u_*$  in qualitative agreement with the data, the quantitative description shown in figure 4 is not yet convincing. For instance the model predicts  $\beta \geq 1$  for all sediment sizes while some of the flat bed experiments indicate  $\beta < 1$ . The fact that the data does not collapse when plotted in this manner also suggests that processes other than those considered in this analysis are most likely important. Some of these additional processes are briefly considered in the next section.

### Dynamic Interaction of Fluid and Sediment

The constant-stress-layer analysis shown in the previous section was based on the assumption that suspended sediment is a passive scalar in a turbulent flow. However this is not usually the case, the presence of suspended sediment is known to change the suspending fluids mean velocity and turbulence profiles from the clear water equivalent. Furthermore, the presence of turbulence may significantly affect the velocity statistics of the suspended sediment due to a process called “selective sampling”. This can lead to the bulk settling velocity of the sediment in turbulence being different from its clear water value, as well as the turbulent fluctuations of the sediment being different from that of the suspending fluid.

### Effect of Suspended Sediment on Fluid Velocity

The addition of a suspended load of heavy particles to a steady, uniform, clear-water, channel flow has been shown to increase the near-bed velocity gradient. This is usually explained by turbulence attenuation resulting from the stable stratification induced by the sediment concentration gradients, [7]. This effect implies that the presence of sediment causes momentum to be less efficiently mixed, which should be accounted for in the calculation of  $\beta$  (Eq. (19)). In order to investigate the importance of this stratification effect the dataset of Coleman [4] was considered. Both velocity and sediment concentration measurements were obtained as sediment load was gradually increased in a series of experiments. In order to simply demonstrate any first-order effects, the following analysis

assumes that a log-law velocity and power-law concentration profile remain valid. Figure 5a shows how the apparent von Karman constant,  $\kappa'$ , varied with suspended sediment concentration (simply a convenient abscissae). Figure 5b compares  $\beta$  obtained assuming  $\kappa = 0.4$  with that obtained allowing for variation,  $\beta'$ . This shows that, in the case of Coleman's data,  $\beta < 1$  in the original analysis can be accounted for by the reduction in velocity gradient. Unfortunately the same explanation does not seem to account for  $\beta < 1$  in Graf and Cellino's [6] data.

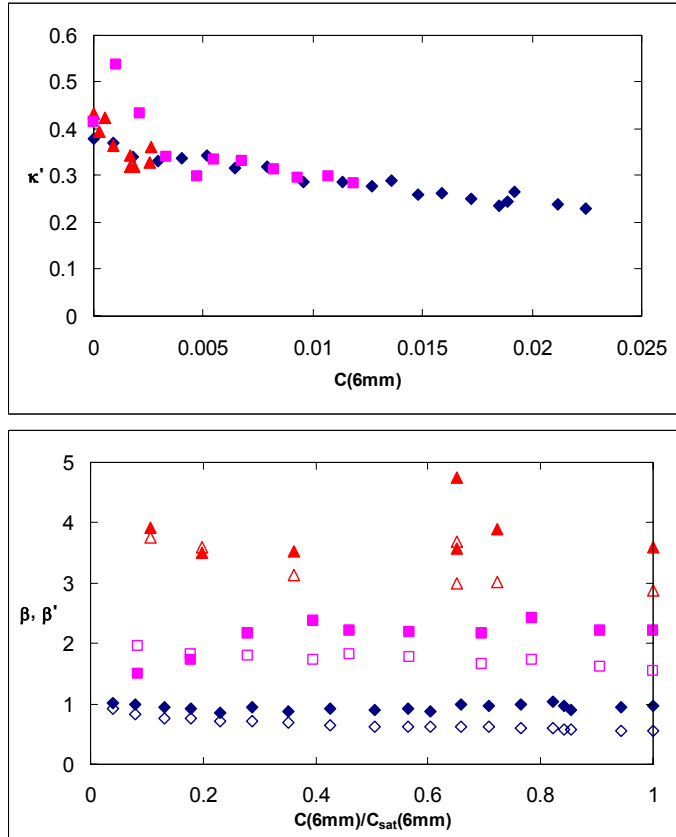


Figure 5a Showing the variation in  $\kappa'$  with increasing sediment load. Data from Coleman (1986) [4].  $\blacklozenge$   $w_s/u_* = 0.2$ ;  $\blacksquare$   $w_s/u_* = 0.6$ ;  $\blacktriangle$   $w_s/u_* = 1.5$ . 5b Comparing  $\beta$  (hollow symbols) and  $\beta'$  (solid symbols). Symbols as for 5a.

### Sediment Velocity

Most models of suspended sediment and many experiments have assumed that the sediment and fluid have essentially identical velocity statistics. However, an interesting experiment by Muste and Patel [8] used a discriminator LDV to measure separate fluid and suspended sediment velocities in dilute sediment-laden flow. Their results suggest that there is a lag between fluid and sediment mean stream-wise velocities of up to 4%. Their most intriguing finding was that stream-wise turbulence intensities of water and sand were very similar, whereas the vertical sediment turbulence intensities were significantly damped compared with the fluid (by approximately 20%). In the context of the FML model this could be interpreted as a reduction of the sediment mixing velocity,  $w_m$ , compared with that of the fluid. This would lead to  $\beta < 1$  for small  $w_s/u_*$ .

This phenomenon could perhaps be explained by the particles "selectively-sampling" the turbulent fluid velocity field. That is, in a fluid velocity field comprising spatially and temporally coherent turbulent structures, suspended particles with inertia differing from that of a fluid particle have been shown to preferentially migrate due to centrifugal action to certain regions of the flow field [5]. This "preferential concentration" implies that the suspended particles are "selectively sampling" the fluid velocity field and therefore different velocity statistics between the fluid and sediment become possible.

Selective sampling has been shown to change the bulk settling velocity of particles in turbulence from its clear water value. For heavy particles in a strong turbulence field this is expected to result in an increase in bulk settling velocity [13]. This increase in settling velocity due to turbulence would have the same effect on the concentration profiles as a reduction in mixing efficiency and thus would manifest itself as  $\beta < 1$ .

### Conclusions

This paper has demonstrated the application of a Finite-Mixing-Length (FML) theory to the case of sediment suspensions in steady, uniform flows. Unlike the Fickian diffusion framework the FML theory is capable of explaining why  $\beta$ -factors are required to be an increasing function of  $w_s/u_*$ . A unified FML description of momentum and sediment mixing in a "constant-stress-layer" was shown to adequately describe the observed trend in the data.

The large scatter in the data for small  $w_s/u_*$  and the occurrence of  $\beta < 1$  was considered in some further detail. The dynamic interaction of fluid and suspended sediment was shown to significantly alter both the momentum and sediment mixing efficiencies. The potential importance of a "selective-sampling" mechanism was also postulated.

### Acknowledgments

The authors gratefully acknowledge support from the CRC Sustainable Tourism Project #52001.

### References

- [1] Anderson, A.G., Distribution of suspended sediment in a natural stream. *Trans Am Geophys Union*, **23(2)**, 1942, 678-683.
- [2] Cellino, M. and H. Graf Walter, Experiments on suspension flow in open channels with bed forms. *Journal of Hydraulic Research*, **38(4)**, 2000, 289-298.
- [3] Coleman, N.L., Flume studies of the sediment transfer coefficient. *Water Resources Research*, **6(3)**, 1970, 801-809.
- [4] Coleman, N.L., Effects of suspended sediment on the open-channel velocity distribution. *Water Resources Research*, **22(10)**, 1986, 1377-84.
- [5] Fessler, J.R., J.D. Kulick, and J.K. Eaton, Preferential Concentration of Heavy-Particles in a Turbulent Channel Flow. *Physics of Fluids*, **6(11)**, 1994, 3742-3749.
- [6] Graf, W.H. and M. Cellino, Suspension flows in open channels; experimental study. *Journal of Hydraulic Research*, **40(4)**, 2002, 435-448.
- [7] McLean, S.R., On the Calculation of Suspended Load for Noncohesive Sediment. *Journal of Geophysical Research*, **97(C4)**, 1992, 5759-5770.
- [8] Muste, M. and V.C. Patel, Velocity profiles for particles and liquid in open-channel flow with suspended sediment. *Journal of Hydraulic Engineering ASCE*, **123(9)**, 1997, 742-751.
- [9] Nielsen, P., *Coastal bottom boundary layers and sediment transport*. Advanced series on ocean engineering ; v. 4., Singapore, World Scientific. 1992.
- [10] Nielsen, P. and I.A.L. Teakle, Turbulent diffusion of momentum and suspended particles: A finite-mixing-length theory. **16(7)**, 2004, 2342-2348.
- [11] Pope, S.B., *Turbulent flows*, Cambridge, Cambridge University Press. 2000.
- [12] van Rijn, L.C., Sediment Transport, Part II: Suspended Load Transport. *Journal of Hydraulic Engineering ASCE*, **110(11)**, 1984, 1613-1641.
- [13] Yang, T.S. and S.S. Shy, The settling velocity of heavy particles in an aqueous near-isotropic turbulence. *Physics of Fluids*, **15(4)**, 2003, 868-880.



## Modelling Gas-Liquid Bubbly Flows

G.H. Yeoh<sup>1</sup> and J. Y. Tu<sup>2</sup>

<sup>1</sup>Australian Nuclear Science and Technology Organisation (ANSTO)  
PMB 1, Menai, NSW, 2234 AUSTRALIA

<sup>2</sup>School of Aerospace, Mechanical and Manufacturing Engineering  
RMIT University, Victoria, 3083 AUSTRALIA

### Abstract

In this paper, modelling gas-liquid bubbly flows is achieved by the introduction of a population balance equation combined with the three-dimensional two-fluid model. An average bubble number density transport equation has been incorporated in the commercial code CFX5.7 to better describe the temporal and spatial evolution of the geometrical structure of the gas bubbles. The coalescence and breakage effects of the gas bubbles are modelled according to the coalescence by the random collisions driven by turbulence and wake entrainment while for bubble breakage by the impact of turbulent eddies. Local radial distributions of the void fraction, interfacial area concentration, bubble Sauter mean diameter, and gas and liquid velocities, are compared against experimental data obtained at Prudue University. Satisfactory agreements for the local distributions are achieved between the predictions and measurements.

### Introduction

The range of applications for two-phase flow systems is immense. In many chemical industries, bubble column reactors are extensively employed for handling processes that require large interfacial area and efficient mixing processes. Engineering systems such as heat exchangers also widely employ the two-phase flow mixture of gas and liquid for efficient removal of heat generation. In the nuclear area, the capability to predict void fraction profile and other two-phase flow parameters in subcooled boiling flows is of considerable importance to ensure the safe operation of the reactor.

In the present state-of-the-art, the two-fluid model can be considered as the most detailed and accurate macroscopic formulation of the thermal-hydraulic dynamics of two-phase flow systems. Within the field equations, expressed by conservation of mass, momentum and energy for each phase, interfacial transfer terms appear in each of the equations. These terms determine the rate of phase changes and the degree of mechanical and thermal non-equilibrium between phases. They represent essential closure relations, which should be modelled accurately. However, the closure relations for the interfacial transfer terms are presently far from resolution and they are still the weakest link in the two-fluid model.

In the two-fluid model, the interfacial transfer terms are strongly related to the interfacial area concentration and the local transfer mechanisms such as the degree of turbulence near the interfaces. Fundamentally, the interfacial transport of mass, momentum and energy is proportional to the interfacial area concentration  $a_{if}$  and driving forces. The interfacial area concentration (interfacial area per unit volume) characterises the kinematic effects; it is related to the geometrical effects of the interfacial structure. Nevertheless, the driving forces for the inter-phase transport characterises the local transport mechanism.

Since the interfacial area concentration  $a_{if}$  represents the key parameter that links the interaction of the phases, much attention have been concentrated towards better understanding the coalescence and breakage effects due to interactions among bubbles and between bubbles and turbulent eddies for gas-liquid bubbly flows. The primary aim is to better describe the temporal and spatial evolution of the two-phase geometrical structure. Some empirical correlations [1], models [2], population balance approaches [3], volumetric interfacial area transport equation [4-6] have been proposed to predict the interfacial area concentration.

The MUSIG (Multiple Size Group) model has been implemented in CFX4.4 to account for the non-uniform bubble size distribution in a gas-liquid mixture. In CFX5.7, it is currently provided as a beta version. The model was developed by Lo [7] and solves a range of bubble classes. Because of the possible wide range of bubble sizes that may exist in the two-phase flow system, it requires a substantial number of equations to adequately track the bubble sizes. From our recent studies [8] of a subcooled boiling flow in an annulus channel, we have employed 15 transport equations in addition to the two sets of conservation equations of mass, momentum and energy to track the range of bubbles sizes ranging from 0 mm to 9.5 mm in diameter. For flows where large bubbles can exist especially in bubble column reactors, this could amount to the consideration of greater than 15 transport equations, which the numerical effort to solve such problem could be enormous. Therefore in practical calculations if the bubble classes chosen are limited, the size distribution of the bubbles cannot be adequately represented.

In this paper, the average number density transport equation is considered. Here, only one additional equation is solved. To demonstrate the possibility of a simpler approach of combining population balance with computational fluid dynamics (CFD), this transport equation is implemented in the generic commercial CFD code CFX5.7. In this equation, the coalescence and breakage mechanisms of the bubble are accommodated for the gas phase. The two-fluid and standard  $k$ - $\epsilon$  models are employed. Within the source terms of the turbulent kinetic energy  $k$ , the energy exchange between the interfacial free energy and liquid turbulent kinetic energy due to bubble coalescence and breakage is incorporated. Respective coalescence and breakage mechanisms by Wu et al. [4], Hibiki and Ishii [5] and Yao and Morel [6], implemented as source terms in the average number density transport equation, are assessed. The model predictions are compared against experimental data of an isothermal gas-liquid bubbly flow in a vertical pipe performed in Prudue University [5].

### Physical Model Governing Equations

The numerical simulations presented are based on the two-fluid model Eulerian-Eulerian approach. The Eulerian modelling framework is based on ensemble-averaged mass and momentum

transport equations for each phase. Regarding the liquid phase ( $\alpha_l$ ) as continuum and the gaseous phase (bubbles) as disperse phase ( $\alpha_g$ ), these equations without mass transfer can be written as:

$$\frac{\partial \rho_k \alpha_k}{\partial t} + \nabla \cdot (\rho_k \alpha_k \bar{u}_k) = 0 \quad (1)$$

$$\begin{aligned} \frac{\partial \rho_k \alpha_k \bar{u}_k}{\partial t} + \nabla \cdot (\rho_k \alpha_k \bar{u}_k \bar{u}_k) = & -\alpha_k \nabla P + \alpha_k \rho_k \bar{g} \\ & + \nabla \cdot [\alpha_k \mu_k^e (\nabla \bar{u}_k + (\nabla \bar{u}_k)^T)] + \bar{F}_k \end{aligned} \quad (2)$$

where  $F_k$  represents the sum of the interfacial forces that include the drag force  $F_D$ , lift force  $F_L$ , virtual mass force  $F_{VM}$ , wall lubrication force  $F_{WL}$  and turbulent dispersion force  $F_{TD}$ . Turbulence of the liquid phase is modelled using a standard  $k$ - $\varepsilon$  model while a zero equation turbulence model is employed for the disperse phase. Bubble induced turbulence caused by wakes of bubbles is accounted according to Sato's bubble-induced turbulent viscosity [9].

Detail descriptions of the interfacial forces that appear in the momentum equation can be found in Anglart and Nylund [10]. Briefly, the inter-phase momentum transfer between gas and liquid due to drag force is given by

$$F_D = \frac{1}{8} C_D a_{if} \rho_l |\bar{u}_g - \bar{u}_l| (\bar{u}_g - \bar{u}_l) \quad (3)$$

In a vertical pipe flow, the non-drag forces that are the lift, virtual mass, wall lubrication and turbulent dispersion are forces that are directed perpendicular to the flow direction. Lift force in terms of the slip velocity and the curl of the liquid phase velocity can be described as

$$F_L = \alpha_g \rho_l C_L (\bar{u}_g - \bar{u}_l) \times (\nabla \times \bar{u}_l) \quad (4)$$

Wall lubrication force, which is in the normal direction away from the heated wall and decays with distance from the wall, is expressed by

$$F_{WL} = \frac{\alpha_g \rho_l (\bar{u}_g - \bar{u}_l)}{D_s} \max \left( 0, C_{wl} + C_{w2} \frac{D_s}{y_w} \right) \bar{n} \quad (5)$$

Turbulence induced dispersion taken as a function of turbulent kinetic energy and gradient of the void fraction of the of liquid yields in the form of:

$$F_{TD} = -C_{TD} \rho_l k \nabla \alpha_l \quad (6)$$

The drag coefficient  $C_D$  in equation (3) has been correlated for several distinct Reynolds number regions for individual bubbles according to Ishii and Zuber [11]. The constant  $C_L$  has been correlated according to Tomiyama [12] – a relationship expressed as a function of the Eotvos number that allows positive and negative lift coefficients depending on the bubble size. The correlation also accounts the effects of bubble deformation and asymmetric wake of the bubble. By default, the virtual mass coefficient  $C_{VM}$  takes the value of 0.5 while the wall lubrication constants  $C_{wl}$  and  $C_{w2}$  are  $-0.01$  and  $0.05$  respectively. The coefficient  $C_{TD}$  is adjusted to 0.5 in the current study.

By definition, the interfacial area concentration  $a_{if}$  for bubbly flows can be determined through the relationship:

$$a_{if} = \frac{6\alpha_g}{D_s} \quad (7)$$

where  $D_s$  is the bubble Sauter mean diameter. From the drag and non-drag forces above, it is evident that the interfacial area concentration  $a_{if}$  as well as the bubble Sauter man diameter in equation (7) are essential parameters that link the interaction between the liquid and gas (bubbly) phases. In most two-phase flow studies, the common approach of prescribing constant bubble sizes through the mean bubble Sauter diameter is still prevalent. Such an approach does not allow dynamic representation of the changes in the interfacial structure; the two-fluid model remains deficient in predicting flow transition behaviour from bubbly to slug regimes. In order to resolve the problem, the average number density transport equation, which allows changes in the two-phase flow structure to be predicted mechanistically, is introduced and described below.

### Average Bubble Number Density Equation

The average bubble number density transport equation can be expressed as

$$\frac{\partial n}{\partial t} + \nabla \cdot (\bar{u}_g n) = \phi_n^{CO} + \phi_n^{BK} \quad (8)$$

where  $n$  is the bubble number density and  $\phi_n^{CO}$  and  $\phi_n^{BK}$  are the bubble number density variations induced by coalescence and breakage. Assuming a single bubble size given by the bubble Sauter mean diameter, the bubble number density for bubbly flow can be defined as

$$n = \frac{\alpha_g}{\pi D_s^3 / 6} = \frac{1}{36\pi} \frac{a_{if}^3}{\alpha_g^2} \quad (9)$$

It is observed that by solving the transport equation for the bubble number density  $n$ , the changes to the interfacial structure is locally accommodated throughout the flow. The inclusion of the source and sink terms in equation (8) caused by the phenomenological mechanisms of coalescence and breakage allows the description of the temporal and spatial evolution of the geometrical structure of the gas phase.

The coalescence and breakage effects due to the interactions among bubbles and between bubbles and turbulent eddies have been the subject of much attention. As far as isothermal bubbly flow is concerned, the coalescence of bubbles is caused by the random collisions driven by turbulence ( $RC$ ) and wake entrainment ( $WE$ ) while the mechanism responsible for bubble breakage is caused by the impact of turbulent eddies ( $TI$ ). These three mechanisms of coalescence and breakage developed by Wu et al. [4] have the form  $\phi_n^{CO} = \phi_n^{RC} + \phi_n^{WE}$  and  $\phi_n^{BK} = \phi_n^{TI}$ :

$$\begin{aligned} \phi_n^{RC} = & -0.021 \frac{\alpha_g^2 \varepsilon^{1/3}}{D_s^{11/3} \alpha_{\max}^{1/3} (\alpha_{\max}^{1/3} - \alpha_g^{1/3})} \left[ 1 - \exp \left( - \frac{3\alpha_{\max}^{1/3} \alpha_g^{1/3}}{\alpha_{\max}^{1/3} - \alpha_g^{1/3}} \right) \right] \\ \phi_n^{WE} = & -0.0073 U_r \frac{\alpha_g^2}{D_s^4} \end{aligned} \quad (10)$$

$$\phi_n^{TI} = 0.0945 \frac{\alpha_g \varepsilon^{1/3}}{D_s^{11/3}} \left( 1 - \frac{We_{cr}}{We} \right) \exp \left( - \frac{We_{cr}}{We} \right)$$



where  $\alpha_{\max}$ ,  $U_r$ ,  $We$  and  $We_{cr}$  are the maximum allowable void fraction (= 0.80), relative velocity between the gas and liquid phases, Weber number and critical Weber number (= 2.0), respectively. It is noted that the relative velocity  $U_r$  is approximated by the consideration of the terminal velocity of a single isolated bubble.

Nevertheless, some experimental observations [13,14] argued that the coalescence due to wake entrainment is only significant between pairs of large cap bubbles (slug flow regime) in fluid sufficiently viscous to maintain their wake laminar; whereas small spherical or ellipsoidal bubbles tend to repel each other. As far as bubbly flows are concerned, Hibiki and Ishii [5] and Yao and Morel [6], therefore, considered only the coalescence of the bubbles governed mainly by the random collisions driven by turbulence. These two models are rather similar as can be observed below in their derivations. However, Yao and Morel [6] introduced the interaction time of the bubbles to coalesce and break-up in addition to the free travelling time as considered in their model as well as in Hibiki and Ishii [5] model. These coalescence and breakage mechanisms developed by Hibiki and Ishii [8] have the form

$$\phi_n^{CO} = -0.03 \frac{\alpha_g^2 \varepsilon^{1/3}}{D_s^{11/3} (\alpha_{\max} - \alpha_g)} \exp\left(-1.29 \frac{\rho_l^{1/2} \varepsilon^{1/3} D_s^{5/6}}{\sigma^{1/2}}\right) \quad (11)$$

$$\phi_n^{BK} = 0.03 \frac{\alpha_g (1 - \alpha_g) \varepsilon^{1/3}}{D_s^{11/3} (\alpha_{\max} - \alpha_g)} \exp\left(-1.37 \frac{\sigma}{\rho_l \varepsilon^{2/3} D_s^{5/3}}\right)$$

while in Yao and Morel [6] model, they have been derived as

$$\phi_n^{CO} = -2.86 \frac{\alpha_g^2 \varepsilon^{1/3}}{D_s^{11/3}} \frac{\exp\left(-1.017 \sqrt{\frac{We}{We_{cr}}}\right)}{\frac{\alpha_{\max}^{1/3} - \alpha_g^{1/3}}{\alpha_{\max}^{1/3}} + 1.922 \alpha_g \sqrt{\frac{We}{We_{cr}}}} \quad (12)$$

$$\phi_n^{BK} = 1.6 \frac{\alpha_g (1 - \alpha_g) \varepsilon^{1/3}}{D_s^{11/3}} \frac{\exp\left(-\frac{We}{We_{cr}}\right)}{1 + 0.42 (1 - \alpha_g) \sqrt{\frac{We}{We_{cr}}}}$$

The maximum allowable void fraction in Hibiki and Ishii [5] and Yao and Morel [6] models retains the value of 0.52, which corresponds to the transition between the finely dispersed bubbly flow and slug flow. The critical Weber number in Yao and Morel [6] model is set to a value of 1.24.

## Experimental Details

The two-phase flow experiment has been performed at the Thermal-Hydraulics and Reactor Safety Laboratory in Prudue University. The test section was a round tube made of acrylic with an inner diameter ( $D$ ) of 50.8 mm and a length ( $L$ ) of 3061 mm. The temperature of the apparatus was kept at a constant temperature (20°C) within the deviation of  $\pm 0.2^\circ\text{C}$  by a heat exchanger installed in a water reservoir. Local flow measurements using the double sensor and hotfilm anemometer probes were performed at three axial (height) locations of  $z/D = 6.0, 30.3$  and  $53.5$  and 15 radial locations of  $r/R = 0$  to  $0.95$ . A range of superficial liquid velocities  $j_l$  and superficial gas velocities  $j_g$  have been performed, which covered mostly the bubbly flow region, including finely dispersed bubbly flow and bubbly-to-slug transition flow regions. Area averaged superficial gas velocity  $\langle j_g \rangle$  was obtained from local void fraction and gas velocity measured by the double sensor probe, whereas area

averaged superficial liquid velocity  $\langle j_l \rangle$  was obtained from local void fraction measured by the double sensor probe and local liquid velocity measured by the hotfilm anemometry. More details regarding the experimental set-up can be found in Hibiki and Ishii [5]. In this paper, numerical predictions have been compared against local measurements at the flow conditions:  $\langle j_l \rangle$  of 0.986 m/s,  $\langle j_g \rangle$  of 0.0473 m/s, inlet void fraction of 5% and inlet bubble size of 3 mm.

## Numerical Details

Solution to the two sets of governing equations for momentum was sought. Radial symmetry has been assumed, so that the numerical simulations could be performed on a  $60^\circ$  radial sector of the pipe with symmetry boundary conditions at both sides. Inlet conditions were assumed to be homogeneous in regards to the superficial liquid and gas velocities, void fractions for both phases and uniformly distributed bubble size in accordance with the flow conditions described above. At the pipe outlet, a relative average static pressure of zero was specified. A three-dimensional mesh containing hexagonal elements was generated resulting in a total of 30000 elements covering the entire pipe domain. Reliable convergence was achieved within 400 iterations for a satisfied convergence criterion based on the RMS (Root Mean Square) residuals of  $1.0\text{e-}4$  and for a physical time scale of the fully implicit solution method of 0.01 s.

## Results and Discussion

The local radial profiles of the void fraction, interfacial area, bubble Sauter mean diameter, vapour and liquid velocities at two axial locations of  $z/D = 6.0$  and  $53.5$  are predicted through the two-fluid and population balance models.

Figure 1 shows the void fraction distributions at the two axial locations for the measured data and results obtained from the various coalescence and breakage models employed in the average bubble number density transport equation. In isothermal gas-liquid bubbly flows, Serizawa and Kataoka [15] classified the phase distribution patterns into four basic types of distributions: “wall peak”, “intermediate peak”, “core peak” and “transition”. The void fraction peaking near the pipe wall represented the flow phase distributions caused by the typical “wall peak” behaviour. From these results, it was observed that a well-developed wall peaking occurred further downstream at the axial location of  $z/D = 53.5$  (near the exit) instead at the location of  $z/D = 6.0$  (near the inlet). The three model predictions of the radial void fraction distributions could be seen to capture the similar behaviour trends with the measurements very well at these two locations.

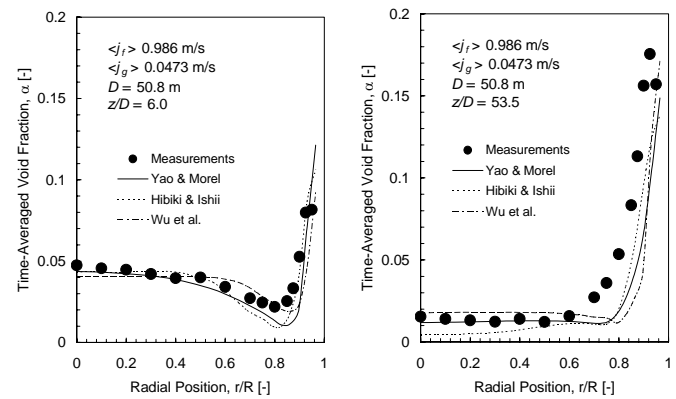


Figure 1. Local predicted and measured void fraction profiles at  $z/D = 6.0$  and  $53.5$ .

Figure 2 illustrates the interfacial area concentration distributions for the respective two axial locations for the measurements and the three model predictions. The measured data followed the similar profile as the void fraction distribution as stipulated in Figure 1. From these results, the three coalescence and breakage models compared very well with the experimental data. Nevertheless, the bubble Sauter mean diameter distribution in

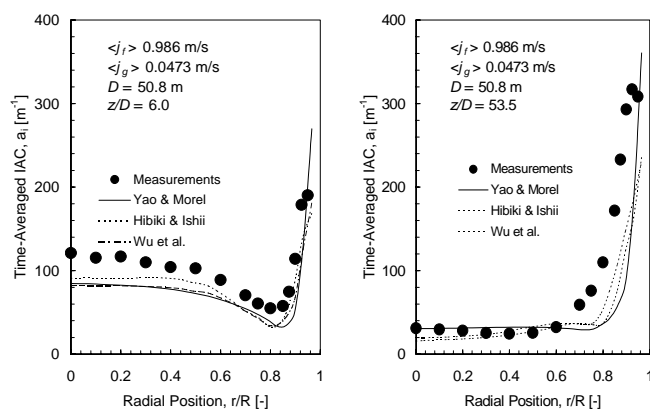


Figure 2. Local predicted and measured interfacial area concentration profiles at  $z/D = 6.0$  and  $53.5$ .

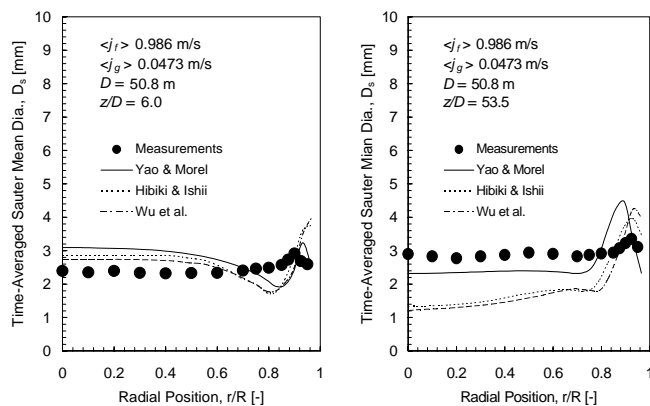


Figure 3. Local predicted and measured bubble Sauter mean diameter profiles at  $z/D = 6.0$  and  $53.5$ .

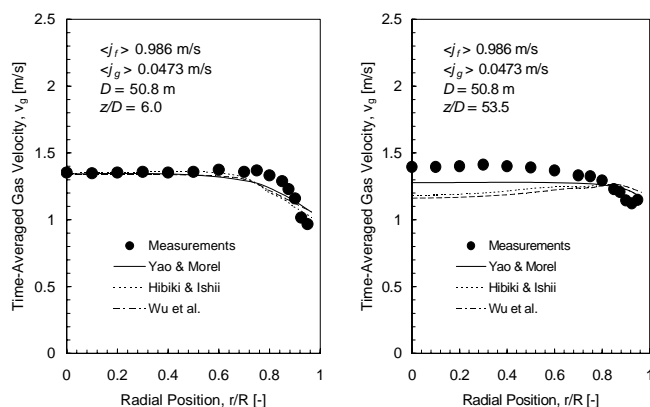


Figure 4. Local predicted and measured gas velocity profiles at  $z/D = 6.0$  and  $53.5$ .

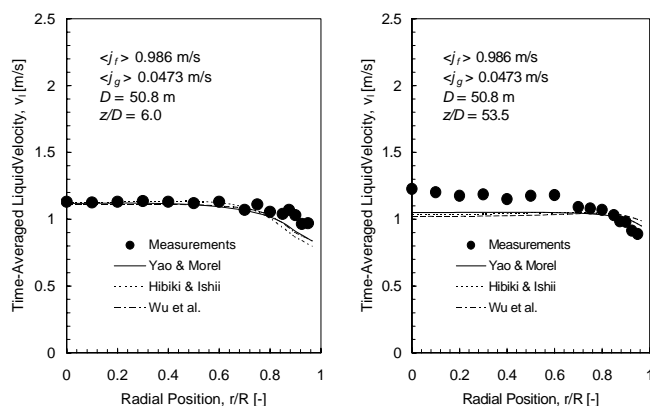


Figure 5. Local predicted and measured liquid velocity profiles at  $z/D = 6.0$  and  $53.5$ .

Figure 3 was better predicted by Yao and Morel [6] model at  $z/D = 53.5$  in comparison to the model predictions made by Wu et al. [4] and Hibiki and Ishii [5].

Figures 4 and 5 show the local radial vapour and liquid velocity distribution at the two axial locations. The introduction of bubbles into the liquid flow had the tendency to flatten the liquid velocity profiles with a relatively steep decrease close to the pipe wall. The same behaviour was also observed for the gas velocity profiles. Overall, all the three model predictions of the gas and liquid velocities were in satisfactory agreement with measurements.

## Conclusions

A two-fluid model coupled with population balance approach is presented in this paper to handle isothermal gas-liquid bubbly flows. The average bubble number density transport equation was formulated and implemented in the CFD code CFX5.7 to determine the temporal and spatial geometrical changes of the gas bubbles. Coalescence and breakage mechanisms by Wu et al. [4], Hibiki and Ishii [5] and Yao and Morel [6] were assessed against experiments performed at Purdue University. Satisfactory agreements were achieved for the void fraction, interfacial area concentration, bubble Sauter mean diameter and gas and liquid velocities against measurements.

## References

- [1] Delhaye, J.M. & Bricard, P., Interfacial Area in Bubbly Flow: Experimental Data and Correlations, *Nuc. Eng. Des.*, **151**, 1994, 65-77.
- [2] Kocamustafaogullari, G., Huang, W.D. & Razi, J., Measurement of Modeling of Average Void Fraction, Bubble Size and Interfacial Area, *Nuc. Eng. Des.*, **148**, 1994, 437-453.
- [3] Lehr, F. & Mewes, D., A Transport Equation for the Interfacial Area density Applied to Bubble Columns, *Chem. Eng. Sci.*, **56**, 2001, 1159-1166.
- [4] Wu, Q., Kim, S., Ishii, M. & Beus, S.G., One-Group Interfacial Area Transport in Vertical Bubbly Flow, *Int. J. Heat Mass Transfer*, **41**, 1998, 1103-1112.
- [5] Hibiki, T., & Ishii, M., Axial Interfacial Area Transport of Vertical Bubbly Flows, *Int. J. Heat Mass Transfer*, **44**, 2001, 1869-1888.
- [6] Yao, W., & Morel, C., Volumetric Interfacial Area Prediction in Upwards Bubbly Two-Phase Flow, *Int. J. Heat Mass Transfer*, **47**, 2004, 307-328.
- [7] Lo, S., Application of Population Balance to CFD Modelling of Bubbly Flow via the MUSIG model, AEA Technology, *AEAT-1096*, 1996.
- [8] Yeoh, G.H. & Tu, J.Y., Population Balance Modelling for Bubbly Flows with Heat and Mass Transfer, *Chem. Eng. Sci.*, 2004, in press.
- [9] Sato, Y., Sadatomi, M. & Sekoguchi, K., Momentum and Heat Transfer in Two-Phase Bubbly Flow-I, *Int. J. Multiphase Flow*, **7**, 1981, 167-178.
- [10] Anglart, H. & Nylund, O., CFD Application to Prediction of Void Distribution in Two-Phase Bubbly Flows in Rod Bundles, *Nuc. Sci. Eng.*, **163**, 1996, 81-98.
- [11] Ishii, M. & Zuber, N., Drag Coefficient and Relative Velocity in Bubbly, Droplet or Particulate Flows, *AIChE J.*, **25**, 1979, 843-855.
- [12] Tomiyama, A., Struggle with Computational Bubble Dynamics, ICMF'98, 3rd Int. Conf. Multiphase Flow, Lyon, France, 1998, 1-18.
- [13] Stewart, C.W., Bubble Interaction in Low-Viscosity Liquids, *Int. J. Multiphase Flow*, **41**, 1998, 1103-1112.
- [14] Otake, T., Tone, S., Nakao, K. & Mitsuhashi, Y., Coalescence and Breakup of Bubbles in Liquids, *Chem. Eng. Sci.*, **32**, 1997, 377-383.
- [15] Serizawa, I., & Kataoka, I., Phase Distribution in Two-Phase Flow, in N.H. Afgan (Ed.), *Transient Phenomena in Multiphase Flow*, Washington DC, 1988, 179-224.

## Numerically Modelling Blockage Effects on the Flow Between Flat Plates

M.D. Griffith, K. Hourigan and M.C. Thompson

Department of Mechanical Engineering  
Monash University, Clayton, VIC, 3800, AUSTRALIA

### Abstract

Results are reported for a two-dimensional numerical investigation of the effect of various semi-circular blockages on the laminar flow between two plates, for Reynolds number between 50 and 3000, and blockage ratio ranging from 0.05 to 0.9. The study is undertaken with the intention of providing a fundamental understanding of blockage effects in arterial constrictions, or stenoses. The results with blockage ratio of 0.5 compare favourably with previous work on the flow over a backward-facing step. The two-dimensional parameter space for Reynolds number and blockage ratio is also mapped out. The analysis suggests that the onset of three-dimensionality of the flow is likely to be closely matched with that previously established for backward-facing step flow. Flow phenomena associated with blockage ratios above and below the customary half-blockage are summarised, including smaller-than-expected flow separation lengths for lower blockages, and vortex shedding and unusual structures within the recirculation zones for higher blockages.

### Introduction

The study of blockage effects in internal flows has typically focused on determining correction factors for small blockage ratios in wind tunnels. The standard study of the flow over a backward-facing step closely matches a half-blocked flow, but such studies tend to be more interested in the various instabilities that occur in the flow, rather than on any effects the step height may have. This study examines the flow behaviour between two flat plates, with the addition of a semi-circular blockage, of variable size, attached to one side. The blockage ratio is defined as  $b = r/D$ , where  $r$  is the radius of the semi-circular blockage and  $D$  is the distance between the two plates. Figure 1 shows one of the computational meshes used, with a blockage ratio of 0.7. Such a study has particular relevance to the flow through arterial constrictions, but also to industrial applications involving pipe flow.

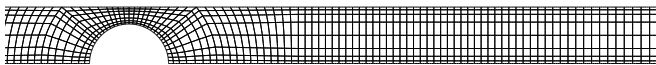


Figure 1: Computational mesh, showing macroelements, used for blockage ratio = 0.7.

The subject of this study bears much similarity to the flow over a backward-facing step, of which there is a far greater availability of literature. This is due to the fact that it offers one of the simplest and most well-defined occurrences of separated flow. The standard test-section geometry is well-known, consisting of a channel with a sudden expansion. This expansion causes an immediate separation of the flow, along with the appearance of a recirculation zone. The work of Armaly *et al.* [1] offers a detailed review of the subject, including an experimental investigation with a fixed expansion ratio of 0.516, and Reynolds numbers ranging through the laminar, turbulent and transitional regimes. With increasing Reynolds number in the laminar regime, the length of the first recirculation zone also in-

creased, and was accompanied by the appearance, downstream, of more recirculation zones on alternating sides of the channel. Three-dimensional effects were also observed.

Numerical studies of the problem, as in [2, 3, 4], give good accounts of the development of unsteadiness and three-dimensionality in the flow, and are important in determining the limitations of two-dimensional analyses. The work of Williams and Baker [10] is particularly useful, in its comparison of two and three-dimensional numerical simulations of backward-facing step flow. For the geometry used in the present two-dimensional study, the exact onset of three-dimensionality in the flow is unknown and must be kept in consideration. The work of Thangam and Knight [8] seems to present the only study of the effects of step height. They found a strong dependence of recirculation length on step height, with a Reynolds number based on the width of, and maximum velocity in, the small inlet, before the expansion.

An investigation focusing on higher blockage effects was carried out by Sahin and Owens' [6], but it used the geometry of a freely suspended cylinder between two plates, and was more interested in how the problem related to cases of unbounded flow past cylinders. Although the geometry bears only a limited similarity to this study (it is symmetrical and creates a wake consisting of twin vortices) Sahin and Owens work showed that the proximity of the walls would increase the critical Reynolds number at which shedding would occur. Also of some interest is the work of Marquillie and Ehrenstein [5], which examines the flow over a bump on a flat plate. Their work, having no blockage effects, showed that at high Reynolds number, the flow became unsteady, with smaller zones of recirculation shedding off the end of the main recirculation zone.

This paper will firstly give a brief outline of the method used in the study, followed by a description of the various flow behaviours occurring over the parameter space.

### Method

#### Problem Definition

Figure 1 shows a section of the macro-element mesh used for the cases run with blockage ratio of 0.7. Similar meshes were produced for blockage ratios from 0.05 to 0.9. The Reynolds number is based on the hydraulic diameter ( $2D$ ) and is described by:

$$Re = \frac{2DU_{ave}}{\nu} \quad (1)$$

where  $U_{ave}$  is the average flow velocity between the plates at inlet and  $\nu$  denotes the kinematic viscosity. Data cited from other studies have been rescaled to fit this Reynolds number definition. A fully-developed Poiseuille profile, with a non-dimensionalised average velocity of 1, and a peak of 1.5, was prescribed at the inlet, such that:

$$U = 6y(1-y) \quad (2)$$

where the bottom and top walls are placed at  $y=0$  and  $y=1$ , respectively. The inlet was placed six plate widths ( $6D$ ) upstream

of the bump, and the outlet 25 widths downstream. Increasing distances beyond these values produced no discernible effect on the near-wake behaviour.

Tests were done over a broad range of Reynolds number, with the main restriction being the higher velocities generated over the semi-circular blockage. Blockage ratios ranging from 0.05 to 0.9 were used. For the lower blockage ratios, runs were made for Reynolds numbers ranging from 50 to 3000, whilst for higher blockages the upper limit was more restricted. The maximum Reynolds number achieved for the blockage ratio 0.9 was 500. This highlights a limitation of the two-dimensional analysis. For the flow between two flat plates, the transition to turbulence is known to begin when  $Re \approx 2000$ . In addition to this, the constriction of the flow over the blockage will act as an additional tripping mechanism for transition.

### Numerical Method

The investigation employed a spectral-element method. Previously, the software for this method has been successfully used and validated in the prediction of wake flows past rings [7] and circular cylinders [9]. The spectral-element code uses high-order Lagrangian polynomial interpolants to approximate the solution variables for each element. Generally, a grid resolution of 49 ( $7 \times 7$ ) nodes per element was used, however for higher blockages and Reynolds numbers, elements comprising of  $8 \times 8$  nodes per element had to be employed, to properly resolve parts of the flow field. Recirculation lengths and downstream vorticity profiles were the flow field characteristics used to analyse the effect of grid resolution. Increasing the nodal concentrations beyond the levels described produced no discernible effect.

### Results

#### Flow Separation Length

Figure 2 shows the streamlines for the flow over a blockage of 0.5, at  $Re = 1000$ . This geometry is the closest to the classic

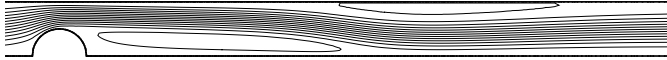


Figure 2: Streamlines for  $b = 0.5$  and  $Re = 1000$ .

backward-facing step case and the flow behaved much as expected. For this case, two flow separation zones (FSZ's) can be seen: immediately after the blockage, and then on the top wall, beginning near where the flow reattaches on the bottom. The initial FSZ is formed by the sudden expansion at the blockage, and the subsequent adverse pressure gradient along the back half of the blockage. The length of this initial flow separation zone,  $L$ , serves as an effective way of characterising the flow behaviour. The end of the first recirculation zone,  $L$ , was determined by locating where the line of zero velocity, emanating from the flow separation point at the blockage, met the lower wall. Dividing by the blockage height,  $r$ , normalises the recirculation length for different blockage ratios.

For this blockage size and up to  $Re \approx 400$ , the recirculation length matched well with the data of previous studies. Above this point, the two-dimensional computational results give a recirculation length lower than previous experimental results for a backward-facing step [1]. Williams and Baker [10] have examined this problem previously in their investigation of two and three-dimensional numerical simulations for backward-facing steps. They found that the flow became three-dimensional at  $Re \approx 400$ , and that recirculation lengths calculated from these three-dimensional results, more closely matched the experimental results of Armaly *et al.* [1]. The onset of this three-

dimensionality can be put down to the effect of the sidewalls of the experimental apparatus. Hence, regardless of any effect caused by the different two-dimensional geometries, a divergence between the experimental and two-dimensional results at this Reynolds number is not wholly unexpected. Data is not available on when the two dimensional flow may become three-dimensional for the other blockage ratios, but the 0.5 blockage gives us some guide.

Figure 3 shows a plot of all normalised recirculation lengths for all blockages. Also depicted on the graph are the results of

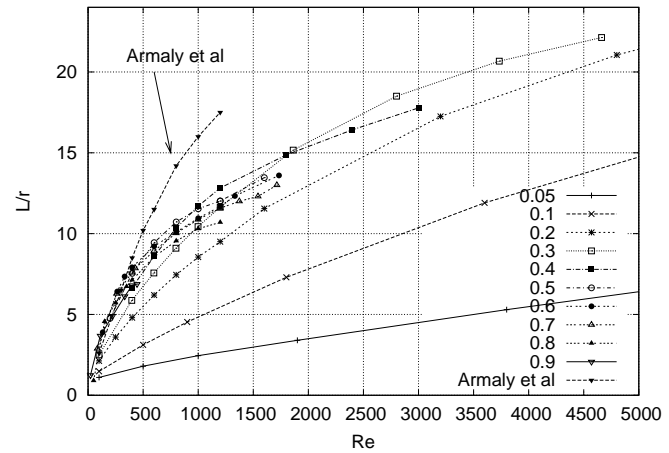


Figure 3: Plot of normalised recirculation length ( $L/r$ ) against upstream Reynolds number ( $Re$ ).

Armaly *et al.* [1], up to  $Re = 1200$ , where they observed the transitional flow regime beginning. The divergence at  $Re \approx 400$  between the two data sets, at which the flow is thought to become three-dimensional, can be clearly seen, and bears a strong similarity to the comparisons made by Williams and Baker [10]. Excepting the lower blockage ratios, the data sets for each ratio appear to follow a similar curve, meaning the normalised recirculation length is largely a function of upstream Reynolds number. The work on step-height effects for a backward-facing step flow by Thangam and Knight [8] showed a much greater dependence on step height, or blockage size. However, the Reynolds number in that study was referenced to the maximum velocity before the step, which did not change with the step height. In this study, the comparable velocity, by continuity, is dependent on the blockage size. For this geometry, referencing the upstream velocity and channel width for the Reynolds number, yielded the most useful form of figure 3.

The lower blockage ratios, 0.05, 0.1 and 0.2, produced recirculation lengths lower than those for higher blockages. These results can largely be put down to the low fluid velocities at these blockage heights. If we examine equation 2, at  $y = 0.05$ , it returns  $U_{y=0.05} = 0.285U_{ave}$ . At these heights, the more rapid parts of the fluid flow over the blockage are largely unperturbed. The low fluid velocity in the vicinity of the blockage results in a smaller recirculation zone. A similar effect is either masked or not reproduced at  $b = 0.9$ , since the entirety of the fluid flow is forced through the tiny gap, meaning a very high velocity around the blockage. Using the local  $U$  velocity at the blockage height, calculated by equation 2, as the reference velocity for the Reynolds number, concentrates the results on figure 3 into a slightly smaller band, but doesn't allow for an easy comparison with other studies and geometries, such as backward-facing steps.

#### Wake behaviour

Apart from the behaviour of the initial flow separation length,

there were other flow phenomena observed in the parameter space. As observed in many backward-facing step studies, the appearance of a second FSZ on the upper wall, near the end of the initial FSZ, would occur as the Reynolds number was increased. This secondary zone results from another adverse pressure gradient, produced when the flow expands near the end of the first recirculation zone. It was found that the secondary zone of recirculation could only be produced with blockages of 0.3 and greater. For  $b = 0.3$ , the secondary zone appeared at  $Re \approx 2200$ , and for  $b = 0.9$ , at  $Re \approx 60$ . By a similar mechanism, a third zone of recirculation could be produced, but only for  $b \geq 0.6$ . No third recirculation zone is observed for  $b = 0.5$ , which is in contrast to the work of Armaly *et al.* [1], who observed the third recirculation zone for Reynolds numbers between 1200 and 2300. However, this experimental range falls within the transitional regime, which is not accounted for in the present two-dimensional investigation. Figure 4 presents a map of the parameter space, presenting the boundaries over which various phenomena occur. It includes the boundaries at which the second and third recirculation zones begin to appear. It is important to note that data is only known at 0.1 blockage intervals, boundary lines are fitted to those data and the precise critical Reynolds number for each phenomenon may not be known.

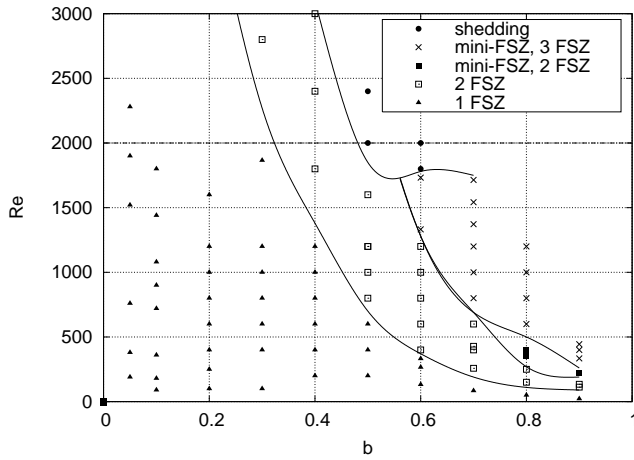


Figure 4: Map of wake behaviour over Reynolds number and blockage. Lines indicate the boundaries of each wake behaviour. Data points are also plotted.

Those data points labelled “mini-FSZ” denote the appearance at the end of the initial recirculation zone of a vortex structure, not observed in the previously cited backward-facing step investigations. This steady vortex structure is never apparent with the 0.5 blockage ratio, which is the closest geometry to the standard backward-facing step. The vortex structure makes a brief appearance with the 0.6 blockage ratio, at  $Re \approx 1500$ . Increasing the Reynolds number to 1800, produces vortex shedding from the blockage. The phenomenon is best observed with the 0.7 and 0.8 blockage ratios. Figure 5 shows plots of the vorticity at  $b = 0.7$  and  $Re = 400, 800, 1200, 1600$ .

The first instance, at  $Re = 400$ , is located below the relevant boundary on figure 4, and the steady vortex structure is not immediately apparent. The next three instances clearly depict the appearance of the vortex structure at the end of the first recirculation zone. The structure seems to consist, initially, of a single smaller zone of recirculating flow, just behind the point at which the flow reattaches to the bottom wall. As the Reynolds number increases, a second smaller recirculating zone can be seen, particularly for  $Re = 1200$ . At  $Re = 1600$ , a third zone is apparent indicating that a series of these zones is developing upstream, as the Reynolds number is increased.

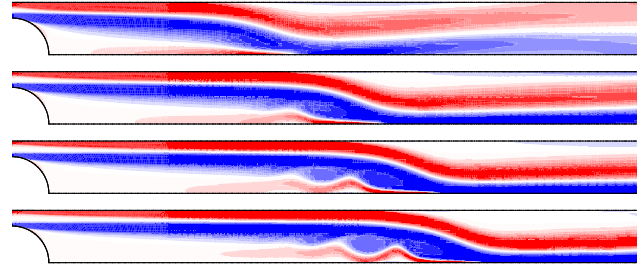


Figure 5: Visualisation of the vorticity field, at  $b = 0.7$  and  $Re = 400, 800, 1200, 1600$ .

Figure 6, on the following page, shows a close-up of another instance of this vortex structure, this time at  $b = 0.8$  and  $Re = 1000$ . Total velocity vectors are overlaid on the vorticity field to give a better indication of the flow behaviour. The vortex structure here seems quite complex. A series of three mini-recirculations is apparent and even the hint of a fourth is present. Closer inspection reveals the presence of further, even smaller recirculations, or mini-flow separation zones, between the obvious ones in figure 6, closer to the bottom wall. If we examine the very end of the first major recirculation zone, there exists a high reverse velocity back along the bottom wall. This flow seems to quickly separate, precipitating the appearance of the first smaller recirculation zone. Figures 5 and 6 suggest that an increase in Reynolds number promotes the continued development of the vortex pattern, right up until the onset of vortex shedding from the blockage. The steadiness of this vortex structure was initially surprising. Tests were performed and the steady state did not respond to small perturbations in the flow, higher mesh resolutions or longer outlet lengths.

The points labelled “shedding” on figure 4 represent those simulations where the flow sheds vortices from the blockage. The different vortex dynamics, on and above the corresponding boundary, have not yet been fully analysed. In comparison to Sahin and Owens work [6], the onset of shedding is delayed to a much higher Reynolds number ( $Re \approx 1800$ , rather than  $Re \approx 340$ ). This is to be expected, as there is only one large vortex forming behind the asymmetric blockage of this study, as compared to the far more unstable twin vortices behind the cylinder in Sahin and Owens’ study. There is a possible comparison here, in the occurrence of delayed shedding. The proximity of the top wall to the blockage may be having a suppressing effect on shedding, much as the proximity of the two walls does on the shedding from the Sahin and Owens cylinder [6]. Looking again at figure 4, we see that, up to the 0.5 blockage, the gradient of the boundary for the appearance of shedding, at least partially, continues in the boundary for the appearance of the apparent new vortex structure in the initial flow separation zone. The appearance and growth of this structure in the initial flow separation zone as Reynolds numbers and blockage ratios increase, may indicate an increasing, yet delayed, propensity for shedding to begin.

If we consider that Armaly *et al.* observed the transition to turbulence commencing at  $Re = 1200$  for a 0.5 blockage ratio on a backward-facing step [1], we could reasonably surmise that the critical Reynolds number for transition would be even lower for higher blockage ratios. The blockage’s effectiveness as a tripping mechanism would only increase with the size of the blockage. Taking this into consideration, it is possible the instability in the initial flow separation zone, as shown in figure 6, only occurs above where the transition to turbulence would occur. The instability may be an indication that the flow at these Reynolds number is no longer two-dimensional and perhaps the same vortex structure would not be reproduced in any three-dimensional



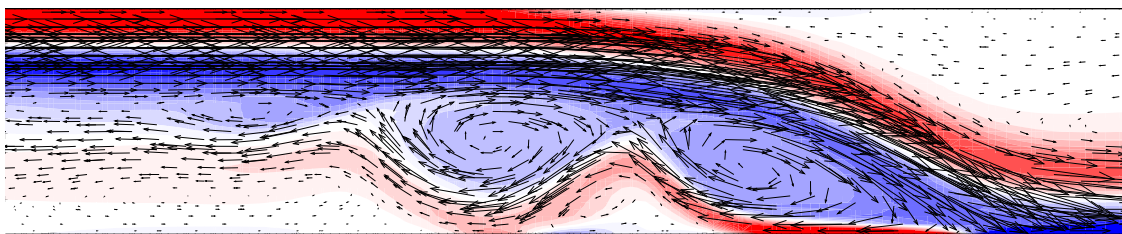


Figure 6: Close-up of the end of the initial FSZ for  $b = 0.8$  and  $Re = 1000$ . Vorticity is plotted, with total velocity vectors overlaid.

simulations or experiments. Work on the similarities and differences between two and three-dimensional simulations for high blockage ratios, similar to that by Williams and Baker [10] on a backward-facing step of 0.5 blockage ratio, is not available and, for now, can only be estimated.

### Conclusions

A numerical investigation of the two-dimensional laminar flow over semi-circular blockages has been carried out. Comparisons have been made with studies of the flow over a backward-facing step, which bears several similarities to the geometry used in this study. The results for  $b = 0.5$  compared favourably with the experimental work of Armaly *et al.* [1] and the numerical simulations of Williams and Baker [10]. The lengths of the initial flow separation were closely matched with the experimental work, up to  $Re \approx 400$ , where the onset of three-dimensionality is thought to occur. Excepting the smaller blockage ratios, for a constant upstream Reynolds number, the normalised recirculation lengths seemed to all behave similarly. For blockage ratios equal to or less than 0.2, it was found that the low velocities around the blockages, close to the channel wall, resulted in a smaller initial recirculation zone. At higher blockage ratios, the reduction in area and the resultant high velocity through the constriction masked or cancelled out any similar effect.

For blockage ratios of 0.4 and greater, vortex shedding from the blockage was observed for higher Reynolds numbers. For blockage ratios of 0.6 and greater the appearance of a vortex structure at the end of the first recirculation zone was observed, before the onset of shedding. It was postulated that the appearance of this vortex structure was an indication of delayed or suppressed shedding. Whether the same vortex structure will be reproduced in any three-dimensional simulations or experiments is currently under investigation.

### Acknowledgements

The research was principally supported by the Australian Research Council, ARC Grant No:DP0452664

### References

- [1] Armaly, B.F., Durst, F., Pereira, J.C.F and Schoenung B., Experimental and Theoretical Investigation of Backward-Facing Step Flow, *J. Fluid Mech.*, **127**, 1983, 473–496.
- [2] Barkley, D., Gomes, M.G.M and Henderson, R.D., Three-Dimensional Instability in Flow over a Backward-Facing Step, *J. Fluid Mech.*, **473**, 2002, 167–190.
- [3] Kaiktis, L., Karniadakis, G.E. and Orszag, S.A., Onset of Three-Dimensionality, Equilibria, and Early Transition in Flow over a Backward-Facing Step, *J. Fluid Mech.*, **231**, 1991, 501–528.
- [4] Kaiktis, L., Karniadakis, G.E. and Orszag, S.A., Unsteadiness and Convective Instabilities in Two-Dimensional Flow over a Backward-Facing Step, *J. Fluid Mech.*, **321**, 1996, 157–187.
- [5] Marquillie, M. and Ehrenstein, U., On the onset of nonlinear oscillations in a separating boundary-layer flow, *J. Fluid Mech.*, **490**, 2003, 169–188.
- [6] Sahin, M. and Owens, R.G., A Numerical Investigation of Wall Effects up to High Blockage Ratios on Two-Dimensional Flow past a Confined Circular Cylinder, *Phys. Fluids*, **16**, 2004, 1305–1320.
- [7] Sheard, G.S., Thompson, M.C. and Hourigan, K., From Spheres to Circular Cylinders: Classification of Bluff Ring Transitions and Structure of Bluff Ring Wakes, *J. Fluid Mech.*, **492**, 2003, 147–180.
- [8] Thangam, S. and Doyle, D. D., Effect of Stepheight on the Separated Flow past a Backward Facing Step (brief communication), *Phys. Fluids A*, **1**, 1989, 604–606.
- [9] Thompson, M.C., Hourigan, K. and Sheridan, J., Three-Dimensional Instabilities in the Wake of a Circular Cylinder, *Exp. Therm. Fluid Sci.*, **12**, 1996, 190–196.
- [10] Williams, P.T. and Baker, A.J., Numerical Simulations of Laminar Flow over a 3D Backward-Facing Step, *Int. J. Numer. Methods Fluids*, **24**, 1997, 1159–1183



# Effects of Turbulence Manipulation in Skimming Flows: An Experimental Study

C.A. Gonzalez and H. Chanson

Department of Civil Engineering  
The University of Queensland, Brisbane QLD, 4072 AUSTRALIA

## Abstract

Current expertise in air-water flow properties in turbulent flows is limited to low to moderate Reynolds numbers and a few types of surfaces (roughness). Highly turbulent air-water flows cascading down a large-size stepped spillway model were systematically investigated with a 22° slope. Several stepped configurations were tested and turbulence manipulation was conducted to enhance interactions between skimming flows and cavity recirculating regions. Systematic experiments were performed with 3 new configurations to complement an initial study [6] with another three configurations. Turbulence modifiers (vanes or longitudinal ribs) were observed to have a strong influence on the air-water flow properties, with wakes or low-speed streaks observed above each vane.

## Introduction

Numerous studies of turbulent flows over rough surfaces were conducted with different approaches [1,10,14]. However, only a limited number of the published papers refer to highly turbulent flows associated with strong free-surface aeration [3,7]. One such flow situation is a high velocity open channel flow skimming down a stepped canal (Figure 1). This type of channel design is common for overflow spillways of gravity and embankment dams [4]. Most structures were designed with flat horizontal steps but some included devices to enhance energy dissipation [6]. There may be some analogy between skimming flows over stepped chutes and skimming flows above large roughness elements, including boundary layer flows past d-type roughness. Chanson and Toombes [7] presented new experimental evidence for the former. Djenidi et al [10] provided a comprehensive review of the latter configuration, while Aivazian [1] studied zigzag strip roughness. Mochizuki et al [13,14] studied turbulent boundary layer past d-type roughness with thin longitudinal ribs. Despite conflicting interpretations of their data, their experiments demonstrated some turbulence manipulation by interfering with the recirculation vortices.

Chanson and Gonzalez [6] demonstrated a strong influence of the vanes on the air-water flow properties of both free-stream and cavity recirculation flows, as the vanes prevented the spanwise translation of cavity recirculating eddies and contributed to the development of low speed streaks above each vane. They also suggested that the microscopic air-water flow structure (bubble/droplet distribution and clustering) was affected by the presence of vanes possibly leading to form drag and energy dissipation enhancement. Their results hinted that more intricate vane arrangements could disturb further the flow.

This paper presents the result of an investigation into the effects at microscopic scales of several vane configurations. The experiments were conducted in a large stepped channel equipped with 3 new vane arrangements operating with Reynolds numbers between 4 and 9 E+5 (Figure 1, table 1). Interactions between free surface and cavity recirculation, as well as turbulence manipulation were systematically investigated in skimming flow regime.

## Experimental Facilities

New experiments were conducted at the University of Queensland in a 3.3 m long, 1 m wide, 21.8° slope chute for flow

rates ranging from 0.10 to 0.22 m<sup>3</sup>/s corresponding to a skimming flow regime with Reynolds numbers between 4 and 9 E+5 (table 1).

The water supply pump was controlled by an adjustable frequency AC motor drive. This enabled for the accurate control of the closed circuit system. Waters were supplied from a feeding basin (1.5 m deep, surface area 6.8 m × 4.8 m) leading to a sidewall convergent with a 4.8:1 contraction ratio. The test section was a broad-crested weir (1 m wide, 0.6 m long, with upstream rounded corner (0.057 m radius) followed by ten identical steps (h = 0.1 m, l = 0.25 m) made of marine ply (Figure 1). The stepped chute was 1 m wide with perspex sidewalls followed by a horizontal concrete-invert canal ending in a dissipation pit. For three series of experiments, vanes (longitudinal thin ribs) were placed among the step cavities in different configurations to modify turbulence and possibly to enhance energy dissipation (Figure 2, table 1).



Figure 1. Skimming flow down a stepped chute (h = 0.1 m) (Configuration 3  $d_c/h = 1.3$ ,  $Re = 7.3 \text{ E}+5$ ). Left: side view. Right: Top view with flow from top to bottom.

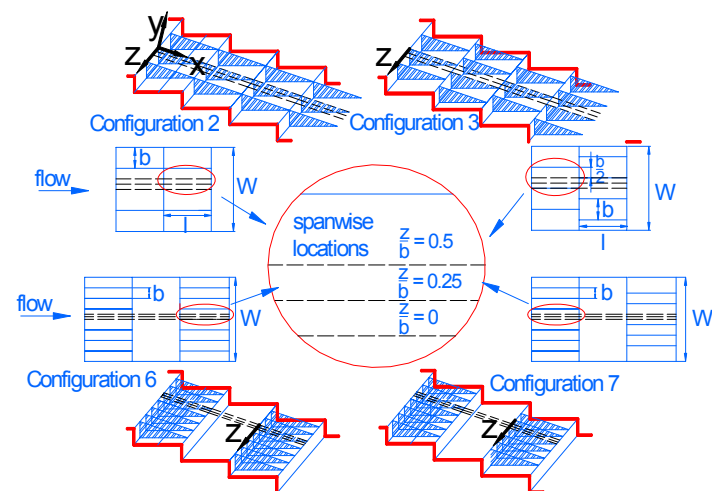


Figure 2. Sketch of a stepped invert with energy dissipation enhancers.

Clear-water flow depths were measured with a point gauge and air-water flow properties with a double-tip conductivity probe ( $\varnothing = 0.025 \text{ mm}$ ) designed at the University of Queensland [2] (Figure 3). The probe sensors were aligned in the free-stream flow direction. The leading tip had a small frontal area (i.e. 0.05 mm<sup>2</sup>) and the trailing tip was offset to avoid wake disturbance from the first tip. Tests showed the absence of wake disturbance during all experiments [2].

An air bubble detector (UQ82.518) excited the probe and its output signal was scanned at 20 kHz for 20 s. The translation of the probes in the direction normal to the channel invert was controlled by a fine adjustment travelling mechanism connected to a Mitutoyo™ digimatic scale unit. The error on the vertical position of the probe was less than 0.025 mm. The accuracy on the longitudinal probe position was estimated as  $\Delta x < \pm 0.5$  cm. The accuracy on the transverse position of the probe was less than 1mm. Flow visualizations were conducted with high-shutter speed digital still and video cameras.

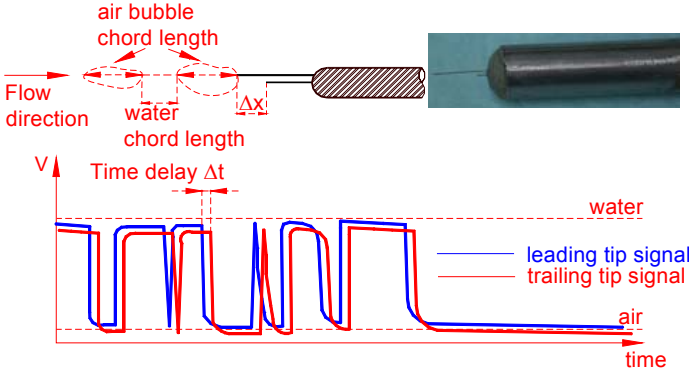


Figure 3. Sketch and photo of the double-tip conductivity probe and corresponding binary signal.

Measurements were performed at step edges and between adjacent step edges within the main flow stream and into the recirculation cavity region observed below the pseudo-bottom formed by the step edges. For the stepped configurations with vanes, measurements were conducted at spanwise locations  $z/b = 0, 0.25$  &  $0.5$ , where  $z$  is the spanwise direction with  $z = 0$  at the centre of the channel above an arrangement of vanes and  $b$  is the spacing between vanes (Figure 2).

Reference	$\theta^\circ$	$q_w$ (m <sup>2</sup> /s)	h (m)	Re	Remarks
(1)	(2)	(3)	(4)	(5)	(6)
Chanson & Gonzalez [6]	21.8	0.1 to 0.22	0.1	4E+5 to 8.7E+5	L=3.3 m, W=1m
Config. 1	b=W=1m (no vane)				
Config. 2	b = W/4 = 0.25 m (3 vanes in line)[6]				
Config. 4	b = W/8 = 0.125 m (7 vanes in line)[6]				
Config. 5	b = W/8 = 0.125 m (7 vanes in zigzag)[6]				
Present Study	21.8	0.1 to 0.22	0.1	4E+5 to 8.7E+5	L=3.3 m, W=1 m
Config. 3	b=W/4=0.25m(3 vanes in zigzag every step)				
Config. 6	b=W/8=0.125m(7 vanes in line every 2 steps)				
Config. 7	b=W/8=0.125m(7 vanes in zigzag every 2 steps)				
Notes: h : step height; W chute width; L : chute length					

Table 1. Detailed experimental investigations on moderate slope stepped chutes with turbulence manipulation.

### Data Analysis

The probe sampled data that provided information about the void fraction, bubble count rate, velocity, turbulence intensity, and air/water chord length distributions [5,10]. The void fraction or air concentration  $C$  is the proportion of time that the probe tip is in the air. The bubble count rate  $F$  is the number of bubbles impacting the probe tip. The bubble chord length provides information on the air-water flow structure. With a double-tip conductivity probe, the velocity measurement is based upon the successive detection of air-water interfaces by both tips.

In turbulent air-water flows, the detection of all bubbles by each tip is highly improbable and it is common to use a cross-correlation technique [9]. The time average air-water velocity equals:

$$V = \frac{\Delta x}{T} \quad (1)$$

where  $\Delta x$  is the distance between tips and  $T$  is the time for which the cross-correlation function is maximum. The turbulent intensity may be derived from the broadening of the cross-correlation function compared to the autocorrelation function:

$$Tu = 0.851 \cdot \frac{\sqrt{\Delta T^2 - \Delta t^2}}{T} \quad (2)$$

where  $T$  is a time scale satisfying :  $R_{xy}(T+\Delta T) = 0.5 \cdot R_{xy}(T)$ ,  $R_{xy}$  is the normalized cross correlation function, and  $t$  the characteristic time for which the normalized autocorrelation function  $R_{xx}$  equals 0.5 [5]. Thin skewed cross-correlation functions correspond to small variation in the interfacial velocity, hence small turbulent levels. Broad cross-correlation functions imply large turbulence levels.

Chord sizes may be calculated from the raw probe signal outputs. The results provide a complete characterization of the stream wise distribution of air and water chords. In turn information on the flow structure may be analyzed in terms of particle clustering and grouping [7]. In this study, two air bubbles are considered to be part of a cluster when the water chord separating the bubbles is less than one tenth of the mean water chord size. The measurement of air-water interface area is a function of void fraction, velocity, and bubble sizes. For any bubble shape, bubble size distribution and chord length distribution, the specific air-water interface area  $a$  defined as the air-water interface area per unit volume of air and water may be derived from continuity:

$$a = 4 \cdot \frac{F}{V} \quad (3)$$

where  $F$  is the bubble count rate and  $V$  the velocity.

### Flow Observations

Skimming flows look similar to self-aerated flows down smooth chutes (Figure 1). At the upstream end, the flow was smooth and transparent. However, a bottom boundary layer developed. When the outer edge of the boundary layer reached the water free surface, turbulence induced strong aeration. Downstream of the point of inception of air entrainment, air-water flow became fully developed and “white waters” were observed. Strong exchanges of air-water and momentum occurred between the main stream and the atmosphere. Intense cavity recirculation was observed also below the pseudo-invert formed by the step edges. The air-water flow mixture consisted of a bubbly region ( $C < 30\%$ ), a spray region ( $C > 70\%$ ) and an intermediate zone in between.

Observations from the sidewall showed some effects of the vanes on cavity recirculation. Vanes appeared to be subjected to strong pressure and shear forces. Fluctuations seemed to be of the same period and in phase with cavity fluid ejections reported by Djenidi et al. [10] for d-type roughness and Chanson et al. [8] for stepped chute flows. Longitudinal troughs above the vanes were also observed possibly associated with wakes or quasi-coherent low speed streaks occurring immediately above each vane.

### Air-Water Flow Properties

A detailed comparison of measured air-water flow properties obtained at  $z/b = 0, 0.25$  and  $0.5$  for stepped configurations with vanes was conducted and compared with data for a stepped geometry without vanes. Figure 4 presents typical results of air concentration  $C$  and velocity  $V/V_{90}$  for configurations 6 & 7 at step edge 9, where  $y$  is the distance normal to the pseudo-bottom formed by the step edges,  $Y_{90}$  the distance where  $C = 0.90$  and  $V_{90}$  is the air-water flow velocity at  $y = Y_{90}$ .

Void fraction distributions observed in Figure 4 suggested negligible effects of the vanes on the rate of air entrainment. Velocity measurements at all transverse positions for each vane

configuration showed some marked difference in presence of vanes within  $y/Y_{90} < 0.6$  to  $0.7$  demonstrating that the effect of the vanes was not limited to the cavity flow but extended into the mainstream, result that is consistent with a wake region observed nearby the wall of each vane.

Figure 5 presents velocity  $V/V_{90}$  and turbulence intensity  $Tu$  distributions obtained for configurations 1 & 7 (7 vanes in zigzag every 2 steps) between step edges 9 and 10 (step cavity without vanes). Results hinted that the streamwise effects of vanes are limited to one downstream cavity as hardly any difference in velocity and turbulence intensity could be observed despite the presence of vanes.

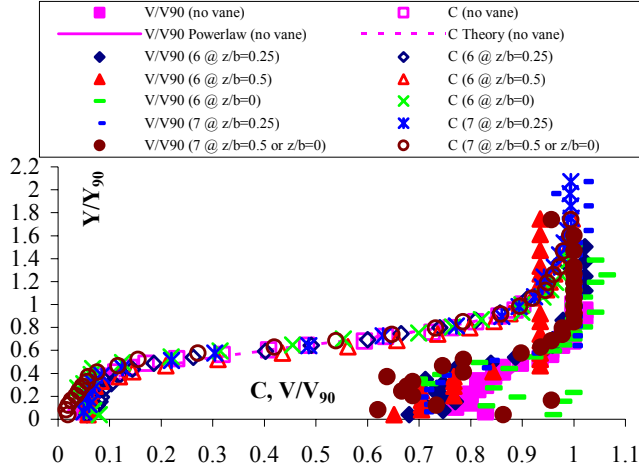


Figure 4. Void fraction and velocity distributions at step edge 9 ( $d_c/h=1.5$ ). Comparison between Configuration 1 (No vane) and every configuration including 7 vanes (Config. 4,5,6,7).

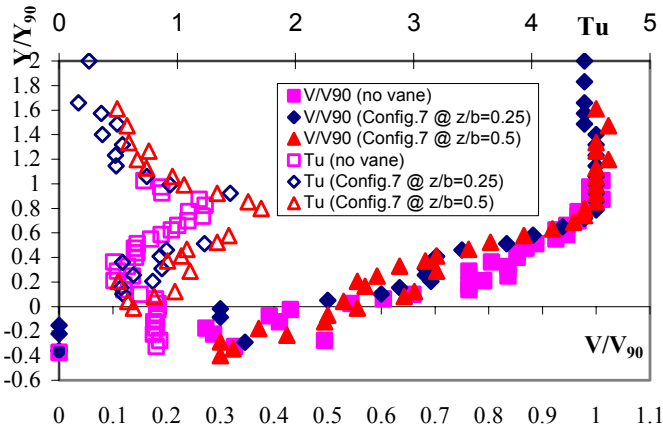


Figure 5. Turbulence intensity and velocity distributions at one quarter of the distance between step edges 9 and 10 ( $d_c/h = 1.5$ ). Comparison between Configuration 1 (No vane) and configuration 7 (7 vanes in zigzag every 2 steps).

### Flow Resistance and Energy Dissipation

Flow resistance was calculated from the average friction slope [8] for all the configurations at  $z/b=0$  (above vanes),  $0.25$  and  $0.5$  (table 2). Results are presented in Table 2 for all configurations. In average they implied equivalent Darcy friction factors of  $0.16$ ,  $0.21$ ,  $0.21$  and  $0.20$  in average for no vane, 3 and 7 vanes inline and 7 vanes in line every 2 steps respectively and  $0.22$ ,  $0.22$  and  $0.21$  in average for 3 and 7 vanes in zigzag and 7 vanes in zigzag every 2 steps respectively suggesting that the presence of vanes increased the flow resistance and the rate of energy dissipation. Maximum values of equivalent Darcy friction  $f_e$  factors were observed for configurations with vanes in zigzag (Configurations 3, 5 & 7). However, results of  $f_e$  obtained for configuration 7 were smaller than those corresponding to configuration 5.

### Air-Water Chord Length Distributions

In highly turbulent air-water flow, measurements with intrusive phase-detection probe, were analysed in terms of streamwise air or water structures bounded by air-water interfaces detected by the probe tip (Figure 3). Figure 6 presents probability distribution functions (PDF) of bubble chord sizes corresponding to configurations 1, 2 and 3 obtained below the pseudo-bottom formed by the step edges ( $y/h < 0$ ). Figure 7 presents PDF of bubble chords for the same configurations in locations above the pseudo-bottom ( $y/h > 0$ ) with similar void fractions. Results showed a greater number of bubbles detected in the mainstream ( $y/h > 0$ ) and a broader range of bubble sizes at locations below the pseudo-bottom, in agreement with previous observations [7]. Note the differences between Figures 6 and 7, where the amount of bubbles detected in the mainstream (Fig. 7) were at least twice as much as that detected in the recirculation region (Fig. 6), for locations with very similar void fraction. The histogram mode (predominant bubble size) was between  $0.5$  and  $1$  mm for all configurations at both locations ( $y/h < 0$  &  $y/h > 0$ ) suggesting that the flow structure did not vary much for configurations 1, 2 & 3 (No vane, 3 vanes in line and 3 vanes in zigzag respectively).

	$f_e$					
Conf.	1	2			3	
	No vane	3 vanes in line			3 vanes in zigzag	
$d_c/h$		$z/b=0$	$z/b=0.25$	$z/b=0.5$	$z/b=0.25$	$z/b=0.5$
1.1	0.1689	0.2384	0.1673	0.1863	0.1412	0.2118
1.3	0.1756	0.236	0.1859	0.1728	0.1506	0.2867
1.5	0.0924	0.3109	0.1446	0.1334	0.2075	0.2882
1.7	0.211	0.2713	0.1911	0.2585	0.2253	0.227
Conf	4			5		
	7 vanes in line			7 vanes in zigzag		
$d_c/h$	$z/b=0$	$z/b=0.25$	$z/b=0.5$	$z/b=0.25$	$z/b=0.5$	
1.1	-	0.1741	0.1704	0.1796	0.2377	
1.3	-	0.1699	0.1755	0.2051	0.3112	
1.5	0.2806	0.1649	0.1656	0.2105	0.2487	
1.7	-	0.1704	0.1628	0.2152	0.1696	
Conf	6			7		
	7 vanes in line every 2 steps			7 vanes in zigzag every 2 steps		
$d_c/h$	$z/b=0$	$z/b=0.25$	$z/b=0.5$	$z/b=0.25$	$z/b=0.5$	
1.1	0.2155	0.177	0.1807	0.1649	0.2047	
1.3	0.2579	0.167	0.191	0.1196	0.2364	
1.5	0.2659	0.1626	0.16	0.136	0.2306	
1.7	0.3735	0.1208	0.1626	0.207	0.3464	

Notes:  $d_c$ : critical depth

Table 2. Flow resistance estimates in air-water flows

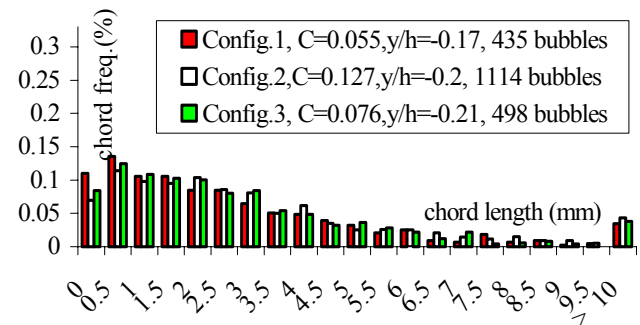


Figure 6. Air-bubble chord length PDF.  $d_c/h=1.5$  between step edges 9 and 10 at  $X=0.25$  and  $z/b=0.25$  ( $y/h < 0$ ).



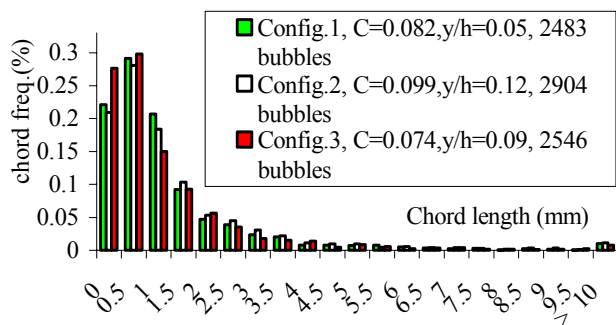


Figure 7. Air-bubble chord length PDF.  $dc/h=1.5$  between step edges 9 and 10 at  $X=0.25$  and  $z/b=0.25$  above pseudo-bottom ( $y/h > 0$ ).

### Bubble Clustering

For configurations 1 and 3, air-bubble and water-droplet clustering analyses were performed at several flow positions (e.g. from bubbly to spray region) and at different streamwise locations along the cavity ( $X = 0.25, 0.5$  &  $0.75$ ). Results demonstrated consistency with previous studies [7,8] confirming that a great proportion of bubbles (typically 30%) clustered mainly in 2 particles. Despite recirculating eddy presence and mixing layer influence the flow structure did not vary much.

### Discussion

Holmes et al [12] proposed the existence of pairs of counter-rotating streamwise eddies next to the wall in turbulent boundary layers, associated with a region of reduced velocity in the stream direction. Above vanes, quasi-coherent wakes, somehow similar to low-speed streaks, were seen interfering with the main stream. It is believed that the effects of the vanes onto the main flow were two-fold. Firstly the presence of vanes prevented the spanwise development of large coherent structures in the step cavities ( $y/h < 0$ ). Secondly they led to the appearance of longitudinal (streamwise) coherent "wake" structures in the mainstream flow ( $y/h > 0$ ). Such coherent structures affects momentum exchange between cavity and stream flows, enhancing vertical mixing between recirculation zones and mainstream and hence the rate of energy dissipation. Such vertical mixing is characterized by irregular fluid ejections, turbulent bursts and sweeps.

In terms of flow resistance maximum equivalent Darcy friction factors  $f_c$  were found for configurations with vanes in zigzag (Configurations 3, 5 & 7). However, results obtained for configuration 7 were smaller than those corresponding to configuration 5. Based upon such finding, it is hypothesized that the behaviour of recirculating vortices is different for every vane arrangement. It is believed that, for configuration 7, the spanwise development of the recirculating eddies in the step cavities reappeared where no vanes existed (every 2 steps) inducing smaller flow resistance than configurations where the vortices remained confined in small cavities at all times (with vanes at each step).

### Conclusion

Interactions between free surface and cavity recirculation, as well as turbulence manipulation were investigated in skimming flow regime down a stepped chute in a large facility operating with highly turbulent flows. Three new turbulence manipulation arrangements were tested and compared with previous data [6]. Results demonstrated that the vane arrangements influence in a different manner the air-water flow properties in both mainstream and recirculating region. Maximum flow resistance was observed for configurations with vanes arranged in zigzag while flow resistance for configuration 7 (zigzagged vanes placed every 2 steps) was smaller than that corresponding to configuration 5 (zigzagged vanes placed every step).

Based upon presented results it is hypothesized that maximum flow resistance and greatest interfacial aeration are achieved with zigzagged geometries placed at each step, rather than inline vane arrangements. It is also suggested that more intricate geometries (e.g. zigzagged vanes every 2 steps) will not further flow resistance. This study provides new information on the complex structure of highly turbulent aerated flows and suggests that turbulence manipulation can be applied to stepped spillways to enhance energy dissipation and to aeration cascades to enhance re-oxygenation.

### Acknowledgments

The writers thank Mr G. Illidge for his assistance. The first author acknowledges the financial support of the National Council for Science and Technology of Mexico (CONACYT).

### References

- [1] Aivazian, O.M., New Investigations and new Method of Hydraulic Calculation of Chutes with Intensified Roughness. *Gidrotekhnicheskoe Stroitel'stvo*, No. 6, 1996, 27-39 (in Russian).
- [2] Chanson, H., Air Bubble Entrainment in Free-surface Turbulent Flows. Experimental Investigations. *Report CH46/95*, Dept. of Civil Engineering, University of Queensland, Australia, 1995.
- [3] Chanson, H., *Air Bubble Entrainment in Free-Surface Turbulent Shear Flows*. Academic Press, 1997.
- [4] Chanson, H., *The Hydraulics of Stepped Chutes and Spillways*. Balkema, 2001.
- [5] Chanson, H., Air-Water Flow Measurements with Intrusive Phase-Detection Probes. Can we Improve their Interpretation ?. *Jl of Hyd. Engrg.*, ASCE, Vol. 128, No. 3, 2002, 252-255.
- [6] Chanson, H., and Gonzalez, C.A., Interactions between Free-surface, Free-stream Turbulence and Cavity Recirculation in Open Channel Flows: *Measurements and Turbulence Manipulation*. *5th International Conference on Multiphase Flow, ICMF'04, Yokohama, Japan*, 2004 Paper No. 104.
- [7] Chanson, H., and Toombes, L., Air-Water Flows down Stepped Chutes: Turbulence and Flow Structure Observations. *Intl Jl of Multiphase Flow*, Vol. 27, No. 11, 2002, 1737-1761.
- [8] Chanson, H., Yasuda, Y., and Ohtsu, I., Flow Resistance in Skimming Flows and its Modelling. *Can. Jl. of Civ. Eng.*, Vol. 29, No. 6, 2002, 809-819.
- [9] Crowe, C., Sommerfield, M., and Tsuji, Y., *Multiphase Flows with Droplets and Particles*. CRC Press, 1998.
- [10] Djenidi, L., Elavarasan, R., and Antonia, R.A., The Turbulent Boundary Layer over Transverse Square Cavities. *Jl Fluid Mech.*, Vol. 395, 1999, 271-294.
- [11] Gonzalez, C.A., and Chanson, H., Interactions between Cavity Flow and Main Stream Skimming Flows: an Experimental Study. *Can Jl of Civ. Eng.*, Vol. 31, 2004.
- [12] Holmes, P., Lumley, J.L., and Berkooz, G., *Turbulence, Coherent Structures, Dynamical Systems and Symmetry*. Cambridge University Press, 1996. pp. 63-77.
- [13] Mochizuki, S., and Osaka, H., Two-Point Velocity Correlation Measurement in a d-type Rough Wall Boundary Layer Modified with the Longitudinal Thin Ribs: *Proc. 9th Symp. On Turbulent Shear Flows*, Kyoto, Japan, (1993), paper 5-2.
- [14] Mochizuki, S., Izawa, A., and Osaka, H., "Turbulent Drag Reduction in a d-type Rough Wall Boundary Layer with Longitudinal Thin Ribs Placed within Traverse Grooves Higher-order Moments and Conditional Sampling Analysis)." *Trans. JSME Intl Journal*, series B, Vol. 39, No. 3, 1996, 461-469.

## Hydrodynamic Performance of a Surfboard Fin

P.A. Brandner<sup>1</sup> and G.J. Walker<sup>2</sup>

<sup>1</sup>Faculty of Maritime Transport and Engineering  
Australian Maritime College, Launceston Tasmania, 7248 AUSTRALIA

<sup>2</sup>School of Engineering  
University of Tasmania, Hobart, Tasmania, 7001 AUSTRALIA

### Abstract

The performance of a generic surfboard fin is investigated in a cavitation tunnel to gain basic understanding of the viscous flows involved for future systematic experimental and computational studies. Measurements of lift and drag forces, pitching moment and results of flow visualisation are presented. Surface flow visualisation studies reveal relatively complex boundary layer transition and separation phenomena although lift and drag characteristics are virtually invariant with Reynolds number in the range tested. A mixed two- and three-dimensional separation behaviour is observed at high incidence.

### Introduction

Increasing competition and professionalism in the sport of wave surfing has created an increasing desire to improve equipment performance. A project is underway at the Australian Maritime College (AMC) to investigate the performance of surfboard fins. The board's fins provide the basis for control and manoeuvrability and for the purposes of this study involve the three-fin configuration typical of modern surfboards – as shown in Figure 1. These consist of two cambered side fins and one symmetric centre fin. The side fins are located near the edge of the surfboard at approximately 80% of the board length from the nose and the centre fin is located on the centreline at approximately 90% of the board length from the nose. The side fins are canted outward at approximately 5 to 10° to maintain verticality in a turn whilst the centre fin is upright. The side fins are also toed in approximately 4 to 8° to achieve zero lift incidence for linear motion. Lift (or side force for manoeuvring of the surfboard) is produced by the combined effects of the centre fin and the fin on the inner side of the turn. However the side fins, being cambered, produce most of the lift and are the subject of the present investigation. They are typically of intermediate to low aspect ratio and have a moderately swept planform [5]. Foils typically have a thickness to chord ratio of approximately 10% with an arbitrarily curved low-pressure surface and a flat high-pressure surface. The leading edges usually have a relatively small radius.

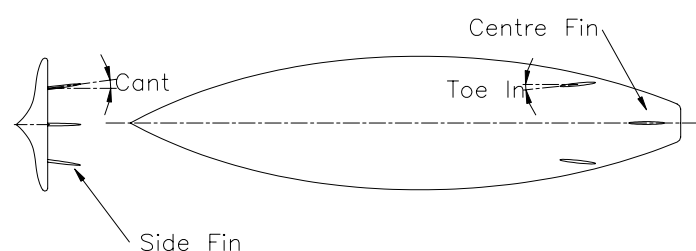


Figure 1. Typical Modern Surfboard Fin Arrangement.

There is currently no definitive information available on surfboard relative speeds and fin incidences and their dependence on wave size. In the absence of this data it is estimated that speeds may reach 10 to 15 m/s. Typical fin chords are of the order of 0.1m giving typical chord based Reynolds numbers, ( $R_n$ )

between  $10^5$  to  $10^6$ . This is a range where transitional flow and separation effects are known to be significant. Given the range and type of manoeuvres performed with surfboards it can be expected that the fins would operate over a wide range of incidence including stall. Preliminary testing on production fins has shown that a range of viscous flow effects may occur including leading and trailing edge separation, laminar separation and laminar bubble bursting. Testing has also shown that significant cavitation phenomena may occur, but this is beyond the scope of the present paper.

Fins designs have to date been based on practical experience of surfboard and accessory manufacturers with significant emphasis on aesthetic considerations and perceived market expectations. Whilst there exists considerable published data on the performance of foil sections and lifting surfaces [5] and some specific studies [4] a literature survey has revealed little information on the performance of lifting devices with this range of flow parameters and geometry. There is therefore considerable scope for characterising viscous and cavitating flows on surfboard fins and identifying how these are affected by foil geometry. The ultimate objective of this work is to optimise fin designs for various Reynolds numbers and incidences. The aim of the present investigation is to characterise performance of a lifting surface typical of a surfboard side fin and to gather data that may form the basis of more detailed investigation and optimisation using experiment and CFD. Observations made include measurements of lift and drag forces, pitching moments and on- and off-body flow visualisation for characterisation of viscous flows.

### Experimental Overview

#### Surfboard Fin Geometry

A simple geometry representative of typical surfboard fins was chosen for the present study. The test foil has an elliptical planform and a NACA 4 digit half section with a flat pressure surface. The fin is swept by offsetting the 65% chord position on a 25° inclined generator line. Geometric parameters are summarised in Table 1. The fin was manufactured using numerically controlled machining from commercially available fibre reinforced plastic sheet and coated with a black coloured epoxy for contrast in flow visualisation tests.

Span, $S$	0.12m
Base Chord, $c$	0.1m
Planform Area, $A$	0.00962m <sup>2</sup>
Sweep angle, $A$	25°
Planform	Elliptical
Aspect ratio, $AR$	3
Thickness/Chord, $t/c$	9% (constant)
Section	Half NACA 0009
Leading edge radius	0.5% of $c$

Table 1. Summary of Surfboard Fin Geometric Parameters.

### **Cavitation Tunnel Experimental Set Up**

All tests were performed in the Tom Fink Cavitation Tunnel, a closed recirculating variable pressure water tunnel. The test section dimensions are 0.6m x 0.6m cross section x 2.6m long. The velocity may be varied from 2 to 12m/s and the centreline static pressure from 4 to 400 kPa absolute. Studies may involve the investigation of steady and unsteady flows, two-phase flows including cavitation, turbulence and hydro-acoustics. Full details of the tunnel and its capabilities are given by Brandner and Walker [2].

The fin was mounted on a 0.16m diameter flush penetration on the ceiling of the test section 1.15m from the entrance to achieve a similar boundary layer thickness to that on a surfboard. Typical surfboard lengths are 1.5m and for the expected Reynolds Number range a turbulent flat plate boundary layer thicknesses would be of the order of 0.02m assuming a  $1/7^{\text{th}}$  power law. This gives a boundary layer thickness/fin span ratio of 1/6.

Parameters measured during testing include tunnel pressure, velocity, temperature and dissolved oxygen content. Online instrumentation is used for automatic control of tunnel pressure and velocity as well as real time data monitoring and acquisition. The test section pressure is measured using 2 *Rosemount* Model 3051C Smart absolute pressure transducers in parallel. Test section velocity is derived from the contraction pressure differential measured using 2 *Rosemount* Model 1151 Smart differential pressure transducers in parallel. One of each pressure transducer pair has a lower range to improve measurement precision at lower pressures and velocities respectively. The estimated precision of the absolute pressure measurement is 0.1 kPa for pressures up to 120 kPa and 0.5 kPa for pressures up to 400 kPa. The estimated precision of the velocity measurement is 0.05 m/s. Water temperature is measured to 0.5°C accuracy using a *Rosemount* Model 244 temperature transducer. Dissolved Oxygen content is measured using a *Rosemount* Model 499 Dissolved Oxygen sensor. Pitot tube pressures relative to the tunnel static pressure (as well as tunnel instrument pressures) were measured sequentially using a *Validyne* Model DP15TL differential pressure transducer via a Model 48J7-1 *Scanivalve* pressure multiplexer.

Measurements of tunnel wall boundary layer profiles were made using a 1.6mm diameter Pitot tube, a wall static tapping and an automated traverse. The velocity profiles closely follow those of the standard law of the wall for turbulent flow. Measurements of lift, drag and pitching moment acting on the fin were performed using a six-component force balance developed at the AMC [1]. Balance calibration data indicates a precision of 0.13 N for the three force components and 0.03Nm for the three moment components. The fin incidence was set using the balance to an estimated absolute precision of 0.05°. For the flow visualisation studies the incidence of the model could be set with an estimated precision of 0.25°.

### **Experimental Procedure**

The following tests were performed:

- (i) Measurement of lift and drag forces and pitching moment;
- (ii) On body flow visualisation using oil flow tests;
- (iii) Off body flow visualisation using air injection.

Measurements of lift, drag and pitching moment were made at incidence angles,  $\alpha$ , varying between -6 to 26° in increments of 1° and Reynolds Numbers between  $2 \times 10^5$  to  $10^6$  in increments of  $2 \times 10^5$ . Reynolds Number is defined by  $R_n = Uc/\nu$  where  $U$  is the freestream velocity,  $c$  the fin base chord and  $\nu$  the kinematic viscosity. To investigate hysteresis effects measurements were made with both increasing and decreasing incidence for all

Reynolds numbers tested. The force balance is calibrated as a six-component linear instrument resulting in a 36 coefficient calibration matrix. A circular penetration for model mounting is used for connecting the model to the measurement side of the force balance. Forces acting on the penetration in addition to those on the fin are therefore measured. The components other than lift, drag and pitching moment have been neglected as a result of this. A tare correction has not been made to the drag measurement for the skin friction acting on the circular penetration. Force balance outputs were recorded at 4 kHz and averaged over 4 seconds. The forces and moments are non-dimensionalised to give coefficients of lift, drag and pitching moment (measured about the base mid-chord) defined by  $C_L = L / \frac{1}{2} \rho U^2 A$ ,  $C_D = D / \frac{1}{2} \rho U^2 A$  and  $C_M = M / \frac{1}{2} \rho U^2 A c$  where  $L$ ,  $D$ , and  $M$  are the lift, drag and pitching moment respectively,  $A$  the reference area (in this case the planform area of the fin) and  $\rho$  the fluid density.

On-body flow visualisation was achieved by oil flow tests using a mixture of titanium dioxide powder and silicone oil. Considerable experience has been gained in this technique from a range of experiments as to the quantity of titanium dioxide and viscosity of silicone oil required. A Typical mixture has a 1/10 ratio of titanium dioxide powder to silicone oil by mass. Silicone oils used have kinematic viscosities of 10, 100, 200, 500, 1000 and 5000 centiStokes depending on the shear stress involved. For the present experiments the 500 centiStoke kinematic viscosity oil was used. Tests were performed with the oil initially uniformly distributed for each incidence; the flow was then rapidly accelerated to the test velocity and the surface pattern allowed to reach equilibrium.

Off-body flow visualisation was by air injection via a reverse Pitot tube located 0.85m upstream of the fin location inserted varying depths into the flow depending upon the features to be visualised. Provided the bubbles are sufficiently small in diameter they are effective for flow visualisation or flow tracking. A procedure for calculating relative bubble velocities based on bubble size, length scales and velocity is given by Brennan [3]. Small bubbles can be produced using a reverse Pitot tube provided its internal diameter is small (in this case approximately 0.3mm) and there is some turbulence present to promote break up of larger bubbles and minimise coalescence. The bubbles were illuminated using a 150W flood lamp and images recorded using a Nikon 300D 35mm SLR digital camera. Both on and off-body flow visualisations were performed at incidences of 4, 8, 12, 14, 16, 18, 20, 22 and 26° at  $R_n = 4 \times 10^5$ .

## **Results**

### **Lift, Drag and Pitching Moment**

The variation of  $C_L$ ,  $C_D$  and  $C_M$  against  $\alpha$ , with  $R_n$  a parameter, is shown in Figure 2. Of particular interest are significant parameters of foil performance including the zero lift incidence for setting of fin angles on the surfboard, any discernible influence of the sharp leading edge, the lift slope and how this compares with published data, maximum lift and the type of stall.

There is relatively little variation of the  $C_L$  and  $C_D$  curves with  $R_n$  except at  $R_n = 2 \times 10^5$  apart from an expected monotonic reduction in maximum  $C_L$  with decreasing  $R_n$ . There is a greater scatter in the data for the latter curves that can largely be attributed to estimated errors of the order of 10% at the lowest velocity. However, the break in the lift curve at around  $\alpha = 12$  to  $14^\circ$  is characteristic of thin aerofoil stall behaviour associated with bursting of a laminar separation bubble at an intermediate incidence. The zero lift incidence is essentially invariant with  $R_n$  in the range tested at approximately  $-3.5^\circ$ , indicating that fin



angles can be set regardless of anticipated velocity. The lift curve slope is also essentially invariant with  $R_n$  and is approximately  $0.05^\circ$  which compares closely with the classical data compiled by Hoerner [5] for an aspect ratio of 3 and reduced for sweep as indicated in [5]. The maximum  $C_L$  varies approximately linearly with  $R_n$  and again compares closely with compiled data in [5] based on thickness and various aspect ratios. The lift curve peak is well rounded in all cases. The presence of a relatively small leading edge radius does not appear to have any deleterious effects on the fin performance. Measurements of both increasing and decreasing incidence showed essentially no effects of hysteresis or instability despite the complex nature of the flows involved.

### Off-body Flow Visualisation

Results of off-body flow visualisations are presented in Figure 3 for 8, 12, 16 and  $20^\circ$  incidences at  $R_n = 4 \times 10^5$ . The general flow pattern is dominated by the induced effect of the trailing tip vortex. At  $\alpha=4^\circ$  (Figure 3a) the inward and outward deflection of streamlines on the suction and pressure sides respectively can be clearly seen with the tip vortex core just becoming visible. Greater spanwise deflection of the streamlines is apparent at  $\alpha=8^\circ$  (Figure 3b) with the tip vortex core clearly evident. At  $\alpha=12^\circ$  (Figure 3c) the origin of the vortex core moves on to the suction surface of the foil inward of the tip. A similar pattern is observed at  $\alpha=16^\circ$  (Figure 3d). At  $\alpha=20^\circ$  (Figure 3e) bulk separation begins with a globally vortical nature about a point at approximately 60% span. At higher incidences the flow becomes fully separated from the leading edge although the vortical nature of the flow remains about a point which moves toward the fin base as incidence increases.

### On-body Flow Visualisation

Results of on-body flow visualisations are presented in Figure 4 for 8, 12, 16 and  $20^\circ$  incidences at  $R_n = 4 \times 10^5$ . In contrast with the off-body visualisation the on-body visualisation indicates a general outward flow on the suction surface, driven by the pressure gradient associated with the foil sweep. At  $\alpha=4^\circ$  (Figure 4a) the suction surface flow is laminar to about 40% chord and transitions without any laminar separation.

At  $\alpha=8^\circ$  (Figure 4b) the prominent attachment line around 30% chord near the base indicates the presence of a laminar separation bubble over the forward part of the foil. The flow at this incidence is essentially 2-D, with the extent of laminar flow decreasing forwards toward the tip. The forward movement of the attachment line (and reduction in extent of laminar flow) near the base is due to interactions with the turbulent boundary layer on the tunnel wall. A greater deflection of the surface streamlines indicates the presence of a secondary flow vortex in this interaction region. The wall boundary layer interaction effects become progressively more pronounced as incidence increases (Figure 4(c) and (d)) and a localised region of trailing edge flow separation appears to develop at the base on the suction surface.

A discontinuity in the attachment line develops near the tip at  $\alpha=12^\circ$  (Figure 4(c)) that is consistent with the off-body visualisation in Figure 3(c). This indicates the appearance of a three-dimensional separation zone near the foil tip as the origin of the tip vortex moves inboard onto the suction surface. These effects become pronounced at  $\alpha=16^\circ$  (Figure 4(d)). At  $\alpha=20^\circ$  (Figure 4(e)) the surface visualisation exhibits a classical focus pattern associated with a spiral point of separation. This tip stall phenomenon, which causes shedding of a part-span vortex sheet, is well known on aircraft with swept wings as described by Lighthill [6]. In this case the separation line issues from a saddle point separation at a part-span position (clearly evident in Figure

4e). The stall mechanism is therefore a combination of developing tip stall and localised trailing edge stall due to secondary flow interactions near the base.

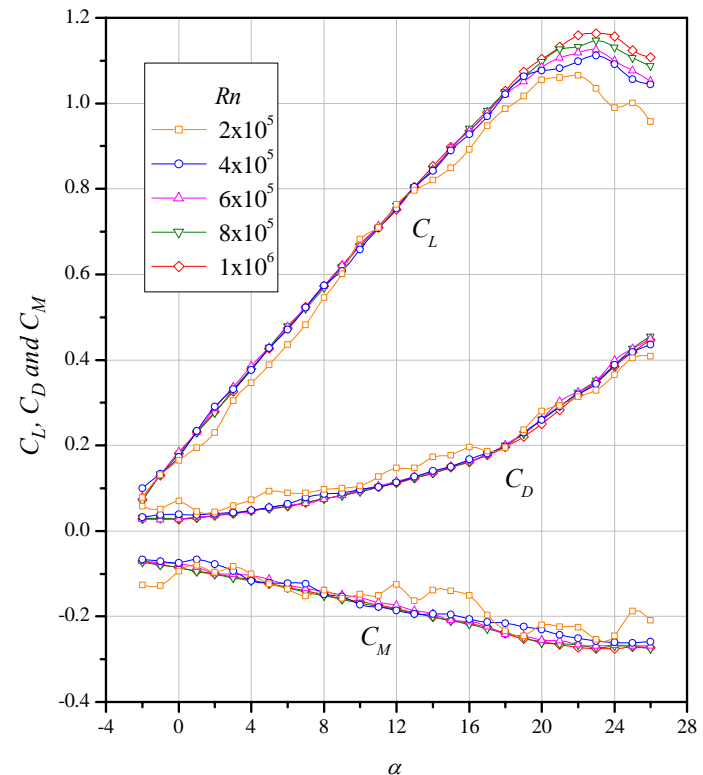


Figure 2. Lift, Drag and Pitching Moment Coefficients as a Function of Incidence with Reynolds Number a Parameter.

### Conclusions

The hydrodynamic performance of a generic surfboard fin has been investigated. The measured forces and moments show relatively stable behaviour despite the presence of transitional flow with laminar separation at low Reynolds number. On and off-body flow visualisation reveal the extent of laminar flow and the influence of the wall boundary layer and tip vortex flow. These reveal that stall occurs as a combination of secondary flow effects at the base and three-dimensional stall at the foil tip.

### Acknowledgments

The authors wish to acknowledge the assistance of Mr David Clarke in formulating the oil flow visualisation technique, Dr Colin Grubb and Mr Robert Wrigley for their assistance in carrying out experiments and the support of AMC, University of Tasmania, Surf Hardware International, Murray Burns & Dovell and the AusIndustry R&D Start Program.

### References

- [1] Brandner, P.A., *AMC Tom Fink Cavitation Tunnel – 6 Component Force Balance Laboratory Notes*, AMC, 2000.
- [2] Brandner, P.A. and Walker G.J., *A Waterjet Test Loop for the Tom Fink Cavitation Tunnel*, International Conference on Waterjet Propulsion III, Royal Institution of Naval Architects, Gothenburg, Sweden, February, 2001, 54-57.
- [3] Brennan, C.E., *Cavitation and Bubble Dynamics*, Oxford University Press, 1995.
- [4] Hajime, Y., Hiroharu, K., Nobuhide, T., Hirofumi, S. and Masahiko, H., *Study on a Finite Span Foil with Sweptback Planform*, International Symposium on Cavitation: CAV95, Deauville, France, 1995, 367-372.
- [5] Hoerner, S.F., *Fluid-Dynamic Lift*, Hoerner Fluid Dynamics, 1985.
- [6] Lighthill, M.J., *Attachment and Separation in Three-dimensional Flow, Laminar Boundary Layers*, Ed. L. Rosenhead, Oxford University Press, 1963, 72-82.



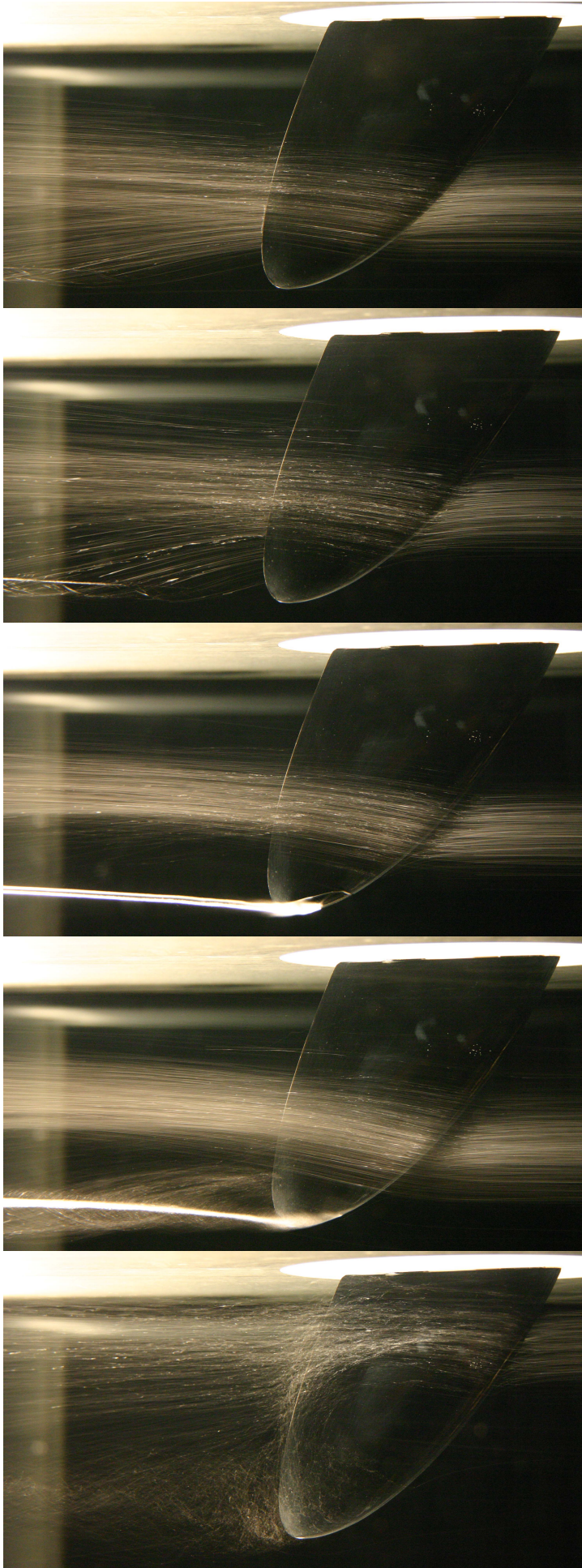


Figure 3. Off-body Flow Visualisation on the Suction Surface Using Air Injection at  $\alpha = 4, 8, 12, 16$  and  $20^\circ$  Incidence for  $R_n=4 \times 10^5$ .

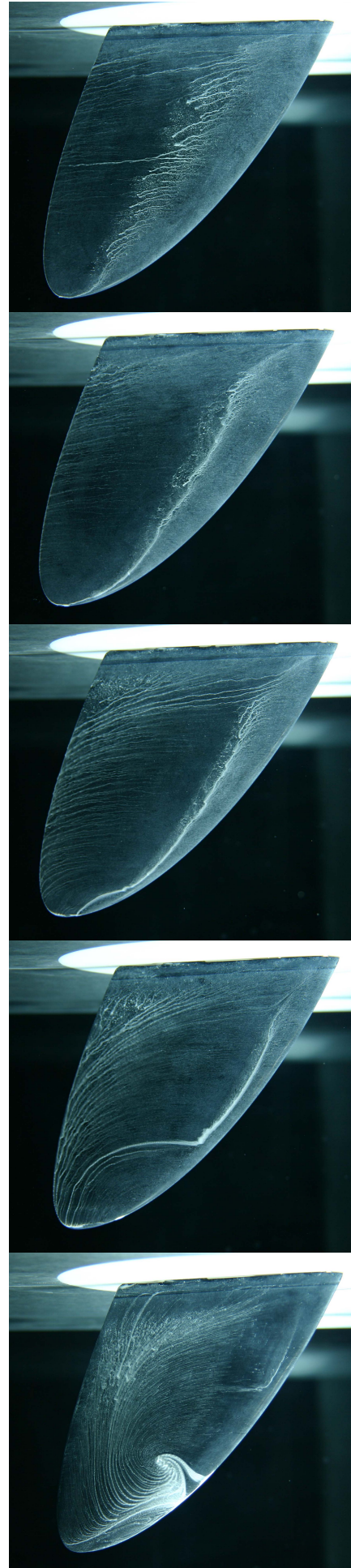


Figure 4. On-body Flow Visualisation on the Suction Surface Using Oil Flow at  $\alpha = 4, 8, 12, 16$  and  $20^\circ$  Incidence for  $R_n=4 \times 10^5$ .

Figures 3a (Left)  
and 4a (Right)  
Off and On-body  
Flow Visualisation  
on the Suction  
Surface @  $\alpha=4^\circ$

Figures 3b (Left)  
and 4b (Right)  
Off and On-body  
Flow Visualisation  
on the Suction  
Surface @  $\alpha=8^\circ$

Figures 3c (Left)  
and 4c (Right)  
Off and On-body  
Flow Visualisation  
on the Suction  
Surface @  $\alpha=12^\circ$

Figures 3d (Left)  
and 4d (Right)  
Off and On-body  
Flow Visualisation  
on the Suction  
Surface @  $\alpha=16^\circ$

Figures 3e (Left)  
and 4e (Right)  
Off and On-body  
Flow Visualisation  
on the Suction  
Surface @  $\alpha=20^\circ$



## Effect of Localised Wall Suction on the Small-scale Motion in a Turbulent Boundary Layer

O. Oyewola, L. Djenidi, P. Burattini and R.A. Antonia

Discipline of Mechanical Engineering  
University of Newcastle, NSW, 2308 AUSTRALIA

### Abstract

Hot wire measurements have been made in a turbulent boundary layer subjected to concentrated suction applied through a porous wall strip in order to examine the influence of suction on the small-scale motion. The suction results show significant departure from the no-suction case of the Kolmogorov normalised spectra and second-order structure functions for  $k^*_1 < 0.2$  and  $r^* > 20$ , respectively, suggesting that suction induces a change in the small-scale motion. This change is a result of the weakening of the large-scale structures. The effect is enhanced as the suction rate is increased.

### Introduction

The response of the large-scale motion to suction applied through a single narrow porous wall strip or slit has received some attention in the past [3,9,10,13]. For example, [3] studied the effect of concentrated wall suction, applied through a short porous wall strip, on a low Reynolds number turbulent boundary layer. They showed that, when the suction rate is sufficiently high, pseudo-relaminarisation occurs almost immediately downstream of the suction strip. Further downstream, transition occurs and is followed by a slow return to a fully turbulent state. Further, [9,10] showed that both the suction rate,  $\sigma$  ( $\equiv V_w b / \theta_0 U_1$ , where  $V_w$  is the suction velocity,  $b$  is the effective width of the strip,  $\theta_0$  is the momentum thickness of the boundary layer at the leading edge of the porous strip with no-suction and  $U_1$  is the free stream velocity), and the momentum thickness Reynolds number,  $R_{\theta_0}$ , played an important role in the relaminarisation process. They argued that the ratio  $R_{\theta_0} / \sigma$  should not exceed a (as yet undetermined) critical value, if relaminarisation is to occur. Recently, the effect concentrated wall suction can have on the anisotropy of the Reynolds stress tensor was examined in [11]. Those results indicated that the large-scale motion of the boundary layer was significantly altered by suction, and that the global anisotropy of the layer increases with the suction rate. For example, they found that the shape of the structures near the wall changed from a cigar to a pancake-shape when suction is applied.

The characteristics of the small-scale motion in a smooth wall turbulent layer have been examined by several authors [1,2,17]. The possibility of local isotropy at various  $R_\theta$  ( $=U_1\theta/v$ , where,  $\theta$  and  $v$  are the momentum thickness and kinematic viscosity of the fluid respectively) and the Taylor microscale Reynolds number  $R_\lambda$  ( $=(\langle u_1^2 \rangle)^{1/2} \lambda / v$ , where  $u_1$  is the longitudinal velocity fluctuation,  $\lambda$  the longitudinal Taylor microscale,  $v$  the viscosity of air) has spawned the introduction of various criteria for local isotropy [4,6,8,19]. For example, [19] used  $S/(\langle \partial u / \partial y \rangle^2)^{1/2}$  (where,  $S \equiv U/\partial y$ ) for characterising the anisotropy of the small-scale motion and suggested that this ratio should not depend on the Reynolds number in the near-wall region. Using direct numerical simulations of a fully developed channel flow, [1] showed that the magnitude of  $R_\lambda$  should have little effect on the degree of isotropy at sufficiently high wave number provided  $S^*(\equiv S/(\langle \epsilon \rangle / v)^{1/2}$ , where  $\langle \epsilon \rangle$  is the mean turbulent energy dissipation rate) is sufficiently small. They argued that the

Corrsin criterion is too restrictive and may be relaxed to  $S^* \leq 0.2$ , provided the high wave number vorticity spectra approach isotropy. However, the general consensus is that local isotropy is best satisfied at high  $R_\theta$  and  $R_\lambda$ . Since changes in the boundary conditions affect  $R_\theta$ , it would be of interest to determine if and how these changes influence the small-scale motion.

The main objective of the present study is to examine the influence of wall suction on the small-scale motion.

### Measurement Details

Measurements were made in a smooth flat plate turbulent boundary layer, which is subjected to concentrated suction applied through a short porous strip. The turbulent boundary layer develops on the floor of the wind tunnel working section (figure 1) after it is tripped at the exit from a two-dimensional 9.5:1 contraction using a 100 mm roughness strip (Norton Bear No. 40, very coarse). Tests showed that the boundary layer was fully developed at the suction strip location, which is about 1200 mm downstream of the roughness strip. The roof of the working section is adjusted to achieve the desired pressure gradient (zero for the present investigation). The free stream velocity  $U_\infty$  was approximately  $7 \text{ ms}^{-1}$ ; corresponding values of the initial momentum thickness Reynolds numbers  $R_{\theta_0}$  are 1400 and the Taylor microscale Reynolds number is in the range  $R_\lambda = 90$ –120. A 3.25 mm thick porous strip with a width of 40 mm and made of sintered bronze with pore sizes in the range 40–80  $\mu\text{m}$  or  $(0.4$ – $0.9)v/U_\tau$  was mounted flush with the test section floor. Allowing for the width of the mounting recess step, the effective width ( $=b$ ) of the strip was 35 mm. Suction was applied through a plenum chamber located underneath the suction strip and connected to a suction blower, driven by a controllable DC motor, through a circular pipe (internal diameter  $D = 130 \text{ mm}$  and  $L/D \approx 38$ , where,  $L$ , is the pipe length). The flow rate  $Q_r$  was estimated directly by radially traversing a Pitot tube located near the end of the pipe, for various values of the pipe centre-line velocity ( $U_c$ ). A plot of  $Q_r$  vs  $U_c$ , allowed the suction velocity ( $V_w$ ) to be inferred via the continuity equation ( $Q_r = A_w V_w$ , where,  $A_w$  is the cross-sectional area of the porous strip).

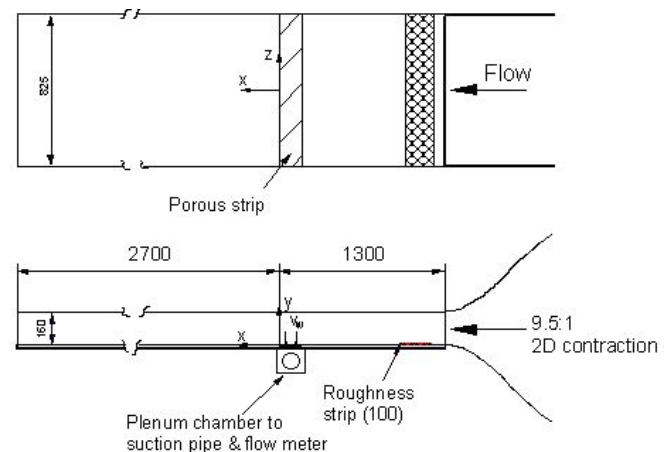


Figure 1: Schematic arrangement of the working section (dimensions in mm).

The suction velocity was assumed to be uniform over the porous surface; this assumption seems reasonable if the variation in the permeability coefficient of the porous material is  $\pm 3\%$ .

Measurements were made for  $\sigma (= V_w b / \theta_0 U_\infty)$ , normalised suction rate or severity index, as introduced by [3]) = 0, 0.8, 1.7, 3.3 and 5.5. The results for  $\sigma = 0$  provided a reference against which the suction data could be appraised. The wall shear stress  $\tau_w$  was measured with a Preston tube (0.72 mm outer diameter), and a static tube located approximately 35 mm above it at the same x position. The Preston tube was calibrated in a fully developed channel flow using a method similar to that described in [3,14].  $\tau_w$  was determined from the relation  $\tau_w = -h(dp/dx)$ , where h is the channel half-width and p is the static pressure. Although the calibration of the Preston tube in the channel flow may not ensure that  $\tau_w$  will be correctly obtained especially if the flow is perturbed, the level of agreement with those inferred from the mean velocity gradient at the wall was about 5%. Measurements of the velocity fluctuations in the streamwise and wall normal directions were made with cross wires, each inclined at  $45^\circ$  to the flow direction. The etched portion of each wire (Wollaston, Pt-10% Rh) had a diameter of  $2.5 \mu\text{m}$ , and a length (l) to diameter ratio of about 200. The separation ( $\Delta$ ) between the inclined wires was about 0.6 mm. The ratios  $l/\eta$  and  $\Delta/\eta$  for no-suction at  $y^+ = 15$  are about 4.0 and 4.9 respectively. The velocity fluctuation in the spanwise direction was also measured by rotating the same X-probe through  $90^\circ$ . All hot wires were operated with in-house constant temperature anemometers at an overheat ratio of 1.5. The analog output signal of the hot wire was low pass filtered (the filter cut off frequency was typically between 5kHz and 8kHz), DC offset and amplified to within  $\pm 5 \text{ V}$ .

### Mean Turbulent Energy Dissipation Rate and Mean Strain Rate

The variation of  $\langle \epsilon \rangle \delta / U_\tau^3$  ( $\delta$  is the boundary layer thickness) across the boundary layer is shown in figure 2 as a function of  $y/\delta$  for both the perturbed and unperturbed boundary layers. The mean turbulent energy dissipation rate,  $\langle \epsilon \rangle$ , was estimated by integrating the dissipation spectrum (e.g., [18]), viz.

$$\langle \epsilon \rangle = 15\nu \int_0^\infty k_1^2 \phi_u(k_1) dk_1, \quad (1)$$

where  $\phi_u(k_1)$  is the one-dimensional spectrum of the streamwise velocity. Taylor's hypothesis was used to obtain the one component wavenumber  $k_1 = 2\pi f / U$ , where U is the local mean velocity and f is the frequency. Because of the contamination due to electronic noise, the high wavenumber part of the spectrum was extrapolated by assuming an exponential decay function for the data corresponding to  $k_1^{5/3} \phi_u$  [7,16]. It should be noted that a more reliable estimate of  $\langle \epsilon \rangle$  would be to measure all the

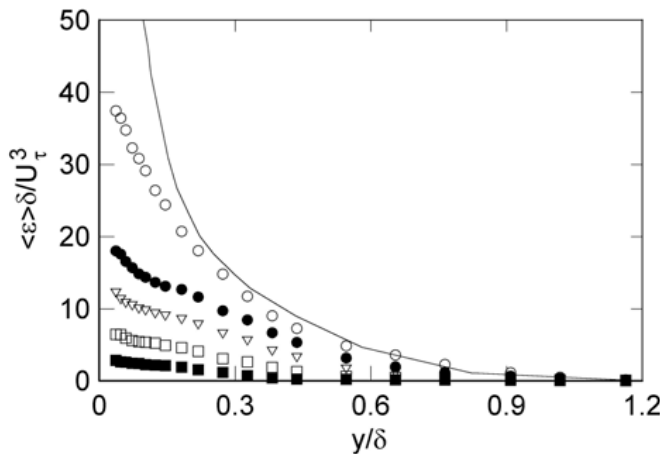


Figure 2: Variation of  $\langle \epsilon \rangle \delta / U_\tau^3$  with  $\sigma$ .  $\circ$ ,  $\sigma = 0$ ;  $\bullet$ , 0.8;  $\nabla$ , 1.7;  $\square$ , 3.3;  $\blacksquare$ , 5.5; —: Spalart ( $R_0 = 1410$ ) [15].

components of  $\langle \epsilon \rangle$  with multiple hot-wires. This is not feasible at the moment in the current laboratory experiment. The present data for  $\sigma = 0$  fall below the DNS data of [15] at  $R_0 = 1410$  in the region  $y/\delta \leq 0.2$  but there is reasonable agreement between the present measurement and the DNS data in the outer layer ( $y/\delta > 0.4$ ). The reason for the discrepancy in the wall region is partly due to the inaccuracy of cross-wire measurements and the expected departure of  $\langle \epsilon \rangle$  from its isotropic value. Because of the increased anisotropy of the near-wall flow, the uncertainty of  $\langle \epsilon \rangle$  was estimated using error analysis to range between 45% and 19%, over the region  $0.05 < y/\delta < 0.2$  for  $\sigma = 0$ . It is interesting to point out that the marginal difference between the present no-suction data of  $\langle \epsilon \rangle$  and the DNS in the region  $y/\delta > 0.2$  gives confidence in the values derived for the Kolmogorov's variables in that region. Thus, the comparison between the suction and no-suction data should be reliable, at least qualitatively, since the measurements were made with the same probe. The measurements should provide some insight into the changes that occur in the boundary layer. However, the comparison between the suction and no-suction data should be interpreted with caution.

Relative to no-suction, there is a considerable reduction in the normalised mean turbulent energy dissipation rate when suction is applied. This is consistent with the significant reduction observed in the production of the mean turbulent kinetic energy (not shown). These results suggest a possible alteration in the mechanism responsible for the energy transfer within the boundary layer, which in turn would affect both large and small-scale motions. This is not surprising since quasi-streamwise vortical structures are the major structural element responsible for turbulence production in the near-wall region. A reduction in  $\langle \epsilon \rangle$  would imply a weakening of these structures. The effect is enhanced as  $\sigma$  is increased. The reduction in  $\langle \epsilon \rangle$  is reflected in the Kolmogorov scales shown in figures 3a and 3b.

The figures are plotted in this manner to highlight the changes that occur in the near-wall region when suction is applied. Interestingly, the measured data agree reasonably well with the DNS data in the region  $y^+ \geq 100$ .  $\eta^+$  varies only slowly nearly up to  $y^+ \leq 100$  ( $y/\delta \approx 0.2$ ).

While the rate of change of  $\eta^+$  with  $y^+$ , relative to  $\sigma = 0$ , increases as  $\sigma$  increases for  $y^+ \geq 100$ , that of  $v_k^+$  is reduced significantly. It seems that  $y^+ = 100$  represents a transition point, above which the rate of change of  $\eta^+$  or  $v_k^+$  is significantly increased for a particular  $\sigma$ . It may be concluded from the results presented here that, relative to no-suction, the near-wall structures of the perturbed boundary layer have been modified, as reflected in the changes in the energy dissipation rate and therefore the Kolmogorov velocity and length scales.

The variations with  $\sigma$  of  $R_\lambda$  and the Kolmogorov normalised shear  $S^*$  are shown in figure 4. All distributions of  $R_\lambda$  show

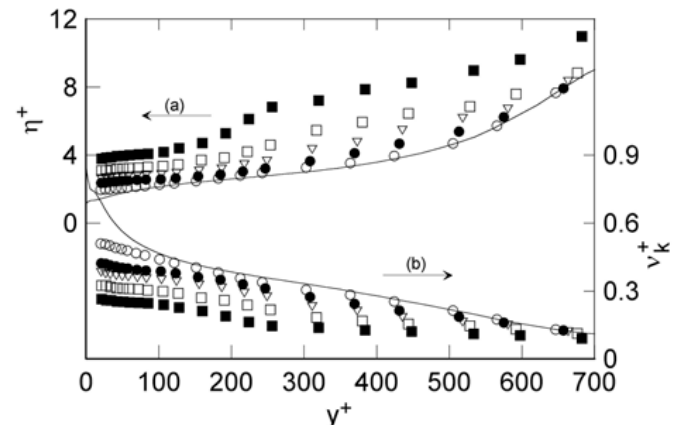


Figure 3: Variations of (a)  $\eta^+$ ; (b)  $v_k^+$  with  $\sigma$ . Symbols are as in figure 2.

almost the same behaviour.  $R_\lambda$  decreases until a minimum is reached, increases again slightly and then decreases towards a constant value. The values are lower in the suction case as compared with no-suction case in the region  $y/\delta \geq 0.05$ . Similarly, relative to no-suction,  $S^*$  increases in the region  $y/\delta < 0.45$  and decreases towards the negative values in the remaining part of the boundary layer when suction is applied.

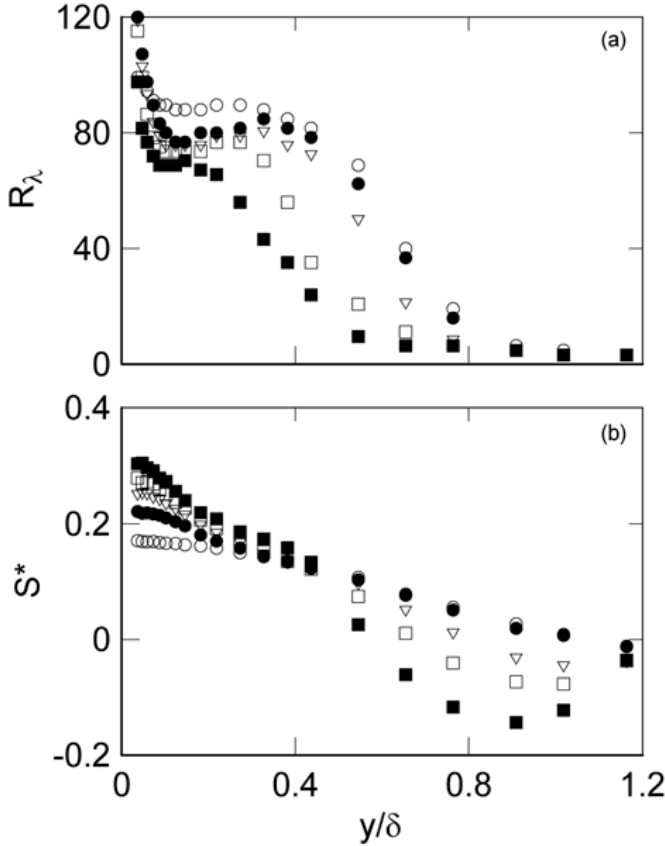


Figure 4: Variation of (a)  $R_\lambda$ ; (b)  $S^*$  with  $\sigma$ . Symbols are as in figure 2

The significant changes in  $R_\lambda$  and  $S^*$  when suction is applied would suggest that the small-scale motion has been altered, and the magnitude of this alteration is increased as  $\sigma$  is increased. For example, relative to no-suction, the change in the region  $y/\delta \leq 0.2$ , where  $R_\lambda$  and  $S^*$  decreases and increases respectively when suction is applied may suggest an increase in the anisotropy of the small-scale. While  $S^*$  is about the same for all  $\sigma$  at  $y/\delta \approx 0.43$ ,  $R_\lambda$  changes appreciably with  $\sigma$ . For example at  $y/\delta \approx 0.43$ ,  $R_\lambda$  is 82, 78, 72, 35 and 24 for  $\sigma = 0, 0.8, 1.7, 3.3$  and  $5.5$ , respectively. The result could suggest that the anisotropy of the layer is the same at  $y/\delta \approx 0.43$ , and beyond this point, the anisotropy decreases below that for no-suction. This is evident in figure 4b where the suction data cross over below those of no-suction data at  $y/\delta \approx 0.43$ .

### Spectra and Second-order Structure Functions

The distributions of  $\langle \epsilon \rangle$ ,  $R_\lambda$  and  $S^*$  reflect a change in the near-wall structure when suction is applied. Figures 5 and 6 show the Kolmogorov compensated spectra and second-order structure functions, respectively, of  $u$ ,  $v$  and  $w$ . Although,  $R_\lambda$  (90-120) is not large enough for the existence of a discernible inertial range, the dependence of  $k_1^{*2}\phi_u^*$ ,  $k_1^{*2}\phi_v^*$  and  $k_1^{*2}\phi_w^*$  on  $\sigma$  is visible at low wavenumbers ( $k_1^* < 0.2$ ), where the suction data depart from the no-suction data at  $y/\delta = 0.125$  as shown in figure 5. The departure increases as  $\sigma$  increases. There is reasonable collapse among all the data sets at larger wavenumbers ( $k_1^* \geq 0.2$ ) for the  $u$  spectra. The quality of the collapsed is poorer for  $v$  and  $w$ . This is not too surprising since the value of  $\langle \epsilon \rangle$  used to calculate the

Kolmogorov scales were inferred from the  $u$  spectrum. However, the collapse should be addressed with some reservation because  $\langle \epsilon \rangle$  obtained from  $\langle \epsilon \rangle_{\text{hom}} \approx \nu \langle (\partial u / \partial x)^2 \rangle + \langle (\partial v / \partial x)^2 \rangle + \langle (\partial w / \partial x)^2 \rangle$  may provide a better estimate than those used here, and therefore, more appropriate. While the attenuations of the spectral at  $k_1^* < 0.2$  by suction highlights a change in large-scale motion, the departure of  $v$  spectra further suggests the anisotropy of the large-scale resulting from an alteration of the large-scale structures. Since coherent structures are present at various scales, the departure from no-suction may suggest the weakening of these structures. Also, the attenuation of  $k_1^{*2}\phi_v^*$  persists more than the other two over a significant fraction of  $k_1^*$  at least for  $\sigma = 5.5$ . Thus, the distributions of  $k_1^{*2}\phi_v^*$  are more affected by suction than  $k_1^{*2}\phi_u^*$  and  $k_1^{*2}\phi_w^*$ . The results are in agreement with [10]. The high-wavenumber variation exhibited among all the data set when displayed on a linear scale (not shown) may reflect the difference in large-scale anisotropy, since anisotropy introduced at the large scales can be felt down to the small scales. The effect of this change in the large-scale anisotropy increases as  $\sigma$  increases.

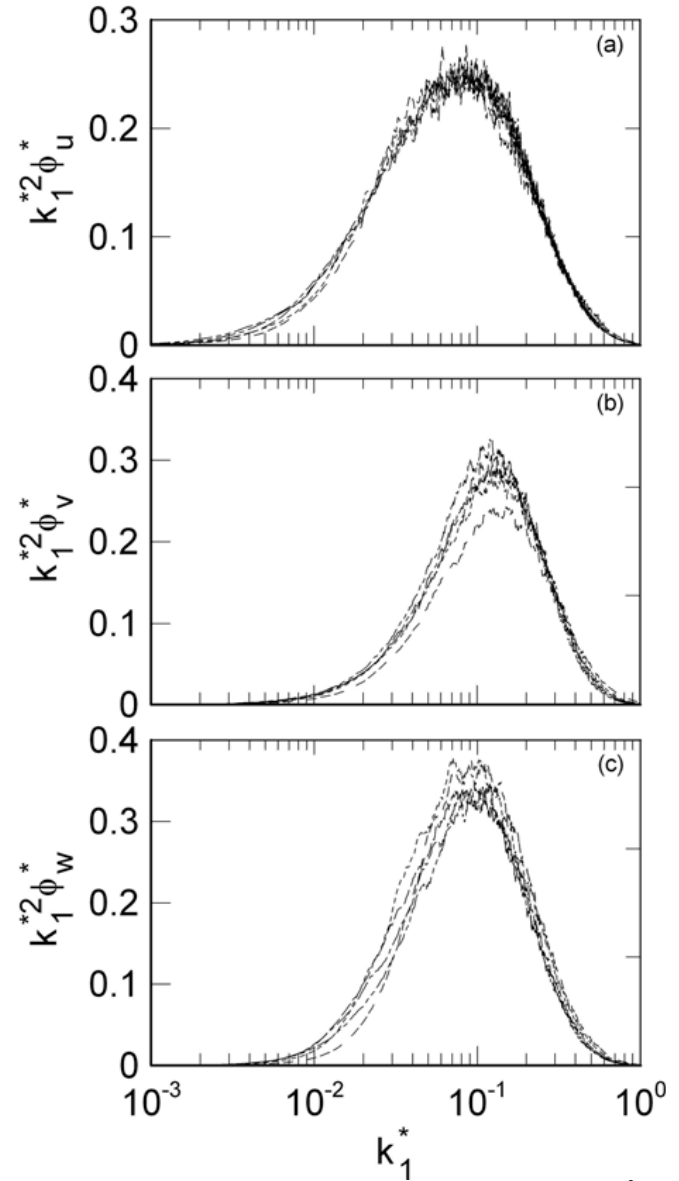


Figure 5: Kolmogorov-normalised spectra multiplied by  $k_1^{*2}$ , of (a)  $u$ , (b)  $v$  and (c)  $w$  for several values of  $\sigma$  at  $y/\delta = 0.125$ . —:  $\sigma = 0$ ; — —:  $\sigma = 0.8$ ; — · —:  $\sigma = 1.7$ ; · · ·:  $\sigma = 3.3$ ; — · —:  $\sigma = 5.5$ .

From figure 6, For  $r^* \leq 10$ , there is fairly good collapse among for  $\langle (\delta u^*)^2 \rangle$ ,  $\langle (\delta v^*)^2 \rangle$  and  $\langle (\delta w^*)^2 \rangle$ , providing support for the validation of Kolmogorov similarity hypothesis [18] in the

dissipative range even when the boundary layer is perturbed strongly.

In all the figures, there exist a region where there is no collapse among all the data set for  $\langle(\delta u^*)^2\rangle$ ,  $\langle(\delta v^*)^2\rangle$  and  $\langle(\delta w^*)^2\rangle$  as  $\sigma$  increases, suggesting a change in the small-scale motion between the perturbed and unperturbed boundary layers. For example, in the range  $r^* \geq 20$ , the suction data depart from  $\sigma = 0$  for  $\langle(\delta u^*)^2\rangle$ ,  $\langle(\delta v^*)^2\rangle$  and  $\langle(\delta w^*)^2\rangle$ , with  $\langle(\delta v^*)^2\rangle$  and  $\langle(\delta w^*)^2\rangle$  exhibiting the greater departures. Since  $v$  is a more sensitive indicator of the large-scale organization than  $u$  [12], the departures may suggest a difference in the anisotropy of the large-scale motion between suction and no-suction. For  $\langle(\delta u^*)^2\rangle$ ,  $\langle(\delta v^*)^2\rangle$  and  $\langle(\delta w^*)^2\rangle$ , the departure increases as  $\sigma$  is increased. It is likely that this large-scale anisotropic behaviour influences the isotropy of the smallest scales as observed in the poorer quality of collapse of the suction and no-suction data of  $\langle(\delta v^*)^2\rangle$  in the region  $r^* \leq 10$  (dissipative range) as compared with a reasonable collapse of  $\langle(\delta u^*)^2\rangle$ , suggesting that the change in the large-scale motion is felt down to the smallest scales. While the lack of collapse of  $\langle(\delta v^*)^2\rangle$  may suggest differences in the anisotropy of the small-scale motion between suction and no-suction, the departures of  $\langle(\delta w^*)^2\rangle$  from  $\sigma = 0$  may not be attributed to a change in the anisotropy of the small-scale motion, but may rather highlight strictly the differences in the large-scale motion between the suction and no-suction. Also, taking into consideration that  $R_\lambda$  and the local mean shear are influenced by suction (see figure 4), the departures observed in  $\langle(\delta u^*)^2\rangle$ ,  $\langle(\delta v^*)^2\rangle$  and  $\langle(\delta w^*)^2\rangle$  would also reflect the influence of these parameters.

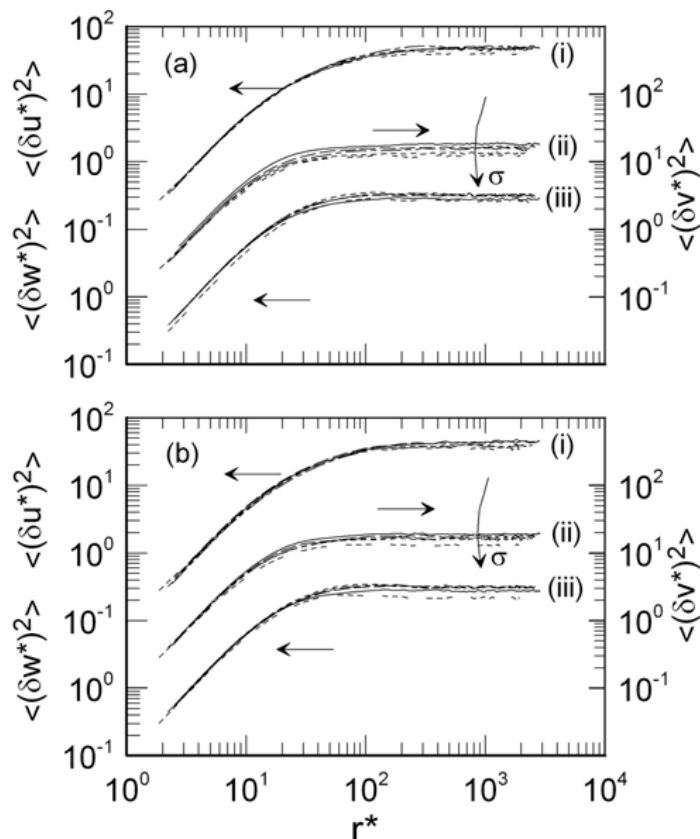


Figure 6: Kolmogorov normalized second-order velocity structure functions for several values of  $\sigma$  at (a)  $y/\delta = 0.065$ ; (b) 0.125. (i)  $\langle(\delta u^*)^2\rangle$ ; (ii)  $\langle(\delta v^*)^2\rangle$ ; (iii)  $\langle(\delta w^*)^2\rangle$ . Symbols are as in figure 5.

## Conclusions

Some characteristics of the small-scale motion in a turbulent boundary layer subjected to concentrated suction, applied through a short porous wall strip, have been examined for a range of suction rates. The results indicate that, relative to no-suction, both  $R_\lambda$  and the normalised mean energy dissipation rate are reduced in the near-wall region when suction is applied,

suggesting that the structures in this region of the boundary layer have been modified. The Kolmogorov similarity hypothesis seem to be reasonably well satisfied for suction and no-suction data by spectra and second-order structure functions for  $k^*_1 > 0.2$  and  $r^* < 10$ . However, Kolmogorov compensated spectra and second-order structure functions for  $k^*_1 < 0.2$  and  $r^* > 20$  depart from those for  $\sigma = 0$ , highlighting that suction induces a change in the small-scale motion as a result of the manipulation of the large-scale structures; the magnitude of this change increases as  $\sigma$  is increased.

## Acknowledgments

The support of the Australian Research Council is acknowledged.

## References

- [1] Antonia, R.A. and Kim, J., A Numerical Study of Local Isotropy of Turbulence, *Phys. Fluids*, **6**, 1994, 834-841.
- [2] Antonia, R.A., Kim, J. and Browne, L.W.B., Some Characteristics of Small-scale Turbulence in Turbulent Duct Flow, *J. Fluid Mech.*, **233**, 1991, 369-388.
- [3] Antonia, R.A., Zhu, Y. and Sokolov, M., Effect of Concentrated Wall Suction on a Turbulent Boundary Layer, *Phys. Fluids*, **7**, 1995, 2465-2475.
- [4] Durbin, P.A. and Speziale, C.G., Local Anisotropy in Strained Turbulence at High Reynolds Numbers, *Trans. ASME I: J. Fluids Engng.*, **113**, 1991, 707-709.
- [5] Kolmogorov, A.N., The Local Structure of Turbulence in Incompressible Viscous Fluid for Very Large Reynolds Number, *Dokl. Akad. Nauk. SSSR*, **30**, 1941, 301-305.
- [6] Lee, M.J., Kim, J. and Moin, P., Structure of Turbulence at High Shear Rate, *J. Fluid Mech.*, **216**, 1990, 561-583.
- [7] Martinez, D.O., Chen, S., Doolen, G.D., Kraichnan, R.H., Wang, L-P. and Zhou, Y., Energy Spectrum in the Dissipative Range of Fluid Turbulence, *J. Plasma Phys.*, **57**, 1997, 195-201.
- [8] Monin, A.S. and Yaglom, A.M., *Statistical Fluid Mechanics*. Vol. 2, 1975, MIT Press, Cambridge, MA.
- [9] Oyewola, O., Djenidi, L. and Antonia, R.A., Effect of Wall Suction on a Turbulent Boundary Layer: Reynolds Number Dependence, in *Proceedings of 14<sup>th</sup> Australasian Fluid Mech. Conf.*, editor B.B. Dally, Adelaide, 2001, 239-243.
- [10] Oyewola, O., Djenidi, L. and Antonia, R.A., Combined Influence of the Reynolds Number and Localised Wall Suction on a Turbulent Boundary Layer, *Expts. in Fluids*, **35**, 2003, 199-206.
- [11] Oyewola, O., Djenidi, L. and Antonia, R.A., Influence of Localised Wall Suction on the Anisotropy of the Reynolds Stress Tensor in a Turbulent Boundary Layer, *Expts. in Fluids*, **37**, 2004, 187-193.
- [12] Papailiou, D.D. and Lykoudis, P.S., Turbulent Vortex and the Entrainment Mechanism of the Turbulent Wake, *J. Fluid Mech.*, **62**, 1974, 11-31.
- [13] Sano, M. and Hirayama, N., Turbulent Boundary Layer with Injection and Suction Through a Slit. First Report: Mean and Turbulence Characteristics, *Bull. JSME*, **28**, 1985, 807-814.
- [14] Shah, D.A. and Antonia, R.A., Scaling of the Bursting Period in Turbulent Boundary Layer and Ducts Flows, *Phys. Fluids*, **A 1**, 1989, 318-325.
- [15] Spalart, P.R., Direct Simulation of a Turbulent Boundary Layer up to  $R_\theta = 1410$ , *J. Fluid Mech.*, **187**, 1988, 61-98.
- [16] Sreenivasan, K.R., On the Fine-scale Intermittency of Turbulence, *J. Fluids Mech.*, **151**, 1985, 81-103.
- [17] Sreenivasan, K.R., On the Universality of the Kolmogorov Constant, *Phys. Fluids*, **7**, 1995, 2778-2784.
- [18] Townsend, A.A. *The Structure of Turbulent Shear Flow*, 2<sup>nd</sup> ed., Cambridge, CUP, 1976.
- [19] Uberoi, M.S., Equipartition of Energy and Local Isotropy in Turbulent Flows, *J. Appl. Phys.*, **28**, 1957, 1167-1170.



## Pressure Measurements on an Automobile Side Rear View Mirror

R. Jaitlee, F. Alam and S. Watkins

School of Aerospace, Mechanical & Manufacturing Engineering  
RMIT University, Melbourne, VIC 3083, AUSTRALIA

### Abstract

The vibration of automotive side rear view mirror is a concern for vehicles safety. Although the primary causes of mirror vibration are due to power train, road/tyre interaction and aerodynamic pressure fluctuations, not many studies have been undertaken on mirror vibration due to aerodynamic inputs. The primary objective of this paper is to study the aerodynamic pressures on mirror surface at various speeds to determine the effects of aerodynamic inputs on mirror vibration. The mean and fluctuating pressures were measured and analysed.

### Introduction

A significant effort has been made by the automobile and component manufacturers to reduce aerodynamic drag, noise and vibration. However, relatively less attention has been drawn to the refinement of performance of automobile side rear view mirrors, especially mirror vibration. The primary function of a side rear view mirror is to provide the driver a clear vision of all objects to the rear and side of the vehicle. However, there are several problems associated with it such as image distortion due to aerodynamically induced and structural vibration, aerodynamically induced noise (due to cavities and gaps) and water and soil accommodation on mirror surface due to complex mirror shapes and airflow around it. An automotive mirror is a bluff body and causes significant periodic flow separation at the housing, which produces oscillating aerodynamic forces (due to hydrodynamic pressure fluctuations) on mirror surface. These pressure fluctuations not only cause the mirror surface to vibrate but also generate aerodynamic noise. Due to excessive vibration, the rear view mirror may not provide a clear image. Thus, vibrations of the wing mirrors can severely impair the driver's vision and safety of the vehicle and its occupants. The rear view mirrors are generally located close to the A-pillar region on the side window. An intense conical vortex forms on the side window close to A-pillar due to complex A-pillar geometry and the presence of side rear view mirror and flow separation from it makes the airflow even more complex. Although some studies ([3], [4], [5], [6], [7]) have been undertaken to investigate the structural input (engine, road/tyre interaction etc) as well as aerodynamic input to mirror vibration, very little or no study was undertaken to quantify the aerodynamic input to mirror vibration. Therefore, the primary objective of this work as a part of a larger study is to measure the aerodynamic pressures (mean and fluctuating) on mirror surface to understand the aerodynamic effects on mirror vibration.

### Experimental Procedure and Equipment

In order to measure the mean and fluctuating pressures on mirror surface, a brand new production mirror was used. The glass of the mirror was replaced with a rigid aluminium plate (2.4 mm thickness) and the mirror case was slightly modified in order to hold the aluminium plate. There are 51 holes on the aluminium plate in a grid pattern. The diameter of the hole was 1 mm. The space between the two holes was 25 mm horizontally and 13 mm vertically. The mirror face was pressure tapped with rubber tubing. The rubber tubing was connected to four pressure sensor

modules, each having 15 channels. All pressure sensor modules were connected to an interface box that provided power and multiplexes the inputs to the data acquisition system. The Dynamic Pressure Measuring System (DPMS) data acquisition software provided mean, rms, minimum and maximum pressure values of each pressure port on mirror. By entering dimensions of the tubing used, the data were linearised to correct for tubing response in order to obtain accurate dynamic pressure measurements. The instrumented mirror was attached with a quarter model of a current production Ford Falcon and placed in the working section of RMIT Industrial Wind Tunnel. The quarter model was used to reduce the blockage ratio and to have representative vehicle geometry and airflow pattern around the mirror. The mean and fluctuating pressures were measured at a range of speeds (60 to 120 km/h with an increment of 20 km/h) at zero yaw angle. The mirror was tested as standard configuration first and then modified configuration. The results for the modified condition are not included in this paper.

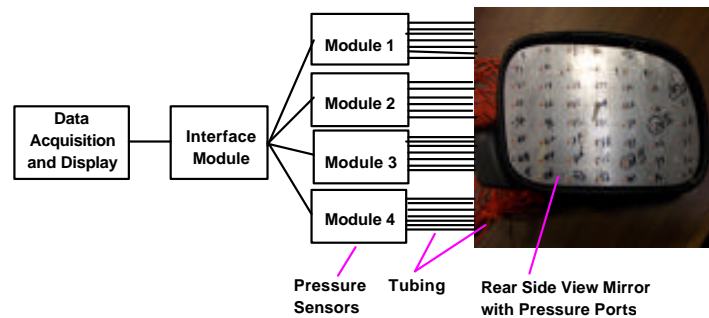


Figure 1 : A Schematic of Pressure Measurement Set Up.

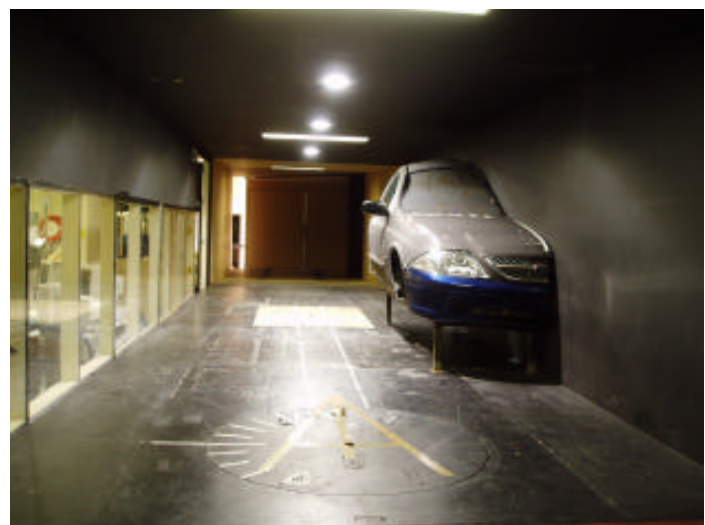


Figure 2: Experimental Set Up of the Mirror with a Ford Quarter Model in the Test Section of RMIT Wind Tunnel.

Figure 2 shows the experimental set up in the wind tunnel test section. In order to simulate real wind condition and A-pillar geometry, the mirror was attached to the quarter model current production car as shown in the figure. Experiments were

performed in RMIT University Industrial Wind Tunnel which is a closed test section, closed return circuit wind-tunnel with a maximum speed of 145 km/h. The rectangular test section dimension is 3 m (wide) x 2 m (high) x 9 m (long). More details about the RMIT Industrial Wind Tunnel can be found in [1, 2]. The tunnel was calibrated before conducting the experiments and tunnel air speeds were measured via a modified NPL (National Physical Laboratory) ellipsoidal head Pitot-static tube (located at the entry of the test section) connected to a MKS Baratron Pressure sensor. The sampling frequency of each channel was 1250 Hz. It may be noted that the peak energy of fluctuating pressure on mirror surface is well below 500 Hz (for more details, refer to [5] and [6, 7]). The dynamic response of the tubing was calibrated in order to minimise the attenuation of frequency.

### Results and Discussion

The mean and fluctuating pressures were converted to non-dimensional parameters such as mean pressure coefficient ( $C_p$ ) and fluctuating pressure coefficient ( $C_p \text{ rms}$ ) by dividing the velocity head ( $q$ ). The mean  $C_p$  and Fluctuating  $C_p \text{ rms}$  were plotted in 3-D and also in contour. The origin of the plot is located at the top left hand corner position, eg., Position 1 (see Figure 3). The x-distance is horizontal and y-distance is vertically down as shown in Figure 3. The contour plots for 60, 80, 100 and 120 km/h for the mean and fluctuating pressure coefficients are shown in Figures 4 to 8, 10-11 and 13. The 3-D plots of fluctuating pressure coefficients ( $C_p \text{ rms}$ ) for 100 and 120 km/h are shown in Figures 7 and 12.

The lowest surface mean pressure was found in the lower part of the mirror for all speeds except for the 80 km/h speed (see Figures 4, 6, 8 & 11). The maximum fluctuating pressure was also measured at the bottom part of the mirror surface at all speeds tested. The 3-D and contour plots clearly show that the fluctuating pressure is not uniformly distributed on the mirror surface rather concentrated at the lower central part of the mirror surface. It is believed to be due to the strong flow separation from the edge. Generally, the higher the magnitude of the fluctuating pressure, the greater possibility of generating intermittent force and aerodynamic noise. With the increase of speed, the affected area and magnitude of fluctuating pressures increase. The contour and 3-D plots for the mean pressure show a significant pressure drop (lowest mean pressure) at the lower right hand corner for all speeds except at 60 km/h. Further investigation is needed to clarify this phenomenon but this is thought to be due to the interaction of the A-pillar vortex. It may be noted that the airflow around the mirror housing is very complex and strongly influenced by the A-pillar vortex. It may be mentioned that when the mean pressure is low, the fluctuating pressure is high, however, the peak fluctuating pressure does not occur at lowest mean pressure. The peak fluctuating pressure shifts from the location of the lowest mean pressure.

A real mirror glass is generally mounted with the base using a primary pivot and two auxiliary supports to stabilize the mirror. The primary pivotal support is located approximately in the centre of the mirror glass. Therefore, intermittent fluctuating pressure acting on any part other than pivotal point causes mirror to vibrate. However, the vibration is neither purely horizontal nor vertical. The mirror glass vibration is generally diagonal (torsional) due to the asymmetric fluctuating pressure on the mirror surface as shown in Figures 5, 7, 9-10 and 12-13.

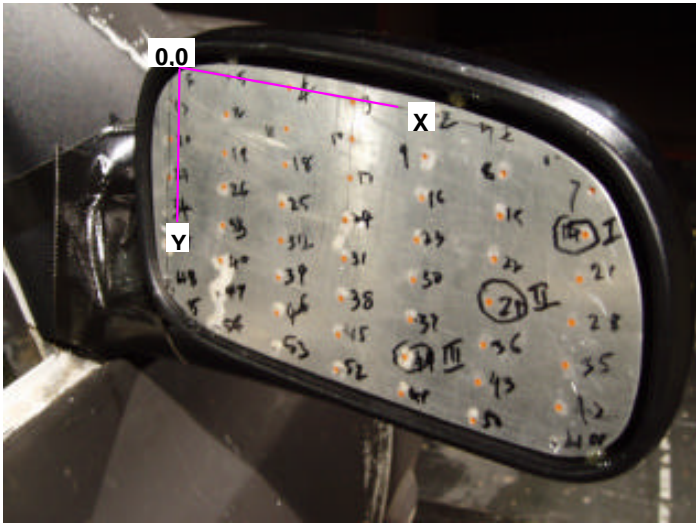


Figure 3: Schematic of Data Representation in Relation to Mirror Geometry and Coordinates.

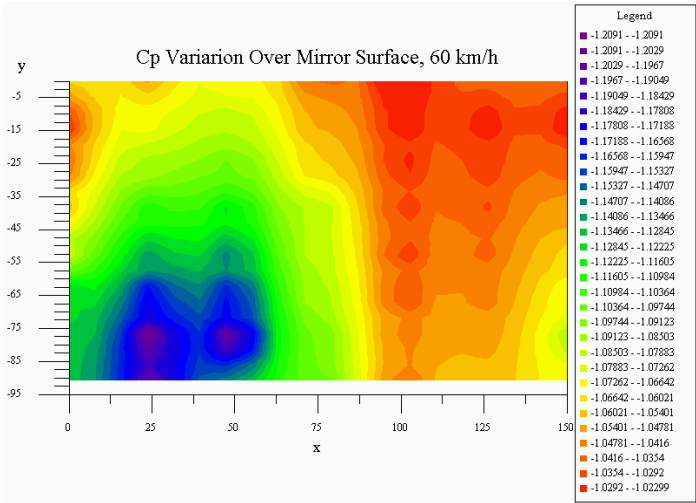


Figure 4: Contour Plot of Mean  $C_p$ , 60 km/h Speed.

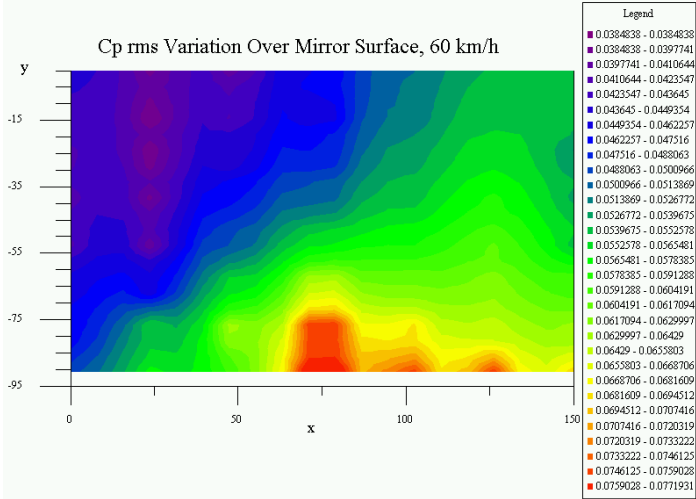


Figure 5: Contour Plot of Fluctuating  $C_p \text{ rms}$ , 60 km/h Speed.

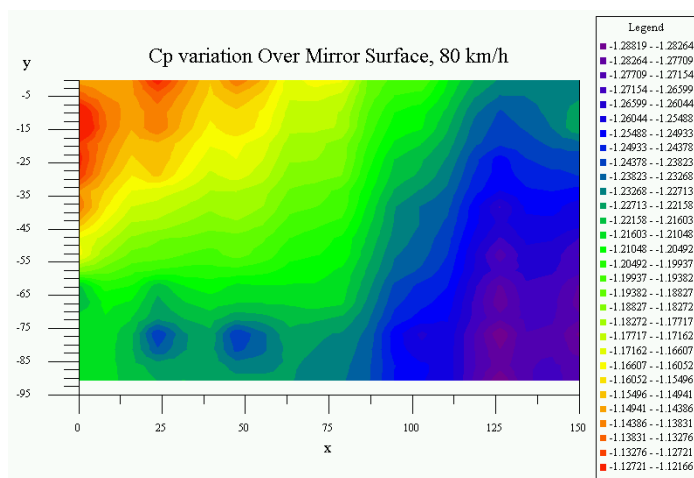


Figure 6: Contour Plot of Mean Cp, 80 km/h Speed.

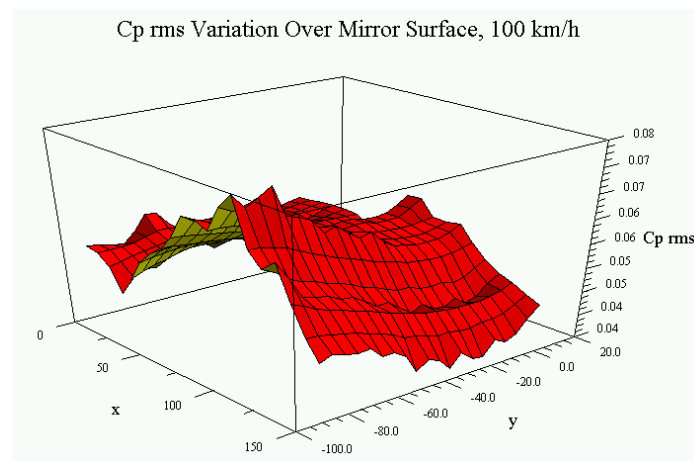


Figure 9: Fluctuating Pressure Cp rms Variation on Mirror Surface, 100 km/h Speed.

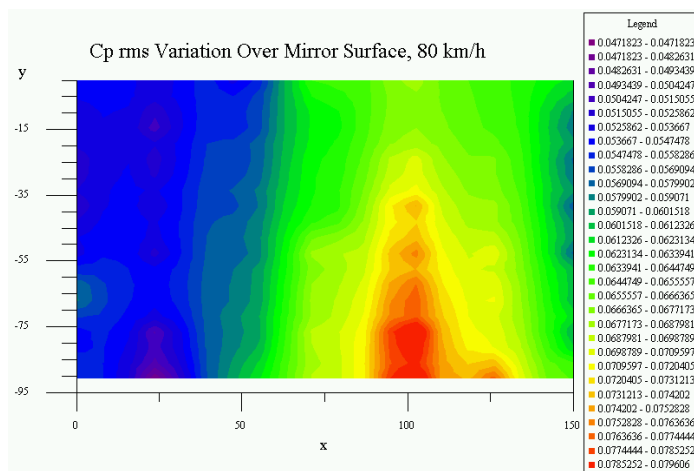


Figure 7: Contour Plot of Fluctuating Cp rms, 80 km/h Speed.

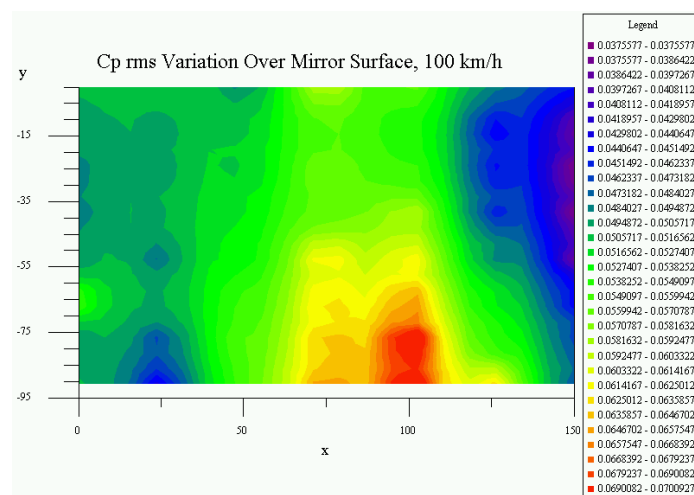


Figure 10: Contour Plot of Fluctuating Cp rms, 100 km/h Speed.

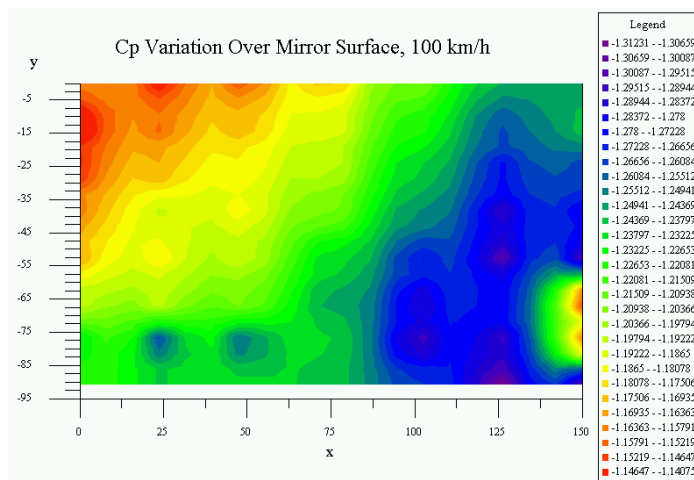


Figure 8: Contour Plot of Mean Cp, 100 km/h Speed.

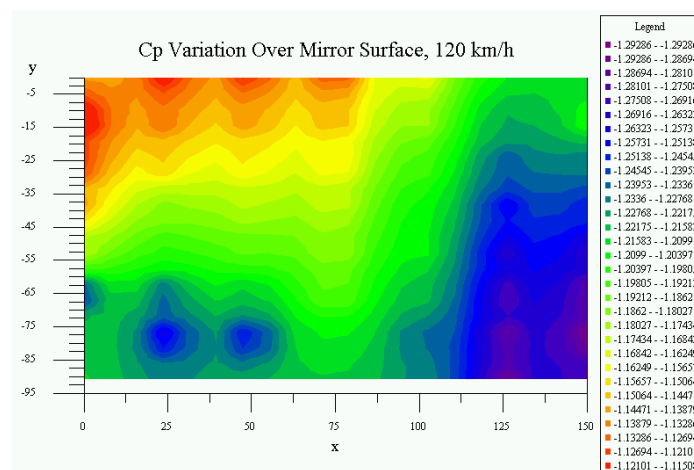


Figure 11: Contour Plot of Mean Cp, 120 km/h Speed.



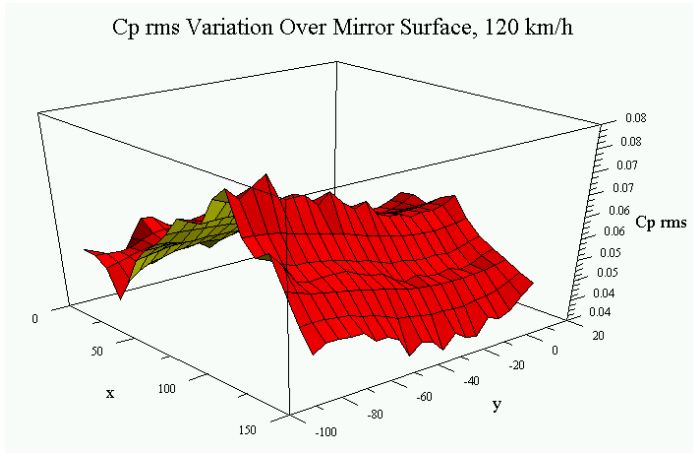


Figure 12: Fluctuating Pressure  $C_p$  rms Variation on Mirror Surface, 120 km/h Speed.

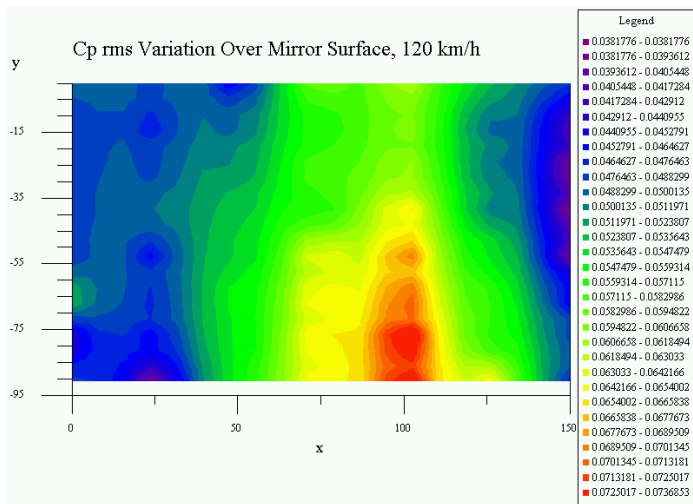


Figure 13: Contour Plot of Fluctuating  $C_p$  rms, 120 km/h Speed.

### Spectral Analysis

Power Spectral Density (PSD) was used to document the energy characteristics of fluctuating pressure signals in the frequency domain. The fluctuating pressure data from the position on mirror surface where the maximum fluctuating pressure occurred was used for PSD analysis and plotted against frequency (see Figure 14). The spectra plot indicates that the fluctuating pressures on mirror glass are broad band type and most energy is located in low frequencies.

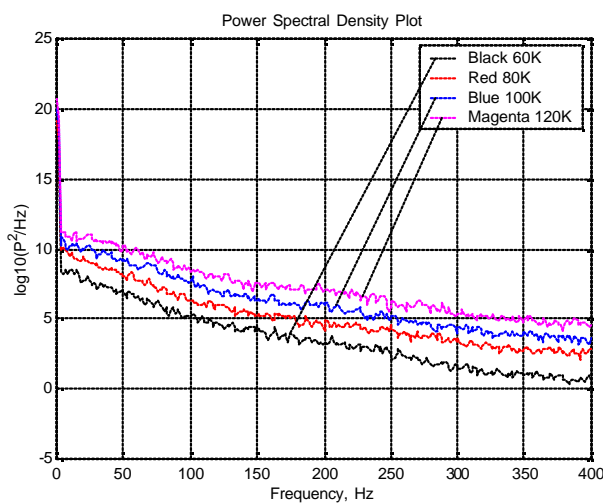


Figure 14: Fluctuating Pressure Spectra Variation with Speeds.

### Concluding Remarks

The following conclusions have been made from the work presented here:

- Fluctuating and mean aerodynamic pressures are not uniformly distributed over an automobile mirror surface.
- The highest magnitude of fluctuating pressure can be found at the central bottom part close to the mirror edge.
- The lowest magnitude of mean pressure was noted at bottom right hand corner of the mirror surface
- The pressure fluctuation on mirror glass is broad band type and most energy is located in low frequencies (below 50 Hz)

### Acknowledgments

The authors would like to express their sincere thanks to Mr G. Vино and Juliette Milbank, Vehicle Aero Group for their assistance with the testing and data processing. Authors are also grateful to Mr Gilbert Atkins, School of Aerospace, Mechanical and Manufacturing Engineering, RMIT University for providing technical assistance.

### References

- [1] Alam, F., Watkins, S. and Subic, A., "The Aerodynamic Forces on a Series of Tennis Balls", Submitted to *The 15<sup>th</sup> Australasian Fluid Mechanics Conference*, 13-17 December, University of Sydney, Sydney, Australia, 2004.
- [2] Alam, F., "The Effects of Car A-pillar and Windshield Geometry on Local Flow and Noise", Ph.D. Thesis, Department of Mechanical and Manufacturing Engineering, RMIT University, Melbourne, Australia, 2000.
- [3] Bannister, M., "Drag and Dirt Deposition Mechanisms of External Rear View Mirrors and Techniques Used for Optimisation", SAE Paper No. 2000-01-0486, also in SP-1524, *SAE World Congress*, March, Detroit, USA, 2000.
- [4] Milbank, J., Watkins, S. and Kelso, R., "Development of a Small-Scale Aeroacoustic Open Jet, Open Return Wind Tunnel for Cavity Noise and Component Testing", SAE Paper No. 2000-01-0867, also in SP-1524, *SAE World Congress*, March, Detroit, USA, 2000.
- [5] Oswald, G., "Influence of Aerodynamics on the operating performance of Automotive External Rear View Mirror", Ph.D. Thesis, Department of Mechanical and Manufacturing Engineering, RMIT University, Melbourne, Australia, 1999.
- [6] Watkins, S., "On the Causes of Image Blurring in External Rear View Mirrors", SAE Papers 2004-01-1309, SP- 1874, *SAE World Congress*, Detroit, Michigan, USA, 2004.
- [7] Watkins, S., Oswald, G. and Czedel, R., "Aerodynamically-Induced Noise and Vibration of Automobile Add-Ons-External Mirrors, Aerials and Roof racks", *The 9<sup>th</sup> International Pacific Conference on Automotive Engineers*, Bali, Indonesia, 1997.

## A Numerical Comparison of Forced and Free Vibration of Circular Cylinders at Low Reynolds Number

J. S. Leontini<sup>1</sup>, M. C. Thompson<sup>1</sup> and K. Hourigan<sup>1</sup>

<sup>1</sup>Department of Mechanical Engineering  
Monash University, Victoria, 3800 AUSTRALIA

### Abstract

Numerical simulations of flow past an elastically-mounted cylinder at  $Re = 200$  have been performed, and the results directly compared to simulations of flow past a pure-tone driven oscillating cylinder at  $Re = 200$ . It is shown that the pure-tone driven oscillation can capture the important VIV characteristics, if the frequency and amplitude of oscillation are closely matched, for a limited range of  $U^*$ . Multi-frequency oscillation simulations have been performed in areas where the pure-tone oscillation is not accurate, and while they show a significant improvement in the lift force history, as yet they provide little improvement in values of phase.

Nomenclature	
$A^*$	Amplitude ratio, $\frac{y}{D}$
$C_E$	Energy transfer coefficient, $\int_T C_L \cdot U \cdot dt$
$C_L$	Lift coefficient, $\frac{F_L}{0.5\rho U^2 D}$
$D$	Cylinder diameter
$F_L$	Lift force / unit length
$f$	Oscillation frequency
$f_N$	Natural structural frequency
$f_V$	Vortex-shedding frequency from a stationary cylinder
$m^*$	Mass ratio, $\frac{m_{cyl}}{\frac{\pi}{4} D^2 \rho L}$
$Re$	Reynolds number, $\frac{UD}{\nu}$
$St$	Strouhal number, $\frac{f_V D}{U}$
$t$	Time, in seconds
$T$	Period of oscillation
$U$	Free-stream velocity
$U^*$	Reduced velocity, $\frac{U}{f_N D}$
$v$	Transverse cylinder velocity
$y$	Transverse cylinder displacement
$\rho$	Fluid density
$\phi_L$	Phase between displacement and lift force (deg.)
$\zeta$	Damping ratio, $\frac{c}{c_{crit}}$

### Introduction

Vortex-induced vibration (VIV) of bluff structures can occur whenever a bluff body is immersed in a fluid stream. If the frequency of vortex shedding is close to the natural structural frequency of the structure, resonance can occur resulting in large-scale oscillations and ultimately structural failure.

Circular cylinders are extensively used in the study of bluff-body fluid dynamics, due to their geometrical simplicity and common use in engineering applications. Capitalising on these attributes, many vortex-induced vibration studies are based on a circular cylinder constrained to vibrate transverse to the free stream, such as the early investigation of Feng [8], and some more recent investigations ([11],[9]). While this system is greatly simplified, it contains the basic elements of coupled fluid-structure interaction.

In an attempt to better understand these systems, the fluid and structural systems are often decoupled. The cylinder can be

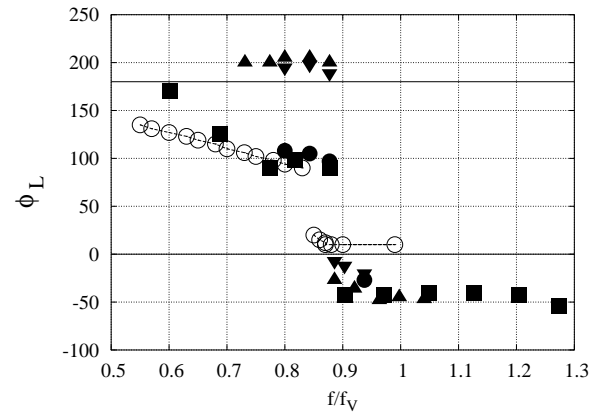


Figure 1: Phase vs frequency ratio  $f/f_V$  for pure-tone driven oscillation and VIV. ■  $A^* = 0.25$ . ●  $A^* = 0.4$ . ▲  $A^* = 0.5$ . ▼  $A^* = 0.6$ . All driven oscillation data from [7] ○ VIV at high  $m^*\zeta$ , that produces peak amplitudes of  $\simeq 0.55$  [9].

driven by some external force at a prescribed amplitude and frequency of sinusoidal oscillation. An extensive map of wake modes with varying amplitude and frequency has been created using this method [16].

While the results gained from driven oscillation experiments match the wake modes and phase difference between the cylinder displacement and lift force well, they do not predict observed levels of energy transfer  $C_E$ , where  $C_E$  is defined as the normalised work done by the fluid on the cylinder over a cycle of oscillation. This can be written as

$$C_E = \int_T C_L \cdot dy = \int_T C_L \cdot v \cdot dt, \quad (1)$$

where  $T$  is a period of oscillation,  $C_L$  is the lift coefficient and  $v$  is the cylinder velocity transverse to the free stream. If it is assumed the non-dimensionalised displacement and resulting lift force coefficient are pure sinusoids, such that  $\frac{y(t)}{D} = A^* \sin(2\pi ft)$  and  $C_L(t) = C_L \sin(2\pi ft + \phi_L)$ , the energy transfer  $C_E$  only varies with the phase angle  $\phi_L$  [5] such that

$$C_E = \pi C_L A^* \sin(\phi_L), \quad (2)$$

where  $A^*$  is the normalised cylinder displacement magnitude,  $\frac{y}{D}$ , and  $\phi_L$  is the phase between the cylinder displacement and generated lift force. Inspection of equation 2 shows that  $C_E$  is positive whenever  $0^\circ < \phi_L < 180^\circ$ . This implies that in vortex-induced vibration  $\phi_L$  always lies between these bounds, whereas during driven oscillation any values of  $\phi_L$  are possible. Measurements of  $\phi_L$  from VIV studies and driven oscillation studies are presented in figure 1.

Figure 1 shows that while the general trend of  $\phi_L$  is the same between the VIV and driven oscillation cases, in that there is a

sudden drop in  $\phi_L$  around  $f/f_V = 0.9$ , almost all of the driven oscillation cases have  $\phi_L$  outside the range  $0^\circ < \phi_L < 180^\circ$ , predicting VIV should not occur. Only the lower amplitudes,  $A^* = 0.25$  and  $A^* = 0.40$ , return a phase such that  $0^\circ < \phi_L < 180^\circ$  at values of  $f/f_V$  below that at which the drop in  $\phi_L$  occurs. However, it is known that VIV does occur at the higher  $A^*$  conditions ([11], [2]). It is clear from these results that while pure-tone driven oscillation captures many of the features of VIV, there are important flow features present during VIV that it does not re-create.

Any efforts to predict VIV using driven oscillation results have met with only mild success. One prediction [14] showed agreement between prediction and results over only a narrow range of flow speeds, and another [13] predicted an amplitude limit of  $A_{MAX}^* = 1$ , a limit later exceeded [10]. The prediction of VIV response from driven oscillation experiments has been investigated over a period of nearly 30 years, and has so far only yielded these mildly successful results. It is for this reason that a more complete driven oscillation model is required.

It is natural that the lower  $Re$  two-dimensional case should be used as a base case, to allow the physics of these flows to be understood. However, due to the practical difficulties of controlling such a low speed experiment, practically no experimental investigations of VIV have been made at  $Re < 200$  ([1] is an exception). However, many numerical results are available ([4], [2]), that compare well to the limited experimental results. Experimental driven oscillation results at  $Re < 200$  have been obtained [12], as well as numerical results ([4], [3]). While a phase change similar to that observed at higher  $Re$  has been reported, the phase at these lower  $Re$  is that between the cylinder displacement and vortex shedding, not between the displacement and lift force, and it has been shown by [6] that these two phases are not always the same. These difficulties mean a direct comparison between existing VIV and driven oscillation data has not been made at low  $Re$ .

This paper attempts to directly compare numerical VIV results with driven oscillation results at the same amplitude and frequency. Pure-tone driven oscillation is compared first, and then multi-harmonic forcing is used where discrepancies between the VIV and pure-tone driven oscillations exist. The improvement in the lift force history is shown, and the advantages and drawbacks of using multi-harmonic driven oscillation to model VIV are discussed.

### Computational method

A two-dimensional, spectral-element method based on an accelerated frame of reference was used for this study. A 508 macro-element, non-deforming mesh was employed, with tensor-product 8th-order Lagrangian interpolation polynomials employed within each macro-element. Details of the method used can be found in [15]. A grid resolution study was performed using the stationary cylinder base case as the benchmark solution to check convergence. The resolution was altered by incrementing the order of the interpolation polynomials. No variation was observed in the value of the Strouhal number,  $St$ , as the polynomial order increased past 8, indicating the grid resolution was adequate.

### Results

#### Vortex-Induced Vibrations

A set of simulations of flow past an elastically-mounted cylinder was run to determine the VIV response. As in low- $Re$  experiments, three amplitude response branches were observed; the initial, upper, and trailing branches. The branches are defined in

figure 2a. The upper branch was the largest amplitude response branch, with amplitudes up to  $A^* \simeq 0.5$ . The upper branch also coincided with the range of  $U^*$  over which synchronisation of the primary response frequency  $f$  and the natural structural frequency  $f_N$  occurred.

The initial branch was characterised by a sharp increase in  $A^*$  with increasing  $U^*$ . While the main response frequency  $f$  was close to the vortex shedding frequency of the stationary cylinder  $f_V$ , a number of frequency components were present, with the displacement showing significant beating over time.

The trailing branch occurred at values of  $U^*$  higher than the synchronisation range. It exhibited low amplitudes of response, and so the frequency  $f \simeq f_V$ . These response results are presented in figure 2a and b.

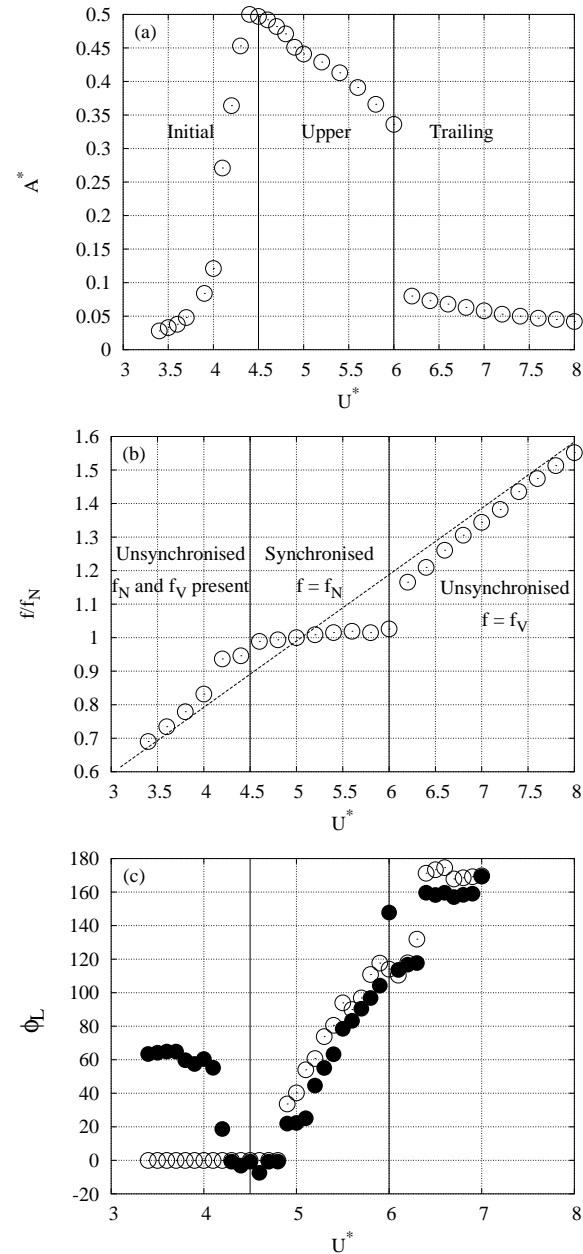


Figure 2: Response of the elastically-mounted cylinder. (a) Amplitude response. (b) Frequency response.  $\circ f/f_N$ ,  $- - f_V/f_N$  (c) Phase between lift force and displacement;  $\circ$  Elastically-mounted cylinder,  $\bullet$  Pure-tone driven cylinder.

Shown in figure 2c are the phase characteristics of this system. Phase was defined as the lag that produced the greatest correlation coefficient, obtained by calculating the cross-correlation between the lift force and displacement. Similar to the high-



Re experimental studies, the phase changed between approximately  $0^\circ$  and  $180^\circ$  over the range of significant response. However, unlike the high-Re experiments, which see the phase change as a sudden jump, this change is an almost linear climb over the upper branch, with smaller jumps at the initial-upper and upper-trailing transitions.

### Pure-Tone Driven Oscillation

To investigate the effectiveness of modelling VIV with driven oscillation, pure-tone driven oscillation simulations were performed at the amplitude and frequencies obtained during the elastically-mounted simulations for a direct comparison. Where the amplitude of response in the VIV case was not steady, the maximum amplitude was used.

The phase of these simulations are compared directly to the VIV phase in figure 2c. It is shown that the phase characteristics of the two set-ups are very similar over the upper branch, especially for  $U^* \geq 5.0$ . Large discrepancies in phase exist throughout the initial branch, even though the amplitude of oscillation is only small,  $O\{0.05D\}$ . Interestingly, the phase results from the pure-tone oscillation match the VIV results closely over the initial-upper transition, even though many frequency components are present during VIV in this region. However, pure-tone driven oscillation cannot capture all the characteristics of VIV in this region, due to the high levels of modulation of cylinder oscillation. The largest oscillations also occur in this region, highlighting the importance of the development of multi-frequency models.

### Multi-Frequency Driven Oscillation

Three cases were selected for multi-frequency driven oscillation testing. A case matching VIV at  $U^* = 4.0$  was selected as a large discrepancy in  $\phi_L$  existed between the VIV and pure-tone driven oscillation at these conditions. It was also observed that two significant frequencies existed in the VIV response of the cylinder at these conditions,  $f_V$  and  $f_N$ .

The second case selected was at  $U^* = 4.6$ . The largest amplitude oscillations occurred here, hence the importance of an accurate model. Significant beating was also evident in the displacement history, indicating the influence of more than one frequency.

The third case selected was at  $U^* = 5.0$ . This case was chosen because the cylinder natural frequency was effectively equal to the vortex-shedding frequency from a stationary cylinder,  $f_N = f_V$ .

The frequencies to include at  $U^* = 4.0$  and  $U^* = 4.6$  were deduced by performing an FFT on the VIV response data. To determine the magnitude of each component, all other components except for the one of interest were filtered out in the frequency domain, and the filtered data transformed back to the time domain with an inverse FFT.

For the  $U^* = 5.0$  case, an FFT was performed on the lift force data, as the second component of oscillation was too small to be detected through FFT analysis of the response. The magnitude of each force component was deduced in the same fashion as the response components at  $U^* = 4.0$ . The linear equation of motion,  $m\ddot{y} + c\dot{y} + ky = F$ , was then solved for each force component, to establish the magnitude of each response component. The input frequencies and respective displacement amplitudes are presented in table 1.

The lift force and phase for the multi-frequency cases are presented in table 2, along with the corresponding VIV and pure-tone driven oscillation results. The values reported were taken

$U^*$	$f_1$	$A_1^*$	$f_2$	$A_2^*$	$f_3$	$A_3^*$
4.0	0.206	0.086	0.230	0.014	-	-
4.6	0.216	0.302	0.209	0.101	0.221	0.101
5.0	0.200	0.491	0.600	0.003	-	-

Table 1: The input parameters for the two multi-frequency driven oscillation cases.

from the steady-state portion of the response in each case.

Simulation	$U^* = 4.0$	$U^* = 4.6$	$U^* = 5.0$
	Peak lift coefficient, $C_{LMAX}$		
VIV	1.22	2.476	0.246
Pure-Tone	1.01	0.682	0.266
Multi-Frequency	1.03	2.681	0.208
	Phase, $\phi_L$		
VIV	0.70	-0.78	42.50
Pure-Tone	60.61	20.69	22.32
Multi-Frequency	58.93	-0.77	46.25

Table 2: Maximum lift coefficient and phase for the multi-frequency driven oscillation cases, compared to the corresponding pure-tone and VIV cases. It can be seen that the extra components added at  $U^* = 4.6$  have a very significant effect on  $C_{LMAX}$ .

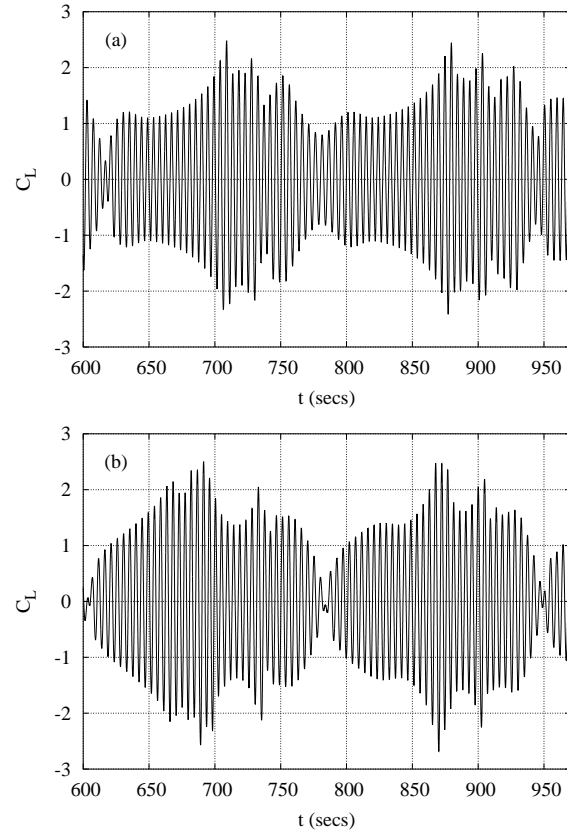


Figure 3: History of the lift force experienced by the cylinder at  $U^* = 4.6$  (a) VIV. (b) Multi-frequency driven oscillation using the primary and two secondary frequency components of the VIV case. The agreement is close, but not perfect.

It can be seen from the values in table 2 that the multi-frequency oscillations have a varying degree of impact compared to pure-tone oscillations. The largest difference between the multi-frequency and pure-tone oscillations occurs in the initial branch and the initial-upper transition region, where extra frequency components are clearly present during VIV.

For  $U^* = 4.0$ , the value of  $C_{LMAX}$  for pure-tone and multi-

frequency oscillation was similar, but the multi-frequency case displayed significant beating, and was a much more accurate recreation of the VIV case. The maximum lift coefficient,  $C_{L_{MAX}}$ , from the multi-frequency oscillation at  $U^* = 4.6$ , matched the VIV case closely, and was markedly better than the pure-tone case. The lift coefficient also showed a constant beating over time, that was not completely regular. A similar phenomenon occurred during VIV. This is illustrated in figure 3.

The phase results obtained were encouraging, but more work is required before any significant conclusions can be drawn from them. While there seems to be a very close agreement between the phase results taken from VIV and multi-frequency oscillation at  $U^* = 4.6$ , they are both negative, which is not expected for a positive energy transfer. Also, the results at  $U^* = 5.0$  indicate the extra frequency component makes the phase vary by approximately  $20^\circ$ . Obtaining phase by cross-correlation is heavily dependent on the accuracy of the frequency of the driving signal, so a discrepancy of this magnitude is not unexpected.

### Conclusions

While pure-tone driven oscillation captures many of the features of VIV, it has been shown that it misses some significant effects, especially in the region where the largest oscillations occur. It is for this reason that a more complete model for VIV has been investigated, namely one that includes extra frequency components.

Specific examples from the initial and upper branches of response have been examined. It was discovered that in the initial branch, at the equivalent of  $U^* = 4.0$ , adding a secondary frequency component to a driven oscillation changed the maximum amplitude of the lift force very little. However, it had the effect of making the lift force history much more similar to the VIV case it was to model.

However, at  $U^* = 4.6$ , adding extra frequency components had a significant effect on the maximum lift coefficient obtained, when compared to the pure-tone oscillation. This lift coefficient was also much closer to the VIV case lift coefficient. This result is important as it shows the magnitude of the lift force is not solely dependent on the peak amplitude of oscillation, but can also be dependent on the oscillation history.

At  $U^* = 5.0$  where  $f_N = f_V$ , adding the small extra frequency component had very little effect on the lift force magnitude. Over the range  $5.0 < U^* < 6.0$ , the cylinder oscillation appears to be a pure-tone oscillation, and it is concluded that a pure-tone driven oscillation in this region is sufficient for the modelling of VIV.

Adding the extra component had little effect on the phase angle in either case, with both still differing when compared to their corresponding VIV cases, except at  $U^* = 4.6$ . However, the sensitivity of the response to minor changes in forcing indicate that to accurately predict the phase difference may require an exceptionally accurate representation of the forcing signal.

It has been shown that multi-frequency driven oscillation offers an improvement over pure-tone oscillation in modelling VIV, especially in the region of largest oscillations. It is envisaged that further work of this nature will lead to a better understanding of the nature of VIV, and an improved capability to predict it.

### Acknowledgements

Primary support for this research program was provided by the Monash University Engineering research committee. Mr. Leontini also acknowledges support from the Department of Me-

chanical Engineering, Monash University, through a Departmental Postgraduate Scholarship.

### References

- [1] Anagnostopoulos, P. and Bearman, P., Response characteristics of a vortex-excited cylinder at low reynolds numbers, *J. Fluids & Structures*, **6**, 1992, 39–50.
- [2] Blackburn, H., Govardhan, R. and Williamson, C., A complementary numerical and physical investigation of vortex-induced vibration, *J. Fluids & Structures*, **15**, 2000, 481–488.
- [3] Blackburn, H. and Henderson, R., A study of two-dimensional flow past an oscillating cylinder, *J. Fluid Mech.*, **1385**, 1999, 255–286.
- [4] Blackburn, H. and Karniadakis, G., Two- and three-dimensional simulations of vortex-induced vibration of a circular cylinder, in *Proceedings of the Third International offshore and polar engineering conference*, Singapore, 1993.
- [5] Carberry, J., *Wake states of a submerged oscillating cylinder and of a cylinder beneath a free surface*, Ph.D. thesis, Monash University, 2001.
- [6] Carberry, J., Sheridan, J. and Rockwell, D., Forces and wake modes of an oscillating cylinder, *J. Fluids & Structures*, **15**, 2001, 523–532.
- [7] Carberry, J., Sheridan, J. and Rockwell, D., Vortex forces on an oscillating cylinder, in *Proceedings of IMECE: ASME International Mechanical Engineering Congress and Exposition*, 2002, 1–7, 1–7.
- [8] Feng, C., *The measurement of vortex-induced effects in flow past a stationary and oscillating circular and D-section cylinders*, Master's thesis, University of British Columbia, 1968.
- [9] Govardhan, R. and Williamson, C., Modes of vortex formation and frequency response of a freely vibrating cylinder, *J. Fluid Mech.*, **420**, 2000, 85–130.
- [10] Khalak, A. and Williamson, C., Dynamics of a hydroelastic cylinder with very low mass and damping, *J. Fluids & Structures*, **10**, 1996, 455–472.
- [11] Khalak, A. and Williamson, C., Motions, forces and mode transitions in vortex-induced vibrations at low mass-damping, *J. Fluids & Structures*, **13**, 1999, 813–851.
- [12] Koopman, G., The vortex wakes of vibrating cylinders at low reynolds numbers, *J. Fluid Mech.*, **28**, 1967, 501–512.
- [13] Sarpkaya, T., Fluid forces on oscillating cylinders, *Journal of the waterways, port, coastal and ocean division of ASCE*, **104**, 1978, 275–290.
- [14] Staubli, T., Calculation of the vibration of an elastically mounted cylinder using experimental data from forced oscillation, *J. Fluids Eng.*, **105**, 1983, 225–229.
- [15] Thompson, M., Hourigan, K. and Sheridan, J., Three-dimensional instabilities in the wake of a circular cylinder, *Experimental Thermal and Fluid Science*, **12**, 1996, 190–196.
- [16] Williamson, C. and Roshko, A., Vortex formation in the wake of an oscillating cylinder, *J. Fluids & Structures*, **2**, 1988, 355–381.

## Vortex Wake and Energy Transitions of an Oscillating Cylinder at Low Reynolds Number

B.E. Stewart, J.S. Leontini, K. Hourigan and M.C. Thompson

Department of Mechanical Engineering  
Monash University, Victoria, 3800 AUSTRALIA

### Abstract

As a means of understanding the phenomenon of vortex-induced vibration, the forced oscillation of a cylinder in cross-flow has been examined. A lack of information regarding the connections between energy transfer and the wake mode of oscillating bodies in low Reynolds number flow prompted a two-dimensional numerical investigation at  $Re = 200$ . The region in which vortex shedding synchronized with the cylinder forcing frequency was defined and the energy transfer calculated. The mode of Kármán vortex shedding incorporated a gradual change from positive to negative energy transfer as the amplitude of the motion was increased. A mode of shedding was detected in the negative energy region in which a pair and a single vortex (P+S) were shed each motion cycle. Energy contours were established in the region of primary lock-in and the boundary of zero energy transfer was defined.

### Introduction

The phenomenon of vortex-induced vibration (VIV) has been studied in some detail over recent years with a common approach being to investigate the near wake and energy transfer characteristics of a bluff body undergoing forced cross-flow oscillation (see reviews in [11]). This approach provides a valuable indication of flow regimes likely to result in VIV. Modern advances in robotics and nano-technology are yielding fluid immersed structures with small characteristic length scales, resulting in low Reynolds number flow regimes. This underlines the need for a greater understanding of the energy transfer characteristics of flows at  $Re < 350$ .

The current numerical investigation attempts to define the region of positive energy transfer for a cylinder undergoing forced oscillation transverse to the flow at a Reynolds number of 200. Experimentation has found that forcing a cylinder to oscillate transverse to a flow caused the vortex shedding of the cylinder to synchronize with the imposed motion along its entire length [7]. In this way, oscillations near the natural shedding frequency,  $f_n$ , extended the laminar flow range from  $Re = 150$  to approximately 350 [7,4], resulting in physical flows that could be accurately approximated by two-dimensional simulations. This region of synchronisation or 'lock-in' near  $f_n$  is termed the primary (or fundamental) lock-in region and the boundaries are dependent on  $Re$  [5]. For frequencies away from  $f_n$ , the flow becomes chaotic and at certain values of amplitude and frequency, synchronisation may be difficult to determine [9].

An examination of the wake at various amplitudes of oscillation was conducted in order to determine specific regions of the near wake influencing the direction of energy transfer. As vortices are shed from the structure, vortex formation takes place from the interaction of four regions of vorticity generated at the body during each motion cycle [12,2]. These regions may then interact to shed two, three or four vortices into the wake each cycle. For oscillations near the fundamental lock-in region, a wake mode shedding two pairs of opposite sign vortices (2P) has been observed [12], but for flows with  $Re$  less than 300 this mode is replaced by a pair and a single vortex (P+S) being shed [2,7,5].

More complex modes have been detected at harmonics and sub-harmonics of  $f_n$  with the wake being encouraged to lock-on at these frequencies [1,12]. During their investigation, Griffin and Ramberg [5] concluded that the appearance of the P+S wake at higher amplitudes was linked to a transition from a drag induced wake to a jet (where thrust dominated). At  $Re \leq 200$  this wake mode was predicted and observed within the synchronization region at amplitudes of oscillation greater than 0.65 cylinder diameters [5,9].

Carberry et al. [3] found experimentally that changes in the lift force, and hence the energy transfer, of a cylinder undergoing forced oscillation was intrinsically linked to the formation of the near wake. When traversing the parameter space defined by frequency versus amplitude of the body motion, a discontinuity in the phase between the lift force and cylinder displacement was perceived. This discontinuity was commented upon by Bishop and Hassan [1] and has since been observed at frequencies both above and below the natural shedding frequency at a range of Reynolds numbers [8,6,2]. Difficulties in detecting the phase jump at low Reynolds number led Blackburn and Henderson [2] to conclude that flows at  $Re < 400$  have viscous dissipation inhibiting the switch and only for values of  $Re$  greater than this can the phenomenon be accurately observed. The phase jump is often associated with a change in sign of energy transfer or shedding mode and when the phase between cylinder displacement and lift force was observed to jump through  $180^\circ$  the direction of energy transfer changed from positive to negative [9,3,12,2,1]. Hover et al. [6] have reproduced energy transfer contours from data at  $Re = 3800$  and 10000 in the non-dimensional amplitude-frequency plane. The authors found that the contour of zero energy transfer agreed reasonably with the data obtained from free vibration of the cylinder at  $Re = 3800$ . This result indicated that analysis of forced vibration might be a useful tool for predicting the regions in which vortex induced vibration is possible and provide an upper limit for the amplitude of oscillation.

### Computational Methodology

The cylinder motion was described by the relationship

$$y(t) = A \cos(2\pi f_o t), \quad (1)$$

where  $A$  is the amplitude of displacement and  $f_o$  is the forcing frequency. Results are described in terms of the scaled amplitude,  $A/D$  and the reduced velocity

$$V_r = \frac{U}{f_o D}, \quad (2)$$

which is equivalent to the wavelength of the cylinder motion scaled by  $D$ . Attention was focused on the primary lock-in region of the parameter space. Throughout the investigation, the scaled amplitude was varied between 0.1 and 1.0 and the reduced velocity between 1.0 and 8.0. No fewer than 80 data sets were collected at irregularly spaced intervals throughout this region. The cylinder was constrained to move transverse to the up stream flow and hence the drag force played no part in the energy transfer. Analysis of the drag force was therefore neglected throughout this study.

Also used to characterise the wake was the Strouhal frequency

$$S_t = \frac{f_n D}{U}. \quad (3)$$

Data analysis was carried out using the lift coefficient,  $C_L$ , and non-dimensional energy transfer per motion cycle,

$$E = -\frac{1}{D} \int_0^T A \sin(2\pi f_o t) C_L(t) dt, \quad (4)$$

as defined in [2].  $E$  indicates the component of  $C_L$  in phase with the cylinder velocity over one period of motion  $T$  and positive  $E$  indicates work done by the fluid on the cylinder. The energy integral given by equation (4) was evaluated using a composite Simpson's Rule. For consistency, the time was scaled by  $U/D$ , giving dimensionless time  $\tau$ .

### Numerical Code

The two-dimensional numerical code utilized a spectral-element scheme with three-step time splitting to solve the incompressible Navier-Stokes equations with an additional forcing term. Eighth-order Lagrangian interpolating polynomials were used to approximate the solution variables within the macro-elements of the mesh. For a more detailed description of the numerical scheme see [10]. The mesh (shown in figure 1) consisted of quadrilateral elements with the domain extending  $23D$  downstream and  $15D$  upstream and to each of the transverse boundaries. The mesh was attached to the non-inertial frame of reference of the cylinder and the free-stream flow and cylinder motion were started impulsively from rest. A no-slip condition was enforced at the cylinder body.

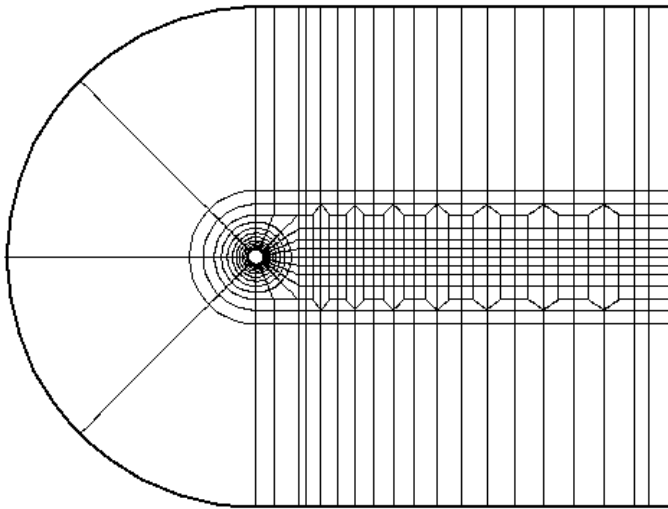


Figure 1. Macro-element mesh used during investigation

Detailed resolution and convergence tests have previously been conducted for this system at a variety of Reynolds numbers and were found to give results that compared well with accepted values [10]. For completeness, a time-step analysis was carried out for the fixed and forced cylinders in the current investigation. Time-steps of  $\Delta\tau = 0.001$  and  $0.002$  were used to check convergence of the solution. In the case of the fixed cylinder, the smaller time-step led to a slightly faster flow development but the vortex shedding frequency for the two solutions was found to be identical to 5 significant figures over any defined time interval. In the case of the cylinder undergoing forced oscillations, the flow development was dictated by the cylinder motion and the lift and drag coefficients were within  $0.1\%$  after  $\tau = 200$ . Consequently  $\Delta\tau = 0.001$  was deemed to give sufficient accuracy and was used

in all subsequent simulations. A fixed cylinder simulation run at  $Re = 200$  for  $\tau > 350$  provided the natural shedding frequency of the cylinder. Using an FFT over the entire lift force data series, equation (3) gave  $St = 0.198$ .

### Results

The wake was considered synchronized with the cylinder motion when a plot of cylinder displacement versus lift traced out a steady, closed loop (see [2]) and the energy transfer per cycle had reached a constant value. For certain forcing frequencies near  $f_n$ , synchronization was difficult to obtain, with a small variation in the frequency altering the lift data from a steady synchronized form to a slowly varying series with a small constant increase in  $E$  each cycle. This behaviour continued for  $\tau > 500$  with no sign of stabilising. Such sensitivity of cylinder wakes near the Strouhal frequency has been observed in previous numerical investigations [2,9].

At reduced velocities below  $4.5$ , wake visualisations showed an apparently stable Kármán wake; however a prominent beating was present between  $f_o$  and  $f_n$ . Although the forcing frequency was dominant, the interaction of these two frequencies led to a beating in the form of the energy transfer per motion cycle and  $E$  consequently varied about a mean value. The varying nature of the energy transfer led this region to be classified as non-synchronised. Areas in which this chaotic nature was particularly apparent were at  $3f_n$  and  $3/2f_n$  and near these frequencies the energy transfer oscillated about a mean value that was becoming increasingly negative. Again, very long time-scale simulations were necessary to determine an equilibrium state. As  $V_r$  increased to values near  $4.5$ , the vortex shedding locked on. This occurred first at amplitudes above  $0.5$  where the effects of cylinder motion were more pronounced. As  $f_o$  approached  $f_n$  synchronisation occurred at all values of  $A/D$ . This lock-on was observed throughout the parameter space until  $V_r > 6.5$ , at which point the wake pattern become totally chaotic. This boundary coincided closely with that established by Williamson and Roshko [12], defining the limits of the fundamental synchronization region.

As the amplitude of oscillation was increased from a value of  $0.2$  in the synchronization region, the lift trace varied continuously from a sinusoidal trace, out of phase with the cylinder displacement, to an asymmetric mode becoming apparent at values of  $A/D > 0.6$ . This represented the progression from the standard Kármán street wake to the P+S mode of shedding. Kármán shedding occurred at low amplitudes and displayed a gradual change from positive to negative energy transfer with increasing amplitude. P+S shedding was observed only in the region of negative energy transfer.

Lift data is shown along with cylinder displacement for  $V_r = 5.0$  at three different amplitudes within the lock-on region (figure 2). It was apparent that although the lift phase experienced a shift between the Kármán shedding in figure 2(d) and the P+S shedding in figure 2(f), the wake mechanism governing this shift was not obvious. During the Kármán shedding the lift progressed from a near sinusoidal trace to one that contained two smaller, secondary peaks per oscillation (figure 2(b)). These peaks became apparent at amplitudes between  $0.40$  and  $0.45$  in the primary lock-on region. The flow remained symmetric with secondary maxima and minima developing in the lift trace each cycle. Following the development of the secondary peaks an increase in the amplitude caused the major peaks and troughs to reduce until all were of approximately equal magnitude. Further increases in  $A/D$  caused a growth in alternate peaks, creating a phase shift between lift and displacement. At this time the wake was still symmetric and shedding in the Kármán street mode. An

increase in amplitude following this switch led to the disappearance of one of the remaining secondary peaks (figure 2(c)) and the development of the asymmetric, P+S mode mentioned previously. One such peak transition occurred at the time indicated by dots in figure 2(a), (b) and (c) at which wake images were obtained. The phase shift corresponded to a change in the direction of energy transfer. Although the switch occurred as the result of a continuous process, the transition took place over a small amplitude range and was completed within a variation of  $A/D < 0.1$ . At the time that images were obtained the cylinder was at maximum downward velocity and the lift data changed dramatically from an extreme negative in figure 2(a) to almost zero in (b) and an extreme positive in (c).

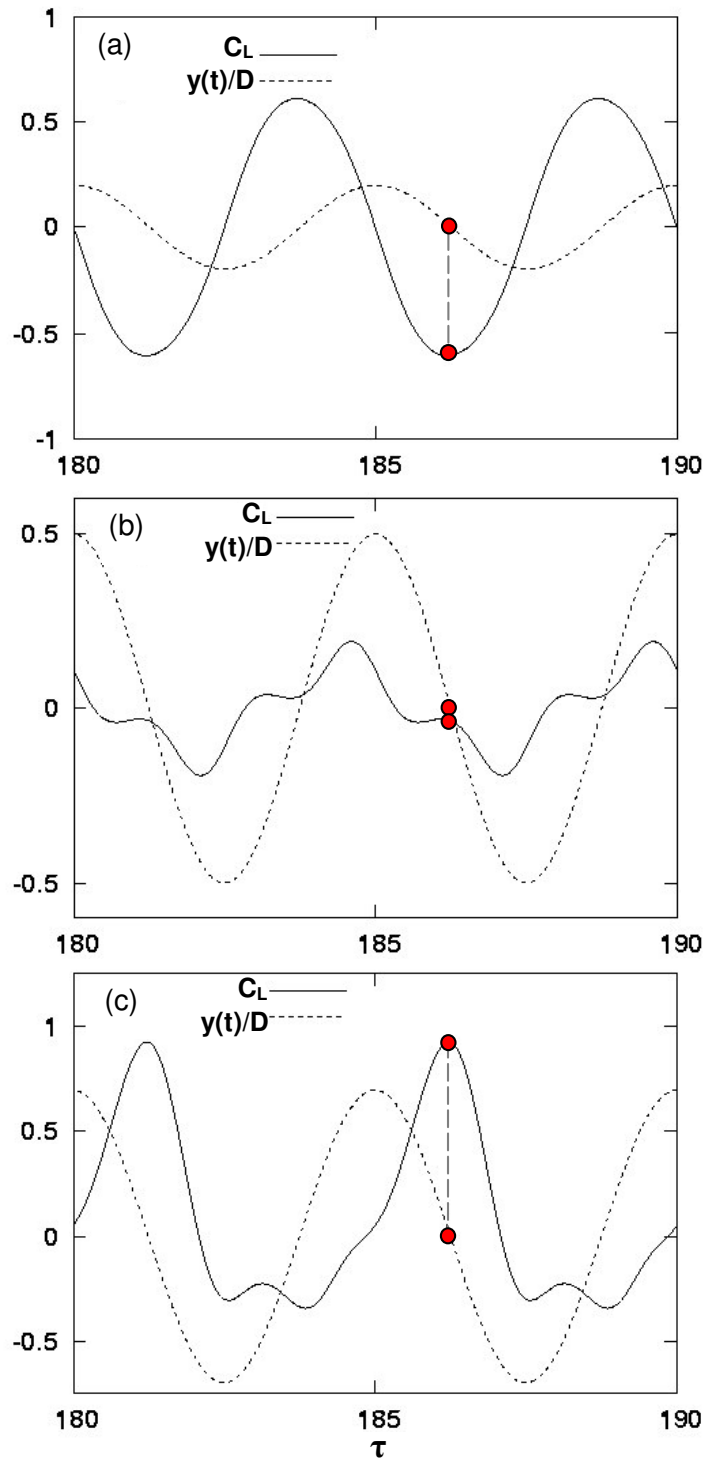


Figure 2. Lift coefficients and corresponding vorticity contours for cylinder oscillating at  $V_r=5.0$ , (a)  $A/D=0.199$ , (b)  $A/D=0.497$  and (c)  $A/D=0.696$ . Red dots indicate point at which images were obtained. Negative vorticity is shown in black and enclosed by dashed contours. H and L show high and low pressure regions respectively.

Three dominant pressure regions affected the lift force on the cylinder. These were the high pressure area at the front stagnation point and the low pressure regions corresponding to the top and bottom shear layers, occurring just before separation. As the amplitude was increased these points were displaced further around the cylinder during maximum velocity (as shown by the high and low pressure regions indicated in figure 2(d), (e) and (f)). This shift made a substantial difference in the overall lift when the pressure forces at the top and bottom of the cylinder were nearly balanced.

In figure 2(d) the cylinder's downward motion caused acceleration of the lower shear layer which created an area of low pressure near the bottom of the cylinder and a net downward lift

force ( $C_L$  negative). This differed from the wake structure at amplitudes near 0.5 (figure 2(e)), when the front stagnation point was shifted towards the bottom of the cylinder. This high pressure region partially offset the low pressure created in the lower shear layer, resulting in a near zero value for  $C_L$ .

At amplitudes in the region of 0.7 the P+S mode of shedding occurred and the elongated region of positive vorticity shown in figure 2(f) separated into two distinct vortices downstream. The elongation of the lower shear structure moved the concentration of vorticity further from the cylinder and the low pressure in the upper shear layer dominated, giving a maximum positive  $C_L$ . During the upwards motion of the cylinder in this asymmetric wake mode, negative vorticity from the upper shear layer formed a low pressure region much closer to the back of the cylinder. This contributed a larger component to the upward lift, resulting in the net downward lift being of much lower amplitude than the net upward lift generated in the previous half cycle.

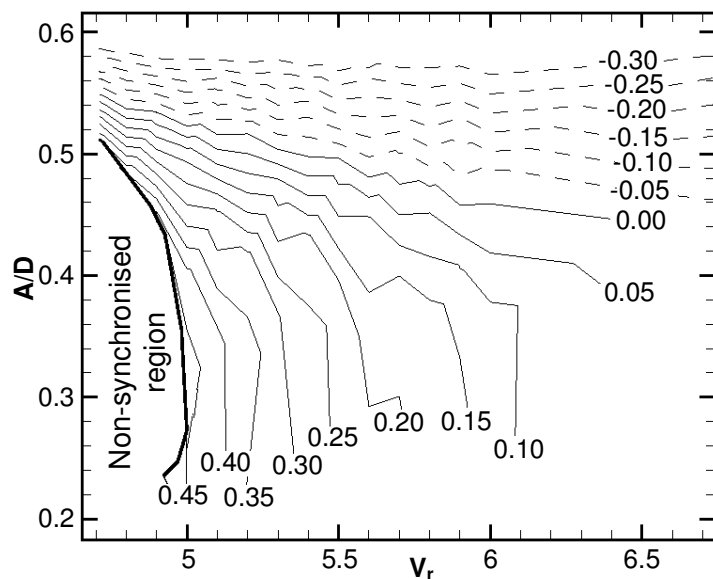


Figure 3. Contours of constant energy transfer in the primary lock-in region. Values of  $E$  are shown and negative energy transfer is indicated with dashed lines

From energy measurements throughout the lock-in region contours of energy transfer per cycle were established (figure 3). These contours of energy,  $E$ , indicated that the energy transition took place between amplitudes of 0.45 and 0.55. For VIV to occur a positive energy transfer is required to account for losses due to structural damping [3,6], hence this boundary represents an upper limit to the observed oscillation amplitude. At amplitudes above the energy transition, values of  $E$  became steadily more negative and were dependent primarily on the amplitude, rather than the reduced velocity. This may be linked to findings in [9] where the P+S wake developed at an almost constant amplitude. The current investigation did not examine the wake mode transition in any detail but it is intended that future work will define this boundary more clearly. The flattened nature of the zero-energy contour may also be representative of the fact that the upper branch of response (see [11] for details) was undetected in the two-dimensional investigation. This was not the case in [6] where a sharp peak occurred in the energy contours for  $V_r$  between 5.0 and 6.0.

## Conclusions

Following an investigation of two-dimensional flow past an oscillating cylinder at  $Re=200$ , information was obtained for the lift force and wake mode occurring at various frequencies and amplitudes of motion. The region in which vortex shedding locked-on to the cylinder motion was determined and energy transfer calculated for all points in the synchronized region. Following analysis of the wake modes, it was discovered that the Kármán shedding displayed a gradual decrease in energy transfer as the reduced velocity and amplitude increased. This was brought about by the development of two secondary peaks in the lift force. At a critical amplitude, these peaks switched prominence, effecting a shift in phase between lift and displacement, and a change in direction of energy transfer. Further increase in amplitude saw the onset of asymmetric P+S shedding in regions of negative energy transfer and amplitudes above 0.6. A plot of energy contours (figure 3) indicated that an energy transition took place over a fairly small range of amplitudes in the primary lock-on region. This result indicated the occurrence of maximum VIV amplitudes of between 0.45 and 0.55 at reduced velocities between 4.5 and 6.5.

## References

- [1] Bishop, R.E.D. and Hassan, A.Y., The Lift and Drag Forces on a Circular Cylinder Oscillating in a Flowing Fluid, *Proc. R. Soc. Lond. A*, **277**, 1964, 51-75.
- [2] Blackburn, H.M. and Henderson, R.D., A Study of Two-Dimensional Flow Past an Oscillating Cylinder, *J. Fluid Mech.*, **385**, 1999, 255-286.
- [3] Carberry, J., Sheridan, J. and Rockwell, D., Forces and Wake Modes of an Oscillating Cylinder, *J. Fluids Struct.*, **15**, 2001, 523-532.
- [4] Griffin, O.M., The Unsteady Wake of an Oscillating Cylinder at Low Reynolds Number, *J. Appl. Mech.*, **38**, 1971, 729-738.
- [5] Griffin, O.M. and Ramberg, S.E., The Vortex-Street Wakes of Vibrating Cylinders, *J. Fluid Mech.*, **66**, 1974, 553-576.
- [6] Hover, F.S., Techet, A.H. and Triantafyllou, M.S., Forces on Uniform and Tapered Cylinders in Crossflow, *J. Fluid Mech.*, **363**, 1998, 97-114.
- [7] Koopmann, G.H., The Vortex Wakes of Vibrating Cylinders at Low Reynolds Numbers, *J. Fluid Mech.*, **28**, 1967, 501-512.
- [8] Lu, X.-Y. and Dalton, C., Calculation of the Timing of Vortex Formation From an Oscillating Cylinder, *J. Fluids Struct.*, **10**, 1996, 527-541.
- [9] Meneghini, J.R. and Bearman, P.W., Numerical Simulation of High Amplitude Oscillatory Flow About a Circular Cylinder, *J. Fluids Struct.*, **9**, 1995, 435-455.
- [10] Thompson, M.C., Hourigan, K. and Sheridan, J., Three-Dimensional Instabilities in the Wake of a Circular Cylinder, *Exp. Therm. Fluid Sci.*, **12**, 1996, 190-196.
- [11] Williamson, C.H.K. and Govardhan, R., Vortex-Induced Vibrations, *Ann. Rev. Fluid Mech.*, **36**, 2004, 413-455.
- [12] Williamson, C.H.K. and Roshko, A., Vortex Formation in the Wake of an Oscillating Cylinder, *J. Fluids Struct.*, **2**, 1988, 355-381.



## Comparison of Flow Characteristics of 45° Forward and 45° Backward Facing Proximal Anastomosis Models: A Particle Image Velocimetry Study

W.F. Ji, L.P. Chua, T. M. Zhou and S. C. M. Yu

School of Mechanical and Production Engineering  
Nanyang Technological University, 639798, Singapore

### Abstract

In order to gain a physical insight on the role of hemodynamics, especially at the proximal anastomosis, in the intimal thickening and graft failure, a two-dimensional Particle Image Velocimetry (PIV) system has been used to map the velocity vector in the actual scale (1:1) 45-degree forward and 45-degree backward proximal anastomosis models under pulsatile flow condition. At the peak flow phase, a low velocity region containing recirculation was found near the heel along the graft inner wall and a stagnation point was found at the graft outer wall. Large spatial wall shear stress variation was found near the heel and the toe for the 45-degree forward facing model. It is recommended that the 45-degree backward facing model is a better arrangement for the bypass operation.

### Introduction

Anastomotic intimal hyperplasia (IH) is a major cause of long-term failure in small diameter vascular prostheses. This process leads to the gradual occlusion of the anastomosis from a sub-intimal proliferation of smooth muscle cells and extracellular matrix [1]. Various hypotheses have been proposed to explain this phenomenon, based upon both mechanical and fluid dynamic mechanisms [2]. It is suggested that these processes may be influenced by biological responses [3], and interactions between blood and the non-endothelialised graft surface [4]. Hemodynamic factors, including flow angle, high wall shear stress variation together with the low wall shear stress level, have long been suggested in causing of vascular disease and have been shown to play an important role on the deformation of arterial wall structure [5, 6, 7]. It is not surprising, therefore, that many studies have tried to relate hemodynamic effects to the localized development of intimal hyperplasia.

However, most of the previous studies were focused on the distal anastomosis and little effort has been put on the proximal side. It is possible that the proximal anastomosis provides the condition to form mitogens and activated platelets, and then they are convected down to the distal part [8]. The effect of flow patterns of the proximal side on the distal part has rarely been reported. Based on the preliminary in-vitro experiment under steady flow condition [9], this study aims to examine the flow structures that occur at the proximal anastomosis under pulsatile flow condition. It is hoped that the study will provide better understanding of the flow structure and its responsibility at the proximal anastomosis.

### Methods

The flow models are designed and fabricated based on the clinical data from the National Heart Centre of Singapore, which had the same geometry as the computational model used in the simulation [10]. The internal diameter of aorta and graft are 20mm and 6mm respectively and the schematic view of the proximal anastomotic model with 45-degree backward facing graft was shown in Figure 1. Note in the present study, 45-degree forward facing graft model was also investigated.

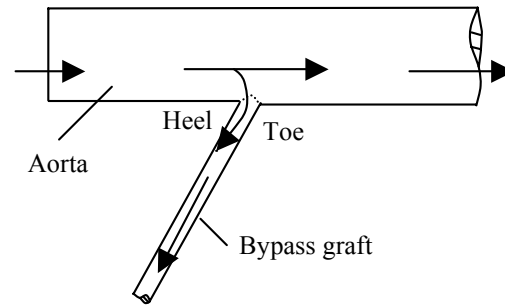


Figure 1: Schematic designs of the proximal anastomotic models.

A solution containing about 30% glycerin and 70% aqueous ammonium thiocyanate ( $\text{NH}_4\text{SCN}$ ) by weight was used to provide a fluid with a viscosity comparable to blood and meet the requirement of refractive index. The aqueous ammonium thiocyanate solution was made up of equal parts of ammonium thiocyanate salt and distilled water by weight. The resulting viscosity and refractive index were measured by means of a controlled shear rate rheometer (Contraves Low Shear 40) and commercial refractometer (ATAGO 3T) respectively. The mixture adapted to yield a viscosity of  $4.08 \times 10^{-3} \text{ Pa} \cdot \text{s}$  and a refractive index of 1.47. Polyamid Seeding Particle (38A2-121 PSP-50, Dantec Measurement Technology) was added into the fluid to highlight the flow field.

Figure 2 is a schematic presentation of the experimental arrangements for Particle Image Velocimetry measurements. The fluid is forced from a sump tank (1) by a centrifugal pump (2) into the reservoir and overflow container (3). Firstly the main flow from the head tank was allowed to fill up the whole circuit, including the piston tube and backpressure tank. Then the valve (4) was closed and the special designed cam device (10) started to generate pulsatile flow profiles. The special designed cam device was fabricated according to the typical flow waveform reported by Nichols and O'Rourke [11] and the pulsatile waveform generated by the cam device in the measurement was shown in Figure 3.

A Q-switched, double cavity pulsed Nd: YAG laser was used as the illumination source, which has a repetition rate of 10Hz and provides two thin (0.3-1mm) green laser sheets ( $\lambda = 532 \text{ nm}$ ). An 80C42 DoubleImage 700 camera with a Nikon AF Micro-Nikkor lens 60/2.8 was used to capture two consecutive images. The images were analyzed using a cross-correlation algorithm yielding the local displacements vector for each interrogation area. The laser-timing unit was triggered to the beginning of the systole by means of the flowmeter signal. The marking dot with number on the curve represents the time interval in the cycle selected to show the velocity vector maps and the wall shear stress.

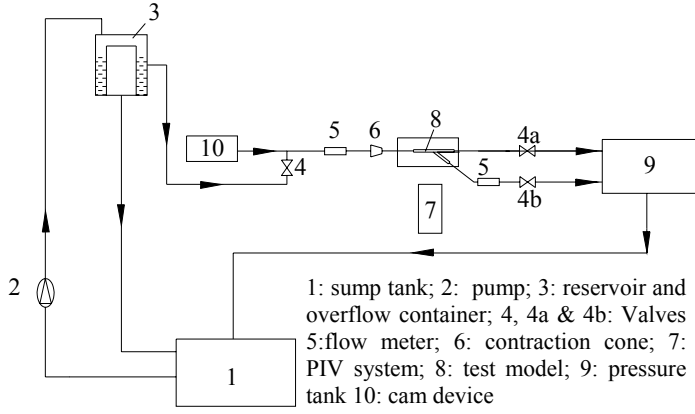


Figure 2: Schematic presentation of in-vitro experimental arrangement.

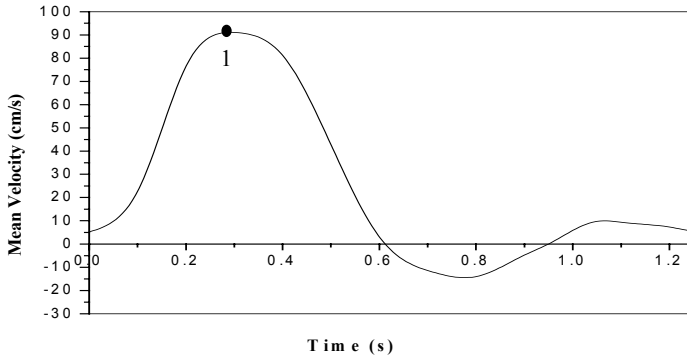


Figure 3: The pulsatile velocity waveform.

Post-processing of the results included the calculation of WSS and spatial WSSG, the two parameters believed to be associated with IH formation [5, 6, 7]. The wall shear stresses,  $\tau_w$ , along the graft inner wall and outer wall were calculated using the following relation:

$$\tau_w = \mu \frac{\partial u}{\partial y} \Big|_{y \rightarrow 0} \quad (1)$$

Where  $\partial u / \partial y$  is the velocity gradient close to the wall. The wall shear stress gradients, WSSG, along the graft inner wall and outer wall were calculated using:

$$WSSG = \partial \tau_w / \partial x \quad (2)$$

## Results and Discussion

The flow measurements as shown in Figure 4 reveal that a recirculation region, which spans a distance of 10 mm (about 1.6 times of graft diameter), is observed along the graft inner wall of 45-degree forward facing model during the peak flow phase ( $t=0.3s$ ). The colour map in Figure 4 represents the velocity magnitude. Note that within the recirculation region, the magnitudes of the velocity vectors are much smaller than the main stream.

Figure 5 shows the flow field of 45-degree backward facing graft model under the peak flow phase ( $t=0.3s$ ). Similarly a small low velocity region was found along the graft inner wall near the heel. Comparing Figure 5 with Figure 4, it was found that the low flow region in 45-degree backward facing graft model occupies a much smaller space. The low flow region which was believed to be suffered from low shear stress may allow prolonged residence times for circulating pro-inflammatory cells to adhere to the endothelial monolayer cells of the vessel, and have thus increased the chances for forming mitogens and activating platelets [12]. Once the mitogens formed and the platelet activated, they may be

transported down to the distal site during the physiological cycle and fastened the formation of the intimal hyperplasia [13].

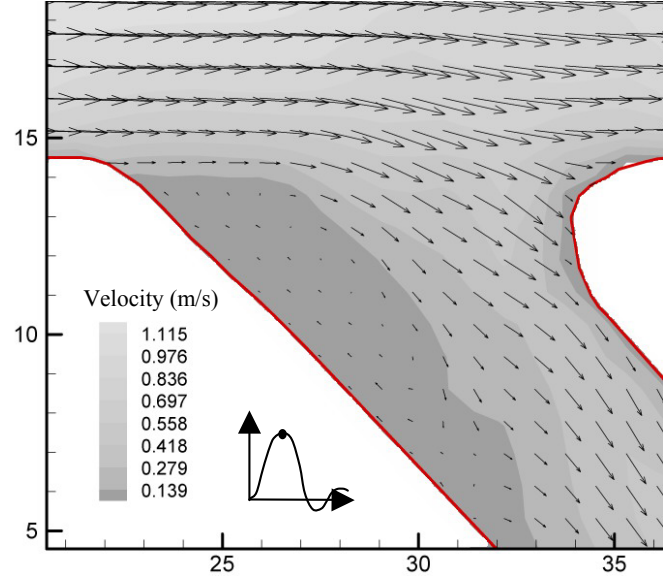


Figure 4: Flow patterns and velocity magnitude distribution in 45-degree forward facing graft model under peak flow phase ( $t=0.30s$ ).

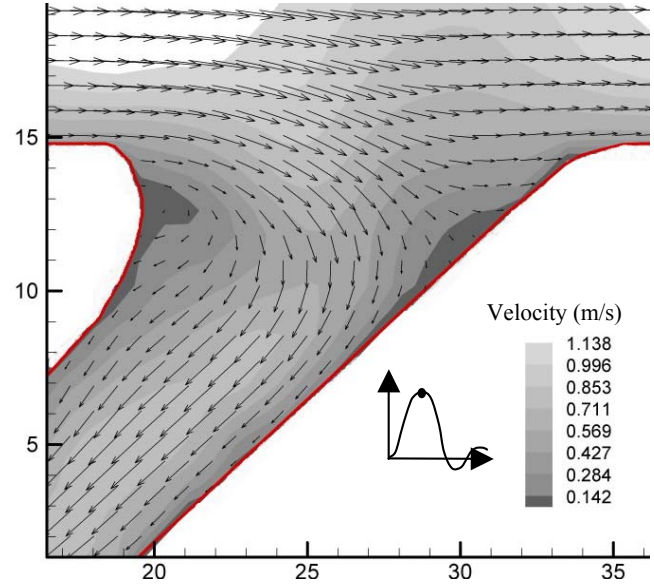


Figure 5: Flow patterns and velocity magnitude distribution in 45-degree backward facing graft model under peak flow phase ( $t=0.30s$ ).

Wall shear stress (WSS) is an important factor which can stimulate and affect the development of intimal hyperplasia [14], and is the main cause for the bypass graft failure. Furthermore, the suture joint is more prone to the intimal thickening. Low WSS [5], high or unidirectional shears [15] were believed to be closely related to the development of intimal hyperplasia at the suture joint. In order to study the effect of anastomotic angle on the wall shear stress distribution, the comparison among the WSS distributions of 45-degree forward and 45-degree backward facing graft models under the peak flow condition has been conducted and presented in Figure 6. This is because the flow fields under peak flow condition were found to be much more complicated than other phases, and have much higher WSS and can correspondingly induce the release of growth factors from the endothelium, followed by smooth muscle cell proliferation [3]. Note the coordinates used to express the wall shear stress profiles are shown schematically at the corner of the figure. The annotation,  $x_1$  and  $x_2$  are the points selected approximately at the end of the straight aortic wall and are going along the direction of the graft inner and outer walls respectively.

From Figure 6 (a) it is observed that the wall shear stress distributions of the two models have the similar trend in general, which is due to the same inlet flow condition. The wall shear stresses reach a peak value and then drop sharply to a low level and maintain at the similar order of magnitude before increasing at further downstream. However, they also have some differences, the low stress region is quite short in the case of 45-degree backward facing model. And a large negative wall shear stress region was found from  $x_1 = 3\text{mm}$  to  $x_1 = 12\text{mm}$  in the 45-degree forward facing graft model, which indicates the existence of the recirculation region there.

Along the graft outer wall, it is noted that the magnitude of wall shear stresses are much higher than those of graft inner wall for the two models, as shown in Figure 6 (b). From the figure it is observed that the stagnation point of the 45-degree forward facing model locates at further upstream ( $x_2 = 2\text{mm}$ ) compared with that of 45-degree backward facing model ( $x_2 = 4.7\text{mm}$ ). It is also noted that 45-degree forward facing model has the highest positive wall shear stress and much steeper increase of WSS along the graft outer wall. Significant flow disturbances which have resulted in locally elevated WSS has been proposed to cause damage to the endothelial cells and endothelium dysfunction, and have also played an important role in platelet activation, and ultimately IH formation [16].

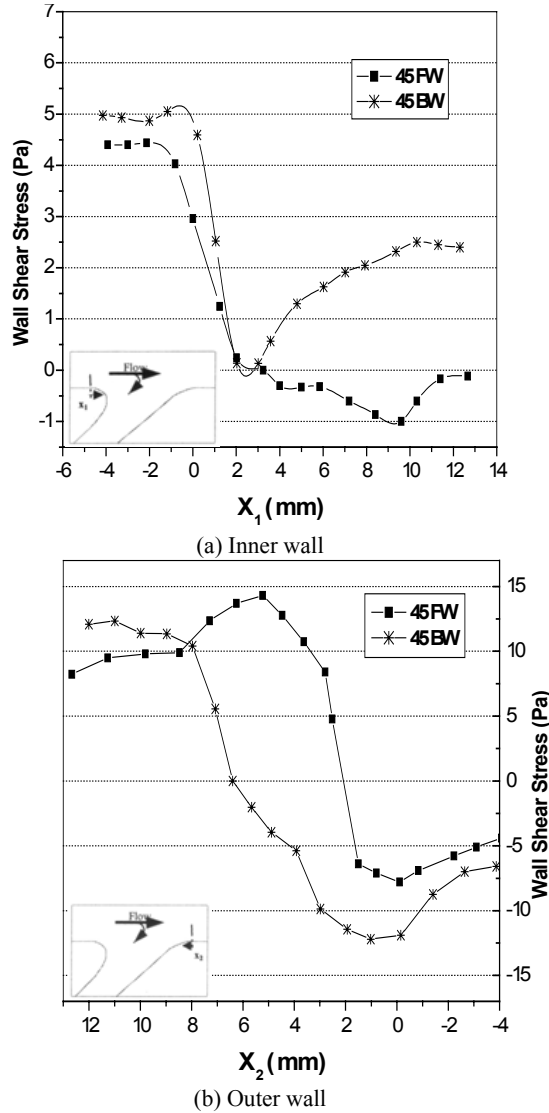


Figure 6: Wall shear stress distributions of the anastomotic joint in different anastomotic models under peak flow condition ( $t=0.30\text{s}$ ). (a) Inner wall; (b) Outer wall.

Spatial wall shear stress gradients (WSSG) along the graft inner wall and outer wall of both models were calculated in the study, as shown in Figure 7. It could be observed in Figure 7(a) that for the two cases there existed a dramatic decrease of WSSG when the flow accessing the heel region. The largest negative WSSG values are  $-2.45\text{Pa/mm}$  and  $-1.6\text{Pa/mm}$  at 45-degree forward facing and 45-degree backward facing models respectively. After the heel region the WSSGs increase which is corresponding to the increase of wall shear stress along the graft. The WSSGs reached an asymptotic value close to zero at the further downstream, which indicated much more uniform flow along the graft. Along the aorta at the toe region, as shown in Figure 7 (b), the WSSGs in both cases are negative in value before increasing sharply when approaching the graft outer wall, which is due to the definition of  $x_2$  coordinate. The magnitude of WSSG of 45-degree forward facing graft was found to be much higher than that of the other model, and reaches its highest value of  $14\text{Pa/mm}$  at  $x_2 = 2.0\text{mm}$ . The peak value of WSSG at 45-degree backward facing graft model appears much more downstream, at  $x_2 = 7.0\text{mm}$ , and smaller in magnitude of only  $6.8\text{Pa/mm}$  when comparing with that of 45-degree forward facing graft model. Large spatial WSSG was found to induce morphological and functional changes in the endothelium, which contribute to elevate wall permeabilities and hence possible atherosclerotic lesions [16]. Therefore the relatively low WSSG values along both inner and outer walls of 45-degree backward facing graft once again suggested that it should be recommended for anastomosis.

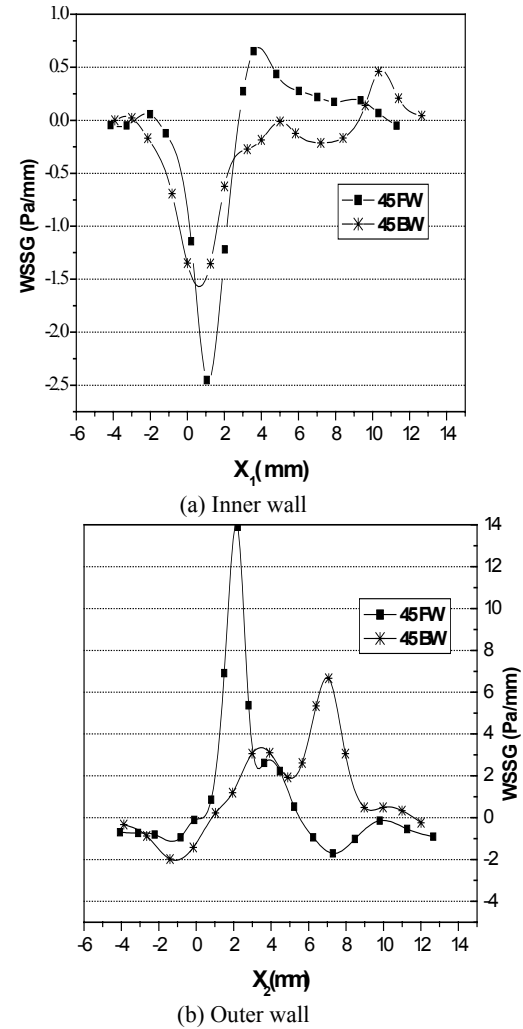


Figure 7: Wall shear stress gradients of the anastomotic joint in different anastomotic models under peak flow condition ( $t=0.30\text{s}$ ). (a) Inner wall; (b) Outer wall.

## Conclusion

At the peak of the pulsatile flow, a low velocity region containing recirculating flow is formed at the graft inner wall in the 45-degree forward facing model and briefly on the 45-degree backward facing model. It is also found that there is a stagnation point at the graft outer wall. The existence of recirculating flow and stagnation point may accelerate the formation of intimal hyperplasia.

The wall shear stress distributions at the peak flow phase also demonstrate significant variations along the walls of the anastomotic joint. Large wall shear stress variation (ranging from  $-15$  Pa to  $14.8$  Pa) was found around the anastomotic joints. The small region near the heel had low wall shear stress level (ranging from  $-0.5$  Pa to  $1$  Pa). In addition, near the stagnation point of the outer wall, there was a small region, which had the low wall shear stress level in the two models. At peak flow phase, the 45-degree forward facing model was found to have the highest positive wall shear stress. The 45-degree forward facing model was found to have the extreme high WSSGs at both heel and toe regions, however, the 45-degree backward model has the lowest WSSG obtained. The high wall shear stress gradient together with the low wall shear stress level were associated with the formation of intimal hyperplasia [5, 6, 7].

In summary, the 45-degree backward model may provide the best conduit between the aorta and coronary artery, which should be able to reduce the potential of IH formation uttermost. This could be useful in the design of sleeve for bypass operation and would be reported in due course.

## Acknowledgments

The financial support of A\*STAR Project Number 0221010023 is gratefully acknowledged

## References

- [1] Hughes, P. E. and How, T. V., Effects of Geometry and Flow Division on Flow Structures in Models of the Distal End-to-Side Anastomosis, *J. Biomechanics*, **29**, 1996, 855-872.
- [2] Rittgers, S. E., Karayannacos, P. E., Guy, J. F., Nerem, R. M., Shaw, G. M., Hostetler, J. R. and Vasko, J. S. Velocity Distribution and Intimal Proliferation in Autologous Vein Grafts in Dogs, *Circ. Res.*, **42**, 1978, 792-801.
- [3] Clowes, A., Intimal Hyperplasia and Graft Failure, *Cardiovasc. Pathol.*, **2**, 1993, 179S-186S.
- [4] LoGerfo, F. W., Quist, W. C., Nowak, M. D., Crawshaw, H. M., Haudenschild, C. C., Downstream Anastomotic Hyperplasia. A Mechanism of Failure in Dacron Arterial Grafts, *Ann. Surg.*, **197**, 1983, 479-483.
- [5] Binns, R. L., Ku, D. N., Stewart, M. T., Ansley J. P. and Coyle, K. A., Optimal Graft Diameter: Effects of Wall Shear Stress on Vascular Healing, *J. Vas. Surg.*, **10**, 1989, 326-337.
- [6] Henry, F. S., Collins, M. W., Hughes, P. E. and How, T. V., Numerical Investigation of Steady Flow in Proximal and Distal End-to-Side Anastomoses, *J. Biomech. Engng.*, **118**, 1996, 302-310.
- [7] Kleinstreuer, C., Lei, M. and Archie J. P. Jr., Flow Input Waveform Effects on the Temporal And Spatial Wall Shear Stress Gradients in a Femoral Graft-Artery Connector, *J. Biomech. Engng.*, **118**, 1996, 506-510.
- [8] Hughes, P. E. and How, T. V., Flow Structures at the Proximal Side-to-End Anastomosis. Influence of Geometry and Flow Division. *J. Biomech. Engng.*, **117**, 1995, 224-236.
- [9] Chua, L. P., Ji, W. F., and Zhou, T. M., In-Vitro Study on the Steady Flow Characteristics of Proximal Anastomotic Models. Proceedings of 10th Asian Congress of Fluid Mechanics (CD-ROM), 2003.
- [10] Zhang, J. M., Numerical Simulation and Measurements of Hemodynamics in Coronary Arterial Bypass, First Year Ph. D. Report, Nanyang Technological University, Singapore, 2002.
- [11] Nichols, W. W. and O'Rourke, M. F., *McDonald's Blood Flow in Arteries*. Philadelphia Lea & Febiger, 1990.
- [12] Glagov, S., Zarins, C., Giddens, D. P. and Ku, D. N., Hemodynamics and Atherosclerosis: Insights and Perspectives Gained from Studies of Human Arteries. *Arch. Pathol. Lab. Med.*, **112**, 1988, 1018-1031
- [13] Yamaguchi, R. and Kohtoh, K., Sinusoidal Variation of Wall Shear Stress in Daughter Tube Through 45 deg Branch Model in Laminar Flow. *J. Biomech. Engng.*, **116**, 1994, 119-126
- [14] Ojha, M., Spatial and Temporal Variations of Wall Shear Stress Within an End-to-Side Arterial Anastomosis Model. *J. Biomechanics*, **26**, 1993, 1377-1388.
- [15] Friedman, M. H., Barger, C. B., Duncan, D. D., Hutchins, G. M. and Mark, F. F., Effects of Arterial Compliance and Non-Newtonian Rheology on Correlations Between Intimal Thickness and Wall. *J. Biomech. Engng.*, **114**, 1992, 317-320.
- [16] Kleinstreuer, C., Hyun, S., Buchanan, J. R., Longest, P. W. Jr., Archie J. P. Jr. and Truskey, G. A., Hemodynamic Parameters and Early Intimal Thickening in Branching Blood Vessels, *Critical Reviews in Biomechanical Engineering*, **29(1)**, 2001, 1-64.

## Dynamic measurement of differential buffet pressure

J.H. Watmuff<sup>1</sup>, G. Vino<sup>1</sup>, S. Watkins<sup>1</sup> and B. Hill<sup>1</sup>

<sup>1</sup>School of Aerospace, Mechanical & Manufacturing Engineering  
RMIT University, VIC, 3001 AUSTRALIA

### Abstract

A technique for measuring the unsteady differential pressure acting across two closely spaced surfaces is successfully demonstrated. The results show that conventional single-surface pressure measurements are likely to provide misleading information about the buffet pressures responsible for unsteady structural loading on fighter aircraft.

### Introduction

Modern high performance aircraft, such as the F/A-18 fighter, are designed to rely on the high lift generated by a vortex system to enhance their manoeuvrability. The behaviour of the vortex system is complex and not well understood. Breakdown of F/A-18 LEX vortices is responsible for severe buffeting, which has resulted in premature fatigue failures of the aircraft frame. The buffet loads are responsible for increased maintenance costs and downtime.

Given that a major DSTO (Defence Science and Technology Organisation) objective is more accurate prediction of aircraft life, and given that the buffeting associated with vortex breakdown is a major contributor to fatigue loading, it is surprising, but true, that only limited and incomplete information exists concerning the buffet pressures responsible for the loads.

### Research Objectives

The long term objective is to create a database from wind tunnel tests that will provide detailed information about the buffet pressures acting on tail fins and other critical components of fighter aircraft at flight Reynolds numbers. Pressure fluctuations that act in common on opposing surfaces will not contribute to the structural loading. On the other hand, pressure fluctuations that are out of phase will result in larger pressure differences than indicated by individual fluctuations experienced on each side. The fluctuating pressure difference across a component will provide a more accurate indication of the structural loads than the pressure fluctuations acting on a single surface.

Creation of the database will not be a trivial task since measurement of the unsteady differential pressure acting across two surfaces will be required. Furthermore, measurements obtained at a single point may not be fully representative. Therefore a useful database will need to consist of multiple unsteady differential pressure measurements at each of a large number of operating points that are representative of the multiple parameters that define the flight of the aircraft.

### Dynamic Pressure Measurement System (DPMS)

At the outset it was recognized that it would be unfeasible to mount multiple dynamic pressure transducers within the components of interest of an aircraft model, which are usually very thin, e.g. the tail fins. A viable alternative is the Dynamic Pressure Measurement System (DPMS) offered by Turbulent Flow Instrumentation Pty Ltd (TFI).

The advantage of the DPMS system is that only relatively minor additional modifications need to be made to a model for dynamic measurement compared to the conventional arrangement where only static pressures are measured. A typical DPMS module consists of 16 or more pressure transducers, with a pressure port for each transducer and a common reference pressure port. The same form of hypodermic tubing could be used to route pressures from taps on a fin to a position outside where flexible tubing would complete the connection to the DPMS module ports. The DPMS module could be mounted in the fuselage of the model to minimize the total length of tubing.

The total length and diameter of the pressure tubing is an important consideration since it introduces frequency dependent amplitude and phase distortion of the pressure fluctuations. The TFI software compensates for the distortion introduced by the external tube and components within the module by using a transfer function to represent the transmission of pressure fluctuations from the tap to the transducer. The theoretical basis for the compensation is a linearized theory first proposed by Iberall [3]. Details of the derivation are provided by Bergh and Tijdeman [1] and they also derived a general recursion relation for the propagation of small amplitude harmonic disturbances through a system consisting of an idealized series of volumes interconnected by thin straight round tubes. They found the predicted response to agree very well with observation. Validation of the predicted transfer functions has also been demonstrated more recently by Hooper & Musgrove [2] and Mousley, Watkins & Hooper [4]. The theory is strictly valid only for simple geometries, but it has been shown that curvature of the pressure tubing has an almost insignificant effect on the transfer function provided that the tubes are not kinked.

In practice, installation of an external tube from the module port to a pressure tap will modify the system transfer function. Acoustic tests could be used to evaluate the modified response of the entire system, including the external tubing and the pressure port, internal tubing between the port and the transducer, and the physical (and electronic) characteristics of transducer. However, in most situations the external tube conforms well to the idealized geometry assumed by the Bergh & Tijdeman model. Hence the TFI software can use the recursion relation to accurately estimate the modified transfer function once the length and internal diameter of the external tubing are known. The tube diameter is a particularly important parameter since it is raised to 6<sup>th</sup> power. In a conventional application the accuracy of the modified transfer function is almost solely dependent on the accuracy of the measurements of the tube diameter and length.

The accuracy requirements of overall system transfer functions used for the compensation are more stringent for differential pressure measurements. Small errors in the amplitude response of each signal could result in a relatively large error after the signals are subtracted, especially if the difference between the two signals is small. Additionally, errors in the phase response will not significantly affect the accuracy of a single point

measurement. However, small errors in the individual phase response of two time records could result in a much larger error after they are subtracted. Furthermore, configurations with sharp corners and other significant departures from the idealized geometry could introduce considerable deviations from the calculated transfer function that can only be fully accounted for by direct calibration. These are important issues that need to be resolved before embarking on the proposed investigation.

One method being considered for creating carefully aligned pairs of taps on either side of a fin is to braze the sidewall of a hypodermic tube onto the inside of each surface. The hole for each tap would then be drilled from outside through the fin surface and the sidewall of the tubing. The minimum thickness of the fin is then only limited to be at least double the thickness of the surface material plus the outside diameter of both tubes. This non-standard tap geometry is likely to significantly depart from the idealized geometry used in the recursive model since the pressure fluctuations will have to negotiate a sharp corner. Another objective of these preliminary tests is to examine the influence of this non-standard form of pressure tap.

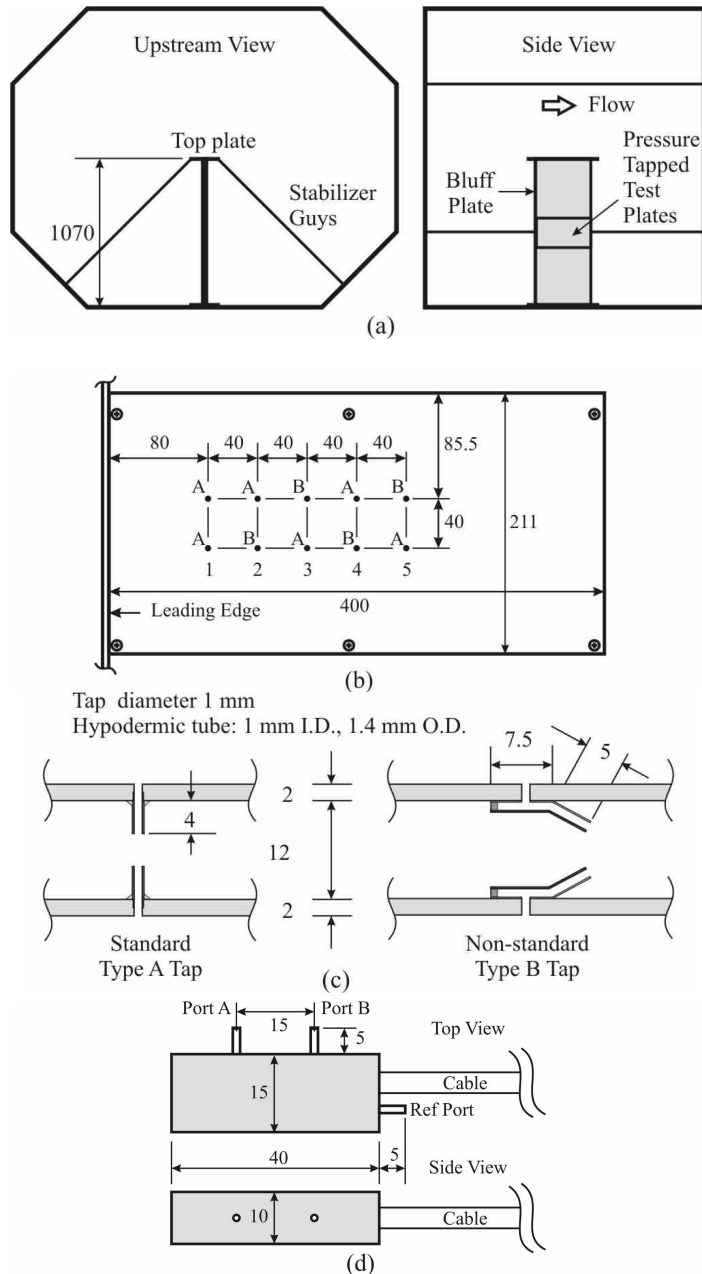


Figure 1. Experimental configuration. (a) Model in DSTO 9x7 ft low speed wind tunnel (b) Definition of pressure taps (LH test plate shown) (c) Details of pressure taps (d) DPMS module. Dimensions in mm.

### Test Model and custom miniature DPMS module

A simple test model has been constructed to investigate the accuracy of the DPMS system for unsteady differential buffet pressure measurements with significant energy up to a frequency of 300 Hz using the non-standard form of pressure taps described in the previous section. This frequency range corresponds to the buffet pressures anticipated on the tail fins of a 1/9<sup>th</sup> scale model of the F/A-18 fighter that is part of future tests being considered in the DSTO 9x7 ft low speed wind tunnel. The model consists of a 32 mm wide bluff plate attached to a 16mm thick splitter plate. Figure 1(a) is a schematic of the model located in the working section of the DSTO 9x7 ft tunnel used for the tests.

The advantage of the model is that both standard and non-standard taps can be used in the same test. Construction details of standard (termed Type A) and non-standard (termed Type B) pairs of pressure taps are shown in figure 1(c). The layout and nomenclature for referencing the tap locations are shown in figure 1(b). It is not possible to conduct tests by swapping between different types of taps at the same location. However, the taps are staggered about the centreline of the 1070 mm tall model and one of the design objectives is to ensure that the flow is acceptably two-dimensional.

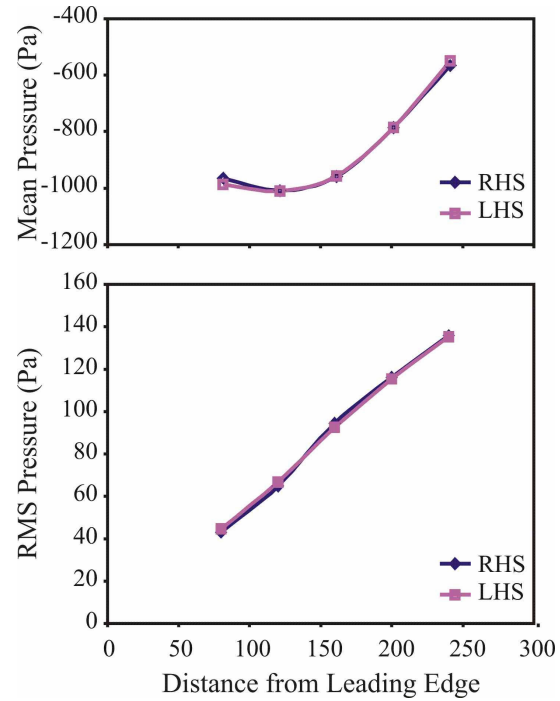


Figure 2. Streamwise development of mean and rms pressure. Upper pressure taps, 600 mm long tubes, 16 channel DPMS module,  $U=50 \text{ ms}^{-1}$ .

Large amplitude pressure fluctuations are generated on each side of the splitter plate by turbulent eddies that are shed from a pair of separation bubbles forming behind the bluff plate. The internal gap between the test plates forming the surfaces on either side of the splitter plate allows a custom-built miniature dual channel DPMS module to be located inside the model. The DPMS module is shown in figure 1(d) and it uses the same pressure transducers and it is functionally equivalent to standard DPMS modules manufactured by TFI.

The configuration allows a range of flexible tubing lengths to be used between the DPMS pressure ports and the hypodermic tubes of the taps. The shortest pair of flexible tubes is limited by the requirement to reinstall the test plates after the installation of the tubing and the minimal length was found to be 30 mm. The other pairs of tubing used in the tests are 140, 300 and 600 mm long. All tests were conducted using nominally the same length tubes on each port.



## Results

Experiments were conducted in the DSTO 9×7 ft wind tunnel located at Fishermens Bend using the two test section velocities of  $U = 50 \text{ ms}^{-1}$  and  $U = 70 \text{ ms}^{-1}$ . Streamwise development of the mean pressure and rms pressure fluctuations for  $U = 50 \text{ ms}^{-1}$  is shown in figure 2. These results were obtained using all the upper row of pressure taps on both sides of the model and 600 mm long flexible tubes were used so that a larger 16 channel DPMS module could be located in the test section but outside the model.

The symmetry of the distributions shown in figure 2 demonstrates that the model is properly aligned with the freestream. One end of a long tube was connected to the reference pressure port and the other open end was located in a still region outside the test section. This was considered more desirable than connecting the reference port to a static pressure source in the test section with the risk of introducing additional pressure fluctuations. The test section is vented to atmosphere so that the minimum pressure coefficient has been estimated to be  $C_{p\min} \approx -0.67$ . The largest rms amplitudes are observed at station 5 corresponding to a distance of 240 mm (30 step heights) from the leading edge. The rms pressure fluctuations at this location are about 10% of the dynamic pressure. The taps at this location have been used for all the subsequent pressure fluctuation measurements with the miniature dual channel DPMS module.

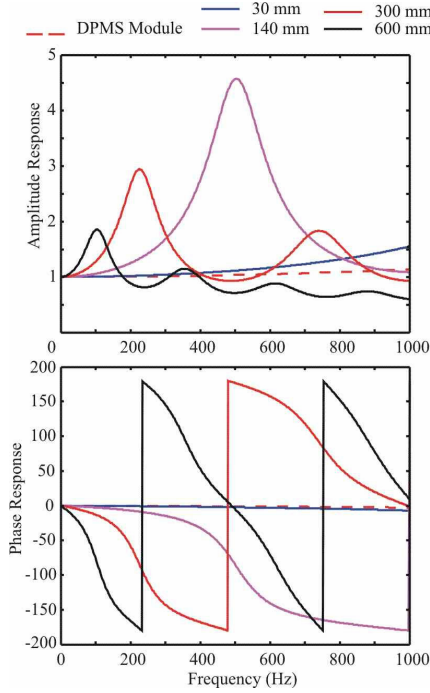


Figure 3. Amplitude and phase response of transfer function of DPMS module alone and the responses with added lengths of pressure tubing.

The transfer function of the dual channel DPMS module alone and with flexible tubing is shown in figure 3. The variations in the amplitude and phase response with the 30 mm long tubes are both very small over the frequency range 0-500 Hz. This configuration is therefore the least likely to be affected by any errors in the compensation so it will act as a baseline for comparing the results obtained with the longer tubes.

The transfer function for the next longest tube,  $L=140 \text{ mm}$ , contains a resonant peak at 500 Hz with an amplitude ratio that is a factor of 4.5 times the response at 100 Hz. Smaller amplitude ratio peaks are also observed with the longer tubes, but these are more significant since they are closely centred in the frequency range to be experienced by the transducers. Note that for the 600 mm long tube, the gradient of the phase response is about 0.7 degrees per Hz in the region of interest.

(a)

$L$ , Tap	$P_L$	$P_R$	$P_{\text{diff}}$	$P_{\text{diff}} / P_L$	$P_{\text{diff}} / P_R$	$R$
30, A	142.1	140.6	201.9	142%	144%	-0.0205
140, A	144.4	141.2	203.5	141%	144%	-0.0151
300, A	140.6	137.8	197.6	141%	143%	-0.0079
300, B	140.4	137.1	197.0	140%	144%	-0.0080
600, A	136.7	134.4	193.5	142%	144%	-0.0185

(b)

$L$ , Tap	$P_L$	$P_R$	$P_{\text{diff}}$	$P_{\text{diff}} / P_L$	$P_{\text{diff}} / P_R$	$R$
30, A	256.1	256.9	366.8	143%	143%	-0.0226
140, A	267.1	261.5	376.1	141%	144%	-0.0122
300, A	251.4	246.3	353.6	141%	144%	-0.0094
300, B	256.6	253.0	362.1	141%	143%	-0.0095
600, A	253.5	249.4	361.2	143%	145%	-0.0319

Table 1. Rms pressures, Pa. (a)  $U=50 \text{ ms}^{-1}$  (b)  $U=70 \text{ ms}^{-1}$ .  $L(\text{mm})$  Tap A/B,  $P_L$ : LHS;  $P_R$ : RHS;  $P_{\text{diff}}$ : difference;  $R$ : correlation coefficient.

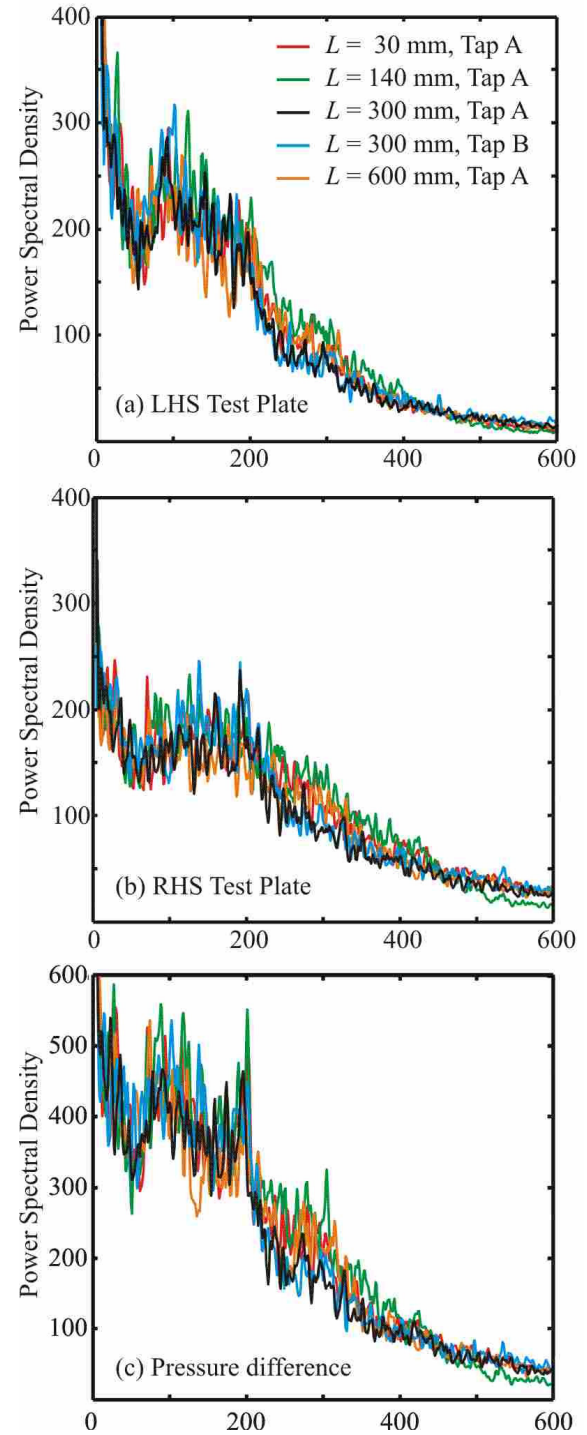


Figure 4. Power spectra corresponding to broadband results in Table 1(b).

A summary of the rms pressures obtained with the miniature dual channel DPMS module is shown in table 1. The rms pressures were calculated using the same time records as those for calculating the spectra shown in figure 4. The agreement between results for different tube length and pressure tap combinations indicates that the transfer functions used to correct for the distortion introduced by the tubing have worked extremely well. In particular, the agreement between the rms values of the pressure difference across the splitter plate using the standard and non-standard taps is excellent, despite the factor of three variation in the correction factor used for the amplitude response for the 300 mm long tubes over this frequency range. The correlation coefficients are close to zero, which indicates that the pressure fluctuations on both sides of the splitter plate can be considered to be random and independent. For truly random fluctuations the ratio of the individual to pressure difference rms fluctuations would be  $\sqrt{2}$ , which is closely observed in the measurements. The most significant observation is that the magnitude of the rms pressure difference is 40% larger than the individual rms pressures on either side of the splitter plate.

The power spectra shown in figure 4 allow a more detailed evaluation of the measurements to be made and they are plotted on a linear scale to clearly distinguish differences between the results. The spectra were evaluated from time records consisting of 40,960 samples obtained at a frequency of 1250 Hz to avoid aliasing, leading to total sampling period of 32.8 s. The spectra are evaluated using 512 samples for the FFT so the rms values in each frequency bin were obtained from 80 realizations.

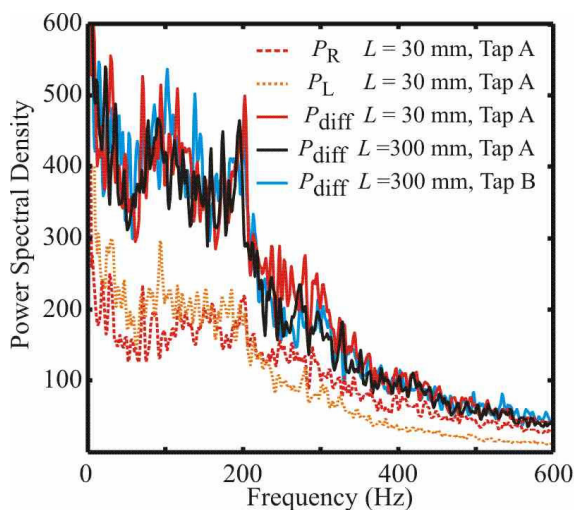


Figure 5. Individual spectra of  $P_L$ ,  $P_R$  and spectra of  $P_{diff}$  for the baseline, and for  $L = 300$  mm tubes with both Type A & B pressure taps.

The spectra on each side of the plate are in reasonable overall agreement; within the scatter arising from incomplete convergence. However the amplitudes on the LHS test plate shown in figure 4(a) are consistently larger than those on the RHS at a frequency around 100 Hz. The differences are nullified in the spectrum of the pressure difference shown in figure 4(c). It appears there is some small differences in the vortex shedding characteristics on each side of the model. The origin of the differences is unknown. However, the most important observation is the consistency between the spectra obtained with standard and no-standard taps and with different length tubes

Spectra obtained on each test plate and spectra evaluated from the result of subtraction of the time records from each test plate are shown in figure 5. As explained previously, the results obtained with standard pressure taps and 30 mm long tubes will be the least in error and provide a baseline for comparison. The spectrum of the pressure difference for the 30 mm long tubes clearly demonstrates that it is the low frequency (long wavelength) fluctuations that are responsible for the larger rms

amplitudes of the pressure difference compared to the individual pressures on each side. The spectra of the pressure difference using standard and non-standard pressure taps with 300 mm long tubes are both in substantial agreement with the baseline result.

## Conclusions

The rms value of the pressure difference acting across the splitter plate has been demonstrated to be about 40% larger than the rms pressure measured on each side of plate. The test model is not representative of an aircraft, and the rms pressure fluctuations are much less than those that can occur on the tail fin of the F/A-18 aircraft (peak values of up to 4 or 5 times the dynamic pressure). Nevertheless, the results demonstrate that standard single-surface pressure measurements are likely to provide misleading information about the buffet pressures responsible for unsteady structural loading on fighter aircraft. For the simple configuration used in these experiments, it is the lower frequency (longer wavelength) fluctuations that are responsible for the larger value of the pressure difference measurements. The DPMS system offered by TFI is capable of providing accurate results in the more demanding situation where dynamic measurement of pressure difference is required. The non-standard pressure taps that will be necessary for dynamic measurements of the pressure difference across the thin fin of an aircraft model do not appear to contaminate the measurements. Lingering doubts that remain about their effect on the transfer function used for the compensation can be removed by direct calibration.

## Acknowledgments

The project is supported by the DSTO / RMIT Centre of Expertise – Aerodynamic Loading (CoE-AL). The encouragement of Dr. Oleg Levinski and Dr. Doug Sherman is acknowledged together with an appreciation of help from other DSTO personnel for operation of the 9x7 ft wind tunnel during the experiments. The 16-channel DPMS module and other TFI components were on loan from DSTO for the duration of the tests. The authors wish to thank Peter Mousley of TFI for his valuable advice regarding the design and manufacture of the custom dual channel DPMS module and for his assistance and cooperation at many stages throughout the project.

## References

- [1] Bergh, H. & Tidjeman, H., Theoretical And Experimental Results For The Dynamic Response Of Pressure Measuring Systems, *National Aero And Aeronautical Research Institute*, 1965, NLR-TR F.238.
- [2] Hooper, J.D. & Musgrave, A. R., Reynolds Stress, Mean Velocity, And Dynamic Static Pressure Measurement By A Four-Hole Pressure Probe, *Experimental, Thermal and Fluid Science*, **15**, 1997, 375-383.
- [3] Iberall, A. S., Attenuation Of Oscillatory Pressures In Instrument Lines, *U.S. Department Of Commerce, National Bureau Of Standards*, **45**, 1950, RP2115.
- [4] Mousley, P.D., Watkins, S. & Hooper, J.D. Use of a Hot-Wire Anemometer to examine the pressure signal of a High-Frequency Pressure Probe, 1998, *13th Australasian Fluid Mechanics Conference*, Monash University, Melbourne, Australia.

## Evidence of the -1-law in a high Reynolds number turbulent boundary layer

T. B. Nickels<sup>1</sup> S. Hafez<sup>2</sup> I. Marusic<sup>3</sup> and M.S. Chong<sup>2</sup>

<sup>1</sup>Department of Engineering  
University of Cambridge  
Trumpington St., Cambridge CB2 1PZ, UK

<sup>2</sup>Department of Mechanical & Manufacturing Engineering  
The University of Melbourne, VIC, 3010 AUSTRALIA

<sup>3</sup>Department of Aerospace Engineering & Mechanics  
University of Minnesota, Minneapolis, MN 55455, USA

### Abstract

Dimensional analysis leads to a prediction of a -1-power-law for the streamwise velocity spectrum in a turbulent boundary layer. This law can be derived from overlap arguments or from physical arguments based on the attached eddy hypothesis of Townsend (1976). Some recent experiments have questioned the existence of this power-law region in wall-bounded flows. In this paper experimental spectra are presented which support the existence of the -1-law in a high Reynolds number boundary layer, measured in the large boundary layer facility in the Walter Basset laboratory at the University of Melbourne. The paper presents the experimental results and discusses the theoretical and experimental issues involved in examining the existence of the -1-law and reasons why it has proved so elusive.

### Introduction

Turbulent wall-bounded flows occur in a wide range of situations that are of interest both for technical, engineering applications and in terms of the general physics of turbulent flows. The practical interest stems from the fact that many flows of engineering importance occur at high Reynolds numbers. Examples are flows over submarines, aircraft and the atmospheric surface layer. The theoretical interest stems from questions regarding the asymptotic behaviour of such flows as the Reynolds number tends to infinity. At present many experiments and direct numerical simulations are limited to lower Reynolds numbers and the important question is how to extrapolate these results to higher Reynolds number flows. There are a few theoretical predictions concerning the likely characteristics of these flows at high Reynolds number which have been used in modelling and predicting real flows. One of these is the -1-power-law for the Power Spectral Density (PSD) of the streamwise fluctuating velocity component. This law can be derived either by simple dimensional reasoning or, more rigorously from asymptotic overlap arguments as described, for example, in Perry *et al.* (1986). These arguments are consistent with the attached eddy hypothesis of Townsend (1976). Essentially, the idea is that there is a range in wavenumber space in which the effects of both viscosity and the outer length-scale (eg. the boundary layer thickness or the pipe radius) are negligible. These arguments are discussed in more detail in the next section. The salient feature is that an overlap region exists where both *inner scaling* and *outer scaling* are simultaneously valid. Inner scaling refers to non-dimensionalisation using the length scale  $z$ , the wall-normal position, and the velocity scale  $U_\tau$ , the friction velocity. Outer scaling uses the length scale  $\delta$ , the boundary layer thickness, and the velocity scale  $U_\tau$ . Despite the fact that the arguments involved in deriving such a region are, at least, very plausible, the experimental evidence for the -1-law has not been completely convincing. This has led to questions regarding the

possible existence of such a region. Recently, Morrison *et al.* (2004) have analysed spectra taken in the Princeton *superpipe* and concluded that for those data no overlap region is observed and therefore no universal -1-law is present. They refer to this as 'incomplete similarity'. Del Alamo *et al.* (2004) interpret the incomplete similarity result as a consequence of a variation of velocity scale between the largest eddies in the flow (scaling with  $\delta$ ) and the eddies that scale with  $z$ , the local distance from the wall. Consequently they show that a logarithmic correction is needed to the -1 law. All of the above arguments agree that the existence of a -1 law depends on a sufficiently large Reynolds number to ensure an overlap region. What remains unclear at this stage is what value of Reynolds number qualifies as sufficiently large, and where measurements should be made in the boundary layer in order to discover such a region. In what follows we present new measurements in the high Reynolds number boundary layer at the University of Melbourne both at high Reynolds number close to the wall. The measurements show evidence of a -1-law region with complete similarity.

### Experimental Details

#### The wind-tunnel facility

The measurements were conducted in the high Reynolds number boundary layer facility in the Walter Basset Aerodynamics Laboratory at the University of Melbourne as shown in figure 1. This unique facility is especially designed for the experimental study of high Reynolds number boundary layers with sufficient thickness to provide for good spatial resolution. The facility is a blower-tunnel driven by a 2m diameter axial flow fan. Air from the fan passes through two vaned corners, through a settling chamber with honeycomb and screens, then through a 6:1 contraction and into the working section. The working section is the unique feature of the tunnel. It has a cross-section of 2m x 1m (horizontal x vertical) and 27m in length. The long working section allows the boundary layer to grow over a long fetch and hence produces a high Reynolds number, thick, boundary layer. The boundary layer near the end of the working section is approximately 330mm thick, providing for good spatial resolution of the measurements. Separate experiments in another wind-tunnel (Jones *et al.* 1995) show that the effect of finite width is negligible as long as the tunnel is wider than six boundary layer thicknesses ( $6\delta$ ). The tunnel is capable of a maximum speed of 45 m/s, although the measurements to be presented here are for lower tunnel speeds. At a speed of 30m/s the free-stream turbulence intensity is 0.05%. The working section is above atmospheric pressure and a zero pressure-gradient is achieved by bleeding air from the tunnel ceiling through adjustable slots. The coefficient of pressure,  $C_p$ , along the working section is constant to within  $\pm 1\%$ .

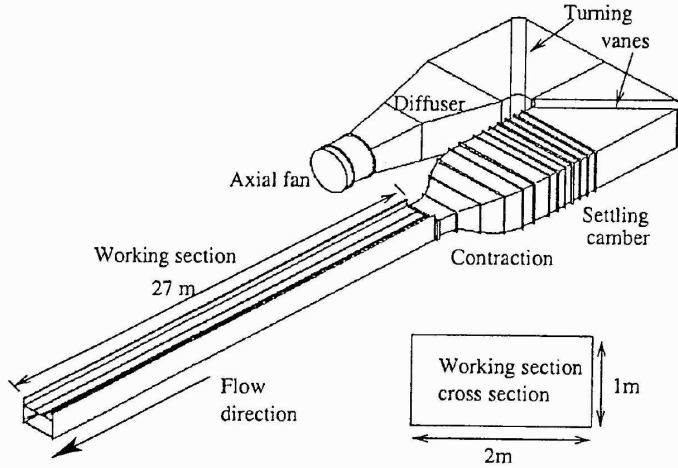


Figure 1: Schematic of wind-tunnel used in this study.

### Hot-wire measurements

The measurements to be presented here have been made using hot-wire probes made from platinum Wollaston wires. All measurements shown were made with wires of  $2.5\mu\text{m}$  diameter etched to  $0.4\text{mm}$  in length (giving a length to diameter ratio,  $l/d=160$ ). The wires were run at constant temperature at an overheat ratio of 1.8 using an AA-labs model AN1003 anemometer. The system was checked to ensure second order impulse response and showed a frequency response of greater than  $150\text{kHz}$ . The wires were calibrated statically by traversing them into the centre of the tunnel in the undisturbed free-stream. They were calibrated using a third-order polynomial fit to the discrete data. The signal was filtered at  $35\text{kHz}$  using 8th order analogue Butterworth filters, to avoid aliasing, and were sampled at  $80\text{kHz}$  using a 16 bit A-D converter board mounted in a PC. The probes were attached to a stepper motor driven traverse run by the computer and could be positioned within the boundary layer with an accuracy of  $3\mu\text{m}$ . The initial wall distance was measured using a video camera with a short focal length lens to image the probe and its image in the polished aluminium floor of the tunnel. The initial position could be determined to an accuracy of  $\pm 5\mu\text{m}$ .

The PSD was determined by sampling bursts (or “records”) of the velocity signal of 3.27 seconds in length at  $80\text{kHz}$  (262,144 points). This was determined to be sufficiently long to capture the lowest wavenumber motions with significant energy content. Each burst is then fast-Fourier-transformed online and the PSD formed from the modulus squared of the transformed signal. In order to ensure convergence of the PSD a series of 500 bursts were taken and the PSDs were ensemble averaged to form the final PSD. Five hundred bursts corresponded with approximately 45 minutes total time to measure a single spectral curve (for a single wall-normal position). Extreme care was taken to ensure accurate and well-converged data for each measurement. One typical wall-normal position of interest was averaged over 5000 bursts (approximately 7.5 hours) and compared with the 500 burst case to ensure that the results were equivalent in all essential details. Calibration drift was checked by re-calibrating at the end of every run and proved to be negligible for all cases (the temperature of the tunnel remained constant to within  $\pm 1^\circ\text{C}$ ). In order to further reduce the scatter in the data points of the original high resolution PSD file (131,072 points), the data was resampled by averaging 27 points of the original file to form one point in the final file (at the centre of the 27 point window). This was done with non-overlapping windows in spectral space so that each point in the file was produced from independent data. This is equivalent to the approach of using a narrow band-

pass filter to evaluate the PSD from an analogue velocity signal (as used before the advent of digital sampling equipment). The final file had 4800 points. It should be noted that at the very lowest wavenumbers a smaller window was used so as to avoid discarding data at the very low end (this is for appearance of the results to show the full PSD curve). No other form of “smoothing” was used on the data.

### Scaling the spectra

As noted earlier the existence of a -1-law, as predicted by the theory, requires, not only a region with a -1-law behaviour, but that this region must scale with both inner and outer flow scaling. Inner flow scaling requires that,

$$\frac{\phi_{11}(k_1 z)}{U_\tau^2} = \frac{\phi_{11}(k_1)}{z U_\tau^2} = f(k_1 z), \quad (1)$$

and outer flow scaling requires that

$$\frac{\phi_{11}(k_1 \delta)}{U_\tau^2} = \frac{\phi_{11}(k_1)}{\delta U_\tau^2} = f(k_1 \delta), \quad (2)$$

where  $\phi_{11}(k_1 z)$  is the PSD of the streamwise velocity fluctuation per unit non-dimensional wavenumber  $k_1 z$  and  $z$  is the wall-normal position. In order to examine this scaling it is necessary to know the mean flow parameters. These were taken from Pitot-tube measurements of the mean velocity profiles. The wall shear stress velocity,  $U_\tau$ , was found using the method of Clauser which assumes a logarithmic region in the mean velocity profile with universal constants. This technique has been shown to be accurate by comparison with direct measurements using oil-film interferometry, in the same wind-tunnel as used in this study, by Jones *et al.* (2001) who also checked and confirmed that the mean velocity variation was logarithmic. The boundary layer thickness definition used is that of Perry *et al.* (2002) i.e.

$$\delta = \delta^* C_1 / S \quad (3)$$

where  $\delta^*$  is the displacement thickness of the boundary layer,  $S = U_1 / U_\tau$  ( $U_1$  is the free-stream velocity) and  $C_1$  is a constant found from integrating the velocity-defect profile i.e.

$$C_1 = \int_0^\infty \frac{U_1 - \bar{U}}{U_\tau} d(z/\delta) \quad (4)$$

The streamwise wavenumber,  $k_1$ , was found from the frequency,  $f$ , using Taylor’s hypothesis of frozen turbulence i.e.

$$k_1 = \frac{2\pi f}{U_c} \quad (5)$$

where  $U_c$  is the convection velocity of the turbulent motions past the probe. Different values of  $U_c$  have been examined and will be discussed later.

### Experimental Results

The results shown here were obtained at a streamwise position 22m downstream from the exit of the contraction tripping device. The boundary layers on all four walls were tripped using grade 40 sandpaper strips located inside the contraction. All profiles were measured with a nominal free-stream velocity of  $20\text{m/s}$  (note that for runs on different days the Reynolds number per unit streamwise distance was matched by varying the tunnel velocity to compensate for any change in viscosity due to changes in ambient conditions). The Reynolds number at this point is  $R_\theta = 37540$  which corresponds with  $\delta_+ = 14380$ .

Figure 2 shows the premultiplied spectra in the vicinity of  $z^+ = z U_\tau / \nu = 100$  scaled with inner (upper plot) and outer



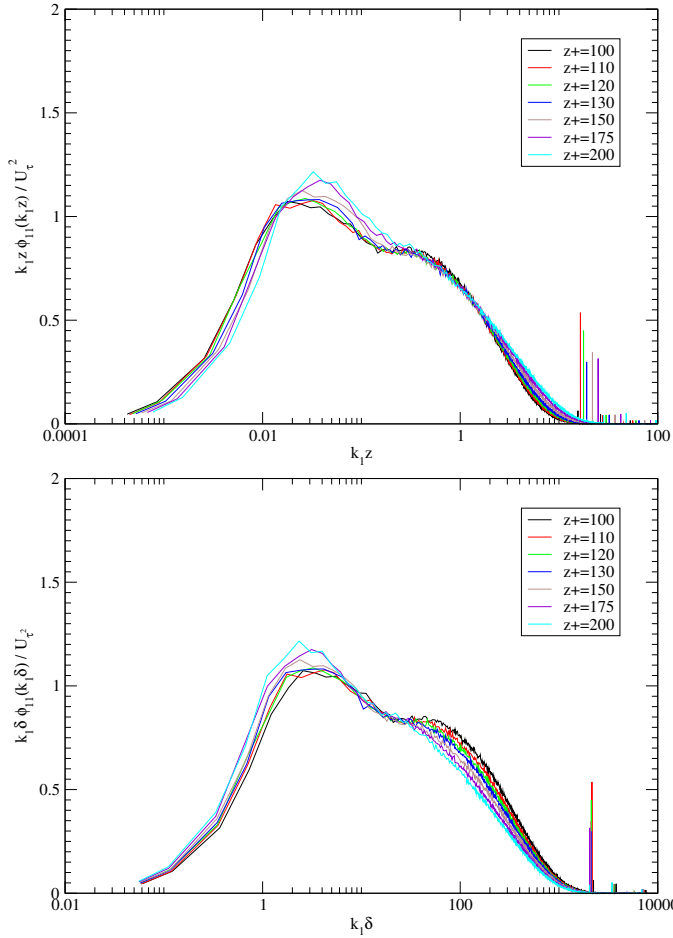


Figure 2: Streamwise spectra in inner (upper plot) and outer (lower plot) scaling. Wavenumber calculated using  $U_c$  equal to local mean velocity at each wall-normal position.

(lower plot) scaling. Here the convection velocity has been taken as the local mean velocity at the wall-normal position of each measurement. This is consistent with standard practice in plotting spectra and hence is shown first: the convection velocity will be discussed further later. It is clear that there is a region where the spectra collapse with both of these scalings. This region corresponds with a plateau in the premultiplied spectra which indicates a -1-power-law behaviour. The region is approximately  $1/3$  of a decade long in the profile closest to the wall. A close-up of this region is shown in figure 3. The behaviour of the spectra in the two plots is also consistent with the expected scaling behaviour since, in the inner-scaled plot, the profiles collapse at the high end of the region and peel off at the low end as the probe moves away from the wall. This peel off is due to the outer flow scaling of the lower end of the region. In outer-flow scaling the behaviour is also expected. Here the spectra collapse at the low end of the region (albeit not perfectly, see later discussion) and peel off at the high end as the wall-normal distance is increased - this is the effect of changing  $z$ . The scaling behaviour of the spectra and the plateau appear to be consistent with complete similiarity arguments and the existence of a -1-law behaviour.

### Convection velocity

More information may be gleaned from these plots. The first issue of interest is the correct choice of convection velocity. In figure 2 the local mean velocity was used. It seems plausible that the smaller structures near the wall (and in the vicinity of the probe) may convect at this velocity. Examining the lowest wavenumbers suggests that the collapse with outer flow scaling is good but not perfect. These structures are of a size equal to, or larger than the boundary layer thickness. If these structures

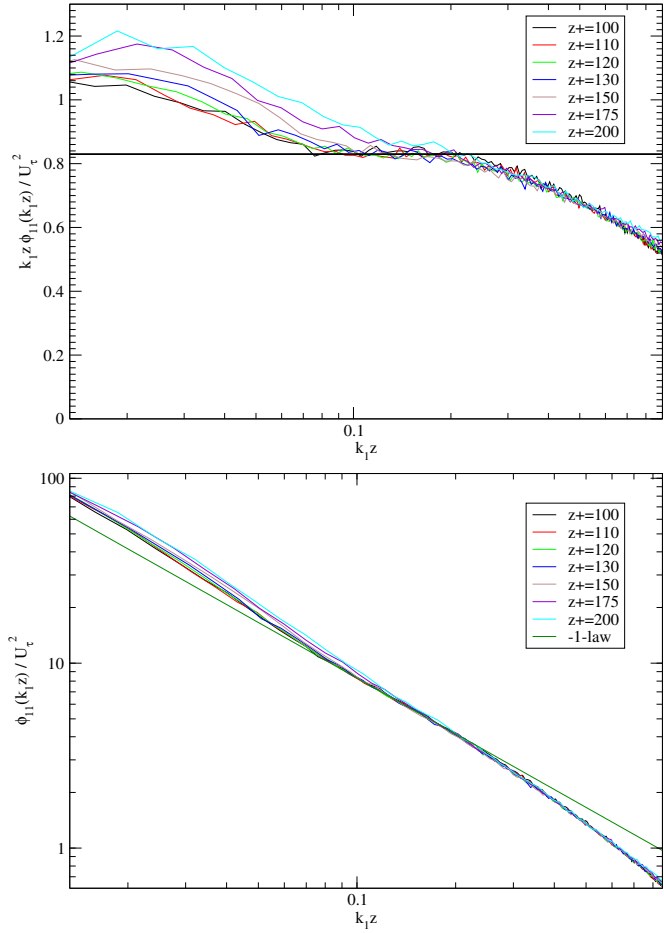


Figure 3: Close up of -1-law region of spectra. Wavenumber calculated using  $U_c = \bar{U}$ . Upper plot premultiplied. Lower plot standard PSD.

extend to the edge of the boundary layer then perhaps a more appropriate convection velocity for the low wavenumbers would be the free-stream velocity,  $U_1$ . Figure 4 shows the same spectra with the wavenumber calculated using  $U_c = U_1$ . The collapse in the low wavenumber range with outer scaling is improved, whereas a very close examination reveals that the collapse of the high wavenumber range with inner-scaling is not quite as good as in figure 2. This suggests the, physically plausible, idea of a spread in convection velocity across wavenumber space. At this stage it is not possible to calculate this spread but it is sufficient to note that it exists. This spread is consistent with the measurements of Krogstad *et al.* (1997) who found a significant spread in convection velocities with the scale of the convected structure. They found that motions of the order of the boundary layer thickness have a  $U_c \approx U_1$  whereas the smaller scales convect at a significantly lower velocity. Note that the existence of a spread does not affect conclusions about the existence of a -1-power-law region, in fact a spread in convection velocity of this nature would have the effect of stretching the plateau in wavenumber space and hence increasing its length.

### Spatial resolution

The spatial resolution of the measurements is important when evaluating the results. In the measurements presented so far the hot-wire length,  $l$ , was 0.4mm which corresponds with  $l^+ = 17.5$  at the Reynolds number of the measurements ( $\delta^+ = 14380$ ). Ligrani & Bradshaw (1987) suggest that there is significant attenuation of the streamwise stress if  $l^+ > 20 - 25$ . There is a way to estimate the point at which spatial resolution limitations start to occur in these measurements. Consider the high wavenumber end of the plots shown in inner-scaling. The different wall-normal positions all collapse though the -1-law

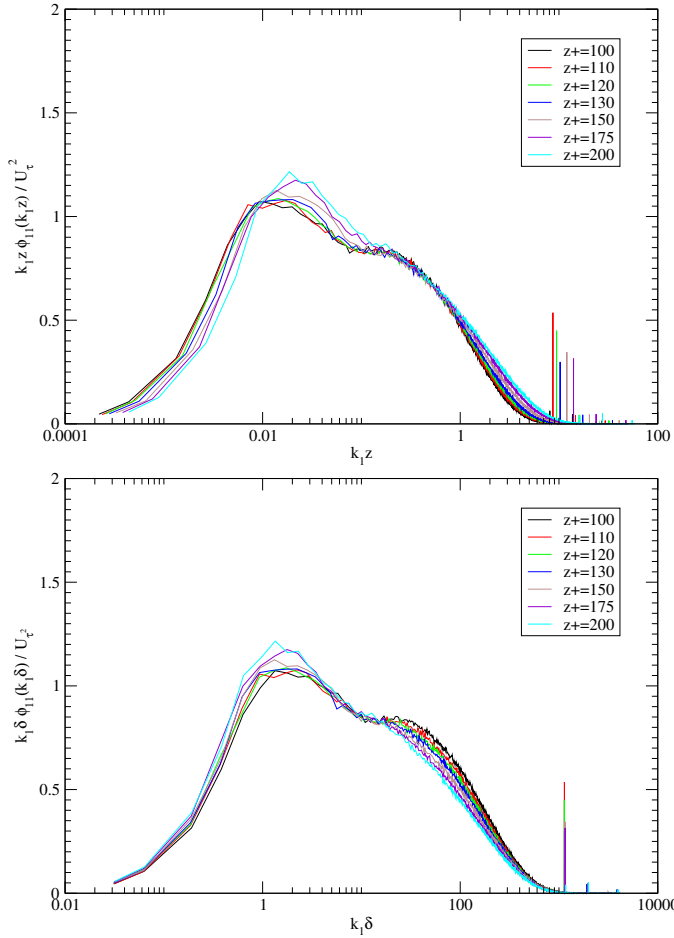


Figure 4: Streamwise spectra in inner (upper plot) and outer (lower plot) scaling. Wavenumber calculated using  $U_c = U_1$ .

region and beyond, up to a point where they start to peel off. If the spatial resolution was a problem below the peel-off position then the spectra *would not collapse with inner scaling*. This suggests that the -1-power-law region itself is well-resolved.

#### The limits of the -1-law region

The experiments shown here allow us to make some assessment of the conditions required to obtain a -1-law in the streamwise spectrum. We will use the values of parameters from the plots where  $U_c = \bar{U}$  since this is the most common choice and hence will be convenient for other researchers. The outer-flow scaled plot shows that the -1-law starts at approximately  $k_1 \delta = 21$  and the inner-flow scaled plot shows that the region ends at approximately  $k_1 z = 0.4$ . Results (not presented here) suggest that a -1-law region is not possible below  $z^+ = 100$ . Below this value the spectra is contaminated by structures in the viscous and buffer zones leading to a hump at the high wavenumber end which becomes larger as the wall-normal distance is reduced. A limit such as this is consistent with the theory since we can argue that below this the effects of viscosity become important - making complete similarity impossible. These numbers allow us to make some predictions about future measurements. Let the highest wavenumber within the -1-law region be  $k_{1up}$  and the lowest wavenumber in the -1-law region be  $k_{1low}$ . If we want to have one decade of -1-law region then we need  $k_{1up}/k_{1low} = 10$ . Using the limits above we find that  $z/\delta = 0.0019$ . Now this value of  $z/\delta$  must correspond with  $z^+ > 100$  (to avoid viscous effects) so the Reynolds number required is  $\delta^+ > 52500$  (corresponding approximately with  $R_\theta = 137700$ ). This is currently beyond the capability of the wind-tunnel used in this study. It is very important to note that the length of the -1-law region depends only on  $z/\delta$  with the restriction that this corresponds with a sufficiently large  $z^+$ . The point to emphasize is that high

Reynolds numbers are only of use in examining this question if it is possible to make measurements very close to the wall (and of course with sufficient spatial resolution). This causes difficulty in many existing high Reynolds number facilities particularly where the largest length scale is moderate to small and the high Reynolds number is achieved by either increasing speed or changing the kinematic viscosity. In these facilities small values of  $z/\delta$  correspond with very small distances from the wall.

#### Conclusions

Measurements in a high Reynolds number boundary layer show the existence of a short region of complete similarity in which a -1-power-law region is evident. The behaviour of the spectra is entirely consistent with the arguments used classically to derive the -1-law for large (infinite) Reynolds numbers. Examination of the length of the region and the position in which it occurs suggest that measurements must be made, not only in high Reynolds number flows, but also sufficiently close to the wall if the -1-law is to be detected. This may, in part, explain why other researchers have had difficulty in identifying this region.

#### Acknowledgements

MSC and SH are grateful for support from an Australian Research Council Discovery Grant. IM would like to acknowledge support from NSF and the Packard Foundation. The measurements were made by Nickels whilst supported by EPSRC overseas travel grant GR/S86303/01.

#### References

- [1] Del Alamo, J.C., Jimenez, J. Zandonade, P. and Moser, R. D. Scaling of the energy spectra of turbulent channels., *J. Fluid Mech.*, **500**, 2004, 135–144.
- [2] Jones, M.B., Marusic, I. and Perry, A.E. The effect of aspect ratio and divergence on the turbulence structure of boundary layers., In *Proc.12th Australasian Fluid Mech. Conf.*, University of Sydney, Australia, 1995, 436–439.
- [3] Jones, M.B., Nishizawa, N. and Chong, M.S. The effect of aspect ratio and divergence on the turbulence structure of boundary layers., In *Proc.14th Australasian Fluid Mech. Conf.*, University of Adelaide, Australia, 2001, 211–214.
- [4] Krogstad, P.-Å., Kaspersen, J. H. and Rimestad, S. Convection velocities in a turbulent boundary layer. *Phys. Fluids*, **10**, 4, 1997, 949–957.
- [5] Ligrani, P.M. and Bradshaw, P. Spatial resolution and measurement of turbulence in the viscous sublayer using sub-miniature hot-wire probes. *Exps. Fluids*, **5**, 6, 1987, 407–417.
- [6] Morrison, J.F., McKeon, B.J., Jiang, W. and Smits, A.J. Scaling of the streamwise velocity component in turbulent pipe flow., *J. Fluid Mech.*, **508**, 2004, 99–131.
- [7] Perry, A.E., Henbest S.M. and Chong M.S. A theoretical and experimental study of wall turbulence., *J. Fluid Mech.*, **119**, 1986, 163–199.
- [8] Perry, A.E., Marusic, I. and Jones, M.B. On the streamwise evolution of turbulent boundary layers in arbitrary pressure gradients., *J. Fluid Mech.*, **461**, 2002, 61–91.
- [9] Townsend, A. A., *Turbulent Shear Flow*, Cambridge University Press, 1976.



## Characterising Roof Ventilators

A. Revel<sup>1</sup> and B.P. Huynh<sup>2</sup>

<sup>1</sup>Ex-Faculty of Engineering, UTS, P.O. Box 123, Broadway 2007, AUSTRALIA

<sup>2</sup>Faculty of Engineering, UTS, P.O. Box 123, Broadway 2007, AUSTRALIA

### Abstract

Extraction performances of roof-mounted ventilators are compared using data from tests based on an Australian/New Zealand Standard. The results show that a single performance curve (embodying air extraction rates, wind speeds, throat size and pressure differentials across the devices) characterises each ventilator. This also shows that the constant parameters specified in the current Standard are far too simplistic to adequately describe a device's performance.

### List of Symbols

$\Delta p$  = pressure difference across ventilator as per figure 1 (Pa)

$\Delta p_v$  = close-range pressure drop across ventilator (Pa)

$V$  = wind speed acting on ventilator (m/s)

$Q$  = measured flow rate through ventilator (m<sup>3</sup>/s)

$A_t$  = ventilator geometric throat area (m<sup>2</sup>)

$v$  = air speed through ventilator throat, calculated as  $v = Q/A_t$  (m/s)

$\rho$  = air density (1.2 kg/m<sup>3</sup>)

### Introduction

Efforts to clear smoke, foul air and damp from dwellings, ships and factories have produced various designs of ventilators, sometimes fitted to assist draft through chimneys but more often mounted on roofs. Wind influenced roof ventilators (also called eductors) such as cowls, swivelling elbows, venturi and turbine types compete with powered fans to clear spaces of vapours and foul air. These ventilators also allow hot gases to escape, as well as exclude rain and vermin. Very few published works on these devices can be found. In 1932 O. Savonius [3] and O. Back [2] published test results comparing cowls and the S-rotor wind-driven fan invented by S. V. Savonius. Back mentions earlier work by Professor Rietschel in Germany (1906 and 1910) and in France ("Concours d'Aspirateurs de Fumes", 1929). The last two tested only with "free suction" or ambient upstream pressure. Savonius and Back tested over a range of "suction pressures". Their methods were similar – a free jet blowing over an eductor which withdrew air from a "suction box" or plenum. Those tests were done at plenum pressures less than or equal to ambient. Back used a "Prandtl tube", set in the  $\Phi$  160 mm x 6 m inlet duct, and micromanometer to measure duct air velocities. Savonius used a cup anemometer in the inlet duct. Apart from these very early works there has been virtually nothing else published since then that the authors are aware of, particularly in English.

Australian/New Zealand Standard, AS/NZS 4740:2000. An industry has been developing around natural ventilation for over a century. Prior to 2000 there was no Australian Standard for natural ventilators. The first such Standard, AS/NZS 4740, was published in March 2000 [1]. It covers classification and testing for wind loading, rain penetration, flow and pressure drop. Louvres and grilles are classified as type 1 and serve as either air inlets or outlets on buildings. Types 2, 3 and 4 withdraw air by the influence of wind (eductors):

- type 2 being static (cowl, ridge, louvred cupola, etc.),

- type 3 being wind directional (swivelling elbow or hood),

- type 4 being turbine type.

This Standard [1] has essentially been an arbiter laying down test procedures and defining the following for ventilators:

- discharge coefficient  $C_i$  at a particular wind speed,

$$C_i = (Q/A_t) \times \sqrt{\rho/2\Delta p_v} \quad (1)$$

which then gives the mean discharge coefficient  $C_{mean}$  for a number  $n$  of wind speeds, and the ventilator's discharge coefficient  $C_d$  as

$$C_{mean} = \sum_{i=1}^n \frac{C_i}{n}, \text{ and } C_d = C_{mean} - \text{errors} \quad (2)$$

- flow coefficient for a particular wind speed,

$$(C_f)_i = \frac{v}{V} \quad (3)$$

A ventilator's flow coefficient  $C_f$  is then the average of a number of such  $(C_f)_i$ .

Results from equations 2 and 3 are then used to estimate extraction by "wind siphonage". So, in effect,  $C_d$  and  $C_f$  are the two parameters used to quantify a ventilator's air extraction performance.

Client and Industry. It was through a request from the Australian Consumers' Association that this work was started. For the ventilation industry, interest is in extraction rate  $Q$ , wind speed  $V$ , and pressure difference  $\Delta p$  - from the space being vented, across the ventilator, to the outside ambient. The request was for a concise and consistent way to assess the ventilators quantitatively, and for the test results to be shown in a manner that will distinguish them.

Responding to this request, experiments have been set up and a variety of these devices tested. Two ways of presenting results will be shown here; neither is mentioned in the current Standard [1]. In particular, it will be seen that a single non-dimensional curve captures succinctly a ventilator's performance, and thus presents a better method of characterizing such a device than the simple, constant parameters specified in the current Standard. In this work, attention is given to type 4; but other simple ventilators are also shown for comparison.

### Experiments

Apparatus. The experimental set-up follows recommendation in the Standard [1], and is shown in figure 1. In the first set up (figure 1(a)), ventilators were fixed on top of a rectangular box or plenum. A variable speed 800 mm diameter axial fan produced the "wind" on the ventilator. Air was supplied to the plenum by a radial fan via a metering nozzle. By changing the supply fan's speed, plenum pressure ( $\Delta p$ ) was varied from a negative to a positive value with respect to ambient. Having a supply fan to overcome duct losses is a practice used in fan testing. Here it was used to provide a wide range of plenum pressures.

As testing proceeded, wind speeds and plenum pressures increased. So did supply air requirements. To achieve required

flow rates, the radial fan's speed (figure 1(a)) was increased until the fan disintegrated. At this stage it was realised that flow rates beyond 6000 litres per minute ( $0.1 \text{ m}^3/\text{sec}$ ) may be required. Such flow rates could be met by a 400 mm axial fan and duct (figure 1(b)). Fan surge had to be watched as the supply flow can become unsteady and the manometers erratic.

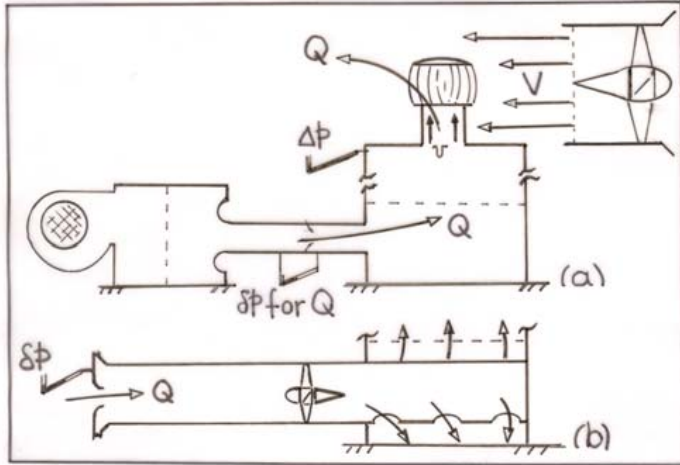


Figure 1: Schematic of eductor test rigs comprising; large wind producing fan, plenum, variable speed supply fan, flow metering and sensitive manometers (0 to 125 Pa).

- (a) original test rig using radial fan,  $\Phi$  100 mm x 4 m duct with  $\Phi$  65 mm metering nozzle,
  - (b)  $\Phi$  400 axial fan and duct replacement for radial fan.
- In both cases the plenum was 1.2 m square x 2.4 m high.

**Method.** The Standard [1] specifies five “minimum required incident air velocities” from 0.72 m/s to 3.6 m/s (2.6 to 12.96 km/hr). Sydney's average wind speed is taken as 12 km/hr hence natural ventilation calculations for extraction are based on a wind speed of 12 km/hr for Sydney. Greater test wind speeds are recommended in case of unusual behaviour beyond 13 km/hr.

By performing calibration runs before each series of tests relationships between fan speed and wind speed are established. This is done with an anemometer placed at the position where the eductor will later be located. A linear relationship between wind speed and fan speed has been obtained, as may be expected, since fan discharge is proportional to fan speed. This allows setting a wind speed without the presence of an anemometer while testing.

**Wind uniformity.** It is prudent to assess wind uniformity. For this a Pitot rake was used to determine a number of velocity profiles across the jet. From these, average wind speeds were estimated. Variation of wind speed was considered acceptable if it was within 2.5% about the average value.

**Four devices.** Four ventilating devices, shown in figure 2, were tested. Turbine eductors are shown in figures 2(a) and (b). Figure 2(c) shows a  $\Phi$  300 mm throat omni-directional venturi formed from two spherical segments spaced 150 mm apart; and figure 2(d) a  $\Phi$  300 mm x 300 mm high open stub.

## Results and Discussion

Test results were first plotted as a series of curves of plenum pressures  $\Delta p$  against flow rates  $Q$  at different wind speeds, rather analogous to fan characteristics; see figures 3(a) to 6(a). This representation does not readily compare eductors; overlaying so many curves became confusing. Following Back and Savonius [2, 3], the measurements are also plotted using the non-dimensional parameters  $v/V$  and  $\Delta p/(1/2\rho V^2)$ . These are shown in figures 3(b) to 6(b). The data collapse very well into single curves, each embodying air extraction rates, wind speeds, throat

size and pressure differentials. Note that in these figures,  $\Delta p$  is as shown in figure 1. Thus  $\Delta p$  is the difference between pressure in the plenum just before the ventilator's inlet, and that of the ambient.

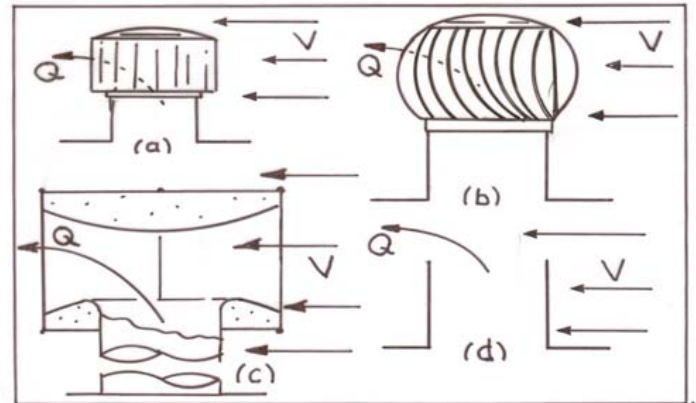


Figure 2: Diagram of the four ventilating devices (eductors) tested;

- (a) 250 mm throat turbine type,
- (b) 300 mm throat turbine type,
- (c) 300 mm throat omni directional venturi,
- (d) 300 mm bore open stub.

On the other hand, it can also be seen from the present measurements that the two parameters  $C_d$  and  $C_f$  recommended in the Standard as bases for quantifying a ventilator's performance are far too simplistic for the purpose.

For example, using data of figure 5(a), and taking the pressure immediately behind the device (in the direction of air extraction) as equal to the plenum pressure at zero flow rate, the following has been obtained:

With 18 km/hr wind, plenum pressure is  $-6.7 \text{ Pa}$  at  $Q = 0 \text{ l/min}$ , and  $-4 \text{ Pa}$  at  $Q = 2000 \text{ l/min}$ . Thus  $\Delta p_v = -4 - (-6.7) = 2.7 \text{ Pa}$ . Equation (1) then gives  $C_i = k \times 2000 / \sqrt{2.7} = 1220 \times k$ , where  $k$  is a constant incorporating the conversion factors, throat area and air density. Similarly, with 8 km/hr wind, the corresponding figures are  $-1 \text{ Pa}$  at  $Q = 0 \text{ l/min}$ ,  $2 \text{ Pa}$  at  $Q = 5000 \text{ l/min}$ . Equation (1) then gives  $C_i = k \times 5000 / \sqrt{3} = 2890 \times k$ . Clearly, such a wide variation of  $C_i$  values would make  $C_d$ , which is based on the average of these values as per equation (2), too simplistic and thus unsuitable as a representative characteristic of a ventilator.

The flow coefficient ( $C_f$ ) can similarly be seen to vary so widely that its average  $C_f$  would be unsuitable as a parameter characterizing a ventilator. This is clearly illustrated in all non-dimensional plots.

Now that individual ventilator's characteristic can be succinctly described by a single curve, relative performances of the four devices tested can be concisely shown. This is done in figure 7. Clearly the open stub withdraws best. In reality, this device is impractical as a roof ventilator, because it had neither vermin mesh nor a “conical top” to exclude rain. It can however stand as a base-line model for eductors. Similarly impractical is the omni directional venturi which had no surrounding mesh to prevent birds nesting. The only practical eductors here are the turbine types shown in figure 2(a) and (b).

## Conclusions

Measurements of air extraction characteristics of 4 wind-influenced ventilators have been presented. The non-dimensionalised data collapse well into single curves, which have been seen to be more suitable as performance indicators than the

simple parameters suggested in the current Standard on these devices. The ventilation industry would thus find these curves useful for specification purposes, and manufacturers for judging the effects of modification to their eductors or when developing new models. It has also been seen that as regards air extraction, the simple stub performs best.

### Acknowledgements

- Chantal Buttini, Mech. Eng. UTS, student 1998,
- Emmanuel Christou, Mech. Eng. UTS, student 2004,
- CHOICE, Australian Consumers' Association,
- Tristan Day, School of Building UTS, Student 1997,
- Prof. J P Gostelow, Engineering, University of Leicester, U K,
- Kim Kennedy, Mech. Eng. UTS, student 2000,
- S. West, School of Architecture and Building UTS.

### References

- [1] Australian/New Zealand Standard AS/NZS 4740:2000, *Natural ventilators – Classification and performance*, Standards Australia, 2000
- [2] Back, O., *Die Ermittlung der relativen Wertigkeit windbetätigter Saughauben*. Gesundheits-Ingenieur, Heft 51, 1932 (in German).
- [3] Savonius, O., *Undersökning av Sughuvar och Rotor-Ventilatorer*, Sartryck ur Teknisk Tidskrift 1932, hafte 38. Mekanik 9 (in Finnish)

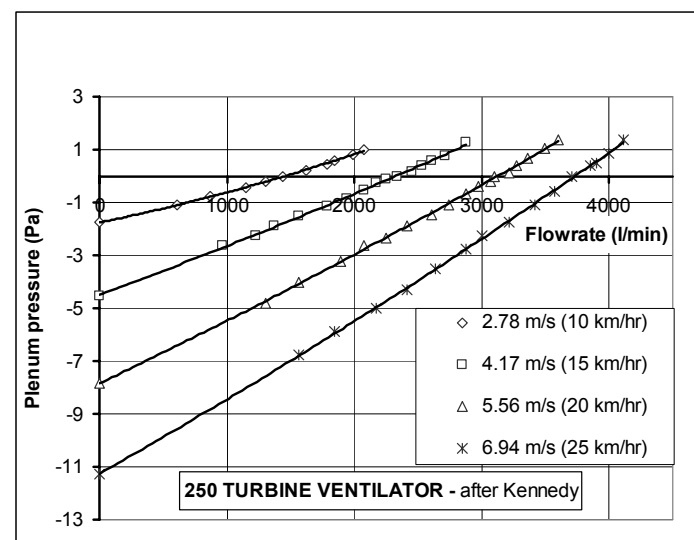


Figure 3(a): Results for 250 mm throat turbine ventilator - plots of plenum pressure ( $\Delta p$ ) against extraction flow rate ( $Q$ ) at set wind speeds.

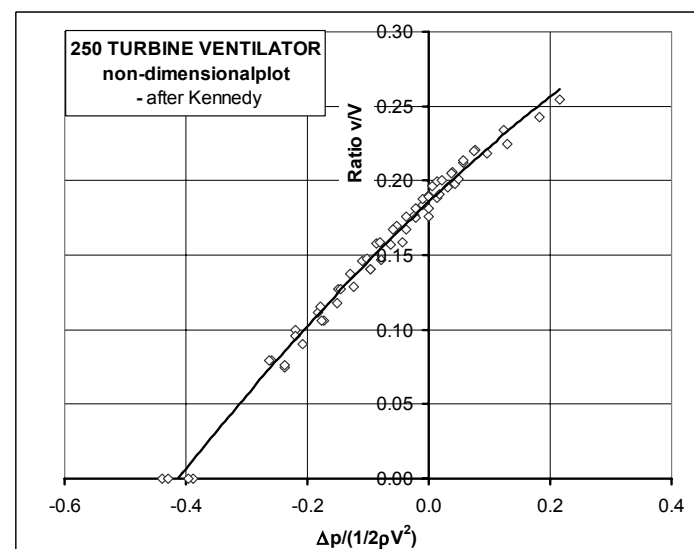


Figure 3(b): Results for 250 mm throat turbine ventilator plotted non-dimensionally (from figure 3(a)).

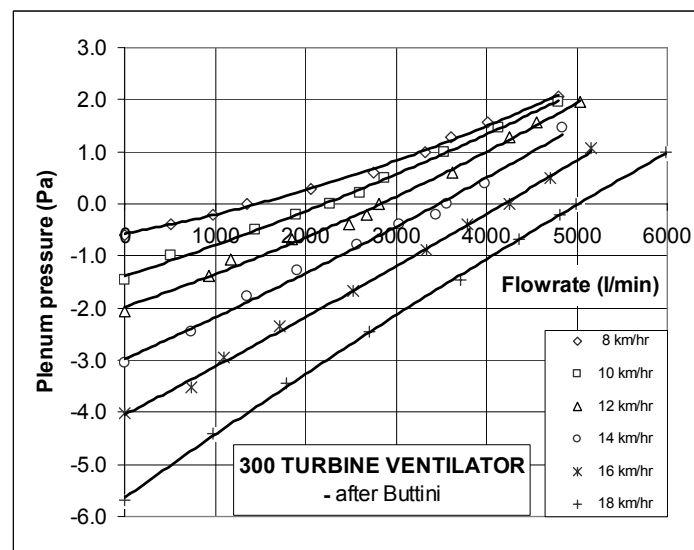


Figure 4(a): Results for 300 mm throat turbine ventilator - plots of plenum pressure ( $\Delta p$ ) against extraction flow rate ( $Q$ ) at set wind speeds.

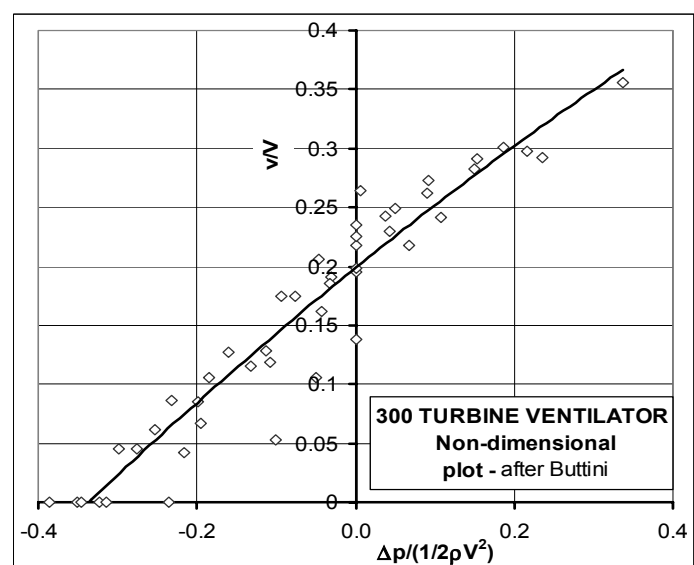


Figure 4(b): Results for 300mm throat turbine ventilator plotted non-dimensionally (from figure 4(a)).

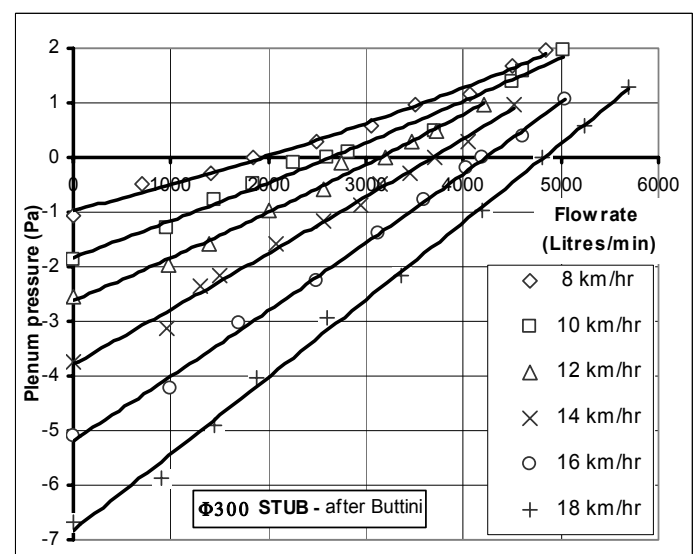


Figure 5(a): Results for Φ300 mm stub x 300 mm high. Each curve is a plot of plenum pressure ( $\Delta p$ ) against flow rate ( $Q$ ) at a set wind speed.

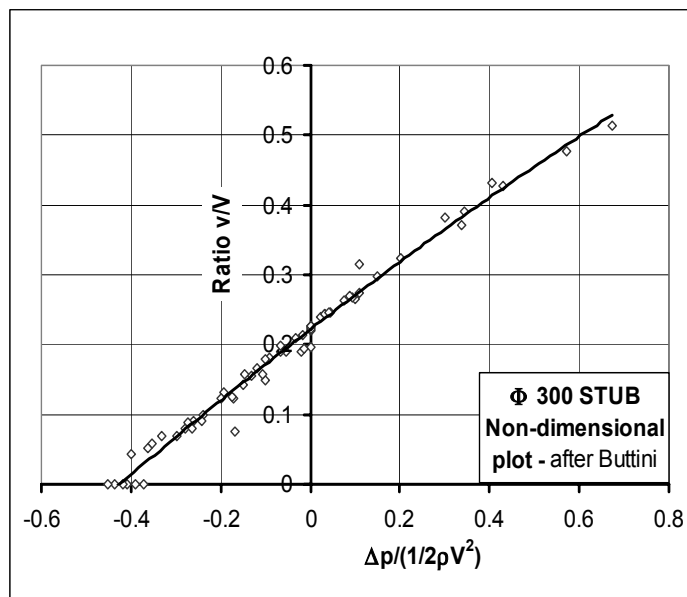


Figure 5(b): Results for  $\Phi$  300 mm stub plotted non-dimensionally (from figure 5(a)).

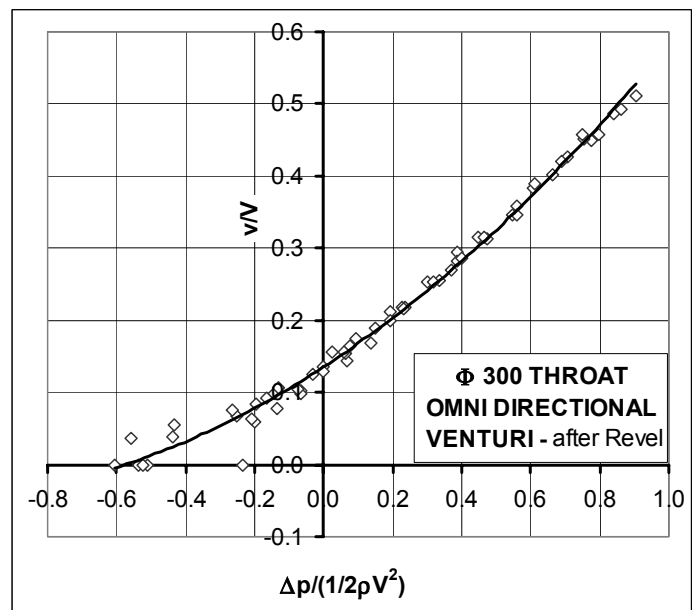


Figure 6(b): Results for  $\Phi$  300 omni directional venturi plotted non-dimensionally (from figure 6(a)).

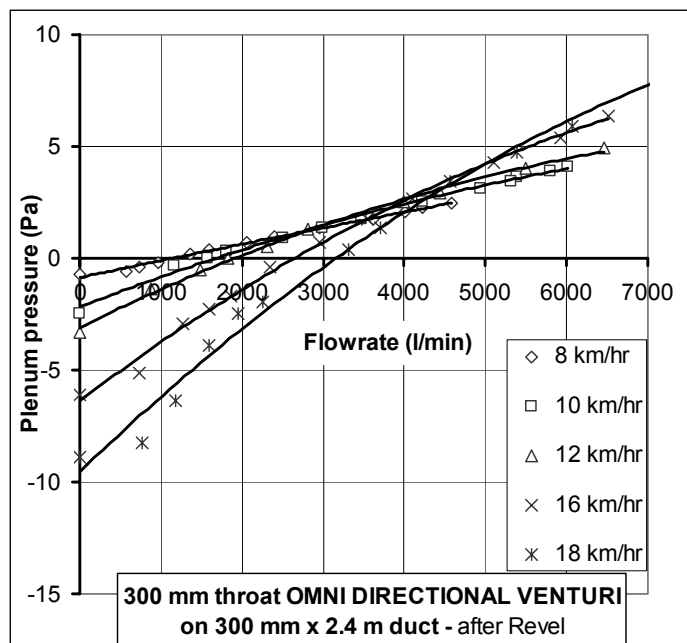


Figure 6(a): Results for  $\Phi$  300 omni directional venturi formed by spherical sectors (see figure 1) mounted onto a  $\Phi$  300 x 2400 mm high duct. – plenum pressure vs flow rate.

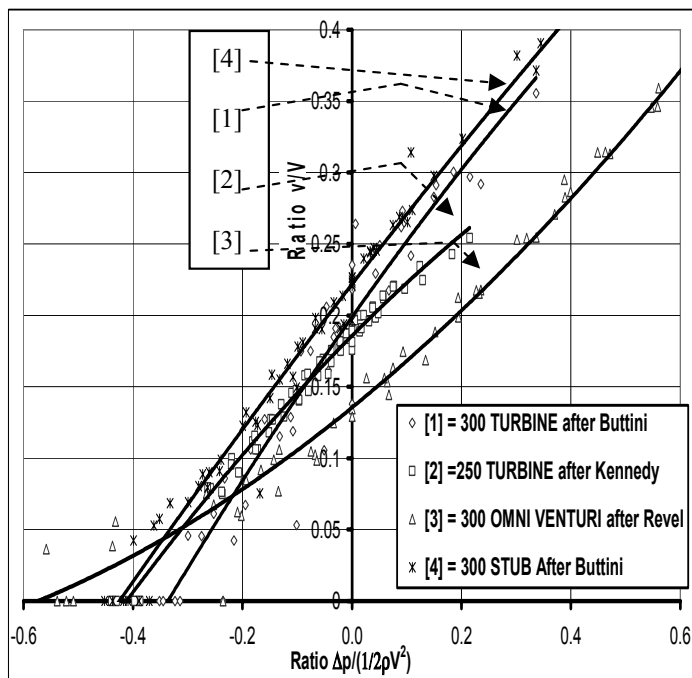


Figure 7: Combined non dimensional curves for the four eductors

# Laminar-Turbulent Transition of a Boundary Layer by a Single Roughness Element in an Inlet Region of a Circular Pipe

M. Ichimiya

Department of Mechanical Engineering  
The University of Tokushima, 2-1 Minami-josanjima, Tokushima, 770-8506 JAPAN

## Abstract

An artificially triggered transition due to a local disturbance source in an inlet region in a circular pipe has been investigated experimentally. To create the disturbance, a single roughness element was installed on the pipe wall, thus forming a steady turbulent region downstream. Hot-wire measurements of the axial mean and fluctuating velocities were obtained. A peripheral development of the turbulent region was examined with the aid of an intermittency factor. The turbulent region was similar to a turbulence wedge formed downstream of a single roughness element in a flat-plate laminar boundary layer.

## Introduction

Because pipe flows have been used in a wide variety of engineering fields, it is important to understand their properties. Flows within a pipe are limited not only by turbulence but also by transitions. For this reason, laminar-turbulent transitions in pipes have long been investigated since the work of Reynolds in 1883 [2].

From a variety of theoretical and experimental investigations [5,3], the flow in a fully developed region has been found to be stable in regard to axisymmetric and small non-axisymmetric disturbances. For this reason, the flow in an inlet region is important with respect to any transition in the pipe. There have not, however, been many investigations into a transition due to disturbances within the inlet region. Such investigations may generally be divided into one of two types: one is focused on the instability process from a perturbation to a hairpin vortex, and the other on established turbulent patches. A turbulent slug in a high Reynolds number and low-turbulence pipe flow, or a turbulent puff in a low Reynolds number and high-turbulence pipe flow corresponds to the turbulent patch. Both can be observed in the region downstream of various disturbances within the pipe, although they have also been observed in a developed flow in many experiments [6,7]. In addition, all such disturbances were constant or periodic in the azimuthal direction.

In the present experiment, however, a local point-like disturbance was introduced in the inlet region, and the resulting turbulent region just behind the disturbance was observed. A single roughness element was employed to create the disturbance. When such an element is introduced in a flat-plate laminar boundary layer, once the Reynolds number exceeds a certain critical value, a wedge-shaped turbulent region (turbulence

wedge) is formed [4]. The vertex of the wedge is at the roughness position. The turbulence wedge does not propagate downstream but exists in a stationary state. In the present pipe flow, a stationary turbulent region was formed just behind the roughness, similar to the one in the flat plate. The present investigation is focused on the developing property in the turbulent region.

## Experimental Apparatus and Methods

A Plexiglas pipe with a diameter,  $D$ , of 60 mm and a total length of approximately 6200 mm ( $=103D$ ) was used in the experiment. A fan downstream of the pipe sucked air into the pipe. Figure 1 shows the coordinate system and roughness element. An axial coordinate,  $x$ , starts from a position where the curvature of an inlet bell-mouth curve becomes straight. The origin of that coordinate is 90 mm downstream from the inlet. The roughness element is a cylinder 2 mm both in diameter ( $d$ ) and height ( $k$ ), and is mounted on the pipe wall. The axis of the roughness element is perpendicular to the wall. The downstream distance of the roughness element from the coordinate origin,  $x_k$ , is 107 mm. The boundary layer at this position without the roughness element is laminar and has a thickness of 3.5 mm. Therefore, the top of the roughness element is kept within the boundary layer. The Reynolds number based on the pipe diameter and the velocity averaged over the cross-section is 20000. The roughness Reynolds number based on the roughness height and the velocity at the top of the roughness is 610. The turbulent level at the pipe centerline is approximately 0.6%. The axial similarity of the velocity is satisfactory.

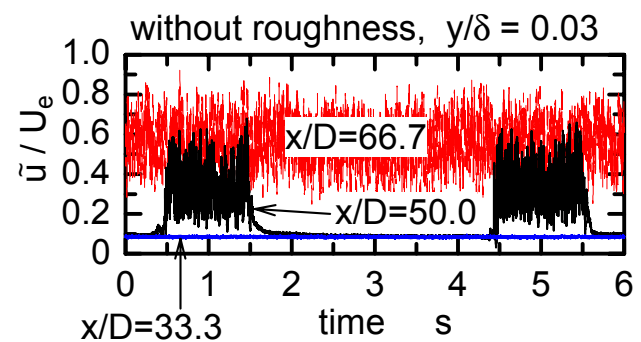


Figure 2. Instantaneous velocity signals.

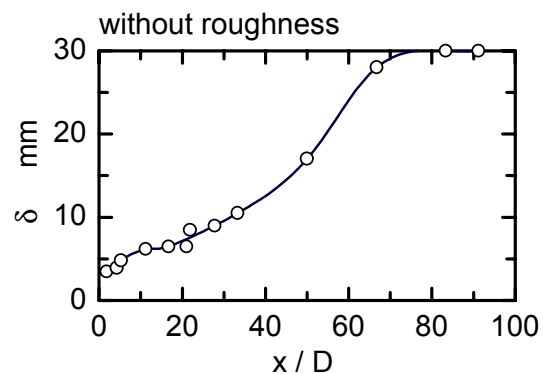


Figure 3. Boundary-layer thickness.

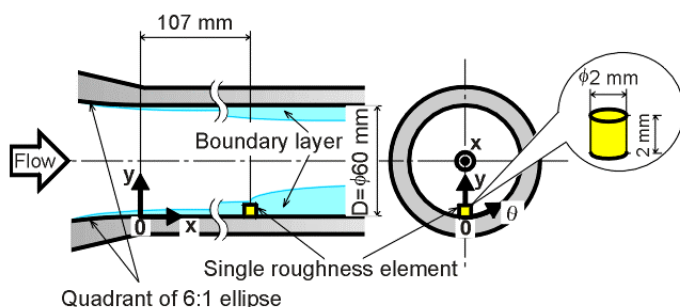


Figure 1. Coordinate system and single roughness element.



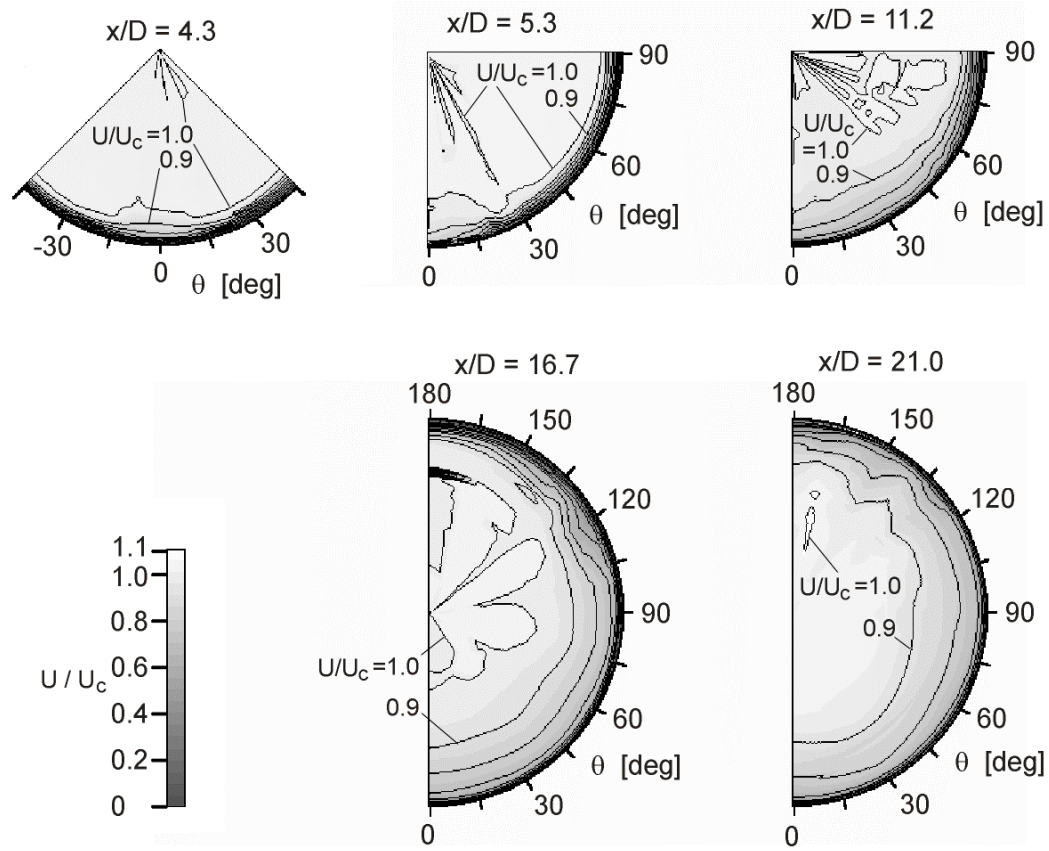


Figure 4. Isocontour maps of mean velocity.

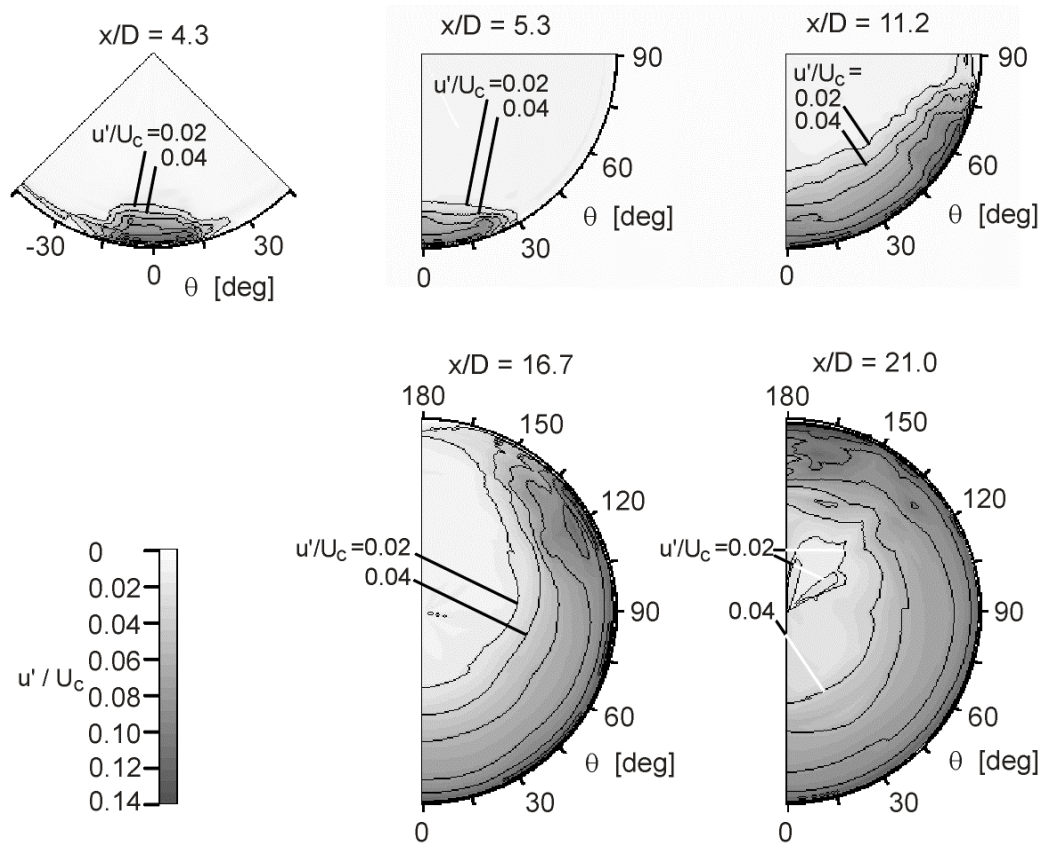


Figure 5. Isocontour maps of fluctuating velocity.

Measurements with a single hot-wire probe were made at five axial stations downstream of the roughness element, i.e.,  $x/D = 4.3, 5.3, 11.2, 16.7$  and  $21.0$ . A single hot-wire probe with a tungsten sensing element  $5\ \mu\text{m}$  in diameter and  $1\ \text{mm}$  in length

was used in the measurements. The output voltage from the hot wire had been digitized at a  $5\ \text{kHz}$  sampling frequency and a  $52$ -second sampling period.



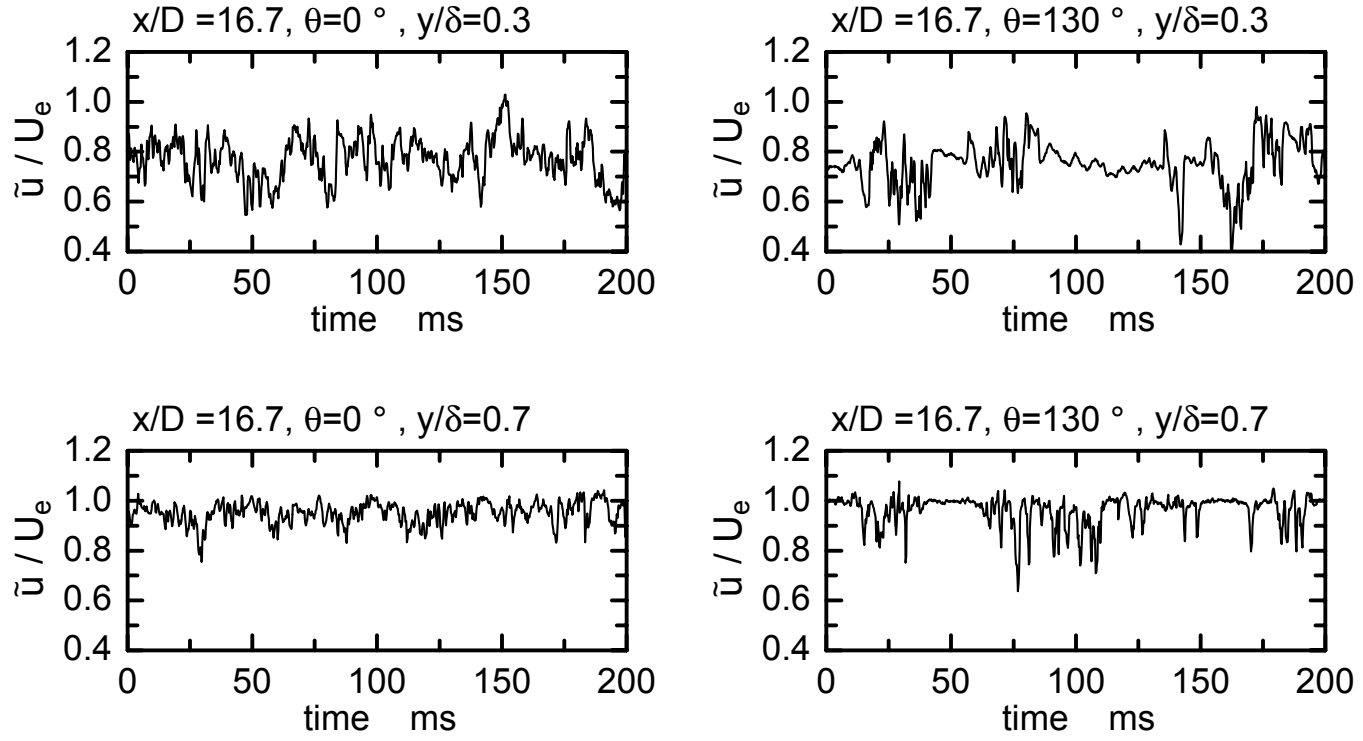


Figure 6. Instantaneous velocity signals.

## Results and Discussion

### Outline of Transition without Roughness Element

First of all, an outline of the natural transition, i.e., the transition without a roughness element, is briefly discussed. Instantaneous velocity signals are shown in Fig. 2 at three axial positions,  $x/D = 33.3, 50.0$  and  $66.7$ , where  $y$  is a normal distance from the pipe wall. The intermittent turbulent patches in  $x/D = 50.0$  appeared to be turbulent slugs based on the sharp leading and trailing edges of the patches and the present high Reynolds number of 20000. Figure 3 shows an axial distribution of a boundary layer thickness. The inlet region, which is fairly maintained downstream, is approximately 70 times the pipe diameter.

### Artificial Transition due to Roughness Element

Next, the experimental results of the transition property due to the single roughness element are discussed. Isocontour maps of an axial mean and of fluctuating velocities in the five cross-sections are shown in Figs. 4 and 5, respectively. An azimuthal position,  $\theta = 0^\circ$ , corresponds to the roughness position. Positive and negative regions of  $\theta$  are measured only in the section  $x/D = 4.3$ . In the other four sections, only the positive region of  $\theta$  is measured, since the symmetry with respect to the position  $\theta = 0^\circ$  at  $x/D = 4.3$  is satisfactory. The turbulent region originates from the position  $\theta = 0^\circ$ . As  $\theta$  increases, the flow changes from turbulent to laminar. The turbulent region expands in both the radial and azimuthal directions in the downstream region, though the azimuthal expansion is faster.

The fluctuating velocity is higher, i.e., it is in the azimuthal region away from  $\theta = 0^\circ$  than in the region of  $\theta = 0^\circ$ , higher than at  $\theta = 0^\circ$  at  $\theta = 10^\circ, 20^\circ, 60^\circ, 120^\circ$  and  $140^\circ$  in  $x/D = 4.3, 5.3, 11.2, 16.7$  and  $21.0$ , respectively. This is a remarkable characteristic that has also been observed in the turbulence wedge downstream of a single roughness element on a flat plate [1]. To examine the fluctuation at these azimuthal positions in detail, instantaneous velocity signals are shown in Fig. 6 at  $x/D = 16.7$ . The signals at  $\theta = 0^\circ$  always fluctuate, whereas those at  $\theta = 130^\circ$  show an intermittent occurrence of turbulent patches. To confirm that the fluctuating velocity is higher within the patches, conditional-averaged fluctuating velocity distributions are shown in Fig. 7. The condition was based on the criterion of whether an

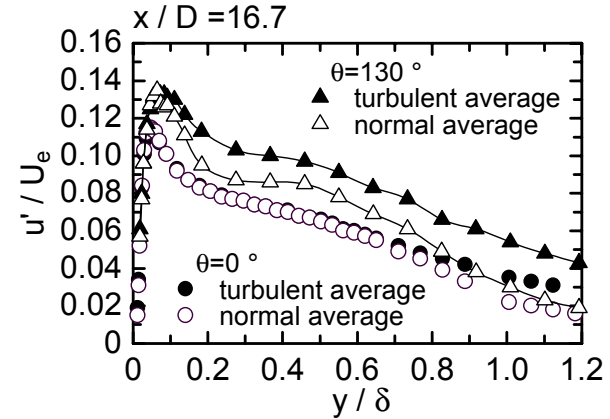


Figure 7. Conditionally averaged fluctuating velocity distribution.

instantaneous flow is turbulent or not. Both turbulent and normal (non-conditioned) averages are shown. Both distributions of  $\theta = 0^\circ$  are quite similar except for those in the outer region of the boundary layer. This is because the flow is always turbulent at  $\theta = 0^\circ$ , so that the turbulent-averaged velocity is almost the same as the normal-averaged one. On the other hand, at  $\theta = 130^\circ$ , the fluctuating velocity of the turbulent average, i.e., within the turbulent patches, is much higher. The large turbulent average at  $\theta = 130^\circ$  makes the normal average greater than the normal average at  $\theta = 0^\circ$ .

Figure 8 shows isocontour maps of an intermittency factor, i.e., time fractions of the turbulent flow. The discrimination between turbulence and non-turbulence was determined according to whether a time derivative of an instantaneous velocity exceeds a prescribed threshold level. The azimuthal expansion is faster than the radial expansion both in the fluctuating velocity in Fig. 5 and the intermittency factor in Fig. 8. At  $x/D = 21.0$ , contour lines whose value exceeds 0.3 fail to reach the pipe center. The lines, however, reach the position of  $\theta = 180^\circ$ , i.e., the turbulent region in the positive  $\theta$  area merges with it in the negative  $\theta$  area and covers the entire periphery of the pipe.

These peripheral expansions of the turbulent region unfolding on a flat plane are shown in Fig. 9. The peripheral distance  $l$  is

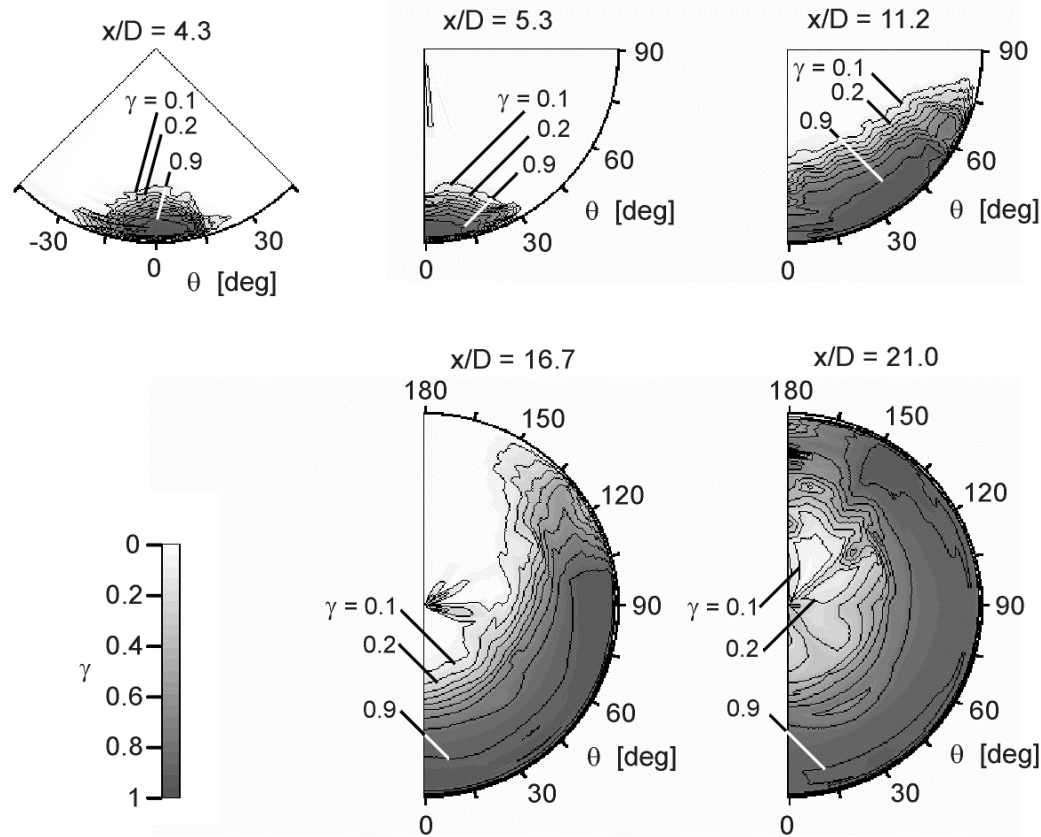


Figure 8. Intermittency contour maps.

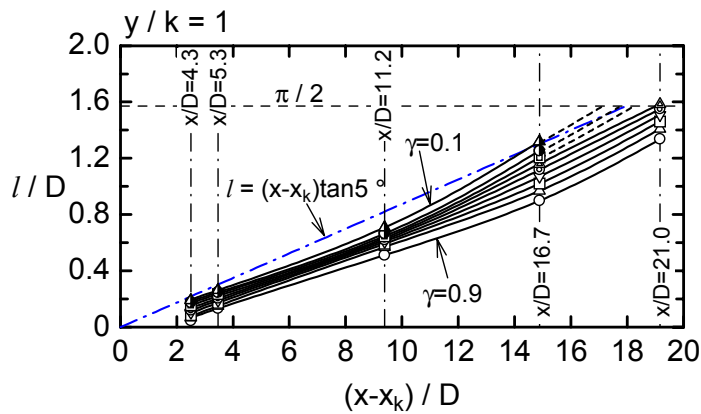


Figure 9. Peripheral expansion of turbulent region.

shown across the axial distance from the roughness element  $x - x_k$ . Note that both scales are different. The contour lines are wedge-shaped. The lines, which are initially straight, then curve to the outside. This condition is similar to that of the turbulence wedge on a flat plate [1]. If the lines are extrapolated to the upstream region, they reach the position  $x - x_k = 0$ , i.e., the virtual origin of the turbulent region equals the roughness position. The present author has found that the half-angle of the lines at the virtual origin  $4.8^\circ$  and  $6.0^\circ$  at  $y/k = 0.25$  and  $2.5$ , respectively [1]. A line corresponding to  $5^\circ$  is also shown in Fig. 9. The present turbulent region expands at approximately the same angle and is similar to the turbulence wedge on a flat plate.

## Conclusions

Experiments were performed to investigate the effects of a single roughness element on a boundary-layer transition in an inlet region in a circular pipe. When the roughness element was absent, turbulent slugs were observed in the transition process; when it was present, however, a stationary turbulent region was formed downstream. The contour lines of the turbulent region were

wedge-shaped once they unfolded onto a flat plane. The lines, which were initially straight, then curved to the outside. This condition is similar to that of the turbulence wedge on a flat plate. The fluctuating velocity was as its maximum not at the center of the region but at a region away from the center. Intermittent turbulent patches existed in the region, and the fluctuation within those patches was large.

## References

- [1] Ichimiya, M., Nakase Y. & Fukutomi, J., Structure of a Turbulence Wedge Developed from a Single Roughness Element on a Flat Plate, *Engineering Turbulence Modelling and Experiments* 2, editors W. Rodi and F. Martelli, Elsevier, 1993, 613-622.
- [2] Reynolds, O., An Experimental Investigation of the Circumstances which Determine Whether the Motion of Water Shall be Direct or Sinuous and of the Law of Resistance in Parallel Channels, *Phil. Trans. R. Soc. Lond.*, **174**, 1883, 935-982.
- [3] Sarpkaya, T., A Note on the Stability of Developing Laminar Pipe Flow Subjected to Axisymmetric and Non-Axisymmetric Disturbances, *J. Fluid Mech.*, **68-2**, 1975, 345-351.
- [4] Schubauer, G. B. & Klebanoff, P. S., Contributions on the Mechanics of Boundary-Layer Transition, *NACA Rep.*, **1289**, 1956.
- [5] Tatsumi, T., Stability of the Laminar Inlet-Flow Prior to the Formation of Poiseuille Regime, *J. Phys. Soc. Jpn.*, **7-5**, 1952, 495-502.
- [6] Wygnanski, I. J. & Champagne, F. H., On Transition in a Pipe. Part 1. The Origin of Puffs and Slugs and the Flow in a Turbulent Slug, *J. Fluid Mech.*, **59-2**, 1973, 281-335.
- [7] Wygnanski, I., Sokolov, M. & Friedman, D., On Transition in a Pipe. Part 2. The Equilibrium Puff, *J. Fluid Mech.*, **69-2**, 1975, 283-304.

## Model for Anomalous Scaling of Turbulent Structure Functions

T.S.Lundgren<sup>1</sup>

<sup>1</sup>Dept. Aerospace Engineering and Mechanics  
University of Minnesota, Minneapolis MN 55455 USA

### Abstract

A model for inertial range intermittency and anomalous scaling of velocity structure functions is proposed. This model is similar to the Kolmogorov log-normal model except that velocity difference statistics are assumed instead of dissipation statistics. The Navier-Stokes equation is used to derive the basic law for the instantaneous velocity difference between two points. This gives incomplete information about the dependence on scale size and requires a statistical hypothesis in order to compute structure functions and other quantities. The specific assumptions made here relate the singular exponent to the velocity amplitude and give results which agree well with experiment.

### Introduction

The purpose of this paper is to study the statistics of the velocity difference between two neighboring points in a turbulent flow. Structure functions of turbulence theory are defined by averages of the velocity difference between neighboring points:

$$B_p(r) = \langle (\mathbf{v} \cdot \hat{\mathbf{r}})^p \rangle \quad (1)$$

where  $\mathbf{v}(\mathbf{r}, \mathbf{x}) = \mathbf{u}(\mathbf{x} + \mathbf{r}) - \mathbf{u}(\mathbf{x})$ . We have restricted to longitudinal components in this definition. The classical result of Kolmogorov[1] is  $B_p = C_p(\epsilon r)^{p/3}$ , where  $\epsilon$  is the mean dissipation at a point. It is convenient to use a length scale  $L$  defined by  $\epsilon = U^3/L$  where  $U$  is the rms velocity fluctuation, then the Kolmogorov result is  $B_p = C_p U^p (r/L)^{p/3}$ . Experimentally it has been found that  $B_p \sim U^p (r/L)^{\zeta_p}$  where  $\zeta_p < p/3$ . This has been interpreted as being caused by extreme intermittency in the instantaneous dissipation which has an effect on velocity difference statistics even at inertial range scales.

### Asymptotic Analysis

#### Partial Lagrangian Coordinate System

The starting point for an analysis of structure functions is an equation for the difference in velocity between two points. Such an equation may be derived by letting one of the points,  $\mathbf{x}$ , be a Lagrangian fluid particle, moving with the fluid. The second point, which is not Lagrangian, is slaved to the motion of the first with fixed separation  $\mathbf{r}$ . It may be easily shown[3] that  $\mathbf{v}$  satisfies the Navier-Stokes equation in the form

$$\frac{\partial \mathbf{v}}{\partial t} + \mathbf{v} \cdot \frac{\partial \mathbf{v}}{\partial \mathbf{r}} = -\frac{1}{\rho} \frac{\partial P}{\partial \mathbf{r}} + \nu \frac{\partial}{\partial \mathbf{r}} \cdot \frac{\partial \mathbf{v}}{\partial \mathbf{r}}, \quad \frac{\partial}{\partial \mathbf{r}} \cdot \mathbf{v} = 0, \quad (2)$$

in which only derivatives with respect to  $\mathbf{r}$  occur, none with respect to  $\mathbf{x}$ . (In an accelerated coordinate system an inertial force appears on the right hand side of (2), which may be absorbed into the pressure.) Since  $\mathbf{v} = 0$  at the origin of  $\mathbf{r}$ , these equations describe a generalized stagnation point flow. It is of some interest to note that Kolmogorov had such a partial Lagrangian system in mind. He considered a coordinate system fixed to a fluid particle and looked at the velocity of another point relative to this moving coordinate system. He did not actually write down (2), but no doubt had this equation in mind.

### Outer Equation

Now express these equations in outer variables, using the rms velocity  $U$  as the characteristic velocity, and  $L = U^3/\epsilon$  as length. Define dimensionless outer variables  $\mathbf{v}_o = \mathbf{v}/U$ ,  $\mathbf{r}_o = \mathbf{r}/L$ ,  $\tau = tU/L$ . Scaling with these variables gives

$$\frac{\partial \mathbf{v}_o}{\partial \tau} + \mathbf{v}_o \cdot \nabla_o \mathbf{v}_o = -\nabla_o P_o + R_L^{-1} \nabla_o^2 \mathbf{v}_o, \quad \nabla_o \cdot \mathbf{v}_o = 0 \quad (3)$$

where  $R_L = UL/\nu$  and  $\nabla_o = \partial/\partial \mathbf{r}_o$ . An outer expansion may be taken in the form

$$\mathbf{v} = U \mathbf{v}_o, \quad \mathbf{v}_o = \mathbf{v}_{o,1} + R_L^{-1} \mathbf{v}_{o,2} + \dots \quad (4)$$

The first term  $\mathbf{v}_{o,1}$  satisfies (3) without the viscous term.

### Inner Equation

Now rescale variables so that the viscous term is retained as  $R_L \rightarrow \infty$ , by defining inner variables

$$\mathbf{r}_i = R_L^{-\alpha} \mathbf{r}_o, \quad \mathbf{v}_i = R_L^{-\beta} \mathbf{v}_o, \quad P_i = R_L^{-2\beta} P_o \quad (5)$$

Then (3) may be rewritten as

$$R_L^{-\beta+\alpha} \frac{\partial \mathbf{v}_i}{\partial \tau} + \mathbf{v}_i \cdot \nabla_i \mathbf{v}_i = -\nabla_i P_i + R_L^{-1-\beta-\alpha} \nabla_i^2 \mathbf{v}_i \quad (6)$$

The conditions that the viscous terms be retained as  $R_L \rightarrow \infty$  gives the condition  $\beta + \alpha = -1$ . Clearly another condition would be required to complete this, but it is left undetermined. Equation(6) takes the form (using  $\beta = -1 - \alpha$ )

$$R_L^{2\alpha+1} \frac{\partial \mathbf{v}_i}{\partial \tau} + \mathbf{v}_i \cdot \nabla_i \mathbf{v}_i = -\nabla_i P_i + \nabla_i^2 \mathbf{v}_i \quad (7)$$

which suggests an inner expansion

$$\mathbf{v} = U R_L^{-1-\alpha} \mathbf{v}_i, \quad \mathbf{v}_i = \mathbf{v}_{i,1} + R_L^{1+2\alpha} \mathbf{v}_{i,2} + \dots \quad (8)$$

### Matching

These two asymptotic expansions describe the same function in different variables. If there is an overlap region where both are valid the method of matched asymptotic expansions can be used. Van Dyke's matching principle states that one should take the inner expansion of the outer expansion and set that equal to the outer expansion of the inner expansion. That prescription was carried out in detail in [3], yielding the functional relation

$$\mathbf{v}_{o,1}(\mathbf{r}_o) = R_L^{-1-\alpha} \mathbf{v}_{i,1}(R_L^{-\alpha} \mathbf{r}_o) \quad (9)$$

This can be satisfied in the limit  $R_L \rightarrow \infty$  only if

$$\mathbf{v}_{o,1} = \mathbf{V} r_o^q \quad \text{and} \quad \mathbf{v}_{i,1} = \mathbf{V} r_i^q \quad (10)$$

Here  $q = -(1 + \alpha)/\alpha$  is undetermined (as is  $\alpha$ ). That is, substituting these into (9), with  $r_i = R_L^{-1/(1+\alpha)} r_o$  satisfies it exactly and any power other than  $q$  would give zero or infinity

as  $R_L \rightarrow \infty$ . In these equations  $\mathbf{V} = \mathbf{V}(\mathbf{x}, t, \hat{\mathbf{r}})$  is a dimensionless random variable;  $\hat{\mathbf{r}}$  is a unit vector in the direction of  $\mathbf{r}$ . The significant result is

$$\mathbf{v} = U\mathbf{V}\left(\frac{r}{L}\right)^q \quad (11)$$

in which both  $\mathbf{V}$  and  $q$  are random variables, i.e. they depend on the realization of the turbulent flow. Longitudinal structure function ensemble averages at a fixed point  $\mathbf{x}$  are then given by

$$B_p = \langle (\mathbf{v} \cdot \hat{\mathbf{r}})^p \rangle = U^p \langle (\mathbf{V} \cdot \hat{\mathbf{r}})^p \left(\frac{r}{L}\right)^{qp} \rangle. \quad (12)$$

Any further conclusions depend on assumed statistics of  $\mathbf{V}$  and  $q$ . This is addressed in the following section.

### Anomalous Scaling

#### Statistical Assumptions

For longitudinal velocity components we take the velocity function in the form

$$v = V_0 U C(q) \left(\frac{r}{L}\right)^q \quad (13)$$

where

$q$  is a random variable with pdf  $f(q)$ ,

$C$  is a random variable which depends only on  $q$ ,

$V_0$  is an independent dimensionless random variable,

$U$  is the rms velocity giving dimension to the expression.

The function  $C(q)$  will be assumed to be large for smaller  $q$  for reasons which will become apparent below.  $C$  can be thought of as a velocity amplitude function which depends on the exponent  $q$ , or perhaps it is better to think of  $q$  as dependent on the amplitude  $C$ . If  $v$  is interpreted as the azimuthal velocity in an axially symmetric vortex, the vorticity would be given by

$$\omega = V_0 \frac{U}{L} C(q) (q+1) \left(\frac{r}{L}\right)^{q-1}, \quad (14)$$

a singular vortex with amplitude which is greater when the singularity is greater (smaller  $q$ ). Therefore  $C(q)$  specifies the distribution of vortex singularities.

Longitudinal structure functions are then given by

$$B_p = \langle v^p \rangle = U^p \langle V_0^p \rangle \int_0^\infty \left(\frac{r}{L}\right)^{qp} C^p f(q) dq. \quad (15)$$

The idea here is that  $f(q)$  has a peak near  $q = 1/3$ . If  $C(q)$  is larger on the left of the peak and smaller on the right then the product  $C^p f$  shifts the peak to smaller values as  $p$  increases, thus selecting a smaller  $q$  in  $(r/L)^{qp}$ . If the selected  $q$  were  $1/3$ ,  $(r/L)^{p/3}$  results, the K41 result. A smaller value than  $1/3$  gives  $(r/L)^{\zeta_p}$  with  $\zeta_p < 1/3$ , an anomalous result.

In order to illustrate this specific assumptions for  $f(q)$  and  $C(q)$  have to be made: the pdf  $f(q)$  is assumed to be log-normal,

$$f(q) = \frac{1}{\sqrt{(2\pi)\sigma^2}} \exp\left(-\frac{(\ln(q/q_0))^2}{2\sigma^2}\right), \quad (16)$$

and  $C$  is assumed to be an inverse power of  $q$

$$C(q) = \left(\frac{q}{q_0}\right)^{-\beta}. \quad (17)$$

The parameter values have been taken to be  $q_0 = .373$  and  $\sigma^2 = .0144$  for reasons to be discussed presently and  $\beta$  is taken to be 2. In Figure 1,  $C^p f$  is plotted versus  $q$  for various values of  $p$ . The curves have been normalized so that each has an integral of unity. This quantity is like an effective pdf for  $q$  which depends on the order of the structure function.

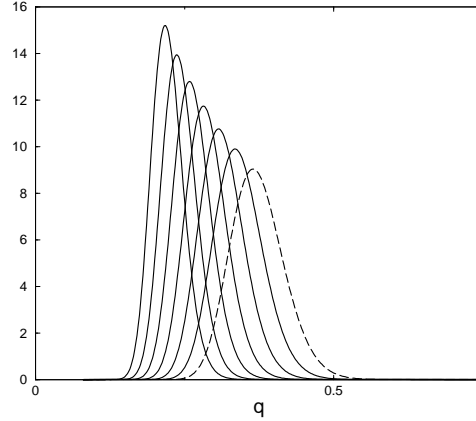


Figure 1: Effective pdf,  $C(q)^p f(q)$ . The dashed line is the actual log-normal pdf. The curves which peak at smaller  $q$  are for  $p = 3, 6, 9, \dots$ .

The structure function exponents have been computed from Eq.(15) with these values. For each value of  $p$  the integration was carried out for  $.02 < r/L < .2$ . The resulting function of  $r/L$  is close to, but not exactly equal, a power law and was curve-fit to a power law formula to determine the best exponent. For  $p = 3$  the result is supposed to be linear,  $\zeta_3 \equiv 1$ , to agree with the exact Kolmogorov "4/5" law,  $B_3 = -.8\epsilon r \equiv -.8U^3(r/L)$ . This was achieved by adjusting the parameter  $q_0$ . The parameter  $\sigma$  was adjusted to give  $\zeta_6 = 1.80$ , which is close to the observed experimental value, and is the usual value assumed. The computed values of  $\zeta_p$  are plotted in Figure 2 for  $p$  as large as 20. The She-Leveque curve agrees with experiments out to about  $p = 18$  and can be regarded here as a surrogate for the experiments. The K62 log-normal result levels off at about  $p = 16$  and decreases after that. The present result agrees well with the present level of experimenta but finally levels off around  $p = 30$ .

It was noticed in doing these computations that the results were not exactly power laws. The  $\zeta_p$  exponents depended slightly on the range of  $r/L$  used for the curve fitting. This can be looked at analytically by letting  $\beta\sigma^2$  be constant as  $\sigma^2$  tends to zero. That is as  $\sigma^2$  gets smaller  $\beta$  becomes larger. This is set up by first writing

$$\begin{aligned} C(q)^p f(q) &= \frac{1}{\sqrt{(2\pi)\sigma^2}} \exp\left(-\beta p \ln(q/q_0) - \frac{(\ln(q/q_0))^2}{2\sigma^2}\right) \\ &= \frac{1}{\sqrt{(2\pi)\sigma^2}} \exp\left(\frac{(\beta\sigma^2 p)^2}{2\sigma^2} - \frac{(\ln(q/q_0) + \beta\sigma^2 p)^2}{2\sigma^2}\right) \end{aligned}$$

The second line follows by completing the square in the first exponent. Then by a simple change of variables in the integral (15) may be written

$$B_p = U^p \langle V_0^p \rangle \exp\left(\frac{(\beta\sigma^2 p)^2}{2\sigma^2}\right) \text{ times}$$

$$\int_{-\infty}^{\infty} \left(\frac{r}{L}\right)^{\zeta_p \exp(\sigma^2 \xi)} \frac{1}{\sqrt{2\pi}} \exp\left(-\frac{\xi^2}{2}\right) d\xi$$

where, jumping ahead for notational purposes,

$$\zeta_p = p q_0 \exp(-\beta\sigma^2 p). \quad (18)$$

Now expanding in powers of  $\sigma$ , the result is

$$B_p = U^p < V_0^p > \exp\left(\frac{(\beta\sigma^2 p)^2}{2\sigma^2}\right) \text{ times} \left(\frac{r}{L}\right)^{\zeta_p} \left(1 + \left(\zeta_p \ln r/L + \zeta_p^2 (\ln r/L)^2\right) \sigma^2/2 \dots\right) \quad (19)$$

Therefore exact power laws result in the limit as  $\sigma^2 \rightarrow 0$  but there are logarithmic corrections for small but finite  $\sigma^2$ .

In the limit  $\zeta_p$  is given by (18). This formula has two adjustable parameters. We want  $\zeta_3 = 1$ , which gives  $q_0 = \exp(3\beta\sigma^2)/3$  and we want  $\zeta_6 = 2 - \mu$ , which gives  $2\exp(-3\beta\sigma^2) = 2 - \mu$ . These therefore result in  $q_0 = (1/3)(1 - \mu/2)^{-1}$  and  $\beta\sigma^2 = -(1/3)\ln(1 - \mu/2)$ . When these are substituted into (18) the result is

$$\zeta_p = (p/3)(1 - \mu/2)^{(p/3)-1}. \quad (20)$$

This is plotted in Figure 2, where it seen to lie slightly below the computed values.

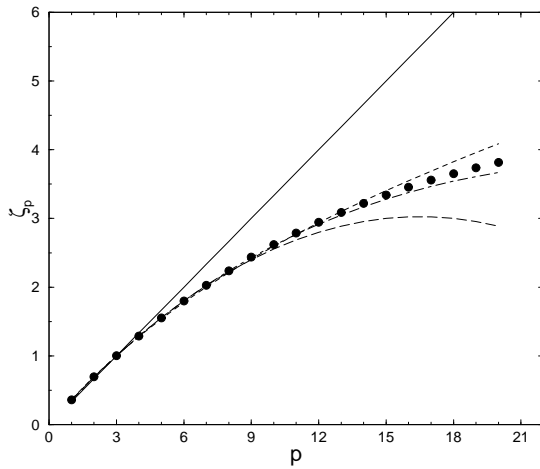


Figure 2: Anomalous exponents  $\zeta_p$  versus  $p$ ; Black dots, present computation; Solid straight line is K41,  $\zeta_p = p/3$ ; Long dashed curve, K62 log-normal model  $\zeta_p = p/3 + \mu(3p - p^2)/18$ ,  $\mu = .2$ ; dashed curve is She-Leveque[4],  $\zeta_p = p/9 + 2 - 2(2/3)^{p/3}$ ; Dot-dashed curve is Eq.(20),  $\zeta_p = (p/3)(1 - \mu/2)^{(p/3)-1}$ ,  $\mu = .2$ .

### Relationship to K62 Theory

The Kolmogorov refined similarity theory (K62) depends on the hypothesis that the instantaneous dissipation averaged over a sphere centered at  $\mathbf{x}$  should replace the mean dissipation in the K41 theory. The average dissipation over a sphere of radius  $l$  is defined by

$$\varepsilon_l = \frac{3}{4\pi l^3} \int_{r < l} 2\nu D_{ij}(\mathbf{x} + \mathbf{r}) D_{ij}(\mathbf{x} + \mathbf{r}) d\mathbf{r} \quad (21)$$

where  $D_{ij}$  is the rate of strain tensor. It was shown in [3] that by using the relative velocity  $\mathbf{v}$  and the energy equation in the partial Lagrangian coordinate system that (21) may be written, as  $R_L \rightarrow \infty$ ,

$$\varepsilon_l = -\frac{3}{4\pi l^3} \int_{r=l} n_i v_i \left(P + \frac{1}{2} v_i v_i\right) dS. \quad (22)$$

This relates the average dissipation in the sphere to the flux of energy into the sphere through the outer surface. Now, using (13), and the equivalent expression for the other velocity components, we get

$$\varepsilon_r = \frac{U^3}{L} A_0 C(q)^3 \left(\frac{r}{L}\right)^{3q-1}, \quad (23)$$

where  $A_0$  is an independent random variable, similar in nature to  $V_0$ , but not simply  $V_0^3$  because other velocity components occur in the surface integral. Equation(23) implies  $\varepsilon_r = (A_0/V_0^3)v^3/r$  or  $v \sim (\varepsilon_r r)^{1/3}$ , which is the Kolmogorov refined hypothesis. It follows from (23) that

$$< \varepsilon_r^n > \sim \left(\frac{r}{L}\right)^{\tau_n} \text{ with } \tau_n = \zeta_{3n} - n, \quad (24)$$

a result which is due to Kolmogorov[2]. Kolmogorov made a statistical assumption for  $\varepsilon_r$  (log-normal), determined  $\tau_n$ , and used (24) to determine  $\zeta_p$ . In the present work the statistical assumptions are on  $v$  and  $\tau_n$  is determined from (24).

### Conclusion

A self consistent derivation of turbulent structure function exponents has been made by the method of matched asymptotic expansions using the Navier-Stokes equation, to determine the velocity power law relation (11). This contains two undetermined parameters, an amplitude and a singularity exponent. Because the equations under consideration are instantaneous, not averaged, these could be random variables depending on the realization of the turbulent flow. Assumptions about the statistical relationship between the amplitude  $C$  and the singularity exponent  $q$  was made at this stage. The choice made gave results which agree with experiment, but this choice is not unique and perhaps a better motivated idea could throw some light on the nature of the cascade process and give similar results.

One result is a simple expression for the structure function exponent  $\zeta_p$ ,

$$\zeta_p = \frac{p}{3} \left(1 - \frac{\mu}{2}\right)^{\frac{p}{3}-1} \quad (25)$$

which satisfies  $\zeta_3 = 1$  and  $\zeta_6 = 2 - \mu$  and agrees with experiments over a wide range.

These results suggest a number of further researches. It should be possible to include viscous effects along the lines of the work done in [3], which should show a slow approach to the limit as Reynolds number tends to infinity.

Given the velocity difference function (13) and the assumed statistics it should be possible to study the velocity pdf. This will require an additional assumption about the independent random variable  $V_0$ .

### References

- [1] Kolmogorov, A.N., The local structure of turbulence in incompressible viscous fluid for very large Reynolds number, *Dokl. Akad. Nauk. SSSR* **30**, 1941, 299-303. Reprinted in *Proc. Roy. Soc. Lond. A* **434**, 1991, 9-13.
- [2] Kolmogorov, A.N., A refinement of previous hypotheses concerning the local structure of turbulence in a viscous incompressible fluid at high Reynolds number. *J. Fluid Mech.* **13**, 1965, 82-85.
- [3] Lundgren, T.S., Kolmogorov turbulence by matched asymptotic expansion, *Phys. Fluids* **15**, 2003, 1074-1081.
- [4] She, Z-S and Leveque, E., Universal scaling laws in fully developed turbulence, *Phys. Rev. Lett.* **72**, 1994, 336-339.

## Noise Emission in Large Aspect Ratio Cavities

G. Guj<sup>1</sup>, R. Camussi<sup>1</sup>, A. Di Marco<sup>1</sup> and A. Ragni<sup>2</sup>

<sup>1</sup>Industrial and Mechanical Engineering Department (DIMI)  
Roma Tre University, Rome, 00146 ITALY

<sup>2</sup>Department of Experimental Aerodynamics Methodologies  
Italian Aerospace Research Centre (CIRA), Capua, 81043 ITALY

### Abstract

This paper describes an experimental test campaign aimed at the study of the influence of surface irregularities on the turbulent boundary layer noise emission. The irregularities were represented by a two-steps large aspect-ratio cavity. The main task of the experiments was to characterize, from the aeroacoustic and fluid-dynamic viewpoint, the effects of the main non-dimensional parameters on the statistical quantities of interest correlated to the wall pressure fluctuations, accounting for the geometrical and dynamical similarity requirements with respect to real conditions. The experiments were performed in the low speed wind tunnel at ENEA-DIMI research centre. Results allowed us to individuate the significant, independent dimensionless groups governing the point wall pressure spectra in-between the double steps discontinuity. Proper scaling relations of local (pressure spectra) and global (Sound Pressure Level - *SPL*) quantities are proposed, and universal form functions modelling the properly normalized spectra and *SPL* are presented. The ability of the proposed model to predict the noise emission is finally validated and tested on experimental data.

### List of Symbols

$\alpha_i$	Power laws coefficients
$B$	Cavity span
$c$	Speed of sound
$\delta$	Boundary layer thickness
$f$	Frequency
$G_{pp}$	Pressure auto-spectrum
$H$	Steps height
$L$	Cavity length
$q$	Dynamic pressure
$Re$	Reynolds number
$St$	Strouhal Number
$U$	Free stream velocity
$x$	Streamwise coordinate
$\Delta$	Thickness ratio
$\Gamma_{pp}$	Universal spectrum
$\Psi$	Universal form function
$\gamma$	Velocity ratio
$\nu$	Cinematic viscosity
$\tilde{u}$	Mean Turbul. level within TBL
$\sigma$	Standard deviation
$\langle \rangle$	Dimensionless quantity
$AR$	Aspect ratio
$\langle \rangle$	Average on the tests
$\overline{\phantom{x}}$	Average on $x$ position

### Introduction

Steps and geometrical irregularities on the exterior surface of modern high-speed passengers aircraft appear for example at skin lap joints or window gaskets, and are recognized as potential sources of aerodynamically generated noise. It is known that the contributions of such aeroacoustic sources to the interior noise is significant and dominate the overall interior noise at the front part of the fuselage. Similar aeroacoustic problems are also encountered in other fields of engineering interest, for example in the vehicles or trains aerodynamics. Even if the subject is of great interest from the viewpoint of practical and basic research applications, it has not been treated in detail and the results available in literature are limited and sometimes contradictory.

The primary motivation of the present work is to cover the lack of experimental results in this field and the main goal is to contribute to a deeper understanding of the physics through a detailed experimental analysis. The surface irregularities were modelled by a backward-facing step (BFS) followed by a forward-facing step (FFS) disposed in an incompressible turbulent boundary layer (TBL). The sketch of the surface irregularities model is exhibited in Fig. 1, together with the main symbols used in present work.

When the flow reaches the BFS, a detachment occurs and a reverse flow zone is generated just after the step. After a distance of about  $5-7H$  there is an oscillating reattachment point of the flow. The reattachment point unsteadiness is recognised a strong noise source [1], [2]. After the reattachment, the flow encounters the FFS and the flow behaviour can be described as follow [3], [4]: there is a flow detachment about  $1H$  before the step, a separation bubble close to the step in which reverse flow occurs, and a second recirculating region bounded downstream by a reattachment point, after which the TBL slowly recovers its characteristics.

### Dimensional Analysis and Scalings

The six significative dimensionless groups governing the point wall pressure spectra in-between the double steps discontinuity are:

$$G'_{pp} = \frac{G_{pp} U}{q^2 H}, \quad St_H = \frac{fH}{U}, \quad Re_H = \frac{UH}{\nu}, \quad \gamma = \frac{\tilde{u}}{U},$$

$$x' = \frac{x}{H}, \quad \Delta = \frac{\delta}{H} \quad (1)$$

with

$$\tilde{u} = \frac{1}{\delta} \int_0^\delta \sigma_u dy \quad (2)$$



The effect of the other non-significative groups, ( $L/H$ ,  $U_\infty/c$  and  $B/H$ ) is neglected.

The study was conducted by means of the hypothesis of the variables separation. Thus the single dimensionless spectrum  $G'_{pp}$  can be represented as a function of the dimensionless groups, leading to the following expressions:

$$\begin{aligned} G'_{pp}(St_H, x', \Delta, Re_H, \gamma) &= G''_{pp}(St_H, x') \Delta^{\alpha_1} Re_H^{\alpha_2} \gamma^{\alpha_3} \\ &= G'''_{pp}(St_H) \Psi(x') \Delta^{\alpha_1} Re_H^{\alpha_2} \gamma^{\alpha_3} \end{aligned} \quad (3)$$

The quantity  $G'''_{pp}(St_H)$  denotes spectra with corresponding unitary  $SPL'''$ . Therefore, the basic hypothesis, which is here made, is the assumption of a universal shape of the spectra  $G'''_{pp}(St_H)$ . The actual amplitude modulation due to the effect of the distance from the steps, is recovered by the function  $\Psi(x')$  which denotes a universal form function representing the normalized  $SPL$  variation along the dimensionless axial variable  $x'$ . So, the problem is if it is possible to determinate the  $\alpha_i$  coefficients and the universal function  $\Psi(x')$  so that the dimensionless spectra  $G'''_{pp}$  collapse on a reasonable unique shape with unitary  $SPL'''$ . Then, a unique spectrum form function  $\Gamma_{pp}$  can be obtained by an average procedure on a very large number of  $G'''_{pp}$ . Details about the data analysis are reported in the following sections. In order to better understand the adopted procedure is useful to define the following quantities:

$$SPL' = 10 \log_{10} \left[ \int_0^{St_{H \max}} G'_{pp} dSt_H \right] \quad (4)$$

$$SPL'' = 10 \log_{10} \left[ \int_0^{St_{H \max}} G''_{pp} dSt_H \right] \quad (5)$$

Integrating the eqn (3), taking the logarithm and using the expression (4), the following relation is obtained:

$$\begin{aligned} SPL' &= \alpha_1 10 \log_{10} \Delta + \alpha_2 10 \log_{10} Re + \alpha_3 10 \log_{10} \gamma \\ &\quad + SPL'' \end{aligned} \quad (6)$$

The unitary  $SPL'''$  is obtained as follows:

$$\begin{aligned} SPL''' &= \langle -10 \log_{10} \Psi(x') + SPL'' \rangle \\ &= \tilde{\Psi}(x') + \langle SPL'' \rangle = 1 \end{aligned} \quad (7)$$

The symbols  $\langle \rangle$  represent the average on the tests. The universal form function of the  $SPL$ ,  $\Psi(x')$ , is calculated from equ. (7).

### Experimental Apparatus

The tests were carried out in the low-speed wind tunnel installed at the aerodynamic laboratory of the Energy Department of ENEA.

The steps were obtained using aluminium plates of the same height  $H$ , which were mounted in different positions to obtain different cavity length  $L$ ; the cavity span  $B$  is much larger than  $H$  ( $B/H \gg 1$ ). Measurements inside the cavity were performed using an aluminium sliding plate as cavity floor. Four microphones can be positioned on the cavity and flush mounted on the floor, three streamwise and one spanwise. TBL of desired characteristics

were obtained with a special designed generator constituted by curved grids placed at the end of the convergent.

The pressure fluctuations measurements were performed using B&K equipment: 1/4'' 4135 & 1/8'' 4138 microphones, Falcon 2670 preamplifiers, Nexus 2690 for sensitivity, amplification and filters settings. The pressure signals were acquired using an 8 channel Yokogawa *Digital Scope* DL708E. Around  $10^5$  samples, with a sampling rate in the range 10kHz-40kHz and a cut-off frequency filter in the range 4kHz-20kHz, were acquired from each channel.

A preliminary TBL aerodynamic characterisation was performed using a hot wire anemometer. The sliding plate was translated by means of a numerically controlled micrometric traversing system driven by a step-by-step motor.

### Test Matrix

The measurements were performed at thirty different positions along the cavity floor (Fig. 1).

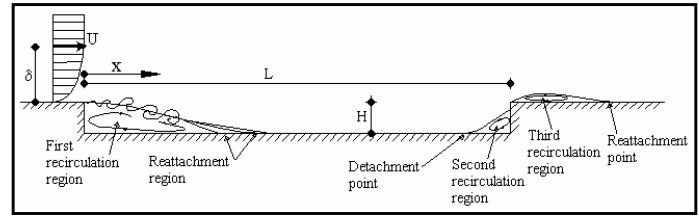


Fig. 1: Sketch of flow conditions over a backward-forward facing step.

The use of more microphones at the wall was useful to check the reliability of the results. Measurements were also performed in fixed positions downstream the FFS. During the whole test campaign a reference microphone was placed in the flow field to measure the background noise. The values assumed by the most important geometrical and aerodynamic parameters during the tests are reported in Tab. 1.

$U$ [m/s]	10, 30, 50
$H$ [mm]	15, 25
$\delta$ [mm]	22, 25, 28, 100, 150, 165
$L$ [mm]	340, 640
$Re_H$ [ $10^4$ ]	1, 1.7, 3.1, 5.1
$Re_\delta$ [ $10^4$ ]	1.9, 5.1, 7.5, 10.3, 20.5, 56.5

Tab.1: Values of the aerodynamic parameters assumed during the tests.

Such values were defined accounting for real conditions experienced by aircraft manufacturers. The low TBL thicknesses are relative to the natural TBL present on the test section floor, whereas the high thicknesses were generated using a curved grid.

### Data Post-processing Procedure

The adopted procedure to analyse the microphone signals is summarised below.

1. The pressure spectra  $G_{pp}$  are calculated, and corrected for the wind tunnel background noise. Details about the adopted conditioning technique can be found in [1].
2. The dimensionless spectra  $G'_{pp}$  (and  $SPL'$ ) are calculated from equ (1).
3. The exponents  $\alpha_1$ ,  $\alpha_2$ ,  $\alpha_3$ , are determined by applying an optimization procedure which minimizes the  $SPL'''$  deviations.
4. The functions  $G''_{pp}$  and  $SPL''$  are then definitively calculated using equ (3) and (6) and the optimum set of esponents  $\alpha_i$ .
5. Using equ (7) the  $\Psi$  function can be calculated at each  $x'$  position, averaging on a large number of tests (order of 400).

6. Once the universal form function  $\Psi$  is calculated, the functions  $G''_{pp}$ ,  $G'''_{pp}$  can be calculated using equations (3).
7. The universal form function  $\Gamma_{pp}$  representing the spectra is obtained as follows, where the over bar indicates the average on  $x'$  positions.

$$\Gamma_{pp} = \langle \overline{G'''_{pp}}(St_H) \rangle \quad (8)$$

## Results

A comparison among normalized spectra  $G'_{pp}(St_H)$  measured at the reattachment point and those by other authors is reported in Fig. 2.

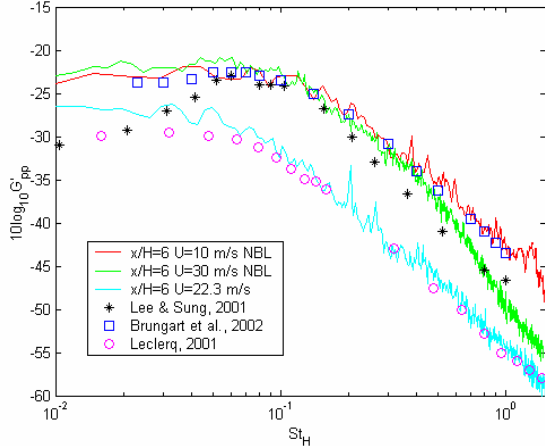


Fig. 2: Spectra comparison.

The reported reference measurements were obtained at the reattachment point downstream BFS, and the agreement with present data is satisfactory for both the natural (NBL) and the artificial boundary layer cases. It is also noticeable that the normalization adopted to obtain the  $G'_{pp}(St_H)$  is not sufficient to collapse the spectra, so the other parameters described in the previous sections have to be taken into account.

A typical spatio-frequency pressure spectrogram in the cavity (Fig. 3) shows that the energy content is concentrated at low frequencies while the spectra amplitude is modulated by the  $SPL$  distribution.

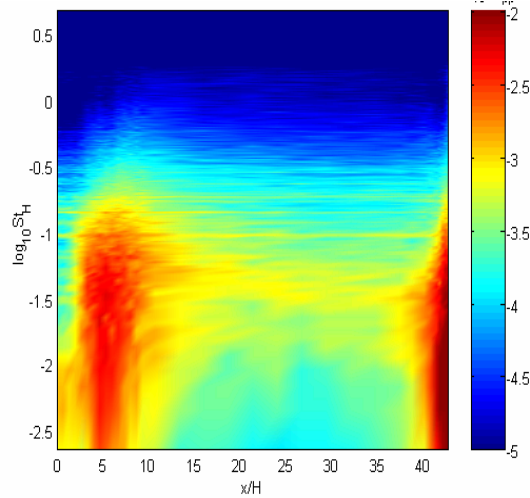


Fig. 3: Pressure spectrogram.

This result supports the idea presented in the previous sections where the scaling of the spectra is obtained by normalizing their amplitudes in terms of the function  $\Psi$ , which reproduces the  $SPL$  distribution along the cavity. The thin horizontal lines that can be observed in the picture represent some background noise not completely eliminated by the correction procedure.

The  $SPL$  distributions along the cavity model, for different flow conditions, are reported in Fig. 4.

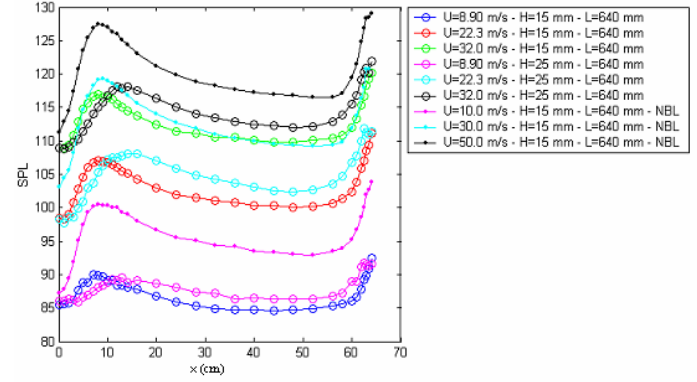


Fig. 4:  $SPL$  distributions along the cavity for different flow conditions.

In the different reported tests, steps' height, free stream velocity, steps' separation and incoming boundary layer thickness were varied and a clear influence on the  $SPL$  amplitude is observable. However, a similarity in shape of the  $SPL(x)$  is exhibited indicating that a collapse of the curves could be obtained by a proper rescaling. From the physical viewpoint, it is stressed that the first maximum of  $SPL$  occurs in the region of the average reattachment point of the separation bubble downstream the BFS (Fig. 1). The second maximum is located at the end of the step floor, just in front of the FFS; this maximum is probably due to the reattachment of the flow on the vertical face of the step. It is also shown that the second maximum is larger than the first one, thus indicating that the FFS configuration is more effective in emitting noise.

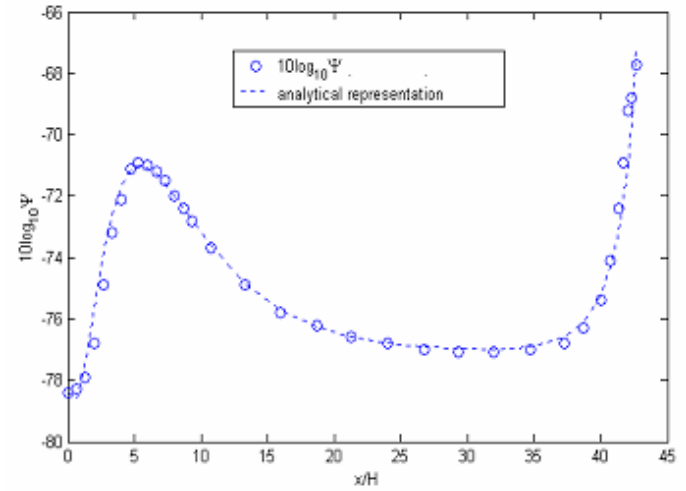


Fig. 5: Universal form function.

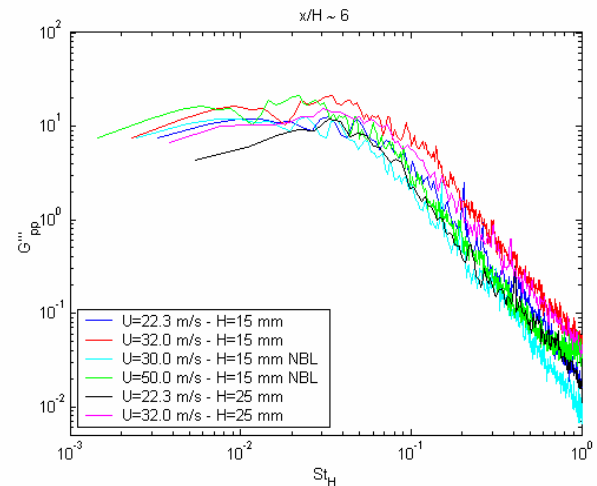


Fig. 6: Normalized spectra.

Applying the procedure described in the previous section the following exponents are obtained:  $\alpha_1 = -1.2$ ,  $\alpha_2 = -0.1$ ,  $\alpha_3 = -3.3$ .

The universal form function  $\Psi$  is exhibited in Fig. 5.

Using the calculated exponents  $\alpha_i$  and the universal function  $\Psi$ , the normalized spectra  $G'''_{pp}$  can be calculated at different  $x'$  positions (Fig. 6).

As it is possible to observe, the shape of the spectra is almost the same and a good collapsing is obtained.

As described in the previous section, averaging the normalised spectra  $G'''_{pp}$  on different test conditions and different  $x'$  positions, the universal form function can be extracted by a best fitting procedure, based on the minimization of the mean square error: all the considered spectra are included, except those ones used for the validation purposes (Fig. 7).

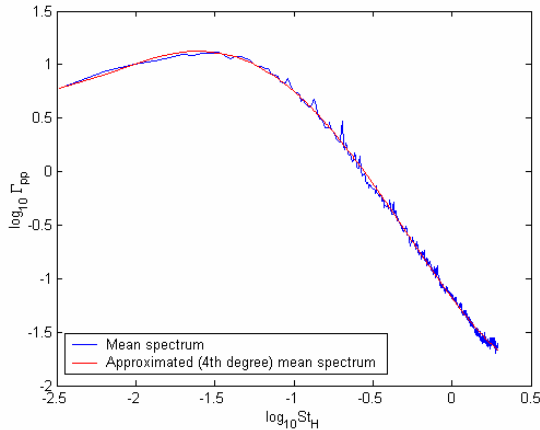


Fig. 7: Universal shape for the pressure spectrum.

The validation of the proposed model for the calculation of the noise  $SPL$  in a cavity is conducted using the model to simulate the considered cases, and comparing the simulated results with the measured and conditioned  $SPL$ . The mean difference between the simulated and measured  $SPL$ , evaluated from all the test cases and positions, is lower than 1.4 dB. An example of the comparison between simulated and measured spectra is reported in Fig. 8. The comparison is relative to a streamwise position where the agreement between measured and simulated quantities is good but (as already mentioned) this is not true very close to the vertical side of the BFS.

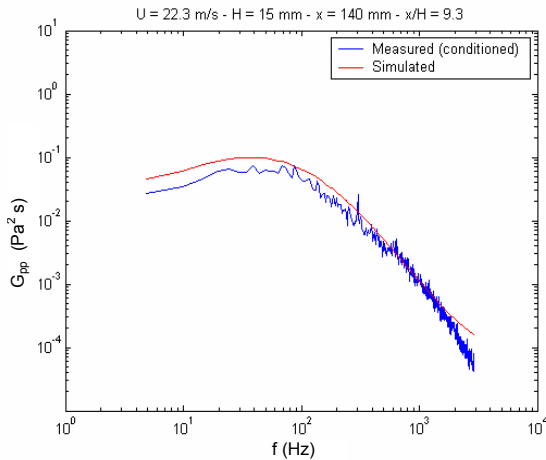


Fig. 8: Measured and simulated pressure spectrum

## Conclusions

In the present report, results aimed to the aeroacoustic characterization of TBL on a surface with geometrical irregularities have been presented. The experimental analysis was conducted on a two-step (backward/forward facing step) large aspect-ratio cavity and the main results obtained are summarized as follows.

- The dimensional analysis allowed individuating six relevant parameters influencing the aeroacoustic behaviour.
- From the physical viewpoint, the  $SPL$  distributions along the plate evidenced that the dimensionless reattachment point downstream the first BFS is weakly influenced by the dimensionless parameters and it is always located at 5-6H. Furthermore it is observed that the maximum  $SPL$  is reached in the vicinity of the second step, thus confirming that the FFS is more effective in emitting noise. We argue that the largest noise emission at the second step are not attributed to localized fluid dynamic events, but rather to acoustic effects probably related to the reattachment of the flow at the vertical wall.
- The experimental results confirmed that the variables separation approach is appropriate. Indeed, both the wall pressure spectra and  $SPL$  distributions along the cavity show a satisfactory similarity in their shape, at least within the regions not too close to the two steps, where re-circulations occur. The spectra dependence upon the dimensionless parameters is determined by power laws (yielding to a linear dependence in terms of  $SPL$ ) and an optimisation procedure was applied to retrieve the best (in terms of minimum error) scaling exponents. Furthermore, it was found that the parameter  $L/H$ , being asymptotic, can be neglected, while the exponent of the  $Re_H$  number is very small and thus this number does play a weak role.

## References

- [1] Bendat, J.S., Piersol, A.G., *Random Data: Analysis and Measurements Procedures*, Wiley Interscience, 1986.
- [2] Efimtsov, B.M., Kozlov, N.M., Kravchenko, S.V., Anderson, A.O., Wall Pressure Fluctuation Spectra at Small Forward-Facing Step, *Proceedings of the 5th AIAA/CEAS Aeroacoustics Conference - AIAA paper 99-1964*, Bellevue, WA, USA, 1999.
- [3] Lauchle, G.C., Kargus, W.A., Scaling of Turbulent Wall Pressure Fluctuations Downstream of a Rearward-Facing Step, *J. Acoust. Soc. Am.*, **107**, 2001, L1-L6.
- [4] Leclercq, D.J.J., Jacob, M.C., Louisot, A., Talotte, C., Forward-backward Facing Step Pair: aerodynamic flow, wall pressure and acoustic characterisation, *Proceedings of the 7th AIAA/CEAS Aeroacoustics Conference - AIAA paper 2001-1249*, Maastricht, The Netherlands, 2001.
- [5] Lee, I., Sung, H.J., Characteristics of Wall Pressure Fluctuations in Separated and Reattaching Flows over a Backward-Facing Step – Part I, *Exp. Fluids*, **30**, 2001, 262-272.

## Analysis of the propeller wake by pressure and velocity correlation

M. Felli<sup>1</sup> and F. Di Felice<sup>1</sup>

<sup>1</sup>INSEAN, Italian Institute for Naval Studies and Testing  
Via di Vallerano 139, 00128 Rome, ITALY

G. Guj<sup>2</sup>, R. Camussi<sup>2</sup>

<sup>2</sup>Department of Mechanical and Industrial Engineering  
"Roma Tre" University, Via della Vasca Navale 79, 00146 Rome, ITALY

### Abstract

In the present study an experimental analysis of the velocity and pressure fields behind a marine propeller, in non cavitating regime is reported. Velocity measurements were performed in phase with the propeller angle by using 2D Particle Image Velocimetry (2D-PIV). Measurements were carried out arranging the light sheet along the mid longitudinal plane of the propeller, to investigate the evolution of the axial and the radial velocity components, from the blade trailing edge up to 2 diameters downstream. The pressure measurements were performed at four radial and eight longitudinal positions downstream the propeller model. Measurements of the pressure field were performed at different advance ratios of the propeller. Pressure data, processed by using slotting techniques, allowed to reconstruct the evolution of the pressure field in phase with the reference blade position. In addition, the correlation of the velocity and pressure signals was performed.

The analysis demonstrated that, within the near wake, the tip vortices passage is the most important contribution in generating the pressure field in the propeller flow. The incoming vortex breakdown process causes a strong deformation of the hub vortex far downstream the slipstream contraction. This process contributes to the pressure generation at the shaft rate frequency.

### Introduction

In the last years, the accurate analysis of the fluctuating pressure and velocity fields, induced by a marine propeller, is required by the increase of both the power of the ship and the demand for a more comfortable vessel.

With the present emphasis on increased ship speeds and consequently much higher propeller thrust, in fact, hydrodynamic-induced noise and vibrations has become a very important problem both in navy and civil naval architecture. Vibratory forces, which are predominantly applied at the blade frequency, have frequently caused local structural failure by producing fatigue and, in many cases, have precluded the occupancy of parts of passengers vessels because of the noise and discomfort correlated to the resonance of decks and bulkheads.

The problem of reducing propeller induced noise and vibration leads to an increased complexity of blade geometry, primarily due to the low aspect ratio and to the skew, and have implied a rising interest on detailed measurements of the propeller flow field, to be used for both new design approach as well as for analysing propulsive, hydro-acoustic and structural performances.

The pressure on the stern bottom of the hull, generated by a propeller, is strictly related to the induced velocity field, therefore a detailed flow field analysis, relating the flow structures and the pressure signal, is required to improve the knowledge on the noise mechanism.

On the other hand, the experimental investigation provides baselines to improve and integrate theoretical predictions and to

support the flow modelling and the validation of computational codes (BEM, RANS, LES).

The flow field analysis around a propeller is complicated by many factors as unsteadiness, three-dimensionality, and high levels of turbulence. These properties has been pointed out in many previous Laser Doppler Velocimetry (LDV) measurements ([1], [2], [3], [4], [5]), but none of previous studies have been aimed in correlating the velocity field with the pressure signal. In the present study the pressure signals were correlated with the flow structures of the propeller slipstream, like the tip and hub vortex and the blade wake. The correlation between the velocity field and the pressure at a point is performed by using 2D-PIV and hydrophones.

A Wageningen modified type model propeller (INSEAN E779A) was selected for the present research project for two main reasons. First, this model propeller has been widely studied with the most advanced flow measurement and visualization techniques, such as LDV ([3], [5]) and PIV [6]. A large amount of data has been collected providing a thorough documentation on the non-cavitating flow characteristics: the propeller geometry, LDV data and PIV data are now freely available for downloading at <http://crm.insean.it/E779A>.

### Facility and propeller model

Measurements were conducted in the Italian Navy Cavitation Tunnel (C.E.I.M.M.). This is a close jet tunnel with a 2.6 m long by 0.6 m span by 0.6 m deep test section. Perspex windows on the four walls enable optical access.

The nozzle contraction ratio is 5.96:1 and the maximum water speed is 12 m/s. The highest free stream turbulence intensity in the test section is 2% and, in the adopted test condition, reduces to 0.6% in the propeller blade inflow at 0.7 r/R, being r the radial coordinate and R the propeller radius. In the test section, the mean velocity uniformity is within 1% for the axial component and 3% for the vertical component.

The four blades propeller model E779A is skewed, with a uniform pitch (pitch/diameter=1.1) and with a forward rake angle of 4° 3". A reference system O-XYZ, with the X axis along the tunnel centerline, the Y axis along the upward vertical, the Z axis along the horizontal towards starboard is adopted.

Two dimensionless groups govern the propeller flow field in non-cavitating conditions: the advance ratio  $J=U_\infty/2nR$ , where  $U_\infty$  is the free stream velocity, n the revolution frequency and 2R the diameter of the propeller, and the Reynolds number  $Re=C_{0.7}V_{0.7}/\nu$ , where  $C_{0.7}$  and  $V_{0.7}$  are respectively the cord of the blade and the velocity at 0.7 r/R and  $\nu$  the kinematic viscosity.

### PIV measurements experimental set up

A sketch of the PIV experimental set up is reported in figure 1. The propeller model is mounted on a front dynamometer shaft. This arrangement of the propeller and the length of the test

section, which is about 15 times the propeller diameter, allows the slipstream to develop freely in the downstream direction as in a real operative condition. An encoder, with a resolution of  $0.1^\circ$ , mounted on the dynamometer shaft, feeds a special signal processor which provides a trigger signal to a special synchronising device for each propeller angular position. The synchroniser provides a TTL trigger signal to a cross-correlation camera (1008 by 1018 pixel), and to a double cavity Nd-Yag laser (200 mJ per pulse at 12.5 Hz each), to allow image acquisitions for each propeller angular position. The digital cross-correlation video camera, allows the recordings of two separate images (one for each laser pulse) within a few microseconds at a maximum camera frame rate of 15.0 Hz. By using cross-correlation, the directional ambiguity is completely removed. The instantaneous velocity fields were acquired from a distance up to 700 mm from the side window, using a 60 mm lens with 2.8 f-number and imaging an area of about 100 mm by 100 mm.

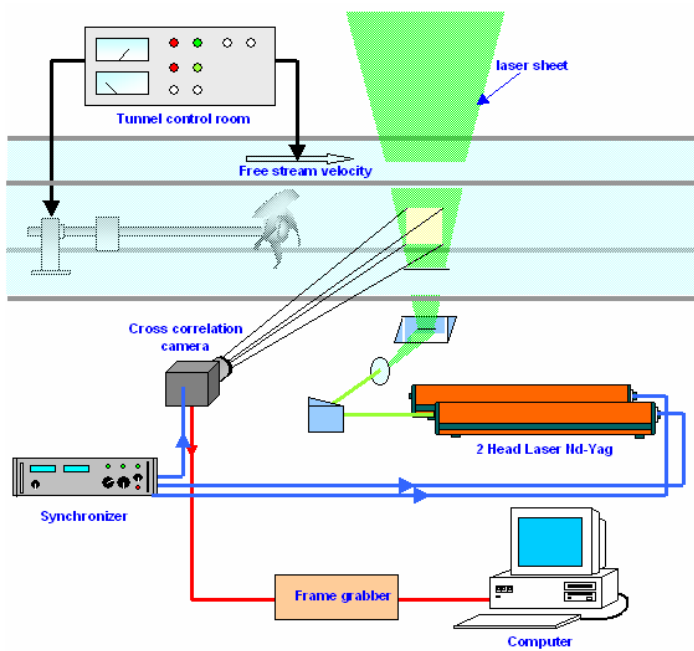


Figure 1. PIV measurements experimental set up.

The tracer particles are one of the critical aspects of the PIV technique, especially in case of large facilities. Since the technique is based on the measurement of particle displacement, it is fundamental that the seed accurately follows the water flow velocity. This requires particles having a diameter on the order of some  $\mu\text{m}$ . At the same time, it is mandatory to achieve a high uniform seeding density in the region of interest, at least 15 particle pairs per interrogation window, in order to accurately perform auto/cross correlation analysis. To this purpose, the water in the tunnel was initially filtered, and then seeded with  $10\text{ }\mu\text{m}$  silver coated hollow glass spherical particles with high diffraction index and density of about  $1.1\text{ g/cm}^3$ . The PIV system was arranged to measure, in the mid longitudinal plane of the propeller, the axial and vertical velocity components simultaneously in the tunnel frame. In view of the symmetry of the propeller inflow and of the steady conditions, when the light sheet is located on the vertical radius (along the z-axis), the axial component of the velocity and the vertical one correspond respectively to the axial and the radial components in the propeller moving frame.

To investigate the propeller wake up to 2 diameters downstream the blades trailing edge, the measurements were performed over 3 adjacent windows by traversing the camera (with an accuracy

of about 0.1 mm). The initial reference position was fixed with an accuracy of about 0.5 mm by imaging a special target device.

### Pressure measurements experimental set up

Pressure measurements have been performed by using hydrophones (Brüel & Kjær 8103 models), with a frequency response flat till 20 kHz and a diameter of 3.5 mm. These transducers are sensitive to the pressure fluctuations in the range from 0.3 Hz to 20 kHz, and hence are capable to measure the fluctuations of the total pressure. Hydrophones have been mounted on a special rake device, shown in figure 2. The transducers outputs were amplified by four conditioner-amplifiers Brüel & Kjær 2650 with band pass filter (0.3 Hz÷20 kHz), connected with the acquisition system and a spectral analyzer. Simultaneously, the TTL signal was acquired to synchronize the angular position of the reference blade. The hydrophones signals were acquired for 50 s at the sample rate of 40 kHz.

The pressure measurements were performed at four radial and eight longitudinal positions downstream the propeller model. Pressure signals acquisition was performed at different propeller conditions  $J=0.748, 0.814, 0.880, 0.940, 1.012$  that correspond to  $Re$  ( $Re \times 10^6$ ) 1.14, 1.15, 1.17, 1.80, 1.20. Correlation between pressure signal and velocity field has been performed only for  $J=0.88$ .

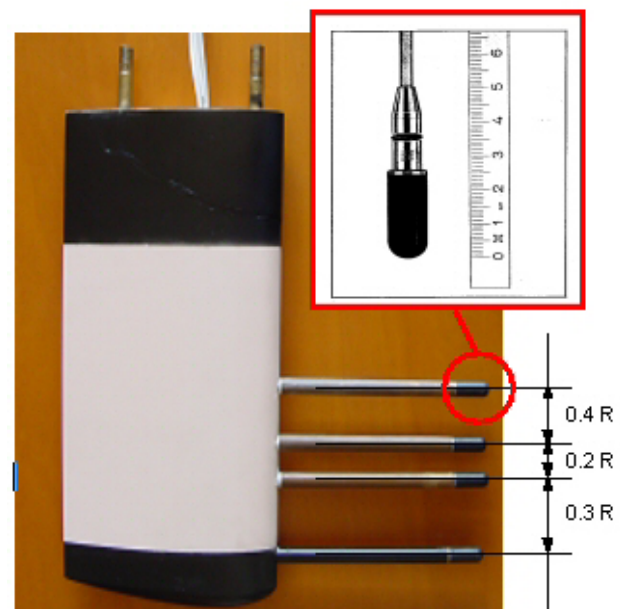


Figure 2. Hydrophones arrangement.

### Experimental results

In the following we will focus on pressure measurement results and in the correlation of the pressure signal with the flow structures.

More information about the flow field measured by PIV can be found in [6].

Figure 3 shows the pressure coefficients at different radial positions, for the longitudinal station  $x/R=1.0$ . The signals show a different behavior and amplitude as a consequence of the different interaction with the flow structures of the propeller wake.

An example of the pressure signals and the flow field measured by PIV for the angular position  $\theta = 20^\circ$  is reported in figure 3 (where  $\theta$  denotes the reference blade angular position).



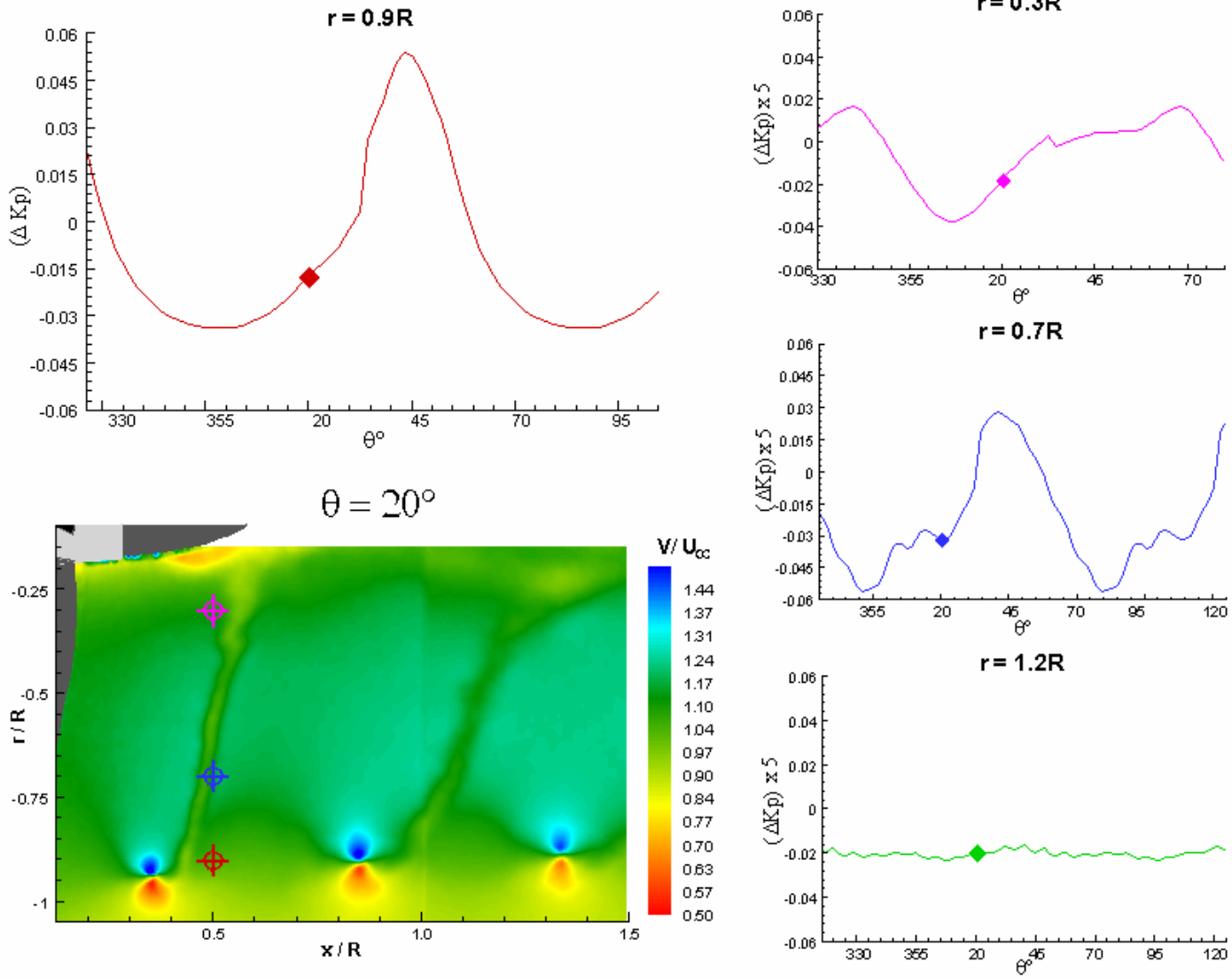


Figure 3. Correlation between velocity field, by PIV images, and pressure signal at  $\theta=20^\circ$ .  
The longitudinal station corresponds to  $x/R=1.0$ .

The contour plot represents the magnitude of the in-plane velocity components normalized with the freestream velocity. The main flow structures, like the viscous wake shed from the blade trailing edge, the tip and the hub vortex, are clearly apparent.

In the same figures the pressure at the hydrophones locations is also highlighted. Specifically, the plots report the angular variation, at different radial positions, of the pressure coefficient fluctuations  $\Delta k_p$  defined as:

$$\Delta k_p = \frac{\Delta P}{\rho \cdot n^2 \cdot D^2} \quad (1)$$

where  $\Delta P$  is the total pressure fluctuations. It is shown that the pressure signal at  $r/R=0.3$  is influenced by the blade wake passages and by the hub vortex evolution. In the same way, at  $r/R=0.7$ , the signal consists of large scale fluctuations caused by the passage at the hydrophone location of the low pressure flow, coming from the face of the propeller and small scale fluctuations due to the passage of the blade wake.

The maximum values of the pressure coefficient are achieved at  $r/R=0.9$  simultaneously to the passage of the tip vortex core, pointing out that the tip vortex is the most important pressure fluctuations source in the propeller wake at  $x/R=1.0$ . In fact pressure fluctuation peaks are one order of magnitude larger at  $r/R=0.9$  with respect the other locations. At  $r/R=1.2$  the pressure fluctuation is very low being the transducer out the slipstream tube. Close to the trailing edge of the propeller and for all the

radial positions the pressure signals are dominated by the blade rate.

The described behaviour changes downstream the contraction due to the vortex breakdown mechanism. At this purpose, figure 4 shows the amplitude of the blade rate and shaft harmonics, for the radial position  $r/R=0.3$  (top of figure 4) and  $r/R=0.9$  (bottom of figure 4). The analysis points out that near the hub ( $r/R=0.3$ ), 2-3 diameters downstream the propeller, a different mechanism is contributing to the generation of the pressure signal. In fact the transfer of the energy from the blade to the shaft rate harmonics is strictly related to the vortex breakdown mechanism, as shown in [6]. Downstream the contraction a separation of the trajectory of the tip vortices, due to the different blades and a strong spiralling and deformation process of the hub vortex, occurs. The slipstream starts to lose its axis-symmetry and blade periodicity but in the first phase of the breakdown still maintains the phase with the shaft revolution. This behaviour is probably due to the mutual tip-hub vortex interaction, as demonstrated by their simultaneous generation.

The phase analysis of the correlation between the turbulence field with the standard deviation of the pressure signal  $(\Delta k_p)_{std}$  has been also conducted. An example of the achieved results is reported in Fig. (5).

This analysis outlined the following points clarifying the wake characteristics:

1. The highest values of the pressure standard deviation are related to the highest values of the turbulence intensity and mainly concentrated, for  $r/R=0.9$ , in the tip vortex core;



2. Turbulent blade wake, downstream of the propeller, is quickly diffused and dissipated by viscous effects. Nevertheless the standard deviation plots show two peaks associated respectively to blade wake and tip vortex passages. The maximum values are achieved in correspondence of the tip vortex core;
3. The standard deviation of the pressure fluctuation in the downstream direction raises as a consequence of the largest turbulent fluctuation achieved in the tip vortex core far downstream the propeller. This effect is related to the vortex breakdown instability as shown in [6].

## Conclusions

The performed experimental study allows correlating the propeller flow field structures, like the blade wake and the tip vortex, with the pressure signal at a point. The results point out that, within the slipstream contraction, the highest values of the pressure fluctuations are in correspondence of radial position  $x/R=0.9$ , in coincidence with the tip vortex passage. Thus this flow structure is the most important one in generating the hydrodynamic pressure field in the propeller flow.

Far downstream the slipstream contraction the vortex breakdown occurs and the strong deformation of the hub vortex contributes in the pressure signal generation at the frequency of the shaft rate.

The standard deviation of the pressure signal shows the presence of two peaks, with different intensity, due to blade wake and tip vortex passage. Furthermore, the increased values of the standard deviation in the downstream evolution point out the vortex instability phenomena as also shown by the turbulence distribution.

## Acknowledgments

The authors are grateful to the CEIMM personnel who supported the PIV measurements. This work was sponsored by Italian Ministero delle Infrastrutture in the frame of INSEAN Research Plan 2000-2002.

## References

- [1] Min K. S. (1978) "Numerical and experimental methods for prediction of field point velocities around propeller blade" *Department of Ocean Engineering Report 78-12*, MIT.
- [2] Kobayashi S. (1982) "Propeller wake survey by laser doppler velocimeter" *First International Symposium on the Application of Laser Anemometry to Fluid Mechanics*, Lisbon.
- [3] Cenedese A., Accardo L., Milone R. (1985) "Phase sampling techniques in the analysis of a propeller wake" *First International Conference on Laser Anemometry: Advances*

and Application, BHRA Fluid Engineering, Manchester.

- [4] Hoshino T., Oshima A. (1987) "Measurement of flow field around propeller by using a 3-component laser doppler velocimeter" *Mitsubishi Tech Rev* 24(1): 46-53.
- [5] Stella A., Guj G., Di Felice F., Elefante M. (2000) "Experimental investigation of propeller wake evolution by means of LDV and flow visualizations" *Journal of Ship Research*, 44 (3): 159-173.
- [6] Di Felice F., Di Florio D., Felli M., Romano G.P. (2004) "Experimental Investigation of the Propeller wake at different Loading Condition by PIV" *Journal of Ship Research*, 48 (2): 168-190.

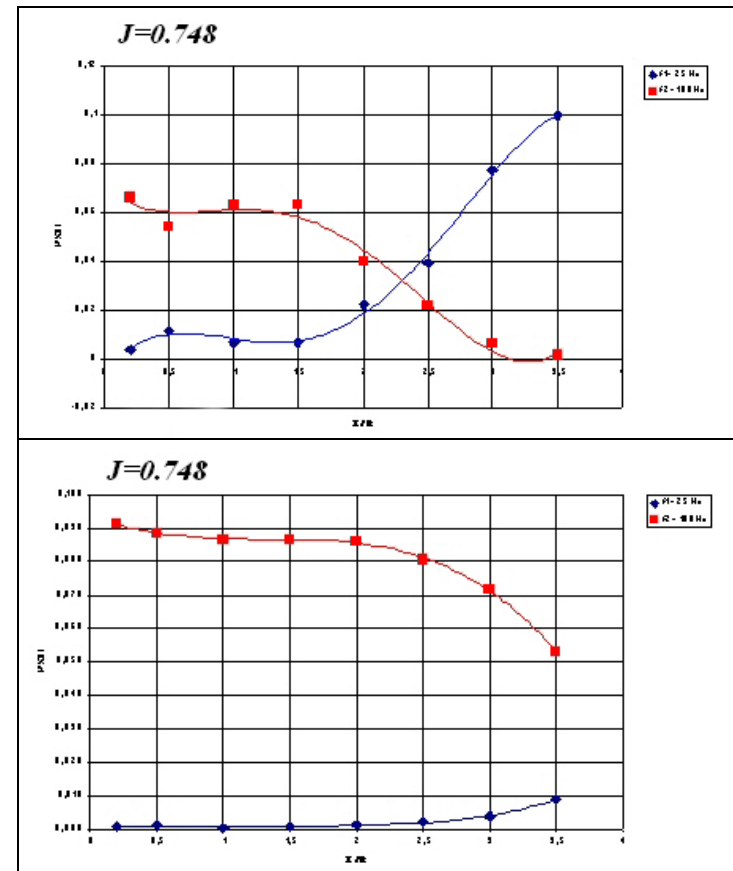


Figure 4. Amplitude of blade rate and shaft harmonics.

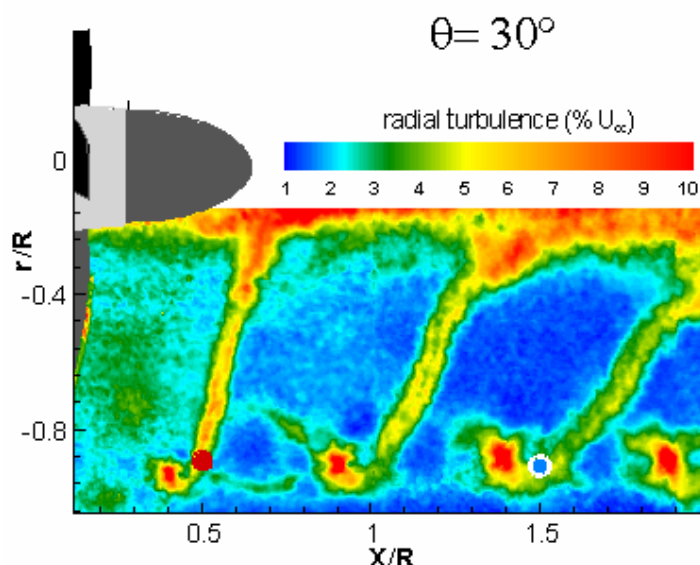
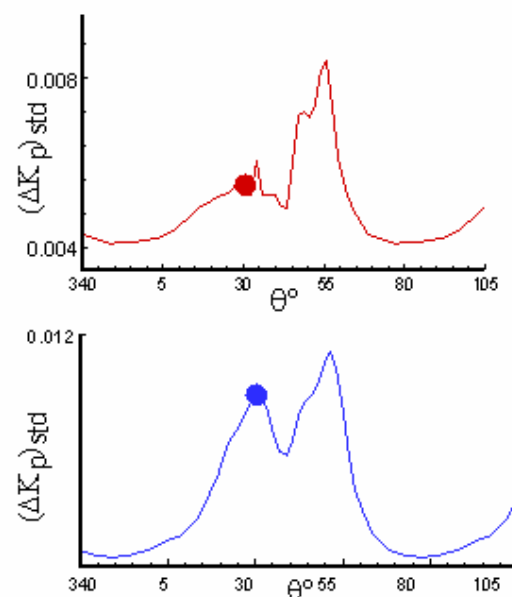


Figure 5. Correlation between turbulence and pressure signal standard deviation at  $\theta=30^\circ$ .



## Dominant spanwise Fourier modes, and the existence of very large scale coherence in turbulent boundary layers

N. Hutchins, B. Ganapathisubramani and I. Marusic

Department of Aerospace Engineering & Mechanics, University of Minnesota, Minneapolis, 55455 MN USA

### Abstract

Multiple plane stereo PIV results and data from a rake of ten hot-wire probes are used to investigate the largest scale structures in a zero-pressure-gradient turbulent boundary layer. Instantaneous vector fields from stereo PIV in spanwise-streamwise planes reveal long low- and high-speed regions, with a length that often exceeds the viewing window ( $> 2\delta$ ). Also evident is a remarkable degree of spanwise organisation, that manifests as a persistent spanwise stripiness in the  $u$  component of the PIV vector field. Almost all trace of such spanwise organisation is lost in the mean statistics, presumably due to the multitude of scales naturally present in wall-bounded turbulence. This can be overcome by ‘de-jittering’ the instantaneous vector fields. By sorting the data according to dominant spanwise Fourier modes, and then applying simple statistical tools to the sorted subsets, we are able to extract a clear view of spanwise organisation. Results are confirmed in the various PIV data-sets. Since the PIV fails to adequately capture the full streamwise extent of the low-speed regions, a rake of hot-wire probes is also employed to capture a continuous view of the spanwise coherence. It is found that the low-speed regions are in fact extremely persistent in the streamwise direction, often exceeding  $20\delta$  in length. The fact that these long features meander appreciably in the spanwise direction will limit the overall streamwise length-scale as witnessed by a single probe or single point statistic. For instance, premultiplied one-dimensional spectra of the streamwise velocity ( $k_x\Phi_{uu}$ ) at this  $z/\delta$  show a peak contribution for characteristic lengthscales of  $5 - 7\delta$ .

### Introduction

It is well documented that a streaky structure with an average spanwise streak spacing of approximately 100 wall units exists in the near-wall region of turbulent boundary layers (See [8] for review). Further from the wall, two-point correlations obtained from hot-wire data ([10, 7]) have consistently indicated a larger spanwise structure in the log and wake regions (scaling on  $\delta$  and increasing in size with distance from the wall). Prior to the advent of PIV, the precise form of these log-region structures was largely unproven, although statistics based on fluctuating  $u$  signals at these heights (particularly the peak in the pre-multiplied energy spectra  $k_x\Phi_{uu}$  and the long tails in the autocorrelations) had long hinted at the existence of long regions of uniform streamwise momentum. PIV measurements in the streamwise-spanwise plane revealed that the log region is indeed characterised by its own streaky structure (eg [9]), albeit of a much larger scale. Long regions of streamwise momentum deficit are found, with high-speed fluid seeming to fill the separation between neighbouring motions. Further PIV investigations have suggested that these long modes of uniform momentum deficit are associated with packets of hairpin vortices [1, 3]. The low speed regions are found to be of the order  $0.4 - 0.5\delta$  wide, and typically have a length that exceeds the streamwise extent of the PIV frame (usually limited to  $\sim 2\delta$ ). More recent analysis of large numerical domain DNS results (in particular 2D spectra) have shown that  $\Phi_{uu}$  energy can reside in very long streamwise modes (certainly  $> 20\delta$ ) for larger  $k_y$  bands [2].

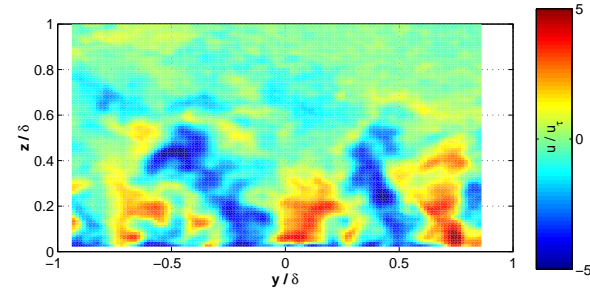


Figure 1: Example streamwise velocity field from  $45^\circ$  inclined plane. Color shading denotes velocity fluctuation.

### Facility

We investigate these scales using three separate datasets, all of which were obtained at the same Reynolds number ( $Re_\tau = 1100$ ) and in the same flow facility (open return suction-type boundary layer wind-tunnel of working section  $4.7 \times 1.2 \times 0.3$  m). The datasets comprise:

- i. Inclined plane cross-stream PIV measurements taken at both  $45^\circ$  and  $135^\circ$  to the  $x$ -axis.
- ii. Streamwise-spanwise plane PIV measurements.
- iii. Hot-wire measurements from a rake of 10 single wire sensors covering approximately  $1.14\delta$  in the spanwise direction.

The axis system  $x$ ,  $y$  and  $z$  refer to the streamwise, spanwise and wall-normal directions, with  $u$ ,  $v$  and  $w$  describing the respective velocity components. Dataset (i) is described in full detail in [5]. Dataset (ii) is described in [3]. Combined correlation results from (i) and (ii) are presented in [4].

### Interpreting two-point correlation $R_{uu}$

Figure 1 is an example streamwise velocity field from the  $45^\circ$  inclined plane. This frame is typical of the many hundreds of captures. Large eruptions of low-speed fluid (marked in blue) extend from the wall, often growing beyond  $z = 0.5\delta$ . Such regions are flanked in the spanwise direction by high-speed fluid (marked in red). There are also signs of weaker high-speed regions crowning the low-speed motions. Such arrangements are typical of inclined hairpin type structures (discussed in [5]). In Figure 1 the complete pattern repeats in the spanwise direction, giving a strong impression of spanwise periodicity. Such repetition is evident in many of the acquired vector fields.

Figure 2 shows the two-point correlation based on the streamwise velocity fluctuations ( $R_{uu}$ ) about the reference point  $z_{ref}/\delta = 0.14$ , for the same  $45^\circ$  inclined plane. The picture we see is familiar. A central region of positive correlation with a spanwise width of approximately  $0.5\delta$  is flanked by anti-correlated lobes, separated by approximately  $0.75\delta$ . These two length-scales seem to approximately correspond to the width and separation between the low- and high-speed regions

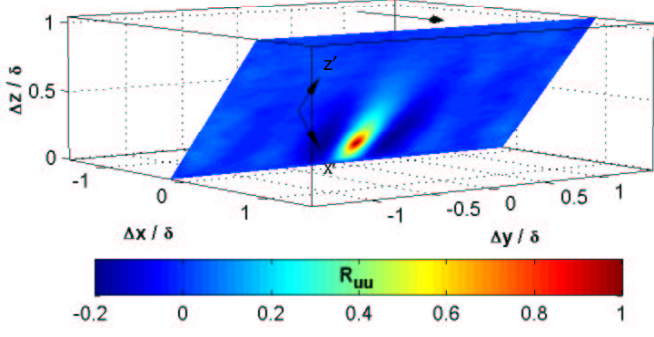


Figure 2:  $R_{uu}$  at  $z_{ref} = 0.14\delta$  for the  $45^\circ$  inclined plane data.

shown in Figure 1. If we calculate the spanwise energy in the streamwise velocity signal, a peak in the pre-multiplied spectra ( $k_y \Phi_{uu}$ ) is noted at a spanwise length-scale of approximately  $0.75\delta$ . It is incorrect at this stage to interpret this peak as signifying a true spanwise periodicity. Indeed it can be shown that a single low-speed region of width  $0.5\delta$ , flanked by similar sized high-speed regions could lead to such an energy peak. In other words, the velocity signature due to a single hairpin or hairpin packet, in the absence of any spanwise repetition of this pattern, could produce a similar two-point correlation and peak in the spectra. So the question we asked is *why doesn't the spanwise repetition so obvious in the instantaneous flow-fields manifest in the two point correlation as a spanwise ringing of the positive correlation region?* The reason of course lies in the multitude of scales that reside in turbulent flows. This causes a statistical smearing that masks any signs of repetition. To overcome this, a very simple method of sorting is proposed.

#### De-jittered data

The method is as follows:

- A spanwise trace of streamwise velocity fluctuation is extracted from each frame at a given reference height (in this case  $z_{ref} = 0.14\delta$ ).
- Fourier analysis of the extracted signal reveals the dominant spanwise mode in that particular frame.
- The frame is sorted or 'binned' according to the dominant mode ( $\lambda_y$ ).
- Two point correlations are conducted on the 'binned' (or de-jittered) sets of frames.

The bin sizes used are relatively broad ( $0.25\delta$  increments from 0 to 1.5). It is found that most of the energy resides in the first 4 modes, with  $0.5 < \lambda_y/\delta < 0.75$  being the most populated bin. Here  $\lambda_y$  is spanwise wavelength. Of the entire data-set, 37% of all frames exhibit a dominant spanwise  $u$  fluctuation of this wavelength. The two-point correlations as calculated on these first four modes are shown in Figure 3 plots (a - d). Note that these modes recover 93% of the total energy (93% of all PIV frames exhibit these spacing modes). With the data sorted in this way, there is clear evidence of ringing in the 'binned' two-point correlations indicating an underlying spanwise periodicity. This is perhaps expected along the line  $z = z_{ref}$ , however it is noted that these spanwise modes extend a considerable distance in the wall-normal direction ( $> 0.5\delta$ ). If we take the bin  $0.5 < \lambda_y/\delta < 0.75$  (plot b), the implication is that 37% of the PIV images have a large-scale spanwise periodicity, of repeating high- and low- momentum regions, extending a considerable distance across the boundary layer. Note that this is raw unfiltered data. Yet 93% of all frames are well described by a

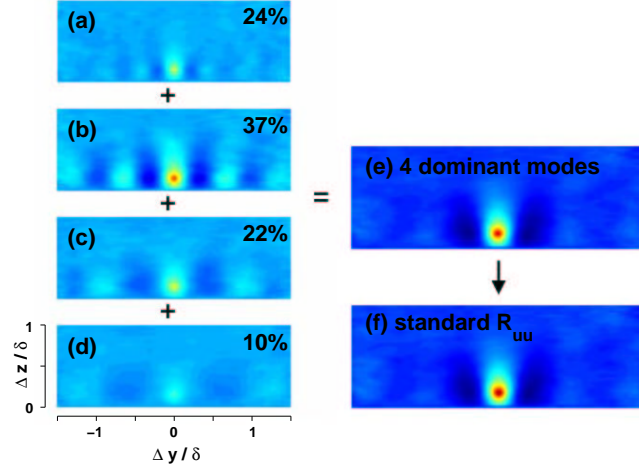


Figure 3:  $R_{uu}$  calculated at  $z_{ref} = 0.14\delta$  for each of the four dominant modes (a)  $0.25 < \lambda_y/\delta < 0.5$ ; (b)  $0.5 < \lambda_y/\delta < 0.75$ ; (c)  $0.75 < \lambda_y/\delta < 1.0$ ; (d)  $1.0 < \lambda_y/\delta < 1.25$ . (e) shows the sum of these four modes as compared to (f) the standard  $R_{uu}$ .

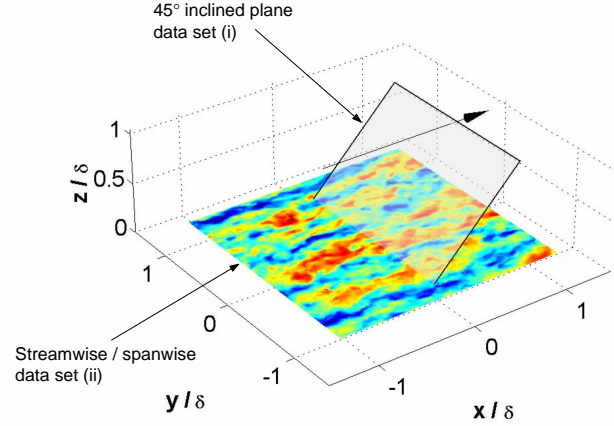


Figure 4: Example  $u$  velocity fluctuations from streamwise / spanwise plane PIV. Color shading as Figure 1.

single sinusoidal mode for all of the log region and slightly beyond (up to  $0.5\delta$ ). It is worth noting that despite the fact that repeating modes characterise the majority of the data, the superposition of the individual modes leads to an  $R_{uu}$  plot that exhibits no obvious sign of spanwise periodicity. Therefore, care must be taken when interpreting statistical quantities, such as  $R_{uu}$ , where multiple scales interactions can mask underlying organization. As a final clarification of this, Figure 3(e) shows the sum of the 4 dominant modes which almost completely recovers the standard  $R_{uu}$  profile included as plot (f).

#### Spanwise-streamwise plane PIV data

The view of this large-scale spanwise periodicity can be further enhanced by applying the same de-jittering technique to data-set (ii). Figure 4 is an example of the  $u$  velocity fluctuation in the streamwise / spanwise plane. The spanwise stripiness observed by [9, 3] is evident. The data set is similarly 'binned' according to the dominant spanwise mode at the centre of the frame ( $x/\delta = 0$ ). Since data set (ii) was obtained at  $z/\delta = 0.14$ , the resulting  $R_{uu}$  results can be matched with the previous plots shown in Figure 3 (where  $z_{ref}/\delta = 0.14$ ), with the planes intersecting at the condition point  $x/\delta = 0$ . Figure 5 shows such a construct for the most populated bin ( $0.5 < \lambda_y/\delta < 0.75$ ).



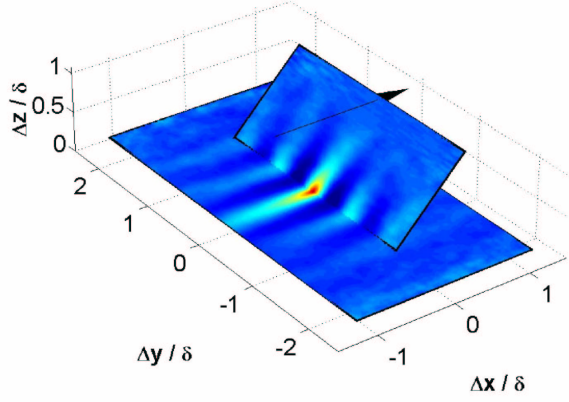


Figure 5:  $R_{uu}$  calculated from datasets (i) & (ii) at  $z_{ref} = 0.14\delta$  for the mode  $0.5 < \lambda_y/\delta < 0.75$

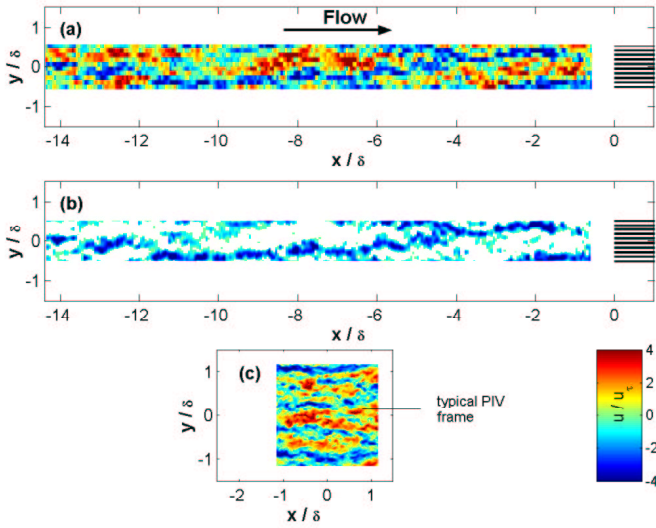


Figure 6: (a) Example signal section from ten sensor hot-wire rake at  $z/\delta = 0.14$ . Spatial view is reconstructed using local mean velocity ( $x = -U_c t$ ); (b) the negative momentum fluctuations only; (c) comparison with typical PIV frame.

Clearly the previously observed spanwise modes actually persist for a substantial distance in the streamwise direction, extending well beyond the  $x = \pm\delta$  view afforded by the PIV data.

#### Hot-wire data

A spanwise rake of ten single sensor hot-wire probes was inserted into the boundary layer at a height from the wall of  $z/\delta \approx 0.14$ . The ten sensors were separated by  $0.114\delta$  in the spanwise direction, such that the entire rake measured a spanwise domain just greater than one boundary layer thickness. The idea here is to use the fluctuating signals from the ten probes to reconstruct the instantaneous spanwise profile of the  $u$  velocity fluctuation. By projecting this signal in time and using Taylor's Hypothesis (frozen convection) a view of the long high- and low-speed regions can be constructed that covers a much larger streamwise domain than that available with PIV. An example section of the reconstructed field is shown in Figure 6(a). A typical size PIV vector field for this Reynolds number is also shown as plot (c). Clearly there are some very long features in the flow that the PIV data will fail to adequately capture. Figure 6(b) highlights the streamwise extent of the low-speed region by shading only those regions of negative velocity fluctuation. A long, meandering low-speed region wanders through the mea-

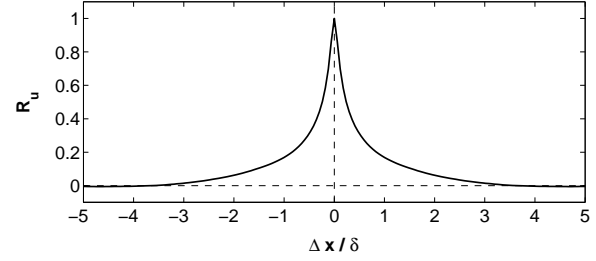


Figure 7: Autocorrelation curve from the fluctuating hot-wire  $u$  velocity signals. The spatial  $x$ -ordinate is obtained using Taylor's hypothesis and a convection velocity based on the local mean  $\bar{U} \approx 0.64U_\infty$ .

surement domain for the entire  $14\delta$  shown. Indeed when we run movies of the frozen turbulence as it advects past the probe array, there are many instances where the length of the low-speed regions exceed  $20\delta$ . There is a problem that the meandering often causes these regions to leave the spanwise limit of the domain ( $y/\delta = \pm 0.5$ ). This tends to curtail the maximum length of low-speed regions that we can track. To overcome this problem, and track the full extent of the very longest meandering features it would be useful to increase the spanwise domain measured by the rake to at least  $2\delta$ . At present we have no concrete statistics on the probability distribution of these large events. However, in the future, it is hoped that streak tracking algorithms can be developed to successfully identify these regions.

Figure 7 shows the autocorrelation for all ten probes. Note that the positive correlation region tends to fall to zero (becoming negative) for signal shifts  $\Delta x > 4\delta$ . Similarly the broad peak in the pre-multiplied streamwise spectra  $k_x \Phi_{uu}$  occurs for comparable length-scales. Such features in classical single point statistics have previously informed our view of the largest energetic scales in turbulent boundary layers. However the rake data, and in particular velocity maps such as those shown in Figure 6 (a & b), demonstrate that much larger scales inhabit the flow. It is proposed that these length-scales are not resolved by classical single point techniques due to a spanwise wandering or meandering in these structures. In fact there is a clue to such behaviour in the autocorrelation result shown in Figure 7, where there are signs of anti-correlated regions beyond signal shifts of approximately  $\pm 4\delta$ . Figure 8 clarifies this behaviour. A simple model of a long meandering low-speed region is shown, flanked on either side by high-speed regions. A region width of  $0.5\delta$  is chosen, with meandering amplitude and wavelength of  $0.6\delta$  and  $16\delta$  respectively. At this stage the precise form is arbitrary. However Figure 8(a) confirms that a long meandering feature would be witnessed by a single-point measurement as a much shorter event. Figure 8(b) shows the autocorrelation calculated on a randomly spaced array of such features (with a normal distribution of lengths about 0 to a maximum  $40\delta$ ). Despite the existence of what is essentially a very large scale feature, the positive correlation region seems to drop to zero (becoming negative) at a signal shift of  $\pm 3\delta$ . This represents something like the average streamwise path-length detectable through the low-speed event by a single-point measurement.

There is additional supporting evidence for these large meandering regions contained within the two-point correlation results. Figure 9(a) shows the  $R_{uu}$  map obtained from the hot-wire rake. Figure 9(b) shows the corresponding  $R_{uu}$  result from the streamwise-spanwise PIV data. Good general agreement is seen between the two, although the limited field of view of the PIV data is again evident. Even with the extended view afforded by the hot-wire data, the central positive correlation region drops to zero relatively quickly. This is previously predicted by the

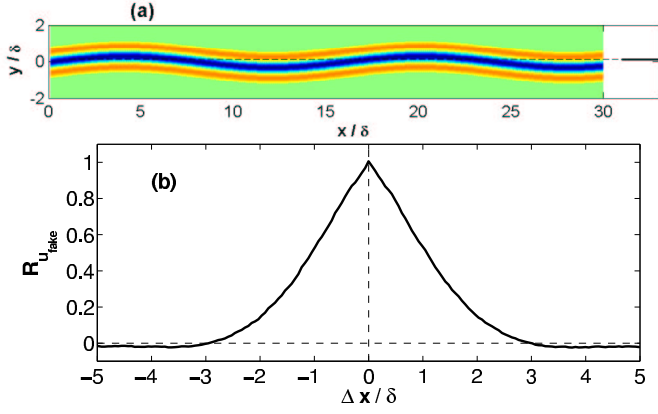


Figure 8: (a) Fake meandering high- and low-speed regions; (b) Autocorrelation associated with random distribution of such regions of varying lengths.

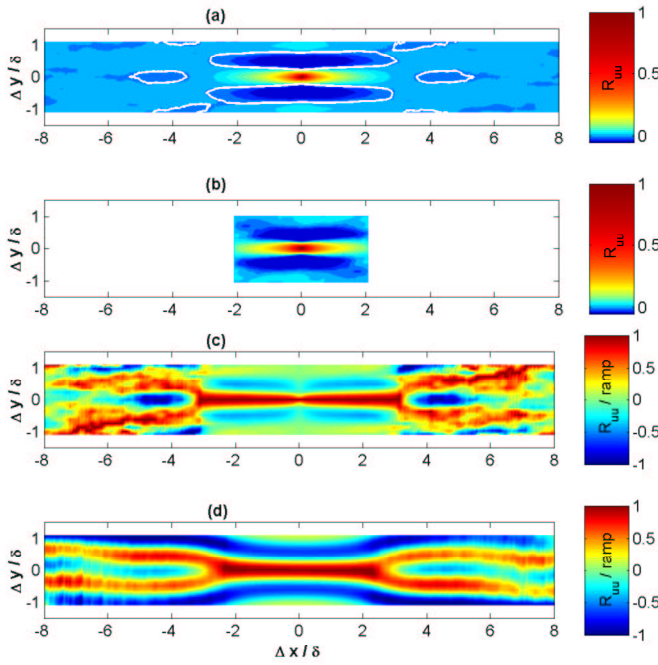


Figure 9: (a) Two-point correlation from hot-wire data (contours show  $R_{uu} = -0.002$ ); (b) same result from streamwise / spanwise PIV; (c) hot-wire correlation normalised by the ramp function ( $\max |R_{uu}(\Delta x)|$ ); (d) fake streak correlation normalised by ramp function.

autocorrelation results of Figure 7. However, there are weakly correlated regions forming a distinctive **X** shape across the  $R_{uu}$  map. Such features could not be resolved from the limited field PIV. These are difficult to see with the colour axis as shown in plot (a). However, we can highlight these features by normalising the  $R_{uu}$  map with the modulus of the maximum correlation value for any given spatial shift  $\Delta x$ . Normalising by this ramp function overcomes the problem of the rapid drop-off in absolute correlation magnitude as  $\Delta x$  is increased from the reference point. Plot (c) clearly exhibits some weak yet significant correlation behaviour in the far field, that could be due to a meandering motion in the largest scales. Figure 7(d) shows a similarly normalised two-point correlation result for the random array of idealised fake low-speed regions as introduced in Figure 8(a). The similarity between plots (c) and (d) would imply that the meandering streak is a reasonable model for these large-scale structures. We can state that a random array of meandering large-scale features can cause a similar two-point correlation result to that obtained from the hot-wire data.

## Conclusions

An analysis of the largest scale features in the log region of a turbulent boundary layer has lead to the following conclusions:

- Instantaneous spanwise  $u$  behaviour is well described by single spanwise sinusoidal modes extending a considerable distance in the wall-normal and streamwise directions
- There is a strong spanwise periodicity associated with the largest streamwise velocity fluctuations. Since, these velocity fluctuations are indicative of a wider vortical structure, such results would seem to have implications to flow control / prediction strategies, and may hold clues to the underlying structural dynamics.
- These large-scale features are extremely long in the streamwise direction (occasionally  $> 20\delta$ ) and seem to meander appreciably. The meandering effectively hides the true length of these features from single point measurement techniques.
- Such large-scale motions have previously been observed in pipe flows from single point measurements [6]. This raises the interesting possibility that the radial nature of pipe boundary layers acts to restrict spanwise meandering.

The authors gratefully acknowledge support from the National Science Foundation (Grant CTS-0324898) and the David and Lucile Packard Foundation.

## References

- [1] Adrian, R. J., Meinhart, C. D. & Tomkins, C. D., Vortex organization in the outer region of the turbulent boundary layer. *J. Fluid Mech.* **422**, 2000, 1–54.
- [2] DEL ALAMO, J. C., JIMENEZ, J., Spectra of the very large anisotropic scales in turbulent channels. *Phys. Fluids* **14**, 2004, 41–44.
- [3] Ganapathisubramani, B., Longmire, E. K. & Marusic, I., Characteristics of vortex packets in turbulent boundary layers. *J. Fluid Mech.* **478**, 2003, 35–46.
- [4] Ganapathisubramani, B., Hutchins, N., Hambleton, W. T., Longmire, E. K. & Marusic, I., Statistical analysis of turbulent boundary layer using two-point correlations. *J. Fluid Mech.* Submitted 2004.
- [5] Hutchins, N., Hambleton, W. T. & Marusic, I., Inclined cross-stream stereo PIV measurements in turbulent boundary layers. *J. Fluid Mech.* Submitted 2004.
- [6] Kim, K. C., Adrian, R. J., Very large scale motions in the outer layer. *Phys. Fluids* **11**, 1999, 417–422.
- [7] Mclean, I. R., The near-wall eddy structure in an equilibrium turbulent boundary layer. PhD thesis, University of Southern California, USA, 1990.
- [8] Robinson, S. K., Coherent motions in turbulent boundary layers, *Annu. Rev. Fluid Mech.* **23**, 1991, 601–639.
- [9] Tomkins, C. D., Statistics and structure of turbulence over smooth and rough walls. PhD thesis, University of Illinois, USA, 2000.
- [10] Wark, C. E., Naguib, A. M. & Robinson, S. K., Scaling of spanwise length scales in a turbulent boundary layer. *AIAA-paper* **91-0235**, 29th Aerospace Sciences Meeting, Reno, Nevada, 1991.

## Dual-plane PIV investigation of structural features in a turbulent boundary layer

I. Marusic, B. Ganapathisubramani and E. K. Longmire

Department of Aerospace Engineering & Mechanics  
University of Minnesota, Minneapolis, MN 55455, USA

### Abstract

Simultaneous dual-plane PIV experiments were performed in streamwise-spanwise planes in the log region of a turbulent boundary layer at a moderate Reynolds number ( $Re_\tau \sim 1100$ ). The acquired datasets were used to resolve all 9 velocity gradients from which the complete vorticity vector and other invariant quantities like 3-D swirl strength were computed. These derived quantities were used to analyze and interpret the structural characteristics and features of the boundary layer. Results of the vorticity vector and the 2-D swirl strength from the two neighbouring planes indicate the existence of hairpin shaped vortices inclined downstream along the streamwise direction. These vortices envelop low speed zones and generate Reynolds shear stress that enhances turbulence production. Plots of full 3D swirl strength indicate the existence of additional vortical structures in the middle of the low speed zones that may represent heads of smaller eddies intersecting the measurement plane. This concept is in accordance with the hierarchy of structure size in a hairpin packet proposed by Adrian *et al.* [2]. Computation of inclination angles of individual eddies using the vorticity vector suggests that most cores are inclined at  $25^\circ$  to the streamwise-spanwise plane with a resulting projected eddy inclination of  $32^\circ$ .

### Introduction

Over the past few decades, researchers have worked toward understanding the eddy structure within turbulent boundary layers in order to develop effective simplifying models. Recently, Adrian *et al.* [2] have reinforced the viewpoint that “hairpin vortices” are a primary feature in turbulence transport and production. The authors performed PIV experiments in streamwise-wall-normal planes of a turbulent boundary layer and found instantaneous signatures of heads of hairpin vortices. Most significantly, they observed that these vortices travelled together in spatially coherent groups, termed “hairpin packets”. Recently, Ganapathisubramani *et al.* [5], with stereoscopic PIV data in streamwise-spanwise planes, concluded that these hairpin packets occupy only a small percentage of the total area in the log layer, but contribute a significant proportion of the total Reynolds shear stress generated, conservatively more than 30%. Therefore, the hairpin packets are a very important mechanism in turbulence production. However, a detailed understanding of the three dimensional structure of hairpin vortices and packets is not yet available, and many questions regarding the shape, size, orientation and dynamics of these structures remain unanswered. The objective of the current experimental study is to obtain the full velocity gradient tensor over a plane in order to begin answering these questions.

### Experiment and methods

Experiments were performed in a suction type boundary layer wind tunnel. Measurement planes were located 3.3 m downstream of a trip wire in a zero-pressure-gradient flow with freestream velocity  $U_\infty = 5.3 \text{ m s}^{-1}$  and  $Re_\tau = 1060$  ( $Re_\tau = \delta U_\tau / \nu$ , where  $\delta$  is the boundary layer thickness,  $U_\tau$  is the skin friction velocity). All measured flow parameters shown in the

results section are normalized using the skin friction velocity ( $U_\tau$ ) and kinematic viscosity ( $\nu$ ) and are denoted with a superscript +. The streamwise, spanwise and wall-normal directions are along the  $x$ ,  $y$  and  $z$  axes respectively.

Two independent PIV systems capture data simultaneously in neighboring streamwise-spanwise planes separated by  $\sim 1 \text{ mm}$  (15 wall units) as shown in figure 1. System 1 is a stereoscopic system used to provide all three velocity components over a plane illuminated by Sheet 1, and System 2 is a single-camera planar PIV system. The single-camera system measures the streamwise-spanwise velocity components in the higher plane illuminated by Sheet 2. Simultaneous measurements are performed utilizing the polarization property of the laser light sheets to isolate one plane to one set of camera/cameras (see e.g. [9, 8, 3]). PIV data were captured in the log layer region of the turbulent boundary layer.

System 1 includes two TSI Powerview  $2k \times 2k$  pixel resolution cameras equipped with Nikon 50 mm lenses. The lenses are fitted with linear polarizers oriented to allow the passage of horizontally polarized light only. Light sheets for System 1 are generated by a pair of Nd:YAG lasers (120 mJ/pulse) that are horizontally polarized. System 2 includes one TSI Powerview camera with  $2k \times 2k$  pixel resolution and a Nikon 50 mm lens. The linear polarizers in this case are oriented to allow the passage of vertically polarized light only. The illumination source for System 2 is a pair of Nd:YAG (120 mJ/pulse) lasers of vertical polarization. The laser pairs in Systems 1 and 2 are aligned independently to illuminate a specific wall-normal location. The timing of each laser/camera system is controlled using a TSI synchronizer box. In order to ensure simultaneous capture of images, an external trigger is provided to both synchronizer boxes for image capture at a frequency of 0.2 Hz. The data from the two systems are streamed continuously to disk.

Vector fields are computed using a  $32 \times 32$  pixel window in both planes. The vectors from each camera in the stereo plane are then combined using suitable magnification factors to compute all three velocity components (see [4]). The vector field from the single camera is resampled and mapped to the grid of the stereo measurement using bi-linear interpolation. The resolution of the resulting vector fields is about  $18 \times 18$  wall units, and the total field size is  $1.8\delta \times 1.8\delta$ .

The single camera vector fields from the upper plane in liaison with the stereoscopic data from the lower plane are then used to compute all velocity gradients in the lower plane. A second order central difference method is used to compute all possible in-plane gradients while a first order forward difference is used to compute the wall-normal gradients of the streamwise and spanwise velocities. Finally, the continuity equation is used to recover the wall-normal gradient of the wall-normal velocity. With the out-of-plane gradients provided by the dual-plane data, we are able to compute the complete swirl strength and vorticity vector.



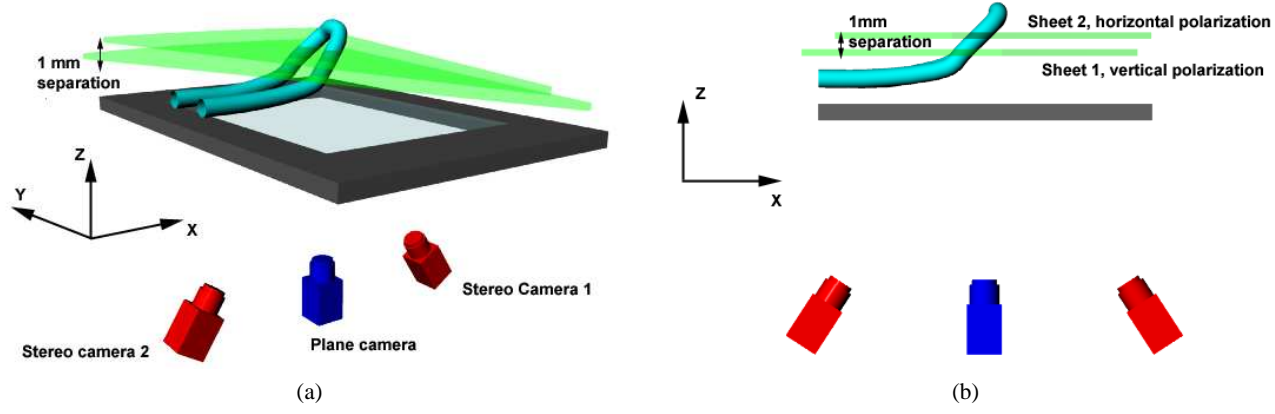
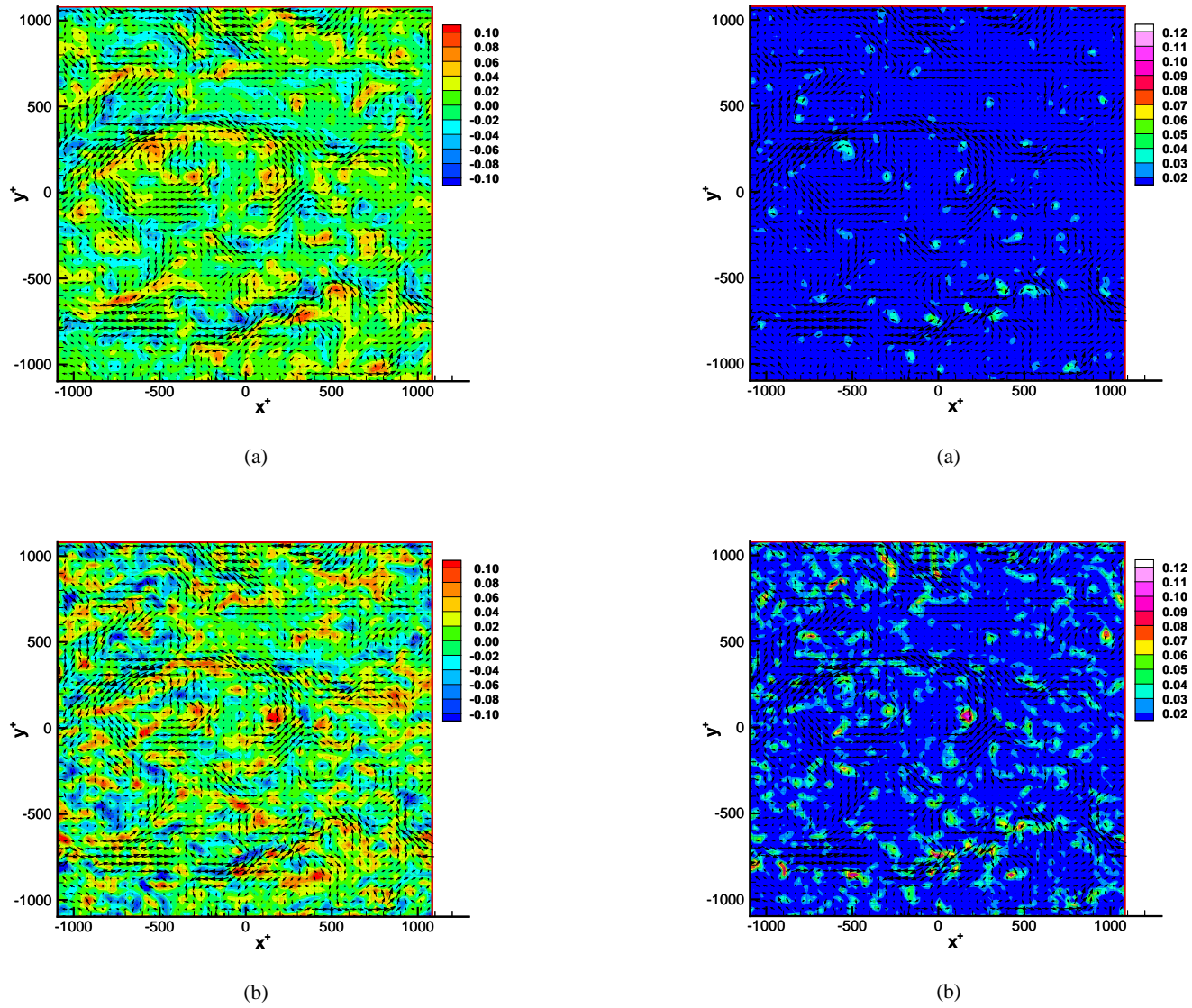


Figure 1: (a) Perspective view (b) side view of the experimental setup



## Results and Discussion

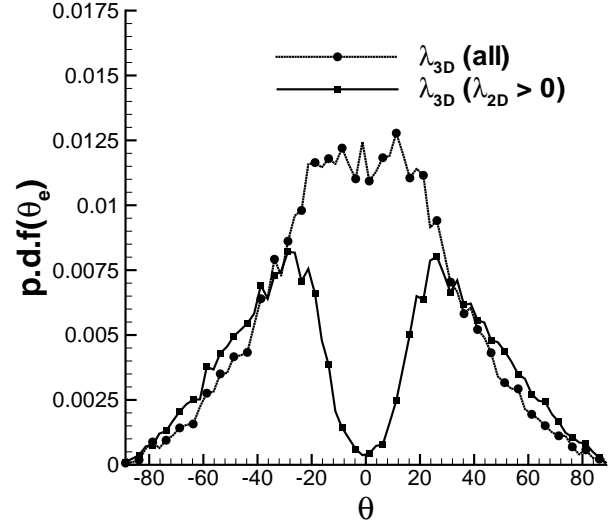
Examination of streamwise and spanwise velocities from the lower and upper planes reveals that the two planes are very well correlated. At this wall-normal position ( $z^+ = 125$ ) the streamwise velocity signature is typically seen to contain long low and high speed regions bordering one another in the spanwise direction. A typical field is shown in figures 2 and 3.

Contours of wall-normal vorticity ( $\omega_z^+$ , figure 2(a)) show that, in this orientation, the tops of low speed regions are typically enveloped by negative values and the bottoms by positive values. Also, the variations in vorticity strength seem to indicate that these regions of vorticity contain swirling motions indicative of vortex cores. These cores are noted as being predominantly inclined to the plane. This point becomes clear from the streamwise vorticity  $\omega_x^+$  plot (figure 2(b)). The regions of positive  $\omega_z^+$  have predominantly positive  $\omega_x^+$ , and regions of negative  $\omega_z^+$  have negative  $\omega_x^+$ . The data thus are consistent with the presence of vortices inclined at an angle with respect to the streamwise direction. We will refer to these inclined vortices broadly as hairpin vortices, which may or may not be symmetric. Note, however, that inclined hairpins are not the only type of instantaneous structures observed. Examination of various vector fields in the two neighbouring planes indicate evidence of some structures that are inclined at 90 degrees to the streamwise direction and others that are completely streamwise.

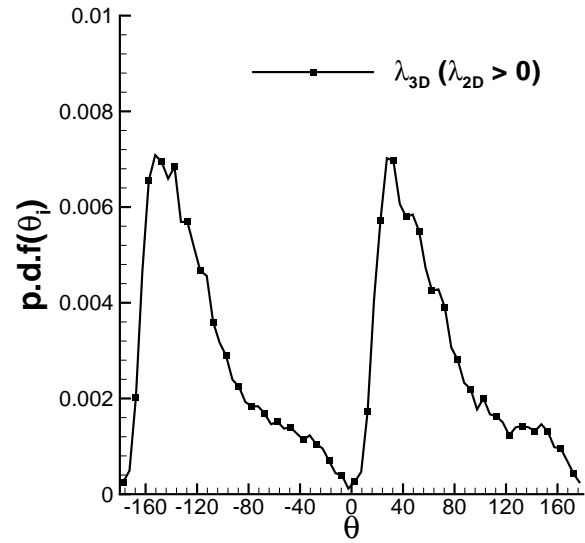
Figure 3(a) reveals the instantaneous two dimensional swirl strength ( $\lambda_{2D}^+$ ) at  $z^+ = 125$ . Two dimensional swirl strength is computed from the eigenvalues of the in-plane (2-D) velocity gradient tensor (see [1]) and is the measure of the swirling tendency of the flow. This plot in tandem with  $\omega_z^+$  (see figure 2(a)) shows that 2-D swirl isolates regions that are swirling about an axis aligned with the wall-normal direction. A visual comparison between the swirl in the lower and upper planes (not shown here) indicates a forward tilt to most structures as they are offset in the positive streamwise direction in the upper plane. It should be noted that  $\lambda_{2D}^+$  cannot identify vortices whose inclination angles to the plane are small. Figure 3(b) presents a plot of the full swirl strength ( $\lambda_{3D}^+$ , computed from the eigenvalues of the complete 3-D velocity gradient tensor [10]). The plot reveals that the 3-D swirl identifies not only the vortices cutting across the plane but also additional regions that are not isolated by 2-D (wall normal) swirl. These regions could possibly coincide with smaller hairpin vortices whose heads are cutting across the measurement volume and hence are not apparent in the 2-D swirl plot.

Having the full three-dimensional information in a plane, it is now possible to study the inclination angle of vortex structures by computing the orientation of the vorticity vector. If the vector angle is computed at every point in the field, the results are noisy partly due to measurement uncertainty, but primarily due to the predominance of small-scale incoherent motions to the instantaneous vorticity, and thus the instantaneous vortex lines in a turbulent flow are not very well organized. By contrast, computation of the vorticity vector averaged over a region identified as a vortex core by the swirl strength  $\lambda_{3D}^+$ , leads to determination of the orientation of the vortex core. This orientation can then be interpreted as the local inclination of that vortex.

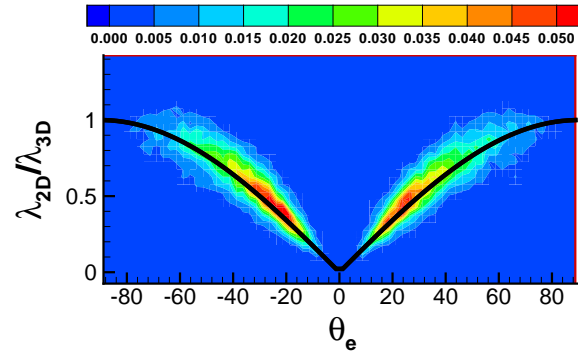
Figure 4(a) reveals the probability density function (p.d.f.) of the inclination angle ( $\theta_e$ ) that vortex cores make with the  $x - y$  plane. The angles were computed for all distinct regions of significant  $\lambda_{3D}^+$ . This distribution (square symbols) includes a wide range of structure angles at this wall-normal location. Note that many structures have small inclination angles. Further study, including the investigation of the azimuthal angle made by the projection of the vorticity vector onto the  $x - y$  plane with the



(a)



(b)



(c)

Figure 4: p.d.f. of (a) Inclination angle ( $\theta_e$ ), (b) Eddy inclination angle ( $\theta_i$ ), (c) Joint p.d.f. of inclination angle and  $\lambda_{2D}/\lambda_{3D}$ , the solid line is the function  $\lambda_{2D}/\lambda_{3D} = |\sin \theta_e|$ .

$x$  axis, reveals that most  $\lambda_{3D}^+$  regions with small inclinations are spanwise structures indicative of heads of smaller hairpin vortices or other in-plane oriented vortices. In order to obtain the inclination angles of cores that are not spanwise heads or streamwise legs, the average vorticity vector in isolated regions of  $\lambda_{3D}^+$  that includes  $\lambda_{2D}^+$  were computed. This additional criterion filters out spanwise and streamwise structures since  $\lambda_{2D}^+$  does not capture them. The resulting p.d.f., shown by circles in figure 4(a)) yields peaks at  $\pm 25^\circ$ . This suggests that most cores are inclined at  $25^\circ$  to the  $x-y$  plane. The angle made by the projection of the vorticity vector in the  $x-z$  plane with the  $x$  axis is defined as the eddy inclination ( $\theta_i$ ). The p.d.f. of the eddy inclination angle (only for regions where  $\lambda_{2D}^+ > 0$ ) is shown in figure 4(b). This p.d.f has peaks at  $\pm 32^\circ$ , which indicates that most of the inclined vortex rods have an inclination of  $32^\circ$ . This is comparable to a  $45^\circ$  hairpin inclination as suggested by various researchers over the past century ([7]). Another measure is the weighted average of  $\theta_e$  and  $\theta_i$  based on the centre of area of the p.d.fs shown in the figures respectively. This reveals that the average inclination angle  $\theta_e$  is  $37^\circ$  and the average eddy inclination ( $\theta_i$ ) is  $57^\circ$  at this wall-normal location.

Figure 4(c) is a plot of the joint probability distribution of the ratio of 2-D swirl strength to 3-D swirl strength and the inclination angle ( $\theta_e$ ). It is worth noting that, mathematically  $\lambda_{2D}$  will always be less than or equal to  $\lambda_{3D}$  for any orientation. The distribution indicates a unique relationship between this ratio and the inclination angle of vortex structure with respect to the cutting plane ( $x-y$  plane in this instance). Velocity fields induced around idealized hairpin vortices (with and without curvature) were computed using Biot-Savart calculations to calculate the ratio  $\lambda_{2D}/\lambda_{3D}$  as a function of the hairpin angle. The results from this computation suggest that the ratio of the two swirl strengths varies as  $|\sin \theta_e|$ . The value of this ratio from the experiments follows this theoretical finding as seen in figure 4(c). Note that this plot does not reveal any information about the streamwise or spanwise oriented structures, since the ratio was computed only for cores where  $\lambda_{2D}$  is greater than zero. The fact that the distribution is dense in the angle range  $20^\circ < \theta_e < 40^\circ$  indicates that most vortex structures in this plane are inclined in that range of angles.

## Conclusions

Simultaneous dual-plane PIV experiments were successfully performed to compute all nine velocity gradients in a turbulent boundary layer. Dual-plane measurements could be used to compute the complete vorticity vector and other quantities like instantaneous Reynolds shear stress production and 3-D swirl strength to study the eddy structure and their dynamics. Contours of different components of the vorticity vector and 2-D swirl strength from the two neighboring planes indicate the existence of hairpin shaped vortices inclined downstream along the streamwise direction. These vortices envelop low speed zones and generate Reynolds shear stress that enhances turbulence production (see [6]). Plots of 3-D swirl strength indicate the existence of additional vortical structures in the middle of low speed zones that may represent heads of smaller eddies intersecting the measurement plane. The dual-plane data were also used to compute typical vortex inclination angles at this wall-normal location. It is worth noting that this study includes just one dataset at one wall-normal location. Datasets at multiple wall-normal locations are required to resolve the complete vortex structure and learn more about the dynamics of a turbulent boundary layer.

## Acknowledgements

The authors gratefully acknowledge support from the Na-

tional Science Foundation through Grants ACI-9982274, CTS-9983933 and CTS-0324898, the Graduate school of University of Minnesota and the David and Lucile Packard Foundation. We are indebted to Dr. Nicholas Hutchins and William Hambleton for their help in data acquisition and many discussions during the course of this study.

## References

- [1] Adrian, R. J., Christensen, K. T. and Liu, Z. C., Analysis and interpretation of instantaneous turbulent velocity fields, *Exp. Fluids*, **29**, 2000, 275–290.
- [2] Adrian, R. J., Meinhart, C. D. and Tomkins, C. D., Vortex organization in the outer region of the turbulent boundary layer, *J. Fluid Mech.*, **422**, 2000, 1–53.
- [3] Christensen, K. T. and Adrian, R. J., Measurement of instantaneous eulerian acceleration fields by particle image accelerometry: method and accuracy, *Exp. Fluids*, **33**, 2002, 759–769.
- [4] Ganapathisubramani, B., Longmire, E. K. and Marusic, I., Investigation of three dimensionality in the near field of a round jet using stereo PIV, *J. Turbulence*, **3**, 2002, 017.
- [5] Ganapathisubramani, B., Longmire, E. K. and Marusic, I., Characteristics of vortex packets in turbulent boundary layers, *J. Fluid Mech.*, **478**, 2003, 35–46.
- [6] Ganapathisubramani, B., Longmire, E. K., Marusic, I. and Pothos, S., Dual-plane PIV technique to resolve complete velocity gradient tensor in a turbulent boundary layer, in *12th International Symposium of Applications of Laser Techniques in Fluid Mechanics*, Lisbon, Portugal, July 12–15, 2004.
- [7] Head, M. R. and Bandyopadhyay, P., New aspects of turbulent boundary-layer structure, *J. Fluid Mech.*, **107**, 1981, 297–337.
- [8] Hu, H., Saga, T., Kobayashi, T., Taniguchi, N. and Yasuki, M., Dual-plane stereoscopic particle image velocimetry: system set-up and its application on a lobed jet mixing flow, *Exp. Fluids*, **31**, 2001, 277–293.
- [9] Raffel, M., Willert, C. and Kompenhans, J., *Particle image velocimetry - A practical guide*, Springer-Verlag, 1998.
- [10] Zhou, J., Adrian, R. J., Balachandar, S. and Kendall, T. M., Mechanisms for generating coherent packets of hairpin vortices in channel flow, *J. Fluid Mech.*, **387**, 1999, 353–396.

## Numerical Study of Flow and Forced Heat Transfer of Robertson-Stiff Fluid Flowing Axially through Concentric Annuli

Aliakbar Heydari Gorji and Fariborz Rashidi

Department of Chemical Engineering,  
The Amirkabir University of Technology (Tehran polytechnic), Hafez Ave., Tehran, Iran

### Abstract

The Steady laminar axial flow of an incompressible and non-Newtonian fluid inside concentric annular spaces is analyzed. The material is supposed to behave as a generalized Newtonian liquid with Robertson-stiff stress-strain relation. Fluid flow is produced by the inner cylinder axial motion and an imposed pressure gradient in the axial direction. Both cases of positive and negative pressure gradient i.e. it assist or oppose the drag on the fluid due to the moving cylinder are studied. Four possible cases with respect to positions of the plug flow regions are considered. Heat transfer in axial flow of this viscosity function is investigated for uniform wall temperature at inner cylinder and adiabatic condition for outer cylinder. The governing momentum and energy equations have been solved iteratively by using a finite difference method. Velocity distribution, temperature profiles and Nusslet number have been obtained and compared for different values of yield stress, flow index and radius ratio in all cases mentioned above.

**Keyword:** Heat transfer, Axial flow, concentric annuli, non-Newtonian, Robertson-Stiff materials, Numerical simulation

### Introduction

Many of the fluids used in industrial purposes are non-Newtonian and flow and heat transfer of such fluids in annuli spaces accounts for a significant part of the flow. Non-Newtonian fluids (i.e. fluid which don't obey Newtonian's law of viscosity and have an effective viscosity which is a function the shear rate) appear in many important applications and different industries including the food, sewage, pharmaceutical industries, polymer industries, cosmetics and lubricants, drilling process of oil wells and extrusion of ceramic catalyst supports. Waxy crude in the oil industry can also form non-Newtonian gels if allowed to cool below their gel-points. In all above processes and applications, the fluids, either synthetic or natural, are mixtures of different stuffs such as water, particles, oils and other long chain molecules; this combination imparts strong non-Newtonian characteristics to the resulting liquids: the viscosity function varies non-linearly with the shear rate. The fluid flows and heat-transfer behavior of non-Newtonian viscoelastic fluids has attracted special interest in recent years due to the wide application of these fluids in above processes. In these processes, heat transfer information is sometimes needed to predict temperature levels or heat transfer rate to be controlled to cause a desired rheology of the flowing material.

When one deals with a practical engineering problem consisting of a non-Newtonian fluid, it is not easy to estimate the heat transfer even in a simple geometry. The reason is that the viscosity of non-Newtonian liquids varies with both shear rate and temperature, a phenomenon which significantly influences the velocity and temperature profiles. Numerous articles about flow and heat transfer of non-Newtonian fluids can be found in the literature.

T. Shigechi et al. investigated the laminar forced convection of Newtonian fluids in concentric annuli with axially moving cores for both thermal entrance and fully developed regions, neglecting the effect of viscous dissipation on heat transfer. The moving wall of the inner cylinder deforms the fluid velocity profile near the wall region, resulting changes in velocity gradient there. Thus, viscous

dissipation may not be neglected in heat transfer involving moving boundaries. Manglik and Fang investigated numerically heat transfer to a power-law fluid through annuli. They found that the power-law index dose not change significantly the Nusselt number for concentric annular spaces [1]. Round and Yu analyzed the effects of reological parameters on velocity and pressure profiles of Herschel-bulkley fluids through concentric annuli.

Soares et al. (1999) studied the developing flow of Herschel-bulkley materials inside tubes for constant and temperature-dependent properties, taking axial diffusion into account. They observed that the temperature-dependent properties do not affect qualitatively pressure drop or the Nusselt number [3].

Soares et al. (2003) investigated the heat transfer in the entrance-region laminar axial flow of viscoplastic materials inside annulus. It is shown that the entrance length decreases as the material behavior departs from Newtonian. Also they observed that the effect of rheological parameters on the inner-wall Nusselt number is rather small [4].

Nascimento et al. analyzed the developing flow of Bingham fluids through concentric annuli. They resulted that the Nusselt number increases with the dimensionless yield stress along thermal entry region, but is nearly insensitive to it at the fully developed region.

Robertson-stiff fluids are non-Newtonian materials possessing a yield value. They are the combination of a Bingham plastic fluid and a pseudoplastic power-law fluid [5].

The constitutive equation for these fluids is as follows:

$$\tau = \left[ K^{\frac{1}{n}} |\dot{\gamma}|^{\frac{n-1}{n}} + \left( \frac{\tau_0}{|\dot{\gamma}|} \right)^{\frac{1}{n}} \right]^n \cdot \dot{\gamma} \quad \tau > \tau_0 \quad (1)$$

It may be represented in below form.

$$\tau = K[\dot{\gamma} + C]^n \quad , \quad \tau > \tau_0 = KC^n \quad (2)$$

Where  $\tau$  is shear stress,  $\tau_0$  is a yield stress,  $\dot{\gamma}$  is the shear rate of strain,  $n$  is the flow behavior index,  $K$  and  $C$  are consistency and material constant respectively.

E. Santoyo et al. (2003) analyzed the Rheological behavior typified by Robertson-stiff model using the experimental rheometric data of some maize flour pastes. Figure 1 shows a schematic diagram of this model.[2]

In this paper, we are concerned with the flow and heat transfer of Robertson-stiff model in the annular space between two concentric cylinders where the inner cylinder is in axial motion and the outer cylinder is at rest. As a first approximation, rheological parameters in Equation 1 are assumed to be independent of temperature. Using a finite difference method, the momentum and energy equations have been solved numerically for a third kind of thermal boundary condition i.e. uniform temperature at inner cylinder; The outer cylinder is assumed to be perfectly insulated (adiabatic). Velocity distribution, temperature profiles and Nusslet number have been obtained and compared for different values of yield stress, flow index and radius ratio in some different cases of flow.

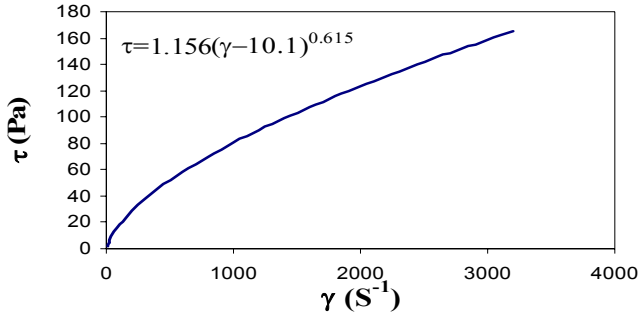


Figure 1: Rheological behavior of DPMF-13 by Robertson-stiff model [2].

### Formulation and Mathematical Analysis of the Problem

A Robertson-stiff fluid confined to the space between two coaxial cylinder surfaces. The outer and inner radiuses of the concentric are  $R$  and  $kR$ , respectively. The outer cylinder is stationary while the cylinder with radius  $kR$  moves with a constant axial velocity  $U$  in the positive  $z$  direction. There is pressure gradient in the  $z$  direction, with pressure gradient being  $P_0$  and  $P_L$  at  $z = 0$  and  $z = L$  respectively. The flow is supposed to be steady, laminar, incompressible and with constant pressure gradient. Local velocity is denoted by  $V_z$  and depends solely to radial distance ' $r$ '.

We consider the rheological equation of state for Robertson-stiff model in cylindrical coordinate as in equation 1.

With considering the dimensionless radius and velocity, equation 1 may be simplified and rewritten in the following dimensionless form:

$$\zeta = \frac{r}{R} \quad \varphi = \frac{V_z}{U} \quad (3)$$

$$\tau_{rz} = K \left( \frac{V}{R} \right)^n \left[ \left| \frac{\partial \varphi}{\partial \zeta} \right|^{\frac{n-1}{n}} + C \left( \frac{R}{V} \right) \left| \frac{\partial \varphi}{\partial \zeta} \right|^{\frac{1}{n}} \right]^n \left( -\frac{\partial \varphi}{\partial \zeta} \right) \quad (4)$$

Under the above assumptions, the momentum equations in the tangential and axial directions with negligible end effects of the cylinders in the cylindrical coordinate system with the origin at the center of the cross section of the annulus are given by

$$\frac{1}{r} \frac{\partial}{\partial r} (r \tau_{rz}) = \frac{\Delta p}{L} \quad \Delta p = p_0 - p_L \quad (5)$$

This equation after simplification to dimensionless state and integration yields the shear-stress distribution as below.

$$\tau_{rz} = \frac{\Delta p R}{2 L} \left( \zeta - \frac{\lambda^2}{\zeta} \right) \quad (3)$$

and boundary conditions are

$$V_z(1) = 0, \quad V_z(k) = U > 0$$

$\lambda^2$  in equation 6 is a dimensionless constant of integration. If  $\lambda$  is real ( $\lambda^2 > 0$ ), then  $\lambda$  corresponds mathematically to a dimensionless zero-shear radius. Equations 4 and 6 are combined and rewritten as

$$K \left( \frac{V}{R} \right)^n \left[ \left| \frac{\partial \varphi}{\partial \zeta} \right|^{\frac{n-1}{n}} + C \left( \frac{R}{V} \right) \left| \frac{\partial \varphi}{\partial \zeta} \right|^{\frac{1}{n}} \right]^n \left( -\frac{\partial \varphi}{\partial \zeta} \right) = \frac{\Delta p R}{2 L} \left( \zeta - \frac{\lambda^2}{\zeta} \right) \quad (7)$$

This equation will be different based on pressure or velocity gradient sign. Some of these different cases will be presented and discussed as follow.

### Pressure gradient assists the drag on the fluid ( $\Delta P > 0$ )

$\lambda_0, \lambda_i$  are the dimensionless boundary values of the plug flow region.  $\varphi_0, \varphi_p, \varphi_i$  are the dimensionless velocity at 1) region between plug flow and inner cylinder,  $k \leq \zeta < \lambda_i$ , 2) plug flow region,  $\lambda_i \leq \zeta \leq \lambda_0$ , 3) region between outer cylinder and plug flow,  $\lambda_0 < \zeta \leq 1$ , respectively.

At this condition ( $\Delta P > 0$ ) and for above regions equation 7 will be converted as below:

case I :  $k \leq \zeta < \lambda_i$

$$\begin{aligned} \frac{\partial \varphi_i}{\partial \zeta} > 0 &\Rightarrow -K \left( \frac{V}{R} \right)^n \left[ \frac{\partial \varphi_i}{\partial \zeta} + C' \right]^n = \frac{\Delta p R}{2 L} \left( \zeta - \frac{\lambda^2}{\zeta} \right) \\ \frac{\partial \varphi_i}{\partial \zeta} &= \left[ \Lambda \left( \frac{\lambda^2}{\zeta} - \zeta \right) \right]^{\frac{1}{n}} - C' \end{aligned} \quad (8)$$

case II :  $\lambda_i \leq \zeta \leq \lambda_0$

$$\frac{\partial \varphi_p}{\partial \zeta} = 0 \quad (9)$$

case III :  $\lambda_0 < \zeta \leq 1$

$$\frac{\partial \varphi_0}{\partial \zeta} < 0 \Rightarrow \frac{\partial \varphi_0}{\partial \zeta} = - \left[ \Lambda \left( \zeta - \frac{\lambda^2}{\zeta} \right) \right]^{\frac{1}{n}} + C' \quad (10)$$

Here,  $\Lambda$  and  $C'$  are denoted as

$$\Lambda = \frac{\Delta p R}{2 L K} \left( \frac{R}{V} \right)^n \quad C' = C \left( \frac{R}{V} \right) \quad (11)$$

### Pressure gradient opposes the drag on the fluid ( $\Delta P < 0$ )

Pressure gradient is negative i.e.  $P_0 < P_L$  and it is caused the fluid flow in opposite direction of inner cylinder axial moving. At this condition and for three regions Equation 7 will be as

case I :  $k \leq \zeta < \lambda_i$

$$\frac{\partial \varphi_i}{\partial \zeta} < 0 \Rightarrow \frac{\partial \varphi_i}{\partial \zeta} = - \left[ \Lambda \left( \frac{\lambda^2}{\zeta} - \zeta \right) \right]^{\frac{1}{n}} + C' \quad (12)$$

case II :  $\lambda_i \leq \zeta \leq \lambda_0$

$$\frac{\partial \varphi_p}{\partial \zeta} = 0 \quad (13)$$

case III :  $\lambda_0 < \zeta \leq 1$

$$\frac{\partial \varphi_0}{\partial \zeta} > 0 \Rightarrow \frac{\partial \varphi_0}{\partial \zeta} = \left[ \Lambda \left( \zeta - \frac{\lambda^2}{\zeta} \right) \right]^{\frac{1}{n}} - C' \quad (14)$$

Finally with considering of above results and equations for different cases, the following general equations are resulted.

$$\frac{\partial \varphi_i}{\partial \zeta} = \Lambda \left| \Lambda \right|^{\frac{1}{n}-1} \left( \frac{\lambda^2}{\zeta} - \zeta \right)^{\frac{1}{n}} - \frac{|\Lambda|}{\Lambda} C' \quad k \leq \zeta < \lambda_i \quad (15)$$

$$\frac{\partial \varphi_0}{\partial \zeta} = -\Lambda \left| \Lambda \right|^{\frac{1}{n}-1} \left( \zeta - \frac{\lambda^2}{\zeta} \right)^{\frac{1}{n}} + \frac{|\Lambda|}{\Lambda} C' \quad \lambda_0 < \zeta \leq 1 \quad (16)$$

Four different cases of velocity distributions between two coaxial cylinders have been studied and mathematically formulated.

### Velocity profile with maximum

In this case where there is maximum in the velocity distribution between two cylindrical surfaces for determination of  $\lambda_0$  we consider the following conditions.

$$\Delta P > 0, \quad \varphi_i(k) = 1, \quad \varphi_0(1) = 0 \quad \varphi_i(\lambda_i) = \varphi_0(\lambda_0)$$

$$\varphi_i = 1 + \int_k^\zeta \Lambda \left[ \left( \frac{\lambda^2}{\zeta} - \zeta \right) \right]^{\frac{1}{n}} d\zeta - C'(\zeta - k) \quad (17)$$

$$-\varphi_0 = - \int_\zeta^1 \Lambda \left[ \left( \zeta - \frac{\lambda^2}{\zeta} \right) \right]^{\frac{1}{n}} d\zeta + C'(1 - \zeta) \quad (18)$$



Equations 17, 18 are combined and rewritten as below:

$$\Lambda^{\frac{1}{n}} \left[ \int_k^{\lambda_0 - \frac{\tau_0}{P}} \left( \frac{\lambda_0 \left( \lambda_0 - \frac{\tau_0}{P} \right)}{\zeta} - \zeta \right)^{\frac{1}{n}} d\zeta - \int_{\lambda_0}^{\left( \zeta - \frac{\lambda_0 \left( \lambda_0 - \frac{\tau_0}{P} \right)}{\zeta} \right)^{\frac{1}{n}}} d\zeta \right] + \quad (19)$$

$$C'(-2\lambda_0 + k + 1 + \frac{\tau_0}{P}) = -1$$

Equation 19 is used for calculating of  $\lambda_0$  in case of maximum velocity profile, but it has limitation at  $\lambda_i = k$ . therefore  $\Lambda_{critical}$  is calculated by the following equation and  $\Lambda > \Lambda_{cr1}$ :

$$\Lambda_{cr1} = \left[ \frac{\left[ 1 + C' \left( k + \frac{\tau_0}{P} - 1 \right) \right]}{\int_{k + \frac{\tau_0}{P}}^1 \left[ \zeta - \frac{k(k + \frac{\tau_0}{P})}{\zeta} \right]^{\frac{1}{n}} d\zeta} \right]^n \quad (20)$$

#### Velocity Profile with Plug Flow on Inner Cylinder

In this case plug flow is attached to inner cylinder and for determination of  $\lambda_0$  we consider the following conditions.

$$\Delta P > 0, \quad \varphi_0(\lambda_0) = 1$$

$$\Lambda^{\frac{1}{n}} \int_{\lambda_0}^1 \left( \zeta - \frac{\lambda_0 \left( \lambda_0 - \frac{\tau_0}{P} \right)}{\zeta} \right)^{\frac{1}{n}} d\zeta + C'(\lambda_0 - 1) - 1 = 0 \quad (21)$$

Equation 21 has limitation at  $\lambda_0 = k$ . therefore  $\Lambda_{cr2}$  is calculated at  $\lambda_0 = k$  by the relevant equation, in common way as previous in equation 20 and  $\Lambda_{cr2} \leq \Lambda \leq \Lambda_{cr1}$

#### Velocity Profile with Minimum

For this case where there is minimum in the velocity distribution, for determination of  $\lambda_0$  we consider the following conditions.

$$\Delta P < 0, \quad \varphi_i(\kappa) = 1, \quad \varphi_0(1) = 0 \quad \varphi_i(\lambda_i) = \varphi_0(\lambda_0)$$

$$\Lambda^{\frac{1}{n}} \left[ \int_k^{\lambda_0 - \frac{\tau_0}{P}} \left( \frac{\lambda^2}{\zeta} - \zeta \right)^{\frac{1}{n}} d\zeta - \int_{\lambda_0}^1 \left( \zeta - \frac{\lambda^2}{\zeta} \right)^{\frac{1}{n}} d\zeta \right] + \quad (22)$$

$$C'(-2\lambda_0 + k + 1 + \frac{\tau_0}{P}) = 1$$

Equation 22 has limitation at  $\lambda_0 = 1$  and  $\Lambda > \Lambda_{cr11}$ .

#### Velocity Profile with Plug Flow on Outer Cylinder

Plug flow is attached to outer cylinder and for determination of  $\lambda_i$ , the following equation is resulted as previous.

$$\Delta p < 0, \quad \varphi_i(\lambda_i) = 0$$

$$\Lambda^{\frac{1}{n}} \int_k^{\lambda_i} \left( \frac{\lambda_i \left( \lambda_i + \frac{\tau_0}{P} \right)}{\zeta} - \zeta \right)^{\frac{1}{n}} d\zeta - C'(\lambda_i - k) = 1 \quad (23)$$

The above equation has limitation at  $\lambda_i = 1$ . In above four cases after calculating of  $\lambda_i$  or  $\lambda_0$ , another parameter will be obtained by  $\lambda^2 = \lambda_i \times \lambda_0$ . By using of finite difference method, the momentum equations have been solved numerically at these four cases.

#### Temperature Profile in Concentric Annuli

The energy equation neglecting the viscous and work terms is given as

$$\rho C_p V_z = \frac{\partial T}{\partial z} = \frac{k_0}{r} \frac{\partial}{\partial r} \left( r \frac{\partial T}{\partial r} \right) \quad (24)$$

The following dimensionless variables are introduced:

$$\zeta = \frac{r}{R}, \quad z' = \frac{z}{L}, \quad \theta = \frac{T - T_w}{T_0 - T_w} \quad D_H = 2R(1-k)$$

$$P_e = \frac{\rho C_p \bar{V} D_H}{k_0} \quad F = \frac{V_z}{\bar{V}} \cdot \frac{P_e \cdot R}{2L(1-k)}$$

and finally dimensionless form of energy equation is

$$F \frac{\partial \theta}{\partial z'} = \frac{1}{\zeta} \frac{\partial}{\partial \zeta} \left( \zeta \cdot \frac{\partial \theta}{\partial \zeta} \right) \quad (25)$$

Here,  $\bar{V}$  is mean velocity and energy equation has been numerically solved, simultaneously with momentum equations, in order to obtain temperature profiles for various flow regimes.

#### Nu number

$$\tau_c = -\frac{dp}{dz} \cdot \frac{D_H}{4} = -\frac{\Delta p}{L} \cdot \frac{R}{2} (1-k) \quad \gamma_c = \frac{\tau_c^n - \tau_0^n}{k^n}$$

$$\eta_c = \eta(\gamma_c) = \frac{\tau_c}{\gamma_c}, \quad R_e = \frac{\rho \bar{V} D_H}{\eta_c}$$

$$Nu_z = \frac{h_z D_H}{k_0} = \frac{2(1-k) \left( \frac{\partial \theta}{\partial \zeta} \right)_{\zeta=k}}{\theta_m} \quad (26)$$

In above equations,  $\tau_c$ ,  $\gamma_c$ ,  $\eta_c$  and  $\theta_m$  are characteristic shear stress, shear rate, viscosity and bulk temperature respectively.

#### f Re for checking the accuracy of numerical results

The product between the friction factor and reynolds number is:

$$f Re = \frac{-16 \frac{dP}{dx} D_H}{\tau_s}, \quad \tau_s = \frac{\tau_{R_0} + k \tau_{R_i}}{1+k}$$

$fRe$  is always equal to 64 regardless the rheological behavior and the duct geometry ( $fRe=64$ ). This matter is used during selecting stage of an appropriate mesh while obtaining numerical solution. The numerical solution was also compared with some axial flows of non-Newtonian materials. The velocity, temperature and Nu profiles obtained numerically were as it is expected theoretically and in agreement with exact / numerical solution of Herschel-Bulkley material with considering of different rheological parameters [3,4]. Our velocity trend was similar in comparison to maximum velocity of Robertson-stiff fluid in annular duct obtained by I. Machac et al. (2003) [7].

#### Results and Discussion

Dimensionless velocity & temperature profiles and results for some governing parameters are presented and discussed.

##### Velocity distribution:

Typical dimensionless axial velocity distributions for fully developed region are shown in Figures 2, 3, 4. As shown in Figure 3, lower flow indexes cause larger dimensionless velocities and wider plug flow region. Figure 4 shows the dimensionless velocity increases and plug flow region decreases with the increase in yield stress. Velocity and finally volumetric flow rate increases for larger pressure gradients and lower radius ratios,  $k$ , as expected.



### Temperature profile:

Dimensionless temperature profiles and Nusselt number variation for thermal boundary condition of uniform temperature at inner moving wall are presented. For different flow regime at  $\Delta P > 0$ , the dimensionless temperature always decreases with axial position (Figure 5), except for  $\Delta P < 0$ , which increase. It is observed that the dimensionless velocity is almost invariant with both yield stress and flow index, Figure 6. The Nusselt variation with different rheological parameters at maximum velocity profile has been studied. It is observed that the Nu is approximately unaffected by the yield stress, but in comparison of calculated data Nu increase with  $\tau_o$ . Figure 7 shows Nusselt number increases as flow index increases. It also increases with Peclet number. Finally, it is concluded that the influence of rheological parameters on nusselt number is rather small.

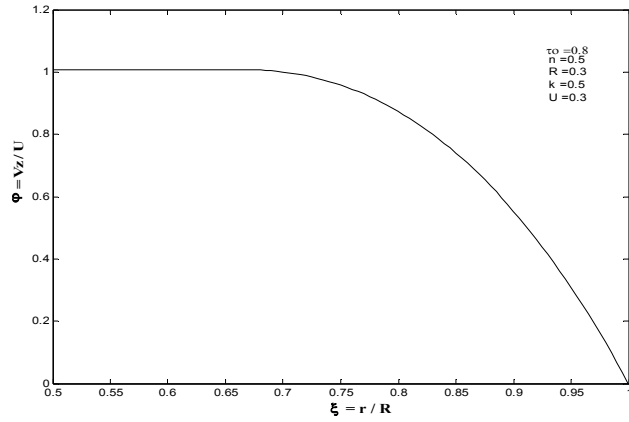


Figure 2: Velocity Distribution with plug flow on inner cylinder (Eq.21).

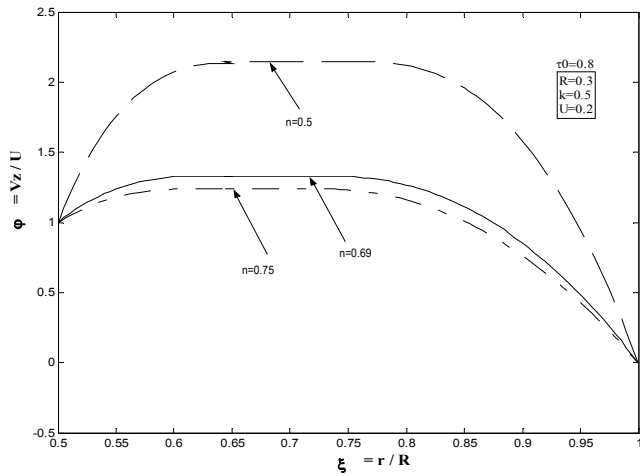


Figure 3: Velocity Distribution for different values of 'n' (Eq. 17,18,19).

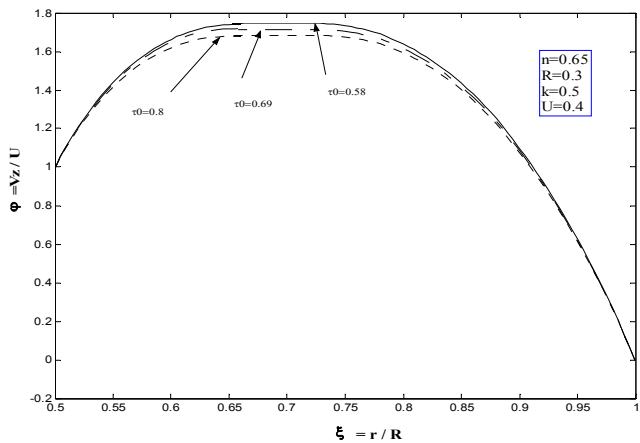


Figure 4: Velocity Distribution for different values of '\(\tau\_o\)' (Eq. 17,18,19).

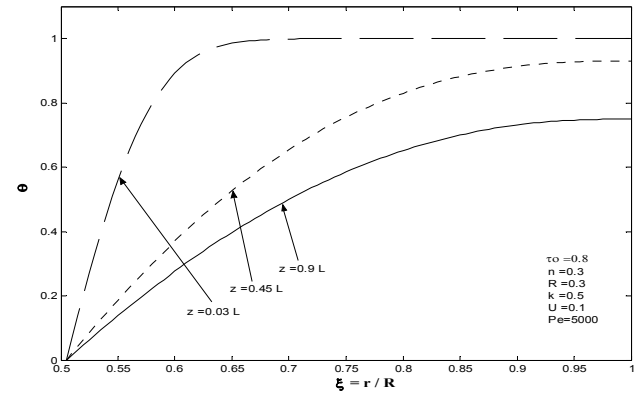


Figure 5: Temperature profile for different axial positions, for velocity distribution with maximum ( $\Delta P > 0$ ), (Eq. 17,18,19,25).

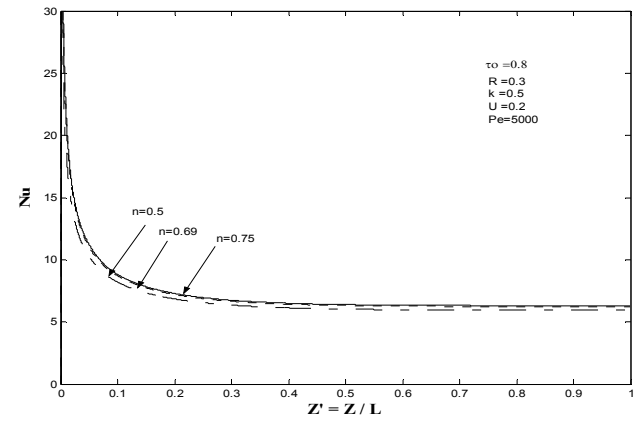


Figure 6: Temperature profile for different values of '\(\tau\_o\)', (Eq. 17,18,19,25).

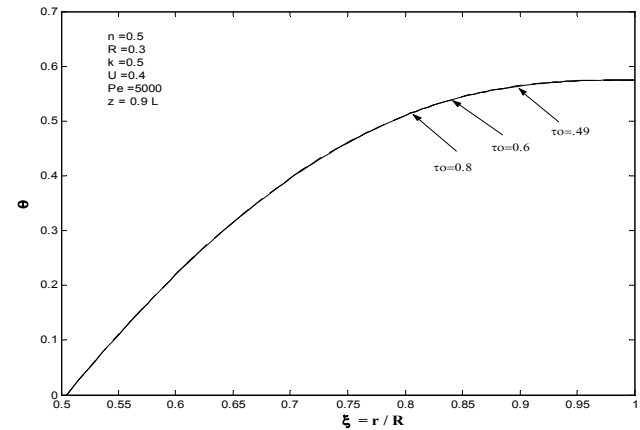


Figure 7: Nusselt number variation for different values of 'n' (Eq. 17,18,19,25,26).

### References

- [1] Manglik, R., Fang, P., Thermal Processing of Various non-Newtonian Fluids in Annular Ducts, *Int. J. Heat and Mass Transfer*, **45**, 2002, 803-815
- [2] Nunez-Santiago M.C., Santoyo E., Rheological evaluation of non-Newtonian Mexican nixtamalised maize and dry processed masa flours, *Journal of Food Engineering*, **60**, 2003, 55-66.
- [3] Soares, E.J., Naccache, M.F., Souza Mendes, P.R., Heat Transfer to viscoplastic liquids flowing laminarly in entrance region of tubes, *Int. J. Heat and Fluid Flow*, **20**, 1999, 60-67.
- [4] Soares, E.J., Naccache, M.F., Souza Mendes, P.R., Heat Transfer to viscoplastic materials flowing axially through concentric annuli, *Int. J. Heat and Fluid Flow*, **24**, 2003, 762-773.
- [5] Robertson, R.E. and Stiff, H.A., An improved rheological Model for Relating Shear Stress to Shear Rate in Drilling Fluids and Cement Slurries, *Trans AIME, Soc. Pet. Eng. J.*, **261**, 1976, 31-37.
- [6] Malik, R. and Uday V. Shenoy, Generalized Annular Couette Flow of a Power-law Fluid, *Ind. Eng. Chem. Res.*, **30**, 1991, 1950-1954.
- [7] Machac I., Dolecek P., Machacova L., Poiseuille Flow of Purely Viscous Non-Newtonian Fluids through Ducts of Non-Circular Cross Section, *Chemical Engineering and Processing*, **38**, 1999, 143-148.

## Numerical Analysis of Turbulent Convective Heat Transfer Processes in a Square-Sectioned U-bend Duct

S. Etemad<sup>1</sup> and B. Sundén<sup>2</sup>

<sup>1</sup>Thermodynamic Analysis, Dept 97613,  
Volvo Car Corporation, SE-405 31 Gothenburg, SWEDEN  
setemad@volvocars.com

<sup>2</sup>Division of Heat Transfer, Lund Institute of Technology, Box 118  
SE-221 00 Lund, SWEDEN

### Abstract

The flow and thermal field in a square-sectioned 180° U-bend were investigated using five turbulence models, namely Suga's quadratic and cubic low-Re k- $\epsilon$ , V2F k- $\epsilon$ , RSM-EVH and RSM-GGDH. All models managed to mimic the general flow and thermal patterns. The V2F-version used in this study, however, over-predicted the pressure-induced secondary flow and seems to need modifications and/or re-tuning of the coefficients to reduce its redistribution of turbulence energy. Suga's two k- $\epsilon$  variants are less CPU-demanding and perform relatively well and, hence are interesting candidates for industrial applications. The RSM models performed best.

### Introduction

The turbulent flow and heat transfer in square-sectioned 180° U-bends give rise to complex three-dimensional motion and heat transfer phenomena which are similar to the phenomena that occur frequently in many engineering applications such as cooling passages in gas turbine blades and automobile engines. The study of generic cases like the U-bend is hence important for the understanding of the flow and heat transfer mechanisms in the industrial applications mentioned above. In the present study the published experimental data [8] were used for the validation of the results for a square-sectioned U-bend. Besides the interest in studying the complex flow and heat transfer phenomena, the other objective for this work is to explore the performance of the methods for accurate prediction of flow-heat transfer behaviour in such generic cases for final use in engineering applications.

### Problem Description

The geometry is a square-sectioned 180° U-bend duct with the side length  $D=88.9$  mm. The bend mid-line radius,  $r$ , was  $3.35D$  as illustrated in figure 1. The Reynolds number was  $Re_D=U_m D/\nu=56000$  where  $U_m=9.11$  m/s is the mean velocity. The Dean number was  $De=Re_D(D/2r)^{0.5}=21634$  (where  $\nu$  is the kinematic viscosity). The bend was provided with a long straight inlet part and a  $4.5D$  straight outlet part as shown in figure 1b. As specified in table 1 the inlet length was tuned for each turbulence model to match the flow conditions at  $-2.2D$  (upstream the bend) to the ones measured by Johnson and Launder [8]. As shown in figure 1(a), the cross-section grid consisting of  $51 \times 51$  grid points expanded from a fine near-wall grid to a coarser off-wall grid. The mean  $Y^+$  was nearly 7 ( $Y^+=Yu_\tau/\nu$  where  $u_\tau=(\tau_w/\rho)^{0.5}$  is the friction velocity,  $\rho$  is the density and  $\tau_w=(\rho\nu\partial U/\partial y)_{at y=0}$  is the wall shear stress). Hence, the grid was compromised to be used for both high- and low-Re models. The grid details appear in table 1. As inlet boundary condition constant temperature, 20°C, and uniform velocity profile was used. Constant heat flux was used on walls.

Turbulence Model	Grid points (Streamwise inlet+bend+outlet)	Inlet length	mean $Y^+$	$Y^+$ range
Suga, Quad	179+91+41	$20D$	6.8	0-11
Suga, Cubic	179+91+41	$20D$	6.8	0-11
V2F	241+91+41	$28D$	6.1	0-11
RSM, EVH	286+91+41	$32D$	7.5	0-14
RSM, GGDH	286+91+41	$32D$	7.6	0-14

Table 1. Grid specifications.

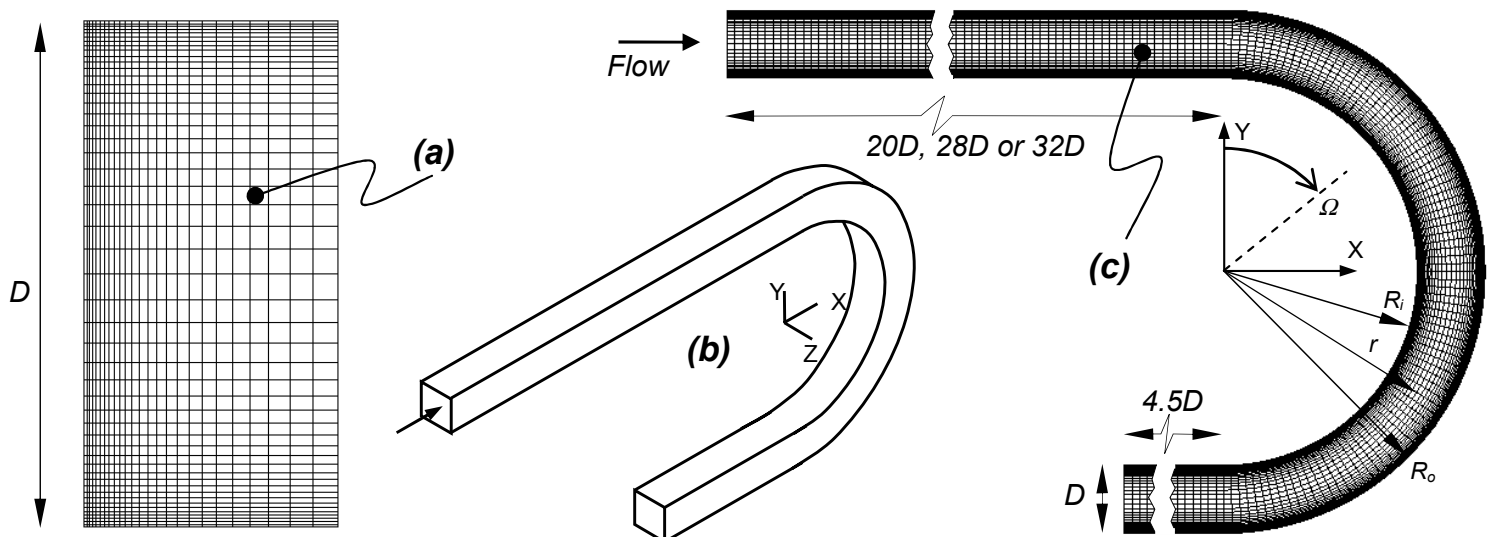


Figure 1. (a) Half of the cross-section mesh, (b) Bend and its co-ordinate system, (c) Streamwise mesh.

## Turbulence Models

The turbulence models used in this work are Suga's quadratic and cubic low-Re k- $\epsilon$  [1-2], V2F k- $\epsilon$  [4,7] and two versions of RSM [9], Reynolds stress model, namely isotropic EVH [10] and anisotropic GGDH [3] (i.e. Eddy Viscosity Hypothesis and Generalised Gradient Diffusion Hypothesis, respectively). The models are briefly explained below. To obtain non-linear eddy viscosity models, like Suga's quadratic and cubic model, and thereby account for the non-isotropic nature of the turbulence, series expansions of functional terms are added to the linear eddy viscosity model (Boussinesq assumption). The general expression for the Reynolds stresses,  $-\rho \overline{u_i u_j}$ , is given below.

$$\begin{aligned} \rho \overline{u_i u_j} = & \frac{2}{3} \rho k \delta_{ij} - 2 \mu_t S_{ij} + \\ & + 4 C_1 \mu_t \tau (S_{ik} S_{kj} - \frac{1}{3} S_{kl} S_{kl} \delta_{ij}) + 4 C_2 \mu_t \tau (W_{ik} S_{kj} + W_{jk} S_{ki}) + 4 C_3 \mu_t \tau (W_{ik} W_{jk} - \frac{1}{3} W_{kl} W_{kl} \delta_{ij}) \\ & + 8 C_4 \mu_t \tau^2 (S_{kl} W_{ij} + S_{ij} W_{kl}) S_{kl} + 8 C_5 \mu_t \tau^2 (S_{kl} S_{kl} - W_{kl} W_{kl}) S_{ij} \end{aligned} \quad (1)$$

$$S_{ij} = \frac{1}{2} \left( \frac{\partial U_i}{\partial x_j} + \frac{\partial U_j}{\partial x_i} \right), \quad W_{ij} = \frac{1}{2} \left( \frac{\partial U_i}{\partial x_j} - \frac{\partial U_j}{\partial x_i} \right), \quad S = \frac{k}{\epsilon} \sqrt{2 S_{ij} S_{ij}}, \quad W = \frac{k}{\epsilon} \sqrt{2 W_{ij} W_{ij}} \quad (2)$$

Note that  $X_i = X, Y, Z$  and  $x_i = x, y, z$  are the streamwise and Cartesian co-ordinates,  $U_i$  and  $u_i$  are the time averaged and fluctuating velocity, respectively, in  $x_i$ -direction and  $\tau = k/\epsilon$  is the turbulent dissipation time scale. The first line in eq. (1) contains only the linear version. By adding the second and the third line containing the quadratic and cubic products of strain and vorticity rate,  $S_{ij}$  and  $W_{ij}$ , the quadratic and cubic model, respectively, is obtained. The coefficients  $C_1$ - $C_5$  and  $C_\mu$ , the turbulent viscosity,  $\mu_t$ , and the damping function,  $f_\mu$ , (in Suga's model) are given below.

$$\mu_t = f_\mu \frac{C_\mu \rho k^2}{\epsilon}, \quad f_\mu = 1 - \exp\left(-\left(\tilde{R}_t / 90\right)^{0.5} - \left(\tilde{R}_t / 400\right)^2\right) \quad (3)$$

$$C_\mu = \frac{0.3}{1 + 0.35 \eta^{1.5}} [1 - \exp(-0.36 \exp(0.75 \eta))] , \quad \eta = \max(\tilde{S}, \tilde{W}) \quad (4)$$

$$\tilde{S} = \frac{k}{2\epsilon} \sqrt{S_{ij} S_{ij}}, \quad \tilde{W} = \frac{k}{2\epsilon} \sqrt{W_{ij} W_{ij}}, \quad \tilde{R}_t = k^2 / (\nu \epsilon) \quad (5)$$

$C_1 = -0.1$ ,  $C_2 = 0.1$ ,  $C_3 = 0.26$ ,  $C_4 = 10.0 \cdot C_\mu^2$  and  $C_5 = 5.0 \cdot C_\mu^2$ .

In the k- $\epsilon$  models two transport equations, one for the turbulent kinetic energy,  $k$ , and another one for its dissipation rate,  $\epsilon$ , are solved. These are expressed in a condensed general form below.

$$\frac{\partial(\rho k)}{\partial t} + \frac{\partial}{\partial x_j} (\rho U_j k) = \frac{\partial}{\partial x_j} \left[ \left( \mu + \frac{\mu_t}{\sigma_k} \right) \frac{\partial k}{\partial x_j} \right] + P_k - \rho \epsilon \quad (6)$$

$$\frac{\partial(\rho \epsilon)}{\partial t} + \frac{\partial}{\partial x_j} (\rho U_j \epsilon) = \frac{\partial}{\partial x_j} \left[ \left( \mu + \frac{\mu_t}{\sigma_\epsilon} \right) \frac{\partial \epsilon}{\partial x_j} \right] + f_1 \frac{C_{\epsilon 1}}{T_s} P_k - f_2 \frac{C_{\epsilon 2}}{T_s} \rho \epsilon + E + Y_c \quad (7)$$

$$P_k = -\rho \overline{u_i u_j} \frac{\partial U_i}{\partial x_j}, \quad \epsilon = \nu \frac{\partial u_i}{\partial x_j} \frac{\partial u_i}{\partial x_j}, \quad T_s = \frac{k}{\epsilon} \quad (8)$$

In Suga's model, as can be seen above the  $k$ -equation has its conventional form while in the  $\epsilon$ -equation two terms,  $E$  and  $Y_c$ , expressed below, are added and  $\epsilon$  is replaced by  $\tilde{\epsilon}$ , as defined below, which is the isotropic part of  $\epsilon$  and is zero at the wall. The model coefficients appear in table 3.

$$E = 0.0022 \tilde{S} \mu_t \frac{k^2}{\tilde{\epsilon}} \left[ \frac{\partial^2 U_i}{\partial x_j \partial x_k} \right]^2, \quad f_1 = 1, \quad f_2 = 1 - 0.3 \exp(-R_t^2) \quad (9)$$

$$Y_c = \max \left[ 0.83 \left( \frac{k^{3/2}}{2.5 \tilde{\epsilon} y} - 1 \right) \left( \frac{k^{3/2}}{2.5 \tilde{\epsilon} y} \right)^2 \frac{\tilde{\epsilon}^2}{k}, 0 \right], \quad \tilde{\epsilon} = \epsilon - 2\nu \frac{\partial \sqrt{k}}{\partial x_i} \frac{\partial \sqrt{k}}{\partial x_i} \quad (10)$$

In the V2F model [4,7] an additional transport equation for the wall-normal turbulence intensity,  $\sqrt{v^2}$ , and an elliptic equation for the redistribution term,  $f$ , in the  $\sqrt{v^2}$ -equation, have to be solved. The time scale,  $T_s$ , length scale,  $L$ , and,  $\mu_t$ , are also give below. No wall function or damping function is used in the V2F model.

$$\frac{\partial(\rho v^2)}{\partial t} + \frac{\partial}{\partial x_j} (\rho U_j v^2) = \frac{\partial}{\partial x_j} \left[ \left( \mu + \frac{\mu_t}{\sigma_k} \right) \frac{\partial v^2}{\partial x_j} \right] + \rho k f - 6 \rho v^2 \frac{\epsilon}{k} \quad (12)$$

$$f - L^2 \frac{\partial^2 f}{\partial x_j \partial x_j} = \frac{0.4}{T_s} \left( \frac{2}{3} - \frac{v^2}{k} \right) + 0.3 \frac{P_k}{k} + \frac{5}{T_s} \frac{v^2}{k} \quad (11)$$

$$f_1 = 1 + 0.045 \sqrt{k / v^2}, \quad f_2 = 1, \quad E = Y_c = 0 \quad (13)$$

$$T_s = \max \left( \frac{k}{\epsilon}, 6 \sqrt{\frac{\nu}{\epsilon}} \right), \quad L = 0.23 \max \left( \frac{k^{3/2}}{\epsilon}, 70 \frac{\nu^{3/4}}{\epsilon^{1/4}} \right), \quad \mu_t = C_\mu \rho v^2 T_s \quad (14)$$

Reynolds Stress Models, RSM, solve directly the transport equations for the Reynolds stresses,  $-\rho \overline{u_i u_j}$ , as expressed below.

$$\frac{\partial(\rho \overline{u_i u_j})}{\partial t} + \frac{\partial}{\partial x_k} (U_k \rho \overline{u_i u_j}) = D_{ij} - \rho \left( \overline{u_i u_j} \frac{\partial U_i}{\partial x_k} + \overline{u_j u_i} \frac{\partial U_j}{\partial x_k} \right) - \frac{2}{3} \delta_{ij} \rho \epsilon + \Phi_{ij} \quad (15)$$

For the diffusion term,  $D_{ij}$ , two alternative models, the isotropic EVH [10] and the anisotropic GGDH [3] are used.  $k$  and  $\epsilon$  are obtained from eqs. (6-7). However, the diffusion terms in eqs. (6-7), here denoted  $D_k$  and  $D_\epsilon$ , respectively, are modified as given below in table 2 together with  $D_{ij}$  for EVH and GGDH.

EVH	GGDH	eq.#
$D_{ij} = \frac{\partial}{\partial x_m} \left( \frac{\mu_{eff}}{\sigma_k} \frac{\partial \overline{u_i u_j}}{\partial x_m} \right)$	$D_{ij} = 0.22 \frac{\rho k}{\epsilon} \frac{\partial}{\partial x_m} \left( \overline{u_m u_n} \frac{\partial \overline{u_i u_j}}{\partial x_n} \right)$	(16)
$D_k = \frac{\partial}{\partial x_m} \left( \frac{\mu_{eff}}{\sigma_k} \frac{\partial k}{\partial x_m} \right)$	$D_k = \frac{\partial}{\partial x_m} \left( 0.22 \frac{\rho k}{\epsilon} \overline{u_m u_n} \frac{\partial k}{\partial x_n} \right)$	(17)
$D_\epsilon = \frac{\partial}{\partial x_m} \left( \frac{\mu_{eff}}{\sigma_\epsilon} \frac{\partial \epsilon}{\partial x_m} \right)$	$D_\epsilon = \frac{\partial}{\partial x_m} \left( 0.18 \frac{\rho k}{\epsilon} \overline{u_m u_n} \frac{\partial \epsilon}{\partial x_n} \right)$	(18)

Table 2. Diffusion terms in RSM,  $k$  and  $\epsilon$  equations.

For the pressure-strain term,  $\Phi_{ij}$ , the SSG model [11] is used.

$$\begin{aligned} \Phi_{ij} = & -(C_1 \epsilon + C_1^* P_k) b_{ij} + C_2 \epsilon (b_{ik} b_{kj} - \frac{1}{3} \delta_{ij} b_{km} b_{km}) + (C_3 - C_3^* \Pi_b^{0.5}) k S_{ij} + \\ & + C_4 k (b_{ik} S_{jk} + b_{jk} S_{ik} - \frac{2}{3} \delta_{ij} b_{kl} S_{kl}) + C_5 k (b_{ik} W_{jk} + b_{jk} W_{ik}) \end{aligned} \quad (19)$$

$$\mu_{eff} = \mu + 0.09 \frac{k^2}{\epsilon}, \quad b_{ij} = \left( \overline{u_i u_j} - \frac{1}{3} \delta_{ij} \overline{u_k u_k} \right) \frac{1}{\overline{u_k u_k}}, \quad \Pi_b = b_{ij} b_{ij} \quad (20)$$

$C_1 = 3.4$ ,  $C_1^* = 1.8$ ,  $C_2 = 4.2$ ,  $C_3 = 0.8$ ,  $C_3^* = 1.3$ ,  $C_4 = 1.25$  and  $C_5 = 0.4$ . With the RSM models the logarithmic wall function given below is used for the wall-adjacent cells with  $E_{wff} = 9.0$  and  $\kappa = 0.42$ .

$$u^+ = (1/\kappa) \ln(E_{wff} Y^+), \quad u^+ = U_i / u_\tau \quad (21)$$

For the thermal field the simple eddy diffusivity model, SED, was used in all cases. The turbulent heat fluxes are expressed as

$$\rho \overline{u_j h} = - \frac{\mu_t}{\sigma_h} \frac{\partial h}{\partial x_j}, \quad \sigma_h = \text{turbulent Prandtl number} = 0.9 \quad (22)$$

Model	$C_\mu$	$\sigma_k$	$\sigma_\epsilon$	$C_{\epsilon 1}$	$C_{\epsilon 2}$
Suga	0.09	1.0	1.22	1.44	1.92
V2F	0.22	1.0	1.30	1.40	1.90
RSM	0.09	1.0	1.30	1.44	1.83

Table 3. Model coefficients.

## Numerical approach

The governing equations were solved using the implicit finite volume non-staggered solver STAR-CD [12]. The SIMPLE algorithm was used for the pressure-velocity coupling. Based on earlier work by Etemad et al. [5-6], the MARS scheme (2nd order) was chosen for velocities and Upwind (1st order) for other quantities. Constant physical properties were assumed.

## Results

The results obtained for all models are condensed in two figures. Figure 2 compares the computed profiles of the streamwise velocity,  $U$ , and temperature,  $T$ , with the existing measured data on the symmetry plane for several cross-sections. Note that the predicted profiles for  $-2.2D$  (upstream the bend),  $2.2D$  and  $5D$  are compared with the experimental data at  $-5D$ ,  $5D$ , and  $10D$ ,

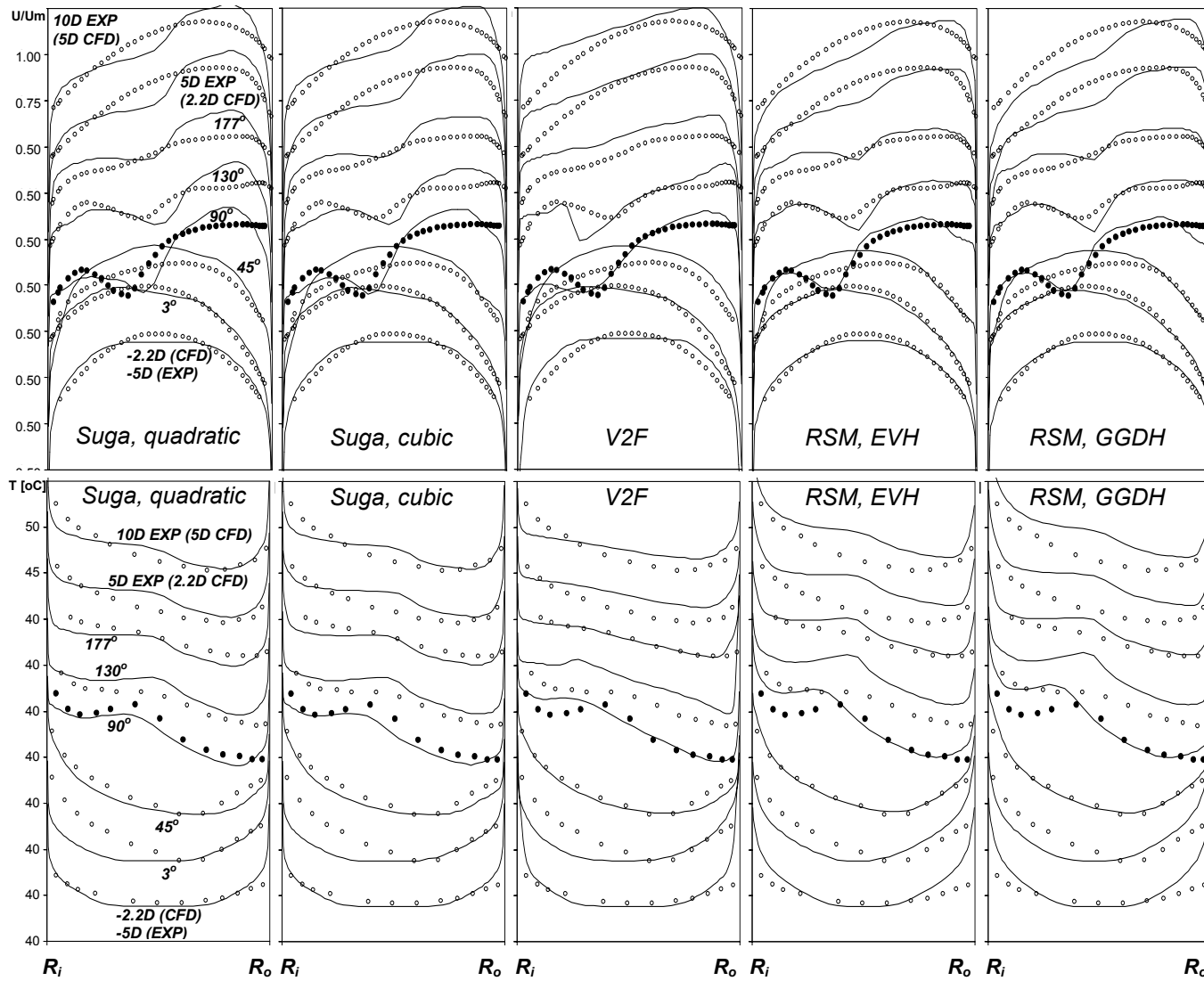


Figure 2. Predicted velocity (top) and temperature (bottom) profiles (lines) on the symmetry plane obtained using Suga's quadratic & cubic model, V2F, RSM-EVH and RSM-GGDH at  $-2.2D$ ,  $3^\circ$ ,  $45^\circ$ ,  $90^\circ$ ,  $130^\circ$ ,  $177^\circ$ ,  $2.2D$  and  $4.5D$  and the experimental data (white circles, black only at  $\Omega=90^\circ$ ).

respectively. The diagrams give a quantitative overview of the results. For the understanding of the predicted physical features, however, it is appropriate to review the plots, presented in figure 3 where the vector plots show the pattern of the complex secondary flow in the duct cross-sections together with the mean velocity magnitude contours and isotherms. The first glance at figure 2 shows that at  $-2.2D$  the velocity profiles are fairly close to the experimental data. This indicates that appropriate inlet length is used for each case. The V2F results, however, differ somewhat from the other models. As it was shown in earlier studies [5-6] the upstream velocity distribution is of great significance for the development of the secondary motion in the bend. Near each side-wall the centrifugal forces, pointing outwards from the bend centre, decrease (due to the friction) and hence, the pressure gradient, which in other regions is in balance with the centrifugal forces, prevails and causes a flow motion near each side-wall towards the bend centre. This initiates the streamwise secondary vortex with a number of smaller satellite-vortices. The velocity distribution upstream the bend dictates the intensity of these vortices which in turn impact the flow and heat transfer in the bend. The V2F prediction of the velocity field upstream the bend deviates most from the other numerical and also experimental data. Hence it is natural to expect that its secondary flow further downstream also deviates most. A closer look at the plots for V2F, especially at  $130^\circ$  in figure 3 implies that this model behaves as the least diffusive among the ones used here. Another general observation is that all models, except V2F, deliver quite similar and reasonable results. It is likely that the V2F version used here needs a re-tuning of coefficients for this kind of flow, because it seems to over-predict the strength

and complexity of the secondary flow and might go too far in redistributing the turbulence energy from the streamwise to wall-normal component. The RSM models mimicked the experimental data best, especially at  $90^\circ$  and  $130^\circ$ , (with no significant advantages for GGDH compared to EVH). Suga's cubic model performs slightly better than its quadratic version. This might be due to the fact that the cubic models are known to improve the predictions of curved flow. None of the models seems to mimic the measured velocity profile at  $45^\circ$ . It is likely that this discrepancy is caused by the fact that predicted velocity profiles upstream the bend are more flat than the measured one. It is known that an inviscid flow with a flat velocity profile upstream a bend causes a free-vortex flow in the bend with a higher velocity near the inner radius and lower velocity near the outer radius. Therefore, the predicted velocity profiles in this work at  $45^\circ$  have their peak closer to the inner radius rather than the outer radius (as in the experimental data). When comparing the predicted and measured temperature profiles in figure 2, it should be noted that the temperatures are not normalised and therefore only the shape of these profiles should be considered rather than their level. The general impression is that the temperature profiles correspond well to their velocity counterpart and this indicates the dominating role of the flow field. Except the V2F-results which differ from the rest, all models managed to predict the trends well. Suga's quadratic and cubic models performed similar. Likewise RSM-EVH and RSM-GGDH gave almost the same results. The review of the plots in figure 3 shows that all the used models could capture the complex secondary motions especially at  $135^\circ$ . The most dominating is, however, the main vortex (here counter-clockwise) which convects the cold high

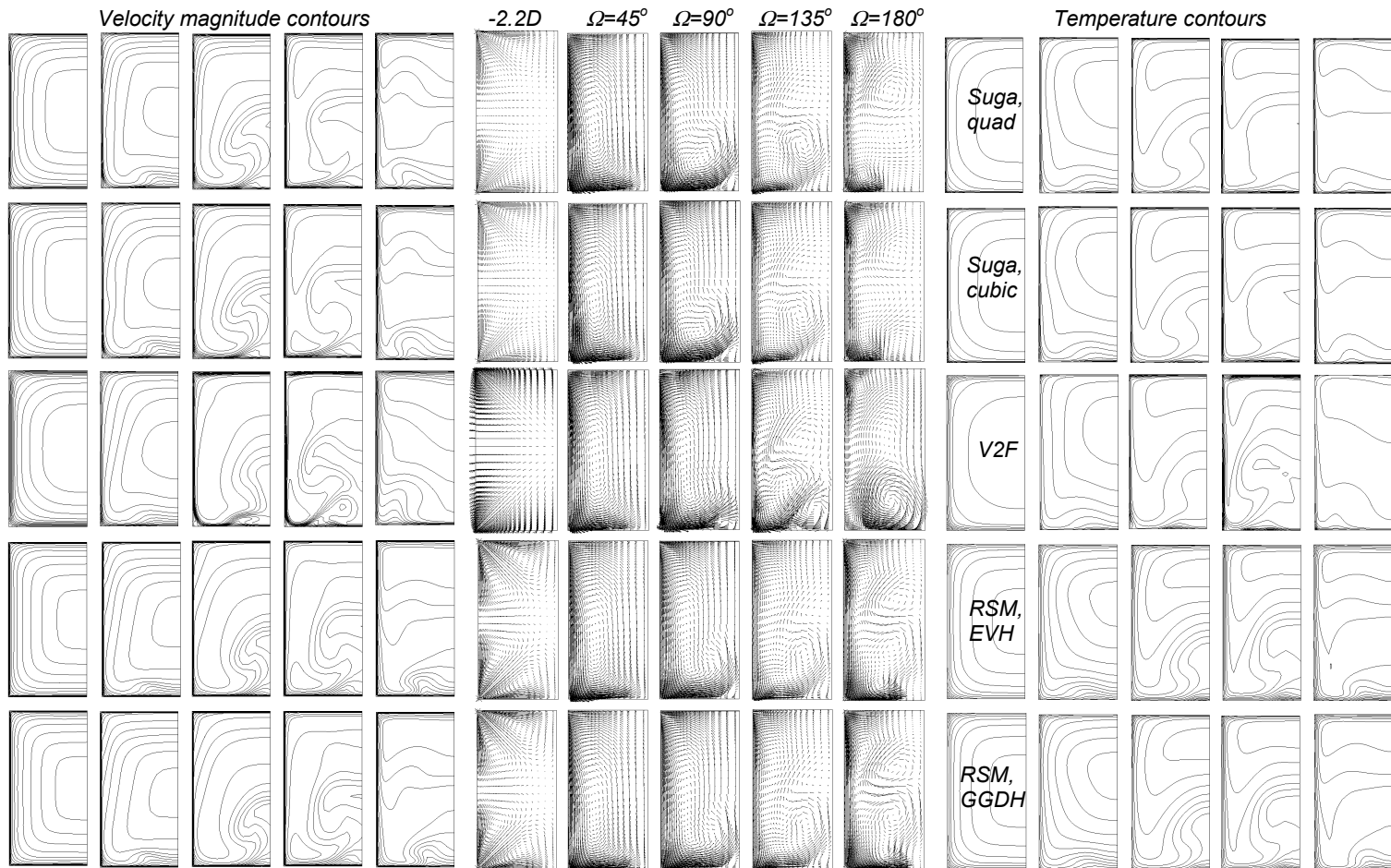


Figure 3. Predicted velocity magnitude contours (left), velocity vectors (middle) & temperature contours (right) obtained using Suga's quadratic & cubic model, V2F, RSM-EVH and RSM-GGDH (top to bottom, respectively) at  $-2.2D$ ,  $45^\circ$ ,  $90^\circ$ ,  $135^\circ$  and  $180^\circ$ . Lower plot edge is the inner radius.

speed flow from the core towards the inner wall corner and later alongside the inner wall back towards the symmetry plane. This process brings cold high speed fluid near the inner wall which explains the double peak in the velocity profile and double dip in the temperature profile especially at  $90^\circ$ . The velocity vectors at  $-2.2D$  also show that, except V2F, all models have accounted for the anisotropy of turbulence in the inlet duct and predicted the turbulence induced secondary motion.

## Conclusions

The flow and thermal fields in a square-sectioned  $180^\circ$ -bend were investigated using five turbulence models, namely Suga's quadratic and cubic low-Re  $k$ - $\epsilon$ , V2F  $k$ - $\epsilon$ , RSM-EVH and RSM-GGDH. All models managed to mimic the general flow and thermal patterns. The V2F-version used in this study seems, however, to need modifications and/or re-tuning of its coefficients to reduce its redistribution of turbulence energy. The RSM models performed best but Suga's two  $k$ - $\epsilon$  variants, despite their simplicity and relatively low computational effort, performed well and might be suitable for industrial applications.

## Acknowledgments

The authors wish to acknowledge Lic. Engn. Olof Daunius for valuable discussions and his support and encouragements. This study is financed by the Swedish Agency for Innovation Systems (VINNOVA) and Volvo Car Corporation.

## References

- [1] Craft, T.J., Launder, B.E., and Suga, K., *Development and application of a cubic eddy viscosity models of turbulence*, Int. J. Heat and Fluid Flow, **17**, 1996, 108-115.
- [2] Craft, T.J., Launder, B.E., and Suga, K., *Extending the applicability of eddy viscosity models through the use of deformation invariants and non-linear elements*, Proc. 5th

- Int. Symp. on Refined Flow Modelling and Turbulence Measurements, 1993, 125-132.
- [3] Daly, B.J. and Harlow, F.H., *Transport equations in turbulence*, Phys. Fluids, **13**(11), 1970, 2634-2649.
- [4] Durbin, P.A., *Separated flow computations with the  $k$ - $\epsilon$ - $v^2$  model*, AIAA Journal, **33**(4), 1995, 659-664.
- [5] Etemad, S., Rokni, M., Sundén, B. and Daunius, O., *Analysis of Turbulent Flow and Heat Transfer in a Square-Sectioned U-Bend*, 4th Int. Symp. on Turbulence, Heat and Mass Transfer, Hanjalic, K., Nagano, Y. and Tummers, M., (Eds), Begell House Inc., 2003, 1171-1178.
- [6] Etemad, S. and Sundén, B., *Prediction of Developing Turbulent Flow in a Rectangular-Sectioned Curved Duct*, HT-FED2004-56193, ASME Heat Transfer/Fluids Eng. Summer Conf., Charlotte, North Carolina, USA, 2004.
- [7] Iaccarino, G., *Predictions of a turbulent separated flow using commercial CFD codes*, J. Fluids Eng., **123**(4), 2001, 819-828.
- [8] Johnson, R.W. and Launder, B.E., *Local Nusselt number and temperature field in turbulent flow through a heated square-sectioned U-bend*, Int. J. Heat and Fluid Flow, **6** (3), 1985, 171-180.
- [9] Launder, B.E. and Sandham, N.D., (Eds.), *Closure strategies for turbulent and transitional flows*, Cambridge Univ. Press, 2002.
- [10] Lien, F.S. and Leschziner, M.A., *A pressure-velocity solution strategy for compressible flow and its application to shock/boundary layer interaction using second-moment turbulence closure*, J. Fluids Eng., **115**, 1993, 717-725.
- [11] Speziale, C.G., Sarkar, S., and Gatski, T.B., *Modelling the pressure-strain correlation of turbulence: an invariant dynamical system approach*, J. Fluid Mech., **227**, 1991, 245-272.
- [12] STAR-CD, *Methodology*, STAR-CD VERSION 3.2, 2004, CD-Adapco Group.



## The Internal Wave Field Generated by the Body and Wake of a Horizontally Moving Sphere in a Stratified Fluid

James W. Rottman<sup>1</sup>, Dave Broutman<sup>2</sup>,  
Geoff Spedding<sup>3</sup> and Patrice Meunier<sup>3</sup>

<sup>1</sup>Science Applications International Corporation  
San Diego, CA 92121 USA

<sup>2</sup>Computational Physics, Inc.  
Springfield, VA 22151 USA

<sup>3</sup>Department of Aerospace and Mechanical Engineering  
University of Southern California, Los Angeles, CA 90089-1191 USA

### Abstract

A combination of ray and Fourier methods is used to describe the linear internal wavefield generated by a horizontally moving, vertically oscillating, source in a stratified fluid. Ray theory is used to approximate the wavefield in a Fourier transform domain. The ray solutions are then superimposed by inverse Fourier transform to produce the spatial solution. This is a more practical approach than calculating the ray solution directly in the spatial domain, and it is general enough to treat background flows with depth dependent shear and stratification. The theory is compared with tank experiments for a towed sphere in a uniformly stratified background.

### Introduction

Obstacles that move through a stratified fluid generate internal waves, either directly by the displacement of the fluid around the obstacle or indirectly by motions in the obstacle's wake. The wake motions consist of turbulent eddies and the collapse of partially mixed regions toward an equilibrium density level.

To gain insight into these generation processes, we study the case of a source travelling horizontally at constant speed through a vertically stratified fluid. We consider moderate Froude number  $Fr = U/(Na)$ , where  $U$  is the speed of the source,  $a$  is its radius, and  $N$  is the buoyancy frequency of the fluid.

The theory, described in more detail in [2], is a modification of the methods developed for topographically generated internal waves by [1] and [2]. Ray solutions are computed in a Fourier transform domain and are then superimposed by inverse Fourier transform to produce a spatial solution. This is a more practical approach than calculating the ray solution directly in the spatial domain, mainly because the Fourier superposition automatically accounts for diffraction effects near caustics and other regions where the spatial ray theory fails.

We present the theory in a form that allows the source to oscillate vertically as well as move horizontally. The vertical oscillations will be used to model the unsteady wave generation by turbulence in the wake of the sphere, as suggested by [3]. The theory is developed for a depth-dependent background, but in this study the results presented are limited to a uniform background. This is to compare with our available data from laboratory experiments, which were conducted by towing a sphere through a background at rest with uniform stratification. Wave reflections from the upper and lower boundaries of the tank are important, so the reflected waves are included in the theory.

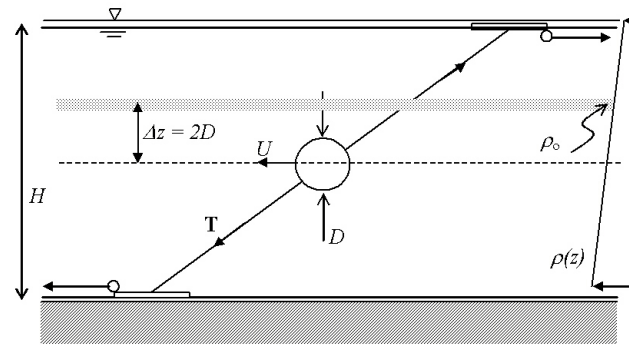


Figure 1: A sphere of diameter  $D$  is towed horizontally at speed  $U$  through a linear density gradient in water of depth  $H$ . Wave motions propagate away from the sphere and through a carpet of neutrally-buoyant polystyrene beads with density  $\rho_0$ . In the experiments reported here, the beads are 2 sphere diameters above the midplane of the sphere. Model vibrations are reduced by operating at high tension  $T$  in the oblique support wires.

### Theory

We consider a stratified Boussinesq fluid. Internal waves are generated by a source that moves horizontally at constant speed while oscillating vertically at constant frequency  $\sigma$ . The coordinate system,  $\mathbf{r} = (x, y, z)$  with  $z$  positive upwards, is fixed to the mean position of the oscillating source. The background flow in this reference frame is  $\mathbf{U} = (U(z), V(z), 0)$ , and the background buoyancy frequency is  $N(z)$ .

The internal waves have wavenumber  $\mathbf{k} = (k, l, m)$  and intrinsic frequency

$$\hat{\omega} = \sigma - kU - lV. \quad (1)$$

The internal-wave dispersion relation is

$$m = \pm (k^2 + l^2)^{1/2} (N^2 / \hat{\omega}^2 - 1)^{1/2}. \quad (2)$$

We derive a solution for the vertical displacement  $\tilde{\eta}(k, l, z)$  of the wavefield at a fixed horizontal wavenumber. The spatial solution is then obtained by inverse Fourier transform:

$$\eta(\mathbf{r}, t) = e^{-i\sigma t} \iint_{-\infty}^{\infty} \tilde{\eta}(k, l, z) e^{i(kx + ly)} dk dl. \quad (3)$$

The factor  $e^{-i\sigma t}$  accounts for all of the time dependence in the present model. This can be considered as the long-time limit



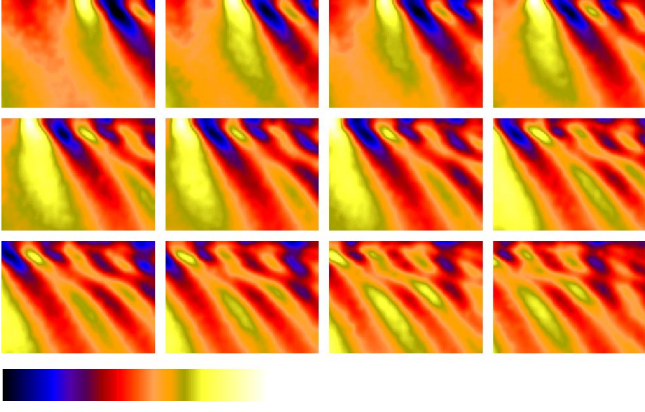


Figure 2: Experimental results for  $u$  in the case of  $Fr = 2$ . Each image is a horizontal cross section of one side of the wake. The 12 images are for equally spaced times over the duration of time  $Nt = 29.8$ . Time increases from left to right and from top to bottom. The total distance traversed by the sphere in this time is  $29.8D$ . The minimum and maximum values for  $u$  are  $-0.2\text{cm/s}$  to  $0.14\text{cm/s}$ .

of an initial value problem in which the motion is started from rest, and the associated transients have decayed or propagated away.

We use a ray approximation for  $\tilde{\eta}(k, l, z)$ , of the form

$$\tilde{\eta}(k, l, z) = b(k, l, z) e^{i \int_0^z m(k, l, z') dz'}. \quad (4)$$

The amplitude  $|b|$  can be derived from the conservation of wave-action  $A$ , which here reduces to the constancy of the vertical flux of wave-action  $c_{g3}A$ , where  $c_{g3} = \partial\hat{\omega}/\partial m$  is the vertical group velocity.

The details of the derivation are given in [2]. Here we quote the result:

$$b = \pi i (Q/\hat{\omega})_0 [G_0/G]^{1/2}. \quad (5)$$

The zero subscript indicates evaluation at  $z = 0$ , the mean depth of the source. We also have

$$G = N^2 c_{g3} / \hat{\omega}, \quad (6)$$

For the source function  $Q$ , we use the following form, from [3],

$$Q(\mathbf{k}, t) = \frac{3}{4} i \pi^{-2} a^3 \left[ U_0 k + h \sigma e^{-i \sigma t} m \right] \frac{j_1(Ka)}{Ka}, \quad (7)$$

where  $K = |\mathbf{k}|$  and  $j_1(z) = (\sin z)/z^2 - (\cos z)/z$  is the spherical Bessel function of order unity. The background flow at the mean position of the source is  $U_0$ , which is aligned in the  $x$ -direction. In the limit of large Froude number  $Fr = U_0/Na$  the source function (7) represents the effects of a horizontally translating, vertically oscillating, solid sphere of radius  $a$ . The amplitude of the vertical oscillation of the sphere is  $h$ , and its vertical velocity is  $h\sigma e^{-i\sigma t}$ .

Modifications of the above results to incorporate buoyancy frequency turning points (where  $\hat{\omega} = N$ ) are given in [1] and [2].

To compute the spatial solution for another variable, such as the  $x$ -component of the perturbation velocity  $u$ , we need only to relate the vertical displacement  $\tilde{\eta}$  to  $\tilde{u}$  by standard ray relations (e.g. [5]) before taking the inverse Fourier transform (3).

## Reflected Waves

So far we have only considered waves that move upward from the source. To compare with our experimental results, we must allow wave reflections from the upper and lower boundaries of the tank. From here on, we will restrict attention to a uniform background, which is the condition of the experiments.

To account for wave reflections, we follow the method of [1], where more details can be found. Consider a fixed height  $z$  above the source and a tank of height  $H$ . Each time a ray returns to that  $z$  after reflecting once from the top of the tank and once from the bottom of the tank, the wave phase  $mz$  is advanced by  $m2H$ . To include the effects of this and subsequent reflections, we must multiply  $\hat{\eta}(k, l, z)$  in (4) by the sum

$$S = \sum_{n=0}^{\infty} e^{in2mH} \quad (8)$$

$$= ie^{imH} / 2 \sin mH. \quad (9)$$

The sum is defined in the sense of generalized functions (see Eq. (1.2.2) of [6]). It diverges for  $mH = \pi$ , the condition for perfect constructive interference between all of the reflected waves. The divergence can be eliminated by adding a small damping factor in the form of an imaginary wavenumber  $m_i$ , as in [1], or by limiting  $S$  to a finite number of terms. The number of terms can be chosen to represent a finite number of reflections at the time of interest, as determined by group velocity calculations. We have so far only experimented with the first method. In the results presented below, we have used a value of  $m_i H = 0.02$ .

The wavefield, including all reflected waves, is modelled by four terms, each with a factor of  $S$ . Two terms represent upward and downward moving rays that initially leave the source moving upward. The other two terms represent upward and downward moving rays that initially leave the source moving downward. The term  $\hat{\eta}(k, l, z)S$ , where  $\hat{\eta}(k, l, z)$  is given by (4), corresponds to the first of those four terms.

## Experiments

Experiments were conducted in a  $2.4 \times 2.4$  m tank filled to a height  $H = 26\text{cm}$  with a linearly stratified salt solution. The density gradient was created by the standard two-tank method, and density values were checked at an array of taps in the side-wall. In the experiments reported here, the buoyancy frequency  $N = 1.88 \pm 2\%$ . The sphere was towed at a height of  $11.3\text{cm}$  above the bottom tank. The sphere diameter is  $D = 2.52\text{cm}$  and  $Fr = N/Ua$  (where  $a = D/2$ ) was varied by varying the tow speed  $U$ . For  $Fr = 1$ , the tow speed was  $U = 2.37\text{cm/s}$ . The Reynolds number  $Re$  varies by the same amount (i.e. for  $Fr = 1, 2, 4$ , we have  $Re = 600, 1200, 2400$ ), but we assume the variations in  $Re$  to be of minor importance for the wavefield. A horizontal (isopycnal) bead sheet is left at a height  $\Delta z = 2D$  above the mid-plane of the sphere, and particle motions are tracked using a custom DPIV technique, detailed in [4] and [7]. The experimental setup is sketched in figure 1.

To improve the spatial and temporal resolution, the image window was centered on one side of the wake only (assuming bilateral symmetry), and exposures were made over fast and slow timescales using a nested pair of short and long exposure times at each timestep. The components of the horizontal velocity field  $u, v$  were calculated directly from the particle image displacements and interpolated onto a regular grid by a two-dimensional smoothing spline.

## Results

We will consider the cases of  $Fr = 1, 2, 4$ . The sphere is towed in the  $x$  direction, and each plot that we present is a horizontal

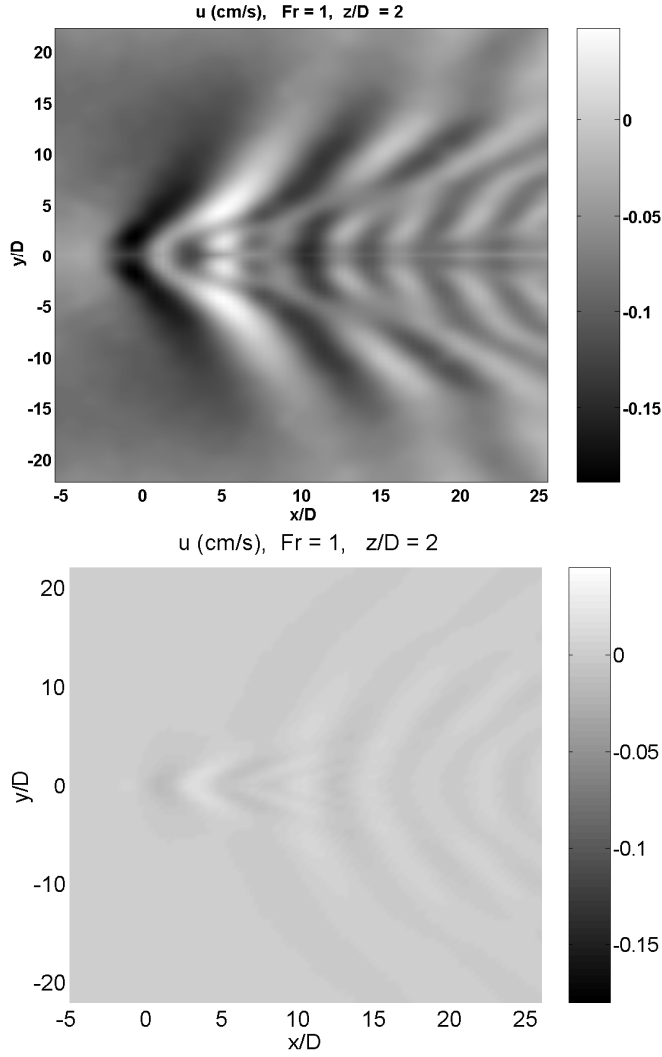


Figure 3: A comparison for  $Fr = 1$  of tank experiments (upper panel) and theory (lower panel). The plotted variable is  $u$ , the  $x$ -component of the velocity of the wavefield, in cm/s.

cross section at a height  $z = 2D$  above the centerplane of the sphere. All plots are of the  $x$  component  $u$  of the wavefield velocity. In all plots except the final figure 6, we have considered a non-oscillating source, i.e.  $\sigma = 0$  in (7).

For the theoretical calculation, the inverse Fourier transform (3) was approximated discretely on a Fourier grid of  $1024 \times 1024$  in  $k, l$ . The corresponding grid spacing in the spatial domain is about 0.8cm. A smaller number of Fourier grid points would have sufficed in some cases. In addition to resolving the flow features, the extent of the Fourier grid must be chosen to limit periodic wrap-around errors, which result from the discrete approximation of the inverse Fourier transform.

A sequence of images of  $u$  from the tank experiment is shown in figure 2 for the case of  $Fr = 2$ . Here and in subsequent figures, the image grid size is  $74 \times 54$ , with spacing 1.072 cm  $\times$  1.056 cm. This gives a 78.3  $\times$  56 cm window (inside a 2.44  $\times$  2.44 m tank). In units of  $D$  the window is  $31D \times 22.2D$ . The window is fixed in space and the sphere moves through it in time.

As noted above, the images from the experiments were taken on one side of the wake only, assuming a symmetric wake. In the following figures, we have flipped the experimental images symmetrically to give the more familiar picture of the full wavefield. The data points directly behind the obstacle, along the line  $y = 0$ , are at the edge of the field of measurement, and this

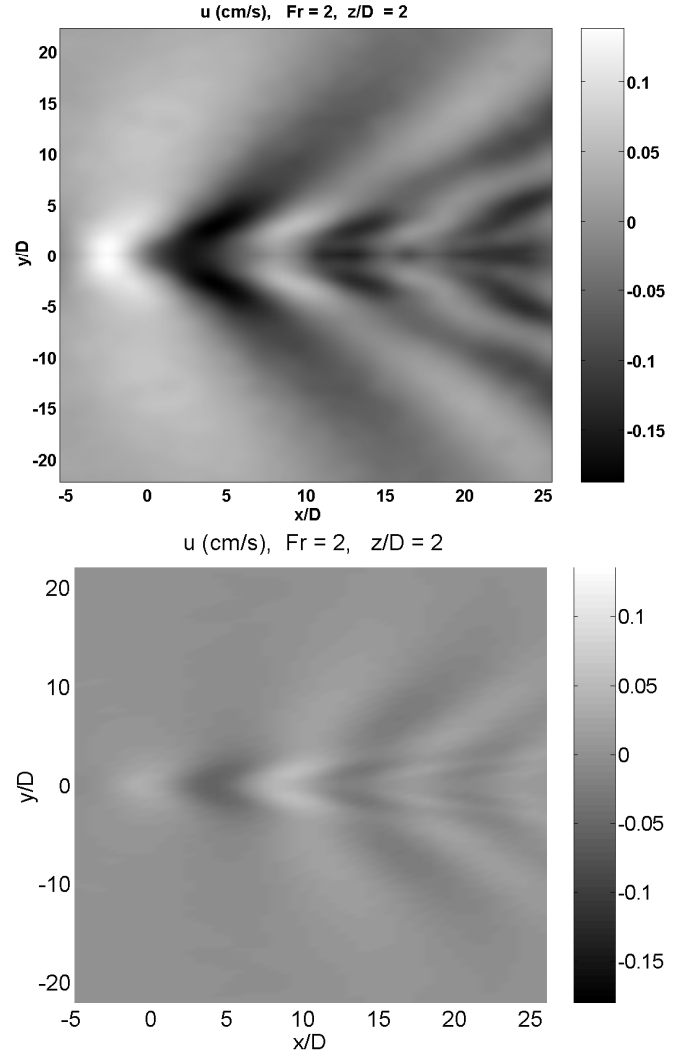


Figure 4: A comparison for  $Fr = 2$  of the experimental result (upper panel) and the theory (lower panel). The plots are of  $u$ .

shows up as an anomaly in the following figures.

Figure 3 is for the case of  $Fr = 1$ . The tank measurement is shown in the top panel, and our linearized theory is shown in the lower panel. At this relatively low Froude number the turbulent eddies in the wake are not strong and are thus not important for the generation of internal waves. (We ignore wake generation until figure 6). However, the source function we have used, (7), is most accurate for the representation of a solid sphere only in the limit of high Froude number. Thus some of the discrepancy between the theory and measurements in this example may be due to the source representation. In the future, we plan to try other source representations that depend on the Froude number.

Figure 4 shows the case of  $Fr = 2$ , again with the experimental results in the upper panel and the theory in the lower panel. The peak theoretical amplitude of the wavefield is lower than the peak amplitude of the experiments, by a factor of about two. This difference in wave amplitudes is maintained in the region closest to the obstacle, so the difference must be due to factors other than turbulent eddy generation in the wake. We have omitted from the theory all eigenfunctions that correspond to evanescent modes. These could be included in the theory, by the usual WKB methods, and might account for some of the difference in the amplitude predictions. Another possibility is the presence of vortical modes, which may be important in the experimental results but are not included in the theory. We plan to check this by comparing the horizontal divergence  $u_x + v_y$  of the experimental data and the theory, which would reveal the

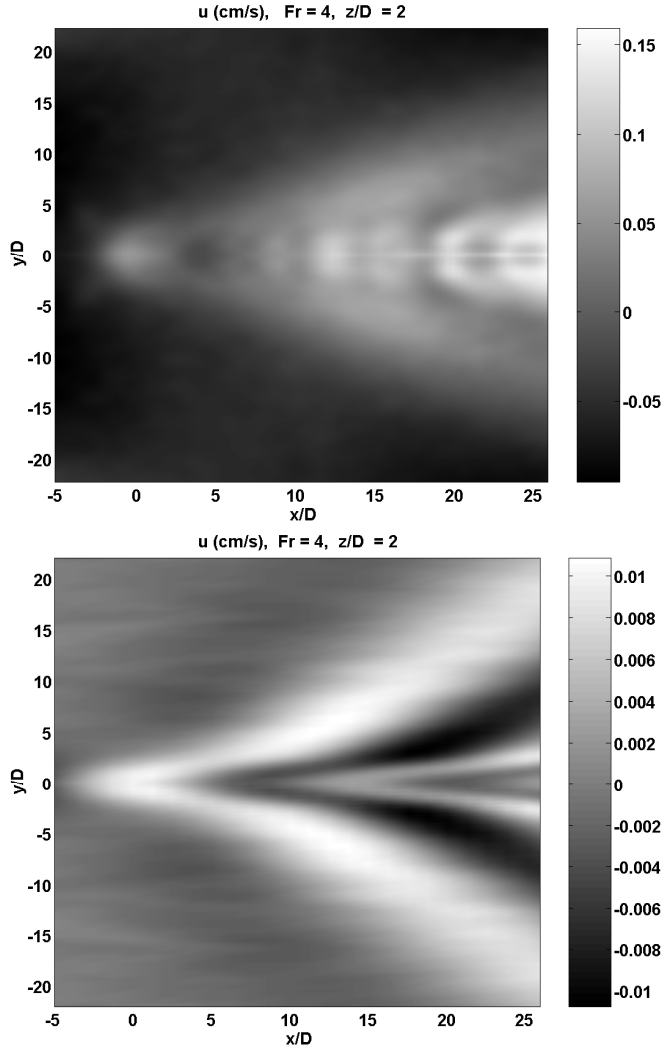


Figure 5: A comparison for  $Fr = 4$  of the experimental result (upper panel) and the theory (lower panel). The plots are of  $u$ .

non-vortical modes only.

Figure 5 shows the results for  $Fr = 4$ . Here our linear theory is a poor representation of the experimental results, though it does give a reasonable prediction for the lateral extent of the wavefield. This is the parameter regime in which eddy-generated internal waves from the wake are important. A better agreement between theory and experiment is obtained by including an oscillating source to model the eddy generation. Previously we had ignored the oscillating term in the source function (7). Here we include the oscillating term, with oscillation amplitude  $h = 0.4a$  and frequency  $\sigma = 2.5N$ , following guidelines in [3]. The result is shown in figure 6, which is a better fit to the data, though the theory predicts a wavefield that is more concentrated around the  $x$ -axis.

## Conclusions

This work is a step toward seeing how far ray theory can go in simulating the internal wavefield generated by an obstacle and its wake. By combining ray and Fourier methods, we have obtained a detailed three-dimensional picture of the wavefield, with far higher resolution than possible in numerical models. The calculation is also fast, taking only a few seconds for each depth on a standard PC. Future needs are a better representation of the source, dependent on the Froude number, and a more detailed study of the effectiveness of modelling wake generated internal waves by an oscillating source.

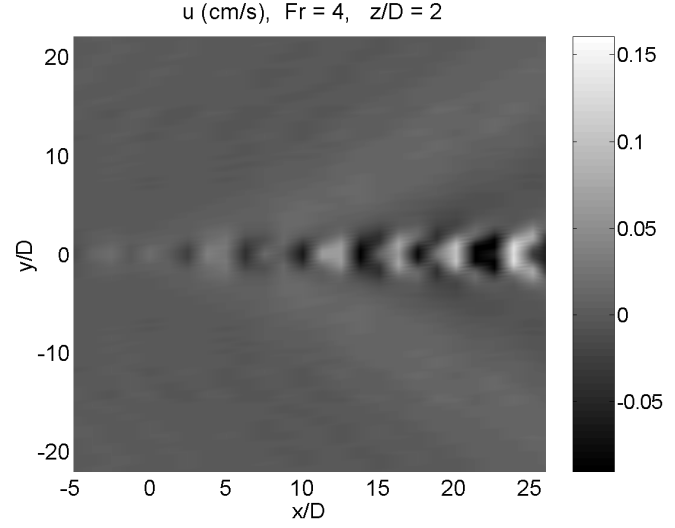


Figure 6: As in Figure 5, lower panel, but with an additional oscillating source term for wave generation by wake eddies.

## Acknowledgements

This research is supported by ONR under contract numbers N00014-01-C-0191 and N00014-96-1-0001. Dr. Ronald Joslin is the program manager.

## References

- [1] Broutman, D., Rottman, J. and Eckermann, S., A simplified fourier method nonhydrostatic mountain waves, *J. Atmos. Sci.*, **60**, 2003, 2686–2696.
- [2] Broutman, D. and Rottman, J., A simplified fourier method for computing the internal wavefield generated by an oscillating source in a horizontally moving, depth-dependent background, *Phys. Fluids*, **16**, 2004, 3682–3689.
- [3] Dupont, P. and Voisin, B., Internal waves generated by a translating and oscillating sphere, *Dyn. Atmos. Oceans*, **23**, 1996, 289–298.
- [4] Fincham, A. and Spedding, G., Low-cost high-resolution dpiv for turbulent flows, *Exps. Fluids*, **23**, 1997, 449–462.
- [5] Gill, A., *Atmosphere-Ocean Dynamics*, Academic Press, 1982.
- [6] Hardy, G., *Divergent Series*, Clarendon, 1949.
- [7] Spedding, G., Browand, F. and Fincham, A., Turbulence, similarity scaling and vortex geometry in the wake of a towed sphere in a stably stratified fluid, *J. Fluid Mech.*, **314**, 1996, 53–103.

## Direct Injection of Natural Gas/Liquid Diesel Fuel Sprays

T.R White, B.E. Milton and M. Behnia

School of Mechanical and Manufacturing Engineering  
The University of New South Wales, Sydney, NSW, 2052 AUSTRALIA

### Abstract

Dual-fuelling provides a suitable method for operating compression-ignition engines on alternative fuels. The CFD package *Fluent* is being used to model the direct-injection of two such fuels simultaneously into an engine. The CFD models have been initially calibrated using high-speed photographic visualisation of the jets. Different orientations and staging of the jets with respect to each other are now being simulated. Salient features of the two fuel jets are being studied to optimise the design of a dual-fuel injector for compression-ignition engines. Analysis of the fuel/air mixture strength during the injection allows the ignition delay to be estimated and thus the best staging of the jets to be determined.

### Introduction

The introduction of alternative fuels such as natural gas (NG), liquefied petroleum gas (LPG) and alcohols for internal combustion engines is likely to occur at an increasing rate. The dual-fuel (DF) concept allows these low cetane number fuels to be used in compression-ignition (CI, diesel) type engines. Most CI engine conversions have pre-mixed the alternative fuel with air in the intake manifold whilst retaining diesel injection into the cylinder. The advantage is simple adaptation but the main disadvantage is that good substitution levels are only obtained at mid-load. This is because at low load, conventional diesel injectors still require a substantial fuel delivery to operate efficiently while at high load, the extended ignition delay and mixed fuel in the end zone exacerbate both diesel and SI type knock. Other disadvantages are that displacement of air in the intake can reduce peak power at any given fuel/air ratio and that fuel can directly short-circuit from inlet to exhaust, thereby increasing UHC emissions.

A solution is to inject both the alternative and diesel fuels directly into the cylinder. Here, the fuel in the end zone is limited and the diesel, injected before the alternative, has only a conventional ignition delay. This improves the high end performance. Modern, very high pressure diesel injectors have good turndown characteristics as well as better controllability and hence offer an improvement at the low end. Several systems exist, mainly for large marine engines but also for smaller, truck size engines. For the latter, the key is to produce a combined injector to handle both fuels which has the smallest diameter possible so that installation is readily achieved.

This paper details research where the spray characteristics of such a combined injector have been modelled using CFD. CFD allows the details that are difficult to assess experimentally to be quantified. The mixing advantages of different nozzle configurations, the starting interval between and the duration of the flows and the best driving pressures can be ascertained. The computational results are being verified experimentally using high-speed photographic visualisation of the injection of the two streams and their subsequent interaction. Some results from the photographic rig are included here.

### Numerical Scheme

The domain used as the basis for the CFD work is based on UNSW's "Rapid Compression Machine" (RCM). The RCM is a constant-volume combustion apparatus and is, in effect, a single-stroke engine simulator [5]. It consists of a cylinder which is the size of that found in an average six or seven litre six-cylinder diesel engine and a piston which can be driven from BDC to TDC at high speed. When the piston reaches TDC it is captured and held, the dual-fuel injector fires and constant-volume combustion occurs. The combustion chamber's pressure and temperature history immediately following the injection is logged for later analysis of the combustion.

Whilst most of the validation of the CFD work will be carried out using high-speed photography, combustion testing of the DF injection will eventually be carried out in the RCM and so the RCM's cylinder was decided upon as the choice for the computational domain. The RCM's simple combustion chamber has a bore of 108mm and a height of 10 to 15mm, depending on the compression ratio used. The computational domain for the results presented here is for the 15mm case which equates to the RCM's lowest compression ratio of about 14:1.

The diesel injector used in these experiments is a mini-sac design with six equi-spaced holes and the gas injector has also been made with six holes. The RCM's cylinder is itself axis-symmetric. Thus, when the two nozzles are oriented so that the holes are co-planar, it is computationally-efficient to model the combustion chamber as a segment of one-sixth of the cylinder.

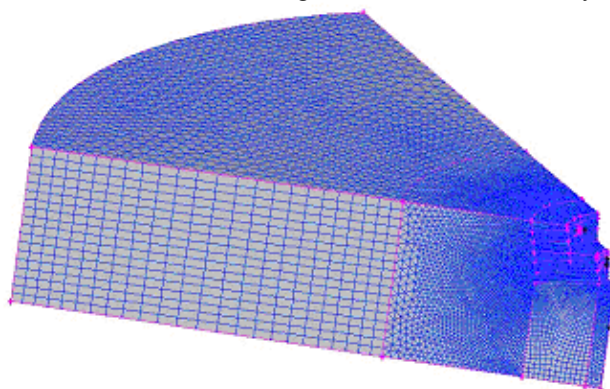


Figure 1. The computational domain used in this study.

### Diesel Injection Model

*Fluent 6.1.18* is the CFD code being used in this study. *Fluent* allows the modelling of the high-speed injection of liquid into a gaseous atmosphere using a "Plain Orifice Atomiser" (POA) model. This model can be used to simulate a diesel injector which is essentially a long, thin orifice that connects a high-pressure reservoir of diesel fuel within the injector to the compressed air in the combustion chamber. In such an atomiser, the liquid is accelerated through a nozzle, forms a jet and then droplets. Using the POA model enables the injection and subsequent atomisation of the diesel jet to be modelled without



the need to create complicated mesh geometry. The location of the actual orifice and the direction it faces are specified and then parameters particular to the nozzle being modelled are entered. The main parameters used in the case modelled here are as follows:

Nozzle diameter:	0.2mm
Nozzle length:	0.8mm
Chamber temperature:	300K (ambient conditions)
Mass-flow rate:	10.36g/s
Injection duration:	425 $\mu$ s

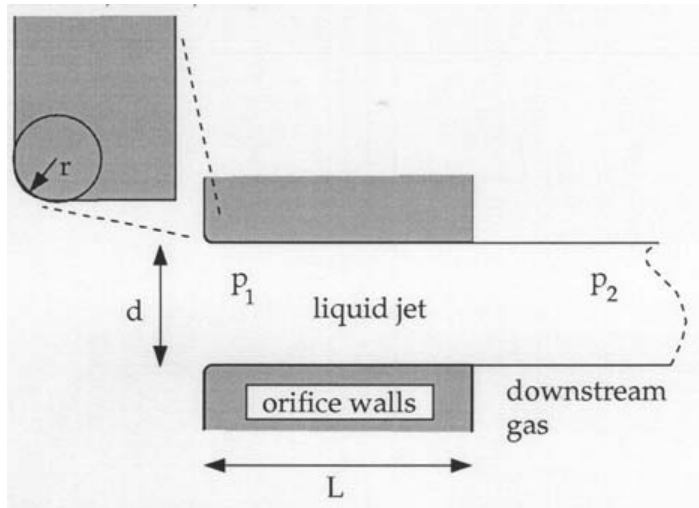


Figure 2. Illustration of the parameters used in *Fluent's* Plain Orifice Atomiser model [1].

### **Diesel Spray Break-Up and Transport Models**

The diesel nozzles being used in this study operate at very high pressures and other researchers support the belief that modern, multi-hole sac-type nozzles usually operate in the cavitating regime [8]. The diesel injector being used in the laboratory work for this study is from a Common-rail, Direct-Injection (CDI) system. It has a multi-hole, mini-sac nozzle and the injection pressure can be set up to 1,800bar. For simulating this nozzle in the CFD, the inlet radius “r” for *Fluent's* POA model was set to a value of 25 $\mu$ m which caused the orifice to cavitate.

*Fluent* offers two spray break-up models: the Taylor Analogy Break-up (TAB) model and the “wave” model. The wave model of Reitz [6] considers the break-up of an injected liquid to be induced by the relative velocity between the liquid and gas phases. This model is popularly used in high-speed fuel injection applications [4, 2] and so is the model chosen for this study. Calibration constants B0 and B1 have been set to 0.61 and 0.20 respectively as suggested by Hong, *et al* [2]. Once the spray has broken-up into droplets, the penetration of the spray depends mainly on the aerodynamic drag of the droplets. *Fluent's* “dynamic drag” model accounts for the effects of droplet distortion by linearly varying the drag between that of a sphere and that of a disc depending on the environmental conditions.

The injection of both the diesel and NG both occur under high pressures and speeds and as a result the jets have high Reynolds’ numbers. The “Realisable” k- $\epsilon$  model has been chosen for this study since, according to the *Fluent* manual, it more accurately predicts the spreading rate of the round jets being studied here.

### **Natural Gas Injection**

Since the NG does not change its state during or after the injection, its introduction into the computational domain is

through a simple “mass-flow” inlet. In *Fluent*, parameters for such inlets include the actual mass-flow of the fluid as well as the fluid’s stagnation temperature. In this study, the gas jet is taken to be choked at a mass-flow of 4.43g/s and thus the stagnation temperature has been set at 343K.

### **Calibration of the CFD Models**

The CFD models are being calibrated using a laboratory rig designed and built by the first author which allows analysis of the dual-fuel jets using a high-speed imaging system. This “Spray Visualisation Rig” (SVR) consists of supply systems for both the diesel and the NG, a prototype DF injector and the imaging equipment.

Diesel is supplied to the DF injector by a pump and accumulator set-up which is based on components taken from a modern CDI system on a commercial vehicle. An electric motor is used to drive the pump and in the absence of the donor vehicle’s engine management system, a needle-valve and pulse generator are used to control the rail pressure and injection timing respectively. NG is supplied from a cylinder via a regulator.

The diesel part of the DF injector consists of a CDI injector taken from the same vehicle as the diesel supply system. The gas nozzles used in this study fit co-axially with the diesel nozzle as a DF injector would be fitted in an engine (figure 3). Control of the gas flow is achieved using another modified CDI injector placed in-line with the gas supply to act as high-speed valve. Extensive calculations were performed during design of the gas valve and nozzles to ensure that the flow would be choked and thus the flow rate dependent only on time.

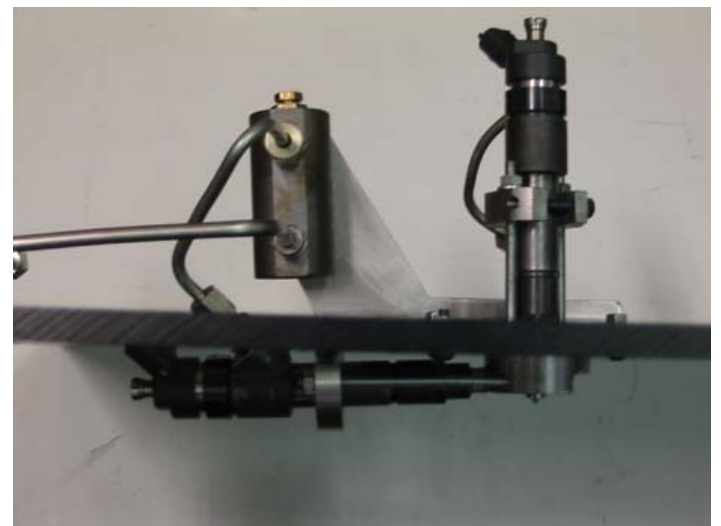


Figure 3. The DF injector assembly. The CDI diesel injector is vertical and fits into the gas nozzle. A second CDI injector (horizontal) controls gas flow into the gas nozzle.

The DF injector has been fitted to a Perspex box to enable photographs of the spray to be taken. Since the NG jet is invisible to the naked eye, special photographic techniques must be employed to capture its image. At first, shadowgraph images were taken using the set-up shown in figure 4. More recently, this shadowgraph equipment has been replaced by schlieren equipment which provides better pictures of the NG jet.

The main parameters used to compare results from the SVR to the CFD are the penetration and shape of the jets at a given time after their respective Start Of injection (SOI). Whilst penetration of the diesel jet depends upon both its injection pressure and its subsequent atomisation, a certain jet penetration for a given injection pressure has been taken to validate the amount of atomisation in the CFD.

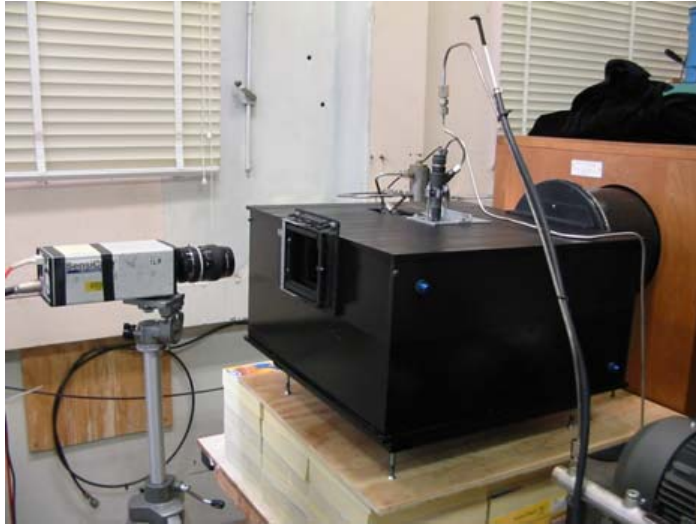


Figure 4. The DF injector fitted to the SVR.

## Results

The case being modelled in the CFD work is for an engine of the equivalent size of several RCM-sized cylinders. This engine is assumed to be running with 75% NG substitution at a total fuel/air equivalence-ratio of 0.75 (ie. close to full-load for a diesel engine). For these conditions, the DF injection parameters are as follows:

Diesel Start/End of Injection (S/EOI):	0ms, 370 $\mu$ s
NG SOI/EOI:	200 $\mu$ s, 4,100 $\mu$ s
Diesel nozzle diameter and mass flow:	0.2mm, 10.36g/s
NG nozzle diameter and mass flow:	0.4mm, 4.43g/s

The diesel and gas nozzles are parallel to each other at 12.5° below horizontal. The diesel injection occurs at 1,600bar which is that found in current-generation common-rail systems. The gas flow simulates that which would occur with an injection pressure of 160bar which is the value suggested by a previous researcher at UNSW [3]. Figure 5 shows the distribution of particles 100 $\mu$ s after SOI for the diesel. The view chosen is a two-dimensional slice taken vertically through the centre of the computational domain and both the gas and diesel nozzles. In this plot, the area-density of the particles is representative of the concentration of the liquid diesel in that plane in the cylinder. Figure 6 shows a schlieren image from the laboratory rig of actual diesel injection at the same time (100 $\mu$ s after SOI). In comparing the CFD results to the photos, a good correlation between the penetration of the two jets may be seen. Also noticeable is the initial “blooming” of the jet near the nozzle.

One of the goals of this study is to find the optimum “staging” for the two fuel jets so that the diesel pilot can be used to virtually eliminate the ignition delay of the NG. Thus the diesel should be igniting at the time of SOI for the NG. Since *Fluent* can simulate the atomisation and subsequent evaporation of the diesel, a plot of the mass-fraction of the diesel vapour relative to the air already in the cylinder can be obtained and is shown in figure 7. This feature of modelling evaporation is useful for helping to predict the ignition delay of the diesel and thus make a good estimate of suitable injection staging. Several researchers in the past who have used CFD to model diesel injection have used non-evaporating models [2, 9]. The availability of the evaporating model in *Fluent* is a distinct improvement over those simulations.

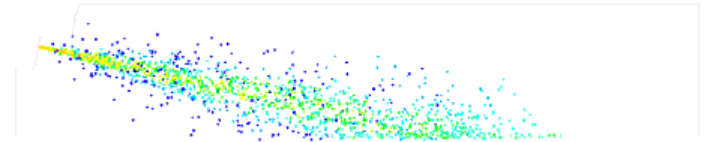


Figure 5. A plot of the diesel particles 100 $\mu$ s after SOI, coloured by the speed of the particles where red is the fastest and blue the slowest.

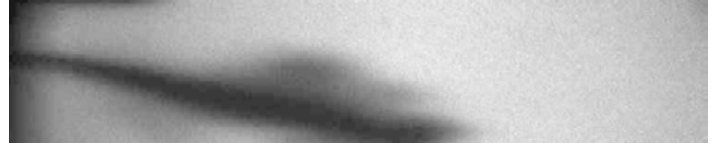


Figure 6. Schlieren image of actual diesel injection at 100 $\mu$ s after SOI. The injection pressure is 1,600bar.

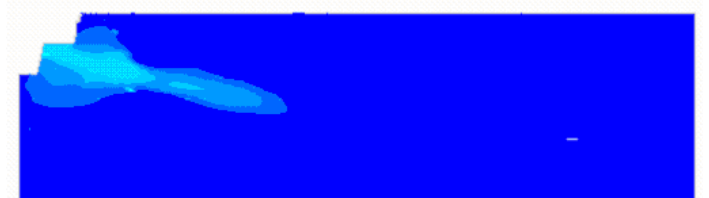


Figure 7. Contour plot of the mass-fraction of diesel vapour in the cylinder at 100 $\mu$ s after SOI. The lighter colours represent higher concentrations.

Figure 8 shows a schlieren image of the NG jet by itself at 100 $\mu$ s after its own SOI (300 $\mu$ s after the diesel’s SOI). Figure 9 shows contours of the mass-fraction of diesel vapour in a diesel-only case at this same time.



Figure 8. Schlieren image of the NG at 100 $\mu$ s after SOI. The injection pressure is 160bar.

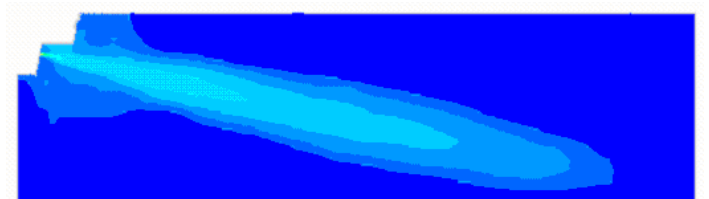


Figure 9. Plot of the contours of diesel mass-fraction at 300 $\mu$ s after diesel SOI.

Figures 10, 11 and 12 show CFD results for the DF case captured 300 $\mu$ s after diesel SOI. Figure 10 shows the contours of diesel vapour whilst figure 11 shows the NG. Figure 12 shows an overlay of the contours of mass-fraction for both diesel and NG. EOI of the diesel occurred shortly after this series of results whilst the NG injection continued for several milliseconds afterwards.

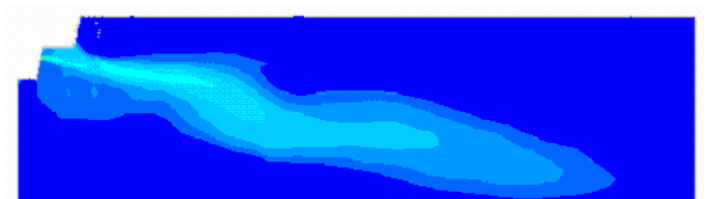


Figure 10. Plot of the contours of diesel mass-fraction at 300 $\mu$ s after diesel SOI and 100 $\mu$ s after NG SOI. The distorting effect of the NG injection can be seen.



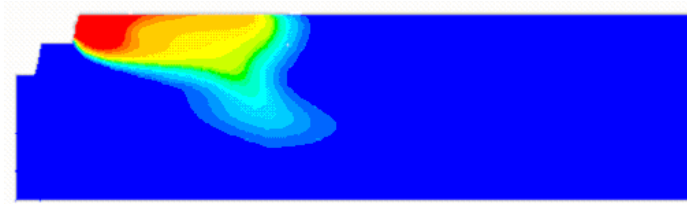


Figure 11. Plot of the contours of NG mass-fraction at 300 $\mu$ s after diesel SOI and 100 $\mu$ s after NG SOI. Red is a high concentration, blue is low.

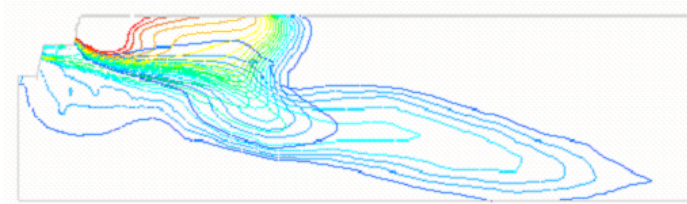


Figure 12. Overlaid contours of both NG and diesel mass-fraction at 300 $\mu$ s after diesel SOI and 100 $\mu$ s after NG SOI. Significant mixing of the two fuels is clearly evident.



Figure 13. Schlieren image of a laboratory test 300 $\mu$ s after diesel SOI and 100 $\mu$ s after NG SOI. Diesel and NG injection pressures are 1,600bar and 160bar respectively.

In a real engine, the duration of the gas injection used in the case studied here (4.1ms) may be a little long (one engine stroke at 2,000rpm is 15ms in duration). In a production injector there would be some benefit in making the gas orifices say, 0.6mm in diameter rather than the 0.4mm modelled here. A 0.4mm nozzle was chosen here to enable controlled switching of the gas in the laboratory environment. By making the nozzle only 0.4mm in diameter, the flow time required to deliver the correct mass of gas through the injector was high enough to be achieved accurately. Having said that, there may actually be a benefit in engines for some applications in having an injection as “slow” as that modelled here. This slow injection rate and subsequent burning would help with control of NO<sub>x</sub> emissions which often occur as a result of the rapid energy release with modern, high-pressure diesel injectors.

### Future Work

Previous studies [7] have shown that the auto-ignition of diesel jets occurs in a diesel vapour concentration band between the equivalence ratios of 1 and 1.5. Subsequent flame development along mixture contours close to stoichiometric then occurs rapidly from there. Thus ignition delay is a function of how quickly the atomised fuel evaporates and forms mixture concentrations conducive to auto-ignition. The evaporation rate depends heavily on conditions into which the fuel is sprayed, especially the temperature and pressure within the cylinder at SOI. The cetane number of the diesel fuel also plays a significant role in cold-start conditions and during warm-up. The staging of the NG injection should therefore be varied depending upon the operating conditions of the engine.

The CFD models developed enable fast and inexpensive testing of operation under these varying conditions. Mesh and time-step independence of the numerical models has not been confirmed at this stage. Such studies are presently being conducted so that

future cases with varying injector orientation and staging can be studied in a way which optimises the computational resources available.

### Conclusions

The CFD models created and now running enable identification inside the cylinder of diesel, NG and air mixtures within the flammability range and the number of such potential ignition sites early in the process. The orientation and staging of the gas injection relative to the diesel jet is being varied and the results assessed to find the case whereby ignition delay of the DF injection can be minimised. From there, the final combustion rate is determined for a variety of engine operating conditions.

This data is to be used to find the optimum parameters for the design and development of a production DF injector. Numerical modelling allows quantitative analysis which is not possible using the high-speed photography alone. The laboratory images are, however, being used to validate the numerical work on a qualitative basis using parameters which can be directly compared, ie. spray penetration and shape. Combustion testing in the laboratory will ultimately be carried out using the Rapid Compression Machine.

### References

- [1] Fluent 6.1.18 User's Guide, © Fluent Inc., 2003.
- [2] Hong, K.B., Department of Thermal Engineering, ChoongJu University, Korea, Ryou, H.S., Ko, G.H. & Lee, H., Department of Mechanical Engineering, ChungAng University, Korea, The Influence of Breakup Time Constant and Cavitation Modeling on Numerical Simulation of High-Pressure Diesel Sprays, ILASS Asia '00, 5<sup>th</sup> Annual Conference on Liquid Atomization and Spray Systems, Tsukuba, Japan, 14-15 December 2000.
- [3] Kloeckner, S., Analysis of a Preliminary Design of a Hydraulically-Actuated Natural Gas Injector, Masters Thesis, The University of New South Wales, June 2002.
- [4] Kong, S.C., Senecal, P.K. & Reitz, R.D., Engine Research Center, University of Wisconsin-Madison, Developments in Spray Modelling in Diesel and Direct-Injection Gasoline Engines, Oil & Gas Science and Technology, Volume 54, 1999.
- [5] Mbarawa, M., Problems Related to the Combustion of the Gaseous Fuel (NG) in Diesel Engines; PhD Thesis, The University of New South Wales, 1998.
- [6] Reitz, R.D. & Bracco, F.V., Mechanism of Atomization of a Liquid Jet, Physics of Fluids, 1982, Volume 25, p.1730-1742.
- [7] Rife, J. & Heywood, J.B., Photographic and Performance Studies of Diesel Combustion with a Rapid Compression Machine, SAE Paper 740948.
- [8] Soteriou, C., Andrews, R. & Smith, M., Lucas Diesel Systems, Further Studies of Cavitation and Atomisation in Diesel Injection, SAE Paper 1999-01-1486.
- [9] Tanner, F.X., Swiss Federal Institute of Technology and Paul Scherrer Institute, Liquid Jet Atomization and Droplet Breakup Modeling of Non-Evaporating Diesel Fuel Sprays, SAE Paper 970050.

The Turbulent Wind Environment of Birds, Insects and MAVs

S. Watkins<sup>1</sup> and G. Vino<sup>1</sup>

<sup>1</sup>School of Aerospace, Mechanical & Manufacturing Engineering  
RMIT University, Melbourne, Australia

Abstract

Measurements are described that document the time-averaged and transient velocities at a height of 4m above the ground that provide insight into the turbulent flow environment of micro flight. These were made using a bank of four multi-hole probes laterally separated by 150 mms on a mast above a test car. Fluctuating pitch angles were investigated and it was found that the variation with lateral separation was significant, even under light winds, and that this did not reduce significantly as the separation reduced. This implies that the roll inputs arising from vertical fluctuations in the atmosphere would increase with reducing wingspan posing considerable control problems for man-made micro air vehicles.

Introduction and Aim

The natural world and the human constructed environment are significantly influenced by the atmospheric boundary layer (ABL) which extends from the ground surface to between 100 and 1000m, depending upon climatic conditions and terrain. The mean (time-averaged) and turbulent effects of the atmospheric wind in the ABL strongly affect the design of land-based structures and they also play a significant role in the design and operation of aircraft. In nature, the upper speed boundary of flight is set by a combination of the mean wind speed and gustiness inherent in the atmosphere. Atmospheric winds present a challenge to insects and birds – with the speed at which they curtail flying set by their capability to negotiate a desired flight path and/or strength limitations on their wings.

There is a considerable body of work on the flight speeds of birds and insects e.g. see Table 1, reproduced from [1]. Under relatively low wind speeds the smaller flying insects remain grounded, and as the wind speed rises, increasingly larger insects, then birds, then aircraft, become grounded. Tennekes [1] comments that there is a considerable difference between the maritime climate and a continental one thus ocean birds, living in a relatively windy environment, tend to have larger wingspans than their more continental counterparts.

Whilst the flying speed of birds and insects has received much attention, data on the turbulent flow environment is relatively scant. Much work has been done on understanding the turbulence inherent in atmospheric winds and its effects on the response of structures and large aircraft; see for example [2] but the small scale structures that are relevant to smaller flying birds and insects remain a mystery to those outside their world.

The design and use of Unmanned Air Vehicles (UAVs) are currently areas of significant interest, including miniaturizing and controlling such vehicles to meet the mission requirements for a wide range of commercial and military operations [3], [4] and [5] and currently there is strong interest on emulating the insect world including replication of a one-inch robotic fly [6].

Micro air vehicles (MAVs) typically have a spans that range from the fly scale to the larger birds. MAV operations are of relatively short flying duration and at low speed close to the ground. Thus they are “immersed” in the lower part of the ABL. Since MAVs are to be flown “over hillside, around street corners or up to a window for reconnaissance and surveillance” [3] they will be operating in the “roughness zone” where the wakes of the local surface obstructions are significant. The wind environment of cities is known to be complex and the wakes of ground-based objects can increase the turbulent energy levels. When the wind is present the operational environments of MAVs are turbulent; far more so than larger aircraft that cruise above the ABL.

Watkins demonstrated outdoor flight of aircraft of 65g, [7]. In addition to the prior documentation, personal experience has shown that the largest challenge to their flight is overcoming the effects of turbulence, particularly small vortices and eddies that are inherent in atmospheric turbulence that produce seemingly random roll and pitch inputs. This seems due to the relative size of structures in atmospheric turbulence as well as the effects the mean atmospheric wind. It is considered that this restriction would curtail the number of possible days per year that they could be used for outdoor activities.

The aim of the work reported here is to further the understanding of the turbulent flow environment by measuring the transient flow vectors at four laterally separated points in space corresponding to a “span” of 150 mms.

0.6			
1	1	Light air	Butterflies
2	2	Light breeze	Gnats, midges, damselflies
3			
4	3	Gentle breeze	Human-powered aircraft, flies, dragonflies
5			
6	4	Moderate breeze	Bees, wasps, beetles, hummingbirds, swallows
8			
10	5	Fresh breeze	Sparrows, thrushes, finches, owls, buzzards
	6	Strong breeze	Blackbirds, crows
	7	Near gale	Gulls, falcons
20	8	Gale	Ducks, geese
	9	Strong gale	Swans, coots
	10	Storm	Sailplanes
30	11	Violent storm	Light aircraft
	12	Hurricane	

Table 1 Flying Speeds of Insects, Birds and Aircraft



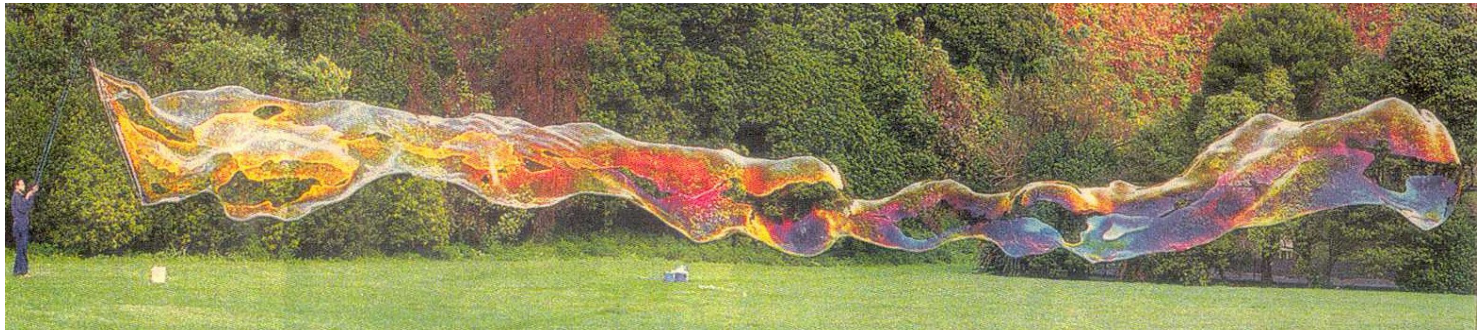


Figure One The Largest Bubble in the World (1998). Photo Courtesy Reuters.

A useful and interesting depiction of atmospheric turbulence very close to the ground is given above in Figure 1 (note the person standing in the left hand side for an indication of scale). Although surface tension effects minimise the influence of the extremely small structures in the atmosphere, distortion of the soap film depicts some of the smaller scale structures in the first few metres of the ABL that influence micro flight. The influence of various scale eddies are apparent, ranging from less than half a metre to approximately 15 metres (the total length of the bubble is 32 metres). Less evident, but arguably more significant to the flight of MAVs, is vorticity about a horizontal axis which is apparent one-third way along the length of the bubble and towards the end.

#### Multi-Point Measurements

Four TF<sup>1</sup> multi-hole probes of 3 mm head dimension were utilised with lateral separations of 150 mm, thus covering a ‘span’ of 450 mm, see Figure 2. The probes provide a more robust alternative to hot-wire anemometers yet, via a dynamic calibration, have a frequency and amplitude response that is flat from 0 to 2,000Hz and are accurate from a mean velocity of about 2-40 m/s. In turbulent flow the velocity vector is constantly fluctuating in angle and to enable resolution of the fluctuating vector the probes are calibrated over a cone of +/-45 degrees. Data that fall outside the acceptance cone are flagged by the software.



Figure 2 The Four Multi-Hole Probes

Details of pressure probe systems, verification and examples of use can be found in Watkins et al [8]. The probes were mounted 4.0 m from the ground on a mast above a vehicle and aligned nominally to the direction of motion, see Figure 3.

#### Calibration and Data Processing

The probes were calibrated by the manufacturer for velocity and frequency response. In order to measure the exact alignment angles of pitch and roll referenced to the horizontal and direction of travel, and to check the velocity calibration, runs were performed at 100 km/h (27.8 m/s) under calm conditions. The

maximum variation in relative velocity averaged over each run between each probe (for several runs) was 0.3 m/s with a typical variation of 0.1 m/s. The maximum variations in averaged pitch and yaw angles between each probe after (minor) offsets had been removed were 0.2 degrees. The proximity effect of the car body on velocity and angle was not accounted for. However prior experience with sensors mounted closer to the car body than was the case for this work, had shown the proximity effect to be relatively minor and is not thought to significantly influence the results.

The four probes were simultaneously sampled at 6,500 Hz and to avoid aliasing data were filtered and down sampled to 375 Hz. This was thought to be a good compromise between excessive data capture and resolving frequency. Prior work had shown that under atmospheric winds of upto 9 m/s and a vehicle speed of 100 km/hr there is little turbulent energy above 100 Hz.

For the moving vehicle runs a sample length of 10 seconds was used. For documenting the atmospheric wind (ie when the vehicle was stationary) 100 seconds samples were used and these data were captured whilst the vehicle was parked close to the start or end of a moving run, on locations that were selected to be away from local effects (buildings, trees etc).

Arithmetic averages of the magnitude of relative velocities were calculated over the duration of each run to determine the average relative velocities. Turbulence intensities, in the three orthogonal directions, were calculated by dividing the standard deviation of each longitudinal, lateral and vertical fluctuation by the averaged relative velocity and expressed as a percent.

#### Test Strategy and Routes

The four sensors were ‘flown’ along various roads in Victoria in order at 40, 60, 80 and 100 km/h either directly into or against the prevailing wind to obtain data relevant to a flying aircraft. Vehicle stationary (relative to the Earth) data were obtained in order to document the atmospheric winds. The terrain would be classed as category 2 in the Australian Wind Code (‘open terrain with well scattered obstructions having heights generally of 1.5 to 10 m’). A large volume of data was recorded and only selected portions are presented here. These selected data were obtained during a 20 minute period and the vehicle stationary data sets (100 seconds duration) were obtained either side of the moving vehicle runs (10 second duration). For the data presented here the mean atmospheric wind was aligned to the road direction within 15 degrees and for most runs this was less than 10 degrees.

#### Results and Discussion

Time averaged data from the vehicle stationary tests indicated that the mean atmospheric wind  $V_w$ , was of 4-5 m/s in strength, details can be found in Watkins and Melbourne [9]. This is very close to the average windspeed at this height. The averaged outputs of each probe indicated that there was not a significant difference in mean speed between the four locations in space, but some slight variation in turbulence intensities was found. The values of longitudinal, lateral and vertical intensities (denoted  $I_u$ ,  $I_v$  and  $I_w$ ) are close to the (limited) existing atmospheric data considering the height of the probes and terrain.

Single point velocity spectra (obtained from one probe output) were found to be closely similar to a von Karman spectra for atmospheric turbulence at this height, Figure 3

<sup>1</sup> Turbulent Flow Pty Ltd

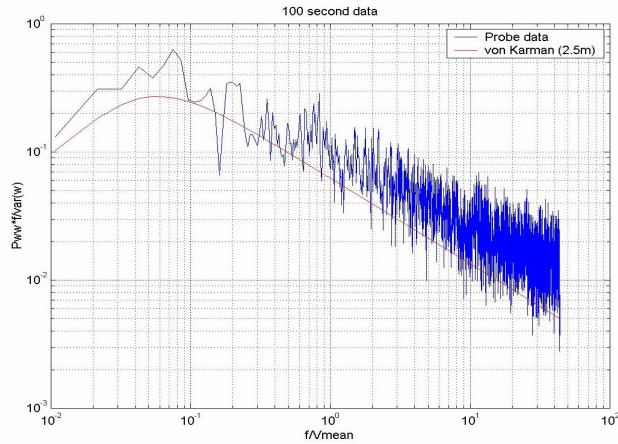


Figure 3 A Typical Spectrum from a Single Probe

Once motion is imposed (via moving the vehicle and probe system) the relative fluctuation magnitude experienced by the relative motion are reduced and the frequencies are increased. Figure 4 shows the relative turbulence intensities for the three orthogonal directions relative to the average direction of flight.

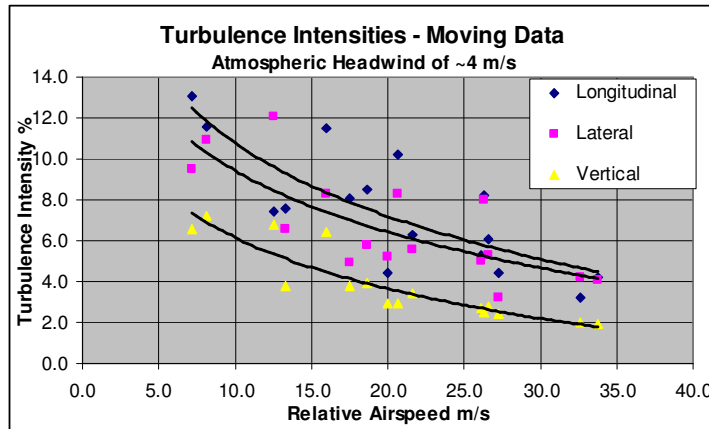


Figure 4 The Influence of Velocity on Turbulence Intensities

For 8 m/s air speed (which is a reasonable flying speed for small birds, see Table 1) relative turbulence intensities are of the order of 7 to 12%. It is interesting to note that for zero forward motion (but still subject to atmospheric winds) a hovering craft and a building will be subject to the same levels of atmospheric turbulence. In the field of building aerodynamics it is considered mandatory to simulate turbulence, whilst for aeronautical testing zero turbulence is strived for!

### Time Histories

For selected data sets the instantaneous velocities and pitch angles are presented. Figure 5 and 6 show the variation of velocities and pitch angles for all four probes as a function of time for case of an 8 m/s flight speed through 4m/s atmospheric winds. Immediately apparent is the large variation in velocity and pitch angles ( $\pm 15$  degrees) with time but all measurement points appear to have instantaneous velocities and pitch angles that are reasonably well correlated. However closer examination reveals that there are considerable differences pitch angles – Figure 7 depict short sections of data. At times there are differences in pitch angles of 20 degrees between Probes 2 and 3 which are laterally spatially removed by 150 mm. This is far greater than experimental error (estimated to be less than one degree).

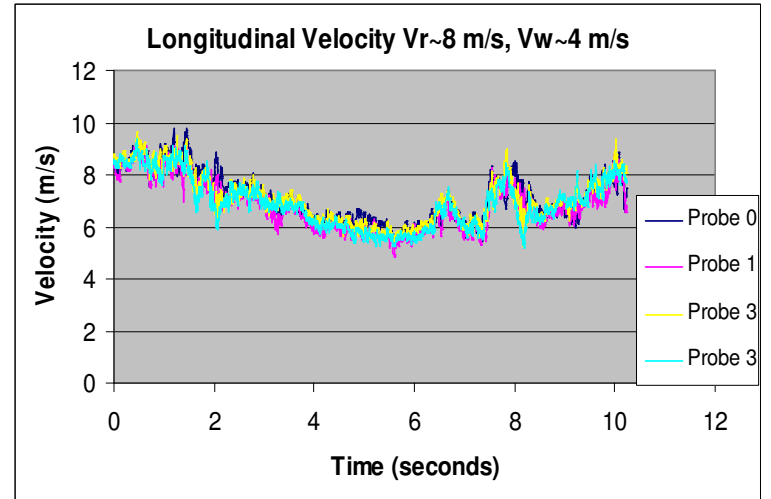


Figure 5 Longitudinal Velocity Time History

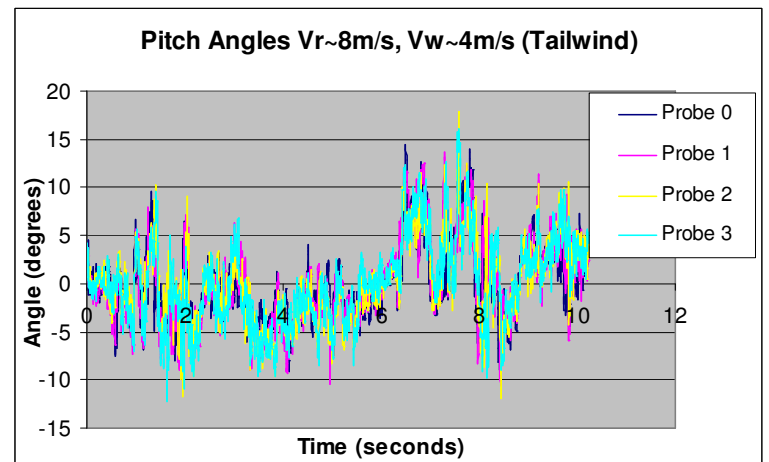


Figure 6 Pitch Angle Variation with Time

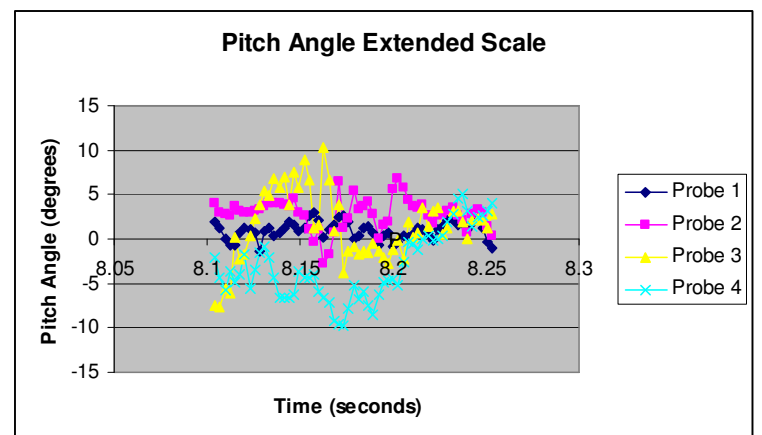


Figure 7 Pitch Angle Variations – Expanded Scale

It is useful to examine the variations in flow pitch angles that would be incident across the span of a MAV, in order to understand transient rolling moments. Plotted in Figures 8 to 10 are the differences in pitch angles between Probe 0 and Probes 1, 2 and 3 respectively for the first data set in Table 2. It can be seen that there seems little difference in variation as a function of lateral spacing.

The standard deviation of variation in pitch angles as a function of spacing is shown in Figure 11. The results for all combinations of probe spacing are plotted but are not readily evident since the points are almost coincident (eg for 150 mm separation data there are 3 data points arising from the three possible data sets Probe 1-0, Probe 2-1, Probe 3-1). It is interesting to speculate on the pitch angle differences at spacings less than 150mm or greater than 450mm.



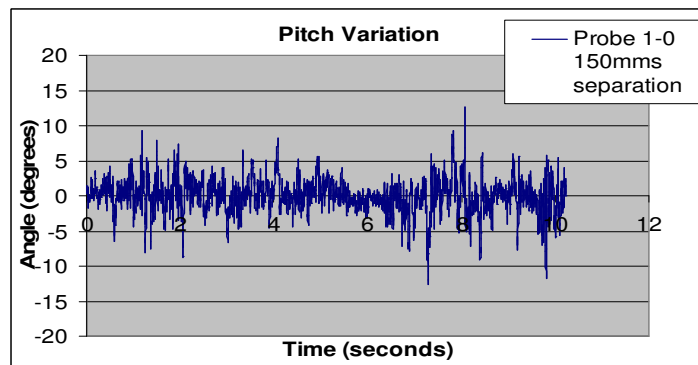


Figure 8 Pitch Angle Variation 150 mms Separation

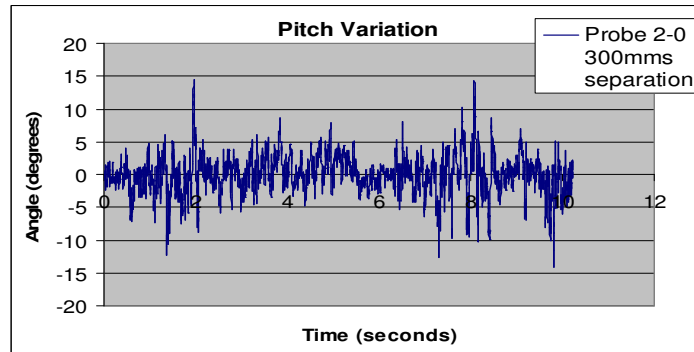


Figure 9 Pitch Angle Variation 300 mms Separation

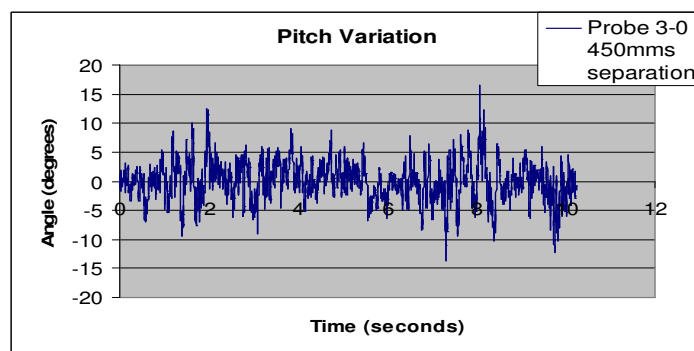


Figure 10 Pitch Angle Variation 450 mms Separation

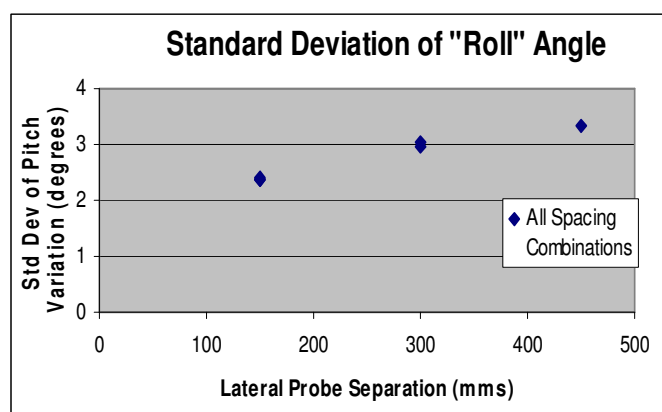


Figure 11 Standard Deviations of Pitch Variation vs Separation

## Conclusions

Atmospheric conditions can vary from calm to cyclonic. Under no wind conditions the flight environment is smooth (aside from the wakes of other moving objects) whereas at the other extreme even large aircraft remain grounded. However days of zero or very low atmospheric winds are rare. An examination of the probability distributions of wind speed for one site<sup>2</sup> reveals that that most probably wind speed is approximately 4 m/s and

average wind speeds below 2 m/s occur for less than 10% of the time. Clearly distribution varies with location height, terrain etc.

Further processing of the data sets gathered here is planned, including investigation of the effects of the turbulence on the motion of MAVs (from measured aerodynamic derivatives). High speeds and high masses will minimise aircraft motion through the ABL but this is in direct conflict with low speed manoeuvrability.

Unlike the majority of wind engineering data sets, the measurements taken here were for elevations that were close to the height of the ABL roughness zone. It should be noted that this is the environment in which MAVs are envisaged to collect data. Since the proposed environment of MAVs is through irregular terrain such as city canyons where very disturbed flow environments exist further work is considered necessary.

It is interesting to note that the variation in pitch angles with lateral separation (a parameter that is thought to influence the roll controllability of aircraft) is complex and that reducing separation from 450mm to 150mm appears to make relatively little difference to the variation, indicating that the roll rates induced by turbulence would increase as span reduces. Further work in this area is planned, including reducing the lateral spacing of the probes to 37.5 mm and analysing an existing data set obtained with a longitudinal probe separation, in order to understand the correlation of disturbances over aircraft of various spans and tail moments.

The potential roll inputs are of such significance it is postulated that it will be very hard to hold a relatively stable viewing platform. Clearly we have some way to go before we can emulate small-scale natural flight and how it has adapted to the turbulent wind environment.

## References

1. Tennekes H., "The Simple Science of Flight", MIT Press, ISBN 0-262-70065-4
2. Holmes J. D., "Wind Loading of Structures", Spon Press, London, 2001, ISBN 0-419-24610-X.
3. Burger, K., "Micro Air Vehicle Demo Approaching", Janes Defence Weekly, Janes Publications, UK, Vol 36, Issue No 14, pp 6, 12 September 2001.
4. Burger, K., "Budget Boost for UAVs and Counter-terrorism", Janes Defence Weekly, Janes Publications, UK, Vol 37, Issue No 1, pp 6, 2 January 2002a.
5. Anon "UAVs Applications are Driving Technology – Micro Air Vehicles", UAV Annual Report, Defence Airborne Reconnaissance Office, Pentagon, Washington, pp 32, 6 November 1997.
6. Wilson and Schnepf, "Micro Air Vehicles – New Military Capability", proc. 16<sup>th</sup> Int Conf on UAVs 2-4 April 2001, Bristol, UK.
7. Watkins S., "Development of a Micro Air Vehicle", The Aeronautical Journal, February 2003.
8. Watkins S, Mousley P and Vino G., "The Development and Use of Dynamic Pressure Probes With Extended Cones of Acceptance (ECA)", 14<sup>th</sup> AFMC, Sydney, Dec 2004.
9. Watkins S. and Melbourne W. H., "Atmospheric Turbulence and Micro Air Vehicles", 18<sup>th</sup> Bristol International Conference on UAV Systems, Bristol University, UK, March 31 - April 2, 2003.
10. Watkins S and Saunders J. W., "A Review of the Wind Conditions Experienced by a Moving Vehicle", SAE Technical Paper 981182 in *Developments in Vehicle Aerodynamics*, 1998, ISBN 0-7680-0138-2

<sup>2</sup> Obtained over 42 years at a height of 10m for a site in Australia, see Watkins and Saunders [10]

# Coherent Structure Dynamics in Jets from Irregular Shaped Nozzles

J. Hart<sup>1,2</sup>, J. Naser<sup>1,2</sup> and P. Witt<sup>1,3</sup>

<sup>1</sup>Cooperative Research Centre for Clean Power from Lignite

<sup>2</sup>School of Engineering & Science, Swinburne University of Technology, VIC, 3122 AUSTRALIA

<sup>3</sup>CSIRO, Division of Minerals, Clayton, VIC, 3169, AUSTRALIA

## Abstract

Computational Fluid Dynamics was used to model spatially developing, initially laminar, gas jets issuing from nozzles of regular and irregular cross-section, using the Large Eddy Simulation (LES) technique. Nozzles were based on bluff jets used in tangentially fired lignite-burning furnaces. Validation of the LES based model was achieved by comparing predicted jet entrainment rates with published experimental and numerical data. Large-scale coherent turbulent structures including ring and braid vortices and other stream wise structures are predicted by the LES model. The shape of the ring vortices formed was found to directly relate to the nozzle geometry. Size and proximity of discontinuities in the vortex rings were observed to determine how strongly a vortex ring deforms, furthermore discontinuities in the ring curvature were found to alter the number of stream wise structures formed. Jets with only a single pair of braid vortices per side were predicted to spread along their axes while those with multiple braids spread more uniformly.

## Introduction

Bluff (rectangular) jets have numerous applications, from low heat-signature jet engines to slot burners in lignite-fired boilers. The entrainment and spreading characteristics of bluff jets are considerably different to those from circular nozzles, due largely to the dynamics of the coherent structures that develop from the nozzle [5]. Bluff jets entrain more fluid and spread more rapidly than circular jets because vortex rings from rectangular nozzles deform more rapidly and to a greater extent than rings from circular nozzles. Coherent structures deform according to (1), the equation for self-induced velocity,  $u$ , of a vortex ring, [1]

$$u \propto C b \log(\sigma^{-1}) \quad (1)$$

where  $C$  is the local curvature of the ring,  $b$  is the binormal to the plane containing the ring and  $\sigma$  is the local vortex ring thickness or cross-section. Circular rings have uniform curvature resulting in a uniform self-induced velocity according to (1) and are therefore quite stable. Rectangular rings contain large differences in curvature between the straight edges and corner regions; the self-induced velocity of the vortex ring is not uniform, leading to increased deformation [5].

Controlled combustion of coal is highly desirable in tangentially fired boilers in order to provide uniform and predictable heat release. Entrainment characteristics determine how well the fuel-laden primary jet is heated by the hot combustion products within the boiler and also how well it mixes with air from co-flowing secondary-air jets. Tangentially-fired boilers are designed such that most of the combustion occurs within a fireball at the centre of the furnace. The near-field entrainment characteristics must be controlled to prevent early combustion and to conserve sufficient momentum for the jet to reach the centre.

The use of coherent structures as a means of controlling shear flows by selective suppression or augmentation of turbulence is discussed in [10]. One possible method of passive control put forward is an alteration to the initial conditions of the shear flow such as altered velocity profiles. The use of intrusive tabs at the

nozzle exit to introduce extra turbulence has been used to increase mixing of rectangular jets with their surroundings [2]. The high rates of wear caused by coal particles make this impractical in coal-burner nozzles. This paper proposes that by combining the properties of circular and rectangular jets the mixing characteristics may be altered, and these characteristics might then be used to selectively enhance or suppress mixing and spreading rates. In order to investigate this, coherent structure dynamics were modelled in jets that are geometrically and hydrodynamically similar to burner jets, with novel semi-circular, semi-rectangular nozzles, hereafter referred to as hybrid nozzles.

## Numerical Methods and Boundary Conditions

Two aspect ratio (AR) rectangular nozzles (PRI/SEC), one circular nozzle (CIRC) and one hybrid nozzle (HYB) are presented here. The two rectangular nozzles were similar to typical primary and secondary jet nozzles in a slot burner. The HYB nozzle was essentially the PRI nozzle but the radius of curvature of the corners on one side was half the nozzle's height.

The same mesh was used for each nozzle, with different top-hat velocity profiles imposed on the mesh boundary. The peak mean velocity was 60 m/s and the thickness,  $\delta_0$ , of the linear shear layer was four mesh elements in all cases. The rectangular corner regions of the nozzle were slightly rounded to ensure a uniform initial vorticity thickness,  $\sigma$ , in (1). To facilitate the roll-up of the shear layer into coherent structures the inlet velocity was perturbed according to a sine function whose frequency resulted in the Strouhal numbers,  $St_\delta = f\delta/U$ , shown in table 1, which were within the range of preferred natural jet frequencies of these jets. The table compares some hydrodynamic properties of these and other jets from the literature, which were used for validation. Reynolds number was based on the nozzle hydraulic diameter,  $D$ .

Run	AR	Re	$St_{\delta_0}$	$D/\delta_0$	M
PRI	1.2	270,000	0.041	10	0.17
PRI2	1.2	270,000	0.0496	10	0.17
SEC	2.2	205,000	0.041	7	0.17
CIRC	1.0	139,000	0.041	8	0.17
HYB	1.2	250,000	0.041	9	0.17
SQ1	1.0	>85,000	0.043	11	0.3
SQ3	1.0	>85,000	0.043	11	0.6
SQ4	1.0	>120,000	0.027	16	0.6

Table 1: Hydrodynamic Properties of Jets.

Jets were modelled using a Large Eddy Simulation model based on that of [15], with the Smagorinsky constant,  $C_s$ , set to 0.1. A finite-volume coupled solver, CFX5.7, was used to solve the equations on an unstructured mesh containing a mixture of hexahedral and tetrahedral elements. Temporal discretisation was achieved using second-order backward-Euler time-differencing. Spatial discretisation used the quadratic the third-order QUICK differencing scheme. The chosen time step resulted in a Courant flow number of 4, which was found to be stable.

## Results

In order to validate the LES model and to provide a source of comparison for the hybrid jet simulations, PRI, PRI2 and SEC



were compared with [5] and [7]. Time-averaged statistics were collected for 36 forcing periods of the inlet velocity perturbation, beginning after 4 initial periods. Figure 1 shows the mass flux in the jet,  $Q$ , normalized to the mass flux at the nozzle,  $Q_0$ , for each simulation and for the experimentally measured mass flux in square, circular and elliptic jets as well as the square jet simulations of [5], who averaged over only eight forcing periods.

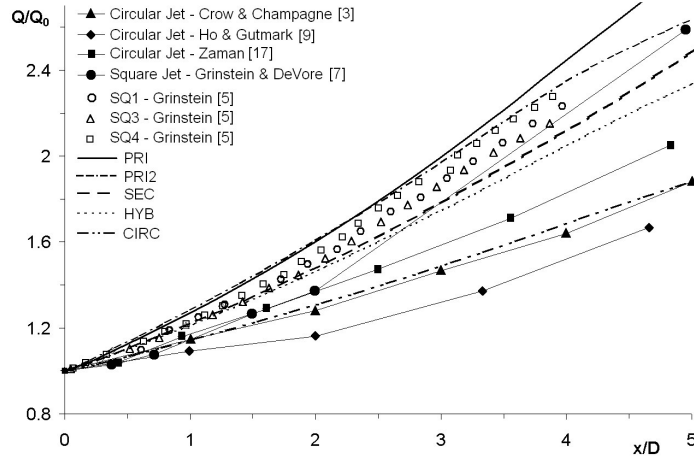


Figure 1: Comparison of Entrainment Rates with Literature.

The entrainment rate (slope of curve) for PRI and PRI2 was very close to the square jets of [5], although slightly higher. The domain modelled here was slightly smaller than in [5], and [6] showed that for a larger computational domain the measured entrainment tends to be reduced, due to an increased contribution from reverse flow in the outer jet region. Figure 1 shows how the rate of entrainment increased in PRI, PRI2 and SEC downstream of the nozzle. For SEC the increase in aspect ratio reduced the entrainment rate, in agreement with [6] for rectangular jets and [14] for elliptic jets. Entrainment rates for circular jets are lower than for rectangular jets of any aspect ratio, and are relatively constant. The entrainment rate of CIRC was within the range of circular jets in the literature.

Separate entrainment curves for the circular side, the rectangular side and the total entrainment in HYB are shown in figure 2. The entrainment was similar to SEC, even though the aspect ratio was the same as PRI. Entrainment by the circular side was significantly higher than in the circular jet of the same diameter. In addition the rate of entrainment was not constant but in fact reduced after three nozzle diameters. Entrainment on the rectangular side was initially very similar to the circular side, although marginally less, but at around three diameters the rate increased and the two curves crossed over. At around four diameters the circular side showed a marked drop in entrainment rate with a corresponding increase on the rectangular side.

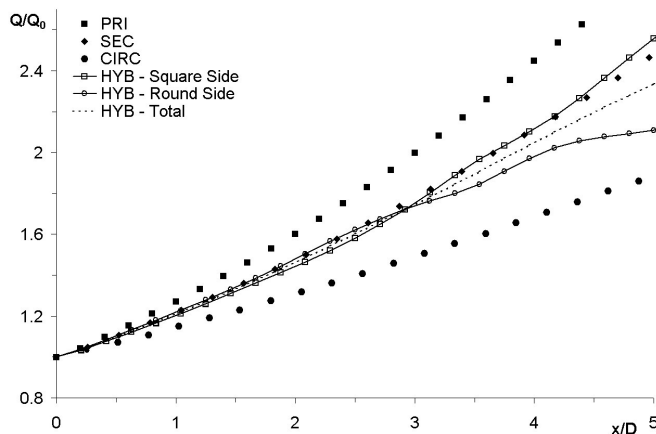


Figure 2: Entrainment Rates for Simulated Jets.

The preceding illustrates how the shape of the nozzle has a large influence on jet entrainment, especially in the near field. What follows is an explanation of this phenomenon by describing the dynamics of the large-scale turbulent structures as they develop within the jet shear layer.

After [11], the black hashed surfaces in figure 3 show regions where the pressure is lower than  $2/3 p_{min}$  and indicate the structure of the vortex rings clearly, while the grey shows isosurfaces of 40% of peak vorticity and indicates the larger turbulent eddies, including vortex rings. The frames cover one full period of oscillation of the inlet velocity. The rings deformed in a manner very similar to the square and rectangular jet simulations of [5], [6] and [7]. The corner regions of the initially planar ring deformed by moving ahead of the plane containing the ring and in towards the jet axis, while the straight sections moved behind and away from the axis; all due to the effects of self-induced velocity (1), with higher self-induced velocity in the corner regions with high curvature, and zero self-induced velocity in the straight sections due to the lack of curvature. A more thorough description of the mechanism can be found in the above papers.

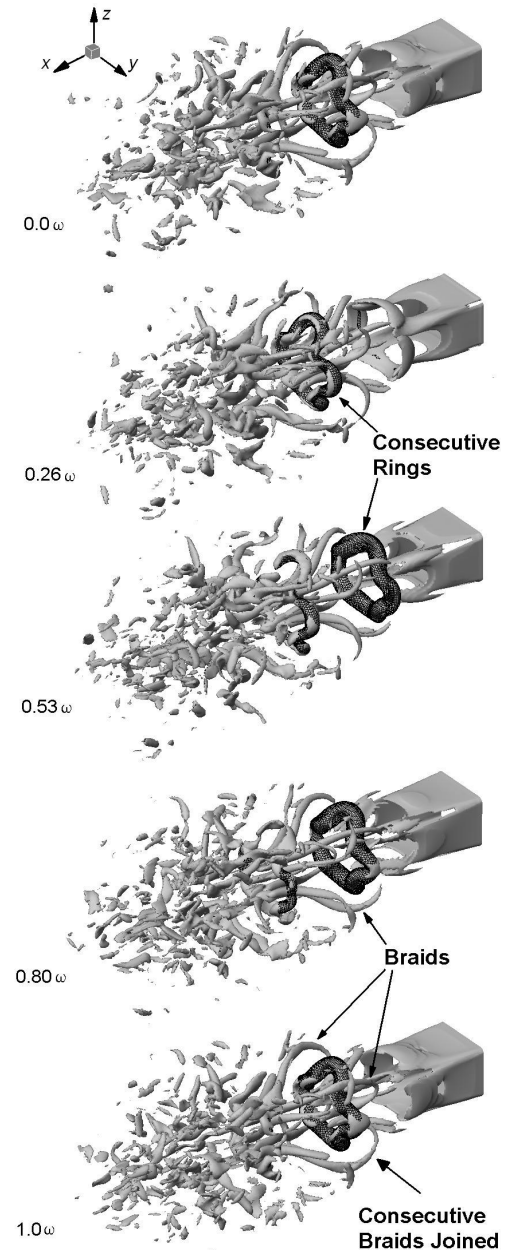


Figure 3: Dynamics of Coherent Structures in PRI as a function of dimensionless time,  $\omega$ .

Long thin structures (braids) appeared between the rings, similar to braid vortices in a mixing layer [12]. Braids are created by instabilities in the mixing layer and are formed in counter rotating pairs. Since a vortex ring is essentially a mixing layer wrapped around onto itself the appearance of these secondary structures between vortex rings is expected and has been noted by the majority of authors investigating coherent structures in jets. In their studies of “side jet ejections” in circular jets, [13] added the contribution of stream-wise vortices to their proposed jet-spreading model of 1989 that only included ring vortices.

The braids were grouped in pairs similar to a mixing layer, one pair per corner, and counter-rotating such that fluid was drawn between them from within the jet core and expelled outwards. The downstream ends of one set of braids on the longer side of the jet periodically joined with braids forming behind the upstream ring on the short sides of the jet, indicated by an arrow in figure 3. No such behaviour could be found in the literature.

Shear layer development in jets occurs due to entrainment of fluid from the surroundings and redistribution of fluid from the jet core. The effect of the different modes of coherent structures on the mean velocity profile of each jet is shown in figure 4. Mean velocity profiles are shown for each jet in the  $yz$  plane at the same distance downstream of the nozzle normalised to  $D_{PRI}$ . A snapshot of the coherent structures in the jet is also shown.

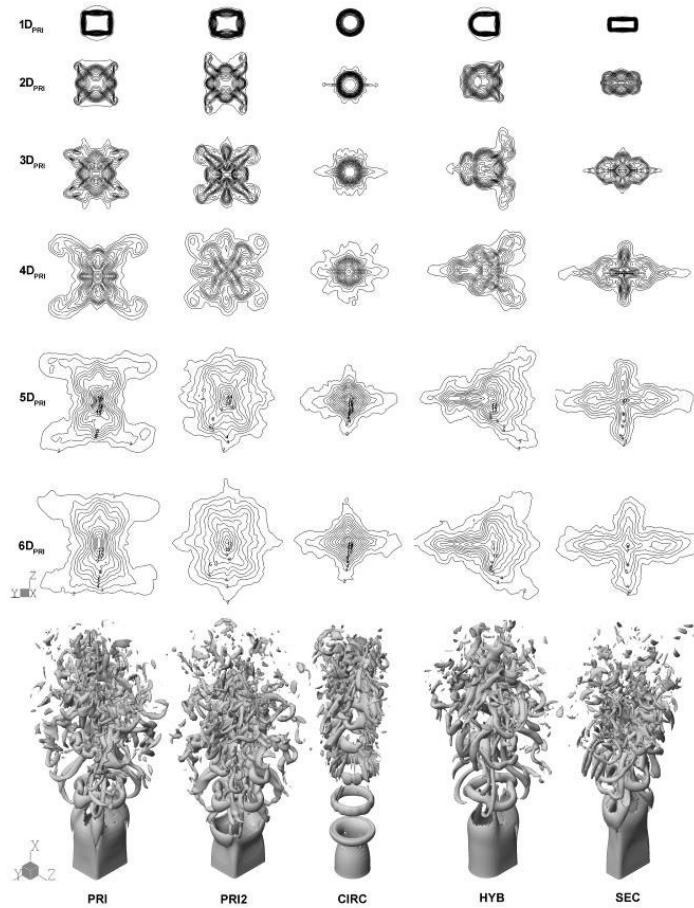


Figure 4: Development of Mean Velocity Profiles.

Although both primary jets produced the same general coherent structure behaviour, i.e. almost square rings and four pairs of counter-rotating braid vortices, the resulting shear layers were notably different. Due to the higher frequency in PRI2 the rings rolled up closer to the nozzle than those in PRI, initiating the shear layer spreading process somewhat sooner. The braid vortices contributed significantly to redistribution of momentum in the diagonal cross-stream directions of the shear layer. In PRI the rings switched axis once and then began to break up, so the

fluid in them continued to convect in the same direction along the minor axis, with little spreading occurring in the major axis. The rings were preserved longer as a coherent structure in PRI2, allowing them to continue deforming and giving a more uniform shear layer by  $6D_{PRI}$ .

The dynamics of the jet SEC were similar to those of the rectangular jets of [5]. Because the corners were closer together the self-induced velocity of the corners was reinforced, compared with PRI where it was retarded by the straight sections. When viewed along the centreline axis, the rectangular ring switched axis by  $90^\circ$ , and remained like this until it dissipated into smaller structures. The stream wise vorticity only maintained one pair of braid vortices on either side of the jet, as opposed to the two pairs in PRI and PRI2. Braids associated with the shorter sides of the ring were consumed by larger structures almost as they were formed. Curiously, the braids actually became joined at the tails, rather than head-to-tail as in PRI and PRI2. Spreading of the shear layer occurred predominantly along the major and minor axes. On the major axis the contribution was dominated by the braid vortices, while on the minor axis it was by the ring vortices.

Instead of spreading uniformly in the radial direction, as one might intuitively expect, the jet CIRC actually exhibited some preferential spreading along the  $y$  and  $z$ -axes. This resulted in velocity profiles which were square, but rotated  $45^\circ$  to the axes. This was due to the peculiar braid structure that formed from the axi-symmetric rings. In PRI and PRI2, the high curvature corner regions provided locations of high stream-wise vorticity from which braid vortices could form. With a uniform initial stream-wise vorticity distribution in CIRC, braids were not triggered until instability waves deformed the ring such that stream-wise vorticity began to grow. This wave instability is well documented for isolated circular vortex rings and circular rings in jets; see for example [16] and [3]. For this simulation pairs of braid vortices of varying strength formed, two strong pairs aligned with the  $y$ -axis and four slightly weaker pairs aligned with the  $z$ -axis, resulting in more spreading on the axes. This is not a detailed investigation of the precise mechanisms of vortex deformation within circular jets, the important point is that the occurrence of the braids occurred much farther downstream in the circular jet than the rectangular ones, and they were much weaker than for the other jets, due to the initially uniform curvature of the rings.

By contrast, braid vortices of nearly equal strength formed in HYB at approximately the same time on the rectangular and circular sides. While there were two counter-rotating pairs on the square side, one for each corner as in jets PRI and PRI2, there was only one pair on the circular side, similar to SEC. The rectangular side deformed in much the same manner as in PRI and PRI2. Although the self-induced velocity of the circular side of the ring was uniform around the circumference due to its uniform curvature, the circular part of this coherent structure was effectively pinned or hinged at the points of joining to the rectangular side and as a result this part of the structure folded in towards the axis as it tried to accelerate ahead of the rest of the ring. This resulted in cross-axis mixing in HYB, the only jet to exhibit such behaviour. This can be seen clearly in the time series of figure 5 in which the circular side folds inwards, eventually crossing the axis at about  $x/D = 4$ . The movement of the ring across the central axis also forced the braids to cross the axis by about  $x/D = 3$ . These correspond to the locations in figure 1 where there was a reduction in entrainment on the round side. Figure 4 shows that HYB spread along the major axis on the circular side, which was due to the convection of the tail ends of the braid vortices in this direction, with no direct contribution from the ring structures. This reinforces the point that stream-wise vortical structures are at least as important as ring vortices in the near-field shear layer development of jets.

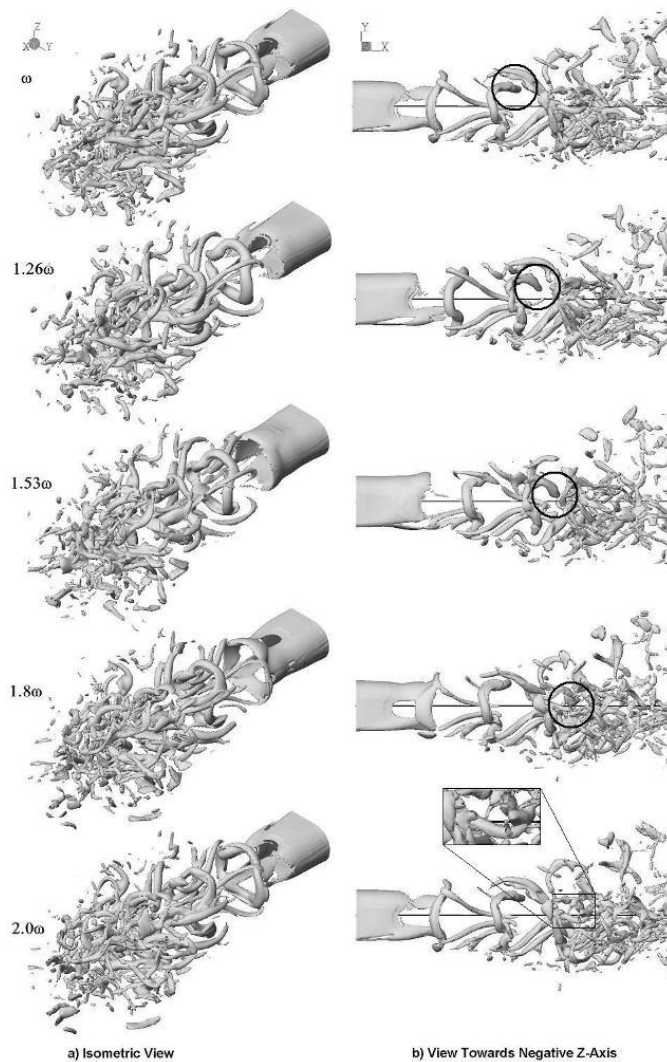


Figure 5: Coherent Structure Dynamics in HYB.

A hybrid jet was simulated with an aspect ratio of 2.2:1 [8], however, the curvature of the circular side was so close to the curvature of the rounded corners of SEC that there was no significant difference between SEC and this geometry. As a result the coherent structure dynamics were almost exactly the same, in terms of vortex ring deformation as well as in the generation and convection of stream wise coherent structures. This lead to virtually the same shear layer development as in SEC, with the shear layer spreading along the major and minor axes. For this reason the results were not shown here.

## Conclusions

For the two aspect ratio nozzles, it was only the lower ratio one that showed any significant change in the shear layer development when one side of the nozzle was rounded. The influence of nozzle geometry can be seen in two areas, the shape of the ring and the number of stream wise structures that formed due to discontinuities in the curvature of the ring.

The size and relative proximity of discontinuities in the vortex ring determine how strongly a vortex ring deforms. There was little difference between PRI and the rectangular side of HYB because  $90^\circ$  bends produce strong deformation behaviour. The circular side of HYB behaved nothing like CIRC because even the small discontinuity where the circular side joined the straight sections dominated over the uniform curvature section and caused the ring to deform in the manner it did.

Spreading of HYB along its major axis on the circular side was due to the single pair of braids that formed on that side. There

appears to be a correlation between those jets that spread along their axes and those jets with only a single pair of braid vortices per side.

## Acknowledgments

The authors gratefully acknowledge the financial received for this research from the Cooperative Research Centre (CRC) for Clean Power from Lignite, which is established and supported under the Australian Government's Cooperative Research Centres program.

The authors would to like to acknowledge the financial and other support of Swinburne University of Technology.

## References

- [1] Batchelor, G. K., *An Introduction To Fluid Dynamics*, Cambridge University Press, London, 1967, 510
- [2] Bohl, D. G., Foss, J. F., *Near Exit Plane Effects Caused By Primary and Primary-Plus-Secondary Tabs*, AIAA Journal, **37**, 2, 1999, 193-201
- [3] Cohen, J., & Wygnanski, I., *The Evolution of Instabilities in the Axisymmetric Jet. Part 2. The Flow Resulting from the Interaction Between Two Waves*, Journal of Fluid Mechanics, **176**, 1987, 221
- [4] Crow, S. C., and Champagne, F. H., *Orderly Structure in Jet Turbulence*, Journal Fluid Mechanics, **48**, 1971, 547-591
- [5] Grinstein, F. F., AIAA Shear Flow Conference, *Vorticity Dynamics in Spatially Developing Rectangular Jets*, 1993, AIAA Paper 93-3286
- [6] Grinstein, F. F., *Vortex Dynamics and Entrainment in Rectangular Free Jets*, Journal Fluid Mechanics, **437**, 2001, 69-101
- [7] Grinstein, F. F. and DeVore, C. R., 28<sup>th</sup> Joint Propulsion Conference and Exhibit, *Coherent Structure Dynamics in Spatially Developing Square Jets*, 1992, AIAA Paper 93-3441
- [8] Hart, J. T., *Numerical Investigation of Isothermal Burner-Jet Aerodynamics*, Ph.D. Thesis, Swinburne University of Technology, Melbourne, 2001
- [9] Ho, C. M., and Gutmark, E., *Vortex Induction and Mass Entrainment in Small Aspect-Ratio Elliptic Jet*, Journal of Fluid Mechanics, **179**, 1987, 383
- [10] Husain, H. S., Bridges, J. E., and Hussain, F., *Turbulence Management in Free Shear Flows by Control of Coherent Structures*, Keynote Paper – International Symposia on Transport Phenomena. Transport Phenomena in Turbulent Flows. Theory Experiment and Numerical Simulation, Hemisphere Publishing Corporation, 1988
- [11] Jeong, J., & Hussain, F., *On the Identification of a Vortex*, Journal of Fluid Mechanics, **285**, 1995, 69
- [12] Lopez, J. M., Bulbeck, C. J., *Behavior Of Streamwise Rib Vortices In A Three-Dimensional Mixing Layer*, Physic Of Fluids A, **5**, 7, 1993, 1694-1702
- [13] Monkewitz, P. A., and Pfizenmaier, E., *Mixing by "side jets" in strongly forced and self-excited round jets*, Physics of Fluids, A, **3**, 5, 1991, 1356-1361
- [14] Schadow, K., Wilson, K., Lee, M., & Gutmark, E., *Enhancement of Mixing in Reacting Fuel-Rich plumes issued from Elliptical Jets*, J. Prop. Powe..., **3**, 1987, 145
- [15] Smagorinsky, J., *General Circulation Experiments With The Primitive Equations. I. The Basic Experiment*, Mon. Weather Rev., **91**, 1963, 99-164
- [16] Widnall, S. E., Bliss, D. B., & Tsai, C.-Y., *The Instabilities of Short Waves on a Vortex Ring*, Journal of Fluid Mechanics, **66**, 1974, 35
- [17] Zaman, K. B. M. Q., *Journal of Sound and Vibration*, 106, 1986, 1-16

## CFD Investigation of Particle Deposition Around Bends in a Turbulent Flow

By A. Hossain and J. Naser

School of Engineering and Science, Swinburne University of Technology  
PO Box 218, Hawthorn, VIC 3122, AUSTRALIA

### Abstract

A comprehensive 3D numerical investigation of hydrodynamics of particles flowing through a horizontal pipe loop consisting of four bends has been modeled. The multiphase mixture model available in Fluent 6.1 [6] is used in this study. In this numerical simulation five different particles have been used as secondary phases to calculate real multiphase effect in which inter-particle interaction has been accounted. The deposition of particles, along the periphery of the wall around bends has been investigated. The effect of bend and fluid velocity on particle deposition has also been investigated. The maximum particle deposition is at the bottom wall in the pipe before entering the bends conversely, downstream of bends the maximum deposition is not at the bottom - as seen upstream of the bends - rather it occurs at an angle of  $60^\circ$  toward the inner side from the bottom. The larger particles clearly showed deposition near the bottom of the wall except downstream of the bends. As expected, the smaller particles showed less tendency of deposition and this is more pronounced at higher velocity. This numerical investigation showed good agreement with the experimental results conducted by CSIRO team [9].

### Introduction

Particle deposition from flowing suspensions is an important process in various fields of engineering and in nature. Analyzing diminutive suspended particles deposition in fluid streams has attracted considerable attention in the past few decades [1-4,9-11,13,19,20]. This is because of particle deposition plays a major role in a number of industrial processes such as filtration, separation, particle transport, combustion, air and water pollution, and many others.

The CFD (computational fluid dynamics) models to simulate the hydraulic behavior of water-distribution systems have been available for many years [10,11,17]. More recently these models have been extended to analyze water quality as well [10,11]. But at earlier days numerical computations were suffered from some serious limitations. The number of particles is one of them, which was fairly small in numerical simulations, and therefore, size effects can become important, especially with low volume fraction. In this study we have introduced water as a primary and 5 different solid spherical particles as secondary phases. The driving force behind this trend is the timely challenge to comply with increasingly stringent governmental regulations and customer-oriented expectations. Modern management of water-distribution systems like South East Water Ltd, Melbourne Water, Sydney Water, need simulation models that are able to accurately predict the hydrodynamics of particles behavior (cause of dirty water) in the water distribution networks around bends. Particle deposition on pipe-surfaces in turbulent flows had attracted the interest of many researchers. Using the stopping distance of a particle near a wall, Friendlander and Johnstone [8] developed the free-flight model for particle deposition process. Davies [5] among others offered an improved theoretical model for particle deposition rate. Liu and Agarwal [15] analyzed the deposition of aerosol particles in turbulent pipe flows. Simplified simulation procedures for deposition of particles in turbulent flows were described by Abuzeid [1], and Li and Ahmadi [14].

Hossain et al [11] represented the circumferential particle deposition in a straight pipe for turbulent flow in which researchers explained the circumferential particle deposition for a straight pipe. But that model is not applicable for circumferential deposition and hydrodynamic behavior of particles around bends. Particle deposition around bends of a circular cross section is important to the sampling and transport of particles in high-purity fluid streams [4,21]. In the recent experimental study Pui [4] revealed that discrepancies still exist between the experimental data and the available theories. These discrepancies are believed to be mainly caused by various flow field assumptions made by different investigators. Even though the problem has been studied both theoretically and experimentally by a number of investigators, it is still unclear at present as to the applicable theory for the different flow regimes. The difficulty of the flow field (3D with strong secondary motion) makes it very difficult to calculate the particle trajectories and deposition in the bend. Unfortunately, detail experiments have not been performed so far for solid-liquid flow excluding experiments for aerosol particles deposition in the bend [8,12], to be validated with this study. This study would be partially validated with the experimental [9] results.

The motivation for this study is to investigate the deposition of solid spherical particles with specific gravity 1.64 as it occurs in water supply network (South East Water Ltd, Melbourne) around bends for a test loop (figure 1). This test loop was investigated by Clive et al [9] in collaboration with South East Water Ltd. The secondary phases of such flows consist of particles with diameters ranging from  $2\text{ }\mu\text{m}$  to approximately  $20\text{ }\mu\text{m}$  for different velocities. The Eulerian description of turbulence and the role of turbulent structures in the dispersion of particles give us a better understanding in the relationship between temporal and spatial properties of turbulent flows.

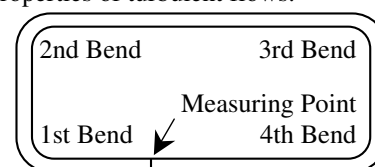


Figure 1: Schematic diagram of the pipe loop with four  $90^\circ$  bends.

To study the hydrodynamics of particles behavior in a turbulent flow field numerically: a geometry (figure 1) comprising 41 m long and 100 mm diameter pipe, close-loop with four  $90^\circ$  bends has been considered with the boundary conditions shown in table 1 that were used in the experiment [9].

Pipe loop length (m)	41.0
Diameter of the pipe D (m)	0.1
Total volume of water ( $\text{m}^3$ )	0.322
No. of phases	6
VF of each secondary phases	$332 \times 10^{-6}$ (332 ppm)
Pump	true axial flow
Average water velocities ( $\text{ms}^{-1}$ )	0.05, 0.1, 0.2, 0.3, and 0.4
Particle density ( $\text{kgm}^{-3}$ )	1640
Particles sizes ( $\mu\text{m}$ )	2, 5, 10, 15, and 20
No of computational cells	129654

Table 1: Physical and hydraulic characteristics of the system used for CFD simulation.

## Governing Equation

The Multiphase Mixture Model of FLUENT 6.1 [6] used in this study solves the continuity and the momentum equation for the mixture. Volume fraction equations are solved for the secondary phases. The model also solves for the well-known algebraic expressions for the relative velocities for secondary phases [7 Chapter 20].

### Continuity Equation for the Mixture

The continuity equation for the mixture is

$$\frac{\partial}{\partial t}(\rho_m) + \nabla \cdot (\rho_m \vec{v}_m) = 0 \quad (1)$$

where  $\vec{v}_m$  is the mass-averaged velocity:

$$\vec{v}_m = \frac{\sum_{k=1}^n \alpha_k \rho_k \vec{v}_k}{\rho_m} \quad (2)$$

and  $\mu_m$  is the mixture density:

$$\rho_m = \sum_{k=1}^n \alpha_k \rho_k \quad (3)$$

$\alpha_k$  is the volume fraction of phase k.

### Momentum Equation for the Mixture

The momentum equation for the mixture can be obtained by summing the individual momentum equations for all phases. It can be expressed as:

$$\frac{\partial}{\partial t}(\rho_m \vec{v}_m) + \nabla \cdot (\rho_m \vec{v}_m \vec{v}_m) = -\nabla p + \nabla \cdot [\mu_m (\nabla \vec{v}_m + \nabla \vec{v}_m^T)] + \rho_m \vec{g} + \vec{F} + \nabla \cdot \left( \sum_{k=1}^n \alpha_k \rho_k \vec{v}_{dr,k} \vec{v}_{dr,k} \right) \quad (4)$$

where n is the number of phases,  $\vec{F}$  is a body force, and  $\mu_m$  is the viscosity of the mixture:

$$\mu_m = \sum_{k=1}^n \alpha_k \mu_k \quad (5)$$

$\vec{v}_{dr,k}$  is the drift velocity for secondary phase k:

$$\vec{v}_{dr,k} = \vec{v}_k - \vec{v}_m \quad (6)$$

### Relative (Slip) Velocity and the Drift Velocity

The relative velocity (also referred to as the slip velocity) is defined as the velocity of a secondary phase (p) relative to the velocity of the primary phase (q):

$$\vec{v}_{qp} = \vec{v}_p - \vec{v}_q \quad (7)$$

The drift velocity and the relative velocity ( $\vec{v}_{qp}$ ) are connected by the following expression:

$$\vec{v}_{dr,p} = \vec{v}_{qp} - \sum_{k=1}^n \frac{\alpha_k \rho_k}{\rho_m} \vec{v}_{qk} \quad (8)$$

The basic assumption of the algebraic slip mixture model is that, to prescribe an algebraic relation for the relative velocity, a local equilibrium between the phases should be reached over short spatial length scales. The form of the relative velocity is given by

$$\vec{v}_{qp} = \tau_{qp} \vec{a} \quad (9)$$

where  $\vec{a}$  is the secondary-phase particle's acceleration and  $\tau_{qp}$  is the particulate relaxation time. Following Manninen et al. [16]  $\tau_{qp}$  is of the form:

$$\tau_{qp} = \frac{(\rho_m - \rho_p) d_p^2}{18 \mu_q f_{drag}} \quad (10)$$

where  $d_p$  is the diameter of the particles of secondary phases p, and the drag function  $f_{drag}$  is taken from Schiller and Naumann [18]:

$$f_{drag} = \begin{cases} 1 + 0.15 \text{Re}^{0.687} & \text{Re} \leq 1000 \\ 0.0183 \text{Re} & \text{Re} > 1000 \end{cases} \quad (11)$$

and the acceleration  $\vec{a}$  is of the form

$$\vec{a} = \vec{g} - (\vec{v}_m \cdot \nabla) \vec{v}_m - \frac{\partial \vec{v}_m}{\partial t} \quad (12)$$

The simplest algebraic slip formulation is the so-called drift flux model, in which the acceleration of the particle is given by gravity and/or a centrifugal force and the particulate relaxation time is modified to take into account the presence of other particles.

### Volume Fraction Equation for the Secondary Phases

From the continuity equation for secondary phase p, the volume fraction equation for secondary phase p can be obtained:

$$\frac{\partial}{\partial t}(\alpha_p \rho_p) + \nabla \cdot (\alpha_p \rho_p \vec{v}_m) = -\nabla \cdot (\alpha_p \rho_p \vec{v}_{dr,p}) \quad (13)$$

### Turbulence Viscosity (The Spalart-Allmaras Model)

Instead of  $\mu_m$  (equation 5) the turbulent viscosity,  $\mu_t$ , is computed from

$$\mu_t = \rho_m \tilde{\nu} f_{v1} \quad (14)$$

where the viscous damping function,  $f_{v1}$ , is given by

$$f_{v1} = \frac{\chi^3}{\chi^3 + C_{v1}^3} \quad (15)$$

where  $C_{v1} = 7.1$  and

$$\chi \equiv \frac{\tilde{\nu}}{\nu} \quad (16)$$

## Results and Discussion

**Model Validation:** In this paper the results have been validated with the experimental result conducted by Clive et al [9]. At CSIRO Clive et al [9] demonstrated an experiment for particle distribution and deposition in a test loop. In order to compare with the experiment results [9] we have used the same geometry and boundary conditions (table 1). Figure 2 represents the cumulative particle volume fraction (summation of all different size particles) as a function of heights across the pipe at a certain location in the loop for both experiment and CFD results. Figure 2 shows the comparison between experimental and CFD results.

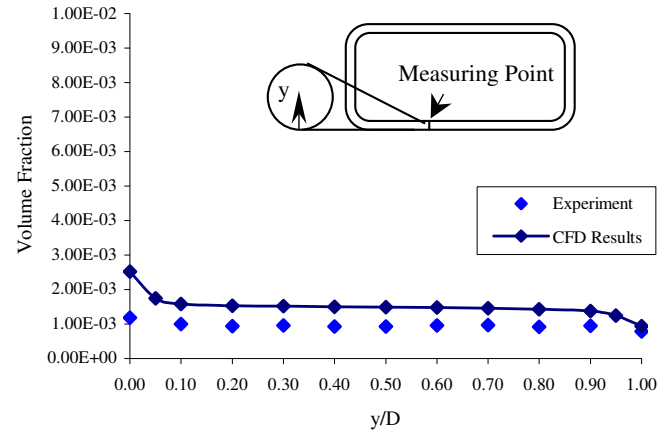


Figure 2: Comparison of CFD results and experimental data [9] for the velocity  $0.4 \text{ ms}^{-1}$  at center of the pipe.

Nevertheless, the trend is similar, but the experimental results show marginally lower volume fraction. This is because of the shortcomings of the measuring instruments that used in the experiment. Clive et al [9] reported that particle larger than  $20 \mu\text{m}$  could not be detected by the instruments although small amount of particles larger than  $20 \mu\text{m}$  still were introduced into the system. Those larger particles, which tend to settle quickly at the bottom, were also out of count during experiment. This may be the cause of lower volume fraction at the very bottom.



## Discussion

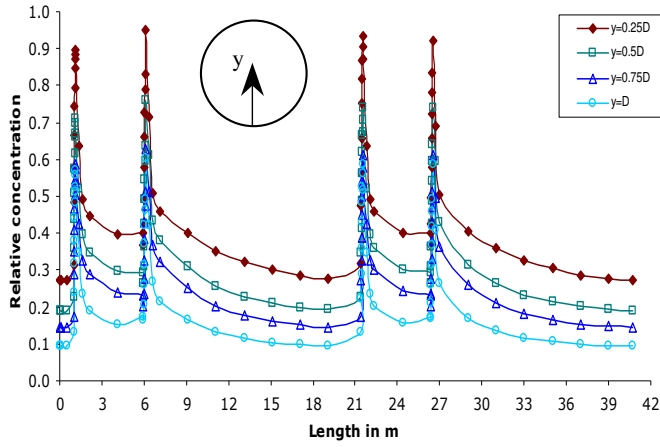


Figure 3a: Relative concentration of particles for different depths along the pipe at  $0.05 \text{ ms}^{-1}$ .

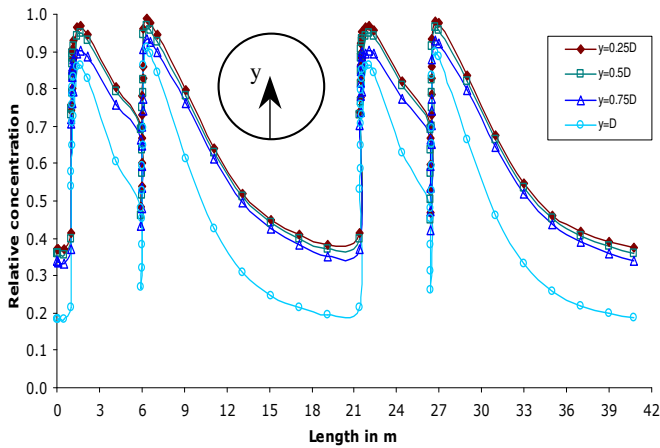


Figure 3b: Relative concentration of particles for different depths along the pipe at  $0.4 \text{ ms}^{-1}$ .

Figures 3a and 3b show the relative concentration plotted along the pipe for different height of  $0.25D$ ,  $0.5D$ ,  $0.75D$ , and  $1D$  from the bottom wall of the pipe. Relative concentration is a dimensionless parameter, which represents the ratio of local particle concentration to that of bottom of the pipe wall. Figures 3a and 3b show more homogeneous distribution of particles at different depths in the bend region. Due to high streamline curvature and associated centrifugal force the fluid at different depths gets well mixed resulting in homogeneous distribution of particles near bend. Down stream of the bend, the streamline curvature and associated centrifugal force disappears and particles start to segregate to different concentration at different depths. This segregation or stratification is more pronounced at lower velocity. At higher velocity the particles do not get enough time to segregate before they reach the next bend. Higher turbulence at higher velocity also contributes to homogeneity of the particles around bends.

Figures 4a-4b show typical circumferential distributions of particles volume fraction for the different velocities ( $0.05$  and  $0.4 \text{ ms}^{-1}$ ) for up and downstream location of bends (1st, 3rd and 4th). The angle  $0^\circ$  starts at the top wall and angle  $180^\circ$  is the bottom wall of the pipe. The upstream profiles exhibit a distinctive variation with the maximum deposition at the bottom of the pipe. Similar trends for entry of the bends were observed from the experimental data of Anderson & Russell [2] and the analytical results of Mols and Oliemans [17] and Laurinat et al [13] and Hossain et al [10]. The peak deposition at the bottom wall is high when the velocity is low. This can be easily explained as particles disperse at higher velocity and can be found higher concentration across the cross-section of the pipe due to high turbulence [13,17]. However, the trends of the particle deposition at

upstream of bends (figures 4a-4b) are not symmetrical along vertical plane. This is because of the particles entrainment in between bends is governed by the particle distribution of previous upstream bend, which is different from straight pipe flow [11,13,17].

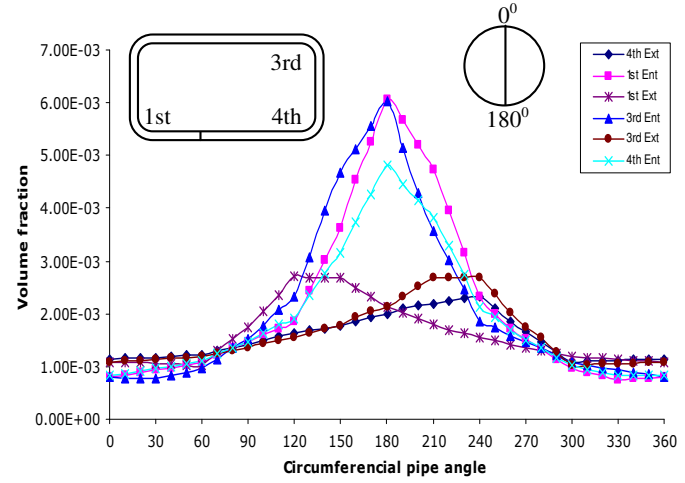


Figure 4a: Cumulative particle deposition (CFD) as a function of circumferential pipe angles at three different up and down stream of bends at  $0.05 \text{ ms}^{-1}$ .

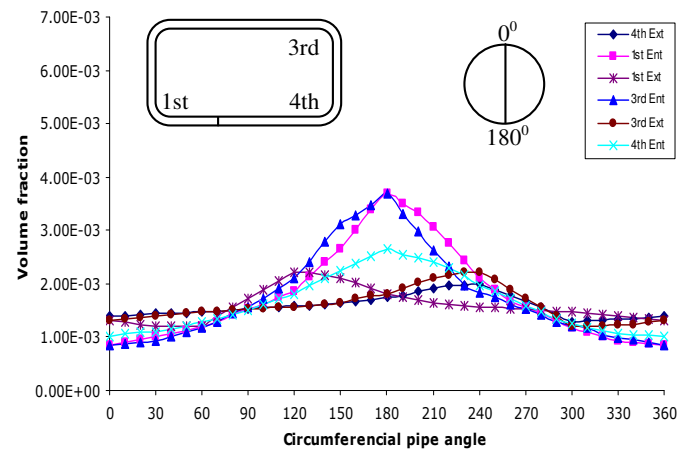


Figure 4b: Cumulative particle deposition (CFD) as a function of circumferential pipe angles at three different up and down stream of bends at  $0.4 \text{ ms}^{-1}$ .

As shown in figures 4a-4b at downstream of the bend the maximum deposition does not occur at the bottom ( $180^\circ$ ) rather it occurs at on the inner wall of the bend. The location of the peak deposition is situated at an angular displacement of  $60^\circ$  with respect to the bottom of the wall. The fluid is subjected to centrifugal force as it flows around the bend. Particles having higher specific gravity get segregation and deposit in the bend region. This deposition is pronounced near the outer wall of the bend entry and inner wall of the bend exit. However, due to the influence of high particle distribution at the inner wall upstream bend exit, the inner wall of the downstream bend entry will receive relatively higher load of particles.

In figures (5a-5b) the volume fraction of particles plotted as a function of circumferential angles for different planes ( $0^\circ$ ,  $22.5^\circ$ ,  $45^\circ$ ,  $67.5^\circ$ , and  $90^\circ$ ) of 4th bend (figure 1) for different velocities ( $0.05$  and  $0.4 \text{ ms}^{-1}$ ).  $0^\circ$  and  $90^\circ$  planes are known also as up and down stream planes respectively. The peak deposition (figures 5a-5b) moves from bottom ( $180^\circ$ ) to  $240^\circ$  ( $60^\circ$  inner wall from bottom) as it goes from upstream plane ( $0^\circ$ ) to downstream plane ( $90^\circ$ ). For a higher velocity (figure 5b), the particle diffusivity increases as a result of fluid diffusivity, which resulted in less particles deposition at the bottom inner wall.



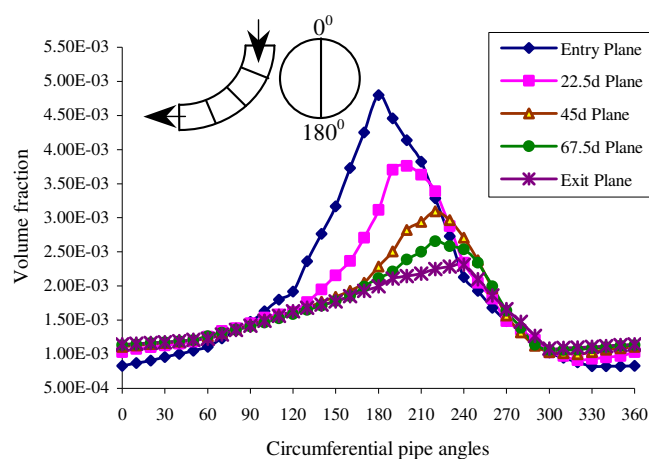


Figure 5a: Particle deposition (CFD) as a function of circumferential pipe angles at different planes of 4th bend at  $0.05 \text{ ms}^{-1}$ .

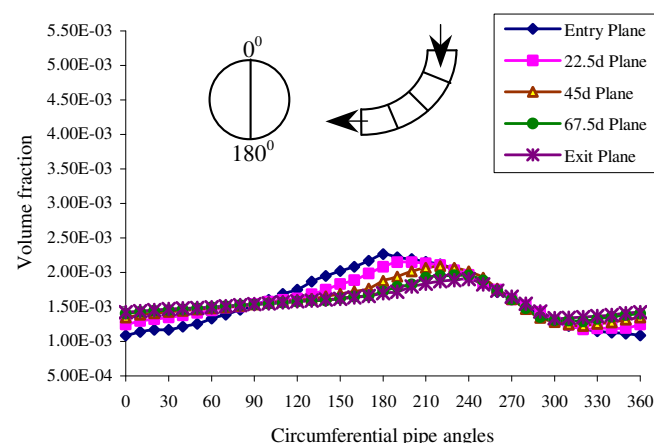


Figure 5b: Particle deposition (CFD) as a function of circumferential pipe angles at different planes of 4th bend at  $0.4 \text{ ms}^{-1}$ .

## Conclusion

The effect of bend and velocities on the deposition of particle in a horizontal test loop (figure 1) has been investigated numerically. This CFD results have also been validated with the experimental results [9] shown in figure 2. A reasonably good agreement between simulation and experiment results has also been established. Relative deposition at various velocities (figures 3a and 3b) indicates that particles are evenly distributed at bends. The circumferential particle deposition for different planes of a bend has also been investigated. Near and around the bends the maximum deposition of particles does not occur at bottom ( $180^\circ$ ) rather it occurs at  $60^\circ$  skewed to the inner wall. The further study would be needed to conclude more comprehensively the particle deposition around periphery at the downstream of bend.

## References

- [1] Abuzeid, S., Busniana, A. A., and Ahmadi, G., Wall deposition of aerosol particles in a turbulent channel flow, *Journal of Aerosol Science*, **22**, 1991.
- [2] Anderson, R. J. and Russell, T. W. F., Circumferential variation of interchange in horizontal annular two-phase flow, *Ind. Engg. Chem. Fundam.*, **9**, 1970.
- [3] Anderson, R. J. and Russell, T. W. F., Film formation in two-phase annular flow, *AIChE JI*, **14**, 1970, 626-633.
- [4] David, Y. H. P., Francisco Romy-Novas, and Benjamin Y. H. Liu, Experimental study of particle deposition in bends of circular cross section, *Aerosol Science and Technology*, **7**, 1987, 301-315..
- [5] C.N. Davies. *Aerosol Science*, London, Academic Press, 1966.
- [6] FLUENT INC., FLUENT, ver. 6.1.22, rel. 2001. USA.
- [7] FLUENT INC. FLUENT Manual. In: Anonymous USA: 2001.
- [8] Friendlander, S. K. and Johnstone, H. F., Deposition of suspended particles from turbulent gas streams, *Industrial and Engineering Chemistry*, **49**, 1957, 1151.
- [9] Grainger, C., Wu, J., Nguyen, B. V., Ryan, G., Jayanratne, A., and Mathes, P., Part 1: Settling , Re-Suspension and Transport, CRC, CFC, Melbourne, Australia, Apr 2003.
- [10] Hossain, A. , Naser, J., and McManus, A. M. K., Analytical turbulent diffusion model for particle dispersion and deposition in a horizontal pipe flow: comparison with CFD simulation, *Journal of Hydraulic Engineering*, (submitted)
- [11] Hossain, A., Naser, J., McManus, A. M. K., and Ryan, G., CFD Investigation of particle deposition and dispersion in a horizontal Pipe, *Third International Conference on CFD in the Minerals and Process Industries*, Dec. 2003.
- [12] Landahl, H. D. and Herrmann, R. G., *Journal of Colloid and Interface Science*, **4**, 1949.
- [13] Laurinat, J. E., Hanratty, T. J., and Jepson, W. P., Film thickness distribution for gas-liquid annular flow in a horizontal pipe, *Phys. Chem. Hydrodynam.*, **6**, 1985, 179-195.
- [14] Li, A. and Ahmadi, G., Deposition of aerosols on surfaces in a turbulent channel flow, *International Journal of Engineering and Science*, **31**, 1993.
- [15] Liu, B. Y. H. and Agarwal, J. K., Experimental observation of aerosol deposition in turbulent flows, *Journal of Aerosol Science*, **5**, 1974, 145.
- [16] Manninen, M., Taivassalo, V., and Kallio, S., On the mixture model for multiphase flow, *VTT Publications 288*, Technical Research Centre of Finland., 1996.
- [17] Mols, B. and Oliemans, R. V. A., A Turbulent diffusion model for particle dispersion and deposition in horizontal tube flow, *International Journal of Multiphase Flow*, **24**, 1998, 55-75.,.
- [18] Schiller, L. and Nuemann, Z., *Z.Ver. Deutsch. Ing.*, **77**, 1935, 318.
- [19] Swailes, D. C. and Reeks, M. W., Particle deposition from a turbulent flow. I. A steady-state model for high inertia particles. *Physics of Fluids*, **6**, 1994, 3392.
- [20] Thomson, D. J., Dispersion of particle pairs and decay of scalar fields in isotropic turbulence. *Physics of Fluids*, **15**, 2003, 801-813.
- [21] Tsai, C. J. and Pui, D. Y. H., Numerical study of particle deposition in bends of a circular cross section laminar flow regime, *Aerosol Science and Technology*, **12**, 1990.

## A steady ‘filling box’ solution with zero net buoyancy flux

G. O. Hughes, R. W. Griffiths and J. C. Mullarney

Research School of Earth Sciences  
The Australian National University, Canberra ACT 0200, AUSTRALIA

### Abstract

We present a simple flow model and solution to describe ‘horizontal convection’ driven by a gradient of temperature or heat flux along one horizontal boundary. Following laboratory observations for the steady-state convection, the model is based on a localized turbulent plume that maintains a stably stratified interior. In contrast to the ‘filling box’ process of Baines and Turner [1], the convective circulation involves vertical diffusion in the interior and a stabilising buoyancy flux distributed over the horizontal boundary. The latter flux causes the density distribution to reach a steady state. Applied to the laboratory experiments of Mullarney *et al.* [5], the solution successfully predicts the top-to-bottom density difference and the thickness of the boundary layer adjacent to the horizontal boundary. We conclude that the turbulent ‘recycling box’ model is a useful way to describe this form of convection.

### Introduction

Horizontal convection driven by a horizontal gradient of temperature or heat flux along the top or bottom boundary of a volume of fluid has been mooted as a model for the global overturning circulation of the oceans in response to net heating at low latitudes and a net cooling at high latitudes [11]. In this form of convection, heat enters over a section of the boundary (such as the ocean surface) and is removed at an equal rate elsewhere on that boundary. The resulting boundary layer flow is observed to feed into a plume that penetrates through the depth of the box, at one end of the box [9, 10, 5, see figure 1]. For sufficiently large Rayleigh numbers the plume is turbulent [5].

In a companion paper [2] we have examined the implications of potential energy generation by the buoyancy fluxes at the horizontal boundary and of the rates of dissipation of energy in the box interior. We have shown that the steady-state buoyancy-driven flow requires a level of turbulence sufficient to mix heat into the interior at a rate equal to the cooling flux delivered by the turbulent plume. On energy grounds alone it is possible to predict the depth of the boundary layer adjacent to the surface at which the heating and cooling is applied, and to estimate the magnitude of the interior mixing rate (the vertical diffusivity). However, in order to predict the temperature (density) distribution and the mass flux (given an imposed heat flux), it is necessary to construct an explicit solution for the flow. This is the purpose of the current paper.

### The ‘recycling box’ model

Horizontal convection has much in common with ‘filling box’ flows [1], where a localised destabilising source of buoyancy maintains a turbulent plume and drives a circulation in the box. Fluid in the plume penetrates rapidly through the depth of the box, whereupon it becomes part of a broad gradual return flow in the box interior towards the level of the plume source. The density anomaly of fluid in the plume is reduced with distance from the source by entrainment and mixing of water from the box interior into the plume. Consequently a density stratification is established throughout the depth of the box. As in the

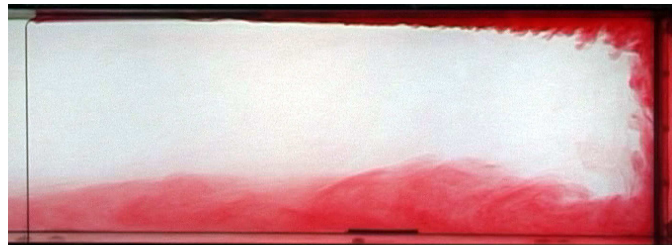


Figure 1: Dye visualisation of the convective flow driven in a box by differential heating along the lid [5]. In this experiment surface heat fluxes  $q_h$  and  $q_c (= -q_h)$  per unit box width are applied over the left- and right-hand halves of the lid, respectively. The field of view shows only the right-hand (cooled) end of the box. The thin vertical line at the left of the photograph corresponds to the centre of box, where dye was introduced into the boundary layer adjacent to the lid. Heat is transferred to/from this boundary layer, maintaining a horizontal density gradient and a flow directed from the heated region to the cooled region (left to right). A turbulent outflow from the plume is visible at the base of the box, directed from right to left. For sufficiently large heat fluxes most of the temperature variation occurs across the lid boundary layer, which occupies a small fraction of the total depth.

case of horizontal convection, the filling box stratification is strongest at levels near the plume source (in the ‘thermocline’) and relatively weak throughout the remainder of the box interior. The analysis of Baines & Turner [1] shows that the filling box flow reaches an asymptotic steady state in which the density gradient and velocity field is constant. Crucially, however, the density field continues to evolve since the filling box flow is driven by a continuous net input of buoyancy.

Here, we develop a steady filling box (which we term a ‘recycling box’) model to describe horizontal convection. We ensure that the density field in the box is in a steady state by applying a stabilising buoyancy source at the same horizontal boundary as the destabilising buoyancy source driving the plume. The stabilising source is of such a strength that the net input of buoyancy into the box is zero. Vertical diffusion in the box interior is then important in maintaining the density distribution.

Without loss of generality, we consider in the remainder of this paper horizontal convection driven by fluxes applied at the upper surface. The destabilising buoyancy source then corresponds to cooling and the stabilising flux to heating, as shown in figures 1 and 2. Although the destabilising and stabilising fluxes were applied symmetrically over a large area either side of the tank centre in figure 1, the resulting flow is highly asymmetric with a tightly confined plume. The global overturning circulation in the oceans displays a similar asymmetry [11]. These observations suggest a useful approximation: we treat the cooling flux at the surface as highly localised, and distribute the heat input uniformly over the remainder of the surface. The exact position of the cooling and the size of the cooling area are assumed not to play an important role in determining the vertical

structure of the flow, provided there is no net heat input. The rate of heat loss  $q_c$  per unit box width at the surface produces a buoyancy flux

$$F_c = \frac{\alpha g q_c}{c_p} \quad (1)$$

per unit box width, where  $\alpha$  is the expansion coefficient,  $g$  is the gravitational acceleration and  $c_p$  is the specific heat capacity of water at constant temperature. The plume is assumed to be turbulent, as in the filling box [1, 4, 8]. Experiments [5] confirm this to be the case (figure 1) at Reynolds and Rayleigh numbers characterising laboratory-scale flows.

We consider here an isolated vertical line plume in a rectangular box (figure 2), and note that our model is equally applicable to a ‘half-plume’ against the boundary (as in figure 1). The ratio of height to length of the box is assumed to be small so that horizontal velocities are much greater than vertical velocities.

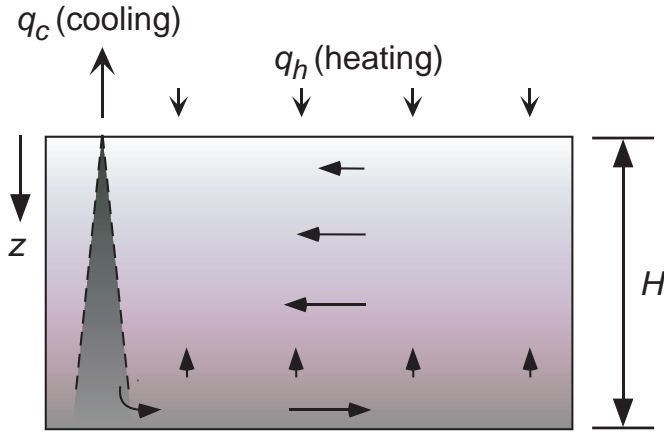


Figure 2: Schematic diagram of the ‘recycling box’ model for horizontal convection. Localised surface cooling at a rate  $q_c$  per unit box width leads to a tightly confined region of downwelling (represented as an isolated vertical line plume) from the surface to the bottom in a box of depth  $H$  and length  $2L$ . By symmetry, a ‘half-plume’ (against the vertical boundary) may be modelled by defining the box length to be  $L$ . Heating at a rate  $q_h = -q_c$  per unit box width is distributed over the surface allowing the flow to reach a steady state. If the sinking is turbulent, entrainment drives recirculation at depth.

### Plume model

We assume here that the plume width is much smaller than the length of the box. For simplicity we shall also assume that the plume does not interact with the confining (vertical) boundary of the box, but note that by symmetry the model can be applied to a ‘half-plume’ (figure 1) that sinks against the vertical boundary. Following Baines & Turner [1], we assume that profiles of mean velocity  $\bar{W}$  and density anomaly  $\bar{\rho} - \rho_e$  through the plume cross-section are similar at all depths and well approximated by a Gaussian form, i.e.

$$\bar{W}(x, z) = W_p(z) \exp \left[ -\frac{x^2}{R^2(z)} \right], \quad (2)$$

and

$$\bar{\rho}(x, z) - \rho_e(z) = [\rho_p(z) - \rho_e(z)] \exp \left[ -\frac{x^2}{R^2(z)} \right], \quad (3)$$

where  $x$  is the distance from the plume axis and  $\bar{\rho} - \rho_e$  is the density anomaly in the plume relative to water in the interior

at the same depth but far removed from the plume. We define the vertical coordinate  $z$  increasing downwards with the plume source at the origin. We have defined  $R$  to be the  $1-\sigma$  plume width and  $\rho_p - \rho_e$  and  $W_p$  to be the mean density anomaly and mean vertical velocity on the plume axis, respectively. Upon integrating in the horizontal plane, the equations describing conservation of volume, momentum and buoyancy in the plume can be written (cf. [1])

$$\frac{d}{dz} [\sqrt{\pi} R W_p] = 2U_e = 2E W_p, \quad (4)$$

$$\frac{d}{dz} \left[ \frac{R W_p^2}{2\sqrt{2}} \right] = R \frac{g(\rho_p - \rho_e)}{\rho_r}, \quad (5)$$

and

$$\frac{d}{dz} \left[ \frac{R W_p g(\rho_p - \rho_e)}{\sqrt{2}\rho_r} \right] = R W_p \frac{d}{dz} \left[ \frac{g(\rho_r - \rho_e)}{\rho_r} \right], \quad (6)$$

where  $\rho_r$  is a reference density and  $E$  is a constant characterising the ratio of an entrainment velocity  $U_e$  to the vertical velocity  $W_p$  in the plume. The entrainment velocity can be interpreted as the rate of increase with  $z$  of the plume volume flux per unit box width, and  $E$  takes a value of approximately 0.1 for a Gaussian plume [1, 12].

### Interior model

As in the filling box model of Baines & Turner [1], conservation of volume in the box interior is expressed as

$$\frac{\sqrt{\pi}}{2} R W_p = -L W_e, \quad (7)$$

where  $W_e$  is the mean vertical velocity in the interior over the cross-sectional area of the box. Equation (7) holds if the box length is defined to be  $2L$  for isolated plumes and to be  $L$  for ‘half-plumes’ against a vertical boundary in the box.

The density field  $\rho_e$  in the box interior must vary with depth (cf. [1]). However, in contrast to the filling box flow,  $\rho_e$  does not vary with time and advection of the density field must instead be balanced everywhere by diffusion of the stratifying species. Thus

$$W_e \frac{d\rho_e}{dz} = \frac{d}{dz} \left[ \kappa^* \frac{d\rho_e}{dz} \right], \quad (8)$$

where  $\kappa^*$  is the diffusivity characterising the vertical transport of the stratifying species. We note at this point that a molecular diffusivity is not necessarily appropriate to the interior since turbulence may be supported internally within the system.

### Boundary conditions

The plume is assumed to be forced purely by a localised (point) source of destabilising buoyancy at  $z = 0$ . The rate at which buoyancy is exchanged per unit box width with the plume at the surface is the buoyancy flux  $F_0$ . The volume flux across the boundary where the plume is forced is zero and, under a point source approximation, both

$$[R W_p]_{z=0} = 0 \quad (9)$$

and

$$R(0) = 0. \quad (10)$$

Therefore,

$$W_e(0) = 0 \quad (11)$$

by equation (7). Equations (9) and (10) show that the vertical velocity in the plume  $W_p$ , and hence the entrainment velocity

$U_e$  (by equation 4), must be zero at  $z = 0$ . We ensure that the flow in the container reaches a steady state by supplying stabilising buoyancy to a half-plume (against a vertical boundary) at a rate  $F_0 = F_c$  per unit box width or to an isolated plume at a rate  $2F_0 = F_c$  per unit box width, where  $F_c$  is given by equation (1). We assume the fluid to have a linear equation of state. As we have developed an interior model that neglects variations in the horizontal, we choose to distribute the stabilising flux uniformly over the forcing boundary at  $z = 0$ . Upon integrating the buoyancy flux per unit box width over the plume cross-section and taking the limit as  $z \rightarrow 0$ , the boundary condition may be written

$$F_0 = \frac{\sqrt{\pi}}{2\sqrt{2}} [RW_p g (\rho_p - \rho_e)] \Big|_{z=0} = gL\kappa^* \frac{d\rho_e(0)}{dz}. \quad (12)$$

Equations (4) – (8) are strictly valid only for the part of the box volume that excludes the plume outflow. Here we assume that the outflow redistributes fluid from the plume over the horizontal boundary at  $z = H$ , whereupon the fluid becomes part of the interior. Thus the densities of fluid in the plume and in the interior must be equal at  $z = H$ , and we expect boundary conditions of zero buoyancy flux in each of the plume and the interior, i.e.

$$F(H) = \frac{\pi}{2} [RW_p g (\rho_p - \rho_e)] \Big|_{z=H} = gL\kappa^* \frac{d\rho_e(H)}{dz} = 0. \quad (13)$$

### Solution

We solve numerically for  $R$ ,  $W_p$ ,  $\rho_p$ ,  $W_e$  and  $\rho_e$  the system given by equations (4) – (8), and subject to the boundary conditions in equations (9) – (13). We note, however, that the plume outflow has been effectively neglected in the model here and the boundary condition in equation (13) cannot be enforced. In practice, we obtain a solution that satisfies the boundary conditions at  $z = 0$  (equations 9 – 12). To a very good approximation, this solution is found to implicitly satisfy the boundary condition in equation (13) over the parameter range of interest. We verify this assumption below.

### Comparison with laboratory data

The recycling box model solutions are presented by way of a comparison with available data from the laboratory experiment in figure 1 [5]. The experimental tank was 1.2 m long, 0.15 m wide and 0.2 m high, and a cooling flux per unit tank width  $q_c = 933$  W/m was supplied over the right-hand half of the tank lid. By equation (1), this cooling flux generates a buoyancy flux per unit tank width of  $F_c = F_0 = 3.6 \times 10^{-4}$  N/m/s, where we have taken  $g = 9.81$  m/s<sup>2</sup>, the specific heat  $c_p = 4184$  J/kg/K and the expansion coefficient  $\alpha = 1.6 \times 10^{-4}$  °C<sup>-1</sup>.

We present in figures 3 and 4 the solutions for the buoyancy flux per unit width in the plume and the vertical velocity and temperature profile in the box interior, since these are the quantities of most practical interest. The solutions have been obtained using an entrainment coefficient  $E = 0.1$  and a diffusivity that is approximately molecular  $\kappa^* = 10^{-7}$  m<sup>2</sup>/s. The vertical velocity in the box interior increases with depth owing to entrainment into the plume (equation 7). The buoyancy flux reduces very rapidly with depth owing to entrainment as the plume passes through the strong density stratification (the thermocline) at the top of the box. The thermocline thickness in this flow is predicted to be less than approximately one-tenth of the box depth, i.e.  $< 2$  cm. Immediately below the thermocline the buoyancy flux is small and continues to decrease with depth (not visible on this scale). Thus it is apparent that the boundary condition at  $z = H$  (equation 13) is indeed approximately satisfied by this solution. The variation with depth of the buoyancy flux is in

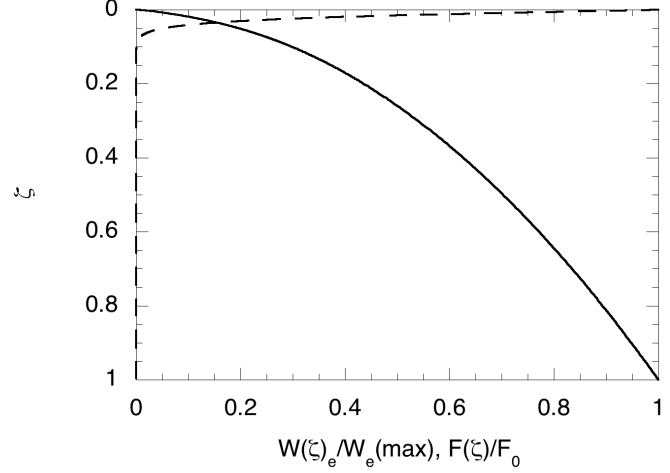


Figure 3: Profiles of vertical velocity (solid line) in the box interior and buoyancy flux (dashed line) in the plume predicted by the recycling box model with a localised cooling flux per unit box width of  $q_c = 933$  W/m. Vertical velocities  $W_e$  have been normalised by the maximum vertical velocity  $W_e(\max) = 0.12$  mm/s and the buoyancy flux has been normalised by the applied buoyancy flux  $F_0 = 3.6 \times 10^{-4}$  N/m/s. The vertical coordinate is the normalised depth  $\zeta = z/H$ .

stark contrast to the filling box flow, where  $F/F_0$  reduces linearly from a value of one at the surface to zero at  $z = H$ .

As the vertical velocities in the tank are very small, only temperatures in the tank interior are readily measurable. Temperatures vary with horizontal position, particularly in the boundary layer adjacent to the applied heating and cooling fluxes. Therefore, to undertake a comparison with the temperature profile predicted by the recycling box model (which ignores horizontal variations in the box interior), we construct a horizontal average of a number of temperature profiles measured at several positions along the length of the tank. The averaged profile is also plotted in figure 4 for direct comparison with the theoretical prediction. Both the thermocline thickness and the top-to-bottom temperature difference are very well predicted. Although it is not visible in figure 4, both profiles show that the box interior (below the thermocline) supports a stable temperature stratification (with the exception in experiments of statically unstable regions immediately below the applied cooling). While the temperature gradient in the interior is many times smaller than in the thermocline, it is dynamically very significant since it forces the plume to penetrate to the bottom of the box.

The predicted maximum vertical velocities of 0.12 mm/s compare very well with numerical simulations undertaken by Mullarney *et al.* for the above experimental parameters [5, figure 10b]. On the basis of the predicted vertical velocity profile in figure 3, we would estimate the ventilation timescale  $\tau \sim 2H/W_e(\max) \approx 30$  min to characterise the recycling of the tank volume through the plume. This timescale is consistent with observations of the time required for the dye in figure 1 to be spread throughout the tank.

### Application to the oceans

Although the global oceans represent a very complex system that is not forced by buoyancy alone, models of horizontal convection can offer insight into the governing dynamics. Here we give only a brief outline of current work (to be presented elsewhere) examining the application of the recycling box model to the oceans. The global thermohaline circulation (or merid-

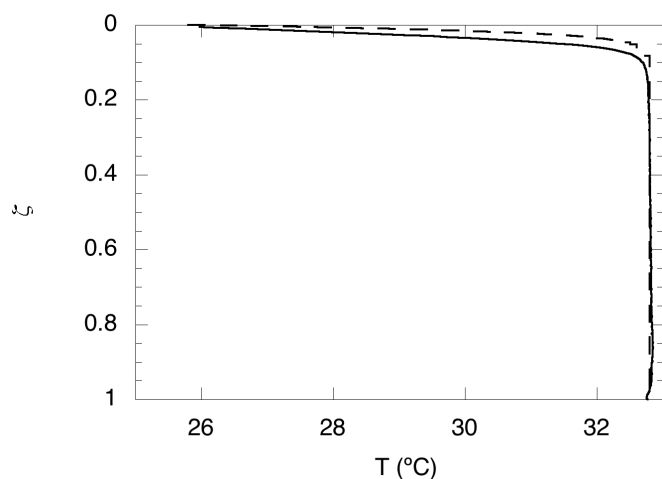


Figure 4: Comparison of temperature profiles predicted by the recycling box model (dashed line) for a line plume with data from the laboratory experiment (solid line) of Mullarney *et al.* [5]. The laboratory temperature profile represents a horizontal average of five vertical profiles taken at various horizontal positions along the length of the tank. The predicted temperature profile is referenced to the measured average temperature at  $\zeta = 1$ .

ional overturning circulation) of the oceans carries heated surface waters poleward, where they are cooled and sink in highly localised downwelling at polar latitudes. In the downwelling plume of largest buoyancy flux (the outflow from the Weddell Sea) the cold water sinks to the bottom, spreads through much of the oceans as Antarctic Bottom Water, and is eventually returned to the surface layers by a broad, slow upwelling in the interior. Laboratory experiments [4, 13] suggest that the plume reaching the bottom will dominate the overall density structure, hence we have developed a first order model using a single plume in the recycling box model. If the ocean is presumed to be in a steady state, the interior upwelling of cold water must be countered by downward mixing of heat (and upward mixing of density). The density structure has been similarly described by a simple one-dimensional balance of advection and diffusion (cf. equation 8), from which the measured abyssal gradients imply a diffusivity of order  $10^{-4} \text{ m}^2\text{s}^{-1}$  [6, 7]. The recycling box model may help to answer two important questions. Much of the heat transport is a consequence of wind-driven surface flows. However, it is not clear whether the heat transport is passive [7, 3, 14, 15], or whether instead the thermal buoyancy flux associated with the meridional heat flux is a significant contribution to the driving forces in the momentum budget for the mean overturning flow. The second question is whether the internal vertical mixing (which maintains the density structure of the oceans in the presence of the vertical components of the circulation) is substantially sustained by energy input from buoyancy-driven flow (hence by the heat flux) or whether the mixing is dominated by energy from tides and winds [6, 7, 3, 14, 15].

## Conclusions

We have developed a model that describes ‘horizontal convection’ driven by a temperature gradient or heat flux applied along one horizontal boundary of a box. A steady circulation evolves, consisting of a localised turbulent plume that penetrates through the depth of the box and a broad gradual return flow to the plume. Important features in our steady model include zero net buoyancy input to the box and a balance between diffusion and advection of the density field in the box interior. The pre-

dictions from the model are in excellent agreement with available data from laboratory experiments and provide a sound basis from which to explore the relevance of the model to the global oceans.

## References

- [1] Baines, W. D. and Turner, J. S., Turbulent buoyant convection from a source in a confined region, *J. Fluid Mech.*, **37**, 1969, 51–80.
- [2] Griffiths, R. W. and Hughes, G. O., The energetics of horizontal convection, *Proc. Fifteenth Aust. Fluid Mech. Conference*.
- [3] Huang, R. X., Mixing and energetics of the oceanic thermohaline circulation, *J. Phys. Oceanogr.*, **29**, 1999, 727–746.
- [4] Killworth, P. D. and Turner, J. S., Plumes with time-varying buoyancy in a confined region, *Geophys. Astrophys. Fluid Dyn.*, **20**, 1982, 265–291.
- [5] Mullarney, J. C., Griffiths, R. W. and Hughes, G. O., Convection driven by differential heating at a horizontal boundary, *J. Fluid Mech.*, in press.
- [6] Munk, W. H., Abyssal recipes, *Deep-Sea Res.*, **13**, 1966, 707–730.
- [7] Munk, W. H. and Wunsch, C., Abyssal recipes II: energetics of tidal and wind mixing, *Deep-Sea Res. I*, **45**, 1998, 1977–2010.
- [8] Pierce, D. W. and Rhines, P. B., Convective building of a pycnocline: laboratory experiments, *J. Phys. Oceanogr.*, **26**, 1996, 176–190.
- [9] Rossby, H. T., On thermal convection driven by non-uniform heating from below: an experimental study, *Deep-Sea Res.*, **12**, 1965, 9–16.
- [10] Rossby, H. T., Numerical experiments with a fluid non-uniformly heated from below, *Tellus*, **50**, 1998, 242–257.
- [11] Stommel, H., On the smallness of sinking regions in the ocean, *Proc. Nat. Acad. Sci., Washington*, **48**, 1962, 766–772.
- [12] Turner, J. S., *Buoyancy effects in fluids*, Cambridge University Press, Cambridge, England, 1973.
- [13] Wong, A. B. D. and Griffiths, R. W., Stratification and convection produced by multiple plumes, *Dyn. Atmos. Oceans*, **30**, 2001, 101–123.
- [14] Wunsch, C., Moon, tides & climate, *Nature*, **405**, 2000, 743–744.
- [15] Wunsch, C. and Ferrari, R., Vertical mixing, energy, and the general circulation of the oceans, *Ann. Rev. Fluid Mech.*, **36**, 2004, 281–314.



## Experimental Investigation of a Rectangular Slot-Burner in the presence of Cross-Flow for different Jet Velocity Ratios

S. Ahmed<sup>1</sup>, J. Naser<sup>1</sup>, J. Nikolov<sup>2</sup>, C. Solnordal<sup>2</sup>, W. Yang<sup>2</sup>, J. Hart<sup>1</sup>

<sup>1,2</sup>Cooperative Research Centre for Clean Power from Lignite

<sup>1</sup>School of Engineering & Science, Swinburne University of Technology, VIC, 3122 AUSTRALIA

<sup>2</sup>CSIRO Minerals, Clayton, VIC, 3169 AUSTRALIA

### Abstract

In a typical coal-fired power station boiler the ignition and the combustion are largely controlled by burner aerodynamics, hence the geometry of the burner and the jet velocity ratio play an important role in achieving stable combustion, high burnout of fuel, low production of pollutants and control of fouling. Slot-burners are used in tangentially fired brown coal boilers in Victoria. To obtain a better understanding of the overall combustion process, it is important to investigate the aerodynamics of the jet development from these burners. The aim of this paper is to investigate a rectangular slot burner in the presence of cross flow for jet velocity ratios of 1.0 and 3.0. A simple burner has been considered for investigation where the jets discharge at an angle of 60° to the wall. The burner consists of three rectangular slots vertically aligned with the centre known as primary nozzle and the top and bottom ones known as secondary nozzles. The velocity ratio ( $\phi$ ) is defined as the ratio of secondary to primary jet velocity. Laser Doppler Anemometry experiments have been carried out at CSIRO Minerals. In the presence of cross flow, both primary and secondary jets deviated significantly from the geometric axis towards the wall.

### Introduction

A jet in cross flow has been the subject of numerous studies because of its wide variety of applications in engineering. Chimney plumes for the dispersion of pollutants in the atmosphere, the cooling of turbine blades, lifting jets for V/STOL aircraft, fuel injection of burners and jets of oil and gas entering the flow in oil wells are just a few important examples. Many researchers have studied a circular jet in cross flow extensively. Foss [6], Andreopoulos [2,3], Andreopoulos and Rodi [4] reported on an extensive investigation of the near field aerodynamics of a round jet issuing normal to the surface and to the cross flow. Catalano *et al.* [5] investigated physically and numerically the development of a system for jet to cross flow velocity ratio equal to 2.0 and 4.0 where the cross flow was confined between two parallel surfaces. Sherif & Pletcher [17] in surveying numerical and physical modelling studies of jets in cross flow, consider that these systems are, generally, more difficult to model numerically than wall boundary-layer flows primarily because of the curvature of the shear layer and the complex turbulent flow pattern in the jet wake region. Sykes *et al.* [19] developed a time marching solution of the incompressible Navier-Stokes equations and discretized them on to a grid using central spatial differencing on a non-uniform grid. The model was used to investigate the details of the flow within the jet in cross flow. Smith and Mungal [18] presented the results from extensive imaging of the concentration field of a jet in cross flow. Lester *et al.* [11] reported on a series of large-eddy simulations of a round jet issuing normally into a cross flow. Simulations were performed at two jet-to-cross flow velocity ratios, 2.0 and 3.3, and two Reynolds numbers, 1050 and 2100, based on cross flow velocity and jet diameter. The mechanisms by which large-scale coherent structures form were described in their investigation. Lim *et al.* [12] also investigated the development of large-scale structures of a jet normal to a cross flow. Peterson and Plesniak [15] studied the evolution of a short

injection-hole jet issuing into a cross flow at low blowing ratio by using PIV technique. It is well-established from all of these investigations that a circular jet in cross flow produces a multitude of vortical structures and the five most significant ones are the leading edge vortices, lee-side vortices, counter-rotating vortex pairs, horseshoe vortices and wake vortices.

There are substantially fewer papers dealing with studies of multiple round jets in cross flow compared to those dealing with a single round jet in the same environment. Examples of the papers dealing with multiple round jets include Isaac & Schetz [10], Makihata & Miyai [13], Isaac & Jakubowski [9] and Savory & Toy [16]. Multi-jet configurations studied include two or three jets aligned in a row transverse to the cross flow direction, two jets in tandem and three jets each located at a corner of an equilateral triangle. Velocity ratios between the jets equal one, and between the jet and cross flow range from 2.0 to 10.0. In recent years, various attempts have been made to improve the mixing efficiency of a jet in cross flow by using non-circular jet geometry such as an ellipse, square and rectangle. New *et al.* [14] studied the flow structures of an elliptic jet in cross flow in a water tunnel using laser-induced fluorescence technique and for a range of jet aspect ratio from 0.3 to 3.0. A similar investigation was conducted by Haven & Kurosaka [8] to examine the effect of hole exit geometry on the near field characteristics of cross flow jets. Hole shapes investigated were round, elliptical, square and rectangular. Hart [7] investigated in detail the formation mechanism of large-scale coherent structures of multiple rectangular slot burners without cross flow and for secondary to primary jet velocity ratio of 1.0. The effect of jet velocity ratio for multiple rectangular slot burners was extensively studied by Ahmed *et al.* [1] without cross flow. Yan & Perry [20] first investigated the jet velocity ratio effect for the rectangular slot burners in the presence of cross flow. They studied the flow by visualization and took measurements for mean velocity by Laser Doppler Anemometry (LDA) in the near field region. The flow pattern in a tangentially fired rectangular slot burner is very complex and needs detailed investigation to understand the mean and turbulent statistics in near and far field region of the jets. The current work was undertaken to produce more detailed data on mean flow and turbulent stresses in such a flow.

The development of the flow field in the near burner region is influenced by burner geometry, velocity ratio and complex rotational flow in the tangentially fired furnace. In a simple isolated burner study it is not possible to faithfully model all of these influences, particularly the furnace flow field. The cross flow in this isolated burner investigation is the representation of the burner flow field similar to the tangentially fired furnace.

### Description of the Burner Model

A simple burner has been considered for investigation where the jets discharge at an angle of 60° to the wall. The burner consists of three nozzles vertically aligned with the centre known as primary nozzle and the outer two known as upper and lower secondary nozzles. The burner model is a large box (1.85mx1.5mx1.6m) made from a frame of aluminium with perspex walls. The dimensions of the cross section of the primary



nozzle and the secondary nozzles (upper and lower) in the cold flow model are (75mm x 58mm) and (75mm x 34mm) respectively. The hydraulic diameter ( $D_e$ ) and the nozzle spacing were 64mm and 27mm respectively. Upstream of the nozzles, the duct length was 1.2m, to give a more developed velocity profile at the exit of the burner. The dimension of the cross section of the cross flow nozzle was (75mm x 252mm) and the duct length was 1.8m. Figure 1(a) and 1(b) show the dimensions of the flow containment box, primary and secondary nozzles respectively.

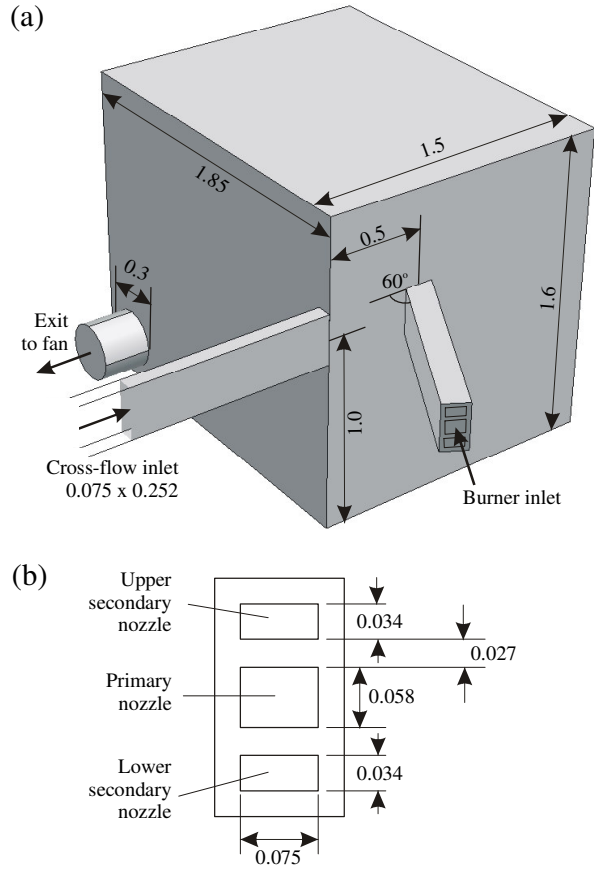


Figure 1. Dimensioned view of flow containment box and burner inlet detail (all units in m)

### Experimental Set-up & Measurement Technique

A Schematic diagram of the experimental set up is shown in figure 2. Air passed into the burner model via ducts A (Burner) and B (cross flow), and exited through duct C. It was driven into the rig from the blower and extracted through the bag house using a fan. A 2-axis traversing mechanism was suspended within the enclosure from the roof. This traverse was used to automatically position a laser with high precision. The velocity in the primary jet was held constant at 8m/s. The value of the secondary jet velocity was 8m/s for  $\phi=1.0$  and 24m/s for  $\phi=3.0$ . The velocity of the cross flow jet was 8m/s and was constant throughout the experiments.

A TSI-Aerometrics 2D Laser Doppler Anemometer (LDA) was used to measure the mean and fluctuating component of velocity. The system consisted of a two-colour four-beam optical arrangement utilising the green (with the wavelength of 514.5 nm) and blue (with wavelength of 488 nm) lines of a 5W Argon-Ion laser. A fibre optic probe had a lens of a 250 mm focal length and a 40 mm beam separation which produced an ellipsoid shaped measuring volume with dimensions of 0.11 mm x 0.11 mm x 1.5 mm. A specially designed 2D traversing mechanism was used inside the containment box to traverse the fibre optic probe.

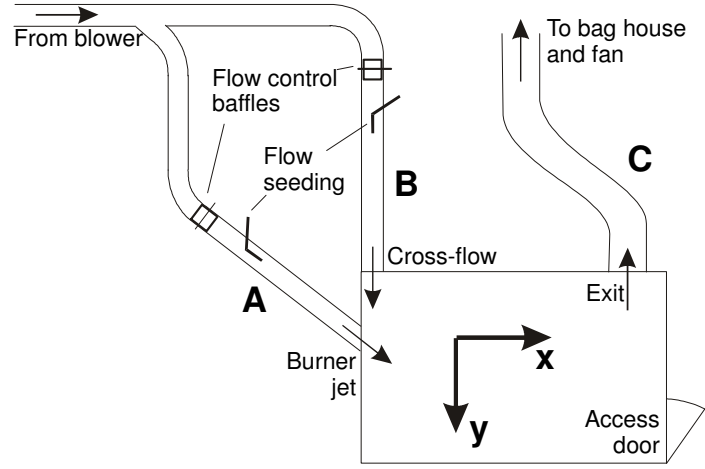


Figure 2. Schematic Diagram of Burner Model and associated ducting

The airflow was seeded with a fine mist of sugar particles introduced into the primary, secondary and cross flow jets. The partially dried sugar particles with a mean diameter about 1  $\mu$ m were generated by a TSI six-jet Atomizer from a 5% sugar solution. For each position inside the burner model, data was taken for 60 seconds. The average data rate was 400 Hz giving a total of around 24,000 particles counted at each position.

### Results and Discussion

Figures 3(a) and 3(b) show the velocity vectors for  $\phi=1.0$  at the centre of the primary nozzle ( $z/D_e=0$ ) and lower secondary nozzle ( $z/D_e=1.14$ ) respectively.

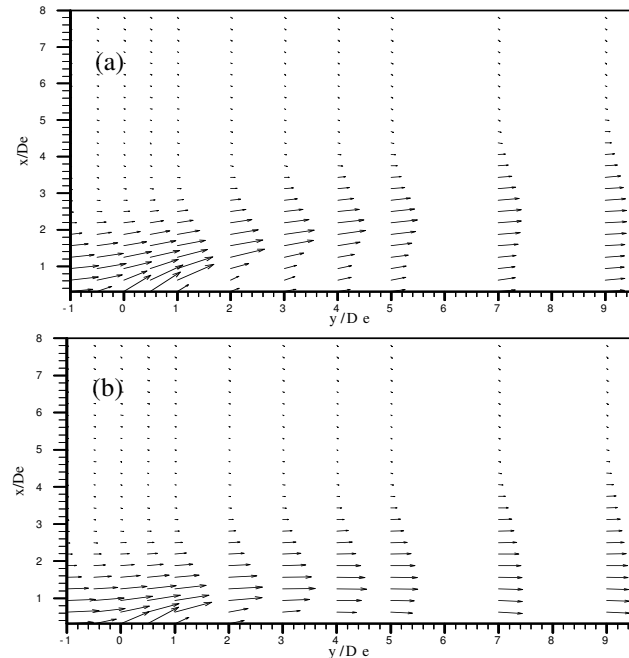


Figure 3(a-b). Velocity vectors at the centre of the primary (a) and lower secondary (b) nozzles for  $\phi=1.0$

The direction of the cross flow jet was in the same direction as the component of the jet velocity parallel to the furnace wall. The cross flow has a profound effect on the developing flow field. For this geometry without cross flow, [7] the three jets were aligned almost along the geometric axis of the burner. In the presence of cross flow, the three jets were pushed towards the wall and remained predominantly within the cross flow. The deflection of the lower secondary jet was slightly greater than the primary jet as shown in figure 3(a) and 3(b). The centreline of the primary and lower secondary jet diverged significantly from the geometric axis towards the wall. Figures 4(a) and 4(b) show the velocity vectors for  $\phi=3.0$  in the same planes as figure 3.

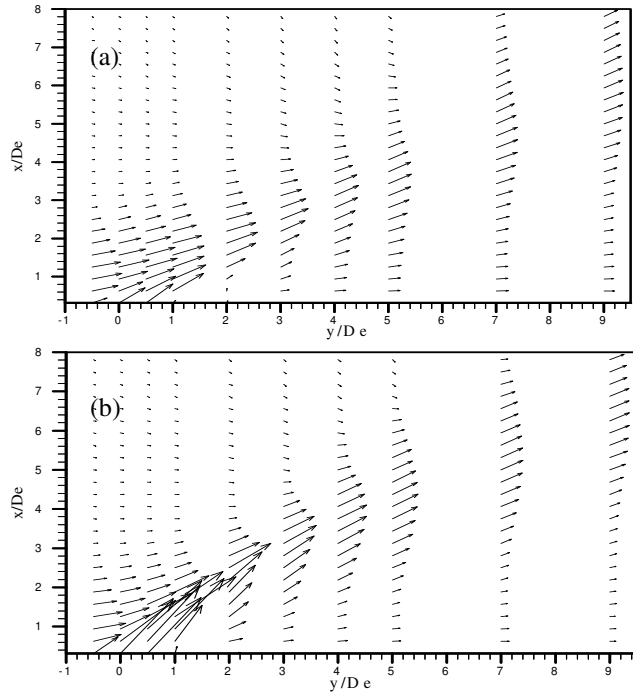


Figure 4(a-b). Velocity vectors at the centre of the primary (a) and lower secondary (b) nozzles for  $\phi = 3.0$

The flow field changed significantly with the increase in jet velocity ratio. The degree of deflection of primary jet towards the wall was reduced which is clear from figure 4(a). The primary jet penetrated through the cross flow layer whereas it was almost entirely within the cross flow for  $\phi=1.0$ . Due to the mixing of the secondary jets with the primary jet, the momentum of the primary jet was increased allowing the penetration of the primary jet through the cross flow. This phenomenon can be understood more clearly in figure 4(b) where the deflection of the lower secondary jet was minor from the geometric axis due to its high momentum showing that the jet pierced the cross flow layer.

Comparisons of the resultant velocity ( $U$ ) at the centre of the primary nozzle are presented in figures 6(a-b) for a number of lines downstream of the primary jet. The lines are  $y/De=0, 1, 3, 5$  and  $9$ . The velocities were measured in two perpendicular directions with  $u$  normal and  $v$  parallel to the cross-flow. All velocities are normalized to the velocity at the exit of the primary nozzle ( $x/De=0, y/De=0, z/De=0$ ). Measurement lines are shown in figure 5.

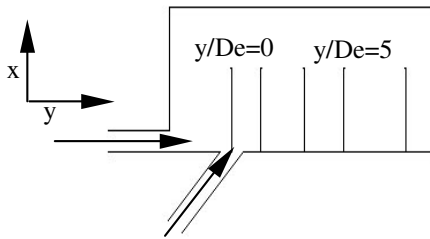


Figure 5. Schematic diagram showing the measurement lines

At  $y/De=0$ , the peak values are at the exit of the nozzle for both jet velocity ratios. At  $y/De=1$ , although the peak values occurred at the same position ( $x/De=0.8$ ) for both jet velocity ratios, the spreading of the jet for  $\phi=3.0$  is greater than for  $\phi=1.0$ . Further downstream ( $y/De=3, 5$  and  $9$ ), the peak value for  $\phi=3.0$  shifted farther from the wall than  $\phi=1.0$  and the difference is clear at  $y/De=5$  where the peak value for  $\phi=1.0$  is at around  $x/De=2.2$  and for  $\phi=3.0$  is at  $x/De=3.8$ . At  $y/De=9$  the difference between the peak values is at a maximum. This clearly indicates more spreading of the primary jet and less deviation from the geometric axis for  $\phi=3.0$ .

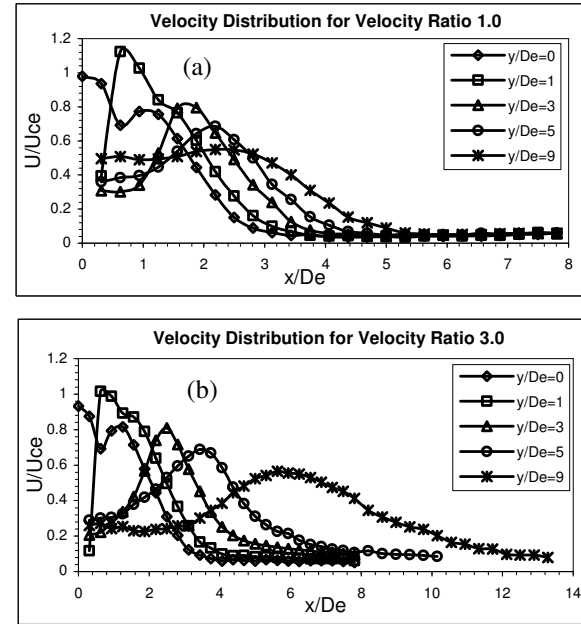


Figure 6(a-b). Velocity distribution at the centre of the primary nozzle for jet velocity ratio 1.0 (a) and 3.0 (b)

Figure 7(a-b) shows  $u_{rms}$  at the centre of the primary nozzle for jet velocity ratios of 1.0 and 3.0 respectively. At  $y/De=0$ , for  $\phi=1.0$ , very near to the wall ( $x/De=0.31$ ), there is a non-zero value (0.06) of  $u_{rms}$ . This non-zero value occurred due to diffusion transport in the cross-stream directions from regions of peak generation. After that there is a sudden peak of  $u_{rms}$  due to interaction between the primary jet and the cross flow. The magnitude then fell, gradually increased and reached the second peak at  $x/De=2.0$ . At  $y/De=1$ , peak value occurred at  $x/De=0.31$  because of the generation of turbulence due to high velocity gradient.

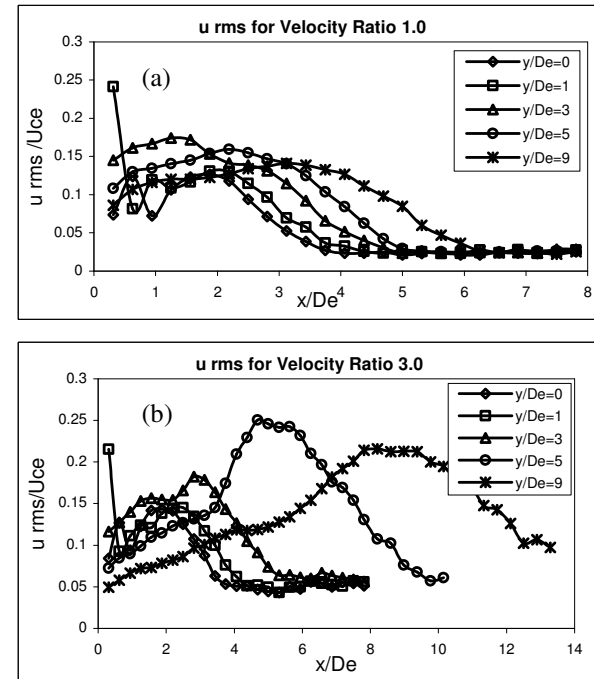


Figure 7(a-b). Comparison of  $u_{rms}$  at the centre of the primary nozzle for jet velocity ratio 1.0 (a) and 3.0 (b)

In this region there was a reverse flow. Further downstream ( $y/De=3, 5$  and  $9$ ) the peak values of  $u_{rms}$  shifted and occurred at the centreline of the jet. The peak values at this region occurred because of the diffusive redistribution of the normal stresses from the cross-stream generation regions. The trend is

similar for  $\phi=3.0$  at  $y/De=0$  and 1 but the magnitude of the peak values at  $y/De=3, 5$  and 9 are higher than those in  $\phi=1.0$ . Figure 8(a-b) shows the  $v_{rms}$  at the same planes for  $\phi=1.0$  and 3.0 respectively. Unlike the  $u_{rms}$ , there is only one peak at  $y/De=0$  both for  $\phi=1.0$  and  $\phi=3.0$ . At  $y/De=1$ , the peak value occurred near to the wall ( $x/De=0.31$ ) because of high velocity gradient as mentioned earlier. Further downstream the peak values shifted and occurred at the centreline of the jet due to the diffusive redistribution from the cross-stream generation regions.

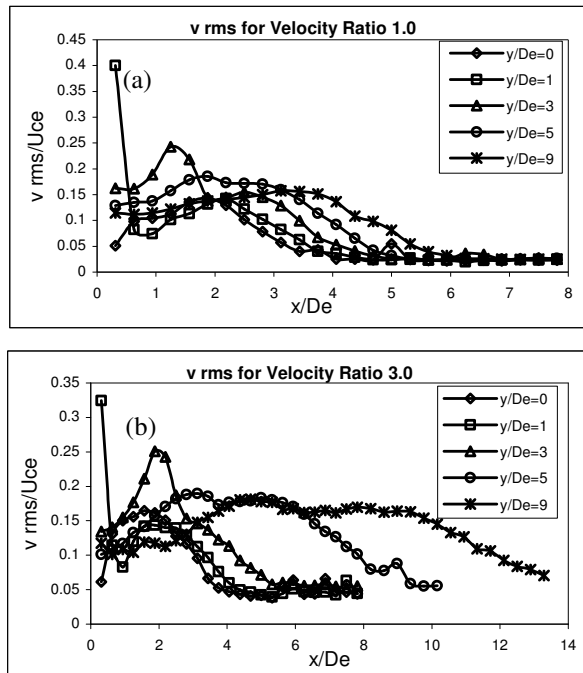


Figure 8(a-b). Comparison of  $v_{rms}$  at the centre of the primary nozzle for jet velocity ratio 1.0 (a) and 3.0 (b)

## Conclusions

The effect of jet velocity ratio on jet development in the presence of cross flow has been investigated in this paper. The burner was at an angle of  $60^\circ$  to the wall. The experiment was conducted for jet velocity ratios of 1.0 and 3.0. The LDA technique was used to measure the mean velocity component and turbulent fluctuation. Cross flow had a significant effect in developing the near field region. In the presence of cross flow both the primary jet and the secondary jet deviated from the geometric axis towards the wall and remained within the cross flow for velocity ratio 1.0. For  $\phi=3.0$ , the primary jet penetrated the cross flow layer due to higher momentum of the secondary jets. The deviation of the jet centreline from the geometric axis was less for  $\phi=3.0$ . The spreading of the jets for  $\phi=3.0$  was more than for  $\phi=1.0$ . There were two peaks for  $u_{rms}$  at  $y/De=0$  both for jet velocity ratios of 1.0 and 3.0. At  $y/De=1$ , near to the wall ( $x/De=0.3$ ),  $u_{rms}$  was high because of high velocity gradient. This investigation of the effect of jet velocity ratio indicates that simple small-scale isothermal models can be a major aid in the interpretation of observations in more complex flow environments.

## Acknowledgments

The authors gratefully acknowledge the financial and other support received for this research from the Cooperative Research Centre (CRC) for Clean Power from Lignite, which is established and supported under the Australian Government's Cooperative Research Centres program.

## References

- [1] Ahmed S., Hart J., Naser J., The effect of jet velocity ratio on aerodynamics of rectangular slot burners in tangentially fired furnace, *Third International conference on CFD in the Minerals and Process Industries*, CSIRO, Melbourne, Australia, 2003.
- [2] Andreopoulos J., Measurements in a jet-pipe flow issuing perpendicularly in to a cross stream. *ASME J. Fluids Eng.*, 104, 1982, 493-499.
- [3] Andreopoulos J. On the structure of jets in a cross flow, *J. Fluid Mech.*, 157, 1985, 163-197.
- [4] Andreopoulos J & Rodi W., Experimental investigation of jets in cross flow. *J. Fluid Mech.*, 138, 1984, 93-127.
- [5] Catalano GD, Chang KS & Mathis JA., Investigation of turbulent jet impingement in a confined cross flow, *AIAA J*, 27, 11, 1989, 1530-1535.
- [6] Foss J. Flow visualization studies of jets in a cross flow, *SFB 80 report/T/161*, Karlsruhe University, 1980.
- [7] Hart J., Numerical Investigation of Isothermal Burner Jet Aerodynamics, *Thesis*, School of Engineering & Science, Swinburne University of Technology, November, 2001
- [8] Haven B.A. & Kurosaka M., Kidney & anti-Kidney vortices in crossflow jets, *J. Fluid Mech.*, 352, 1997, 27-64.
- [9] Issac KM & Jakubowski AK., Experimental study of the interaction of multiple jets with a cross flow, *AIAA J*, 23, 1985, 1679-1683.
- [10] Issac KM & Schetz JA., Analysis of multiple jets in cross-flow, *ASME J. Fluids Eng.*, 104, 1982, 489-492.
- [11] Lester L. Yuan, Robert L. Street & Joel H. Ferziger., Large-eddy simulations of a round jet in crossflow, *J. Fluid Mech.*, 379, 1999, 71-104.
- [12] Lim T.T., New T. H. & Luo S.C., On the development of large-scale structure of a jet normal to a crossflow, *Physics of Fluids*, 13, 3, 2001, 770-775.
- [13] Makihata T & Miyai Y., Prediction of the trajectory of triple jets in a uniform cross flow, *ASME J. Fluids Eng.*, 105, 1983, 91-97.
- [14] New T. H., Lim T. T. & Luo S.C., Elliptic jets in cross-flow, *J. Fluid Mech.*, 494, 2003, 119-140.
- [15] Peterson S. D. & Plesniak M. W., Evolution of jets emanating from short holes into crossflow, *J. Fluid Mech.*, 503, 2004, 57-91.
- [16] Savory E & Toy N., Real time video analysis of twin jets in a cross flow, *ASME J. Fluids Eng.*, 113, 1991, 68-72.
- [17] Sherif SA & Pletcher RH., Measurements in the flow and turbulence characteristics of round jets in crossflow, *ASME J. Fluids Eng.*, 111, 1989, 165-171.
- [18] Smith S. H. & Mungal M. G., Mixing, structure and scaling of the jet in crossflow, *J. Fluid Mech.*, 357, 1998, 83-122.
- [19] Sykes RI, Lewellyn WS & Parker SF., On the vorticity dynamics of a turbulent jet in a cross flow, *J. Fluid Mech.*, 168, 1986, 993-413.
- [20] Yan H., Perry J.H., Two-Phase Flow Development in Slot Burners - Part 2 Detailed Flow Measurement and Numerical Model Validation, *ESAA Report No. ES/94/01*, August, 1994.

## Direct and Large Eddy Simulation of a turbulent channel flow with roughness on one wall.

S. Leonardi<sup>1</sup>, F. Tessicini<sup>2</sup>, P. Orlandi<sup>1</sup> and R.A. Antonia<sup>3</sup>

<sup>1</sup>Dipartimento di Meccanica e Aeronautica  
Università La Sapienza, Via Eudossiana 16, I-00184, Roma

<sup>2</sup>Dep. of Aer. Imperial College of London  
London UK

<sup>3</sup>Discipline of Mechanical Engineering,  
University of Newcastle, NSW 2308 Australia

### Abstract

Large and Direct Numerical Simulations (LES, DNS) of a turbulent channel flow with square bars on one wall have been carried out at  $Re = 10400$ . Two sub-grid models have been used: Smagorinsky with Van Driest damping and Dynamic. There is satisfactory agreement between the two types of simulations for the pressure and skin friction on the wall and the *rms* streamwise velocity. Comparison for the *rms* normal and spanwise velocities is poor but the sub-grid models are a significant improvement relative to the no model (which corresponds to an unresolved DNS). A further DNS at  $Re = 18000$  has been performed with the aim of comparing the results with the experiment by Hanjalic & Launder [1]. The Reynolds number dependence ( $Re$  ranging from 4200 to 18000) has been discussed. The pressure on the wall and hence the form drag does not depend on  $Re$  and the velocity profile changes slightly for  $Re > 10400$ .

### Introduction

Flows over rough surfaces are of interest in many practical applications, ranging from shipbuilding and aviation, the flows over blades in different types of turbomachines and the flows over vegetated surfaces in the atmospheric surface layer. In all these cases, the Reynolds number is high and the roughness is very small relative to the characteristic length of the outer flow. Jiménez [2] claimed that numerical or laboratory experiments should have at least  $\delta/k > 50$  and  $k^+ = ku_\tau/\nu$  in the fully rough regime ( $\delta$  represents either the diameter of the pipe, the thickness of the boundary layer or the half-width of a duct, and  $k^+$  is the height of the roughness elements in wall units). Therefore, numerical simulations require a large number of points. For this reason, to date, numerical simulations have been carried out only at low Reynolds numbers ( $Re = U_c h/\nu < 10000$ ,  $h$  is the channel half-width,  $U_c$  is the centerline velocity and  $\nu$  is the kinematic viscosity) e.g. DNS, [3], [4], [5] and LES, [6]. Although these simulations have provided useful results, it is important to increase the Reynolds number. In the present paper, LES and DNS results of a turbulent channel flow with square bars on the bottom wall and a smooth upper wall are discussed. One of the aims is to compare the results with those of the experiment by Hanjalic & Launder [1] for a turbulent channel flow with square bars on the bottom wall with  $\lambda/k = 10$ , where  $\lambda$  is the distance between successive elements. DNSs have been carried out at  $Re = 10400$  and  $Re = 18000$ . The computational box is  $8h \times 2.125h \times 6.25h$  in the streamwise ( $x$ ) wall-normal ( $y$ ) and spanwise ( $z$ ) direction respectively. The additional  $0.125h$  increase in the channel height is due to the cavity height where the square elements ( $k = 0.125h$ ) are placed. In this context, the development of reliable LES sub-grid models remains an important objective.

The grid used for the LES, ( $240 \times 160 \times 49$  in  $x, y, z$  respectively), is much coarser than that used for the DNS ( $513 \times 177 \times 193$  and  $769 \times 161 \times 193$  for  $Re = 10400$  and  $Re = 18000$  respectively). The models used are the standard Smagorinsky model with Van Driest damping ( $C_s = 0.1$ , hereafter SM10) and the dynamic model (DYN). To underline the effect of the sub-grid model, a simulation without model has been carried out (NOM). The latter would correspond to an unresolved DNS.

### Numerical Procedure

The non-dimensional Navier-Stokes and continuity equations for incompressible flows are:

$$\frac{\partial U_i}{\partial t} + \frac{\partial U_i U_j}{\partial x_j} = -\frac{\partial P}{\partial x_i} + \frac{1}{Re} \frac{\partial^2 U_i}{\partial x_j^2} + \Pi, \quad \nabla \cdot U = 0 \quad (1)$$

where  $\Pi$  is the pressure gradient required to maintain a constant flow rate,  $U_i$  is the component of the velocity vector in the  $i$  direction and  $P$  is the pressure. The Navier-Stokes equations have been discretized in an orthogonal coordinate system using the staggered central second-order finite-difference approximation. Here, only the main features are recalled since details of the numerical method can be found in Orlandi [7]. The discretized system is advanced in time using a fractional-step method with viscous terms treated implicitly and convective terms explicitly. The large sparse matrix resulting from the implicit terms is inverted by an approximate factorisation technique. At each time step, the momentum equations are advanced with the pressure at the previous step, yielding an intermediate non-solenoidal velocity field. A scalar quantity  $\Phi$  projects the non-solenoidal field onto a solenoidal one. A hybrid low-storage third-order Runge-Kutta scheme is used to advance the equations in time. The roughness is treated by the efficient immersed boundary technique described in detail by Fadlun *et al.* (2000). This approach allows the solution of flows over complex geometries without the need of computationally intensive body-fitted grids. It consists of imposing  $U_i = 0$  on the body surface which does not necessarily coincide with the grid. Another condition is required to avoid that the geometry is described in a stepwise way. Fadlun *et al.* (2000) showed that second-order accuracy is achieved by evaluating the velocities at the closest point to the boundary using a linear interpolation. This is consistent with the presence of a linear mean velocity profile very near the boundary even for turbulent flows, albeit at the expense of clustering more points near the body.

### Results and discussion

The square element on the bottom wall induces a separation at the trailing edge of the elements ( $x/k \simeq 1$  Fig.1). In agreement with the results of Leonardi *et al.* [4] obtained for larger ele-

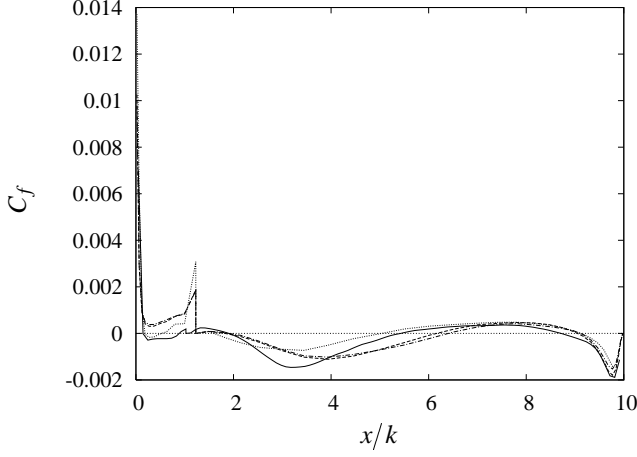


Figure 1: Frictional drag on the horizontal walls of a roughness element at  $Re = 10400$ . — DNS, ..... NOM, ---- Smagorinsky, -.-.- Dynamic.

ments (DNS  $k = 0.2h$ ) the flow reattaches on the bottom wall at about  $x/k \simeq 5$  (where  $x = 0$  is taken at the leading edge of the element). On the other hand, LES simulations predict a larger recirculating region, with a smaller intensity. As the next element is approached, a separation occurs at about  $x/k \simeq 9$ , one roughness height upstream of the element. The LESs, in this case, yield a good approximation for the  $C_f$  with respect to the DNS. This behaviour is due to the non-uniform grid used for the LES with a larger number of points very near the element, and a very coarse resolution within the cavity. The element leads to a large increase of velocity and a presence of the friction peak at the leading edge of the element. Above the crest, as shown in Leonardi *et al.* [4] for  $\lambda/k > 8$  a separation occurs. LES and NOM are not able to reproduce this separation which was also observed in the experiment of Liu, Kline and Johnston [9].

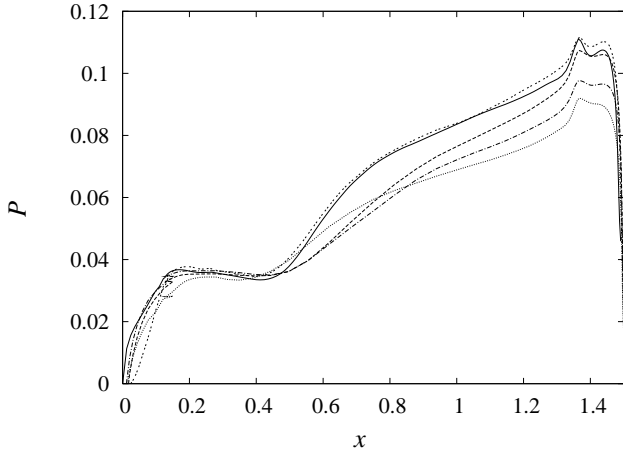


Figure 2: Pressure along the walls of a roughness wavelength.  $Re = 10400$ : — DNS, ..... NOM, ---- Smagorinsky, -.-.- Dynamic.  $Re = 18000$  ..... DNS.

Pressure distributions along the horizontal and vertical walls are shown in Fig. 2 over one wavelength. Very near the element ( $0 < x < 0.25$  and  $1.25 < x < 1.5$ ) LES and DNS results are in good agreement. At the center of the cavity, larger differences are found. This is again due to the non-uniform grid used. Since the difference between pressure distributions on the vertical walls, corresponds to the form drag for this roughness element, approximately, the LES and DNS yield values of the form drag that agree. On the other hand, NOM yields a different pressure distribution over most of the wavelength and

a different (smaller) form drag. The pressure distributions for  $Re = 10400$  and  $Re = 18000$  are close to each other. The form drag, is  $\overline{P_d} = 6.46E - 03$  and  $6.6E - 03$  for  $Re = 10400$  and  $Re = 18000$  respectively ( $\overline{P_d} = \lambda^{-1} \int_0^\lambda \langle P \rangle \vec{n} \cdot \vec{x} ds$ , angular brackets denote averaging in time and  $z$ ). This is an extension of the results of Leonardi *et al.* [4]. In a previous paper, they defined  $C_d = \overline{P_d}/k$  and showed that for several values of  $\lambda/k$ ,  $C_d$  does not depend on  $Re$  (which was varied between  $Re = 4200$  to  $Re = 10400$ ) and on  $k$  (in the range  $0.1h$  to  $0.2h$ ). For large values of  $\lambda/k$  (e.g.  $\lambda/k > 3$ ), the total drag is almost entirely due to the form drag. Therefore, the value of the friction velocity,  $U_\tau \equiv (\overline{P_d} + \overline{C_f})^{1/2}$ , does not change with the Reynolds number, ( $\overline{C_f} = \lambda^{-1} \int_0^\lambda \langle C_f \rangle ds$ ). As a consequence, we believe that, for this type of roughness, the flow physics near the wall can be investigated through numerical simulations at moderate Reynolds numbers.

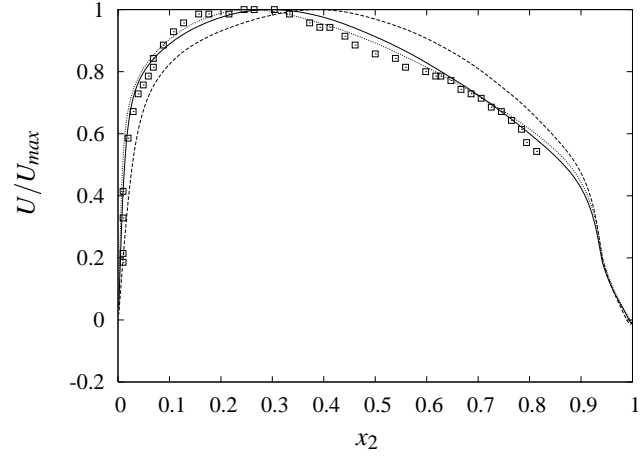


Figure 3: Mean velocity distribution. Symbols, experiment by Hanjalic & Launder [1], lines DNS. ----  $Re = 4200$ , —  $10400$ , .....  $18000$ .

The mean velocity distribution shown in figure 3 for different Reynolds numbers, are compared with the measurements of Hanjalic & Launder [1] at  $Re = 18000$ . The agreement between experiment and DNS is satisfactory. The DNS results show that by increasing  $Re$  the maximum velocity is shifted upwards (towards the smooth wall). However, whereas the changes to the velocity profile are large between  $Re = 4200$  and  $Re = 10400$ , only slight differences are observed between  $Re = 10400$  and  $Re = 18000$ . Therefore, the dependence on the Reynolds number, for intermediate values of  $Re$  is weak even in the outer layer, so that DNS is a useful tool for providing insight into rough flows.

The velocity profile in wall units is:

$$U^+ = \kappa^{-1} \ln y^+ + C - \Delta U^+, \quad (2)$$

where  $C$  and  $\kappa$  are constants and “+” denotes normalization by either  $U_\tau$  or  $v/U_\tau$ . The origin for  $y$  is at  $0.15k$  above the bottom wall. With respect to the smooth wall the velocity profile is shifted downward by a factor  $\Delta U^+$ , known as the roughness function. In Figure 4, the mean velocity profiles in wall units for DNS, LES and NOM are compared to the smooth wall distribution by Moser, Kim & Mansour [10]. As expected, the mean velocity profile is shifted downward, and the agreement between LES and DNS is reasonable. The roughness function is indeed due essentially to the increase of  $U_\tau$ . For this value of  $\lambda/k$ ,  $U_\tau$  is mostly due to the pressure distribution which was shown to be similar for DNS and LES (Fig.2). On the other hand, the pressure drag for NOM was different from that relative to the DNS,

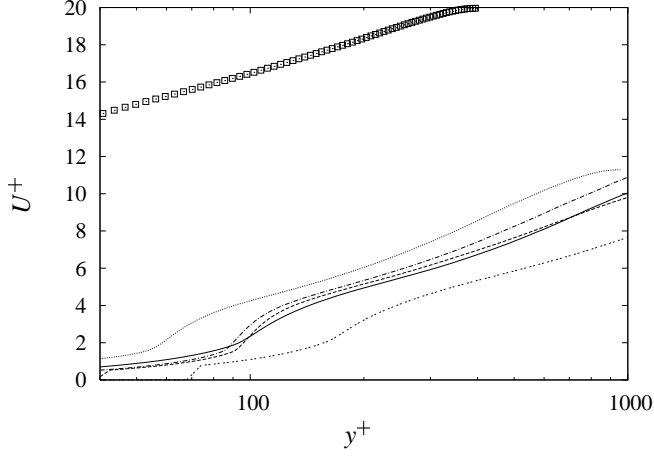


Figure 4: Mean velocity distribution in wall units. Symbols smooth channel Moser, Kim & Mansour [10].  $Re = 10400$ : — DNS, ..... NOM, ---- Smagorinsky, —·— Dynamic.  $Re = 18000$ : ..... DNS.

then larger differences to the velocity profile are expected. Even if  $U_\tau$  does not change, the roughness function for  $Re = 18000$  is larger than that for  $Re = 10400$ . As the origin in  $y$  is the same, and  $k^+$  increases, the velocity distribution is shifted downward. In fact, Perry, Schofield & Joubert [11] showed that, for large  $\lambda/k$  (k-type roughness),

$$\Delta U^+ = \kappa^{-1} \ln k^+ + B. \quad (3)$$

The value of  $k^+$  is 80, 103 and 180 for  $Re = 4200$ , 10400 and  $Re = 18000$  respectively. The corresponding values of  $\Delta U^+$  are 12.9, 13.5 and 14.8 respectively, in agreement with equation 3 and  $B = 2.2$ . For these values of  $k^+$  we are in the fully rough regime (Bandyopadhyay [12]).

Turbulent intensities are shown in Figure 5. For  $\langle uu \rangle$ , both the Large Eddy Simulations performed with Smagorinsky and dynamic models agree reasonably well with the DNS. However, for the other two stresses, the agreement is poor, especially for  $\langle ww \rangle$ . Near the rough wall ( $x_2 = -1$ ), there is reasonable agreement for  $\langle vv \rangle$  but significant differences can be discerned in the inner part of the channel. Perhaps surprisingly, the agreement between DNS and LES is not satisfactory near the upper smooth wall. Since sub-grid models work well for a smooth wall, this result should mean that the grid is too coarse to simulate the interaction between the two walls. In fact, roughness increases the communication between the wall and the outer layer. The improvement brought by the sub-grid models that have been tried is encouraging. Indeed, with respect to NOM, Large Eddy Simulations compare much better with the DNS results. While  $\langle uu \rangle$  on the rough-wall is about the same as that on the smooth wall,  $\langle vv \rangle$  and  $\langle ww \rangle$  increase by about 2.5 times. This means that isotropy is better approximated over rough wall, as noted by Smalley *et al.* [13].

DNS results at  $Re = 18000$  are compared with the experiment of Hanjalic & Launder [1] in Fig.6. Despite the uncertainty in the determination of  $U_\tau$  the agreement is reasonable. In particular,  $\langle uu \rangle$  and  $\langle ww \rangle$  are in reasonable agreement, while there is poor agreement for  $\langle vv \rangle$ , especially near the wall.

## Conclusions

Direct and Large Eddy Simulations have been performed for a turbulent channel flow with square bars on the bottom wall with a pitch to height value of  $\lambda/k = 10$  at  $Re = 10400$ . For the pressure, skin friction and *rms* streamwise velocity the agreement between DNS and LES is satisfactory. On the other hand, for

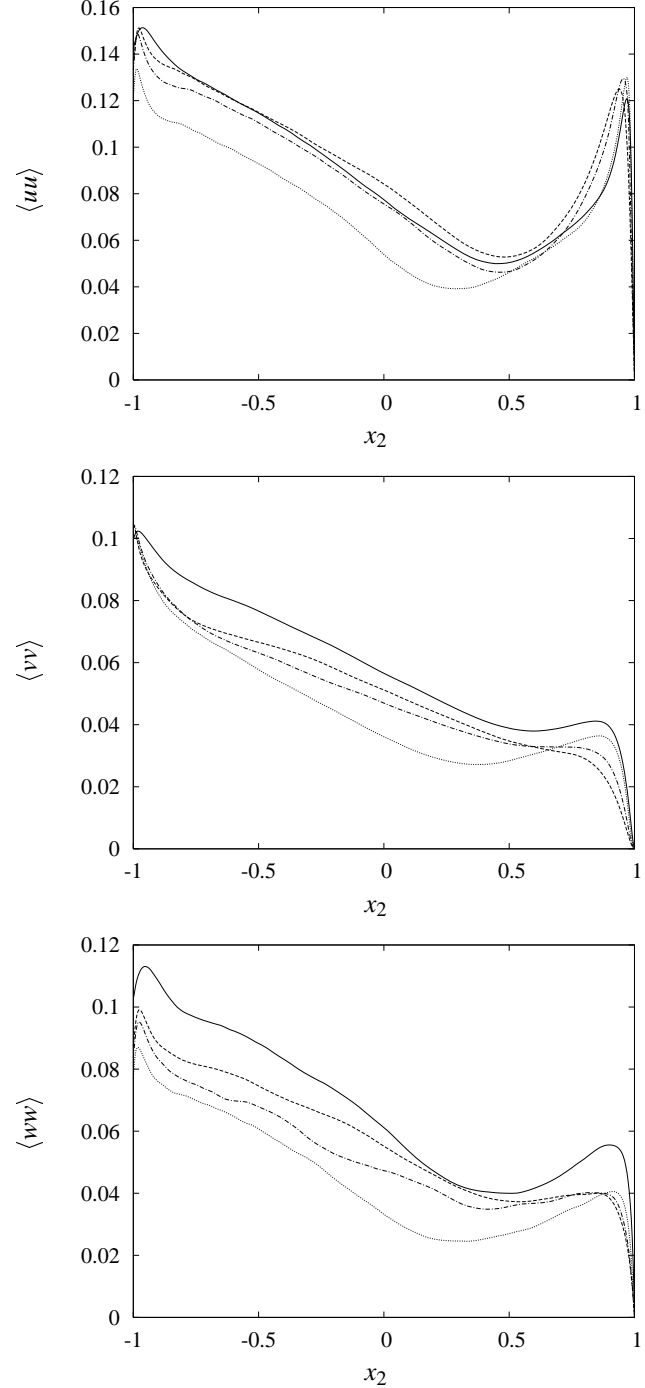


Figure 5: Normal turbulent intensities,  $Re = 10400$ : — DNS, ..... NOM, ---- Smagorinsky, —·— Dynamic.

the *rms* spanwise and normal velocity, the agreement is poor. The improvement brought by the sub grid model is encouraging. The DNS at  $Re = 18000$  showed a reasonable agreement with experimental results by Hanjalic & Launder [1]. The Reynolds number dependence for intermediate Reynolds is very weak, then we speculate that DNS can be very useful in the study of rough flows.

## Acknowledgments

We acknowledge the support of the Australian Research Council, and the Ministero dell' Istruzione, dell' Università e della Ricerca and Centro di Eccellenza di Meccanica Computazionale, Politecnico di Bari.

## References



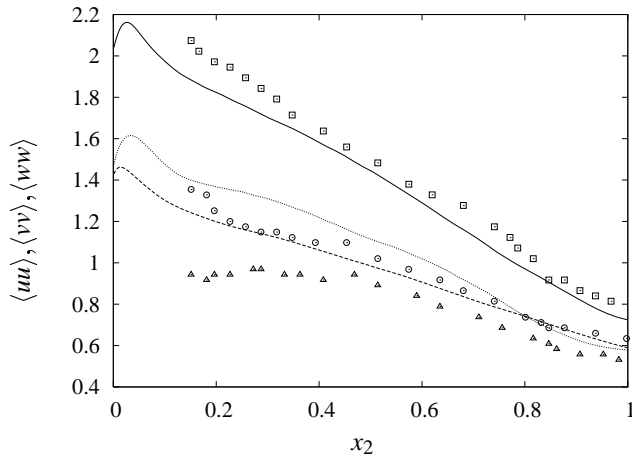


Figure 6: *rms* velocity fluctuation in wall units. Lines DNS at  $Re = 18000$ , symbols experiment by Hanjalic & Launder [1]: —  $\square \langle uu \rangle$ , ---  $\triangle \langle vv \rangle$ , .....  $\circ \langle ww \rangle$ .

- [1] Hanjalic & Launder. Fully developed asymmetric flow in plane channel. *J. Fluid Mech.* **51**, 1972, 301–335.
- [2] Jiménez, J. Turbulent flows over rough walls. *Ann. Rev. Fluid Mech.* **36**, 2004, 173–196.
- [3] Miyake Y., Tsujimoto K. & Nagai N. Numerical simulation of channel flow with a rib-roughened wall. *J. Turb.* **3**, 2002, 35.
- [4] Leonardi, S., Orlandi, P., Smalley, R.J., Djenidi, L. & Antonia, R.A. Direct numerical simulations of turbulent channel flow with transverse square bars on one wall. *J. Fluid Mech.* **491**, 2003, 229–238.
- [5] Ashrafiyan A. & Anderson H.I. (2003). DNS of Turbulent Flow in a Rod-Roughened Channel. Proceedings of the Turbulent and Shear Flow Phenomena 3, Sendai, Japan. N. Kasagi, J. K. Eaton, R. Friedrich, J. A. C. Humphrey, M. A. Leschziner, T. Miyauchi. **Vol I**, 2003, 117–123.
- [6] Cui J., Virendra C. Patel & Ching-Long Lin. Large-eddy simulation of turbulent flow in a channel with rib roughness. *Int. J. of Heat and Fluid Flow* **24**, 2003, 372–388.
- [7] Orlandi, P. Fluid flow phenomena, a numerical toolkit. *Kluwer Academic Publishers*. 2000.
- [8] Fadlun E.A., Verzicco, R., Orlandi P. & Mohd-Yusof, J. Combined immersed boundary finite-difference methods for three-dimensional complex flow simulations. *J. Comput. Phys.* **161**, 2000, pp.35–60.
- [9] Liu, C.K., Kline, S.J. and Johnston, J.P. An experimental study of turbulent boundary layers on rough walls. Report MD-15, 1966, Department of Mechanical Engineering, Stanford University.
- [10] Moser R.D., Kim J. & Mansour N.N. Direct numerical simulation of turbulent channel flow up to  $Re_\tau = 590$ . *Phys. Fluids* **11**, 1999, 943–945.
- [11] Perry, A. E., Schofield, W. H. & Joubert, P. N. Rough wall turbulent boundary layers. *J. Fluid Mech.* **37**, 1969, 383–413.
- [12] Bandyopadhyay, P.R. Rough-wall turbulent boundary layers in the transition regime. *J. Fluid Mech.* **180**, 1987, pp.231–266.
- [13] Smalley, R.J., Leonardi, S., Antonia, R., Djenidi, L. & Orlandi, P. Reynolds stress anisotropy of turbulent rough walls layers. *Expts in Fluids* **33**, 2002, 31–37.

## Evolution of a Turbulent Wedge from a Streamwise Streak

J.H. Watmuff<sup>1</sup>

<sup>1</sup>School of Aerospace, Mechanical & Manufacturing Engineering  
RMIT University, VIC, 3001 AUSTRALIA

### Abstract

A narrow streamwise low-speed streak is deliberately introduced into an otherwise extremely uniform Blasius boundary layer. The streak shares many of the characteristics of Klebanoff modes known to be responsible for bypass transition at moderate Free Stream Turbulence (FST) levels. However, for the low background disturbance level of the free stream ( $u'/U_1 < 0.05\%$ ), the layer remains laminar to the end of the test section ( $R_x \approx 1.4 \times 10^6$ ) and there is no evidence of bursting or other phenomena associated with breakdown to turbulence. A harmonic disturbance is used to excite a sinuous form of instability, which grows over a considerable streamwise distance before breakdown of the streak occurs, which leads to the formation of a turbulent wedge. Detailed measurements show that new streaks are formed on either side during the breakdown process. The characteristics of the wedge are examined over a considerable streamwise distance. A similar mechanism appears to be responsible for the spanwise growth of the wedge since a spanwise succession of new streaks is observed in the early stages of its development.

### Introduction

The current experiment was motivated by observations during a series of flow quality improvements by Watmuff [6] in which the background unsteadiness,  $u'/U_1$ , in a Blasius boundary layer was reduced by a factor of 30. The effectiveness of the improvements was judged by examining contours of hot-wire data in spanwise planes through the layer. The contours demonstrated a form of three-dimensionality in which locally concentrated regions of elevated background unsteadiness appeared to be correlated with small spanwise variations of the layer thickness. The characteristics of the unsteadiness (e.g. low frequency spectral content) in the concentrated regions were much the same as at other spanwise positions, where the  $u'/U_1$  distribution was more uniform and the Blasius wall distance of the  $u'/U_1$  maxima was  $\eta \approx 2.3$ . These characteristics have much in common with Klebanoff modes observed by Klebanoff [4], Kendall [2, 3] and Westin et al. [8] at elevated FST levels.

The most significant reductions in  $u'/U_1$  were realised after painstaking improvements were made to the uniformity of the porosity of wind tunnel screens. Watmuff found that even almost immeasurably small Free Stream Nonuniformity (FSN) variations (e.g.  $\Delta U/U_1 \approx 0.05\%$ ) appeared to be associated with local concentrations of elevated unsteadiness. During the final stages, further improvements to the screen system produced only a relatively minor reduction in the FST level, but the additional decrease in the FSN led to a three-fold reduction of  $u'/U_1$  within the layer. The extraordinary sensitivity to weak FSN encouraged Watmuff to develop a means of deliberately embedding a streak with Klebanoff-mode-like characteristics into the boundary layer in order to perform detailed studies in a controlled manner.

Boiko et al. [1] demonstrated that the combination of vibrating ribbon generated Tollmien-Schlichting (TS) waves and grid generated Free Stream Turbulence (FST) leads to transition at lower Reynolds numbers than when the FST is present alone. These results prompted Watmuff [7] to use a vibrating ribbon to examine the interaction between the streak and TS waves. He found that the deformation of the mean flow associated with the streak is responsible for substantial phase and amplitude distortion of the TS waves. He used pseudo-flow visualization of hot-wire data to show that the breakdown of the distorted waves is more complex and that it occurs at a lower Reynolds number than the breakdown of the *K*-type secondary instability that was observed when the FSN is not present.

However, breakdown of the flow was not observed unless the wave amplitude was sufficiently large to reach a level for the onset of secondary instability when the FSN is not present. In this paper the stability of the streak alone is considered.

### Introduction of streak into Blasius boundary layer

The base-flow consists of a highly spanwise uniform Blasius boundary layer. The development of the mean flow closely follows the Blasius similarity solution. The background unsteadiness levels are extremely low: in the free-stream,  $u'/U_1 < 0.05\%$ ; and within the layer,  $u'/U_1 < 0.08\%$ . Vibrating ribbon experiments by Watmuff [7] demonstrate the growth of distortion-free Tollmien-Schlichting waves closely follow predictions from the linearized Parabolized Stability Equations (PSE) provided by Bertolotti [private communication].

A narrow low-speed streak (i.e. region of elevated thickness) is deliberately introduced into the Blasius boundary layer as a result of the interaction of a laminar wake with the leading edge of the flat plate. The wake is generated by stretching a fine wire across the full extent of the test section and it is aligned perpendicular to the freestream and to the leading edge. A range of wire diameters, at varying distances from the leading edge have been used by Watmuff [7] to produce streaks with different properties. For the results in this paper, the wire diameter,  $d = 50.8 \mu\text{m}$  and it is located 184 mm upstream of the leading edge.

The wake profile is shown in figure 1(a) at a location 63.5 mm upstream of the leading edge. The measurements were obtained using a flattened total pressure tube which was connected directly to a high accuracy differential pressure transducer and a fixed total pressure tube was used as the reference pressure. The velocity defect compares very well with the theoretical distribution predicted using a linearized theory which is shown as a solid line. The unit Reynolds number for the experiments is  $6.68 \times 10^5 \text{ m}^{-1}$  ( $U_1 \approx 10 \text{ ms}^{-1}$ ), giving  $R_d = 34$ . Streamwise development of the spanwise variation of displacement thickness resulting from interaction of the wake with the leading edge is shown in figure 1(b) for 16 streamwise positions, ranging from  $x = 0.3$  to 1.8 m. The results clearly demonstrate the narrow region of elevated thickness, i.e. the low-speed streak.

A rather surprising result is that the shape factor of the layer affected by the streak remains close to the Blasius value,  $H=2.59$ , despite the large spanwise thickness variation. Another feature that is not shown here, is that regions of elevated background unsteadiness occur on either side of the peak layer thickness, which share many of the characteristics of Klebanoff modes identified by Kendall [2, 3] that are observed at elevated Free Stream Turbulence (FST) levels. However, for the low background disturbance level of the free stream, the layer remains laminar to the end of the test section ( $R_x \approx 1.4 \times 10^6$ ) and there is no evidence of bursting or other phenomena associated with breakdown to turbulence.

The advantage of using a steady free-stream disturbance in the current experiments is that the streak is almost single stationary, which allows its features to be examined in detail using a hot-wire probe, with 0.5  $\mu\text{m}$  diameter and 0.5 mm long filaments.

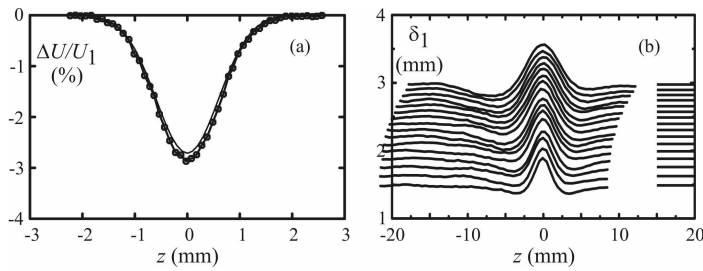


Figure 1. (a) Wake profile 63.5 mm upstream of leading edge.  $z$ -coord. relative to wire centreline. (b) Streamwise growth of spanwise variation of displacement thickness,  $\delta_1$ .  $z$ -coord. relative to the peak  $\delta_1$  values. Lines in range  $15 < z < 20$  are Blasius values, i.e.  $\delta_1 = 1.7208 (v_x/U_1)^{1/2}$ .

### Excitation of the streak

It was discovered by experiment that a harmonic disturbance could be used to excite a sinuous form instability in the streak. The source of the disturbance is a 0.5 mm diameter hole in the test surface located beneath the streak at a point  $x = 0.38$  m from the leading edge. The response of the streak was found to be remarkably sensitive to the excitation frequency. A nondimensional frequency,  $F = 2\pi f v/U_1^2 = 185 \times 10^{-6}$  ( $f \approx 265$  Hz) was found to introduce the strongest response. This is larger than the frequency corresponding to the Branch II of the neutral stability curve at this location,  $f \approx 165$  Hz, so small amplitude disturbances should decay according to linear stability theory.

For small disturbance amplitudes, the magnitude of the instability was found to grow and then decay with streamwise distance. However, for moderate disturbance amplitudes, the streamwise growth of the instability reached a threshold leading to breakdown of the streak. The streamwise distance between the source and the breakdown of the streak is dependent on the magnitude of the disturbance. Selection of the disturbance magnitude for detailed study was a compromise between using smaller amplitudes (to minimize the initial nonlinearity) and larger amplitudes (to limit the distance between the source and the breakdown and minimize phase jitter in the measurements).

When the streak is not present (wire removed from test section), measurements have demonstrated that a low amplitude harmonic disturbance at  $F = 60 \times 10^{-6}$  generates a 3D TS wave pattern that closely match the pattern calculated by Mack & Herbert [5] using the Parabolized Stability Equations. Similar measurements have been performed using the larger amplitude disturbance at nondimensional frequency of  $F = 185 \times 10^{-6}$ , corresponding to the parameters for the streak study, but without the presence of the streak. The results are not shown here, but they demonstrate that the disturbance has larger amplitude and is of a more complex form than the 3D Ts wave pattern of Mack & Herbert. However, the disturbance remains confined in the spanwise direction. The magnitude of the disturbance,  $u''/U_1 \approx 3\%$ , but the amplitude

decays with streamwise distance. When the streak is excited by the harmonic disturbance the phase-averaged velocity fluctuations reach an amplitude of  $u''/U_1 \approx \pm 25\%$  at the point of breakdown, given by  $x=0.63$  m, i.e. about 0.25 m from the source of the disturbance.

### Form and growth, and breakdown of streak instability

Detailed 64-interval phase-averaged measurements have been made with a single hot-wire to investigate the spatial form of the streak instability during the growth period and the final breakdown process. Contours of the total phase-averaged streamwise velocity,  $\bar{U} + u_\phi$ , in two cross-stream planes are shown in figure 2(a-b). Spanwise meandering of the outer region of the streak is evident in the results, as shown for the two phase intervals in each plane. A more complete depiction of the streak instability can be made by using pseudo-flow visualization, i.e. the use of phase as the streamwise coordinate. Pseudo-flow contours of  $\bar{U} + u_\phi$  and the phase-averaged unsteadiness,  $u''_\phi$  are shown in planes parallel to wall in figures 3(a-b). The velocity contours possess a local kink that is associated with a region of elevated phase-averaged unsteadiness. This region reveals the onset of randomness of instability with streamwise distance. Two localized regions of elevated unsteadiness appear in the contours in figure 3(b) which suggest that additional kinks may form with streamwise growth.

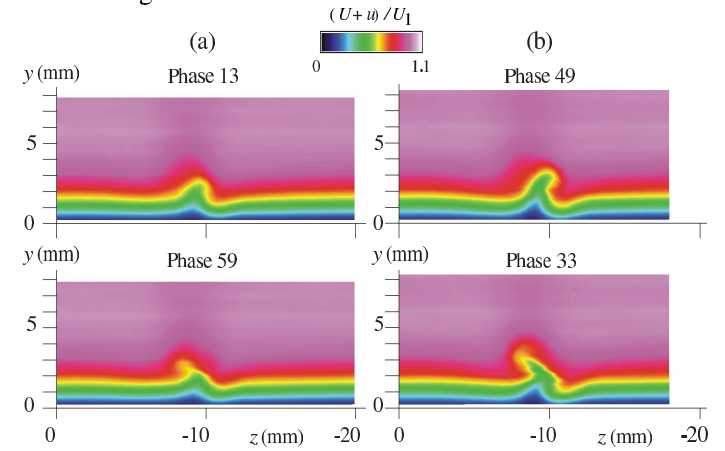


Figure 2. Total phase-averaged velocity,  $(\bar{U} + u_\phi)/U_1$ , in cross-stream planes (a)  $x=0.52$  m,  $\phi=13$  &  $\phi=59$  (b)  $x=0.58$  m,  $\phi=49$  &  $\phi=33$ .

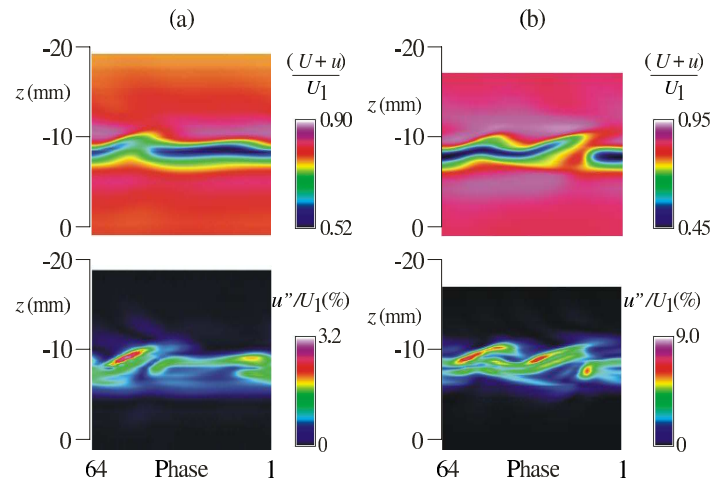


Figure 3. Pseudo-flow contours of  $(\bar{U} + u_\phi)/U_1$  and  $u''_\phi/U_1$  at fixed wall distance. (a)  $x = 0.52$  m,  $y = 2.2$  mm (b)  $x = 0.58$  m,  $y = 2.6$  mm.

True spatial contours representing the final stages of growth and the ultimate breakdown of the streak are shown in figures 4(a-c). The sinuous shape of the streak remains much the same while the phase-averaged unsteadiness level increases in the region corresponding to the pseudo-flow contours in figures 3(a-b). Washout of the contours of the total phase-averaged streamwise velocity is evident in figure 4(a) in the vicinity of the streak centreline for  $x > 0.6$  m. (Note that the streak is located about 10 mm away from the centreline of the test plate.) This region also corresponds with an increase in the phase-averaged unsteadiness level as shown in figure 4(b). These features demonstrate the onset of randomness associated with the instability as the streak undergoes breakdown to turbulence. Also visible in figure 4(b) are two regions with elevated phase-averaged unsteadiness levels that appear on either side of the centreline of the streak for  $0.65 < x < 0.70$  m. The breakdown on the centreline and the formation of two regions of highly unsteady flow on either side of the streak are most clearly evident in the contours of the broadband unsteadiness shown in figure 4(c).

The sudden appearance of the two concentrated regions of highly unsteady flow on either side of the streak centreline is consistent with the notion that streak is responsible for introducing a new pair of streaks on either side via some instability mechanism. It is likely that the sinuous shape of the streak is responsible for introducing cross-flow velocity perturbations. Hence a plausible mechanism responsible for the appearance of the new streaks is cross-flow instability.

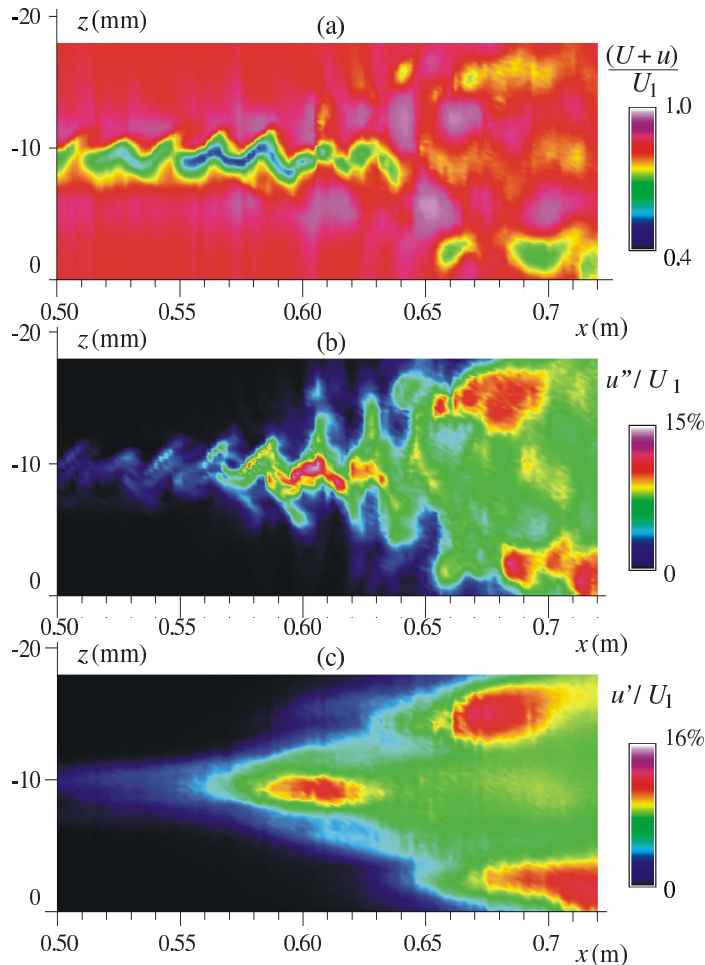


Figure 4. True spatial contours in plane,  $y=2$ mm (a)  $(\bar{U} + u_\phi)/U_1$ ,  $\phi=21$ . (b)  $u''_\phi/U_1$ ,  $\phi=21$ . (c) Broadband unsteadiness,  $\bar{u}'/U_1$ .

## Features of turbulent wedge

The contours in figures 4(a-c) demonstrate that the randomness associated with the breakdown of the streak precludes the use of phase-averaged data to examine the flow structure further downstream. However, broadband hot-wire measurements are useful for examining the structure of the turbulent wedge that develops downstream of the breakdown.

Contours of the temporal mean streamwise velocity are shown in figure 5. A smaller fixed wall distance of the measurement grid ( $y=0.5$  mm) has been used for these results compared to the grid used to produce figure 4 ( $y=2.0$  mm) since the central portion of the flow is fully turbulent. The grid is wedge-shaped to avoid time consuming measurements in the regions of inactive flow.

A series of streamwise streaks are clearly evident in the mean flow contours at this early stage of development. The streaks persist in the mean flow for considerable streamwise distance, despite the fully turbulent characteristics of the central region of the wedge. The innermost pair of streaks, located at  $x = 0.7$  m, are the result of the growth and breakdown of the instability shown in figure 4. Another pair of streaks can be seen to form at successive spanwise positions near the border of the wedge as it develops with streamwise distance.

The overall features of the wedge are shown in the contours of the mean flow, and broadband turbulence intensity in the expanded view of the entire measurement grid in figure 6. The spreading rate of the wedge is shown by the half-angle of  $8^\circ$ , which is close to that observed in previous studies of roughness generated turbulent wedges. Contours of these quantities are also shown in a streamwise sequence of cross-stream planes in figure 7 and the streaks are clearly visible in the mean velocity distribution in the planes located at  $x=0.8$  and  $0.9$  m. The maximum turbulence levels are experienced near the wall in the central region, and profiles (not shown) are similar to those observed in a turbulent boundary layer. However the distribution near the edge is spread over a larger wall distance and profiles (not shown) have a secondary maximum.

It is plausible that the spanwise growth of the wedge is the result of the formation of a spanwise succession of streaks, where the formation of each in turn is the result of an instability introduced by the streak immediately preceding it upstream. Streaks are not observed in the mean flow contours near the border of the wedge further downstream. However this does not preclude the preceding notion that the spanwise growth of the wedge is the result of a succession of streaks. Any randomness in the streak formation process will lead to increased randomness in the formation of downstream streaks because of their successive dependency on the streaks forming upstream. Increased randomness associated with the location of successive streaks would result in a smearing of data thereby causing washout of the streaks in the contours.

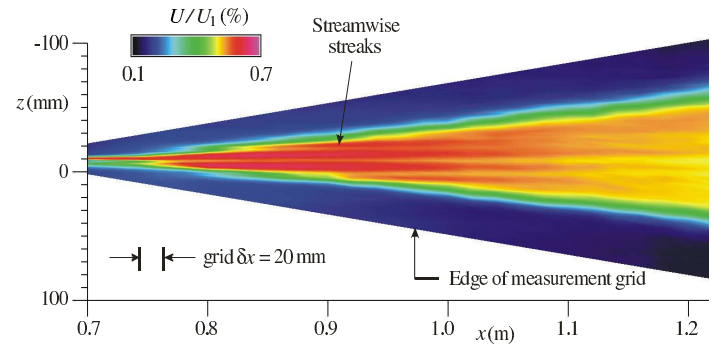


Figure 5. Contours of  $\bar{U}/U_1$ , in plane,  $y = 0.5$  mm.

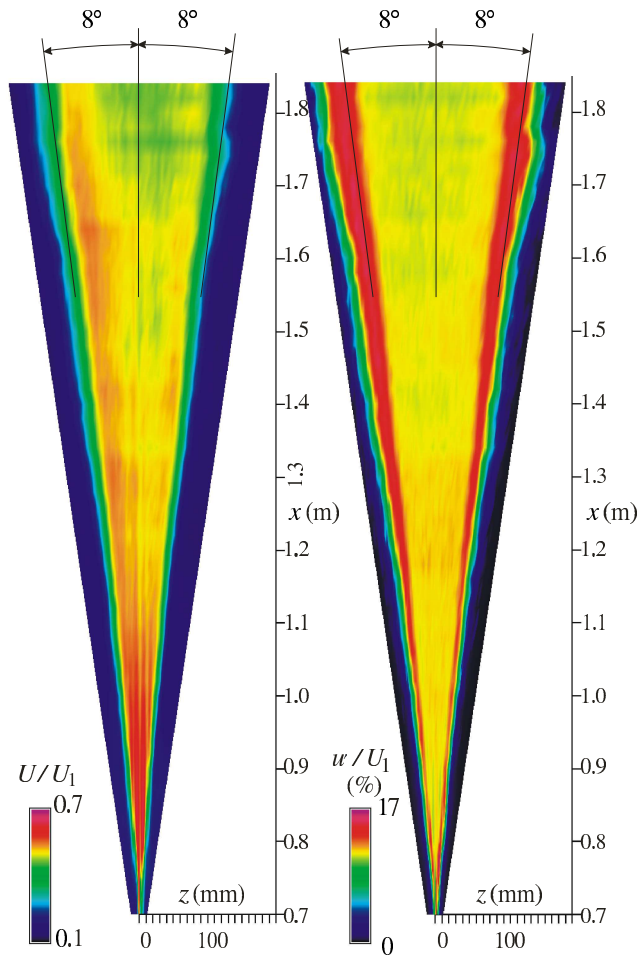


Figure 6. Contours of  $\bar{U}/U_1$ , broadband turbulence intensity,  $\bar{u}'/U_1$ , in the plane,  $y = 0.5$  mm. Grid:  $(N_x, N_z) = (56, 73)$ ; 4088 data points.

## Conclusions

The breakdown process resulting from excitation of the steady streak leads to the formation of new streaks on either side. A similar mechanism also appears to be responsible for the spanwise growth of the wedge since a spanwise succession of new streaks is observed in the early stages of its development. A plausible mechanism that is common to both the breakdown of the streak and growth of the wedge is cross-flow instability.

## Acknowledgments

The measurements were obtained in the Fluid Mechanics Laboratory, at NASA Ames Research Center, in California. Much of the subsequent analysis has been performed at the School of Aerospace, Mechanical Manufacturing Engineering at RMIT University in Australia.

## References

- [1] Boiko, A. V., Westin, K. J. A., Klingmann, B. G. B., Kozlov, V. V. & Alfredsson, P. H., Experiments in a boundary layer subject to free stream turbulence. Part 2. The role of TS-waves in the transition process, *J. Fluid Mech.*, **281**, 1994, 193-218.
- [2] Kendall, J. M., Boundary layer receptivity to freestream turbulence, 1990, *AIAA Paper 90-1504*.

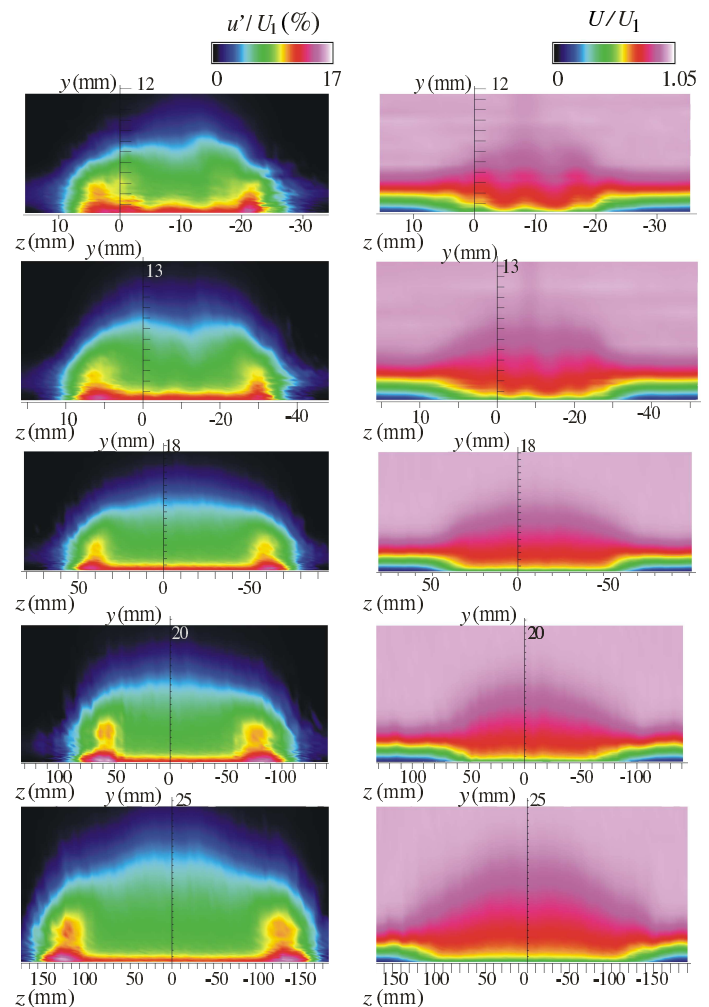


Figure 7. Streamwise development of  $\bar{U}/U_1$  and  $\bar{u}'/U_1$  contours in cross-stream planes. From top to bottom:  $x = 0.8, 0.9, 1.2, 1.5$  and  $1.8$  m.

- [3] Kendall, J. M., Experimental study of disturbances produced in a pre-transitional laminar boundary layer by weak free-stream turbulence, 1985, *AIAA Paper 85-1695*.
- [4] Klebanoff, P. S., Effect of free-stream turbulence on a laminar boundary layer, *Bull. Amer. Phys. Soc.*, **10**, 1971, 1323.
- [5] Mack, L. M. & Herbert, T., Linear wave motion from concentrated harmonic sources in Blasius flow. 1995, *AIAA Paper 95-0774*.
- [6] Watmuff, J. H. Detrimental Effects of Almost Immeasurably Small Free-Stream Nonuniformities Generated by Wind Tunnel Screens, *AIAA J.*, **36**, No. 3, 1988, 379-386.
- [7] Watmuff, J. H. Effects of weak free stream nonuniformity on boundary layer transition, 2003, *ASME Proc. FEDSM'03*, Honolulu, Hawaii.
- [8] Westin, K. J. A., Boiko, A. V., Klingmann, B. G. B., Kozlov, V. V. & Alfredsson, P. H. Experiments in a boundary layer subject to free stream turbulence. Part 1. Boundary layer structure and receptivity. *J. Fluid Mech.*, **281**, 1994, 219-245.



## Response of Ocean Circulation to Variable Wind Forcing

A.E. Kiss<sup>1,2</sup> and C. Ménesguen<sup>3</sup>

<sup>1</sup>formerly: Research School of Earth Sciences,

The Australian National University, Canberra, ACT 0200 AUSTRALIA

<sup>2</sup>currently: Discipline of Oceanography, School of Physical, Environmental and Mathematical Sciences,  
University of New South Wales at ADFA, Canberra, ACT 2600 AUSTRALIA

<sup>3</sup>Ecole Normale Supérieure, Paris, FRANCE

### Abstract

An idealised model is used to investigate the effects of variable wind forcing on basin-scale wind-driven ocean circulation. The circulation displays a rapid poleward current along the western coast which separates to form a free jet. Parameters are chosen so that the jet has a periodic time-variation under steady wind forcing, and we investigate how this intrinsic periodicity can be disrupted by a periodic variation in the wind forcing.

We show that the intrinsic oscillation is a linear instability of the jet which has saturated at finite amplitude, and eddy shedding occurs when negative streamfunction anomalies arrive at the terminus of the jet. When the forcing is periodic, Rossby waves carry the flow adjustment westward across the basin and the arrival of maxima produces periodic variations in the strength of the jet. If the forcing variation is sufficiently large and has a period close to a rational multiple of the intrinsic period, it can drive the jet instability, resulting in eddy shedding which is locked onto a rational multiple of the forcing period (nonlinear resonance). With weaker variations the eddy-shedding period may remain independent of the forcing, yielding a quasiperiodic flow. Chaotic or partially locked states are also observed, with variability on timescales far exceeding either the natural or forcing periods.

### Introduction

The large-scale horizontal flow of subtropical oceans takes the form of a recirculating gyre in each ocean basin. Gyre circulations are highly asymmetric: a slow equatorward wind-driven flow (Sverdrup drift) occupies most of each basin, and this fluid returns poleward in a much faster and narrower current along each western boundary. These western boundary currents (WBCs), such as the Gulf Stream and East Australian Current, are among the most energetic features of ocean circulation. WBCs are climatically important due to their heat transport, and their variability has been implicated in climate fluctuations.

Dynamical-systems studies of idealised WBCs [1, 6, 3, 9] have revealed periodic, quasiperiodic and chaotic behaviour under steady wind forcing, with variability on seasonal to decadal timescales. Thus WBC variations may result from ocean-only dynamics, but since these intrinsic timescales overlap with those of the atmospheric forcing (e.g. the annual cycle, and the North Atlantic Oscillation) it is likely that variable wind forcing also plays a role.

An unstable WBC under variable forcing can be regarded as a forced nonlinear oscillator, and we may expect some of the behaviour typical of a forced nonlinear pendulum [1, 4]. The frequency of a nonlinear oscillator depends on its amplitude, and can therefore be shifted to allow resonance with a mismatched forcing frequency. Nonlinear oscillators can also resonate with forcing at a rational multiple of their natural frequency, or display a chaotic or quasiperiodic response to variable forcing.

These nonlinear effects may explain the response of ENSO to the annual cycle [7]. We investigate the relevance of these processes to WBC variability using an idealised model of a gyre driven by wind with a periodic component. We model the horizontal flow using the barotropic vorticity equation

$$\frac{\partial Q}{\partial t} + J(\psi, Q) = W - \delta_s \zeta + \delta_M^3 \nabla^2 \zeta, \quad (1)$$

where  $\psi$  is the streamfunction for the horizontal velocity,  $\zeta = \nabla^2 \psi$  is the relative vorticity,  $Q = \delta_r^2 \zeta + y$  is the potential vorticity,  $y$  is the northward position,  $J$  is the Jacobian operator and  $W(t) = -1 + A \sin(f_w t)$  is the forcing by a spatially uniform anticyclonic wind stress curl with a periodic perturbation of amplitude  $A$  and frequency  $f_w$ .  $y$  is scaled by the basin width  $L$ ,  $\psi$  is scaled by Sverdrup transport  $\psi_{SV} = \tau/(\rho\beta H)$ , and the time  $t$  is scaled by  $L^2/\psi_{SV}$ , where  $\tau$  is the surface wind stress,  $\rho$  is the fluid density,  $\beta$  is the northward gradient of the planetary vorticity<sup>1</sup> and  $H$  is the depth. The flow is governed by three dimensionless parameters:  $\delta_s = (\beta L H)^{-1} \sqrt{A_v f/2}$  and  $\delta_M = L^{-1} (A_H/\beta)^{1/3}$  control the strengths of bottom and lateral friction, respectively, and  $\delta_r = \sqrt{\psi_{SV}/\beta L^3}$  controls the importance of advection.  $A_v$  and  $A_H$  are the coefficients of vertical and horizontal turbulent diffusion and  $f$  is the Coriolis parameter.

Flow governed by equation (1) has been studied numerically and in the laboratory in a basin with a circular no-slip boundary under steady forcing ( $A = 0$ ) [2, 5, 8], and has a Hopf bifurcation from steady flow to periodic eddy-shedding from the WBC jet at a critical  $\delta_r$  depending on  $\delta_s$  and  $\delta_M$ . We fixed  $\delta_s = 1.01 \times 10^{-2}$ ,  $\delta_M = 8.67 \times 10^{-3}$  and  $\delta_r = 2.78 \times 10^{-2}$ , to give periodic flow (with “natural” frequency  $f_n$ ) when  $A = 0$ , and surveyed the behaviour in the  $(f_w, A)$  parameter space with over 230 runs (see figure 1). We studied the perturbation problem by writing  $\psi = \bar{\psi} + \psi'$ ,  $Q = \bar{Q} + Q'$ ,  $\zeta = \bar{\zeta} + \zeta'$ , where the overbars denote the unstable steady state solution to (1) with  $A = 0$  (obtained numerically by Sheremet’s method [10]), and the dashed quantities are the solution to the perturbation equation

$$\begin{aligned} \frac{\partial Q'}{\partial t} + J(\bar{\psi}, Q') + J(\psi', \bar{Q}) + J(\psi', Q') \\ = A \sin(f_w t) - \delta_s \zeta' + \delta_M^3 \nabla^2 \zeta'. \end{aligned} \quad (2)$$

This system was solved in polar coordinates using the finite-volume code described by [8]. The linear stability was also investigated, by neglecting the nonlinear term  $J(\psi', Q')$ .

### Results and Discussion

Figure 2 shows the periodic eddy-shedding cycle under steady forcing. The slow southward interior flow is returned in a rapid WBC which separates from the boundary to form an unstable

<sup>1</sup> $\beta$  is a weak function of  $y$  to match the laboratory experiments of [5]



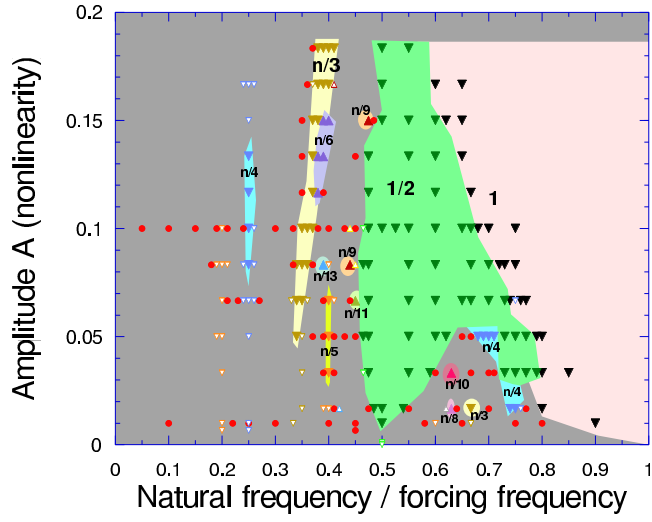


Figure 1: Locked regimes with various frequency ratios in the  $(f_n/f_w, A)$  plane (the points outside the labelled regions yielded quasiperiodic or chaotic flow).

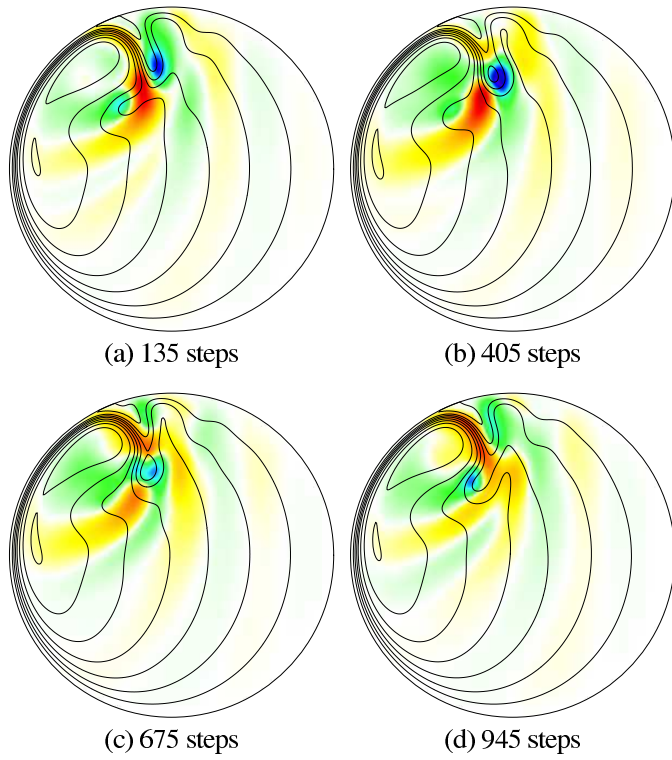


Figure 2: One eddy-shedding cycle under steady forcing. Streamlines indicate  $\bar{\psi} + \psi'$  and colours indicate  $\psi'$  (blue, green  $< 0 <$  yellow, red).

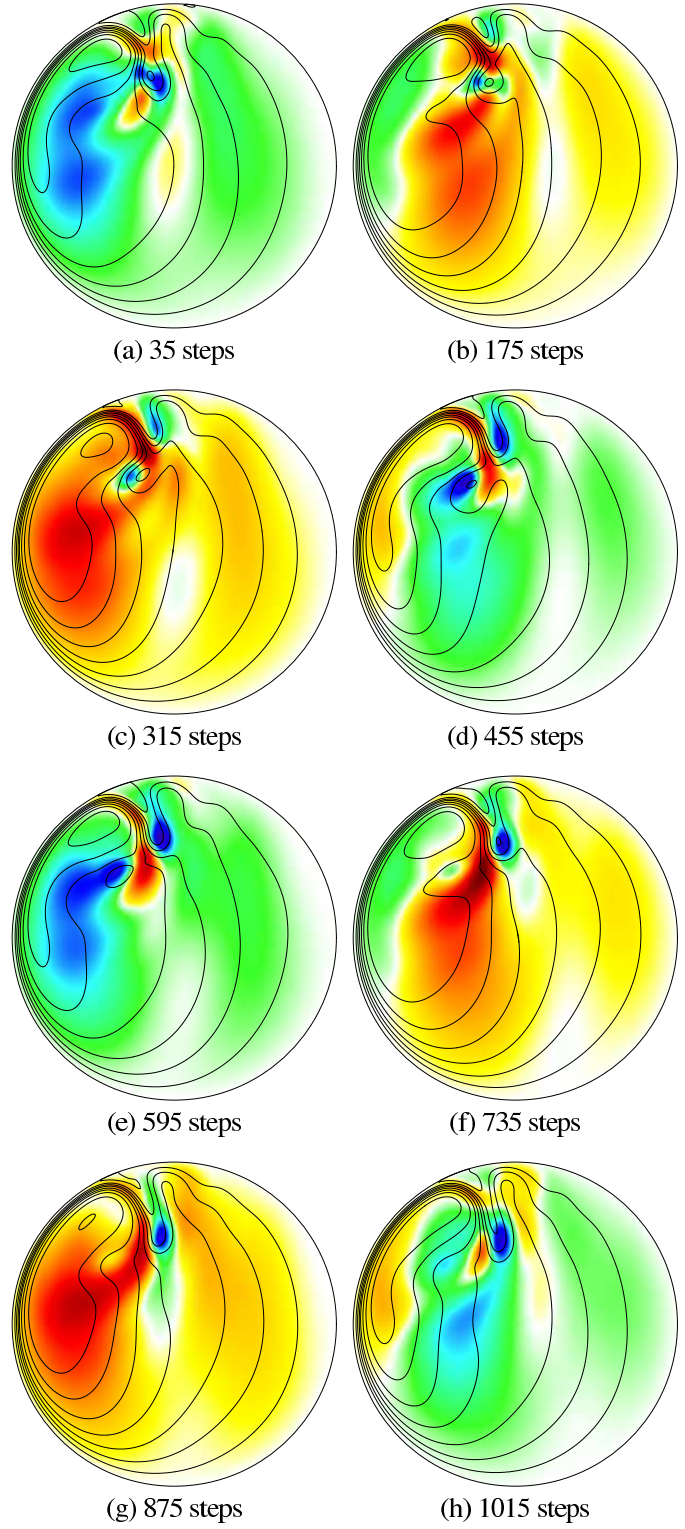


Figure 3: Eddy-shedding locked to double the forcing period, with  $f_n/f_w = 0.52$ ,  $A = 0.10$ . The frames show two forcing periods, over which the flow completes one cycle. Streamlines indicate  $\bar{\psi} + \psi'$  and colours indicate  $\psi'$  (blue, green  $< 0 <$  yellow, red).

jet. The finite-amplitude perturbation in figure 2 closely resembles the most unstable linear eigenmode (not shown) but has an asymmetry between positive and negative perturbations. Eddy shedding corresponds to the arrival of negative streamfunction anomalies  $\psi'$  at the terminus of the jet. It appears that the instability growth saturates at finite amplitude due to energy loss by Rossby wave radiation (visible as the waves in the interior).

Figure 4(a) shows the flow's response to switching on the forcing perturbation (upper curve:  $W$ ; lower curve: perturbation kinetic energy  $K$ ). The “natural” oscillation under steady forcing changes to a larger-amplitude, higher-frequency oscillation locked to  $f_w = 1.35f_n$ . This locking is evident in the plot of  $K$  vs.  $W$  (figure 4(b)), and has also been observed in a laboratory realisation of this system. Physically, the eddy-shedding is locked to  $f_w$  via forced fluctuations of the WBC mediated by Rossby waves, whose transit time across the basin produces a lagged response.

Locking at a wide variety of other rational frequency ratios was also observed; various locking ratios occur in complicated interleaved regimes in the  $(f_n/f_w, A)$  plane (figure 1), reminiscent of “Arnol'd tongues” which occur with a forced nonlinear pendulum [1, 4]. Increasing the driving amplitude  $A$  increases the nonlinearity of the flow perturbation and allows locking to occur with a larger mismatch between  $f_w$  and  $f_n$ .

Figure 5 shows an example of eddy-shedding locked to  $f_w/2 = 0.89f_n$  (the power spectrum in figure 5(c) shows the shift in the fundamental frequency from its (dashed) natural value). Figure 3 shows how westward-propagating Rossby waves mediate this locking by driving WBC perturbations which trigger eddy shedding. Locking may be absent when  $A$  is small and the mismatch large ( $f_n/f_w$  far from a simple rational), giving a quasiperiodic response (having a line spectrum with two incommensurate fundamental frequencies) as in figure 6. In other cases chaos was observed: figure 7 shows a response with partial locking onto  $f_w/5 \approx f_n/4$ , but unpredictable variations and broad-band noise in the spectrum. Note the large amount of power at frequencies well below both  $f_w$  and  $f_n$ .

## Conclusions

Despite the high dimensionality of this fluid system, the nonlinear response of an unstable WBC to variable forcing shows a remarkable concurrence with low-dimensional driven pendulum theory. Locked “Arnol'd tongues” are observed, as well as chaotic states with low-frequency variability which is absent from the forcing or ocean in isolation. These results suggest that these nonlinear effects could contribute to low-frequency western boundary current variability.

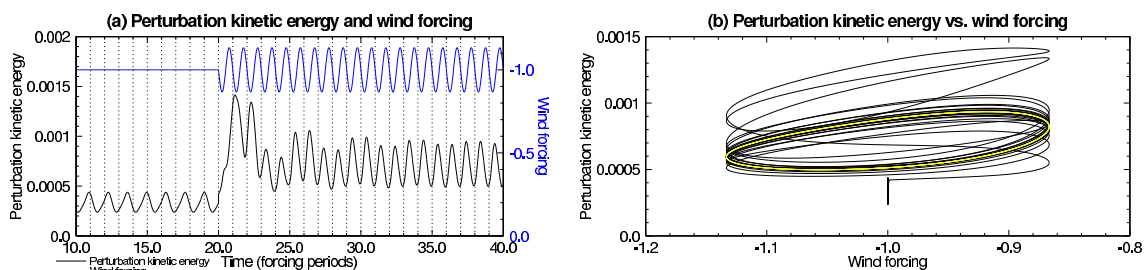


Figure 4: Locking to forcing frequency:  $f_n/f_w = 0.74$ ,  $A = 0.133$ . The final attractor in (b) is shown in yellow.

## References

- [1] Bak, P., Bohr, T. and Jensen, M. H., Mode-locking and the transition to chaos in dissipative systems, *Physica Scripta*, **T9**, 1985, 50–58.
- [2] Beardsley, R. C., A laboratory model of the wind-driven ocean circulation, *J. Fluid Mech.*, **38**, 1969, 255–271.
- [3] Dijkstra, H. A. and Katsman, C. A., Temporal variability of the wind-driven quasi-geostrophic double gyre ocean circulation: Basic bifurcation diagrams, *Geophys. Astrophys. Fluid Dyn.*, **85**, 1997, 195–232.
- [4] Glazier, J. A. and Libchaber, A., Quasi-periodicity and dynamical systems: an experimentalist's view, *IEEE Trans. Circuits and Systems*, **35**, 1988, 790–809.
- [5] Griffiths, R. W. and Kiss, A. E., Flow regimes in a wide ‘sliced-cylinder’ model of homogeneous  $\beta$ -plane circulation, *J. Fluid Mech.*, **399**, 1999, 205–236.
- [6] Jiang, S., Jin, F.-F. and Ghil, M., Multiple equilibria, periodic, and aperiodic solutions in a wind-driven, double-gyre, shallow-water model, *J. Phys. Oceanogr.*, **25**, 1995, 764–786.
- [7] Jin, F. F., Neelin, J. D. and Ghil, M., El Niño/Southern Oscillation and the annual cycle: Subharmonic frequency-locking and aperiodicity, *Physica D*, **98**, 1996, 442–465.
- [8] Kiss, A. E., Potential vorticity “crises”, adverse pressure gradients, and western boundary current separation, *J. Mar. Res.*, **60**, 2002, 779–803.
- [9] Primeau, F. W., Multiple equilibria of a double-gyre ocean model with super-slip boundary conditions, *J. Phys. Oceanogr.*, **28**, 1998, 2130–2147.
- [10] Sheremet, V. A., A method of finding unstable steady solutions by forward time integration: relaxation to a running mean, *Ocean Modelling*, **5**, 2002, 77–89.
- [11] Speich, S., Dijkstra, H. A. and Ghil, M., Successive bifurcations in a shallow-water model applied to the wind-driven ocean circulation, *Nonlin. Process. Geophys.*, **2**, 1995, 241–268.

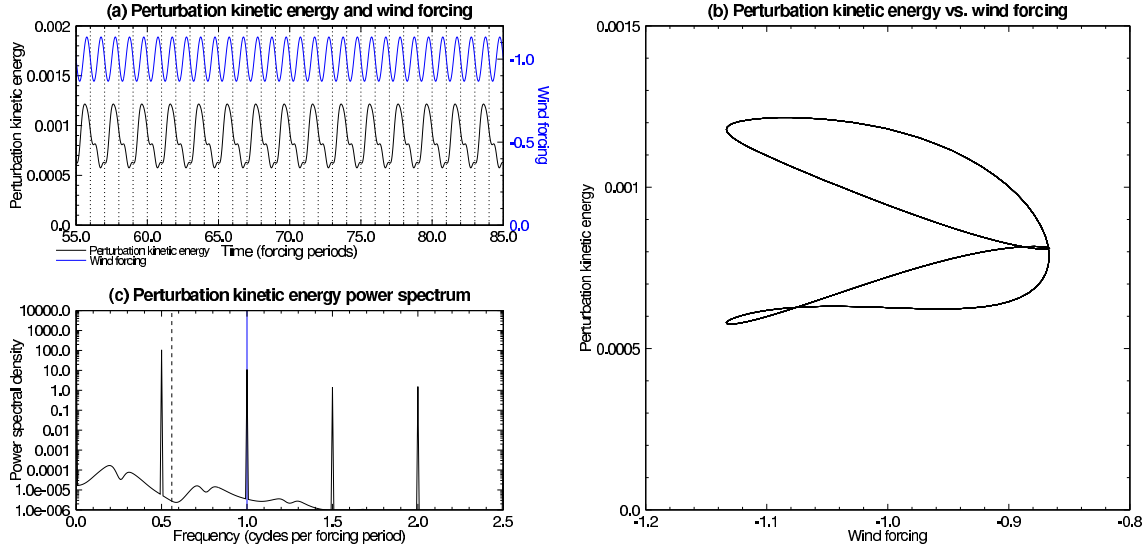


Figure 5: Locking to 1/2 forcing frequency:  $f_n/f_w = 0.56$ ,  $A = 0.133$

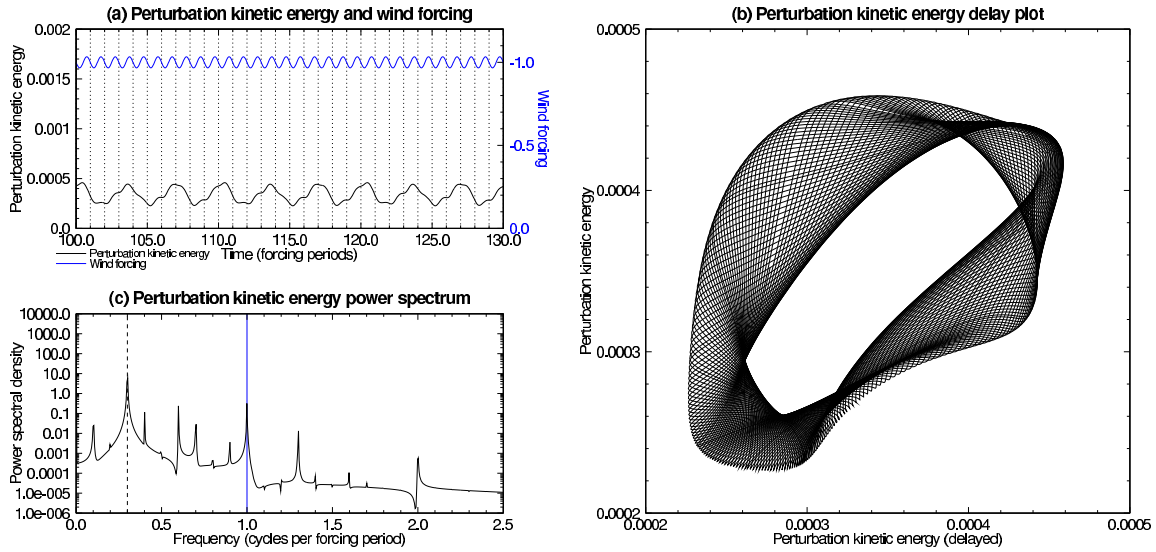


Figure 6: Quasiperiodic state:  $f_n/f_w = 0.30$ ,  $A = 0.0333$

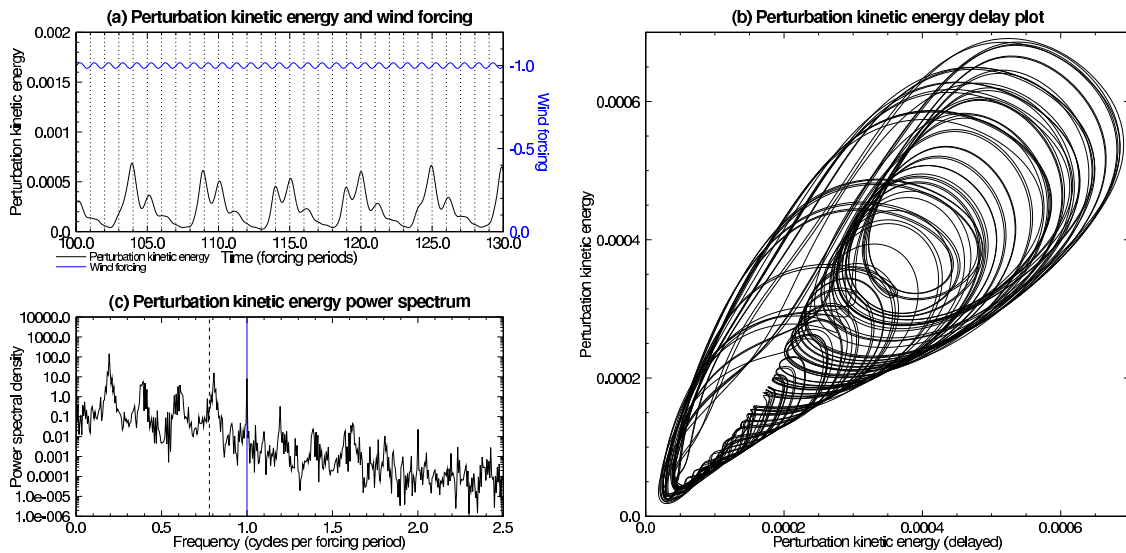


Figure 7: Chaotic state:  $f_n/f_w = 0.78$ ,  $A = 0.0167$

## A Directional Event Detector for Conditional Laser Imaging

P. V. Lanspeary<sup>1</sup> and S. K. Lee<sup>1</sup>

<sup>1</sup>School of Mechanical Engineering  
The University of Adelaide, Adelaide, South Australia, 5005 AUSTRALIA

### Abstract

Conditional sampling of laser-image data in bi-directional non-periodic unsteady flows requires an event detector which can resolve the characteristic direction of the flow. To avoid storing data which does not contain events of interest, event detection must be performed in real time. This paper describes a mixed analogue-TTL circuit which determines the characteristic flow direction from signals at three analogue inputs. When the analogue inputs indicate an event arriving from the preferred direction, the detector allows trigger signals to reach the imaging camera.

The event detector has been used for conditionally-sampled PIV of the internal flow in an oscillating-jet nozzle. In this particular example, streamlines of the conditionally-averaged flow have a spiral focus and two half saddles which are not resolved by conventional time averaging.

### Introduction

Conditional sampling is a well-established method for investigating the structure of unsteady flows. Van Atta [9] provides an early history, and Antonia [1] describes a number of variations on the technique. Before the development of laser imaging for experimental research, conditional sampling was most often used in conjunction with hot-wire anemometry or cold-wire thermometry.

The essence of conditional averaging is to detect an event in the flow and to use the time or location of the event as an origin or reference point for ensemble averaging. The conditional-averaging process therefore has two components, (a) ensemble averaging, and (b) event-detection. For the measured parameter  $u$ , a simple form of ensemble average can be written as

$$\langle u(\mathbf{x}, t) \rangle = \frac{1}{N} \sum_{i=1}^N u(\mathbf{x}, t + \tau_i), \quad (1)$$

where  $\mathbf{x}$  is the space domain,  $t$  is the time domain, and events are detected at  $N$  points in time,  $\{\tau_i : 1 \leq i \leq N\}$ . The average may include a weighting function. For quasi-periodic flows such as oscillating jets, time between adjacent events may be mapped onto the interval  $[0, 2\pi]$  so that the conditionally-averaged parameter  $\langle u(\mathbf{x}, t) \rangle$  becomes periodic [11].

Event detection is less easy to summarise because the available choice of detection criterion is virtually unlimited, especially if the data is recorded continuously and the detection algorithm is applied to the recorded data. Some of the simpler schemes only compare the instantaneous event signal with a fixed discriminator level. Readers interested in a more detailed discussion of event-detection may wish to consult reviews and other articles on conditional sampling [1, 2, 6, 8, 9, 10].

In years before 1990, conditional sampling was used with hot-wire and other point-measurement sensors. The usual procedure was to store a continuous data record first; then a conditional-sampling filter would selectively extract data from the record and deliver it to the averaging algorithm. For PIV, the volume of data from the apparatus is so high that data not containing

events of interest cannot be stored, and event detection must be performed in real time.

Of published investigations making use of conditionally-sampled PIV, the largest proportion ( $\approx 53\%$ ) synchronise the PIV sampling with the phase of mechanically or acoustically driven unsteadiness in the flow (for example, Li et al. [5]). Another 37% are investigations of flow produced by turbines, rotary pumps or helicopter rotors where PIV is phase-locked to the rotation of a shaft.

At the time of writing, the authors know of only five examples (i.e. the remaining 10% of articles) of conditionally-sampled PIV where there was no apparent external excitation of the unsteady flow and the event-detection signal was obtained from the flow itself. Of these only one oscillating flow, the precessing-jet flow of Wong et al. [12] was bi-directional. Wong used an Atmel 8-bit microprocessor to resolve the direction of oscillation. In this paper, we present an alternative method of sensing direction — that is, with a TTL circuit.

### Design Requirements

The specific requirement is for a device which controls the conditional sampling of PIV in a naturally oscillating-jet flow. The oscillating jet is produced by flow through an orifice into a short but larger diameter chamber (Figure 1). Flow from the inlet orifice reattaches asymmetrically and precesses around the circumference of the chamber [4]. For the tests described in this paper the event detector receives signals from an array of three pressure sensors which are distributed over part of the circumference and are turned to face the inlet orifice.

It is important not to bias the conditional average by using a detection algorithm which does not account for asymmetry of the unsteady flow. If, for example, precession in either direction were equally probable, a detection scheme which lacks sensitivity to direction would produce false symmetry in the conditional averages [3]. We therefore require that sampling occur only when precession is in a specified direction (i.e. clockwise or counter-clockwise). With three sensors, the event detector can also perform a crude form of spatial correlation so that small-scale features in the flow are less likely to be accepted as events.

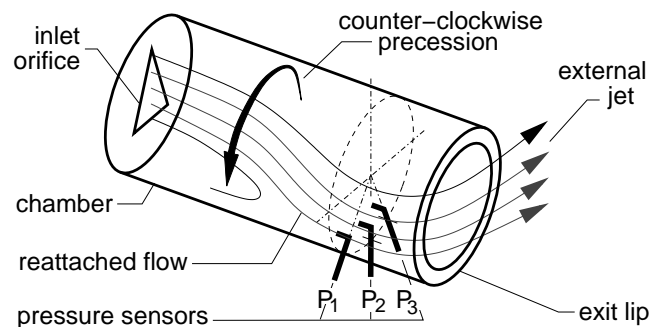


Figure 1: Schematic diagram of oscillating-jet device, with event-detecting pressure sensors.

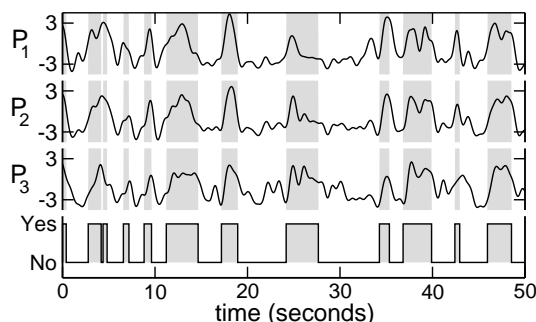


Figure 2: Comparison of pressure-sensor signals  $P_1$ ,  $P_2$ ,  $P_3$  (Volts) and directly observed alignment of flow reattachment with the pressure sensors (Yes/No).

The pressure sensors produce a well defined signal peak when flow reattachment is aligned with the sensors (Figure 2) and so the initial step in event detection is to compare the signal with a suitable threshold level. To obtain the results shown in Figure 2, the alignment of flow reattachment is observed by using air bubbles as a flow-visualisation tracer. The working fluid is water.

The main operational requirement is that the event detector be installed as a switch in the camera-trigger line. The state of the switch is determined by the analogue signals from the pressure sensors. Figure 3 shows a typical arrangement of equipment for PIV. Recording the analogue signals and the conditioned camera trigger (via an A/D converter) is strongly recommended.

### Description of Event Detector

The functional blocks of the event detector are a “threshold source”, a “comparator” for each analogue-signal input, and a “direction-detector logic” block (Figure 4). The circuit elements which, under control of the detection logic, enable and disable the camera trigger are little more than an “AND” logic gate.

The text which follows only describes how the most important parts of the circuit work. Many standard details and refinements familiar to technicians are omitted.

### Adjustable threshold source

The circuit shown in Figure 5 produces rising-edge and falling-edge threshold voltages for the comparators. The comparator output is low when the pressure signal is below the falling-

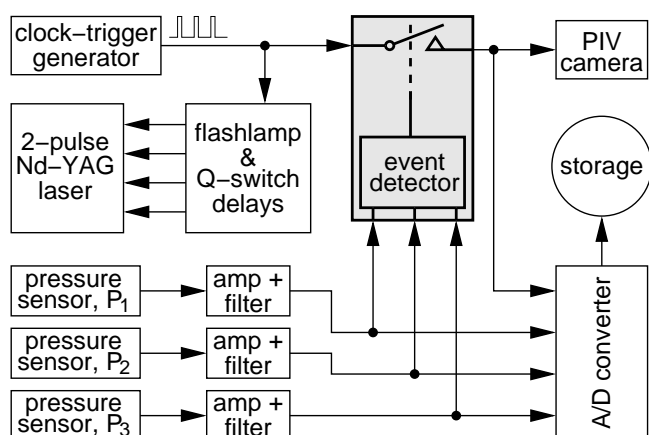


Figure 3: Installation of event detector for conditionally sampled PIV.

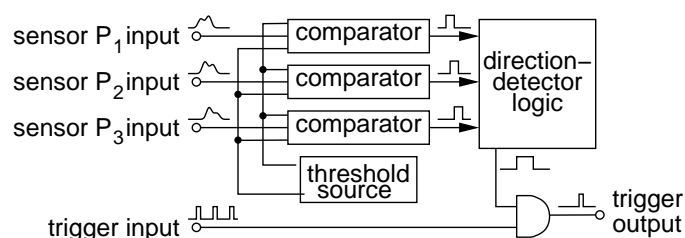


Figure 4: Event-detector functional blocks.

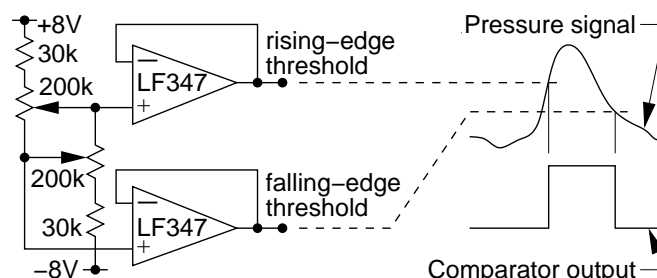


Figure 5: Adjustable threshold-source circuit.

edge threshold, and is high when the pressure signal is above the rising-edge threshold. For stability of the comparator output, the rising-edge threshold must always be higher than the falling-edge threshold.

### Comparator

The main elements of the comparator circuit are shown in Figure 6. The output of the circuit is connected to the control input of a two-way (CMOS 4053) multiplexer so that a low output selects the rising-edge threshold and a high output selects the falling-edge threshold.

Instability or oscillation is a common problem with analogue comparators because of their high gain and bandwidth [7]. Both the LF347 and “positive feedback network” in the circuit diagram are intended to reduce instability. Details of the “positive feedback network” are given in Figure 1 of the National Semiconductor datasheet [7]. The network provides sufficient hysteresis for sharp output transition with signals of only a few Hertz. Small oscillations, which appear at slew rates lower than 100 mV/s, are cleaned up by adding a 40106 Schmitt trigger. The second Schmitt trigger serves only as an inverter.

### Direction-detector logic

Figure 7 is a TTL circuit for detecting the counter-clockwise precession portrayed in Figure 1. Timing sequences for counter-

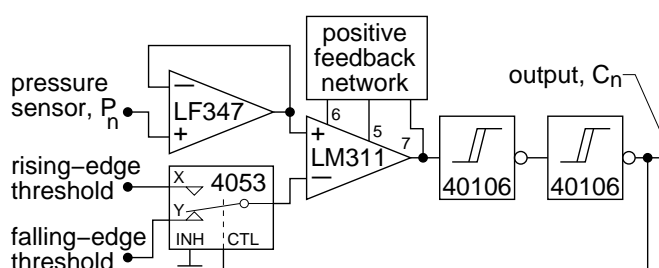


Figure 6: Comparator circuit (one of three); “LF347” is an op-amp, “4053” is a two-way multiplexer (i.e. switch), “LM311” is a comparator, “40106” is an inverting Schmitt trigger.



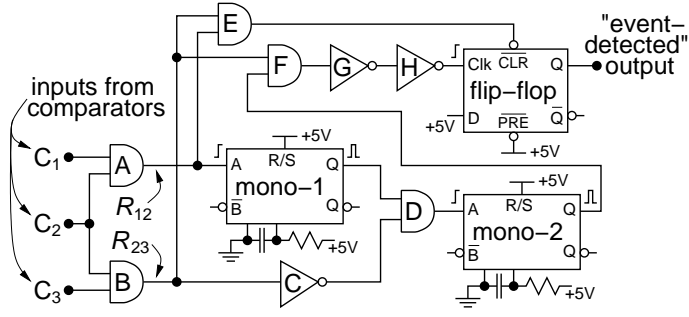


Figure 7: Direction-detector circuit; “mono” is a monostable multivibrator; “flip-flop” is a 7474 D-type flip flop; A, B, D, E and F are “AND” gates; C, G and H are inverters.

clockwise and clockwise precession are shown in Figure 8. Via the comparators, there are inputs from the three pressure sensors. Logic gates A and B combine signals from adjacent pressure sensors so that the distance between sensors determines the minimum physical size of flow feature which is likely to be detected. The outputs of gates A and B are

$$R_{12} = C_1 \text{ and } C_2, \quad (2)$$

$$R_{23} = C_2 \text{ and } C_3 \quad (3)$$

respectively. When  $R_{12}$  rises to a logic TRUE state, the first monostable (mono-1) produces a pulse which has a width of only a few microseconds. If the pulse passes through gate D, it “tells” the second monostable (mono-2) that an event has arrived at sensors  $P_1$  and  $P_2$ , but has not arrived at sensors  $P_2$  and  $P_3$ . Mono-2 then generates a pulse which, for a “detection lag” time equal to the pulse width, allows a rising edge at  $R_{23}$  to set the “event detected” output of the flip flop. If  $R_{23}$  does not produce a rising edge within the duration of the pulse from mono-2, an event is not detected. Inverters G and H provide the necessary “settling-time” delay from the  $\overline{\text{CLR}}$  input to the Clk input of the flip flop. In summary, an event begins when  $R_{23}$  becomes TRUE, but only if this transition occurs within a specified “detection lag” time of a rise in  $R_{12}$ . When either of  $R_{12}$  or  $R_{23}$  become FALSE, the flip-flop is cleared and the event ends.

If precession is clockwise,  $R_{23}$  rises while  $R_{12}$  is already TRUE, the pulse from mono-1 is suppressed by gate “D”, and an event is not detected. In this case, mono-1 prevents mono-2 from being triggered at the *trailing* edge of  $R_{23}$ .

### Experimental Test Results

Conditionally-sampled PIV measurements were made of the flow inside an oscillating-jet device of the type shown in Figure 1. The working fluid was water seeded with 20  $\mu\text{m}$ -diameter polyamid spheres. The Reynolds number based on flow at the inlet orifice was 70,000. Pulsed illumination of the seed particles was from a laser-light sheet normal to the axis of the chamber, and so only the non-axial components of velocity ( $V$ ,  $W$ ) were measured. The location of the laser-light sheet, pressure sensors and PIV camera are given in Figure 9. The area expansion ratio from the inlet orifice to the chamber is  $3.5^2$ .

Seven hundred and twenty PIV-image pairs were obtained by unconditional sampling at the laser-pulse rate of 10 Hz. Another data set of the same size was obtained by conditional sampling with the event detector. Velocity vectors were calculated by cross-correlation with  $32 \times 32$ -pixel interrogation windows having 50% overlap. The mean and r.m.s. velocity magnitudes, and the mean streamlines of each data set are plotted in Figure 10. It is important to note that the much larger axial velocity component ( $U$ ) is not measured by the PIV. The confidence intervals

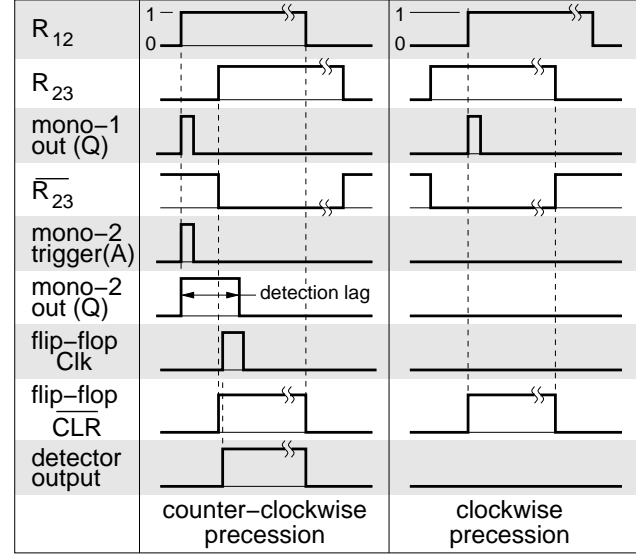


Figure 8: Schematic waveforms of the direction-detector signals for counter-clockwise and clockwise precession.

for the mean velocity magnitudes vary from  $\pm 0.012$  to  $\pm 0.015$ . Most of the non-axisymmetry in Figure 10(a-c) may therefore be due to insufficient data, and most of the variation in the magnitude of the mean flow (Figure 10(a)) is likely to be statistical scatter.

The mean-flow streamlines in Figure 10(b) show that the only detail preserved by the non-conditional averaging is a star node. Flow streamlines for the conditionally sampled data are clearly different because they contain an additional focus and two half saddles. The fluctuation levels shown in Figure 10(f) are fairly typical of turbulent jet flow. This is expected because, conditional sampling partly filters out fluctuations due to large-scale jet oscillation, but does not filter out turbulence fluctuations.

### Conclusions

The authors have designed and tested an event detector to perform real-time conditional sampling of laser-image data in bi-directional unsteady flows which are not produced by the motion of a mechanical device. The event detector is a mixed analogue-TTL circuit and has three analogue inputs. When the analogue inputs indicate an event arriving from the preferred direction, the detector allows trigger signals to reach the imaging camera.

The event detector has been used for conditionally-sampled PIV in a chamber which produces oscillating jet flow. Streamlines of the conditionally-averaged flow have a spiral focus and two half saddles which are not resolved by simple time averaging.

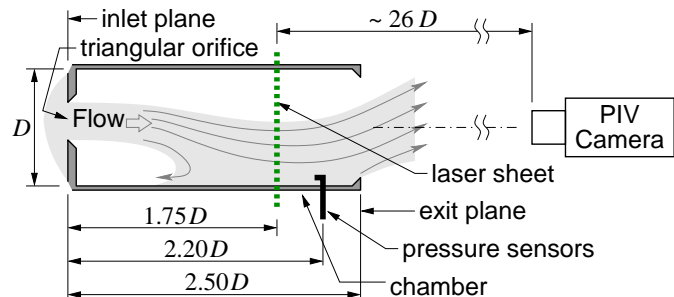


Figure 9: Arrangement for PIV measurements; azimuthal separation between pressure sensors is  $30^\circ$ .



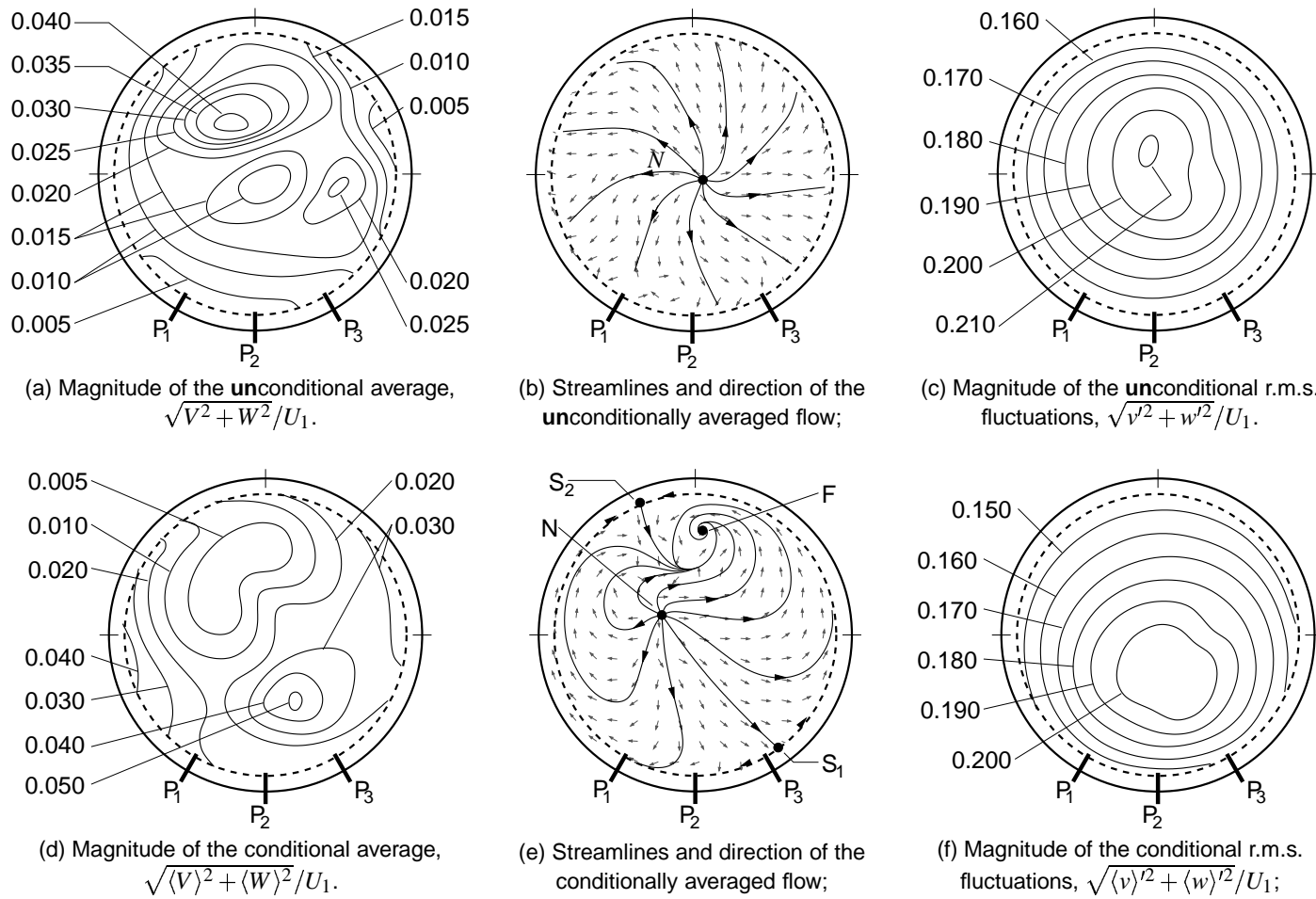


Figure 10: Averaged non-axial ( $V\mathbf{i} + W\mathbf{j}$ ) component of non-dimensional velocity; (a), (b), (c) — unconditionally sampled data; (d), (e), (f) — conditional sampled data;  $U_1$  is mean flow speed at the inlet orifice; only 1 in every 16 of the direction vectors is plotted.

## Acknowledgements

The authors offer their thanks to Silvio De Ieso, Derek Franklin and Joel Walker for advice on electronics and for etching the printed circuit, to George Osborne for the pressure sensors, and also to Peter Kalt for setting up and nursing the PIV optics.

## References

- [1] Antonia, R. A., Conditional sampling in turbulence measurement, *Annu. Rev. Fluid Mech.*, **13**, 1981, 131–156.
- [2] Blackwelder, R., On the role of phase information in conditional sampling, *Phys. Fluids*, **20**, 1977, S232–S242.
- [3] Guezennec, Y. G., Piomelli, U. and Kim, J., On the shape and dynamics of wall structures in turbulent channel flow, *Phys. Fluids A*, **1**, 1989, 764–767.
- [4] Lee, S. K., Lanspeary, P. V., Nathan, G. J., Kelso, R. M. and Mi, J., Low kinetic-energy loss oscillating-triangular-jet nozzles, *Exp. Therm. Fluid Sci.*, **27**, 2003, 553–561.
- [5] Li, Y., Zhao, H., Peng, Z. and Ladommatos, N., Particle image velocimetry measurement of in-cylinder flow in internal combustion engines - experiment and flow structure analysis, *P. I. Mech. Eng. D – J. Aut.*, **216**, 2002, 65–81.
- [6] Marshall, B. J., Marwood, R., Belcher, R. E. and Wood, C. J., Laser doppler anemometry and conditional sampling, *J. Wind. Eng. Ind. Aerod.*, **79**, 1999, 209–231.
- [7] National Semiconductor Corporation, Santa Clara, California, U.S.A., *LM111/LM211/LM311 voltage comparator, datasheet*, 2001.
- [8] Subramanian, C. S., Rajagopalan, S., Antonia, R. A. and Chambers, A. J., Comparison of conditional sampling and averaging techniques in a turbulent boundary layer, *J. Fluid Mech.*, **123**, 1982, 335–362.
- [9] Van Atta, C. W., Sampling techniques in turbulence measurements, *Annu. Rev. Fluid Mech.*, **6**, 1974, 75–91.
- [10] Wernert, P. and Favier, D., Considerations about the phase-averaging method with application to ELDV and PIV measurements over pitching airfoils, *Exp. Fluids*, **27**, 1999, 473–483.
- [11] Wong, C. Y., Lanspeary, P. V., Nathan, G. J., Kelso, R. M. and O'Doherty, T., Phase-averaged velocity in a fluidic precessing jet nozzle and in its near external field, *Exp. Therm. Fluid Sci.*, **27**, 2003, 515–524.
- [12] Wong, C. Y., Nathan, G. J. and Kelso, R. M., PIV of the unsteady flow emerging from a fluidic precessing jet nozzle using direction and phase triggers, in *Proceedings of 7th Asian Symposium on Visualisation*, National University of Singapore, Singapore, 2003, 22.1–22.6, 22.1–22.6.

# Investigations on the Closure of Laminar Separation Bubbles

R.L. Thomas<sup>1</sup> and J.P. Gostelow

Department of Engineering, The University of Leicester, Leicester, LE1 7RH, U.K.

<sup>1</sup>Now at The Whittle Laboratory, Cambridge University, Cambridge, CB3 0DY, U.K.

## Abstract

Laminar separation was investigated experimentally on a flat plate under a strongly diffusing self-similar pressure distribution. This gave a long and thin laminar separation bubble. Boundary layer velocity traverses were performed at numerous longitudinal stations. An array of microphones was used to give instantaneous contours of pressure perturbation. Reattachment was caused by transition of the separated shear layer. Intermittency values for the flow in the reattachment region are well represented by the Narasimha intermittency distribution, supporting the use of intermittency-based predictions in calculating the closure of separation bubbles.

## Introduction

Flows undergoing laminar separation, and possible reattachment, take many different forms. There are various classifications of laminar separation bubbles, an important one being the distinction between long and short bubbles [13]. Furthermore there are different candidates for the physical mechanism of the transition leading to bubble closure. Flows with incipient laminar separation will inherit the tendency to viscous instability, especially under the amplifying influence of an adverse pressure gradient and the viscous mechanisms of Tollmien-Schlichting (T-S) waves, which break down into turbulent spots. For thin laminar separation bubbles it may be anticipated that this mechanism will predominate. For thicker bubbles the inflectional influences resulting in Kelvin-Helmholtz (K-H) instability will become the more aggressive mode and this will result in transition and bubble closure. Furthermore the receptivity to external influences and by-pass mechanisms may intervene, resulting in an earlier and often relatively sudden transition. In the context of a separated flow this may result in the sudden collapse of a laminar separation bubble [5]. All of these mechanisms are, of course, strongly Reynolds number dependent so that a wide range of candidate scenarios is available.

In 1957 Narasimha [11] introduced the concept of intermittency as a basis for the phenomenological description of transition to turbulence in attached shear layers. Four decades later he suggested [12] that the intermittency approach might also be of value in predicting laminar separation bubble closure.

Under the strong adverse pressure gradients conducive to laminar separation the shape of the turbulent spot is quite far removed from the characteristic 'arrow-head' shape of the zero pressure gradient spot [2]. The universal intermittency distribution is still satisfied over the complete range of adverse pressure gradients for attached laminar flows and also over a wide range of free stream turbulence levels. Furthermore the use of intermittency has made it possible to produce transition length correlations that are robust in application for design purposes and computational fluid dynamics procedures [15].

The physical mechanism of boundary layer transition [18] varies according to the level of adverse pressure gradient

sustained. Whereas under zero pressure gradient conditions the behaviour is quite stochastic, with random external influences largely determining the transition phenomenon and transition occurring in 'sets' or packets of T-S waves, under a strong adverse pressure gradient each wave participates in its own local transition process. This results in a transition region much shorter in length than under a zero pressure gradient but one which, nevertheless, is still very well represented by the universal intermittency distribution.

The broad context of this investigation was the large scale simulation of transition phenomena occurring in turbomachines, providing evidence on similarities between turbomachinery and wind tunnel flows [4]. Flows over blades are particularly dependent on the transition modes occurring on the suction surface of the blade. For Reynolds numbers below a million, characteristic of aircraft cruise conditions, laminar flow is present over a significant portion of the blade surface and the general nature of the flow is both unsteady and transitional. A triggered turbulent spot harbours an attendant calmed region [3] and the very similar interactions of blade wakes sweeping over blade boundary layers result in a very strong calmed region. This phenomenon is in use in aircraft engines to significantly reduce cost and weight.

The periodic passage of wakes from upstream blade rows also affects transition and could cause the boundary layer to undergo transition ahead of any laminar separation. Studies such as those of Halstead *et al.* [6] and Mayle [10] have documented this. In some meticulous work Hughes and Walker [8] used wavelet conditioning to identify instability phenomena in periodic transitional flows on compressor blades. In these flows the transition process was found to be mainly of the natural growth type, rather than of the bypass type.

The purpose of the present experiments was to establish a parameter space in which more than one of the routes to transition and bubble closure could be investigated. An experiment was set up in which different transition mechanisms could be compared directly. These included natural transition of a separation bubble in an undisturbed boundary layer, early natural transition resulting from a wake interaction, and by-pass transition from a different and more turbulent wake.

The work described here was limited to investigating the applicability of intermittency-based approaches to the closure of undisturbed laminar separation bubbles. The method of Solomon *et al.* [15] had predicted transition length under varying pressure gradients, based on spot formation rates and spreading angles. That model is based on intermittency to describe the transition process and thus addresses Narasimha's hypothesis concerning the application of intermittency to separated flows. Intermittency had given a robust basis for predicting the length of attached flow transition and it was a logical extension to enquire whether this approach could be extended to predict separated flow transition and bubble closure.

## Experimental Arrangement

The experiments were performed in the 1.00m × 1.15m working section of the University of Leicester low-speed research wind tunnel, shown in figure 1. The Reynolds number, based on the flat plate length of 2.41m, was constant at  $1.4 \times 10^6$ . The free stream velocity was around 9m/s and the turbulence level less than 0.2%.

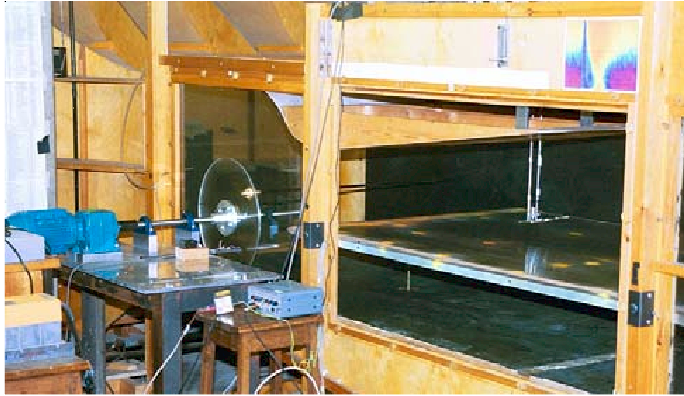


Figure 1. Flat plate installation with fairing, hot wire traverse and upstream wake generator

The top wall of the test section was contoured to provide the desired strong adverse pressure gradient with a similarity distribution having a Hartree parameter  $\beta$  of -0.221. This induced laminar separation in the form of a long laminar separation bubble which was sufficiently thin to barely influence the pressure distribution.

The tunnel had the capability to produce wakes generated by rotating a tapered spanwise rod upstream of the working section. The rod was cantilevered from a disc and was mounted at a radius of 270mm. The disc was rotated at 60 rpm, resulting in the introduction of two dissimilar wakes each second. The influence of these wakes is the subject of ongoing study and does not relate directly to the present work.

## Hot Wire Data

Hot wire data were acquired continuously using a single wire probe mounted on a computer-controlled traverse mechanism. Centreline phase-averaged velocity traces were determined at 27  $x$  locations along the plate and  $y$  distances up to 50mm normal to the flat plate surface. A photodiode, mounted near the wake generator, acted as a triggering mechanism for the purposes of activation of data acquisition routines, continuous signal discretization and processes such as phase averaging.

Phase averaging was performed over 128 repetitions, each record consisting of one full rotation of the wake generator producing two individual wakes. The spacing between these was sufficient that large portions of data were generated under steady conditions and these are reported in the current work as time-averaged data.

## Microphone Data

Using a single hot wire it is not possible to track individual instabilities as they convect downstream. In most of this and the previous work a combination of individual traces, phase averaging and time averaging has been used. It was, however, found useful to instal an array of microphones to investigate the time dependent features of the undisturbed boundary layer and its separation bubble. These were mounted internal to the flat plate, as shown in figure 2.

The microphones were dynamically calibrated and a blind microphone was used for vibration compensation. Individual voltage traces have been acquired and a typical record is shown in figure 3. This covers  $x$  values from 0.675m to 0.850m in steps of 0.025m. The disturbances are depicted in contour form over a broader streamwise range in the  $x-t$  diagram of figure 4.

The most prominent feature is the clear detection of developing instabilities through the transition region. The fundamental frequency was found to be 91Hz and the traces, which have been amplified by the adverse pressure gradient, are clearly strongest at transition inception and through transition. Once the coherence is lost, in a turbulent layer, the amplitude is diminished.

Walker [17] produced an equation that has allowed the prediction of the most likely T-S frequencies:

$$\frac{\omega v}{U_\infty^2} = 3.2 \text{Re}_\delta^{-1.5} \quad (1)$$

Estimated values using this approach closely match the measured frequencies for instability occurrence observed in the data. The 91Hz frequency corresponds to an  $x$  of 0.325m and it is hypothesized that this is the location of inception of the instabilities. Figure 4, along with the finer resolution data of figure 3, should relate quite directly to the Walker model of breakdown [17]. Although it does provide evidence that each T-S wave participates in its own breakdown process there is also some randomness in the inception location. The evidence tends to broadly confirm the Walker model, but with a degree of scatter. The data of figures 3 and 4 have also produced valuable information on the propagation rates of the T-S disturbances and these will be the subject of a future report.

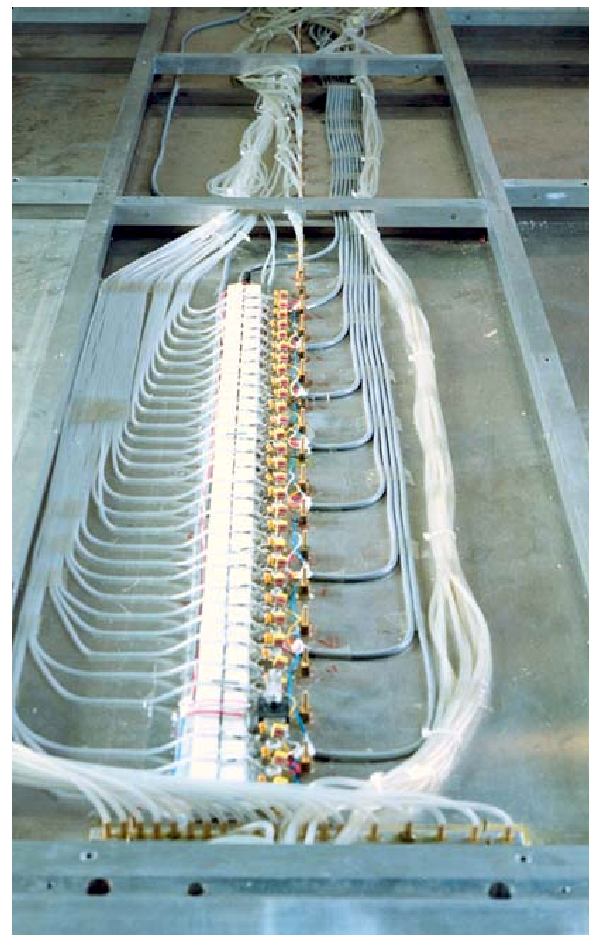


Figure 2. Microphone installation inside flat plate.

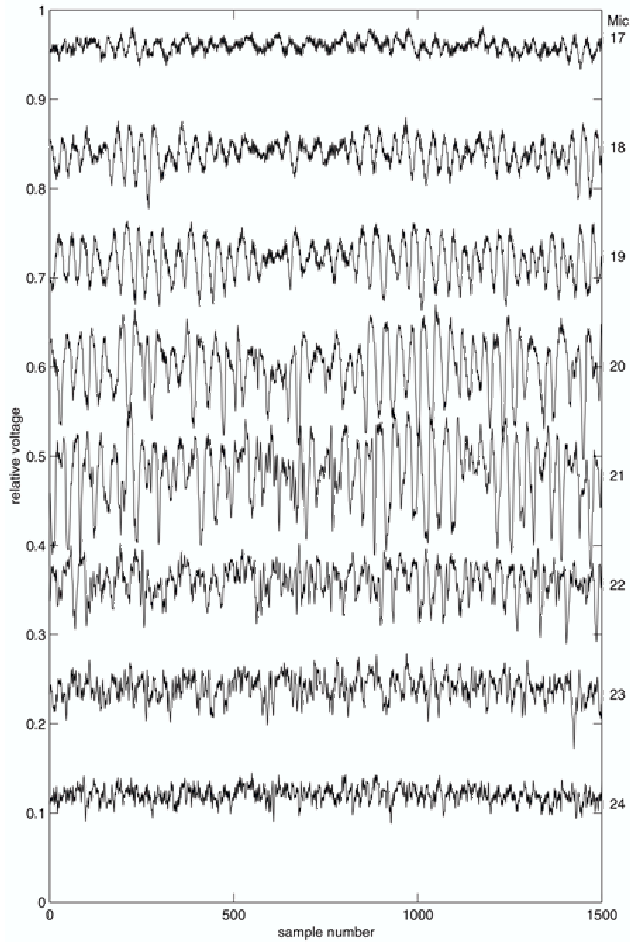


Figure 3. Simultaneous microphone voltage traces for streamwise locations  $x = 675\text{--}850\text{mm}$ .

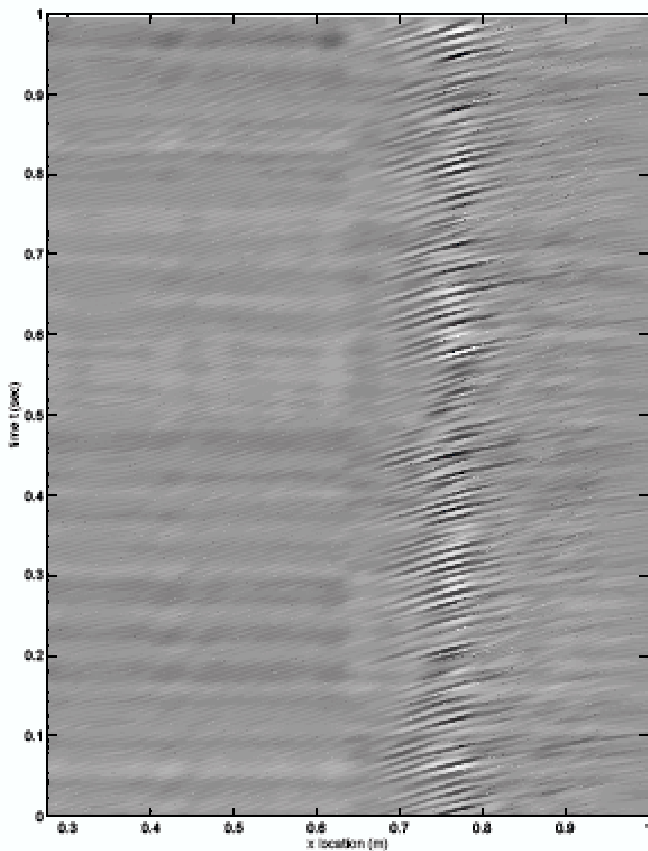


Figure 4. Microphone amplitude contour plot.

## Intermittency

In earlier work on intermittency detection in transition and turbulent spots the TERA routine of Falco and Grendrich [1], based on  $(u \times \partial u / \partial t)$  as a discriminant, has proved to be versatile and robust. However in the present investigation it failed to accurately discriminate the calmed region following each turbulent patch. This is due to the high velocities with steep gradients that exist at the beginning of the particularly strong calmed regions following a wake before they rapidly subside towards their undisturbed values. Accordingly, for these experiments on wakes, with particularly strong velocity gradients in stable flows, the temporal velocity gradient alone,  $(\partial u / \partial t)$ , was used to promote detection of high gradients only.

The calmed region itself has a high gradient, but very little velocity fluctuation; a high pass filter was therefore applied to the data, retaining the high frequency content of the turbulent regions whilst reducing the aggressive gradient inherent in the relaxation process. A moving average smoothing with an eight-sample window was introduced to improve the continuity of the detected regions. Calibration was performed by visual selection of turbulent regions from velocity traces to derive the correct threshold.

In order to establish an appropriate  $y$  value for sampling intermittency the variation of intermittency with height was determined (figure 5). Although a constant value of  $y/\delta$  would have been preferred, in practice it was determined that a constant  $y$  of  $2\text{mm}$  would well represent the peak intermittency for a wide streamwise extent.

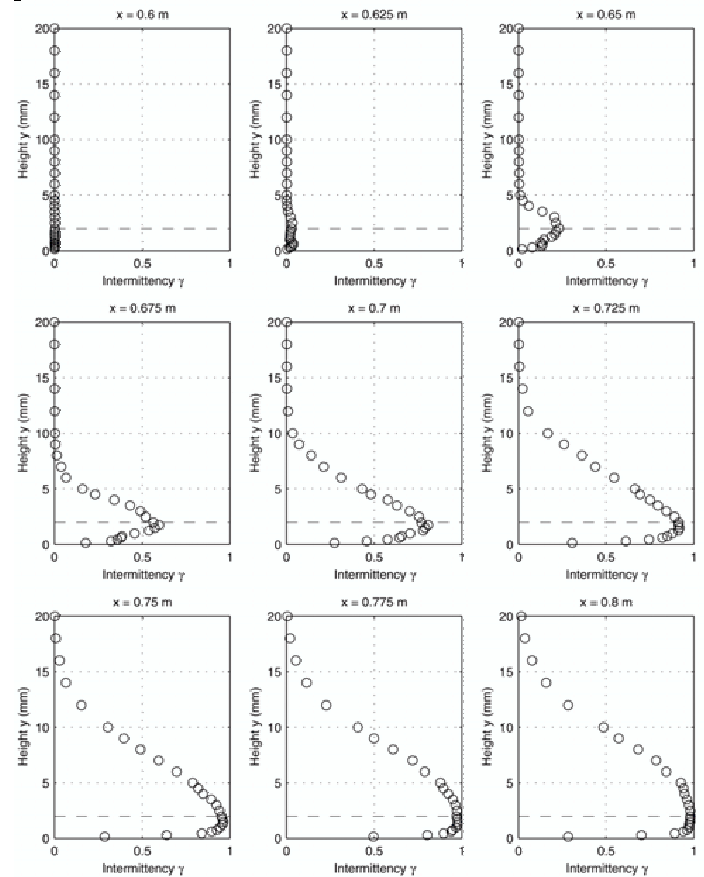


Figure 5. Time-averaged intermittency profiles for  $y = 2\text{mm}$  and increasing streamwise locations.

The Narasimha [11] universal intermittency distribution has proved to be a robust basis for predicting transition. Figure 6 shows the time-averaged intermittency for the undisturbed

transition region. The test data show good agreement with Narasimha's intermittency ( $\gamma$ ) distribution:

$$\gamma = 1 - \exp(-0.412\xi^2), \quad (2)$$

where  $\xi = (x - x_i)/\lambda$

The value for  $x_i$  is determined from the values of intermittency plotted as

$$F(\gamma) = [-\ln(1-\gamma)]^{0.5} \quad (3)$$

against  $x$  and equating the left hand side of a straight line fit to zero to find the  $x$  axis intercept.  $\lambda$  is the distance between the  $x$  locations for  $\gamma = 0.25$  and  $\gamma = 0.75$ .

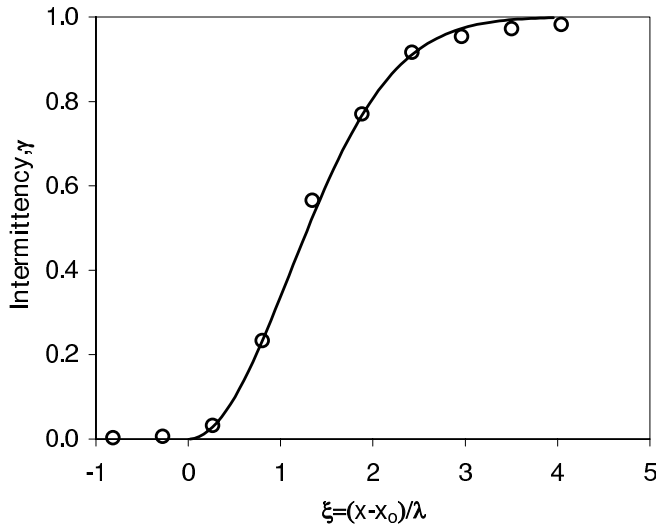


Figure 6. Time-averaged intermittency distribution for the reattachment region at  $y = 2\text{mm}$ .

This finding confirms the earlier findings of Malkiel and Mayle [9] and of Volino and Hultgren [16], who also observed agreement with the universal intermittency distribution in the reattachment region of a laminar separation bubble. It also justifies the extension of intermittency-based transition region prediction procedures such as those of Solomon *et al.* [4] to flows having laminar separation bubbles. Good examples of such a practice are given in the work of Sanz and Platzer [14] and Hobson and Weber [7].

## Conclusions

The adverse pressure gradient causes strong amplification of instabilities detected far upstream of the separation point. Driven at a particular frequency, matching those of the predicted T-S waves, these instabilities grow into turbulent spots that develop in the shear layer of the separation bubble. This ultimately progresses into fully three-dimensional turbulence. The traces indicate that the undisturbed flow experiences a natural transition. At this low free-stream turbulence level, transition inception is predicted best by stability methods developed for natural growth transition.

The universal intermittency distribution for predicting the development of transition in a boundary layer has proven to accurately represent the transition process closing a laminar separation bubble. This relationship provides support for the use of intermittency-based predictive routines, such as the approach of Solomon *et al.* [15] even in flows involving separation bubbles.

## Acknowledgment

The work was funded by a research grant from the Engineering and Physical Sciences Research Council.

## References

- [1] Falco, R.E. & Grendrich, C.P., The turbulence burst detection algorithm of Z. Zaric, in *Near-wall turbulence* eds. Kline, S.J. and Afgan, N.H., 1988 Zoltan Zaric Memorial Conf., Hemisphere, New York, 1990, 911-931.
- [2] Gostelow, J.P., Melwani, N. & Walker, G.J., Effects of streamwise pressure gradient on turbulent spot development, *ASME J. Turbomachinery*, 118, 1996, 737-743.
- [3] Gostelow J.P., Walker G.J., Solomon W.J., Hong, G. & Melwani, N., Investigation on the calmed region behind a turbulent spot, *ASME J. Turbomachinery*, 119, 1997, 802-809.
- [4] Gostelow, J.P. & Thomas R.L. Response of a laminar separation bubble to an impinging wake. *ASME Paper 2003-GT-38972*. In press, *J. Turbomachinery*.
- [5] Gostelow, J.P., On the role of intermittency in the closure of laminar separation bubbles. Invited Address, *Symposium. on Fluid Mechanics, Indian Institute of Science, Bangalore* (July 2003).
- [6] Halstead D.E., Wisler D.C., Okiishi T.H., Walker G.J., Hodson H.P. & Shin H-W, Boundary layer development in axial compressors and turbines: Part 1-4, *ASME J. Turbomachinery*, 119, 1997, No.1, 114-127 and 128-139, No. 2, 234-246, No. 3, 426-444.
- [7] Hobson, G.V. & Weber, S., Prediction of a laminar separation bubble over a controlled-diffusion compressor blade, *ASME Paper 2000-GT-277*, 2000.
- [8] Hughes J. D. & Walker G. J., Natural transition phenomena on an axial compressor blade, *ASME J. Turbomachinery*, 123, 2001, 392-401.
- [9] Malkiel, E. & Mayle, R.E., Transition in a separation bubble, *ASME J. Turbomachinery*, 118, 1996, 752-759.
- [10] Mayle R. E., The role of laminar-turbulent transition in gas turbines, *ASME J. Turbomachinery*, 113, 509-537, The 1991 IGTI Scholar Lecture.
- [11] Narasimha, R., On the distribution of intermittency in the transition region of the boundary layer, *J. Aero. Sci.*, 24, 1957, 711-712.
- [12] Narasimha, R., Post-Workshop Summary, Minnowbrook II Workshop on Boundary Layer Transition in Turbomachines 1997, eds. LaGraff, J.E. and Ashpis, D.E., *NASA CP 1998-206958*, 485-495.
- [13] Owen, P.R. & Klanfer, L., On the laminar boundary layer separation from the leading edge of a thin aerofoil, *ARC C.P.* 220, 1953.
- [14] Sanz, W. & Platzer, M.F., On the Navier-Stokes calculation of separation bubbles, *ASME Paper 96-GT-487*, 1996.
- [15] Solomon W.J., Walker G.J. and Gostelow J.P., Transition length prediction for flows with rapidly changing pressure gradients, *ASME J. Turbomachinery*, 118, 1996, 744-751.
- [16] Volino, R.J. & Hultgren, L.S., Measurements in separated and transitional boundary layers under low-pressure turbine airfoil conditions, *ASME Paper 2000-GT-260*, 2000.
- [17] Walker, G.J., Transitional flow on axial turbomachine blading, *AIAA J.*, 27, 1989, 5, 595-602.
- [18] Walker, G.J. & Gostelow, J.P., Effects of adverse pressure gradients on the nature and length of boundary layer transition, *ASME J. Turbomachinery*, 112, 1990, 196-205.

## Flow Measurements in Microchannels Using a MicroPIV system

Wing T. Lai and Rajan K. Menon  
TSI Incorporated  
500 Cardigan Rd  
Shoreview, MN 55126

### Abstract

High quality PIV experiments in micro-channel flow geometries to get detailed and accurate flow measurements can be difficult and involves paying attention to a variety of aspects. In the experiments, the reasons could be ranging from uncontrolled transients in the fluidic flows systems to fouling of the micro-channels by impurities, bubbles, the seed particles themselves. Another factor which could have a significant effect is the distortion of the boundary of the channel caused by the difference in the refractive indices. Experimental measurements were taken on two channels in a PDMS (polydimethylsiloxane) micro-channel test facility shown in Figure 1. The two micro-channels under study were (a) the expansion channel with fully developed flow in a 150  $\mu\text{m}$  wide rectangular section to a 750  $\mu\text{m}$  wide channel, and (b) a 'T' junction with two 100  $\mu\text{m}$  wide outflow channels branch at two 90 degree elbow turns from a 100  $\mu\text{m}$  inflow channel. Both micro-channels are 100  $\mu\text{m}$  deep across the entire channel length. The measurements were performed for Reynolds number of 1, based on the centerline velocity of the channels. The experiments were performed using a PIV system equipped with an inverted microscope. Fluorescent particles of about 1  $\mu\text{m}$  in size were employed as seed particles. Typical particle number concentration was around 2 to 3 particles per interrogation volume. Hence, the ensemble average of the correlation function was used to obtain the velocity vectors. Channel geometry imperfections, fouling and bubble formation affect the flow development and the nature of the flow, especially near the wall.

### Introduction

Flows in micro-channels are of interest in a wide range of areas such as aerodynamics, fluid mixing, propulsion, microsprays, chemical and biological analysis, bio-MEMS applications and bio-fluid mechanics [1]. The high surface-to-volume ratio and the small volume of flow associated with microchannels provide unique advantages in the area of transport, especially heat transfer.

Generally, micro-channels are defined to be smaller than 1mm, and for measurement purposes, more than tens of microns. Fabrication of the channels is a complex process that can have strong impact on the surface texture, cross sectional geometry and hence the affect the velocity field, especially, close to the wall boundaries. In microflows, unlike in ordinary flows, the entire flow field is influenced by the presence of wall boundaries. Hence, the entire flow field could be affected by the imperfections in the channels caused during the manufacturing process.

Various types of fabrication techniques are used to obtain different desired microchannel (cross section) properties [2]. Lithography is one of the most common techniques for fabricating microchannels. Although the channels could be made out of different polymeric materials, PDMS (polydimethylsiloxane) is often chosen for the many properties it exhibits that are suitable for flow measurement applications. Transparency to laser light illumination, mechanical durability, good surface chemistry and stability against humidity and temperature are among them. A rapid prototyping method based on lithography is used to fabricate the microchannels [3 - 5]. The microchannel flow model used here is a test bed that contains multiple flow elements or channels of different geometries. Velocity measurements are carried out in two different channels in the test bed.



## Experimental details

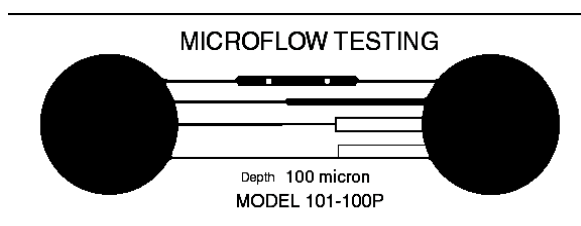
The microchannel flow model used here for the experiments is a Model 101-100P test bed. The details of the construction of the Model 101-100P PDMS test facility are as follows.

The mask for photolithography containing a negative image of the micro-channel device is created in a CAD program then printed on a transparency by a high-resolution printer. The mold is made from a silicon wafer coated by a 100 micron thick layer of photo resist (Nano XP SU-8 100, Microchem Corp., Newton, MA) by spin-coating at 2900 rpm for 30 s, followed by a soft-bake (95C for 30 min.), UV lithography (650 mJ/cm<sup>2</sup>), a post-bake (95C for 30 min), and development for 10 min. A pre-polymer of PDMS is then cast onto the mold and cured. The PDMS replica is then peeled from the silicon wafer leaving the channels cast into the surface of the cured PDMS.

To create closed channels a cover glass slip is bonded to the PDMS surface by oxidizing both the surface of the PDMS replica and glass by oxygen plasma treatment (70W, 85mTorr for 20s). When the two oxidized surfaces are brought into contact they bond covalently creating a seal, which can withstand up to 5 bars. The tightly sealed channels are necessary for pressure driven flow experiments to be conducted over a wide range of speed. Since the surfaces of the glass and the PDMS are each hydrophilic, filling the channels with liquids is relatively easy.

A gravity feed approach (pressure driven) was used to generate the flow in the microchannel. The two reservoirs (Fig.1) in the test bed provide a stable pressure differential to drive the flow.

The two micro-channels in the test bed used are (a) expansion channel with fully developed flow in a 150  $\mu\text{m}$  wide rectangular section to a 750  $\mu\text{m}$  wide channel and (b) 'T' junction with two 100  $\mu\text{m}$  wide outflow channels branch at two 90 degree elbow turns from a 100  $\mu\text{m}$  inflow channel.



Both micro-channels are 100  $\mu\text{m}$  deep across the entire channel

Figure 1: PDMS Microchannel test bed

length. Distilled water was used as the fluid medium. The flow was seeded using fluorescent particles of about 1  $\mu\text{m}$  in size.

Since volume illumination (as opposed using a light sheet illumination in macro flow PIV applications) is used in measuring microflows, the number concentration of seed particles need to be controlled [6]. The out-of-focus images becomes the background noise that, if not properly controlled, could overwhelm the particle images and hence can result in poor signal quality. The number of out-of-focus images can be reduced by controlling the seed number concentration,  $C$  or selecting the proper depth,  $L$ , of the channel. The visibility  $V$  of the in-focus images [6] is

$$V \sim 1/(CL) \quad (1)$$

In the present study, the approach was to rely on the depth of the channel (100 microns) to reduce the background or out-of-focus images. The Reynolds number based on the channel hydraulic diameter is about unity.

## MicroPIV system

An inverted microscope-based MicroPIV system was used for making measurements in the channels. It uses a multiport design that allows for different illumination and imaging systems. The components include a binocular with eyepiece; universal stage holder and traverse; nosepiece sextuple; illumination lamp kit; F-mount adaptor; epioptics attachment housing; and microscope objectives. This approach, using epifluorescence, allows illumination and scattered light collection to use the same optical access to the flow channel. A 12-bit, 4 Megapixel camera (POWERVIEW 4M) was mounted on the side of the microscope optical system to get the greatest flexibility, stability and ease of use. A lens system attached between the microscope and the camera increases the image field magnification and allows more uniform illumination of the flow field. A light guide system was used for the convenient delivery of the laser light. It consists of a light guide, a diffuser and lens to provide uniform beam intensity, along with adaptors for the microscope and the laser. A laser light attenuator used with the laser provides good control of the laser energy.

INSIGHT Data Analysis and display software was used to analyze the image fields. Iterative processing combined with window shifting was used to get high spatial resolution. Both local and global signal enhancement techniques were used. A TSI Synchronizer system provided precise timing and synchronization for the operation of the Dual-YAG Laser and the 2K x 2K camera and other hardware.

Since the typical particle number concentration was around 2 to 3 particles per interrogation volume, the approach of ensemble averaging of the correlation function was used. This approach improves the signal-to-noise level of the image, and increases the spatial resolution of the measurement [7]. The flows in this channel are steady and hence ensemble correlation approach can be advantageously used. An ensemble average of the correlation

of 100 captures was used to calculate the velocity vector on each interrogation region. The background reference image computed using the mean intensity was used for background subtraction. This improves the signal quality of the images and/or the removal of “unwanted objects” in the image field. Other tools that are part of the *Micron Resolution Particle Image Velocimeter* patent are also incorporated into the INSIGHT software package [8]. The typical spatial resolution obtained in the experiments was about 4 microns.

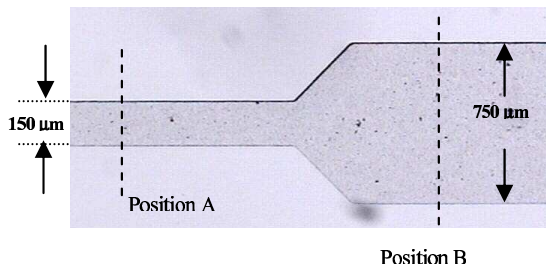


Figure 2: Diffuser channel

The measurements in the diffuser channel are shown below. Position A is 1500 microns upstream of the diffuser. Measurements were carried out in two different planes in the Z-direction (depth of the channel).  $Z = 50$  micron corresponds to the mid-plane of the channel.

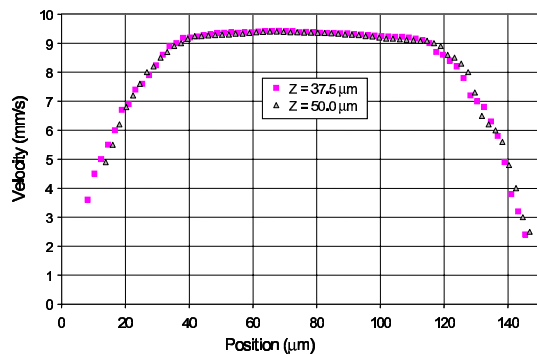


Figure 3: 1500 mm upstream of diffuser

The velocity profile (Figure 3) indicates the expected behavior in the center region of the channel. The measured velocity values near the wall indicate some departure from the ideal distribution.

It appears that the deviations of the velocity profile are caused by a variety of factors relating to geometrical imperfections and potential fouling of the channel.

Figure 4 shows the velocity distribution downstream of the expansion. Here, the velocity distribution is close to the expected profile.

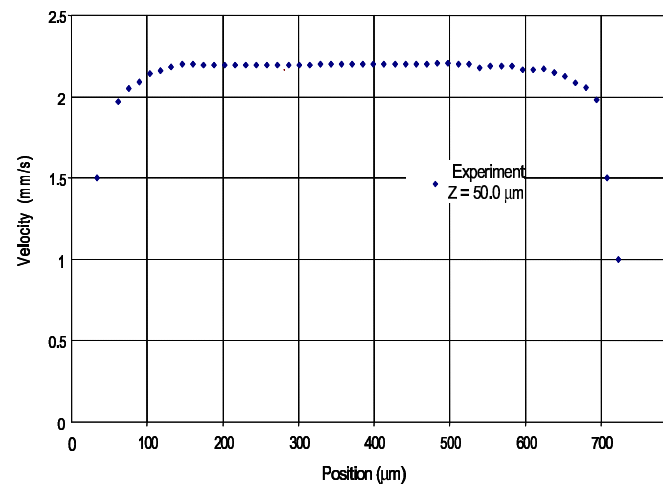


Figure 4: 750 microns downstream of diffuser

The dimensions and the measurement locations in the T-channel are shown in Fig.5. Measurements were carried out at multiple locations upstream and downstream of the t-junction.

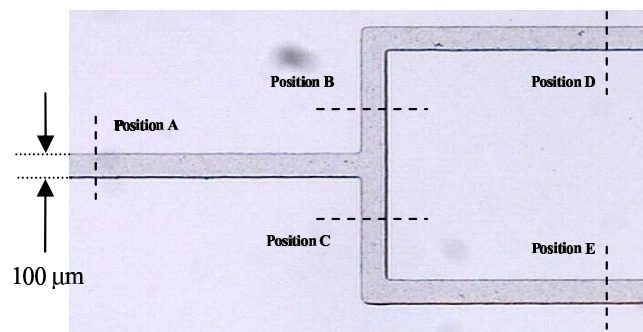


Figure 5: T- channel

Velocity profiles in the T-channel are shown below. They represent measurements at different channel depths ( $Z$ ).

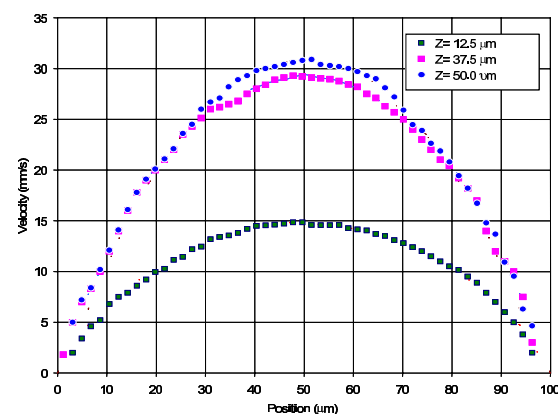


Figure 6: 2000 microns upstream of junction – position A

Position A corresponds to a location 2000microns upstream of the junction. Velocity profiles obtained at three different  $Z$  values are shown in Figure 6.  $Z = 50$  corresponds to the mid-plane of the channel.

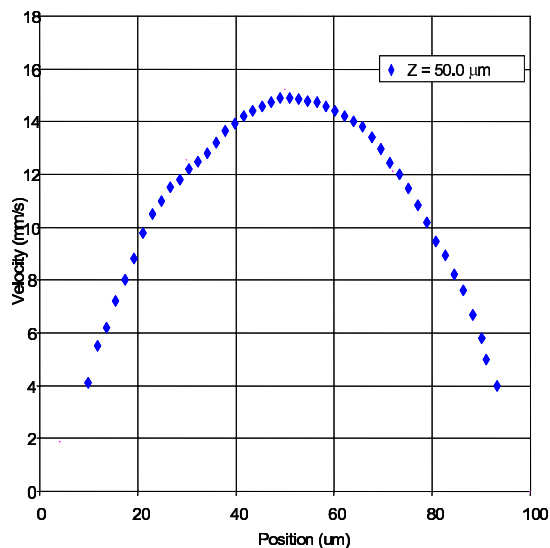


Figure 7: 200 microns downstream of junction – pos. B

Measurements at a location 200 microns downstream of the junction are shown in Figure 6. The velocity profile at this location show that the flow has not fully recovered from the influence of the corner or the junction on the flow. In addition, three dimensional effects due to out-of-plane motion downstream of the 90 degree corners can also influence the velocity profiles.

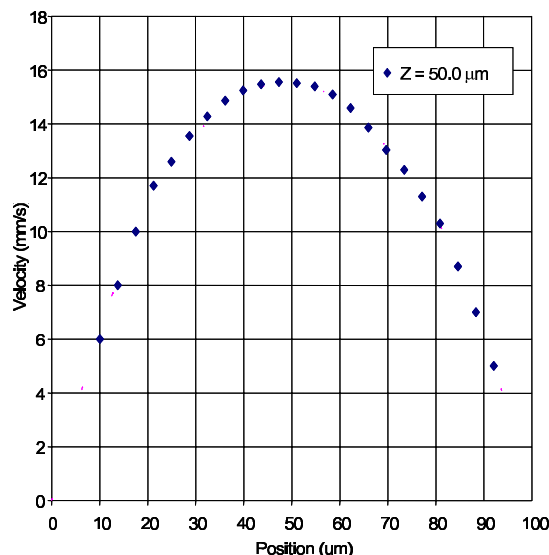


Figure 8: Velocity profile at position D  
2000 microns downstream of junction

The velocity profile at 2000 microns downstream of the junction is shown in Figure 8. The flow field appears to have fully recovered from the influence of the junction on the flow profile. In microchannel flows, the surface fouling due to accumulation of particles and other material on the wall affects the velocity profile near the wall. It is also known that bubbles that develop in the channel can aggregate and adversely affect flow development. This in turn affects the velocity profile. These practical aspects associated with the microflow experiments can limit the accuracy of the results obtained.

## Conclusions

Measurements in microchannels require careful consideration of the seed concentration. Special analysis techniques combined with other tools are used to reduce the background “noise” influence and enhance the signal quality. The operation of the channel so as to reduce or prevent fouling of the surfaces becomes important in getting accurate near wall flow details. In addition to fouling due to particles, formation and development of bubbles can noticeably affect the flow profiles. These aspects along with the wall roughness of the PDMS model demands special attention to detail in order to get accurate detailed measurements in microchannel flows.

## References

- [1] Gad-el-Hak, M., *The MEMS Handbook*, CRC Press, 2002
- [2] Madou, M., *Fundamentals of Microfabrication; The Science of Miniaturization*, 2<sup>nd</sup> ed., Boca Raton, Fla., CRC Press, 2002
- [3] Nguyen, N and Wereley, S. T., *Fundamentals and Applications of Microfluidics*, Artech House, 2002
- [4] Whitesides, G. M., Stroock, A.D., Flexible methods for microfluidics, *Physics Today*, 42-48, June (2001)
- [5] Beebe, D. J., Adrian R. J., Olsen, M. G., Stremmer, M. A., Aref, H. and Jo B. H, Passive mixing in micro-channels: Fabrication and flow experiments, *Mechaniques Industrie*, **2**, 343-348 (2001).
- [6] Olsen M. and R. J. Adrian, Out-of-focus effects on particle image visibility and correlation in microscopic PIV, *Exp. Fluids*, **29**, S166-S174 (2001).
- [7] Meinhart, C. D., Wereley, S.T. and Santiago, J. G., A PIV Algorithm for Estimating Time-Averaged Velocity Fields, *J. Fluid Engg.*, Vol. 122, pp.285, 2000
- [8] Measuring Microflows using Particle Image Velocimetry, P/N 2980249, TSI Inc, 2003.

## Experimental Investigation of Impinging Axisymmetric Turbulent Fountains

Paul Cooper<sup>1</sup> and Gary R. Hunt<sup>2</sup>

<sup>1</sup>School of Mechanical, Materials and Mechatronic Engineering, University of Wollongong, NSW 2522, Australia.

<sup>2</sup>Department Civil and Environmental Engineering, Imperial College London, London, SW7 2AZ, UK.

### Abstract

The behaviour of a turbulent, axisymmetric, Boussinesq, vertical fountain that impinges on a horizontal plate a distance  $H$  from the fountain source is investigated. Images from Light Induced Fluorescence visualisation of the flow provide a clear picture of the internal structure of the impinging flow. The interaction between the impinging fountain and the plate results in a buoyant radial wall jet that spreads horizontally before separating from the surface at a radius  $R_{sp}$ . The transient development of the flow and behaviour of  $R_{sp}$  with time is described. The steady-state flow is modelled theoretically and a correlation of the non-dimensional spread of the impinging fountain is presented that successfully relates  $R_{sp}/H$  to the source-plate separation and the source characteristics of the fountain.

### Background

The characteristics of turbulent plumes are of interest in many industrial and geophysical fluid flows. Frequently a prediction of the distribution of fluid density, velocity and concentration of contaminants, or other products, in the flow is needed for engineering design purposes. Plumes that develop from sources of buoyancy and momentum that act in opposite directions are known as fountains. Turner [1] reported experiments and presented an analytical model of a fountain developing in a uniform and quiescent environment. Baines, Turner and Campbell [2] extended this work to fountains within enclosures and determined the manner in which a fountain and a “filling box” interact. Bloomfield and Kerr [3] have more recently reported on the behaviour of axisymmetric and line fountains in an environment that is initially stratified.

The basic flow configuration for a positively-buoyant fountain developing in a homogeneous environment is shown in figure 1a. The outer, upward flowing, stream entrains fluid from both the surrounding ambient and from the downward moving buoyant jet. The focus of the present study is the situation where a fountain impinges on a horizontal plate as shown schematically in figure 1b. This situation is of interest both as a fundamental issue in fluid mechanics and also as the flow is central to a number of practical applications. The latter include the heating of large building spaces by warm jets of air directed downward from the ceiling (e.g. warm air curtains); flow from the jets of vertical takeoff aircraft; modelling of the dispersion of welding fume, as in gas metal arc welding (GMAW) where the plume of welding fume is initially directed downwards and outwards by shielding gas ejected from the GMAW nozzle towards the welding workpiece.

In the case of the impinging fountain, the buoyant fluid is forced radially outwards before rising as it impacts on the horizontal plate and thus the flow is wider than the free fountain (figure 1). The major objective the present work is to determine the way in which the presence of the solid plate changes the nature of the fountain and to investigate the flow both in the near field, close to the plate, and in the far field plume that rises above. Researchers who have looked at this problem and similar situations in the past include Lawrence and MacLachy [4] who investigated the radial spread of a positively-buoyant plume release beneath the surface

of a body of water. However, in this situation the stratification setup by the impinging plume is intrinsically stable, unlike the present case where the radial out-flowing jet (shown in figure 1b) is positively buoyant. More recently, Holstein and Lemckert [5] reported a set of experiments on impinging saline fountains. Their work focussed on how the radius of spread,  $R_{sp}$ , of the impinging fountain was related to the source conditions of the fountain, the source radius,  $R_0$ , and source-plate separation,  $H$ .

### Theoretical Framework

The two length scales that determine the behaviour of a free fountain, are the “jet length” ( $l_M = M_0^{3/4}/B_0^{1/2}$ ) and the “acceleration length” ( $l_Q = Q_0/M_0^{1/2} = \pi^{1/2}R_0$ ), where  $B_0$ ,  $Q_0$  and  $M_0$  are the source buoyancy, volume and specific momentum fluxes, respectively. The fountain source Froude number is then  $Fr_0 = (l_M/l_Q)$ . Turner [1] determined by experiment that the steady rise height,  $z_m$ , of a free fountain from a source with  $Fr_0 \gg 1$  is given by  $z_m = 1.85l_M$ . In the present situation the distance of the source from the plate,  $H$ , represents the third length scale. The behaviour of the impinging fountain might therefore be expected to be determined by these three length scales and the source Reynolds number,  $Re_0 = D_0V_0/\nu$ , ( $D_0 = 2R_0$ ).

After impinging on the plate one might expect the fountain to transform into a radial wall jet as discussed by many authors, e.g. Rajaratnam [6]. However, in the present case the radial outflow is positively buoyant and will separate from the plate when the Coanda effect has diminished sufficiently. In a 2D geometry, the separation distance between the source of a positively-buoyant wall jet flowing over a horizontal surface and the point where the jet detaches from the surface has been briefly reported by Sandberg *et al.* [7] who found the non-dimensional separation distance  $R_{sp}/H$  to be a function of the source Archimedes number,  $Ar_0 = (Fr_0)^2$ .

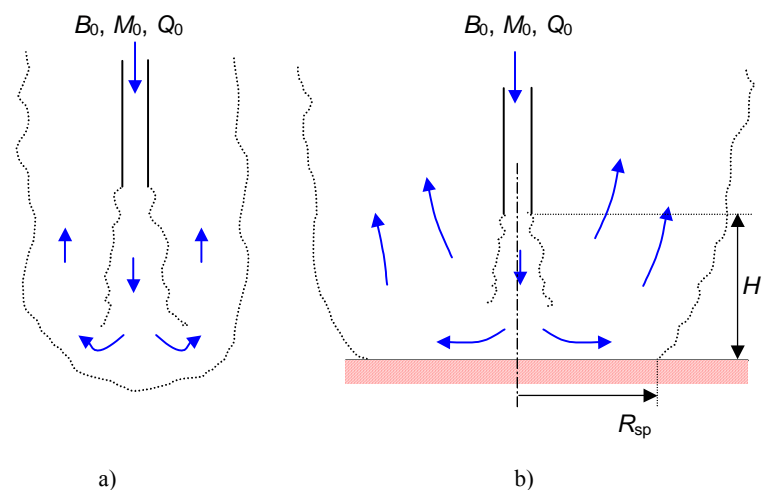


Figure 1. a) Turbulent fountain in a homogeneous environment;  
b) Turbulent fountain impinging on a horizontal plate.

In the present situation the impinging flow forms the “source” of the buoyant radial wall jet. Since we require  $H \leq 1.85 l_M$  for a



fountain to impinge on the plate, we shall assume that at the plate the flow properties are similar to that of a free jet. In particular, the momentum flux at the plate ( $M_H$ ) is approximately equal to that at the fountain source and the volume flux ( $Q_H$ ) and velocity radius ( $b_v$ ) are:

$$Q_H = 2^{3/2} \pi^{1/2} \alpha (H/l_Q) Q_0 \quad \text{and} \quad \frac{db_v}{dz} = 2\alpha \quad (1)$$

where  $\alpha = 0.0535$  is the entrainment constant applicable to jets (Papanicolaou and List [8]) and  $z$  is the vertical coordinate with origin at the fountain source. We assume that a fraction,  $\gamma$ , of the vertical momentum of the mean flow in the down-flowing fountain is transformed to radial momentum in the radial wall jet. Invoking conservation of volume it can be shown that the source Archimedes number of the radial jet,  $Ar_{rad} = g'_{rad} \delta_{rad} / u_{rad}^2$  is related to the Archimedes number of the source of the fountain,  $Ar_0 = g'_0 R_0 / W_0^2$  as follows:

$$Ar_{rad} = 2^{5/2} \alpha^2 \gamma^{-3} (H/R_0)^2 Ar_0 \quad (2)$$

where  $g'_{rad}$ ,  $\delta_{rad}$  and  $u_{rad}$  are the buoyancy, thickness and velocity of the radial wall jet at its “source” at radius  $b_v$ , and  $g'_0$ ,  $R_0$  and  $W_0$  are the buoyancy, radius and velocity at the fountain source.

## Experiments

Initial experiments were carried out at both the University of Wollongong and Imperial College London to determine the radius of spread ( $R_{sp}$ ) of the radial wall jet. Preliminary experiments were visualised using a shadowgraph and then further experiments were conducted with sodium fluorescein dye added to the source fluid and the tank lit from below with a light sheet. The latter technique allowed the internal flow structure of the impinging fountains to be clearly visualised. A glass-walled tank measuring  $1.4 \times 1.4$  m in plan was filled, with salt water as the ambient fluid, to a depth of approximately 1.2 m. A wide range of experiments were conducted with fresh water injected through nozzles with diameters between  $3 \text{ mm} \leq D_0 \leq 10 \text{ mm}$ , held at distances of  $25 \text{ mm} \leq H \leq 200 \text{ mm}$  above the plate. The light sheet was generated by means of a line of dichroic incandescent 12v bulbs that were directed at a 1 mm wide slit in black cardboard sheeting attached to the lower glass surface of the tank. In the field of view it is estimated that the light sheet varied in thickness between 2 and 3 mm over the field of view. Images were captured by means of a digital CCD video camera (JAI CV-M4 monochrome,  $1380(\text{h}) \times 1030(\text{v})$  pixel read out) and processed using the DigiFlow software system (Dalziel [9]).

## Results and Discussion

The structure of the impinging fountain flow is somewhat different than might have been surmised from the observations of previous research that used shadowgraph or basic dyed fluid. The present Light Induced Fluorescence (LIF) experiments allowed a vertical section through the impinging fountain to be clearly visualised. Figure 2 is an enhanced and annotated image of a typical experiment taken after the flow had reached a quasi-steady state and shows the main flow features. One of the most striking features of the flow (as observed for  $H/l_M \ll 1$ ) is that when the buoyant radial jet separates from the plate it does not form a line plume (circular in plan), but rather the separated flow is re-entrained into the radial outflow and the descending fountain forming a large toroidal vortex. After the initial transients, which are discussed in more detail below, a steady, turbulent plume rises above the toroidal vortex. The initial radius of this plume varies considerably with time during the transients.

The basic flow structure of the impinging fountain was found to depend primarily on the non-dimensional nozzle-plate separation,

$H/l_M$ . Figure 3 shows examples of the different flow structures once steady state had been reached. The majority of the results presented herein are for experiments where  $H/D_0 \gg 1$ .

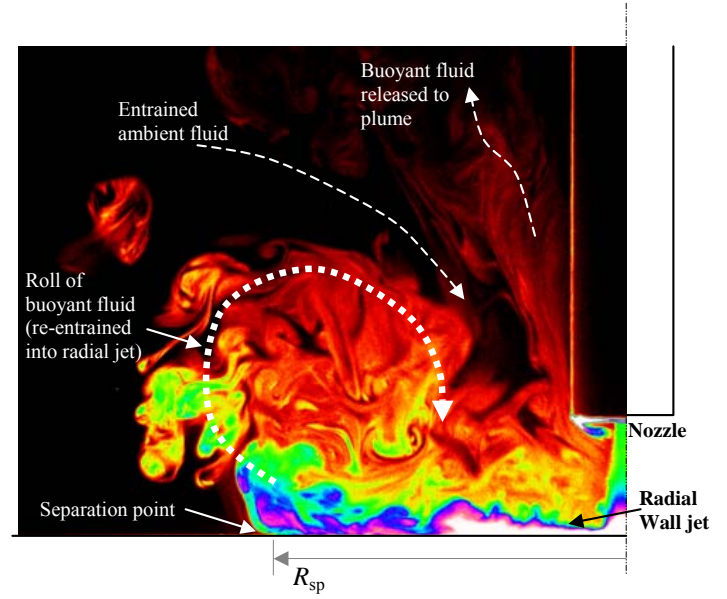


Figure 2. Digitally enhanced/annotated image illustrating the main characteristics of the flow field (only left half shown for clarity).  $H/l_M = 0.10$ ,  $H/D_0 = 8.3$ .

For  $H/l_M \ll 1$  the steady-state flow behaved in a fashion similar to that of an energetic, isothermal, turbulent jet impinging on a plate. Outside the impingement zone the thickness,  $\delta$ , of the radial jet appeared to increase linearly with radius,  $r$ , as shown in figure 4. (However, one might expect the rate of growth,  $d\delta/dr$ , to be greater since the radial jet shear layer is effectively unstably stratified in the case of impinging fountains, as compared to the usual isothermal or filling box situations). Vortices aligned circumferentially were generated in the jet impingement zone and swept outward. These are visible in figure 4. The presence of these vortices cause the high local turbulence intensities reported by Cooper *et al.* [10] and other researchers investigating isothermal impinging jets. With increasing radius the buoyancy forces became dominant and resulted in the separation of the buoyant radial jet from the plate at the critical radius  $R_{sp}$ .

The transient development of the impinging fountains showed that for  $H/l_M < 1.5$  there were three distinct stages of development as illustrated in the sequence of images in figure 5.

i) First, the starting fountain impacts with the plate and the horizontal radial flow is established. The front of the radial jet-like flow is a vortex ring, the major radius of which increases with time. The front observed is quite different from that observed for the spreading gravity current arising from an impinging, negatively buoyant plume (as in the case of the classic “filling box” situation, for example). During this initial transient very little buoyant fluid escapes re-entrainment and the majority is drawn back into the axisymmetric down-flowing fountain and radial outflow. Moreover, the ambient fluid immediately adjacent to the down-flowing fountain is co-flowing with the respect to the radial jet at this time.

ii) The separation radius of the attached radial jet reaches a maximum. At approximately this point in time a bulk upward motion of buoyant fluid occurs above the zone  $r < R_{sp}$ , and a starting plume develops with the radial jet acting as a distributed source of buoyancy.

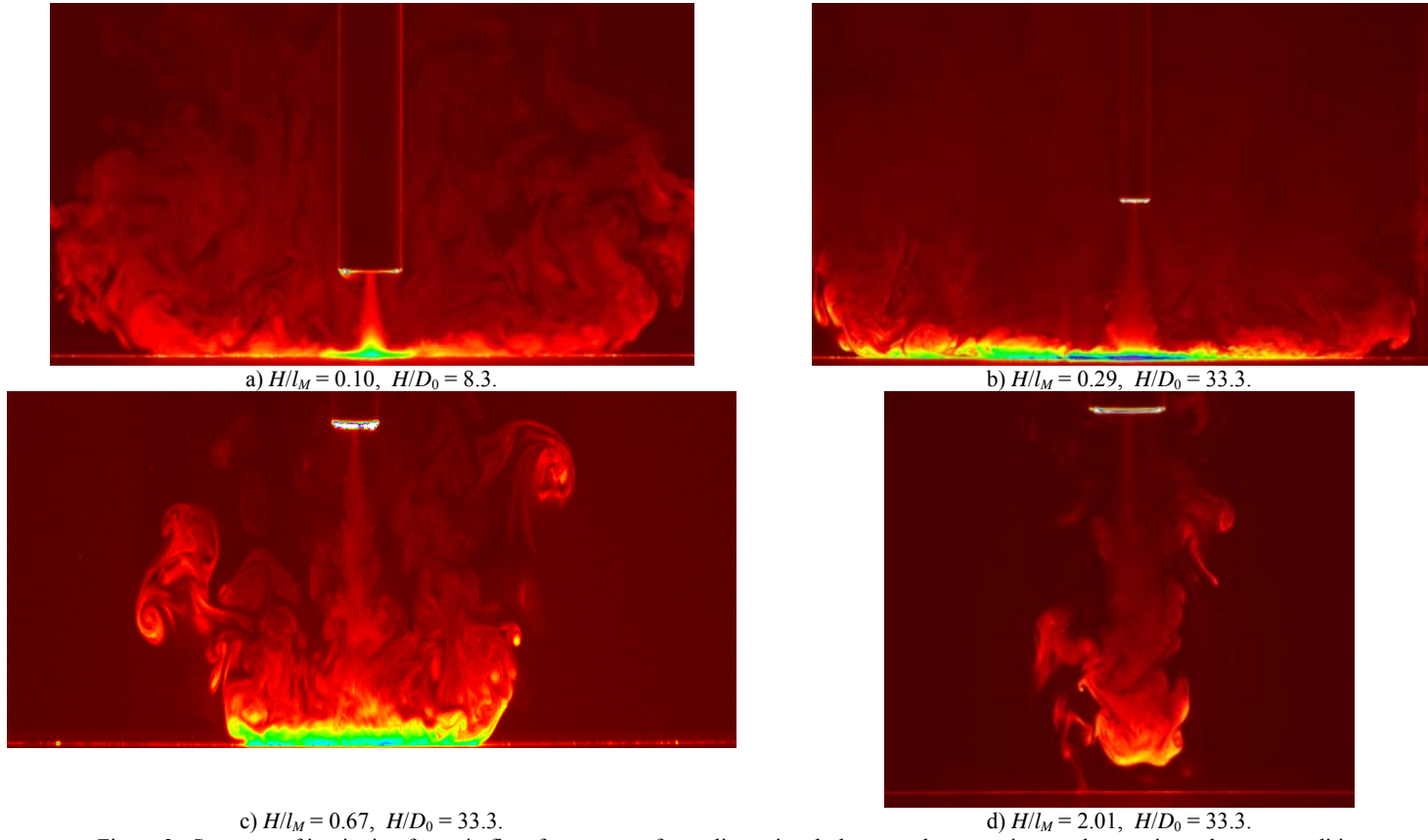


Figure 3. Structure of impinging fountain flow for a range of non-dimensional plate-nozzle separations under quasi-steady state conditions.

iii) Finally, the bulk plume flow above the nozzle,  $z > H$ , acts to reduce, and sometimes reverse, the direction of flow of ambient and re-entrained buoyant fluid adjacent to the fountain. Thus, the momentum flux of the fountain when it reaches the plate is reduced and the separation radius decreases and settles to a quasi-steady-state value.

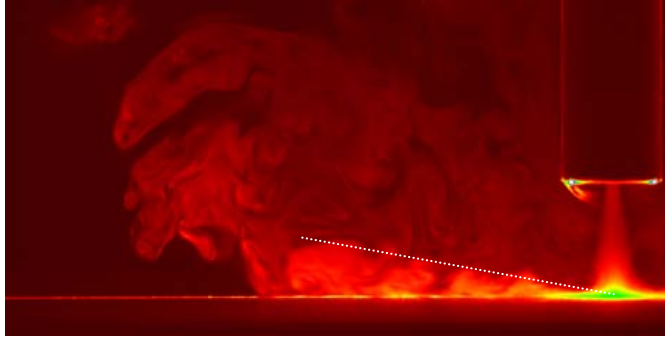


Figure 4. Buoyant radial wall jet development.  $H/l_M = 0.10$ ,  $H/D_0 = 8.3$ .

A time-series image showing the variation of  $R_{sp}$  with time is shown in figure 6. This image was generated by processing the digital movie of a typical experiment so that a horizontal line of pixels just above the flat plate has been extracted from each frame of the movie and placed one above the other to give time on the vertical axis and a well-defined horizontal boundary indicating  $R_{sp}$ . For the case shown  $R_{sp} \approx 240\text{mm}$  at 120s.

With increasing  $H/l_M$  the radial jet becomes thicker and less energetic, and the non-dimensional radius of separation,  $R_{sp}$ , decreases until at approximately  $H/l_M \sim 2$  the fountain no longer maintains continuous contact with the plate, as shown in figure 3c. When the nozzle-plate separation  $H/l_M \sim 2$  the fountain initially makes contact with the plate but subsequently detaches and may make periodic contact in the quasi-steady state.

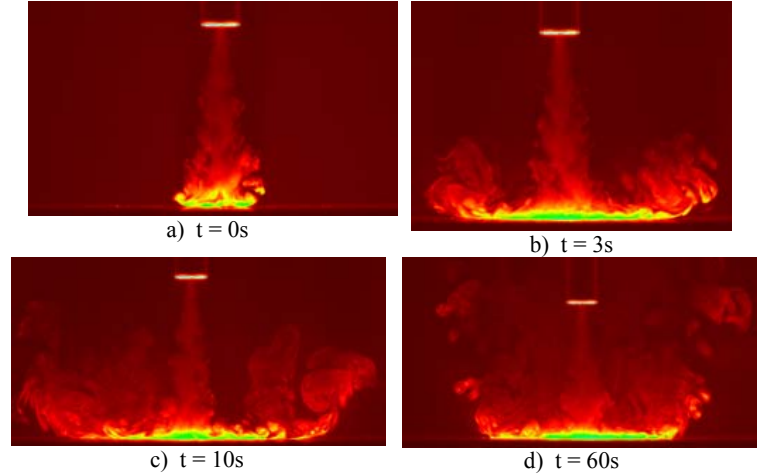


Figure 5. Initial development of the impinging fountain flow field for  $H/l_M = 0.69$ ,  $H/D_0 = 20.0$ .

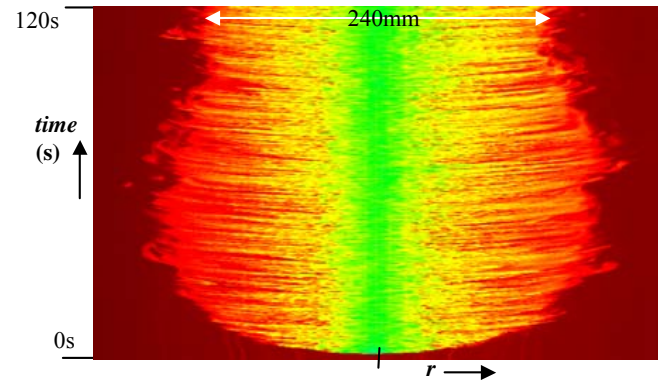


Figure 6. Typical time series of the intensity of light viewed in a line just above the flat plate for  $H/l_M = 0.69$ ,  $H/D_0 = 20.0$ .

Figure 7 is a time-series image showing this transient. The figure was generated by taking a vertical line of pixels from the nozzle outlet to the plate from each frame of the digital movie of the experiment shown in figure 3d.



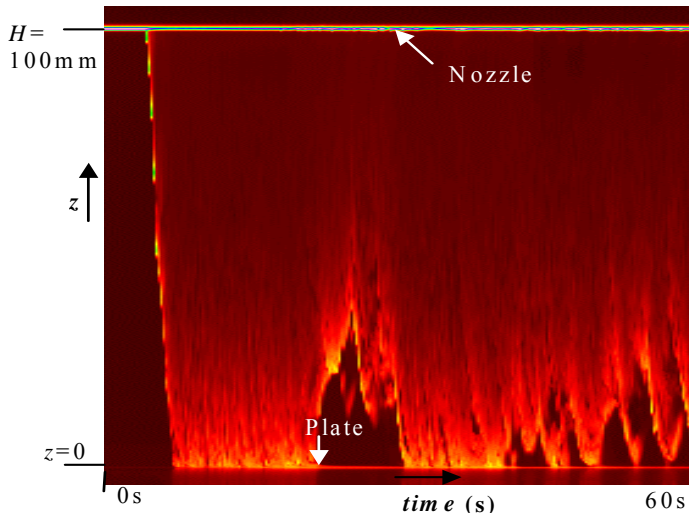


Figure 7. Time series of the intensity of light viewed in a vertical line between the nozzle outlet and the plate ( $H/l_M = 2.01$   $H/D_0 = 33.3$ ).

The non-dimensional spread of the radial jet is successfully correlated by the scaling developed by the present authors as discussed above. Figure 8 shows a plot of the data from virtually all the shadowgraph experiments carried out over a wide range of source conditions and nozzle-plate separations. The solid line in this figure has a gradient of  $-0.75$  which is the same as found by Sandberg *et al.* [7] for the case of a simple 2D buoyant jet introduced with horizontal momentum immediately above a horizontal surface. The numerical value of  $\gamma$  has a very strong influence on the properties of the radial jet (thickness, velocity, etc) and on the relationship between the Archimedes number of the fountain source and the radial jet source. A value of  $\gamma \sim 0.3$  correlates the data most closely with that of Sandberg (which is for a different geometry). This is also consistent with the work of Witze and Dwyer [11] who found that assuming conservation of momentum “severely overpredicts” the radial jet momentum.

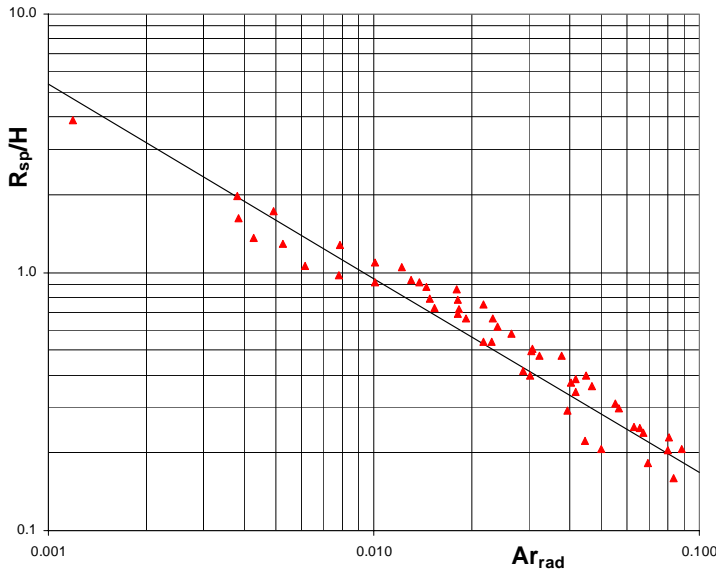


Figure 8. Radial spread of the buoyant radial jet as a function of the Archimedes number at the radial jet ‘source’ deduced from the source conditions of the fountain and assuming  $\gamma = 1$  in (2). Symbols are experimental data and the solid line is a best fit with gradient  $-0.75$  (the same power law dependency as reported in Sandberg *et al.* [7] for the separation of a plane buoyant jet injected across a horizontal surface).

The maximum Archimedes number in the experiments is  $Ar_{rad} \sim 0.01$ . This is the maximum value (approx.) for impinging fountains since it can be shown to be equivalent to a non-dimensional nozzle-plate separation of  $H/l_M \sim 1.7$  beyond which the fountain will no longer impinge on the plate in a steady manner (*cf.* Turner [1]).

## Conclusions

This work has shown that the flow structure within a fountain impinging on a horizontal plate is complex and is primarily dependent on the fountain source Archimedes (or Froude) number and the non-dimensional separation  $H/l_M$  of the nozzle and plate. The impinging fountain generates a buoyant radial wall jet that spreads out across the plate until buoyancy forces overcome the effects of momentum and the flow separates from the plate at a radius  $R_{sp}$ .

Light Induced Fluorescence experiments have shown that the upward flow from the impinging fountain cannot be modelled as a line plume arising from a ring of radius  $R_{sp}$ , owing to re-entrainment of the separating fluid by the fountain and radial jet.

The authors have developed a theoretical framework whereby the steady-state spreading radius ( $R_{sp}$ ) of an impinging fountain may be predicted from the fountain source Archimedes number.

The transient development of the impinging fountain has been investigated and it is found that the fountain reaches the quasi-steady separation radius after an initial period where the plume rising from the impingement zone is not fully developed, thus, the separation radius is initially larger than in the steady state since the ambient fluid is co-flowing with, rather than counter-flowing against, the vertical fountain flow.

## Acknowledgments

The authors would like to acknowledge the Engineering and Physical Sciences Research Council (UK) for partial support of the work described herein. They would also like to thank G.R.Slater and M.Gaston for carrying out the shadowgraph experiments. We are grateful to William Bobinski and Tony Allen at IC for constructing apparatus for the LIF experiments.

## References

- [1] Turner, J. S., Jets and plumes with negative or reversing buoyancy, *J. Fluid Mech.*, **26**, 1966, 779-792.
- [2] Baines, W. D., Turner, J. S. and Campbell, I. H., Turbulent fountains in an open chamber, *J. Fluid Mech.*, **212**, 1990, 557-592.
- [3] Bloomfield, L. J. and Kerr, R. C., Turbulent fountains in a stratified fluid, *J. Fluid Mech.*, **358**, 1998, 335-356.
- [4] Lawrence, G. A. and MacLachy, M. R. Radially spreading buoyant flows, *J. Hydraulic Res.*, **39**, no. 6, 2001, 583-590.
- [5] Holstein, D. M. and Lemckert, C. J., Spreading of energetic submerged fountains impinging on a rigid surface, *Proc. 14<sup>th</sup> Australasian Fluid Mech. Conf.*, Adelaide, 2001, 749-752.
- [6] Rajaratnam, N. *Turbulent Jets*, Elsevier, 1976.
- [7] Sandberg, M., Wirén, B. and Claesson, L., Attachment of a cold plane jet to the ceiling – length of recirculation region and separation distance, *Proc. ROOMVENT 92*, Denmark, 1992, 489-499.
- [8] Papanicolaou, P. N. and List, E. J., Investigations of vertical turbulent buoyant jets, *J. Fluid Mech.*, **195**, 1988, 341-391.
- [9] Dalziel, S.B. Rayleigh-Taylor instability: experiments with image analysis. *Dyn. Atmos. Oceans*, **20**, 1993, 127-153.
- [10] Cooper, D., Jackson, D. C., Launder, B. E. and Liao, G. X., Impinging jet studies for turbulence model assessment – I. Flow-field experiments, *J. Heat Mass Transfer*, **36**, 1993, no. 10, 2675-2684.
- [11] Witze, P. O. and Dwyer, H. A., The turbulent radial jet, *J. Fluid Mech.*, **75**, part 3, 1976, 401-417.

## Axisymmetric Jet Control Using Passive Grids

R. Lehman, S. Rajagopalan, P. Burattini and R. A. Antonia

Discipline of Mechanical Engineering, School of Engineering  
The University of Newcastle, NSW, 2308 AUSTRALIA

### Abstract

The structure of a circular jet, modified by placing grids of two different configurations near the nozzle exit plane, was investigated by using a single hot wire probe. An annular grid which perturbed mainly the axisymmetric shear layer and a circular disk grid which covered most of the potential core were used to modify the jet passively. Behind the annular mesh, the width of the shear layer is reduced and a significant decrease in turbulence intensity is observed. Spectra of the velocity fluctuation show the suppression of the formation of organised structures in the jet mixing layer. In contrast to the annular grid, the influence of the disk grid on the mean velocity and turbulence intensity is not as significant. Evidence for the presence of large scale structures downstream of the edges of the grids is presented.

### Introduction

Turbulence control or management in different flows is a rapidly expanding field of research because of potential benefits in industry. In particular, in plane and axisymmetric jets, extensive investigations have been carried out by using active techniques for turbulence enhancement as well as suppression, but investigations using passive techniques are not as extensive. The main objective in jet turbulence control is to target and interfere with the organised vortical structures that are formed due to Kelvin–Helmholtz instability in the mixing layer. Tong and Warhaft [11] and Parker et al [8] obtained a significant reduction of turbulence intensity by placing a thin wire ring in the shear layer near the nozzle exit plane. The width of the shear layer was reduced and the spectra of velocity fluctuations indicated the suppression of organised large structures in the mixing layer of the jet. Stephens [9] and Stephens et al [10] used grids and honeycombs to completely cover the nozzle exit and obtained similar results. Burattini et al [2] suggested that the grids suppress the shear layer instability and damp the jet column instability. Another passive technique employed in a plane jet is to place a bluff body like a cylinder in the potential core and use the vortex shedding behind it as a feed back mechanism to control the shear layer instability [6, 3, 5, 1]. Antonini and Romano [1] disturbed a circular jet by placing a long, thin cylinder parallel to the nozzle exit plane and obtained an increase in mixing.

In jet turbulence control using a grid, apart from the influence of the mesh size and wire diameter of the grid, the circular edge is also likely to have an impact on the jet development. By using wire screens to partially cover the test section of a wind tunnel, Oguchi and Inoue [7] produced a mixing layer similar to that developing behind a splitter plate. Smoke flow visualisation indicated the presence of large scale structures downstream of the grid in the mixing layer. When a thin wire was attached to the screen edge, vortex shedding behind the wire also dominated the flow. Use of a narrow rectangular mesh or a small diameter disk grid yielded a wake. Spectra of velocity fluctuations in the wake produced by a rectangular screen (Zhou and Antonia [12]) clearly showed the presence of organised vortical structures even though

there was no primary vortex street. Hydrogen bubble flow visualisation (Finlay [4]) in the wake of a rectangular grid (Figure 1) shows the formation of large structures downstream.



Figure 1: Hydrogen bubble flow visualisation of structures behind a grid (from [4]).

The main aim of the present work is to investigate the effect of placing an annular grid and a disk grid at the nozzle exit plane on the development of a circular jet by using a single hot wire probe. The annular grid perturbs the initial shear layer and a small peripheral part of the potential core; the disk grid covers most of the potential core.

### Experimental Conditions

The jet was produced by a 55 mm diameter ( $d$ ) circular nozzle to which air was supplied by a variable speed centrifugal blower via a diffuser, settling chamber and contraction which had an area ratio of 85:1. Two annular and two disk grids were used in this

Case	Grid	Wire dia. (mm)	Aperture size (mm×mm)	Outer dia. (mm)	Inner dia. (mm)
1	Annular	0.5	1.25×1.25	100	30
2	Annular	0.2	0.54×0.54	100	30
3	Disk	0.5	1.25×1.25	30	–
4	Disk	0.2	0.54×0.54	30	–

Table 1: Summary of mesh geometry for disturbed flow conditions.

study and Table 1 gives the details of the grid geometry, mesh and wire size. Hereafter, measurement conditions will be referred to as Cases 1, 2, 3 and 4. The grid was isolated from the body of the jet by mounting it on a separate frame which was placed at a distance of 2 mm downstream of the nozzle exit plane. Figure 2 shows the nozzle, the coordinate axes and the four grids. Measurements of the mean velocity ( $U$ ) and the longitudinal velocity fluctuation ( $u$ ) were made by using a single hot wire probe operated in a constant temperature mode. The hot wire, made of 90% Pt-10% Rh, had diameter was 2.5  $\mu\text{m}$  and the wire length to diameter ratio was nearly 200. A height gauge with a resolution of 0.01 mm was used to move the probe in the y-

direction. The hot wire signals were digitised using a 12 bit A/D converter and stored on a PC for further processing.

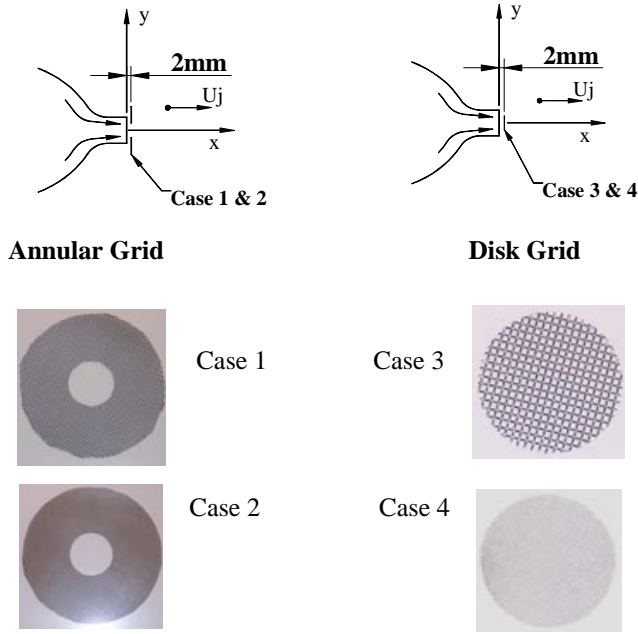


Figure 2: Co-ordinate system and grid configuration.

The jet exit velocity ( $U_j$ ) was 10 m/s which yielded a Reynolds number  $Re_d = 3.7 \times 10^4$ . For the annular grid measurements,  $U_j$  was determined by placing a Pitot tube close to the nozzle exit plane in the potential core. For the disk grid,  $U_j$  was set at 10 m/s at  $x/d = 2$  since the flow immediately downstream of the grid is unsteady due to the vortex shedding from the mesh. Burattini et al [2] also employed a similar approach to set  $U_j$  in their measurements behind a grid. Distributions of mean velocity ( $U$ ) and rms velocity fluctuation ( $u'$ ) were obtained at several locations up to  $x/d = 10$ . The nozzle exit boundary layer was laminar and exhibited a small deviation from the Blasius profile. The shape factor was 2.2 which is smaller than the value of 2.59 for the Blasius distribution. The shear layer instability frequency  $f_0$  (Kelvin – Helmholtz instability frequency) was approximately 600 Hz which yielded a Strouhal number  $St_{\theta_0} (= f_0 \theta_0 / U_j, \theta_0$  is the nozzle boundary layer momentum thickness) = 0.013 which is in agreement with the values available in the literature.

## Results and Discussion

### Mean Velocity Distribution

The normalised mean velocity distributions  $U/U_j$  of the undisturbed jet and the jet with grids are shown in Figure 3 and 4 for  $x/d = 0.2, 1, 2, 4, 6$  and  $10$  to include parts of the mixing layer and the transition zone of the jet. At  $x/d = 2, 4, 6$  and  $10$ , the distributions with the annular mesh (Figure 3, Case 1) have a reduced lateral spread which is reflected in a smaller width of the shear layer which is consistent with the results of Burattini et al [2] and Stephens et al [10]. At  $x/d = 0.2$  and  $0.4$ ,  $U/U_j$  profiles exhibit a discontinuity with a rapid decrease between  $y/d \approx 0.35$  and  $0.5$ . This region of a rapid change in  $U$  corresponds to the interphase between the potential core and the inner edge of the annular mesh which produces a mixing layer type of flow, somewhat similar to the two-stream mixing layer obtained by Oguchi and Inoue [7]. This layer disappears rapidly and cannot be identified for  $x/d > 4$ . The mean velocity gradient inside this layer is smaller for the grid with a finer mesh and wire size (Case 2) compared to Case 1 which implies that the fine mesh produces a rapid mixing and results in a reduced velocity gradient. Another possibility is that the width of the shear layer formed by the mesh is smaller for the fine grid compared to that for the coarse grid

(Case 1). For this flow at  $x/d = 6$  and  $10$ , the value of  $U/U_j$  on the centreline is

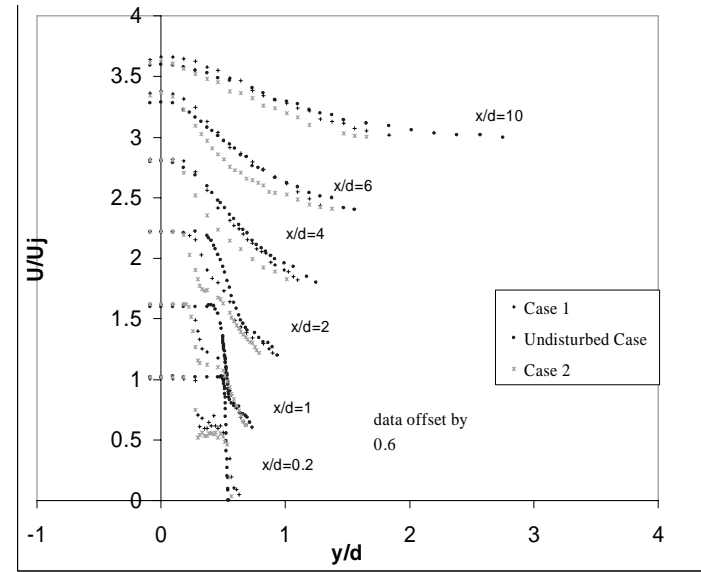


Figure 3: Mean velocity distribution with annular grids.

slightly larger than that of the undisturbed jet whereas for Case 2, there is a small excess at  $x/d = 6$  which disappears at  $x/d = 10$ . This observation suggests that the influence of the coarse grid persists for a larger downstream distance compared to that of the fine grid. Distributions of  $U/U_j$  for the disk grids (Cases 3 and 4) indicate a negligible influence on the width of the jet while, in the potential core region, the mean velocity is smaller compared

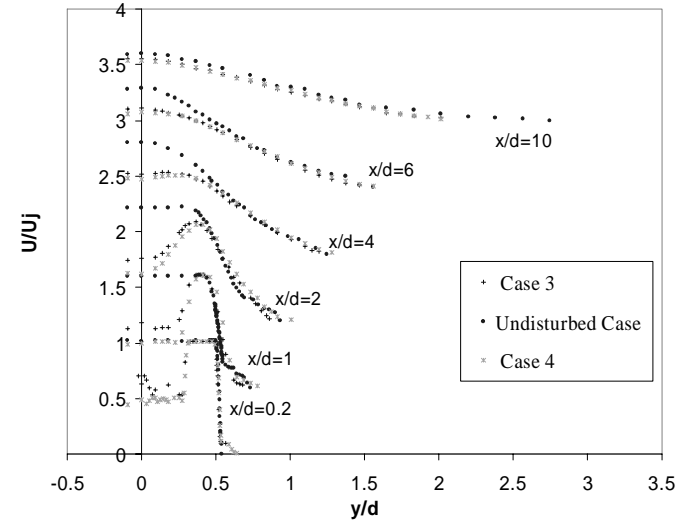


Figure 4: Mean velocity distribution with disk grids.

to the undisturbed jet (Figure 4). At  $x/d = 0.2$ , the mixing zone at the outer edge of the disk grid yields a rapid increase in  $U/U_j$ , which disappears for  $x/d > 4$ .

### RMS Velocity Fluctuation $u'$

Distributions of  $u'/U_j$  at different downstream locations for the annular grid (Figure 5) show that these grids produce a significant amount of turbulence suppression. For example, at  $x/d = 1$ , the maximum value of  $u'/U_j$  is reduced by 60 % and 50 % respectively for Cases 1 and 2. Large reductions can be observed at other downstream locations also. A significant feature of  $u'/U_j$  distribution for the flows with annular grids is the presence of two maxima at  $x/d = 1$  and  $2$ ; at other downstream locations, the peaks are still discernible. The peak at small  $y/d$  can be identified with the presence of the mixing zone produced by the inner edge of the mesh whereas the peak at large  $y/d$  is due to the jet mixing layer. Unlike the inner edge, the outer edge protrudes into the ambient region and does not produce a mixing zone. The grid with a finer mesh exhibits a peak in  $u'/U_j$  at the outer edge of the

jet (large  $y/d$ ) compared to the coarse grid. The influence of both annular grids decreases as  $x/d$  increases.

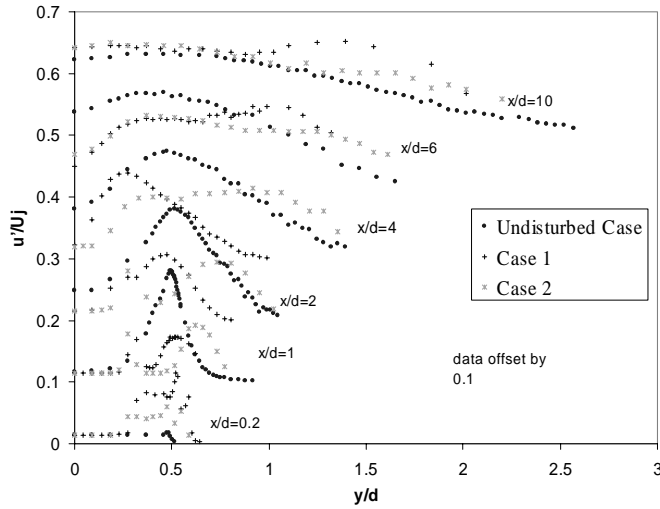


Figure 5: Distribution of rms velocity fluctuation with annular grids.

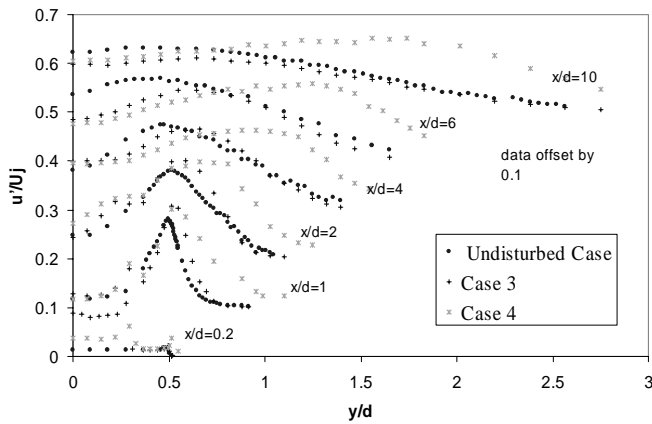


Figure 6: Distribution of rms velocity fluctuation with disk grids.

For the disk grids placed in the potential core (Cases 3 and 4),  $u'/U_j$  increases slightly at  $x/d = 1$  and 2 (Figure 6). The distributions have two maxima – one associated with the mixing zone of the edge of the grid and the other inside the jet mixing layer. At  $x/d = 4, 6$  and 10, the distributions exhibit a broad maxima. For the fine mesh disk (Case 4), the maxima occur at larger  $y/d$  values compared to the other two conditions. As  $x/d$  increases, the distribution for Case 4 deviates from those of the undisturbed and Case 3 flows. Antonini and Romano [1] also observed two peaks in  $u'/U_j$  distributions in their modified jet measurements. They observed an increase in  $u'/U_j$  and a lateral shift in the location of the maximum value compared to an undisturbed jet. In a plane jet disturbed by placing a cylinder in the potential core, Hsiao et al [6] observed an induced self sustaining oscillation at the cylinder vortex shedding frequency; in this flow, Chou et al [3] obtained an enhanced mixing. In a plane jet with a cylinder in the potential core, Henry et al [5] obtained a large amplitude peak in the mixing layer spectra at the cylinder vortex shedding frequency instead of the instability frequency, suggesting a resonant interaction between the jet exit and the cylinder vortex shedding. However, for this to occur, an intense vortex shedding from a relatively large diameter cylinder was necessary since small diameter cylinders produced only weak vortex shedding.

### Centreline Distributions

Centreline distributions of  $U/U_j$  for the undisturbed and all the disturbed (Case 1–4) flows are shown in Figure 7. The annular

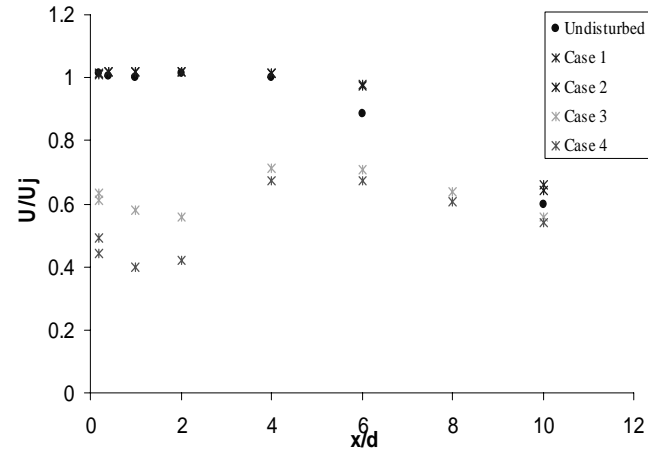


Figure 7: Centreline mean velocity distribution.

mesh extends the potential core to  $x/d = 6$  from a value of 4 for the undisturbed jet which reflects a contraction of the shear layer for the jets with the annular mesh. The mesh and wire size have little influence on the centreline velocity. For the disk grids with a coarse mesh,  $U/U_j$  decreases slightly from a value of 0.6 (Case 3) up to  $x/d = 2$  followed by an increase up to  $x/d = 6$ . Downstream of this location,  $U/U_j$  decreases continuously, similar to the undisturbed jet. For the disk with fine mesh (Case 4), centreline velocities are smaller, but the distribution has a shape similar to that of Case 3. The initial decrease in  $U_j$  up to  $x/d = 2$  is characteristic of the flow behind a grid. Between  $x/d = 2$  and 4, the increase in  $U_j$  might be linked to the growth of the jet which is associated with a reduction in the size of the central core. For the jet with the disk grids, it is not possible to identify a potential core in the conventional sense.

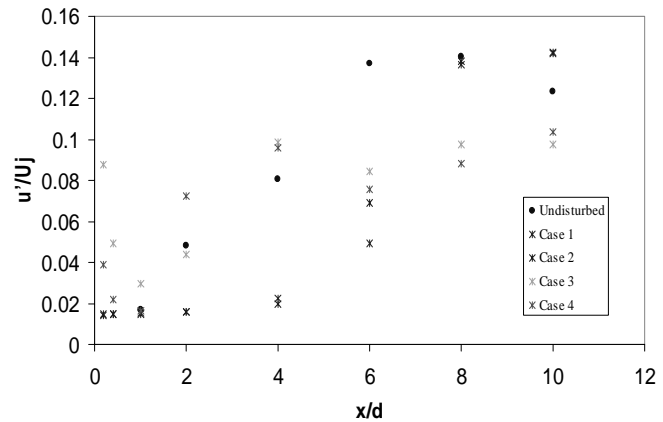


Figure 8: Centreline rms velocity fluctuation distribution.

For Cases 1 and 2, the centreline distributions of  $u'/U_j$  are almost identical (Figure 8), but are different to the distribution for the undisturbed jet. The maximum value of  $u'/U_j$  is nearly the same (14.5%) for the undisturbed and disturbed flows, but the maximum for the grid flows occurs at  $x/d = 6$ , compared to  $x/d = 4$  for the undisturbed jet. This result provides additional support for the extension of the potential core. The two disk meshes also produce almost identical centreline distributions of  $u'/U_j$ , with a local minimum at  $x/d = 1$  followed by a maximum at  $x/d = 4$ .

### Spectra of u

For the undisturbed jet,  $u$  spectra at  $x/d = 0.2$  and 0.4 and  $y/d = 0.5$ , which is in line with the nozzle tip (Figure 9), indicate the presence of organised large structures at the instability frequency of approximately 600 Hz.



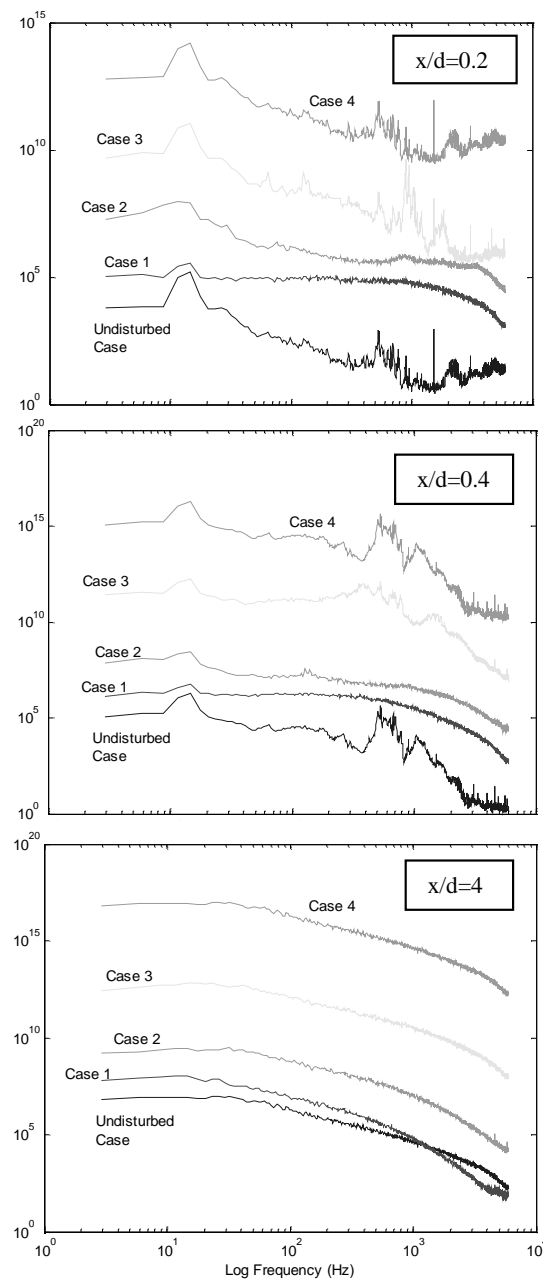


Figure 9: Spectra of  $u$  with annular and mesh grids.

With the annular grids in place, the spectral peak at this frequency cannot be identified, indicating that the grids suppress the formation of organised vortical structures near the nozzle exit. This result is similar to that of Burattini et al [2] and Stephens et al [10] when the jet nozzle was completely covered by grid and honeycomb. Lack of organised structures results in a reduced growth rate and a smaller shear layer width. At  $x/d = 4$ , the spectra for the undisturbed flow and Cases 1 and 2 are almost identical and the lack of spectral peaks indicates the absence of an organised motion. The disk grids have no influence on the formation of organised structures at  $x/d = 0.2$  and the spectral peak near 600 Hz can be identified for the undisturbed and the grid flows. However, at  $x/d = 0.4$ , additional peaks can be seen in the spectra for these grids (Cases 3 and 4). The additional peaks may be associated with the shear layer produced at the edge of the disk grid, but further investigation is needed to confirm this. At  $x/d = 4$ , all the three spectra are almost identical.

## Conclusions

The two annular grids used in this investigation suppress the formation of the shear layer (Kelvin-Helmholtz) instability and

inhibit the formation of organised vortical structures. This leads to a reduction in the growth rate and an extension of the length of the potential core. The mean velocity distributions close to the nozzle exit exhibit a discontinuity which can be identified with the mixing zone formed at the inner edge of the grid. Distributions of  $u'$  exhibit two peaks, one of which is inside the jet mixing layer whilst the other one occurs closer to the jet axis, due to the mixing (shear) zone mentioned previously. The absence of a spectral peak confirms the suppression of the organised motion in the jet mixing layer. The disk grids have negligible influence on the development of the jet. The organised vortices are not suppressed and the growth rate of the undisturbed and disturbed jets is nearly the same. The value of  $u'$  was slightly larger compared to the undisturbed jet which yields an enhanced mixing. Similar to the annular grid, the distributions of  $U$  exhibit a discontinuity and  $u'$  distributions exhibit two peaks. These observations are related to the mixing zone formed at the outer edge of the disk which is inside the potential core. Both the annular grids and disk grids have potential in the context of jet turbulence control. The disk grid increases the turbulence level which yields an enhanced mixing. On the other hand, the annular grid suppresses turbulence which is also achieved by a full grid. However, the annular grid produces a smaller pressure drop at the exit compared to a full grid.

## References

- [1] Antonini, I. and Romano, G.P., Passive Control of the Turbulent Flow at the Outlet of a Circular Jet by Means of a Cylinder, *Turbulent Shear Flow Phenomena -2*, editors E. Lindborg, A. Johansson, J. Eaton, J. Humphrey, N. Kasagi, M. Leschziner, & M. Sommerfeld, 2001, Sweden.
- [2] Burattini, P., Antonia, R.A., Rajagopalan, S. and Stephens, M., Effect of Initial Conditions on the Near Field Development of a Round Jet, *Exp. Fluids*, **37**, 2004, 56-64.
- [3] Chou, Y-W., Hsiao, F-B., Hsu, C-C. and Huang, J-M., Vortex Dynamics and Energy Transport of a Plane Jet Impinging Upon a Small Cylinder, *Exp. Thermal Fluid Sci.*, **26**, 2002, 445-454.
- [4] Finlay, S., *Development of Flow Visualisation Facilities*, B.E. Thesis, University of Newcastle, 1999.
- [5] Henry, P., Olsen, J. and Rajagopalan, S., Passive Control of the Shear layer Turbulence in a Plane Jet, *Proc. 8th Asian Congress of Fluid Mechanics*, editor E. Cui, Shenzhen, China, 1999, 559-562.
- [6] Hsiao, F-B., Chou, Y.-W. and Huang, J-M., The Study of Self-Sustained Oscillating Plane Jet Flow Impinging Upon a Small Cylinder, *Exp. Fluids*, **27**, 1999, 392-399.
- [7] Oguchi, H. and Inoue, O., Mixing Layer Produced by a Screen and its Dependence on Initial Condition, *J. Fluid Mech.*, **142**, 1984, 217-231.
- [8] Parker, R., Rajagopalan, S. and Antonia, R.A., Control of an Axisymmetric Jet Using a Passive Ring, *Proc. Fourteenth Australasian Fluid Mechanics Conference*, editor B. Dalley, 2001, Adelaide.
- [9] Stephens, M., *Axisymmetric Shear Layer Behind a Grid*, B.E. Thesis, University of Newcastle, 2002.
- [10] Stephens, M., Rajagopalan, S., Burattini, P. and Antonia, R.A., Axisymmetric Shear Flow Behind a Honeycomb, *Proc. Tenth Asian Congress of Fluid Mechanics*, editor J.J. Wijetunge, 2004, Sri Lanka, Paper No. D16.
- [11] Tong, C. and Warhaft, Z., Turbulence Suppression in a Jet by Means of a Fine Ring, *Phys. Fluids*, **6**, 1994, 328-333.
- [12] Zhou, Y. and Antonia, R.A., Memory Effects in a Plane Turbulent Wake, *Exp. Fluids*, **19**, 1995, 112-120.

## Flows Within a Cylindrical Cell Culture Bioreactor with a Free-Surface and a Rotating Base

J. Dusting, J. Sheridan and K. Hourigan

Fluids Laboratory for Aeronautical and Industrial Research (FLAIR), Department of Mechanical Engineering  
Monash University, Victoria, 3800 AUSTRALIA

### Abstract

Experimental studies have been conducted in order to identify and investigate flows that are potentially more suited to culturing cells than those commonly found in bioreactors. The tested model has a cylindrical working section with a free surface and a rotating base. Flow visualisation confirms the presence of vortex breakdown bubbles at  $Re \geq 780$  for an aspect ratio of 1.5. The central bioreactor region has been characterised using Particle Image Velocimetry and Stereoscopic Particle Image Velocimetry. Shear stress, an important parameter for cell culture applications, has been plotted at various Reynolds numbers, showing a pattern related to the geometry of the vortex breakdown bubble.

### Introduction

Strong recent advancements in tissue engineering and cell-based therapeutic research have driven a push to find alternative methods of culturing cells, with the aim to increase the efficiency and productivity of the process. Lately, the development of various perfused vessel and rotational bioreactors has received interest, with some promising results [1, 4]. Progress is still to be made, however, in controlling the fluid dynamic conditions within mixed flask bioreactors. Depending on the cell phenotype, hydrodynamic forces may provide an important stimulatory effect on cell aggregation processes, however excessive shear will impede cell proliferation. Ideally, the bioreactor flow conditions would suit these and other factors such as mixing.

A simplified experimental model has been developed to enhance flow control. The model has a flat bottom disk capable of producing swirling flows far steadier than those produced by standard bioreactor impellers and magnetic stirrers [7]. The working section consists of a cylindrical volume of media devoid of protruding objects that might disturb the flow. A free surface rather than a closed lid is used so as to provide greater aeration while minimising the extent of high-shear boundary regions. This model is suited to the application because it has the potential to produce flows that contain appropriate shear levels, can be adequately mixed and can be characterised experimentally. Detailed studies of flows within such vessels are scarce and so flow visualisation and Particle Image Velocimetry studies were undertaken to characterise the flow and measure shear levels within it.

### Bioreactor Flow Visualisation

#### Experimental Model Configuration

A purpose-built rig has been constructed to allow flow visualisation and measurement while also producing the desired flow conditions of the bioreactor model described above. As illustrated in Figure 1, the rig consists of a polished Perspex container mounted on a rigid base with a 65mm diameter cylindrical hole drilled through its centreline to form a working section. The outer surface of the block is kept flat with square walls so that refraction effects are minimised, preventing optical dis-

tortions which may impair the image-based measurement techniques used. For similar reasons Perspex, which has a refractive index close to that of water, is used as the container material.

The swirling motion within the working section is controlled by a flat turntable rotated at constant speed using a high-resolution stepper motor. Precise mounting of the turntable and high accuracy in the rotation rate help to minimise turbulence and allow accurate control of Reynolds number. In addition, the model stand and motor bracket are screwed directly onto a precision flat steel optical table in order to reduce mechanical vibration.

Flows within cylindrical vessels driven by a rotating bottom are known to produce vortex breakdown under certain conditions. Flows are generally classified in terms of two parameters—the container height ratio ( $H/R$ ) and the Reynolds number ( $Re = \omega R^2/\nu$ ), where  $H$  is the height of the free surface above the impeller,  $R$  is the radius of the working section,  $\omega$  is the rotational velocity of the bottom disc, and  $\nu$  is the kinematic viscosity.

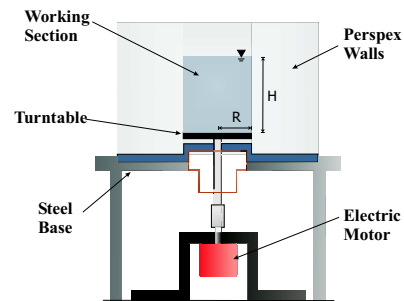


Figure 1: Test rig configuration, indicating height ratio

For the current study, experiments were conducted at  $500 \leq Re \leq 3000$  and  $H/R = 1.5$ . It is in this range that the flow is expected to be most suitable for cell culture, being not overly turbulent whilst still providing adequate mixing. For the configuration used, with a low Froude number and a Capillary number of order  $10^{-4}$ , free-surface deformations were restricted to the extent that they were not detected macroscopically and are thus unlikely to greatly affect the bioreactor flow conditions. The free surface is not stress-free, as minor contamination is known to induce a Marangoni stress. However, the implications of this do not seem to be severe, as results produced numerically with a slip boundary condition are qualitatively similar to our experimental results [8].

#### Visualisation of Vortex Breakdown Development

The flows observed within the bioreactor have a dominant azimuthal component. However it is the secondary flow pattern, which is best viewed on a vertical plane through the rig centreline, that provides much of the mixing effect. While there is high shear along the bottom and side boundary layers acting in three dimensions, the component of shear stress aligned along



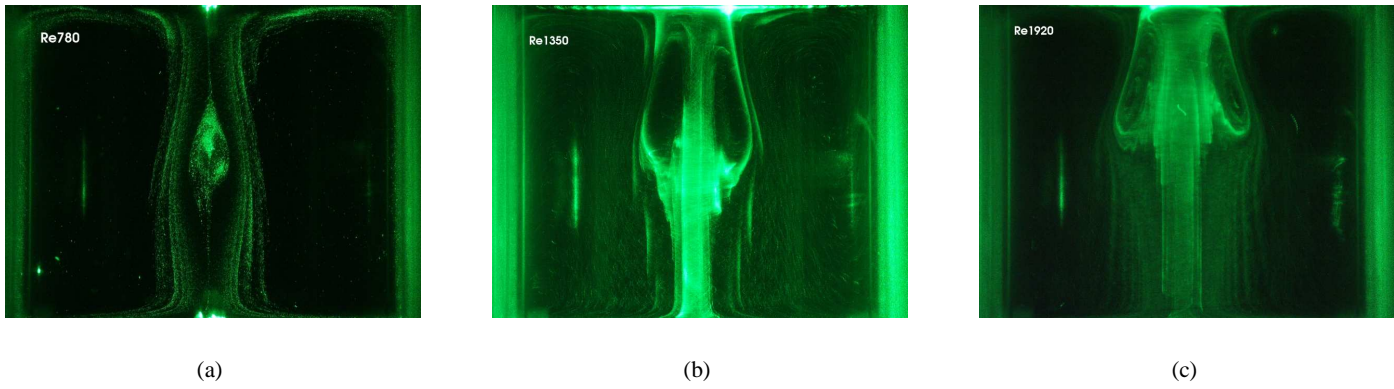


Figure 2: Laser particle visualisation of VB bubble development for (a)  $Re = 780$ , (b)  $Re = 1350$ , and (c)  $Re = 1920$

the  $x - z$  plane is a good indicator of the stresses caused by the occurrence of vortex breakdown (VB).

Flow visualisation experiments were conducted using tracer particles illuminated by a high-powered laser. The particles produce distinctive streaklines as long-exposure images are captured; this can be seen in the results presented in Figure 2. The visualisation images produced were found to correspond well with Spohn et al.'s [5] observations of vortex breakdown (VB) in a cylindrical vessel with a free surface, although in the present investigation a greater number of  $Re$  cases were studied for a reduced  $H/R$  range.

The lowest Reynolds number at which VB was observed at this  $H/R$  was approximately 780. VB can be identified on the secondary flow plane by a separate region of recirculating flow moving in an opposing direction to the larger recirculation region. There is a stagnation point upstream of this VB bubble for cases where it is fully submerged. At higher  $Re$ , the bubble may be attached to the free surface, as can be seen in Figure 2, in which case the stagnation point is replaced by a stagnation ring. Once attached to the free surface, a noticeable widening of the bubble occurs as  $Re$  increases. At  $Re \geq 2000$ , an increasing flow unsteadiness was observed. Below this  $Re$ , the flow retains its near-axisymmetric geometry. However, as the flow takes on a more oscillatory nature, asymmetries appear to be exacerbated. These asymmetries may arise from the development of a rotating wave instability [2] or the imperfections which are inherent in any experimental rig [9].

## Flow Characterisation

### Flow Measurement Technique

The flow was characterised using Particle Image Velocimetry (PIV) and Stereoscopic Particle Image Velocimetry (SPIV). PIV is a well-documented technique involving the measurement of a two-dimensional velocity field by correlating the relative positions of laser-illuminated, neutrally-buoyant particles, across two images separated by a known time interval. SPIV utilises two cameras placed at a known angle to resolve all three velocity components.

For the current SPIV study, the two cameras were placed an angle of  $45^\circ$  from the centreline in an angular displacement configuration similar to that described by Prasad [3]. In this configuration, the  $x$ -axis of the image is stretched in relation to the  $y$ -axis, so the effective field of view is reduced by a factor of  $\sqrt{2}$  in the cylinder's axial direction.

While the velocity fields measured using each technique were similar, the SPIV results are more reliable for several reasons. Firstly, for a single-camera view, the azimuthal velocity component appears as an erroneous radial velocity component. This is particularly a problem towards the central axis of the cylinder, where in-plane velocities are low, and the laser light-sheet is relatively thick compared with the path distance of a particle swirling about the central axis. Secondly, the out-of-plane velocity component adds error to in-plane velocity measurements, particularly towards the outer edges of the image. As the flow is predominantly azimuthal in this case, the ratio of the out-of-plane flow velocity to in-plane velocity is severe. This effect was eliminated to some extent in PIV experiments by using a telecentric lens.

Aside from reasons of accuracy, SPIV measurements provided a superior flow characterisation because information pertaining to the azimuthal-component of velocity is of interest to this application. Therefore the results discussed in this section are those measured using SPIV.

### Secondary Flow Pattern

Spohn et al. [6] previously measured the secondary flow pattern within a cylindrical vessel with a free surface driven by a rotating disk. Their results failed to resolve all the details of the flow observed by flow visualisation. The current study, undertaken using a more precise SPIV technique, produced a velocity field which contains substantially more detail, albeit with a reduced field of view.

The flow field was measured for  $H/R = 1.5$  and  $500 \leq Re \leq 3000$  between horizontal positions of  $0.25 \leq x/D \leq 0.75$  and axial positions of  $0.56 \leq z/H \leq 0.94$ . Figures 3 and 4 contain the flow field at a Reynolds number of 1200 averaged, for the sake of clarity, over 2 seconds (equivalent to approximately one third of a disk rotation). In Figure 3 streamlines illustrate the flow topology near the centre of the bioreactor. Towards the centre of the vessel ( $x/D = 0.5$ ), the clockwise rotating recirculation region observed during flow visualisation is apparent. This distinguishing feature of the flow has seldom been captured by flow measurement. Streamlines on the right-hand side of the plot trace a portion of the counter-clockwise rotating flow region.

In Figure 4, in-plane velocity component vectors are superposed onto contours of the azimuthal velocity component. Upon detailed examination of these results and the instantaneous vector fields, it is noticeable that the VB region contains several vec-

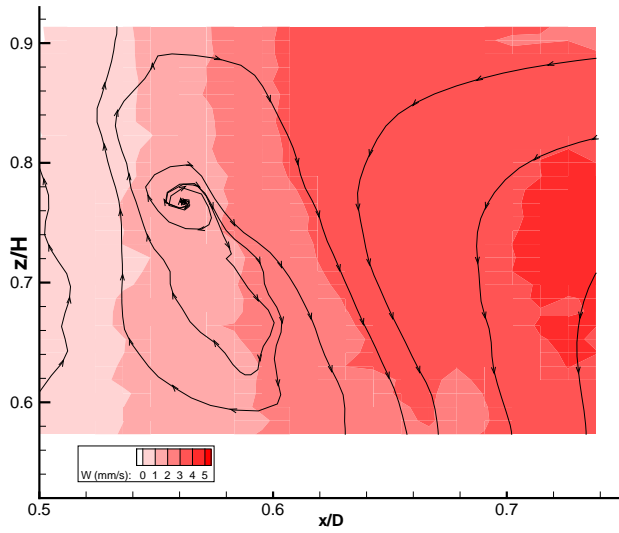


Figure 3: Flow topology in the central region of the bioreactor for  $Re = 1200$ . Red contours indicate the magnitude of the azimuthal velocity component. Measured streamlines indicate the flow in the diametral plane.

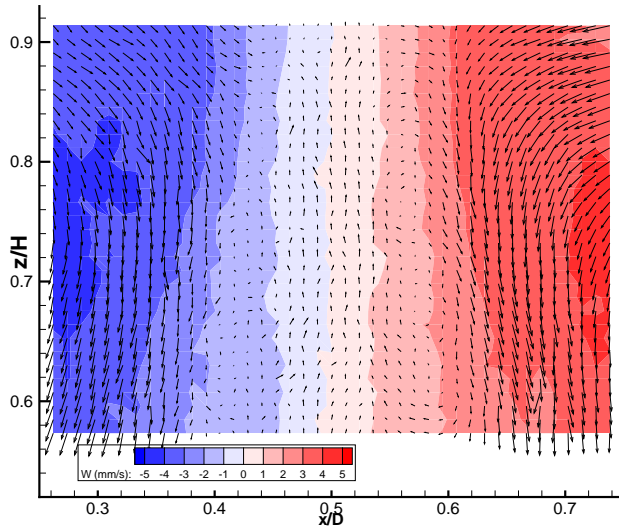


Figure 4: Measured velocity vector field in the central region of the bioreactor for  $Re = 1200$ . Coloured contours indicate the magnitude and direction of the azimuthal velocity component.

tors pointing away from the typical flow. While it is difficult to be certain of the reason for this, experimental noise resulting from the small displacement measurements is a possible explanation. In some cases the PIV measurements were  $\ll 1$  pixel, although this could not be avoided due to difficulties in measuring flows of this nature.

In general, the velocity field shows a high degree of axisymmetry, particularly in the axial component of velocity. It is also apparent that cells within the VB region of a bioreactor will be exposed to far lower velocities than those in the standard recirculation region. The issue of whether particles can be contained within this region for long periods of time is a significant one, especially at high  $Re$  where instabilities and the increased opening of the downstream end of the bubble may cause cells

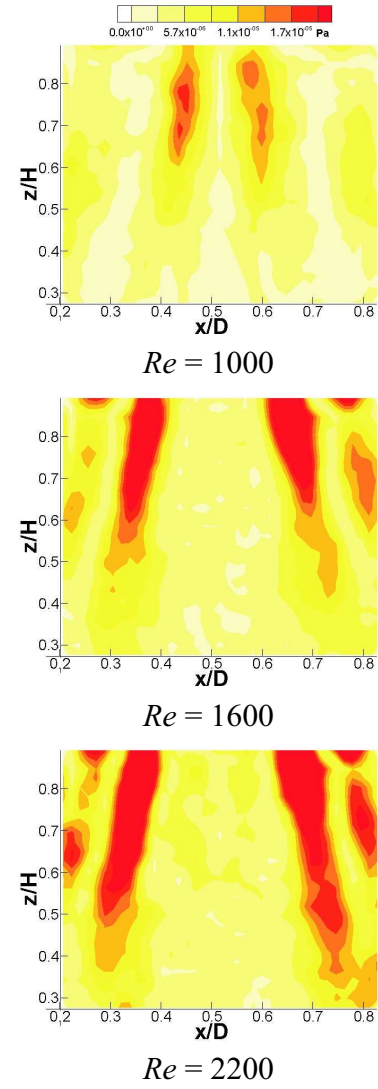


Figure 5: Time-averaged two-dimensional shear stress contours in the central region of the bioreactor for  $Re = 1000, 1600, 2200$ .

to escape into the high-velocity region.

#### Azimuthal Velocity Component

The azimuthal velocity contours plotted in Figure 4 confirm that the primary flow is axisymmetric about the central axis of the cylinder, and that the magnitude of the azimuthal velocity component is much greater than the axial and radial velocity components.

There is some limited dependency of azimuthal velocity on axial position, particular at the outer radial positions. This possibly arises from the shift in the direction of flow momentum near the free surface, or the influence of the bubble region.

#### Shear-Stress Fields

Shear stress is the flow characteristic of primary interest to researchers studying cell cultures. For this reason, the velocity fields measured experimentally have been used to compute shear stress contour maps for the region of the bioreactor that was investigated. If the assumption is made that time-averaged shear within the azimuthal plane is negligible, then SPIV data provides all the flow gradients required to estimate the full stress tensor, and therefore the principal stresses, at each vector loca-

tion. At the time of publication, the means of presenting these values is being developed.

The shear stress fields shown in Figure 5 are contours of time-averaged shear-stress in the vertical diametral plane ( $\tau_{xz} = \mu[\frac{\partial v_x}{\partial z} + \frac{\partial v_z}{\partial x}]$ , where  $\mu$  is dynamic viscosity), measured using PIV. These results are useful in that they reflect the trends observed for the principle stresses in the central region of the bioreactor. While these measurements are not as accurate as the SPIV measurements towards the center of the vessel, they encompass a significantly larger field of view ( $0.28 \leq z/H \leq 0.89$ ). The results presented have also been validated by two dimensional numerical flow simulations that produced  $\tau_{xz}$  contours of similar magnitude and geometric pattern [8].

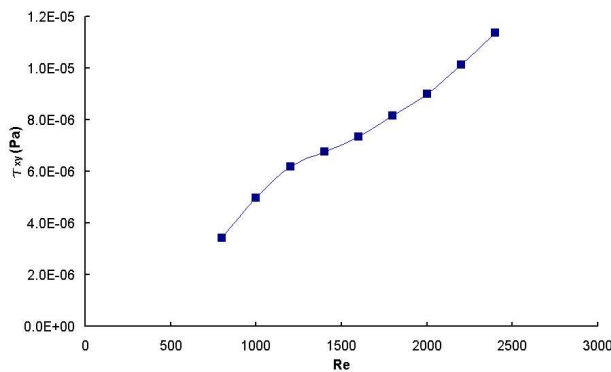


Figure 6: Mean shear levels at various  $Re$

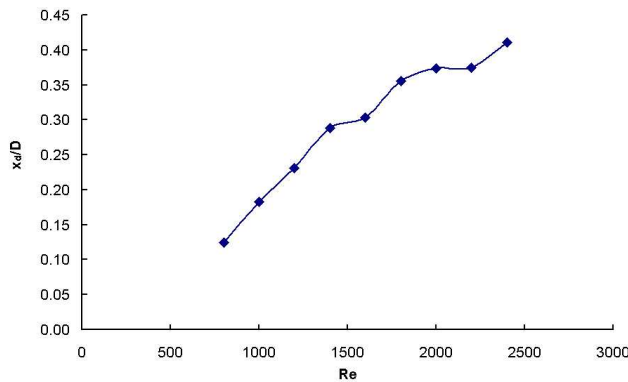


Figure 7: Horizontal distance between local shear level maxima at various  $Re$

The VB bubble causes a heterogeneous stress distribution in the central region of the bioreactor. High stress bands mark the boundary of the breakdown bubble, where the high and low velocity regions border one another. In each case studied, time-averaged stress magnitudes were less in the breakdown region than in the standard recirculating flow region, although temporal fluctuations were higher in this region.

As can be expected, the mean stress levels are highly dependent on  $Re$ . Figure 6, in which the spatial mean  $\tau_{xz}$  is plotted against  $Re$  provides another illustration of this. Reynolds number also controls the width of the breakdown region, and so it follows that the internal low stress region increases in volume as  $Re$  increases. At an axial position of  $z/H = 0.6$ , the horizontal distance  $x_d$  between peak shear levels increases with  $Re$ , although this increase tapers off at higher  $Re$  values, where the

breakdown region tends towards its maximum width. This trend is presented in Figure 7, with  $x_d$  normalised against cylinder diameter.

All recorded levels of  $\tau_{xz}$  are orders of magnitude below those typically observed for cell disruption, although use of a cell culture medium with a higher viscosity than water would directly increase these magnitudes. They also represent stresses in a conveniently located plane, and are thus only indicative of the principal stress trends measured using SPIV, rather than a quantitative measure of the maximum stresses experienced by cells. Indeed, cell geometry and orientation would also be expected to influence shear stress.

## Conclusions

Laser-particle visualisation, PIV, and SPIV techniques have been employed to study how low shear swirling flows within a cylindrical bioreactor may be controlled to provide conditions suitable for cell culture applications. The flow in the vicinity of VB bubbles contained within the flow field has been found to affect conditions relevant to suspension cell culture, including mixing patterns and local shear stress. In particular, shear stress magnitudes increase rapidly as Reynolds number increase, and alter their spatial distribution as the VB region changes shape.

## Acknowledgements

Funding for this research was provided by Monash University through the Monash University Research Fund and an Australian Research Council Discovery Grant (DP0452664).

## References

- [1] Freed, L. and Vunjak-Novakovic, G., Tissue engineering bioreactors, in *Principles of Tissue Engineering*, editors R. Lanza, R. Langer and J. Vacanti, Academic Press, San Diego, USA, 2000, 143–156.
- [2] Hirs, A., Lopez, J. and Miraghaie, R., Symmetry breaking to a rotating wave in a lid-driven cylinder with a free surface: experimental observation, *Physics of Fluids*, **14**, 2002, L29–L32.
- [3] Prasad, A., Stereoscopic particle image velocimetry, *Experiments in Fluids*, **29**, 2000, 103–116.
- [4] Sen, A., Kallos, M. S. and Behie, L. A., Effects of hydrodynamics on cultures of mammalian neural stem cell aggregates in suspension bioreactors, *Ind. Eng. Chem. Res.*, **40**, 2001, 5350–5357.
- [5] Spohn, A., Mory, M. and Hopfinger, E. J., Observations of vortex breakdown in an open cylindrical container with a rotating bottom, *Experiments in Fluids*, **14**, 1993, 70–77.
- [6] Spohn, A., Mory, M. and Hopfinger, E. J., Experiments on vortex breakdown in a confined flow generated by a rotating disk, *Journal of Fluid Mechanics*, **370**, 1998, 73–99.
- [7] Sucosky, P., Osorio, D. F., Brown, J. B. and Neitzel, G. P., Fluid mechanics of a spinner-flask bioreactor, *Biotechnology and Bioengineering*, **85**, 2004, 34–46.
- [8] Tan, B. T., Personal correspondence.
- [9] Thompson, M. C. and Hourigan, K., The sensitivity of steady vortex breakdown bubbles in confined cylinder flows to rotating lid misalignment, *Journal of Fluid Mechanics*, **496**, 2003, 129–138.

## Effect of Initial Conditions on the Far Field of a Round Jet

P. Burattini, R. A. Antonia and S. Rajagopalan

Discipline of Mechanical Engineering  
University of Newcastle, NSW, 2308 AUSTRALIA

### Abstract

The effect of initial conditions on the far field of a turbulent round jet ( $R_\lambda \simeq 450$ ) has been examined using hot-wire measurements. Two types of initial conditions have been examined: the unperturbed jet, issuing from a nozzle in a laminar state, and the perturbed jet, where a woven grid is placed at the jet outlet in order to interfere with the initial development of the jet. Turbulent integral quantities and small scale characteristics show that the flow is partly reminiscent of the initial stages of the jet development, as modified by the grid. While the first- and second-order velocity statistics are affected only in terms of the virtual origin, length scales (such as the Kolmogorov and the Taylor scale) show also a different decay rate, under modified initial conditions. The similarity of the second-order structure functions is unaltered by the grid.

### Introduction and Background

The concept of similarity has played a central role in fluid dynamics research. Blasius applied this approach to the study of the laminar boundary layer over a flat plate, showing that there is compatibility between the equations of motion and a universal velocity profile. From this, the actual profile at any streamwise station can be derived. The Blasius approach for *laminar flow* paved the way for its extension to the similarity analysis of *turbulent flows* (e.g., plane and axisymmetric jets and wakes, [16, 20, 21, 22, 24]).

Similarity of multi-scale statistics (as opposed to one-point statistics), such as spectra or structure functions of turbulent quantities, has been the subject of more recent attention. An attempt to investigate the similarity of multi-point statistics of homogeneous isotropic turbulence, starting from the spectral dynamical equation, has been made by George [10]. He showed that self-similarity of the velocity spectra, normalized by the Taylor scale and mean kinetic energy, is compatible with this equation. More recently, a similar conclusion was obtained for velocity structure functions by Antonia et al. [2].

However, the validity of universal similarity in turbulent flows has been criticised from time to time. George [9, 10] noted that there is no *a priori* reason why the influence of initial conditions should be ruled out from the outset. If true, this argument would preclude *universal* (namely, unchanged from one realization of the same flow to another) similarity solutions. Even though George's suggestion remains qualitative in nature, since there is no formal way of taking explicitly into account the initial conditions, it seems plausible, considering the large scatter in experimental data in nominally identical flows.

Besides the role of initial conditions, but perhaps not separately from these, is the effect coherent structures may have on the achievement of similarity. The evolution of the large scales could preclude a state of similarity for the complete spectrum, because the energy may be concentrated in a few modes with strong interactions between them. The available evidence seems convincing. For instance, it has been noticed that in far field of a 2D wake behind a bluff body the flow properties depend on the coherent structures and how they were created in rela-

tion to the geometrical details of the wake generator (solidity, shape) [25, 3]. Arguably, the role of coherent structures can be assessed in a more specific manner compared to that of the initial conditions. Direct measurements, say of coherent vorticity or spatial correlation, can show the influence of the large scale structures.

In the round jet, evidence of the relationship between initial conditions, coherent structures, and similarity is not yet complete. If we discard comparisons between different experimental set-ups (since the results may be biased by different arrangements and experimental techniques) there is not much left in the literature from which a sound conclusion can be drawn on this issue. Although many studies have been indeed devoted to the modification of initial conditions and their effect on velocity and scalar in the developing region of the flow ([11, 17, 23, 28]), the extension of the analysis to the far field has not previously been considered. When the developed region is explored, the initial conditions are, usually, only briefly discussed. For instance in two of the most recent investigations on the far field of a round jet [12, 19] the initial conditions are not described in great detail.

In previous works [5, 8] we examined the effect of different initial conditions on the developing region of a round jet (within 12 diameters from the exit). The disturbances created by a grid at the exit inhibited the shear layer mode and delayed the preferred mode. The extension of the potential core was increased by nearly 50% in the disturbed case. The effects of disc and annular-shaped grids have been also investigated in connection to the near field of a round jet, [14]. Here we want to document the possible influences of the initial conditions on the far field of a jet. This problem has been discussed in two recent papers [26, 27], where two jets (one issuing from a contraction nozzle and the other from a pipe) were compared. The authors concluded that there was no appreciable effect on the turbulent energy distribution, due to the different initial conditions, at 20 diameters downstream from the exit.

A check of the effect of the initial and boundary conditions is apparently more within the reach of direct numerical simulation. The work of Boersma et al. [4] (see also [15]) has tried to address this issue by investigating the effect of two different initial conditions: a top-hat exit velocity profile and another with the streamwise velocity overshooting in proximity of the boundary layer. The authors claimed that: "evidence is presented in support of the suggestion by George [9] that the details of self-similarity depend on the initial conditions". However, these authors ran simulations only up to 45 diameters, where the flow is only starting to be similar [22]. In a recent work [7] the similarity properties of the velocity spectra and structure functions have been studied experimentally in a turbulent round jet. It was shown that the collapse of these quantities was best when the Taylor microscale and the mean turbulent kinetic energy were adopted as similarity scales.

### Experimental Details

The jet was generated using an open circuit wind tunnel, located



in a relatively large laboratory. The tunnel contains a variable speed centrifugal blower, a diffuser, a settling chamber, and a contraction with an area ratio of 85:1. Screens and a honeycomb are fitted inside the settling chamber to reduce the turbulence level and to straighten the flow. The outlet circular nozzle has a diameter  $D = 55$  mm. The velocity probe could be traversed along the streamwise ( $x$ ), lateral ( $y$ ), and vertical ( $z$ ) directions with a resolution of 0.1 mm, 0.1 mm and 0.01 mm respectively. Two velocity components were measured:  $u$ , in the streamwise direction, and  $v$  in the lateral (or radial) direction. The corresponding uppercase quantities refer to the time-averaged values and a prime denotes the rms value.

Two types of exit conditions are investigated: the unperturbed jet (or case *A*), as it exits from a smooth contraction, and the perturbed jet (case *B*). The modification of the initial conditions was achieved by placing a grid at the jet outlet. Details of the grid, composed of rigid woven round steel wires, are given in table 1. The reference exit velocity,  $U_j$ , was fixed at  $\approx 35$  ms<sup>-1</sup> and 32.5 ms<sup>-1</sup> for case *A* and *B*, respectively. This yielded an exit Reynolds number,  $Re_D = DU_j/\nu$  ( $\nu$  is the kinematic viscosity of the air), of  $1.3 \times 10^5$  and  $1.2 \times 10^5$ , for the two cases. Further details on the initial conditions of the perturbed and unperturbed cases can be found in [5]. Measurements were carried out in the far field of the jets for  $30 \leq x/D \leq 90$  (see also [7] for a detailed description of the flow field characteristics).

The velocity was acquired by means of in-house hot wires and DISA anemometers (55M01 model). X-wire probes, with an angle between the wires of nearly 90° and a lateral separation between the wires of approximately 0.8 mm, were operated at an overheat of 1.5. The hot wires were etched from Pt-10% Rh to a diameter of  $d_w = 2.5 \mu\text{m}$  and the active length  $l_w$  was chosen so as to have an aspect ratio  $l_w/d_w$  of nearly 200.

Velocity and angle calibrations were carried out *in situ* at the jet exit plane. The X-wire was calibrated at several values of speed and angle in the ranges of 40° (in steps of 10°) and 0.9 – 17.2 ms<sup>-1</sup>, respectively. This set of values was used as a look-up-table (LUT), during the data reduction step, to estimate the velocity through spline interpolations. The LUT method was verified to give, for mean longitudinal velocities below 6 ms<sup>-1</sup>, more reliable results than the common effective angle method [6], which assumes a constant coefficient of sensitivity for the lateral velocity. Single wire data were used as a check of the X-wire response, and differences in the mean values of the streamwise velocity were always below 2%. The anemometer signals were acquired by means of a 16-bit AD board. Uncertainties in the mean and rms fluctuation velocities were about 0.8% and 4%, respectively, as calculated by repeating the measurements 30 times at 60D and applying standard error estimations (1:20 odds) [18].

### Velocity and Length Scales

The decay of the mean longitudinal velocity,  $U_0$ , along the axis is shown in figure 1. Data were least squares fitted according to the model equation  $\alpha = C_\alpha^{-1}(x - x_{0_\alpha})/D$ , where  $\alpha$  refers to a generic quantity (a length or a velocity scale),  $C_\alpha$  represents the decay rate (or growth rate, for the length scales) coefficient and  $x_{0_\alpha}$  is the virtual origin. From this figure, it is clear that the decay rate (measured by the slope of the least squares fit to the data) is unchanged between the two jets (see also table 2). There is, however, a downstream shift in the decay origin for case *B*. This can be appreciated better from the inset in figure 1, which focuses on the initial region of the jet, from [5]. In this reference it was shown that the grid delayed by nearly two diameters the start of the decay in the axial direction. The axial decay of  $u'$  (figure 2) is inversely linear, as expected, with an

almost identical decay rate for both cases, but different virtual origins. Again, the inset in the figure shows that the initial stage of the jet is responsible for the shift.

It is worth comparing the mean turbulent energy decay of the jets with that of grid turbulence. In the latter case,  $u'^2$  decays following a power law with decay rates varying according to the initial conditions, a typical range being  $-1.1 < m < -1.3$  [20] ( $m$  is the coefficient of the power law). Parameters such as grid solidity, geometry (planar, biplanar, woven) and shape of the grid elements have a discernible influence on the decay rate of the mean energy in the equilibrium region ( $x/M \geq 40$ ,  $M$  is the mesh size) [13]. At variance with grid turbulence, the decay rate of  $u'^2$  for the jet is unaltered by the initial conditions, the effect being restricted to a shift in the origin.

The ratio of the turbulence intensities in the streamwise and radial directions,  $u'/v'$ , is provided in figure 3. The two jets attain almost exactly the same constant value ( $\approx 1.25$ ) along the axis, showing that, in the range investigated, an equilibrium between the two components is reached in both cases. The ratio of the integral scales (which are defined by the first zero-crossing of the autocorrelation function of the velocity fluctuation),  $L_u/L_v$ , is about 1.75 (same figure), but it shows a comparatively larger scatter. This can be partly related to the definition of the integral scale, which is somewhat ill-conditioned. Note that the isotropic value of this ratio is 2, thus significantly higher than in the present cases. The ratio  $u'/v' (\approx 1.2)$ , although typical for a round jet [12], is also far from the isotropic value ( $=1$ ). In figure 3, we also report the turbulence intensity,  $u'/U_0$ : its value is around 25%, as expected for an unconfined jet [12, 19].

The rate of growth of the Kolmogorov length scale ( $\eta \equiv (\nu^3/\langle \epsilon \rangle)^{1/4}$ , where  $\langle \epsilon \rangle$  is the mean energy dissipation rate and angular brackets denote time averaging) and the Taylor microscale ( $\lambda \equiv u' / (\partial u / \partial x)$ ) is given in figure 4. Compared to the velocity scales, the behaviour of  $\eta$  and  $\lambda$  is more sensitive to the initial conditions. Case *B* has a faster decay rate for these two quantities, while the virtual origin is located further downstream (table 3), compared to case *A*. This is in the same direction as the shift for  $U_j/U_0$  and  $U_j/u'$ . The circular jet is one of the (few) flows for which the turbulent Reynolds number,  $R_\lambda = \lambda u' / \nu$ , is considered to be constant along the streamwise direction [22]. However, it is clear that this is true only if the virtual origins of  $\lambda$  and  $u'$  are the same, zero being a special case. From the present results, it seems that this is not generally valid. However, it can be noted that, as  $x/D$  becomes larger, the product of  $\lambda$  and  $u'$  becomes less sensitive to the value of the virtual origins. Thus  $R_\lambda$  approaches a constant value.

Case	$U_j$ (ms <sup>-1</sup> )	$M$ (mm)	$t$ (mm)	$D/M$	$\sigma$
A (unperturbed)	35.0	—	—	—	—
B (perturbed)	32.5	3.2	0.7	$\approx 16$	0.44

Table 1: Jet configurations investigated.  $M$ : mesh size;  $t$ : mesh wire diameter;  $\sigma$ : solidity.

Case	$C_{U_j/U_0}$	$x_{0_{U_j/U_0}}/D$	$C_{U_j/u'}$	$x_{0_{U_j/u'}}/D$
A	5.98	4.32	1.51	-1.43
B	6.06	5.68	1.50	1.01

Table 2: Decay rate characteristics of the velocity scales.

### Similarity of the Structure Functions

The second-order structure functions of the turbulent kinetic energy,  $\langle (\delta q)^2 \rangle = \langle (\delta u)^2 \rangle + 2\langle (\delta v)^2 \rangle$ , where  $\delta \bullet \equiv \bullet(x+r) -$

Case	$C_\eta$ ( $\text{m}^{-1}$ )	$x_{0_\eta}/D$ —	$C_\lambda$ ( $\text{m}^{-1}$ )	$x_{0_\lambda}/D$ —
A	$3.38 \times 10^5$	-1.79	$8.08 \times 10^3$	-3.03
B	$3.08 \times 10^5$	1.96	$7.64 \times 10^3$	-0.08

Table 3: Decay rate characteristics of the length scales.

$\bullet(x)$  is the difference of a quantity  $\bullet (= u \text{ or } v)$  between two points separated by  $r$  along the streamwise direction are given in figure 5. Since  $R_\lambda$  is constant along the axis (with the specifications given before), in each case these functions are in similarity [7]. This is reflected in the collapse of the normalized profiles of  $\langle (\delta q)^2 \rangle$  measured at different axial locations. However, the initial conditions do not alter the collapse; this would have been apparent had the structure functions not been shifted to improve clarity. The third-order structure function  $\langle (\delta u)(\delta q)^2 \rangle$  (not shown here) indicate that the similarity is also valid at this order, even though the scatter is larger, as expected for odd-order moments. It is worth noting that the similarity condition of the structure functions involves both velocity and length scales, since they are both used to normalize the profiles. Thus, even though the length scales are more sensitive to the initial conditions, the normalized form of  $\langle (\delta q)^2 \rangle$  can absorb these variations to yield a unique self-similar profile.

### Conclusions

Similarity ideas continue to play a central role in the description of fluids dynamics. Recently, it has become evident that universal similarity solution are not possible for certain types of flows [1, 2, 9, 10]. For instance, grid turbulence, arguably the most basic type of turbulent flow that can be set up in a laboratory, shows a dependence on the initial generation of the flow [13]. In this regard, it can be speculated that the details of the large scales production behind the grid can have a lasting influence on the subsequent evolution of the flow [9] in terms of the redistribution of energy among the velocity components and the mean energy decay rate. The present results, for the far field of a perturbed and an unperturbed round jet, show that, on one hand, basic quantities, such as the decay rate of the mean velocity and mean energy, are not influenced by a modification in the initial conditions in a significant way; for these two quantities, only a shift in the virtual origin is detected. On the other hand, the decay of the Kolmogorov and Taylor length scales is modified in terms of the growth rate and virtual origin, even though the former remains linear. Profiles of the normalized second-order velocity structure functions indicate that similarity is not affected by the initial conditions. This is at odds with grid turbulence, where the initial conditions have an influence on the shape of the second-order structure functions even at large distance from the grid. It is plausible that, in the case of the jet, the coherent structures generated in the developing region evolve more rapidly towards an equilibrium state, compared to grid turbulence. This is compatible with the observed self-similarity of the multi-scale distribution of the turbulent energy measured at different axial locations.

### Acknowledgments

The support of the Australian Research Council is gratefully acknowledged.

### References

- [1] Antonia, R. A. and Burattini, P., Small-scale turbulence: How universal is it?, in *15th Australasian Fluid Mechan-*

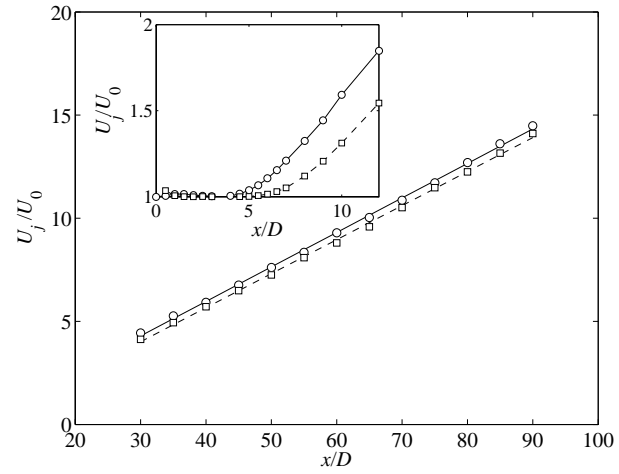


Figure 1: Mean longitudinal velocity along the axis: —○, case A; —□, case B. Inset: developing region (from [5]).

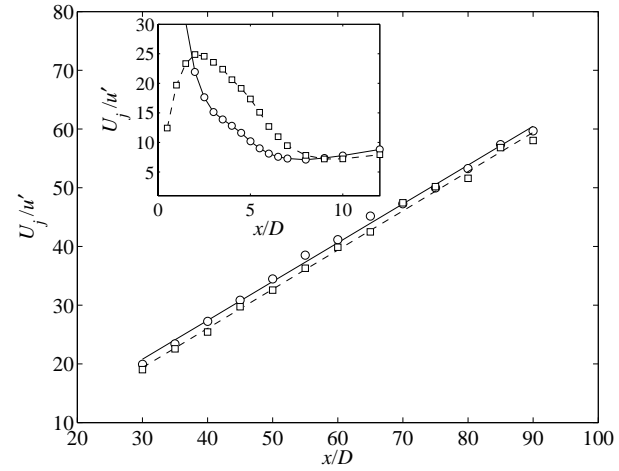


Figure 2: Rms longitudinal velocity along the axis: —○, case A; —□, case B. Inset: developing region (from [5]).

ics Conference, University of Sydney, 2004.

- [2] Antonia, R. A., Smalley, R. J., Zhou, T., Anselmet, F. and Danaïla, L., Similarity of energy structure functions in decaying homogeneous isotropic turbulence, *J. Fluid Mech.*, **487**, 2003, 245–269.
- [3] Antonia, R. A., Zhou, T. and Romano, G. P., Small-scale turbulence characteristics of two-dimensional bluff body wakes, *J. Fluid Mech.*, **459**, 2002, 67–92.
- [4] Boersma, B. J., Brethouwer, G. and Nieuwstadt, F. T. M., A numerical investigation on the effect of the inflow conditions on the self-similar region of a round jet, *Phys. Fluids*, **10**, 1998, 899–909.
- [5] Burattini, P., Antonia, R., Rajagopalan, S. and Stephens, M., Effect of initial conditions on the near-field development of a round jet, *Exp. Fluids*, **37**, 2004, 56–64.
- [6] Burattini, P. and Antonia, R. A., The effect of different X-wire calibration schemes on some turbulence statistics, *Accepted for publication in Exp. Fluids*, 2005.
- [7] Burattini, P., Antonia, R. A. and Danaïla, L., Similarity in the far field of a turbulent round jet, *Accepted for publication in Phys. Fluids*, 2005.



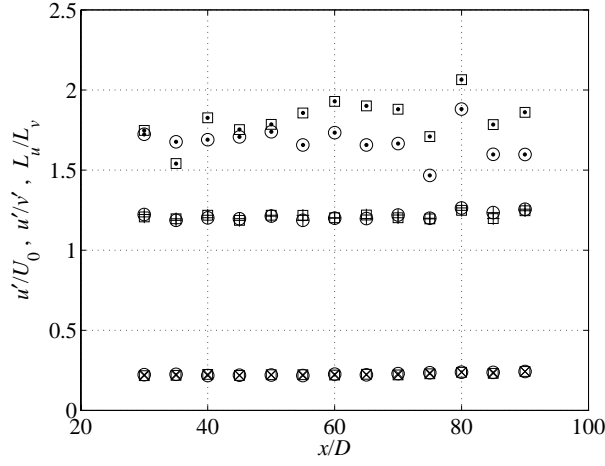


Figure 3: Axial variations of  $u'/v'$ ,  $u'/U_0$  and  $L_u/L_v$ . +,  $u'/v'$ ;  $\times$ ,  $u'/U_0$ ;  $\bullet$ ,  $L_u/L_v$ .  $\circ$ , case A;  $\square$ , case B.

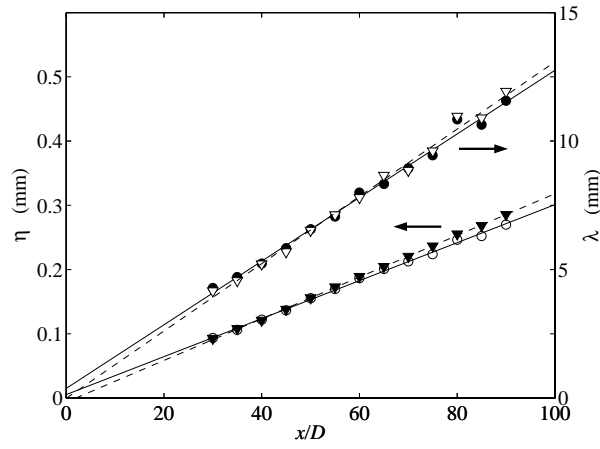


Figure 4: Axial growth of the Kolmogorov and Taylor microscales.  $\circ$ ,  $\eta$  case A;  $\nabla$ ,  $\eta$  case B;  $\bullet$ ,  $\lambda$  case A;  $\nabla$ ,  $\lambda$  case B.

- [8] Burattini, P. and Djenidi, L., Velocity and passive scalar characteristics in a round jet with grids at the nozzle exit, *Flow Turbul. Combust.*, **72**, 2004, 199–218.
- [9] George, W. K., The self-preservation of turbulent flows and its relation to initial conditions and coherent structures, in *Advances in turbulence*, editors W. K. George and R. Arndt, Springer, Berlin, 1989, 39–74.
- [10] George, W. K., The decay of homogeneous isotropic turbulence, *Phys. Fluids A*, **4**, 1992, 1492–1509.
- [11] Husain, Z. D. and Hussain, A. K. M. F., Natural instability of free shear layers, *AIAA J.*, **21**, 1983, 1512–1517.
- [12] Hussein, H. J., Capp, S. P. and George, W. K., Velocity measurements in a high-Reynolds-number, momentum-conserving, axisymmetric, turbulent jet, *J. Fluid Mech.*, **258**, 1994, 31–75.
- [13] Lavoie, P., Antonia, R. A. and Djenidi, L., Effect of grid geometry on the scale-by-scale budget of decaying turbulence, in *15th Australasian Fluid Mechanics Conference*, University of Sydney, 2004.
- [14] Lehman, R., Rajagopalan, S., Burattini, P. and Antonia, R. A., Axisymmetric jet control using passive grids, in *15th Australasian Fluid Mechanics Conference*, University of Sydney, 2004.

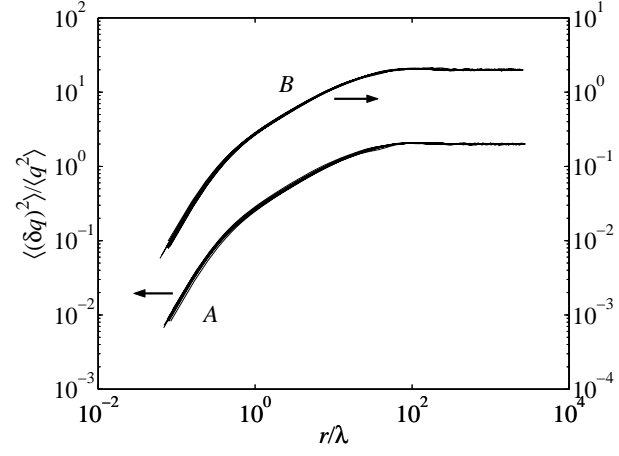


Figure 5: Second-order structure functions of the turbulent kinetic energy along the axis of the jet ( $30 \leq x/D \leq 90$ ) for cases A and B.

- [15] Lubbers, C. L., Brethouwer, G. and Boersma, B. J., Simulation of the mixing of a passive scalar in a round turbulent jet, *Fluid Dyn. Res.*, **28**, 2001, 189–208.
- [16] Mathieu, J. and Scott, J., *An Introduction to Turbulent Flow*, Cambridge University Press, Cambridge, 2000.
- [17] Mi, J., Nobes, D. S. and Nathan, G. J., Influence of jet exit conditions on the passive scalar field of an axisymmetric free jet, *J. Fluid Mech.*, **432**, 2001, 91–125.
- [18] Moffat, R. J., Describing the uncertainties in experimental results, *Exp. Therm. Fluid Sci.*, **1**, 1988, 3–17.
- [19] Panchapakesan, N. R. and Lumley, J. L., Turbulence measurements in axisymmetric jets of air and helium. Part 1. Air jet, *J. Fluid Mech.*, **246**, 1993, 197–223.
- [20] Pope, S. B., *Turbulent Flows*, Cambridge University Press, Cambridge, 2000.
- [21] Schlichting, H., *Boundary-layer Theory*, McGraw-Hill, New York, 1979.
- [22] Tennekes, H. and Lumley, J. L., *A First Course in Turbulence*, MIT Press, Cambridge, MA, 1972.
- [23] Tong, C. and Warhaft, Z., Turbulence suppression in a jet by means of a fine ring, *Phys. Fluids*, **6**, 1994, 328–333.
- [24] Townsend, A. A., *The Structure of Turbulent Shear Flow (2nd edition)*, Cambridge University Press, Cambridge, 1976.
- [25] Wygnanski, I., Champagne, F. and Marasli, B., On the large-scale structures in two-dimensional, small-deficit, turbulent wakes, *J. Fluid Mech.*, **168**, 1986, 31–71.
- [26] Xu, G. and Antonia, R. A., Effect of different initial conditions on a turbulent round free jet, *Exp. Fluids*, **33**, 2002, 677–683.
- [27] Xu, G. and Antonia, R. A., Effect of initial conditions on the temperature field of a turbulent round free jet, *Int. Comm. Heat Mass Transfer*, **29**, 2002, 1057–1068.
- [28] Zaman, K. B. M. Q. and Hussain, A. K. M. F., Vortex pairing in a circular jet under controlled excitation. Part 1. General jet response, *J. Fluid Mech.*, **101**, 1980, 449–491.

## Numerical Analysis of a Hydrocyclone in a Recirculating Aquaculture System

Eunpil Kim, Gul Chang, and Jung In Yoon

School of Mechanical Engineering, Pukyong National University  
Busan, South Korea

### Abstract

This study investigated the performance of a vortex hydrocyclone for solid removal in a recirculating aquaculture system. In a fish-breeding industry, effluent water is mainly disposed by gravity sedimentation. Thus, a large settling tank and a lot of water are needed to purify effluent water. However, this typical method does not show consistent efficiency. In case of low efficiency, discharged water contains a lot of feeding sediments. This causes environmental problems. Instead of this typical method a hydrocyclone is tested to discharge water which contains a lot of feeding sediments. In this paper, a hydrocyclone with low velocity and pressure drop in a recirculating aquaculture system is investigated.

### Introduction

A recirculating aquaculture system is used to purify contaminated water in a fish breeding nursery. The disposal of effluent water in an aquaculture system depends on gravity deposition. This system requires a large amount of water and a large installed area. The efficiency of this system varies with respect to different aquaculture systems. Exhausted water with low separation efficiency produces an adverse effect to the environment due to the release of wastages and fecal solid to environment. A sediment tank with a hydrocyclone can not reduce the installed area of a tank compared to the typical system, but expect a stable efficiency. This means that applying a vortex hydrocyclone in a recirculating aquaculture system is more effective than the traditional system. Also, the method of removing excrements of fish in a fish nursery industry can protect environment.

Madhumita et al. [8] studied the separating efficiency of particles in a gas cyclone with a commercial size. In case of the particles with a diameter below 0.5  $\mu\text{m}$ , they suggested a good design to develop an active swirl in a flow. Dia et al. [3] performed a numerical analysis on the sample of a hydrocyclone with a diameter of 40 mm. They presented the results of inside flow in a cyclone, because a cyclone's efficiency depends on a swirl flow. Franchon and Chlliers [5] studied a flow pattern and a separation efficiency in a gas cyclone numerically. They researched on particles of size 1-3  $\mu\text{m}$  and compared with experimental results. Dirgo and Leith [4] performed an experimental study for two cases of cyclone; the first cyclone has a fluid guide vain along a tangent line, the second case has the shape of creating a vortex by a guide. Mothes and Loffer [9] conducted an experiment with a cyclone extensively for a laboratory test. They measured velocity components in three-directions using LDV and studied particles which were being separated into gas and solid forms. Griffiths and Boysan [6] compared the methods presented by previous researchers. They presented a flow pattern and analysed a cyclone's efficiency with respect to particle movement.

The previous studies mostly investigated patterns of flow in a high velocity and pressure drop situation. On the contrary, present paper investigates the fluid flow in a low velocity and pressure drop in a large system. In addition to this, current study deals with a variation of a fluid flow and separation efficiency in

a recirculating separation devices particularly used in an aquaculture system.

### Mathematical model

Because a real geometry of a hydrocyclone is complicated, the geometry is simplified for computation (see Figure 1). The assumptions to analyze the flow characteristics of a vortex separator are in the following: The flow is three-dimensional and incompressible, viscosity and density of a fluid remain constant, and a buoyancy force is negligible.

For a numerical simulation of a hydrocyclone, the governing equations in tensor notation can be written as follows:

$$\frac{\partial u_i}{\partial x_i} = 0 \quad (1)$$

$$u_j \frac{\partial u_i}{\partial x_j} = (\nu + \nu_t) \frac{\partial}{\partial x_j} \left( \frac{\partial u_i}{\partial x_j} + \frac{\partial u_j}{\partial x_i} \right) - \frac{1}{\rho} \frac{\partial p}{\partial x_i} \quad (2)$$

$$\nu_t = C_\mu \frac{K^2}{\varepsilon} \quad (3)$$

Here,  $u_i$  is the velocity,  $p$  is the pressure, the ranges of  $i$  and  $j$  are from 1 to 3,  $\rho$  is density, and  $\nu$  is dynamic viscosity.

A RNG  $k-\varepsilon$  model is used due to strong swirl flows. The transport equations for the kinetic energy of turbulence and its dissipation rate are

$$u_i \frac{\partial K}{\partial x_i} = \frac{\partial}{\partial x_i} \left( \frac{\nu_t}{\sigma_\varepsilon} \frac{\partial K}{\partial x_i} \right) + P + G - \varepsilon \quad (4)$$

$$u_i \frac{\partial \varepsilon}{\partial x_i} = \frac{\partial}{\partial x_i} \left( \frac{\nu_t}{\sigma_\varepsilon} \frac{\partial \varepsilon}{\partial x_i} \right) + C_1 \frac{\varepsilon}{K} P - C_2 \frac{\varepsilon^2}{K} + C_3 \frac{\varepsilon}{K} G \quad (5)$$

Here,  $P$  is the production of turbulent energy, and  $G$  is the dissipation rate of turbulent energy. The definitions of parameters and model constants in the above equations are described in the paper of Kim and Kim [7].

For the collection efficiency of particles, a droplet motion equation is solved. The motion equation of the trajectory of a particle is

$$\frac{d\vec{v}_p}{dt} = -\frac{18\eta_f}{\rho_p \phi^2} C_D \frac{\text{Re}}{24} (\vec{v}_p - \vec{v}_f) + \vec{g} \quad (6)$$

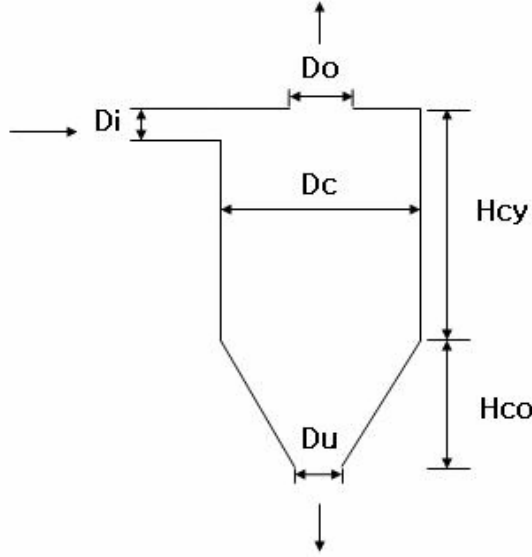


Figure 1. Schematic diagram of a hydrocyclone geometry. Dc-Cylinder diameter, Di-Inflow diameter, Do-Overflow diameter, Du-Underflow diameter, Hcy-Cylinder height, Hco-Cone height.

Here,  $\eta_f$  is the dynamic viscosity of a fluid,  $\bar{v}_p$  is the velocity of a particle,  $\bar{v}_f$  is the velocity for a fluid,  $\phi$  is the diameter of a particle,  $g$  is the acceleration due to gravity, Di is the diameter of the inlet, Do is the diameter of the upper outlet, Du is the diameter of the bottom outlet, Dc is the diameter of the cylinder, Hcy is the height above the cone section and Hco is the height of the cone section of the hydrocyclone.

The Reynolds number is defined as follows:

$$Re = \frac{\rho_f \phi |\bar{v}_p - \bar{v}_f|}{\eta_f}$$

with following Clift et al. [2]

$$C_D = \frac{24}{Re_p} (1 + 0.15 Re_p^{0.687}).$$

A finite volume method is applied to flow prediction. The detailed descriptions of a numerical method are described in the paper [7].

## Results and discussion

To test the correctness of the solution, it was compared with the experimental solution [3]. Figure 2 shows comparative results of velocity profiles. In this case the vortex finder is installed at the overflow section. At each section, the velocity distribution obtained in the study agrees well with experimental results. It can be seen that high velocities are encountered near the air-core. In the centre of the cyclone, the fluid exits to the vortex finder. Near the outer wall of the cyclone, the negative velocity distribution is established. This means that the flow at the outer wall of the cyclone go down to the downflow exit. Figure 3 displays the average velocity and pressure profiles with varying inlet velocity conditions. Though not shown in figure 3, the velocity flow at different inlet velocity profiles shows similar swirling patterns. As the inlet velocity increase, the velocity profile of internal flow of a hydrocyclone increase linearly. The flow phenomena of a cyclone show very complex flow patterns of vortex and turbulent flow. However, the fluid is well satisfied the conservation of mass, because the fluid is incompressible. Overall pressure distribution increases almost linearly as the inlet velocity increases.

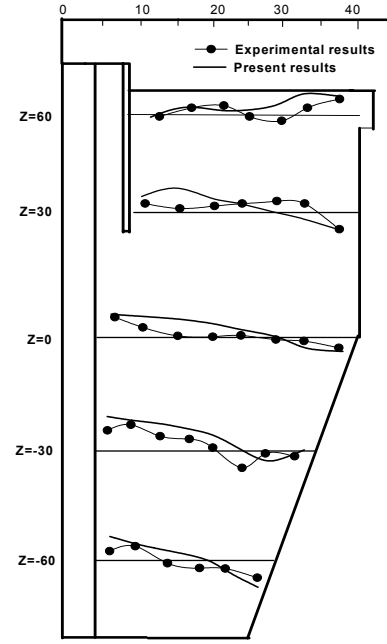


Figure 2. Comparative results of velocity profiles.

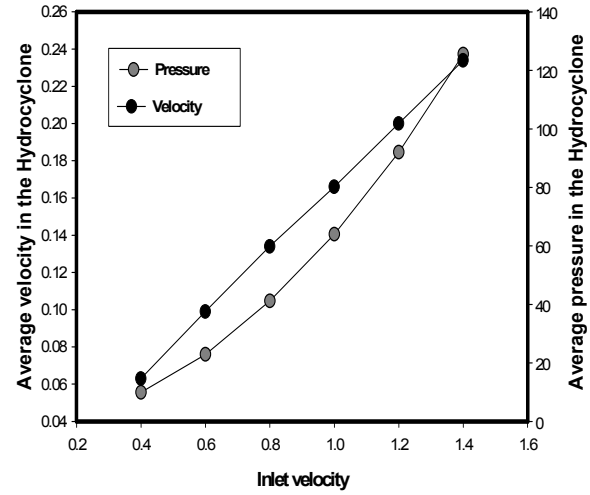


Figure 3. Average velocity and pressure profiles in a hydrocyclone.

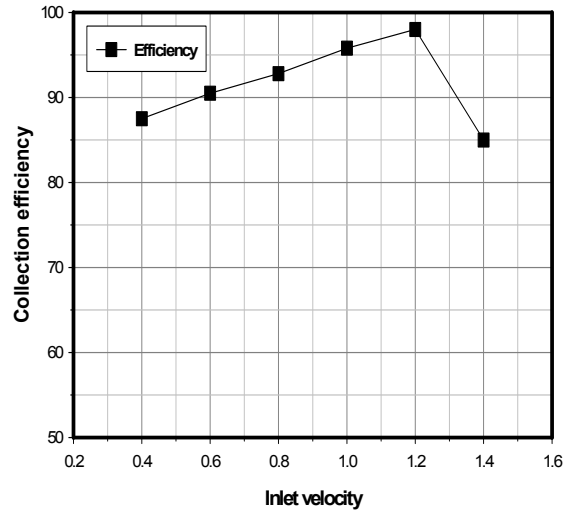


Figure 4. Collection efficiencies with varying of inlet velocities.

Figure 4 shows the collection efficiencies with varying inlet velocities. For this calculation, the droplet motion equation is used, and we assume that a particle is uncoupled with fluid properties. This means the flow governing equations are first solved. Based on those results, the motion equation is solved. The definition of particle efficiency is shown in the paper [1]. The collection efficiency initially increases as the inlet velocity increases to the inlet velocity of 1.2 m/s. After 1.2 m/s of inlet velocity, the efficiency decreases. At 0.4 m/s of small inlet velocity, it is expected the increase of the efficiency by gravitational sedimentation. However, in the study, the efficiency is low. The efficiency of a hydrocyclone is related to a geometry which effects flow mechanism within a cyclone. Figure 5 shows the mass flow rate and efficiency with varying underflow diameters at 1.2 m/s of inlet velocity which shows the best result in Fig. 4. When the underflow diameter increases the efficiency increases. However, after 50 mm, the efficiency approaches a constant value.

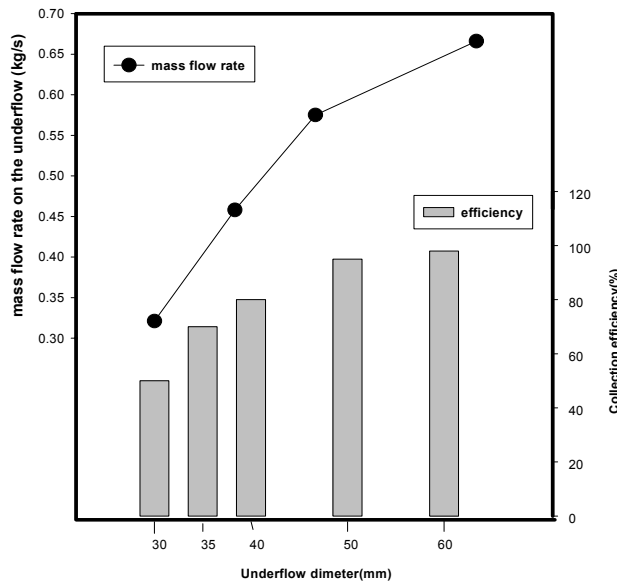


Figure 5. Mass flow rate and collection efficiency.

Figure 6 displays the collection efficiency at different particle sizes. The maximum efficiency occurs at 2.5 mm. For large particle sizes (1.6, 2.0, 2.2 mm) the effect of gravitational

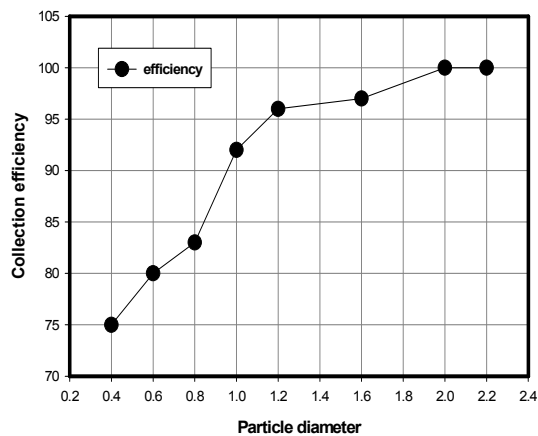


Figure 6. Collection efficiency at different particle.

sedimentation will increase. It can be seen from figure 6 that the collection increases up to the particle sizes of 2 mm diameter. .

### Conclusions

In a fish-breeding industry, effluent water is disposed by gravity sedimentation. Thus, a large settling tank and a lot of water are needed to purify effluent water. Instead of the typical method a hydrocyclone is tested to discharged water which contains a lot of feeding sediments. We investigated design parameters for good performance of a hydrocyclone. The results can be used to construct a vortex cyclone which is expected to be a system capable of protecting environment maintaining a stable efficiency.

### References

- [1] Berlemont, A., Grancher, M.S. & Gouesbet, G. Heat and Mass Transfer Coupling between Vaporizing Droplets and Turbulence using a Lagrangian Approach, *Int. J. Heat Mass Transfer*, **38**, 1995, 3023-3034.
- [2] Clift, R. Grace J.R. & Weber, M.E., *Bubbles, Drops and Particles*, Academic Press, 1987.
- [3] Dai, G., Li J.M. & Chen, W.M., Numerical Prediction of the Liquid Flow within a Hydrocyclone, *Chem. Eng. J.*, **74**, 1999, 217-223.
- [4] Dirgo, J., & Leith, D., Cyclone Collection Efficiency: Comparison of Experimental Results with Theoretical Predictions, *Aerosol Sci. Technol.*, **4**, 1985, 401-410.
- [5] Frachon, M. & Chlliers J.J., A General Model for Hydrocyclone Partition Curves, *Chem. Eng. J.*, **73**, 1999, 53-59.
- [6] Griffiths, W.D., & Boysan, F., Computational Fluid Dynamics and Empirical Modelling of the Performance of a Number of Cyclone Samplers, *J. Aerosol Sci.*, **27**, 1996, 281-304.
- [7] Kim, H. & Kim, E., Characheristics of an Entrainment into the Turbulent buoyant Jet in a Cross Flow, *KSME J.*, **23**, 1999, 342-351.
- [8] Madhumita, B.R., Improving the Removal Efficiency of Industrial-scale Cyclones for Particles Smaller than five Micrometre, *Int. J. Miner. Process.*, **53**, 1998, 39-47.
- [9] Mothes, R., & Loffer, F., Prediction of Particle Removal in Cyclone Separators, *Int. Chem. Eng.*, **28**, 231-240.

## Turbulence Models and Boundary Conditions for Bluff Body Flow

M. E. Young<sup>1</sup> and A. Ooi<sup>2</sup>

<sup>1</sup>Flight Systems Branch, Air Vehicles Division, Defence Science and Technology Organisation  
Fishermans Bend, Victoria, 3207 AUSTRALIA

<sup>2</sup>Department of Mechanical and Manufacturing Engineering  
Melbourne University, Victoria, 3000, AUSTRALIA

### Abstract

Two aspects of turbulence modelling were addressed with respect to a single cylinder in crossflow. Firstly, the effect of varying the turbulent length scale at the inlet was investigated at a high subcritical Reynolds number of  $1.4 \times 10^5$ . Variations of up to 14% were noted in the flow properties such as mean drag and Strouhal number, but significant discrepancy between experimental and computational results remained. Secondly, a modification to the standard  $k$ - $\omega$  turbulence model was assessed. This time-limit model modified the turbulent viscosity term, inhibiting production of turbulent kinetic energy in areas of high strain rates. Tuning of an empirical term was required to match flows at various Reynolds numbers. The time-limit model appeared to offer improvements at some Reynolds numbers compared to the standard  $k$ - $\omega$  model by reproducing real flow structures such as separation bubbles at a transcritical Reynolds number. Use of the time-limit model is in its infancy, especially in unsteady flows, but appears to have some potential.

### Introduction

The complex nature of the flow around a cylinder makes it an excellent case to assess the ability of computational packages to reproduce real flow conditions. At very low Reynolds numbers, the flow around a cylinder is symmetric and steady. As the Reynolds number is increased, asymmetric vortex shedding occurs. This shedding is periodic, therefore requiring an unsteady time dependent solution. The non-dimensional frequency of the vortex shedding is represented by the Strouhal number. The shedding alters the wake behind the cylinder and impacts on the flow properties: drag and lift are now periodic and the mean drag changes from the steady solution. At higher Reynolds numbers, as investigated here, the wake or boundary layer becomes turbulent — requiring a turbulence model. Two-equation models such as the  $k$ - $\omega$  and  $k$ - $\epsilon$  families offer the ability to introduce turbulence into a flow with minimal additional computational overhead.

This paper assesses the ability to computationally predict the mean flow parameters around a bluff body. The accurate prediction of flow parameters such as drag coefficient and Strouhal number hinges on accurate calculation of the separation point. This is because, in broad terms, the point of separation will generally define the width of the wake which, in turn, is a major contribution to the drag experienced by a body.

The two-equation eddy-viscosity turbulence models as used in this paper require two boundary conditions. The first is satisfied by the turbulence intensity,  $I$  (or by turbulent kinetic energy,  $k$  which is related to  $I$  by  $k = 3/2(U_{avg}I)^2$ ). Experimental studies will generally provide an estimate of the upstream turbulence intensity ( $I = Tu = \overline{u'^2}^{1/2}/u_\infty$ ) that has been measured in the experimental facility. The second boundary value can be posed in various ways such as turbulent length scale,  $l$ ; dissipation terms,  $\omega$  or  $\epsilon$ ; or viscosity ratio,  $r_\mu = \mu_t/\mu$ . However, these

values are often not available, and must therefore be estimated. Tutar and Holdø [9] assume a single value for turbulent length scale based on various suppositions. Other papers by Bosch and Rodi [1], and Lakehal and Thiele [6] look at variations in  $l$  to a limited degree. These studies found that the variation in turbulence conditions at the inlet had a marked effect on the flow. The current study aims to compare the estimated flow properties and flow field about a single cylinder using the  $k$ - $\omega$  Shear Stress Transport ( $k$ - $\omega$  SST) turbulence model for a range of turbulent inlet conditions.

The study of bluff body flow was continued by introducing the time-limit turbulence model modification as proposed by Durbin [3]. The new model purportedly addresses one of the shortcomings of two-equation turbulence models, that of overproduction of turbulent kinetic energy. Application of the time-limit model to unsteady flows has been limited and therefore the results presented are largely of an exploratory nature.

### Numerical Model

The unsteady Reynolds-averaged Navier Stokes equations were solved using the commercial CFD code Fluent (version 6.1.22, [5]). Variations of the  $k$ - $\omega$  two-equation eddy-viscosity turbulence models were used, with Menter's [8]  $k$ - $\omega$  SST model being used for part one of this study. This model offers improved performance with respect to adverse pressure gradients. It was chosen to fully resolve the boundary layer thereby requiring the quadrilateral mesh be created such that  $y^+ = yu_\tau/\nu$  was less than one. This required the distance from the wall to the first grid point,  $y$ , to be between  $0.01\%D$  (for Reynolds numbers  $10^3$  and  $1.4 \times 10^5$ ) and  $0.0005\%D$  ( $Re = 3 \times 10^6$ ). The stretching ratio for the mesh was approximately 1.08 in most instances and less than 1.1 in all cases. The meshed domain is presented in figure 1. The upstream boundary was defined as a velocity inlet, allowing inflow velocity and the two turbulence boundary conditions to be defined. The downstream boundary was modelled as a simple outflow. The lateral boundaries were defined such that there was zero normal velocity and zero normal gradients.

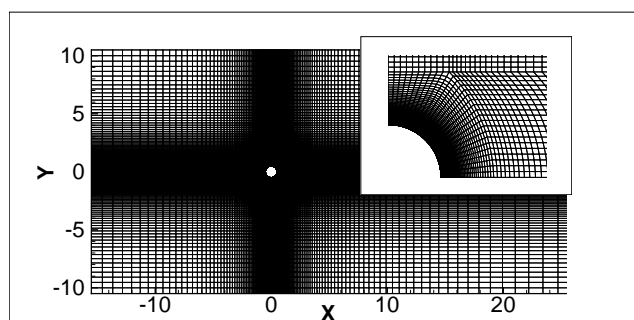


Figure 1: Computational domain arrangement, with detail of the mesh close to the cylinder. Inlet is at  $x = -15.5D$ ; outlet is at  $x = 25.5D$ ; and lateral boundaries are at  $y = \pm 10.5D$ .

Cantwell and Coles [2] note that the freestream turbulence intensity in their tunnel was less than or equal to 0.6%. Therefore, turbulence intensity,  $I$ , was set to 0.6% at the inlet. There is no data on the appropriate length scale in [2] and this must therefore be estimated on the basis of other arguments. As outlined in the introduction, [1] and [6] have noted that selection of different length scale boundary conditions does impact the subsequent flow downstream, and hence this formed the focus of the first part of this study.

Solutions were instigated by developing the flow in the steady solver before introducing an asymmetric perturbation into the flow. The unsteady solver was used subsequent to the introduction of the disturbance, ensuring the timestep was of the order of one hundredth of the expected period (known from experimental measurement of Strouhal number:  $\Delta t = 0.01D/(StU)$ ). The transients resulting from the perturbation were allowed to exit the domain before any data was recorded. To ensure the solution was independent of the starting conditions (i.e. the perturbation), a case was run allowing the asymmetry to grow naturally over time. This gave the same flow properties ( $\overline{C_D}$  and  $St$ ) as the result obtained by perturbing the flow artificially. Mesh independence was tested with higher density meshes in both the radial and tangential directions, and resulted in variations in the mean flow parameters of less than 1 percent. The mean flow conditions were obtained by time-averaging the flow over three periods once the transients had exited the domain.

The same mesh and procedure was used to assess the time-limit model. However, the standard  $k-\omega$  model (Wilcox [10]) was used as the basis for the time-limit modification.

The two-dimensional formulation of Durbin's time-limit turbulence model is briefly presented here (see [3]). Consider the turbulent viscosity in the form:

$$\mu_t = C_\mu \rho u^2 T \quad (1)$$

In the standard  $k-\omega$  model, the velocity scale  $u^2$  is equal to  $k$ , and the timescale,  $T = 1/(C_\mu \omega)$ . A timescale bound is developed in [3] by applying a realizability constraint in order to ensure that the square of the normal components of the Reynolds stress tensor are always positive. This defines the timescale in the two-dimensional case thus:

$$T \leq \frac{2k}{3u^2 C_\mu} \frac{1}{\sqrt{2|S|^2}} \quad (2)$$

Durbin [3] suggests that an empirical constant of value less than one may be used in order to tune the model to experimental flows. This constant was expressed as  $\alpha$  in Medic and Durbin [7]. Therefore, reducing (2), gives

$$T \leq \frac{\sqrt{2}\alpha}{3C_\mu |S|} \quad (3)$$

or, for a computational application:

$$T = \min \left[ \frac{1}{C_\mu \omega}, \frac{\sqrt{2}\alpha}{3C_\mu |S|} \right] \quad (4)$$

The time-limit modification was included through a user defined function that defined the turbulent viscosity by using equation (4) in equation (1).

## Results and Discussion

### Turbulent Inlet Boundary Conditions

To investigate the effect of the turbulent length scale boundary condition, the length scale was varied by orders of magnitude from  $l = 0.0001D$  to  $0.1D$ . Various mean and fluctuating flow properties have been compared with the study of Cantwell and Coles [2]. Table 1 summarises the results from the present study and table 2 presents experimental data from [2], as well as additional computational results from [9].  $\overline{C_D}$  and  $\overline{C_L}$  are the periodic fluctuations in the force coefficients.

Length scale	$r_\mu = \mu_t/\mu$	$\overline{C_D}$	$St$	$\overline{C_D}$	$\overline{C_L}$
0.1D	102.9	0.692	0.238	0.0074	0.297
0.05D	51.4	0.685	0.248	0.0096	0.327
0.01D	10.3	0.729	0.260	0.0204	0.470
0.001D	1.03	0.799	0.257	0.0363	0.671
0.0001D	0.103	0.776	0.258	0.0348	0.642

Table 1: Results of varying turbulent length scale ( $Re = 1.4 \times 10^5$ ,  $I = 0.6\%$ ).

Study	Length scale	$\overline{C_D}$	$St$	$\overline{C_L}$
Exp. [2]	n/a	1.237	0.179	n/a
$k-\epsilon$ [9]	0.02D	0.71	-	-
RNG $k-\epsilon$ [9]	0.02D	0.98	0.167	0.51
LES [9]	0.02D	1.40	0.184	0.65

Table 2: Experimental and computational results ( $Re = 1.4 \times 10^5$ ,  $I = 0.6\%$ ).

The present study's results underestimate mean drag coefficient and overestimate Strouhal number. Similarly, the  $k-\epsilon$  results from [9] also underestimate  $\overline{C_D}$ , however the standard  $k-\epsilon$  model does not predict any vortex shedding, and the RNG model underpredicts Strouhal number. The large eddy simulation (LES) results from [9] provide a closer match to experiment.

Figure 2 presents the distribution of pressure coefficient about the cylinder. On the front side of the cylinder, the reduction in pressure in the experimental data is small in comparison to the computational predictions, and the experimental results indicate an earlier separation point. The computational results are quite similar in this region except at the low pressure minima, where smaller length scales predict a lower pressure coefficient. The predominant difference between the pressure distributions predicted with the use of varying length scales is the different base pressures on the aft side of the cylinder. [2] cites a base pressure coefficient of -1.21. In this region, the small length scales offer an improved match — the closest computational result is for  $l = 0.001D$ , with a value of -0.918, which is markedly better than for  $l = 0.1D$  where  $C_{p_b} = -0.637$ .

It is suggested that the improvement in estimation of the  $C_p$  distribution on the aft side of the cylinder can be attributed to the fact that, with greater length scales, the flow has higher eddy viscosity according to the relationship  $\mu_t = \rho k^{1/2} l$ . This increased viscosity results in a higher velocity gradient at the wall, energising the boundary layer and consequently delaying separation.

The results presented here cover length scales over a range of four orders of magnitude, with the predicted  $\overline{C_D}$  values varying -7 to +8.5% of the value averaged across all length scales. Strouhal number varies -5.6 to +3.1%. This suggests that the selection of length scale has only limited implication on the overall time-averaged flow properties. That is, incorrect estimation of length scale by an order of magnitude does not nec-



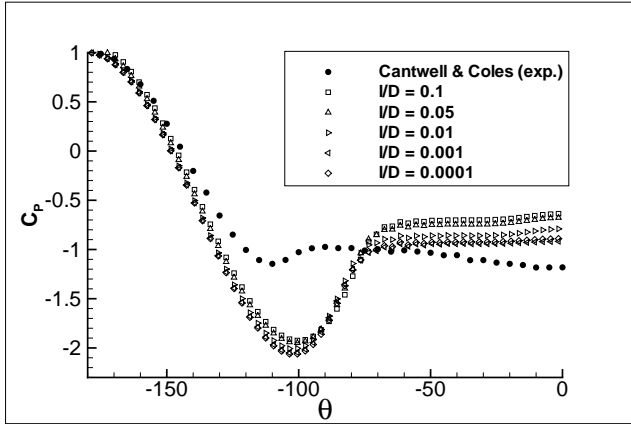


Figure 2: A comparison of the  $C_p$  distributions for different length scales at  $Re = 1.4 \times 10^5$ .

essarily convey with it a result that is in error by a similar order. However, this is contingent on the fact that the model in use is capable of accurately predicting the flow. For the cylinder in crossflow as presented here, the poor showing of computational results cannot be attributed to selection of incorrect length scale. Therefore, further improvements need to be made on the modelling of such flows.

#### Time-Limit Turbulence Model Modification

Durbin [3] proposed this modification (referred to as a time-scale bound) for eddy-viscosity turbulence models to overcome the tendency for overprediction of turbulent kinetic energy,  $k$ , around the stagnation point - the so-called stagnation point anomaly. Durbin proposed that it is not the stagnation point as such, but the large strain rates at this location, that result in the overproduction of  $k$ .

The time-limit model was first implemented in this study for the same  $Re = 1.4 \times 10^5$  case as used above and it was found that the flow was very sensitive to the value of  $\alpha$ , dramatically varying the entire flow structure such that mean drag varied from approximately 0.2 to 1.2.

When used with  $\alpha = 0.7$  at  $Re = 1.4 \times 10^5$ , it was found that the model gave an improved estimation of drag coefficient,  $\overline{C_D} = 1.223$  compared to 1.237 in [2]. However, further investigation revealed that this is not due to correct modelling of the flow. In fact, the mechanism for the high drag was not early separation together with a wide wake (as seen experimentally at this Reynolds number), but late separation in combination with a very low base pressure region. Figure 3 illustrates the variations in pressure distribution between the experimental data, the standard  $k-\omega$  model and the time-limit model, for which the low base pressure at  $\theta = 0$  is evident.

Figure 4 illustrates the regions in which the modified time-scale and conventional  $k-\omega$  formulations are active. In the modified time-scale region the turbulent viscosity was noted to be greatly reduced compared to the standard  $k-\omega$  model. This resulted in a reduction in the turbulence intensity around the cylinder as seen in figure 5.

The time-limit model was subsequently tested over a range of Reynolds numbers from  $10^3$  to  $3 \times 10^6$ . Figure 6 illustrates the trend in drag coefficient and Strouhal number across the Reynolds number range. Data computed using the standard  $k-\omega$  model can be seen plotted in the figure, showing a negative, almost log-linear relationship as  $Re$  increases, but not capturing the reduction in drag nor subsequent drag increase. Using the time-limit model with  $\alpha = 0.7$ , the CFD still does not capture

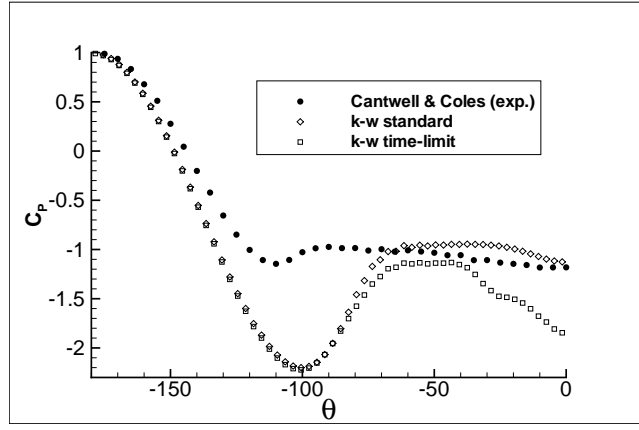


Figure 3: A comparison of the  $C_p$  distribution of different turbulence models at  $Re = 1.4 \times 10^5$ .

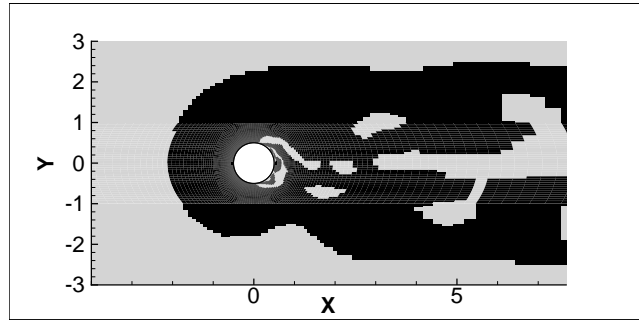


Figure 4: Representation of where the time-limit model is activated (dark region).

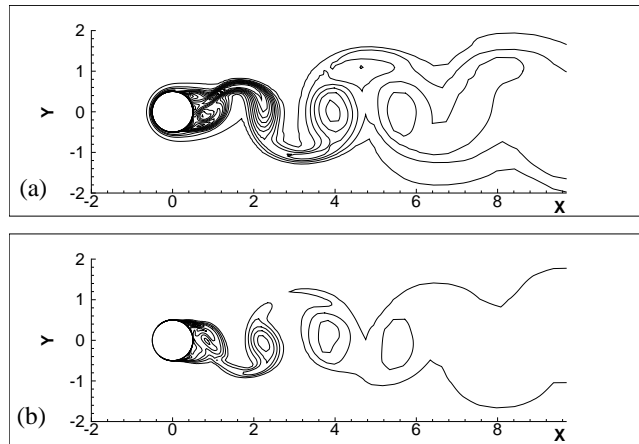


Figure 5: A comparison of the turbulence intensities — (a)  $k-\omega$  standard, (b)  $k-\omega$  time-limit. Contours are from 2% to 24% in increments of 2%.

the drag crisis, although it does give improved results either side of the critical region. By changing the empirical constant,  $\alpha$ , to a value of 0.433, the low drag values at the critical Reynolds number of  $5 \times 10^5$  can be modelled. This is of significance because the flow structure appears to match that seen in experiments. This can be seen in figure 7b where the separation bubble can be seen on the aft side of the time-limit model, which delays separation resulting in a narrower wake.

Figure 8 compares the pressure distribution about the cylinder at critical Reynolds numbers where the computational result at  $Re = 5 \times 10^5$  is compared with experimental data from Farell and Blessman [4] at  $Re = 3.8 \times 10^5$  — both in the critical Reynolds number regime according to figure 6.

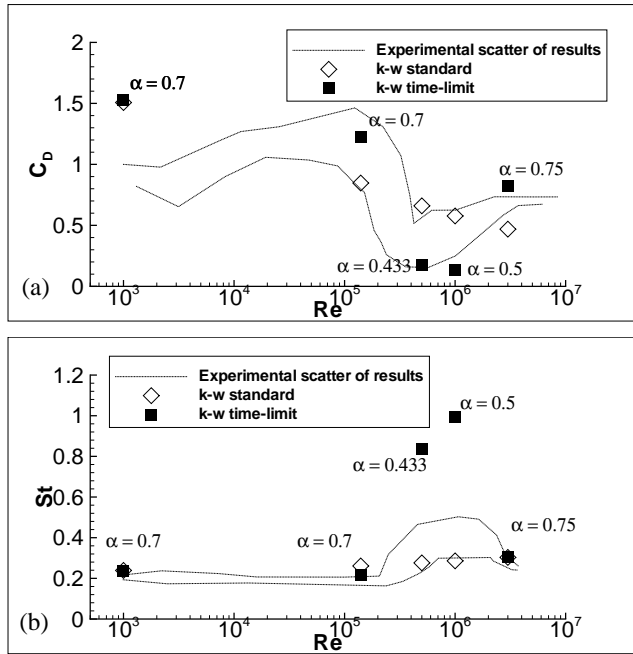


Figure 6: Experimental and computational results of (a) mean drag coefficient, and (b) Strouhal number, on a cylinder in cross-flow at various Reynolds numbers.

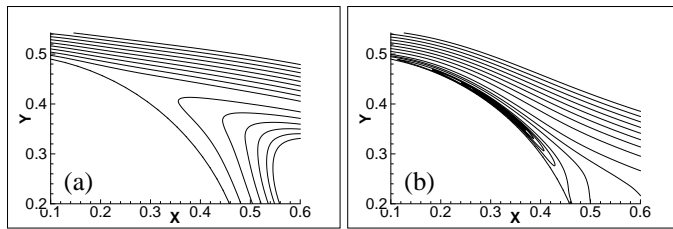


Figure 7: Detail of the flow structure around a cylinder at  $Re = 5 \times 10^5$  — (a)  $k-\omega$  standard, (b)  $k-\omega$  time-limit.

Both the standard and time-limit model compare well with the experimental pressure distribution on the forward part of the cylinder. The low pressure peak is slightly too high for the standard model, and slightly too low for the time-limit model. The pressure in the wake of the standard model is lower than the experimental data whilst the time-limit model overpredicts the pressure recovery.

As Reynolds number exceeds  $1 \times 10^6$ , the transcritical regime is being approached and experimental results (refer figure 6) suggest the drag should begin to increase. This result was not obtained with the time-limit model. It was found that at  $Re = 1 \times 10^6$  (using  $\alpha = 0.5$ ), the time-limit model predicted a similar flow structure as at  $Re = 5 \times 10^5$  but with lower drag.

When applied with  $\alpha = 0.75$ , the time-limit model gave a reasonable match with experimental data at  $Re = 3 \times 10^6$ , where it estimated a drag coefficient of 0.822.

## Conclusions

It was found that the variation in flow parameters such as mean drag coefficient and Strouhal number were influenced by changes in the turbulent boundary conditions. However, large changes in turbulent length scale of several orders of magnitude did not translate into variations of the same magnitude in the measured flow properties. The performance of CFD was quite poor regardless of the chosen boundary conditions, and it is evident that improvements to eddy-viscosity modelling are required for such bluff body flows at high subcritical Reynolds

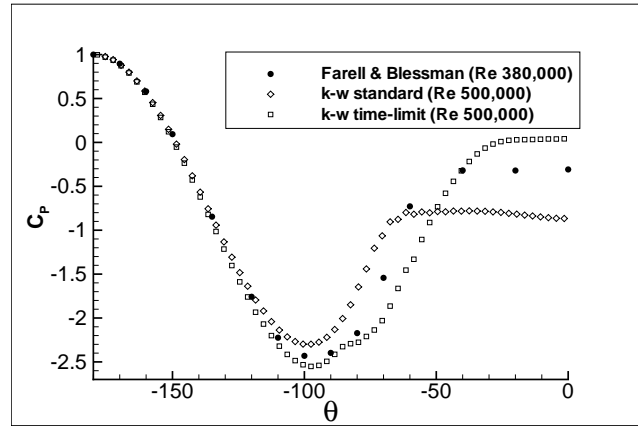


Figure 8: Comparison of pressure coefficient distribution about the cylinder in the critical Reynolds number regime.

numbers. The time-limit turbulence model modification appears to offer some improvement over the standard  $k-\omega$  model, especially in its ability to correctly model some flow structures. However, this improvement is contingent on operation at suitable Reynolds number and the chosen  $\alpha$  values.

## Acknowledgements

This work was supported by DSTO and the authors would like to thank Jan Drobik and Greg McKenzie for their assistance.

## References

- [1] Bosch, G. and Rodi, W., Simulation of Vortex Shedding Past a Square Cylinder With Different Turbulence Models, *Int. J. Numer. Meth. Fluids*, **28**, 1998, 601–616.
- [2] Cantwell, B. and Coles, D., An Experimental Study of Entrainment and Transport in the Turbulent Near Wake of a Circular Cylinder, *J. Fluid Mech.*, **136**, 1983, 321–374.
- [3] Durbin, P.A., On the  $k-3$  Stagnation Point Anomaly, *Int. J. Heat and Fluid Flow*, **17**, 1996, 89–90.
- [4] Farell, C. and Blessman, J., On Critical Flow Around Smooth Circular Cylinders, *J. Fluid Mech.*, **136**, 1983, 375–391.
- [5] Fluent Inc. *FLUENT 6.1 User's Guide*, Fluent Inc., Lebanon, USA, 2003.
- [6] Lakehal, D. and Thiele, F., Sensitivity of Turbulent Shedding Flows to Non-Linear Stress-Strain Relations and Reynolds Stress Models, *Computers and Fluids*, **30**, 2001, 1–35.
- [7] Medic, G. and Durbin, P.A., Toward Improved Prediction of Heat Transfer on Turbine Blades, *Journal of Turbomachinery*, **124**, 2002, 187–192.
- [8] Menter, F.R., Two-Equation Eddy-Viscosity Turbulence Models for Engineering Applications, *AIAA Journal*, **32**, 1994, 1598–1605.
- [9] Tutar, M. and Holdø, A.E., Computational Modelling of Flow Around a Circular Cylinder in Sub-critical Flow Regime with Various Turbulence Models, *Int. J. Numer. Meth. Fluids*, **35**, 2001, 763–784.
- [10] Wilcox, D.C., *Turbulence Modelling for CFD*, DCW Industries, La Cañada, 1998.

## Non-Newtonian flow behaviour in particulate suspensions under magnetic fields

H. See

Department of Chemical Engineering  
The University of Sydney, NSW, 2006 AUSTRALIA

### Abstract

Magneto-rheological fluids are particulate suspensions which show a dramatic increase in viscosity when placed under an external magnetic field. This is due to the magneto-static interaction forces induced between the particles by the external field, which lead to the formation of elongated aggregates of particles aligned in the field direction. The highly non-Newtonian flow behaviour of these fluids can be represented by the Bingham fluid model, where there is solid-like behaviour with a field-dependent yield stress. We have experimentally examined the small strain behaviour of this solid-like, pre-yielded state, and observed a linear, elastic stress-strain response up to the yield point. The corresponding modulus  $G_0$  was found to depend on the magnetic flux density  $B$  as  $G_0 \sim B^{0.7}$ . A theoretical calculation of this modulus was also performed, based on the interacting dipole approach.

### Introduction

A magneto-rheological suspension (MRS) consists of polarisable particles dispersed in a non-polarisable carrier fluid, and displays a dramatic increase in flow resistance under a magnetic field. The basic mechanism is that the field induces a magnetic dipole within each particle, and the resulting interaction forces between particles lead to the formation of elongated aggregates which increase the viscosity (Fig. 1). There are several recent review papers available [1-3]. It should be noted there is also an analogous suspension system, electro-rheological fluid (ERF), whereby an external electric field induces electrostatic polarization of each particle, the interparticle forces again leading to aggregates and an increased viscosity.

These materials are currently the object of intense research attention, as well as considerable applications development work in industry (eg tunable vibration damping systems, based on the adjustable flow properties). A key outstanding issue in our fundamental understanding of these systems is a theoretical constitutive framework within which predictions can be made about the flow behaviour under arbitrary field and flow conditions. Careful measurements are required of the rheological response in closely controlled flow conditions, and this is the contribution of the present work.

We have carried out a series of rheological tests on MRS using laboratory prepared magneto-rheological samples and a modified controlled stress rheometer, with particular focus on the response at the start-up of shear flow. The following sections will describe the materials and apparatus used, and then present the results and discussion.

### Experimental Material

The particles were carbonyl-iron powder (average particle size  $4\mu\text{m}$ ), manufactured by ISP Corp (grade S3700). These were dispersed in a 0.1Pas silicone oil (Dow Corning). The volume fraction was 30%. The particles were mixed thoroughly, and prior to any testing the bottle was vigorously shaken to re-

disperse the system. Inspection of the samples after the tests showed minimal clumping of particles.

### Equipment

The Paar Physica MCR300 rheometer was used in the parallel plate mode (diameter 20mm, typically 1mm gap), as illustrated in Fig. 2. The rheometer has been modified so that a uniform magnetic field can be applied to the sample (perpendicular to the plates) which is produced by an electromagnet under the bottom plate. This consists of a coil of 495 windings, through which is passed a DC current of up to 2A. The test cell is enclosed in a chamber comprising of iron elements, which redirect the magnetic field to the bottom stage, thus generating a magnetic circuit.

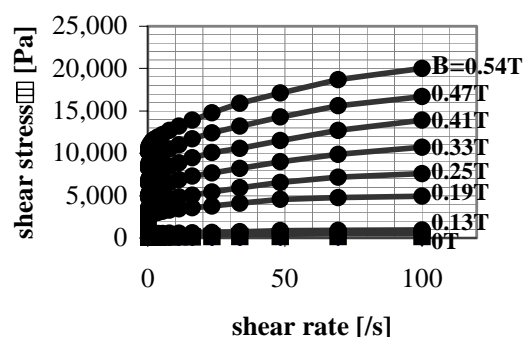


Figure 1. Flow curves for a typical magneto-rheological suspension, consisting of carbonyl-iron particles dispersed in silicone oil (volume fraction 30%). Each curve corresponds to a particular magnetic field strength  $B$  – magnitudes indicated on graph (units : Teslas).

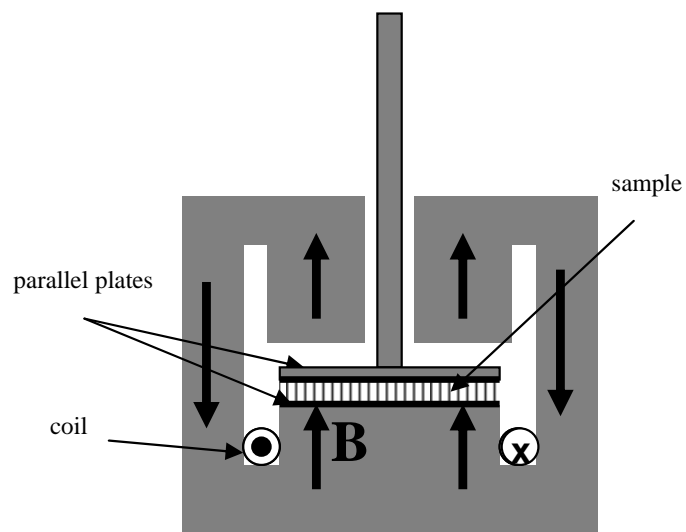


Figure 2. Schematic of the magneto-rheological test cell. The sample is sandwiched between the parallel circular plates, with a magnetic flux ( $B$ ) applied normally to the plates. The upper disk is rotated, inducing shear flow in the sample.

## Procedure

Prior to the commencement of the tests below, the constant magnetic field was applied to the sample for 5 minutes (with no deformation) to enable the particulate columnar microstructure to fully develop. The following tests were performed :

- (i) Steady shear flow – shear rates up to  $100\text{s}^{-1}$  (under constant magnetic field).
- (ii) Transient response after shear start-up under slow constant shearing (yielding behaviour). Typical shear rates :  $\sim 0.01$  to  $\sim 1\text{s}^{-1}$ .

## Results and Discussion

The steady shear results are shown in Fig 1. These are similar to previous reports in the literature [5-7], and it is confirmed that the sample does indeed show the magnetorheological response. The presence of a yield stress, with a magnitude dependent on the magnetic field strength, is apparent.

A typical result from the shear start-up tests is illustrated in Fig. 3, for the case of applied shear rate of  $0.01\text{s}^{-1}$  and constant magnetic flux density of  $0.47\text{T}$ . It is seen that as the strain is increased, there is an elastic-type deformation at low strains (due to the tilting and deformation of the particle columns, spanning the two rheometer plates – Fig. 6). However, as the strain reaches a critical value (approximately 0.3 in the case of Fig. 3), the stress begins to plateau, eventually reaching a steady state value (corresponding to steady shear behaviour). At this stage the microstructural deformation process has likely reached a steady state, involving the rupture and re-formation of the chains or columns under the constant shearing.

Similar curves were obtained at different shear rates over the range  $0.01\text{s}^{-1}$  to  $10\text{s}^{-1}$ . Under small strains, the shear stress  $\tau$  was

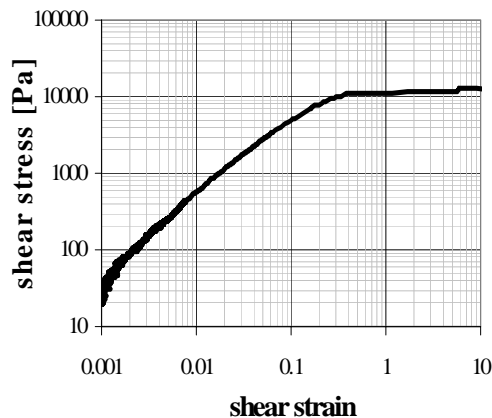


Figure 3. A typical shear start-up test, with stress plotted as a function of strain. The shear rate was  $0.01\text{s}^{-1}$  and the magnetic field  $0.47\text{T}$ .

found to increase linearly with strain  $\gamma$  : that is, the exponent  $\alpha$  in  $\tau \sim \gamma^\alpha$  was found to lie in the range 0.95 to 1.05 for all tests carried out. Therefore, we can use a modulus of elasticity  $G_0$  to describe the linear response at small strains, defined as follows :  $G_0 = \tau / \gamma$ . The variation of  $G_0$  with magnetic flux density  $B$ , evaluated at a strain of 0.01, is plotted in Fig. 4. Fig. 4 shows that  $G_0$  increases with magnetic flux density  $B$ . This result is expected since the interparticle interaction forces become stronger as  $B$  is raised. The exponent  $b$  in the relationship  $G_0 \sim B^b$  was found to be 0.70. Following is a theoretical treatment of this solid-like deformation of MRS under small strains, to examine the origin of this exponent of 0.70.

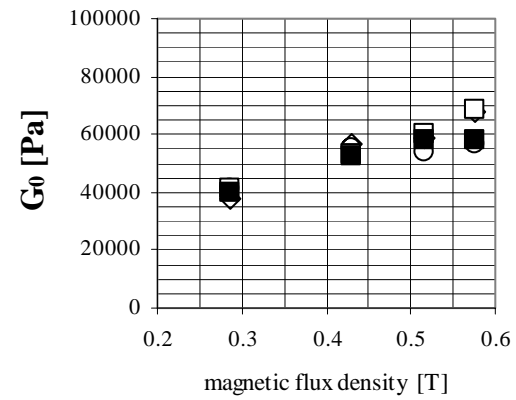


Figure 4. Variation with magnetic flux density  $B$  of modulus  $G_0$  which characterizes the initial solid-like response in the shear start-up curves. Measurements performed under different shear rates are shown: shear rate of  $0.01\text{s}^{-1}$  (open circles),  $0.1\text{s}^{-1}$  (open diamonds),  $1\text{s}^{-1}$  (open squares) and  $10\text{s}^{-1}$  (filled squares).

## Theory

The starting point for the theoretical modelling is the magnetostatic interaction force between two spherical particles of radius  $a$  under a magnetic flux density of  $B$ , as illustrated in Fig. 5.

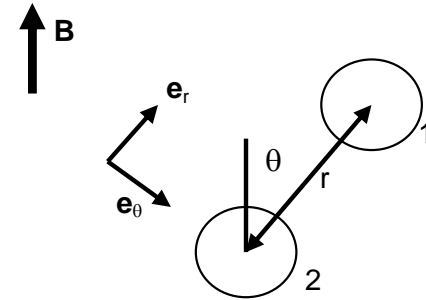


Figure 5. Two polarised spherical particles, under the magnetic flux density  $B$ .

The angle  $\theta$  is measured from the field direction, and  $r$  is the centre-to-centre separation. Using the unit vectors  $\mathbf{e}_r$  and  $\mathbf{e}_\theta$  as shown, the interaction force experienced by sphere 2 due to sphere 1 ( $\mathbf{F}_{12}$ ) is given by

$$\mathbf{F}_{12} = k P^2 r^{-4} [ f_1(\theta)\mathbf{e}_r + f_2(\theta)\mathbf{e}_\theta ] \quad (1)$$

$P$  is the strength of the electric dipole induced in each particle (ie the magnitude of the particle's polarisation, assumed constant), and is given by  $P = 4\pi a^3 \beta B$  where  $\beta = (\mu_p - \mu_c) / [\mu_0 \mu_c (\mu_p + 2\mu_c)]$  and  $\mu_p$  and  $\mu_c$  are the magnetic permeabilities of the particle material and the carrier fluid respectively. The functions  $f_1(\theta)$  and  $f_2(\theta)$  describe the orientational dependence of the interaction force and are given by  $f_1(\theta) = 3\cos^2\theta - 1$  and  $f_2(\theta) = \sin 2\theta$ . The constant  $k$  is given by  $k = (\mu_0 \mu_c) / 4\pi$  where  $\mu_0$  is the vacuum permeability.

The force given by eq(1) will act to attract particles which are aligned parallel with the field direction. The particles will be repelled if they are placed side-to-side, perpendicular to the field

direction. This model is often referred to as the “point dipole model”.

We now turn to the case where we have a single-width chain of particles, with the particles held to their neighbours by the interaction force ( $\mathbf{F}_{12}$  - eq(1)). As illustrated in Fig. 6, this chain is subject to a shear strain through application of a horizontal shearing force  $F$ .

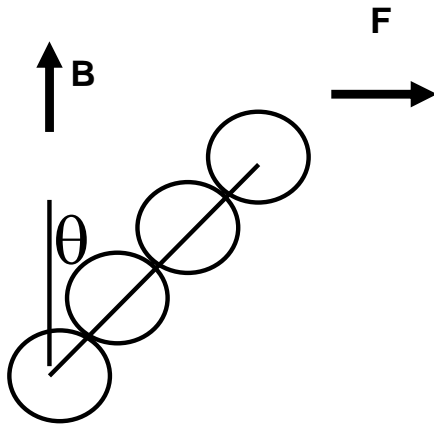


Figure 6. Chain of particles held together by the electrostatic interaction force (eq(1)). A shearing force  $F$  is applied to the chain, which is assumed to deform affinely as shown for small strains.

For small values of shearing strain (ie small values of  $\theta$ ) it is possible to analytically calculate the force-strain relationship. This enables us to obtain the elastic modulus, if we assume that the system consists of similarly strained chains connecting the plates of the rheometer, and which do not interact with each other. (isolated chains). Writing  $\phi$  for the volume fraction of the particles, we obtain the following theoretical result for the modulus  $G_0$ :

$$G_0 = 3/(16\pi) \phi k P^2 / a^6 \quad (2)$$

Substituting typical values for the experimental parameters we find that eq(2) predicts  $G_0$  to be of the order of  $10^4$  Pa under a 0.5 T magnetic flux density. This result underestimates the magnitude of the modulus (cf Fig. 4). In addition, the quadratic dependence on  $P$  (the dipole strength of each particle) implies a quadratic dependence on the flux density  $B$ . This is different to the  $\beta=0.7$  exponent observed experimentally (see Fig 4 and discussion thereof). Even a more sophisticated model, accounting for magnetic saturation effects in the region of the interparticle gap, predicts an exponent of  $\beta=1.5$  [8].

Clearly, the exponent in the experiments (0.70) is much lower than the exponents predicted by these theories. The most likely explanation for this is that the particles may have gone into the magnetic saturation regime under the fields used—in fact this would be more likely to happen with concentrated suspensions as used here. Indeed, magnetisation measurements by Martin and co-workers [9] on a similar particulate system (but at a lower volume fraction of 0.028) indicate that under 0.2 T fields the material is already heavily in saturation (Fig. 12 of that paper). Another factor leading to the discrepancy between the exponents may be that interactions other than field-induced forces, such as excluded volume interactions between the particles as they rearrange themselves within the aggregates, are also contributing to the solid-like mechanical resistance to shearing at the small strains. Indeed, it has been observed microscopically [1,2] that, rather than single-width chains (as we have modelled – Fig. 6),

the particles tend to arrange themselves into thicker columnar structures aligned in the field direction.

## Conclusions

Magneto-rheological fluids show a distinctive, Bingham plastic-type response under magnetic fields, with the yield stress depending on the field strength. We have examined the small strain behaviour of the pre-yielded, solid-like material. We observed a linear stress-strain response up to the yield point, with the corresponding ‘elastic’ modulus  $G_0$  depending on the magnetic flux density  $B$  as  $G_0 \sim B^{0.7}$ . This exponent was significantly less than those obtained from theoretical calculations based on the single-width chain model, indicating that interactions other than the induced magnetostatic dipole-dipole forces may be playing a role in the mechanical resistance of the particle aggregates to an applied shear strain.

## Acknowledgments

Ms R. Chen is thanked for her assistance in the experiments. This work has been supported by the Australian Research Council.

## References

- [1] Klingenberg, D., *AIChE Journal*, **47**, 2001, 246.
- [2] Rankin, P., Ginder, J. & Klingenberg, D., *Curr. Opin. Colloid Interface Sci.*, **3**, 1998, 373.
- [3] See, H., *Appl. Rheol.*, **11**, 2001, 70.
- [4] See, H. & Tanner, R., *Proc. Australian-Korean Rheology Conference*, Melbourne Australia, 20-21 Sept. 2001, 10.
- [5] Chin, B., Park, J., Kwon, M. & Park, O., *Rheol. Acta*, **40**, 2001, 211.
- [6] See, H., *Rheol. Acta*, **42**, 2003, 86.
- [7] Rankin P., Horvath, A. & Klingenberg, D., *Rheol. Acta*, **38**, 1999, 471.
- [8] Ginder, J. & Davis, L., *Appl Phys Lett*, **65**, 1994, 3410.
- [9] Martin, J.E., Venturini, E., Odinek, J & Anderson, R.A., *Phys. Rev. A*, **61**, 2000, 2818.

## Modelling of Solid Wall Boundaries in Computational Acoustics

R. C. Z. Cohen, A. Ooi and R. Widjaja

Department of Mechanical & Manufacturing Engineering  
The University of Melbourne, VIC, 3010 AUSTRALIA

### Abstract

This paper details an investigation into the Impedance Mismatch Method (IMM) as a means of modelling solid-wall boundaries for both one- and two-dimensional computational aeroacoustics (CAA) simulations. The main attraction of this method is its ability to model curved shaped bodies on a cartesian grid. Firstly, the IMM is used to model a solid wall within a one dimensional domain. In its given form the IMM is seen to allow the transmission of small acoustic waves through the solid region. A modification involving damping within the solid region is shown to be an effective improvement. The modified IMM was also used to simulate acoustic scattering off a rectangular block. The results compare well with those obtained using the Tam and Dong wall boundary technique.

### Introduction

Computational aeroacoustics (CAA) is a subfield of computational fluid dynamics (CFD) that has seen rapid growth over the past decade. This has been primarily due to the development of algorithms for the spatial and temporal discretizations of the governing equations that have minimal numerical dispersion and dissipation errors. In this investigation many of the more recent numerical techniques are employed in the investigation of different solid wall boundary modelling. In general, the governing equations of acoustics are the compressible Navier–Stokes equations. However, for the acoustic field, viscous effects are usually neglected, so the Euler equations can be used. The linearized, nondimensionalized Euler equations with a mean flow Mach number of  $M$  in the x-direction are given by:

$$\frac{\partial U}{\partial t} + [A] \frac{\partial U}{\partial x} + [B] \frac{\partial U}{\partial y} = 0 \quad (1)$$

where:

$$U = \begin{bmatrix} \rho \\ u \\ v \\ p \end{bmatrix} \quad [A] = \begin{bmatrix} M & 1 & 0 & 0 \\ 0 & M & 0 & 1 \\ 0 & 0 & M & 0 \\ 0 & 1 & 0 & M \end{bmatrix} \quad [B] = \begin{bmatrix} 0 & 0 & 1 & 0 \\ 0 & 0 & 0 & 0 \\ 0 & 0 & 0 & 1 \\ 0 & 0 & 1 & 0 \end{bmatrix}$$

### Numerical Methods

The following subsections detail the numerical methods that are used in this investigation.

#### Time and Spatial Discretization

A standard 4th order accurate Runge-Kutta time marching scheme is used in this investigation. Small time steps are used to avoid issues of temporal dispersion error. Explicit finite difference schemes for spatial derivatives are generally given in the form:

$$\left( \frac{\partial f}{\partial x} \right)_i \simeq \frac{1}{\Delta x} \sum_{j=-N}^M a_j f_{i+j} \quad (2)$$

where  $a_j$  are the coefficients of the particular scheme. For CFD calculations, such coefficients are typically chosen to satisfy some formal accuracy of the Taylor series expansions.

In CAA however, the dispersion relation of the discretization scheme is of equal importance to the formal accuracy. Tam and Webb [9] developed the so called Dispersion Relation Preserving (DRP) finite difference scheme that uses a wide stencil with some coefficients chosen to minimise the dispersion error. This scheme has higher resolution than standard central differencing schemes, allowing the use of less gridpoints per wavelength in order to achieve the required accuracy. Both the central and one sided 4th order DRP coefficients used in this investigation are given by Tam [5].

#### Absorbing Boundary Layer

The infinite physical domain is necessarily modelled on a finite computational grid. This requires the introduction of absorbing boundary conditions that allow outgoing waves to exit the computational grid without reflection. One method that achieves this is known as the Perfectly Matched Layer (PML) technique of Hu [3]. This methodology employs a buffer region at the edge of the grid that theoretically perfectly absorbs waves of all frequencies independent of the angle of incidence. Further development by Hu led to a more stable formulation [2] that also doesn't require the physical variables to be split as done in earlier versions. It is this formulation that is used in the study.

#### Solid Wall Boundaries

In the literature there are two methods of treating solid wall boundaries. Tam and Dong [7] discussed wall boundary conditions for computational acoustics. They concluded that the main physical wall boundary conditions to be implemented are:

$$v_n = 0 \quad (3)$$

$$\frac{\partial p}{\partial n} = 0 \quad (4)$$

That is, the fluid velocity normal to the wall is zero and the pressure gradient normal to the wall is zero. To implement these conditions, one sided and partially one sided stencil coefficients for the spatial derivatives were developed. The initial value of the velocity normal to the wall is explicitly set to zero. A row of ghost points for pressure are added inside the wall. The values of these ghost pressures are continuously set to ensure the pressure gradient at the wall is zero.

Chung and Morris [1] developed the so called Impedance Mismatch Method (IMM) for modelling solid wall boundaries. In this scheme each point on a cartesian grid is assigned a mean density  $\rho$  and a sound speed  $a$ . The solid wall is modelled with a markedly different characteristic impedance ( $\rho a$ ) to that of the fluid region. Curved solid bodies may be adequately modelled by assigning grid points as either inside or outside the body. At the interface between two regions waves are perfectly reflected if the impedance ratio is infinite. Due to instabilities that arise in having a ratio that is too large, the finite impedance ratio they recommend to use is around 1/30. According to Laik and Morris [4], the amplitude of the reflected wave ( $p_r$ ) to the incident



wave ( $p_i$ ) is given by:

$$R = \left| \frac{p_r}{p_i} \right| = \frac{\rho_2 a_2 - \rho_1 a_1}{\rho_1 a_1 + \rho_2 a_2} \quad (5)$$

where  $\rho_1$  and  $\rho_2$  are the mean densities and  $a_1$  and  $a_2$  are the speeds of the sound in the two media. IMM requires the reformulation of the Euler equations to include the density terms inside the spatial derivative operators. The density in the acoustic regions of the grid is set to unity and inside the solid wall regions it is set to a much smaller value, depending on the particular density ratio to be used. The following are the two dimensional IMM Euler equations with mean flow Mach number  $M$  in the  $x$  direction:

$$\frac{\partial U}{\partial t} + \frac{\partial E}{\partial x} + \frac{\partial F}{\partial y} = 0 \quad (6)$$

where:

$$U = \begin{bmatrix} \rho \\ u \\ v \\ p \end{bmatrix} \quad E = \begin{bmatrix} M\rho + \rho_0 u \\ Mu + p/\rho_0 \\ Mv \\ Mp + \rho_0 u \end{bmatrix} \quad F = \begin{bmatrix} \rho_0 v \\ 0 \\ p/\rho_0 \\ \rho_0 v \end{bmatrix}$$

### Artificial Selective Damping

Solid wall boundaries, especially ones with sharp edges often result in spurious waves being generated. Due to the limited resolution of finite difference schemes these waves will travel at supersonic speeds and contaminate the solution. Tam and Dong [6] studied these short wave components and developed an artificial selective damping technique that can be used to remove these high frequency waves from the calculations. Tam and Shen [8] improved this with a variable artificial damping technique. The amount of damping in their method is controlled by a parameter called the stencil Reynolds number ( $R_{stencil}$ ).

### One Dimensional Simulations

The one dimensional Euler equations are to be used to model the arrangement given in the figure 1. The effectiveness of the IMM solid wall is to be tested with the use of the following initial conditions:

$$p(x, t=0) = e^{-\ln(2)x^2/25} \quad (7)$$

$$v(x, t=0) = 0 \quad (8)$$

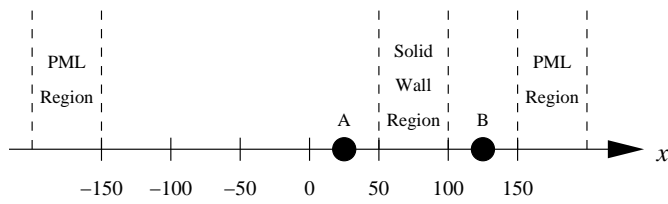


Figure 1: One dimensional arrangement.

Chung and Morris [1] performed an investigation into the IMM in one dimension. They showed that the pressure amplitude of the reflected wave was comparable to that of the incident wave and the transmitted pressure wave had small amplitude. The pressure distribution plot in figure 2 shows results that are almost identical to those obtained by Chung and Morris. Further investigation into the  $u$  velocity wave reveals that it is transmitted into the second medium in an amplified form. Plotting the pressure time histories of the points A and B from figure 1 reveals the unexpected results shown in figure 3. This plot shows

that the point in front of the object, point A, has extra pressure waves passing through it. The source of these waves is the pressure wave bouncing around inside the solid wall medium. Behind the solid wall, point B, waves are observed to pass through to this point. These transmitted waves could be eliminated by decreasing the density ratio, however Chung and Morris advise that decreasing the density ratio too much may make the system numerically unstable.

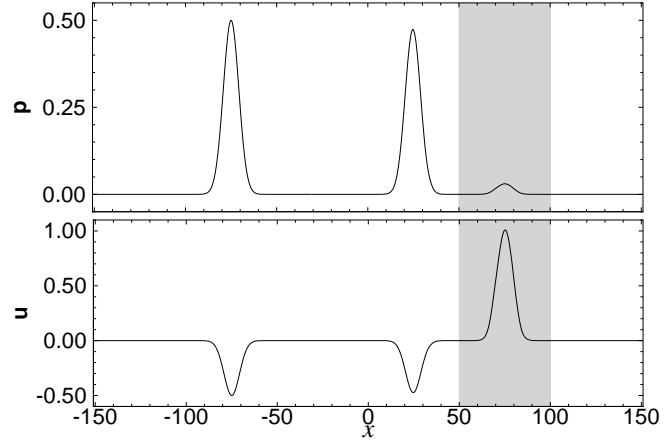


Figure 2: Pressure and velocity at time  $t=75$ , the reflected and transmitted waves are clearly visible.

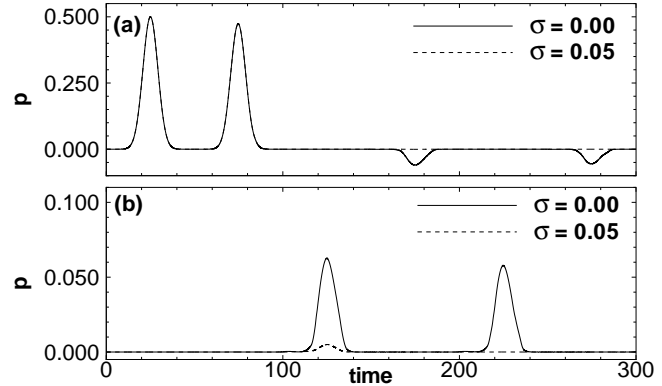


Figure 3: Pressure histories for different values of internal IMM damping (a) Point A in front of the solid object and (b) Point B behind the solid object.

### Improvement to the IMM

To prevent the waves bouncing around inside the solid wall region from periodically emitting waves into the rest of the domain, the following damping was added to the governing equations within the solid wall region:

$$\frac{\partial p}{\partial t} = \dots - \sigma p \quad (9)$$

$$\frac{\partial u}{\partial t} = \dots - \sigma u \quad (10)$$

where  $\sigma$  is some damping ratio between zero and one. The experiment was rerun with the extra damping added, the markedly improved results are shown in 3.

### Two Dimensional Scattering off a Rectangular Block

In this section acoustic scattering off a rectangular block is to be investigated using the arrangement shown in figure 4. The

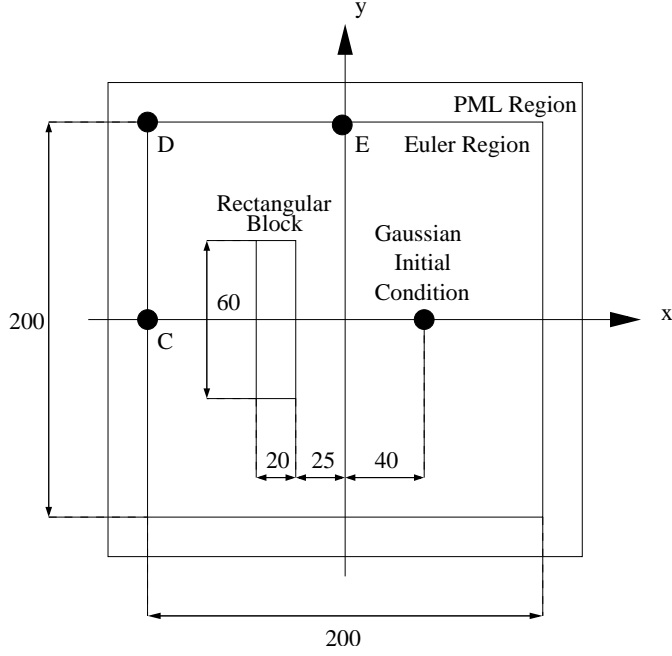


Figure 4: Two dimensional arrangement.

initial condition is to be given by:

$$\rho(x, y, t = 0) = e^{-\ln(2)((x-40)^2+y^2)/3^2} \quad (11)$$

$$u(x, y, t = 0) = 0 \quad (12)$$

$$v(x, y, t = 0) = 0 \quad (13)$$

$$p(x, y, t = 0) = e^{-\ln(2)((x-40)^2+y^2)/3^2} \quad (14)$$

The solid wall boundary was modelled using both the Tam and Dong [7] method and the IMM. The sharp corners of the rectangular object give rise to the development of spurious waves that contaminate the solution. Artificial selective damping will be used to damp these waves, the amount of damping being controlled by the parameter  $R_{stencil}$ . For the IMM modelling, the parameters that may be adjusted are the density ratio  $\rho$  and the IMM internal damping coefficient  $\sigma$ . The test cases to be investigated are given in table 1.

Test Case	Wall Boundary	$R_{stencil}$	IMM $\rho$	IMM $\sigma$
TAM	Tam and Dong	0.1	-	-
IMM1	IMM	0.1	0.030	-
IMM2	IMM	0.1	0.030	0.05
IMM3	IMM	0.1	0.030	0.10
IMM4	IMM	0.1	0.015	0.05
IMM5	IMM	0.2	0.030	0.05

Table 1: Two dimensional test cases.

## Results

Using the TAM test case results, contour plots of pressure are shown at different times in figure 7. The block successfully reflects sound off its surface. The pressure histories at point C directly behind the block for several different test cases are shown in figure 5. IMM1 shows poor results without any extra damping inside the block region. IMM2 and IMM3 show how the result is improved as  $\sigma$  is increased. IMM4 shows improvement over IMM2 by having a smaller density ratio. Figure 6 shows the pressure history for point D at the corner of the domain. IMM3 shows marked improvement over IMM1 due to

the addition of damping inside the block region. Finally, figure 8 shows the pressure histories at point E in front of the block. The IMM2 results show high frequency fluctuations in the result. These are due to spurious waves generated when the sound impinges upon the block. These waves may be eliminated by increasing the artificial selective damping coefficient  $R_{stencil}$  as shown by IMM5.

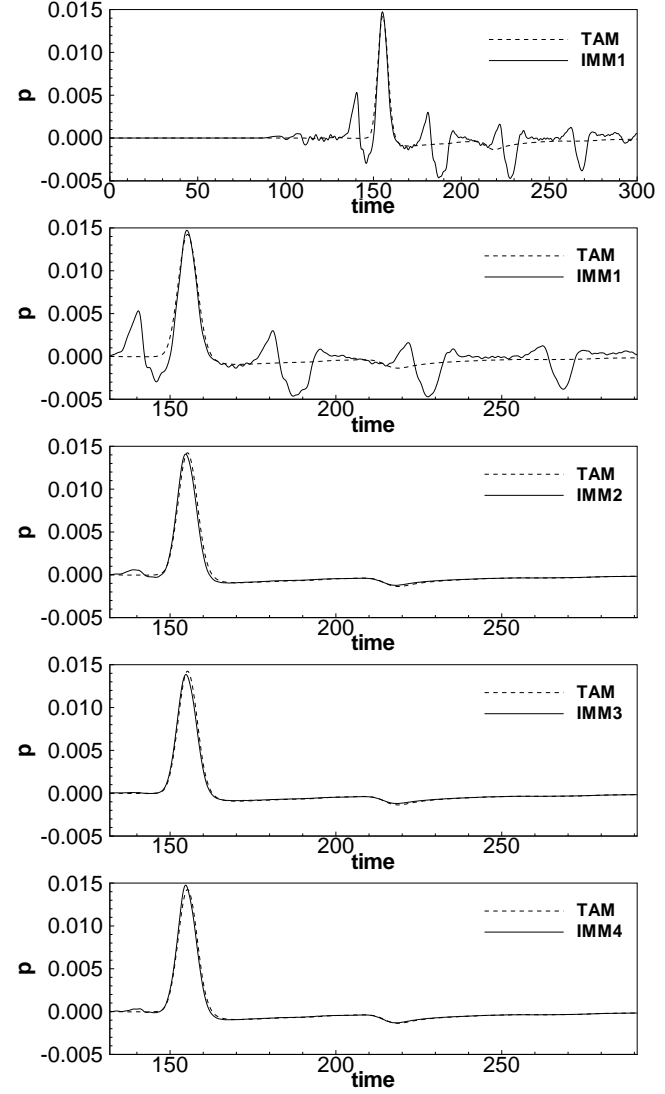


Figure 5: Pressure fluctuations at point C.

## Conclusions

An improvement to the Impedance Mismatch Method (IMM) has been suggested for use in both one- and two-dimensional acoustics simulations. This improvement leads to results close to those obtained using the Tam and Dong wall boundary condition.

## Acknowledgements

Special thanks to the Defence Science and Technology Organisation for supplying additional funding for this project.

## References

- [1] Chung, K. and Morris, P. J. Acoustic Scattering from Two- and Three-Dimensional Bodies, *J. Comput. Acoust.*, **6**, 1998, 357–375.

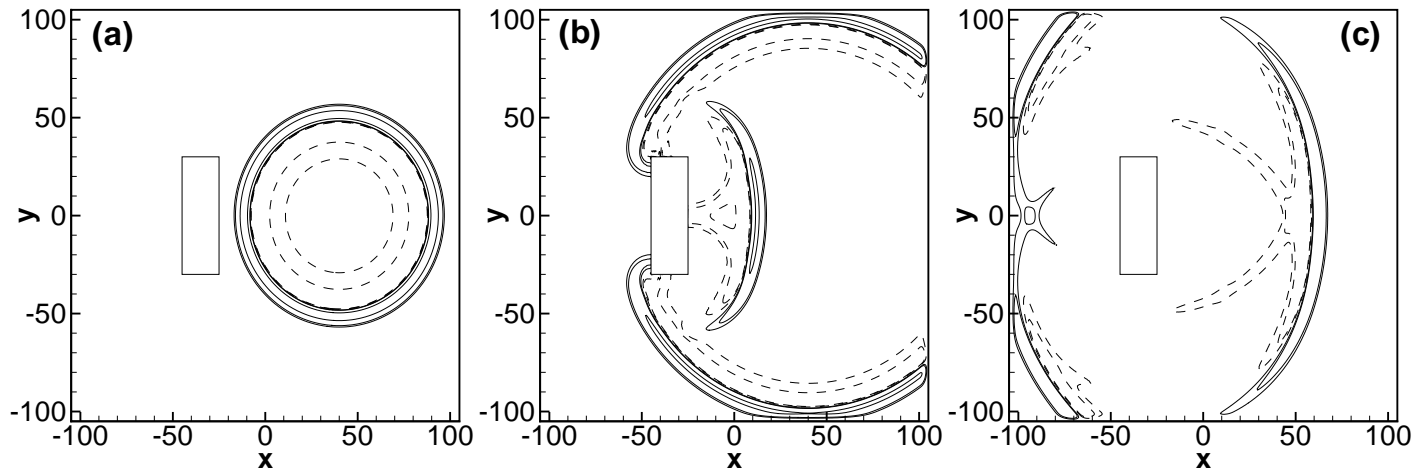


Figure 7: Contours of pressure for the TAM test case (a)  $t=50$ , (b)  $t=100$ , (c)  $t=150$ .

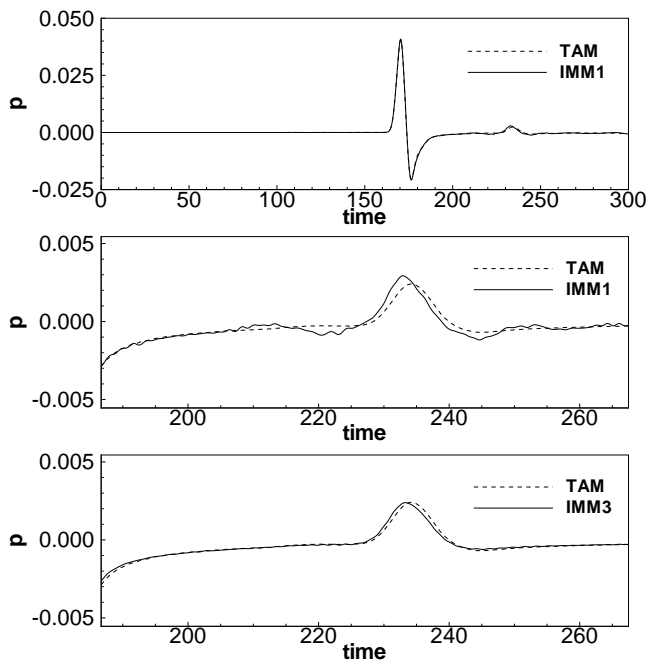


Figure 6: Pressure fluctuations at point D.

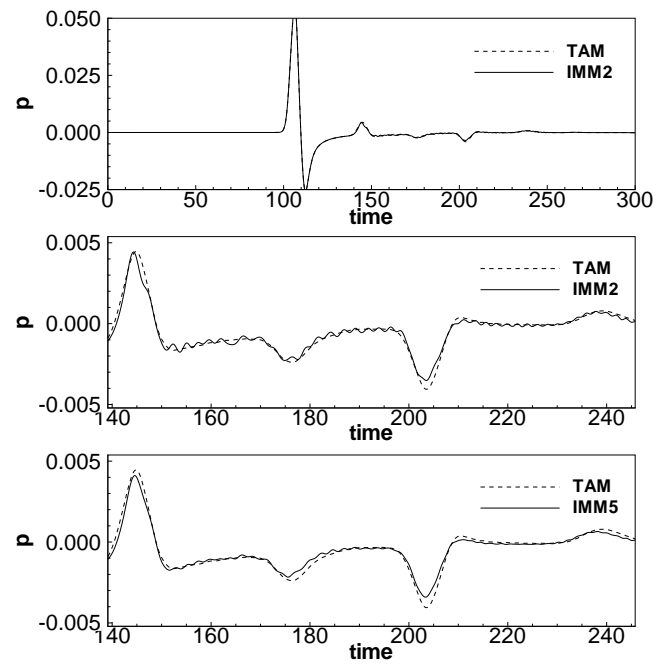


Figure 8: Pressure fluctuations at point E.

- [2] Hu, F.Q., A stable, Perfectly Matched Layer for Linearized Euler Equations in Unsplit Physical Variables, *J. Comput. Phys.*, **173**, 2001, 455–480.
- [3] Hu, F.Q., On Absorbing Boundary Conditions for Linearized Euler Equations By a Perfectly Matched Layer, *J. Comput. Phys.*, **129**, 1996, 201–219.
- [4] Laik, O.A. and Morris, R.J., Direct Simulation of Acoustic Scattering by Two- and Three-Dimensional Bodies, *J. Aircraft*, **37**, 2000, 68–75.
- [5] Tam, C.K.W., Computational Aeroacoustics: Issues and Methods, *AIAA J.*, **33**, 1995, 1788–1796.
- [6] Tam, C.K.W. and Dong, Z., A Study of the Short Wave Components in Computational Acoustics, *J. Comput. Acoust.*, **1**, 1993, 1–30.
- [7] Tam, C.K.W. and Dong, Z., Wall Boundary Conditions for High-Order Finite-Difference Schemes in Computational

Aeroacoustics, *Theor. Comput. Fluid Dyn.*, **6**, 1994, 303–322.

- [8] Tam, C.K.W. and Shen, H., Direct Computation of Non-linear Acoustic Pulses Using High Order Finite Difference Schemes, AIAA 93-4325, 15th AIAA Aeroacoustics Conference, 1993.
- [9] Tam, C.K.W. and Webb, J.C., Dispersion-Relation-Preserving Finite Difference Schemes for Computational Acoustics, *J. Comput. Phys.*, **107**, 1993, 262–281.

## Unsteady RANS Simulation of High Reynolds Number Trailing Edge Flow

D. Ang<sup>1</sup>, L. Chen<sup>2</sup> and J. Tu<sup>1</sup>

<sup>1</sup>School of Aerospace, Mechanical & Manufacturing Engineering  
Royal Melbourne Institute of Technology, VIC, 3083 AUSTRALIA

<sup>2</sup>Defence Science & Technology Organisation  
Aeronautical and Maritime Research Laboratory, VIC, 3001 AUSTRALIA

### Abstract

Unsteady vortex shedding at a trailing edge may cause pressure fluctuations and strong tonal noise which can have important consequences to the performance of marine and aeronautical type lifting surfaces. This paper presents data from unsteady RANS simulation of high Reynolds number trailing edge flow. It aims to identify and quantify dominant features of the trailing edge flow field over a two-dimensional hydrofoil at Reynolds numbers of chord ( $Re$ ) from  $1.4 \times 10^6$  to  $8.0 \times 10^6$ . The foil section is a NACA0015 profile with a trailing edge cut at 0.2% chord from the trailing edge.

It is found that the onset of vortex shedding occurs at a bluntness parameter  $h/\delta^* \geq 0.28$  and  $Re_h \geq 1.9 \times 10^4$ , where  $h$  is the characteristic length scale of the trailing edge bluntness,  $\delta^*$  is the boundary layer displacement thickness and  $Re_h$  is the Reynolds number based on  $h$ .

### Introduction

The flow of an incompressible viscous fluid over a submerged lifting surface at high Reynolds numbers induces a variety of fluid phenomena. Laminar boundary layers form at the leading edge and depending on the viscosity of the flow, may quickly transition into turbulence which completely envelops both sides of the lifting surface near the trailing edge. Turbulent boundary layers near the trailing edge generate broadband scattering noise as well as surface pressure fluctuations which tend to excite structural vibration and fatigue [1]. Furthermore, separation of the turbulent boundary layer at the trailing edge can cause sustained shedding of vortices into the wake and generate tonal noise. An accurate prediction of trailing edge flows is therefore crucial to estimate the associated noise.

The onset of vortex shedding at the trailing edge is closely related to the characteristics of the boundary layer flow near the trailing edge and its bluntness,  $h/\delta^*$  [1]. Thus significant changes in Reynolds number and slight modifications to trailing edge geometry may lead to fundamental changes in the trailing edge boundary layer flow. This, in turn, affects the near wake flow and modifies the shedding of vorticity into the wake [2].

This type of turbulent flow over hydrofoils or aerofoils is of particular interest to designers of propellers, control surfaces and lifting devices seeking quiet high performance components. Examination of the two-dimensional flows over hydrofoils can give insight into how the trailing edge geometry influences performance measures such as lift, drag and pressure loss, as well as the magnitude and nature of damaging structural vibration and the generated noise from surface pressure fluctuations. Numerical simulation provides an avenue for potentially accurate prediction of this damaging phenomenon. However, despite the rapid increase of computer power, analysis of such complex flows by Direct Numerical Simulation (DNS) and the alternative technique, Large-Eddy Simulation (LES), remains

computationally expensive. Thus, the modelling of high Reynolds number flows continues to be based on the solution of the Reynolds-averaged Navier-Stokes (RANS) equations despite the claims of experts that the noise generating eddies over a wide range of length scales cannot be adequately represented by RANS equations [3].

This paper presents the development of a numerical prediction method using the commercial computational fluid dynamics (CFD) code of FLUENT based on RANS equations to determine the extent to which RANS modelling can predict trailing edge flow and tonal noise. The following will thus be a close examination of the trailing-edge and near wake flow over a hydrofoil at high Reynolds numbers to verify the relationship between the trailing edge parameter  $h/\delta^*$ , and the occurrence of vortex shedding. The validation of the turbulence model used for high Reynolds number hydrofoil flows has been reported by Mulvany et. al. [4]. The time-averaged results of displacement thickness are compared to semi-empirical data on flat plate boundary layer growth. The computed results are then used to obtain the unsteady turbulent flow field around the trailing edge and the time history of surface pressure fluctuations and velocity changes in the wake. The frequency spectra of the pressure fluctuations can thus be calculated and the resultant Strouhal numbers compared with published data from Blake [1].

The case under study is a two-dimensional hydrofoil with a NACA0015 section and chord length of 540mm. This symmetrical profile represents a generic section shape used on submerged control surfaces for submarines and ships. Limitations on current manufacturing equipment make it impossible to produce a perfectly sharp trailing edge. To accommodate this, the hydrofoil is 'cut' at 0.2% chord from the trailing edge resulting in a blunt edge with a vertical height of just over 2mm. The hydrofoil is aligned at zero degrees to the incident uniform stream of 2, 5, 7, and 11.5m/s which correspond to Reynolds numbers of chord based on freestream velocity  $U_{ref}$  of  $1.4$ ,  $3.5$ ,  $4.9$ , and  $8.0 \times 10^6$  respectively.

Figure 1 shows the trailing edge geometry under investigation and a close-up on the blunt edge. Stations A, B, C, D and E refer to measurement stations of pressure fluctuations on the upper surface of the hydrofoil. They are located 100mm from the trailing edge  $x_A=438.92$ , 70mm from the trailing edge  $x_B=468.92$ , 40mm from the trailing edge  $x_C=498.92$ , 0.95 chord lengths from the leading edge  $x_D=513$  and at the trailing edge  $x_E=538.92$  respectively. Station F refers to the horizontal line offset 0.5mm above the chord line which runs from the blunt edge, through the wake and to the rear end of the control region. The time-history of the vertical velocity along this line is recorded to give an assessment of the fluctuating vorticity in the wake. The value of displacement thickness,  $\delta^*$  used to calculate the bluntness parameter,  $h/\delta^*$  is calculated from the boundary layer velocity profile at a distance of  $0.2Y_f$  as defined in Blake for the edge geometry under investigation [1].

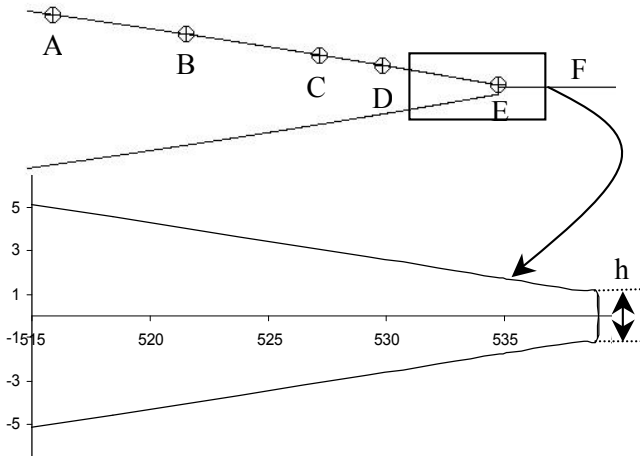


Figure 1. Hydrofoil geometry and measurement stations located at  $x_A=438.92$ ,  $x_B=468.92$ ,  $x_C=498.92$ ,  $x_D=513$ ,  $x_E=538.92$  and F which is a horizontal line running from the blunt edge and through the wake.

### Computational Methodology

The solution of the flow field is achieved using the commercial CFD code FLUENT. The unsteady segregated solver is utilised with 2<sup>nd</sup> order implicit approximation of the governing equations. Pressure-velocity coupling is achieved using the SIMPLE method. The time advancement is determined by the fixed time step size  $\Delta t$ , which is initially set to a sufficiently small value to achieve convergence of the residuals after 25 iterations. FLUENT provides a range of Reynolds-averaged turbulence models. Based on published results, the realizable k- $\epsilon$  model with enhanced wall treatment was chosen as it provides superior performance over the other available models under adverse pressure gradients, separation and recirculation [4].

The computational domain contains the full hydrofoil section within a rectangular control region. The control region which is 1.5 chord lengths in front, above and below the leading edge of the hydrofoil and 3.5 chord lengths behind the trailing edge is sufficiently distanced from the hydrofoil's surface as to have negligible effect on the solution. 'Velocity inlet' boundary conditions are specified at the front, upper and lower boundaries of the control region to allow the definition and variation of flow upstream of the hydrofoil. The 'outflow' boundary condition is used at the outlet and no-slip wall boundary conditions are defined for the surfaces of the hydrofoil.

The computational grid is meshed with quadrilateral cells using a structured multi-block method. The control region is thus divided into fifty, four-sided map meshed faces. Strong control over the density and distribution of cells is achieved through independent meshing of each block using edge mesh stretching schemes. Special care is given to the near-wall region with appropriate clustering to resolve the viscous sublayer of the boundary layer. As required by the enhanced wall treatment, the wall-adjacent cells should be of the order of  $y^+ = 1$  and have at least 10 cells within the viscous sublayer [4]. To reduce the computational cost, the mesh is stretched in the near-wall regions and increase in area away from the wall. Furthermore, transitional cells are utilised to reduce the fine mesh close to the hydrofoil to achieve a coarse mesh in the outer region. The wake region is meshed with a greater density of cells. The near wake and trailing edge region is refined further through hanging node grid adaption. Attention is required in critical regions of the flow where it is important that the mesh is mostly orthogonal to the flow, has minimal skewness and acceptable aspect ratios.

A steady state solution is first obtained to set the initial conditions for the time-dependent solution. 10,000 iterations are

sufficient for the lift and drag coefficients to converge. To stimulate the unsteady flow field, the hydrofoil is given an initial perturbation of small vertical velocity for 100 time steps at a very small time interval of  $5 \times 10^{-5}$  seconds. After this initial perturbation, the hydrofoil is again subjected to uniform flow to allow the perturbation to convect out of the computation domain before data sampling is activated to obtain the time-averaged result.

### Simulation Results

The grid independence test was conducted on five meshes for  $Re=8.0 \times 10^6$ . Table 1 details the maximum node  $y^+$  and drag coefficients of each mesh. Mesh 3, 4 and 5 predict almost identical drag coefficients, suggesting that grid independence is achieved. Mesh 4 is selected considering that the maximum  $y^+$  is approximately one as required [4].

Mesh	No. of Cells	Maximum $y^+$	$C_d (x10^{-3})$
1	69,844	7.993	5.786
2	111,394	5.481	5.674
3	178,852	3.373	5.178
4	<b>279,216</b>	<b>1.005</b>	<b>5.161</b>
5	329,968	1.017	5.159

Table 1. Maximum wall  $y^+$  and drag coefficients achieved for grid independence analysis.

The overall flow field around the hydrofoil is well behaved as expected for a symmetrical section of moderate thickness. In the viscous region close to the surface of the hydrofoil, laminar boundary layers develop at the leading edge, thicken and quickly transition to turbulence. The transition to turbulence is characterised by a large increase in wall shear stress which occurs at approximately 0.01 chord lengths from the leading edge for all Reynolds numbers investigated in this study. Thus, the upper and lower surface of the hydrofoil are nearly completely enveloped in turbulent boundary layer flow, which separates at the salient edge and interacts to form a turbulent wake downstream.

Due to the convergence of the pressure and suction surface of the hydrofoil aft of the point of maximum thickness, the flow close to the surface decelerates, causing a gradient of increasing static pressure. This is particularly evident in the region of the trailing edge as illustrated in Figure 2. This adverse pressure gradient causes a greater thickening of the boundary layer compared to that expected over a flat plate.

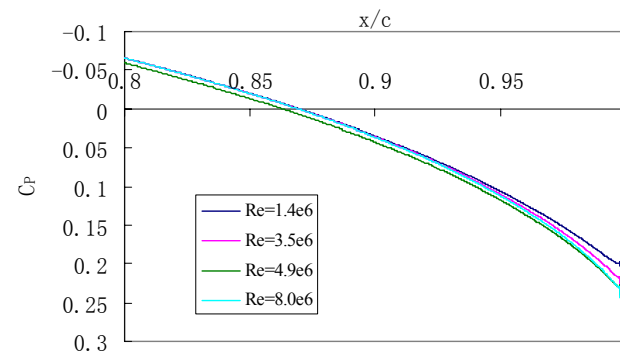


Figure 2. Mean surface pressure coefficient distribution over the pressure surface near the trailing edge for all Reynolds numbers under investigation.



Figure 3 shows the displacement thickness of the boundary layer as it develops over the trailing edge. In comparison, the displacement thickness for a fully turbulent flat plate in a uniform stream of 11.5m/s is only slightly thinner than that for the equivalent hydrofoil case at 80% chord but differs significantly as the trailing edge is approached. This rapid thickening of the boundary layer at the trailing edge influences the Reynolds number at which vortex shedding occurs. Several trends are observed with the increase in Reynolds number. Clearly, there is a general thinning of the boundary layer over the hydrofoil. This is due to the diminishing viscous effects of the flow which also results in a reduction of skin friction drag. Close examination of Figure 2 and the base pressure coefficient measured at the centre of the blunt edge, Figure 4, shows that the pressure at the trailing edge increases with Reynolds number which offsets the pressure drag and further reduces the overall drag coefficient.

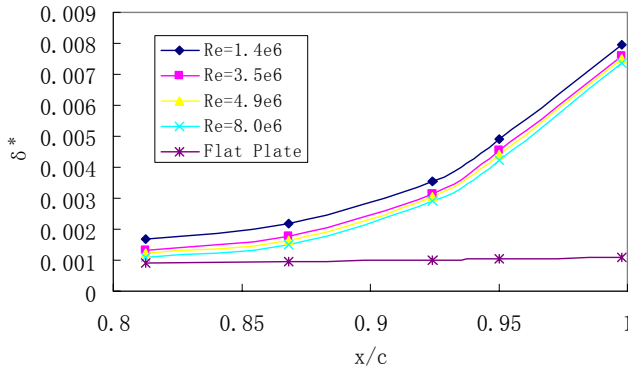


Figure 3. Displacement thickness of the boundary layer as it develops over the trailing edge of the hydrofoil compared to that of a flat plate for  $U_{ref}=11.5\text{m/s}$ .

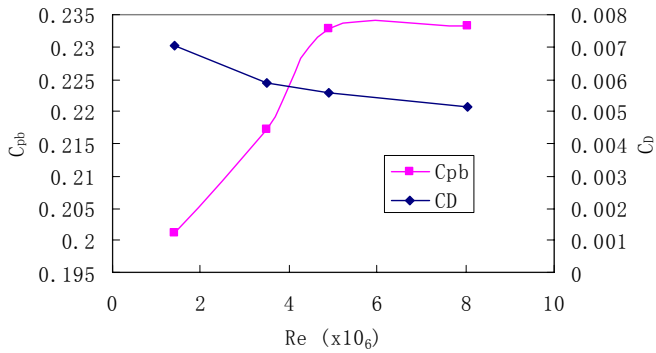


Figure 4. Variation of drag coefficient,  $C_D$  and base pressure coefficient  $C_{pb}$ , with increasing Reynolds number.

For examination of the unsteady flow characteristics, the instantaneous vorticity magnitude contours in the region of the near wake for the Reynolds numbers under investigation are shown in Figure 5. Figure 5a and 5b clearly show that for  $Re=1.4 \times 10^6$  and  $Re=3.5 \times 10^6$ , vortex shedding does not occur and the separated flow past the trailing edge combines to form two standing eddies of opposite sign but equal magnitude in the near wake. On the other hand, the vorticity fields in Figure 5c and 5d show evidence of vortex shedding in the wake for  $Re=4.9 \times 10^6$  and  $Re=8.0 \times 10^6$ , which decays in strength with increasing distance from the trailing edge.

The time history of vertical velocity fluctuations through the wake is plotted in Figure 6. In response to the initial perturbation, the oscillating flow of the wake is damped and clearly subsides with time for the case of  $Re=1.4 \times 10^6$  and  $3.5 \times 10^6$ , whereas the sustained shedding of vorticity is observed for  $Re=4.9 \times 10^6$  and  $Re=8.0 \times 10^6$ . This result will be further validated using LES simulation.

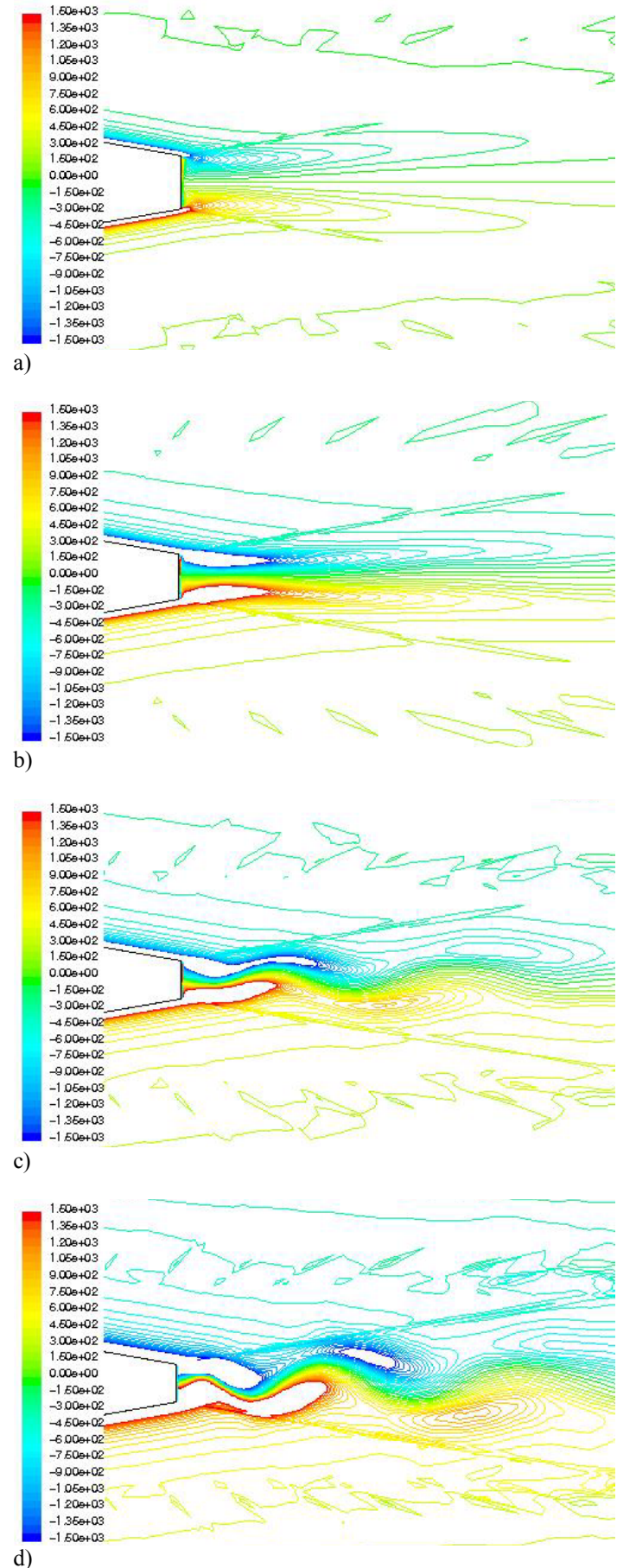


Figure 5. Instantaneous vorticity fields computed from RANS for: a)  $Re=1.4 \times 10^6$ , b)  $Re=3.5 \times 10^6$ , c)  $Re=4.9 \times 10^6$  and d)  $Re=8.0 \times 10^6$  (contour levels from -1500→1500 of vorticity magnitude).



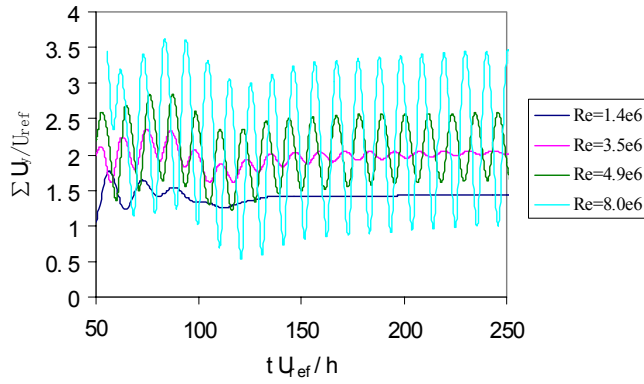


Figure 6. Time history of the vertical velocity along the horizontal line defined as station F in Figure 1, for  $Re=1.4 \times 10^6$ ,  $3.5 \times 10^6$ ,  $4.9 \times 10^6$  and  $8.0 \times 10^6$ .

The pressure differentials induced by vortex shedding across the surface of the hydrofoil were observed to be a maximum at the trailing edge. Figure 7 shows the corresponding frequency spectrum of the surface pressure fluctuation at “station E” obtained through Fast Fourier Transformation (FFT). The largest peak in the frequency spectrum corresponds to the vortex shedding Strouhal number. The discontinuities in the broadband spectral noise may be attributed to the limited number of pressure data used for the spectral analysis.

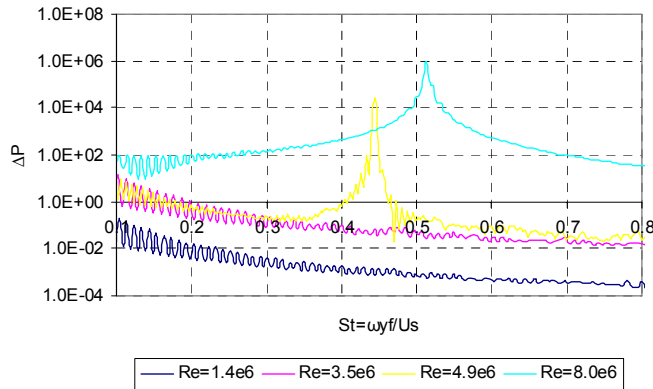


Figure 7. Spectrum analysis of surface pressure fluctuations at the trailing edge, Station E, for  $Re=1.4 \times 10^6$ ,  $4.9 \times 10^6$  and  $8.0 \times 10^6$ .

Table 2 contains a summary of the displacement thickness at the trailing edge, the bluntness parameter,  $h/\delta^*$  and the observed tonal frequency generated at each Reynolds number calculated with reference to the blunt edge height. Figure 8 shows the variation of time-averaged wake dimensions  $L_f/h$  and  $Y_f/h$  with increasing Reynolds number.

$Re_h$ ( $\times 10^4$ )	$\delta^*$ (mm)	$h/\delta^*$	Vortex Shedding	$f_s$ (Hz)	St
0.538	7.916	0.263	No	-	-
1.345	7.554	0.275	No	-	-
1.883	7.445	0.279	Yes	298	0.444
3.094	7.301	0.285	Yes	527	0.513

Table 2. Summary of vortex shedding strouhal number and bluntness parameters.

Thus the onset of vortex shedding occurs at  $h/\delta^* \geq 0.28$  which is comparably close to Blake’s prediction of  $h/\delta^* \geq 0.3$ . This corresponds to a  $Re_h$  of  $1.8 \times 10^4$  and wake dimension  $Y_f/h$  of 0.70. Compared to the published results in Blake [1] for a similar blunt edge geometry, the onset of vortex shedding occurs at  $Re_h$  of  $0.4 \times 10^4$  and the corresponding value of  $Y_f/h$  and St are 1.0 and 0.85 respectively. Note, that the experimental results were based

on a significantly larger bluntness parameter,  $h/\delta^*$  of 5.88 which may be the reason for the differences in the compared results. Also, the rapid thickening of the boundary layer at the trailing edge decreases  $h/\delta^*$  and thus delays the onset of vortex shedding until higher  $Re_h$  values are achieved.

Several similarities of the wake dimensions are observed compared to the wakes of cylinders just before and after the onset of vortex shedding. As Reynolds number of the flow increases, the length of the formation region  $L_f/h$  initially increases and then decreases upon the onset of vortex shedding. Furthermore, the intensity of the generated tone increases, characterised by a larger peak in the frequency spectrum [1].

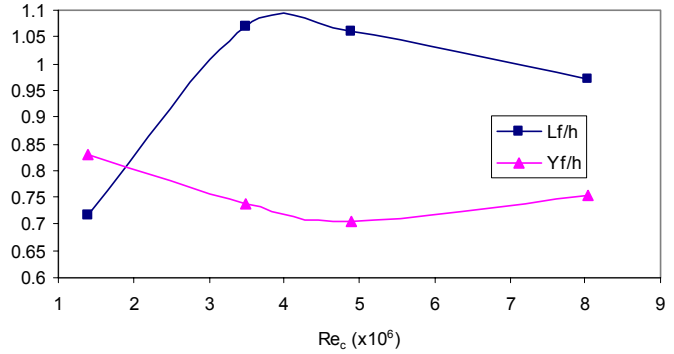


Figure 8. Variation of wake dimensions  $L_f/h$  and  $Y_f/h$  with increasing Reynolds number.

## Conclusions

The dynamic trailing edge and near wake flow have been successfully simulated using unsteady RANS turbulence models. It is found that the onset of vortex shedding is strongly related to  $Re_h$  and the characteristics of the trailing edge. For a given trailing edge geometry, the increase of  $Re_h$  thins the boundary layer at the trailing edge which increases the likelihood of vortex shedding.

Overall, the RANS equations appear to reasonably predict the onset of vortex shedding. This occurs at  $h/\delta^* \geq 0.28$  which is comparably close to results in Blake [1]. However the observed Strouhal numbers do not correlate well with published experimental results for a similar blunt edge geometry. This may be attributed to the inability of the RANS model to accurately obtain the time-averaged wake dimensions of the unsteady wake, which are used as scaling factors for the calculation of the Strouhal number.

## References

- [1] Blake, W. K., *Mechanics of Flow-Induced Sound and Vibration*, Vols. 1 and 2, Academic, London, 1986.
- [2] Bourgoyne, D. A., Hamel, J. M., Ceccio, S. L. & Dowling, D. R., Time-averaged flow over a hydrofoil at high Reynolds number, *J. Fluid Mech.*, **496**, 2003, 365-404.
- [3] Wang, M. & Moin, P., Computation of Trailing-Edge Flow and Noise Using Large-Eddy Simulation, *AIAA Journal*, **38**, 2000, 2201-2209.
- [4] Mulvany, N., Tu, J.Y., Chen, L., Anderson, B., Assessment of Two-Equation Turbulence Modelling for High Speed Reynolds Number Hydrofoil Flow, *Int. J. Numer. Methods Fluids*, **45**, 2004, 275-299.

## Air Entrainment by Free Falling Streams of Particles

Zejin Liu, Paul Cooper and Peter W Wypych

School of Mechanical, Materials and Mechatronic Engineering, University of Wollongong, NSW 2522, Australia

### Abstract

This paper describes a study of free falling streams of particles or “particle plumes”. Experiments in air were carried out to determine the volumetric flow rate of entrained air as a function of drop height, mass flow rate and particle properties. Flow visualisation observations of the particle plumes are presented that show how the stream of particles descends in a dilating “core” of relatively constant radius after an initial contraction immediately below the source. The void fraction of the falling particle stream appears to increase homogeneously with height to a given point, but then the stream breaks up into a train of distinct particle “clouds” that descend and disperse. A theoretical model of the flow in such particle plumes is described whereby both entrained air flow rate and particle velocities are predicted for the situation where the core dilates homogeneously.

### Introduction

Powders and granulated solid handling systems are widely used in industry for bulk solid materials storage, handling and transportation. Industries relying heavily on these systems include agriculture, mining, chemical engineering, power plants, cement and food processing. There are many bulk solids handling processes that involve free fall of the particles (e.g. silo filling, conveyor transfers, powder mixing/processing). When a stream of particles free fall, the surrounding air is induced to flow with the particle stream as the bulk solid accelerates and expands. The entrained air forms a jet or boundary layer around the falling “core” of bulk material. The radius of this boundary layer grows with increasing drop height and may carry with it fine, fugitive dust particles.

Relatively little fundamental research has been carried out on the fluid and particle mechanics of these “particle plumes” which have some similarities with other plume and jet flows such as bubble plumes and water sprays [1,2] in that they are two-phase, non-Boussinesq problems. The purpose of the present research is to develop predictive tools for designers of dust control systems and to further the understanding of an important fundamental fluid flow situation. Articles have appeared in the past literature on air entrainment by falling streams of particles, notable that by Hemeon [3] who predicted air entrainment rates by extrapolating from the case of air entrained by a single, isolated particle free-falling through quiescent ambient air. The theory of Hemeon was later applied and modified by Morrison [4] and Tooker [5]. More recently work in the US by Plinke *et al.* [6] and at the University of Wollongong has focussed on quantifying the practical situation where falling streams of common bulk materials entrain air and work on determination of the velocity profile of the entrained air has been previously reported [7]. In this paper results of recent experiments are presented and the development of a theoretical model of the behaviour of particle plumes is discussed.

### Experimental Apparatus

The experimental rig was designed to permit the quantitative evaluation of the flowrate of air entrained by a falling stream of bulk material by allowing the stream to pass into a sealed enclosure through an aperture (Figure 1). Induced and displaced air was extracted from the enclosure and the extraction flow rate

was adjusted so that there was no static pressure difference between the chamber and the ambient air. The experimental methodology was validated by first replicating the results of Ricou and Spalding [8] by measuring the induced air flowing through the aperture from an isothermal jet generated by a nozzle where the hopper is located in Figure 1 [9]. The mass flowrate of bulk materials was maintained approximately constant during each test by means of the double-hopper arrangement, the test bin being flooded by the storage bin. The entire hopper system was suspended from a frame so that the mass flow rate of material could be measured directly by means of load cells attached to the suspension cables.

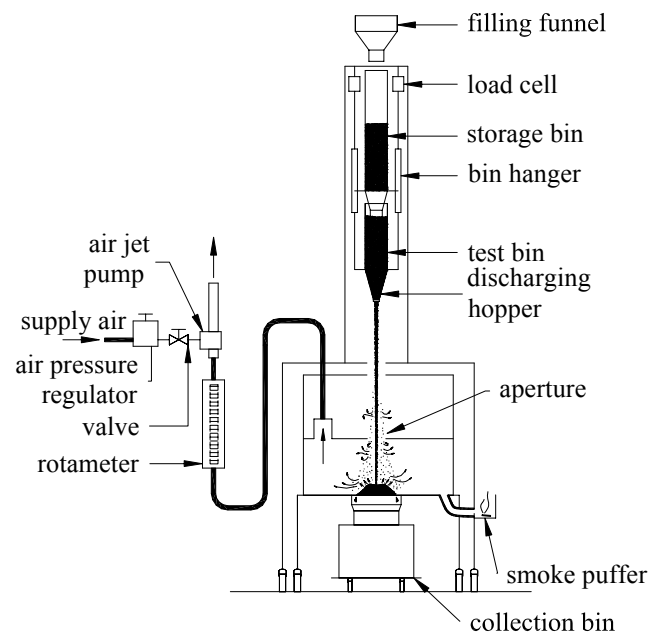


Figure 1. Schematic of the experimental apparatus.

Pressure equilibrium between the surrounding air and the inside of the chamber was determined by smoke visualization at a pressure observation port. To maintain a constant height of stockpile during each experiment, a collection bin was installed to receive the excess particles from the stockpile through an annular slot. The rig frame could be lifted up to adjust drop heights for various tests. The particulate mass flow rate was varied by changing the diameter of the outlet of the discharging hopper. Three bulk materials were tested: alumina powder, sand, and corvic vinyl powder with median particle diameters of  $96\mu\text{m}$ ,  $367\mu\text{m}$  and  $116\mu\text{m}$  and particle densities of  $2465\text{kg/m}^3$ ,  $1400\text{kg/m}^3$  and  $1487\text{kg/m}^3$ , respectively. Bulk solid mass flow rates between  $10\text{grams/s}$  and  $83\text{grams/s}$  were employed for this section of the work.

A visualisation study of the nature of the particle stream flow was also undertaken. The velocity of the free-falling particles was estimated by video recording the particle stream using a Phantom high speed video camera with a frame rate of  $1635\text{Hz}$ . Consecutive images were then analysed to estimate particle velocities using the Insight PIV software system (TSI Inc.). The quantitative accuracy of this system was relatively limited due to the limited resolution of the high speed video camera. However, the data provided important information on both the qualitative

and quantitative behaviour of the free falling particle stream. The bulk solid material mass flow rates for this work were relatively small ( $\sim 1\text{gram/s}$  where the hopper outlet radius  $1.0\text{mm} < r_0 < 2.5\text{mm}$ ).

### Experimental Results

The volume of entrained air increased with increasing drop height and the specific entrainment volume (volume of air entrained per mass of particulate) decreased significantly with increasing mass flow rate. The results for a series of tests on the alumina powder are shown in Figure 2.

Figure 2. Air entrainment variation with drop height and mass flow rate for alumina powder.

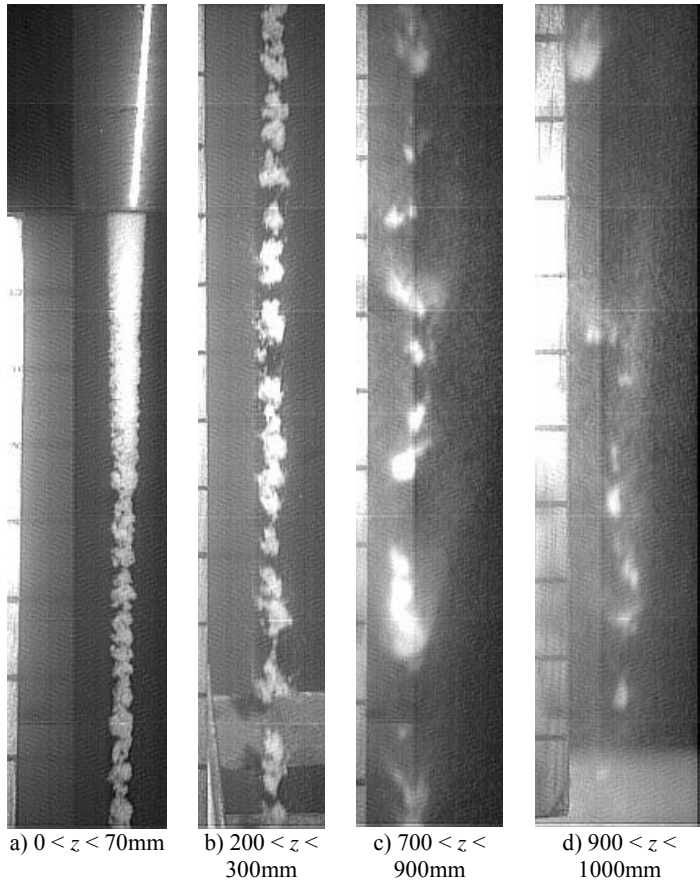
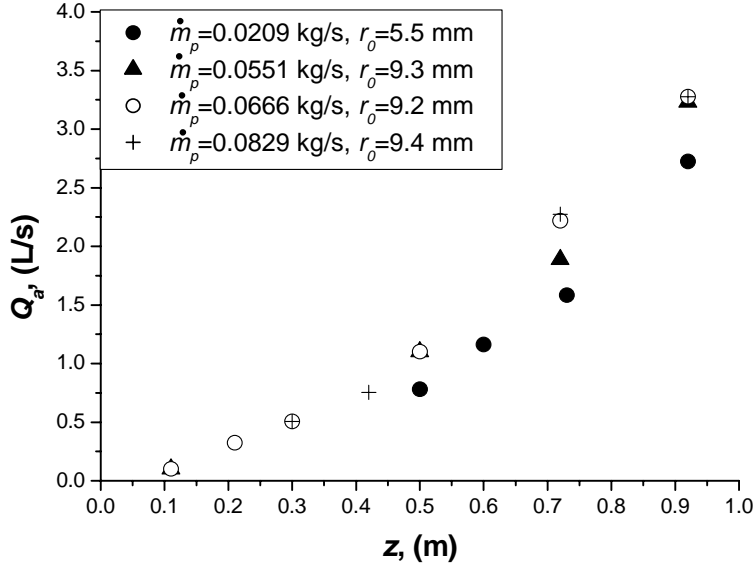


Figure 3 Free-falling alumina particle stream:  $r_0 = 2.5\text{mm}$ ,  $\dot{m}_p = 3.8\text{g/s}$  (scale to the left is marked in 10mm increments)

An example of images of the falling stream recorded by means of the high speed digital camera are shown in Figures 3 and 4. The falling streams of particles appeared to have three zones of development. In the initial stages of free fall, Zone 1 (Figure 3a),

the radius of the particle stream contracted immediately after leaving the hopper. This contraction is most likely to have been due to the fact that the conical sides of the hopper outlet imposed an initial inward radial velocity on the outer particles in the stream.

After the initial contraction, the radius of the core of falling particles remained relatively constant (Zone 2) over a very large elevation (to at least  $z/r_0 \sim 200$ ). A significant feature of the flow was the fact that the dilation of the particulate material was not homogeneous, and the core of the stream appeared to break into a series of individual particle “clouds”, as shown in Figures 3 and 4. Often this breakup appeared to have a preferred length scale, analogous to the breakup of a thin stream of liquid falling through air under gravitational forces where surface tension plays a role in determining droplet size. The particle clouds appeared to disperse with increasing drop height and were more readily dispersed at low particle mass flow rates,  $\dot{m}_p$ .

At large  $z$ , in Zone 3, the particle “clouds” were no longer evident as distinct elements. This region was only observed if there was a sufficiently large drop height or a sufficiently small particle mass flow rate. Moreover, it was difficult to capture the behaviour of this region with the video recording apparatus available. The behaviour of the particle-driven plumes clearly had characteristics similar to that of particle-driven thermals as described by Rahimipour and Wilkinson [10].



Figure 4. Corvic vinyl particle stream:  $r_0 = 2.5\text{mm}$ ,  $\dot{m}_p = 2.0\text{g/s}$

The breakup behaviour of the particle stream was also dependent to some extent on the properties of the bulk material. This is illustrated by a comparison of Figures 3 and 4. Figure 4a shows an energetic breakup event close to the hopper outlet and Figures 4b-d indicate that the corvic vinyl clouds may disperse more rapidly than those of alumina.

### Theoretical Model

The following one-dimensional analysis was developed by considering the momentum equations for both the falling

particles and the induced air, which are coupled through the aerodynamic drag forces. Clearly the particle plume flow is complex and a one-dimensional model to predict particle velocities, air entrainment velocity and volumetric flow rate must involve simplification of the flow phenomena. The aerodynamic force acting on a single particle within a stream of particles, for example, is very different from that acting on a single, isolated, falling particle. The inter-particle distances can be very small, particularly near the source of the particle plume, and the drag force acting on a particle is far from constant with respect to drop height. Moreover, the experimental results reported above show that the dilation of the particle stream may not be homogeneous beyond a given drop height. Nevertheless, the authors believe that the theoretical model represents valuable step toward the goal of understanding the behaviour of the particle plumes.

Consider a particle stream released from a source of radius  $r_0$  where  $n$  is the number of particles released per unit time. If at some elevation  $z$  the particles move with velocity  $v_p$  then the total drag force acting on these particles is given by [9]:

$$F^* = n \times f_d \times C_s \quad (1)$$

where  $f_d$  is the drag that would act on a single, isolated particle falling at velocity  $v_p$  through quiescent air, and  $C_s$  is a “stream coefficient”, which we have introduced to represent the ratio of the drag force acting on a particle within a stream of particles compared to that for an isolated particle. If all particles are then treated as being aerodynamically equivalent to spheres of diameter  $d_p$  and density  $\rho_p$ , then:

$$F^* = \frac{3\pi}{4d_p} \beta_0 v_0 r_0^2 \rho_a (v_p - v_a)^2 C_D \times C_s \quad (2)$$

where,  $\beta_0$  is the volume fraction of solid particles in the bulk solid,  $v_0$  is the bulk solid velocity at the source,  $\rho_a$  and  $\mu_a$  are the density and dynamic viscosity of air, respectively,  $v_a$  is the local characteristic vertical velocity of the air in the falling stream and  $C_D$  is the drag coefficient for a single isolated particle.

We have utilised the results of Wen and Yu [11] who carried out an experimental study on fluidized beds. We have assumed that their results are representative of the present situation in the core of the unconfined particle plume and that the stream coefficient  $C_s$  is a function only of the volumetric void fraction,  $\varepsilon = (\rho_p - \rho_b)/(\rho_p - \rho_a)$ , such that  $C_s = \varepsilon^{-4.7}$ . The net buoyancy force acting on the  $n$  particles released in one second,  $B^*$ , is then given by:

$$B^* = (\rho_p - \rho_a) \pi g \beta_0 v_0 r_0^2 \quad (3)$$

Invoking conservation of momentum on the particles falling under the influence of gravitational forces gives the rate of change of particle velocity with height:

$$\frac{dv_p}{dz} = \frac{B^* - F^*}{\dot{m}_p v_p} \quad (4)$$

The development of the jet or boundary layer of entrained air may be modelled in the same way as for miscible jets/plumes by making the assumption that the horizontal velocity of the entrained air is directly proportional to a local vertical velocity scale [12]. The constant of proportionality being the “entrainment constant” ( $\alpha$ ) so that:

$$\frac{d}{dz} (\pi r_a^2 v_a) = 2\pi r_a \alpha v_a \quad (5)$$

where  $r_a$  and  $v_a$  are the “top hat” radius and velocity of the entrained air jet. The rate of change of momentum flux of the entrained air with height may then be determined. Since the flow is isothermal only drag forces from the particles act on the air and the drag force on the air per unit height is then  $F^*/v_p$ . The rate of change of momentum flux is then:

$$\frac{d}{dz} (\rho_a \pi r_a^2 v_a^2) = \frac{F^*}{v_p} \quad (6)$$

Figure 5. Schematic of the particle stream with the dilating stream of particles of constant stream radius,  $r_p$ , and surrounding entrained air.

The determination of the local value of void fraction is an important issue in the theoretical model, because this influences the magnitude of drag forces on the particles. The model above quantifies the particle velocity but the radius of the particle stream,  $r_v$ , also needs to be known. From the visualisation experiments described above it is clear that this radius is constant with respect to height for at least for much of Zones 1 and 2. We have therefore assumed that  $r_v \sim r_0$ . However, for this model the complexities of the particle clouds have been put aside and the particle stream is assumed to dilate homogeneously. Equations (4)-(6) were then solved using a finite difference scheme.

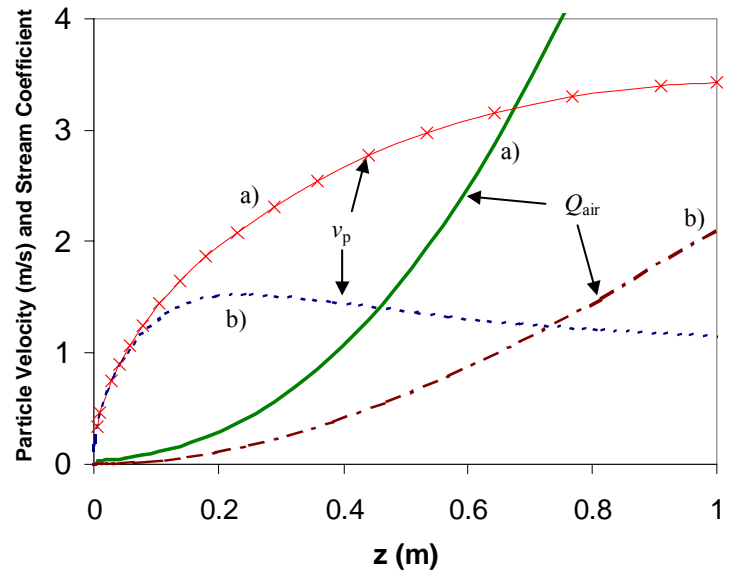


Figure 6. Entrained air flow rate and particle velocities predicted by the theoretical model for an arbitrary bulk solid ( $d_p = 100 \mu\text{m}$ ,  $\rho_p = 1500 \text{ kg/m}^3$ ,  $\rho_b = 500 \text{ kg/m}^3$ ,  $\alpha = 0.03$ ) with two different solid mass flow rates: a)  $\dot{m}_p = 20 \text{ g/s}$ ; b)  $\dot{m}_p = 0.2 \text{ g/s}$ .

The results of this theoretical model are shown in Figures 6 and 7 for a bulk solid of arbitrary physical properties. Figure 6 shows how the particle velocity as a function of elevation is critically dependent on the particulate mass flow rate. At the higher mass



flow rate the particles continue to accelerate over the full height of the simulation (1.0m). However, at the smaller mass flow rate the particles reach a maximum velocity at  $z \sim 0.2\text{m}$  and thereafter tend towards a lower velocity. This behaviour has been observed qualitatively in the flow visualisation experiments as shown in Figure 8. A further insight into the behaviour of the plume can be seen in Figure 7 where the velocity of the particles relative to the air approaches the terminal velocity as expected.

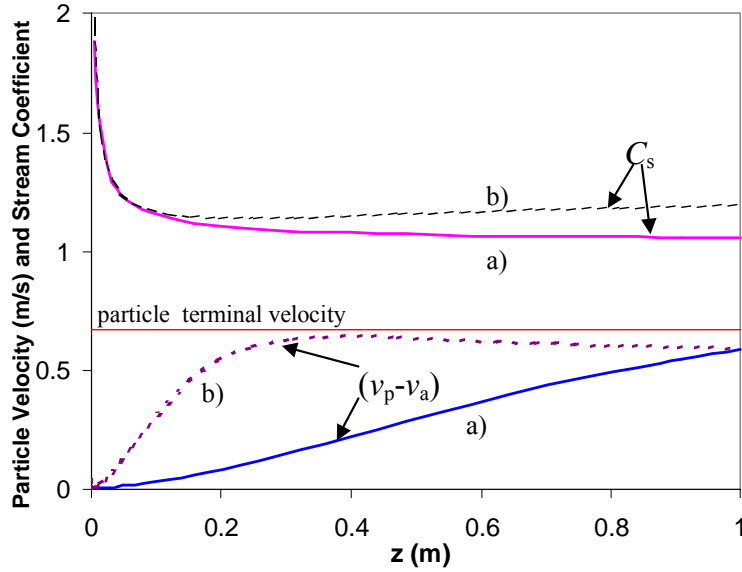


Figure 7. Relative velocity of particles ( $v_p - v_a$ ) and stream coefficient,  $C_s$ , predicted by the theoretical model for an arbitrary bulk solid (details as for Figure 6).

The entrainment constant  $\alpha$  for each material was determined by fitting the theoretical model to the air entrainment experimental data using the least squares method. Figure 8 shows a comparison of the predicted and measured entrained air flow rates for typical set of experiments on alumina. Note that the particle diameter used in the numerical model was taken to be the median particle size of a representative sample of the bulk material. The theoretical model above provided a good correlation of the experimental data with a single entrainment constant for each material. However,  $\alpha$  did vary significantly between the materials:  $\alpha_{\text{alumina}} = 0.0196 \pm 0.004$ ;  $\alpha_{\text{sand}} = 0.0210 \pm 0.007$ ;  $\alpha_{\text{coriv\_vinyl}} = 0.0326 \pm 0.006$ . These entrainment rates are less than for miscible jets and plumes ( $\alpha_{\text{jet}} \approx 0.0535$ ,  $\alpha_{\text{plume}} \approx 0.083$ ).

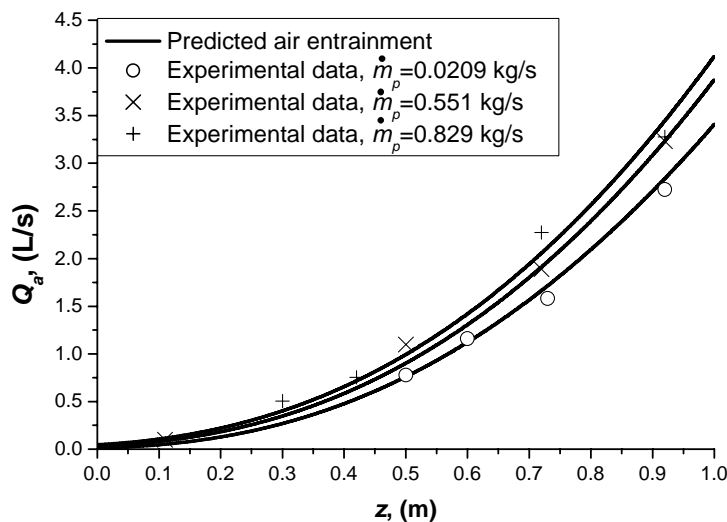


Figure 8. Variation of entrained air flowrate against particle drop height, alumina ( $\alpha = 0.0196$ ,  $d_p = 96 \mu\text{m}$ ).

Further work is required on the theoretical analysis to incorporate some of the details of the flow not covered above, while there is also a need for further experimental work to determine the particle velocities within the falling stream over all three zones.

## Conclusions

Free falling particle streams, or particle plumes, are important in many industrial situations. This paper has outlined a program of experimental work that has determined the characteristics of such falling streams in air, at laboratory scale, with respect to the quantity of air entrained as a function of height, particulate mass flow rate and physical properties.

High speed video imaging of the free-falling particle stream has also shown that the bulk material does not dilate in a homogeneous manner, but rather the core stream of bulk material appears to break up into a series of particle "clouds" that disperse with increasing drop height. There also appears to be three major zones in the vertical development of the particle plume. In Zone 1 near the source the core stream of particles descends with a slight decrease in radius and appear to dilate homogeneously. Below this region, in Zone 2 the core stream breaks up into distinct particle clouds. And finally in Zone 3 these clouds become increasingly dispersed and the core stream radius increases markedly.

A theoretical analysis of the air entrainment process has been developed that models the drag forces on the particles within the falling stream and predicts the particle velocity and entrained air flow as a function of drop height, particulate mass flow rate and particulate properties.

## References

- [1] Leitch, A. M. and Baines, W. D., Liquid volume flux in a weak bubble plume, *J. Fluid Mech.*, **205**, 1989, 77-98.
- [2] Gosh, S., Hunt, J.C.R., Phillips, J.C. and Miller, P.C.H., Dynamics of turbulent air-flow in droplet driven sprays, *Appl. Scientific Res.*, **51**, 1993, 257-262.
- [3] Hemeon, W. D. L., *Plant and process ventilation*, Industrial Press, N.Y., 1963.
- [4] Morrison, J. N., Controlling Dust Emissions at Belt Conveyor Transfer Points, *Society of Mining Engineers, AIME, Transactions*, **250**, 1971, 47-52.
- [5] Tooker, G. E., Controlling fugitive dust emissions in material handling operations, *Bulk Solids Handling*, **12**, no. 2, 1992, 227-232.
- [6] Plinke, M.A.E., Leith D., Holstein D.B. and Boundy, M.G. *Am. Ind. Hyg. Assoc. J.*, **52**(12), 1991, 521-528.
- [7] Cooper, P., Liu, Z. and Wypych, P. W., Plumes Driven by Free-Falling Streams of Solid Particles, *Proc. 14th Australasian Fluid Mechanics Conference*, Adelaide, 2001, 649-652.
- [8] Ricou, F.P. and Spalding, D.P., Measurements of entrainment by axisymmetrical turbulent jets, *J. Fluid Mech.*, **8**, 1961, 21-32.
- [9] Liu, Z., *Air entrainment in free falling bulk materials*, PhD thesis, University of Wollongong, Australia, 2003.
- [10] Rahimpour, H. and Wilkinson, D., Dynamic behaviour of particle clouds, *Proc. 11th Australasian Fluid Mech Conf., Hobart, Australia*, 1992, 743-746.
- [11] Wen, C. Y. and Yu Y. H., Mechanics of Fluidization, *Chemical Engineering Progress, Symposium Series*, **62**, 1966, pp. 100-111.
- [12] Morton, B., Taylor, G.I. and Turner, J.S., Turbulent gravitational convection from maintained and instantaneous sources, *Proc. Royal Soc. London, A*, **234A**, 1956, 1-22.

## Experimental Investigation of Flow-Induced Vibration in a Parallel Plate Reactor Fuel Assembly.

Mark Ho, Guang Hong and A.N.F. Mack

Mechatronics and Intelligence Systems, Faculty of Engineering  
University of Technology, Sydney, Broadway, NSW, 2007 AUSTRALIA

### Abstract

This research aims to experimentally investigate the critical flow velocity of light-water coolant in a reactor parallel-plate fuel-assembly. The critical flow velocity is the speed at which rectangular fuel-plates will buckle and collapse onto each other as a result of flow-induced vibration and consequent asymmetric pressure distribution. Although fuel plates do not rupture during plate collapse, the excessive permanent lateral deflection (buckling) of a plate can cause flow blockage in the reactor core, which may lead to over-heating. This is an important consideration in reactor core designs with parallel plate fuel assemblies. The Replacement Research Reactor (RRR) currently under construction at the Australian Science and Technology Organisation (ANSTO) is of such a design.

A simple physical model of a parallel-plate fuel-assembly composed of two parallel plates was constructed and tested in a closed-loop water tunnel (figure 1). Plate vibration was measured at low flow speeds and the critical flow velocity was recorded. Test results show plate collapse occurring, in 25°C light water, at an average flow velocity range of 11.9 - 12.0m/s. For the first time, cavitation was observed as a result of leading-edge deformation during plate collapse. The experimental results attained support Miller's [4] critical-velocity calculation for plate collapse. However, it must be stressed that the flow characteristics of the RRR are significantly different to the results reported here due to the presence of a lateral-support comb at the RRR fuel assembly inlet. This comb greatly reduces any vibrations and increases the critical velocity for the fuel assembly.

### Introduction

Plate collapse phenomenon was first observed in the Engineering Test Reactor (ETR) in the 1950s. It was noted that some fuel-plates gave warning before buckling by a slight bending or warping. Later, Miller [4] used wide-beam theory to equate the pressure differences between coolant channels with the elastic restoring force of the plate to estimate the critical-velocity ( $U_d$ ) at which plates collapsed. Plate collapse is a *static-instability* type-failure occurring at a moderate velocity, identified by Kim and Davis [3] as the "critical static divergent velocity  $U_d$ ". Static-instability type failure is not to be confused with the high velocity *dynamic instability* experienced at the "critical resonance velocity  $U_r$ " when flow excitation frequency coincides with the in-fluid natural frequency of the fuel plate.

Notable experimental investigations were undertaken by Groninger and Kane [2], Scavuzzo [5] and Smisseart [6] to verify Miller's critical flow velocity (critical static divergent velocity). The experiments gave mixed findings, including: (1) Plates deflecting slightly below Miller's critical-velocity and (2) an absence of Miller's predicted sudden plate collapse at or beyond the 'critical-velocity' mark. What was shown though was a gradual movement of the plates from their mean position with each incremental increase in velocity. Thus plate collapse is actually the moment at which the plates touch after a gradual movement of plates. Also, Smisseart showed that plate collapse

produced alternately open and closed conduits, with plates collapsing in opposite directions.

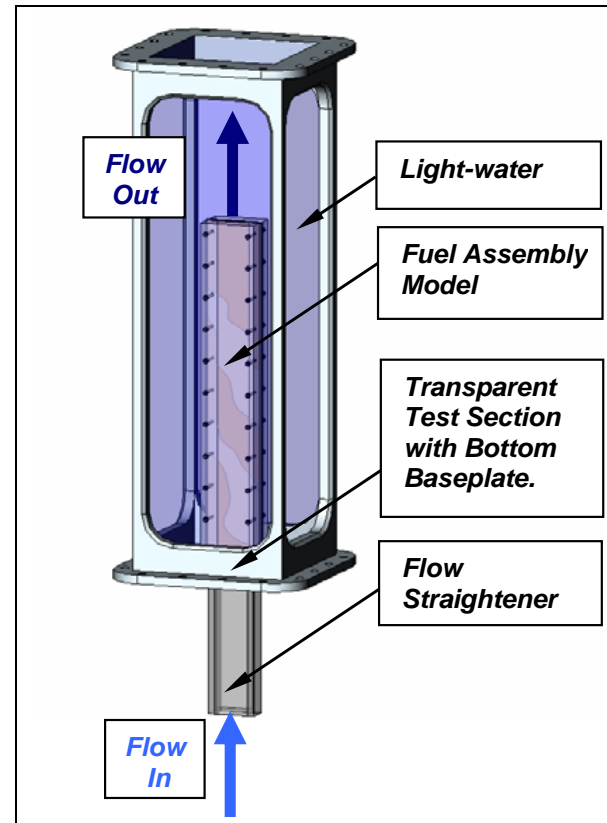


Figure 1 – Isometric view of fuel-assembly-model inside the test section.

### Failure mechanism in parallel plate fuel assemblies.

The main interest of this research is the observation and recording of the plate collapse phenomenon as this data can be used to appraise the oft-quoted Miller's critical velocity, common in critical static-divergent velocity calculations.

Most reactor cores have less than ideal flow conditions, characterised by turbulence, imperfect axial-flow and pressure fluctuations produced by pump and other plant equipment. As such, equal flow through each channel of a parallel plate fuel assembly cannot be assumed. Miller, one of the pioneers of flat-plate fuel stability research described fuel collapse as due to the difference in velocities of adjacent channels. This difference produces a pressure difference on either sides of a plate. When the net pressure on the plate is too large for the plate to resist, the plate buckles and deforms.

Fuel plate collapse originates from plate vibration. As flow passes through a narrowing channel, the pressure head is converted to a velocity head and creates a suction force on the wall. Should the wall be moveable as is the case for parallel fuel plates, the channel cross section can decrease to obstruct the flow. Flow obstruction increases local pressure as flow from the inlet tries to overcome the constriction. Thus pushing apart the



fuel plates and increasing the channel cross section. This pushing and pulling action acts periodically, vibrating the structure which can lead to large plate deflections and localised overheating. ANSTO [1]

### The theoretical collapse velocity

Miller [4] derived a theoretical expression to predict the critical flow velocity ( $U_d$ ) at which long parallel-plate assemblies collapse. This expression is a function of the plate, channel and fluid characteristics, as shown below:

$$U_d = \left[ \frac{15 \cdot E \cdot t_p^3 \cdot t_w}{\rho \cdot W^4 (1 - \nu^2)} \right]^{0.5} \quad (1)$$

Where:

$U_d$  = Miller's critical velocity (m/s)

$E$  = plate Elastic Modulus (kPa)

$t_p$  = plate thickness (mm)

$t_w$  = coolant channel thickness (mm)

$\rho$  = coolant density (kg/m<sup>3</sup>)

$W$  = coolant channel width (mm)

$\nu$  = plate's Poisson's ratio

Physical properties of parallel-plate fuel-assembly model	
Elastic Modulus of Aluminium	70.0 x 10 <sup>6</sup> kPa
Plate thickness	1.2mm
Poisson's ratio of Aluminium plate	0.33
Channel Width	78.2mm
Channel Height	4.3mm
Coolant (H <sub>2</sub> O) density	998.2 kg/m <sup>3</sup> (at 25°C)
Calculated Miller's Collapse Velocity	15.4 m/s

Table 1. Calculated Miller's critical velocity for this parallel-plate fuel-assembly.

Although Miller's theoretical collapse velocity is a basic representation of a complicated system and is known to be outmoded when compared with CFD and FEA techniques, it remains a widely used theory because of its ease in giving an approximate velocity at which plate collapse will occur. However, to allow for uncertainties, reactor designers usually place a large margin between Miller's critical-velocity and the designed operational coolant velocity. The need to impose a margin of safety was shown in an analytical investigation conducted by Kim and Davis [3], which showed plate collapse occurring below Miller's collapse-velocity, at  $0.9U_m$  in the absence of a steadying-comb.

### ANSTO Water Tunnel facility

The water tunnel facility used in our experiments is located at ANSTO, Lucas Heights Research Laboratories in Sydney. The water tunnel is one of only a few test facilities in Australia capable of delivering the power necessary to investigate plate collapse phenomenon. The water tunnel is a closed loop flow rig used for flow visualisation, velocity measurement and pressure loss characteristics testing of hydraulic fittings. The transparent test section is vertical, with internal measurements 0.3m x 0.3m x 1.3m. Water capacity of the rig is approximately 3000L, which is circulated by a double suction pump driven by a 75 kW AC motor and variable speed controller. The motor and pump can achieve a flow of 230 L/s with no flow impediment inside the water tunnel or a maximum head pressure of 350kPa if the exit of the pump were to be blocked.

### Fuel assembly model

This physical fuel-assembly model was designed to simulate a generic light-water cooled parallel-plate fuel assembly. The model is comprised of two identical Aluminium plates dividing a single rectangular conduit into three identical channels. The plates are rigidly clamped along the two long sides, with the two shorter sides free and have a dimension of 780mm x 78mm x 1.2mm. As shown in Figure 2, the fuel-assembly-model is a sandwich structure of 40mm thick Perspex plates, 4.3mm thick Perspex lengths and 1.2mm thick Aluminium plates. The whole structure is clamped together by nuts and threaded rod equally spaced along the long edges of the model. Also, the mock fuel-assembly is mounted vertically in the water tunnel and is preceded by a plain rectangular duct mounted flush to the model.

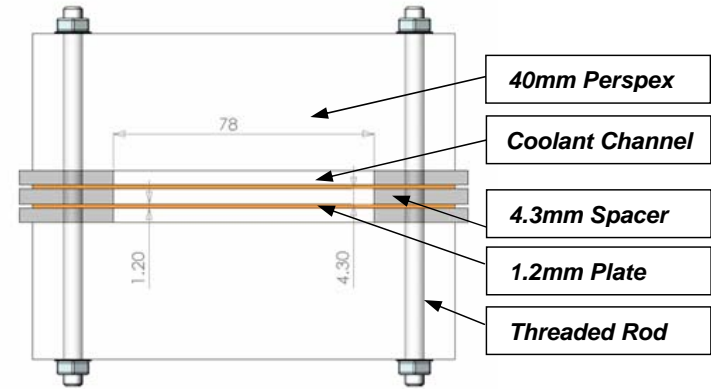


Figure 2 – Top view of the flat plate fuel-assembly-model, dimensions are in millimetres.

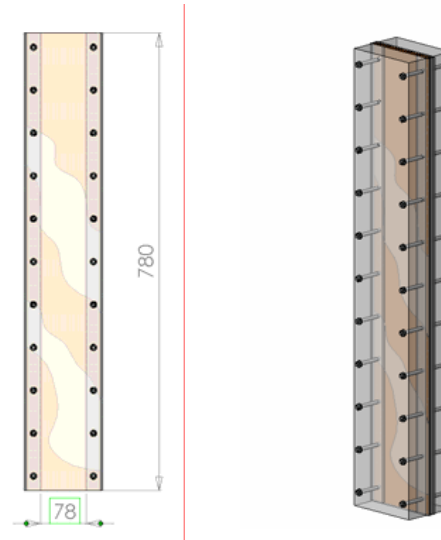


Figure 3 – Front and isometric view of the flat plate fuel-assembly-model, dimensions are in millimetres.

Most flat-plate fuel assemblies are equipped with a stabilisation comb at the plate's leading edged. This comb, mounted at the mid point of the leading edge, helps to stabilise the fuel plate against flow induced vibration mechanisms such as turbulence, vortex shedding and fluidelastic instability. For a conservative test of Miller's Critical Collapse Velocity, there was no reason to install a stabilisation comb and none was installed in this model.

As shown in figure 1, light-water at 25°C enters the flow straightener and passes into the fuel-assembly-model. A base plate at the bottom of the test section prevents any flow bypass. Thus, all flow through the closed-loop facility must enter the fuel-assembly-model. Having passed between the plates, the flow exits the top of the fuel-assembly-model and travels through a flowmeter further downstream. Consequently, the flowmeter is able to measure the aggregate flow through the model.

Instrumentation

In the fuel-assembly model, one of the two plates is instrumented with strain gauges at three positions: the leading edge, the middle of the plate and the trailing edge. At each position two strain gauges on either side of the plate detect vibration and deflection at different flow speeds. Strain gauges serve as the primary method for plate-deflection detection because they are in direct contact with the plate. The strain gauges were epoxied into a 0.4mm ditch milled into the plate and sealed by Araldite. The analogue voltage signal produced by the strain-gauges is directly proportional to the deformation on the plate.



Figure 4 – Close-up photograph of strain gauge embedded inside an Aluminium plate and pressure tapings drilled into the side of the 40mm Perspex plate.

Data Acquisition Equipment	
Strain Gauge	Copper-Nickel alloy measuring-grid ; Measurable Strain: 2–4% max.
Strain Gauge Amplifier	RS Components No. 846-171
Data Acquisition Card	Fast Card : LabView No. NI6071E ; PCI Bus ; 1.25x10 <sup>6</sup> Samples/Sec; Slow Card : LabView No. NI6033E ; PCI Bus ; 100x10 <sup>3</sup> Samples/Sec
Data Acquisition Software	LabView 6.1
Data Acquisition Hardware	IBM Personal Computer, WinNT Operating System.

Table 2 : List of Equipment for plate vibration and deflection monitoring.

In addition, the mock fuel-assembly is equipped to measure static pressure at 100mm intervals along the axis of the plate. Measuring pressure drop serves as a secondary method in detecting plate collapse, as the flow-loss characteristics of the fuel assembly-model changes once the plate has deformed. Pressure loss data can also be collected and used to verify CFD simulations in the future.

As mentioned previously, aggregate flow through the fuel-assembly model is measured by an electromagnetic flowmeter mounted in the water tunnel. To validate the correct physicality of our experiment, it is necessary to check that equal flow is observed through each of the three channels before plate collapse. This was done by using Laser Doppler Velocimetry (LDV) to sample the maximum flow-velocity exiting each channel.

Vibration tests

Tests were conducted in air and quiescent water to ascertain the dynamic characteristics of this model fuel plate. To measure the in-air fundamental vibration of the Aluminium plate, stain gauges and accelerometers were used. The plucking method was used to

find the in-air fundamental frequency of the model fuel plate. Examination of the accelerometer and strain gauge results show a close agreement between the two measurements, with the accelerometer measuring a fundamental frequency of 684 Hz and the strain gauge measuring a fundamental frequency of 685Hz.

Satisfied with our in-air plucking test, the strain gauge and accelerometer can be confidently used to examine the in-water response of the model-fuel-plates. The fuel-assembly-model was placed horizontally and covered with water. A set of strain gauge and accelerometers were fixed on the same location on the plate and the plucking method was used to obtain the plate’s dynamic response. Examination of the accelerometer and strain gauge results for the quiescent water test shows near-identical results. The model fuel plate in quiescent water has a fundamental frequency of 100Hz, a first harmonic at 225Hz and second harmonic at 430Hz.

Vibration monitoring of fluid-elastic instability.

Following the in-air and in-water plucking test, the fuel-assembly-model was flow tested in the water tunnel. Before a model fuel plates was tested to destruction, it was vibration tested from 0 m/s to 8 m/s at 1m/s intervals to observe fluid-elastic instability effects. Monitoring was performed via the use of a LabView data acquisition card & software. The analogue voltage signal was passed through a low-pass filter, recorded then processed using Fast Fourier Transform (FFT) method. Results were averaged over 50 samples to reduce the effects of white noise.

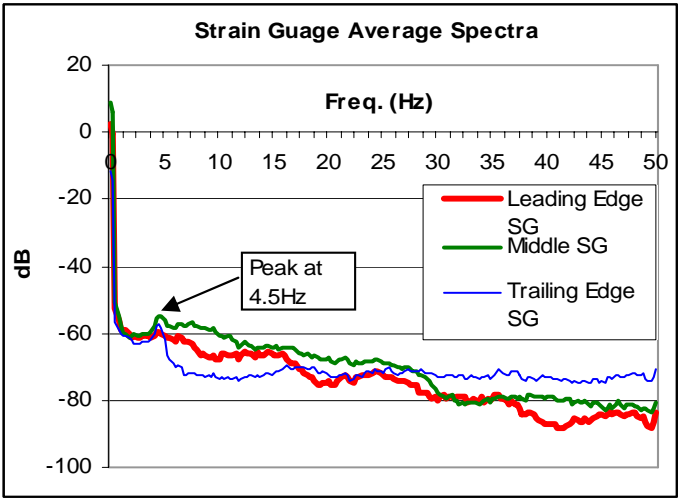


Figure 5 – Average spectra of strain gauges with flow velocity at 6.0m/s (Re 48,360) . Results show a distinct peak at 4.5Hz.

Results attained agree with the push-pull fluid-elastic effect described in The Preliminary Safety Analysis Report prepared by ANSTO [1]. The vibration is low in frequency and appears to remain constant at 4.5Hz in turbulent flow. Also, the graphs show that the amplitude of the vibration increases with flow velocity, which supports the notion that an increase in flow speed is accompanied by increasing plate exacerbation until plate collapse is brought about.

Plate collapse flow tests.

To detect the plate collapse phenomenon, the model was gradually subjected to higher flows at average-velocity increments of 0.5m/s until plate collapse occurred. Plate collapse was observed in a variety of ways. The most accurate method was by recording the voltage output of the strain gauge at the leading edge of the plate where plate collapse was most severe. As the plate catastrophically buckled out, the voltage would change sharply as the resistance changed in the strain gauge - until it was out of the ±5V range of the data acquisition card.

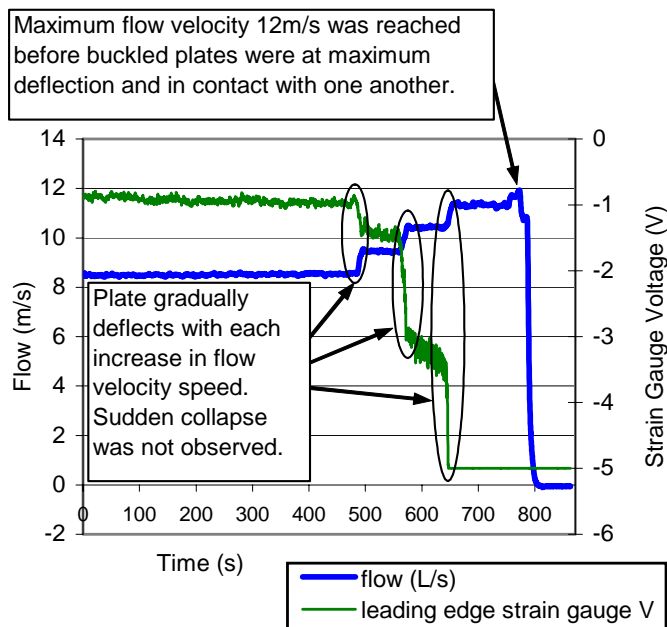


Fig. 6 Flow velocity and pump head pressure versus time.

As shown in figure 6, the leading edge of the plate experienced a gradual buckling outwards as observed by Smislaert [6]. A maximum flow velocity of 12m/s ( $Re\ 108,716$ ) was reached before the plates buckled far enough to be in contact with one another and thus achieving “plate collapse”.

An indirect method of observing plate collapse was by recording the aggregate flow speed through the fuel-assembly model as plate collapse occurred. With the pump delivering a steady pressure, the aggregate flow speed through the fuel-assembly model dropped by approximately 1m/s after the plates collapsed as shown in figure 7. This drop in flow speed was due to the increased flow resistance of the plates as it flexed out into the path of the flow (figure 8). Also, as a consequence of plate collapse, cavitation bubbles in the form of a fine mist were observed departing the coolant channel exit.

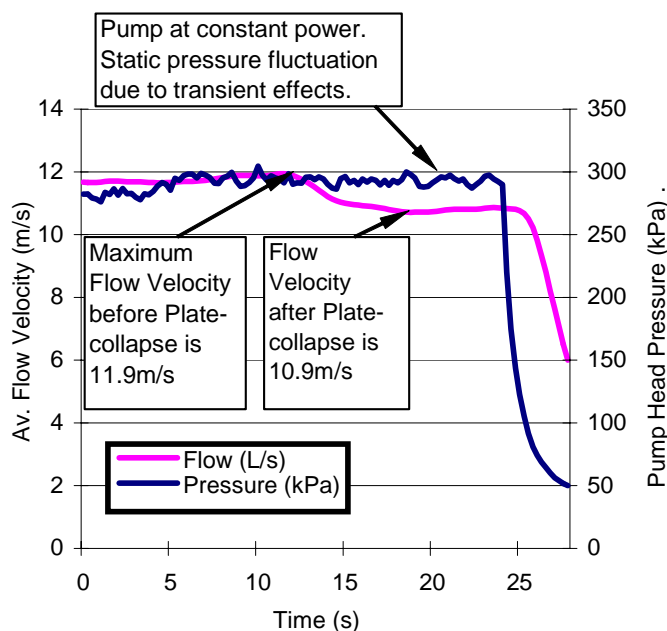


Fig. 7 Flow velocity and pump head pressure versus time.



Figure 8 – Post-failure end view of the flat plate fuel-assembly-model. Note: both plates' leading edges have buckled and plastically deformed away from each other.

## Conclusion

Preliminary results show plate collapse occurring at an average flow velocity between 11.9m/s to 12m/s in 25°C light-water, which is 78% of Miller's critical velocity. It is lower than the collapse velocities reported in past experiments conducted with light-water at 50°C. The shape of the plate collapse seems random, either with both plates collapsing onto each other or with both plates collapsing away from each other. In the case of the plates collapsing away from each other, cavitation was observed. The results attained in the experiment compare well with the calculated Miller's [4] Critical-velocity of 15.4m/s, keeping in mind that analytical analysis by Kim and Davis [3] predicts plate collapse at  $0.9U_d$ . As such, this experimental undertaking has shown the relevance and usefulness of Miller's Critical Velocity for the safe design of flat plate type research reactors.

## Acknowledgments

I would like to sincerely thank ANSTO Reactor Operations, for providing me with the scholarship for this project. Of much importance was their generous supply of laboratory facilities and equipment needed in this experimental investigation. In particular I would like to thank Mr. David Wassink, manager of the Water Tunnel Facility for his expert opinion, Dr. Greg Storr for his keen interest in the project, as well as everyone in Nuclear Analysis Section for their input and advice.

## References

- [1] ANSTO, Summary of the Preliminary Safety Analysis Report (PSAR) for the ANSTO Replacement Research Reactor Facility, 1 and 2, Sydney, ANSTO, 2002.
- [2] Groninger, R. D. and Kane, J. J., Flow Induced Deflections of Parallel Flat Plates, *Nuclear Science and Engineering*, **16**, 1963, 218-226.
- [3] Kim, G. and Davis, D. C., Hydraulic Instabilities in Flat-Plate-Type Fuel Assemblies, *Nuclear Science and Engineering*, **158**, 1995, 1-17.
- [4] Miller, D. R., Critical Flow Velocities for Collapse of Reactor Parallel-Plate Fuel Assemblies, *Journal of Engineering for Power*, **April**, 1960, 83-95.
- [5] Scavuzzo, R. J., Hydraulic Instability of Flat Parallel-Plate Assemblies, *Nuclear Science and Engineering*, **21**, 1965, 463-472.
- [6] Smislaert, G. E., Static and Dynamic Hydro-elastic Instabilities in MTR-Type Fuel Elements Part I. Introduction and Experimental Investigation, *Nuclear Engineering and Design*, **7**, 1968, 535-546.



## Flow past a Cylinder with Free Hemispherical Ends: Comments on Grid Independence and Wake Symmetry Characteristics

G. J. Sheard<sup>1</sup>, Mark C. Thompson<sup>1</sup> and K. Hourigan<sup>1</sup>

<sup>1</sup>Fluids Laboratory for Aeronautical and Industrial Research (FLAIR)  
Department of Mechanical Engineering, Monash University, VIC 3800, AUSTRALIA

### Abstract

A grid independence study and numerical computations are reported for the flow past cylinders with free hemispherical ends. A novel modelling technique is used whereby a spectral-element method is employed with an azimuthal Fourier expansion around the symmetry axis of the cylinder. The flow direction is then normal to the axis of symmetry, rather than in the axial direction. For benchmarking purposes, results using the proposed grids are compared to accurate computations of the flow past a sphere, and an accuracy of better than 0.5% is obtained up to a Reynolds number  $Re = 300$ . Plots showing alterations in the symmetry characteristics of the wakes are provided for length ratios up to  $L_R = 10$ .

### Introduction

In this paper the suitability of a spectral-element method with an azimuthal Fourier expansion to study the flow past a cylinder with hemispherical ends (hereafter referred to simply as a “cylinder”) is considered.

The cylinder may be described by a ratio between its overall length  $L$ , and its diameter  $d$ , giving the length ratio parameter  $L_R = L/d$ . Clearly then,  $L_R = 1$  describes a sphere, whereas as  $L_R \rightarrow \infty$ , the straight circular span of the cylinder becomes the dominant geometric feature, and the flow properties should approach those of a straight circular cylinder. This paper considers only the case where the flow is normal to the symmetry axis of the cylinder. A Reynolds number is defined as  $Re = U_\infty d/\nu$ , based on the cylinder diameter  $d$ , the freestream velocity  $U_\infty$  and the kinematic viscosity of the fluid  $\nu$ . A schematic diagram that shows the relevant dimensions of the cylinder is provided in figure 1.

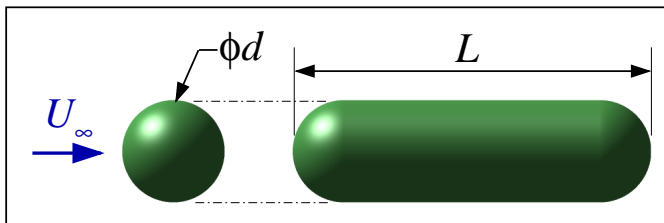


Figure 1: Schematic diagram showing the relevant dimensions of a cylinder with free hemispherical ends, and the relative direction of flow.

The low-Reynolds-number transitions for a sphere and a circular cylinder are somewhat different: [6] describes how the steady separated wake behind a circular cylinder becomes unsteady through a Bénard–von Kármán instability at approximately  $Re = 47$  based on the cylinder diameter, and [16, 17, 18] describes the subsequent development of three-dimensional spanwise-periodic instabilities in the wake, beginning with the Mode A instability at approximately  $Re = 180$ . For a sphere, [15, 3] provided accurate measurements of a regular transition to a steady non-axisymmetric wake at  $Re \approx 212$ , and [2, 14]

have shown that the subsequent transition to unsteady flow occurs at  $Re \approx 272$  through a continuous supercritical bifurcation.

Short cylinders with hemispherical ends have been the subject of experimental studies in recent years [10, 7], driven largely by an interest in the variation in the transition Reynolds number for the development of unsteady flow, the subsequent variation in Strouhal frequency of shedding, and the interaction of wakes behind pairs of bluff bodies [9, 8]. The study of cylinders with hemispherical ends is also relevant to the study of circular cylinders of low aspect ratio (length/diameter) [5, 4]. In [10] the critical Reynolds numbers for the development of periodic flow in the wake behind cylinders with free hemispherical ends was measured for a range of cylinders  $0 \leq L_R \leq 5$ . They observe that the critical Reynolds number was approximately  $Re_c = 270$  for a sphere ( $L_R = 1$ ), and decreased with an increase in length ratio. At  $L_R = 5$  a critical Reynolds number  $Re_c \approx 85$  was measured. This value is still significantly higher than the value for a straight circular cylinder ( $Re \approx 47$ ) measured by [6], suggesting that longer length ratios need to be considered. A benefit of the present numerical formulation is the ease with which larger length ratios can be modeled. The significant difference in flow properties between a cylinder with  $L_R = 5$  and a straight circular cylinder can also be perceived from the measured Strouhal–Reynolds number profiles provided in [10, 7]. The Strouhal–Reynolds number profile for the cylinder with  $L_R = 5$  initiates at the critical Reynolds number  $Re_c \approx 85$  with a shedding frequency  $St \approx 0.095$ . This is approximately 21% below the Strouhal frequency at the critical Reynolds number for the onset of unsteady flow ( $St \approx 0.12$ ) in the wake of a straight circular cylinder, and approximately 41% below the Strouhal frequency at the same Reynolds number.

Whereas the previous experimental studies have provided substantial data relating to the Strouhal–Reynolds number relationships for cylinders with  $1 \leq L_R \leq 5$ , little flow visualisation has been provided. The present numerical study will add significantly to our understanding of the structure of the flows following the development of unsteady and spanwise-asymmetric flow.

### Numerical Formulation

The spectral-element scheme used in this study has been successfully applied to model the flow past axisymmetric bodies such as a sphere [14] and rings [11, 13]. These references should be consulted for further details of the numerical method.

The method employed here uses the same Fourier expansion of the velocity and pressure fields about an axis of symmetry as in the previous studies, but with the important distinction in that the flow direction is now normal to the axis of symmetry, rather than in the axial direction. The mesh required to adequately resolve the wake using this method has some unavoidable inherent inefficiencies. The use of a Fourier expansion of the flow field around the cylinder requires that a large number of Fourier planes be used to resolve details in the flow across the wake. In addition, the computational domain must extend sufficiently

far from the cylinder to minimise both transverse blockage effects, and the deterioration of the wake structure in the vicinity of the downstream domain. Using previous numerical studies as a guide [1, 14], a family of meshes was constructed that varied only in terms of the addition of elements between the hemispherical ends to model the cylinder span. The mesh employed to model a cylinder with  $L_R = 1$  did not require any of these additional elements as the straight-span section of the cylinder had zero length. The meshes consistently employed 10 elements in the radial direction, and 5 elements between the axis and the straight span section around the cylinder ends. As an example, a plot of the mesh employed to model a cylinder with  $L_R = 5$  is provided in figure 2.

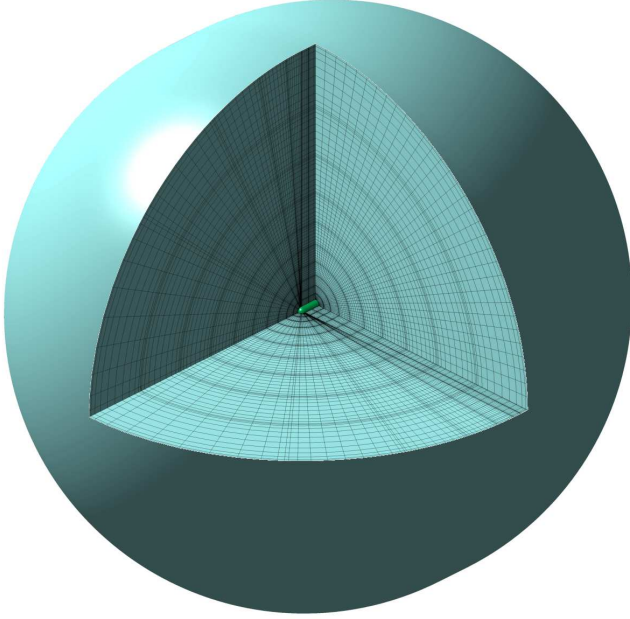


Figure 2: A cutaway view of the computational domain showing the mesh employed to model the flow past a cylinder with free hemispherical ends and a length ratio  $L_R = 5$ . Sub-elements are shown, and the domain extends  $30d$  from the cylinder.

A grid independence study was performed at  $Re = 300$  using the  $L_R = 1$  mesh to allow comparison with previous sphere studies. Meshes with  $P = 64$  and 128 Fourier planes were tested, to determine the number of planes required to resolve the wake, and the number of nodes per element was varied from  $N^2 = 25$  to 144. The graph in figure 3 shows the convergence characteristics with increasing number of mesh nodes ( $N^2P$ ) for the simulations with 64 and 128 planes. Notice that with 64 planes, the pressure and viscous components of the drag coefficient seem to converge to within a few percent of the accurate sphere computations (repeated from an earlier study [13]) indicated by the dotted lines, but the Strouhal frequency is 7% higher. This discrepancy indicates that 64 planes is insufficient to resolve the wake. Notice that with 128 planes, each of the parameters converges to within 0.5% of the accurate numerical values. Based on these findings, the meshes employed for this study each employed  $P = 128$  planes, and  $N^2 = 121$  nodes per element.

To improve the stability of the time-integration of the computations, a filter was applied to the azimuthal Fourier modes to reduce the number of modes in the vicinity of the axis of symmetry ( $r \rightarrow 0$ ). This treatment reduces the limiting effect of the Courant condition on the time-step  $\Delta t$ .

### Sphere Wake Comparison

A visual comparison of the wakes behind a sphere at  $Re = 300$

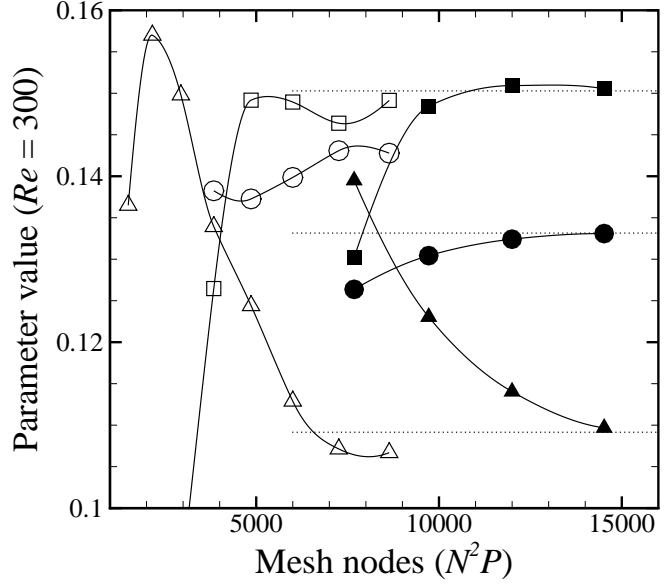


Figure 3: Convergence with increasing nodes per element ( $N^2$ ) of a cylinder with  $L_R = 1$  (a sphere) at  $Re = 300$ . Meshes with  $P = 64$  and 128 planes (open and filled symbols, respectively) are investigated, and the parameters  $C_{Dp}$  (□),  $C_{Dv}$  (△) and  $St$  (○) are monitored. The dotted lines show the corresponding parameter values from previous accurate studies of a sphere.

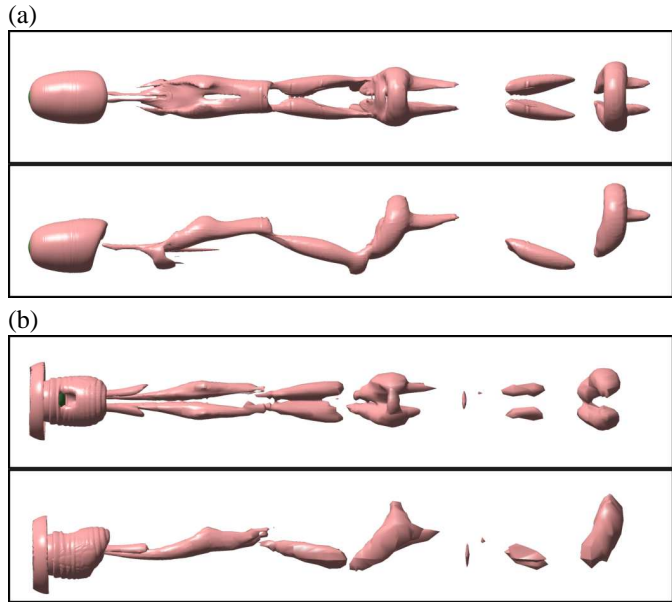


Figure 4: Isosurface plots showing the vortical structures in the wake behind a sphere. In (a), the wake is computed using the present crossflow grids, and in (b), a traditional axial-flow grid is used. The wake in each case is viewed from above and the side, and flow is from left to right.

computed using the present crossflow mesh and previous axial-flow meshes is provided in figure 4. Notice that although the flow quantities have converged to a high degree of accuracy using the crossflow method, an appreciable loss of fine detail in the wake has occurred. Despite this, the convergence of the flow quantities in the previous section suggests that meaningful quantitative predictions of the flow regimes up to  $Re \approx 300$  can be made.

To confirm that the accuracy predicted at  $Re = 300$  extends to lower Reynolds numbers, components of the mean drag were computed. These values are compared to the accurate results from [11, 12] in figure 5.

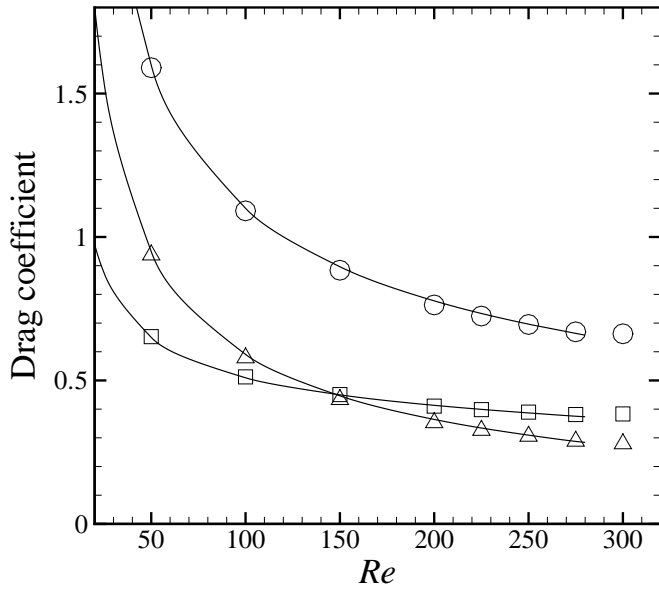


Figure 5: A comparison between the drag coefficient for a sphere using the present numerical technique (symbols), and from the accurate numerical computations of the flow by [11, 12] (lines). The mean pressure, viscous and total drag are shown by  $\square$ ,  $\triangle$  and  $\circ$ , respectively.

#### Cylinder with Hemispherical Ends at $Re = 300$

One of the primary goals of the present study is to determine how the hairpin shedding observed in the flow past a sphere relates to the Kármán vortex street behind a straight circular cylinder. The unsteady wakes behind cylinders with  $L_R = 1, 2, 3, 4$  and  $5$  were computed at  $Re = 300$ . The variation in the pressure and viscous forces acting on the cylinders were monitored in three dimensions.

Chief among the interesting observations that have been made to date is the link between the frequency of the hairpin shedding from a sphere, and a spanwise oscillation computed in the flow past cylinders. The frequency of this oscillation decreases with an increase in  $L_R$ , as depicted in figure 6. The near-periodic oscillations became weaker in magnitude as the length ratio increased, and were replaced by a chaotic force response at  $L_R = 5$ . The decrease in the amplitude of the low-frequency oscillation in the spanwise direction contrasted a measured increase in the force response in the transverse direction normal to the plane of the wake. This fluctuation is thought to be consistent with the Kármán shedding process.

Included in figure 7 are isosurface plots showing the wakes behind cylinders with length ratios up to  $L_R = 10$ . The cylinders with length ratios in the range  $0 \leq L_R \leq 5$  were computed at  $Re = 300$ , while the cylinder with  $L_R = 10$  was computed at  $Re = 100$ . It can be seen that at smaller length ratios the wakes are not symmetrical about the cylinder mid-span. This asymmetry is associated with the Strouhal frequency of the spanwise component of force acting on the cylinder shown in figure 6. The development of a symmetry about the mid-span occurs between  $L_R = 5$  and  $10$ . This observed symmetry development with increasing length ratio is concurrent with the corresponding decrease in the strength of the spanwise force component.

Coinciding with the development of spanwise symmetry is the development of Kármán-like shedding in the vicinity of the cylinder mid-span, and within approximately  $1d$  to  $3d$  downstream. Evidence of this is shown by solid vertical bands in the isosurface plots, and can be seen in figure 7(d–f), although it is more pronounced at the larger length ratios shown in figure 7(e,

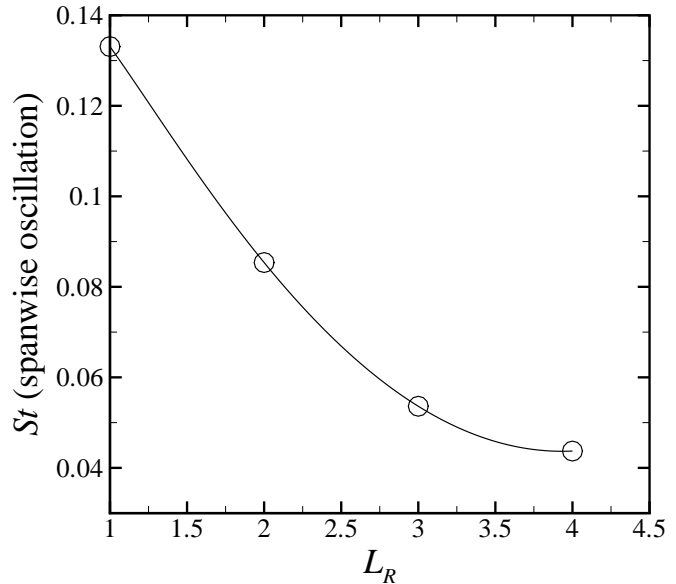


Figure 6: Strouhal frequency of the periodic oscillation in the spanwise body force at  $Re = 300$ . Variation with length ratio.

f).

It is interesting to observe that even with a length ratio  $L_R = 10$ , the influence of the free hemispherical ends on the two-dimensional vortex street is significant. Downstream of the cylinder (to between  $4d$  and  $5d$  downstream), evidence of an approximately parallel vortex street can be observed. Further downstream, the rollers in the wake are deformed by the three-dimensional effects induced by the flow around the free hemispherical ends, and a symmetrical three-dimensional wake replaces the quasi-two-dimensional wake in the vicinity of the mid-span.

#### Conclusions

A novel implementation of a spectral-element method has been employed to model the flow past a cylinder with hemispherical ends. Computations of the flow past a sphere using the current crossflow implementation were compared with previous accurate numerical computations that used the more traditional axial-flow method. For comparison, isosurface plots, Strouhal frequencies and drag coefficients were monitored, and errors were within 0.5% throughout the Reynolds number range  $Re \lesssim 300$ . A limited number of computations of cylinders with length ratios in the range  $1 \leq L_R \leq 5$  provide tantalising hints to the diverse flow regimes to be found.

#### Acknowledgements

This research is supported by an ARC Linkage International grant. These simulations were performed using the resources of the Victorian Partnership for Advanced Computing (VPAC) consortium.

#### References

- [1] Barkley, D. and Henderson, R. D., Three-dimensional Floquet stability analysis of the wake of a circular cylinder, *J. Fluid Mech.*, **322**, 1996, 215–241.
- [2] Ghidersa, B. and Dušek, J., Breaking of axisymmetry and onset of unsteadiness in the wake of a sphere, *J. Fluid Mech.*, **423**, 2000, 33–69.



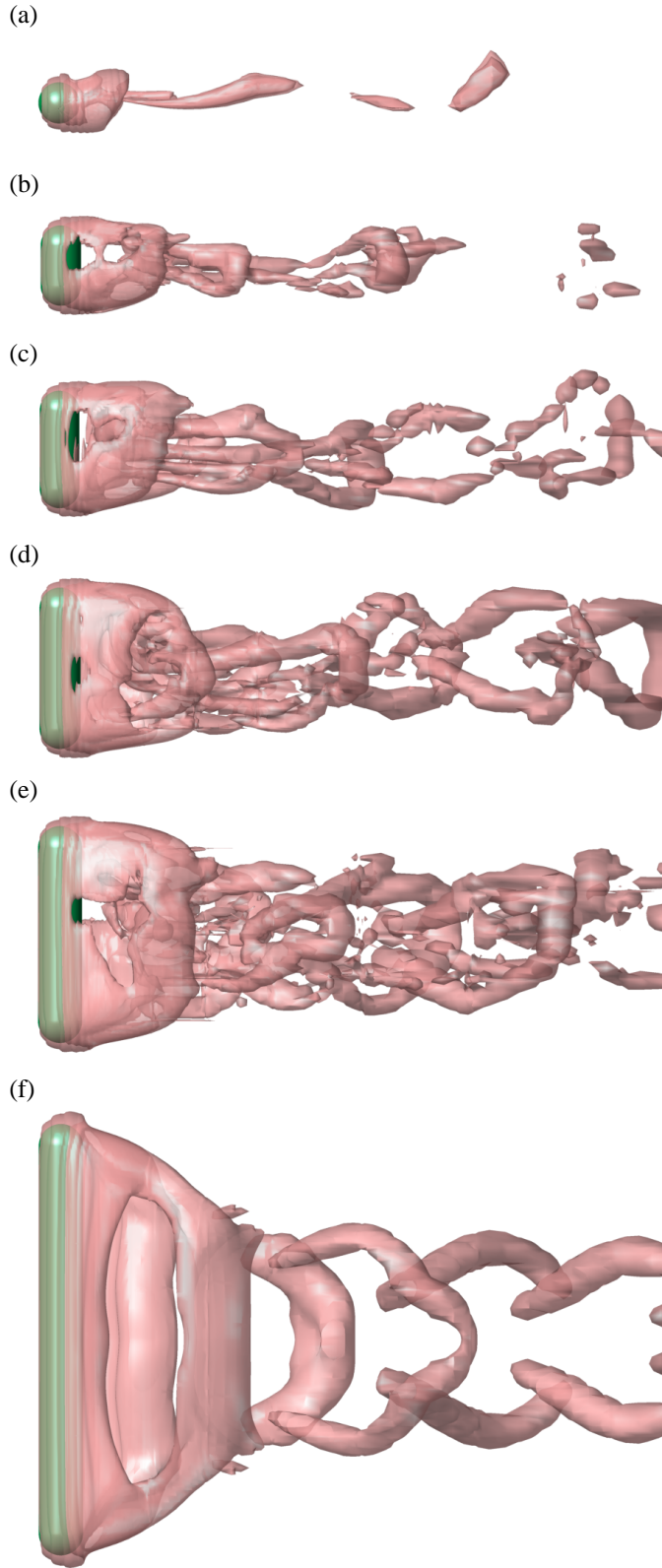


Figure 7: Isosurface plots of the vortical structure of the wakes behind cylinders with free hemispherical ends. Parts (a–e) show length ratios  $L_R = 1, 2, 3, 4$  and  $5$ , respectively, at  $Re = 300$ , and part (f) shows a length ratio  $L_R = 10$  at  $Re = 100$ .

- [3] Johnson, T. A. and Patel, V. C., Flow past a sphere up to a Reynolds number of 300, *J. Fluid Mech.*, **378**, 1999, 19–70.
- [4] Ko, N. W. M., Law, C. W. and Lo, K. W., Mutual interference on transition of wake of circular cylinder, *Phys. Fluids*, **12**, 1962, 1–34.
- [5] Norberg, C., An experimental investigation of the flow

around a circular cylinder: Influence of aspect ratio, *J. Fluid Mech.*, **258**, 1994, 287–316.

- [6] Provansal, M., Mathis, C. and Boyer, L., Bénard-von Kármán instability: Transient and forced regimes, *J. Fluid Mech.*, **182**, 1987, 1–22.
- [7] Provansal, M., Schouveiler, L. and Leweke, T., From the double vortex street behind a cylinder to the wake of a sphere, *Euro. J. Mech. B (Fluids)*, **23**, 2004, 65–80.
- [8] Schouveiler, L., Brydon, A., Leweke, T. and Thompson, M. C., Interactions of the wakes of two spheres placed side by side, **23**, 2004, 137–145.
- [9] Schouveiler, L., Brydon, A., Leweke, T. and Thompson, M. C., Interaction of the wakes of two spheres placed side by side, in *Proceedings of the Conference on Bluff Body Wakes and Vortex Induced Vibrations (BBVIV3)*, editors K. Hourigan, T. Leweke, M. C. Thompson and C. H. K. Williamson, Published by Monash University, Melbourne, VIC 3800, Australia, Port Douglas, Australia, 2002.
- [10] Schouveiler, L. and Provansal, M., Periodic wakes of low aspect ratio cylinders with free hemispherical ends, *J. Fluids Struct.*, **14**, 2001, 565–573.
- [11] Sheard, G. J., *The Stability and Characteristics of the Flow Past Rings*, Ph.D. thesis, Monash University, Melbourne, Australia, 2004.
- [12] Sheard, G. J., Hourigan, K. and Thompson, M. C., Quantitative computations of the drag coefficients for the low Reynolds number flow past rings, *Under consideration for publication in J. Fluid Mech.*
- [13] Sheard, G. J., Thompson, M. C. and Hourigan, K., From spheres to circular cylinders: Non-axisymmetric transitions in the flow past rings, *J. Fluid Mech.*, **506**, 2004, 45–78.
- [14] Thompson, M. C., Leweke, T. and Provansal, M., Kinematics and dynamics of sphere wake transition, *J. Fluids Struct.*, **15**, 2001, 575–585.
- [15] Tomboulides, A. G., Orszag, S. A. and Karniadakis, G. E., Direct and large-eddy simulation of the flow past a sphere, in *Proceedings of the Second International Conference on Turbulence Modeling and Experiments (2nd ICTME)*, Florence, Italy, 1993.
- [16] Williamson, C. H. K., Defining a universal and continuous Strouhal-Reynolds number relationship for the laminar vortex shedding of a circular cylinder, *Phys. Fluids*, **31**, 1988, 2742–2744.
- [17] Williamson, C. H. K., The existence of two stages in the transition to three-dimensionality of a cylinder wake, *Phys. Fluids*, **31**, 1988, 3165–3168.
- [18] Williamson, C. H. K., Mode A secondary instability in wake transition, *Phys. Fluids*, **8**, 1996, 1680–1682.

## Three-Dimensional Instabilities and Transition in Pulsatile Stenotic Flows

H. M. Blackburn<sup>1</sup> and S. J. Sherwin<sup>2</sup>

<sup>1</sup>CSIRO Manufacturing and Infrastructure Technology,  
Highett, Vic., 3190, AUSTRALIA

<sup>2</sup>Department of Aeronautics, Imperial College London,  
South Kensington Campus, London, SW7 2AZ, UK

### Abstract

A straight tube with a smooth axisymmetric constriction is an idealised representation of a stenosed artery. We examine the three-dimensional instability of steady flow plus an oscillatory component in a tube with a smooth 75% stenosis using both linear stability analysis and direct numerical simulation. These flows become unstable through a subcritical period-doubling bifurcation involving alternating tilting of the vortex rings that are ejected from the throat with each pulse. These tilted vortex rings rapidly break down through a self-induction mechanism within the confines of the tube. While the linear instability modes for pulsatile flow have maximum energy well downstream of the stenosis, we have established using direct numerical simulation that breakdown can gradually propagate upstream until it occurs within a few tube diameters of the constriction, in agreement with previous experimental observations.

### Introduction

Atherosclerosis, the formation of plaques within the arterial wall, continues to be a major cause of death in the developed world. The associated narrowing, or stenosis, of the artery can lead to potential significant restriction of blood flow to downstream vessels. Related to this condition is the potential of plaque ruptures and thrombosis formation leading to particles becoming lodged in smaller vessels possibly inducing myocardial infarction or stroke.

This association of arterial disease with flow related mechanisms, such as wall shear stress variation, has motivated the study of steady and pulsatile flow within both idealised axisymmetric and anatomically correct arterial model stenoses [4]. Under standard physiological flow conditions most arterial flows are usually considered to be laminar, although typically separated and unsteady. However in the case of a stenotic flow the increase in local Reynolds number at a contraction can lead to transitional flow associated with the early stages of turbulence. The occurrence of turbulence-like flow phenomena makes the numerical simulation of these flows particularly challenging especially when considering the large range of parameters required to describe both the geometrical and flow features.

In the current work, we turn our attention to the stability of pulsatile flows in an axisymmetric stenotic tube. The approach adopted is to analyse the global linear stability of the axisymmetric flows to arbitrary three-dimensional perturbations. As the problem has rotational symmetry about the cylindrical axis, it is natural to use Fourier decomposition in the azimuth direction in order to break the general three-dimensional linear stability problem into a set of two-dimensional ones, dramatically reducing the size of each individual problem. Once we have the most unstable mode, we then use full three-dimensional direct numerical simulation (DNS) in order to examine the evolution of their instability modes, onset of turbulence, and nonlinear dynamics.

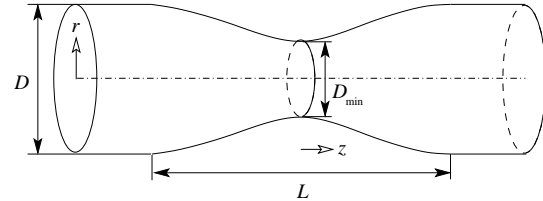


Figure 1: Geometrical parameters that define the axisymmetric sinusoidal stenosis.

### Parameter Space

We will take our length scale  $D$  as the tube diameter and base the Reynolds number on the temporally and spatially averaged inflow velocity  $\bar{u}$ . The axisymmetric stenosis shown in figure 1 is described by a sinusoidal shape which can be described by two geometric parameters: the stenosis degree  $S = 1 - (D_{\min}/D)^2$  and the stenosis length  $\lambda = L/D$ . We have considered the geometry defined by  $S = 0.75$  and  $\lambda = 2$ .

To complement the geometric factors we also need to consider the physiological flow parameters. If we permit the inflow to have a pulsatile waveform of period  $T$  and restrict attention to cases of non-reversing, spatially averaged flow we can identify three important flow parameters: the Reynolds number,  $Re$ ; the Womersley number,  $\alpha = (D^2\pi/(2\nu T))^{1/2}$  and the peak to mean flow ratio  $U_{pm} = Q_{\text{peak}}/Q_{\text{mean}}$ , where  $Q$  is the volume flux. The Womersley number can be interpreted as the ratio of the diameter (or radius) to the viscous boundary layer growth in time period  $T$  which is the ratio of two sectional length scales. An alternative parameter commonly used in fluid mechanics is the reduced velocity  $U_{red} = \bar{u}T/D$  which is the ratio of the convective length the mean flow moves in time  $T$  to the diameter. For geometries where there is a length scale in the flow direction, as is the case of the stenosis, this non-dimensional parameter can prove to be a useful alternative to the Womersley number. We note that  $U_{red}$  and  $\alpha$  are dependent parameters related by the Reynolds number according to  $U_{red} = \pi Re / (2\alpha^2)$ .

### Governing Equations

We consider the flow to be governed by the incompressible Newtonian Navier–Stokes equations

$$\partial_t \mathbf{u} = -\mathbf{A}(\mathbf{u}) - \nabla P + \nu \nabla^2 \mathbf{u}, \quad \text{with} \quad \nabla \cdot \mathbf{u} = 0, \quad (1)$$

where  $\mathbf{u} = \mathbf{u}(z, r, \theta, t) = (u, v, w)(t)$  is the velocity field,  $\mathbf{A}(\mathbf{u})$  represents nonlinear advection terms,  $P = p/\rho$ , and where  $p$  is the pressure,  $\rho$  and  $\nu$  are respectively the fluid density and  $\nu$  kinematic viscosity. The variables  $z$ ,  $r$ ,  $\theta$  and  $t$  are respectively the axial, radial, azimuthal and time coordinates and  $u$ ,  $v$ ,  $w$  the velocity components in the axial, radial and azimuthal directions. We can consider the nonlinear terms either in convective form  $\mathbf{A}(\mathbf{u}) = \mathbf{u} \cdot \nabla \mathbf{u}$ , conservative form  $\mathbf{A}(\mathbf{u}) = \nabla \cdot \mathbf{u}\mathbf{u}$ , or skew-symmetric form  $\mathbf{A}(\mathbf{u}) = (\mathbf{u} \cdot \nabla \mathbf{u} + \nabla \cdot \mathbf{u}\mathbf{u})/2$ , which are

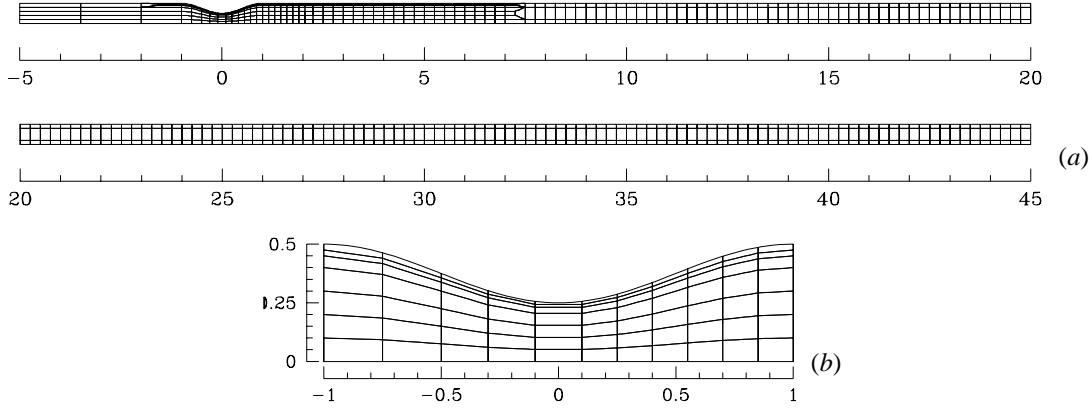


Figure 2: Spectral element outlines of computational mesh, dimensions given in terms of tube diameter  $D$ . Panel (a) shows elements for the first mesh with an outflow at  $45D$ . Panel (b) shows a close-up of the throat, with curved element edges.

all equivalent in a continuum setting. Equation (1) is subject to no-slip boundary conditions at the walls, a prescribed velocity at the inflow (steady or periodic), conditions of zero pressure and zero outward normal derivatives of velocity at the outflow and consistent regularity boundary conditions at the axis as explained in [7].

Taking the pressure to represent the solution of a Poisson equation that has the divergence of the advection terms as forcing, we can consider the Navier–Stokes equations in symbolic form as

$$\partial_t \mathbf{u} = -(\mathbf{I} - \nabla \nabla^{-2} \nabla \cdot) \mathbf{A}(\mathbf{u}) + \nu \nabla^2 \mathbf{u} = \mathbf{N}(\mathbf{u}) + \mathbf{L}(\mathbf{u}) \quad (2)$$

where the nonlinear operator  $\mathbf{N}$  contains contributions from both pressure and advection terms, while the linear operator  $\mathbf{L}$  corresponds to viscous diffusion.

When analysing the linear stability of a flow in terms of its normal modes, we decompose the velocity  $\mathbf{u}$  into a base flow  $\mathbf{U}$  and perturbation flow  $\mathbf{u}'$ :  $\mathbf{u} = \mathbf{U} + \mathbf{u}'$ , and examine the stability of the perturbation linearised about the base flow. In this decomposition, the original nonlinear advection terms are replaced with their linearised equivalent (here for the convective form)  $\partial_{\mathbf{U}} \mathbf{A}(\mathbf{u}') = \mathbf{U} \cdot \nabla \mathbf{u}' + \mathbf{u}' \cdot \nabla \mathbf{U}$  and in symbolic form we write

$$\partial_t \mathbf{u}' = \partial_{\mathbf{U}} \mathbf{N}(\mathbf{u}') + \mathbf{L}(\mathbf{u}') \quad (3)$$

for the evolution of the linear perturbation. If the base flow is  $T$ -periodic in time,  $\partial_{\mathbf{U}} \mathbf{N}$  is linear time-periodic, and

$$\mathbf{u}'(t_0 + T) = \exp \left[ \int_{t_0}^{t_0+T} (\partial_{\mathbf{U}} \mathbf{N} + \mathbf{L}) dt \right] \mathbf{u}'(t_0). \quad (4)$$

The eigenpairs of this Floquet problem are  $\{\mu, \tilde{\mathbf{u}}(t_0)\}$  where  $\mu$  is a Floquet multiplier and  $\tilde{\mathbf{u}}(t_0)$  is the  $T$ -periodic Floquet eigenfunction, evaluated at phase  $t_0$ . The equivalent to the eigenvalues  $\gamma$  of the time-invariant case are the Floquet exponents  $\sigma$ , related to the multipliers by  $\mu = \exp \sigma T$ . In general, the Floquet multipliers/exponents and eigenfunctions occur in complex-conjugate pairs.

Since the geometry is axisymmetric, the velocity must be  $2\pi$ -periodic in  $\theta$  and can be projected exactly onto a set of two-dimensional complex Fourier modes by

$$\hat{\mathbf{u}}_k(z, r, t) = \frac{1}{2\pi} \int_0^{2\pi} \mathbf{u}(z, r, \theta, t) \exp(-ik\theta) d\theta \quad (5)$$

where  $k$  is an integer wavenumber. The Fourier-transformed equations of motion and axial boundary conditions for the velocity and pressure (and their perturbations) in cylindrical coordinates are described in detail in [5, 7]. Our base flows are

both axisymmetric/two-dimensional, i.e.  $\hat{\mathbf{U}}_k = \mathbf{0}$ ,  $k \neq 0$ , and two-component, i.e.  $\mathbf{U} \equiv (U, V, 0)$ . In the numerical stability analysis we take advantage of linearity, which decouples the stability problem for each  $\hat{\mathbf{u}}'_k$ .

### Numerical Methods

For time evolution of both the full and linearised Navier–Stokes equations, we relied on standard (nodal–Gauss–Lobatto–Legendre) spectral elements in  $(z, r)$  and Fourier expansions if required in the azimuthal  $\theta$ -direction. This spatial discretisation was coupled with a second-order-time velocity correction time-integration scheme. The development of this numerical method for DNS has been described in detail in [7]. The application of the method to linearised Navier–Stokes evolution, including appropriate boundary conditions, has also previously been described in [5].

The computational mesh used in the calculations is shown in figure 2. The domain consists of 743 elemental regions. In each element, two-dimensional mapped tensor-product Lagrange-interpolant shape functions based on the Gauss–Lobatto–Legendre nodes were applied. At  $P = 7$  this elemental discretisation corresponds to approximately 38 000 local degrees of freedom in each meridional semiplane. The domain extended  $5D$  upstream and  $45D$  downstream of the throat. As shown in figure 2 (b) a fine radial mesh spacing was adopted in the region of the stenosis where two layers each of 5% of the local radius were applied. At  $z/D \approx 7$  the radial mesh spacing was coarsened to allow a uniform axial spacing of  $0.5D$  to be applied to the outflow. The mesh was refined until both the axisymmetric base flows and Floquet multipliers converged to four significant figures. Typically this also gives enough mesh refinement in the meridional semi-plane for non-axisymmetric DNS as well, with the number of planes of data in azimuth selected to provide a three-order or better reduction in kinetic energy from azimuthal mode 1 to the highest mode.

The numerical methods employed for stability analysis of both steady and pulsatile flow follow those outlined in [10], and previously described and used in other works [3, 5, 6]. The analysis is based on a Krylov-subspace iteration of successive finite increments of (initially random) perturbations through the operator of (4) using an Arnoldi method to extract the dominant eigenpairs of the exponential operators in the equations. The data used to supply the  $T$ -periodic base flow are approximated through Fourier-series reconstruction from a limited number (typically 256) of time-slices obtained from two-dimensional DNS.

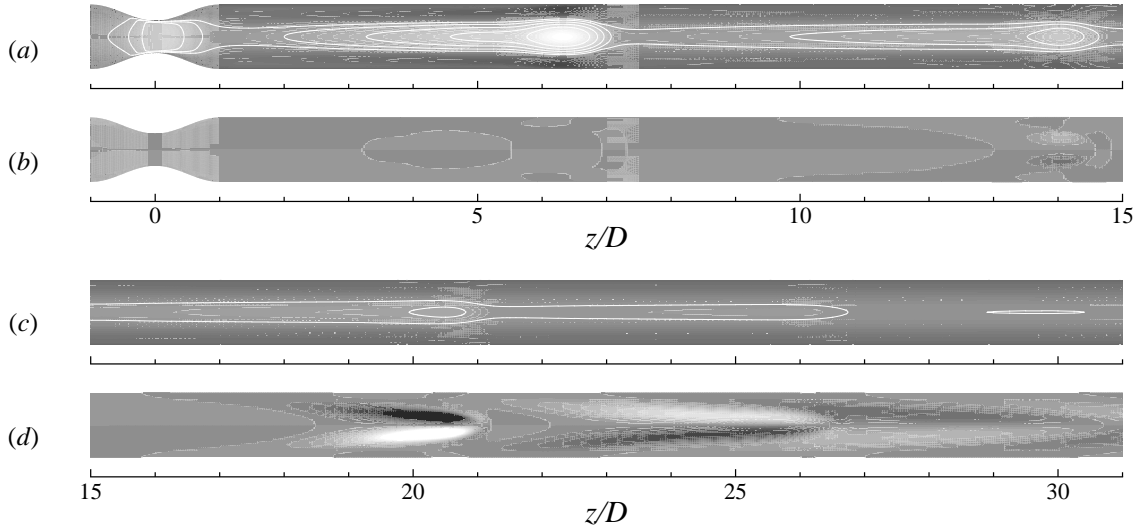


Figure 3: The base flow and the leading eigenmode for one phase in the flow cycle for the unstable pulsatile flow at  $Re = 400$ ,  $U_{red} = 2.5$ , on a vertical centreplane. Panels (a, c) show contours of axial velocity of the base flow, while (b, d) show contours of axial velocity of the eigenmode.

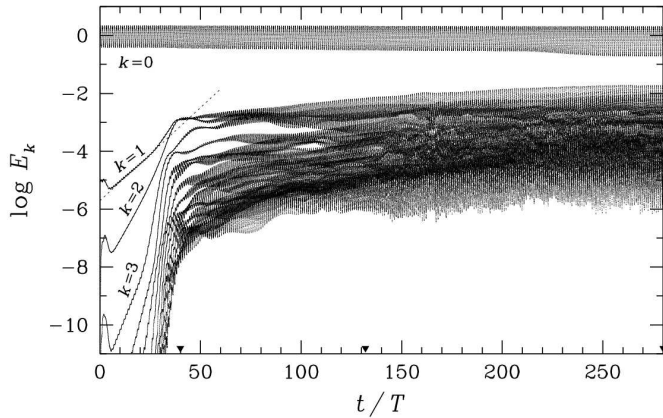


Figure 4: Growth to saturation of the pulsatile inlet flow solution at  $U_{red} = 2.5$ ,  $Re = 400$ , approximately 3% above  $Re_c$ , represented by kinetic energies in azimuthal Fourier modes, with  $N_k = 16$ . An initial exponential growth phase (indicated by the dotted line) is followed by faster than exponential growth near  $t/T \sim 35$ , an initial nonlinear saturation at  $t/T \approx 40$ , then a final slow growth to an asymptotic state, reached at  $t/T \sim 250$ .

## Results

Floquet analysis was carried out at  $U_{pm} = 1.75$  and for three values of reduced velocity:  $U_{red} = 2.5$ , 5, and 7.5, i.e. successively longer dimensionless base flow periods. The corresponding critical Reynolds numbers were found to be  $Re_c = 389$ , 417 and 500. In all three cases, the instability arose through a period-doubling bifurcation in the  $k = 1$  azimuthal Fourier mode. The shape and location of the Floquet instability mode for  $U_{red} = 2.5$ ,  $Re = 400$  is shown in figure 3, where it is compared to the base flow at the same instant in time. The alternating sign of the Floquet mode growing on successive base flow pulses for a streamwise traverse at any fixed radius is related to the period-doubling nature of the instability. The perturbation exerts alternating tilting moments on the vortex rings associated with each pulse of the base flow.

Following the stability analysis, full three-dimensional DNS of the instability at  $U_{red} = 2.5$ ,  $Re = 400$  was initiated by perturbing the base flow with a small amount of the leading Flo-

quet eigenmode and evolving in time. The time-evolution of energies in the azimuthal modes is shown in figure 4. After a brief equilibration, there is an exponential growth phase in the non-axisymmetric components, lasting until  $t/T \approx 35$ , following which the perturbation grows faster than exponentially with time before an initial saturation at  $t/T \approx 40$ , signalling that the bifurcation is subcritical. Then there is an extended slow change until an asymptotic state is approached at  $t/T \sim 250$ .

The evolution of the flow through time is illustrated by the instantaneous isosurfaces shown in figure 5. The first set of panels, in figure 5 (a), shows the flow state after the initial saturation at  $t/T = 40$ . In the side view, the tilting of the third vortex ring in the view can be seen, while the fourth and fifth rings in the view are further advanced in their breakdowns to a packet of  $\Lambda$ -vortices. In figure 5 (b) we see two instances in time leading to the asymptotic state: the slow final growth seen in figure 4 is associated with an upstream movement of the vortex ring breakdown. At  $t/T = 280$ , the flow still has the symmetry of the Floquet mode, but at that point a small random symmetry-breaking perturbation was added to the first azimuthal mode, and the flow further evolved in time, leading to another asymptotic, but now asymmetric state seen in figure 5 (c). At large length and time scales, the flow still has a period-doubling nature, indicating that this is a robust feature.

## Discussion

The experimental results of [1, 2, 9] provide a basis for comparison to our DNS results. These were performed at a higher value of  $U_{red}$ , but similar Reynolds number ( $Re \approx 600$ ) and peak-to-mean flow ratio ( $U_{pm} \approx 1.7$ ).

In [2] it is stated that ‘turbulence was found only for the 75% stenosis and was created only during part of the cycle’, whereas in [1] these fluctuations, which are strongest for  $2.5 < z/D \leq 6$ , are characterised as non-turbulent owing to the presence in the conditional velocity spectra of a band of dominant frequencies associated with ‘vortex shedding and a turbulent front’. These findings are in quite good agreement with the dye-front flow visualisation and interpretation provided by [9]. For the 75% stenosis, they found four post-stenotic zones: Zone I, reaching to  $z/D = 3$ , is called the ‘stable jet region’, although some indication of (apparently axisymmetric) wavy structure can be ob-

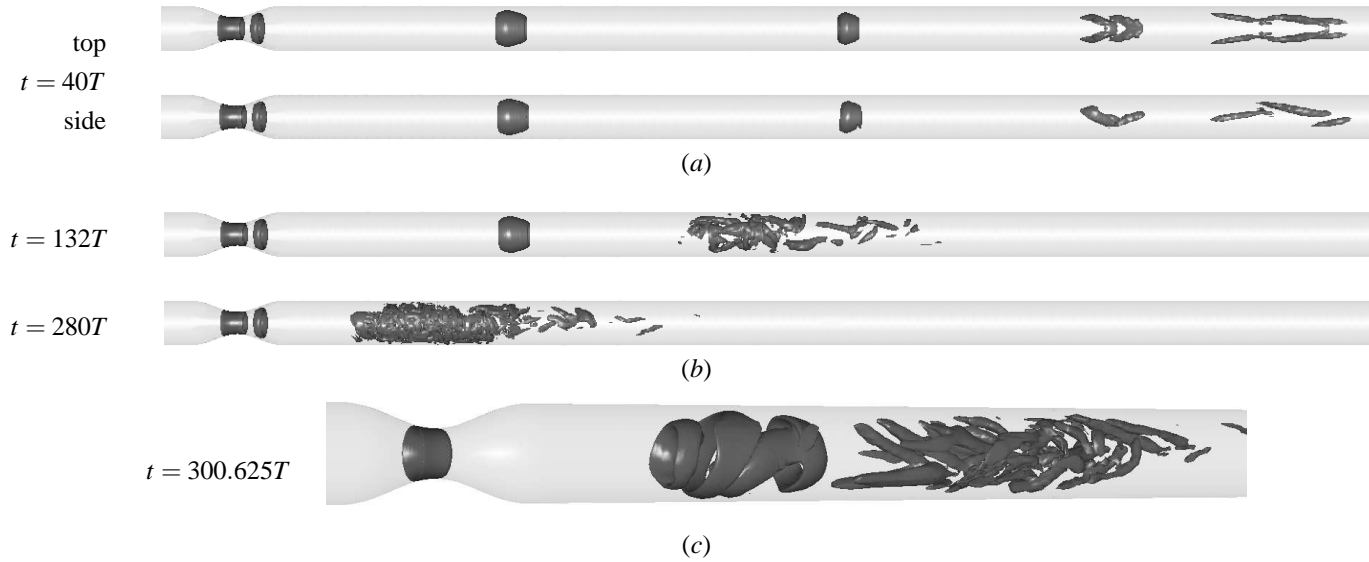


Figure 5: Visualisations for the DNS of pulsatile flow at  $U_{red} = 2.5$ ,  $Re = 400$ . Isosurfaces are extracted using the  $\lambda_2$  criterion [8]. (a) top and side views of the flow just after the initial saturation seen at  $t/T = 40$  in figure 4. (b) Two visualisations at later times in the progression to the asymptotic state. Note the upstream movement of breakdown. (c) A detail perspective view of the breakdown of vortex rings in the cycle following  $t = 300T$ . Downstream of the stenosis, the first group of structures shows a ring deforming during the final stages of the tilting process, while the second group shows the decaying breakdown of the previous ring.

served on the jet front in this region; Zone II,  $3 < z/D \leq 4.5$  is called the ‘transition region’, where the waves become larger; in Zone III, the ‘turbulent region’,  $4.5 < z/D \leq 7.5$ , the front rapidly distorts; Zone IV,  $z/D > 7.5$  is labelled ‘relaminarization’.

These experimental results are thus in reasonable agreement with the kind of asymptotic behaviour we have observed in DNS, as can be seen in figure 5 (b, c): a rapid distortion of a vortex ring becoming evident a few diameters downstream of the stenosis, leading to a highly unsteady/transitional breakdown at  $z/D \sim 6$ , following which relaminarisation takes place further downstream.

## Conclusions

Floquet analysis of three axisymmetric pulsatile flows shows that they become three-dimensionally unstable through period-doubling bifurcations involving alternating tilting of the vortex rings that are ejected from the stenosis during each pulse cycle. Direct numerical simulation shows that the instability evolves to vortex ring breakdown, which moves progressively upstream until it occurs a comparatively few tube diameters downstream of the stenosis. As the bifurcations are subcritical, hysteretic effects can be expected with respect to changes in Reynolds number, reduced velocity, or peak-to-mean pulsatility near the onset of three-dimensionality. The breakdowns are energetic turbulent events, and will lead to regions of high temporal and spatial gradients of wall shear stress where they occur. For the Reynolds numbers studied here, the flow relaminarises further downstream, and will eventually recover the conditions of the pulsatile inflow. These findings are in good agreement with available experimental results.

## Acknowledgements

This work was supported by the Australian Partnership for Advanced Computing, the Royal Academy of Engineering, and the UK Engineering and Physical Sciences Research Council.

## References

- [1] Ahmed SA. An experimental investigation of pulsatile flow through a smooth constriction. *Exptl Thermal & Fluid Sci*, **17**: 309–318, 1998
- [2] Ahmed SA & Giddens DP. Pulsatile poststenotic flow studies with laser Doppler anemometry. *J Biomechanics*, **17**(9): 695–705, 1984
- [3] Barkley D & Henderson RD. Three-dimensional Floquet stability analysis of the wake of a circular cylinder. *J Fluid Mech*, **322**: 215–241, 1996
- [4] Berger SA & Jou LD. Flows in stenotic vessels. *Annu Rev Fluid Mech*, **32**: 347–384, 2000
- [5] Blackburn HM. Three-dimensional instability and state selection in an oscillatory axisymmetric swirling flow. *Phys Fluids*, **14**(11): 3983–3996, 2002
- [6] Blackburn HM & Lopez JM. The onset of three-dimensional standing and modulated travelling waves in a periodically driven cavity flow. *J Fluid Mech*, **497**: 289–317, 2003
- [7] Blackburn HM & Sherwin SJ. Formulation of a Galerkin spectral element–Fourier method for three-dimensional incompressible flows in cylindrical geometries. *J Comput Phys*, **197**(2): 759–778, 2004
- [8] Jeong J & Hussain F. On the identification of a vortex. *J Fluid Mech*, **285**: 69–94, 1995
- [9] Ojha M, Cobbold RSC, Johnston KW & Hummel RL. Pulsatile flow through constricted tubes: An experimental investigation using photochromic tracer methods. *J Fluid Mech*, **203**: 173–197, 1989
- [10] Tuckerman LS & Barkley D. Bifurcation analysis for timesteppers. In E Doedel & LS Tuckerman, editors, *Numerical Methods for Bifurcation Problems and Large-Scale Dynamical Systems*, 453–566. Springer, 2000

## Three-Dimensional Quasi-Periodic Instabilities of Two-Dimensional Time-Periodic Flows

H. M. Blackburn,<sup>1</sup> J. M. Lopez<sup>2</sup> and F. Marques<sup>3</sup>

<sup>1</sup>CSIRO Manufacturing and Infrastructure Technology,  
Highett, Vic., 3190, AUSTRALIA

<sup>2</sup>Department of Mathematics and Statistics,  
Arizona State University, Tempe, AZ 85287, USA

<sup>3</sup>Departament de Física Aplicada,  
Universitat Politècnica de Catalunya, 08034, Barcelona, SPAIN

### Abstract

Three-dimensional synchronous instabilities of two-dimensional time-periodic wake flows, such as the so-called modes A and B of the circular cylinder wake, are now well-known. On the other hand, quasi-periodic three-dimensional instabilities are just as generic, but have as yet not received such wide-spread recognition, partly as a consequence of the predominance of attention given to flows, such as the cylinder wake, in which the synchronous modes happen to dominate at onset of three-dimensionality. Here we provide an introduction to the quasi-periodic modes, which can manifest either as modulated standing waves, or modulated travelling waves.

### Introduction

Three-dimensional instabilities of flows with an underlying two-dimensional time-periodic state became a topic for investigation following experimental studies of secondary instabilities of the circular cylinder wake (figure 1), see e.g. [7]. The following analytical works, e.g. [1, 6] concentrated on Floquet stability analysis of wake flows, particularly those of the circular and square cylinders. The initial investigations dealt with the synchronous three-dimensional modes, i.e. those for which the critical Floquet multipliers pass through the unit circle at  $\mu = +1$ , along the positive real axis in the complex plane. For these wake flows, there were two synchronous modes: long-wavelength mode A, and short-wavelength mode B, as illustrated in figure 2. Modes A and B have different symmetry properties — mode A preserves, while mode B breaks, the spatio-temporal symmetry of the base flow — but these properties are the same across the two flows. The onset Reynolds number for mode A ( $Re_c = 188$ ) is lower than that of mode B ( $Re_c = 259$ ), but as Reynolds numbers increase, mode B becomes dominant, and a mixed-mode model for this behaviour has appeared [2].

The Floquet analysis of Barkley & Henderson [1] suggested the presence of another intermediate-wavelength Floquet mode for the circular cylinder wake, but with complex-conjugate-pair multipliers, and which would possibly bifurcate from the two-dimensional basic state at Reynolds numbers above those for either mode A or mode B. Addressing the wake of the square cylinder, Robichaux et al. [6] also suggested the existence of an intermediate-wavelength mode, but this time subharmonic, i.e. a mode for which the critical Floquet multiplier is  $\mu = -1$ . Later analysis [3] showed that for the square cylinder, this mode in fact also had complex-conjugate-pair multipliers, therefore the three-dimensional bifurcation scenarios for the wakes of the circular and square cylinder wakes are the same.

In general, we might expect that critical Floquet multipliers could emerge anywhere around the unit circle, i.e. at  $\mu = +1$ ,  $\mu = -1$ , or  $\mu = \exp \pm i\theta$ . The wake flows have only a single control parameter (Reynolds number), and it happens that

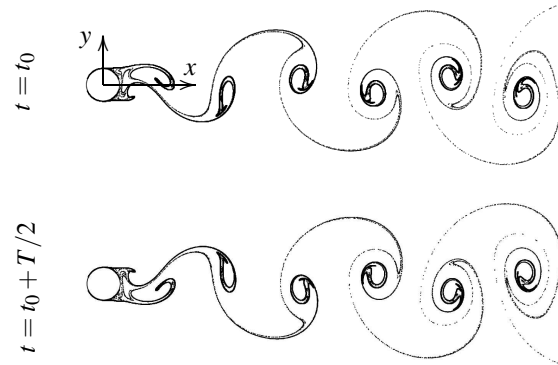


Figure 1: Computed locations of marker particles, illustrating the spatio-temporal symmetry of a two-dimensional circular cylinder wake for  $Re = 188.5$  at times  $t_0$  and  $t_0 + T/2$  ( $t_0$  is arbitrary,  $T$  is the Strouhal period).

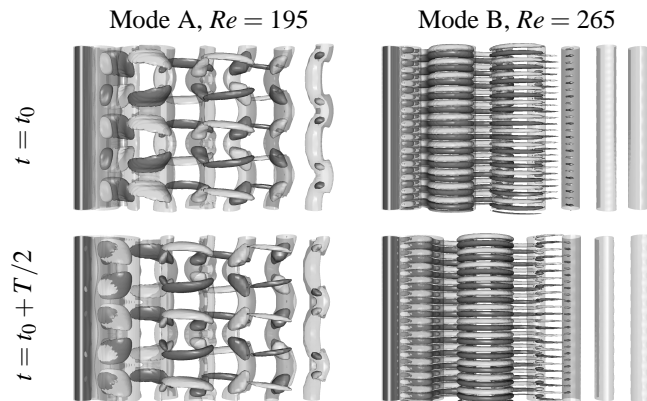


Figure 2: Vorticity isosurfaces for the synchronous wake modes of the circular cylinder, shown for a  $10D$  spanwise domain extent, and viewed from the cross-flow direction. Translucent isosurfaces are for spanwise vorticity component, solid surfaces are for streamwise component.

the first modes to bifurcate from the two-dimensional basic state are synchronous. However, many other flows share the same symmetry group as the wake flows, and hence will have instability modes with the same symmetries. The flow in a rectangular cavity, infinite in spanwise extent, driven by a wall in periodic tangential motion (as illustrated in figure 3) is such an example, and further, possesses two independent control parameters; Reynolds and Stokes numbers. The Floquet analysis for this flow was presented in [4], where it was shown that within certain control-parameter regimes, either a



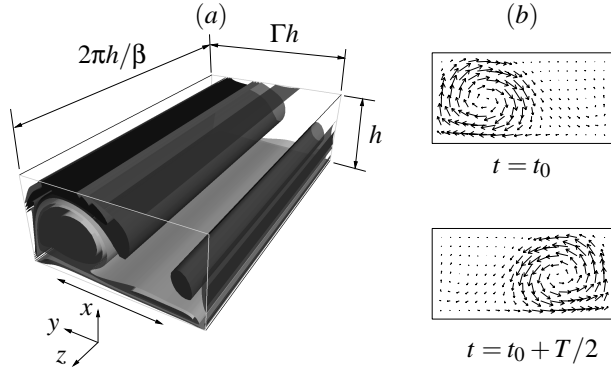


Figure 3: (a) Schematic of the fluid domain for the periodically driven cavity flow, periodic in the  $z$ -direction and forced in the  $y$ -direction, with isosurfaces representing different values of spanwise vorticity. (b) Two snapshots of velocity vectors of the base flow, half a forcing period apart, illustrating its spatio-temporal symmetry.

long-wavelength mode A, a short-wavelength mode B, or an intermediate-wavelength mode QP would be the first to become unstable. Interestingly, the symmetry properties of the synchronous modes (A and B) for this non-autonomous flow are the opposite to those of the same relative wavelengths for the circular and square cylinder wakes.

More recently, the complete analysis for all codimension-1 (generic) bifurcations for these flows was presented [5]. An important result of that work is that, if the base flows have  $Z_2$  spatio-temporal symmetry (a time-shift of  $T/2$ , combined with a spatial reflection, regenerates the original flow, as in figures 1 and 3), then period-doubling bifurcations, while not suppressed, become codimension-2, i.e. can only be produced by careful simultaneous manipulation of two control parameters, and are unlikely to be observed when only one parameter is varied.

Another outcome was a more complete exposition of the nature of quasi-periodic modes. In general, there is no reason to expect that the synchronous modes will be dominant in all flows or parameter regimes, and it is just as likely that flows will arise in which the quasi-periodic modes are dominant. In the remainder of this paper, we give examples of these instability modes, and describe their properties.

### Symmetries of the Quasi-Periodic Modes

When the Floquet multipliers occur in complex-conjugate pairs, then a new secondary period arises in the three-dimensional state, and the solution is quasi-periodic. In the cases under discussion, this period is associated with spanwise motion of the mode. In the physical domain, there are two ways that the quasi-periodic modes can manifest themselves, either as travelling waves (TW), which are unsymmetric but bifurcate in reflection-symmetric pairs, or as standing waves (SW), which have reflection symmetry but can be centred at arbitrary fixed spanwise locations. It is important to realise that in the nonlinear case (in DNS), the SW and TW evolve on distinct solution branches, with separate stability characteristics. The possible stability scenarios at a quasi-periodic bifurcation [5] are illustrated in figure 4.

Since the basic states have a spanwise translation symmetry, we use Fourier expansions in that direction to describe three-dimensional instabilities. The spanwise coordinate is  $z$ , the planar coordinates  $x$  and  $y$ , and the velocity  $\mathbf{u} = (u, v, w)(x, y, z, t)$ . Then

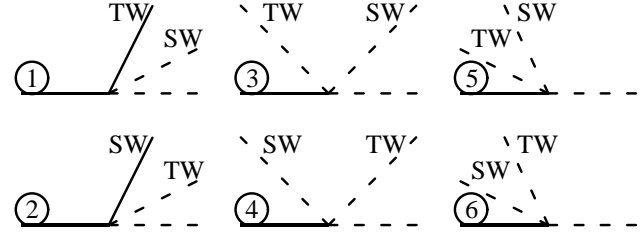


Figure 4: Bifurcation diagrams corresponding to the six scenarios in the QP bifurcation. Solid (dashed) lines represent stable (unstable) states, the horizontal line corresponds to the  $T$ -periodic base state. The horizontal axis is the bifurcation parameter ( $Re$ ), and the vertical axis is the amplitude squared of the 3D components of the solution.

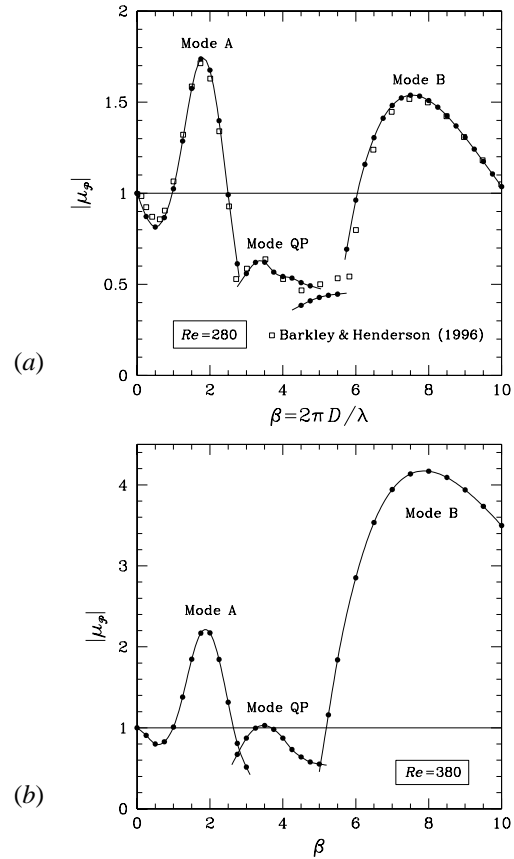


Figure 5: Moduli of the Floquet multipliers,  $|\mu_p|$ , for the three-dimensional instability modes of the two-dimensional wake of a circular cylinder at (a)  $Re = 280$  and (b)  $Re = 380$ . The  $Re = 280$  results are compared with those of [1] at the same  $Re$  (open squares). Multipliers for mode QP occur in complex-conjugate pairs.

the following forms (which have a reflection symmetry in  $z$ ) pass unchanged through the Navier–Stokes equations:

$$\mathbf{u}(x, y, z, t) = (u \cos \beta z, v \cos \beta z, w \sin \beta z)(x, y, t) \quad (1)$$

$$\mathbf{u}(x, y, z, t) = (u \sin \beta z, v \sin \beta z, w \cos \beta z)(x, y, t), \quad (2)$$

where  $\beta$  is a spanwise wavenumber:  $\beta = 2\pi D/\lambda$ , where  $\lambda$  is a spanwise wavelength and  $D$  a characteristic length scale. If the Floquet multipliers are real, then it is sufficient to use one of either of these forms, or a fixed linear combination of the two, to describe one of the infinite set of possible solutions. On the other hand, if the multipliers occur in complex-conjugate pairs, then restriction to any of these forms implies that the solutions

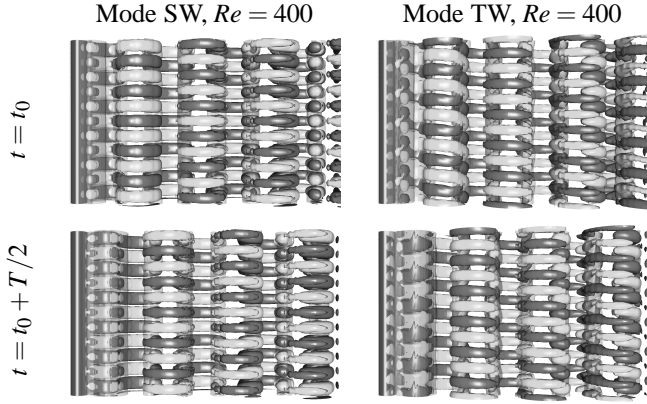


Figure 6: Vorticity isosurfaces for the quasi-periodic wake modes of the circular cylinder, shown for a  $10D$  spanwise domain extent, and viewed from the cross-flow direction. Translucent isosurfaces are for spanwise vorticity component, solid surfaces are for streamwise component.

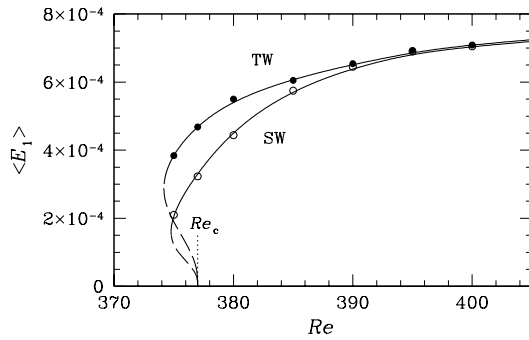


Figure 7: Time-average kinetic energies in the first spanwise Fourier mode of the TW and SW nonlinear solutions of the wake of a circular cylinder, as functions of Reynolds number. Solid (open) circles correspond to stable (unstable) solutions, relative to each other. Dashed lines indicate the unstable segments of the two solution branches, taken individually.

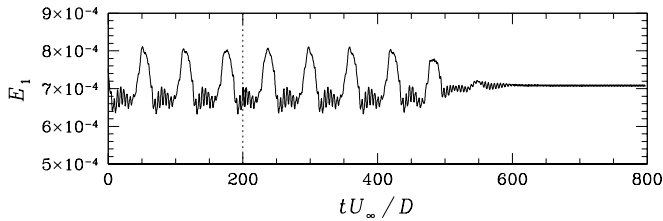


Figure 8: Time series of kinetic energy in the first spanwise Fourier mode for a quasi-periodic circular cylinder wake. Initially, the flow is in a SW state, in a subspace with spanwise reflection symmetry. At  $tU_\infty/D = 200$ , it is perturbed with a small amount of white noise, after which it evolves to a stable, asymmetric, TW state.

are SWs (which can remain in that state unless perturbed), and more generally we must consider non-symmetric expansion sets to allow for TW-type solutions [3, 4].

#### Quasi-Periodic Modes of the Circular Cylinder Wake

In figure 5 we show results from Floquet analysis for the wake of a circular cylinder, both at  $Re = 280$ , recreating results in [1], and at  $Re = 380$ . At  $Re = 280$ , the intermediate-wavelength mode QP is subcritical, while at  $Re = 380$ , it has just bifurcated from the basic state. At bifurcation, the complex-conjugate-pair Floquet multipliers lie quite close to the negative real axis.

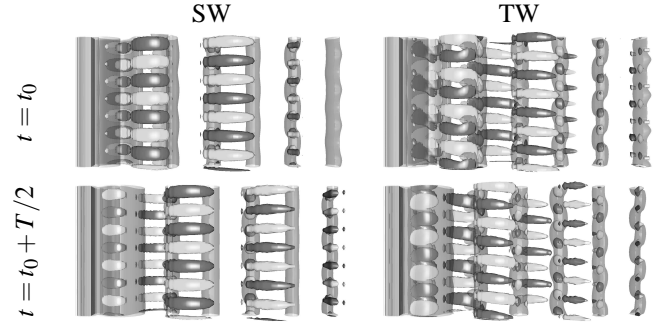


Figure 9: Vorticity isosurfaces for the quasi-periodic wake modes of the square cylinder at  $Re = 220$ , shown for a  $10D$  spanwise domain extent, and viewed from the cross-flow direction. Translucent isosurfaces are for spanwise vorticity component, solid surfaces are for streamwise component.

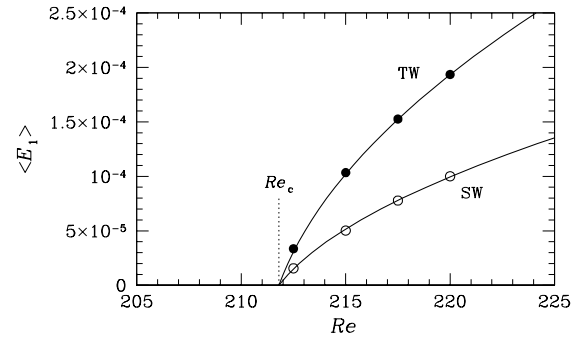


Figure 10: Time-average kinetic energies in the first spanwise Fourier mode of the TW and SW instability modes of the wake of a square cylinder, as functions of Reynolds number. The energy of the SW is smaller, and in accordance with the theory, the SW flow is unstable to perturbations.

In figure 6, isosurfaces of vorticity from  $Re = 400$  DNS studies of the SW and TW circular cylinder wake modes are displayed. The TW shown is the downwards-travelling case. The visual distinguishing characteristic of the TW is that the streamwise vortices on opposite sides of the wake interlace one another by  $\lambda/4$ , while in all other cases (A, B, SW) they are in-line. Apart from that, in this flow they bear a number of visual similarities to mode B, and probably arise from a similar physical mechanism.

#### Growth and Relative Stability of the SW and TW Solutions

To highlight the point that the TW and SW solution branches are distinct under nonlinear evolution, we show in figure 7 the time-averaged energies in the first spanwise mode of the SW and TW solutions as functions of the bifurcation parameter,  $Re$ . Both bifurcations are subcritical, and the energy of the TW solutions is always larger: we have bifurcation scenario 6 in figure 4.

Typically, solutions on at most one of the two branches (SW, TW) are stable *relative to* those on the other branch. This means that if we slightly perturb a solution on the unstable branch, it will evolve to a solution on the other branch. The theory suggests that solutions on the lower-energy branch are those which are relatively unstable. This is exactly what is observed if a solution on the SW branch is slightly perturbed, as seen in figure 8, derived from a perturbation study at  $Re = 400$ . At  $tU_\infty/D = 0$ , the solution is a SW, with long-period oscillations in the energy of the first spanwise mode (the long period is closely related to the imaginary part of the corresponding Floquet multiplier). At  $tU_\infty/D = 200$ , a small [ $O(10^{-4})$ ] perturba-

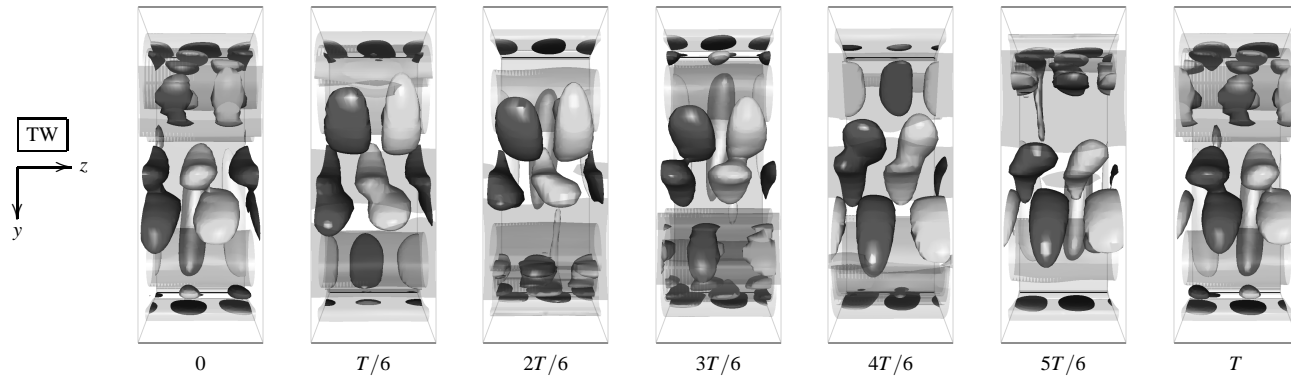


Figure 11: Vorticity dynamics of modulated  $+z$ -traveling waves in the periodically driven cavity flow [4], shown in a spanwise ( $z$ ) domain extent of one wavelength, at ( $St = 100$ ,  $Re = 1225$ ). Solid isosurfaces are of the out-of-page ( $x$ ) component of vorticity, positive and negative of equal magnitude, while translucent isosurfaces represent the  $z$  component of vorticity. The driven cavity wall lies further into the page than the structures, and oscillates in the  $\pm y$  direction.

tion is administered to the real and imaginary parts of the first spanwise mode. For a further  $\Delta t U_\infty/D \approx 200$ , there is little observable change in the energy, but by  $t U_\infty/D = 500$  the system has settled down to a stable TW state, and the long-period fluctuation in energy disappears. The TW is a three-dimensional solution that translates in the spanwise direction with constant kinetic energy (modulo  $T$ ).

#### Quasi-Periodic Modes of the Square Cylinder Wake

The quasi-periodic bifurcation of the wake of a square cylinder provides very similar behaviour [3]. In figure 9, instantaneous vorticity isosurfaces for the SW and TW modes of this wake, computed at  $Re = 220$ , are displayed. Again, the TW state shown is a downwards-travelling wave, and, corresponding to the fact that in this case the critical Floquet multipliers do not lie so close to the negative real axis, the isosurfaces have a more oblique character. Once again, for the TW the streamwise isosurfaces on opposite sides of the wake interlace each other by  $\lambda/4$ .

The bifurcation diagram for the quasi-periodic modes of the square cylinder wake are shown in figure 10. In this case, the bifurcations are supercritical, and we have scenario 1 from figure 4. As for the circular cylinder case, the SW solutions are relatively unstable to the TW solutions.

#### TW Mode of the Driven Cavity

The vorticity dynamics of a spanwise-travelling mode can be seen in an example drawn from the computational study of the periodically driven cavity [3]. In figure 11 we see vorticity isosurfaces of the TW mode over one floor period, as seen from above the cavity. The wave travels via successive merging of braid vortices produced on opposite ( $\pm y$ ) main rollers. As for the wake flows, the braid vortices produced on opposite sides of the cavity have an initial  $\lambda/4$  interlacing. After period  $T$  has elapsed, the vortex structures are exactly the same as in the initial frame, but translated in the  $+z$ -direction — by an amount that can be derived from the secondary period, which in the TW case is related to wave propagation speed.

#### Conclusions

Quasi-periodic instability modes of time-periodic two-dimensional flows are just as generic as synchronous modes, and may in fact already have been observed in existing flows. This is possible because (a) in general, there is no physical necessity, even in single-parameter flows, that synchronous modes will be the

first to become unstable and (b) the initially bifurcating modes do not necessarily remain dominant as the control parameter is increased. We have pointed out some of the salient features that enable TW modes to be discriminated from SW modes, and synchronous modes. When considering the computation of these flows, it is important to recognise that SW and TW modes belong to separate solution branches in the nonlinear case, and to check the relative stability of the two types of solution.

#### Acknowledgements

This work was supported by the Australian Partnership for Advanced Computing, the Australian Academy of Science, NSF Grant CTS-9908599 (USA) and MYCT Grant BFM-2001-2350 (Spain).

#### References

- [1] Barkley D & Henderson RD. Three-dimensional Floquet stability analysis of the wake of a circular cylinder. *J Fluid Mech*, **322**: 215–241, 1996
- [2] Barkley D, Tuckerman LS & Golubitsky MS. Bifurcation theory for three-dimensional flow in the wake of a circular cylinder. *Phys Rev E*, **61**: 5247–5252, 2000
- [3] Blackburn HM & Lopez JM. On three-dimensional quasi-periodic Floquet instabilities of two-dimensional bluff body wakes. *Phys Fluids*, **15**: L57–60, 2003
- [4] Blackburn HM & Lopez JM. The onset of three-dimensional standing and modulated travelling waves in a periodically driven cavity flow. *J Fluid Mech*, **497**: 289–317, 2003
- [5] Marques F, Lopez JM & Blackburn HM. Bifurcations in systems with  $Z_2$  spatio-temporal and  $O(2)$  spatial symmetry. *Physica D*, **189**: 247–276, 2004
- [6] Robichaux J, Balachandar S & Vanka SP. Three-dimensional Floquet instability of the wake of a square cylinder. *Phys Fluids*, **11**: 560–578, 1999
- [7] Williamson CHK. Three-dimensional wake transition. *J Fluid Mech*, **328**: 345–407, 1996

# Fire Behaviour Studies of Combustible Wall Linings Applying Fire Dynamics Simulator

A. Z. Moghaddam\*, K. Moinuddin, I. R. Thomas, I. D. Bennetts and M. Culton

Centre for Environmental Safety and Risk Engineering, Victoria University of Technology

P.O.Box 14428, Melbourne City MC, Victoria 8001, Australia

\*Visiting Research Fellow Tarbiat Modarres University, Tehran, Iran

## Abstract

In this paper the results of a large eddy simulation of an ISO 9705 room corner fire are presented. The field model, Fire Dynamics Simulator (FDS) was used to study the corner fire with and without combustible wall linings. Comparison of the results from simulations with prescribed heating and published experiments showed that with 50 mm grid spacing it is possible to quite accurately reproduce the experimental temperature data locations inside the room. When a combustible wall lining is included a T-shaped flame pattern similar to that observed in the experimental study was obtained but only with a particular grid size and reaction model. Inconsistent results were obtained with varying grid sizes and reaction models when combustible wall lining tests were modelled.

## Introduction

Fire modelling is a highly desirable tool for fire safety design engineers. Since the introduction of the early version of FDS in 2000 with its relatively accurate pool-fire simulation results and free accessibility via the NIST website it has found widespread applications in fire engineering design and research. FDS is a computational fluid dynamics (CFD) model of fire driven flow, and a detailed description of the model is provided in the FDS manual and also by others [1-3]. FDS applications reported in the literature are almost exclusively aimed at verification of FDS results with experimental data using a single fuel, usually comprising the burning of a liquid fuel in pool form or gas from a burner. For ISO 9705 room corner fire scenarios, FDS has only been applied to a sand burner with propane [4], not to a liquid pool fire. Moreover, to the best of our knowledge no report on the application of FDS for multiple fuel scenarios has been published.

In this work two separate FDS simulations of the ISO room with a liquid fuel fire were conducted. The first simulation involves a tray of methylated spirit (consisting of 93% of ethanol and 7% of methanol) as a corner fire source in order to develop base line data for the later ISO room simulations with combustible wall linings. It is referred to herein as the pool fire. It is necessary to successfully reproduce the pool fire experimental results to then be able to carry out successful FDS calculations of the same room with combustible wall linings.

In the second simulation methylated spirit was the source-fire fuel and plywood as wall linings was the main fuel. The outputs of both simulations are compared with the experimental results [5]. In FDS, when two types of fuel are involved, the specification of the governing combustion reaction needs to be considered very carefully.

The FDS package includes Smokeview, a graphical program that allows visual observation of the FDS results. In room lining fire simulations, due to the availability of the large combustible surface area it is possible to observe from Smokeview animations

the important stages of fire development including the flame spread pattern, the approach of flashover and the post flashover stage. These observations provide valuable information on the prediction ability of FDS.

## Experimental work

The experimental data used here are from previous work carried out at the Fire SERT Centre, University of Ulster [5]. Here only a brief summary of the test method is provided.

The experiments were conducted in an ISO 9705 room the west wall of which was modified to include three windows which enabled a direct view of the north and east wall. Double-glazing was employed to ensure the integrity of the enclosure boundary was maintained up to and beyond flashover, thus facilitating observation and video recording. The remaining enclosure walls and the ceiling consisted of masonry construction and were lined internally with 15 mm thick ceramic fibre insulating board. The floor surface was covered with concrete blocks. The primary fuel source used was a 0.55 m × 0.55 m × 0.1 m deep pool of methylated spirit located in the northeast corner of the room and placed 0.4 m above the floor and 0.05 m away from both walls. For each test 8 kg of methylated spirit was used.

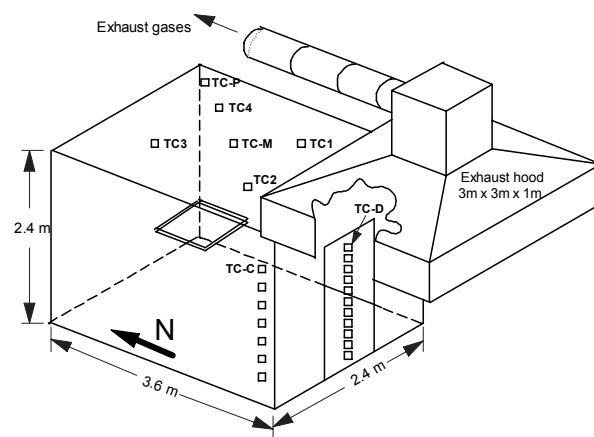


Figure 1. Schematic diagram of ISO 9705 fire test room

A doorway 2 m high × 0.8 m wide was located at the centre of the south wall. The doorway was fully open in all tests providing free passage of entering air and the outgoing products of combustion which were then collected by an exhaust hood and directed to an oxygen analysing system.

Gas temperatures were measured using type K thermocouples. Six thermocouples were placed on the ceiling, one directly above the burner to record plume temperature, another in the centre of the ceiling with the remaining four were located symmetrically around this central thermocouple as shown in figure 1. A thermocouple tree consisting of ten thermocouples

was located in the middle of the doorway. Another thermocouple tree was placed inside the room in the southwest corner in accordance with the ISO standard to measure the variation of temperature with height off-the-floor [6]. To allow visual observation of surface flame and char development, lines were drawn horizontally and vertically on the east and north wall combustible lining surface at 0.2 m spacing. Prior to the main lining test a series of pool-fire tests were conducted to determine the HRR from the pool fire.

### Overview of FDS Simulation

For the current FDS simulation the LES method of calculation is used. This uses a mixture fraction combustion model. In this method since the reactants are not premixed it is assumed that the reaction is diffusion controlled. Consequently the progress of the reaction depends on the degree of mixing. This is represented by a parameter defined as the mixture fraction ( $Z$ ). An infinite rate of reaction between the fuel and oxygen is assumed when the mixture fraction is at the stoichiometric value. This assumption together with the Hoggets relationship [7] for the heat release rate as a function of oxygen consumption leads to the correlation

$$\dot{q}''_c = \Delta H_o \left. \frac{dY_o}{dZ} \right|_{z=z_f} (\rho D) \nabla Z \cdot n \quad (1)$$

Where  $\dot{q}''_c$  is the heat release rate per unit area of the flame sheet,  $Y_o$  is the oxygen mass fraction,  $\rho$  is density of the air,  $D$  is diffusivity,  $n$  is the unit normal facing outward from the fuel [1].

Burning takes place (at a distance from the fuel surface) only where the mixture fraction is at the stoichiometric value. Just above the fuel surface the mixture is mostly fuel and the mixture fraction  $Z$  is close to the maximum value of 1. Moving away from fuel surface  $Z$  begins to reduce and at some point its value will equal the stoichiometric value. This is where it is assumed that burning takes place and where the flame sheet is located

In FDS mixture fraction combustion calculations, the reaction of only one fuel is considered. In the ISO room-lining test, even though two fuels are actually involved only one of them can be modelled. In this work two reactions were considered: 'Ethanol' and 'Wood'. The results of both are presented below.

The objective of lining tests is to determine the contribution that combustible lining materials make to the growth of a room fire. Similarly with the FDS simulation, in order to calculate the fire behaviour and contribution of lining materials to the heat release rate (HRR) an FDS simulation of the pool (source) fire is required.

An FDS model was constructed to resemble the experimental set-up for the ISO room, initially for the pool fire test. The computational domain was 2.4 m high by 2.4 m wide and 5.0 m long. Since calculations up to the flashover stage were intended the overall domain size was selected as minimum possible to avoid prolonged calculation times at small grid sizes. The burner was modelled as an obstruction with the dimensions similar to the actual size, placed at the north-east corner of the room, 0.05 m off the north and east walls. The top section of the obstruction was used to simulate the source fire, this was done in two ways: firstly simulating as methylated spirit fuel which was allowed to burn by itself and secondly by assigning a ramped heat release rate per unit area (HRRPUA) closely modelled on the experimental findings.

The internal surfaces were modelled as a thermally thick solid. Wall surfaces and the ceiling were covered with 12 mm thick layer of Kaowool and the floor was assumed to be of concrete. The thermal diffusivity and the thermal conductivity of Kaowool used were  $1.80 \times 10^{-6} \text{ }^\circ\text{K m}^2/\text{s}$  and  $0.135 \text{ W/m}^\circ\text{K}$  respectively [5,8].

## Results and Discussions

### Pool fire test

Figure 2 shows a comparison of the experimental heat release rate (HRR) and the FDS simulations. The experimental heat release rate shows an initial rapid raise changing to a lower slope about 100 s after ignition. The maximum HRR was about 190 kW about 800 s after ignition.

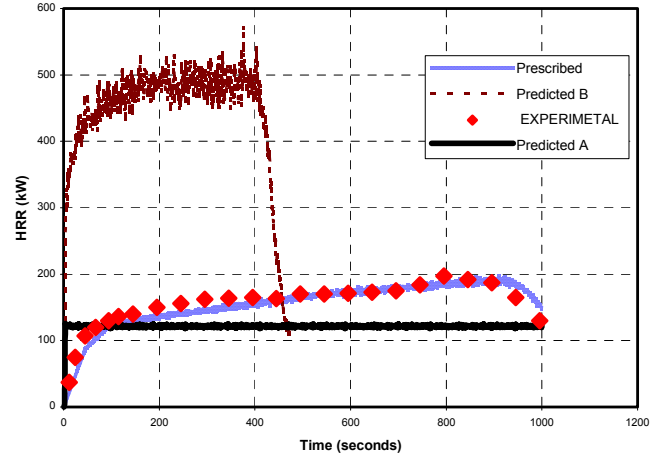


Figure 2. HRR profiles from FDS and experimental results

The HRR calculated in the FDS simulations was affected by input variables such as grid spacing and maximum burning rate. The initial estimate of HRR (Prediction A in figure 2) attained a maximum value of 120kW, well below the experimental value, and remained constant on this value. This unvarying result was unexpected, but after checking it was realised that it was the consequence of a maximum burning rate ( $15 \text{ g/m}^2/\text{s}$ ) incorporated in the data for ethanol in FDS3 database. A similar limitation is also incorporated for other fuels. This limitation was incorporated based on a study by McGrattan *et al.* [2], which showed that the FDS predicted burning rate of methanol was much higher than the experimental values. Setting such a limitation they could reasonably reproduce temperatures found experimentally.

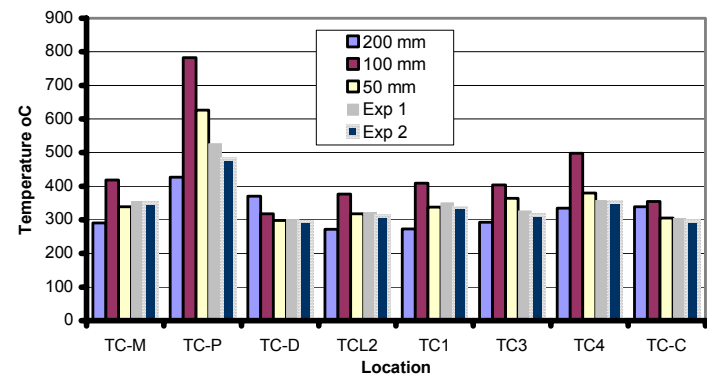


Figure 3. Comparison of temperatures predicted by FDS with the prescribed HRR and measured temperatures

However in enclosure fires the burning rate may be strongly influenced by radiative and convective heat feedback. When the burning rate limitation was removed the resulting HRR estimate (Prediction B in figure 2) was much higher with a maximum value of 500 kW and the fuel was consumed in a much shorter period than found experimentally. Rather than persist with attempting to model the experimental HRR with a pool fire simulation it was simulated using a prescribed ramped heating rate (figure 2).



This pool fire case was then checked for grid convergence. In figure 3 the experimental maximum gas temperature at each labelled point shown in figure 1 is compared with the corresponding temperatures calculated using FDS with three grid spacings. It is notable that at nearly all locations the best agreement with the experimental results is provided by the smallest grid size 50 mm. Due to the long computational time taken for the simulation the run with 25 mm grid spacing was stopped at 200 seconds. With the larger grid spacings the maximum temperature is found at about 950 seconds. Calculated time-temperature curves for the thermocouple near the centre of the ceiling are presented in figure 4. It shows that altering the grid size from 50 mm to 25 mm resulted in little change in the temperature profile, inferring convergence at the 50 mm grid spacing.

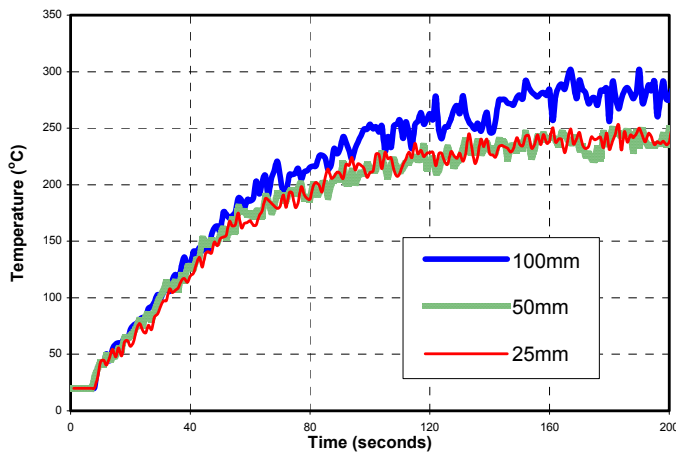


Figure 4. Calculated temperature profiles at the ceiling midpoint (TC-M) for different grid sizes

#### Fire Spread on Wall linings

Following the pool fire simulations, FDS simulations were conducted with the same enclosure but with plywood used as wall lining over part of the wall. In these FDS simulations the upper part of the north and east walls were partially lined with plywood whilst the remainder of the walls were lined with 12 mm thick gypsum plasterboard as shown in figure 5. Initially the reaction used was specified as 'Ethanol', as in the previous simulations, this was then changed to "Wood" from the FDS database. Similar temperature predictions as described for the pool fire simulations were made.

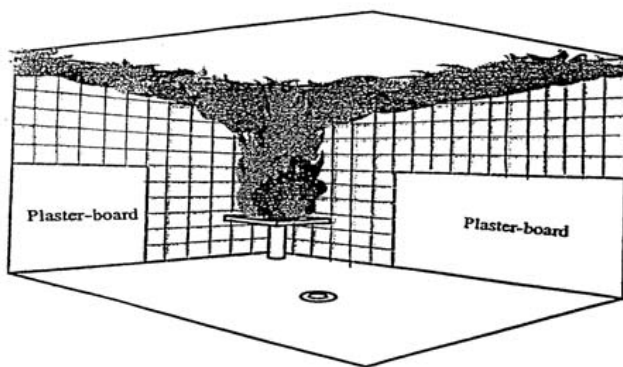


Figure 5. Typical flame spread patterns observed experimentally (schematic view is drawn based on video recording and the figure is reproduced from [5]).

In order to use the FDS calculations effectively, the combustion parameters of plywood as input data were selected carefully. From the available sources three main parameters; ignition temperature, heat of gasification and heat of combustion

were found to be 270 °C, 1800 and 18000 KJ/Kg respectively [9-11]. These values were adopted in all of the FDS calculations.

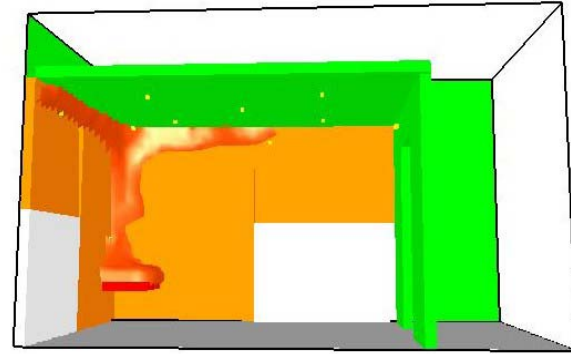


Figure 6. Smokeview flame spread on lining surface at 100 Sec.

Observations made of the experimental tests using video recordings suggest that the ignition of the plywood lining material began at the area adjacent to the source flame about 200-300 mm above the base of the pool fire. After ignition the flame spread vertically towards the ceiling, then horizontally at the intersection of the ceiling and walls (where the gas temperatures are highest, figure 5). Horizontal flame spread continued until the flame front approached the corners of the enclosure at which time the flames started to descend. This heralded the onset of flashover. The Smokeview animations of both mixture fraction and HRR outputs from ignition until the time at which the HRR reaches 1 MW (taken as an indication of flashover) were analysed. The observations showed that the spread of flame after reaching the ceiling follows a similar T-shaped pattern as observed experimentally. At the stage when HRR reached 1 MW flames descended down the wall to approximately the midpoint and flames emerged from top of the doorway. In figure 6 a snapshot from Smokeview shows the shape of the T-shaped propagation of the flame front.

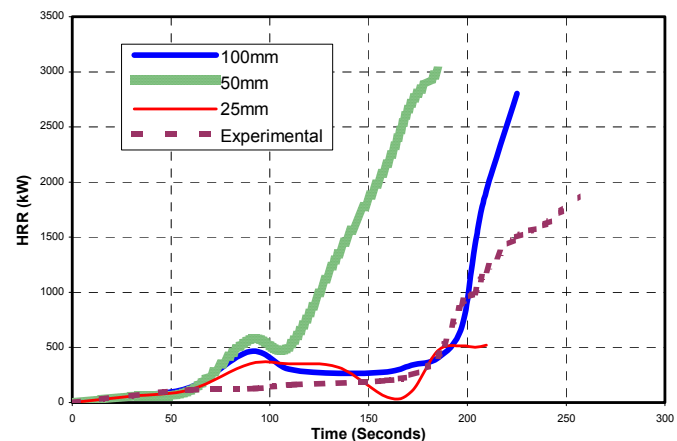


Figure 7. Experimental and FDS, HRR profiles when stoichiometry of reaction is 'Ethanol'.

In figure 7, the HRR profiles resulting from FDS calculations using the "Ethanol" reaction at different grid sizes are presented. It should be noted that as the grid size is reduced the main events relating to HRR occur more rapidly after ignition.

In table 1 the time to flashover is presented utilizing three different flashover criteria [12,13]. With 100 mm grid size the predicted time to flashover was found to approximately be in agreement with the experimental data. However, when a finer grid size (50 mm) was used the predicted time became more



inaccurate, and when the 25 mm grid spacing was used the inaccuracy increased too the extent that the HRR remained below 500 kW (figure 7) and never approached any of the flashover criteria.

Table 1 FDS and experimental time to flashover parameters

Test	Time to flashover Seconds		
	1 MW HRR	600°C	HF20 kW/m <sup>2</sup>
Experimental	200	200	207
FDS 50mm	127	103	128
FDS 100mm	201	199	203

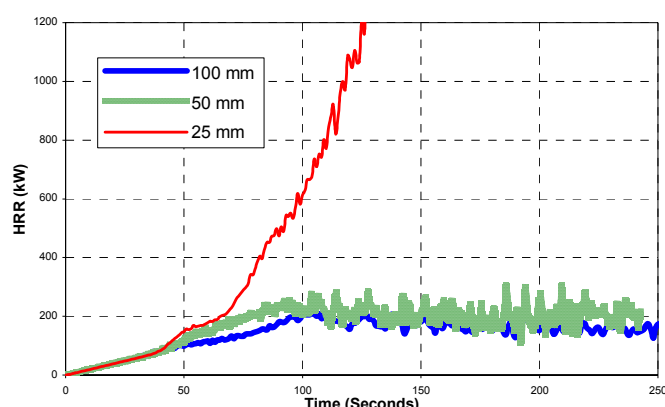


Figure 8. Experimental and FDS, HRR profiles when stoichiometry of reaction is ‘Wood’.

When the reaction was set to “Wood” in the FDS calculations, the Smokeview animation showed a similar surface flame spread pattern as explained previously. However the HRR profiles with wood reaction were found to be quite different from those obtained when the ‘Ethanol’ reaction was used. As shown in figure 8 flashover is reached only with the finest grid spacing (25 mm) is used. With 50 mm and 100 mm grid spacings the fire did not grow sufficiently to reach flashover. Adjustment of the plywood combustion parameters did not change the overall results.

## Conclusions

FDS simulations of the ISO room pool fire test showed that with the prescribed heating rate and fine grid spacing the temperature at different locations could be reproduced in close agreement with the experimental data. Comparison of time-temperature curves obtained at different grid sizes show that convergence is approached at 50 mm grid spacing.

Reproduction of the experimental ISO room pool-fire test by prescribing the HRR made it possible to simulate the ISO room lining test with two fuel: methylated spirit as the source fire and plywood wall lining as the main fuel. With plywood as the wall lining, when the reaction was taken as that of “Wood” an increase in the HRR sufficient for flashover was predicted only with the finest grid spacing (25mm). By contrast when the

“Ethanol” reaction was used, FDS simulated flashover with grid spacings of 50 mm and above, but not with the 25 mm grid spacing.

In conclusion the FDS surface flame spread modelling results show significant inconsistency, with grid size variation and choice of the fuel reaction.

## References

- [1] McGrattan, K. B. and Forney, G. P., Fire Dynamics Simulator Users Manual NISTIR 6469, National Institute of Standards and technology, U.S. Department of Commerce, Gaithersburg, MD 20899.
- [2] Hostikka, S., McGrattan, K. and Hamins, A., Numerical Modelling of Fires Using LES and Finite Method of Radiation, in *Proceedings of Fifth SFPA Conference* 2003, 383-395.
- [3] McGrattan, K., Floyd J., Forney, G., Baum, H. and Hostikka, S., Improved radiation and combustion routines for a large eddy simulation fire model, in *Fire Safety Science - Proceedings of the Seventh International Symposium* 2002, 827-838.
- [4] Floyd, J. and Lattimer, B., Validation of FDS V4 Boundary Heat Flux Predictions for a Corner Fire, in *Proceedings of INTERFLAM Conference* 2004, 1281-1292.
- [5] Shields, T. J., Silcock G. W. H., Moghaddam, A. Z., Azhakesan, M. A. and Zhang, J., A comparison of fire retarded and non-fire retarded wood-based wall linings exposed to fire in an enclosure, *Fire and Materials* **23**, 1999, 17-25.
- [6] International Organisation for Standardization, 1993 Fire tests. Full-scale Room Test for Surface Products, Designation ISO 9705: 1993(E), American National Standards Institute, Boston, MA.
- [7] Huggett, C., Estimation of rate of heat release by means of oxygen consumption measurements, *Fire and Materials* 1980, 4:61-65.
- [8] Consolidated Refractories Australasia PTY. LTD. Australia Thermal Ceramics Data Sheet.
- [9] DiNenno Philip J. (editor), *SFPE Handbook of Fire Protection Engineering* Third Edition 2002 NFPA, ISBN 087765-451-4.
- [10] Drysdale, D., *An Introduction to Fire Dynamics* John Wiley and Sons 1986 ISBN 0471906131.
- [11] Harmathy, T. Z. (editor), *Fire Safety Design and Concrete*, Longman Group UK Limited 1993 ISBN 0582076870.
- [12] Patrick, M. Kathryn, C. and John, A., Flashover and fire analysis a discussion of the practical use of flashover analysis in fire investigations, in *Proceedings of INTERFLAM Conference* 2004, 1101-1114.
- [13] Dietenberger, M. A., Grexa, O., White, R. H., Sweet, M. and Janssen, M., Room/corner tests of wall-linings with 100/300 kW burner, in *Proceedings of Fourth International Fire and Materials Conference* 1995, 53-62.

## Free Surface Monitoring Using Image Processing

P.D.M. Brady<sup>1</sup>, M. Boutounet<sup>2</sup> and S. Beecham<sup>1</sup>

<sup>1</sup> Faculty of Engineering  
University of Technology Sydney, NSW, 2007 AUSTRALIA

<sup>2</sup> Département de Génie Mathématique et Modélisation  
INSA Toulouse, 31077 Toulouse Cedex 4, FRANCE

### Abstract

We present an alternate method of data capture based on a consumer grade digital video camera combined with commonly available image processing techniques. The capture/analysis technique was developed to provide experimental data for the validation of free surface Computational Fluid Dynamics (CFD) models and records the wave motion along the inside of the flume walls. A sample data set is presented as validation of the capture/analysis technique.

### Introduction

The validation of free surface Computational Fluid Dynamics models requires more data than can be supplied by Laser Doppler Velocimetry (LDV), Constant Temperature Anemometry (CTA) or Particle Image Velocimetry (PIV) alone. LDV, CTA and PIV are very expensive to both set up and run and as a result access is restricted to those institutions that have the resources to purchase and maintain these types of sensors. They also require a high level of expertise to operate and only provide data on the structure of the velocity field. Additional validation data can be obtained by measurement of the free surface using manual or automatic point probes although these approaches also have their limitations.

Figure 1 shows an image of free surface CFD data that requires validation. The flow is representative of water draining out of a flume around a square cylinder that is piercing the free surface. The free surface is shown within the wire frame walls and is coloured by the velocity magnitude of the particles in the vicinity.

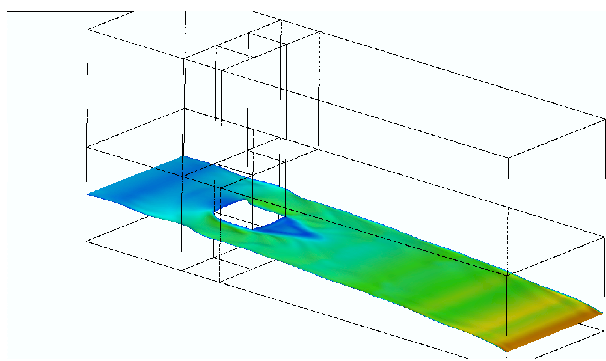


Figure 1: Example CFD data with waves along the walls, only the free surface is shown which has been coloured by speed. The flow is from left to right

Alternatively the use of a consumer grade digital video camera and off the shelf image processing software can provide detailed information on the wave motion, which in turn provides direct, quantitative validation data for CFD validation studies.

The increase of image quality of consumer grade digital cameras means that they can directly compete with commercial PIV systems in terms of pixel resolution. The system discussed in

this paper has several advantages over PIV: the lack of flow seeding and seed resolution. There are experimental configurations where it is impractical, if not impossible, to adequately seed the flow for the use of PIV techniques such as a recirculating flume where the particles may damage the pump or other devices. As the technique presented here does not use seed particles it will be suitable in these situations. A further limitation of PIV systems that they are based on mathematical correlations of seed particles, which generally require a window of at least 5x5 pixels for correlation. However, the optical technique presented in this paper is limited by the resolution of the camera used rather than the pixel window of the correlation function.

The image processing described in this paper was undertaken using MATLAB<sup>TM</sup> [2] and the MATLAB Image Processing Toolbox<sup>TM</sup> because they are available within the Faculty of Engineering, UTS. However all the methods described below could be implemented on alternative software packages.

### Hardware Configuration and Data Capture

The experimental testing was undertaken using the 13m tilting open channel flume located in the Hydraulics Laboratory at the Faculty of Engineering, UTS. The flume is 305mm wide by 305mm deep, has a smooth opaque floor and transparent glass walls. An inlet diffuser is installed to evenly distribute the flow from the incoming pipe, while an adjustable overflow weir provides outlet control. Feed water is provided by a recirculating ring main system that is supplied by a Worthington 52R-13A type pump fed from a return sump.

The image capture process was undertaken using a Sony miniDV camcorder, model DCR-PC110E, which was connected to a computer via an IEEE 1394b (Firewire) interface. Two methods of data capture were tested: direct computer capture and recording to a miniDV tape.

The computer used for the data capture was a Macintosh G4 Powerbook running MACOS<sup>TM</sup> 10. Analysis of the images was undertaken on the Faculty of Engineering Research Computing Cluster using MATLAB<sup>TM</sup> release 6.5 in a Linux environment. The Linux cluster is a collection of workstations dedicated to high speed computing based on Pentium 4 3GHz processors with an 800MHz front side bus and 2Gb of 400MHz DDR-RAM.

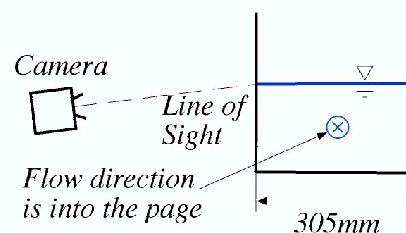


Figure 2: Schematic of the camera location relative to the flume

The focal plane of the camera was set up slightly under the flume so that the camera was looking up to the free surface. This is necessary so that the analysis, which is based on an image detection routine, detects the free surface on the wall and not a wave moving through the centre of the channel. The camera was set back approximately 1m from the walls as shown in Figure 2. Several methods of illuminating the flume were tested and included:

- Room fluorescent lighting only,
- Room fluorescent lighting augmented with a 200W floodlight,
- Floodlight only.

In this case the optimal lighting configuration was the floodlight only. We infer that this was because we had direct control of the direction and intensity of the light. The floodlight would have also eliminated stray light sources from the rest of the laboratory that might have introduced additional shadowing. We suspect that the lighting may need to be tailored for each experimental application.

A 50mm grid was attached to the side of the flume to be filmed. An image of the grid was then taken and used to transform the image to eliminate the curvature introduced as a result of the camera lens.

## Data Analysis

### Image Rectification

The first step in reducing the raw video data as recorded by the camera was to coordinate and rectify the base image. This allows the free surface as captured by the edge detection methods to be expressed in real world coordinates rather than a pixel-based coordinate scheme.

To begin the transformation a selection of control points are graphically selected as shown in Figure 3. The interface allowed the user to simply click at the selected grid intersections.

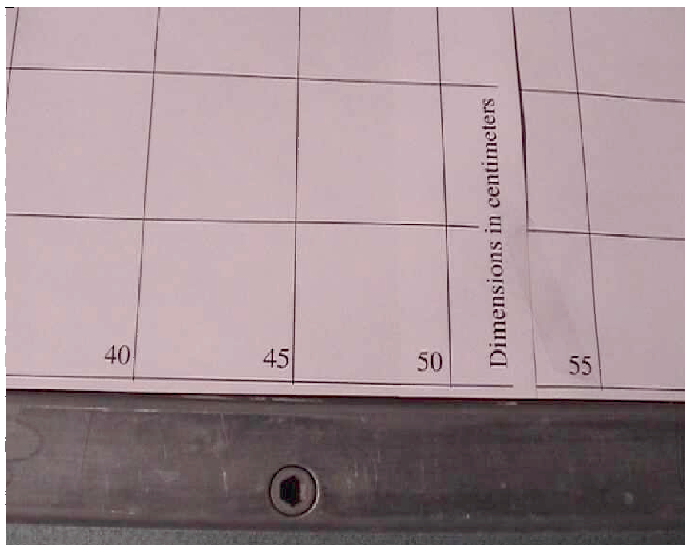


Figure 3: Image registration grid

These points were then assigned their real cartesian coordinates for the transformation. The transformation was based on the discrete linear transform (DLT) method presented by Abdel-Aziz and Karara [1]. A set of control points, entered by the user, were used to define eight parameters, which is the minimum required for a two-dimensional problem. At least four pairs of points are required to compute the transform which was based on a least squares method. A discussion of the accuracy of this method is presented below. A colour image of the transformed grid is shown in Figure 4.

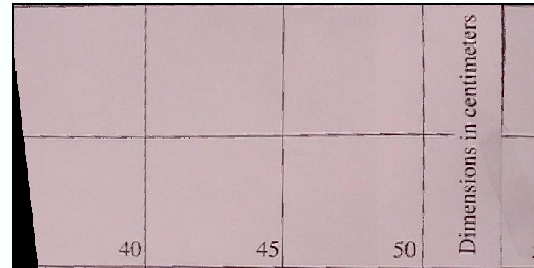


Figure 4: Rectified image of the grid

The next step in analysing the data was to reduce the number of colours in the data from Red/Green/Blue (RGB) to black and white (BW). Four BW reductions were tested: the combined RGB image and the three individual colour channels. Computationally there is little difference in processing overheads from working with the combined or individual channel data. The single green channel, when reduced to black and white, produced the cleanest BW edge. Figure 5 shows the black and white reduction of the green channel data.



Figure 5: Black and white reduction of the green channel data, note the metallic base of the flume with bolts along the bottom of the image. The ellipsoid indicators show where marks on the flume need to be masked. The flow is moving from left to right in this image

Once the image had been reduced to black and white a mask was applied to hide the areas that are not of interest or that contained potentially spurious data. For example there are several marks shown on Figure 5 that are on the flume walls and are not part of the required data set. This mask, like the transform function, was applied to the whole data set and therefore it had to be carefully selected so that the free surface did not infringe on the masked area during the transient data series.

### Edge Detection

The black and white image is stored as a logical array with the black and white pixels represented by FALSE (0 or off) and TRUE (1 or on) respectively. Using the logical array allows the edge detection to be based on the location of the change from FALSE to TRUE.

The edge detected by the edge detection routine is saved in a  $n \times nframes$  array where the  $n$  dimension represents the number of pixels in the image and  $nframes$  is the number of still images that have been analysed. Usually the maximum frame rate for consumer digital video cameras is 25Hz and 29.97Hz for PAL and NTSC respectively. The value stored in the array at location  $n_i$  is the height of the free surface in pixels. Figure 6 shows a typical view of the free surface data as it is extracted from the edge detection routine and before any transforms are applied.

Spurious data points may be introduced as a result of the logical array at the boundaries. This is shown in Figure 6 for the highest time frame and between the 400 and 600 points on the  $x$  pixel axis. An interpolation function, combined with boundary filtering can be implemented at this stage to eliminate these data points. See the sample data section for a detailed discussion and example of these errors.

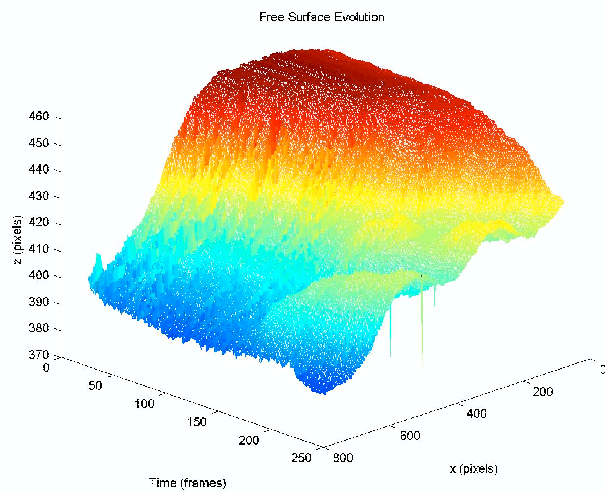


Figure 6: The raw processed data after extraction of the free surface and before applying the transforms to real time and space.

A transformation, which is based on the original coordination points, is then used to translate the measured coordinates from pixel space to physical space. These transformed coordinates are then based in the coordinate system used for the rectification step.

### Sample Data

#### Experimental Configuration

Sample data for validating the software were collected for a hydraulic jump moving upstream as shown in Figure 7. The upstream flow rate was set to 4l/s and the flume was set at a 1/250 slope. Supercritical flow was generated using an adjustable sluice gate set at a 20mm opening while the downstream control was provided by an adjustable weir.

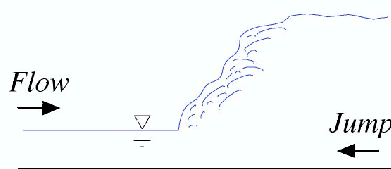


Figure 7: Sketch of the relative motion of the hydraulic jump and flow

Initially the downstream control was relaxed so that the flow remained supercritical for the entire length of the flume downstream of the sluice. Once the flow had been established the weir was lifted to approximately three times the height of the critical depth. This backpressure caused the formation of a hydraulic jump, which then moved upstream and through the data capture window.

#### Analysis

The data captured was reduced to black and white and the edge detected as outlined above. A plot of this raw data is shown in Figure 8, which clearly shows the boundary errors introduced at the left and right edges of the frame. Stray pixel data, visible as vertical lines extending a large distance below the surrounding points, are also visible at around the 450 pixel mark on the distance axis, occurring over intermittent time steps.

Stray pixels can be removed from the data set via an interpolation scheme based on the adjacent data. This method is discussed below in the *Image Errors* section.

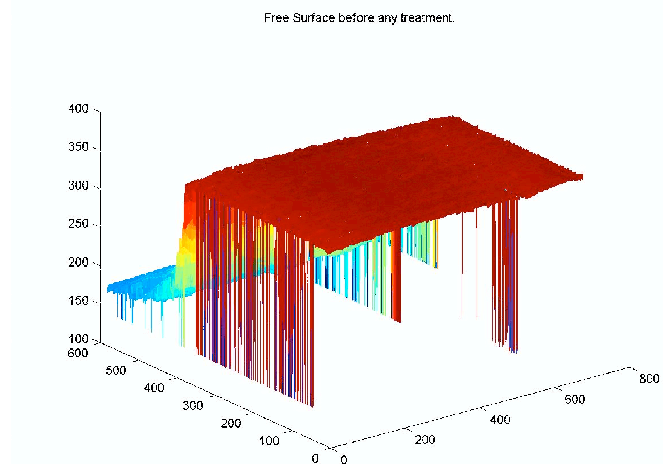


Figure 8: Raw pixel data with the vertical, left and right axes representative of image height (pixels), frame number and distance (pixels) respectively

The edge filtering allows for the removal of a fixed number of data points from either side. This filtering process is subjective and must be undertaken by the operator to ensure that spurious data are removed only. Figure 9 shows the results of the transformed and smoothed data.

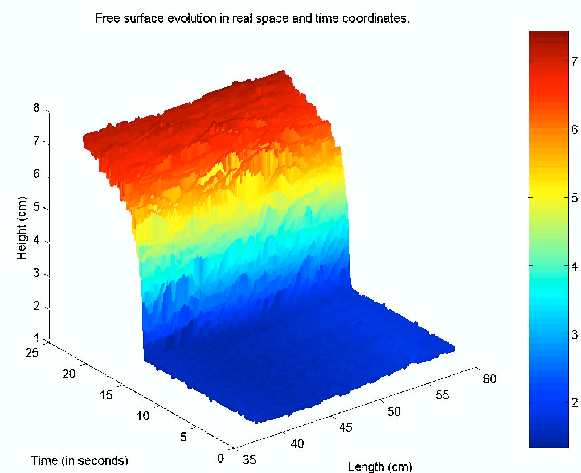


Figure 9: Transformed and filtered data, coloured by depth in centimetres

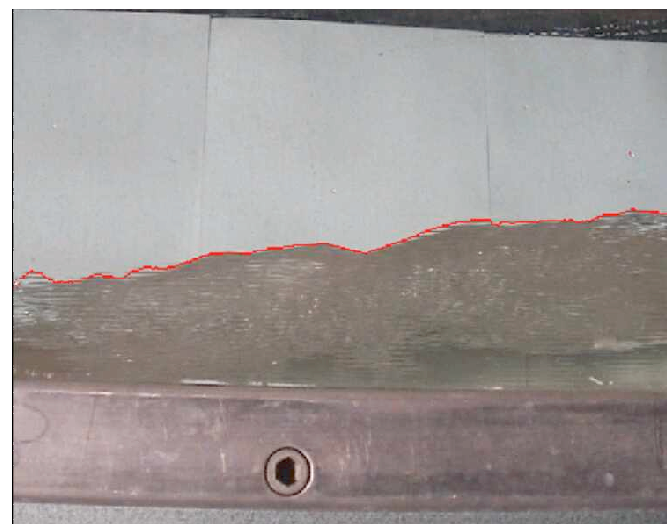


Figure 10: Image of the free surface superimposed over the original data

Figure 10 shows an inspection image of the free surface data superimposed over the original image data. This allows for a quick visual inspection to test the accuracy of the analysis.



### Potential Numerical Inaccuracies

It should be stressed that this method is not as accurate as single point probe techniques. However the strength of the method is that it provides data across the entire field of view. This gives the potential to capture the entire shape of the wave as opposed to measuring the wave passage only. Some of the factors that will affect the accuracy of the procedure are discussed below.

### Rectification

The discrete linear transform used to rectify the images directly calculates an estimate of the numerical error using the mean of the Euclidean norms of vectors,

$$x_{real}(i) - transformed(x_{pixels}(i)), 1 \leq i \leq n_p, \quad (1)$$

where  $n_p$  is the number of coordination points used. For example the grid shown in Figure 3, which was approximately 200x100mm, when transformed with a four point transform had an estimated error of 3.66mm and an error of 2.95mm for ten points. This equates to a 20% reduction in the estimated error.

A test was undertaken with a larger field of view, in this case a 350x200mm grid. For a four and six point transformation the estimated error came to 4.16 and 4.9mm respectively. Examination of this result showed that at larger grids the user selection becomes dominant in the error magnitude rather than the transformation process.

It may be possible to reduce the error introduced by the user selection process by converting the hollow grid currently used to that of a filled checkerboard grid. This would allow the use of a corner detection routine with the user entering the appropriate coordinates for the points found by the routine. Investigation of this method will be a topic for future research.

### Parallax Error

A parallax error will be introduced as the light rays pass at an oblique angle through the glass of the flume. Given an approximate refractive index of glass, relative to air, of  $n=1.50$  and the maximum angle of incidence ( $\theta_i$ ) of  $45^\circ$  (based on a focal length of 42mm at the widest angle [3],  $\theta_r$  is the angle of refraction) the maximum offset ( $o$ ) would be 4.2mm based on the 5mm ( $t$ ) thickness of glass installed in the flume, see Figure 11. The parallax error would be reduced when using the camera at higher focal lengths or when it is located closer to the flume.

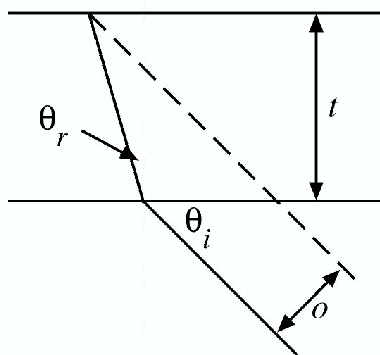


Figure 11: Parallax error

Care must be taken when choosing both the camera type and its location for the experiment to ensure the pixel error is appropriate. The maximum accuracy of the free surface detection is to the pixel that it is in. As an example using a 640x480 video pixel camera, which is common for consumer video cameras, and shooting a 20cm by 10cm window for width and depth respectively yields an approximate pixel size of 0.3mm. These dimensions correspond roughly to the data illustrated above in the sample section and this accuracy is an order of magnitude less than the errors introduced by parallax or

the meniscus however they may become a problem for larger applications or when a macro lens is used.

### Image Errors

Stray pixel data can accumulate as shown in Figure 8 and can be removed using an interpolation scheme. The interpolation scheme used here was based on linear interpolation between the adjacent points that were considered real.

As the user has little control over the implementation of this interpolation scheme care must be taken when examining the final data for inaccuracies.

### Computational Requirements

The sample data processed took an average of 0.7s per frame for analysis. This time is inclusive of image rectification and converting back to an animation.

In order to eliminate the need for the user to be at the program, the software has been configured to run in either a graphical or batch mode. Thus this run time can be undertaken overnight using the batch settings.

### Alternate Implementation Schemes

An alternate capture technique aimed to provide validation data of the flow field around the square cylinder, shown in Figure 1, is being developed. The technique uses a transparent cylinder mounted in the flume and has a fixed mirror in the centre of the cylinder. The camera would then be mounted above the cylinder so that the free surface image is reflected via the mirror to the camera for capture. This technique is currently under development with details to be published upon completion of the development.

### Conclusions

We have presented an alternative data capture and analysis technique based on a consumer quality digital video camera and readily available image processing software. Possible applications of the technique include providing validation data for free surface CFD models and experimental wave analysis. A sample data set has been presented for validation of the method, which shows that the method is applicable within the constraints outlined.

A limitation of the system was identified in that the capture is based on the boundary of the flow rather than the middle of the flow domain. This indicates that the method does provide useful information but is not a complete analysis system in itself and should be used in conjunction with other methods such as PIV or LDV.

### Acknowledgments

This work would not have been possible without the collaborative relationship between Institut National des Sciences Appliquées (INSA), Toulouse and the Faculty of Engineering, UTS. The MATLAB Image Processing Toolbox was made available within the Faculty of Engineering, UTS by Professor Hung Nguyen.

### References

- [1] Abdel-Aziz, Y. I. and Karara, H. M., Direct Linear Transform From Comparator Coordinates Into Object Space Coordinates in Close-Range Photogrammetry, presented in *Symposium on Close Range Photogrammetry*, Falls Church, Virginia, USA, 1971.
- [2] Mathworks, MATLAB 6.5, 6.5.0.180913a Release 13 ed. Natick, Massachusetts, USA: The Mathworks Incorporated, 2002.
- [3] Sony, *Sony Digital Video Camera Recorder - Model DCR-PC110*. Park Ridge, New Jersey, USA: Sony, 2000.

## A Numerical Study of Enhanced Micro-channel Cooling Using a Synthetic Jet Actuator

V. Timchenko, J. Reizes and E. Leonardi

School of Mechanical and Manufacturing Engineering  
The University of New South Wales, Sydney 2052, Australia.

### Abstract

The use of micro synthetic jets to disrupt a laminar flow in forced air convection micro-channels and improve a heat transfer to the cooling air has been studied numerically. The effectiveness of the proposed cooling strategy was evaluated by comparing heat transfer rates with and without the synthetic jet. Simulation results indicate that the location of the synthetic jet is important and that synthetic jets have the potential to significantly improve heat transfer from integrated circuits.

### Introduction

The evolution of integrated electronic devices has led to substantial increases of heat generation rates and requires the development of innovative cooling techniques. Forced air convection in silicon micro-channels etched in the rear side of the silicon substrate has the potential to remove heat directly from the chip and has been developed as one of the strategies for cooling of integrated circuits after micro-channel heat sink concept was first introduced in Tuckerman and Pease [1] pioneering study. However, airflow in such conduits is laminar with the result that the heat transfer rate is quite low. In addition, if the upper surface of the micro-channels is a hot surface, the heat transfer rate may be further reduced by the appearance of separations near the inlets on the upper surfaces of the channels.

A synthetic jet [2], so-called because the jet is synthesized from the working fluid without introducing a fluid from another source, can be used for disrupting the laminar flow in the channels as well as for interfering with the stagnant zones. In fact, the unsteady flow from the jet creates a quasi-turbulent flow, thereby possibly significantly increasing the rate of heat transfer. The synthetic jet is developed in the cooling fluid by a micro-pump actuator [3] which consists of an oscillating diaphragm in a cavity with a small orifice in the face opposite the diaphragm as may be seen in Figure 1. Under appropriate operating conditions this actuator provides a fluctuating flow away from the orifice into the cooling channel. The actuator thus has a zero net mass flow, but a non-zero net momentum transfer over an entire cycle of the diaphragm oscillation.

Utturkar *et al.* [4] suggested the jet formation criterion  $1/St = Re/S^2 > K$ , in which the constant  $K$  was said to be approximately 2 for two-dimensional jets and approximately 0.16 for axisymmetric jets. The non-dimensional parameters used in their analysis of synthetic jet actuators were the Reynolds number,  $Re = \bar{V}_j d / \nu$ , in which,  $\bar{V}_j$ , is the average orifice expulsion velocity,  $d$  is the orifice width, and  $\nu$  is the kinematic viscosity, the Stokes number,  $S = \sqrt{\omega d^2 / \nu}$ , in which  $\omega = 2\pi f$  is the angular velocity and  $f$  is the frequency of the diaphragm motion and the Strouhal number,  $St = \omega d / \bar{V}_j$ .

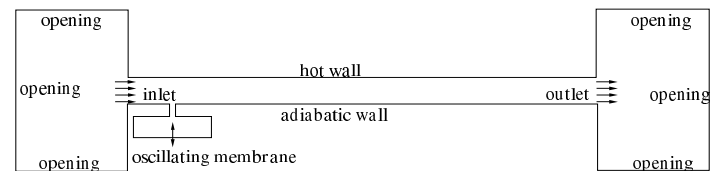


Figure 1. Sketch of computational domain.

An experimental study of periodic disturbances on the penetration and mixing of synthetic jets in cross-flow was performed by Eroglu and Breidenthal [5]. They observed that periodic forcing of the jet stream effects mixing by creating vortex loops whose strength and spacing are determined by the frequency of the forcing and the jet to cross-flow velocity ratio. The main parameter characterizing the jet in cross-flow has been found to be the jet-to-cross-flow momentum ratio [6].

In this paper we study numerically the feasibility of using synthetic jet actuators to enhance heat transfer rates in micro-channels. A two-dimensional micro-channel 200  $\mu m$  high and 4.2 mm long is considered with a top surface hot and all the other walls adiabatic (Figure 1). The effectiveness of the proposed cooling procedure is evaluated by comparing the heat transfer rates with and without the synthetic jet.

### Mathematical and numerical model

For micro sized devices the flow is dependent on the Knudsen number,  $Kn$ , which is defined as ratio of the mean free path to the characteristic geometry length ( $Kn = \lambda/L$ ). In this study flows with  $Kn < 0.01$  are modeled, so that the continuum approach using conventional conservation equations is still valid [7].

The flow generated by synthetic jet actuators has been simulated using a commercial package, CFX-5.6. Unsteady computations of compressible laminar flow have been performed for two-dimensional numerical formulations. The basic set of the unsteady conservation equations for laminar flow comprises the continuity equation

$$\frac{\partial \rho}{\partial t} + \nabla \cdot (\rho \tilde{V}) = 0, \quad (1)$$

the Navier-Stokes equation

$$\frac{\partial \rho \tilde{V}}{\partial t} + \nabla \cdot \rho \tilde{V} \tilde{V} = -\nabla p + \nabla \cdot (\mu \nabla \tilde{V} + \mu (\nabla \tilde{V})^T) + \rho \tilde{g} \quad (2)$$

and the energy equation



$$\frac{\partial \rho h}{\partial t} + \nabla \cdot (\rho \tilde{V} h) - \nabla \cdot (k \nabla T) = 0, \quad (3)$$

in which  $\rho$ ,  $\tilde{V}$ ,  $p$ ,  $\mu$ ,  $h$ ,  $T$ ,  $k$ , and  $t$  denote density, velocity vector, pressure, viscosity, enthalpy, temperature, thermal conductivity and time respectively. The compressibility of the air was taken into account by treating it as an ideal gas with an equation of state given by

$$\rho = \frac{M(p + p_{ref})}{R_u T}, \quad (4)$$

in which  $M$  is the molecular mass of the gas,  $R_u$  is the universal gas constant,  $T$  is the absolute temperature and  $p_{ref}$  is the absolute ambient pressure.

The displacement of the membrane  $Y_m$  was assumed to be a parabola which varies sinusoidally in time, viz,

$$Y_m = A(1 - (x/r)^2) \sin(2\pi f t) \quad (5)$$

in which  $A$  and  $f$  are the amplitude and the frequency of oscillation respectively and  $r$  is the radius of the membrane.

A second order backward Euler differencing scheme was used for the transient term, whereas a second order upwind differencing scheme was used for the advection terms in the Navier Stokes equation. At each time step (equal to one hundredth of a cycle), the internal iterations were continued until the mass and momentum residuals had been reduced to  $10^{-6}$ .

The number of grid points used in the orifice of the synthetic jet generator was  $50 \times 20$  in the stream-wise and transverse directions respectively, so mesh size was kept to  $2.5 \mu m$  in the orifice. Outside the orifice grid was gradually expanded with maximum mesh size equal to  $5 \mu m$ . The total number of mesh points was equal to 164316.

To study the effect of synthetic jets on the enhancement of heat transfer in the micro channel we introduce the factor of heat transfer effectiveness  $F$ , defined as  $F = \dot{Q} / [(1/2)\dot{m}U^2]$ , in which  $\dot{Q}$  is the average heat transfer rate from the upper wall,  $\dot{m}$  is the mass flow rate,  $U$  is an average axial velocity in the channel. This factor represents a ratio of the heat transferred to the total flow kinetic energy.

## Results and discussion

Two two-dimensional cases are presented here. In the first (Case 1) an orifice  $50 \mu m$  wide and  $100 \mu m$  long was placed  $400 \mu m$  downstream from the inlet. The width of the diaphragm was  $0.7 mm$  and the cavity depth was  $250 \mu m$ . As inflow temperature and velocity distributions affect the heat transfer in the channel, external domains  $1 mm$  long and  $1.5 mm$  high were included at either end of the channel (Figure 1). In Case 1, an average velocity in the channel of about  $1 m/s$  was obtained with a pressure drop of  $25 Pa$ , the temperature was set to  $20^\circ C$  at the inlet of the (left) external domain. In Case 2, the pressure was increased to  $250 Pa$  with the temperature remaining at  $20^\circ C$  at the inlet of the external domain. At the outlet (right) of the external domain, in both cases, the pressure was fixed to zero with  $p_{ref}$  equal to  $100 kPa$  and the temperature set to  $30^\circ C$ . The upper wall of the channel was isothermal at the  $50^\circ C$ .

To evaluate the effectiveness of the proposed cooling strategy the steady flow heat transfer was used as the standard. In this particular case we wanted to observe an ability of the synthetic

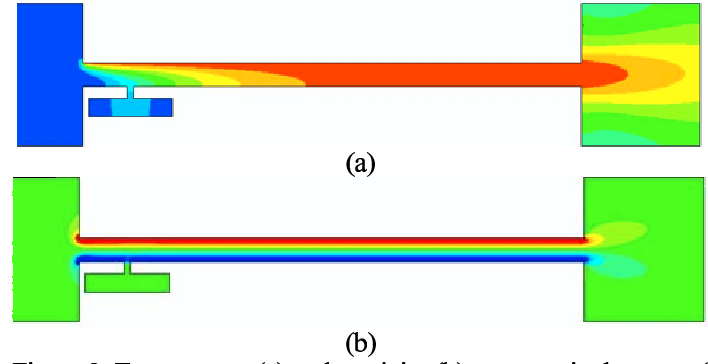


Figure 2. Temperature (a) and vorticity (b) contours in the case of steady flow (Case 1).

jet to disrupt the laminar flow near the inlet of the channel. Thus we positioned it  $1.2 mm$  from the inlet.

Figure 2 shows temperature and vorticity contours in the case of steady flow with the jet not active. Horizontal contours of vorticity correspond to a laminar, parabolic flow with no mixing occurring. The heat transfer rate from the hot upper wall in the case of the steady flow with mass flow rate,  $\dot{m} = \rho AU$  equal to  $0.24 \times 10^{-3} kg/s$  and  $\dot{Q}$ , the rate of heat transfer was  $59.0 \times 10^{-1} W/m$ . The resulting heat transfer effectiveness factor was  $F = 4600$ . It should be noted from the temperature contours in Figure 2 that the average fluid temperature reaches the very close value to that of the upper wall about  $1.8 mm$  from the inlet, so that there is little heat transfer between that point and the outlet.

Enlarged views of the temperature and vorticity contours at various instants of the cycle are shown in Figures 3–4. A jet was produced by the displacement of membrane with frequency  $5 kHz$  and the amplitude  $23.6 \mu m$ . During the expulsion stage a vortex is created near the orifice. It travels a short distance towards the upper wall of the channel thereby interfering with the boundary

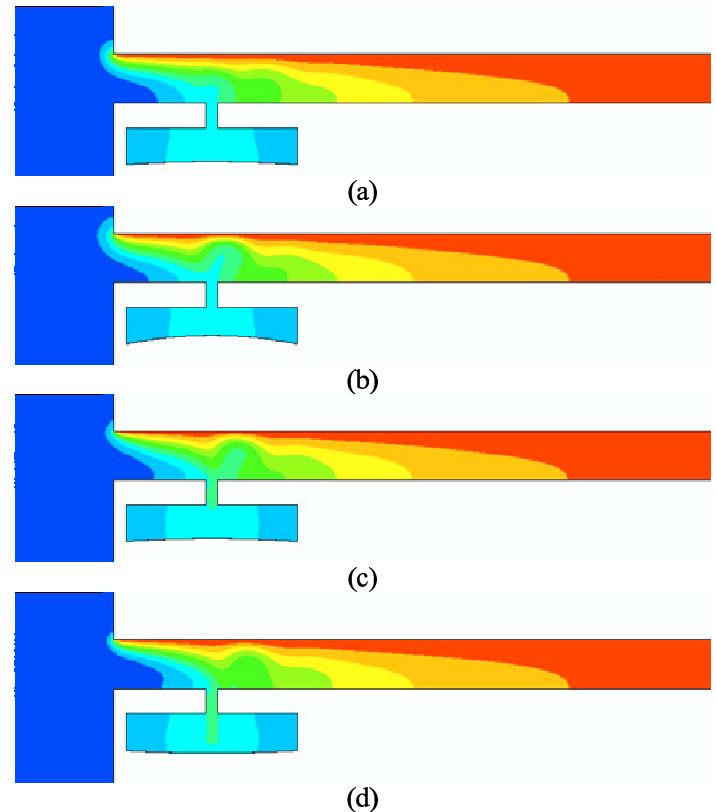


Figure 3. Temperature contours at the Maximum Expulsion (a), Minimum Volume (b), Maximum Ingestion (c) and Maximum Volume (d) stages (Case 1).

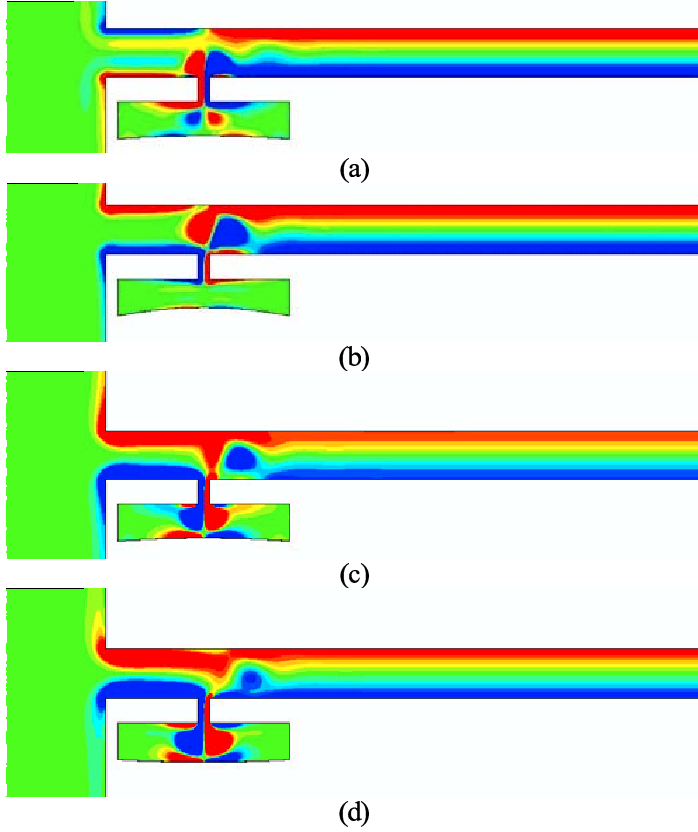


Figure 4. Vorticity contours at the Maximum Expansion (a), Minimum Volume (b), Maximum Ingestion (c) and Maximum Volume (d) stages (Case 1).

layer in which heat transfer occurs. Unfortunately, the disturbance does not propagate very far downstream. In Case 1 the heat transfer rate cannot be increased very much above that in the steady state with the result that  $\dot{Q} = 60.8 \times 10^{-1} W/m$  when average mass flow rate becomes is  $0.242 \times 10^{-3} kg/sm$  and average downstream flow velocity  $U = 1.022 m/s$  with  $F = 4813$ . Thus, for Case1 the heat transfer effectiveness factor increased by only about 5% when the membrane was activated.

By actuating with the chosen forcing membrane parameters a synthetic jet with  $Re=15$  and  $1/St=2.8$  was produced. It should be noted that when there is a cross-flow, the jet is not continuous despite the fact that in a still atmosphere a continuous synthetic jet with would have been produced [8]. The jet-to-cross-flow momentum ratio during expulsion stage defined as  $C_{exp} = d\bar{V}_j^2 / DU^2$  where  $D$  is the height of the channel equal to 5.

Because in Case 1 substantial changes were generated by the jet on the inflow temperature and velocity distributions (see Figures 3-4), in Case 2, the orifice has been moved further downstream to a position 1.2 mm from the inlet of the channel. The pressure drop was increased to 250 Pa to obtain a higher mass flow rate. It may be seen from Figure 5, that in Case 2, the steady flow temperature distribution indicates that it should be possible to significantly increase the rate of heat transfer. In steady flow, the heat transfer rate from the hot upper wall was 30.6W/m, whilst the mass flow rate was  $1.81 \times 10^{-3} kg/sm$  and the average velocity in the channel was 8.06m/s. The resultant heat transfer effectiveness factor was 520.

In case 2, the width of the diaphragm was 1mm and the cavity depth was  $400 \mu m$  so as to keep jet-to-cross-flow momentum ratio

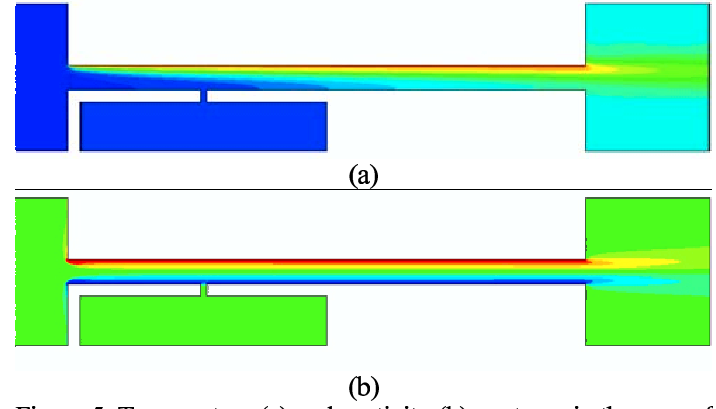


Figure 5. Temperature (a) and vorticity (b) contours in the case of steady flow (Case 2).

during expulsion stage equal to 5, the frequency was increased to 10kHz with the amplitude of  $42 \mu m$ . This led to a jet with  $Re= 125$  and  $1/St=12$ . Temperature and vorticity contours at various stages in the cycle may be seen in Figures 6 and 7. It can be seen that moving the orifice further away from the inlet together with increasing of mass flow rate resulted in substantially deeper penetration into the channel main flow of the vortices created during the expulsion stage thereby significantly enhancing mixing.

As a consequence, the heat transfer rate from the hot upper wall averaged over period of oscillation is 36.05W/m with average mass flow rate equal to  $1.68 \times 10^{-3} kg/sm$  and average downstream flow velocity of 7.09m/s. The heat transfer effectiveness factor is  $F = 853$ . Thus in the Case 2 the heat transfer effectiveness factor in the case of oscillating jet increased by approximately 64%.

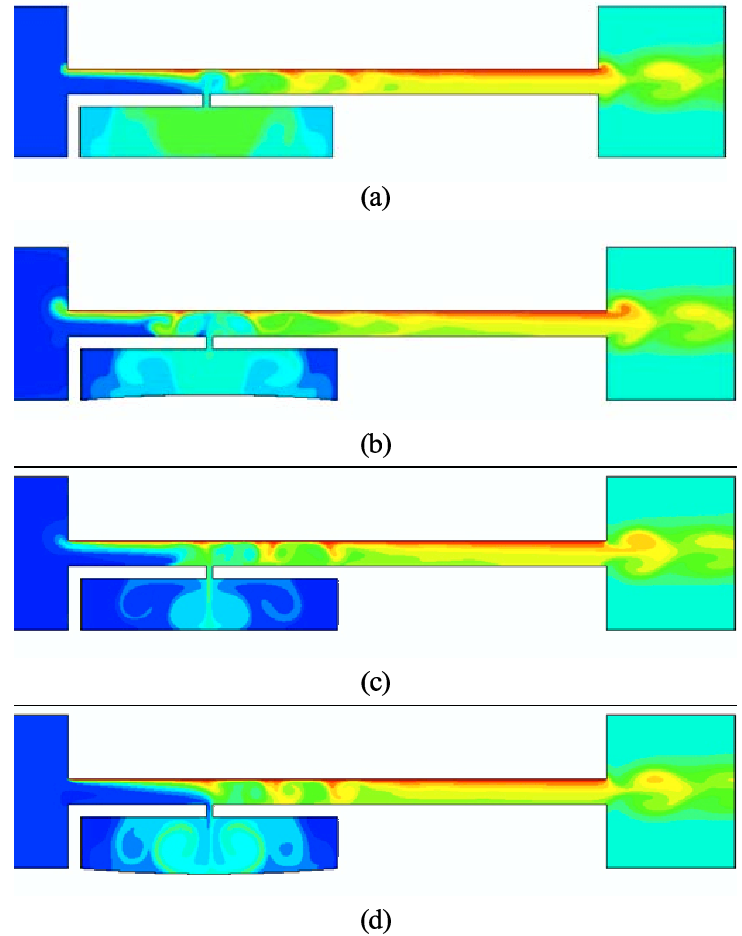


Figure 6. Temperature contours at the Maximum Expansion (a), Minimum Volume (b), Maximum Ingestion (c) and Maximum Volume (d) stages (Case 2).

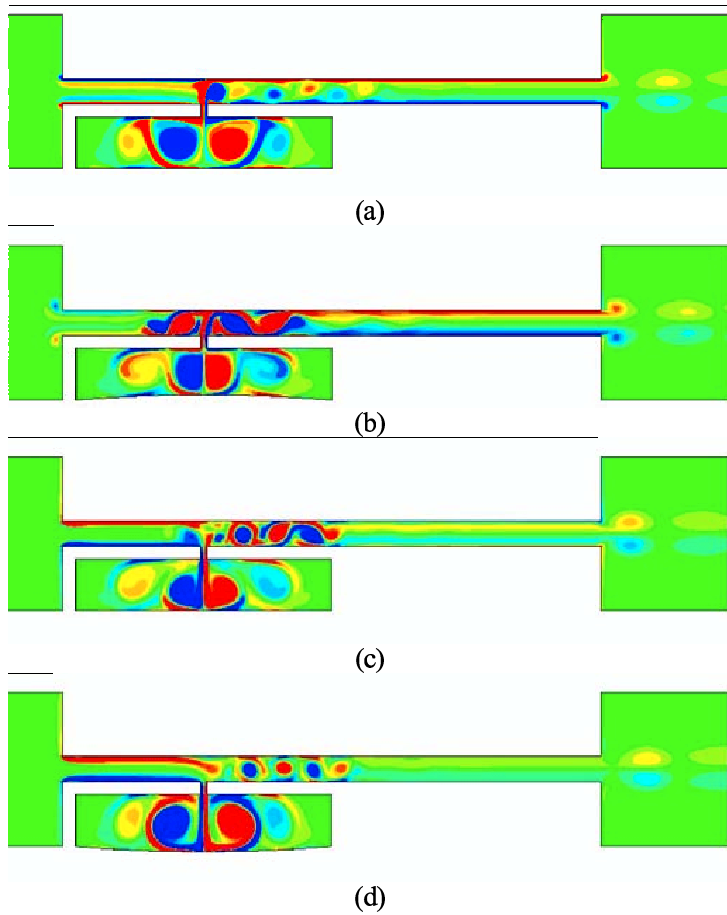


Figure 7. Vorticity contours at the Maximum Expulsion (a), Minimum Volume (b), Maximum Ingestion (c) and Maximum Volume (d) stages (Case 2).

## Conclusion

In this preliminary study simulations have been performed to evaluate the feasibility of using micro synthetic jet actuator to disrupt a laminar flow and enhance heat transfer in micro-channels. The initial results indicate that a fully optimized synthetic jet has the potential to significantly improve heat transfer from an integrated circuit to the cooling fluid. A detailed parametric study will be performed in order to find the optimal parameters, which lead to the largest enhancement of heat transfer.

## Acknowledgments

The authors would like to acknowledge with thanks the support of the Australian Research Council.

## References

- [1] Tuckerman D.B. and Pease R.F.W., , High performance Heat Sinking for VLSI, *IEEE Electron Device Letters*, Vol. EDL-2, No5, 1981, 126-129.
- [2] Glezer A. and Amitay M., , Synthetic jets, *Ann. Rev. Fluid Mech.*, 34, 2002, 503-529.
- [3] Mallinson S.G., Kwok C.Y. and Reizes J.A., Numerical simulation of micro-fabricated zero mass-flux jet actuators, *Sensors and Actuators A* 105, 2003, 229-236.
- [4] Utturkar Y., Holman R., Mittal R., Carrol B., Sheplak M. and Cattafesta L., A jet formation criterion for synthetic jet actuators, 41<sup>st</sup> Aerospace Sciences Meeting and Exhibit, 6-9 January Reno NV, AIAA 2003-0636, 2003.
- [5] Eroglu A. and Breidenthal R.E., *AIAA Journal*, 39, No3, 2001, 417-423
- [6] M. Gordon and J. Soria, "Scalar mixing of zero-net-mass-flux jets in crossflow," in *Proc. 14th Australasian Fluid Mech. Conf.*, 2001, 729-732.
- [7] Kamiadakis G., Beskok A., *Micro flows: fundamentals and simulation*, Springer-Verlag New York Inc., 2002.
- [8] V.Timchenko, J. Reizes , E. Leonardi and G.de Vahl Davis, A Criterion for the Formation of Micro Synthetic Jets, IMECE2004-61374, 2004.

## Identification of aerodynamic sound source in the wake of a rotating circular cylinder

A. Iida<sup>1</sup>, A. Mizuno<sup>1</sup> and R.J. Brown<sup>2</sup>

<sup>1</sup> Department of Mechanical Engineering, Kogakuin University,  
2665 Nakanomachi, Hachioji, Tokyo 192-0015, JAPAN

<sup>2</sup> School of Mechanical, Manufacturing and Medical Engineering,  
Queensland University of Technology, 2434 BRISBANE QLD 4001 AUSTRALIA

### Abstract

In order to reduce aerodynamic noise radiated from the turbulent wake of bluff bodies, vorticity structures and flow field around a rotating circular cylinder at Reynolds numbers between  $10^2$  and  $10^4$  were numerically investigated. Vorticity structures and resultant aerodynamic noise is strongly dependant on the velocity ratio, which is defined as flow velocity over rotational speed to the cylinder. At low velocity ratio, the noise level and aerodynamic forces increase and an anti-symmetric vorticity structure is observed. On the other hand, the absolute value of lift-drag ratio becomes small and alternative vorticity structure disappears as the velocity ratio exceeds about 2. As a result, the fluctuating aerodynamic forces become weak and the resulting aerodynamic sound becomes small. The noise level of the rotational cylinder is 10 dB lower than that of the conventional circular cylinder. Source terms of aerodynamic sound were also visualized by using vortex sound theory. The intensity of the source term of the separated shear layer rapidly changes as the shear layers roll up. Therefore, the separated shear layers play an important role in generating aerodynamic sound at low velocity ratio. Since the anti-symmetric vorticity structure disappears at high velocity ratio, vorticity fluctuation and resultant aerodynamic noise is restrained. As a result, very interestingly, in the case of the high velocity ratio the intensity of the source term generated by the separated shear layer is maintained, however, the noise level gradually decreases. This reveals that cylinder rotation is an effective method for reducing the aerodynamic noise radiated from a turbulent wake.

### Introduction

The maximum speed of high speed trains has been in an upward trend for several years [1]. Cooling flow rates inside air conditioners and computers are also increasing. Aerodynamic noise radiated from these products rapidly increases, because it is proportional to the sixth power of flow velocity. Aerodynamic noise must therefore be reduced if these products are to be further developed. Much research has been directed at noise reduction and prediction in product development. In the case of low Mach number flow, aerodynamic noise is generated by the fluctuating aerodynamic forces. Therefore aerodynamic noise from the wake of the bluff bodies depends on the large-scale eddy structures such as the Karman vorticities which cause the fluctuating lift force and flow induced vibration. In order to reduce the aerodynamic noise, control of the large vortex structures is important. It is well known that tripping wires and small holes are effective devices to reduce flow induced noise.

In this paper we discuss the effect of the rotation to reduce flow induced noise radiated from a circular cylinder in a uniform flow. In the case of potential flows, the downstream stagnation points are merged into one stagnation point when the velocity ratio of 2. Then, flow separation and vorticity structure can be controlled with the cylinder rotation. In this paper, the effect of noise reduction and vorticity break up were numerically investigated for Reynolds number between  $10^2$  to  $10^4$  at various rotational

speeds. The velocity ratio,  $\alpha = u/r\omega$ , defined as the ratio of the rotational speed,  $\omega$ , and the uniform velocity,  $u$ , plays an important roll in noise reduction. The numerical results show the large-scale vorticities broke down at  $\alpha > 2.0$  and resultant aerodynamic noise can therefore be reduced by cylinder rotation.

### Numerical Methods

The governing equation used for the flow field around the rotating circular cylinder is the continuity equation and incompressible Navier-Stokes equations. The standard Smagorinsky model is adopted as the sub-grid scale model for turbulence. The Van-Driess wall-damping function is also used for modeling of near-wall effects. The Smagorinsky constant is fixed to 0.15 and the grid-filler size is computed as the cube-root of the volume of each finite element. The spatially filters of governing equations are solved by a stream-upwind, second order finite element formulation [2]. The far field sound pressure radiated from a low-Mach number flow can be calculated from Lighthill-Curle's equation [3].

$$P_a = \frac{1}{4\pi} \frac{\partial^2}{\partial x_i \partial x_j} \int_V T_{ij} \left( y, t - \frac{r}{c} \right) d^3 y + \frac{1}{4\pi} \frac{\partial}{\partial x} \int_S \frac{n_i}{r} p \left( y, t - \frac{r}{c} \right) ds, \quad (1)$$

where  $c$  denotes the speed of sound,  $P_a$  is the far field sound pressure,  $p$  denotes the surface pressure.  $x_i$  and  $y$  denote the location of the observation point and coordinates at the noise source, respectively.  $r$  denotes the distance between the sound source and the observation point,  $n_i$  denotes the outward unit vector normal to the boundary surface.  $T_{ij}$  denotes the Lighthill's acoustic tensor, its contribution is negligibly small compared to that from the second term of equation at low Mach number flow. Moreover, if the body size is much smaller than the wave length of the resulting sound, equation can be written as follows;

$$P_a = \frac{1}{4\pi c} \frac{x_i}{r^2} \frac{\partial}{\partial t} \int_S n_i p \left( y, t - \frac{r}{c} \right) ds, \quad (2)$$

The surface pressure fluctuation of  $p$  is numerically estimated by using LES. The instantaneous far-field sound is obtained from equation (2). One of the authors [2] attempted to simulate the noise levels and sound spectra radiated from a turbulent wake of a circular cylinder with LES and Lighthill-Curle's acoustic analogy. The results showed that the difference between the predicted sound levels and the experimental values were within 3 dB. Moreover the predicted spectra of radiated sounds were in good agreement with those actually measured up to ten times the fundamental frequency [2]. The results showed that this method is useful for estimating aerodynamic noise level from turbulent wakes. Recent research done by Mohseni, K., Colonius, T., and Freund, J.B. [4] suggests that in some cases Lighthill's analogy may not be acceptable. But further research stills need to be done. Thus for this paper, Lighthill's analogy is adopted.

## Numerical Condition

Figure 1 shows the computational mesh of the circular cylinder. The total number of three dimensional finite element meshes is about 400 thousand. At the upstream boundary of the inlet, a uniform velocity was prescribed. At the downstream boundary, the fluid traction was assumed to be zero (traction free condition). On the cylinder surface, rotational speed or non-slip condition was prescribed to simulate cylinder rotation. Symmetric boundary condition was used for both side of spanwise direction. The distance of spanwise direction is equal to 2 times the diameter.

Flow field around a rotational circular cylinder was calculated by incompressible viscous, unsteady flow simulation. To solve the fine flow structures, Large Eddy Simulation (LES) are used to simulate the unsteady turbulent flow field around a rotating circular cylinder at  $Re = 10^3$  to  $10^4$ . Numerical simulations were carried out at the velocity ratios from 0 to 3. Aerodynamic forces, pressure fluctuation, vorticity distribution and induced noise were calculated under these conditions.

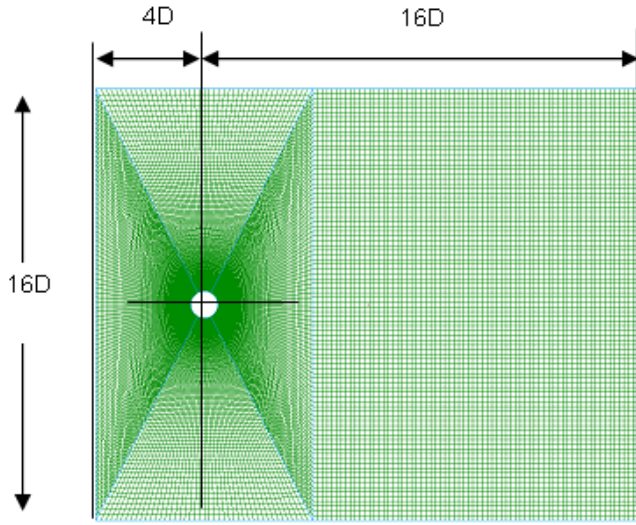


Figure 1: Computational mesh for flow around a circular cylinder.

## Numerical Results

### Flow Field

Figure 2 shows the separation points of the cylinder surface at  $\alpha = 0.5$  and  $\alpha = 2.0$ . Two separation points are observed in figure 2. Since the circular cylinder is rotating counter clock wise, the bottom-side separation point  $S2$  moves counter clock wise. At  $\alpha = 2.0$ , the separation point  $S2$  is located near the downstream stagnation point of the stationary cylinder. As a result, the width of the wake is decreasing with the velocity ratio.

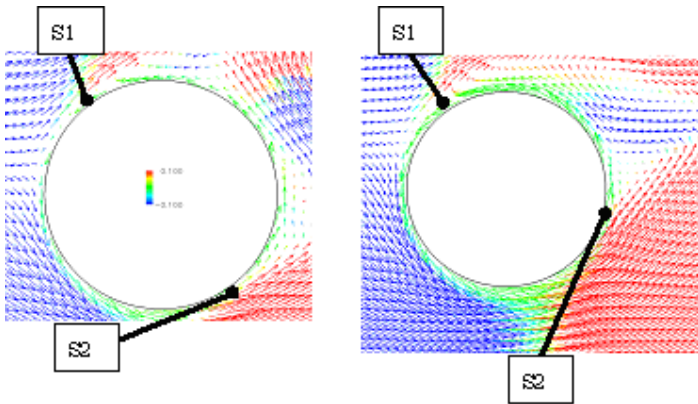


Figure 2: Separation points of a rotating cylinder at  $Re=10^3$ .

Figures 3 to 5 show the vorticity structures around a circular cylinder at Reynolds number of  $10^3$ . In the case of low velocity ratio, large-scale vorticity structures are observed and the separated shear layers roll up at just behind the cylinder. On the other hand, alternative vorticity structures disappear at the high velocity ratio. In the case of  $\alpha = 3.0$ , coherent structure is not observed.

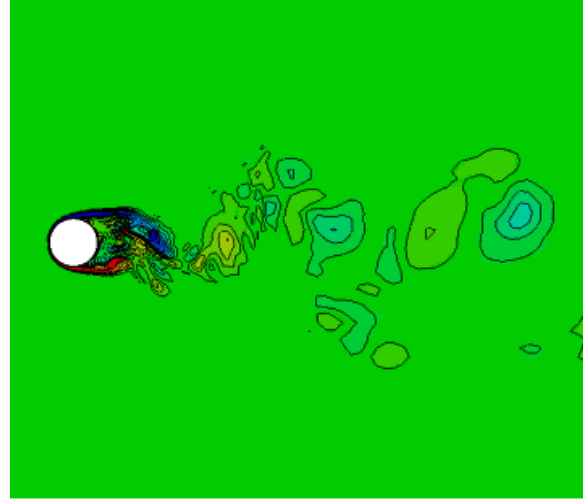


Figure 3: Contours of vorticity around a rotating cylinder at  $Re=10^3$ ,  $\alpha = 0.0$ .

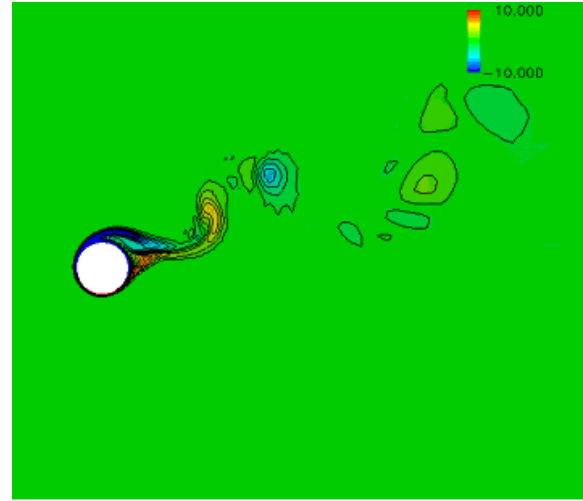


Figure 4: Contours of vorticity around a rotating cylinder at  $Re=10^3$ ,  $\alpha = 2.0$ .

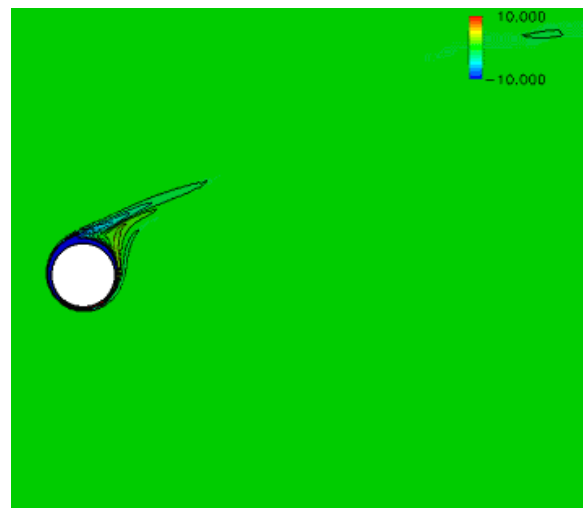


Figure 5: Contours of vorticity around a rotating cylinder at  $Re=10^3$ ,  $\alpha = 3.0$ .



The aerodynamic forces strongly depend on the vorticity structures as shown in Figure 6. The ratio of lift and drag forces increases with the velocity ratio up to  $\alpha = 2.0$ . This corresponds to the velocity ratio of the upper limit of the large-scale structure in existence. The ratio of lift and drag forces decrease over  $\alpha = 2.0$ . This tendency is almost equal to numerical results with the vortex method [5]. In the case of the high velocity ratio, lifting force decreases because the large scale vorticity disappeared. However, friction drags of the cylinder surface increase with the speed of rotation. Therefore, the lift and drag ratio is decreases at high velocity ratio and the fluctuating lifting force also decreases.

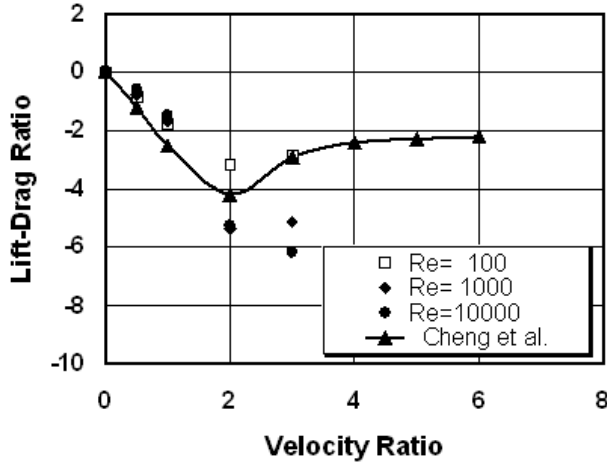


Figure 6: Lift-drag ratio of a rotating circular cylinder.

### Aerodynamic Noise

Figure 7 shows the aerodynamic noise from a rotating circular cylinder. The far-field noise is calculated from equation (2). These simulations are carried out under the compact body assumption, the refraction and reflection is neglected. The predicted noise level does not depend on the Reynolds number, but strongly depends on the velocity ratio of the cylinder rotation. When the alternative vorticity structures exist, noise levels increase in comparison to noise level of non-rotating cylinder. On the other hand, sound levels decrease at high velocity ratio of  $\alpha > 2.0$ . The aerodynamic noise from a rotational circular cylinder at  $\alpha = 3.0$  is 10dB lower than that of the stationary circular cylinder. It revealed that the rotational speed is one of the control factors of aerodynamic noise reduction.

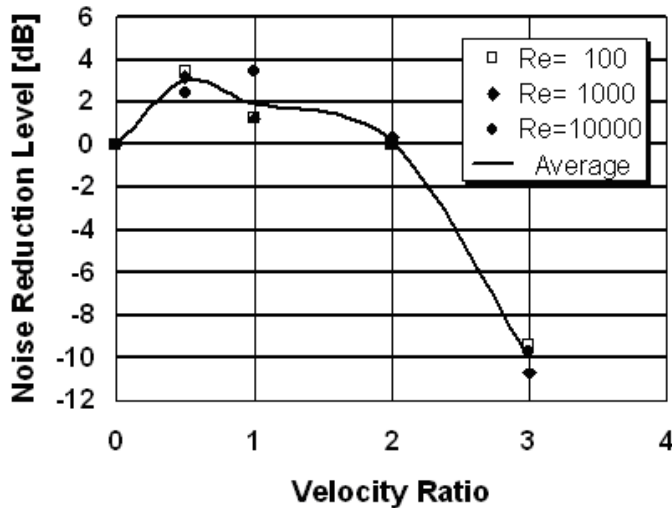


Figure 7: Noise reduction effect on velocity ratio of a rotating circular cylinder.

### Noise Source Identification

Figures 8 to 10 are aerodynamic noise source term calculated by the Powell's theory [6]. The Lighthill-Curle's theory is useful to estimate the aerodynamic noise; however the Lighthill-Curle's theory gives us no information about the relationship between unsteady vorticity fluctuation and aerodynamic sound. In order to control the aerodynamic sound generation, vorticity contribution of sound generation is important to formulate an algorithm of noise control. The Powell's vortex sound theory directly reflects the aerodynamic aspects of the aerodynamic sound generation. Aerodynamic sound can be written as follows:

$$\left( \frac{1}{c_0} \frac{\partial^2}{\partial t^2} - \nabla^2 \right) P_a = \rho_0 \text{div}(\mathbf{\omega} \times \mathbf{v}). \quad (3)$$

The above equation shows that the aerodynamic noise is calculated by using the wave equation with a source term of  $\rho_0 \text{div}(\mathbf{\omega} \times \mathbf{v})$ . Figures 8 and 10 show the source term of the rotating circular cylinder. In the case of non-rotating cylinder, the aerodynamic sound source lies the just behind the cylinder. It is remarkable that the aerodynamic sound source is concentrated in a small region. In this region, the alternating vortices come from both sides of the cylinder, and the separated shear layer is stretched by this vortex motion. The separated shear layer therefore rolls up at this region.

In case of  $\alpha = 2.0$ , the source term declines due to the effect of the rotation, however, the distribution of the source term is almost the same as  $\alpha = 0.0$ . Then noise level of  $\alpha = 2.0$  is almost same as the noise of  $\alpha = 0.0$ . In contrast, distribution of a sound source is different in the case of  $\alpha = 3.0$ . The sound source only exists and around the cylinder surface and source term is not seen in the wake of the cylinder.

Figure 11 shows the iso-surface of sound source term of the circular cylinder. The iso-surface has three-dimensional complicated structure at  $\alpha = 0.0$ . Because the structure of the wake is unstable, the sound source changes in time domain. If the source term has a high velocity ratio, the sound source term has two-dimensional structure as shown in Figure 11 (b). Then noise source fluctuation is not so large. The generated sound is therefore small in the case of  $\alpha = 3.0$ .

The origin of the aerodynamic source comes from the separated shear layers, because the velocity gradient is large at the boundary layer of the cylinder surface. In the case of rotating cylinder, velocity gradient is large compared with the stationary cylinder. The intensity of the source term due to the separated shear layer is large at the high velocity ratio; however, aerodynamic sound is small at the high velocity ratio. Since the aerodynamic noise is caused by the unsteady vortex motion, the aerodynamic sound generation depends on not only on the source term intensity of shear layers but also in the source term fluctuation in time and spatial domains. It is revealed that the vorticity stretching and roll up is important to generate aerodynamic sound.

### Conclusions

Vorticity structures and flow field around a rotating circular cylinder at Reynolds numbers between  $10^2$  and  $10^4$  were numerically investigated. The fluctuating aerodynamic becomes weak and the resulting aerodynamic sound becomes small. The noise level of the rotational cylinder is 10 dB lower than that of the non-rotating cylinder. Aerodynamic sound source terms were numerically visualized by using Powell's theory. The result of the sound source identification shows the aerodynamic sound generated at the formation region of Karman vorticities.



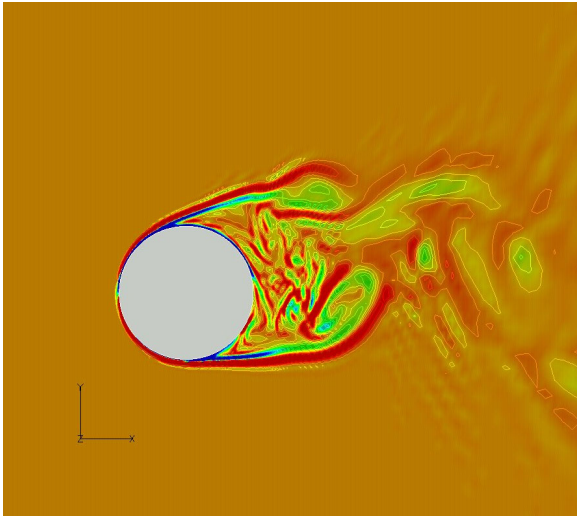


Figure 8: Distribution of aerodynamic sound source term around a rotating circular cylinder at  $\alpha = 0.0$ .

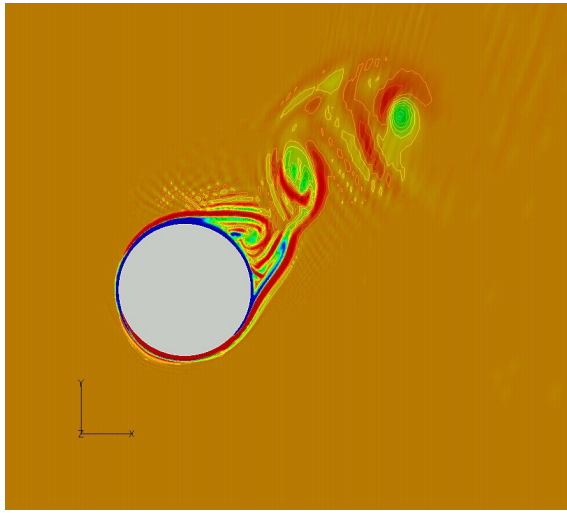


Figure 9: Distribution of aerodynamic sound source term around a rotating circular cylinder at  $\alpha = 2.0$ .

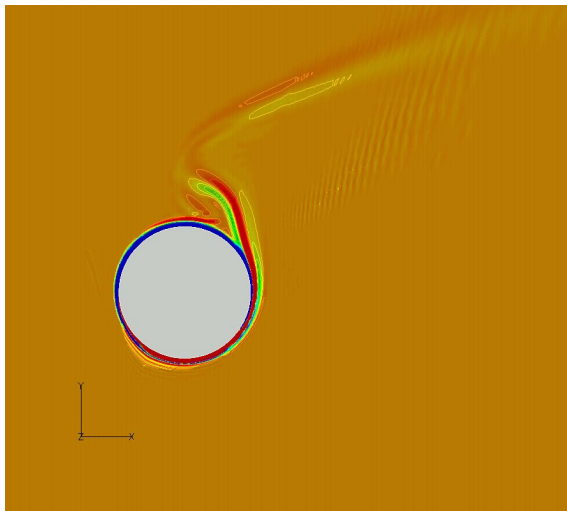
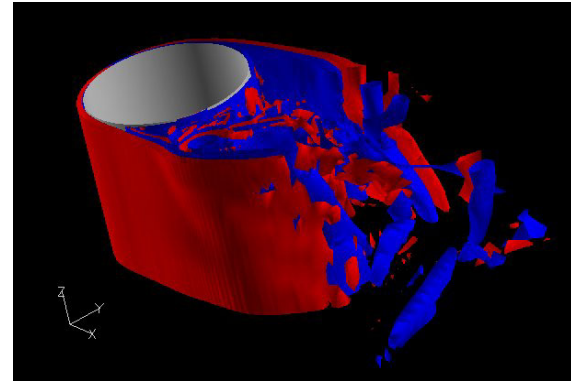
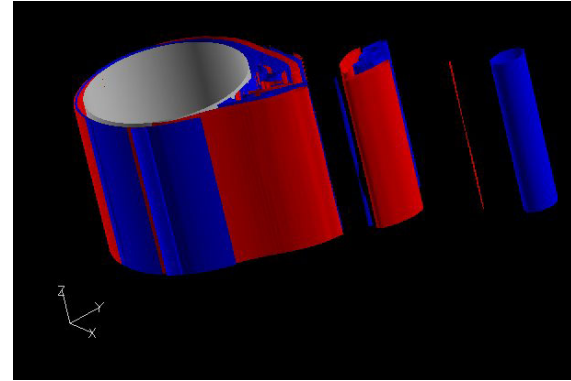


Figure 10: Distribution of aerodynamic sound source term around a rotating circular cylinder at  $\alpha = 3.0$ .



(a)  $\alpha = 0.0$



(b)  $\alpha = 2.0$

Figure 11: Iso-surface of aerodynamic sound source term around a rotating circular cylinder at  $Re = 10^3$ .

Therefore, the separated shear layers play an important role in generating aerodynamic sound at low velocity ratio. Since the aerodynamic noise is caused by the unsteady vortex motion, the aerodynamic sound generation depends on not only source term intensity of the shear layers but also the source term fluctuation in time and spatial domains. The resultant aerodynamic noise is therefore restrained at high velocity ratio. It reveals that cylinder rotation is an effective method to reduce the aerodynamic noise radiated from a turbulent wake.

#### Acknowledgements

The authors thank Professor Chisachi Kato, Institute of Industrial Science, University of Tokyo for his many fruitful discussions on the generation mechanism of aerodynamic sound and technical advice on numerical simulations.

#### References

- [1] King III, W. F., A Precise of Development in the Aeroacoustics of Fast Trains, *J. Sound Vibration*, **193**(1), 1996, 349-358.
- [2] G Kato, C., *et al.*, Numerical Prediction of Aerodynamic Sound by Large Eddy Simulation, *Trans. Jpn. Soc. Mech. Eng.* (in Japanese), **Vol. 60** No.569, **B**, 1994, 126-132.
- [3] Curle, N., The Influence of Solid Boundaries upon Aerodynamic Sound, *Proc. Roy. Soc. London*, **A231**, 1955, 505-514.
- [4] Mohseni, K., Colonius, T., and Freund, J.B., An evaluation of linear instability waves as sources of sound in a supersonic turbulent jet, *Physics of Fluids*, **14**(10), 2002, 3593-3600.
- [5] M. Cheng, Y. T. Chew and S.C. Luo., Numerical simulation of Rotational Circular Cylinder, *Finite Elements in Analysis and Design*, **Vol.18**, 1994, 225-236.
- [6] Powell, A., Theory of vortex sound, *J. Acoustical Society of America*, **36**, 1964, 177-195.

## Dynamic Analysis of Airflow Features in a 3D Real-Anatomical Geometry of the Human Nasal Cavity

H. Tang<sup>1</sup>, J.Y. Tu<sup>1</sup>, H.F. Li<sup>1</sup>, B. Au-Hijleh<sup>1</sup>, C.C. Xue<sup>2</sup>, C.G. Li<sup>2</sup>

<sup>1</sup>School of Aerospace, Mechanical & Manufacturing Engineering

<sup>2</sup>School of Health Sciences

RMIT University, Melbourne, VIC, 3083 AUSTRALIA

### Abstract

Drug delivery in the human respiratory tract is a long standing challenge due to the complexity of the geometry and materials properties. This paper presents a brief summary of flow features in the human respiratory system and simulates an airflow field based on a 3D real-anatomical geometry of the human nasal cavity. A Lagrangian particle-tracking approach is adopted in the flow field solver for the dispersed phase. The dispersion characteristics of particles through the airflow are investigated under the quiet breathing. The particles passing through the domain sections for different value of particle density, diameter and flow rate are investigated. The particle deposition efficiency is also studied. These were compared with experimental data, and results of previous simulations. It is noted that the transportation, dispersion and deposition of particles can be controlled by the particle properties and flow rate. The numerical results show good agreement with previous experimental and computational studies, which are useful for the optimisation design of therapy methodologies, treatment devices and drug materials.

### Introduction

Drug delivery in the human respiratory tract is a long standing challenge due to the complexity of the geometry and materials properties. Inhaling micronized drugs is highly effective and convenient. Information on the velocity distribution and local concentration of solid particle is very important in the design of inhalers that deliver the drugs into lung airways. Scaled-up laboratory models can be used to study the flows in the human respiratory tract; however, the time consuming and expensive nature of experiments carried out in this area mean that computational studies of the processes taking place will become more important. Furthermore, numerical analysis allows investigators to “test” various models under different conditions in relatively short time and at reduced cost. For the past decade, advancements in computational models employing the Computational Fluid Dynamics (CFD) techniques have emerged from the simultaneous modelling of the airflow field distribution, particle trajectory and deposition in human airways. Some of the notable works are: Balashazy and Hofmann [1], Yu *et al.* [2], Zhang *et al.* [3, 4], Martonen *et al.* [5], Gemci *et al.* [6] and Matida *et al.* [7]. In parallel with these computational efforts, a number of important experimental works on particle deposition in the human airways have also been performed, for example, Hahn *et al.* [8], Swift and Strong [9] and Hörschler *et al.* [10].

The nose is a major component of the human respiratory system and also performs important functions in drug delivery. In this paper, we present a brief summary of flow features in the human respiratory system and simulate an airflow field based on a 3D real-anatomical geometry of the human nasal cavity. A Lagrangian stochastic particle-tracking approach is adopted in the flow field solver for the particle dispersion and continuous phases. The dispersion characteristics of particles through the airflow are investigated under the quiet breathing. The particles

passing through the sampling planes for different value of particle density, diameter and flow rate are investigated.

### Fluid Dynamic Perspective of the Human Respiratory System

#### Flow Features

The flow features of the airway in the human respiratory system are extremely complex, involving characteristics of multiple-phase flows in laminar, turbulent and interactive conditions as summarized in Table 1.

A solo simulation approach is difficult to cover all flow features as shown in table 1. Therefore, what's simulation approaches should be taken is depend on main concerns of investigation; physical model was established on a simplified concept and coupled with suitable mathematic algorithms. However, the computational domain should be close to the real-anatomical geometry in order to capture real flow feature. It is worth emphasizing that the geometry of the nasal cavity is a major determination factor of the particle deposition pattern and airflow field.

#### Anatomical Geometry and Computational Domain

The nasal cavity is a complex structure as shown in Figure 1, an anatomical illustration of a left nasal cavity of adult. A 3D real-anatomical geometry reconstructed from a CT fine-scanned data is shown on Figure 2. The surface of this real nasal cavity has complex boundary features, is desirable for the investigation. However, numerous detail boundary features result in hung mesh grids and computation time consuming leading to impracticable at this stage.

An anatomically corrected model of an adult nose was used as a computational domain in present study as shown in Figure 3. It is reconstructed from a CT scanned data via CAD solid model design software, but has been smoothed due to less slice data. This model was developed originally by Prof. Scherer and his bioengineering research group at the Department of Bioengineering, University of Pennsylvania and used in several of their published works [7, 11, 12] and further improved on mesh construction by present study.

#### Flow Configuration

The range of computational domain is shown in blue coloured area of the anatomical illustration in Figure 1. The model of computational domain is shown in Figure 3. The domain is divided into 9 sections.

The airflow rate  $\dot{V}$  is corresponding to normal quiet breathing for a single nostril. Laminar flow is simulated. Drug delivery is assumed to be particulate flow with a uniform diameter  $D_p$  from 1~40 $\mu\text{m}$ , particle density  $\rho_p$  is varied from 500 kg/m<sup>3</sup> to 2000 kg/m<sup>3</sup>.

Breathing conditions		Behaviour &Symptoms	Related locations	Main flow features	Simulation approaches
1	Normal: -quiet -resting -sleeping	Inspiration Expiration Flow rate of 125-200 ml/s	a. nasal cavity b. larynx c. trachea d. bronchi	Periodic flow, Laminar flow, Gap flow, small deformation at the junction of b and c.	sinusoidal velocity profiles, single phase approach
2	Abnormal: -exertion -sickness -physical exercise	-asthma -nasal polyp -heavy vibrissae -foreign-body -sneezing Flow rate of 200-625 ml/s		constriction flow, obstruction flow, extra mucus flow, high flow rate, turbulent flow, deformation at the conjunction of a to d.	single phase approach, multiphase approach, turbulent model free surface model, Fluid-Structure Interaction (FSI) approach,
		-morbidity surface		excessive dry/secretion of the mucousal surface permeation flow	liquid film flow model specific boundary model porous media model
		-cough -snore -yawn	a.-d. e. mouth	high flow rate with deformations and vibrations in c or d-e	FSI approach, acoustic approach
3	Drug delivery: -inhaler -collunarium	Therapy spray	a. nasal cavity b. larynx c. trachea d. bronchi	aerosol flow, droplet flow, free surface flow permeation flow biological reaction	multiphase approach, FSI approach, porous media model,
4	Air pollutions: -dust air: inorganic dust, organic dust, synthetic material dust -chemical gas	Silicosis Asbestosis chronic obstructive pulmonary diseases, COPD			

Table 1. Fluid dynamic perspective of the human respiratory

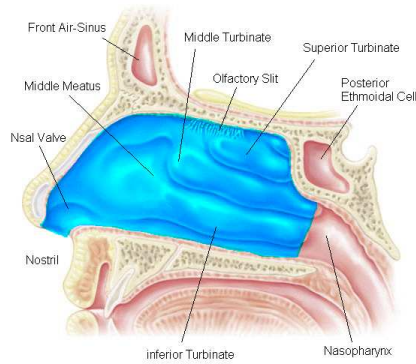


Figure 1. An anatomical illustration of left nasal cavity, shaded (blue) area show the range of computational domain in present study.

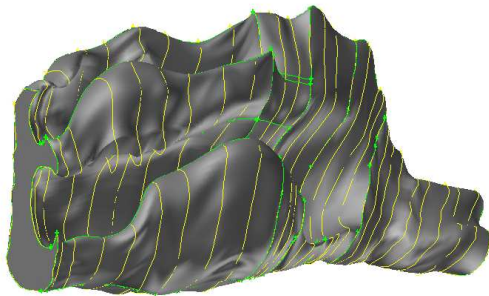


Figure 2. A 3D real-anatomical geometry reconstructed from CT fine-scanned data show the complex boundary details.

The particle deposition is defined in term of Local Particle Deposition efficiency (LPD) = ([number of particles entering the section  $n$ ]-[number of particles exiting section  $n$ ])/ number of

particles entering section  $n$ , and Total Particle Deposition efficiency (TPD) = ([number of particles entering the domain]

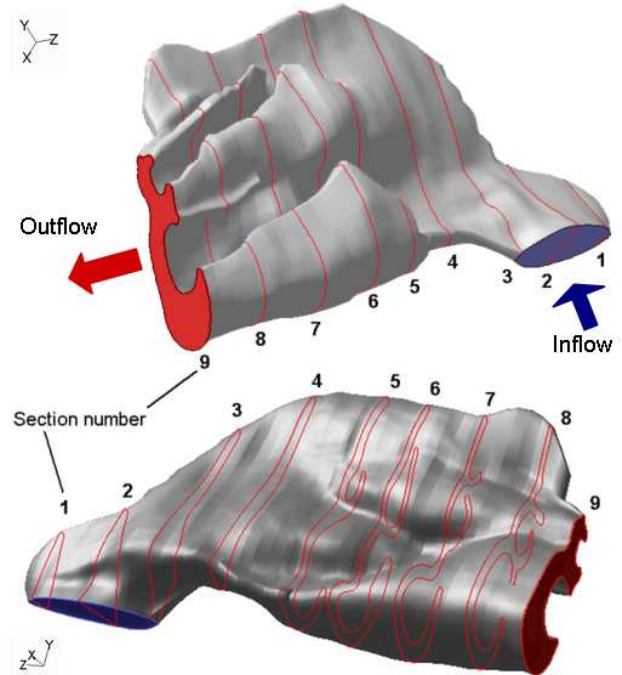


Figure 3. Computational domain is an anatomically corrected model of an adult nose built from CT slice data.

-[number of particles exiting section 9])/ number of particles entering section 9. Stokes number  $St_{Amin}$  is defined:

$St_{Amin} \equiv \frac{\pi^{0.5} d_a \sqrt{\rho_p}}{18 \mu A_{min}^{1.5}}$ ,  $d_a \equiv D_p \sqrt{\frac{\rho_p}{\rho_0}}$ , where  $d_a$  is the aerodynamic diameter and is a function of the particle diameter and density.

The particle density is normalized by the reference density ( $\rho_0$ ) which is equal to 1000 kg/m<sup>3</sup> for the SI units used in the current study.

### Numerical Methods

Dynamic analysis of airflow in the human nasal cavity is conducted in numerical simulation through a commercial package Fluent. Simulation of flow fields is performed by solving full Navier-Stokes equations. In order to track individual particle behaviour, discrete phase model (DPM) Lagrangian method is used to trace the dispersion of particles about the trajectory. The Lagrangian scheme treats the particle phase as a discrete phase, and the fluid phase as a carrier phase in a Eulerian frame. Trajectories of individual particles can be tracked by balancing the forces acting on them. The Lagrangian scheme is most popular in engineering applications for the prediction of particulate flows because it can easily be combined with a stochastic scheme, albeit with high computational cost. In the Lagrangian model, the fluid phase is solved by Eulerian equations, and then integrates Lagrangian equations of motion for the dispersed phase, tracking individual particles through the flow field

### Governing Equations

Under the assumption that the ambient air is incompressible, has constant density and viscosity, and the flow is steady and laminar, the governing equations can be expressed in the following form:  
the continuity equation:

$$\nabla \cdot \vec{V} = 0 \quad (1)$$

and the Navier–Stokes equation:

$$\nabla \cdot (\rho \vec{V} \vec{V}) = -\nabla P + \nabla \cdot (\bar{\tau}) + \vec{F} \quad (2)$$

where  $\rho$  is the gas density,  $P$  the static pressure,  $\bar{\tau}$  the stress tensor and  $\vec{F}$  the external body force.

The equations are discretized in space using a cell-centered finite volume formulation. The coupling between pressure and velocity is solved using the Semi-Implicit Method for Pressure Linked Equations (SIMPLE) algorithm. Time integration is performed using a fully implicit procedure. The linear system which results is solved using a line Gauss–Seidel (LGS) iterative scheme. A multigrid scheme, which involves four automatic successive coarsenings of the original grid, is used to enhance convergence of the pressure correction equation.

### Lagrangian Dispersed Phase Model

The Lagrangian dispersed phase model [14] is used for the prediction of the trajectory of a particle. This is done by integrating the force balance on the particle. The force balance equates the particle inertia with the force acting on the particle, and can be written as:

$$\frac{du_p}{dt} = F_D(u - u_p) + g_x(\rho_p - \rho)/\rho_p + F_x \quad (3)$$

where  $F_D(u - u_p)$  is the drag force per unit particle mass and

$$F_D = \frac{18\mu}{\rho_p D_p^2} \frac{C_D \text{Re}}{24} \quad (4)$$

$$\text{Re} = \frac{\rho D_p |u_p - u|}{\mu} \quad (5)$$

The term  $F_x$  represents additional forces such as thermophoretic force, Saffman's lift force or virtual mass force. However, provided that the particles meet the condition that  $\rho_p > \rho$ , these terms can be neglected, except for the force caused by the pressure gradient in the fluid when there are high acceleration forces present:

$$F_x = \left( \frac{\rho}{\rho_p} \right) u_p \frac{\partial u}{\partial x} \quad (6)$$

The term  $g_x$  is the gravitational body force. The drag coefficient,  $C_D$  is given by:

$$C_D = a_1 + \frac{a_2}{R_e} + \frac{a_3}{R_e^2} \quad (7)$$

where the constants are given by Moris and Alexander [15], and take account of ultra-Stokesian drag.

The momentum transfer from the continuous phase to the particle phase is computed by examining the change in momentum of a particle as it passes through each control volume.

### Results and Discussions

Numerical computations are focused on flow behaviour of particle transportation and deposition through the sections, which can be used by pharmaceutical companies and clinicians who need to predict and optimise inhaled therapies.

#### Particle Transportation through Domain Sections

Particle transportation through the domain section is numerically predicted as shown in Figure 4, which is mainly controlled by particle size and density. It is notice that nasal cavity has a filtering and carrying function depending on different properties of particle. It can be concluded that such numerical simulation can provide the convenient way to optimise various range materials to be inhaled.

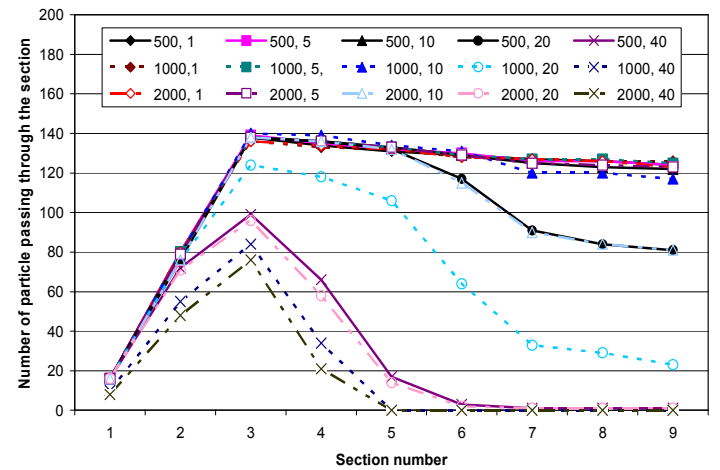
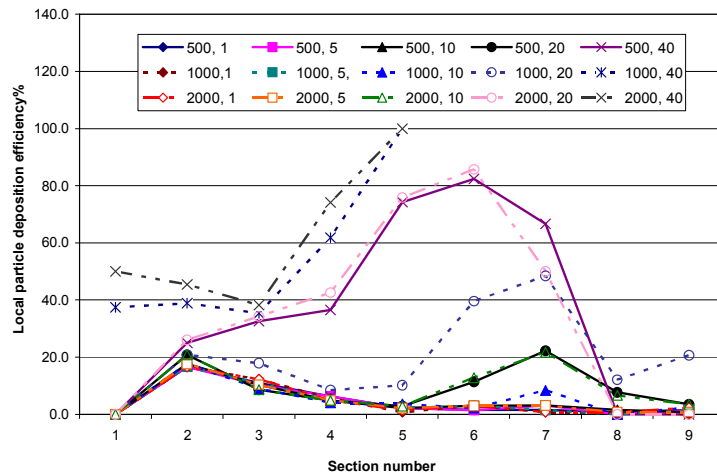


Figure 4. Particle transportation through domain sections at the 125ml/s of airflow rate, comparing with different material properties of particle, e.g. (500, 1) = (density, diameter).

#### Particle Deposition Efficiency

Particle depositions along the flow channel are shown in Figure 5. a concentration peak is appeared at the middle section for high density particle, the peak move into downstream sections.





Figures 5. Particle deposition efficiency on domain sections at the 125ml/s of airflow rate, comparing with different materials properties of particle, e.g. (500, 1) = (density, diameter).

### Comparisons of velocity profiles

Comparison of velocity profile at the section 8 is shown in Figure 6, with previous experimental [8] and computational [11] results.

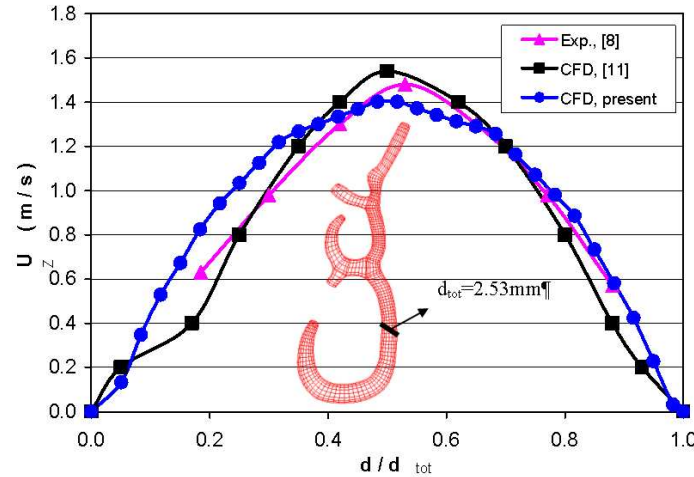


Figure 6. Comparison of velocity profile at the section 8 in Z direction with previous experimental [8] and computational [11] results.

### Comparisons of total deposition efficiency

Comparison of total particle deposition efficiency is shown in Figure 7, with previous experimental [16, 17] and calculated [13] results. The discrepancy shown that different approaches are difficult to replicate the nasal flow processes.

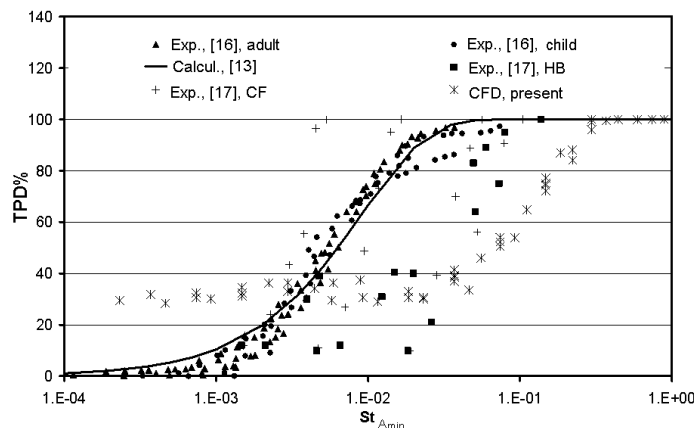


Figure 7. Comparison of total particle deposition efficiency with previous experimental [16, 17] and calculated [13] results.

### Conclusions

Airflow features in the human nasal cavity have a strongly influence on the drug delivery process and particle physical

characteristics. Numerical simulation provides the convenient way to optimise various drug materials to be inhaled.

### Acknowledgments

The financial support from ARC Linkage grant and RMIT-VRII grant on this work is gratefully acknowledged.

### References

- [1] Balashazy, I. and Hofmann, W., Particle Deposition in Airway Bifurcations – I. Inspiratory Flow, *J. Aerosol Sci.*, 1993, **24**, 745-772.
- [2] Yu, G., Xhang, Z. and Lessmann, R., Fluid Flow and Particle Diffusion in the Human Upper Respiratory System, *Aerosol Sci. Technol.*, 1998, **28**, 146-158.
- [3] Zhang, Z., Kleinstreuer, C. and Kim, C. S., Cyclic Micron-Size Inhalation and Deposition in a Triple Bifurcation Lung Airway Model, *J. Aerosol Sci.*, 2002a, **33**, 257-281.
- [4] Zhang, Z., Kleinstreuer, C. and Kim, C. S., Micro-Particle Transport and Deposition in a Human Oral Airway Model, *J. Aerosol Sci.*, 2002b, **33**, 1635-1652.
- [5] Martonen, T. B., Zhang Z., Yue, G., and Musante, C. J., 3-D Particle Transport Within the Human Upper Respiratory Tract, *J. Aerosol Sci.*, 2002, **33**, 1095-1110.
- [6] Gemci, T., Shortall, B., Allen, G.M., Corcoran, T. E. and Chiger, N., A CFD Study of the Throat During Aerosol Drug Delivery Using Heliox and Air, *J. Aerosol Sci.*, 2003, **34**, 1175-1192.
- [7] Matida, E. A., Finlay, W. H., Lange, C. F. and Grgic, B., Improved Numerical Simulation of Aerosol Deposition in an Idealized Mouth-Throat, *J. Aerosol Sc.*, 2002, **35**, 1-19.
- [8] Hahn, I., Scherer, P. W. and Mozell, M. M., Velocity Profiles Measured for Airflow through a Large-scale Model of the Human Nasal Cavity, *Modeling in Physiology*, 1993, **75**, 2273-2287.
- [9] Swift, D. L. and Strong, J. C., Nasal Deposition of Ultrafine  $^{218}\text{Po}$  Aerosols in Human Subjects, *J. Aerosol Sci.*, 1996, **27**, 1125-1132.
- [10] Hörschler, I., Meinke, M. and Schröder, W., Numerical Simulation of the Flow Field in a Model of the Nasal Cavity, *Comp. Fluids*, 2003, **32**, 39-45.
- [11] Keyhani, K., Scherer, P.W., and Mozell, M.M. Numerical simulation of airflow in the human nasal cavity. *J. Biomech. Eng.*, 1995, **117**, 429-441.
- [12] Keyhani, K., Scherer, P.W., and Mozell, M.M., A numerical model of nasal odorant transport for the analysis of human olfaction, *J. Theoretical Biology*, 1997, **186**, 279-301.
- [13] Cheng, Y.S. , Aerosol Deposition in the Extrathoracic Region. *J. Aerosol Sci. Tech.*, 2003 , **37**, 659-671.
- [14] Migdal, D, Agosta, D.V., A source flow model for continuum gas-particle flow, *Trans. ASME J. Appl. Mech.* 1967, 34E 860.
- [15] Morsi, S.A, Alexander, A.J., An investigation of particle trajectories in two-phase flow systems, *J. Fluid Mech.*, 1972; 55: 193-208.
- [16] Swift, D.L., Inspiratory Inertial Deposition of Aerosols in Human Airway Replicate Casts: Implication for the Proposed NCRP Lung model. *Radiat. Prot. Dosim.*, 1991, **38**, 29-34.
- [17] Häußermann, S., Bailey, A.G., Baily, M.R., Etherington, G., and Youngman, M., The influence of breathing patterns on particle deposition in a nasal replicate cast. *J. Aerosol Sci.*, 2002, **33**, 923-933.

## Nonlinear dynamics of thermoacoustic instability using a kinematic, premixed flame model

N. Karimi, M.J. Brear and S.H. Jin

Department of Mechanical and Manufacturing Engineering,  
University of Melbourne, Parkville, 3010, Australia

### Abstract

This paper considers a simple, nonlinear model of a ducted laminar flame. Ducted flames are susceptible to thermoacoustic instability, in which perturbations in the flame heat release drive acoustic modes of the duct that, in turn, drive the flame perturbations. Both the forced response of the flame and the self-excited response of system are studied numerically. The form of the self-excited system behaviour is found to be strongly dependent on both the flame position and duct length. In particular, two basic forms of unstable behaviour are observed, in which the system either experiences a limit cycle or where the flame flashes back. These two responses feature very different time histories in heat release rate. This final result infers that the use of a saturation element to model the flame non-linearity is inappropriate.

### Introduction

Thermoacoustic instability in different systems has been studied extensively over the last fifty or so years [1, 2]. During this time, the applications have varied a great deal, and include solid and liquid fuelled rockets, ramjets, gas turbines and industrial burners. Nonetheless, the essential mechanisms of this instability are the same in all these cases and feature a coupling between the unsteady heat release and the chamber acoustics. In recent years, environmental concerns regarding NO<sub>x</sub> emissions have created considerable interest in the use of premixed flames in natural gas fired gas turbines. Due to the sensitivity of premixed flames to imposed velocity fluctuations, combustion instabilities have appeared again as a problem of considerable practical importance, and have spawned significant research effort worldwide.

Central to the contemporary problem of understanding thermoacoustic instability is the development of accurate and practical *predictive* tools for determining both the stability and (if unstable) the steady-state amplitude of the fluctuations in a given system. This is being approached in, effectively, two ways. The first is to attempt to model the physics of the problem directly with accurate numerical models of combustion in premixed flames. This typically involves LES or DNS codes with simplified reaction kinetics, and has the benefit of the model being more physically representative but also has the drawback of being computationally intensive [2]. Such approaches, whilst potentially accurate, are therefore not truly practical design tools at the moment since the designer often needs to perform parametric studies before settling on a final design.

An alternative approach is to develop simple models of the flame, the duct acoustics and their interaction. For example, the widely-observed sensitivity of premixed flames to low frequency disturbances, and their relative insensitivity to high frequency disturbances, has lead to several investigators modelling the flame as a kind of linear, low-pass filter [1-5]. The duct acoustics are then usually assumed to be linear and one-dimensional, thereby completing the model. Of course, such models only

address the linear stability of the system. More complex models are required to study the nonlinear dynamics.

Following this simple approach, the next level of sophistication that can capture a form of flame nonlinearity is usually to replace the dynamic model of the flame with a kinematic flame model [1, 4, 5]. These models typically consider the flame motion and heat release to be determined only by the local burning velocity and the axial velocity upstream of the flame. Importantly, the effects of vorticity, which is either transported into the flame or created by the flame itself, is not usually modelled. Whilst not studied in this paper, the authors consider that this omission is one of the main shortcomings of such models.

Dowling [3] makes the further claim that a linear dynamic model, combined with a saturation element, models the nonlinear flame dynamics reasonably. The saturation limits of the flame heat release rate are zero when the instantaneous velocity just upstream of the flame is less than or equal to zero, and twice the mean heat release rate when this instantaneous velocity is greater than twice the mean duct velocity. In her later paper that uses a kinematic flame model, Dowling [4] states that her prior use of this saturation element is reasonable, but in the present authors' view, does not verify this rigorously.

The dynamics of such models is relatively easy to analyse using numerical software such as Matlab/Simulink. However, any practical benefit in their speed must be weighed up against their inevitably diminished accuracy. Furthermore, whilst these models are relatively common in the literature, the authors consider that their accuracy has not been clearly established. It is therefore not presently clear where in this broad range of modelling choices, from 'slow and more accurate' LES/DNS to 'fast and less accurate' simple models, that a practical and accurate predictive tool actually lies.

This paper is therefore part of the authors' overall, longer-term aim to determine the requirements for *accurate and practical* predictive tools for studying thermoacoustic instability. The paper is concerned first with Dowling's [4] kinematic flame model applied to a ducted, laminar, premixed flame, and combines this with a simple model of the duct acoustics that was first presented by Dowling in [3]. Two basic forms of unstable behaviour are observed, in which the system either goes into a limit cycle, or where the flame flashes back. These two responses feature very different time histories in heat release rate. As such, they cannot in general be modelled using a simple saturation element integrated into a linear model as Dowling [3] argued.

### Model Flame model

Figure 1 shows a schematic diagram of the present problem. The flame is stabilised behind a flame holder of radius  $a = 17.5 \text{ mm}$ , the end of which is referred to as the gutter, and extends to the duct wall of radius  $b = 35 \text{ mm}$ . The duct has uniform cross-section and open upstream and downstream boundaries. The duct



velocity  $u(x, t)$  is assumed uniform across the duct and purely axial with mean  $\bar{u} = 1.0 \text{ m/s}$ . Given the low Mach number of the upstream flow and assuming that the flame holder is acoustically compact, the velocity at the gutter  $u_g(t)$  is related to the duct velocity just upstream of the flame holder by continuity

$$u_g(t) = u(0, t) / (1 - a^2 / b^2). \quad (1)$$

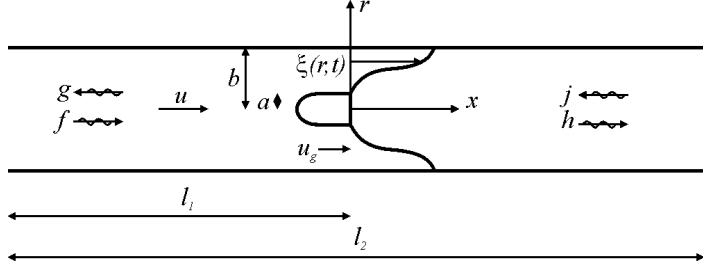


Figure 1: Schematic of the flame, flame holder and duct.

The present geometry is axisymmetric, and it is assumed that combustion occurs within a thin sheet whose instantaneous position  $\xi(r, t)$  is a function of radius and time only. The flame surface is therefore described by another function  $G(x, r, t) = 0$ , such that

$$G(x, r, t) = x - \xi(r, t). \quad (2)$$

The flame surface propagates with a speed  $(\underline{u} \cdot \hat{n} - S_L)$  in the direction of its surface normal  $\hat{n}$ , where  $S_L$  is the laminar flame speed. It is assumed that  $S_L = 0.4 \text{ m/s}$  for an ethylene/air mixture with an equivalence ratio  $\phi = 0.7$  [6]. The propagation of the surface  $G(x, r, t) = 0$  is therefore described by the well-known ‘G equation’ [1, 2, 4, 5],

$$\frac{\partial G}{\partial t} + \underline{u} \cdot \nabla G = S_L |\nabla G|. \quad (3)$$

Dowling [4] and Fleifil et al. [5] both argue that the vertical component of the flow velocity vector is negligible at the flame surface. Accepting their arguments, combination of equations (2) and (3) gives a nonlinear PDE for the flame position

$$\frac{\partial \xi}{\partial t} = u_g - S_L \sqrt{1 + (\partial \xi / \partial r)^2}. \quad (4)$$

It is noted that this expression models the axial velocity just upstream of the flame as equal to the gutter velocity  $u_g$ . This assumes that the flame is compact relative to the duct acoustics, which is reasonable in most cases.

Boundary conditions for equation (4) are quite involved since there is a possibility that the flame surface will flash back when the flow velocity is less than burning velocity. It is also assumed that the flame cannot blow out. Boundary conditions that incorporates these considerations are

$$\xi(a, t) = 0 \quad (5)$$

if  $\xi(a, t^-) = 0$  and  $u_g(t) \geq S_L$ , and

$$(\partial \xi / \partial t)_{r=a} = u_g - S_L \quad (6)$$

otherwise. The initial condition for the simulations is the average surface position  $\bar{\xi}(r)$ , which can easily be shown from equation (4) to be a truncated cone that extends from the gutter to the duct wall

$$\bar{\xi}(r) = (r - a) \sqrt{u_g^2 - S_L^2} / S_L. \quad (7)$$

Equation (4) was integrated using a 2<sup>nd</sup> order accurate spatial difference for  $\partial \xi / \partial r$  and fourth-order Runge-Kutta timestepping for obtaining  $\xi$  from  $\partial \xi / \partial t$ . The spatial resolution was  $0.09 \text{ mm}$  and the timestep was  $100 \mu\text{s}$ , which were found to give solutions that were independent of both the spatial and temporal discretisation.

The instantaneous flame surface area is

$$A(t) = 2\pi \int_a^b r \sqrt{1 + (\partial \xi / \partial r)^2} dr \quad (8)$$

and the heat release rate  $Q(W)$  is

$$Q(t) = \eta \rho_u S_L \Delta H_R A(t), \quad (9)$$

where  $\eta = 0.8$  is a combustion efficiency,  $\rho_u$  is the density of the reactants ( $1.2 \text{ kg/m}^3$ ) and  $\Delta H_R$  is the enthalpy of reaction, which for an ethylene/air mixture with  $\phi = 0.7$  was set to  $2.14 \text{ MJ/kg}_{\text{mixture}}$  [6].

For linear, harmonic perturbations of frequency  $\omega$ , Dowling [4] also solves equation (4) analytically, and integrates it across the duct to obtain the dynamic response of the complex, overall heat release perturbations  $\hat{Q}$  to imposed complex, velocity perturbations  $\hat{u}_g$  at the gutter,

$$\frac{\hat{Q} / \bar{Q}}{\hat{u}_g / \bar{u}_g} = \frac{2}{i\Omega(a+b)} \left[ a - b e^{-i\Omega} + \frac{(b-a)}{i\Omega} (1 - e^{-i\Omega}) \right]. \quad (10)$$

The corresponding real perturbations are given by  $Q' = \text{Re}(\hat{Q} e^{i\omega t})$  and  $u'_g = \text{Re}(\hat{u}_g e^{i\omega t})$  with mean values  $\bar{Q}$  and  $\bar{u}_g$ . The term  $\Omega$  is a Strouhal number, defined by

$$\Omega = \omega(b-a) / S_L \sqrt{1 - (S_L / \bar{u}_g)^2}.$$

### Duct acoustics model

Figure 1 also shows acoustic waves

$$\begin{aligned} p'(x, t) &= f(t - x / (\bar{c}_1 + \bar{u}_1)) + g(t + x / (\bar{c}_1 - \bar{u}_1)), \\ u'(x, t) &= [f(x, t) - g(x, t)] / (\bar{\rho}_1 \bar{c}_1), \end{aligned} \quad (11)$$

upstream of the flame (region 1 i.e.  $x < 0$ ) and

$$\begin{aligned} p'(x, t) &= h(t - x / (\bar{c}_2 + \bar{u}_2)) + j(t + x / (\bar{c}_2 - \bar{u}_2)), \\ u'(x, t) &= [h(x, t) - j(x, t)] / (\bar{\rho}_2 \bar{c}_2), \end{aligned} \quad (12)$$

downstream (region 2 i.e.  $x > 0$ ), where  $\bar{c}$  is the mean sonic velocity ( $\text{m/s}$ ). The flame also produces entropy fluctuations, but as the duct exit is open, these convect out of the domain without having any (first order) effect on the duct pressure and velocity, and so are neglected.

Application of the condition that  $p' = 0$  at the upstream and downstream boundaries gives

$$\begin{aligned} f(0, t) &= -g(0, t - \tau_u), \\ j(0, t) &= -h(0, t - \tau_d). \end{aligned} \quad (13)$$

The terms  $\tau_u$  and  $\tau_d$  are time lags that represent the time taken for a wave to travel from the flame, reflect from the upstream or downstream boundary and return to the flame:

$$\begin{aligned} \tau_u &= 2l_1 / [\bar{c}_1 (1 - \bar{M}_1^2)], \\ \tau_d &= 2(l_2 - l_1) / [\bar{c}_2 (1 - \bar{M}_2^2)], \end{aligned} \quad (14)$$

where  $\bar{M}$  is the mean Mach number in that region.

Dowling [3] combines equations (13) and (14) with the equations for mass, momentum and energy conservation applied across the (assumed acoustically compact) flame to obtain the following matrix equation

$$\mathbf{X} \begin{pmatrix} g(0,t) \\ h(0,t) \end{pmatrix} = \mathbf{Y} \begin{pmatrix} g(0,t-\tau_u) \\ h(0,t-\tau_d) \end{pmatrix} + \begin{pmatrix} 0 \\ (Q(t)-\bar{Q})/\pi b^2 \bar{c}_1 \end{pmatrix}, \quad (15)$$

where matrices  $\mathbf{X}$  and  $\mathbf{Y}$  are given in the appendix. Solving equations (15), (11), (12) and (1) for the velocity perturbation at the flame, the instantaneous heat release in equation (9) can then be determined by the numerical integration of equation (4), thereby closing the integrated model of the flame and the duct acoustics.

## Results and discussion

Figure 2 shows the steady state flame response to sinusoidal velocity forcing (i.e. ignoring the duct acoustics) with an amplitude of 1% of the mean velocity. The numerical simulation's amplitude and phase responses were calculated by least-squares curve fitting a sinusoid with the same frequency as the excitation to the observed, closely sinusoidal response. As expected, the simulations are in close agreement with the linear, analytic dynamic response given by equation (10). The commonly reported [1-5] behaviour of the flame as a kind of low-pass filter to small amplitude excitation is also clear.

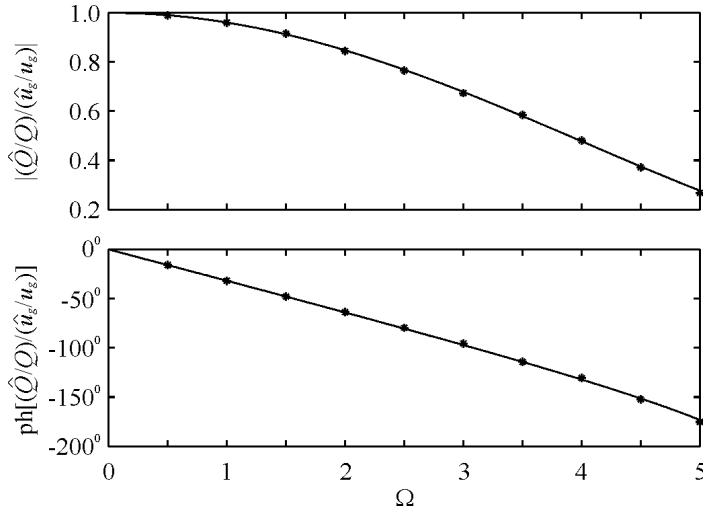


Figure 2: Dynamic response of the flame (solid line: equation (10), points: nonlinear simulations with  $|u'_g/\bar{u}_g| = 0.01$ ).

Figure 3 shows the variations in the heat release, gutter velocity and gutter pressure with time for the integrated flame/acoustic model, for a duct length  $l_2$  of 1.0 m and the gutter placed at  $l_1 = 0.6$  m. The system can be seen to undergo at first a roughly exponential, self-excited disturbance growth in all three quantities until it settles into a constant amplitude limit cycle. The frequency and growth rate of the oscillations during the period of disturbance growth should correspond closely to the unstable duct modes predicted by a linear stability analysis of the system using equation (10) e.g. [7].

The time traces in Figure 3 show relatively small amplitude limit cycle fluctuations in the static pressure, but appreciable velocity fluctuations. Dowling [3] explains this behaviour by noting that since  $u' \sim O(p'/\rho c)$  in equation (11), it follows from the ideal gas law that

$$p'/\bar{p} \sim O(u'\bar{\rho}c/\bar{p}) = O(\gamma \bar{M} u'/\bar{u}). \quad (16)$$

Thus, the fractional pressure fluctuations remain small in a low Mach number flow even when  $u'/\bar{u} \sim O(1)$ . The flame heat release fluctuations are also relatively small. Animations show

that the flame remains anchored at the gutter, oscillating around its undisturbed position given by equation (7).

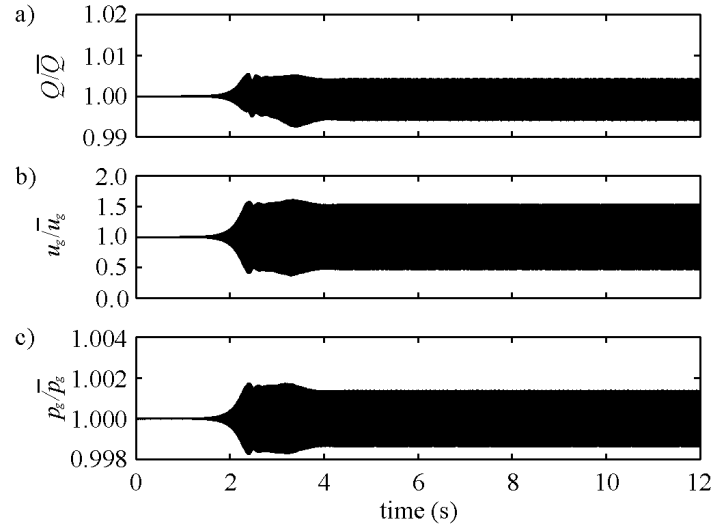


Figure 3: Time series of a)  $Q/\bar{Q}$ , b)  $u_g/\bar{u}_g$  and c)  $p_g/\bar{p}_g$  for  $l_1 = 0.6$  m and  $l_2 = 1.0$  m.

Figure 4 shows that very different behaviour is observed when the length of the duct and gutter position are doubled ( $l_2 = 2.0$  m,  $l_1 = 1.2$  m). The pressure fluctuations remain relatively small, although larger than previously, but the velocity perturbations are now large enough that reversed flow is observed as part of the oscillation. Interestingly, the mean flame heat release departs from that given by equations (7), (8) and (9) and must be an inherently nonlinear effect.

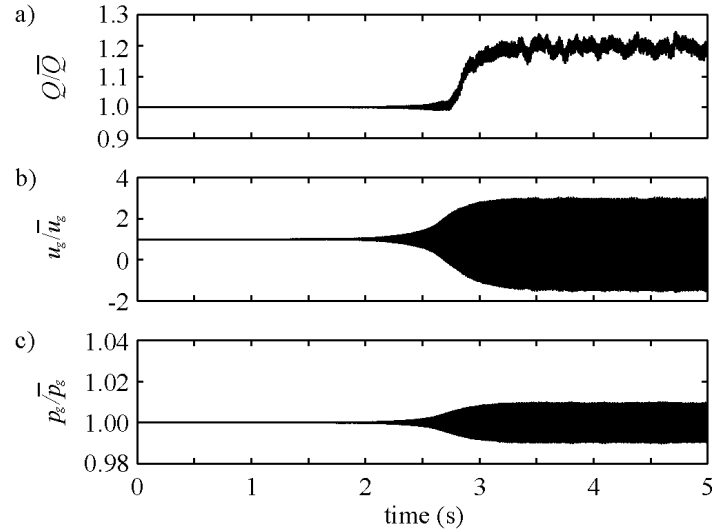


Figure 4: Time series of a)  $Q/\bar{Q}$ , b)  $u_g/\bar{u}_g$  and c)  $p_g/\bar{p}_g$  for  $l_1 = 1.2$  m and  $l_2 = 2.0$  m

Animations of the flame motion in this instance reveal that the flame is no longer anchored to the gutter, but instead progresses gradually upstream as it oscillates in response to the acoustic excitation (eg. Figure 5). This type of behaviour can be called 'flashback', and is a common problem in premixed combustors. A surprising but reasonable result in the present study is that the heat release fluctuation amplitude in Figure 4, which is dependent on the flame surface area, does not change greatly as the flame gradually moves upstream.

A criterion for determining when flame flashback occurs is not obvious, since it is related to both the amplitude and frequency of the acoustic forcing (Figure 5). Both the nonlinear numerical

simulations and linear theory showed that the flame heat release, which drives the duct acoustics, is relatively insensitive to high frequency excitation, regardless of the forcing amplitude. Thus, the flame tends to either limit cycle or flashback in longer ducts, where the fundamental acoustic mode of the duct is relatively low and hence more likely to drive significant flame motion and heat release perturbations (Figure 6).

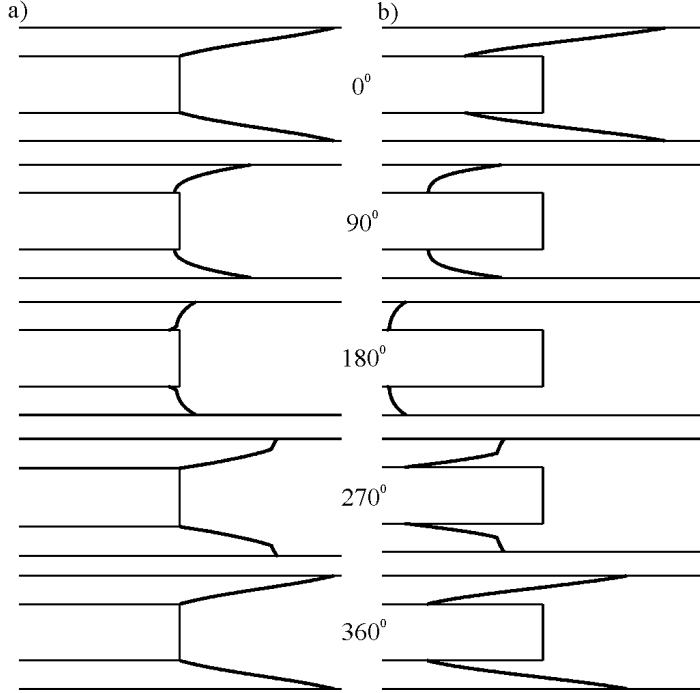


Figure 5: Instantaneous flame surface during steady state sinusoidal forcing,  $\Omega = 2.5$  and a)  $|u'_g / \bar{u}_g| = 1$ , b)  $|u'_g / \bar{u}_g| = 2$ .

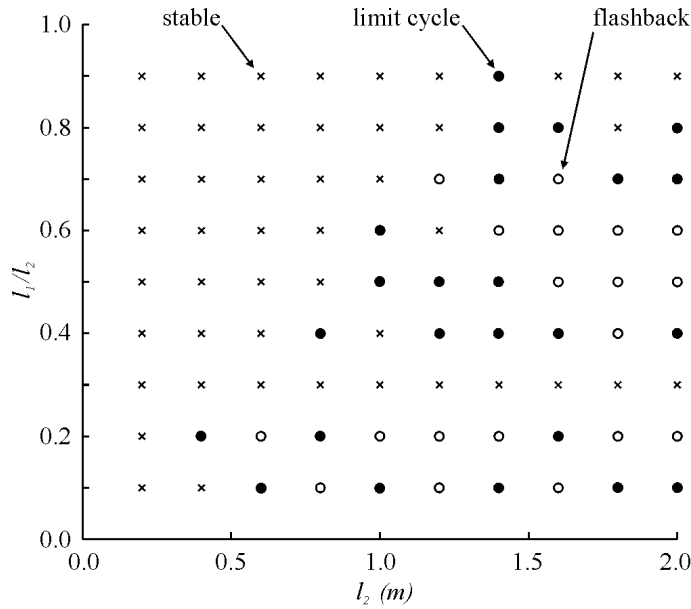


Figure 6: Stability map for different combinations of  $l_1$  and  $l_2$ .

The kinematic flame model predicted that the steady state amplitude of the heat release fluctuations during thermoacoustic instability of either form never exceeded roughly 10% of the mean heat release. Furthermore, Figure 3 and Figure 4 showed that the heat release fluctuation amplitude was strongly dependent on the form of unstable behaviour. Both these amplitudes are significantly smaller than that proposed by Dowling [3], who argued that heat release fluctuations of the same order as the mean heat release were reasonable. Indeed, the use of Dowling's [3] saturation limits and the linear model in equation (10), as Dowling suggests, were observed to cause excessive velocity perturbations in the duct, well in excess of any

predicted by the nonlinear, kinematic flame model. It is also not obvious how to determine *a priori* whether the flame flashes back or goes into limit cycle given knowledge only of the duct's mean flow. Thus, this range of possible nonlinear responses cannot in general be modelled using a linear flame model with saturation as Dowling [3] argued.

## Conclusions

This paper presented an analysis of an integrated kinematic model of a ducted, laminar, premixed flame combined with a simple model of the duct acoustics. Depending on the system parameters, two basic forms of unstable behaviour were observed. The flame either maintained its position around its stabilisation point on the flame holder, in which case the acoustic velocity perturbations excited by the flame were relatively small, or the flame 'flashed back' by moving upstream of the flame holder. This latter response featured significantly larger duct velocity perturbations and periods of reversed duct flow.

In both cases, the kinematic flame model predicted that the steady state amplitude of the heat release fluctuations was significantly smaller than that suggested by Dowling [3] as a reasonable saturation limit for this instability. It is also not obvious how to determine *a priori* whether the flame flashes back or goes into limit cycle given knowledge only of the duct's mean flow. Thus, the range of observed nonlinear responses cannot in general be modelled using a linear flame model with saturation as Dowling [3] argued.

## References

1. Lieuwen, T., *Modeling premixed combustion - acoustic wave interactions: a review*. Journal of Propulsion and Power, 2003. **19**(5): p. 765-781.
2. Candel, S. *Combustion dynamics and control: progress and challenges*. in *Proceedings of the Combustion Institute*. 2002.
3. Dowling, A.P., *Non-linear self excited oscillations of a ducted flame*. Journal of Fluid Mechanics, 1997. **346**: p. 271-290.
4. Dowling, A.P., *A kinematic model of a ducted flame*. Journal of Fluid Mechanics, 1999. **394**: p. 51-72.
5. Fleifil, M., Annaswamy, A.M., Ghoniem, Z. and Ghoniem, A.F., *Response of a laminar premixed flame to flow oscillations: A kinematic model and thermoacoustic instability results*. Combustion and Flame, 1996. **106**: p. 487-510.
6. Glassman, I., *Combustion*. 3rd ed. 1996: Academic Press, San Diego, California.
7. Hield, P.A., Brear, M.J. and Moase, W. *A parametric, linear stability analysis of thermoacoustic oscillation*. in *2003 Australian Symposium on Combustion*. 2003. Monash University: Monash University.

## Appendix

The matrices in equation (15) are

$$\mathbf{X} = \begin{bmatrix} -1 + \bar{M}_1 \left( 2 - \frac{\bar{u}_2}{\bar{u}_1} \right) - \bar{M}_1^2 \left( 1 - \frac{\bar{u}_2}{\bar{u}_1} \right) & 1 + \bar{M}_1 \frac{\bar{\rho}_1 \bar{c}_1}{\bar{\rho}_2 \bar{c}_2} \\ \frac{1 - \gamma \bar{M}_1}{\gamma - 1} + \bar{M}_1^2 - \bar{M}_1^2 (1 - \bar{M}_1) \frac{1}{2} \left( \frac{\bar{u}_2^2}{\bar{u}_1^2} - 1 \right) & \frac{\bar{c}_2}{\bar{c}_1} \frac{(1 + \gamma \bar{M}_2)}{(\gamma - 1)} + \bar{M}_1 \bar{M}_2 \frac{\bar{\rho}_1}{\bar{\rho}_2} \end{bmatrix},$$

$$\mathbf{Y} = \begin{bmatrix} - \left[ 1 + \bar{M}_1 \left( 2 - \frac{\bar{u}_2}{\bar{u}_1} \right) + \bar{M}_1^2 \left( 1 - \frac{\bar{u}_2}{\bar{u}_1} \right) \right] & 1 - \bar{M}_1 \frac{\bar{\rho}_1 \bar{c}_1}{\bar{\rho}_2 \bar{c}_2} \\ - \left[ \frac{1 + \gamma \bar{M}_1}{\gamma - 1} + \bar{M}_1^2 - \bar{M}_1^2 (1 + \bar{M}_1) \frac{1}{2} \left( \frac{\bar{u}_2^2}{\bar{u}_1^2} - 1 \right) \right] & - \frac{\bar{c}_2}{\bar{c}_1} \frac{(1 - \gamma \bar{M}_2)}{(\gamma - 1)} - \bar{M}_1 \bar{M}_2 \frac{\bar{\rho}_1}{\bar{\rho}_2} \end{bmatrix}.$$

## Mean Flow Characteristics of a Micro-injector Induced Swirling Jet

I. K. Toh, P. O'Neill, D. Honnery and J. Soria

Laboratory for Turbulence Research in Aerospace & Combustion  
Department of Mechanical Engineering  
Monash University, Melbourne, Victoria 3800, AUSTRALIA

### Abstract

A novel method of generating a swirling jet using micro-injectors to introduce the required tangential component into an axial jet has been developed. This method allows the flow rate of the axial jet and the tangential micro-injectors to be varied independently. Thus the controlling parameters, Reynolds number ( $Re$ ) and swirl number ( $S$ ), can be varied precisely. This level of control enables detailed investigation of the phenomena associated with swirling jets.

### Introduction

The large scale effects of swirl in fluid flow have been appreciated for many decades. It affects the jet growth, entrainment and decay of non-reacting jets, and flame size, shape and stability of combustor jets. There are a number of ways of generating a swirling jet; namely axial plus tangential entry, guided vanes and direct rotation. Chigier and Chervinsky [1] have carried out experiments using an axial plus tangential entry swirl generator. They were able to generate jets with no swirl to strongly swirling with reverse flow. Gore and Ranz [2] imparted rotation to axial pipe flow by means of a rotating perforated plate in which holes were drilled either parallel to the axis or at  $45^\circ$  to the axis. They found that the flow generated was not axisymmetric and the flow field was complicated by additional secondary flow induced by the vanes. Rose [3], on the other hand, rotated a pipe of 100 diameters in length at 9500 RPM to generate a fully developed swirling jet. The swirl motion is generated solely by the friction force between the air and the inner wall of the pipe. Due to the relatively low viscosity of the air, Rose was only able to generate relatively weak swirl.

In the experiment conducted here, a swirl velocity component is induced in an axial jet by micro-injectors. The combined flow is then discharged through an orifice. This method allows for independent and precise control of the resulting flow and its structure. In the present study, jets with different Reynolds numbers ( $Re$ ) and swirl numbers ( $S$ ), which define the characteristics of the flow, are investigated using particle image velocimetry (PIV).

### Experimental Methods

In this experimental study, velocity field measurements were taken in a jet with micro-injector induced swirl. Figure 1 shows the coordinate system used. Figure 2 shows the micro-jet swirl generator and the experimental apparatus. The air supply to the main jet was separate from the micro-jets supply. This allowed the flow rate of the axial jet and the micro-jets to be varied independently. To enable PIV measurements, the main axial jet supply was seeded with olive oil droplets around  $1\mu\text{m}$  in diameter. The unseeded micro-jets supply was directed into the reservoir, figure 2, before it was injected tangentially into the settling chamber through eight  $0.5 \times 0.5\text{mm}$  square cross section micro-injectors. The combined flow then passed through a contraction with an area ratio of 25, thence through an 8mm diameter orifice at the exit of the nozzle. The nozzle was

mounted in a vertical wind tunnel, figure 2. This set up permits investigation of the effect of co-flow on the swirling jet. In the present study, no co-flow was used.

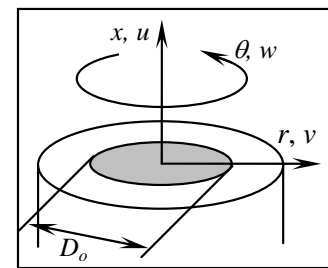


Figure 1: Coordinate system.

A Quanta system dual Nd:YAG laser with the wavelength of 532nm was used to illuminate the seeding particles. The laser is capable of producing two 200mJ pulses of 6 ns duration at a repetition rate of up to 10Hz. System timing was controlled by a computer running Real Time Linux. Time intervals between each laser pulse ranged from 7-40 $\mu\text{s}$  depending on the experiment.

The images required for PIV analysis were acquired using a PCO Sensicam 12bit cooled digital camera that operates in a double shutter mode. Images obtained from the camera were stored in the image acquisition computer. Images in the both the vertical ( $x-r$ ) and azimuth plane ( $r-\theta$ ) were acquired. Orientation of the camera was such that a CCD array of  $1280 \times 1024$  pixels was used for images in vertical plane, while CCD array of  $1024 \times 1024$  pixels was used for images in azimuth plane. A 105mm Nikkor lens was used for images acquired in the vertical plane, while a 200mm Micro-Nikkor lens was used in the azimuth plane.

Figure 2 shows the configuration where the images in the azimuth plane were acquired. A high reflective mirror at  $45^\circ$  was placed above the nozzle to direct the light from the seed particles illuminated by the horizontal laser sheet. For acquiring images in the vertical plane, the mirror was removed and laser sheet rotated by  $90^\circ$  along the axis of the aperture.

The image pairs were analysed using the Multi-grid Cross Correlation Digital Particle Image Velocimetry (MCCDPIV) algorithm described in Soria et al [4], which has its origin in an iterative and adaptive cross-correlation algorithm introduced by Soria [5] and [6]. Details of the performance, accuracy and uncertainty of the MCCDPIV algorithm with applications to the analysis of a single exposed PIV and holographic PIV (HPIV) images have been reported in [7] and [8].

The present single exposed image acquisition experiments were designed for a two-pass MCCDPIV analysis. The first pass used typically an interrogation window  $IW = 32$  pixels, while the second pass used an  $IW = 24$  pixels with discrete  $IW$  offset to minimize the measurement uncertainty [9]. The sampling spacing between the centres of the  $IW$  was 24 pixels. The MCCDPIV

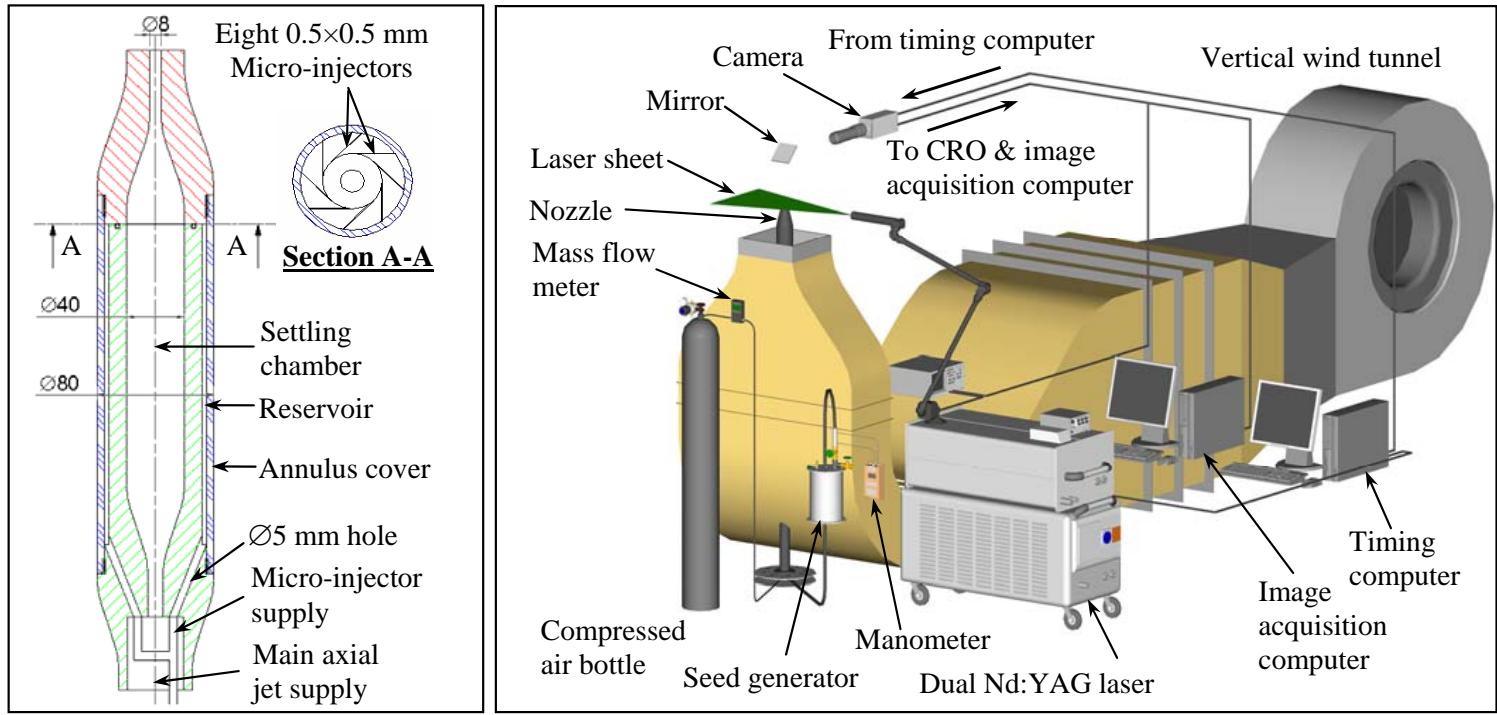


Figure 2: Drawing of nozzle design (left) and schematic diagram of experimental apparatus (right).

algorithm incorporates the local cross-correlation function multiplication method introduced by [10] to improve the search for the location of the maximum value of the cross-correlation function. For the sub-pixel peak calculation, a two dimensional Gaussian function model was used to find, in a least square sense, the location of the maximum of the cross-correlation function [5]. The MCCDPIV data field was subsequently validated by applying: (i) a global histogram operator check [11], (ii) a median test [12], and (iii) the dynamic mean value operator test described in [12]. The tests were applied in the specified order. Following data validation, the in-plane velocity components ( $u, v$ ) in the ( $x, r$ ) coordinate directions respectively were computed by dividing the measured MCCDPIV displacement in each interrogation window by the time between the exposures of the image pair. The uncertainty relative to the maximum velocity in the velocity components at the 95% confidence level for these measurements is 0.3%.

## Results

Two non-dimensional numbers can characterize a swirling jet: the Reynolds number and the swirl number. The Reynolds number used is based on the average axial velocity ( $U_o$ ) at the orifice and the orifice diameter ( $D_o$ ),

$$Re = \frac{\rho U_o D_o}{\mu} \quad (1)$$

The swirl number is normally defined as the axial flux of swirl momentum divided by the axial flux of axial momentum times the equivalent nozzle radius [13]:

$$S = \frac{G_\theta}{G_x D_o / 2} \quad (2)$$

This characterization is often very difficult to measure with certainty. Thus, simplification of the equation is necessary. One common assumption made is to treat the flow as a solid body rotation plug flow at the nozzle. The turbulent stress term is also often neglected [13]. The swirl number can then be simplified to,

$$S = \frac{G/2}{1 - (G/2)^2} \quad (3)$$

where  $G$  is the ratio of the maximum tangential velocity to maximum axial velocity measured at the nozzle. This equation is valid up to a swirl number of about  $S \approx 0.2$  [13].

Figure 3 shows the radial distribution of the normalised mean axial velocity for a set of four experimental conditions. The corresponding non-dimensionalised tangential velocity profiles are shown in figure 4. PIV data processing parameters are listed in table 1 and 2 respectively. In this experiment, The Reynolds number was kept at a fairly constant level, (ranges from 3773 to 3982) while the swirl number was varied progressively.

In figure 3, axial velocity ( $u$ ) is normalised by the local maximum velocity ( $u_m$ ). The radial position  $r$  is normalised by ( $x+a$ ), where  $a$  is the apparent distance of the origin of the jet from the orifice. According to Chigier and Chervinsky [1], the apparent distance of the jet's origin from the orifice can be obtained by extrapolating the line of the reciprocal of centre line axial velocity,  $1/u_m$  against  $x$ . The value of  $a$  is given by the value of  $x$  at  $1/u_m = 0$ . The linear function was fitted to the data points at the far field (self similarity region) in order to obtain a more accurate  $a$  value. Only the data points where  $x > 4D_o$  were used for the linear extrapolation.

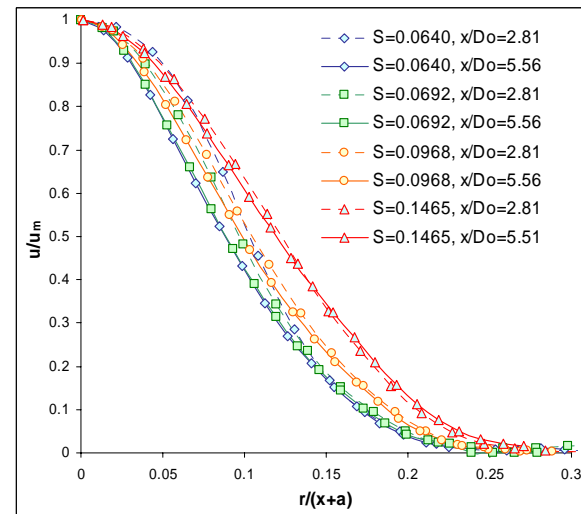


Figure 3: Radial distributions of normalised axial velocity (constant  $Re$ , varying  $S$ ).

The velocity profiles shown in figure 3 exhibit typical Gaussian profiles, which is consistent with previous results for weakly swirling jets [1]. The increased spread of the jet when swirl intensity is increased is clearly evident in figure 3. The velocity profiles exhibit self similarity within the experimental region.

This agrees well with the results of Chigier and Chervinsky (1967) [1], who observed self similarity within 4 diameters of the orifice of weakly swirling jets.

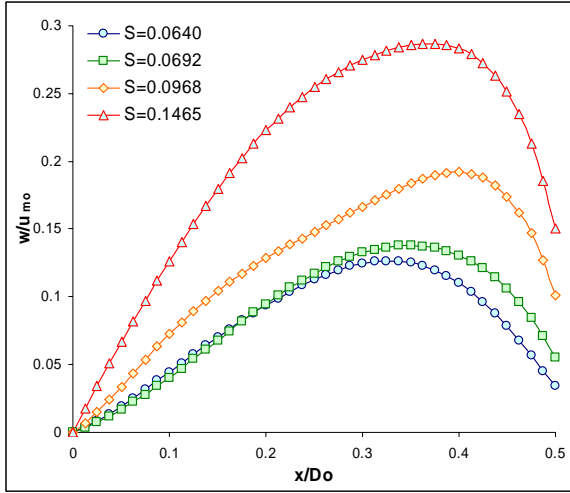


Figure 4: Radial distribution of mean tangential velocity (constant  $Re$ , varying  $S$ ).

Figure 4 shows the radial distribution of integrated mean tangential velocity of the swirling jets. The tangential velocity profiles plotted are in the  $r$ - $\theta$  plane. The tangential velocity is normalised by the maximum axial velocity. The magnitude of the tangential velocity of the jet with higher swirl number is obviously higher and it peaks at a normalised radius closer to the edge of the jet. The inner region of the profile is almost linear and corresponds to solid body rotation plug flow.

Position	$0D_o - 5.8D_o$
Image area	$46.7 \times 37.4\text{mm}^2$ $5.8D_o \times 4.7D_o$
CCD array	$1280 \times 1024\text{pixel}^2$
Spatial resolution	$27.4\text{pixels/mm}$ $219.2\text{pixels}/D_o$
Number of image pairs	1120
Vectors spacing	24pixels
First interrogation window size	$32 \times 32\text{pixels}^2$
Second interrogation window size	$24 \times 24\text{pixels}^2$

Table 1: MCCDPV parameters ( $x-r$  plane).

Position	0.47mm 0.06 $D_o$ above the nozzle
Image area	$8.7 \times 8.7\text{mm}^2$ $1.09D_o \times 1.09D_o$
CCD array	$1024 \times 1024\text{pixel}^2$
Spatial resolution	$118.3\text{pixels/mm}$ $946\text{pixels}/D_o$
Number of image pairs	1100
Vectors spacing	24pixels
First interrogation window size	$32 \times 32\text{pixels}^2$
Second interrogation window size	$24 \times 24\text{pixels}^2$

Table 2: MCCDPV parameters ( $r-\theta$  plane).

Figure 5 shows the radial distribution of the normalised mean axial velocity for a different set of four experimental conditions. The corresponding non-dimensionalised tangential velocity profile is shown in figure 6. The PIV data processing parameters are similar to those listed in table 1 and 2. The swirl number is fixed in the range of 0.0631 to 0.0648 while the Reynolds number is varied progressively.

The decrease in jet width as Reynolds number increases is clearly shown in figure 6. The effect of Reynolds number is counteracting the effect due to the increase in swirl intensity.

Figure 6 shows that swirling jets with different Reynolds number exhibit similar normalised tangential velocity profile. Increase in Reynolds number shifts the location of maximum tangential velocity towards the edge of the jet.

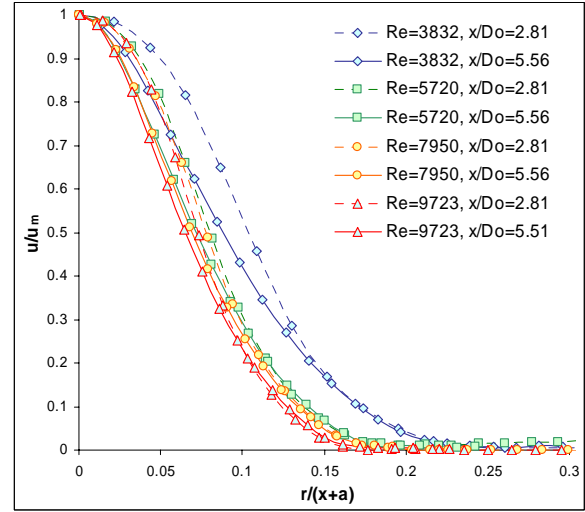


Figure 5: Radial distributions of normalised axial velocity (constant  $S$ , vary  $Re$ ).

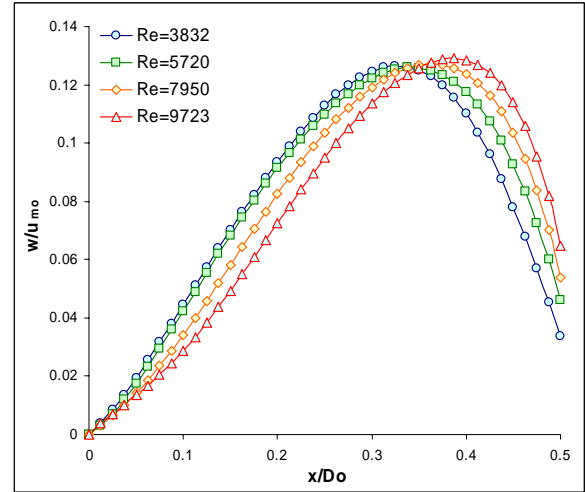


Figure 6: Radial distribution of mean tangential velocity (Constant  $S$ , vary  $Re$ ).

Velocity profile in the self similar region can be approximated using Gaussian curve according to the following equation [1]

$$u / u_m = \exp(-k_u \xi^2), \quad (4)$$

where  $\xi = r/(x+a)$ ,

$k_u$  = Gaussian velocity error curve constant.

$k_u$  is determined from the measured value of  $\xi$  and  $u/u_m$  when  $u/u_m = 0.5$ . The experimental determined  $k_u$  is plotted against swirl number in figure 7. In the region of swirl number investigated,  $k_u$  decreases almost linearly with  $S$ . The data collected in this study is consistency with previous literature [1].

The angle of spread,  $\alpha$  is defined as [14]

$$\alpha = \tan^{-1} \left( \frac{r_{1/2}}{(x+a)} \right). \quad (5)$$

where  $r_{1/2}$  is the radial coordinate where  $u/u_m = 0.5$ . The angle of spread obtained in the experiment is graphed in figure 8. Figure 8 shows that as swirl number increases, the angle of spread increases. Thus, the jet width increases. Angle of spread obtained from this study agrees well with previous literature [1] and [3].

The amount of fluid entrained from the surrounding is given by  $m-m_o$  and an entrainment constant can be defined such that



$$K_e = \left( \frac{m}{m_o} \right) \left( \frac{D_o}{x} \right). \quad (6)$$

The entrainment constants obtained from this study are plotted in figure 9. The amount of surrounding fluids entrained increases as swirl number increases. The entrainment constants determined are higher than the results obtained by [1] and [2].

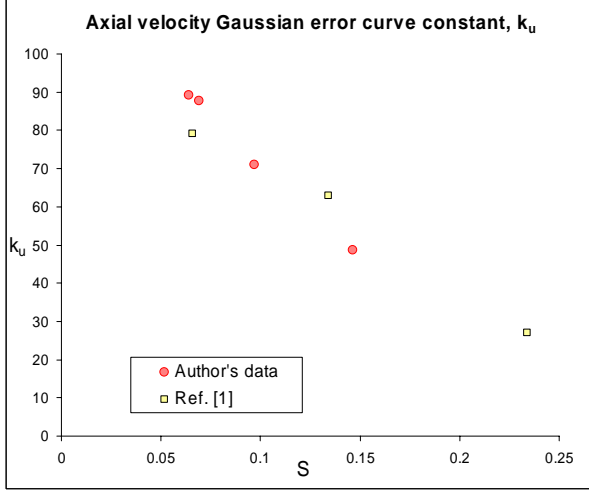


Figure 7: Axial velocity Gaussian error curve constant ( $k_u$ ) versus  $S$ .

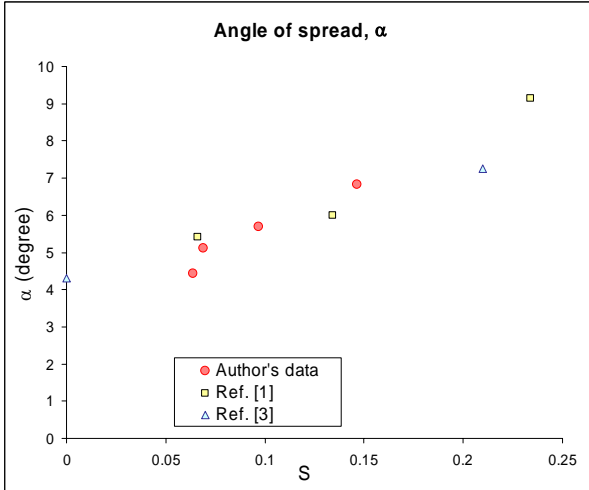


Figure 8: Angle of spread ( $\alpha$ ) versus  $S$ .

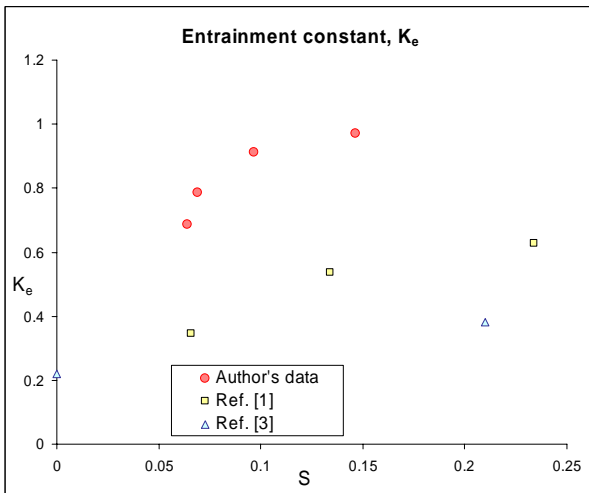


Figure 9: Entrainment constant ( $K_e$ ) versus  $S$ .

## Conclusion

A simple method of generating swirling jet with high degree of control of the governing parameters is developed. The experimental investigation conducted covers a range of weak swirling jets. The characteristics of the swirling jets produced are

similar to those of previous studies. Empirical constants that describe the swirling jet have been determined. These constants are Gaussian velocity curve constant, angle of spread and entrainment constant. Further investigation is required to determine behaviour of a swirling jet, particularly those with higher degree of swirl.

## Acknowledgement

The authors are grateful for the financial support provided by the Monash Research Fund to undertake some of this research.

## References

- [1] Chigier, N. and Chervinsky, A., Experimental Investigation of Swirling Vortex Motion in Jets, *J. Appl. Mech.*, **34**, 1967, 443 – 451.
- [2] Gore, R.W. and Ranz, W.E., Back Flows in Rotating Fluids Moving Axially Through Expanding Cross Sections, *A.I.Ch.E. J.*, **10**, 1964, 83 – 88.
- [3] Rose W.G., A Swirling Round Turbulent Jet, *J. Appl. Mech.*, **84**, 1962, 615 – 625.
- [4] Soria, J., Cater, J. and Kostas, J., High Resolution Multi-grid Cross Correlation Digital PIV Measurements of a Turbulent Starting Jet Using Half-frame-image-shift film Recording, *Optics & Laser Tech.*, **31**, 1999, 3 – 12.
- [5] Soria, J., Digital Cross Correlation Particle Image Velocimetry measurements in the near wake of a circular cylinder, in: *Int. Colloquium on Jets, Wakes and Shear Layers*, CSIRO, Melbourne, Australia, 1994, 25.1 – 25.8.
- [6] Soria, J., An Adaptive Cross Correlation Digital PIV Technique for Unsteady Flow Investigations, in: *Masri, A., Honnery D.(Eds.), 1<sup>st</sup> Australia Conference on Laser Diagnostics in Fluid Mechanics and Combustion*, University of Sydney, NSW, Australia, 1996, 29 – 45.
- [7] Soria, J. Multi-grid Approach to Cross Correlation Digital PIV and HPIV Analysis, in: *13th Australasian Fluid Mechanics Conference*, Monash University, Melbourne, 1998, 381 – 384.
- [8] Ellenrieder, K.von, Kostas, J. and Soria, J., Measurements of a Wall-bounded, Turbulent, Separated Flow Using HPIV, *J. Turbulence – selected papers from the 8th European Turbulence Conference*, 2001.
- [9] Westerweel, J., Dabiri, D., and Gharib, M., The Effect of a Discrete Window Offset on the Accuracy of Cross Correlation Analysis of Digital PIV Recording, *Exp. Fluids*, **23**, 1997, 20 – 28.
- [10] Hart, D., The Elimination of Correlation Error in PIV Processing, in: *9th International Symposium of Applications of Laser Techniques to Fluid Mechanics*, Lisbon, Portugal, 1998, I:13.3.1 – 13.3.8.
- [11] Raffel, M., Willert, C., and Kompenhans, J., Particle Image Velocimetry. A practical guide, Springer, 1998.
- [12] Westerweel, J., Efficient Detection of Spurious Vectors in Particle Image Velocimetry Data, *Exp. Fluids*, **16**, 1994, 236 – 247.
- [13] Gupta. D. Lilley and Syred, N., *Swirling Flows*, Abacus Press, 1984, 1 – 3.
- [14] Pope, S. B., *Turbulent Flows*, Cambridge University Press, 2000, 97 – 133.

## Simulation of Vehicle A-Pillar Aerodynamics of Various Yaw Angles

N.M. Murad<sup>1</sup>, J. Naser<sup>1</sup>, F. Alam<sup>2</sup> and S. Watkins<sup>2</sup>

<sup>1</sup>School of Engineering and Science  
Swinburne University of Technology, VIC, 3122 AUSTRALIA

<sup>2</sup>School of Aerospace, Mechanical and Manufacturing Engineering  
RMIT University, VIC, 3083, AUSTRALIA

### Abstract

Vortices formed around the A-pillar region dictate the pressure distribution on the side panels of a passenger vehicle and also can lead to aerodynamic noise generation. This paper analysed and compared qualitative flow visualization of airflow behavior based on the A-pillar region. Two simplified vehicle models with different A-pillar geometry were simulated using Computational Fluid Dynamics (CFD) under laboratory operating conditions. Commercial software (SWIFT) was used. In SWIFT, the simplified vehicle model was generated using Fame Hybrid. CFD simulations were carried out using SWIFT under steady state conditions using the HTM2 turbulence model. Investigations were carried out at velocities of 60, 100 and 140km/h and at 0, 5, 10 and 15 degree yaw angles. Results of  $C_p$  values were also compared against available experimental data. Results obtained using CFD modeling provided reasonable agreement against available experimental data.

### Introduction

Vortices formed around the vehicle A-pillar region can lead to aerodynamic noise generation [3, 6]. Noise generated from the A-Pillar region is transferred to the passenger cabin causing annoyance and much discomfort to the vehicle occupants [3]. Over the years, research studies concerning A-pillar aerodynamics have focused mainly on understanding the mechanics of airflow behaviour when exposed to various A-pillar and windshield configurations to help further reduce aerodynamic noise. Previous research studies conducted, used predominantly experimental and/or numerical methods [1, 2, 3, 5, and 6].

Reviews from past literatures suggest that the key in A-pillar design to achieve low aerodynamic noise lies on having a slender A-pillar angle with round windshield radius. However, design and safety constraints damper this progress [1] and hence, current vehicle design still utilises the traditional A-pillar design with minimum windshield curvature giving it a quasi-sharp slanted edge shape. This type of design resulted in the generation of complex three-dimensional turbulent flow separation behind the A-pillar region.

In 2004, Murad [7] conducted a study of a simplified vehicle model with slanted edge A-pillar geometry design at 0-yaw angle using CFD simulation. The main reason of the study was to develop an appropriate numerical tool to capture the A-pillar vortex. From the study, Murad obtained reasonable result correlation with available experimental data and developed an appropriate numerical tool for studying A-pillar vortex by using CFD. Results from the study showed helical three-dimensional vortex generated behind the A-pillar region of the slanted edge model. The vortex close to the vehicle wall surface was elongated and spanned out diagonally following the A-pillar shape due to high values of Reynolds stresses in the U and W component of flow. The results also show high vortex intensity at

the base of the A-pillar, where the helical vortex originates, based on high amount of kinetic energy obtained at that region.

In this study, a simplified model with rectangular shaped A-pillar geometry at varying yaw angles similar to Alam [1] was simulated and qualitatively analysed in order to understand the mechanics of the airflow behaviour behind the rectangular A-pillar region. In addition, airflow behaviour behind a slanted A-pillar model, similar to Murad [7], at varying yaw angles was also simulated using CFD and qualitatively analysed. Surface coefficient of pressure ( $C_p$ ) plots of both A-pillar models obtained through the CFD simulations were compared against available experimental data for validation purposes and to further assist in the understanding of A-pillar vortex behaviour close to the A-pillar/side window wall.

### Vehicle Geometry and Boundary Conditions

Geometry configurations, boundary conditions and experimental data used in these simulations were obtained from Alam [1]. In his wind tunnel tests, Alam used a simplified model of a vehicle (40% scale) with varying windshield/A-pillar configurations. Two rows of pressure tapings (96.0 mm apart) were constructed close to the A-pillar region to capture static pressure values on the vehicle surface. The static pressure was then used to calculate the  $C_p$  values. Each row had 16 pressure tapping points, which were 32.0 mm apart. The simplified model was exposed to various flow velocities and yaw angles. In this study, CFD simulations were carried out on the rectangular edge A-pillar model at yaw angles of 0, 5, 10 and 15 degrees with respect to the tunnel in the computational domain, while simulations carried out on the slanted edge A-pillar model were at 5, 10 and 15 degrees yaw angles respectively. The commercial CFD package used for the simulations was SWIFT AVL. Fame Hybrid AVL was used as the grid generator.

Boundary conditions at the velocity inlet were set at 60, 100 and 140 km/h respectively (Correspond to Reynolds number of  $2.169 \times 10^6$ ,  $3.615 \times 10^6$  and  $5.061 \times 10^6$  respectively). The windshield for the rectangular edge model was 90 degrees from the vertical axis while on the slanted edge model, the windshield was at 60 degrees from the vertical axis.

For simulations in SWIFT, the calculation of kinetic energy and dissipation rate ( $k$  and  $\epsilon$ ) were based on the turbulence Intensity and turbulence length scale values of 1.8% and 5.8 mm (1.0% model height) respectively. The values for kinetic energy and dissipation rate varied accordingly with the inlet velocity.

### Mesh Generation

Fame Hybrid in SWIFT uses an advance meshing system called the Arbitrary Cell Technology (ACT) where a blend of polyhedral grids was used to mesh and refine complex 3-D computational domain. An initial coarse mesh of around 250,000 grid cells were generated using Fame Hybrid. The final mesh

after refinement was slightly more than 1.0 million grid cells with a total of around 400,000 grid cells generated around the A-pillar region after refinement. Initial coarse surface mesh (100 mm in size) was generated on the wind tunnel wall. An initial surface mesh of 10 mm in size was generated on the vehicle model surface. A final surface mesh of 3.0 mm was generated around the A-pillar region after refinement. In addition, 10 boundary layer mesh were constructed from the model surface with each one measuring 2.0 mm in size. Grid independency test was performed after each grid refinements were made until error was restricted to a maximum of 5.0% relative to previous adaptation results.

### **Numerical Scheme and Strategy**

In SWIFT, the calculation was first done using first order upwind scheme and central differencing scheme. Once convergence was reached, the AVL smart bound higher order scheme was then used. The convergence level for residuals was set to 0.1% with SIMPLE pressure-velocity coupling used together with 3-dimensional, steady and incompressible flow environment. Throughout the calculation, under-relaxation values were reduced whenever solution showed instability and divergence. The under-relaxation performed varied from one A-pillar model to the other. Turbulence models used in SWIFT was the Hybrid Turbulence Model 2 (HTM2).

### **Discussion of Results**

CFD simulations on both the rectangular and slanted edge A-pillar models were carried out and Cp data values were obtained along the A-pillar region. Results from the Cp plots were within reasonable agreement with available experimental data.

#### **Rectangular Model at 0-yaw angle**

Results from relative pressure contour analysis showed that the A-pillar vortex increased in size and magnitude when exposed to an increase in velocity. At velocity of 100 km/h the A-pillar vortex appeared to be approximately 1/5 of the vehicle roof length. At 140 km/h, the A-pillar vortex appeared to be approximately 1/4 of the vehicle roof length.

Top view results of relative pressures contour showed a decrease in negative pressure magnitude along the y-axis (from A-pillar base to the roof). The area of separation at the A-pillar base was smaller and concentrated close to the A-pillar region due to its high intensity. The vortex expanded away from the side window and became larger as it moved upwards to a distance of approximately 2/3 from the base. At the same time the vortex core shifted downstream. As the vortex activity reached the roof of the model, the area of separation again became smaller and stretched. This resulted in the vortex core moving further downstream of the flow.

Top view results of turbulent kinetic energy contours showed a significant increase in magnitude at velocity of 140 km/h when compared to velocity at 60 km/h. At 140 km/h, high concentration of turbulent kinetic energy close to the A-pillar region but was decreasing in magnitude as it moved at 2/3 distance upwards from the base. As the A-pillar vortex mixed with separated flow from the roof region, it generated a high region of turbulent kinetic energy of similar magnitude to that at the base of the A-pillar region.

Further analysis from the Reynolds stress contours showed that the vortex was dominantly stronger in the  $vv'$  (y-direction) component followed by the  $ww'$  (z-direction) component. This was similar to the Reynolds stress component of the slanted edge

model at 0 yaw angle [7]. This showed that the A-pillar vortex was circulating diagonally and moving downstream to the flow. Surface streamline analysis of the rectangular model further showed that the A-pillar vortex reattachment region was around 45 degrees angle with respect to the A-pillar. This angle was halfway between the A-pillar and the vehicle bonnet. Surface streamline analysis by Murad [7] using the slanted edge model at 0 yaw also exhibited similar finding with the A-pillar vortex reattachment region at halfway (15 degrees) distance between the A-pillar and the vehicle bonnet (30 degrees).

Front view (z-axis) analysis of the CFD results taken of the turbulent kinetic energy contour showed that the airflow separation started from the corner between the bonnet and the A-pillar. As the airflow separated and started moving and circulating downstream to the rear of the vehicle, the vortex started to increase in size and evolved upwards until it reached the roof region of the vehicle (Figure 1). At the same time, the core of the A-pillar vortex was pushed outwards, away from the A-pillar. This phenomenon could be traced back due to the rectangular geometry of the A-pillar, forcing the A-pillar vortex to circulate at a steeper angle (45degrees) making it reach the roof region faster. In comparison, the A-pillar vortex of the slanted edge model at 0 degree yaw circulated downstream at a more acute angle. This resulted in a higher magnitude of turbulent kinetic energy (compared to the rectangular model) concentrated around a smaller region, placing the core of the A-pillar vortex closer to the driver/front passenger window.

CFD data analysis of Cp for the rectangular model taken along the bottom and top row region showed that the Cp values of the rectangular model showed a slow exponential decrease throughout the downstream region of the flow, a strong evidence of a large A-pillar vortex size surrounding much of the A-pillar and side window region. For the slanted edge model at 0 yaw angle, the Cp value plot for the bottom and top row region was more intense than the rectangular model but showed a faster exponential decrease throughout the downstream region of the flow, evidence of a smaller in size, but a more intense A-pillar vortex.

#### **Rectangular Model at 5, 10 and 15 degrees yaw angles**

Results from the rectangular model at varying yaw angles showed different characteristics to the rectangular model at 0 yaw angle. Different vortex size were developed on both sides of the A-pillar. In addition, results showed variations in vortex intensity at different yaw angle.

Top view results of turbulent kinetic energy contour for the 5, 10 and 15 degree yaw angle model showed that the A-pillar vortex formed around the vehicle A-pillar region at the windward side was smaller and compact in size due to the smaller area of separation and re-attachment downstream to the flow compared to the A-pillar vortex formed on the leeward side. Furthermore, the windward side exhibits a high magnitude in turbulent kinetic energy, with the A-pillar vortex core formed near to the A-pillar/side window region. On the leeward side, the A-pillar vortex core was formed further away from the A-pillar/side window region. Both A-pillar vortex on the windward and leeward side rotated in a clockwise direction (Figure 2). This is different from the model at 0 yaw angle where the vortex rotated in opposite direction to each other.

Front view results of relative pressure contour and streamline analysis showed that due to different yaw angles, the A-pillar vortex on the windward side was spread more towards the roof region next to the A-pillar and not much to the side window region. As the A-pillar vortex moved downstream, it became

larger in size, eventually connected with the turbulent boundary layer flow on the roof region and the A-pillar vortex on the leeward side. The A-pillar vortex on the leeward side originated from the A-pillar/bonnet corner region. As the flow moved downstream, flow separation evolved from the roof/side window region, eventually mixing with the flow separation from the A-pillar/bonnet region, resulted in a bigger A-pillar vortex. Relative pressure contour also showed very low pressure region downstream of the flow at area away from the A-pillar-side window, which also contained the core for the A-pillar vortex (Figures 3 & 4).

However, relative pressure contour analysis on the vehicle surface showed considerable high pressure spread on the vehicle wall. This phenomenon resulted from the thin viscous boundary layer effect developed close to the wall side window surface. On average, a  $C_p$  difference of -0.6 was observed between the low pressure region of the A-pillar vortex and the high pressure region of the boundary layer.

Reynolds stress analysis showed that the vortex on the windward and leeward side was stronger in the  $vv'$  and  $ww'$  component, evidence of the vortex moving and rotating downstream and upwards at approximately 45 degrees with respect to the A-pillar.

Results obtained from various yaw angles analysis of the rectangular model showed variations in vortex intensity. At 0 yaw angle, the vortex intensity was equally spread throughout the A-pillar/side window region. From the  $C_p$  analysis of the bottom and top row points, at 5 degree yaw, the windward side of the A-pillar started to show a steeper exponential decrease in  $C_p$  values during the first six bottom row points with a minimum of -1.50 before reaching a plateau. At 10 degree yaw, the  $C_p$  plot showed a steep exponential decrease during the first five bottom row points with a minimum of -1.51. At 15 degrees, a minimum of -1.0 was obtained from the first four points  $C_p$  plot of steep exponential decrease. This showed that as the yaw angle increased, the A-pillar vortex size on the windward side became smaller, resulting in an increase in vortex intensity, reaching peak intensity at 10 degree yaw before weakening back at 15 degree yaw. During this time, the leeward side experienced a steady exponential decline in vortex intensity with a leaner decline at every yaw angle increase. This is to further support the fact that the A-pillar vortex in the leeward side is bigger in size but smaller in intensity at the region close to the A-pillar/window area.

#### **Slanted Edge Model at 5, 10 and 15 degrees yaw angles**

Results from the slanted edge model at varying yaw angles also showed different characteristics to the slanted edge model at 0 yaw angle in that it exhibited A-pillar vortex at varying intensity and size on both sides of the A-pillar. The A-pillar vortex generated from the slanted edge model at varying yaw angle also showed several difference characteristics to the yawed rectangular model.

Top view (y-axis) CFD analysis of the relative pressure and turbulent kinetic energy contour showed that, due to the slanted edge geometry of the A-pillar, the A-pillar vortex intensity close to the A-pillar/side window wall was greater on the leeward side as oppose to the windward side on the rectangular model. The  $C_p$  data analysis showed a progressive increase in vortex intensity of the slanted edge model from 5 degree yaw angle until 15 degree yaw angle as oppose to a drop in vortex intensity at 15 degree yaw angle with the rectangular model.  $C_p$  data analysis also showed that with increase in vortex intensity, the vortex size at 5,

10 and 15 degree yaw angle on the leeward side was slightly smaller than the rectangular model. In addition, it was also observed that the A-pillar vortex formed at 5 and 10 degree yaw angle could only managed to sustain its intensity only for a short distance before reattaching itself to the side window wall but at 15 degree yaw angle, the separation area at low  $C_p$  values were spread out even much further downstream of the flow (Figure 5).

The front view relative pressure contour and streamline analysis showed that for the slanted edge model at various yaw angle, the airflow separation started on the side window on the windward side of the flow and not from the roof region as experienced by the rectangular model. On the leeward side, separation starts from the A-pillar to the side window. As the A-pillar vortex became larger downstream of the flow, it rotated beyond the boundary of the vehicle roof, mixing with turbulence boundary layer on the roof and reaching the A-pillar vortex on the windward side of the vehicle (Figure 6 & 7).

Reynolds stress analysis showed that the vortex on the leeward side was stronger in the  $uu'$  and  $ww'$  component, evidence that the vortex moved and rotated downstream and sideways. As the A-pillar vortex developed further and became established, the Reynolds stress analysis showed that the  $vv'$  and  $ww'$  component was stronger, evidence that the A-pillar vortex were rotating upwards and downstream to the flow. The A-pillar vortex on the windward side on the other hand, started of stronger in the  $vv'$  and  $ww'$  component and remained strong in that component all throughout the flow, evidence of the flow moving upwards and downstream to the flow.

#### **Conclusions**

A simplified vehicle model with rectangular and slanted A-pillar geometry was simulated and analysed to replicate flow behind a vehicle A-pillar region under laboratory operating conditions. Commercial CFD software, SWIFT was used for the simulations. In SWIFT, the simplified vehicle model was generated and meshed using Fame Hybrid. CFD simulations were carried out using SWIFT HTM2 turbulence model at steady state condition. Investigations were carried out at velocities of 60, 100 and 140km/h and at 0, 5, 10 and 15-degree yaw angle. Results showed that for the rectangular model, the A-pillar vortex generated was bigger in size when compared to the slanted edge model at 0 yaw but with less intensity. Results for the rectangular at various yaw angles showed that at the windward side, the A-pillar vortex generated had more intensity than the leeward side but was smaller in size. Results for the slanted edge model from various yaw angles showed that at the leeward side, the A-pillar vortex generated had a higher intensity and in size when compared to the A-pillar vortex in the windward side. Results for both model was greatly influenced by the yaw angles and also by the A-pillar geometry.

#### **Acknowledgments**

The authors would like to thank the Swinburne Centre for Astrophysics and Supercomputing for providing assistance with computing support and resources.

#### **References**

- [1] Alam, F., *The Effects of Car A-Pillar and Windshield Geometry and Yaw Angles on Local Flow and Noise: PhD Thesis*, RMIT University, Australia, 2000.
- [2] George, A.R., *Automobile Aerodynamic Noise, SAE Paper*, No 900315, 1990.
- [3] Hucho, W.H (editor), *Aerodynamics of Road Vehicles*, 2<sup>nd</sup> edn, Butterworths, London, 1998.

- [4] Murad, N.M, Naser, J, Alam, F, Watkins, S, Simulation of Vehicle A-Pillar Aerodynamics using various Turbulence Models, *SAE Paper*, No 2004-01-0231, 2004.
- [5] Popat, B.C., *Study of Flow and Noise Generation From Car A-Pillars: PhD Thesis*, University of London, 1991.
- [6] Watkins, S., Gusts and Transients, in *Topics In Wind Noise and its Measurement Part 2-SP1457*, SAE, USA, 1999.

## Appendices

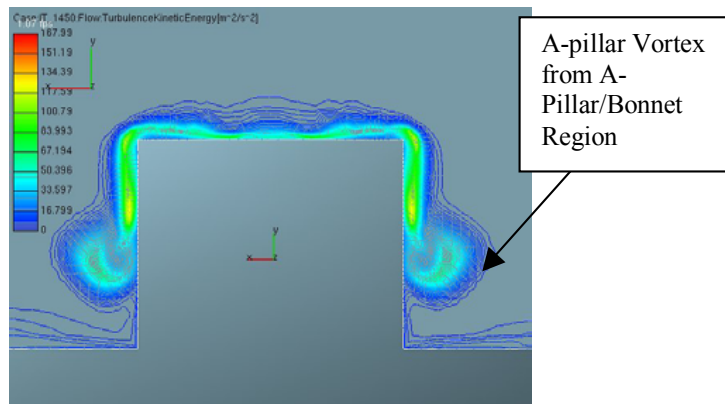


Figure 1. Front View (74 mm from Windshield) Turbulence Kinetic Energy Contour, Rectangular Model at 0 yaw, 140 km/h.

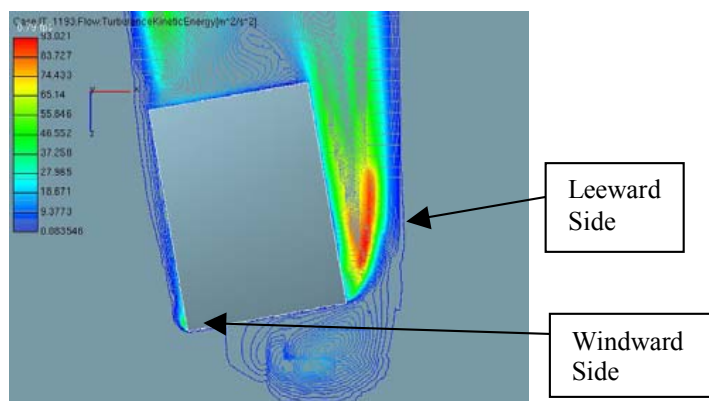


Figure 2. Top View (Bottom Row) Turbulence Kinetic Energy Contour, Rectangular Model at 10 yaw, 140 km/h.

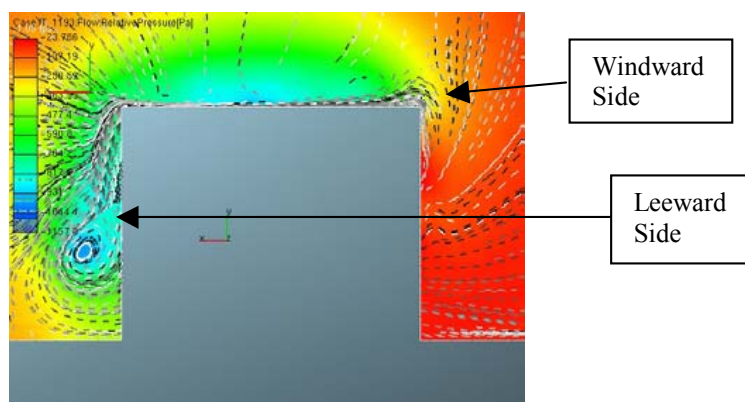


Figure 3. Front View (138 mm from Windshield) Relative Pressure Contour with Streamline, Rectangular Model at 10 yaw, 140 km/h.

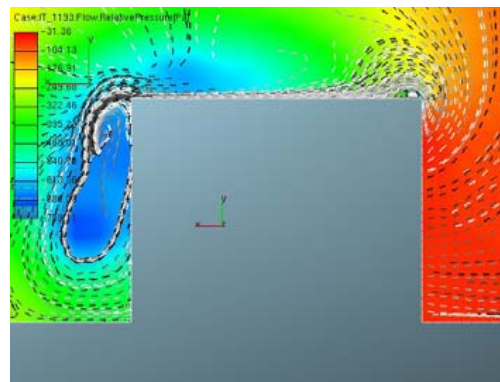


Figure 4. Front View (330 mm from Windshield) Relative Pressure Contour with Streamline, Rectangular Model at 10 yaw, 140 km/h.

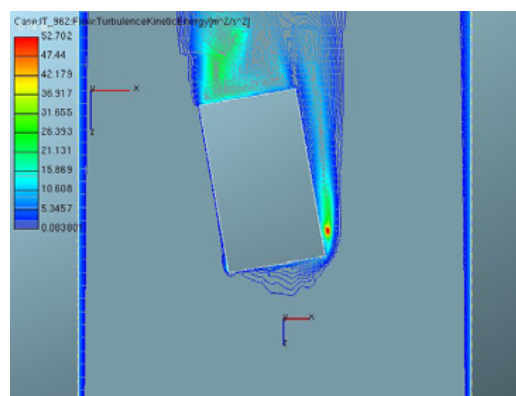


Figure 5. Top View (Bottom Row) Turbulence Kinetic Energy Contour, Slanted Edge Model at 10 yaw, 140 km/h.

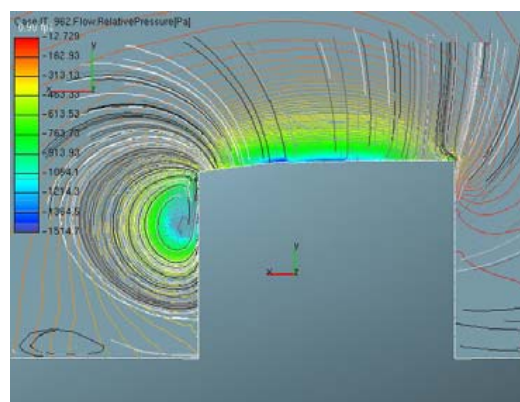


Figure 6. Front View (138 mm from Windshield) Relative Pressure Isolines with Streamline, Slanted Edge Model at 10 yaw, 140 km/h.

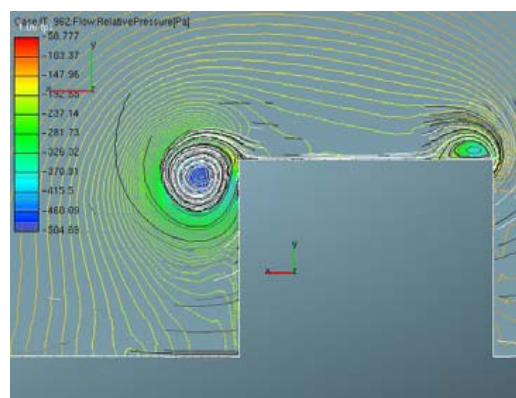


Figure 7. Front View (330 mm from Windshield) Relative Pressure Isolines with Streamline, Slanted Edge Model at 10 yaw, 140 km/h.



## Active Flow Control over a NACA 0015 Airfoil using a ZNMF Jet

A. Tuck and J. Soria

Laboratory for Turbulence Research in Aerospace and Combustion (LTRAC)  
Department of Mechanical Engineering, Monash University, Melbourne, AUSTRALIA 3800

### Abstract

The effect of using a wall-normal, zero-net-mass-flux (ZNMF) jet located at the leading edge of a NACA 0015 airfoil as an active flow control device was investigated. Experiments were conducted over a two-dimensional airfoil in a water tunnel at a Reynolds number of  $3.08 \times 10^4$  for parametric investigations and particle image velocimetry (PIV) and at a Reynolds number of  $1.54 \times 10^4$  for flow visualisations. The largest lift increases were observed when a non-dimensional frequency of 1.3 and an oscillatory momentum blowing coefficient of 0.14% were employed. Under these forcing conditions the stall angle of the airfoil was mitigated from an angle of attack of  $10^\circ$  to an angle of attack of  $18^\circ$ , resulting in a maximum lift coefficient increase of 46% above the uncontrolled lift coefficient. Planar laser induced fluorescence (PLIF) and PIV revealed that the lift increments were the result of the generation of a train of large-scale, spanwise lifting vortices that convected over the suction surface of the airfoil. The presence of these structures resulted in the flow seemingly remaining attached to the upper surface of the airfoil for a wider range of angles of attack.

### Introduction

Flow control over airfoils is primarily directed at increasing the lift and decreasing the drag produced by the airfoil. This is usually achieved by manipulating the boundary and shear layer flows in order to minimise the separation region over the suction surface of the airfoil. Active flow control refers to the process of expending energy in order to modify the flow [2]. This is distinct from passive techniques where flow control is provided without expending energy through means such as geometric shaping. One of the main advantages of active, rather than passive, flow control is that the control device can be switched on and off when required.

Many techniques for implementing active flow control have been proposed previously. These include: piezoelectric devices, vibrating flaperons, oscillating wires, boundary layer suction and blowing devices and the ZNMF jet that was studied here. A ZNMF jet 'transfers linear momentum to the flow system without net mass injection across the system boundary' [7]. ZNMF jets are commonly formed using a sinusoidally oscillating membrane to alternatively force fluid through an orifice into the external flow field and entrain fluid back through the orifice. During the forcing stroke the ejected fluid separates at the sharp edges of the orifice, forming a shear layer that rolls up to form a vortex ring for the case of a round synthetic jet or a vortex pair for the case of a plane synthetic jet. By the time the membrane begins its intake stroke, the vortex pair is 'sufficiently distant from the orifice that it is virtually unaffected by the entrainment of fluid into the cavity' [3,7].

The flow around an airfoil actively controlled by a ZNMF jet can be characterised using the following non-dimensional groups. Firstly, the non-dimensionalised excitation frequency is defined as:

$$F^+ \equiv \frac{fc}{U_\infty} \quad (1)$$

Where  $c$  is the chord length of the airfoil and  $f$  is the excitation frequency. The second parameter of significance is the oscillatory momentum blowing coefficient; a measure of the momentum imparted on the flow field by the ZNMF jet normalised by a characteristic momentum for the unexcited flow field, namely:

$$c_\mu \equiv 2 \frac{h}{c} \left( \frac{u_{j \text{ rms}}}{U_\infty} \right)^2 \quad (2)$$

Where  $h$  is the height of the slot and  $u_{j \text{ rms}}$  is the rms velocity of the jet in the exit plane. An alternative measure of the strength of the ZNMF jet is the velocity ratio, defined as:

$$VR \equiv \frac{u_{j \text{ rms}}}{U_\infty} \quad (3)$$

The use of ZNMF jets as an active flow control device has been shown in a number of studies to effectively delay the stall angle of an airfoil [1,2,4,5]. In delaying the stall angle the maximum lift coefficient produced by the airfoil is invariably increased. The power required to produce equivalent increases in the lift coefficient have been found to be approximately an order of magnitude lower for oscillatory control rather than for steady blowing techniques [5]. It has been reported that the actively controlled flow field shows little dependence on Reynolds number, except in the case where laminar-turbulent transition effects are significant [6]. Studies where the control actuators were placed closest to the separation point have reported the most beneficial results. The magnitude of the jet momentums found to be most effective has been varied, owing primarily to differences in the location and application of the control. Optimal results have generally been found when excitation at non-dimensional frequencies in the range of 0.58-2 was employed [2,5]. However, other researchers have had success operating at non-dimensional frequencies an order of magnitude higher.

The motivation for the work presented in this paper was to determine the most effective excitation parameters for increasing the post-stall lift produced by the particular airfoil geometry employed, and to characterise the flow structure around the controlled airfoil when these optimum excitation parameters were applied.

### Experimental Apparatus and Method

A re-circulating water tunnel, having a 5m long test section with a cross sectional area of 500mm x 500mm was used in this investigation. Water was used as the working fluid in these experiments as by virtue of its lower kinematic viscosity when compared to air, velocities (and hence characteristic frequencies) a factor 18 lower are inherent for the same Reynolds number flows. This affords for much more relaxed acquisition and excitation timescales.

All experiments were conducted using a Perspex NACA 0015 airfoil with a chord length of 100mm and a span of 510mm. The airfoil was mounted vertically in the test section of the water tunnel such that the base of the airfoil maintained a slight



clearance (2-5mm) with the base of the water tunnel. In this configuration the top of the airfoil protruded above the free surface of the working fluid at all times. This arrangement ensured that the flow-field around the airfoil was ideally free from 3-Dimensional effects due to the generation of tip vortices.

A slot of height 0.15mm, oriented normal to the surface at the leading edge, extended the entire span of the airfoil. This slot intersected a 5mm diameter hole through which pressure oscillations were supplied to generate the ZNMF jet, as shown in figure 1. The relative slot height of  $h/c = 0.15\%$  used in this investigation was smaller than those used in previous research. The slot height was minimised in order to maximise the jet exit velocity for the same displacement of fluid, as it was postulated that the control would be more effective for higher jet exit velocities.

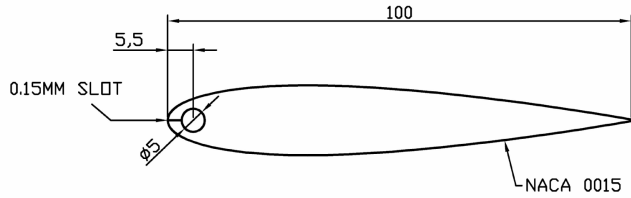


Figure 1. Cross-sectional view of the NACA 0015 airfoil tested (all dimensions in mm).

The pressure oscillations were supplied by a 20mm diameter piston/cylinder arrangement that was driven by a computer-controlled stepper motor via a Scotch-Yoke mechanism. The frequency of the pressure oscillations was controllable by altering the rotational speed of the stepper motor, whilst the magnitude of the oscillations was adjusted by varying the crank length of the Scotch-Yoke mechanism.

The airfoil was mounted on a force transducer, which allowed the lift and drag forces acting on the airfoil to be measured with a resolution of 0.1N. All force measurements reported have been averaged over 500 samples obtained from the force sensor. In order to isolate the fluidic forces from the external forces acting on the airfoil (for example forces arising from the nylon hose connection between the airfoil and the excitation system) force measurements collected with a stationary free stream were subtracted from the dynamic test results.

The zero degree angle of attack position of the airfoil was defined as being the angle for which the measured lift force for the uncontrolled airfoil was zero. As the airfoil used was symmetric, this condition corresponded to the airfoil being aligned with the freestream.

The structure of the flow field was examined by introducing a small amount of Kiton Red 620 fluorescent dye into the ZNMF jet cavity. This dye was ejected from the jet orifice into the external flow during the expulsion phase of the excitation cycle. An Nd:YAG laser sheet, incident on the mid-plane of the airfoil, resulted in fluorescence of the dye. The addition of a constant mass flow of dye to the jet violated the zero-net-mass-flux condition imposed, however it was assumed that the mass of the additional fluid was negligible relative to the total mass flux through the jet orifice during the excitation period. Instantaneous, randomly averaged and phase averaged images of the flow structure were captured using a monochrome digital camera with a CCD array size of 1280 x 1024 pixels.

For the PIV investigation the tunnel was seeded with 11µm hollow glass spheres. An identical laser and camera configuration to that used for the PLIF study was used in this phase of the investigation. The resulting PIV image pairs had a

spatial resolution,  $\Delta/c$ , of 0.075%. These image pairs were analysed using a multi-grid cross-correlation digital PIV algorithm. For more details of the algorithm used refer to [8]. Each image pair was segregated into interrogation windows with a characteristic dimension of  $1.2\%c$ , which resulted in a  $64 \times 80$  vector field being obtained for each realisation of the flow. 50 velocity fields were computed and averaged for every flow configuration investigated. Velocity fields were obtained for a plane immediately surrounding the airfoil and a plane exactly one image plane width downstream of the initial plane. Following processing, these velocity fields were patched together to form a vector field of twice the original aspect ratio.

## Results and Discussion

### Parametric Study

The dependence of the effectiveness of the control on the excitation frequency was evaluated by maintaining a constant jet momentum and varying the excitation frequency at a post-stall angle of attack of  $18^\circ$ . A relatively broad range of forcing frequencies between  $F^+ = 0.6$  and  $F^+ = 1.4$  were effective in enhancing the post-stall lift coefficient. The optimal forcing frequencies were determined to be a pair of frequencies symmetrically offset from a non-dimensional frequency of unity at  $F^+ = 0.7$  and  $F^+ = 1.3$ .

The effect of varying the jet momentum at an angle of attack of  $18^\circ$  for both of the optimum excitation frequencies identified above appears in figure 2. For both frequencies the lift coefficient increase was approximately proportional to the square root of the jet momentum, and hence linearly proportional to the jet velocity ratio. A peak was found in the effectiveness of the active control for  $F^+ = 1.3$  at a jet momentum corresponding to  $c_\mu = 0.14\%$  ( $VR = 0.65$ ). No such peak was observed for an excitation frequency of  $F^+ = 0.7$  in the range of jet momentums investigated. A possible explanation for the presence of such a peak is that at  $c_\mu = 0.14\%$  the maximum reattachment effect was realised from the ZNMF jet. Above this momentum the velocity of the jet may have been large enough to force the boundary layer to separate locally, resulting in the loss of lift demonstrated in figure 2.

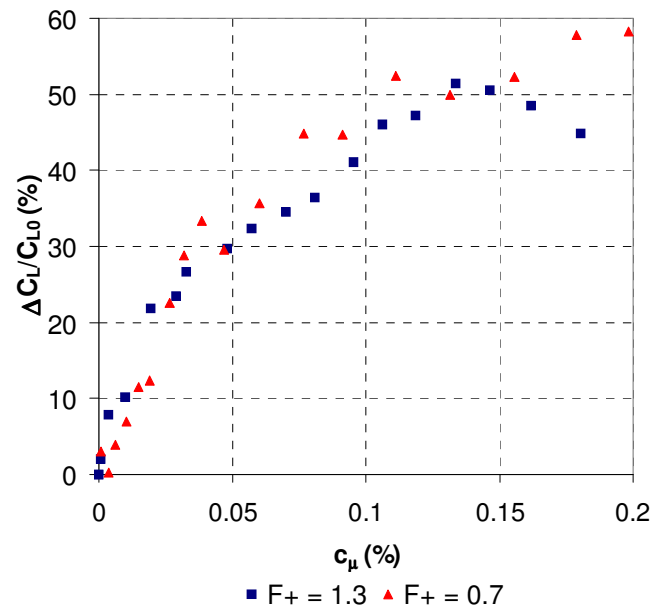


Figure 2. Percentage lift increment above the uncontrolled case for various jet momentums at  $\alpha = 18^\circ$ .

The optimum forcing parameters employed throughout the remainder of the investigation were defined as  $F^+ = 1.3$  and  $c_\mu = 0.14\%$ , despite the fact that slightly greater lift gains were noted for  $F^+ = 0.7$  than for  $F^+ = 1.3$ . This was due to the fact that the lift increments were found to be less repeatable, especially at

lower Reynolds numbers, if the lower effective forcing frequency were employed. Good repeatability was however found for  $F^+ = 1.3$ , hence its use as the optimum excitation frequency.

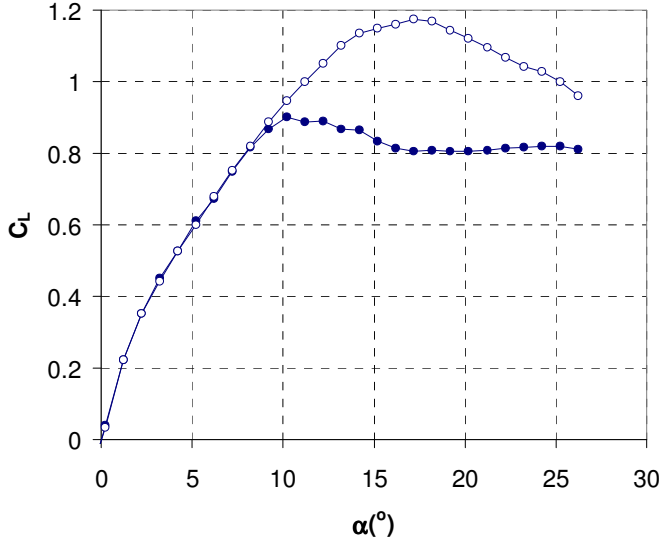


Figure 3. Controlled ( $F^+=1.3$ ,  $c_\mu=0.14\%$ ) airfoil (open circles) and uncontrolled airfoil (closed circles) lift coefficients.

The optimally controlled and the uncontrolled lift curves are presented in figure 3. Activation of the control is noted to result in the stall angle of the airfoil being mitigated from an angle of attack of  $10^\circ$  up to an angle of attack of  $18^\circ$ . Under these controlling parameters a maximum lift coefficient increase of 46% above the uncontrolled lift coefficient is observed at an angle of attack of  $18^\circ$ . The drag force acting on the airfoil was also significantly reduced for angles of attack between  $10^\circ$  and  $18^\circ$ . Significant lift increments were noted throughout the post-stall region investigated, however for angles of attack less than the uncontrolled airfoil stall angle no lift enhancement was realisable by activation of the control. Hence, it was concluded that the control must work by affecting the separated shear layer dynamics.

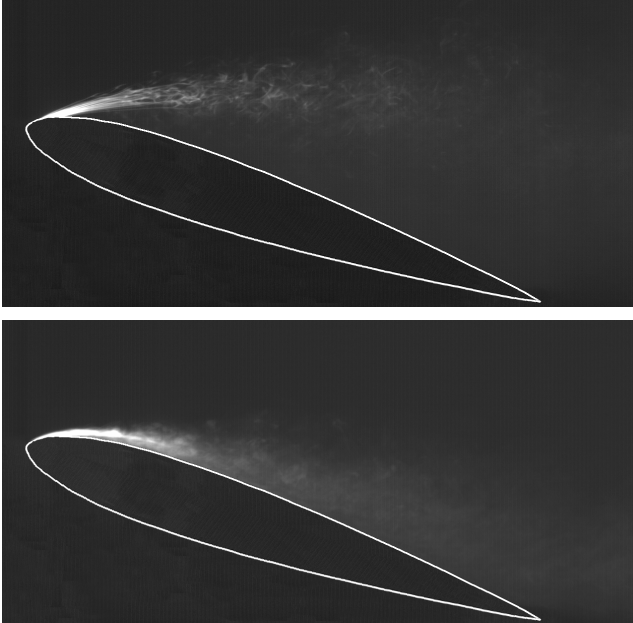


Figure 4. Averaged PLIF visualisation of the uncontrolled (top) and controlled (bottom) airfoils at  $\alpha = 18^\circ$ .

### Flow Characterisation

Flow characterisation was undertaken at  $\alpha = 18^\circ$ , as the lift and drag measurements suggested the greatest difference between the uncontrolled and the controlled flow fields at this angle of attack. It must however be noted that at an angle of attack of  $18^\circ$  the adverse pressure gradient on the suction surface of the airfoil is

such that the excitation is on the verge of losing effectiveness in controlling the flow.

The PLIF images shown in figure 4 demonstrate that the boundary layer of the uncontrolled airfoil has separated right at the leading edge to form a clearly defined separated shear layer that is unable to overcome the adverse pressure gradient required for reattachment to occur. From the trajectory of the separated shear layer it can be inferred that a massive separation region exists above the uncontrolled airfoil at this angle of attack. In contrast, the flow appears to be attached over the entire length of the suction surface of the controlled airfoil.

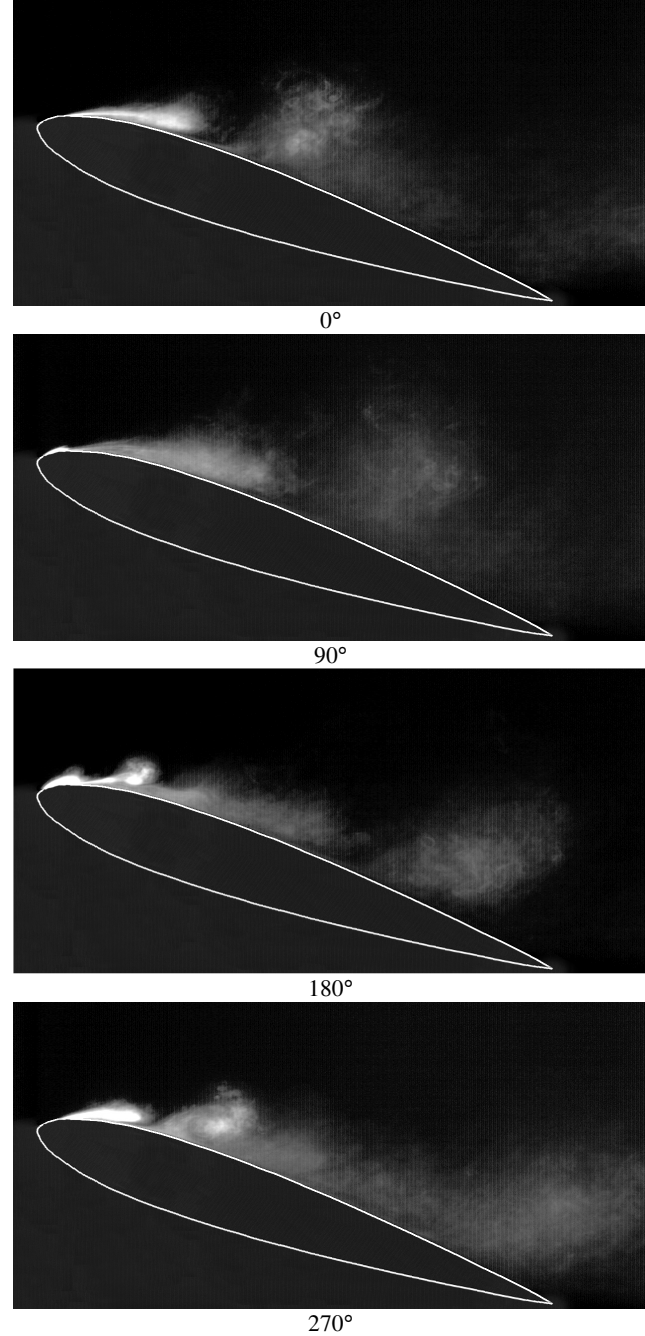


Figure 5. Phase averaged visualisations of the controlled airfoil

Examination of the phase averaged PLIF visualisations of the controlled airfoil presented in figure 5 reveals that the generation of a train of large, spanwise, coherent structures was responsible for the apparent reattachment of the flow. In these images  $0^\circ$  phase is defined as the point in the excitation cycle where fluid begins to be expelled from the jet orifice. The fluid ejected from the ZNMF jet orifice is first observed in the external flow field at a phase angle of  $90^\circ$ . At a phase angle of  $180^\circ$  the presence of multiple vortices is just discernable in the image. Between a phase of  $180^\circ$  and a phase of  $270^\circ$  these smaller vortices are observed to coalesce to form a single, larger, more intense

vortex. It is suspected that a vortex pairing event, or a series of vortex pairing events, that resulted in the formation of the larger vortex occurred in between these two phase angles. By virtue of its larger size, the core of the resulting single vortex is offset a significant distance further from the surface than those of the multiple, smaller vortices.

For the forcing frequency used in figure 5,  $F^+ = 1.3$ , the structures required almost two entire excitation periods to convect from their origin at the leading edge to the trailing edge. This translates to two structures residing over the suction surface of the airfoil at any time; one from the current excitation period that exists over the forward half of the airfoil and one generated during the previous excitation period that is evident over the aft portion of the airfoil. In contrast, for the lower effective forcing frequency,  $F^+ = 0.7$ , the vortices generated required just one excitation period to convect over the same distance.

Streamlines were determined from the PIV results by integrating across the velocity vector field from the inflow conditions. Figure 6 shows phase averaged streamlines for the controlled airfoil at a phase angle of  $180^\circ$ . It is apparent from the streamlines presented that the vortices generated over the upper surface of the airfoil are of negative sign. Being of the same sign as the lifting vortex, the vortex is able to 'roll' over the surface of the airfoil. It is postulated that this rolling motion is what allowed the vortex to move away from the leading edge at a faster rate than the bulk of the fluid ejected from the leading edge orifice - a phenomenon that was noted in the PLIF visualisations displayed in figure 5.

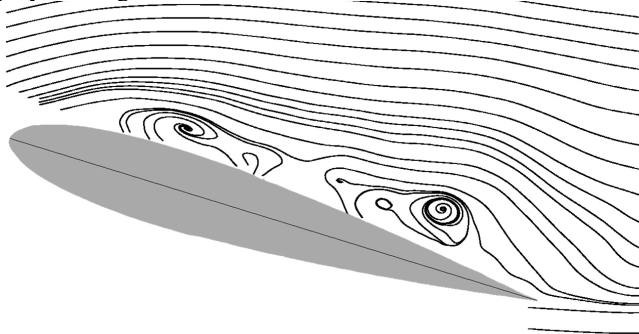


Figure 6 – Phase averaged streamlines around the controlled airfoil for a phase angle of  $180^\circ$ .

Only negative sign vortices were ever observed over the suction surface of the airfoil, however a vortex pair consisting of both a positive and a negative sign vortex is created when the flow separates at the sharp edges of a planar ZNMF jet orifice. The explanation offered for this behaviour is that the positive half of the vortex pair is annihilated by superposition of vorticity of a negative sign, which is inherent in the boundary and shear layers for this flow configuration. Meanwhile, the negative vorticity of the natural flow creates a favourable environment for the amplification of the negative sign vortex created by the ZNMF jet. This in turn results in the negative sign vortex being amplified to the point where it is observed to be two orders of magnitude larger than the characteristic dimension of the jet orifice; a size that is clearly large enough to affect the global airfoil flow field dynamics.

In describing the flow field around the controlled airfoil it is tempting to refer to it as being attached to the airfoil surface. Despite the fact that it is significantly more attached than the equivalent uncontrolled flow it must be noted that it is not fully attached, as at any point in time at least one recirculation region exists above the upper surface of the airfoil. It is the reduction of the massive recirculation region characteristic of the uncontrolled airfoil to a single, or a pair, of much smaller, controlled

recirculation regions that results in the performance benefits noted for the controlled airfoil.

Three mechanisms through which the generated vortices affect reattachment of the flow field are proposed. Firstly, the addition of large-scale structures significantly enhances the entrainment of the shear layer. It is also postulated that the negatively rotating vortex transfers rotational momentum to the shear layer via viscous forces. Both of these mechanisms act to deflect the shear layer towards the airfoil surface. The final mechanism identified assists the reattached shear layer to remain attached for phase angles where no large-scale structure is resident over the forward portion of the airfoil; the presence of the vortex deflects streamlines away from the surface, which results in alleviation of the local upstream pressure gradient, thereby reducing the forces promoting boundary layer separation.

## Conclusions

The optimum forcing frequencies for active flow control to be implemented using a wall-normal ZNMF jet located at the leading edge of a NACA 0015 airfoil were identified to be  $F^+ = 0.7$  or  $F^+ = 1.3$ . When a forcing frequency of  $F^+ = 1.3$  was employed the most effective jet momentum was found to be  $c_\mu = 0.14\%$  ( $VR = 0.65$ ). Using these forcing parameters the airfoil stall angle was mitigated from  $\alpha = 10^\circ$  to  $\alpha = 18^\circ$ , resulting in a maximum lift coefficient increase of 46% above the uncontrolled lift coefficient. Improvement of the lift-to-drag ratio was also noted throughout the range of post-stall angles of attack investigated. Activation of the control resulted in the flow over the suction surface of the airfoil being seemingly more attached for a wider range of angles of attack. The reattachment of the flow was attributed to the generation of a train of spanwise lifting vortices that appeared to roll down the upper surface of the airfoil. The lower effective forcing frequency was observed to result in a single vortex being present over the suction surface of the airfoil at any point in time, whereas the upper effective frequency resulted in two vortices residing over the airfoil surface throughout the excitation period. A number of potential mechanisms through which the spanwise vortices affected reattachment of the flow were identified.

## References

- [1] Chang, R., Hsiao, F. and Shyu, R., Forcing Level Effects of Internal Acoustic Excitation on the Improvement of Airfoil Performance, *Journal of Aircraft*, **29** (5), 1992, 823-829.
- [2] Donovan, J., Kral, L. and Cary, A., *Active Flow Control Applied to an Airfoil*, AIAA Paper 98-0210, 1998.
- [3] Lee, C., Ha, Q.P., Hong, G. and Mallinson, S., A piezoelectrically actuated micro synthetic jet for active flow control, *Sensors and Actuators A* 108, 2003, 168-174.
- [4] Seifert, A., Bachar, T., Shepshelovich, M. and Wygnanski, I., Oscillatory Blowing: A Tool to delay Boundary Layer Separation, *AIAA Journal*, **31** (11), 1993, 2052-2060.
- [5] Seifert, A., Darabi, A. and Wygnanski, I., Delay of Airfoil Stall by Periodic Excitation, *Journal of Aircraft*, **33** (4), 1996, 691-698.
- [6] Seifert, A. and Pack, L., Active Flow Separation Control on Wall Mounted Hump at High Reynolds Numbers, *AIAA Journal*, **40** (7), 2002, 1363-1372.
- [7] Smith, B and Glezer, A., The formation and Evolution of Synthetic Jets, *Physics of Fluids*, **10** (9), 1998, 2281-2297.
- [8] Soria, J., An investigation of the near wake of a circular cylinder using a video-based digital cross-correlation particle image velocimetry technique, *Experimental Thermal Fluid Science*, 1996, **12**, 221-233.

## Velocity Distribution in an Asymmetric Diffuser With Perforated Plates

M.N. Noui-Mehidi, J. Wu and I. Sutalo

Fluids Engineering Division, CSIRO, Manufacturing and Infrastructure Technology  
PO Box 56, Graham Rd, Highett, Vic, 3190 AUSTRALIA

### Abstract

An experimental investigation has been carried out to study the use of perforated plates to control the velocity distribution at the outlet of a wide-angle asymmetric diffuser. The diffuser was half a pyramidal diffuser, the inner wall of which was parallel to the flow, while the other was inclined. The diffuser opening angles were horizontally  $45^\circ$  and vertically  $30^\circ$  and the area ratio was equal to 7. A combination of four perforated plates with porosities of 45% resulted in differing velocity distributions at the outlet of the diffuser. Laser Doppler velocimetry measurements and wall static pressure results indicated the existence of different flow regimes when the perforated plates were placed at different locations. Velocity distributions investigated within the diffuser showed a complicated flow pattern between the different combinations of perforated plates.

### Introduction

Flow control involving perforated plates and wire gauze screens in internal flows has been extensively investigated for more than 50 years [1]. Particular interest has been given to wide-angle diffusers because of their association in many applications, for example in electrostatic precipitators (ESPs) and wind tunnels. There is a natural tendency of a wide-angle diffuser to develop a highly non-uniform velocity distribution at the outlet. Therefore, there is a need to control the flow for industrial applications, such as ESPs. Many studies were concerned with the use of wire gauze and perforated plates as flow control devices [2–3]. They showed that flow is very sensitive to the nature of the screens involved and their positions within the diffuser. Space limitation in practical situations is an important issue, and diffusers used in ESP installations have area ratios greater than 6. Sahin and Ward-Smith [4] and Sahin *et al.* [5] studied flow control by perforated plates in wide-angle diffusers of ESPs with larger area ratios up to 10. In a systematic investigation of the flow distributions at the outlet of wide-angle diffusers with area ratio of 10, Ward-Smith *et al.* [6] showed that good flow uniformity can be achieved at the outlet by using only two perforated plates or wire gauze screens with appropriate porosities and locations. They proposed that two perforated plates with porosities of between 40% and 50% be used, with the first one placed at a location near one-third of the diffuser length from the inlet, and the other one at a location just prior to the diffuser exit. In the present study, the flow within a wide-angle diffuser, which can be schematically represented as half a classical pyramidal diffuser, is investigated. The inner wall is aligned with the flow and the outer wall has an opening angle of  $45^\circ$ . Miller [7] referred to this type of diffuser as asymmetric, but presented only a few data points since they have not been previously investigated. The purpose of this study is to investigate the effect of perforated plates on the flow distributions within this asymmetric wide-angle diffuser model. A combination of different perforated plates permitted the investigation of flow control, and the velocity distribution at the outlet of the diffuser.

### Test Rig

A water circulation loop was set up to join a half-pyramidal diffuser with the inner wall parallel to the flow and the outer wall inclined with a horizontal opening angle of  $\alpha = 45^\circ$ . The total divergence angle of the top and bottom walls was vertically  $\beta = 30^\circ$ . The resulting outlet to inlet area ratio was therefore equal to 7. The diffuser was connected to a stainless steel box with a rectangular section of  $225 \times 250$  mm, as shown schematically in Fig. 1. The diffuser had a length  $L_1$  of 137 mm and the box had a length  $L_2$  of 250 mm.

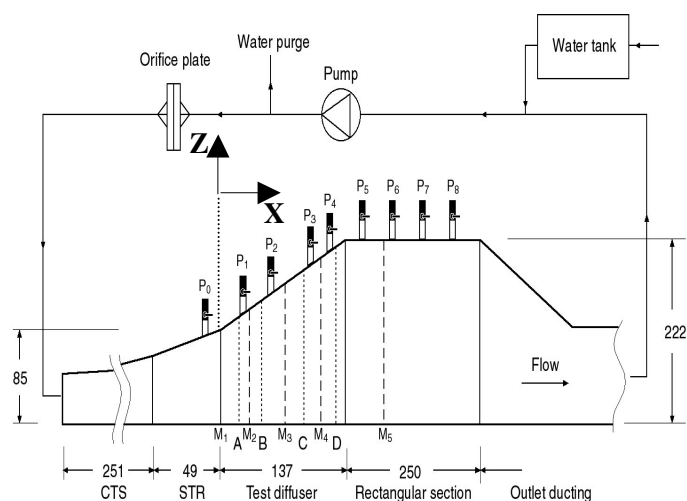


Fig.1 Experimental test rig.

Two transition ducts assured the connection of the diffuser to the upstream ducting circular pipe. The first one permitted the transition from a circular section to a semi-circular one (denoted CTS in Fig. 1), and the second duct connecting a semi-circular section to a rectangular one (denoted STR in Fig. 1). The STR duct inner wall and the diffuser inner wall, both parallel to the flow, were made from the same acrylic plate for visual access and laser Doppler velocimetry (LDV) measurements. The coordinates were defined in the Cartesian system X, Y and Z, where any (Y–Z) plane represented a section perpendicular to the flow, Y being the vertical axis; X was the downstream flow direction axis. Four slots machined into the inner sides of the diffuser stainless steel outer wall and acrylic plate (inner wall) allowed four perforated plates to be rigidly clamped vertically within the diffuser at locations  $X/L_1 = 0.05, 0.25, 0.59$  and  $0.95$ ; the origin was defined at the diffuser inlet plane ( $M_1$ ). The locations of the plates denoted A, B, C and D respectively, are presented in Fig. 1. The perforated plates all had the same porosity (total open area to total plate area) of 45%.

Tap water was used in the test rig. A small draining flow was placed downstream of the pump in order to avoid building up heat in the water body. A stream filled by an overhead tank permitted water loss to be compensated for.

The typical operating velocity at the diffuser inlet ( $M_1$ , Fig. 1) was 1.2 m/s, corresponding to a Reynolds number of  $Re = 1.25 \times 10^5$ , based on the inlet hydraulic diameter. The flow rate was measured by an orifice-plate installed downstream of the pump.

Static pressure taps were installed along the central horizontal plane of the diffuser, in order to quantify pressure variations along the flow direction. A Honeywell STD 130-EIN pressure transducer was used for pressure measurements. The locations of the pressure taps were fixed at  $X/L_1 = -0.74, 0.02, 0.23, 0.56, 0.91, 1.18, 1.55, 2.01$  and  $2.39$ , and were denoted by  $P_0, P_1, P_2, P_3, P_4, P_5, P_6, P_7$  and  $P_8$  respectively. The pressure distribution is represented here by the wall static pressure loss coefficient,  $C_p$ , defined by (cf. Ward-Smith [9]):

$$C_p = \frac{P - P_r}{\frac{1}{2} \rho U_1^2} \quad (1)$$

where  $P$  is the static pressure measured at a certain location,  $P_r$  is the reference pressure located upstream to the diffuser,  $\rho$  is the water density, and  $U_1$  is the average velocity determined at the diffuser inlet plane.

Velocity measurements were carried out using an Aerometrics one-component optical fibre LDV system. The LDV probe, which had built-in transmitting and receiving optics, was mounted on an industrial robotic arm, permitting the laser beam to be automatically positioned at the desired position within the diffuser/box combination. A 610 mm focal length lens was used for both transmitting the laser beams and collecting the scattered light from reflective magnepearl seed particles of 5–10  $\mu\text{m}$  diameter. The Aerometrics system's real-time analyser allowed the reading of the mean, standard deviation and acquisition rate of the axial velocity component  $U$  along the axis  $X$ . The obtained time-mean velocity data was found to be repeatable within  $\pm 1\%$ .

## Results and Discussion

In the literature, the velocity distributions have only been measured at the outlet of diffusers. Sahin and Ward-Smith [9] discussed qualitatively the flow pattern within a wide-angle diffuser based on pressure measurements. In the present investigation, the use of a transparent inner wall for both the diffuser and box allowed axial velocity  $U$  ( $X$ ) distribution measurements to be made within the diffuser and the box at different locations, indicated in Fig. 1 by  $M_1, M_2, M_3, M_4$  and  $M_5$ . The velocity measurements were carried out using different mesh grids at each location  $M_i$  in the ( $Y$ - $Z$ ) plane. The measuring points were placed in a uniform rectangular mesh grid at each measurement section.

### Empty Diffuser Flow Characteristics

In the absence of flow control, an axial jet develops within a wide-angle diffuser in the core region, and separation takes place just at the inlet due to the development of an adverse pressure gradient caused by the sudden expansion (cf. Ward-Smith [8]). In Fig. 2, mean axial velocity contours measured by LDV in a horizontal section ( $Y = 130 \text{ mm}$ ) through the empty diffuser in the ( $X$ - $Z$ ) plane are plotted. The figure clearly shows that the flow separates at a location of approximately  $X/L_1 = 0.08$  from the inlet of the diffuser when there is no screen. A large recirculating zone develops in the region near the outer wall and occupies almost half the area of the measurement plane where velocity magnitudes are negative. The wall static pressure coefficient, which was negative in value as seen in Fig. 3, decreased slightly along the downstream direction within the diffuser and remained unchanged in the rectangular section.

In a study of a wide-angle classical pyramidal diffuser with an expansion angle of  $60^\circ$ , Ward-Smith *et al.* [6] showed that the wall static pressure increased just beyond the diffuser inlet from negative to positive. This pressure recovery was not observed in our measurements.

This is probably due to the fact that our diffuser was asymmetric and had an area ratio equivalent to 14 in a pyramidal

diffuser, whilst the area ratio was 10 in the work of Sahin *et al.* [5] and Ward-Smith *et al.* [6].

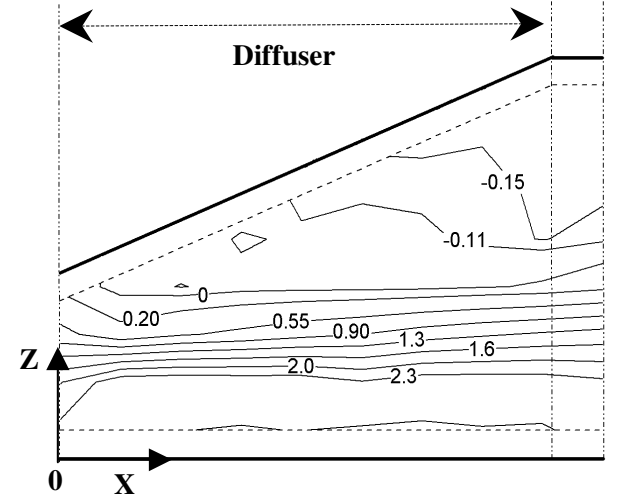


Fig.2 Velocity distribution in the asymmetric diffuser without screens in a  $X$ - $Z$  plane ( $Y=130\text{mm}$ ).

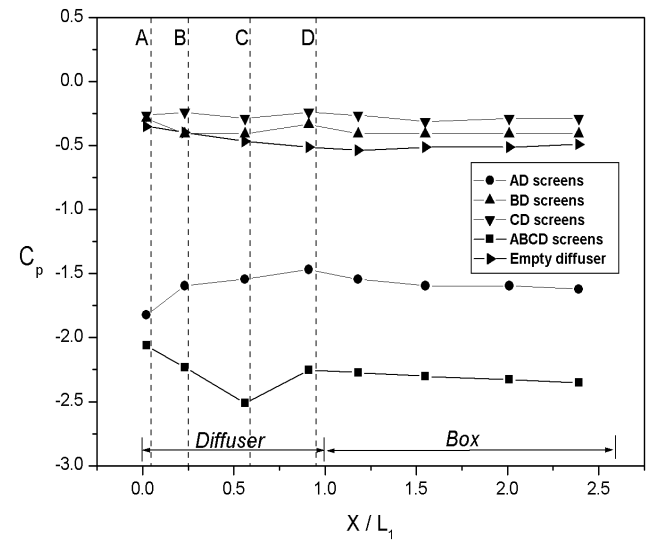


Fig.3 Downstream evolution of the pressure loss coefficient in the studied configurations.

### Flow Distributions Within the Diffuser With Screens Installed

In symmetrical pyramidal diffusers Sahin and Ward-Smith [9] observed that optimal flow control could be achieved by installing a perforated plate close to the diffuser exit, with a second plate installed in an upstream location between  $0.15 < X/L_1 < 0.29$  according to the present system dimensions. In the present work, four screen combinations were investigated: the first configuration had four screens installed, denoted configuration ABCD (Fig. 1). It has been studied as a limit case for comparison to the other two perforated plate configurations. In the three other configurations, screen D was fixed close to the exit of the diffuser, while another screen was installed upstream. These configurations were denoted AD, BD and CD (cf. Fig. 1). The contour plots of the mean axial velocity component  $U$  distribution within the diffuser are displayed in Figs 4–7. In each figure, four velocity distributions are presented for each of the four screen combinations studied. Each contour plot corresponds



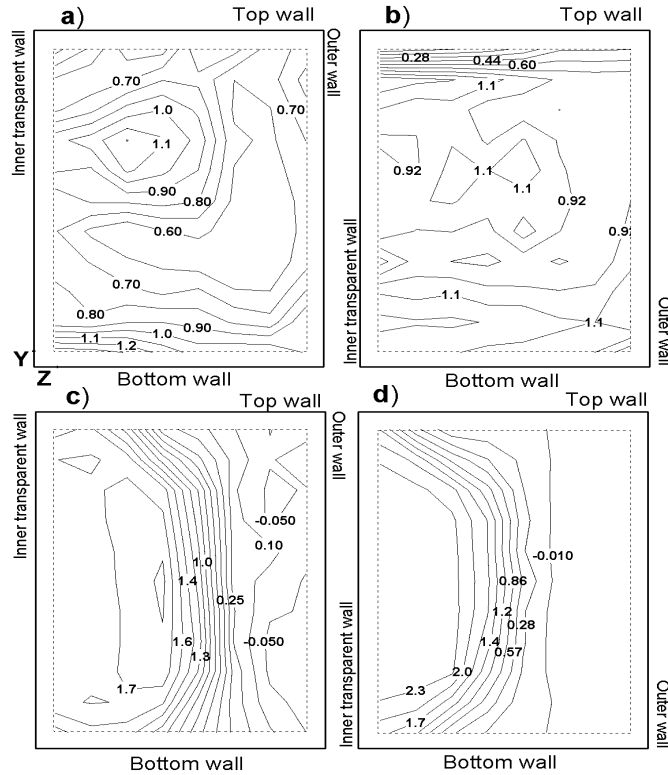


Fig.4 Velocity distributions at the section  $M_2$ .  
(a) ABCD, (b) AD, (c) BD and (d) CD

to a section in the (Y–Z) plane; the velocity magnitude is given in m/s, the flow is outwards to the reader.

Figs 4a–4d represent velocity distributions taken at location  $M_2$  for the four plate configurations. In Figs 4a and 4b the separation observed in Fig. 2 as starting at approximately  $X/L_1 = 0.08$  was not seen due to the presence of screen A. In configuration ABCD (Fig 4a), a jet existed at the upper left corner of the section; this jet occupied the centre region in configuration AD (Fig.4b). In Figs 4c and 4d where there is no screen A, the flow separation can be clearly seen. In both configurations BD and CD, a recirculating zone developed near the outer wall, while a jet was observed near the inner wall. However, the recirculating zone in configuration CD was larger than in BD, since screen C was downstream of screen B.

In the next measuring section  $M_3$  (Fig.5) the velocities were slowed by the second blockage corresponding to screen B in the ABCD configuration. Higher velocities are observed near the inner and outer walls (Fig.5a). In configuration AD, high velocities are confined to the core region in the measuring section, as can be seen in Fig. 5b.

In configuration BD (Fig.5c), the effect of the existence of a recirculating zone upstream of screen B can still be seen. The recirculating zone, however, is deflected from the outer wall to occupy the lower central region of the measuring section.

The velocity distribution in configuration CD observed in Fig. 5d is similar to the one observed previously in Fig. 4d, with large recirculating zones near the outer wall. There is a decrease in the velocity magnitude as the measuring section gets closer to screen C. These results suggest that the presence of screen A prevented separation occurring and the flow remained attached downstream. In the other configurations when separation occurred, even the presence of screen B did not eliminate the recirculating zone downstream as it was deflected from the outer wall to the centre region.

Velocity distribution obtained at  $M_4$  between the locations of screens C and D showed that the flow in configuration ABCD (Fig. 6a) was pushed towards the outer wall where high velocities existed. In configuration AD, the core region presented higher

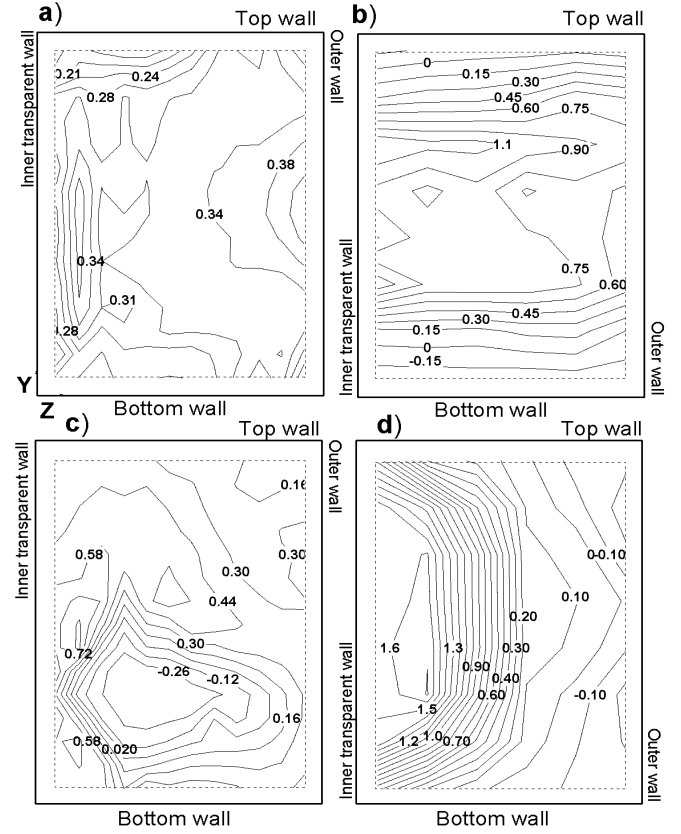


Fig.5 Velocity distributions at the section  $M_3$ .  
(a) ABCD, (b) AD, (c) BD and (d) CD

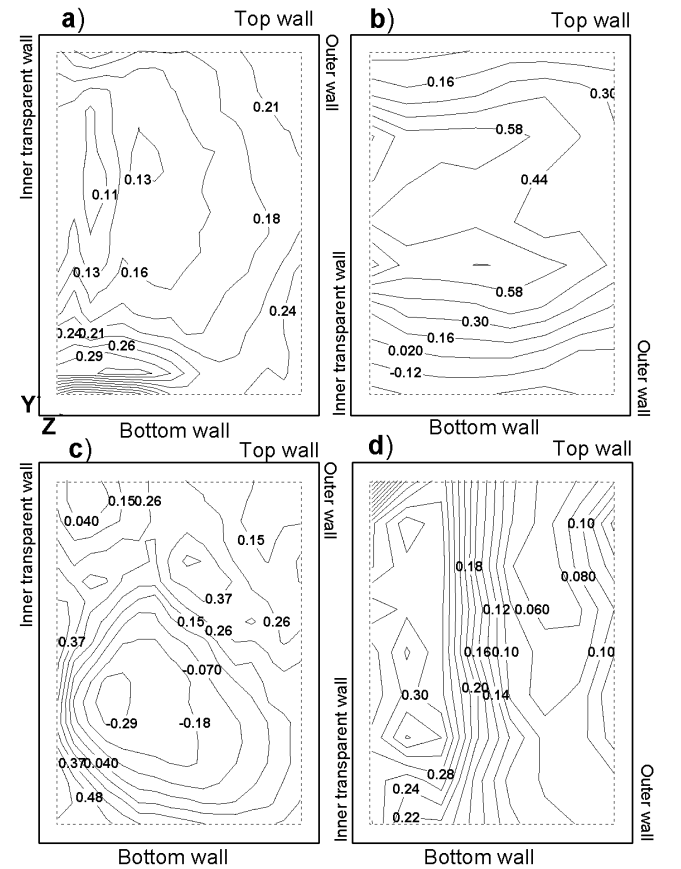


Fig.6 Velocity distributions at the section  $M_4$ .  
(a) ABCD, (b) AD, (c) BD and (d) CD

velocities in the measuring section (Fig. 6b). The recirculating zone observed previously in Fig. 5c is still present in Fig. 6c for



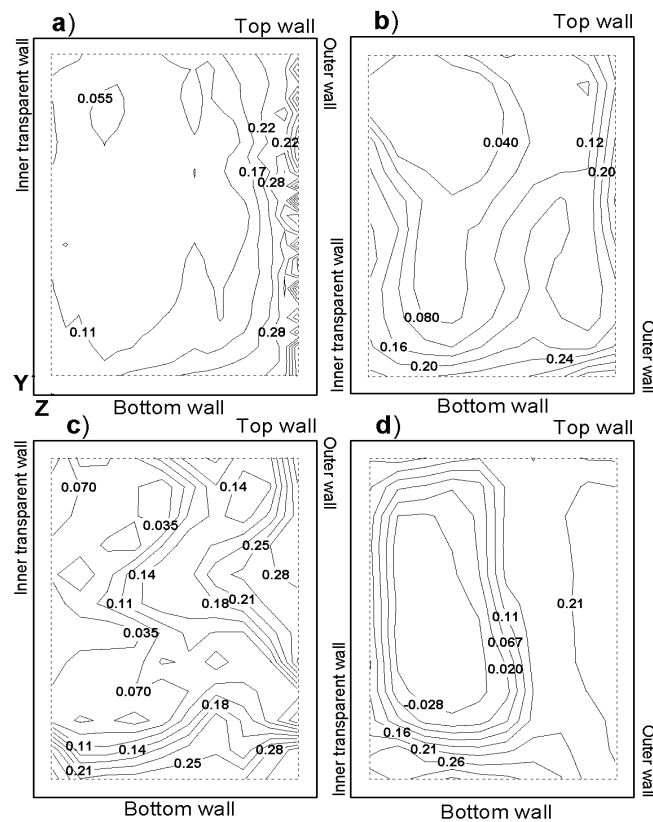


Fig.7 Velocity distributions at the section  $M_5$   
(a) ABCD, (b) AD, (c) BD and (d) CD

configuration BD, but was more confined to the inner wall of the diffuser. In the other parts of the measuring section, the flow seemed to reorganise as higher velocities occupied the upper part of the section.

In Fig.6d the presence of screen C in configuration CD eliminated the recirculating zone observed in Fig. 5d, which was probably weakened by the distance from the diffuser inlet and presented higher velocities from the central region of  $M_4$  towards the inner wall.

#### Velocity Distribution at the Diffuser Outlet

Velocity plot contours presented in Figs 7a–7d permitted the effect of different screen combinations to be determined at the outlet of the diffuser (section  $M_5$ ). Configuration ABCD presented a velocity distribution with a depleted core region and high-velocity wall layers at the inner wall. Different authors have observed a similar behaviour in diffusers with high-velocity wall layers about the periphery of the diffuser section. Ward-Smith *et al.* [6] described it as wall-jet flow. This wall-jet flow existed for high blockage within the diffuser. In Fig. 7a, the central region of the measuring section had a velocity 60% slower than the one obtained near the inner wall. Configuration AD presented lower velocities near the outer wall and also a relatively depleted central region (Fig. 7b). The flow distribution at the diffuser outlet in configuration CD (Fig.7d) presented a dramatic situation where a large recirculating zone took place near the inner wall. The most uniform velocity distribution obtained, in the present study, was for the configuration BD (Fig.7c) where screen D eliminated the confined recirculating zone observed previously in Fig. 6c.

#### Static Pressure Distribution

The static pressure loss coefficient profiles for the different configurations can be seen in Fig. 3. Sahin and Ward-Smith [9] reported that perforated plates of low porosity cause high pressure loss and the loss increases as the perforated plates are moved further upstream within the diffuser. As can be seen in

Fig. 3, the largest pressure loss occurred in configuration ABCD within the diffuser, even though there was a slight pressure recovery in the region  $X/L_1 = 0.6–1.0$ , corresponding to the space between screens C and D. In configuration AD, as the flow remained attached the pressure loss coefficient increased within the diffuser. The pressure losses were the lowest in configurations BD and CD. The present results have shown that static pressure measuring at the wall does not give information on the recirculating zones existing between screens in the core region. This fact can be observed in configuration BD where a recovery is observed between locations C and D as the flow was attached to the outer wall, while a recirculating zone existed in the centre region (Fig. 6c). The present pressure results are in good agreement with those obtained by Sahin and Ward-Smith [9] on the use of two perforated plates for flow control within wide-angle diffusers.

#### Conclusion

Velocity distributions and pressure profiles measured along an asymmetric  $30^\circ$  wide-angle diffuser with an area ratio of 7, were presented for different screen configurations used to achieve flow uniformity at the diffuser outlet. The velocity distributions measured within the diffuser at different locations highlighted the complicated effect of the different blockages seen by the flow within the diffuser. It was found that the location of the first screen had some influence on the velocity profile at the inlet of the diffuser. When the first plate was placed before the separation point at the diffuser inlet, the recirculating zone did not exist downstream, but if the first plate was placed beyond the separation point, the recirculating zone that developed upstream could have some effect on the flow downstream and beyond the perforated plate. A combination of two screens with the same porosity of 45% placed at  $X/L_1 = 0.25$  and  $0.95$  achieved the best velocity uniformity at the outlet for the diffuser under the present study. These results suggest that even an asymmetric diffuser can be used adequately in applications like ESPs where, in most cases, the space and shape allocated to the device depends on other built-up installations. From a fundamental point of view, more theoretical and experimental studies should be devoted to flows within asymmetric diffusers to compare their performance with symmetric systems.

#### References

- [1] Baines, W.D. & Peterson, E.G., An Investigation of Flow Through Screens, *Trans. AMSE*, **50**, 1951, 467–480.
- [2] Gibbings, J.C., The Pyramidal Gauze Diffuser, *Ing. Arch. Bd.*, **42**, 1973, 225–233.
- [3] Hancock, P.E., Plane Multiple Screens in Non-Uniform Flow With Particular Application to Wind Tunnel Settling Chamber Screens, *Eur. J. Mech. B/Fluids*, **17**, 1998, 357–369.
- [4] Sahin, B. & Ward-Smith, A.J., The Use of Perforated Plates to Control the Flow Emerging from a Wide-Angle Diffuser, with Application to Electrostatic Precipitator Design, *J. Heat & Fluid Flow*, **8**, 1987, 124–131.
- [5] Sahin, B., Ward-Smith, A.J. & Lane, D., The Pressure Drop and Flow Characteristics of Wide-Angle Screened Diffusers of Large Area Ratio, *J. Wind Eng.*, **58**, 1995, 33–50.
- [6] Ward-Smith, A.J., Lane, D.L., Reynolds, A.J., Sahin, B. & Shawe, D.J., Flow Regimes in Wide-Angle Screened Diffusers, *Int. J. Mech. Sci.*, **33**, 1991, 41–54.
- [7] Miller, D.S. *Internal Flow Systems*, BHRA, UK, 1990.
- [8] Ward-Smith, A.J., *Internal Fluid Flow: The Fluid Dynamics of Flow in Pipes and Ducts*, Clarendon Press, Oxford, 1981.
- [9] Sahin, B. & Ward-Smith, A.J., The Pressure Distribution in and Flow Characteristics of Wide-Angle Diffusers Using Perforated Plates for Flow Control with Application to Electrostatic Precipitators, *Int. J. Mech. Sci.*, **35**, 1993, 117–127.

## Gap Effect on Taylor Vortex Size Between Rotating Conical Cylinders

M.N. Noui-Mehidi<sup>1</sup>, N. Ohmura<sup>2</sup> and K. Kataoka<sup>3</sup>

<sup>1</sup>Thermal & Fluids Engineering Division, CSIRO, Manufacturing and Infrastructure Technology  
PO Box 56, Graham Rd, Highett, Vic, 3190 AUSTRALIA

<sup>2</sup>Department of Chemical Science and Engineering, Kobe University,  
Rokkodai, Nada Kobe 657-8501, JAPAN

<sup>3</sup>Kansai Chemical Engineering CO., Ltd., 2-chome,  
9-7 Minaminanamatsu-cho, Amagasaki-city, Hyogo 660-0053, JAPAN

### Abstract

The present paper is concerned with an experimental study of the occurrence of Taylor vortices between conical cylinders, the inner one rotating and the outer one at rest. Gap effect on the non-uniqueness of the Taylor vortex flow mode is investigated. Six different flow modes are observed according to the gap width, the acceleration of the inner rotating conical cylinder and Reynolds number. In one of the observed flow modes very large Taylor vortices are obtained with a wavelength up to 3.5 times the gap width. This kind of Taylor vortices has not been observed before in our knowledge.

### Introduction

The non-uniqueness of flow states with Taylor vortices has been largely investigated in the circular Couette flow. Coles [1] conducted a deep investigation on the non-uniqueness of the Taylor vortex flow and showed that a large number of flow modes can be reached. He noticed that these flow states are sensitive to the flow history. The geometric effects have been particularly studied for Couette-Taylor flow systems with finite length [2-4]. The non-uniqueness of the Taylor vortex flow in systems other than circular cylinders has also been discussed. Wimmer [7] obtained different Taylor vortex flow modes between conical cylinders when the inner cylinder was rotating and the outer at rest. In recent years an increasing interest has been accorded to the study of flow mode selection related to Taylor vortices due to the acceleration effect of the inner rotating body in both circular cylinders and conical cylinders. Lim et al. [5] discovered the existence of a Taylor-vortex flow in a region where wavy Taylor vortices were expected according to the Reynolds number. Noui-Mehidi et al. [6] investigated the acceleration effect on the Taylor vortex flow mode observed between conical cylinders when the inner conical cylinder was accelerated linearly with different acceleration rates.

In the classical Couette-Taylor system, different studies have reported that the maximal size of a Taylor vortex was less than 1.1 times the gap width [2-4]. The main objective of this work was to investigate Taylor vortex size between conical cylinders in a wide gap configuration since in the early studies, vortices larger than twice the gap width were observed.

### Experimental Setup

The experimental apparatus consists of a stainless steel machined inner conical cylinder and an outer conical cylinder made of Plexiglas. The square outer wall of the outer cylinder permits a good visualization and eliminates the effect of wall curvature leading to mis-observation. The outer stationary conical cylinder has an upper radius  $R_{oh} = 50$  mm. Two inner conical cylinders are used with the upper radius  $R_{ih} = 34$  and 42 mm respectively. The outer conical cylinder and the inner ones have the same apex angle  $\phi = 16.38$  degrees. Thus two configurations are obtained with axially constant gap of  $d_I = 8$  mm for configuration I

(denoted CI) and  $d_2 = 16$  mm for configuration II (denoted CII) in a horizontal direction respectively. At the top of the flow system the radius ratio is  $\eta_1 = R_{ih} / R_{oh} = 0.84$  for CI and  $\eta_2 = R_{ih} / R_{oh} = 0.68$  for CII. Both top and bottom end plates are fixed in the experiments. The aspect ratio  $\Gamma = L / d$  is fixed to 15.62 in CI and 7.81 in CII ( $L$  is the vertical height of the fluid column). The Reynolds number estimated with an accuracy better than 2.5%, is defined at the upper base for the largest radius, as:

$$Re = \frac{R_{ih} \Omega d}{\nu} \quad (1)$$

$\nu$  is the kinematic viscosity and  $\Omega$  the rotational speed of the inner conical cylinder. In CI the working fluid is a 66% solution of glycerol in filtered water and in CII the working fluid is a 33 % solution of glycerol in filtered water. For flow visualization, 2% of Kalliroscope AQ 1000 is added to each of the working fluids. The temperature is measured by a thermo-couple of Copper-Constantan with accuracy better than 0.1 °C. The kinematic viscosity  $\nu$  for each fluid solution is respectively 14.82 cS and 4.62 cS for CI and CII at 25 °C.

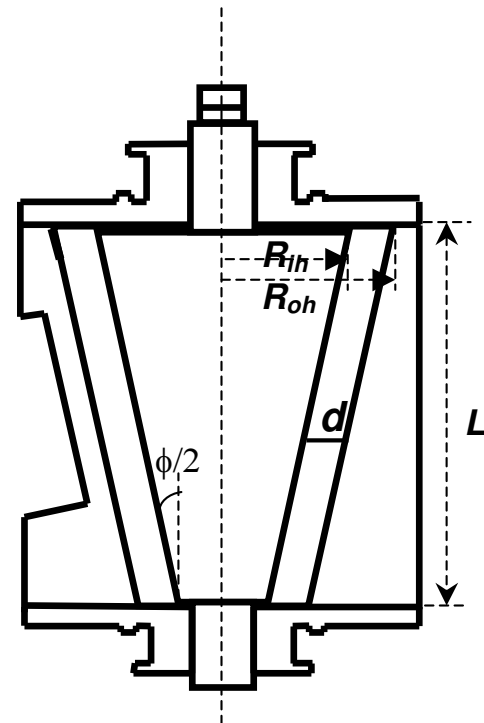


Fig.1. Experimental system.

In the present study, a computer controls the DC motor rotating the inner body. A program written in Visual Basic permits to fix the acceleration path as an output voltage sent to the motor. Thus the acceleration rate  $\beta$  (rad/s<sup>2</sup>) is related to the slope of the linear increase in the angular velocity from zero to the chosen speed. When the desired final value is reached, the inner conical

cylinder is rotated with a constant speed. The speed counter gives readings with accuracy better than 1%. Sudden accelerations are not investigated in the present study. The observations are repeated many times to ensure the reproduction of the observed flow states. The regimes investigated here correspond to Reynolds numbers between 0 and 1000.

## Experimental Results

Previous studies [6][7] have shown that the laminar-turbulent transition of flow between conical cylinders is more sensitive to the geometrical and dynamical parameters than the flow between concentric cylinders. The transition is mainly marked by a bifurcation branching, which occurs at the early observed instabilities.

### Transition to Taylor Vortices

The transition scenario in the present flow system has been previously reported by Noui-Mehidi *et al.* [6]. The basic flow is three-dimensional, the meridional flow being upward along the inner rotating conical cylinder and downward along the outer fixed one. At the critical Reynolds number of 132, a first vortex rotating inwards to the end plate appears at the top of the flow system where the radius is the largest. When  $Re$  is increased further a pair of counter-rotating vortices takes place below the first vortex. For further increase of  $Re$  more vortices are observed below the previous ones. When  $\frac{3}{4}$  of the fluid column is filled with these vortices, according to the acceleration rate two transitions can occur when  $Re$  is increased: 1. For acceleration rates less than  $0.07 \text{ rad/s}^2$  a helical structure takes place in the flow system. The motion is downwards and the helical vortices are counter-rotating two by two. This structure winds around the inner rotating body like a coil giving the effect of the “barber-pole” for a stationary observer. 2. The second transition occurs for acceleration rates higher than  $0.07 \text{ rad/s}^2$ . The previously observed first vortices move upwards until they fill completely the fluid column. Periodically a new pair of vortices is born at the bottom of the flow system while at the top the third vortex below the end plate disappears due to the upward motion and the two neighbouring cells merge to form a big vortex. For higher  $Re$  and acceleration rates, the upward motion stops and regimes of Taylor vortices are observed. The number of Taylor vortices obtained depends on the acceleration rate and the Reynolds number.

### Taylor Vortices Wavelength

Taylor vortices have been investigated widely in the system of concentric cylinders. The wavelength limits have been studied numerically and experimentally. Dominguez-Lerma *et al.* [3] showed that the wavelength in the Taylor vortex flow mode can be different from the critical wavelength calculated theoretically when  $Re$  is changed slightly near its critical value  $Re_c$ . The larger wavelength obtained in their experiments did not exceed 2.4 times the gap width.

Taylor vortex size in the flow between conical cylinders is not constant axially [6][7]. The definition of a wavelength is quite delicate since a pair of counter-rotating vortices is formed of one large cell and a one smaller cell, the larger cell being below as can be seen in Figs.2 and 3. The sizes of the large and small cells even vary from one axial position to the other. The vortex at the bottom of the flow system is the largest compared to the other large vortices above. The larger vortices are rotating in the same sense as the meridional flow i.e. upwards along the inner rotating body and downwards along the fixed one. The smaller vortices are counter rotating to the meridional flow. On the other hand the large vortex size decreases from the bottom to the top of the system, the smaller vortices have the same behaviour.

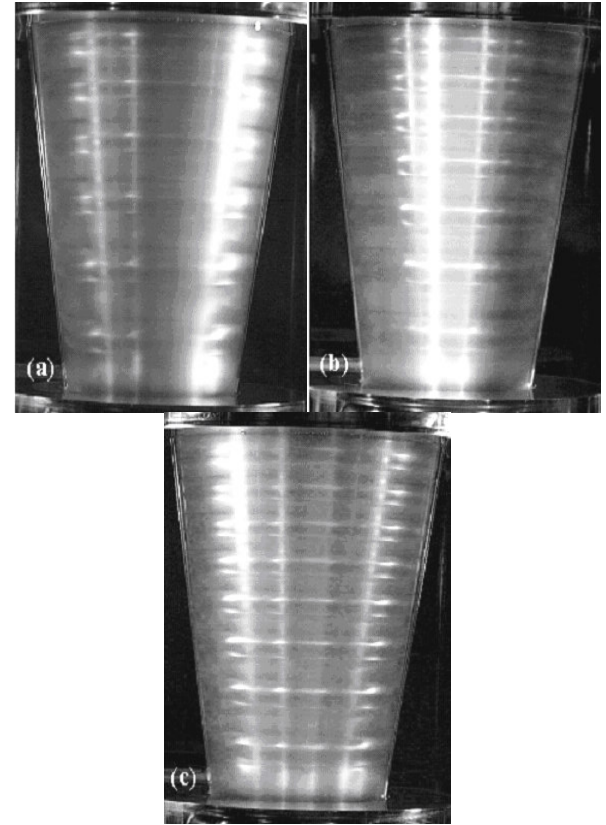


Fig.2. Vortex flow modes observed in CI, (a)  $Re=347$ , (b)  $Re=516$  and (c)  $Re=672$ .

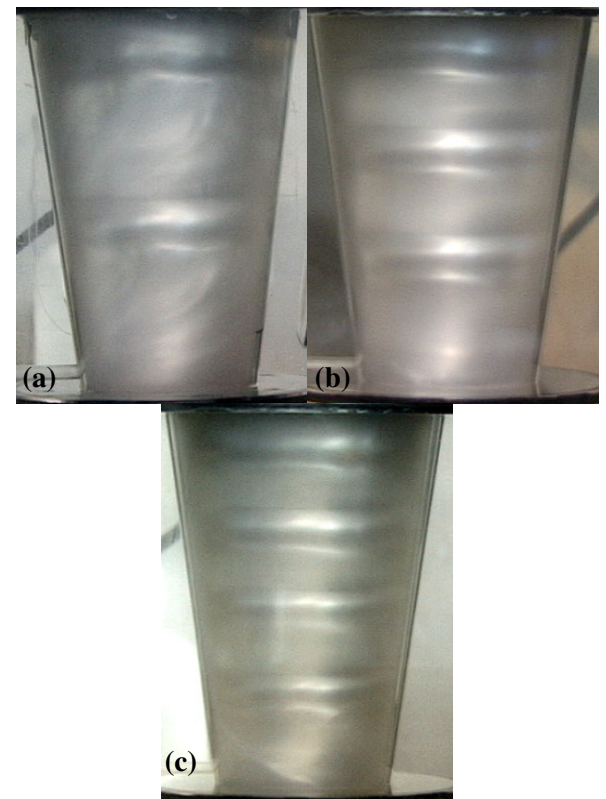


Fig.3. Vortex flow modes obtained in CII, (a)  $Re=92$ , (b)  $Re=88$  and (c)  $Re=85$ .

The wavelength can be defined as the size of a vortex pair, one large and the adjacent counter rotating small one. The mid-point

of an imaginary line joining the vortex centres is taken as the axial location of the wavelength measurements. The flow modes observed in CI are shown in Fig.2. As can be seen there are three different Taylor vortex flow modes with 6-pair, 7-pair and 8-pair of Taylor vortices. The wavelength axial evolution is presented in Fig.4 ( $N$  is the number of vortices). The non-dimensional wavelength  $\lambda^*$  is defined as the ratio of the local wavelength  $\lambda$  to the gap width  $d$ .  $\lambda^*$  is plotted against the axial position  $z^*=z/L$ ,  $L$  being the vertical fluid column height and  $z=0$  at the bottom of the flow system.

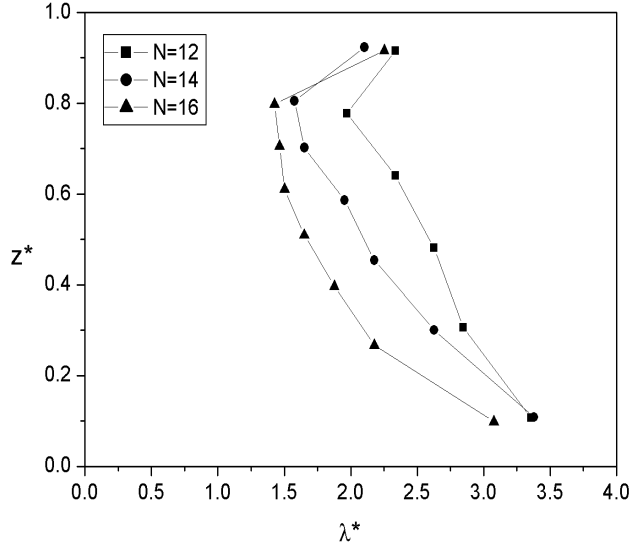


Fig.4. Axial evolution of the non-dimensional wavelength  $\lambda^*$  in CI.

It is worth noting that the size of the first pair of vortices at the bottom of the system in the three modes forms a wavelength varying between 3 and 3.5 times the size of the gap width. The wavelength decreases from the bottom to the top in the three observed modes 6-pair, 7-pair and 8-pair. In the 6-pair flow mode the wavelength decreases from 3.5 to 2.2, which corresponds to values still above the critical wavelength known in the Taylor-Couette system ( $\lambda^*=2$ ). The situation in the 7-pair and 8-pair flow modes is different. In the 7-pair flow mode the wavelength decreases from a value of 3.5 to 1.7 except at the top where the vortex near the end plate has a larger size. In the 8-pair flow mode,  $\lambda^*$  decreases from 3 to values near 1.5 at the top of the flow system except the top vortex at the end plate. The wavelength decrease in the 8-pair flow mode is characteristic to this system since it decreases from a value above the critical  $\lambda^*$  to values lower than the critical one. The top vortex near the end plate in the three modes is related to the Ekman layer thus presents sizes larger than the vortices below.

The experiments performed in the system configuration CII resulted in uncommon vortex flow modes. With a gap size of 16 mm three flow modes could be generated with 2-pair, 4-pair and 6-pair of Taylor vortices only as can be seen in Fig.3.

The same definition of the wavelength is adopted in the configuration CII to represent the axial evolution of the vortices size. As shown in Fig.5 the wavelength decreases from the bottom to the top in both 3-pair and 4-pair flow modes.

In the 3-pair flow mode the wavelength decreases from 3 to 2, which indicates that one pair of vortices has a size larger than the critical value while the two other pairs above have a wavelength corresponding to the critical known value.

The 3-pair flow mode is shown in Fig.3b for  $Re=88$ . In the 4-pair vortex mode, obtained at a Reynolds number of 85 (Fig.3c),

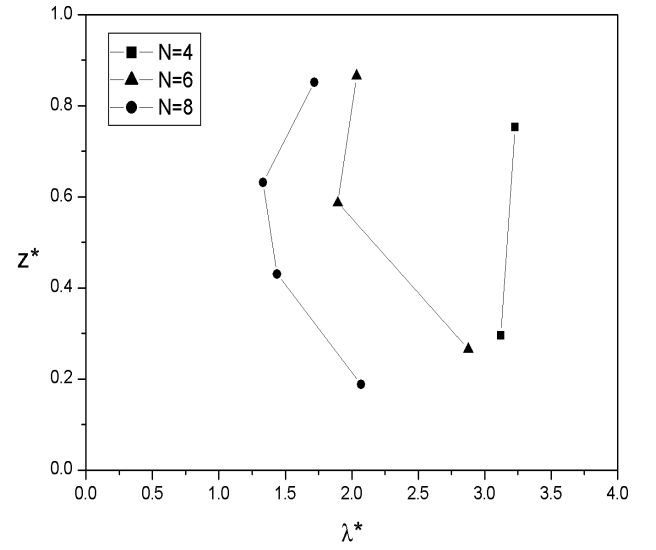


Fig.5 Axial evolution of the non-dimensional wavelength  $\lambda^*$  in CII.

the wavelength decreases from 2 to 1.5 giving values of the wavelength smaller than the critical  $\lambda^*$ . It can be remarked that in both 3-pair and 4-pair modes the wavelength formed by the top vortices is slightly larger than the one below as observed previously in CI.

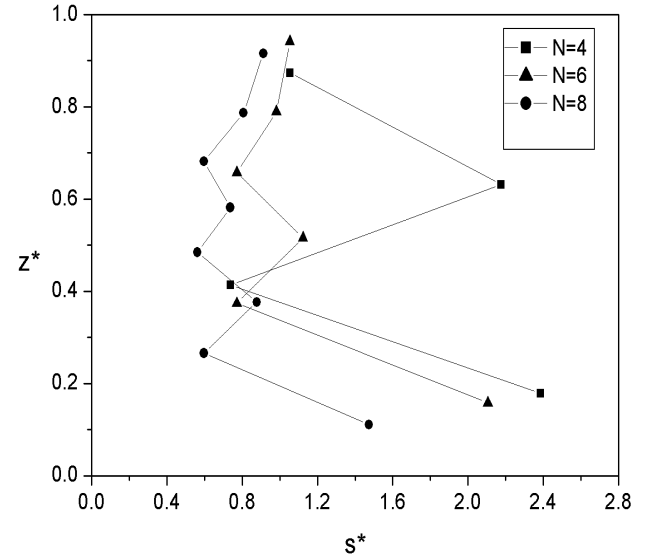


Fig.6 Non-dimensional vortex size axial variation in CII.

The situation is completely different in the case of 2-pair vortex mode. As seen in Fig.5 each of the two pair of vortices forms a very large wavelength  $\lambda^*$  with a value around 3.2. These two pairs of vortices can be seen in Fig. 3a for  $Re=92$ . It can be remarked that this type of vortices (2-pair) is obtained for a Reynolds number value higher than the one related to the 3-pair and the 4-pair modes. In order to compare individual vortices obtained in the configuration CII, the non-dimensional vortex

size  $s^*=s/d$  is presented in Fig.6 for each of the three modes 2-pair, 3-pair and 4-pair. In the 2-pair mode, the first vortex at the bottom of the flow system has almost 2.4 times the size of the gap width  $d$ , while the next small vortex above has only 0.8 times the size of the gap  $d$ . The difference in size between the larger vortices and the smaller ones is less important in the 4-pair flow mode except at the bottom of the system where the vortex is the largest. As deduced from Fig.6 the gap effect on the vortices size can be better expressed in terms of single vortex size than in terms of wavelength presented in Fig.5.

The present results have shown that Taylor vortices with a very large size can be generated between the conical cylinders when the gap is wide. These flow properties are specific to the studied system and have not been observed in other flow systems.

## Conclusions

In the present work, flow visualization has shown that Taylor vortices generated between conical cylinders, the inner rotating and the outer at rest, can reach sizes up to 2.4 times the gap width. This kind of vortices has not been observed before between rotating circular cylinders or other rotating systems. The present results constitute a good challenge for more experimental and numerical investigation of the different effects leading to the occurrence of such vortices.

## References

- [1] Coles, D., Transition in Circular Couette Flow, *J. Fluid. Mech.*, **21**, 1965, 385-425.
- [2] Cannel, D.S., Dominguez-Lerma, M.A. & Ahlers, G., Experiments on Wave Number Selection in Rotating Couette-Taylor Flow, *Phys. Rev. Lett.*, **50**, 1983, 1365-1368.
- [3] Dominguez-Lerma, M.A., Cannel, D.S. & Ahlers, G., Eckhaus Boundary and Wave-Number Selection in Rotating Couette-Taylor Flow, *Phys. Rev. A*, **34**, 1986, 4956-4970.
- [4] Linek, M. & Ahlers, G., Boundary Limitation of Wave Numbers in Taylor-Vortex Flow, *Phys. Rev. E*, **58**, 1998, 3168-3174.
- [5] Lim, T.T., Chew, Y.T. & Xiao, Q., A New Flow Regime in a Taylor-Couette System, *Phys. Fluids*, **10**, 1998, 3233-3235.
- [6] Noui-Mehidi, M.N., Ohmura, N. & Kataoka, K., Mechanism of Mode Selection for Taylor Vortex Flow Between Coaxial Conical Rotating Cylinders, *J. Fluids & Struct.*, **16**, 2002, 247-262.
- [7] Wimmer, M., An Experimental Investigation of Taylor Vortex Flow Between Conical Cylinders, *J. Fluid Mech.*, **292**, 1995, 205-227.

## A Blob Insertion Technique for the Vortex Blob Method

C. Macaskill

School of Mathematics & Statistics  
The University of Sydney, NSW, 2006 AUSTRALIA

### Abstract

This paper describes a new vortex blob method for the solution of problems in 2D vortex dynamics. In contrast to traditional vortex blob methods, this approach incorporates the distortion of the blobs, by the solution of two additional ODEs for each vortex blob, giving the evolution of the aspect ratio and orientation for an equivalent elliptical patch of constant vorticity in response to the locally linearised, but time-dependent, strain and vorticity fields. When the aspect ratio of the equivalent ellipse reaches a pre-determined limit, the circular vortex blob is split in two, with the centres of the new blobs aligned along the principal axis of the ellipse, thus providing a consistent approach to vortex blob insertion, so that fine-scale features such as vortex filamentation can be followed in an efficient way.

### Introduction

Lagrangian methods have a fundamental advantage over Eulerian or grid-based methods for problems in 2D vortex dynamics, in that the calculations are carried out only where the flow velocities are non-zero. This is particularly so for cases where there are strongly nonlinear interactions, giving rise to small-scale, but localised structures. Thus a vortex patch in a strain field (due to the presence of other vortices nearby e.g.) may deform and eventually produce filaments of vorticity. As time progresses, these filaments may quickly become very long and thin, and are advected by the local velocity field, giving rise to long sinuous streaks of vorticity. For inviscid, or near-inviscid flow, the cross-filamentary scales may be extremely small. Resolving such features is extremely difficult with uniform grids, and even with non-uniform grids there is the requirement of changing the grid very quickly in time as the flow evolves. In response to this, vorticity contour following methods have been developed, starting with the contour dynamics technique of Zabusky et al [13], and evolving to hybrid methods such as the Contour Advective Semi-Lagrangian (CASL) method of Dritschel and Ambaum [4], where the stream-function is inverted on a relatively coarse grid, but the vorticity contours (represented by nodes) are advected using Lagrangian techniques by interpolating the velocity field on to the contour nodes at each time-step. Because of the fact that vorticity contours very quickly lengthen as filamentation takes place, these methods must continuously insert new nodes along the vorticity contours, and this growth in the number of nodes can quickly limit the usefulness of such approaches. Accordingly, the techniques of ‘contour surgery’ [3] have been developed, where contours of vorticity are broken when they become very thin, and equal-valued contours merged when they approach closely.

An alternative Lagrangian approach for such problems is to represent the initial vorticity distribution with point-vortices (each has a  $\delta$ -distribution of vorticity) and then

to determine the motion of each point-vortex in response to all other vortices, so giving the evolution of the vorticity field. This technique was first introduced by Rosenhead [9], in his study of the evolution of a vortex sheet. Difficulties encountered with random motions of such point-vortices are to some extent mitigated by desingularising in some way, i.e. replacing the  $\delta$ -distribution of vorticity with some smeared non-infinite distribution with a characteristic small scale, the so-called vortex blob approach of Chorin and Bernard [2]. These vortex blob methods all introduce some numerical dissipation, but are generally accepted as being superior to point-vortex techniques, and we focus on such methods here. In order to resolve fine-scale vorticity features, the vortex blob methods require techniques of artificial blob insertion, that play a role equivalent to the node insertion on contours for contour dynamics techniques. When a single blob is replaced by two others, say, then each of the new blobs will have half the circulation of the old blob. It is clear that any initially circularly symmetric blob should actually distort in response to the local velocity shear. To account for this, Rossi [11] introduced Gaussian elliptical blobs, and determined ODEs for their evolution, to be solved simultaneously with the ODEs describing the motion of the centroids of the blobs. Typically, the aspect ratio of an elliptical blob increases with time, until eventually it must be replaced by a number of elliptical blobs of smaller circulation. The equations for this are non-trivial, however, and in the present work we develop a similar, but simpler scheme. We use fixed size blobs (i.e. no account is taken of viscosity) but for each blob simultaneously follow an equivalent constant vorticity patch of constant area in response to the first order approximation to the local strain and vorticity fields. The two ODEs describing the evolution of the orientation and aspect ratio of the elliptical patch have been obtained by Kida [6], who showed that such a patch remains elliptical for all time. When the aspect ratio reaches some pre-determined quantity, we can replace our initial blob with two blobs, each with half the circulation, aligned along the principal axis of the equivalent patch, thus providing a robust and simple technique for introducing blobs in a way consistent with the evolution of the flow-field. Eventually the growth in the number of blobs can be limited by discarding blobs after some suitable number of splittings: again, this introduces numerical dissipation, but this is quantifiable and can be chosen to be consistent with the computational resources available. Note that in general, although not employed here, blob merger should also be allowed, but as our blobs are circular, standard techniques can be used (see Rossi [11]).

This paper reviews the basic equations for the vortex blob approach and then goes on to show how to incorporate the Kida solution for the equivalent elliptical patches. Some preliminary results are provided, and suggestions made for future work.



## Mathematical Formulation

### Governing Equations

We consider 2-D incompressible, inviscid flow in an unbounded domain, with the flow field governed by the Euler equation

$$\frac{\partial \mathbf{u}}{\partial t} + \mathbf{u} \cdot \nabla \mathbf{u} = 0, \quad (1)$$

where  $\mathbf{u} = (u, v)$  is the fluid velocity and we use rectangular cartesian coordinates  $(x, y)$ . The corresponding vorticity is thus a scalar, satisfying

$$\frac{D\omega}{Dt} = \frac{\partial \omega}{\partial t} + \mathbf{u} \cdot \nabla \omega = 0 \quad (2)$$

and it is convenient to introduce a stream-function  $\psi$  with

$$\nabla^2 \psi = \omega. \quad (3)$$

Then  $(u, v) = (-\psi_y, \psi_x)$ . We define the circulation  $\Gamma$ , associated with any distribution of vorticity  $\omega(x, y)$  over a region  $R$  by

$$\Gamma = \iint_R \omega(x, y) dx dy. \quad (4)$$

The 2-D Green's function for Laplace's equation is

$$G(\mathbf{x}, \mathbf{x}') = \frac{1}{2\pi} \log |\mathbf{x} - \mathbf{x}'|. \quad (5)$$

Therefore, by Green's second identity on our unbounded domain

$$\begin{aligned} \psi(\mathbf{x}) &= \iint \nabla^2 \psi(\mathbf{x}') G(\mathbf{x}, \mathbf{x}') dx' dy' \\ &= \frac{1}{2\pi} \iint \omega(x', y') \log |\mathbf{x} - \mathbf{x}'| dx' dy' \end{aligned} \quad (6)$$

and hence the fundamental equations for the time evolution of the velocity components are

$$\begin{aligned} \frac{dx}{dt} &\equiv u = -\frac{\partial \psi}{\partial y} = -\iint \omega(x', y') \frac{\partial G(\mathbf{x} - \mathbf{x}')}{\partial y} dx' dy' \\ &= \frac{1}{2\pi} \iint \omega(x', y') \frac{(y' - y)}{(x - x')^2 + (y - y')^2} dx' dy' \end{aligned} \quad (7)$$

and similarly

$$\frac{dy}{dt} \equiv v = \frac{1}{2\pi} \iint \omega(x', y') \frac{(x - x')}{(x - x')^2 + (y - y')^2} dx' dy'. \quad (8)$$

All Lagrangian methods solve equation (1) by determining  $u$  and  $v$  at time  $t$  in some way, e.g. from expressions like equations (7) and (8) (point-vortex [9] and vortex-blob [2] methods), by evaluating a line integral over the Green's function (contour dynamics [13] methods) or by inverting equation (3) numerically to find a stream function (the CASL method [4]; [8]). This velocity field is then used to advect the vorticity out to the next timestep.

### Point-Vortex and Vortex Blob Methods

Consider the evolution of a patch of vorticity, non-zero on some region  $D$ . If we represent this as

$$\omega(\mathbf{x}) = \sum_{j=1}^N \Gamma_j \delta(\mathbf{x} - \mathbf{x}_j) \quad (9)$$

then we have the so-called point-vortex method. Here we represent  $\omega(\mathbf{x})$  by the linear superposition of  $N$  point vortices, located at positions  $\mathbf{x}_j$ ,  $j = 1, \dots, N$  and with associated circulation

$$\Gamma_j = \iint \Gamma_j \delta(\mathbf{x} - \mathbf{x}_j) d\mathbf{x}. \quad (10)$$

Substitution of equation (9) in equations (7) and (8) gives explicit expressions for  $dx/dt$  and  $dy/dt$  for each of the point vortices and then setting  $\mathbf{x} = \mathbf{x}_i$  gives the velocity with which point vortex  $i$  is advected by the flow field corresponding to all the other vortices. Use of a standard ODE solving routine (4th-order Runge-Kutta is used here) provides an algorithm for the evolution of the original patch of vorticity. This is the method first used by Rosenhead [9].

There are two fundamental issues/difficulties associated with the point-vortex method. One is the degree to which a general distribution of vorticity can be accurately represented by the point vortices. This can be addressed by using more vortices, but of course that increases the cost of the calculation. Perhaps more significantly, the interaction of four or more vortices gives rise to intrinsically chaotic motions [1], so that in general the long-time behaviour of such models tends to be unreliable.

One way to deal with these problems is to 'desingularise' the point vortices, leading to so-called vortex blobs. This idea goes back to Chorin and Bernard [2], but the explicit model we use here is due to Krasny [7] (his  $\delta$ -equation method):

$$\omega(\mathbf{x}) = \frac{1}{\pi} \sum_{j=1}^N \Gamma_j \frac{\delta^2}{((x - x_j)^2 + (y - y_j)^2 + \delta^2)^2}. \quad (11)$$

There is no longer a singularity at  $\mathbf{x} = \mathbf{x}'$  but the  $\delta$ -function representation is regained in the limit when  $\delta \rightarrow 0$ . Here  $\delta$ , where  $\omega$  has dropped to one quarter of its maximum (central) value, can be thought of as the radius of the blob. The smearing of the point vortex introduced in this way acts to reduce the tendency to chaotic motion, essentially because there is an effective dissipation introduced. Even with this desingularisation, however, there is a tendency for individual vortex blobs to move chaotically, particularly in cases where filamentation takes place and the separation between blobs becomes large. This problem can be overcome to some extent by splitting blobs, or by introducing new blobs and renormalising the circulation.

### Blob-Splitting Determined by the Local Strain Field

The contribution of the present work is a method that allows vortex blob insertion in a dynamically consistent fashion. The approach is motivated by the work of Rossi ([11], [12]), who introduced the idea of using elliptical Gaussian basis functions (or blobs) that deform according to the prevailing velocity field. Once the blobs become significantly elongated, they can be split and replaced by a number of smaller elliptical blobs. In addition, diffusive spreading due to viscosity (not treated here) can be included. However, the equations describing the deformation of the elliptical blobs are non-trivial, so that there is an associated increase in computational load. On the other hand, this is more than compensated for by the increased spatial accuracy.

The simpler idea invoked here is to work with non-deforming circular blobs, but to keep track of their po-

tential deformation under the prevailing strain field due to all the other blobs. To implement this, it is necessary to integrate two ODEs for each blob. These ODEs determine the axis-ratio ( $p$ ) and orientation ( $\theta$ ) as a function of time for the corresponding ‘equivalent elliptical patch’ of uniform vorticity, initially circular with radius  $\delta$  and with the same circulation, in response to the local linearisation of the velocity field induced by all the other vortex blobs. This is possible because exact ODEs for this problem have been determined by Kida [6] for this situation. Two new blobs, with half the circulation, and with centres separated by distance  $2\delta$  and aligned along the major axis of the ellipse equivalent to the vortex blob, are used to replace a vortex blob when the effective aspect ratio for a blob  $p_i$  exceeds the critical value  $p_{\text{crit}}$ . In this way we can resolve fine-scale features of the flow, such as filamentation, by introducing new blobs as required by the local nature of the velocity field. As this procedure will eventually lead to an exponential growth in the number of blobs, some way of limiting the growth is required. The natural technique is to discard blobs after a certain number of splittings (say 9 or 10) when their individual contribution to the circulation is reduced to  $1/512$  or  $1/1024$  respectively of that of an original blob. Note that although the constant vorticity elliptical patch is not exactly equivalent to the corresponding vortex blob, there is no additional error introduced, as we are only using this representation as an aid to deciding when and how to split the vortex blob.

### Implementation of the Kida Solution for Elliptical Patches

For any given vortex blob we expand the external velocity field due to the other blobs to first order as:

$$\mathbf{u} - \mathbf{u}_B \approx A\mathbf{x} = \begin{bmatrix} u_x & u_y \\ v_x & v_y \end{bmatrix}_B \mathbf{x} \quad (12)$$

where  $\mathbf{u}_B$  and all the shear components are evaluated at the centre of the blob and where the coordinate origin here is at the centre of the blob. This corresponds to the external shear field considered by Kida [6], but, of course, here these quantities are not fixed in time but vary as the vorticity field and the corresponding velocity field evolve.

From continuity  $u_x = -v_y$  and then

$$\begin{aligned} \begin{bmatrix} u_x & u_y \\ v_x & -u_x \end{bmatrix} &= \begin{bmatrix} u_x & 0 \\ 0 & -u_x \end{bmatrix} + \frac{1}{2} \begin{bmatrix} 0 & (u_y + v_x) \\ (u_y + v_x) & 0 \end{bmatrix} \\ &+ \frac{1}{2} \begin{bmatrix} 0 & -(v_x - u_y) \\ (v_x - u_y) & 0 \end{bmatrix} \\ &= \begin{bmatrix} e & 0 \\ 0 & -e \end{bmatrix} + \begin{bmatrix} 0 & \beta \\ \beta & 0 \end{bmatrix} + \begin{bmatrix} 0 & -\gamma \\ \gamma & 0 \end{bmatrix} \end{aligned} \quad (13)$$

where  $\gamma = (v_x - u_y)/2$  is half the local vorticity,  $e$  is the strain rate and  $\beta = (u_y + v_x)/2$ . By rotating coordinates to align with the principal strains (following Kida [6]) we find

$$P(\mathbf{u} - \mathbf{u}_B) = D\bar{\mathbf{x}} + \Lambda\bar{\mathbf{x}} \quad (14)$$

where

$$D = \begin{bmatrix} e_{\text{eff}} & 0 \\ 0 & -e_{\text{eff}} \end{bmatrix} \text{ and } \Lambda = \begin{bmatrix} 0 & -\gamma \\ \gamma & 0 \end{bmatrix}, \quad (15)$$

and the coordinates  $\bar{\mathbf{x}}$  are rotated by an angle  $\phi$  from the original coordinates  $\mathbf{x}$ . In fact

$$D = PAP^T \quad (16)$$

where  $D$  is the diagonal matrix of eigenvalues of the matrix  $A$  and

$$P = \begin{bmatrix} \cos \phi & -\sin \phi \\ \sin \phi & \cos \phi \end{bmatrix} \quad (17)$$

with the columns of  $P$  the (suitably normalized) orthonormal eigenvectors of  $A$ . Here the eigenvalues

$$e_{\text{eff}} = \pm \sqrt{e^2 + \beta^2} = \pm \sqrt{u_x^2 + \left(\frac{u_y + v_x}{2}\right)^2}. \quad (18)$$

It turns out that the transformation of velocities implied by equation (14) can be ignored as the only inputs to the Kida model are  $e_{\text{eff}}$  and  $\gamma$  (see below).

The equations for the evolution of the  $i$ th elliptical patch are

$$\begin{aligned} \dot{p}_i &= 2e_{\text{eff}}p_i \cos 2\theta_i \\ \dot{\theta}_i &= -e_{\text{eff}} \left( \frac{p_i^2 + 1}{p_i^2 - 1} \right) \sin 2\theta_i + \frac{\Gamma_i}{2\pi} \frac{p_i}{(p_i + 1)^2} \\ &+ \gamma_i, \end{aligned} \quad (19)$$

with  $p_i = a_i/b_i$  the ratio of the lengths of the major and minor semi-axes of the ellipse. These are Kida’s equations (3.2) and (3.3) with minor changes of notation. Note that  $\theta_i$  is the angle relative to the principal axes of strain, so the orientation  $\theta_{i,\text{ellipse}}$  of the principal axis of the elliptical patch relative to the original axes is given by

$$\theta_{i,\text{ellipse}} = \theta_i + \phi_i \quad (20)$$

where  $\phi_i$  is obtained for each vortex blob from the eigenvector corresponding to the eigenvalue  $e_{i,\text{eff}}$ , i.e.

$$\phi_i = \cos^{-1} \left( \frac{\beta_i}{\sqrt{(e_{i,\text{eff}} - e_i)^2 + \beta_i^2}} \right) \quad (21)$$

and clearly all angles are functions of time. Finally we note that the initial value of  $\theta_i$  can be chosen to be zero, corresponding to an alignment with the local principal axes of strain, as the blobs are all circular.

### A Numerical Example

As a test case we consider the interaction of two circular patches of uniform unit vorticity (Rankine vortices) of radius  $R = 1$ , with their centres separated by a relatively short distance  $3R$ , so that merger is expected. Each vortex is represented initially by 7 rings of vortex blobs and one central blob, all with equal strength and with ‘radius’  $\delta = 1/15$ , so covering the vortex. As each blob represents an equal area of the patch, there are  $8n$  blobs in ring  $n$ , giving 225 blobs initially for each vortex, following Hume [5]. A fourth-order variable time-step Runge-Kutta routine is used (`ode45.m` in MATLAB), and ‘re-blobbing’ carried out every 0.5 time units. The area of blobs in the figures is shown as proportional to the associated circulation, thus giving a visual representation of the relative dynamic significance of each blob.

In figure 1 the results at times  $t = 10, 20$  and  $30$  are given, with  $p_{\text{crit}} = 5$ . Frames (a), (b) and (c) show the blobs, with area proportional to their associated circulation. In frames (d), (e) and (f), the corresponding contour plots of vorticity are given, with the colour bar giving vorticity magnitude. (To smooth the contours of vorticity, we have used a value of  $\delta = 0.2$  when *evaluating* the vorticity from the blob distribution using equation (11)). Also

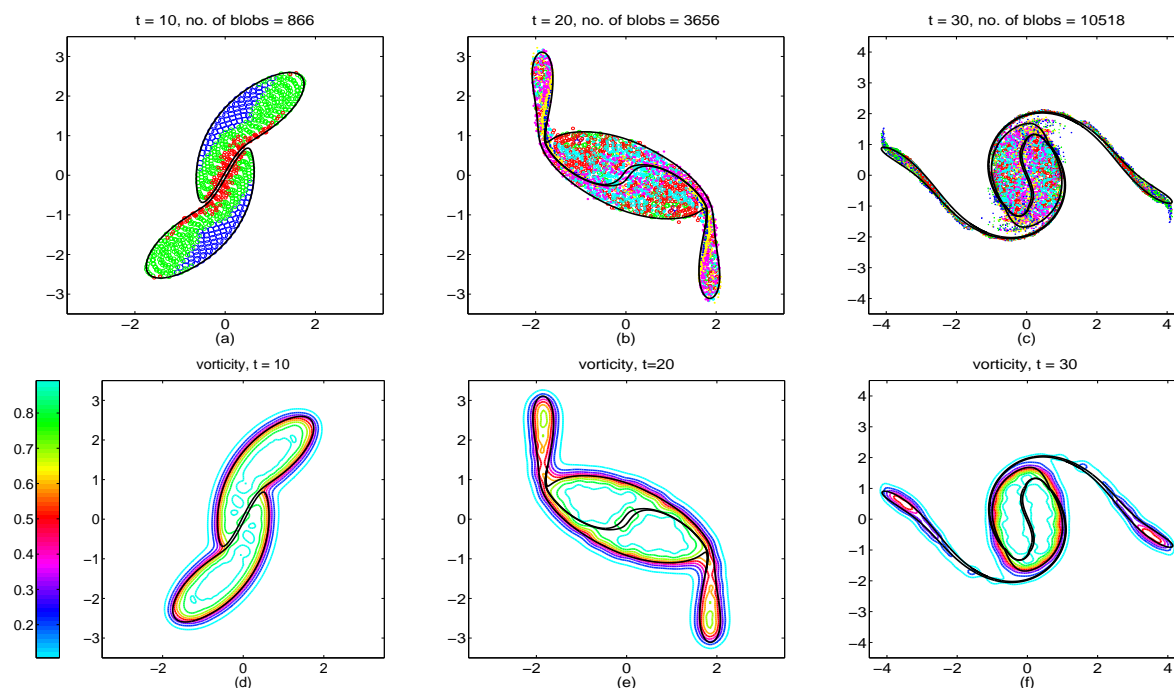


Figure 1: The behaviour at times  $t = 10, 20$  and  $30$  for the merger of two Rankine vortices, with unit radius and centres separated by three radii. Panels (a), (b) and (c) show the vortex blobs, colour coded and with areas proportional to their corresponding circulations, while panels (d), (e) and (f) show the corresponding contour plots of vorticity. In all cases the corresponding contour dynamics calculation (Dritschel [3]) is shown as a solid black curve.

shown are the contours corresponding to the vorticity jump from zero to unity in a planar high resolution contour dynamics calculation, with minimal contour surgery (Dritschel [3]). Very good agreement is achieved, with the filaments of vorticity well resolved, but at this stage the vortex blob code is not very efficient.

## Conclusions

This paper has provided a novel technique for adjusting the resolution of vortex blob methods by introducing new blobs as required, according to the time evolution of an equivalent elliptical patch for each circular blob, thus resolving fine-scale features of the vorticity. Because only circular blobs are used, it is expected that this technique can be quantified accurately, and that simple models for the transfer of enstrophy to high wavenumbers, and its associated final dissipation at the smallest scales resolved, may be possible.

## Acknowledgements

The idea for this work arose out of discussions with David Dritschel after we had listened to the talk by Lou Rossi about deforming elliptical Gaussian blobs at ICIAM 2003 in Sydney. The contour dynamics calculations were made using a code kindly provided by David Dritschel.

## References

- [1] Aref, H., Integrable, Chaotic and Turbulent Vortex Motion in 2-D Flows, *Ann. Rev. Fluid. Mech.*, **15**, 1983, 345–389.
- [2] Chorin, A. J. and Bernard, P. S., Discretisation of a Vortex Sheet with an Example of Roll Up, *J. Comput. Phys.*, **13**, 1973, 423–429.
- [3] Dritschel, D. G., Contour Dynamics and Contour Surgery: Numerical Algorithms for Extended, High-resolution Modelling of Vortex Dynamics in Two-dimensional, Incompressible Flow, *Comp. Phys. Rep.*, **10**, 1989, 77–146.
- [4] Dritschel, D. G. and Ambaum, M. H. P., A Contour-Advection Semi-Lagrangian Algorithm for the Simulation of Fine-Scale Conservative Fields, *Quart. J. Roy. Meteorol. Soc.*, **123**, 1997, 1097–1130.
- [5] Hume, G., Regularisation of Point-Vortex Methods by the Inclusion of Viscous Effects, *Proceedings of the 11th Australasian Fluid Mechanics Conference*, Hobart, Australia, 1992, 479–482.
- [6] Kida, S., Motion of an Elliptic Vortex in a Uniform Shear Flow, *J. Phys. Soc. Japan*, **10**, 1981, 3517–3520.
- [7] Krasny, R., Desingularisation of Periodic Vortex Sheet Roll Up, *J. Comput. Phys.*, **65**, 1986, 292–313.
- [8] Macaskill, C., Padden, W. E. P. and Dritschel, D. G., The CASL Algorithm for Quasi-Geostrophic Flow in a Cylinder, *J. Comput. Phys.*, **188**, 2003, 232–251.
- [9] Rosenhead, L., The Formation of Vortices from a Surface of Discontinuity, *Proc. R. Soc. London A*, **134**, 1931, 170–192.
- [10] Rossi, L. F., Resurrecting core spreading methods: A new scheme that is both deterministic and convergent, *SIAM J. Sci. Comp*, **17**, 1996, 370–397.
- [11] Rossi, L. F., High Order Vortex Methods with Deforming Elliptical Gaussian Blobs 1: Derivation and Validation, Tech. Rep. 2001–11, University of Delaware, 2002.
- [12] Rossi, L. F., A Comparative Study of Lagrangian Methods Using Axisymmetric and Deforming Blobs, Tech. Rep. 2003–09, University of Delaware, 2003.
- [13] Zabusky, N. J., Hughes, M. H. and Roberts, K. V., Contour Dynamics for the Euler Equations in Two Dimensions, *J. Comput. Phys.*, **30**, 1979, 96–106.

# Design and calibration of a wind tunnel with a two dimensional contraction

J.E. Sargison<sup>1</sup>, G.J. Walker<sup>1</sup> and R. Rossi<sup>2</sup>

<sup>1</sup>School of Engineering  
University of Tasmania, TAS, 7001 AUSTRALIA

<sup>2</sup>Ecole Polytechnique de l'Universite de Nantes, FRANCE

## Abstract

A low speed, open circuit, laboratory wind tunnel has been redesigned for use in turbine blade cooling experiments. The two dimensional contraction was designed using a sixth order polynomial. This paper outlines the process of design optimisation, using Computational Fluid Dynamics (CFD) to model the contraction. The parameters that were varied were the location of the point of inflection and the curvature at the contraction inlet. The optimisation was based on flow uniformity at the working section midplane, prevention of separation in the contraction and minimising the boundary layer thickness at entrance to the working section. Calibration of the wind tunnel after construction has demonstrated the value of the design process and validated the CFD predictions.

## Nomenclature

$P$	Pressure, reference pressure (Pa)
$a, b, c, d, e, f, g$	Polynomial coefficients
$h$	Contraction inlet half height-exit half height (m)
$i$	Axial distance to point of inflection (m)
$l$	Total length of contraction (m)
$\rho$	Density (kg/m <sup>3</sup> )
$\tau_w$	Wall shear stress
$u^*$	$u^* = (\tau_w / \rho)^{1/2}$
$w$	Parameter vector
$x, y, z$	Cartesian coordinates (streamwise, vertical, transverse)
$y^+$	$y^+ = y u^* / \nu$
$\alpha$	Curvature at inlet (/m)
$\epsilon$	$d/dx$

## Introduction

Based on evidence in current literature, aerodynamic research is poised between experimental and computation techniques. The two are closely linked and as progress is made in the development of more advanced computational fluid models, more comprehensive experimental data are required to validate the models. In the present situation a wind tunnel was remodelled for the purpose of turbine blade cooling research. The new facility is required for detailed studies of turbulent mixing processes associated with the injection of a simulated cooling jet through the wall of the working section. The data obtained will be used to improve CFD modelling of these complex flows.

Traditionally, the design of wind tunnel contractions has been based on a pair of cubic polynomials, and the parameter used to optimise the design for a fixed length and contraction ratio, has been the location of the joining point [2, 3]. The computation of flow field within the contraction has previously utilised

incompressible, inviscid flow equations and co-ordinate transformation techniques to solve the difference equations. Published, parameterised data in the form of design charts [2] are also available to avoid the need to repeat these computations, for axisymmetric contractions.

Currently, more flexibility in the design of wind tunnel contractions can be exhibited, with the use of CFD to enable rapid testing of designs to optimise contractions of arbitrary cross-section and wall profile. The use of CFD allows for the use of higher order polynomials, and non-zero curvature or slope at inlet to the contraction. However, the performance of the contraction still requires testing after construction, as the level of CFD used for this application is typically insufficient to detect the development of longitudinal vortices through the working section such as were measured by [4].

This paper describes the design of a 2D contraction with 6<sup>th</sup> degree polynomial wall profile for a wind tunnel with a square working section and its subsequent experimental validation.

## Description of the facility

The purpose of this work was to design a wind tunnel using the inlet, honeycomb and, potentially, screens of an existing facility. The working section dimensions were increased from 125 x 225 mm to 225 x 225 mm, requiring an increase in the exit area of the contraction. The contraction inlet was 1200 x 225 mm resulting in a new area ratio of 5.3. This was lower than the limit of recommended area ratios [1], and a full analysis of the design was considered necessary. The maximum velocity in the working section was 20 m/s. The original contraction length of 2 m was retained, but the profile definition was changed from a pair of cubic curves to a 6<sup>th</sup> order polynomial. The wall curvature at inlet and the location of the point of inflection in the wall profile were chosen as design parameters.

## Parameterisation of the profile

The coordinate system for the contraction profile is defined with origin on the tunnel centre line at the contraction inlet plane, and  $x$  coordinate increasing in the downstream direction. The  $y$  coordinate defines the contraction profile and  $z$  is in the spanwise direction. A sixth order polynomial was chosen to define the profile shape:

$$y = ax^6 + bx^5 + cx^4 + dx^3 + ex^2 + fx + g \quad (1)$$

The chosen profile has 7 parameters ( $a-g$ ). Five of these are specified by the inlet and outlet height, zero slope at the inlet and outlet and zero curvature at outlet. This leaves two parameters available for optimisation. These are specified by the inlet curvature and the axial position of the point of inflection relative to the contraction length. The 7 conditions defining the profile are thus:

$$\begin{aligned}
y(x=0) &= h & y''(x=i) &= 0 \\
y'(x=0) &= 0 & y(x=l) &= 0 & y''(x=l) &= 0 \\
y''(x=0) &= \alpha & y'(x=l) &= 0
\end{aligned} \quad (2)$$

where:

$h$  = inlet half height – exit half height

$\alpha$  = inlet curvature

$i$  = axial location of inflection point

$l$  = length of contraction

The conditions specified by (2) directly provide the following constants for the polynomial (1):

$$g = h; f = 0; e = \alpha/2$$

The other constants are defined by the equation:

$$Aw = B \quad (3)$$

where, for  $\alpha = 0$  for the standard case (with no inlet curvature):

$$A = \begin{bmatrix} 30i^4 & 20i^3 & 12i^2 & 6i \\ l^6 & l^5 & l^4 & l^3 \\ 6l^5 & 5l^4 & 4l^3 & 3l^2 \\ 30l^4 & 20l^3 & 12l^2 & 6l \end{bmatrix}, B = \begin{bmatrix} 0 \\ -h \\ 0 \\ 0 \end{bmatrix}, w = \begin{bmatrix} a \\ b \\ c \\ d \end{bmatrix} \quad (4)$$

The range of the variable,  $i$ , distance to the point of inflection, which gives a sensible, monotonically decreasing curve is 0.4-0.6  $l$ . Figure 1 shows that with a lower or higher value of  $i/l$ , the profile under or overshoots respectively. This was deemed to be impractical for a contraction profile. In order to optimise the shape, the optimal position of the point of inflection was determined first, and the degree of curvature at inlet was varied for this optimal design.

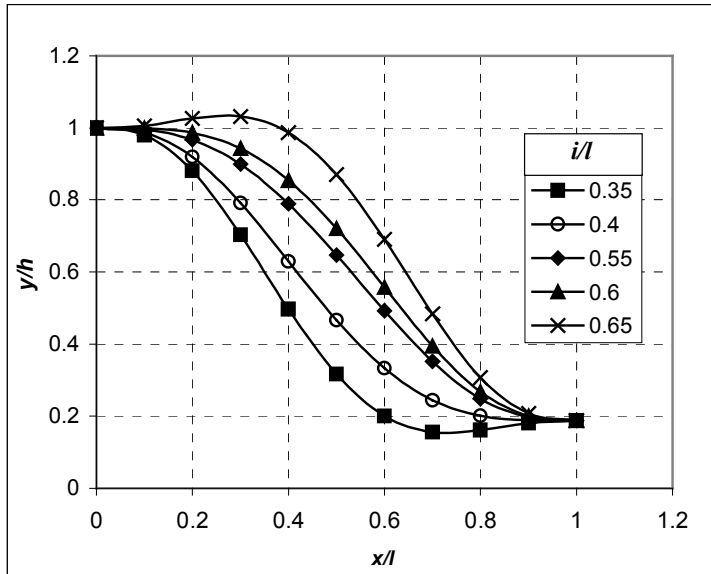


Figure 1: Contraction profiles, variation with inflection point location.

### Computational models

The commercial CFD software package CFX [5] was used to mesh, solve and postprocess the contraction model. The contraction shape was specified by the polynomial curve, with the parameter values outlined in Table 1 below. One quarter of the contraction was modelled, using the horizontal and vertical symmetry planes to reduce the size and computational load of the model. A working section of length 0.5 $l$  was modelled at the end of the contraction to provide a model of the flow development beyond the end of the contraction.

Model	$i/l$	$\alpha$
1	0.4	0
2	0.55	0
3	0.60	0
4	0.60	+0.5
5	0.60	-0.5
6	0.60	+0.2
7	0.60	-0.2

Table 1: Parameters used in model study.

The Reynolds Shear Stress Transport (SST) model of turbulence was used with a specified turbulence level of 1%. A constant total pressure of 280 Pa above atmospheric pressure (or reference pressure) was used to define the inlet boundary condition, with a constant static pressure outlet boundary condition of atmospheric pressure. This generated a mainstream flow velocity of 20 m/s, which is typical of the maximum required of the facility. In the physical wind tunnel, a bellmouth inlet section is followed by a 50 mm length of honeycomb to straighten the flow. These flow manipulators were not modelled in the CFD analysis.

The model was meshed using an unstructured, tetrahedral mesh, with ten layers of mesh inflation (rectangular elements) on the walls. The minimum  $y^+$  value for the models presented in this paper was 10. The model geometry and mesh are shown in Figure 2. The mesh is shown on the inlet plane and on a plane downstream representing the middle of the working section.

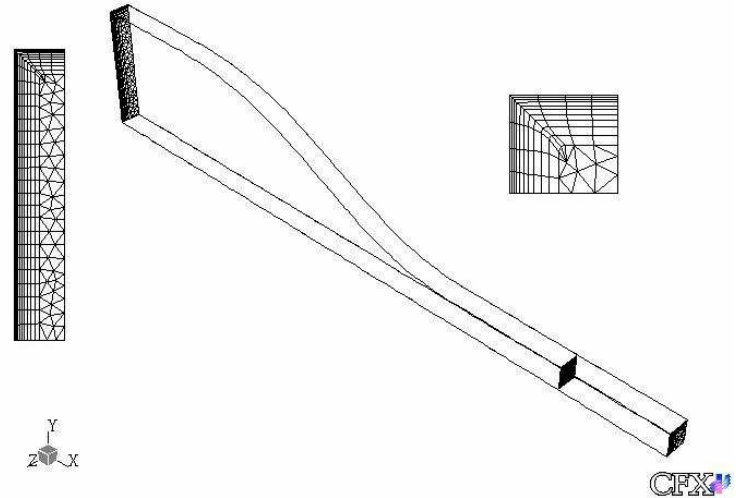


Figure 2: Model of contraction and working section, with inlet and outlet mesh (not to scale).

### Optimisation of model design

The contraction length and width were held fixed for this design, due to the existing facility geometry. The original inlet height was retained, for the practical purpose of using the existing bellmouth inlet and honeycomb. The exit height was increased compared with the existing facility in order to provide a larger working section height. This resulted in a contraction ratio of 5.3, slightly below the recommended range for an aerodynamic facility of 6-10 [1], but considered acceptable following analysis of the CFD models.

The parameters varied in the model were the location of the point of inflection, and the curvature at contraction inlet. The criteria for selection of the optimal design were maximum uniformity of the flow at mid working section (0.5m from the end of the contraction), with prevention of separation at the contraction wall.



## Computational results

The computational models were reviewed to test for uniformity of flow in the working section, and the presence of separation. It was found that none of the models tested experienced separation. In Figure 3, a typical wall shear plot for model 3 ( $i/l = 0.6$ ) demonstrates the lack of separating flow (indicated by positive values of wall shear over the entire wall).

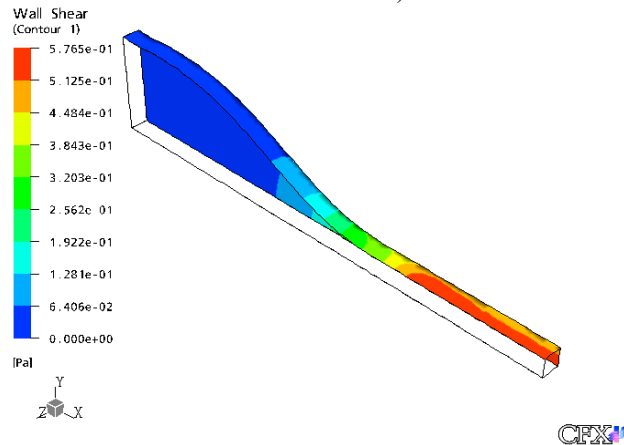


Figure 3. Wall shear (Pa), model 3.

The uniformity of the flow was compared at the mid working section shown as a shaded plane in Figure 2. The velocity profiles at this plane are shown in Figure 4. All models demonstrated reasonably uniform flow across the wind tunnel mid plane, but models 3, 5, 6 and 7 appeared to have a more uniform velocity profile. Comparison of the flow development through the working section, demonstrated model 3 to have the most uniform flow of these four models, and hence it was selected for manufacture. This profile has  $i/l = 0.6$ , and  $\alpha = 0$ .

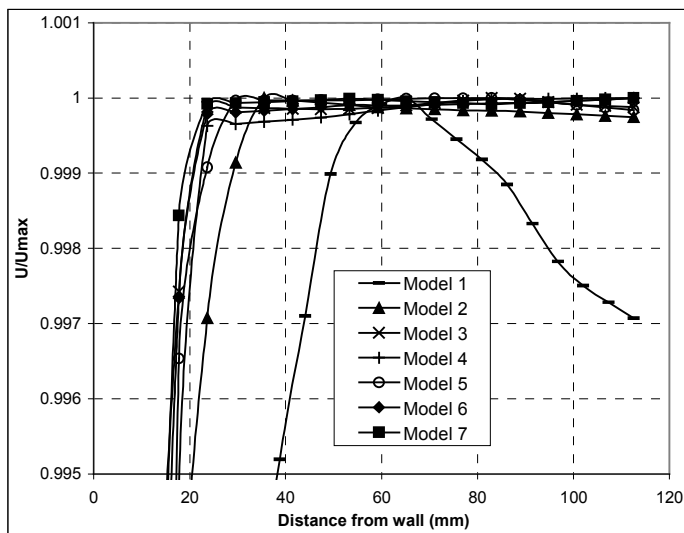


Figure 4: Velocity profile at mid working section on horizontal plane.

## Physical calibration of the facility

Following construction of the optimal design (model 3, Figure 5), experimental measurements were conducted to verify the CFD model and calibrate the facility. Calibration measurements included time mean flow, wall shear stress, flow direction and streamwise turbulence intensity in the working section. The boundary layer was tripped using a 3 mm diameter wire, 200 mm upstream of the start of the working section, in order to obtain a stable, turbulent boundary layer on all walls of the working section. Before the trip wire was installed, the boundary layer was intermittent on the side walls and laminar on the floor and top wall of the working section, resulting in a non-uniform wall shear stress distribution on the working section walls.

The mid plane of the working section was traversed with a 1.6 mm diameter pitot probe to determine the uniformity of the flow in the working section. A wall tapping in the plane of the pitot tube was used to measure static pressure, and reference static

pressures P1 and P2 were measured at the start and end of the contraction, respectively. The nominal working section flow speed was 20 m/s and Reynolds number based on working section width and flow 30 000, the maximum for the facility and equal to the flow speed obtained in the CFD analysis. The pressures were measured to  $\pm 0.005$  Pa using a Furness FC012 micromanometer, with a Furness FCS421 pressure scanner to measure the total and static pressures in differential mode (relative to P1 or Pstat).



Figure 5: Wind tunnel as constructed.

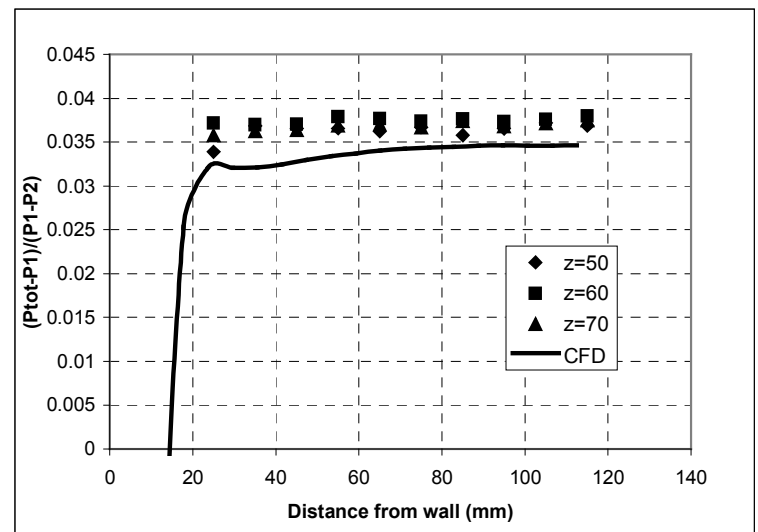


Figure 6: Pressure coefficient at mid working section measured on vertical lines.

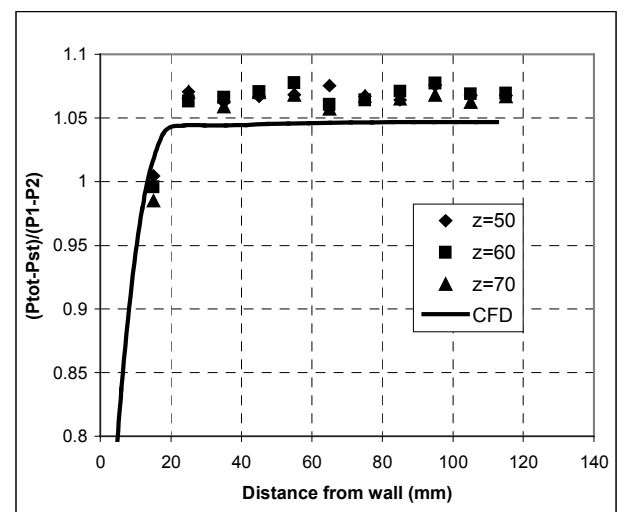


Figure 7: Relative velocity at mid working section measured on vertical lines.

Figures 6 and 7 compare the profiles of pressure coefficients and relative velocity profile, respectively at the mid working section, with the CFD model. The total pressure was measured using vertical ( $y$ ) traverses from the floor of the wind tunnel, at a number of locations in the transverse ( $z$ ) direction in the working section mid plane. The experimental results indicate that the total pressure distribution is uniform, within the experimental



uncertainty of the measurements. The CFD underpredicts the pressure coefficients in both cases (0.004 for pressure coefficient related to P1 and 0.001 for relative velocity). The uncertainty in pressure coefficient measurements was  $\pm 0.007$  (95 %) which is greater than the variation in the experimental measurements shown in Figures 6 and 7. This may be due to the CFD overpredicting the static pressure drop over the contraction (P1-P2). The pressure P1 is higher in the CFD because the honeycomb upstream of the contraction were not modelled.

The streamwise turbulence intensity was measured using a single sensor hotwire probe (Dantec 55P11) with wire axis normal to the flow and a DISA 55M constant temperature anemometer. The hot wire probe was calibrated in situ against a pitot tube and wall static tapping. The RMS voltage measured was corrected for the electrical noise in the instrument. Traverses were made in the horizontal and vertical directions in the centre of the working section, to measure the free stream turbulence. It was expected that the turbulence would be slightly above normal levels for research wind tunnels because of the reduced contraction ratio, and the lack of screens in the inlet section. This was a design parameter of the system for the intended research application, as the inlet turbulence experienced in turbine blade cooling problems is relatively high.

The turbulence profile was found to be very uniform, as shown in Figure 8, at an average level of 0.6%. The profile was symmetric in both the horizontal and vertical planes, with the larger boundary layer thickness on the sidewalls demonstrated by the horizontal traverse results.

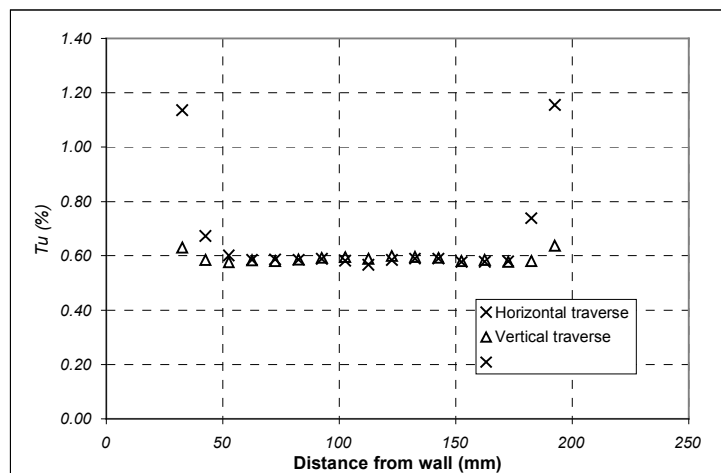


Figure 8: Turbulence profile in centre of working section.

Flow direction was measured using a three-hole probe, based on a wedge design with a rounded nose, shown in Figure 9. The probe was calibrated in a closed circuit wind tunnel. The flow direction was uniform to within  $1.1^\circ \pm 0.7^\circ$  (95%). CFD predicted a flow direction in the mid plane of maximum  $0.15^\circ$  from horizontal.

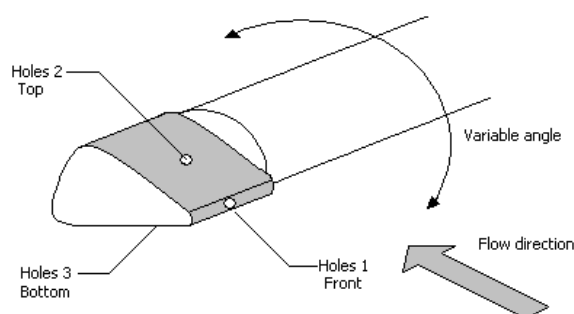


Figure 9: Three hole probe schematic.

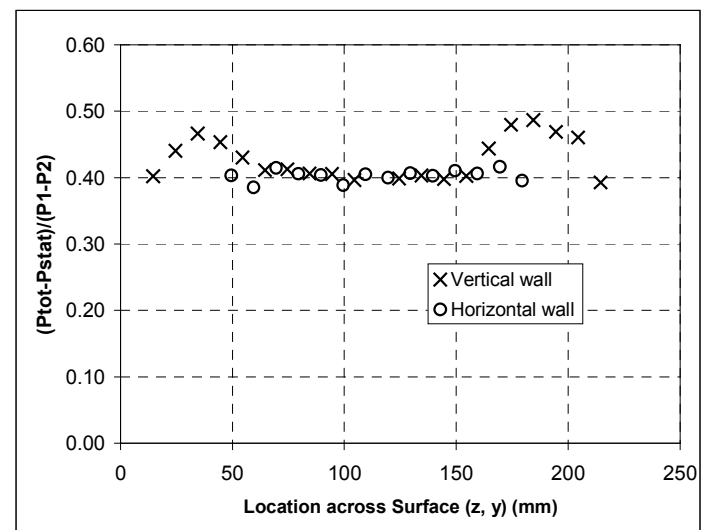


Figure 10: Development of wall shear stress with downstream distance.

Figure 10 shows the wall pressure coefficient measured using a Preston tube on the side wall and floor of the wind tunnel. The uniformity of this pressure coefficient across both walls of the wind tunnel indicates the absence of large vortices in the mainstream flow and is indicative of the uniformity of the wall shear stress in the same region. Greater secondary flow effects are evident in the corner regions on the vertical walls.

## Conclusions

CFD has been used to optimise the design of a wind tunnel contraction. The use of CFD has increased the flexibility of shapes considered, and allowed the use of a sixth order polynomial to define the profile. The parameters of the profile that were varied were the location of the point of inflection and the curvature at the contraction inlet. It was found that the best result, producing the most uniform velocity profile at inlet to the working section, and preventing separation of the flow within the contraction, was obtained when the point of inflection was located as far downstream as possible.

Physical calibration of the facility has validated the CFD methods used and demonstrated that the technique can be used for future wind tunnel designs.

## Acknowledgements

This work is supported by Rolls Royce plc, an IRGS grant from the University of Tasmania, and by the provision of an academic licence for CFX by Australian Trade Development P/L and CFX-ANSYS.

## References

- [1] Mehta, R.D. and Bradshaw, P., 1979, *Design rules for small low speed wind tunnels*, Aeronautical Journal, November 1979, 443-449
- [2] Morel, T., 1975, *Comprehensive Design of Axisymmetric Wind Tunnel Contractions*, ASME Journal of Fluids Engineering, June 1975, 225-233
- [3] Ramaseshan, S. and Ramaswamy, M.A., 2002, *A Rational Method to Choose Optimum Design for Two-Dimensional Contractions*, ASME Journal of Fluids Engineering **124** 544-546
- [4] Kim, W.J., and Patel, V.C., *Origin and Decay of Longitudinal Vortices in Developing Flow in a Curved Rectangular Duct*, Journal of Fluids Engineering **116**, 1994, 45-52
- [5] CFX user manual, ANSYS

## Radiant heating of a Bio-oil droplet: A quest for a suitable model and scaling of pre-explosion conditions

J.Y.Hristov<sup>1</sup>, V.Stamatov<sup>2</sup>, D.R. Honnery<sup>2</sup> and J.Soria<sup>2</sup>

<sup>1</sup>Department of Chemical Engineering  
University of Chemical Technology and Metallurgy, Sofia 1756, BULGARIA  
<sup>2</sup>Laboratory for Turbulence Research in Aerospace & Combustion  
Department of Mechanical Engineering  
Monash University, VIC 3800, AUSTRALIA

### Abstract

A suitable model for radiant heated single drop of bio-oil is discussed. The main efforts of the study are stressed on a discussion of models of droplet heating and scaling of the pre-explosion conditions.

### Introduction

Bio-oil is a liquid fuel produced by the pyrolysis of biomass. In Australia, research on bio-oil production has been undertaken on the slow pyrolysis of a number of indigenous tree species (i.e., *Eucalyptus globulus* and *Eucalyptus camaldulensis*) that can be grown sustainably in plantations. The bio-oil produced is a dark, viscous liquid with smoky odour, it contains negligible sulphur, and it is relatively high in oxygenated compounds. Due to its plantation origins, it is a renewable resource and can be greenhouse gas neutral when used as a fuel. These attributes make bio-oil an alternative liquid fuel source for both power generation and transport. The composition and properties of bio-oil depend on the biomass source and pyrolysis rate used in its production. The elemental composition of bio-oil resembles that of biomass [1-3]. Bio-oil fuel-related characteristics are provided in [4-6].

The oxygen-rich nature of the principle components of wood (lignin, cellulose and hemicellulose [7]) affects the combustion behaviour of these pyrolysis derived liquids. The high oxygen content results in low-energy heating value that is less than 50% of that for conventional fuels. In general, these liquids are combustible, but not flammable (from safety point of view) due to the high content of non-volatile components that require high energy for ignition. Combustion tests on single bio-oil droplets derived from oak and pine [8-9] indicated: (a) A multistep process: ignition, quiescent burning emitting blue radiation, droplet micro-explosion, disruptive sooty burning of droplet fragments emitting bright yellow radiation, formation and burnout of cenosphere particles; (b) A very wide range of boiling temperatures, which is a result of the bio-oil chemical composition. The oils start boiling below 100°C, the distillation stops at 250-280°C, leaving 35-50% of the starting material as residue. Therefore, the bio-oils do not exhibit complete vaporisation before combustion, unlike the mineral hydrocarbons; (c) Droplets of less severely cracked pyrolysis oils exhibit shorter pre-explosion time and less effective micro-explosion. Oils that underwent severe cracking during the pyrolysis exhibit large pre-explosion times and more violent micro-explosions that results in more rapid burnout unlike the lighter oils. This behaviour depends on the oxygen content and pyrolysis process. Severe cracking reduce both the organic liquid yields and the oxygen content; (d) A strong relation between the moisture content and bio-oils combustion behaviour. The moisture content varies over a wide range (15-30%). It is a product of the original moisture in the feedstock and also the

water produced from dehydration reactions occurring during pyrolysis. At this concentration, water is usually miscible with the oligomeric lignin-derived components, because of the solubilising effect of other polar hydrophilic compounds (low molecular weight acids, alcohols, hydroxyaldehydes and ketones) mostly originating from the decomposition of carbohydrates. Despite the high moisture content, the adiabatic flame temperature of the bio-oil is relatively high, 1700-2000 K compared to 2200-2300 K for standard fuels [10].

The present communication considers scaling of the pre-explosion conditions. The paper is developed as follows: (a) Analysis of existing models of explosive boiling of liquid droplet and their adequacy to behaviour of bio-oils; (b) Creating of physical and mathematical model for scaling and definition of dimensionless groups controlling the process; (c) Analysis of the pre-explosion conditions and an attempt to derive scaling estimates.

### Models

#### Explosive boiling of liquid droplets

There are existing models of explosive boiling of droplets [11-13] that are verified by experiments [14-15]. The applicability of these models is discussed below.

Shusser and Weihs [13] proposed a model (see Figure 1a) based on the assumption of a constant evaporation rate equal to its maximal possible value. The kinetic theory [16] limits the maximal evaporation rate to the mass flux through the core (bubble)

$$J_v = p_s \sqrt{\frac{M}{2\pi RT_s}} \quad (1)$$

where  $J_v$  is the evaporation rate,  $T_s$  is the boiling temperature for the droplet liquid,  $p_s$  is the saturation pressure at this temperature,  $M$  is the molar mass of the vapour and  $R$  is the universal gas constant. Shusser and Weihs [13] analysed and simplified the model of Prosperetti [17] to yield equations for the gas density,  $\rho_G = J_v / \dot{R}_1$ , and pressure,  $p_i = \rho_G (R/M) T_s$  inside the core. Here  $\dot{R}_1$  is the core (bubble) growth rate

$$\dot{R}_1 = b_0 \left( \frac{2 J_v R}{3 \rho_1 M} T_s \right)^{1/3} \quad (2)$$

$\rho_1$  is the density of the host fluid,  $b_0$  is an empirical constant that is 0.96 for butane, 0.97 for water, 0.94 for pentane. Shusser and Weihs [13] suggested that  $b_0 = 1$  in equation 2, can be considered as a good approximation for the bubble growth rate.

Fu et al. [18] proposed a model of micro-explosions suitable for both oil-in-water (O/W) and water-in-oil (W/O) emulsified droplets. The authors suggested an empirical model (see Figure 1b) and a criterion for explosion expressed as

$$\frac{4}{3}\pi(R_0^3 - R_1^3)(1 - \phi) = \frac{4}{3}\pi[(R_1 + d)^3 - R_1^3] \quad (3)$$

where  $R_0$  is the initial radius of the emulsion droplet,  $R_1$  is radius of the emulsion core and  $d$  is the diameter of the dispersed micro droplet,  $\phi$  is the water volumetric percentage.

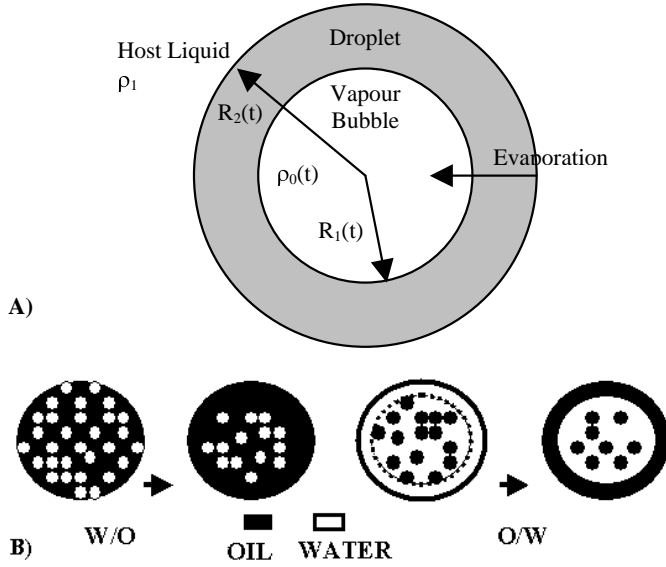


Fig. 1 Existing models of explosive boiling of bi-component droplets: a) Shusser and Weihs [13]; b) Fu et al. [18].

Fu et al. [18] suggested that a micro-explosion occurs when an oil membrane covers the water inside the micro droplets. Equation (3) implies that the volume of the membrane equals the volume of pure oil in the droplet.

## Equivalent Models applicable to Bio-oils

### Assumptions

The models commented above have been tested with pure liquids and hydrocarbons. These conditions differ significantly from those existing in bio-oil droplets. First of all, the bio-oil droplets are neither bi-component with gaseous cores, nor emulsion ones. Combustion experiments [8] show a shell formation that is relatively dry with respect to the remaining part of the droplet liquid. Looking at the pre-explosion process it can be assumed that the droplet diameter remains practically unchanged ( $\dot{r}(t) = \text{const}$ ). This is a very strong simplification since Wornat et al. [8] reported droplet swelling by up factor of 3 in diameter prior to rupture. However for the preliminary scale analysis this fact and the hydrodynamic conditions might be ignored. The further analysis look for an equivalent model that simultaneously satisfies two major conditions: (i) to be geometrically identical to the bio oil droplets and (ii) to permit the use the ideas of the two models commented above. The basic geometric assumption of the equivalent model is that the entire water forms a core with expanding radius and growing pressure, while the rest of the bio-oil material forms a membrane (shell).

Accepting of this equivalent bi-spherical model we attain several advantages: (a) In a situation of scarce physical data and large variations of properties of bio oils the first attempt to solve the

problem is to use macroscopic data relevant to the water content; (b) Both, the water content of the bio-oil and the drop size can be experimentally found; (c) In general, droplet burning (or evaporation) results in moving boundary problems. However, the assumption of a constant droplet size allows applying the classical heat transfer equation with fixed boundaries [19,22], and scaling methods [20] and results from the combustion of W/O emulsions [21].

### Heating of a single droplet - basic equations and approximations

Assuming a spherically symmetrical temperature distribution inside the droplet of a radius  $R_d$  and an external radiation flux rate,  $\dot{q}''$  [22], the transient heat conduction equation for the internal droplet volume is

$$c_o \rho_o \frac{\partial T}{\partial t} = k_o \left( \frac{\partial^2 T}{\partial r^2} + \frac{2}{r} \frac{\partial T}{\partial r} \right) + \dot{q}'''(r) \quad (4)$$

where  $\dot{q}'''(r) = \partial \dot{q}'' / \partial r$ ,  $r$  is the radial distance,  $c_o$ ,  $\rho_o$  and  $k_o$  are the liquid specific heat capacity, density and thermal conductivity. It can be assumed that the Bouguer law is valid [20], i.e.  $\dot{q}''(r) = \dot{q}'' \exp(-\mu r)$ , where  $\mu$  ( $\text{m}^{-1}$ ) is the effective average radiation absorption coefficient. If the droplet is heated by radiation only by the feedback from the surface flame and the convection is ignored the energy balance at the surface ( $r = R_d$ ) is the Stefan boundary condition (SBC) [20, 23]

$$\dot{q}'' + \rho_o L \dot{r}(t) = k_o \frac{\partial T}{\partial r} \Big|_{r=R_d} \quad (5)$$

where  $L$  is the specific heat of evaporation. The second boundary condition is  $(\partial T / \partial r)_{r=0} = 0$ . The initial condition is  $T = T_\infty$  at  $t = 0$ .

### Scaling

The classical approach is to accept a dimensionless temperature  $\Theta = (T - T_\infty) / (T_s - T_\infty)$  and the droplet radius as a length scale ( $\tilde{r} = r / R_d$ ). Therefore, the dimensionless forms of equations (4) and (5) are

$$\frac{\partial \Theta}{\partial \tilde{t}} = Fo \left( \frac{\partial^2 \Theta}{\partial \tilde{r}^2} + \frac{2}{\tilde{r}} \frac{\partial \Theta}{\partial \tilde{r}} \right) + \frac{\mu \dot{q}''(\tilde{r}) \tau_0}{\rho_o c_o (T_s - T_\infty)} \exp[-(\mu R_d) \tilde{r}] \quad (6)$$

$$\underbrace{\frac{\dot{q}'' R_d}{k_o (T_s - T_\infty)}}_{B_{SA}} = \underbrace{\frac{L}{c_o (T_s - T_\infty)}}_{Ste} \underbrace{\frac{R_d \dot{r}(t)}{a_o}}_{Pe} - \frac{\partial \Theta}{\partial \tilde{r}} \Big|_{\tilde{r}=1} \quad (7)$$

where,  $B_{SA}$  is a dimensionless number analogues to the Biot number in case of forced convection (the subscript means *Surface Absorption*) [20],  $Ste$  and  $Pe$  are the Stefan and Peclet numbers. Equation (6) provides three dimensionless groups: Fourier number ( $Fo = t / \tau_0$ ), where  $\tau_0 = R_d^2 / \alpha_o$  is the thermal diffusion time; Bouguer number ( $Bu = \mu R_d$ ) and

$$N_{VA} = \frac{\mu \dot{q}'' \tau_0}{\rho_o c_o (T_s - T_\infty)} = \underbrace{(\mu R_d)}_{Bu} \underbrace{\left[ \frac{\dot{q}'' R_d}{k_o (T_s - T_\infty)} \right]}_{N_0} \quad (8)$$

Here  $N_{VA}$  (the subscript means *Volumetric Absorption*) is a radiation-conduction number [22] analogous to the Stark number [23], that can be presented as a product  $N_{VA} = Bu N_0$  since  $\dot{q}'''(r) = \partial \dot{q}'' / \partial r$ .

### Dimensionless groups and functional relationships

The classical dimensionless solution provides a relationship

$$\Theta = \Phi(Bu; N_0, Ste, Pe) \quad (9)$$

Considering the evaporation rate  $J_v$  (from equation 1) and fixing  $T = T_s = T_L$ , the kinetic superheat limit can be defined.

At  $T = T_L$ ,  $\Theta$  becomes a constant  $\Theta = \Theta_L$ . If the time of the micro-explosion,  $t_e$  is known, then a pre-explosion Fourier number can be defined as  $F_o^e = t_e / \tau_0$  that yields

$$F_o^e = \Psi(\Theta_L Bu, N_0, Ste, Pe) \quad (10)$$

The function  $\Psi = \Phi^{-1}$  depends on the type of the analytical solution.

### Minimisation of the number of dimensionless groups

Minimisation of the number of dimensionless groups performed in [20] yields a new dimensionless number

$$H_p = \frac{B_{SA} Ste}{Pe} = \frac{\dot{q}''}{\rho_o \dot{r} L}. \quad \text{This allows } F_o^e \text{ to be expressed as}$$

$$F_o^e \approx H_p^n Bu^m N_0^s \quad [19], \text{ since the relationship between } F_o^e \text{ and}$$

$Bu$  and  $N_0$  is defined in equation (7) while  $H_p$  from SBC defines the pre-factor of the power-law relationship. The exponents ( $n, m, s$ ) can be defined through scaling of experimental data.

### Alternative scales

The analysis provided in [20] yields that for radiation-conduction problems with SBC at the interface (liquid-flame) a more adequate length scale is  $Z_0 = \frac{k_o(T_s - T_\infty)}{\dot{q}''}$ , which automatically

leads to SBC in a form  $1 = \frac{1}{H_p} - \frac{\partial \Theta}{\partial \tilde{r}}$ . The time scale is

$$\tau_a = (\mu \alpha_o^2)^{-1} \text{ that defines } \tilde{F}_o^e = \mu \alpha_o^2 t_e = Bu^2 F_o^e.$$

### Analysis

#### Approximate solutions

As reported in [24] the approximate solution of equations (4) and (5) is

$$T - T_\infty = \frac{\alpha \dot{q}'' R_d}{k_o} \left[ 1 - \exp\left(-3 \frac{k_o t}{\rho_o c_o R_d^2}\right) \right] \quad (11)$$

where  $\alpha$  is a dimensionless coefficient (in terms of the present analysis  $\alpha = Bu$ ). The dimensionless form of equation (11) is

$$\Theta = \frac{T - T_\infty}{T_s - T_\infty} = Bu N_0 [1 - \exp(-3 F_o^e)] \quad (12)$$

When  $T = T_L$  the RHS of (12) becomes the parameter  $\Theta_L$  and the time  $t_L$  can be scaled as

$$F_o \Big|_{T=T_L} \equiv \underbrace{H_p^m}_{BC} n \underbrace{\frac{1}{1 - \Theta_L / Bu N_0}}_{\text{heat diffusion in the droplet}} \quad (13)$$

### Asymptotic (extreme) situations

Two asymptotic situations relevant to the two term of RHS of equation (4) may be considered [22]: (a) Heat conduction dominating mechanism (HCD) with a surface absorption

( $\dot{q}'''(r) = 0$ ) only; and (b) Heat absorption dominating mechanism (HAD) with a dominating source term.

Following the analysis of [20], the HCD requires a condition  $N_{VA} \ll 1$  that leads to  $Bu N_0 \ll 1$  or  $N_0 \ll 1/Bu$ . The HAD

mechanism with dominating source term imposes the condition  $\frac{Bu}{N_0} \frac{1}{\exp(-\mu S_L \tilde{r})} \ll 1$  where  $S_L$  is the process length scale.

Here  $\exp(-\mu S_L \tilde{r}) \leq 1$ , where 1 corresponds to the droplet surface. Taking into account that  $1/\exp(-\mu S_L \tilde{r}) > 1$ , a more weak, but sufficient condition is  $Bu/N_0 \ll 1$  or  $N_0 \gg Bu$ .

These inequalities permit to estimate the magnitude of  $N_0$  if the values of  $Bu$  are known. The HAD mechanism yields

$$\Theta = \left( \frac{N_0}{Bu} \right)^2 \left[ \tilde{F}_o^2 - \frac{Pe}{N_0} \tilde{F}_o \right]. \quad \text{The result can be simplified as}$$

$$\tilde{F}_o \approx \sqrt{\Theta} \frac{Bu}{N_0} \text{ since } Pe/N_0 \ll 1 \text{ (the hard shell implies low values of } Pe).$$

Furthermore, since  $\tilde{F}_o^e = Bu^2 F_o^e$ ,  $F_o^e$  becomes  $F_o^e \approx \sqrt{\Theta} \frac{1}{Bu} \frac{1}{N_0} \propto \frac{1}{Bu}$ . Therefore, this scale analysis

yields that

$$F_o^e \propto \frac{1}{Bu} H_p \quad (14)$$

The condition  $N_0 \gg Bu$  applied to (13) through the weak condition  $1/Bu N_0 \ll 1/Bu$ , which leads to

$$F_o^e \propto \frac{\Theta_L}{Bu} H_p \quad (15)$$

The further analysis will use the relationship given in equation (1). Generally equation (1) provides that  $T_L \approx (1/J_v)^2 (T_s)$  is replaced by  $T_L$  to avoid ambiguities, since at  $T = T_s$ ,  $\Theta$  becomes unity). Thus,  $\Theta \approx \alpha (1/J_v)^2$  (following the definition of  $\Theta$ ) that yields (via equation 15)

$$F_o^e \propto (1/J_v)^2 \frac{1}{Bu} H_p \quad (16)$$

In an explicit form equation (16) leads to  $t_e \propto (1/J_v)^2$ .

Physically equation (16) implies that high evaporation rates lead to shorter pre-explosion times and *vice versa*. The other components of equation (16),  $Bu$  and  $H_p$  affect the pre-explosion time through: (a) High values of  $Bu$  implies high droplet absorptivity, a dominating HAD mechanism, higher evaporation rates and as a result shorter pre-explosion times. Low values of  $Bu$ , implies a dominating HCD mechanism and larger pre-explosion times; (b) The  $H_p$  number controls the radiation-conduction heat transfer through the droplet surface. Generally, the HAD mechanism is physically relevant to high water contents of the droplets, where occurrence of volume heat sources and nucleation evaporation can be expected. If the water content is not high, the head conduction is the dominating mechanism, which does not lead to intensive vapour nucleation. This comment is consistent with the experiments analysed in [21] where the evaporation rate increases linearly with the increase of the water content (emulsion volume).

### Remarks on the scaling estimates

As commented in [21] the increase of the water content (emulsion volume) leads to higher evaporation rates and shorter

pre-explosion times. It is likely that the micro-explosions would be ruled primary by the explosive evaporation of water for low volatile fuels. Water is only superheated inside less volatile hydrocarbons-based emulsions. Bio-oils behave similarly because of the high amount of low volatile and non-volatile components [9]. The estimate given in equation (16) is consistent with these facts [21]. The analysis in [8], show that oak oil droplets with 16.1 wt% water content explode after 34.8 ms, while droplet of diesel fuel #2 (a negligible water content) has a pre-explosion time of 149 ms.

The scaling estimate derived here is based on the analysis of heat transfer equations, which allows to define the controlling parameters. If a dimensionless nucleation rate is defined as  $N_J = J/J_V$ , where  $J$  is a nucleation rate at temperature  $T < T_s$  for water, equation (16) can be expressed as

$$F_o^e \equiv \left( \frac{1}{N_J} \frac{1}{J_V} \right)^2 \frac{1}{Bu} H_p \quad (17)$$

The main idea of equation (17) is that via analysis of experiments the value of  $N_J$  can be determined. Such analysis would estimate the apparent values of  $J$  for bio oils, since  $J_V$  is known for water and pure liquids [23] only. The latter would allow evaluating the applicability of the homogeneous nucleation theory to bio oils.

### Special mathematical symbols:

$\propto$  - proportional to;

$O$  - order of magnitude;

$\approx$  - about equal;

$\equiv$  - identical (equivalent to);

$a \sim b$  -  $a$  scale to  $b$  as well as;

$\Rightarrow$  - it follows that (implies);

$a \rightarrow b$  -  $a$  approaches  $b$ ;

$||$  - absolute value.

### References

1. Peacocke, G.V.C., Russel, P.A., Jenkins, J.D., Bridgwater, A.V., Physical properties of Flash Pyrolysed Liquids, Biomass & Bioenergy, 1994, 7, pp. 169-178.
2. Sipila, K., Kuoppala, E., Fagernas, L., Oasmaa, A., Characterization of Biomass-based Flash Pyrolysis Oils, Biomass & Bioenergy, 1998, 14, (2), pp. 103-113.
3. Oasmaa, A., Czernik, S. Fuel Oil Quality of Biomass Pyrolysis Oil - The state of Art for the End Users, Energy & Fuel, 13, 1999, pp. 914-921.
4. Stamatov, V., Honnery, D., Fung, P., Soria J. A combustion characterisation of bio-oil from South-Australian blue gum eucalyptus tree (*Eucalyptus globulus*), Proceedings of the 2<sup>nd</sup> International Workshop on Pyrolysis, Notre Dame University, Western Australia, 2003, 8p.
5. Stamatov, V., Honnery, D., Fung, P., Soria J. Atomisation and combustion of blends of Australian bio-oil with ethanol, Proceedings of the 2<sup>nd</sup> World Conference on Biomass for Energy, Industry and Climate Protection, Rome, 2004, 4p.
6. Stamatov, V., Honnery, D., Fung, P., Soria J. (2004) Origin of NO<sub>x</sub> emission from bio-oil flames, Paper No 153, Science in Thermal and Chemical Biomass Conversion, Victoria, BC, Canada, 2004, 8p.
7. Haygreen, J.G., Bowyer, J.L., Forest Products and Wood Science, Iowa State University Press, Ames, IA, 1982.
8. Wornat, M.J., Porter, B.G., Yang, N.Y.C. Single droplet Combustion of Biomass Pyrolysis Oils, Energy & Fuel, 8, 1994, pp. 1131-1142.
9. Czernik, S., Bridgwater, A.V. Overview of Applications of Biomass Fast Pyrolysis Oil, Energy & Fuel, 18, 2004, pp. 590-598.
10. Czernik, S., Bridgwater, A. Applications of bio-oil from fast pyrolysis of biomass, Proceedings of the 2nd International Workshop on Pyrolysis, Notre Dame University, Western Australia, 2003, 14p.
11. Avedisian, C.T. Bubble Growth in Superheated Liquid Droplets, in Gas-Liquid Flows, Encyclopaedia of fluid mechanics, ed. Cheremisinoff, N.P., 1986, Butterworth-Heinemann, vol. 3, 1985, pp. 130-190.
12. Chitavnis, S.M. Explosive Vaporization of Small Droplets by High-energy Laser Beam, J. Appl. Phys., 62, 1987, pp. 4387-4393.
13. Shusser, M., Weihs, D. Explosive Boiling of a Liquid Droplet, Int. J. Multiphase Flow, 25, 1999, pp. 1561-1573.
14. Frost, D. Dynamics of Explosive Boiling of a Droplet, Phys. Fluids, 31, 1988, pp. 2544 - 2561.
15. Shepherd, V.P., Sturtevant, B. Rapid Evaporation at the Superheat Limit, J. Fluid. Mech., 1982, 121, pp. 379-402.
16. Van Carey, P. Liquid-vapor Phase-change Phenomena, Hemisphere, Washington, DC, 1992.
17. Prosperetti, A., Plesset, M.S. Vapor Bubble Growth in a Superheated Liquid, J. Fluid. Mech., 85, 1978, pp. 349-368.
18. Fu, W.B., Hou, L.Y., Wang, L., Ma, F.H. A Unified Model for the Micro-Explosion of Emulsified Droplets of Oil and Water, Fuel. Proces. Technol., 79, 2002, pp. 107-119.
19. Bridgman, P.W. Dimensional Analysis, Cambridge, MA, Harvard University Press, 1931.
20. Hristov, J., Planas-Cuchi, E., Arnaldos, J., Casal, J. Accidental Burning of a Fuel Layer on a Waterbed: A Scale Analysis of the Models Predicting the Pre-Boilover Time and Tests to Published Data, Int. J. Therm. Sci., 43, 2004. pp. 221-239.
21. Kadota, T., Yamsaki, H. Recent Advances in the Combustion of Water Fuel Emulsion, Prog. Energ. Comb Sci., 28, 2002, pp. 385-404.
22. Carslaw, H.S., Jaeger, J.C. Conduction of Heat in Solids, Oxford Univ. Press, 1947.
23. Schneider, P.J. Conduction (chapter 4), in Handbook of Heat Transfer Fundamentals, eds. Rohsenow, J., Hartnett, E. Ganic, McGraw-Hill, 1985, 4-43, 4-44.
24. Sleicher Jr., C.A., Churchill, S.W. Radiant heating of Dispersed Particles, Ind. Eng. Chem, 48, 1956, pp. 1819-1824.

## Thin-Film Flow in Open Helically-Wound Channels

Y. M. Stokes<sup>1</sup>, S. K. Wilson<sup>2</sup> and B. R. Duffy<sup>2</sup>

<sup>1</sup>Applied Mathematics, School of Mathematical Sciences  
The University of Adelaide, SA, 5005 AUSTRALIA

<sup>2</sup>Department of Mathematics  
University of Strathclyde, Glasgow, G1 1XH UK

### Abstract

The study of flow in open helically-wound channels has application to many natural and industrial flows, including those in static spiral separators. The flow consists of a primary axial component and a secondary cross flow and, in spiral separators, the fluid depth is typically small making experimental investigation difficult. Mathematical models are therefore of great value for determining how such flows are influenced by fluid properties and geometrical parameters and, hence, for predicting and improving the performance of these separators. A thin-film approximation is appropriate and yields an explicit expression for the fluid velocity in terms of the free-surface shape. The latter satisfies an interesting non-linear ordinary differential equation that can easily be solved numerically and in some cases analytically. The semi-analytic predictions of the thin-film model are found to be in good agreement with much more computationally expensive solutions of the Navier–Stokes equations.

### Introduction

Considerable literature exists concerning mathematical modelling of fully-developed flow in *closed* helically-wound pipes [1, 2, 3, 10, 19]. These studies have been motivated by a desire to better understand flows in curved geometries such as arise in many piping systems, and the human blood circulation system in particular. They have shown that, for this type of flow, a steady-state solution can be computed, comprising a velocity component along the axis of the pipe and a secondary cross flow.

Flows in *open* helical channels (figure 1) differ most significantly from their closed-pipe counterparts in having a free surface. They have been studied in the context of river flow and sediment transport [17], distillation of petroleum products [13] and, of particular interest here, spiral particle separation [4, 5, 7, 8, 9, 11, 15, 16]. They are also used in the separation of liquids of different densities (e.g. oil from seawater) or solids and liquids (e.g. in the case of wastewaters) [14].

Spiral particle separators are used in the coal and mineral processing industries to segregate and concentrate particles of different sizes and densities [6, 18]. Considerable advances have been made over the past 40 years in understanding the operation of these and improving their design. Nevertheless, fine mineral separation may yet be further improved with a better understanding of the flow in helical channels [18]. It can also assist with the understanding of flow in more general curved channels, such as occur in rivers and pipe networks that run only partly full.

Experimental studies of helical flows, as in spiral separators, are difficult because of problems with visualisation of the flow [7, 8], so that theoretical and computational fluid dynamics are of great value for predicting performance of new and existing spirals. Experimental work has indicated that the fluid depth is small and that some regions of the flow are not laminar [7].

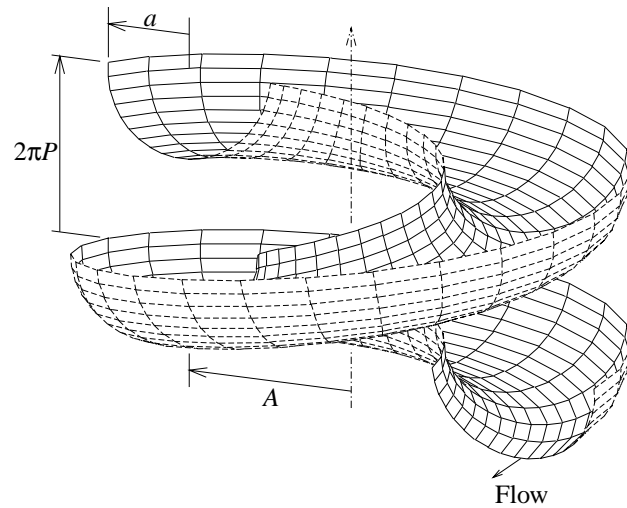


Figure 1: A right-handed helically-wound channel.

Some CFD simulations have been done [9, 12] but systematic parameter studies to determine how laminar flows in spiral separators are affected by variation of fluid properties and geometrical parameters such as curvature and torsion of the helix, and channel cross-section geometry, have yet to be done. A good understanding of the laminar flow is a necessary precursor to a study of the conditions which lead to turbulence or to the (possibly undesirable) phenomena that develop in the transition to turbulence.

As in [1, 2, 3, 10], we consider laminar flow and seek a steady-state solution that is also independent of axial position. This permits a two-dimensional analysis in the cross-section plane. As part of the solution process, we must determine the free-surface profile of the fluid in the channel, making this analysis significantly different from and more complex than fully developed flows in closed pipes. The shape of the free surface will be primarily determined by the curvature of the helix and the flow rate, so that, at this stage, we ignore surface tension. Since flows in spiral separators are known to be shallow, we concentrate here on thin-film flow. Some consideration to full channels has been given in [15, 16].

### Mathematical Model

As in [15, 16] we consider a channel of half-width  $a$ , helically wound about a vertical axis with helix radius  $A$  and pitch  $2\pi P$  (see figure 1). The angle of inclination of the channel to the horizontal is given by  $\tan \alpha = P/A$ , and the Reynolds and Froude numbers are given by  $R = Ua/\nu$ ,  $F = U/\sqrt{ga}$ , where  $U$  is a characteristic axial flow velocity,  $\nu$  is the kinematic viscosity of the fluid and  $g$  is gravitational acceleration. We also assume small dimensionless curvature  $\epsilon = aA/(A^2 + P^2)$  and sufficiently small torsion ( $\tau = \epsilon \tan \alpha$ ) such that  $R\tau = O(\epsilon)$ , i.e.  $R \tan \alpha = O(1)$ .



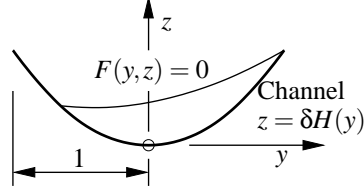


Figure 2: Cross section of channel showing the coordinate system. The  $x$ -axis is directed out of the page in the direction of the primary axial flow.

We use a Cartesian coordinate system with the  $x$ -axis in the direction of the primary axial flow and  $y$  and  $z$  axes in the cross-section of the channel as shown in figure 2. Lengths are normalised to give a channel half-width of 1. Then, at leading order in  $\epsilon$ , the continuity and Navier–Stokes equations give (cf. [15, 16])

$$\frac{\partial v}{\partial y} + \frac{\partial w}{\partial z} = 0, \quad (1)$$

$$v \frac{\partial u}{\partial y} + w \frac{\partial u}{\partial z} = \nabla^2 u + \frac{R \sin \alpha}{F^2}, \quad (2)$$

$$v \frac{\partial v}{\partial y} + w \frac{\partial v}{\partial z} - \frac{1}{2} K u^2 = -\frac{\partial p}{\partial y} + \nabla^2 v, \quad (3)$$

$$v \frac{\partial w}{\partial y} + w \frac{\partial w}{\partial z} = -\frac{\partial p}{\partial z} + \nabla^2 w - \frac{R^2 \cos \alpha}{F^2}, \quad (4)$$

where  $u$  is the primary axial flow velocity (scaled with  $U$ ),  $v$  and  $w$  are the secondary flow velocity components (scaled with  $U/R$ ) in the  $y$  and  $z$  directions respectively,  $p$  is the pressure (scaled with  $\rho U^2/R^2$ ), and  $K = 2\epsilon R^2$  is the Dean number associated with the centrifugal force acting on the flow.

The system (1)–(4) must be solved subject to the conditions for an impermeable, no-slip channel wall, zero stress and the kinematic condition at the free surface, and some prescribed volume flux  $Q$  down the channel, to give the velocity and pressure distributions in the flow domain and the free-surface shape  $F(y, z) = 0$ . In practice it is simpler to prescribe the cross-sectional area  $\Omega$  of the flow domain, rather than the volume flux; then  $Q$  is computed as an output by integrating  $u(y, z)$  over the flow domain, once it has been determined.

In general the solution must be obtained numerically and a method employing finite-element techniques is discussed and demonstrated in [15, 16]. As discussed in those papers, it is necessary to determine the contact points of the free surface with the no-slip wall *a priori* or have a means of adjusting them during the solution process. Here, we use our thin-film solution (discussed below) to obtain first (and very good) estimates of the contact points, and then adjust them iteratively until the required accuracy is achieved.

### Thin-Film Approximation

We obtain approximate equations for flows of small depth by defining new variables  $z = \delta \tilde{z}$ ,  $v = R \delta \tilde{v}$ ,  $w = R \delta^2 \tilde{w}$  and  $p = R \tilde{p}/\delta$ , where  $\delta \ll 1$  is a small aspect ratio. We also choose  $\delta^2 R/F^2 = 1$ , i.e. velocity scale  $U = \delta^2 \rho g a^2/\mu$ . Substituting into equations (1)–(4) gives, at leading order in  $\delta$ ,

$$\frac{\partial \tilde{v}}{\partial y} + \frac{\partial \tilde{w}}{\partial \tilde{z}} = 0, \quad (5)$$

$$\frac{\partial^2 u}{\partial \tilde{z}^2} + \sin \alpha = 0, \quad (6)$$

$$-\frac{\partial \tilde{p}}{\partial y} + \frac{\partial^2 \tilde{v}}{\partial \tilde{z}^2} + \chi u^2 = 0, \quad (7)$$

$$-\frac{\partial \tilde{p}}{\partial \tilde{z}} - \cos \alpha = 0, \quad (8)$$

where  $\chi = \delta K/2R$  is taken to be  $O(1)$ . Under the thin-film scaling, the boundary conditions on the free surface  $F(y, \tilde{z}) = 0$  become

$$\frac{\partial u}{\partial \tilde{z}} = 0, \quad \frac{\partial \tilde{v}}{\partial \tilde{z}} = 0, \quad \tilde{p} = 0 \quad \text{and} \quad \tilde{v} \frac{\partial F}{\partial y} + \tilde{w} \frac{\partial F}{\partial \tilde{z}} = 0.$$

Let the channel shape be given by  $\tilde{z} = H(y)$  and the fluid depth be  $h(y)$  so that the free surface is at  $\tilde{z} = H(y) + h(y)$ . Then we may write the solution to the thin-film equations in terms of the functions  $H(y)$  and  $h(y)$ . Thus, integrating (6) and (8), substituting  $u$  and  $\tilde{p}$  into (7) and integrating for  $\tilde{v}$  we obtain

$$\begin{aligned} u &= \frac{\sin \alpha}{2} (\tilde{z} - H)(H + 2h - \tilde{z}), \\ \tilde{p} &= \cos \alpha (H + h - \tilde{z}), \\ \tilde{v} &= -\frac{\chi \sin^2 \alpha}{120} (\tilde{z} - H) \times \\ &\quad \left[ (\tilde{z} - H)^3 [(H + 2h - \tilde{z})(H + 4h - \tilde{z}) + 2h^2] - 16h^5 \right] \\ &\quad - \frac{\cos \alpha}{2} \frac{d}{dy} (H + h) \times (\tilde{z} - H)(H + 2h - \tilde{z}). \end{aligned}$$

Writing the continuity equation (5) in the alternative form

$$\int_H^{H+h} \tilde{v} d\tilde{z} = 0,$$

substituting for  $\tilde{v}$  and integrating yields a first-order ordinary differential equation for  $h$  for any prescribed channel shape  $\tilde{z} = H(y)$ :

$$\cos \alpha \frac{d}{dy} (H + h) = \frac{6\chi \sin^2 \alpha}{35} h^4. \quad (9)$$

Defining the stream function  $\psi$  such that  $\partial \psi / \partial \tilde{z} = \tilde{v}$  and  $-\partial \psi / \partial y = \tilde{w}$ , substituting for  $\tilde{v}$ , integrating and requiring  $\psi = 0$  on  $\tilde{z} = H(y)$  we obtain

$$\begin{aligned} \psi &= \frac{\chi \sin^2 \alpha}{840} (\tilde{z} - H)^2 (H + 2h - \tilde{z})^2 (H + h - \tilde{z}) \times \\ &\quad \left[ (H + h - \tilde{z})^2 - 5h^2 \right]. \end{aligned} \quad (10)$$

The volume flux  $Q = \delta \tilde{Q}$  down the channel is given by

$$\tilde{Q} = \int_{\ell}^r \int_H^{H+h} u d\tilde{z} dy = \frac{\sin \alpha}{3} \int_{\ell}^r h^3 dy, \quad (11)$$

while the cross-sectional area of the flow domain  $\Omega = \delta \tilde{\Omega}$  is given by

$$\tilde{\Omega} = \int_{\ell}^r h dy, \quad (12)$$

where  $y = \ell$  and  $y = r$  are the left and right ends of the free surface, respectively.

To obtain a thin-film solution for any given channel shape  $\tilde{z} = H(y)$  we must solve (9) subject to either (11) or (12) for the fluid depth  $h(y)$ . Let  $h(\ell) = h_{\ell}$  and  $h(r) = h_r$  be the fluid depth at the contact points, i.e.  $(\ell, h_{\ell})$  and  $(r, h_r)$  determine the points of contact of the free surface with the channel wall and  $\ell \leq y \leq r$ . For any channel geometry, two of the four values  $\ell, r, h_{\ell}, h_r$  will be known and two must be determined as part of the solution; which two are known depends on the specific channel geometry. In this paper we will consider two different cases, as follows.

1. A rectangular cross section,  $H(y) = 0$ ,  $-1 \leq y \leq 1$ . In this case the left and right ends of the free surface are on the left and right walls of the channel, so that  $\ell = -1$ ,  $r = 1$ . However, the fluid depths  $h_\ell, h_r$  are unknown.
2. A parabolic cross section,  $H(y) = y^2$ . In this case we have zero fluid depth at each end of the free surface, i.e.  $h_\ell = h_r = 0$ , but the positions  $y = \ell, r$  are unknown.

For simple cross sections (such as the rectangular one) we can obtain the thin-film solution analytically, but for more general cross sections (such as the parabolic one) we must solve the thin-film equations numerically, for which we use *Matlab* as follows.

We first guess the unknown value at the left end of the free surface,  $h_\ell$  for the rectangular channel or  $\ell$  for the parabolic channel. Then,  $(\ell, h_\ell)$  together with (9) defines an initial value problem that is readily solved using the built-in 4th-order Runge-Kutta solver, to give  $h(y)$ . Finally, we compute the volume flux  $\tilde{Q}$  from (11), iteratively adjusting the initial value to give the required flux. Alternatively we may compute the cross-section area  $\tilde{\Omega}$  from (12) to adjust the initial value.

Having solved for  $h(y)$  we are able to determine the primary axial velocity  $u$  and the pressure  $\tilde{p}$ , and compute streamlines from (10). If desired the cross-flow components  $\tilde{v}, \tilde{w}$  may also be calculated.

#### Comparison of Full Computational and Thin-Film Results

Because of the ease with which we can solve the full Navier-Stokes equations for a specified flow-domain area (and the difficulty in *a priori* prescribing a specified volume flux), it is convenient to compare thin-film solutions and finite-element solutions of the full Navier-Stokes equations for a specified flow domain area  $\tilde{\Omega}$  rather than the volume flux  $\tilde{Q}$ . Thus, we choose the left boundary  $(\ell, h_\ell)$  for the thin-film solution to give the required area  $\tilde{\Omega}$ . We then use the thin-film solution  $h(y)$ ,  $\ell \leq y \leq r$  as input to our Navier-Stokes model, which we then solve iteratively for the flow velocities, pressure and (modified) free-surface shape. Depending on the desired accuracy this can be a time-consuming process.

The difference in the volume flux  $\tilde{Q}$  between the thin-film and Navier-Stokes models gives one (global) measure of comparison. In addition, we may compare contour plots of pressure  $p$ , primary axial velocity  $u$ , and so on, from each model. Comparing the cross-flow streamlines  $\psi = \text{constant}$  is particularly informative.

Solutions for both rectangular and parabolic channels have been obtained with a flow domain area  $\tilde{\Omega} = 2$  and aspect ratio  $\delta = 0.1$ . For the thin-film model we already have  $\delta^2 R/F^2 = 1$  and we now choose

$$\frac{\chi \sin^2 \alpha}{\cos \alpha} = 1.$$

For the Navier-Stokes model, if we take  $\tan \alpha = 4/3$ , then we must have

$$\frac{R \sin \alpha}{F^2} = \frac{\sin \alpha}{\delta^2} = 80,$$

and we further choose

$$\frac{R^2 \cos \alpha}{F^2} = \frac{R \cos \alpha}{\delta^2} = 1200.$$

Together, these imply that  $R = 20$  and  $K = 375$ .

The cross-flow streamlines and free surface for the rectangular channel for both thin-film and Navier-Stokes models are plotted in figure 3. The volume flux given by the thin-film model is

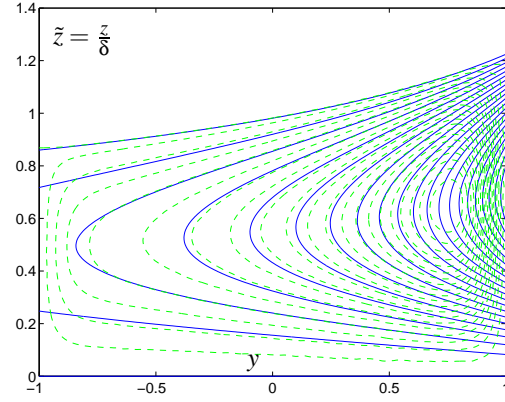


Figure 3: Streamlines of the cross flow in the rectangular channel. Blue (solid) curves correspond to the thin-film model and green (dashed) curves correspond to the Navier-Stokes model.

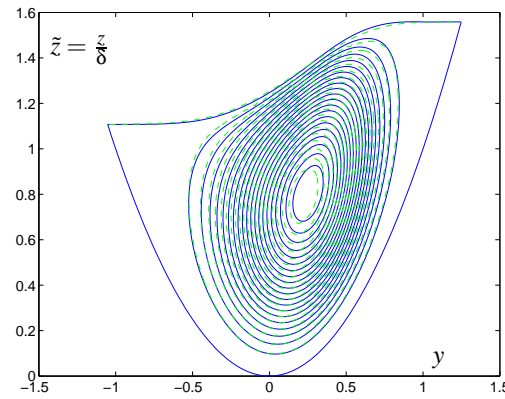


Figure 4: Streamlines of the cross flow in the parabolic channel. Blue (solid) curves correspond to the thin-film model and green (dashed) curves correspond to the Navier-Stokes model.

$\tilde{Q} = 0.55$ , while the Navier-Stokes model gives  $\tilde{Q} = 0.51$ . The differences in the two solutions are primarily due to the vertical side-wall channel boundaries, which are not captured by the present simple thin-film model. In reality there is a thin boundary layer along these walls which the thin-film solution does not show, but which is shown in the solution to the Navier-Stokes model. The thickness of these boundary layers reduces with the aspect ratio  $\delta$ , and in the thin limit approaches zero thickness. Hence the smaller the value of  $\delta$  used for our Navier-Stokes solution, the better the agreement with the thin-film solution. The effect of this boundary layer is greater at the wall on the outside of the channel curve, where velocities are greatest, than at the wall on the inside of the curve, where velocities are much smaller. For the case shown ( $\delta = 0.1$ ) we note that, despite the difference between the two models shown by the streamlines, the free-surface shape is quite similar over 85% of its length. Only near the wall at the outside of the channel curve is there any substantial difference.

For smooth channel cross sections (such as the parabolic one) both models incorporate the impermeable, no-slip boundary conditions over the entire channel wall, so we expect to see better agreement between them in this case. The agreement is indeed very good, as shown in figure 4 where the cross-flow streamlines and free surface for both models are plotted. The free-surface shape differs only slightly between the two models, and the streamlines are also quite similar. The thin-film model gives a volume flux of  $\tilde{Q} = 0.62$  and the Navier-Stokes model gives  $\tilde{Q} = 0.61$ , again showing good agreement.

## Conclusions

Flow in helically-wound channels of small curvature is governed by the Navier–Stokes equations with an extra term representing the centrifugal force. These equations must, in general, be solved numerically. In some practical applications the flows in such channels are shallow for which a thin-film approximation is appropriate. We have derived a thin-film model and shown that the flow solution can be written in terms of the free-surface shape and the prescribed channel geometry. The free-surface shape is given by a non-linear ordinary differential equation. Solutions are readily obtained for a wide range of channel geometries.

Comparison of results from the Navier–Stokes and thin-film models for rectangular and parabolic channels have been obtained. For the rectangular channel, which has vertical wall boundaries that are handled differently by the two models, the general character of the flow solutions is similar, but they differ near these boundaries, most significantly near the wall on the outside curve of the channel. However, for a channel with a smooth cross section (such as the parabolic one) the two models effectively impose the same boundary conditions and the solutions are in close agreement. For the parabolic channel the thin-film model gives a solution of excellent accuracy at a fraction of the computational effort required to solve the Navier–Stokes equations. This leads us to believe that our thin-film model has excellent potential to provide valuable information on practical open-channel flows (such as occur in spiral separators) both quickly and cheaply. Work is being continued to determine the parameter range over which our thin-film model is valid.

## Acknowledgements

Funding from the UK EPSRC (Research Grant GR/S71873) and the University of Adelaide Special Studies Program to support a visit by YMS to the University of Strathclyde is gratefully acknowledged.

## References

- [1] Berger, S.A., Talbot, L. and Yao, L.-S., Flow in curved pipes, *Ann. Rev. Fluid Mech.*, **15**, 1983, 461–512.
- [2] Germano, M., On the effect of torsion on a helical pipe flow, *J. Fluid Mech.*, **125**, 1982, 1–8.
- [3] Germano, M., The Dean equations extended to a helical pipe flow, *J. Fluid Mech.*, **203**, 1989, 289–305.
- [4] Holland-Batt, A.B., Spiral separation: theory and simulation, *Trans. Instn Min. Metall. (Sect C: Mineral Process. Extr. Metall.)*, **98**, 1989, C45–C60.
- [5] Holland-Batt, A.B. and Holtham, P.N., Particle and fluid motion on spiral separators, *Min. Eng.*, **4**, 1991, 457–482.
- [6] Holtham, P.N. and Stitt, P.H., Developments in Australian spiral separator technology, *Minerals and Exploration at the Cross Roads, Aus. IMM Annual Conf.*, Sydney, 1988, p. 165.
- [7] Holtham, P.N., Flow visualisation of secondary currents on spiral separators, *Min. Eng.*, **3**, 1990, 279–286.
- [8] Holtham, P.N., Primary and secondary fluid velocities on spiral separators, *Min. Eng.*, **5**, 1992, 79–91.
- [9] Jancar, T., Fletcher, C.A.J., Holtham, P.N. and Reizes, J.A., Computational and experimental investigation of spiral separator hydrodynamics, *Proc. XIX Int. Mineral Proc. Congress*, San Francisco, 1995, 147–151.
- [10] Kao, H.C., Torsion effect on fully developed flow in a helical pipe, *J. Fluid Mech.*, **184**, 1987, 335–356.
- [11] Matthews, B.W., Fletcher, C.A.J., Partridge, A.C. and Jancar, T., Computational simulation of spiral concentrator flows in the mineral processing industry, *Chemeca '96*.
- [12] Matthews, B.W., Fletcher, C.A.J. and Partridge, A.C., Computational simulation of fluid and dilute particulate flows on spiral concentrators, *Inter. Conf. on CFD in Mineral & Metal Processing and Power Generation*, CSIRO, 1997, 101–109.
- [13] Morton, F., King, P.J. and McLaughlin, A., Helical-coil distillation columns Part I: Efficiency studies, *Trans. Instn Chem. Engrs*, **42**, 1964, T285–T295.
- [14] NASA Patent No 5 248 421, Spiral fluid separator, Marshall Space Flight Center, Technology Transfer Program.
- [15] Stokes, Y.M., Flow in spiral channels of small curvature and torsion, in *IUTAM Symposium on Free Surface Flows, Proceedings of the IUTAM Symposium*, Birmingham, United Kingdom, 10–14 July 2000, editors A.C. King and Y.D. Shikhmurzaev, Kluwer, 2001, 289–296.
- [16] Stokes, Y.M., Computing flow in a spiral particle separator, *Proceedings of the 14th Australasian Fluid Mechanics Conference*, Adelaide University, Australia, 9–14 December 2001, 677–680.
- [17] Thomson, J., On the origin of windings of rivers in alluvial plains, with remarks on the flow of water round bends in pipes, *Proc. R. Soc. Lond. Ser. A*, **5**, 1876, 5–8.
- [18] Weldon, B., Fine Coal Beneficiation: Spiral separators in the Australian industry, *The Australian Coal Review*, Nov. 1997, 25–28.
- [19] Zabielski, L. and Mestel, A.J., Steady flow in a helically symmetric pipe, *J. Fluid Mech.*, **370**, 1998, 297–320.

## Effect of pulsation rate on spray-spreading rate in an isothermal environment

L. Stamatova, D. Honnery, V. Stamatov, J. Ghojel, J. Soria

Laboratory for Turbulence Research Aerospace & Combustion (LTRAC)  
Department of Mechanical Engineering  
Monash University, VIC 3800, AUSTRALIA

### Abstract

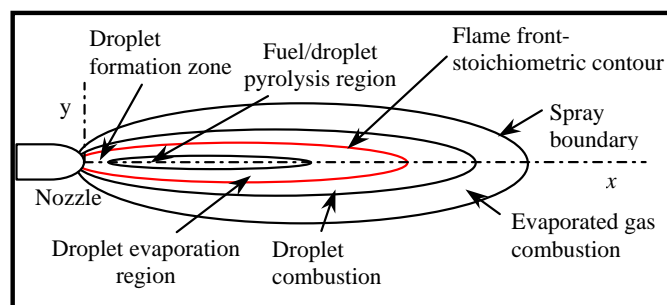
Preliminary results from Planar Laser Induced Fluorescence (PLIF) measurements of pulsed and continuous sprays at isothermal conditions indicate that, at otherwise identical conditions (constant Reynolds number and constant ratio between the injection duration and cycle period), pulsation leads to an increase of the spray-spreading rate of up to four times. Furthermore, the increased pulsation frequency leads to an increase of the spray-spreading rate. PIV measurements are required to provide quantitative data about in-plane velocity and out-of-plane vorticity flow fields.

### Introduction

The diesel engine is well known to offer superior fuel consumption compared to the gasoline engine. It is also less complicated, has better torque performance (i.e. over its engine speed range) and is able to run on a wider range of fuels. It is therefore the dominating power plant for heavy-duty transportation needs. However, compared to the conventional, catalyst equipped, gasoline engines, diesel engines emit higher level of oxides of nitrogen ( $\text{NO}_x$ ) and particulate matter. Particulate matter can accumulate in the respiratory system and is associated with numerous adverse health effects, possibly including cancer. Carbon monoxide enters the bloodstream through the lungs and forms carboxyhemoglobin, a compound that inhibits the blood's capacity to carry oxygen to organs and tissues. Infants, elderly persons, and individuals with heart and/or respiratory diseases are particularly sensitive to carbon monoxide poisoning. Hydrocarbons together with nitrogen oxides react in sunlight to form ground-level ozone, a major component of smog. A number of exhaust hydrocarbons are also toxic, with the potential to cause cancer [1, 2, 3, 4].

Overall performance of diesel engines is influenced by various flow mechanical factors, such as in-cylinder gas flows, fuel spray characteristics, mixing between fuel and gas, combustion characteristics and so on. Among them, the fuel spray characteristics often impose a commanding influence on the combustion phenomena, which in turn control the emission rate of nitrogen oxide and diesel particulate. The fundamental background for the high emissions of  $\text{NO}_x$  and soot from the diesel engine, despite an overall lean operation, is the fuel heterogeneity in the combustion chamber [5], [6]. This fuel heterogeneity stems from the procedure to introduce the fuel into a high temperature atmosphere when the piston is near dead centre. Diesel fuel autoignites readily when heated and the mixing between fuel and air is very limited before combustion commences. This creates a mixing controlled combustion situation with very hot combustion zones where the fuel and oxygen meet. The production of  $\text{NO}_x$  is favoured here. Fuel rich regions are encountered in the central parts of the reacting fuel spray and these promote the formation of soot. A schematic illustration of a spray flame structure is shown in Figure 1.

Greater mixing is required to reduce pollutants emission, but in diesel engines the degree of mixing is fixed by the geometry of the combustion chamber (which may provide swirl and tumble of the two streams) and spray nozzle (cone angle and droplet size). One way of overcoming this limitation may be to pulse the spray during combustion. In pulsing sprays the supply of external fluid is not steady. These sprays consist of periodic pockets of fluids injected into the surrounding air.



Combustion chamber boundary

Fig. 1. A schematic illustration of a spray flame structure.

The structures at the boundary of the spray are responsible for the mixing of droplets with the surroundings. The radial spread is sensitive to the initial conditions including the supply of liquid, which in pulsing sprays is not constant and periodically oscillates. Mixing rate can be quantified using the spray-spreading rate and the decay of droplets number and velocity along the spray trajectory [7].

Important non-dimensional groups characterising pulsing sprays are Reynolds ( $Re_d = \rho U d / \mu$ ) and Strouhal ( $St_d = f d / U$ ) numbers. Here  $\rho$  and  $\mu$  are the density and viscosity of the liquid,  $U$  is the relative velocity between gas- and liquid-phases,  $d$  - diameter of the orifice and  $f$  is the frequency of pulsation. The jet exit velocity,  $U$ , is determined on the basis of mass conservation over the one pulse cycle.

A comparison of round fully pulsed jets has been performed in the laser Doppler anemometry measurements of Bremhorst [8]. The experiments have shown, that like a continuous round jet, a fully pulsed jet has a centreline velocity that decays inversely with stream-wise distance. However, the rate of decay is much slower than comparable "steady jets". This decrease in stream-wise velocity is balanced by an increase in the volume flow-rate. Bremhorst [8] measured significantly higher Reynolds stresses for the pulsed turbulent jets and an increased entrainment, up to twice the value for a continuous stream.

The primary aim is to determine via measurement the degree to which mixing is enhanced in a spray by pulsation. Questions to be examined are: (i) What rates of pulsation increase spray and surrounding gas mixing and by what degree;

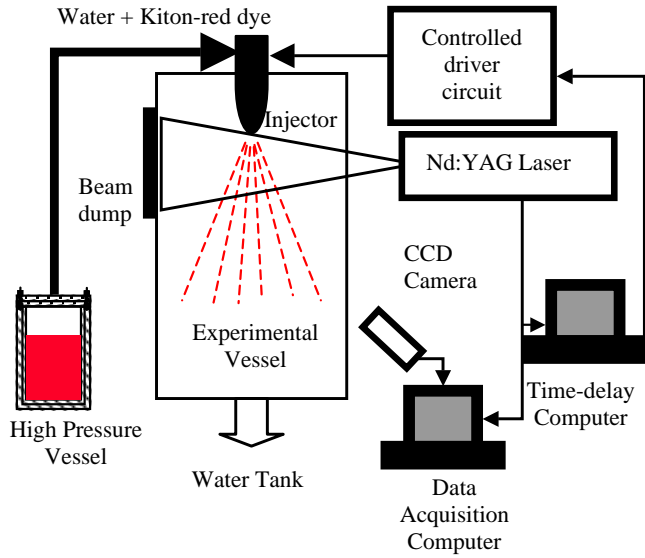


Fig. 2. A schematic diagram of the experimental setup.

(ii) What is the influence of the pulsation time ratio (fluid pulse to total pulse cycle time ratio) on mixing.

To overcome the difficulties of the high pressure, intermittent combustion environment found in engines, current investigation considers a non-reactive, single, round sprays in an isothermal environment. The PLIF technique was used to provide qualitative data about the spray evolution, decay and mixing with the surrounding air. The Reynolds number based on the orifice diameter was kept constant. The frequency of pulsation and the injection duration,  $S$ , were varied. Here the injection duration is defined as that fraction of the cycle period for which the spray was turned on. Note that the ratio  $S/T$ , where  $T$  is the cycle period, was kept constant at 0.7 to ensure a constant flow rate during time-averaging experiments.

### Experimental approach

The LTRAC's isothermal spray system was used for the current experiments. A schematic diagram of the experimental setup is given in Figure 2.

The spray was produced by sending a high-pressure stream of liquid (water) to a pintle type, fuel injector. The operating pressure of the injector can vary from 500 to 1500 kPa, the maximal frequency of pulsation is 230 Hz, and the minimal injection duration is 2 ms. A current controlled driver circuit (CCDC) controlled the motion of the liquid (water) through the injector, ensuring very short ( $<1$  ms) response time. Due to the inertia effect of the mass of the fluid being pumped, there is a delay, leading to a ramp up of the nozzle exit velocity from zero to the constant velocity, even when CCDC has a response time of  $<1$  ms. In order to take into account the inertia effect of the mass of the fluid, the fluid velocity was determined from the accumulated mass injected during multiple ( $>1000$  times) pulsation of the jet.

A single cavity, Q-switched, pulsed Nd:YAG laser model "Brilliant B" was used to irradiate the spray. The fundamental wavelength of the laser, 1064 nm, was frequency doubled to 532 nm. Kiton Red, which emits at 584 nm for a 532 nm incident wavelength was used as the fluorescent dye. Suitable optics was used to create a laser sheet about 1 mm thick. The light sheet was aligned to pass along the central axis,  $x$ , of the spray.

A 12-bit, 1280 x 1024 pixels Pixel-Fly CCD camera coupled with a Pentium based PC with data processing software was used for image acquisition. Illumination of the spray results in the spray droplets scattering both incident and fluorescent wavelengths. The camera was fitted with a suitable filter to separate scattered 532 nm and fluorescent 584 nm signals. Only the fluorescent signal was collected.

In order to obtain phase-matched data, the performance of the injector, lasers and cameras need to be precisely synchronised. The Nd:YAG laser sent triggering impulses to the data acquisition equipment and time-delay computer. The time-delay computer used Real-time Linux software to send TTL signals to CCDC that turns the injector on.

### Experimental results

Four different cases were studied. In all of the cases, the line pressure was kept constant at 1000 kPa, which corresponds to  $Re_d = 3567$  (based on the diameter of the orifice of 1 mm). The experimental conditions are summarised in Table 1.

	Case 1	Case 2	Case 3	Case 4
$f$ (1/s)	167	83	42	21
$T$ (ms)	6	12	24	48
$Re_d$	3567	3567	3567	3567
$St_d$	0.0468	0.0233	0.0118	0.0059
$S$ (ms)	4	8	17	34
$S/T$	0.7	0.7	0.7	0.7

Table 1. Summary of the experimental conditions.

A typical spray evolution is shown in Figure 3. Case 1 (Table 1) was considered. Instantaneous images were taken every 1 ms. The multistage interaction between the liquid-phase and the surrounding gas-phase includes the following steps: (a) the emerging jet becomes partly mixed with the surrounding gas-phase due to jet turbulence; (b) shortly after the start of injection, the jet spreads out in the  $y$ -direction, this leads to velocity decrease in the  $x$ -direction; (c) the degree of atomisation increases due to the break-up of large droplets as the jet moves further along the  $x$  axis; (d) an outer vortex deflects the droplets outwards and opens the spray cone.

Time-averaged contour plots were used to calculate the spray-spreading rate. 256 instantaneous images were taken per plot. Here the spray-spreading rate is defined as  $L_y/L_x$  where  $L_y$  and  $L_x$  are the limits of the spray in the radial,  $y$ , and central,  $x$ , directions. For the purposes of the current work, the limits are defined as the length and width of a contour for which the intensity of the fluorescence signal from the spray decays to 27% ( $2/e^2$ ) from the maximum intensity of the signal from the same spray. These contours are plotted in Figure 4 for the four cases of interest for the current work. The contour of a continuous spray taken at the same  $Re_d$  number is shown for comparison. The spray-spreading rate,  $L_y/L_x$  of the continuous spray was 0.04. The spray-spreading rates of the pulsed sprays, cases 1-4 were found to be much higher ( $\sim 0.16$ ), being independent of the frequency of pulsation. The shape of the spray changes as the frequency of pulsation decreases, showing gradually more of the features of the continuous spray.



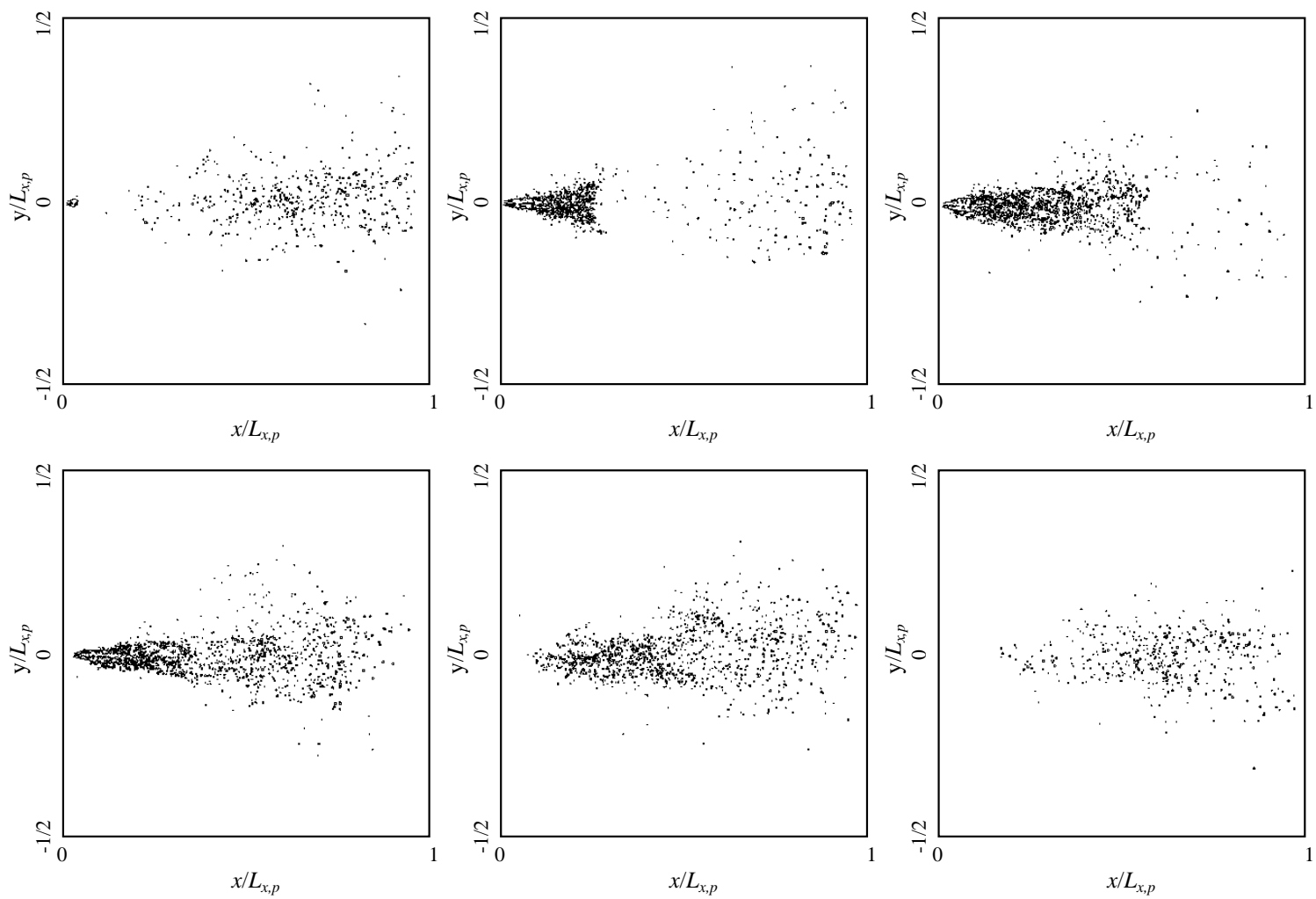


Fig. 3. A typical pulsed spray evolution,  $Re_d = 3567$ ,  $St_d = 0.0468$ ,  $S = 4$  ms.  $L_{x,p}$  is the maximal length of the spray.

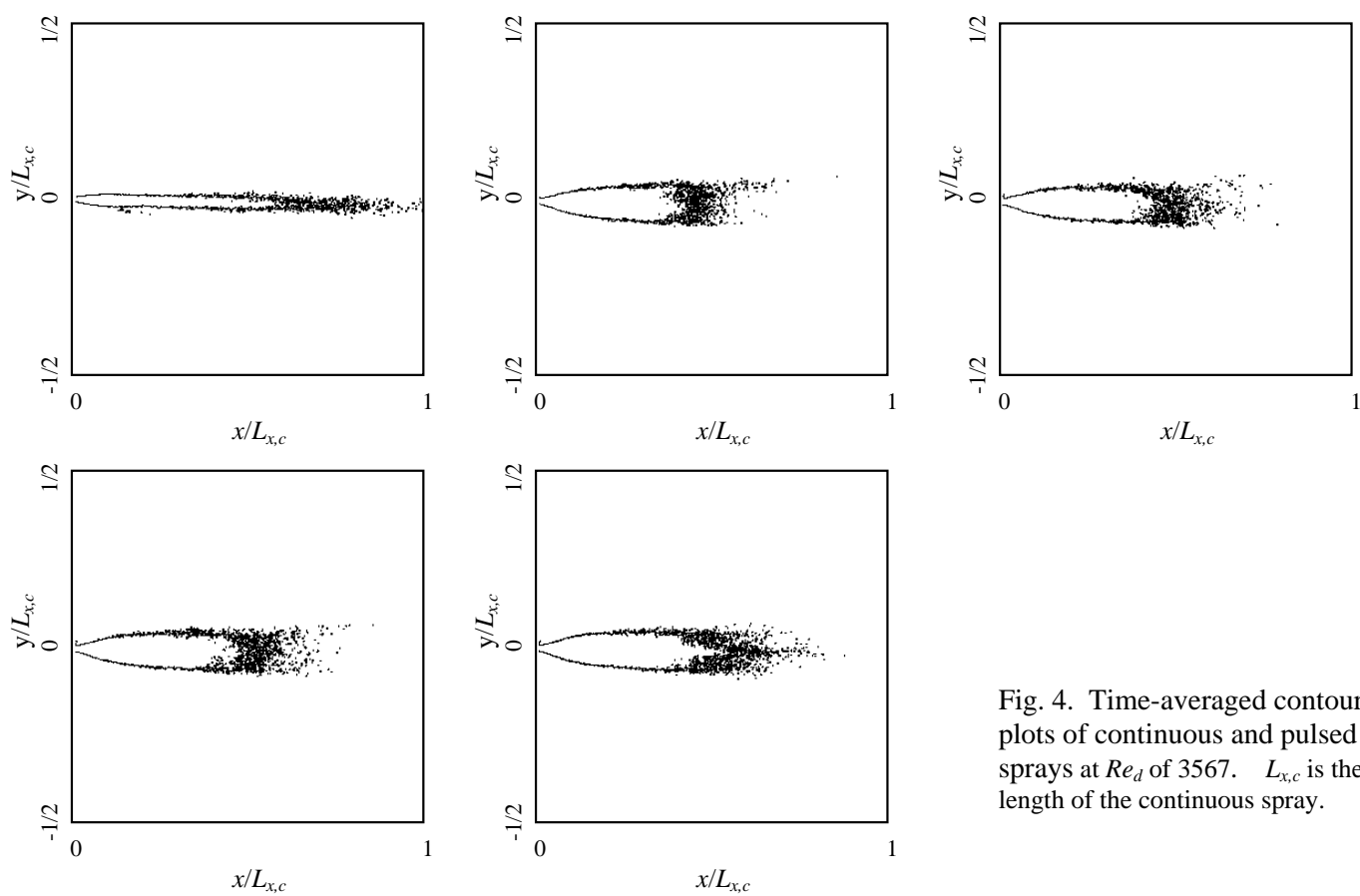


Fig. 4. Time-averaged contour plots of continuous and pulsed sprays at  $Re_d$  of 3567.  $L_{x,c}$  is the length of the continuous spray.



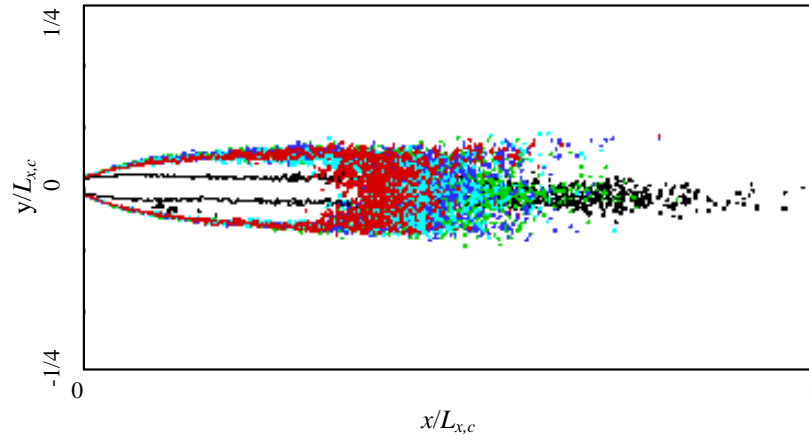


Fig. 5. Limits of pulsed sprays 1-4 compared with this of the continuous spray (marked in black) at  $Re_d$  of 3567. Spray 1 is marked in red, spray 2 – in cyan, spray 3 – in blue, and spray 4 – in green.  $L_{x,c}$  is the length of the continuous spray.

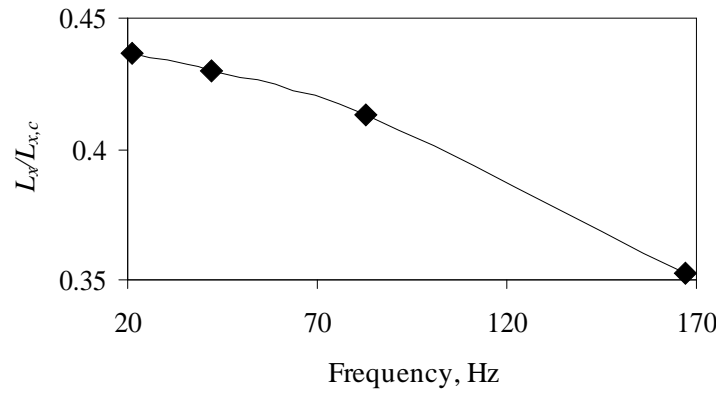


Fig. 6. Normalised length of pulsed sprays 1-4,  $L_x/L_{x,c}$ , versus frequency of pulsation.  $L_{x,c}$  is the length of the continuous spray.

The size of sprays 1-4 is compared with that of the continuous spray in Figures 5 and 6. The sprays limits were calculated on the base of the 27% decay from the maximal signal intensity of the continuous spray. It can be seen that the pulsed sprays are shorter and wider compared with the continuous spray (Figure 5), which in turn should ensure better mixing between the spray and the surrounding air. Furthermore, while the width of the pulsed sprays remains approximately constant, the length of the sprays is inversely proportional to the pulsation frequency, Figure 6. At otherwise identical conditions (constant Reynolds number and constant ratio between the injection duration and cycle period), the increased pulsation frequency leads to an increase of the spray-spreading rate.

## Conclusions

Preliminary results from PLIF measurements of pulsed and continuous sprays at isothermal conditions indicate that, at otherwise identical conditions (constant Reynolds number and constant ratio between the injection duration and cycle period), pulsation leads to an increase of the spray-spreading rate of up to four times. Furthermore, the increased pulsation frequency leads to an increase of the spray-spreading rate. PIV measurements are required to provide quantitative data about in-plane velocity and out-of-plane vorticity flow fields.

## References

- 1 US Environmental Protection Agency, *Study of Exhaust Emissions from Diesel Trucks and Commercially Available Idle-Reducing Devices*, Certification and Compliance Division, Office of Transportation and Air Quality, EPA420-R-02-025, October, 2002.
- 2 Mage, D.T. & Zali, O., *Motor vehicle air pollution*, World Health Organisation, Geneva, 1992.
- 3 World Health Organisation: *Diesel Fuel and Exhaust Emissions*, Stuttgart, Environmental health criteria, 171, 1996.
- 4 Sher, F. (Editor) *Handbook of Air Pollution from Internal Combustion Engines*, Academic Press, London, 1998.
- 5 Turns, S.R., *An Introduction to Combustion: Concepts and Applications*, 2nd Ed., McGraw-Hill, Singapore, 2000.
- 6 Glassman, I., *Combustion*, Academic Press Inc. Ltd., London, 1987.
- 7 Cater, J., *An experimental investigation of viscous vortex rings and zero-net-mass flux jets*, PhD thesis, Monash University, 2002.
- 8 Bremhorst, K. & Hollis, P., Velocity field of an axisymmetric pulsed, subsonic air jet, *AIAA Journal*, **28** (12), 1990, 2043-2049.

## Flow Structure Around A Finite-Length Square Prism

H.F. Wang<sup>1,2</sup>, Y. Zhou<sup>1,#</sup>, C.K. Chan<sup>3</sup>, W. O. Wong<sup>1</sup> and K.S. Lam<sup>4</sup>

<sup>1</sup> Department of Mechanical Engineering

<sup>3</sup> Department of Applied Mathematics

<sup>4</sup> Department of Civil and Structural Engineering

The Hong Kong Polytechnic University

<sup>2</sup>National Laboratory of Coal Combustion, Huazhong University of Science and Technology

#Email: mmyzhou@polyu.edu.hk

### Abstract

Turbulent flow structure around a square prism of finite length is experimentally investigated in a closed-circuit low speed wind tunnel. Hotwire and PIV data indicate that the near wake structure is dependent on the aspect ratio of the prism and characterized by vigorous interactions between base and tip vortices when the cylinder aspect ratio is 3 or less, but among spanwise vortices, tip vortices and base vortices at an aspect ratio of 5 and above. The counter-rotating base vortices dominate the near wake close to the prism base and attain maximum vorticity at  $1d$  (prism width) downstream of the prism and decay rapidly downstream. Both the maximum strength and size of these vortices grow with increasing aspect ratio due to weakening interaction between the tip and base vortices. Based on the present data and those in the literature, the flow structure models for different prism aspect ratios are proposed.

### Introduction

Flow around bluff bodies with finite length is important and of practical significance in many branches of engineering, such as aerodynamic force on cooling towers, pollutant transport and dispersion around high-rise buildings, forces on under water structures and even heat transfer of printed electronic circuit boards. As such, flow around a finite-length prism has attracted a considerable attention in the literature.

It is now well established that the flow over a finite-length circular cylinder is strongly three dimensional due to the interaction of tip vortex sprung from the free end of the cylinder and the horse-shoe vortex formed at the base (Zdravkovich et al. [15], Okamoto and Sunabashiri [10] and Martinuzzi and Tropea [7]). Etzold and Fielder [2] and Kawamura et al. [4] found that the ratio of cylinder height ( $H$ ) to diameter ( $d$ ), i.e., the aspect ratio, has a great influence on the flow structure. When the aspect ratio is less than 4, the wake near the free end of the cylinder is dominated by the down-wash tip vortices, and no periodic Karman vortex shedding occurs. For aspect ratio greater than 4 or 5, alternate Karman vortex shedding occurs along the cylinder except near the free end and the base. More recently, Pattenden et al. [11] investigated the flow structure of tip vortices and horseshoe vortices of a very short cylinder ( $H/d = 1$ ), and found that the counter-rotating tip vortices move downwards with the descending shear layer, and expand while being advected downstream until attaching the wall at  $x/d = 2$ .

Hussein and Martinuzzi [3] carried out flow visualization and LDV measurement of a wall mounted cube in a fully developed channel flow. A reattachment region is formed downstream of the cube by the downwash shear flow originating at the top leading edge. The horseshoe vortex is drawn towards the plane of symmetry up to the reattachment region, and then dispersed outwards by the downwash flow. Krajnovic [5] provided detailed flow visualization of a surfaced-mounted cube and showed a pair of counter-rotating streamwise vortices downstream of the prism base. Lyn et al. [6] studied unsteady turbulent flow around a 2D square prism based on phase-averaged velocities by a two-component LDV. They suggested that, in the base region, the periodic component was governed by the streamwise extent of the vortex formation region, while the turbulent

component was governed by the wake width.

In spite of previous investigations, many aspects of the flow structure around a finite-length prism have yet to be better understood. For example, how is the flow dependent upon  $H/d$ ? How do the tip, spanwise and base vortices interact with each other? This work aims to address these issues and focuses on a finite-length square prism. The aspect ratio examined ranges from 3 to 7. The flow is measured using hotwire and PIV techniques. Based on the experimental data, a schematic flow structure model is proposed.

### Experimental Set-up

Fig. 1 shows a schematic diagram of the experimental setup and coordinate system. Experiments were conducted in a closed-loop wind tunnel with a 2.4 m long working section ( $0.6m \times 0.6m$ ). The prism is mounted on a 10mm-thick horizontal flat plate ( $0.5m \times 1.2m$ ) at 30mm downstream of the leading edge. The width,  $d$ , of the square prism is 20mm. The cylinder height to width ratio,  $H/d$ , is chosen to be 3, 5 and 7. The leading edge was rounded to avoid flow separation. The boundary layer thickness is estimated to be about 2mm at  $L = 30$  mm, resulting in a negligibly small effect on the wake of the prism. The measurements were conducted at a free-stream velocity,  $U_\infty$  of 7m/s. The corresponding Reynolds number,  $Re$ , based on  $d$  is 9,300. The free-stream turbulent intensity is about 0.7%.

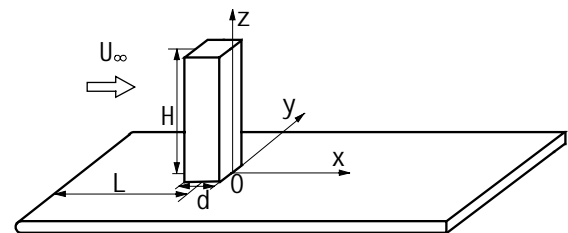


Fig.1 Schematic diagram of the experimental setup.

A single hotwire was placed at  $x/d = 5$  and  $y/d = 2.5$  for various  $z/d$  to monitor the dominant frequencies in the wake. A DANTEC particle imaging velocimetry (PIV) was used to measure the flow in the  $x$ - $z$  plane at  $y = 0$  and in the  $y$ - $z$  plane at  $x/d = 1, 3$  and 5. The CCD camera of the PIV system was placed about  $50d$  downstream of the prism to ensure a negligibly small effect on the near wake of the prism.

### Results and Discussion

#### Dominant vortical structures

In order to investigate the features of the turbulent wake, power spectra of velocities in the  $x$ -direction is obtained. Fig. 2 shows the smoothed power spectrum,  $E_u$ , of streamwise fluctuating velocity  $u$  at various spanwise locations for the three  $H/d$  values. At  $H/d = 3$ , there is a broad peak occurring at  $f^* = 0.09$ , where the asterisk stands for the normalization by  $U_\infty$  and  $d$ . On the other hand, a pronounced sharp peak occurs at  $f^* \approx 0.12$  and  $0.13$  for  $H/d = 5$  and 7, respectively,

close to that (0.135) of dominant vortices in a two-dimensional (2-D) square cylinder wake, Okajima [9]. The observation suggests that the flow behind the prism of  $H/d = 5$  and 7 may be dominated by spanwise vortices, whereas that at  $H/d = 3$  may not. The present result conforms to the reports by Kawamura et al. [4] and Brede et al. [1] that, when  $H/d$  was less than a critical value, 3 to 4, depending on incoming flow condition, no periodic vortex shedding occurred behind the entire prism and the near wake is characterized by the tip vortex generated at the free end and the horse shoe vortex formed at the base of the prism; however, at  $H/d > 3-4$ , the periodic spanwise vortex shedding was observed.

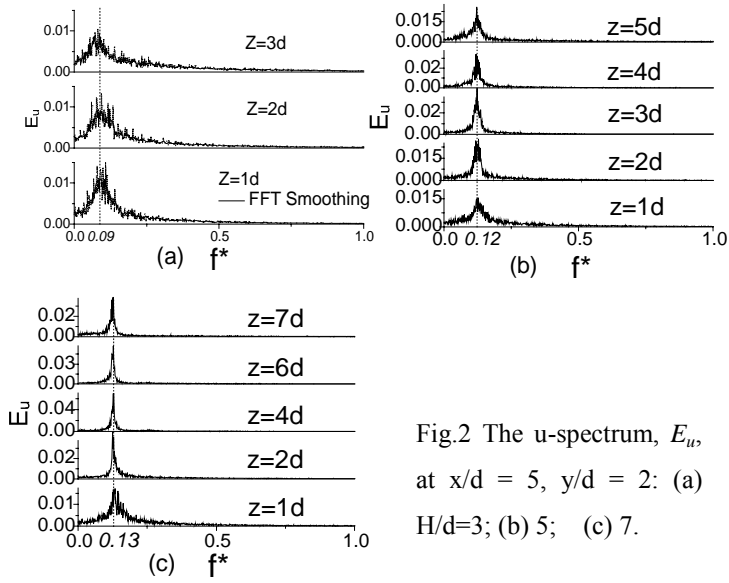


Fig.2 The u-spectrum,  $E_u$ , at  $x/d = 5$ ,  $y/d = 2$ : (a)  $H/d=3$ ; (b) 5; (c) 7.

## PIV Measurements

Fig. 3 presents sectional streamlines obtained from the PIV data, averaged from about 200 images, in the  $(x, z)$  plane for different  $H/d$ , where the reference frame is fixed on the prism. For simplicity, the sectional streamlines are hereinafter referred to as streamlines. The averaged streamlines have been compared with instantaneous ones (not shown) and found to be indeed representative of the typical flow structure. It is evident that the flow structure is qualitatively the same, irrespective of the  $H/d$  value. The approaching flow moves upwards, accelerates towards the free end of the prism and then separates from the leading edge.

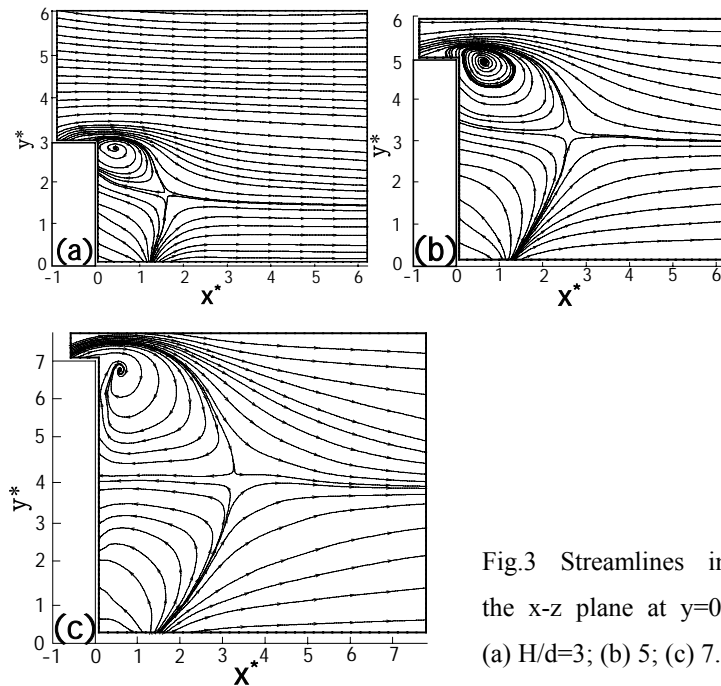


Fig.3 Streamlines in the  $x$ - $z$  plane at  $y=0$ . (a)  $H/d=3$ ; (b) 5; (c) 7.

The separated shear layer descends towards the wall while moving downstream. A focus is formed by the downwash flow downstream of the prism free end. In the region near the prism base, the streamlines do not appear affected by the downwash flow separation. This region, along with the downwash flow, grows for a higher  $H/d$ . Interestingly, all the streamlines near the prism base merge to a point downstream of the prism. The topology of these streamlines is consistent with the occurrence of a saddle point as illustrated in Fig. 4, which is supported by our oil-film flow visualization results (not shown here). One saddle point is formed near the mid-span downstream of the prism by the downwash flow from the free end and the up-wash flow from the saddle point near the base.

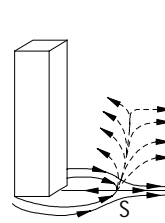


Fig.4 Sketch of the saddle point.

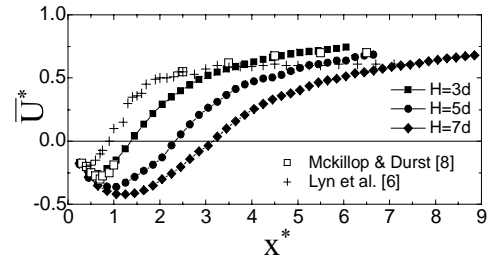


Fig.5 Averaged centerline streamwise velocity measured at mid span of the cylinder.

Figure 5 shows the streamwise velocity  $\bar{U}^*$ , obtained from the averaged PIV data in the  $x$ - $z$  plane, along the centerline at mid-span of the prism, together with Lyn et al.'s [6] and McKillop and Durst's [8] data obtained in the wake of a 2-D cylinder. As  $H/d$  increases, the negative  $\bar{U}^*$  region grows, indicating that the recirculation zone is increased. At  $H/d = 3$ , the up-wash flow appears overwhelming; however, the downwash flow becomes more important for higher  $H/d$ . The downwash flow from the free end brings in high speed fluid contributing to the growing recirculation region. Furthermore, both the maximum magnitude of the reversed flow velocity and the length of the recirculation region are larger presently than those in a 2-D cylinder wake. In the 2-D cylinder wake, the end effects are negligibly small, resulting in a smaller recirculation region.

The  $\bar{\omega}_x^*$ -contours obtained from the averaged PIV data (200 images) in the  $y$ - $z$  plane (Fig. 6) at  $x/d = 1$  display a pair of counter-rotating vortices near the prism base.

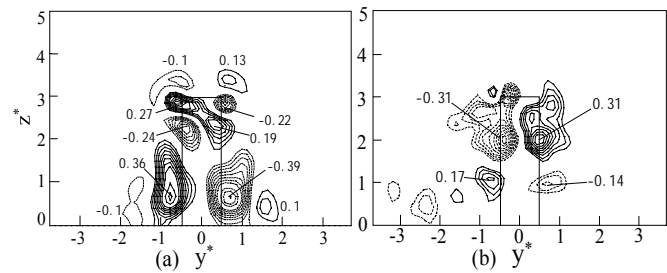


Fig.6  $\bar{\omega}_x^*$ -contours of  $H/d = 3$ . (a)  $x/d=1$ , (b) 3.

As  $x/d$  increases, this pair of vortices (Figs. 6a and 6b) ascends, in consistence with the streamlines in  $x$ - $z$  plane (Fig. 3), where the upward moving flow meets the downwash stream from the free end at  $x/d = 1.5$  at about the mid-span of the prism. The base vortices decay rapidly in both strength and size. It is worth commenting that the rotational senses of

the base vortices are opposite to those of horseshoe vortices described by Kawamura et al. [4] and Simpson [14]. In fact, this pair of base vortices is surrounded by a pair of weaker vortices, which show the characteristics of horseshoe vortices.

The vorticity distribution near the free end of the prism is quite symmetrical and three pairs of oppositely signed vortical structures are identifiable in Fig. 6a. The upper vortex pair with a peak vorticity of -0.1 and 0.13 is attributed to the downwash shear layer separating at the leading edge. The other two pairs of vortices occur at the corner of the free end and have larger magnitude of vorticity. Their occurrence is consistent with the flow structure, as illustrated in Fig. 7. This flow structure was numerically observed behind a cube by Saha [13]. The two pairs of vortices occur slightly below the free end, probably due to the downwash shear flow. At  $x/d = 3$ , the three pairs of vortices appear to have merged into one pair of higher peak vorticity and larger size. One difference between the tip and base vortices is that the tip vortex grows downstream whereas the base vortex decays rapidly.

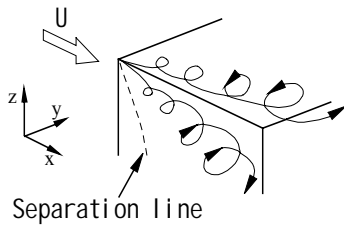


Fig.7 Tip vortex development.

The averaged  $\bar{\omega}_x^*$  - contours at  $x/d = 1$  for  $H/d = 5$  (Fig.8a) are rather different from those for  $H/d = 3$  (Fig. 6a). One pair of opposite-signed vortices only occurs near the free end, and the pair of vortices near the base is spanwise stretched considerably. The strength and size of the latter are much larger than those at  $H/d = 3$ .

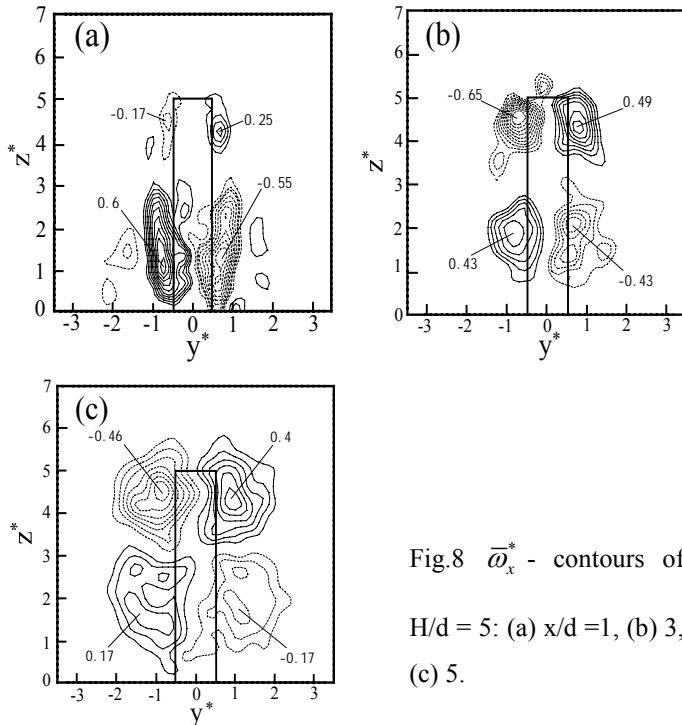


Fig.8  $\bar{\omega}_x^*$  - contours of  $H/d = 5$ : (a)  $x/d = 1$ , (b) 3, (c) 5.

At  $H/d = 5$ , the base vortices perhaps develop into the alternately shedding Karman vortices, which are present along most of the prism (Fig. 2b), thus being spanwise stretched at  $x/d = 1$  (Fig 8a). As  $x/d$  increases, the vortices decays gradually downstream in the maximum  $\bar{\omega}_x^*$ , but grow considerably in size, exhibiting one pair of less stretched opposite-signed  $\bar{\omega}_x^*$  concentrations. On the other hand, the tip vortices are overwhelmed by the present of spanwise

vortices, as confirmed by examining the instantaneous  $\bar{\omega}_x^*$  -contours, and consequently display one pair of relatively weak counter-rotating vorticity concentrations near the free end. But they grow downstream in both strength and size, reaching the maximum  $\bar{\omega}_x^*$  at  $x/d = 3$  (Fig 8b). At  $x/d = 5$ , their size grows larger, though the maximum  $\bar{\omega}_x^*$  appears reducing.

The averaged  $\bar{\omega}_x^*$  -contours at  $H/d = 7$  (Fig 9) are qualitatively similar to those at  $H/d = 5$ . However, there are differences. First, the upper pair of opposite signed concentrations is more spanwise stretched and characterized by a higher vorticity strength at  $x/d = 1$ . Like the  $H/d = 5$  case, the maximum  $\bar{\omega}_x^*$  increases from  $x/d = 1$  to 3 and then decays slowly downstream. Secondly, the lower pair of vortices are also more stretched and stronger than at  $H/d = 5$ . The differences are apparently linked to the enhanced spanwise vortices at a larger  $H/d$ .

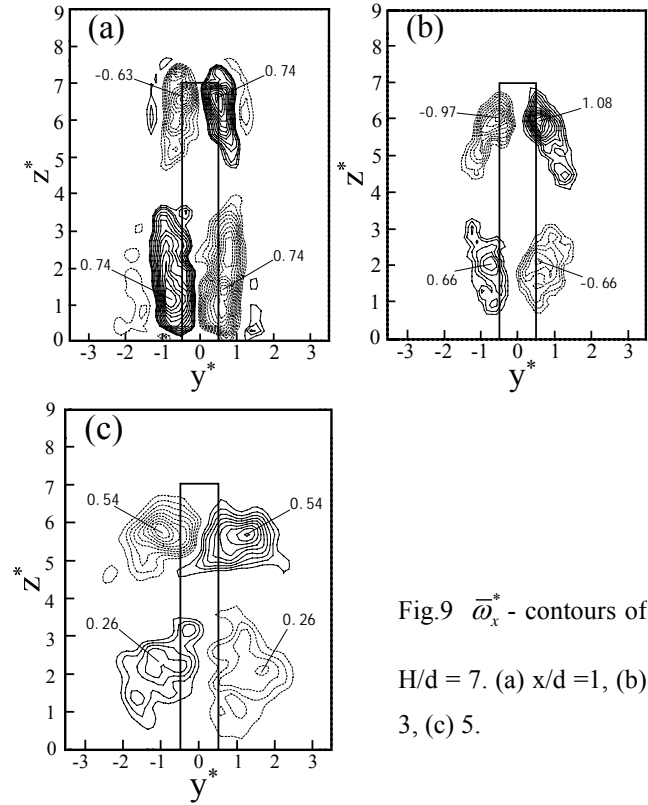


Fig.9  $\bar{\omega}_x^*$  - contours of  $H/d = 7$ . (a)  $x/d = 1$ , (b) 3, (c) 5.

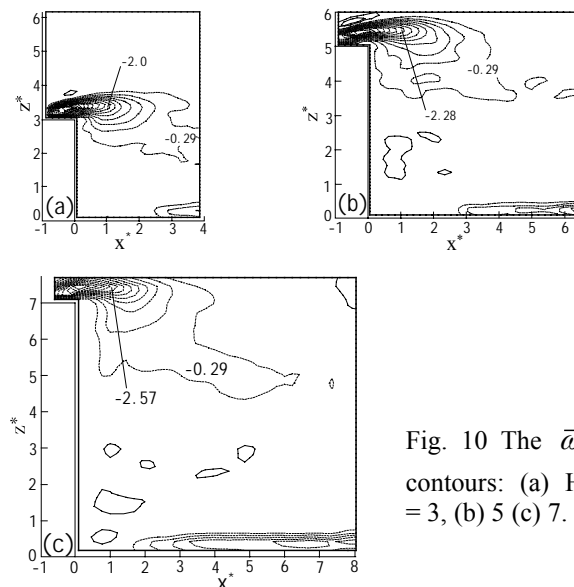


Fig. 10 The  $\bar{\omega}_y^*$  - contours: (a)  $H/d = 3$ , (b) 5 (c) 7.

The averaged  $\bar{\omega}_y^*$ -contours in the x-z plane are presented in Fig. 10. The same scale has been used for the three aspect ratios to facilitate comparison. At  $H/d = 3$ , the maximum  $\bar{\omega}_y^*$  concentration is  $-2.0$  and occurs at  $x/d \approx 1$ . As  $H/d$  increases, this concentration increases in both magnitude and size, probably due to the diminishing interaction between the tip and base vortices.

## Conclusions

The flow around a finite-length prism has been experimentally investigated. The investigation, though preliminary, leads to the following conclusions:

- 1 At  $H/d = 3$ , spanwise vortex shedding is largely suppressed and the near wake is dominated by the tip and the base vortices. At  $H/d = 5$  and 7, periodic spanwise vortex shedding occurs over almost the whole span except very close to the wall. The flow structure is schematically proposed in Fig. 11 for the two cases.
- 2 While the tip vortex grows in both size and strength downstream, the base vortex decays.
- 3 The recirculation region grows for a higher  $H/d$  probably due to the downwash flow from the free end, which brings in high-speed fluid. However, this region is smallest in a 2-D cylinder case, where the end effects are negligibly small.

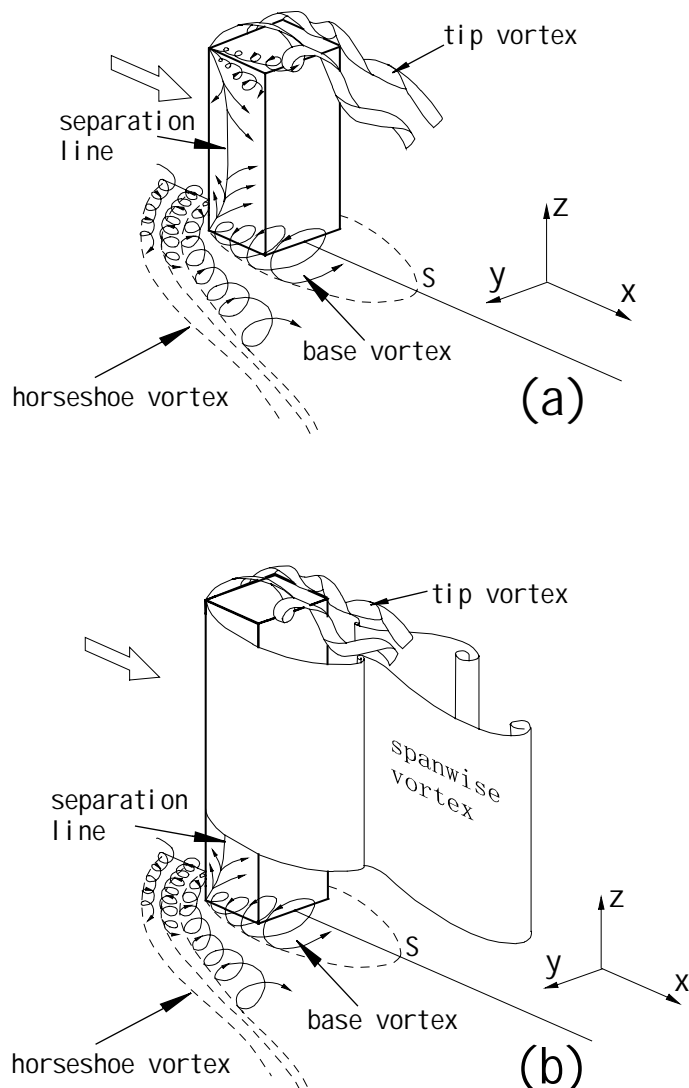


Fig. 11 Flow structure behind a square prism:

(a)  $H/d = 3$ ; (b)  $H/d \geq 5$ .

## Acknowledgements

The authors wish to acknowledge the support given to them by the Central Research Grants of The Hong Kong Polytechnic University through Grant G-YD69 and G-T679, and Research Grants Council of HKSAR through grant B-Q862.

## References

- [1] Brede, M., Eckelmann, H. & Rockwell, D., On the secondary vortices in the cylinder wake, *Phys. Fluids*, **8**, 1996, 2117-2124.
- [2] Etzold, F. & Fiedler, H., The near-wake structure of a cantilevered cylinder in cross flow, *Z. Flugwiss.*, **24**, 1976, 77-82.
- [3] Hussein, H.J. & Martinuzzi, R.J., Energy balance of turbulent flow around a surface mounted cube placed in a channel, *Phys. Fluids*, **8**(3), 764-780.
- [4] Kawamura, T., Hiwada, M., Hibino, T., Mabuchi, I. & Kumada, M., Flow around a finite circular cylinder on a flat plate, *Bull. of JSME*, **27**, 1984, 2142-2151.
- [5] Krajnovic, S., Large eddy simulation of the flow around a three-dimensional bluff body, *PhD thesis*, Dept. of Thermo and Fluid Dynamics, Chalmers Univ. of Tech., Gothenburg, Sweden.
- [6] Lyn, D.A., Einav, S., Rodi, W. & Park, J.H., A laser-Doppler velocimetry study of ensemble-averaged characteristics of the turbulent near wake of a square cylinder, *J. Fluid Mech.*, **304**, 1995, 285-319.
- [7] Martinuzzi, R. & Tropea, C., The flow around a surface-mounted prismatic obstacles placed in a fully developed channel flow, *J. Fluid Eng.*, **115**, 1993, 85-92.
- [8] McKillop, A.A. & Durst, F., A laser anemometry study of separated flow behind a circular cylinder, *In Laser Anemometry in Fluid Mechanics II*, LADOAN-IST, Lisbon, Portugal 1986.
- [9] Okajima, A., Strouhal numbers of rectangular cylinders, *J. Fluid Mech.*, **123**, 1982, 379-398.
- [10] Okamoto, K. & Sunabashiri, Y., Vortex shedding from a circular cylinder of finite length placed on a ground plane, *JSME Int. J. Ser. II*, **114**, 1992, 512-521.
- [11] Pattenden, R.J., Turnock, S.R. & Bressloff, N.W., An experimental and computational study of three-dimensional unsteady flow features found behind a truncated cylinder, *24<sup>th</sup> Symposium on Naval Hydrodynamics*, Fukuoka, Japan, 8-13 July 2002.
- [12] Roshko, A., Perspectives on bluff body aerodynamics, *J. Wind Ind. Aerodyn.*, **49**, 1986, 79-100.
- [13] Saha, A.K., Three dimensional numerical simulation of transition flow past a cube, *Physics of Fluids*, **16**, 2004, 1630-1646.
- [14] Simpson R.L., Junction Flow, *Annu. Rev. Fluid Mech.*, **33**, 2001, 415-443.
- [15] Zdravkovich, M.M., Brand, V.P., Mathew, G. & Weston, A., Flow past short circular cylinders with two free ends, *J. Fluid Mech.*, **203**, 1989, 557-575.

## Active Control of Vortex-Airfoil Interactions

Zhang, M M, Zhou Y & Cheng L  
Department of Mechanical Engineering  
The Hong Kong Polytechnic University  
Hung Hom, Kowloon, Hong Kong

### Abstract

It is well known that interactions between the leading edge of a blade and incoming vortical structures produce a sharp rise in pressure, contributing significantly to the noise production in fans, turbine machines, etc. Active control of interactions between an airfoil and incoming cylinder-generated vortices has been presently investigated. The essence of the control is to create a local perturbation, using piezo-ceramic actuators, on the surface near the leading edge of the airfoil, thus modifying the airfoil-vortex interactions. Both open- and closed-loop controls are used, where the surface perturbation was controlled by an external sinusoidal wave and a feedback pressure signal from a pressure transducer installed at the leading edge, respectively. Experiments were carried out in a wind tunnel. It was observed that the closed-loop control was superior to the open-loop one; the closed- and open-loop controls achieve a maximum reduction in the pressure fluctuation at the dominant vortex frequency by 73% and 44%, respectively.

### Introduction

When a blade, foil, wedge or fin is subjected to an incoming vortical flow, the incident vortices may distort rapidly due to interactions with the solid surface, which is often accompanied by the generation of an intense impulsive sound at the leading edge of the body and subsequent radiation to the far field. This aerodynamic sound is often called blade-vortex interaction (BVI) noise and has become one of the important noise sources for many engineering products, for example, helicopter blades, tails of aircrafts and rotors of turbo-machines, fans, and so on. This noise may hurt human ears in a long term and even lead to the malfunction of machines. Naturally, the BVI noise and its control have attracted the interests of many researchers in the past [1-4].

The passive method is frequently used to control the BVI, which requires no external energy input to the blade-vortex system, and often relies on modifying the blade shape, introducing winglets to the blade, increasing the number or the length of blades, or adding curvature to the blade surface [5-7].

The active control requires external energies to bring about desired changes in the blade-vortex system, and can be open- or closed loop. Using an open-loop system, Kaykayoglu [8] changed interactions between upstream vortices and a downstream airfoil by oscillating the leading edge of the airfoil, which was controlled by an independent external disturbance signal. The vortex strength and the BVI noise were effectively suppressed when the excitation frequency of the external control signal coincided with the instability frequency of the vortex-airfoil system. Peter *et al.* [9] used actuators, which were made of piezo-ceramic or fibre composites and attached on the airfoil surface, to twist the airfoil. They managed to obtain a 10 dB reduction in the BVI noise level. In the so called closed-loop control, the actuators are activated by a feedback-signal. Ziada [10] introduced acoustic disturbances to vortices in order to effectively attenuate the global oscillations of incident jet vortices on a wedge and hence the BVI noise. This was realized by loudspeakers, located near vortex separation edge and activated by a feedback fluctuating pressure signal of flow measured with a microphone. The control action was based on an

adaptive digital controller and a recursive root-mean-square algorithm. A reduction of 30 dB in the noise pressure was achieved.

The actuation mechanism is an important component in an active control system. Cheng *et al.* [11] proposed a novel perturbation technique to control the fluid-structure interaction. The essence of the technique was to create a perturbation on the structural surface using piezo-ceramic actuators, which altered interactions between vortex shedding from a square cylinder and structural vibration. Both open- and closed-loop systems were investigated [11,12]. Both were found to be effective in reducing the vortex strength and structural vibration. One naturally wonders whether this technique could be used for reducing the BVI noise since the noise generation was linked to interactions between vortices and airfoil.

This work aims to investigate the effective control of the BVI noise using the perturbation technique developed by Cheng *et al.* [11] This technique was used to control interactions between vortices generated from a cylinder and a downstream airfoil. The investigation was conducted in a wind tunnel. Both open- and closed-loop controls were used. The fluctuating flow velocity and pressure near the leading edge of the airfoil were monitored using the hotwire and pressure transducers, respectively. The flow structure alteration was also measured using a particle image velocimetry, which is not reported here due to the limitation in pages.

### Experimental Setup

Experiments were carried out in a closed circuit wind tunnel with a square test section of 0.6 m  $\times$  0.6 m, and 2.4 m long. The free-stream turbulence intensity is less than 0.4%. Readers can refer to Zhou *et al.* [13] for more details of the tunnel. A circular cylinder with a diameter  $d = 10$  mm made of stainless steel and an NACA0012 airfoil with a chord length  $c = 150$  mm were horizontally mounted in tandem on the working section of the wind tunnel (Figure 1). The angle of attack of the airfoil was  $0^\circ$ . The distance between the cylinder and the leading edge of the airfoil was  $10d$ . Measurements were conducted at a free-stream velocity  $U_\infty = 11$  m/s. The corresponding Reynolds numbers,  $Re_d$  ( $\equiv U_\infty d / \nu$ , where  $\nu$  is the kinematic viscosity) based on the cylinder diameter and  $Re_c$  ( $\equiv U_\infty c / \nu$ ) based on the chord length of the airfoil were 7300 and 109000, respectively.

A curved piezo-ceramic actuator [11] was embedded in a slot of 200 mm length, 3 mm width and 3 mm depth on the upper surface and was less than 1 mm from the airfoil leading edge (Figure 1). The actuator (THin layer composite UNimorph piezoelectric Driver and sEnsoR) was developed by the NASA Langley Research Centre. The actuator, deforming out of plane under a voltage (Figure 2), is characterized by many advantages such as high displacement, high load capacity and small size [14,15]. Typically, without any loading, the actuator (THUNDER-11R) of 76.2 mm length, 2.54 mm width and 0.74 mm thickness may vibrate at a maximum displacement of about 2 mm and a frequency up to 2 kHz, which is due to a particular fabrication process [15]. One end of the actuator was glue-fixed on the bottom side of the slot, whilst the other end is free. The



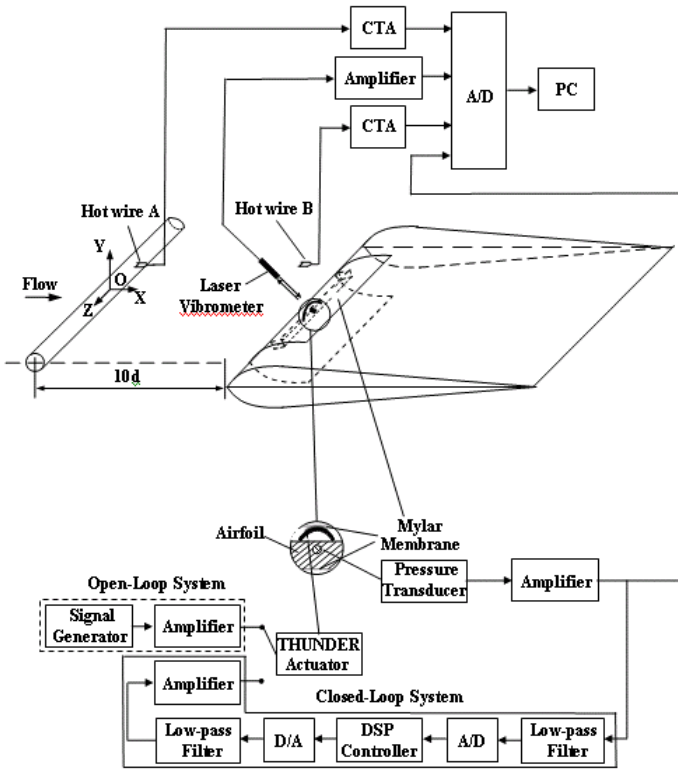


Figure 1. Experimental Setup.

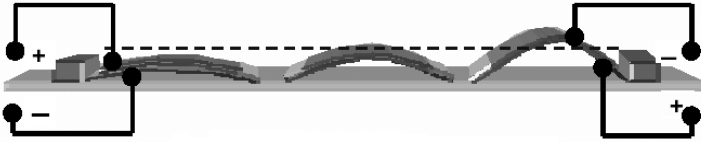


Figure 2. The relationship between typical deformation of THUNDER and applied voltage.

actuators and the walls of the slot around the actuators were well lubricated to reduce contact friction. A Mylar membrane, with superior strength, good heat resistance and insulation, was pasted on the top of actuator for smoothing the airfoil shape. Driven by the actuator, this membrane will oscillate to create the local perturbation on the airfoil surface.

In the open-loop control, the actuator is activated by a signal generated from a signal generator (HP-DS345) and amplified by a dual channel piezo-driver amplifier (Trek PZD 700-2); in a closed-loop control, a fluctuating flow pressure signal measured on the airfoil surface was used to drive the actuator. A pressure transducer (model 151-01), with a sensitivity of 1 volts/ $\mu$ Bar and a frequency response of 1 kHz, was installed at the central part of the leading edge of the airfoil to measure the fluctuating flow pressure on the airfoil surface (Figure 1). After amplification, the feedback pressure signal was filtered at a cut-off frequency of 200 Hz and then sent to a Digital Signal Processor (DSP) controller fitted with 16-bit AD and DA converter. The sampling frequency of the AD converter is self-defined to be a few kHz, which satisfies the present experimental requirements. The converted analog signal was amplified by the dual channel piezo-driver amplifier to activate the actuators. The use of the two low-pass filters for both the feed-forward and feedback passages is to remove high frequency noises from turbulence and electronic components. The controller is developed and executed based on a real-time system, dSPACE, which has rapid control prototyping, production code generation, and hardware-in-the-loop tests. A digital signal processor (DSP) with SIMULINK function of MATLAB and software (ControlDesk 2.0) was applied to sample and process the feedback signal.

In order to evaluate the control effect, the streamwise fluctuating velocities along with the fluctuating flow pressure were measured using two tungsten hot wires, i.e. A and B (Figure 1), placed at  $x/d = 1.5$ ,  $y/d = 1.5$ ,  $z/d = 0$  and  $x/d = 10$ ,  $y/d = 1.5$ ,  $z/d = 0$ , respectively. The coordinates  $x$ ,  $y$  and  $z$  correspond to streamwise, transverse and spanwise directions, respectively (Figure 1). The perturbation displacement of membrane on the top of the actuator was recorded by a Polytec Series 3000 Dual Beam laser vibrometer. The four signals were simultaneously conditioned and digitized using a 12-bit A/D board at a sampling frequency of 3.5 kHz per channel. The duration of each record was 20 s.

### Parameters Optimization and Control Performances

The parameters of the controller were first optimized in order to minimize the pressure fluctuation ( $p$ ) at the leading edge of the airfoil. The optimization was achieved based on manually tuning. For the open-loop control, the tuning parameters include the frequency and voltage of the excitation signal ( $Y_p$ ), perturbation frequency ( $f_p$ ) and perturbation voltage ( $V_p$ ); for the closed-loop control, the amplitude ratio ( $A_{Y_p p}$ ) and phase shift ( $\phi_{Y_p p}$ ) between  $Y_p$  and  $p$  were tuned. The general tuning procedure for closed-loop method is as follows: first vary  $A_{Y_p p}$  by keeping  $\phi_{Y_p p} = 0^\circ$  to find a  $A_{Y_p p}$ , i.e.,  $A_{Y_p p, opt}$ , leading to the smallest  $p$ ; then given  $A_{Y_p p, opt}$  vary  $\phi_{Y_p p}$  within a cycle to determine the  $\phi_{Y_p p, opt}$ , under which  $p$  reaches the minimum. The  $A_{Y_p p, opt}$  and  $\phi_{Y_p p, opt}$  were used as optimal parameters for closed-loop controller. These tuning processes led to an optimal configuration for each control method with the parameters:  $Y_p = 120$  volts,  $f_p = 319$  Hz for the open-loop control;  $A_{Y_p p} = 1.4$ ,  $\phi_{Y_p p} = 143^\circ$  for the closed-loop control.

Figure 3 shows typical time histories of  $p$  under control. Compared with the unperturbed case (Figure 3(a)), the amplitude of  $p$  decreases by up to 33% for the open-loop case (Figure 3(b)) and 73% for the closed-loop case (Figure 3(c)). The  $p$ -spectrum,  $E_p$  (Figure 4), under the optimal condition displays in the absence of control a pronounced peak at the normalized vortex shedding frequency  $f_s^* (= f_s d / U_\infty = 0.205)$ , which is apparently due to the Kármán vortices generated by the cylinder.  $E_p$  has been normalized by the root mean square value ( $p_{rms}$ ) of  $p$  so that

$$\int_0^\infty E_p(f) df = 1.$$

Once the open-loop control is imposed, the peak value of  $E_p$  at  $f_s^*$  is reduced by 30%. One additional peak at a magnitude of 0.021 occurs in  $E_p$  at  $f_p^* (= f_p d / U_\infty = 0.29)$ , apparently due to the perturbation. The closed-loop control leads to an even more impressive performance, resulting in a reduction by 76%. These results demonstrate not only the effectiveness of the present control technique on reducing the BVI noise but also the superiority of the closed-loop method to the open-loop one.

Note that since  $E_p$  is normalized by  $p_{rms}$ , the variation in the peak value may not accurately indicate the actual energy decrease caused by the active control because of the inclusion of external energy in  $p_{rms}$ . One way to estimate more accurately the energy ( $E_{p, \Delta f}$ ) of  $p$  associated with  $f_s$  is to integrate  $E_p$  over a -3dB bandwidth about  $f_s$ , which is subsequently multiplied by  $p_{rms}$ . Use  $E_{p, \Delta f}$  to represent the resulting quantity, calculated from Figure

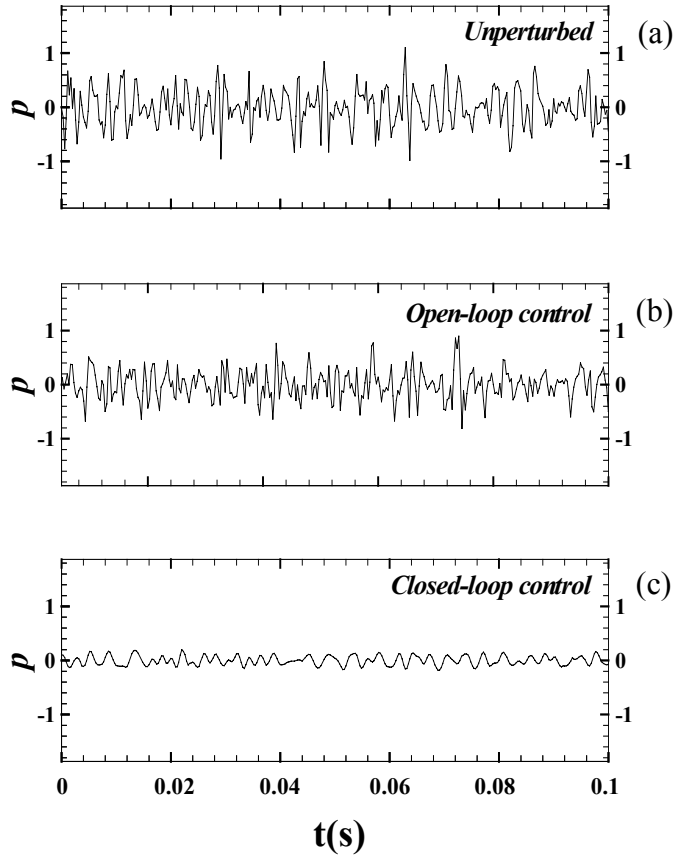


Figure 3. Typical time history of pressure signal ( $p$ ) measured near the leading edge of the airfoil: (a) unperturbed; (b) open-loop control; (c) closed-loop control. The time origin is arbitrary.

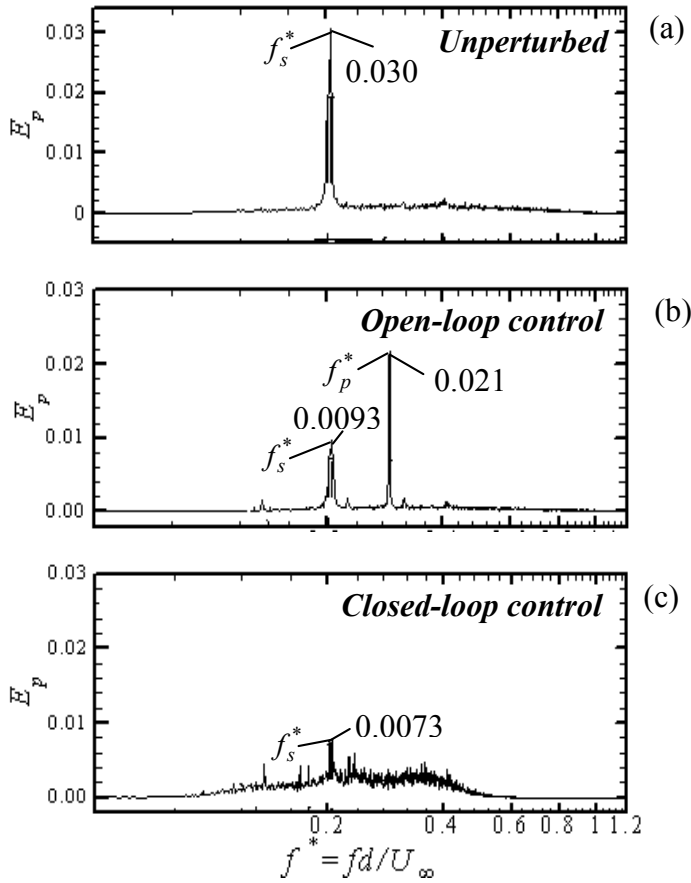


Figure 4. The  $p$ -spectrum  $E_p$ : (a) unperturbed; (b) open-loop control; (c) closed-loop control.

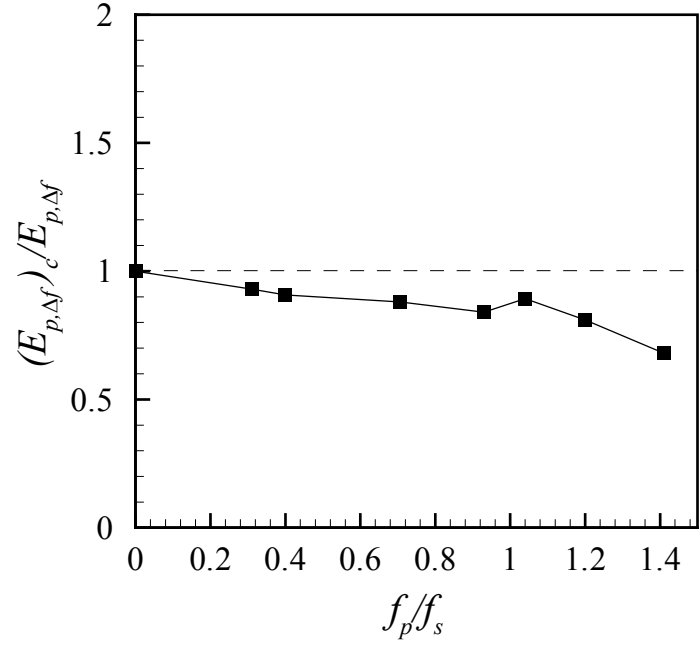


Figure 5. Dependence of the energy ratio,  $(E_{p,\Delta f})_c / E_{p,\Delta f}$ , on the perturbation frequency ( $f_p$ ) in the open-loop control ( $Re_d = 7300$ ).

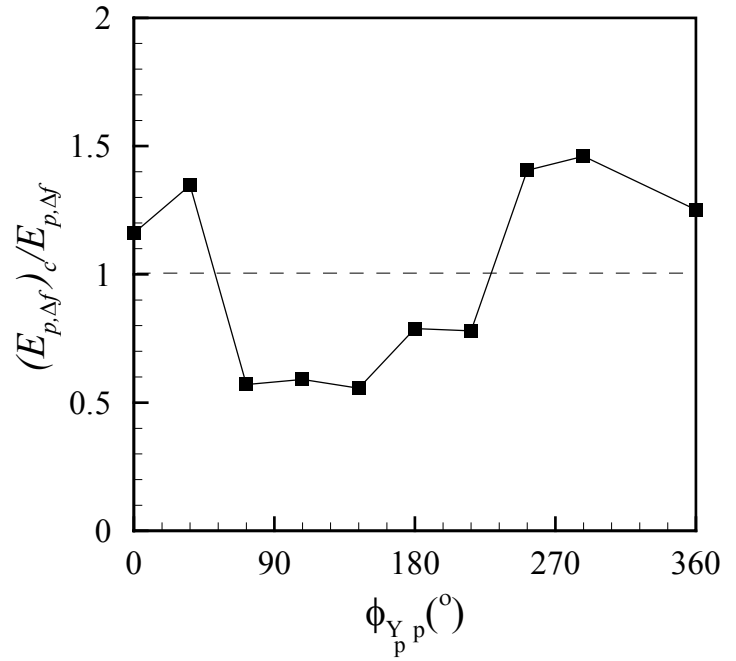


Figure 6. Dependence of the energy ratio,  $(E_{p,\Delta f})_c / E_{p,\Delta f}$ , on the phase shift ( $\phi_{Y_p p}$ ) between the perturbation signal ( $Y_p$ ) and the pressure signal ( $p$ ) in the closed-loop control ( $Re_d = 7300$ ).

4(a), in the absence of control and  $(E_{p,\Delta f})_c$  to denote that calculated from Figure 4(b) or 4(c), in the presence of control. Figure 5 shows the dependence of the energy ratio,  $(E_{p,\Delta f})_c / E_{p,\Delta f}$ , on  $f_p/f_s$  in the open-loop control. Here  $V_p$  was set at 120 volts. As  $f_p/f_s$  increases,  $(E_{p,\Delta f})_c / E_{p,\Delta f}$  drops, indicating more reduction in the BVI noise. At  $f_p/f_s = 1.41$ ,  $(E_{p,\Delta f})_c / E_{p,\Delta f}$  is 67% of the unperturbed case ( $(E_{p,\Delta f})_c / E_{p,\Delta f} = 1$  at  $f_p/f_s = 0$ ). In the closed-loop control case ( $A_{Y_{pp}}$  is fixed at 1.4),  $(E_{p,\Delta f})_c / E_{p,\Delta f}$  (Figure 6) exceeds 1 for  $\phi_{Y_{pp}} < 51^\circ$  or  $\phi_{Y_{pp}} > 229^\circ$ ; its maximum reaches 147% of the uncontrolled energy. On the other hand, for  $51^\circ < \phi_{Y_{pp}} < 229^\circ$ ,  $(E_{p,\Delta f})_c / E_{p,\Delta f}$  is significantly reduced, reaching a minimum of 0.44, i.e. 44% of the unperturbed energy, at  $\phi_{Y_{pp}} \approx 143^\circ$ . Apparently, the closed-loop control out-performs its open-loop counterpart.

## Conclusions

The active control of vortex-airfoil interactions has been experimentally investigated. It can be concluded that the presently proposed control schemes can reduce markedly the fluctuating pressure associated with the vortex-airfoil interactions. The closed- and open-loop controls achieve a maximum reduction by 73% and 44%, respectively, indicating a superiority of the closed-loop scheme to the open-loop one.

The investigation points to a great potential of the present control technique for the BVI noise control. Further investigation is underway to understand the physics behind the control performances.

## Acknowledgement

The authors wish to acknowledge support given to them by the Research Grants Council of HKSAR through Grant PolyU 5294/03E.

## References

- [1] Rockwell, D., Vortex-Body Interactions, *Annu. Rev. Fluid Mech.*, **30**, 1998, 199-229.
- [2] Howe, M.S., *Acoustics of Fluid-Structure Interactions*, Cambridge University Press, 1998.
- [3] Walker, J.D.A., Smith, C.R., Doligalski, T.L. & Cerra, A.W., Impact of a Vortex Ring on a Wall, *J. Fluid Mech.*, **181**, 1987, 99-140.
- [4] Casalino, D., Jacob, M. & Roger, M., Prediction of Rod-Airfoil Interaction Noise Using the Fflowcs-Williams-Hawkins Analogy, *AIAA J.*, **41**, 2003, 182-191.
- [5] Longhouse, R.E., Control of Tip-Vortex Noise of Axial Flow Fans by Rotating Shrouds, *J. Sound Vib.*, **58**, 1978, 201-214.
- [6] Schmitz, F.H., Boxwell, D.W., Lewy, S. & Dahan, C., Mode-to-Full-Scale Comparisons of Helicopter Blade/Vortex Interaction Noise, *J. Am. Helicopter Soc.*, **29**, 1984, 16-25.
- [7] Hardin, J.C. & Lamkin, S.L., Concepts for Reduction of Blade/Vortex Interaction Noise, *J. Aircraft*, **24**, 1987, 120-125.
- [8] Kaykayoglu, C.R., Active Control of a Mixing Layer by Upstream Influence from an Oscillating Edge, *J. Fluids Struct.*, **3**, 1989, 1-16.
- [9] Peter, C.C., James, D.B., Robert, A.D.E. & John, N., Blade-Vortex Interaction Noise Reduction with Active Twist Smart Rotor Technology, *Smart Mater. Struct.*, **10**, 2001, 77-85.
- [10] Ziada, S., Feedback Control of Globally Unstable Flows: Impinging Shear Flows, *J. Fluids Struct.*, **9**, 1995, 907-923.
- [11] Cheng, L., Zhou, Y. & Zhang, M. M., Perturbed Interaction between Vortex Shedding and Induced Vibration. *J. Fluids Struct.*, **17**, 2003, 887-901.
- [12] Zhang, M. M., Cheng, L. & Zhou, Y., Closed- Loop-Controlled Vortex Shedding from a Flexibly Supported Square Cylinder under Different Schemes. *Phy. Fluids*, **16**, 2004, 1439-1448.
- [13] Zhou, Y., Zhang, H.J. & Liu, M.W., The Turbulent Wake of Two Side-by-Side Circular Cylinders, *J. Fluid Mech.*, **458**, 2002, 303-332.
- [14] Pinkerton, J.L. & Moses, R.W., A Feasibility Study to Control Airfoil Shape Using THUNDER. *NASA Technical Memorandum* 4767, 1997.
- [15] Copeland, B.M., Buckley, J.D., Bryant, R.G., Fox, R.L. & Hellbaum, R.F., THUNDER – an Ultra-High Displacement Piezoelectric Actuator. *NASA Langley Research Center*. Hampton, VA, 1999, 23681-0001.

## A Two-Dimensional Analysis of the Effect of a Rotating Cylinder on an Inverted Aerofoil in Ground Effect.

S. Diasinos<sup>1</sup>, T.J. Barber<sup>1</sup>, E. Leonardi<sup>1</sup> and S.D. Hall<sup>1</sup>

<sup>1</sup>School of Mechanical & Manufacturing Engineering  
The University of New South Wales, NSW, 2052 AUSTRALIA

### Abstract

The effect of a front wheel behind a front wing (on an open wheel racing car) was studied using Computational Fluid Dynamics (CFD). Results are presented for a 2D analysis conducted on an aerofoil and cylinder. CFD models are used to compare and demonstrate the effect that these two objects have on each other, when operating in close proximity. From the CFD analysis it was determined that the aerofoil generates lift, instead of the desired downforce in several of the configurations studied and only in certain positions is the aerofoil beneficial. This may explain the reduction in the front wing span that teams adopted after the Formula One (F1) regulation changes for the 1998 season.

### Introduction

In modern open wheeler racing cars, aerodynamics plays a critical role in determining the competitiveness of the vehicle. This is most evident in F1 where teams spend a large portion of their budget tailoring and perfecting their vehicles aerodynamics in an attempt to obtain a crucial advantage over their opposition. As a result, research conducted by teams is rarely made public. The majority of research that has been published on open wheeler aerodynamics, until this point, has focused on individual components studied on their own. This has included aerofoils and wings [7], cylinders [5], wheels [4] and diffusers [6]. Several publications have also presented a general overview of the aerodynamic aspects of an open wheeler racing car [3].

This paper attempts to explain the effect and interaction that the front wing and wheel (two common components of all open wheeler racing cars), have on each other. A 2D CFD analysis of a Cylinder and Aerofoil (A&C) was the preliminary study for this complex aerodynamic interaction. In the near future, a 2D experimental analysis will be used to verify the results presented in this paper. Later studies will also include a 3D CFD analysis and a 3D experimental analysis. Experimental techniques that will be used include flow visualisation and advanced laser diagnostics (LDV and PIV).

### CFD Model

A commercially available CFD package (Fluent 6.1.22) was used. The model consisted of an inverted NACA 4412 aerofoil in front of a circle in contact with the ground, as depicted in figure 1. An extensive verification study was conducted prior to the CFD model being used [2] which included grid refinement. The total number of elements in the CFD model ranged from 240000 to 260000. Grids that utilised up to 550000 elements were found to have no significant improvement on the accuracy of the model. Similar studies were also undertaken ensuring that the results obtained were independent of the positions of the boundaries and that of the convergence levels used.

During the CFD modelling results were obtained at angles within the range of  $-6^\circ$  to  $24^\circ$  in increments of  $3^\circ$ . Results were obtained at ground clearance values of 0.05c (chord), 0.13c, 0.25c and 0.50c. All results presented here are for a cylinder separation of 0.13c as defined by figure 1. The circle diameter was kept the

same as the aerofoil chord. This is also the reference length that was used for the Reynolds number, and lift and drag coefficients. All the results for the A&C were obtained at Reynolds number of  $4.1 \times 10^5$ , ensuring turbulent flow.

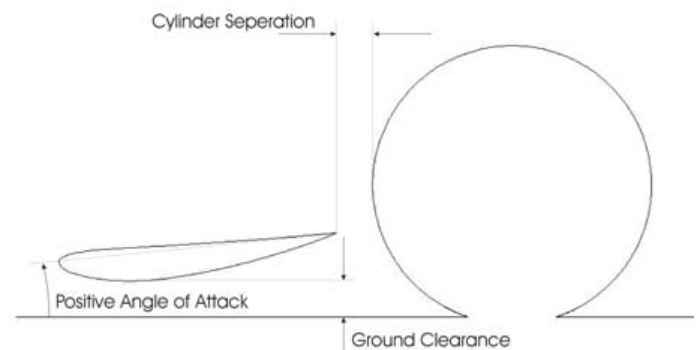


Figure 1. Parameters adjusted during analysis

The cylinder and aerofoil surfaces were modelled as smooth walls (no roughness). Even though this may not accurately depict the surface of a tyre, this is an accurate representation of the surface of the experimental apparatus that will be used to verify the CFD. A k-epsilon, RNG turbulence model was used, with enhanced, pressure gradient wall treatment so that the boundary layer over the aerofoil and cylinder could be monitored. The RNG turbulence model was chosen as it is an improved version of the standard k-epsilon turbulence model and is better suited to small levels of turbulence.

Lift values were obtained for a NACA 4412 aerofoil in free stream at a Reynolds number of  $3.0 \times 10^6$  using the same CFD model for a range of angles of attack of  $-6^\circ$  to  $18^\circ$  and these were found to agree within 5% to the results published by Abbott & Von Doenhoff [1]. Drag data followed the correct trend, however the actual error was larger.

### Results

#### Aerofoil Pressure Coefficients

From figure 2, it can be seen that the pressure beneath an inverted aerofoil in ground effect reduces as the aerofoil approaches the ground. The camber in the aerofoil allows the air flow to be

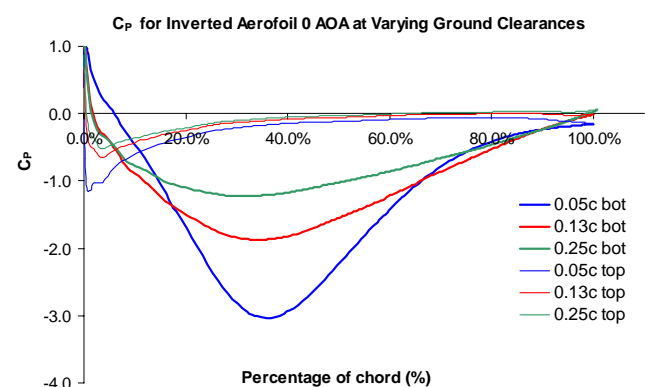


Figure 2. Aerofoil Coefficient of Pressure plots for Aerofoil bottom side at different Ground Clearances for an  $0^\circ$  angle of attack.

accelerated between the aerofoil and the ground. The rear of the aerofoil acts as a diffuser, the lower pressure region behind the aerofoil assisting with increasing the speed of the airflow between the aerofoil and the ground. Both these factors contribute to lowering the pressure beneath the aerofoil and this is the reason that an inverted wing in ground effect has improved performance in comparison to an aerofoil in free stream. As the angle of attack is increased, the lift also increases until stall is achieved at a much smaller angle in comparison to the free stream aerofoil. Zerihan and Zhang[7] obtained similar results during their experimental analysis explaining why an inverted aerofoil experiences improved performance near the ground.

### Cylinder Pressure Coefficients

Figure 3 shows that there was a large pressure acting at the base of the cylinder near the front of the contact patch, as well as behind the rear contact patch. Over the top of the cylinder, a lower pressure exists and because of this, a spinning cylinder in contact with the ground generates lift.

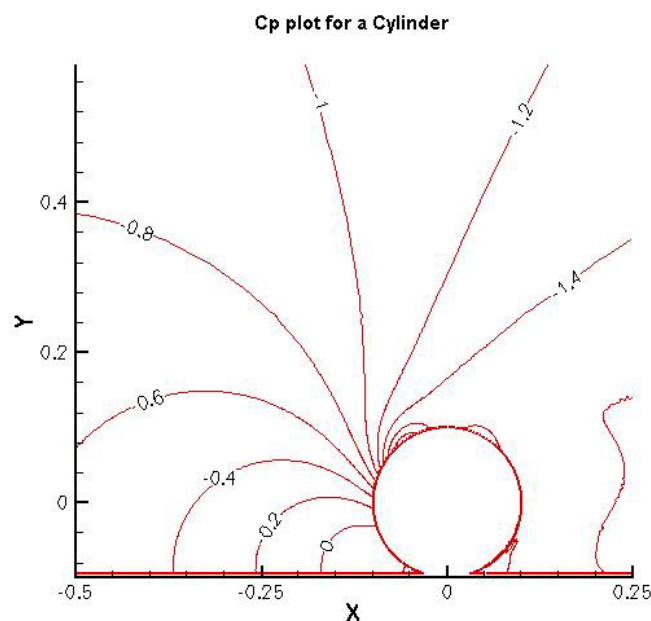


Figure 3. Coefficient of Pressure Contour plot for a cylinder.

This high pressure region is not confined to just the front contact patch of the cylinder, but also extends forward. Another important feature that is evident from the Coefficient of Pressure contour plot (fig 3) is the separation point that is located slightly forward of the top of the cylinder.

### Aerofoil and Cylinder Pressure Coefficients

The high pressure region forward of the front contact patch that was discussed earlier (figure 3) was also evident in results obtained for the aerofoil and cylinder case (figure 4). This high pressure region acts on the bottom surface of the aerofoil and for this reason the aerofoil was generating lift as opposed to the desired downforce. This could potentially be the reason why the front wings on F1 cars have had a reduced span after the regulation changes imposed for the 1998 season. The regulation changes required that the maximum width of the car be reduced from 200cm to 180cm and this would have further increased the interaction between the front wheel and wing.

Similarly, this is the reason that the aerofoil was experiencing a forward force, or a negative drag, in most positions tested in the presence of the cylinder. As the angle of attack was increased, more area was exposed to the high pressure region generated

forward of the cylinder contact patch and hence the lift and the negative drag increased in magnitude (figure 4).

Changing the angle of attack of the aerofoil has relatively little difference on the pressure generated at the contact patch, as this is always a stagnated flow. This is not the case for the front of the cylinder where the pressure decreases as the aerofoil angle of attack was increased. For this reason the drag of the cylinder was affected more by the aerofoil angle of attack than the lift generated by the cylinder was.

Cp plot for Aerofoil and Cylinder at various Aerofoil Angle of Attack

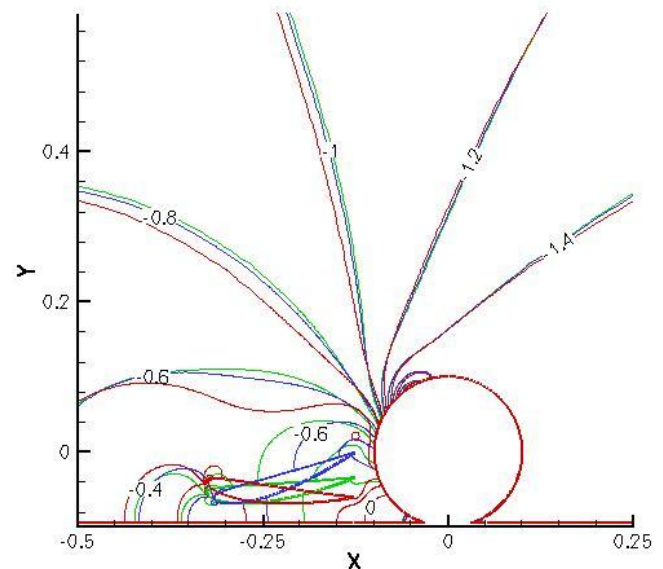


Figure 4. Aerofoil and Cylinder Coefficient of Pressure contour plot a various angles of attack for the aerofoil at a ground clearance of 0.13c

### Wing Lift Results

The lift curve slope obtained for an inverted wing in ground effect on its own, using the CFD model is compared to the experimental results obtained by Zerihan and Zhang[7] in figure 5. As the angle of attack is increased, the down force generated increases until the wing reaches stall. After this occurs, the downforce generated by the aerofoil reduces steadily. As the aerofoil ground clearance is reduced, the stall angle also reduces. These trends are evident in both the results obtained using the CFD model and also those obtained by Zerihan and Zhang[7]. The values for the coefficient of lift and the stall positions differ slightly because two different aerofoil have been used in the two studies since the coordinates of the aerofoil used by Zerihan and

CL of Aerofoil for Aerofoil AOA Comparison to Zerihan

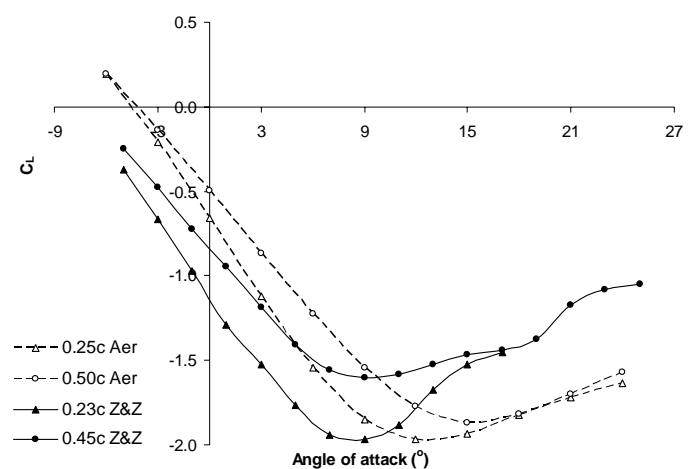


Figure 5. Lift curve slope comparing results by Zerihan and Zhang[7] (Z&Z) with those obtained using the Aerofoil model (Aer).



Zhang were not included in this reference and it is an aerofoil developed by an F1 team.

The lift curve slope for the aerofoil varied significantly when placed in close proximity to a spinning cylinder. Figure 6 shows the lift curve slope for a NACA 4412 aerofoil with a separation of  $0.13c$  from the cylinder at different ground clearances. For the lower ground clearances the lift curve slope is reversed compared too that of the aerofoil working in ground effect on its own. As the aerofoil is raised further from the ground, the lift curve slope gradually changes direction until it is in the same direction as the aerofoil on its own. When comparing the lowest ground clearance for the two cases, the greatest downforce is generated at an angle of attack of  $12^\circ$  for the aerofoil on its own and at the greatest negative angle of attack tested ( $-6^\circ$ ) for the aerofoil and cylinder.

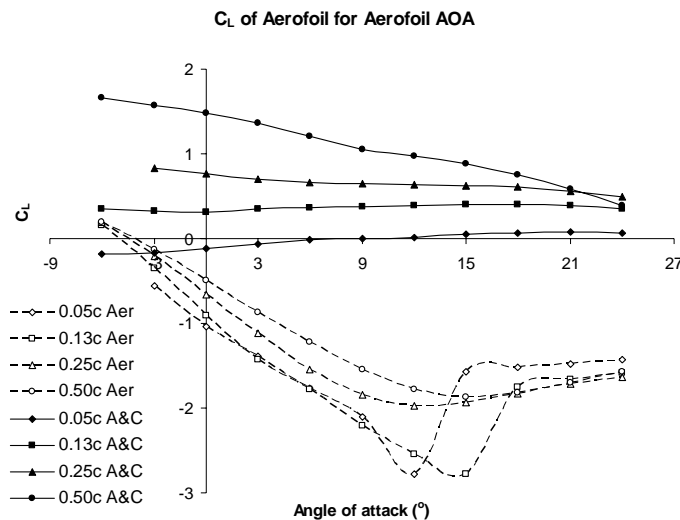


Figure 6. Lift curve slope comparing aerofoil on its own and aerofoil with cylinder separation of  $0.13c$

The magnitude of the downforce generated by the aerofoil in close proximity to the cylinder is also affected. The greatest level of downforce was still generated when the aerofoil was in the closest proximity to the ground tested, but the magnitude was small in comparison to the aerofoil on its own. As the aerofoil ground clearance increases, the aerofoil begins to generate lift instead of downforce.

### Wing Drag Results

The drag that the aerofoil develops is also affected by the presence of the cylinder. The aerofoil on its own has a steadily increasing drag as the angle of attack is increased up until the stall position. For the lower heights, the drag drops after the stall position and then continues to rise. The two greater ground clearances tested on the other hand, continued to rise and no drop in drag was evident after stall was achieved. As the aerofoil ground clearance is increased, the drag magnitude for all angles of attack reduces.

In the presence of the cylinder, the aerofoil drag decreases with an increase in angle of attack. As can be seen from figure 7, this trend is the opposite of that obtained for the aerofoil on its own, at similar ground clearances. The drag values for all the positive angles tested were also found to be negative implying that the high pressure region forward of the cylinder is pushing the aerofoil forward in most positions tested.

At the lowest ground clearance tested, the angle of attack had little change on the drag of the aerofoil. As the ground clearance was increased for the aerofoil, this becomes more pronounced,

but the minimum drag value was obtained at a lower AOA

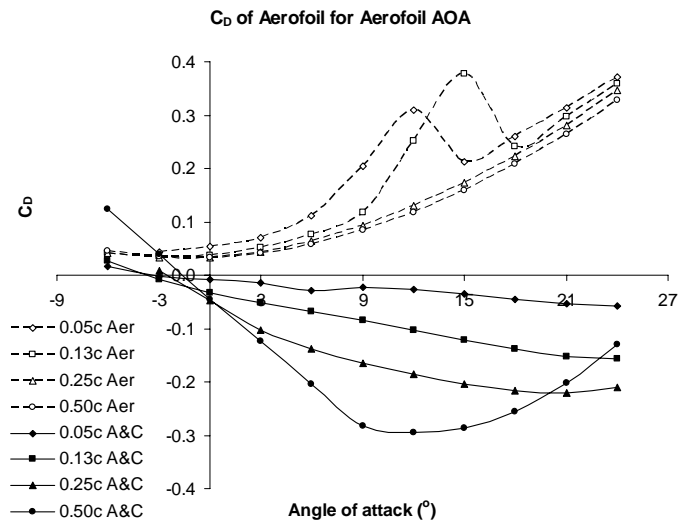


Figure 7. C<sub>D</sub> comparing aerofoil in ground effect (Aer) with aerofoil in the presence of a cylinder (A&C) at different ground clearances

### Cylinder Lift Results

The cylinder lift varied little as the aerofoil angle of attack was varied at the lowest ground clearance tested. As the ground clearance was increased, a change in the angle of attack of the aerofoil would result in a more significant change to the cylinder lift. These results are shown in figure 8. The presence of the cylinder drastically reduces the lift generated by the cylinder, as represented by the broken line in figure 8.

The results obtained at the three lowest ground heights all follow similar trends, were the maximum lift generated by the cylinder occurs when the aerofoil has an angle of attack of approximately  $12^\circ$ . When the aerofoil has a much greater clearance of  $0.5c$ , at the same angle of attack, the minimum lift case occurs. At the larger ground clearance as the angle of attack of the aerofoil is increased, a larger amount of air is deflected away from the cylinder and this reduces the speed of the air over the top of the cylinder and therefore the lift of the cylinder. In the lower positions, no angle of attack is large enough to create a similar effect and for this reason the trend is reversed for the larger ground clearance.

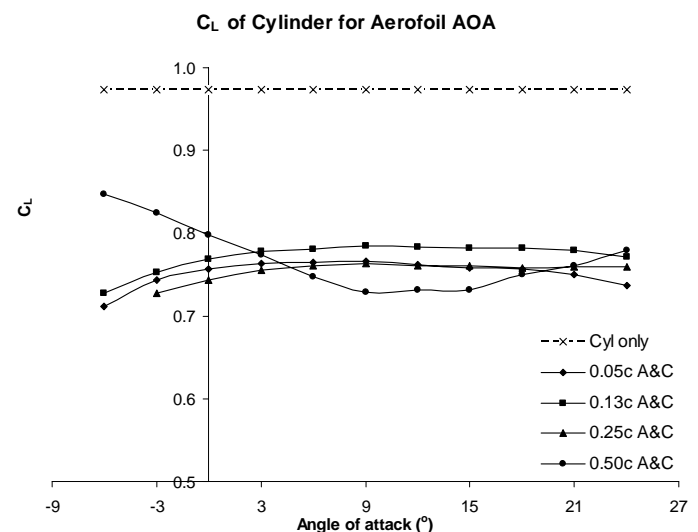


Figure 8. Lift coefficients of the cylinder on its own (Cyl) and with an aerofoil in front (A&C) at different ground clearances and angles of attack of the aerofoil.

### Cylinder Drag Results

The effect that the aerofoil angle of attack has on the cylinder becomes more pronounced as the aerofoil ground clearance is



increased. The drag curves shown in figure 9 exhibit opposite trends to that of the aerofoil drag discussed previously (figure 7). While the aerofoil drag values decrease with an increasing angle of attack and an increase in the ground clearance, the cylinder experiences an increase in drag with increasing aerofoil ground clearance and angle of attack. Only for a small number of positions tested did the cylinder have a reduced drag in comparison to the cylinder on its own. This is represented in figure 9.

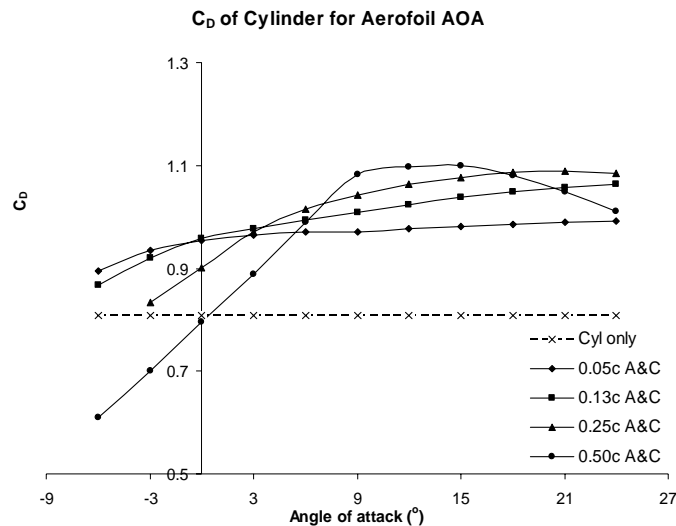


Figure 9. Drag coefficients of the cylinder on its own (Cyl) and the cylinder in the presence of the aerofoil (A&C) at different ground clearances and angles of attack for the aerofoil.

### Total Lift and Drag Results

Also of great interest was how the two components performed together as both the wing and the wheel contribute to the lift and drag generated by a racing car. For this reason, minimising the lift and drag of both is more important than reducing the lift or drag for each individual component. These results have been included in this paper as the optimum compromise between drag and lift varies depending on the characteristics of the track that the open wheeler will compete at.

The total lift of these two objects can be controlled by careful placement of the aerofoil relative to the cylinder. To minimize the lift generated by the two bodies combined, it was found that the best combination of angle of attack and ground clearance was at the lowest ground clearance and the most negative angle of attack tested (0.05c,  $-6^\circ$ ). This can be seen in figure 10 where the broken line represents the lift that the cylinder would experience

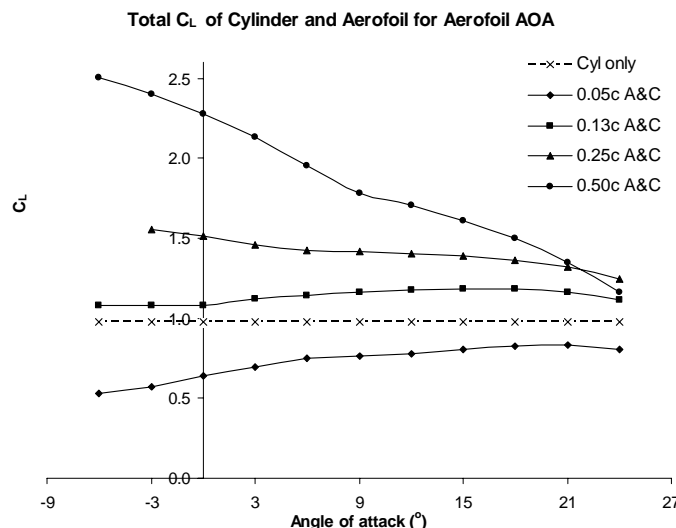


Figure 10. Total lift for aerofoil and cylinder compared to the cylinder on its own.

on its own. In this position it is possible to reduce the lift generated by the cylinder alone by approximately 50% by placing the aerofoil forward of the cylinder and for a small drag penalty.

The total drag result for a given ground clearance did not change significantly with a changing angle of attack. The only significant change occurs with a change in the aerofoil ground clearance. In order to minimize the drag of the two objects it would be necessary to increase the ground clearance of the aerofoil. The best result obtained, amongst the positions tested, for minimizing the drag was found to occur at a ground clearance of 0.5c and an angle of attack of  $-6^\circ$ . Unfortunately the same position would result in a significant increase in lift.

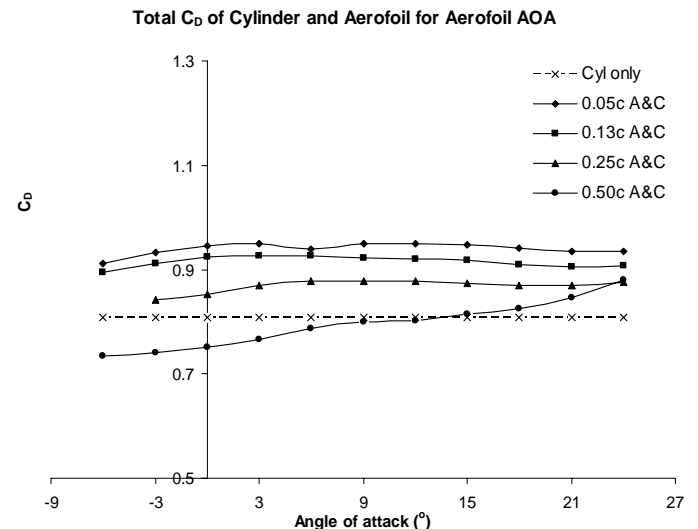


Figure 11. Total drag for aerofoil and cylinder (A&C) at different ground clearances for the aerofoil compared to the cylinder (Cyl) on its own.

### Conclusion

This analysis suggests that the cylinder has a substantial affect on the performance of the aerofoil. The main reason for the significant change found for the aerofoil performance in the presence of the cylinder was due to the large pressure region that is created forward of the contact patch of the cylinder. While the analysis thus far has only been conducted using CFD, in the near future experimental results will be used to verify the CFD results. The results obtained during this analysis imply that it would be beneficial to continue this research so that it may include a 3D CFD and experimental model of a finite width wing and wheel.

### References

- [1]. Abbot, I.H. & Von Doenhoff, A.E., Theory of Wing sections
- [2]. AIAA, Guide for Verification and Validation of Computational Fluid Dynamics Simulations AIAA G-077-1998
- [3]. Dominy, R.G., Aerodynamics of Grand Prix Cars, *Proceedings of the Institution of Mechanical engineers, Part D: Journal of Automobile Engineering*, Vol. 206, no.D4, 1992, pp. 267-274
- [4]. Fackrell, J.E., & Harvey, The Aerodynamics of an Isolated Road Wheel, No. 8 *Proceedings of the Second Symposium on Aerodynamics of Sports and Competition Automobiles*, collection of AIAA papers published by western Periodicals Co., North Hollywood, CA, 1975
- [5]. Mittal, S. & Kumar, B., Flow Past a Rotating Cylinder, *J. Fluid Mech* (2003), Vol 476 pp. 303-334
- [6]. Sovran, G., and Klomp, E.D., Experimentally Determined Optimum Geometries for Rectilinear Diffusers with rectangular, Canonical or Annular Cross-Section, *Fluids Mechanics of internal Flows*, Elsevier Publishing Co., N.Y., 1967 pp. 270-319.
- [7]. Zerihan, J. & Zhang, J., Aerodynamics of a Single Element Wing in Ground Effect, *Journal of Aircraft*, Vol 37, No 6, pp.1058 – 1064, November-December 2000

## PIV measurements in a square backward facing step

M. Piirto, A. Karvinen, H. Ahlstedt, P. Saarenrinne and R. Karvinen

Energy and Process Engineering Laboratory  
Tampere University of Technology, P.O. Box 589, FI-33101 Tampere, FINLAND

### Abstract

The measurements with both 2D/2C and 2D/3C (stereo) particle image velocimetry (PIV) are carried out in a square channel backward-facing step (BFS) in a turbulent water flow at three Reynolds numbers of about 12000, 21000, and 55000 based on the step height  $h$  and the inlet streamwise maximum mean velocity  $U_0$ . The inlet flow is fully developed before the step change with the expansion rate of 1.2. The effect of the velocity spatial sampling resolution is verified with four different two-dimensional PIV measurement sets in location  $x/h = 4$  by comparing maximum Reynolds stresses, rms and Reynolds shear stress profiles are compared with DNS and RSM data having similar Reynolds number with experimental flow of the slowest velocity. The shapes of the profiles agree well with each other on the separated shear layer region of the backward-facing step but in these profiles both DNS and RSM data show higher values than PIV data. PIV results show that the mean and rms velocity profiles between the experimental flow cases are almost identical when they are non-dimensionalized by  $U_0$ .

### Introduction

Comparison of PIV data with the computational fluid dynamics (CFD) data is important when there exists remarkable differences in the results but also many similarities. Compared to the previous experimental study of Piirto *et al.* [7] lot of emphasis is given in the design of backward-facing step (BFS) channel loop to guarantee that the inlet flow before the step is fully developed i.e. the channel length is  $100 \times$  channel height  $y_0$  (or width) and expansion rate  $ER = y_1/y_0 = 1.2$  ( $y_1 = y_0 + h$ ) is exactly the same with the DNS and Reynolds stress model (RSM) tests. In this work, the emphasis is in the PIV turbulence characterization and the results are compared with both DNS of Le *et al.* [3] and computational data of RSM [2].

### PIV system

The stereo PIV system consists of an Nd:YAG double cavity laser with light sheet optics and a  $2 \times$  CCD camera of resolution  $1280 \times 1024$  pixels. Water flow is seeded by the glass sphere particles with an average size of  $10 \mu\text{m}$ . The seeding density is about 10 particles / interrogation area when the laser sheet thickness is about 0.5 mm and the size of the interrogation area is  $32 \times 32$  pixels. In the computation of the velocity vectors, the standard discrete window shift (DWS) method is applied. If the discrete part of the window displacement can be determined within 0.5 pixel, the accuracy of the results after the final iteration is very high, even 0.04 pixel [10]. Only few (1-20) erroneous velocity components conflicting with local median criteria are detected. The spurious spanwise velocity vector components are replaced by interpolation. In stereo PIV measurements, an angle of  $30^\circ$  is set between the cameras with Scheimpflug adapters, and a procedure of Soloff [8] is applied to correct the camera images. The sampling interval between the measurements is 0.25 s, and thus the statistical independency in time domain can be assumed. The measurement samples are 1000 and for the spatial sampling resolution test 2000 vector fields / location. However, spatial averaging in the streamwise

direction over seven lines increases these numbers to 7000 and 14000 samples, respectively. This distance of seven vectors corresponds to  $0.2h$ , and in practice within it, the values of the estimates do not change except the noise is decreasing.

### Inlet flow

The physical size of the square-channel is  $47 \times 47$  mm and the step height is  $h = 10$  mm. The flow directions 1, 2, 3 are streamwise ( $x$ ), vertical ( $y$ ), and spanwise ( $z$ ), respectively. The corresponding velocities are denoted either by plain variables  $U$ ,  $V$ ,  $W$ , and their fluctuating parts  $u$ ,  $v$ ,  $w$  (in graphics). The inlet streamwise maximum mean velocities are  $U_0 \cong 1.2$  m/s,  $U_0 \cong 2.1$  m/s, and  $U_0 \cong 5.5$  m/s and the boundary layer thickness is defined as channel half width (height)  $\delta = \frac{1}{2}y_0$ . The corresponding turbulent boundary layer properties at  $x/h = -4$ , i.e. before the step are shown in Table 1. The inlet flow is measured with the same PIV setup as the other measurements in BFS. Due to the distances close to the wall, reliable measurements could not be conducted closer than 0.5 mm to the wall. Thus, a rough estimate of the friction velocity  $u_\tau$  is solved by fitting the mean inlet velocity profile measured with PIV with Spalding's universal velocity profile for boundary layers [9]. In the flow Case A, the result of the fitting of Spalding's velocity profile to the PIV profile is shown in Figure 1. Inlet velocity rms profiles for the streamwise component in  $x/h = -3$  are shown in Figure 2 and it is compared with DNS of Le *et al.*, DNS of Moser [4] with  $Re_\tau = 590$  and with two-dimensional RSM. Reynolds number for RSM is  $Re_\tau = 1170$  and it is same with the PIV Case A. In addition, both the DNS computations are performed in the infinite wide channel causing lower turbulence intensities than the corresponding results should be in the bounded channel.

PIV experimental cases – inlet flow		
Case A	Case B	Case C
$U_0 \cong 1.2$ m/s	$U_0 \cong 2.1$ m/s	$U_0 \cong 5.5$ m/s
$u_\tau \cong 0.051$ m/s	$u_\tau \cong 0.085$ m/s	$u_\tau \cong 0.2$ m/s
$Re_\tau = u_\tau \delta / \nu \cong 1170$	$Re_\tau = u_\tau \delta / \nu \cong 2000$	$Re_\tau = u_\tau \delta / \nu \cong 4700$

Table 1. Inlet flow boundary layer properties.

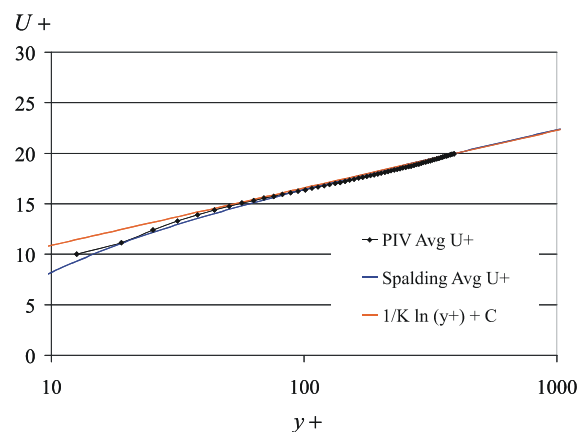


Figure 1. Fitting of Spalding's velocity profile to the PIV mean velocity profile in flow Case A. Log-law parameters are  $K = 0.405$  and  $C = 5.2$ .

As can be noticed here, and will be noticed in the turbulence characterization after the step, the upper boundary conditions, i.e. no-stress wall, limit the results in Le *et al.* Even so, the turbulence intensities by the PIV experiments show lower values than the DNS ones. Especially in DNS of Le *et al.* turbulence intensity maximum is remarkably higher than with DNS of Moser. Because of the square shape of the channel, the sidewalls increase turbulence intensity of the PIV experiments, and for this reason streamwise velocity rms could be about 10% higher than rms of DNS results of Moser between  $y/\delta = 0.2 - 1.0$ , as can be seen in Figure 2.

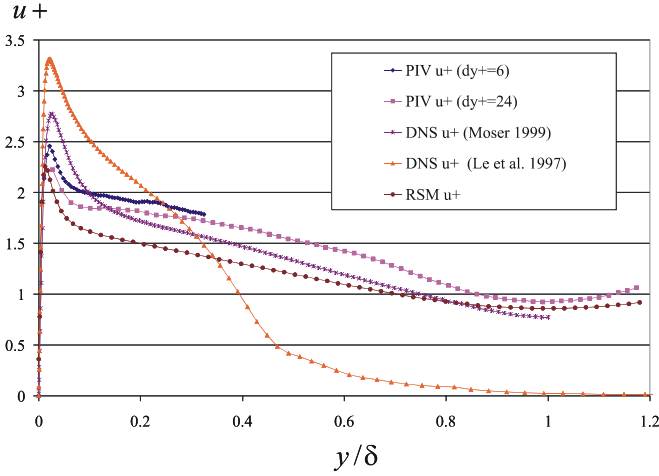


Figure 2. Inlet rms velocity profiles for PIV Case A, DNS of Moser, DNS of Le *et al.* and RSM at  $x/h = -4$ . Spatial sampling resolutions for PIV experiments are  $\Delta y = 0.0125h$  ( $\Delta y^+ = 6$ ) and  $\Delta y = 0.05h$  ( $\Delta y^+ = 24$ ).

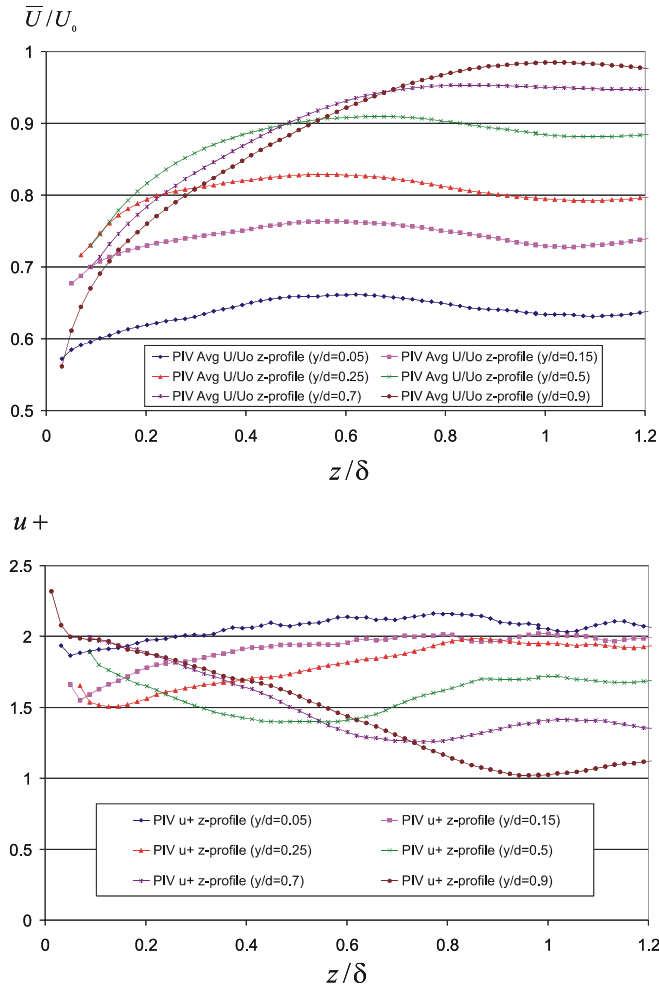


Figure 3. Off-center inlet mean and rms velocity profiles at  $x/h = -3$  and  $y/\delta = 0.05, 0.15, 0.25, 0.5, 0.7$ , and  $0.9$  for PIV flow Case B. Spatial sampling resolution is  $\Delta y = 0.05h$ .

In addition to this, in the PIV results the higher measurement resolution  $\Delta y = 0.0125h$  ( $\Delta y^+ = 6$ ) gives slightly higher turbulence intensity than the lower resolution of  $\Delta y = 0.05h$  ( $\Delta y^+ = 24$ ) which is the spatial distance between two measurement samples (overlapping 50%) and also the half size of the interrogation area. With the higher resolution also the turbulence intensity peak is found and it is about  $u^+ = 2.5$ . For DNS of Moser it is  $u^+ = 2.7$  and for RSM it is  $u^+ = 2.25$ . In Figure 3 is shown the off-center profiles for the streamwise mean velocity and rms for the Case B and the lower resolution of  $\Delta y = 0.05h$ .

### Re-attachment point

Reattachment point after the step change in flow Cases A, B and C are  $5.3h$ ,  $5.6h$ , and  $5.7h$ , respectively. In the previous study of Piirto *et al.* [7] it is  $6.2h$  but the flow geometry is slightly different and inlet flow is not fully developed. According to DNS of Le *et al.* it is  $6.3h$  but again no-stress wall upper boundary condition may have an increasing effect on it. In Figure 4 is shown streamwise mean velocity and the location in which the direction of flow changes. The distance from the wall is approximately the highest spatial resolution  $\Delta y = 0.0125h$  which is in the wall units  $\Delta y^+ = 6$  for the Case A,  $\Delta y^+ = 11$  for B,  $\Delta y^+ = 25$  for C. With the computational model corresponding to the Reynolds number of PIV Case A, RSM gives re-attachment length  $4.5h$ , and in three-dimensional case the effect of the sidewalls will only decrease it.

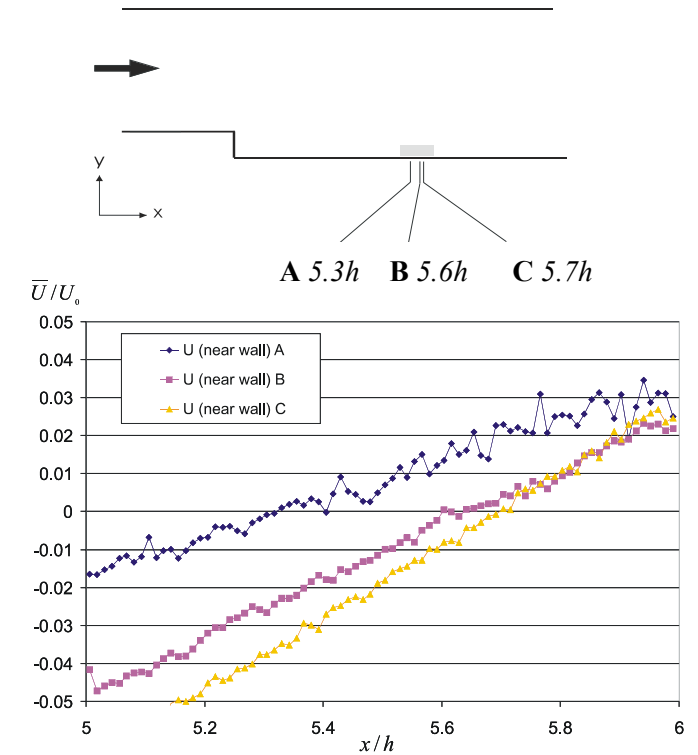


Figure 4. Streamwise mean velocity by the re-attachment point with the highest spatial sampling resolution  $\Delta y = 0.0125h$  which is also the rough distance from the wall.

### Turbulence profiles after the step

The shapes of the profiles for mean velocity, rms and Reynolds shear stress agree well with the DNS study of Le *et al.* in the separated shear layer part of flow, but outside that area, the results are not comparable with each other because of the DNS conditions. With RSM, the shape of the profiles agree well with PIV but especially turbulence intensity in vertical direction and Reynolds shear stress are remarkable higher than the corresponding PIV and DNS estimates and their maxima are closer to the wall than the corresponding maxima of PIV and DNS. In addition to this, there exists sudden change in velocity mean of RSM by the wall after about  $x/h = 3.5$ , and the peak is

too low which is also found in [5]. With PIV and DNS backward streamwise mean velocity peak is about  $U/U_0 = -0.15$ . Streamwise rms maximum at  $x/h = 4$ , after non-dimensionalized with  $U_0$ , is  $u_0 = 0.151$  for PIV,  $u_0 = 0.175$  for DNS, and  $u_0 = 0.188$  for RSM. The non-dimensional average, rms, and Reynolds shear stress profiles are compared with DNS and RSM at  $x/h = 4$  in Figures 5, 6, 7, 8, and 9. The PIV spatial sampling resolution for these results is  $\Delta y = 0.05h$ . As can be noticed, the shapes of the profiles fit well with each other except DNS between  $y/h = 1.5 - 6.0$ . Both the upper boundary condition with stress and the sidewall effects would only increase the maximum of rms of DNS. Thus, it means that there exists clear difference between the experimental values and DNS results. For the spanwise velocity rms, the difference is the opposite, and the higher estimates of PIV than of DNS can be explained by the sidewall effect of the square-channel. It is interesting to compare the RSM results with the three-dimensional RSM for the square-channel, because it will give an certain understanding about the the sidewalls effects in turbulence quantities, especially at the re-circulation region. According to the initial two-dimensional and three-dimensional air computations, which computational time is much less than with water, the increase is between 5 – 10% for the velocity rms profile maxima and about 20% for the Reynolds shear stress maximum at  $x/h = 4$ . These values are only hints, but anyhow the effect of the sidewalls will only take DNS and RSM turbulence intensity and Reynolds shear stress profiles further off from the PIV ones, except the spanwise velocity rms profile which will get closer with the PIV profile. Unfortunately, the three-dimensional RSM computations by water have not been finished yet.

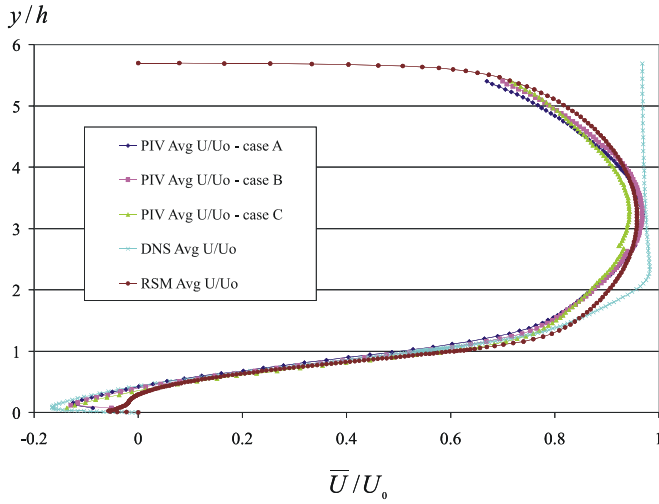


Figure 5. Mean velocity profiles at  $x/h = 4$  for PIV, DNS and RSM.

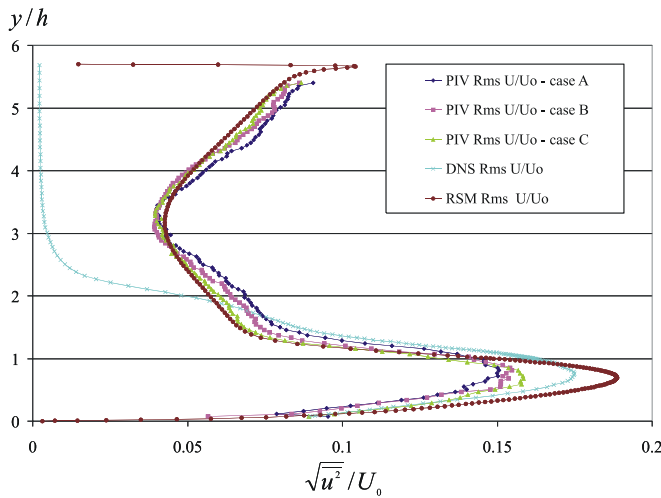


Figure 6. Streamwise velocity rms profiles at  $x/h = 4$  for PIV, DNS and RSM.

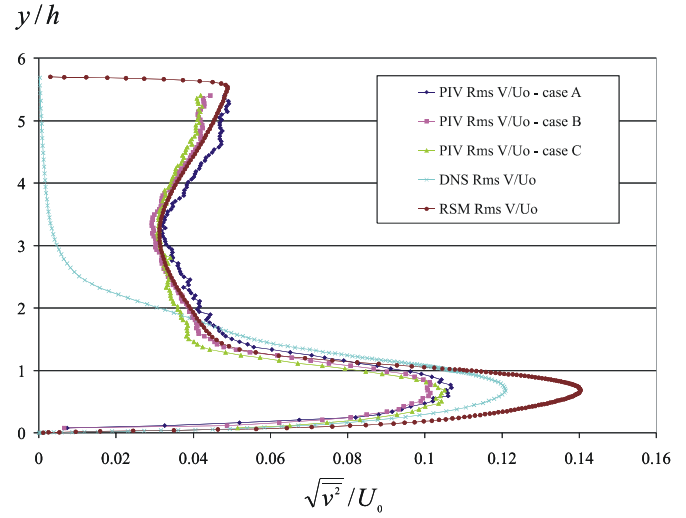


Figure 7. Vertical velocity rms profiles at  $x/h = 4$  for PIV, DNS and RSM.

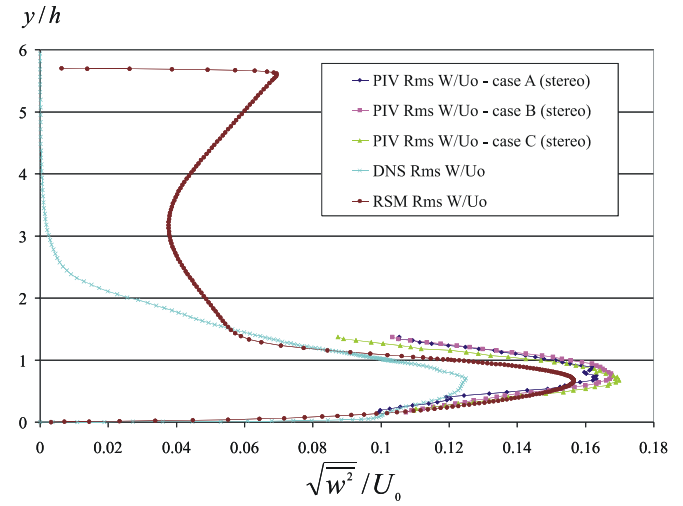


Figure 8. Spanwise velocity rms profiles at  $x/h = 4$  for PIV, DNS and RSM.

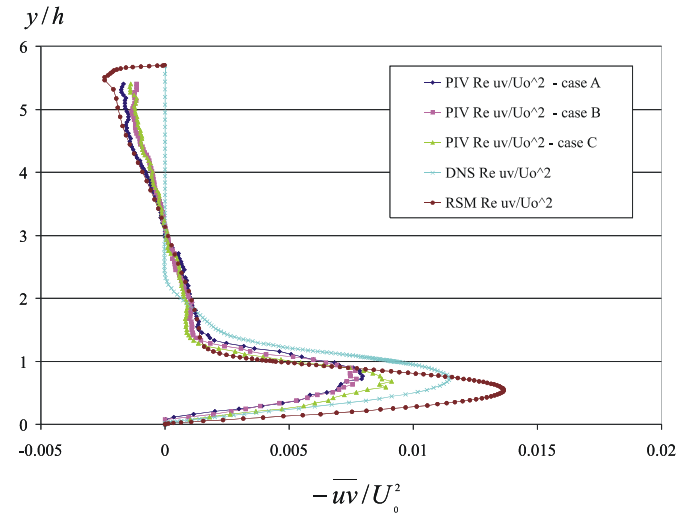


Figure 9. Reynolds shear stress profiles at  $x/h = 4$  for PIV, DNS and RSM.

### Spatial sampling resolution and rms error

When the PIV results are compared with CFD, the increased spatial sampling resolution and the measurement rms error are important factors as they have an increasing effect on turbulence intensity. Even in turbulence intensity, the effect is remarkable while in contrast with the velocity gradients the effect of the



spatial resolution must be analysed [1]. If the resolution is high, the smaller turbulence scales are included in the estimates and they will be more realistic. However, if the measurement spatial resolution passes the capacity of the PIV system and the number of the particles is too few in a particular interrogation area, it also has an increasing effect in the estimates because of the measurement error. Thus, it is important to prove that the data sets are stationary at least in rms sense [6] and also verify that the measurement rms error do not increase when the spatial resolution increases. This is verified, and the rms error with all the resolutions are about 0.1 pixel for velocity components  $U$  and  $V$ , and 0.3 pixel for  $W$ . These are estimated by zero-flow tests [7] provided for each one of the resolutions of the following spatial sampling resolutions and for the resolution used with the measurements of the previous page. One kind of estimate for the uncertainty is if these rms errors are divided by rms maxima. In location  $x/h=4$  these maxima are about 1.4 pixels, 1.4 pixels and 2.3 pixels for streamwise, vertical, and spanwise velocity rms estimates, leading to uncertainty error of 7%, 7%, and 13%, respectively. In practice, the rms error increases turbulence rms. However, this uncertainty estimate is rather the maximum than the average because velocities are much higher on non-shear regions, typically between 2 – 10 pixels. The effect of the spatial resolution is plotted in Figures 10 and 11 for streamwise velocity rms and Reynolds shear stress. According to this test, the effect of the spatial sampling resolution is about 5-10% for streamwise velocity rms depending on the case, and about 5% for Reynolds shear stress  $\overline{uv}$  when the resolution increases from  $\Delta y = 0.05h$  to  $\Delta y = 0.0125h$ .

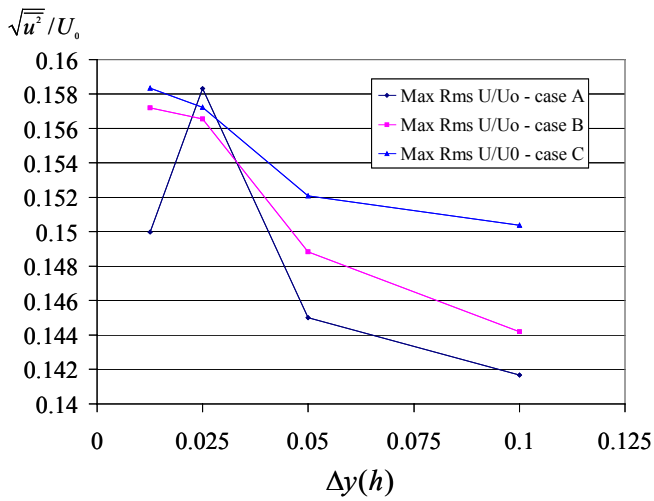


Figure 10. Streamwise velocity rms maxima at  $x/h = 4$  with 2D/2C PIV test data sets of different spatial sampling resolutions.

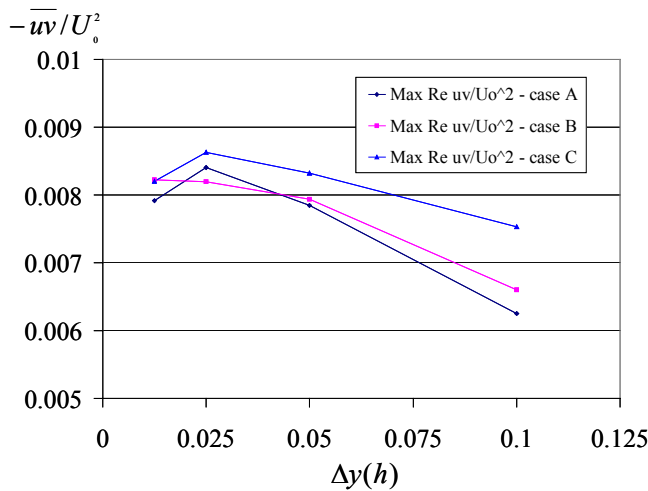


Figure 11. Reynolds shear stress maxima at  $x/h = 4$  with 2D/2C PIV test data sets of different spatial sampling resolutions.

As was mentioned, this resolution  $\Delta y = 0.05h$  is used with 2D/2C and 2D/3C measurements in the results of the previous Section. This increased spatial resolution will take the PIV results a bit closer with the CFD results.

## Conclusions

Turbulent backward-facing step flow of a square-channel is measured by conventional PIV system and stereo PIV system at three Reynolds numbers of about 12000 (Case A), 21000 (Case B), and 55000 (Case C), based on the step height  $h$  and the inlet streamwise maximum mean velocity  $U_0$ . The inlet flow before the step is fully developed and the expansion rate of the step is  $ER = 1.2$ . The turbulence intensity profiles are almost identical between the experimental cases at different Reynolds numbers. The PIV results are compared with DNS and RSM for infinite width of the channel that have similar Reynolds number with the Case A. The shapes of the profiles agree well with each other in the separated shear layer part  $y/h = 0 - 1.5$ . The most remarkable difference is the spanwise velocity rms maximum, which probably depends more on the sidewalls than the other turbulence intensities. In addition, the re-attachment length with PIV Case A is  $5.3h$  whereas with DNS, it is  $6.3h$  and with RSM, it is  $4.5h$ . The effect of the PIV spatial sampling resolution is analysed with the four test data sets. When this effect is taken account, the quantities between PIV and DNS are almost the same. However, it can be assumed that some difference exists between PIV and CFD results when the effect of the sidewalls will be analysed by three-dimensional RSM computations.

## References

- [1] Fouras, A. & Soria, J., Accuracy of out-of-plane vorticity measurements derived from in-plane field data, *Exp. Fluids* **25**, 1998, 409-430.
- [2] Launder, B.E., Second-Moment Closure: Present... and Future? *Int. J. Heat Fluid Flow* **10**:4, 1989, 282-300.
- [3] Le, H., Moin, P. & Kim, J., Direct numerical simulation of turbulent flow over a backward facing step. *J. Fluid. Mech.* **330**, 1997, 349-374.
- [4] Moser, R.D., Kim, J. & Mansour, N.N., Direct numerical simulation of turbulent channel flow up to  $Re_\tau=590$ , *Phys. Fluids* **11**:4, 1999, 943-945.
- [5] Parneix, S., Laurence, D., & Durbin, P.A., A Procedure Using DNS Database, *Trans ASME* **120**, 1998, 40-47.
- [6] Piirto, M., Ihalainen, H., Eloranta, H. & Saarenrinne, P., 2D Spectral and Turbulence Length Scale Estimation with PIV, *Journal of Visualization* **4**:1, 2001, 39-49.
- [7] Piirto, M., Saarenrinne, P., Eloranta, H. & Karvinen, R., Measuring turbulence energy with PIV in a backward-facing step flow, *Exp. Fluids* **35**, 2003, 219-236.
- [8] Soloff, S.M., Adrian, R.J. & Liu, Z.C., Distortion compensation for generalized stereoscopic particle image velocimetry. *Meas. Sci. Technol.* **8**, 1997, 1441-1454.
- [9] Spalding, D.B., A single formula for the law of the wall. *J. Appl. Mech.* **28**, 1961, 455-457.
- [10] Westerweel, J., Dabiri, D. & Gharib, M., The effect of a discrete window offset on the accuracy of cross-correlation analysis of digital PIV recordings. *Exp. Fluids* **23**, 1997, 20-28.

# Stabilisation of a Trapped Vortex for Enhancing Aerodynamic Flows

A. Bouferrouk<sup>1</sup>, S. I. Chernyshenko<sup>1</sup>

<sup>1</sup>AFM Research Group, School of Engineering Sciences  
Southampton University, Southampton, SO17 1BJ, United Kingdom

## Abstract

This study reports on the technologically important application of active stabilisation control of a trapped vortex concept for improving the aerodynamic characteristics of a Lighthill's airfoil. The flow under consideration is two-dimensional, incompressible and inviscid solved using a suitably designed Discrete Vortex Method (DVM) code. With suction, various techniques were implemented for stabilisation resulting in reduced drag and increased lift. Stabilisation was also achieved via a feedback control law which kept the vortex stable with respect to large-scale vortex shedding.

## Introduction

Large-scale vortex structures usually tend to travel downstream to the wake, and continuously maintain a chain of vortices forming behind them, see figure 1. Consequently, the drag increases and both the wake and the loads on the body become unsteady. However, using specific technologies such as vortex cells (cavities) allows the vortex structure to be held near the body at all times. This is what is known as a trapped vortex as depicted in figure 2. In figure 2 the trapped vortex is identified by the enclosed organised streamlines. Although not a new idea, only

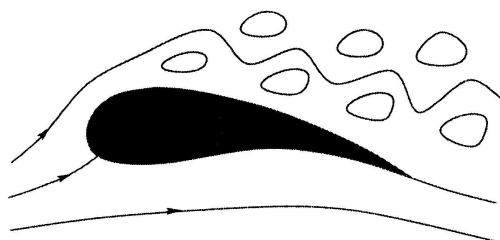


Figure 1: Vortex Shedding from a Generic Airfoil

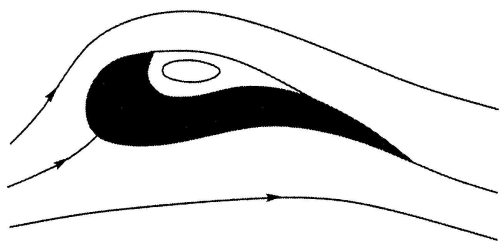


Figure 2: Airfoil with a Cavity and a Trapped Vortex

few articles are available on trapped vortices. Unfortunately, compared to other pursued ideas, it is much less known within the academic community. Research into trapped vortex flows began following Kasper's seminal efforts in designing a glider having a significant lift improvement at low speeds (without corresponding change in drag), which he attributed to a massive vortex residing over the upper surface of the wing [6]. A trapped vortex is also a useful tool for drag reduction because it could postpone/prevent vortex shedding from bodies of aircraft, racing cars, and helicopters. Also, by maintaining a vortex near a wing's surface it is possible to extend the post-stall performance by increasing the maximum obtainable lift. For a racing

car, this translates into increased downforce as found by Garcia et al. [9]. Bunyakin et al. [5] considered trapped vortices for separation control which is extremely important in internal systems such as a compressor. There is also the opportunity of using a trapped vortex for vehicle control.

Unfortunately, previous studies concluded that a trapped vortex is unstable, or at best has a very limited region of stability [11], and as such the slightest form of perturbation may cause it to become unstable. Although a trapped vortex minimises unsteadiness, other forms of unpredictable perturbations and/or intrinsic instability mechanisms are always present in a flow making the vortex susceptible to being easily displaced. Therefore, to fully achieve the potential benefits of a trapped vortex, it must be stable at all times.

The intention of the ongoing work is to demonstrate the feasibility of stabilising a trapped vortex using active flow control. The main objective is to maximise the benefits of stabilisation by exploring reliable and cost effective techniques for enhancing aerodynamic flows.

## Novelty of the Research Study

In past numerical work the modelling and stability of a trapped vortex was always based on a single point vortex. In this study, the vortex is modelled by a very large number of elemental blob vortices due to a DVM. However, use of single vortices enabled the application of linear stability theory for characterising the stability of the vortex while this is extremely difficult with a large number of vortices. Therefore, characterisation of stability will be different to old methods but not without proper physical justification. With the exception of the work of Iollo et al. [7] on optimal control of a single point trapped vortex, stabilisation has always been passive. The present work is a unique application of feedback control to the stabilisation of a trapped vortex.

## Formulation of the Problem

The flow model for the study is the two-dimensional, inviscid, incompressible flow, while the simulation model for a body with a trapped vortex is a Lighthill's airfoil. The body shape was determined from a classical inverse problem. The inverse problem is that of determining the body shape for a given velocity distribution on its surface. For the present geometry, the desired velocity distribution ensures no separation takes place except at a single point on the upper surface. Such point could be replaced by a cavity for vortex trapping [4], see figure 3. Thus, the Lighthill's airfoil has a naturally desirable distribution of velocity and is potentially able to trap a large vortex. Because of these characteristics of the Lighthill's airfoil it was selected as the simulation model. The flow solution was obtained using the inviscid version of a DVM due to Spalart [12]. Figure 4 shows a convergence study for the main parameters. The set of results suggests that a choice of 1300 vortices and a time step of 0.004 should provide reasonable estimates. The numerical scheme was initially found to be ill-posed. The application of a Tikhonov regularisation [3] technique made the problem well-posed.



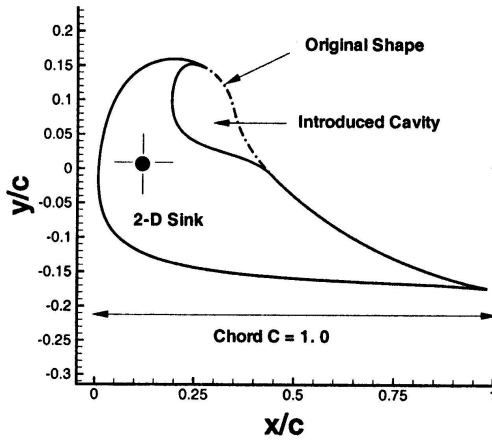


Figure 3: Lighthill's Airfoil Geometry

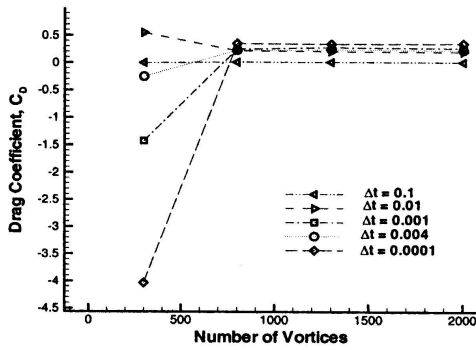


Figure 4: Choice of Numerical Parameters

## Flow Control

### Stabilisation by Continuous Steady Suction

The DVM was modified to simulate suction effects using a 2-D potential sink introduced inside the body, see figure 3. Uniform suction was applied using the spacing between two consecutive wall points  $x_k$  and  $x_{k+1}$  as suction panels. For each panel ( $x_k$ ,  $x_{k+1}$ ), the suction flow rate  $Q_k$  is obtained as

$$\psi(x_{k+1}, t) - \psi(x_k, t) = Q_k \quad (1)$$

where  $\psi$  is a stream function. In order to determine the best location for suction, the numerical simulation was performed with a constant distributed suction at two distinctive locations; one towards the airfoil's trailing edge and the other along the cavity's surface. The results for the drag history are shown in figure 5. Averaged numerical values of drag and lift coefficients,  $C_{D_{av}}$ , and  $C_{L_{av}}$ , are also shown. Compared with the result with no control, the placement of the suction system along the cavity was effective in stabilising the trapped vortex by reducing the amplitudes of the unsteady drag force, resulting in a substantial enhancement of the aerodynamic performance. On the contrary, trailing edge suction seems to have a counter productive effect exhibited by the disruption in the flow field even more than in the uncontrolled case, causing higher drag oscillations and reduced lift (from 1.8365 to 1.4469). Figure 6 shows velocity vector plots of the flow with and without suction. The cavity becomes completely filled with an organised vortex bubble when a strong suction is applied compared to the case with no suction.

### Force Behaviour with Suction

Figure 7 illustrates the variations in lift and drag forces with increasing suction: the drag decreases and lift increases. This improvement was due to the fact that as suction increases it

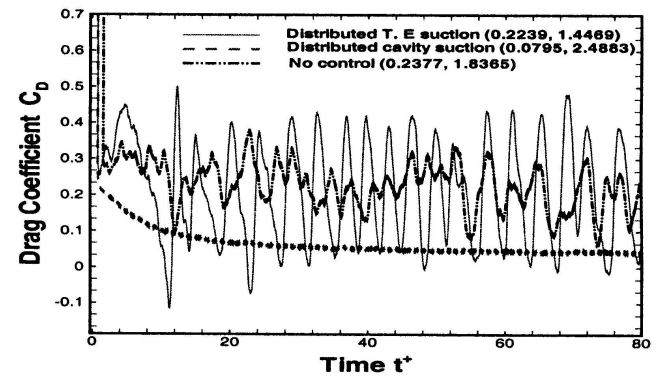


Figure 5: Choice of Best Suction Location

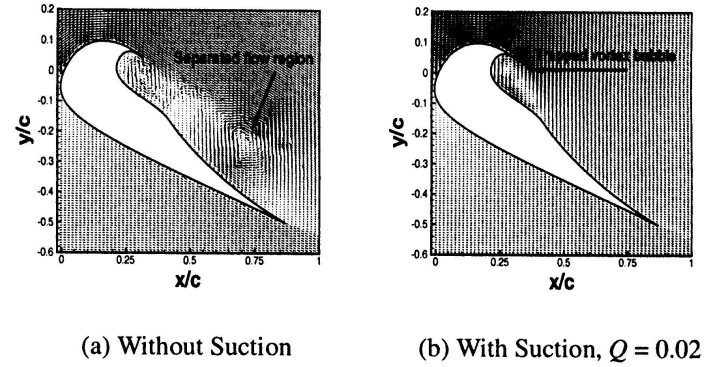


Figure 6: Vortex Trapping with Suction

gradually weakens the vortex shedding process (gradual stabilisation). However, beyond a suction rate of about  $Q = 0.017$  further increases in suction leads to a decrease in performance.

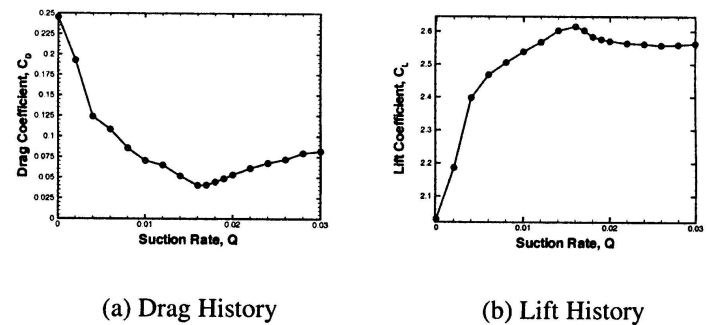


Figure 7: Force Histories with Suction

### Stabilisation by Unsteady Suction

The main idea behind this was to cease suction completely once the trapped vortex was stabilised then switch it back on at a later time. This technique relies on the fact that the self rotational behaviour of the trapped vortex enables it to remain stable for some time before its stability is lost. When suction was switched between  $Q_{total} = 0.02$  and zero the trapped vortex was kept in the cavity with no shedding and a 13% reduction in the required suction was achieved. Interestingly, compared to the case with continuous suction, the  $C_{L_{av}}$  remained the same but  $C_{D_{av}}$  was reduced from 0.078 to 0.020 using unsteady suction.

### Stability of the Trapped Vortex

The results presented for the Lighthill's airfoil have clearly shown that with a strong suction a forming massive vortex struc-

ture is withheld permanently in the vicinity of the airfoil and the flow reaches and maintains a steady state. Despite this evidence, we seek a convincing mathematical argument for stability. From the work of Saffman [11], the equilibrium location of a stationary vortex is considered stable if the vortex returns to it after being subjected to a small perturbation. This means that the response of a system to a given perturbation does not develop an instability which destabilises the system, but one which decays with time. Such behaviour is true for a system described by a decaying exponential of the form

$$v(t) = a_0 + a_1 \exp(\lambda t), \quad \lambda < 0. \quad (2)$$

where  $v(t)$  is any flow variable,  $a_0$  and  $a_1$  are constant coefficients. In order to establish such behaviour for the trapped vortex, it is sufficient to register in time any flow variable like velocity (at a given location) and to see whether it can be represented by a decaying exponential. At a suction rate of 0.02, a sample of registered data for the normal velocity  $v$  is fitted with the exponential model as depicted in figure 8. Figure 8

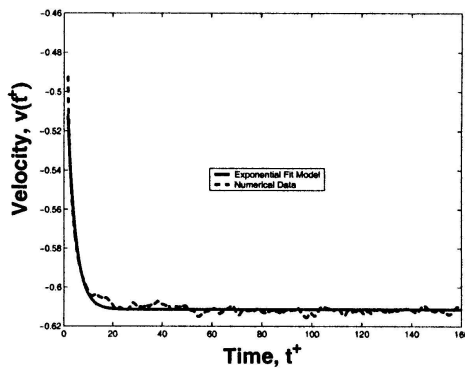


Figure 8: Characterising Stability by an Exponential Model

clearly shows that the velocity behaviour asymptotes to a constant value, implying a steady state situation. For suction rates  $Q \geq 0.02$ , similar behaviour was seen.

### Feedback Control

#### Pre-control Issues

The presence of a high noise level severely limits the effectiveness of a flow control strategy [8]. Vortex methods are known for being particularly noisy. We used a Tikhonov regularisation technique to achieve some noise reduction in the numerical scheme, see Bouferrouk et al. [2]. The trapped vortex system was found to possess an interesting behaviour depending on the initial conditions. For impulsive starts, the drag values obtained as suction was varied from 0.0 to 0.02 are higher than those obtained when the flow was started from a stable state with  $Q = 0.02$  after which suction was slowly reduced to  $Q = 0.0$ . Figure 9 shows that for the same given suction rate the drag obtained with the slow suction reduction technique is lower than that obtained from the impulsive start. This is not, however, a hysteresis behaviour: when suction is started at  $Q = 0.0$  then increased slowly to  $Q = 0.02$  and then reduced back to  $Q = 0.0$  the drag traces the same path. This could be specific to the current airfoil geometry as results from another Lighthill's geometry with a different cavity shape (not shown) reveal that the two paths were slightly different, i.e, there is some form of hysteresis. This may potentially be useful in future trapped vortex stabilisation studies.

#### The Active Control Law

The aim is to stabilise the flow and to delay the onset of vortex shedding for as long as possible. Also, it is desired to achieve

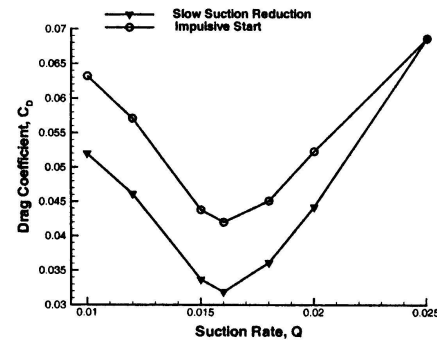


Figure 9: Drag Reduction by Slow Suction Reduction

this with minimum possible suction. The reasons for this are numerous. In a more realistic turbulent flow with a suction system applied at the wall, removal of fluid accelerates the loss of flow momentum with the consequence of increased skin friction drag. Minimising suction also minimises the weight needed to have a suction pump installed. We propose to use a feedback control law, based on an *artificial stabilising parameter* such that stability is maintained while slowly reducing the suction from a reference stable point. We consider a Single Input Single Output (SISO) standard linear (small perturbation) controller design with a constant gain parameter  $G$  (the stabilising parameter) in the form

$$Q_{total} = Q_0 + G \cdot (V_t - V_{bias}) \quad (3)$$

where  $V_t$  is the signal (or sensor variable) taken as the tangential velocity,  $V_{bias}$  is the constant biased velocity (averaged velocity of a flow run without control),  $Q_0 = 0.02$ , and  $Q_{total}$  is the control variable representing the total suction rate to be varied. This representation implies that the system is only stable for small perturbations and these are modelled in the form of a slow reduction in suction flow rate. Then, by introducing various values of  $G$  it is possible to change suction such that the stability of the trapped vortex is maintained for as long as possible before the onset of vortex shedding (the unstable system). The best  $G$  would be the one which delays the instability with as little suction as possible.

Figures 10 and 11 illustrate respectively the drag behaviour with two selected values of  $G = -0.05$  and  $-0.09$ , at a fixed monitoring point. It is concluded from the figures that with active control the large perturbations which correspond to large-scale vortex shedding only appear after a more prolonged period of time compared with the uncontrolled case. When large-scale vortex shedding sets in the trapped vortex system is said to have lost its stability. Prior to this, whether control is or is not implemented, some occasional small-scale vortex shedding was observed. Despite this, the main bulk of the trapped vortex flow remains within the cavity and so it is considered stable. Positive values of  $G$  were found to be destabilising. However, there seems to be a critical value of  $G = -0.09$  beyond which the control actually promotes vortex shedding. A total of 20 sensor positions were investigated in search for an optimum sensor position which delays vortex shedding with the least amount of suction. In terms of suction, the case with  $G = -0.09$  consumed more suction compared with  $G = -0.05$ . The averaged drag coefficient for the case of  $G = -0.09$  was 0.0367 while that for  $G = -0.05$  was 0.0338.

#### Power Balance for the Flow Control

It is important to evaluate the balance between the power saved by delay of vortex shedding and that consumed by the control flow. This is currently being investigated. Based on the work of Rioual et al. [10] the components of the power balance consist

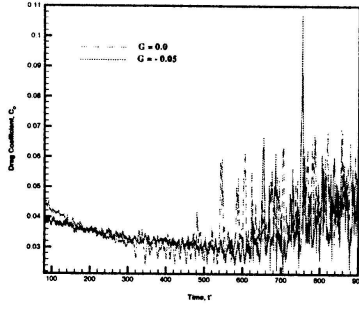


Figure 10: Active Control with  $G = -0.05$

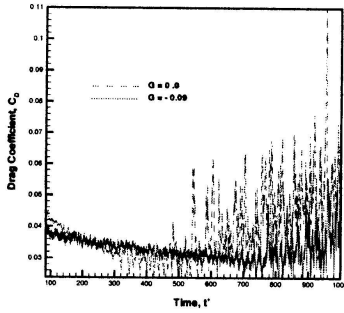


Figure 11: Active Control with  $G = -0.09$

of power consumption due to the pressure drag and the power needed to suck fluid through the various panels. The power to account for the momentum loss at the surface of the suction panels may be ignored. The power required to overcome the drag by a propulsive system is given by

$$P_{drag} = D \frac{U_{\infty}}{\eta_p} \quad (4)$$

and that required to drive the suction system is expressed as

$$P_{suc} = \frac{1}{2\eta_s} \dot{m} U_s^2 + L \quad (5)$$

where  $\eta_p (< 1)$ ,  $\eta_s (< 1)$  are coefficients reflecting the efficiency of the propulsive and suction systems, respectively,  $\dot{m}$  the total suction mass flow rate,  $U_s$  the suction velocity, and  $L$  represents energy losses due to friction across the suction surface, and is expressed as (see Bieler et al. [1])

$$L = \frac{\dot{m}}{\rho \eta_s} \sum \Delta p_i \quad (6)$$

where  $\Delta p_i$  is the pressure drop across a suction panel  $i$  and measured as

$$\Delta p_i = \frac{1}{2} \rho C \left( \frac{U_s}{P} \right)^2 + 32 \mu K \frac{h}{d^2} \frac{U_s}{P} \quad (7)$$

In (7),  $C$  and  $K$  are empirical constants,  $d$  is a typical diameter of the hole in the panel,  $h$  is the panel thickness,  $P$  the panel porosity. The values for the various parameters used in (4)-(7) will have to be chosen with suitable assumptions in order to have a reasonable power estimate. This is under investigation.

## Conclusions

The stabilisation problem of a large-scale vortex structure trapped in a Lighthill's airfoil cavity has been studied using a DVM. While the cavity entrains the large vortex, continuous increase of suction was required to trap the vortex and inhibit

vortex shedding. As a result, the drag decreased and lift increased. However, this is only possible up to a critical suction rate beyond which performance decreases. Because of the rotational character of the trapped vortex, unsteady suction achieved 13% reduction in total suction rate needed for stabilisation. The trapped vortex was shown to be stable using a simple decaying exponential model. By starting at a stable position then slowly reducing the suction rate it is possible to reduce suction further (hence drag) while keeping the vortex stably trapped. Stability is only defined with respect to large-scale vortex shedding of the main trapped vortex as small-scale shedding may occur. The stabilisation was then investigated using a feedback control law based on a constant stabilising parameter. There is evidence that such control retains the vortex stability (with respect to large-scale vortex shedding) for longer periods of time compared with the case of no control. Open questions remain on the optimisation of such control and power balance requirements.

## Acknowledgement

This research was supported in part by the Royal Society grant (Ref. 13872) and partly by a PhD studentship from the School of Engineering Sciences, University of Southampton.

## References

- [1] Bieler, H., and Priest, J., HLFC for Commercial Aircraft—First ELFIN Test Results, *Proceedings of the First European Forum on Laminar Flow Technology*, 1992, 558–594.
- [2] Bouferrouk, A. and Chernyshenko, S.I., Tikhonov Regularisation in Discrete Vortex Methods, *Computers and Fluids*, **34**, 275–281.
- [3] Tikhonov, A., Goncharsky, A.V., Stepanov, V.V., and Yagoda, A.G., Numerical methods for the solution of ill-posed problems, *Dordrecht, Kluwer*, 1995.
- [4] Buldakov, E.V., Chernyshenko, S.I., and Stepanov, G.Y., Inviscid Batchelor-model Flow Past an Airfoil with a Vortex Trapped in a Cavity, *Journal of Fluid Mechanics*, **323**, 1996, 367–376.
- [5] Bunyakin, A.V., Chernyshenko, S.I., and Stepanov, G.Y., High-Reynolds-number Batchelor-model Asymptotics of a Flow Past an Aerofoil with a Vortex Trapped in a Cavity, *Journal of Fluid Mechanics*, **358**, 1998, 283–297.
- [6] Cox, J., The Revolutionary Kasper Wing, *Soaring*, **37**, 1973, 20–23.
- [7] Iollo, A., and Zannetti, L., Trapped Vortex Optimal Control by Suction and Blowing at the Wall, *European Journal of Mechanics/B-Fluids*, **20**, 2001, 7–24.
- [8] Gad-el-Hak, M., Flow Control: Passive, Active and Reactive Flow Management, *Cambridge University Press*, 2000.
- [9] Garcia, D.L. and Katz, J., Trapped Vortex in Ground Effect, *AIAA Journal*, **41**, 2003, 674–678.
- [10] Rioual, J.-L., Nelson, P.A., Hackenberg, P., and Tutty, O.R., Optimum Drag Balance for Boundary-Layer Suction, *Journal of Aircraft*, **33**, March–April 1996, 435–438.
- [11] Saffman, P.G., and Sheffield, J.S., Flow over a Wing with an Attached Free Vortex, *Studies in Applied Mathematics*, **57**, 1977, 107–117.
- [12] Spalart, P.R., A Discrete Vortex Method for Separated Flows, *NASA Technical Memorandum 100068*, 1988.

## Development of a Fast Response Pressure Probe for Use in a Cavitation Tunnel

P. A. Brandner<sup>1</sup>, D. B. Clarke<sup>2</sup> and G. J. Walker<sup>3</sup>

<sup>1</sup>Faculty of Maritime Transport and Engineering  
Australian Maritime College, Launceston Tasmania, 7248 AUSTRALIA

<sup>2</sup>Maritime Platforms Division  
Defence Science and Technology Organisation, Maribyrnong, Victoria, 3032, AUSTRALIA

<sup>3</sup>School of Engineering  
University of Tasmania, Hobart, Tasmania, 7001 AUSTRALIA

### Abstract

The performance of a prototype fast response probe designed for use in a cavitation tunnel is investigated. The probe consists of a total head tube with an embedded miniature pressure sensor. Miniaturisation allows installation of the pressure transducer close to the head of the head of the instrument and improves frequency response through reducing inertia of fluid in the connecting tube. Measurements made with the fast response probe are compared with those of a Pitot tube connected to a slow response transducer and a hot film probe in a thickened turbulent boundary layer on the tunnel ceiling. Measurements of both streamwise velocity and turbulence made with the probe were found to compare well with those of a Pitot tube and a hot film probe. A useful frequency response up to 2.5kHz in water was demonstrated without any frequency compensation for pressure tube response.

### Introduction

Fast response probes, (FRPs) have been in use for some time for measuring velocity and turbulence in situations where thermal anemometry or other methods are either inappropriate or inconvenient. These include environments where hostile conditions exist or applied laboratories where cost and convenience of use can be a consideration such as transonic, combustion or cavitation test facilities [9]. In the cavitation tunnel environment relatively large ranges of pressure and velocity as well as the presence of cavitation are possible. These difficulties generally relate to model and equipment costs in terms of structural and mechanical design complexity and facility time required for experiments. At the Australian Maritime College (AMC) cavitation tunnel, Pitot and hot film probes have been used to date for velocity and turbulence measurements. Pitot probes with slow response pressure transducers, whilst very reliable and convenient for time-mean velocity measurement, cannot be used for turbulence measurement. The problems associated with the use of hot film probes are well known including their fragility and accuracy and stability of calibration.

For the reasons mentioned above and the desire for simultaneous measurement of both velocity and turbulence it was decided to develop a one-dimensional FRP for use in the cavitation tunnel. The design concept chosen is similar to other devices developed for aerodynamic [2, 6, 9, 10] and hydrodynamic measurements [1]. These are based on the measurement of unsteady pressures from which the velocity and turbulence components can be derived. The present investigation compares results from a prototype FRP with those from a Pitot tube and a hot film probe. The flow used to compare the probes is a thickened turbulent boundary layer in zero pressure gradient. Comparisons are made of streamwise mean velocity, turbulence intensity and wave number spectrum.

### Experimental Overview

#### Fast Response Probe Design

The FRP has been conceived as a total head tube with an embedded pressure sensor similar to those used in transonic and combustor flow applications [2, 9]. The FRP general arrangement is shown in Figure 1. A modular design has been developed consisting of interchangeable probe head or tip, sensor housing and support stem. Each section can be changed depending on the flow to be investigated, range of velocity/turbulence to be measured and distance to be traversed. The sensor body is glued into the housing with epoxy resin and the periphery of the sensor head is surrounded by silicone filler as per manufacturer's suggestions.

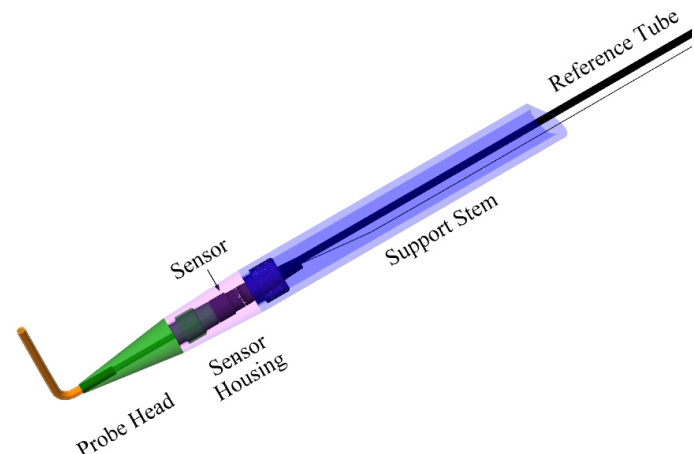


Figure 1. FRP General Arrangement.

The size of the probe head or tip for this application is based on considerations of spatial resolution and frequency response. Bradshaw [3] suggests that quasi-steady measurements in turbulent flows are possible provided the tube size is small compared with the size of energy containing eddies and that eddy traversal time is larger than the ratio of probe size to mean velocity. For the present application involving boundary layers and wakes of the order of 50 to 100mm thick and velocities up to 10m/s a probe head size of 1mm diameter has been chosen. For a velocity of 10m/s this gives a tube diameter to velocity ratio of the order of 0.1ms or frequencies of the order of 10kHz. The frequency response required for hydrodynamic measurements are generally much less than those encountered in aerodynamic problems. Experience in the cavitation tunnel suggests that turbulent frequencies of interest for momentum transfer do not exceed 2kHz. The influence of yaw on a simple Pitot tube is insignificant for angles up to 15°; hence the use of a one dimensional probe for streamwise property measurement in the present study appears reasonable considering that the amplitude



of incidence excursions should seldom exceed  $15^\circ$  based on typical zero pressure gradient boundary layer rms turbulent velocities.

Whilst there are a range of so called sub-miniature pressure sensors, of the order of 1mm diameter, available for applications in gases there are very few available for use in liquids. There are however so called miniature pressure sensors, of the order of 3mm diameter, available for use in liquids. These sensors must be embedded some distance from the probe tip to maintain a small head size, thus introducing problems of frequency response and viscous damping in the probe head. Estimations of acoustic natural frequencies derived from the speed of sound in water and the probe head length show that for this application frequencies of interest are significantly lower than the first acoustic natural frequency. However the added inertia of the contained water significantly reduces the natural frequency from that of the sensor alone. Damping involving viscous losses in the tube and at entry and exit is also significant. The tube length and sensor diaphragm can be modelled as a single degree of freedom system with the mass, damping and stiffness constants calculated or derived empirically. From this model, tube lengths and diameters have been chosen that provide satisfactory response. A tube with internal and external diameters of 0.8 and 1.2mm respectively was chosen for the present study. The chosen tube length of 32mm gives a natural frequency of mass oscillation of approximately 2.5kHz. This is sufficient to provide meaningful results for the present study, but is significantly lower than the 50 kHz natural frequency of the transducer.

For the present application an *Entran* EPB-B01-1.5B/Z2 miniature pressure sensor was chosen for the FRP. It has an overall diameter of 3.2mm, a pressure range of 150 kPa and is a differential sensor for which it is necessary to use an air reference due to exposed strain gauges that is incompatible with conducting liquids. The tunnel maximum speed is 12m/s, corresponding to a maximum mean dynamic pressure of 72 kPa, and the static pressure range is 4 to 400 kPa making a differential sensor necessary for acceptable resolution. To achieve an air reference the sensor is connected to a convenient static tapping via a volume containing a thin latex diaphragm separating the water and air. Through a process of design optimisation it was possible to size the diaphragm, adjacent volumes and connecting tubing such that the system responded quickly and only small deflections of the diaphragm resulted from static pressure changes.

### **Cavitation Tunnel Experimental Setup**

All tests were performed in the Tom Fink Cavitation Tunnel, a closed recirculating variable pressure water tunnel. The test section dimensions are 0.6m x 0.6m cross section x 2.6m long. The velocity may be varied from 2 to 12m/s and the centreline static pressure from 4 to 400 kPa absolute. Studies may involve the investigation of steady and unsteady flows, two-phase flows including cavitation, turbulence and hydro-acoustics. Full details of the tunnel and its capabilities are given by Brandner and Walker [4].

Tests were performed in a thickened boundary layer created by a saw toothed device chosen from a range of tested devices as being the most efficient and that with the lowest inception cavitation number [4]. This thickener has been used in many studies in the cavitation tunnel and has been investigated in detail by wind tunnel tests of Sargison et al. [11]. The test section was set up with the thickener and probe located on the ceiling 0.3m and 1.15m from the test section entrance respectively. The thickener produces a nominally 50mm thick boundary layer equating to measurements being made at 17 boundary layer

thicknesses downstream of the device. Measurements were made of the thickened boundary layer, on the test section vertical centre plane, with a Pitot tube, a hot film probe and the FRP. The probes were traversed using a computer controlled automated traverse with an estimated precision of better than 0.01mm. The wall static reference tap used for the Pitot tube and FRP was located on the test section ceiling in the plane of the probe head 75mm from the centre plane. The Pitot tube head diameter is 0.7mm and pressures relative to the tunnel static pressure (as well as tunnel instrument pressures) were measured sequentially using a slow response *Validyne* Model DP15TL differential pressure transducer via a Model 48J7-1 *Scanivalve* pressure multiplexer. The hot film probe used was *Dantec* R36 wedge probe with a *TSI* model 1750 constant temperature anemometer.

Parameters measured during testing include tunnel pressure, velocity, temperature and dissolved oxygen content. Online instrumentation is used for automatic control of tunnel pressure and velocity as well as real time data monitoring and acquisition. The test section pressure is measured using 2 *Rosemount* Model 3051C Smart absolute pressure transducers in parallel. Test section velocity is derived from the contraction pressure differential measured using 2 *Rosemount* Model 1151 Smart differential pressure transducers in parallel. One of each pressure transducer pair has a lower range to improve measurement precision at lower pressures and velocities respectively. The estimated precision of the absolute pressure measurement is 0.1 kPa for pressures up to 120 kPa and 0.5 kPa for pressures up to 400 kPa. The estimated precision of the velocity measurement is 0.05 m/s. Water temperature is measured to 0.5°C accuracy using a *Rosemount* Model 244 temperature transducer. Dissolved Oxygen content is measured using a *Rosemount* Model 499 Dissolved Oxygen sensor.

### **Experimental Procedure**

The boundary layer traverses for each probe consisted of 50 positions up to 75mm from the wall graded with a log distribution. The Pitot tube and FRP were traversed onto the wall for Preston tube measurement of the wall skin friction and wall friction velocity (used for reduction of profiles to compare with the log law of the wall). The Preston tube calibration used is that by Head and Ram as presented by Goldstein [5]. The hot film probe was traversed to within 0.4mm from the wall and the wall friction velocity and wall skin friction were derived from at least squares fit to the log law of the wall using the 20 closest points to the wall.

Pitot tube traverses were performed at 9 Reynolds numbers between the test section minimum and maximum speeds. Hot film probe and FRP measurements were made at 5 and 6 Reynolds numbers respectively, limited by structural loading or electronic instrument considerations. All probe measurements were corrected for small temporal changes in test section velocity using the contraction pressure differential. The hot film was calibrated at the beginning and end of measurements using a non-dimensional relationship between the Nusselt number and the Reynolds number. The FRP was calibrated from measurements in the free stream using velocities derived from the contraction calibration. Data from slow response Pitot tube measurements was acquired at 800Hz over 6 s and hot film and FRP data was acquired at 16384Hz over 8s. Hot film and FRP turbulence data were both corrected for base electronic noise. For the present investigation instantaneous velocities for the FRP were derived from the unsteady total pressure measurements relative to the wall static reference assuming zero unsteady static pressure.

## Results

### Boundary Layer Parameters

A summary of boundary layer parameters measured with each probe are presented in Tables 1 to 3 and a comparison of derived skin friction coefficients are presented in Figure 2. The boundary layer thickness  $\delta$  measured with the Pitot tube is that corresponding to 99% of the freestream velocity. The data generally compare favourably although the skin friction coefficients reflect the expected lack of accuracy of the hot film probe for mean data.

$R_\theta$	$\delta$ , mm	$\delta^*$ , mm	$\theta$ , mm	$H$	$C_f$
12400	51.7	6.32	4.94	1.278	0.00281
16200	51.5	6.26	4.94	1.268	0.00271
19200	50.3	5.94	4.69	1.268	0.00269
22800	48.5	5.87	4.63	1.267	0.00261
27400	51.3	5.98	4.76	1.258	0.00248
30900	51.0	5.90	4.69	1.258	0.00246
34400	50.4	5.80	4.61	1.258	0.00239
38400	50.4	5.81	4.63	1.257	0.00237
41700	50.0	5.79	4.62	1.252	0.00232

Table 1. Boundary Layer Parameters Measured Using Pitot Tube, where  $R_\theta$ =momentum thickness Reynolds number,  $\delta$ =boundary layer thickness at 99% of freestream velocity,  $\delta^*$ =displacement thickness,  $H$ =shape factor and  $C_f$ =wall friction coefficient.

$R_\theta$	$\delta^*$ , mm	$\theta$ , mm	$H$	$C_f$
12400	6.64	5.33	1.245	0.00301
16200	6.66	5.38	1.239	0.00278
19200	6.56	5.32	1.234	0.00267
22800	6.95	5.58	1.247	0.00250
27400	6.27	5.04	1.244	0.00243

Table 2. Boundary Layer Parameters Measured Using Hot Film Probe.

$R_\theta$	$\delta^*$ , mm	$\theta$ , mm	$H$	$C_f$
19200	6.14	4.95	1.240	0.00255
22800	6.10	4.94	1.234	0.00248
27400	5.95	4.83	1.232	0.00244
30900	5.86	4.77	1.228	0.00240
34400	5.88	4.80	1.226	0.00235
38400	5.82	4.76	1.222	0.00232

Table 3. Boundary Layer Parameters Measured Using FRP.

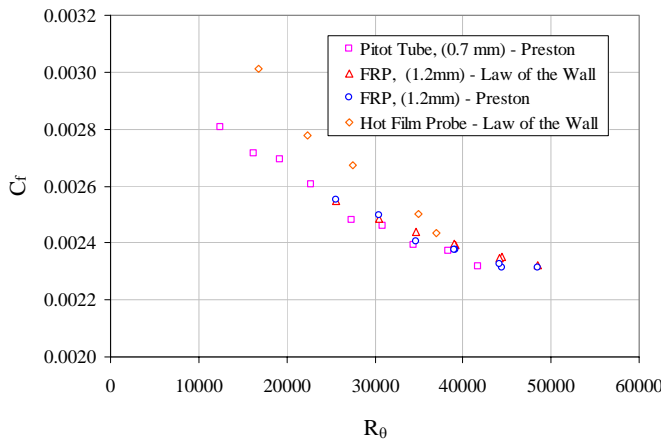


Figure 2. Comparison of Thickened Boundary Layer Wall Friction Coefficient Measured Using a Pitot Tube, Hot Film Probe and FRP.

### Boundary Layer Velocity Profiles

The measured boundary layer profiles for each probe are presented as staggered plots in Figure 3. A comparison of each probe at a common Reynolds number is also shown. The data

from all the probes show that the thickened boundary layer closely follows the law of the wall although there is a slight undershoot in the outer part, also reported in [11]. These data also show little change with Reynolds number. The Pitot tube and FRP data show better overall agreement with the law of the wall compared with the hot film which, as mentioned above, can be attributed to less accuracy in velocity determination and hence the wall friction estimate.

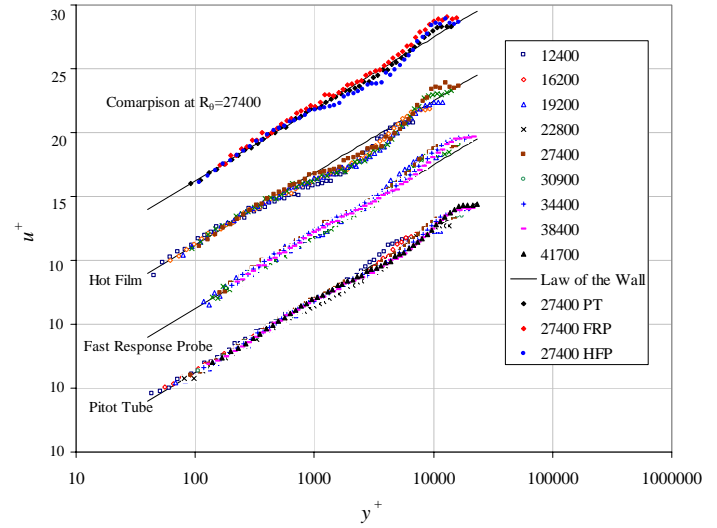


Figure 3. Comparison of Thickened Boundary Layer Velocity Profiles Measured Using a Pitot Tube, Hot Film Probe and FRP.

### Boundary Layer Turbulence Profiles

Turbulence profiles measured with the hot film probe and FRP, for the range of Reynolds numbers tested, are shown as staggered plots in Figure 4, together with the profile by Klebanoff [7]. The profile from [7] appears to be based on a boundary layer thickness definition for 100% of the freestream velocity and has been adjusted by 15% for a compatible definition in this case of 99%. The difference in the magnitude of the profiles can in part be due to differences in Reynolds numbers. From [7] the experiments in [8] were performed at a much lower momentum thickness Reynolds number - approximately one order of magnitude less than the current measurements. There may also be some slight increase in turbulence intensity in the centre of the boundary layer as a result of boundary layer thickener. Higher freestream turbulence intensity of about 0.6% in the water tunnel as compared to 0.02 to 0.04% for [7] would have contributed to the higher boundary layer turbulence level observed in present study.

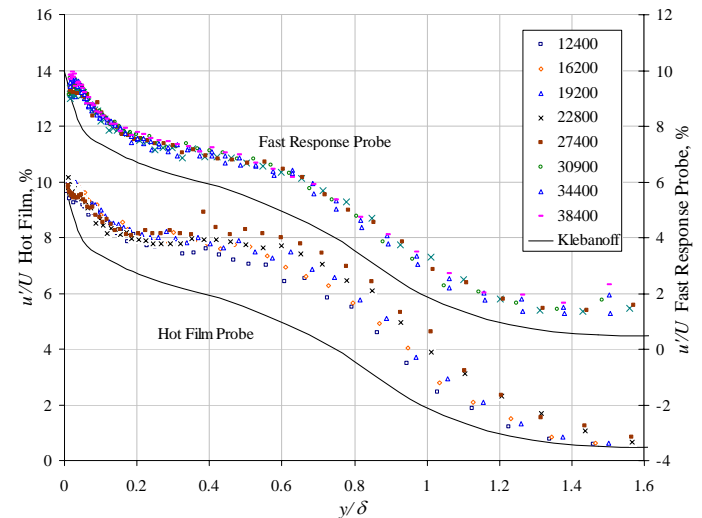


Figure 4. Thickened Boundary Layer Turbulence Intensity Profiles Measured Using a Hot Film Probe and FRP.



The FRP data shows a small monotonic increase of turbulence intensity with Reynolds number increase whereas the hot film data displays a much greater increase. Both the lack of variation with Reynolds number and the overall reduced value of the turbulence intensity for the FRP results, compared with the hot film, can be attributed to filtering of higher frequency turbulent energy. In the wake region the FRP over predicts the turbulence intensity, compared with the hot film probe, and examination of spectra shows that the outer most 3 points were affected by probe stem vibration and are therefore unreliable. The data at the lower Reynolds numbers agree overall to within few percent growing to a maximum of 15 to 20 % at the higher Reynolds Numbers. The greatest difference being through the middle of the boundary layer with excellent agreement near the wall for all cases.

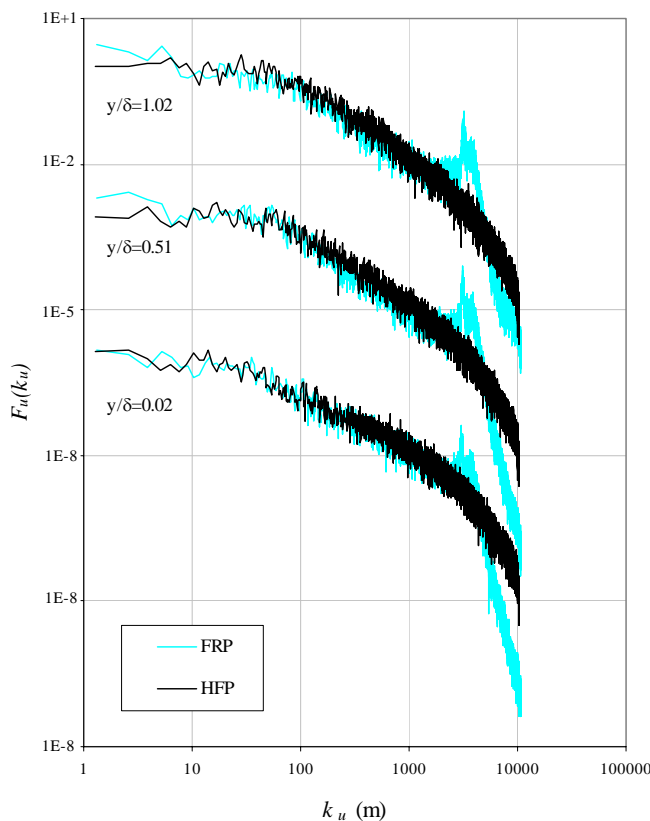


Figure 5. Comparison of Thickened Boundary Layer Wave Number Spectra at  $y/\delta = 0.02, 0.50$  and  $1.02$  Measured Using FRP and Hot Film Probe.

### Wave Number Spectra

Wave number spectra for 3 positions across the boundary layer at  $R_\theta = 27400$ , measured with the hot film probe and FRP, are shown in Figure 5. The spectra are presented using the quantities described in [7, 8]. The spectra for the two probes match closely for wave numbers up to approximately  $2000 \text{ m}^{-1}$  ( $\sim 2.5 \text{ kHz}$ ) after which two resonant peaks at approximately  $3500$  and  $3900 \text{ m}^{-1}$  develop. The first peak is possibly due to head resonance in a torsional mode while the second is attributable to response of the sensor combined with the mass of water contained in the probe head. The straight line roll-off of the curve clearly demonstrates the effects of damping due to the viscous loss of the water contained in the head. As discussed above the typical frequency range of interest in the cavitation tunnel does not exceed  $2 \text{ kHz}$  which is well within the normal response range of the FRP. The attenuation at high frequencies probably explained the slight reduction in turbulence intensity measured by the FRP compared to the hot film data.

### Conclusions

The present investigation has demonstrated the use of a prototype FRP for use in a cavitation tunnel. Streamwise velocity and turbulence measured with the FRP compare well with those measured with a Pitot tube and a hot film probe in a thickened turbulent boundary layer. The FRP exhibited resonance phenomena due to possible probe head vibration and mass oscillation of the water contained within the head combined with sensor diaphragm flexibility. The occurrence of damping beyond the resonance peak due to viscous losses associated with the movement of the water contained within the probe head was also discernable. A useful frequency response up to  $2.5 \text{ kHz}$  in water was demonstrated without any frequency compensation for pressure tube response. This is an order of magnitude improvement over the performance of hydrodynamic probes reported in [1] and also exceeds the performance of frequency compensated aerodynamic probes reported in [6].

### Acknowledgement

The authors acknowledge the assistance of Mr Robert Wrigley and Dr Colin Grubb in manufacturing of equipment and carrying out experiments and the support of the DSTO, AMC and UTas.

### References

- [1] Arndt, R. E. A. and Ippen, A. T., *Turbulence Measurements in Liquids Using an Improved Total Pressure Probe*, Journal of Hydraulic Research, Vol. 8, pp131-158, 1970.
- [2] Biagioni, L. and d'Agostino, L., *Measurement of Energy Spectra in Weakly Compressible Turbulence*, AIAA 99-3516 30th AIAA Fluid Dynamics Conference, 28 June - 1 July, 1999 / Norfolk, VA
- [3] Bradshaw, P., *An Introduction to Turbulence and its Measurement*, Pergamon Press, 1971.
- [4] Brandner, P.A. and Walker G.J., *A Waterjet Test Loop for the Tom Fink Cavitation Tunnel*, International Conference on Waterjet Propulsion III, Royal Institution of Naval Architects, Gothenburg, Sweden, February, 2001, 54-57.
- [5] Goldstein, R. J., *Fluid Mechanics Measurements*, Springer-Verlag, 1983.
- [6] Hooper, J. D. and Musgrove, A. R., *Reynolds Stress, Mean Velocity and Dynamic Pressure Measurement by a Four-Hole Pressure Probe*, Exp Thermal & Fluid Science, Vol 15, pp 375-383, 1997.
- [7] Klebanoff, P. S. and Diehl, Z. W., *Some Features of Artificially Thickened Fully Developed Turbulent Boundary Layers With Zero Pressure Gradient*, NACA Report 1110, 1952.
- [8] Klebanoff, P. S., *Characteristics of Turbulence in Boundary Layers With Zero Pressure Gradient*, NACA Report 1247, 1955.
- [9] LaGraff, J. E., Oldfield, M. L. G., Biagioni, L., Moss, R. W. and Battelle, R. T., *Measurement of Turbulent Pressure and Temperature Fluctuations in a Gas Turbine Combustor*, NASA/CR—2003-212540, Sept, 2003.
- [10] Moss, R. W. and Oldfield, M. L. G., *Comparisons Between Turbulence Spectra Measured with Fast Response Pressure Transducers and Hot Wires*, Symposium on Aerodynamic Measuring Techniques for Transonic and Supersonic Flows in Cascades and Turbomachinery, VKI, Brussels, 1990.
- [11] Sargison, J.E., Walker, G.J., Bond, V., and Chevalier, G., *Experimental Review of Devices to Artificially Thicken Wind Tunnel Boundary Layers*, 15<sup>th</sup> AFMC, Sydney, Dec, 2004.

## Linear stability of natural convection on an evenly heated vertical wall

G. D. McBain and S. W. Armfield

School of Aerospace, Mechanical, & Mechatronic Engineering  
The University of Sydney, Darlington NSW 2006 AUSTRALIA

### Abstract

A collocation technique is applied to the equations governing the linear stability of the anabatic layer on an evenly heated vertical wall in a stratified fluid. Marginal stability curves and critical heat fluxes are obtained for Prandtl numbers from 0 to 1000. As in other cases of vertical natural convection, two kinds of instability are observed, depending on the Prandtl number: at lower Prandtl numbers, the modes are short slow waves and the critical parameter is roughly proportional to the local Reynolds number, whereas at higher Prandtl numbers, the critical Reynolds number decreases rapidly and the waves are longer and faster.

### Introduction

One of the simplest solutions of the Oberbeck [14] equations of natural convection was discovered by Prandtl [15, pp. 422–425]. It describes the flow parallel to a vertical (or inclined) plane held at a constant temperature difference above the neighbouring stratified fluid. The linear stability of this flow has been studied by Gill & Davey [7].

A more realistic boundary condition, however, is that of a uniform heat flux at the wall. Since Prandtl's [15] base solution is independent of height, it also applies in this case. The flow may be realized in a cavity with evenly heated and cooled vertical walls [9], and its mass transfer-analogue occurs in electrochemical cells [6]. The stability properties differ, however, due to the replacement of the Dirichlet condition,  $\theta(0) = 0$ , on the thermal perturbation with a Neumann one,  $\theta'(0) = 0$ . The authors have recently investigated the linear stability of this modified problem for Prandtl number  $\sigma = 7$  [11], and shown that both the critical Reynolds number and the form of the critical disturbance agree with direct numerical simulations. The present paper extends the linear stability results to the range  $0 \leq \sigma \leq 10^3$ .

### Mathematical formulation

Let the  $x$ -axis be normal to the wall and the  $y$ -axis vertical. Denote the fluid properties by  $\nu$ ,  $\alpha$ , and  $\beta$  for the coefficients of kinematic viscosity, thermometric conductivity, and thermal expansion, respectively. Denote the normal temperature gradient at the wall by  $\Gamma_w$ , the far-field stratification by  $\Gamma_s$ , and the gravitational field strength by  $g$ . Then if

$$\delta = \left( \frac{4\alpha\nu}{g\beta\Gamma_s} \right)^{1/4} \quad (1)$$

$$U = \Gamma_w \left( \frac{4g\beta}{\nu} \right)^{1/4} \left( \frac{\alpha}{\Gamma_s} \right)^{3/4} = \frac{2\alpha\Gamma_w}{\Gamma_s\delta} \quad (2)$$

$$\Delta T = \Gamma_w\delta \quad (3)$$

are the scales for length, speed, and temperature [7, 11], the governing parameters are the Prandtl number,  $\sigma = \nu/\alpha$  and the Reynolds number

$$R = \frac{U\delta}{\nu} = \frac{2\Gamma_w}{\Gamma_s\sigma}, \quad (4)$$

and the Oberbeck equations governing the evolution of the ve-

locity  $\mathbf{u}$ , pressure  $p$ , and temperature  $T$  in time  $t$  are

$$R \left( \frac{\partial}{\partial t} + \mathbf{u} \cdot \nabla \right) \mathbf{u} = -R\nabla p + \nabla^2 \mathbf{u} + 2T\hat{\mathbf{e}}_y, \quad (5)$$

$$R\sigma \left( \frac{\partial}{\partial t} + \mathbf{u} \cdot \nabla \right) T = \nabla^2 T, \quad (6)$$

subject to the velocity vanishing at the wall

$$\mathbf{u} = \mathbf{0} \quad (x = 0), \quad (7)$$

the wall heat flux being specified

$$\frac{\partial T}{\partial x} = -1 \quad (x = 0), \quad (8)$$

and general decay far from the wall

$$|\mathbf{u}|, \left( T - \frac{2y}{R\sigma} \right) \sim 0 \quad (x \rightarrow \infty). \quad (9)$$

The system (5)–(9) admits Prandtl's [15, 7, 11] steady one-dimensional solution  $\mathbf{u} = V(x)\hat{\mathbf{e}}_y$ ,  $T = \Theta(x) + 2y/R\sigma$  where

$$V(x) = e^{-x} \sin x \quad (10)$$

$$\Theta(x) = e^{-x} \cos x. \quad (11)$$

The stability of small plane perturbations with streamwise wavenumber  $\kappa$  and wave speed  $c$  of the form

$$\delta \mathbf{u} = \Re \hat{\mathbf{e}}_z \times \nabla \psi(x) e^{i\kappa(y-ct)} \quad (12)$$

$$\delta T = \Re \theta(x) e^{i\kappa(y-ct)} \quad (13)$$

are governed by [7]

$$[E^2 + i\kappa R \{ (V - c)E + V'' \}] \psi + 2D\theta = 0 \quad (14)$$

$$[2D - i\kappa R \sigma \Theta'] \psi + [E + i\kappa R \sigma (V - c)] \theta = 0, \quad (15)$$

subject to

$$\psi(0) = \psi'(0) = \theta'(0) = \psi(\infty) = \theta(\infty) = 0, \quad (16)$$

where  $D = d/dx$  and  $E = \kappa^2 - D^2$ . For the temporal linear stability problem,  $\kappa$  is taken as real,  $\psi$  and  $\theta$  are the eigenvectors, and  $c$  is the complex eigenvalue.

### Discretization and solution procedure

As in the previous study [11], (14)–(15) were discretized using orthogonal collocation based on weighted generalized Laguerre functions, the algebraic generalized eigenvalue problem  $(L - cM)q = 0$  converted to standard form as  $(M^{-1}L - c)q = 0$ , and solved by the QR algorithm. The flow is regarded as unstable at a given  $\sigma$ ,  $R$ , and  $\kappa$  if any part of the  $c$ -spectrum lies in the upper-half complex plane.

This approach needed modification at  $\sigma = 0$ , however, since then  $c$  disappears from (15); i.e. the 'mass matrix'  $M$  becomes

singular, prohibiting the usual conversion to standard form. Instead, we used a shift-and-invert technique [1, 12] with the shift taken near the critical complex wave speed found for small but finite Prandtl numbers. The zero Prandtl number limit for this problem differs from that for the isothermal slot [3], since there the  $\psi$ -perturbation equation (14) becomes uncoupled from the  $\theta$ -equation (15); the reason is that the length scale there is fixed by the slot width, but here (1) depends on  $\alpha$ .

A Reynolds number close to both a value of  $R$  for which the flow is stable and one for which it is unstable is a *marginal* Reynolds number for that  $\sigma$  and  $\kappa$ ; the locus of marginal Reynolds numbers and  $\kappa$  is the *stability margin*. Margins for various  $\sigma$  were traced using our adaptive skirting algorithm [10].

The least marginal Reynolds number for a given  $\kappa$  and  $\sigma$  is the critical Reynolds number for that  $\sigma$  number. After roughly locating the turning points of the margins, the critical Reynolds numbers were found by Golden Section search [8, p. 37].

The method converges exponentially (as is to be expected from an orthogonal collocation method) for number of collocation points  $n$  up to about 60; for higher  $n$ , a levelling-off occurs, probably due to the high condition number of the differentiation matrices. This is illustrated in figure 1, which shows the

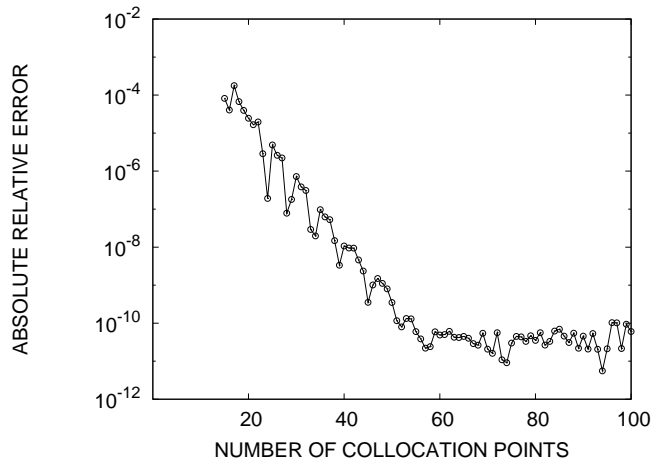


Figure 1: Convergence of the collocation method with bisection for the marginal Reynolds number at  $\sigma = 7$  and  $\kappa = 0.4612$ .

absolute relative error in the marginal Reynolds number computed for  $\sigma = 7$  and  $\kappa = 0.4612$  (taking the true value to be  $R = 8.581336650$  as assessed from all data at  $10 < n < 100$ ).

Another check on the method and code was made by reproducing Gill & Davey's results [7] for the critical Reynolds numbers with the fixed temperature boundary condition; i.e. they assumed  $T(0) = 1$  in place of (8), and so replaced  $\theta'(0) = 0$  in (16) with  $\theta(0) = 0$ . Their results, originally obtained with a finite difference shooting method, were found to be correct to the stated accuracy of three significant figures.

All computations were programmed in Octave [5] and executed on a heterogeneous openMosix cluster. Computations at each Prandtl number were performed serially, but several such programs were executed simultaneously.

## Results

The variation of critical Reynolds number with Prandtl number is plotted in figure 2 and some critical modes in figure 3.

At  $\sigma = 0$  the marginal stability curve is simple (figure 4a) but by  $\sigma = 0.1$  a second lobe, representing a second mode of instability, appears at small wavenumbers (figure 4b). The crit-

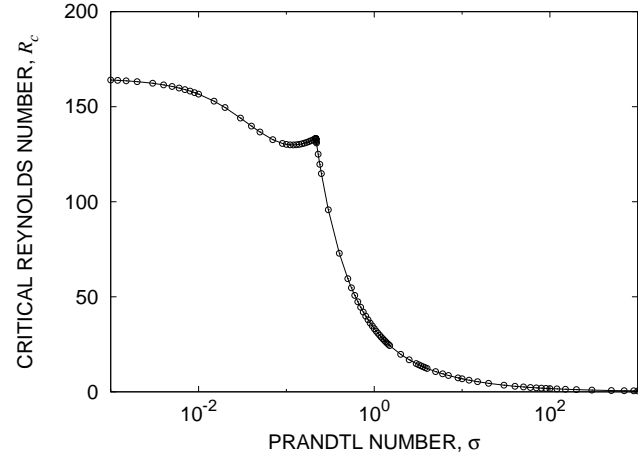


Figure 2: Critical Reynolds numbers.

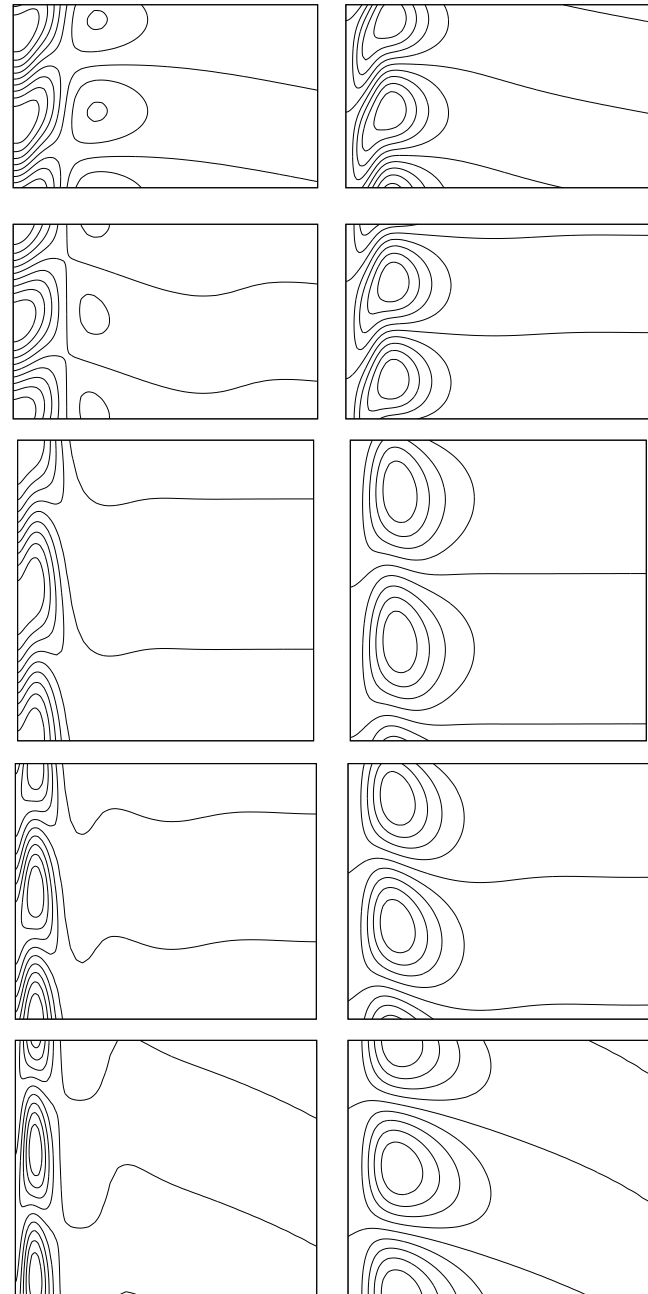


Figure 3: Isotherms (left) and stream-lines (right) of the critical mode for  $\sigma = 0, 0.1, 0.7, 7$ , and 100 (rows, downward), drawn over  $0 \leq x < 16$  and  $-\pi/\kappa_c < y < \pi/\kappa_c$ .

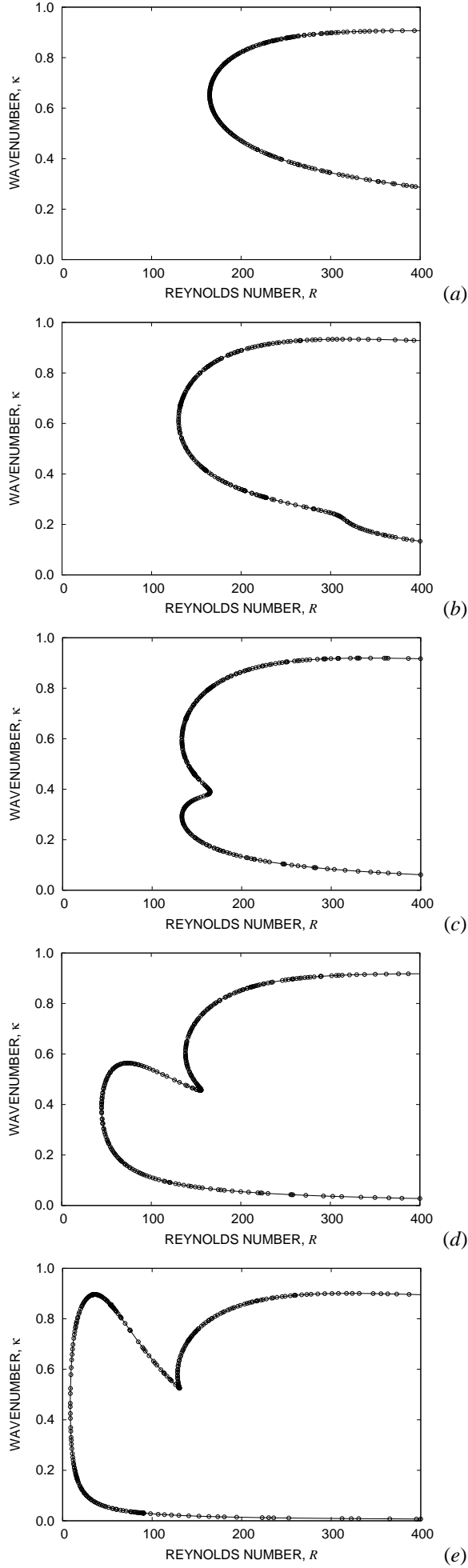


Figure 4: Marginal stability curves:  $\sigma = (a) 0, (b) 0.1, (c) 0.2163, (d) 0.7, (e) 7$ .

ical Reynolds number decreases with increasing  $\sigma$ , reaching a minimum of about 130 near  $\sigma = 0.12$ , then increases again (figure 2). The critical Reynolds number of the second mode decreases faster with increasing Prandtl number, and there is a cusp in the critical curve at  $R_c = 133$  near  $\sigma = 0.2163$  at which the second mode passes the first (figures 2, 4 c). Thereafter,  $R_c$  enters a steep decline which continues up to the highest Prandtl numbers investigated ( $\sigma = 10^3$ ).

### Discussion

The phenomenon of the low Prandtl number mode of instability giving way to one with longer wavelength and greater speed (see figure 5) also occurs in the linear stability of convection in

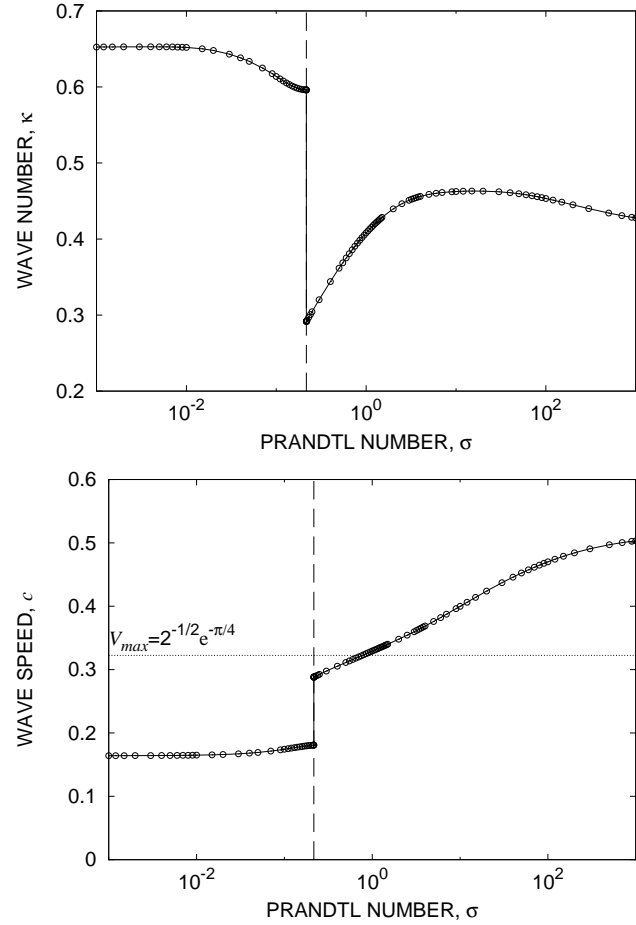


Figure 5: Critical wave numbers (above) and wave speeds (below, also showing the maximum speed of the base flow). The dashed vertical line marks  $\kappa = 0.2163$ .

a vertical slot [4, 12], in a stratified vertical slot [2], in the fixed-temperature-excess plate problem [7], and for a hot isothermal plate in a cold isothermal fluid [13]. Here, however, the transition occurs at quite a low Prandtl number:  $\sigma \approx 0.216$ ; cf.  $\sigma = 12.454$  for the slot [12] and somewhere in  $0.4 < \sigma < 0.72$  for the fixed-temperature-excess plate [7]. Roughly speaking, we suspect this is because the Neumann condition on the temperature perturbation is less restricting to the ‘thermal’ mode. We call the first and second modes ‘hydrodynamic’ and ‘thermal’ since the first sets in at roughly a constant boundary layer Reynolds number, while the latter is strongly dependent on the Prandtl number.

In order to investigate the effect of the thermal boundary condition on the stability of the anabatic layer, our critical Reynolds numbers are compared with those of Gill & Davey [7] in figure 6. It is evident that the low Prandtl number ( $\sigma < 0.2163$ ) critical mode is slightly stabilized by the change to the

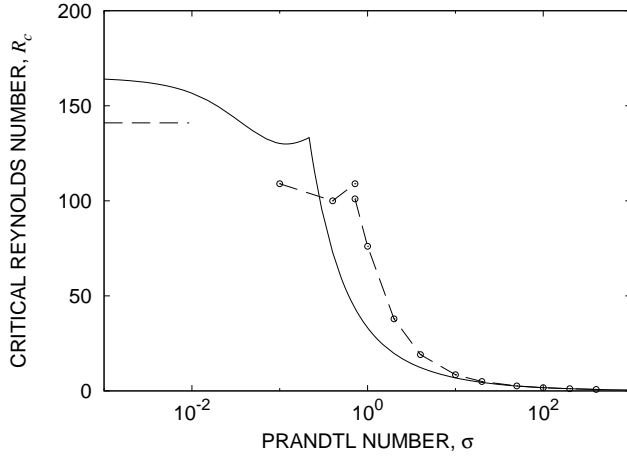


Figure 6: Comparison of critical Reynolds numbers for the linear stability of a vertical anabatic layer for heat flux (present work, curve) and temperature (Gill & Davey [7], points joined by line segments) thermal boundary conditions.

flux boundary condition, though at moderate Prandtl numbers ( $0.2163 < \sigma < \sim 10^1$ – $10^2$ ) the base flow is destabilized with respect to the ‘thermal’ mode by the change: the critical Reynolds numbers at large Prandtl numbers are less, and this mode becomes the critical one at a lower Prandtl number. At large Prandtl numbers, the difference disappears; e.g. Gill & Davey’s  $R_c = 1.70$  at  $\sigma = 100$ , which coincides with the figure in table 1. This is because the hot and cold spots in the critical modes are increasingly localized, away from the wall and near the maximum of the base velocity profile; both the value and gradient of the temperature perturbation are small near the wall so the two boundary conditions are equivalent. This may be seen by comparing Gill & Davey’s figure 11 with the lower isotherm plots in our figure 3.

## Conclusions

The specially developed collocation method based on generalized Laguerre functions provides accurate solutions to the linear stability equations for this flow with modest computational requirements.

Like other vertical natural convection flows, the anabatic layer on an evenly heated wall in a stratified fluid has two different critical modes, depending on the Prandtl number.

The present flow system is particularly suitable for linear stability studies, since, unlike the boundary layer in an isothermal fluid, it has a parallel base flow; unlike the unstratified slot, it has boundary layer behaviour in the base solution; and compared to the stratified slot, it depends on only two parameters rather than three.

For future reference, some selected critical values are listed in table 1.

## Acknowledgements

McBain and Armfield acknowledge funding from The University of Sydney’s Sesqui Postdoctoral Fellowship scheme and the Australian Research Council’s Discovery scheme, respectively.

## References

[1] Bai, Z., Demmel, J., Dongarra, J., Ruhe, A. and van der Vorst, H., editors, *Templates for the Solution of Algebraic Eigenvalue Problems*, SIAM, Philadelphia, 2000.

$\sigma$	$R$	$\kappa$	$c$
0	164.89414	0.6523	0.1641
$10^{-3}$	164.0357	0.6525	0.1642
$10^{-2}$	156.6220	0.6520	0.1650
$10^{-1}$	130.19156	0.6138	0.1743
(0.2163)	(133.2506)	(0.5962)	(0.1809)
0.2163	133.2403	0.2917	0.2882
0.7	44.48526	0.3858	0.3200
7	8.58134	0.4612	0.3874
10	6.859748	0.4625	0.3999
$10^2$	1.7001183	0.4533	0.4702
$10^3$	0.4841815	0.4278	0.5033

Table 1: Critical data. The data are believed accurate to the stated precision.

[2] Bergholz, R. F., Instabilities of steady natural convection in a vertical fluid layer, *J. Fluid Mech.*, **84**, 1978, 743–768.

[3] Birikh, R. V., On small perturbations of a plane parallel flow with cubic velocity profile, *J. appl. Math. Mech.*, **30**, 1966, 432–438.

[4] Birikh, R. V., Gershuni, G. Z., Zhukhovitskii, E. M. and Rudakov, R. N., On oscillatory instability of plane-parallel convective motion in a vertical channel, *J. appl. Math. Mech.*, **36**, 1972, 707–710.

[5] Eaton, J. W., *GNU Octave Manual*, Network Theory, 2002.

[6] Eklund, A., Alavyoon, F., Simonsson, D., Karlsson, R. I. and Bark, F. H., Theoretical and experimental studies of free convection and stratification of electrolyte in a copper refining cell, *Electrochimica Acta*, **36**, 1991, 1345–1354.

[7] Gill, A. E. and Davey, A., Instabilities of a buoyancy driven system, *J. Fluid Mech.*, **35**, 1969, 775–798.

[8] Greig, D. M., *Optimisation*, Longman, 1980.

[9] Kimura, S. and Bejan, A., The boundary layer natural convection regime in a rectangular cavity with uniform heat flux from the side, *J. Heat Transfer*, **106**, 1984, 98–103.

[10] McBain, G. D., Skirting subsets of the plane, with application to marginal stability curves, *ANZIAM J.*, **45(E)**, 2004, C78–C91.

[11] McBain, G. D. and Armfield, S. W., Instability of the buoyancy boundary layer on an evenly heated vertical wall, submitted for publication in *J. Fluid Mech.*, 2004.

[12] McBain, G. D. and Armfield, S. W., Natural convection in a vertical slot: Accurate solution of the linear stability equations, *ANZIAM J.*, **45(E)**, 2004, C92–C105.

[13] Nachtsheim, P. R., Stability of free-convection boundary-layer flows, Tech. Note D-2089, NASA, 1963.

[14] Oberbeck, A., Ueber die Wärmeleitung der Flüssigkeiten bei Berücksichtigung der Strömungen infolge von Temperaturdifferenzen, *Ann. Phys. Chem.*, **7**, 1879, 271–292, neue Folge.

[15] Prandtl, L., *Essentials of Fluid Dynamics*, Blackie, 1952.



## An Investigation of Flow over a Two-Dimensional Circular Cavity

C.C. Beves, T.J. Barber, E. Leonardi

School of Mechanical & Manufacturing Engineering  
The University of New South Wales, Sydney, NSW, 2052 AUSTRALIA

### Abstract

The flow structure within a two-dimensional spherical cavity on a flat plate has been studied numerically. A verification analysis of the grid spacing has been conducted; and a validation of the turbulence schemes has been performed by comparing with experimental results obtained using flow visualisation techniques.

### Nomenclature

$\delta$  depth of the cavity  
 $D$  effective diameter of the cavity  
 $Re$  Reynolds Number  
 $T.I.$  Turbulence Intensity

### Introduction

The application of spherical cavity wells to enhance heat transfer by turbulent mixing of the boundary layer has been investigated both numerically [2, 4] and experimentally [1, 6]. The benefits of using spherical cavity wells, as opposed to more conventional techniques e.g. vortex generators, comes from the improved hydrodynamic characteristics which result from the reduced drag since the cavities do not protrude into the boundary layer.

Previous work [1-7] focused primarily on the benefits to heat transfer by using an array of such cavities. Several main findings were consistent among the literature:

- Flow separation exists within a cavity of  $\delta/D > 0.2$
- A vortex leaving the cavity pushes oncoming external flow away from the cavity
- Rounding the edges of the cavity reduced hydraulic friction.

An inconsistency was reported by [3], which refers to the limited understanding of the detailed structural characteristics of the vortices shed from the cavities. A detailed verification and validation analyses on the work conducted may lead to a better understanding of this.

In this paper, two major factors affecting numerical results, namely grid spacing and turbulence modelling are considered. Numerical simulations are conducted using the commercially available CFD package Fluent 6.1.22. A simplified two-dimensional representation of the cavity will be used as a preliminary step, with the aim of building on this knowledge to a three dimensional representation.

### Flow Structure Characteristics

A region of flow recirculation exists for cavities with  $\delta/D > 0.22$ . For the most part the centre of this recirculation exists (at approximately  $0.5\delta$ ) below the surface within which the cavity sits and towards the upstream face of the cavity, as shown in figure 1. For the problem studied Reynolds number is in the order of  $3.0 \times 10^3$  with respect to the cavity diameter ( $D$ ).

The location of this recirculation zone is largely dependent on Reynolds number. As  $Re$  is increased to the values near  $3.0 \times 10^5$ , the recirculation zone moves closer to the free surface but does not protrude above the free surface and shifts towards the downstream face of the cavity.

There exists a point at which the flow separates from the cavity which is reasonably consistent for the range of Reynolds number solved ( $2.7 \times 10^3$  to  $3.0 \times 10^5$ ). For the most part this coincides with the point at which the edge radius and the upstream face of the cavity become tangent.

As the edge radius decreases this clearly impacts on the flow separation point by bringing it closer to the surface within which the cavity is located. This affects the flow structure within the cavity as the flow recirculation zone and the flow separation point are heavily linked, therefore is within the wake of the flow separation that the recirculation zone exists.

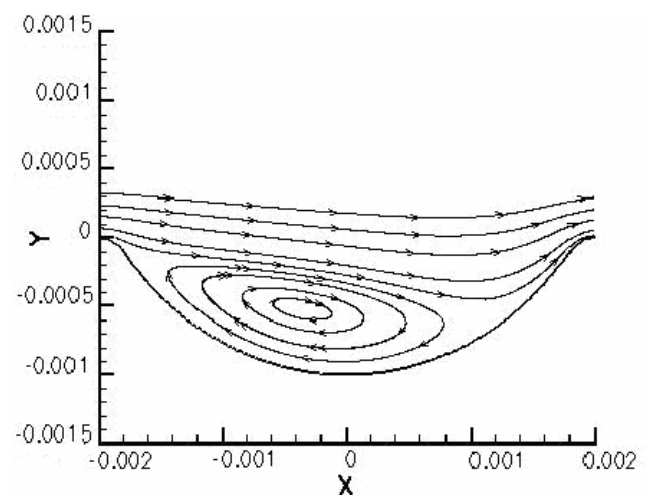


Figure 1 Velocity Streamline plot of the flow within the cavity  $\delta/D=0.22$   
 $Re = 2.7 \times 10^3$   $k-\epsilon$  realisable turbulence model at  $T.I.$  10%.

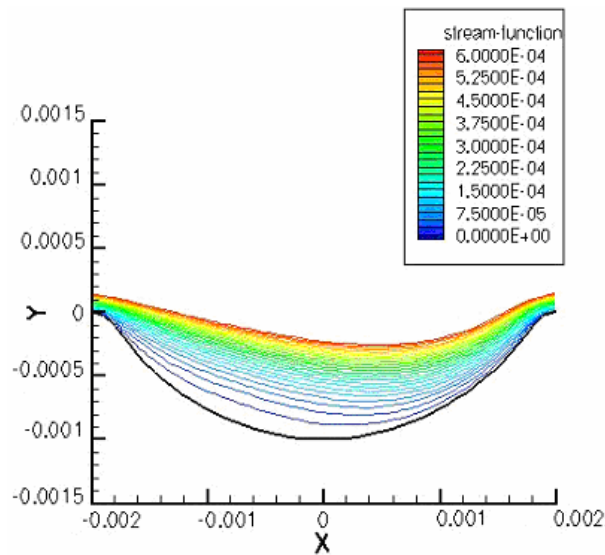


Figure 2 Stream function plot of the flow in the cavity  $\delta/D=0.22$   $Re = 2.7 \times 10^3$  for grid spacing 0.1 mm  $\kappa$ - $\epsilon$  realisable turbulence model at T.I. 10%.

### Grid Spacing within the Cavity

Initial steps were taken to ensure the accurate modelling of the flow within the cavity; this focused on how fine the grid spacing within the cavity should be.

Five different grid spacings were used within the cavity (4 mm in diameter and 1 mm in depth): 0.02 mm, 0.04 mm, 0.06 mm, 0.08 mm and 0.1 mm. This corresponded to 192 064, 107 996, 71 571, 49 276 and 45 958 elements respectively throughout the domain (measuring 50 mm x 244 mm).

Changing the grid spacing along the face of the cavity yielded some interesting results; the first of which was that for the coarsest spacing (0.1 mm) there was no presence of any flow recirculation within the cavity, see figure 2. As the grid spacing was further refined to 0.08 mm, this yielded a stalled region of flow within the upstream face of the cavity. From 0.06 mm to 0.02 mm the flow recirculation clearly exists, however as there are more cells located within the cavity the centre of the flow recirculation migrates towards the central part of the cavity, see figure 3. The change in location and size of the recirculation zone did not vary greatly between the 0.04mm and 0.02mm cases, thus it was concluded that sufficient grid convergence was achieved.

The intensity of the recirculation increases for finer grids, as the recirculation region becomes clearly defined and the flow that travels back up the upstream face of the cavity is accelerated locally compared to the coarser grids.

Investigation of the static pressure profile within the cavity shows that for the coarsest grid spacing, there is a larger region of positive pressure that covers most of the surface of the cavity and extends out of the cavity. As the grid spacing is refined, the size of the high static pressure region retracts to where there is only a localised region on the downstream face of the cavity where the edge radius and the cavity are tangent.

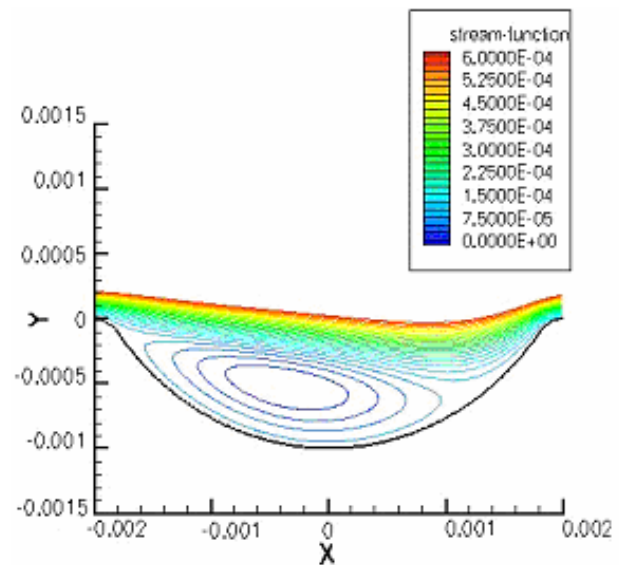


Figure 3 Stream function plot of the flow in the cavity  $\delta/D=0.22$   $Re = 2.7 \times 10^3$  for grid spacing 0.02mm  $\kappa$ - $\epsilon$  realisable turbulence model at T.I. 10%.

Not only does the size of the high static pressure region retract but the strength of it increases (from 2.61 Pa to 5.7 Pa). This mirrors the increase in recirculation strength due to local flow acceleration as the grid spacing becomes finer.

### Turbulence Modelling

Considering the complex flow structure and the low level of mass transfer within the cavity, a turbulence model validation analysis was conducted using the commonly available turbulence models, namely  $\kappa$ - $\epsilon$  Realisable, RNG  $\kappa$ - $\epsilon$  and Reynolds stress. This was to ensure that when validating the results with those obtained experimentally the most correct model would be used.

A cavity of  $\delta/D = 0.5$  was chosen both in the experiments and computational analysis due to ease of manufacture, and also because the flow separation and recirculation zones would be more pronounced for lower experimental  $Re$  numbers (as a smoke will be used for visualisation in this initial study).

### $\kappa$ - $\epsilon$ Realisable

Ranges of turbulence intensity (T.I.) levels were used, from 5% to 20% in 5% intervals ( $Re = 8.2 \times 10^2$ ). The results showed no discernable change in the location of the centre of the flow recirculation zone for all turbulence intensity values.

The location of this centre was approximately  $0.36\delta$  and  $0.6D$  for the height as a percentage of cavity depth from the free surface and the longitudinal placement as a percentage of the cavity diameter from the upstream edge point tangent to the free surface, see figure 4.

With a change in  $Re = 2.9 \times 10^4$  for T.I. = 10% the centre of recirculation zone migrated to  $0.38\delta$  and  $0.57D$ , that is to say it shifted down and towards the upstream face.

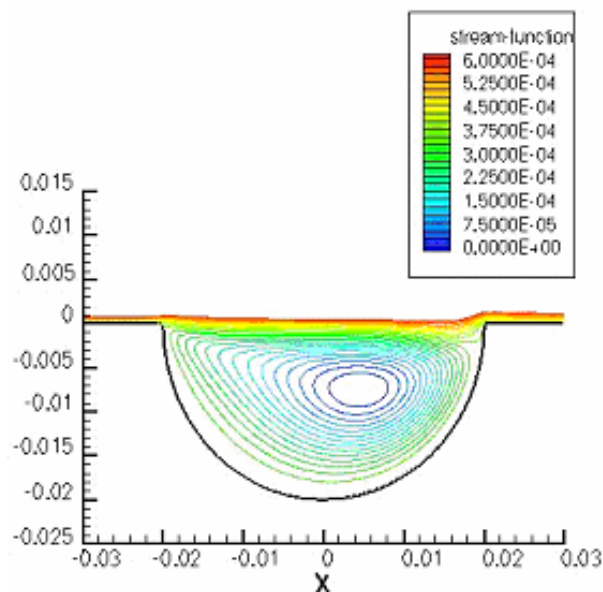


Figure 4 Stream function plot of the cavity  $\delta/D = 0.5$   $Re = 8.2 \times 10^2$   $\kappa$ - $\epsilon$  realisable turbulence model at T.I. 10%.

#### **$\kappa$ - $\epsilon$ RNG**

A 10% turbulence intensity level was used to compare it to the same T.I. 10% for the  $\kappa$ - $\epsilon$  realisable model as a conservative compensation for the turbulence in the wind tunnel was used. The result exhibited a fairly similar solution to the  $\kappa$ - $\epsilon$  realisable 10% T.I.

The centre of flow recirculation existed at  $0.43\delta$  and  $0.6D$  from the same point, that is to say the recirculation zone migrated  $0.13\delta$  away from the free surface for the RNG T.I. 10% model, but the flow separation point and stagnation points remained relatively unchanged. Thus there is little difference between  $\kappa$ - $\epsilon$  RNG and Realisable  $\kappa$ - $\epsilon$  turbulence models for the flow within a cavity of  $\delta/D = 0.5$  for low Reynolds Numbers ( $8.2 \times 10^2$ ).

#### **Reynolds Stress (Re- $\sigma$ )**

A 10% turbulence intensity level was again used to compare with the 10% RNG and 10% Realisable model. The results show the recirculation zone at  $0.34\delta$  and  $0.40D$ , which indicates that for the same  $Re$  the Reynolds stress turbulence model predicted the recirculation zone to be slightly higher and significantly further towards the upstream face of the cavity compared with the  $\kappa$ - $\epsilon$  realisable and  $\kappa$ - $\epsilon$  RNG models, which gave fairly similar results. These solutions must now be validated with experimental results.

#### **Experimentation**

Initial experimentation was centred on flow visualisation techniques to validate the numerical models. The information to be retrieved included the flow structure and location of the recirculation position. Also there was additional task to determine if the centre of rotation was changing a position within the cavity with time.

For the experimentation an existing wind tunnel was used, which was of open circuit, closed test section design (see figure 5). The tunnel was made from Perspex to allow the laser sheet to pass into the test section.

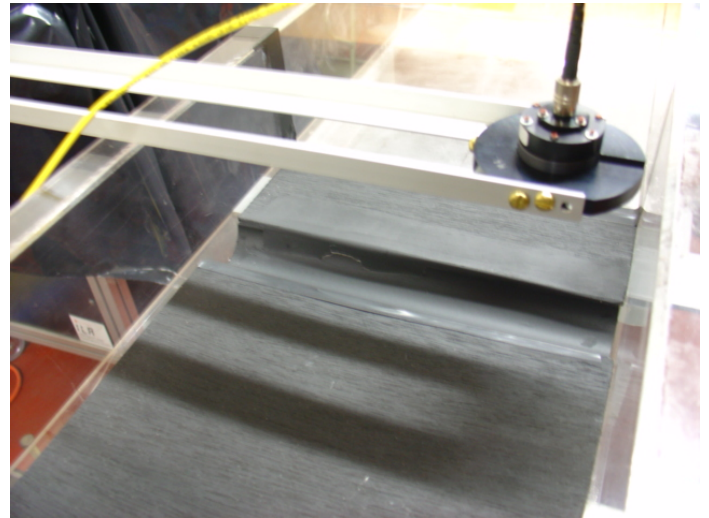


Figure 5 Experimental set-up, showing laser line generator on arm and channel for the two-dimensional cavity

A 25mW JDS 'Uniphase' Model 1145 He-Ne laser was used to generate the laser sheet and a Sony DSC-V1 digital camera used to capture the pictures. A digital manometer was used to determine the free stream velocity in the tunnel. For visualisation a Le Maitre G100 smoke generator was used to seed the tunnel.

The test piece consisted of a channel running across the tunnel. A dimple depth to effective dimple diameter ratio of  $\delta/D = 0.5$  was chosen due to the ease of manufacture and the visualisation benefits resulting from the more pronounced flow recirculation. The image in figure 6 shows the instance at which the recirculation zone forms within the cavity.

Several observations were made:

- The recirculation zone took quite a while to develop, as the momentum within the cavity is quite small.
- The recirculation zone did slightly reciprocate around itself.
- The interaction of the fluid ejecting from the rear of the cavity and the boundary layer on the surface (within which it sits) caused an oscillation within the boundary layer even at low  $Re$ .
- Once the smoke developed in the cavity it remained locally for several minutes without the introduction of additional smoke.

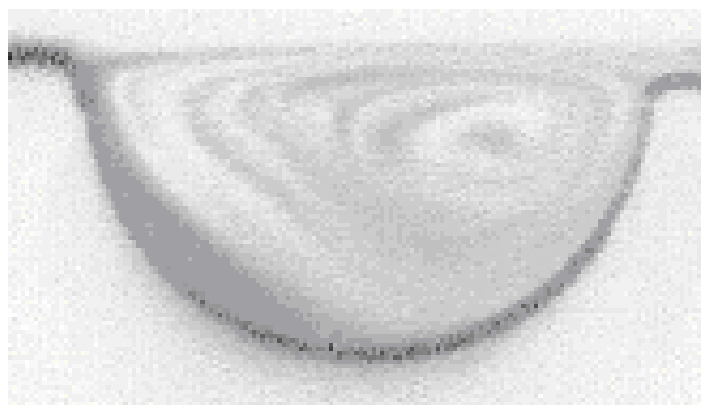


Figure 6 Flow visualisation within cavity  $\delta/D = 0.5$   $Re = 8.2 \times 10^2$ .

Turbulence model	$\Delta\delta$ with respect to experiments	$\Delta D$ with respect to experiments
Realisable 5%	+0.05	+0.03
Realisable 10%	+0.05	+0.03
Realisable 15%	+0.05	+0.03
Realisable 20%	+0.05	+0.03
RNG 10%	-0.12	-0.03
$R_e-\sigma$	+0.03	-0.14

Table 1 Change in the position of recirculation centre with respect to experimental result.

The recirculation zone of the experiment and the numerical result are overall fairly consistent with each other. For the K- $\epsilon$  Realisable turbulence model the results were the most consistent with the experimental result with the deviation in the recirculation centre shown in Table 1.

### Conclusions

The flow structure within a two-dimensional spherical cavity on a flat plate has been studied numerically. A two-dimensional configuration was used to develop a consistent turbulence model and ensure that sufficient grid spacing for the three-dimensional case is used. Vortex shedding was not observed, possibly due to a two-dimensional nature of the experiment. However the oscillation of the flow exiting the 'two-dimensional' cavity may cause a similar phenomenon three-dimensionally.

The stability of the flow within the cavity over time suggests that the assumption of a steady state analysis (for such low Reynolds numbers) is appropriate. Although an unsteady solution was obtained, it was observed that once the recirculation zone had formed off the upstream edge of the cavity it stabilised to a position consistent with the steady-state case.

The grid spacing has a significant effect on the flow structure within the cavity, as seen in figures 2 and 3. There need not be too much refinement in the grid for flow recirculation to exist, from meshed edge length 0.1mm to 0.8mm a recirculation zone was established, and the overall flow field within the cavity was approximate to the finer spaced grids, albeit the static pressure profile and recirculation centre changed. For accuracy in modelling the flow within the cavity this requires fairly strong computing power, especially as the simulation progresses from two-dimensional to three-dimensional cases.

The turbulence model validation suggests that a  $\kappa-\epsilon$  realisable scheme is the most consistent to the experimental situation. The turbulence intensity levels did not have too much of an effect within the numerical cases, although more accurate modelling of the turbulence levels within the tunnel may yield a more accurate representation of the recirculation centre for the numerical solution.

### References

- [1] Ekkad S.V., Nasir H., Dimple Enhanced Heat Transfer in High Aspect Ratio Channels, Proceed. of IMECE: 2001 ASME International Mechanical Engineering Congress & Exposition Nov 1-16, 2001, New York
- [2] Isaev S.A., Leont'ev A.I., Baranov P.A., Identification of Self-Organised Vortexlike Structures in numerically Simulated Turbulent Flow of a Viscous Incompressible Liquid Streaming around a Well on a Plane, Technical Physics Letters. **26** (1), 2000.
- [3] Jongmyung Park, Desam P.R., Ligrani P.M., Numerical Predictions of Flow Structure above a Dimpled Surface in a Channel, *Journal of Numerical Heat Transfer, Part A*, **45** Part A, 2004, 1-20.
- [4] Lin, Y.-L., Shih T.I.-P. Chyu M.K., Computations of Flow and Heat Transfer in a Channel with rows of Hemispherical Cavities, *ASME Paper* No. 99-GT-263.
- [5] Mahmood G.I., Hill M.L., Nelson D.L., Ligrani P.M., Moon H.K., Glezer B., *ASME Trans. Turbomachinery* **123**, 2001, 115.
- [6] Mahmood G.I., Ligrani P.M., Heat Transfer in a Dimpled Channel: Combined Influences of Aspect Ratio, Temperature Ratio, Reynolds Number and Flow Structure, *International Journal of Heat and Mass Transfer*, **45**, 2002, 2011-2020.
- [7] Schukin A.B., Kozlov A.P., Chudnovskii Ya.P., Agachev R.S., Intensification of Heat Exchange by Spherical Depressions. A Survey, *Applied Energy: Russian Journal of Fuel, Power, and Heat Systems*, **36** (3), 1998, 45-62.



## Mixing Characteristics of a Notched-Rectangular Jet and a Circular Jet

J. Mi, P. Kalt and G. J. Nathan

School of Mechanical Engineering, The University of Adelaide, South Australia 5005, Australia

### Abstract

This paper reports an experimental investigation of the near-field mixing characteristics of two single air/air turbulent jets issuing, respectively, from a notched-rectangular orifice and a circular orifice with identical opening areas. Planar particle image velocimetry (PIV) was used for measurements of the velocity field. Present experiments for the two jets were conducted under the same nominal conditions with the exit Reynolds number of 72,000.

Consistent with previous investigations of other noncircular jets, the notched jet is found to have an overall superior mixing capability over the circular counterpart. Immediately downstream of the nozzle exit, it entrains, and then mixes with, the surroundings at a higher rate. This jet has a shorter potential core and higher rates of decay and spread than the circular jet. The phenomenon of axis switching is also found to occur in this jet.

### Introduction

Extensive research into noncircular jets has been performed in the past two decades or so (e.g., [1-21]), largely due to their potential to entrain ambient fluid more effectively than comparable circular jets. The superior mixing capability of such jets is experimentally related either to the non-uniform curvature of their initial perimeter, relative to the evenness for the circular configuration, or to the instabilities produced by the initial perimeter's sharp corners through the asymmetric distribution of pressure and mean flow field [3]. Both phenomena are deduced to accelerate three-dimensionality of the jet structures, therefore causing greater entraining and mixing. For elliptic and rectangular jets, azimuthal curvature variation of initial vortical structures produces non-uniform self-induction and three-dimensional structures. As a result, these flows spread more rapidly in the minor axis plane than in the major axis plane, causing 'axis switching' at a certain distance from the nozzle exit (e.g., [3,21]). For corner-containing configurations, the corners promote the formation of fine-scale turbulence and thus enhance fine-scale mixing [4,9]. The above experimental results have also been demonstrated in a number of numerical simulations (e.g. [1,2,12]). The review of Gutmark and Grinstein [3] summarizes both experimental and numerical studies in the context of noncircular jets.

Note however that previous investigations on noncircular jets, e.g.[1-22], have focussed predominantly on elliptical, rectangular (including square), and triangular configurations. Few detailed measurements and simulations have been performed for other shapes. Although Mi et al. [11] provided hot-wire measurements in nine different-shaped jets, their data were limited only to the centreline mean and rms of the axial velocity.

The present study carried out planar PIV measurements of two single jets issuing respectively from a circular and a four-notched rectangular orifice, with the same opening area ( $A$ ) and thus an identical equivalent diameter  $D_e [\equiv 2(A\pi)^{1/2}]$  of approximately 12 mm (Fig. 1). The aspect ratio (AR) of the notched orifice, i.e., the ratio of the long to short axes of symmetry of the orifice cross-section, is  $AR = 1.5$ . The main objective of the present

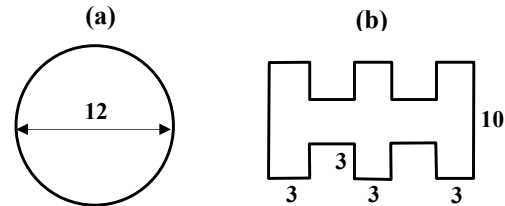


Fig. 1. Present orifice shapes and dimensions (mm). (a) Circle:  $D_e = D_h = 12$  mm,  $D_e/D_h = 1$  and  $AR = 1$ ; (b) Notched-rectangle:  $D_e = 12$  mm,  $D_h = 9.12$  mm,  $D_e/D_h = 1.32$  and  $AR = 1.5$ .

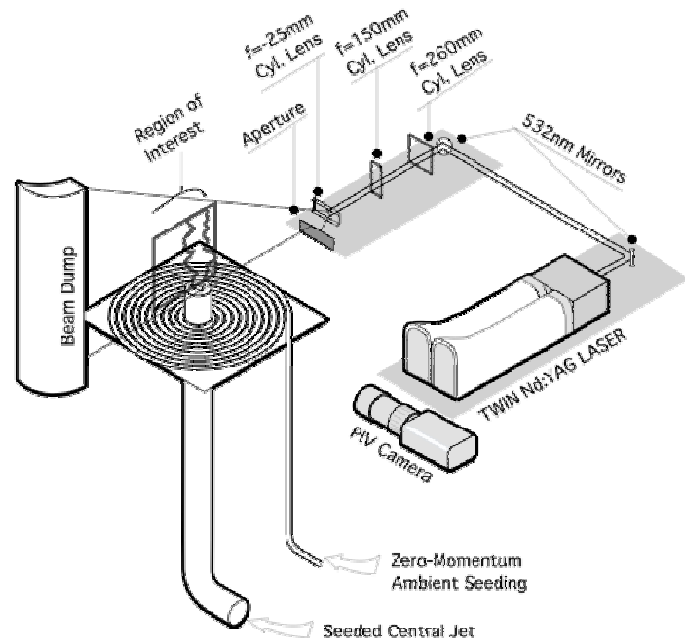


Fig. 2. Experimental set-up of the PIV system.

report is to compare the mean flow fields of the two jets to identify their similarity and difference.

### Experimental details

The PIV experiments were conducted at the Laser Laboratory of Turbulence, Energy & Combustion Group, The University of Adelaide. Fig. 2 shows schematically the experimental set-up. A compressor with an operating pressure of up to 650 kPa supplied conditioned air to the test rig. The two orifice plates (Fig. 1) were separately attached to the vertical tube of 25.4 mm i.d. and 1000 mm in length. The flow rate through the tube, which was used to calculate the jet exit bulk velocity and Reynolds number, was obtained by a flow meter. Good axisymmetry of the tube flow immediately upstream of each orifice plate attached was achieved since nearly identical and symmetric radial profiles of the mean velocity at the tube exit for different orientations (not presented here) were found. The tube flow at the exit was not fully developed so that its mean velocity profile did not follow the one-seventh power-law as for the fully-developed pipe flow. The axial turbulence intensity was about 3% at the centre and up to 26% near the tube edge. Both jets were measured at the same nominal Reynolds number of  $Re = 72,000$ , where  $Re \equiv U_e D_e / \nu$ ,

with  $U_e$  being the exit bulk velocity,  $D_e$  the exit equivalent diameter and  $\nu$  the kinematic viscosity of fluid.

The air jet flows were seeded with small olive oil droplets, with a mean diameter of about  $1\ \mu\text{m}$ , generated by a Laskin nozzle particle generator. This type of seeding follows the bulk flow well and is suitable for the present velocity range [16]. The droplets from the generator were divided into two streams, one used for seeding the core jet flow and the other through a plastic tube coil with fine holes upwards for seeding ambient air with very low ejecting speed ( $< 1\% U_e$ ). The whole rig was positioned under an extraction hood and was further surrounded by a curtain of black cloth to reduce the effects of room draughts and stray laser scattering.

PIV measurements were realised by a Quantel Brilliant Twins double-head Nd:YAG laser at a frequency of 10 Hz and power of 250 mJ per pulse at  $\lambda = 532\ \text{nm}$ . This laser is specially designed for PIV applications, each of the laser heads being independently triggerable. The temporal separation between laser pulses was adjusted from 10 to 40  $\mu\text{s}$ , depending on the flow-field. The camera is a MegaPlus ES1.0 PIV camera operated in triggered double exposure mode. The CCD in this camera is 1008 pixels wide by 1018 pixels high. The collection optics comprised a Nikon ED 70-300 mm (set to 110 mm) telephoto lens coupled to the camera C-mount with an adapter. The aperture was fully opened ( $f^\# = 4$ ). The imaging region was 100 mm by 100 mm, each pixel corresponding to  $10\ \mu\text{m}$ . Data were collected from the camera at 20 Hz into a memory buffer on the data storage computer. At the end of a run, the entire dataset of PIV image pairs were saved to hard disk for later processing.

The time delay between laser pulses was selected so that the interrogation region could be set to 32 by 32 pixels, with a 50% offset. This resulted in an effective resolution for the velocity measurements of 3 mm. The resulting vector field is comprised

of FIL by FIL vectors. A 2-pass Hart correlation algorithm was used to correlate the two image pairs. The correlation image scanned for peaks using a centroid-hunting algorithm on a roaming  $3 \times 3$  pixel mask. This gives sub-pixel accuracy for the determined velocity. Outliers (erroneous vectors) were detected by comparison to the neighbourhood average. Outliers were replaced by a suitable, alternative correlation peak where possible, and were otherwise replaced by interpolation from valid neighbouring vectors. This is only recommended when outlying vectors occur only infrequently within any given vector field.

Mean vector fields were found from an ensemble of 520 vector fields for each condition. Downstream measurements of the flow were made by axially translating the nozzle relative to the camera and laser sheet.

## Results and discussion

Figures 3(a) and 3(b) show the mean velocity ( $\langle U \rangle / U_e$ ) contours and mean streamlines in the two symmetric (i.e.,  $xy$  and  $xz$ ) planes of the notched jet, respectively, while those results obtained from the central plane of the circular jet are presented in Fig. 3(c) for comparison. We also present the mean vorticity contours in Fig. 4. The measurement area shown here is in the near-field region at  $0.4 \leq x/D_e \leq 8.2$ . For the notched jet, the  $xy$  and  $xz$  planes are the minor and major axis planes as indicated on the plot.

Comparison of Figs. 3(a)-(c) and 4(a)-(c) suggests significant differences in the mean flow field between the two jets. Apparently, the core (bounded with yellow contours) of the mean notched jet initially contracts over a short distance  $x \leq 1.0 D_e$  in the minor axis ( $xy$ ) plane while simultaneously it spreads out in the major axis ( $xz$ ) plane. Interestingly, in the minor axis plane, the jet 'edge' spreads very rapidly over the region  $0.5 < x/D_e < 2$ ; further downstream, the spreading speed slows down but still remains high relative to the circular case (Fig. 3(a)). In the major

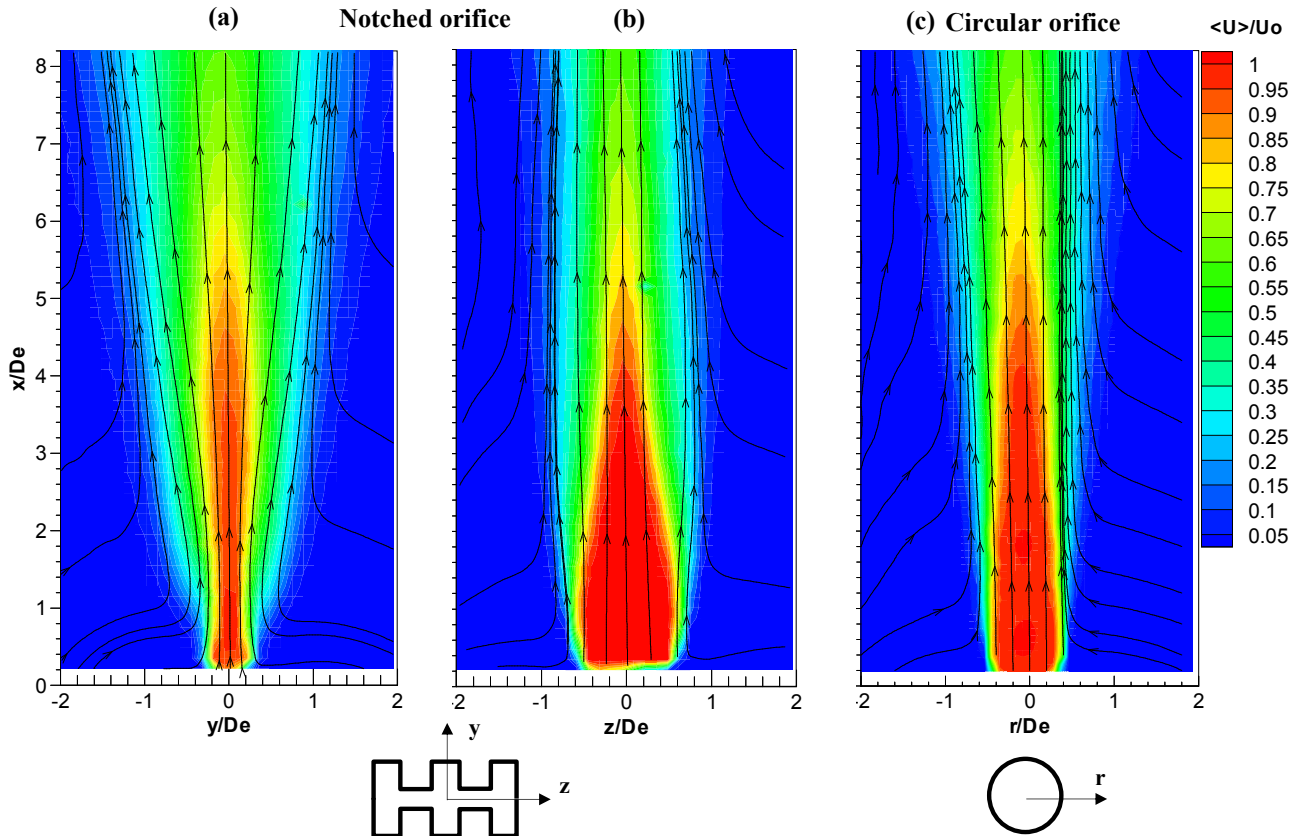


Fig. 3. Mean velocity contours and streamlines. (a) notched jet in the  $xy$  plane; (b) notched jet in the  $xz$  plane; (c) circular jet.



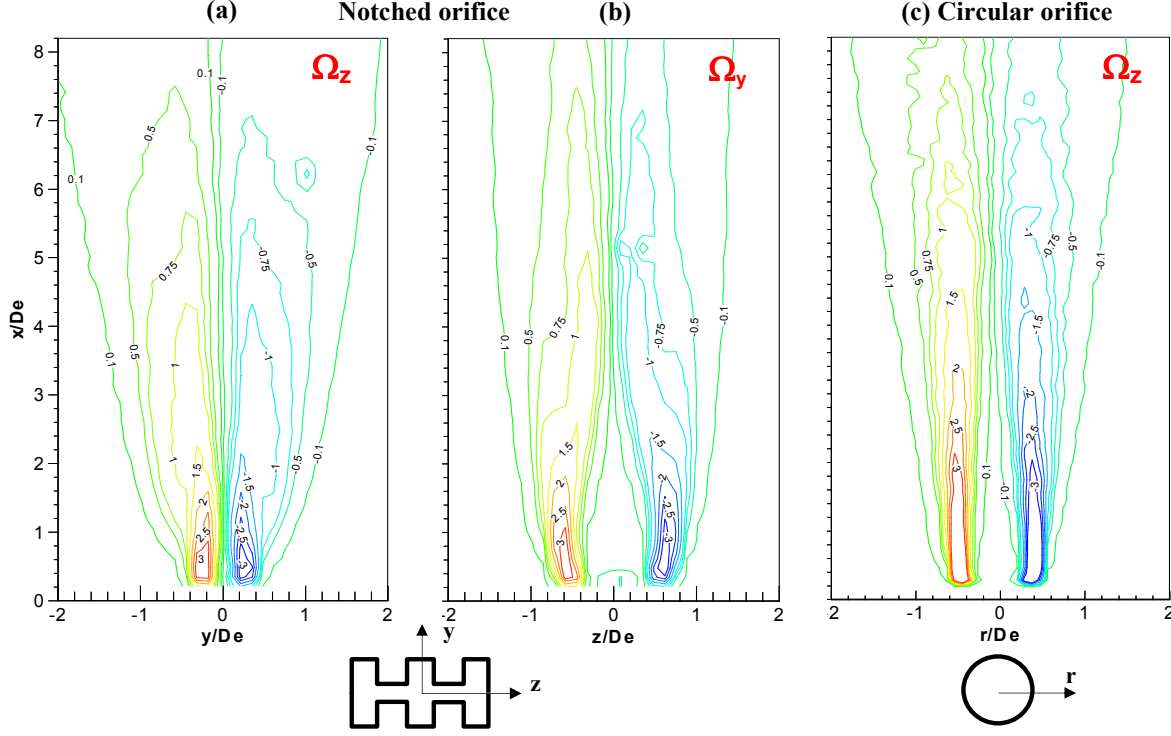


Fig. 4. Mean vorticity contours. (a)  $\Omega_z$  in the  $xy$  plane, notched jet; (b)  $\Omega_y$  in the  $xz$  plane, notched jet; (c)  $\Omega_z$ , circular jet.

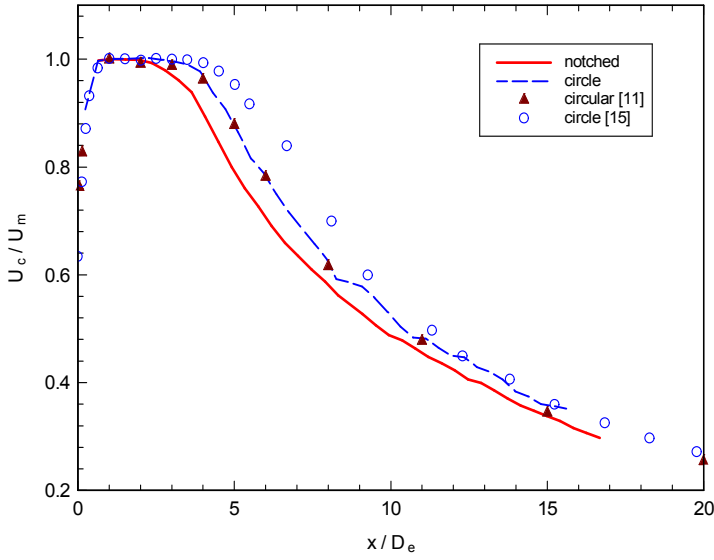


Fig. 5. Mean velocity decay along the jet centreline.

axis plane, however, the notched core jet contracts slowly from  $x/D_e \approx 1.0$  to  $x/D_e \approx 6.0$  and starts to spread further downstream. By comparison, the circular jet spreads out all the way in all lateral directions, yet with a relatively low rate. Moreover, as indicated by red to yellow colour scales in Figs. 3(a)-(c), the mean velocity of the notched jet decreases with  $x$  at a higher rate than that of the circular jet. It is hence clear that overall the notched jet spreads and decays more rapidly than does the circular jet. This implies that it entrains (and then mixes) ambient fluid at a higher rate. This is consistent with previous observations for other noncircular jets [3-9].

The above conclusion is made based only on the measurements in the  $xy$  and  $xz$  planes rather than for the entire field of the notched jet. However, further support for this deduction can be derived from the streamwise variations of the normalized centreline velocity,  $U_c/U_m$ , and half-velocity widths ( $y_{1/2}$  and  $z_{1/2}$ ), shown in Figs. 5 and 6. Here,  $U_m$  is the maximum of  $U_c(x)$  occurring near

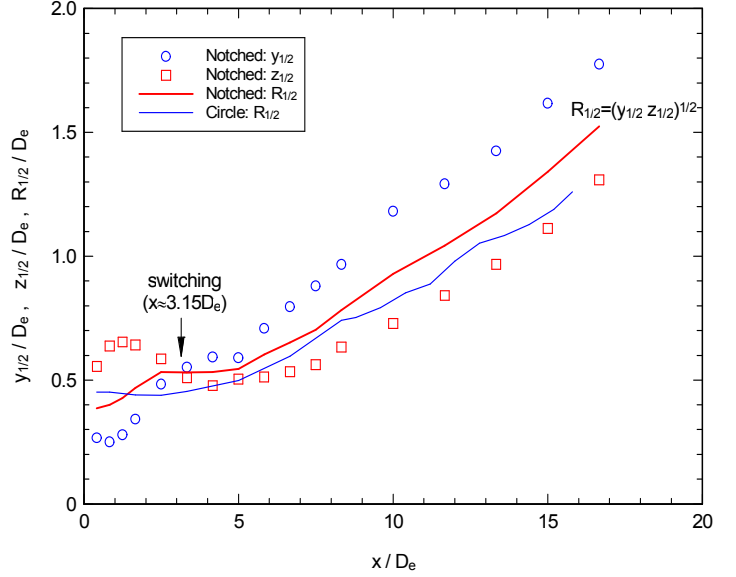


Fig. 6. Half-velocity widths of the notched jet and their comparison with the circular counterpart.

to the orifice exit; the half-velocity width is the lateral distance from the jet axis to a location at which the mean velocity  $\langle U \rangle$  is half the centreline mean velocity  $U_c$ , i.e.,  $\langle U \rangle = U_c/2$ . The data reported in Figs. 5 and 6 were extracted from the PIV measurements over the range  $0.4 \leq x/D_e < 17$ . For comparison with previous work, the hot-wire data of  $U_c/U_m$  of Mi et al. [11],  $Re \approx 15000$ , and Quinn [15],  $Re \approx 200000$ , for a circular orifice jet are also included in Fig. 5. It is interesting to note that the present data for the circular jet agree very well with [11] while Quinn's data differ quite significantly at  $x/D_e < 12$ . The difference between the present results and those of [15] is likely associated with very distinct upstream flow configurations used in the two studies. While the present study utilized an industry-type pipe, without conditioning, to supply compressed airflow to the orifice, Quinn adopted a conventional jet facility, which has a large settling chamber fitted with honey-comb and mesh-wire screens and a three-dimensional contraction, to achieve a low-turbulence-intensity uniform flow upstream of the orifice.

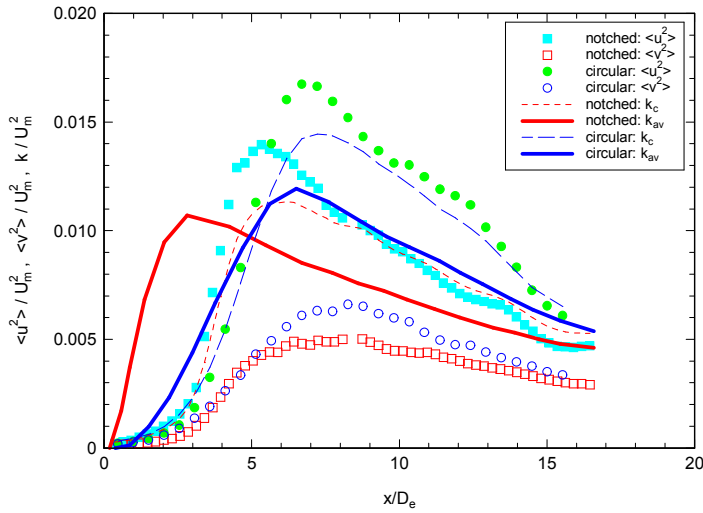


Fig. 7. Centreline distributions of the normal stresses ( $\langle u^2 \rangle$ ,  $\langle v^2 \rangle$ ) and turbulence kinetic energy ( $k_c$ ).

The centreline velocity decreases more rapidly with axial distance (Fig. 6), while the half-velocity equivalent radius,  $R_{1/2} = (y_{1/2} z_{1/2})^{1/2}$ , spreads faster (Fig. 7), in the notched jet than in the circular jet. (Note that  $R_{1/2}$  was adopted by Hussain and Husain [7] for elliptic jets.) Consistently, the potential core is shorter for the former, with length of  $L_{pc} \approx 2.2D_e$ , relative to  $L_{pc} \approx 3.5D_e$  for the latter. Figure 6 also demonstrates that for the notched jet the half-width in the minor axis plane,  $y_{1/2}$ , develops from being initially smaller than that in the major axis plane,  $z_{1/2}$ , to exceeding the latter, i.e.,  $y_{1/2} > z_{1/2}$ , at  $x \approx 3.15D_e$ . That is, there is axis-switching occurring in the notched jet with AR = 1.5, similar to rectangular jets initially with or without disturbance of tabs [21].

Figure 7 shows the centreline Reynolds normal stresses,  $\langle u^2 \rangle$  and  $\langle v^2 \rangle$ , of the two jets, where  $u$  and  $v$  represent the axial and lateral components of the fluctuating velocity. Also reported are the centreline distributions ( $k_c$ , dashed lines) of the turbulence kinetic energy  $k = (\langle u^2 \rangle + \langle v^2 \rangle + \langle w^2 \rangle)/2$  and the streamwise variations of the averaged  $k$  over the cross-section ( $k_{av}$ , solid lines). Note that  $k_{av}$  was obtained in the  $xy$  and  $xz$  planes for the notched jet while for the circular case it was estimated from the central plane. As expected, the magnitude of  $\langle u^2 \rangle$  is much greater than that of  $\langle v^2 \rangle$  in both jets. In the near field, as  $x$  increases, both  $\langle u^2 \rangle$  and  $\langle v^2 \rangle$  increases. This increase results from the high production of turbulence in the shear layers; the turbulence is then diffused from the shear layers to the jet centreline. For the notched jet,  $\langle u^2 \rangle$  and  $\langle v^2 \rangle$  peak at  $x/D_e \approx 5.5$  and  $7.5$ , respectively, while the corresponding peaks occur at  $x/D_e \approx 7$  and  $8.5$  for the circular counterpart. Consequently, the kinetic energy  $k_c$  peaks nearly at the same location as  $\langle u^2 \rangle$  in both jets.

One important finding extracted from Fig. 7 is that the averaged kinetic energy  $k_{av}$  evolves very distinctly in the two jets. This reflects a significant difference in their mixing mechanisms. Clearly,  $k_{av}$  grows much faster until  $x/D_e \approx 3$  in the notched jet than in the circular counterpart, indicating that, in the very near region, the former jet mixes far more intensively with its surroundings. The stronger mixing is accompanied by a faster spreading of the mean velocity field, Fig. 3, and thus a shorter potential core region, Fig. 4. The overall kinetic energy  $k_{av}$  turns to decrease from  $x/D_e \approx 3$  in the notched jet and much farther downstream from  $x/D_e \approx 6.5$  in the circular jet. This is because large-scale coherent structures formed in the former are more three-dimensional in more complex flow patterns and have stronger interactions with each other and the ambient flow, thus breaking down faster. As a result,  $k$  is dissipated more rapidly in

this jet. It follows that, downstream of  $x/D_e = 5-6$ ,  $k$  is higher in the circular than notched jet.

## Conclusions

In this study we carried out planar PIV measurements of two single jets issuing respectively from a circular and a notched rectangular orifice with same opening areas. Comparison has been made between the near-field mixing characteristics of the two jets. It has been found that, in general, the notched jet entrains the ambient fluid at a higher rate than does the circular counterpart. Specifically, the former jet both decays and spreads faster, yielding a shorter potential core. Immediately downstream from the nozzle exit ( $x < 3.0D_e$ ), it mixes the surroundings much faster and, hence, the cross-sectional averaged kinetic energy grows far more rapidly relative to the circular case. In addition, the phenomenon of axis switching occurs (at  $x \approx 3.15D_e$ ) in the notched jet.

## Acknowledgment

The authors gratefully acknowledge the support of the Australian Research Council.

## References

- [1] Grinstein, F.F., Self-induced vortex ring dynamics in subsonic rectangular jets, *Phys. Fluids* **7**, 1995, 2519-2521.
- [2] Grinstein, F.F., Gutmark, E. and Parr, T., Near field dynamics of subsonic free square jets, A computational and experimental study, *Phys. Fluids*, **7**, 1995, 1483-1497.
- [3] Gutmark, E. & Grinstein, F. F., Flow control with noncircular jets, *Ann. Rev. Fluid Mech.*, **31**, 1999, 239-272.
- [4] Gutmark, E., Schadow, K.C., Parr, T.P., Hanson-Parr, D.M., & Wilson, K.J., Noncircular jets in combustion systems, *Expts Fluids* **7**, 1989, 248-258.
- [5] Ho, C.M. & Gutmark, E., Vortex induction and mass entrainment in a small-aspect-ratio elliptic jet, *J. Fluid Mech.* **179**, 1987, 383-405.
- [6] Husain H. S. & Hussain F., Controlled excitation of elliptic jets *Phys. Fluids* **26**, 1983, 2763-2766.
- [7] Hussain, F. and Husain, H.S., Elliptic jets. Part 1. Characteristics of unexcited and excited jets, *J. Fluid Mech.* **208**, 1989, 257-320.
- [8] Husain, H.S. and Hussain, F., Elliptic jets. Part 2. Dynamics of coherent structures: pairing, *J. Fluid Mech.* **233**, 1991, 439.
- [9] Koshigoe, S., Gutmark, E. & Schadow, K., Initial development of non-circular jets leading to axis switching, *AIAA J.* **27**, 1989, 411.
- [10] Krothapalli, A., Baganoff, D. & Karamcheti, K., On the mixing of rectangular jets, *J. Fluid Mech.* **107**, 1981, 201-220.
- [11] Mi, J. Nathan, G.J. and Luxton, R.E., Centreline mixing characteristics of jets from nine differently shaped nozzles, *Expts. Fluids* **28**, 2000, 93-94.
- [12] Miller, R.S., Madnia, C.K. and Givi, P., Numerical simulation of non-circular jets, *Computers & Fluids* **24**, 1995, 1-25.
- [13] Quinn, W.R., On mixing in an elliptic turbulent free jet, *Phys. Fluids* **A1**, 1989, 1716-1722.
- [14] Quinn, W.R., Mean flow and turbulence measurements in a triangular turbulent free jet, *Int. J. Heat & Fluid Flow* **11**, 1990, 220-224.
- [15] Quinn, W.R., Development of a large-aspect-ratio rectangular turbulent free jet, *AIAA J.* **32**, 1994, 547-554.
- [16] Raffel M., Willert C. & Kompenhans J., *Particle image velocimetry—A Practical Guide*, Springer, Germany, 1998.
- [17] Schadow, K.C., Gutmark, E., Parr, D.M. and Wilson, K.J., Selective control of flow coherence in triangular jets, *Expts. Fluids* **6**, 1988, 129-135.
- [18] Sforza, P.M., Steiger, M.H. and Trentacoste, N., Studies on three dimensional viscous jets, *AIAA J.* **4**, 1966, 800.
- [19] Trentacoste, N. and Sforza, P.M., Further experimental results for three dimensional free jets, *AIAA J.* **5**, 1967, 885.
- [20] Tsuchiya, Y., Horikoshi, C. and Sato, T., On the spread of rectangular jets, *Exps. Fluids* **4**, 1986, 197-204.
- [21] Zaman, K.B.M.Q., Axis switching and spreading of an asymmetric jet: the role of coherent structure dynamics, *J. Fluid Mech.* **316**, 1996, 1-27.
- [22] Zaman, K.B.M.Q., Spreading characteristics of compressible jets from nozzles of various geometries, *J. Fluid Mech.* **383**, 1999, 197-228.

## Preliminary Investigations of Vortex Rings and Jets in Cross Flow

E.R. Hassan, R.M. Kelso, G.M. Schneider and T.C.W. Lau

School of Mechanical Engineering  
The University of Adelaide, S.A, 5005 AUSTRALIA

### Abstract

A piston-cylinder arrangement has been designed and tested for the generation of continuous jets, fully modulated jets and individual vortex rings in cross flow. Hydrogen bubble visualisation, Acoustic Doppler Velocimetry and dye visualisation have been implemented to test the validity of the equipment. Mean trajectories of the vortex rings and continuous jets were determined by time averaging video footage of the spatial and temporal evolution of the vortex rings and jets interacting with the cross flow. These trajectories were found to be in close agreement with trajectories quoted in the literature.

### Introduction

The jet in cross-flow (JICF) is a commonly occurring flow in both industry and nature. An appealing aspect of the jet in cross flow is its enhanced mixing over the free jet. A thorough review of the topic is given by Margason [12] citing over 300 references. More recent considerations of the JICF have been Kelso, Lim and Perry [11], Smith and Mungal [14] and Cutler [3]. Jets in cross flow are primarily classified by the Jet Reynolds number,  $Re_j$  and the square root of the ratio of momentum fluxes from the jet and the cross flow. The latter term is usually referred to as the velocity ratio,  $R$ , because in the cases of same jet and cross flow fluids  $R$  is approximately equal to the ratio of the jet to cross flow velocities. Figure 1 shows the jet and cross flow velocities, the coordinate system, the jet apparatus used in the experiment and definitions of  $Re_j$  and  $R$ . The jet diameter is denoted as  $d$  and the kinematic viscosity of the fluid is  $\nu$ . Many studies have established that the variation of the temporal velocity profile of a modulated transverse jet changes the characteristics of the resulting flow. Particular attention has been devoted to fully modulated jets. Full modulation of a jet "breaks" the jet up into discrete vortex rings [1]. Hermanson *et al.* [9], Johari *et al.* [10] and others have demonstrated that the stronger the modulation, the deeper the jet penetrates into the cross flow. A recent study on pulsed jets by Eroglu and Breidenthal [5] demonstrated that for a fixed duty cycle (ratio of time the jet is pulsed to total time between pulses), variation of pulsation frequency varied the penetration and mixing rate of the jet. Recently zero-net-mass-flux (ZNMF) jets in cross flow were investigated by Gordon *et al.* [8]. It was observed that, under certain conditions, the ZNMF JICF penetration lacked the velocity ratio dependence of the continuous JICF. Due to the differences between the steady jet and vortex ring it is necessary to define a characteristic Reynolds number for the vortex ring. Normalizing a vortex ring's circulation,  $\Gamma$ , by  $\nu$  results in a parameter that can be considered a Reynolds number of the vortex ring [6]. This Reynolds number,  $Re_\Gamma$  shown in figure 1, takes into account the velocity and duration of the pulse in generating the vortex ring. Apart from low pulsing frequencies considered in Chang and Vakili [1], there have been few studies of individual vortex ring trajectories in cross flow. The current study is investigating individually pulsed vortex rings and continuous jets - two extremes of the pulsed jet duty cycle.

### Experimental Arrangement

The experiments were conducted in a 500mm x 500mm working section of a closed-return water channel located at the School of Mechanical Engineering at The University of Adelaide. The frequency-controlled pump allowed steady operation at velocities below 20mm/s and up to 450mm/s. Before issuing into the cross flow, the jet fluid passed through a flow conditioning section. This section, shown in figure 1, consisted of a 9:1 conical expansion, followed by a settling section and flow straightener and a 9:1 axisymmetric contraction. See Cutler [3] for further details. The discharge pipe had a diameter of 50mm and a length to diameter ratio,  $(L/d)$ , of 4. This diameter could be further reduced using an insert consisting of a smooth contraction and a 25mm pipe of  $L/d=4$ . A circumferential dye injection port was located in the pipe wall at least 4 jet diameters upstream of the jet exit. This method of dye injection into the jet boundary layer allowed the shear layer of the jet to be uniformly marked.

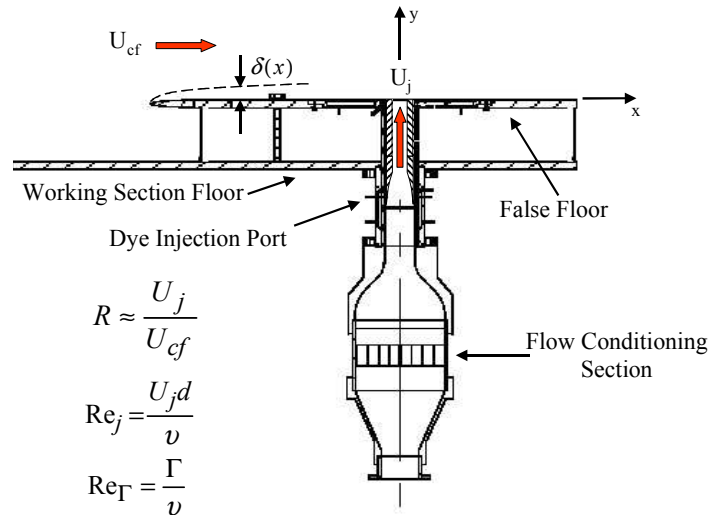


Figure 1. The jet apparatus used in the experiment showing the coordinate system.  $\delta(x)$  denotes the boundary layer thickness. Reproduced and modified after Cutler and Kelso [4].

### Vortex generating system

A Bellofram<sup>TM</sup> cylinder was used to generate the modulated jet flow. Fluid expelled from the cylinder travelled along a 1.5m long, 25mm diameter hose into the settling chamber and eventually issued into the working section transversely to the cross flow. A stepper motor was used in conjunction with a lead screw to advance and retract the shaft of the piston in a controlled manner. Two lead screws of pitch 2mm and 5mm were utilised. The motor controller allowed various user inputs of motor speed, drive time, pause time (and thus duty cycle) and direction. This allowed the generation of impulsively started continuous and fully modulated jets as well as individual and trains of vortex rings. Having two jet diameters of  $d=25\text{mm}$  and  $50\text{mm}$  as well as two lead screws of pitches 2mm and 5mm provides a large range of jet velocities and Reynolds numbers. The available jet velocities ranged from 10mm/s to 650mm/s with corresponding Reynolds numbers of 500 and 16,000.



## Velocity Profiles

Both the spatial and temporal jet centre-line velocities were investigated as a means of verification of the jet apparatus.

## Hydrogen bubble visualisation

Hydrogen bubble visualisation (see Smith *et al* [13]) was used to observe the spatial velocity profile of the jet. The timelines were generated by a Hydrogen bubble wire mounted across the jet exit. Figure 2 shows timelines at different times after the generation of a long duration pulse. Figures 2a and 2b show the early stages of the jet and figure 2c shows the jet at a relatively well-developed stage with two successive timelines clearly visible. The images are digitally enhanced and a 5mm by 5mm grid superimposed. Hydrogen bubble visualization was conducted in this fashion over the full range of operating conditions. The results indicate a top hat velocity profile is obtained for the jet in absence of a cross flow and show symmetric roll up of the shear layer.

## Acoustic Doppler Velocimetry

Three-dimensional Acoustic Doppler Velocimetry was used to measure the temporal velocity profile of the pulsed jets. The measurements were conducted using a SonTek<sup>TM</sup> Acoustic Doppler Velocimeter (ADV), which had a measurement volume of 5 cubic centimetres. The measurement volume of the ADV was aligned with the centre of the jet and was located approximately one jet diameter upstream of the jet exit. The ADV supplied not only velocity components in the x, y and z directions but also correlation coefficients and signal to noise ratios for velocity signals in all three directions. A sample velocity trace of a one second pulse ( $\tau=1$  sec) with three different jet velocities is shown in figure 3. As can be seen, the profile structure, although not exactly square, is adequate of the purposes of generating fully modulated jets. The limiting property of the equipment was the rise time of the velocity from zero to the desired value. The time axis on figure 3 is normalised relative to the pulse time,  $\tau$ , and the velocity axis is normalised relative to the velocity that the steady state jet would attain if continually driven at the set speed,  $V_{ss}$ .

## Experiment

Dye visualization of jets and vortex rings in cross flow was conducted. The continuous jet was marked with neutrally buoyant dye. For all cases presented, the jet diameter is 25mm. Several minutes were allowed to elapse between each run to let the dye in the jet pipe diffuse to a relatively uniform concentration and to allow any secondary flows in the jet pipe to dissipate. The cross-flow velocity was held constant at 32mm/s for all flow cases, thereby keeping the cross-flow boundary layer thickness at the jet exit constant at  $\delta/d=0.7$ . Table 1 shows flow cases considered as well as the number of the times each flow case was run.

Flow	R	$U_j$ mm/s	$Re_j$	$Re_\Gamma$	No. of runs	mean at $x/d=10$	$U_{95\%}$ (+/-)
Jet	2	69	1,700	-	5	3.84	0.12d
Jet	4	127	3,200	-	5	5.79	0.26d
Jet	6	195	4,900	-	5	10.40	0.48d
Jet	8	252	6,300	-	5	13.48	1.10d
Ring	2	69	1,700	1,400	10	3.02	0.075d
Ring	4	127	3,200	4,800	10	8.13	0.090d
Ring	6	195	4,900	11,400	9	14.74	0.232d

Table 1. Details of the cases investigated.

## Data Analysis

Video footage was digitised into a series of images and then analysed using *MATLAB*<sup>TM</sup> software. Images were averaged to obtain a normalised "time exposure".

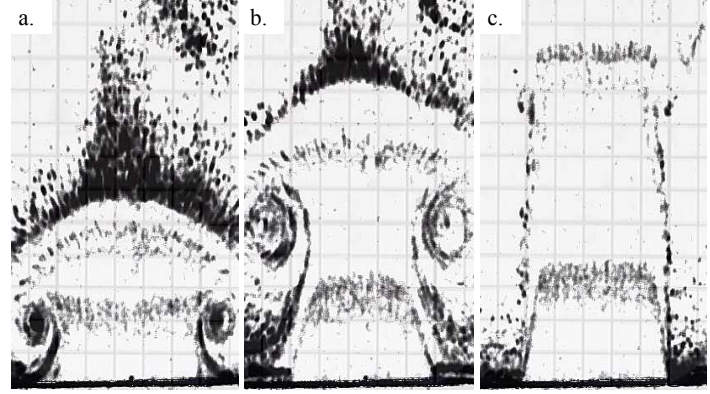


Figure 2. Time lines of an impulsively started jet. Images a, b and c correspond to times  $t=0.8$ sec,  $t=1.1$ sec and  $t=3.3$ sec respectively. The jet velocity is 123mm/s and the jet diameter is 25mm.

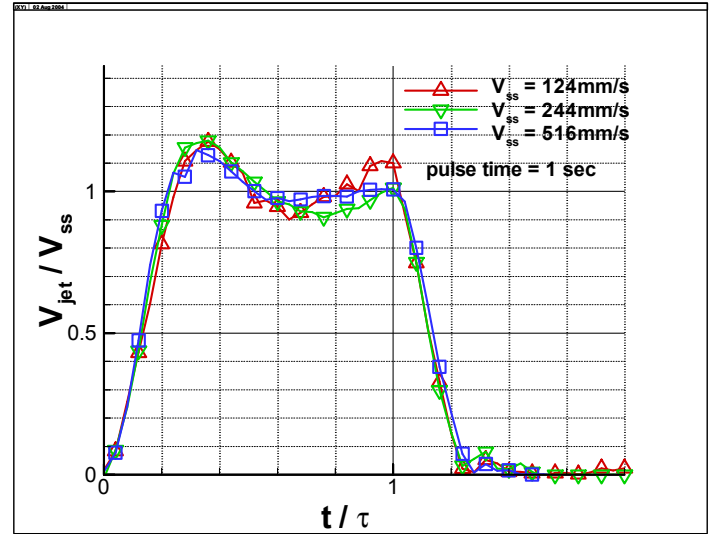


Figure 3. A characteristic temporal velocity profile of a 1 second pulse at three different jet velocities.

Mean trajectories of each flow case were obtained using a similar technique used by and Cutler [3] and Gordon [7]. The maximum concentration in vertical direction along each point on the x-axis was identified, as was maximum concentration in the horizontal direction at each point on the y-axis. This provides two approximations to the jet and vortex ring trajectories. Figure 4 and figure 5 show samples of jet and vortex ring mean image contours with the maxima in concentration in the vertical and horizontal directions overlaid. As can be seen in figure 4 the maxima in the vertical direction seem to provide a much better indication of the jet trajectory than the maxima in the horizontal direction. For the vortex ring sample, figure 5, it can be seen that both approximations to the vortex ring trajectory are consistent with the mean image. This is primarily due to the fact that the spread of the vortex ring as it travels downstream is much less than for the jet at a similar velocity ratio. The vortex ring mean image does not seem to grow more than one or two jet diameters in the range examined. Hence, the trajectories derived from maxima in the vertical direction were used exclusively to define the jet and vortex ring trajectories for this study. Table 1 shows 95% confidence intervals for the flow cases presented here based on the scatter of the maximum concentration trajectory data at  $x/d=10$ . It can be seen that the worst case scatter is approximately  $\pm 8\%$ . It should be noted that there are two sources of uncertainty in the mean trajectory for each case. The first is the uncertainty based on the determination method used in estimating the trajectory. The second is the deviation of the trajectory from jet to jet or ring to ring at a fixed set of flow parameters. No attempt has been made as of yet to investigate the individual uncertainty associated with each of these two sources.

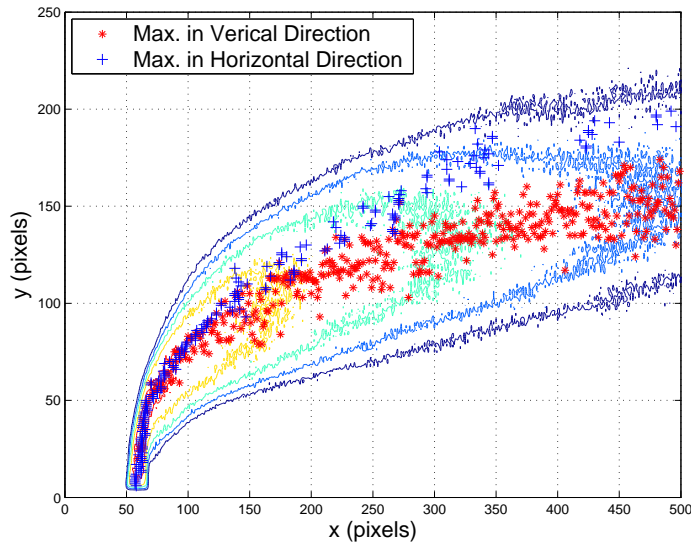


Figure 4 Trajectories based on maximum concentration in the horizontal and vertical directions overlaid on a mean jet contour plot. The velocity ratio is  $R=4$  and jet velocity is 127mm/s.  $Re_j = 3,200$ .

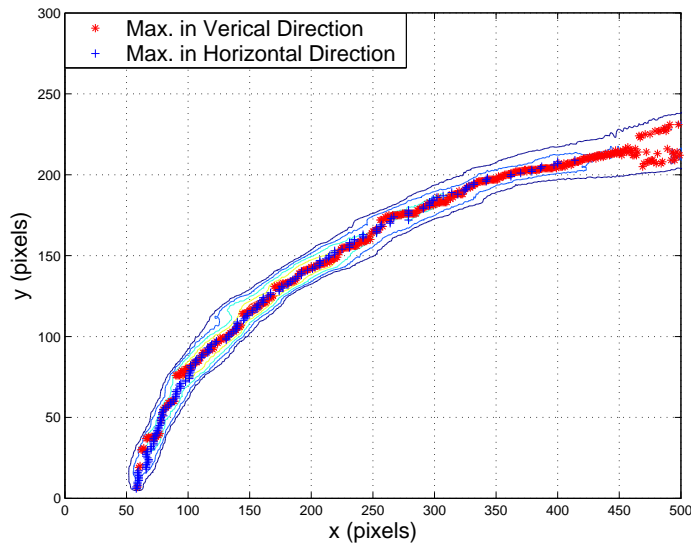


Figure 5. Trajectories based on maximum concentration in the horizontal and vertical directions overlaid on a mean vortex ring contour plot. The velocity ratio is  $R=4$  and jet velocity is 127mm/s.  $Re_j = 3,200$ ,  $Re_\Gamma = 4,800$ .

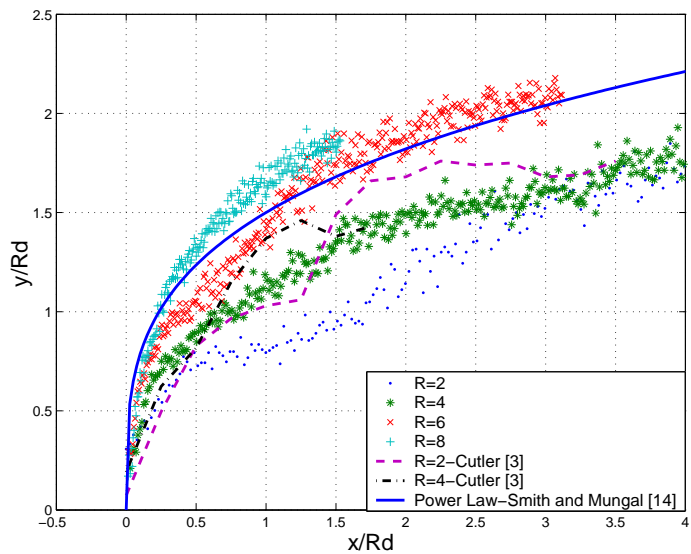


Figure 6. Rd scaling of jet trajectories based on maximum concentration in the vertical directions for  $R = 2, 4, 6$  and  $8$  compared to results from Cutler [3] for  $R = 2$  ( $Re_j = 4,000$ ) and  $R = 4$  ( $Re_j = 8,000$ ) and the power law obtained by Smith and Mungal [14].

## Results and Discussion

### Jet Trajectory

Figure 6 shows the concentration data plotted using Rd scaling, and compared with data from Cutler [3] and a power law obtained by Smith and Mungal [14]. The current data are consistent, with the trajectory height increasing with velocity ratio. The trajectories for  $R = 2$  and  $4$  appear to be slightly lower than those found by Cutler [3]. The power law curve of Smith and Mungal [14] can only be used as a guide as it represents data obtained for  $5 < R < 25$ .

### Counter Rotating Vortex Pair

The counter-rotating vortex pair (CVP) is a large scale vortex system occurring in the jet in cross flow. This vortical structure is aligned and embedded in the jet and has been shown to originate from the jet shear layer, [2,11]. As the CVP develops and the jet bends over, the jet fluid is entrained into the CVP. Studies by Smith and Mungal [14] and Cutler [3] among others have shown that the CVP core fluid concentration is higher than the centre plane concentration. Furthermore, due to the “kidney” shape of the jet cross section and the up-wash of cross flow fluid into the underside of the jet, we expect the trajectories of the CVP to be somewhat lower than the trajectory of the jet fluid on the centreline. Figures 7 and 8 show the current data plotted with centreline and CVP trajectories from Cutler [3]. The data obtained by Cutler [3] indeed show the centreline trajectory to be higher than the CVP trajectory. The data from the present study were obtained from a side-view of the jet under uniform illumination. Thus it is expected that this method should deliver jet trajectories that lie somewhere between the CVP trajectory and the jet trajectory. Indeed, the present data show trends that match closely the data presented by Cutler [3] for a similar  $Re_j$  and in general lie closer to the CVP data. The  $R=2$  case presented in figure 7 is also compared with centreline data from Kelso *et al* [11] and shows reasonable agreement. This provides further evidence that the new experimental equipment is adequate for the further investigation of pulsed and continuous jets in cross flow.

### Vortex Ring Trajectory

Figure 9 shows comparisons between the trajectories of continuous jets and individual vortex rings. The cases for  $R=4$  and  $R=6$  reinforce the results obtained by Chang and Vakili [1] that the trajectories of individual vortex rings are significantly higher than those of a continuous jet for the same velocity ratio. It is interesting to note the seemingly low trajectory of the vortex ring at  $R=2$ . It was observed that, for vortex rings at  $R=2$ , the vortex ring broke down very soon after its initial formation at the jet exit. Within approximately 2 jet diameters downstream of the jet exit the vortex ring structure broke down so that the ring was apparently devoid of any vortical structure. A possible cause of this is the interaction between the low circulation vortex rings and the boundary layer fluid in the vicinity of the jet exit. It is possible that vorticity cancellation occurs between the vortex ring and the boundary layer fluid resulting in a lower vortex ring trajectory. For all of the velocity ratios considered in this study, the vortex rings left a trail of ring fluid from the jet exit to the centre of the ring. Due to the stretching of these “structures” and the subsequent thinning of the dye it is unclear whether or not they contain any vorticity. This is consistent with observations made by Chang and Vakili [1] as was the observation of a slight tilt in the higher velocity ratio rings as they moved into the cross flow.



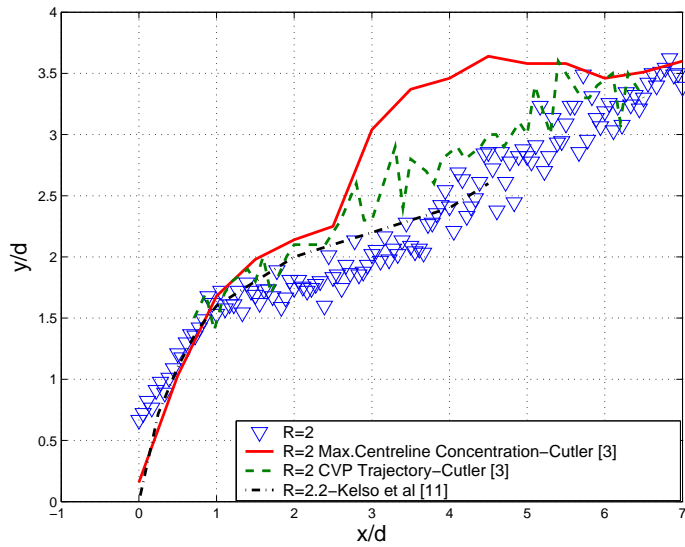


Figure 7. Jet trajectory for  $R=2$  ( $Re_j = 1,700$ ) compared to centreline and CVP trajectories from Cutler [3] for  $R=2$  ( $Re_j = 4,000$ ) and hotwire measurements from  $R=2.2$  from Kelso *et al* [11].

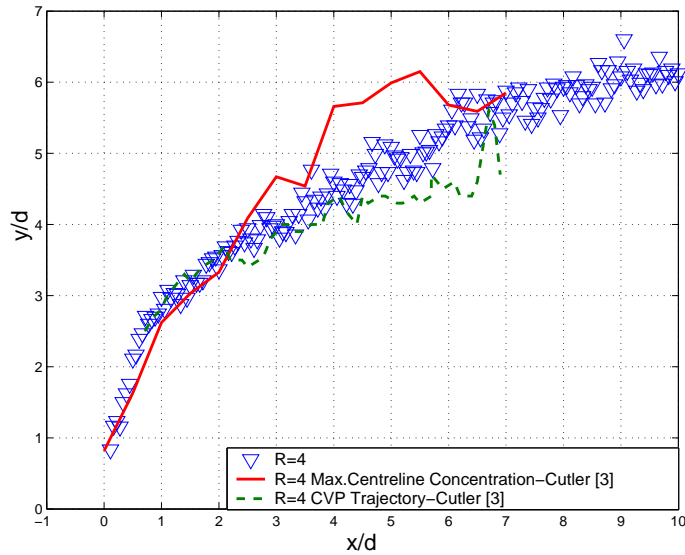


Figure 8. Jet trajectory for  $R=4$  ( $Re_j = 3,200$ ) compared to centreline and CVP trajectories from Cutler [3] for  $R=4$  ( $Re_j = 8,000$ ).

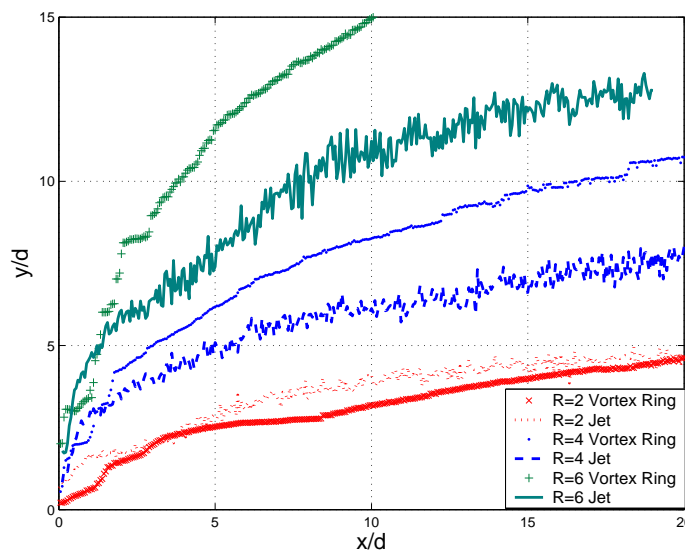


Figure 9. Jet trajectories for  $R=2, 4$  and  $6$  compared to vortex ring trajectories for  $R=2, 4$  and  $6$ .

## Conclusions

The implementation of equipment to study continuous and pulsed jets has been presented. Acoustic Doppler Velocimetry and Hydrogen bubble wire visualisation have been used to examine the spatial and temporal velocity profile of short duration pulses and continuous jets at the jet exit. Dye visualisation of jets and vortex rings has shown that the equipment generates flows consistent with previous work in this area. This current work has provided framework for more detailed studies of continuous jets, pulsed jets and individual vortex rings in cross flow.

## Acknowledgments

Financial support in the form of a departmental scholarship from School of Mechanical Engineering at the University of Adelaide and the Frank Perry Scholarship from the University of Adelaide Postgraduate Office are acknowledged and appreciated.

## References

- [1] Chang, Y.K. and Vakili, A.D., Dynamics of Vortex Rings in Cross-flow. *Phys. Fluids*, **7**(7), 1995, 1583–1597.
- [2] Cortezzi, L. and Karagozian, A.R., On the Formation of the Counter-rotating Vortex Pair in Transverse Jets. *J. Fluid Mech.*, **446**, 2001, 347–373.
- [3] Cutler, P.R.E., On the Structure and Mixing of a Jet in Cross-Flow. *Ph.D. Thesis*. Department of Mechanical Engineering. The University of Adelaide, 2002.
- [4] Cutler, P.R.E. and Kelso, R.M., On the Structural Differences Between Elevated and Flush-mounted Transverse Jets. *14<sup>th</sup> Australasian Fluid Mechanics Conference*, The University of Adelaide, 9–14 December, 2001.
- [5] Eroglu, A. and Breidenthal, R.E., Structure, Penetration and Mixing of Pulsed Jets in Cross Flow. *AIAA J.*, **39**(3), 2001, 417–423.
- [6] Glezer, A., The Formation of Vortex Rings. *Phys. Fluids*, **31**, 1988, 3532–3542.
- [7] Gordon, M., Investigation of Zero-net-mass Flux Jets in Cross-flow using Planar-laser-induced Fluorescence, *Masters Thesis*, Department of Mechanical Engineering, Monash University, 2001.
- [8] Gordon, M., Cater, J.E., and Soria, J., Investigation of the Mean Passive Scalar Field in Zero-net-mass-flux Jets in Cross-flow using Planar-laser-induced Fluorescence, *Phys. Fluids*, **16**(3), 2004, 794–808.
- [9] Hermanson, J.C., Wahba, A. and Johari, H., Duty-cycle Effects on Penetration of Fully Modulated, Turbulent Jets in Cross Flow. *AIAA J.*, **36**(10), 1998, 1935–1937.
- [10] Johari, H., Pacheco-Tougas, M., and Hermanson, J.C., Penetration and Mixing of Fully Modulated Turbulent Jets in Cross-flow. *AIAA J.*, **37**(7), 1999, 842–850.
- [11] Kelso, R.M., Lim, T.T. and Perry, A.E., An Experimental Study of Round Jets in Cross-flow, *J. Fluid Mech.*, **306**, 1996, 111–144.
- [12] Margason, R.J., Fifty Years of Jet in Cross Flow Research. *Computational and Experimental Assessment of Jets in Cross Flow*, AGRAD, 1993.
- [13] Smith, C.R., Seal, C.V., Praisner, T.J. and Sabatino, D.R., Hydrogen Bubble Visualisation in *Flow Visualisation*, editors T.T. Lim and A.J. Smits, Imperial College Press, 2000, 27–42.
- [14] Smith, S.H. and Mungal, M.G., Mixing, Structure and Scaling of the Jet in Cross-Flow. *J. Fluid Mech.*, **357**, 1998, 83–122.

## Observations on High Reynolds Number Turbulent Boundary Layer Measurements

S. Hafez<sup>1</sup>, M.S. Chong<sup>1</sup>, I. Marusic<sup>2</sup> and M.B. Jones<sup>3</sup>

<sup>1</sup>Department of Mechanical & Manufacturing Engineering  
The University of Melbourne, VIC, 3010 AUSTRALIA

<sup>2</sup>Department of Aerospace Engineering & Mechanics  
University of Minnesota, Minneapolis, MN 55455, USA

<sup>3</sup>School of Mathematical Sciences  
Queensland University of Technology - Gardens Point Campus  
GPO Box 2434

### Abstract

An experimental study that examines spatial resolution effects on the measured streamwise velocity component is presented. Normal hot-wire measurements for mean flow velocity profiles, streamwise turbulence intensity profiles in addition to their respective spectra at different levels within the turbulent boundary layers will be presented. Measurements were carried out at Reynolds number based on momentum thickness,  $R_\theta = 20,000$ . Matching the same Reynolds number of the flows is achieved by varying the measuring station and consequently the reference freestream velocity. Wires of non-dimensional lengths  $l^+$ , ranging from 11–54, were used. These measurements show that attenuation in hot-wire signals for long wires extend not only deep within the boundary layer, but also to the low wavenumber part of the spectra. It is conjectured that wires with the same  $l^+$ , will be prone to further attenuation due to the increase of end conduction loss with increasing freestream velocity.

### Introduction

Hot-wire anemometry is one of the most commonly used measuring techniques for turbulence research. The measured signal is the spatial average of the signature of eddies moving past the wire. Eddies of smaller size than the wire length will not correctly contribute to the higher order statistics of the flow. The inability to resolve these small eddies, commonly known as spatial resolution effects, is relevant to turbulence measurements for flows at high Reynolds number and for measurements close to solid boundaries. This is a direct result of the reduction in the size of the small scale viscous dissipative eddies and the anisotropy of the flow.

The limiting size of eddies in turbulent flows is the Kolmogoroff length scale,  $\eta$ . Within the turbulent wall region of wall-bounded flows it can be estimated as  $\eta = (\nu^3 \kappa z / U_\tau^3)^{1/4}$  (see Perry *et al.* [8]). Here  $z$  is the wall-normal distance,  $\nu$  is the kinematic viscosity,  $\kappa$  is the Karman constant and  $U_\tau$  is the friction velocity. Ligrani & Bradshaw [6] carried out extensive normal hot-wire measurements in a boundary layer flow with  $R_\theta = 2620$ . Near-wall measurements with sub-miniature normal hot-wire sensors revealed that a wire of length,  $l^+ = l/(v/U_\tau) < 20\text{--}25$  is sufficient to yield 'true' turbulence intensity measurements to within 4%. They suggest that wires with an aspect ratio (length/diameter) of approximately 200 will produce a uniform temperature along the wire length that will reduce the end conduction effect and improve the temporal resolution of the wire. These limits are commonly used as a guide for selecting sensors for turbulence measurements.

The effect of the sensor size in turbulence measurements has been recently investigated by Hites [5]. Normal hot-wire

measurements were carried out along a cylindrical model with a diameter of 45.7cm and length of 900cm. Different wires with diameters ranging from 0.6 $\mu\text{m}$ –3.8 $\mu\text{m}$  were tested at two measuring stations. The first measuring station was located at 184cm from the tripping device. At this station  $R_\theta$  varied from 4100–9720, corresponding to viscous length,  $\nu/U_\tau$ , of 26 $\mu\text{m}$ –11 $\mu\text{m}$ . The second measuring station was 733cm from the tripping device with freestream velocity of 28.6m/s,  $R_\theta = 19,300$  and  $\nu/U_\tau = 17\mu\text{m}$ . Turbulence intensity profiles measured with two different wires,  $l^+ = 6$  and 31, which should not collapse due to the large difference in  $l^+$ , showed complete collapse. This implies that a wire length of  $l^+ = 30$  is sufficiently small to resolve turbulent flows which is not consistent with the findings of Ligrani & Bradshaw [6].

A new wind tunnel has recently been constructed at the University of Melbourne to study turbulent boundary layer flow at high Reynolds number. Attention was given at the design stage to produce flows that can be measured and resolved adequately. The wind tunnel was built to be "big and slow" and the high Reynolds number of the flow which can be achieved, is the outcome of having a long development length and relatively low freestream velocity.

Mean flow measurements by Hafez *et al.* [4], have shown mean flow characteristics to be dependent only on  $R_\theta$ . Also, the velocity defect plots showed self-similar profiles for  $R_\theta > 20,000$ . This behaviour is consistent with the calculated Coles' wake factor, which approaches an asymptotic value for large  $R_\theta$ .

The main objective of this study is to produce detailed normal hot-wire measurements for the streamwise velocity component at high Reynolds number. These measurements will include mean flow velocity profiles, turbulence intensity profiles for the streamwise velocity component and their respective spectra. Carrying out these measurements at the same Reynolds number, with controlled variation of spatial resolution, will help explain the observed discrepancy in recent studies and provide a framework for further hot-wire measurements. It can also be used to check recently proposed similarity laws for the mean flow, Reynolds stresses and spectra.

### Apparatus and Techniques

The test facility is an open return blower wind tunnel with a 27m working length and a 2m x 1m cross section. Measurements were carried out for boundary layers developing on the tunnel floor, which is covered by aluminium plates of 6m x 2m and 6mm in thickness. The measured surface roughness of these plates is 1.5 $\mu\text{m}$  (rms). All boundary layers developing along the inner surface of the nozzle were tripped using grade 40 sandpaper sheets, of 115mm width, glued on the nozzle inner surface, 750mm upstream from the exit. Figure 1 shows the main features of the test facility.

Measurements were limited to three reference unit Reynolds numbers of  $U_\infty/\nu = 6.48 \times 10^5$ ,  $1.03 \times 10^6$  and  $1.59 \times 10^6/\text{m}$ , where  $U_\infty$  is the reference free-stream velocity. They corresponding to nominal reference freestream velocity of 10m/s, 16m/s and 24m/s, respectively. Ambient flow conditions were measured using a calibrated thermocouple and an electronic barometer.

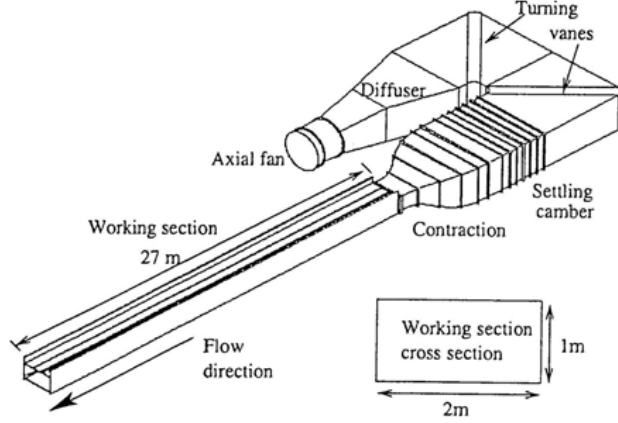


Figure 1: Isometric view of wind tunnel.

A nominally zero pressure gradient was maintained along the working section. The pressure coefficient  $C_p$ , which can be written as

$$C_p = 1 - \left( \frac{U_1}{U_\infty} \right)^2, \quad (1)$$

is kept constant along the entire 26m measuring section of the tunnel to within  $\pm 1\%$ , or better, for the velocity range covered in this study.

The normal single sensor (DANTEC 55P05) is used with a constant temperature anemometer system (AN-1003 from AA lab systems). Wollaston wires are soldered to the probe and etched to give a platinum filament with core diameters of  $5.0\mu\text{m}$  and  $2.5\mu\text{m}$ , with active lengths of approximately  $0.9\text{mm}$  and  $0.55\text{mm}$  respectively. A static calibration technique, with a third order polynomial curve fit, is used to convert the measured anemometer output voltage into velocity. The normal hot-wire is calibrated against a Pitot-static tube pair, located within the mid height of the tunnel and about  $5\text{cm}$  apart. A CCD camera fitted with a macro lens is used to check that the wire is parallel to the wall and to make a first estimate of the distance of the wire from the wall. The counted number of pixels between the wire and its image on the tunnel surface is converted into distance using a conversion ratio from a calibration of the optical system. The uncertainty in the wall distance is estimated to be  $\pm 5\mu\text{m}$ .

Following calibration, the wire is positioned at the first measuring point, based on an initial estimate from the optical system. The measured mean velocity at that level is used to find a more accurate wall distance assuming that the Reichardt [9] formulation for the mean velocity profile is valid within the viscous sub-layer. No further adjustment is made to the wall distance. The validity of the measuring technique is verified by comparing the near wall data with other reliable and independent data. The friction velocity is obtained using the Clauser chart technique, with  $\kappa = 0.41$  and  $A = 5.0$ , where  $A$  is the smooth wall constant.

Hot-wire signals were sampled on-line with an IBM compatible personal computer, using a Microstar 16 bit data acquisition board model DAP3000a/21. Turbulence intensity measurements were taken in burst of 8000 samples of 200Hz. Four bursts were sufficient to obtain converged results to within 1%. The u-spectra were measured with calibrated normal wires. The signals were sampled at three sampling rates of 500, 5,000 and 50,000Hz and

low-pass filtered at 200, 2,000 and 20,000Hz respectively, using Frequency Devices filter model LP00. A fast Fourier transform algorithm was used to calculate digitally the power spectral density of the signal. The three spectra files were then matched, joined and smoothed to form a single spectrum file. Taylor's hypothesis of frozen turbulence was used to transform the spectral argument from the frequency domain,  $f$ , to the wave number domain  $k_1$ , such that

$$k_1 = \frac{2\pi f}{U_c}, \quad (2)$$

where  $U_c$  is the local mean convection velocity, which is assumed to be equal to the local mean velocity. The spectra were normalized such that

$$\int_0^\infty \Phi_{11}[k_1] dk_1 = \overline{u^2}, \quad (3)$$

where  $\Phi_{11}[k_1]$  is the power spectral density per unit stream-wise wave-number  $k_1$ .

## Results and Discussion

### Preliminary measurements

Preliminary measurements were carried out at low Reynolds number to check and validate the current measuring technique and instrumentation. The measuring station is located at  $1.5\text{m}$  downstream the tripping device. The reference freestream velocity is  $10\text{m/s}$ , which produced a boundary layer of thickness  $\delta_c = 38.6\text{mm}$  and  $R_\theta = 2600$ . The mean flow velocity profile and streamwise turbulence intensity profiles, normalised with inner flow variables, are shown in figure 2 and compared with the LDA data of DeGraaff & Eaton [2] at  $R_\theta = 2900$ . Good agreement is observed down to the first measuring point. The difference in the mean flow in the outer flow region is related to the slight difference in  $R_\theta$ . The lack of agreement of turbulence intensity profiles in the outer flow region is not known. These measurements show that the current approach for positioning, calibrating and measuring the wall distance for the wires is valid and accurate and can be used with confidence at other measuring stations.

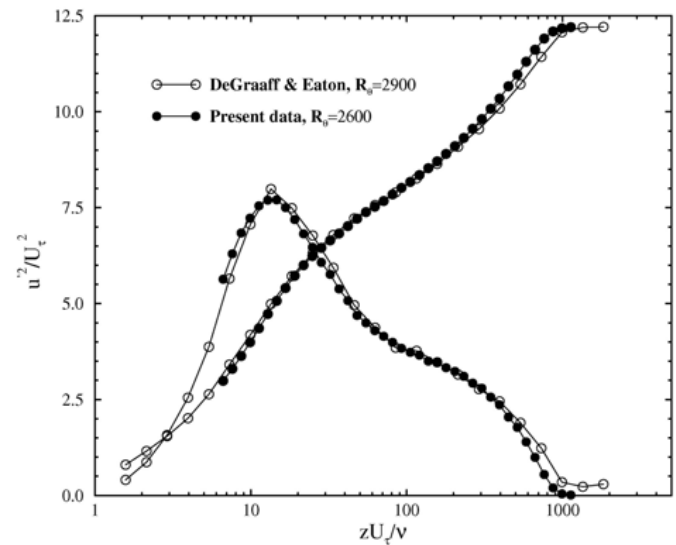


Figure 2: Comparison between normal hot-wire and LDA at low Reynolds number, with inner flow scaling. The vertical-axis label and values are shown for turbulence intensity profiles only. Mean flow velocity profile values are scaled down by 2.

### Mean flow velocity profiles

Measurements for matched Reynolds number were carried out at three stations along the symmetry plane of the tunnel. The

Reynolds number,  $R_0$ , for the most downstream station at the lowest reference velocity is approximately 20,000. This value is kept constant within  $\pm 0.7\%$  for the other two measuring stations. Mean flow parameters used for scaling the measurements are shown in Table 1.

Table 1: Mean flow parameters.			
X (m)	21.7	13.7	8.7
$\delta_c$ (mm)	335.9	214.9	140.5
$\nu/U_\tau$ ( $\mu\text{m}$ )	46.8	28.6	18.5
$U_\infty$ (m/s)	10.0	16.0	24.0
$\eta$ ( $\mu\text{m}$ )*	118.4	72.4	46.8
$l/\eta$	4.2 & 7.6	8.3 & 13.8	12.8 & 21.8
$l^+$	10.9 & 19.2	21.1 & 34.9	32.4 & 53.4

\*Estimated value of  $\eta$  at  $z^+=100$ .

Mean flow velocity profiles, scaled with inner flow variables, are shown in figure 3. Profiles show complete collapse throughout the whole layer. The DNS data of Spalart [11], for  $R_0=1410$  is also shown. The agreement is excellent for  $z^+ < 100$ ,  $z^+ \equiv z U_\tau/\nu$ . The difference of approximately 1% between Pitot-static tube measurements and hot-wire measurements is acceptable. This difference can be reduced by applying a turbulence correction to the data collected by the impact pressure probe. This has not been done to the Pitot tube data shown in figure 3. The turbulence correction is more important for increasing Reynolds number. Developing similarity laws without such corrections may lead to wrong conclusions. Normal hot-wire data, plotted in the velocity defect form show complete collapse throughout the boundary layer. This result is consistent with the mean flow measurements using Pitot-static tube in the same wind tunnel (see Hafez *et al.* [4]). The velocity defect similarity arguments proposed by Castillo *et al.* [1] are not supported by our finding. They argued that for a certain tripping device type and location, different reference free stream velocities will yield different velocity defect curves.

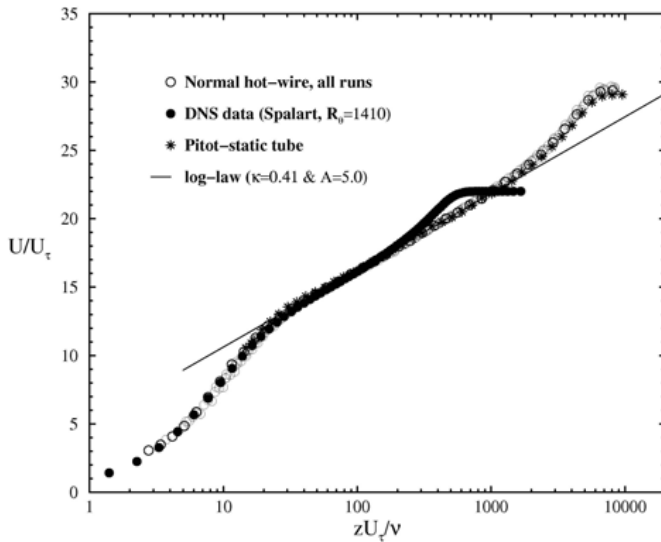


Figure 3: Mean flow velocity profiles, inner flow scaling.

### Streamwise turbulence intensity

Figures 4 and 5 show the streamwise turbulence intensity profiles taken at the three measuring stations with different wire lengths. The spatial resolution effects can be seen up to relatively high  $z^+$  values of about 300. Moving towards the wall the differences between profiles become more significant and account for about 40% of the near-wall maximum peak values. The 10m/s case represents the most resolved measurement in our study (with  $l^+$  of 11 and 19) and differences are limited to small values of  $z^+ < 15$ . This result is in agreement with the finding of

Ligrani & Bradshaw [6], but not with Hites [5]. The data of Hites at  $R_0=19,000$  (as discussed earlier), were measured with wires of length  $l^+$  of 6 and 31. Hites' data gave a peak value of about 7.3 at about  $z^+=15$ , and roughly constant value of 5.8 for  $70 < z^+ < 700$ . These values agree well with the present measurements at 24m/s and wire length  $l^+$  of 32.4. This indicates that Hites' data with the short wire,  $l^+=6$ , may represent unresolved flow.

The wire length is found to have a major effect on the present results. However, close examination reveals differences between wires of similar  $l^+$ , but different freestream velocity. The increase in freestream velocity appears to adversely affect the measurements leading to further attenuated results. The reason for this could be an increase in end conduction heat loss.

An interesting feature of the plots is the continued attenuation of the measured turbulence intensity for  $z^+$  up to about 300. The highly attenuated profile, for  $l^+=53$ , can be seen to have double peaks, one close to the wall and the other at  $z^+$  of about 300. This behaviour represents loss of turbulent energy over a large portion of the boundary layer. Similar trends have been observed in boundary layer flows by Fernholz & Finley [3] and more recently by Morrison *et al.* [7], and is probably due to the lack of spatial resolution.

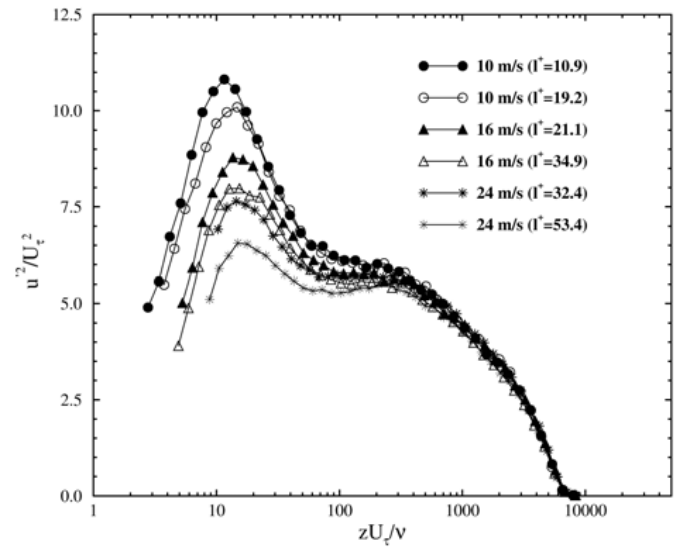


Figure 4: Streamwise turbulence intensity profiles, inner flow scaling.

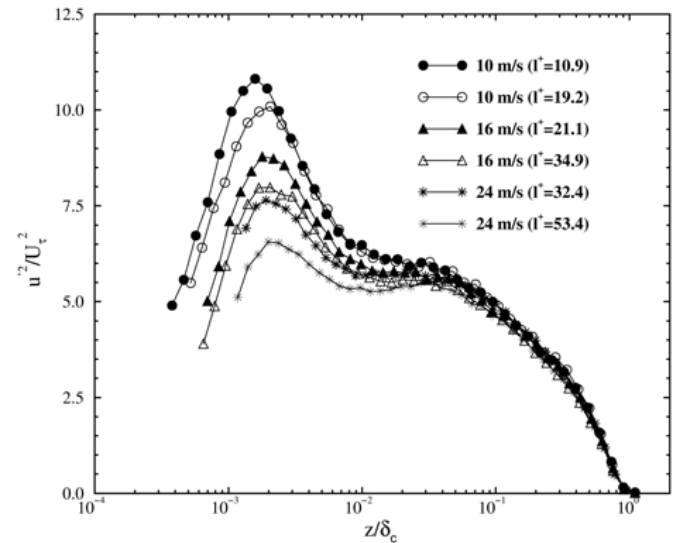


Figure 5: Streamwise turbulence intensity profiles, outer flow scaling.

### Spectra

In this paper spectra measurements for the streamwise turbulence intensity are presented at  $z^+=100$ , for  $R_0=20,000$  and for different freestream velocities, and hence different  $l^+$ . Measured spectra are presented in the outer flow scaling and its respective pre-multiplied form in figures 6 and 7, respectively. According to

Perry *et al.* [8], within the turbulent wall region, spectra with outer and inner flow scaling should collapse onto the  $-1$  or inverse power law envelope. Since the present measurements are collected at the same value of  $z^+$  and the same  $Re_\theta$ , they should follow the same spectrum, provided that the flow is adequately resolved.

The plots demonstrate qualitatively the effect of using long wires. Figure 6 shows the peeling off trend for increasing wire length. Figure 7 shows the effect on the inverse power law plateau in the premultiplied spectra. These results highlight the difficulty of measuring highly resolved spectra.

The lack of spatial resolution could be a major factor and as pointed out by Smits & Dussauge [10]: “For long wires, the effects, spatial resolution, are more severe and begin at lower wave numbers”.

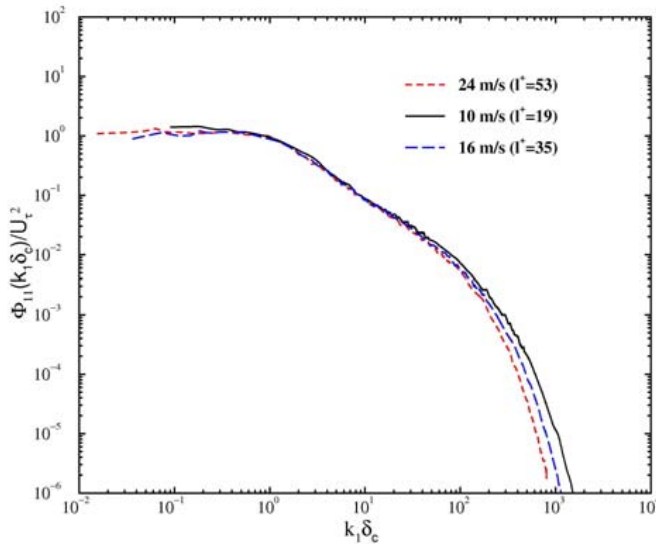


Figure 6: u-spectra with outer flow scaling at  $z^+=100$ .

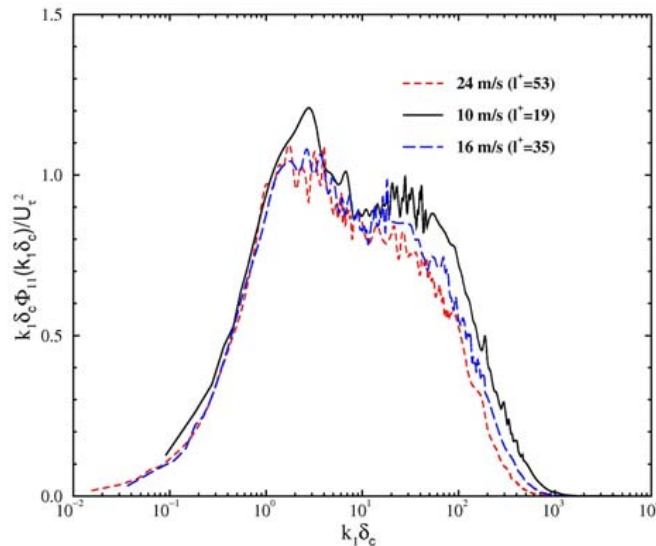


Figure 7: Pre-multiplied u-spectra with outer flow scaling at  $z^+=100$ .

## Conclusions

An experimental study of the effects of spatial resolution on turbulent boundary layers measurements at high Reynolds number has been presented. Measurements are carried out at  $Re_\theta=20,000$  with wires non-dimensional length,  $l^+$ , ranging from 11–54.

Mean flow measurements showed that turbulence correction might improve agreement between Pitot-tube and hotwire measurements. The mean flow velocity defect profiles showed independence of relevant freestream velocity. This finding is consistent with previous measurements in the same facility using Pitot-static tube but do not support the mean flow velocity defect similarity laws proposed by Castillo *et al.* [1].

Ligrani & Bradshaw [6] criterion for selecting hotwires suitable for resolving turbulent flows is found to be adequate, provided that flow velocity is low. However, with increasing bulk velocity even for properly selected wires may have further attenuations. This may be a result of increasing end conduction loss which reduces the effective length of the wire. The presence of a second peak, away from the wall in the turbulence intensity profiles, observed at high Reynolds number flows, may be due lack of spatial resolution.

Spectra measurements have shown that spatial resolution may be a serious problem, even with the limited range of  $l^+$  employed in this study.

## Acknowledgments

SH, MSC and MBJ wish to acknowledge the financial assistance of the Australian Research Council. IM would like to acknowledge support from NSF and the Packard Foundation.

## References

- [1] Castillo, L., Seo, J., Hangan, H. and Johansson, T.G., Smooth and rough turbulent boundary layers at high Reynolds number. *Exp. Fluids*, **36**, 2004, 759-774.
- [2] DeGraaff, D.B. & Eaton, J.K., Reynolds-number scaling of the flat-plate turbulent boundary layer, *J. Fluid Mech.*, **422**, 2000, 319-346.
- [3] Fernholz, H.H. & Finley, P.J., The incompressible zero-pressure-gradient turbulent boundary layers: An assessment of the data. *Prog. Aerospace. Sci.*, **32**, 1996, 245-311.
- [4] Hafez, S., Jones, M.B. and Chong, M.S., The zero pressure gradient turbulent boundary layer and its approach to equilibrium, Proc. of the 10<sup>th</sup> AFMC, Peradeniya, Sri Lanka, 2004.
- [5] Hites, M.H., Scaling of High-Reynolds number Turbulent Boundary Layers in the National Diagnostic Facility, Ph.D. thesis, Illinois Institute of Technology, 1997.
- [6] Ligrani, P.M. & Bradshaw, P., Spatial resolution and measurement of turbulence in the viscous sublayer using subminiature hot-wire probes, *Expt. Fluids*, **5**, 1987, 407-417.
- [7] Morrison, J.F., McKeon, B.J., Jiang, W. and Smits, A.J., Scaling of the streamwise velocity component in turbulent pipe flow, *J. Fluid Mech.*, **508**, 2004, 99-131.
- [8] Perry, A.E., Henbest, S. and Chong, M.S. A theoretical and experimental study of wall turbulence. *J. Fluid Mech.*, **165**, 1986, 163-199.
- [9] Reichardt, H, Volständige darstellung de turbulenten geschwindigkeitsverteilung in glatten leitungen. *Zeitschrift für Angewandte mathematik und mechanik*, **31**, 1951, 208.
- [10] Smits, A.J. & Dussauge, J.P., *Turbulent Shear Layers in Supersonic Flow*. AIP Press, 1996.
- [11] Spalart, P.R., Direct simulation of a turbulent boundary layer up to  $Re_\theta=1410$ , *J. Fluid Mech.*, **187**, 1988, 61-98.



# The Effect of Density Ratio on the Mean Spread Rate of a Low Pressure Drop Oscillating Jet Nozzle

G. England, P.A.M. Kalt, G.J. Nathan and R.M. Kelso

School of Mechanical Engineering  
The University of Adelaide, SA, 5005 AUSTRALIA

## Abstract

Particle Image Velocimetry measurements were obtained in the highly unsteady turbulent flow issuing from a triangular oscillating jet (TOJ) nozzle into a fluid of different density. The TOJ nozzle comprises a triangular jet partially confined within an axi-symmetric chamber that produces a large-scale flow oscillation which is analogous to that in a precessing jet nozzle previously investigated. The initial spreading angle of the emerging jet was found to depend upon the density ratio, but in a more complex and different way to that of an unconfined jet. Instead, an increase in the density ratio of the jet fluid to the surroundings is found to be analogous to a decrease in the ratio of the nozzle length to diameter.

## Introduction

Fluidic precessing jet (FPJ) flames of natural gas have high radiant heat transfer, high burn-out and low emissions of oxides of nitrogen ( $\text{NO}_x$ ) and are therefore attractive in industrial applications such as cement and lime production. In such applications, FPJ flames have been demonstrated to reduce  $\text{NO}_x$  emissions by between 40-70% [10] while achieving a fuel saving of up to 5% for an equivalent product output. Additionally, the product quality is improved due to the shift in heat transfer profile toward the front of the kiln [6]. More recently they have been applied to pulverised fuels, with promising results [8,12].

The FPJ flow has been studied extensively at the University of Adelaide because of its scientific interest and immediate relevance to industrial applications. However the flow is highly unsteady and complex, making its characterisation and optimisation difficult. The unsteadiness allows more rapid initial spread and decay than is possible for a steady jet, and is deduced to be the primary cause of the benefits [9]. However, the large expansion ratio within the nozzle results in a large pressure drop across the burner. While this is not an obstacle when firing natural gas, which is usually available at high pressure, it is a significant barrier in pulverised fuel applications where air must be pressurised on-site.

A new burner, known as the triangular oscillating jet (TOJ) nozzle, has been developed to provide an oscillating flow which is closely related to that of the FPJ nozzle but with a lower pressure drop. The TOJ nozzle has been shown to produce large-scale oscillations, large initial spreading and rapid near-field velocity decay rate of similar trend, but reduced magnitude, to those observed from the FPJ nozzle [4]. However, the temperature of the co-flowing (secondary) combustion air in a rotary kiln is high – typically 600-1200°C, and this temperature varies both during operation and from site to site. The high temperature leads to a density difference between the jet fluid and the co-flow fluid. The influence of this density difference on the internal or emerging flows has not been investigated previously. The present study seeks to address this by measurement of the near-field jet spreading from the TOJ nozzle using a range of jet fluids of different density.

## Experimental Method

Velocity measurements were performed using a digital cross-correlation particle image velocimetry (DPIV) system at the Turbulence Energy and Combustion Laboratory of the University of Adelaide.

## Experimental Setup

The TOJ nozzle is similar to that described by Lee *et al.* [4]. It utilises a triangular orifice partially confined by an axisymmetric chamber with a small lip at the nozzle exit (Figure 1). The chamber diameter,  $D$ , is 26.5 mm and the exit lip diameter,  $d_2$ , is 21.8 mm. The triangular orifice is equilateral, its size described by the diameter of a circular orifice with equivalent cross-sectional area,  $d_{eq}$ . In this study, non-reacting TOJ flows with an expansion ratio,  $D/d_{eq}$ , of 3.5 are examined.

The length of the nozzle,  $L$ , is, for most of the work, selected to satisfy the ratio  $L/D = 2.49$ . This is based on the work of Lee *et al.* [4], who determined this to be the optimum length to diameter ratio for maximum spread when the density ratio  $\rho_f/\rho_a = 1$ . However for the case with carbon dioxide as the working fluid,  $L/D$  ratios of 2.11, 2.30 and 2.68 are also examined.

The working fluids, carbon dioxide, argon, air and a helium-air mixture, were introduced through the nozzle into ambient air. This gives density ratios,  $\rho_f/\rho_a$ , of 1.56, 1.39, 1 and 0.57 respectively. The jet Reynolds number, calculated using the effective orifice diameter;  $\text{Re} = \rho d_{eq} u / \mu = 60,000$ . Both the jet, and an ambient air co-flow of negligible momentum, were seeded with atomised olive oil with a nominal droplet diameter of 0.6  $\mu\text{m}$ . These droplets are effective flow tracers even in the high shear regions at the edge of the jet.

The laser sheet was aligned with the nozzle centreline and configured to provide sufficiently uniform intensity through the exit plane. The orientation of the triangular orifice with respect to the light sheet is shown in Figure 1. The camera was positioned to capture the emerging flow over the range  $0 < x/D \leq 4$ .

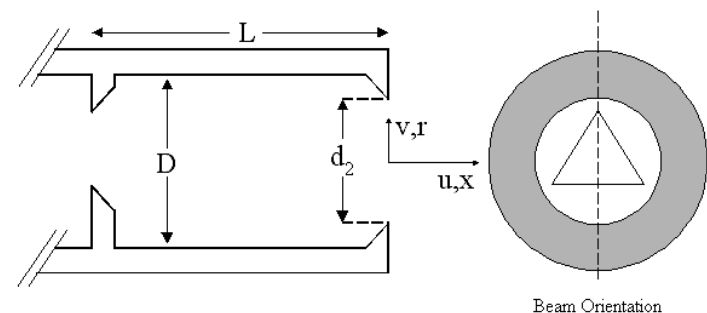


Figure 1. Notation for the Triangular Oscillating Jet (TOJ) nozzle and the laser beam orientation.

## Lasers and Optics

The particles are illuminated by the second harmonic ( $\lambda = 532$  nm) of a Quantel Brilliant Twins double-cavity pulsed Nd:YAG laser. The output energy of each pulse is ~250 mJ. The laser beams are directed towards the imaged area using 2 dichroic mirrors, and are formed into a laser sheet approximately 1.9 mm

thick in the imaged area using a series of cylindrical lenses. This thickness of the laser sheet is necessary to avoid significant loss of image pairs due to the large out-of-plane motion in these unsteady flows. The light sheet thickness thus becomes a limiting dimension in the spatial resolution of the measurement.

A Kodak MegaPlus ES1.0 PIV camera, operated in the triggered double exposure mode, was used to record the Mie-scattered particle images. The images were collected through a Nikon ED 70-300 telephoto lens. The dimensions of the CCD array are 1008 pixels by 1018 pixels. The imaged region was 100 mm by 101 mm, with each pixel corresponding to a region measuring 100  $\mu$ m by 101  $\mu$ m. The time delay between laser pulses was set to 20  $\mu$ s, which was optimised for a PIV interrogation window of  $32 \times 32$  pixels, with a 50% overlap. This results in an effective resolution for the velocity measurements of 3.2 mm, which is comparable with the light sheet thickness. The resulting vector field contains 62 by 62 vectors.

### Timing

A Hamag signal generator producing 10 Hz TTL output initiated the timing of data collection. This 10 Hz output was used to trigger a Stanford Research Systems DG-535 delay generator which, in turn, triggered both the laser flash-lamps and the camera. The delay between the laser flash-lamp and the Q-Switch was set by internal timing electronics, so that the delay between laser pulses could be altered without adjusting the Q-switch delay or the laser energy. Data were transferred from the camera at 20 Hz into a memory buffer on the data storage computer. After each run, the entire dataset of PIV image pairs was saved to hard disk for subsequent processing. The size of the data set was limited by the buffer size to 360 image pairs.

### PIV Processing

Processing of the PIV image pairs was performed using Pivtec's PivView (v 1.7.5) software. A 2-pass Hart correlation algorithm was used to correlate between the image pairs. The correlation image was scanned for peaks using a centroid-hunting algorithm on a roaming  $3 \times 3$  pixel mask. This method gives sub-pixel accuracy.

Outliers (erroneous vectors) are detected by comparison with the neighbourhood average. Where possible, outliers are replaced by a suitable, alternative peak from the correlation plane but are otherwise deleted. The total proportion of deleted vectors is less than 2% in the worst case.

## RESULTS

Data analysis is carried out for the axial component,  $u$  of the time averaged velocity field. Normalisation is typically applied relative to the bulk mean orifice velocity  $u_{or}$ . Figure 2 shows the time averaged flow field,  $u/u_{or}$ , for the TOJ with  $L/D = 2.49$  and  $\rho_f/\rho_a = 1.56$ . This is typical of the time averaged flow field in all cases. Half widths are used to assess the spreading angle of the emerging TOJ jet. Half widths are obtained from the time averaged flow field. The mean spread,  $r_{1/2}$ , is taken to be the average of that on either side of the nozzle axis noting the asymmetry resulting from the triangular orifice [4]. The orientation of the light is such that the left side of the image is aligned with an apex of the orifice.

### Effect of $\rho_f/\rho_a$

Figure 3 shows the mean half widths,  $r_{1/2}$ , for the TOJ nozzle at each of the density ratios,  $\rho_f/\rho_a$ , investigated. This figure shows that the greatest spread rate of the jet emerging from the nozzle is achieved when the density ratio,  $\rho_f/\rho_a$ , is 1. At first sight, this appears to contradict the well known dependence of the spreading angle for a free jet, which decreases with an increase in

the density ratio, as determined by Era and Saima [2] and Richards and Pitts [11].

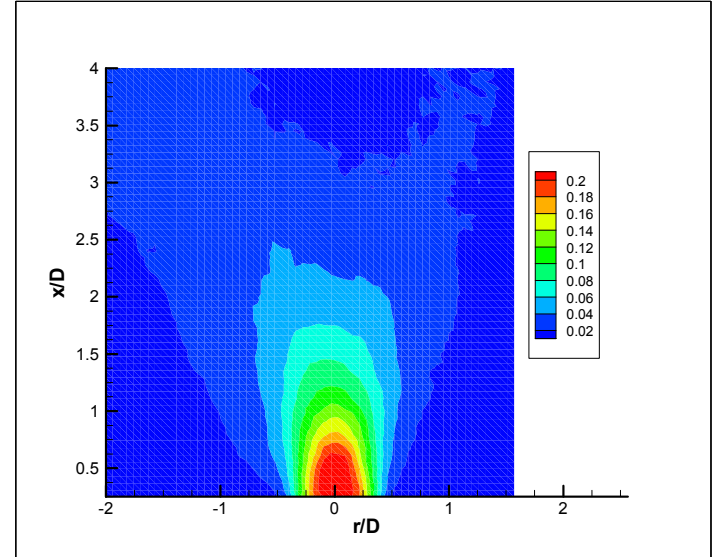


Figure 2. Time averaged flow field,  $u/u_{or}$ , for TOJ with  $L/D = 2.49$  and  $\rho_f/\rho_a = 1.56$ .

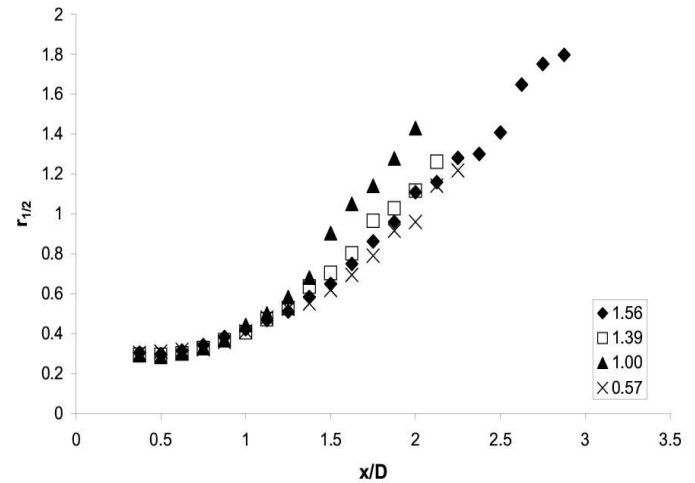


Figure 3. Mean half widths for TOJ at various  $\rho_f/\rho_a$  as determined from the mean flow field.

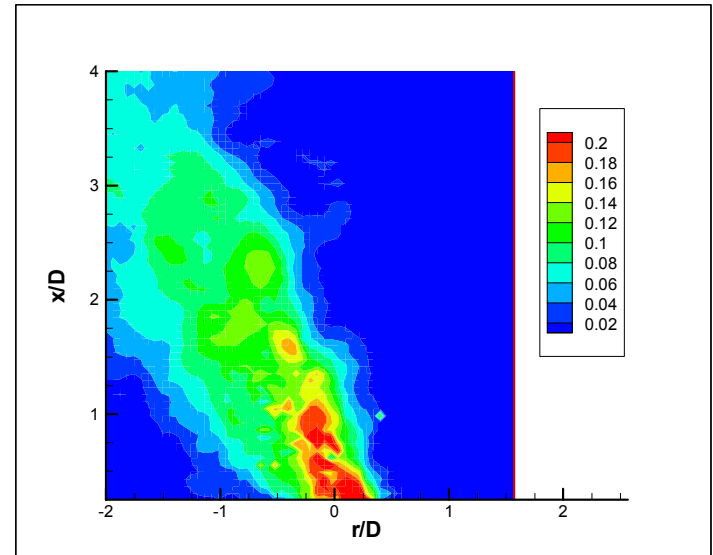


Figure 4. Conditionally averaged flow field,  $u/u_{or}$ , for TOJ with  $L/D = 2.49$  and  $\rho_f/\rho_a = 1.56$ .

Deflection angles of the instantaneous emerging jet were determined by conditionally averaging the data. Since the angle of the jet within the plane of the light sheet depends upon its phase, those images with the greatest angles are taken to be within the plane of the light sheet. On this basis, a representative, although not absolute, measure of the instantaneous angle is taken as the average of the five image pairs with the greatest angle of deflection toward the left. These were selected by determining the slope of the linear line of best fit for maximum axial velocity for each image pair. Figure 4 shows the conditionally averaged flow field,  $u/u_{or}$ , for the TOJ with  $L/D = 2.49$  and  $\rho_j/\rho_a = 1.56$ . This is typical of a conditionally averaged flow field. Once the conditionally averaging was complete, the spread angle was determined from the slope of the linear line of best fit for maximum axial velocity. Figure 5 shows the spread angle of the TOJ as a function of the density ratio,  $\rho_j/\rho_a$ . The result shown is consistent with the trend shown in figure 3.

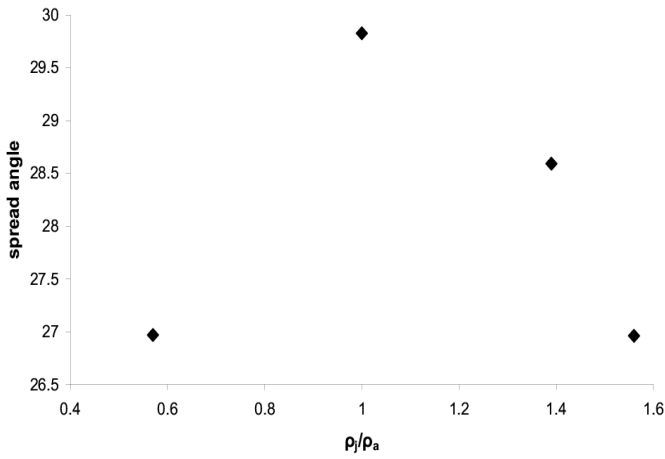


Figure 5. Deflection angle of the instantaneous emerging jet as a function of density ratio,  $\rho_j/\rho_a$ .

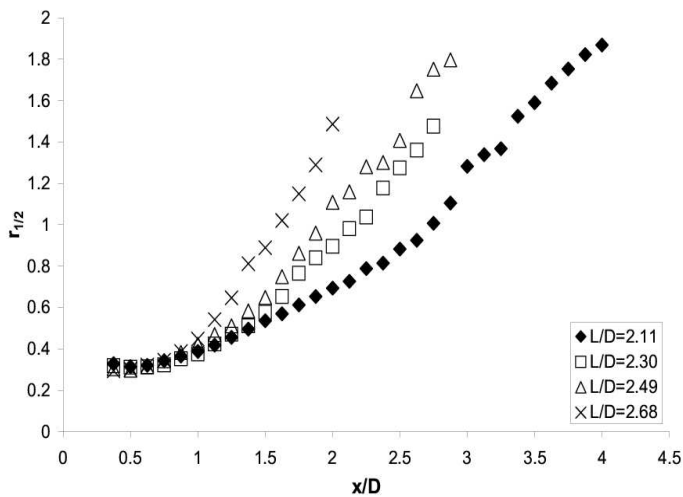


Figure 6. Mean half widths for TOJ at various  $L/D$  ( $\rho_j/\rho_a = 1.56$ ), as determined from the time-averaged flow field.

### Effect of $L/D$

Figure 6 shows the mean half widths,  $r_{1/2}$ , for the TOJ nozzle at  $L/D = 2.11, 2.30, 2.49$  and  $2.68$  when the working fluid is carbon dioxide ( $\rho_j/\rho_a = 1.56$ ). This shows that increasing  $L/D$  results in an increased rate of spread. This is consistent with Lee *et al.* [4] for  $L/D$  less than the optimum for maximum spread. However Lee *et al.* [4] showed that when  $\rho_j/\rho_a = 1$  this optimum  $L/D$  is  $2.49$ . Figure 4 clearly shows that this is not the case when  $\rho_j/\rho_a = 1.56$  since greater spread is achieved for  $L/D = 2.68$  than  $L/D = 2.49$ . This also shows that the density ratio has an effect on the spread of the jet emerging from the TOJ nozzle.

### Discussion

The apparent discrepancy between the effect of density ratio on spreading angle can be explained by consideration of the complex flow within the chamber. Lee *et al.* [4] have investigated the effect of varying the length to diameter ratio of the TOJ using air as the working fluid ( $\rho_j/\rho_a = 1$ ). They found that as  $L/D$  was increased from zero the spread rate of the jet initially increases also. Eventually a maximum rate of spread is reached at some  $L/D$ , which is then defined as the optimum  $L/D$ . Further increasing  $L/D$  leads to a decrease in the rate of jet spread. A simplified representation of this is shown in figure 7. Also shown in figure 7 is the spread inside the chamber.

Wong [13] shows that just beyond the exit plane of a FPJ nozzle the emerging jet is “kidney” shaped (although it evolves toward a circular cross-section further downstream). The lateral spreading of a jet upon reattachment to a wall is well known and can explain the evolution of a “kidney shape” within the chamber [3]. Clearly the longer the chamber, the greater this interaction with the chamber wall will be. A similar trend can be expected to occur for the TOJ nozzle. Therefore as  $L/D$  is increased the spread of the jet inside the chamber is also increased, resulting in the jet both filling more of the exit plane and increasing its interaction with the chamber walls and the exit lip (Figure 7). This implies that the spreading angle of the external jet depends upon the extent to which the emerging jet fills the exit plane of nozzle and by the interaction of the emerging jet with the exit lip.

By analogy then, it can be expected that the spreading angle of the emerging jet will also depend upon the rate of spread of the jet within the nozzle chamber, and hence on the internal density ratio. Now figure 3 shows that for the TOJ with  $L/D = 2.49$  the greatest external spread rate is achieved when the density ratio,  $\rho_j/\rho_a$ , is 1. This result simply reflects the fact that these dimensions were optimised for a density ratio of unity, while the flow is dependent upon the density ratio.

Nathan [7] observed that surrounding fluid is continually drawn into the FPJ chamber and entrained into the main jet. A similar phenomenon was observed for the TOJ nozzle by Lee *et al.* [5]. This induced reverse flow allows a density gradient to occur inside the nozzle chamber. It follows that when the density ratio,  $\rho_j/\rho_a$ , inside the chamber is lowest the internal spread will be the greatest [2,11], and will therefore result in the emerging jet filling more of the nozzle exit plane and interacting more with the chamber walls and exit lip. Hence increasing the density ratio,  $\rho_j/\rho_a$ , has the same effect on the external spread rate as decreasing the chamber length to diameter ratio,  $L/D$ .

Density gradients between the jet and surroundings rapidly decrease with downstream distance due to entrainment [1,11]. Therefore any gradient existing between the jet and the surroundings as the jet exits the nozzle will be decreased in magnitude from the initial gradient due to entrainment within the nozzle chamber. Any density gradient external of the nozzle will still have an effect on the rate of jet spread. However it is likely that this will be secondary to the interaction that take place inside the nozzle chamber where the jet shear layer is the thinnest and the density gradients are likely to be the largest.

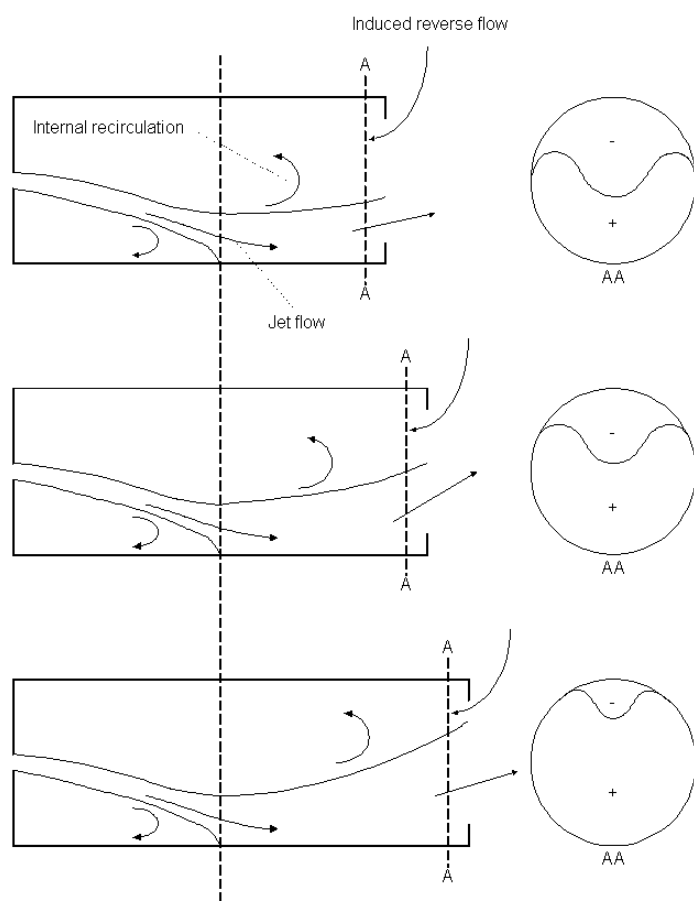


Figure 7. A simplified diagram showing the trends of the effect of varying  $L/D$  on the flow field within the TOJ chamber and the exit angle.

## Conclusion

The measurements of jet half widths show that, for the triangular oscillating jet nozzle whose dimensions are optimised for a unity density ratio [4], i.e. with  $L/D = 2.49$ , the maximum spread occurs with this same density ratio. That is, variation of the density ratio,  $\rho_f/\rho_a$ , to values above or below one led to a decrease in the rate of spread.

By reference to the flow patterns within the chamber it was deduced that the effect of increasing the density ratio,  $\rho_f/\rho_a$ , on the spread rate is broadly analogous to the effect of decreasing the chamber length to diameter ratio,  $L/D$ .

Further work is required to determine the optimum  $L/D$  for maximum spread as a function of density ratio. More detailed investigations of the flow inside the nozzle chamber are also required to verify and quantify the proposed explanations.

## Acknowledgments

The work has been undertaken with the joint support of the Australian Research Council and FCT-Combustion through the SPIRT scheme.

## References

- [1] Brown, G.L. and Roshko, A., On density effects and large structure in turbulent mixing layers, *J. Fluid Mech.*, **64**(4), 1974, 775-816.
- [2] Era, Y. and Saima, A., Turbulent mixing of gases with different densities, *B. JSME*, **20**(139), 1977, 63-70.
- [3] Law, A.W.K. and Herlina., An Experimental Study on Turbulent Circular Wall Jets, *J. Hydraul Eng.*, **128**(2), 2002, 161-174.
- [4] Lee, S.K., Lanspeary, P.V., Nathan, G.J., Kelso, R.M. and Mi, J., Low kinetic-energy loss oscillating-triangular-jet nozzles, *Exp. Therm Fluid Sci.*, **27**, 2003, 553-561.
- [5] Lee, S.K., Lanspeary, P.V., Nathan, G.J. and Kelso, R.M., Surface-Flow Patterns in Oscillating-Triangular-Jet Nozzles, *15<sup>th</sup> Australasian Fluid Mechanics Conference*, Sydney, Australia, December, 2004, 13-17.
- [6] Manias, C.G., and Nathan, G.J., The Precessing Jet Gas Burner – a low  $\text{NO}_x$  burner providing efficiency and product quality improvements, *World Cement*, March, 1993, 4-11.
- [7] Nathan, G.J., The enhanced mixing burner, PhD thesis, Department of Mechanical Engineering, University of Adelaide, Australia, 1988.
- [8] Nathan, G.J., and Hill, S.J., Full Scale Assessment of the Influence of a Precessing Jet of Air on the Performance of Pulverised Coal Flame in a cement Kiln, *FCT Internal Report*, 2002.
- [9] Newbold, G.J.R., Mixing and Combustion in Precessing Jet Flows, PhD Thesis, Department of Mechanical Engineering, University of Adelaide, Australia, 1998.
- [10] Parham, J. J., Nathan, G. J. and Alwahabi, Z. T., Quantification of Mixing Characteristics for the Optimisation of Combustion in Rotary Kilns, *14<sup>th</sup> Australasian Fluid Mechanics Conference*, Adelaide, Australia, December, 2001, 10-14.
- [11] Richards, C.D. and Pitts, W.M., Global density effects on the self-preservation behaviour of turbulent free jets, *J. Fluid Mech.*, **254**, 1993, 417-435.
- [12] Smith, N.L., Megalos, N.P., Nathan, G.J., Zhang, D.K., and Smart, J. P., Precessing Jet Burners for Stable and Low  $\text{NO}_x$  Pulverised Fuel Flames - Preliminary results from small-scale trials, *Fuel*, **77**, 1998, 1013-1016.
- [13] Wong, C.Y., The flow within and in the near external field of a fluidic precessing jet nozzle, PhD thesis, Department of Mechanical Engineering, University of Adelaide, Australia, 2004.

## Flow visualisation of a pitching and heaving hydrofoil

Timothy C. W. Lau, Richard M. Kelso and Eyad R. Hassan

Department of Mechanical Engineering,  
The University of Adelaide, North Terrace Campus, SA, 5005 Australia

### Abstract

A fish-inspired heaving and pitching foil was investigated in a water tunnel using dye visualisation, at Reynolds numbers between 870 and 3480 (based on the chord length) and Strouhal numbers between 0.06 and 1.37. The variation of the wake pattern with respect to the Strouhal number was investigated. Three different wake regimes were observed - a drag wake, a transition wake and a thrust wake. The drag wake consisted of a combination of a regular Karman street and an array of 'primary' stop-start vortices, whereas the thrust wake consisted of a reverse Karman vortex street, commonly observed in swimming fish. The transition wake regime, which occurs at approximately  $0.2 < St < 0.3$ , is interpreted as a momentum balanced wake, where the thrust developed by the foil approximately balances its produced drag. This wake was observed to either consist of an in-line vortex street, or a paired vortex pattern.

### Introduction

Interest in the swimming of aquatic animals took on a scientific edge with the publication of the now famous Gray's Paradox, which states that using standard steady-state fluid mechanics concepts, a swimming dolphin would have to produce more muscular power than was believed possible, or conversely, a swimming dolphin would have to be able to reduce its hydrodynamic drag. The latter possibility has large potential for application. Although the steady-state concepts used in Gray's Paradox have been shown to be inapplicable to swimming fish [7], the question remains whether swimming aquatic animals have capabilities of reducing drag (or of increasing efficiency) beyond what exists in man-made aquatic applications [2].

Although there are many forms of aquatic animals, here we concentrate on carangiform locomotion, or rather the interaction between the carangiform tails and the their wake, as the wake dynamics will provide clues as to how force production occurs during fish swimming. In many instances (such as [1]), carangiform tails (which generate the majority of the fish's total thrust) are modelled as heaving and pitching foils, and this is the concept adopted here.

Heaving and pitching foils have been demonstrated to produce thrust very efficiently (over 80% efficiency under certain conditions), and this occurs at a Strouhal number ( $St$ , see definition later) of approximately 0.25, where the wake is shown to be of a reverse von Karman vortex street form [1]. Interestingly, it appears that carangiform swimmers also swim at approximately the same  $St$  and produce the same wake form - the reverse Karman street [8, 10]. This would seem to suggest that fish "excite" the fluid-structure system at the system's "favoured" normalised frequency (i.e.  $St$ ), analogous to a wave exciting a plate at its resonance frequency. At this juncture it also has to be noted that the commonly investigated flow past a stationary cylinder produces a "regular" von Karman vortex street wake, with a  $St$  of approximately 0.2 [6]. Taking into account the different parameter definitions, it is reasonable to wonder if the two  $St$  are linked.

The concept of a preferred operating condition is not limited to heaving and pitching foils - it also has been shown to some extent in the generation of vortex rings, whereby the vortex

rings reach a maximum circulation at a non-dimensional 'formation time' of approximately 4, regardless of the geometry of their cylinder/piston setup [3]. As this formation time is loosely linked to  $St$ , it can be speculated that at  $St \approx 0.25$ , the circulation of the vortices developed by a foil may be maximised [9].

In other experiments, the effect of the body movements - as opposed to solely the tail movements considered thus far - is scrutinised. Lighthill [4] has shown mathematically that to produce thrust, the wavespeed of an undulating body ( $V$ ) has to be slightly more than the speed of the free stream ( $U$ ). The ratio of these two speeds ( $\frac{V}{U}$ ) is of particular interest, as Triantafyllou *et al.* [9] quotes that  $\frac{V}{U}$  values of approximate 1.2 - 1.5 give best results for reduction in turbulence intensity, and thus drag, for an undulating plate, and Muller *et al.* [5] show that the forward momentum of an undulating swimming fish is most considerable when  $\frac{V}{U}$  is approximately 1.4. Furthermore, for the latter case, it can also be shown that at  $\frac{V}{U} \approx 1.4$ , the Strouhal number is approximately 0.25.

As can be seen, there are pockets of evidence which suggests that efficient force production develops when the system is excited at its preferred states. However, more evidence is needed before complete understanding is achieved. Therefore, the aim of this experiment is to investigate the effect of the Strouhal number on the wake dynamics of a heaving and pitching foil, to determine whether the foil could possibly produce efficient propulsion at  $St \approx 0.25$ , and why this  $St$  value is of significance. Particular attention will be given to the wake, as the experiments described above by Anderson *et al.* [1], and Muller *et al.* [5] show that the shift from the inefficient generation of forces to efficient generation of forces also corresponds to a shift in the wake form.

### Experimental Setup

A NACA 0026 hydrofoil, with a chord length,  $c$  of 50mm and a span,  $l$  of 200mm (giving an aspect ratio of 4), is placed in a water tunnel with a working section of 1500mm x 500mm x 500mm. The foil is independently heaved and pitched harmonically, using a scotch yoke mechanism and a cam respectively, driven by two stepper motors (see figure 1). The heave amplitude,  $h_0$  can be set to five discrete values, corresponding to  $\frac{h_0}{c} = 0.0, 0.25, 0.5, 0.75, 1.0$ . The amplitude of pitch angle  $\theta_0$ , can be set to ten discrete settings by changing the offset of the cam, leading to pitch angle amplitudes from  $\theta_0 = 0^\circ$  to  $\theta_0 = 45^\circ$  in 5 degree intervals. The motion of the heave is sinusoidal, whereas the pitch motion is near-sinusoidal due to the effect of the shifting contact point on the cam-follower interface (maximum error  $\approx 2\%$ ). The phase difference between the heave and pitch is defined as  $\Psi$ , and in these experiments is nominally set to  $90^\circ$ .

The Strouhal number, based on the trailing edge excursion, is defined as  $St = \frac{fA}{U}$ , where  $f$  is the frequency (Hz),  $A$  is the peak to peak trailing edge excursion (consistent with [1]) and  $U$  is the free stream velocity. The frequency  $f$  of heaving and pitching can be directly controlled using a signal generator. The flow speed of the water tunnel can be set within a range of  $U = 0 - 250\text{mm/s}$ . Therefore, by setting all the above values beforehand,  $St$  can be determined prior to the experiments.



Dye is gravity-fed via a 1mm probe, which is fixed along the leading edge of the hydrofoil (see figure 1) at a depth corresponding to the mid-span of the foil. This allows the dye to be fed to both sides of the foil at the same time, and allows the dye probe to move with the foil when the foil is heaving. Food colouring diluted with the operating fluid from the water tunnel was used to visualise the flow, which in turn was recorded using a video camera (Sony DCR - TRV900E, 25 frames per second). The recordings are then digitally captured onto a computer for post processing.

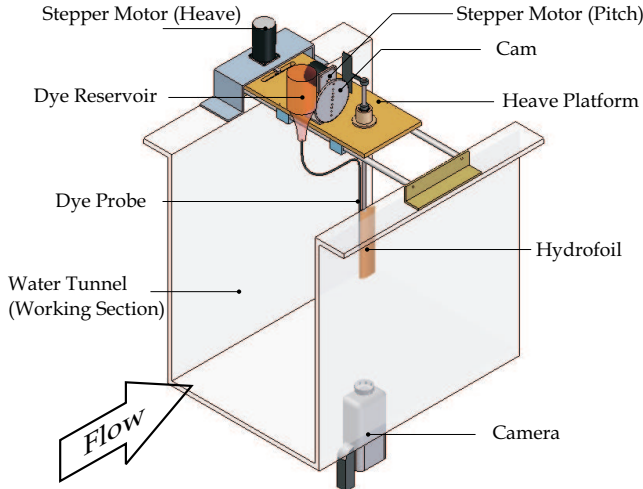


Figure 1: Experimental setup.

## Results and Discussion

Altogether 113 different flow cases were investigated, captured in approximately 3 hours of digital video information (approximately 270000 frames). These flow cases consisted of combinations of different heave and pitch amplitudes, as well as different flapping frequencies and water tunnel flow velocities. The minimum and maximum  $St$  obtained were 0.06 and 1.37 respectively. The Reynolds number,  $Re$ , based on the foil chord ranged from 870 (for  $U = 19.5\text{mm/s}$ ) to 3480 (for  $U = 78\text{mm/s}$ ). All flow cases are cyclic, i.e., every cycle is identical to the previous cycle, however a few cases show asymmetry, whereby the upstroke and downstroke do not necessarily produce the same pattern of vortices (e.g. figure 4b). Nonetheless, the majority of the cases examined show symmetry, which would be expected since the motion of the foil is symmetrical as well.

A number of different wake patterns were observed. In particular we observe an in-line vortex wake pattern (figure 4c), a vortex pairing pattern (figure 4d) and a reverse Karman vortex street (figure 4e). The former two cases shed two vortices per cycle, whereas the latter case sheds four vortices per cycle. We also observe a “drag” wake pattern, whereby the wake pattern consists of a regular Karman vortex street which is slightly rotated from the streamwise axis (figure 4a). Many cases examined also show signs of additional vortices, which we denote “tertiary vortices”. Figure 2 shows a reverse Karman wake with the clear existence of tertiary vortices. These vortices, which are usually shed between the half cycles, are differentiated from the vortices shed at the ends of the half cycles, which we call the “primary” vortices. The primary vortices are almost always noticeably stronger than the tertiary vortices.

The existence of the primary vortices can be explained using classical wing theory. The primary vortices are simply a combination of the stopping vortex of the previous half cycle, and the starting vortex of the subsequent half cycle, and hence they



Figure 2: Tertiary vorticity ( $St = 0.51$ ).

are sometimes called start-stop (or stop-start) vortices. On the other hand, tertiary vortices are generated due to the instability of the shear layer near at the trailing edge of the wing - an area where the velocity gradients are high. Intuitively, the experiments also show that more tertiary vortices are produced at higher flapping speeds ( $= f \cdot A$ ). We also define the secondary vortices, which are the vortices that are shed in the wake of an unforced or mildly forced drag producing body (see figure 3).



Figure 3: Secondary vorticity ( $St = 0$ ).

In general, the differing wake patterns presented in figure 4 can be arranged into three different wake regimes - a drag wake, a transition or balanced wake and a thrust wake (see figure 5). The transition from a drag wake to a thrust wake occurs via the transition or balanced wake, and is strongly dependent on  $St$ . At low  $St$  ( $<0.2$ ), the foil produces a wake indicative of drag - generally producing a pattern of the regular Karman street form. At very low  $St$  ( $<0.1$ ), and at low to moderate heave amplitudes, the wake consists of a phase-rotated regular Karman street wake, whereby the vorticity is generated at the leading edge of the wing (figure 4c). At large heave amplitudes ( $\frac{h_0}{c} = 1.0$ ), the pattern becomes complex and will be discussed in later publications.

Within this drag regime exists a wake pattern that is unexpected - an asymmetrical wake pattern (see figure 4b), which occurs at approximately  $0.1 < St < 0.2$ . This wake pattern consists of a pair of counter rotating vortices, plus an additional vortex per cycle. This asymmetry is cyclic, but the initial onset of the asymmetry is random. This asymmetrical wake pattern is also seen in experiments with oscillating cylinders [11], which the authors call the “P+S” (Pair + Single) vortex mode. This asymmetry is attributed to the generation of secondary vortices, which combine with the primary stop-start vorticity shed at the trailing edge of the wing. The vortex shedding frequency is synchronised with the flapping frequency of the wing, however there is a phase difference between the generation of these vortices, such that one drag vortex is shed freely into the wake while the other combines with the start-stop vortex, generating the pattern shown in

figure 4b. At slightly higher  $St$ , the competition between the two modes of vortex generation is balanced, either producing an in-line wake pattern or a vortex pairing pattern; this wake regime is called the balanced or transition wake regime (discussed below).

The balanced or transition wake regime occurs in the range  $0.2 < St < 0.3$ , where the wake shows evidence of an approximate momentum balance. This occurs when the drag forces on the wing balances the thrust produced by the wing. For this case, neither a momentum deficit nor a momentum surplus should be observed in the wake, and the wake patterns reflect this. Two wake patterns are observed in this  $St$  band; the first is the in-line wake pattern (see figure 4a), whereby two counter rotating vortices are shed along the centreline per cycle. The second wake pattern is the vortex pair pattern, whereby two pairs of counter rotating vortices are shed per cycle (figure 4d). Both wake patterns appear to be combinations of regular vortex shedding due to drag and the start-stop vortices shed at the trailing edge, following the asymmetrical case discussed above. The in-line wake pattern occurs when the start-stop vortices combine with the drag vortices of the same sign - therefore only generating two vortices per cycle. On the other hand, the vortex pair pattern occurs when the start-stop vortices and the drag vortices do not combine immediately - they are formed and shed separately. The arrangement and axial alignment of these shed vortices in both cases suggest that there is little momentum excess or deficit in the wake. Hence, it is likely that the wing is generating large side forces, but little thrust or drag. The strength of these vortices should be proportional to the magnitude of the side forces, which do not contribute to useful work.

At  $St > 0.3$ , the wake pattern consists of a reverse Karman street, indicating that the foil is generating forward thrust. Evidence of the development of thrust is also provided by the shed tertiary vortices, which are accelerated away from the foil when they enter the jet region of the foil - a phenomenon not observed in the other two wake regimes. As  $St$  increases, so does the apparent strength of the primary vorticity and, we expect, the magnitude of thrust. This flow regime also shows the greatest tendency to produce tertiary vortices.

The variation of the wake patterns with respect to  $St$  is summarised in figure 5, which is plotted against the maximum angle of attack of the wing. This angle is calculated from both heave and pitch angle amplitudes. The plot allows the direct comparison to the wake map produced by Anderson *et al.* [1], at  $Re = 1100$ . There are some major differences between the two plots. Firstly, Anderson *et al.* do not observe a transition regime at  $0.2 < St < 0.3$ . At this  $St$  range they observe a reverse Karman street. Secondly, they do not observe an in-line wake pattern, and the vortex pairing pattern they observe occurs either at high angles of attack ( $> 50^\circ$ ) at all  $St$ , or at  $St > 0.5$  at all angles of attack above  $10^\circ$ . The first difference can be accounted for by the fact that the wake map produced by Anderson *et al.* is only for high heave values ( $\frac{h_0}{c} = 1.0$ ), whereas the wake map produced here is for all heave values. In our study, high heave values account for five out of the six cases where a reverse Karman street is observed within the transition regime. The second major difference is, so far, inexplicable. Nevertheless, the results of Anderson *et al.* do indicate that at  $St < 0.2$ , low or negative thrust (drag) develops on the foil, with good agreement with the results presented here.

In general, our results indicate that, at  $St < 0.2$ , the secondary, or vortex shedding mode dominates the flow, and the foil generates drag. As  $St$  increases, the influence of the flapping increases, and at a certain point the relative influence of both the flapping and the vortex shedding is balanced, and both vortex generating modes are phase-locked. This occurs approximately at  $0.2 < St < 0.3$ , and it appears that little or no net thrust or

drag is developed. At  $St > 0.3$ , the flapping dominates the flow and the foil develops net thrust. Therefore, to maintain steady propulsion, the parameters of the flapping foil have to be chosen such that  $St \approx 0.25$ , where the thrust and drag developed by the foil is balanced. This concurs with the observation that steadily swimming fish swim approximately at  $St = 0.25$  [8]. However, there is no proof, as yet, that efficient propulsion can be developed at this  $St$ . The next part of our study, which will include laser imaging, will eventually allow the measurement of the wake parameters (most notably the strength of the primary vortices, and the geometry of the wake patterns), which would potentially provide important information regarding the generation of the wake vortices and also provide clues whether fish do in fact, swim with exceptional efficiency.

## Conclusion

Flow visualisation of a heaving and pitching hydrofoil has revealed different wake patterns at various Strouhal numbers. These wake patterns can be classified into three regimes - a drag regime, a transition or balanced regime and a thrust regime. The transition regime occurs approximately at  $0.2 < St < 0.3$ , the  $St$  band at which fish have been observed to swim steadily.

## References

- [1] Anderson, J. M., Streitlien, K., Barrett, D. S. and Triantafyllou, M. S., Oscillating foils of high propulsive efficiency, *Journal of Fluid Mechanics*, **360**, 1998, 41–72.
- [2] Barrett, D. S., Triantafyllou, M. S., Yue, D. K. P., Grosenbaugh, M. A. and Wolfgang, M. J., Drag reduction in fish-like locomotion, *Journal of Fluid Mechanics*, **392**, 1999, 183 – 212.
- [3] Gharib, M., Rambod, E. and Shariff, K., A universal time scale for vortex ring formation, *Journal of Fluid Mechanics*, **360**, 1998, 121–140.
- [4] Lighthill, J., *Mathematical Biofluidynamics*, Society for Industrial and Applied Mathematics, Pennsylvania, 1975.
- [5] Muller, U. K., Stamhuis, E. J. and Videler, J. J., Riding the waves: the role of the body wave in undulatory fish swimming, *Integrative and Comparative Biology*, **42**, 2002, 981 – 987.
- [6] Nakamura, Y., Vortex shedding from bluff bodies and a universal strouhal number, *Journal of Fluids and Structures*, **10**, 1996, 159–171.
- [7] Schultz, W. W. and Webb, P. W., Power requirements of swimming: Do new methods resolve old questions?, *Integrative and Comparative Biology*, **42**, 2002, 1018 – 1025.
- [8] Triantafyllou, G. S., Triantafyllou, M. S. and Grosenbaugh, M. A., Optimal thrust development in oscillating foils with application to fish propulsion, *Journal of Fluids and Structures*, **7**, 1993, 205–224.
- [9] Triantafyllou, M. S., Techet, A. H., Zhu, Q., Beal, D. N., Hover, F. S. and Yue, D. K. P., Vorticity control in fish-like propulsion and maneuvering, *Integrative and Comparative Biology*, **42**, 2002, 1026 – 1031.
- [10] Triantafyllou, M. S., Triantafyllou, G. S. and Yue, D. K. P., Hydrodynamics of fishlike swimming, *Annual Review of Fluid Mechanics*, **32**, 2000, 33 – 53.
- [11] Williamson, C. H. K. and Roshko, A., Vortex formation in the wake of an oscillating cylinder, *Journal of Fluids and Structures*, **2**, 1988, 355 – 381.

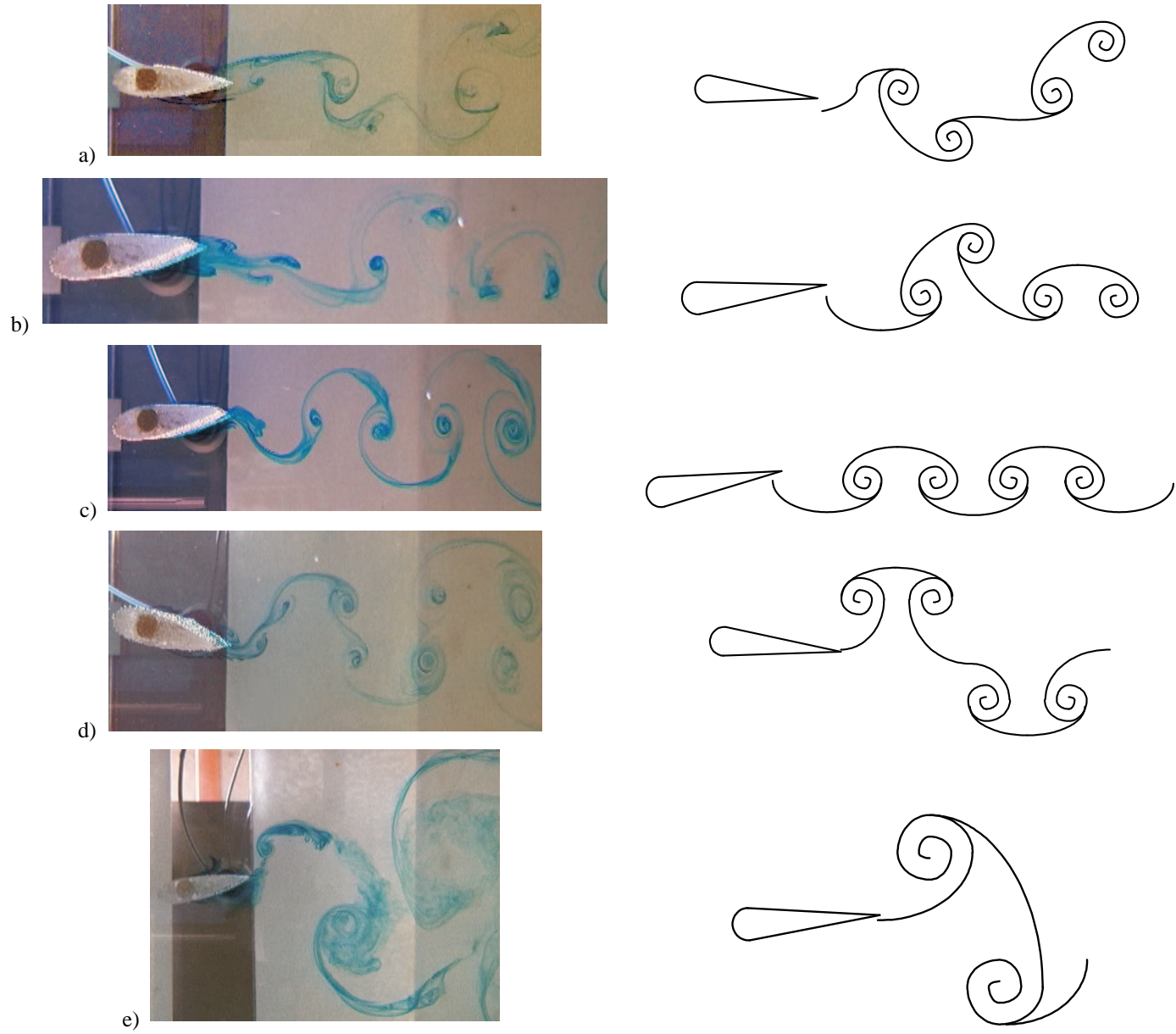


Figure 4: Vortex wake patterns. Flow is from left to right. Case a) Drag ( $St = 0.09$ ) b) Drag ( $St = 0.12$ ) c) In-line ( $St = 0.19$ ) d) Vortex Pair ( $St = 0.23$ ) e) Reverse Karman ( $St = 0.53$ ).

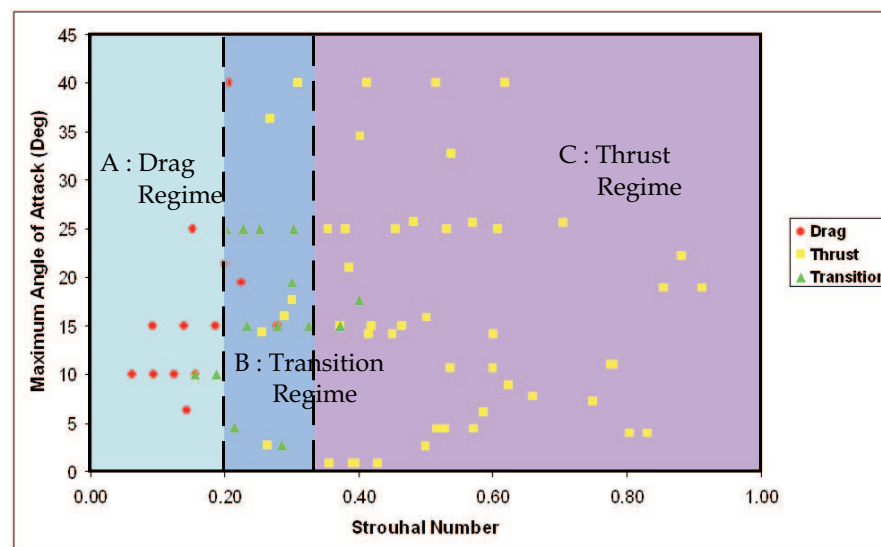


Figure 5: Vortex wake map.

## A Numerical Study Of A Circular Cylinder In The Wake Of An Airfoil

C. Y. Zhou<sup>1</sup>, C. W. Sun<sup>1</sup>, Y. Zhou<sup>2</sup>, L. Huang<sup>2</sup>

<sup>1</sup>Shenzhen Graduate School, Harbin Institute of Technology  
Xili Shenzhen University Town, Shenzhen 518055, China

<sup>2</sup>Department of Mechanical Engineering, The Hong Kong Polytechnic University  
Hung Hom, Kowloon, Hong Kong, China

### Abstract

A circular cylinder in the near wake of NACA 4412 airfoil in a cross flow is numerically studied using finite volume method for Reynolds Number  $Re=200$  based on the cylinder diameter. The effects of the attack angle of the airfoil, the longitudinal and lateral spacing between the airfoil and the cylinder on the unsteady loading, vortex shedding frequency and vortex patterns of the cylinder are examined.

### Introduction

A circular cylinder in an airfoil wake in a cross flow arises in many engineering applications, for example, in cooling fan applications where motor is supported by simple struts made of circular cylinders. The rotor wake impinges on the struts and the struts themselves experience vortex shedding. The interaction of rotor with a downstream cylindrical strut has been found to be the main noise source for cooling fans [2]. With the aim to investigate the rotor-strut interaction in order to understand the mechanism of noise generation in a cooling fan, Zhang et al. [6] carried out an experimental work to study the interaction of a circular cylinder with an airfoil near-wake by considering a stationary airfoil with a downstream cylinder where the effects of the lateral distance between the airfoil and the cylinder, the Reynolds number and the incidence angle on the aerodynamic loading on the cylinder were investigated. With the application of cooling fans in mind, their attention was focused on configurations of a cylinder being in close proximity of the blade trailing edge. The effect of the in-line distance between airfoil and cylinder was not investigated.

The flow field for a configuration of a circular cylinder in the wake of an airfoil has not been widely studied. The most relevant study is the research on the flow field with two cylinders in tandem arrangement or staggered in a cross flow, such as the work of Mochizuki et al [3] where the aerodynamic noise generation by the interaction of two tandem cylinders with different diameters was experimentally studied. A good review on the effects of interaction between circular cylinders in cross flow was given by Zdravkovich [5]. Recently Akosile & Summer [1] carried out an experimental work where the aerodynamic forces and the vortex shedding frequencies were measured for staggered two circular cylinders immersed in a uniform shear flow. The wake-body interaction and several critical incident angles were studied in detail. The mutual interference effect of two cylinders in tandem arrangement is very strong and this effect leads to a significant change in fluid forces acting on the cylinders depending on the spacing between them. There is a critical spacing at which fluid forces jump from a low value to a high value and then intermittently switch between those values. This is known as the jump phenomenon. The interactions between two or more cylinders have been extensively investigated. However the wake of bluff body behaves rather differently from that of a streamline body and the results of the investigation cannot be simply extrapolated to the situation to be studied in the present work.

In this paper a numerical study has been carried out for the configuration of a circular cylinder in an airfoil wake using the finite volume method. It is known that the longitudinal, lateral spacing and the attack angle of the airfoil are the important parameters in this configuration. The three groups of calculations are carried out to investigate the effects of the attack angle, the longitudinal and the lateral spacing on flow vortex patterns and the unsteady loading on the circular cylinder. The present work is of both practical and fundamental significance since the configuration is related to a number of engineering applications and also itself represents the generic fluid-structure interaction having important implication for fluid induced vibration and noise generation. The Reynolds number  $Re$  based on the diameter of the cylinder  $d$  is kept at 200 for all calculations.

### Computational Modelling

An airfoil NACA4412 and a circular cylinder are arranged in a staggered configuration in a cross flow shown in figure 1, where  $d$  is the diameter of the cylinder,  $c$  the chord length of the airfoil,  $U_\infty$  the velocity of the uniform flow,  $\alpha$  the attack angle of the airfoil,  $l$  and  $T$  are the longitudinal and lateral spacing between the airfoil and the cylinder respectively, and  $c/d=7$ .

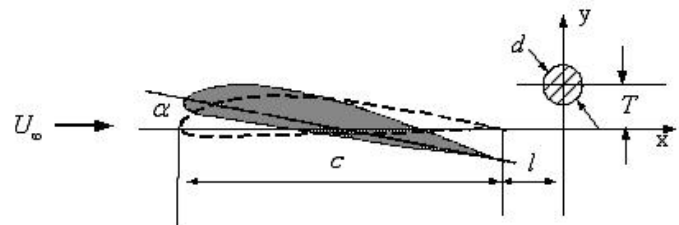


Figure 1: The configuration of a circular cylinder and an airfoil.

The flow is assumed to be unsteady, two-dimensional and laminar, and the incompressible fluid flow can be described by the following continuity and Navier-Stokes equations (non-dimensionalized):

$$\frac{\partial u}{\partial x} + \frac{\partial v}{\partial y} = 0 \quad (1)$$

$$\frac{\partial u}{\partial t} + u \frac{\partial u}{\partial x} + v \frac{\partial u}{\partial y} = -\frac{\partial p}{\partial x} + \frac{1}{Re} \left( \frac{\partial^2 u}{\partial x^2} + \frac{\partial^2 u}{\partial y^2} \right) \quad (2)$$

$$\frac{\partial v}{\partial t} + u \frac{\partial v}{\partial x} + v \frac{\partial v}{\partial y} = -\frac{\partial p}{\partial y} + \frac{1}{Re} \left( \frac{\partial^2 v}{\partial x^2} + \frac{\partial^2 v}{\partial y^2} \right) \quad (3)$$

where  $u$  and  $v$  are the velocities in  $x$ - and  $y$ - directions, Reynolds number  $Re$  is defined as  $Re=U_\infty d/\nu$ ,  $\nu$  is the kinematic viscosity.

The equations are numerically solved using finite volume method where the pressure-velocity coupling is achieved using the SIMPLEC method [4]. These procedures are implemented within a CFD code Fluent 6.0 used in the present study. Unstructured mesh is employed and the computational domain is a rectangle with  $60d$  length and  $24d$  width. The velocity at upstream



boundary of the computational domain is set as the uniform velocity  $U_\infty$  and the outflow boundary condition is used at the downstream boundary. Time dependent simulation is conducted with the initial conditions of  $u=1$  and  $v=0$  in the entire computing domain. Computations are carried out in PENTIUM IV PCs with run times on the order of 40-60 hrs for grids with typical  $10^5$  computational cells and run of 50000 time steps.

The drag and lift coefficients are defined as

$$C_d = \frac{2F_x}{\rho U_\infty^2 d} \text{ and } C_l = \frac{2F_y}{\rho U_\infty^2 d}$$

where  $F_x$  and  $F_y$  are the force components in  $x$ - and  $y$ - direction and  $\rho$  is the density of the fluid.

To validate the code and also obtain a baseline for comparison, a single circular cylinder in a cross flow and an isolated airfoil in a cross flow are first calculated respectively. The results of force coefficients, Strouhal number  $St$  and the vortex pattern for the single cylinder are compared with previous experimental and computational results reported [7] and good agreement is obtained. Calculations are then carried out in three groups:

- ♦ to investigate the effect of the attack angle  $\alpha$ , where  $\alpha$  varies from  $-10^\circ$ ,  $0^\circ$ ,  $7^\circ$ ,  $10^\circ$ ,  $15^\circ$  and  $20^\circ$  with  $l/d=2.5$  and  $T/d=0$  fixed;
- ♦ to investigate the effect of the in-line distance  $l/d$ , where  $l/d$  varies from 1, 1.5, 2, 2.5, 3, 4, 5, 6 and 9 for  $\alpha=5^\circ$  &  $15^\circ$  with  $T/d=0$  fixed;
- ♦ to investigate the effect of lateral spacing  $T/d$ , where  $T/d$  varies from -2, -1, 0, 1 and 2 with  $l/d=1.5$  and  $\alpha=0^\circ$  fixed.

The effects of these parameters on unsteady forces, vortex shedding frequency and vortex patterns of the downstream circular cylinder are examined.

### Effects of Attack Angle $\alpha$

The results for the isolated airfoil show that the flow is attached when  $\alpha=0^\circ$  and flow separates when  $\alpha=5^\circ$  however no big vortex shed from the airfoil. As  $\alpha$  increases the separation point moves upwards from the trailing edge and separation region becomes larger. As  $\alpha$  increases further vortices shed forming a vortex street behind the airfoil. When  $\alpha=15^\circ$  the shedding frequency of this vortex street is 0.1102.

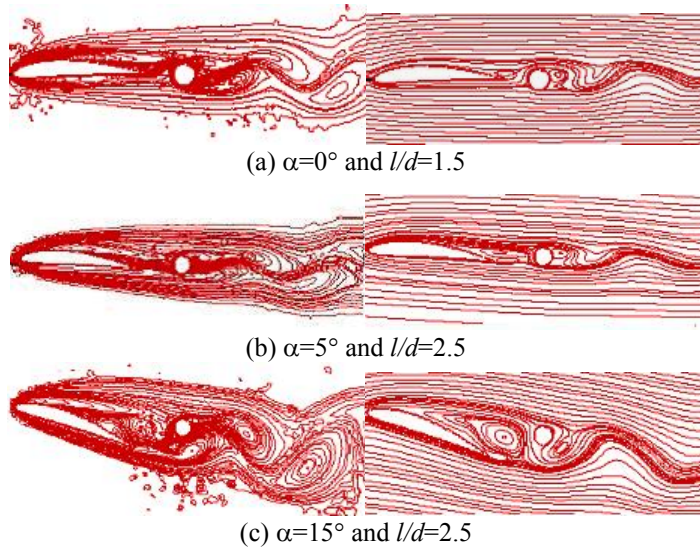
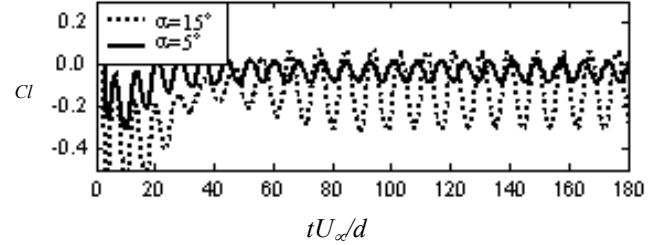


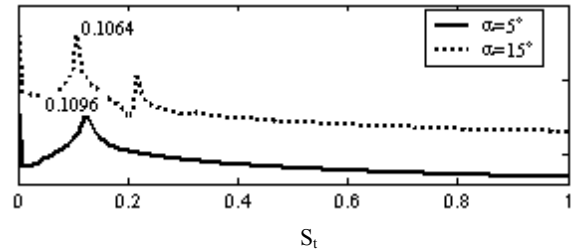
Figure 2: Vorticity contours and streamlines for  $\alpha=0^\circ$ ,  $5^\circ$  and  $15^\circ$ .

When a circular cylinder is placed in the near wake of the airfoil, the flow separates from the airfoil earlier and separation point occurs more upwards. The flow separates from the surface of the

airfoil and reattaches on the front surface of the cylinder when the attack angle is very small, and forms a separation region between the airfoil and the cylinder (see figure 2 for  $\alpha=0^\circ$  and  $5^\circ$ ). The flow separates again from the cylinder and shed vortices generating a vortex street after the cylinder. As the cylinder experiences a much slower incident velocity the shedding frequency appears much lower than the value of 0.1885 for an isolated cylinder. This frequency is 0.1448 for the case of  $\alpha=0^\circ$  and  $l/d=1.5$ , and 0.1096 for  $\alpha=5^\circ$  and  $l/d=2.5$ . Obviously for the latter case the separation region is relatively larger and the influence of the separation region is therefore stronger. This influence can be seen from the power spectrum of the lift force on the cylinder where the peak of the shedding frequency is slightly broad-banded (see figure 3).



(a) Time histories of the lift force coefficient.



(b) Power spectrum from the lift time histories.

Figure 3: Time history of lift force coefficient and power spectrum from the histories for  $\alpha=5^\circ$  and  $\alpha=15^\circ$ .

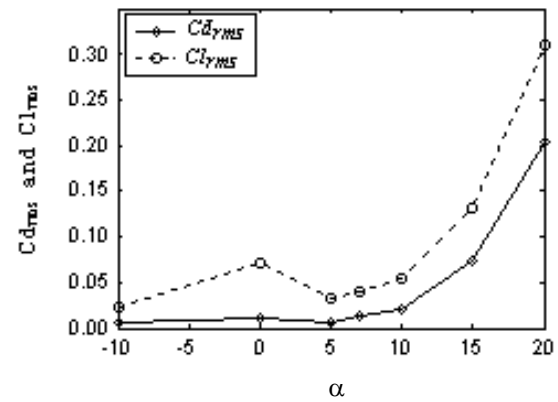
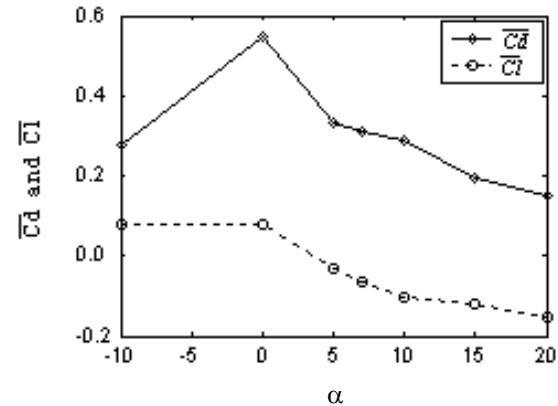


Figure 4: Variation of the force coefficients of the cylinder with  $\alpha$ .

When the attack angle increases, the separation region of the airfoil becomes larger. When the  $l/d$  is small enough, the cylinder

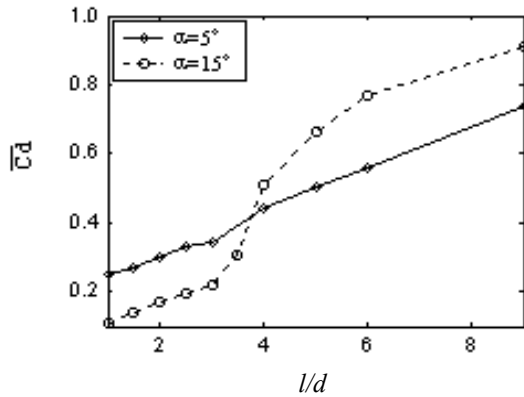


can be wrapped in the separation region. The vortex shedding from the cylinder is then suppressed. The airfoil with the separation region and the cylinder becomes a whole. Big vortices shed and form a Karmen vortex street behind the separation region with a shedding frequency very close to the one for an isolated airfoil. The case with  $\alpha=15^\circ$  and  $l/d=2.5$  shown in the figures is in this situation where the shedding frequency is 0.1064 which is very close to the value 0.1102 for an isolated airfoil. The feature of the flow field is dominated by the characteristics of the airfoil in this situation.

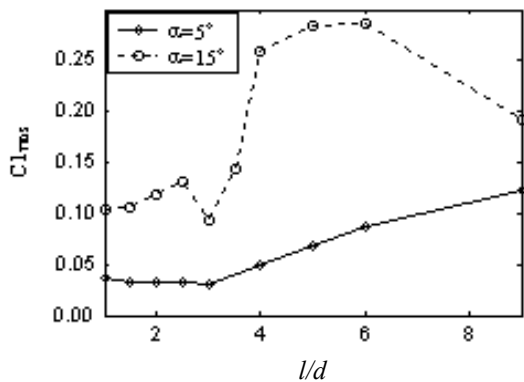
The drag coefficient appears to be much smaller than the value 1.3375 for the isolated cylinder for all cases studied in this section (see figure 4) due to the shadow effect of the upstream airfoil. Not surprisingly the maximum value occurs at  $\alpha=0^\circ$  since the cylinder has minimum influence from the airfoil. The drag coefficient reduces quickly as the attack angle increases as expected. It is seen in figure 4 that  $Cl_{rms}$  is very small and does not change much when  $\alpha$  varies from  $0^\circ$  to  $10^\circ$ . However  $Cl_{rms}$  increases rapidly as  $\alpha$  increases from  $10^\circ$  to  $20^\circ$ . This might be because the unsteady force is mainly due to the cylinder generated vortices when  $\alpha$  varies from  $0^\circ$  to  $10^\circ$ , while for  $\alpha>10^\circ$ , the unsteady force exerted on the cylinder is due to the more violent shedding of vortices from the separation region with high vorticity density and the impingement of large-scale vortices generated from the separated shear flow from the leading edge (see figure 2 for  $\alpha=15^\circ$  and  $l/d=2.5$ ).

#### Effects of In-line Distance $l/d$

Figure 5 show the variation of  $C_d$  and  $Cl_{rms}$  on the cylinder with  $l/d$  for  $\alpha=5^\circ$  &  $\alpha=15^\circ$ . The drag coefficient for  $\alpha=15^\circ$  increases as  $l/d$  and reaches a value of 0.9059 at  $l/d=9$  which is still much smaller than the value 1.3375 for an isolated cylinder. The rms value of  $Cl$  behaviours differently for the two attack angles with



(a) Drag force



(b) Lift force

Figure 5: The variation of force coefficients on cylinder with  $l/d$ .

$l/d$ . For  $\alpha=5^\circ$   $Cl_{rms}$  remains unchanged until  $l/d=3$  and then starts to increase with  $l/d$ . However for  $\alpha=15^\circ$  where the flow has a large separation region, the value of  $Cl_{rms}$  reaches a

minimum value at  $l/d=3$  and then increases rapidly to a high value at  $l/d=4$  (see figure 5). This, to some extent, shows a similarity to the case of two tandem cylinders. At an in-line spacing of  $l/d > 3.5$ , the upstream cylinder sheds vortices and the force fluctuation on the downstream cylinder is larger than that at a smaller  $l/d$  when upstream cylinder fails to shed vortices.

The effect of  $l/d$  on the vortex shedding frequency is investigated by examining the power spectra of the lift time history and drag time history on the cylinder. The vortex shedding frequency varies with  $l/d$  and  $\alpha$ , and very much depends on the value of  $\alpha$ . The frequency value decreases and the separation region of the airfoil becomes larger and wider as  $\alpha$  increases (see figure 6 also figure 3). The influence of airfoil wake lasts for a long distance. When  $\alpha=0^\circ$ , the vortex shedding frequency of the cylinder is 0.1597 at  $l/d=9$  which is still much lower than the value 0.1885 for the isolated cylinder.

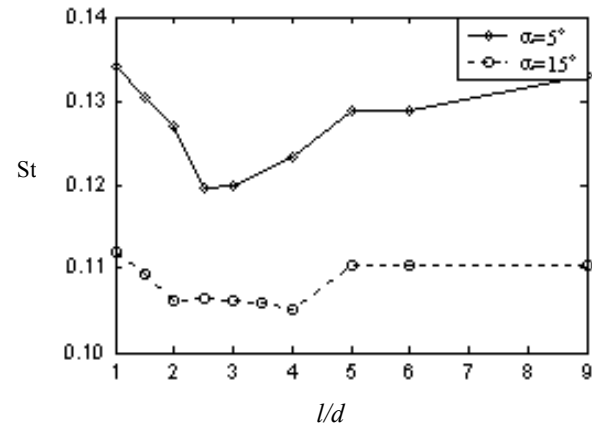
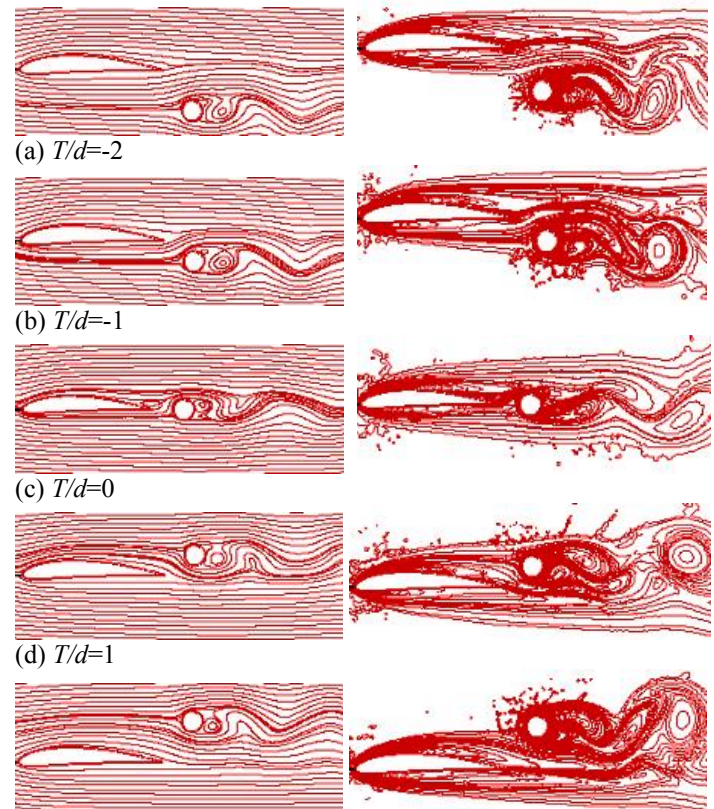


Figure 6: The variation of vortex shedding frequency with  $l/d$ .

#### Effects of Lateral Distance $T/d$

Figure 7 shows the streamlines and the vortex contours for different value of  $T/d$ . At  $T/d=0$  shear layers formed from the upper and lower sides of the airfoil reattach on the front surface



(e)  $T/d=2$

Figure 7: Streamlines and vortex patterns with different  $T/d$ .

of the cylinder and vortices shed from the cylinder and form a Karmen vortex street (see figure 7(c)). The drag force reaches a low value of 0.5329 (see figure 8) and the shedding frequency also reaches a low value 0.1448 (see figure 9).

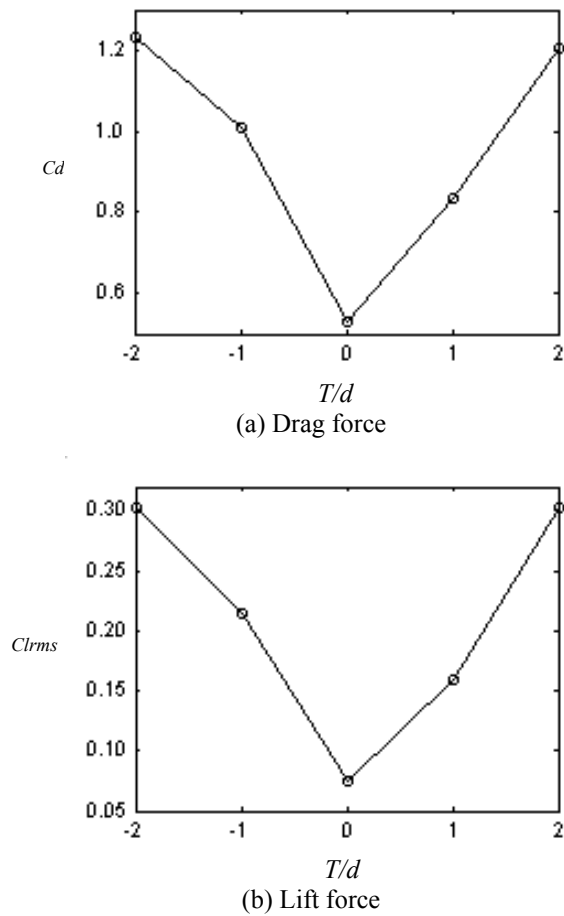


Figure 8: The variation of drag and lift coefficients with  $T/d$ .

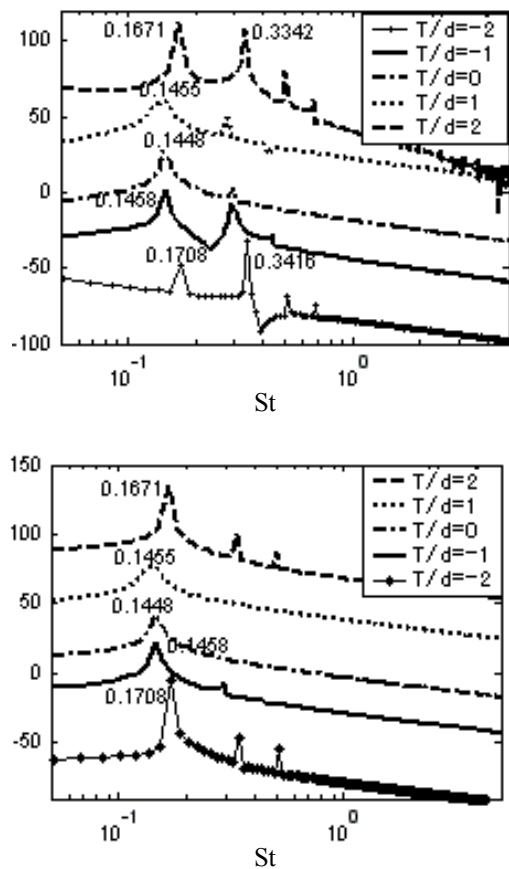


Figure 9: The power spectrums of lift and drag coefficients with different  $T/d$

It is obvious that the influence of the airfoil wake on the cylinder becomes weaker as the distance increases. The drag coefficient and the rms value of lift coefficient increase rapidly with  $T/d$ . When  $T/d=\pm 2$ , the value of drag force coefficient and the shedding frequency are very close to the values of 1.3375 and 0.1885 respectively for an isolated cylinder (see figure 8 and 9). It is found that the vortex shedding frequency peak is small and noticeably broad-banded when  $T/d=1$ , and the value of the frequency is low and almost the same value for  $T/d=0$ . This lowering of  $St$  is attributed to the enlargement of the separation region in near wake of the airfoil due to the presence of the cylinder. This does not happen when  $T/d=-1$  as the airfoil is not symmetrical.

## Conclusions

The interaction between an airfoil wake and a downstream circular cylinder has been numerically examined using finite volume method for  $Re=200$ . The results indicate that the existence of an upstream airfoil has significant impacts on the drag and lift on the cylinder, the vortex pattern and the vortex shedding frequency, and also the presence of a circular cylinder in the near wake of the airfoil can cause flow to separate earlier and the separation point to move upwards. Many parameters play important roles in the interaction. The effects of the attack angle of the airfoil, the in-line and the lateral distances between the cylinder and the airfoil are investigated in this paper. The following conclusions are drawn.

For the cylinder in the near wake of the airfoil (e.g.  $l/d=2.5$  studied in the present paper) when the attack angle is small, cylinder generated vortex street persists but with a much lower frequency than the value for an isolated cylinder; when the attack angle is larger the cylinder is wrapped by the separation bubble of the airfoil and the cylinder vortex shedding can be suppressed; increasing the attack angle will cause the drag force on the cylinder reduced and the lift enlarged.

There is a rapid rise in drag coefficient on the cylinder at  $l/d\approx 3.5$  for the case of  $\alpha=15^\circ$ , which shows, to some extent, a similarity to the case of two tandem cylinders; force coefficients on the cylinder and shedding frequency increases with  $l/d$ .

As the lateral distance increases the influence of the airfoil wake on the cylinder declines quickly. When  $T/d=\pm 2$ , the value of drag force coefficient and the shedding frequency are very close to the values of 1.3375 and 0.1885 respectively for an isolated cylinder.

## References

- [1] Akosile, O.O. and Summer, D., Staggered Circular Cylinders Immersed in a Uniform Planar Shear Flow, *Journal of Fluids and Structures*, **18**, 2003, 613-633.
- [2] Huang, L., Characterizing Computer Cooling Fan Noise, submitted to *J. Acoust. Soc. Am.* (2003).
- [3] Mochizuki, O., Kiya, M., Suzuki, S. and Komiyama, K., Aerodynamic Noise Generated by Two Circular Cylinders Arranged in Tandem, *J. of Wind Eng. Industrial Aerodynamics*, **50**, 1993, 107-115.
- [4] Patankar, S.V., *Numerical Heat Transfer and Fluid Flow*, Hemisphere, Washington D. C., 1980.
- [5] Zdravkovich, M.M., The Effects of Interaction Between Circular Cylinders in Cross Flow, *ASME Journal of Fluids Engineering*, **1**, 1987, 239-263.
- [6] Zhang, H.J., Huang, L. and Zhou, Y., Aerodynamic Loading on a Cylinder Behind an Airfoil, submitted to *Physics of Fluids* (2003).
- [7] Zhou, C.Y., So, R.M.C. and Lam, K., Vortex-induced Vibrations on an Elastic Circular Cylinder, *Journal of Fluids and Structures*, **13**, 1999, 165-189.

## The Influence of Mass Loading on Particle Distribution in the Near Field of a Co-Annular Jet

C.H. Birzer<sup>1,2</sup>, P.A.M. Kalt<sup>1</sup>, G.J. Nathan<sup>1</sup> and N.L. Smith<sup>2</sup>

<sup>1</sup>School of Mechanical Engineering  
The University of Adelaide, SA, 5005 AUSTRALIA

<sup>2</sup>School of Chemical Engineering  
The University of Adelaide, SA, 5005 AUSTRALIA

### Abstract

The effects of mass loading on the distribution of spherical particles in the near field of a co-annular jet have been investigated using planar laser light nephelometry. Particle concentrations were measured for nine different mass loading ratios ranging from  $\phi = 0.19$  to 1.88, in the first 15 nozzle diameters downstream. Results indicate that particle mass loading has a significant effect on the near field region. The length of the initial triangular core region of approximately uniform particle distributions varies by more than a factor of two, as does its shape. The mass loading ratio also influences the centreline particle concentration decay rates. The effects of mass loading on the signal attenuation are also assessed.

### Introduction

Two-phase co-annular jets are widely used, for example to mix fuel and air in pulverised fuel combustion systems. The distribution of particles in the emerging jet stream plays a controlling influence on their subsequent combustion performance. However only limited data are available of particle distributions in such systems. Data for single phase co-annular jets exist [1], however the presence of particles can have a pronounced effect on the structure of the underlying gas flow field [2]. Furthering the understanding of the particle distribution will enable improvements into the combustion of co-annular pulverised fuel systems.

The mass loading ratio,  $\phi$ , is defined as the ratio of solid phase mass flow rate to gas phase mass flow rate,

$$\phi = \frac{\dot{m}_p}{\dot{m}_f} \quad (1)$$

where subscripts p and f designate particle and fluid respectively.

Di Giacinto *et al.* [3] investigated the effect of  $\phi$  on velocity and pressure by a simulation of a pressure metering device. These results highlight the coupling between particles and fluid. Fan *et al.* [4, 5] used a Laser Diffraction Method (LDM) to measure particle concentration in the fully merged, self-similar region of co-annular jet flows, 10 to 30 nozzle diameters downstream. Their work comprised three different values of mass loadings for different velocities of the central jet (and therefore particles) and of particle diameters. They found that the fully merged zone for a two-phase turbulent co-axial jet exhibits self similarity in particle concentration and that the rate of particle dispersion is decreased with an increase in particle loading. Black *et al.* [6] used phase Doppler particle anemometry (PDPA) to measure the velocity of spherical and non-spherical particles emerging from co-axial and swirling flows. Their results pertain specifically to velocity. However, they highlighted that particle momentum in the region immediately downstream from the jet plays a significant role in

velocity variations between gas, spherical and non-spherical particles.

To the authors knowledge no published results exist which isolate the influences of solid particle mass loading and particle momentum on the particle distribution in the near field of a co-annular jet. The near field has particular importance in the stabilisation of pulverised fuel flames.

Previous measurements of particle concentration have been obtained from particle counting. Planar nephelometry (a method of measuring concentration based on scattered light) does not appear to have been used for measuring particle distributions in jet flows before, probably because they are subject to errors associated with attenuation of the incident and scattered light beams. Where they are viable, however, planar imaging techniques have the advantage of providing addition information of the instantaneous flow structures, such as regions of local and/or temporal preferential concentration. These issues can not be successfully identified from single point techniques. The effects of particle mass loading on attenuation is therefore of interest, but has also yet to be assessed. The current work provides preliminary data to determine the extent of attenuation for different mass loading ratios.

### Background

Particles suspended in a flow will respond to, and cause disturbances in, the suspending flow. Analysis of the motion of particles in a fluid can be based on the inertia of a particle, using the Stokes number, [7], particle dispersion, using the turbulent Schmidt number [5] and the mass loading ratio [3].

The Stokes number is defined as the ratio of particle relaxation time,  $\tau_p$  to fluidic time scale,  $\tau_f$  [8]

$$St = \frac{\tau_p}{\tau_f} \quad (2)$$

Used to predict how individual particles respond to the localised fluid flow, the Stokes number neglects the influence of surrounding particle induced fluid perturbations.

The turbulent Schmidt is defined as,

$$Sc_p = \frac{\nu_t}{\epsilon_p} \quad (3)$$

where  $\nu_t$  is the effective turbulent kinematic viscosity of the gas and  $\epsilon_p$  is the diffusivity of the particles due to turbulence. Fan *et al.* [5] determined that the influence of mass loading was minimal. They calculated that the turbulent Schmidt number varies only between 1.4 and 1.5 with changes in mass loading over the range of 0.5 to 1.5.

To avoid the above complications, the present investigation into the effects of mass loading on particle dispersion is conducted with fixed values of Stokes number. Instantaneous planar concentration measurements of the particle distribution from the central jet of a co-annular nozzle were recorded for a range of mass loadings up to 17 diameters downstream.

### Equipment

Experiments were conducted in a purpose built open loop wind tunnel with 650mm x 650mm square cross section as shown in figure 1. It is vertically down fired to avoid any bias due to gravity. A bell-mouth inlet and flow conditioning screens (not shown) were used to provide a co-flow with steady and uniform velocity of approximately 8m/s.

Q-Cel™ hollow glass spheres with a particles diameters range from 25-45 microns with a density of approximately 700kg/m<sup>3</sup> were introduced into the central jet via a fluidised bed feeder. Mass loadings were determined by the change in mass of the feeder, as measured by a load cell and fulcrum and recorded on a computer. Calibration of the feeder was conducted before and after each experimental run.

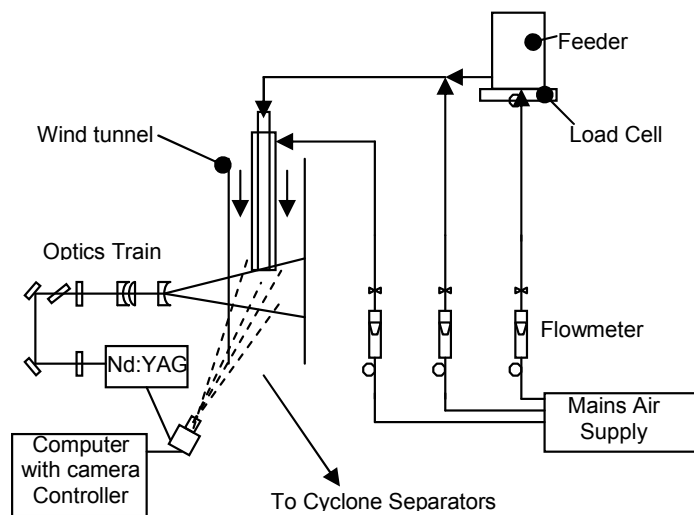


Figure 1. A schematic representation of the experimental layout.

Controlling of the particle mass flow rate was achieved by varying the amount of fluidising air as measured by a Fisher & Porter FP ¼-10-SS flow meter. The resulting variation of total air flow through the central jet was measured to be  $\pm 0.5$ m/s, which equates to less than a 2% error.

The nozzle and dimensions are shown in figure 2. The development length of the central and annular nozzles is in excess of 100 diameters to avoid bias and allow fully developed initial flow. Constant flow velocities of  $U_1 = 42$ m/s and  $U_2 = 73$ m/s were obtained using FP ½-27-G-10/83 with GSVT 44 float and FP-1-27-G-10/83 with a GSVT 64 float. The fluid based momentum ratio ( $G_1/G_2$ ) for the configuration is 0.115. The addition of particles results in a momentum ratio ranging from 0.116 to 0.118. Tabulated data are given in table 1.

A frequency doubled Nd:YAG laser, pulsed at 10Hz was used to produce a light sheet approximately 3mm thick through the central plane of the jet. Light scattering was recorded on a Kodak Megaplug Class 1 CCD, with exposure time of 6.487 msec and trigger by the laser flashlamp. Each experiment yielded 448 images with 10 bit resolution.

### Technique

Instantaneous planar concentration measurements were conducted using planar nephelometry. As the particles are much larger than the laser beam wavelength the Mie scattering theory, as outlined by Becker [9] may not apply. The CCD was aligned at 90 degrees to the incident beam to minimise image distortion. Variations in laser sheet intensity have been accounted for by using a mean image of the laser sheet profile, obtained by filling the tunnel with smoke (with the fan not operating).

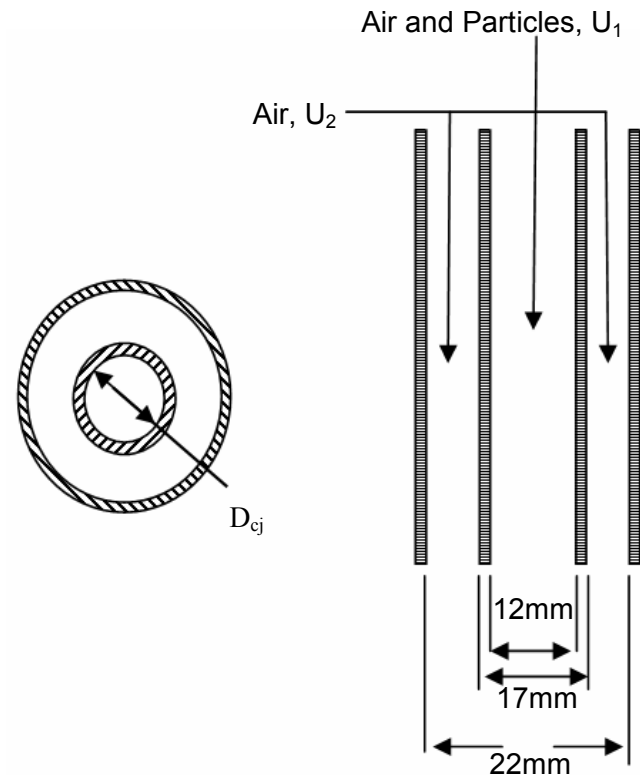


Figure 2. The nozzle design.

### Results and Discussion

#### Centreline Distribution / Decay Rates

Figure 3 presents a set of mean particle distribution images for a range of mass loading ratios. A colour map has been used for clarity.

The higher momentum of the annular jet, relative to the central jet, results in a necking of the flow so that the region of maximum particle concentration is located not at the nozzle exit, but some distance downstream. Figure 4 plots the centreline particle concentration normalised to the maximum concentration for each mass loading ratio. There is a distinct difference between centreline particle decay rates for varying mass loading ratios. Fan *et al.*[5] showed that the higher mass loading cases had a reduction in jet spread, which complements a lower decay rate. The effect of mass loading on the axial location of the peak concentration is presented in figure 5. It can be seen that increasing the mass loading by an order of magnitude causes the location of the maximum concentration to move downstream by almost two nozzle diameters. Mean images shown in figure 3 indicate that the overall shape of the potential core is also elongated by an increase in mass loading. The increase in mass loading ratio equates to an increase of less than 0.5% to the central jet momentum. Particle inertia may have an influence on near field structure, however the current data has isolated mass loading from individual particle inertia.



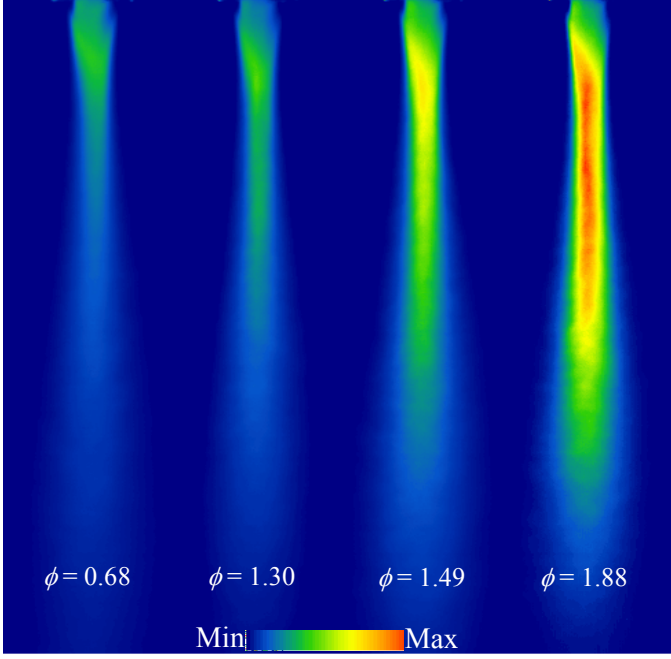


Figure 3. A set of images of the mean particle distributions for, from left to right,  $\phi = 0.68, 1.30, 1.49, 1.88$ . Colour map used to highlight variation in particle concentration.

It is expected that the virtual origin of the jet also depends on the change in mass loading. However, the current data is limited to 15 nozzle diameters downstream so that reliable measurements of the virtual origin cannot be obtained.

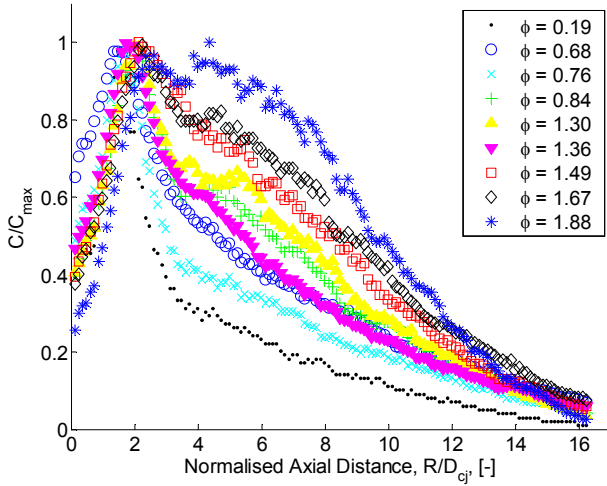


Figure 4. Centreline concentration profiles for all mass loading ratios normalised to the maximum concentration.

### Radial Profiles

Figure 6 shows a series of radial profiles for the  $\phi = 1.30$  case. The concentration has been normalised to the maximum radial concentration. Radial distances ( $R/D_{cj}$ ) have been normalised by the axial distance from the nozzle,  $x/D_{cj}$ , in the absence of an accurate measurement of the location of the virtual origin. Here  $R$  is the radial distance from the centre of the jet,  $D_{cj}$  is the inside diameter of the central jet and  $x$  is the axial distance downstream.

Further downstream, the radial profiles collapse to be self similar. The current findings indicate that the location at which mean similarity begins is approximately 5 diameters from the nozzle. Previous findings [5] only detailed radial profiles between  $x/D_{cj} = 10$  to 30.

At  $x/D_{cj} = 1$  the radial concentration is expected to follow a top-hat profile. The effect of attenuation to the incident beam can be

clearly seen by the asymmetrical concentration with respect to the incident laser sheet as discussed in Errors

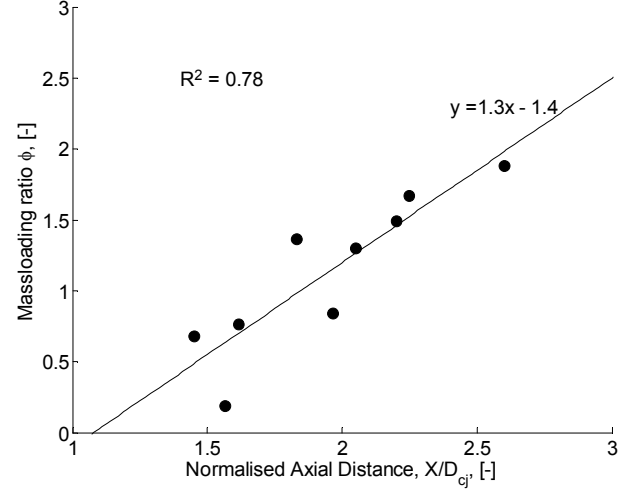


Figure 5. Location of the maximum centreline concentration peak for all mass loading ratios normalised to the exit concentration.

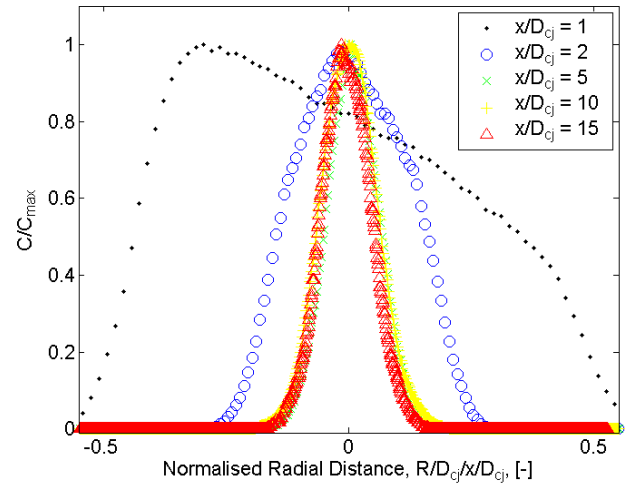


Figure 6. Radial profiles for the case of  $\phi = 1.30$ .

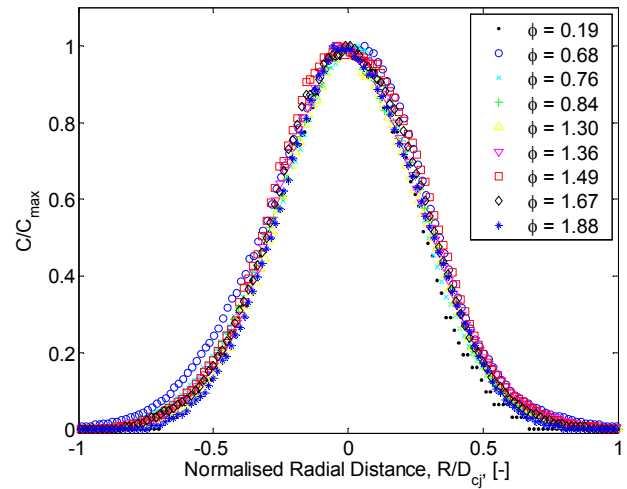


Figure 7. Radial profiles at  $x/D_{cj} = 5$  for varying mass loading ratios.

The radial profiles of the 9 mass loading ratios at  $x/D_{cj} = 5$  are shown in figure 7. Concentration is normalised to the maximum concentration and the radial distance is normalised to the central jet inside diameter. The radial profiles of all mass loadings at  $x/D_{cj} = 10$  and 15 also appear to collapse. However, this does not necessarily contradict the finding of Fan *et al.* [5] that spreading rate decreases with mass loading. Since the location of the virtual origin also shifts with mass loading, the similarity of spread any given axial location cannot be considered in isolation.



## Errors

It is argued that the largest source of error is from attenuation of light which can be seen indirectly the near nozzle regions in figure 3. An increase in mass loading causes an increase in particle volume fraction and surface area, attenuating both the laser beam and the scattered signal.

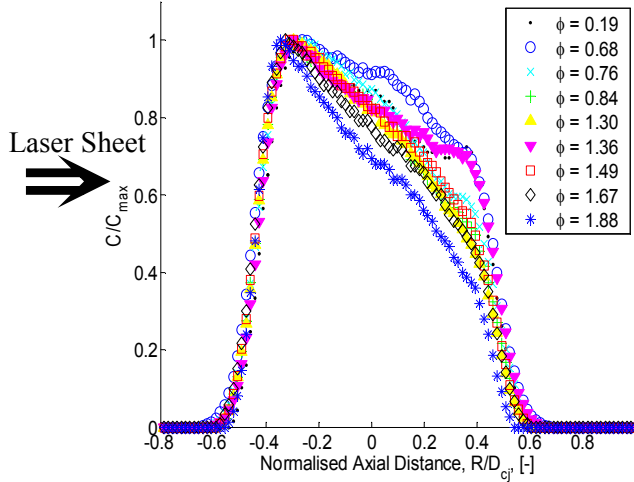


Figure 8. Radial profiles at  $x/D_{cj} = 1$  indicating the attenuation.

Figure 8 presents radial profiles at  $x/D_{cj} = 1$  for the 9 cases. In this region particle concentration is high and therefore any effects of attenuation are severe. Uniform particle concentration and no effects of attenuation would be represented by symmetry about the centreline. A reduction in normalised concentration can be seen from left to right of the graph, the direction the beam travels. The general trend is that lower mass loadings have a lower absolute rate of change of the normalised concentration. If the above mentioned effect was a result of biased particle concentration then the rate of change in normalised concentration of the different loading cases would be similar. Any major bias of particle concentration would also be prominent further downstream, where attenuation effects are reduced by particle dispersion. It can be seen in figure 6, that bias downstream is not significant. Furthermore, during the experimentation, no bias in particle concentration was seen visually.

Flow Conditions		
	Fan <i>et al.</i> [5]	Current work
Particle Diameter	70 microns	25 - 45 microns
Particle Density	1250 kg/m <sup>3</sup>	700 kg/m <sup>3</sup>
Stokes Number	77	37
Central Jet Diameter	40mm	12mm
Annular Jet Diameter	68mm	20mm
Central Jet Velocity	20 m/s	42 m/s
Central Jet Reynolds Number	52,000	28,000
Annular Jet Velocity	30 m/s	73 m/s
Annular Jet Reynolds Number	134,000	110,000

Table 1. Particle and flow data of current work and that of Fan *et al.* [5].

## Conclusions

The effects of particle mass loading on particle concentration in co-annular jets have been assessed. Planar nephelometry was used to investigate mass loading ratios ranging from  $\phi = 0.19$  - 1.88 at fixed fluid velocities and particle Stokes numbers. Data of the first 15 nozzle diameters downstream have yielded the following observations:

- 1) A necking region occurs downstream from the nozzle exit where the particle concentration increases significantly above the exit value.
- 2) The length of the “potential core” region of uniform concentration increases by almost two diameters with an order of magnitude increase in mass loading.
- 3) The mean rate of centreline particle concentration decreases with increase mass loading.
- 4) The mean radial profiles are approximately self similar beyond  $x/D = 5$  for each mass loading investigated.
- 5) For the present particles, the effects of attenuation on measurement accuracy are diminished beyond  $x/D_{cj} = 2$ .

## Acknowledgments

The authors acknowledge the financial assistance provided to this project by the Australian Research Council through its large grant scheme.

The authors also thank Mr Grant England, Miss Sarah Crook and Mr Billy Constantine of the School of Mechanical Engineering, The University of Adelaide, Adelaide, for the assistance with data collection and analysis.

## References

- [1] Wall, T.F., Nguyen, H., Subramanian, V., Mai-Viet, T. and Howley, P., Direct Measurements of the Entrainment by Single and Double Concentric Jets in the Regions of Transition and Flow Establishment, *Trans. IChemE*, **58**, 1980, 237-241.
- [2] Fan, J., Zhang, X., Chen, L. and Cen, K., New Stochastic Particle Dispersion Modeling of a Turbulent Particle-Laden Round Jet, *Chem. Eng. J.*, **66**, 1997, 207-215.
- [3] Di Giancinto, M., Sabetta, F., and Piva, R., Two-Way Coupling Effects in Dilute Gas-Particle Flows, *J. of Fluids Eng.*, **104**, 1982, 304-312.
- [4] Fan, J., Zhao, H. and Cen, K., An Experimental Study of Two-Phase Turbulent Coaxial Jets, *Exp. Fluids*, **13**, 1992, 279-287.
- [5] Fan, J., Zhao, H. and Cen, K., Particle Concentration and Size Measurements in Two-Phase Turbulent Coaxial Jets, *Chem. Eng. Comm.*, **156**, 1996, 115-129.
- [6] Black, D.L., and McQuay, M.Q., Laser-based Particle Measurements of Spherical and Nonspherical Particles, *Int. J. Multiphase Flow*, **27**, 2001, 1333-1362.
- [7] Aggarwal, S., Relationship between Stokes Number and Intrinsic Frequencies in Particle-Laden Flows, *AIAA J.*, **32**, 1993, 1322-1324.
- [8] Kulick, J.D., Fessler, J.R., and Eaton, J.K., On the Interactions between Particles and Turbulence in a Fully-Developed Channel Flow in Air, *Internal Report Stanford University, Stanford, California*, **MD-66**, 1993.
- [9] Becker, H.A. Mixing, Concentration Fluctuations, and Marker Nephelometry, in *Studies in Convection, Vol 2. Theory, Measurements and Applications*, editor, Launder, B.E., Academic Press, 1977, 45-139.

## Flow visualisation of forced flow control over inclined aerofoils

K.L. Powell, K. Parker and J. Soria

Laboratory for Turbulence Research in Aerospace and Combustion (LTRAC)

Mechanical Engineering Monash University

Clayton Campus, Victoria, 3800 AUSTRALIA

### ABSTRACT

Dye Flow visualisation experiments are used to investigate the forced flow around a symmetrical aerofoil at various angles of attack. An oscillating cylinder upstream of the aerofoil provides the flow forcing at a Strouhal number of 0.2 and Reynolds number ( $Re$ ) of 290, based on the cylinder diameter. The effect of the upstream forcing frequency of the flow is achieved by oscillating the upstream cylinder at its natural shedding frequency. This effect is investigated for various spacing ( $l/d$ ) between the cylinder and aerofoil. Two spacing cases, 2 and 10 diameter are presented here at a pre-stall, stall and post stall angles of attack of  $7^\circ$ ,  $12^\circ$  and  $17^\circ$  respectively. These visualisations suggest a degree of control that allows manipulation of the downstream flow structure through an upstream-induced mechanism.

### INTRODUCTION

In nature certain species of cetaceans are able to utilise the effect of upstream oscillatory flow conditions to improve their propulsive efficiency. This effect is known as the Katzmayer effect, and was described in 1922 by the Austrian Aerodynamicist Dr Katzmayer. It was noted by [4] that an oscillating wind could reduce the drag on an aerofoil. The Katzmayer effect utilises an upstream oscillating flow condition to reduce aerofoil drag.

It was noted by Tokumaru et al. [5] that a circular cylinder undergoing rotary oscillations about a fixed axis of symmetry can exert a degree of control over the structure of the wake. The wake produced by cylinders in cross flow is known as a von Karman vortex street and is made up of equally spaced vortices of the same strength but alternating in sign. As lift and drag forces are caused by vortex shedding at the surface of the cylinder, the structure of the wake is strongly dependent on the driving frequency of the cylinder. From previous studies it has been found that the frequency of these vortex shedding can be characterised by a dimensionless parameter, the Strouhal number. For a cylinder the Strouhal frequency is approximately 0.21 for any Reynolds number greater than 400. Moretti [3] showed that under forced oscillation two frequencies of vortex shedding exist: one being the same frequency as the unforced cylinder and the other at the forcing frequency.

Experimental studies on cylinders in lock-on synchronisation by Jarza et al. [2] has concluded that oscillations in the incident flow alter the geometry of the vortex street behind an aerofoil. Aerofoils naturally produce lift. Thus the application of the Katzmayer effect on an aerofoil arrangement provides significant potential for application in aerodynamics and hydrodynamics.

Gopalkrishnan et al. [1] experimented with a heaving and pitching NACA0012 aerofoil downstream of a transversely oscillating cylinder. The separation distance between the aerofoil and cylinder was sufficient not to interfere with the vortex formation. In the experiments, the phase between heave and pitch oscillations was varied. The results of these experiments suggested three primary

modes of interaction between the separated flow from the cylinder and the aerofoil.

The work presented in this paper is part of a study to characterise the nature of the interaction between the controlled upstream shedding process on the downstream wake behaviour over an aerofoil. The results presented here describe unique features observed in the tandem arrangement. The effects of an initial angle of attack on a stationary aerofoil, as well as the effect of an aerofoil oscillating at multiples of the Strouhal frequency of the cylinder will be examined, and changes in the cylinder centre to aerofoil leading edge ratio.

The purpose of this investigation is to gain a qualitative understanding through dye flow visualisation, the interactions of periodic disturbances of the incident stream with various parameters as a form of active control for potential thrust optimisation.

### EXPERIMENTAL APPARATUS

The experiments were performed in a re-circulating water tunnel at the LTRAC laboratories at Monash University. The tunnel has a five metre long working section, measuring 500mm x 500mm in cross section. The Reynolds number, based on a cylinder diameter of 9.6mm and the steady post acceleration flow velocity of 30mm/s, is equal to 298. Figure 1 shows a schematic drawing of the water tunnel layout.

A cylinder of diameter,  $d = 9.6\text{mm}$  was used to form the von Karman vortex street. Downstream a NACA0012 aerofoil with chord,  $c = 12\text{mm}$  and  $AR = 5.63$ , with a maximum thickness,  $t$ , equal to the cylinder diameter,  $d = t = 9.6\text{mm}$  was used. The aerofoil has an angle of incidence to the freestream of 7 degrees, 12 degrees and 17 degrees. The cylinder contains two dye holes separated by 30 degrees, allowing dye traces in both directions above and below the aerofoil. An optical trigger is used to determine the centre position for both the cylinder and aerofoil. A motion control program was developed to allow controlled, timed shedding of the vortices from the cylinder by oscillating the cylinder at its natural Strouhal frequency. The aerofoil and cylinder are vertically mounted from above the test section. The current experimental setup allows for synchronised oscillations of the downstream aerofoil with the upstream cylinder. The spacing between the aerofoil aerodynamic centre (quarter chord location) and cylinder centre is divided by the cylinder diameter,  $L/d$  (spacing/diameter) and is varied to 2, and 10.

The cylinder is oscillated by a stepper motor capable of 80 000 micro-steps per revolution. The stepper motor drivers are controlled by TTL pulses from a Parker AT6400 Indexer. The in-house software allows various oscillation profiles to be achieved by the

cylinder. In the data presented here, the cylinder oscillates sinusoidally accordingly:

$$\theta = \theta_0 \sin(\omega t)$$

where:  $\theta_0 = 10^\circ$ ,  $\omega$  = frequency of oscillation. Dye is used in order to visualise the behaviour of the flow. The dye is introduced gently into the flow using a needle valve arrangement. Blue and red, are used to highlight the interaction of the upstream disturbance on the wake produced by the aerofoil. Dye flow visualisation is a particle tracing technique, thus the dye follows the path lines in the flow. In an unsteady flow the path lines do not coincide with the instantaneous streamlines and so one must use caution when trying to identify flow features such as vortices. Despite this, dye flow visualisations can provide an idea about the structure of the flow and can be used as a basis to determine areas where more detailed quantitative study can be useful.

The flow is captured on a SONY 120x digital zoom video recorder. In order to adequately capture the field of view the camera is mounted horizontally below the test section. A 45 mirror is used to capture the flow in a wingtip view of the aerofoil and cylinder. In order to identify the phase at which the flow images are captured an optical trigger is used to actuate a LED in the captured video images. Using MGI video wave III, images can be acquired at different phases of the oscillating cylinder from the captured video.

## RESULTS AND DISCUSSION

Tests with a circular cylinder in cross flow with forced and unforced oscillation were performed and can be seen in Figures 2 and 3 respectively. It has been shown that oscillating a cylinder at its natural frequency produces controlled timing of the release of vortices behind the cylinder and that two separate frequencies of shedding exist. It can be seen here that the applied forcing on the cylinder appears to form more compact vorticity then compared to the un-forced cylinder, suggesting more intense vorticity that dissipates further downstream due to viscosity when compared to the unforced case. This is in agreement with Moretti [3] who noted that two frequencies of vortex shedding exist at the same time and coexists for a region downstream before other instability affect their superposition and the flow is reorganised into the two vortex patterns. Thus for forcing at the natural Strouhal frequency the superposition of the vortices would suggest more intense vorticity which was observed in the experiments.

In order to compare the effect of the oscillatory flow on the aerofoil, the streamlines of the aerofoil alone was first investigated at a pre-stall, stall and post-stall condition. The stall angle for a NACA 0012 aerofoil is 12 degrees. It was chosen to examine the effect of the stall condition and condition  $\pm 5^\circ$ . Figure 4 a-c shows the aerofoil at an angle of incidence of 7 degrees, 12 degrees and 17 degrees respectively.

Figure 5, Figure 6 and Figure 7 represents the evolution of a forced oscillatory flow on an aerofoil inclined at seven, twelve and seventeen degrees respectively at 2 diameter spacing at a regular interval through one period of forcing.

The forcing of the cylinder on an aerofoil at 2 diameter spacing causes a stagnation region to exist between the aerofoil and the cylinder. The forcing of the cylinder appears to pulse the stagnation region and shedding can be seen above and below the aerofoil,

although the majority of the dye flow travels above the cylinder. Regions of more intense dye concentration can be seen at periodic spacings downstream along the surface of the aerofoil. The flow appears to stay attached over the entire surface of the aerofoil at all angles of attack, even when the aerofoil is at its characteristic stall angle, twelve degrees. The evolution of the flow as seen in Figure 5-8 is quite similar in structure suggesting repetitious conditions. The mixing of the dyes in the flow visualisation suggest some interaction/mixing between the oscillatory flow and flow from the aerofoil. The flow structure for the forced flow over the aerofoil at the various angles of attack are similar; however the size of the flow structure over the aerofoil increases with increasing angle of attack.

The two-diameter spacing appears to be advantageous in increasing the angle of attack without stall. At this spacing the usual von-Karman vortex street associated with cylinders in cross flow cannot be seen. However, a periodic train of vortices travel down the surface of the aerofoil. The oscillatory flow appear to promote increased mixing down the surface of the aerofoil due to the slower fluid at the boundary layer surface mixing with the free stream velocity, re-energising the boundary layer. In the twelve and seventeen degree angle of attack case the effect of the vortex train acts to promote reattachment of the separated flow by removing the velocity deficit at the boundary layer, delaying stall.

Figure 8, Figure 9 and Figure 10 represents the evolution of a forced oscillatory flow on an aerofoil inclined at seven, twelve and seventeen degrees respectively at 10 diameter spacing at a regular interval through one period of forcing.

The 10 diameter spacing shows various forms of flow that differs from the 2 diameter spacing case. As the angle of incidence increase over this spacing, the wake profile becomes larger. A lower frequency disturbance is notable in the flow at the higher angles of attack (twelve degrees and seventeen degrees) that sinusoidally oscillated the von Karman vortex street. This effect is more prominent as the angle of attack increases and is most likely due to the upstream effect of the stalled aerofoil. Less mixing is evident between the flow from the leading edge and the oncoming vortex street compared with the tow diameter spacing case. This flow does not look as favourable as the 2 diameter spacing case and is most likely due to the dissipation of vorticity in the von-Karman vortex street, disabling penetration of the boundary layer.

## CONCLUSION

This present experimental study suggests through flow visualisation that it is possible to alter the lift coefficient in pre-stall and post-stall cases via an upstream oscillatory disturbance. The 2 diameter spacing appeared to be the most favourable condition for increase of the stall angle, as the flow still remained attached down a portion of the aerofoil at the 17 degree case. An increase in the spacing revealed that stall occurred earlier than in the 2 diameter spacing case. However, a secondary lower frequency disturbance is evident at the higher angles of attack, twelve and seventeen degrees, which made the flow pattern unsteady with time, producing an oscillating von-Karman vortex street. This effect attached and separated the flow from the surface of the aerofoil at this lower secondary frequency. The von-Karman vortex street oscillated at an angle of  $\pm 30$  degrees to the free stream.

## REFERENCES

- [1] Gopalkrishnan, R., Triantafyllou, M.S., Triantafyllou, G.S. & Barrett, D., Active vorticity control in a shear flow using a flapping foil., *Jour. Fluid Mech.*, **Vol 7, No. 2**, 1994, 1-21.
- [2] Jarza, A. & Podolski, M., (2004) Turbulence structure in the vortex formation behind a circular cylinder in lock-on conditions, *Euro. Jour. Mech. B/Fluids.*, **Vol 23**, pp.535-550.
- [3] Moretti, P..M., Flow induced vibrations in arrays of cylinder, *Ann. Rev. Fluid Mech.*, **25**, 1993, 99-114.
- [4] Ober, S. (1925) Note on the Katzmayr effect on aifoil Drag, *NACA.*, **No. 214**.
- [5] Tokumaru, P.T. & Dimotakis, P.E., Rotary oscillation control of a cylinder wake, *Jour. Fluid Mech.*, **Vol 224**, pp.77-90.

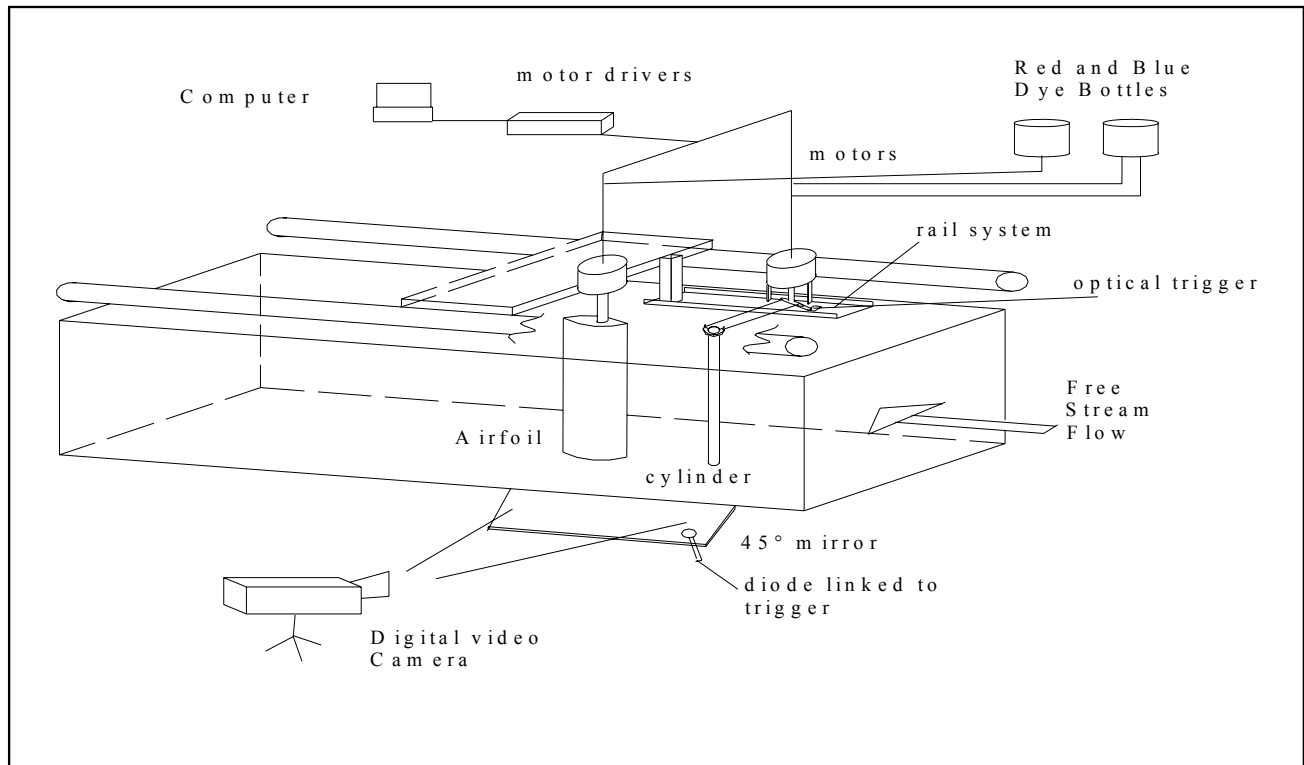


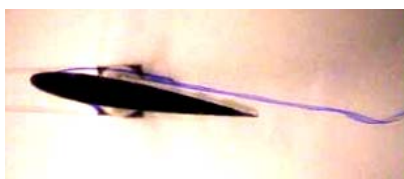
Figure 1: Experimental Setup.



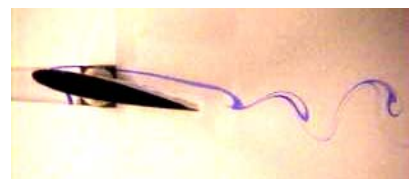
Figure 2: Flow visualisation of the von Karman vortex street produced by forced flow behind a cylinder in cross flow.



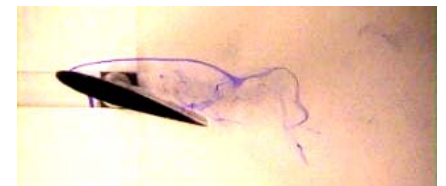
Figure 3: Flow visualisation of the von Karman street formed behind a cylinder in cross flow.



(a)



(b)



(c)

Figure 4 (a-c): Flow visualisation of a NACA0012 aerofoil at 7, 12 and 17 degree angle of attack respectively.





Figure 5: Evolution of the interaction of a forced oscillatory flow with a NACA 0012 aerofoil at a seven degree angle of attack and two-diameter spacing.



Figure 6: Evolution of the interaction of a forced oscillatory flow with a NACA 0012 aerofoil at a twelve degree angle of attack and two-diameter spacing.



Figure 7: Evolution of the interaction of a forced oscillatory flow with a NACA 0012 aerofoil at a seventeen degree angle of attack and two-diameter spacing.



Figure 8: Evolution of the interaction of a forced oscillatory flow with a NACA 0012 aerofoil at a seven degree angle of attack and ten-diameter spacing.



Figure 9: Evolution of the interaction of a forced oscillatory flow with a NACA 0012 aerofoil at a twelve degree angle of attack and ten-diameter spacing.



Figure 10: Evolution of the interaction of a forced oscillatory flow with a NACA 0012 aerofoil at a seventeen degree angle of attack and ten-diameter spacing.



## 15th Australasian Fluid Mechanics Conference: On Collective Oscillations of Bubble Chains and Arrays

E. M. B. Payne<sup>1</sup>, R. Manasseh<sup>2</sup> and A. Ooi<sup>3</sup>

<sup>1</sup>The University of Melbourne, VIC, 3010 AUSTRALIA

<sup>2</sup>CSIRO Manufacturing & Infrastructure Technology

Energy and Thermofluids Engineering, Highett, VIC, 3190 AUSTRALIA

<sup>3</sup>Department of Mechanical and Manufacturing Engineering  
The University of Melbourne, VIC, 3010 AUSTRALIA

### Abstract

A number of different models have previously been developed to describe the collective oscillatory behaviour of gas-filled bubbles in a liquid medium. In this paper we perform an eigenanalysis on two mathematical models and discuss which is more physically realistic for the case of a chain of bubbles. The modal structures of both a bubble chain and bubble array are investigated, as well as the corresponding complex eigenfrequencies. For the case of two spherical bubbles located between two rigid parallel plates, we show how the eigenfrequencies change as the plate spacing is varied.

### Introduction

Much work has been done towards the development of a model to describe the oscillations of gas bubbles in a liquid domain [1, 2, 3, 4, 5, 6], mostly analysing pairs of bubbles. The acoustically-coupled volumetric oscillations of bubbles are relevant in many fields, such as process engineering, ocean physics, microtechnology and medicine. Two different models for an arbitrary number of bubbles will be considered in this paper. The first model follows from work done by Manasseh *et al* [8], which has been developed for the particular case of a chain of bubbles. The second model, what we will call the standard model, is a simplified version of Feuillade's model [7], based on the theory of Tolstoy [2], and is applicable for any general configuration of bubbles. Both models appeared capable of predicting basic experimental trends [8, 9]. The models are discussed in the theory section of this paper. Numerical solutions for the eigenmodes and eigenfrequencies of a bubble chain are generated using each model. The results are compared and contrasted so that the most physically realistic model can be used.

We then look at an array of bubbles using the simplified standard model. A few modal structures are shown graphically, for the case of a square array of bubbles. The standard model is then modified to account for the presence of two rigid parallel plates between which two bubbles are trapped. The plates are modelled using the method of images. Using this very simplistic approach, we show that as the plates are brought together, the resonant frequencies (symmetric and asymmetric) decrease, which follows from work done by Strasberg [10]. The paper concludes with a summary of findings and outlines further work that is presently underway.

### Theory

All the models used in this paper can be written in the following form:

$$\mathbf{M}\ddot{\mathbf{X}} + \mathbf{C}\dot{\mathbf{X}} + \mathbf{K}\mathbf{X} = \mathbf{0}, \quad (1)$$

where  $\mathbf{M}$ ,  $\mathbf{C}$ , and  $\mathbf{K}$  represent inertial, damping, and stiffness matrices respectively and  $\mathbf{X}$  is related to a differential bubble radius (i.e., the difference between the instantaneous and equilibrium bubble radii).

Each model described below represents a system of second order differential equations with constant coefficients, the solution of which is harmonic in nature. Furthermore, equation 1 is a homogeneous equation (there is no driving term on the RHS) since we only require the natural frequencies and natural modes of a given bubble configuration. The coefficient matrices are determined by the assumptions made about the coupling between bubbles in the chain. For simplicity, it is assumed that all bubbles have equal radii.

### Model 1

This is the model proposed by Manasseh *et al* [8]. To enable comparison with the standard model, equation 4 of [8] is reproduced here, and called Model 1A,

$$\ddot{\delta}_i + b_i \dot{\delta}_i + \omega_{0i}^2 \delta_i = - \sum_{j \neq i} \frac{R_0}{s_{ji}} \left( \omega_{0j}^2 \delta_j + b_j \dot{\delta}_j \right), \quad (2)$$

where  $\delta$  is the change in bubble radius from an equilibrium radius  $R_0$ ,  $b = \omega_0^2 R_0 / c$  is a radiative damping term,  $\omega_0$  is the radian frequency of a single, linearly oscillating spherical bubble in an unbounded liquid,  $s_{ji}$  denotes the spacing between centres of bubbles  $i$  and  $j$ , and  $c$  is the speed of sound in the liquid.

Model 1 was derived by assuming the coupling is due to the monopole superposition of the pressures from other bubbles. The bubbles can in principle have finite radii, whereas in the standard model, the bubbles are essentially point sources. Furthermore, there are no coupling terms arising from the velocity fields of neighbouring bubbles. In the course of Model 1's derivation, the liquid was first assumed to have a finite compressibility, and the compressibility was then made negligible. However the sign of the coupling term was negative because the bubbles were assumed from the outset to oscillate in a perfectly incompressible liquid. This appears to be an inconsistency, but since Model 1A had predicted experimental data, it was not clear if Model 1A was inappropriate. A self-consistent version is Model 1B,

$$\ddot{\delta}_i + b_i \dot{\delta}_i + \omega_{0i}^2 \delta_i = \sum_{j \neq i} \frac{R_0}{s_{ji}} \left( \omega_{0j}^2 \delta_j + b_j \dot{\delta}_j \right), \quad (3)$$

and in this paper, both 1A and 1B will be analysed to judge which is more appropriate.

### Model 2

The model developed by Feuillade [7] was simplified by assuming that the acoustic wavelengths are much larger than the spacing between bubbles (effectively also neglecting liquid compressibility). Equation 7 in [7] has also been arranged to have the same form as equations 2 and 3 above, yielding:

$$\ddot{\delta}_i + b_i \dot{\delta}_i + \omega_{0i}^2 \delta_i = - \sum_{j \neq i} \frac{R_0}{s_{ji}} \left( \ddot{\delta}_j \right). \quad (4)$$

Feuillade couples each bubble by scattered pressure fields from all other bubbles and then relates the pressure to the inertial mass of each bubble. This effectively couples the bubbles by velocity fields assumed continuous throughout a multiphase domain. Inherent in the model is that the bubbles act as radiating point sources. The pressure due to damping stress from other bubbles is not included. As an aside, this model is identical to that of Hsiao *et al* [5] when damping is neglected.

### Numerical Method

A computer program was developed to find the eigenvalues (eigenfrequencies) and eigenvectors (eigenmodes) for a system of differential equations of the form given by equation 1. To do so, the system of equations was converted into state-space coordinates of the form:

$$\dot{\mathbf{Z}} = \mathbf{AZ}, \quad (5)$$

where

$$\mathbf{Z} = \begin{bmatrix} \mathbf{X} \\ \mathbf{Y} \end{bmatrix}, \quad \mathbf{Y} = \dot{\mathbf{X}}, \quad \mathbf{A} = \begin{bmatrix} \mathbf{0} & \mathbf{1} \\ -\mathbf{M}^{-1}\mathbf{K} & -\mathbf{M}^{-1}\mathbf{C} \end{bmatrix}. \quad (6)$$

The program makes use of the numerical routines in *Numerical Recipes in C* as well as *CLAPACK* routines and libraries to calculate the eigenvalues and eigenvectors of equation 5. The required output was coded in C so as to produce a MATLAB-readable file (i.e., an M-file). The M-file was run in MATLAB to produce the plots shown in this paper.

The program reads an input file containing parameters of interest (e.g. bubble size, bubble separation, number of bubbles in the chain, etc.), creates the coefficient matrices from these values and according to the desired model, constructs the state-space matrix, then calculates the eigenvalues and eigenvectors.

### Chains of Bubbles

A number of interesting plots were generated to show the similarities and differences between the models using a chain of bubbles. Firstly, the program was tested for the case of an undamped two-bubble chain to see if it reproduced the analytic natural frequencies. Once the numerical output was verified, the chain was extended to thirty bubbles, and plots of the modal structures were generated.

#### Two-bubble Chain

For Model 1A the analytic low-frequency eigenmode is given by,  $\omega_1 = \sqrt{(1 - R_0/s)}\omega_0$ , while the high-frequency mode is given by,  $\omega_2 = \sqrt{(1 + R_0/s)}\omega_0$ . For the standard model,  $\omega_1 = \omega_0/\sqrt{(1 + R_0/s)}$  and  $\omega_2 = \omega_0/\sqrt{(1 - R_0/s)}$ . Figures 1 and 2 show the agreement between the analytical expressions and the numerical values generated by the program, as a function of the ratio of bubble separation to bubble radius, for each model.

As expected, figures 1 and 2 have the same general behaviour. The most important point is that the models break down when the bubbles are brought close together (the two natural frequencies rapidly diverge). In reality the bubbles would coalesce to form a single, larger bubble. (For a physical intuition behind the frequency shift of the two modes see [7].)

#### Eigenmodes for a Chain of Thirty Bubbles

Figures 3 and 4 show the first five consecutive modes with every fifth mode shown thereafter, for a chain of thirty bubbles. A bubble radius of 2.605 mm was used in the computation and the bubble separation was calculated such that all thirty bubbles fit within a chain of length 0.535 m. The centreline on each

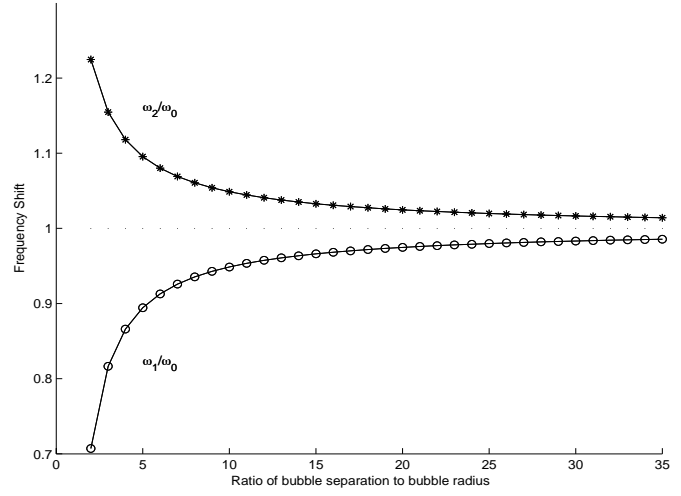


Figure 1: Frequency shifts of the natural frequencies for a two-bubble chain using Model 1A. The horizontal axis represents a non-dimensional ratio scaled in terms of bubble radii. The vertical axis scales the modal resonance frequency relative to the resonance frequency of a single bubble in free space. The solid lines represent the analytic solutions. The points denoted “o” and “\*” are the results from the numerical eigenvalue solver.

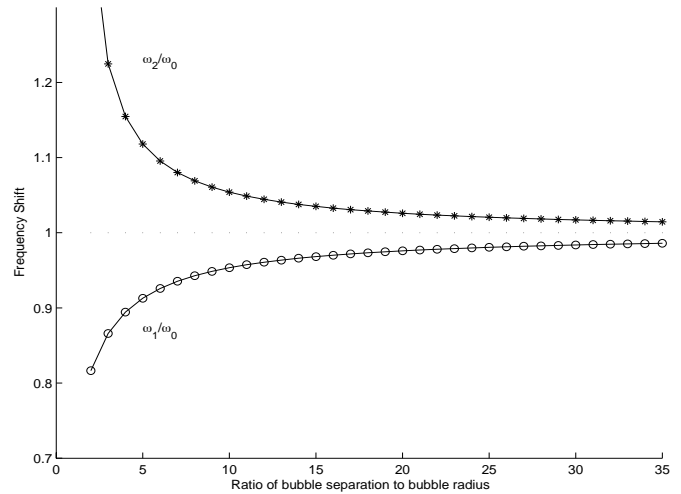


Figure 2: Frequency shifts of the natural frequencies for a two-bubble chain using Model 2. The same notation as shown in figure 1 is used.

plot represents the condition where bubble radii are at equilibrium. Also note that damping has been neglected since it has very little effect on the modal structures. Here we see a fundamental difference between models. For Model 1A, the lowest frequency mode corresponds to the most complicated mode structure, whilst the highest frequency mode corresponds to the simplest eigenmode (in which all bubbles oscillate in phase). This is contrary to physical intuition. For the standard model, however, the opposite is true; the lowest frequency mode corresponds to the simplest eigenmode, whilst the highest frequency mode corresponds to the most complicated mode. This is true of most harmonic situations (e.g. harmonics of a plucked string). When Model 1B is used, the eigenmode structure has a form consistent with physical intuition, like that of Model 2.

Also worth noting is that the bubbles towards the ends of the chain oscillate at a lower amplitude than those in the middle. This is analogous to a system of masses connected by springs, in which the masses in the middle have more flexibility than those on the end.

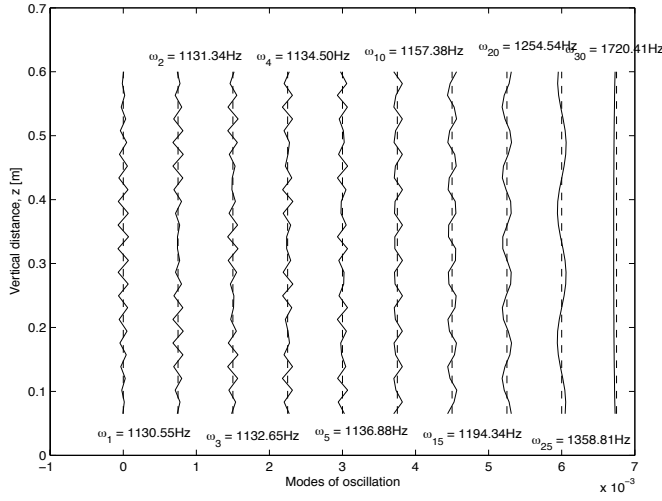


Figure 3: Modal structures for Model 1A for a chain of thirty bubbles. A chain height of 0.535 m was used. The lowest frequency mode has the most complicated mode structure. The highest frequency mode occurs when all bubbles oscillate in phase.

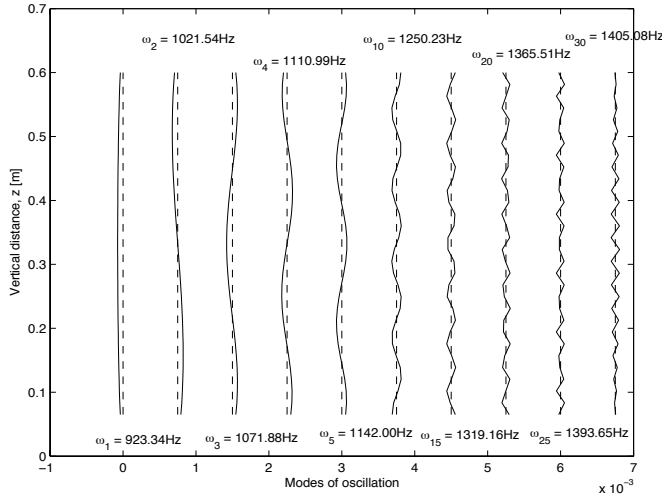


Figure 4: Modal structures for Model 2 for a chain of thirty bubbles. A chain height of 0.535 m was used. The lowest frequency mode has the simplest mode structure and corresponds to all bubbles oscillating in phase.

For each of Models, 1A, 1B and 2, it can be shown that the low-frequency mode is less damped than the high-frequency mode. This agrees with physical intuition that low frequency oscillations generally survive longer than higher frequency oscillations; the model of Hsiao *et al* [5] predicts the opposite. An interim conclusion is that Model 2 is both physically realistic and self-consistent and should be used in preference, although more comparison with experiment is warranted.

#### Arrays of Bubbles between Parallel Plates

This section of work is based on the standard model approach to the coupling between spherical bubbles. This model was used because it can be easily extended to any configuration of bubbles. However, it does mean that the bubbles are modelled as point sources, and so the model is invalid when the bubbles become too close.

To simulate the presence of top and bottom plates, the method of images was used. The configuration for the case of two bubbles is shown in figure 5. The plates are simulated by the presence of bubble images and therefore act as mirrors. Each bubble im-

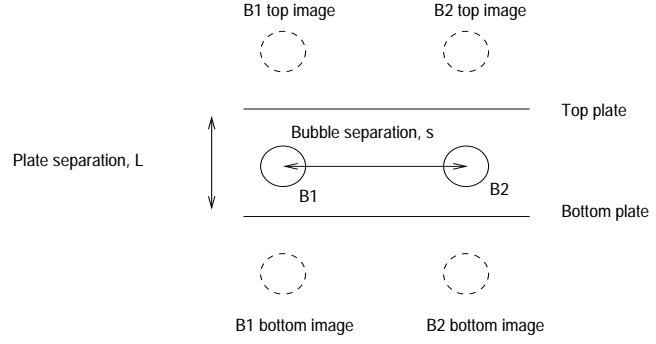


Figure 5: Configuration of the bubble image model for two bubbles, B1 and B2.

age is in phase with its respective original (i.e., B1's top and bottom images are in phase with itself). Note that only primary images have been considered. In fact, for a source between parallel plates the streamfunction is made up of an infinite series of images. Neglecting the other images is justified since they are further away and thus have less effect on the mass loading of the surrounding fluid.

To generate meaningful results, the first task was to modify the numerical code developed earlier (for the bubble chain) for the case of a bubble array with no images. This involved re-specifying the spacing between each and every bubble so as to produce an array rather than a chain configuration. An example of some of the eigenmodes that can be generated from such a configuration is shown in figure 6. This plot represents the situation in which the plates are infinitely far apart.

The standard model was then modified to include the presence of the bubble images. This meant adding extra inertia terms (due to the bubble images) to each bubble between the plates. The result was a set of  $N$ -coupled equations describing the oscillation of an  $N$ -bubble array between plates. The numerical code was adapted to take this into account by altering the inertia matrix.

The effect of the plate separation on the resonant frequencies is best shown for the case of two bubbles. This is shown in figure 7. As the ratio of plate separation to bubble radius ( $L/R_0$ ) decreases, the two resonant frequencies decrease. This is supported by work done by Strasberg [10], in which he looks at the effect of a rigid boundary on the pulsation frequency of a spherical bubble. An intuitive way of explaining the above result is that the presence of the bubble images oscillating in phase with the original bubbles increases the mass loading, retards the motion and therefore reduces the resonant frequencies [7].

#### Conclusions

We have performed an eigenanalysis to determine the eigenfrequencies and eigenmodes of spherical bubbles in both chain and array configurations. The models assume that the bubbles are of identical radii and oscillate linearly, remaining spherical in form. For small ratios of bubble separation to bubble radius, the models clearly break down.

In comparing the two models, it has been noted that Model 2, the standard model, assumes that the bubbles act as point sources, whereas this assumption is not necessary for Model 1. From a physical point of view, both models agree with the intuition that lower frequency oscillations survive longer than higher frequency ones. However, considering the eigenmode structures for a chain of bubbles, Model 2 agrees with what is generally seen in nature (the lowest frequency mode has the simplest structure and the highest frequency mode the most

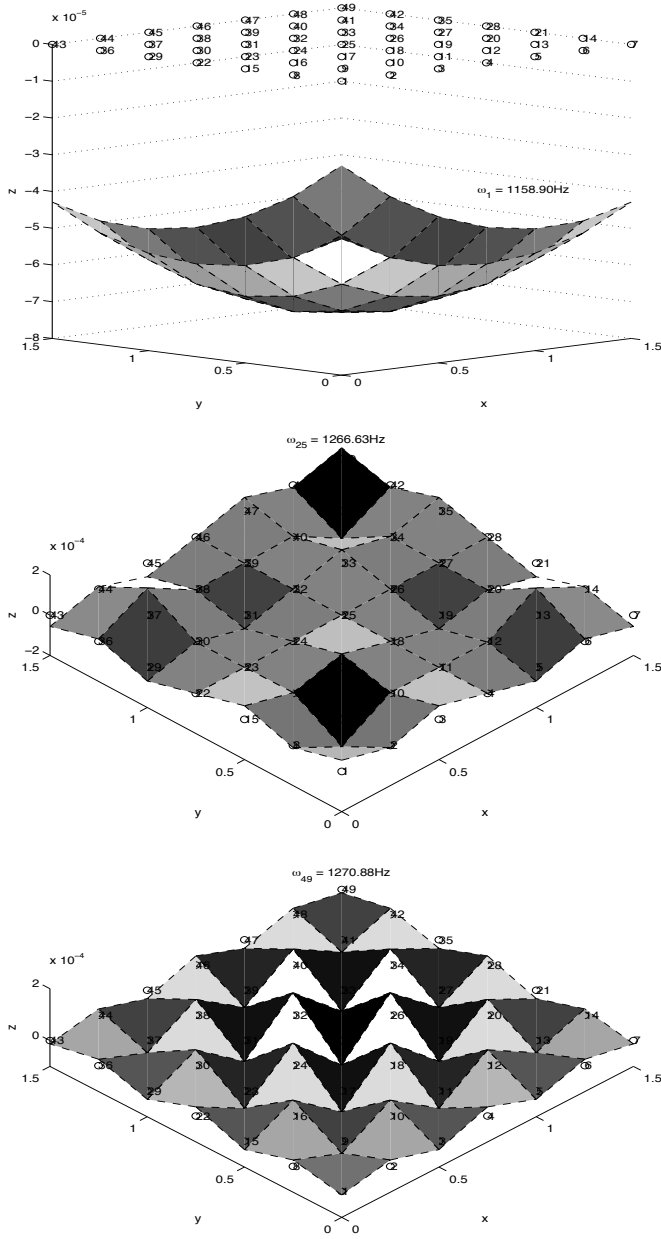


Figure 6: Eigenmode structures for the 1st, 25th and 49th modes of a  $7 \times 7$  array of 49 bubbles. This was generated for identical bubble radii of 2.605 mm and without damping. The spacing between bubble 1 and bubble 2 is 0.25 m.

complex), whereas Model 1A predicts the opposite. A corrected version of Model 1, Model 1B, removes this problem. An interim conclusion is that the ‘standard’ Model 2 should still be used.

For the case of two bubbles bounded by parallel plates, we have shown that the resonant frequencies decrease as the plates are brought closer together. However, the analysis becomes inappropriate for small plate spacings, where the bubbles would no longer be spherical. On this note, current work in progress is aimed at investigating the resonant frequencies of bubbles which are trapped between parallel plates, not just bounded by them. Thus the bubbles are shaped more like cylinders than spheres. This work will hopefully determine what happens to the resonant frequencies of such bubbles as the plate spacing is varied. To some extent, the modified standard model for the case of two bubbles bounded by parallel plates offers some guidance for this work.

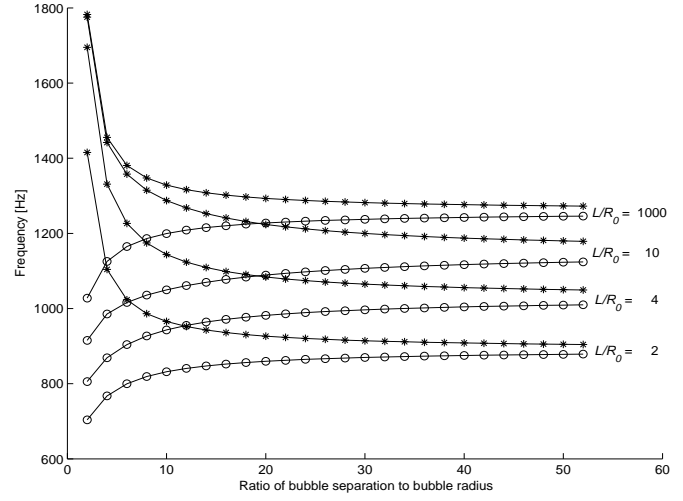


Figure 7: The resonant frequency curves for the two modes as plates with dimensionless spacing  $L/R_0$  are brought closer together. This was generated for identical bubble radii of 2.605 mm and without damping.

### Acknowledgements

The authors would like to thank CSIRO Manufacturing & Infrastructure Technology for providing financial assistance towards this work. Alexander Doinikov of the Byelorussian State University, Belarus, provided important insight.

### References

- [1] Zabolotskaya, E. A., Interaction of gas bubbles in a sound field, *Sov. Phys. Acoust.*, **30**(5), 1984, 365–368.
- [2] Tolstoy, I., Superresonant systems of scatterers. I., *J. Acoust. Soc. Am.*, **80**(1), 1986, 282–294.
- [3] Ogüz, H. and Prosperetti, A., A generalization of the impulse and virial theorems with an application to bubble oscillations, *J. Fluid Mech.*, **218**, 1990, 143–162.
- [4] Doinikov, A. A. and Zavtrak, S. T., On the mutual interaction of two gas bubbles in a sound field, *Phys. Fluids*, **7**(8), 1995, 1923–1930.
- [5] Hsiao, P.Y., Devaud, M. and Bacri, J.C., Acoustic coupling between two air bubbles in water, *Eur. Phys. J. E*, **4**, 2001, 5–10.
- [6] Ida, M., A characteristic frequency of two mutually interacting gas bubbles in an acoustic field. *Physics Letters A*, **297**(3–4), 2002, 210–217.
- [7] Feuillade, C., Scattering from collective modes of air bubbles in water and the physical mechanism of superresonances, *J. Acoust. Soc. Am.*, **98**, 1995, 1178–1190.
- [8] Manasseh, R., Nikolovska, A., Ooi, A. and Yoshida, S., Anisotropy in the sound field generated by a bubble chain, *Journal of Sound and Vibration*, 2004, *J. Sound Vibration*, **278**, 2004, 807–823.
- [9] Nikolovska, A., Ooi, A., Widjaja, R., and Manasseh, R., Resonant scattering from a chain of air bubbles in water, *Seventh European Conference on Underwater Acoustics, ECUA 2004, Delft, The Netherlands*, 5–8 July 2004.
- [10] Strasberg, M., The Pulsation Frequency of Nonspherical Gas Bubbles in Liquids, *J. Acoust. Soc. Am.*, **25**, 1953, 536–537.

## ROLE OF PLANT BUILDINGS IN A POWER STATION ACTING AS BARRIER TO THE WIND AFFECTING THE NATURAL DRAFT COOLING TOWER PERFORMANCE

Ghulam Amur, Brian Milton, John Reizes, Jafar Madadnia, Simon Beecham, Peter Brady, and Homa Koosha

Faculty of Engineering University of Technology Sydney  
Sydney 2007 Australia  
([Ghulam.Amur@uts.edu.au](mailto:Ghulam.Amur@uts.edu.au))

### Abstract

The effect of wind on the performance of a cooling tower has been investigated taking into consideration plant buildings and the presence of another tower. The results include measurements from a full scale tower, wind tunnel testing and numerical simulations. It has been found from these data that the plant buildings can significantly improve tower performance depending on the wind direction relative to the buildings. However, surprisingly, when the wind is blowing from the direction of the second cooling tower, the performance of the first cooling tower drops. This paper presents some results which demonstrate the importance of buildings in predicting cooling tower performance.

### Introduction

The performance of natural draft cooling towers depends heavily on weather conditions. This includes the ambient temperature and humidity, which affect the density of atmospheric air and its ability to absorb water vapour. Winds, on the other hand, create uneven pressure distributions at the tower inlet and outlet thereby affecting the velocity distribution within the tower and the overall mass flow rate. Although atmospheric air temperatures and humidity can not be controlled, the adverse consequences of wind can be mitigated to some extent by the use of suitable barriers. Little information is available on wind effects on the cooling tower performance [6] and remedial barriers [4, 5]. In most studies the effect of wind has been reported in terms of variation in the approach temperature, often called approach and defined as the difference between the outlet cooling water temperature of the tower and the wet bulb temperature of the incoming air. Unfortunately, the accompanying information does not include any indication as to whether there were any obstructions to the wind due to plant buildings and other topographical features.

The approach temperature of an isolated tower has been found to increase whenever there is any wind; indicating an increase in the outlet cooling water temperature. A 1K rise in that temperature has been reported when wind speed increases from 2 to 4ms<sup>-1</sup> [9]. In another study changes in approach temperatures by up to 14K were observed in dry cooling towers for wind speeds up to 15ms<sup>-1</sup> and 4K in wet towers for wind speeds up to 12.5ms<sup>-1</sup> [6].

It is therefore necessary that while investigating the effects of wind on the natural draft cooling towers, the role of buildings in creating a barrier to the wind before it reaches the towers need to be studied in detail.

The present study therefore included the installation of instrumentation in a wet cooling tower at Mt Piper Power Station in NSW. Arrays of thermocouples and anemometers were installed in the tower and a remote data collection system was developed for data acquisition. The turbine load, the volumetric flow rate through the tower and water temperatures were obtained from the control room data acquisition system. The

mass flow rate of air was calculated by integrating the anemometer data.

A 1/1000 isothermal scaled model of the tower was developed for wind tunnel testing. A duct was attached to the top of the model tower so that the flow rate of air could be controlled by an external fan. The performance of the tower was evaluated in terms of the pressure loss through the model tower. The surrounding buildings and the second tower were also reduced to the same scale and mounted on a turntable in similar positions to those in the full scale power station as may be seen in Figure 1 below.

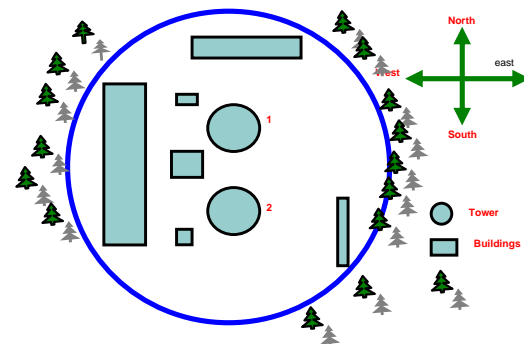


Figure 1: Cooling Tower Layout in relation to Plant Buildings.

The study was further extended by constructing a 2D numerical model of the plant to gain an understanding of the wind flow patterns around the cooling tower area in relation to the other plant buildings.

### Full scale measurements

The instruments for data collections at the tower were installed above the cooling tower fill. These included calibrated anemometers and thermocouples installed on ropes extending from the centre to the outer surface of the tower at approximately 30° around the tower azimuth. In addition, the cooling water temperatures entering and leaving the tower and dry bulb and wet temperatures were also recorded. The data were collected at a frequency of 2000Hz and averaged over 5 minute intervals on a 24 hour cycle. The wind speed and direction and air temperature data was measured at 10 meters height at the metrological station situated 500 meters from the cooling tower and outside the plant buildings. The power generation data was obtained from the plant control room data.

### Tower performance with wind from plant building side

For a typical day when the wind direction and the output of the turbine were reasonably constant the data are given in Figure 2.

Although the wind speed at the plant reached velocities up to 10m/s, reliable data were only available for wind speeds up to



4m/s. Since there is wind direction and the power demand fluctuate during the day, the data to be used were obtained from records on a day during which wind direction and the power remained fairly constant. This leads to a more reliable correlation between the wind and the approach. Unfortunately, data at constant wind direction and power were only available for wind speed up to  $4ms^{-1}$ .

It can be seen in the Figure 2 that when the wind blows from the building side the approach temperature decreased from 13K to about 10 K as the wind speed increases. A decrease of about 3K

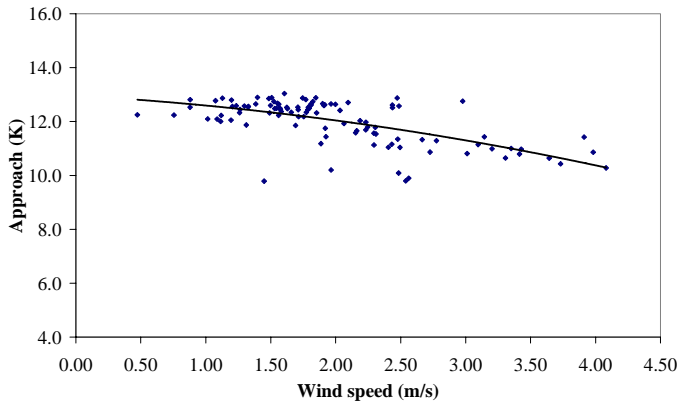


Figure: 2 Effect of wind on tower approach temperature. (Wind from plant building side)

has been obtained when plant buildings act as barrier to the wind blowing towards the tower. As a result the water leaving the tower could be 3K lower than when there is no wind. This condition is in direct contradiction to some of the previous studies in which the approach increased with the wind speed [6]. This is supported by *Dreyer et alia* [10], who studied evaporative natural draft cooling towers. They found that the approach temperature decreased from 14K to 12K when the wind speed increased from 0 to  $6 ms^{-1}$ ; regrettably, they do not mention whether there were any barriers in front of the tower. One possible explanation is that not only do buildings shield the tower intake, thereby reducing any velocity distribution; the wind also provides suction at the tower outlet, thereby increasing the available pressure drop and the resulting air mass flow rate through the tower. It follows that a judicious placement of power station buildings can actually have a favourable influence on the performance of cooling towers during windy periods.

#### Wind from the direction of the second cooling tower

A wind from the direction of the second tower has been found in this work to increase the approach temperature as can be seen in Figure 3. There is considerable scatter in the data in Figure 3, however, the line of best fit of the approach temperature has a minimum of approximately 6K when there is a wind of  $0.5ms^{-1}$ , to a maximum of approximately 12K at a wind speed of  $2.8ms^{-1}$ . Beyond that velocity there is a slight decrease but the approach temperature remains well above its zero velocity value. Since the two towers are of the same size, and they are completely open at ground level, the second tower does not provide any shielding for the other tower at ground level. Further, the wake from the second tower would reduce the suction effect at the top of the first tower. The result is a decreased air mass flow rate with a consequent reduction in the performance represented by a substantial increase in the approach temperature. Unfortunately this phenomenon cannot be fully investigated in wind tunnel tests because the flow through the model tower is provided by an external fan, but could be modelled numerically.

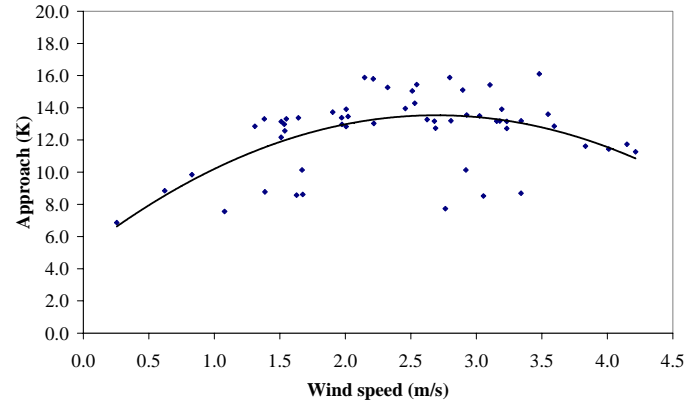


Figure: 3 Effect of wind on tower approach temperature. (Wind from second cooling tower side)

#### Wind tunnel results

A 1/1000 scale model of the tower was tested in the wind tunnel together with all the buildings and the second tower placed at the correct positions relative to the tower as may be seen in Figure 1. Tests were carried out at different velocity ratios,  $VR$ , defined as the ratio of the velocity at the tower throat to the wind velocity, and some of those are reported in Figure 4. The effect has been described in terms of the inlet pressure loss coefficient ( $C_{pi}$ ) of the tower as a function of the velocity ratio ( $VR$ ).

$C_{pi}$  is defined as

$$C_{pi} = \frac{\Delta p_o}{0.5 \rho V_{ct}^2},$$

in which,  $C_{pi}$  is pressure loss coefficient at the inlet;  
 $\Delta p_o$  is the pressure loss in the tower;  
 $V_{ct}$  is the velocity inside the cooling tower;  
and  
 $\rho$  is the density of air.

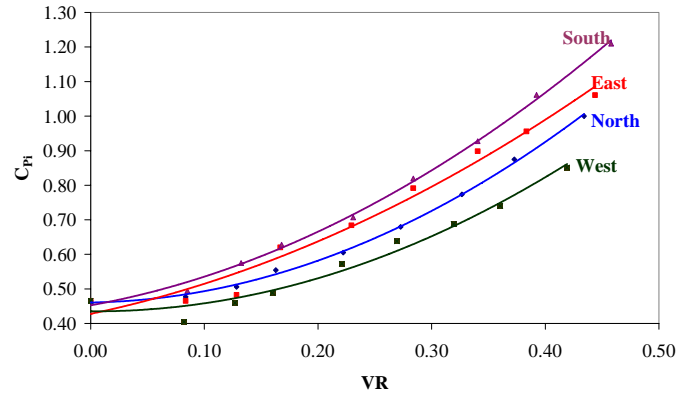


Figure: 4 Variation of  $C_{pi}$  with building and tower obstruction.

As may be seen in Figure 4,  $C_{pi}$  is much larger with a value of about 1.20 when the wind reaches the tower from the south, which is the second cooling tower side, than its value of about 0.45 when there is no wind. This loss of performance is accompanied by the fact that it has been reported that in windy conditions, when in tandem arrangement, the pressure fluctuation on the downstream tower can be as high as 40% [2]. However,  $C_{pi}$  is approximately 0.90 when the wind blows from the boiler house side buildings; which is about 33% lower than that obtained when the wind blows from the south or second cooling tower side for a similar velocity ratio. Surprisingly, when the wind blows from the east where there is no obstruction in the path of the oncoming wind (see in Figure 1) there is a lesser loss

of performance that when the wind blows from the south and the cooling tower is sheltered by the second cooling tower. The minimum loss of performance occurs when the cooling tower is protected by the massive boiler house building which lies to its west. The northerly approach is also protected by the water treatment building which, however, is smaller than the boiler house so that it gives less protection.

It should be noted that  $C_{pi}$  really only represents the inlet losses of the model tower and these are always increased when the wind blows. Because the development of a hot small scale cooling tower model is not really possible, a cold model is used, thereby not allowing the wind effects at the top of the tower to be modelled at all. Thus, the effects of wind suction mentioned in the discussion concerning the full scale plant cannot be reproduced, which means that the improved performance shown in Figure 2 is not seen in the model results.

The model results qualitatively indicate that the tower performance is differently affected when the wind blows from different directions and that this is due the different obstructions present. Surprisingly, the second cooling tower has by far the major effect on the tower performance as can be seen in the full scale and wind tunnel results. It seems that sheltering the inlet reduces  $C_{pi}$  so that all other effects being equal it is expected that a reduction in  $C_{pi}$  will lead to an improvement in the tower performance. Thus, wind tunnel test on remedial devices designed to improve the inlet flow to the cooling tower will still yield valuable information, but the surrounding buildings need to be included in the model.

### Numerical simulations

A two-dimensional numerical simulation of the wind tunnel model has been performed to improve the understanding of wind flow around the cooling tower area in the presence of plant buildings. Although the numerical model studies are in a preliminary stage and have not yet been completely validated, they are given here for information to indicate that the flow pattern is greatly affected by the arrangement of the surrounding buildings and complement the physical modelling results.

The commercial code CFDACE was used to perform the numerical work. The wind tunnel physical arrangement has been simulated in this work. The numerical model was prepared using a total number of 175000 mesh points on an unstructured grid. Since it was expected that the flow would not be steady, a transient solution was sought with a time step of  $10^{-4}$ s and an upwind differencing scheme was used on the advective terms in the Navier-Stokes Equation and a central differencing scheme used on the other terms. The  $\kappa$ - $\epsilon$  turbulence model was used. At the inlet, a uniform velocity of 11 m/s was used. At each time step convergence of the velocity and pressure residuals were reduced to  $10^{-6}$  of their initial values. Since the work is still in the progress there are several refinements in the process of being included, the full details would be available after validation. These results here are presented for an indicative purpose only.

The preliminary results may be seen in the Figures 5 to 7 (wind from the small building direction) and Figures 8 to 10 (wind blows from the second tower direction) at various times. In agreement with the full scale and the wind tunnel results, it can be seen that the small building provides shelter to the first cooling tower whereas when the wind is blowing from the second cooling tower there is no shelter. The exact effect of the obstructions need to be averaged overall a long period, however, the general pattern does not change enormously as may be seen in the Figures 5 to 10.

The high stream of air caused by the upstream building affects the eastern side of the second tower. The detached boundary layer on the eastern side of the large building results in a low velocity stream around the western side of the second tower.

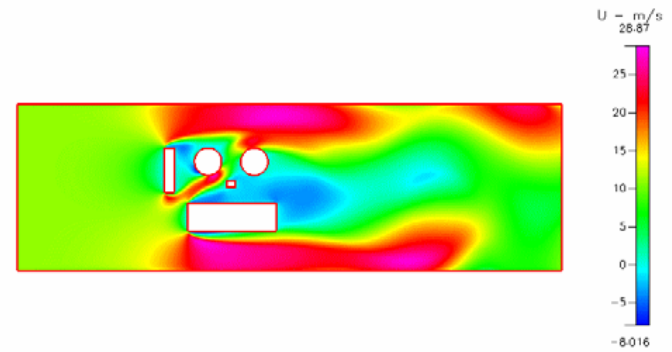


Figure 5: Flow pattern when the wind blows from the direction of a building.

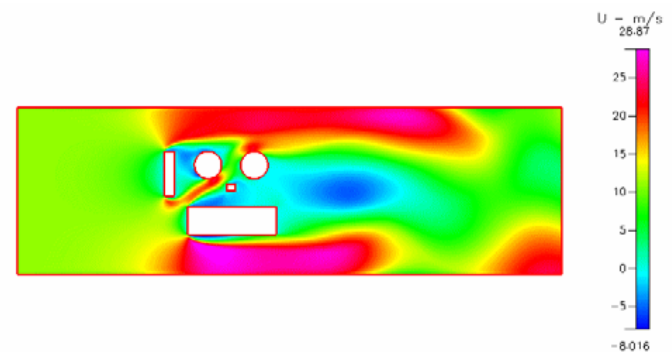


Figure 6: Flow pattern when the wind blows from the direction of a building.

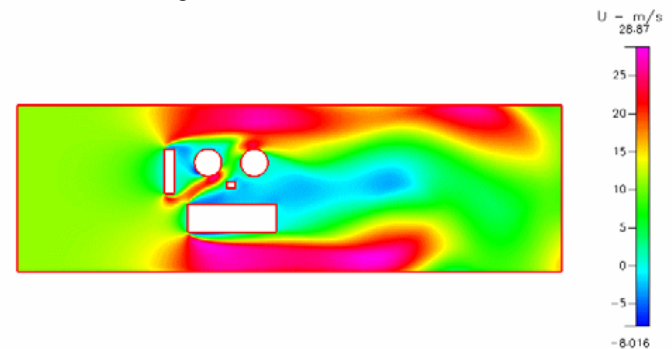


Figure 7: Flow pattern when the wind blows from the direction of a building.

In the second case of wind from the south, as shown in Figures 8 to 10, the two towers are arranged in tandem with a building on the down stream side of the two towers and the large boiler building on one side of both towers. In this case both towers are affected by the wind with the upstream tower having higher surrounding velocity than the down stream tower. However, the upstream tower provides some little shelter to the down stream tower. Although the up stream tower provides some shelter to the down stream tower, the flow pattern created by the large building in fact increases the wind speed on the second tower.

The simulation results, although not yet validated, support the full scale and wind tunnel results in the sense that the tower performs better when the plant buildings provide shelter from the wind. The interaction of the flows around the cooling towers and buildings is much more easily understood from the numerical calculations and their effects quantified. However, it should be understood that a cooling tower in isolation is not an adequate

model for the evaluation of its performance in windy conditions without taking account of nearby buildings.

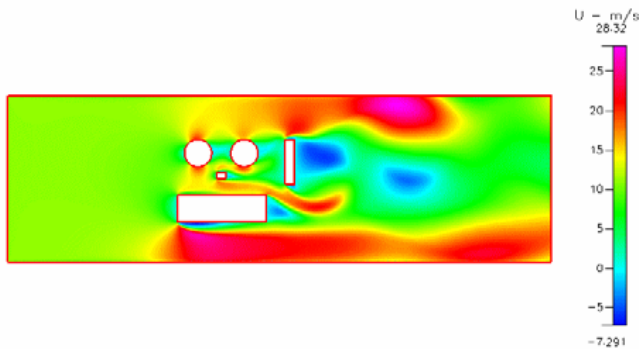


Figure 8: Flow pattern when the wind blows from the direction of the second cooling tower.

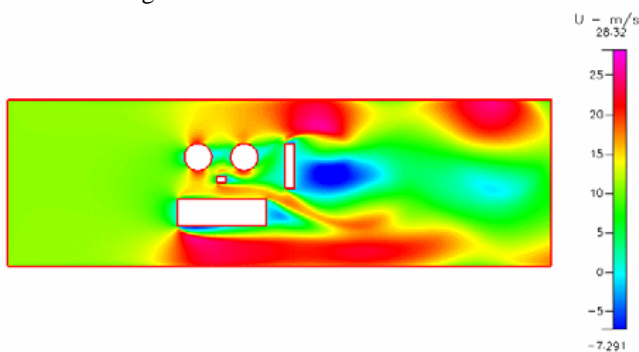


Figure 9: Flow pattern when the wind blows from the direction of the second cooling tower.

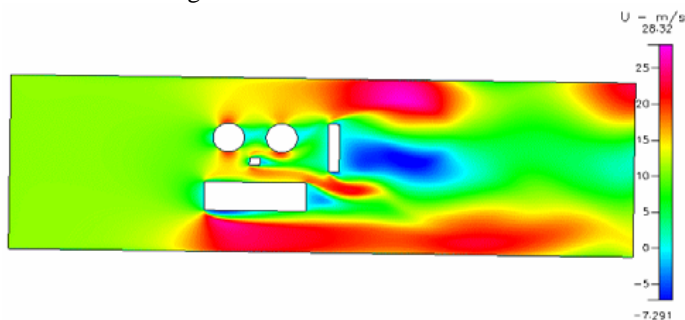


Figure 10: Flow pattern when the wind blows from the direction of the second cooling tower.

## Conclusion

The performance of natural draft cooling towers is significantly affected by wind. The plant buildings depending upon the orientation can significantly help to improve the cooling tower performance by sheltering the tower from wind. The effect depends upon the size and orientation and arrangements of the buildings.

The tower performance is reduced when the wind blows from the direction of a second tower or from a direction without any buildings to shelter the tower.

## Acknowledgements

The authors thank to Delta Electricity for providing funding for this project and the ARC for providing the research grant.

## Reference:

- [1] Preez Du A.F (1992) "The influence of Cross-winds on the performance of Natural Draft dry cooling towers" PhD Thesis University of Stellenbosch, Stellenbosch, RSA
- [2] Sun T.F et al (1992), "Full Scale Measurement and Wind Tunnel Testing of Wind Loadings on two Neighbouring Cooling Towers", *Journal of Wind Engineering and Industrial Aerodynamics*, 41-44 (1992) 2213-2224 ELSEVIER
- [3] Qing-ding Wei et al (1995), "A study of unfavourable effects of wind on the cooling efficiency of dry cooling towers", *Journal of Wind Engineering and Industrial Aerodynamics* 54/55 pp 633-643, ELSEVIER
- [4] Derksen, D.D et al (1996), "A study on the effects of wind on the air intake flow rate of a cooling tower: Wind wall study" ", *Journal of Wind Engineering and Industrial Aerodynamics* 64 pp 47-59, ELSEVIER
- [5] Preez Du A.F. and Kroger D.G (1995), "The effects of the heat exchanger arrangement and wind-break walls on the performance of natural draft dry-cooling towers subjected to cross winds" *Journal of Wind Engineering and Industrial Aerodynamics* 58 pp 293-903, ELSEVIER
- [6] Kroger Deltev (1998) "Chapter 9.2: Effect of wind on cooling towers", *Aircooled heat Exchangers and Cooling Towers*, University of Stellenbosch, Stellenbosch, RSA
- [7] Rennie, E.J and Hay, N., 1990 "Analysis of full-scale natural-draft tower measurements to develop and validate tower performance computer codes" *International Association for Hydraulic Research 7<sup>th</sup> Cooling tower and spray pond symposium, Leningrad, USSR*
- [8] Burger, Robert 1995, "Cooling Tower Technology" The Fairmont Press Inc, 700 Indian Trail Gilburn GA30247
- [9] Valente, J, 1996, private communication, Pacific Power, NSW Australia
- [10] Dreyer, A.A, Oosthuizen, P.C, Van Standen, M.P 1998, "The effect of wind on the performance of counter flow natural draft evaporative cooling towers, *Proceedings of the 11<sup>th</sup> IAHR cooling tower symposium, Cottbus, Germany*

## Towards a Universal Criterion for Predicting Vortex Breakdown in Swirling Jets

A. J. Fitzgerald, K. Hourigan and M. C. Thompson

Fluids Laboratory for Industrial and Aeronautical Engineering (FLAIR),  
Department of Mechanical Engineering, PO Box 31,  
Monash University, Clayton, VIC, 3800, AUSTRALIA

### Abstract

Previous studies of unconfined swirling jets have shown that when the ratio of the axial to azimuthal velocity exceeds a critical value ( $S_c$ ), the vortex core undergoes vortex breakdown [4]. In this paper, critical swirl ratios are determined numerically for a wide range of different upstream axial velocity distributions and Reynolds numbers to determine the general applicability of the proposed *critical swirl ratio* criterion. While it predicts the onset of vortex breakdown reasonably well, a modified version based on averaged axial and azimuthal velocities, improves the prediction of the onset of breakdown from 60% to better than 10% over a large part of the parameter space considered.

### Introduction

Vortex breakdown is a flow phenomenon that can affect vortex cores over a wide range of flow parameters. Vortex breakdown and its control have importance to flows in mixing vessels [5], meteorological phenomena (e.g. tornados) [1], military [16] and civil aviation [15], and combustion [17]. Three main vortex breakdown topologies have been identified in the literature [6]: the bubble, spiral and double helix. Recently, a new type has been added to this list, which has been designated *conical breakdown* due to its conical (near) axisymmetric expansion about the vortex core [4]. The critical swirl ratio criterion described in the abstract, and in more detail below, has been applied to breakdown types including conical breakdown. Refer to the recent review of Lucca-Negro and O'Doherty for details [14].

Early vortex breakdown research was conducted experimentally in diverging pipes [19] and with somewhat less success over delta wings [11]. Numerical studies have allowed an often more detailed analysis of the mechanisms and dynamics of vortex breakdown beginning with the quasi-cylindrical approximation of Hall in 1972 [10]. The quasi-cylindrical approximation allowed prediction of the occurrence and position of vortex breakdown, but not the internal dynamics or the upstream and downstream influences. The use of the quasi-cylindrical approximation is hence limited. Parallel with the increase in computing power came more sophisticated simulations utilising the Navier-Stokes equations with steady [8] and unsteady [9] axisymmetric approximations. Later the need for full 3D time-dependent solutions to the Navier-Stokes equations became more apparent [21]. State of the art direct numerical simulations have successfully shown a variety of vortex breakdown states including the bubble, the spiral, combined bubble and spiral, and combined bubble and helical modes [18].

Despite decades of research, the physical mechanism of vortex breakdown remains under dispute. Three main theories have been put forward, which are supported to varying degrees by experimental observations and measurements. These are: (i) an axisymmetric analogy to a two-dimensional hydraulic jump, where there is a jump transition between the supercritical upstream vortex and the downstream sub-critical conjugate state [2, 3, 19, 18]; (ii) an analogy with two dimensional bound-

ary layer separation, where the quasi-cylindrical approximation of the equations of motion is assumed to be analogous to 2D boundary layer equations, such that a breakdown in the approximation indicates the occurrence of a local separation and hence vortex breakdown [10]; and (iii) through a hydrodynamic instability, that uses stability analysis based on a columnar Q-vortex [17, 12, 13].

Proceeding in parallel with research into the mechanism of vortex breakdown, research has also attempted to find the critical parameters (critical states) that can be used to determine whether breakdown will occur. Most of these critical conditions have been related to axial and azimuthal velocities, or axial and azimuthal momenta [7]. One parameter, the Rossby number,  $Ro = U/r_c\Omega$ , where  $U$ ,  $r_c$  and  $\Omega$  are the characteristic axial velocity, radius and rotation rate respectively, was used to interpret past experimental and numerical results as well as new numerical results [20]. Collation of the data for the onset of breakdown showed a trend to asymptote to a critical  $Ro_c \approx 0.65$  for  $Re \geq 250$ . Generally, these classifications are based on characteristics of a whole vortex core. Alternatively, the swirl angle, defined as  $\phi = \tan^{-1}(W/U)$  [10], where  $U$  and  $W$  are the local axial and azimuthal velocities, has been used as a local indicator to predict the downstream occurrence of breakdown.

One form of critical parameter—the swirl ratio, has been argued to provide a better indicator of the onset of breakdown than the Rossby number [4]. An analysis based on Bernoulli's equation applied along the core centreline, and the assumption that the pressure in the breakdown region matches the far field pressure, leads to the prediction that breakdown will occur under the following condition

$$S \equiv \frac{2W_{(R/2, z_0)}}{U_{(0, z_0)}} \gtrsim \sqrt{2}. \quad (1)$$

Here,  $S$  is the *swirl ratio*,  $W_{(R/2, z_0)}$  is the azimuthal velocity at radius  $r = R/2$  and a small distance downstream of the nozzle exit at  $z = z_0$ ,  $R$  is the nozzle radius and  $U_{(0, z_0)}$  is the axial velocity at the nozzle centreline (hereafter referred to as  $U_{cl}$ ). Results of swirling jet experiments [4] showed that for  $300 < Re < 1200$ , vortex breakdown first occurred at  $S \approx 1.4$ , consistent with the theoretical prediction. Note that equation 1 has been simplified by assuming a Rankine vortex, i.e. solid body rotation and a top-hat axial velocity profile.

Figure 1 shows the variation of the centreline, flow-rate-averaged and momentum-averaged jet velocity as a function of swirl ratio for the swirling jet studied experimentally by Bilant *et al.* [4]. As expected, the averaged velocities are almost constant with swirl ratio, since the experimental rig was supplied with a constant head. Of interest, the axial velocity profiles (with radius) show a variable height local peak in the axial velocity at the centreline depending on the relative swirl ratio, however, further out from the axis the axial velocity is relatively uniform before dropping smoothly to zero at the edge of the jet. It is expected that the relatively small mass flow associated with

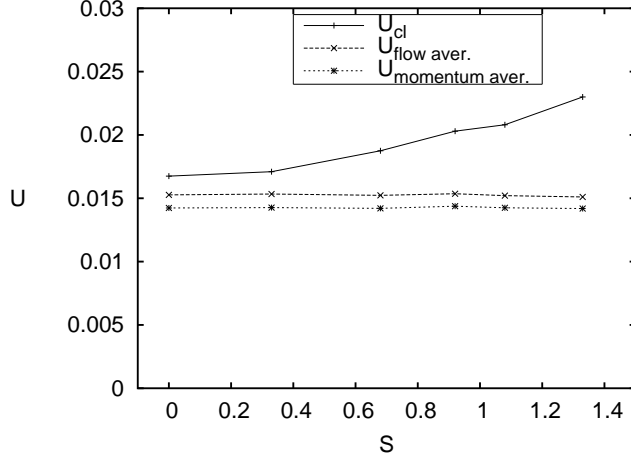


Figure 1: The magnitude of the centreline axial velocity used in the swirl ratio  $S$ , as compared with the flow and momentum averaged velocities.

this local peak should not have a great influence on the tendency for the jet to breakdown. Despite this, but with some theoretical support, the centreline velocity was the measure used by Billant *et al.* [4] to represent the axial flow in equation 1.

The aims of this research were to determine the sensitivity of critical swirl ratio ( $S_c$ ) to changes to the axial velocity profile and, if the critical swirl ratio was found not to be constant, then to attempt to find a modified version of the swirl ratio for which this would be the case.

### Numerical Method

Axisymmetric numerical simulations were performed using a spectral-element code previously developed and validated [22]. The method employs high-order tensor-product Lagrangian polynomials as shape functions within the discretisation elements. Accurate and efficient integration over each element is achieved by matching the node points of the Lagrangian polynomials to the Gauss-Legendre-Lobatto quadrature points. The method is second-order accurate in time.

The computational grid has six macro elements across the swirling jet with mesh compression towards the outer radius ( $R$ ) to help resolve the jet shear layer. There are thirteen macro elements expanding out from the nozzle radius to the outer radial boundary at  $r = 10R$ . The axial domain length is  $l = 46R$  and there are thirty macro-elements that expand away from the nozzle. The number of internal nodes was fixed for all cases at 36 ( $6 \times 6$ ), limiting the error in flow field characteristics, such as Strouhal number and point velocities, to  $\leq 3\%$ . This error estimate was determined through a series of simulations with higher numbers of internal nodes per element. At the inflow boundary the axial and azimuthal velocity profiles were specified. At the outlet boundary the normal component of velocity were set to zero. Initial problems with divergence of the solution as the jet reached the outlet were resolved by the inclusion of a *viscous sponge* region of very high relative viscosity. This was applied in the last three rows of elements before the outlet. A free-slip condition was specified to the outer wall. The flow was evolved until it reached either a steady, periodic or asymptotic state (dependent on flow parameters). Typically this involved  $1-2 \times 10^5$  timesteps.

In order to investigate the effect of velocity profile on the critical swirl ratio, four quite different axial velocity profiles were chosen (figure 2). These profiles will be referred to as "medium", "flattened", "peaked" and "top-hat". The medium, peaked and

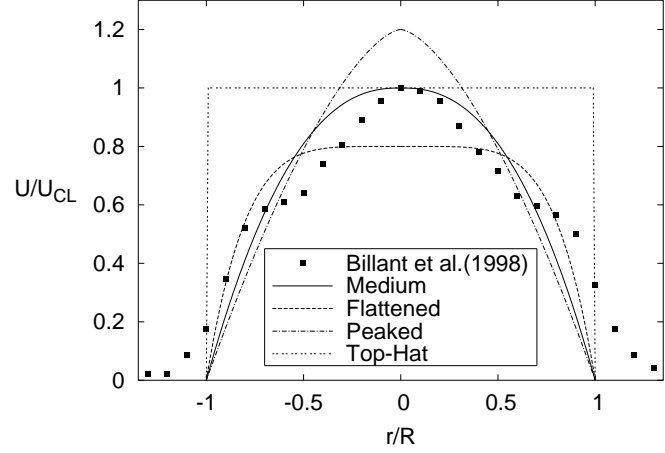


Figure 2: Axial velocity profiles tested (medium, flattened, peaked and top-hat) as compared with the profile given by Billant *et al.* (1998)[4] (■) for  $S = 1.33$ , a swirl ratio near the critical swirl ratio  $S_c$ .

flattened profiles have been momentum matched to the profile of Billant *et al.* (1998) (figure 2). The flattened and peaked profiles have centreline velocities decreased and increased by 20% from that of the medium case. The top-hat profile has the same centreline velocity as the medium case but significantly higher momentum. This profile also has the same averaged velocity as its centreline velocity ( $\bar{U} = U_{cl}$ ). All profiles simulated were generated using the  $U(r) = U_{cl}(1 - (r/R)^n)$  where the exponent  $n$  describes the profile. The peaked, medium, flattened and top-hat profiles had  $n = 1.55, 2.39, 5.1$  and  $1000$ , respectively.

Azimuthal velocity profiles follow a sinusoidal curve described by  $W(r) = W_{R/2,0} \sin(\pi r/R)$ , where  $W_{R/2,0}$  is the peak azimuthal velocity at the nozzle exit. The radial velocity ( $V$ ) was set to zero at the inlet. The Reynolds number ( $Re$ ) was defined as  $Re = 2R\bar{U}/\nu$ , where  $\bar{U}$  is the mass-flow averaged axial velocity. Locating  $S_c$  was accomplished by running a series of independent simulations at increasing azimuthal velocity with sufficient resolution, such that the critical swirl ratio for the onset of vortex breakdown could be determined to within  $S_c \pm 0.02$ .

### Results

Predicted vortex breakdown structures showed good qualitative correlation with experiments as seen in figure 3 and 4. At  $Re < 600$ , the bubble was the first breakdown state formed. In all cases the bubble progressed into a cone with increasing  $S$ . The transition from bubble to cone with increasing swirl involves a state where both the cone and bubble alternately appear in an unsteady fashion. With further increases in swirl a steady cone appears, however at high  $Re$ , the "tails" of the cone experience a shear layer instability causing a form of vortex shedding, as can be seen in figure 3. At  $Re > 600$ , the cone type was the first breakdown state to form and no real bubble was subsequently formed.

The critical swirl ratios determined from the numerical simulations are shown in figure 5. The numerical predictions (+, \*, x, □) have hyperbolic trendlines determined using the least squares method. The experimental values from [4] are shown (■) without a trendline. Figure 5 (a) shows predictions based on the definition of the swirl ratio given in equation 1.

The critical swirl ratio ( $S_c$ ) for vortex breakdown for the simulated medium case (the case most similar to the experimental work), demonstrates convergence on  $S_c \approx 1.28$ . This correlates with the measured range of  $1.22 \lesssim S_c \lesssim 1.57$  published by Bil-



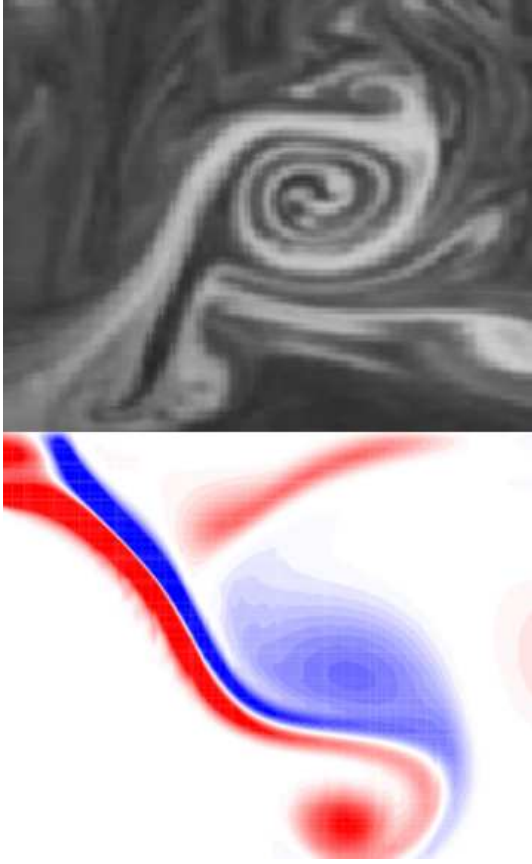


Figure 3: Comparison of unsteady conical vortex breakdown between dye visualisations of Billant *et al.* (1998) at  $Re = 626$ ,  $S = 1.31$  and simulated contours of azimuthal vorticity at  $Re \approx 650$ ,  $S = 1.45$ .

lant *et al.* [4], and corresponds to their experimental data also shown in the figure. The most notable difference between the simulations and the experimental data is the trend toward higher critical swirl ratios at lower  $Re$ . This trend has been noted previously in an extensive review of both numerical and experimental results [20], and is an effect that becomes apparent at  $Re < 300$ . Some evidence of this effect can be seen in the experimental data shown here although most of the results are for higher Reynolds numbers.

Figure 5(a) reveals that the critical swirl ratio is dependent on the axial velocity profile and there is a significant shift to higher critical swirl ratios at lower Reynolds numbers. For example,  $S_c$  for the flattened and peaked profiles were respectively higher and lower than the base case by up to 20%, and up to 60% higher for the top-hat case. This effect is not surprising when the jet is considered in terms of flow rate or momentum. Looking at the flattened case, the total axial momentum is unchanged from the medium case, however the denominator of the swirl ratio ( $U_{cl}$ ) has decreased, causing an increase in the critical ratio. The opposite occurs with the peaked profile. A similar situation applies to a top-hat profile, where  $\bar{U} = U_{cl}$ ,  $S_c$  increases to  $\approx 2$ . As expected, the significantly larger momentum in this jet is causing a significant increase in the critical swirl ratio.

However, the significant differences in  $S_c$  for the medium, flattened and peaked cases suggests that neither the upstream centreline axial velocity nor the axial momentum are the appropriate scaling parameters influencing the downstream vortex breakdown state. In fact, the average flow rates are  $\bar{U} = 1.217$ , 1.265, 1.335 and 2.323 for the peaked, medium, flattened and top-hat profiles, respectively, despite the constancy of axial momentum for the first three of these profiles. This suggests that a

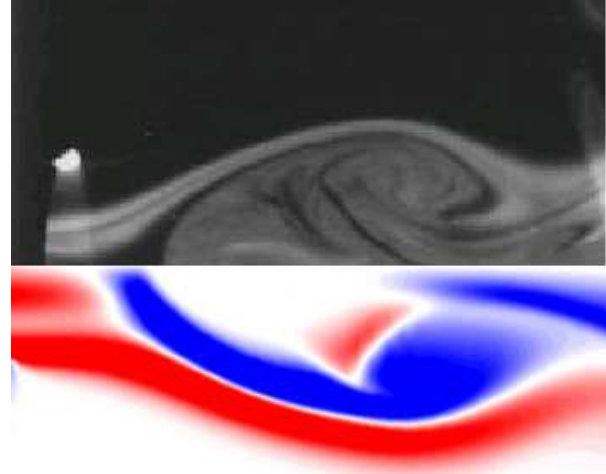


Figure 4: Comparison of unsteady bubble vortex breakdown between dye-visualisation from Billant *et al.* (1998)  $Re = 600$  and  $S = 1.42$  and simulated contours of azimuthal vorticity at  $Re \approx 600$ ,  $S = 1.32$ .

critical swirl ratio based on averaged axial and azimuthal velocities may be more successful at collapsing the data. Following through this line of reasoning, the following swirl ratio parameter is suggested as an alternative to the definition used in equation 1

$$S_* \equiv \frac{2\bar{W}_{(z_0)}}{\bar{U}_{(z_0)}}. \quad (2)$$

Here,  $\bar{W}_{(z_0)}$  is the mass-flow averaged azimuthal velocity evaluated at the upstream position  $z = z_0$ .

Figure 5(b) shows the critical swirl ratio based on this definition of the swirl ratio. Clearly, the use of averaged axial and azimuthal velocities in the formulation significantly improves the collapse of the data. For a particular Reynolds number, the critical swirl ratio varies by less than 10%, despite significant changes to the axial velocity profile. The critical swirl ratio increases slightly at Reynolds number below approximately 400. For  $Re > 400$ ,  $S_c \approx 1.2 - 1.3$ .

Figure 5(b) also yields further support for the idea that the centreline velocity may not be the optimal scaling parameter even with respect to the axial velocity profiles given by Billant *et al.* [4]. The critical swirl ratios determined from their experiments are almost exactly coincident with the predictions for a top-hat profile. In retrospect, this should not be wholly unexpected, as the local axial velocity peak at the centreline contributes only slightly to the overall jet mass or momentum flux. Recall that their axial velocity profiles resemble a top-hat distribution, except for the appearance a localised increase in velocity near the centreline. While the new formulation does not eliminate the slight Reynolds number dependence at low Reynolds numbers, the effect is considerably less for the swirl ratio based on integrated parameters.

## Conclusions

The results of the present numerical simulations of axisymmetric vortex breakdown of a swirling jet using the spectral-element method show good correlation with those obtained from the experiments of [4]. Axisymmetric solutions show both the bubble and the cone type of vortex breakdown as seen in these experiments. The simulations are successful at replicating the ob-

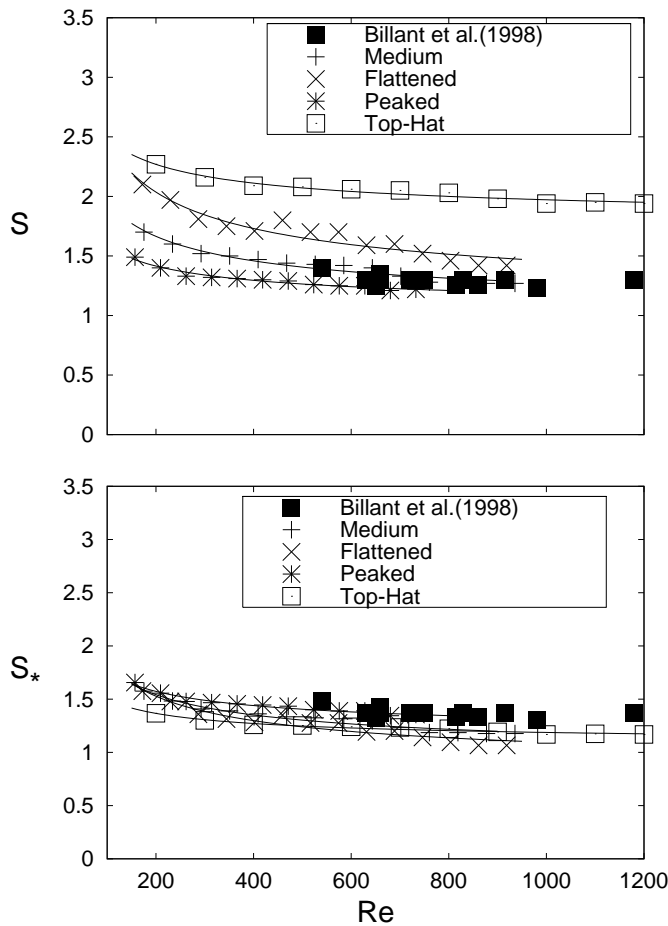


Figure 5: Comparison of critical swirl ratio for vortex breakdown between data and present numerical simulations. ■ denotes experimental data[4]. +, \*, ×, □ show present simulation data. Figures show swirl ratio as interpreted (a) using  $S$  and (b) using  $S_*$ .

served behaviour of the critical swirl ratio when a similar axial velocity profile to that seen in the experiments is used. This allowed us to extend on the experimental work by observing the effect of swirl ratio definition on jets with different axial velocity profiles. It was seen that the swirl ratio definition originally used in interpreting the experimental data (equation 1) did not produce a profile-independent critical swirl ratio for the range of profiles tested. The inclusion of an averaged azimuthal velocity and an averaged axial flow velocity in the definition of the swirl ratio (equation 2) yielded an excellent collapse of data, so that the critical swirl ratio was in the range  $S_c \approx 1.2 - 1.3$ .

At present the authors are trying to develop a theoretical understanding of these observations.

#### Acknowledgements

Mr. Fitzgerald acknowledges the support of the Department of Mechanical Engineering, Monash University, through a Departmental Scholarship.

#### References

- [1] Althaus, W., Brücker, C. and Weimer, M., Breakdown of slender vortices, In *Fluid Vortices* (ed. S. Green), 373–426.
- [2] Benjamin, B. T., Theory of the vortex breakdown phenomenon, *J. Fluid Mech.*, **14**(4), 1962, 593–629.

- [3] Benjamin, B. T., Some developments in the theory of vortex breakdown, *J. Fluid Mech.*, **28**(1), 1967, 65–84.
- [4] Billant, P., Chomaz, J.-M. and Huerre, P., Experimental study of vortex breakdown in swirling jets, *J. Fluid Mech.*, **376**, 1998, 183–219.
- [5] Escudier, M., Observations of the flow produced in a cylindrical container by a rotating endwall, *Exps. Fluids*, **2**, 1994, 189–196.
- [6] Faler, J. and Leibovich, S., An experimental map of the internal structure of a vortex breakdown, *J. Fluid Mech.*, **86**, 1978, 313–335.
- [7] Farokhi, S., Taghavi, R. and Rice, E., Effect of initial swirl distribution on the evolution of a turbulent jet, *AIAA Journal*, **27**(6), 1988, 700–706.
- [8] Grabowski, W. and Berger, S., Solutions of the navier-stokes equations for vortex breakdown, *J. Fluid Mech.*, **75**, 1976, 525–544.
- [9] Hafez, M., Ahmad, J., Kuruvila, G. and Salas, M., Vortex breakdown simulation, *AIAA Journal*, **7**-1343.
- [10] Hall, M., Vortex breakdown, *Ann. Rev. Fluid Mech.*, **4**, 1972, 195.
- [11] Lambourne, N. and Bryer, D., The bursting of leading edge vortices, *Aeronaut. Res. Coun., R and M*, **3282**.
- [12] Leibovich, S., Vortex stability and breakdown, In *Aerodynamics of Vortical Type Flows in Three Dimensions* (ed. A.D. Young), AGARD Conference Proceeding, **342**, 1983, Paper 23.
- [13] Leibovich, S., Vortex stability and breakdown: Survey and extension, *AIAA Journal*, **22**(9), 1984, 1192–1206.
- [14] Lucca-Negro, O. and O'Doherty, T., Vortex breakdown: A review, *Prog. Energy Combust. Sci.*, **27**, 2001, 431–481.
- [15] Mager, A., Dissipation and breakdown of a wing-tip vortex, *J. Fluid Mech.*, **55**(4), 1972, 609–628.
- [16] Özgören, M., Sahin, B. and Rockwell, D., Vortex structure on a delta wing at high angle of attack, *AIAA Journal*, **40**, 2002, 258–292.
- [17] Panda, J. and McLaughlin, G., Experiments on the instabilities of a swirling jet, *Phys. Fluids*, **6**, 1994, 262–276.
- [18] Ruith, M., Chen, P., Meiburg, E. and Maxworthy, T., Three-dimensional vortex breakdown in swirling jets and wakes: Direct numerical simulation, *J. Fluid Mech.*, **486**, 2003, 331–378.
- [19] Sarpkaya, T., On stationary and travelling vortex breakdowns, *J. Fluid Mech.*, **45**(3), 1971, 545–559.
- [20] Spall, R., Gatski, T. and Grosch, C., A criterion for vortex breakdown, *Phys. Fluids*, **30**(11), 1987, 3434–3440.
- [21] Spall, R., Gatski, T. and Grosch, C., The structure and dynamics of bubble-type vortex breakdown, *Proc. Roy. Soc. Lond. A*, **429**, 1990, 613–637.
- [22] Thompson, M., Leweke, T. and Provansal, M., Kinematics and dynamics of sphere wake transition, *J. Fluids Structures*, **15**, 2001, 575–585.

## A Numerical Study of Heat Transfer from a Cylinder in Cross Flow

K. Szczepanik<sup>1</sup>, A. Ooi<sup>1</sup>, L. Aye<sup>2</sup> and Gary Rosengarten<sup>1</sup>

<sup>1</sup>Department of Mechanical and Manufacturing Engineering  
The University of Melbourne, VIC, 3052 AUSTRALIA

<sup>2</sup>International Technologies Centre (IDTC)  
Department of Civil and Environmental Engineering  
The University of Melbourne, VIC, 3052 AUSTRALIA

### Abstract

This paper presents numerical investigations into the characteristics of heat transfer from a cylinder in cross flow. Two dimensional Steady State as well as Unsteady RANS (Reynolds-Averaged Navier Stokes) simulations are presented and compared with experimental results from the literature. Experimental data is compared with numerical results which utilise a standard  $k - \omega$  turbulence model as well as a  $k - \omega$  model for which the calculation of some turbulent quantities has been modified. Significant improvements upon the prediction of heat transfer were found with the modified  $k - \omega$  turbulence model.

### Introduction

Heat transfer from a cylinder in cross flow can be found in a multitude of thermal-fluid applications containing heat sinks, heat exchangers or even thermal storage devices and the accurate prediction of such heat transfer using computational methods has not always proved successful. RANS simulations especially have proved difficult to calibrate for accurate heat transfer. The inherently unstable and fluctuating nature of vortex shedding within the velocity field of a cylinder in cross flow makes it additionally difficult to predict instantaneous heat transfer which will also fluctuate in such a flow. Numerical simulations allow excellent visualization and quantification of flow properties however if accurate prediction of heat transfer is not possible their usefulness will be limited. The Reynolds numbers studied in this paper are out of the range of DNS (Direct Numerical Simulation) and thus RANS simulations are used. The ability of RANS simulations to predict heat transfer accurately is dependent, amongst other things, upon the turbulence model used. This paper shows numerical results which include the use of a two-equation RANS turbulence model which was modified to improve heat transfer characteristics. To evaluate success of the simulations, their results are compared with experimental data from the literature. Scholten and Murray [3] and [4] have investigated the mechanism of heat transfer over the circumference of a cylinder in cross flow and some of their results will be used for such comparison.

### Numerical Method and Model

The unmodified turbulence model employed in this study is the  $k - \omega$  SST turbulence model. For numerical solution of the flow equations a commercial software package FLUENT was employed. FLUENT uses finite volume, implicit techniques to solve the governing equation which were solved sequentially. Flow across the cylinder was solved as an incompressible problem with air being the fluid. Pressure discretization utilised the Standard method whereas velocity-pressure coupling discretization was achieved with the SIMPLEC method. The QUICK discretization scheme was employed for the momentum, turbulent kinetic energy, specific dissipation rate and energy equations. The SST  $k - \omega$  turbulence model utilises

a calculation of turbulent viscosity which varies slightly from what is known as the standard  $k - \omega$  model. Thus the closure coefficients and other relations also differ slightly. Nonetheless for the current study the SST  $k - \omega$  turbulence model is considered the ordinary or unmodified turbulence model. The basic  $k - \omega$  transport equations used are as follows:

Turbulent Kinetic Energy ( $k$ ):

$$\frac{\partial}{\partial t}(\rho k) + \frac{\partial}{\partial x_i}(\rho k u_i) = \frac{\partial}{\partial x_j} \left[ \left( \mu + \frac{\mu_t}{\sigma_k} \right) \frac{\partial k}{\partial x_j} \right] - \rho \overline{u'_i u'_j} \frac{\partial u_j}{\partial x_i} - \rho \beta^* k \omega \quad (1)$$

Specific Dissipation Rate ( $\omega$ ):

$$\frac{\partial}{\partial t}(\rho \omega) + \frac{\partial}{\partial x_i}(\rho \omega u_i) = \frac{\partial}{\partial x_j} \left[ \left( \mu + \frac{\mu_t}{\sigma_\omega} \right) \frac{\partial \omega}{\partial x_j} \right] - \alpha \frac{\omega}{k} \rho \overline{u'_i u'_j} \frac{\partial u_j}{\partial x_i} - \rho \beta \omega^2 \quad (2)$$

The modified  $k - \omega$  turbulence model investigated in this study is that proposed by Durbin [1] and Medic and Durbin [2]. The modification was born from the unfortunate tendency of two equation turbulence models to over-predict levels of turbulent kinetic energy close to a stagnation point. In [1] Durbin outlines his method for modifying two equation models based on a realisability constraint for the Reynolds stress tensor i.e., that the eigenvalues of the stress tensor should be non negative. The purpose of such turbulence model modifications is to reduce the calculated levels of turbulence by either increasing the production of dissipation  $\omega$  or decreasing the production of turbulent kinetic energy  $k$ . Having had observed spuriously high values of the turbulent time scale  $T_t$  as well as  $k$  close to stagnation points, Durbin's and Medic's modification develops a limiting criterion for this turbulent time scale. Turbulent time scale  $T_t$  appears in the formula for eddy viscosity (or turbulent viscosity)  $\mu_t$  expressed as:

$$\mu_t = C_\mu \rho u^2 T_t \quad (3)$$

and in an unmodified or ordinary  $k - \omega$  turbulence model  $T_t = 1/(C_\mu \omega)$ . Durbin and Medic's turbulent time scale limit is as follows:

$$T_t = \min \left[ \frac{1}{C_\mu \omega}, \frac{\alpha}{\sqrt{6} C_\mu |S|} \right] \quad (4)$$

Placing a limiting criterion on  $T_t$  will subsequently limit turbulent viscosity  $\mu_t$  which will then have an effect on the production and dissipation of  $k$  and  $\omega$  and importantly on the solution of the energy equation and heat transfer. It is not intended here to describe in detail the derivation of the  $T_t$ -limit equation and the reader should refer to its original publications [1] and [2]. Solutions utilising this modified  $k - \omega$  turbulence model will be hence referred to as the T-limited  $k - \omega$  solutions. To solve with the T-limited  $k - \omega$  model the T-limiting criterion (equation 4) was coded into FLUENT as a user defined function (UDF) for the turbulent eddy viscosity  $\mu_t$ .

The simulated model consisted of a 2-dimensional mesh, with the cylinder centered at the origin. The computational domain extended 25D (D = cylinder diameter) in the positive (downstream) X-direction, 15D in the negative (upstream) X-direction and 10D in both positive and negative Y-directions. 180 cells were modelled around the circumference of the cylinder allowing a circumferential resolution of  $2^\circ$ . Consistent with the literature, convective heat transfer coefficient and surface Nusselt number are calculated as follows:

$$h_{conv} = \frac{q}{T_w - T_\infty} \quad (5)$$

$$Nu = \frac{h_{conv} D}{k_{fluid}} \quad (6)$$

Where  $k$ =conductivity,  $D$ =diameter and  $q$ =heat flux. Reynolds numbers, Prandtl numbers and boundary conditions were all set to preserve similarity with experimental results in [3]. For the three Reynolds numbers simulated Prandtl number was held at  $Pr=0.7$ , cylinder wall temperature was maintained at  $310^\circ C$  and free stream temperature was maintained at  $310^\circ C$ . To match experimental values, inlet turbulence intensity at different Reynolds numbers was set as follows:  $T_u = 1.6\%$  for  $Re = 7190$ ;  $T_u = 0.46\%$  for  $Re = 21580$ ; and  $T_u = 0.34\%$  for  $Re = 50350$ .

### Vortex Shedding Results

Two comparisons arise from the present results. Firstly steady state results for the Nusselt number ( $Nu$ ) distribution around the cylinder will be compared to unsteady simulations which were time averaged over a single vortex shedding period. Secondly, results using the T-limited  $k - \omega$  turbulence model will be compared with those using the ordinary  $k - \omega$  model.

Unsteady simulations were conducted at a Reynolds number of 21580 and depicted vortex shedding well. Figure 1 shows the sinusoidal behaviour of coefficient of drag  $C_d$  for the  $k - \omega$  solution at  $Re = 21580$  and the constant frequency and amplitude indicate a steady and periodic simulation of vortex shedding. Strouhal number calculated from data of figure 1 is  $S_t = 0.2146$  which compares well with the experimental value of  $S_t = 0.213$  from [3].

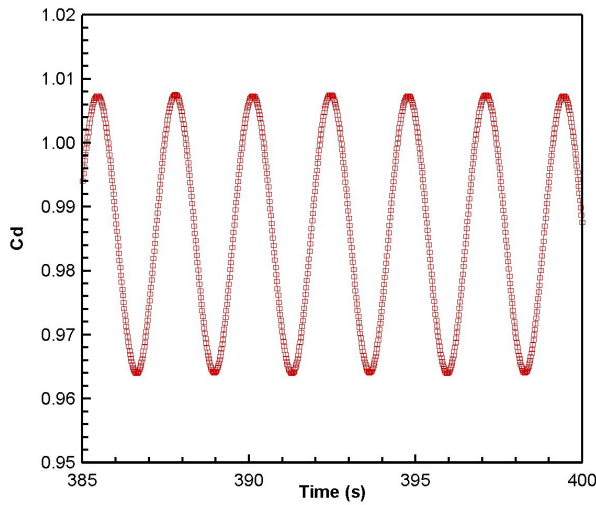


Figure 1: Coefficient of drag ( $C_d$ ) vs Time for  $Re = 21580$  unsteady  $k - \omega$  solution.

Figure 2 shows the clearly sinusoidal behaviour of  $C_d$  when the T-limited  $k - \omega$  model is employed and these results yield

a Strouhal number of  $S_t T-limited = 0.197$  for  $Re=21580$ . Although being lower than the relevant experimental Strouhal number from [3] periodic vortex shedding is nonetheless being well represented. Given the objective for the T-limited modification, it is the heat transfer results which will determine the models usefulness. The mean  $C_d$  for both ordinary and T-limited  $k - \omega$  are slightly higher than the expected values for this Reynolds number but nonetheless still close to the  $C_d$  curve for a smooth cylinder.

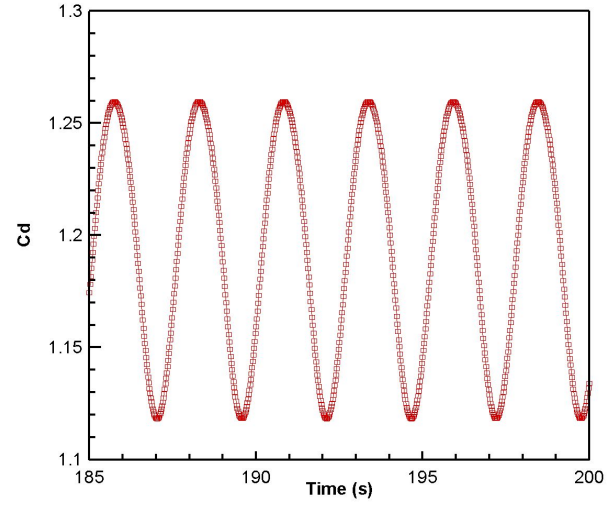


Figure 2: Coefficient of drag ( $C_d$ ) vs Time for  $Re = 21580$  unsteady T-limited  $k - \omega$  solution.

### Turbulent Kinetic Energy Results

Figure 3 and figure 4 show the difference in turbulent kinetic energy  $k$  when the T-limited  $k - \omega$  model is used. The original function of the T-limited model was to restrict high levels of  $k$  close to the stagnation point and this can clearly be seen in figure 4 where stagnation point turbulent kinetic energy is two orders of magnitude lower compared to the ordinary  $k - \omega$  simulation. Given that both T-limited and ordinary  $k - \omega$  cases have equal inlet  $k$ , the T-limited  $k - \omega$  case predicts a significantly reduced increase in  $k$  close to the stagnation point.

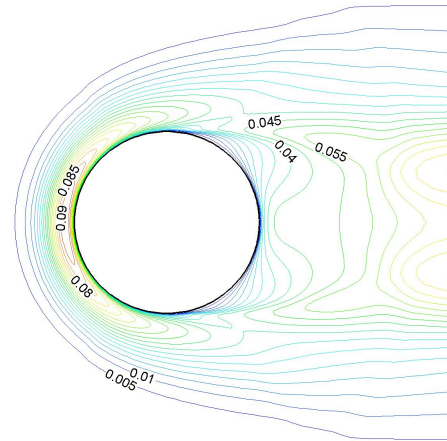


Figure 3: Contours of Turbulent Kinetic Energy ( $m^2/s^2$ ) for  $Re = 21580$  steady state  $k - \omega$  solution.

In the wake however levels of  $k$  are comparable for the T-limited and ordinary  $k - \omega$  models. Although contours of turbulent kinetic energy are shown only for  $Re = 21580$ , for all Reynolds numbers studied it was observed that when using the ordinary



$k - \omega$  model the local maximum of  $k$  near the stagnation point was in fact the solution maximum. This stagnation point maximum is precisely the incorrect result which the T-limited  $k - \omega$  model ameliorates. When the T-limited  $k - \omega$  model is employed levels of  $k$  at the stagnation point drop significantly and overall maximums of  $k$  occur within the wake region.

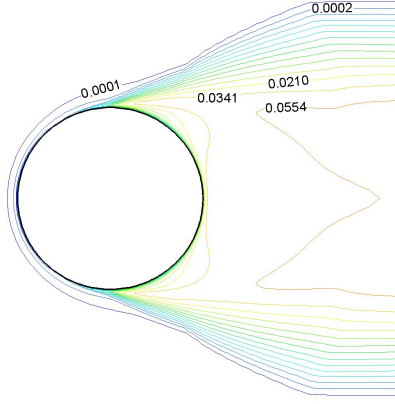


Figure 4: Contours of Turbulent Kinetic Energy ( $m^2/s^2$ ) for  $Re = 21580$  steady state T-limited  $k - \omega$  solution.

By observing  $k$  we can witness the T-limited model's effects upon turbulence but it is the heat transfer in which we're ultimately interested.

### Heat Transfer Results

In general all cases displayed the correct characteristic shape of surface  $Nu$  around the cylinder. A local maximum of  $Nu$  at or close to stagnation point is preceded by a decreasing  $Nu$  as one moves towards the top (or bottom) of the cylinder. A minimum  $Nu$  occurs close to the top of the cylinder which is associated with separation, where local recirculation could restrict heat transfer away from the surface. Moving further into the wake region  $Nu$  increases as the turbulent wake allows heat to again be removed more effectively. Figures 5 to 7 show the  $Nu$  profiles for the three Reynolds numbers studied including experimental data from [3] and considering the overall comparison between experiment and simulation, a perfectly accurate matching remains elusive. The horizontal axis in figures 5 to 7 is circumferential angle in degrees, where zero degrees is the leading edge or front stagnation point of the cylinder and 180 degrees is the trailing edge or rear.

A flow's capacity for convective heat transfer will be affected by, amongst other factors, levels of turbulence close to the heat transfer surface. Qualitatively it makes sense that abnormally high levels of turbulence will lead to abnormally high heat transfer due to turbulence affecting the flow's ability to transport heat away from the wall. Thus the ordinary  $k - \omega$  turbulence model which over predicts levels of  $k$  close to the stagnation point also over predicts stagnation point heat transfer. This can be seen in figures 5, 6 and 7 where ordinary  $k - \omega$  cases all display over predicted levels of Nusselt number at the front stagnation point  $Nu_{fsp}$ .

Figures 5, 6 and 7 also clearly show the significant reduction in front stagnation point Nusselt number,  $Nu_{fsp}$ , when the T-limited  $k - \omega$  model is employed. Reduced stagnation point heat transfer is obviously related to the reduced levels of  $k$  at the stagnation point but specifically it is through the heat transfer relation that the T-limited model is able to achieve improved heat transfer results. Eddy viscosity  $\mu_t$  appears in the heat flux

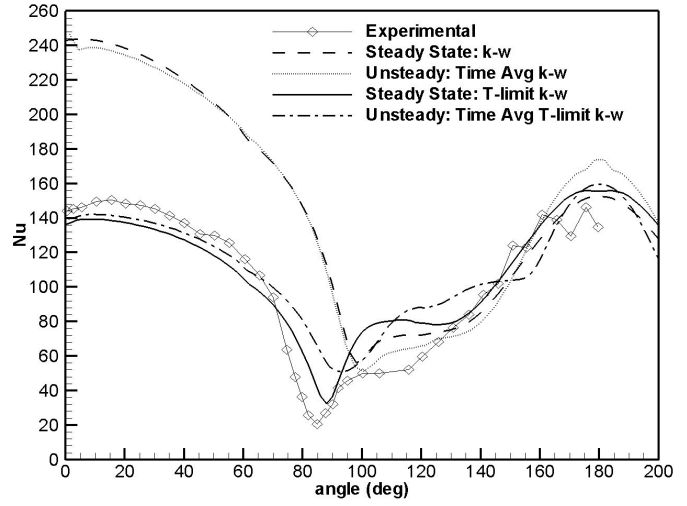


Figure 5: Surface Nusselt number for  $Re = 21580$ . Experimental data from [3].

tensor as follows:

$$\dot{q}_t = \frac{\mu_t C_p}{Pr_t} \nabla T \quad (7)$$

where  $T$ =temperature. With its reformulation of  $\mu_t$  the T-limited model is able to influence heat transfer directly through the heat flux tensor. In this way, combined with its effect on levels of turbulence, the new T-limited turbulent viscosity  $\mu_t$  plays its part in reducing heat transfer.

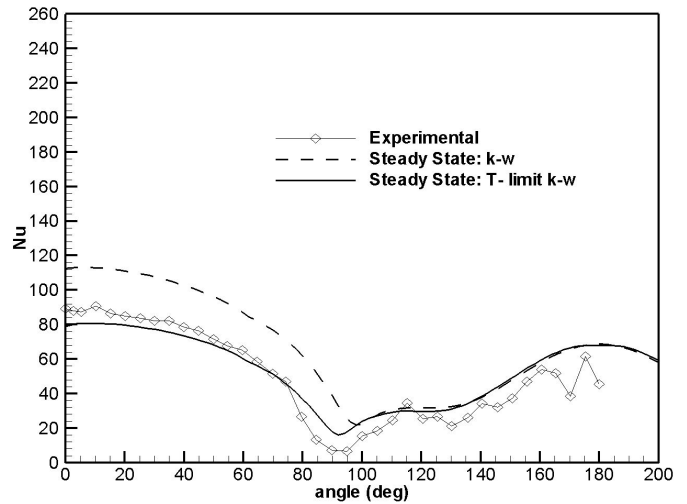


Figure 6: Surface Nusselt number for  $Re = 7190$ . Experimental data from [3].

These improvements in the simulation of heat transfer are significant due the erroneously high results obtained using ordinary  $k - \omega$  models. Table 1 summarizes the results across the three Reynolds numbers considered. Unsteady results were completed for  $Re=21580$  only.  $Nu_{fsp}$  refers to the Nusselt number at the front stagnation point (fsp) and  $Nu_{avg\ circ}$  is the circumferentially averaged surface Nusselt number.

It should be noted that higher Reynolds numbers yielded a greater relative error in  $Nu$  compared to the experimental values. Furthermore the T-limited  $k - \omega$  models bore less favourable results at high Reynolds number. This is also evident



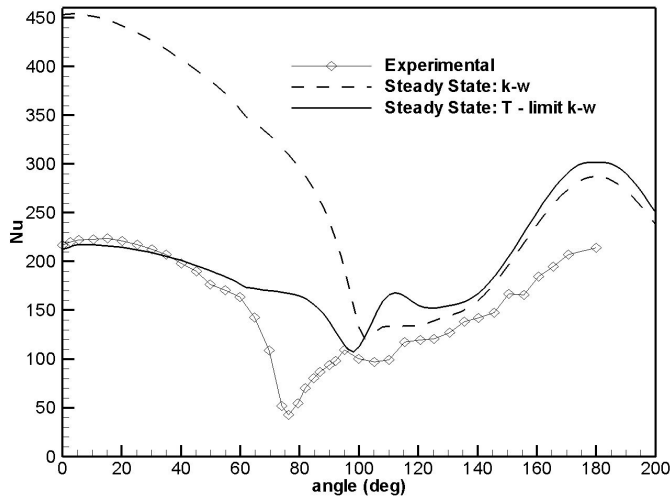


Figure 7: Surface Nusselt number for  $Re = 50350$ . Experimental data from [3].

	steady $k-\omega$	unsteady $k-\omega$	steady $k-\omega$ T-lim	unsteady $k-\omega$ T-lim	Exp [3]
<b>Re=7190</b>					
$Nu$ (fsp)	112.6	—	79.0	—	89.1
% diff from exp	26.4%		-1.2%		
$Nu$ (avg circ)	67.3	—	52.5	—	51.0
% diff from exp	32.0%		2.9%		
<b>Re=21580</b>					
$Nu$ (fsp)	243.1	247	136.2	139.7	148
% diff from exp	64.2%	66.9%	-8.0%	-6.0%	
$Nu$ (avg circ)	149.3	148	105.7	108.8	103.4
% diff from exp	44.4%	43.1%	2.2 %	5.2%	
<b>Re=50350</b>					
$Nu$ (fsp)	453.3	—	212.5	—	216.8
% diff from exp	109.1%		-2.0%		
$Nu$ (avg circ)	284.5	—	191.1	—	149.9
% diff from exp	89.8%		27.5%		

Table 1:

in figure 7 where the  $Nu$  plot has a poorer qualitative comparison with the experimental data. Assuming the minimum  $Nu$  is associated with separation it is evident from figure 7 that the highest  $Re$  simulation displayed the greatest error in the location of separation. Indeed the best alignment of minimum  $Nu$  with the experimental minimum occurred for the lowest Reynolds number investigated,  $Re=7190$ .

### Comparing Unsteady and Steady State Simulations

The purpose of conducting unsteady simulations was to test the solution's ability to depict vortex shedding accurately and to compare time averaged  $Nu$  results with their steady state counterparts. Figure 5 shows all unsteady and steady state results together. The unsteady plots of  $Nu$  v Theta were time averaged over several vortex shedding periods. Although it was shown earlier how the unsteady results depicted vortex shedding reasonably well this did not transfer into advantageous heat transfer results. For  $Re=21580$  the  $Nu$  v Theta plot for the time averaged unsteady ordinary  $k-\omega$  case did not differ drastically from the steady state ordinary  $k-\omega$  plot. Figure 5 also shows how the unsteady time averaged T-limited  $k-\omega$  plot of  $Nu$  v Theta is qualitatively worse than the steady state T-limited  $k-\omega$  case. However Table 1 shows that the circumferential average and  $Nu_{fsp}$  for the unsteady T-limited case is nonetheless well matched with the experimental data.

### Concluding Remarks

In general the T-limited  $k-\omega$  turbulence model fulfilled its objective to reduce heat transfer close to the stagnation point. Heat transfer in the wake region however was not significantly altered by the T-limited  $k-\omega$  model. The reduction in stagnation point heat transfer nonetheless had a significant reducing effect on circumferentially averaged Nusselt numbers due to the fact that stagnation point over-prediction was largely responsible for over predicted averages.

Unsteady simulations of the cylinder depicted vortex shedding behaviour satisfactorily. However when compared with steady-state simulations, and for Reynolds numbers studied, unsteady simulations did not yield significant benefits in predicting heat transfer.

The highest Reynolds numbers studied produced heat transfer results least similar to experiments. This was the case for both the ordinary  $k-\omega$  turbulence model at  $Re=50350$  and the T-limited  $k-\omega$  model. Thus further high Reynolds number studies would be recommended in order to test the capabilities and limitations of these type of numerical models.

### Acknowledgements

For their support of the current work the author would like to thank Fantec, Environmental Controls and Bassett Kuttner Collins.

### References

- [1] P. A. Durbin, On the  $k-\epsilon$  Stagnation Point Anomaly, *Int. J. of Heat and Fluid Flow*, 1996, **17**, 89–90.
- [2] G. Medic and P. A. Durbin, Toward Improved Prediction of Heat Transfer on Turbine Blades, *Journal of Turbomachinery*, 2002, **Vol. 124**, 187–192.
- [3] J. W. Scholten and D. B. Murray, Unsteady Heat Transfer and Velocity of a Cylinder in Cross Flow- I. Low Freestream Turbulence, *Int. J. of Heat and Mass Transfer*, 1998, **41**, (10), 1139–1148.
- [4] J. W. Scholten and D. B. Murray, Unsteady Heat Transfer and Velocity of a Cylinder in Cross Flow- II. High Freestream Turbulence, *Int. J. of Heat and Mass Transfer*, 1998, **41**, (10), 1149–1156.
- [5] A. Zukauskas and N. J. Ziugda, Heat Transfer of a Cylinder in Cross Flow. *Springer-Verlag*, 1985, 97–127.

## Impact of Outlet Boundary Conditions on the Flow Properties within a Cyclone

St. Schmidt, H. M. Blackburn and M. Rudman

CSIRO Manufacturing & Infrastructure Technology  
PO Box 56, Highett, Victoria, 3190 AUSTRALIA

### Abstract

In this study the influence of the exit tube geometry on the overall flow properties of cyclones is investigated using detached eddy simulation. The results for different exit pipe shapes and lengths reveal that under certain conditions the outlet has an upstream effect on the flow behaviour within the cyclone. This can in turn result in poor build-up of swirl in the crucial region of the cyclone and substantially reduce the efficiency of the cyclone as a particle-separation device.

### Introduction

Cyclones are widely used in the industrial cleaning process, where particles are removed from particle-laden carrier flows without the need for using particle filters. The performance of these maintenance-free devices depends to a large extent on the swirl velocity within the cyclone as this quantity directly determines the centrifugal force imposed on the particles and at the same time limits the ability to separate particles from the flow. In cyclone design it is therefore vital to accurately calculate the flow in order to be able to predict the overall performance of the cyclone. The work here deals only with single-phase flow of carrier fluid, as this must be correctly predicted before the solids phase can be considered.

Owing to the technological relevance of cyclones, flow simulations have been carried out in the last decades, as appropriate computational techniques have been developed [1, 2]. Since the Reynolds numbers for cyclone flows are usually in the order of  $Re = 10^6$  and the flow itself is inherently very complex due to strong streamline curvature and anisotropic turbulent structures, these flows require sophisticated turbulence modelling in order to obtain reliable and trustworthy results. Of the available models to be applied to the Reynolds-averaged Navier-Stokes (RANS) equations, full Reynolds-stress transport models (RSTM) are best able to cope with turbulence anisotropy and satisfactorily predict these flows [1].

Wall-resolving large eddy simulation (LES), which directly resolves the main turbulent flow structures down to the wall, while potentially the most accurate approach, remains extremely expensive in terms of computational effort and is therefore not useful in product design. However, combinations of RANS and LES, such as detached eddy simulation (DES, [7]) provide attractive alternatives, since this numerical method combines the advantages of LES and RANS. Like LES, DES is capable of resolving unsteady flow features but utilises wall models similar to RANS in order to reduce the spatial resolution in the crucial near-wall region.

Previous results based on LES and DES revealed differences in the flow predictions depending on the inflow conditions, and exhibited deficiency in predicting the swirl level in the cyclonic part of the cyclone [3]. Perhaps more importantly, the results in the present study show that in order to successfully predict flow within the cyclone, care must be paid to the treatment given to the exit tube, downstream of the vortex finder, and external to

the cyclone body. It will be demonstrated that the swirl velocity within the cyclone can be influenced dramatically by changing the length and shape of the vortex finder. Highly swirling flows can promote propagation of flow information upstream, against the mean flow direction, by pressure waves, similar to pressure waves in compressible flows [10].

Our results further suggest that the performance of the cyclone in an industrial environment will be greatly influenced by the actual inflow and outflow conditions. Hence, cyclone design should not be restricted to the cyclone itself, but also encompass the surrounding ductwork.

### Detached Eddy Simulation

This numerical technique based on the solution of the three-dimensional unsteady Navier-Stokes equations was first introduced by Spalart et al. [7] for the simulation of flows past airfoils at high angles of attack, which feature massive flow separation and the shedding of large vortical structures into the wake.

In terms of numerical modelling, this approach combines methods solving the Reynolds-averaged Navier-Stokes (RANS) equations with large-eddy simulation (LES). Owing to the fact that (like LES) DES resolves the turbulence spectrum up to a certain cut-off wavenumber, it is capable of capturing helical vortices which form around the centreline of a cyclone, a feature common to many swirling flows. At the same time, by avoiding the necessity for fine (eddy-resolving) mesh structure near the walls, DES is substantially cheaper than LES.

From a turbulence modelling point of view, DES is obtained by a slight modification of the destruction term in the Spalart-Allmaras one-equation RANS model [6], resulting in a limitation of the length scale by the grid spacing. This hybrid approach employs the unmodified RANS model in wall areas while turning itself into a one-equation subgrid-scale model in regions located off the wall. The model has been implemented and validated for internal and external high Reynolds number flows [4, 5].

### Numerical Method

The Navier-Stokes equations are discretised using a cell-centered finite-volume method based on block-structured grids [11]. All diffusive fluxes are approximated with a central-differencing scheme (CDS). For the convective fluxes, the use of blending functions ensures that in the RANS region a third-order upwind-biased QUICK scheme is used, while in the LES region, CDS is recovered [8]. The time integration is of second order, using a fully implicit three-level scheme, ensuring CFL stability even in coarse regions of the mesh where the CDS would produce unphysical solutions owing to high Peclet numbers. The flow solver is parallelised using a blockwise domain decomposition technique employing message passing library MPI for inter-block communication. Computations were carried out using 28-34 nodes on the APAC Alpha cluster with the same set of boundary conditions, timestep and total integra-

tion time for each configuration, allowing valid comparisons to be made.

### Flow Configuration

The cyclone (figure 1a) features an outer diameter  $D = 2R$  and a half-angle of  $\alpha = 20^\circ$  in the conical region and an underflow-exit pipe at the bottom end for the collection of particles. In this study this outflow is closed for all simulations as only the carrier flow is investigated. Hence only the outflow through the vortex finder with a diameter  $d$  at the top of the cyclone is used and convective outflow boundary conditions are imposed on this outlet plane.

All velocities presented here are normalised by the bulk velocity in the inlet duct. The kinematic viscosity of the fluid was set so that the Reynolds number based on this velocity and the cyclone body diameter  $D$  was  $Re = 1 \times 10^6$ , matching the corresponding experiments [9]. Dimensions are normalised by  $R$ , and the reference axial location,  $z_0$ , is placed in line with the bottom of the cylindrical cyclone outer body. The vortex finder terminates at  $z^*/R = (z - z_0)/R \approx 0.5$ .

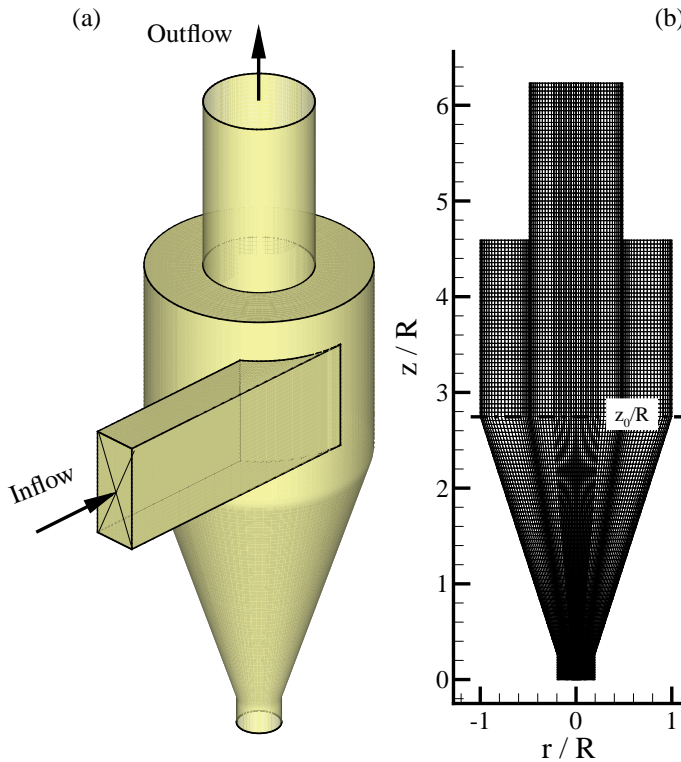


Figure 1: Cyclone geometry and block-structured grid.

### Exit Tube Geometries

The results of previous cyclone LES [3] using a spectral-element method on a domain comparable to the one shown in figure 2a, showed a strong under prediction of the swirl velocity component in the cyclone. DES results confirmed that the choice of a short exit tube length (cf. figure 2a) has an adverse effect on the swirl velocity within main part of the cyclone and contributed to the lack of agreement with the experiments [9].

The main goal of this paper is therefore to examine the effects of different outflow geometries on the swirl velocity in the cyclone. The work concentrated on both the extension of the axisymmetric exit tube as well as different outlet geometries, namely a short, medium and long straight exit (figures 2a-c), an outlet with centre-body blocking the core of the flow at the exit (figure 2d), a radial outlet ring surrounding the exit area (figure 2e), a short/long straight pipe with an additional bend and extension tube (figures 2f/g). The original experimental setup included an elongated rectangular inlet duct and a outlet geometry similar to the one depicted in figure 2g.

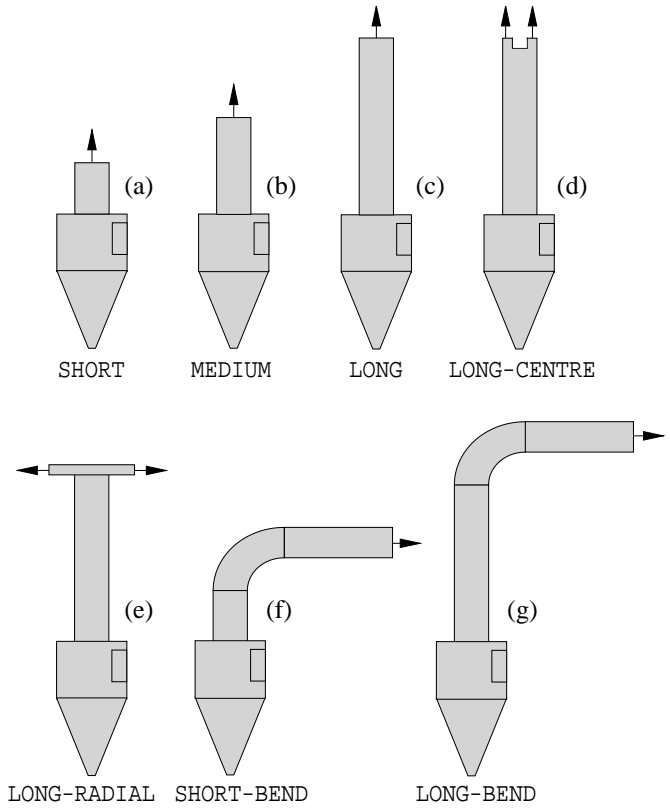


Figure 2: Cyclone outlet geometries: short (a), medium (b) and long (c) straight outlet; long with blocked centre part (d); long with radial outlet (e); short with bend (f) and long outlet with bend similar to the experimental setup (g); arrows indicate outflow direction.

ure 2e) as well as a short/long straight pipe with an additional bend and extension tube (figures 2f/g). The original experimental setup included an elongated rectangular inlet duct and a outlet geometry similar to the one depicted in figure 2g.

### Results

The figures 3a-c show the distribution of the time-averaged swirl velocities at three locations within the cyclone for all geometries including the previously mentioned simulation based on the SHORT geometry (cf. fig. 2a). Obviously the simulations based on geometries with a longer exit are in much closer agreement with the measurements, except the geometry with the long vortex finder and the blocked centre (cf. figure 2d), which gives swirl velocity profiles comparable to those for the SHORT geometry. In part, this setup was chosen because in the previous spectral element LES an axisymmetric centre body was placed in the outlet area in order to prevent any flow re-entering the domain and de-stabilising the numerical scheme. The DES of this configuration suggests that this body slows down the swirl velocity in the cyclone and contributes to the poor quality of the results. Comparing the results of the other geometries, it becomes clear that beyond a certain exit tube length, the shape of the geometry does not have a strong impact on the swirl in the cyclone. Even the inclusion of the bend does not affect the solution significantly.

The mean axial velocities are shown in figures 4a-c. Below the entry plane of the vortex finder (figure 4a) the results are mainly influenced by the length of the exit tube as the solutions tend to approach the results with bend included in the outlet geometry. The shorter the outlet, the more the velocity peak drops and evens out the steep velocity gradients. In the conical part of the cyclone (figure 4b,c) the differences become

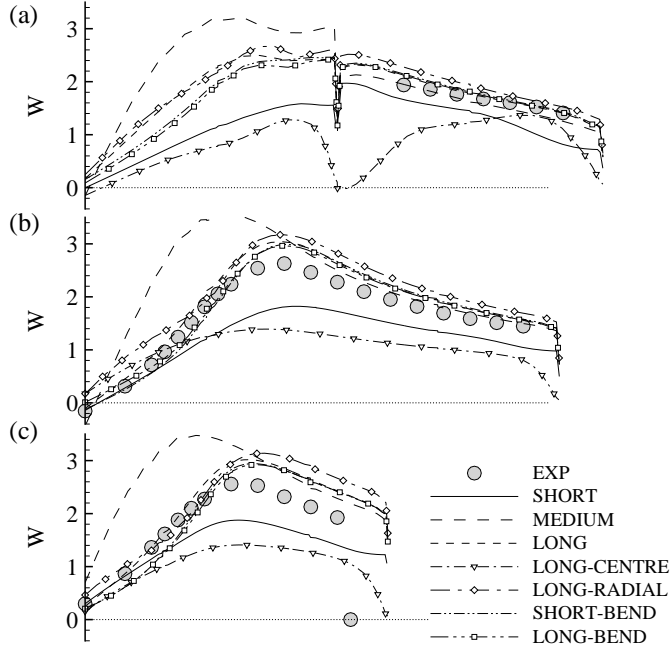


Figure 3: Time-averaged tangential velocity profiles at: (a)  $z^*/R = 1.0$ , (b)  $z^*/R = -0.25$  and (c)  $z^*/R = -1.25$ .

larger and two areas can be identified: a near-axis region, which gives good overall agreement of all solutions, and an internal part, located between the axis and the surrounding walls. In the latter region, the axial velocities of all solutions miss the experiments and tend to flow counter to the experimental results. The computations exhibit three radial locations where the velocity changes direction, whereas the experiments do not suggest such behaviour. As only the solutions where swirl velocities are under-predicted exhibit this behaviour, the results indicate that depending on the swirl more than one flow pattern may exist in the cyclone body.

At the lower end (figure 4c), these differences become more obvious and the geometries with longer exit tubes tend to agree more with the experimental data than the low-swirl solutions.

#### Influence of Exit Tube Geometry

The differences in the results of the shorter cyclone geometries (SHORT/MEDIUM) compared to the other cases can be traced to figure 5, where tangential velocity is represented by grey tones ranging from  $W = 0$  (black) to  $W = W_{\max}$  (white). The location of the vortex core can be clearly identified as the dark region meandering around the centre line of the cyclone. It can be seen that especially for the shorter geometries (figures 5a/b) the core becomes increasingly perturbed and non-axial.

In part, this behaviour can be linked to flow at the entry to the vortex finder where, for the shorter geometries, the vortex core is inclined to the exit plane, thereby promoting localised reverse axial flow. As the solution evolves in time these instabilities eventually wash away for the longer domains (figures 5c/d) but prevail in the shorter domains and prevent the flow from settling into a stable flow pattern. This state can be classified in terms of flow criticality as a high swirl-number case, as discussed in [10]. According to their findings, swirling flows can have either a low or a high swirl number called either supercritical or subcritical respectively. In *supercritical* flows no information from a downstream point can be transported upstream, whereas in *subcritical* flows a downstream disturbance can propagate upstream hence changing the flow patterns there.

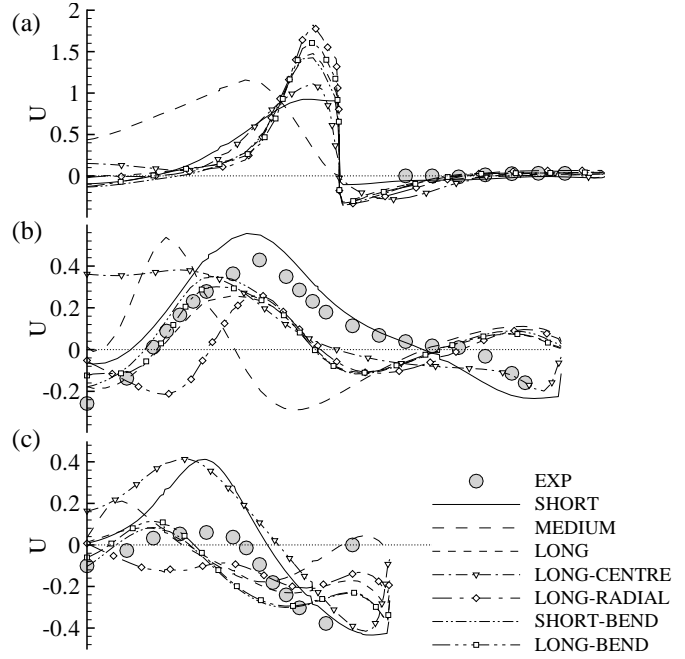


Figure 4: Time-averaged axial velocity profiles at: (a)  $z^*/R = 1.0$ , (b)  $z^*/R = -0.25$  and (c)  $z^*/R = -1.25$ .

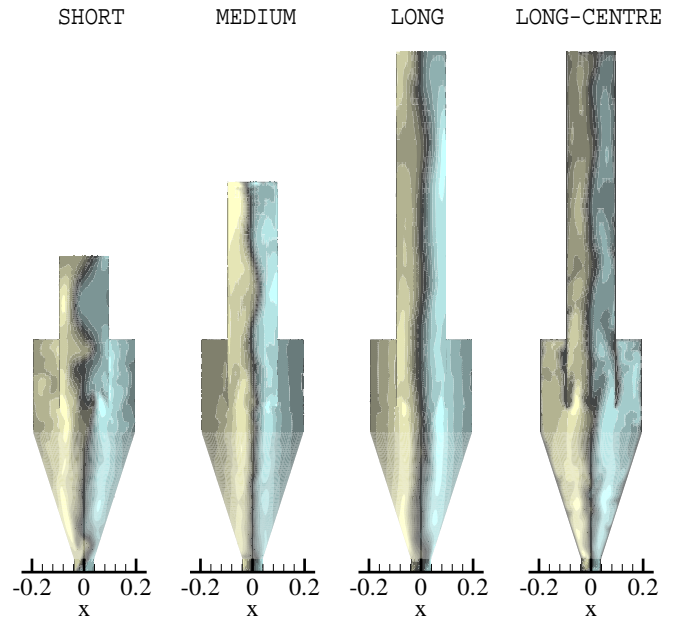


Figure 5: Location of the centre vortex for different exit tube geometries visualised by time-averaged swirl velocity: short (a), medium (b) and long (c) straight outlet; long with blocked centre part (d)

Figure 6 displays the axial velocity profiles in the vortex finder starting just downstream of the entry plane at  $z^*/R \approx 0.5$ . The velocity evens out the asymmetry linked to the swirl velocity and begins a recovery towards a rotating pipe flow. At the most downstream location (figure 6c) massive reverse flow occurs in the central part, resulting from by the strong vortex and the low pressure associated with it. As even the geometries with the longest exit tube have reverse flow at these locations, this reverse flow in itself cannot be the main reason for the lack of swirl observed in the short geometries. As only the blockage in the LONG-CENTRE geometry prevents this backflow, it seems to be entirely driven by low pressure in the vortex core.

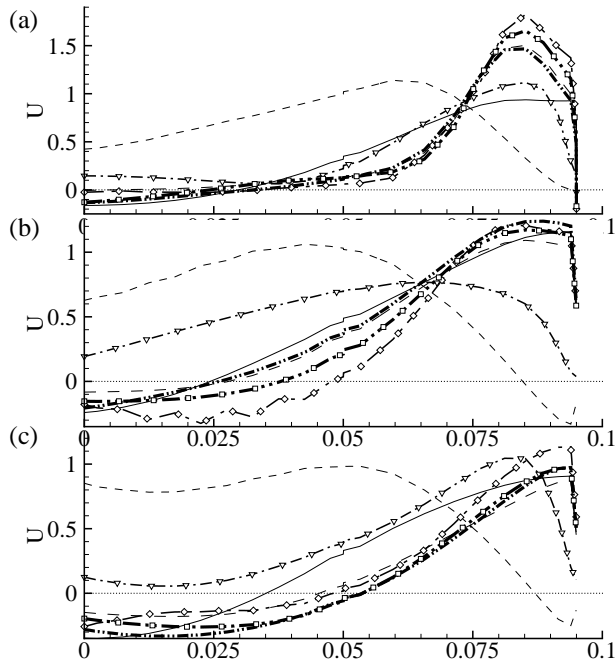


Figure 6: Time-averaged axial velocity profiles in the vortex finder at: (a)  $z^*/R=1.0$ , (b)  $z^*/R=2.0$  and (c)  $z^*/R=3.1$ .

In figure 7 the swirl numbers  $\langle S \rangle = (\int_0^R w u r^2 dr) / (R \int_0^R u^2 r dr)$  in the vortex finder (averaged in the circumferential direction) are shown. While most solutions have rather high but almost constant swirl numbers just above  $\langle S \rangle = 2$ , the low swirl of the SHORT domain can also be seen. The swirl number drops significantly in the short vortex finder (cf. figure 2a), indicating some kind of non-settled behaviour. The cases with longer exit tubes apparently have a more stable flow pattern owing to the distance of the exit from the cyclone itself, and hence disturbances originated in the outlet area do not tend to feed back into the main part of the cyclone chamber.

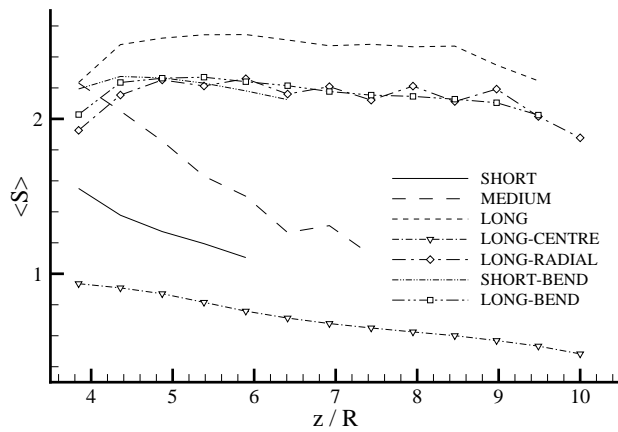


Figure 7: Swirl number  $\langle S \rangle$  in the vortex finder averaged in the azimuthal direction at downstream locations; note that these values are only determined in the straight part of the exit tube.

## Conclusions

Flow simulations of cyclones with different exit tube geometries have been carried out using detached eddy simulation. The DES method predicts the main flow properties quite accurately, however, depending on the length of the vortex finder two different flow pattern can be identified. In case of a short vortex

finder, flow can enter the domain and alter the dynamics in the main cyclone chamber resulting in poor swirl velocities. In geometries with a longer vortex finder, these effects do not arise, although even for the geometries which include a bend, reverse flow can occur without any serious consequence on the overall results.

## Acknowledgements

The support of the Australian Partnership for Advanced Computing (APAC) is gratefully acknowledged. Thanks are also due to R. Weber for his helpful suggestions.

## References

- [1] Boysan, F., Swithenbank, J. and Ayers, W. H., Mathematical modeling of gas-particle flows in cyclone separators, in *Encyclopedia of Fluid Mechanics*, editor N. P. Chermisnoff, Gulf, 1986, volume 4, 1307–1329.
- [2] Griffiths, W. and Boysan, F., Computational fluid dynamics (CFD) and empirical modelling of the performance of a number of cyclone samplers, *J. Aero. Sci.*, **27**, 1996, 281–304.
- [3] Schmidt, S., Blackburn, H., Rudman, M. and Sutalo, I., Simulation of Turbulent Flow in a Cyclonic Separator, in *3rd Int. Conf. CFD Minerals and Proc. Ind.*, editors P. Witt and M. Schwarz, CSIRO, Dec 10–12, Melbourne, Australia, 2003, 365–369, ISBN 0 643 09037 1 (Printed Book).
- [4] Schmidt, S. and Thiele, F., Comparison of numerical methods applied to the flow over wall-mounted cubes, *Intl J. Heat Fluid Flow*, **23**, 2002, 330–339.
- [5] Schmidt, S. and Thiele, F., Detached Eddy Simulation of Flow around A-Airfoil, *J. Flow Turbulence & Combustion*, **71**, 2003, 261–278.
- [6] Spalart, P. and Allmaras, S., A one-equation turbulence model for aerodynamic flows, *La Rech. Aéronautique*, **1**, 1994, 5–21.
- [7] Spalart, P., Jou, W.-H., Strelets, M. and Allmaras, S., Comments on the feasibility of les for wings, and on a hybrid rans/les approach, in *Advances in DNS/LES*, editors C. Liu and Z. Liu, Greyden Press, Columbus, OH, USA, 1997.
- [8] Strelets, M., Detached Eddy Simulation of Massively Separated Flows, in *39th AIAA Aerospace Sciences Meeting and Exhibit*, AIAA, Reno, Nevada, 2001, number 2001-0879 in 2001-0879, #2001-0879.
- [9] Sutalo, I. and Merrell, J., Pressure loss measurements on physical models of cyclones, Report 99/095, CSIRO BCE, 1999.
- [10] Weber, R., Visser, B. and Boysan, F., Assessment of turbulence modeling for engineering prediction of swirling vortices in the near burner zone, *Intl J. Heat Fluid Flow*, **11**, 1990, 225–235.
- [11] Xue, L., *Entwicklung eines effizienten parallelen Lösungsalgorithmus zur dreidimensionalen Simulation komplexer turbulenter Strömungen*, Dissertation, Technische Universität Berlin, 1998.



## An Experimental Study of the Jet of a Boat Propeller

A. Loberto<sup>1</sup>, R.J. Brown<sup>1</sup>, M.K. Kwek<sup>1</sup>, A. Iida<sup>2</sup>, H. Chanson<sup>3</sup>, and S. Komori<sup>4</sup>

<sup>1</sup>School of Mechanical, Manufacturing, and Medical Engineering  
Queensland University of Technology, Brisbane QLD 4001, AUSTRALIA

<sup>2</sup>Department of Mechanical Engineering, Kogakuin University  
2665 Nakanomachi, Hachioji, Tokyo 192-0015, JAPAN

<sup>3</sup>Department of Civil Engineering  
The University of Queensland, Brisbane QLD 4072, AUSTRALIA

<sup>4</sup>Department of Mechanical Engineering, Kyoto University  
Kyoto 606-8501, JAPAN

### Abstract

An experimental study of the velocity and concentration (scalar) fields of a propeller is presented. Field and laboratory measurements were undertaken. The former were up to 50 diameters downstream. Important findings were that the mean velocity and scalar fields quickly become Gaussian while further downstream they both become irregular sometimes approaching approximately linear profiles. Propeller turbulence causes rapid mixing giving an initial concentration dilution factor of 1/20,000 after fifty propeller diameters. Some preliminary comparisons with field measurements of an actual boat in a natural waterway are made. Considerably more work is needed to gain a full understanding of the complex problem of propeller mixing.

### Introduction

In Queensland alone, boats and ships release approximately 4.5 ML of oil into marine environment each year, while this figure is about 1.0 million tonnes world wide [4]. In addition, significant quantities of unburned fuel, toxic combustion by-products and well over 14 M tonnes of antifouling agents (tri-butyl tin) are directly released into the water and dispersed by the vessels' propellers annually. Such pollutants have been shown to impact directly on Australia's coastlines, including the Great Barrier Reef. Inland waterways, dams, and estuaries are even more critically affected by pollution from vessels because dispersion is drastically limited by weak background flows and small water volumes. In all situations, propellers create considerable turbulence, which thoroughly mixes pollutants and chemicals into the water. It is of great importance to quantify pollutant concentrations in the jet region, and hence to estimate the effective contaminant concentrations emitted by vessels. Figure 1 shows a schematic diagram of dispersion of emissions in the propeller jet of a vessel. While there has been considerable research on propellers for ship propulsion, very little research has been done on the dispersing action of the propeller. We report results of the first study of its kind to experimentally quantify the dilution of a conserved scalar by a vessel type propeller. The present work aims to comprehend the fundamentals of mixing processes occurring in a propeller jet.

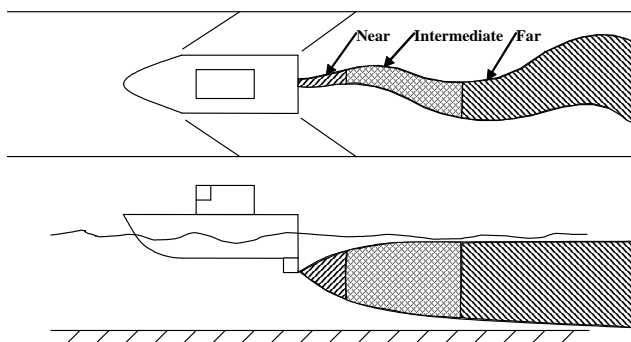


Figure 1: Schematic of boat propeller jet plume and regions of interest.

### Experimental Method and Data Collection

New experiments were conducted to measure both the velocity and scalar concentration fields in a propeller jet. The introduced scalar was dye (Methylene Blue). No horizontal profile was performed because of experimental limitations, but flow visualisations indicated approximately horizontal symmetry of the flow field. Measurements were performed at several longitudinal locations ranging from near-field,  $x/D=2$ , to far-field,  $x/D=50$ , where  $x$  is the distance downstream of the propeller and  $D$  is the propeller diameter (tip-to-tip).

The tests were conducted in the closed loop flume of the Department of Mechanical Engineering at Kyoto University, Japan. The flume dimensions were 12 m (L) x 0.4 m (W) x 0.2 m (H). The water level was controlled by a sharp-crested weir at the channel downstream end. The water depth ( $h_1+h_2$ ) was 0.150 m and held constant for all experiments (Fig. 2). The volume flow rate was held constant and resulted in a water surface velocity of 0.040 m/s, used for all experiments. The background turbulence intensity was low (rms/mean < 1%).

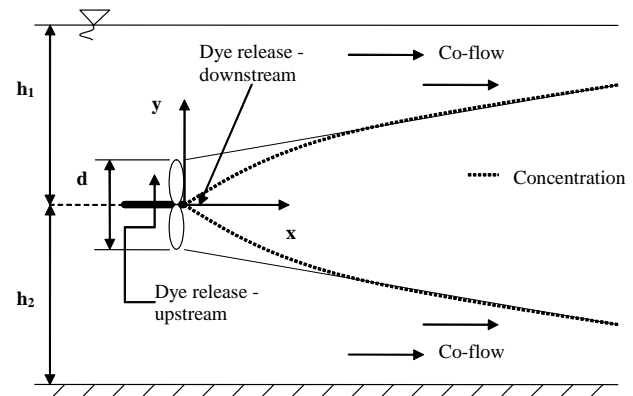


Figure 2: Schematic diagram of experimental set-up.

The experimental set up comprised a two-bladed propeller, powered by a variable speed electric motor with flexible cable transmission, held in space by a wing shaped frame where the long axis coincided with direction of flow. The propeller diameter,  $D$  was 20 mm. Velocity measurements were conducted with a 2D Dantec Laser Doppler Anemometer.

Dye concentrations (mean and fluctuations) were measured with a Komori concentration probe [5] held in place by an adjustable frame. The Komori probe has a sample rate of 1 kHz and a frequency response of up to 100 Hz. The data collection was conducted with a Sony PC208Ax digital recorder. The dye was released upstream of the propeller, 8 mm above the rotation axis and 4 mm upstream of the propeller blades (Fig. 2). The inside diameter of injection pipe was 1 mm. The flow of injected dye

was maintained constant by a syringe pump. Experimental conditions are shown in Table 1 listing initial dye concentration,  $C_o$  and injected flow rate,  $Q$ . The background concentration of dye steadily increased over time because the flume volume was fixed and the water was recirculated. The upward drift in background concentration was accounted for by measuring the background concentration in between each profile, about every thirty minutes. At each measurement point, the measured background concentration was subtracted from the reading to give the true concentration. Background fluctuations were eliminated by mixing the flow in a tank with an impeller. Spectral analysis was used to compare fluctuations in the flume before and after dye injection. No significant differences were observed even with relatively high background concentrations. The Komori probe exhibited a linear voltage response to variations in concentration. The probe was calibrated in clean water (0 ppm) and in solutions of known concentration up to the maximum range of the instrument (8 ppm).

The total experimental campaign consisted 600 point measurements. At each point, 120,000 instantaneous measurements were recorded with a sampling rate of 1 kHz. The data were processed by a FORTRAN program to obtain the concentration statistics, including the first four moments of the scalar concentration, although the paper focuses on mean concentration results. Velocity and scalar experiments were conducted separately.

$x/D$	$C_o$	$Q$	Sample time
	ppm	mL/min	minutes
2	4000	5	2
10	4000	10	2
20	25000	10	2
50	25000	10	2

Table 1: Experimental conditions for upstream dye injection at 3000 rpm.

### Velocity field

The mean velocity field was recorded in the longitudinal and tangential axes from  $x/D = 2.5$  to  $x/D = 50$  for two propeller speeds, 1500 and 3000 rpm. Downstream of the propeller, the evolving jet can be represented by a Gaussian profile once it is established [1]. Typical results are shown in Figure 3 for 3000 rpm. The data have been presented in a normalised format to emphasise jet flow field evolution. The data are compared with the Gaussian equation:

$$\bar{U} = U_m \exp \left[ -\frac{1}{2} \left( \frac{r-r'}{\sigma} \right)^2 \right] \quad (1)$$

as used by Brown and Bilger [2] for a study of reactive plumes in grid turbulence where  $U_m$ ,  $r$ ,  $r'$  and  $\sigma$ , are the maximum jet velocity, radial distance from centreline (shown as  $y$  on the figures), radial offset of curve centerline from  $x=0$  and standard deviation of Gaussian profile, respectively. Overbars represent mean for velocity. Gaussian curves were fitted (with a least squares criteria) to the data, using a steepest descent, unconstrained multivariable curve fitting procedure. Equation (1) was chosen because it comprised fundamental parameters that are clear descriptors of the jet shape.

A power law was fitted to  $\sigma$  obtained from Eq (1) (Fig. 4, Table 2):

$$\frac{\sigma}{D} = k \left( \frac{x}{D} \right)^m \quad (2)$$

and a similar expression for decay of  $U_m$ :

$$\frac{U_m}{U_p} = k \left( \frac{x}{D} \right)^m \quad (3)$$

where  $U_p$  is the jet velocity immediately downstream of the propeller.

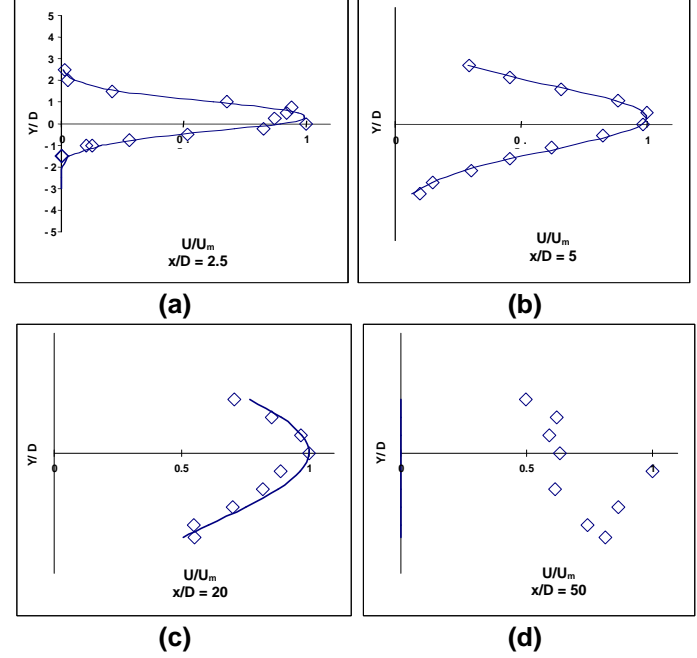


Figure 3: Mean velocity field  $\bar{U}/U_m$  at 3000 rpm with profiles from Eq (1); (a), (b), (c), (d):  $x/D = 2.5, 5, 20, 50$ , respectively.

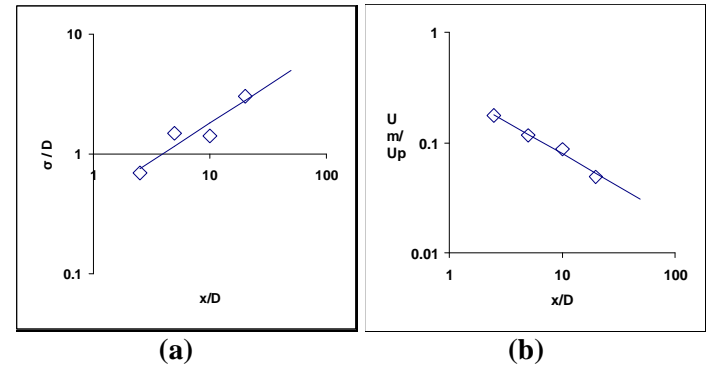


Figure 4: Evolution of Gaussian Profile statistics for mean velocity at 3000 rpm: (a), standard deviation; (b) mean.

At 3000 rpm, the jet velocity data exhibited some scatter in relation to the Gaussian profile. In particular, at the farthest downstream position ( $x/D=50$ ), the velocity data exhibited a breakdown in jet profile whereas a slower jet (1500 rpm, results not shown) maintained a Gaussian distribution. There are a few likely causes of jet breakdown in this far field. It is conceivable that the jet was interacting with the wall. It is important to note that both jets shared a same rate of spread and that the jet did not break down in the far-field at 1500 rpm, although it touched the walls somewhat. Hence the evidence available did not support some jet impingement on the flume wall. The writers hypothesise instead that the higher velocity and flow of the 3000 rpm jet may have induced some instabilities leading to the jet break down observed at 3000 rpm. This matter is under further investigation.

### Scalar Concentration Field

Since it was shown that submerged jets exhibit a Gaussian velocity profile ([1] and present study), the distributions of

conserved scalar were compared also with Gaussian curves using a similar method to Eq (1):

$$C = C_p \exp \left[ -\frac{1}{2} \left( \frac{r-r'}{\sigma} \right)^2 \right] \quad (4)$$

where  $C$  and  $C_p$  are the concentration at a point  $P(x,r)$  and peak concentration, respectively.

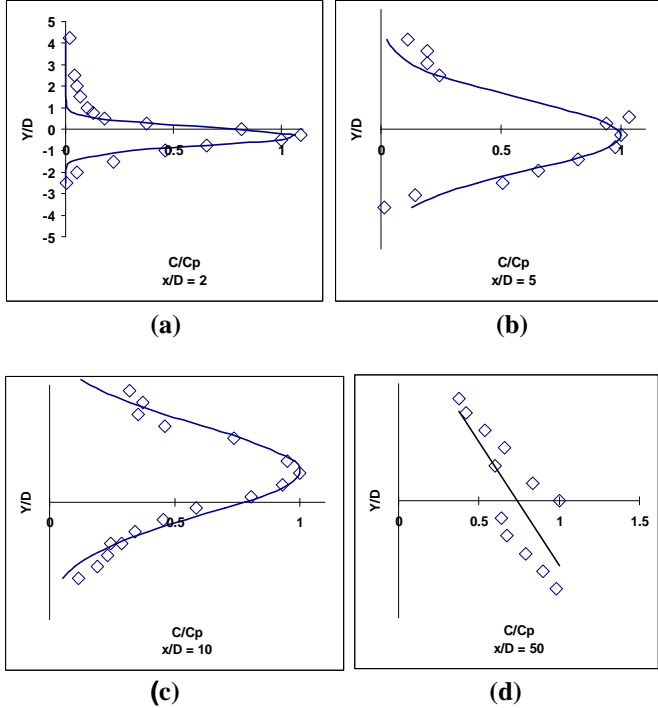


Figure 5: Vertical profiles of normalised mean centreline concentration at 3000 rpm.

Figure 5 shows vertical profiles for consecutive downstream locations, for  $x/D=2, 5, 10$  and  $50$ . The downstream location,  $x$ , and the radial location,  $y$ , are normalised against propeller diameter,  $D$ . Concentration,  $C$ , is normalised with the peak Gaussian concentration,  $C_p$ .

Drift of the plume centerline,  $r'$  has not been subtracted from the data so the reader can see the variability of the experiment. The maximum drift was less than  $D$  for all experiments. Despite some scatter, most data (Fig. 5a,b,c) compared favourably with Equation (4). Yet there were two obvious experimental variables that contributed to data scatter. Both were addressed through careful experimental procedure and post-processing of the results. First, the calibration of concentration probe was prone to drift, as expected of high frequency measuring probes. The calibration was re-checked over consistent periods in time during the experiment and systematic data were available to make corrections during the processing phase. Second, the background concentration of dye increased with time. Although the background concentration was measured periodically, the inherent randomness of the process and the limiting resolution of the equipment contributed toward some data scatter that could not be completely accounted for.

The evolution of dye concentration plume is of significant interest. Figure 5 illustrates that the plume originated, in the near-field region, with an approximately Gaussian shape (Fig. 5a) and evolved by outward spreading, eventually developing into an approximately linear distribution (Fig. 5d). The initial Gaussian shape was expected, based on previous results of near-field propeller jet. However, the observed linear profile in the far field

( $x/D=50$ ) was a new finding. It is hypothesised that greater longitudinal dispersion of dye took place in the high-velocity flow region next to the free-surface, while, next to the bottom, dye transited at lower flow velocities in the boundary layer, hence with a higher concentration. The influence of swirl may also contribute to this effect. Indeed the data showed that, next to the bottom, the scalar concentration was approximately fifty per cent larger than that next to the free surface (Fig. 5). Such a result would be amplified in a rough, coarse natural channel leading possibly to a greater concentration gradient between lower and upper flow regions.

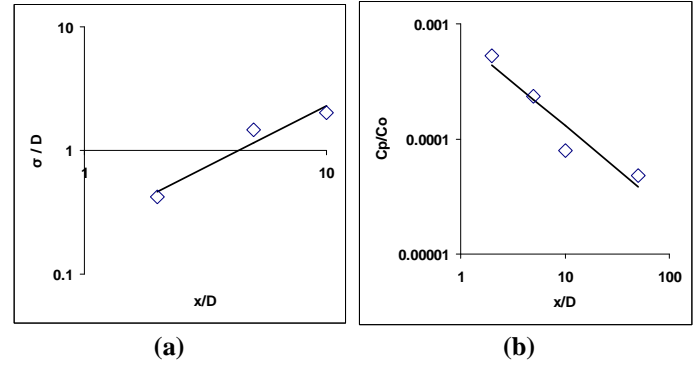


Figure 6: Evolution of Gaussian profile statistics for mean concentration; (a) standard deviation,  $\sigma$ ; (b) mean on centreline,  $C_p$ .

	Velocity		Scalar	
	$\sigma/D$	$U_m/U_p$	$\sigma/D$	$C_p/C_0$
m	0.63	-0.59	1.00	-0.76
k	0.42	0.31	0.23	7.40E-04

Table 2: Coefficients for line of best fit for axial change of mean velocity and mean scalar concentration at 3000 rpm corresponding to Figures 4 and 6, respectively.

Figure 6 shows the longitudinal variations of Gaussian profile properties,  $\sigma$  and  $C_p$ . The downstream change in radial offset of the plume (not shown) drifts by approximately one propeller diameter

Figure 6(a) shows the growth in plume width,  $\sigma$ , with increasing downstream distance, using a Log-Log scale. A power-law curve was fitted to the growth trend of  $\sigma/D$ :

$$\frac{\sigma}{D} = k \left( \frac{x}{D} \right)^m \quad (5)$$

The least squares fit was carried out to ascertain the magnitudes of the coefficients,  $k$  and  $m$ , where  $m$  is the gradient of the straight line in Figure 6(a) and  $k$  takes the value of  $10^c$  where  $c$  is the y- intercept of the same straight line of best fit. The values of  $m$  and  $k$  are shown in Table 2.

Figure 6(b) shows the decay in peak concentration,  $C_p$ , with increasing downstream distance, using a Log-Log scale. As with Figure 6(a), a power-law curve was fitted to the growth trend of  $C_p/C_0$ :

$$\frac{C_p}{C_0} = k \left( \frac{x}{D} \right)^m \quad (6)$$

The values of  $m$  and  $k$  for best data fit in Figure 6(b) are shown in Table 2. The total dilution of the peak concentration is of

significant interest. In Figure 6(b), the peak concentration was reduced by a factor of  $1.48\text{E-}6$  (i.e.  $\sim 1/20,000$ ) by  $x/D=50$ .

It should be noted that since the results at  $x/D=50$  did not exhibit a Gaussian profile, the graphs in Figure 6(a) does not include data from this axial location. Furthermore, in Figure 6(b), for the data point at  $x/D=50$ , the measured data at the propeller centreline was used as an estimate of  $C_p$  since the profile exhibited did not allow a Gaussian profile to be fitted. It should also be noted that in Figure 6, graphs (a) and (b), both axes have been normalised against  $D$ .

Corresponding experiments with reduced propeller speed (1500 rpm) exhibited similar trends to the 3000 rpm results with an increased growth of  $\sigma$  and faster decay  $C_p$ . Further experiments with a dye release point downstream of the propeller and with the same propeller speed produced results (not shown) that supported those described above and shown in Figure 5 and Figure 6. The results from the downstream dye release showed a less pronounced shift of the centreline, a similar rate of change of plume width (although with slightly lower magnitudes) and similar decay rate of peak concentration. However, the difference in peak concentration between the free surface and bottom was more pronounced, with a three-fold change, fifty per cent higher than that exhibited by the upstream experiment.

Present results can be used to quantify the dispersion and mixing of scalars by a propeller. As shown in Figure 6(b) and Table 2, the decay exponent for  $C_p/C_0$  is  $m=-0.76$  in the range  $2 < x/D < 50$ . Such a result is lower than that for a plume for which  $m=-1$  [2], but larger than that typically obtained for a jet. However, in the range  $x/D < 10$  the exponent  $m$  was considerably greater: i.e.,  $m=-1.5$ , suggesting that the near flow field is characterised by a greater decay of peak concentration. Overall significant mixing occurs with a dilution of approximately  $1/20,000$  by  $x/D=50$ .

### Field Experiment

In parallel with the present study a series of field tests [3] were conducted in cooperation with the Environmental Protection Authority and the University of Queensland to contribute to a broad environmental assessment of Eprapah Creek, Brisbane, which included: continuous water quality sampling, creek velocity measurements, bird and fish activity monitoring. All measurements were maintained for up to 8 hours continuously.

During the course of the field test several different outboard motor / boat combinations were driven past the sampling area at different load/velocity combinations which were carefully monitored. Boats with outboard motors were driven past the measurement point for a range of speeds and configurations. Figure 7 shows the effect of a non planing outboard motor on the velocity field at the point of measurement which was 0.5 m below the surface and approximately 1 m from the passing boat horizontally. The results in figure 7 showed high turbulence caused by both propeller and bow wave corresponding to that observed in the present study. These effects were detected in the turbulent velocity data for a period of less than one minute typically, but the velocity autocorrelation function showed some effects lasting at least eight minutes, while water quality observations showed some important levels of fluctuations for several minutes after boat passage (e.g. in terms of turbidity, conductivity and temperature [3]). Overall the data suggested some mixing induced by wake waves and by the propeller.

Further comparison of the velocity and scalar fields in the laboratory and field are continuing.

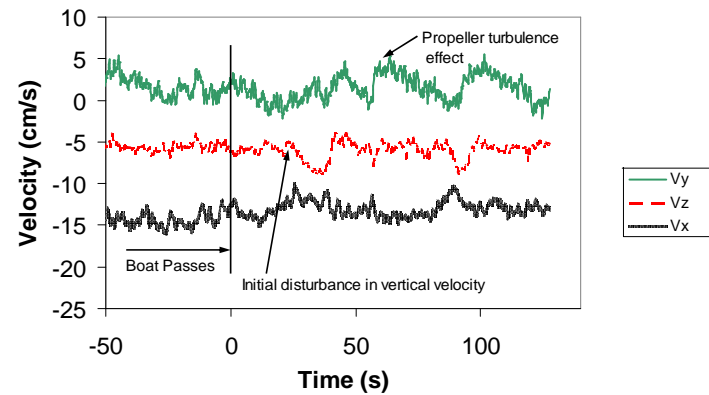


Figure 7: Instantaneous velocity disturbance caused by an outboard motor. (coordinates:  $x, y, z$ ; parallel to creek, transverse, vertical, respectively).

### Summary and Conclusion

The initial conclusion of this study of dye mixing by a propeller indicates that contaminant mixing is rapid giving a reduction in peak Gaussian concentration by a factor of  $1.48\text{E-}6$  after fifty propeller diameters. With an actual boat in a natural waterway, the situation will be different because the incoming velocity to the propeller will be higher and interactions with low level environmental turbulence will occur. Considerably more work is needed to gain a full understanding of the complex problem of propeller mixing.

### Acknowledgments

We gratefully acknowledge the expert assistance of Dr K Nagata and Mr Y Ito, and staff in the conduct of these experiments at Kyoto University. Support for Dr. Richard Brown under a Research Fellowship from the Japan Society for the Promotion of Science and the Australian Research Council is gratefully acknowledged.

### References

- [1] Albertson, M.L., Dai, Y.B., & Jensen, R.A., *et al.*, Diffusion of Submerged Jets, in *ASCE Transactions* (Fort Collins, 1948, 639-664.
- [2] Brown, R.J. & Bilger, R.W., An Experimental Study of a Reactive Plume in Grid Turbulence. *J Fluid Mech.*, **312**, 1996, 373-407.
- [3] Chanson, H., Brown, R., Ferris, J., & Warburton, K., "A Hydraulic, Environmental and Ecological Assessment of a Sub-tropical Stream in Eastern Australia: Eprapah Creek, Victoria Point QLD on 4 April 2003", *Report No. CH52/03*, Dept. of Civil Eng., Univ. Queensland, Australia, 2003.
- [4] Kelly, C.A., Ayoko, G.A. & Brown, R.J., Under Water Emissions from a 2-Stroke Outboard Engine: a Comparison between EAL and Equivalent Mineral Lubri-cant. *Proc 2nd Internl Conf on Tribology in Environ Design* 8th-10th September 2003, Bournemouth, UK., (Eds M. Hadfield & Y. Wang) ISBN: 1-86058-415-2., 2003, 171-180
- [5] Komori, S., Hunt, J.C.R., & Kanzaki, T., *et al.*, The Effects of Turbulent Mixing on the Correlation between Two Species and on Concentration Fluctuations in Non-Premixed Reacting Flows. *J. Fluid Mech.*, **228**, 1991, 629-659.



## Airflow Distribution through the Radiator of a Typical Australian Passenger Car

H. Jama, S. Watkins, C. Dixon and E. Ng

School of Aerospace, Mechanical & Manufacturing Engineering  
RMIT University, VIC, 3081 AUSTRALIA

### Abstract

The airflow distribution and non-uniformity across the radiator of a full-size, Australian made Ford falcon was tested at the RMIT Industrial Wind Tunnel. The cooling air intakes of the vehicle were shielded by a quarter, one-half and three-quarters and fully blocked. Four different possibilities of shielding methods were investigated with the aim of determining the best method of shielding to be employed. Results from these tests have shown the optimum method for shielding the front-end of the vehicle in terms of airflow uniformity to be the horizontal method followed by the vertical method. These shielding methods also produced the higher average airflow velocity across the radiator which is analogous to better cooling.

### Introduction

The aerodynamic drag coefficient of most passenger vehicles is now around 0.3. The use of body shape and external detail optimisation has led to this low drag coefficient. The remaining areas of exploration and optimisation are the underbody and cooling system. The cooling system of a typical passenger vehicle contributes between 6 and 10 percent to the overall drag of the vehicle [5]. Furthermore engine cooling systems are designed to meet two rare and extreme conditions. Firstly, driving at maximum speed and secondly driving up a specified gradient at full throttle while towing a trailer of maximum permitted mass. At all times, in fact the majority of the time, the cooling system operates below maximum capacity while incurring a drag penalty [4].

A system that matches the required cooling airflow through the radiator to the operating condition of the vehicle has been recently proposed. It involves the varying of the cooling air intakes by the use of servomotors and controllers such that in the majority of the cases described above, the cooling air intake areas are less than the baseline condition.

It is generally known that the velocity of the airflow through the radiator is a function of the vehicle speed and the "heat transferred by a radiator is a function of the airflow rate across the radiator" [6]. However, the non-uniformity is another factor to determine in engine cooling. Others like Chiou [2] have suggested that radiator heat transfer effectiveness "deteriorates due to two-dimensional flow non-uniformity on both the air and coolant sides". Therefore an experimental program was designed that investigated methods of reducing the airflow through the radiator and engine compartment by shielding the front-end of a passenger vehicle. The velocity distributions as well as the non-uniformity of the cooling airflow across the radiator were also measured.

### Test Vehicle and Experimental Set up

The vehicle used in this investigation was an Australian made Ford Falcon AU. This vehicle is a middle range family vehicle that weights approximately 1550kg. It comes with a four-speed automatic transmission as standard equipment. The air

conditioning and engine-cooling components that are pertinent to this investigation consisted of a condenser, fitted in front of the radiator, and a mechanically driven centrifugal water pump, dual electric fans with shroud combination and an airdam. The airdam aids in engine cooling by creating a favourable pressure gradient for the cooling airflow. The front-end cooling air intakes consist of a decorative grille and a lower intake area.

To study the variable front-end geometry, four front-end shielding methods were employed. In each of the methods the front-end cooling air intakes were shielded by an area of  $\frac{1}{4}$ ,  $\frac{1}{2}$ ,  $\frac{3}{4}$  and totally shut. These shielding methods employed were vertical, horizontal, side-to-side and side-to-centre as illustrated in Figure 1 to Figure 4. In the vertical shielding method evenly distributed vertical strips were used. The underlying principle for this type of shielding is that many vehicles already have vertical strips as part of their decorative grille and lower cooling intakes. To implement this type of shielding one could envisage plates sliding behind each other that would change the area of the cooling air intakes.

However, other vehicles exhibit the opposite by having decorative grilles and lower cooling air intake openings that are covered by horizontally placed strips. The analogous method of shielding that is envisaged is that of having horizontal plates sliding behind each other. The other configuration investigated was closing the intake opening from one side to the other. This configuration was chosen as it can be applied to small vehicles that have very small radiators and even smaller condensers placed in front of these radiators. Instead of this normal arrangement, it is envisaged that the condenser could be placed besides the radiator. Then, in periods of extended non-operation of the condenser like winter, one could entirely block off the condenser side to the cooling airflow. The last option considered is to symmetrically shield both the grille and lower cooling air intake from both sides to the centre. This last method was used to investigate the interaction between external and internal flows.

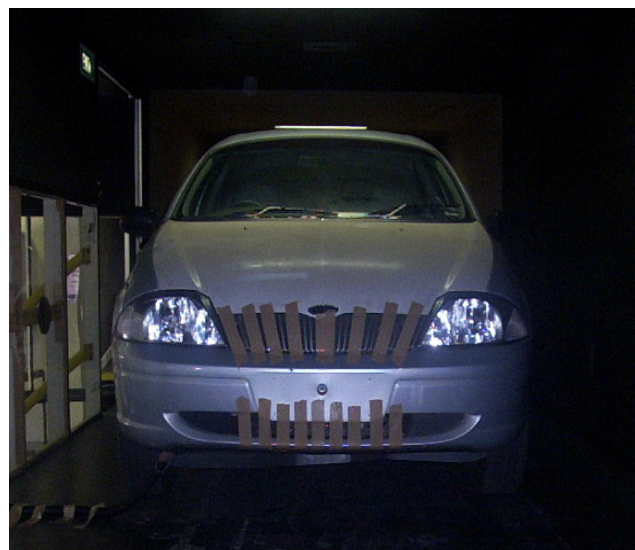


Figure 1: Vertical method (1/2 cooling air intake area shielded).





Figure 2: Horizontal method (1/2 cooling air intake area shielded).



Figure 3: Side-to-side method (1/2 cooling air intake area shielded).



Figure 4: Side-to-centre method (1/2 cooling air intake area shielded).

### Test Facilities, Equipment and Parameters

The vehicle was tested at the RMIT Industrial Wind Tunnel. This tunnel has a 3m wide, 2m high and 9m long working test section and a 2:1 contraction ratio. It has been described in detail in the works of Watkins [10] and Ng et al. [8]. This tunnel has a blockage ratio of 0.35 for a full-size Australian passenger vehicle. Although this blockage is very high for aerodynamic

testing, it was shown by Ng et al. [8] that it can be used adequately for evaluating the cooling performance of a passenger vehicle. Others [3, 7] had earlier shown that it could be used to evaluate the cooling performance of the front section of a passenger vehicle.

The choice of equipment available to quantify airflow distribution across the radiator was limited by the cost and complexities involved. A pressure based technique established by Ng et al. [9] to quantify airflow distribution across an automotive radiator was used in this investigation. The equipment consisted of 24 pairs of hypodermic tubes inserted into the radiator and condenser assembly, a pressure measuring unit, a PC computer and the associated software. The technique is relatively low cost, robust and suitable for measuring complex airflow. For a detailed description please refer to Ng et al. [9].

The airflow non-uniformity index ( $i$ ) was used to quantify the non-homogeneity of the airflow. If the radiator is segmented into a finite number  $n$  of areas elements. The non-uniformity was then defined by Lee and Hong [6] as follows;

$$i = \frac{1}{n} \sum_{k=0}^n \frac{|\dot{m}_K \frac{A_R}{A_K} - \dot{m}_{tot}|}{\dot{m}_{tot}} \quad (1)$$

Where;

$A_K$  = size of one area section,

$A_R$  = Area of radiator matrix,

$\dot{m}_K$  = mass flow rate through one section and

$\dot{m}_{tot}$  = Total mass airflow.

When the sectioned areas are of equal size then the non-uniformity simplifies to;

$$i = \frac{1}{n} \sum_{k=0}^n \frac{|V_K - V_{av}|}{V_{av}} \quad (2)$$

Where;

$V_K$  = the airflow velocity of one section and

$V_{av}$  = the average airflow velocity across the radiator.

### Results and Discussion

Once the results were obtained both contour plots of the velocity distributions as well as the average velocity of the airflow and the airflow non-uniformity index were analysed. The velocity distributions were plotted using a commercial software called Tecplot. The data points were extrapolated to the full area of the radiator using the Kriging method of spatial statistical interpolation available in the software. The Kriging method uses a general trend and a specified number of points to weigh from and adds a random noise component to find the value of the point being interpolated [1].

Figure 5 in the following pages shows the airflow distribution at the radiator as being highly non-uniform. This is for the baseline configuration for the simulated road speed of 100km/h. It can be seen that the top and bottom sections show higher airflow velocities. This was due to the fact that these regions are behind the flow inlets and is consistent with the physical location of the decorative grille panel and lower intake area. The middle section exhibits very low velocities due to being located directly behind the bumper bar. It was found that the airflow velocities ranges between 2.6m/s and 7.5m/s compared to a free-stream velocity of 22.8m/s. These velocities are the average for each location recorded over a 30 second period. As the area of the front-end

cooling air intakes were shielded the distribution of the airflow across the radiator changed.

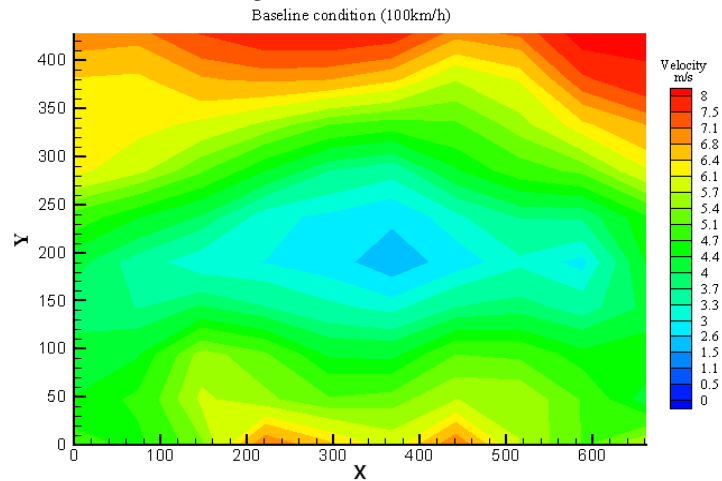


Figure 5: Baseline vehicle airflow distributions (100km/h road speed).

Presented in Figure 6 to Figure 9 are the airflow distributions across the radiator when one-half of the cooling intake areas are shielded. These velocity contour plots are for the simulated road speed of 100km/h. Due to the blockage of the tunnel a lower air speed of 82km/h was used which was confirmed by previous on-road tests to be equal to 100km/h road speed [8]. Figure 6 and 7 show a comparatively uniform airflow than Figure 8 an9. The vertical and horizontal shielding methods show a higher degree of airflow uniformity and are comparable to the baseline configuration but exhibit some dead zones. These dead zones are mainly the signature of the engine block.

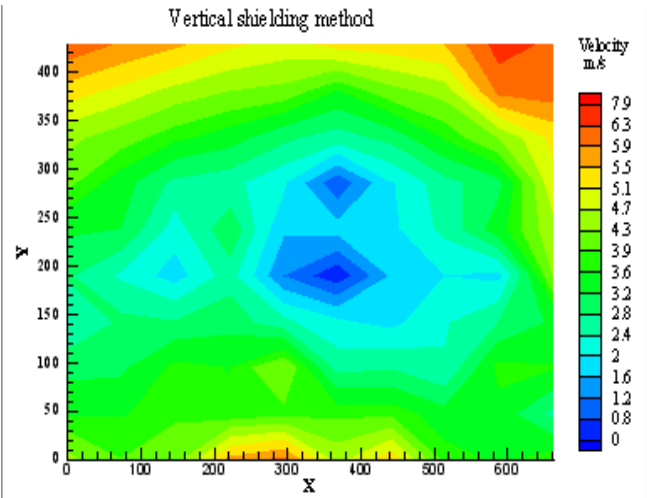


Figure 6: Airflow velocity distribution 1/2 intake area shielded (Vertical).

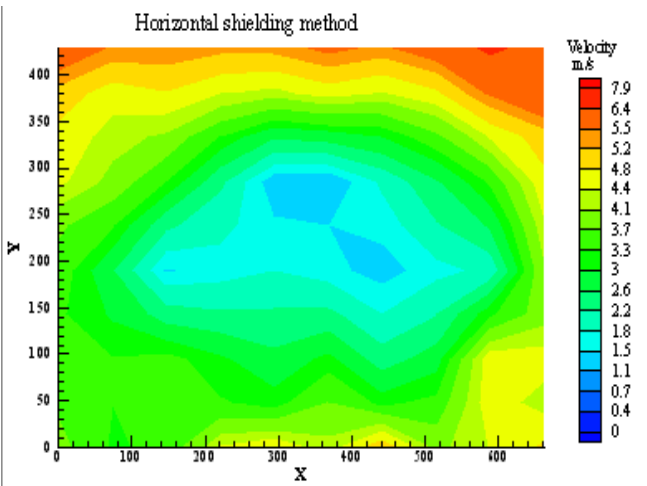


Figure 7: Airflow velocity distribution 1/2 intake area shielded (Horizontal).

However, the side-to-side and side-to-centre shielding methods show a high level of non-uniformity. Figure 8 shows the region directly behind the shield to be a dead zone with little or no flow. Similarly, Figure 9 shows the side-to-side shielding method produces areas with no or little airflow directly behind the areas where the shields were employed. It should also be noted for each case the average cooling airflow velocity was 2.6m/s and 3.2m/s respectively.

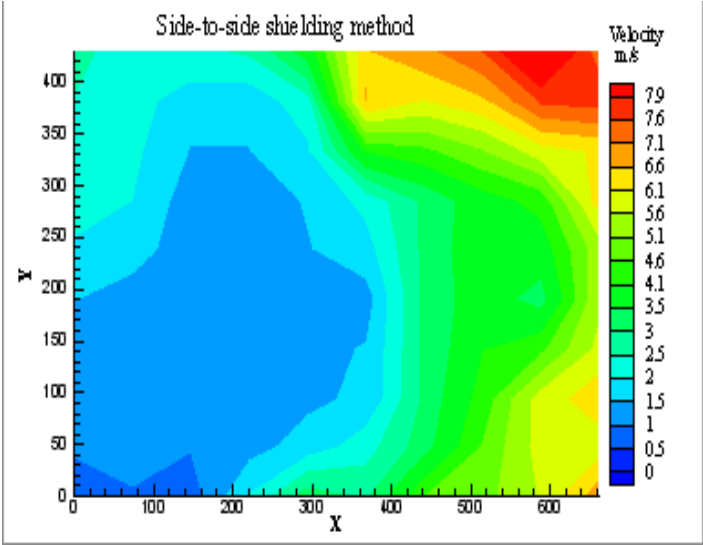


Figure 8: Airflow velocity distribution 1/2 intake area shielded (Side-to-side).

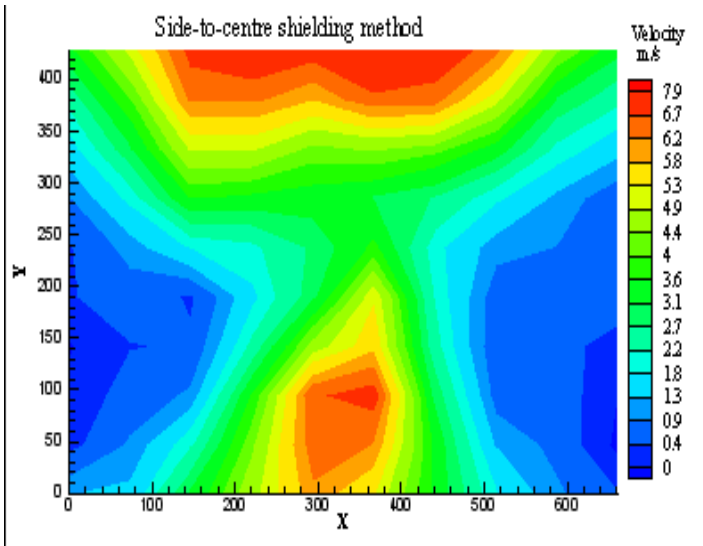


Figure 9: Airflow velocity distribution 1/2 intake area shielded (Side-to-centre).

It is important to note that the errors arising from the pressure – based system greatly increased as the velocities being measured reduce. It was found that as more areas of the front-end intakes were shielded, the average airflow velocities across the radiator decreased and the errors involved increased. Using a vane anemometer, it was found that the pressure-based technique resulted in an error of about 5% when the velocities being measured were higher than 2m/s. This is simply as a result of the measured pressure being reduced significantly as the front-end intake area is reduced. As with any pressure-based measuring systems as the quantity being measured reduces significantly, the accuracy of the system diminishes.

Significant differences between the methods were found when plotting the velocity contours for the different configurations. However, this was not replicated when the average cooling air

velocity through the radiator were analysed. It should be noted that the cooling fans were not operating throughout the tests but were in place together with the fan shroud. Figure 9 shows the vertical shielding method yields the lowest velocity while the horizontal shielding method consistently produced the higher velocities. This is explained by the fact that the vertical strips used in shielding the front-end allow the airflow, while passing over the upper and lower intake area, to stay attached as it travels over the bonnet. This diverts the airflow from entering the engine bay and results in less internal flow and increased external flow. In a contrary fashion, it was observed (with the aid of wool tufts) that the horizontal strips allow the airflow to split and be ingested into the cooling system. This explains the higher velocities recorded for the horizontal shielding method. It was surprising to observe the side-to-side shielding method leads to higher average core velocities than the side-to-centre method.

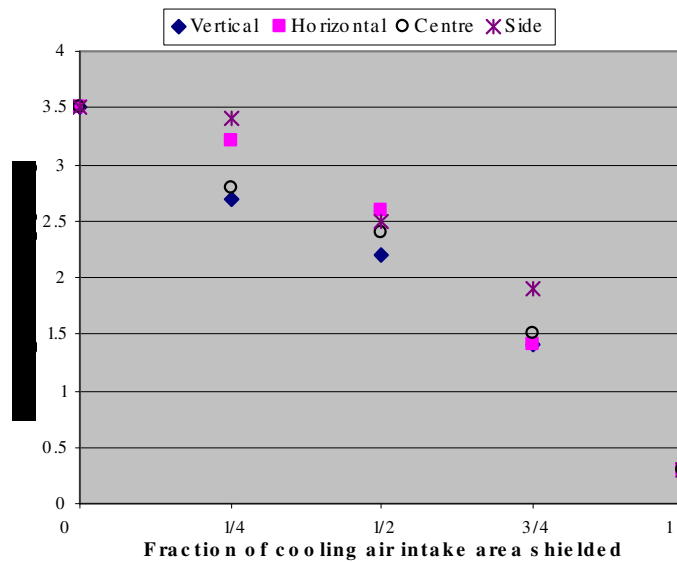


Figure 9: Average airflow velocities behind the radiator for the simulated road speed of 100km/h.

The cooling airflow non-uniformity index was also calculated as the front-end intake areas were shielded. AS defined before, airflow is highly non-uniform when  $i$  is low and vice versa. The vehicle at the baseline condition had a non-uniformity index of about 0.3. This rises to more than 0.8 when the side-to-centre shielding method is employed and  $\frac{3}{4}$  of the intake area is shielded. It can be seen in Figure 10 that the vertical followed by the horizontal shielding method contribute to a more uniform and hence better airflow distribution across the radiator. In contrast, the side-to-centre shielding method performs poorly in terms of airflow velocity distribution across the radiator.

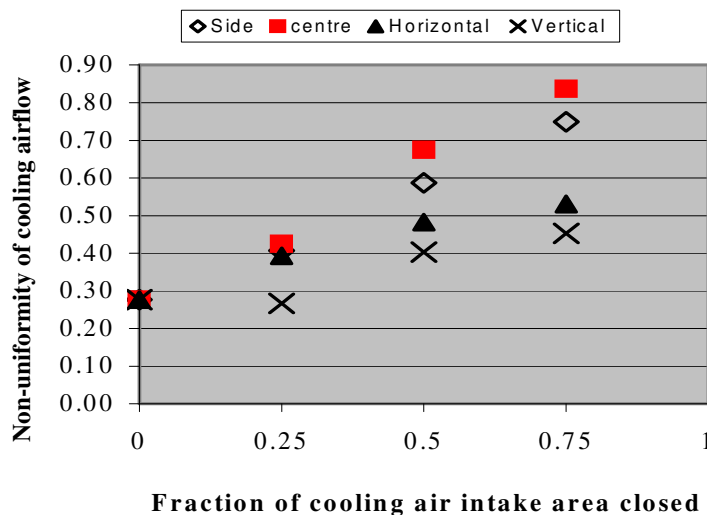


Figure 10: Fraction of cooling intake area shielded vs airflow non-uniformity index.

## Conclusions

The results showed that the best method to shield the front-end of a passenger vehicle would be to employ a horizontal method. This shielding method produced the more uniform cooling airflow distribution compared to the other methods. By extension it should also produce the least reduction in cooling capacity for a given intake area.

It was found and was expected that the non-uniformity index increased significantly as the front-end air intake area was shielded. This increase in the non-uniformity index is expected to correlate with reduced cooling capacity of the vehicle.

## Acknowledgments

The authors would like to acknowledge the generous financial assistance of the Australian federal government in the form of an Australian Postgraduate Award – Industry. We would also like to thank the Ford Motor Company of Australia for proving financial and material support during this research.

## References

- [1] Amtec Engineering Inc. Tecplot Users Manual Version 7, Amtec Engineering, 1996.
- [2] Chiou, J.P. The Effect of Flow Non-uniformity on the Sizing of Engine Radiators, SAE 800035, *SAE World Congress and Exhibition*, 1980.
- [3] Dib, S. Parametric Study of the Front-end of Australian Cars and its Effects on Cooling, M.Eng. thesis, RMIT University, Melbourne, 1997.
- [4] Hoffmann, R. Engine Cooling – State of the Art in Hucho W. H. and Weideman, J. (Eds) *Progress in Vehicle Aerodynamics II Thermo-management*, Expert Verlag, 2002.
- [5] Hucho, W.H., Aerodynamics of Road Vehicles, 4<sup>th</sup> Edition, SAE International, 1998.
- [6] Lee, Y.L. & Hong, Y.T, Analysis of Engine Cooling Airflow including Non-uniformity over a Radiator, in *International Journal of Vehicle Design*, **24**, 1, 2000, 121-135.
- [7] Lin, C.H. Specific Dissipation as a Technique for Evaluating Motor Car Radiator Cooling Performance, PhD thesis, RMIT University, Melbourne, 1999.
- [8] Ng, E., Watkins, S., Johnson, P.W., & Grant, L. Wind Tunnel Tests of Vehicle Cooling Performance at High Blockage, SAE 2000-01-0351, *SAE World Congress and Exhibition*, 2000.
- [9] Ng, E., Watkins, S., Johnson, P.W., & Mole, L. Use of a Pressure-based Technique for Evaluating the Aerodynamics of Vehicle Cooling Systems, SAE 2002-01-0712, *SAE World Congress and Exhibition*, 2002.
- [10] Watkins, S. Wind-tunnel Modelling of Vehicle Aerodynamics; with Emphasis on Turbulent Wind effects on Commercial Vehicle Drag, PhD thesis, RMIT University, Melbourne, 1990.



## Spreading Radius of Fountains After Impinging on a Free Surface

C. J. Lemckert

School of Engineering  
 Griffith University, Queensland, AUSTRALIA

### Abstract

Laboratory experiments and dimensional considerations were used to investigate the spreading radius of axisymmetric fountains after they impinged upon the free surface of the initially homogeneous and quiescent ambient environment. The distance to which the fountain fluid spread, before plunging downwards as the result of negative buoyancy, was found to be a function of the source radius, the source Froude number and the depth at which the fluid was injected. For example, the greater the source Froude number (and hence initial momentum) the greater the spread of the surface flow for the same injection depth and source radius. Experimental data and simple scaling considerations were used to an equation for predicting the spreading distance. The results show the need for further studies to quantify mixing processes and dilution rates.

### Introduction

When a dense fluid is steadily injected vertically upward into a miscible and less dense fluid, a fountain-type structure forms [1,2,3,4]. The denser fluid penetrates to a finite height, whereupon it stops, and then falls back as an annular plunging plume around the upward flow. Surrounding ambient fluid is constantly being entrained into the plunging plume, while the rising inner jet can entrain only outer plume fluid. The net result is that, as the injected fluid travels through the ambient, its volumetric flow rate increases and its mean density decreases. Fountains also occur in the reverse case, when lighter fluid is injected vertically downward into a denser ambient [5].

For submerged fountains with a relatively large momentum in comparison to the negative buoyancy, the maximum height of rise will be considerably greater than the radius of the source [4]. This means that the source is effectively a point and the virtual origin of the flow is at the injection point. The maximum height of rise of a submerged vertical fountain within a homogeneous quiescent ambient,  $z_m$ , can therefore be written as (following the notation of [4]):

$$\frac{z_m}{r_o} = C Fr_o \quad (1)$$

here  $r_o$  is the source radius,  $C$  is a constant,  $Fr_o = w_o / (r_o g' o)^{1/2}$  is the source Froude number,  $w_o$  is the average flow velocity,  $g' o = g(r_o - r_a)/r_a$  is the reduced gravity,  $r_o$  is the initial fountain density,  $r_a$  is the density of the ambient and  $g$  is the acceleration due to gravity, all of which are defined at the source. The value of  $C$  has been found to be in the range 2.46-3.7 [3,4,6,7,8].

When  $z_m$  exceeds the depth ( $H$ ) of a homogeneous quiescent ambient with a free surface, the momentum contained within the negatively buoyant fountain fluid will deform the surface upwards. The resultant horizontal pressure gradient and remaining momentum then forces the fluid to spread laterally as a radial surface jet. At some radius, the negative buoyancy of the jet will cause it to fall below the surface and plunge downwards (see Figure 1). Impinging fountain-type structures are found in many engineering applications; for example, the heating of large open structures is often achieved by using fan-driven heaters at the ceiling level [4]. It is expected that as  $Fr_o$  increases (for the same  $H$  and  $r_o$ ) the plunge point radius will increase, as is the case for energetic bubble plumes (eg [9]). Baines et al. [4] found that for impinging fountains in a confined tank (where the side-walls play an important role in the overall mixing behaviour) there was an expansion in diameter of the surface flow as the ratio  $z_m/H$  was increased. However, no values or relations were given for this in their work.

While various studies have examined the height to which a fountain can rise no experimental or numerical work has been sighted that specifically examines the lateral spread of impinging fountain fluid as it moves along a free surface. Using laboratory experiments and scaling considerations this paper examines this issue when the receiving ambient is initially quiescent and homogeneous.

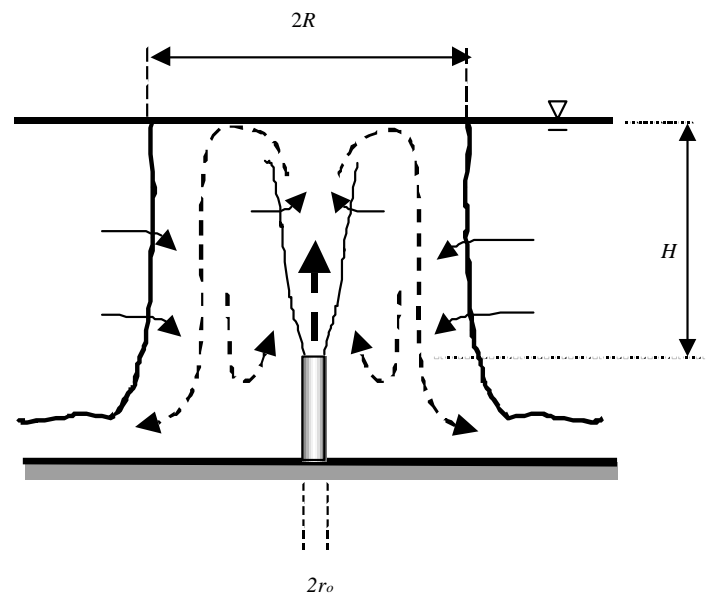


Figure 1. Schematic representation of a vertical fountain impinging on a free surface. Dashed arrows indicate dominant flow directions while dashed arrows indicate dominant entrainment paths..

## Experimental Methodology

To support the experimental objectives of this study, detailed experiments were conducted within a 2 x 2 x 0.4 m glass sided tank. This tank was found to be large enough to avoid strong recirculation patterns developing in the ambient by the fountain flow, given that experiments were run only for short periods once the fountain flow was well established. Trials revealed that strong convection cells did not establish (even though the Rayleigh number was high), which again was the result of the short experiment times.

A solution of salty water (initial fountain fluid) was pumped upward into the fresh water-filled tank through a vertical tube of 1 cm diameter and length of 10 cm. Before entering the tube the water passed through a 2 m long 1 cm diameter hose. Only one inlet diameter was chosen for this study, as past investigations of jets have shown that the behaviour can be readily characterised using non-dimensional expressions such as Eq. [1]. Fountain fluid inflow rates were monitored using a calibrated rotometer, with the flow rates adjusted so that the fountain always impinged on the free upper surface. A total of 33 experiments were completed with  $6 < Fr_o < 54$ ,  $5 < H < 25$  cm and  $756 < Re < 3182$ , where  $Re = 2w_o r_o / \nu$  is the source Reynolds number and  $\nu$  is viscosity.

The radius at which the impinging fluid plunged below the surface, which was always significantly less than the width of the tank, was determined from data collected 5 mm below the water surface by horizontally traversing a calibrated in situ microscale conductivity and temperature probe across the tank. Transects were always conducted using the same azimuthal and radial angles and commenced shortly after pumping commenced when it appeared a steady state developed (which usually took only about 30 sec). The microscale probe (Precision Measurement Engineering, USA, Model 125) has sensor resolutions of  $1 \times 10^{-3}$  °C and  $2 \times 10^{-5}$  Sm<sup>-1</sup>, spatial resolution of  $\pm 2$  mm, and time responses of approximately 0.02 and 0.004 s respectively, with the traversing mechanism having a spatial resolution  $< 1$  mm. Signals from the probe were recorded electronically and stored for analysis. A number of traverses (typically 6 at 4 cms<sup>-1</sup>) were made for each experiment and the average width value determined. Traverses were performed at intermittent steps to avoid adding significantly to mixing across the fountain and within the tank. The amount of fountain fluid injected into the tank was small in relation to the initial tank volume; meaning changes in total water depth during an experiment were negligible. Further the water within the tank was changed and monitored on a regular basis to ensure the water surface was not contaminated.

## Results and Discussion

Figure 2 presents an example of a vertical impinging fountain striking a free surface (ie  $z_m > H$ ). The dyed rising jetting water was issuing upwards from the nozzle before striking the surface and spreading radially outwards (along the free surface). At some radial distance ( $R$ ) the spreading fountain water detached from the free surface and plunged downwards into the ambient as an annular plume that had some degree of unsteadiness. That is, the water did not fall as a simple stream, but instead it had a blobby type nature (as typically found in any annular plume type flows

– eg. [9]). Visual observations of the plunging point indicated that it experienced some wandering, but that the mean radius appeared to remain constant with time.

Figure 3 presents an example of the conductivity signal recorded as the microscale probe was traversed across the tank. For clarity, the conductivity signal recorded during each traverse has been displaced sequentially by 0.05 Sm<sup>-1</sup>. The region of highest conductivity marks the central core of the fountain, while adjacent to this is the zone of lower conductivity marking the plunging annular ring. The conductivity is lower because the fluid has had more time to entrain the surrounding ambient fluid. Adjacent to the plunging fluid is the ambient region having the lowest constant conductivity values. In keeping with general unsteady nature of jet/plume behaviour, the central region was found to wander from one traverse to another. The outer radius of the falling fluid is clearly marked by a conductivity signal (the radius for traverse 5 is shown). While the probe sensors were positioned 5 mm below the water surface, it is expected that there would be little change in diameter of the plunging radius was observed from when it initially falls below the free surface. In this study, the constant  $C$  from Eq [1] had to exceed 3 in order for the development of impinging fountains. As discussed earlier, this is in keeping with previously published works.

If the properties of submerged fountains impinging on a free surface are governed by  $r_o$ ,  $Fr_o$  and  $H$  then dimensional reasoning and Eq. [1] suggest that the average radius to which the fluid can spread out across the surface ( $\bar{R}$ ) for a given set of initial conditions would be given by:

$$C_1 Fr_o^n = f\left(\frac{\bar{R}}{r_o}, \frac{H}{r_o}\right) \quad (2)$$

where  $C_1$  and  $n$  are constants.

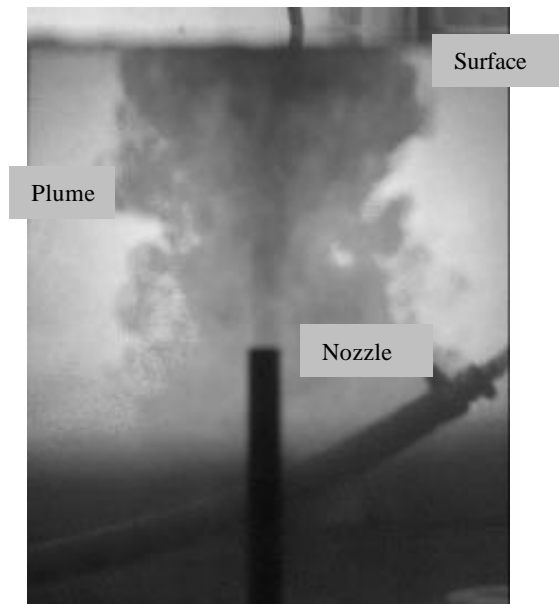


Figure 2. Example of a negatively buoyant fountain impinging of a free surface. For clarity the fountain fluid is dyed.



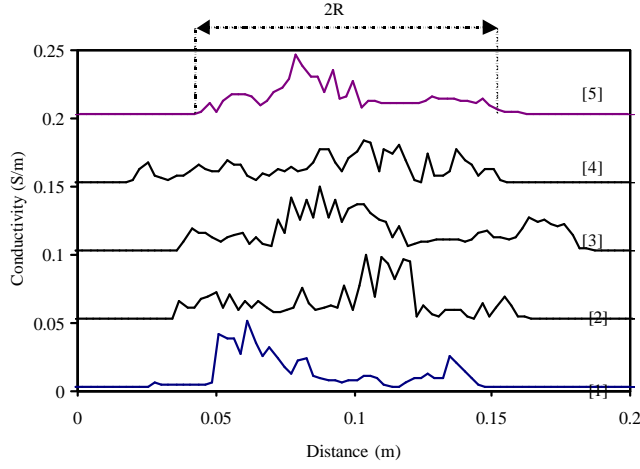


Figure 3. Surface conductivity as a function of distance traversed by the microscale probe as it moved backwards and forwards through a fountain impinging on the free surface. Each line represents one traverse (traverse number is shown in square brackets) with each line sequentially displaced vertically by 0.05 S. In this experiment  $Fr_o = 22$ ,  $H = 11.8$  cm and  $Re = 3200$ .

Now, in the first instance if it is considered that the fluid elements within the fountain travels a distance  $R+H$  ( $= z_m$  in a vertically unbounded system when  $R = 0$ ) before negative buoyancy dominates, causing the fluid to plunge downwards, than Eq. [3] becomes:

$$\frac{H + \bar{R}}{r_o} = C_1 Fr_o^n, \quad (3)$$

Figure 4 presents the experimentally derived data. The line of best fit to the data shows how that Eq [3] can be used to predict the spreading radius with  $C_1 = 4.8$  and  $n = 0.74$ , and a squared correlation coefficient of 0.921. That is:

$$\frac{H + \bar{R}}{r_o} = 4.8 Fr_o^{0.74}, \quad (4)$$

Eq [4] will have an upper limit of application, which are yet to be determined. This limit is reached when the fountains have sufficient momentum to break through the free surface and exit the ambient. Recently, [9] found a similar formulation for submerged fountains impinging on a rigid surface. However in their study  $n$  ( $=0.4$ ) was different and  $C_1$  was found to be dependant upon the ratio  $H/r_o$ , such that they found for a rigid surface  $(H + R)/r_o = 2.7(H/r_o)Fr_o^{0.4}$ . In this study the extra dependence on  $H/r_o$  was not observed, suggesting the type of surface on which the fountain impinges plays a significant role in the spreading dynamics. Further studies are required to quantify this.

## Conclusions

Detailed laboratory experiments and simple dimensional considerations have been used to investigate the spreading radius of water fountains when they impinge on the free surface of the receiving ambient. It was observed that as the fountains struck the free surface the fountain fluid spread out radially before plunging below the surface. The plunging distance was found to be a function of the source radius, the ambient fluid depth and the source Froude number.

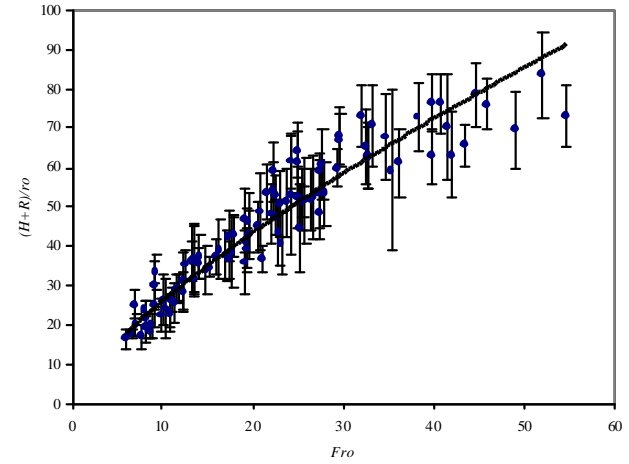


Figure 2. Normalised radius of fountain as a function of  $Fr_o$ . The solid line is the line of best fit  $(H + R)/r_o = 4.8 Fr_o^{0.74}$  with a squared correlation coefficient of 0.921. The vertical error bars indicate one standard deviation.

This investigation indicates that a number of important aspects of fountains striking a free surface warrant further investigation. Yet to be determined is the amount of energy lost in the formation of surface motions generated by impinging fountains, the dilution rates within the fountain flow and a formulation to describe the behaviour of the observed plume wondering. The influence of viscosity and diffusion rates (which are different for air and water systems) on the spreading distance also warrants further investigation, so that universally applicable relations can be derived.

## Acknowledgments

The author would like to thank the School of Engineering, Griffith University Gold Coast Campus, and the School of Engineering and Technology, Deakin University, for supporting this investigation. This project was partially funded through the Australian Research Council Large Grant Scheme.

## References

- [1] Morton, B. R., Forced plumes, *J. Fluid Mech.*, **5**, 1959, 151-163.
- [2] Turner, J. S., Jets and plumes with negative or reversing buoyancy, *J. Fluid Mech.*, **26**, 1966, 779-792.
- [3] Mizushima, T., Ogino, F., Takeuchi, H. and Ikawa, H., An experimental study of vertical turbulent jet with negative buoyancy, *Warne and Stoffubertragung*, **16**, 1982, 15-21.
- [4] Baines, W. D., Corriveau, A. F. and Reedman, T. J., Turbulent fountains in a closed chamber, *J. Fluid Mech.*, **255**, 1983, 621-646.
- [5] Holstein, D. M. and Lemckert, C. J., Spreading of energetic submerged fountains impinging on a rigid surface, 14th Australasian Fluid Mechanics Conference, Adelaide University, Adelaide, Australia, 10-14 December 2001, CD ROM
- [6] Lindberg, W. R., Experiments on negatively buoyant jets, with and without cross-flow, in *Recent Research Advances in*

the Fluid Mechanics of Turbulent Jets and Plumes, Davies, P. A. and Naves, V. (eds), Kluwer Academic, 1994, 131-145.

- [7] Zhang, H. and Baddour, R. E., Maximum penetration of vertical round dense jets at small and large Froude numbers, *J. Hydraul. Engrg*, **124**, 1998, 550-552.
- [8] Bloomfield, L. J., and Kerr, R. C., A theoretical model of a turbulent fountain, *J. Fluid Mech.*, **424**, 2000, 197-216
- [9] Lemckert, C. J. and Imberger, J., Energetic bubble plumes in arbitrary stratification, *J. Hydraulic Engineering*, **119** (6), 1993, 680-703.

## Preliminary Estimation Methods for Sizing Detention Basins in Queensland

C. J. Scraggs and C. J. Lemckert

School of Engineering,  
Griffith University, QLD, 4215 AUSTRALIA

### Abstract

The Queensland Urban Drainage Manual gives four methods for the preliminary sizing of detention basins, but it does not give any guidelines as to when to use each method. This paper develops some guidelines based upon the modelling of numerous detention basins and comparing the modelled detention volumes to the estimates given by each of the four methods.

### Introduction

Urban stormwater management systems typically include detention and retention facilities (basins) to mitigate the negative impacts of urbanisation on stormwater drainage. These basins act as a filter mechanism and are primarily designed to hold water and slowly release it at a rate similar or less than that of encountered before urbanisation. That is, the intent is to allow water out of the urbanised region at an artificial, but pseudo natural, rate.

To size a basin for the quantity control of stormwater runoff an initial estimate is obtained from one of the numerous preliminary sizing methods described in literature, (eg. [1, 2, 3, 4, 5, 6, 7, 8, 9]). From this preliminary estimate and the site topography, the basin, including the outlet structure can then be designed. To determine the efficiency of the basin, various runoff hydrographs are then routed through the basin using stormwater management software. The basin and the outlet structure are then reconfigured until the outflow hydrograph satisfies the criteria set by the designers.

The Queensland Urban Drainage Manual (QUDM) [10] gives four methods for the preliminary sizing of a detention basin. However, QUDM does not give any guidelines as to when to use each method, but it does state 'these procedures may give widely different answers and should be used with care'. This paper develops some guidelines as to which method to use for any given situation.

### Queensland Urban Drainage Manual

The four methods for the preliminary sizing of detention volumes given in QUDM [4] yield the following four equations:

$$\frac{V_s}{V_i} = \frac{r(1+2r)}{3} \quad (1)$$

$$\frac{V_s}{V_i} = r \quad (2)$$

$$\frac{V_s}{V_i} = \frac{r(3+5r)}{8} \quad (3)$$

$$\frac{V_s}{V_i} = \frac{r(2+r)}{3} \quad (4)$$

where  $V_s$  is the storage volume,  $V_i$  is the inflow volume, and  $r$  is a reduction ratio calculated by:

$$r = \frac{(Q_i - Q_o)}{Q_i} \quad (5)$$

$Q_i$  and  $Q_o$  are the peak inflow and outflow rates of the detention basin.

Equations 1-4 are referred to, after the authors of which each method is based, as the Culp, Boyd, Carroll and Basha methods respectively.

### Method Comparisons

The pre- and post-development catchment hydrology details were obtained for several urban developments using the rational method as described in QUDM [10]. A detention basin for each catchment was then designed to reduce the post development flow rates to below the pre-development flow rates.

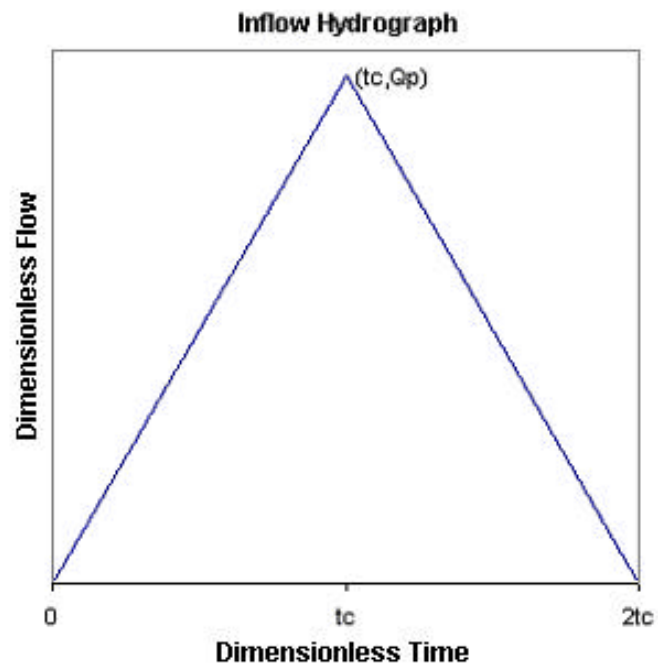


Figure 1. The general shape of the inflow hydrographs that were routed through the detention basins.

To model the detention basins, a commercial software package entitled XP-SWMM was used. XP-SWMM is a link-node model that performs hydrology, hydraulics and quality analysis of stormwater and wastewater drainage systems including sewage treatment plants, water quality control devices and Best Management Practices (BMP's). For the modelling of detention basins, the stage versus area relationship and the outlet structure were defined set. The software uses the St. Venant dynamic flow equations to route flows through the basin.

The flows that were routed through the basins were hydrographs from storm events up to a 1 in 100 year storm. These hydrographs were derived from the rational method. A triangular hydrograph as shown in Figure 1 was used, with a peak flow rate of  $Q_p$  (from the rational method), and the time to peak flow being equal to the time of concentration of the catchment. Typical peak flow rates through the basin ranged between  $0.3$  and  $8.0 \text{ m}^3\text{s}^{-1}$ , however some basins had flow rates up to  $15 \text{ m}^3\text{s}^{-1}$  routed through them.

The typical basin shape consisted of a square base, and side slopes equal to 1 vertical to 6 horizontal. The length of the basin base was determined so that the storage from a 1 in 20 year storm was chosen to be no deeper than 1.2 m. The lengths ranged between 8 and 55 m, but the majority were between 10 and 20 m.

A typical outlet structure of the detention basins consisted of two pipes and a weir. For smaller reductions in the flow, a greater number of pipes were used, the greatest consisting of six pipes and a weir.

The preliminary estimates from Equations 1-4, an average of these estimates, and the detention volume given by the stormwater management software for each storm event were then compared. For each of the basins the typical results are shown in Figure 2. These results show that the modelled detention volumes lie between the estimates obtained by using the Basha and Boyd methods. However, there was one catchment where the modelled volume was better represented by the Carroll method. Figure 3 shows these results.

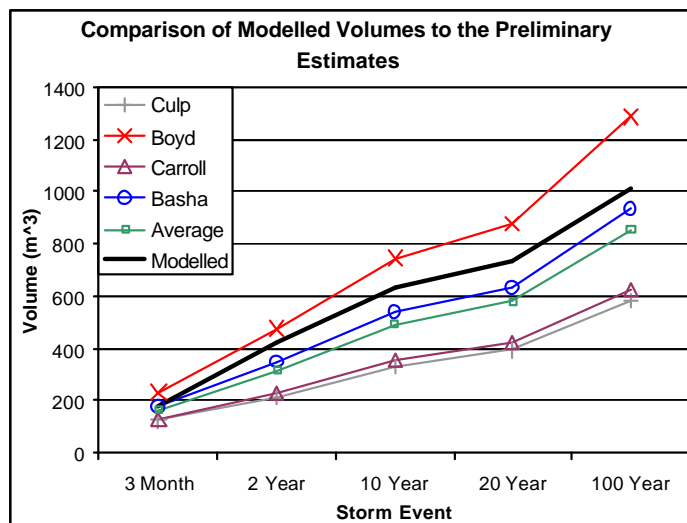


Figure 2. Typical results obtained from the comparison of the preliminary and modelled detention volumes.

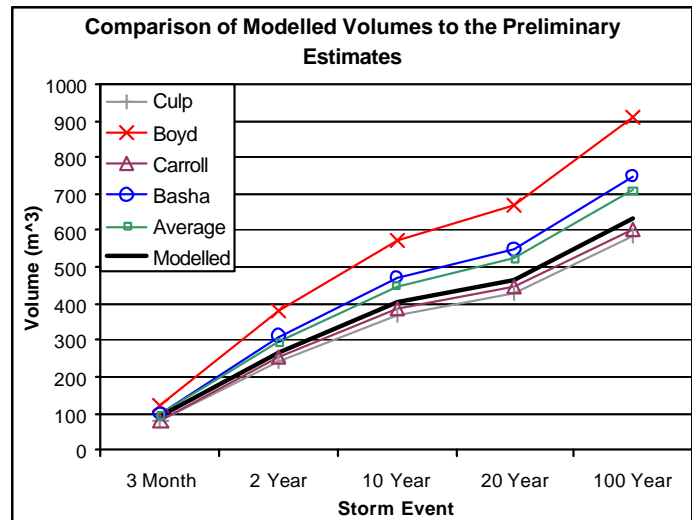


Figure 3. Results showing the modelled detention volumes are more accurately estimated by the Carroll method.

A comparison of the catchment data, including size, slopes and shape showed that this catchment did not differ greatly from the majority of the others. However, the extent of the development of this catchment did differ greatly being that it was the sole catchment that is completely contained within the development. Due to this a greater reduction in the post-development flow rate was needed. Figures 4 and 5 show the pre and post development hydrographs calculated by using the rational method, along with the outflow hydrographs given by the flood routing software. What should be noted is that the reduction in the post-development peak flow rates in Figure 5 is much greater than that of Figure 4.

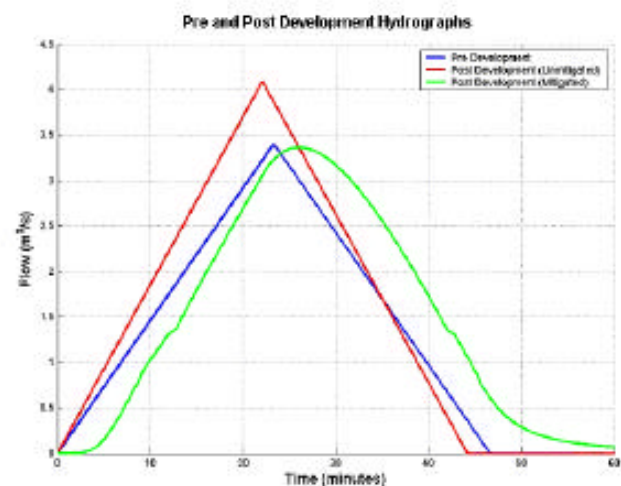


Figure 4. Typical hydrographs where the modelled detention volume is best estimated by the Basha or Boyd methods.

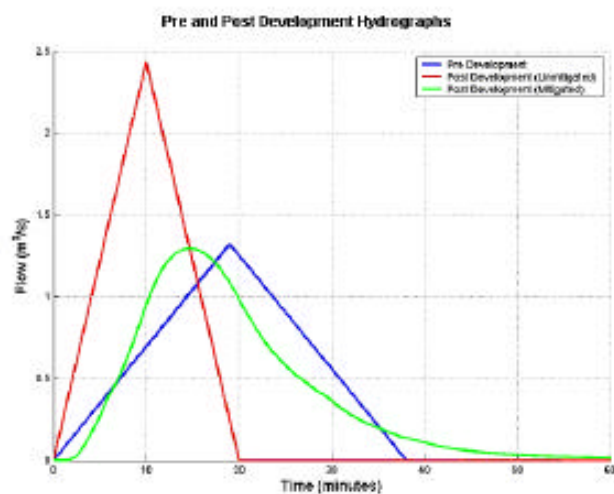


Figure 5. Hydrographs from the same catchment as that for figure 3.

The results suggest that there may be a relationship between the accuracy of each preliminary method and the reduction in the flow that is to be achieved. However, the majority of the catchments that were modelled had reduction ratios between 0.2 and 0.3. To determine the relationship between the preliminary methods and the reduction ratio,  $r$ , numerous detention basins were designed and modelled for a number of catchments with reduction ratios between 0.05 and 0.95. Figures 6 through 8 show the modelled and preliminary estimates of the detention volume for a single catchment with detention basins designed for varying reductions in the peak flow rate. Figure 6 shows the results after a reduction of 15%, and as can be seen the modelled volume is best represented by the Basha estimates. As the reduction in the flow increases the modelled volumes decrease with respect to the preliminary estimates.

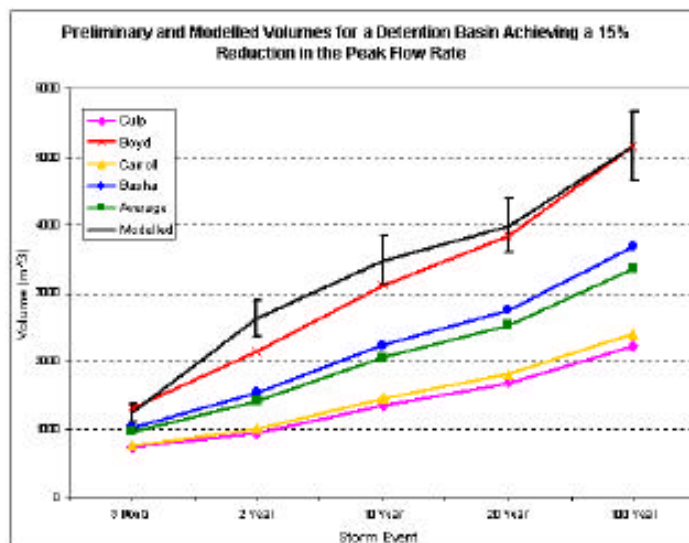


Figure 6. A comparison of the preliminary and modelled detention volumes showing the Boyd method produces the best approximation for a reduction ratio of 0.15 for this catchment.

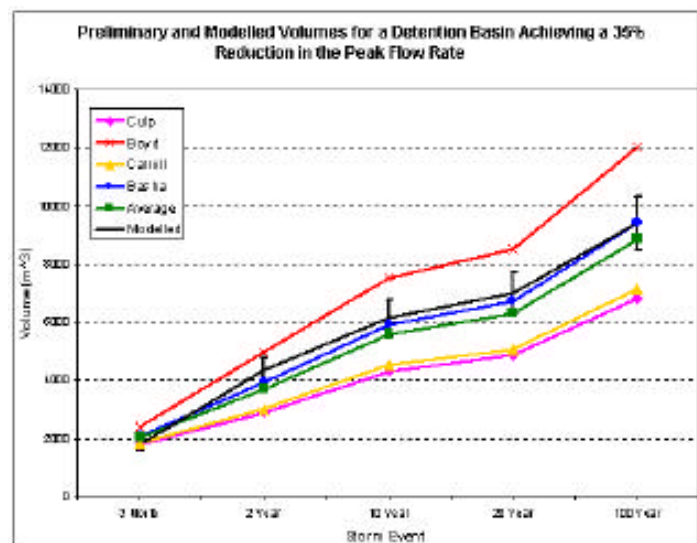


Figure 7. A comparison of the preliminary and modelled detention volumes showing the Basha method produces the best approximation for a reduction ratio of 0.35 for this catchment.

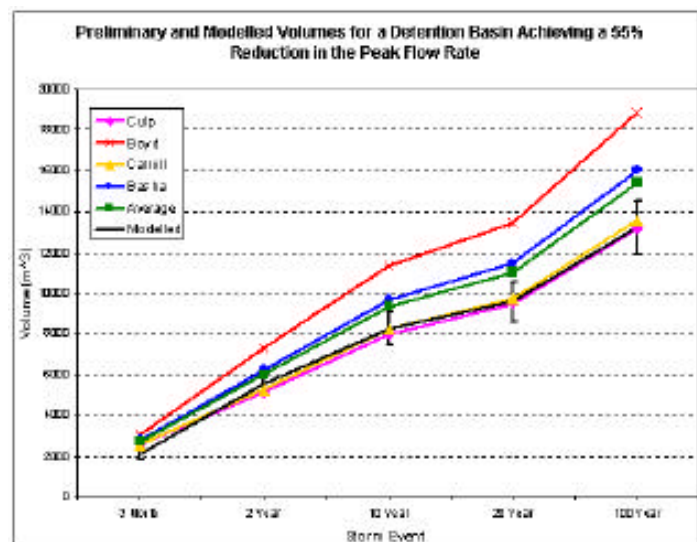


Figure 8. A comparison of the preliminary and modelled detention volumes showing the Carroll and the Culp methods produce the best approximation for a reduction ratio of 0.55 for this catchment.

This trend was typical of each of the catchments that were modelled. As the reduction ratio increased the modelled volume tended towards the smaller estimates obtained from the Carroll and the Culp methods.

Using the results from the catchments obtained from the urban developments, and the results from the additional catchments with varying degrees of reduction, guidelines for the use of each preliminary estimation method were produced and are given in Table 1.



Table 1. Recommendations for the use of the preliminary detention storage methods given in QUDM [1].

Condition	Method
$0.00 = r = 0.25$	Boyd Method
$0.25 = r = 0.45$	Basha Method
$0.45 = r = 0.60$	Carroll Method
$0.60 = r = 1.00$	Culp Method

## Conclusion

By modelling numerous detention basins, and comparing the modelled detention storage volumes to the preliminary estimates obtained by four methods outlined in the Queensland Urban Drainage Manual, it was found that the use of each preliminary method was dependent on the required mitigation of the flow. Recommendations for the use of each equation, based on the reduction ratio, have been presented in table 1. The results show that no one method was suitable for all cases.

## References

- [1] Abt, S.R., & N. S. Grigg, An Approximate Method for Sizing Retention Reservoirs, *Water Res. Bull.*, **4**, 1978, 956-965.
- [2] Akan, A.O., Detention Pond Sizing for Multiple Return Periods, *J. Hydraul. Engn*, **115**, 1989, 650-654.
- [3] Akan, A.O., Single-Outlet Detention-Pond Analysis and Design, *J. Irrig. Drainage Eng*, **116**, 1990, 527-536.
- [4] Aron, G. & D. F. Kibler, Pond Sizing for Rational Formula Hydrographs, *Water Res. Bull.*, **26**, 1990, 255-258.
- [5] Donahue, J. R., R. H. McCuen, & T. R. Bondelid, Comparison of Detention Basin Planning and Design Models, *Journal of the Water Resource Planning and Management Division*, **107**, 1981, 385-400.
- [6] Kessler, A., & M. H. Diskin, The Efficiency Function of Detention Reservoirs in Urban Drainage Systems, *Water Resources Res.*, **27**, 1991, 253-258.
- [7] Mays, L. W., & Y. K. Tung, *Hydrosystems Engineering and Management*, McGraw-Hill, 1992.
- [8] McEnro, B.M., Preliminary Sizing of Detention Reservoirs to Reduce Peak Discharges, *J. Hydraul. Engn*, **118**, 1992, 1450-1459.
- [9] Wycoff, R.L., & V. P. Singh, Preliminary Hydrologic Design of Small Flood Detention Reservoirs, *Water Res. Bull.*, **2**, 1976, 337-349.
- [10] Queensland Urban Drainage Manual (QUDM), Neville Jones & Associates, Australian Water Engineering, Queensland Department of Primary Industries, 1994.

## Design and Experimental Issues with Heat Exchangers for Microfluidics

G. Rosengarten<sup>1</sup>, J. Cooper-White<sup>2</sup> and Guy Metcalfe<sup>3</sup>

<sup>1</sup>Department of Chemical and Biomolecular Engineering  
University of Melbourne, 3010, AUSTRALIA

<sup>2</sup>Division of Chemical Engineering  
University of Queensland, QLD, 4072, AUSTRALIA

<sup>3</sup>Energy and Thermofluids Engineering  
CSIRO, Melbourne, 3190, AUSTRALIA

### Abstract

In this paper we explore issues in designing a heat exchanger for a microfluidic channel. Among important issues specific to heat exchangers in microfluidics are axial conduction and shear rate dependant phenomena. A heat exchanger has been designed for use in a further study to examine the effect of liquid contact angle on the convective heat transfer coefficient. We show that by applying a constant heat flux to the outer channel wall surface, axial conduction causes the boundary conditions to change from uniform temperature at lower Reynolds numbers, to approach uniform heat flux at higher Reynolds numbers.

### Introduction

Microfluidics, the generic name given to the study of fluid flow in confined channels with dimensions generally less than approximately 1mm, has exploded onto the fluid mechanics scene in the last 5 years or so [1]. In general, microfluidics research has been driven by two main application areas: high surface area heat sinks for high-flux computer chip cooling using multiple microchannels arrays [2]; and functional devices on a chip for biotechnology (lab-on-a-chip or micro total analytical systems) that increase the speed and sensitivity of processes that often involve heating and temperature control of reagents and products [3]. As both these applications involve convective heat transfer from a solid to a fluid, a fundamental understanding of microscale processes is required for device design. The question then arises: Can we use standard macro scale heat transfer correlations for microscale flows?

There has been considerable debate in the literature over the applicability of macro scale Nusselt number (non dimensional heat transfer coefficient) correlations to microfluidic flow. This is due, primarily, to the particularly large variation in experimental data (see for example [4-9]). There are various reasons for the lack of consistency in the experimental data but most are due to the following:

- Approximations and assumptions made due to the difficulty in measuring bulk fluid temperatures where it is almost impossible to place a temperature measurement device in a microchannel without effecting the flow [5, 8]
- Heat loss due to the increased surface area to volume ratio in microchannels relative to macrochannels [10]
- Relative dimensional tolerances in fabrication (e.g one micron tolerance in a 30 micron channel is significant compared to a 0.1mm tolerance in a 100mm channel)
- Axial conduction due to the thickness of the wall relative to the channel destroying ideal conditions [10, 11]
- Ill-defined surface variability such as roughness and hydrophobicity [9]

Slip flow, where there exists a non zero fluid velocity at a solid wall, has been well documented in the literature both experimentally [12-15] and by using molecular dynamics simulations [16-18]. Slip flow is important as it may allow a significant reduction in the friction pressure drop and thus the pumping power required for micro heat-exchangers and other microfluidic devices. While the underlying physical cause of slip is not fully understood, what is clearly known is that an apparent slip occurs more readily on non-wetting surfaces (hydrophobic), on rough surfaces, and at high shear rates. The last two phenomena are why slip may become important in microchannels, for it is in microchannel flow where surface roughness becomes significant relative to the channel size and where it is possible to obtain large shear rates (see shear rate section below).

Given that there must be a weaker interaction between the fluid and wall molecules for slip to occur, the corollary to the reduced pressure drop is a reduced heat transfer coefficient. To date in the literature there is only one study that investigates the effect of hydrophobicity on the heat transfer rate [9]. This study is limited to flow inside silicon and hydrophilic glass microchannels, and it shows an increase in the Nusselt number for the glass microchannels, relative to the silicon channels equal to approximately 10% (depending on the Reynolds number).

In this paper we consider several issues in the design of a heat exchanger for a microchannel that will be used for testing the effect of different fluid/wall contact angles on heat transfer coefficient. The main design considerations were surface access prior to assembly to allow surface modification via plasma polymerisation, small enough hydraulic diameters to obtain high enough shear rates to expect slip, the ability to measure the heat transfer surface temperature accurately and the minimisation of expensive microfabrication techniques.

### Experiments

Figure 1 shows the schematic design of the heat exchanger. It has been designed to mimic flow between parallel plates (width  $\gg$  channel depth) with one wall at a constant heat flux (or temperature depending on the flow rate) and the other wall adiabatic. This corresponds to a well studied geometry for which the Nusselt number is a constant 5.35 (or 4.86) [19].

The heat transfer surface consists of 2mm thick brass that has been imbedded into a Poly(methyl methacrylate), (PMMA or its trade name Perspex) base and polished flat using a Logitech PM5 precision lapping and polishing machine (the RMS roughness as measured by an atomic force microscope was found to be approximately 50nm). PMMA is a good thermal insulator (see table 1) meaning that the flow should be hydrodynamically fully developed before flowing over the brass heat transfer surface.

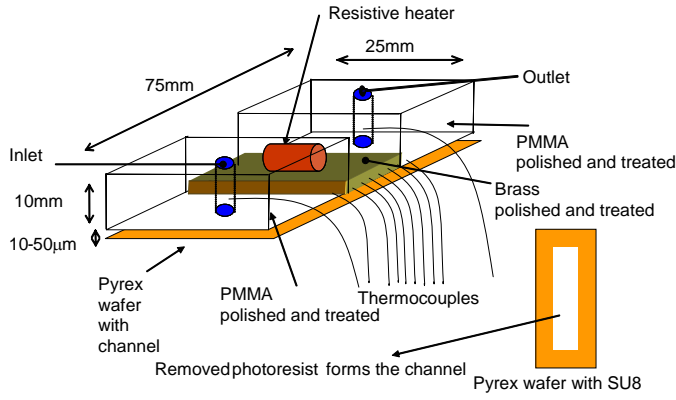


Figure 1: Schematic of the microfluidic heat exchanger.

The channel is formed by spinning a photoresist (in this case we used SU8, due to its excellent mechanical strength and solvent resistance) on to a 100mm diameter Pyrex wafer to the desired thickness (10-50μm) and removing the 8mm by 50mm channel (by UV exposure through a mask and developing). The wafer was then cut into the desired size (75mm by 25mm). The glass wafer with channel was sealed to the heat exchanger with a clamping system. The channel depth was measured with a microscope after sealing. Heating was provided by a 10W 47Ω resistor bonded to the back of the brass using high thermal conductivity epoxy (Tra-Con 2902) and heated with a calibrated HP power supply. Six 70μm diameter type T thermocouples were imbedded in the brass, and one thermocouple was imbedded on each side of the brass in the PMMA, with their tips at the centre of the channel. Small diameter wires were used to minimise conduction losses. A thermocouple was also placed at the centre of the inlet and outlet channels.

	PMMA	Brass
Thermal Conductivity (W/m.K)	0.18	112
Thermal Expansion coeff (m/m/°K)	73e-6	18.5e-6
Specific heat (J/kg.K)	1460	380
Density	1160	8500

Table 1: Physical properties of heat exchanger material.

The temperature measurement system was calibrated against a traceable platinum resistance thermometer in a uniform temperature water bath. Data was captured to computer via a high precision National Instruments 4350 data logger and a constant temperature terminal block.

## Theory

### Shear rate

The velocity profile for flow between parallel plates is given by [19]

$$\frac{u}{u_m} = \frac{3}{2} \left( 1 - \left( \frac{y}{w} \right)^2 \right) \quad , \quad (1)$$

where  $u$  is the velocity,  $u_m$  is the mean velocity,  $y$  is the distance between the channel walls with the origin at the centre of the channel, and  $w$  half the channel height. The maximum shear rate is at the wall and is

$$\left. \frac{du}{dy} \right|_{y=w} = \dot{\gamma}_{\max} = \frac{3u_m}{w} = \frac{3\text{Re}_{Dh}\nu}{2w^2} \quad , \quad (2)$$

where  $\text{Re}_{Dh}$  is the Reynolds number based on the hydraulic diameter,  $D_h=2w$ , and  $\nu$  is the kinematic viscosity. Equation (2) illustrates the fact that for the same Reynolds number the maximum shear rate scales as the reciprocal of the channel height

squared. That is why it is much more likely to observe slip in microchannels. In fact there tends to be a critical value where slip has been observed as summarised in Table 2.

	Critical shear rate ( $\text{s}^{-1}$ )	Comments
Wu and Cheng, 2003 [9]	~50,000	Roughness ~10nm
Zhu and Granick 2002 [13]	~10,000	Roughness ~10nm
Choi et al 2002 [12]	~10,000	

Table 2: Example of some critical shear rates extracted from the literature from which either a critical slip length was specified or for which it has been inferred from the departure of hydrophobic and hydrophilic data.

The maximum channel height used for this heat exchanger is approximately 50μm, which, with the available flow rates from our pump corresponds to a maximum shear rate of approximately  $10^6 \text{s}^{-1}$ .

### Axial conduction

The ratio of conduction heat transfer through a channel wall, to the convective heat transfer to the fluid from the wall, assuming the same temperature difference for the two processes, has been presented previously as a non-dimensional number to define compact heat exchanger efficiency [20] (see equation 3). This number, re-arranged, has been recently applied to microfluidics where walls are generally thicker than the fluid channels [11, 21] and is given by:

$$\lambda = \frac{A_s D_h \kappa_s}{A_f L \kappa_f} \frac{1}{\text{Pe}} \quad , \quad (3)$$

where  $A_s$  and  $A_f$  are the cross sectional areas of the solid wall and fluid respectively,  $L$  is the channel length,  $\kappa$  is the thermal conductivity, and  $\text{Pe}$  is the Peclet number given by  $\text{Re}_{Dh}\text{Pr}$ . Given a constant heat flux on a channel outer wall (as in Figure 1) for low values of  $\lambda$  ( $<0.01$ ) axial conduction can be considered negligible, and the fluid/solid surface boundary condition can be considered as having constant heat flux. For higher values of  $\lambda$  axial conduction becomes more important, and the boundary conditions approach constant temperature for infinite  $\lambda$ . Microfluidic channels are generally characterised by large  $A_s/A_f$  and low  $\text{Pe}$ , hence the tendency for axial conduction to become significant.

### Numerical Simulations

In order to aid in the understanding of the heat transfer processes in the heat exchanger design the commercial package CFD-ACE (ESI-Group) was used to solve the coupled flow, convection and conduction heat transfer. The mass conservation, the Navier-Stokes and the energy -in the form of total enthalpy- equations were solved by numerically integrating over each of computational cells or control volumes defined by the grid.

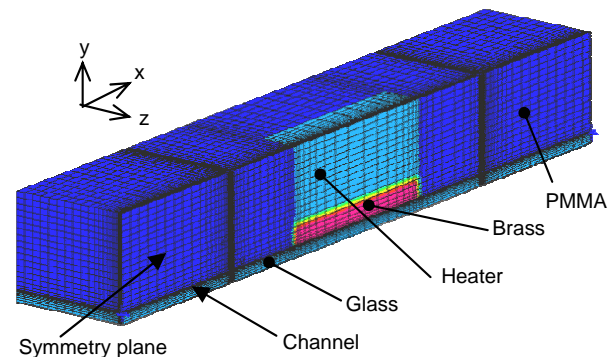


Figure 3: Three dimensional grid used for the numerical modelling.

## Results and Discussion

### Inlet configuration

In order to assume flow between parallel plates, the flow from a single inlet should spread evenly along the width of the channel. The 3D CFD model was used to determine the uniformity of the flow under various conditions. Numerical simulations and flow visualisation experiments indicate that a spreader at the inlet is not required. It has been found that with the flow entering the microchannel from the top through an inlet with diameter much greater than the channel height, the impinging jet tends to spread the liquid evenly across the channel width. This was verified experimentally with streak line visualisation using fluorescent  $2\mu\text{m}$  particles. Figure 4 shows a superposition of streak lines from experiments with those from CFD results for  $Re = 2$  (note that the inlet was not perfectly centred in the channel for the experimental streaklines).

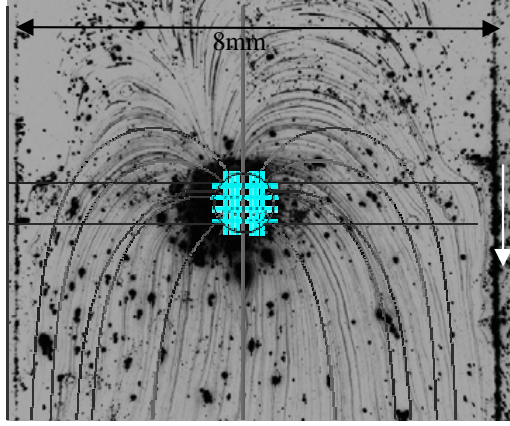


Figure 4: Streak line images taken using a long working distance fluorescent microscope and by using CFD simulations for  $Re = 2$ . Flow from the inlet in the direction as indicated by the arrow.

Figure 5 shows the predicted velocity profiles at the centre plane in the  $y$  direction (middle of the channel depth) for a range of Reynolds numbers. The excellent uniformity along the width of the channel further than  $200\mu\text{m}$  from the wall indicates that the assumption of flow between parallel plates is reasonable. Figure 5b shows that the flow becomes fully developed within 5mm from the inlet, before which little heat is transferred to the fluid (see next section).

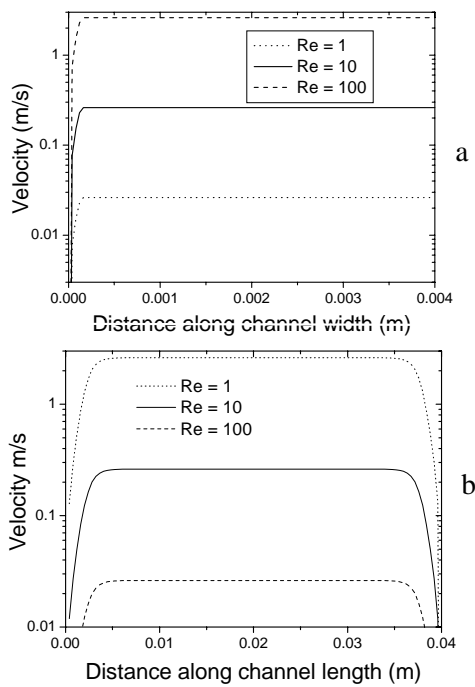


Figure 5: Plots of velocity profile from CFD simulations across the width (a) and the length (b) of the channel. In both plots the data is taken in the centre line of the channel.

### Heat transfer results

The effect of different Reynolds numbers on the wall temperature distribution in the heat exchanger is shown in Figure 6 from both experiments and from the simulations. For the low Reynolds number where the effect of wall conduction is more significant the simulations tend to under-predict the amount of heat being transferred axially to the PMMA. This discrepancy requires further investigation but it is most likely at least partly due to the fact that the heat transfer coefficient is not uniform over all the external surface area. Future experiments with more insulation should help reduce the axial conduction. The agreement between experiments and the simulations is better for the higher Reynolds number case where heat loss and axial conduction effects are reduced. In general however the results show that the brass wall is almost at a constant temperature at  $Re = 2$  and slightly increasing at  $Re = 20$ .

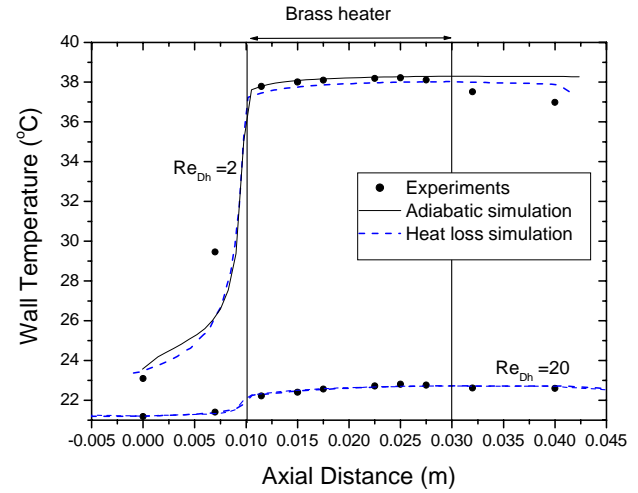


Figure 6: Measured and simulated wall temperatures along the wall of the heat exchanger with a heat input of  $0.53\text{W}$ , for two different Reynolds numbers. The simulation includes a perfectly insulated case (adiabatic) and a simulated heat loss case that assumed a convective heat transfer coefficient of approximately  $1\text{W/m}^2\cdot\text{K}$  (calculated from cooling experiments).

The Nusselt number is the standard non-dimensional heat transfer coefficient and is defined as:

$$Nu_x = \frac{hD_h}{\kappa} = \frac{q''D_h}{\kappa(T_w(x) - T_m(x))}, \quad (4)$$

where  $h$  is the convective heat transfer coefficient,

$T_m = \frac{1}{UA_c A_c} \int uT dA_c$  is the mean fluid temperature,  $T_w$  is the

wall temperature,  $q''$  is the wall heat flux and  $\kappa$  the thermal conductivity of the fluid. One of the major issues with experimental evaluations of the Nusselt number in microfluidics is that it is almost impossible to measure the mean fluid temperature, especially because the temperature gradients, like the velocity gradients, are so large across the channel. Thus it is probably not the most useful number to use for experimental micro heat exchanger data.

Figure 7 shows the normal heat flux distribution from the channel wall into the fluid along with the Nusselt number calculated using equation (4) from numerical simulations. Due to axial conduction the brass plate is closer to a uniform temperature boundary condition than to the uniform heat flux boundary condition that was applied to the outer wall. As the Reynolds number is increased, however, the heat flux becomes more

uniform along the channel length due to the decrease in the axial conduction effect (see equation (3)).

An interesting feature of the Nu results is the drop to a negative value just before the brass heater. As the glass lid has a thermal conductivity five times higher than the PMMA, heat is conducted axially towards the inlet. In the region adjacent to the heater the glass wall is hotter than PMMA surface and the fluid is heated primarily from the glass. Thus the fluid temperature is slightly warmer than the PMMA surface adjacent to the brass. This gives rise to the negative Nusselt number shown in figure 7.

The important feature from figure 7 is the fact that although a uniform heat flux was applied to the external wall the internal wall is essentially at a uniform temperature with a Nusselt number very close to the theoretical value of 4.86. In the PMMA which heated via conduction from the brass, the Nusselt number is very close to the uniform heat flux theoretical value of 5.35, although an insignificant amount of heat is transferred in that region.

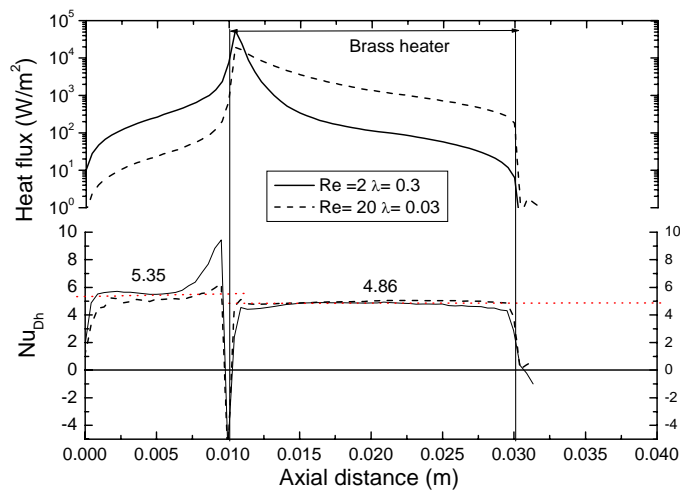


Figure 7: Local heat flux and Nusselt number distributions for the same cases given in Figure 6.

## Conclusions

We have demonstrated a heat exchanger design for microfluidics that will allow the testing of the effect of contact angle on the heat transfer coefficient at high wall shear rates. We have shown using CFD that due to the large channel wall cross-sectional area relative to the fluid channel dimensions, the affect of axial heat conduction becomes important. In fact, when the Reynolds number, or more importantly the axial conduction ratio,  $\lambda$ , is small, it is not possible to achieve the preferred constant heat flux boundary condition on the channel wall. However at higher Reynolds numbers and thus shear rate, where apparent wall slip effects will become visible,  $\lambda$  increases and the boundary conditions tend to constant heat flux, which is more desirable to measure small changes in temperature due to slip. Finally the complex nature of the Nusselt number variation along the flow direction indicates how experimental studies of heat exchangers for microfluidics can become rather confused if detailed coupled simulations are not carried out simultaneously.

## Acknowledgments

We would like to thank Kevin Smeaton for an excellent job of fabricating the heat exchanger, and for his useful suggestions, and the University of Melbourne's CSIRO collaborative grant scheme and early career grant scheme for funding.

## References

- [1] Nguyen, N. and S. Wereley, *Fundamentals and Applications of Microfluidics*. 2002, Norwood: Artech House.
- [2] Madawar, I., Assessment of high-heat-flux thermal management schemes. *IEEE. Trans. Comp. Pack. Technol.*, **24**(2), 2001, 122-141.
- [3] Northrup, A. and e. al. DNA Amplification with a Microfabricated Reaction Chamber. in *7th International Conference on Solid-State Sensors and Actuators*. 1993. Yokohama, Japan.
- [4] H.Herwig and O. Hausner, Critical view on "new results in micro-fluid mechanics":an example. *Int. J. Heat Mass Transfer*, **46**, 2003, 935-937.
- [5] Owhaib, W. and B. Palm, Experimental investigation of single-phase convective heat transfer in circular microchannels. *Exp. Therm. Fluid Science*, **28**, 2004, 105-110.
- [6] Peng, X.F., G.P. Peterson, and B.X. Wang, Heat transfer characteristics of water flowing through microchannels. *Exp. Heat Transfer*, **7**, 1994, 265-283.
- [7] Choi, S.B., R.F. Barron, and R.O. Warrington, Fluid Flow and Heat Transfer in Microtubes, in *Micromechanical Sensors, Actuators and Systems*, D.C.e. al, Editor. 1991, ASME. p. 123-134.
- [8] Qu, W., G. Mala, and D. Li, Heat transfer for water flow in trapezoidal silicon microchannels. *Int. J. Heat Mass Transfer*, **43**, 2000, 3925-3936.
- [9] Wu, H.Y. and P. Cheng, An experimental study of convective heat transfer in silicon microchannels with different surface conditions. *Int. J. Heat Mass Transfer*, **43**, 2003, 2547-2556.
- [10] Tiselj, I., et al., Effect of axial conduction on the heat transfer in micro-channels. *Int. J. Heat Mass Transfer*, **47**, 2004, 2551-2561.
- [11] Maranzana, G., I. Perry, and D. Maillet, Mini- and micro-channels:influence of axial conduction in the walls. *Int. J. Heat Mass Transfer*, **47**, 2004, 3993-4004.
- [12] Choi, C., K. Westin, and K. Breuer. To slip or not to slip-water flow in hydrophilic and hydrophobic microchannels. in *International Mechanical Engineering conference and exposition*. 2002. New Orleans.
- [13] Zhu, Y. and S. Granick, Limits of Hydrodynamic No-Slip Boundary Condition. *Phys. Rev. Let.*, **88**(10), 2002, 106102-1-4.
- [14] Barrat, J. and L. Bocquet, Large Slip effect at a Nonwetting Fluid-Solid Interface. *Phys. Rev. Let.*, **82**(3), 1999, 4671-4674.
- [15] Tretheway, D. and C. Meinhart, Apparent fluid slip at hydrophobic microchannel walls. *Phys. Fluids*, **14**(13), 2002, 9-12.
- [16] Nagayama, G. and P. Cheng, Effects of interface wettability on microscale flow by molecular dynamics simulation. *Int. J. Heat Mass Transfer*, **47**, 2004, 501-513.
- [17] Thomson, P. and S. Troian, A general boundary condition for liquid flow at solid surfaces. *Nature*, **389**, 1997, 360-362.
- [18] Xue, L., et al., Effect of liquid layering at the liquid-solid interface on thermal transport. *Int. J. Heat Mass Transfer*, **47**, 2004, 2004.
- [19] Shah, R.K. and A.L. London, *Laminar flow forced convection in ducts*. Adv. Heat Transfer. 1978: Academic Press.
- [20] Chiou, J.P. The advancement of compact heat exchanger theory considering the effects of longitudinal heat conduction and flow nonuniformity. in *Symposium on compact heat exchangers*. 1980. NY: ASME.
- [21] Guo, Z.Y. and Z.X. Li, Size effects on single-phase channel flow and heat transfer at microscale. *Int. J. Heat Fluid Flow*, **24**, 2003, 284-298.



## Investigation of the Mean Flow Pattern in Zero-Net-Mass-Flux Elliptical-Jets in Cross-Flow using Planar-Laser-Induced Fluorescence

J. Arnaud, S. Tomar and J. Soria

Laboratory for Turbulence Research in Aerospace & Combustion (LTRAC),  
Department of Mechanical Engineering,  
Monash University, Melbourne, VIC 3800, Australia

### Abstract

Planar-laser-induced fluorescence (PLIF) measurements have been used to investigate the mean flow pattern of a zero-net-mass-flux elliptical jets in cross-flow (ZNMF-EJICF). This particular jet is generated using the working fluid without net transfer of mass across the system boundary during one period of oscillation. The investigation involves the measurement of the mean jet profiles of the elliptical JICF. Two distinct flow regimes are observed namely single trajectory and multiple trajectory jets. Single trajectory jets demonstrate mixing of the bulk of the fluid outside the upstream boundary layer, while multiple trajectory ZNMF-JICF can penetrate more deeply into the ambient cross-flow. Ensemble-averaged PLIF images of two elliptic jets of aspect ratios (AR) of 2 and 3 exhausting normally into a cross flow with velocity ratios (VR) ranging from 2 to 5 have been studied and compared.

### Introduction

Jets in cross-flow (JICF) have many important practical and industrial applications, a few of which include combustion, industrial mixing, injection cooling, pollution transport, cooling of turbine blades, missile control system, etc. Over the past few decades, the JICF has attracted a considerable amount of research interest. Substantial research has been done on jets over the years to reveal their trajectory, spreading and mixing as a function of various flow parameters such as Reynolds number, Strouhal number and ratio of jet-flow to cross-flow momentum [1,2,5]. Previous research based on continuous, pulsed or Zero-Net-Mass-Flux jets suggest that a presence of cross flow enhances the mixing of the jet as compared to a free jet [4,14].

A ZNMF jet is a fluid stream with non-zero mean stream wise momentum formed by the interaction of vortices. The vortices are generated by the periodic oscillation of a fluid. Since there is no net mass of fluid added to the system, the jet formation occurs within the working fluid stream. In the present study, the time-averaged flow across the jet orifice is equal to zero, thus forming a zero-net-mass-flow jet in cross-flow (ZNMF-JICF).

While most studies on JICF phenomenon concentrated their efforts on the circular jet geometry, it is believed that jets of other geometries can also be of immense potential, especially in the area of passive mixing. Previous studies have shown that even in the free jet configuration, continuous or pulsed non-circular geometries (i.e., square, rectangular, elliptic and lobed) exhibit higher mixing rates than a circular geometry [6-13]. Therefore the motivation of this study is to investigate qualitatively the flow pattern of ZNMF-EJICF.

### Experimental Apparatus And Method

The experimental investigation was carried out in a square 250 mm closed-circuit vertical water tunnel at the Laboratory for

Turbulence Research in Aerospace and Combustion (LTRAC) at Monash University, Melbourne, Australia.

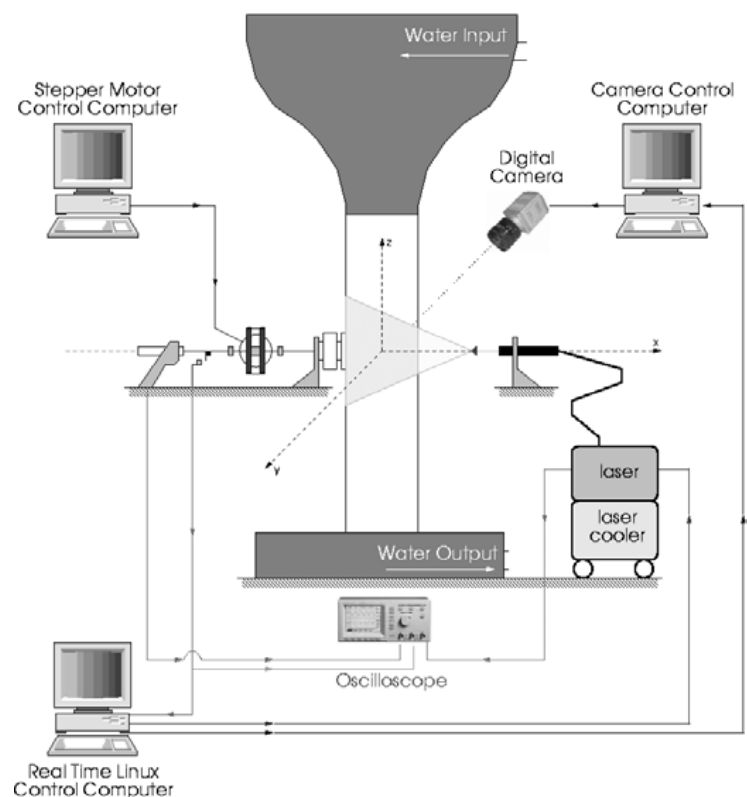


Fig. 2. The experimental setup used for firing the laser and acquiring images using a digital camera.

The tunnel, shown in figure 1, has a 1.5m long working section made of 15mm thick Perspex. Water is introduced into the settling chamber using a spray system at the top, which is then passed through a perforated plate, four stainless steel wire screens, a honeycomb and a 16:1 contraction before entering the working section of the water tunnel.

The creation of the ZNMF jet is produced through an orifice by a piston oscillating in a cylinder. The piston is connected through a scotch-yoke mechanism driven by a stepper motor. The entire set-up is mounted on a horizontal support plate bolted to the tunnel test section wall 550mm below the contraction exit. The arrangement of the apparatus is shown in figure 2.

The scotch-yoke mechanism, which is driven by a stepper motor is controlled by a software program running in Windows operating system. The scotch-yoke mechanism can be driven at amplitudes of 1, 2, 4, 6, 10, 14 and 22mm. It is capable of producing frequencies as low as 0.01Hz. The upper limit of frequencies depends on the choice of the amplitude of motion of the piston and is shown in the table 1.

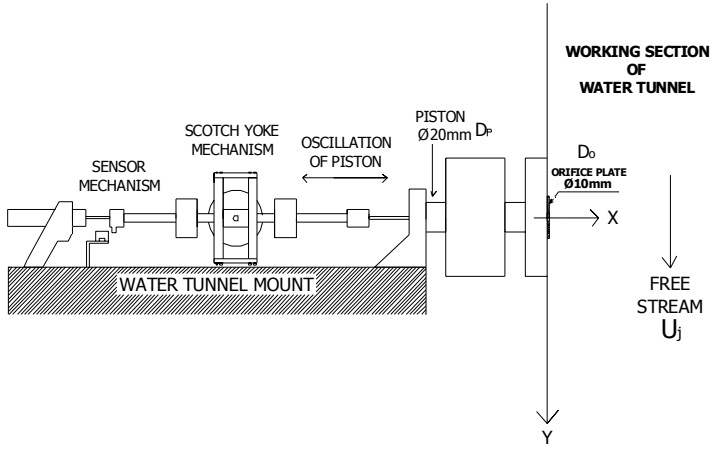


Fig. 2. Arrangement and details of zero-net-mass-flux injection apparatus in the vertical water tunnel [15].

a (mm)	1	2	4	6	10	14	22
$f_{max}$ (Hz)	5	6	8	8	6	4	2

Table 1. The upper limit of frequencies depends on the choice of the amplitude of motion of the piston

### PLIF Technique

Fluorescent dye flow visualizations were carried out to provide a qualitative picture of these ZNMF-EJICF using a laser sheet generated by a Quanta System 200 mJ dual cavity Nd: YAG laser at a wavelength of 532nm. The sheet was aligned with the orifice center in the  $z=0$  plane.

The entire PLIF image acquisition system was controlled using an in-house developed Real-time Linux (RTAI) computer program. The trigger signal, coming from the sensor mechanism, references the maximum forward position. This signal is sent to the Real-time Linux Computer Program, which synchronizes the images acquisition and the laser firing with a time delay corresponding to the phase of interest.

24 instantaneous flow visualization images of the ZNMF-JICF, at 12 different phases ( $N\pi/12$ ,  $N$  integer number,  $1 \leq N \leq 12$ ) and in a region measuring 250 x 180 mm, were recorded using a 12 bit 1.3 Mega Pixel (1280 x 1024) PCO Pixelfly CCD camera. The camera was mounted on a vertical rail and the position was measured using a set of rulers installed in the x, y and z-axes. In addition, 256 images of the dye fluorescence in a region measuring 250 x 180 mm were also acquired at random points in the jet cycle. These were then averaged to reveal the mean flow pattern for each jet.

### Flow parameterization

The dimensional parameters governing the flow are the hydraulic diameter of the elliptical orifice  $D_0 = 10$  mm, the diaphragm diameter  $D_p = 20$  mm, the frequency of oscillation  $f$ , the amplitude of oscillation  $a$ , the characteristic jet velocity  $U_j$ , and the cross-flow velocity  $U$ . These form the non-dimensional groups shown below. These groups are identified as: the Reynolds number (Re), the Strouhal number (St), and the Velocity Ratio (VR), respectively.

$$St = \frac{f D_0}{U_j} \quad (1)$$

$$Re = \frac{U_j D_0}{\nu} \quad (2)$$

$$R = \frac{U_j}{U} \quad (3)$$

The momentum jet velocity,  $U_j$ , through the orifice can be calculated from the root mean square piston velocity  $V_{rms}$  using equation (4):

$$U_j = \frac{V_{rms} D_p}{D_0} \quad (4)$$

Making use of the following relationship between the root mean square and peak velocity for a pure sinusoidal oscillation,

$$V_{rms} = \frac{V_{max}}{\sqrt{2}} \quad (5)$$

$$V_{max} = \omega a \quad (6)$$

And after substituting Equations (4), (5) and (6) appropriately into equations (1), (2) and (3), the following equations were obtained,

$$St = \frac{D_0^2}{a \sqrt{2} \pi D_p} \quad (7)$$

$$U_j = \frac{\sqrt{2} \pi f a D_p}{D_0} \quad (8)$$

$$Re = \frac{\sqrt{2} \pi f a D_p}{\nu} \quad (9)$$

Equations (7), (8) and (9) indicate that the above parameters depend entirely on the geometrical aspects of the experimental set-up and the frequency of motion of the piston.

### Experimental Conditions

To identify the various flow regimes of the ZNMF-EJICF, 40 different jets were formed by varying the tunnel speed  $U$ , the oscillation frequency, the amplitude of the diaphragm oscillations and the aspect ratio.

VR	Re	a (mm)	St	f (Hz)	$U_j$ (m/s)	$U$ (m/s)
2	1066	2	0.563	6.00	0.107	0.053
2	1066	4	0.281	3.00	0.107	0.053
2	1066	6	0.188	2.00	0.107	0.053
2	1066	10	0.113	1.20	0.107	0.053
2	1066	14	0.080	0.86	0.107	0.053
3	1066	2	0.563	6.00	0.107	0.053
3	1066	4	0.281	3.00	0.107	0.053
3	1066	6	0.188	2.00	0.107	0.053
3	1066	10	0.113	1.20	0.107	0.053
3	1066	14	0.080	0.86	0.107	0.053
4	1066	2	0.563	6.00	0.107	0.027
4	1066	4	0.281	3.00	0.107	0.027
4	1066	6	0.188	2.00	0.107	0.027
4	1066	10	0.113	1.20	0.107	0.027
4	1066	14	0.080	0.86	0.107	0.027
5	1066	2	0.563	6.00	0.107	0.027
5	1066	4	0.281	3.00	0.107	0.027
5	1066	6	0.188	2.00	0.107	0.027
5	1066	10	0.113	1.20	0.107	0.027
5	1066	14	0.080	0.86	0.107	0.027

Table 2. Jet parameters used for qualitative PLIF experiments.

The generation parameters for elliptical jets of  $AR = 2$  and  $AR = 3$  are summarized in Table 2. Only certain necessary characteristics of the ZNMF-EJICF have been discussed in this study.

## Results

### Instantaneous Flow Pattern

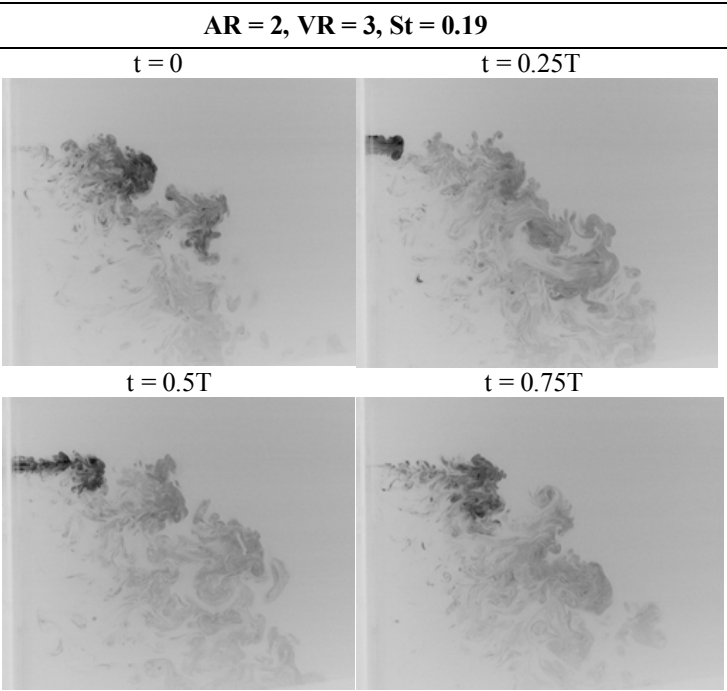


Fig 3. Instantaneous PLIF measurements of a single trajectory.

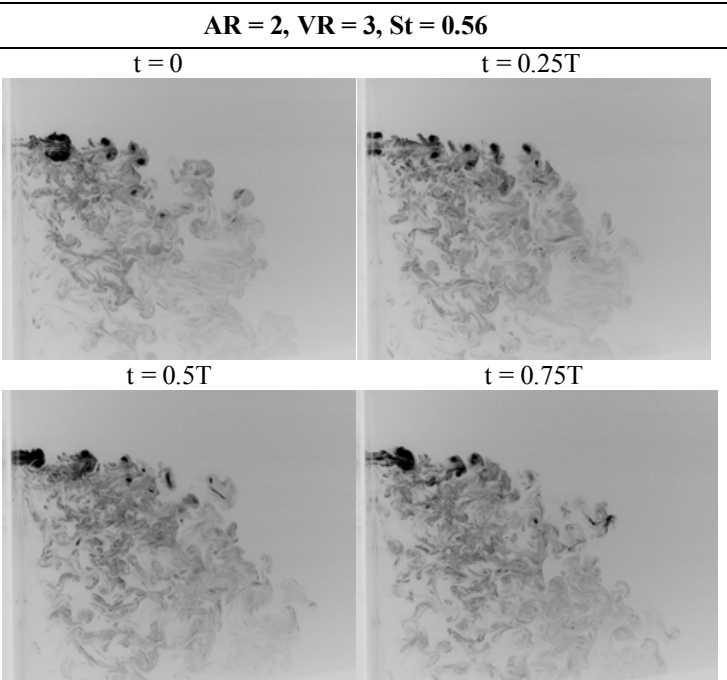


Fig. 4 Instantaneous PLIF measurements of a multiple trajectory.

The instantaneous PLIF measurements of single and multiple trajectory ZNMF elliptical-JICF are shown in figures 3 and 4 respectively. They clearly show the emergence of the jet and formation of a vortex ring pair that is gradually carried into the cross flow. At cycle start time,  $t = 0$ , the piston is at its maximum back position in the cylinder and hence, the velocity of the piston is zero at this particular point. The backward stroke of the piston caused the fluid to be “sucked in” from the mainstream into the

cylinder. At  $t = 0.25T$ , the piston is moving forward in the cylinder and hence “pushing” the fluid out of the orifice plate, which results in the generation of the ZNMF jet. At the next phase,  $t = 0.5T$ , the entire fluid in the cylinder has been expelled for the creation of the jet. The piston is at its maximum forward position in the cylinder and is at zero velocity. As a result there is no sucking or pushing occurring. At the last phase,  $t = 0.75T$ , the piston is moving back towards the trigger signal [15].

The major differences in the instantaneous patterns of the two jets were the frequency of shedding of the vortex ring pair and the concentration of the dye in the flow frame captured. In the multiple trajectory jets, the dye is convected away by the free-stream fluid a lot slower than the single trajectory jets. This last difference is critical as explained further in the mean flow pattern in the next section.

### Main Flow Pattern

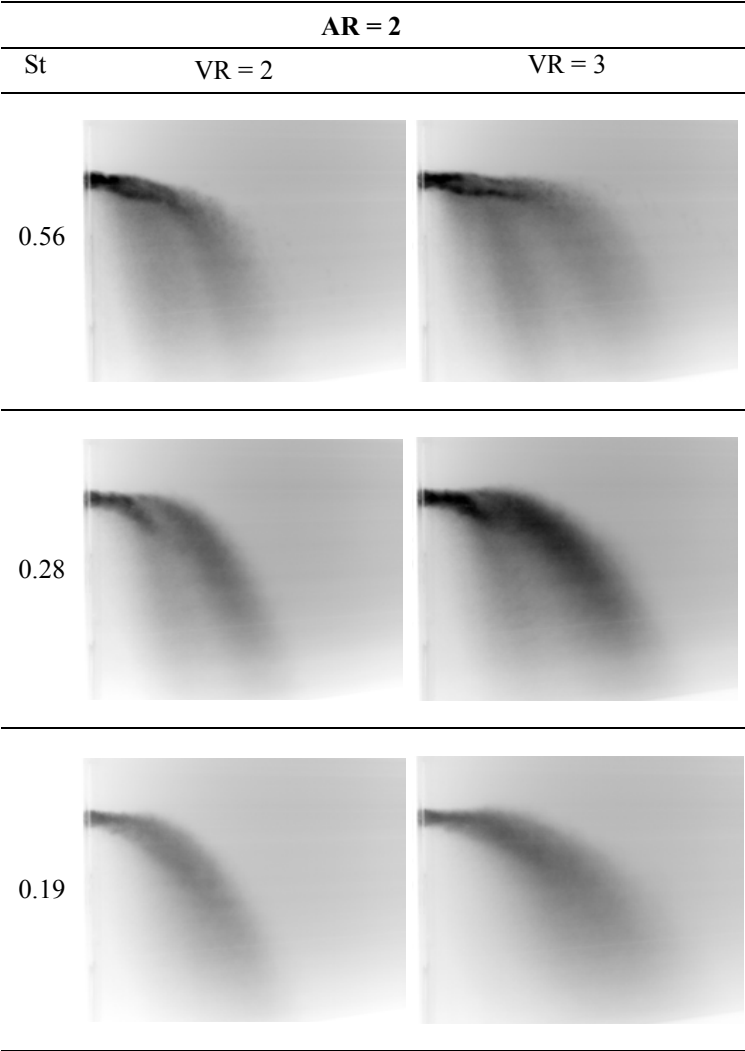


Fig. 5 Main flow pattern for elliptical jets of aspect ratio  $AR = 2$  and velocity ratio  $VR=2$  and  $VR = 3$ , and  $St = 0.56$ ,  $St = 0.28$  and  $St = 0.19$ .

The different mean flow patterns are obtained by an ensemble average of 256-single exposed dye flow visualization images and are shown in figures 5 and 6 for the single and multiple trajectory ZNMF-EJICF respectively. The obvious observation made is the dependence between the jet penetration, the elliptical aspect ratio  $AR$  and the velocity ratio  $VR$ . Penetration of the jet increases with orifices of less aspect ratio as expected. As seen from figures 5 and 6, the mean penetration of the dye also increases with increase in the velocity ratio. A critical Strouhal number was found for the generation apparatus that can be used to distinguish between the two regimes: single trajectory ZNMF-EJICF and

multiple trajectory ZNMF-EJICF. By comparing the main flow pattern of figure 5 with those of figure 6, it seems the critical Strouhal number is dependant on the aspect ratio AR. Indeed whereas the critical Strouhal number is for AR = 2:  $0.19 < St_{crit} < 0.28$ , for AR = 3 the value of the critical Strouhal number increases:  $0.28 < St_{crit} < 0.56$ . This shows that the critical Strouhal number is dependant on the aspect ratio of the orifice chosen to perform the experiment.

In the two elliptical jets, AR = 2 and AR = 3, the two flow structures: single trajectory and multiple trajectory are only dependent on Strouhal number when  $2 \leq VR \leq 5$ .

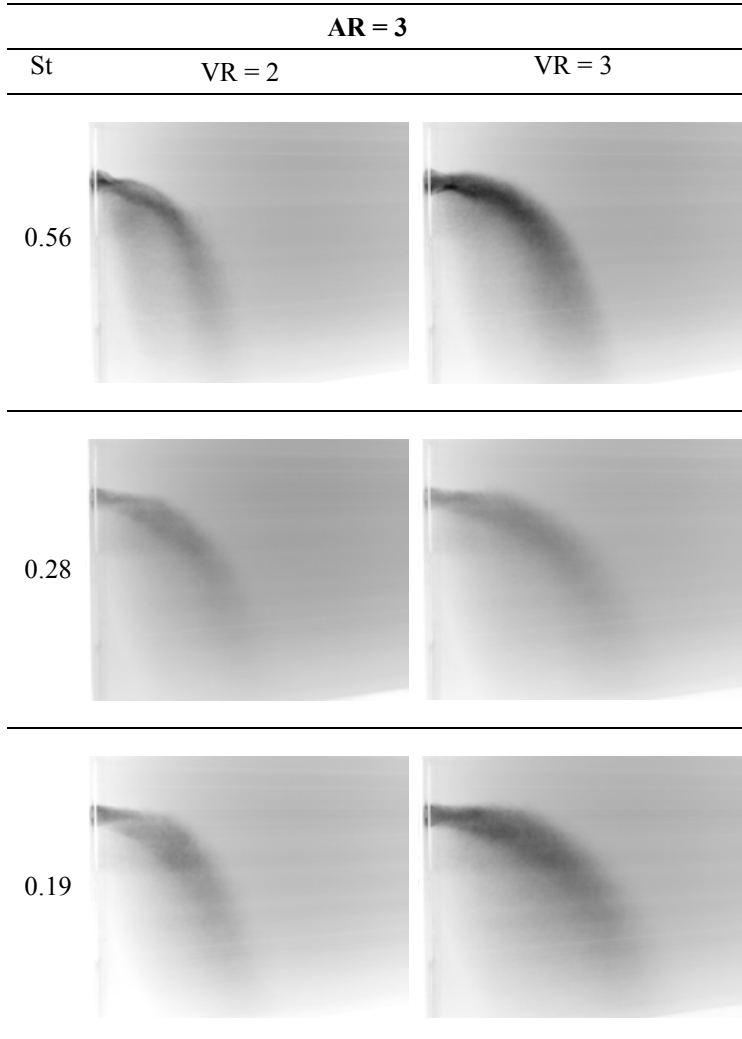


Fig. 6 Main flow pattern for elliptical jets of aspect ratio AR = 3 for velocity ratios of VR=2 and VR = 3, and St = 0.56, St = 0.28 and St = 0.19.

## Conclusions

As for circular ZNMF-JICF, single trajectory jets are characterized by a single section of high concentration along the trajectory of the jet whereas multiple trajectory jets are seen to have multiple areas of high concentration. In this case, the multiple trajectory jets are seen to have two distinct areas of maximum concentration, one parallel to the cross flow and the other in the direction of the jet trajectory.

Yet, for elliptical jets the aspect ratio seems to influence the penetration and the value of the critical Strouhal number: the penetration increases with a low aspect ratio and the critical Strouhal number increases with aspect ratio.

Finally, for a fixed aspect ratio and for  $2 \leq VR \leq 5$ , the two flow structures: single trajectory and multiple trajectory are only

dependent on Strouhal number. As decreasing VR increases the distance between the upper and the lower trajectories of multiple trajectory jets, more experiments should be done to investigate the eventual dependence between the critical Strouhal number  $St_{crit}$  and the velocity ratio VR.

## Acknowledgments

I would like to thank Prof Julio Soria and Mr. Kamal Parker for their help, supervision and patience throughout this project.

## References

- [1]Cater, J.E. and Soria, J., The evolution of round zero-net-mass-flux-jets, *J. Fluid Mech.*, **472**, 2002, 167-200.
- [2]Chang, Y.K., and Vakili, A.D., Dynamics of Vortex Rings in Crossflow, *Physics of Fluids*, **7**, 1995, 1583-1597.
- [3]Dhanak, M. and de Bernardinis, B., The evolution of an elliptic vortex ring, *J. Fluid Mech.*, **109**, 1981, 189-216.
- [4]Eroglu, A., and Breidenthal, R.E., Effects of Periodic Disturbances on Structure and Flame Length of a Jet in a Cross Flow, *AIAA Paper 91-0137*, Jan. 1991.
- [5]Gordon, M. and Soria, J., PIV measurements of a zero-net-mass-flux jet in cross flow, *Experiments in Fluids*, **33**, 2002, 863-872.
- [6]Grinstein, F., Vortex dynamics and entrainment in rectangular free jets, *J. Fluid Mech.*, **437**, 2001, 69-101.
- [7]Gutmark, E. and Grinstein, F., Flow control with non-circular jets, *Annu. Rev. Fluid Mech.*, **31**, 1999, 239-272.
- [8]Ho, C. and Gutmark E., Vortex induction and mass entrainment in a small-aspect-ratio elliptic jet, *J. Fluid Mech.*, **179**, 1987, 383-405.
- [9]New, T.H., Lim, T.T. and Luo S.C., A visual study on elliptic jets in cross flow, in: Proceedings of 9th International Symposium of Flow Visualisation, 2000, Paper 224.
- [10]New, T.H., T.T. Lim, S.C. Luo, J. Soria, "Particle image velocimetry on elliptic jets in cross flow", in: Proceedings of PIV'01, 2001.
- [11]New, T.H. and Soria J., Near-field pairing of leading-edge vortices in elliptic jets in cross flow, *European Journal of Mechanics B/Fluids*, **23**, 2004, 551-569.
- [12]Ruggeri, R., Callaghan, E. and Bowden D., Penetration of air jets issuing from circular, square and elliptic orifices directly perpendicularly to an air stream, in: NACA TN 2019, 1950.
- [13]Weston, R. and Thames, F., Properties of aspect-ratio 4.0 rectangular jets into a subsonic crossflow, *J. Aircraft* **16**, **10**, 1979, 701-707.
- [14]Wu, J.M., Vakili, A.D., and Yu, W.K., Mixing of an Acoustically Pulsed Air Jet with a Confined Crossflow, *AIAA Journal*, **26**, No.8, 1988, 940-947.
- [15]Tomar S. and Soria J., MCCDPIV Measurements of a ZNMF JICF, published in the proceedings of PIV'03, Busan, South Korea, 2003

## Flow Past An Impulsively Started Oscillating Elliptical Cylinder

T.L. Chng, T. T. Lim, J. Soria<sup>1</sup>, K. B. Lua and K. S. Yeo

Fluid Division, Department of Mechanical Engineering,  
National University of Singapore,

10 Kent Ridge Crescent, Singapore 119260.

<sup>1</sup>LTRAC, Monash University, Melbourne, Victoria 3800, Australia.

### Abstract

The current experimental study on a two-dimensional oscillating aerofoil aims to isolate and explore the effects of wing twisting, one of the most basic aspects of insect locomotion. Particle Image Velocimetry (PIV) is employed to study the effects of reduced frequency as well as angular amplitude on an impulsively started aerofoil oscillating which is initially at rest. The forced oscillation is of a sinusoidal nature about a mid-chord, spanwise axis and all investigations are carried out at a Reynolds number of 1000, with amplitudes in the range of 20° to 60°, typical of the regime that insects tend to operate within. A piston tank facility is used to generate the impulsively started motion. The ensemble averaged results obtained suggest that both the reduced frequency and angular amplitude are important governing parameters which influence the development of leading edge structures and subsequent wake vortices. In the limiting case (i.e. fixed angle of attack), the resulting flow field is one fairly similar to that of a bluff body, with the distinct, periodic formation of a von Karman vortex street. In the lower reduced frequency cases, the flow displays characteristics similar to the former, except that the effect of the aerofoil oscillation imposes a velocity component on the flow which seems to retard the leading edge separation. In contrast, in the higher reduced frequency cases, where the velocity component imparted by the oscillatory motion is much higher than that of the freestream, the effect of the freestream velocity seems to be almost non-existent. Vortices are generated in an anti-symmetric manner at both the leading and trailing edges, but whilst the trailing edge vortices are advected downstream, the leading edge vortices are negated before advection can occur.

### Introduction

Over the past two decades, the advancement of non-intrusive experimental techniques and DNS solvers has given scientists the impetus to undertake the study of unsteady aerodynamic problems with newfound resolve. Peculiar to this class of flows is the topic of oscillating aerofoils. Traditionally one which has been applied to flutter analysis, gust response and regarded as a possible avenue of alternative thrust production, this field has incited renewed interest due to its applications to aircraft maneuverability and relevance to insect flight.

From the perspective of the former, the attractiveness of a pitching aerofoil mainly stems from the fact that studies have shown that such a motion is able to generate high levels of lift even when operating beyond the stall angle [1]-[3]. This phenomenon is very similar to the lift overshoot observed during the nascent stages of the flow past a fixed incidence aerofoil [4]. Yet, from a totally different dimension, wing oscillation has also been known to be an integral part of insect wing motion. In recent times, scientists have begun to explore the possibility of applying this concept of dynamic wing motion to future Micro Aviation Vehicles (MAVs). This has in turn contributed to a surge in studies hoping to piece together a sufficiently workable model of insect flight which can subsequently be applied to these man-made vehicles [5]-[6].

Fundamentally speaking, the investigation of both these applications primarily differs in the incidence angles and the Reynolds number regimes that they operate in. Whilst

conventional aerodynamic applications usually span the order of  $10^6$ - $10^8$ , insect flight is centred around a relatively lower range of  $10$ - $10^4$ . Additionally, insects typically flap their wings at mean angles of attack in excess of 40° [7], well within the deep stall regime of most aircraft.

The focus of the current study is on the flow past an impulsively started elliptical cylinder subjected to a sinusoidal oscillation at a nominal Reynolds number of 1000. Such a configuration is aimed at mimicking the twisting motion of an insect wing, one of the basic elements of insect flight. Whilst attempts have been made at producing dynamically scaled models to study the motion of such creatures in their entirety [8], here our emphasis is on examining the artefacts of wing twisting in isolation. Particle Image Velocimetry (PIV) is employed to study the effects of the reduced frequency and angular amplitude on the flow. For the purpose of comparison, the flow past an elliptical cylinder at fixed incidences is also investigated.

Extensive flow visualization studies have previously been conducted to examine the effect of parameters such as the reduced frequency and angular amplitude on the flow field of an oscillating aerofoil [9, 10]. The reduced frequency has generally been found to have a more pronounced effect on the evolving flow structures compared to other parameters like the angular amplitude. In addition, studies have also found that the flow field of an oscillating aerofoil at low reduced frequencies is very similar to that of an aerofoil in static stall whilst at higher reduced frequencies, the flow is primarily due to the rotational motion of the wing. Computational studies have also shown good agreement with the above [11, 12].

### Experimental Setup

The experiments were carried out in a piston tank facility shown in figure 1. The entire setup consists of a stepper motor-driven square piston used to generate the impulsively started flow, and an additional stepper motor used to generate the sinusoidal oscillation. The test section has a square cross section of 198mm by 198mm and a length of about 400mm. In addition, the motion of the piston is restricted to a maximum horizontal displacement of 300mm.

An elliptical cylinder made of brass, with a chord of 60mm, thickness 7.5mm and aspect ratio of 3.25, is used throughout the experiments and spans the entire width of the water tunnel.

A Nd:YAG laser capable of generating 2x300mJ pulses of 5ns duration is used as the illumination source, and produces a uniform light sheet of 2mm thickness. Polyamide particles with a mean diameter of 20µm are used to seed the flow. Images are captured via a 12 bit digital CCD camera with a 1280px by 1024px resolution.

The stepper motors, CCD camera and laser are all computer controlled and linked via an Ethernet interface. TTL signals are used to synchronize all the devices and ensure that they are triggered off simultaneously.

A multigrid cross correlation digital PIV (MCCDPIV) algorithm [13] is used to analyse and process the captured single exposed images. Data validation is carried out using three techniques, the global histogram test, median value operator test and the dynamic mean value operator test. A velocity vector is rejected unless all the criteria are met.



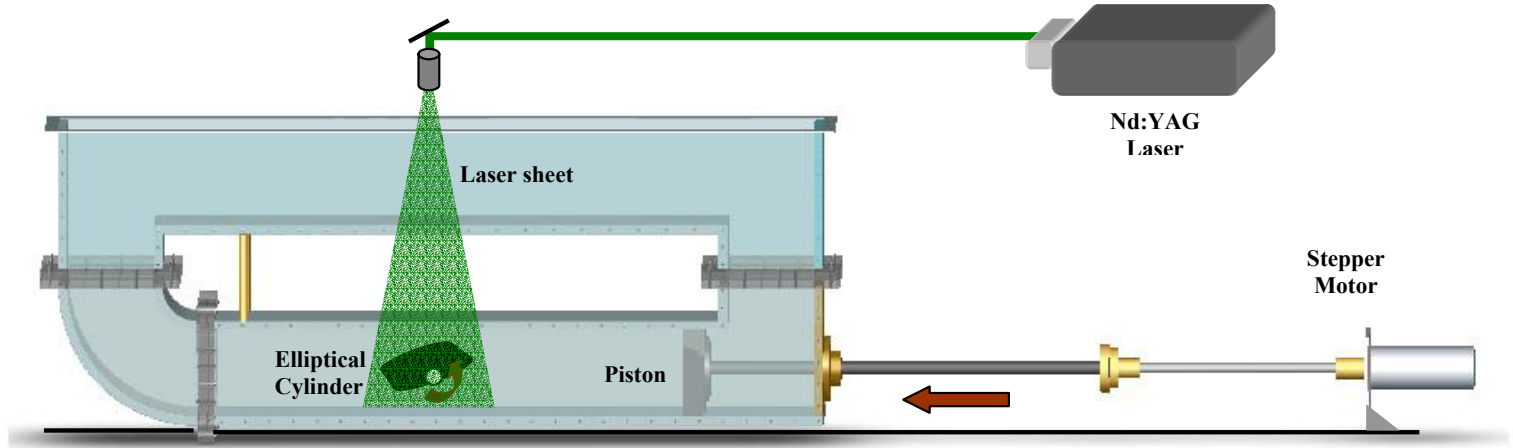


Figure 1: Schematic of piston tank facility.

The opacity of the elliptical cylinder results in a lack of illumination beneath the wing. In order to obtain a complete field of data, two sets of experiments are performed: one with the orientation and motion of the wing reversed and the other as per normal. The two datasets are then merged together. Each realization is repeated a total of 100 times and ensemble averaging is performed.

### Experimental Conditions

For all experiments conducted, the flow is impulsively started from rest with an initial linear acceleration,  $a_0$ , of  $100\text{mm/s}^2$ . The Reynolds number,  $Re$ , is defined as

$$Re = \frac{U_\infty c}{\nu} \quad (1)$$

where  $U_\infty$  is the constant, post acceleration, freestream velocity,  $c$  is the aerofoil chord and  $\nu$  is the kinematic viscosity of water.

For the oscillatory cases, the imposed oscillation is that of a sinusoidal nature, given by the equation:

$$\theta = \theta_0 \sin \omega t \quad (2)$$

where  $\theta$  is the angular displacement,  $\theta_0$  the angular amplitude,  $\omega$  the temporal frequency of oscillation and  $t$  is the time elapsed. The varied parameters are the angular amplitude,  $\theta_0$ , and the oscillation frequency, which is represented by the dimensionless reduced frequency,  $\kappa$ . The reduced frequency is defined as,

$$\kappa = \frac{fc}{2U_\infty} \quad (3)$$

where  $f = \omega/2\pi$  is the oscillation frequency. The time elapsed is also non-dimensionalized by the freestream velocity and aerofoil chord to give,

$$t^* = \frac{tU_\infty}{c} \quad (4)$$

## Results & Discussion

### Fixed Incidence Case

The case of an elliptical aerofoil at a fixed incidence of  $40^\circ$  is presented here for reference. The flow is impulsively started from rest and attains a constant velocity corresponding to a Reynolds number of 1000 at  $t^*=0.048$ . The PIV results reveal a flow field typical of an aerofoil in deep stall. During the initial stages of the flow, a starting vortex is seen to emanate from the trailing edge of the wing. This is accompanied by a corresponding separation at the leading edge which culminates in the formation of the well-known leading edge vortex or separation bubble. The consequent flow is then characterized by shear layer instabilities of a Helmholtz nature just above the leading edge, which result in the eventual shedding of the leading edge vortex. At the same time, the flow is marked by the growth of a secondary vortex, opposite in sign to that of the leading edge vortex, at around the quarter chord position. One possibly attributes the occurrence of this vortex to the adverse pressure

gradient encountered by the flow entrained by the leading edge vortex. Figure 2 clearly shows the presence of this secondary vortex as well as the growth of a new leading edge vortex. Finally, as the initial leading edge vortex is advected downstream beyond the visual field, the growth of a vortex at the trailing edge marks the development of a periodic von Karman vortex street often associated with bluff bodies.

### Oscillatory Case: $\kappa = 0.1$ , $\theta_0 = 40^\circ$

An investigation is carried out for two different reduced frequencies of  $\kappa=0.1$  and  $\kappa=0.5$ , both with a corresponding angular amplitude of  $40^\circ$ .

The lower reduced frequency configuration results in a flow field which is distinguished by its resemblance to the static case described above. The vortical structures such as the initial starting vortex as well as the consequent growth of the leading edge and secondary vortex are all similarly observed (see figure 3A). However, a few differences are worthy of mention. The rotational velocity imposed by the sinusoidal oscillation appears to inhibit the separation characteristics of the aerofoil. Primarily, one observes a delay in the formation of the leading edge vortex during the pitching up motion which is in good agreement with other studies. Similarly, apart from the initial starting vortex, the shedding of trailing edge vortices seems to be practically negated, and is instead replaced by a wavy-like structure. In addition, the pitching motion of the aerofoil repositions both the leading edge and secondary vortex, which traverse the top surface of the aerofoil and are shed into the wake during the course of an oscillation cycle.

### Oscillatory Case: $\kappa = 0.5$ , $\theta_0 = 40^\circ$

In contrast to the above case where the translational flow seems to adapt fairly well to the variation in incidence, the flow pattern for the reduced frequency of  $\kappa=0.5$  is dominated by the rotational motion of the aerofoil. This is due to the fact that the tip velocities of the aerofoil are much larger than that of the freestream. As such, vortices are generated in an anti-symmetric manner as shown in figure 3B, with the growth of secondary vortices perceptibly missing. Also, it is interesting to note that the vortices produced in the vicinity of the leading edge are not advected downstream as in the previous cases. The low pressure region at the leading edge caused by the forceful pitching motion seems to provide a suction effect which prevents these vortices from moving downstream. These vortices are then periodically annihilated during the ensuing motions of the aerofoil. It is also observed that the wake is characterized by the formation of a reverse von Karman jet structure due to the shedding of trailing edge vortices.

### Oscillatory Case: $\kappa = 0.5$ , $\theta_0 = 20^\circ$

A brief investigation of the effect of angular amplitude is conducted for the case of  $\kappa=0.5$ , with  $\theta_0=20^\circ$ . Interestingly, the results display a combination of characteristics of both the oscillatory cases mentioned above. The leading edge vortices are

repositioned by the aerofoil and shed downstream whilst the trailing edge vortices form a reverse von Karman street (see figure 3C).

The foregoing discussion suggests that the ratio of the maximum tip velocity of the aerofoil to that of the freestream plays an important role in determining the characteristics of the flow. More specifically, this dimensionless number establishes the degree of modification of the effective angle of attack at the leading edge. This is evident in a comparison of the two different reduced frequency cases shown in figures 3A and 3B. In the case of the former, the additional velocity component imparted by the aerofoil oscillation is small and only serves to retard the flow evolution characteristics. However, its influence in the latter case is much larger and the flow is virtually dictated by the oscillatory motion.

To a certain extent, the reduced frequency as defined in this study provides a reasonable approximation for this ratio, but a more accurate representation of the aerofoil tip velocity should include the angular amplitude and account for any differences in the location of the pitching axis.

### Concluding Remarks

A preliminary study of an impulsively started elliptical cylinder in oscillatory motion has been conducted. The results show that the ratio of the aerofoil tip velocity to that of the freestream is the main parameter which governs the flow. When this ratio is small, as in the reduced frequency case of  $\kappa=0.1$ , the flow continues to display characteristics reminiscent of an aerofoil in static stall, albeit with a delay in the separation at the leading edge during the pitch up motion. This brings to mind the classical, linearized theory of oscillating aerofoils which predicts that the solutions of an aerofoil conducting small amplitude oscillations are merely functions of the static cases with a certain phase difference.

When this ratio is large, the flow is dominated by the pitching motions of the aerofoil and characterized by the formation of a reverse Von Karman vortex street. Although the reduced frequency provides a reasonable estimate of this ratio, it is proposed that a more complete representation should include the angular amplitude of the oscillation, as well as the location of the pitching axis.

### References

- [1] Visbal, M. R. & Shang, J. S., Investigation of the Flow Structure Around a Rapidly Pitching Airfoil, *AIAA J.*, **27**, 1989, 1044-1051.

- [2] Currier, J. M. & Fung, K. Y., Analysis of the Onset of Dynamic Stall, *AIAA J.*, **30**, 1992, 2469-2477.
- [3] Chandrasekhara, M. S., Carr, L. W. & Wilder, M. C., Interferometric Investigations of Compressible Dynamic Stall Over a Transiently Pitching Airfoil, *AIAA J.*, **32**, 1994, 586-593.
- [4] Katz, J., Yon, S. & Rogers, S. E., Impulsive Start of a Symmetric Airfoil at High Angle of Attack, *AIAA J.*, **34**, 1996, 225-230.
- [5] Ellington, C. P., The Novel Aerodynamics of Insect Flight: Applications to Micro-air Vehicles, *J. Exp. Bio.*, **202**, 1999, 3439-3448.
- [6] Sane, S. P. & Dickinson, M. H., The Aerodynamic Effects of Wing Rotation and a Revised Quasi-steady Model of Flapping Flight, *J. Exp. Bio.*, **205**, 2002, 1087-1096.
- [7] Willmott, A. P. & Ellington, C. P., The Mechanics of Flight in the Hawkmoth *Manduca Sexta*. I. Kinematics of Hovering and Forward Flight, *J. Exp. Bio.*, **200**, 1997, 2705-2722.
- [8] Ellington, C. P., Berg, C. V., Willmott, A. P. & Thomas, L. R., Leading-edge Vortices in Insect Flight, *Nature*, **384**, 1996, 626-630.
- [9] Ohmi, K., Coutanceau, M., Loc, T. P. & Dulieu, A., Vortex Formation Around an Oscillating and Translating Airfoil at Large Incidences, *J. Fluid Mech.*, **211**, 1990, 37-60.
- [10] Ohmi, K., Coutanceau, M., Daube, O. & Loc, T. P., Further Experiments on Vortex Formation Around an Oscillating and Translating Airfoil at Large Incidences, *J. Fluid Mech.*, **211**, 1990, 37-60.
- [11] D'Alessio, S. J. D., Dennis, S. C. R. & Nguyen, P., Unsteady Viscous Flow Past an Impulsively Started Oscillating and Translating Elliptic Cylinder, *J. Eng. Math.*, **35**, 1999, 339-357.
- [12] Akbari, M. H. & Price, S. J., Simulation of the Flow Over Elliptic Airfoils Oscillating at Large Angles of Attack, *J. Fluid & Struc.*, **14**, 2000, 757-777.
- [13] Soria, J., Lim, T. T., Hou, K. C. & Sengupta, T. K., Investigation of Accelerated Flow over an Airfoil at an Angle of Attack using Multigrid Cross-Correlation Digital PIV, *4th International Symposium on Particle Image Velocimetry*, 2001.

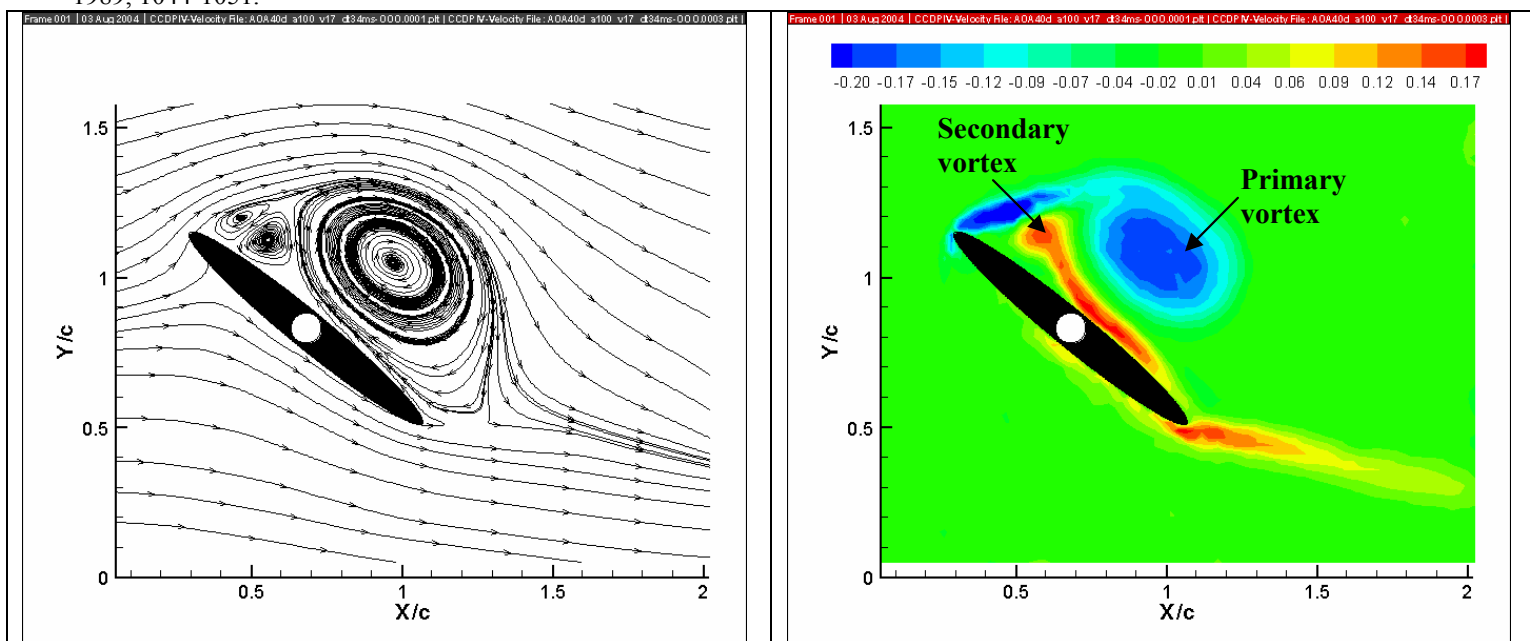


Figure 2: Streamline and vorticity plots for an elliptical aerofoil at 40° incidence,  $Re=1000$ ,  $t^*=1.7$ . Flow is from left to right.

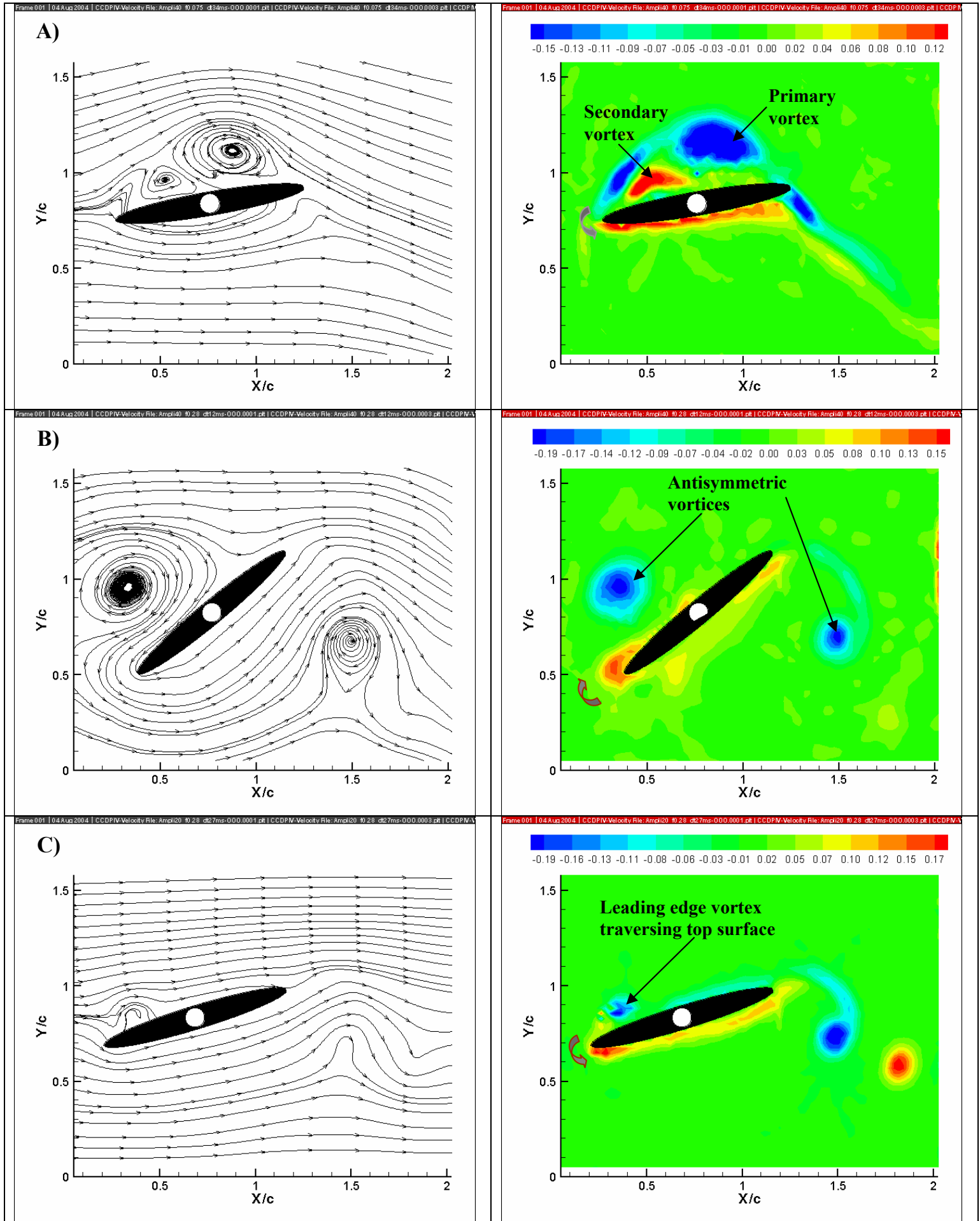


Figure 3: Streamline and vorticity plots for an elliptical aerofoil in sinusoidal oscillation. A)  $Re=1000$ ,  $\kappa=0.1$ ,  $\theta_0=40^\circ$ ,  $\theta=-10^\circ$ ,  $t^*=2.04$ . B)  $Re=1000$ ,  $\kappa=0.5$ ,  $\theta_0=40^\circ$ ,  $\theta=-40^\circ$ ,  $t^*=1.76$ . C)  $Re=1000$ ,  $\kappa=0.5$ ,  $\theta_0=20^\circ$ ,  $\theta=-17^\circ$ ,  $t^*=0.85$ .

## Wake structures of a heaving airfoil

G.Y. Oo, K.B. Lua, K.S. Yeo and T.T. Lim

Department of Mechanical Engineering  
National University of Singapore 10 Kent Ridge Crescent, Singapore 119260

### Abstract

Two-dimensional wake structures of a sinusoidally heaving airfoil are investigated using Particle Image Velocimetry at a Reynolds number of about 1000. The advance ratio and reduced frequency are varied from 0.0919 to 0.276 and 0.1 to 2.0, respectively. Results show that thrust generation occurs consistently at moderately low reduced frequency of between 0.25 and 0.5 for all the advance ratios investigated.

### Introduction

An airfoil in a heaving motion perpendicular to a uniform free stream can under certain conditions, produce thrust. In this paper, we examine the effect of the variation of the advance ratio and the reduced frequency on the wake structures behind a heaving airfoil. The objective is to determine the conditions under which a thrust generating reverse von Karman vortex street is produced.

In the case of a pitching and oscillating airfoil, high thrust efficiency of up to 87% have been obtained by Anderson et al. [1] for advance ratio of 0.15, phase angle of 75 degrees and a heave to chord ratio of 0.75. He also found that optimal thrust production occurred when the advance ratio was between 0.125 and 0.20 and the heave to chord ratio was of the order of one. A subsequent study by Read et al. [4] obtained a thrust efficiency of 71.5% for a similar motion with a phase angle of 90 to 100 degrees between the pitching and oscillating motions.

In a simply heaving airfoil, the thrust-generating flow was also investigated by Freymuth [2] using flow visualization for an advance ratio of 0.17 and reduced frequency of 0.86. And he found that increasing the plunge amplitude or advance ratio led to some severe leading edge vortex separation, causing deterioration in the thrust generation. Moreover, a reduction in reduced frequency led to wider spacing of the vortices, causing the propulsive wake to be overcome by the drag of the airfoil profile.

Computational studies by Wang [6] on single wing strokes of simple heaving wing motion show that the optimal advance ratio is linked to maximizing the angle of attack during the motion. For a fixed advance ratio, it is found that the reduced frequency determines the time window available for vortex growth and leading edge vortex shedding. Peak results are obtained at maximum relative angles of attack of 45 to 60 degrees, which correspond to advance ratios of 0.16 and 0.276, respectively.

In a study on a simply pitching airfoil, Koochesfahani [3] observed a case whereby double wake vortical structures of the same rotational sense were produced in the same half cycle for amplitude of 4 degrees and frequency of 1.85, corresponding to a reduced frequency of 0.53.

In this paper, Particle Image Velocimetry is used to study a simply heaving wing with no pitching motions. The Reynolds

number based on chord length and free stream velocity is about 1000. The advance ratios considered are 0.0919, 0.16 and 0.276, which correspond to maximum relative angle of attack of 30, 45 and 60 degrees, with the reduced frequency ranging from 0.1 to 2.0.

### Experimental method and setup

The experiments were conducted in a recirculating water tunnel using an elliptical airfoil of 20mm chord, 2mm thick, and 196mm long. The airfoil spanned the Perspex test section with additional endplates mounted 2mm from both ends of the airfoil to reduce three dimensional effects and spanwise flow. A further horizontal Perspex plate was placed in contact with the free surface of the water so as to minimise free surface effects.

A servo motor which is linked to a linear actuator was used to control the heaving motion of the airfoil. The motor was in turn controlled by a Labview program through National Instrument DAQ cards which sent out pulse train of positional signals to achieve a motor spatial resolution of 0.1mm.

The water was seeded with 10 micrometer diameter hollow glass beads and illuminated with the laser sheet from a pair of Nd-YAG lasers at the mid-span of the airfoil. A Kodak MegaPlus ES1.0/ Type 16 (30Hz) 1 Megapixel PIV camera was used to capture the image pairs of dimensions 130.9mm by 131.9mm (or 1008 by 1016 pixels). Both the lasers and the camera were coordinated by a Dantec PIV system and were triggered by the same Labview program upon commencement of motion.

The time interval between each image pair was set at 8.309 milliseconds or the time taken for a particle to travel 20% of the length of the 16 by 16 pixel interrogation area. All the image pairs were then masked to remove the shadow cast by the airfoil and processed with 3 step adaptive correlation of interrogation area of 16 by 16 pixels and with a 25% overlap. The resultant vectors were further smoothed with moving average validation and average filtering over an area of 3 by 3 pixels.

A total of 20 runs were conducted for each case, and the results were then ensemble-averaged over 20 realizations. A further 20 runs were conducted with the wing in a reverse motion, the purpose is to provide the flow field within the shadow cast by the airfoil. The two averaged results were then combined to produce complete streamline and vorticity plots for all the 18 cases.

### Results

The advance ratio and reduced frequency used here are defined as follows:

$$St_a = fA / U \quad (1)$$

$$St_c = fc / U \quad (2)$$

Where  $f$  is the sinusoidal heaving frequency in Hz,  $A$  the maximum heaving amplitude,  $c$  the chord length (20mm) and  $U$  the free stream velocity (fixed at 50mm/s).

Three types of wake structures were observed. The first type was a normal Karman vortex street similar to that observed behind a stationary bluff body, an indication of a drag profile. The second type was a reverse Karman vortex street, which caused the flow between the vortices to be directed downstream as a jet, thus generating a thrust. The third type was a double wake structure, where vortices of the same sign were shed on each half cycle of the oscillation, thus creating a pattern of near vertical twin vortices of identical circulation alternating with twin vortices of the opposite circulation. In some cases, the shed vortices were found to dissipate rapidly downstream.

The results obtained here are summarised in Tables 1-3 for differing advance ratio. The first column shows the reduced frequency, followed by a heaving frequency, heave to chord amplitude and the resulting wake structures observed.

Stc	f (Hz)	A/c	Wake structures
0.1	0.25	0.919	Dissipation
0.25	0.625	0.3676	Weak thrust
0.5	1.25	0.184	Double wake
0.75	1.875	0.092	Weak drag
1.0	2.5	0.046	Thrust
2.0	5	0.023	Alternating vortices

Table 1. Parameters and observations for  $Sta = 0.0919$ .

Stc	f (Hz)	A/c	Wake structures
0.1	0.25	1.6	Dissipation
0.25	0.625	0.64	Thrust
0.5	1.25	0.32	Double wake/ Thrust
0.75	1.875	0.16	Weak thrust
1.0	2.5	0.08	Weak thrust
2.0	5	0.04	Weak thrust

Table 2. Parameters and observations for  $Sta = 0.16$ .

Stc	f (Hz)	A/c	Wake structures
0.1	0.25	2.76	Dissipation
0.25	0.625	1.104	Thrust/ Dissipation
0.5	1.25	0.552	Double wake/ Thrust
0.75	1.875	0.276	Thrust
1.0	2.5	0.138	Weak thrust
2.0	5	0.069	Weak thrust

Table 3. Parameters and observations for  $Sta = 0.276$ .

Streamline and vorticity plots for two of the cases studied are presented in fig 1-5, with the time  $t$  given in periods  $T$  of heaving oscillations. The flow direction is from left to right. Fig. 1-3 show the double wake structures which occur when the advance ratio is 0.16 and the reduced frequency is 0.5. Likewise, fig. 4 and 5 show the thrust producing reverse Karman vortex street structure when the advance ratio is 0.276 and reduced frequency is 0.75.

## Discussion

It was observed that thrust generation was generally present at reduced frequencies of between 0.25 and 0.5 for all the three advance ratios studied.

At lower reduced frequencies, the vortices took longer to rollup, resulting in an increased distance between them. Also, for the high amplitude to chord ratio cases, severe leading edge vortex

separation was found, resulting in the vortices dissipated within 2 to 3 chord lengths downstream. Based on the wake structure, very little thrust was produced in this case.

Although the reverse Karman vortex street structure was generally seen for higher reduced frequencies, the lower amplitude to chord ratio meant that the vertical separation between the top and bottom row decreased, thus limiting the amount of thrust generated. The transition to drag producing structures was not observed for the advance ratios of 0.16 and 0.276, even at the maximum reduced frequency of 2.0. At this point, the heaving cycle was just at the limit of the time window suggested by Wang [6]. For advance ratio 0.0919 and reduced frequency 2.0, the vertical separation was virtually nonexistent; yielding a pattern of a single row of alternating signed vortices.

At the reduced frequency of 0.5, the double wake structure was observed for all the advance ratios. This was similar to the flow visualization results of Koochesfahani [3] for a pitching airfoil of 4 degrees amplitude and equivalent reduced frequency of 0.53. For the advance ratio of 0.16, a "pure" case of vertical alternating pairs of same signed vortices was observed. And for advance ratios of 0.276 and 0.0919, the pair was slightly tilted and the one further downstream was found to have a higher strength. The double wake structures have previously been found in a pitching case only [3], and as far as we are aware, this is probably the first time that they have been observed in the heaving case. The mechanism for their generation, and the role they play in thrust production remain unclear.

For the advance ratio of 0.0919, and at the reduced frequencies of 0.5 and 1.0, a thrust generating reverse Karman vortex street structure was observed. Interestingly, at the intermediate reduced frequency of 0.75, a normal Karman vortex street was found instead. Why this is the case remains unclear. This anomaly requires further investigation

The advance ratios of 0.16 and 0.276 tended to have a wider range of reduced frequency for which thrust was produced. At the advance ratio of 0.0919 when heave to chord ratio is small, a smaller vertical separation of the top and bottom vortices is likely to lead to a smaller average horizontal thrust force.

## Conclusion

For an elliptical airfoil at constant zero angle of attack in sinusoidal heaving motion and Reynolds number 1000, the parameters of advance ratio and reduced frequency were found to govern the type of wake structures produced.

Thrust generating conditions were observed for most of the cases but primarily for moderate reduced frequencies of 0.25 and 0.5 for the three advance ratios of 0.0919, 0.16 and 0.276. Weaker thrust conditions were also found for higher reduced frequencies of up to 2.0 for advance ratios 0.16 and 0.276. Double wake structures appeared consistently for all advance ratios at the reduced frequency of 0.5.

Although the present study provides valuable information about the wake structure, quantitative thrust forces are needed before a clearer insight into optimizing the choice of the two parameters can be better obtained.

## References

- [1] Anderson J. M., Streitlien K., Barrett D. S. & Triantafyllou M. S., Oscillating foils of high propulsive efficiency, *J. Fluid Mech.*, **360**, 1998, 41-72.
- [2] Freymuth P., Propulsive Vortical Signature of Plunging and Pitching Airfoils, *AIAA journal*, **26**, 1988, 881-883.



- [3] Koochesfahani M. M., Vortical Patterns in the Wake of an Oscillating Airfoil, *AIAA journal*, **27**, 1989, 1200-1205.
- [4] Read D. A., Hover F. S. & Triantafyllou M. S., Forces on oscillating foils for propulsion and maneuvering, *J. Fluids Structures*, **17**, 2003, 163-183.
- [5] Triantafyllou M. S., Triantafyllou G. S. & Gopalkrishnan R., Wake mechanics for thrust generation in oscillating foils, *Phys. Fluids*, **A3**, 1991, 2835-2837.
- [6] Wang Z. J., Vortex shedding and frequency selection in flapping flight, *J. Fluid Mech.*, **410**, 2000, 323-341.

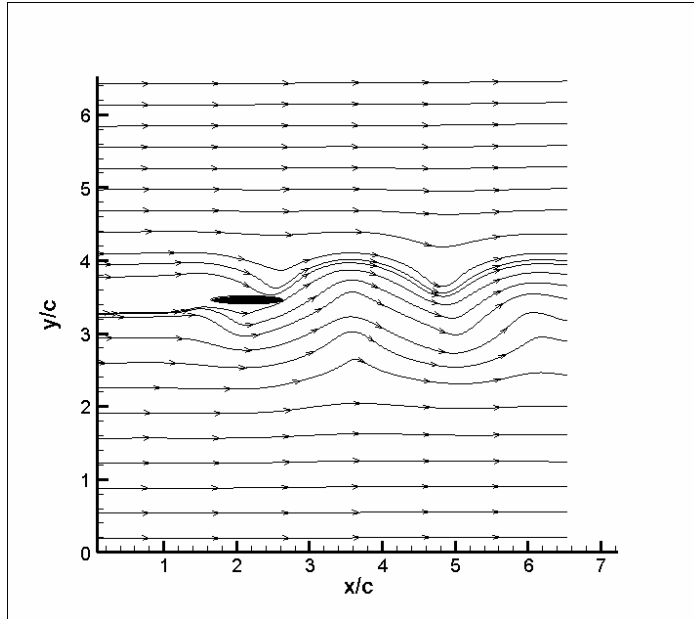


Figure 1a. Streamline plot  $Sta=0.16$ ,  $Stc=0.5$ ,  $t = 5T$ , airfoil descending.

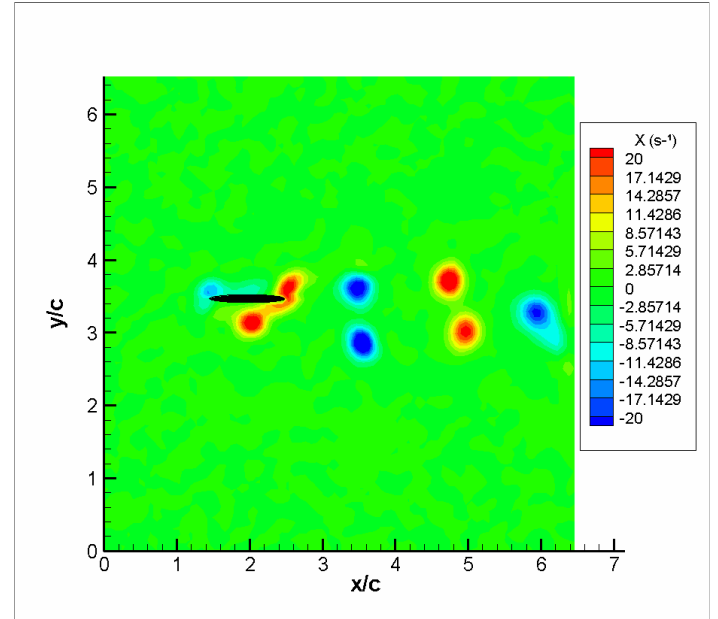


Figure 1b. Vorticity plot  $Sta=0.16$ ,  $Stc=0.5$ ,  $t = 5T$ , airfoil descending.

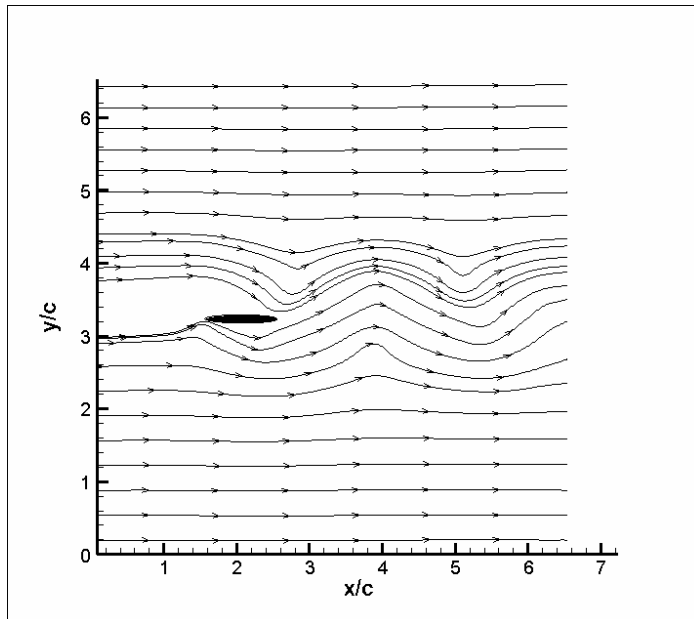


Figure 2a. Streamline plot  $Sta=0.16$ ,  $Stc=0.5$ ,  $t = 5.125T$ , airfoil descending.

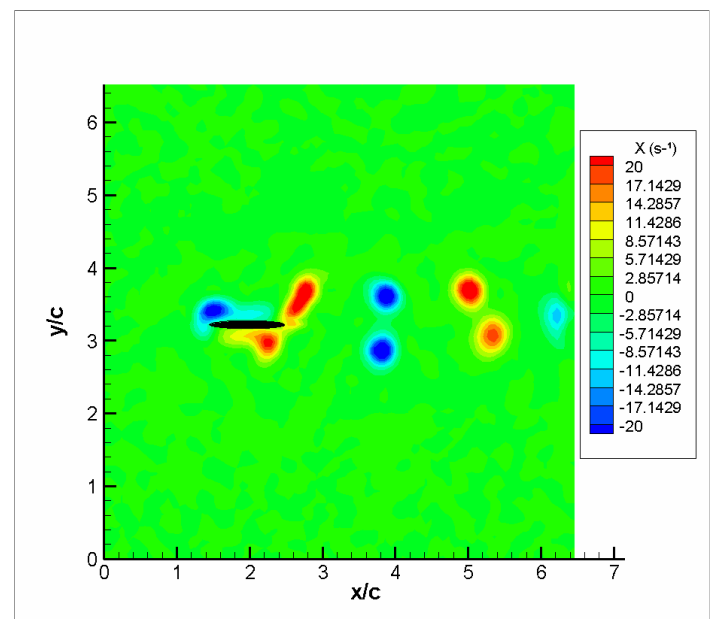


Figure 2b. Vorticity plot  $Sta=0.16$ ,  $Stc=0.5$ ,  $t = 5.125T$ , airfoil descending.

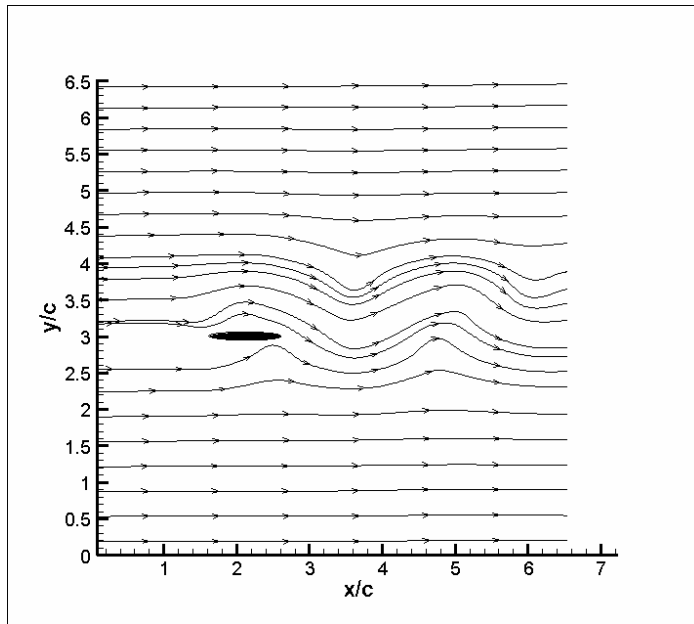


Figure 3a. Streamline plot Sta=0.16, Stc=0.5,  $t = 5.5T$ , airfoil ascending.

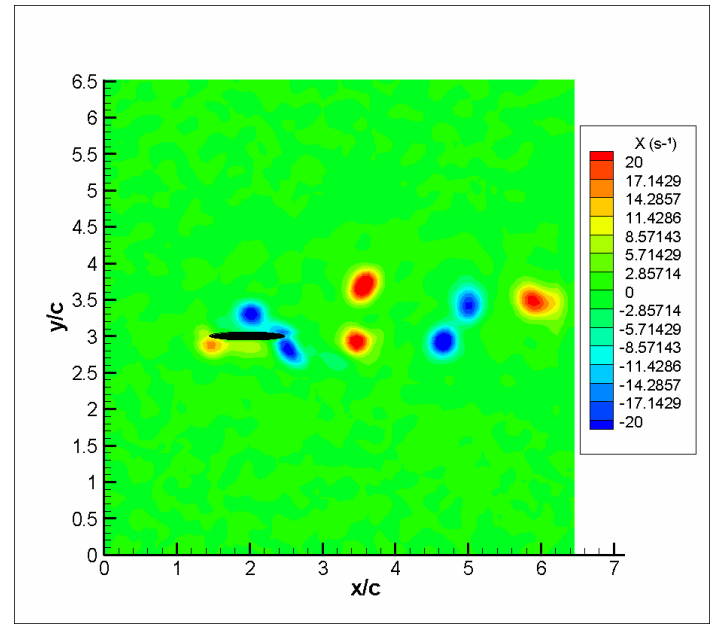


Figure 3b. Vorticity plot Sta=0.16, Stc=0.5,  $t = 5.5T$ , airfoil ascending.

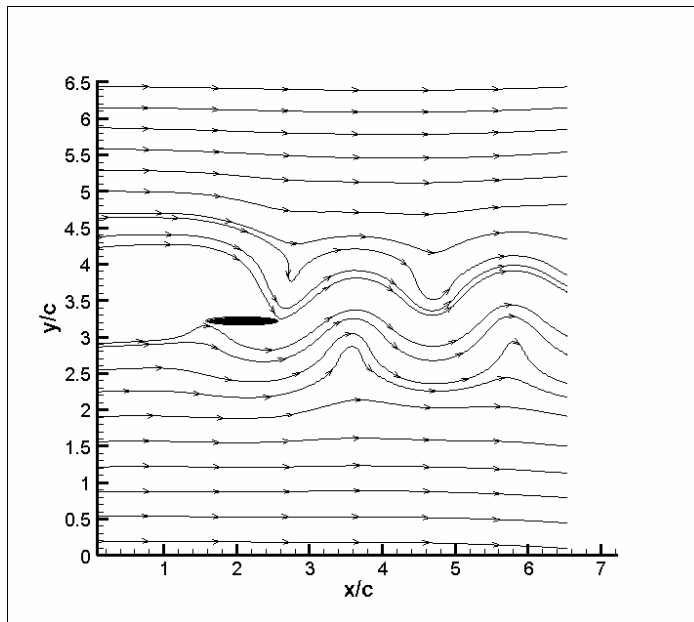


Figure 4a. Streamline plot Sta=0.276, Stc=0.75,  $t = 5.0625T$ , airfoil descending.

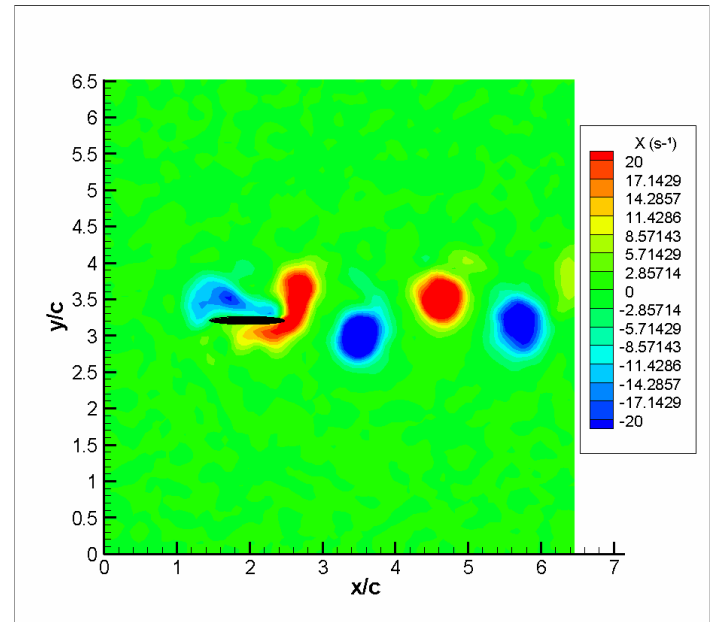


Figure 4b. Vorticity plot Sta=0.276, Stc=0.75,  $t = 5.0625T$ , airfoil descending.

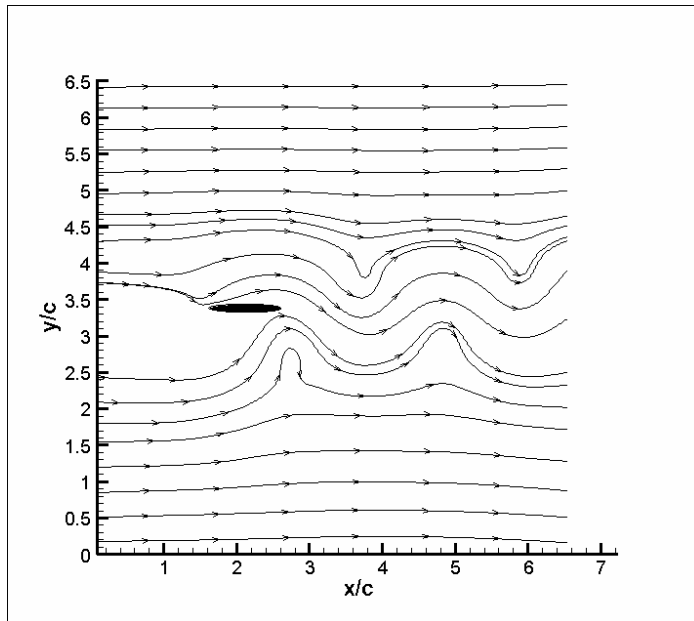


Figure 5a. Streamline plot Sta=0.276, Stc=0.75,  $t = 5.625T$ , airfoil ascending.

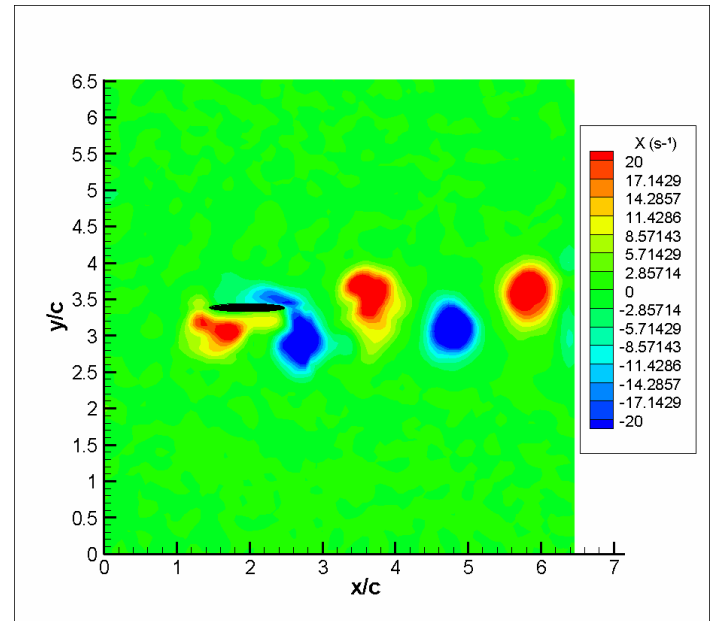


Figure 5b. Vorticity plot Sta=0.276, Stc=0.75,  $t = 5.625T$ , airfoil ascending.

## Structure of a Zero-net-mass-flux round jet in crossflow

S. Tomar, J. Arnaud and J. Soria

Laboratory for Turbulence Research in Aerospace & Combustion (LTRAC),  
Department of Mechanical Engineering, Monash University,  
Melbourne, AUSTRALIA 3800

### Abstract

Planar laser induced fluorescence (PLIF) has been used to investigate the mean structure of circular Zero-Net-Mass-Flux Jet in Crossflow (ZNMF-JICF). The flow structure of these jets is primarily characterized by the Reynolds number ( $Re$ ), the Strouhal number ( $St$ ) and the velocity ratio ( $VR$ ). The prime focus of this study is to investigate the effect of different  $VR$  and  $St$  numbers on the mean structure of the ZNMF-JICF. The Reynolds number for all the ZNMF-JICF experiments was kept constant at 1066. Four velocity ratios,  $VR = 2, 3, 4$  and  $5$  were used in the investigation of the ZNMF-JICF. For each  $VR$ , the ZNMF-JICF experiments were carried out for Strouhal numbers ranging from  $0.08$  to  $0.56$ . PLIF experiments revealed that there is a critical Strouhal number in the range between  $0.11$  to  $0.19$  that separates the mean structure of the ZNMF-JICF into a single trajectory ZNMF-JICF for  $St < 0.11$  and a multiple trajectory ZNMF-JICF for  $St \geq 0.19$ .

### Introduction

The flow of turbulent jets in crossflow is encountered in a variety of applications including pollutant discharges, STOL (Short Take off Vertical Landing), combustion processes, film cooling of turbine blades and missile control systems. Even though extensive research has gone in the investigation of jets in crossflow many aspects of the flow remain unexplored. The primary reason being that these flows are difficult to predict accurately due to the inherent complexity of the jet-crossflow interaction.

The majority of the studies reported in the 1970's and 1980's were motivated by VSTOL-related applications and several flow visualization and experimental studies were conducted to understand the characteristics of the jet-crossflow interactions.

This study reports the measurements of a zero-net-mass-flux jet in crossflow (ZNMF-JICF). A zero-net-mass-flux jet is a mechanically excited fluid stream formed by no addition of external fluid to the system during the generation of the jet. These jets have non-zero mean streamwise momentum formed by the interaction of vortices. The vortices are generated by the periodic oscillation of a fluid boundary and propagate due to the non-linear term in the governing equations of motion. [2] found that the spreading rate of a round turbulent ZNMF jet is greater than an equivalent continuous jet throughout the measured domain. Previous research based on continuous, pulsed or ZNMF jets suggest that a presence of cross flow enhances the mixing of the jet as compared to a free jet. Pulsing the flow further improves the mixing of the jet [9,10]. Investigation reported by [8] revealed that a fully modulated jet always penetrates more than the corresponding steady jet at the same time-averaged velocity. Recent studies of ZNMF jets show that they have a higher entrainment rate compared to their continuous counterparts [2,11]. The present study investigates the observed characteristics of single and multiple-trajectory ZNMF jets created using a piston-cylinder assembly coupled with a scotch-yoke mechanism.

### Experimental Setup

The experimental investigation was carried out in a square 250 mm closed-circuit vertical water tunnel at the Laboratory for Turbulence Research in Aerospace and Combustion (LTRAC) at Monash University, Melbourne, Australia. The tunnel has a 1.5 m long working section made of 15mm thick Perspex. Water is introduced into the settling chamber using a spray system at the head of the tunnel, which is then passed through a perforated plate, four stainless steel wire screens, a honeycomb and a 16:1 contraction before entering the working section of the water tunnel. The contraction provides smooth, uniform flow in the working section of the tunnel with the freestream turbulence intensity of less than 1% [1]. Sinusoidal oscillation of a 20 mm diameter piston ( $D_p$ ) in a cylindrical bore through a 10mm diameter orifice ( $D_o$ ) generated the ZNMF-JICF. The piston-cylinder apparatus was mounted on a horizontal rail and attached the water tunnel wall. This setup is shown in Figure 1. The piston is connected via a coupling to a scotch-yoke mechanism, which is driven by a PC controlled stepper motor. The ZNMF apparatus was specifically constructed to achieve low excitation frequencies ranging from  $0.5 - 6$  Hz. The displacement history of the piston was recorded by a LVDT axially aligned with the piston-cylinder setup. The static pressure of the water column in the tunnel did not have an effect on the motion of the piston [3].

The water tunnel flow was seeded with  $11 \mu\text{m}$  diameter hollow glass spheres with a density of  $1100 \text{ kg/m}^3$  prior to the PIV experiments. The ratio of the relaxation time for the particles to the excitation frequency of 5Hz was in the order of  $10E-6$  and even smaller for lower excitation frequencies. This suggests that the particles will follow the fluid motion in the tunnel with high fidelity. These particles were illuminated using a 2 mm thick pulsed laser light sheet produced with an appropriate cylindrical/spherical lens arrangement and a Quanta System dual cavity Nd: YAG laser. It is capable of producing 6-ns, 200-mJ pulses at a repetition rate of 15Hz

The mean jet velocity ( $U_j$ ) was 106.6mm/s for all the experiments and the velocity ratio was adjusted by changing the velocity of the freestream fluid ( $U_\infty$ ). The jet velocity was kept the same to allow exactly the same flowrate of dye through the orifice.

The single exposed images of the seed particles were acquired with a 12 bit 1.3 Mega Pixel ( $1280 \times 1024$ ) PCO Pixelfly CCD camera. The camera was mounted on a bevel-gear vertical railing system and the position was measured using a set of rulers positioned in the x, y and z-axes. A micrometer installed in the z direction controlled the minute motion of the camera in that direction. An optical sensor monitoring the stepper motor was used to trigger the laser. The entire image acquisition system was controlled using an in-house developed Real-time Linux (RTAI) computer program.

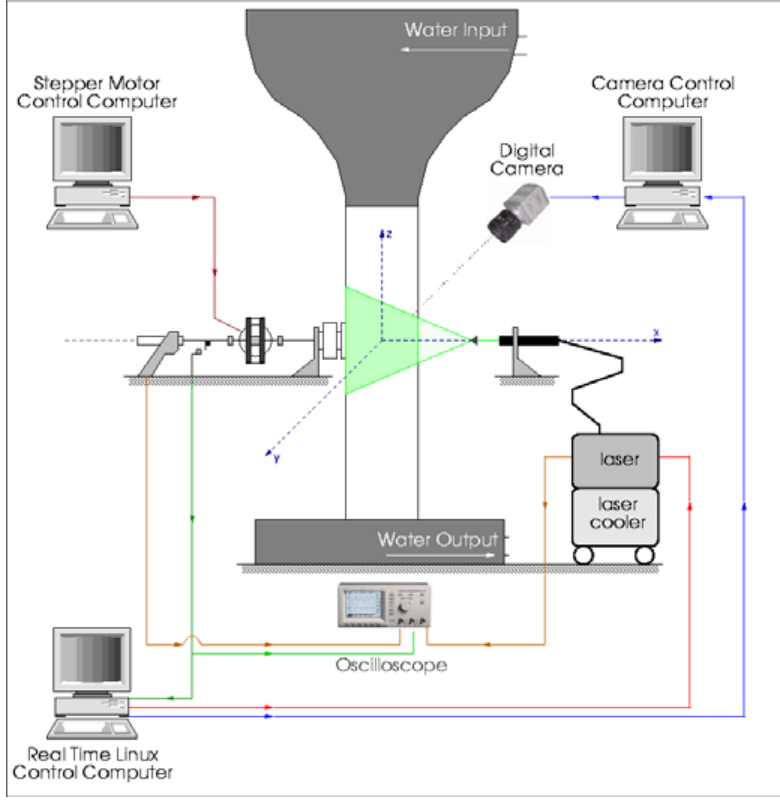


Fig 1. Vertical Water Tunnel Setup

The flow was visualized using Kiton Red 620 fluorescent dye, which has a Schmidt number of approximately 5000. Eight dye injection ports are located on the circumference of the cylinder in which the piston oscillates. The Kiton Red dye, driven by a gravity-based system, enters the cylinder via these ports. During the injection of the dye in the cylinder the piston is oscillated at the required frequency ( $f$ ) and amplitude ( $a$ ) to facilitate mixing of the dye in the cylinder. After the cylinder is completely filled with dye, an injection valve is turned off to preserve the zero net mass flux nature of the system. The piston is oscillated for about 30 seconds after the valve has been shut to allow the steady dye flow through the orifice. The co-ordinate axes have been shown in Figure 2 relative to the location of the orifice plate and the tunnel.

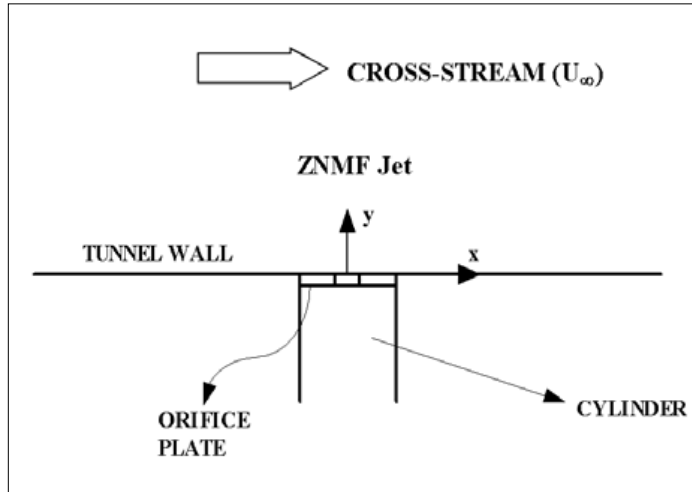


Fig. 2. Schematic of ZNMF-JICF in the test section and coordinate axes the tunnel.

## Flow Parameterization

The parameters governing the flow are shown by equations 1-6 .

$$St = \frac{f D_o}{U_j} ; Re = \frac{U_j D_o}{\nu} \quad Eq(1)$$

From [3], the angular velocity ( $\omega$ ) of the piston is given by

$$\omega = 2\pi f \quad Eq(2)$$

The maximum velocity of the piston ( $V_{max}$ ) is given by

$$V_{max} = \omega a = 2\pi f a \quad Eq(3)$$

The rms velocity of the piston ( $V_{rms}$ ) is equal to  $V_{max}/\sqrt{2}$ . From [3],

$$V_{rms} D_p = U_j D_o \quad Eq(4)$$

Hence,

$$U_j = \frac{\sqrt{2} \pi f a D_p}{D_o} \quad Eq(5)$$

Substituting Eq (5) into Eq (1), St and Re are modified as shown in Eq (6),

$$St = \frac{D_o^2}{\sqrt{2} \pi D_p a} ; Re = \frac{\sqrt{2} \pi f a D_p}{\nu} ; VR = \frac{U_j}{U_\infty} \quad Eq(6)$$

The Strouhal number shown by Eq(6) does not depend directly on the frequency of oscillation. The reason is that the product of frequency and amplitude is a constant as shown by Table 1.

The jet velocity,  $U_j$ , is a velocity scale chosen based on the mean momentum flow of the jet through the orifice. Table 1 shows the parameters for the twenty ZNMF-JICF.

VR	A (mm)	f (Hz)	St
2	2	6	0.56
2	4	3	0.28
2	6	2	0.19
2	10	1.2	0.11
2	14	0.86	0.08
3	2	6	0.56
3	4	3	0.28
3	6	2	0.19
3	10	1.2	0.11
3	14	0.86	0.08
4	2	6	0.56
4	4	3	0.28
4	6	2	0.19
4	10	1.2	0.11
4	14	0.86	0.08
5	2	6	0.56
5	4	3	0.28
5	6	2	0.19
5	10	1.2	0.11
5	14	0.86	0.08

Table 1. The table of parameters for the ZNMF-JICF.

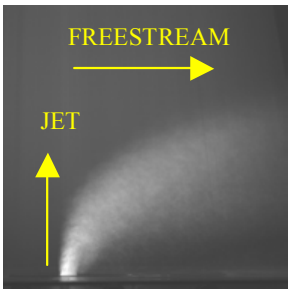

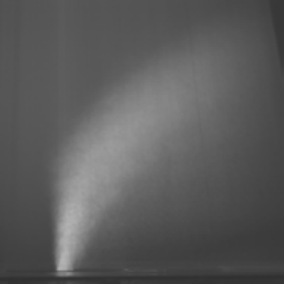
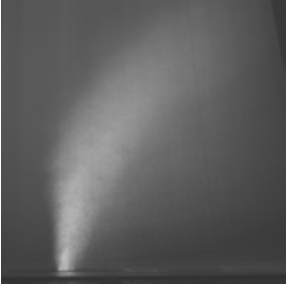
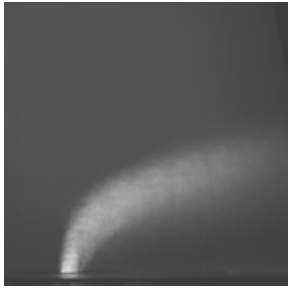

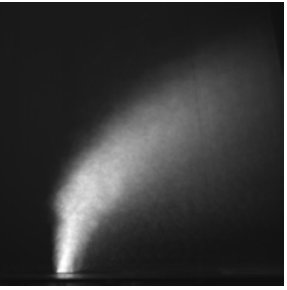
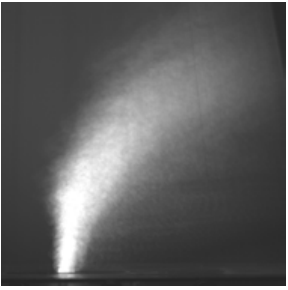
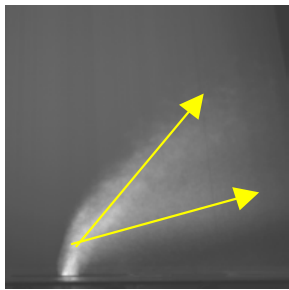
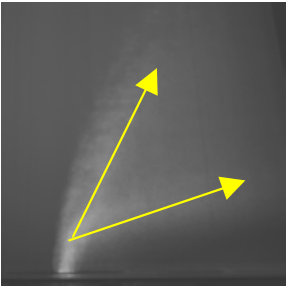
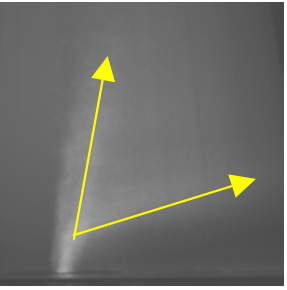
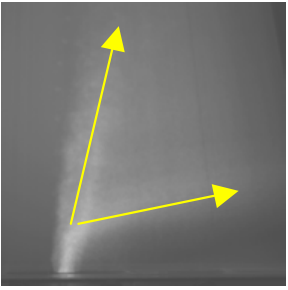
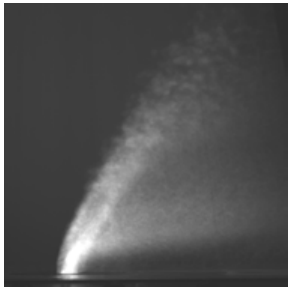
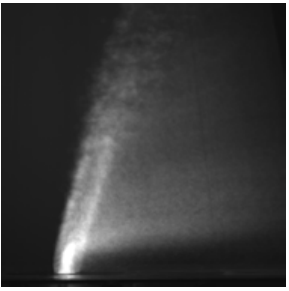
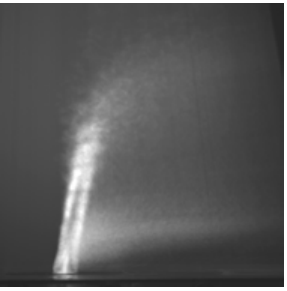
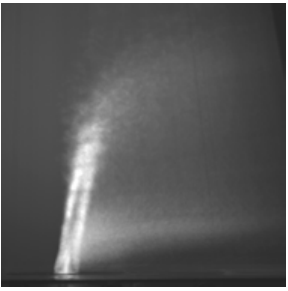
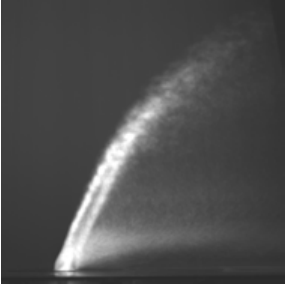



	VR = 2	VR = 3	VR = 4	VR = 5
St = 0.08				
St = 0.11				
St = 0.19				
St = 0.28				
St = 0.56				

Table 2. The structure of twenty round ZNMF-JICF at different Strouhal numbers and velocity ratios.



## Results

The mean intensity images of the twenty ZNMF-JICF obtained from the PLIF experiments are shown in table 2. The area of interest is 225 mm x 180 mm which corresponds to  $22.5 D_o \times 18.0 D_o$ . The main emphasis is on the structure of the jets and its interaction with the crossflow and hence the analysis is purely of a qualitative nature. As a result the spatial resolution of the flow field is quite low to record the evolution of the complete jet structure. As seen from equation 1, the Strouhal number is a function of amplitude and not the frequency of oscillation of the piston. As seen from table 2, five different St numbers were chosen for a particular VR. The freestream fluid was flowing from left to right as shown in the table. For  $0.08 \leq St \leq 0.11$ , it can be seen that there is only a primary trajectory of the jet issuing out of the orifice. As the jet penetrates into the crossflow, it bends and tries to align with the freestream fluid. With increase in VR, the ZNMF jet tends to align more axially with the orifice. This is because at higher velocity ratio the jet momentum is more dominant than the freestream momentum and as a result the mean dye concentration in regions away from the jet center increases. In this range of Strouhal numbers, the jet is known as the single trajectory jet by virtue of its solitary trajectory issuing out of the orifice.

As the Strouhal number is increased, there is a definite transition from the single trajectory structure to a multiple trajectory structure. This is shown by the flow visualizations at  $St = 0.19$  in table 2. The primary trajectory is one that penetrates further into the freestream but there is a secondary trajectory that emerges from the primary one forming an acute angle. This angle between the two trajectories increases with increase in VR due to the progressive alignment of the primary trajectory with the axis of the orifice.

For  $St \geq 0.19$ , there is a well defined multiple trajectory structure. The angle between the two jet trajectories can be seen to be a function of St and VR.

In continuous jets, the trajectory based on the maximum velocity represents the streamline originating at the orifice center. This is not the case with the ZNMF-JICF. This is due to the intermittent formation of the jet with a duty cycle of 50%. For half the jet cycle, cross-flow fluid moves unrestrained through the jet trajectory. Hence, although injected fluid penetrates far into the cross-flow instantaneously, in an ensemble average, the cross-flow fluid at the jet center is displaced from the wall by a much smaller amount.

A quantitative study in [5] shows that the penetration of the jet does not depend on VR and their experiments reported the same penetration for  $VR = 5$  and  $VR = 30$ . The results obtained in this study show that increase in VR increases mean dye penetration slightly.

## Concluding Remarks

The qualitative nature of twenty ZNF-JICF have been studied for a range of Strouhal numbers  $0.08 \leq St \leq 0.56$  and velocity ratio  $2 \leq VR \leq 5$ . Two definite jet trajectories were found for the ZNMF-JICF when the Strouhal number was varied. A critical range of St was found to lie between  $0.11 - 0.19$  where the transition from single to

multiple trajectory takes place. Single trajectory jets are characterized by a single maximum concentration across the width of the jet along the trajectory while multiple trajectory jets are characterized by multiple regions of high concentration issuing from the orifice.

## References

- [1] Nicolaides, D., Measurement of spatial quantities in grid turbulence using particle image velocimetry, *Master's thesis*, Monash University, Melbourne, Australia, 1997.
- [2] Cater, J.E. and Soria, J., The evolution of round zero-net-mass-flux jets, *J. Fluid Mechanics*, **472**, 2002, 167-200.
- [3] Gordon, M. and Soria, J., PIV measurements of a zero-net-mass-flux jet in cross flow, *Experiments in Fluids*, **33**, 2002, 863-872.
- [4] Tomar, S. and Soria, J., MCCDPIV Measurements of a ZNMF JICF, published in the proceedings of PIV'03, Busan, South Korea, 2003.
- [5] Tomar, S. and Soria, J., Multi-grid Cross Correlation Digital Particle Image Velocimetry Measurements of a Zero Net Mass Flux Jet in Cross-flow, published in the Proceedings of 7th Asian Symposium on Visualization, 2003.
- [6] Gordon, M., Cater, J.E. and Soria, J., Investigation of the mean passive scalar field in zero-net-mass-flux jets in cross-flow using planar-laser-induced fluorescence, *Phys. Fluids*, **16(3)**, 2004, 794-808.
- [7] Morton, B. R. and Ibbetson, A., Jets Deflected in Crossflow, *Experimental Thermal and Fluid Science*, **12**, 1996, 112 – 133.
- [8] Hermanson, J.C., Wahba, A. and Johari, H, Duty-Cycle effects on Penetration of Fully Modulated, Turbulent Jets in Crossflow, *AIAA Journal*, **36**, No. 10, 1998.
- [9] Eroglu, A., and Breidenthal, R.E., Effects of Periodic Disturbances on Structure and Flame Length of a Jet in a Cross Flow, *AIAA Paper 91-0137*, 1991.
- [10] Wu, J.M., Vakili, A.D., and Yu, W.K., Mixing of an Acoustically Pulsed Air Jet with a Confined Crossflow, *AIAA Journal*, **26**, 1988, 940-947.
- [11] Smith, B. H. and Glezer, A., The Formation and Evolution of Synthetic Jets, *Phys. Fluids*, **10**, 1998, 2281-2297.

## Dynamic Testing of Aircraft Models in a Water Tunnel

Lincoln P. Erm

Air Vehicles Division, Defence Science and Technology Organisation  
506 Lorimer Street, Fishermans Bend, Victoria, 3207 AUSTRALIA

### Abstract

An existing water tunnel, used for testing stationary aircraft models, is being upgraded so that it will be possible to carry out tests with the model in motion. Precise yaw, pitch and roll motions of a model can now be obtained independently. A special roll mechanism has been designed so that dye can be discharged from ports on an aircraft and water can be sucked through the intake(s) on the aircraft, while it undergoes continuous roll, i.e. there is no twisting of dye or suction tubes. A sensitive five-component strain-gauge balance is currently being manufactured. It will be possible to measure forces and moments and capture corresponding images of the flow while the model undergoes a specified dynamic manoeuvre. The dynamic rig will be used to study unsteady aerodynamic effects associated with aircraft motion and to obtain data for use in aircraft flight-dynamic models. Some preliminary flow-visualization images are presented.

### Introduction

Forces and moments on an aircraft model in a tunnel are generally measured with the model stationary and set at a known orientation, and similarly for the visualization of flow patterns over the model. This static testing is the most common form of testing carried out in tunnels and there is an abundance of useful static measurements reported in the literature.

On the other hand, dynamic testing of an aircraft simply means that measurements are taken while the aircraft is in motion. Reported dynamic measurements are somewhat limited compared with static measurements. There is a need to carry out dynamic testing on combat aircraft in tunnels to study unsteady aerodynamic effects associated with aircraft motion, which may have a major impact on the manoeuvrability and controllability of aircraft, especially at high angles of attack. The ongoing interest in flying at high angles of attack to improve aircraft control necessitates developing testing techniques to investigate dynamic flow situations in this flow regime. In a single manoeuvre, an advanced fighter aircraft can experience attached flows, vortex and vortex bursting flows, and totally separated flows. In particular, these vortical and highly separated flows can be very sensitive to unsteady or time variant effects—see Suárez *et al.* [5]. A clear understanding of the behaviour of the flow is an essential requirement for solving flight mechanics problems in the advanced manoeuvring regime. Dynamic force/moment data are also needed to determine approximate stability control derivatives, used in aircraft equations of motion in flight-dynamic models of aircraft. Dynamic data taken in tunnels can be used in the models to supplement data from flight trials on full-sized aircraft.

Most of the experimental dynamic studies reported in the literature have been limited to motion in one plane, either yaw,  $\psi$ , pitch,  $\theta$ , or roll,  $\phi$ . Huang & Hanff [3] indicate that since the behaviour of a vortex and its breakdown are non-linear, it is not valid to superimpose the effects due to the motion in different planes. There is a need for dynamic testing in which motions in all three planes can be obtained simultaneously.

In this paper, details are given of how an existing water tunnel at the Defence Science and Technology Organisation (DSTO), used

for testing stationary models, is being upgraded to measure flow-induced loads on a model and simultaneously capture images of the flow over the model, while it undergoes a specified dynamic manoeuvre, with independent yaw, pitch and roll motions. The DSTO dynamic testing system has similarities to that developed by Suárez *et al.* [5] for their water tunnel, but contains significant new features compared with their system. For the DSTO system, water can be sucked through the intake(s) of an aircraft to simulate flow through the engine(s) while the aircraft undergoes continuous roll.

Some preliminary images of the flow over an aircraft, obtained in the DSTO tunnel, are also given in this paper.

### Effects of Motion on Measured Data

The instantaneous flow pattern over an aircraft as it passes through a given orientation is different from that on the aircraft when it is stationary at that orientation, and likewise for the loading on the aircraft. This is due to the fact that the flow over the aircraft and the associated loading take some time to stabilize when the aircraft is moved to a new orientation, i.e. the flow lags the motion. According to Brandon & Shah [1], there can be a lag time of up to 30 convective time units (one convective time unit is the time required for a fluid particle to travel across the wing) before the flow re-establishes itself to the stationary condition.

Figure 1 shows a plot of normal force coefficient vs angle of attack,  $C_N$  vs  $\alpha$ , for a 70° delta wing in a wind tunnel, as obtained by Brandon & Shah. Both static and dynamic data are shown. The dynamic data corresponds to the wing oscillating in pitch by  $\pm 18^\circ$  about 4 different mean values of  $\alpha$ . The measured dynamic  $C_N$  vs  $\alpha$  data for increasing  $\alpha$  is different from that for decreasing  $\alpha$ , creating a hysteresis loop in the plotted data. The instantaneous loading on the model at say  $\alpha = 40^\circ$  varies over a wide range, depending on the motion of the model.

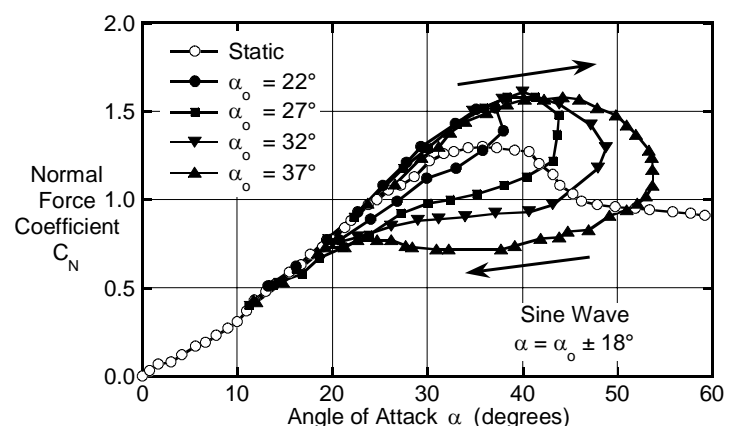


Figure 1. Dynamic wind-tunnel tests for a 70° delta wing, as obtained by Brandon & Shah [1].

For real combat aircraft,  $\alpha$  is continuously changing during manoeuvres so that static data taken in tunnels has limited applicability to aircraft in flight. The work program at DSTO is concerned with many aspects of aircraft in flight and there was a need to develop a dynamic testing system to obtain dynamic data for use in investigations undertaken by researchers. The question

that had to be answered was “do we develop our dynamic testing system for a wind tunnel or for a water tunnel”.

### Wind Tunnel vs Water Tunnel

A fundamental principle of dynamic testing is that the non-dimensional rotation rate,  $Q = qC/2U_0$ , of an aircraft model in a tunnel must be the same as that for a full-sized aircraft, where  $q$  is the rate of rotation of the aircraft,  $C$  is a characteristic length of the aircraft and  $U_0$  is the free-stream velocity –see Brandon & Shah [1]. Table 1 summarizes parameters for a typical full-sized aircraft, a model in a wind tunnel and a model in a water tunnel. For typical values of pitch rate, characteristic length and free-stream velocity for a full-sized aircraft (see table 1), the value of  $Q$  is 0.0188. Applying this to tests carried out in a wind tunnel and a water tunnel, for a 1/9 scale model in a wind tunnel operating at 60 m/s, the pitch rate of the model is 330 deg/s, but for a 1/48 scale model in a water tunnel operating at 0.1 m/s, the pitch rate of the model is only 3 deg/s.

	Full-sized aircraft	Wind-tunnel model	Water-tunnel model
Non-dimensional pitch rate of aircraft $Q$	0.0188	0.0188	0.0188
Free-stream velocity $U_0$ (m/s)	65	60	0.1
Mean aerodynamic chord of aircraft $C$ (m)	3.51	0.39	0.07
Pitch rate of aircraft $q$ (rad/s) $q$ (deg/s)	0.698 40	5.760 330	0.052 3

Table 1. Modelling parameters for a high-performance aircraft.

The required rotation rate in a wind tunnel to simulate a scaled dynamic manoeuvre is over 100 times that for a water tunnel. This suggests that problems may occur carrying out dynamic tests in wind tunnels, and that there would be significant advantages in undertaking such tests in water tunnels. The fast model rotation rates required for wind tunnel tests are mechanically difficult to implement ( $q = 330$  deg/s) and the effects of model inertia on the measured forces and moments are significant, necessitating the need for inertial tare measurements when calibrating a strain-gauge balance –see Suárez & Malcolm [4]. The fast model rotation also places demanding requirements on the data acquisition system to acquire data at high sample rates. In contrast, the model rotation rates required in a water tunnel are low ( $q = 3$  deg/s), so that the effects of model inertia on the measured loads are negligible, and there is no need for inertial tare measurements when calibrating a strain-gauge balance [4]. The response rates for the data acquisition system are also less demanding than for a wind tunnel and are more easily managed.

Although most of the limited number of reported investigations on dynamic testing have been carried out in wind tunnels, rather than water tunnels, there are clearly definite advantages in using a water tunnel.

### Features of Dynamic Testing System

#### Water Tunnel

The Eidetics Model 1520 flow-visualization water tunnel, shown diagrammatically in figure 2, has a horizontal-flow test section 1520 mm long, 510 mm deep and 380 mm wide, and the free-stream velocity can be varied between 0 and 0.6 m/s. It is a closed-circuit tunnel, in which the same water is recirculated, and there is a free water surface in the test section. Further details of the tunnel are given by Erm [2].

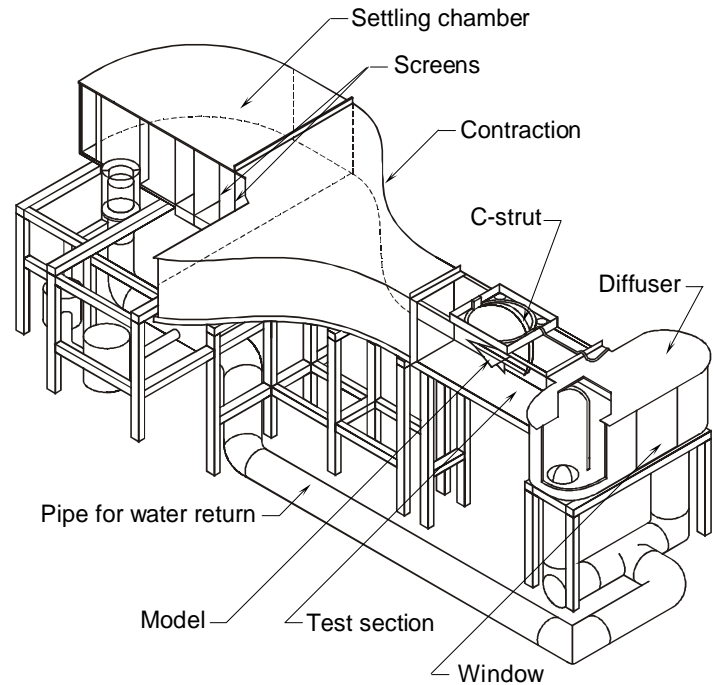


Figure 2. Diagrammatic representation of Eidetics Model 1520 flow-visualization water tunnel.

### Control of Model Motion

Models are mounted on a sting attached to a C-strut and are positioned so that all model angular motion is about the centre of rotation of the model. In the original tunnel, it was only possible to alter the yaw and pitch angles of a model and this was done manually using motors controlled by a joystick, so that model motion could not be accurately controlled. A roll mechanism (see below) has now been fitted and three PC-controlled stepper motors have been installed so that precise specified yaw, pitch and roll motions can now be obtained independently. The setup of the upgraded model motion system is shown diagrammatically in figure 3. Yaw, pitch and roll angles can be varied between  $-20^\circ$  and  $+20^\circ$ ,  $0^\circ$  and  $45^\circ$ , and  $0^\circ$  and  $360^\circ$  respectively. The input commands to the stepper motors consist of the required yaw, pitch and roll angles at chosen instants of time, say each 1/15th of a second, as shown in figure 4 for a test dynamic manoeuvre. Input commands can correspond to linear ramped or sinusoidal functions. It is possible to oscillate the model in yaw, pitch and roll, with maximum rotational speeds of 8, 6 and 12 %/s respectively throughout the cycle. With the current system, it is not possible to impart plunging or coning motion to the model.

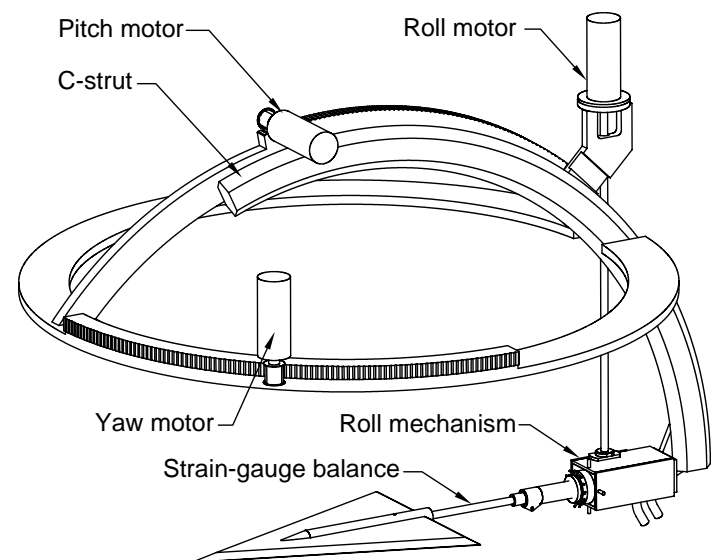


Figure 3. Diagrammatic representation of upgraded model motion system.

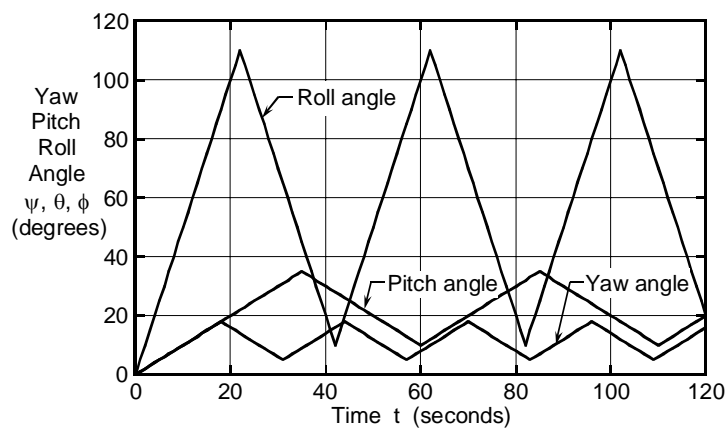


Figure 4. Required yaw, pitch and roll angles for a test manoeuvre.

### Roll Mechanism

A special roll mechanism has been designed so that dye can be discharged from circular ports on an aircraft and water can be sucked through the intake(s) on the aircraft, to simulate flow through the engine(s), while the aircraft undergoes continuous roll, i.e. there is no twisting of dye or suction tubes. The roll mechanism is shown in figure 5. The chassis of the mechanism is attached to the C-strut and does not rotate. An input shaft from a stepper motor rotates the central shaft, the strain-gauge balance (see below) and the model via a worm wheel and pinion. A dye reservoir is located between adjoining fixed and rotating parts, with the interface sealed with O rings, enabling dye to be transmitted to dye tubes, which rotate with the model. The central shaft on the mechanism is hollow and is connected to the exhaust(s) on an aircraft using a suction adaptor, which can also rotate. The adaptor shown is for an aircraft with twin exhausts, but adaptors can be made to suit the aircraft under test. The adaptor fits inside the exhaust(s) of an aircraft, but does not actually touch with the aircraft, since this would bridge the strain-gauge balance and invalidate measured loads on the aircraft. The central shaft has been partitioned into two halves, enabling suction through each of the two water circuits to be controlled independently by suction pumps, if required. The features of the system that enable a model to undergo continuous roll without twisting of dye or suction tubes are believed to be unique.

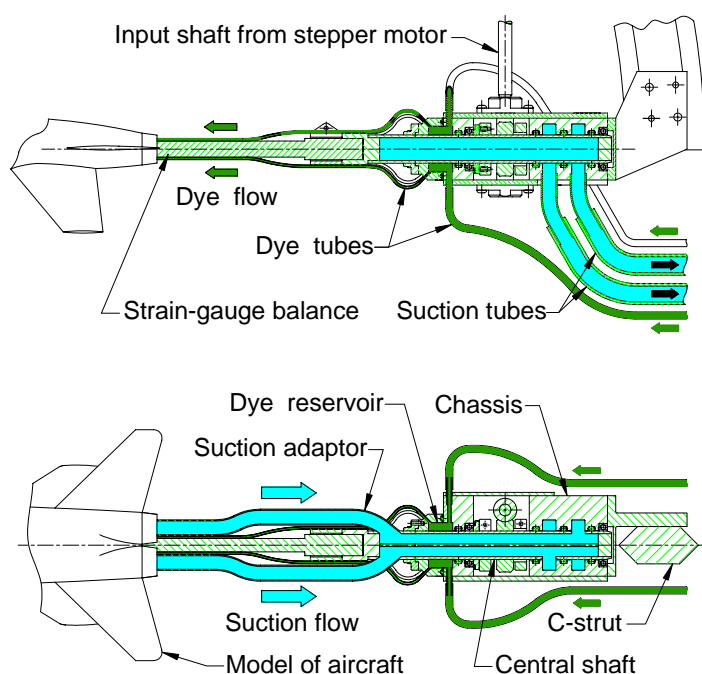


Figure 5. Cross-sectional side- and plan-views of the roll mechanism.

### Strain-Gauge Balance

A sensitive five-component strain-gauge balance is currently being manufactured and will measure downwards and sideways forces, and yawing, pitching and rolling moments. The balance, shown in figure 6, will be an integral unit. Semi-conductor strain gauges are to be used, having a resistance of  $1000\ \Omega$ , a gauge factor of 145, and dimensions of 2.03 mm by 0.15 mm (length by width). The positioning of the gauges on the balance for each of the five components will be as shown (note that some gauges are obscured). Gauges of this type have been successfully trialed at DSTO on a simplified two-component balance. The gauges will be waterproofed using microcrystalline wax covered with silicon rubber. The balance will be mounted in a sleeve, using the tapered attachment, and the sleeve will be inserted into a model, such as the delta wing shown. The flow-induced loads on a representative 1/48 scale model of a combat aircraft are very small by conventional standards and the balance has been designed to measure downwards and sideways forces of 1.0 N, yawing and pitching moments of 0.017 Nm and a rolling moment of 0.007 Nm (greater loads can be measured by the balance, due to inbuilt safety factors).

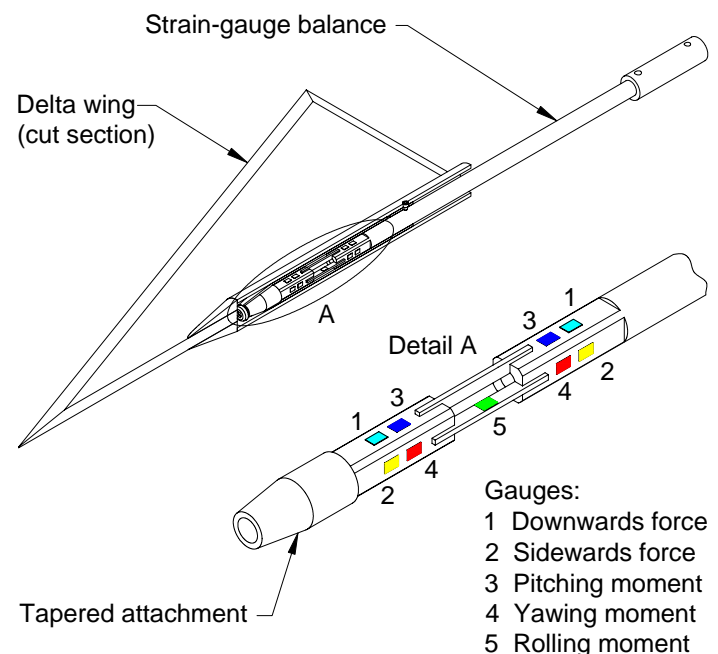


Figure 6. Five-component strain-gauge balance

### Output Data From System

For each chosen instant of time during a dynamic manoeuvre, an output file is created which contains yaw, pitch and roll angles, together with corresponding downwards and sideways forces, and yawing, pitching and rolling moments. For each of the instants of time, side- and plan-view images of the flow are also captured with digital cameras using synchronization software. Thus it is possible to correlate precisely the instantaneous flow patterns over a model and the flow-induced loads on the model.

### Preliminary Experimental Results

The dynamic testing system has been completed to the stage where it is possible to capture images of the flow over an aircraft, with or without suction through the intake(s), while the aircraft undergoes preset motions in yaw, pitch and roll. It is not yet possible to measure forces and moments with the five-component strain-gauge balance. Samples of typical instantaneous flow patterns over a 1/48 scale modern high-performance aircraft during a test dynamic manoeuvre are given in figure 7. The flow was visualized using sodium fluorescein dye and there was no suction through the intakes of the aircraft.



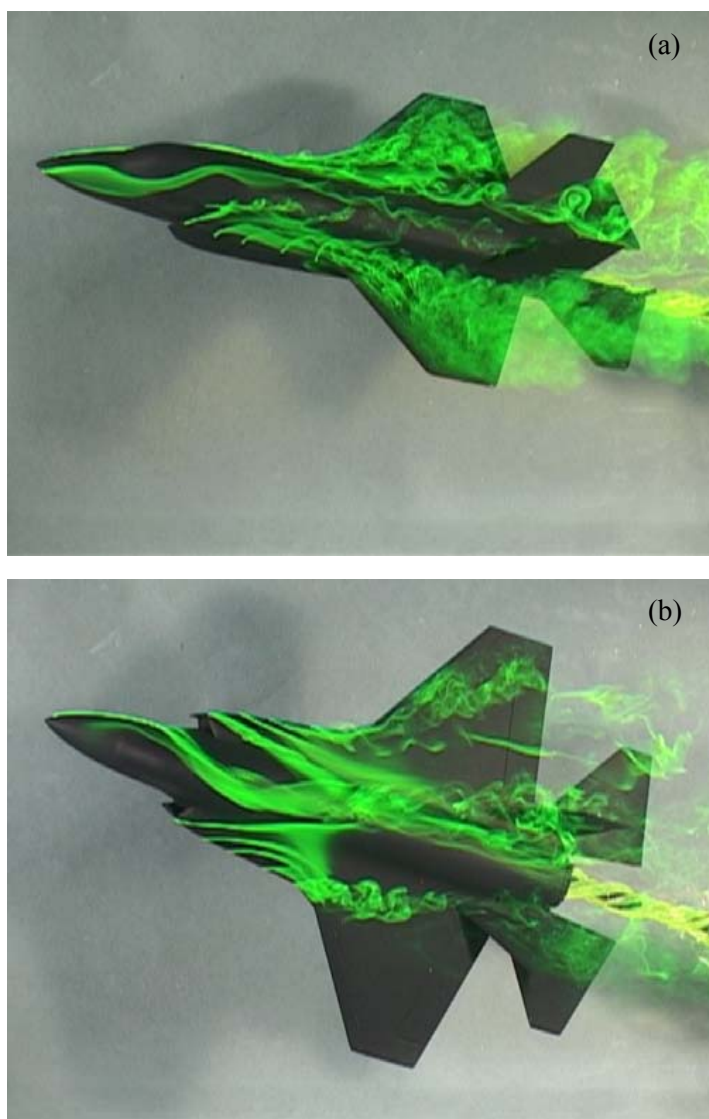


Figure 7. Instantaneous images for the test manoeuvre shown in figure 4.

(a)  $t = 7.6$  s;  $\psi = 7.6^\circ$ ,  $1^\circ/\text{s}$ ;  $\theta = 7.6^\circ$ ,  $1^\circ/\text{s}$ ;  $\phi = 38.2^\circ$ ,  $5^\circ/\text{s}$ .

(b)  $t = 64.3$  s;  $\psi = 12.3^\circ$ ,  $1^\circ/\text{s}$ ;  $\theta = 14.3^\circ$ ,  $1^\circ/\text{s}$ ;  $\phi = 98.6^\circ$ ,  $-5^\circ/\text{s}$ .

As can be seen, the flow over the aircraft is complex and is dominated by vortices formed by the rolling up of the flow as it separates along the leading edges of the aircraft. The vortical flow field and associated loading on the aircraft change continuously throughout a dynamic manoeuvre. Due to the low pressure in the cores of vortices, high-performance aircraft generate high lift at high angles of attack and this improves aircraft manoeuvrability and controllability when operating at extreme attitudes. However, in this flight regime, the cores of vortices can become unstable and break down or “burst”. The breakdown is characterised by a sudden expansion in the size of the vortex core, a rapid deceleration of the axial velocity in the core, a steep increase in the pressure and an increase in the turbulence downstream of the breakdown region. The increase in the core pressure after the breakdown reduces the lift contributed by these vortices, which can cause the wing to stall, and the increased turbulence can result in significant wing buffeting. The location of vortex breakdown is known to fluctuate in the stream-wise direction and the breakdown can be asymmetric. This behaviour results in significant loss of stability in roll and yaw.

Many uncertainties exist when studying vortical flow behaviour over manoeuvring aircraft. Questions remain about how aircraft instability in the extreme manoeuvring regime is influenced by

the prevailing flow patterns over the aircraft. Instabilities need to be explained in terms of the physics of the flow processes involved. Hopefully, using the dynamic rig, the ability to correlate precisely the instantaneous flow patterns over an aircraft with the flow-induced loads experienced by the aircraft will help us resolve some of these issues.

### Concluding Remarks

This paper describes how an existing water tunnel, used for testing a stationary model, is being upgraded so that it will now be possible to carry out tests with the model in motion. There is a need to carry out dynamic testing on aircraft in tunnels to study unsteady aerodynamic effects associated with aircraft motion, which will lead to a better understanding of the behaviour of aircraft, especially in the advanced manoeuvring regime. Dynamic force/moment data are also needed for use in the data bases of flight-dynamic models of aircraft to predict their performance.

Precise yaw, pitch and roll motions of a model can now be obtained independently. A special roll mechanism has been designed so that dye can be discharged from circular ports on an aircraft and water can be sucked through the intake(s), while the aircraft undergoes continuous roll, i.e. there is no twisting of dye or suction tubes. A sensitive five-component strain-gauge balance that uses semi-conductor strain gauges is currently being manufactured. Some flow-visualization images corresponding to a test dynamic manoeuvre are given, but no force/moment measurements are yet available.

Using the dynamic rig, it will be possible to directly correlate measured forces and moments with observed flow patterns when a model is undergoing a specified dynamic manoeuvre, and this may be beneficial when trying to understand and solve flight-mechanics problems of manoeuvring aircraft.

### Acknowledgments

The author is grateful to David Graham, Neil Matheson and Jan Drobik for supporting the project, to Owen Holland for work done on the model motion system, and to Phil Ferrarotto for work done on the strain-gauge balances.

### References

- [1] Brandon, J.M. & Shah, G.H., Unsteady Aerodynamic Characteristics of a Fighter Model Undergoing Large-Amplitude Pitching Motions at High Angles of Attack, *AIAA 28th Aerospace Sciences Meeting*, Reno, NV, Jan 8-11 1990.
- [2] Erm, L. P., An Investigation into the Feasibility of Measuring Flow-Induced Pressures on the Surface of a Model in the AMRL Water Tunnel, *DSTO-TN-0323*. Aeronautical and Maritime Research Laboratory, Defence Science and Technology Organisation, Melbourne, Australia, Nov 2000.
- [3] Huang, X.Z., Hanff, E.S., Motion Effects on Leading-Edge Vortex Behaviour Over Delta wings and Generalized Modeling, *Symposium on Vortex Flow and High Angle of Attack Aerodynamics*, Loen, Norway, May 7-11 2001.
- [4] Suárez, C.J., & Malcolm, G.N., Dynamic Water Tunnel Tests for Flow visualization and Force/Moment Measurements on Maneuvering Aircraft, *AIAA-95-1843-CP*, *13th Applied Aerodynamics Conference*, San Diego, CA, Jun 19-22 1995.
- [5] Suárez, C.J., Malcolm, G.N., Kramer, B.R., Smith, B.C. & Ayers, B.F., Development of a Multicomponent Force and Moment Balance for Water Tunnel Applications, Volume I and II, *NASA Contractor Report 4642*, Dec 1994.



## Stereoscopic PIV measurements behind a 3D flapping foil producing thrust

Parker, K.<sup>1</sup>, von Ellenrieder, K. D.<sup>2</sup> and Soria, J.<sup>1</sup>

<sup>1</sup>Laboratory for Turbulence Research in Aerospace & Combustion (LTRAC)

Mechanical Engineering, Monash University  
Clayton Campus, Victoria, 3800 AUSTRALIA

<sup>2</sup>Dept. Ocean Engineering  
Florida Atlantic University

Dania Beach, FL 33004-3023, USA

### Abstract

Past qualitative dye flow visualizations behind a finite-span flapping foil have led to a model of the vortex skeleton. Subsequent 2D PIV experiments have highlighted some salient features in the proposed model but the 2D measurements reveals limited information about a highly 3D flow. This study proposes to use 3C 3D SPIV to quantitatively describe the flow geometry and test the proposed model of the vortex skeleton. This information is used to investigate the mechanisms responsible for thrust production. Preliminary results from 2D 3C SPIV behind a 3D NACA0012 flapping foil with an aspect ratio of 3, at a Strouhal number of 0.35 at the plane of symmetry reveal qualitative information about the reverse Karman vortex street. The structure as seen in the single measured plane, is phase locked with the forced flapping motion of the foil, in agreement with previous flow visualisations.

**Keywords:** *Strouhal number, stereoscopic particle image velocimetry, flapping/oscillating airfoil, vortical structures, unsteady aerodynamics*

### Introduction

An understanding of the fluid dynamic interactions that exist in the flow behind 3D flapping foils is paramount to harnessing the potential technology that is available in the field of unsteady propulsion. Vorticity control plays an important role in manipulating the evolution of large scale structures in the flow, thereby controlling the transport of momentum in the flow. An understanding of the mechanisms responsible for vortex interactions behind heaving and pitching foils is important from a control as well as thrust-production perspective [3].

In this study a deeper understanding of any momentum transport mechanisms, that result from modification to the vortical structure behind a flapping foil, is sought. Much of our present understanding in this field comes from past research using airfoils of infinite-span (2D airfoils). Parameters have been identified for optimal thrust production using flapping foils, with up to 80% recorded [1]. The dimensionless Strouhal number has been identified as a suitable parameter to describe the thrust producing ability of a flapping foil. In a Strouhal regime of  $0.25 \leq St \leq 0.35$  2D airfoils produce thrust with maximum efficiency. The flow behind a thrust producing foil is described by a 'reverse' Karman vortex street in which the mean velocity profile resembles a jet and momentum is added to the flow. In reality, wings are three dimensional and have finite spans. In this case the wingtip vortices add another dimension of complication to the vortical interactions and structure of the flow. Cheng and Murillo [2] first raised concerns that results from studies on 2D airfoils were over-estimated. Figure 1a shows a typical qualitative flow visualizations as observed from the wingtip of the airfoil. In contrast, the presence of wingtip vortices signif-

icantly alter the typical 2D vortex sheet as shown in the flow visualisations of von Ellenrieder *et al* in figure 2. In both cases the  $St = 0.35$ . The flow visualizations in figure 2 suggest that the vorticity shed from the leading edge, trailing edge and wingtips are connected. Based on these flow visualisation experiments the authors propose a model of the vortical skeleton for a 3D thrust producing foil [7] shown in figure 1b.

Since dye is a passive scalar and flow visualizations are restrictive in the information that they provide, more quantitative experiments will be carried out. The purpose of this paper is to report on SPIV measurements that provide 3C 2D information of the flow for comparison with the previous flow visualisations. Of interest is the relationship between the phase averaged structure of the flow, represented by the model of the vortex skeleton in figure 1b and the forcing introduced into the flow.

### Experimental Technique

#### Apparatus & method

The experiments are conducted in a water tunnel at the Laboratory for Turbulence Research for Aerospace & Combustion. The working section measures  $500\text{mm} \times 500\text{mm} \times 1000\text{mm}$ . The turbulence intensity levels in the core region is less than 0.35%. A full description of the experimental rig is provided in [4].

A NACA0012 airfoil with chord,  $c = 25\text{mm}$  and  $AR = 8$  is suspended vertically above the test section. The airfoil performs angular (pitch) and lateral (heave) oscillations using stepper motors. The airfoil heaves in the y direction and simultaneously pitches about the quarter-chord position. The heave-stepper motor performs the oscillations by virtue of a scotch yoke. The scotch yoke wheel can be adjusted to accommodate different heave oscillation amplitudes. The scotch yoke moves a platform on which the pitch motor is mounted. The pitch motor drives the airfoil directly. A motion control program was created in such a manner to allow different motion parameters (such as frequency,  $f$ , maximum pitch oscillation amplitude,  $\theta_0$  and phase angle between heaving and pitching oscillations,  $\psi$ ) to be independently varied. Thereby allowing for various motion profiles. Potentiometers are mounted along the heave and pitch axes. These provide accurate feedback of the output trajectory of the foils. Optical triggers have been placed at various locations along the airfoil trajectory to provide the trigger signals to the laser and cameras.

The entire oscillating mechanism is mounted on a railing system above the water tunnel, allowing the airfoil setup to be moved to different locations, while the cameras and laser arrangement is kept fixed. Further details of the motion parameters of the experiment is provided in [4].

## Data Acquisition

In order to quantitatively analyze the flow, digital particle image velocimetry is utilized. PIV measurements are conducted in the near wake region of the foil. A region  $3.5c$  (y-direction) by  $3c$  (x-direction) is captured at a magnification of 0.095. Flow visualizations by von Ellenrieder *et al* [7] suggest this to be adequate to capture the large scale structures in the flow over 1 complete forced oscillation cycle of the foil.

Two Pixelfly CCD cameras, with array sizes of  $1280px \times 1024px$  each, are mounted vertically onto a 3-axis translation stage, below the test section. An angular-displacement stereo-configuration is utilized with the cameras at  $65^\circ$  to each other. The cameras are fitted with  $55mm$  Micro Nikkor Nikon lenses at  $f\#2.8$ . To satisfy the Scheimpflug condition each camera axis is tilted by  $3^\circ$ .  $11\mu m$  seed particles are illuminated by laser light from a dual-cavity New Wave Nd:Yag laser, pulsing  $532nm$  light at  $32mJ$ . A  $3mm$  thick horizontal light sheet is created in the midspan region of the airfoil using the necessary collimating optics. The SPIV setup is optimised for good image quality. A beam collector is placed on the far side wall of the test section to collect light from the laser.

## Stereo Acquisition

An in-situ calibration technique is utilized similar to [5]. Calibration images are acquired for the right and left camera at several planes across the thickness of the laser sheet. Using a template-matching digital image correlation approach, the exact positions of calibration markers are found. A polynomial with cubic dependence on the in-plane components,  $x$  and  $y$  and quadratic dependence on the out-of plane component,  $z$  is used to map the displacement in the object plane to an image plane displacement. This is adequate to remove any higher order distortions one expects to encounter [5]. A least squares approach is used to determine the mapping function for the cameras and also to calculate the final displacements of the flow field.

Double exposed images are acquired in a horizontal plane bisecting the span of the wing. The laser firing is synchronized with the motion of the foil. A trigger signal from a stepper motor is sent via a breakout box, to a RT Linux control computer that regulates a return signal to activate the laser firing and the camera acquisitions. This setup is shown in figure 1c. Phase-averaged measurements are made at 8 locations within 1 heave cycle. The period of 1 heave cycle is  $640ms$ . 500 instantaneous images are acquired to achieve a statistical confidence of 99%, that the error in the mean is 1%. The acquired image pairs are analyzed using a multigrid cross-correlation algorithm from Soria [6]. From the stereo images, the three components of velocity  $u$ ,  $v$  and  $w$  are calculated in each plane and the vorticity is derived from the velocity gradients.

## Discussion of Results

The results of the stereo-PIV experiments are presented for  $Re = 637$ ,  $\psi = 90^\circ$ ,  $\theta_0 = 5^\circ$  and  $St = 0.35$ . Phase averaged measurements are taken at 8 locations shown in figure 1d. The data for every 2nd phase location is presented here, representing the motion reciprocating motion of the foil in 1 cycle. The visualisations in figure 2 are at the same phase locations in order to compare to the SPIV measurements. The preliminary measurements are made in a plane bisecting the midspan of the foil where the flow exhibits greatest complexity.

From the integrated streamline patterns of figure we observe many critical points including nodes, saddle points and foci in the in-plane field. Here the convection velocity has been removed from the flow field. The orientation and location of the

airfoil in the flapping trajectory has been indicated by the inclusion of the airfoil in the right of each image. As in the case of the flow visualisation images, flow is from right to left. These results compare favourable with previous 2D PIV measurements [4]. The location and orientation of the airfoil in the flow field gives a sense of the disturbance introduced by the forcing motion of the foil. Figure shows iso-contours of the out of plane vorticity. Regions of intense vorticity. Vorticity of opposite sign is shed into the flow in 1 cycle. The vortex formations produces a reverse Karman vortex street of counter-rotating vortex pairs. From this measurement in the symmetry plane the results support the argument of phase locked vorticity control from von Ellenrieder *et al*[7]. The flow is characterized by a sequence of coherent structures of positive and negative vorticity which shed and evolve in relation to the phase of the foil. Vorticity of opposite rotation is shed at the extreme heave and pitch positions of the airfoil.

## SUMMARY

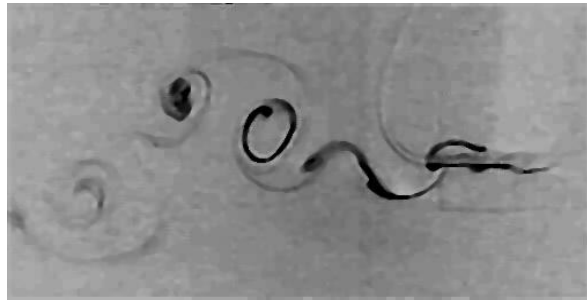
The flow measured at the midspan of the foil is inherently complex and three dimensional. The flow sequence from the PIV measurements differ from the flow visualizations images. These differences are ascribed firstly, to the general limitation of flow visualizations, as passive scalar measurements. Secondly, with the current single-plane information further elaboration of the mechanisms responsible for momentum transport or vorticity evolution is speculative at best. Consequently, 3C 3D measurements are planned for the future.

## ACKNOWLEDGEMENTS

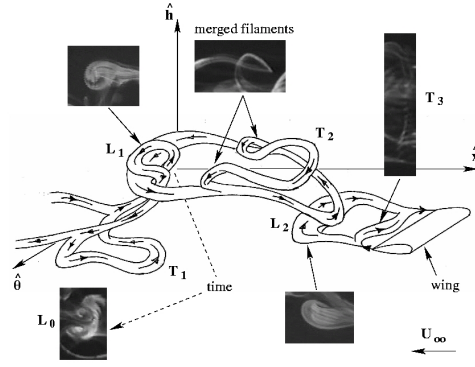
The authors would like to acknowledge the support of Dr. Phillipa O'Neil and Dr. Simon Clarke in the formulation of the stereo reconstruction algorithm. Also Mr. Ivor Mackay, Mr. Eric Wirth and Mr. Adam Castle for the fabrication of the SPIV experimental rig

## References

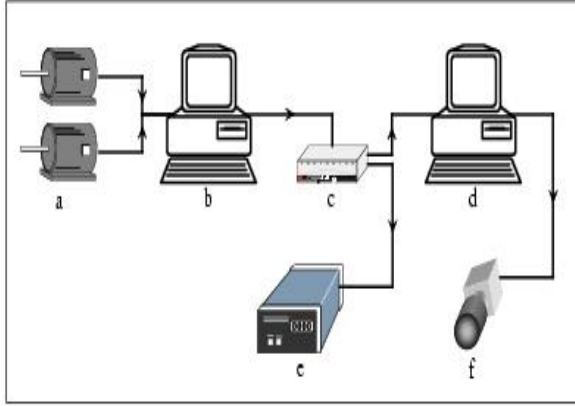
- [1] J. M. Anderson, K. Streitlien, D. S. Barrett, and M. S. Triantafyllou. Oscillating foils of high propulsive efficiency. *J. Fluid Mech.*, 360:41–72, 1998.
- [2] H.K Cheng and L. E Murillo. Lunate-tail swimming propulsion of a curved lifting line in unsteady flow. *J. Fluid Mech.*, 143:327–350, 1984.
- [3] R. Gopalkrishnan, M. S. Triantafyllou, G. S. Triantafyllou, and D. Barrett. Active vorticity control in a shear layer using a flapping foil. *J. Fluid Mech.*, 274:1–21, 1994.
- [4] Soria J. Parker K., von Ellenrieder K. D. A description of the vortical skeleton behind an finite-span flapping wing. In *Twelfth International Symposium on Applications of Laser Techniques to Fluid Mechanics*, Lisbon, Portugal, 2004.
- [5] Liu Z. C. Soloff S. M., Adrian R. J. Distortion compensation for generalized stereoscopic particle image velocimetry. *Meas. Sci. Technol.*, 8:1441–1454, 1997.
- [6] J. Soria. Multigrid approach to cross-correlation digital PIV and HPIV analysis. In *Proceedings of 13th Australasian Fluid Mechanics Conference*. Monash University, 1998.
- [7] Soria J. von Ellenrieder K. D., Parker K. Flow structures behind a heaving and pitching finite-span wing. *J. Fluid Mech.*, 490:129–138, 2003.



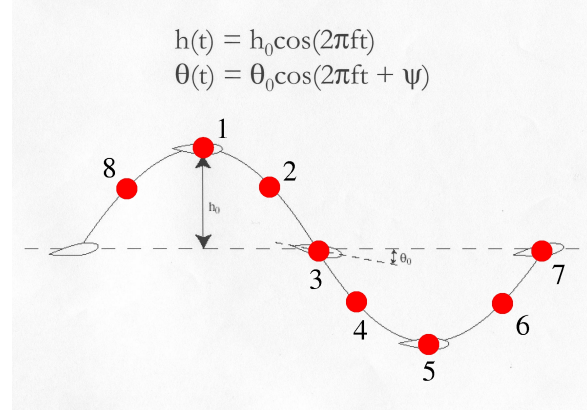
(a)



(b)

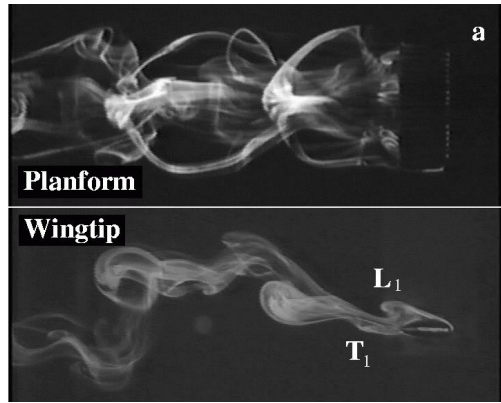


(c)

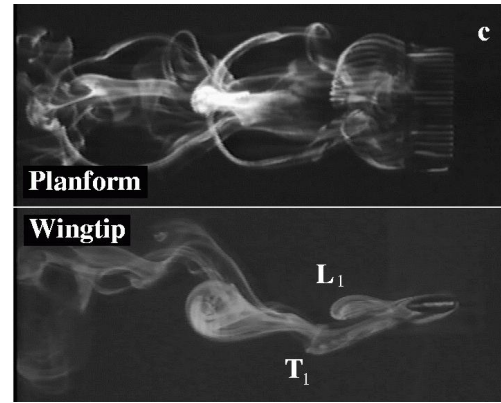


(d)

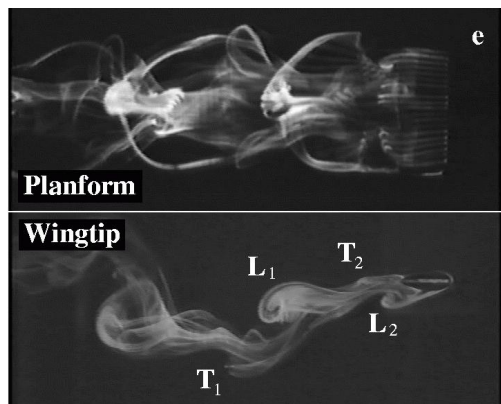
Figure 1: (a) Dye flow visualization of the flow behind a 2D flapping airfoil, (b) Proposed 3D structure of the vortex skeleton behind a 3D flapping wing. For the condition shown,  $St = 0.35$ ,  $\theta_0 = 10^\circ$  and  $\psi = 90^\circ$ , (c) Schematic of the data acquisition and PIV control system- a) heave and pitch motor trigger signal, b) RTLinux control PC, c) breakout box, d) camera control PC, e) CCD camera, f) Nd:Yag laser, (d) Motion profile of the flapping foil highlighting the location of the phase averaged measurements.



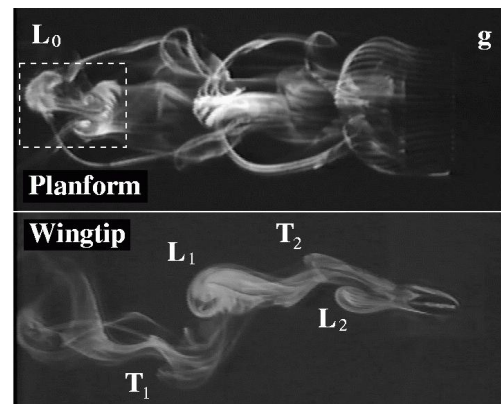
(a)



(b)



(c)



(d)

Figure 2: Dye flow visualisation of the flow behind a 3D flapping foil at  $St = 0.35$ . instantaneous images at: (a) phase 1, (b) phase 3, (c) phase 5, (d) phase 7.

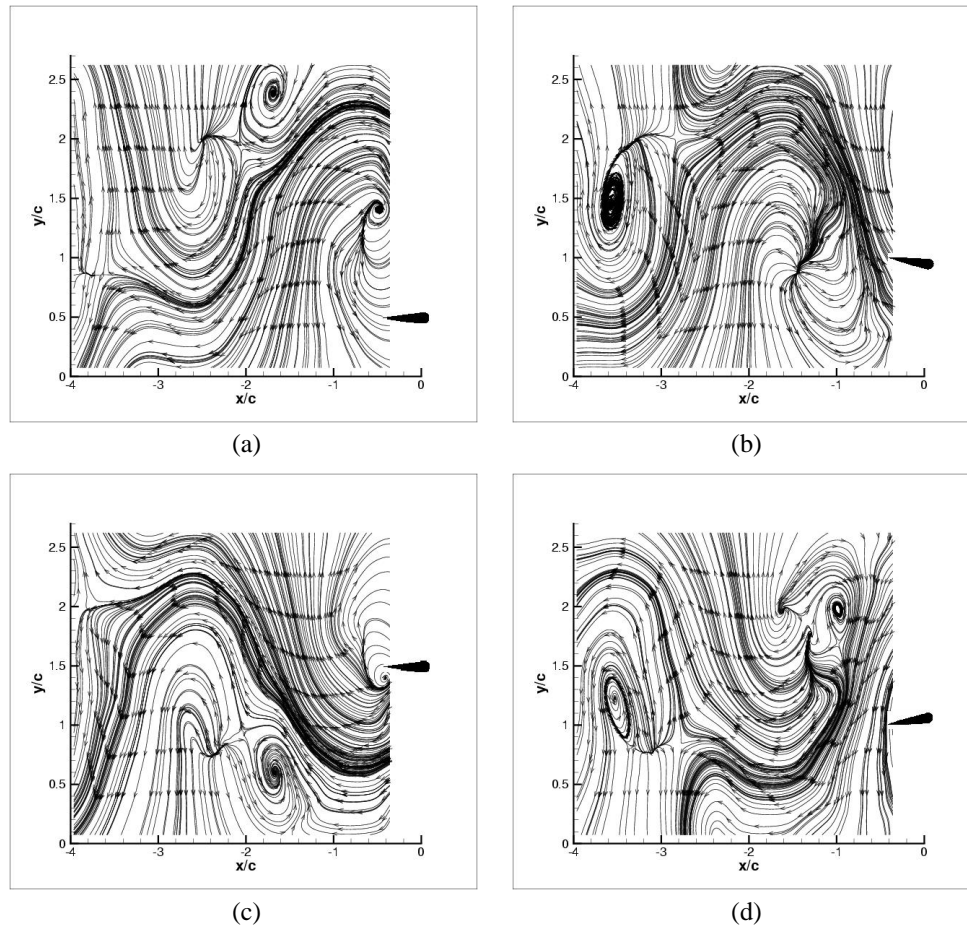


Figure 3: Integrated streamline pattern for the  $u, v$  in-plane velocity components measured behind a 3D flapping foil at (a) phase 1, (b) phase 3, (c) phase 5, (d) phase 7. In both cases the velocity components are non-dimensionalised by the freestream velocity,  $u_\infty$ .

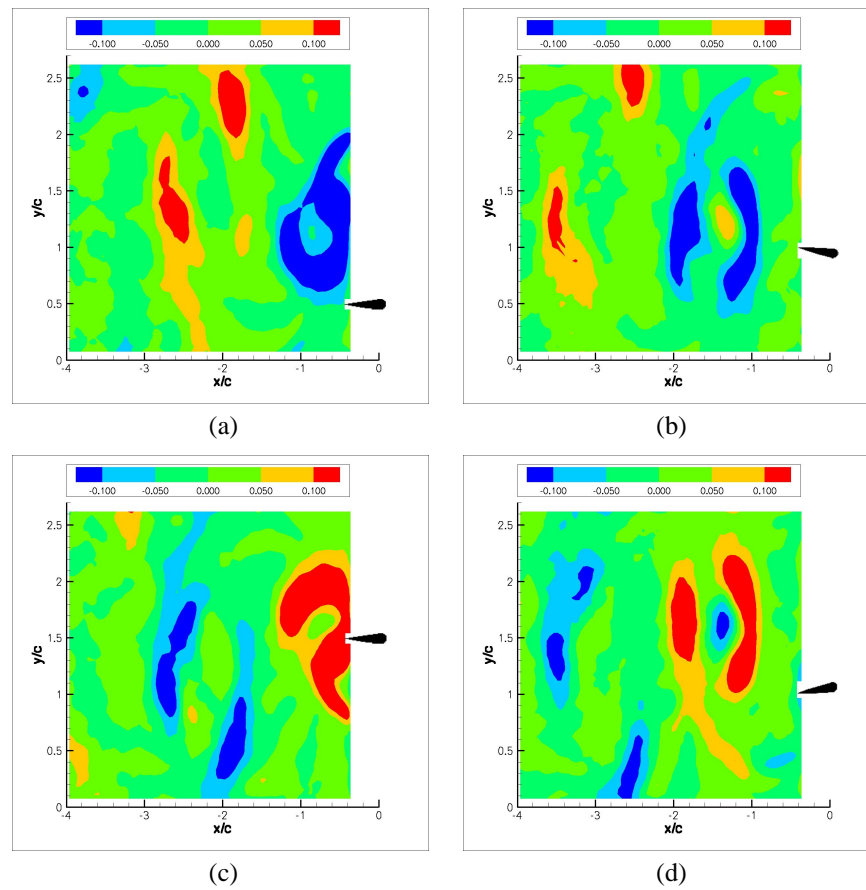


Figure 4: Contour plot of the out-of-plane vorticity  $\omega_z/\omega_0$  behind a 3D flapping foil at (a) phase 1, (b) phase 3, (c) phase 5, (d) phase 7; where vorticity is non-dimensionalised by the angular velocity of the pitching oscillation of the flapping foil.



## Analysis of Local Flame Propagation in Gas Explosions with Multiple Obstacles

D.J. Park<sup>1</sup>, A.R. Green<sup>1</sup> and Y.C. Chen<sup>2</sup>

<sup>1</sup>School of Safety Science, Faculty of Science, The University of New South Wales, NSW 2052, AUSTRALIA

<sup>2</sup>School of Mechanical & Manufacturing Engineering, Faculty of Engineering, The University of New South Wales, NSW 2052, AUSTRALIA

### Abstract

Experimental investigations were performed in a top-venting explosion chamber to assess the effects of multiple obstacles on local flame propagation. The chamber dimension is 235 mm in height with a  $1000 \times 950 \text{ mm}^2$  rectangular cross section and a large vent area of  $1000 \times 320 \text{ mm}^2$ . Multiple cylinder obstacles with blockage ratio of 30 % were used. Temporally resolved flame front images were recorded by a high speed video camera to investigate the interaction between the propagating flame and the obstacles. The propagation velocity of local flame fronts around the obstacles was estimated.

### Introduction

Gas explosions have a considerable implication on the safety in terms of potential loss of life, asset and business interruption risks. In particular, explosions occurring in confined and partially-confined regions of are of special concern due to the potential for domino effects and more serious consequences [1]. The interaction between the flame and the local blockage caused by the presence of equipments such as pip-work and vessels causes local flame acceleration of the propagating flame front [2]. The influences of such local blockage on explosion process were performed through laboratory-scale studies by many investigators [3,4,5,6].

The studies based on large length to diameter (L/D) ratio revealed that there is a strong interaction between the turbulence level formed behind the obstacle and the resulting peak pressure, and the turbulent flame and turbulence interaction trapped behind the obstruction greatly enhance the speed of flame propagation and hence increase the rate of pressure rise. However, the more detailed data of the flame displacement velocities due to the propagating flame front and obstacles have not been reported.

The present work aims at providing the experimental data of the local flame propagation velocities around the obstacle and investigating the underlying mechanisms of local flame/obstacles interactions in a partially confined enclosure with small L/D ratios and a large vent area.

### Experimental Set-Up

Figure 1 shows a schematic diagram of the experimental set-up consisting of an explosion chamber, 235 mm in height,  $1000 \times 950 \text{ mm}^2$  in cross section and with a large top-venting area of  $1000 \times 320 \text{ mm}^2$ . This gives a total volume of 223 liters of explosive mixture and a  $A_v/V^{2/3}$  ratio of 0.8695. The rig was made of 20 mm thick transparent chemiglass restrained by bolted flanges and strong adhesives. Flammable gas (99.95 %  $\text{CH}_4$  by vol.) entered the box through the valve placed in the bottom of the side wall of the chamber. The fuel volume flow rates were monitored using a calibrated gas flow control system (TEI, Model GFC 521).

Before gas filling, the large rectangular vent of area  $1000 \times 320 \text{ mm}^2$  was covered with thin plastic film (household plastic wrap). The film was sealed on a layer of blue tar lined around the vent. Air within the chamber during the filling sequence was continuously withdrawn via the open sample ports positioned at three different locations. The fuel/air mixture was circulated through the explosion chamber using a recirculation pump for several minutes to ensure a completely homogeneous mixture and then allowed to settle for several minutes before ignition. The fuel concentration was monitored by an infrared gas analyzer (GDA, Model LMSx) with an accuracy of  $\pm 0.3\%$ . The calibration of the apparatus was periodically checked by injecting calibration gases of known composition into the measurement system.

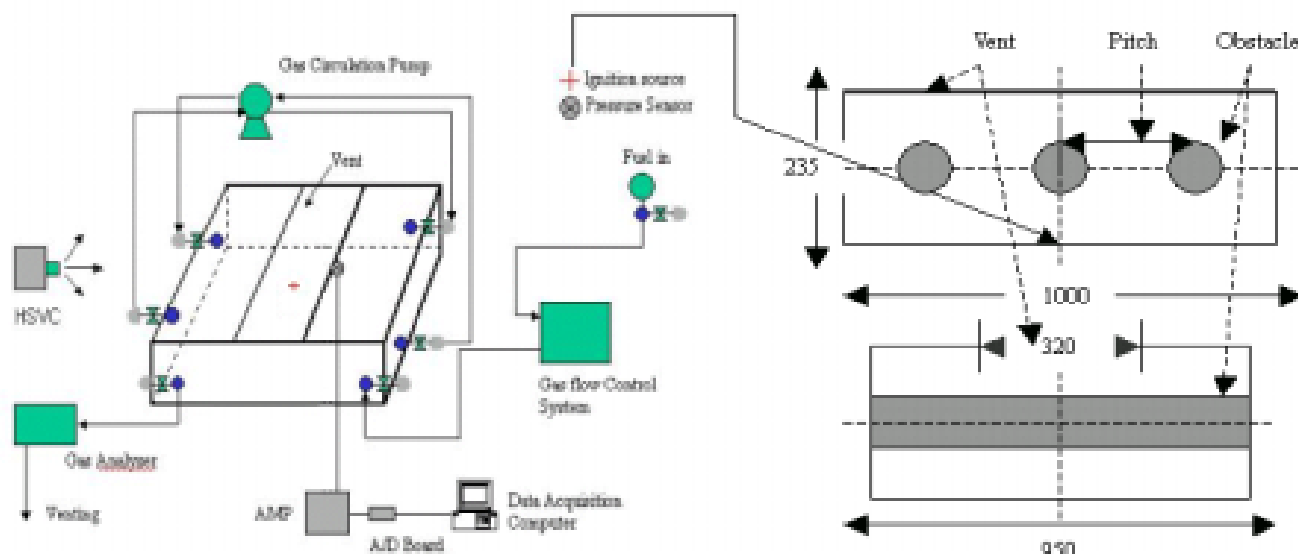


Figure 1: Schematic diagram of the experimental arrangements and the rig.



The flammable mixture in the chamber was ignited by a 15.5 KV electric spark positioned near the centre of the bottom wall, when the contact switch was closed. The flame images were photographed with a high speed video camera (KODAK Motion Recorder Analyzer, SR-ULTRA-C) operating at the rate of 500 frame/s, providing a temporal resolution of 2 ms. The pressure was recorded using a dynamic pressure transducer with a range of 0-2.5 bar (KISTLER type 701 A). Signals from the pressure transducer were logged on a 16 bit A/D converter sampling at 2 kHz, and a channel charge amplifier (KISTLER type 5019 B) and data acquisition computer were used to record pressure data.

As shown in figure 1, multiple solid obstructions with blockage ratio of 30% were mounted inside the chamber and centred 117.5 mm from the bottom of the chamber. The estimation of blockage ratio is an area percentage defined as the largest cross-sectional area blocked by positioning the obstruction in the explosion chamber divided by the cross-sectional area of the explosion chamber which is  $1000 \times 950 \text{ mm}^2$  [5].

The methane concentration in air was  $(10 \pm 0.2) \%$ , a slightly richer mixture than a stoichiometric methane/air mixture. Each test was repeated at least five times in order to ensure reproducibility and the results were averaged and the average results were presented. The reproducibility between all tests was found to be reasonable: the error was  $\pm 5\%$  in time and  $\pm 5\%$  in pressure.

### Image Processing and Flame Front Tracking

The procedures to study the local flame-front characteristics are divided into the following three steps:

#### (1) Identification of the region of interest.

As shown in Fig. 2 (a), the local region of interest selected here was around the left obstacle. The sub-region area was  $100 \times 100 \text{ pixels}^2$  with the centre of the obstacle coincide with that of the region of interest.

#### (2) Image processing.

Fig. 2 (b) shows one example of image processing applied in the area of interest to the original flame image obtained at 120ms after ignition. Image analysis was done by using the Optical Multi-channel Analyser (OMA) program for all the images obtained from the high speed video camera. A 5 by 5 smoothing filter is applied initially before the image is made binary. The red colour represents the burnt area and the black one is the unburnt area including the circular obstacle. A sequence of images can be processed to study the flame propagation behaviour at the vicinity of the obstacles and the flame-front boundary is determined for each individual image.

#### (3) Flame front tracking.

The flame-front contour coordinates of each image can be extracted by using an in-house FORTRAN code. All points along the contour are separated by 1 pixel, and one pixel here is 2 mm. With the coordinates of the contour, the flame front length and local flame front displacement in the normal direction between two consecutive images were calculated. Local flame propagation velocity was determined along the flame front by dividing the distance along the normal line at each point by the time between images.

### Results and Discussions

Figure 3 shows a sequence of temporally resolved flame-front images in the region of interest. The time shown below each image represents the elapsed time after ignition and subsequent flame images are at 2 ms intervals.

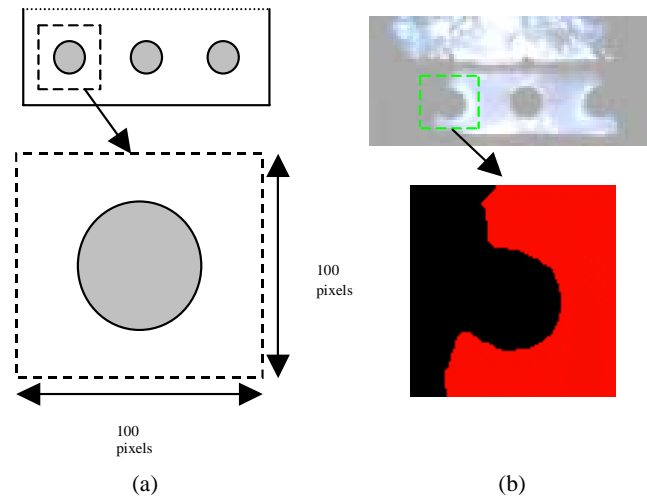


Figure 2: (a) Selection of a local area of interest; (b) Example of image processing applied to the original flame image in the area of interest.

The propagating flame front moves laterally toward the left obstacle and reaches the right side of the obstacle at about 96 ms after ignition. After impinging on the obstacle, the segment of flame front above the obstacle was found to propagate slower than the lower segment of the flame front.

With increasing time after impingement, the flame starts to roll up around the obstacle, and the flame decelerates. This is seen in figure 4 (a) where the temporal increase of the burnt area,  $A$ , slows down slightly with time. After flame deceleration, the flame burns into the wake and the propagation flame front reconnects, the flame accelerates again. The flame surface area is greatly increased at this stage and hence the burning rate. Flame reconnection in the wake of the obstacle occurred at about 134 ms after ignition.

Figure 4 (b) shows a comparison of the average of the local flame propagation velocity,  $S_{av}$ , derived via two different methods from 80 ms to 140 ms after ignition. The first one is from the incremental burnt area,  $\Delta A$ , divided by the flame front length,  $L$ ; the second is from the average of the local propagation velocity determined at each point along the flame front. In the first method, the flame front length touched with the obstacle is not included at the calculation of the flame front length. The results from both methods show good consistency, as expected.

The local flame propagation velocity remains fairly constant at approximately 2 m/s before the flame impinges onto the obstacle. The much higher value of the flame propagation velocity than the laminar burning velocity is due to the expansion effect as actually it is the burnt gas velocity that is measured here.

Much higher burning velocity is found at the early stage of flame impingement onto the obstacle. Despite some fluctuations, the general trend of the local propagation velocity is decreasing when the flame passes over the obstacle from 96 ms to 126 ms after the ignition. Only when the flame has passed over the obstacle does the local burning velocity rise again most likely due to turbulent generated at the wake of the obstacle.

### Conclusions

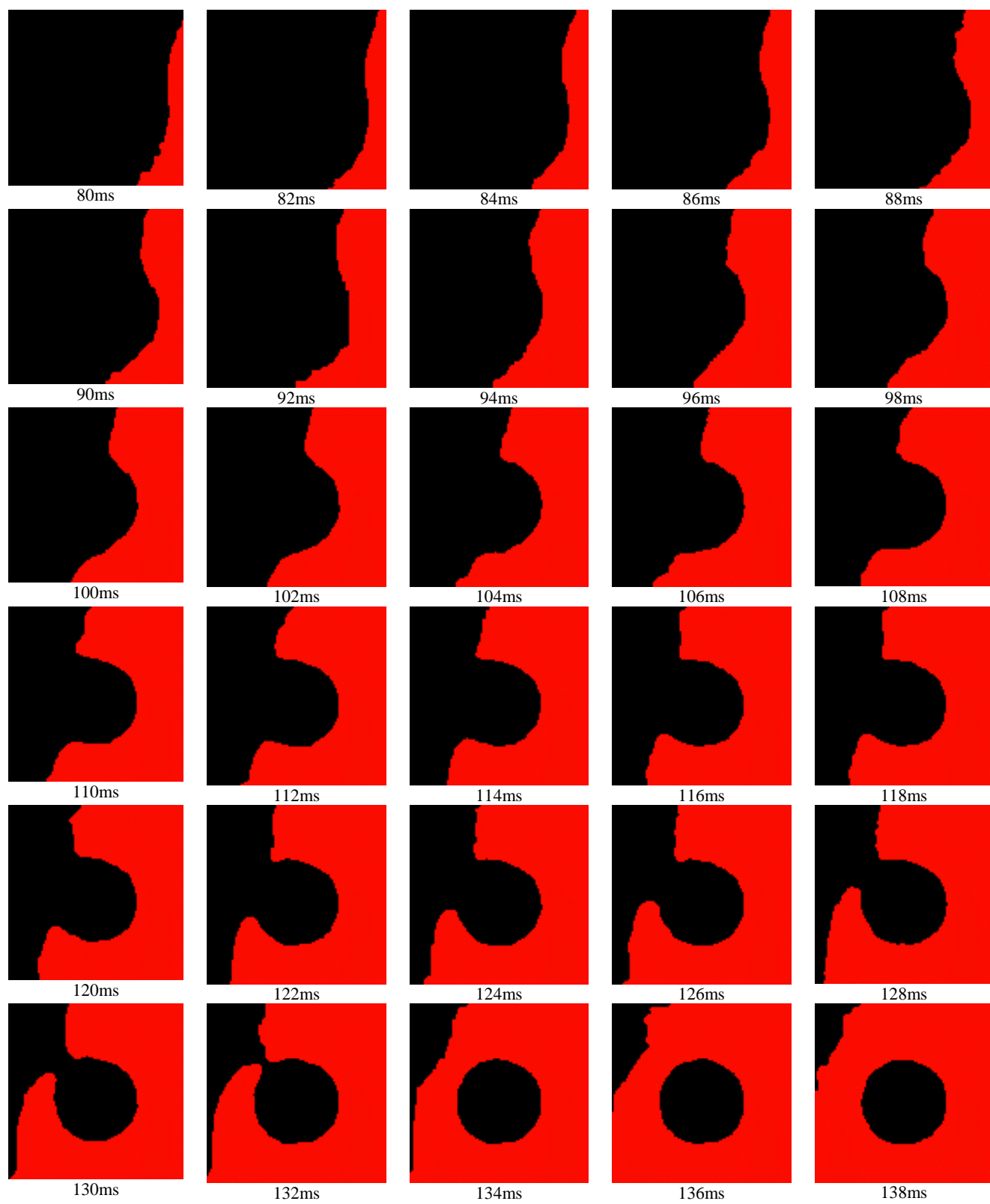
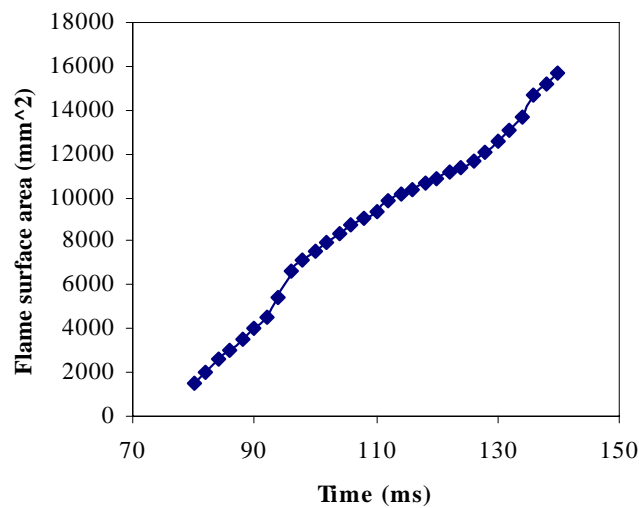
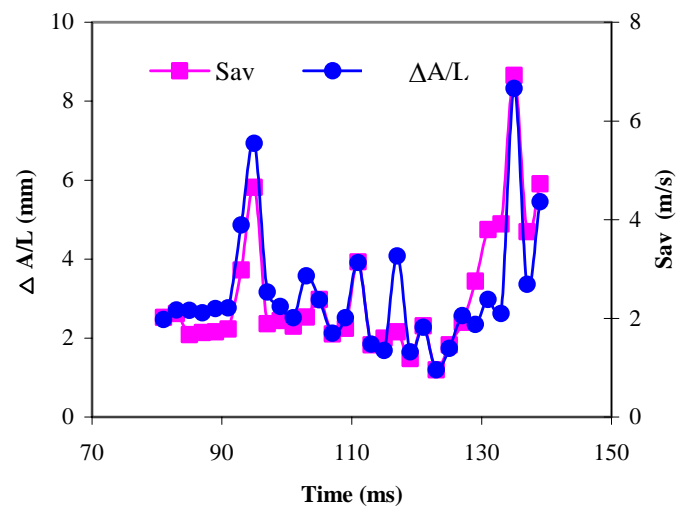


Figure 3: A temporal sequence of flame-front images in the region of interest showing flame propagation around the left obstacle during the course of the explosion.



(a)



(b)

Figure 4: (a) The flame area of local burnt area with time and (b) The incremental burnt area ( $\Delta A$ ) divided by the flame front length ( $L$ ) and the average of the local flame propagation velocity ( $S_{av}$ ) versus time after ignition for the local area

High-speed images have been acquired for a propagating premixed flame interacting with multiple obstacles in an explosion chamber. The images were processed to obtain the temporally resolved flame-front contours in the region of interest around the obstacle. An in-house FORTRAN code is further developed to determine the local flame propagation velocity.

The results show that overall the flame propagation slows down slightly after impinging onto the obstacle and accelerates again after flame front reconnection. The average of the local flame propagation velocity increases drastically when the flame impinges onto the obstacle. It follows then a decreasing trend and rises again after flame reconnection behind the obstacle wake.

### Acknowledgments

The authors gratefully acknowledge the financial support by R&D Training Centre, Korea Gas Corporation.

### References

- [1] Green, A.R. & Nehzat, N., Experimental studies of flame propagation and pressure rise in a 1:54 scale coal mine model, *Australian Symp. on Combustion and The Sixth Australian Flame Days*, 1999, 170-174 August..
- [2] Hargrave, G.K., Jarvis, S.J. and Williams, T.C., A study of transient flow turbulence generation during flame/wall interactions in explosions, *Meas. Sci. Technol.*, **13**, 2002, 1036-1042.
- [3] Moen, I.O., Donato, M., Knystautas, R. & Lee, J.H., Flame Acceleration Due to Turbulence Produced by Obstacles, *Combust. Flame*, **39**, 1980, 21-32.
- [4] Masri, A.R., Ibrahim, S.S., Nehzat, N., & Green, A.R., Experimental study of premixed flame propagation over various solid obstructions, *Experimental Thermal and Fluid Science*, **21**, 2000, 109-116.
- [5] Ibrahim, S.S. & Masri, A.R., The effects of obstructions on overpressure resulting from premixed flame deflagration, *J. Loss Prev. in the Process Ind.*, **14**, 2001, 213-221.

- [6] Phylaktou, H., & Andrews, G.E., Gas Explosions in Long Closed Vessels, *Combust. Sci. and Tech.*, **77**, 1991, 27-39.

## Stereoscopic PIV measurements of the flow past a circular cylinder at Reynolds number 15000

Parker, K.<sup>1</sup>, von Ellenrieder, K. D.<sup>2</sup> and Soria, J.<sup>1</sup>

<sup>1</sup>Laboratory for Turbulence Research in Aerospace & Combustion

Mechanical Engineering, Monash University

Clayton Campus, Victoria, 3800 AUSTRALIA

<sup>2</sup>Dept. Ocean Engineering

Florida Atlantic University

Dania Beach, FL 33004-3023, USA

### Abstract

Stereoscopic PIV measurements are conducted on a 2D stationary circular cylinder at Reynolds number 15000, based on cylinder diameter. The experiments form part of the validation of an in-house developed stereoscopic PIV reconstruction procedure. The purpose of this paper is to discuss the difficulties associated with stereo PIV measurements in liquid flows in the context of high Reynolds flow measurements past a cylinder. A liquid filled prism can be used to correct for the radial distortions of SPIV for liquid flows. This method significantly improves the stereo-image focusing ability. The stereo method utilised here is able to provide high quality data of the flow past the cylinder.

### Introduction

Standard 2D PIV allows one to measure two components of velocity with a single camera oriented orthogonally to the plane of measurement. In reality most flows are 3D in nature. Due to the physical nature of any experiment, even 2D flows experience some out-of-plane components. In these cases more information about the velocities in all 3 principal directions,  $u$ ,  $v$  and  $w$  would be useful. The principles of stereoscopic imaging is well established and documented and is omitted here [1, 3].

The 3D PIV technique can be divided into measurement of the velocity fields in a three-dimensional domain (3D 3C) and measurement of the three velocity components in a two-dimensional domain (3C 2D). This paper will focus on the latter. There are two basic SPIV configurations. The translation method [2, 5], which is omitted here and the angular offset method. The Angular offset configuration shown in figure 1 uses two cameras with lens axis perpendicular to the imaging sensor. The problem is that the best plane of focus is parallel to the image plane, not in the plane of the laser sheet. In order to have the entire field in focus a sufficiently large depth of field is required. This can be achieved by decreasing the lens aperture, but this decreases the image intensity as defined in the depth of field equation 1,

$$\delta z = 4(1 + M^{-1})^2 f\#^2 \lambda, \quad (1)$$

where  $M$  is the camera magnification,  $f\#$  is the f-number, and  $\lambda$  is the wavelength of the illuminating laser. As a result an increase in laser intensity is required to adequately illuminate particles in the object plane. When the camera angle is increased the required depth of field increases as well. An optimal range of camera angle between  $30^\circ$  and  $45^\circ$  is found to minimise the error in the measured velocity components,  $e_T$ , defined in equation 2.

$$e_T = (e_x^2 + e_y^2 + e_z^2)^{1/2}, \quad (2)$$

where each term in the expression represents the mean square difference between the measured and actual velocity for a par-

ticular component of velocity. In order to obtain particles in good focus over the entire image plane, the Scheimpflug condition must be satisfied [2, 5]. The Scheimpflug condition is satisfied when the object plane, image plane and lens principle plane intersect at a common point. This can be achieved by mounting the camera at an angle and rotating the lens with respect to the images sensor until all particles are in good focus. The combination of the Scheimpflug condition, sufficient laser intensity and adequate depth of field provides good quality stereo data with an out-of-plane velocity component resolved to a high degree of accuracy [2].

The aim of this study is to increase the accuracy of the measured out-of-plane velocity component by optimising the SPIV methodology applicable to liquid flows. This is as much dependent on the ability to acquire good quality PIV images from each stereo camera as the ability to account for the physical limitations of the experimental setup through optical or mathematical methods. In liquid flows, specifically with large contained test sections the air-glass-liquid interfaces is a major source of radial distortions that affects negatively the ability for the correlation the PIV images from the stereo cameras. Utilising a liquid filled prism corrects this distortion [5].

When viewing in liquid flows the variable index of refractions further introduces radial distortions which transform circular particles into ellipses which are smeared. This results in distorted correlation peaks and erroneous measurement of the particle displacement from the image correlations. Furthermore, the magnification varies over the entire field. This variation can be accounted for in the mathematical mapping of the images from distorted to undistorted space, discussed in section , but the radial distortion remains. The radial distortion creates blurred images that affect the quality of the PIV images from each camera. Poor image quality at this level is further deteriorated during the reconstruction procedure resulting in very high out-of-plane velocity error [5].

The purpose of this paper is to report on validation of a stereoscopic technique applied at the Laboratory for Turbulence research in Aerospace & Combustion. The paper will focus on the experimental technique as well as report on the results from calibration and validation experiments. These experiments are used to optimise the experimental methodology by 'fine-tuning' the optical and mathematical algorithms used. Furthermore, as a test case, some flow measurements behind a 2D cylinder at high Reynolds number are presented.

### Experimental Technique

#### Apparatus and method

The experiments are conducted in a water tunnel at the Laboratory for Turbulence Research for Aerospace & Combustion.

tion. The perspex working section measures  $500\text{mm} \times 500\text{mm} \times 1000\text{mm}$ . The turbulence intensity in the core region of the test section is less than 0.35% at the freestream velocity of  $92\text{mm/s}$ . Figure 2 illustrates the experimental layout. For the test case, a 2D cylinder of diameter,  $d = 25\text{mm}$  is suspended vertically above the test section as shown in figure 2. The cylinder is mounted to an oscillating rig that can be towed along the top of the test section on a railing system. The cylinder has a bow of  $0.5\text{mm}$  over  $500\text{mm}$  span due to machining.

CCD cameras are mounted vertically onto a 3-axis translation stage, below the test section. An angular-displacement stereo-configuration is utilized. The cameras are fitted with  $55\text{mm}$  Micro Nikkor Nikon lenses. For SPIV acquisitions, the lens aperture is operated at  $f\#11$ . The Scheimpflug angle is  $3^\circ$ . The cameras view a common region in the test section through two separate liquid filled prisms.  $11\mu\text{m}$  Potter's hollow glass fibre beads are used to seed the water tunnel. The particles are illuminated by laser light from a dual-cavity New Wave Nd:Yag laser, delivering  $32\text{mJ}$  at a wavelength of  $532\text{nm}$ . Using appropriate collimating optics and mirrors, a  $3\text{mm}$  thick horizontal light sheet is created in the midspan region of the cylinder as shown in figure 2).

### Stereo Acquisition

The ability to accurately determine the particle displacements is dependent on how accurately one is able to map from distorted image space to undistorted object space. This is dependant on the calibration process. An in-situ calibration technique, similar to Solof *et al*[6] it utilised here as it does not rely on accurate knowledge of the geometry of the stereo-camera setup and is able to account for all distortions encountered during the actual experiment. Each camera acquires calibration images in multiple planes over a distance corresponding to the thickness of the laser sheet. Using a template-matching digital image correlation scheme, the exact locations of calibration markers in distorted image space are found.

The calibration data is used to calculate the mapping function,  $f$ , using a least squares approach. A vector-valued polynomial with cubic dependence on the in-plane components,  $x$  and  $y$  and quadratic dependence on the out-of plane component,  $z$  is used. This function is expected to adequately track any distortions one expects to encounter in PIV images and is discussed in greater detail in Solof *et al*[6].

Double exposed images are acquired in a single planes along the span of the cylinder ( $z$ -direction). Based on the variance in the measured velocity 1000 instantaneous images are acquired. The bias error in the measurements is 1% at 99% confidence level. The acquired image pairs are analyzed using a adaptive multi-grid cross-correlation algorithm from Soria [7]. From the stereo images, the three components of velocity  $u$ ,  $v$  and  $w$  and the out of plane vorticity,  $(\omega_z)$  is derived from the velocity gradients using a local Chi-Sq fit of 13 data points. From the instantaneous velocity fields, the mean velocity field is derived. The stereo reconstruction algorithm, StereoMagik<sup>©</sup>, interpolates the displacement information from the two separate PIV images onto a user defined regular grid by applying the mapping function. A reverse mapping combines the two component image displacements to three components of fluid displacements. The experimental setup is discussed in detail in [4].

### Solid Body translations

In order to validate the SPIV technique a method similar to Bjorkquist [2] is adopted in which a known displacement is measured using SPIV. A PIV test surface is translated by a fixed distance. The displacement is measured using the SPIV tech-

nique and the variation between the actual and measured values is calculated. 80 grit sandpaper is used as a test surface.

### Discussion of Results

The results from translating the sandpaper  $1\text{mm}$  in all principle directions is shown in table 1. The values shown represent the RMS of the difference between the measured and actual value. It can be seen that the worst case is when the test block is translated in the  $z$  direction. In this case the RMS error in the translated direction is up to 4 times as high as the measured  $y$  displacement.

RMS	$\sigma\Delta x$	$\sigma\Delta y$	$\sigma\Delta z$
1mm X	0.056	0.005	0.101
1mm Y	0.01	0.064	0.088
1mm Z	0.053	0.023	0.193

Table 1: RMS [ $px$ ] error from solid body translations of  $1\text{mm}$ .

Table 2 indicates the RMS error in locating the calibration markers accurately from the distorted calibration images. These values translate directly into the mapping of particles from distorted to undistorted space. This quality is dependant on the method employed to identify local points in the field of view, The adopted template correlation scheme is the latest in several improvements.

$\Delta X^1$	$\Delta Y^1$	$\Delta X^2$	$\Delta Y^2$
0.102	0.080	0.209	0.106

Table 2: RMS [ $px$ ] mapping error.

Table 3 indicates the RMS residual error from the final calculation of the fluid displacements. This quantity indicates how accurately the SPIV reconstruction algorithm is able to determine the displacements by recalculating the location of the particles in image space once the displacements are determined. The superscripts 1 and 2 indicate the X or Y location of a particle as seen in camera 1 and camera 2 respectively.

$\Delta X^1$	$\Delta Y^1$	$\Delta X^2$	$\Delta Y^2$
0.0008	0.0064	0.0006	0.0063

Table 3: RMS [ $px$ ] residual error.

The largest residual error originates from the  $y$ -component of each camera yet the mapping error is greater for the  $x$ -component. In general, the values are small compared to  $32px$ , the interrogation window size selected for the PIV analysis. If the perspective distortions are actually linear then the use of higher order polynomials as is the case here, would introduce error into the solutions for the fluid displacements. The largest RMS error obtained is 10 times larger than those obtained by Bjorkquist. [2]

### Summary

The radial distortions associated with SPIV measurements in large volume liquid flows can be alleviated by using liquid-filled prisms. While the values obtained for both the mapping and residual errors are larger than those SPIV errors obtained by others, the errors are low. Furthermore, the validation experiments show that the technique and setup has been 'tuned' to measure and resolve the three components of velocity in a 2D plane to within  $0.2px$  for the worst case. In the case of the measured test flow case at RE 15000, the mean profiles are similar



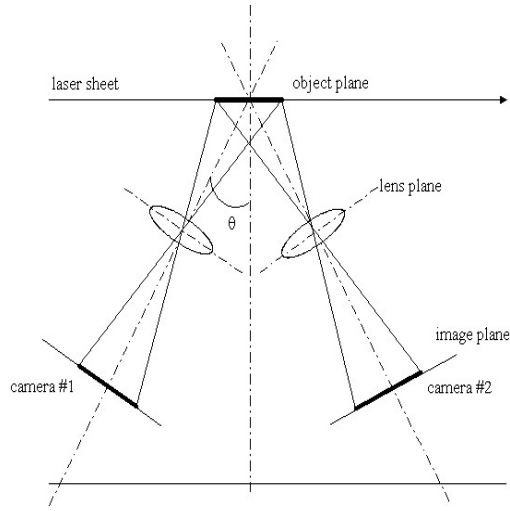


Figure 1: Stereo-camera angular offset configuration.

to other measured profiles for this flow regime. The RMS error is greatest in the core region of the wake but at overall low levels indicative of the quality of the measurement and methodology. Further refinement and adaptation of the SPIV technique is ongoing.

#### Acknowledgments

The authors would like to acknowledge the support of Dr. Phillipa O'Neil and Dr. Simon Clarke in the formulation of the stereo reconstruction algorithm. Also Mr. Ivor Mackay, Mr. Eric Wirth and Mr. Adam Castle for the fabrication of the experimental rig.

#### References

- [1] Greated C. A. Arroyo M. P. Stereoscopic particle image velocimetry. *Meas. Sci. Technol.*, 2:1181–1186, 1991.
- [2] Bjorkquist D. Design and calibration of a stereoscopic piv system. In *9<sup>th</sup> International Symposium on Applied Laser Techniques to Fluid Mechanics*, Lisbon, Portugal, July 13–16 2001.
- [3] Kompenhans J. Kahler C. J. Fundamentals of multiple plane stereo particle image velocimetry. *Exp. Fluids*, 30:70–77, 2000.
- [4] Soria J. Parker K., von Ellenrieder K. D. The flow of a three-dimensional thrust producing wing. In Krogstad P. A. and Andersson H. I., editors, *Advances in Turbulence X. Proceedings of the 10th European Turbulence Conference*, volume 49 of *Fluid Mechanics and its Applications*, pages 11–14, Trondheim, Norway, June/July 2004. CIMNE.
- [5] Jensen K. Prasad A, K. Scheimpflug stereocamera for particle image velocimetry in liquid flows. *Appl. Optics*, 34(30):7092–7099, 1995.
- [6] Liu Z. C. Soloff S. M., Adrian R. J. Distortion compensation for generalized stereoscopic particle image velocimetry. *Meas. Sci. Technol.*, 8:1441–1454, 1997.
- [7] J. Soria. Multigrid approach to cross-correlation digital PIV and HPIV analysis. In *Proceedings of 13th Australasian Fluid Mechanics Conference*. Monash University, 1998.

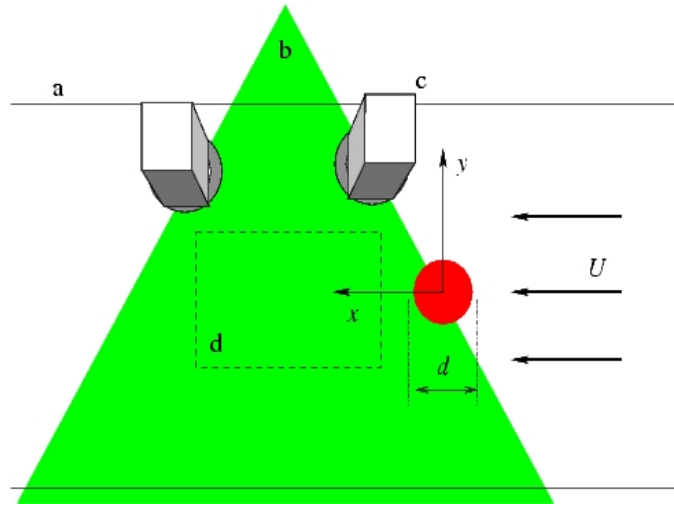


Figure 2: Schematic of the experimental apparatus: a) test section, b) laser sheet, c) stereo-CCD camera arrangement, d) imaged region of interest.

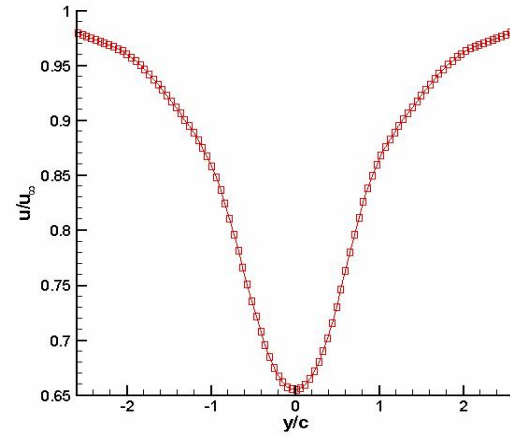


Figure 3: Mean velocity profile of  $u$ -component velocity behind a 25mm cylinder measured  $6d$  from cylinder centre. Velocity is non-dimensionalised by the freestream velocity,  $u_\infty$ .

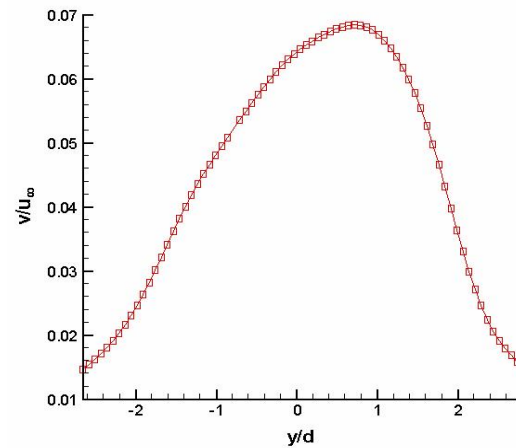


Figure 4: Mean velocity profile of  $v$ -component velocity behind a 25mm cylinder measured  $6d$  from cylinder centre. Velocity is non-dimensionalised by the freestream velocity,  $u_\infty$ .

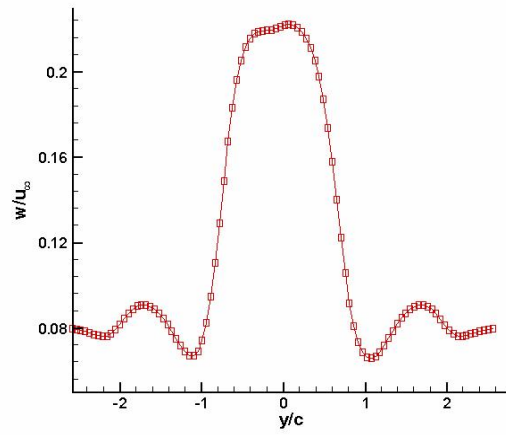


Figure 5: Mean velocity profile of  $w$ -component velocity behind a  $25mm$  cylinder measured  $6d$  from cylinder centre. Velocity is non-dimensionalised by the freestream velocity,  $u_\infty$ .

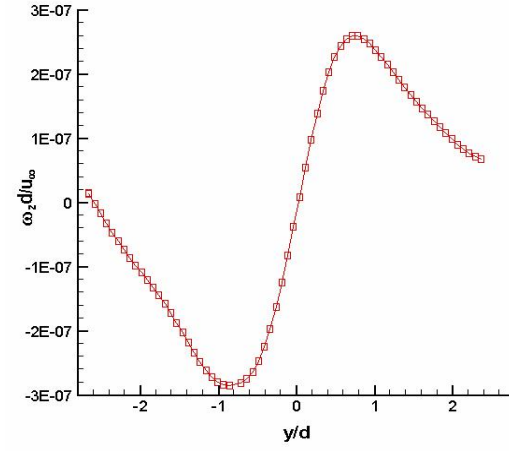


Figure 8: Mean out-of-plane vorticity profile behind a stationary cylinder of diameter  $25mm$  measured  $6d$  from cylinder centre. Vorticity is non-dimensionalised by the convective time scale,  $u_\infty/d$ .

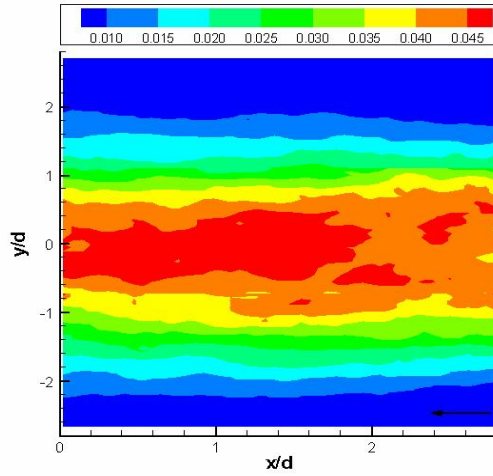


Figure 6: Iso-contour of the mean square error in  $u$ -component velocity, non-dimensionalised by the square of the freestream velocity,  $u_\infty^2$ . Arrow indicates flow from right to left

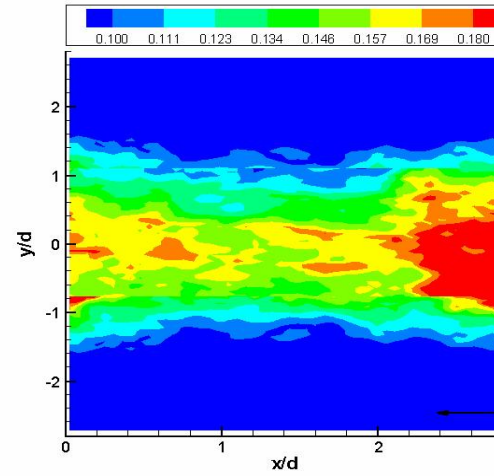


Figure 9: Iso-contour of the mean square error in  $w$ -component velocity, non-dimensionalised by the square of the freestream velocity,  $u_\infty^2$ . Arrow indicates flow from right to left

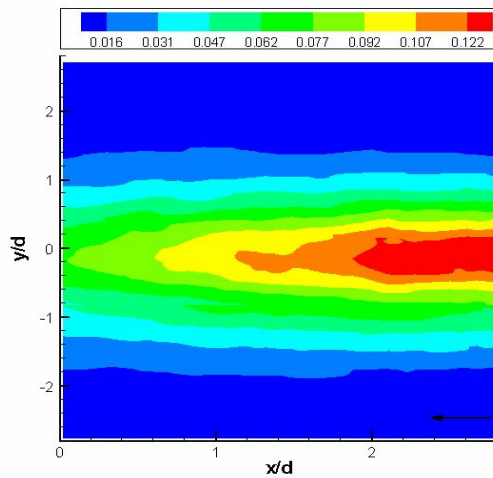


Figure 7: Iso-contour of the mean square error in  $v$ -component velocity, non-dimensionalised by the square of the freestream velocity,  $u_\infty^2$ . Arrow indicates flow from right to left

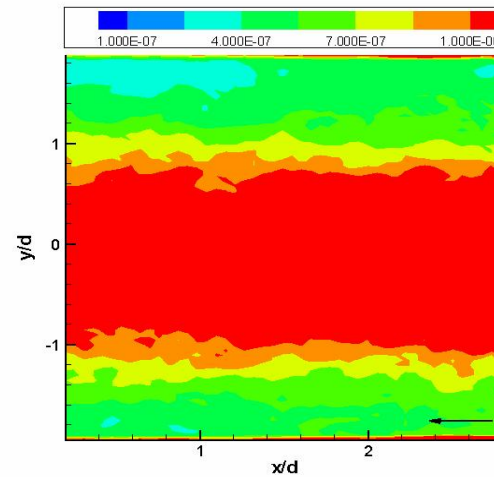


Figure 10: Iso-contour of the mean square error in out-of-plane vorticity components,  $\omega_z$ , non-dimensionalised by the square of the convective timescale,  $(u_\infty/d)^2$ . Arrow indicates flow from right to left

## Further Study of Spray Combustion in a Simple Turbulent Jet Flow

Yung-Cheng Chen, Sten H. Stårner, and Assaad R. Masri

School of Aerospace, Mechanical & Mechatronic Engineering  
The University of Sydney, NSW, 2006 AUSTRALIA

### Abstract

A laboratory burner has been developed to study the combustion characteristics of dilute sprays dispersed in a turbulent round jet flow of air. The burner design is intended to extend previous work with piloted jet diffusion flames into turbulent combustion of spray jets. In this paper, the characteristics of a methanol spray flame are compared with those of an acetone spray flame and a non-reacting acetone spray jet. The Phase Doppler Anemometry technique is applied to measure droplet size, two-component velocity, number density and the axial volume flux. The results show that, when the droplet carrier is air, spray flames are premixed in nature with most of the droplets consumed in the vicinity of local flame fronts and have quite different droplet velocity profiles from those of the non-reacting spray jet.

### Introduction

Spray combustion has a wide range of applications in power generation, including internal combustion engines and airborne propulsion. Its physical and chemical processes are made more complex by the largely unknown interactions between droplets, the turbulence, and chemical reactions involved. The capabilities of numerical predictions are often limited by the empiricism in the sub-models used for droplet evaporation, combustion and turbulence, and also by the lack of suitable experimental data for detailed comparison. A laboratory burner based on the spray jet configuration has been recently developed [1] to avoid some of the modelling difficulties often encountered in the near field, such as high initial velocity, flow recirculation, steep axial gradients, and non-uniform drop distribution. The well-defined boundary and initial conditions provided by this burner are particularly suitable for model validation purpose. Experimental data of this kind are very much needed by the spray combustion community [2].

The burner design extends the previous work with piloted jet diffusion flames [3] into turbulent combustion of spray jets. A nebulizer is placed upstream to generate droplets of different sizes, the distribution of which becomes fairly uniform at the burner exit. The slender shear flow field developed downstream is fluid mechanically well understood. Such flow fields are easily predicted with existing commercial CFD codes, so that the focus can be placed on evaporation and other aspects of droplet dynamics in turbulent spray flames. Similar burner design has also been used to investigate effects of the droplet-size distribution [4], burning modes of droplet clusters [5], and droplet/turbulence interactions [6,7].

Salient features of droplet dispersion and evaporation in non-reacting [1] and reacting [8] acetone spray jets generated by this burner have been reported recently. The aim of this work is to extend the current database to a different fuel and to investigate its effects on turbulent spray combustion. Methanol is chosen here because of the small difference in liquid density by less than

1%. It has also the same index of refraction at 1.36 as acetone, but a lower vapour pressure and a larger binary diffusion coefficient in air. This results in a longer evaporation time for methanol than acetone droplets of the same diameter for a single droplet in an infinite oxidizing environment.

The Phase Doppler anemometry (PDA) technique is applied to measure droplet size, two-component velocity, number density and the axial volume flux. The mean and rms velocities conditional on different size classes are compared for methanol and acetone spray flames. The differences in droplet dispersion between non-reacting and reacting sprays are also explored. Both the Sauter Mean Diameter (SMD) and the integrated liquid flux are then compared to reveal the controlling factors on the bulk fuel consumption rate.

### Experimental Conditions

The schematic diagrams of the spray jet nozzle and burner are shown in Fig. 1. A co-flowing air stream at a mean velocity of 3 m/s and less than 2 per cent turbulence intensity is applied to shroud the spray jet and spray flame and to provide a well-defined boundary condition. The inner diameter of the main fuel tube,  $D$ , is the same at 9.8 mm. The main fuel tube is 75 mm long for the spray jet nozzle and is 50 mm long for the spray burner. Pressurized liquid fuel is fed into the nebulizer and its flow rate is measured by rotameters to be within 3% accuracy.

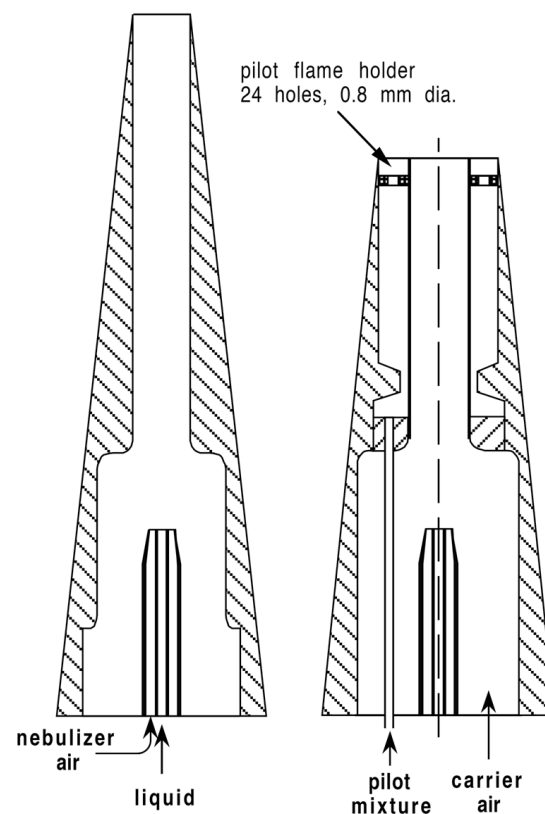


Figure 1: Spray jet nozzle (left) and burner (right) design.

On the thin burner lip, an annular premixed pilot flame anchors the spray flames. The pilot flame is a stoichiometric  $H_2/C_2H_2$ /air mixture such that the C/H ratio equals that of the main fuel, and its contribution to total heat release is 3.2 and 2.9 percent for flames MHF and AHF, respectively.

The global conditions for the methanol spray flame MHF, the acetone spray flame AHF, and the non-reacting spray jet LFS are listed in Table 1. The carrier air flow rate is maintained the same for both MHF and AHF flames to keep the jet Reynolds number the same.

	MHF	AHF	LFS
liquid fuel injected	methanol	acetone	acetone
liquid fuel injection rate (g/min)	26.3	21.1	7.0
carrier air flow rate (g/min)	170.4	170.4	135
overall fuel/air equivalence ratio	0.99	1.17	0.49
integrated vapour flux at nozzle exit (g/min)	-	11.4	5.9
gas-phase equivalence ratio at nozzle exit	-	0.63	0.41
$D_{32}$ at nozzle exit ( $\mu m$ )	19.2	18.0	13.7
mean flame height ( $x/D$ )	15 ~ 20	15 ~ 20	

Table 1: Global operation conditions.

PDA measurements have been carried out that scan along the radial direction at several axial stations downstream until less than 5% of the injected fuel remains as liquid. Droplet diameters as well as the axial,  $x$ -, and radial,  $r$ -, components of droplet velocities are recorded with a PDA instrument (Aerometrics, RSA 3100) arranged in  $45^\circ$  forward scattering mode, with 3 micron fringe spacing. More details about the settings for the PDA system can be found in Ref. [8].

## Results and Discussion

The thermal structure of methanol and acetone spray flames is first compared in Fig. 2. Mean flame temperature measured with a R-type thermocouple is shown at two axial stations. The bead diameter is approximately 0.2 mm. At the near burner exit location of  $x/D = 5$ , the methanol spray flame remains at ambient temperature close to the jet centreline; whereas the acetone flame is already at a higher temperature of approximately  $300^\circ C$ . The much lower temperature near the centreline for the methanol flame is attributed to both its longer droplet evaporation time and relatively higher liquid fuel injection rate. Substantial droplet evaporation is expected to occur at this axial station and reduces the gas phase temperature. Further downstream at  $x/D = 15$  in the flame zone, the radial temperature profile becomes very similar for the methanol and acetone flames.

The centreline axial mean,  $\bar{U}_{CL}$ , and rms,  $u'_{CL}$ , velocities conditional on a particular size class are compared in Fig. 3 between the spray flame MHF and AHF. At axial locations of  $x/D < 15$ , both spray flames have almost the same droplet velocity for the same droplet size class. This indicates that

response of droplet dispersion to turbulent convection is almost the same in both spray flames. Because the liquid density is the same for methanol and acetone, the droplet relaxation time is expected to be also the same for droplets of the same diameter.

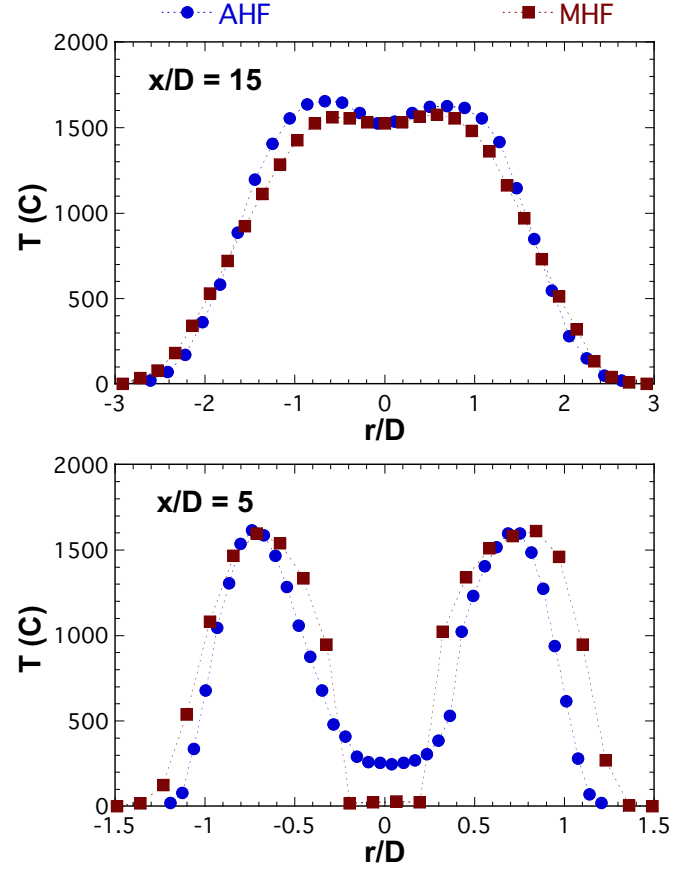


Figure 2: Comparison of the radial profiles of flame temperature at two axial stations for flames AHF and MHF.

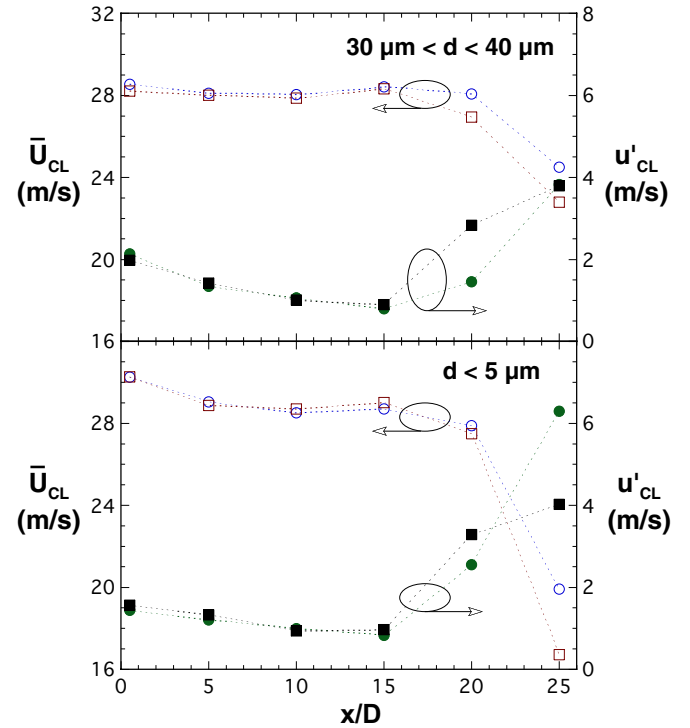


Figure 3: Comparison of the axial mean,  $\bar{U}_{CL}$ , and rms,  $u'_{CL}$ , velocities of droplets conditional on different size classes along the centreline for flame AHF:  $\circ$  and  $\bullet$ ; and MHF:  $\square$  and  $\blacksquare$ . The open symbols represent the mean velocities and the closed symbols represent the rms velocities.

However, the methanol spray flame shows a faster decline of  $\bar{U}_{CL}$  as well as the corresponding earlier rise of  $u'_{CL}$  than the acetone flame at axial stations of  $x/D > 15$  for both small and large droplets. This is consistent with a slightly shorter flame length for flame MHF as is also observed in the faster rise of temperature along the centreline shown in Fig. 4. Despite a smaller droplet evaporation time, the longer acetone flame length is attributed to its slightly rich overall fuel/carrier air equivalence ratio of the jet, as seen in Table 1. The corresponding laminar burning velocity can be higher in the MHF than the AHF flame. This is related to the premixed-dominated nature for both spray jet flames investigated here.

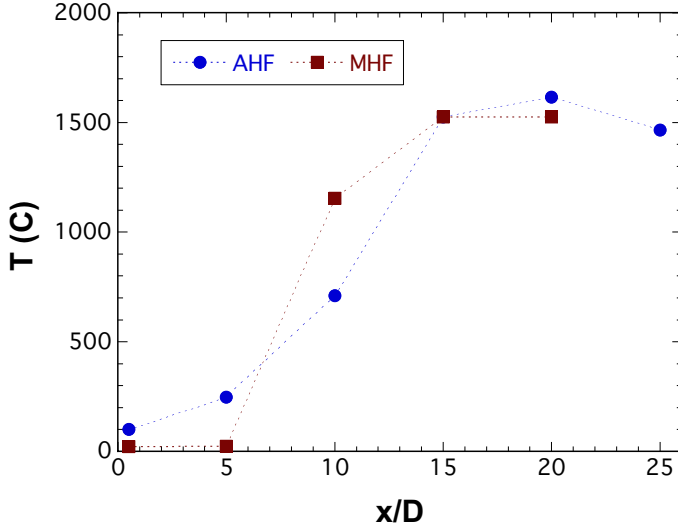


Figure 4. Comparison of the centreline flame temperature for flames AHF and MHF.

The droplet velocity distributions measured in non-reacting spray jets are quite different to those in the spray flames. Figure 5 compares the centreline axial mean and rms velocities of the spray jet LFS with the corresponding spray flame AHF. The axial mean velocity remains almost unchanged along the centreline up to  $x/D = 20$  for the spray flames. In contrast, the decline of  $\bar{U}_{CL}$  occurs already at axial locations of  $x/D > 5$  for LFS in Fig. 5, indicating substantial droplet dispersion effects. The different trends for both  $\bar{U}_{CL}$  and  $u'_{CL}$  are clearly associated with the much longer potential core in the spray flame than in the non-reacting counterpart. A similar extension of the potential core length has been observed before in turbulent premixed jet flames [9] where the turbulent flame brush is located at a smaller radius than the mixing layer, and thus retards the inward transport of turbulence generated at the mixing layer.

The resemblance to a premixed jet flame of the spray flames investigated here has been confirmed by OH-LIF imaging [10]. Almost all of the droplets are observed to evaporate within 1-2 mm of the local, instantaneous OH-fronts, irrespective of the fuel type. As the gas flow does not decay within the lengthened potential core, no apparent mean slip velocity is developed in the axial direction. Thus, the values of  $\bar{U}_{CL}$  for droplets of all the size classes remain the same as the mean droplet velocity at the jet centreline for  $x/D < 20$  in spray flames.

The droplet Sauter Mean Diameter (SMD),  $D_{32}$ , relative to that at the burner exit is compared in Fig 6 for flames AHF and MHF. The general behaviour of  $D_{32}$ , and the other mean droplet diameters as well, is the same for both flames. At a particular axial location,  $D_{32}$  remains almost constant in the jet core region

and increases gradually towards the flame zone as small droplets are quickly consumed. Also,  $D_{32}$  increases monotonically along the axial direction. At the near burner exit axial station of  $x/D = 5$ , the relative SMD remains the same for both flames. This indicates that the difference in the droplet evaporation time and the liquid injection rate does not change substantially the mean droplet diameter.

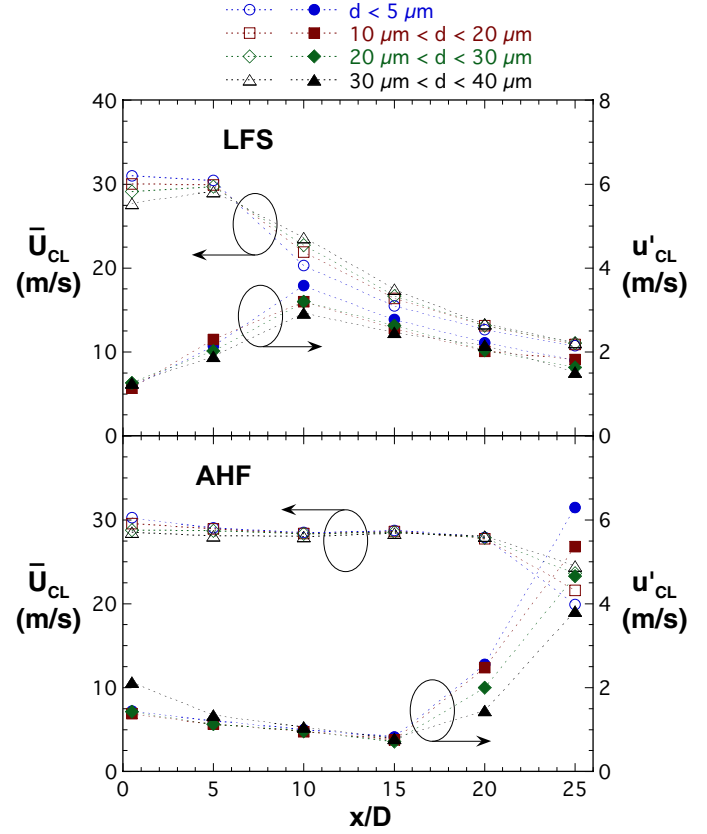


Figure 5: Comparison of the axial mean,  $\bar{U}_{CL}$ , and rms,  $u'_{CL}$ , velocities of droplets conditional on different size classes along the centreline for the non-reacting LFS spray jet and the reacting AHF spray flame. The open symbols represent the mean velocities and closed symbols represent the rms velocities.

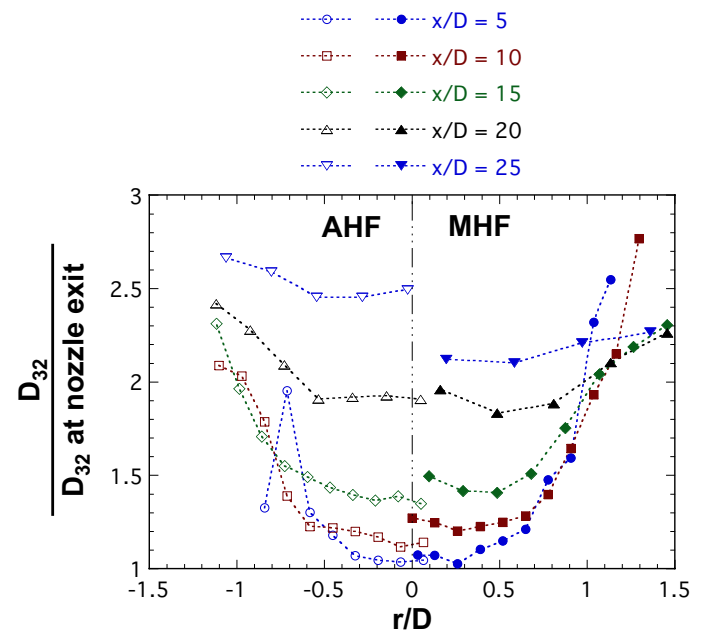


Figure 6: Comparison of the radial profiles of the Sauter mean diameter,  $D_{32}$ , at different axial stations for flames AHF and MHF.



Further downstream from  $x/D = 10$  to  $x/D = 20$ , the mean droplet diameter is greater in the methanol flame than in the acetone flame in Fig. 6. This difference in the Sauter mean diameter suggests that small droplets are consumed faster in the former than the latter flame. This is counter-intuitive since, by vapour pressure consideration alone, acetone droplets are expected to evaporate faster than methanol. A higher burning velocity of the methanol flame than acetone flame may be responsible for the faster depletion of the small drops for the methanol spray jet. At the axial location of  $x/D = 25$ , higher Sauter mean diameter is found for the methanol spray jet and can be attributed to the faster evaporation of acetone droplets.

Compared with the acetone flame AHF, the methanol spray flame MHF has a higher fuel injection rate, but is slightly shorter in flame height. The flame zones are located at approximately the same radius at all axial stations judging from the temperature measurements. All these imply a faster bulk fuel consumption rate for the flame MHF. This is also supported by the integrated droplet mass flux plotted along the flight time,  $t$ , in Fig. 7. The flight time at a given axial location is obtained by integrating the reciprocal of the centreline mean axial velocity along the axis. A faster decline of the integrated droplet mass flux with time is found for spray flame MHF. Dashed lines in Fig. 7 indicate the erroneous PDA measurements at  $x/D = 0$  and 10, where the liquid flux shows an unphysical increasing trend with increasing axial distance.

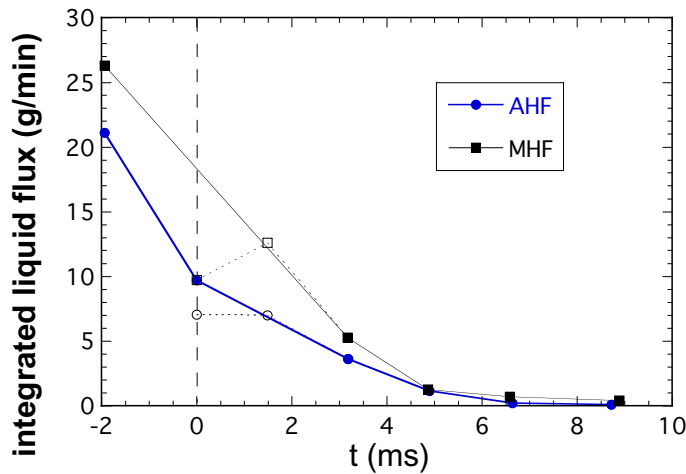


Figure 7: Comparison of the integrated liquid flux for flames AHF and MHF. Data points at  $x/D = 0$  and 10 are plotted in open symbols to indicate that they may be susceptible to PDA measurement error.

## Conclusions

The Phase Doppler Anemometry technique is applied to measure the droplet size, two-component velocity, and the axial volume flux in a methanol spray flame. Comparison is also made with an acetone flame and a non-reacting acetone spray jet. Despite the longer droplet evaporation time and higher liquid fuel injection rate for methanol than acetone flame, the methanol spray flame shows a faster bulk fuel consumption rate. This indicates that the premixed flame nature dominates the droplet evaporation process, which occurs mostly in the vicinity of the local flame front.

The premixed flame nature also affects strongly the droplet velocity profiles in the spray flames in comparison with those measured in the non-reacting spray jets. The axial mean velocity remains almost the same along the axial axis until reaching the

flame tip near  $x/D = 20$ . Droplet dispersion and its interactions with the mixing layer are substantially suppressed in the spray flames than in non-reacting jet flows.

## Acknowledgments

This work is supported by the Australian Research Council.

## References

- [1] Chen, Y.-C., Stårner, S.H., & Masri, A.R., Combined PDA/LIF Measurements in Simple, Evaporating Turbulent Spray Jets, in *Proceedings of the Fourteenth Australasian Fluid Mechanics Conference*, Adelaide, Australia, 2001, 267-270.
- [2] Widmann, J.F. & Presser, C., A Benchmark Experimental Database for Multiphase Combustion Model Input and Validation, *Combust. Flame* **129**, 2002, 47-86.
- [3] Bilger, R.W., Advanced Laser Diagnostics: Implications of Recent Results for Advanced Combustor Models, in *Aerothermodynamics in Combustors*, editors R.S.L. Lee, J.H. Whitelaw and T.S. Wung, Springer-Verlag, Heidelberg, 1992, 3-16.
- [4] Bossard, J.A. & Peck, R.E., Droplet Size Distribution Effects in Spray Combustion, *Proc. Combust. Inst.* **26**, 1996, 1671-1677.
- [5] Akamatsu, F., Mizutani, Y., Katsuki, M., Tsushima, S., Cho, Y.D., & Nakabe, K., Group Combustion Behavior of Droplets in a Premixed-Spray Flame, *Atomization and Sprays*, **7**, 1997, 199-218.
- [6] Karpetis, A.N. & Gomez, A., Self-Similarity, Momentum Scaling and Reynolds Stress in Non-Premixed Turbulent Spray Flames, *J. Fluid Mech.* **397**, 1999, 231-258.
- [7] Sornek, R.J., Dobashi, R., & Hirano, T., Effects of Turbulence on Dispersion and Vaporization of Droplets in Spray Combustion, *Proc. Combust. Inst.* **28**, 2000, 1055-1062.
- [8] Chen, Y.-C., Stårner, S.H., & Masri, A.R., Characteristics of Turbulent Spray Combustion in a Piloted Jet Flame Burner, *Proc. Combust. Inst.* **29**, 2002, 625-632.
- [9] Chen, Y.-C., Peters, N., Schneemann, G.A., Wruck, N., Renz, U., & Mansour, M.S., The Detailed Flame Structure of Highly Stretched Turbulent Premixed Methane-Air Flames, *Combust. Flame* **107**, 1996, 223-244.
- [10] Stårner, S.H. & Masri, A.R., Mass Flux Measurements in Simple, Evaporating Turbulent Spray Jets, in *Proceedings of the Third Australian Conference on Laser Diagnostics in Fluid Mechanics and Combustion*, Brisbane, Australia, 2002, 114.

## Laminar Flow in a Periodic Serpentine Channel

N.R. Rosaguti, D.F. Fletcher, B.S. Haynes

Department of Chemical Engineering  
The University of Sydney, NSW, 2006 AUSTRALIA

### Abstract

This paper presents a study of laminar flow in serpentine channels with periodically repeating elements, with application to heat transfer passages within complex compact heat exchangers. A methodology has been developed to determine the fully-developed flow and heat transfer behaviour in such channels with a constant wall heat flux using Computational Fluid Dynamics (CFD). Utilising this approach, flow characteristics are investigated for a fixed geometry, with  $L/d = 4.5$  and  $R_c/d = 1$ , for a range of Reynolds numbers up to 200. Pressure loss and heat transfer within a repeating module is compared with that expected from fully-developed flow in a straight pipe of equivalent path length. Dean vortices are generated in the flow and their rotation sense and intensity are dependent on the bend direction and Reynolds number. They are shown to suppress recirculation around bends and to be responsible for the high heat transfer rate with a relatively low pressure drop. The effect of the length to diameter ratio ( $L/d$ ) on pressure loss and heat transfer performance is also reported for a Reynolds number of 110, with  $R_c/d = 1$ .

### Introduction

This paper describes a method to study fully-developed flow in geometries that are periodic in the flow direction. The geometry under examination is a serpentine duct of circular cross-section with a constant heat flux applied at the walls. A serpentine channel geometry, as shown in Figure 1, has been studied as it is representative of the channel geometries used in complex compact heat exchangers. The work presented in this paper focuses on flow characteristics, with some comments also on heat transfer.

The definition of serpentine channels follows the work of Liu *et al.* [8]. The channel consists of a number of repeating modules that are periodic in nature. We analyse the fully-developed flow in this system, as this is analogous to a heat exchanger passage, consisting of many modules in series.

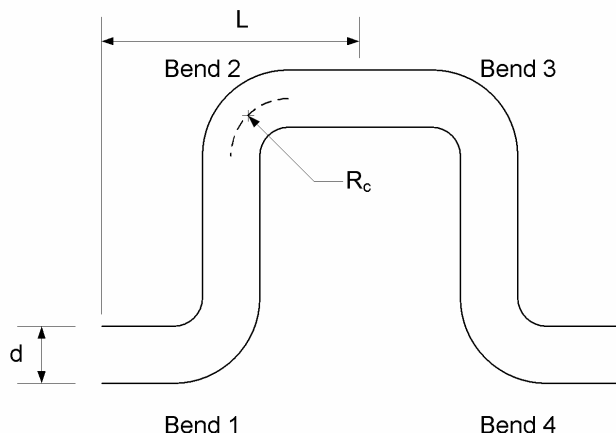


Figure 1: Repeating module of the serpentine geometry. Non-dimensional geometrical parameters of interest are  $L/d$  and  $R_c/d$ .

### Relevant Literature

A method to study fully-developed flow and heat transfer in channels with periodically varying shape was first developed by Patankar *et al.* [11] for the analysis of an offset-plate fin heat

exchanger. Their method takes advantage of the repeating nature of the flow field to minimise the extent of the computational domain. The method of Patankar *et al.* [11] assumes that for a periodic geometry, the flow is periodic with a prescribed linear pressure gradient being applied to drive the flow. The outlet velocity field and its gradient are wrapped to the inlet to produce periodic boundary conditions. Flow velocities within the geometry are then calculated using momentum and mass conservation equations, assuming constant fluid properties.

Webb and Ramadhyani [16] and Park *et al.* [10] analysed fully-developed flow and heat transfer in periodic geometries following the method of Patankar *et al.* [11]. Webb and Ramadhyani [16] studied parallel plate channels with transverse ribs; they presented a comparison with the performance of a straight channel, and reported an increase in both the heat transfer rate and pressure drop as the Reynolds number is increased. Park *et al.* [10] incorporated optimisation of the heat transfer rate and pressure drop into their study of the flow and thermal fields of plate heat exchangers with staggered pin arrays.

A significant amount of research has focussed both on channels with internal obstructions and tortuous channels. The rationale behind this work has been to determine the configurations that lead to the most vigorous mixing and highest rates of heat transfer. Examples of research into such wavy channels are provided by Popiel and van der Merwe [12] and Popiel and Wojtkowiak [13] who studied experimental pressure drops for geometries with an undulating sinusoidal shape or U-bend configuration. In these papers, the effects of Reynolds number, curvature, wavelength and amplitude on the friction factor were investigated in laminar and low-Reynolds-number turbulent flow. An interesting observation made by these authors is that when the friction factor is plotted against the Reynolds number, there is either no definite transition from laminar to turbulent flow, or a delayed transition relative to that of a straight pipe. This is also reflected in the work of Johnston and Haynes [6], whose results demonstrate a smooth transition from laminar to turbulent flow in plots of both friction factor and Colburn  $j$ -factor versus Reynolds number. It is hypothesised by Popiel and van der Merwe [12] that a smooth transition to turbulence occurs due to the secondary flows produced within the complex geometry. Dean [3] originally observed that the mixing effects of these secondary flows are steadily replaced by the development of turbulent secondary flow. This effect of secondary flows is also discussed in the work of Chen *et al.* [2].

Shah and London [14] investigated laminar flow forced convection in ducts of various cross-sectional shapes. Many other researchers have investigated channels or ducts with undulating or corrugated surfaces, including the work of Fabbri [4], Greiner *et al.* [5] and Tauscher and Mayinger [15].

### Modelling Methodology

The work of Patankar *et al.* [11] stands out as the formative reference for the calculation of fully-developed velocity and temperature fields in two-dimensional streamwise-periodic geometries. Here we describe a method to calculate fully-developed flow and heat transfer in a broader range of geometries

than that considered by [11], such as the serpentine channel, where the flow is not aligned with the streamwise coordinate. We use ANSYS CFX-5.7, a finite-volume code that solves the Navier-Stokes equations using a coupled solver. All calculations are performed using a second order bounded differencing scheme for the convective terms. The method has been developed for steady, laminar, incompressible, single phase flow of a Newtonian fluid with constant physical properties.

In order to model the periodic behaviour computationally, one of two methods may be adopted. The first method is similar to that of Patankar *et al.* [11], where the components of velocity and their gradients at the outlet of the geometry are re-applied to the inlet ('wrapping'). This requires the use of periodic boundary conditions for the flow variables and temperature, coupled with the ability to prescribe the mass flow rate and to wrap a normalised temperature profile. This option is not currently available in ANSYS CFX-5.7.

A second method to achieve a fully-developed periodic solution forms the basis of the methodology presented in this paper. The flow variables ( $u, v, w, T$ ) at the outlet are reapplied to the inlet without any corresponding gradient information. For the case of constant wall heat flux, outlet temperatures are scaled to yield the desired bulk mean temperature at the inlet, and then applied. The solution then approaches the fully-developed state iteratively, but is never perfectly developed because the gradients are not wrapped. To overcome this, a sufficient number of repeating units of geometry need to be included in order to ensure that the flow is fully-developed in the unit of interest.

For computational efficiency and accuracy, a structured mesh has been utilised in the discretisation of the model domain. This discretisation is carried out to allow reduction of the system of differential equations that govern fluid flow and heat transfer to a set of coupled algebraic equations. Grid independence studies have been conducted to ensure that the mesh generated for each model is refined to the extent that the resulting solution is no longer influenced by the size of the grid. The resulting grid-independent mesh contains 1600 cells in any cross-section perpendicular to the axial direction. An indication of the mesh resolution is shown in Figure 2.

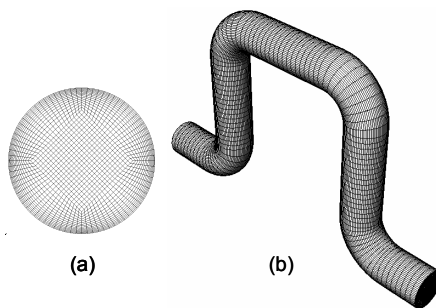


Figure 2: Mesh density (a) on the duct cross-section, (b) along the duct.

Studies were also performed to assess the required entrance length to ensure a fully-developed solution in the unit of interest. Flow and heat transfer was assessed in two, three and four repeating units. The method of Patankar *et al* [11] was also used as a reference to assess the velocity fields for the current geometry. Results from the entrance length study show that as the entrance length is extended (i.e. the number of repeating units is increased) the difference between the wrapped solution and the truly period one decreases. Improved levels of agreement were seen with an increase in the number of units up to three, with little difference beyond this. Typically, we find that three repeating units are sufficient to achieve fully developed flow, with all data being taken from the central unit.

## Results and Discussion

We present results for  $L/d = 4.5$  and  $R_c/d = 1$ , with Reynolds numbers up to 200. At higher Reynolds numbers the flow becomes unsteady. We measure performance of the serpentine channel by comparing pressure drop and rate of heat transfer in these channels to that achieved by fully-developed flow in a straight pipe of equal path length. We define a measure of the pressure loss with a normalised friction factor given by:

$$f^* = \frac{(p_{0,m} - p_{i,m})_{\text{serpentine}}}{(p_{0,m} - p_{i,m})_{\text{straight}}} \quad (1)$$

where  $p_{0,m}$  and  $p_{i,m}$  the mean outlet and inlet pressures, respectively.

The heat transfer performance is measured by:

$$Nu^* = \frac{Nu_{\text{serpentine}}}{Nu_{\text{straight}}} \quad (2)$$

where  $Nu_{\text{serpentine}}$  and  $Nu_{\text{straight}}$  are the average Nusselt numbers for the serpentine channel and an equivalent length of pipe, respectively.

Figure 3 shows the normalised friction factor and heat transfer performance for the geometry studied for a range of Reynolds numbers. It can be seen that the normalised friction factor increases only slightly with increasing Reynolds number. The heat transfer performance, however, is increased by a factor of three over the range of Reynolds numbers studied.

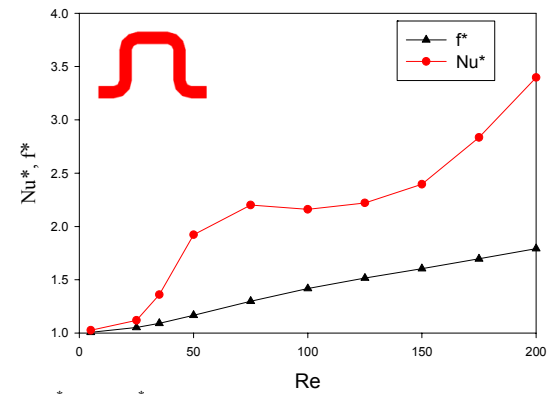


Figure 3:  $f^*$  and  $Nu^*$  as a function of Reynolds number for  $L/d = 4.5$ ,  $R_c/d = 1$  and  $Pr = 6.13$ .

A detailed examination of the flowfield shows that a number of interesting flow phenomena arise in these channels. A transfer of momentum towards the outer wall following each bend causes rotation of the fluid transverse to the bulk flow. These secondary flows, first observed by Dean [3] in helical channels, are known as Dean vortices. Every second bend in the serpentine geometry alternate in direction, i.e. bends 2 and 3 in Figure 1 are in the same sense. The direction of rotation of the Dean vortices also alternates after every second bend. Examples of the secondary flows, as well as directional change in vortex rotation, are shown in Figure 4.



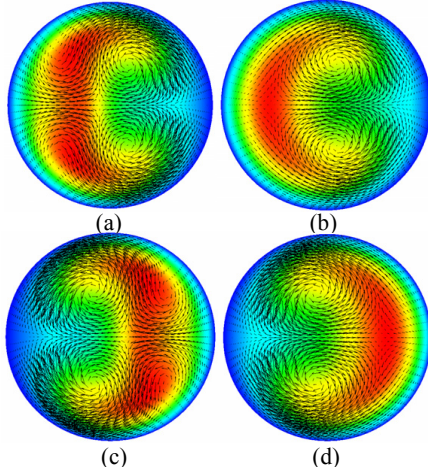


Figure 4: Speed contours, with tangential velocity vectors superimposed, at various downstream locations for a Reynolds number of 200 for  $L/d = 4.5$  and  $R_c/d = 1$  at: (a) Inlet, (b) 1d downstream of bend 1, (c) 1d downstream of bend 2, (d) 1d downstream of bend 3.

The effect of Reynolds number on the secondary flow patterns at the entrance of a repeating unit (2.5d upstream of bend 1) is shown in Figure 5. The work of Dean [3] characterised the behaviour of secondary flow in helical channels by defining a non-dimensional number (the Dean number) given by:

$$Dn = Re \left( \frac{d}{R_c} \right)^{1/2} \quad (3)$$

For a fixed ratio of duct size ( $d$ ) to radius of curvature ( $R_c$ ), the Dean number is directly proportional to the Reynolds number. At low Reynolds numbers, shown in Figure 5(a), there is negligible secondary flow. The flow tends towards the straight pipe solution in this case, as the viscous forces are large in comparison with inertial forces, and act to suppress secondary flow formation. As the Reynolds number increases, inertial forces become more significant, and a pair of vortices develops. The strength of these vortices increases with Reynolds number, as is evident by the tangential velocities vectors seen in Figures 5 (b) to (d). As the Reynolds number increases further, a second pair of vortices develops on the inside of the bend (see Figure 6). A similar transition has been seen by others, for example, Mees *et al.* [9]. In this case the emergence of the second pair of vortices corresponds with the plateau in the heat transfer performance observed in Figure 3. Development of the second pair of vortices creates regions of slower flow at the walls, decreasing the rate of heat transfer.

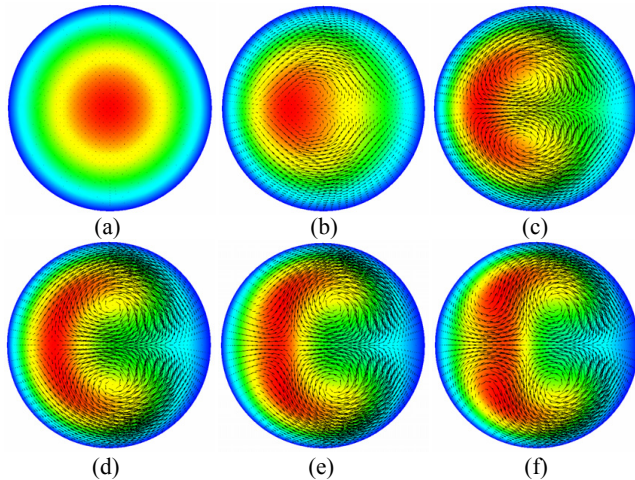


Figure 5: Speed contours, with tangential velocity vectors superimposed, at the inlet for  $L/d = 4.5$ ,  $R_c/d = 1$  and Reynolds numbers of: (a) 5, (b) 50, (c) 100, (d) 150, (e) 175, and (f) 200.

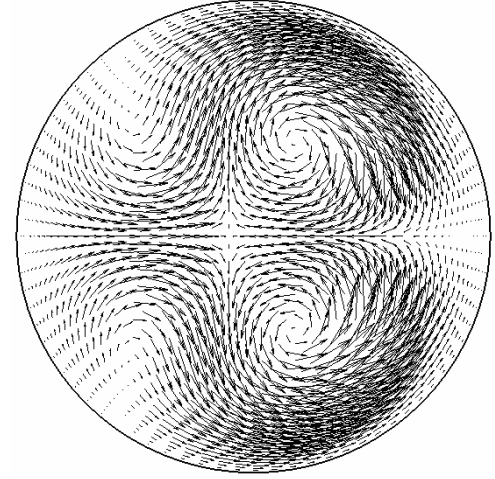


Figure 6: A tangential velocity vector plot at the inlet for a Reynolds number of 200 for  $L/d = 4.5$ ,  $R_c/d = 1$  showing two vortex pairs.

Levy *et al.* [7] proposed a method for detection and visualisation of vortex cores. They identified a correlation between velocity and vorticity in that, near vortex cores, the angle between these two vectors is small. They defined “normalised helicity” as:

$$H_n = \frac{\mathbf{v} \cdot \boldsymbol{\omega}}{|\mathbf{v}| |\boldsymbol{\omega}|} \quad (4)$$

This quantity has limiting values of  $\pm 1$ , where the angles between the velocity and vorticity vectors are zero, and the sign depends on the direction of rotation.

The volume-average of the absolute value of helicity, given by:

$$\bar{H}_v = \frac{1}{V} \int_V |H_n| dV = \frac{1}{V} \int_V \frac{|\mathbf{v} \cdot \boldsymbol{\omega}|}{|\mathbf{v}| |\boldsymbol{\omega}|} dV \quad (5)$$

is shown in Figure 7. The absolute value of helicity excludes rotation direction information from these results, and a high value corresponds to strong vortical structures. An increase in the volume-averaged helicity is seen up to a Reynolds number of approximately 125. The ensuing decline can be attributed to the development of the second pair of vortices. These vortices are not closed, and lead to a reduction in the volume average of the absolute value of helicity but do give rise to the improved heat transfer performance seen at higher  $Re$  in Figure 3.

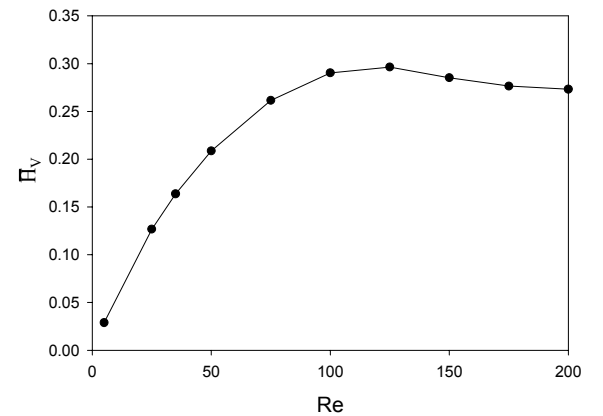


Figure 7: Effect of Reynolds number on the volume integral of the absolute value of normalised helicity for  $L/d = 4.5$ ,  $R_c/d = 1$ .

Flow structures exhibiting a single pair of vortices display the highest vortex strength immediately after bends 1 and 3 (Figure 1). This occurs because vortices are allowed to progress through bends with the same direction of rotation, thus acting to increase the vortex strength. Flow development within straight sections of the geometry after each bend causes a decrease in vortex strength. For this reason, as the vortex strength increases, the distance that vortices progress into the straight sections of the pipe also increases, as shown in Figure 8.

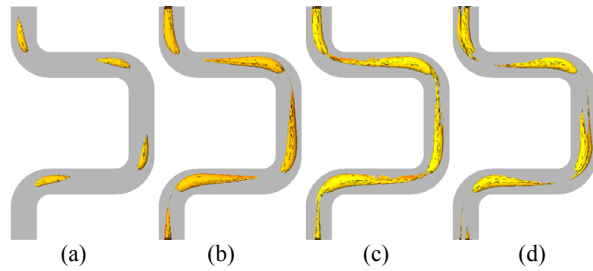


Figure 8: Isosurface plots of regions where the absolute value of helicity is 0.8 for Reynolds numbers of: (a) 50, (b) 100, (c) 150, and (d) 200.

The development of two pairs of vortices at Reynolds numbers above 150 occurs only after bends 2 and 4, which turn in an alternating direction from the previous bend. Bends 1 and 3 act to re-form the two-cell vortex structure, thus resulting in decreased vortex strength.

The influence of the ratio of unit size to diameter ( $L/d$ ) on  $f^*$  and  $Nu^*$  is shown in Figure 9 for a Reynolds number of 110. It can be seen that up to  $L/d = 12.5$ , an increase in  $L/d$  leads to an increase in heat transfer performance and a reduction in the normalised friction factor.

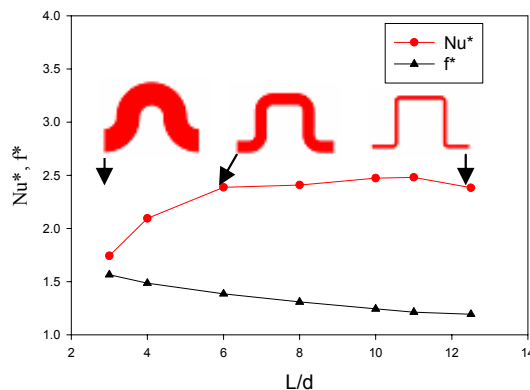


Figure 9:  $f^*$  and  $Nu^*$  as a function of  $L/d$  for a Reynolds number of 110,  $R_c/d = 1$  and  $Pr = 6.13$ .

Geometries with high values of  $L/d$  have longer straight sections, in which flow development reduces the strength of the vortices, reducing their influence at the following bend. Ultimately, for large  $L/d$ , the flow in the straight sections becomes fully-developed, and the normalised friction factor and heat transfer performance are independent of the bend direction and upstream behaviour. The pressure drop approaches that of fully-developed flow in a straight pipe due to the increase in flow development as  $L/d$  increases. Dean vortices are evident in the flow, but the Reynolds number is too low for the development of a four-cell vortex structure.

A significant observation of this study is that flow separation does not occur. This is true for the studies in which the Reynolds number and  $L/d$  were varied. We explain this by the presence of Dean vortices. Recirculation was expected to occur on the inside wall after each bend, particularly at higher Reynolds numbers, due to the centrifugal shift of momentum to the outside wall. However, the Dean vortices direct flow back toward the inside wall, and act to suppress the onset of recirculation. The absence of recirculation zones accounts for the small increase in  $f^*$ . Increased heat transfer performance may therefore be obtained with a surprisingly low pressure drop penalty.

## Conclusions

A methodology has been developed and validated to study fully-developed flow behaviour in serpentine channels. Flow characteristics within such channels are complex, leading to high rates of heat transfer, whilst low pressure loss is maintained. Dean vortices act to suppress the onset of recirculation around each bend, and are the main contributing factor to these high

levels of heat transfer performance, and low normalised friction factor. For  $L/d = 4.5$ ,  $R_c/d = 1$  and  $Pr = 6.13$ , two pair of vortices are observed at Reynolds numbers above 150. This flow structure occurs immediately after bends that turn in an opposite direction to the one previous.

The influence of  $L/d$  on heat transfer and pressure drop has been shown for a fixed Reynolds number. Increasing  $L/d$  increases the rate of heat transfer and decreases the pressure drop relative to that of fully-developed flow in a straight pipe.

## Acknowledgments

The authors would like to acknowledge Meggitt UK, the ARC for an APAI scholarship for Nathan Rosaguti and Patrick Sharkey of CFX for assistance with the wrapping code.

## References

- [1] ANSYS, Inc., CFX Computational Fluid Dynamics (CFD) software, [www.ansys.com/cfx](http://www.ansys.com/cfx), 2004.
- [2] Chen, I.Y., Lai, Y.A. & Wang, C-C., Single-Phase and Two-Phase Frictional Characteristics of Small U-Type Wavy Tubes, *Int. Comm. in Heat & Mass Transfer*, **31**(3), 2004, 303-314.
- [3] Dean, W.R., Note on the Motion of Fluid in a Curved Pipe, *The London, Edinburgh and Dublin Philosophical Magazine*, **7** (14), 1927, 208-223.
- [4] Fabbri, G., Heat Transfer Optimisation in Corrugated Wall Channels, *Int. Journal of Heat and Mass Transfer*, **43** (23), 2000, 4299-4310.
- [5] Greiner, M., Fischer, P.F., Tufo, H.M. & Wirtz, R.A., 3D Simulations of Enhanced Heat Transfer in a Flat Passage Downstream from a Grooved Channel, *34<sup>th</sup> National Heat Transfer Conference*, 2000, Pittsburgh, Pennsylvania.
- [6] Johnston, A.M. & Haynes, B.S., Design Considerations for Compact Heat Exchangers, *Proc. of the Int. Symposium on Compact Heat Exchangers*, 2002, Grenoble, France.
- [7] Levy, Y., Degani, D. & Seginer, A., Graphical Visualization of Vortical Flows by Means of Helicity, *AIAA Journal*, **28** (8), 1990, 1347-1352.
- [8] Liu, R.H., Stremler, M.A., Sharp, K.V., Olsen, M.G., Santiago, J.G., Adrian, R.J., Aref, H. & Beebe, D.J., Passive Mixing in a 3D Serpentine Microchannel, *Journal of Microelectromechanical Systems*, **9** (2), 2000, 190-197.
- [9] Mees, P.A., Nandakumar, K. & Masliyah, J.H., Instability and Transitions of Flow in a Curved Square Duct: The Development of Two Pairs of Dean Vortices, *Journal of Fluid Mechanics*, **314**, 1996, 227-246.
- [10] Park, K., Choi, D-H. & Lee, K-S., Design Optimisation of Plate Heat Exchanger with Staggered Pins, *14<sup>th</sup> Int. Symp. on Transport Phenomena*, Bali, Indonesia, 6-9 July 2003.
- [11] Patankar, S.V., Liu, C.H. & Sparrow, E.M., Fully-Developed Flow and Heat Transfer in Ducts Having Streamwise-Periodic Variations in Cross-Sectional Area, *Journal of Heat Transfer*, **99**, 1977, 180-186.
- [12] Popiel, C.O. & van der Merwe, D.F., Friction Factor in Sine-Pipe Flow, *Journal of Fluids Engineering*, **118**, 1996, 341-345.
- [13] Popiel, C.O. & Wojkowiak, J., Friction Factor in U-Type Undulated Pipe Flow, *Journal of Fluids Engineering*, **122**, 2000, 260-263.
- [14] Shah, R.K. & London, A.L., Laminar Flow Forced Convection in Ducts, *ed. Irvine, T.F & Hartnett, J.P.*, 1978, Academic Press, New York.
- [15] Tauscher, R. & Mayinger, F., Heat Transfer Enhancement in a Plate Heat Exchanger with Rib Roughened Surfaces, *NATO ASI Series E Applied Sciences*, **355**, 1999, 207-222.
- [16] Webb, B.W. & Ramdhyani, S., Conjugate Heat Transfer in a Channel with Staggered Ribs, *Int. Journal of Heat and Mass Transfer*, **28** (9), 1985, 1679-1687.



## Simulating the Deformation of Newtonian and Non-Newtonian Drops through a Micro-Fluidic Contraction

D.J.E. Harvie<sup>1</sup>, M.R. Davidson<sup>1</sup> and J.J. Cooper-White<sup>2</sup>

<sup>1</sup>Department of Chemical and Biomolecular Engineering  
The University of Melbourne, VIC, 3010 AUSTRALIA

<sup>2</sup>Division of Chemical Engineering  
The University of Queensland, QLD, 4072 AUSTRALIA

### Abstract

A numerical parametric study of droplet deformation within an axisymmetric micro-fluidic contraction is performed. Both Newtonian and Non-Newtonian shear-thinning fluids are considered for the droplet phase. Droplet deformation is found to be largest when surface tension forces are lowest, and inertial forces highest. The Non-Newtonian droplets behave quite differently to their Newtonian counterparts, primarily because the high strain rates experienced within the contraction result in low internal viscosities. This can allow instabilities to develop on the droplet surface.

### Introduction

In the field of two phase micro-fluidics, the simple contraction is a tool that can be used to stretch, shear, break or otherwise deform a droplet. Droplet behaviour within such micro-sized devices differs from that within larger sized systems because surface effects, such as surface tension forces, assume greater importance. Knowledge of droplet behaviour within such contractions would be beneficial to applications such as micro-reactors, where the controlled deformation of droplets to enhance mixing, heat or mass transfer rates is desirable.

There have been few experimental studies concerned with immiscible fluids passing through micro-fluidic contractions. An exception to this is the work of [1] who used a micro-fluidic contraction as a 'flow focusing' device to break a stream of disperse phase fluid into droplets. The deformation of larger, millimetre sized droplets moving through contractions has been studied experimentally by several researchers, including [4]. Numerical investigations of droplets moving through contractions have generally employed the creeping flow approximation, however, [10] used the full Navier-Stokes equations when simulating droplet deformation through millimetre sized contractions. Droplet deformation in general extensional and shear flows has been extensively studied both experimentally and numerically. [3] and [8] give good reviews of this topic.

The purpose of this study is to perform a parametric numerical study of droplet deformation in an axisymmetric contraction, focusing in particular on regimes relevant to micro-fluidic devices. Due to the importance of organic and polymer suspensions in micro-fluidic applications, we consider shear thinning Non-Newtonian fluids for the disperse phase as well as Newtonian fluids.

### Problem Description

As shown in figure 1, the problem under consideration consists of a droplet entrained in a continuous liquid phase passing through a 4 : 1 axisymmetric contraction. All lengths are non-dimensionalised by the radius of the inlet  $R$ , so that the contraction radius is  $1/4$ , the contraction length is 5 and the initial droplet diameter is 1.

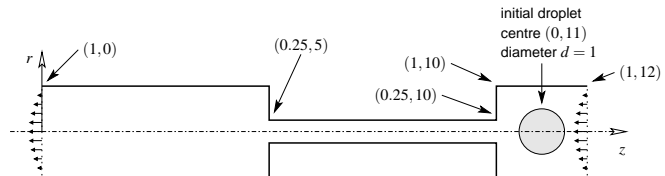


Figure 1: The geometry used in the computational problem. All lengths are normalised by the inlet radius  $R$  and cylindrical co-ordinates  $(r, z)$  are used.

Three equations are used to describe motion throughout the disperse (ie, droplet) and continuous phases; a continuity equation, a volume-averaged incompressible Navier-Stokes momentum equation, and an advection equation which describes the evolution of the disperse phase volume fraction  $\phi$ ,

$$\nabla \cdot \mathbf{u} = 0 \quad (1)$$

$$\frac{D_u \rho \mathbf{u}}{Dt} = -\nabla p + \frac{1}{We} \kappa \delta(x) \mathbf{n} + \frac{1}{Re} \nabla \cdot \mu [\nabla \mathbf{u} + (\nabla \mathbf{u})^T] \quad (2)$$

$$\frac{D_u \phi}{Dt} = 0 \quad (3)$$

All three equations are employed in a non-dimensional form. Velocity is scaled by the average inlet velocity,  $\bar{v}$ , length by the inlet radius  $R$ , density by the disperse phase density  $\rho_d^*$  and viscosity by the disperse phase viscosity  $\mu_d^*$ . The asterisk in these equations implies a dimensioned quantity.

The second term on the right of equation (2) is a surface tension induced stress jump which occurs at the disperse-continuous phase interface. In this term  $\kappa$  is the signed local curvature of the interface,  $\delta(x)$  is the Dirac delta function, non-zero only on the interface, and  $\mathbf{n}$  is a unit vector directed normal to the interface and into the disperse phase. As the equations are applied over both phases, the viscosity  $\mu$  is a function of the local volume fraction,  $\phi$ . The density  $\rho$  is not a function of  $\phi$  however as it is assumed to be equal in both phases. Gravitational forces have been neglected as their effect in liquid-liquid micro-sized flows is small.

In this study the behaviour of the droplet as it passes through the contraction is determined by a balance between three types of forces — inertial, viscous and surface tension. Ratios between these forces are given by the Reynolds (Re), Weber (We) and capillary (Ca) numbers, defined by

$$Re = \frac{\rho_d^* \bar{v} R}{\mu_d^*}, \quad We = \frac{\rho_d^* \bar{v}^2 R}{\sigma} \quad \text{and} \quad Ca = \frac{We}{Re} = \frac{\bar{v} \mu_d^*}{\sigma},$$

respectively. A simple order of magnitude analysis on momentum equation (2) shows that the strength of surface tension forces relative to both viscous and inertial forces can be mea-

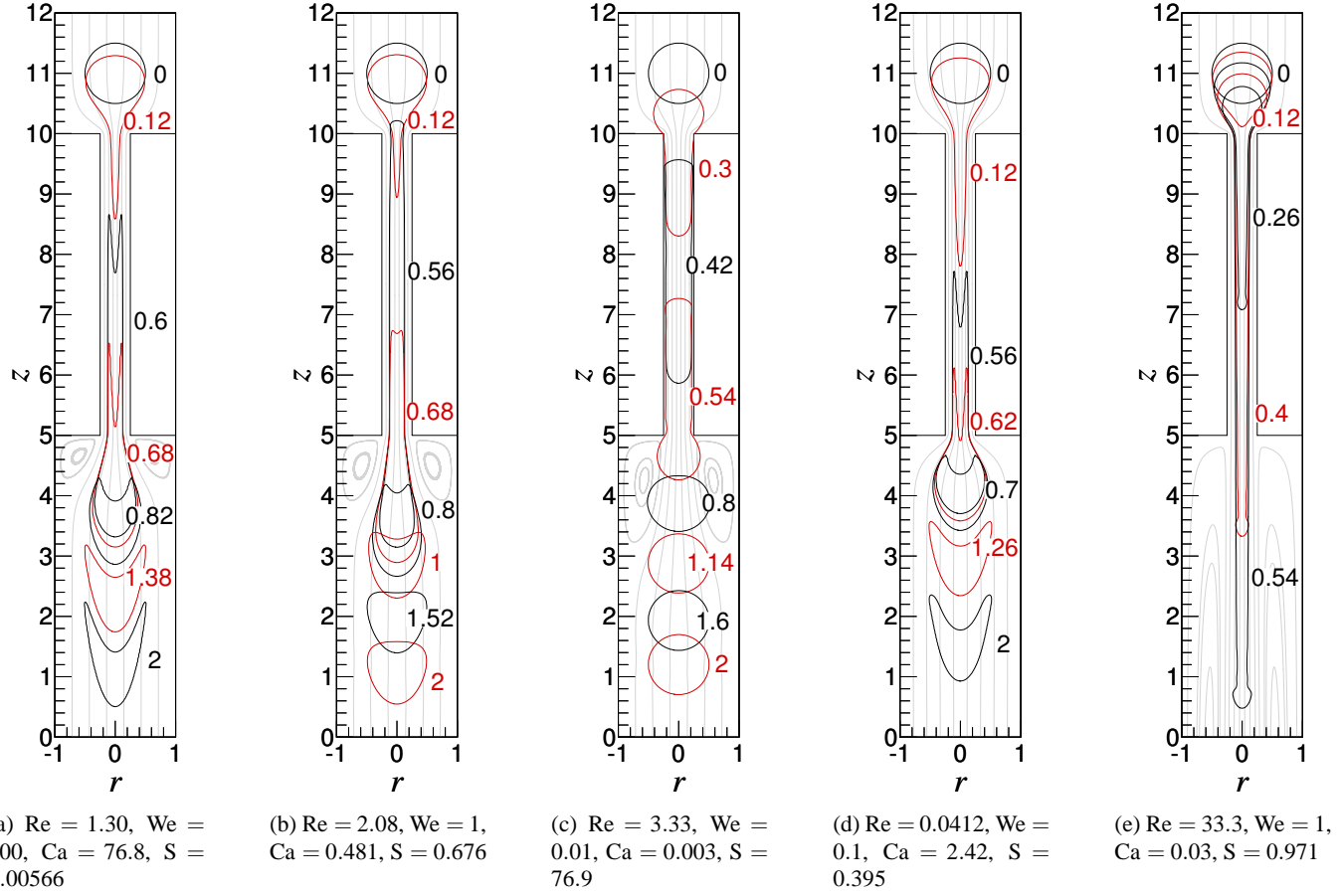


Figure 2: Images of droplet shapes produced by the Newtonian simulations. Each image was produced by reflecting the two dimensional cylindrical data around the  $z = 0$  centreline. In each figure several droplet shapes are shown at the indicated non-dimensional times. The streamlines shown in faint grey were produced by tracing massless particles over a stationary velocity field corresponding to  $t = 2$ .

sured via another number, termed  $S$ . Formally this number is defined as

$$S = \frac{1}{We + Ca} = \frac{\sigma}{\bar{\nu}\mu_d^* + \rho_d^*\bar{\nu}^2R}.$$

As a balance between three forces determines droplet behaviour, only two of the above non-dimensional numbers are required to classify a particular flow regime. In the following we use  $Re$  and  $S$  —  $Re$  specifies the ratio of inertial to viscous forces acting in the flow, while  $S$  specifies the magnitude of surface tension present, relative to the other forces combined.

Both Newtonian and Non-Newtonian drops are simulated in this study. For the Newtonian cases, we let the continuous phase viscosity equal the disperse phase viscosity so that  $\mu = \mu_d = \mu_c = 1$  everywhere. This assumption could be applicable in modelling a light oil droplet entrained in a continuous water phase.

For the Non-Newtonian cases we employ the Carreau model to describe a shear-thinning droplet phase. The Carreau model relates the non-dimensional local disperse phase viscosity  $\mu_d$  to a non-dimensional ‘infinite shear rate’ viscosity  $\mu_{d,\infty}$  via

$$\frac{\mu_d - \mu_{d,\infty}}{1 - \mu_{d,\infty}} = [1 + (\lambda\dot{\gamma})^2]^{(n-1)/2}, \quad (4)$$

where  $\lambda$  is a time constant,  $n$  is a ‘power-law exponent’ and the total shear rate is given by  $\dot{\gamma} = \sqrt{\nabla u : [\nabla u + (\nabla u)^T]}$ . For the Non-Newtonian cases all viscosities are scaled against the ‘zero shear rate’ disperse phase viscosity  $\mu_{d,0}^*$  instead of  $\mu_d^*$ . In this study we have chosen  $\mu_{d,\infty} = 0$ ,  $\lambda = 1$  and  $n = 0.2$ . Such values could represent a droplet consisting of a semidilute polystyrene

particulate suspension, for example.

### Simulation Method

The simulations were performed using a finite volume code due to [7], adapted to model shear-thinning fluids. This code has been successfully used to model the formation and subsequent ‘pinch-off’ of both Newtonian and Non-Newtonian pendant drops [2] and the deformation of Newtonian droplets through millimeter sized contractions [10]. The Volume of Fluid (VOF) technique is used to track the disperse-continuous phase interface, and surface tension forces are applied using a variation of the Continuum Surface Force (CSF) model. The VOF function is advected using the Youngs scheme. The domain is discretised using a structured, uniform and staggered mesh.

For all of the simulations presented here, a mesh of dimensions  $64 \times 768$  was used. It was found that using a finer mesh did not significantly alter droplet deformation behaviour. The fluid entering the domain was assumed to have a fully developed Newtonian profile, however tests showed that droplet behaviour within the contraction was quite insensitive to the form of this profile. At the exit the pressure gradient normal to the outlet port was chosen to ensure global mass conservation. All domain walls were non-slip, and non-wetting with respect to the disperse phase liquid. The simulations were performed in series on a Beowulf cluster of Linux boxes with each simulation typically requiring several weeks to complete.

### Results: Newtonian Droplets

Figure 2 shows selected droplet shapes at various non-dimensional times for a variety of  $Re$  and  $S$  numbers. Figure

2(a) shows the results of a simulation conducted with a moderate  $Re$  but low  $S$ . The low value of  $S$  implies that surface tension forces are small here and as a result, surface tension has only a small effect on the deformation of this droplet. A characteristic feature of this simulation is the forked tail that the droplet develops within the contraction. This tail develops because the centreline velocity within the contraction is higher than that near the walls of the contraction. This causes the interface of the droplet near the centreline to move faster through the contraction than the interface located at positions of larger  $r$  resulting in the observed ‘fork’. As surface tension effects are very weak, the droplet does not return to the form of a sphere before reaching the outlet port.

Figure 2(b) shows a simulation with a similar  $Re$  to that shown in figure 2(a), but now with a moderate value for  $S$ . The higher surface tension forces act to smooth interface regions of high curvature. As a result, the tail that the previous droplet developed within the contraction is almost absent, and after the droplet leaves the contraction, it returns to a more spherical shape. Figure 2(c) shows a simulation where  $S$  has been increased to a high value. Surface tension effects here are so great that significant shape changes only occur when the droplet is constrained by the contraction walls. Thus, within the contraction the droplet forms a long capsule having approximately the same radius of the contraction, while beyond the contraction, it quickly reforms back to its initial spherical state.

Two other moderate  $S$  number simulations are shown in figure 2. Figure 2(d) shows a simulation conducted with a  $S$  number that lies between that of figure 2(a) and 2(b). As a result the surface tension forces present in this example are greater than those in figure 2(a), but less than those in figure 2(b). Consequently the droplet shapes in figure 2(d) are generally smoother in form than those in figure 2(a), but less spherical than those of figure 2(b). The low  $Re$  of figure 2(d) relative to 2(a) appears to have little effect on droplet behaviour, implying that inertial forces in both simulations are almost absent.

Figure 2(e) shows a case with a slightly higher value for  $S$  than in figure 2(b), but with a substantially higher  $Re$ . The larger inertial effects experienced in this case result in a strong jet of fluid emerging from the contraction, and this jet drives large recirculation zones that extend beyond the computational boundaries. As the recirculation zones extend beyond the computational domain, their behaviour may not be well resolved. However, tests conducted using a variety computational domain sizes have shown that the shape of these recirculation zones does not significantly affect droplet deformation here, most probably because the droplet does not enter these zones during the simulation.

The larger inertial effects present in figure 2(e) mean that the droplet requires a longer time to accelerate at the entrance to the contraction. Once within the contraction however, the droplet forms a fine thread of fluid whose leading tip moves at approximately the contraction centreline velocity, significantly faster than observed in the lower  $Re$  cases. As the inertia of this filament is high, its shape remains substantially intact after leaving the contraction.

A characteristic feature of this example is the bulging of the leading tip of the droplet as it moves through the domain. This bulging is the result of surface tension forces which increase the pressure inside the high curvature region at the tip of the thread, in turn pulling this tip back towards the main body of the droplet. The development of this type of bulging has been studied numerically by [5] for the case of low inertia fluids, however a corresponding study for inertial flows is not available.

## Results: Non-Newtonian Droplets

Figure 3(a) shows results for a Non-Newtonian droplet. The  $Re$  and  $S$  numbers used in this simulation, although now based on the zero shear rate disperse phase viscosity, are the same as those used in the example of figure 2(b). At the entrance to the contraction, the fluid experiences both high extensional and shearing strain rates and this causes the viscosity of the droplet phase to decrease. In fact, between the heights of  $z = 11$  and  $z = 9$  in this example, the viscosity within the droplet decreases by approximately two orders of magnitude. This level of decrease is typical of all of our Non-Newtonian contraction simulations and means that the droplets in these simulations behave in a largely inviscid manner.

An interesting characteristic of shear thinning fluids is that the viscosity generally decreases more than one might expect based on Newtonian strain rate calculations. As the strain rate of a shear thinning fluid increases, its viscosity decreases, leading to smaller viscous stresses. This decrease in viscous stresses generally increases the strain rate, in turn reinforcing the decrease in viscosity. In the droplet shown in figure 3(a) for example, although the strain rate in the continuous phase at the bottom of the computational domain is quite low, the strain rates within the droplet phase are significant as the fluid here is almost inviscid. These high strain rates reinforce the low viscosity, with the result that the viscosity of the leading tip of the droplet remains low for a considerable distance below the lower edge of the contraction. Indeed, the behaviour of this leading tip is quite different to that shown in the Newtonian case of figure 2(b). It is closer to the behaviour displayed in the higher Reynolds number Newtonian case of figure 2(e).

Figure 3(a) also shows that at the indicated time, small disturbances have developed along the interface of the stretched droplet. As both inertial and viscous effects may be important in the continuous phase here, neither the low Reynolds number stability analysis of [9] or the solely inviscid disperse phase analysis of [6] are relevant in predicting the dominant wavelength at which disturbances might grow along this cylinder.

The next three frames, figures 3(b), 3(c) and 3(d), show the movement of a lower  $Re$  droplet as it exits the contraction. In this example the strain rates at the contraction entrance are higher than in figure 3(a), so that the viscosity of the droplet phase within the contraction is lower. The two most striking features of this deformation are the large instabilities which grow along the extended droplet, and the unusual ‘arrow’ shape that forms once the leading tip of the droplet exits the contraction.

As the Reynolds number that characterises this flow is very low, inertial forces within both phases are small relative to viscous forces within the continuous phase, so the behaviour of the droplet is largely determined by the continuous phase viscous forces. This means that the creeping flow stability analysis of [9] is now relevant in predicting the wavelength of maximum capillary wave growth rate on the droplet surface when it is in the contraction. Assuming a constant viscosity ratio of 0.001 within this cylinder, [9]’s analysis suggests that the wavelength of disturbance having the maximum growth rate on the surface of this cylinder would be around 1.0 non-dimensional length units. This appears to be slightly larger than the wavelengths of disturbances displayed in the figure, but of a similar magnitude.

Figures 3(b) through to 3(d) show the development of the leading tip of the droplet as it exits the contraction. As the viscosity of the droplet is low within this region, the deformation of the droplet front is largely determined by the low Reynolds number flow pattern of the surrounding fluid. Thus, as the tip exits the contraction, its front is decelerated and its edges expand radi-

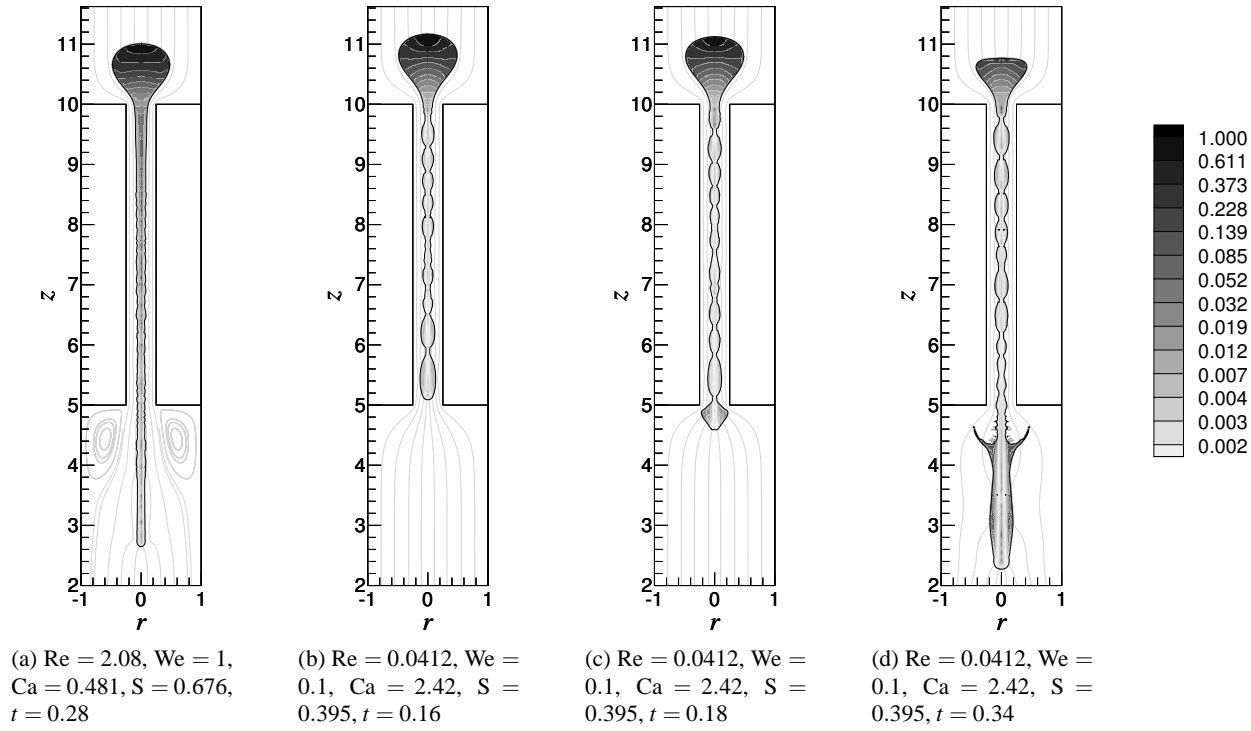


Figure 3: Droplet shapes produced by the Non-Newtonian simulations. The streamlines shown in faint grey were produced by tracing massless particles over the instantaneous velocity field of the continuous phase from the indicated time. The shading shows the non-dimensional local viscosity within the drop.

ally, causing it to shorten and ‘bulge’ (figure 3(c)). After some time elapses however the higher velocity that the droplet experiences along the centreline of the domain advances the centre of the tip further than its slowly advancing radial ‘wings’. This results in the unusual ‘arrow’ type shape seen in figure 3(d). Shapes similar to this have been observed in higher Reynolds number simulations conducted by [10, unreported]. It is interesting to note that even after the tip of the droplet has reached approximately five contraction diameters from the lower edge of the contraction, the viscosity of the droplet is still around three orders of magnitude below the zero shear rate value.

At later times, small amounts of fluid separate from the main droplet just below the contraction exit, as is evident in Figure 3(d). This behaviour is caused by waves along the fluid filament shortening and expanding radially as the droplet exits the contraction and decelerates. While this behaviour appears to be mesh independent, due to the small size of the ejected fluid elements its existence should be treated with caution until experimentally validated.

## Conclusions

The deformation of both Newtonian and shear-thinning Non-Newtonian droplets as they pass through an axisymmetric micro-fluidic contraction has been simulated over a range of  $Re$  and  $S$ . Depending on the balance of inertial, viscous and surface tension forces acting in the fluid, a variety of droplet shapes were simulated including thick ‘capsules’, thin ‘rods’ and unstable filaments. Future work will extend the analysis to systems where the viscosity ratio between the two phases is not one, and where droplet breakup is known to occur.

## References

- [1] Anna, S. L., Bontoux, N. and Stone, H. A., Formation of dispersions using ‘flow focusing’ in microchannels, *Applied Physics Letters*, **82**, 2002, 364–366.
- [2] Davidson, M. R., VOF prediction of drop formation of shear-thinning and yield stress fluids, in *5th International Conference on Multiphase Flow, ICMF’04*, Yokohama, Japan, 2004, paper No. 501.
- [3] Eggers, J., Nonlinear dynamics and breakup of free-surface flows, *Reviews of Modern Physics*, **69**, 1997, 865–929.
- [4] Funatsu, C. D. H. K., An experimental study of droplet deformation and breakup in pressure-driven flows through converging and uniform channels, *Journal of Rheology*, **22**, 1978, 113–133.
- [5] Powers, T. R., Zhang, D., Goldstein, R. E. and Stone, H. A., Propagation of a topological transition: The rayleigh instability, *Physics of Fluids*, **10**, 1998, 1052–1057.
- [6] Rayleigh, Lord., On the capillary phenomena of jets, *Proceedings of the Royal Society of London*, **29**, 1879, 71–97.
- [7] Rudman, M., A volume-tracking method for incompressible multifluid flows with large density variations, *International Journal for Numerical Methods in Fluids*, **28**, 1998, 357–378.
- [8] Stone, H. A., Dynamics of drop deformation and breakup in viscous fluids, *Annual Review of Fluid Mechanics*, **26**, 1994, 65–102.
- [9] Tomotika, S., On the instability of a cylindrical thread of a viscous liquid surrounded by another viscous fluid, *Proceedings of the Royal Society of London, Series A*, **150**, 1935, 322–337.
- [10] Whyte, D. S., Cooper-White, J., Davidson, M., Lunqvist, A. and Schaerringer, P., Deformation of a droplet passing through a contraction, in *Proceedings of FEDSM2002: 2002 ASME Fluids Engineering Division Summer Meeting*, ASME, Montreal, Quebec, Canada, 2002.

## DNS of Turbulent Heat Transfer in a Channel Flow with a Streamwisely Varying Thermal Boundary Condition

Y. Seki<sup>1</sup> and H. Kawamura<sup>1</sup>

<sup>1</sup>Department of Mechanical Engineering,  
Tokyo University of Science, 2641 Yamazaki Noda-shi, Chiba-ken, 278-8510, JAPAN

### Abstract

Effect of thermal boundary condition is examined. The direct numerical simulation of turbulent heat transfer in a fully developed turbulent channel flow has been carried out for streamwisely varying thermal boundary conditions ( $Re_\tau = 180$ ) with  $Pr = 0.71$  to obtain the statistical mean temperature, the temperature variance, their budget terms and the time scale ratio etc. The obtained results have indicated that the time scale ratio varies along a stream direction.

### Introduction

With the aid of recent developments in super and parallel computers, direct numerical simulation (DNS, hereafter) of turbulent flow is now often performed. The DNS is able to provide with a large amount of detailed data on the turbulent heat transfer with various thermal boundary conditions. Several experiments [4, 2] and turbulent modelling studies [7] for the streamwisely varying thermal boundary conditions had been carried out in the past studies. However, no DNS has been done for streamwisely varying thermal boundary conditions.

In the present study, effect of thermal boundary condition is examined. The DNS of turbulent heat transfer in a fully developed turbulent channel flow has been carried out for streamwisely varying thermal boundary conditions with  $Pr = 0.71$ ,  $Re_\tau = 180$ , which is based on the friction velocity  $u_\tau$  and channel half width  $\delta$ ,  $Re_c = 6600$ , which is based on the center velocity  $u_c$  and  $2\delta$ . The computational domains are given in figure 1. The computational domain is divided into three parts; the entrance region, the test region and the cooling (fringe) region. In the fringe region, an extra damping function is added in the energy equation to attenuate the temperature. Thus the periodic boundary condition can be applied in the streamwise direction with maintaining the inlet temperature to be zero.

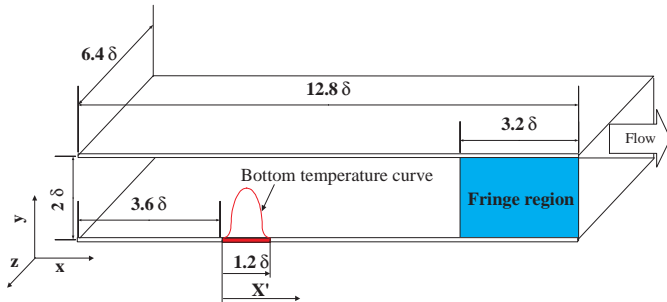


Figure 1: Configuration.

### Numerical procedure

The DNS of turbulent heat transfer in a channel flow have been performed with Reynolds number of  $Re_\tau = 180$  ( $Re_c = 6600$ ) with  $Pr = 0.71$ . The computational domain is given in figure 1. Two infinite parallel plates are assumed. The buoyancy effect is not taken into consideration to examine the fundamental nature of the convective turbulent heat transfer in this research.

The coordinates and flow variables are normalized by the

channel half width  $\delta$ , the kinematic viscosity  $\nu$ , the friction velocity  $u_\tau$ , and the maximum temperature of the bottom wall  $T_{max}$ . The fundamental equations are the continuity equation:

$$\frac{\partial u_i^+}{\partial x_i^*} = 0, \quad (1)$$

and the Navier-Stokes equation:

$$\frac{\partial u_i^+}{\partial t^*} + u_j^+ \frac{\partial u_i^+}{\partial x_j^*} = -\frac{\partial p^+}{\partial x_i^*} + \frac{1}{Re_\tau} \frac{\partial^2 u_i^+}{\partial x_j^{*2}} + \frac{\partial \bar{p}^+}{\partial x_1^*} \delta_{i1}. \quad (2)$$

Here,  $i = 1, 2$  and  $3$  indicate the streamwise, wall-normal and spanwise directions, respectively. The variables  $t$  and  $p$  are the time and the pressure. The superscript  $*$  indicates that the variables are normalized by  $\delta$ . The third term in the right-hand side of Eq. (2) is the streamwise mean pressure gradient. The boundary condition for the momentum field is

$$u_i^+ = 0, \quad \text{at } y = 0 \text{ and } 2\delta. \quad (3)$$

The energy equation for the instantaneous temperature  $T^+(x^*, y^*, z^*)$  is expressed as

$$\frac{\partial T^*}{\partial t^*} + u_j^+ \frac{\partial T^*}{\partial x_j^*} = \frac{1}{Re_\tau \cdot Pr} \frac{\partial^2 T^*}{\partial x_j^{*2}} - Q(x). \quad (4)$$

The endothermal term ( $Q(x) = \lambda(x)T^*$ ) is non-zero only in the fringe (cooling) region, where fringe function  $\lambda(x)$  is the strength of the cooling with a maximum of inverse number of the time step  $\Delta t^{*-1}$ . The form of  $\lambda(x)$  is designed to minimize the upstream temperature influence. The heating condition at the bottom wall is

$$T_{wall}(\xi) = T_{max} (\sin \pi \xi)^2 \\ \text{if } 0 \leq \xi \leq 1, \text{ else } T_{wall}(\xi) = 0 \text{ at } y = 0, \\ \text{where } \xi = x - x_o, \quad x_o = 3D_L = 3.6\delta. \quad (5)$$

where  $D_L$  is the heated streamwise length of  $1.2\delta$ . Figure 2 shows the thermal boundary condition given by equation (5) at the bottom wall. On the other hand, the thermal boundary condition at the top wall is assigned to be zero.

$L_x \times L_y \times L_z$	$N_x \times N_y \times N_z$	$\Delta x^+$	$\Delta y^+$	$\Delta z^+$
$12.8\delta \times 2\delta \times 6.4\delta$	$512 \times 128 \times 256$	4.5	0.2 ~ 5.9	4.5

Table 1: Computational conditions.

The simulation has been made with the use of the finite difference method in which special attention is paid to the consistency between the analytical and numerical differential operations [5]. The method was confirmed to give good agreement with the spectral method [6]. The present numerical scheme consistent with the analytical operation ensures the balance of the transport



equations for the statistical correlations such as the temperature variance and the turbulent heat flux. A fourth-order central difference scheme is adopted in the streamwise and spanwise directions, and the second-order central difference scheme is used in the wall-normal direction. Further details of the method can be found in [1], [5] and [6]. The computational condition is shown in table 1. The computation has been performed with the use of 8 processing elements of VPP5000 at Kyushu University.

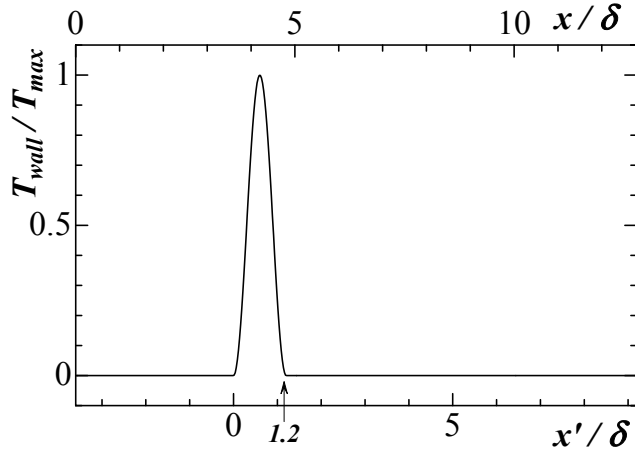


Figure 2: Variation of bottom wall temperature.

## Results and discussion

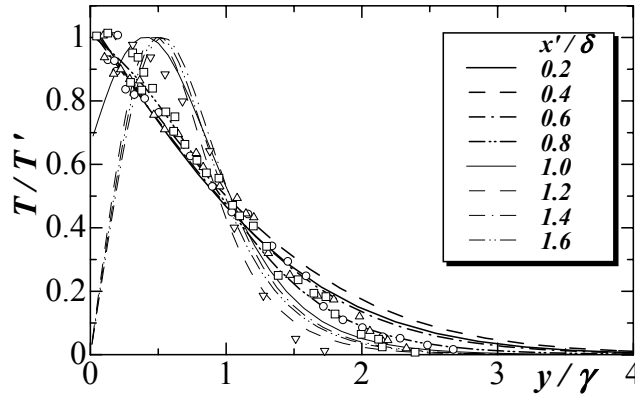


Figure 3: Mean temperature, symbols are experimental data [9],  $x' = 9.6$ ,  $x' = 37.2$ ,  $x' = 75.6$ ,  $x' = 122.4$ .

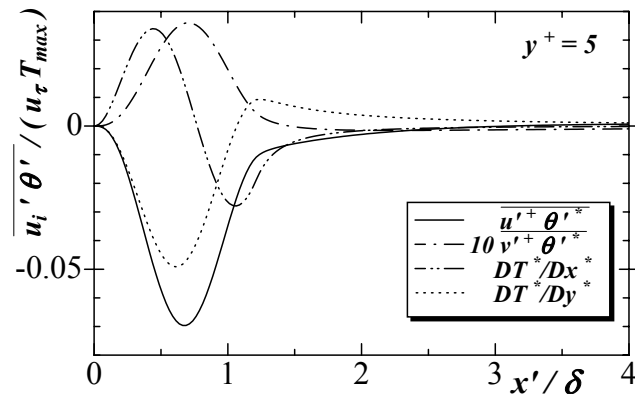


Figure 4: Turbulent heat flux.

Mean temperature profiles are shown in figure 3. If the maximum temperature (above ambient)  $T'$  and the normal distance  $\gamma$  from the wall where  $T = 0.5T'$  occurs are chosen as the temperature and length scales respectively, the values of DNS (up-

stream of  $x'/\delta = 0.8$ ) are similar to experimental data [9] of heated wall-Cylinder immersed in a turbulent boundary layer.

Figure 4 shows the turbulent heat flux  $\overline{u'\theta'}$  and  $\overline{v'\theta'}$  in the near wall region. The interesting feature of figure 4 is that the counter gradient diffusion exists for  $\overline{u'\theta'}$  behind  $x'/\delta = 0.8$ . The counter gradient diffusion is observed behind  $x'/\delta = 1.1$  for  $\overline{v'\theta'}$  as well.

## Turbulent Prandtl number

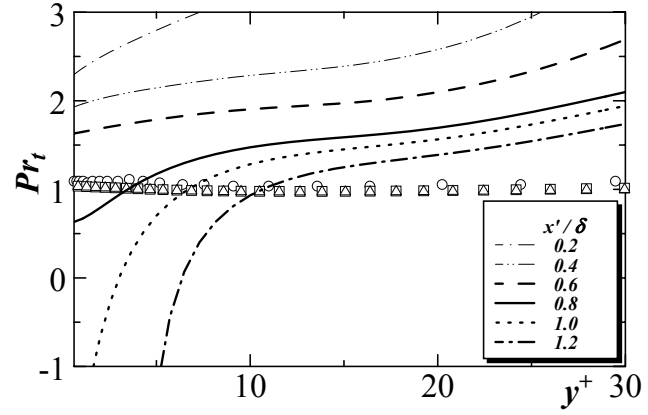


Figure 5: Turbulent Prandtl number,  $\circ$ :Uniform heat source [3],  $\square$ :Constant wall temperature difference [8],  $\triangle$ :Uniform heat flux heating [8].

The turbulent Prandtl number  $Pr_t$ , defined as the ratio;

$$Pr_t \equiv \frac{\overline{u^+v^+} d\bar{T}^*/dy^+}{\overline{v^+\theta^*} d\bar{u}^+/dy^+} \quad (6)$$

of momentum diffusivity to thermal diffusivity, has been evaluated from the present data at several stations and is shown in figure 5. The calculated results [3] for uniform heat source is plotted in figure 5. The other calculated results of the constant wall temperature difference and the uniform heat flux heating by authors' group [8] are also plotted in figure 5. In most of the existing studies,  $Pr_t$  tends to be the constant value of 1.0 for several thermal boundary conditions [3, 8]. In the case of the present streamwisely varying thermal boundary condition, however, figure 5 shows that  $Pr_t$  is totally different than the constant value of 1.0. This tendency is qualitatively similar to that reported in [2]. Generally,  $Pr_t$  is used to obtain the turbulent heat flux from the mean temperature gradient. Figure 5, however, indicates that it cannot be used for the estimation of the turbulent heat flux in case of the thermal boundary condition with rapid streamwise variation, because it changes significantly along the streamwise direction.

## Time scale ratio

The time scale ratio  $R$  is expressed as the ratio of the scalar time scale  $\tau_\theta (= k_\theta/\epsilon_\theta)$  to the momentum one  $\tau_u (= k/\epsilon)$ ;

$$R = \frac{\tau_\theta}{\tau_u} = \frac{k_\theta}{\epsilon_\theta} \frac{\epsilon}{k}. \quad (7)$$

Because the velocity field is the fully developed turbulent channel flow in this study, the momentum time scale  $\tau_u (= k/\epsilon)$  is constant along the streamwise direction. Therefore, the scalar time scale  $\tau_\theta (= k_\theta/\epsilon_\theta)$  determines  $R$  along the streamwise direction. Figure 6 shows the distribution of the time scale ratio. The wall-asymptotic value of  $R$  is analytically equal to the molecular Prandtl number. The near-wall limiting value of  $R$

given in figure 6 becomes indeed the molecular Prandtl number irrespective of the streamwise direction. On the other hand, the obtained result in figure 6 has indicated that the time scale ratio varies along the streamwise direction in the outer region.

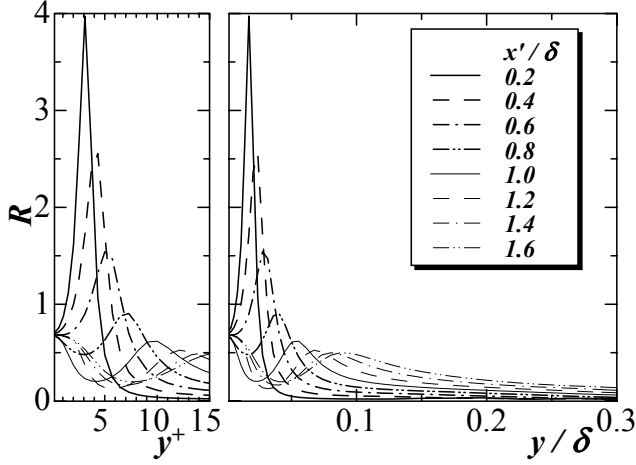


Figure 6: Time scale ratio.

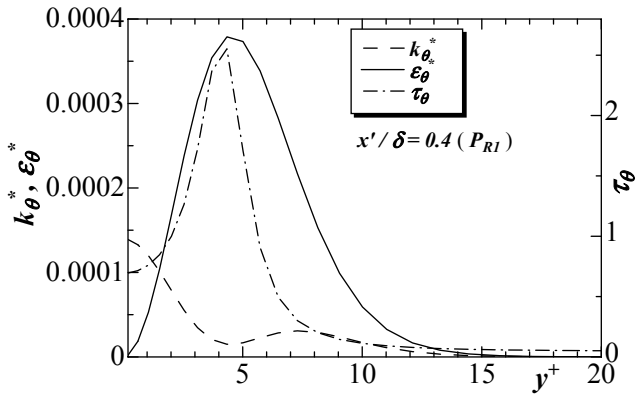


Figure 7:  $k_\theta^*$  and its dissipation rate.

The value of  $R$  at the position  $x'/\delta = 0.4$  is significantly higher than the unity at  $y^+ = 4.3$  in figure 6. As can be seen from figure 7, it results from the value of the temperature variance  $k_\theta$  in excess of those of other height at  $y^+ = 4.3$ . Moreover, the local minimal value of its dissipation rate  $\epsilon_\theta$  is also observed at  $y^+ = 4.3$  in figure 7. The local maximal value around  $y^+ = 0, 7.5$  occurs to dissipate the energy transported from the portion of large energy by the molecular and turbulent diffusion. In fact, the local minimal value of the dissipation rate necessarily exists at the peak of the temperature variance. Therefore, the peak of the time scale ratio surely occurs at  $y^+ = 4.3$ .

$R$  is shown in figure 8 where a abscissa axis is assigned to the streamwise direction. It indicates that the time scale ratio varies along the streamwise direction. To examine the peak of both  $P_{R1}$  and  $P_{R2}$ , the budget for  $k_\theta^*$  is shown in Fig. 9. The positions where the maximal and minimal peaks of the time scale ratio exist are in agreement with those of the production term for  $k_\theta^*$ . In the case of the present streamwisely varying thermal boundary condition, the specific feature of  $P_{k_\theta}$  is that the negative value of  $P_{k_\theta}$  exists in latter half of the heated section. To explain the negative value of the production term  $P_{k_\theta}$ , the terms which constitute  $P_{k_\theta}$  in the transport equation of  $k_\theta^*$  are examined. It is given by

$$P_{k_\theta} = -\overline{u'\theta'} \frac{d\bar{T}}{dx} - \overline{v'\theta'} \frac{d\bar{T}}{dy}. \quad (8)$$

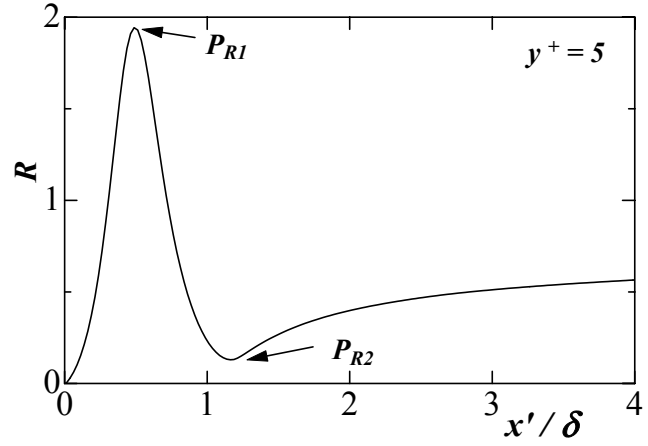


Figure 8: Time scale ratio at the inner region.

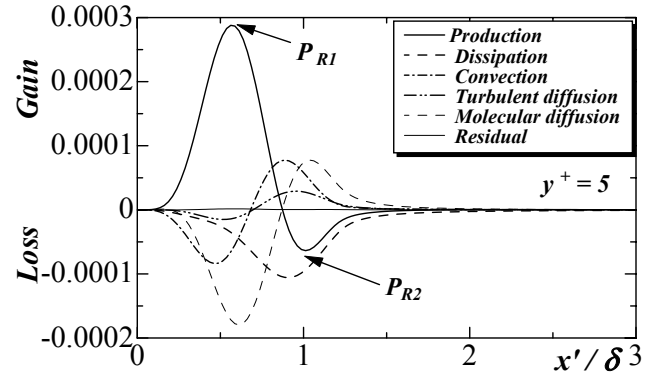


Figure 9: Budget of  $k_\theta^*$ .

The relation among  $\overline{u'\theta'}$ ,  $d\bar{T}/dx$ ,  $\overline{v'\theta'}$ ,  $d\bar{T}/dy$  is seen in figure 4. In the position of the negative value of  $P_{k_\theta}$ ,  $\overline{u'\theta'}$  and  $d\bar{T}/dx$  stay negative value. Moreover, other constitutive terms stay positive value in the region.

Figure 10 shows the two dimensional distribution for the production term  $P_{k_\theta}$  of the  $k_\theta^*$ . Solid line shows the positive value and Dashed line shows the negative value, respectively. The negative region of the production term occupies a fairly large area behind the heated section. This is because the hot convection is transported from the upstream, and thus the mean temperature gradient is inverted in the near-wall region. The two dimensional distribution of  $R$  is also shown in figure 11. The specific feature of  $R$  is that the local maximum exists in the heated section and the local minimum in latter half of the heated section. A noticeable agreement in the profiles of  $P_{k_\theta}$  and  $R$  is observed through the comparison of figures 10 and 11. The region of the negative of  $P_{k_\theta}$  is in good agreement with that of the local minimum of  $R$ .

Figure 12 indicates that the tendency of the balance between  $k_\theta$  and  $\epsilon_\theta$  is the same at any downstream position. It is also shown that the peaks of both  $k_\theta$  and  $\epsilon_\theta$  are transported to the central region of the channel along the streamwise direction. One can notice that, in general,  $\epsilon_\theta$  is high where  $k_\theta$  is large. More detailed inspection indicates that the contour of  $\epsilon_\theta$  possesses a large number of inflection points than that of  $k_\theta$ . We have seen in figure 8 that the position of the local minimum in  $\epsilon_\theta$  corresponds to the maximum point of  $k_\theta$ . This trend can be observed also in the two-dimensional contour of  $\epsilon_\theta$ , which causes the more complex profile of  $\epsilon_\theta$  than that of  $k_\theta$ .

## Conclusions

The DNS of turbulent heat transfer in a fully developed turbulent channel flow has been carried out for streamwisely varying thermal boundary conditions with  $Pr = 0.71$ ,  $Re_\tau = 180$  ( $Re_c = 6600$ ). The thermal turbulence statistics such as the mean temperature, temperature variance, its dissipation terms, turbulent Prandtl number, time scale ratio have been discussed.

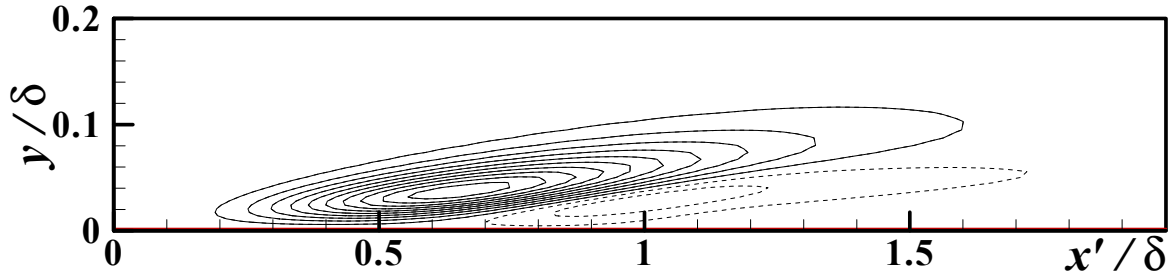


Figure 10: Side views of the production term for  $k_\theta^*$ . Solid line are the positive value and dashed line are the negative one. Contour level is from  $-1.0 \times 10^{-4}$  to  $3.0 \times 10^{-4}$  with increments of  $5.0 \times 10^{-5}$ .

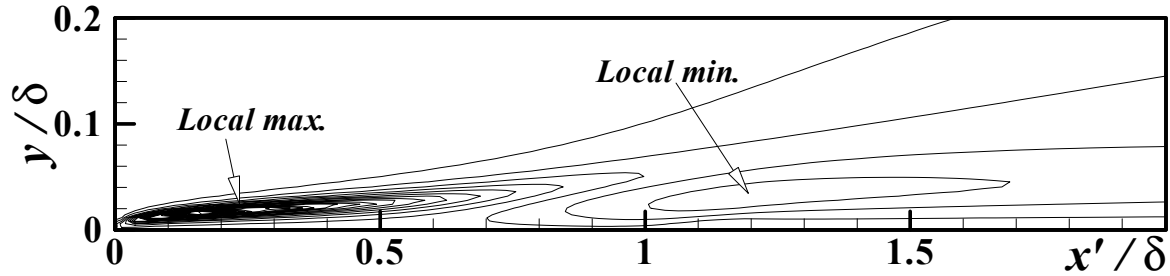


Figure 11: Side views of the time scale ratio  $R$ . Contour level is from 0.2 to 4 with increments of 0.2.

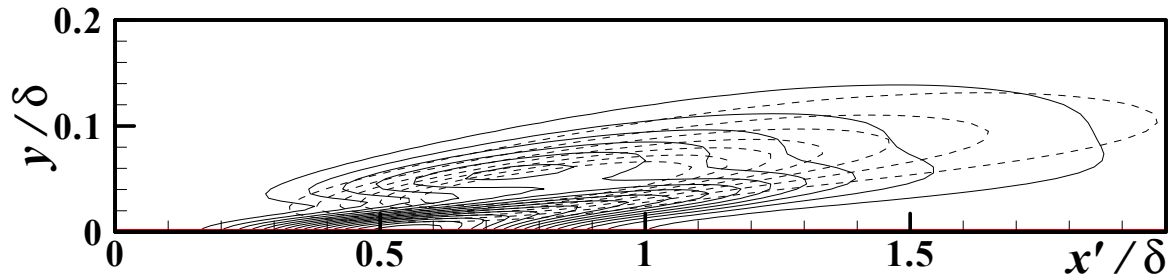


Figure 12: Side views of  $k_\theta^*$  (dot line) and  $\epsilon_\theta^*$  (solid line). Contour level for  $k_\theta^*$  is from  $1.7 \times 10^{-4}$  to  $8.7 \times 10^{-4}$  with increments of  $1.0 \times 10^{-4}$ , while that of  $\epsilon_\theta^*$  is from  $1.1 \times 10^{-6}$  to  $1.7 \times 10^{-4}$  with increments of  $1.0 \times 10^{-5}$ .

In this present study, the presented turbulent Prandtl number cannot be used for estimating because it changes rapidly with  $x$  due to the rapid variation in the thermal boundary condition. The time scale ratio also varies along the streamwise direction in the outer region. It results from the tendency that the value of  $k_\theta$  tends to become rapidly smaller than that of  $\epsilon_\theta$  in the near-wall region behind the heated section. Moreover, it has been confirmed that the local minimal value of  $\epsilon_\theta$  necessarily exists at the peak of the temperature variance.

#### Acknowledgements

This calculations were performed with the use of the VPP-5000 at Kyushu University.

#### References

- [1] Abe, H., Kawamura, H. and Matsuo, Y., Direct numerical simulation of a fully developed turbulent channel flow with respect to Reynolds number dependence, *ASME J. Fluids Eng.*, **123**, 2001, 382–393.
- [2] Antonia, R.A., Danh, H.Q. and Prabhu, A., Response of a Turbulent Boundary Layer to a Step Change in Surface Heat Flux, *J. Fluid Mech.*, **80**, 1977, 153–177.
- [3] Antonia, R.A. & Kim, J., Reynolds shear stress and heat flux calculations in a fully developed turbulent duct flow, *Int. J. Heat Mass Transfer*, **34**, No. 8, 1991, 2013–2018.
- [4] Johnson, D.S., Velocity and Temperature Fluctuation Measurements in a Turbulent Boundary Layer Downstream of a Stepwise Discontinuity in Wall Temperature, *J. Appl. Mech., Trans. A.S.M.E.*, **26**, 1959, 325–336.
- [5] Kawamura, H., Direct numerical simulation of turbulence by finite difference scheme, In: Zhang, Z. S. & Miyake, Y. (Eds.), *The Recent Developments in Turbulence Research*, International Academic Publishers, 1994, 54–60.
- [6] Kawamura, H. and Kondoh, Y., Application of consistent finite difference scheme to DNS of turbulent heat transfer in channel flow, *Proc. 3rd KSME/JSME Therm. Eng. Conf., Kyongju, Korea*, **1**, 1996, 53–58.
- [7] Nagano, Y., Hattori, H. and Abe, K., Modeling the Turbulent Heat and Momentum Transfer in Complex Flows under Various Thermal Conditions, *Proc. of Int. Symp. on Math. Modelling of Turbulent Flows, Tokyo, Japan*, 1995, 79–86.
- [8] Seki, Y., Abe, H. and Kawamura, H., DNS of turbulent heat transfer in a channel flow with different thermal boundary conditions, *Proc. 6th ASME/JSME Therm. Eng. Conf., USA*, 2003, 248.
- [9] Sreenivasan, K.R., Danh, H.Q. and Antonia, R.A., Diffusion from a heated wall-cylinder immersed in a turbulent boundary layer, *Proc. of Thermo-fluids Conf., Hobart*, 1976, 103–106.

## Numerical Simulation of Heat and Mass Transfer in a Natural Draft Wet Cooling Tower

N. Williamson<sup>1</sup>, M. Behnia<sup>2</sup> and S. Armfield<sup>1</sup>

<sup>1</sup>School of Aerospace, Mechanical & Mechatronic Engineering  
The University of Sydney, NSW, 2006 AUSTRALIA

<sup>2</sup>Dean of Graduate Studies, The University of Sydney, NSW, 2006 AUSTRALIA

### Abstract

A 2D axisymmetric two-phase simulation of the heat and mass transfer inside a natural draft wet cooling tower using the commercial CFD package *Fluent* has been conducted. The water droplets in the spray and rain zones are represented with droplet trajectories written in Lagrangian form with heat and mass transfer coupled with the continuous phase. The heat and mass transfer in the fill is represented using source terms controlled through user defined subroutines. These functions solve basic heat and mass transfer equations with the transfer coefficients written in terms of the Poppe equations. The functional dependence of the transfer coefficients are included in the empirical relationship. The model has the capability to model non-uniformities in fill layout and water distribution, which traditional analytical and empirical models are unable capture.

### Introduction

Natural draft wet cooling towers (NDWCT) are commonly used in thermal power stations to cool the condenser feed water. Improving the performance of these structures can reduce turbine back-pressure and improve generation efficiency. Even a small reduction in cooling water temperature can result in a large savings in fuel costs. This leads to a desire to understand the operation of the cooling tower and to optimise its design parameters.

Current design procedures still make use of the traditional 1D analytical cooling tower models [1], relying on extensive empirical relationships for loss coefficients and transfer coefficients. The most widely used 1D model is the original Merkel model [1]. By dropping a few terms in the heat balance Merkel was able to reduce the driving for heat and mass transfer down to an enthalpy difference, allowing the calculation to be performed by hand. Poppe [1, 2, 3] later proposed a complete and more accurate set of equations accounting for the evaporation of water. Either of these models can be quite accurate and incorporate a great deal of detail, however they cannot capture the non-uniformities through the tower. Numerical models are required to assess the effects of major design layout changes [1].

The model developed here attempts to bring together the two approaches with the goal of understanding the limitations of the traditional design process and to optimise the cooling tower design with respect to these non-uniformities. This desire for a comprehensive comparison has influenced the development of the model, in particular the representation of the fill.

No numerical models reported on to date explicitly model the fill, instead researchers have employed source terms to model the effect of the fill on the continuous phase [4, 5, 6, 7]. Recently numerical models of NDWCTs have been developed using this approach supported with a variety of experimental data. Fournier and Boyer [4] presented a proprietary code with the capability to employ either Merkel or Poppe [1] transfer coefficients. Hawlader and Liu [5] developed a 2D axisymmetric model employing the Merkel fill characteristics.

Recently Kloppers and Kröger [8, 2] suggested a new empirical form of the equations for fill loss coefficients and fill transfer coefficients with full functional dependence. These have been found to provide a much better fit to experimental data than traditional forms of the equations and are valid under a wider range of operating conditions. This is essential for cooling tower modeling where the dependent conditions can vary considerably from the tower center to the tower outer edge.

Most previous studies have been performed on very coarse grids and have employed an algebraic turbulence model [5, 6, 7]. This study presents a more detailed model of the cooling tower fill within a commercial CFD package *Fluent*. It is the future goal of this investigation to create a numerical model and use it to optimise the design of cooling towers by varying the fill depth and water flow rate in the tower.

### Fluent Numerics

*Fluent* is a general purpose CFD code. The code has been used to solve the steady Reynolds Averaged Navier-Stokes Equations closed with the standard k-epsilon turbulence model with buoyancy terms included. The semi-implicit method for pressure linked equations (SIMPLE) was employed with second order upwind discretisation employed for the spatial derivatives. A segregated implicit solver was used.

A cooling tower is a cylindrical structure so a 2d axisymmetric steady representation is valid under no wind conditions. This representation was used to reduce computational requirements. The steady 2D axisymmetric momentum and transport equations can be written in general form as follows:

$$\nabla \cdot (\rho u \phi - \Gamma_{\phi} \nabla \phi) = S_{\phi} \quad (1)$$

where ( $\rho$ ) is the density, ( $u$ ) is the velocity vector, ( $\phi$ ) is the flow variable ( $k$ ,  $\epsilon$ ,  $\omega$  ( $h_2O$  species concentration),  $u$ ,  $v$ ,  $h$  (enthalpy)).  $\Gamma_{\phi}$  is the diffusion coefficient and  $S_{\phi}$  is the source term.

The humid air-water mixture is taken to be an ideal gas and an incompressible fluid. The density is computed using,

$$\rho = \frac{p_{op}}{\frac{R}{M_w} T} \quad (2)$$

where  $p_{op}$  is the user specified constant operating pressure for the entire domain and is set at 101kPa.

The buoyancy term in the momentum equation is given as  $(\rho - \rho_0)g$ , where  $g$  is the gravitational acceleration and  $\rho_0$  is the constant operating density specified at the inlet fluid conditions of 295k and 50% humidity.

### Simulation

The geometry of the tower is that of the unit 1 cooling tower at Mt. Piper Power Station in Lithgow NSW. The computational domain is discretised with approximately 250,000 2D unstructured mesh elements. The computational domain extends 90

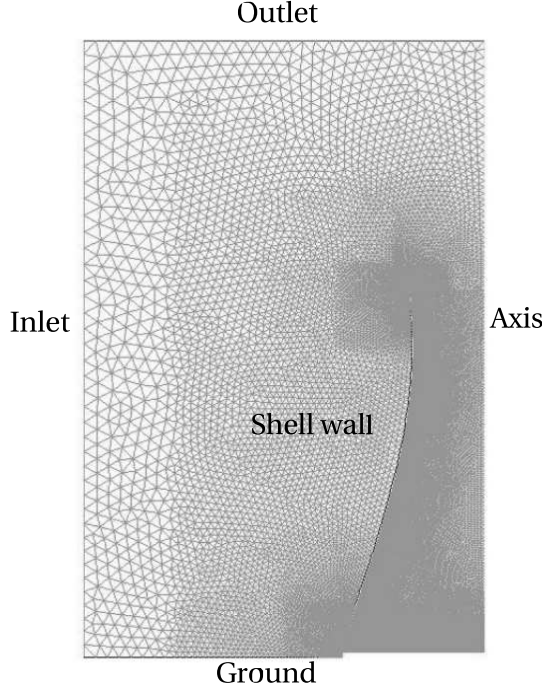


Figure 1: Computational domain with boundary conditions.

meters beyond the cooling tower inlet and 90 meters above the cooling tower outlet allowing for the determination of the inlet velocity profile and the effect of the plume. The tower has a total water flow rate of 17,000kg/s at 313K. The tower has a height of 131m and a base diameter of 49m.

### Modelling

In a NDWCT there are three heat and mass transfer regions that need to be modeled, the spray region below the spray nozzles, the fill (with compact film type fill) and the rain region below the fill.

### Droplet Modelling

In the spray and rain regions the water flows in droplet form. This has been represented with Lagrangian particle tracking with coupled heat and mass transfer between the droplets and the continuous phase. Most previous models [4, 5, 6, 7] assumed the 1D motion of the droplets.

The change in droplet temperature and mass are found through equations (3) and (4), where  $N_i$ , the molar flux of mass and  $h$  the heat transfer coefficient are evaluated through empirical correlations [9]. Variables  $m_p$ ,  $c_p$ ,  $A_p$ ,  $T_p$  are the particle mass (kg), specific heat (J/kgK), surface area ( $m^2$ ) and temperature (K) respectively.  $h_{fg}$  is the latent heat of vapourisation (J/kg)

$$m_p c_p \frac{dT_p}{dt} = h A_p (T_\infty - T_p) + \frac{dm_p}{dt} h_{fg} \quad (3)$$

$$m_p(t + \Delta t) = m_p(t) - N_i A_p M_{w,i} \Delta t \quad (4)$$

The energy ( $Q$ ) and mass ( $M$ ) transfer are coupled with the continuous phase through equations (5) and (6) [9].

$$Q = \left[ \frac{\bar{m}_p}{m_{p,0}} c_p \Delta T_p + \frac{\Delta m_p}{m_{p,0}} \left( -h_{fg} + \int_{T_{ref}}^{T_p} c_{p,i} dT \right) \right] \dot{m}_{p,0} \quad (5)$$

$$M = \frac{\Delta m_p}{m_{p,0}} \dot{m}_{p,0} \quad (6)$$

$m_{p,0}$ ,  $\bar{m}_p$  and  $\dot{m}_{p,0}$  are the initial mass of the particle, the average mass of the particle in the cell and the initial mass flow rate of particles in the trajectory respectively.

Lagrangian particle trajectories are initiated from spray nozzle locations. At the surface of the fill these droplet trajectories are terminated and the droplet temperature and mass flow rate are stored. In the rain region the droplets are initiated from the center of each face on the bottom surface of the fill. The temperature and water mass flow rate of the droplets are determined by the subroutine that describes the heat and mass transfer on the fill. The droplets are given a uniform distribution of 2.5mm in the rain zone.

### Fill Modelling

In the fill, the water flows in complex film type motion across the closely packed parallel wavy plates in the counter direction to air flow. It would be computationally prohibitively expensive to model the fill explicitly so the effect of the fill on the continuous phase is represented using source terms. The change in water temperature is calculated through the fill using a user defined subroutine which tracks the water properties through the fill to balance the heat and mass transfer to the continuous phase.

The water flow through the fill is physically one-dimensional as it is constrained to film flow descending along the vertical plates. This requires that the heat and mass transfer in the fill to also be a 1 dimensional process. This simplification allows the water flow to be represented solely by two variables at each point, its temperature and mass flow rate. The fill region in the tower is considered as a number of discrete columns, each one being equivalent to a 1D grid, overlaying the computational domain. Across each layer in these columns, or between points on the 1D grid, the change in water temperature and mass are computed based on the traditional analytical methods. This approach is depicted in figure (2). The water flow through the tower fill is represented by 87 of these columns with each one discretised into 10 layers or nodes.

### Momentum Source Terms

The pressure loss through the fill is modeled using source terms in the momentum equation. This momentum sink is given as:

$$S_v = -K_{fi} \times \frac{\rho_m V^2}{2} \quad (7)$$

where  $K_{fi}$  is the fill loss coefficient per meter depth of fill. The empirical correlation for  $K_{fi}$  is expressed as a function of the air ( $m_a$ ) and water ( $m_w$ ) flow rates through the fill and the depth of the fill ( $L_{fi}$ ) (equation 8) as described by Kloppers [2].

$$K_{fdm1} = (5.154914 m_w^{0.877646} m_a^{-1.462034} + 10.806728 m_w^{0.226578} m_a^{-0.293222}) \times L_{fi}^{-0.236292} \quad (8)$$

The pressure loss due to the cooling tower shell supports, the water distribution piping network and the drift eliminators was modeled in a manner similar to the fill. The loss coefficients used were  $K_{cts} = 0.5$ ,  $K_{wdn} = 0.5$  and  $K_{de} = 3.5$  respectively as taken from [1].

### Heat and Mass Transfer in the Fill

The heat and mass transfer characteristics are governed by the volumetric mass transfer coefficient and the wetted contact area between the phases. The product of these two values  $h_d A$  can be found from the Merkel number [1] for a particular fill type. The transfer coefficients used are in the Poppe form, which means that the Poppe equations [3] are used to interpret the experimental data and form the empirical equation for the coefficient.



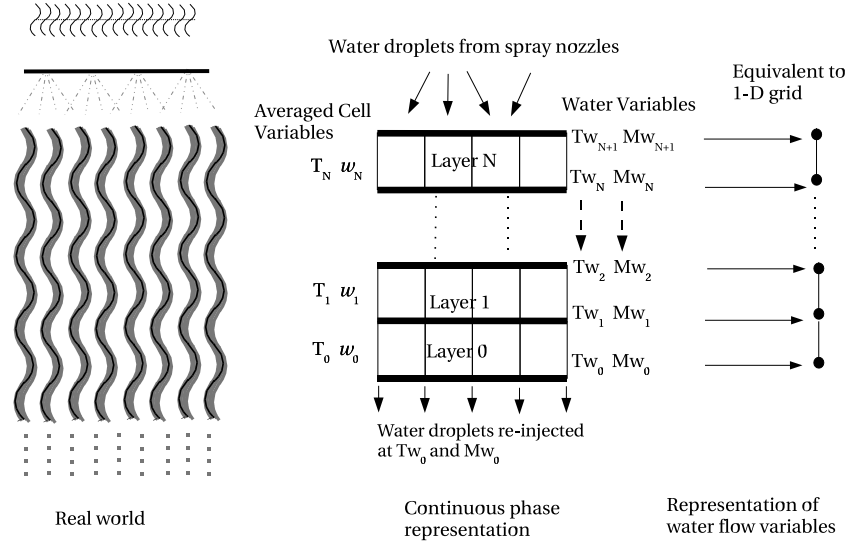


Figure 2: Incremental control volume of the fill.

Kloppers [2] gives a detailed analysis of the Poppe model. The methods used to derive the coefficients are replicated here to find the change in water properties.

The transfer coefficient used here is written in terms of inlet flow rates for water and air as shown in equation (9). The functional dependence on air wet and dry bulb inlet temperature was shown by Kloppers [2] to be insignificant so this dependency can be excluded. Although the coefficient is a function of both water inlet temperature and fill depth [2], these are both held constant in this investigation so a more general relation was not sought.

$$\frac{Me_{Poppe}}{L_{fi}} = \frac{h_d A}{m_w} = 1.380517 m_w^{0.112753} m_a^{0.698206} - 0.517075 m_w^{0.461071} m_a^{0.681271} \quad (9)$$

The heat transfer coefficient can then be found using the Lewis factor relationship given in equation (10).

$$Le_f = \frac{h}{h_d C_{pa}} \quad (10)$$

where  $h_d$  is the mass transfer coefficient for the fill with units  $kg/m^2 s$  and  $h$  is the heat transfer coefficient for the fill with units  $W/m^2 K$ . The Lewis factor is determined using Bosnjakovics formula [10] given in equation (11). Under saturation conditions, the formula is modified to equation (12).

$$Le_f = 0.865^{2/3} \cdot \frac{\left( \frac{\omega_{sw} + 0.622}{\omega + 0.622} - 1 \right)}{\ln \left( \frac{\omega_{sw} + 0.622}{\omega + 0.622} \right)} \quad (11)$$

$$Le_{f,sat} = 0.865^{2/3} \cdot \frac{\left( \frac{\omega_{sw} + 0.622}{\omega_{sa} + 0.622} - 1 \right)}{\ln \left( \frac{\omega_{sw} + 0.622}{\omega_{sa} + 0.622} \right)} \quad (12)$$

### Coupling Procedure

The calculations across each layer take place between the averaged continuous phase flow variables and the upstream (with

respect to water flow) water flow variables. The heat and mass transfer from the water phase is computed first and then the energy and mass source terms which balance this change in water temperature and mass flow rate are evaluated. The source terms calculated are identical for all the cells across the layer. The maximum column width in the model is 1m, the smallest being 0.1m.

The water evaporated  $m_{evap}[n]$  across fluid layer  $n$  is determined using equation (13), where  $\omega_{sat,Tw}$  is the specific humidity of saturated air evaluated at the water temperature ( $kg/kg$ ) and  $\omega_{ave,fluid}$  is the average specific humidity in the fluid zone.

$$m_{evap} = h_d A (\omega_{sat,Tw} - \omega_{ave,fluid}) \quad (13)$$

The volumetric transfer coefficients are specified per meter depth of the fill and the heat and mass transfer is being evaluated across a small increment in the fill  $\Delta L_{fi}$ , so the transfer coefficients must be reduced to allow for the smaller area over which the heat transfer is taking place using,

$$h_d \cdot A = (h_d \cdot A)_{calc} \cdot \Delta L_{fi} \quad (14)$$

The new water mass flow rate is found using equation (15).

$$m_w[n] = m_w[n+1] - m_{evap}[n] \quad (15)$$

The latent and sensible heat transfer is evaluated using equations (16) and (17) respectively.

$$q_{latent} = m_{evap} \cdot h_{fg} \quad (16)$$

$$q_{sensible} = hA \cdot (Tw[n+1] - T_{ave,air}) \quad (17)$$

where  $T_{ave,air}$  is the average temperature of the continuous phase in the layer. The water temperature at the inter-facial layer  $n$  is determined using equation (18).

$$Tw[n] = Tw[n+1] - \frac{(q_{sensible}[n] + q_{latent}[n])}{C_{pw} m_w[n]} \quad (18)$$

where  $Tw[n+1]$  is the water temperature corresponding to the fluid boundary above the fluid layer  $n$ ,  $m_w$  is the mass flow rate of water in the column in  $kg/s$ ,  $C_{pw}$  is the specific heat of water  $J/kgK$ .

When the flow becomes super-saturated then additional energy is released in the flow, as the latent heat of vapourisation is released when the water vapour condenses as mist. It has been

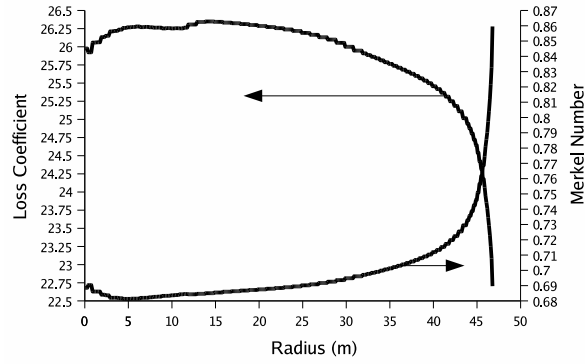


Figure 3: Merkel number and loss coefficient with radial location in the fill.

assumed for this investigation, as in the Poppe model [3], that vapour condenses as mist when the vapour pressure rises above the saturation vapour pressure although in reality it may reach very high levels of supersaturation before this occurs.

The mass source  $M_{source}$  ( $kg/m^3s$ ) and enthalpy source  $Q_{source}$  ( $W/m^3$ ) per unit volume are given by equations (19 and 20):

$$M_{source} = \frac{m_{evap}}{\Delta L_{fi}} \quad (19)$$

$$Q_{source} = \left( m_w \cdot C_{pw} \cdot \Delta T_w + m_{evap} \cdot (C_{pv} \cdot (T_w - T_{ref}) - h_{fg}) \right) / \Delta L_{fi} + m_{condense} \cdot h_{fg} \quad (20)$$

where  $C_{pw}$  is the specific heat of water and has units  $J/kg$ , ( $h_{fg}$ ) and ( $C_{pv}$ ) are the latent heat of vapourisation and the specific heat of saturated water vapour respectively.

### Preliminary Results

The implementation of the cooling tower fill subroutine was validated against the traditional analytical models used and also against the experimental data obtained from Kloppers [2]. Full validation of the model has not yet been performed so the following results are therefore deemed preliminary.

The results indicate a significant deviation from the assumptions of 1D analytical models. A radial cut through the tower exhibits significant temperature, velocity,  $h_2o$  species concentration, and pressure gradients. Errors in the determination of the outlet condition will lead to erroneous computation of the tower draft and therefore heat transfer through the fill.

The Merkel number varies between 0.85 to 0.75 from the center to the outer edge of the tower as depicted in figure (3). Loss coefficients also vary throughout much of the tower, from 22.6 in the center to 24 near the outer edge where there is a low air to water flow rate ratio.

These results are of course numerically obtained and therefore do not represent any blockages or non-uniformities in the fill. Some published data [11] indicates that these non-uniformities can partially eliminate any variation in the temperature and humidity profile across the fill.

### Conclusions

A commercial package can be successfully implemented with user defined subroutines to model a natural draft wet cooling tower. Preliminary results show room for improvement in cooling tower design and highlight the non-uniformities that exist

in the fill inlet conditions. The future goal of this work is to quantify the effect of these non-uniformities on the accuracy of traditional cooling tower design and specification and to also determine where improvements can be made in cooling tower design.

### Acknowledgements

Chris Kloppers (SASOL South Africa), Delta Electricity (NSW Australia).

### References

- [1] Kröger, D.G., *Air Cooled Heat Exchangers and Cooling Towers Thermal Flow Performance: Evaluation and Design*, Begell House, 1998.
- [2] Kloppers, J.C., A Critical Evaluation and Refinement of the Performance of Wet-Cooling Towers, PhD Thesis, University of Stellenbosch, Stellenbosch, South Africa, 2003.
- [3] Poppe, M. and Rogener, H., Berechnung von Ruckkühlwerken, VDI-Wärmeatlas, pp. Mi 1-Mi 15, 1991.
- [4] Fournier, Y. and Boyer, V., Improvements to the N3S-AERO Heat Exchanger and Cooling Tower Simulation Code, *12th IARH Symposium in Cooling Tower and Heat Exchangers*, 11-14 November 2001, UTS, Sydney, Australia.
- [5] Hawlader, M.N.A. and Liu, B.M., Numerical study of the thermal-hydraulic performance of evaporative natural draft cooling towers, *Applied Thermal Eng.*, **22**, 2002, 41–59.
- [6] Radosavljevic, D., The Numerical Simulation of Direct-Contact Natural-Draught Cooling Tower performance under the influence of cross-wind, PhD Thesis, University of London, London, England, 1990.
- [7] Majumdar, A.K., Singhal, A.K. and Spalding, D.B., Numerical Modeling of Wet Cooling Towers - Part 1: Mathematical and Physical Models, *J. Heat Transfer*, **105**, 1983, 728–735.
- [8] Kloppers, J.C. and Kröger, D.G., Loss coefficient correlation for wet-cooling tower fills, *Applied Thermal Eng.*, **23**, 2003, 2201–2211.
- [9] FLUENT, *User's Guide*, Fluent Inc. Lebanon, USA, 2003.
- [10] Bosnjacovic, F., *Technische Thermodynamik*, Theodor Steinkopf, Dresden, 1965.
- [11] Sirok, B., Blagojevic, B., Novak, M., Hochevar, M. and Jere, F., Energy and Mass Transfer Phenomena in Natural Draft Cooling Towers, *Heat Transfer Eng.*, **24**, 2003, 66–75.

## Three-dimensional transition in the buoyancy boundary layer on an evenly heated vertical wall

S. W. Armfield and G. D. McBain

School of Aerospace, Mechanical and Mechatronic Engineering  
Sydney University, New South Wales, 2006 AUSTRALIA

### Abstract

The three-dimensional structure of the thermal boundary layer adjacent to an evenly heated vertical wall with imposed stable background density stratification is investigated using direct numerical simulation. The wall is considered to extend infinitely in the vertical and spanwise directions, with the heating imposed as a constant flux boundary condition. Flow behaviour is determined by a Reynolds number based on the ratio of the boundary flux gradient to the background gradient. For low Reynolds numbers the flow is stable with variation in the wall normal direction only. For Reynolds numbers greater than a critical value the flow is unstable and supports a two-dimensional wave travelling vertically up the plate, in the direction of fluid flow. A further increase in Reynolds number sees the generation of a three-dimensional spanwise structure on the two-dimensional travelling wave.

### Introduction

Flows generated by the transfer of heat from a vertical wall to an adjacent fluid are known as natural convection flows and occur widely in nature and engineering. The rate of heat transfer is strongly dependent on the character of the flow, that is whether it is laminar or turbulent, with turbulent natural convection boundary layer flows having heat transfer rates several times that of a laminar natural convection boundary layer. The transition from laminar to turbulent flow is believed to occur via the generation of rapidly growing three-dimensional waves associated with an initial two-dimensional transition, although the mechanism is not fully understood. In this paper the onset of three-dimensional travelling waves is investigated for the case of an infinite plate having a uniform heat flux, subjected to a stable linear background temperature stratification. For a constant Prandtl number the behaviour of this flow is determined by the ratio of the horizontal temperature gradient imposed at the plate, and the background stable vertical temperature gradient. Below a critical value of this control parameter the flow is steady, one-dimensional and independent of the control parameter. Above a critical value the flow is two-dimensional and oscillatory, exhibiting waves travelling in the vertical direction. A further increase in the control parameter leads to a spanwise, three-dimensional, structure super-imposed on the two-dimensional travelling waves.

The governing equations for this flow are the three-dimensional Navier–Stokes equations with the Oberbeck–Boussinesq approximation for buoyancy, together with a temperature transport equation,

$$u_t + uu_x + vu_y + wu_z = -p_x + \nu(u_{xx} + u_{yy} + u_{zz}), \quad (1)$$

$$v_t + uv_x + vv_y + wv_z = -p_y + \nu(v_{xx} + v_{yy} + v_{zz}) + g\beta T, \quad (2)$$

$$w_t + uw_x + vw_y + ww_z = -p_z + \nu(w_{xx} + w_{yy} + w_{zz}), \quad (3)$$

$$u_x + v_y + w_z = 0, \quad (4)$$

$$T_t + uT_x + vT_y + wT_z + \nu\Gamma_s = \alpha(T_{xx} + T_{yy} + T_{zz}), \quad (5)$$

where  $u$ ,  $v$  and  $w$  are the velocity components in the directions  $x$ ,  $y$  and  $z$  respectively, with  $x$  the horizontal direction,  $y$  the vertical and  $z$  the spanwise,  $t$  is the time,  $p$  the pressure,  $\beta$ ,  $\alpha$  and  $\nu$  are the coefficients of thermal expansion, thermal diffusivity and kinematic viscosity respectively and  $g$  is the acceleration due to gravity. The temperature is represented as the sum of a background temperature  $\bar{T}$  and a perturbation temperature  $T$ . The background temperature is assumed to be  $x$  and  $z$  independent and linear with  $\bar{T}_y = \Gamma_s$  a positive constant. The domain is  $-\infty < y < \infty$ ,  $-\infty < z < \infty$ ,  $0 \leq x < \infty$ , with boundary conditions,

$$u = v = w = 0, \quad T_x = -\Gamma_w \quad \text{on} \quad x = 0, \quad (6)$$

$$u, v, w, T \rightarrow 0 \quad \text{as} \quad x \rightarrow \infty. \quad (7)$$

A one-dimensional steady analytic solution may be found for this flow. Under the assumption that  $v = V(x)$  and  $T = \Theta(x)$ , the governing equations reduce to,

$$0 = \nu V_{xx} + g\beta\Theta, \quad (8)$$

$$V\Gamma_s = \alpha\Theta_{xx}, \quad (9)$$

with the solution,

$$V(x) = \sqrt{2}\Gamma_w \left( \frac{g\beta\alpha^3}{\nu\Gamma_s^3} \right)^{1/4} \times \dots \exp \left\{ - \left( \frac{g\beta\Gamma_s}{4\alpha\nu} \right)^{1/4} x \right\} \sin \left\{ \left( \frac{g\beta\Gamma_s}{4\alpha\nu} \right)^{1/4} x \right\}, \quad (10)$$

$$\Theta(x) = \Gamma_w \left( \frac{g\beta\Gamma_s}{4\alpha\nu} \right)^{-1/4} \times \dots \exp \left\{ - \left( \frac{g\beta\Gamma_s}{4\alpha\nu} \right)^{1/4} x \right\} \cos \left\{ \left( \frac{g\beta\Gamma_s}{4\alpha\nu} \right)^{1/4} x \right\}. \quad (11)$$

This suggests the appropriate dimensional velocity, length and temperature scales for this problem are,

$$U = \sqrt{2}\Gamma_w \left( \frac{g\beta\alpha^3}{\nu\Gamma_s^3} \right)^{1/4}$$

$$H = \left( \frac{4\alpha\nu}{g\beta\Gamma_s} \right)^{1/4},$$

$$\Delta T = \Gamma_w H.$$

Using these quantities to non-dimensionalise (1) to (5) above gives,

$$u_t + uu_x + vu_y + wu_z = -p_x + \frac{1}{Re}(u_{xx} + u_{yy} + u_{zz}), \quad (12)$$

$$v_t + uv_x + vv_y + wv_z = -p_y + \frac{1}{Re}(v_{xx} + v_{yy} + v_{zz}) + \frac{2}{Re}T, \quad (13)$$

$$w_t + uw_x + vw_y + ww_z = -p_z + \frac{1}{Re}(w_{xx} + w_{yy} + w_{zz}), \quad (14)$$

$$u_x + v_y + w_z = 0, \quad (15)$$

$$T_t + uT_x + vT_y + wT_z = \frac{1}{RePr}(T_{xx} + T_{yy} + T_{zz}), \quad (16)$$

where all quantities are now non-dimensional, the Reynolds number  $Re = \frac{UH}{\nu} = \frac{2\Gamma_w}{\Gamma_s Pr}$  and the Prandtl number  $Pr = \frac{\nu}{\alpha}$ . The Reynolds number can also be expressed in terms of a Grashof number  $Gr = \frac{g\beta\Delta TH^3}{\nu^2} = \frac{4\Gamma_w}{\Gamma_s Pr}$  as  $Re = \frac{Gr}{2}$ , and thus the Reynolds number is also a Grashof number. The boundary conditions for the non-dimensional quantities are,

$$u = v = w = 0, T_x = -1 \quad \text{on} \quad x = 0, \quad (17)$$

$$u, v, w, T \rightarrow 0 \quad \text{as} \quad x \rightarrow \infty. \quad (18)$$

The stability of the one-dimensional flow, given by (10) and (11) has been investigated using two-dimensional linear stability analysis employing a Laguerre collocation scheme. The stability analysis has provided the critical Reynolds number, and other properties, and has been shown to accurately predict the behaviour of a full nonlinear solution obtained via a two-dimensional direct numerical solution [7, 8]. At  $Pr = 7$ , the critical Reynolds number for the onset of an oscillatory solution consisting of two-dimensional travelling waves was found to be  $Re_{cr} \simeq 8.6$ .

The heat flux boundary condition solution given above is similar to that of the vertical slot with different temperatures on the walls and a uniform vertical gradient, which exhibits boundary layers near either wall, investigated by Elder [4]. The stability of these temperature boundary conditions flows has been examined by Bergholz [2], Christov & Homsy [3], and that of the stratified fluid near a single wall by Gill & Davey [5].

The transition to turbulence in thermal boundary layers is associated with the generation of three-dimensional structures within the boundary layer. Surprisingly however, very few investigations of the three-dimensional stability properties of vertical natural convection boundary layers have been carried out. The definitive experiment was performed by Jaluria & Gebhart [6] for the boundary layer on a vertical plate heated by a constant heat flux. A transverse ribbon near the leading edge was vibrated to trigger instabilities in both the streamwise and spanwise directions; the spanwise structures led to double vortex structures aligned with the streamwise flow during the early stages of transition. The wave number of the spanwise structures was found to be determined by the lateral length scales present in the ribbon itself; however these structures were clearly present and were unstable in the sense that their amplitude increased downstream. The flow associated with the heat flux boundary condition combined with a stable background temperature gradient, investigated here, is considered to be an ideal flow for the further investigation of three-dimensional transition.

In this paper a full numerical nonlinear three-dimensional solution will be obtained using an unsteady Navier–Stokes solver. The results are consistent with those of McBain & Armfield [7] in that they show that, with increasing  $Re$ , the initial instability is a two-dimensional travelling wave. A further increase in Reynolds number then leads to a three-dimensional spanwise structure.

## Results and Discussion

The equations given above are solved in the domain  $0 \leq x \leq X, 0 \leq y \leq Y, 0 \leq z \leq Z$  with initial conditions;

$$u = v = w = T = 0, \quad \text{at all} \quad x, y, z \quad \text{and} \quad t = 0; \quad (19)$$

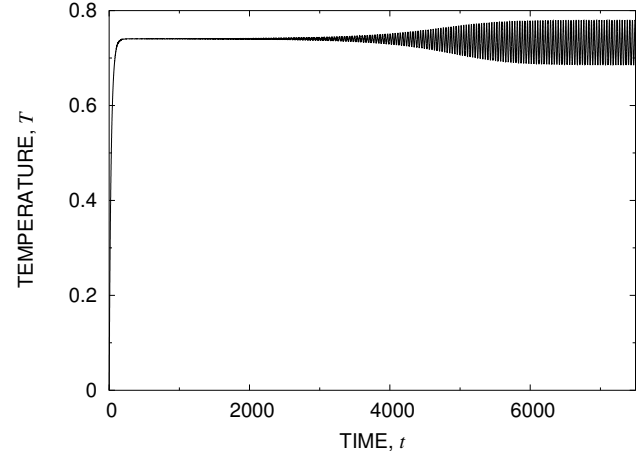


Figure 1: Temperature time series for  $Re = 9$

boundary conditions on  $x = 0, X$ ;

$$u = v = w = 0, T_x = -1 \quad \text{on} \quad x = 0, \quad (20)$$

$$u_x = v = w = T_x = 0 \quad \text{on} \quad x = X; \quad (21)$$

with periodic boundary conditions on  $y = 0, Y, z = 0, Z$ ;

$$\cdot|_{y=Y} = \cdot|_{y=0}, \cdot|_{z=Z} = \cdot|_{z=0}, \quad (22)$$

for variables  $u, v, w, T$

A second order fractional step Navier–Stokes solver defined on a non-staggered rectangular grid is used. Time integration is accomplished using an Adams–Bashforth scheme for the non-linear terms and Crank–Nicolson for the viscous and diffusion terms. All spatial terms are discretised using centred second order differences. Continuity is enforced and pressure obtained using a pressure correction equation. All the discrete equations are inverted using a pre-conditioned conjugate gradient solver. The three-dimensional solver is similar to a two-dimensional solver that has been used for the investigation of natural convection flow for a number of years [1, 7], and the code may be run in either two- or three-dimensional form.

The results presented in figures 1 to 3 were obtained using the code in two-dimensional form. These results were obtained with the domain  $X = 16, Y = 13.84$ . The  $x$  extent of the domain has been chosen to ensure that the large  $x$  boundary conditions do not adversely influence the solution, while the  $y$  extent has been chosen to match the most unstable wavelength, based on a linear stability analysis, at  $Re = 10$ . The grid is uniform in  $y$  with  $\Delta y = 0.25$  and non-uniform in  $x$  with  $\Delta x = 0.025$  at  $x = 0$  and a maximum stretching of 1.025 in the increasing  $x$  direction, giving a grid of  $119 \times 55$  in  $x$  and  $y$ . The time step is  $\Delta t = 5 \times 10^{-4}$ . This grid size and time step has been shown to be fine enough to provide asymptotic second order convergence for this flow.

The temperature time series, shown in figure 1, was obtained with an initial random perturbation added to the temperature field in the range  $-0.005$  to  $0.005$ . The use of an initial perturbation reduces the time required for the unsteady solution to reach full development; however all other features of the flow, such as frequency, growth rate and fully developed amplitude, are independent of the initial perturbation. As can be seen the flow shows an initial large growth, associated with the base flow development. A sinusoidal oscillation is then seen to develop, growing slowly, and reaching full development by approximately  $t = 7000$ . The early stages of growth of the sinusoidal oscillation and the frequency are accurately predicted

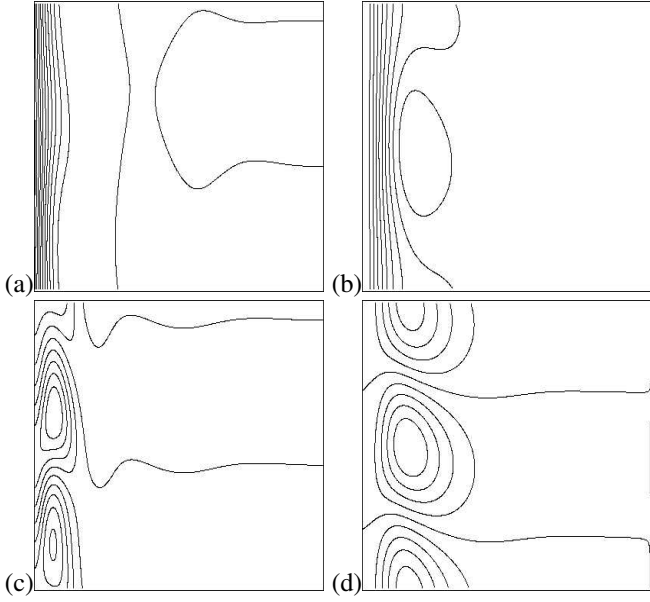


Figure 2: Two-dimensional temperature (a,c) and stream-function (b,d) contours for  $Re = 9$ ; total temperature and stream-function shown in (a,b) and difference from streamwise mean shown in (c,d).

by the linear stability analysis [7], while the final amplitude is determined by nonlinear effects.

Figure 2 shows the temperature and stream-function contours for the  $Re = 9$  flow, where the wave structure is clearly seen in both fields. The waves travel vertically with a wave velocity of 0.38—approximately the same as the speed of the critical mode in linear theory. The difference from the streamwise mean is also plotted, clearly showing the wave structure of the perturbation.

Figure 3 shows the temperature contours for the cases  $Re = 19$  and  $Re = 20$ , also obtained with the code in two-dimensional form. Once again the travelling wave structure of the flow is clear, with a noticeable increase in amplitude when compared to the  $Re = 9$  results. It is also clear that nonlinear effects have also increased as evidenced by the strong asymmetry seen in the waves.

Results obtained with the code in three-dimensional form are shown in figures 4 and 5. These results were obtained on the domain  $X = 16, Y = 13.84, Z = 16$ . Once again the  $x$  extent of the domain was chosen to ensure large  $x$  boundary effects did not adversely influence the flow, the  $y$  extent was chosen to match the domain used for the two-dimensional results given above. The  $z$  extent was chosen arbitrarily and will be discussed below. The grid used has  $\Delta x = 0.1, \Delta y = 1.0, \Delta z = 1.0$  with stretching in the increasing  $x$  direction of 1.1 and timestep  $\Delta t = 2 \times 10^{-3}$ . This considerably coarser grid and larger time step, than those used for the two-dimensional simulations, was required to ensure reasonable computation times.

Figure 4 shows temperature contours obtained with the three-dimensional code on constant  $x$  and  $z$  planes for  $Re = 19$ . The constant  $z$  plane result clearly shows a travelling wave structure, while the constant  $x$  result shows no spanwise variation indicating that the solution is two-dimensional. This solution may be compared directly to the equivalent two-dimensional solution shown in figure 3(a) where it is seen that the wave structure is nearly identical. The  $Re = 19$  result is therefore a genuinely two-dimensional flow, and it is clear that relatively coarse grid and time step used for the three-dimensional solution is having only a small effect on the overall flow character.

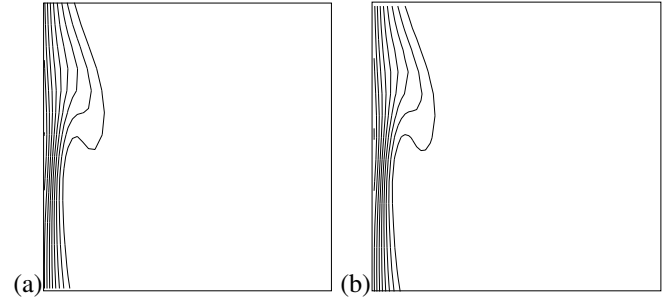


Figure 3: Temperature contours for  $Re = 19$ , (a), and  $Re = 20$ , (b) obtained with two-dimensional code.

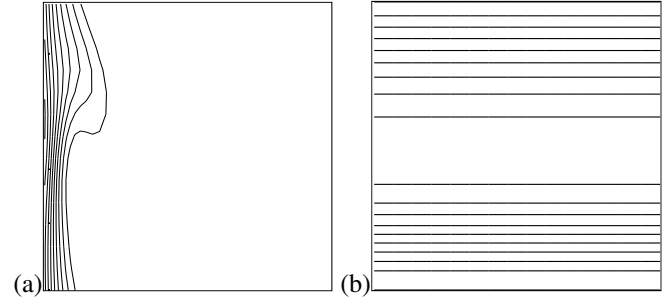


Figure 4: Temperature contours for  $Re = 19$  shown on  $z = Z/2$  (a), and  $x = 0.1$  (b) obtained with three-dimensional code.

Figure 5 shows temperature contours obtained with the three-dimensional code on constant  $x$  and  $z$  planes for  $Re = 20$ . The constant  $z$  plane result again shows a travelling wave structure, while the constant  $x$  plane result now shows a spanwise structure. The flow has clearly undergone a three-dimensional transition between  $Re = 19$  and  $Re = 20$  and is now exhibiting a wave structure in both the  $y$  and  $z$  directions. Once again the combined  $y$  and  $z$  wave structure is travelling vertically. It is interesting to note that the amplitude of the wave as seen in the constant  $z$  plane results has reduced from  $Re = 19$  to  $Re = 20$ , and also in comparison to the two-dimensional  $Re = 20$  result shown in figure 3(b).

Figure 6 contains the Fourier power spectra of time series for the two- and three-dimensional solutions for  $Re = 20$ . For consistency in this case both solutions were obtained on the same, coarse, grid used for the three-dimensional simulation. Both solutions have a dominant frequency of approximately 0.02, however there are considerable differences in the structure of the two power spectra. The three-dimensional signal is marginally lower in amplitude at frequency 0.02, and considerably lower at the first harmonic, frequency 0.04. Additionally the three-dimensional signal shows a low frequency mode, at approximately 0.002, that is not seen at all in the two-dimensional signal. The three-dimensional signal also shows

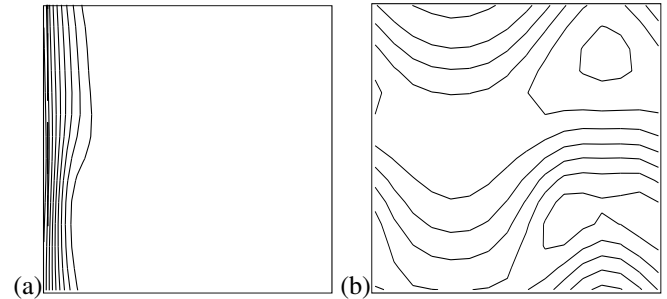


Figure 5: Temperature contours for  $Re = 20$  shown on  $z = Z/2$  (a), and  $x = 0.1$  (b) obtained with three-dimensional code.



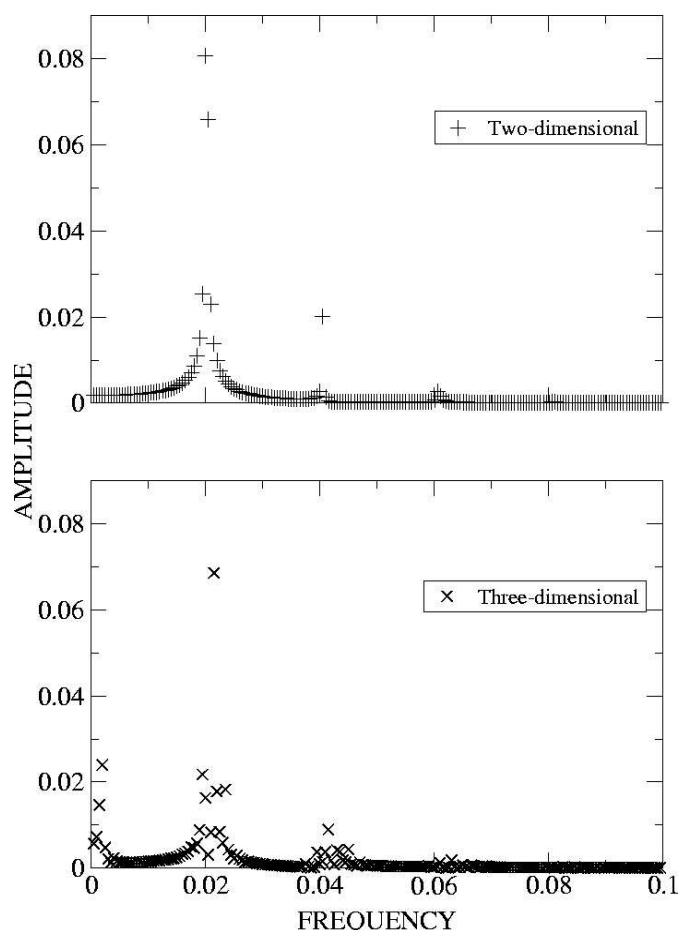


Figure 6: Fourier power spectra of temperature time series for two-dimensional and three-dimensional solutions for  $Re = 20$

additional modes close to 0.02 and 0.04 that are not present in the two-dimensional result. The lower amplitude of the three-dimensional signal at 0.02 and 0.04 is associated with the reduced amplitude of the wave seen in the temperature contours, noted above, and is very likely to be a result of the transfer of energy to the spanwise mode, leading to the hypothesis that the three-dimensional transition is associated with a nonlinear transfer of energy from the base two-dimensional mode to the spanwise mode. A single measure of the effect of the travelling waves is the Nusselt number, defined as the mean ratio of the heat transfer coefficient to that prevailing under the base flow. The Nusselt number for the two-dimensional flow at  $Re = 20$  is approximately 3% greater than that for the three-dimensional flow, again with both solutions obtained on the coarse mesh used for the three-dimensional simulation. The reduction in Nusselt number seen with the three-dimensional flow is again believed to be a result of the reduced amplitude of the 0.02 and 0.04 frequency modes.

### Conclusions

The flow generated by a constant temperature gradient boundary condition on a vertical plate with constant stable background vertical temperature gradient has been found very useful for the investigation of stability and transition in natural convection boundary layers. The sub-critical flow is one-dimensional, with no variation in the  $y$  and  $z$  directions, allowing the use of parallel flow stability analysis techniques. Direct numerical simulations may be carried out on a reduced domain using periodic boundary conditions in the  $y$  and  $z$  directions.

The results obtained by McBain & Armfield [7] demonstrated that accurate information about the behaviour of the super-critical flow could be obtained via linear stability analysis. This

provided the critical Reynolds number for transition to oscillatory two-dimensional flow, as well as information about the wave-length and velocity of the fully nonlinear super-critical flow. The three-dimensional results presented above have shown that the initial transition is genuinely two-dimensional, with a further increase in Reynolds number required to generate a three-dimensional, spanwise, transition.

The results presented here indicate that the critical Reynolds number for three-dimensional transition is between  $Re = 19$  and  $Re = 20$ . These results were obtained for a domain with spanwise extent approximately equal to the resolved vertical wave-length, and it is not immediately clear that this will be the critical spanwise wave-length. The use of a finite domain with periodic boundary conditions does limit the resolvable modes to those with wavelengths that are an integral divisor of the domain size, and some care must be taken to examine a number of domains to determine critical values. Some initial tests with smaller and larger spanwise extent domains have indicated that the critical spanwise mode has a wave-length approximately equal to that of the base two dimensional streamwise mode, as shown here, giving support to these results, although more work is required to verify this hypothesis.

### Acknowledgements

This work was supported by the Australian Research Council Discovery scheme and the University of Sydney Sesqui Post-doctoral Fellowship scheme.

### References

- [1] Armfield, S. W. and Patterson, J. C., Wave properties of natural convection boundary layers, *J. Fluid Mech.*, **239**, 1992, 195–211.
- [2] Bergholz, R. F., Instability of steady natural convection flow in a vertical fluid layer, *J. Fluid Mech.*, **84**, 1978, 743–768.
- [3] Christov, C. I. and Homsy, G. M., Nonlinear dynamics of two-dimensional convection in a vertically stratified slot with and without gravity modulation, *J. Fluid Mech.*, **430**, 2001, 335–360.
- [4] Elder, J. W., Laminar free convection in a vertical slot, *J. Fluid Mech.*, **23**, 1965, 77–98.
- [5] Gill, A. E. and Davey, A., Instabilities of a buoyancy driven system, *J. Fluid Mech.*, **35**, 1969, 776–798.
- [6] Jaluria, Y. and Gebhart, B., An experimental study of nonlinear disturbance behaviour in natural convection, *J. Fluid Mech.*, **61**, 1973, 337–365.
- [7] McBain, G. D. and Armfield, S. W., Instability of the buoyancy boundary layer on an evenly heated vertical wall. *J. Fluid Mech.*, submitted.
- [8] McBain, G. D. and Armfield, S. W., Linear stability of natural convection on an evenly heated vertical wall, this conference.

## Transient Behaviour of the Fuel Spray from an Air-Assisted, Direct Fuel Injector

S.H. Jin<sup>1</sup>, M.J. Brear<sup>1</sup>, G. Zakis<sup>1</sup>, H.C. Watson<sup>1</sup> and C. Xavier<sup>2</sup>

<sup>1</sup>Department of Mechanical and Manufacturing Engineering  
University of Melbourne, VIC, 3010 AUSTRALIA

<sup>2</sup>Orbital Engine Company (Australia) Pty. Ltd.  
Balcatta, Western Australia, 6021 AUSTRALIA

### Abstract

The transient behaviour of the fuel spray from an air-assisted fuel injector in a constant volume chamber has been investigated experimentally. The relative Sauter mean diameter (SMD) of the spray droplets was determined using planar laser induced fluorescence (PLIF) and planar Mie scattering. Planar images of the ensemble averaged relative SMD with various injection conditions were obtained by calculating the ratio between the two laser light intensities at a given point. The penetration length and the spray shape factor were also obtained. The ensemble averaged results suggest the existence of vortices that are shed from the injector tip, and which entrain the smaller droplets. Results also show that the characteristics of the injector vary weakly with several particular injection parameters, notably the fuel injection pressure and the delay between fuel and air injection.

### Introduction

In order to meet ever-tightening emissions regulations whilst simultaneously minimising fuel consumption and CO<sub>2</sub> emissions, many efforts have been made recently to improve the performance of gasoline fuelled spark ignition engines. Such efforts include the manipulation of in-cylinder flow, optimisation of the electronic control systems, and optimisation of direct injected spark ignition (DISI) fuel systems [1,2]. The improvements in fuel economy obtained by using DISI have prompted an increased adoption of this technology in passenger vehicles. Further study of fuel sprays in SI engines aims in particular to minimise the emissions of hydrocarbons (HC), oxides of nitrogen (NO<sub>x</sub>) and particulate matter (PM) and improve efficiency through more complete combustion. Since the fuel injection pressure of a DISI engine is typically lower than that of a diesel engine, larger fuel droplets can exist in the cylinder, and so poor fuel distribution and slow evaporation may result. This is particularly the case during cold engine starting and warm-up, when the highest levels of HC emissions over the entire drive-cycle usually occur. For these reasons, air-assisted direct injectors with improved fuel atomisation are currently under development.

The air-assisted direct injection fuel system has many unique features compared with single fluid systems. The most obvious difference is the addition of air, which is injected directly into the combustion chamber with the fuel. The pressure and quantity of the air influence the characteristics of spray. The characteristics of the fuel spray play an important role in mixture preparation, which has an effect on combustion and emissions, so it is important to understand the spray characteristics within the combustion chamber.

The droplet diameter of the spray is one of the most important aspects of spray characteristics. Laser diffraction particle analysis (LDPA) and phase Doppler particle analysis (PDPA) are generally used to measure the droplet size, but there are disadvantages to both methods. LDPA is not suitable for dense spray measurement because of multiple diffraction phenomena,

and PDPA is used for point measurement, so it needs a great deal of time and effort to obtain the droplet size distribution across the whole spray. It is therefore worthwhile developing alternative methods, such as the present, planar imaging technique using a laser sheet, to study the transient spray characteristics [3-5].

This paper presents an experimental study of an air-assisted, direct injection (DISI) system. The technique of 'laser sheet drop-sizing' (LSD) is used to examine the transient behaviour of the fuel spray. These results are compared to back-illuminated images at the same conditions, and the spray-tip penetration and shape factor are also determined.

### Experimental methods

The Sauter mean diameter (SMD) can be determined for liquid droplets by combining the well established techniques of Mie scattering and laser induced fluorescence (LIF). The intensity of the fluorescence signal measured by LIF is proportional to the concentration of the fluorescing molecules. As such, the observed fluorescence originates almost entirely from molecules in the liquid phase. As shown in equation (1), the fluorescence intensity per unit area  $I_{LIF}$  of the emitted light is *ideally* proportional to the cube of the particle diameter, assuming negligible light absorption and negligible optical amplification [4].

$$I_{LIF} = C_1 I_0 e^{-kx} \int_0^\infty D^3 \frac{dn}{dD} dD, \quad (1)$$

where  $I_0$  is the intensity of the incident laser beam,  $x$  is the distance travelled by the incident laser beam,  $k$  is an attenuation factor,  $D$  is the droplet diameter,  $dn$  is the droplet number density between  $D$  and  $D+dD$  and  $C_1$  is a constant that depends on the experimental configuration. In the case of significant absorption or optical amplification,  $I_{LIF}$  has been observed to vary with particle diameter to a power varying between 2.4 and 3.1 [4]. The exact relationship can only be established by examining a range of droplets of known diameter, and the ideal cubic relationship for the fluorescence is therefore assumed.

According to Lorenz-Mie theory, the intensity of Mie scattering is a function of droplet diameter, the reflection rate of the droplet, polarization, and the wavelength of the incident beam. In the case of spherical droplets with a diameter larger than 1  $\mu\text{m}$  and illuminated with a beam of wavelength 355nm, the intensity is approximately proportional to the square of droplet diameter [4], and can be expressed as:

$$I_{Mie} = C_2 I_0 e^{-kx} Q_{sca} \int_0^\infty D^2 \frac{dn}{dD} dD, \quad (2)$$

where  $C_2$  is a coefficient determined by the characteristics of the detecting optical system and  $Q_{sca}$  is related to the angle between the direction of incident laser beam and the detecting direction. Using equations (1) and (2), it is then found that the SMD is proportional to the ratio between the LIF and Mie intensities:

$$\frac{I_{LIF}}{I_{Mie}} = \frac{C_1}{C_2 Q_{sca}} \frac{\int_0^\infty D^3 \frac{dn}{dD} dD}{\int_0^\infty D^2 \frac{dn}{dD} dD} = \frac{D_{32}}{C}, \quad (3)$$

where  $C=C_2Q_{sca}/C_1$  has the units of length and could be determined with an appropriate calibration method, such as laser diffraction particle analysis (LDPA) or phase Doppler particle analysis (PDPA) [6]. The simultaneous measurement of the LIF and Mie scattering signals also yields a relative SMD of the spray that is not related to the intensity of the incident laser sheet or the absorption of the laser sheet.

### Experimental layout

A schematic of the experimental set-up is shown in figure 1. The light source used was a Nd:YAG laser (Quantel, TwinsB). The laser pulse duration was 5ns and the maximum energy was 120mJ at a wavelength of 355nm. A sheet beam was formed using a set of cylindrical lenses and the optical system was carefully aligned to minimize unwanted stray light such as reflections from the chamber wall. The fluorescence and Mie scattered signals were imaged at a right angle to the laser beam using an ICCD camera (LaVision, FlowMaster3 with intensifier) with a UV Nikon lens (f/# 4.5) and a gate width of 100ns. A GG-400 Schott glass filter was used for the fluorescence signal and a 355nm band-pass filter for Mie scattering. Images of the LIF and Mie scattering at a given instant during subsequent injection events were ensemble averaged. The ensemble averaged distributions obtained using 100 and 1000 ensemble averages were very similar, so all the results presented in this paper used 100 ensemble averages.

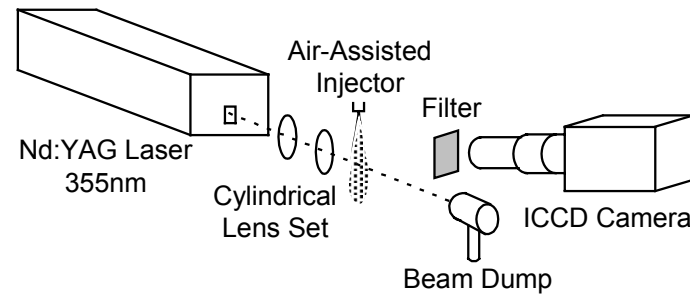


Figure 1. Schematic of experimental set-up.

Standard, unleaded petrol (ULP) with an octane number of 91 was used as the fuel during experiments. The LIF spectrum of this particular ULP blend is broadband, and ranges from 380nm to 440nm, with a peak at 405nm. Absorption and emission bands are spectrally well separated, ensuring the absence of fluorescence trapping and making possible the separation of the Mie scattered and the fluorescence signals.

The air-assisted injection system comprises two main components: a fuel metering injector, similar to a port fuel injector, and an air injector, which delivers a mixture of metered fuel and air into the combustion chamber (figure 2a). The fuel injector delivers fuel into a reservoir that is internal to the injector. The air injector then delivers this (metered) fuel into the combustion chamber. This system has been reported previously to exhibit the favourable quality of small fuel droplet size [7]. A unique feature of the system is the decoupling of the direct injection event with the fuel-metering event (figure 2c). This allows the direct injection event to be tailored to the combustion requirements, rather than being limited by also needing to perform the fuel metering, as is the case in high-pressure single fluid injection systems. The air-assisted injection system, installed in the constant volume chamber, has the capability of varying the chamber pressure and uses a nominal injection air pressure of 650kPa and a fuel pressure of either 720 or 800kPa. Both fuel and air injection pressures were controlled by adjusting pressure regulators. Table 1 outlines the experimental conditions of the air-assisted fuel injector. With a fuel injection duration of 4.1ms at 720kPa fuel pressure and 3.1ms at 800kPa,

about 10mg of fuel was injected at a frequency of 1Hz. Injection timing, laser triggering and ICCD camera control were controlled by LABVIEW software. The times that are reported in this paper refer to the time after the trigger pulse was sent to the injector driver. This means that the first appearance of fuel is somewhat later due to delays within the injector driver and the mechanical properties of the injector. These unavoidable delays are typically a few hundred microseconds long and will be discussed later in the paper. The experiments were performed with the chamber at ambient temperature and pressure and quiescent gas conditions.

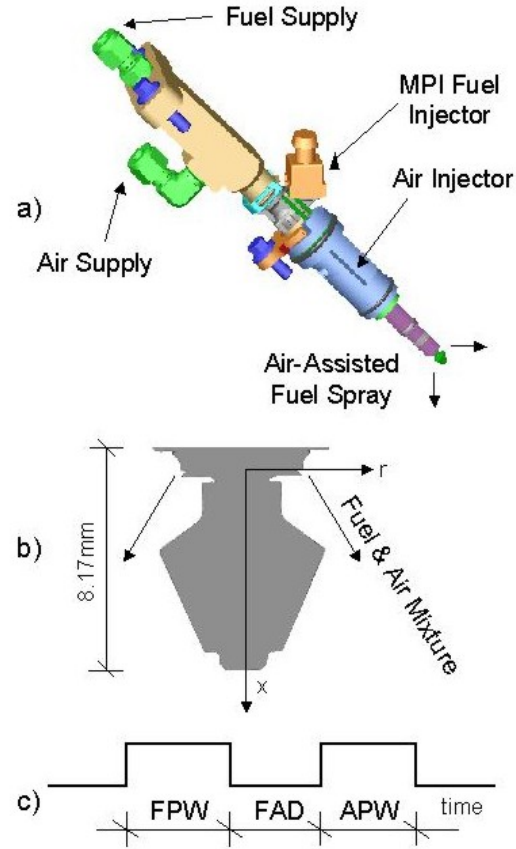


Figure 2. The air-assisted direct fuel injection system, showing a) overall configuration, b) the injector tip and c) timing schedule

Fuel injection pressure (FIP)	720 & 800kPa gauge
Air injection pressure (AIP)	650kPa gauge
Fuel pulse width (FPW)	4.1ms & 3.1ms
Air pulse width (APW)	3ms
Fuel metering gain (FMG)	10mg/pulse
Air metering gain (AMG)	8.43mg/pulse
Fuel and air injection delay (FAD)	-1, 0 and 1ms
Ambient pressure	101kPa abs.

Table 1. Experimental conditions.

### Results and Discussion

The relative SMD of an air-assisted direct fuel injector has been measured using LIF and Mie scattering. Figure 3 shows ensemble averaged LIF, Mie scattering and relative SMD images collected separately. These images were obtained at 1.8ms after the start of air injection for 720kPa fuel injection pressure and 650kPa air injection pressure. Both LIF and Mie scattering images were not corrected for laser profile variation since the images and the profiles are divided to produce the relative SMD. The systematic laser profile features could therefore be cancelled across both the laser height and thickness of the laser sheet. The LIF image shows the liquid volume fraction, with most of the fuel mass in the centre of the spray. The Mie scattering image also has a strong signal in the centre of the spray but is narrower in width compared to the LIF image. The relative SMD image possesses a

small degree of asymmetry about the injector centreline, and such behaviour was seen throughout the present set of experiments (eg. figure 7). Previous experiments showed that similar, asymmetric results were reflected when the injector was rotated  $180^\circ$ , thus showing that this was due to non-axisymmetry in the experimental set-up, rather than in the measurement technique.

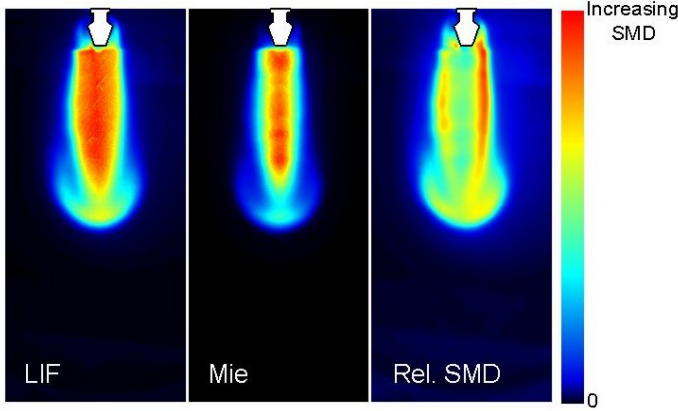


Figure 3. Time-averaged images of LIF signal (left), Mie scattering signal (middle) and relative SMD (right).

The relative SMD image shows that the edge of the spray contains larger droplets, whilst there are smaller droplets in the centre. Near the nozzle tip, the signal is not well defined due to the presence of fuel ligaments and surface scattering of the incident laser beam. Each of the three images in figure 3 shows that the spray roughly resembles a downward pointing arrow; the Mie scattered result shows this most clearly. This behaviour is thought to be due to the shedding of a vortex ring from the injector at the start of injection. Such behaviour is common in studies of pulsing, single phase injection. In the present, two phase case, the smaller droplets are presumably entrained more by the vortex ring, and are wrapped around the ring as it translates, leading to this ‘arrowhead’ shape. This behaviour, if true, highlights the coupling between the gas and liquid phases in this injection system, and is very different to that of a liquid-only injector. Further experiments (in particular particle image velocimetry) and ongoing numerical simulations will determine whether this vortex structure actually exists.

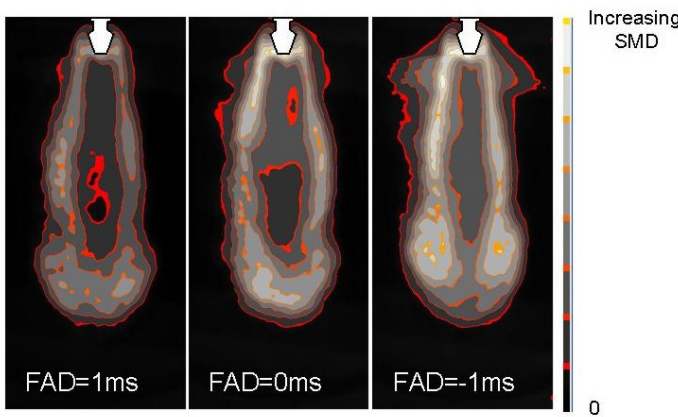


Figure 4. Comparison of relative SMD for different time interval between fuel and air injection (FAD).

Figure 4 shows the effect of fuel air delay (FAD) on the ensemble averaged SMD. These images were measured 2.0ms after the start of air injection with a 720kPa fuel injection pressure and 650kPa air injection pressure. As can be seen in this figure, there is a difference in droplet size between locations such as the centre and periphery of the spray, and the droplet size is larger away from the spray centreline. This is thought to be due to the larger droplets maintaining their initial trajectory better

because of their greater inertia. The smaller droplets are deflected more by the air, and so can migrate to the injector centreline. The relative SMD also increases as the FAD decreases. Reasons for this trend in FAD are not clear, and are presently being studied using numerical simulations.

Spray characteristics of interest also include the spray tip penetration length, the spray cone angle and the overall spray SMD. The spray tip penetration length was measured directly from the spray images and obtained by measuring the distance from the injector exit (figure 2b) to the lowest intensity Mie scattering contour in the axial direction. Figure 5 shows the spray tip penetration length as a function of time for the two different fuel injection pressures (FIP) and delay between fuel and air injection (FAD). The effects of varying the FIP and FAD are relatively small. This is to be expected for positive FAD's, since the fuel and air injection events are then separate, with the fuel being dumped into the internal reservoir and then injected by the air into the chamber. The spray penetration is also expected to decrease for negative FAD's, and figure 5 shows this beginning to occur by FAD=-1ms.

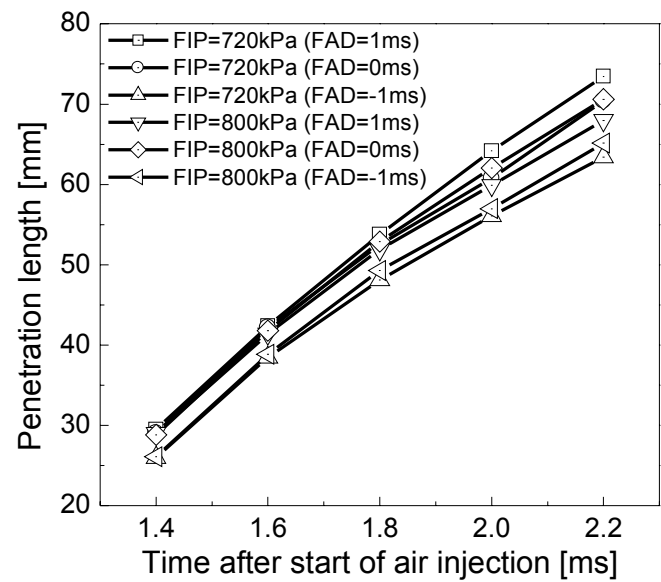


Figure 5. Spray tip penetration length for different fuel injection pressure (FIP) and time interval between fuel and air injection (FAD).

The spray shape factor is defined as

$$\text{spray shape factor} = \tan^{-1} \left( \frac{\text{maximum spray width}}{\text{spray penetration length}} \right) \quad (4)$$

Figure 6 shows that the spray shape factor decreases rapidly after the start of injection at all the conditions studied. As figure 7 shows, this is due to the width of the spray remaining relatively contained as the spray penetrates into the chamber. This highlights once again the effect of the air-assist on the spray development [7].

Figure 7 displays a collection of back-illuminated and relative SMD spray images for different times after the start of air injection. The relative SMD results for later times are not shown due to the charge impinging on the chamber walls and filling the chamber. As mentioned earlier, there is a delay between the electrical triggering of the start and end of injection and the mechanical response of the injector. The opening and closing delays for this injector were approximately 1.0ms and 0.6ms respectively. The back-illumination passes through the entire spray and is therefore a projection of an (ideally) axisymmetric problem, rather than a planar image such as those shown for the relative SMD. Nonetheless, the penetration of the spray in both



cases is similar, and there is some suggestion of the aforementioned spray ‘arrowhead’ in the back-illuminated results at 1.8ms.

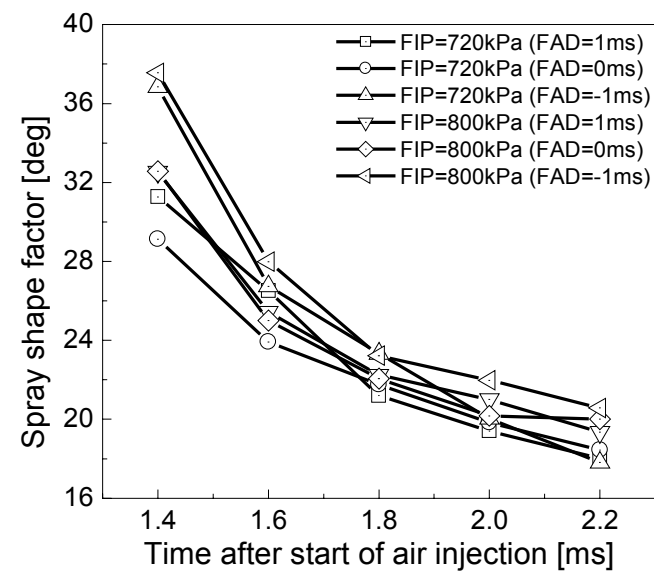


Figure 6. Spray shape factor for different fuel injection pressure (FIP) and time interval between fuel and air injection (FAD).

### Conclusions

The characteristics of the fuel spray from an air-assisted, gasoline direct fuel injector have been performed using optical techniques. The technique of ‘laser sheet drop-sizing’ (LSD), which required the combined use of Mie scattering and laser induced fluorescence (LIF), allowed determination of the relative Sauter mean diameter (SMD) of the fuel spray. Both the Mie and LIF images were ensemble averaged over separate injection events, thereby permitting study of the transient development of the ensemble averaged spray.

Several, interesting aspects of the transient spray behaviour were noted. The previously reported spray containment enabled by the air-assist was observed, with the spray maintaining a narrow

width as it penetrated into the chamber. The largest droplets were also observed to lie away from the spray centreline, which was considered reasonable. Finally, there was also some evidence that a vortex ring was shed from the injector at the start of injection, although further, planned experimental and numerical studies are required to confirm this.

### Acknowledgments

This work was supported by the Orbital Engine Company, Holden Limited and the Australian Research Council. The authors are particularly grateful for the strong co-operation of their industrial partners, as well as the technical support from Mr T. Grange and Mr D. Halpin.

### References

- [1] Zhao, F.Q., Lai, M.C. & Harrington, D.L., The Spray Characteristics of Automotive Port Fuel Injection – A Critical Review, *SAE Paper* 950506, 1995.
- [2] Sampson, M.J. & Heywood, J.B., Analysis of Fuel Behaviour in the Spark-Ignition Engine Start-Up Process, *SAE Paper* 950678, 1995.
- [3] Yeh, C., Kosaka, H. & Kaminoto, T., Fluorescence / Scattering Image Technique for Particle Sizing in Unsteady Diesel Spray, *JSME Trans.*, B **59**, 1993, 308-313.
- [4] LeGal, P., Farrugia, N. & Greenhalgh, D.A., Laser Sheet Dropsizing of Dense Sprays, *Opt. Laser Technol.*, **31**, 1999, 75-83.
- [5] Stojkovic, B.C. & Sick, V., Evolution and Impingement of an Automotive Fuel Spray Investigated with Simultaneous Mie/LIF Techniques, *Appl. Phys.*, B **73**, 2001, 75-83.
- [6] Jermy, M.C. & Greenhalgh, D.A., Planar Dropsizing by Elastic and Fluorescence Scattering in Sprays Too Dense for Phase Doppler Measurement, *Appl. Phys.*, B **71**, 2000, 703-710.
- [7] Cathcart, G. & Xavier, C., Fundamental Characteristics of an Air-Assisted Direct Injection Combustion System as Applied to 4-Stroke Automotive Gasoline Engines, *SAE Paper* 2000-01-0256, SP-1499, 2000.

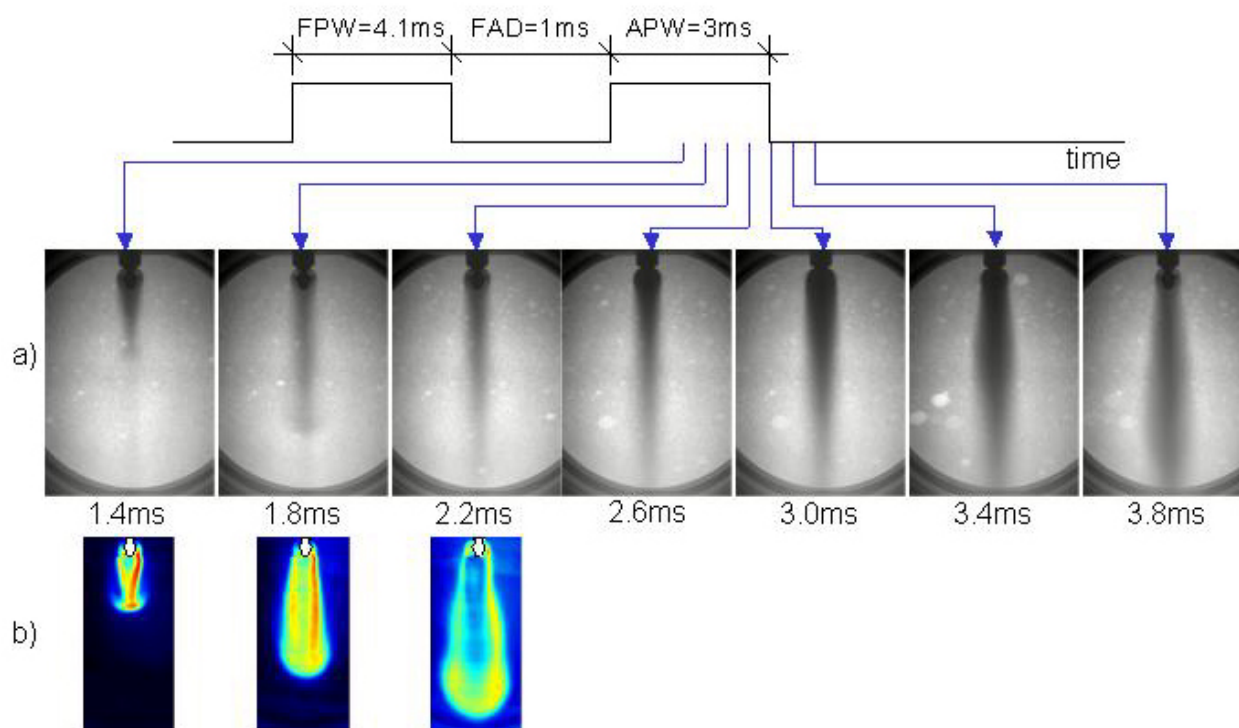


Figure 7. Spray profiles after the start of air-injection showing a) back-illumination and b) relative SMD results (key as in figure 3).



## How to describe turbulent energy distributions without the Fourier transform

P. A. Davidson<sup>1</sup>, B. R. Pearson<sup>2</sup> & P. Staplehurst<sup>1</sup>

<sup>1</sup>Department of Engineering, University of Cambridge.  
Cambridge CB2 1PZ, UNITED KINGDOM.

<sup>2</sup>School of Mechanical, Materials, Manufacturing Engineering & Management.  
University of Nottingham, Nottingham NG7 2RD, UNITED KINGDOM.

### Abstract

It has been noted that the scale-by-scale distribution of kinetic energy in a turbulent flow is more readily observed in spectral space, using  $E(k)$ , than in real space, using the second-order structure function. For example, the 5/3rds law is usually easier to identify in experimental data than the equivalent 2/3rds law. We argue that this is not an implicit feature of a real-space description of turbulence. Rather, it is because the second-order structure function mixes small and large-scale information. In order to remedy this problem, Davidson[1] introduced a real-space function,  $V(r)$ , which plays the role of an energy density function, somewhat analogous to  $E(k)$ . In this paper we examine data taken in a variety of flows and determine the form of  $V(r)$  in intermediate Reynolds number turbulence. We find that dissipation-range phenomena, such as the bottleneck effect, and the energy injection range are clearly evident in the signature function, but are absent in the structure function.

### A Problem with the second-order Structure Function.

There are two common methods of describing how kinetic energy is distributed amongst the hierarchy of eddy sizes in isotropic turbulence. These are the three-dimensional energy spectrum,  $E(k)$ , and the second-order structure function, defined as,

$$\langle [\delta u(r)]^2 \rangle = \langle [u_x(\mathbf{x} + r\hat{\mathbf{e}}_x) - u_x(\mathbf{x})]^2 \rangle.$$

The utility of the energy spectrum rests, in part, on three useful properties of  $E(k)$ :

1. it is positive;
2. it integrates to give the kinetic energy; and
3. a random distribution of eddies of fixed size  $l_e$  produces an energy spectrum of the form,

$$E(k) \sim \langle \mathbf{u}^2 \rangle l_e (kl_e)^4 \exp \left[ -(kl_e)^2 / 4 \right],$$

which exhibits a peak at  $k \sim \pi/l_e$  (see, for example, Ref.[1]).

The first two properties tells us that we may regard  $E(k)$  as an energy distribution in spectral space, while the third suggests that we may loosely associate eddy size with  $\pi/k$ , at least in the range  $\eta < \pi/k < l$ , where  $l$  and  $\eta$  are the integral and Kolmogorov scales[2], respectively.

The second-order structure function can also be used to describe the distribution of energy over different scales. However, it has profound limitations, as we now show. The usual explanation for using  $\langle [\delta u(r)]^2 \rangle$  as a measure of energy density is the following. Eddies of size much less than the separation  $r$  can induce a large signal at  $\mathbf{x}$  or  $\mathbf{x}' = \mathbf{x} + r\hat{\mathbf{e}}_x$ , but not

at both points simultaneously. Thus eddies smaller than  $r$  tend to induce a contribution to  $[\delta u]^2$  which is of the order of their kinetic energy. On the other hand, eddies much greater than  $r$  tend to produce similar velocities at both  $\mathbf{x}$  and  $\mathbf{x}'$ , and so make little contribution to the velocity difference,  $\delta u$ . So we might think of the structure function as a sort of filter, suppressing information from eddies of size greater than  $r$ . Given that  $\frac{3}{4} \langle [\delta u]^2 \rangle \rightarrow \frac{1}{2} \langle \mathbf{u}^2 \rangle$  for large  $r$  we might expect that,

$$\begin{aligned} \frac{3}{4} \langle [\delta u(r)]^2 \rangle &\sim [\text{energy in eddies of size } < r] \\ &\sim \int_{\pi/r}^{\infty} E(k) dk, \end{aligned} \quad (1)$$

and indeed such estimates are commonly made[3]. This led Townsend[3] to propose  $V_T(r) = d \langle \frac{3}{4} [\delta u]^2 \rangle / dr$  (the subscript  $T$  to indicate Townsend) as a kind of energy density which plays a role analogous to  $E(k)$ . However, this is a deeply flawed view. Eddies whose sizes are much greater than  $r$  produce a contribution to  $\frac{3}{4} [\delta u]^2$  of the order of  $\frac{3}{4} \langle (\partial u_x / \partial x)^2 \rangle r^2 = \frac{1}{10} \langle \frac{1}{2} \omega^2 \rangle r^2$ , so that we should replace Eq. (1) by the estimate,

$$\begin{aligned} \frac{3}{4} \langle [\delta u(r)]^2 \rangle &\sim [\text{energy in eddies of size } < r] + \left( r^2 / 10 \right) \\ &\quad \times [\text{enstrophy in eddies of size } > r]. \end{aligned} \quad (2)$$

Indeed it is readily confirmed, using the transform pair which relates  $E(k)$  to  $\langle [\delta u(r)]^2 \rangle$ , that a good approximation to the relationship between these two quantities is[1],

$$\frac{3}{4} \langle [\delta u(r)]^2 \rangle \approx \int_{\pi/r}^{\infty} E(k) dk + (r/\pi)^2 \int_0^{\pi/r} k^2 E(k) dk, \quad (3)$$

which is precisely what we would expect from Eq. (2) [see Ref.[1] for a more detailed discussion of the progression from Eq. (1) to Eq. (3)]. Thus  $\langle [\delta u(r)]^2 \rangle$  mixes large- and small-scale information, as well as information about energy and enstrophy. It follows that  $V_T(r)$  is not a satisfactory estimate of the kinetic energy density. This failure of  $V_T(r)$  led Davidson[1] to introduce a new function, called the *signature function*, which seeks to eliminate the large-scale information contained in Eqs. (2) and (3).

### An Alternative to the Structure Function: The Signature Function.

The signature function is defined for isotropic turbulence only. It is:

$$V(r) = -\frac{1}{2} r^2 \frac{\partial}{\partial r} \frac{1}{r} \frac{\partial}{\partial r} \left\{ \frac{3}{4} \langle [\delta u(r)]^2 \rangle \right\}. \quad (4)$$

It may be shown that  $V(r)$  has the following properties[1]:

1.

$$\int_0^r V(r) dr \geq 0;$$

2.

$$\int_0^\infty V(r) dr = \frac{1}{2} \langle \mathbf{u}^2 \rangle;$$

3. a random distribution of eddies of fixed size  $l_e$  gives rise to the signature function,

$$V(r) \sim \langle \mathbf{u}^2 \rangle l_e^{-1} (r/l_e)^3 \exp(-r^2/l_e^2),$$

which has a peak around  $r \sim l$ .

If we compare these properties with those of  $E(k)$  we see that, like the energy spectrum,  $V(r)$  may be thought of as an energy density, with  $r$  interpreted as eddy size. The formal relationship between  $E(k)$  and  $V(r)$  is readily shown to take the form of a Hankel transform[1],

$$rV(r) = \frac{3\sqrt{\pi}}{2\sqrt{2}} \int_0^\infty E(k)(rk)^{1/2} J_{7/2}(rk) dk, \quad (5)$$

from which it may be shown that,

$$rV(r) \approx [kE(k)]_{k=\hat{\pi}/r},$$

where  $\hat{\pi} = 9\pi/8$ . For example, the difference between  $rV(r)$  and  $[kE(k)]_{k=\hat{\pi}/r}$  can be shown to be less than 4% for power-law spectra of the form[1],

$$E = Ak^n, \quad -2 < n < 1.$$

One illustration of this is the 2/3rds law,

$$\langle [\delta u(r)]^2 \rangle = \beta \varepsilon^{2/3} r^{2/3}, \quad (6)$$

(where  $\beta$  is the Kolmogorov constant and  $\varepsilon$  the mean turbulent energy dissipation rate) whose spectral equivalent is

$$E(k) = 0.761 \beta \varepsilon^{2/3} k^{-5/3}.$$

In terms of  $V(r)$  we have, from Eq. (4),

$$rV(r) = \frac{1}{3} \beta \varepsilon^{2/3} r^{2/3} = 1.016 [kE(k)]_{k=\hat{\pi}/r}. \quad (7)$$

The aim of the present work is to evaluate  $V(r)$  for data taken from various flows. We will demonstrate that  $V(r)$  is a superior diagnostic tool to  $\langle [\delta u(r)]^2 \rangle$  for examining the energy structure of turbulence in the scale range  $\eta < r < L$ . Although this paper limits itself to “second-order” quantities, it is possible to define “higher-order” signature functions[1, 4]. For example, the natural progression from  $V(r)$  is to define a signature function that, in some way, corresponds to the turbulent kinetic energy transfer flux and is comparable to the third-order structure function.

### An Analytical Example

A simple example which demonstrates the utility of Eq. (4) is the following. Batchelor[5, 6] introduced a model expression for the second order structure function in the equilibrium range. It is exact in the limit  $r \ll \eta$  and  $r \gg \eta$ , and interpolates between these limits. It is:

$$15 \langle [\delta u(r/\eta)]^2 \rangle / u_\kappa^2 = \frac{(r/\eta)^2}{[1 + (15\beta)^{-3/2} (r/\eta)^2]^{2/3}}, \quad (8)$$

where  $\eta (\equiv \nu^{3/4} \varepsilon^{-1/4})$  and  $u_\kappa (\equiv \nu^{1/4} \varepsilon^{1/4})$  are the Kolmogorov length and velocity scales respectively. Figure 1 shows both Eq. (8) [with  $\beta = 2.06[10]$ ] and 3 times Eq. (4) normalized by  $\varepsilon^{2/3} r^{2/3}$ . A viscous bottleneck effect[11, 12, 13] is clearly observed for the signature function in the cross-over region between the dissipative and inertial ranges. In the dissipative range, the signature function, unlike the structure function, quickly decays to zero as  $r/\eta \rightarrow 0$ . Both functions begin to display the required 2/3rds scaling from the same value of  $r/\eta \approx 100$ .

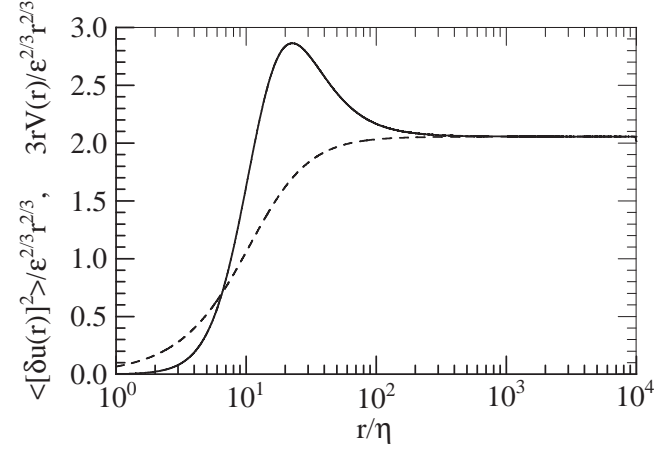


Figure 1: Curves of  $3rV(r)$  and  $\langle [\delta u(r)]^2 \rangle$ , normalized by  $\varepsilon^{2/3} r^{2/3}$  and plotted against  $r/\eta$ , for Batchelor’s parametric form, Eq. (8). —,  $3rV(r)$ ; ---,  $\langle [\delta u(r)]^2 \rangle$ .

### The Experimental Determination of the Signature Function.

#### The Experimental Data

The experimental data used for the present study are measurements made in fully developed turbulent wakes flows. Detailed experimental conditions can be found in Refs. [7, 8, 9] and need not be repeated here. The majority of data is acquired in a simple inexpensive geometry, which we call a NORMAN grid, that “stirs” vigorously on large scales. The geometry is composed of a perforated plate superimposed over a bi-plane grid of square rods. The grid is located in a blow-down wind-tunnel[7] of test section dimensions  $35 \times 35 \text{ cm}^2$  and 2 m length. The central three rows of the original bi-plane grid (mesh size  $M = 50 \text{ mm}$ , original solidity  $\sigma = 33\%$ ) have alternate meshes blocked (final  $\sigma = 46\%$ ). As well as the NORMAN grid geometry, normal plate and circular cylinder wake data are re-evaluated here with original details also found in Ref.[7]. The measurements are made on the centreline of the wake formed behind each geometry at a downstream measurement station of  $x/d \approx 40$ . For all flows, signals of  $u$  are acquired on the mean shear profile centreline.

All data are acquired using the constant temperature anemometry (CTA) hot-wire technique with a single-wire probe made of  $1.27 \mu\text{m}$  diameter Wollaston (Pt-10% Rh) wire. The instantaneous bridge voltage is buck-and-gained and the amplified signals are low-pass filtered  $f_{lp}$  with the sampling frequency  $f_s$  always at least twice  $f_{lp}$ . The resulting signal is recorded with 12-bit resolution. Throughout this work, time differences  $\tau$  and frequencies  $f$  are converted to streamwise distance  $r (\equiv \tau U)$  and 1-dimensional longitudinal wavenumber  $k_1 (\equiv 2\pi f/U)$  respectively using Taylor’s hypothesis. The mean dissipation rate  $\varepsilon$  is estimated assuming isotropy of the velocity derivatives

i.e.  $\varepsilon \equiv \varepsilon_{\text{iso}} = 15\nu \langle (\partial u / \partial x)^2 \rangle$ . We estimate  $\langle (\partial u / \partial x)^2 \rangle$  from the average value of  $E_{1D}(k_1)$  [the 1-dimensional energy spectrum of  $u$  such that  $u^2 = \int_0^\infty E_{1D}(k_1) dk_1$ ] and from finite differences  $\langle (\partial u / \partial x)^2 \rangle = \langle u_{i+1} - u_i \rangle^2 / (U f_s)^2$ . For most of the data, the worst wire resolution is  $\approx 2\eta$  where  $\eta$  is the dissipative length scale  $\equiv \nu^{3/4} \varepsilon_{\text{iso}}^{-1/4}$ . We have chosen not to correct for the decrease in wire resolution that is associated with an increase in  $Re_\lambda$ , since all methods known to us rely on an assumed distribution for the 3-dimensional energy spectrum. For most of the data, the worst wire resolution is  $\approx 2\eta$ . For the NORMAN grid data, the worst wire resolution is  $\approx 4\eta$ .

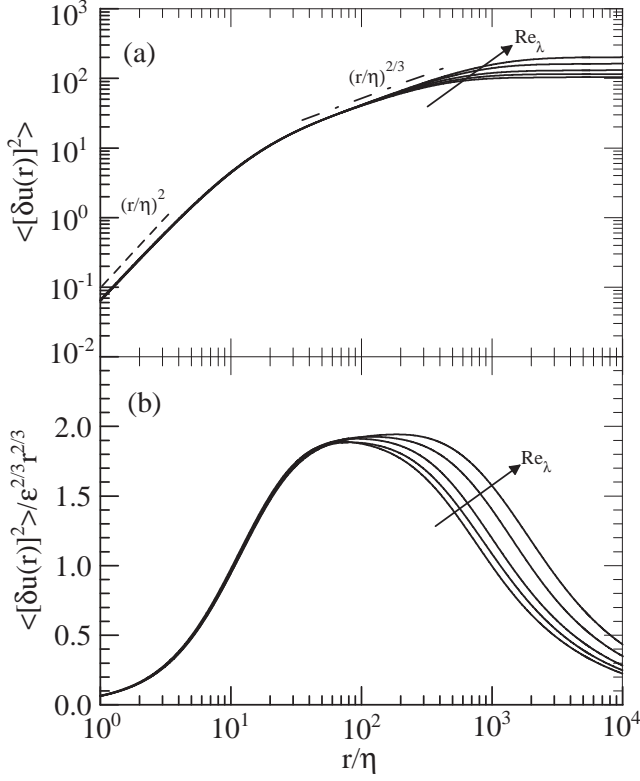


Figure 2: The  $Re_\lambda$  dependence of (a),  $\langle [\delta u(r)]^2 \rangle$ ; and (b),  $\langle [\delta u(r)]^2 \rangle / \varepsilon^{2/3} r^{2/3}$  and plotted against  $r/\eta$ , for NORMAN grid turbulence over the range  $Re_\lambda = 200 - 400$ . The  $\nearrow$  arrow points in the direction of increasing  $Re_\lambda$ .

## Results

Figures 2 and 3 show the  $Re_\lambda$  dependence of  $\langle [\delta u(r)]^2 \rangle$  and  $3rV(r)$  respectively. The data are calculated from the measurements made in the NORMAN grid experiment[8, 9] over the range  $Re_\lambda = 200 - 400$ . Figure 2(a) shows that  $\langle [\delta u(r)]^2 \rangle \sim r^2$  as  $r \rightarrow 0$  and  $\langle [\delta u(r)]^2 \rangle \sim r^{2/3}$  in the inertial range while Figure 3(a) shows that  $3rV(r) \sim r^4$  as  $r \rightarrow 0$  and  $3rV(r) \sim r^{2/3}$  in the inertial range. The scaling behavior in the range  $\eta \ll r \ll L$  can be more easily gleaned from Figs. 2(b) and 3(b). For both quantities,  $Re_\lambda$  dependent behaviors are observed. The signature function has a higher amplitude at large  $Re$ , and has acquired the characteristic double hump shape seen in energy spectra, e.g. see Fig. 5 in Ref. [14]. This second hump occurs in the region of  $r \approx L$ .

In Figure 4 we compare  $3rV(r)$  and  $\langle [\delta u(r)]^2 \rangle$ , both normalized by  $\varepsilon^{2/3} r^{2/3}$ , for NORMAN grid turbulence at  $Re_\lambda = 255$ . According to Eq. (7) the inertial range in such compensated

plots should show up as a plateau with a numerical value equal to  $\beta$ . It is clear that, because of the modest value of  $Re_\lambda$ , only a limited inertial range is discernable in the signature or structure functions. Never-the-less, the expected overshoot in energy at the junction of the inertial and dissipation ranges shows up clearly in the signature function, though not in the structure function. The cause of this overshoot, which has become known as the bottleneck effect[11, 12, 13], are the viscous forces[1].

Figure 5 shows compensated plots of  $rV(r)$  for NORMAN grid turbulence ( $Re_\lambda = 255$ ) and for wakes behind a plate ( $Re_\lambda = 248$ ) and a cylinder ( $Re_\lambda = 254$ ). This time we use a linear plot and restrict ourselves to  $r < L$ , which corresponds to  $r/\eta \sim 300$ . The inertial range shows up more clearly in these plots, with a Kolmogorov constant of around  $\beta \approx 2.0$  in good agreement with the consensus value[10]. More details of the experimental determination of  $V(r)$  may be found in Ref. [4].

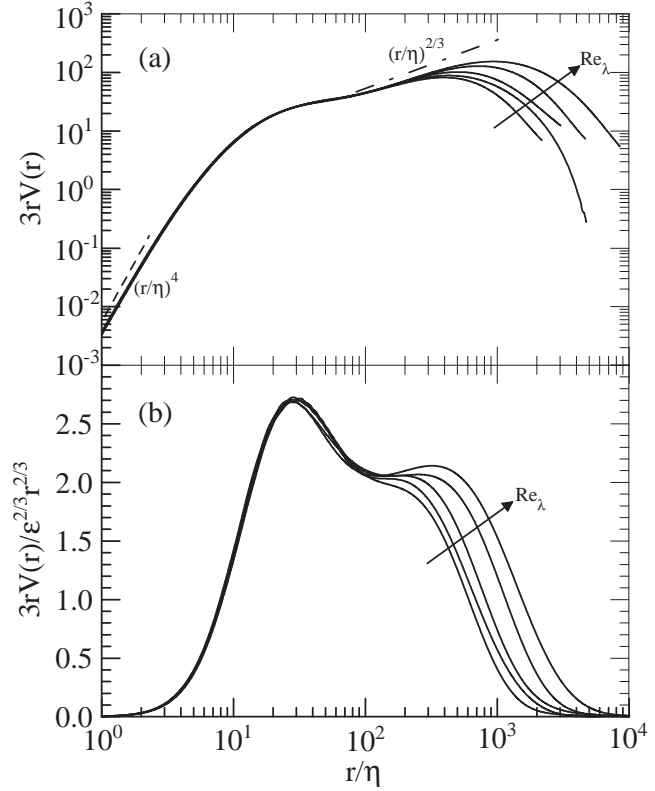


Figure 3: The  $Re_\lambda$  dependence of (a),  $3rV(r)$ ; and (b),  $3rV(r) / \varepsilon^{2/3} r^{2/3}$  and plotted against  $r/\eta$ , for NORMAN grid turbulence over the range  $Re_\lambda = 200 - 400$ . The  $\nearrow$  arrow points in the direction of increasing  $Re_\lambda$ .

## Final remarks and conclusions

We have explored the utility of the signature function  $V(r)$  as an alternative to the structure function  $\langle [\delta u]^2 \rangle$  in describing turbulent kinetic energy in real space. At small separations  $r$ , the signature function  $V(r)$ , unlike  $\langle [\delta u]^2 \rangle$ , captures the bottleneck behavior seen in Fourier space[11, 12, 13]. At large  $r$ , e.g.  $r = L$ , the signature function  $V(r)$  indicates the region of large scale energy input. For the range of  $Re_\lambda$  investigated in the present work  $V(r)$  clearly indicates that the large and small turbulent scales have insufficient separation for a “true” inertial range to exist.

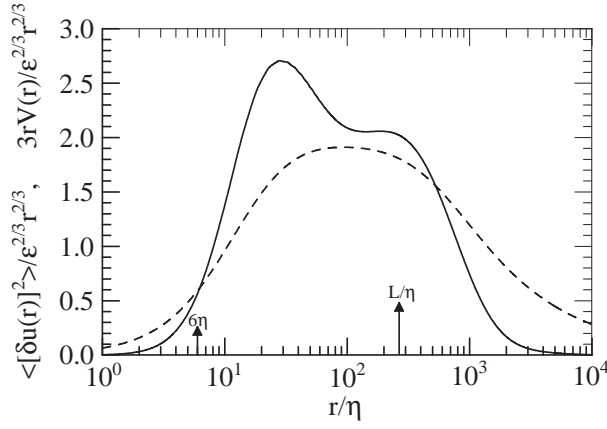


Figure 4: Curves of  $3rV(r)$  and  $\langle [\delta u(r)]^2 \rangle$ , normalized by  $\epsilon^{2/3} r^{2/3}$  and plotted against  $r/\eta$ , for NORMAN grid turbulence,  $Re_\lambda = 255$ . —,  $3rV(r)$ ; ---,  $\langle [\delta u(r)]^2 \rangle$ . The first  $\uparrow$  arrow indicates the average size of a dissipative structure and the second  $\uparrow$  arrow indicates the integral length scale  $L$ .

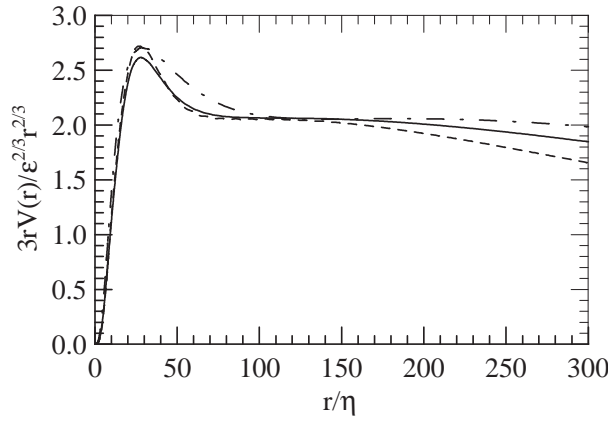


Figure 5: Compensated plots of  $3rV(r)$  for: —, plate wake turbulence  $Re_\lambda = 248$ ; ---, Cylinder wake turbulence  $Re_\lambda = 254$ ; and — · —, NORMAN grid turbulence  $Re_\lambda = 255$ .

## References

- [1] Davidson, P. A., *Turbulence*, Oxford University Press, 2004, p. 386-410
- [2] Kolmogorov, A. N., The local structure of turbulence in an incompressible fluid for very large Reynolds numbers, *Dokl. Akad. Nauk. SSSR*, **30**, 1941, 299-303.
- [3] Townsend, A. A., *The Structure of Turbulent Shear Flow*, Cambridge University Press, 1976.
- [4] Davidson, P. A. and Pearson, B. R., Identifying turbulent energy distributions in real, rather than Fourier, space, *Phys. Rev. Lett.*, *sub judice*, 2004.
- [5] Batchelor, G. K., *The Theory of Homogeneous Turbulence*, Cambridge University Press, 1953.
- [6] Batchelor, G. K., Pressure fluctuations in isotropic turbulence, *Proc. Cambridge Philos. Soc.* **47**, 1951, 359-378.
- [7] Antonia R. A. and Pearson, B. R., Effect of initial conditions on the mean energy dissipation rate and the scaling exponent, *Phys. Rev. E* **62**, 2000, 8086-8090.
- [8] Pearson, B. R., Krogstad, P. -Å. and van de Water, W., Measurements of the turbulent energy dissipation rate, *Phys. Fluids*, **14**, 2002, 1288-1290.
- [9] Pearson, B. R., Krogstad, P. -Å. and Johnson, G. R.,  $Re_\lambda$  dependence of the Kolmogorov constant and scaling, in *Reynolds Number Scaling in Turbulent Flow* (Ed. A. J. Smits) Kluwer Academic Publishers, 2003, 229-336.
- [10] Sreenivasan, K. R. On the universality of the Kolmogorov constant, *Phys. Fluids*, **7**, 1995, 2778-2784.
- [11] Falkovich, G., Bottleneck phenomenon in developed turbulence, *Phys. Fluids*, **6**, 19942, 1411-1414.
- [12] Coantic, M. and Lasserre, J. -J., On pre-dissipative bumps and an Re-number-dependant spectral parameterization of turbulence. *Eur. J. Mech. B/Fluids*, **18**, 1999, 1027-1047.
- [13] Dobler, W., Haugen, N. E. L., T. A. Yousef and A. Brandenburg, Bottleneck effect in three-dimensional turbulence simulations, *Phys. Rev. E*, **68**, 2003, 026304-1.
- [14] Kaneda, K., Ishihara, T., Yokokawa, M., Itakura, K. and Uno, A., Energy dissipation rate and energy spectrum in high resolution direct numerical simulations of turbulence in a periodic box, *Phys. Fluids*, **15**, 2003, L21-L24.



## Oscillations of the Horizontal Intrusion in a Side-Heated Cavity

F. Xu, J.C. Patterson and C. Lei

School of Engineering, James Cook University, QLD 4811, AUSTRALIA

### Abstract

In this study, a two dimensional numerical simulation of natural convection in a side-heated cavity is carried out. The evolution of the hot horizontal intrusion is observed and its physical properties are described. The results show that after the hot intrusion reaches the cold wall, due to the hot fluid accumulation and the associated buoyancy effect in the cold top corner, a flow opposing the cold boundary layer flow firstly appears and then forms a local circulation. This circulation then moves back to the hot wall, and eventually a cavity-scale oscillation is formed between the hot and cold walls underneath the ceiling of the cavity.

### Introduction

Natural convection in a rectangular side-heated cavity is a problem of fundamental interest to fluid mechanics, with many industrial applications such as electronic cooling systems, heat exchangers, solar water heaters and crystal growth procedures. Studies of this topic have been conducted for many years since Batchelor [1] first presented natural convection in a cavity of a large aspect ratio with a temperature difference between the sidewalls. Based on a detailed scaling analysis, Patterson & Imberger [2] portrayed the physical processes and features of the natural convection caused by abruptly heating and cooling two sidewalls respectively, and classified the laminar transient flow from the start-up to the steady state into different flow regimes. Major flow regimes include the vertical boundary layer growth, the horizontal intrusion and approach to steady state, which have been validated by experimental measurements [3] and numerical simulations [4]. Accompanying the above-mentioned theoretical analyses [1, 2], many significant experimental and computational results have been subsequently obtained in the context of the basic flow in a side-heated cavity. A representative experiment by Ivey [3] firstly and rather comprehensively described certain kinematic properties of the transient flow. The basic flow field was visualized in [3], and separation of the horizontal intrusion from the horizontal boundary was observed. Another comprehensive numerical and experimental description of the flow evolution in a side-heated cavity was reported in [5], and some basic physical properties of the transient flow were discussed.

It is known that a vertical boundary layer flow firstly appears when the sidewall of a cavity is abruptly heated or cooled. A distinct feature of the transient boundary layer flow is the leading-edge effect (LEE), which is characterised by high-frequency oscillations and even turbulence of natural convection in the side-heated cavity [6, 7]. A major discrepancy between the theoretical predictions and experimental measurements of the arrival time of the LEE was resolved by Armfield & Patterson [6] and Patterson et al [7] who confirmed that the arrival time of the LEE was determined by the velocity of the travelling waves which comprised the LEE. Another important feature of the vertical boundary layer is entrainment, which was discussed by Wright & Gebhart [8]. It is expected that the entrainment play a

key role in the transition of the vertical boundary layer from the start-up to quasi-steady state.

The horizontal intrusion is another important physical process in the side-heated cavity. The flow structure of the horizontal intrusion was visualized using the shadowgraph technique [9]. Contradictory explanations have been given in the literature for the mechanism responsible for the separation of the transient intrusion. Ivey [3] suggested that an internal hydraulic jump resulted in the separation. This explanation was supported by Paolucci & Chenoweth [4], but questioned by Patterson & Armfield [5] and Ravi et al [10]. It was suggested in [10] that the separation resulted from thermal effects; that is, the relatively cold fluid detached from the ceiling under the action of buoyancy forces when it reached the hot top corner. However, this explanation is not convincing because the fluid in the cavity core is not stratified in the early intrusion stage, and thus there is no 'colder' part of the intrusion relative to the ambient fluid near the hot top corner. The authors are currently investigating the dynamic mechanisms that are responsible for the separation of the horizontal intrusion flow, and the outcomes will be reported separately.

Despite of a large body of literature devoted to the transient natural convection boundary layer flow in a side-heated cavity over the last two decades, limited attention has been paid to the evolution of the horizontal intrusion after the start-up, which will be the primary focus of the present investigation.

### Numerical procedures

Under consideration is a two-dimensional rectangular domain. The dimensions of the physical domain are based on the experimental model described in [11], that is, 0.24-m high ( $H$ ) by 1-m long ( $L$ ). The working fluid is water. The two-dimensional Navier-Stokes and energy equations with Boussinesq approximation to be solved are as follows

$$u_x + v_y = 0, \quad (1)$$

$$u_t + uu_x + vv_y = -\rho^{-1}p_x + \nu(u_{xx} + v_{yy}), \quad (2)$$

$$v_t + uv_x + vv_y = -\rho^{-1}p_y + \nu(v_{xx} + v_{yy}) + g\beta(T - T_m), \quad (3)$$

$$T_t + uT_x + vT_y = \kappa(T_{xx} + T_{yy}), \quad (4)$$

where  $T$  is the temperature,  $p$  pressure,  $u$  the velocity in the  $x$ -direction,  $v$  the velocity in the  $y$ -direction,  $g$  the acceleration due to gravity,  $\beta$  the coefficient of thermal expansion,  $\kappa$  the thermal diffusivity, and  $\nu$  the kinematic viscosity. Subscripts represent partial differentiation except that  $T_m$  denotes a mean temperature. The SI units are adopted for all quantities throughout the paper.

The boundary conditions are shown in figure 1 along with the coordinate system, with the origin located at the center of the cavity. Initially, the fluid in the cavity is motionless and isothermal.

The above equations are solved using the SIMPLE scheme, where the spatial derivatives are discretized with a second-order upwind scheme. In order to accurately capture the features of the boundary layer flows, a non-uniform grid system is constructed with finer grids in the vicinity of wall boundaries. A 165 ( $H$ )  $\times$



463 ( $L$ ) mesh is adopted with the smallest cells of  $0.2 \times 0.2 \text{ mm}^2$  at the corners and a mesh expansion factor of 1.04 along both the horizontal and vertical directions toward the center of the domain (a similar mesh system was used in [5]). In addition, a finer mesh ( $199 \times 563$ ) and a coarser mesh ( $133 \times 387$ ) are also tested. The results of the mesh dependence test are shown in figure 2, which plots the time series of the calculated temperature at a point within the hot boundary layer for each mesh. Clearly, the two finer meshes produce almost identical results, and thus the medium fine mesh ( $165 \times 463$ ) is eventually adopted. Time marching is done by a second order implicit scheme. It is found that a time step of 0.4 second (smaller than that used in [5]) is sufficiently small to capture the features of the intrusion, and the stability of the scheme is also guaranteed for the non-uniform grids.

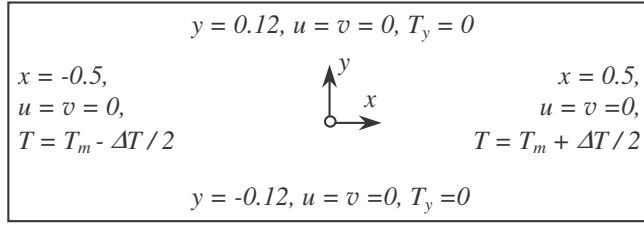


Figure 1: Physical domain and boundary conditions.

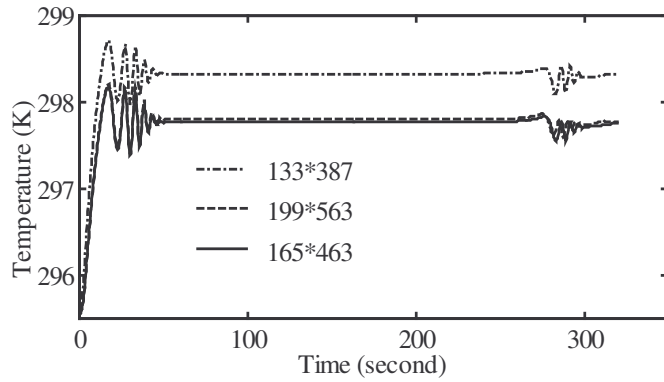


Figure 2: Time series of the temperature at ( $x = 0.498$ ,  $y = 0.09$ ) obtained with different meshes.

In the present investigation, the temperature difference between the two sidewalls is fixed at 16 K and the mean temperature is 295.55 K. The corresponding Rayleigh number and Prandtl number, which are defined below, are  $3.77 \times 10^9$  and 6.64, respectively,

$$Ra = \frac{g\beta\Delta TH^3}{\nu\kappa}, \quad (5)$$

$$Pr = \frac{\nu}{\kappa}. \quad (6)$$

## Results and Discussions

The present study focuses on the horizontal intrusion. Since the intrusion flow impacts on other flows within the core and the boundary layers, naturally, some kinematic properties of other flows in the side-heated cavity are also described.

Figure 3 shows plots of the temperature contours and stream functions at different times of the early stage of the flow development. In all the figures, the hot wall is to the right. It is seen in figure 3(a) that a group of trailing waves of the hot intrusion appear in the upper-right corner. In the meantime, a large anticlockwise circulation (hereinafter referred to as the *front circulation*) under the intrusion front is generated by a strong shear as seen in 3(b). With the passage of time, those trailing waves gradually regress to the hot top corner as shown in

3(c), and the *front circulation* arrives at the cold sidewall in 3(d). The *front circulation* then moves downstream along the cold sidewall in 3(f) and eventually dissipates into the core 3(h). Since the cold sidewall cannot cool and entrain all the hot intrusion to the bottom, increasing hot fluid is accumulated in the cold top corner (the upper-left corner). As a consequence, a tilted flow field forms near the cold top corner as shown in 3(h). In addition, the intrusion front stretches gradually downward along the cold sidewall, as indicated by the temperature contours shown in 3(e) and 3(g).

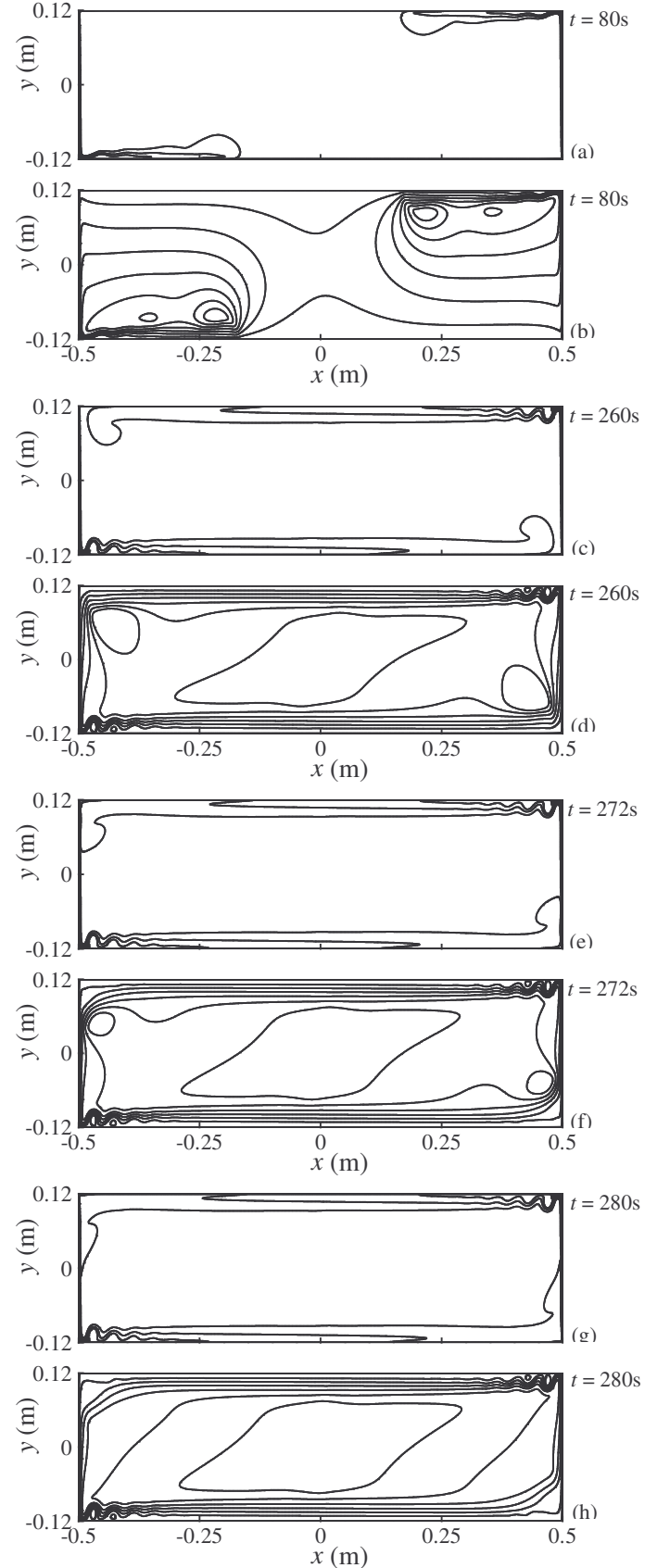


Figure 3: (a), (c), (e) and (g) temperature contours. (b), (d), (f) and (h) streamlines.

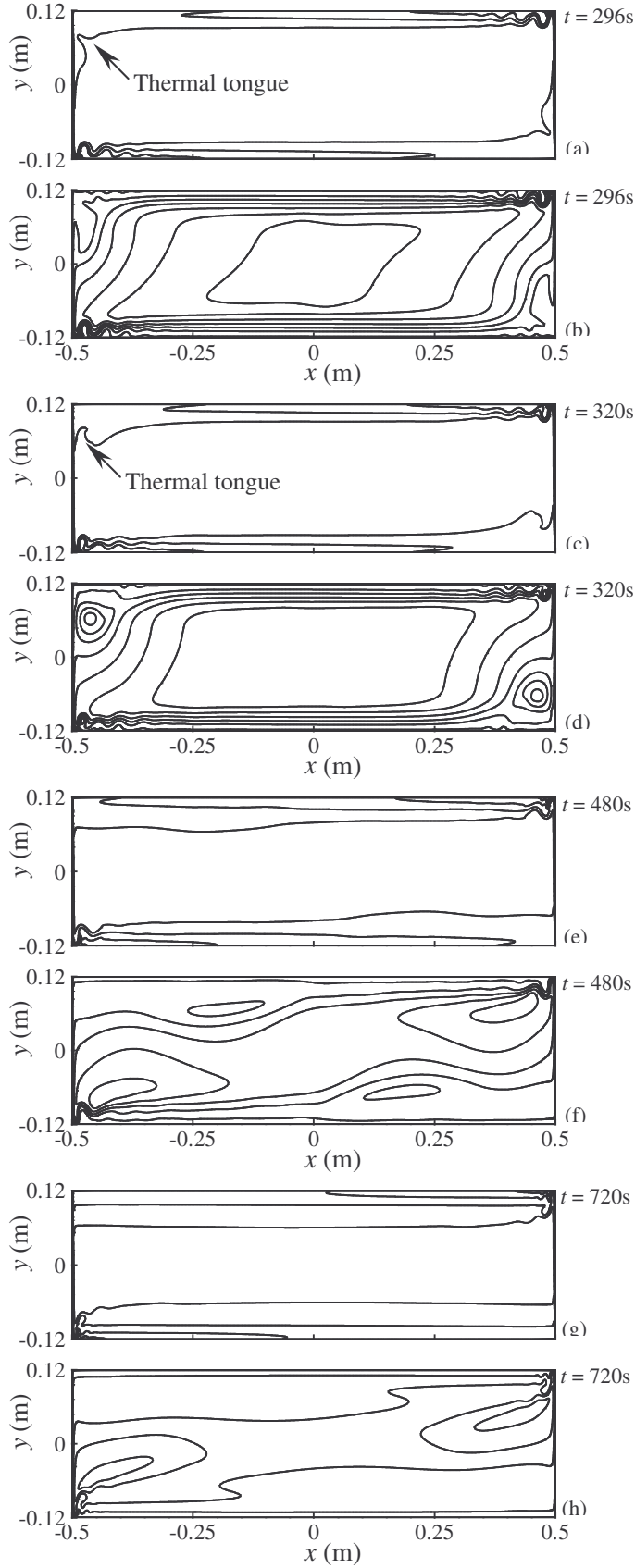


Figure 4: (a), (c), (e) and (g) temperature contours. (b), (d), (f) and (h) streamlines.

Likewise, a tilted density field is also generated near the cold top corner as can be seen in figure 3(g), and some buoyancy forces are associated with the tilted density field.

The subsequent flow development is shown in figure 4. As a consequence of the above-mentioned buoyancy effect, a reverse flow near the cold sidewall is generated as shown in 4(b). At this time, the temperature contours exhibit an upward ‘thermal tongue’ near the upper corner of the cold sidewall in 4(a). As the

hot intrusion further accumulates in the cold top corner, the increasing buoyancy effect forces the thermal ‘tongue’ to rotate in the clockwise direction 4(c), and eventually, a clockwise circulation as shown in 4(d) is formed in the region.

Figure 4(f) shows that this clockwise circulation is travelling toward the hot sidewall, although it has been weakened significantly. Moreover, the clockwise circulation splits the hot intrusion into two parts, one of which continues to run to the cold sidewall along the ceiling and the other jets into the core as seen in 4(f). After about 720 seconds, the clockwise circulation is completely dissipated and forms a reverse flow relative to the hot intrusion as shown in 4(h). This reverse flow then pushes the trailing waves near the hot (upper-right) corner closer to the hot sidewall (4g). It also impacts on the flow properties and structure of the hot vertical boundary layer. In addition, it is clear in figure 4 that the temperature contours in the upper part of the cavity move downward toward the core as the reverse flow moves back to the hot sidewall. This implies that the reverse flow speeds up the core stratification.

For the purpose of gaining insights into the details of the flow near the cold top corner when the hot intrusion reaches the cold wall, figure 5 shows the velocity vector field at the same time as of figure 4(d). It is seen in this figure that the strong shear between the clockwise circulation and the hot intrusion underneath the ceiling induces some smaller scale circulations in the region as well as some waves in the coming hot intrusion. A detailed discussion on the corresponding kinematic and dynamic mechanisms as well as the evolution of these waves will be reported separately.

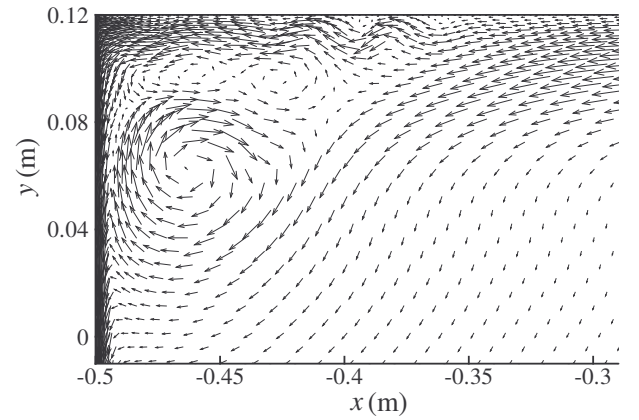


Figure 5: Velocity field in the cold top corner at 320s.

As shown in figure 4(h), the reverse flow has been significantly dissipated when it moves toward the hot sidewall. However, this flow does not disappear, and eventually it causes a cavity-scale oscillation in the upper part of the cavity (a back and forth flow between the hot and cold walls). Figure 6(a) shows this cavity-scale horizontal oscillation using a time series of the horizontal velocity obtained at the point ( $x = 0$ ,  $y = 0.07$ ). It is seen that the amplitude of the oscillations decreases significantly after the first oscillation cycle as indicated by I in figure 6(a). The first two cycles (I and II in figure 6a) are completed by 1400 seconds, but the oscillation actually lasts for a longer time with reduced amplitude. At the point shown, the time duration for which the velocity is positive (the reverse flow) is more than 200 seconds. Despite of the reduced intensity of the cavity-scale oscillation, it plays a key role in the stratification of the core, as shown in figure 4.

Similarly, there always exists a symmetrical oscillation of the cold intrusion in the lower part of the cavity. Figure 6(b) shows the horizontal velocity profile at  $x = 0$  at different times. Two symmetrical oscillations, one in the upper part and the other in

lower part of the cavity respectively, can be clearly observed in figure 6(b).

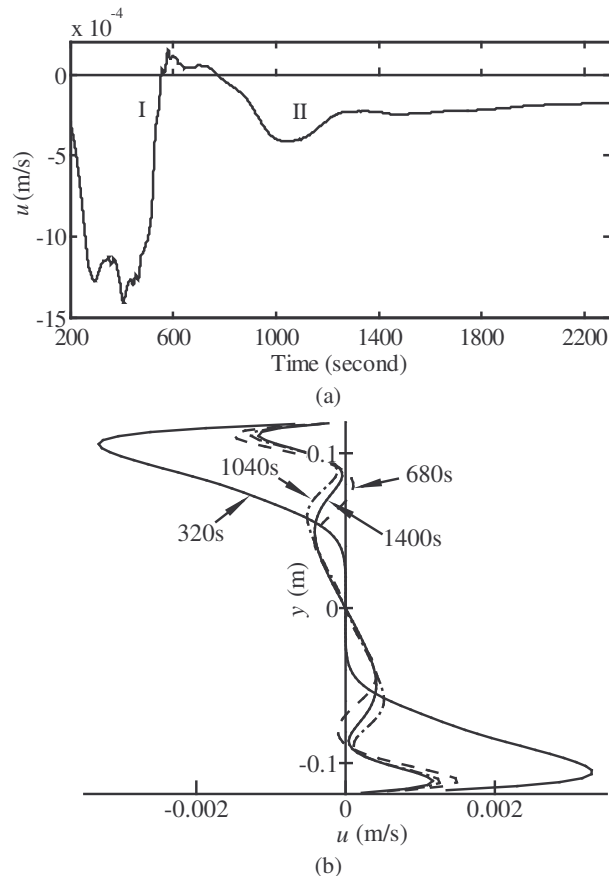


Figure 6: (a) Horizontal velocity ( $u$ ) against time at the point ( $x=0$ ,  $y=0.07$ ). (b) Horizontal velocity profile at  $x=0$  at 320, 680, 1040 and 1400s.

## Conclusions

This paper focuses on the horizontal intrusion generated in the suddenly heated and cooled cavity. The physical properties of the intrusion are described, and a back and forth flow between the hot and cold walls is observed.

The numerical results show that some trailing waves initially evolve from the intrusion and a large anticlockwise circulation below the hot intrusion front forms. With the passage of time, this anticlockwise circulation moves horizontally to the cold sidewall and eventually dissipates. Subsequently, another clockwise circulation, close to the cold sidewall, is generated. This clockwise circulation produces a strong shear with the hot intrusion underneath the ceiling, inducing some smaller scale circulations and waves in the hot intrusion. The clockwise circulation moves back to the hot sidewall and forms an oscillation (a back and forth flow between the hot and cold walls). The oscillation is typical of the internal gravity wave of natural convection in a side-heated cavity, and can impact on both the vertical boundary layer flow and stratification of the

fluid in the core to some extent. This is because, on one hand, the oscillation can push the trailing waves in the hot top corner closer to the hot wall, thus changing the properties and structure of the hot vertical boundary layer flow; on the other hand, the hot intrusion into the core is split by the back and forth flow and speeds up the core stratification.

In conclusion, oscillations of the horizontal intrusion can play a key role in the transition of natural convection in a side-heated cavity. A more detailed kinematic description and dynamic discussion related to this issue will be reported separately.

## Acknowledgments

Useful discussions with Steve Armfield and Yong Sha and the financial support by the Australian Research Council are gratefully acknowledged.

## References

- [1] Batchelor, G.K., Heat Transfer by Free Convection across a Closed Cavity between Vertical Boundaries at Different Temperatures, *Quart. Appl. Math.*, **12**, 1954, 209-233.
- [2] Patterson, J.C. & J. Imberger, Unsteady Natural Convection in a Rectangular Cavity, *J. Fluid Mech.*, **100**, 1980, 65-86.
- [3] Ivey, G.N., Experiments on Transient Natural Convection in a Cavity, *J. Fluid Mech.*, **144**, 1984, 389-401.
- [4] Paolucci, S. & D. R. Chenoweth, Transition to Chaos in a Differentially Heated Vertical Cavity, *J. Fluid Mech.*, **201**, 1989, 379-410.
- [5] Patterson, J.C. & S.W. Armfield, Transient Features of Natural Convection in a Cavity, *J. Fluid Mech.*, **219**, 1990, 469-497.
- [6] Armfield, S.W. & J.C. Patterson, Wave Properties of Natural-Convection Boundary Layers, *J. Fluid Mech.* **239**, 1992, 195-211.
- [7] Patterson, J.C., Graham, T., Schöpf, W. & S.W. Armfield, Boundary Layer Development on a Semi-Infinite Suddenly Heated Vertical Plate, *J. Fluid Mech.*, **453**, 2002, 39-55.
- [8] Wright, N.T. & B. Gebhart, The Entrainment Flow Adjacent to an Isothermal Vertical Surface, *Int. J. Heat and Mass Transfer*, **37**, 1994, 213-231.
- [9] Schöpf, W. & J.C. Patterson, Visualization of Natural Convection in a Side-Heated Cavity: Transition to the Final Steady State, *Int. J. Heat Mass Transfer*, **39**, 1996, 3497-3509.
- [10] Ravi, M.R., Henkes, R.A.W.M. & C.J. Hoogendoorn, On the High-Rayleigh-Number Structure of Steady Laminar Natural-Convection Flow in a Square Enclosure, *J. Fluid Mech.*, **262**, 1994, 325-351.
- [11] Brassington, G.B., Lee, M. & J.C. Patterson, Observations of a Transient Stratified Laminar Intrusion, in *Proc. 7<sup>th</sup> Australian Heat and Mass Transfer Conference*, editor G.B. Brassington and J.C. Patterson, Chalkface Press, 2000, 45-51.

## Numerical studies of contoured shock tube for murine powdered vaccine delivery system

Y. Liu\*, N. K. Truong and M.A.F. Kendall

The PowderJect Centre for Gene and Drug Delivery Research  
Department of Engineering Science, University of Oxford  
Oxford OX2 6PE, United Kingdom  
\*Email: yi.liu@eng.ox.ac.uk

### Abstract

A unique form of powdered delivery system, a biolistic system, has been developed. This novel technology is to accelerate particles in micro-particle form by a gas flow behind a travelling shock wave, so that they can attain sufficient momentum to penetrate the skin and thus achieve a pharmacological effect. One of the most recent developments is a mouse biolistic system, used in immunological studies. These studies require powdered vaccine to be delivered into the epidermis of the mouse with a narrow and highly controllable velocity distribution and a uniform spatial distribution. In this paper, Computational Fluid Dynamics (CFD) has been utilized to characterize the complete operation of a prototype mouse biolistic system. The key features of the gas dynamics and gas-particle interaction are discussed.

### Introduction

A needle-free epidermal powdered delivery system, a biolistic system, has been developed at University of Oxford (Bellhouse et al, 1994, [1]). The underlying principle of the system is to accelerate a pre-measured dose of vaccine and drugs in micro-particle form to an appropriate momentum by a high speed gas flow in order to penetrate the outer layer of the skin to achieve a pharmacological effect.

The biolistic system has shown many advantages over conventional needle and syringe, in terms of effectiveness, cost and health risk. The system can deliver powdered vaccine into a desired layer of skin or tissue to achieve the optimal effect. When antigenic compounds are delivered to skin or mucosa, the biolistic system requires less material to elicit the equivalent immune response [2, 12]. The formulation of vaccines in powder form can also improve stability, making transport and storage simple and inexpensive.

Recently, the mouse biolistic system, has been used in particle impact and immunological studies [7, 13, 14]. These studies require powdered vaccine preferably to be delivered into specific epidermis of the mouse skin with a narrow and controllable velocity range and uniform spatial distribution.

In this paper, Computational Fluid Dynamics (CFD) is utilized to simulate the gas and particle dynamics of a mouse biolistic system. The performance of this system is investigated in a series of numerical simulations. The main features of the starting process are presented. Predicted gas and particles characteristics within prototype system are compared with experimental data. The primary emphasis of this study is to gain new insights into the nozzle starting process and the interaction between the gas and particles. Representative results for a variant of the nozzle contour are given.

### Murine biolistic system

Figure 1 shows a schematic of the mouse biolistic system, a variation of the Contoured Shock Tube system(CST). Key as-

pects of principles of operation are described by Kendall (see reference [6]). Essentially, the rupture of the diaphragms forms a primary shock wave, which propagates downstream and initiates an unsteady gas flow, as in a classical shock tube [15]. A quasi-state supersonic flow (QSSF) is subsequently established. In the course of these processes, particles are entrained in the gas flow and accelerated towards the nozzle exit. The gas is deflected, while the particles maintain a sufficient momentum to breach the stratum corneum and target the underlying cells in the viable epidermis.

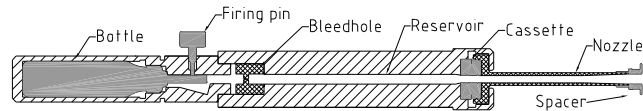


Figure 1: A schematic of the murine biolistics system.

The system is optimized such that the bulk of the particle cloud is accelerated in the QSSF and not in the starting process. This is achieved by the choice of system geometry, gas species, operation pressure and particles. The upstream termination boundary of the particle delivery window is defined by the reflected expansion wave. Therefore an emphasis is placed upon gaining new insights in to the nozzle starting process and the gas-particle interactions.

The characteristics of the steady flow generated by the prototype mouse biolistic system have been analyzed theoretically with ideal shock relations. For a nominal diaphragm burst pressure of 2070 kPa, the primary shock Mach number ( $Ma_s$ ) is 2.343, the pressure for both Regions 2 and 3 in the shock tube is 632 kPa, and Mach numbers for Regions 2 and 3 (using standard shock tube nomenclature) are 1.133 and 0.787, respectively. The correctly expanded Mach number for helium at the nozzle exit is 2.11.

### The CFD Model

In order to better understand the physical mechanics and help optimize the design, CFD is utilized to characterize the operation of the mouse biolistic system, illustrated in Figure 1.

For the solution, Fluent, a commercial available CFD software package [3], is employed to numerically simulate the multi-species gas flow and the interaction with the particles. Discrete and numerical solutions can be obtained by solving the governing partial differential equations (PDEs) using the finite volume method to determine the real gas flow field. The convective flux is discretized by an upwinding Roe vector difference splitter, and viscous term by the central difference. Time integration has been explicitly performed. Due to the unsteady motion of the shock wave process, a coupled explicit solver is chosen. An overall second order scheme is satisfied spatially and temporally. For an efficient, time-accurate solution of the preconditioned equations, a multi-stage scheme is employed.



Modelling of particle dynamics requires knowledge of the fluid flow field as well as the variation of the drag coefficient with relative Reynolds and Mach numbers. It is evident that there is great discrepancy between the correlations proposed for the particle drag coefficient. These discrepancies stem from the different ranges of Reynolds and Mach number covered, gas flows, particle sizes and density ranges and the particle concentration.

Regarding to our particular application, which consists of both subsonic and supersonic unsteady flow region, the correlation of Igra and Takayama [5], covering a wider range of Reynolds number (200 to 101,000), is implemented to determine the unsteady drag coefficient.

Some validation of this approach with prototypes of biolistic systems have been conducted through extensive comparison with experimental data [9, 10, 11] and computational results from the CFX calculations [4].

## Results and discussion

The flow fields under consideration have circular cross sections and are assumed to be axisymmetric. The emphasis is on the events after diaphragm rupture, thus the gas filling process is not simulated. The diaphragm (shown in Figure 1) initially separates high-pressure driver gas (mixture of helium and air) and driven gas (air) at atmospheric pressure. In this study, a single diaphragm is assumed for simplicity, and no attempt is made to consider the effects of non-ideal diaphragm rupture. Similarly, we have not included the effects of tissue surface deformation, studied by Kendall et al [8]. The calculation is started with the instant rupture of the diaphragm when the driver mixture gas pressure reaches the pressure of 2.07 MPa, which has been approximately determined from the experiments.

### Gas flow

The calculated and experimental history of the static pressure in the driver chamber (23 mm upstream of the diaphragm), is shown in Figure 2. The time zero is taken as the rupture of the diaphragm. The measured pressure is rather oscillatory and the level is higher than that CFD prediction. This discrepancy is attributed to the assumption of a closed gas filling system after diaphragm rupture, and perhaps a weak area change influence caused by the ruptured diaphragm and the unsteady expansion. This phenomenon is consistent with other biolistic systems [9, 4].

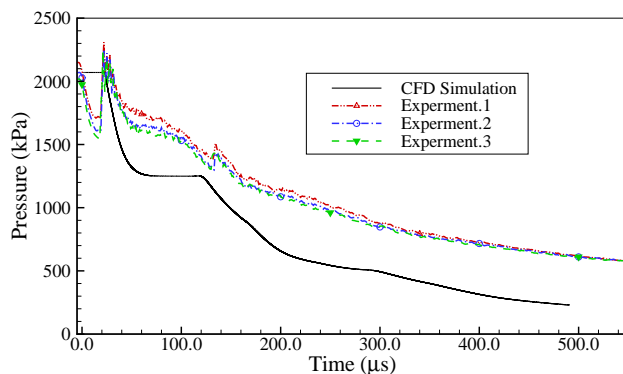


Figure 2: Calculated and measured pressure history.

In Figure 3, the simulated Pitot pressure history is compared with corresponding measurements from a centrally located Pitot probe of 3 mm downstream of the nozzle exit. The CFD has overestimated the Pitot pressure. This is largely due to poor spatial sensitivity of the probe in the supersonic flow (the diameter of the Pitot probe is about 2 mm, comparing with 4 mm of

nozzle exit diameter), which is not considered in the simulation.

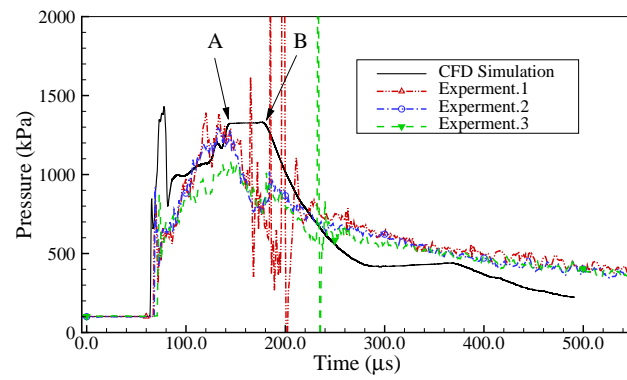


Figure 3: Calculated and measured Pitot pressure history.

In general, however, all the simulated pressure histories in Figure 2 and 3 are in good agreement with the measurements. The termination time of the starting process ("A" in Figure 3) is reasonable modelled. It demonstrates that shock, compression, expansion waves, and interactions between waves and the boundary layer are reasonably predicted by the numerical method employed.

Further investigation is obtained through examining the sequences of the flow field. Closer examination of the formation of the secondary shock is achieved at time of 89.3  $\mu$ s and 107.4  $\mu$ s after diaphragm rupture as shown in Figure 4.1 and 4.2. The contact surface between the primary shock and the secondary shock can be identified in the lower half of flow field. The contours within the QSSF, identified in Figure 3 to be 152.5  $\mu$ s., are shown in Figure 4.3.

### Particle flow

The particle trajectories are advanced simultaneously with the generated gas flow field. In the calculation, the particles are assumed to be initially arranged in a matrix representing all the different possible positions within the vaccine particle cassette.

Figure 5 plots the calculated particle impact velocity as a function of radius. Particles were assumed as sphere with a density of 19,320  $kg/m^3$ . The velocity plots clearly show that the particles are achieved velocity of approximately 640 m/s with a reasonably uniform.

Finally, the key gas flow regimes and the particles cloud trajectories are shown together in the calculated space-time (x-t) diagram, Figure 6. The representation of the gas flow is achieved by plotting the CFD calculation, in the typical form of contours of pressure. It can be seen that the particles have been accelerated to the nozzle exit, avoiding the starting process secondary shock and the reflected expansion wave, and thereby remaining in the quasi-steady supersonic flow (QSSF).

### Alternative nozzle design

The other feature of Figure 6, illustrates oblique shocks associated with a weak overexpanded nozzle flow, and resulting separated flow. This observation leads to a new design of the supersonic nozzle to achieve a quasi-steady correctly expanded supersonic flow and a more uniform particle impact velocity. The results are present here.

Figure 7 shows the instantaneous velocity contours in the QSSF state obtained with an alternative, correctly expanded nozzle design. The uniformity of gas velocity distribution is further illustrated in Figure 8.



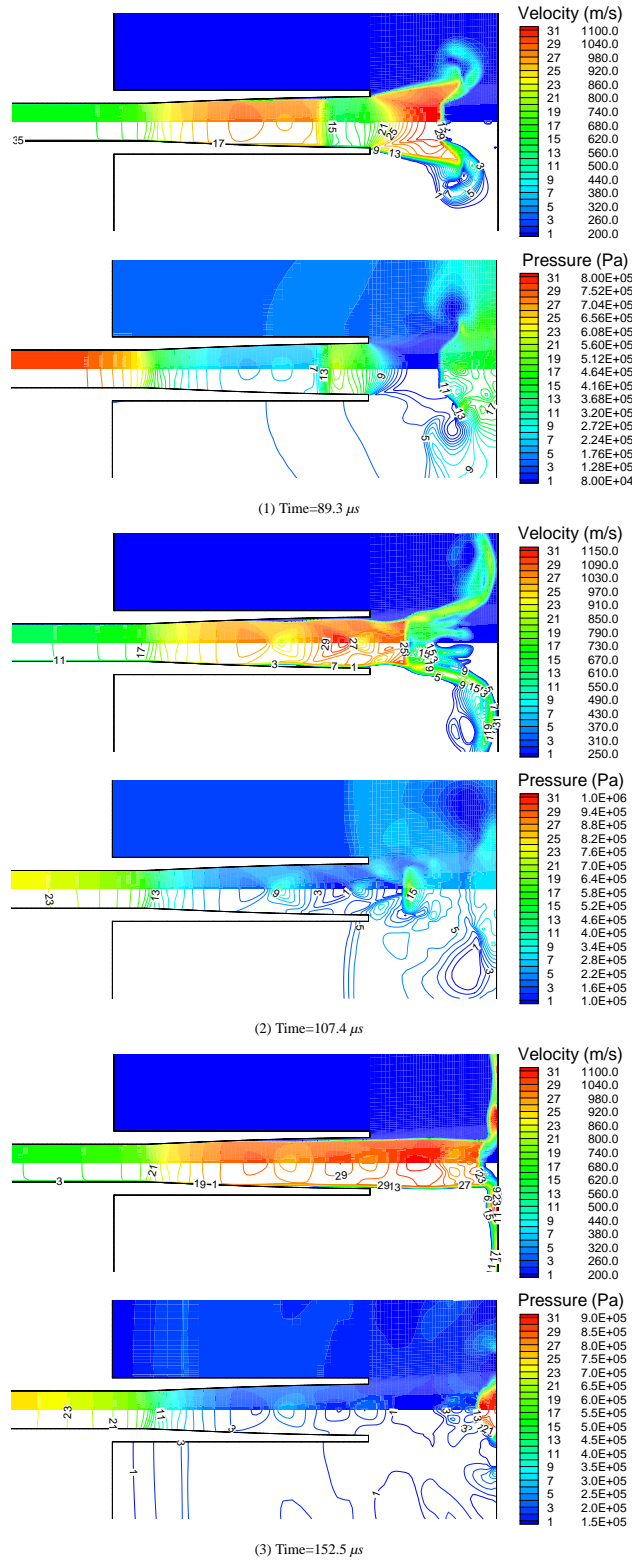


Figure 4: Instantaneous contour plots of velocity and pressure.

Figure 9 plots the calculated particle trajectories. The velocity plots clearly show that the particles are accelerated to a more uniform velocity. The improvement in impact velocity distribution is further illustrated by comparison with Figure 5. It is worthwhile to mention that the nozzle exit diameter has been reduced to 3.8 mm, still achieving an equivalent impact area. A statistic analysis of impact velocity, shown in Figure 10, provides 626 m/s of a mean velocity, with 1.61 m/s standard deviation.

## Conclusions

A CFD model has been implemented to gain new insights into the mouse biolistic system used to accelerate vaccines in micro-

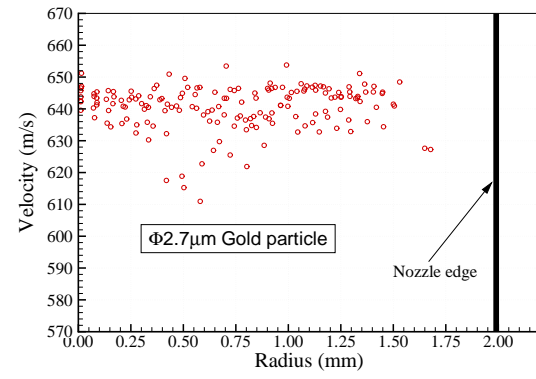


Figure 5: Calculated impact velocity of murine device.

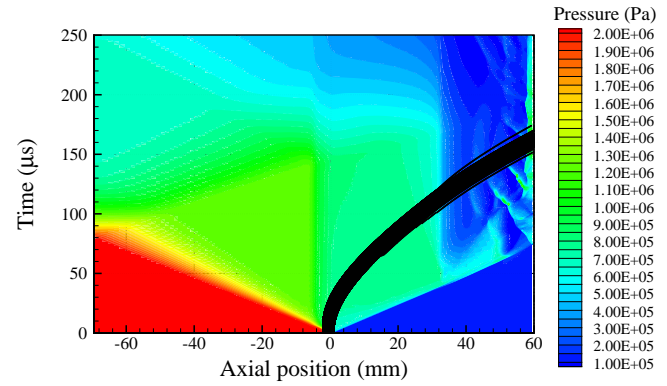


Figure 6: Constructed x-t characteristics from simulations.

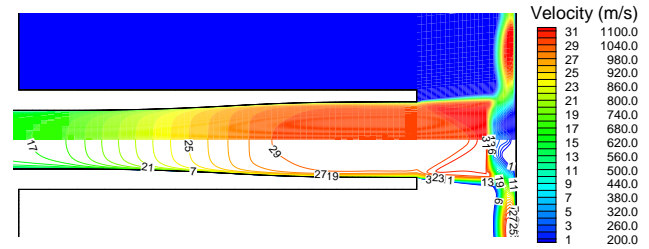


Figure 7: The Contour plot of velocity.

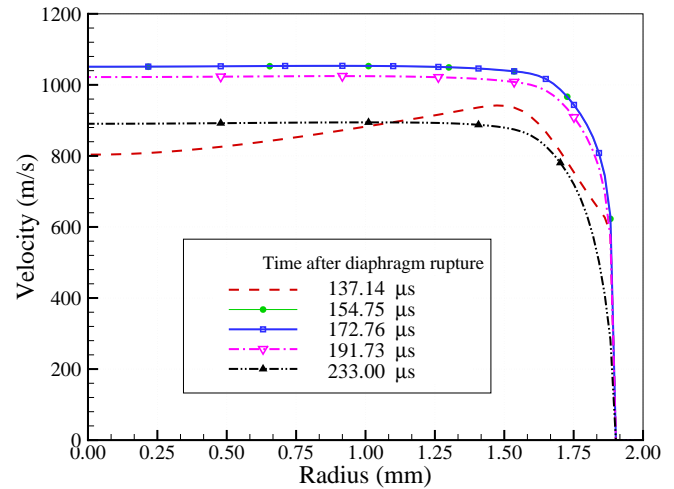


Figure 8: Velocity profiles along radius.

particle form to impart the skin. Fluent is utilized to simulate the unsteady gas flow and the interaction with the particles by a coupled explicit solver.

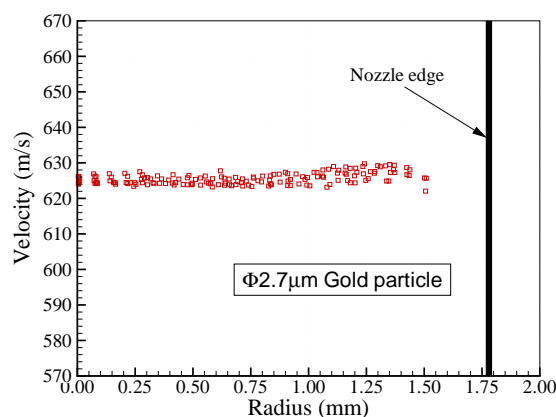


Figure 9: The impact velocity of new design murine device.

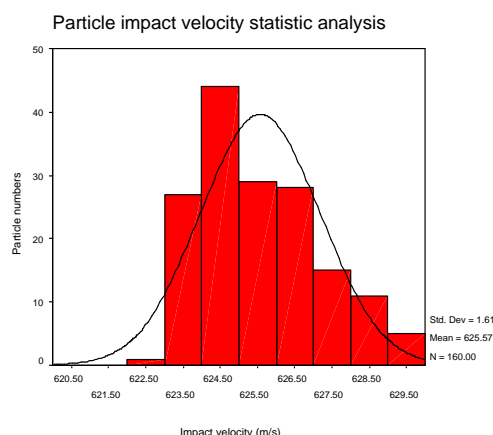


Figure 10: The statistic analysis of new design murine device.

Simulated pressure histories agree well with the corresponding static and Pitot pressure measurements. These calculations have been used to further explore the gas flow field, with an emphasis on the nozzle starting process. The quasi-steady supersonic flow window has been accordingly determined. The action of the gas flow in accelerating the particles was calculated within the modelled flow field. The main features of the gas dynamics and gas-particle interaction are presented.

The preliminary results demonstrate the overall capability of a new designed supersonic nozzle to deliver the particles to the skin targets with a more uniform velocity and spatial distribution.

### Acknowledgements

The authors wish to thank professor B. J. Bellhouse, Powderject Centre for Gene and Drug Delivery Research, University of Oxford, for his encouragement of this work. This work was supported by PowderJect plc. and Chiron Vaccines. Their support is gratefully acknowledged.

### References

- [1] Bellhouse B.J., Sarphie D.F. and Greenford J.C., Needleless syringe using supersonic gas flow for particle delivery. *Int. Patent WO94/24263*. 1994.
- [2] Chen D.X., Endres R.L., Erickson C.A., Weis K.F., McGregor M.W., Kawaoka Y. and Payne1 L.G., Epidermal

immunization by a needle-free powder delivery technology: Immunogenicity of influenza vaccine and protection in mice. *Nature Medicine* 2002, (6):1187–1190.

- [3] Fluent user's guide volume, Fluent Inc. or see: <http://www.fluent.com/>.
- [4] Hardy, M.P., Kendall, M.A.F., Quinlan, N.J. and Bellhouse, B.J., Numerical study of a prototype needle-free powdered vaccine delivery system. *Proc. 23rd Int. Symp. on Shock Waves, Austin, USA*. 2001.
- [5] Igra, O., Takayama, K., Shock tube study of the drag coefficient of a sphere in a non-stationary flow. *Proc R. Soc. Land. A* 1993, **442**():231–2467.
- [6] Kendall, M.A.F., The delivery of particulate vaccines and drugs to human skin with a practical, hand-held shock tube-based system. *Shock Waves Journal* 2002, **12**(1):22–30.
- [7] Kendall M.A.F., Mulholland W.J., Tirapur U.K., Arbuthnott E.S. and Armitage M., Targeted delivery of micro-particles to epithelial cells for immunotherapy and vaccines: an experimental and probabilistic study, *The 6th International Conference on Cellular Engineering*, Sydney, Australia, 2003.
- [8] Kendall M.A.F., Mitchell T.J., Hardy M.P. and De Focatiis D.S.A., Mucosal deformation from an impinging transonic gas jet and effects on biolistic particle impact velocity. *Submitted to Biomaterials Journal* 2004.
- [9] Liu, Y., Kendall, M.A.F., Truong, N.K. and Bellhouse, B.J., Numerical and experimental analysis of a high speed needle-free powdered vaccines delivery device. AIAA-2002-2807. *Proc. 20th AIAA Applied Aerodynamics Conference, St. Louis, MO, USA*. 2002.
- [10] Liu, Y., Kendall, M.A.F., Numerical simulation of heat transfer from a transonic jet impinging on skin for needle-free powdered drug and vaccine delivery. *Journal of Mechanical Engineering Science, Proceedings of the Institution of Mechanical Engineers Part C*. (Accepted on 15 July, 2004, Article in press)
- [11] Liu, Y., Kendall, M.A.F., Numerical study of a transient gas and particle flow in a high-speed needle-free ballistic particulate vaccine delivery system. *Journal of Mechanics in Medicine and Biology* (Accepted on 7 May, 2004, Article in press)
- [12] Loehr, B.I., Wilson, P., Babiuk, L.A. and S. van Drunen Little-van den Hurk Gene gun-mediated DNA immunization primes development of mucosal immunity against bovine herpes virus 1 in cattle, *J. Virol.* 2000,**74**:6077–6086.
- [13] Mcsloy N.J., Raju P.A. and Kendall M.A.F., The effects of shock waves and particle penetration in skin on cell viability following gene gun Delivery. *1st British Society for Gene Therapy Conference, Oxford, UK*, 2004.
- [14] Mitchell, T.J., Kendall, M.A.F. and Bellhouse, B.J. A ballistic study of micro-particle penetration to the oral mucosa, *International Journal of Impact Engineering* 2003, **28**(6): 581–599.
- [15] Smith, C.E., The starting process in a hypersonic nozzle. *Journal of Fluid Mechanics* 1966, **24**(4):625–641.

# Application of Transport PDF Approach for Modelling MILD Combustion

F.C. Christo<sup>1</sup> and B.B. Dally<sup>2</sup>

<sup>1</sup>Weapons Systems Division  
Defence Science and Technology Organisation  
P O Box 1500, Edinburgh, SA 5111 AUSTRALIA

<sup>2</sup>School of Mechanical Engineering  
Adelaide University, SA 5001

## Abstract

A transport PDF (TPDF) approach was used for modelling turbulent non-premixed Methane/Hydrogen (1/1 by volume) flames issuing from a jet in hot, oxygen-diluted coflow. A comparison between the TPDF results and detailed experimental data of  $\xi$ , temperature, major species and OH is presented for flames with different oxygen level in the hot coflow (oxygen mass-fraction of 6%, and 3%). Results from a previous study using the eddy-dissipation concept (EDC) solver, is also presented. A comparison in performance between the TPDF and EDC models is presented.

## Introduction

In moderate and intense low-oxygen dilution (MILD) Combustion [2,17], fuel is mixed with highly diluted and heated air to create a distributed reaction zone with a reduced peak temperature. Attractive features of these flames include a semi-uniform temperature field, higher radiation flux and low emission of pollutants. Whilst MILD combustion can be classified as non-premixed jet flames, studies of diffusion flames cannot be directly extended to characterise MILD combustion. This is because most studies of non-premixed flames are conducted in cold air surroundings. Although the concept of MILD combustion has been extensively studied experimentally [5,6,10,11], mathematical modelling of this regime has received relatively little attention [4,7,9]. At first glance this regime seems relatively straightforward to model as it does not feature high-density gradients and complex turbulence-chemistry interactions processes, which are prominent in conventional turbulent jet flames. However, the conditions of elevated and uniform temperature distribution and low oxygen concentration in MILD regime, lead to slower reaction rates and enhances the influence of molecular diffusion on flame characteristics. These two effects in particular challenge the applicability of simple combustion models that assume fast chemistry and neglect the effects of differential diffusion.

## Motivation

In a previous study [3] the authors used Reynolds-Averaging Navier-Stokes (RANS) approach to model the flow, compositions and temperature fields of a fuel jet issuing into a hot, oxygen-diluted coflow. That study focused on modelling Jet in Hot Coflow (JHC) flames measured by Dally et al. [5], and examined the effects of various combustion and turbulence models, chemical kinetics mechanisms, thermal radiation and differential diffusion, on the accuracy of the predictions. It was shown [3] that the standard  $k-\epsilon$  turbulence model with a modified dissipation equation constant ( $C_{\epsilon_1}$ ) provided the best agreement with the experiment. Differential diffusion effects were found to have a strong influence on the accuracy of the predictions and therefore should always be accounted for. It was also found that conserved scalar based models, i.e. the  $\xi$ /PDF and flamelet

models, are inadequate for modelling jet in hot coflow (JHC) flames. The representation of the chemistry in the model was also found to play an important role in accurately predicting flame characteristics. Using detailed chemical kinetics, rather than global or skeletal mechanisms, with the eddy-dissipation concept (EDC) model was found to improve the accuracy significantly. In general, the EDC model performed reasonably well for flames with higher O<sub>2</sub> concentration in the hot coflow, such as flames with 9% O<sub>2</sub> and 6% O<sub>2</sub>. The agreement with the measurements however was poor for the 3% O<sub>2</sub> case. However, the largest discrepancy was noted at the 120mm axial location where the model did not perform well, particularly for 3% and 6% cases. This is due to the intermittent localised flame extinction that the EDC model could not capture. This paper is an extension of our previous study [3] and focuses on examining the performance of transport PDF (probability density function) approach in modelling JHC flames.

## Model Description

The numerical model constructed for this study is based on the geometry and dimensions of the experimental JHC burner used by Dally et al. [5], which is designed to emulate the MILD combustion regime. The details of the burner geometry, computational domain, boundary and inlet conditions, and convergence criteria are presented in Ref. [3,5] and are not repeated here. The flames of interest that were modelled here composed of Methane/Hydrogen (1/1 by volume), issuing into a hot coflow with species composition as shown in Table 1.

Test Case	YO <sub>2</sub> %	YN <sub>2</sub> %	YH <sub>2</sub> O %	YCO <sub>2</sub> %
1	3	85	6.5	5.5
2	6	82	6.5	5.5

Table 1. Species composition in the hot coflow. The jet Reynolds number is approximately 10,000 and the nominal fuel jet and coflow temperatures are 305K and 1300K, respectively.

## Composition Transport PDF Model

In the RANS approach species equations are Reynolds-averaged, which leads to unknown terms for the turbulent scalar flux and the mean reaction rate. The turbulent scalar flux is modelled by gradient diffusion, treating turbulent convection as enhanced diffusion. The mean reaction rate is modelled by the finite-rate EDC model. Since the reaction rate is invariably highly non-linear, modelling the mean reaction rate in a turbulent flow is difficult and prone to error. An alternative to Reynolds-averaging the species and energy equations is to derive a transport equation for their single-point, joint PDF. This PDF, denoted by  $P$ , can be considered to be proportional to the fraction of the time that the fluid spends at each species, temperature, and pressure state. By solving this transport PDF equation, any thermochemical moment (e.g., mean or RMS temperature, mean reaction rate) can

be easily computed. The composition PDF transport equation [12] is derived from the Navier-Stokes equations as:

$$\frac{\partial}{\partial t}(\rho P) + \frac{\partial}{\partial x_i}(\rho u_i P) + \frac{\partial}{\partial \psi_k}(\rho S_k P) = -\frac{\partial}{\partial x_i}[\rho \langle u_i'' | \psi \rangle] + \frac{\partial}{\partial \psi_k} \left[ \rho \left\langle \frac{1}{\rho} \frac{\partial J_{i,k}}{\partial x_i} \middle| \psi \right\rangle P \right] \quad (1)$$

where  $P$  is the Favre joint PDF of composition,  $\rho$  is the mean fluid density,  $u_i$  is the Favre mean fluid velocity vector,  $S_k$  is the chemical reaction rate for species  $k$ ,  $\psi$  is the composition space vector,  $u_i''$  is the fluid velocity fluctuation vector, and  $J_{i,k}$  is the molecular diffusion flux vector. The notation of  $\langle \dots \rangle$  denotes expectations, and  $\langle A|B \rangle$  is the conditional probability of event  $A$ , given the event  $B$  occurs. In Equation (1), the terms on the left-hand side are closed, while those on the righthand side are not and require modelling. The first term on the left-hand side is the unsteady rate of change of the PDF, the second term is convection by the mean velocity field, and the third term is the reaction rate. The principal strength of the PDF transport approach is that the highly non-linear reaction term is completely closed and requires no modelling. The two terms on the right-hand side represent scalar convection by turbulence (turbulent scalar flux), and molecular mixing/diffusion, respectively.

Molecular mixing of species and heat was modelled using the Euclidean Minimum Spanning Tree (EMST) model [15]. Physically, mixing occurs between fluid particles that are adjacent to each other. The Modified Curl and IEM (interaction by exchange of momentum) mixing models take no account of this localness, which can be a source of error. The EMST model mixes particle pairs that are close to each other in composition space. The particle pairing is determined by an EMST, which is the minimum length of the set of edges connecting one particle to at least one other particle. The EMST mixing model is more accurate than the Modified Curl and IEM mixing models, but incurs a slightly greater computational expense.

The transport PDF (TPDF) equation is solved using a Monte Carlo method, which is ideal for high-dimensional equations since the computational cost increases linearly with the number of dimensions. The disadvantage is that statistical errors are introduced, and these must be carefully managed. The Monte Carlo algorithm involves notional particles that move randomly through physical space due to particle convection, and also through composition space due to molecular mixing and reaction. For the representation of the chemistry into the TPDF model, a GRI2.11-based augmented reduced mechanism (ARM) kinetics [16] is used. To reduce computational cost of time-integration of chemical reactions, the ISAT (*is-situ* adaptive tabulation) model of Pope [13], is used.

## Results

Calculations were performed for the 6% and 3%  $O_2$  flames using the FLUENT6 package [8]. For comparison purposes the modelling results obtained using the EDC model [3] are also presented here. It is worth noting that in the EDC model the GRI3.0[14] kinetics mechanism was used. This use of different mechanism is not expected to have any effect on the conclusions drawn from this study. The computational expense of using GRI3.0 with the TPDF is prohibitive. Due to space constraints only sample of the results are presented, and plotted against mixture fraction ( $\xi$ ) computed using Bilger's formulation [1].

Figure 1 shows comparison between measured and calculated mean temperature profiles at 120mm from the jet exit. The figure shows that for both the 3% and 6%  $O_2$  flames, the TPDF model yields better agreement with the experiment than the EDC model. It predicts the peak temperature and its location (in  $\xi$ -space) more

accurately than the EDC model. Similarly, the TPDF predictions of species e.g. OH and CO mass fraction are significantly closer to the experimental results than the EDC model, as shown respectively in Fig.2 and Fig.3. The figures also show that the EDC model tends to over-predict the peak values of temperature and mass fractions. This behaviour however is not erroneous; rather the EDC model tends to capture the peak values of the instantaneous measurements.

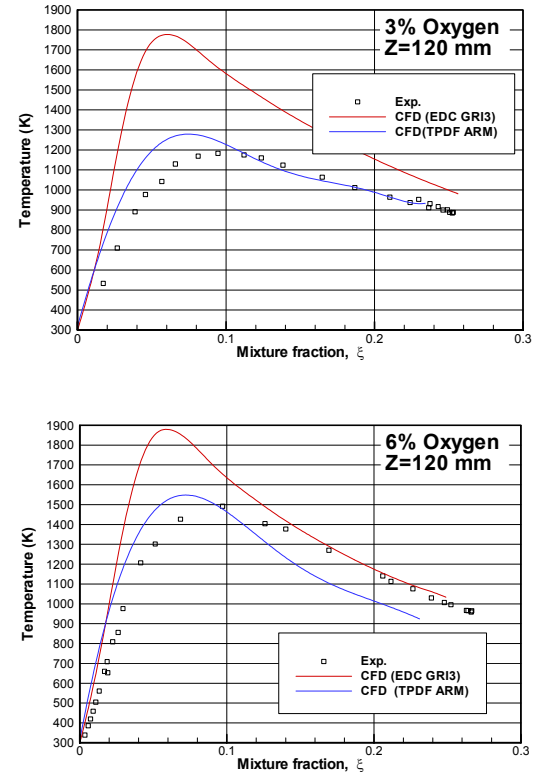


Fig. 1: A comparison between mean measured and calculated temperature at 120mm from the jet exit for 3% and 6%  $O_2$  flames.

It is worth mentioning that when using the Modified Curl or the IEM mixing models in the TPDF model, the flame has been completely blown off. A stable flame could only be achieved using a slightly adjusted EMST mixing model. It was necessary to increase the number of the randomly selected pairs of Monte Carlo particles at each iteration. The number of pairs ( $N_{pair}$ ) is defined as

$$N_{pair} = \frac{1.5 C_\phi N \Delta t}{\tau_t} \quad (2)$$

where  $N$  is the total number of particles in each computational cell,  $C_\phi$  is an empirical mixing constant, and  $\tau_t$  is a turbulent time scale (for the  $k-\epsilon$  turbulence model this is  $k/\epsilon$ ). It was necessary to increase the value of  $C_\phi$  from the default value of 2 to 5 to stabilise the flame. Despite increasing the number of particles per cell from 20 to 40 particles, the solution was not significantly affected. To maintain low statistical error, 40 particles per cell were used in all the calculations (resulting of approximately 4 million particles been tracked at each iteration).

The results in Figs. 1-3 show that the 6%  $O_2$  flame produces higher CO levels than the 3%  $O_2$  flame. This is an unexpected behaviour since higher  $O_2$  in the coflow stream is expected to yield higher conversion of CO into  $CO_2$ . Similar trends were also observed in laminar MILD flame measurements and calculations (not presented). It is believed that at MILD combustion conditions the current chemical pathways of CO conversion into



CO<sub>2</sub> do not hold, and a different kinetics mechanism might be required. This issue is beyond the scope of this paper.

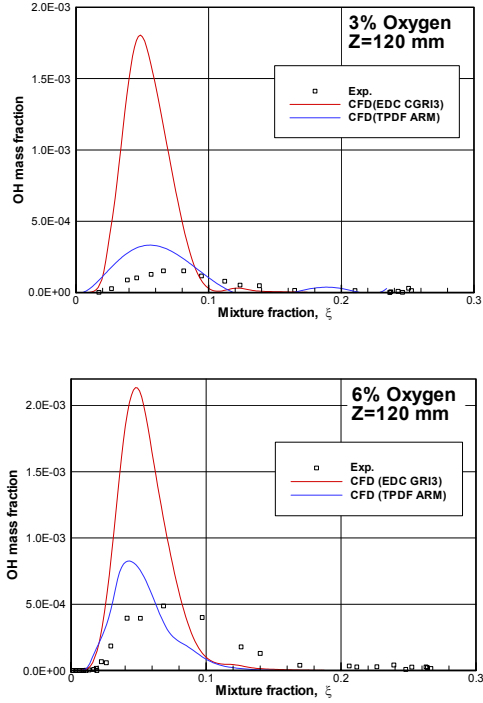


Fig. 2: A comparison between mean measured and calculated OH mass fraction at 120mm from the jet exit for 3% and 6% O<sub>2</sub> flames.

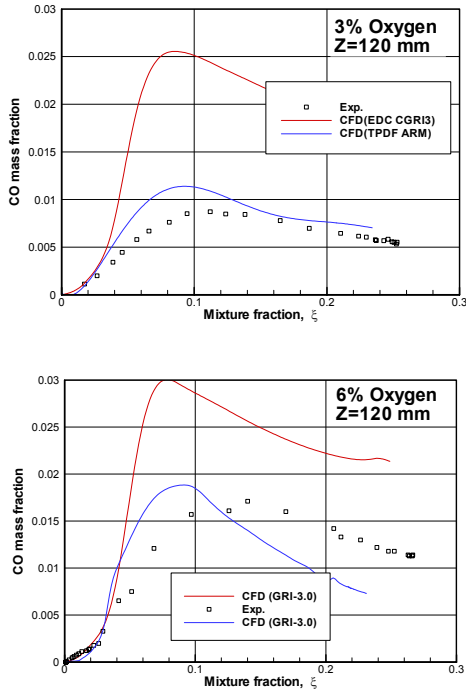


Fig. 3: A comparison between mean measured and calculated CO mass fraction at 120mm from the jet exit for 3% and 6% O<sub>2</sub> flames.

Considering that the EDC model is based on Reynolds averaging and it does not resolve the fluctuations in mixture fraction, it cannot therefore account for the bias in mean profiles due to localised extinction or intermittency. The TPDF model on the other hand contains a complete statistical representation for each species (mean, RMS and higher moments), therefore it resolves scalar fluctuations and hence its mean predictions are closer to the measured values. Figure 4 illustrates this point clearly; showing the EDC biased tendency towards peak values while the TPDF model is closer to the (mean) measured values.

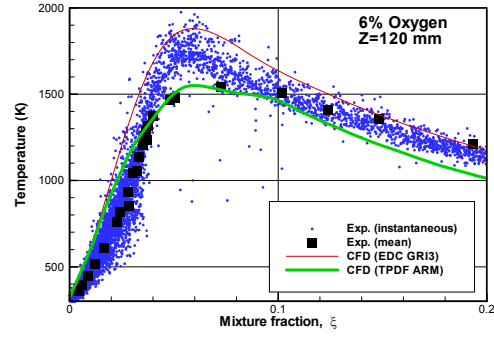


Fig. 4: A comparison between instantaneous and mean measured and calculated temperature at 120mm from the jet exit for 6% O<sub>2</sub> flame.

Interestingly, the performance of the TPDF model at upstream axial locations of 30mm and 60mm from the jet exit was not accurate. The TPDF predictions at these locations were either comparable to or slightly better than the EDC model. The majority of the TPDF results at the upstream locations tend to under-predict the temperature and species concentration. This is clearly illustrated in Fig. 5, which shows profiles of H<sub>2</sub>O mass fraction at 60mm for 3% and 6% O<sub>2</sub> flames.

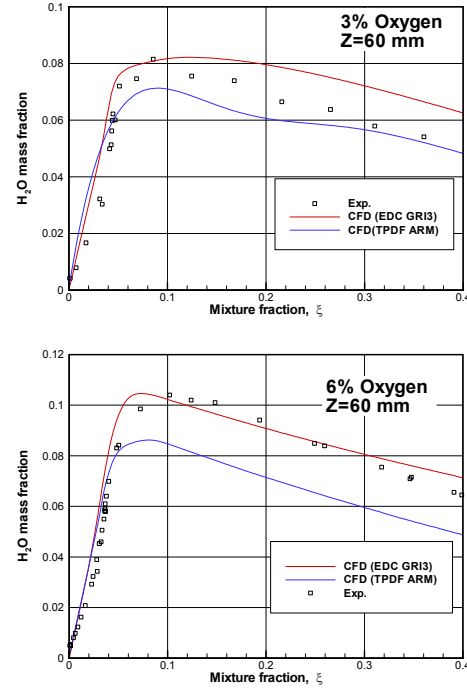


Fig. 5: A comparison between mean measured and calculated H<sub>2</sub>O mass fraction at 60mm from the jet exit for 3% and 6% O<sub>2</sub> flames.

Whilst the TPDF peak OH prediction is better than that of the EDC, it is still off by a factor of four from the peak-measured value for the 3% O<sub>2</sub> case. This is illustrated in Fig. 6, which indicates that the flame is not anchored close to the jet exit plane. Figure 7 is a contour plot of OH mass fraction for the 3%O<sub>2</sub> case, showing the flame-stabilisation location at approximately 120mm from the jet exit.

Although similar observation was noted in the experiment, neither model was accurate enough in predicting the flame-stabilisation distance. The experimentally observed distance was only of a few jet-diameters (~10mm), whilst the model shows a distance of ~30 jet-diameter.



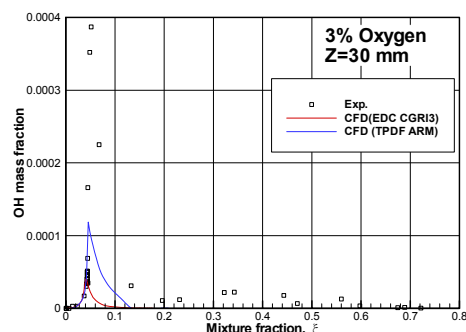


Fig. 6: Profiles of mean OH mass fraction at 30mm from the jet exit for 3% flame.

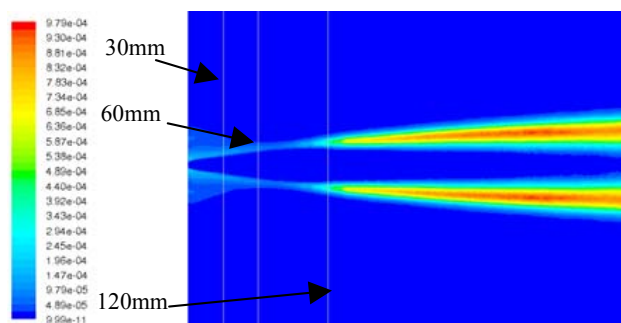


Fig. 7: Contours of mean OH mass fraction for the 3% flame showing the location of flame stabilisation above the jet exit plane.

## Conclusions

For the 3% and 6% O<sub>2</sub> flames the TPDF model is proved more accurate than the EDC model, particularly at 120mm. This conclusion however does not extend to the TPDF performance at upstream locations of 30mm and 60mm, where both models have comparable accuracy. Considering that turbulent mixing is predicted accurately (see Ref [3]), and that oxidation of the fuel is represented in the TPDF model by the best available kinetics mechanism, we can only speculate (at this stage) on possible causes for these discrepancies. One possibility is that the TPDF model is highly sensitive to fluctuations in velocity field, which the current turbulence model may not be resolving accurately. One suggestion to assess this assumption is to model the JHC flames using a joint velocity-composition transport PDF approach. Another possible contributing factor is that for low-oxygen concentration flames the molecular mixing becomes extremely sensitive to composition fluctuations that even the EMST model is unable to reflect/capture accurately. This assumption is based on the fact that the TPDF prediction is reasonably accurate in the downstream location (120mm). ‘Leakage’ of high-concentration oxygen from the outer shroud air into the oxygen-diluted region, maybe reducing the sensitivity of molecular mixing to variations in compositions.

Accurately predicting flame-stabilisation location in JHC combustion remains a modelling challenge. Whilst the TPDF results are encouraging, establishing a model that can accurately predict JHC flames across the entire combustion domain remains a challenge.

## Acknowledgement

The authors thank Dr Graham Goldin from Fluent Inc. for his valuable suggestions.

## References

- [1] Bilger, R.W., On reduced mechanisms for methane---air combustion in nonpremixed flames, *Combustion and Flame* **80**, 1990, 135-149.
- [2] Cavaliere A., de Joannon, M., Mild Combustion, *Progress in Energy and Combustion Science*, **30**, 2004, 329-366.
- [3] Christo, F.C. and Dally, B.B., Modelling Turbulent Reacting Jets Issuing into a Hot and Diluted Coflow, *Combustion and Flame*, under review, July 2004.
- [4] Coelho, P. J. and Peters, N., Numerical simulation of a MILD combustion burner, *Combustion and Flame*, **124**, 503-518, 2001.
- [5] Dally, B.B. Karpetsis, A.N. and Barlow, R.S., Structure of Turbulent Nonpremixed Jet Flames in a Diluted Hot Coflow Proceedings of the Combustion Institute, Volume **29**, 2002, pp.1147-1154.
- [6] Dally, B. B., E. Riesmeier, and Peters, N., Effect of fuel mixture on mild combustion, *Combustion and Flame*, **137**, 2004, 418-431.
- [7] Evrard, P., Pesenti, B. and Lybaert, P., NO<sub>x</sub> production and radiative heat transfer from an auto regenerative flameless oxidation burner, 6<sup>th</sup> European Conference on Industrial Furnaces and Boilers, Portugal, 2002.
- [8] FLUENT6 User Guide, 2003, Lebanon NH 03766, USA.
- [9] Kim, S. H., Huh, K. Y. and Dally, B., Conditional Moment Closure Modeling of Turbulent Nonpremixed Combustion in Diluted Hot Coflow, Proceedings of the Combustion Institute, Vol. **30**, 2004, in print.
- [10] Mancini, M., Weber, R. and Bollettini, U., Predicting NO<sub>x</sub> emission of a burner operated in Flameless Oxidation mode, Proceedings of the Combustion Institute, Vol. **29**, 2002, pp. 1155-1163.
- [11] Plessing, T. Peters, N. and Wüning, J.G., Laser optical Investigation of Highly Preheated Combustion with Strong Exhaust Gas Recirculation, Twenty-Seventh Symposium (International) on Combustion, Combustion Institute, Pittsburgh, PA, 1998, vol. **2**, pp. 3197-3204.
- [12] Pope S. B., Pdf methods for turbulent reactive flows. *Progress Energy Combustion Science*, **11**:119, 1985.
- [13] Pope, S.B., Computationally Efficient Implementation of Combustion Chemistry using *in situ* adaptive tabulation, *Combustion Theory and Modeling*, **1**:41-63, 1997.
- [14] Smith, G.P., Golden, D.M., Frenklach, M., Moriarty, N.W., Eiteneer, B., Goldenberg, M., Bowman, C.T., Hanson, R.K., Song, S., Gardiner, Jr. W.C., Lissianski, V.V. and Qin, Z., [http://www.me.berkeley.edu/gri\\_mech](http://www.me.berkeley.edu/gri_mech).
- [15] Subramaniam, S. and Pope S. B., A Mixing Model for Turbulent Reactive Flows based on Euclidean Minimum Spanning Trees, *Combustion and Flame*, v. **115** (No. 4). pp. 487-514, 1998.
- [16] Sung C. J., Law, C. K. and Chen, J. Y., Augmented Reduced Mechanisms for NO Emission in Methane Oxidation, *Combustion and Flame*, **125**, 906, 2001.
- [17] Tsuji, H., Gupta, A.K., Hasegawa, T., Katsuki, M., Kishimoto, K. and Morita, M., High Temperature Air Combustion, CRC Press, 2003.

## The Transient Behaviour of a Differentially Heated Cavity with Isoflux Boundaries

S. Jiracheewanun<sup>1</sup>, S. W. Armfield<sup>1</sup>, M. Behnia<sup>2</sup> and G. D. McBain<sup>1</sup>

<sup>1</sup>School of Aerospace, Mechanical and Mechatronics Engineering,  
University of Sydney, NSW, 2006 Australia

<sup>2</sup>Dean of Graduate Studies, University of Sydney, NSW, 2006 Australia

### Abstract

In this study we investigate, using direct numerical simulation, the transient two-dimensional natural convection flow in a square cavity with isoflux side walls and adiabatic top and bottom boundaries. The equations of motion were solved using a non-iterative fractional-step pressure correction method which provides second-order accuracy in both time and space. Several features of the flow are identified and discussed in detail, in particular, the flow behaviour in the vertical thermal boundary layers along the side walls and in the horizontal intrusions adjacent to the top and the bottom boundaries. The results show that the transient flow features obtained for the isoflux cavity are similar to the flow features for the isothermal case. However, the fully developed flow features of the isoflux cavity are very different from the isothermal case.

### Introduction

Natural convection in closed cavities has received a lot of attention because of its wide range of engineering applications. In the past, natural convection in a rectangular enclosure with vertical isothermal walls has been studied extensively, both experimentally and numerically. A classification of the development of the flow by Patterson & Imberger [1], a series of experiments by Ivey [2], and a comparison of numerical and experimental results by Patterson & Armfield [3] and Armfield & Patterson [4,5] are examples of previous isothermal cavity investigations. On the other hand, the cavity with isoflux walls has received much less attention. Kimura & Bejan [6] examined this case, but details of the flow features were not reported. The objectives of this study are to investigate the flow features from initiation until full development and compare the results with the isothermal cavity results of Patterson & Armfield [3].

### Numerical Method

#### Governing Equations

The square cavity configuration is given in figure 1. The cavity is of width  $L$ , a uniform heat flux is specified along the no-slip side walls with isoflux in on the left wall and isoflux out on the right wall. The horizontal walls are adiabatic and no-slip. The governing equations are the two-dimensional Navier-Stokes and energy equations based on the Boussinesq assumption. The equations are written in non-dimensional form as follows:

$$\frac{\partial u}{\partial x} + \frac{\partial v}{\partial y} = 0 \quad (1)$$

$$\frac{\partial u}{\partial t} + u \frac{\partial u}{\partial x} + v \frac{\partial u}{\partial y} = -\frac{\partial p}{\partial x} + \left( \frac{\partial^2 u}{\partial x^2} + \frac{\partial^2 u}{\partial y^2} \right) \quad (2)$$

$$\frac{\partial v}{\partial t} + u \frac{\partial v}{\partial x} + v \frac{\partial v}{\partial y} = -\frac{\partial p}{\partial y} + \left( \frac{\partial^2 v}{\partial x^2} + \frac{\partial^2 v}{\partial y^2} \right) + \frac{Ra}{Pr} T \quad (3)$$

$$\frac{\partial T}{\partial t} + u \frac{\partial T}{\partial x} + v \frac{\partial T}{\partial y} = \frac{1}{Pr} \left( \frac{\partial^2 T}{\partial x^2} + \frac{\partial^2 T}{\partial y^2} \right) \quad (4)$$

where  $u$  and  $v$  are the velocity components in the  $x$ - and  $y$ -direction,  $t$  is time,  $p$  is pressure and  $T$  is temperature. In these equations, velocity is non-dimensionalized by  $U = \nu/L$ , length by

$L$ , time by  $L^2/\nu$ , pressure by  $\rho(\nu/L)^2$ , and  $(T-T_0)$  by  $q''L/k$ . Prandtl number and Rayleigh number are defined as,

$$Pr = \frac{\nu}{\alpha}$$

$$Ra = \frac{g\beta q'' L^4}{\alpha \nu k} \quad (5)$$

where  $\beta$  is the coefficient of volume expansion,  $q''$  is heat flux,  $\alpha$  is the thermal diffusivity,  $\nu$  is the kinematic viscosity and  $k$  is the thermal conductivity.

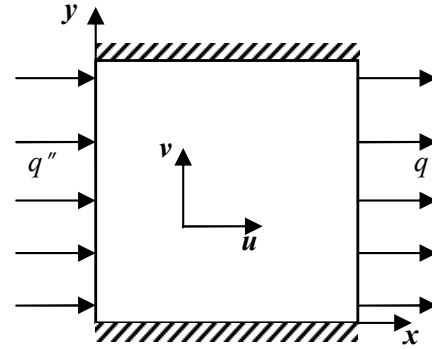


Figure. 1 Computational domain and coordinate system.

The corresponding dimensionless initial and boundary conditions are

$$\begin{aligned} T = u = v = 0 & \quad \text{at all } x, y \text{ and } t < 0 \\ T_x = -1 & \quad \text{on } x = 0, 1 \\ T_y = 0 & \quad \text{on } y = 0, 1 \\ u = v = 0 & \quad \text{on } x = 0, 1 \text{ and } y = 0, 1 \end{aligned} \quad (6)$$

### Discretization

Because of the large variation in length scales it is necessary to use a mesh that concentrates points in the boundary layer and is relatively coarse in the interior. The meshes are constructed using an exponentially stretched grid. The basic mesh uses 110x110 grid points, which are distributed symmetrically with respect to the domain half-width and half-height. The smallest grid size, near the boundaries, is 0.002. Away from the boundaries, the mesh stretching factor is 1.05. The mesh is generated with this expanding rate until it reaches half of the domain, resulting in a coarse mesh in the interior. The time step used was  $1 \times 10^{-5}$ .

The direct numerical simulations have been carried out using a finite volume method. The governing equations are discretized on a non-staggered mesh, with standard second-order central differencing used for the viscous, pressure gradient, and divergence terms, whereas the QUICK third-order upwind scheme is used for the advective terms. The momentum and temperature equations are solved using an ADI scheme. The second-order Adams-Bashforth scheme and Crank-Nicolson scheme are used for the time integration of the advective terms and the diffusive terms, respectively. To enforce continuity, the non-iterative fractional-step pressure correction method is used to construct a Poisson equation, which is solved using the Preconditioned Conjugate Gradient method.

## Results

Results will be obtained with the isoflux boundary condition for  $Ra=1 \times 10^{10}$  and  $Pr=7.5$ , with the general flow structure and behaviour compared to those presented in Patterson & Armfield [3] for isothermal boundary conditions. The Patterson & Armfield [3] results were presented in dimensional form for a square cavity of height 0.24 m ( $h=0.24$ m) and obtained for  $Ra^*=3.26 \times 10^8$  and  $Pr=7.5$  where  $Ra^*=g\beta\Delta Th^3/\nu\alpha$ . A summary of the results obtained by Patterson & Armfield [3] is as follows.

Patterson & Armfield [3] divided the flow development into two stages; the first stage from 0 to 150 s and the second stage from 150 s to full development, at approximately 1500 s. The first stage is associated with the development of thermal boundary layers on the heated and cooled walls, which can be seen in figure 2, which shows the temperature in the boundary layer at  $y = 0.12$  m and  $x = 0.002$  m from the hot wall, plotted against time, with both numerical and experimental results shown.

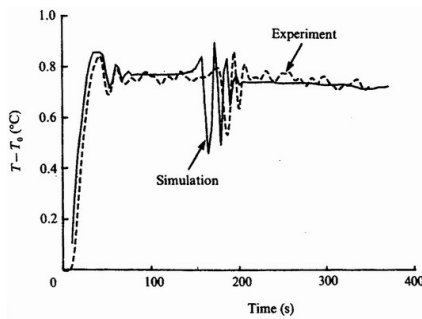


Figure. 2 Time traces of temperature at mid-height of the cavity for isothermal case with  $Ra^*=3.26 \times 10^8$  [3].

The initial rapid increase in temperature shows the thermal boundary layer growth, which at this height has reached full development by time 100 s. It is also observed that transition to full development in the boundary layer is associated with an oscillation in the signal, at approximately 40 s. This oscillation is caused by a series of waves travelling up the heated boundary layer, generated by the impulsive start-up of the system. The thermal boundary layers eject heated and cooled intrusions at the top and bottom of the hot and cold walls respectively. These intrusions travel across the cavity, with the heated intrusion in contact with the upper boundary and the cooled intrusion in contact with the lower boundary, striking and interacting with the base of the far wall boundary layer. This interaction perturbs the boundary layer, producing a second set of travelling waves that transit the boundary layer in the flow direction, seen in the second set of oscillations in figure 2, at approximately 170 s. The boundary layers are only able to entrain part of the intrusion flow, with the remainder rebounding from the far wall and setting up a seiching motion in the cavity. The development of the flow from this stage is associated with considerable activity in the intrusions, which gradually fill the cavity with stratified fluid. As the flow approaches full development the intrusion activity gradually diminishes, with the steady state flow consisting of a fully stratified interior with a cavity scale circulation, as shown in figure 3, where the flow is shown with the hot wall on the left.

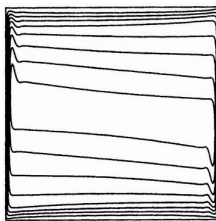


Figure 3. The mirror stream function contour in the isothermal cavity of Patterson & Armfield [3] at near steady state.

As noted above the isoflux boundary condition results presented here have been obtained with  $Ra=1 \times 10^{10}$ . This value was chosen because it gave approximately the same thermal boundary layer thickness (3% of the cavity width) as the  $Ra^*=3.26 \times 10^8$  isothermal boundary condition case (compare figure 9(a), below, with figure 2(a) of Patterson & Armfield [3]). Figure 4 presents a temperature time series obtained at  $x=0.01$  and  $y=0.5$ . Comparing this to figure 2 above, it is seen that the thermal boundary layer shows a qualitatively similar development, with an initial growth accompanied by a decaying oscillation followed by a second decaying oscillation. Both these sets of oscillations represent travelling waves, as in the isothermal case, with the initial set generated by the impulsive start-up and the second set generated by the intrusion striking the far wall. The general development for the isoflux boundary condition is therefore similar to that of the isothermal boundary condition.

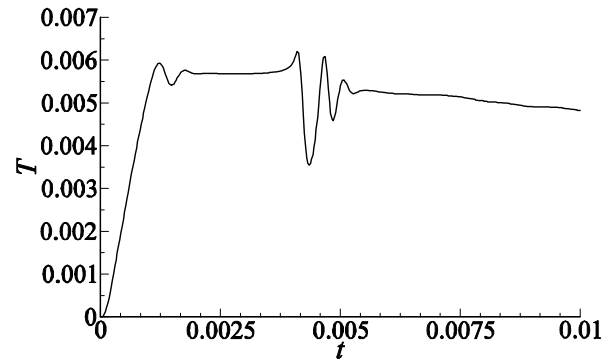


Figure. 4 Time traces of temperature at  $x=0.01$ ,  $y=0.5$  cavity for isoflux case with  $Ra=1.0 \times 10^{10}$ .

Detailed flow development for the isoflux boundary condition is shown in figure 5, in the form of streamfunction contours. Figures 5(a-f) show 12 equally spaced contours between the maximum and minimum values, while figures 5(g-i) show 30 equally spaced contours, with the latter contour value chosen to more clearly demonstrate the features of the latter part of the development. In all cases the heated wall is on the left.

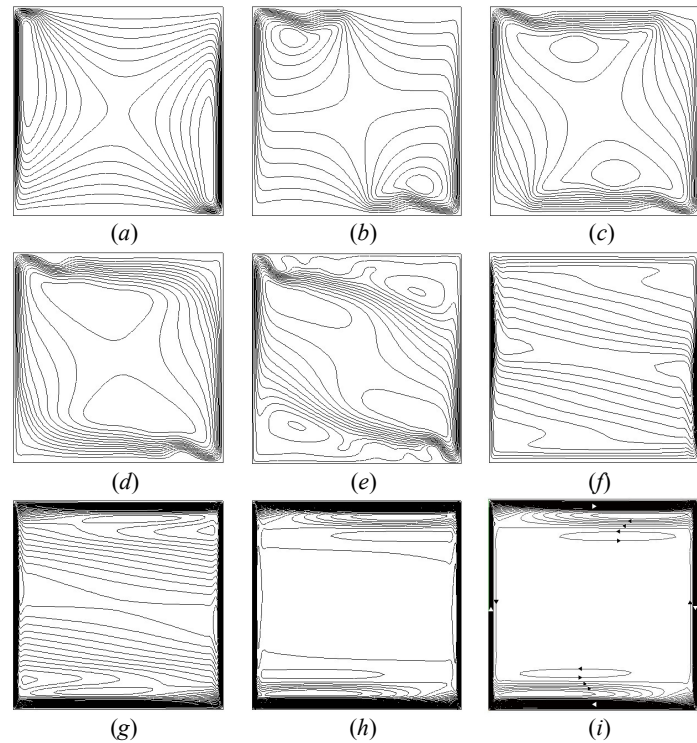


Figure. 5 Time evolution of the contours of stream function fields in the domain for  $Ra=1 \times 10^{10}$ ,  $Pr=7.5$  at various times. (a)  $t=0.001$ ; (b)  $t=0.002$ ; (c)  $t=0.003$ ; (d)  $t=0.004$ ; (e)  $t=0.006$ ; (f)  $t=0.025$ ; (g)  $t=0.1$ ; (h)  $t=0.55$ ; (i)  $t=2.5$ .

For the isoflux boundary condition the flow development is most appropriately divided into three stages. The first stage, figures 5(a-c), is associated with the development of the thermal boundary layers, the generation of the intrusions, which are clearly seen travelling from the top of the heated wall towards the cooled wall, and vice-versa for the cooled wall, and the establishment of two circulations. The second stage, shown in figures 5(d-f), shows the intrusion striking the far walls, the generation of a separated backward flowing region within intrusions, and finally a cavity scale flow. The third stage, shown in figures 5(g-i), shows the full development of the flow in which the interior circulation gradually decays until finally the interior is quiescent, with flow only in the regions of the boundaries. This fully developed flow is complex, with an outer clockwise circulation following the boundary and an inner reverse circulation, as may be seen by the flow direction arrows included in figure 5(i). This reverse flow is accompanied by closed circulations adjacent to the horizontal boundaries, with additional interior reverse circulations also seen. However away from the horizontal boundaries the flow adjacent to the vertical boundaries is parallel to the boundaries. Temperature contours, presented in figure 6, show that at full development the cavity is fully stratified. The structure of the boundary layer adjacent to the vertical wall is seen in figure 7, which shows a horizontal profile of the vertical velocity at  $y=0.5$ . The inner region of reversing flow is clearly visible in the region  $x=0.027-0.055$ .



Figure. 6 Temperature contour of fully developed flow  $t=2.5$ .

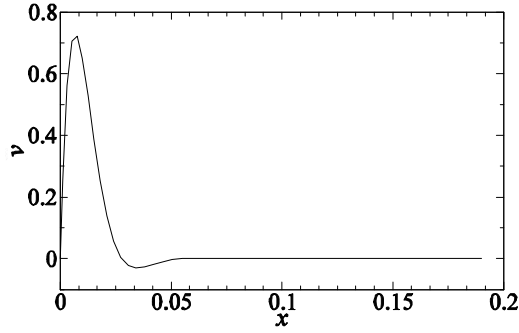


Figure. 7 Profile of vertical velocity along horizontal distance from the hot wall at  $y=0.5$ .

The first two stages of flow for the isoflux boundary condition are very similar to the isothermal boundary condition, with similar boundary and intrusion growth, two sets of travelling boundary layer waves with the same generation mechanisms, unsteady intrusion activity and eddy formation. The third stage however is quite different, indicating different heat transfer characteristics and scaling. It is therefore of interest to determine appropriate scalings for the isoflux boundary condition flow and compare them to scalings for the isothermal boundary condition flow. Scalings for the isoflux boundary condition flow may be obtained as follows. Combining the one-dimensional solution of Lietzke [7] with an energy balance relation [6] allows scalings to be obtained for the length, velocity and temperature for an evenly heated cavity of the following form;

$$\delta : 2^{5/9} Ra^{-2/9} \quad (7)$$

$$U : 2^{5/3} Ra^{1/3} Pr^{-1} \quad (8)$$

$$\Delta T : 2^{14/9} Ra^{-2/9} \quad (9)$$

It is expected that these scalings will apply to the boundary layers on the cavity walls far enough away from the floor and ceiling such that the flow is approximately parallel. As observed above at  $Ra=1 \times 10^{10}$  parallel regions of flow are observed adjacent to the walls and these scalings will therefore be tested for the boundary layer profiles obtained at the wall half height.

Figure 8 contains the profiles of the vertical velocity at four Rayleigh numbers at steady state at  $y=0.5$ , with the raw data shown in figure 8(a). The profiles show the typical structure of the natural convection boundary layer. The scaling obtained indicates that velocity will scale with the  $1/3$  power of the Rayleigh number, while the boundary layer thickness will scale with the  $-2/9$  power of the Rayleigh number. Scaled results are shown in figure 8(b). As can be seen the scaling brings all results onto a single curve indicating that the numerical velocity solution obeys the scaling relations.

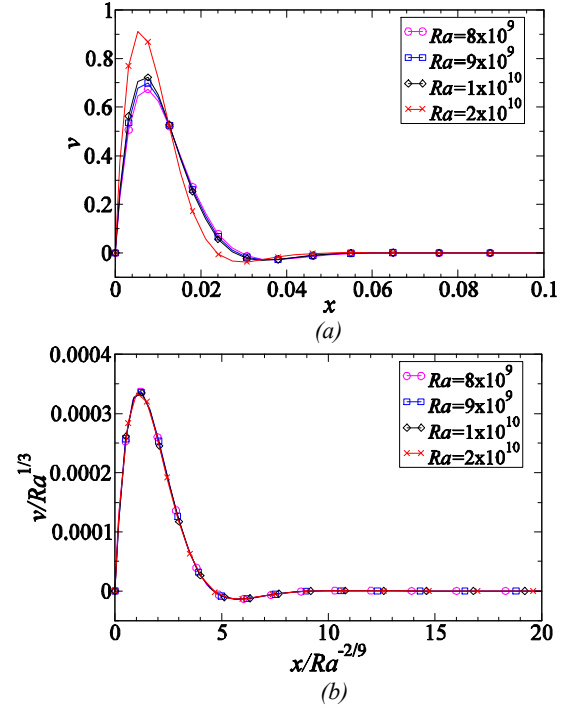


Figure. 8 Vertical velocity profiles of fully developed flow at various  $Ra$ ; (a) raw data, (b) scaled data.

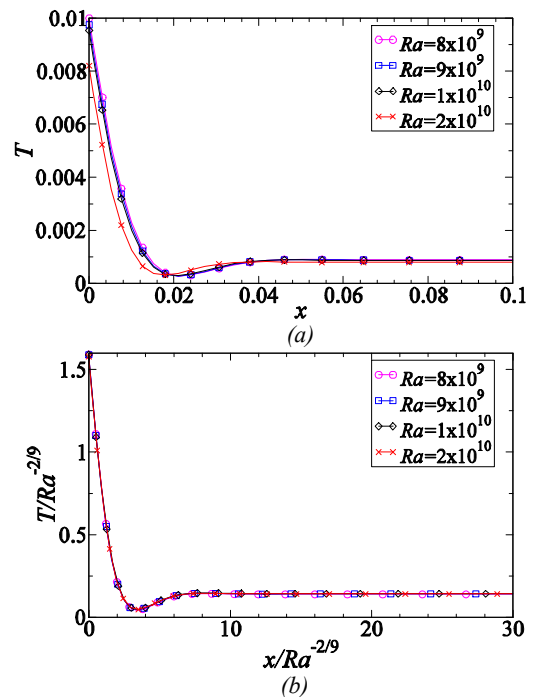


Figure. 9 Temperature profiles of fully developed flow at various  $Ra$ ; (a) raw data, (b) scaled data.

The temperature profiles near the hot wall at steady state of four Rayleigh numbers at  $y=0.5$  is shown in figure 9(a). The scaling obtained indicates that temperature will scale with the  $-2/9$  power of the Rayleigh number, while the boundary layer thickness, again, will scale with the  $-2/9$  power of the Rayleigh number as shown in figure 9(b). Again the scaling is seen to bring all the temperature profiles onto a single curve, validating the scaling relations.

The scaling results of the length and velocity for the natural convection in the cavity with isoflux boundaries at steady state can be compared with the isothermal boundaries scalings of Patterson & Imberger [1] as summarized in table 1. It shows that the scaling results of the isoflux case differ from of the isothermal case [1] in every case. Thus, the  $Ra$  chosen for the present study is larger than  $Ra^*$  used for isothermal case [3] to yield approximately the same boundary layer thickness and development time as the isothermal case [3].

	Types of boundary	
	Isothermal [1]	Isoflux
Length scale	$x \sim Ra^{*-1/4}$	$x \sim Ra^{-2/9}$
Velocity scale	$v \sim Ra^{*1/2}$	$v \sim Ra^{1/3} Pr^{-1}$

Table 1. The comparison of length and velocity scaling results of the isothermal case [1] and of the isoflux case.

## Conclusion

The flow features in the first two stages of flow development, described above, are similar to those for the isothermal boundary condition case, described by Patterson & Armfield [3]. However the fully developed flow is quite different with the isoflux boundary condition cavity having a flow only in the vicinity of the boundaries, with a quiescent core. The isothermal boundary condition cavity displays cavity scale circulation with a non-quiescent core. Clearly the interaction of the isoflux boundary condition with the cavity flow is different to that of the isothermal boundary condition. The scalings for the fully developed isoflux boundary condition flow have also been found to be different to those of the isothermal boundary condition flow. The length scale for the isoflux case will be reduced more rapidly with increasing Rayleigh number, while the velocity scale will be increased more rapidly.

## References

- [1] Patterson, J. and Imberger, J., Unsteady natural convection in a rectangular cavity, *J. Fluid Mech.*, **100**, 1980, 65-86.
- [2] Ivey, G. N., Experiments on transient natural convection in a cavity, *J. Fluid Mech.*, **144**, 1984, 389-401.
- [3] Patterson, J.C. and Armfield, S.W., Transient features of natural convection in a cavity, *J. Fluid Mech.*, **219**, 1990, 469-497.
- [4] Armfield, S.W. and Patterson, J.C., Direct simulation of wave interactions in unsteady convection in a cavity, *Int. J. Heat Mass Transfer*, **34**, 1991, 929-940.
- [5] Armfield, S.W. and Patterson, J.C., Wave properties of natural-convection boundary layers, *J. Fluid Mech.*, **239**, 1992, 195-211.
- [6] Kimura, S. and Bejan, A., The boundary layer natural convection regime in a rectangular cavity with uniform heat flux from the side, *J. Heat Transfer*, **106**, 1984, 98-105.
- [7] Lietzke, A. F., Theoretical and experimental investigation of heat transfer by laminar natural convection between parallel plates, Report 1223, NACA, 1955.



## Flow Response to Periodic Heating and Cooling in a Reservoir

Chengwang Lei, John C. Patterson and Yong Sha

School of Engineering, James Cook University,  
Townsville, QLD 4811, AUSTRALIA

### Abstract

An unsteady model is formed and solved numerically in order to investigate the transient circulations in a reservoir subject to periodic heating and cooling. The numerical results reveal that there is a time lag in the response of the overall flow to the switch of the thermal forcing, and thermal instabilities play an important role in breaking the residual circulation and reversing the flow in deep waters.

### Introduction

Large-scale convective circulations in response to the transient daytime heating and night-time cooling take place in the sidearm of reservoirs or shallow littoral waters with gently sloped bottoms. These convective circulations greatly influence the transport of nutrients and pollutants between the shallow region and the bulk deep water [1, 2]. When the shallow and deep regions are exposed to a uniform rate of surface cooling under the night-time condition, the shallow water cools faster than the deep water. The difference in the cooling rate then results in a horizontal temperature gradient which in turn drives a downward dense gravity current along the sloping bottom [2, 3]. A similar but converse statement can be made for the daytime heating condition [1, 4, 5].

In general the flow response in reservoirs is characterized by unsteady forcing and large scale circulations in field situations. Of particular interest is the response of the convective circulation to the switch between the daytime heating and night-time cooling. This will be the major focus of this paper.

### Model Formulation and Normalisation

A two-dimensional (2D) reservoir model consisting of a region with a sloping bottom and another region of a uniform water depth is considered here (see figure 1). Here,  $h$  is the maximum water depth in the reservoir. Previous investigations suggested that 2D numerical models can reproduce major flow features observed in both heating and cooling experiments [5, 6].

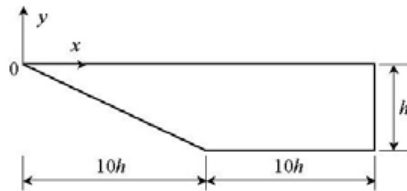


Figure 1 Sketch of the flow domain and coordinate system.

Two types of thermal forcing are constructed for the reservoir model in order to simulate the diurnal cycle in field situations. Assume the period of the thermal forcing is  $P$ . During the first half of every forcing cycle, solar radiation with a time-dependent intensity of  $I_0 \sin(2\pi t/P)$  is imposed at the water surface. Here  $I_0$  is the maximum intensity of the solar radiation at the water surface and  $t$  is the time. The solar radiation entering from the water surface is absorbed by the water body according to the Beer's law:

$$I = I_0 e^{-\eta y} \sin(2\pi t/P) \quad (y \leq 0) \quad (1)$$

where  $I$  is the radiation intensity at a given water depth ( $-y$ ), and  $\eta$  is the attenuation coefficient of water. The attenuation

coefficient can be regarded as a constant [4, 5]. It is assumed in this study that any radiation reaching the bottom is fully absorbed by the bottom and the absorbed energy is then released back into the water as a boundary heat flux. Moreover, it is assumed that the heat loss through the water surface during the heating phase is negligible, and all the radiation entering through the water surface is ultimately absorbed by the water.

During the second half of the forcing cycle, heat is lost through the water surface, and an unsteady heat flux  $H$  defined below is imposed uniformly across the water surface:

$$H = H_0 \sin(2\pi t/P) \quad (2)$$

where  $H_0$  is the maximum heat flux during the cooling period. The construction of the heating and cooling conditions through the water surface ensures a smooth transition from one type of forcing to the other, and the combination of these two types of thermal forcing allows us to simulate an entire diurnal cycle. Moreover, it is assumed that the heat absorbed by the water body during the heating phase is in a balance with the heat released by the water body during the cooling phase, and thus  $H_0 = I_0$ .

The evolutions of flow and temperature in the reservoir are governed by the Navier-Stokes and energy equations as follows:

$$u_x + v_y = 0 \quad (3)$$

$$u_t + uu_x + vv_y = -\rho_0^{-1} p_x + \nu \nabla^2 u \quad (4)$$

$$v_t + uv_x + vv_y = -\rho_0^{-1} p_y + \nu \nabla^2 v + g\beta(T - T_0) \quad (5)$$

$$T_t + uT_x + vT_y = \alpha \nabla^2 T + Sr \quad (6)$$

where  $u$  and  $v$  are the velocity components along  $x$  and  $y$  direction respectively,  $p$  the pressure,  $T$  the temperature,  $\rho_0$  the density at the reference temperature  $T_0$ ,  $g$  the acceleration due to gravity,  $\nu$  kinematic viscosity,  $\alpha$  the thermal diffusivity, and  $\beta$  the thermal expansion coefficient.  $Sr$  is the internal heat source term quantifying the radiation absorption by the water body under the daytime condition, and it is set to zero for the night-time cooling period. Thus,

$$Sr = \begin{cases} \frac{I_0}{\rho_0 C_p} \eta e^{-\eta y} \sin(2\pi t/P) & \text{if } \sin(2\pi t/P) \geq 0 \\ 0 & \text{if } \sin(2\pi t/P) < 0 \end{cases} \quad (7)$$

where  $C_p$  is the specific heat of water.

The governing equations are subject to the following initial and boundary conditions:

- (1) At  $t = 0$ ,  $u = v = 0$ ,  $T = T_0$ .
- (2) At the deep end ( $x = 20h$ ), an insulated and rigid non-slip boundary condition applies, i.e.  $u = v = 0$ , and  $T_x = 0$ .
- (3) The water surface ( $y = 0$ ) is assumed to be stress-free ( $v = 0$  and  $u_y = 0$ ). The thermal boundary condition is given by

$$-k \frac{\partial T}{\partial y} = \begin{cases} 0 & \text{if } \sin(2\pi t/P) \geq 0 \\ -H_0 \sin(2\pi t/P) & \text{if } \sin(2\pi t/P) < 0 \end{cases} \quad (8)$$

where  $k$  is the thermal conductivity.

- (4) The sloping and horizontal bottom is rigid and non-slip ( $u = v = 0$ ). The thermal boundary condition is given by

$$-k \frac{\partial T}{\partial n} = \begin{cases} I_0 e^{y\eta} \sin(2\pi t/P) & \text{if } \sin(2\pi t/P) \geq 0 \\ 0 & \text{if } \sin(2\pi t/P) < 0 \end{cases} \quad (9)$$

where  $n$  is the direction normal to the bottom.

In this study, the governing equations are normalized using the following scales:

Length ( $x, y$ ):	$\sim h$ ;
Velocity ( $u, v$ ):	$\sim \alpha/h$ ;
Time ( $t, P$ ):	$\sim h^2/\alpha$ ;
Temperature variation ( $T - T_0$ ):	$\sim I_0 h/k$ ;
Pressure gradient ( $p_x, p_y$ ):	$\sim \rho_0 g \beta I_0 h/k$ ;
Attenuation coefficient ( $\eta$ ):	$\sim 1/h$ .

The normalised governing equations are rewritten as:

$$u_x + v_y = 0 \quad (10)$$

$$u_t + uu_x + vv_y = -(Pr^2 Gr) p_x + Pr \nabla^2 u \quad (11)$$

$$v_t + uv_x + vv_y = -(Pr^2 Gr) p_y + Pr \nabla^2 v + (Pr^2 Gr) T \quad (12)$$

$$T_t + uT_x + vT_y = \nabla^2 T + Sr \quad (13)$$

where the Grashof ( $Gr$ ) and Prandtl ( $Pr$ ) numbers are defined as:

$$Gr = \frac{g \beta I_0 h^4}{\nu^2 k} \quad \text{and} \quad Pr = \frac{\nu}{\alpha}, \quad (14)$$

and the source term is given by

$$Sr = \begin{cases} \eta e^{y\eta} \sin(2\pi t/P) & \text{if } \sin(2\pi t/P) \geq 0 \\ 0 & \text{if } \sin(2\pi t/P) < 0 \end{cases} \quad (15)$$

All the variables in equations (10) ~ (15) are now dimensionless. The initial and boundary conditions are also normalised accordingly. For brevity, details are not given here.

### Numerical Considerations

The normalised governing equations are solved using a finite difference scheme. Standard second-order central differencing is used for all spatial derivatives except the non-linear terms in the momentum and energy equations, which are approximated with a modified second-order upwind scheme. The time integration for the velocity components and temperature is by a second-order time accurate backward differencing scheme. Details of the numerical schemes can be found in [4].

Since the present investigation is relevant to reservoirs or lakes with water as the medium, the Prandtl number is fixed at 7. The numerical simulations are based on a laboratory scaled model with a maximum water depth of 0.1 m and a bottom slope of 0.1 in the sloping region. Consider a peak intensity of 50 W/m<sup>2</sup> for the thermal forcing with a cycle period of approximately 4 hours. The corresponding dimensionless period of forcing is set to 0.2, and the Grashof number is calculated to be  $1.73 \times 10^7$  based on a room temperature of 20°C. The dimensionless attenuation coefficient is set to 0.62 according to the experimental measurement reported in [5]. A less-than-unity value for the dimensionless attenuation coefficient implies that the maximum water depth is less than the penetration length scale of the radiation, and thus a significant portion of the radiation entering through the water surface will penetrate all the way through the water depth and reach the bottom. For the purpose of examining the dependence of the flow response on the Grashof number, another case with  $Gr = 10^6$  is also calculated.

The results presented here were obtained using a non-uniform mesh of  $201 \times 61$  and a time step of  $10^{-6}$ . In order to test the dependence of numerical solutions on the grid resolution, a coarser mesh of  $121 \times 61$  and a finer mesh of  $301 \times 91$  are also adopted to calculate the case with the higher Grashof number. It

is found that all three meshes gave similar results in terms of the overall response of the flow to the periodic forcing.

For the discussion of the numerical results, a horizontal volumetric flow rate is defined in a 2D domain as [4]

$$Q(x) = 0.5 \int_{-h_x}^0 |u| dy, \quad (16)$$

where  $h_x$  is the local water depth.  $Q(x)$  quantifies the intensity of the horizontal exchange flow at a given  $x$  location. Here, the dimensional quantity has been normalised using the scales  $Q \sim \alpha$ . By integrating  $Q(x)$  along the horizontal direction as follows:

$$Q = L^{-1} \int_0^L Q(x) dx, \quad (17)$$

an averaged volumetric flow rate  $Q$  is obtained. Here,  $L$  is the total length of the domain.

### Flow Response to Periodic Forcing

The numerical results obtained for  $Gr = 1.73 \times 10^7$  are reported here. The simulation covers 10 full thermal forcing cycles in order to minimize the effect of the start-up flow, and the results of the last cycle are presented. In this paper, we only examine the flow response to the daytime heating process corresponding to the first-half of the forcing cycle. Figure 2 plots the temperature contours at representative time instances, and Figure 3 plots the corresponding streamlines. The times indicated in these two figures are relative to the end of the ninth or the beginning of the tenth forcing cycle ( $t = 9P$ ).

At the beginning of this cycle ( $t = 0.00P$ ), the surface cooling is switched off and the radiation heating is switched on at the same time. However, residual temperature and flow structures formed in the previous cooling phase are still present. Figure 2(a) clearly shows that a cold gravity current is flowing downward along the sloping bottom and into the main water body along the flat bottom. The downwelling gravity current is a major feature expected in coastal waters during the night-time cooling process. Corresponding to this downwelling flow, a cavity-wide large-scale circulation is present, as can be seen in figure 3(a). Here the solid streamlines indicate a counter-clockwise circulation. Conversely, dashed streamlines indicate a clockwise circulation (see for example figures 3b, 3c). It is also seen in figure 3(a) that the cavity-wide circulation has multiple cores, indicating the residual effect of plunging plumes formed during cooling.

As the radiative heating intensifies, the water temperature across the entire domain increases as a consequence of the absorption of radiation entering from the water surface. Of particular interest is the growth of a thermal boundary layer along the sloping and flat bottom (see figure 2b). The thermal boundary layer forms because, in shallow waters, a significant portion of the radiation reaches the bottom (the so-called residual radiation) and is absorbed by the bottom. The absorbed energy is then re-emitted back into the water through a boundary heat flux. The combined effects of the bottom boundary heat flux and the topography in the sloping region result in an upward flow along the slope [4, 5], as indicated by the dashed lines in figure 3(b). This upwelling flow is in the opposing direction to the residual flow formed during the previous cooling phase. It is seen in figure 3(b) that, at this time, the reverse flow appears only in the region near the tip and the slope. In the region with a flat bottom, the bottom boundary heat flux does not produce any flow at this stage due to the absence of the topographical effect.

Further to the previous description, the thermal boundary layer continues to grow (figure 2c), and the region with the reverse flow expands toward the core (figure 3c). At this time ( $t = 0.07P$ ), the flow in the region above the slope is almost reversed completely, and the residual flow has been pushed toward the

deep-end wall. It is worth noting that the thermal boundary layer is stable until this time.

As the thermal boundary layer grows further, it eventually becomes unstable to the Rayleigh-Benard type instabilities. As a consequence, rising hot-water plumes occur all the way along the bottom thermal boundary layer, as can be seen in figure 2(d). The thermal instability in the form of rising plumes is the same as the instability observed in shallow waters under constant radiative heating [4, 5]. As the hot-water plumes move upward, they generate secondary flows by pushing and entraining the nearby fluid. The rising thermals also break up the residual circulation and form a cellular flow structure in the domain (see figure 3d).

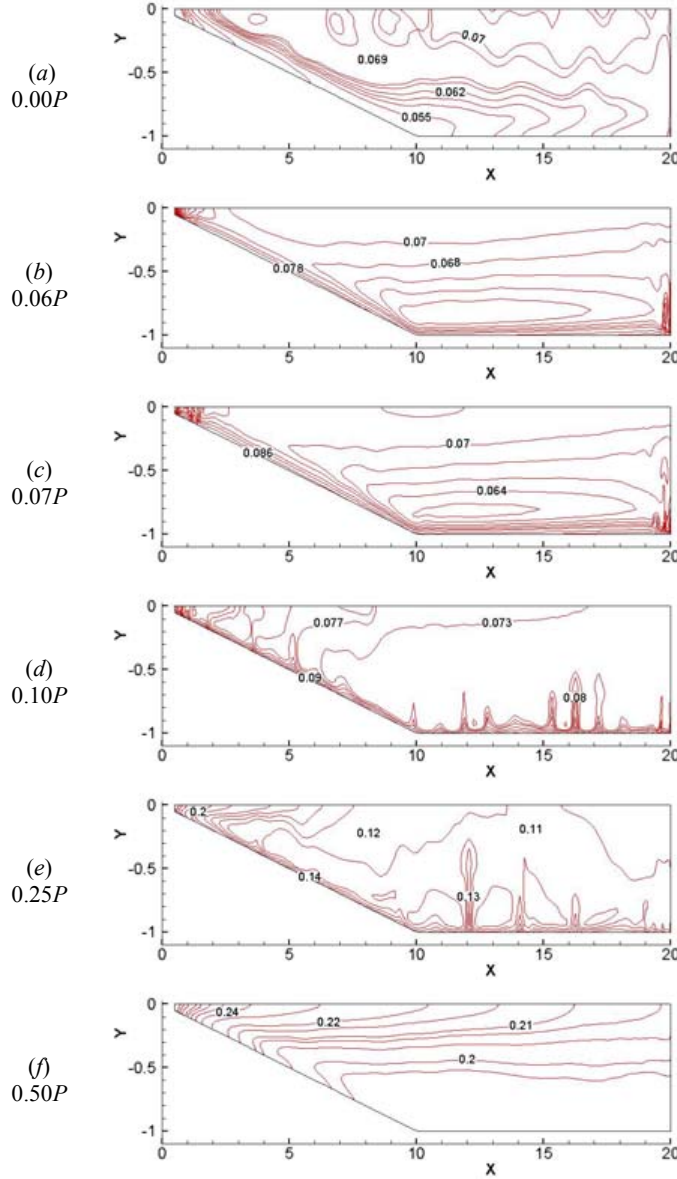


Figure 2 Temperature contours at different stages of the flow response to radiative heating ( $Gr = 1.73 \times 10^7$ ).

The subsequent flow response in the domain is dominated by the occurrence of the thermal instability. Figure 2(e) plots the temperature contours at  $t = 0.25P$  when the intensity of the radiative heating peaks, and figure 3(e) plots the corresponding streamlines. The occurrence of the rising thermals is clearly seen in figure 2(e), and accordingly, the cellular flow structure persists (see figure 3e). Another effect of the thermal instability in the form of rising thermals is to accelerate the vertical mixing in the domain, which in turn reduces the temperature gradient over the local water depth and tends to weaken the thermal instability.

After the time  $t = 0.25P$ , the intensity of the radiative heating starts to decline. However, it is observed that the bottom boundary heating mechanism discussed above, along with the

associated thermal layer instability and the resulting cellular flow structure, persists for a relatively long time. Eventually, the thermal instability dies out when the radiation entering from the water surface becomes very weak. At this stage, the flow response is dominated by the topographic effect in the sloping region. Since the radiation entering from the surface is uniform across the length of the domain, but the water depth increases gradually in the sloping region, the averaged absorption of the radiation over the local water depth increases toward the tip. Therefore, a horizontal temperature gradient is established in the domain, which drives a cavity-wide circulation up the slope and out of the tip region along the surface. The representative temperature and flow structures at this stage is shown in figures 2(f) and 3(f), which plot the contours of temperature and streamlines at  $t = 0.50P$ . Clearly, a temperature gradient exists along the slope and the water surface, and in the majority of the core region, the water is stably stratified (refer to figure 2f). The corresponding streamlines indicate a clockwise circulation across the entire domain (see figure 3f).

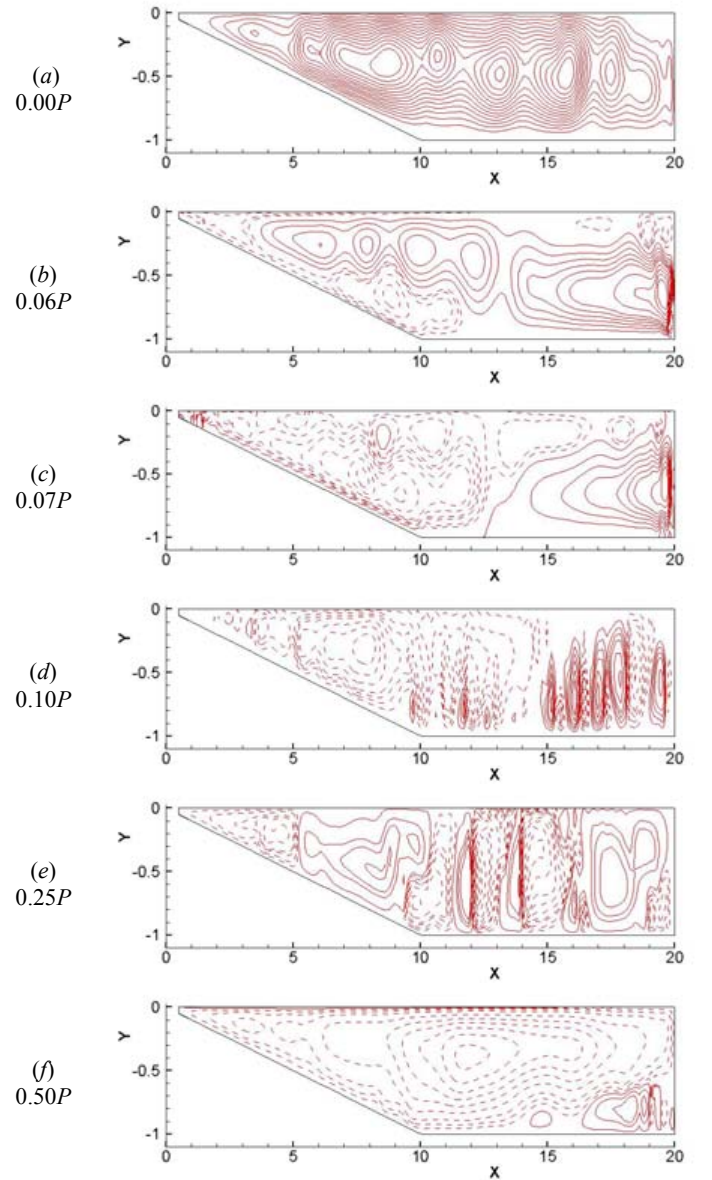


Figure 3 Streamlines at different stages of the flow response to radiative heating ( $Gr = 1.73 \times 10^7$ ).

The temperature and flow structures shown in figures 2(f) and 3(f) respectively also represent the residual structures from the daytime heating phase since the radiative heating is switched off and at the same time the surface cooling is switched on at  $t = 0.50P$ . The flow response during the second-half of the forcing cycle ( $0.50P < t < P$ ) may be described in a similar way. For brevity, the detailed description is not included here. In general,



the flow response during the surface cooling phase is very similar to the radiative heating phase. The major difference between the heating and cooling phases is that there is no thermal boundary layer growing along the bottom. Instead, a thermal boundary layer grows underneath the water surface. It is this surface layer that eventually becomes unstable, and the thermal instability in the form of sinking cold-water plumes breaks the residual circulation and promotes vertical mixing. At the end of the cooling phase, temperature and flow structures identical to those shown in figures 2(a) and 3(a) are formed, and the previously described flow response is repeated in the following cycle.

### Time History of Horizontal Exchange Flowrate

Features of the flow response to the diurnal forcing can also be observed from the time history of the horizontal exchange flowrate, which is presented in figure 4 for two different Grashof numbers along with the corresponding thermal forcing. A positive value of the thermal forcing in figure 4(a) represents the daytime radiative heating, whereas a negative value represents the night-time surface cooling. In figure 4,  $t = 1$  is the beginning of the sixth cycle, and  $t = 2$  is the end of the tenth cycle. At  $t = 1$ , the thermal forcing is switching from the night-time cooling to the daytime heating, and since then, the intensity of the radiative heating increases for a quarter of the cycle.

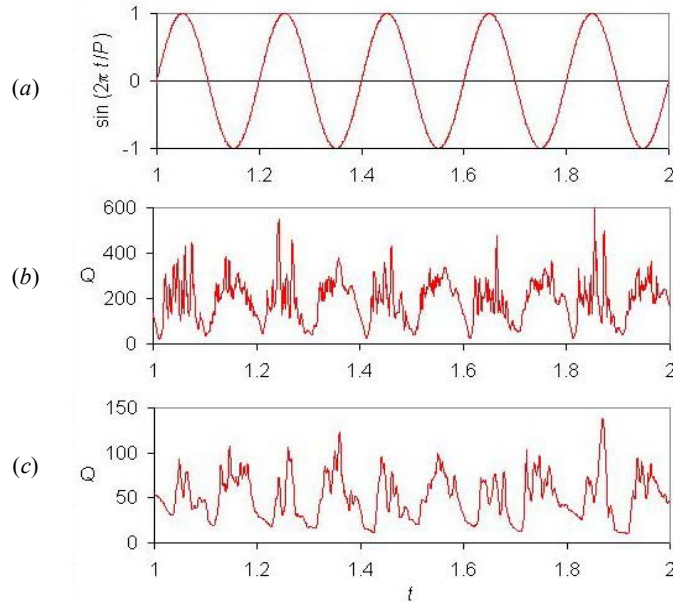


Figure 4. Time history of (a) the thermal forcing; (b) the averaged horizontal exchange flowrate for  $Gr = 1.73 \times 10^7$ ; (c) the averaged horizontal exchange flowrate for  $Gr = 10^6$ .

Consider first the case with  $Gr = 1.73 \times 10^7$  shown in figure 4(b). It is seen in this figure that, in contrast to the increasing thermal forcing, the averaged horizontal flowrate decreases from  $t = 1$  until  $t = 1.012$ . This is due to the effect of the residual circulation formed in the precedent cooling phase. After  $t = 1.012$ , the averaged horizontal flowrate starts to increase, which is in phase with the thermal forcing. The above observation indicates that the lag time of the flow response to the switch of the thermal forcing from cooling to heating is approximately 6% of the forcing period ( $P = 0.2$ ). As the radiative heating intensifies, thermal instabilities associated with the bottom heating start to occur, which cause the fluctuations of the horizontal exchange flowrate. It is seen in figure 4(b) that the thermal instabilities dominate most of the heating phase and persists until well after the radiative heating peaks. When the radiative heating becomes sufficiently weak, the thermal instability dies out, and the overall flowrate decreases until a certain time after the cooling phase

starts. Similarly, there is a lag of the reversal of the overall flow relative to the switch of the thermal forcing from heating to cooling, and the thermal instabilities dominate the flow response for most of the cooling phase.

It is also noticeable in figure 4(b) that the overall strength of the circulation in the heating phase is relatively weaker than that in the cooling phase although the imposed surface heat fluxes are of equal amounts. This is because part of the radiation entering from the water surface is absorbed by the water body, which results a stable stratification in the reservoir.

The time history of the averaged horizontal exchange flowrate obtained for  $Gr = 10^6$  (see figure 4(c)) exhibits similar features. However, three additional features in comparison with the higher Grashof number case are worth noting. First, the strength of the overall circulation is much weaker than the previous case. Second, the thermal instability becomes weaker, and the frequency is also reduced at  $Gr = 10^6$ , as shown in figure 4(c). Finally, the lag time of the flow response to the switch of the thermal forcing is longer for the lower Grashof number case. The lag time for the switch from cooling to heating is estimated to be about 17% of the forcing period for  $Gr = 10^6$ .

### Summary

The flow response to diurnal thermal forcing in shallow waters is described based on numerical simulations. It is observed that there is a time lag of the flow response to the switch of the thermal forcing from surface cooling to radiative heating. The lag time estimated in the present study is significantly shorter than that reported in [1] and in field situations. This is mainly attributed to the shallow water assumption in the present investigation. The flow response in deep waters with a water depth beyond the penetration length scale of the radiation is worth investigating.

It is also observed that the thermal instabilities associated with the bottom heating during the daytime phase and the surface cooling during the night-time phase play an important role in breaking the residual circulation and reversing the flow in deep waters. These instabilities are also the dominant mechanism responsible for the vertical mixing in field situations.

### Acknowledgement

This research was supported by the Australian Research Council and the Australian Partnership for Advanced Computing.

### References

- [1] Farrow D.E., Periodically forced natural convection over slowly varying topography, *J. Fluid Mech.*, **508**, 2004, 1–21.
- [2] Sturman J. J., Oldham C. E. & Ivey G. N., Steady convective exchange flows down slopes, *Aquat. Sci.*, **61**, 1999, 260–278.
- [3] Horsch G.M. & Stefan H.G., Convective circulation in littoral water due to surface cooling, *Limn. Ocean.*, **33**, 1988, 1068–1083.
- [4] Lei C. & Patterson J.C., Unsteady natural convection in a triangular enclosure induced by absorption of radiation, *J. Fluid Mech.*, **460**, 2002, 181–209.
- [5] Lei C. & Patterson J.C., A direct three-dimensional simulation of radiation-induced natural convection in a shallow wedge, *Intl J. Heat Mass Transfer*, **46**, 2003, 1183–1197.
- [6] Horsch G.M., Stefan H.G. & Gavali S., Numerical simulation of cooling-induced convective currents on a littoral slope, *Intl J. Num. Meth. Fluids*, **19**, 1994, 105–134.

## Numerical Method for the Simulation of Front Evolving Fibre Suspension Flow Using Level Set Method

H.-S. Dou<sup>1</sup>, N. Phan-Thien<sup>1</sup>, B. C. Khoo<sup>1</sup>, K. S. Yeo<sup>1</sup>, R. Zheng<sup>2</sup>

<sup>1</sup>Fluid Mechanics Division, Department of Mechanical Engineering  
National University of Singapore, Singapore 119260, SINGAPORE

<sup>2</sup>Moldflow Pty. Ltd, 259-261 Colchester Road, Kilsyth, Vic 3137, Australia

### Abstract

Numerical method for simulating the front evolution of fibre suspension flow is developed using projection and level set methods. The semi-dilute suspensions of short fibres in Newtonian fluids are considered. The governing equation for the fibre motion is the Jeffery equation and that for velocity field is the Navier-Stokes equation. The velocity field is solved using the projection method with finite difference scheme, and the fibre equations are solved with the Runge-Kutta method. Flows with two groups of parameters of semi-dilute suspension flows are simulated in a duct. These results are compared with those of Newtonian flows. It is shown that the numerical method is able to deal with the complexity due to fibre effects and to track the front of the flow. Because the fibre orientation in the flow and the shape of the flow front are of great significance to the quality of the product, this study has wide background of engineering applications.

**Keywords:** Level set; Projection; Fibre suspension; Semi-dilute; Simulation; Front flow.

### Introduction

Simulation of fibre suspensions can be used in the injecting moulding technique to improve the product quality. The quality of simulation of fibre suspension depends upon the appropriate description of the constitutive equations to the fibre properties in the flows and the correct prediction of property of the fibre flows. In the past years, several micro-structural models have been proposed for dilute suspensions and various numerical methods have been developed [1-5]. Generally, most simulations in the literature use a traditionally continuous mechanics method to solve the Navier-Stokes equations, and the contribution of the fibre motion is included in the stress terms. There are currently three kinds of numerical methods for stress contribution from the fibre suspension. One is using the assumption that the fibre is in full-alignment along with the velocity vector [6]. The second method solves the stress tensor in the flow field, and the fibre stress is modelled by a constitutive equation of the fibre orientation tensor [2,7]. The third method is that the orientation tensor of fibre is modelled by Brownian configuration field method [4,8]. Azaiez and Gulbali [9] compared the fibre aligned-assumption and the solution of orientation tensors which is defined as dyadic products of the orientation vector through their FEM solution for contract problem. Their results show that the coupling between the flow and the fibre orientation is very important in the modelling.

The level set method has been developed and used in the tracing of the flow front evolution, and it demonstrated to be very useful and convenient [10,11]. However, it has not been yet applied to the fibre suspension flows. We have used this method for simulating the film flows of shear thinning flows on an inclined plates [12]. In this paper, Numerical method for simulating the front evolution of fibre suspension flow is developed using projection and level set methods. The semi-dilute suspensions of short fibres in Newtonian fluids are

considered. The Brownian configuration field method in [4,8] is employed to solve the fibre motion and their contributions. The purpose of the study is to study the effect of fibre behaviour on the front shape because it strongly influences the quality of the moulding products. Computation examples are given and the result is discussed.

### Governing Equations

The conservations of mass and momentum for an isothermal flow of fibre suspension can be expressed with the following equations,

$$\nabla \cdot \mathbf{u} = 0, \quad \rho \left( \frac{\partial \mathbf{u}}{\partial t} + \mathbf{u} \cdot \nabla \mathbf{u} \right) = -\nabla p + \nabla \cdot \boldsymbol{\tau}_f + \mu_N \nabla^2 \mathbf{u} + \rho \mathbf{g}, \quad (1)$$

where  $\rho$  is the fluid density,  $\mathbf{g}$  the gravity acceleration,  $t$  the time,  $\mathbf{u}$  the velocity vector,  $p$  the hydrodynamic pressure, and  $\boldsymbol{\tau}_f$

the stress tensor from the fibre suspension, and  $\mu_N \nabla^2 \mathbf{u}$  the stress tensor from the Newtonian fluid with  $\mu_N$  being the fluid viscosity.

The constitutive equation for the fibre stress is [3,4],

$$\boldsymbol{\tau}_f = \eta_N f(\phi) [A \dot{\gamma} : \langle \mathbf{p} \mathbf{p} \mathbf{p} \mathbf{p} \rangle + 2D_r F \langle \mathbf{p} \mathbf{p} \rangle], \quad (2)$$

with

$$f(\phi) = \frac{\phi(2 - \phi/\phi_m)}{2(1 - \phi/\phi_m)^2}, \quad A = \frac{a_r^2}{2(\ln 2a_r - 1.5)}, \quad F = \frac{3a_r^2}{\ln(2a_r - 0.5)}, \quad (3)$$

where  $\dot{\gamma} = (\nabla \mathbf{u}^T + \nabla \mathbf{u})/2$  is the rate-of-strain tensor,  $\mathbf{p}$  a unit vector along the axis of the fibre,  $D_r$  the diffusion coefficient,  $\langle \dots \rangle$  denotes the ensemble average over the orientation space of fibres,  $\langle \mathbf{p} \mathbf{p} \rangle$  and  $\langle \mathbf{p} \mathbf{p} \mathbf{p} \mathbf{p} \rangle$  are the second and forth-order structure tensors, respectively, and  $\phi$  the volume concentration.

The parameter  $\phi_m$  express the maximum volume packing of fibres, and it can be approximated by the following empirical linear function of the aspect ratio,

$$\phi_m = 0.53 - 0.013a_r, \quad 5 < a_r < 30. \quad (4)$$

In Eq.(2), the first term on the right hand side expresses the stress contribution from the fibre motion, rotation and interactions (dissipative), and the second term represents the stress contribution due to the momentum transport caused by random motion of fibres (entropic). Generally, the first term plays a dominating role over the second term.

The second and fourth order structure tensors of fibres in Eq.(2) have to be calculated after the unit vector  $\mathbf{p}$  is solved for each fibre. The evolution of the unit vector  $\mathbf{p}$  is expressed by the Jeffery equation [13],

$$\frac{d}{dt} \mathbf{p}(i) = \mathbf{L} \cdot \mathbf{p}(i) - \mathbf{L} : \mathbf{p}(i) \mathbf{p}(i) \mathbf{p}(i) + (\mathbf{I} - \mathbf{p}(i) \mathbf{p}(i)) \cdot \mathbf{F}^{(b)}(i). \quad (5)$$

Here, a diffusion term has been added to Jeffery equation according to Folgar-Tucker [1]. In Eq.(5),  $\mathbf{p}(i)$  is the unit vector along the axis of the  $i$ th fibre,  $\mathbf{L}$  the effective velocity tensor,



$\mathbf{L} = \nabla \mathbf{u}^T - \zeta \dot{\gamma}$ , with  $\zeta = (a_r + 1)^{-1}$ .  $\mathbf{F}^{(b)}(t)$  is a random force, with properties

$$\langle \mathbf{F}^{(b)}(t) \rangle = 0, \quad (6)$$

and

$$\langle \mathbf{F}^{(b)}(t+s) \mathbf{F}^{(b)}(t) \rangle = 2D_r \delta(s) \mathbf{I}, \quad (7)$$

where  $\delta(s)$  is the Dirac delta function and  $\mathbf{I}$  the unit tensor.  $D_r$  is a diffusion factor mentioned in Eq.(2). Folgar and Tucker assumed that

$$D_r = C_i \dot{\gamma}, \quad (8)$$

where  $\dot{\gamma} = \sqrt{\text{tr} \dot{\gamma}^2} / 2$  is the generalized strain rate,  $C_i$  is the interaction factor, which may be a function of  $\phi$  and  $a_r$ . Phan-Thien et al. have given a correlation of a semi empirical equation [14]. The random force can be expressed in terms of the white noise,

$$\mathbf{F}^{(b)}(t) = \sqrt{2C_i \dot{\gamma}} \frac{d\mathbf{w}_t}{dt}, \quad (9)$$

where  $\mathbf{w}_t$  is the Wiener process and it is a Gaussian random function.

After the Eq.(5) for  $\mathbf{p}(i)$  is solved, one can calculate the structure tensor using the ensemble average:

$$\langle \mathbf{p} \mathbf{p} \rangle = \frac{1}{N} \sum_{i=1}^N \mathbf{p}(i) \mathbf{p}(i), \quad \langle \mathbf{p} \mathbf{p} \mathbf{p} \mathbf{p} \rangle = \frac{1}{N} \sum_{i=1}^N \mathbf{p}(i) \mathbf{p}(i) \mathbf{p}(i) \mathbf{p}(i), \quad (10)$$

where  $N$  is the number of fibres. Now, introducing that,

$$\mathbf{q}(i) = q(i) \mathbf{p}(i) \quad (11)$$

with  $q(i)$  being the modulus of  $\mathbf{q}(i)$ . Equation (5) becomes

$$\frac{d}{dt} \mathbf{q}(i) = \mathbf{L} \cdot \mathbf{q}(i) + q(i) \mathbf{F}^{(b)}(t). \quad (12)$$

Rewriting Eq.(12),

$$\frac{\partial}{\partial t} \mathbf{q}(i) = -\mathbf{u} \cdot \nabla \mathbf{q}(i) + \mathbf{L} \cdot \mathbf{q}(i) + q(i) \sqrt{2C_i \dot{\gamma}} \frac{d\mathbf{w}}{dt}. \quad (13)$$

This equation can be solved using the time marching scheme with the evolution of the flow field for each fibre at all the nodes.

### Level Set Method for Two-Phase Flows

The level set method is to solve the following convective equation,

$$\frac{\partial \phi}{\partial t} + \mathbf{u} \cdot \nabla \phi = 0, \quad (14)$$

where  $\phi$  is the level set function and  $\mathbf{u}$  is the “unified” fluid velocity. The interface between the two fluids is expressed by a zero value of a function  $\phi$ ; the function is positive in one phase and is negative in another phase. In the computing, the level set function is initialized as a signed distance function from the interface. Then, it is evolved according to Equation (14), which is solved by a time marching scheme. After each time step, the zero level set function should represent the position of the new interface. However, because of the numerical approximation, the level set function may not remain a distance function at later time steps; in particular after a long time. Therefore, it is suggested that the level set function is re-initialized after a time step so that it remains a distance function without changing its zero level set. Generally, this is achieved by solving the following partial differential equation [10,11],

$$\frac{\partial \phi}{\partial \tau} = \text{sign}(\phi)(1 - |\nabla \phi|) \quad (15)$$

with initial conditions

$$\phi(x, 0) = \phi_0(x), \quad (16)$$

where  $\text{sign}(\phi)$  is a sign function, and  $\tau$  is the (artificial) time, and  $\phi_0(x)$  is the initial value of  $\phi$  given at the beginning of calculation for all of the domain.

The Navier-Stokes equations for two-fluid flows can be modified to include the surface tension force. Thus, the governing equation for the fluid velocity,  $\mathbf{u}$ , along with the boundary conditions can be combined in a single equation,

$$\rho(\phi) \frac{D\mathbf{u}}{Dt} = -\nabla p + \nabla \cdot \boldsymbol{\tau}_f + \mu(\phi) \nabla^2 \mathbf{u} + \rho(\phi) \mathbf{g} - \sigma k(\phi) \delta(\phi) \nabla \phi, \quad (17)$$

where  $\rho(\phi)$  and  $\mu(\phi)$  are the density and viscosity, respectively, which are functions of  $\phi$ , and they are expressed by a smoothed heaviside function at the interface.  $\delta(\phi)$  is the Dirac delta function,  $\sigma$  is the surface tension factor, and  $k(\phi)$  is the curvature of the interface.

The equation (17) is rewritten as the dimensionless form,

$$\mathbf{u}_t + \frac{\nabla p}{\rho(\phi)} = \mathbf{F}, \quad (18)$$

where

$$\mathbf{F} = -\mathbf{u} \cdot \nabla \mathbf{u} - \frac{\mathbf{e}}{Fr} + \frac{1}{\rho(\phi)} \left( \frac{1}{Re} \nabla \cdot \boldsymbol{\tau}_f + \frac{1}{Re} \nabla \cdot (2\mu(\phi) \dot{\gamma}) - \frac{1}{We} k(\phi) \delta(\phi) \nabla \phi \right), \quad (19)$$

and  $\mathbf{e}$  is the unit vector of the gravitational force.

Sussman et al [11] described a variable density projection method. In this method, it is assumed that

$$\nabla \cdot \mathbf{u}_t = 0 \quad (20)$$

Thus, according to the Hodge decomposition, one can uniquely decompose the quantity  $\mathbf{F}$  found in Equation (18) into a divergence free part ( $\mathbf{u}_t$ ) and the gradient of a scalar divided by density ( $\nabla p / \rho(\phi)$ ). Since  $\mathbf{u}_t$  is divergence free we can write it as for two-dimensional flow,

$$\mathbf{u}_t = (\partial \psi_t / \partial y, -\partial \psi_t / \partial x, 0)^T \quad (21)$$

where  $\psi_t$  is the stream function corresponding to  $\mathbf{u}_t$ .

For two-dimensional flows, if we multiply both sides of Equation (18) by  $\rho$  and take the curl of both sides, we then obtain,

$$-\nabla \cdot (\rho \nabla \psi_t) \mathbf{k} = \nabla \times (\rho \mathbf{F}), \quad (22)$$

where  $\mathbf{k}$  is the unit vector in the  $z$  direction.

For given smooth boundary conditions and initial conditions, Eq.(22) can be solved for the stream function for a prescribed time increment.

### Numerical Discretization and Algorithm

The discretization is based on a staggered grid arrangement, as shown in Fig. 1. Here,  $\mathbf{u}$ ,  $\mathbf{q}$ ,  $\rho$ ,  $\mu$ ,  $\phi$ , are given at the primary grid points denoted by open circles, and  $\psi_t$ ,  $\nabla \mathbf{u}$ , and  $\boldsymbol{\tau}$  are defined on the dual grid points denoted by “ $\times$ ”. Actually, the dual grid points lie on the wall boundary of the physical domain for the imposition of the no-slip boundary conditions (Fig. 1). The numerical discretization has been described in [11-12].

The projection equation (22) is solved using a preconditioned conjugate gradient (PCG) method. Then,  $u_t$  is obtained by Eq.(21) using the central difference scheme. The

time marching of the dependent variable  $u$ ,  $v$ , and  $\phi$  are calculated by using a high order Total Variation Diminishing (TVD) Runge-Kutta scheme. The time step  $\Delta t$  is determined by restrictions due to CFL condition, gravity, viscosity and surface tension.

The total numerical procedure can be summarized as below:

- (1) Initialize all the parameters. Give initial  $\phi$  in the domain.
- (2) For given  $\phi^n$ ,  $\mathbf{u}^n$ ,  $\rho(\phi)$ ,  $\mu(\phi)$ , solve the Eq.(5) using the time march scheme, and obtain the fibre orientation distribution and the configuration tensor.
- (3) For given  $\phi^n$  and  $\mathbf{u}^n$ , calculate  $\rho(\phi)$  and  $\mu(\phi)$  etc., then calculate the convective term, viscous term and fibre stress term (Central difference), source term (coordinate components), and tension term in Eq.(19).
- (4) Solve equation (22) using a preconditioned conjugate gradient (PCG) method to get  $\psi_i$ . Calculate  $\mathbf{u}_i$  expressed by Eq.(21) by differencing  $\psi_i$ .
- (5) Determine the time step  $\Delta t$  using the criteria given; Do the time marching step for variables  $u$ ,  $v$ , and  $\phi$  using a high order total variation diminishing (TVD) Runge-Kutta scheme to obtain  $u^{n+1}$ ,  $v^{n+1}$ , and  $\phi^{n+1}$  (like  $\mathbf{u}^{n+1} = \mathbf{u}^n + \mathbf{u}_i \Delta t$ ).
- (6) Re-initialize the level set function for  $\phi^{n+1}$  following the equations (16).
- (7) Take the new  $u^{n+1}$ ,  $v^{n+1}$ , and  $\phi^{n+1}$  as the old ones, and then return to step (2).

### Simulation Results and Discussions

An annoying feature in the application of the projection/level set method is that it is required that the initial condition for the computational domain is divergence free. This requirement is only satisfied for few situations. Unfortunately, this condition is not satisfied for most open flow problems. In this study, first, we assign a continuous smooth distribution of stream function. Then, a divergence free velocity field is obtained from this stream function and is taken as the initial flow field.

The computing domain is shown in Fig.2 as a rectangular area with inlet AD, and BC the outlet. AB and CD are solid walls and EF is the interface of the two fluids. AB is taken as 4 times of AD, and AF is taken as 0.25 times of AD. The fluid flow is driven by a pressure gradient at the inlet in a two-dimensional channel. Initially, the fluid stays in the area enclosed by AFED. At time  $t=0$ , the fluid is allowed to flow as the given velocity distribution. At the first few steps, the flow will automatically adjust itself to obey the governing equations. After a long enough time and far enough from the inlet, the effect of initial flow field becomes small. The flow is dominated by the pressure gradient and viscous and fibre forces as well as the surface tension. For the laminar flow of a Newtonian fluid, it is thought that the velocity distribution in the duct far from the front obeys parabolic distribution, in which the effect of interface and surface tension can be neglected. In the simulation, we hope to track the evolution of the flow front, and to find the effect of fibre suspension properties. The boundary condition is taken such that AB and CD are solid surfaces and hence no-slip boundary condition applies. Boundary conditions at inlet for velocities are given at AD and Neumann boundary condition applies on BC. At the wall, the level set function is extrapolated to the wall from interior domain. The contact angle is not given as in most level set methods. The slope of the interface at the wall is directly obtained from the simulation. The BC on  $\mathbf{p}$  at the wall is given that the fibre is parallel to the wall ( $p_1=0$ ,  $p_2=1$ , and  $p_3=0$ ). The initial condition for  $\mathbf{p}$  within the domain is random (AFED in Fig.2). With the fluid flowing and the time involving, the orientation of the fibres will automatically adapt to the velocity

field. The simulation is carried out for given concentration and number of fibres. They are set to be constants in the domain as in [4,8]. Generally, there is no number limitation of fibres in principle, provided that the computer resources are sufficient large. Eq.(5) is solved for each fibre, and then assemble average is employed to calculate the stresses. Thus, it is better for the simulation to be carried out using a large number. However, the simulation results will be about the same when the number of fibres is larger than a sufficient large number. A large number for the fibres avoids the oscillation of the solutions. Numerical limitation is encountered when the concentration is high which leads to high stress gradients near the interface.

Simulation results for two examples are shown in Fig.3 to Fig.5 for Newtonian flow and fibre flow ( $\phi = 0.08$ ,  $a_r = 10$ ,  $\sigma = 0.01$ , and  $N=500$ ). The flow is from top to bottom. It can be seen that the addition of fibres makes the flow front more distorted. Compared to Newtonian flow, the presence of fibres affects the shapes of flow fronts and the flow front changes gradually with the increase of fibre concentration. The simulation results show that the fibres near the walls (high shear rate) generate high stresses, slow down the streamwise velocity, and increase the transverse velocity. This make the flow near the front form a fountain flow. Although the surface tension increases the strength of the "fountain," the primary reason of this front shape is due to the influence of fibre stresses. The velocity field is shown in Fig.3 and Fig.4 for Newtonian and fibre suspension cases. The difference is clearly demonstrated. The effect of fibres makes the front near the walls moving faster than that for Newtonian flow (Fig.5). After the flow evolving a long enough time, the flow front should approach steady-state geometries owing to the balance of various forces including surface tension. In Fig.5, the flow front is still under development at  $t=17$ .

Finally in conclusion, the front flow evolution in fibre suspension flows can be simulated with the projection scheme and the level set method. Using this algorithm, the effect of various material parameters on the flow properties and front shapes as well as the final fibre orientation can be obtained. This study will help to improve the product quality in injection moulding and other process industries.

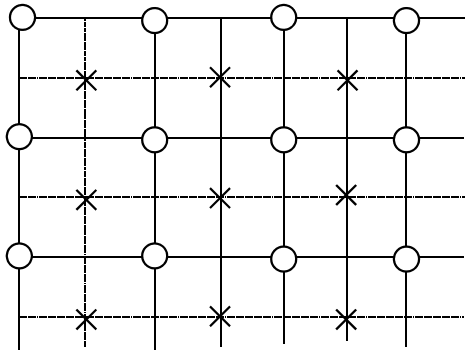
### Acknowledgements

The authors are grateful to X-J Fan (The University of Sydney) for his helpful discussions and suggestions.

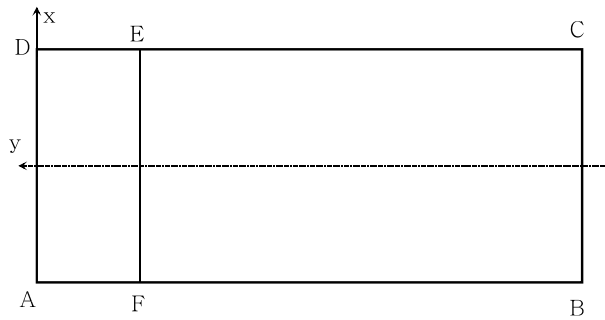
### References

1. Folgar, F.P. & Tucker, C.L., Orientation behavior of fibers in concentrated suspensions, *J. Reinforced Plastics and Composites*, 3, 1984, 98-119.
2. Advani, S.G. & Tucker, C.L., The use of tensors to describe and predict fibre orientation in short fibre composites, *J. of Rheol.*, 31, 1987, 751-784.
3. Phan-Thien, N. & Graham, A.L., A new constitutive model for fibre suspensions: flow past a sphere, *Rheol. Acta*, 30, 1991, 44-57.
4. Fan X.J., Phan-Thien, N. & Zheng R., Simulation of fibre suspension flows by the Brownian configuration field method, *J. Non-Newt. Fluid Mech.*, 84, 1999, 257-274.
5. Petrie, C.J.S., The rheology of fibre suspensions, *J. Non-Newt. Fluid Mech.*, 87, 1999, 369-402.
6. Baloch, A. & Webster, M.F., A computer-simulation of complex flows of fiber suspensions, *Comput. Fluids*, 24, 1995, 135-151.
7. Reddy, B.D. & Mitchell, G.P., Finite element analysis of fibre suspension flows, *Comput. Method Appl. Mech. & Eng.*, 190, 2001, 2349-2367.
8. Hulsen, M.A., van Heel, A.P.G. & van den Brule, B.H.A.A., Simulation of viscoelastic flows using Brownian configuration fields, *J. non-Newt. Fluid Mech.*, 70, 1997, 79-101.

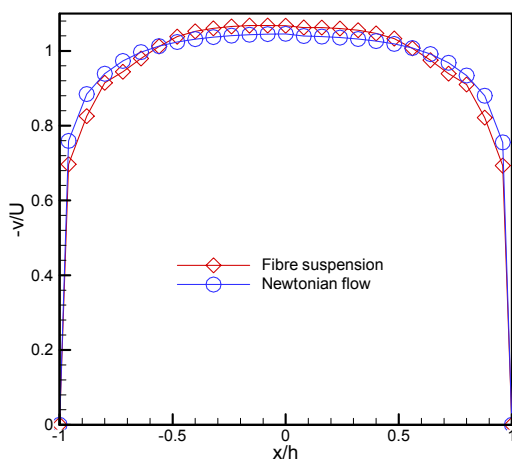
9. Azaiez, J. & Guette, R., Numerical Modelling of the Flow of Fibre Suspensions through a Planar Contraction, *Canadian J of Chem. Engineering*, 80, 2002, 1115-1125.
10. Sethian, J.A. & Smereka, P., Level set methods for fluid interfaces, *Annu. Rev. Fluid Mech.*, 35, 2003, 341-372.
11. Sussman, M., Fatemi, E., Smereka, P. & Osher, S., An improved level set method of incompressible two-fluid flows, *Comput. Fluids*, 27, 1998, 663-680.
12. Dou, H.-S., Phan-thien, N., Khoo, B.C., Yeo, K.S. & Zheng, R., Simulation of front evolving liquid film flowing down an inclined plate using level set method, *Comput. Mech.*, 34, 2004, 271-281.
13. Jeffery, G.B., The motion of ellipsoidal particles immersed in viscous fluid, *Proc. Roy Soc. Lond.*, A102, 1922, 161-179.
14. Phan-Thien, N., Fan, X.J., Tanner, R.I. & Zheng, R., Folgar-Tucker constant for a fibre suspension in a Newtonian fluid, *J. Non-Newt. Fluid Mech.*, 103, 2002, 251-260.



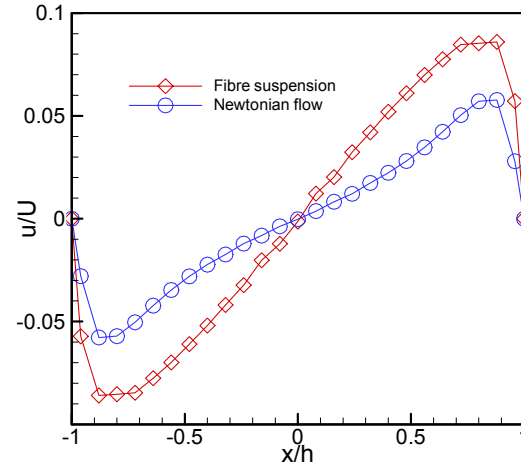
**Fig.1.** Schematic of the grid arrangement. Primary grid points O: for  $\mathbf{u}$ ,  $\mathbf{q}$ ,  $\rho$ ,  $\mu$ ,  $\phi$ ; Dual grid points  $\times$ : for  $\psi_t$ ,  $\nabla \mathbf{u}$ ,  $\boldsymbol{\tau}$ , and the resulting  $p$ .



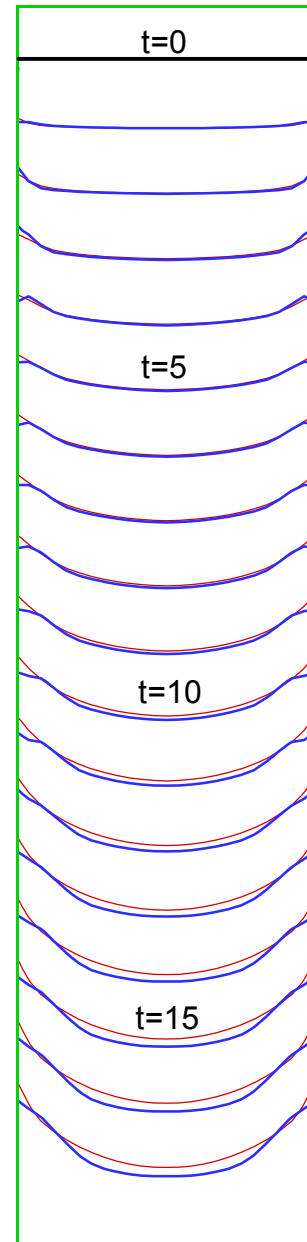
**Fig.2.** Schematic of the computing domain



**Fig.3** Streamwise velocity profile at the position just behind the front for  $t=15$ .



**Fig.4.** Velocity profile in transverse direction at the position just behind the front for  $t=15$ .



**Fig.5** Computing results for the flow front evolution for Newtonian flow (red thin line) and fibre suspension flow (blue thick line,  $\phi = 0.08$ ,  $a_r = 10$ ,  $N = 500$ ,  $C_i = 0.01$ ). Reynolds number is 60 based on the viscosity of the solvent; Grid is  $27_i \times 100_j$ ; Time interval of the front contour is  $\Delta t = 0.01$  second. Surface tensor coefficient is  $\sigma = 0.01$  N/m.

# Instability of Fluid Material Systems

H.-S. Dou and N. Phan-Thien

Fluid Mechanics Division, Department of Mechanical Engineering  
National University of Singapore, Singapore 119260, SINGAPORE

## Abstract

Transition to turbulence is due to the instability of a laminar flow subject to a disturbance. This complicated problem can be explained using a new proposed energy gradient theory in our previous study. This theory is extended to the instability of fluid material systems in this study. The instability of fluid material systems may lead to the evolution of natural environments and the occurrence of catastrophic events in the world. To better describe these phenomena and to understand the physical mechanism behind them are very important. In order to more generally describe the instability of fluid material systems, *laws of energy gradient* are summarized for static and motion systems, respectively. These laws could be applicable to various flow problems and material systems. Examples are shown that many events in the world could be explained using these laws.

**Keywords:** Fluid materials system; Instability; Energy gradient; Catastrophic events; Laws of energy gradient.

## Introduction

Turbulence is a very complex phenomenon which has a history of more than 120 years. The mechanism of turbulence generation is still unknown so far. Earlier researches include theory, experiments and semi-empirical theory. In recent 30 years, numerical simulation for this topic has obtained large advance with the aid of the computer techniques. However, the understanding of the flow physics of turbulence is still limited. Even some experts assert that our research on turbulence is still at the infant stage after 100 years [1]. Although we noticed that it is still lacking of theoretical unity in many respects, Tatsumi [2] stated that it is the time for constructing a unified physical theory of turbulence from the enormous amount of information obtained during this century.

Newtonian mechanics founded the basis of modern science and technology. However, even though using that, many phenomena could not be explained in the macro-world so far. The most typical one is the generation of turbulence as stated. This is the most difficult problem in classical mechanics.

Researches have shown that turbulence generation is resulted from the instability of laminar flows. All of the theories of flow instability, including linear theory, energy method, weak nonlinear theory, and secondary instability theory, could not satisfactorily explain the problem of flow instability in parallel flows [3-8]. Recently, Dou [9] proposed a new theory of energy gradient for flow instability and turbulence transition. The energy gradient theory obtains consistent results for the subcritical transition of parallel flows. Dou showed that the energy gradient theory is a better method for the description of subcritical flow transition than the others.

Many phenomena occurring in the nature have similar behaviour as the generation of turbulence. Many material systems have the feature of flow like fluid. This is as described in [10]: everything flows. Therefore, these systems may be described using same theory as for turbulence.

In this paper, we show that energy gradient theory is suitable for stability of various fluid material systems in nature. This theory may be used for the prediction of catastrophic events in the nature. New laws are proposed for the Newtonian mechanics.

## Energy Gradient Theory

Dou (2004) [9] proposed an energy gradient theory with the aim to clarify the mechanism of transition from laminar to turbulence. It is thought that the gradient of total energy in the transverse direction of the main flow and the viscous friction in the streamwise direction dominate the instability phenomena and hence the flow transition. The energy gradient in the transverse direction has the potential to amplify a velocity disturbance, while the viscous friction loss in the streamwise direction can resist and absorb this disturbance energy. The transition to turbulence depends on the relative magnitude of the two roles of energy gradient amplifying and viscous friction damping to the initial disturbance. Based on such, a new dimensionless parameter,  $K$  (the ratio of the energy gradient in the transverse direction to that in the streamwise direction), can be written as,

$$K = \frac{\partial E / \partial n}{\partial E / \partial s} \quad (1)$$

Here,  $E = p + \frac{1}{2} \rho V^2 + \rho g \xi$  is the total energy for incompressible flows with  $\xi$  as the coordinate perpendicular to the ground,  $n$  denotes the direction normal to the streamwise direction and  $s$  denotes the streamwise direction.  $\rho$  is the fluid density,  $g$  the gravity acceleration,  $V$  the velocity, and  $p$  the hydrodynamic pressure. The parameter  $K$  in Eq.(1) is a field variable. The occurrence of instability depends upon the magnitude of this dimensionless parameter  $K$  and the critical condition is determined by the maximum value of  $K$  in the flow. For a given flow geometry and fluid properties, when the maximum of  $K$  in the flow field is larger than a critical value  $K_c$ , it is expected that instability would occur for certain initial disturbance [9]. The analysis showed that the transition to turbulence is due to the energy gradient and the disturbance amplification, rather than a linear eigenvalue instability type [11, 12]. Both Grossmann [11] and Trefethen et al.'s [12] commented that the nature of the onset-of-turbulence mechanism in parallel shear flows must be different from an eigenvalue instability of linear equations of small disturbance. Dou (2004) demonstrated that the criterion has obtained excellent agreement with the experimental data for plane Poiseuille flow and pipe Poiseuille flow as well as plane Couette flow, see Table 1 [9]. It can be found that the turbulence transition takes place at a critical value of  $K_c$  of about 385 for both plane Poiseuille flow and pipe Poiseuille flow, and about 370 for plane Couette flow, and they obtained a consistent value. This result proved that the flow instability is resulted from the action of energy gradients, but not the kind of eigenvalue instability of linear equations. The



comparison of theory with experiments is shown in Table 1 for wall bounded parallel flows (Fig.1).

The proposed principle can be used to both pressure and shear driven flows. If we assume that there is no energy input (such as shear) to the system or energy output from the system, this criterion can predict that the viscous flow with inflectional velocity is unstable. This is because if there is an inflection point in the velocity profile, the value of maximum of  $K$  in the flow will be infinite. Therefore, the flow is unstable at the inflection point. Following this principle, it is proved that viscous parallel flow with inflectional velocity profile is sufficient for flow instability for both two-dimensional and axisymmetrical flows [14].

Flow type	Re expression	Linear theory, $Re_c$	Exp $Re_c$	$K_{max}$ at Exp $Re_c$
Pipe Poiseuille	$Re = \rho U D / \mu$	$\infty$	2000	385
Plane Poiseuille	$Re = \rho U L / \mu$	7696	1350	389
	$Re = \rho u_0 h / \mu$	5772	1012	389
Plane Couette	$Re = \rho U h / \mu$	$\infty$	370	370

Table 1 Comparison of the critical Reynolds number and the energy gradient parameter  $K_{max}$  for plane Poiseuille flow and pipe Poiseuille flow [9] as well as for plane Couette flow [13].

Although laminar-to-turbulent transition can occur through several mechanisms, such as in linear instability, bypass transition (skip linear instability), Gortler instability (flow on concave surface), and cross-flow instability (flow over swept wing) [15], all of these instabilities can be included in the frame of instabilities resulted by energy gradient.

The instability mechanism can also get some hint from solid mechanics. As is well known, the damage of a metal component generally starts from some area such as manufacturing fault, crack, stress concentration, or fatigue position, etc. In fluid mechanics, the breaking down of a steady flow should also start from some most dangerous position first. For example, for the flow around an airfoil at a large attack angle, the flow instability first starts from the rear part on the suction side where the pressure gradient is large. For the flow around a cylinder, it is known that the flow instability begins first from the two inflection points near the rear stagnation point.

## Laws of Energy Gradient For Flow Instability

The Newtonian mechanics as a basic subject has been developed for more than 300 years since this subject was established (1664-1684). The Newton's three laws (Law of inertia, law of acceleration, and law of action and reaction) established the foundation of modern mechanics and becomes the backbone of modern science and technology [16].

In these laws, it is not shown why a fluid material system becomes of motion from static (or why a phase change occurs), and why the flow of materials becomes unstable from stable. Now, we describe the laws for the stability of fluid material systems using the energy gradient theory.

### First law of energy gradient (static system)

*If a material system is static, when the energy gradient in some direction is larger than a critical value, the system will become unstable and the phase change or flow would occur.*

The unstable condition can be expressed as

$$\frac{\partial E}{\partial x} > C, \quad (2)$$

where  $C$  is the critical value which is related to the material properties (friction factor, density, etc.) of the material and the geometry of the problem. This law may be restated as: when the energy gradient in some direction is larger than the work which should be done to overcome the resistance for the material moving, the material will be unstable and the material may flow or the phase change may occur. Thus, this law may be expressed as that the unstable condition of a system is,

$$D = \frac{\partial E / \partial x}{\partial A / \partial x} > 1, \quad (3)$$

where  $\partial A / \partial x = C$  is the work needed to make the material moving for unit volume media. Actually, this law is consistent with the first law and second law of Newton. Newton's first and second laws describe the system from the roles of forces, while the first law of energy gradient describes the system from the viewpoint of energy field.

### Second law of energy gradient (moving system)

*If a material system flows, when the ratio of the energy gradient in the transverse direction and that in the streamwise direction is larger than a critical value, the system will become unstable.*

The unstable condition for a moving system can be expressed as

$$K = \frac{\partial E / \partial y}{\partial E / \partial x} > K_c, \quad (4)$$

where  $K_c$  is the critical parameter which is related to the material properties and the flow geometry. The instability of plane Poiseuille flow, pipe Poiseuille flow, and plane Couette flow are typical examples of instability of moving systems.

These laws could be thought as that they are supplements to Newton's three laws. *Any fluid system violating these laws will become unstable.* The energy gradient laws enriched the system of classical mechanics. They can deal with problems which could not be resolved by Newton's laws. This will be demonstrated in later section for use in various instability problems. From these laws, it can be found that the reason of a material system moving in some cases is due to energy gradient, and not simply to the role of forces. For example, fluid cell formation in Rayleigh-Benard problem is not resulted in by forces, but by energy gradient (we will show the detail later). Energy gradient is the power of motion of material when there is no external force acting on it. Further, it is found that the motion of media from one state to another state is due to the role of energy gradient. The instability of the media state is caused by energy gradient, and a new state is then formed through the motion of the media under the energy gradient.

### Examples of Material System Instabilities

We take  $x$  is horizontal and  $y$  is upward. The total energy per unit volume fluid for incompressible fluids can be written as

$$E = p + \frac{1}{2} \rho V^2 + \rho g y. \quad (5)$$

**Static fluid in a container:** (a) If the fluid in the container is single fluid (Fig.2a), there is  $\frac{\partial E}{\partial x} = 0$  and  $\frac{\partial E}{\partial y} = 0$  in everywhere of the domain. Thus, the energy of fluid in the domain is uniform. Because there is no energy gradient in the



domain, the fluid is stable. (b) If one fluid ( $\rho_1$ ) is over another fluid ( $\rho_2$ ) in the container, the energy gradient will be formed at the interface (fig.2b). When  $\rho_1 < \rho_2$ , there are  $\frac{\partial E}{\partial x} = 0$  and  $\frac{\partial E}{\partial y} < 0$  at the interface, the fluid state is stable. When  $\rho_1 > \rho_2$ , there are  $\frac{\partial E}{\partial x} = 0$  and  $\frac{\partial E}{\partial y} > 0$  at the interface, the fluid state is unstable (Rayleigh-Taylor instability).

**Uniform flow will be stable:** For uniform flow, the velocity is a constant in the domain (Fig.2c). If the fluid gravity is neglected, there are  $\frac{\partial E}{\partial x} = 0$  and  $\frac{\partial E}{\partial y} = 0$  in everywhere of the flow field, and thus the flow is stable.

**Kelvin-Helmholtz instability:** Free shear flow displays an instability called Kelvin-Helmholtz instability (Fig.2d). There are  $\frac{\partial E}{\partial x} = v \nabla^2 V$  and  $\frac{\partial E}{\partial y} = V \frac{\partial V}{\partial y}$  in the flow field if the fluid gravity is neglected. The flow stability depends on the magnitude of  $K$  calculated by Eq.(1). Because an inflection point exists in the interface of free shear flow, we have  $K = \infty$  at the inflection point from Eq.(1). Therefore, free shear flow is always unstable.

**Rayleigh-Bernard problem:** When the fluid is placed on a horizontal plate and it is heated from below. Then, the fluid will become unstable, and fluid cells of vortices will be formed (Fig.2e). This kind of pattern of roll formation can be explained using the energy gradient theory. If we treat the fluid as incompressible,  $E = p + \frac{1}{2} \rho V^2 + \rho g y$ , then  $\frac{\partial E}{\partial x} = 0$  and  $\frac{\partial E}{\partial y} = g y \frac{\partial \rho}{\partial y} > 0$  in the fluid domain because the fluid density in the bottom becomes low. If  $\frac{\partial E}{\partial y}$  is larger than a critical value, the

flow will become unstable. It is noticed that there is no role of forces, but there is an energy gradient in the vertical direction.

**Stratified flows:** When two layers of fluids with different densities flow along one direction, instability due to stratified density will occur. This is because an energy gradient is formed at the interface (Fig.2f). The formulation is similar to that as for Fig.2e.

**Wall bounded Parallel flows:** Plane Poiseuille flow, pipe Poiseuille flow, and plane Couette flow are all the examples of instabilities of parallel flows resulted by energy gradients, as shown in Table 1 and Fig.1. These flows have been studied in [9] and [13].

**Inflectional instability:** Flows behind a cylinder display instability at higher Reynolds number. It is known that this instability is caused by the inflection points near the rear stagnation points. Kelvin-Helmholtz instability is another example of inflectional instability produced by jet-wake (Fig.2d) as stated before.

**Granular material instability (Fig.3):** (a) Avalanche of piled sands or phase change (Fig.3a): A sand pile is placed on an inclined plate. When the inclined angle exceeds a critical value, the avalanche of sand pile will occur due to the energy gradient influence (gravitational energy).

**Migration of stone in the bottom of a river bed (Fig.3b):** Stones on the bottom of a river is moved by water flow. This process could be explained using the energy gradient theory (pressure energy).

**Migration of sands in desert (Fig.3c):** Sand piles in desert moves due to the role of windings around them. This movement could be explained using the energy gradient theory (pressure energy).

The experimental data for material system is very limited and the critical value also depends on the material property. The analyses for instabilities of granular materials in literature are mostly qualitative. Here, we summarize the comparison of laws of energy gradient with experimental observations for a few cases in Table 2.

Fluid system	Experiments observations	Laws of Energy gradient
Single fluid, Fig.2a	Stable	Stable
Two fluids, $\rho_1 > \rho_2$ , Fig.2b	Unstable	Unstable
Uniform flow, Fig.2c	Rec= $\infty$ , stable	Rec= $\infty$ , stable
Free shear flow, Fig.2d	Rec=0, unstable	Rec=0, unstable

Table 2 Comparison of theory with experiments.

Energy gradient is not only the mechanism of turbulence generation, but also the rule of generation of many unstable phenomena in nature. For example, evolution of cosmic stars, motion of mantle of earth, earthquake occurrence, land shift, mountain coast, snow avalanche, dam breaking, change of atmosphere, etc, all can be explained and described using the energy gradient laws. The breakdown of the process of these mechanical systems can be universally described in detail using this theory. Sornette (2002) described a unifying approach for modelling and predicting these catastrophic events or “ruptures,” that is, sudden transitions from a quiescent state to a crisis [17]. He stated that such ruptures involve interactions between structures at many different scales. He believes that it is possible to develop universal theory and tool for predicting these catastrophic events. The energy gradient laws can be used to predict the flow-system breakdown and the catastrophic events too [18]. The energy gradient theory [9] describes a mechanism of failure of mechanical system in a simple way. It will demonstrate its powerfulness in the application of catastrophic predictions in near future.

## Conclusion

Energy gradient theory was proposed for laminar-turbulence instability [9]. In present work, it is shown that this theory is also suitable for instabilities of various material systems in nature. Laws are proposed for describing these instabilities. These laws can be considered as a supplement to the Newtonian mechanics, which enriched the theoretical system of the classical mechanics. Newton’s first and second laws described the rules of body motion from the equilibrium of forces. Laws of energy gradient describe the rules of fluid material stability from the viewpoint of energy field. These laws are more general because it described the stability of moving fluids and those under no force. Listed examples have been shown that the validity of the proposed laws. On the other hand, using laws of energy gradient we can control the evolution of fluid material systems.

## References

1. Lumley, J. L. & Yaglom, A. M., A Century of Turbulence, *Flow, Turbulence and Combustion*, **66**, 2001, 241-286.
2. Tatsumi, T., Turbulence in the turn of the century, *Laminar-Turbulent Transition*, Eds. HF Fasel and WS Saric, Springer, Berlin, 2000, 3-8.
3. Schmid, P. J. & Henningson, D. S., *Stability and transition in shear flows*, New York: Springer-Verlag, 2000.
4. Drazin, P. G. & Reid, W. H., *Hydrodynamic Stability*, Cambridge, Cambridge University Press, 1981.

5. Huerre, P. & Rossi, M., Hydrodynamic instabilities in open flows, In: *Hydrodynamics and Nonlinear Instabilities*, Edited by C.Godreche and P.Manneville, Cambridge, Cambridge University Press, 1998, 81-294
6. Lin, C. C., *The theory of hydrodynamic stability*, Cambridge, Cambridge Press, 1955, 1-153.
7. Stuart, J. T., Nonlinear Stability Theory, *Annual Review of Fluid Mechanics*, **3**, 1971, 347-370.
8. Bayly, B. J., Orszag, S. A. & Herbert, Th., Instability mechanism in shear-flow transition, *Annu. Rev. Fluid Mech.*, **20**, 1988, 359-391.
9. Dou, H.-S., Energy gradient theory of hydrodynamic instability, *The Third International Conference on Nonlinear Science*, Singapore, 30 June -- 2 July, 2004.
10. Owens, R. G. & Phillips, T.N., *Computational rheology*, Imperial College Press, London, 2002.
11. Grossmann, S., The onset of shear flow turbulence, *Reviews of modern physics*, **72**, 2000, 603-618.
12. Trefethen, L. N., Trefethen, A. E., Reddy, S. C. & Driscoll, T. A., Hydrodynamic stability without eigenvalues, *Science*, **261**, 1993, 578-584.
13. Dou, H.-S., Khoo, B. C., Phan-Thien, N. & Yeo, K.S., Instability of plane Couette flow, *Technical Report of the National University of Singapore*, April, 2004.
14. Dou, H.-S., Viscous instability of inflectional velocity profile, *Proc. of the 4<sup>th</sup> International conference on Fluid Mechanics*, Dalian, China; Springer-verlag, 2004, 76-79.
15. Mankbadi, R. R., *Transition, Turbulence, and noise*, Kluwer, Boston, 1994, 21-49.
16. Chandrasekhar, S., *Newton's principia for the common reader*, Oxford Press; Reprint edition, 2003.
17. Sornette, D., Predictability of catastrophic events: Material rupture, earthquakes, turbulence, financial crashes, and human birth, *PNAS*, **99**, 2002, 2522-2529.
18. Dou, H.-S., Predicting the flow-system breakdown and the catastrophic events, *The Journal of Global Issues & Solutions*, The BWW Society, ISBN #1544-5399, No.6, 2003, 1-3.

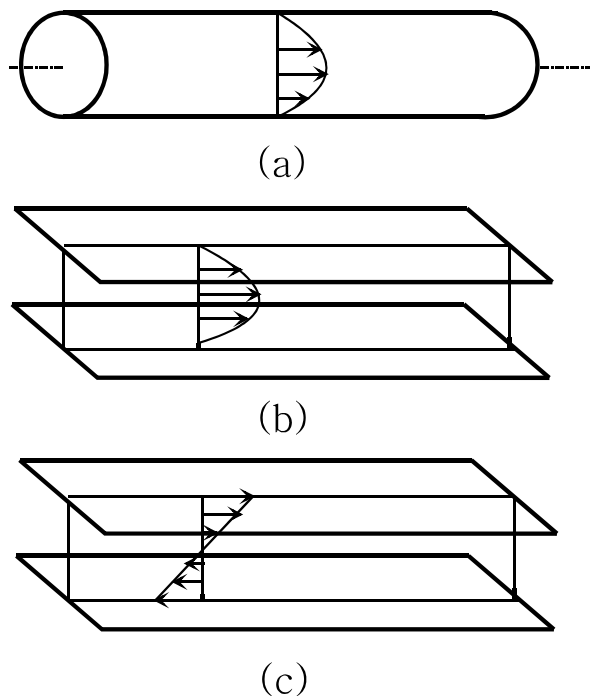


Fig.1 Wall bounded parallel flows. (a) Pipe Poiseuille flow; (b) Plane Poiseuille flow; (c) Plane Couette flow.

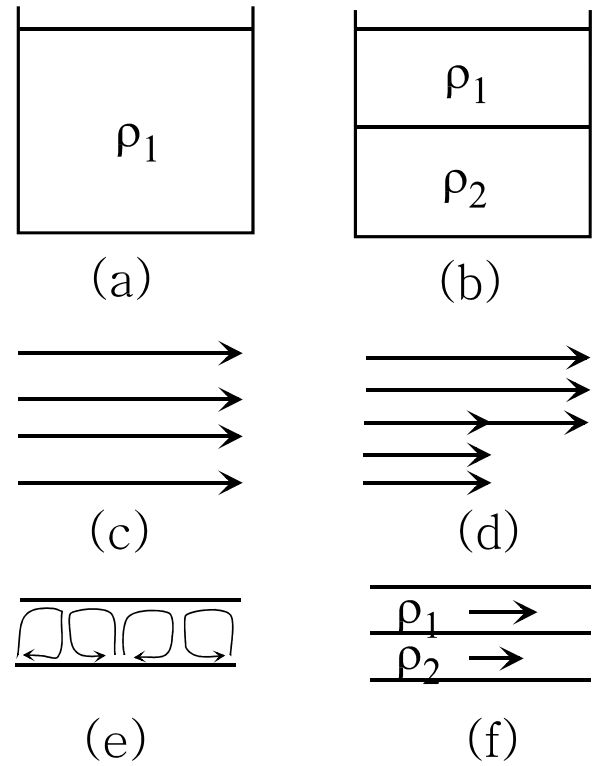


Fig.2 Flow instabilities resulted by energy gradient. (a) Single fluid in a container; (b) Two fluids in a container; (c) Uniform flow; (d) Free shear flow; (e) Rayleigh-Bernard flow; (f) Stratified flow by density.

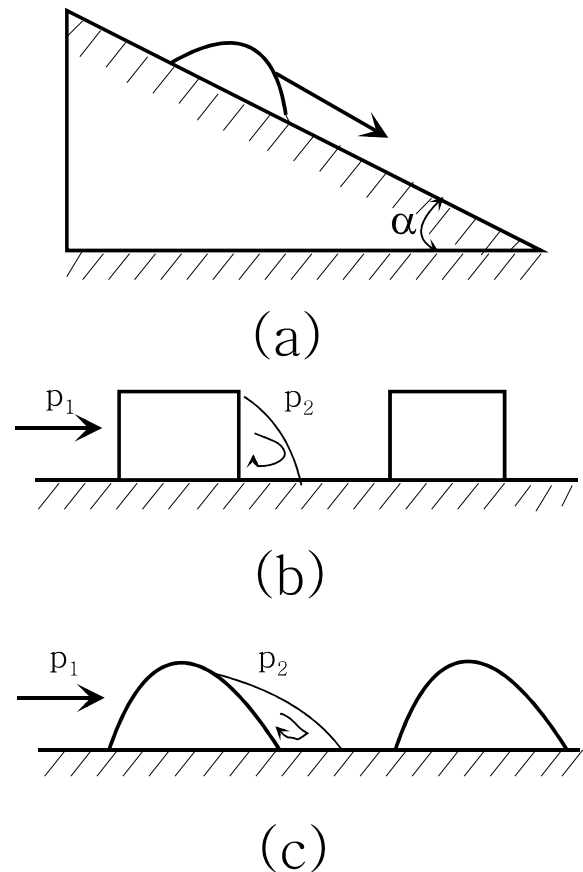


Fig.3 Materials moving under energy gradient. (a) Granular material avalanching on an inclined plate; (b) Stone moving in a river bed. (c) Sand pile moving in a desert.

## Simulation of Turbulence Pressure Fluctuations on Cylinders In Axial Flow

M.J. Woods and M.K. Bull

Department of Mechanical Engineering  
The University of Adelaide, SA, 5005, AUSTRALIA

### Abstract

Direct numerical simulations have been made of the turbulent boundary layer developed in axial flow over long cylinders. In the frequency spectra of surface-pressure fluctuations on the cylinders, characteristic frequency ranges, which are the counterparts of similar ranges in flat-plate flow, have been identified. Forms of similarity scaling in these ranges have been determined. They are considerably more complicated than the flat-plate scaling, with length and time scales additionally dependent on curvature parameters, but are consistent with existing numerical simulations of and experimental data for cylinder flows.

At the low cylinder Reynolds numbers considered, the rms surface-pressure in terms of the mean wall shear stress is found to be smaller than in flat-plate flow; it increases towards flat-plate values as the cylinder Reynolds number increases, in accord with experiment.

### Introduction

Properties of the axisymmetric turbulent boundary layer that develops on a very long cylinder with its axis aligned with the direction of a uniform flow of fluid have been determined by direct numerical simulation. Details of the numerical method are given by Woods and Bull [8]. The procedure is similar to that used by Neves, Moin and Moser [5], with the exception that the boundary conditions at the cylinder surface and at the outer edge of the boundary layer have been set in terms of vorticity rather than velocity.

Here, attention is concentrated on the pressure fluctuations generated at the cylinder surface. The cylinder radius is denoted by  $a$ , the fluid kinematic viscosity by  $\nu$ , the free-stream velocity by  $U_1$ , and the boundary layer thickness by  $\delta$ . Flows with cylinder Reynolds numbers of  $Re_a = U_1 a / \nu = 311, 492, 674$  and 1300 and various values of the ratio  $\delta/a$  have been considered. Two of the Reynolds number values, 311 and 674 are the same as those used in [5]. At  $Re_a = 311$ , calculations have been made for a systematic variation of  $\delta/a$  over the range  $4.0 \leq \delta/a \leq 28.3$ . So far in the present work, direct calculations of frequency spectra and convection velocities have not been made. The frequency spectra presented have been obtained from calculated wavenumber spectra by application of Taylor's hypothesis, whereby the wavenumber  $k$  is replaced by  $\omega/U_c$ , the radian frequency  $\omega$  divided by the convection velocity  $U_c$ . The convection velocity has been taken as the value obtained by Neves et al. [5], namely  $U_c = 0.65 U_1$ . The flow conditions considered are shown in Table 1.

Of direct interest is the effect of curvature on the frequency spectrum and the mean square pressure, as compared with the much more extensively investigated case of flow over a flat plate.

$Re_a$ / Ref.	$\delta/a$	$\delta^+$	Symbol	$Re_a$ / Ref.	$\delta/a$	$\delta^+$	Symbol
311	3.95	88.3	.....	[5]	5	214	■ ■ ■
311	7.25	160	-----	[5]	11	239	■ ■ ■
311	14.8	310	-----	[3]	0	1169	.....
311	28.3	573	-----	[3]	0	2010	- . - .
492	7.85	247	.....	[6]	0	556	○
674	3.66	157	- . - .	[1]	3.2	563	- - -
674	8.09	330	- - -	[1]	6.6	1101	.....
1300	3.63	270	-----	[1]	11.5	1829	■ ■ ■
[4]	0	590	■ ■ ■ ■	[7]	5.04	892	■ ■ ■

Table 1. Flow parameters and symbols used for figures.

Analysis of experimental investigations of surface-pressure fluctuations generated by the turbulent boundary layer on a flat plate (for example, Farabee and Casarella [3], Bull [2]) have shown that the power spectral density of the pressure  $\phi$  scales in different ways in different frequency ranges. The following four frequency ranges and their associated forms of spectral scaling can be identified:

1. Low-frequency range:  $\omega \delta^* / U_1 \leq 0.03$ ,  
 $\phi U_1 / q^2 \delta^* = k_1 (\omega \delta^* / U_1)^2$ ;
2. Mid-frequency range:  $5 \leq \omega \delta / U_\tau \leq 100$ ,  
 $\phi U_\tau / \tau_w^2 \delta = f_2 (\omega \delta / U_\tau)$ ;
3. Universal range:  $100 \leq \omega \delta / U_\tau \leq 0.3 \delta^+$ ,  
 $\omega \phi / \tau_w^2 = k_3$ ;
4. High-frequency range:  $\omega^+ = \omega \nu / U_\tau^2 \geq 0.3$ ,  
 $\phi^+ = \phi U_\tau^2 / \tau_w^2 \nu = f_4 (\omega \nu / U_\tau^2)$ ;

where  $\delta^*$  is the displacement thickness of the boundary layer,  $\tau_w$  the wall shear stress,  $U_\tau = \sqrt{\tau_w / \rho}$ ,  $\rho$  is the fluid density,  $q = (1/2)\rho U_1^2$ ,  $\delta^+ = \delta U_\tau / \nu$ ,  $k_1$  and  $k_3$  are constants, and  $f_2$  and  $f_4$  represent functions. These scalings and frequency ranges make an obvious point of reference for the examination of similar results for axisymmetric boundary layers.

### Low-frequency Range

The present cylinder calculations are based on periodic boundary conditions in the streamwise direction, with a periodic streamwise length in all cases of  $66\pi a$ . This limits the lowest attainable wavenumber to  $k = 1/33a$  and the lowest attainable value of both  $k\delta$  and  $\omega \delta / U_c$  to  $(\delta/a)/33$ . The minimum possible value of  $\omega \delta^* / U_1$  (for  $\delta/a \approx 4$ ,  $\delta/\delta^* \approx 6$ ,  $U_c/U_1 = 0.65$ ) is therefore about 0.013. For larger values of  $\delta/a$ , the parameter  $\omega \delta^* / U_1$  exceeds the upper limit (0.03) of the flat-plate low-frequency range. Consequently comparison of axisymmetric-flow similarity and flat-plate similarity in this frequency range cannot usefully be made.

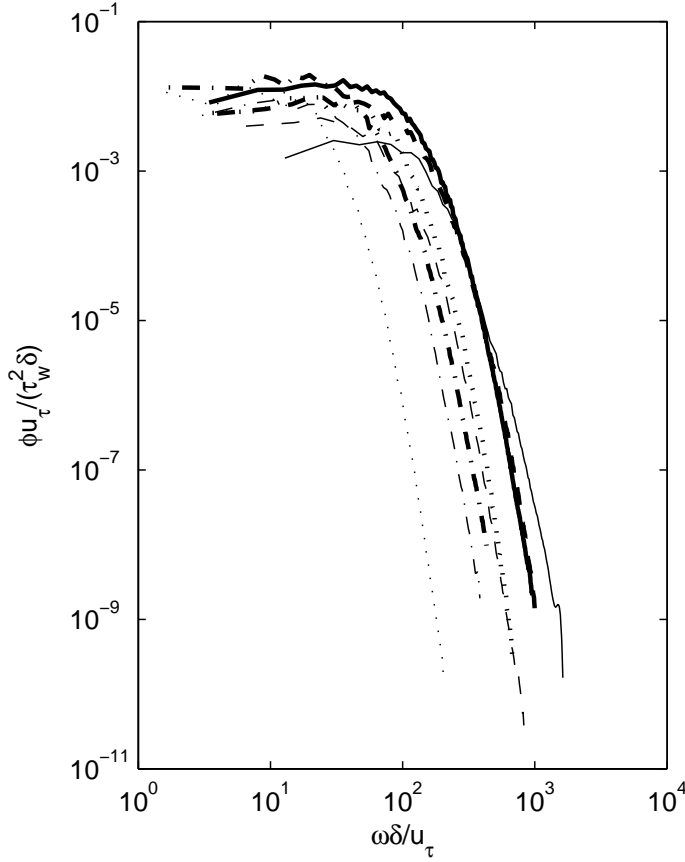


Figure 1. Pressure spectra of present simulations in flat-plate mid-frequency-range form. Symbols are defined in table 1.

### Medium-frequency Range

When plotted in the flat-plate medium-frequency-range (MFR) form,  $\phi U_\tau / \tau_w^2 \delta$  as a function of  $\omega \delta / U_\tau$  (figure 1), the calculated data do not exhibit similarity.

Since it is to be expected that the greatest contributions to the wall pressure come from the regions closest to the wall, contributions from the outer part of the boundary layer can be expected to become less and less significant as  $\delta/a$  increases. This suggests that the boundary layer thickness itself is unlikely to be the most appropriate length scale for this frequency range. In fact, the data collapse quite well when the radius of curvature, the cylinder radius, is used as the length scale instead of the boundary layer thickness. However, in the limiting case of very small  $\delta/a$ , when the cylinder becomes effectively a flat plate with  $a = \infty$ , the radius of curvature ceases to be a useful length scale and must be replaced by the boundary-layer thickness. A possible composite length scale  $L$  that meets the limiting requirements at the extremes of very large and very small  $\delta/a$  can be defined as

$$L = \delta / [1 + (\delta/na)] = Fa, \quad (1)$$

where

$$F = (\delta/a) / [1 + (\delta/na)], \quad (2)$$

and  $n$  is a constant factor, an appropriate value of which is a low integer. A similar factor has been used by Neves et al. [5], although in their case to increase the length scale to a value larger than  $\delta$  rather than to decrease it as in the present case. Equation (1) has the property that  $L \rightarrow na$  as  $\delta/a \rightarrow \infty$  and  $L \rightarrow \delta$  as  $\delta/a \rightarrow$

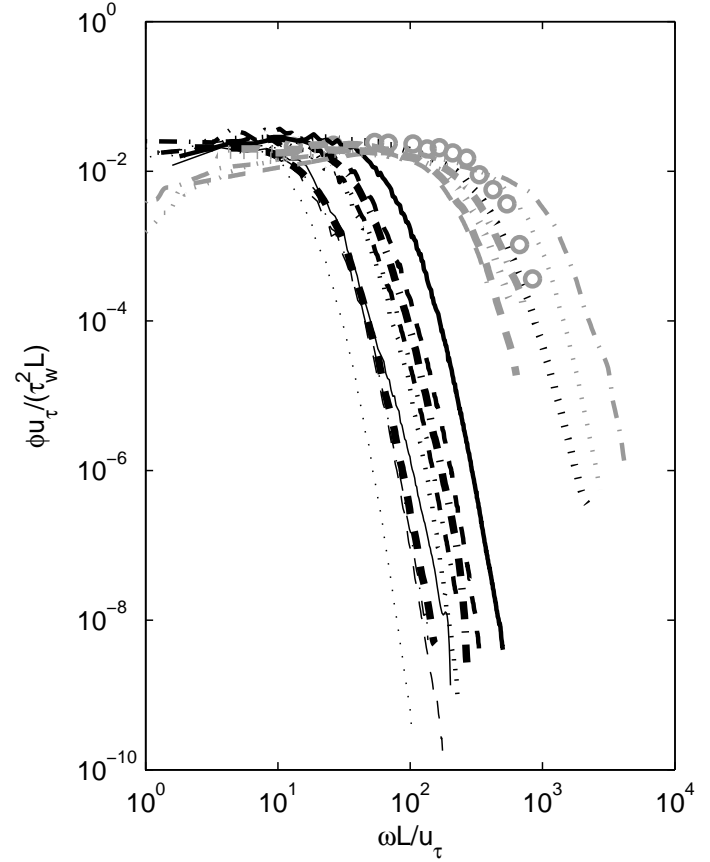


Figure 2. Pressure spectra in modified mid-frequency form, with  $L = \delta / [1 + \delta/4a]$  (see equation 1). Symbols are defined in table 1.

0. Similarity of the results of the present calculations is not very sensitive to the value of  $n$ : it is quite close for values of  $n$  from about 1 to 4. A value of  $n = 4$  has been chosen as this seems to give the most satisfactory agreement with flat-plate data. For  $\delta/a$  as low as 4,  $L = 2a = \delta/2$ ,  $L$  is still heavily biased towards the cylinder radius.

The data in the modified form  $\phi U_\tau / \tau_w^2 L = \phi U_\tau (1 + \delta/4a) / \tau_w^2 \delta$  as a function of  $\omega L / U_\tau = \omega \delta / (1 + \delta/4a) U_\tau$  are shown in figure 2. In this form there is similarity, with  $\phi U_\tau / \tau_w^2 L$  constant over the lower part of the frequency range. The calculations indicate that the constancy persists at least down to a frequency corresponding to  $\omega L / U_\tau \approx 0.2$ , while the upper limit is Reynolds-number dependent and given approximately by  $\omega L / U_\tau = 0.2L^+$  (where  $L^+ = LU_\tau/\nu$ ). The range can therefore be tentatively taken as  $0.2 \leq \omega L / U_\tau \leq 0.2L^+$ . This contrasts with the approximate constancy of  $\phi U_\tau / \tau_w^2 \delta$  over the flat-plate mid-frequency range of  $5 \leq \omega \delta / U_\tau \leq 100$ . Other cylinder data — the results of the numerical simulations of Neves et al. [5] and the experimental results of Snarski and Lueptow [7] and Berera [1] — are consistent with this, as figure 2 indicates. The Reynolds-number dependency of the upper limit of this frequency range is a reflection of the fact that at these low Reynolds numbers the overall rms pressure fluctuation is strongly dependent on the cylinder Reynolds number.

### High-frequency Range

At a given value of the cylinder Reynolds number ( $Re_a$ ), spectral plots (figure 3) in the flat-plate high-frequency (HFR) form,  $\phi^+ = \phi U_\tau^2 / \tau_w^2 \nu$  as a function of  $\omega^+ = \omega \nu / U_\tau^2$ , show close similarity that is almost independent of the value of  $\delta/a$ . For all the Reynolds numbers considered, the similarity occurs for  $\omega^+$  greater than

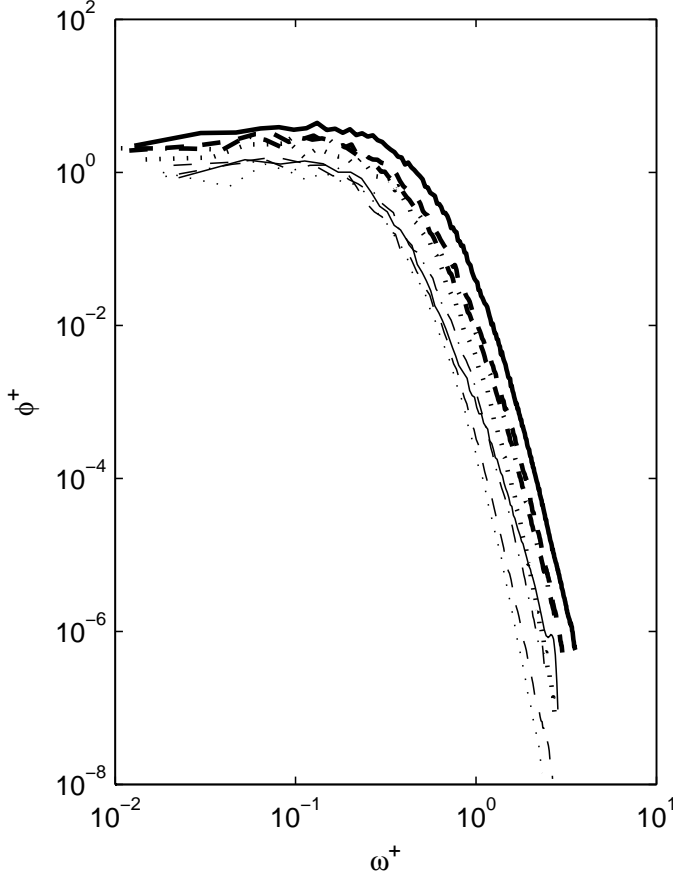


Figure 3. Pressure spectra of present simulations in flat-plate high-frequency-range form. Symbols are defined in table 1.

0.2–0.3, a value very similar to that for high-frequency similarity in the flat-plate case. However, the similarity curve is not the same at all Reynolds numbers, the spectral levels increasing with  $Re_a$  (or  $a^+ = aU_\tau/\nu$  or  $L^+$ ), a further reflection of the fact that at these low Reynolds numbers  $p'/\tau_w$  is quite strongly dependent on  $Re_a$ . Nevertheless, the curves do have similar forms, and those for the various Reynolds numbers can be brought together if the data are plotted in the form of  $G^2\phi^+$  against  $G\omega^+$  (figure 4), where  $G$  is primarily a function of  $a^+$  (although also expressible in terms of  $F$  and  $L^+$ );  $G$  can be represented empirically as

$$G = (1 + 120/a^+)^{1/2} \\ = (1 + 120F/L^+)^{1/2}. \quad (3)$$

As  $a^+$  and  $L^+$  increase, the function  $G$  approaches unity, so that for large values of these parameters the standard flat-plate spectral form of  $\phi^+$  as a function of  $\omega^+$  is recovered.

### Universal Frequency Range

The flat-plate universal range represents an overlap of the mid-frequency and high-frequency ranges. Such an overlap implies that, in this range, the spectral density is independent of any frequency scale, which in turn implies that  $\phi \propto \omega^{-1}$  or  $\omega\phi = \text{constant}$ . For the present cylinder data, the character of the variation of the spectral density with increasing frequency — a transition from a constant value to a rapidly falling value — inevitably means that over some part of the frequency range the spectral density will vary inversely as the frequency. The frequency range over which this form of variation occurs is in fact very small, and there is certainly no extended region of overlap as found in high-Reynolds-number measurements on flat

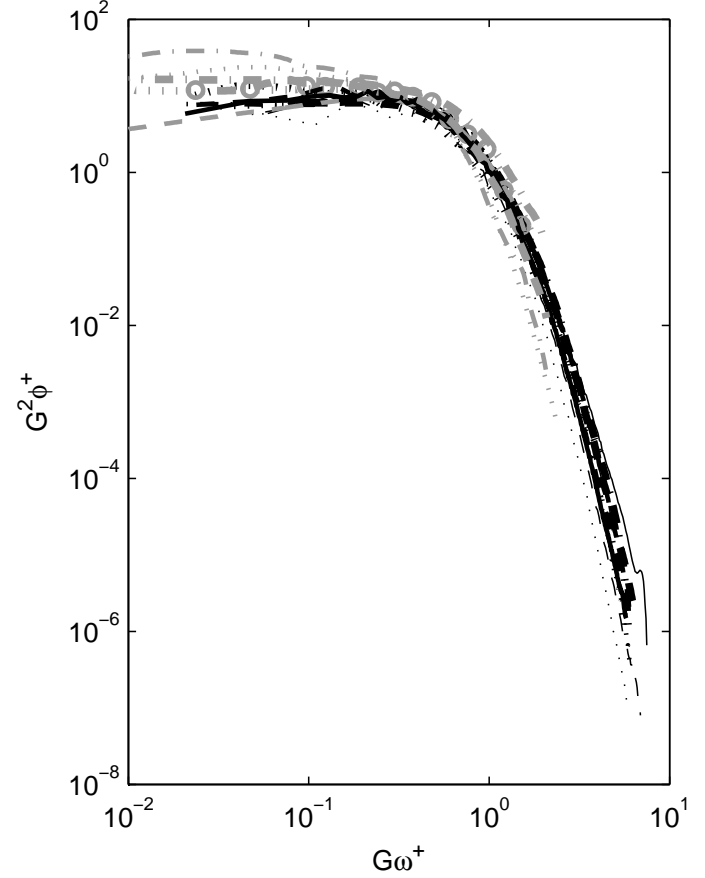


Figure 4. Pressure spectra in modified high-frequency form, with  $G$  given by equation 3. Symbols are defined in table 1.

plates. For the low Reynolds numbers under consideration, the upper limit of the mid-frequency range and the lower limit of the high-frequency range can therefore be taken to be coincident. The high-frequency range can then be defined by  $G\omega^+ \geq 0.2G$ , that is  $\omega^+ \geq 0.2$ .

### Mean-square Pressure

Calculated and experimental values of the rms wall-pressure fluctuation  $p'$ , expressed in the form of  $p'/\tau_w$  (where  $\tau_w$  is the mean shear stress at the cylinder surface), are shown in figure 5 as a function of  $L^+$ . An empirical expression for  $p'/\tau_w$  can be obtained from the values of the non-dimensional spectral levels in the frequency ranges that have been identified and the corresponding non-dimensional extents of those ranges. Thus, the contribution of the "mid"-frequency range (where  $\phi U_\tau/\tau_w^2 L = \text{constant} = 0.020$ ) to the mean square pressure is

$$(\overline{p^2/\tau_w^2})_{\text{MFR}} = (0.020) (0.2L^+) = 0.0040L^+. \quad (4)$$

(This assumes that the constant value of  $\phi U_\tau/\tau_w^2 L$  also extends over the frequency range  $0 \leq \omega L/U_\tau \leq 0.2$ , but the contribution from this range will generally be insignificant).

With the extent of any overlap region assumed to be negligible, the contribution of the high-frequency range to the mean square pressure is

$$(\overline{p^2/\tau_w^2})_{\text{HFR}} = (1/G^3) \int_{0.2G}^{\infty} (G^2\phi^+) d(G\omega^+). \quad (5)$$



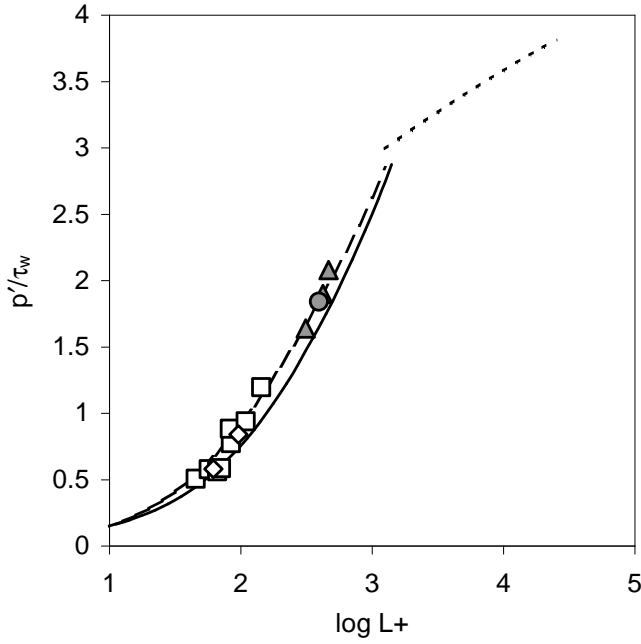


Figure 5. Root-mean-square pressure normalised by mean wall shear stress as a function of length scale  $L^+$ . Equation (7): ---  $\delta/a=4$ ; —  $\delta/a=30$ . Equation (8): - - - ( $L^+=\delta^+$ ). Simulations:  $\square$  present study;  $\diamond$  [5]. Experiments:  $\triangle$  [1];  $\bullet$  [7].

Evaluation of the integral leads to the result

$$(\overline{p'^2/\tau_w^2})_{\text{HFR}} = 5.75/G^3 - 1.60/G^2. \quad (6)$$

The total mean square pressure is then given by

$$\begin{aligned} p'/\tau_w &= [(\overline{p'^2/\tau_w^2})_{\text{MFR}} + (\overline{p'^2/\tau_w^2})_{\text{HFR}}]^{1/2} \\ &= [0.0040L^+ + 5.75/G^3 - 1.60/G^2]^{1/2}. \end{aligned} \quad (7)$$

This relation is compared with the available low-Reynolds-number experimental and numerical data for cylinders in figure 5. Its form implies a weak dependence on  $\delta/a$ , as the curves for  $\delta/a = 4$  and 30 (the approximate range of this parameter for the data considered) shown in the figure illustrate. In the limiting case of the flat plate, the scale  $L$  becomes the boundary layer thickness, and  $L^+ = \delta^+$ . The figure therefore also shows the form of the dependence on  $\delta^+$  of the rms pressure for flat plates at high Reynolds numbers as determined by Farabee and Casarella [3], namely

$$p'/\tau_w = [6.5 + 1.86 \ln(\delta^+/333)]^{1/2}. \quad (8)$$

## Conclusions

Direct numerical simulations of the pressure fluctuations on the surface of a cylinder in axial flow show that the pressure spectra exhibit characteristic frequency ranges that are the counterparts of the frequency ranges previously identified for flow over flat plates. The cylinder ranges, however, show considerably more complicated similarity scaling relations than the flat-plate ranges,

as a result of the effects of curvature on the flow. These effects introduce a dependence on  $\delta/a$  and  $a^+$  in addition to the parameters governing flat-plate flow. Empirical forms for the spectral scaling have been obtained from the numerical simulations. These are consistent with available experimental data for cylinders in axial flow, and asymptotically approach the flat-plate relations as the radius of the cylinder increases. In particular, it is found that, for the low Reynolds numbers considered, the counterparts of the mid-frequency and high-frequency flat-plate ranges are:

$$\begin{aligned} \text{Mid-frequency range: } 0.2 \leq \omega L/U_\tau \leq 0.2L^+, \\ \phi U_\tau/\tau_w^2 L = f_2(\omega L/U_\tau); \end{aligned}$$

$$\begin{aligned} \text{High-frequency range: } \omega^+ \geq 0.2, \\ G^2 \phi^+ = f_4(G\omega^+). \end{aligned}$$

There appears to be no significant universal range in a region of overlap of the mid-frequency and high-frequency ranges.

At low cylinder Reynolds numbers  $Re_a$ , the ratio of mean-square surface-pressure to wall shear stress  $p'/\tau_w$  is found to be considerably smaller than the values typical of flat plates, but to increase towards flat-plate values with increasing  $Re_a$ ,  $a^+$ , and the scale  $L^+$ .

## Acknowledgments

The support of this work by the Australian Research Council and Thales Underwater Systems is gratefully acknowledged.

## References

- [1] Berera, F., *An Investigation of the Flow along and Induced Vibration of Long Cylinders*, Ph.D. thesis, Department of Mechanical Engineering, University of Adelaide, Australia, 2004.
- [2] Bull, M.K., Wall-pressure fluctuations beneath turbulent boundary layers; some reflections on forty years of research, *J. Sound Vib.*, **190**, 1996, 299–315.
- [3] Farabee, T.M. and Casarella, M.J., Spectral features of wall pressure fluctuations beneath turbulent boundary layers, *Phys. Fluids A*, **3**, 1991, 2410–2420.
- [4] Moser, R.D., Kim, J. and Mansour, N.N., Direct numerical simulation of turbulent channel flow up to  $Re_\theta=590$ , *Phys. Fluids*, **11**, 1999, 943–945.
- [5] Neves, J.C., Moin, P. and Moser, R.D., Effects of convex transverse curvature on wall-bounded turbulence, *J. Fluid Mech.*, **272**, 1994, 349–406.
- [6] Schewe, G., On the structure and resolution of wall-pressure fluctuations associated with turbulent boundary layer flow, *J. Fluid Mech.*, **134**, 1983, 311–328.
- [7] Snarski, S.R. and Lueptow, R.M., Wall pressure and coherent structures in a turbulent boundary layer on a cylinder in axial flow, *J. Fluid Mech.*, **286**, 1995, 137–171.
- [8] Woods, M.J. and Bull, M.K., Computation of the turbulent boundary layer on a long circular cylinder in axial flow with a vorticity boundary condition, in proceedings of ICCFD3, Springer, 2004.

## An Experimental Study of Sudden Release of Bentonite Suspensions down an Inclined Chute

H. Chanson<sup>1</sup>, S. Jarny<sup>2</sup>, L. Tocquer<sup>2</sup> and P. Coussot<sup>2</sup>

<sup>1</sup>Dept of Civil Engineering, The University of Queensland,  
Brisbane QLD 4072, AUSTRALIA

<sup>2</sup>Laboratoire des Matériaux et Structures du Génie Civil, Unité Mixte de Recherche (LCPC-ENPC-CNRS),  
2 allée Kepler, 77420 Champs-sur-Marne, FRANCE

### Abstract

Bentonite suspensions, used in the construction industry, are non-Newtonian fluids with a thixotropic behaviour. Sudden releases of bentonite suspensions were systematically investigated down a sloping chute, to quantify the effects of bentonite concentrations and initial rest period on flow motion. Experiments observations highlighted four types of flows, that differ substantially from Newtonian fluid motion. Quantitative informations were documented in terms of the fluid thickness, wave front position and wave front curvature during motion and after stoppage. It is believed that the present study is the first systematic study of its kind in a large-size facility.

### Introduction

Bentonite suspensions are commonly used in the construction industry for drilling and tunnelling. They are non-Newtonian fluids with a thixotropic behaviour. Such a behaviour is also found in liquid concrete, pasty cements, clay-water mixtures used by the beauty industry for skin treatment, and some forms of mud flows and debris flows [2,6,7]. Thixotropy is the characteristic of a fluid to form a gelled structure over time when it is not sheared and to liquefy when agitated. The apparent viscosity of the fluid is a function of both shear intensity and current state(s) of structure of the material, sometimes called degree(s) of jamming of the fluid [3].

In this paper, an experimental study of sudden releases of bentonite suspensions was conducted down a sloping channel. The effect of bentonite mass concentrations and initial rest periods were systematically conducted. The results provide an unique databank of thixotropic fluid motion in highly unsteady flow conditions.

### Bibliography

Although non-Newtonian fluid mechanics has been studied for sometimes [2,4], thixotropy was understood relatively recently [6]. Up to date, experimental studies were often limited to very simplistic conditions to study primarily the fluid rheology [5,7]. Sudden releases of thixotropic fluids have not been studied despite the relevance to industry: e.g., L-ring concrete tests for self-compacting concrete.

### Experimental Setup

New experiments were performed in a 2 m long, 0.34 m wide, tilting flume (Fig.1). The sidewalls were made of polycarbonate panels, while the invert was covered with grade 150 sand paper to minimise slippage. A removable gate was installed and tilted 15° with the direction normal to the channel invert. All experiments were conducted with a fixed bed  $\theta_b = 15^\circ$  for which the sluice gate was vertical.

The channel slope was measured with an electronic inclinometer Digital Protactor Pro360 with an accuracy of 0.1°. For the preparation of the suspensions, bentonite and water were weighted with a balance Sartorius LP3200D with an accuracy of less than 0.01 g. During experiments, the mass of bentonite

suspension was weighted with a balance Metler PM16 with an error less than 1 g. The rheological properties of suspensions were measured with a Rheometer Bohlin Instruments C-VOR 200 NF, equipped with two rough circular disk ( $\varnothing = 40$  mm). Flow visualisations were performed with four digital video-cameras with high-shutter speed : Canon MV500i (25 fr/s, shutter: up to 1/8,000 s), Sony CDR-TRV950E 3CCD (25 fr/s, shutter: up to 1/10,000 s), Olympus Camedia C700 (15 fr/s, shutter: up to 1/1,000 s) and a CCD camera (25 fr/s) connected to a computer system. Unsteady free-surface elevations were measured using the CCD camera at the intersection of a series of laser beams (He/Ne 10mW) illuminating the free-surface at low incidence. The data were analysed using a Mourier projection method. Further details on the experiments were given by Chanson et al. [1].

### Fluid preparation

Great care was taken to prepare systematically and consistently the bentonite suspension using the procedure described by Huynh et al. [5]. Solid mass concentrations between 10 and 20% were used. The bentonite solutions were prepared with distilled water and industrial grade bentonite (Impersol powder, Société Française des Bentonites et Dérivés, France) with no chemical additives. The bentonite-water suspensions were first agitated continuously for about 3 h to ensure complete homogenisation. The suspensions were then left to rest for at least 48 h to allow hydration and dispersion of bentonite particles.

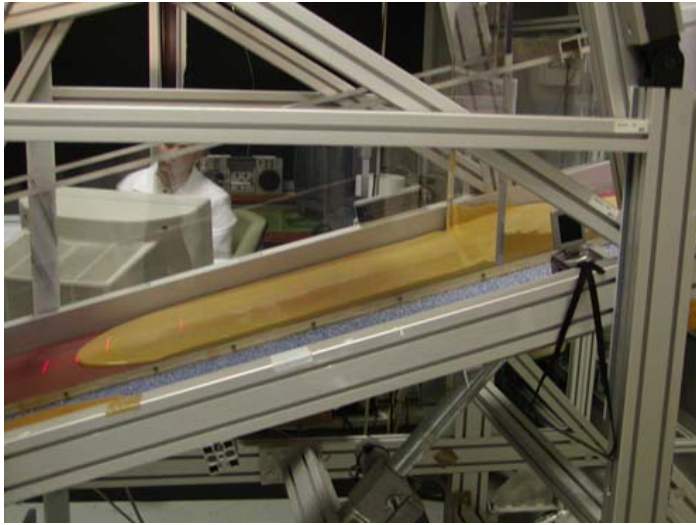
Herein the mass concentration  $C_m$  is defined as the ratio of mass of bentonite to mass of bentonite plus water. The density  $\rho$  of bentonite suspension equals :

$$\rho = \frac{\rho_w * \rho_b}{C_m * \rho_w + (1 - C_m) * \rho_b} \quad (1)$$

where  $\rho_w$  is the water density and  $\rho_b$  is the bentonite density (2600 kg/m<sup>3</sup>).

Basic properties of bentonite suspensions were measured with the rheometer equipped with rough circular disks separated by a 1 mm gap. The tests were performed under controlled stress for relatively short durations at constant temperature (25 Celsius). For each test, a small sample of well-stirred liquid was pre-sheared at constant a shear rate of 500 s<sup>-1</sup> for 20 s. It was then rested for a known period  $T_0$  before being subjected to a controlled stress loading and unloading of 1 minute each.

Results provided some information on the apparent yield stress of the fluid  $\tau_c$  and the effective viscosity  $\mu$  as functions of bentonite suspension mass concentrations and rest times. The apparent yield stress and viscosity were estimated during the unloading phase, to be consistent with the inclined plate experiments. Experimental results showed an increase in apparent yield stress with increasing rest time for a given mass concentration, as well as a marked increase in apparent yield stress with mass concentration for a constant rest period. Viscosity data indicated little effect of mass concentration and rest period. In average over all tests, the apparent viscosity was 0.34 Pa.s for  $1 < T_0 < 900$  s and  $0.10 < C_m < 0.17$ .



(A) Flow type II, Test 03,  $C_m = 0.15$ , rest period:  $T_o = 60$  s



(B) Flow type II, Test 05,  $C_m = 0.15$ , rest period:  $T_o = 60$  s -  
View in elevation of the leading edge



(C) Flow type III, Test 08,  $C_m = 0.15$ , rest period:  $T_o = 2400$  s -  
Sideview of the head packet

Fig. 1 - Photographs of experimental tests (taken after stoppage).

### **Preparation of experiments**

Prior to each test, the bentonite suspension was stirred for about 1 hour to ensure that the fluid was completely de-structured. The

suspension was poured upstream of the closed sluice gate where it formed a quasi-two-dimensional, triangular reservoir with a horizontal free-surface. The suspension was rested for a given period of time  $T_o$  before the gate was suddenly opened. The gate removal was rapid (less than 0.05 s). All measurements were conducted in ambient conditions (i.e. 20 Celsius).

### **Basic Flow Patterns**

Experiments were performed with mass concentrations of 0.10, 0.13, 0.15, 0.17 and 0.20, rest times between 20 s and 17 h, and initial mass of fluid between 1.6 and 4.1 kg. For that range, the results demonstrated four basic fluid flow patterns. Some are illustrated in Figure 1.

For small bentonite mass concentrations ( $C_m \leq 0.15$ ) and short relaxation times ( $T_o \leq 30$  s), the fluid flowed rapidly down the constant slope all along the plate length, and it spilled into the overflow container (Flow Type I). During the initial instants immediately following gate opening, inertial effects were dominant and the flow was subjected to a very-rapid acceleration (see below).

For intermediate concentrations and rest periods, the suspension flowed rapidly initially (as described above), decelerated relatively suddenly, continued to flow slowly for sometimes and later the flow stopped, often before the plate downstream end (Flow Type II). Observations suggested distinct flow periods. Immediately after gate opening, the fluid was rapidly accelerated and quasi-two-dimensional. Then the suspension continued to flow rapidly although sidewall effects started to develop with a slower front propagation at and next to the walls. Later the fluid decelerated relatively rapidly, and this was followed by a significant period of time during which the suspension continued to flow slowly before stopping ultimately. During and after fluid deceleration, careful video analysis suggests that the front propagation was subjected to some form of perturbations. That is, the wave front (on centreline) seemed to accelerate and decelerate with periods of about 0.1 to 0.25 s.

For relatively large mass concentrations and rest periods, the mass of fluid stretched down the slope, until the head separated from the tail (Flow Type III). After separation, a thin film of suspension connected the head and tail volumes which could eventually break for long travelling distance of the head. The head had a crescent shape (Fig. 1C). For long rest periods (i.e. several hours), several successive packets were sometimes observed (Flow Type IIIb).

The last flow pattern (Type IV) corresponded to an absence of flow. That is, for very large bentonite concentrations and the longest rest times, the fluid may not flow at all after gate opening, even after waiting 30 to 60 minutes.

### **Transition between flow regimes**

The characteristic conditions for the transition between flow regimes were functions of the mass concentration of bentonite suspension, rest time and initial mass of fluid  $M$ . A summary of the observations is shown in Figure 2 for a fixed mass  $M$ . Basically the type of flow regime changed from no flow (Type IV) to a rapid flow (Type I) with increasing mass  $M$ , decreasing mass concentration  $C_m$  and decreasing rest period  $T_o$ . Figure 2 illustrates the trend in terms of mass concentration and rest period for a given mass of fluid (and constant plate slope).

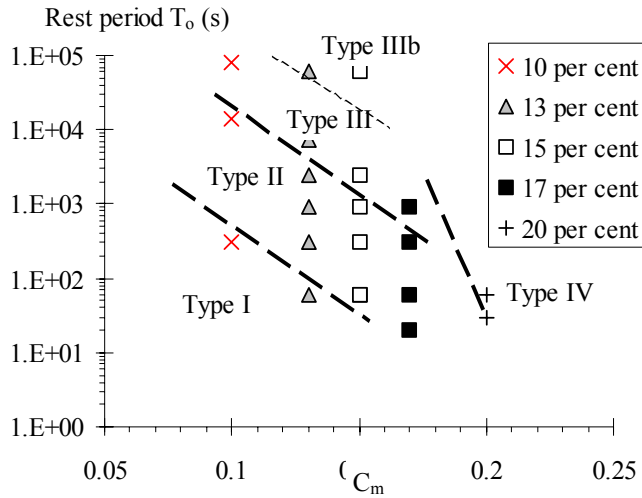
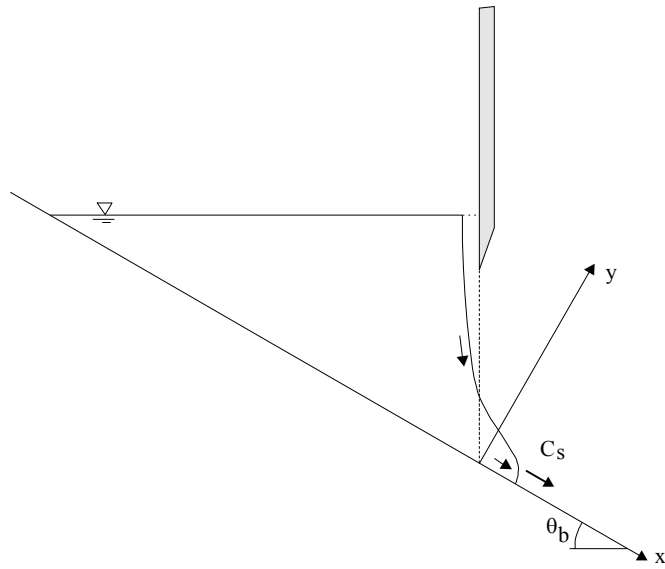
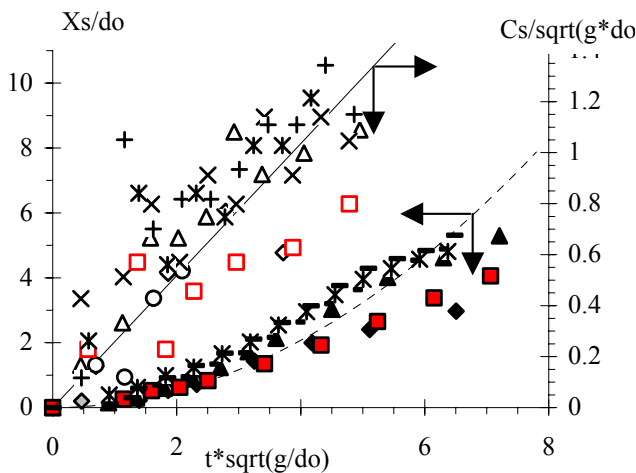


Fig. 2 - Chart of flow regimes : rest time as function of the mass concentration for a given mass of fluid ( $M = 3.7$  kg). Comparison with experimental flow conditions.



(A) Definition sketch



(B) Experimental results

Fig. 3 - Initial jet flow : wave front propagation immediately after gate opening.

## Experimental results

### Initial jet flow

For Flow Types I and II (possibly some Flow Type III), the initial instants following the gate opening were characterised by a very-rapid acceleration of the fluid, somehow similar to a two-

dimensional jet flow motion. Experimental data demonstrated that the flow acceleration derived solely from the gravity force component in the longitudinal direction (Fig. 3). That is, immediately after gate opening, the fluid was subjected to an acceleration component parallel to the plate of about  $-g \sin \theta_b$ , where  $g$  is the gravity acceleration, and flow resistance was negligible. Within these assumptions, the equation of motion compared favourably with the data for  $t^* \sqrt{g/d_0} < 4.5$  to 6 (e.g. Fig. 3B). In Figure 3B, the dimensionless wave front location  $X_s/d_0$  and wave front celerity  $C_s/\sqrt{g^*d_0}$  are plotted as functions of the dimensionless time  $t^* \sqrt{g/d_0}$ , where  $d_0$  is the initial reservoir height measured normal to the gate, and  $t$  is the time. Experimental observations showed further that the initial jet flow motion was quasi-two-dimensional and that it was little affected by bed friction.

### Discussion

For all experiments, the maximum shock celerity was recorded at the end of the initial jet flow motion. The results were basically dependent only upon the Flow Type. The Reynolds number estimated in terms of the maximum shock celerity  $(C_s)_{\max}$ , initial reservoir height  $d_0$  and measured fluid properties was  $\rho^*(C_s)_{\max} * d_0 / \mu = 310, 150$  and  $73$  for Flow Types I, II and III respectively, where  $\mu$  is the effective viscosity of the destructured fluid.

The lesser maximum shock celerity observed in Flow Types II and III may indicate some incomplete destructuration of the fluid at gate opening. Note that the Reynolds number in Flow Type I was significantly high. Turbulent flows may be observed for such Reynolds numbers with large roughness, and it is conceivable that turbulent flow motion was experienced during the present study in Flow Type I.

### Shock front curvature

After the initial jet flow motion, the flow became rapidly three dimensional with the development of a marked front curvature, viewed in elevation, for all investigated flow conditions. This is well illustrated in Figures 1B and 4. The results showed that the front curvature increased with time, hence the travelled distance  $X_s$ , for a given experiment (Fig. 4). Further video-observations demonstrated slower fluid motion next to the sidewalls. For all experiments, the flow curvature developed very rapidly, and it exhibited a power law profile that was best fitted by :

$$\frac{Z}{d_0} \sim \left( \frac{X}{d_0} \right)^{0.4} \quad (2)$$

where  $X = X_s - x$ ,  $Z$  is the transverse distance measured from the centreline and  $x$  is the longitudinal coordinate of the front (Fig. 4). Basically  $X = 0$  and  $Z = 0$  at the shock front on the channel centreline. Equation (2) was obtained independently of time  $t$ , initial mass  $M$ , mass concentration, rest period and flow regime. It is compared with experimental observations in Figure 4.

Since the polycarbonate panels of sidewalls were much smoother than the invert, it was probable that sidewall friction did not play a preponderant role in the very-rapid development of front curvature. Calculations showed that sidewall boundary layers were thin and could not explain the brisk development of curved profile over short distances, as observed in the present study. The front curved profile might in fact result from interactions between sidewall and bottom boundary layers. Indeed the flow was quasi-two-dimensional as long as flow resistance had little effect on the fluid motion.

Interestingly Huang and Garcia [4] presented a photograph showing a similar front curvature with kaolinite suspension mud flows, but they did not elaborate on the shock front curvature.



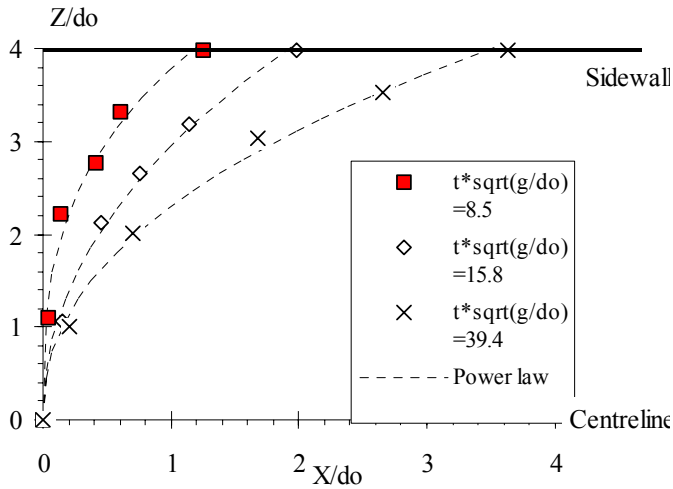


Fig. 4 - Curved profiles of the shock front, viewed in elevation : Test 23,  $C_m = 0.13$ ,  $M = 3.7$  kg,  $T_0 = 60$  s, Flow Type I.

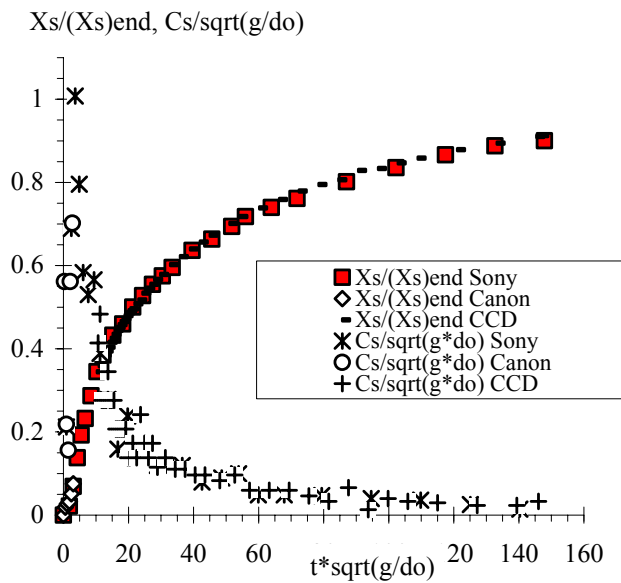


Fig. 5 - Wave front propagation on the channel centreline as function of the dimensionless time : Flow Type II. Test 6,  $\theta_b = 15^\circ$ ,  $C_m = 0.15$ ,  $M = 3.7$  kg, rest period: 300 s.

### Shock front propagation

The propagation of the wave front was investigated with video-cameras. A typical result is presented in Figure 5 for a Flow Type II, with the dimensionless wave front location  $X_s/(X_s)_{end}$  and wave front celerity  $C_s/\sqrt{g^*d_0}$  as functions of the dimensionless time  $t^*\sqrt{g/d_0}$ , where  $(X_s)_{end}$  is the final location of the front after stoppage on the plate. In Figure 5, data from several cameras are presented showing good agreement between all data, independently of camera location and type.

For the Flow Type II, and possibly some Flow Types I and III, the extrapolation of present results to an infinitely long inclined plate yields a relationship between wave front location and time that is characterised by five characteristic periods before stoppage. (1) The initial instants following the gate opening are characterised by a very-rapid acceleration of the fluid: i.e., the initial jet flow motion. (2) When the wave front starts to become three-dimensional (Fig. 1B & 4), the relationship between front location and time becomes nearly linear, and the flow motion

remains rapid. (3) For  $t^*\sqrt{g/d_0} \sim 10$  to 20, a relatively strong flow deceleration is observed, which is seen by a sharp change in the shock celerity (e.g. Fig. 5). It is thought that the fluid motion at the wave front is characterised by a shear-dominated region next to the invert, an upper fluid layer and an interfacial zone. In the upper flow zone, the fluid is subjected to much less stress, it has time to restructure and its apparent viscosity increases significantly. After the marked flow deceleration, experimental observations suggest (4) a relatively slower flow motion, followed by (5) a very-slow flow motion. The latter is nearly a "creeping" motion, until stoppage.

### Conclusions

This study is focused on the highly unsteady flow motion of a thixotropic fluid with a free-surface. The phenomenon is a shock during which the interactions between flow motion and fluid rheology are very strong, and the fluid is subjected to a continuous transition from a liquid to a solid behaviour.

Physical experiments were performed by pouring a given volume of bentonite suspension in a dam reservoir at the top of an inclined channel ( $15^\circ$  slope). The mass of fluid was left at rest for a controlled time  $T_0$  before the gate was abruptly lifted. Systematic experiments were performed for a range of rest periods  $T_0$  during which the fluid restructured, for various solid volume fractions  $C_m$ , and initial mass of fluid  $M$ . Qualitatively, four flow types were observed. Quantitative informations were documented in terms of wave front curvature and initial jet flow motion. The results highlight the complexity of the interactions between flow motion and fluid rheology.

It is believed that the present study is the first experimental study of highly unsteady flow motion of thixotropic fluid in a large-size flume. Further works may include the effects of bed slope and inner velocity field in the shock flow. Theoretical developments outlined by Chanson et al. [1] may provide additional insights into the complex interactions between fluid motion and rheology.

### Acknowledgments

The writers acknowledge the technical assistance of the L.M.S.G.C..

### References

- [1] Chanson, H., Coussot, P., Jarny, S., and Toquer, L., "A Study of Dam Break Wave of Thixotropic Fluid: Bentonite Surges down an Inclined plane." *Report No. CH54/04*, 2004, Dept. of Civil Engineering, The University of Queensland, Brisbane, Australia, June, 90 pages (ISBN 1864997710).
- [2] Coussot, P., *Mudflow Rheology and Dynamics*, IAHR Monograph, Balkema, The Netherlands, 1997.
- [3] Coussot, P., Nguyen, A.D., Huynh, H.T., and Bonn, D., "Avalanche Behavior in Yield Stress Fluids", *Physics Review Letters*, 2002, Vol. 88, p. 175501.
- [4] Huang, X., and Garcia, M., "A Herschel-Bulkley Model for Mud Flow Down a Slope", *Jl of Fluid Mech.*, 1998, Vol. 374, pp. 305-333.
- [5] Huynh, H.T., Bonn, D., and Coussot, P., "Caractérisation de la Thixotropie de Fluides Pâteux", *Proc. 36th Colloque Annuel du Groupe Français de Rhéologie GFR*, Marne-la-Vallée, France, 2001, pp. 72-77.
- [6] Mewis, J., "Thixotropy - A General Review", *Jl of Non-Newtonian Fluid Mech.*, 1979, Vol. 6, p. 1.
- [7] Wilson, S.D.R., and Burgess, S.L., "The Steady, Spreading Flow of a Rivulet of Mud", *Jl Non-Newtonian Fluid Mech.*, 1998, Vol. 79, pp. 77-85.



## Comparing RANS Models for Flow and Thermal Analysis of Pin Fin Heat Sinks

B. Moshfegh<sup>1</sup> and Robert Nyiredy<sup>2</sup>

<sup>1</sup>Division of Energy Systems, Department of Mechanical Engineering, Linköping University, S-581 83 Linköping, Sweden

<sup>2</sup>Fluent Sweden AB, S-416 64 Göteborg, Sweden

### Abstract

The paper discusses various levels of numerical modelling of turbulent flow that are relevant to electronic cooling. Five well-known turbulence models are investigated, i.e., four different eddy-viscosity models; the standard  $k$ - $\epsilon$ , RNG, the realizable and the  $k$ - $\omega$ , as well as the Reynolds stress model, RSM. Different near-wall treatments have been employed. The accuracy of the numerical schemes has been discussed. The model under consideration is a 3-D model of circular pin fin heat sinks in bypass flow conditions. The experimental data presented by Jonsson and Moshfegh [1] has been used for comparison. Three different inlet velocities have been considered corresponding to a channel  $Re = 5000$  to 14500. Results are presented for the base plate temperature, the pressure drop, as well as the influence of flow bypass, and the leakage from the interfin region to the bypass regions of the domain. The result shows that choosing the right turbulence model and near-wall treatments have a great influence on the heat transfer coefficient and the pressure drop.

### Introduction

The current trends towards miniaturization, greater functionality and faster processors are resulting in a steady increase in the amount of heat dissipated per unit surface area or unit volume of the electronic components. Usually extended surfaces are used to increase the heat dissipation from electronic components to the ambient air and have been the topic of many studies in recent years. One of the most common types of extended surfaces is the pin fin heat sink. The main advantage of this type of heat sinks is independent of the direction of the incoming flow and it is suitable for the situations where the flow paths are hard to predict. Traditionally, the research in the field of electronic cooling has been dominated by experiments. The performance of pin fin heat sinks in forced convection has been studied quite extensively. Recently a comprehensive experimental investigation, which considered pin fins of different cross shapes, sizes and bypass conditions, was carried out by Jonsson and Moshfegh [1]. Jonsson [2] has also presented a comprehensive literature survey. However, interest has now also turned to numerical investigations, mostly due to the increasing capability of performing CFD simulations. CFD predictions of pin fin heat sinks in forced convection are still quite rare. Yokono and Hisano [3] and Behnia et al. [4] performed CFD analysis on pin fin heat sinks without a flow bypass. Nowadays, thermal management engineers in electronic industries use CFD as a design tool to predict the details of flow and heat transfer. During the past decades, too many turbulence models have been developed and introduced into the market. Thus, it is a rather challenging task to choose the right turbulence model for a specific application. The objective of this study is to investigate the performance of five well-known turbulence models to predict the air flow and heat transfer for pin fin heat sinks under bypass flow conditions. The employed models are four eddy-viscosity models, i.e., the standard  $k$ - $\epsilon$ , the RNG, the Realizable and the  $k$ - $\omega$ , and the RSM. A steady-state 3-D model is used for simulating the flow and the heat transfer of the pin fin heat sinks under bypass conditions, see Figure 1. The experimental data presented by Jonsson and Moshfegh [1] is used for comparison. It is shown that choosing the right turbulence model and near-wall treatments have a great influence on the heat transfer coefficient and the pressure drop.

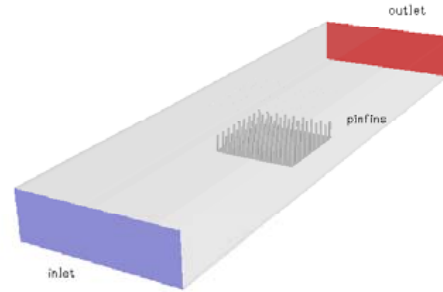


Figure 1. Pin fin heat sink in bypass flow conditions.

### Mathematical Modelling

This part of the paper presents the turbulence models used for analysing the flow and heat transfer in a package of circular pin fins under bypass flow conditions. The buoyancy effect is assumed to be negligible and the radiation heat transfer is not included. Based on the above assumptions for steady state, three-dimensional, incompressible turbulent flow the continuity, time-averaged Navier-Stokes and energy equations are given by

$$\frac{\partial U_i}{\partial x_i} = 0 \quad (1)$$

$$\frac{\partial (U_j U_i)}{\partial x_j} = -\frac{\partial \bar{P}}{\partial x_i} + \nu \nabla^2 U_i + \frac{\partial}{\partial x_j} (-\overline{u'_i u'_j}) \quad (2)$$

$$\frac{\partial (U_j T)}{\partial x_j} = \alpha \nabla^2 T + \frac{\partial}{\partial x_j} (-\overline{u'_j \theta}) \quad (3)$$

where  $\bar{P}$  is the modified kinematic pressure and the unknowns,  $\overline{u'_i u'_j}$ ,  $\overline{u'_j \theta}$  constitute the *second-moments* statistical correlation or so-called Reynolds stresses and turbulent heat fluxes. These unknowns must be modelled to close the system of equations. The most popular models to approximate these terms are the eddy-viscosity turbulence models and RSM.

### The Eddy Viscosity Turbulence Hypothesis

The aim is to analogise the turbulent transport phenomenon to viscous transport and to introduce an *eddy-viscosity* for turbulence by the Boussinesq assumption. Boussinesq eddy-viscosity assumption for  $\overline{u'_i u'_j}$ ,  $\overline{u'_j \theta}$  are given by

$$\overline{u'_i u'_j} = -2\nu_t S_{ij} + \frac{2}{3}\delta_{ij}k, \quad \overline{u'_j \theta} = -\frac{\nu_t}{\sigma_t} \frac{\partial T}{\partial x_j} \quad (4)$$

where  $\nu_t$  is the eddy viscosity,  $\sigma_t$  is the turbulent  $Pr$  number,  $k$  is turbulent kinetic energy and  $S_{ij} = 0.5(\partial U_i / \partial x_j + \partial U_j / \partial x_i)$ .

### Two-equation model

This model implies that the length and velocity scales of the mean flow and of the turbulence are proportional and can be related by means of dimensional reasoning to turbulent kinetic,  $k$ , energy and its dissipation rate,  $\epsilon$ ,  $u=k^{0.5}$ ,  $l=k^{1.5}\epsilon^{-1}$ . Considering the above assumption, the turbulent eddy viscosity can be derived as,  $\nu_t=C_\mu k^2 \epsilon^{-1}$ , and it is valid only when local isotropy in the turbulence field is assumed.  $\epsilon$  is given by

$$\epsilon = \nu \frac{\partial u'_i}{\partial x_j} \frac{\partial u'_i}{\partial x_j} \quad (5)$$

Thus two-equation eddy-viscosity models require two additional transport equations for  $k$  and  $\varepsilon$  to solve the spatial and temporal variation of the local velocity scale and the length scale.

### The Standard $k$ - $\varepsilon$ Model

The following transport equations for  $k$  and  $\varepsilon$  are obtained from Reynolds stress transport equation and a model version of the exact transport equation derived from the second moment

$$\frac{\partial(U_j k)}{\partial x_j} = \nabla^2 k - \frac{\partial}{\partial x_j} \left( \frac{1}{2} \overline{u'_i u'_j u'_i} + \frac{\overline{p' u'_j}}{\rho} \right) - \overline{u'_i u'_j} \frac{\partial U_i}{\partial x_j} - \varepsilon \quad (6)$$

$$\begin{aligned} \frac{\partial(U_j \varepsilon)}{\partial x_j} = & \nabla^2 \varepsilon - \nu \frac{\partial}{\partial x_k} \left( u'_k \frac{\partial u'_i}{\partial x_m} \frac{\partial u'_i}{\partial x_m} + \frac{2}{\rho} \frac{\partial p'}{\partial x_m} \frac{\partial u'_k}{\partial x_m} \right) \\ & - 2\nu \left( \frac{\partial u'_j}{\partial x_i} \frac{\partial u'_j}{\partial x_k} + \frac{\partial u'_i}{\partial x_j} \frac{\partial u'_k}{\partial x_j} \right) \frac{\partial U_i}{\partial x_k} - 2\nu u'_k \frac{\partial u'_i}{\partial x_j} \frac{\partial^2 U_i}{\partial x_k \partial x_j} \\ & - 2\nu \frac{\partial u'_i}{\partial x_k} \frac{\partial u'_i}{\partial x_m} \frac{\partial u'_k}{\partial x_m} - 2\nu^2 \frac{\partial^2 u'_i}{\partial x_{km}^2} \frac{\partial^2 u'_i}{\partial x_{km}^2} \end{aligned} \quad (7)$$

These equations are accurate for turbulent kinetic energy and turbulent dissipation rate. Quantities such as Reynolds stresses are still unknown and have to be modelled. The equations of  $k$  and  $\varepsilon$  after approximation are modelled in the high  $Re$  models as

$$\frac{\partial(U_j k)}{\partial x_j} = \left( \nu + \frac{\nu_t}{\sigma_k} \right) \nabla^2 k + \nu_t S^2 - \varepsilon \quad (8)$$

$$\frac{\partial(U_j \varepsilon)}{\partial x_j} = \left( \nu + \frac{\nu_t}{\sigma_\varepsilon} \right) \nabla^2 \varepsilon + C_{\varepsilon 1} \frac{\varepsilon}{k} \nu_t S^2 - C_{\varepsilon 2} \frac{\varepsilon^2}{k} \quad (9)$$

where  $C_\mu = 0.09$ ,  $C_{\varepsilon 1} = 1.44$ ,  $C_{\varepsilon 2} = 1.92$ ,  $\sigma_k = 1.0$ ,  $\sigma_\varepsilon = 1.3$  and  $S = (2S_{ij}S_{ij})^{0.5}$ . The  $k$ - $\varepsilon$  model (hereafter called  $k$ - $\varepsilon$ ) is the most popular of the two-equation eddy viscosity models, but various others have been developed.

### The RNG $k$ - $\varepsilon$ Model

The coefficients of the  $k$ - $\varepsilon$  are determined from a number of case studies of simple turbulent flows. Thus the  $k$ - $\varepsilon$  has a limited board of applicability, which yields poor performance for cases with complex flows. This poor performance is suspected to be due to inaccuracies in the  $\varepsilon$ -equation. The Renormalization Group  $k$ - $\varepsilon$  model (RNG) introduces an additional term in the  $\varepsilon$ -equation, which improves the performance of it. The basic idea is to systematically filter out the small-scale turbulence to a degree that the remaining scales can be resolved. This is done by the parameter,  $\eta$ , which is the ratio between the time scales of the turbulence and the mean flow. The  $\varepsilon$ -equation is given by

$$\frac{\partial(U_j \varepsilon)}{\partial x_j} = \left( \nu + \frac{\nu_t}{\sigma_\varepsilon} \right) \nabla^2 \varepsilon + C_{\varepsilon 1} \frac{\varepsilon}{k} \nu_t - C_{\varepsilon 2}^* \frac{\varepsilon^2}{k} \quad (10)$$

where  $\eta = Sk/\varepsilon$ ,  $\eta_0 = 4.38$ ,  $\beta = 0.012$ ,  $C_\mu = 0.0845$ ,  $C_{\varepsilon 1} = 1.42$ ,  $C_{\varepsilon 2} = 1.68$ ,  $\sigma_k = \sigma_\varepsilon = 0.7178$  and  $C_{\varepsilon 2}^* = C_{\varepsilon 2} + \frac{C_\mu \eta^3 (1 - \eta/\eta_0)}{1 + \beta \eta^3}$ .

### The Realizable $k$ - $\varepsilon$ Model

"Realizable" means that by numerical clipping, which is introduced in the code, one can remove unphysical values of variables, e.g. negative normal stresses, from the predictions. To achieve the realizability effect the  $C_\mu$  is no longer constant but a function of the turbulence fields, mean strain and rotation rates. The  $k$  equation is identical with Eq. (8) and  $\varepsilon$  equation is given by

$$\frac{\partial(U_j \varepsilon)}{\partial x_j} = \left( \nu + \frac{\nu_t}{\sigma_\varepsilon} \right) \nabla^2 \varepsilon + C_1 S \varepsilon - C_2 \frac{\varepsilon^2}{k + \sqrt{\nu \varepsilon}} \quad (11)$$

where  $C_1 = \max [0.43, \eta/(\eta+5)]$ ,  $C_2 = 1.0$ ,  $\sigma_k = 1.0$ ,  $\sigma_\varepsilon = 1.2$ .

### The $k$ - $\omega$ Model

The standard  $k$ - $\omega$  model with low  $Re$  effects has been used. The  $k$ - $\omega$  model is based on model transport for the turbulent kinetic energy,  $k$ , and the specific dissipation rate,  $\omega = \varepsilon/k$ . The  $\omega$  equation is defined as

$$\frac{\partial(U_j \omega)}{\partial x_j} = \left( \nu + \frac{\nu_t}{\sigma_\omega} \right) \nabla^2 \omega + C_{\omega 1} \frac{\omega}{k} \nu_t S^2 - C_{\omega 2} \omega^2 \quad (12)$$

### Reynolds Stress-Transport Model, RSM

The RSM is one of the most sophisticated tools currently used by engineers to predict turbulent flows with complex strain fields or significant body forces. RSM or a so-called second-moment model is based on modelled versions of the exact but intractable Reynolds stress transport equations. The aim is to solve the unknowns introduced when averaging Navier-Stokes equations. For non-isothermal 3-D turbulent flows, it is necessary to solve nine full partial differential transport equations for six unknown Reynolds stresses and three turbulent heat fluxes and one equation for transport of  $\varepsilon$ .  $k$  is found by adding the three normal stresses. Equation for the transport of  $R_{ij} = \overline{u'_i u'_j}$  is given by:

$$\begin{aligned} \frac{\partial(U_j R_{ij})}{\partial x_j} = & \left( \nu + \frac{\nu_t}{\sigma_k} \right) \nabla^2 R_{ij} - R_{ik} \frac{\partial U_j}{\partial x_k} - R_{jk} \frac{\partial U_i}{\partial x_k} \\ & - \frac{2}{3} \delta_{ij} \varepsilon - \frac{p'}{\rho} \left( \frac{\partial u'_i}{\partial x_j} + \frac{\partial u'_j}{\partial x_i} \right) \end{aligned} \quad (13)$$

where the terms on the right side of the equation are the molecular and turbulent diffusion (after modelling), stress production (no need for modelling), dissipation (after modelling) and pressure strain. Linear pressure strain model is used to model the pressure strain term in this study. The  $\varepsilon$  equation is given by:

$$\frac{\partial(U_j \varepsilon)}{\partial x_k} = \left( \nu + \frac{\nu_t}{\sigma_\varepsilon} \right) \nabla^2 \varepsilon - C_{\varepsilon 1} R_{ij} \frac{\partial U_i}{\partial x_j} \frac{\varepsilon}{k} - C_{\varepsilon 2} \frac{\varepsilon^2}{k} \quad (14)$$

where  $C_\mu = 0.09$ ,  $C_{\varepsilon 1} = 1.44$ ,  $C_{\varepsilon 2} = 1.92$ ,  $\sigma_k = 0.82$ ,  $\sigma_\varepsilon = 1.0$ .

### Near-Wall Treatments

For high  $Re$  models (i.e.  $k$ - $\varepsilon$ , RNG, Realizable and RSM), three different near-wall treatment options have been used in the present investigation that is the Standard wall function (SW) proposed by Launder and Spalding, the Enhanced wall function (EW) and the Non-equilibrium wall approach (NW). The SW is well known and will not be discussed here. The EW subdivides the near wall region into a viscous sub-layer and a fully turbulent flow. In the viscous sub-layer region, only the  $k$  equation is solved, while in the fully turbulent flow the  $k$ - $\varepsilon$  or RSM is computed. The term wall distance is introduced to compute the interface between the two layers. The idea behind the non-equilibrium wall function not only considers the equilibrium assumption (production=dissipation) for computing the budget for the kinetic energy adopted by the SW, but also takes into account the budget of kinetic energy, which can vary widely in highly non-equilibrium flows involving strong pressure gradients. This effect can be implemented by introducing the pressure gradient term in the log law in order to sensitise the mean velocity. For the  $k$ - $\omega$ , the near wall approach will be employed. This means that the near-wall region will be completely resolved all the way down to the viscous sub-layer.

### Geometry and boundary conditions

The problem domain consists of a heated base plate with circular pin fin heat sinks placed on the floor of a rectangular channel. A sketch of the set-up is shown in Figure 1. The  $x$ ,  $y$  and  $z$  directions are in stream-wise, normal and span-wise directions, respectively. The channel dimensions are, length by width by

height, 350×100×30 mm. The base plate has the following dimensions, length by width by thickness, 52.8×52.8×3 mm. Only one pin fin heat sink configuration is modelled with the following dimensions, a pin diameter of 1.5 mm and a fin-to-fin distance of 4.9 mm. The selected heat sink is an inline 9×9 circular pin fin heat sink with a fin height of 10 mm. The distance from the inlet to the leading edge of the heat sink is 150 mm and the distance from the trailing edge of the heat sink to the domain outlet, is 147.2 mm. For validation of the numerical model, three experimental cases, see Jonsson and Moshfegh [1] have been used. The simulations were conducted under the same boundary conditions as the experiments were performed, see Table 1.

	Case 1	Case 2	Case 3
$U_{in}$ , [m/s]	1.57	3.00	4.59
$T_{in}$ , [°C]	17.5	17.5	17.5
$q_{in}$ , [W]	9.19	9.42	9.52
$q''_{in}$ , [W/m <sup>2</sup> ]	3298	3342	3411

Table 1. Set-up boundary conditions for the numerical model.

The inlet turbulence intensity is assumed to be 5%. The simulations were performed for the following  $Re$ ,  $Re_d = \rho U_{in} d_h / \mu$ , 5000, 9500 and 14500, based on the channel hydraulic diameter,  $d_h$ . The physical properties of air and aluminium are summarised in Table 2 and are constant during the simulation.

	Air	Aluminium
$\lambda$ , [W/m K]	0.0242	202.4
$\mu$ , [kg/m s]	$1.789 \cdot 10^{-5}$	-
$\rho$ , [kg/m <sup>3</sup> ]	1.225	2719
$C_p$ , [J/kg K]	1006.43	871

Table 2. Physical properties of air and aluminium.

For a detail discussion about the experimental errors see Jonsson [2]. The resulting maximum relative errors for the cases 1-3 vary between 4.6 to 37.6% and 3.0 to 3.6% for  $T_b$  and  $\Delta p$  respectively.

### Computational Grids

The Gambit [5] grid generation package is used to generate the 3-D unstructured grid. Due to symmetry conditions in the span-wise direction, only half of the channel is considered. Two grids of different density are used for computation of the test cases. The coarse grid has 360 333 hexahedral cells. The mesh close to the pins is finer with a mesh distribution of 108×52×35. The mesh is non-conformal at the interface between fine and coarse region. The grid distribution for the coarse mesh has been effectively controlled by clustering the mesh towards the walls and edges in such a way that the wall function can be applied properly, i.e. the first numerical point was always located at  $y^+ > 15$ . The finer grid ensured that the wall nearest  $y^+$  is kept close to one near the walls and edges. The finer grid consists of 1 710 027 cells and is used for computation with the  $k-\omega$ . Figure 2 zooms up the coarse and fine computational grids.

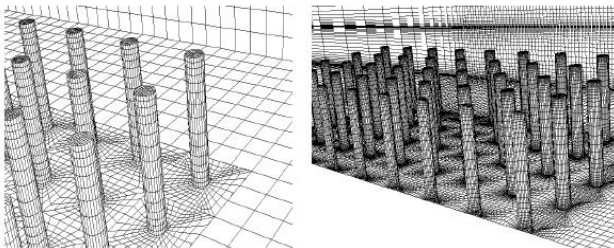


Figure 2. Non-conformal (left) and conformal (right) grid structures are used for coarse and fine mesh respectively.

### Numerical Accuracy

FLUENT 6.0 [6] is used to numerically simulate the airflow and thermal behaviour of the heat sinks under bypass flow conditions. The governing equations are solved with a segregated scheme.

The governing equations are discretized spatially with first and second order upwind as well as with the Quick schemes for checking the dependency of the results on a scheme level. The SIMPLE algorithm solves the pressure-velocity coupling. The following under relaxation factors are used for the  $p$ ,  $U$ ,  $k$ ,  $\varepsilon$  and  $T$ , 0.3, 0.7, 0.8, 0.8 and 1.0. With the fine grid, it takes about 8 hours CPU-time on a 1.4 GHz Pentium-4 to get the result.

## Results

### Effect of the near-wall treatments on the base plate temperature and pressure drop

Table 3 illustrates the influence of the near-wall treatments on different  $k-\varepsilon$  models. All turbulence models with Standard and Enhanced wall functions over-predict both the mean base plate temperature,  $T_b$ , and the pressure drop,  $\Delta p$ . Generally, both the  $k-\varepsilon$  and RNG yield similar results with a small advantage for the RNG compared with the measured case. The SW provides the best agreement with the experimental measurement. The non-equilibrium wall treatments over-predict the  $\Delta p$  and under-predict the  $T_b$ , which indicates poor agreement with the measured case.

	Case 2	$k-\varepsilon$			RNG			Realizable		
		SW	EW	NW	SW	EW	NW	SW	EW	NW
$T_b$ , [°C]	35.8	38.8	39.6	34.6	38.6	39.4	34.4	39.7	39.7	34.9
CFD/Exp	-	8.3	10.5	-3.4	7.7	9.8	-4.0	10.7	10.7	-2.7
$\Delta p$	2.38	2.70	2.69	3.65	2.61	2.67	3.26	2.58	2.71	3.89
CFD/Exp	-	13.3	13.2	53.4	9.6	12.1	37.1	8.4	13.9	63.6

Table 3. The effect of the near-wall treatments on  $T_b$  and  $\Delta p$ .

### Effect of the discretization schemes on the base plate temperature and pressure drop

Table 4 shows that the second order upwind discretization provides a significant improvement on the magnitude of the  $\Delta p$  compared to the first order upwind scheme. However, the lower pressure drop will raise the base plate temperature according to Reynolds analogy. In general, the second order upwind is recommended for complex flows such as those presented in this study. As it is shown in Table 4, the Quick discretization did not influence the magnitude of the pressure drop and only reduced the mean base plate temperature with 0.3°C. Thus the accuracy of the second order scheme is quite acceptable for the present study.

	Case 2	First order	Second order	Quick
$T_b$ , [°C]	35.8	37.9	39.4	39.1
CFD/Exp	-	5.7%	9.8%	9.0%
$\Delta p$ , [N/m <sup>2</sup> ]	2.38	3.18	2.67	2.67
CFD/Exp	-	33.7%	12.0%	12.0%

Table 4. The effect of the discretization schemes on  $T_b$  and  $\Delta p$ .

### Comparing all turbulence models for Case two

Table 5 compares the predictions obtained by different turbulence models with the experimental data for the  $T_b$  and the  $\Delta p$  for Case two. EW treatments have been used as near-wall approach for high  $Re$  models. For the  $T_b$  the  $k-\omega$  gives a better prediction while the  $\Delta p$  prediction by RNG shows the best agreement with the experimental one. Surprisingly, the RSM predictions are nearly the same as the employed two-equation models. One possible clue can be the usage of the isotropic eddy-viscosity hypothesis employed in the present study for RSM instead of the non-linear eddy viscosity modelling.

	Case 2	Coarse mesh				Fine mesh
		$k-\varepsilon$	RNG	Real.	RSM	$k-\omega$
$T_b$ , [°C]	35.8	39.6	39.4	39.7	39.6	38.8
CFD/Exp	-	10.5%	9.8%	10.7%	10.5%	8.2%
$\Delta p$ , [N/m <sup>2</sup> ]	2.38	2.69	2.67	2.71	2.69	2.93
CFD/Exp	-	13.2%	12.1%	13.9%	13.2%	22.9%

Table 5. The effect of the turbulence modelling on  $T_b$  and  $\Delta p$ .

### Comparing Case 1-3 with RNG, RSM and $k-\omega$

Table 6 compares the experimental results for three different inlet velocities with the numerical one. As it is shown, better agreement has been obtained between the CFD predictions and experimental data by increasing the channel  $Re$ . The RNG shows better overall agreement compared to the other models.

		Exp	RNG	RSM	$k-\omega$
Case 1	$T_b$ , [°C]	44.9	50.2	50.1	49.5
	CFD/Exp	-	11.9%	11.8%	10.3%
	$\Delta p$ , [N/m <sup>2</sup> ]	0.71	0.77	0.85	0.91
	CFD/Exp	-	7.9%	19.3%	28.4%
Case 2	$T_b$	35.8	39.4	39.5	38.8
	CFD/Exp	-	9.8%	10.3	8.2%
	$\Delta p$	2.38	2.67	2.7	2.93
	CFD/Exp	-	12.1%	14.5	22.9%
Case 3	$T_b$	31.9	34.5	34.6	33.8
	CFD/Exp	-	8.0%	8.2%	5.8%
	$\Delta p$	5.72	6.07	6.05	6.40
	CFD/Exp	-	6.0%	5.8%	12.0%

Table 6. Comparison between the CFD and experimental data.

### Effect of the inlet velocity on the frontal bypass ratio, tip and side leakage

Table 7 illustrates the influence of the inlet velocity on the frontal bypass ratio, the tip and side leakage, respectively; for more information about the definition of the bypass ratio and leakage, see Jonsson and Moshfegh [1]. As can be seen in the table below, the frontal bypass ratio decreases by increasing the inlet velocity, which means that more air is passing through the heat sink package. About 37% of the flow entering the heat sink leaks from the tip to the bypass area and is nearly constant for the three simulated cases. The side leakage also varies with the inlet velocity. An increase of the inlet velocity will increase the side leakage. At the lowest inlet velocity, almost 8.5% of the flow entering the heat sink leaks out from the side.

	Bypass Ratio	Tip Leakage	Side Leakage
Case 1	24.3%	37.2%	8.5%
Case 2	22.4%	37.7%	10.9%
Case 3	21.4%	37.5%	12.9%

Table 7. The effect of inlet velocity on the frontal bypass ratio, tip and side leakage for all three cases.

Figure 3 shows the flow and temperature behaviour of the air entering the heat sink and the side and tip leakage predicted by RNG for Case two. A wave motion has been observed at the top of the heat sink, which is damped in the stream-wise direction. Most of the turbulent kinetic energy is produced along the first rows in the stream-wise direction. The air-flow pattern at the side of the heat sinks also shows sinusoidal motion. A small recirculation cell has also been observed between the pins close to the base plate in the stream-wise direction. The surface temperature of the pins and the air temperature increase in the stream-wise direction.

Figure 4 shows the pressure and velocity as well as the temperature contours in  $xz$  plane at  $y = 5$  mm predicted by RNG for Case two. Larger pressure drop are observed at the first rows in the stream-wise direction. The contour of the pressure field shows also multiple contractions and expansions as well as redevelopment of the boundary layers in the stream-wise direction causing higher pressure drop compared to the other heat sinks such as plate fin heat sink. In some region, the magnitude of the velocity in the bypass region is higher than the inlet velocity. The penetration of the hot air from interfin to the side bypass is clearly presented in Figure 4.

### Conclusions

Four eddy viscosity models and Reynolds stress model are used to predict the airflow and heat transfer in a pin heat sink

configuration under bypass flow conditions. The RNG performed the best agreement with the experimental data. The validation of the numerical results has been limited to the static pressure drop before and after the heat sinks and average base plate temperature. Nevertheless, the differences are considerable in some cases, especially at the lower upwind level. It should be noted that more detailed experimental data are necessary for a comprehensive validation analysis. The non-equilibrium wall approach indicates poor agreement with the measured case, while the Standard wall function and Enhanced wall functions provide good agreement with the experimental measurement. Numerical predictions show that about 37% of the flow entering the heat sink leaks from the tip to the bypass area and is nearly constant for the three simulated cases. The side leakage is about 8.5% of the flow entering the heat sink at the lowest velocity and increases by increasing the inlet velocities.

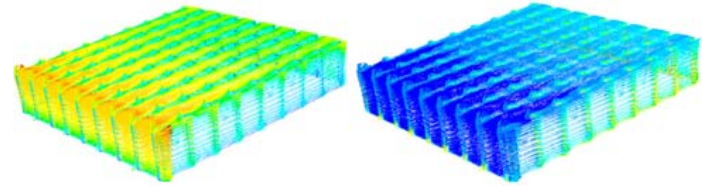


Figure 3. The velocity vector coloured with velocity (left) and temperature (right) values for the bypass domain.

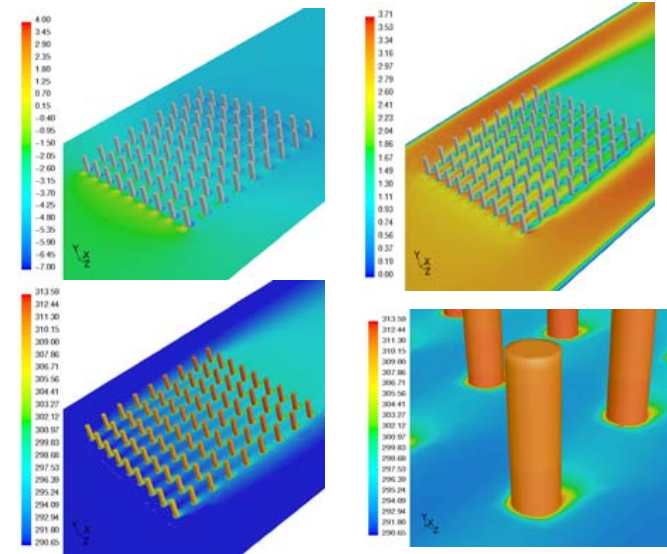


Figure 4. The pressure, velocity and temperature field predicted at  $y = 5$  mm through by RNG for Case two.

### References

- [1] Jonsson, H. and Moshfegh, B., CFD Modeling of the Cooling Performance of Pin Fin Heat Sinks Under Bypass Flow Conditions, *Proceedings of the InterPACK 2001*, Kauai, Hawaii, USA, 2001.
- [2] Jonsson, H., *Turbulent Forced Convection Air Cooling of Electronics with Heat Sinks Under Flow Bypass Conditions*, Doctoral Thesis, Royal Institute of Technology, Department of Energy Technology, Stockholm, Sweden, ISSN 1102-0245, ISRN KTH/REFR/R-01/28-SE, 2001.
- [3] Yokono, Y., Hisano, K., Numerical Simulation for Thermal Resistance of Finned LSI Packages, *Advances in Electronic Packaging*, **EEP-Vol. 4-2**, ASME, 1973.
- [4] Behnia, M., Copeland, D., Soodphakdee, D., A Comparison of Heat Sink Geometries for Laminar Forced Convection: Numerical Simulation of Periodically Developed Flow, *Proc. 6th InterSociety Conf. on Thermal and Thermomechanical Phenomena in Electronic Systems (ITherm 1998)*, IEEE, 310-315, ISBN 0-7803-4475-8, 1998.
- [5] Gambit 2.0, *Gambit Manuals*, Fluent Inc. December 2001.
- [6] Fluent 6.0, *Fluent Manuals*, Fluent Inc, December 2001.



## A Study of the Global Differences between Axisymmetric Turbulent Free Jet Flames from a Smooth Contraction and a Pipe with Well Defined Boundary Conditions

A.S. Langman<sup>1</sup>, G.J. Nathan<sup>1</sup> and P.J. Ashman<sup>2</sup>

<sup>1</sup>School of Mechanical Engineering, <sup>2</sup>School of Chemical Engineering  
The University of Adelaide, Adelaide, SA, 5005, AUSTRALIA

### Abstract

A quantitative assessment is undertaken of the global differences between axisymmetric turbulent free jet flames from a smooth contraction and pipe nozzle by measurement of the radiant fraction, mean flame length, lift-off height and blow-off. The results show that the differences in these parameters are significant. The smooth contraction nozzle produces a flame less radiant, longer and more stable flame than the pipe. It resists lift-off at higher velocities and is self-sustaining at velocities 17% greater than that for the pipe. Similarly, lift-off is prevented till a velocity 40% higher compared to the pipe. The 25% higher radiant fraction of the smooth contraction is also significant.

These results show that the trends found in previous studies [4,5] in non-reacting jets, where differences in the initial flow conditions are found to propagate throughout the flow, also apply for reacting flows. Thus the accepted approach of normalising global parameters based solely on bulk mean velocity and nozzle diameter is inadequate.

### Introduction

The general behaviour of simple round jets is well established. Hawthorne *et al.* [2] developed a formula to describe flame length for all round jets employing the classical assumption of universal similarity in their mixing characteristics. Similar assumptions were employed more than 30 years later by Becker and Liang [1] who proposed refined models which also unify the behaviour of round jets. Likewise, the pioneering measurements of Kalghatgi [3] of lift-off and blow-off employ similar assumptions in their normalisation, which are reproduced in many text books, e.g. Turns [9]. All of these measurements have been performed with a single set of initial conditions, as have measurements of global emissions [8] and radiant fraction [7]. In each the tacit assumption is that the same results will occur for any round nozzle of the same diameter, e.g. for a pipe and a smooth contraction. However this assumption is yet to be tested.

Recent works [4,5] found both near and far field differences in three non-reacting round jets with different initial conditions. The existence of these far field differences suggested the possibility of global differences in reacting jets. The aim of the present study is therefore to compare the global characteristics of flames from straight pipe and smooth contraction nozzles.

### Experimental Method

Global performance is assessed here by measurements of radiant fraction, flame length and lift-off height. The stability limits and the heat transfer characteristics of a flame are significant indicators of performance. Measurements of the flame width and area, axial radiant profiles and emissions of CO, CO<sub>2</sub>, NO and NO<sub>2</sub> were taken but are not presented here.

#### Burner Arrangement

To provide consistent ambient flow for both nozzles, which have different *external* shapes, the burner tips were set into a 450 mm

round metal plate. The presence of the plate also avoids having an unknown co-flow, since any ambient flow at the nozzle tip must be radial. It is noted that this configuration will provide a more stable flame than most studies in the literature that do not have such a plate.

Careful control of the initial conditions is of key importance in the present comparison. Both nozzles had an exit diameter of 5.00mm. The pipe nozzle had a length of 500mm and was attached in-line to a series of 8 honeycomb sections and mesh screens to ensure symmetrical initial flow without swirl (Figure 1). This satisfies the criteria that  $l/d$  exceed 100 for fully-developed turbulent pipe flow [6]. The smooth contraction was mounted to the end of a 20mm ID  $\times$  1000mm long supply pipe fitted to the same flow conditioning system. The initial velocity profile of the smooth contraction approximates a “top hat” profile in contrast to that of the of the pipe with its fully-developed turbulent flow.

Fire retardant curtains were used to both limit the ingress of light into the laboratory area and to minimise the effect of draughts.

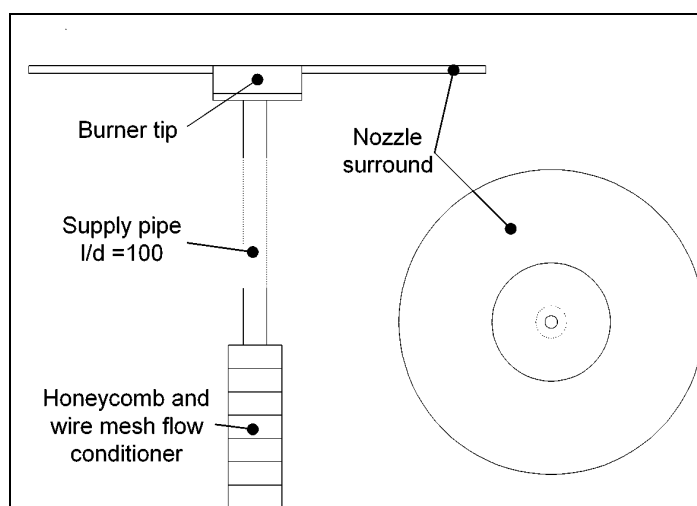


Figure 1: Burner and supply pipe arrangement.

#### Radiant Heat Flux

A radiant heat flux transducer (Medtherm, 64P-0.5-24-T) was mounted to an automated vertical traverse with a 2.3-metre span via a support frame. This provides good resolution of the axial heat flux profile for flame lengths of up to approximately 1.2 metres. This method is to be preferred over the single point measurement techniques developed by Sivathanu & Gore [7] for the present study, since single point measurements rely on the assumption that the flames are self-similar.

The signal from the transducer is transferred to an amplifier via shielded, low-impedance cabling. The signal then enters a data acquisition card in a PC (National Instruments, Lab-PC-1200). The experimental layout is shown in Figure 2.



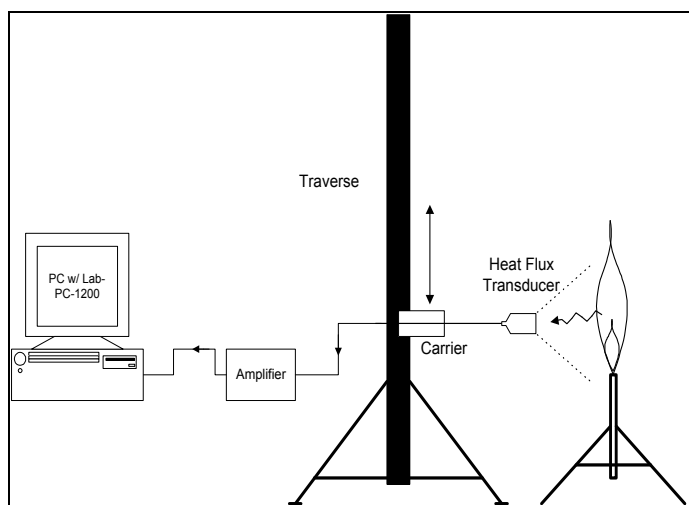


Figure 2: The apparatus used for radiant heat flux measurements.

Purpose written software is used to control the traverse, to capture data and to synchronise these processes.

A statistical study was used to determine the number of measurements required for reliable measurement of the mean and rms at each height along the axis of the flame. This showed that 400 measurements, sampled for 2 minutes at 3.33 Hz, provides convergence of the rms to within 2%.

The axial radiant profile was typically measured at 20 heights. The transducer was initially placed in a position where it registered only background radiation (i.e. below the burner exit plane) and was then traversed along the flame axis until, again, only background radiation was detected (typically 1.2-1.5 times the flame height).

As discussed by previous studies [7], the total radiant emission is assumed to be dominated by the axial radiant profile (for these long, thin flames) and thus the radial profile is ignored. The temperature of the flat plate surrounding the burner tip (Figure 1) was measured but never exceeded the ambient temperature by more than 10°C during any test and its influence has been neglected.

### Flame Size Measurements

A time series of visual images has been recorded with a digital video camera (Sony, DCR-TRV900E). The camera has a three colour (RGB) CCD recording system with manual control of exposure setting and is capable of shutter speeds of up to 1/10000<sup>th</sup> of a second, allowing instantaneous flame images to be captured without blurring. The camera is operated in progressive scan mode to eliminate image interlacing.

To allow direct comparisons of different flames a series of video clips was recorded at standard exposures, shutter speeds and frame sizes. The amount of background light was sufficiently reduced using blackout curtains to allow for a valid comparison of intensity. Each flame was recorded for 30-40 seconds (750-1000 frames) to ensure statistically significant results.

To determine flame dimensions the video footage was imported and processed by computer. Edge determination from time-lapse images has always been a contentious issue due to low intensity gradients. With this in mind, video footage is recorded at fast shutter speeds and analysed frame by frame. The instantaneous images are clear and importantly have very sharp edge definition. Typically, image intensity at the flame edge increases from a background intensity of approximately zero to over 80% of the maximum intensity in the space of 2-4 pixels (~0.2-8mm actual distance). Thus an overall spatial accuracy of better than 1.1%,

ignoring errors associated with parallax, can be achieved using this technique. The mean flame length and mean lift-off height are defined as the arithmetic average of the instantaneous positions, with reference to the burner exit planes.

The use of a frame-by-frame approach means that the arbitrary threshold value used in determining the edge position is of minor importance. For footage with a high overall exposure, such as in Figure 3, varying the threshold value between 30 and 200 resulted in only a 3% change in the calculated flame tip position.

Using this frame-by-frame approach, flame length, width and lift-off height detection was unambiguous. Since each frame is analysed individually it is also possible to obtain a histogram of flame position, as opposed to only a mean value, as shown in Figure 3 & Figure 4.



Figure 3: Example of instantaneous flame length measurement performed by software using frame-by-frame approach.

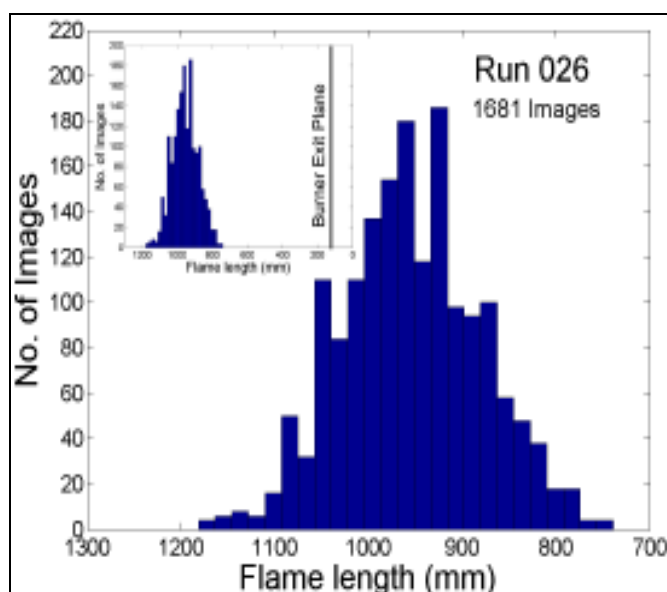


Figure 4: Histogram of flame tip position using frame-by-frame approach. Inset, histogram of flame tip position, showing burner exit plane at 122 mm.

The computer analysis calculates the flame tip position for each of the three colour channels independently. The red channel is used to measure the length of yellow-to-red radiant flames. Whereas footage of flames which are predominately blue in colour, such as lifted flames, are analysed using the blue channel. This approach maximises the signal to noise ratio in the video data, which is an important consideration when processing footage taken at high shutter speeds of flames with low luminosity.

## Results & Discussion

### Radiant Fraction

A comparison of the radiant fraction for the two burners is presented in Figure 5. The trends are similar for both nozzles. An increase in jet velocity causes in initial rapid drop in radiant

intensity as the flame lifts off, before converging asymptotically to their ultimate value. The effect of lift-off correlates with the visual observation of less yellow/orange colour in the flame associated with the presence of soot. At their respective blow-off velocities the relative difference in the radiant energy emitted from the two flames is 36%. The maximum velocity used for each of the nozzles was the largest velocity sustainable for the duration of the measurements (typically 45 minutes per flame). These maximum velocities are expected to be slightly smaller than the minimum blow-off velocities.

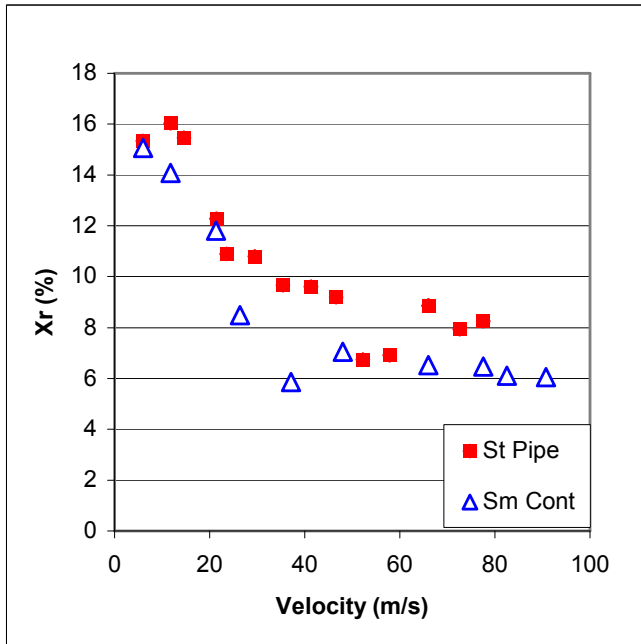


Figure 5: Radiant fraction ( $X_r$ ) vs. nozzle exit velocity.

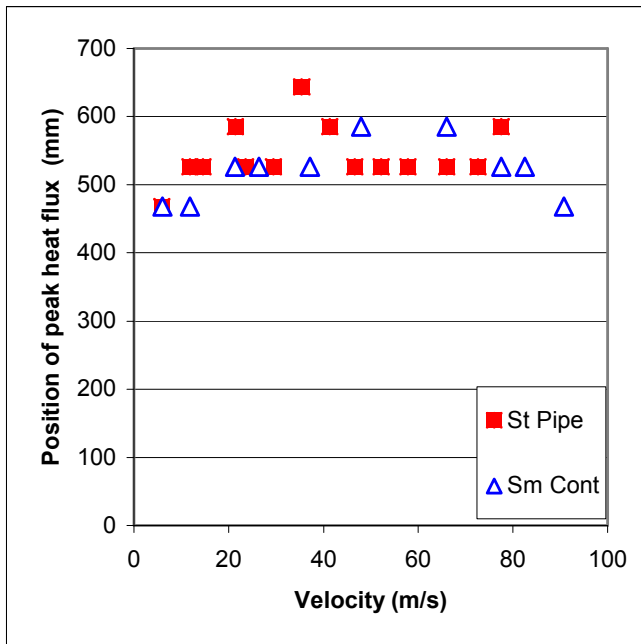


Figure 6: Position of the peak heat flux height vs. velocity.

Figure 6 shows that there is little difference in the position of the peak heat flux relative to the exit plane for the two burners. Previous work [7] suggests a method to approximate the total heat flux of a flame from a single point measurement at axial and radial positions equal to half the flame height, which is to coincide with the position of maximum heat flux. This single point measurement technique has since become prevalent in research, notably, [8]. The results of Fig. 6, when viewed with the flame length data in Figure 8, can not be reconciled with

these findings and indeed lend support to the method used in this study. The position of maximum radiant heat release is relatively constant across the range of heights measured that differ by up to 27%. Figure 7 shows that the positions of the peak heat flux for both flames is neither equal to 0.5 nor constant. Further, some of the data points are outside of the 0.5-0.7 range quoted as typical for the single point method.

The accuracy of the single point method was assessed to be 20% [7]. It can be seen that this level of accuracy is insufficient for this study.

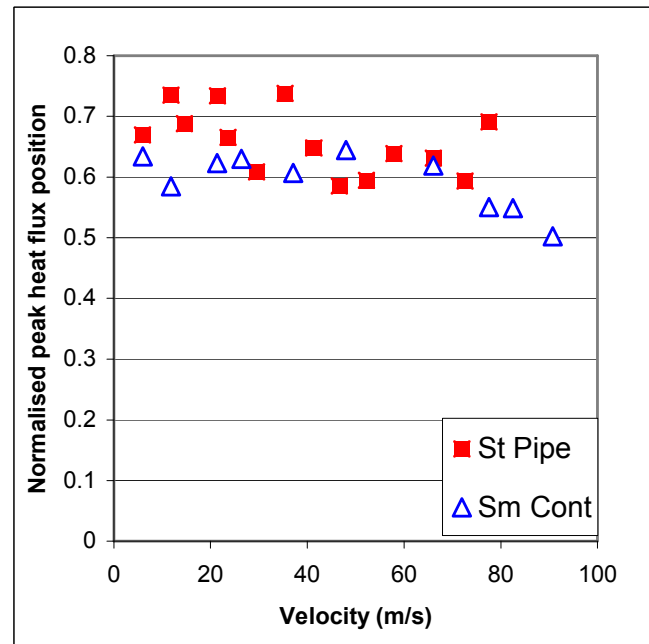


Figure 7: Normalised position of peak heat flux vs. velocity.

### Flame Length

The flame lengths from the two burners are shown in Figure 8. The mean flame length from the smooth contraction burner have a maximum length 17% longer than those from the pipe. The burners can be seen to yield a similar trend up to a velocity of 50 m/s. The straight pipe then converges to a constant length, while the smooth contraction nozzle flames continue to lengthen. In general, the length of the straight pipe flame is shorter than that from the contraction. This result conflicts with expectation based on the cold flow measurements [4,5], since the pipe jet has a lower rate of centre-line decay.

It is possible that the unexpected differences in flame length arise from slight differences in buoyancy. A possible explanation for this effect could be due to the difference in the radiant heat released from the two flames (Figure 5). Due to the lower radiation emitted from the smooth contraction nozzle it can be expected that higher flame temperatures will be experienced. The higher temperatures will result in a larger degree of gas expansion and hence, a potential increase in flame size. However, further investigations are required to confirm this effect and explanation. In any case it is clear that the presence of the flame changes the behaviour of the system from what may be expected from cold flow tests.

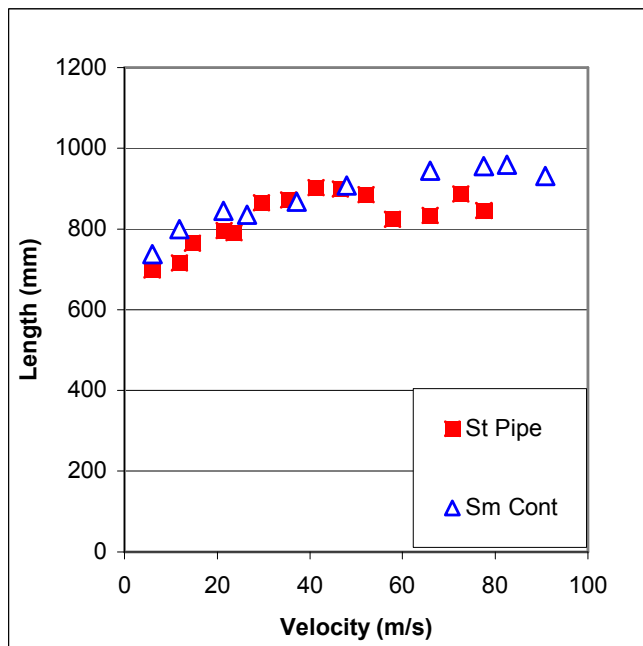


Figure 8: Mean flame length vs. velocity.

### Flame Lift-off Height

A clear difference in lift-off and blow-off behaviour can be seen in Figure 9. The smooth contraction burner is shown to exhibit a greater degree of stability in terms of initial lift-off velocity and lift-off height achieved before blow-off. The lift-off velocity was measured by starting with an attached flame and slowly increasing the flow rate. This was repeated ten times and the results averaged. The same method was used to determine blow-off. Due to the susceptibility of the flames to minor external disturbances at the point of blow-off this may not be an ideal method. Differences in the rate at which the flowrate is increased, as well as fluctuations in the lift-off height with time, are probably significant. However, an advantage is that the method is repeatable and uncomplicated.

The difference in the lift-off velocities is 40%, with the smooth contraction flame remaining attached at higher velocities. The blow-off velocity of the smooth contraction burner was found to be 17% greater.

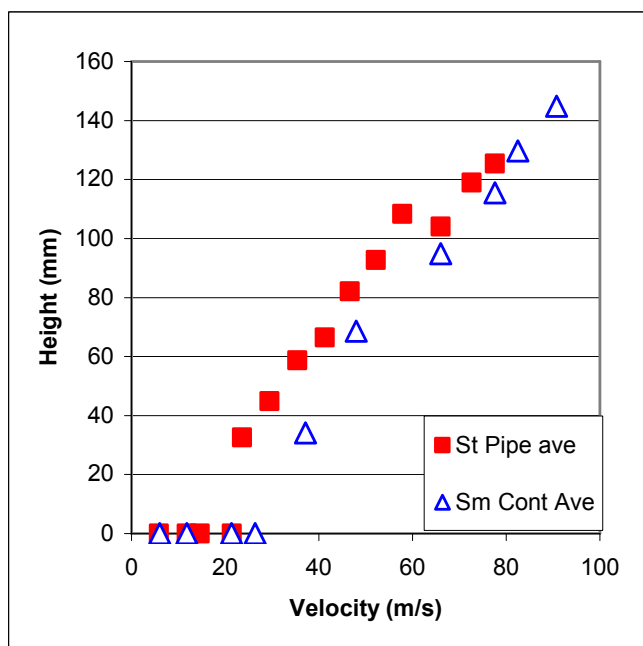


Figure 9: Lift-off height vs. velocity.

The present values of lift-off and blow-off are lower than previously reported data due to the flat plate surrounding the nozzles.

### Conclusion

This study has found that there are non-negligible differences between the flames from a smooth contraction and a straight pipe with the same exit diameter.

The following differences were found between the two burners:

1. The blow-off velocity of the smooth contraction nozzle exceeds that of the straight pipe by 17%
2. The smooth contraction nozzle has a mean flame length 13% longer than the straight pipe
3. The maximum stable lift-off height of the smooth contraction nozzle is 17% greater than the straight pipe.
4. The lift-off velocity of the smooth contraction exceed that for the pipe by 40%
5. The radiant energy released for a give fuel flow was always lower for the smooth contraction nozzle. This resulted in approximately a 36% difference at blow-off conditions.

This work is consistent with previous findings [4,5] that found both near and far field differences in their cold flow experiments with the same nozzles used in this study. It supports the idea that far field differences influence global performance. This work also has implications for combustion modelling as it is becoming apparent that circular burners can not be seen a being globally self similar.

Further work will be done to assess the impact of initial conditions on other aspects of global performance, such as emissions of CO, CO<sub>2</sub>, NO and NO<sub>2</sub>.

### References

1. H. A. Becker, D. Liang, Visible Length of Vertical Free Turbulent Diffusion Flames, *Combust Flame*, **32**, 1978, 115-137
2. W. R. Hawthorne, D. S. Weddell, H. C. Hottel, Mixing and Combustion in Turbulent Gas Jets, Third symposium on combustion, flame and explosion phenomena, 1949, 266-288
3. G. T. Kalghatgi, Blow-out Stability of Gaseous Jet Diffusion Flames. Part I: In Still Air, *Combust Sci Technol*, **26**, 1981, 233-239
4. J. Mi, D. S. Nobes & G. J. Nathan 2000, Influence of Jet Exit conditions on the Passive Scalar Field of an Axisymmetric Free Jet, *J. Fluid Mech.*, 2001, **432**, 91-125
5. J. Mi, G. J. Nathan & D. S. Nobes 2001, Mixing characteristics of Axisymmetric Free Jets From a Contoured Nozzle, an orifice Plate and a Pipe, *Trans. ASME*, **123**, December 2001, 878-883
6. Munson, B. R., Young, D. F. & Okiishi, T. H. Fundamentals of Fluid Mechanics, 3rd Edn, John Wiley, 1989, 483-488
7. Y. R. Sivathanu, J. P. Gore, Total Radiative Heat Loss in Jet Flames from Single Point Radiative Flux Measurements, *Combust Flame*, **94**, 1993, 265-270
8. S. R. Turns, F. H. Myhr, R. V. Bandaru, E. R. Maund, Oxides of Nitrogen Emissions from Turbulent Jet Flames: Part I – Fuel Effects and Flame Radiation, *Combust Flame*, **87**, 1991, 319-335
9. S. R. Turns, An Introduction to Combustion; Concepts and Applications 2<sup>nd</sup> Ed., McGraw-Hill, 2000, 502 & 506

## Control of Liquid Sloshing in Flexible Containers: Part 1. Added Mass

Birhan U. Güzel, Marija Gradinscak, S. Eren Semercigil and Özden F. Turan

School of Arch. Civil and Mechanical Engineering, Victoria University (F113)  
PO BOX 14428 MC Melbourne, VIC, 8001 AUSTRALIA

### Abstract

Liquid sloshing is the low frequency oscillation of a liquid in a partially full container. Intentional container flexibility has been employed in this study to suppress excessive levels of liquid sloshing. Part 1 of this two-part paper is regarding the effectiveness and optimization of added mass for this purpose.

### Introduction

The liquid in an open container can oscillate at discrete natural frequencies. The liquid motion, sloshing, at the lowest of these frequencies is of concern in this study as shown in Figure 1. In this figure,  $L$  indicates the width of the container (wavelength), and  $H$  the height of the static liquid. The shaded area of the diagram illustrates the shape of the free surface at the fundamental mode. It is critical to predict and to control liquid sloshing in order to maintain safe operation in ground and marine transport of liquid cargo, aerospace vehicles and earthquake-safe structures. A numerical model is presented in this study, which enables prediction of liquid sloshing. With this model, the use of container flexibility is investigated in order to control sloshing. Tuning is achieved with added masses.

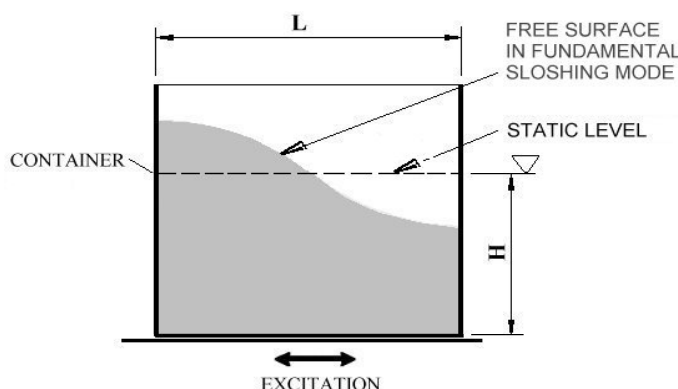


Figure 1. Sloshing in a rigid container.

Anderson [1], first investigated the possibility of using container flexibility for the control of liquid sloshing. Gradinscak et al. [3] investigated the design of flexible containers and observed significant reduction of sloshing amplitudes when the container natural frequency is tuned to the liquid sloshing frequency. The effect of container flexibility is previously studied [4] to provide insight for the tuning process. In this paper, further findings are presented towards an optimal flexible container design. The objective is to explore the possibility of enhancing the control action.

### Numerical Model and Procedure

An aluminum rectangular prism of 1.6 m x 0.4 m x 0.4 m has been chosen as the container. The wall thickness of the container is 1 mm. With this 0.4 m by 0.4 m cross section, the liquid level is fixed at 0.3 m (in the Z direction). Working liquid is water. A

finite element analysis (FEA) package, ANSYS, is used to model both the container and liquid dynamics [2]. A schematic view of the geometric model is given in Figure 2.

The container walls are modelled with standard shell elements of 0.05 m x 0.05 m size. A 1 % equivalent viscous critical damping is used to represent structural energy dissipation in the first two modes. Three dimensional cubic fluid elements are used for the liquid of the same size as the container. Grid independence has been verified. Similarly, a 10-ms integration step has been found to be sufficiently small for the accuracy of numerical predictions.

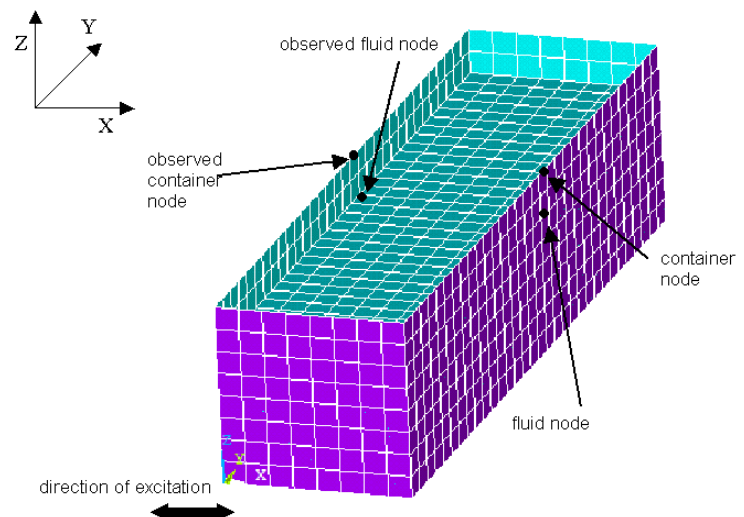


Figure 2. The numerical model and the location of the observed nodes.

A conventional tuned absorber is an auxiliary oscillator attached to a structure to be controlled. Normally, the natural frequency of the absorber is tuned to that of the structure to maintain minimum oscillation amplitudes, while the absorber is put in resonance intentionally. Here, the sloshing liquid is taken to be analogous to the structure to be controlled, whereas the flexible container acts like the tuned absorber. The objective is to tune the container's dynamics in such a way as to minimize liquid sloshing.

The tuning process may be implemented with the addition of masses to the container [4]. Varying point masses, of 1 kg to 45 kg each, are added on the container walls, at the two locations marked as the observed container nodes in Figure 2. These nodes have also been chosen to represent the container's response in the X direction. Liquid response is represented by the displacement of the two nodes at the free surface, directly aligned with those of the container nodes, in the Z direction.

Sloshing is induced by imposing a sinusoidal base displacement of one cycle in the X direction. The peak-to-peak base displacement is 10 mm with a frequency of 1.34 Hz. This frequency corresponds to the theoretical sloshing frequency of a rigid container of the same dimensions [5].



In the numerical model, the starting instant corresponds to the sudden presence of a rather large amount of water in the undeformed container. In response, the container immediately attempts to assume a deformed shape to accommodate the water's presence. This attempt results in oscillations of the container and the fluid. However, these fluid oscillations are simply an up-and-down motion of the flat surface, and quite different than sloshing. Originally, simulations were performed for 40 seconds to allow the container to assume its static equilibrium for the first 20 seconds, and then, the transient base disturbance mentioned earlier was applied. However, due to relatively poor energy dissipation, a 20 second period was insufficient to reach the static equilibrium. As a result, the in-phase displacements of the free surface continued, along with the out-of-phase sloshing displacements. The difference between the vertical displacements of the two free surface nodes, allowed the extraction of the out-of-phase motion of the free surface, which is referred as the "sloshing history".

When the same cases were simulated starting with the application of the base disturbance without waiting to reach the static equilibrium first, it was observed that the out-of-phase "sloshing history" of the free surface was virtually identical to the earlier ones. For these cases, in-phase and out-of-phase liquid motion took place simultaneously. However, the subtraction process made it possible to observe the relevant "sloshing history" avoiding the initial 20-second idle period. In this paper, selected cases are presented for a total duration of 20 seconds where the base disturbance is given at the start of the simulation period. This point is further examined in Part 2.

## Results and Discussion

Sloshing histories and the corresponding frequency spectra for selected cases of a rigid container and a flexible container with no added mass, 7-kg, and 21-kg added masses, are presented in Figures 3(a) to 3(d). Sloshing histories given in the first column of Figure 3, represent the out-of-phase displacement of the free surface.

The sloshing history for the rigid container in Figure 3(a), sustains a peak amplitude of around 40 mm. This amplitude is approximately the same for the flexible container case in Figure 3(b) with no added mass. The gradual decay is due to 1% critical damping of the structure. The optimal tuning range is around 7 kg of added mass [4]. For this case, the peak sloshing amplitude decreases to 10 mm - 15 mm in Figure 3(c). Sloshing amplitude further increases to about 30 mm with 21-kg added mass in Figure 3(d).

In the second column of Figure 3, the frequency spectra of the container displacement (—) and sloshing (.....) are presented. For the rigid container in Figure 3(a), the fundamental liquid sloshing frequency is indicated to be around 1.4 Hz, quite close to 1.34 Hz [5]. Another small spectral peak is around 2.3 Hz, possibly corresponding to a harmonic of the fundamental mode.

The frequency of the highest sloshing peak in Figure 3(b), is around 1.2 Hz. The flexible structure seems to be driven strongly by the liquid at this frequency. In addition to the sloshing driven structural peak at 1.2 Hz, there are two major spectral peaks, one around 0.75 Hz and the other around 1.7 Hz. In Figure 3(b), spectral peaks around 1.4 Hz and 2.3 Hz can still be noticed for sloshing.

With 7-kg added mass in Figure 3(c), the structure appears to have two dominant spectral peaks. These peaks are around 0.7 Hz and 1.1 Hz. The magnitude of second spectral peak at 1.1 Hz, is comparable to that of the first peak. The control effect on

sloshing of the second structural peak is clear, practically eliminating any response from the liquid motion between frequencies of 0.9 Hz and 1.4 Hz. In contrast to the second spectral peak, the first spectral peak of the structure at 0.7 Hz seems to have an adverse effect on sloshing control. The structure seems to drive the liquid at this frequency.

In Figure 3(d), for 21-kg added mass, sloshing around 1.4 Hz becomes significant again, indicating that the interaction of the structure and liquid is being lost. The result of this loss is the appearance of independent spectral peaks for both the structure and liquid separately.

In Figures 4(a) to 4(c), the left column is the cross-correlation between sloshing amplitude and structural displacement for a flexible container with no added mass, 7-kg added mass and 21-kg added mass, respectively. The horizontal axis represents the number of integration steps of 10 ms each over the total time of 20 s. The right column is the corresponding cross-spectrum for the same cases. In the cross-correlation graphs, it is seen that the fluid-structure interaction is significantly lost after 7 kg added mass.

In the cross-spectrum plots, the dominant frequency of communication can be viewed at different added masses. As the structure and fluid strongly drive each other, a clear large spectral peak is observed. For the no added mass case and within the tuning region, there is a clear dominant frequency as seen in Figures 4(a) and 4(b). The dominant frequency for the no added mass case in Figure 4(a) is close to the fundamental fluid frequency. This result suggests that the system is mainly driven by the fluid. The dominant spectral peak in the tuning range, on the other hand, is around that of the structural fundamental frequency, which similarly is an indication that the fluid is being driven by the container at this time.

From Figures 3(c) and 4(b), it is seen that the structure is significantly affecting the liquid response in the tuning range. In addition to suppressing the liquid response at certain frequencies, the structure is driving the liquid at other frequencies, as previously mentioned. Therefore, if this second detrimental effect can be eliminated, it should certainly be possible to improve the design of a flexible container. Current work is in this direction to identify the structural mode shapes to encourage the control effect, and to discourage the driving effect on liquid sloshing.

A summary of the tuning process is presented in Figure 5 with the root mean square averages of sloshing amplitudes. The minimum sloshing amplitude is for about 7 to 8-kg added mass on the flexible container, corresponding to better than 80% attenuation as compared to the rigid container (solid red line). Considering the respective slopes of the trend line on either side of the best case, the control effect is more sensitive as the tuning is approached from the left. Therefore, it may be advantageous to be on the right hand side of the best performance where the added mass may be allowed to be somewhat larger than the optimal without significant loss of effectiveness.

## Conclusions

With proper tuning of a flexible container, a net reduction of about 80% is possible in the rms liquid sloshing amplitudes, as compared to that in the rigid container. An optimal value of added mass exists around 7 kg for the dimensions used here. This paper represents a progress report on attempts to improve the control effect on sloshing.



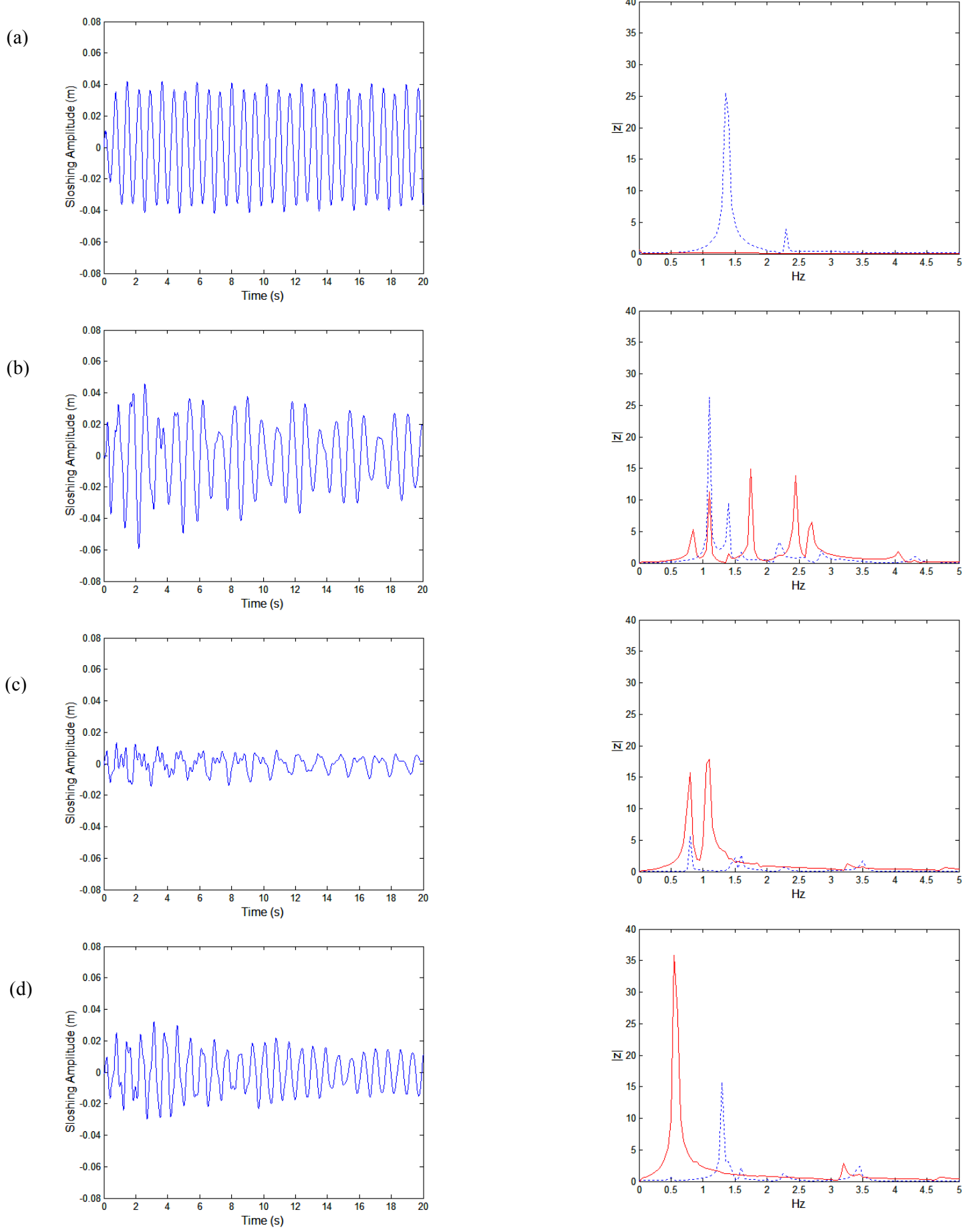


Figure 3. First column: Predicted sloshing histories (a) Rigid container. Flexible container with added point masses: (b) 0 kg, (c) 7 kg, (d) 21 kg. Second column: FFT of sloshing liquid (dashed) and structural vibration (solid) for the same cases.

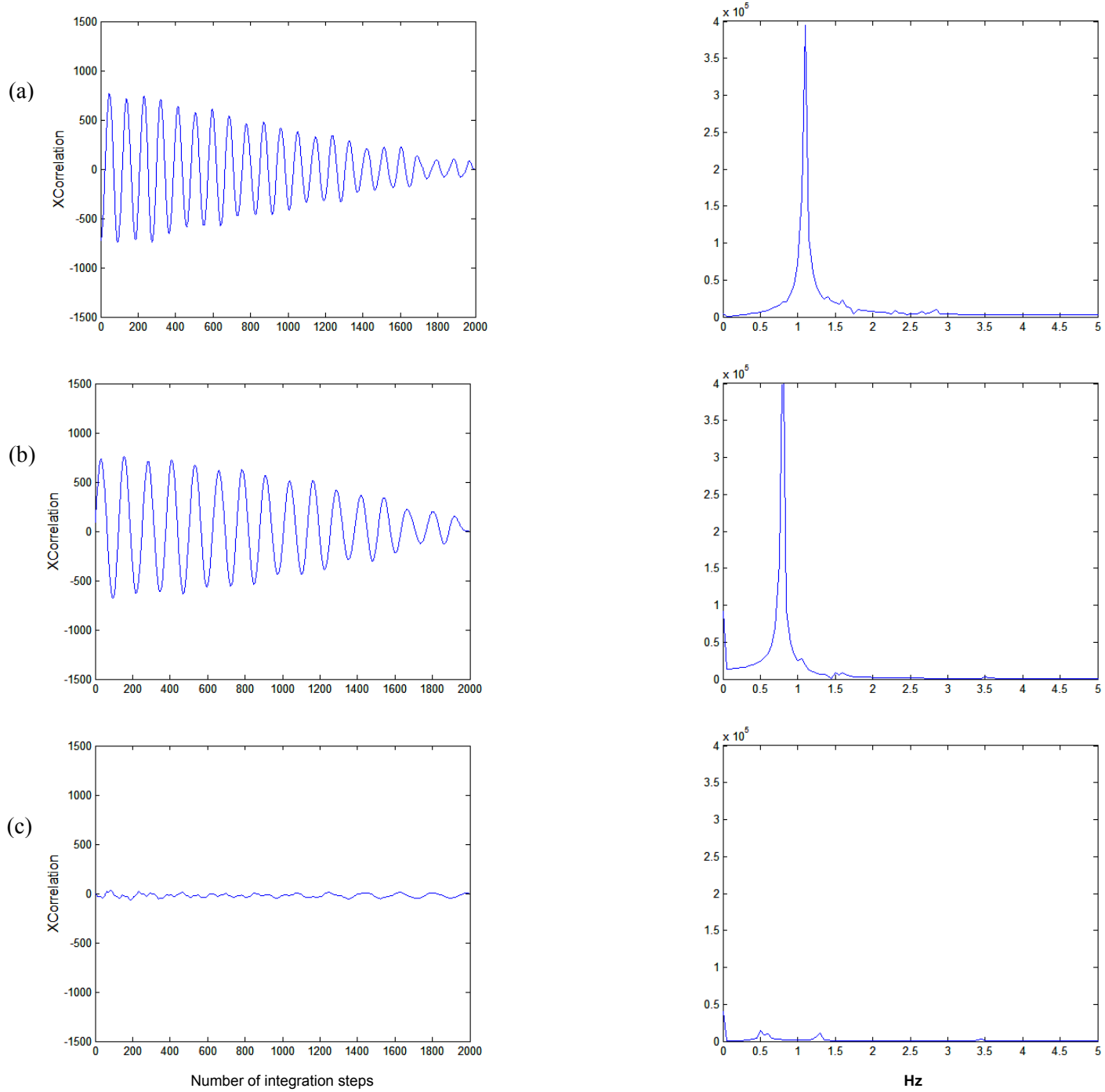


Figure 4. First column: Cross-correlation between sloshing and structural displacement for flexible container with added point masses: (a) 0 kg, (b) 7 kg, (c) 21 kg. Second column: Cross spectrum for the same cases.

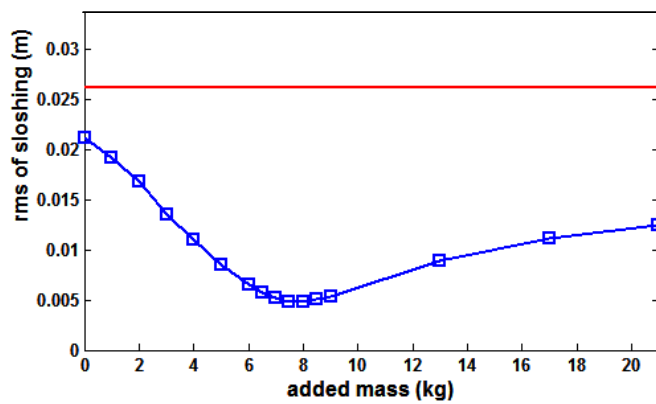


Figure 5. Variation of the rms of sloshing magnitude with mass for rigid (—) and flexible (□) containers.

## References

- [1] Anderson, J. G., *Liquid Sloshing in Containers, Its Utilisation and Control*, Ph.D. thesis, Victoria University, Melbourne, Victoria, Australia, 2000.
- [2] ANSYS 6.1 Users Manual, ANSYS Inc. Houston, Texas, USA, 2002.
- [3] Gradinscak, M., Semercigil, S. E., & Turan, Ö. F., Design of Flexible Containers for Sloshing Control, Proceedings of ASME Fluids Eng. Div. Summer Meeting, Montreal, Canada, Paper No. FEDSM2002-31424, 2002.
- [4] Güzel, B. U., Gradinscak, M., Semercigil, S. E., & Turan, Ö. F., Tuning Flexible Containers for Sloshing Control, IMAC XXIII, 2004, Orlando, Florida, USA.
- [5] Milne-Thomson, L.M., *Theoretical Hydrodynamics*, 5<sup>th</sup> ed. Macmillan Press, 1968, 427-442.

## Control of Liquid Sloshing in Flexible Containers: Part 2. Top Straps

Marija Gradinscak, Birhan U. Güzel, S. Eren Semercigil and Özden F. Turan

School of Arch. Civil and Mechanical Engineering, Victoria University (F113)  
PO BOX 14428 MC Melbourne, VIC, 8001 AUSTRALIA

### Abstract

As described in Part 1, sloshing is the low frequency periodic motion of the free surface of a liquid in a partially filled container. The dynamic response of structures containing liquid can be significantly influenced by these low frequency oscillations, and interaction with the sloshing liquid could lead to instabilities. The authors' earlier work indicates that container flexibility can be effective in sloshing control. In Part 2, the added advantage of top straps is discussed towards a more practical optimal container design.

### Introduction

Liquid in an open container can move back and forth across the basin in standing (or travelling) waves at discrete natural frequencies, as described in Part 1. This low frequency oscillation of the liquid is defined as sloshing. In Part 2 of this two-part paper, the effect of horizontal straps is investigated in controlling liquid sloshing in a flexible container. A schematic view of such a container is shown in Figure 1. As further illustrated below, a flexible container with straps on top, is chosen as a practical way to implement tuning with added masses without excessive wall deflection. Straps on top of a flexible container, reduce static deflection due to the addition of liquid and point masses.

Liquid sloshing and its control have attracted attention in engineering research due to the consequences of uncontrolled sloshing. Welt and Modi [9] showed that the sloshing resulting from external forces is often critical when the excitation frequency is near the liquid natural frequency. The methods of determining natural frequencies and mode shapes of such flexible structures could be found in the works of Kana and Abramson [7], Chen and Haroun [3] and Jeong and Kim [6]. Further investigations on using structural flexibility for the control of liquid sloshing using finite element analysis are reported by Anderson [1] and Gradinscak et al. [4, 5].

### Numerical Model

The container used for this part of the study, is identical to that described in Part 1. It has a rectangular shape, 1.6 m in length, 0.4 m in width and 0.4 m in high. The wall thickness is 1 mm. The material properties for aluminum are used for the container. As in Part 1, the ANSYS FEA [2] program has been used to create the numerical model of the flexible container and liquid using finite elements, simulate liquid sloshing in the container and obtain displacement values at different nodes for the container and liquid.

The container is modelled with two-dimensional rectangular shell elements. Such an element has constant thickness, and it is defined by four nodes, with six degrees of freedom at each node. 1% critical damping is applied to the structure without liquid. In addition, three link elements are attached at the top of the container at three points as straps. A link element is defined by two nodes, the cross-sectional area and material properties. The material properties for aluminum are used also for the link

elements. The numerical model is illustrated in Figure 1 with the top straps.

Three dimensional brick finite elements are used to model the liquid. This element is defined by eight nodes having three degrees of freedom at each node. The parameters are chosen for a homogeneous, inviscid, irrotational and incompressible liquid. The material properties for the liquid are defined by the fluid elastic modulus and the density. The liquid depth is 0.3m. The liquid is kept undamped throughout the simulations.

Two structural mass elements are added to each long side of the container, on either side of the middle strap, in order to tune the natural frequency of the container with that of the fundamental sloshing mode. A structural mass element is defined as a single node that has a concentrated mass acting along the element's own coordinate directions.

Fluid-structure interaction is achieved by coupling the liquid displacement with that of the container walls in the direction normal to the walls. The container and liquid parameters are adjusted to ensure that the frequency of the structure and liquid are close numerically to guarantee strong interaction. Eigenvalue analysis is used to determine natural frequencies and mode shapes, and direct numerical simulation is used to determine the displacement histories of the liquid and container.

The disturbance used is the same as in Part 1. Sloshing is induced by imposing a transient sinusoidal displacement of one cycle to the base of the container in the X direction, as defined in Figure 2 of Part 1. The peak-to-peak base displacement is 0.01 m with frequency of 1.34 Hz. This frequency corresponds to the theoretical sloshing frequency of a rigid container of the same dimensions [8].

As described in Part 1, simulations were performed previously for 40 seconds, by allowing the container time for the first 20 seconds to assume its static equilibrium, and then, by imposing to the base a transient disturbance along the X axis. Two sample results are presented in Figure 2 for 40-second simulations. In Figure 2(a), the container and liquid free surface displacement histories are presented for the case of 9-kg total added mass without top straps. In Figure 2(b), the histories are given for the 9-kg added mass case with top straps. In both of these figures, the right column represents the liquid sloshing history, obtained as the difference between the vertical displacements of the top middle liquid nodes, as defined in Part 1. During the first 20 seconds, the liquid surface simply bobs up-and-down with an amplitude comparable to that of the container displacement. With the 40-second runs, liquid sloshing starts only after the transient base disturbance is applied at the twentieth second. As described in Part 1, when the liquid sloshing amplitude is compared with 20-second simulations with disturbance applied at the start, similar out-of-phase liquid sloshing histories are obtained, indicating that 40-second simulations with a settling down

period, are not needed. Therefore, the rest of the results presented here are from 20-second simulations.

## Results and Discussion

From a comparison between the static container displacements with and without straps within the first 20 seconds, the practical significance of top straps can be observed. As described in Part 1, added mass is needed to tune the container flexibility to liquid sloshing for optimal control. As indicated in Figure 2(a), with a 9-kg added mass, a static deflection of about 6 cm occurs in the container. With the addition of three straps at the top, the static deflection reduces to about 1 cm.

It is known that the sloshing due to external forces becomes critical when the excitation frequency is close to the fluid sloshing frequency [1]. Ideally, to control sloshing, the objective is to tune the container natural frequency to the exact sloshing frequency. As described in Part 1, tuning is achieved by attaching different amounts of mass to the container to decrease its natural frequency, while keeping all other parameters the same. Tuning for the cases presented in this paper has been achieved by adding structural mass elements at two points on either side of the middle strap, as described in the previous section. The presence of significant energy transfer between the liquid and container is considered to be a sign of appropriate tuning. Such energy transfer is detected by a beat in the displacement history of the container walls or liquid.

As shown in Figure 3(a) of Part 1, for the rigid container (with no added mass and no straps), the sloshing amplitude does not decay, after the excitation is applied for the first 0.74 seconds. As in Part 1, this case is taken as the comparison base here for the flexible wall cases with and without additional elements to demonstrate the effectiveness of sloshing control.

In Part 1, the best tuning case is shown to be around an added mass of 7 to 8 kg without straps. With straps, a series of numerical trials has been conducted to determine the most promising case. In Figure 3, the histories are presented for selected cases of the horizontal oscillations of the top middle nodes of the long container walls, and the vertical oscillations of the corresponding liquid nodes. Figures 3(a) to 3(e) correspond to cases of 0, 6 kg, 10 kg, 14 kg and 18 kg added mass, all with three top straps. The right column in each figure is the corresponding sloshing history, calculated as the difference between the vertical displacements of the two liquid nodes at the top middle of the long sides of the container.

From a comparison of Figures 3(a) to 3(e), it is seen that with added masses of 6 kg and 10 kg, the peak sloshing amplitude drops significantly with respect to the no added mass case and the case of the rigid container. The best result is obtained for the 10-kg added mass case. By adding masses of 14 kg or more, the tuning effect is lost, and the liquid sloshing amplitude starts to increase.

In Figure 4, the rms liquid sloshing amplitudes of different cases are shown as a function of added mass for all the cases presented in Parts 1 and 2. The rms amplitudes are normalized by the rms sloshing amplitude in the rigid container. This figure is obtained by adding the strapped cases to Figure 5 of Part 1. As seen in this figure, the optimal control achieved with straps corresponds to a decrease in the sloshing amplitude of about 80 % between 6 to 10

kg added mass. Similar to the cases of sloshing control without straps, but only with added mass, the control is more sensitive for smaller added mass cases than for larger ones, as indicated by the steeper slope to the left of the best control.

## Conclusion

The effect of additional elements, along with container flexibility, in sloshing control is presented. The results from these simulations have shown that the sloshing amplitude is significantly lower in comparison with the rigid container case. With three straps on top and for the dimensions chosen here, the best suppression is obtained for the 6 to 10-kg added mass on the flexible container.

The fluid-structure interaction model presented here is based on numerical modelling. The model allows for an unlimited number of parameters to be examined, so that a comprehensive investigation of various elements used for sloshing suppression can be undertaken. The results presented require experimental verification, and this work is currently underway.

## References

- [1] Anderson, J.G., *Liquid Sloshing in Containers, Its Utilisation and Control*. Ph.D. thesis, Victoria University, Melbourne, Victoria, Australia, 2000.
- [2] ANSYS 6.1 Users Manual, ANSYS Inc. Houston, Texas, USA, 2002.
- [3] Chen, W. & Haroun, M.A., Dynamic Coupling Between Flexible Tanks and Seismically Induced Nonlinear Liquid Sloshing, *Fluid Transients, ASME FED 198/PVP-Vol.291*, 1994.
- [4] Gradinscak, M., Semercigil, S. E. & Turan, Ö.F., Design of flexible Containers for Sloshing Control, *Proceedings of ASME Fluids Eng. Div. Summer Meeting, Montreal, Canada, Paper No. FEDSM2002-31424*, 2002.
- [5] Gradinscak, M., Semercigil, S. E. & Turan, O.F., Sloshing Control with Container Flexibility, *14 Australasian Fluid Mechanics Conference, Adelaide University Adelaide, Australia*, 2001.
- [6] Jeong, K.H. & Kim, K.J., Free Vibration of a Circular Cylindrical Shell Filled with Bounded Compressible Fluid, *Journal of Sound and Vibration*, **217**(2), 1998, 197-221.
- [7] Kana, D. D. & Abramson, H. N., Experimental Study of Liquid Instability in a Vibrating Elastic Tank, *Journal of Spacecraft*, **3**(8), 1966, 1183-1188.
- [8] Milne-Thomson, L.M., *Theoretical Hydrodynamics*, 5<sup>th</sup> ed. Macmillan Press, 1968, 427-442.
- [9] Welt, F. & Modi, V.J., Vibration Damping Through Liquid Sloshing, Part 1: A Nonlinear Analysis, *Transactions of the ASME, Journal Vibration and Acoustics*, **114**, 1992, 10-16.

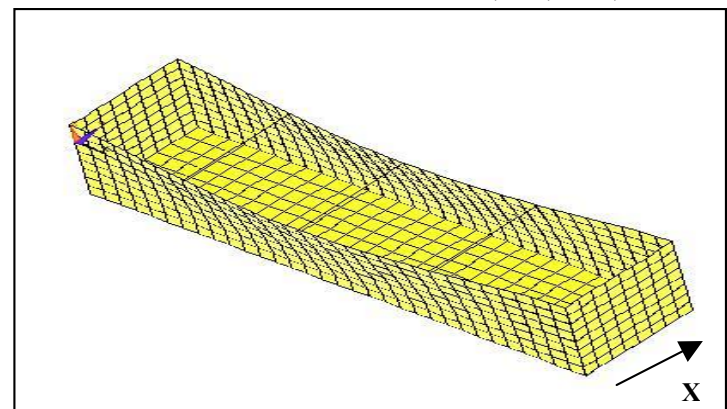


Figure 1. The first mode shape of the flexible container without water, showing the locations of the three straps.

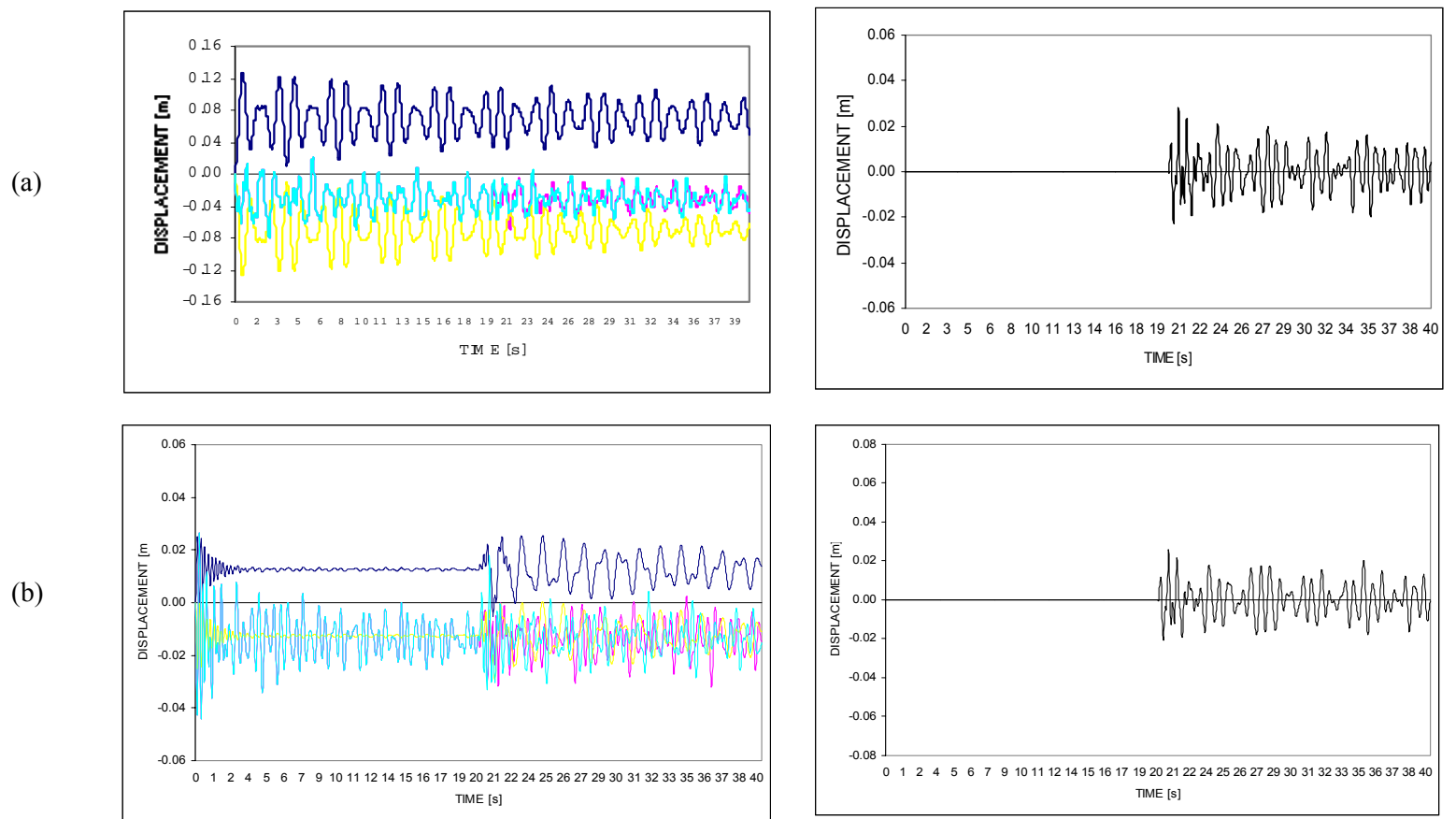


Figure 2. Selected 40-second simulations. (a) 9-kg added mass without straps. (b) 10-kg added mass with straps. Left column, displacement (top and bottom, horizontal displacement of the two sides of the structure; two in the middle, vertical displacement of the adjacent liquid nodes); and right column, sloshing histories.

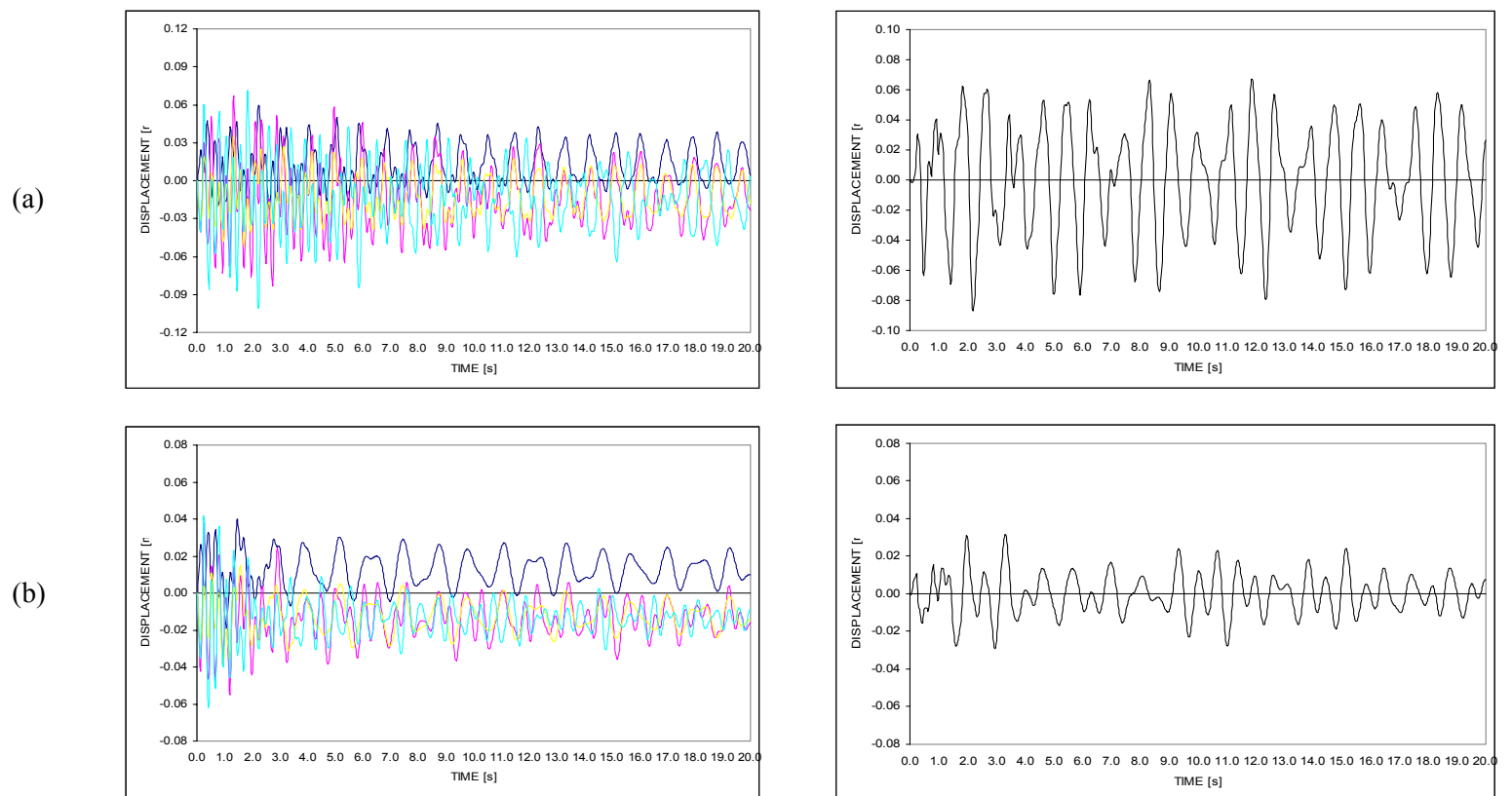
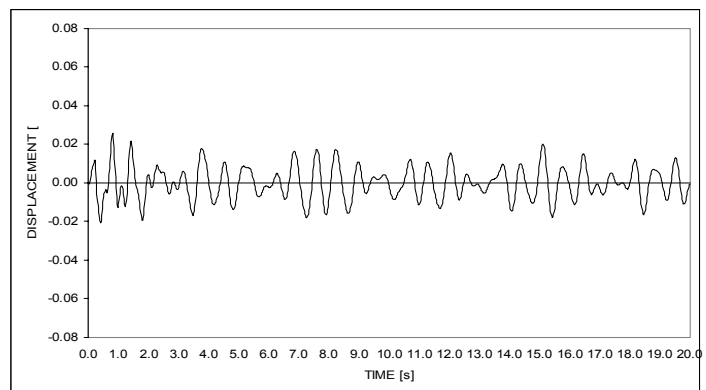
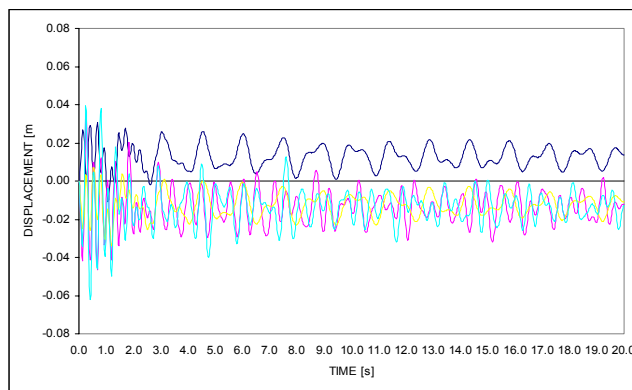


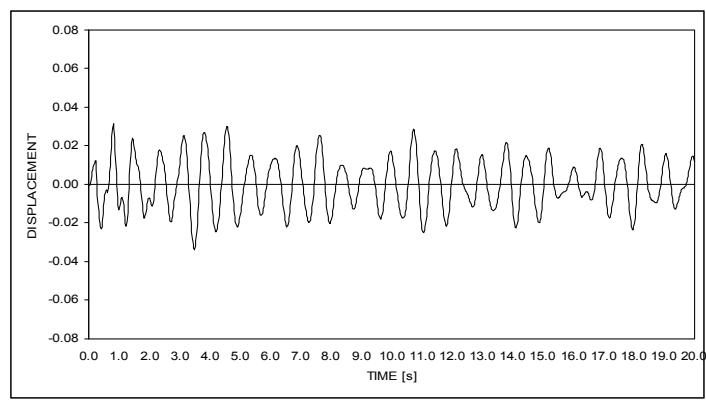
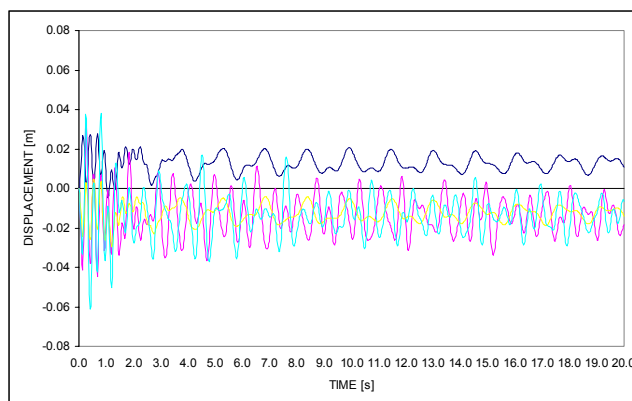
Figure 3. Strapped cases. (a) no mass; added masses of (b) 6 kg; (c) 10 kg; (d) 14 kg; (e) 18 kg.



(c)



(d)



(e)

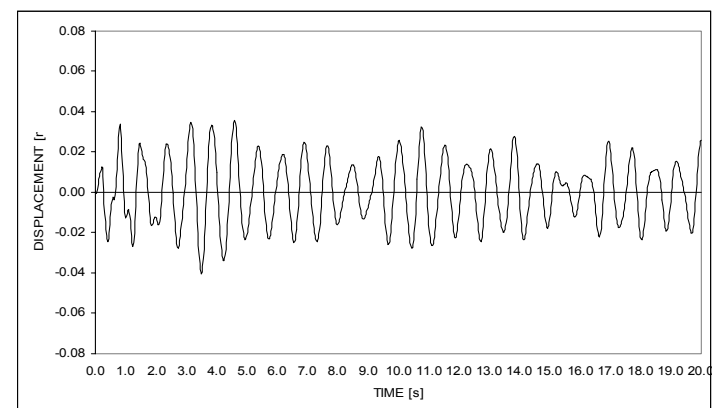
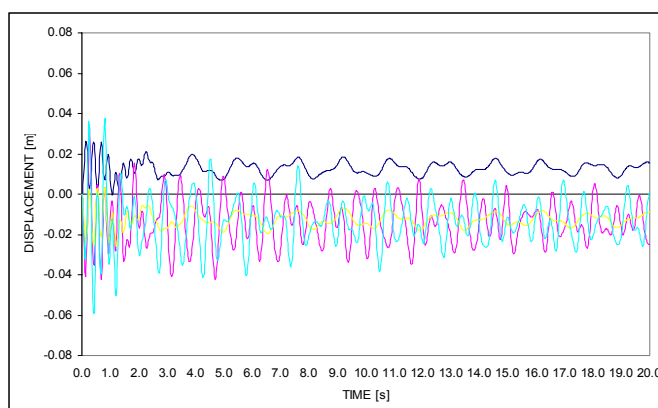


Figure 3. Continued.

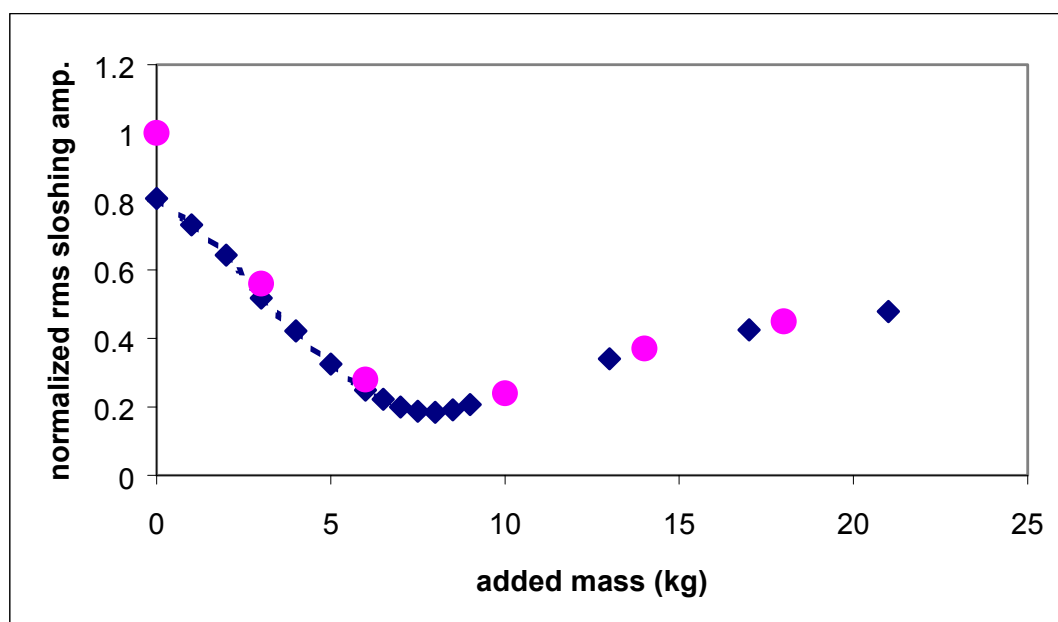


Figure 4. Variation of rms sloshing amplitude with added mass for cases without (◆) and with (●) straps.

## Towards a Valveless Electro-Rheological Valve

Tam D. Truong, S. Eren Semercigil and Özden F. Turan

School of Arch. Civil and Mechanical Engineering, Victoria University (F113)  
PO BOX 14428 MC Melbourne, VIC, 8001 AUSTRALIA

### Abstract

Electro-Rheological (ER) fluids can change phase from liquid to a solid-like gel in response to being exposed to electric field. This property makes ER fluids useful in motion control applications. The motivation of this paper is to present a technique such that ER fluids may be used in designs of valves where “valving” can be achieved without any moving mechanical components. Such designs should be attractive as control agents.

### Introduction

Electro-Rheological (ER) fluids have the desirable feature of being able to change phase between a liquid and a solid-like gel. These are normally suspension fluids, mostly made up of some variety of semi-conducting particles and a suspending oil. There are literally hundreds of different recipes to make ER fluids [3], and the one used in this work is a corn starch – mineral oil suspension.

Normally, an ER fluid has its particles suspended in quite random fashion as shown in Figure 1(a). When an electric field is applied across the fluid, however, the semi-conducting particles are polarised electrically, and form chains. These chains are shown in Figure 1(b). The flat regions shown at the top and the bottom in Figure 1, are the conductor plates through which the electric potential is applied. The required electric field strength is in the order of kilo Volts per mm. The phase change takes place in milliseconds. More importantly, the liquid phase is recovered upon removal of the electric field.

When the conductors required to apply the electric field, are kept at a fixed distance from each other, there are two different modes of operation, namely the shear mode and the flow mode. In the shear mode, the two electrodes are given a relative motion to cause shearing of the fluid placed between them. In the flow mode, the electrodes are kept stationary to form a channel, and the fluid is pushed through them. In the shear mode, the application of electric field increases the shear resistance, or shear strength, of the fluid. In the valve mode, the application of electric field increases the pressure drop along the length of the conductors.

A typical set of results are shown in Figure 2, where the shear resistance of a corn starch-mineral oil ER fluid is given for different strain rates [5]. The solid to liquid weight ratio of the ER fluid suspension is 0.70 for this case. Details of the shear stress measurements are given in Reference 5.

Five sets of shear stresses are plotted in Figure 2 corresponding to five different electric fields, including zero. For zero electric field, the behaviour may be represented with that of an ideal Newtonian fluid where the shear stress,  $\tau$ , is linearly proportional to the rate of strain,  $\dot{\gamma}$ , and the proportionality constant represents the dynamic viscosity,  $\mu$ :

$$\tau = \mu \dot{\gamma} \quad (1)$$

Note that the curve fit for the linear behaviour is also given next to the trend line. The value of  $R^2$  indicates the reliability of the linear trend, in mean square sense, to the experimental points where an  $R^2$  of unity would correspond to a perfect fit.

When an electric field is applied, the shear stress variation seems to shift up, approximately parallel to the zero-field trend. What is of significance here is the presence of an intercept on the vertical axis, representing shear resistance for a zero rate of strain. This intercept may be interpreted as an “equivalent stiffness” as a result of the level of solidification. Stiffness, or resistance to deformation, is, of course, the property of a solid.

Although the  $R^2$  reliability of the existence of the linear trend of the new cases, is somewhat lower than that of the zero-field case, the shear stress may still be expressed as

$$\tau \approx \tau_b + \mu \dot{\gamma} \quad (2)$$

Here,  $\tau_b$  represents the intercept to indicate the effect of applied electric field [2, 4-6].  $\tau_b$  may be expressed as

$$\tau_b = \alpha E^\beta \quad (3)$$

where  $\alpha$  and  $\beta$  are the material properties of the fluid, and  $E$  is the electric field strength [2, 4-6]. Equation 2 also represents the condition for Bingham Plastic Flow [2, 4-7]. It should be mentioned here that there is also a class of ER fluids (such as those of liquid crystal type) which behave quite differently than what is suggested in Equation 2. These fluids do not acquire an intercept in response to an electric field. They maintain a shear stress variation similar to that of a Newtonian fluid, but they experience an increase in their viscosity.

In the next section, the treatment of the Bingham model is extended into the valve mode of operation. The objective of this extension is to demonstrate the possibility of controlling the pressure loss, with the electric field as the control parameter. The further objective is to compare this control process against the performance of a generic pump.

### Behaviour In Valve Mode

In Figure 3, the thick lines at the top and bottom indicate the conductors which form the channel in which the ER fluid flows from left to right. The length of the channel is  $L$ .  $\Delta P$  is the pressure drop along the length  $L$ . The width and the depth of the channel are  $h$  and  $b$ , respectively, where  $b$  is in the direction normal to the view given in Figure 3. The profile of the velocity  $u(y)$  is also indicated in the flow direction. The middle section of the channel acquires a plug, of total thickness,  $\delta$ , in response to

the gradual solidification of the fluid. The plug thickness grows as the electric field strength increases [2, 4-7].

Establishing the force balance between the shear force and the force due to pressure drop, once at the wall and once at the interface of the plug, leads to the following expression:

$$\frac{\tau_b}{\tau_w} = \frac{\delta}{h} \quad (4)$$

indicating that the ratio of the plug thickness,  $\delta$ , to the width of the channel,  $h$ , is the same as the ratio of the static shear strength,  $\tau_b$ , to the shear stress at the wall of the channel,  $\tau_w$ . Further rather lengthy manipulations lead to [4,5,7]

$$4\left(\frac{L}{h\Delta P}\right)^3 \tau_b^3 - 3\left(\frac{L}{h\Delta P}\right) \tau_b + \left(1 - \frac{12\mu LQ}{bh^3\Delta P}\right) = 0 \quad (5)$$

In this expression, the parameters  $L$ ,  $b$  and  $h$  are the dimensions of the channel;  $\mu$  is the Newtonian viscosity of the fluid;  $Q$  is the amount of flow through the channel; and  $\Delta P$  is the resulting loss of pressure. The ER effect is represented only through  $\tau_b$  whose value may be determined as a function of the applied electric field as suggested in Equation 3.

The relationship between  $\Delta P$  and  $Q$  for zero electric field may be obtained by setting the  $\tau_b$  term to zero in Equation 5. The resulting equation is analogous to Equation 1:

$$\Delta P = 12 \frac{\mu L}{bh^3} Q \quad (6)$$

For increasing values of the electric field strength  $E$ , or equivalently, for increasing values of  $\tau_b$ , the variation of  $\Delta P$  with  $Q$  is similar to the variation of the shear stress,  $\tau$ , with the strain rate. As illustrated in Figure 4, increasing  $E$  shifts up the linear relationship of the zero-field case. The intercept with the  $\Delta P$  axis may be obtained to be

$$\frac{L}{h\sqrt{3/4}} \tau_b \quad (7)$$

from Equation 5, by setting  $Q$  to zero.

In Figure 5, the variation of  $\Delta P$  with  $Q$  from Figure 4, is repeated along with a generic performance curve of a pump to provide the flow in the channel. This pump curve indicates the amount of possible  $Q$  as a function of the amount of pressure loss  $\Delta P$  which the pump has to overcome. Amongst all possible pairs of  $(\Delta P_i, Q_i)$  which the pump can provide, the point of operation is obtained by the simultaneous solution of the pump (supply) and system (demand) characteristics. This simultaneous solution is represented graphically by the intersection of the two such characteristic curves.

For a zero electric field, the intersection with the pump curve indicates  $Q_0$  as the volume flow rate at the operating point. When an electric field is applied, however, the point of intersection moves towards left, effectively increasing the amount of pressure loss to be overcome by the pump. This decrease in  $Q$  continues monotonically with increasing  $E$ , until such a point that the

pressure demand of the “ER valve” is so large as to stall the pump and to completely shut off the flow.

## Conclusions

A brief summary is presented in this paper of an extensive study to model the shear and flow modes of a particular ER fluid. The suggested procedure indicates that the amount of flow through a channel may be valved by varying only the applied electric field, and with no moving mechanical components.

## Acknowledgement

T. D. Truong was a recipient of a Victoria University Postgraduate Scholarship during the course of this work.

## References

- [1] Gandhi, M.V. & Thompson, B. S., *Smart Materials and Structures*, Chapman & Hill, Boundary Row, London, 1992, 144.
- [2] Lee, H.G. & Choi, B. Dynamic Properties of an ER Fluid under Shear and Flow Modes. *Mat. and Design*, **23**, 2002, 69-76.
- [3] Mäkelä, K.K., Characterization and Performance of Electro-Rheological Fluids based on Pine Oils. Ph.D. thesis, University of Oulu, 1999.
- [4] Peel, D.J. & Bullough, W.A., Prediction of Electro-Rheological Valve Performance in Steady Flow, *Proceedings of International Mechanical Engineering*, **208**, 1994, 253-266.
- [5] Truong, T.D., An Investigation of Electro-Rheological Fluids in Engineering. Ph.D. thesis, Victoria University of Technology, 2004.
- [6] Truong, T.D., Semercigil, S.E. & Turan, Ö.F., Performance of an Electro-Rheological Fluid Shock Absorber: Predictions and Observations. Accepted for presentation at IMAC-XXII International Model Analysis Conference, Jan 31 – Feb. 3<sup>rd</sup>, 2004. Orlando, Florida, USA.
- [7] Winslow, M.W. *Induced Vibration of Suspensions*. *J. Applied Phys.*, **12**, 1949, 1137-1140

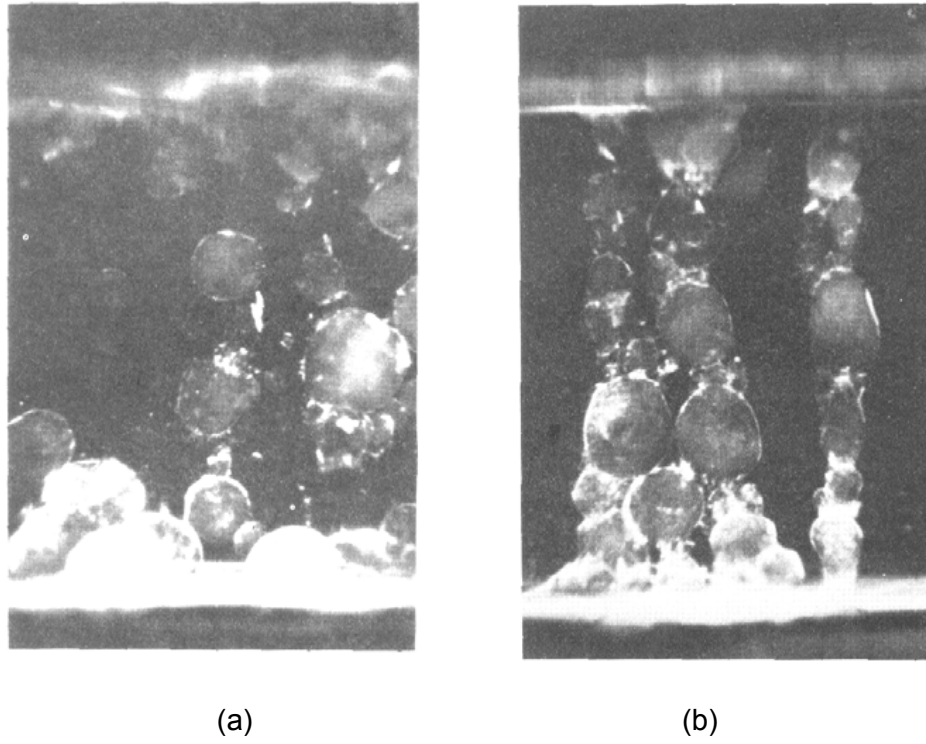


Figure 1. Electron-microscope photograph of an ER fluid (a) without, (b) with an electric field from Reference 2.

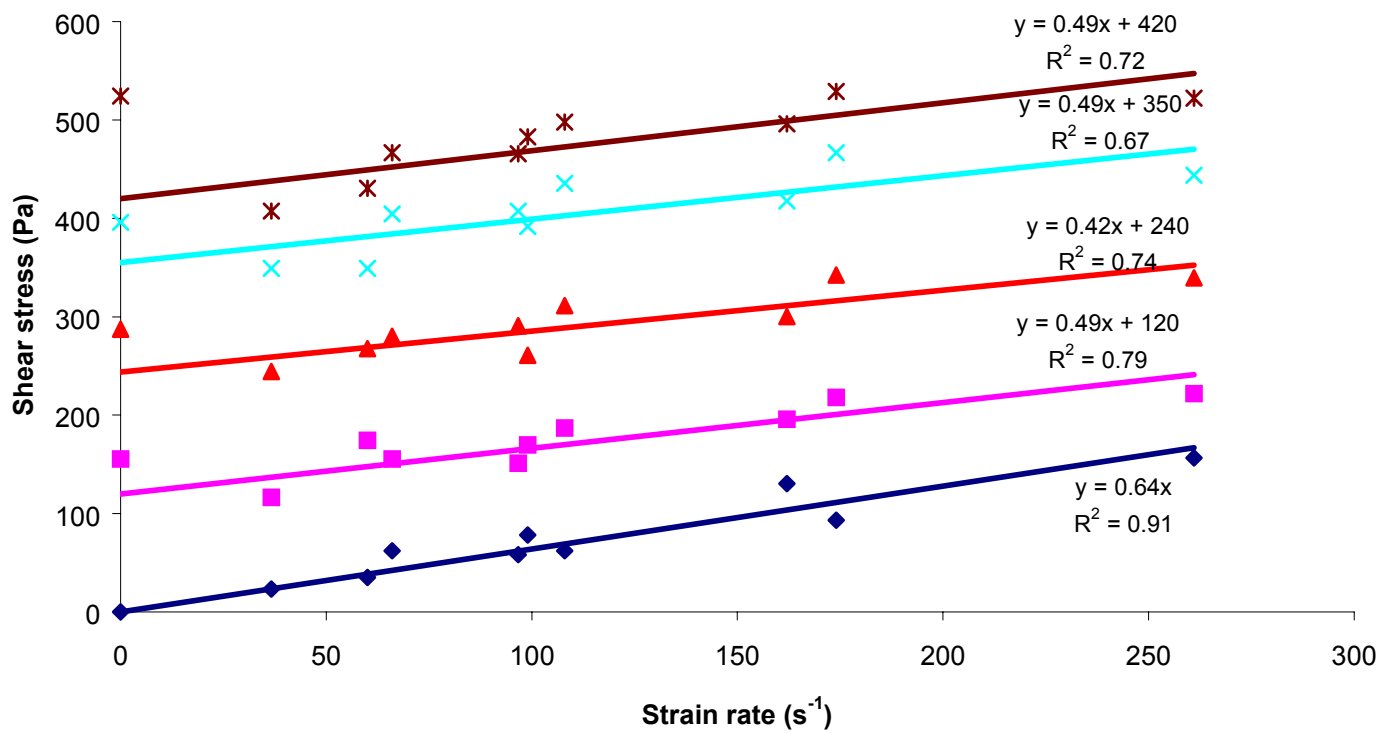


Figure 2. Variation of shear stress with strain rate for 70% weight fraction [3].  
 (◆) 0 V/mm, (■) 333 V/mm, (▲) 667 V/mm, (×) 1000 V/mm and (\*) 1333 V/mm

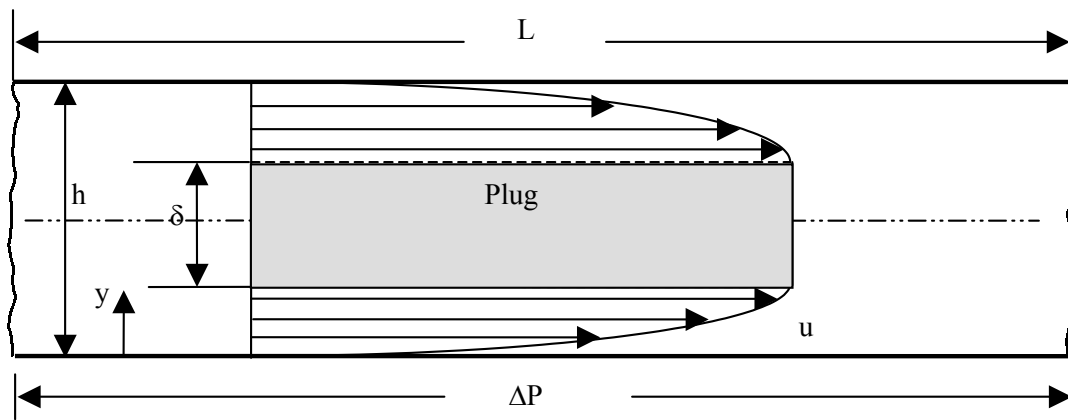


Figure 3. Showing the Bingham plastic valve flow and relevant parameters

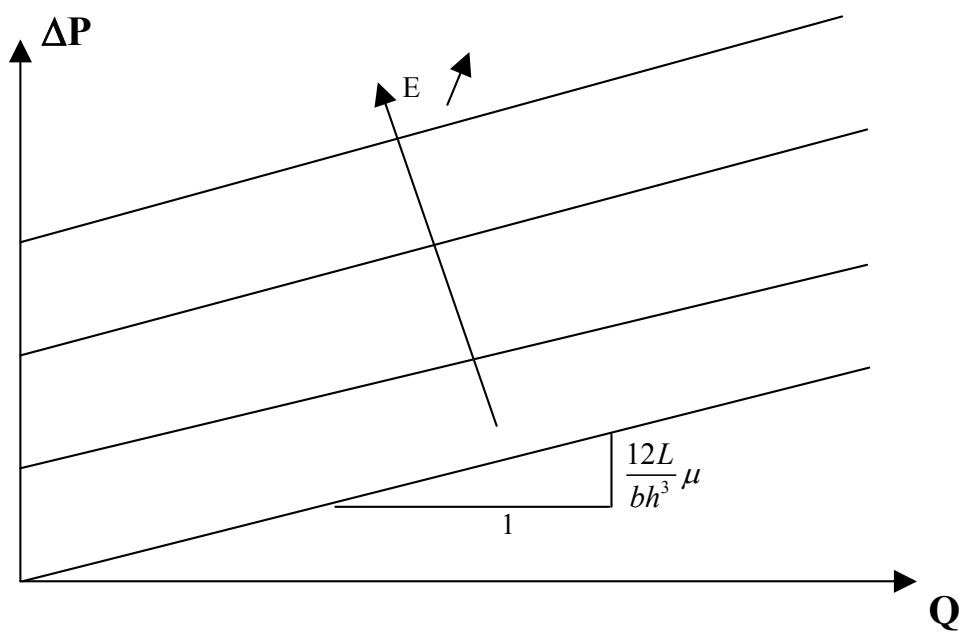


Figure 4. Variation of pressure drop with volumetric flow rate for a Bingham fluid in valve mode.

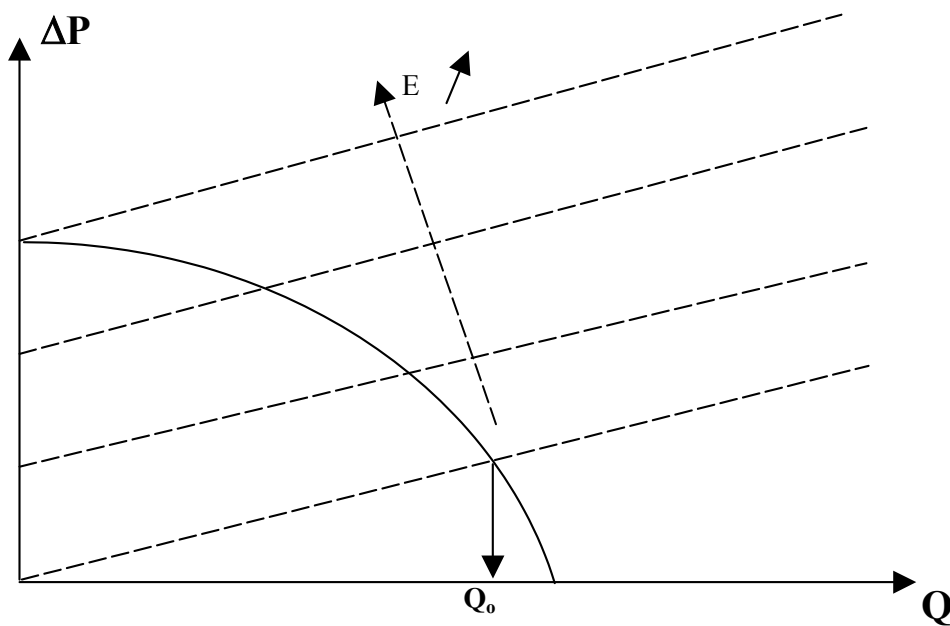


Figure 5. Same as in Figure 4, but with a generic pump characteristic curve.



## Adverse Pressure Gradient Turbulent Boundary Layer Flows: Part 1: Flow Development

C.M. Anderson, Ö.F. Turan,

School of Architectural, Mechanical and Civil Engineering  
Victoria University (F113), P.O. Box 14428 MC, Melbourne, VIC, 8001, AUSTRALIA

B. Brzek and L. Castillo

Department of Mechanical Engineering, Aeronautical and Mechanics,  
Rensselaer Polytechnic, Troy, NY, 12180, USA

### Abstract

A progress report is presented of the authors' recent work on the scaling of adverse pressure gradient turbulent boundary layer flows. In the first part, flow classification is presented based on mean deficit scaling. A fully developed equilibrium condition is defined based on the Zagarola and Smits scaling. This definition agrees with the constant pressure parameter definition of Castillo and George.

### Introduction

Adverse pressure gradient boundary layers have been of interest due to their common presence in engineering applications. The challenges associated with the development of proper scales with which to describe these flows, have attracted considerable attention [Clauser, Castillo and George]. Extensive work of the authors [1, 2, 5, 6, 8] has shown that the classical scaling of the mean deficit profiles with the friction velocity,  $u_*$ , does not hold for these flows. Neither does the Castillo and George scale of  $U_e$  where  $U_e$  is the free stream velocity. It has been shown by the authors that using the scale of Zagarola and Smits [17, 18], as suggested by Castillo and George [7], it is possible to observe the flow development to a fully developed stage. It has been further shown that this fully developed stage is the one referred as the equilibrium stage in data from the earlier APG work of Clauser [9], Bradshaw [3, 4] and Newman [15]. The objective of this two-part paper is to give a progress report of the authors' recent work, while providing additional insight. In the first part, flow development is described based on the characterization of mean deficit profiles. In the second part, Reynolds stresses are examined with a view to the development of a new scale.

### Experimental Setup and Pressure Gradient

Two new flows, Flow A and B, have been generated using the Victoria University Research Wind Tunnel. The wind tunnel is a blower-type with a 1.3m diameter fan. The 4.5 m long test section is fitted with an adjustable, flexible top that is set to form a plane diffuser shape. By changing the top shape, it is possible to generate different adverse pressure gradient conditions on the boundary layer that is growing on the bottom floor. The pressure distribution is measured by a series of static pressure taps along the centerline of the floor. In Figure 1, the dimensionless pressure distribution is presented as the pressure coefficient,  $C_p$ , for four flows. Flow A and Flow Han [11] were designed to have a similar pressure distribution to that of Flow 141 of the 1980 Stanford Conference [12] contributed by Samuel and Joubert [16]. Flows A, B and Han were generated in the Victoria University Wind Tunnel. Flows 141, Han and A are *increasingly* APG flows, as seen in Figure 1. Flow B was designed to contrast with these flows by having only a short *increasingly* APG region followed by a longer *decreasingly* APG region. The experimental data from these four flows are compared in detail below with the data of Clauser [9], Bradshaw [3, 4] and Newman [15].

For Flows Han, A and B, a reference velocity of 22 m/s was held constant at the test section inlet. DANTEC 55P05 boundary layer type single wire probes and DANTEC 55R51 x-wire probes were used for hot-wire measurements with a DANTEC streamline CTA system and Streamware software. On the single wire probes, the sensing wires are defined with gold plating on a platinum plated tungsten core of 5  $\mu$ m nominal core diameter. The x-wire probes have nickel film deposited on 70 $\mu$ m diameter quartz core. For single wire measurements, 524,288 samples were collected at each point at 100 kHz. For x-wire measurements, 262,144 samples were collected with a sampling frequency of 10 kHz. For single wire calibration, look-up tables are used. For x-wire calibration, the pitch/yaw method suggested in [19] as detailed in [14] is used.

### Mean Velocity Deficit Scaling

In Figure 2, the classical APG data of Clauser [9], Bradshaw [3, 4] and Newman [15] are presented with the Zagarola and Smits scaling of  $U_e \delta^*/\delta$ . These flows all have decreasingly APG. They are referred as Flows 2200, 2300, 2500, 3300, and 3500, respectively, in the 1968 Stanford Conference [10].

In Figure 2, a collapse of the mean deficit profiles is evident. Statistical means are applied to the data from these flows to define a curve representing the average collapse. The standard error of this curve is used to define a band of the acceptable collapse. The average line and upper and lower limit are also shown in Figure 2. This band is used to classify developing APG boundary layer flows. Similarly, 12 velocity profiles from the favorable pressure gradient (FPG) flow of Ludweig and Tillman [13] is used to determine an average FPG behavior.

In Figure 3,  $U_e \delta^*/\delta$  scaling has been applied to the mean velocity deficit of Flows 141, Han, A and B. The average APG and FPG lines are given to indicate the predicted behavior for these flows. All the flows demonstrate velocity profile behaviours that range from FPG to APG behavior. Even though based on the pressure distribution, Flows A, B and Han exhibit short regions of FPG, none of the velocity profiles presented come from an FPG region. Thus, it is evident all flows are demonstrating flow development from FPG type behavior to APG type behavior.

In Figure 4, the mean deficit profiles that fall within the acceptable range in Figure 3, are repeated. The acceptable range is as defined in Figure 2. These profiles are considered to be in the fully developed region, defining a state of equilibrium. In Flows 141, Han, A and B, this region corresponds to consecutive longitudinal locations towards the end of the test section. The upstream measurements do not fall within the APG band, indicating that the flow had not developed to an APG equilibrium state.

### Pressure Parameter $\Lambda_\theta$

In Castillo and George [7], equilibrium is defined with the pressure parameter,  $\Lambda_\theta$ , given in Equation (1). When  $\Lambda_\theta$  is constant, the boundary layer flow is expected to reach an equilibrium state. Three different constants are expected for ZPG, FPG and APG boundary layers.

$$\Lambda_\theta = \frac{\theta}{U_e} \frac{dU_e}{d\theta/dx} \frac{dU_e}{dx} \quad (1)$$

In Figure 5 the pressure parameter is presented for Flows 141, Han, A and B. The shaded band highlights where the parameter becomes almost constant, and hence, where equilibrium is reached. The onset of equilibrium as defined in this manner, agrees with the definition of the acceptable band of  $U_e \delta^*/\delta$  scaling. A star is used to indicate the position of the first mean deficit profile which lies within the acceptable APG equilibrium band. For all four flows, the location of the star coincides with the point where  $\Lambda_\theta$  is seen to have become constant.

### Conclusions

An equilibrium state for adverse pressure gradient boundary layer flows can be defined by a constant pressure parameter,  $\Lambda_\theta$ . When the flow is in this equilibrium state, the mean velocity deficit profiles, collapse to a single profile when scaled with  $U_e \delta^*/\delta$ .

### Acknowledgments

The support of this international collaboration has been possible from the Office of Naval Research, monitored by Dr. R. Joslin. C.M. Anderson is a recipient of a Victoria University Vice-Chancellor's Scholarship.

### References

- [1] Anderson, C.M., Turan, Ö.F. & Castillo, L., New Measurements in an Increasingly Adverse Pressure Gradient Turbulent Boundary Layer, American Physical Society Division of Fluid Dynamics, 56th Annual Meeting November 23-25, 2003, East Rutherford, New Jersey. Paper No. FA.003.
- [2] Anderson, C.M., Brzek, B., Castillo, L. & Turan, Ö.F., An Investigation of the Outer Flow Scaling of Developing Adverse Pressure Gradient Turbulent Boundary Layers: Part 1. Mean Deficit and Reynolds Stress Behavior, American Physical Society Division of Fluid Dynamics, 57th Annual Meeting, November 21-23, 2004, Seattle, Washington. Paper No. FA.004.
- [3] Bradshaw, P. *The Turbulence Structure of Equilibrium Boundary Layers*, NPL Aero. Rep 1184, 1966. Tabulated data reproduced in 'Proceedings Computation of Turbulent Boundary Layers -1968 AFOSR-IFP-Stanford Conference' as 'Flow 2500'.
- [4] Bradshaw, P., *The Response of a Constant Pressure Turbulent Boundary Layer to the Sudden Application of an Adverse Pressure Gradient*, NPL Aero. Rept 1219, 1967. Tabulated data reproduced in *Proceedings Computation of Turbulent Boundary Layers -1968 AFOSR-IFP-Stanford Conference* as 'Flow 3300'.
- [5] Brzek, B., Anderson, C.M., Castillo, L. & Turan, Ö.F., An Investigation of the Outer Flow Scaling of Developing Adverse Pressure Gradient Turbulent Boundary Layers: Part 2. Flow Development and Characterization, American Physical Society Division of Fluid Dynamics, 57th Annual Meeting, November 21-23, 2004, Seattle, Washington. Paper No. FA.005.

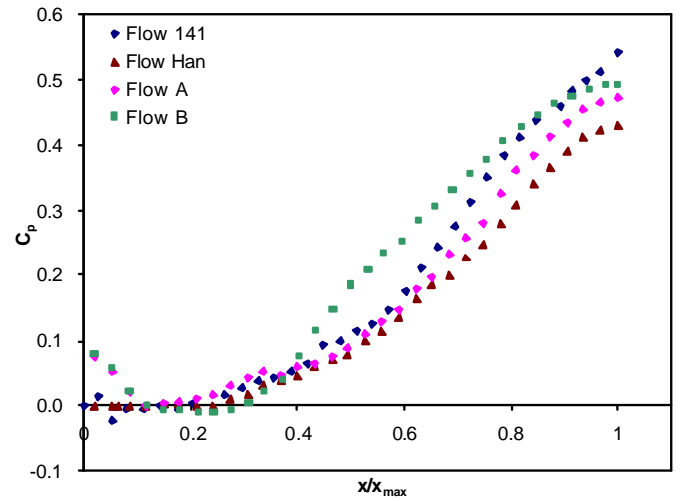


Figure 1. Pressure distribution for Flows 141, Han, A and B.

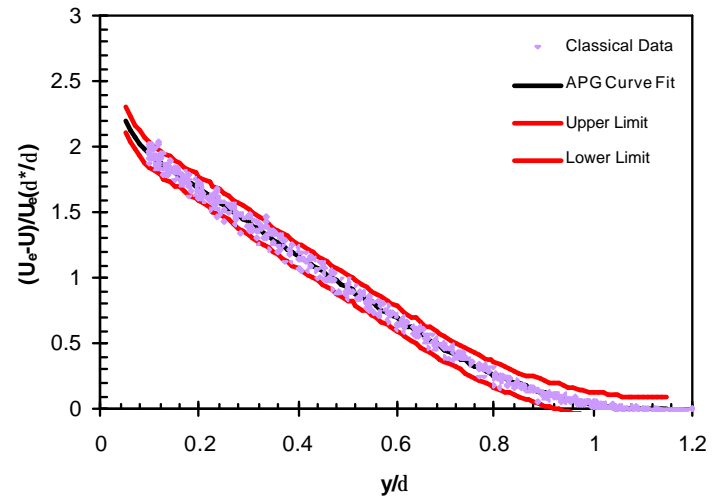
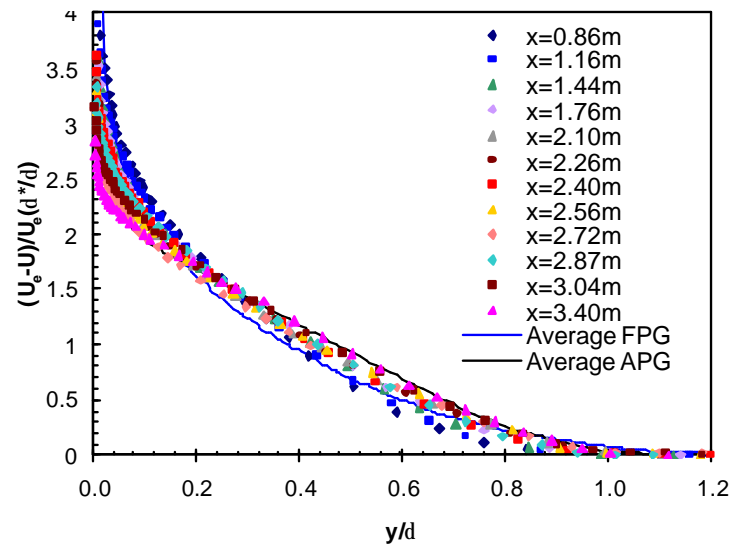
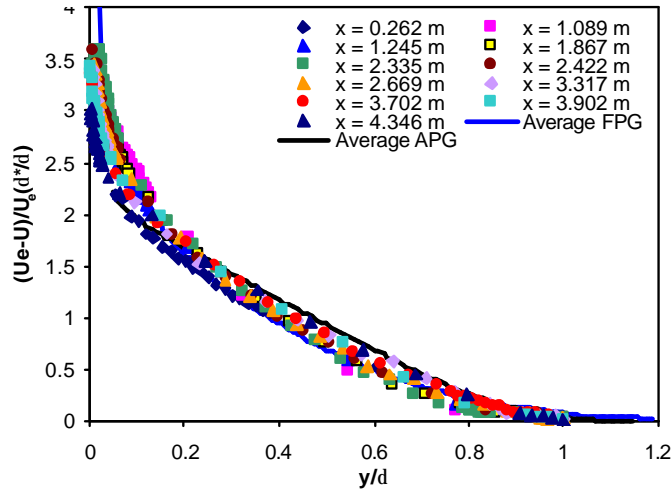


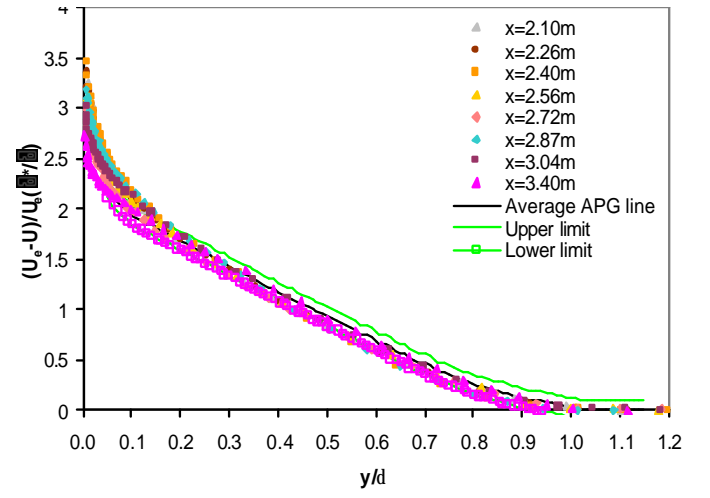
Figure 2. Mean velocity deficit profiles scaled with  $U_e \delta^*/\delta$  Flows 2500, 3300, 2200, 2300 and 3500 [10] of Bradshaw [3, 4], Clauser [9] and Newman [15], respectively. The upper and lower limits shown with the line of average collapse, are used to define the acceptable collapse of APG flow data.



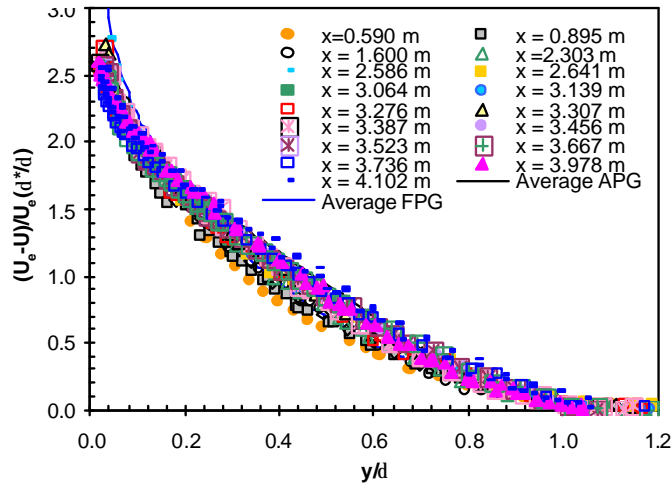
3a) Flow 141



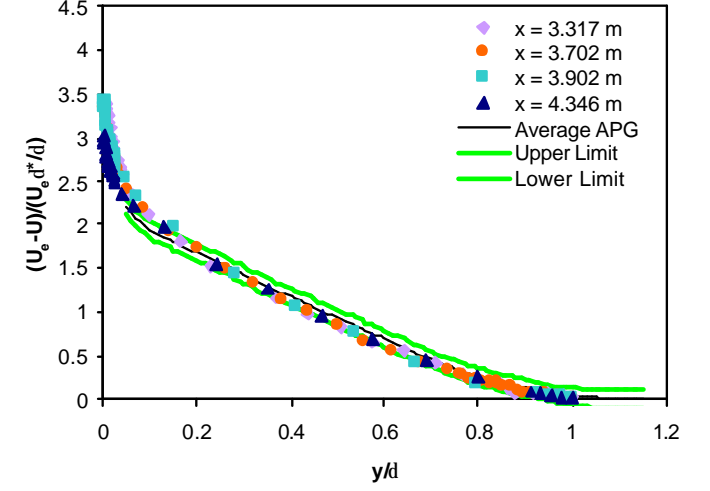
3b) Han



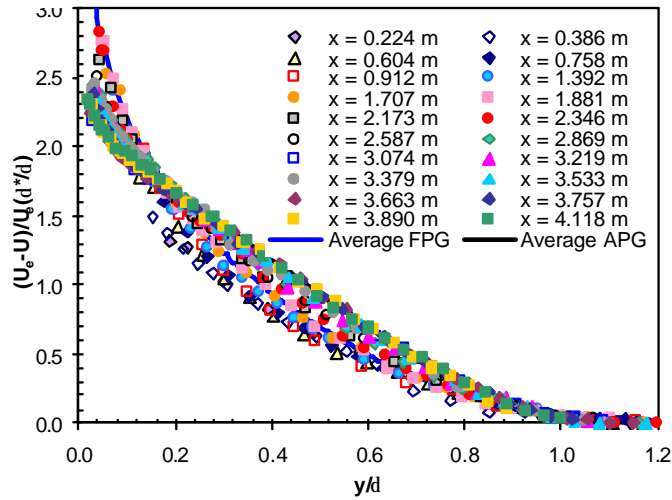
4a) Flow 141



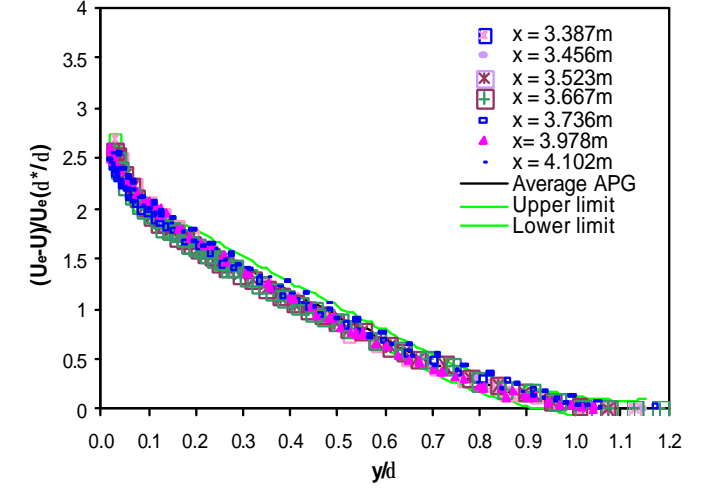
3c) Flow A



4b) Flow Han

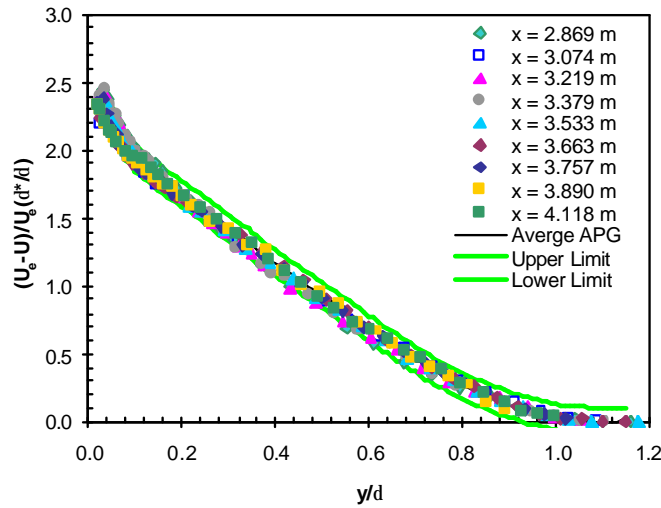


3d) Flow B



4c) Flow A

Figure 3. Mean velocity deficit profiles scaled with  $U_e^*/\delta$ . The solid lines correspond to the average collapse of classical APG data of Clauser [9], Bradshaw [3, 4] and Newman [15], and average collapse of FPG data from Ludweig and Tillman [13].



4d) Flow B

Figure 4. Mean velocity deficit profiles scaled with  $U_e \delta^* / \delta$  for Flow 141 4a), Flow Han 4b), Flow A 4c) and Flow B 4d). Only the velocity profiles which fall within the acceptable APG equilibrium band are given.

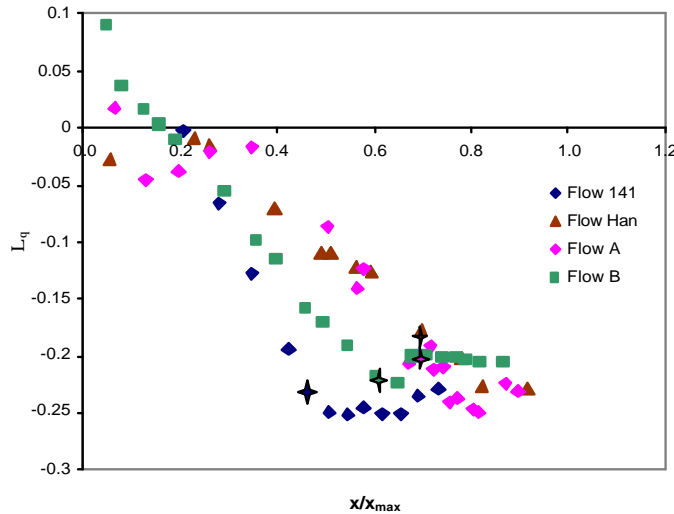


Figure 5. Pressure parameter  $\Lambda_\theta$  for Flows 141, Han, A and B. The star represents the first longitudinal location which is within the acceptable APG equilibrium band with  $U_e \delta^* / \delta$  scaling.

## References, continued

- [6] Brzek, B., Anderson, C.M., Castillo, L. & Turan, Ö.F., Scaling Laws and Measurements on Adverse Pressure Gradient Turbulent Boundary Layers, 43rd AIAA Aerospace Sciences Meeting and Exhibit, 10 - 13 Jan 2005, Reno, Nevada. Paper No. AIAA-2005-0111
- [7] Castillo, L. & George, W.K., Similarity Analysis for Turbulent Boundary Layer with Pressure Gradient: Outer Flow, *AIAA Journal*, **39**(1), 2001, 41-47.
- [8] Castillo, L. & Turan, Ö.F., Equilibrium, Self-Similar and Self-Preserving Solutions in Diffuser Flows with Developing Inlet, American Physical Society Division of Fluid Dynamics, 56th Annual Meeting November 23-25, 2003, East Rutherford, New Jersey. Paper No. FA.002.
- [9] Clauser, F.H., Turbulent Boundary Layers in Adverse Pressure Gradients, *J. Aero. Sci.*, **21**(2), 1954, 91-108. Tabulated data reproduced in *Proceedings, Computation of Turbulent Boundary Layers – 1968 AFOSR-IFP-Stanford Conference* as 'Flow 2200' and 'Flow 2300'.
- [10] Coles, D.E. & Hirst, D.E., *Proceedings, Computation of Turbulent Boundary Layers – 1968 AFOSR-IFP-Stanford Conference*, Volume II. Mech Eng Dept, Stanford University, 1969.
- [11] Han, J. Y., *Pressure Signature in Adverse-Pressure-Gradient Wall Bounded Turbulent Flows*, M.Eng. Thesis, Victoria University, 2000.
- [12] Kline, S. J., Cantwell, B.J. & Lilley, G.M., eds., *The 1980-81 AFOSR-HTTM-Stanford Conference on Complex Turbulent Flows*, Mech. Eng Dept., Stanford University, 1981.
- [13] Ludweig, H. & Tillmann, W., Investigations of the Wall Shearing Stress in Turbulent Boundary Layers, *Ing-Arch.*, **17**, 1949. Tabulated data reproduced in *Proceedings, Computation of Turbulent Boundary Layers – 1968 AFOSR-IFP-Stanford Conference* as 'Flow 1300'.
- [14] Lueptow, R.M., Breuer, K.S. & Haritonidis, J.H. Computer Aided Calibration of x-Probes Using a Look-up Table, *Experiments in Fluids*, **6**, 1988, 115-118.
- [15] Newman, B.G., Some Contributions to the Study of the Turbulent Boundary Layer Near Separation, *Austr. Department Supply Rept. ACA-53*, 1951. Tabulated data reproduced in *Proceedings, Computation of Turbulent Boundary Layers – 1968 AFOSR-IFP-Stanford Conference* as 'Flow 3500'.
- [16] Samuel, A.E. and Joubert, P.N., A Boundary Layer Developing In An Increasingly Adverse Pressure Gradient, *J. Fluid Mech.*, **66**(3), 1974, 481-505. Tabulated data reproduced in *Proceedings, Computation of Turbulent Boundary Layers – 1980 AFOSR-IFP-Stanford Conference* as 'Flow 141'.
- [17] Zagarola, M.V. & Smits, A.J., A New Mean Velocity Scaling for Turbulent Boundary Layers, *Proceedings of FEDSM'98*, Washington D.C., 1998.
- [18] Zagarola, M.V. & Smits, A.J. Mean Flow Scaling of Turbulent Pipe Flow, *J. Fluid Mech.*, **373**, 1998, 33-79.
- [19] Zilberman, M. *On the Interaction of Transitional Spots and Generation of a Synthetic Turbulent Boundary Layer*. Ph.D. Thesis, Tel-Aviv University, 1981.

## Adverse Pressure Gradient Turbulent Boundary Layer Flows: Part 2: Scaling of Reynolds Stresses

**B. Brzek, L. Castillo**

Department of Mechanical Engineering, Aeronautical and Mechanics,  
Rensselaer Polytechnic, Troy, NY, 12180, USA

**C.M. Anderson and Ö.F. Turan**

School of Architectural, Mechanical and Civil Engineering  
Victoria University (F113), P.O. Box 14428 MC, Melbourne, VIC, 8001, AUSTRALIA

### Abstract

A fully developed state has been defined for APG boundary layer development corresponding to an equilibrium state. The Reynolds stresses data are examined within the fully developed region. A new set of scales are examined for mean deficit and Reynolds stress profiles.

### Introduction

As shown in Part 1 of this paper, the mean deficit profiles of developing adverse pressure gradient (APG) flows can be scaled with  $U_e \delta^*/\delta$  of Zagarola and Smits [10, 11] as suggested by Castillo and George [4]. It is shown in Part 1 that as a result, it is possible to define a fully developed equilibrium state for these flows. In Part 2, the corresponding scale is examined for Reynolds stresses.

### Flow Details

The flows presented here are the same as the ones used in Part 1, namely Flows 2500 and 3300 of Bradshaw [1, 2], and Flows 2200 and 2300 of Clauser [5] and Flow 3500 of Newmann [8]. The flow classification number is as reported at the 1968 Stanford Conference [6]. Two new flows generated in the Victoria University Wind Tunnel are also used, Flows A and B as described in Part 1. The increasingly adverse pressure gradient flow of Samuel and Joubert [9] denoted Flow 141 at the 1980 Stanford Conference [7], is also used.

### Scaling Velocity Deficit

Applying the Zagarola and Smits scaling of  $U_e \delta^*/\delta$  to mean velocity deficit profiles can remove the Reynolds number dependence, and it is expected to result in a collapse of profiles [4]. The collapse is dependent on the pressure gradient, and three possible collapses have been reported, namely, one each for APG, favorable pressure gradient (FPG) and zero pressure gradient (ZPG) flows. In Part 1 of this paper, it is shown that this collapse could only be expected in fully developed flows.

In Figure 1, the mean velocity deficit profiles are scaled with  $U_e \delta^*/\delta$  for all flows listed in the previous section. As discussed in Part 1, whilst all these flows are APG flows, FPG behavior is also evident. Flow development is causing this spread. Only after the flow reaches equilibrium, a good collapse is produced. In Part 1 the pressure parameter  $\Lambda_\theta$  is used to further confirm this equilibrium state.

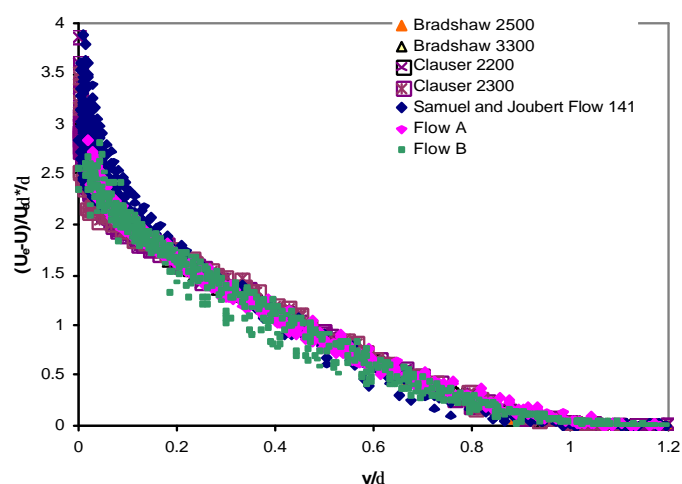


Figure 1 Mean velocity deficit scaled with  $U_e \delta^*/\delta$  for Flows 2500, 3300, 2200, 2300, 3500, 141, A and B.

### New Scaling

The similarity analysis technique of Castillo and George [4] has been applied to the mean continuity and x-momentum equations using  $\delta^*/\delta$  as the similarity parameter. The result is a set of new mean deficit and Reynolds stress scales which include the term  $\delta^*/\delta$ , as well the pressure parameter,  $\Lambda_\theta$ . The solution is valid for the outer flow (typically  $y/\delta > 0.1$ ) of a 2-D, incompressible boundary layer that is statistically steady in the mean. With this process, the outer scale for the mean velocity deficit becomes,  $U_{so} = U_e (\delta^*/\delta)^{1-\Lambda_\theta}$  whilst the outer scale for the normal Reynolds stresses,  $u'$  and  $v'$  is  $R_u = R_v = U_e^2 (\delta^*/\delta)^{1-\Lambda_\theta}$ . For the shear stress,  $uv$ , the scale is  $R_{uv} = U_e^2 (\delta^*/\delta)^{1-\Lambda_\theta} \cdot (d\delta/dx)$ .

In Figure 2 the new scale of  $U_e (\delta^*/\delta)^{1-\Lambda_\theta}$  is applied to the mean velocity deficit for the same flows as in Figure 1. When compared with the Zagarola and Smits [10, 11] scale of  $U_e (\delta^*/\delta)$ , the new velocity deficit scale produces less scatter. The developing region of the flow scales to the same profile as that of the fully developed flow.



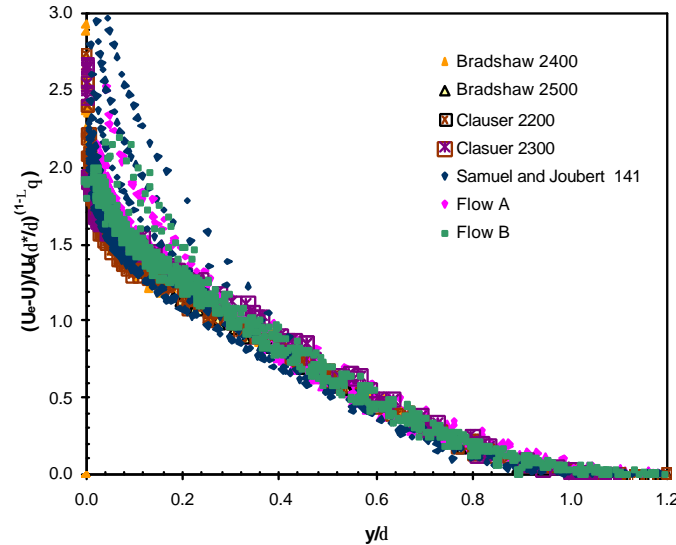


Figure 2. Mean velocity deficit profiles scaled with  $U_e(\delta^*/\delta)^{1-A_s}$  for all flows.

### Scaling Reynolds Stresses

In Figure 3 the normal Reynolds stresses,  $u'^2$  and  $v'^2$  are scaled with  $U_e^2$  for Flows A and B, and  $uv$  is scaled with  $U_e^2 d\delta/dx$ . These scales correspond to the Zagarola and Smits scale of  $U_e \delta^*/\delta$  for the mean deficit. Although some clustering of the data is evident, a complete collapse is not obtained. For  $u'^2$  and  $v'^2$ , the arrow on the figure indicates the flow direction. The profiles increase in magnitude downstream. The shading in this figure highlights the region of equilibrium as defined in Part 1. There is better clustering of the data within this region than outside of it. Even in this region the profiles do not collapse.

In Figure 4, the new scales are applied to the Reynolds stress data from Flows A and B. In comparison with Figure 3, the scatter is reduced. Similar to the comparison between Figures 1 and 2, better collapse of data is obtained both within and outside of the fully developed region.

### Conclusions

The Zagarola and Smits scaling is applied to Reynolds stress data of Flows A and B. The resulting collapse is not as satisfactory as for the mean deficit profiles. A new set of scales is being developed. The results are encouraging.

### Acknowledgments

The support of this international collaboration has been possible from the Office of Naval Research, monitored by Dr. R. Joslin. C.M. Anderson is a recipient of a Victoria University Vice-Chancellor's Scholarship.

### References

- [1] Bradshaw, P. *The Turbulence Structure of Equilibrium Boundary Layers*, NPL Aero. Rep 1184, 1966. Tabulated data reproduced in 'Proceedings Computation of Turbulent Boundary Layers – 1968 AFOSR-IFP-Stanford Conference' as 'Flow 2500'.
- [2] Bradshaw, P., *The Response of a Constant Pressure Turbulent Boundary Layer to the Sudden Application of an Adverse Pressure Gradient*, NPL Aero. Rept 1219, 1967. Tabulated data reproduced in *Proceedings Computation of Turbulent Boundary Layers – 1968 AFOSR-IFP-Stanford Conference* as 'Flow 3300'.

- [3] Brzek, B., Anderson, C.M., Castillo, L. & Turan, Ö.F., An Investigation of the Outer Flow Scaling of Developing Adverse Pressure Gradient Turbulent Boundary Layers: Part 2. Flow Development and Characterization, American Physical Society Division of Fluid Dynamics, 57th Annual Meeting, November 21-23, 2004, Seattle, Washington. Paper No. FA.005.
- [4] Castillo, L. & George, W.K., Similarity Analysis for Turbulent Boundary Layer with Pressure Gradient: Outer Flow, *AIAA Journal*, **39**(1), 2001, 41-47.
- [5] Clauser, F.H., Turbulent Boundary Layers in Adverse Pressure Gradients, *J. Aero. Sci.*, **21**(2), 1954, 91-108. Tabulated data reproduced in *Proceedings, Computation of Turbulent Boundary Layers – 1968 AFOSR-IFP-Stanford Conference* as 'Flow 2200' and 'Flow 2300'.
- [6] Coles, D.E. & Hirst, D.E., *Proceedings, Computation of Turbulent Boundary Layers – 1968 AFOSR-IFP-Stanford Conference*, Volume II. Mech. Eng. Dept, Stanford University, 1969.
- [7] Kline, S. J., Cantwell, B.J. & Lilley, G.M., eds., *The 1980-81 AFOSR-HTTM-Stanford Conference on Complex Turbulent Flows*, Mech. Eng. Dept., Stanford University, 1981.
- [8] Newman, B.G., Some Contributions to the Study of the Turbulent Boundary Layer Near Separation, *Austr. Department Supply Rept. ACA-53*, 1951. Tabulated data reproduced in *Proceedings, Computation of Turbulent Boundary Layers – 1968 AFOSR-IFP-Stanford Conference* as 'Flow 3500'.
- [9] Samuel, A.E. and Joubert, P.N., A Boundary Layer Developing In An Increasingly Adverse Pressure Gradient, *J. Fluid Mech.*, **66**(3), 1974, 481-505. Tabulated data reproduced in *Proceedings, Computation of Turbulent Boundary Layers – 1980 AFOSR-IFP-Stanford Conference* as 'Flow 141'.
- [10] Zagarola, M.V. & Smits, A.J., A New Mean Velocity Scaling for Turbulent Boundary Layers, *Proceedings of FEDSM'98*, Washington D.C., 1998.
- [11] Zagarola, M.V. & Smits, A.J. Mean Flow Scaling of Turbulent Pipe Flow, *J. Fluid Mech.*, **373**, 1998, 33-79.

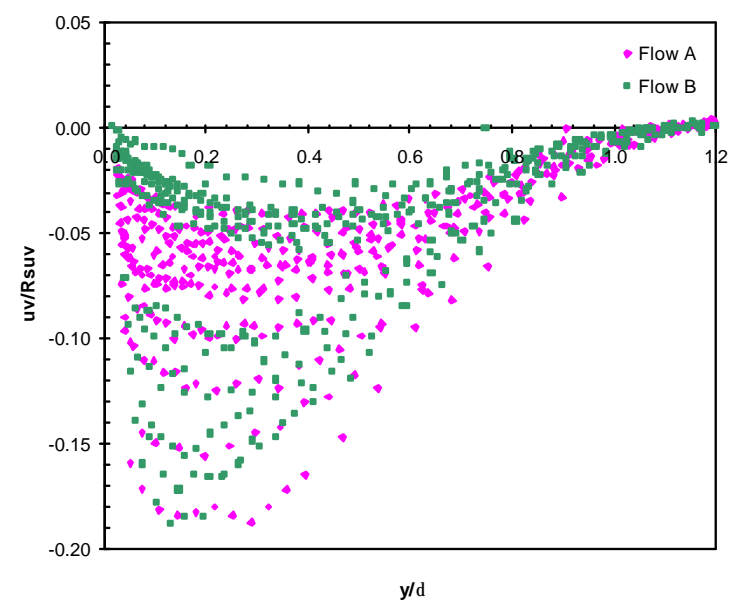
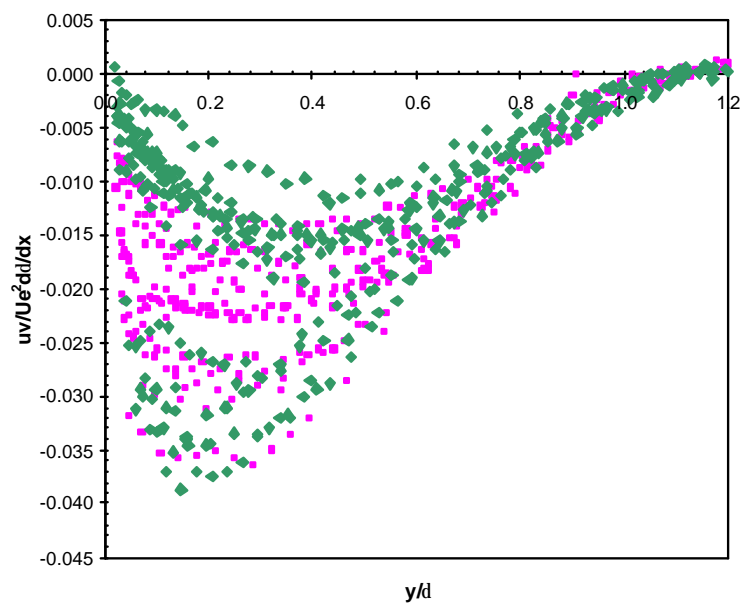
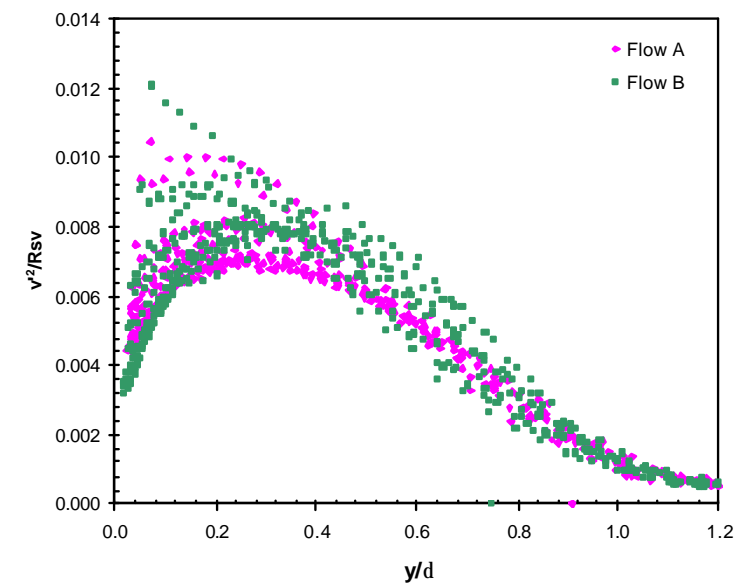
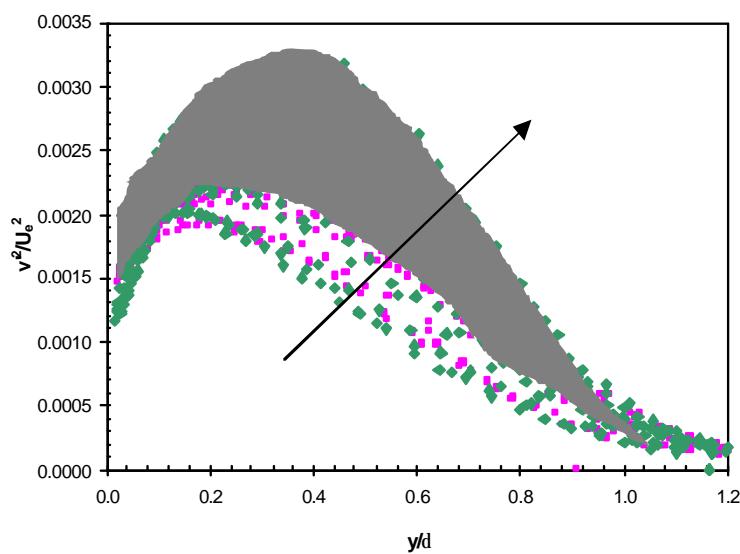
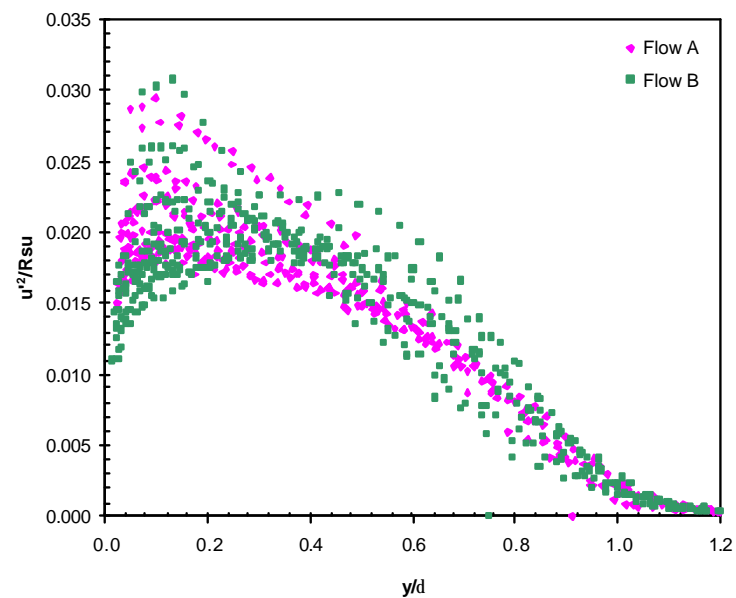
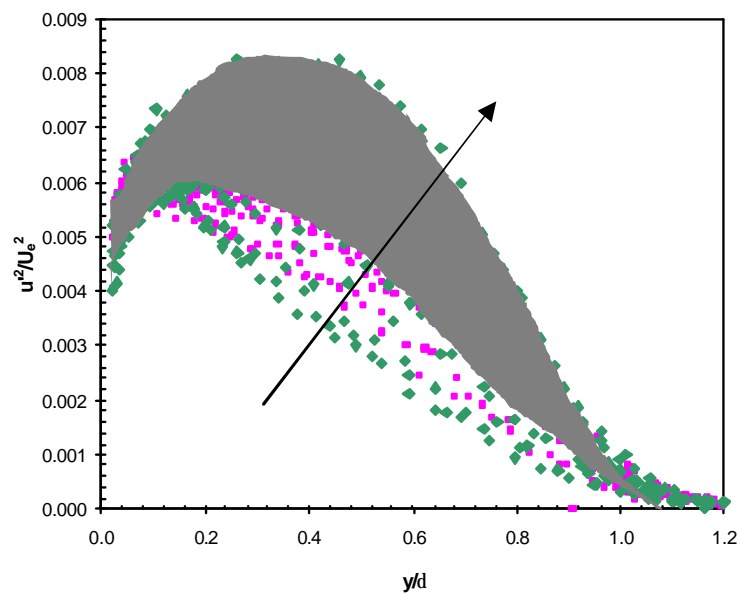


Figure 3 Reynolds stresses  $u'$ ,  $v'$  and  $uv$  scaled with  $U_0^2$ .

Figure 4 Reynolds stresses  $u'$ ,  $v'$  and  $uv$  with the corresponding new scaling.

